AD-A200 210

Journal of APPLIED PHYSICS

Proceedings of the Thirty-Second Annual Conference on Magnetism and Magnetic Materials

Pages 3621–4358

Volume 63 | 15 April 1988 | Number 8, Part IIB

DTIC ELECTE MAY 17 1988 S D

a publication of the American Institute of Physics

DISTRIBUTION STATEMENT A
Approved for public release
Distribution Unlimited

88 5 16 009

CODEN: JAPIAU

ISSN: 0021-8979

Journal of APPLIED PHYSICS

Lester Guttman, Editor

Robert E. Holland and Steven J. Rothman, Associate Editors

Catherine M. Krippel, Assistant to the Editor

Editorial Board

Term ending 31 December 1988	*Term ending 31 December 1989*	*Term ending 31 December 1990*
Rolf Landauer	John S. Blakemore	Tsuneya Ando
C. Kumar N. Patel	Karl Hess	M. R. Beasley
James J. Rhyne	George I. Stegeman	J. M. Cowley
		J. M. Poate

AIP EDITORIAL STAFF: Janis Bennett, *Managing Editor;* Elizabeth Belmont, *Chief Copy Editor*

The *Journal of Applied Physics* is published semimonthly by the American Institute of Physics (AIP) with the cooperation of The American Physical Society. It is devoted to general physics and its applications to other sciences, to engineering, and to industry. (Prior to 1937, the Journal carried the name *Physics.*) The Editor welcomes manuscripts describing significant new experimental or theoretical results in applied physics or manuscripts concerning important new applications of physics to other branches of science and engineering.

Information for Contributors

Submit manuscripts to Lester Guttman, Editor, *Journal of Applied Physics,* Argonne National Laboratory, P.O. Box 8296, Argonne, IL 60439-8296. Submission is a representation that the manuscript has not been published previously nor currently submitted for publication elsewhere. The manuscript should be accompanied by a statement transferring copyright from the authors (or their employers—whoever holds the copyright) to AIP; a suitable form for copyright transfer is occasionally printed in the back of this journal and is available from the Editor's office or AIP. This written transfer of copyright, which previously was assumed to be implicit in the act of submitting a manuscript, is necessary under the 1978 U.S. copyright law in order for AIP to continue disseminating physics research results as widely as possible. Further information may be obtained from AIP.

Publication Charge: To support the cost of wide dissemination of research results through publication of journal pages and production of a data base of articles, the author's institution is requested to pay a *page charge* of $45 per page (with a one-page minimum) and an *article charge* of $20 per article. The page charge (if honored) entitles the author to 100 free reprints. For **Errata** the minimum page charge is $10, with no article charge and no free reprints. Nonpayment of the publication charge may lead to delays in publication.

Two categories of manuscripts are acceptable, **full-length articles** and **Communications.** The latter are short contributions not generally exceeding in length nine double-spaced typewritten pages or approximately 2500 words of text reduced, however, by allowances for equations, tables, and figures. Abstracts are required for manuscripts of both types. Being short, *Communications are often published more* quickly than full-length articles. Instructions for preparation of **manuscripts** will be found in the January issue of this journal and occasionally in later issues. In brief and incomplete summary: Two copies of the manuscript, including clear copies of the figures, are required, double-spaced throughout on one side of 21.6×28 cm (8½×11 in.) paper. The original should be retained by the author until it is requested, after review. The *abstract, references, figure captions,* and *tables* are similarly to be double-spaced each on its separate sheets. The original *figures* should be original line drawings or high-contrast glossy prints not larger than 21.6×28 cm and should be included with the original submission. *References* should conform to the style used in AIP journals including this one. Unusual mathematical symbols should be clarified with marginal notes.

AIP's **Physics Auxiliary Publication Service (PAPS)** is a low-cost depository for material which is part of and supplementary to a published paper, but is too long to be included in the journal; inquire of the Editor.

Proofs and all correspondence concerning papers in the process of publication should be addressed to: Managing Editor, *The Journal of Applied Physics,* American Institute of Physics, 335 East 45th Street, New York, NY 10017. In all correspondence reference should be made to title, author, journal, and scheduled date of issue. A limited number of **alterations in proof** are unavoidable, but the cost of making extensive alterations after the article has been set in type will be charged to the author.

Copyright 1988, American Institute of Physics. Individual teachers, students, researchers, and libraries acting for them are permitted to make copies of articles in this journal for their own use in research or teaching, including multiple copies for classroom or library reserve use, provided such copies are not sold. Copying for sale is subject to payment of copying fees. (See "Copying Fees" paragraph elsewhere in this journal.) Permission is granted to quote from this journal with the customary acknowledgment of the source. To reprint a figure, table, or other excerpt requires in addition the consent of one of the original authors and notification to AIP. Reproduction for advertising or promotional purposes, or republication in any form, is permitted only under license from AIP, which will normally require that the permission of one of the authors also be obtained. Direct inquiries to Office of Rights and Permissions, American Institute of Physics, 335 East 45th Street, New York, NY 10017.

Second-class postage rates paid at Woodbury, N.Y. and at additional mailing offices

12/1/87

PROCEEDINGS OF THE THIRTY-SECOND ANNUAL CONFERENCE ON MAGNETISM AND MAGNETIC MATERIALS

PART B

Accesion For
NTIS CRA&I ☑
DTIC TAB ☐
Unannounced ☐
Justification
$32.00
By per call
Distribution /
Availability Codes
Dist Avail and / or Special
A-1 21

Sold by: American Institute of Physics
500 Sunnyside Blvd.
Woodbury, N.Y. 11797

9–12 November 1987
Chicago, Illinois

Edited by N. C. Koon, J. D. Adam, I. A. Beardsley, and W. M. Saslow

Journal of Applied Physics
Volume 63, Number 8, Part II, 1988

Library of Congress Catalog Number: 59-2468
International Standard Book Number: 0-88318-564-4
CONF-871126--Vol. 2
Copyright © 1988 by the American Institute of Physics
Published by the American Institute of Physics
335 East 45th Street, New York, New York 10017
Printed in the United States of America

All papers in this volume, and in previous Proceedings of the Conference on Magnetism and Magnetic Materials published in this series, have been reviewed for technical content. The selection of referees, review guidelines, and all other editorial procedures are in accordance with standards prescribed by the American Institute of Physics.

Subscription Prices (1988)	U.S.A. & Poss.	Foreign (incl. Can. & Mex.)	Optional air freight Europe, Mideast, N. Africa	Asia & Oceania	Microfiche (1st class/ airmail)
Members*	$90.00	$130.00	$190.00	$190.00	$90.00
Reg. rate	$725.00	$765.00	$825.00	$825.00	$725.00

*AIP Member and Affiliated Societies.

Back-Number Prices. Single copies from Vol. 24 (1953) through Vol. 55 (1984): $32.00; Vol. 56 (1984) and thereafter: $32.00. Special Supplements: $50.00. Volumes 1–23 (1931–1952) are available only on microfilm.

The *Journal of Applied Physics* (ISSN: 0021-8979) is published semimonthly by the American Institute of Physics, 500 Sunnyside Blvd., Woodbury, NY 11797. Second-class postage paid at Woodbury, NY, and additional mailing offices. POSTMASTER: Send address changes to *Journal of Applied Physics*, 500 Sunnyside Blvd., Woodbury, NY 11797.

Subscriptions, renewals, address changes, and single-copy orders should be addressed to *AIP Subscription Fulfillment Division, 335 East 45th St., New York, NY 10017.* Allow at least six weeks advance notice. For address changes please send both old and new addresses and, if possible, include a mailing label from the wrapper of a recent issue. For your convenience a **change of address form is included in every issue of *Physics Today;* please use it.** Requests from subscribers for missing journal issues will be honored without charge only if received within six months of the issue's actual date of publication; otherwise, the issue may be purchased at the single copy price. (AIP Headquarters are located at 335 East 45th St., New York, NY 10017; Subscription Fulfillment offices are located at 500 Sunnyside Blvd., Woodbury, NY 11797.)

Reprints of individual articles in this journal may be ordered singly at $10.00 per article copy (postage included) for articles up to 20 pages. Beyond 20 pages there is a surcharge of $0.20 per page. Air mail delivery is available. Orders are filled within one week of receipt or of the date of publication, whichever is later. Send orders to the American Institute of Physics, *Current Physics Reprints,* 335 East 45th St., New York, NY 10017.

Copying Fees: The code that appears on the first page of articles in this journal gives the fee for each copy of the article made beyond the free copying permitted by AIP. (See statement under "Copyright" elsewhere in this journal.) If no code appears, no fee applies. The fee for pre-1978 articles is $0.25 per copy. With the exception of copying for advertising and promotional purposes, the express permission of AIP is not required provided the fee is paid through the *Copyright Clearance Center, Inc. (CCC), 21 Congress St., Salem, MA 01970.* Contact the CCC for information on how to report copying and remit payment.

Microfilm subscriptions of complete volumes of the *Journal of Applied Physics* are available on 16 mm and 35 mm. The *Journal of Applied Physics* also appears on a monthly basis in *Current Physics Microform* (CPM) Section 1 along with 29 other journals published by the American Institute of Physics and its member societies. A *Microfilm Catalog* is available on request. The *Journal of Applied Physics* is indexed quarterly in *Current Physics Index,* a subject and author index (with abstracts) to all journals published by AIP and its member societies.

Journal of **APPLIED PHYSICS** Vol. 63, No. 8, Part II B, 15 April 1988

Thin Films: Perpendicular Recording

2897	CoCr double-layered media with NiFe and CoZrNb soft-magnetic layers (invited)	J. P. C. Bernards, C. P. G. Schrauwen, V. Zieren, S. B. Luitjens
2902	A comparison of perpendicular and longitudinal recording	C. M. Perlov, J. A. Christner, O. Lopez
2905	Magnetic-structural development in Co-Cr films for perpendicular recording media	J.-W. Lee, B. G. Demczyk, K. R. Mountfield, D. E. Laughlin
2908	Influence of oxygen on recording characteristics in vacuum-evaporated Co-Cr thin films	F. Kugiya, M. Suzuki, F. Kanno, Y. Yoshida, O. Kitakami, H. Fujiwara, D. E. Speliotis
2911	Studies on coercivity in Co-Cr thin films by means of a multilayer technique	Shigeki Nakagawa, Makoto Sumide, Yoshitaka Kitamoto, Yoshiro Niimura, Masahiko Naoe
2914	Torque analysis of the perpendicular magnetic anisotropy in Co-Cr films	K. Ishibashi, Y. Uchiyama, U. Hwang, T. Suzuki
2917	Stress-induced anisotropy in Co-Cr thin films	P. V. Mitchell, K. R. Mountfield, J. O. Artman
2920	Magnetic aftereffect in CoCr films	Daniel K. Lottis, E. Dan Dahlberg, J. A. Christner, J. I. Lee, R. L. Peterson, R. M. White
2923	Magnetization decay in Co-Cr films	Bucknell C. Webb, S. Schultz, S. B. Oseroff
2926	Annealing effect on microstructure and magnetic properties in Fe-Cr sputtered films	*Masatoshi* Ohkoshi
2929	Magnetic properties and microstructure of Co-Cr-Pr vertically magnetized films	T. Suzuki, N. Yoshida, U. Hwang, Y. Uchiyama, K. Ishibashi

Force Microscopy and Domain Effects

2932	A specific model for domain-wall nucleation in thin-film Permalloy microelements (invited)	Neil Smith
2938	Magnetics of nonlaminated, bilaminated, and multilaminated permalloy stripes	C. Tsang, P. Kasiraj, M. Krounbi
2941	Effects of magnetic history on the domain structure of small NiFe shapes	B. W. Corb
2944	Domain wall pinning in sputtered soft amorphous magnetic thin films	Wing Kei Ho, Floyd B. Humphrey
2947	Magnetic imaging by atomic force microscope (invited) (abstract)	P. Grütter, E. Meyer, H. Heinzelmann, L. Rosenthaler, H. R. Hidber, H.-J. Güntherodt
2947	Theory of magnetic imaging by STM force microscopy (invited) (abstract)	J. J. Sáenz, N. García
2948	High-resolution magnetic imaging by force microscopy (invited) (abstract)	H. K. Wickramasinghe, Y. Martin
2948	Magnetoresistive measurement of the exchange constant in varied thickness Permalloy films (abstract)	N. Smith, D. Markham, W. Doyle, D. LaTourette

Molecular Magnetism

2949	The quest for a polymeric ferromagnet: A new polymorph of 1,4-bis(2,2,6,6-tetramethyl-4-oxy-4-piperidyl-1-oxy)butadiyne (invited)	Joel S. Miller, Joseph C. Calabrese, Daniel T. Glatzhofer, Arthur J. Epstein
2952	Ferromagnetism in molecular materials: Decamethylferrocenium tetracyanoethanide (DMeFc) (TCNE) (invited)	A. J. Epstein, Sailesh Chittipeddi, A. Chakraborty, Joel S. Miller
2957	Mössbauer spectroscopy studies of molecular magnets (invited)	William Michael Reiff

2962	Ferromagnetic interactions in organic solids: An overview of theory and experiment (invited)	J. B. Torrance, P. S. Bagus, I. Johannsen, A. I. Nazzal, S. S. P. Parkin, P. Batail

Soft Magnetic Materials: Technical Properties

2966	Magnetic properties and domain structures in domain refined grain-oriented silicon steel (invited)	T. Nozawa, Y. Matsuo, H. Kobayashi, K. Iwayama, N. Takahashi
2971	7-mil-thick high-permeability grain-oriented silicon steel sheet	K. Iwayama, K. Ueno, Y. Yoshitomi, H. Nakayama, T. Kumano
2974	Microanalysis of nonoriented P containing silicon steel	Puru Liu, Fulin Li, Liang Chen, Zhenchun Li
2977	The effect of nickel content on the ac magnetic properties of [illegible]-49Co-2V alloys	P. M. Novotny
2980	The influence of size and morphology of eutectoid carbides on the magnetic properties of carbon steels	D. C. Jiles
2983	Effects of the viscosity field on the Barkhausen noise of amorphous ferromagnetic materials	M. Celasco, P. Mazzetti, A. Masoero, A. Stepanescu
2986	Use of resistivity and magnetic measurements to monitor recrystallization of metallic glasses	G. E. Fish, R. Hasegawa
2989	Harmonic signal generation from metallic glasses	Ryusuke Hasegawa
2992	Magnetic state of Mn in $Fe_{40-x}Ni_{40}Mn_xB_{12}Si_8$ before and after crystallization	R. Krishnan, K. Le Dang, P. Veillet

Hysteresis and Eddy Current Modeling

2995	Vector Preisach hysteresis models (invited)	I. D. Mayergoyz
3001	Determination of the bilinear product Preisach function	György Kádár, Edward Della Torre
3004	Vector Preisach and the moving model	Edward Della Torre, György Kádár
3007	Modeling of velocity effects in eddy current applications	Nathan Ida
3010	Linear-exponential functions for eddy current analysis	Konrad Weeber, Samuel Vidyasagar, S. Ratnajeevan H. Hoole
3013	Perturbations in the adaptive refinement of boundary elements	S. Jayakumaran, S. Ratnajeevan H. Hoole
3016	Singularity and corner effects in a boundary element model for a short, linearly magnetic conducting cylinder	M. R. Ahmed, P. E. Burke, J. D. Lavers
3019	A hybrid method for eddy current open-boundary field computation	M. V. K. Chari, G. Bedrosian
3022	The natural finite element formulation of the impedance boundary condition in shielding structures	S. Ratnajeevan H. Hoole, Konrad Weeber, N. Ratnasuneeran G. Hoole
3025	Spectrally correct finite element operators for electromagnetic vector fields	A. R. Pinchuk, C. W. Crowley, P. P. Silvester, R. L. Ferrari

Phase Transition

3028	Magnetic properties of the copper trimer chains 4-picolinium$_2$ Cu_3Cl_8 and 4-*picolinium*$_2$ Cu_3Br_8	C. E. Zaspel, Gerald V. Rubenacker, Stuart L. Hutton, John E. Drumheller, R. S. Rubins, R. D. Willett, Marcus R. Bond
3031	Magnetic tricritical behavior of ethylammonium tetrachlorocuprate	Jerome R. Long, Donald N. Haines, John E. Drumheller
3034	Magnetic study of acetamidinium tetrachlorocuprate II	L. Landenburger, Gerald V. Rubenacker, John E. Drumheller, Wan Ke Lin, K. Emerson
3036	Unusual finite size effects on critical temperature in fcc Ising antiferromagnets	J. Pommier, H. T. Diep, A. Ghazali, P. Lallemand
3039	Nonequilibrium relaxation of the Ising square lattice at the percolation threshold	D. P. Landau, S. Wansleben

3041	Examination of the cluster variational method for the Ising model and some possible corrections (abstract)	H. Leidecker, J. Harnden, J. Condon
3041	*Phase transition in Ising ferromagnetic lattices with fixed spins (abstract)*	A. Labarta, J. Marro, J. Tejada, B. Martínez
3042	Mean-field treatment of three component spin Hamiltonian with high-order cubic anisotropy: Generic phases and sequences of order-order transitions (abstract)	Z. Pawlowska, J. Oliker, G. F. Kventsel, J. Katriel

Itinerant Magnetism

3043	Precision measurements of the magnetization and its temperature derivative of Ni and dilute Ni alloys at 290 K	D. Hunter, A. S. Arrott, R. I. Grynszpan, P. Dassonvalle, P. Langlois
3046	Band structure of cobalt by an empirical approach	J. S. Nelson, C. Y. Fong, C. M. Perlov
3049	Electronic properties of $Co_{1-x}Cr_x$	J. S. Nelson, C. Y. Fong, Inder P. Batra
3052	Spin-polarized relativistic LMTO method	H. Ebert, P. Strange, B. L. Gyorffy
3055	Theory of circularly polarized x-ray absorption by ferromagnetic Fe	H. Ebert, P. Strange, B. L. Gyorffy
3058	Fractional quantized nesting for the spin-density waves induced by a magnetic field	G. Faini, F. Pesty, P. Garoche
3061	Thermodynamic investigations of the field-induced spin-density wave: Significant departure from Bardeen–Cooper–Schrieffer behavior at high field	F. Pesty, G. Faini, P. Garoche
3064	The role of hybridization in U(Ru,Rh)Al	P. A. Veenhuizen, J. C. P. Klaasse, F. R. de Boer, V. Sechovsky, L. Havela
3067	Electronic properties of UNi(Al,Ga)	V. Sechovsky, H. Maletta, L. Havela, P. A. Veenhuizen, F. R. de Boer
3070	5*f* magnetism in (U,Th)CoSn	V. Sechovsky, L. Havela, G. Hilscher, N. Pillmayr, A. V. Andreev, P. A. Veenhuizen, F. R. de Boer
3073	Thermodynamics of free electrons in helical magnetic fields	Miguel Calvo
3076	Electromagnetic gauge invariance and orbital motion in field-induced spin-density-wave collective modes: Magnetorotons (abstract)	P. Lederer, D. Poilblanc
3076	The contribution of Cu^{2+}-Cu^{2+} pairs to EPR (abstract)	Guo-Yin Shen, Chang-qing Xu, Gui-Ru Bai

Critical Phenomena

3077	Surface and size effects in magnetic phase transitions (invited)	D. P. Landau, K. Binder
3082	Bond randomness at Ising criticality	Rajiv R. P. Singh, Michael E. Fisher
3083	First-order phase transition induced by quantum fluctuations in Heisenberg helimagnets	A. B. Harris, E. Rastelli
3086	Critical properties of helical magnets and triangular antiferromagnets	Hikaru Kawamura
3089	Spin fluctuations in EuS above T_C: Comparison with asymptotic renormalization-group theory	P. Böni, G. Shirane, H. G. Bohn, W. Zinn
3092	On the ferro-cone-fan magnetic transitions in MnP	C. C. Becerra, N. F. Oliveira, Jr., A. C. Migliano
3095	^{31}P NMR relaxation study of spin dynamics in layered transition-metal compounds MPX_3	J. Ziolo, S. Torre, A. Rigamonti, F. Borsa
3098	Crossover of the spectral weight function: A new interpretation of some large *q* neutron scattering data (abstract)	Lee Chow, David Fisher
3098	Multicritical point in the magnetic phase diagram of $CsNiCl_3$ (abstract)	A. Caillé, L. M. Plumer, Kevin Hood

Magneto-optic Isolators and Materials

3099	Thin-film garnet materials with zero linear birefringence for magneto-optic waveguide devices (invited)	R. Wolfe, V. J. Fratello, M. McGlashan-Powell
3104	Anisotropy of the linear magnetic birefringence in erbium iron garnet	M. Guillot, H. Le Gall, P. Feldmann, A. Marchand
3107	Magnetization anomalies and temperature-dependent hole localization in the $Ca^{2+}Fe^{4+}Ga^{3+}$: yttrium iron garet system	M. Pardavi-Horváth, A. Thavendrarajah, P. E. Wigen, P. De Gasperis
3110	Photomagnetism in $Ca^{2+}Fe^{4+}$-doped yttrium iron garnet	M. Pardavi-Horváth, P. E. Wigen, G. Vértesy
3113	Temperature dependence of Faraday rotation in Bi-substituted terbium iron garnet films	H. Umezawa, Y. Yokoyama, N. Koshizuka
3116	Kerr rotation spectra of Bi-substituted polycrystalline YCaVIn iron garnets	Shoukhrat Egamov, Guiqin Wang, Shiyuan Zhang, Hao Wang, Hongru Zhai
3118	Overview of magneto-optic isolator materials and devices (invited) (abstract)	K. Tsushima
3118	Faraday rotator materials for lasers (invited) (abstract)	M. J. Weber

Symposium on Rare-Earth Iron Magnets

3119	Magnetic and structural studies of erbium-iron-manganese-boron alloy (invited)	C. D. Fuerst, G. P. Meisner, F. E. Pinkerton, W. B. Yelon
3124	Multi-ion crystal field analysis: Methodology and application to $(Er_xPr_{1-x})_2Fe_{14}B$ (invited)	E. B. Boltich
3130	Structure and properties of some novel ternary Fe-rich rare-earth intermetallics (invited)	K. H. J. Buschow
3136	Disclinations: The magnetism and the magnetic anisotropies of the rare-earth–*3d* transition-metal hard magnets (invited)	R. E. Watson, L. H. Bennett, M. Melamud
3139	Magnetic anisotropy energy *in single* crystal $Y_{1.8}Er_{0.2}Fe_{14}B$ (invited) (abstract)	C. M. Williams, N. C. Koon, B. N. Das

Bubbles, Bloch Lines, and Other Magnetic Memories

3140	Epitaxial Fe films on GaAs for hybrid semiconductor-magnetic memories	Ernst Schloemann, Randal Tustison, Jehoshua Weissman, H. Jerrold Van Hook, Thomas Varitimos
3143	Performance improvement of bubble memories using Bi-substituted bubble films	P. Thayamballi
3146	A Permalloy-access bubble-memory dual-function gate	J. R. Kelly
3149	Magnetoresistivity in NiFeCo multilayer films	J. H. Hur, C. S. Comstock, A. V. Pohm, L. A. Pearey
3151	Thermal noise limitations to 2×20-μm^2 magnetoresistive memory element thresholds	R. I. Waite, A. V. Pohm, C. S. Comstock
3153	Direct Bloch line optical observation (invited)	A. Thiaville, F. Boileau, J. Miltat, L. Arnaud
3159	Direct investigations of Bloch line memory functions by wall resonance spectroscopy	J. Heidmann, H. Krause, J. Engemann
3162	Wide domain walls and Bloch lines in Permalloy and Co-Fe films using Kerr effect microscopy	P. J. Ryan, T. B. Mitchell
3165	Generation of vertical Bloch lines in ion-implanted (111) garnet films	J. J. Fernandez-de-Castro, F. J. Friedlaender
3168	Nonuniform wall motion in magnetic stripe domains and its effect on vertical Bloch line propagation	M. R. Lian, F. B. Humphrey
3171	Controlling Bloch lines and domain chopping for multiple stripes aligned in parallel	K. Matsuyama, K. Nakamura, H. Asada, T. Suzuki, K. Fujimoto, S. Konishi

Eddy Current Application and Coupled Phenomena

3174	Modeling of magnetization characteristics and faster magnetodynamic field computation (invited)	Y. Saito, Y. Kishino, K. Fukushima, S. Hayano, N. Tsuya
3179	Numerical micromagnetics by the finite element method. II	D. R. Fredkin, T. R. Koehler
3182	Finite element optimization of field configuration for the eddy current testing of roller bearing rib rings	R. Palanisamy, O. J. Varonis
3185	A coupled field finite element for magnetostructural analysis	Dale F. Ostergaard
3188	Electromagnetic field analysis of unbalanced regimes of synchronous machines	I. D. Mayergoyz, F. P. Emad, M. A. Sherif
3191	Magnetic field gene-ated by lightning protection system	A. Geri, G. M. Veca
3194	Eddy current losses in composite and/or multibodies with $\mu_r \geq 1$	M. Taher Ahmed, J. D. Lavers, P. E. Burke
3197	Finite element modeling of electromagnetic resonators and absorbers	J. R. Brauer, R. H. Vander Heiden, A. B. Bruno
3200	Scattering from an infinite, finitely conducting cylinder by finite element analysis	A. B. Bruno, J. R. Brauer

Composition Modulation and Multilayers

3203	Magnetic properties and film structures of Fe/C multilayers	Toshio Kobayashi, Ryoichi Nakatani, Shigekazu Ootomo, Noriyuki Kumasaka
3206	Magnetic properties of amorphous Fe-Si compositionally modulated thin films	B. Martinez, M. A. Moreu, A. Labarta, X. Obradors, J. Tejada
3209	Magnetization of Ni-Si, Co-Si, and Fe-Si layered systems	C. L. Foiles, J. M. Slaughter
3212	Enhancement of perpendicular anisotropy in amorphous GdCo and TbFe films prepared by alternative bias sputtering	Hiroshi Yamamoto, Masaichi Tanaka, Masahiko Naoe
3215	Ellipsometric and magneto-optic properties of sputtered dysprosium-iron multilayers	Thomas E. Tiwald, John A. Woollam, D. J. Sellmyer
3218	Magnetic properties, anisotropy, and microstructure of sputtered rare-earth iron multilayers	Z. S. Shan, S. Nafis, K. D. Aylesworth, D. J. Sellmyer
3221	Structural, electrical, and magnetic properties of Fe/Pd superlattices (abstract)	A. Boufelfel, R. M. Emrick, J. L. Makous, Charles M. Falco, Charles Majkrzak
3221	Structural and magnetic studies of Fe/W metallic superlattices (abstract)	A. Boufelfel, Roy M. Emrick, Charles M. Falco
3222	Hyperfine field measurements of Co-Cr multilayered films (abstract)	M. B. Stearns, Y. D. Zhang, J. I. Budnick
3223	Magnetic aftereffect in textured Ni/Cu compositionally modulated alloys (abstract)	U. Atzmony, L. J. Swartzendruber, L. H. Bennett, D. Lashmore, R. E. Watson, M. Rubinstein, P. Lubitz

Thin Films, Sandwiches, and Small Particles

3224	Magnetic and structural studies in Co-Al thin films	A. Tsoukatos, B. Dale, J. Strzeszewski, G. C. Hadjipanayis
3227	X-ray diffraction determination of stress in magnetron-sputtered Permalloy films	C. D. England, C. M. Falco, J. A. Aboaf
3230	Iron nitride thin films prepared by facing targets sputtering	A. Morisako, K. Takahashi, M. Matsumoto, M. Naoe
3233	The dependence of coercivities of ultrafine Fe particles on packing fraction and microstructure	K. Bridger, J. Watts, C. L. Chien
3236	Magnetic anisotropy and granulometry of Ni/CeO_2 catalyst	A. Mauger, M. Escorne, V. Paul-Boncour, A. Percheron-Guegan, J. C. Achard, J. Barrault
3239	Magnetic filtration of submicron hematite particles	M. F. Haque, R. Aidun, C. Moyer, S. Arajs
3241	Nonlinear magnetic susceptibility tensors of ferromagnetic films	Longpei Shi

3244	Exchange coupling between a soft and a hard ferromagnetic thin film	K. Ounadjela, G. Suran
3247	Magnetic profile in Tb-Fe and Tb-Fe/Ni-Fe bilayer films (abstract)	R. O. Hilleke, G. P. Felcher, F. Hellman, E. M. Gyorgy
3247	The structural model of the interglobular voids in chains of magnetic metal powders (abstract)	D. R. Mehandiev, I. D. Dragieva, M. S. Slavcheva, D. T. Buchkov

Thin Films: Longitudinal Recording

3248	Micromagnetic studies of thin metallic films (invited)	Jian-Gang Zhu, H. Neal Bertram
3254	Density dependence of noise in thin metallic longitudinal media	Jaekyun J. Moon, L. Richard Carley, Romney R. Katti
3257	Relationship between the transition width and the zigzag wavelength	X. Y. Zhang, H. Suhl, P. K. George
3260	Low-noise metal medium for high-density longitudinal recording	J. A. Christner, R. Ranjan, R. L. Peterson, J. I. Lee
3263	The effect of Cr and W nucleation layers on the magnetic properties of CoPt films	J. K. Howard
3266	Micro/magnetic structural development in Co-Ni-Cr and Co-Ni-Cr/Cr films for longitudinal recording media	J.-W. Lee, K. R. Mountfield, D. E. Laughlin
3269	The crystal growth and magnetic properties of sputtered Co-Ni films on bcc polycrystalline underlayers	Hyung J. Lee
3272	The microstructure of iron oxide thin films	Cherngye Hwang, Mao-Min Chen, Gilbert Castillo
3275	Wear resistance of iron oxide thin films	Mao-Min Chen, Judy Lin, Tsai-Wei Wu, Gilbert Castillo
3278	Spacing dependence of magnetic recording with a single thin-film head and disk (abstract)	C. Michael Jefferson, I. A. Beardsley
3278	Microstructure of oblique incidence CoNi thin films (abstract)	H.-M. Ho, G. Thomas, J.-S. Gau

Magnetic Semiconductors

3279	Fe-based semimagnetic semiconductors (invited)	Andrzej Mycielski
3285	Diluted magnetic semiconductor superlattices for magnetic studies of dimensional crossover (invited)	J. M. Hong, D. D. Awschalom, L. L. Chang, Armin Segmüller
3291	Activated dynamic scaling and magnetic ordering in $Cd_{1-x}Mn_xTe$: Spin glass or random antiferromagnet? (invited)	S. Geschwind, A. T. Ogielski, G. Devlin, J. Hegarty, P. Bridenbaugh
3297	Spin dynamics in $Zn_{1-x}Mn_xTe$	T. M. Giebultowicz, J. J. Rhyne, W. Y. Ching, D. L. Huber, J. K. Furdyna
3300	Electroreflectance and wavelength-modulated reflectivity spectra of $Zn_{1-x}Mn_xSe$ alloys	Jolanta Stankiewicz, José R. Fermín
3303	Magnetic and crystallographic characterization of $Zn_{0.78}Fe_{0.22}Se$ and FeSe films on GaAs (001)	B. T. Jonker, J. J. Krebs, S. B. Qadri, G. A. Prinz, F. Volkening, N. C. Koon
3306	The mechanism of the high conduction state in the $Ca^{2+}Ge^{4+}$:YIG system	S. H. Yuan, M. Pardavi-Horváth, P. E. Wigen, P. De Gasperis
3309	Magnetoreflectivity study of excitons in $Zn_{1-x}Fe_xSe$ epilayers (abstract)	X. Liu, A. Petrou, G. A. Prinz, B. T. Jonker, J. J. Krebs, J. Warnock

R-Fe-B Magnetic Hardening and Microstructure

3310	Domain wall pinning versus nucleation of reversed domains in R-Fe-B magnets (invited)	George C. Hadjipanayis, A. Kim
3316	Demagnetization process of sintered $R_{17}Fe_{83-x}B_x$ magnets (R = Nd or Pr)	Y. Otani, H. Miyajima, S. Chikazumi, S. Hirosawa, M. Sagawa
3319	Effect of heat treatment on grain-boundary microstructure in Nd-Fe-B sintered magnet	Y. Tsubokawa, R. Shimizu, S. Hirosawa, M. Sagawa
3321	Evidence for domain wall pinning by a magnetic grain-boundary phase in sintered Nd-Fe-B based permanent magnets	K. J. Strnat, H. F. Mildrum, M. Tokunaga, H. Harada

3324	Hard magnetic properties of melt-spun Nd-Co-Fe-B materials	C. D. Fuerst, J. F. Herbst
3327	Magnetic properties and microstructure of iron-based rare-earth magnets with low-temperature coefficients	S. Z. Zhou, C. Guo, Q. Hu
3330	Crystallization and texturing in rapidly quenched $Nd_2Fe_{14}B$, and $Nd_{15}Fe_{77}B_8$	Guo-hau Tu, Z. Altounian, D. H. Ryan, J. O. Ström-Olsen
3333	Evidence for particle interaction effects in Nd-Fe-B ribbons (abstract)	F. E. Pinkerton
3333	Al_2O_3 additions to Fe-Nd-B magnets: Can pinning be achieved? (abstract)	R. Ramesh, G. Thomas, B. M. Ma
3334	Al-Fe-Nd-B magnets: Where does the Al go? (abstract)	R. Ramesh, J. K. Chen, G. Thomas, B. M. Ma

Microwave Propagation, Resonance, and Devices

3335	Second-order term effect on the dispersion characteristics of a magnetostatic delay line	P. De Gasperis, R. Marcelli, G. Miccoli
3338	Propagation of an extraordinary wave in a thin ferrite film in the absence of an external magnetic field	David J. Halchin
3341	Magnetostatic resonance of holes	J. C. Peuzin, J. C. Gay
3344	Brillouin light scattering detection of ferromagnetic resonance in thin films	G. Srinivasan, C. E. Patton, J. G. Booth
3347	Photothermal characterization of inhomogeneous ferromagnetic resonance absorption in ferrites	O. V. Geisau, U. Netzelmann, J. Pelzl
3350	A contribution to the ferromagnetic resonance linewidth of *M*-phase barium ferrite	E. Tsantes, L. M. Silber
3353	Effective linewidth measurements at 36 GHz in hexagonal and cubic ferrites	W. D. Wilber, L. M. Silber
3356	A three-octave-band bandwidth Y circulator (abstract)	Young Mouh Duh

Magnetic Field Computation

3357	Toward an algorithm to make cuts for magnetic scalar potentials in finite element meshes	P. R. Kotiuga
3360	Variational principles for three-dimensional magnetostatics based on helicity	P. R. Kotiuga
3363	Forces in finite-element magnetostatics using co-energy related estimation of field accuracy	S. McFee, D. A. Lowther, J. P. Webb
3366	The strategic dual image method: An extremely simple procedure for open field problems	Y. Saito, K. Takahashi, S. Hayano
3369	A meaningful post-processing method based on a locally orthogonal discretization	Y. Saito, S. Ikeguchi, S. Hayano
3372	Head saturation in magnetic recording	J. P. Peng, J. R. Varner
3375	Three-dimensional finite-element analysis of recording heads	D. A. Lowther, T. M. Coughlin
3378	Erasing magnetic recording media	K. C. Wiesen, R. R. Katti, S. H. Charap, M. H. Kryder
3381	Analytical solutions for the three-dimensional side-fringing field of magnetic recording heads	I. D. Mayergoyz, Dan S. Bloomberg
3384	Automatic field problem formulation for CAE stations	S. Ratnajeevan H. Hoole, Samuel Vidyasagar, Konrad Weeber
3387	Reassessment of matrix solvers in repeated solution (abstract)	A. W. Anandaraj, S. Ratnajeevan H. Hoole

Amorphous Materials and Magnetization

3388	Magnetic moment suppression in rapidly solidified Co-TE-B alloys	A. Mitra Ghemawat, M. E. McHenry, R. C. O'Handley
3391	The thermal behavior of the critical magnetic field in amorphous ribbons	R. Montes de Oca, E. Amano, R. Valenzuela
3394	Miniaturization limit of a cloth inductor	H. Matsuki, H. Miyazawa, K. Murakami, T. Yamamoto

3397	Low-temperature magnetic susceptibility of Fe-B amorphous alloys (abstract)	R. Puźniak, W. Dmowski
3397	Magnetic properties of Co-B-C amorphous alloys melt-quenched beyond the eutectic regime (abstract)	Montse Pont, K. V. Rao, A. Inoue, T. Masumoto
3398	Temperature hysteresis and relaxation effects in amorphous Fe-Ni-Zr alloys (abstract)	C. E. Violet, R. J. Borg, K. V. Rao, J. Noques, R. D. Taylor, A. P. Batra

Rare Earths and Actinides

3399	Electron-hole interaction in $TmSe_{1-x}Te_x$ under pressure	J. Neuenschwander, P. Wachter, W. Bührer, P. Fischer
3402	Variational ground state for the periodic Anderson model	Samuel P. Bowen, Jay D. Mancini
3405	Heavy fermion behavior in CePtSi and CeRuSi	L. Rebelsky, K. Reilly, S. Horn, H. Borges, J. D. Thompson, J. O. Willis, R. Aikin, R. Caspari, C. D. Bredl
3408	Magnetic susceptibilities of actinide 3*d*-metal intermetallic compounds	R. Bechara Muniz, J. d'Albuquerque e Castro, A. Troper, A. A. Gomes
3411	CeSi: A non-Kondo trivalent Ce compound	S. A. Shaheen
3414	Anisotropy of the upper critical field in the magnetic heavy-fermion superconductor URu_2Si_2	V. V. Moshchalkov, F. Aliev, V. Kovachik, M. Zalyaljutdinov, T. T. M. Palstra, A. A. Menovsky, J. A. Mydosh
3417	Magnetic order in the Kondo-lattice compound CePdIn	E. Brück, M. van Sprang, J. C. P. Klaasse, F. R. de Boer
3420	Field-dependent behavior of longitudinal ultrasonic attenuation in UPt_3	M.-F. Xu, A. Schenstrom, H.-P. Baum, Y. J. Qian, J. B. Ketterson, D. Hinks, M. Levy, Bimal K. Sarma
3422	A resistance minimum in an alloy of only "impurity" atoms (abstract)	Warren E. Henry
3422	Narrow bands and magnetic properties of heavy fermions (abstract)	F. Marabelli, P. Wachter

Particulate Recording Materials

3423	Micromagnetic predictions for barium ferrite particles (invited)	R. H. Victora
3429	Overwrite modulation in Ba-ferrite particulate media	D. E. Speliotis
3432	Magnetization reversal in Ba-ferrite particulate media	D. E. Speliotis
3435	The mechanism of nucleation in uniaxial ferromagnets	Ching-Ray Chang, D. R. Fredkin
3438	Overwrite temperature dependence for magnetic recording	Takayuki Takeda, Katsumichi Tagami, Takaaki Watanabe
3441	Orientation of acicular particles in magnetic tape	D. I. Paul, B.I. Finkelstein
3443	Recording characteristics of tapes prepared using iron oxide particles treated with organic titanate	S. Aoyama, K. Sumiya, M. Kishimoto, M. Amemiya
3446	Temperature dependence of magnetization time decay in particulate magnetic media (abstract)	S. B. Oseroff, Z. Dai, C. H. Chan, V. M. T. Bin, S. Schultz

Crystalline Magnetic Multilayers

3447	Magnetic rare-earth superlattices (invited)	C. F. Majkrzak, Doon Gibbs, P. Böni, Alan I. Goldman, J. Kwo, M. Hong, T. C. Hsieh, R. M. Fleming, D. B. McWhan, Y. Yafet, J. W. Cable, J. Bohr, H. Grimm, C. L. Chien
3453	Interlayer exchange in magnetic superlattices (invited)	Y. Yafet, J. Kwo, M. Hong, C. F. Majkrzak, T. O'Brien
3458	Magnetic characterization of Er/Y superlattices	J. A. Borchers, M. B. Salamon, R. Du, C. P. Flynn, J. J. Rhyne, R. W. Erwin

3461	Magnetoelasticity and structure of Er/Y superlattices	R. W. Erwin, J. J. Rhyne, J. Borchers, M. B. Salamon, R. Du, C. P. Flynn
3464	Magnetic properties of sandwiches and superlattices of fcc Fe(001) grown on Cu(001) substrates	J. R. Dutcher, B. Heinrich, J. F. Cochran, D. A. Steigerwald, W. F. Egelhoff, Jr.
3467	Magnetic and structural properties of Fe(100)/Ag(100) single-crystal multilayer films with ultrathin Fe layers	J. J. Krebs, B. T Jonker, G. A. Prinz
3470	Structures and magnetic properties of Fe/Ag multilayer films prepared by sputtering and ultrahigh-vacuum depositions	Y. Kozono, M. Komuro, S. Narishige, M. Hanazono, Y. Sugita
3473	Static and dynamic magnetic properties of Fe-Cr-layered structures with antiferromagnetic interlayer exchange	F. Saurenbach, U. Walz, L. Hinchey, P. Grünberg, W. Zinn
3476	Co-Mo thin films with an artificially layered structure	Noboru Sato
3479	Perpendicular anisotropy in Pd/Co multilayers	H. J. G. Draaisma, F. J. A. den Broeder, W. J. M. de Jonge

Itinerant Magnetism and Electronic Structure

3482	Local spin-density functional theory of noncollinear magnetism (invited)	J. Kübler, K.-H. Höck, J. Sticht, A. R. Williams
3487	Mn magnetism and magnetic structures in RMn_2	R. Ballou, J. Deportes, R. Lemaire, B. Ouladdiaf
3490	Effects of chemical and magnetic disorder in $Fe_{0.50}Mn_{0.50}$	D. D. Johnson, F. J. Pinski, G. M. Stocks
3493	All-electron study of $c(2\times2)$ S chemisorbed above magnetic Fe(001)	S. R. Chubb, W. E. Pickett
3496	Spin fluctuations in Ni above T_C	P. Rusek, J. Callaway
3499	Spin-resolved photoemission from Fe_3Pt(001) Invar and γ-Fe films (invited)	C. Carbone, G. S. Sohal, E. Kisker, E. F. Wassermann
3503	The near-edge x-ray absorption spectroscopy of RT_2Si_2 and RT_2Ge_2 compounds	P. H. Ansari, B. Qi, G. Liang, I. Perez, F. Lu, M. Croft
3506	Spin-polarized photoelectron diffraction: A new probe of short-range magnetic order (*invited*) (abstract)	C. S. Fadley, B. Sinkovic, B. D. Hermsmeier, J. Osterwalder

R-Fe Alloying and Processing

3507	Effects of silicon and aluminum additions on magnetic properties of rapidly quenched Nd-Fe-B permanent magnets	F. Matsumoto, H. Sakamoto, M. Komiya, M. Fujikura
3510	Magnetizability of Nd-Fe-B-type magnets with Dy additions	M. Tokunaga, M. Endoh, H. Harada, S. R. Trout
3513	Misch-metal-iron based magnets	W. Gong, G. C. Hadjipanayis
3516	The effects of various alloying elements on modifying the elevated temperature magnetic properties of sintered Nd-Fe-B magnets	Y. Xiao, S. Liu, H. F. Mildrum, K. J. Strnat, A. E. Ray
3519	High coercivity Nd-Fe-B magnets with lower dysprosium content	A. S. Kim
3522	Elevated temperature study of Nd-Fe-B–based magnets with cobalt and dysprosium additions	D. R. Gauder, M. H. Froning, R. J. White, A. E. Ray
3525	Fe-Nd-B permanent magnet prepared by hot extrusion of rapidly solidified melt-spun filaments	C. J. Yang, R. Ray
3528	Grain growth and alignment in hot deformed Nd-Fe-B magnets	Raja K. Mishra, Earl G. Brewer, Robert W. Lee
3531	A texture study of anisotropic sintered Nd-Fe-B magnets	W. C. Chang, T. B. Wu, K. S. Liu
3534	X-ray determination of alignment in FeNdB magnets	S. Z. Zhou, Y. X. Zhou, C. D. Graham, Jr.
3537	Radiation-induced changes in magnetic properties of Nd-Fe-B permanent magnets (abstract)	R. D. Brown, J. R. Cost
3537	Thermal aging and storage characteristics of rapidly solidified Nd-Fe-B powder (abstract)	E. E. Welker, M. S. Guthrie

Low-Dimensional Magnetism

3538	Quantum energy gap in two quasi-one-dimensional $S=1$ Heisenberg antiferromagnets (invited)	J. P. Renard, M. Verdaguer, L. P. Regnault, W. A. C. Erkelens, J. Rossat-Mignod, J. Ribas, W. G. Stirling, C. Vettier
3543	Quantum spin chains and the conformal anomaly	Jill C. Bonner, John B. Parkinson
3546	The Ising model between one and two dimensions	M. A. Novotny
3548	Magnetic birefringence of two $S=1/2$ Heisenberg antiferromagnetic chains	A. C. Lamas, C. P. Landee
3551	Low-dimensional magnetic systems; from 1D to 3D ferrimagnets	M. Drillon, E. Coronado, M. Belaiche, R. L. Carlin
3554	Neutron scattering investigation of a quasi-two-dimensional planar ferromagnet	D. G. Wiesler, H. Zabel
3557	Quasi-one- and two-dimensional antiferromagnetism in α-$FeC_2O_4 \cdot 2H_2O$ and α-$MnC_2O_4 \cdot 2H_2O$	Satoru Simizu, S. A. Friedberg
3560	Scaling behavior in the $S=1$ antiferromagnetic XXZ chain (abstract)	J. C. Bonner, G. Müller, J. B. Parkinson
3560	Thermodynamics of the diluted classical spin Heisenberg chain with single ion anisotropy (abstract)	X. Y. Dong, S. Ahmed, A. R. McGurn

Compounds and Magnetochemistry

3561	Effects of electric and magnetic fields on the convective heat transfer in gaseous O_2 and N_2O	M. F. Haque, Sigurds Arajs, C. A. Moyer, E. E. Anderson, E. Blums
3563	Magnetic properties, hyperfine interactions, and spin dynamics in the layer compounds $CsVF_4$ and $RbVF_4$	J. Ziolo, M. Corti, F. Borsa, A. Rigamonti, A. Paleari, G. Spinolo
3566	Single-crystal ac susceptibility measurements on $[Co(NH_3)_6][CuCl_5]$, a 3D, $S=1/2$ Heisenberg antiferromagnet	Mary C. Morón, Fernando Palacio, Josefina Pons, Jaime Casabo, K. E. Merabet, Richard L. Carlin
3569	Magnetic and structural properties of $Mn(SCN)_2(ROH)_2$ compounds	G. C. DeFotis, E. M. McGhee, K. R. Echols, R. S. Wiese
3572	Crystal structure and magnetic properties of $[Co(py)_2(H_2O)_2Br_2]$	Richard L. Carlin, Danny Shum, Ekk Sinn
3575	Magnetic ac susceptibilities of $CsMnF_4 \cdot 2H_2O$ and $NH_4MnF_4 \cdot 2H_2O$ weak ferromagnets (abstract)	Mercedes Andrés, Fernando Palacio, Fernando Lahoz
3575	Magnetochemistry of chromium (III) (abstract)	K. E. Merabet, R. Burriel, Richard L. Carlin
3576	Magnetic properties of some $FeCl_4^-$ salts (abstract)	Carol Lowe, J. A. Zora, K. R. Seddon, Richard L. Carlin

Magnetic Compounds and Alloys. I

3577	Magnetic phase transition in $Y_{0.97}Dy_{0.03}$	J. A. Gotaas, J. J. Rhyne, L. E. Wenger, J. A. Mydosh
3580	X-ray scattering study of the magnetic phase transformation in GdB_6	R. M. Galera, D. P. Osterman, J. D. Axe, S. Kunii, T. Kasuya
3583	Anomalous electrical and magnetic properties of gadolinium hexaboride	Naushad Ali
3586	Magnetic properties of $YCo_{12}B_6$ and $GdCo_{12}B_6$ intermetallics	M. Rosenberg, M. Mittag, K. H. J. Buschow
3589	Crystal structure of $R(Ti,Fe)_{12}$(R = Nd,Sm) compound	N. C. Liu, N. Kamprath, L. Wickramasekara, F. J. Cadieu, H. H. Stadelmaier
3592	A $CaCu_5$-type samarium-iron phase stabilized by zirconium addition	Chin Lin, Yun-Xi Sun, Zheng-Hua Lou
3595	On the anisotropy energies for YCo_5, RCo_5, Y_2Co_{17}, and R_2Co_{17}	H. Takahashi, K. Hikosaka, S. Ohtsuka, A. Seo, T. Ukai, N. Mori
3598	Neutron inelastic experiments on actinide dioxides: Search for crystal-field levels in NpO_2	S. Kern, J. Morris, C. K. Loong, G. L. Goodman, G. H. Lander, B. Cort

3601	Studies of the magnetization densities in Pu compounds; determination of the degree of localization	G. H. Lander, M. Wulff, J. Rebizant, J. C. Spirlet, P. J. Brown, O. Vogt
3604	Magnetic structure of UCu_2Si_2 and $U(Cu_{0.75}Mn_{0.25})_2Si_2$	A. L. Giorgi, A. C. Lawson, J. A. Goldstone, K. J. Volin, J. D. Jorgensen

Magnetic Compounds and Alloys. II

3606	Determination of the absolute magnetic moment direction in Cr_2O_3 using generalized polarization analysis	F. Tasset, P. J. Brown, J. B. Forsyth
3609	On magnetic transitions in dilute Cr-Ga and Cr-Ge alloys	P. Smit, H. L. Alberts
3611	On the magnetic structure of noncollinear γ-$Fe_{70}Mn_{30}$	T. Takahashi, T. Ukai, N. Mori
3614	Magnetic anisotropy induced by magnetic field cooling in Ni_3Mn alloys	T. Yamauchi, H. Miyajima, S. Chikazumi
3617	Neutron scattering and magnetic susceptibilities of dilute *Pt*Co alloys calculated by Monte Carlo methods	R. E. Parra, R. A. López
3620	Temperature hysteresis and time-dependent effect in the initial susceptibility of rapidly solidified Monel (abstract)	U. Atzmony, L. J. Swartzendruber, L. H. Bennett
3620	Magnetic and structural properties of $MMNi_{4.15}Fe_{0.85}$ and its hydride (abstract)	F. W. Oliver, W. Morgan, E. C. Hammond, L. Bang-Zheng, L. Meng-Zhao, A. Thorpe

Thermo-magneto-optic Materials

3621	The TM dependence of the magneto-optic signal in GdTb-TM thin films	D. K. Hairston, M. H. Kryder
3624	The effects of deposition conditions on microstructure and magnetic properties of TbFeCo	J.-W. Lee, H-P. D. Shieh, M. H. Kryder, D. E. Laughlin
3627	Microstructure and stability of rf-diode sputtered GdTbFeCo thin films	H-P. D. Shieh, M. Hong, S. Nakahara
3630	Characterization of amorphous TbFeCo films for magneto-optical media	M. F. Ruane, J. Calkins
3633	Single ion model for magnetostriction in rare-earth–transition-metal amorphous films	Yoshio Suzuki, Norio Ohta
3636	Magneto-optical properties of PtMnSb films prepared by facing targets sputtering	M. Naoe, N. Kitamura, M. Shoji, A. Nagai
3639	Microstructure of sputtered garnet films for magneto-optical recording media	K. Shono, H. Kano, N. Koshino, S. Ogawa
3642	Improvement in optical and magnetic properties of Bi-substituted garnet sputtered films for magneto-optical recording	M. Gomi, K. Satoh, M. Abe
3645	Magnetic anisotropy in TbFe thin films prepared at oblique incidence	Sung-Chul Shin, Ashok K. Agarwala
3648	Materials for magneto-optic data storage (invited) (abstract)	Alan E. Bell

Surface and Interfacial Magnetism

3649	Long-range magnetic reconstruction of ferromagnetic films with diffused interfaces	J. R. Cullen, K. B. Hathaway, J. M. D. Coey
3652	Monolayer ferromagnetism of Fe(110) on W(110) studied by Mössbauer spectroscopy	M. Przybylski, U. Gradmann
3655	Structural and magnetic properties of Au/Pd/Au sandwiches: A total energy all-electron approach	Soon C. Hong, C. L. Fu, A. J. Freeman
3657	Magnetic proximity effects for Fe films across a thin Ag barrier	Z. Q. Qiu, H. Tang, Y. W. Du, G. P. Stern, J. C. Walker
3659	Effects of magnetic surface anisotropy near the (110) Fe/MnF_2 interface	H. Tang, Z. Q. Qiu, Y. W. Du, G. P. Stern, J. C. Walker
3662	Magnetic properties of molecular-beam epitaxial grown (100) iron films	D. K. Lottis, J. Florczak, E. Dan Dahlberg, S. Batra, A. M. Wowchak, P. I. Cohen
3664	Surface magnetism of oxygen and hydrogen adsorption on Ni(111)	H. J. Elmers, U. Gradmann

3667	Ferromagnetic order at Tb surfaces above the bulk Curie temperature	C. Rau, C. Jin, M. Robert
3669	Magnetization depth profiling with low-energy electron spectroscopy and MOKE	J. Woods, A. Ushioda, M.M. Donovan, S. W. Sun, M. Tobise, R. C. O'Handley
3672	Substrate modified growth of epitaxial Fe films (abstract)	S. Batra, A. M. Wowchak, P. I. Cohen, D. K. Lottis, E. D. Dahlberg

Valence Fluctuations and Heavy Fermions

3673	Collective density fluctuations in heavy-fermion systems (invited)	P. Fulde, K. W. Becker
3676	Electronic structure of the light actinide oxides from electron spectroscopy (invited)	O. Gunnarsson, D. D. Sarma, F. U. Hillebrecht, K. Schönhammer
3680	Photoemission study of 5*f* localization in $UPd_{3-x}(Pt,Rh)_x$	A. J. Arko, D. D. Koelling, B. D. Dunlap, A. W. Mitchell, C. Capasso, M. del Giudice
3683	Basis of strong change of hybridization-induced magnetic ordering between CeSb and CeTe	N. Kioussis, B. R. Cooper, J. M. Wills
3686	Shift in maximum of sound attenuation with magnetic field in UPt_3	H.-P. Baum, M.-F. Xu, Y. J. Qian, A. Schenstrom, J. B. Ketterson, D. H. Hinks, M. Levy, B. K. Sarma
3689	Magnetization measurements on $(Ce,Gd)Al_3$	A. S. Edelstein, R. L. Holtz
3692	Unstable valence rare earths ion implanted into transition metals: Valence variation studies	F. Lu, S. Gunapala, M. Croft, N. G. Stoffel, M. L. den Boer
3695	Photoemission and BIS spectra of narrow-band uranium systems (abstract)	P. S. Riseborough

R-Fe New Phases and Intrinsic Properties

3696	The magnetic properties of Sm-Ti-Fe and Nd-Ti-Fe hard and soft sputtered phases	N. Kamprath, L. Wickramasekara, H. Hegde, N. C. Liu, J. K. D. Jayanetti, F. J. Cadieu
3699	Magnetic properties of rapidly quenched and annealed $Fe_{10}RTi$ and related alloys	Z. R. Zhao, Y. G. Ren, K. D. Aylesworth, D. J. Sellmyer, E. Singleton, J. Strzeszewski, G. C. Hadjipanayis
3702	Intrinsic magnetic properties of $SmTiFe_{10}$	Ying-chang Yang, Lin-shu Kong, Shu-he Sun, Dong-mei Gu, Ben-pei Cheng
3704	Magnetic properties of rare-earth transition-metal borides	S. H. Aly, E. Singleton, G. C. Hadjipanayis, D. J. Sellmyer, Z. R. Zhao
3707	The enhancement of the magnetic properties of Fe-Cr-Co-Mo polycrystalline permanent magnet alloys by cold rolling and annealing	S. Sugimoto, M. Okada, M. Homma
3710	The effect of Ga substitution on the magnetic properties of $Nd_2Fe_{14}B$, $Pr_2Fe_{14}B$, and $PrCo_5$	A. T. Pedziwiatr, S. G. Sankar, W. E. Wallace
3713	Analysis of high-field magnetization measurements on $R_2Fe_{14}B$ single crystals (R = Tb, Dy, Ho, Er, and Tm)	D. Givord, H. S. Li, J. M. Cadogan, J. M. D. Coey, J. P. Gavigan, O. Yamada, H. Maruyama, M. Sagawa, S. Hirosawa
3716	Electronic structure and spin density of $Gd_2Fe_{14}B$	W. Y. Ching, Zong-Quan Gu
3719	An NMR study of tetragonal $Nd_2Fe_{14}B$ and $Nd_2Fe_{14-x}Co_xB$	Y. D. Zhang, J. I. Budnick, E. Potenziani II, A. T. Pedziwiatr, W. E. Wallace, P. Panissod
3722	Mössbauer study of the permanent-magnet material $Nd_2(Fe_{1-x}Ni_x)_{14}B$	S. Dai, A. H. Morrish, X. Z. Zhou, B. P. Hu, S. G. Zhang
3725	Neutron determination of the magnetic order and site preference in $Er_2(Co_xFe_{1-x})_{17}$	R. Kumar, W. B. Yelon, C. D. Fuerst
3728	Sublattice magnetization and spin reorientation in $Nd_2Fe_{14}B$ (abstract)	K. Muraleedharan, G. Kaindl, G. Wortmann, B. Perscheid, N. C. Koon

Random Anisotropy, Random Fields

3729	Magnetic-wave-like excitations and cluster modes in randomly disordered $Rb_2Mn_xCr_{1-x}Cl_4$ (invited)	D. Sieger, H. Tietze, R. Geick, P. Schweiss, G. Heger, W. Treutmann
3735	Spin-glass transition in the random anisotropy axis model	Amitabha Chakrabarti
3738	Critical behavior of weakly diluted frustrated antiferromagnets	Julio F. Fernandez
3740	Transition behavior in Gd-Co based alloys with strong anisotropy	K. M. Lee, M. J. O'Shea
3743	Magnetic transitions and phases in random-anisotropy magnets	D. J. Sellmyer, S. Nafis, M. J. O'Shea
3746	Random-anisotropy ferromagnetism in amorphous $U_{27}Fe_{73}$ films	P. P. Freitas, T. S. Plaskett, T. R. McGuire
3749	Low-temperature spin waves in amorphous $Fe_{90-x}Ni_xZr_{10}$	J. A. Fernandez-Baca, J. W. Lynn, J. J. Rhyne, G. E. Fish
3752	Small-angle neutron scattering from amorphous $ErFe_2$ and $HoFe_2$ alloys	M. L. Spano, J. J. Rhyne
3755	Evidence for a spin-glass behavior in the diluted antiferromagnet $Fe_xZn_{1-x}F_2$	F. C. Montenegro, S. M. Rezende, M. D. Coutinho-Filho
3758	Tricritical point in dilute Ising antiferromagnets in magnetic field	P. Azaria, H. T. Diep, Serge Galam
3760	Reorientations, freezing, and plastic phase	Serge Galam

Ferrites

3762	Effect of demagnetizing fields on Kerr effect in ferrites	Prabhat K. Singh, P. K. Singh, S. Prasad
3765	Generalization of Snoek's limit for modeling initial permeability of magnetic materials	Gary G. Bush
3768	Validation of mixture equations for dielectric-magnetic composites	H. M. Musal, Jr., H. T. Hahn, G. G Bush
3771	Microwave susceptibility and effective linewidth of iron-carbonyl powders	G. A. Naziripour, C. E. Patton, M. V. Kogekar
3774	Ferrite-organic multilayer film for microwave monolithic integrate circuits prepared by ferrite plating based on the spray-spin-coating method	M. Abe, T. Itoh, Y. Tamaura, M. Gomi
3777	Molecular-field coefficients of $MnFe_2O_4$ and $NiFe_2O_4$ spinel ferrite systems	Gerald F. Dionne
3780	Dielectric and magnetic properties of polycrystalline cobalt-substituted LiTi ferrites	B. K. Kuanr, P. K. Singh, P. Kishan, N. Kumar, S. L. N. Rao, Prabhat K. Singh, G. P. Srivastava
3783	Charge transport in Li-Ni ferrospinels	P. Venugopal Reddy
3786	A novel low-temperature preparation of Ni-Zn ferrite and the properties of the ultrafine particles formed	C. J. Chen, K. Bridger, S. R. Winzer, V. PaiVerneker
3789	Studies on high-density nickel zinc ferrite and its magnetic properties using novel hydrazine precursors	T. T. Srinivasan, P. Ravindranathan, L. E. Cross, R. Roy, R. E. Newnham, S. G. Sankar, K. C. Patil
3792	New routes for the synthesis of iron oxide based magnetic materials	Sushama Joshi, D. M. Phase, S. M. Kanetkar, S. B. Ogale
3795	^{57}Fe-YIG: Narrow x-ray linewidth epitaxial layers on $Gd_3Ga_5O_{12}$	D. M. Gualtieri, W. Lavender, S. L. Ruby
3798	Simplified Mie series calculation of dipole moments for artificial dielectric constituents	Gary G. Bush
3801	Missing magnetic moment in spinel iron oxide films (abstract)	C. Ortiz, G. Vurens, M. M. Chen, M. Salmeron

Spin Waves

3802	Magnetic resonance experiments on ion beam sputtered {100} Fe films	S. A. Oliver, C. Vittoria, E. Schloemann, H. J. Van Hook, R. W. Tustison
3805	Spin-wave resonance in FeNiBSi films	J. Xia, J. S. Ryu, C. Vittoria

3808	Spin-wave FMR in annealed NiFe/FeMn thin films	A. Layadi, J.-W. Lee, J. O. Artman
3811	Ferromagnetic antiresonance transmission through pure iron at 73 GHz	J. M. Rudd, J. F. Cochran, K. B. Urquhart, K. Myrtle, B. Heinrich
3814	Light scattering from thermal magnons in thin metallic ferromagnetic films	J. F. Cochran, J. R. Dutcher
3817	Optical observation of evanescent surface magnons in thin magnetic films	G. Srinivasan, P. R. Emtage, J. G. Booth, C. E. Patton
3820	The dynamics of longitudinal spin fluctuations	U. Balucani, R. Vaia, A. Federighi, V. Tognetti
3823	Zero point motion and magnetic field effects on the spin configuration in a Heisenberg rhombohedral antiferromagnet. Application to solid oxygen	E. Rastelli, A. Tassi
3826	Dynamic susceptibility and damping rate of magnetic excitations in hybridizing cerium systems	Gong-Jia Hu, Bernard R. Cooper
3829	Ferromagnetic and spin-wave resonance in multilayer films (abstract)	R. F. Soohoo
3829	Ferromagnetic resonance measurements on epitaxial iron and cobalt films of ZnSe/GaAs substrates (abstract)	S. A. Oliver, C. Vittoria, J. J. Krebs, G. A. Prinz
3830	Spin-wave energies in ferromagnetic nickel alloys (abstract)	R. Bechara Muniz, J. d'Albuquerque e Castro, D. M. Edwards

Thermo-magneto-optic Recording

3831	Magnetization reversal dynamics in magneto-optic media (invited)	M. Mansuripur, T. W. McDaniel
3835	Micromagnetics of magnetization reversal in amorphous Tb-Fe films by *Lorentz microscopy*	C.-J. Lin, J. C. Suit, R. H. Geiss
3838	Numerical simulation of recorded domain shapes on a rotating magneto-optical disk	Masahiko Takahashi, Hirofumi Sukeda, Masahiro Ojima, Norio Ohta
3841	A study of the thermal switching behavior in GdTbFe magneto-optic films using two laser beams	F. J. A. M. Greidanus, W. F. Godlieb, P. M. L. O. Scholte
3844	*Performance of magneto-optical recording media with direct overwrite capability*	M. D. Schultz, H-P. D. Shieh, M. H. Kryder
3847	Design and performance of magnetic heads for magneto-optic recording with magnetic field modulation	J. J. M. Ruigrok, F. J. A. M. Greidanus, W. F. Godlieb, J. H. M. Spruit
3850	Improvement of the *C/N* ratio and corrosivity of TbFeCo amorphous films by controlling their microstructure	M. Naoe, N. Kitamura, H. Ito
3853	Corrosion-resistant-rare-earth–transition-metal amorphous films with high recording sensitivity for magneto-optical disks	A. Kawamoto, K. Nagato, R. Kuzuo, T. Yorozu
3856	Compositional dependence of recording noise in amorphous rare-earth–transition-metal magneto-optical disks	K. Nagato, A. Kawamoto, T. Sato, T. Yorozu
3859	Simulation of bit jitter in magneto-optic recording	T. W. McDaniel
3862	Domain shapes of field modulation recorded TbFeCo and GbTbFeCo magneto-optical disks (abstract)	Shigenori Okamine, Takeshi Nakao, Takeshi Maeda, Masahiko Takahashi, Norio Ohta

Symposium on Surface Anisotropy

3863	Large surface anisotropies in ultrathin films of bcc and fcc Fe(001) (invited)	B. Heinrich, K. B. Urquhart, J. R. Dutcher, S. T. Purcell, J. F. Cochran, A. S. Arrott, D. A. Steigerwald, W. F. Egelhoff, Jr.
3869	Hyperfine fields and spin orientations in (Fe^{57}/Ag) superlattices from conversion electron Mössbauer studies (invited)	F. A. Volkening, B. T. Jonker, J. J. Krebs, N. C. Koon, G. A. Prinz
3874	Mechanisms of exchange anisotropy (invited)	A. P. Malozemoff
3880	Brillouin scattering from collective spin waves in magnetic superlattices (invited)	B. Hillebrands, A. Boufelfel, C. M. Falco, P. Baumgart, G. Güntherodt, E. Zirngiebl, J. D. Thompson

3885 Theory of magnetic surface anisotropy and exchange effects in the Brillouin scattering of light by magnetostatic spin waves (invited) — G. T. Rado, R. J. Hicken

Heavy Electrons, Magnetic and Transport Properties

3890 Observation of high-temperature spin fluctuations in UBe_{13} by nuclear-spin relaxation — W. G. Clark, W. H. Wong, W. A. Hines, M. D. Lan, D. E. MacLaughlin, Z. Fisk, J. L. Smith, H. R. Ott

3893 Magnetic field dependence of the cyclotron effective mass in the Kondo lattice CeB_6 — W. Joss, J. M. van Ruitenbeek, G. W. Crabtree, J. L. Tholence, A. P. J. van Deursen, Z. Fisk

3896 Hall effect for Kondo systems — P. M. Levy, Wei Guo, D. L. Cox

3899 Transport properties of $CeAl_3$ under pressure — Ch. Fierz, D. Jaccard, J. Sierro, J. Flouquet

3902 Magnetic order and superconductivity in heavy fermion systems (invited) (abstract) — G. Aeppli

3902 Two-impurity Kondo problem: Relevance to heavy fermions (invited) (abstract) — B. A. Jones

3903 Spatially dependent correlation functions in the Anderson model (abstract) — Kan Chen, C. Jayaprakash, H. R. Krishnamurthy

3903 Solutions of the magnetic Eliashberg equations for heavy fermion superconductors (abstract) — M. R. Norman

Magnetoelastic Properties

3904 Magnetoelastic effects on antiferromagnetic phase transitions (invited) — W. P. Wolf, C. H. A. Huan

3910 Magnetostriction "jumps" in twinned $Tb_{0.3}Dy_{0.7}Fe_{1.9}$ — A. E. Clark, J. P. Teter, O. D. McMasters

3913 Magnetoelasticity and magnetovolume of dilute Cr-Si alloys — H. L. Alberts, J. A. J. Lourens

3915 Nonlinear magnetization in magnetostrictive amorphous metal ribbons — M. D. Mermelstein, A. Dandridge

3918 Improved calculations of magnetoelastic properties in collinear metamagnets — J. A. Tuszyński

3921 Magnetovolume in fcc ferro- and antiferromagnetic 3*d*-metal alloys — M. Acet, H. Zähres, W. Stamm, E. F. Wassermann

3924 Simulation of the magnetostrictive performance of Terfenol-D in mechanical devices — G. Engdahl, L. Svensson

3927 Magnetoelastic-surface-acoustic-wave attenuation peaks in thin ferromagnetic films — D. Walikainen, R. F. Wiegert, M. Levy

3930 A model for the effect of stress on the low-frequency harmonic content of the magnetic induction in ferromagnetic materials — M. J. Sablik, G. L. Burkhardt, H. Kwun, D. C. Jiles

3933 Magnetic field dependence of the elastic constants in Nd_3Se_4 (abstract) — H. Fütterer, T. Yohannes, H. Bach, J. Pelzl, K. Nahm

New Techniques and Applications

3934 Electron spin injection and detection at a ferromagnetic-paramagnetic interface (invited) — Mark Johnson, R. H. Silsbee

3940 An alternating-gradient magnetometer (invited) — P. J. Flanders

3946 Integrated on-line instrumentation for simultaneous automated measurement of magnetic field, induction, Barkhausen effect, magnetoacoustic emission, and magnetostriction — D. C. Jiles

3949 Large Barkhausen discontinuities in Co-based amorphous wires with negative magnetostriction — J. Yamasaki, F. B. Humphrey, K. Mohri, H. Kawamura, H. Takamure, R. Mälmhäll

3952 Training of Barkhausen emission in nickel and iron — H. Weinstock, T. Erber

3955 Acoustic emission along the hysteresis loops of various ferro- and ferrimagnets — M. Guyot, T. Merceron, V. Cagan

3958 Modified magnetic properties in laser welded materials — N. Smith, R. Bird

3961	rf sputtered CoCr for magnetography	D. Jeanniot, J. C. Bouchand, G. Sache

Hard Magnets and Applications

3964	Prediction of magnetic phase diagrams of selected $(R_xR'_{1-x})_2Fe_{14}B$ systems	E. B. Boltich, F. Pourarian, R. T. Obermyer, S. G. Sankar, W. E. Wallace
3967	Spin reorientation in $(Y_{1-x}Sm_x)_2Fe_{14}B$	Chin I · Zun-Xiao Liu, Yun-Xi Sun, Zheng-Hua Lou, Bayinqilao
3969	Spin reorientation in substituted Nd_2Co_{17} compounds	H. Y. Chen, S. G. Sankar, W. E. Wallace
3972	Structure and magnetic properties of quaternary $Pr_{2-x}R_xCo_{14}B$ (R = Dy and Er) systems and their hydrides	F. Pourarian, S. Y. Jiang, S. G. Sankar, W. E. Wallace
3975	Magnetic properties of NdDyFeCoAlB alloys	A. S. Kim
3978	Giant intrinsic coercivities in as-cast RFe_2Ni_2B alloys	J. Strzeszewski, A. Nazareth, G. C. Hadjipanayis
3981	The effect of Lorentz demagnetization field (LDF) on the saturation magnetization of $SmCo_5$ magnets	Shiang-Jiun Heh, Swe-Kai Chen
3984	Thermal stability of five sintered rare-earth–cobalt magnet types	D. Li, H. F. Mildrum, K. J. Strnat
3987	Design applications of magnetic mirrors	H. A. Leupold, E. Potenziani II
3989	A magnetostrictive motor	N. Ida, L. E. Roemer
3991	Field enhancement in traveling wave tubes with tapered pole pieces	John P. Clarke, Herbert A. Leupold
3993	SEM study of the effect of Zr additive on the microstructures of $Sm(Co,Cu,Fe,Zr)_{7.64}$ magnets (abstract)	Ying-Chun Lin, Jiang-Ching Lin, Da-Pun Chiang, Kang-Ming Fan, Wen Cheng Chang

Spin Glass Theory, Mostly

3994	Short-range Ising spin glasses in general dimensions	Rajiv R. P. Singh, Michael E. Fisher
3997	Chiral order in a two-dimensional *XY* spin glass	*Hikaru Kawamura, Masaharu* Tanemura
3998	Introduction of spin disorder by exchange defects	G. Parker, W. M. Saslow
4001	Phase diagram for the Bethe lattice spin glass (abstract)	J. M. Carlson, J. T. Chayes, L. Chayes, J. P. Sethna, D. J. Thouless
4001	Reentrant ferromagnetism in a two-dimensional Ising model with random nearest-neighbor interactions (abstract)	N. Benayad, A. Benyoussef, N. Boccara
4002	The antiferromagnetic spin glass with frustrations (abstract)	M. Blazej, S. Krzeminski, P. Rusek

Symposium on High T_c Superconductivity

4003	High T_c thin-film superconductivity: Science and technology (invited)	T. H. Geballe
4005	Magnetism and superconductivity in $La_{2-x}Sr_xCuO_{4-y}$ (invited)	D. Jérome, W. Kang, S. S. P. Parkin
4009	The effect of lanthanide substitution on the superconductivity in $Ba_2YCu_3O_7$ and $(La,Sr)_2CuO_4$ (invited)	H. Takagi, S. Uchida, H. Eisaki, S. Tanaka, K. Kishio, K. Kitazawa, K. Fueki
4015	Antiferromagnetism in the high-T_c related compounds (invited)	S. K. Sinha, D. E. Moncton, D. C. Johnston, D. Vaknin, G. Shirane, C. Stassis
4019	Theoretical studies of high T_c superconductors (invited) (abstract)	D. J. Scalapino

Magnetic Recording Heads

4020	Laminated CoZr amorphous thin-film recording heads	James L. Su, Mao-Min Chen, Jerry Lo, Rod E. Lee
4023	CoZrMo amorphous films as a soft adjacent layer for biasing magnetoresistive elements with a current shunt layer	K. Yamada, T. Maruyama, M. Ohmukai, T. Tatsumi, H. Urai

4026	The track-edge bias profile in shunt-biased magnetoresistive heads	D. E. Heim
4029	Behavior of thin-film magnetic recording heads and their application to micromagnetics (invited)	I. R. Walker, A. S. Arrott
4033	Bloch line influence on wall motion response in thin-film heads	B. E. Argyle, B. Petek, M. E. Re, F. Suits, D. A. Herman
4036	Study of field-driven wall-configuration conversions for laminated Permalloy in the easy-axis state	D. A. Herman, Jr., B. E. Argyle, P. L. Trouilloud, B. Petek, L. T. Romankiw, P. C. Andricacos, S. Krongelb, D. L. Rath, D. F. Canaperi, M. L. Komsa
4039	Measured fields and performance of recording heads	J. A. Brug, H. S. Gill, E. Murdock, S. Naberhuis, G. Tarnopolsky, R. Simmons
4042	Effect of pole tip alignment on magnetic fringing fields from recording heads	P. V. Koeppe, M. E. Re, M. H. Kryder

Metastable Phases, Quasi-Crystals, and Nonequilibrium Growth

4045	Magnetism of metastable phases: Band theory and epitaxy (invited)	P. M. Marcus, V. L. Moruzzi
4051	Ferromagnetism in ultrathin metastable films of fcc Fe, Co, and Ni (invited)	R. F. Willis, J. A. C. Bland, W. Schwarzacher
4057	Magnetic structure of bcc and fcc manganese	N. E. Brener, G. Fuster, J. Callaway, J. L. Fry, Y. Z. Zhao
4060	Stoner theory of magnetic structure of alternate cubic phases of transition metals	J. L. Fry, Y. Z. Zhao, P. C. Pattnaik, V. L. Moruzzi, D. A. Papaconstantopoulos
4063	Substitutional site preference in a quasicrystal	M. Eibschütz, M. E. Lines, H. S. Chen, J. V. Waszczak, G. Papaefthymiou, R. B. Frankel
4066	Epitaxial film growth and metastable phases of single crystal Dy by molecular beam epitaxy	Kai-Yueh Yang, Hitoshi Homma, Ivan K. Schuller
4069	Spin-polarized electron energy-loss spectroscopy of metastable bcc cobalt films (abstract)	D. M. Lind, Y. U. Idzerda, G. A. Prinz, B. T. Jonker, J. J. Krebs
4070	Local structure of $Al_{75}(Mn,Cr,Ru,Re,Si)_{25}$ icosahedral alloys studied by pulsed neutron scattering (abstract)	W. Dmowski, T. Egami, P. A. Bancel, P. A. Heiney, K. Volin
4070	Specific-heat measurements for the quasi-crystalline, first cubic approximant and hexagonal phase in AlMnSi (abstract)	K. Wang, P. Garoche, Y. Calvayrac

Reentrant Spin Glasses

4071	Magnetic structure and dynamics anomalies in "reentrant" spin glasses (invited)	M. Hennion, B. Hennion, I. Mirebeau, S. Lequien, F. Hippert
4077	Field cooling and demagnetizing field influence on the magnetic structure observed in reentrant spin glasses	I. Mirebeau, M. Hennion, S. Lequien, F. Hippert
4080	Magnetic correlations in amorphous Fe-Zr alloys	J. J. Rhyne, R. W. Erwin, J. A. Fernandez-Baca, G. E. Fish
4083	Spin-wave excitations in amorphous $Fe_{78}B_{13}Si_9$	S. C. Yu, J. W. Lynn, J. J. Rhyne, G. E. Fish
4086	The domain and the domain wall structures of an $Fe_{90}Zr_{10}$ reentrant alloy	S. Senoussi, S. Hadjoudj, P. Jouret, J. Bilotte, R. Fourmeaux
4089	"Zero" frequency spin relaxation in reentrant magnets	E. M. Jackson, S. M. Bhagat, S. B. Liao, M. A. Manheimer
4091	Quenching of ferrimagneticlike ordering in $SrCr_8Fe_4O_{19}$ hexagonal ferrite	X. Obradors, A. Labarta, J. Tejada, M. Pernet, J. L. Tholence, M. Saint-Paul, B. Barbara
4094	Magnetic behavior of $CeFe_2$: Effects of ruthenium substitution	S. B. Roy, B. R. Coles
4096	High-pressure study of the magnetic states of disordered Ni-Mn alloys	R. G. Aitken, K. Daneshvar
4099	Spin dynamics of the reentrant spin-glass system amorphous $(Fe_xCr_{1-x})_{75}P_{15}C_{10}$ (abstract)	P. Mangin, D. Boumazouza, B. George, R. W. Erwin, J. J. Rhyne

4099	Double-phase transition in $Au_{82.5}Fe_{17.5}$? (abstract)	L. D. Rakers, Paul A. Beck

Hyperfine Fields, Mössbauer Effect, and NMR

4100	A Mössbauer study of fine iron particles (invited)	Z. Q. Qiu, Y. W. Du, H. Tang, J. C. Walker
4105	Mössbauer investigation of zinc ferrite particles	H. Tang, Y.-W. Du, Z.-Q. Qiu, J. C. Walker
4108	Isomer shift and magnetic properties of EuO under pressure	R. D. Taylor, J. N. Farrell
4110	Probing molecular cages in polymeric gels using paramagnetic ions: Internal motion of cupric ion in a cage	Darbha Suryanarayana
4113	A NMR study of $YCo_{12}B_6$ and $GdCo_{12}B_6$ intermetallic compounds	K. Erdmann, M. Rosenberg, K. H. J. Buschow
4116	A NMR study of $R_2(TM)_{14}B$ compounds with R = Sm, Gd, or Lu and TM = Fe or Co	K. Erdmann, M. Rosenberg, K. H. J. Buschow
4119	NMR spin-echo studies in sputtered Heusler alloy films	K. Le Dang, P. Veillet, R. Krishnan, A. Morisako, M. Matsumoto, M. Naoe
4121	Magnetic clustering in $LaNi_{5-x}Fe_x$ compounds	M. Escorne, J. Lamloumi, A. Percheron-Guegan, J. C. Achard, A. Mauger, G. Jehanno
4124	Local atomic structure in amorphous Fe-P alloys	R. L. McCally, J. S. Morgan, T. J. Kistenmacher, K. Moorjani
4127	Unusual magnetic and lattice transformation in UNiSn, a possible half-metallic ferromagnetic system	N. Bykovetz, Warren N. Herman, T. Yuen, Chan-Soo Jee, C. L. Lin, J. E. Crow
4130	Environmental influence on the nuclear spin-lattice relaxation rate in Cu_xPt_{1-x}	J. Banhart, P. Weinberger, H. Ebert, J. Voitländer
4133	Crystal/chemical structures and magnetic properties of naturally occurring $Mn_{1.7}Fe_{1.3}O_4$	B. J. Evans, W. R. Dunham, C. Porter, S. M. Abernathy, C. Bluncson

Solitons and Spin-Wave Instabilities

4136	Microwave solitons in magnetic garnet films (invited)	P. De Gasperis, R. Marcelli, G. Miccoli
4141	One-dimensional Dzyaloshinski–Moriya antiferromagnets in an applied field	Qing Xia, Peter S. Riseborough
4144	Two-magnon excitations in quantum spin chains	Jian-Min Liu, Jill C. Bonner
4147	Spin-wave instabilities and their revival by nonlinear mechanics (invited)	H. Suhl, X. Y. Zhang
4151	Instabilities of spin waves in parallel-pumped easy plane ferromagnets	S. P. Lim, D. L. Huber
4154	Chaos in spin clusters: Correlation functions and spectral properties	Niraj Srivastava, Charles Kaufman, Gerhard Müller
4157	Chaos in magnetic garnet thin films	P. E. Wigen, H. Doetsch, Y. Ming, L. Baselgia, F. Waldner
4160	Excitation spectra of generalized antiferromagnetic Heisenberg spin chains (abstract)	J. B. Parkinson, J. C. Bonner
4160	Spin-wave instability and "true" foldover in single-crystal YIG films (abstract)	Y. T. Zhang, C. E. Patton, G. Srinivasan

Superconductivity and Magnetism of High T_c Superconductors. I

4161	Superconductivity and spin-glass ordering in $RBa_2(Cu_{1-x}Fe_x)_3O_z$: R = Y,Gd; $0 \le x \le 0.12$	K. Moorjani, J. Bohandy, B. F. Kim, F. J. Adrian, Y. W. Du, H. Tang, Z. Q. Qiu, J. C. Walker
4164	Stabilization of the tetragonal phase of $YBa_2Cu_3O_{7-\delta}$ through the addition of Fe impurities	M. T. Causa, S. M. Dutrús, C. Fainstein, H. R. Salva, L. B. Steren, M. Tovar, R. Zysler
4167	Magnetic properties of Y-Ba-Cu-O superconductors	T. R. McGuire, F. Holtzberg, D. L. Kaiser, T. M. Shaw, S. Shinde

4170	Low-field characterization of $YBa_2Cu_3O_{7-\delta}$ single crystals	H. Claus, G. W. Crabtree, J. Z. Liu, W. K. Kwok, A. Umezawa
4173	Flux creep in high T_c superconductors	C. Giovannella, P. Rouault, I. A. Campbell, G. Collin
4176	On the critical fields and current densities of $YBa_2Cu_3O_7$ and $La_{1.85}Sr_{0.15}CuO_4$ superconductors	S. Senoussi, M. Oussena, S. Hadjoudj
4179	Constricted diamagnetic hysteresis loops observed for the high T_c superconductors	U. Atzmony, R. D. Shull, C. K. Chiang, L. J. Swartzendruber, L. H. Bennett, R. E. Watson
4182	New glassy features in high-T_c superconductors	Y. Yeshurun, Y. Wolfus, I. Felner
4185	Multiple coil pulsed NMR method for measuring the multipole moments of particle accelerator bending magnets	W. G. Clark, T. W. Hijmans, W. H. Wong
4187	Superconducting and magnetic properties of $RBa_2Cu_3O_{7-x}$ compounds	S. A. Shaheen, N. Jisrawi, Y. H. Lee, M. Croft, W. L. McLean, H. Zhen, L. Rebelsky, S. Horn
4190	X-ray absorption spectroscopy studies of high-T_c superconductors	Y. Jeon, F. Lu, H. Jhans, S. A. Shaheen, M. Croft, P. H. Ansari
4193	Correlation between electronic states of O, Cu, and Ba in several high-T_c superconductors	S. Horn, J. Cai, S. A. Shaheen, M. Croft, C. L. Chang, M. L. denBoer
4196	Superconductivity and magnetism in transition-element-substituted $YBa_2Cu_3O_7$ compounds	Gang Xiao, F. H. Streitz, A. Gavrin, M. Z. Cieplak, C. L. Chien, A. Bakhshai
4199	Magnetic behavior of both superconducting thin films and their deposition targets	K. Moorjani, J. Bohandy, F. J. Adrian, B. F. Kim, U. Atzmony, R. D. Shull, C. K. Chiang, L. J. Swartzendruber, L. H. Bennett
4202	EPR, magnetization, and resistivity studies in doped (4-*f* or 3-*d* ions) and undoped $RBa_2Cu_3O_y$ high T_C superconductors (R = Y,Pr,Nd,Eu,Gd,Ho,Er, or Yb) (abstract)	D. C. Vier, J. F. Smyth, C. T. Salling, S. Schultz, Y. Dalichaouch, B. W. Lee, K. N. Yang, M. Torikachvili, M. B. Maple, S. B. Oseroff, Z. Fisk, J. D. Thompson, J. L. Smith, E. Zirngiebl
4202	Magnetic ordering and crystal field effects in $REBa_2Cu_3O_{7-x}$ (RE = Gd, Dy, Ho, Er) (abstract)	B. D. Dunlap, M. Slaski, D. G. Hinks, C. Segre, K. Zhang, L. Soderholm, M. Beno, G. W. Crabtree, W. K. Kwok, S. K. Malik, I. K. Schuller, J. D. Jorgensen, Z. Sungaila
4203	A new method for determining superconducting transition temperature T_c (abstract)	Ronghua Xue, Quan Lu

Superconductivity and Magnetism of High T_c Superconductors. II

4204	Magnetic behavior of Y-Ba-Cu-O superconductors prepared under different oxygen anneals	T. Datta, Carmen Almasan, J. Estrada, C. E. Violet, D. U. Gubser, S. A. Wolf
4207	Effect of vacuum annealing on the superconducting transition temperature of the Y-Ba-Cu-O system	Dajian Wang, Guobin Wu, Shengtao Huang, Chenghuan Tang, Wanqiu Cei, Peng Dan
4209	Effective electron interactions due to virtual charge and spin excitations in an extended Hubbard model for Cu-O superconductors	H.-B. Schüttler, A. J. Fedro
4212	Magnetization of high-temperature superconductors (abstract)	Sang Boo Nam
4212	Correlation between the superconducting properties and the oxygen stoichiometry in $Y_1Ba_2Cu_3O_x$ (abstract)	J. F. Marucco, K. Wang, P. Garoche
4213	Are the high T_c superconducting materials bulk superconductors or grain boundary percolating network superconductors? (abstract)	N. Garcia, S. Vieira, A. M. Baro, J. Tornero, L. Vazquez, J. Gomez, A. Aguilo, S. Bourgeal, A. Buendia, M. Hortal, M. A. Lopez de la Torre, M. A. Ramos, R. Villar, K. V. Rao, D-X. Chen, J. Nogues, N. Karpe

4213	Properties of high T_c superconductors with modified compositions (abstract)	S. Jin, R. C. Sherwood, T. H. Tiefel, K. B. van Dover, R. A. Fastnacht, M. Yan
4214	Superconductivity above 110 K in the orthorhombic phase of the Y-Ba-Cu-O ceramic compounds (abstract)	J. Baszyński
4214	Pairing and magnetic instabilities in high T_c systems with finite U (abstract)	A. J. Fedro, S. K. Sinha
4215	Some novel melt-spun superconducting materials (abstract)	Akihisa Inoue, Kunio Matsuzaki, T. Masumoto, K. V. Rao, Han Zeng He, D-X. Chen

Recent Developments in High T_c Superconductivity

4216	Studies at IBM on anisotropy in single crystals of the high-temperature oxide superconductor $YBa_2Cu_3O_{7-x}$ (invited)	W. J. Gallagher
4220	Electronic structure, charge transfer excitations, and high-temperature superconducting oxides (invited)	A. J. Freeman, Jaejun Yu, S. Massidda, C. L. Fu, J.-H. Xu
4226	One-dimensional Hubbard model with first- and second-neighbor hopping	T. A. Kaplan
4229	Magnetic susceptibility of rapidly solidified $YBa_2Cu_3O_{7-x}$ superconductors	M. E. McHenry, J. McKittrick, S. Sasayama, V. Kwapong, R. C. O'Handley, G. Kalonji
4232	Field ion microscopy of the high T_c superconductor $Ba_2YCu_3O_{7-x}$ (abstract)	A. J. Melmed, R. D. Shull, C. K. Chiang, H. A. Fowler
4233	Spin excitations in La_2CuO_4 (title only)	C. Peters
4233	Electronic anisotropy and magnetism in $YBa_2Cu_3O_7$ and $La_{2-x}Sr_xCuO_4$ measured using the techniques of muon spin rotation and positron annihilation (title only)	D. Harshman
4233	Observation of hexagonally ordered flux quanta on $YaBa_2Cu_3O_7$ (title only)	D. J. Bishop, P. L. Gammel, G. J. Dolan, J. R. Kwo, C. A. Murray, L. F. Schneemeyer, J. V. Waszczak
4233	Resonating valence bands and d-wave superconductivity (title only)	G. Kotliar
4233	Superconductivity and magnetic ordering in the $YBa_2(Cu_{1-x}Fe_x)_3O_{9-\delta}$ system (title only)	Z. Q. Qiu, H. Tang, Y. W. Du, J. C. Walker, K. Moorjani, J. S. Morgan, W. A. Bryden
4233	Metallic, but not superconducting, La-Ba (and La-Sr) copper oxides (title only)	J. B. Torrance, Y. Tokura, A. Nazzal, S. S. P. Parkin

Fine Particles

4234	Macroscopic quantum tunneling in single domain magnetic particles	A. DeFranzo, I. Klik, L. Gunther, A. G. Swanson, J. S. Brooks
4237	Hysteresis of submicron permalloy particulate arrays	J. F. Smyth, S. Schultz, D. Kern, H. Schmid, Dennis Yee
4240	Particle size dependence of the magnetic properties of ultrafine granular films	S. H. Liou, C. L. Chien
4243	Preparation and properties of sputter-deposited crystalline ultrafine particles	S. Ohnuma, A. Kunimoto, T. Masumoto
4246	Variation of magnetic properties with composition in $(Fe\text{-}Ni)_{76}Si_8B_{16}$ amorphous ultrafine particles	S. Ohnuma, M. Mitera, C. D. Graham, Jr., T. Masumoto
4249	Particulate metallic glass composite magnetostrictors for interferometric magnetometry	D. Brugel, M. R. J. Gibbs, P. T. Squire
4252	Enhanced magnetic coercivity in magnetic granular solids	Gang Xiao, C. L. Chien
4255	Magnetic properties of gas atomized powders of $Al_{74}Mn_{20}Si_6$	M. E. McHenry, R. A. Dunlap, R. Chatterjee, A. Chow, R. C. O'Handley
4258	Noncollinear magnetic structure of $CoFe_2O_4$ small particles	K. Haneda, A. H. Morrish
4261	Magnetic properties of thin-film Ag + iron-oxide granular metals	R. D. Shull, U. Atzmony, A. J. Shapiro, L. J. Swartzendruber, L. H. Bennett, W. J. Green, K. Moorjani

4264	The application of sodium amalgam to prepare ferrofluids containing iron particles in mercury	L. Takács
4267	Effect of magnetic field cooling and magnetization anomaly in magnetic fluids near melting point	H. Miyajima, N. Inaba, S. Taketomi, M. Sakurai, S. Chikazumi

Transport Properties

4270	Magnetotransport: An ideal probe of anisotropy energies in epitaxial films (invited)	E. Dan Dahlberg, Kevin Riggs, G. A. Prinz
4276	Exchange forces between domain wall and electric current in permalloy films of variable thickness	C.-Y. Hung, L. Berger
4279	Electrical and magnetic properties of semiconducting ternary U compounds: UTSn and UTSb	T. T. M. Palstra, G. J. Nieuwenhuys, R. F. M. Vlastuin, J. A. Mydosh, K. H. J. Buschow
4282	The electrical resistance of Cr films	J. A. J. Lourens, S. Arajs, H. F. Helbig, L. Cheriet, El-Sayed A. Mehanna
4285	Magnetic properties across the metal-insulator transition (invited)	Subir Sachdev, R. N. Bhatt, M. A. Paalanen
4291	Electrical transport properties of thin epitaxially grown iron films on GaAs	F. J. Rachford, M. Rubinstein, G. A. Prinz
4294	Magnetothermal conductivity of $ErAl_2$ for cryogenic applications	C. B. Zimm, C. K. Campenni, J. A. Barclay
4297	Enhanced spin-density waves in Co-Cr superlattices	Shihui Ge, M. B. Stearns
4300	Magnetoresistance of very thin cobalt-gold multilayers with perpendicular anisotropy	C. Dupas, J. P. Renard, J. Seiden, E. Vélu, D. Renard
4303	Transport and magnetic properties of amorphous $Fe_{80-x}M_xB_{14}Si_6$ (Mn = Mn, V, Cr)	S. U. Jen, S. M. Yang

Soft Magnetic Materials and Domain Effects

4306	A new type of high-resistive soft magnetic amorphous films utilized for a very high-frequency range	H. Karamon
4309	Effects of hydrogen and nitrogen ion bombardments on soft magnetism of iron films during double-ion-beam sputtering	M. Nagakubo, T. Yamamoto, M. Naoe
4312	Effects of boron implantation in films of iron-nickel	J. Ryu, K. Castell, W. Nowak, C. Vittoria
4315	Magnetic properties of ion-beam sputter-deposited Fe-Ni-B-Si films	J. Ryu, Y. Huang, C. Vittoria
4318	Induced magnetic anisotropy related to the local atomic order: A study in amorphous Co-Zr and Co-Zr-M thin films	G. Suran, M. Naili, J. Sztern
4321	Perturbations to the Stoner–Wohlfarth threshold in $2 \times 20\ \mu m$ *M-R* memory elements	C. S. Comstock, H. Y. Yoo, A. V. Pohm
4324	On the pinning of domain walls in low magnetization materials	C. H. Wörner, J. E. Valdés
4327	Period competition in a stripe domain structure subjected to a periodic field	P. Molho, J. L. Porteseil, Y. Souche
4330	A theory of the three-dimensional solenoidal magnetization configurations in ferro- and ferrimagnetic materials	R. Vlaming, H. A. M. van den Berg
4333	Effect of preannealing on the kinetics of the reorientation of the field-induced anisotropy in CoZr thin films (abstract)	Tomasz Jagielinski

Spin Glass: Experiment

4334	$Rb_2Cu_{1-x}Co_xF_4$, a two-dimensional Ising spin glass	C. Dekker, A. F. M. Arts, H. W. de Wijn
4337	Spin-glass behavior in mixed metal oxides with a rutile-type structure	A. Labarta, X. Obradors, J. Tejada, F. J. Berry, M. Sarson
4340	Spin-glass behavior of cubic $Tb_{0.3}Y_{0.7}Ag$: A scaling of the thermoremanence	M. R. Said, J. S. Kouvel, T. O. Brun
4343	Nonstationary spin glass dynamics from susceptibility and noise measurements	Ph. Refregier, M. Ocio, J. Hammann, E. Vincent

4346	Isothermal anisotropy rotation in a Au-Fe spin-glass alloy	Kh. Ziq, J. S. Kouvel
4349	Torque relaxation in a *Cu*Mn spin glass	C. Giovannella, I. A. Campbell
4351	Spin-glass dynamics in $Fe_{2-x}Ti_{1+x}O_5$	R. L. Lichti, S. Kumar, C. Boekema
4354	Energy gap in concentrated spin glasses	S. B. Liao, S. M. Bhagat, M. A. Manheimer, K. Moorjani
4357	Spin-density wave in spin glasses (*Cu*Mn) and other dilute alloys (*Y*Gd) (invited) (abstract)	J. A. Mydosh
4357	Magnetic susceptibility in the spin glass system, $[(CH_3)_3NH]CO_{1-x}Ni_xCl_3 2H_2O$ (abstract)	Gerald V. Rubenacker, Donald N. Haines, John E. Drumheller
4358	Asymmetric hysteresis cycles as a probe of local fields in metallic spin glasses (abstract)	Laurent P. Lévy, Hélène Bouchiat

The TM dependence of the magneto-optic signal in GdTb-TM thin films

D. K. Hairston and M. H. Kryder
Carnegie Mellon University, Pittsburgh, Pennsylvania 15213

The magneto-optic polar Kerr rotation for various GdTb-TM thin films was measured at room temperature as a function of TM composition and was found to correlate with the Slater–Pauling curve. In spite of the fact that the temperature dependence of magnetization is a complicating factor, the data clearly establish the above-mentioned correlation. The TM compositions ranged from Mn through Fe and Co to Ni. The Fe-based films had Curie temperatures covering a range from 100 to 300 °C in contrast to the Co-based films whose Curie temperatures were clearly much greater than 300 °C. Neither the Mn- nor the Ni-based films exhibited desirable magneto-optic activity when fabricated under the same conditions as the Fe- and/or Co-based films. When the Fe constituent of the GdTbFe films was gradually substituted with Mn or Co the room-temperature magneto-optic signal was found to decrease and increase, respectively. In a similar manner, when the Co constituent of GdTbCo films was gradually substituted with Fe or Ni the room-temperature magneto-optic effect was found to increase and decrease, respectively. However, when the Co constituent of GdTbCo films was gradually substituted with Mn the room-temperature magneto-optic effect also decreased, clearly establishing the correlation to the Slater–Pauling curve. These results are further evidence that the magneto-optic effect of traditional RE-TM thin films is dominated by the TM composition and explain the fact that the magneto-optic signal is largest in GdTbFeCo thin films. New data supporting the correlation between magneto-optic effect and perpendicular anisotropy was also obtained.

I. INTRODUCTION

The magneto-optic effect of amorphous rare-earth–transition-metal (RE-TM) films traditionally used for magneto-optic recording depends upon film composition. In general, these films have compositions where the RE elements are Gd and/or Tb and TM elements are Fe and/or Co. The magneto-optic effect of RE-FeCo films has generally been found to be larger than the magneto-optic effect of any other RE-TM composition.[1-3]

It is generally known that the magneto-optic effect of RE-TM films is dominated by the TM magnetization. Stated another way, it is reasonable to describe the polar Kerr rotation and hence the magneto-optic effect of these films as being proportional to the TM magnetization.

The well-known Slater–Pauling curve[4,5] relates the magnetic moment at 0 K of various TM alloys to the valence state of the alloy as determined by its composition. The Slater–Pauling curve has a maximum peak for FeCo alloys. The coincidence of this peak and the peak in the magneto-optic effect for RE-FeCo alloys suggests the possibility of a correlation.

II. EXPERIMENTAL METHOD

A variety of GdTb-TM films were fabricated using nearly the same rf sputtering parameters with the significant process variable being the TM composition of the mosaic target. The other process parameters, such as target and substrate voltage, were held constant and are typical for these films. Substrates made of soda lime glass were used and a film thickness of approximately 1000 Å was thick enough to make the films opaque. The backing plate of the target was made of either Fe or Co. Rare-earth tiles of either Gd or Tb were epoxied to the face of these targets in such a way that the ratio of Gd:Tb was always 2 : 1. The total surface of the Co target covered by RE material was 33.0% while this number was 30.5% for the Fe target. At times, appropriate TM tiles of Mn, Fe, Co, or Ni were epoxied onto the target to vary the TM composition. In this way five different alloys: GdTbCoFe, GdTbCoNi, GdTbCoMn, GdTbFeCo, and GdTbFeMn were fabricated for characterization.

The films were all characterized using a polar Kerr effect hysteresis loop tracer to measure the polar Kerr rotation as a function of temperature. The Fe-based films, denoted here as GdTbFeX, were also characterized using a torque magnetometer to directly measure their effective perpendicular anisotropy,

$$K_u - 2\pi M^2.$$

III. RESULTS

The temperature dependence of the polar Kerr rotation for various GdTbFeX compositions is shown in Fig. 1. These films were deposited from a target where the RE composition was constant at 30.5% and the TM percentages within the target TM composition were those indicated in the legend. From past experience, a target such as this would yield films with a composition near $Gd_{0.14}Tb_{0.07}$-$TM_{0.79}$. In that

 0021-8979/88/083621-03$02.40 © 1988 American Institute of Physics

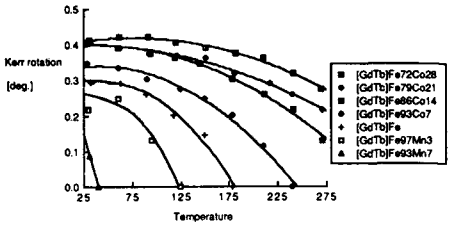


FIG. 1. Temperature dependence of the polar Kerr rotation for various GdTbFeX compositions.

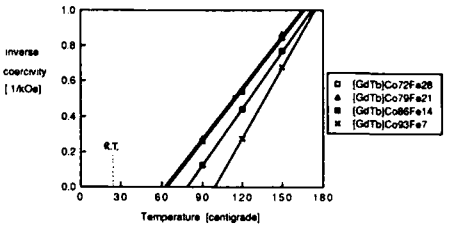


FIG. 3. Temperature dependence of inverse coercivity for GdTbCoFe films. The data are extrapolated to show their compensation points.

figure it is seen that GdTbFe has a room-temperature polar Kerr rotation of 0.3° and a Curie temperature of around 180 °C. As the TM composition changes by the substitution of small amounts of Co for Fe, both the room-temperature polar Kerr rotation and the Curie temperature are seen to increase. However, when Mn is substituted for Fe the room-temperature polar Kerr rotation and the Curie temperature are seen to decrease.

The room-temperature polar Kerr rotation for the GdTbFeX films is summarized in Fig. 2. The figure also shows the trend in effective perpendicular anisotropy, $K_u - 2\pi M^2$, for the same films. It can be seen here that the MO signal and perpendicular anisotropy show a high correlation as functions of film composition.

The various Co-based films, denoted here as GdTbCoX, were observed to have polar Kerr rotations that were relatively temperature independent over the temperature range from room temperature to 200 °C. This is a result of the fact that the GdTbCoX films had extremely high Curie temperatures compared to the GdTbFeX films. Figure 3 shows the inverse coercivity of the various GdTbCoFe films. It is seen there that the compensation temperatures of these films is between 60 and 100 °C. In general, the compensation temperatures of all the films were in the vicinity of room-temperature. Figure 4 summarizes the composition dependence of the room-temperature polar Kerr rotation for the various GdTbCoX compositions. In that figure it can be seen that a GdTbCo film has a room-temperature polar Kerr rotation just under 0.4°. The polar Kerr rotation decreases from 0.4° with the substitution of Co by small amounts of either Ni or Mn and increases beyond 0.4° with the substitution of Co by Fe.

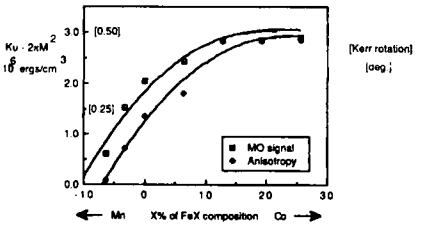


FIG. 2. Composition dependence of the room-temperature polar Kerr rotation and effective perpendicular anisotropy for various GdTbFeX compositions.

A summary of the composition dependence of the room temperature polar Kerr rotation for both the GdTbFeX and GdTbCoX films is shown in Fig. 5. These data are overlaid upon the data which historically verified the Slater–Pauling curve, thus showing the qualitative correlation between the room temperature MO signal and magnetic moment at 0 K as functions of composition. It should be noted that the correlation is strongest for the GdTbCoX films, where the magnetization of those films is relatively temperature independent up to and beyond room temperature.

IV. DISCUSSION

The strong correlation between the magneto-optic effect and effective perpendicular anisotropy, $K_u - 2\pi M^2$, for GdTbFeX films shown in Fig. 2 is presumably a correlation between magneto-optic effect and composition-dependent perpendicular anisotropy, K_u, which is proportional to magnetization. Because the GdTbFeX films had compensation points near room temperature, the perpendicular anisotropy constant can be assumed to be the dominant term in the expression for effective perpendicular anisotropy $K_u - 2\pi M^2$.

The qualitative correlation between the magneto-optic effect of RE-TM films and the Slater–Pauling curve shown in Fig. 5 is reasonable in light of several complicating facts. Although the Slater–Pauling curve was derived for bulk crystalline alloys near 0 K it can be assumed to qualitatively describe the TM moment of RE-TM thin films which are amorphous but nonetheless highly ordered magnetically. Also, the dilution of the TM valence state by the RE conduction electrons is considered to be relatively insignificant since the total RE composition is only 20% of the metallic

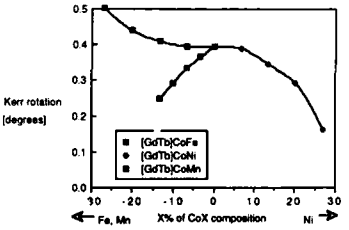


FIG. 4. Composition dependence of the room-temperature polar Kerr rotation for various GdTbCoX alloys.

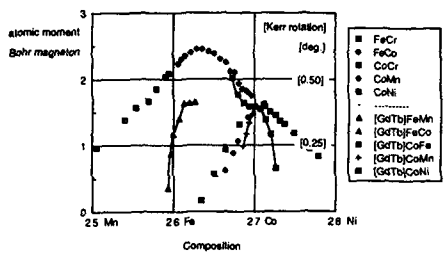


FIG. 5. Qualitative correlation of the magneto-optic effect in GdTb-TM thin films with the Slater–Pauling curve.

(RE + TM) composition. The data shown for FeCr alloys are assumed to be closely matched to that of FeMn alloys which are not shown, given that the data shown for CoCr and CoMn alloys are closely matched. The extrapolation of the room-temperature magneto-optic effect back to absolute zero temperature is expected to be most accurate when the magnetization is nearly temperature independent over this range which is the case with the GdTbCoX films which show the strongest correlation.

V. CONCLUSIONS

The magnetic and optical propeties of RE-TM films are both process and composition dependent. The films characterized here exhibit a wide range of values even though they were fabricated under nearly the same set of rf sputtering conditions.

For GdTb-TM films the magneto-optic effect qualitatively correlates with the Slater–Pauling curve. This fact explains the observed maximal magneto-optic effect of GdTbFeCo alloys.

ACKNOWLEDGMENT

Support from the IBM Corporation and from the Magnetic Materials Research Group, through the Materials Research Groups Program, Division of Materials Research, National Science Foundation, under grant No. DMR-8613386 is gratefully acknowledged.

[1] S. Masui, T. Kobayoshi, S. Tsunashima, and S. Uchiyama, IEEE Trans. Magn. **MAG-20**, 1036 (1984).
[2] Y. Sakurai, K. Onishi, T. Numata, H. Tsujimoto, and K. Saiki, IEEE Trans. Magn. **MAG-19**, 1734 (1983).
[3] H. Tsujimoto, M. Shouji, and Y. Sakurai, IEEE Trans. Magn. **MAG-19**, 1757 (1983).
[4] S. Chikazumi and S. H. Charap, *Physics of Magnetism* (Krieger, Huntington, NY, 1978), Chap. 4.3, p. 73.
[5] A. R. Williams, V. L. Moruzzi, A. P. Malozemoff, and K. Terakura, IEEE Trans. Magn. **MAG-19**, 1983 (1983).

The effects of deposition conditions on microstructure and magnetic properties of TbFeCo

J-W. Lee, H-P. D. Shieh, M. H. Kryder, and D. E. Laughlin
Magnetics Technology Center, Carnegie Mellon University, Pittsburgh, Pennsylvania 15213

Transmission electron microscopy (TEM) has been employed to characterize micro/magnetic structural details of magneto-optical (MO) recording TbFeCo thin films as a function of dc-magnetron sputtering parameters using bright/dark field imaging, selected area diffraction, convergent beam electron diffraction, and Lorentz electron microscopy. It is found that the preparation conditions have a strong impact on both microstructure and magnetic properties of the films. The microstructures of the films deposited at low argon bleeding pressures (< 10 mTorr) are featureless, and their magnetic domains are of the "stripe" type with a perpendicular anisotropy. In contrast, high argon pressures (> 20 mTorr) give rise to microvoids surrounding "honeycomblike" networks and in-plane domains with "ripple type" contrast. The microstructure and magnetic domain structures are related to the films' magnetic properties as characterized by a MO loop tracer.

I. INTRODUCTION

Tb-Fe-Co amorphous thin films have been studied extensively as a promising candidate for magneto-optical (MO) recording media because of their perpendicular magnetic anisotropy as well as their high readout signal-to-noise ratio.[1,2] It is known that perpendicular magnetic anisotropy is closely associated with micro/magnetic structures which depend on deposition parameters such as argon pressure (P_{Ar}) and substrate bias voltage (V_b). The investigation of structural changes in Tb-Fe-Co has been reported as a function of P_{Ar}[3] and of oblique incidence angle.[4] However, few attempts have been made to correlate the micro/magnetic structural changes with magnetic properties of sputtered Tb-Fe-Co films as a function of deposition parameters. Hence, this paper describes further results of micro/magnetic structural changes and magnetic properties in Tb-Fe-Co films as a function of P_{Ar}.

II. EXPERIMENT

The films were prepared from a FeCo based Tb-Fe-Co mosaic target by a dc-magnetron sputtering system on carbon-coated Cu grids for direct observation by transmission electron microscopy (TEM).[5] They also were deposited on glass substrates for cross-sectional TEM observation and magneto-optical (MO) measurements. The sputtering was carried out at the following P_{Ar}: 2, 10, 20, and 40 mTorr. The deposition rate at cathode power density of 2.2 W/cm^2 was 120 nm/min and the nominal area composition of the target was $Tb_{27}(Fe_4Co_1)_{73}$. The nominal thickness of the films is 50 nm. TEM was performed using a Philips EM420T analytical electron microscope. The magnetic domain structures were observed by the Fresnel mode imaging in Lorentz electron microscopy (LEM) at 120 kV. The MO hysteresis loops were measured through the glass substrate of films at room temperature with a 633-nm He-Ne laser in fields up to 7 kOe.

III. RESULTS AND DISCUSSION

Transmission electron micrographs of plane view and cross-sectional specimens of Tb-Fe-Co films deposited at four different P_{Ar} are shown in Figs. 1 and 2. The structures change with P_{Ar} reflecting a variation in the mechanism by which the film grows. In Fig. 1(a) ($P_{Ar} = 2$ mTorr), the film structure is shown to be relatively smooth and featureless. At 10 mTorr, the film morphology is even smoother [Fig. 1(b)]. As the P_{Ar} increases further (20 mTorr), the morphologies change in that the film now contains microvoids surrounding amorphous islands [Fig. 1(c)]. Further increase in P_{Ar} (40 mTorr) leads to a large increase in the density of microvoids [Fig. 1(d)].

Cross-sectional samples also reveal smooth and featureless morphologies for films deposited at lower P_{Ar}, i.e., 2 and 10 mTorr [Figs. 2(a) and 2(b)]. Also, the microvoids are observed to be perpendicular to the film plane at higher P_{Ar}; i.e., 20 and 40 mTorr [Figs. 2(c) and 2(d)]. The smooth morphology at lower P_{Ar} and the high density of perpendicular microvoids causing a columnar microstructure at higher P_{Ar} are consistent with the zone model proposed by Thornton.[6]

Figures 3 and 4 are selected area diffraction (SAD) and convergent beam electron diffraction (CBED) patterns, respectively. At low P_{Ar} (2 mTorr), the SAD pattern exhibits a broad halo [Fig. 3(a)]. Similarly, the CBED pattern reveals only one broad halo [Fig. 4(a)]. It should be noted, however, that the halo in the CBED pattern appears to contain weak spots (arrowed). This may indicate that the amorphous phase coexists with microcrystals. With increasing

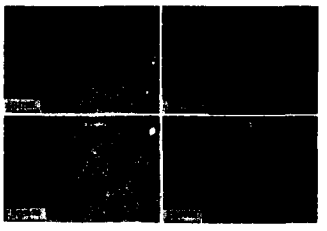


FIG. 1. Bright field TEM images of Tb-Fe-Co films (plane view): (a) 2, (b) 10, (c) 20, and (d) 40 mTorr.

 0021-8979/88/083624-03$02.40 © 1988 American Institute of Physics

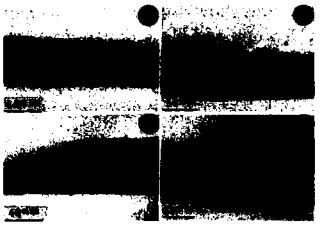


FIG. 2. Bright field TEM images of cross-sectioned Tb-Fe-Co films: (a) 2, (b) 10, (c) 20, and (d) 40 mTorr.

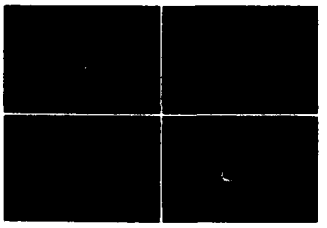


FIG. 4. CBED patterns of Tb-Fe-Co films: (a) 2, (b) 10, (c) 20, and (d) 40 mTorr.

P_{Ar} (10 mTorr), the SAD pattern shows one broad halo as well as the weak contrast of a second halo [Fig. 3(b)]. The corresponding CBED pattern contains only one halo [Fig. 4(b)]. However, the CBED pattern still displays weak spots within the halo. At 20 mTorr P_{Ar}, the contrast of the second halo becomes stronger [Fig. 3(c)], as do the microcrystalline reflections within the first halo [arrowed in Fig. 4(c)]. As the P_{Ar} increases even further (40 mTorr), the same observation can be made as shown in Figs. 3(c) and 4(c) [see Figs. 3(d) and 4(d)]. These results suggest that the films contain microcrystals. The size of the crystals is less than 1.5 nm. In addition, as the P_{Ar} increases, the number of microcrystals appears to increase.

The presence of the crystalline reflections could be due to either oxides of the rare earth element Tb or microcrystals of the ternary alloy. However, Tb oxides have larger d spacings[7] than the spacings that we observe in SAD patterns. This rules out the interpretation of the reflections as "oxides." Experimentally, it has been confirmed[8] that "the increase in P_{Ar} increases the exit temperature of the deposited metal, i.e., 64 °C at 1 mTorr P_{Ar} and 106 °C at 25 mTorr P_{Ar}." Thus the crystallization of the amorphous phase is more likely to occur at higher argon pressure. This inference is consistent with our results since the increasing P_{Ar} leads to sharper contrast of microcrystalline reflections.

Figure 5 reveals that the magnetic domain structures of films is dependent upon P_{Ar}. At 2 mTorr P_{Ar}, the domains are "stripe type" associated with white and black dots typical of perpendicular magnetization [Fig. 5(a)]. Increasing P_{Ar} to 10 mTorr [Fig. 5(b)] does not significantly change the domain configurations. However, the domain width increases, showing more widely spaced black and white domains. As the P_{Ar} increases further (20 mTorr), the domain structures exhibit a "featherlike" ripple configuration associated with small domains containing an in-plane component of magnetization [Fig. 5(c)]. However, a few white and black dots associated with a perpendicular component of magnetization remain. Thus, at larger P_{Ar}, a greater amount of in-plane magnetization exists even though the microstructure is more columnar. This suggests that the columnar microstructure is not the major cause of perpendicular anistropy. Furthermore, the decrease of perpendicular magnetization is not unexpected with increasing P_{Ar} since the microstructures show a high density of microvoids as well as a higher number of microcrystals.

At 40 mTorr, one cannot see any evidence for the formation of domains [Fig. 5(d)]. This may be associated with deposition parameters. Results (Figs. 1 and 2) indicate that the increase in P_{Ar} increases the density of microvoids. Oxygen may react with Tb along the microvoids to form nonmagnetic oxides. Thus the oxides may shield the magnetic portions of the amorphous phases. This leads to further separation between magnetic portions so that the interaction energy between the magnetic regions is greatly reduced. This reduction in interaction energy would give rise to a low magnetization and hence weak Lorentz force, not capable of producing images in LEM.[9]

The influence on the perpendicular magnetization of P_{Ar} shown in Fig. 5 can also be observed through MO hysteresis loops. At 2 and 10 mTorr [Figs. 6(a) and 6(b)], the loops are rectangular, typical of materials with an easy axis normal to the film plane. Further increase in P_{Ar}

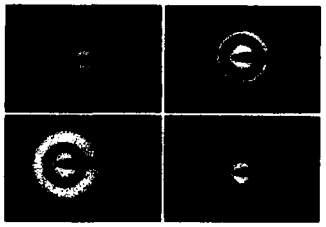


FIG. 3. SAD patterns of Tb-Fe-Co films: (a) 2, (b) 10, (c) 20, and (d) 40 mTorr.

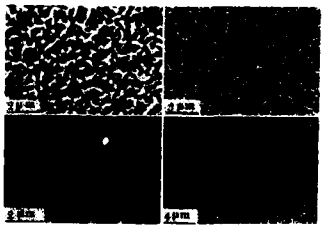


FIG. 5. Lorentz images of Tb-Fe-Co films: (a) 2, (b) 10, (c) 20, and (d) 40 mTorr.

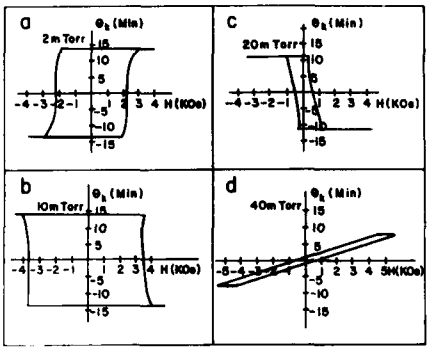


FIG. 6. MO hysteresis loops of Tb-Fe-Co films: (a) 2, (b) 10, (c) 20, and (d) 40 mTorr.

(20 mTorr) decreases the coercivity to 0.7 kOe. At 40 mTorr, the loop becomes sheared (squareness < 1) indicating that the film is dominated by in-plane magnetization components.

IV. CONCLUSIONS

(1) Low P_{Ar} produces films with microstructures that are smooth and featureless while high P_{Ar} produces films with microvoids surrounding the amorphous islands.

(2) Films grown at high P_{Ar} contain columnar shape morphologies.

(3) It is suggested that TbFeCo films contain a mixture of amorphous and microcrystalline (< 1.5 nm) phases.

(4) At low P_{Ar}, the films show "stripe type" magnetic domains associated with white and black dotted domains. In-plane "featherlike" domains are observed at high P_{Ar}.

(5) MO loops indicate that low P_{Ar} gives rise to perpendicular magnetization while higher P_{Ar} is dominated by in-plane magnetization.

ACKNOWLEDGMENTS

This research was funded in part by International Business Machines Corporation (IBM) and also supported by the Magnetic Materials Research Group at Carnegie Mellon University, Pittsburgh, PA 15213, through the Division of Materials Research, National Science Foundation, under Grant No. DMR-8613386. One of the authors (H-P.D. Shieh) would like to acknowledge the support of an IBM post-doctoral fellowship.

[1]Y. Togami, K. Kobayashi, M. Kajimura, K. Sato, and T. Teranishi, J. Appl. Phys. **53**, 2334 (1982).
[2]F. Tanaka, Y. Nagao, and N. Imamura, IEEE Trans. Magn. **MAG-20**, 1033 (1984).
[3]M. Hong, E. M. Gyorgy, R. B. van Dover, S. Nakahara, D. D. Bacon, and P. K. Gallaghen, J. Appl. Phys. **59**, 551 (1986).
[4]S-C. Shin, J. Appl. Phys. **61**, 3340 (1987).
[5]H-P. D. Shieh, M. Hong, and S. Nakahara (these proceedings).
[6]J. A. Thornton, J. Vac. Sci. Technol. **11**, 666 (1974).
[7]S. Nakahara, M. Hong, R. B. van Dover, E. M. Gyorgy, and D. D. Bacon, J. Vac. Sci. Technol. **A4**, 543 (1986).
[8]D. P. Ravipati, W. G. Heines, and J. L. Dockendorf, J. Vac. Sci. Technol. A **5**, 1968 (1987).
[9]T. Chen and G. B. Charlan, J. Appl. Phys. **50**, 4285 (1979).

Microstructure and stability of rf-diode sputtered GdTbFeCo thin films

H-P. D. Shieh
Dept. of Electrical and Computer Engineering, Carnegie Mellon University, Pittsburgh, Pennsylvania 15213

M. Hong and S. Nakahara
AT&T Bell Laboratories, Murray Hill, New Jersey 07974

The correlation of deposition parameters, microstructure, and stability of rf-diode sputtered magneto-optical thin films has been studied by using transmission electron microscopy and a magneto-optical hysteresis loop tracer. Among the sputtering parameters, we found that both argon bleeding pressure and substrate bias have strong influences on microstructure and consequently the oxidation resistance of the films. Sputtering using moderate argon pressure and substrate bias produces dense and smooth films. The bare films are strongly resistant to oxidation. In contrast, low or high argon pressure and substrate table bias result in films of high porosity, columnar "islandlike" structure, or "spongelike" morphology. They degrade rapidly in air.

I. INTRODUCTION

Magneto-optical (MO) recording is emerging as a technology for high-density, high-capacity erasable data storage applications.[1] Amorphous rare earth-transition metal (RE-TM) thin films fabricated by sputtering are the most promising MO recording materials so far. Long-term stability of the RE-TM thin films due to the high oxygen affinity of the rare earth constituents is, however, still one of the very critical issues.[2,3] Among the various proposed solutions, the most fundamental and important one is to enhance the environmental stability of RE-TM thin films. It has been reported that there are strong correlations of the deposition process, microstructure, magnetic properties, and oxidation resistance of sputtered thin films.[4]

rf-diode sputtering is commonly used to fabricate RE-TM thin films. To maintain a high ionization efficiency, the argon bleeding pressure (P_{Ar}) used in the rf-diode mode is typically several times higher than that applied in the dc-magnetron mode. Moreover, a negative rf-substrate bias voltage (V_b) with respect to ground is often applied to influence the film growth by inducing resputtering during deposition of the film. In this work, we investigate whether rf-diode sputtering can produce dense and smooth RE-TM thin films which have desirable magnetic and MO properties and at the same time possess high oxidation resistance.

II. EXPERIMENT

Quaternary RE-TM thin films of GdTbFeCo were deposited by using rf-diode sputtering from a 6-in.-diameter Fe-base mosaic target. The nominal areal composition of the target is $(Gd_1Tb_1)_{30}(Fe_4Co_1)_{70}$. The substrates are Corning 0211 1-in.-sq glass and 3-mm-diam copper grids coated with amorphous carbon for the transmission electron microscopy (TEM) studies. Both the target and substrate table were water-cooled and the spacing between them was 2-in. The chamber, equipped with a liquid-nitrogen cold trap, was evacuated to 2×10^{-7} Torr prior to introducing argon to a predetermined dynamic pressure monitored by a capacitor monometer. The target voltage was fixed at -1.2 kV. By varying V_b, P_{Ar}, and deposition time, films of different properties could be obtained. All the films on copper grids and glass substrates in the same run were about 50 nm thick. There were no passivative overcoats on them and the films were exposed to air after they were removed from the sputtering chamber. The polar Kerr MO hysteresis loops of the films on glass substrates were measured from both film and glass sides at a HeNe laser wavelength. For microstructure and morphology characterizations, we used a Philips 420 TEM operating at 120 kV to obtain bright field imaging and selective area electron diffraction patterns.

III. RESULTS AND DISCUSSION

From the TEM micrographs, it is noted that both V_b and P_{Ar} have strong effects on film morphology. At $|V_b|$

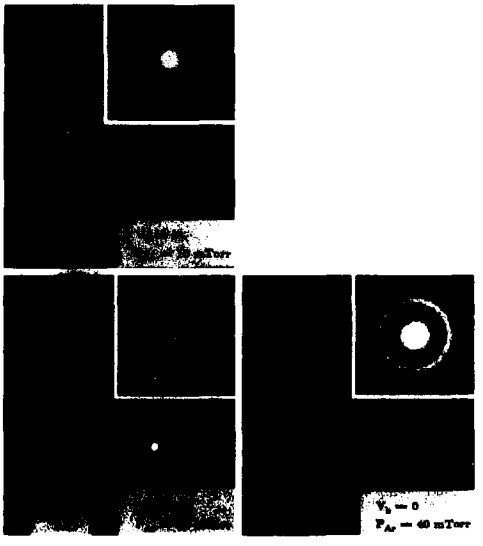


FIG. 1. TEM micrographs of films rf-diode sputtered at $V_b = 0$ and P_{Ar} = 10, 20, and 40 mTorr.

 0021-8979/88/083627-03$02.40 © 1988 American Institute of Physics

= 0, the films deposited at 20 and 40 mTorr display columnar "islandlike" structure, surrounded by discontinuous and continuous chains of voids, as shown in Fig. 1. The micrograph of the 10 mTorr film does not reveal void regions. At the other extreme of $V_b = -200$ V, the microstructure very much depends upon P_{Ar}, as seen in Fig. 2. In all cases, the micrographs reveal "micrograin" structures; the "grain" size of the 10 mTorr film is on the order of several nm; yet the "grains" become much finer as P_{Ar} increases to 20 mTorr. We should note that the term "micrograin" or "grain" used in this paper is a description of the film region(s) surrounded by the voids. These film regions are amorphous, not crystalline. As P_{Ar} reaches 40 mTorr, the structure becomes a porous and "spongelike" mixture of large size voids and micrograins. Such peculiar morphology may be caused by intense argon bombardment at a high P_{Ar} as well as by high resputtering effects on the growing films due to a high V_b.

On the other hand, smooth and morphologically featureless films can be made by using moderate V_b, as illustrated in Fig. 3, showing two sets of micrographs. Careful inspection of the microstructures shows that the films sputtered at 20 mTorr have finer and smoother morphology than the 10 mTorr ones, where micrograins are still visible in the TEM micrographs at a scale of nm.

The microstructure of dc-magnetron sputtered films is a simple function of P_{Ar}. The films become less dense and smooth as P_{Ar} increases.[5] The morphology of the films varies from featureless at 10 mTorr or less to columnar features surrounded by fine chains of voids at 20 mTorr, and to pronounced continuous void chains at 40 mTorr.[6] In the rf-diode mode without substrate bias, the trends are quite similar to those of dc-magnetron sputtering, as seen in Fig. 1, although isolated columns are still discernible for the films sputtered at low P_{Ar}. The regions of white chains surrounding the columns increase with increasing P_{Ar}, but the argon inclusion in the deposited films actually decreases with increasing P_{Ar}.[7] Because of the shorter mean free paths of argon ions at high P_{Ar}, argon ion bombardment on the growing films thereby increases with decreasing P_{Ar}. The result suggests that the increase in void regions is not directly related to the trapping of argon, but more likely is due to the change of growth processes by dominant argon ion impingement on the substrates. At high P_{Ar}, argon bombardment on the growing films is less intense and thus the vertical growth of the films is enhanced, as seen from the distinct columnar features in Fig. 1. Lowering P_{Ar}, however, increases argon bombardment on the film surface by the energetic argon ions and neutral species to promote surface diffusion processes. Therefore, the columnar structure becomes less pronounced. However, with the presence of substrate bias, the dependence of microstructure on P_{Ar} is quite different. The columnar structure does not appear any more, instead, films deposited at low P_{Ar} show micrograins. The grains become much finer as P_{Ar} is increased to 20 mTorr. The marked difference in the influence of microstructure by V_b suggests the dominant role of V_b in rf-diode sputtering.

In rf-diode sputtering, V_b is very effective in modifying the characteristics of the films. The reflectivity of rf-diode sputtered films can be made to vary by as much as 5% by applying V_b from 0 to -200 V,[7] implying a significant topo-

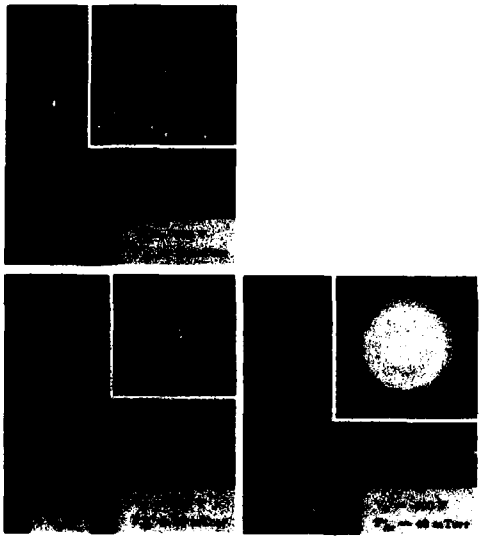


FIG. 2. TEM micrographs of films rf-diode sputtered at $V_b = -200$ V and $P_{Ar} = 10$, 20, and 40 mTorr.

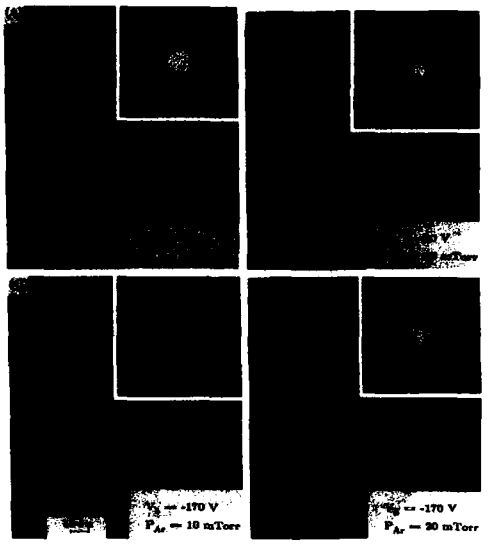


FIG. 3. TEM micrographs of films deposited at moderate P_{Ar} and V_b. Samples A and B were fabricated at $V_b = -90$ V and $P_{Ar} = 10$ and 20 mTorr, respectively. Samples C and D were deposited at $V_b = -170$ V and $P_{Ar} = 10$ and 20 mTorr, respectively.

logical change in the films. The application of V_b induces resputtering on the growing films. Due to the difference in resputtering rates, RE constituents are preferentially resputtered producing RE-deficient films as $|V_b|$ increases. Moreover, V_b also affects magnetic properties of the films such as perpendicular anisotropy.[3] Among all these effects induced by V_b, there is an underlying mechanism which affects the characteristics of the films. From the TEM micrographs in Figs. 1–3, it is quite clear that microstructural changes in the films are very significant. It is possible that these microstructural changes are responsible for the change in magnetic properties of the films.

It is also noted that in spite of the fact that the argon content is higher in the films aputtered at V_b,[7] the void regions shown in the micrographs of the films sputtered at no-bias voltage do not appear. This result suggests that argon is not trapped in the void regions. However, the bombardment processes on the films should be optimized since the intense impingement by energetic ions can damage the films and cause high porosity which significantly weakens the stability of the films.

The strength of oxidation resistance of bare RE-TM thin films can be indirectly evaluated by monitoring the change in coercivity and MO signal by using a MO hysteresis loop tracer. As shown in Fig. 4, the coercivity change as a function of the number of days of exposure to air for dense and smooth films ($V_b = -170$ V) are far less than porous films with rough surfaces ($V_b = -200$ V). The morphologic void regions provide an easy path for oxygen to diffuse into the films and to react with the rare earth constituents. Moreover, the oxygen content in the films deposited at no bias voltage is a factor of 2–3 higher than the films deposited at moderate V_b.[8] Both factors result in adverse effects on the stability of the films. By applying a moderate V_b, it is possible to deposit void-free films whose oxygen content is dramatically reduced.

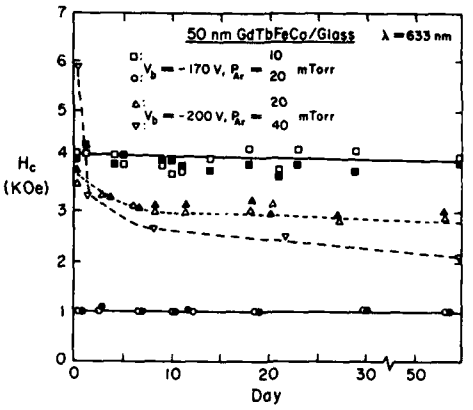


FIG. 4. The magneto-optically measured coercivities of films as a function of the number of days of exposure to air. Open and filled symbols represent values as measured from substrate and film sides, respectively.

IV. CONCLUSION

There are strong correlations of film deposition conditions, magnetic properties, microstructure, and stability. Both P_{Ar} and V_b strongly affect the magnetic and structural properties of rf-diode sputtered films. Distinct changes in film morphology, microstructure, and oxidation resistance can be obtained by using different P_{Ar} and V_b. It is possible to "engineer" the microstructure of the amorphous films to be dense, smooth, and morphologically featureless by using moderate P_{Ar} and V_b in the rf-diode sputtering. The films deposited at these conditions possess superior oxidation resistance, in spite of a high argon inclusion in the films (< 10 at. %). On the other hand, films with columnar features and chains of void degrade rapidly in air, although the argon content is less than that in the former films. These results demonstrate the importance of the microstructure on the stability of the sputtered amorphous RE-TM thin films.

ACKNOWLEDGMENT

One of us (H-P.D.S.) would like to acknowledge the support of an IBM post-doctoral Fellowship.

[1]M. H. Kryder, J. Appl. Phys. **57**, 3913 (1985).
[2]R. B. van Dover, E. M. Gyorgy, R. P. Frankenthal, M. Hong, and D. J. Siconolfi, J. Appl. Phys. **59**, 1291 (1986).
[3]F. E. Luborsky, IEEE Trans. Magn. **MAG-22**, 937 (1986).
[4]M. Hong, E. M. Gyorgy, R. B. van Dover, S. Nakahara, D. D. Bacon, and P. K. Gallagher, J. Appl. Phys. **59**, 551 (1986).
[5]S. Nakahara, M. Hong, R. B. van Dover, E. M. Gyorgy, D. D. Bacon, J. Vac. Sci. Technol. A **4**, 543 (1986).
[6]J-W. Lee, H-P. D. Shieh, M.H. Kryder, and D. E. Laughlin (these proceedings).
[7]H-P. D. Shieh, Ph.D. dissertation, Carnegie Mellon University (1987).
[8]M. Ohkoshi, M. Harada, T. Tokunaga, S. Honda, and Kusuda, IEEE Trans. Magn. **MAG-21**, 1635 (1985).

Characterization of amorphous TbFeCo films for magneto-optical media

M. F. Ruane and J. Calkins
Department of Electrical, Computer, and Systems Engineering, Boston University, Boston, Massachusetts 02215

Sputter-deposited amorphous TbFeCo films can exhibit magneto-optical Kerr rotation and are leading candidates for erasable optical storage media. Thirty-two TbFeCo samples, deposited on quartz substrates in four different sputtering runs, were characterized by RBS, VSM, Kerr loop tracing, and polarization microscope photographs. Both Tb- and Fe-rich samples were deposited, with room-temperature coercivities ranging from 1 kOe to over 6 kOe. Kerr rotations varied from 14 to 32 min of arc (film side) and from 19 to 21 min of arc (substrate side). Domain photographs, using fields just below coercivity to initiate reversal at inherent nucleation sites, show domain shapes that vary from irregular structures with internally striped reversal to rather circular, well-reversed domains. The shape of observed domains and their internal magnetization patterns are related to composition and compared with important magneto-optical properties such as coercive field H_c and Kerr rotation θ_K. Variability of these properties across different sputtering runs and within the same run are also discussed.

I. INTRODUCTION

During the rf-sputter deposition process, controllable process factors such as target compositions, target-substrate geometries, bias voltages, Ar pressure, and rf power levels, interact in a complex fashion to determine the composition, magnetic properties, and magneto-optical (MO) behavior of deposited samples.[1] Developing reproducible MO media capable of reliable high-density data storage requires a rich characterization of deposited films,[2,3] so that factors contributing to domain creation, stability, and erasure can be identified and related to sputtering conditions. This paper describes characterization experiments on a series of TbFeCo films.

Thirty two rf-sputter-deposited samples of amorphous TbFeCo have been studied using Rutherford backscattering (RBS), a Kerr effect hysteresis loop tracer, a vibrating sample magnetometer (VSM), and a modified polarization microscope. This paper first describes the samples that were studied and the conditions under which they were deposited. Next the apparatus used to characterize the samples will be described. Observations on the samples will then be given, followed by a summary.

Samples consisted of approximately 900 Å of TbFeCo sputtered in Ar from 8-in. diameter cathodes onto 1-in.-diameter, 0.5-mm-thick quartz substrates, with a protective overcoat of about 4000 Å of Al_2O_3 deposited *in situ*. Four sputtering runs, denoted *A*, *B*, *C*, and *D*, were made with different substrate and target bias voltages. Substrates were on a rotating substrate carrier at three radii; radius 4 substrates passed directly under the center of the targets, while radius 2 substrates were 2 in. inward, and radius 6 substrates were 2 in. outward from the center. Sample composition was determined by RBS analysis (Table I) using a single carbon substrate included in each radial group. VSM substrates were also sputtered with each radial group.

II. EXPERIMENTAL APPARATUS

Hysteresis loops, Kerr rotation θ_K, and coercivity H_c were collected by a computer-controlled loop tracer[4] using a polarized HeNe laser ($\lambda = 632.8$ nm) and maximum field strength of about 5.7 kOe. A temperature-controlled stage heated samples from room temperature to 130 °C for measuring compensation temperature T_{comp}.

A commerical VSM was used to measure remanence field, B_r, and H_c for the VSM substrate samples. Because the VSM was designed for samples with relatively large magnetization, signals from our 900 Å samples were sometimes comparable to system noise levels and required calculations of B_r and H_c directly from VSM hysteresis curves.

A standard polarization microscope, modified to hold a *± 3.6-kOe electromagnet below its sample stage* was used to photograph domain structures created at inherent nucleation centers by fields just below the coercive field. Many such centers appear to coincide with visible defects in the film. Density of nucleation centers is a function of composition as well as of the field applied and the depth of the saturating field.[5] Samples were usually saturated in one direction using the microscope magnet; field strength was then increased in the opposite direction until nucleation was observed, usually at or below the bulk coercive field. Returning the field to zero allowed photographs with the domain structures "frozen" in place. Films with H_c above 3.6 kOe were reversed externally and then observed under the microscope in the area where domains had just begun to nucleate.

TABLE I. RBS sample compositions by run (*A,B,C,D*) and radial position (2,4,6) using carbon substrate.

Run Group ID	Tb%	Co%	Fe%	Ar%
A-radius 2	19.7	8.3	62.8	9.2
A-radius 4	20.9	8.5	62.1	8.5
A-radius 6	21.3	8.7	61.2	8.8
B-radius 2	22.2	8.8	59.6	9.4
B-radius 4	22.9	9.4	58.4	9.3
B-radius 6	22.8	11.2	55.6	10.4
C-radius 2	23.3	8.7	58.8	9.2
C-radius 4	23.4	8.5	57.6	10.5
C-radius 6	23.5	8.5	57.2	10.8
D-radius 4	17.2	7.4	60.3	15.2

 0021-8979/88/083630-03$02.40 © 1988 American Institute of Physics

III. EXPERIMENTAL CHARACTERIZATIONS

A. Room-temperature Kerr loops

Film-side room-temperature measurements of θ_K and H_c showed *A*, *B* and *C* to be Tb rich while *D* was Fe rich. Samples within each run tended to be similar in H_c, while different runs showed different H_c. Film-side θ_K (Fig. 1) varied widely, with samples within B showing nearly a factor of 2 difference in θ_K. Note that *A* had a room temperature T_{comp} for several subsrates. Film-side θ_K variability is believed to arise from interference effects at the overcoat layer. Substrate-side θ_K for all runs was 20 ± 1 min of arc and is comparable to that of other TbFeCo films with similar compositions.

Observed film-side room-temperature H_c varied from substrate-side values by as much as several hundred Oersteds. This difference might be due to a film-side oxidation layer, but more likely arises from field measurement calibration errors arising from the finite size of the gaussmeter probe area, the errors in estimating the distance from the film to the magnet tip creating the field.

B. Temperature dependence of H_c

Kerr hysteresis loops were used to measure H_c from 20 to 130 °C. Table II shows data for samples from each radial group in *A* and representative samples from *B*, *C*, and *D*. A-2 has T_{comp} near room temperature, where its H_c exceeded the Kerr loop tracer's maximum field. *A*-4 had T_{comp} near 80 °C and its hysteresis loops showed the usual conversion from Tb to Fe-rich orientation. *A*-6 has its compensation point above 130 °C and exhibited only Tb-rich loops. This variation of over 100 °C in T_{comp} within the same sputtering run is attributed to the differences in target-substrate geometry, and the resulting compositional differences.

B-2 showed compensation point behavior similar to *A*-6, although its H_c increase near 120 °C was steeper. Samples in the *B*-4 and *B*-6 radial groups showed no sign of T_{comp} and had H_c steadily decrease with increasing temperatures. *C*-2 showed no T_{comp} in the temperature range studied, nor did samples studied in the *C*-4 or *C*-6 groups. *D*-4 suggests a T_{comp} below room temperature.

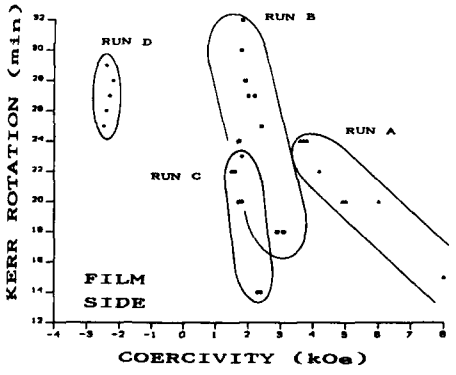


FIG. 1. Kerr loop tracer θ_K and H_c data for film side.

TABLE II. Kerr loop tracer H_c vs temperature for representative samples in different runs and radial groups.

Temperature (°C)	*A*-2 (kOe)	*A*-4 (kOe)	*A*-6 (kOe)	*B*-2 (kOe)	*C*-2 (kOe)	*D*-4 (kOe)
20	> 5.7	3.8	3.5	2.7	2.2	2.5
40	> 5.7	4.7	3.8	2.8	2.0	2.0
60	> 5.7	> 5.7	4.1	2.9	2.0	1.5
80	3.1	> 5.7	4.6	3.1	1.8	1.2
100	1.9	> 5.7	5.7	3.5	1.7	0.9
120	1.2	2.7	> 5.7	> 5.7	1.6	0.8
130	1.0	1.8	> 5.7	> 5.7	1.5	0.7

C. VSM measurements

VSM H_c measurements were made with the VSM substrates sputtered with the groups in Table II. VSM results had lower T_{comp} values and broader ranges of high H_c. In comparison with the Kerr loop tracer results, some differences would be expected due to the variability of film compositions with position on the sputtering platform, even at the same radius. Other differences arise because the VSM measures only bulk properties, while the Kerr loop tracer observes localized characteristics. Nonuniformity of H_c, which was observed to increase with radial position on individual substrates as much as 50% from center to edge, could also contribute to Kerr-VSM differences.

VSM measurement of remanence magnetization, B_r, indicated room-temperature values near 4×10^{-4} emu for VSM substrates from *A*, *B*, and *C*, while the *D* VSM substrate had B_r nearer to 2×10^{-4} emu.

D. Polarization microscope observations

Room-temperature coercive field domain structures provide another, qualitative method for distinguishing among samples deposited in the same run. Domain nucleation and growth seems to be dominated by the microstructure, both in terms of the density and location of nucleation centers, and the manner in which domain walls propagate and create a reversed region. Thermomagnetic writing creates nucleation centers at each mark, but the shape and uniformity of the domain is dictated both by the isotherms of the writing laser and the film's preferred mode of wall propa-



FIG. 2. Sample coercive field domains, run *B*, radius 2. Field of view 160 μm. $H_c = 3.1$ kOe, VSM $B_r = 6 \times 10^{-4}$ emu.

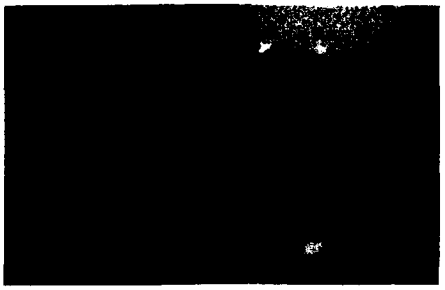


FIG. 3. Sample coercive field domains, run *B*, radius 4. Field of view 160 μm. $H_c = 3.1$ kOe, VSM $B_r = 4\times10^{-4}$ emu. Note nucleation at defect site.



FIG. 4. Sample coercive field domains, run *B*, radius 6. Field of view 160 μm. $H_c = 3.1$ Oe, VSM $B_r = 6\times10^{-4}$ emu.

gation. Coercive field domain photographs indicate differences in wall propagation among samples.

When initially deposited, films generally exhibit a random up-down minimum energy structure. With a saturating field the pattern becomes uniform, and as the opposite coercive field is approached, domains begin to appear. While domain wall velocity can be controlled by varying the field strength, the nature of the wall growth depends on domain energetics and is characteristic of the film.

Local domain wall growth (smooth, or jagged with dendritic structure), the overall shape of the domains, and the internal structure (completely reversed or striped) varied widely. Domains tended towards being either smooth walled, round, and completely reversed internally, or jagged, with dendritic structures at the wall and striped internal structure. The jagged structure is favored by domains with high demagnetizing energy compared to wall energy. High demagnetizing energy also favors the striped internal structure. Conversely, the smoother walls and complete internal reversal is associated with higher wall enegy and lower demagnetizing energy.[6,7] All samples produced square hysteresis loops, including those exhibiting jagged domains.

Domains in samples within *A* were difficult to initiate and control because of their room temperature T_{comp} and high H_c. Domains from all samples in *D*-4 tended to be round and well reversed internally. Figures 2, 3, and 4 show coercive field domains of samples from the three radii of run *B*. The sample at radius 2 is rounded and completely reversed internally, while the domains in the sample at radius 4 have jagged edges and striped internal structure. Domains from the sample at radius 6 were even more random, growing in a jagged fashion, and leaving behind striped internal structures. A similar pattern was seen for *C*, with the radius 2 group being rounded and well reversed, while groups at radii 4 and 6 were striped.

The dendritic structures become more pronounced at domain edges, such that the localized readout of the Kerr loop tracer quickly becomes dominated by the internal structure of the domain under the laser spot. As long as the internal patterns become fully reversed with increasing field, square loops would be expected. When the readout beam diameter is on the order of the domain size, noise will be introduced by jagged edges.

IV. SUMMARY

RBS, Kerr loop tracing, VSM, and coercive domain photographs have been used to characterize amorphous TbFeCo films that could be used for magneto-optical recording media. Variation in sample properties, even in the same run, has been apparent in all the characterizations. This suggests that predicting MO properties of an individual sample from sputtering process parameters such as substrate and target bias voltages or Ar pressure alone will be difficult. Target-sample geometry, exhibited here by radial groupings and positioning within the same group, can play an important role.

ACKNOWLEDGMENTS

The authors wish to thank N. Jubb and T. Rieth of IBM General Products Division, Tucson, AZ, for sample preparation and their helpful discussions.

[1]M.H. Kryder, H. P. Shieh, and D. K. Hairston, IEEE Trans. Magn. MAG-23, 165 (1987).
[2]J. C. Suits, R. H. Geiss, C. J. Lin, D. Rugar, and A. E. Bell, Appl. Phys. Lett. 49, 419 (1986).
[3]M. Takahashi, N. Ohta, and S. Takayama, IEEE Trans. Magn. MAG-22, 931 (1986).
[4]P. Wolniansky, S. Chase, R. Rosenvold, M. Ruane, and M. Mansuripur, J. Appl. Phys. 68, 346 (1986).
[5]J. Calkins, M. Mansuripur, and M. Ruane, MRS Symposia Proc. 80, 435 (1987).
[6]M. Mansuripur and G. A. N. Connell, J. Appl. Phys. 55, 3049 (1984).
[7]M. Mansuripur, J. Appl. Phys. 61, 1580 (1987).

Single ion model for magnetostriction in rare-earth–transition-metal amorphous films

Yoshio Suzuki and Norio Ohta
Central Research Laboratory, Hitachi Ltd., Kokubunji 185, Tokyo, Japan

The mechanism of magnetostriction in rare-earth–transition-metal amorphous films was investigated based on a single ion anisotropy model for rare-earth atoms using a point charge approximation. The theory was compared with the observed magnetostriction in $(Gd_{0.75}R_{0.25})_{19}Co_{81}$ films with various rare-earth elements R. The dependence of the observed magnetostriction on substitutional rare-earth elements R is well explained with this model. Screening of an electric field was found to be essential for magnetostriction, and a screening function was determined from the observed magnetostriction. The screening was found to be of the type in which an electric field decreases more rapidly with an increase of distance than a Coulombic interaction.

I. INTRODUCTION

Perpendicular magnetic anisotropy K_u in rare-earth–transition-metal (RE-TM) amorphous films can be separated into two components, a part due to inverse magnetostriction and an intrinsic anisotropy.[1–3] In a previous paper[4] we have shown that the intrinsic anisotropy can be explained with a single ion anisotropy model of rare-earth atoms using a point charge approximation, and that such an intrinsic anisotropy can be induced by an anelastic deformation during deposition of a film. We also pointed out that magnetostriction is closely related to the single ion anisotropy of rare-earth atoms. In this study we investigated magnetostriction in RE-TM amorphous films based on a point charge approximation. A point charge model without any screening is known to lead to zero magnetostriction in amorphous structures.[5] We determined the screening function for the crystal field from the observed magnetostriction in $(Gd_{0.75}R_{0.25})_{19}Co_{81}$ film with various rare-earth elements R.

II. POINT CHARGE MODEL OF MAGNETOSTRICTION IN AMORPHOUS STRUCTURES

By applying a point charge model[6] in amorphous structure, the crystal field energy $W_c(i)$ associated with the $4f$ electrons of a rare earth atom at a site i was calculated. The term related to uniaxial anisotropy along z axis can be written as[4]

$$W_c(i) = -A\left(\cos^2\theta_M - \frac{1}{3}\right)\sum_j \frac{q_j(3\cos^2\theta_{ij}-1)}{R_{ij}^3} \tag{1}$$

with

$$A = \tfrac{3}{4}|e|\langle r^2\rangle\alpha(J^2 - J/2), \tag{2}$$

where e is the electron charge, $\langle r^2\rangle$ is the size of the $4f$ orbit, α is the Stevens factor,[7] J is the total angular momentum, θ_M is the polar angle of the direction of magnetization, R_{ij} and θ_{ij} are polar representation of the position of the nearest-neighbor ion j, q_j is the charge of the ion j, and the sum is taken over the nearest-neighbor ions of i.

We define the local magnetic anisotropy $K_u(i)$ at the site i by the following equation:

$$W_c(i) = -K_u(i)n^{-1}(\cos^2\theta_M - \tfrac{1}{3}), \tag{3}$$

where n is the number of rare earth atoms in a unit volume. Then the bulk anisotropy K_u can be obtained as the average of $K_u(i)$ as $K_u = \langle K_u(i)\rangle$ where $\langle\ \rangle$ means a configurational average over all sites i. Comparing Eqs. (1) and (3), we get an expression for $K_u(i)$:

$$K_u(i) = An\sum_j \frac{q_j(3\cos^2\theta_{ij}-1)}{R_{ij}^3}. \tag{4}$$

In the following analysis we use a uniform strain approximation in which all atomic positions change with a strain tensor

$$\epsilon_{xx} = \epsilon_{yy} = -\epsilon/2, \quad \epsilon_{zz} = \epsilon, \quad \text{others} = 0. \tag{5}$$

This represents a pure shear part of a uniaxial deformation along z axis.

We define the local magnetoelastic coupling constant $B(i)$ as

$$B(i) = \frac{dK_u(i)}{d\epsilon}. \tag{6}$$

Then, the magnetic and elastic energy per unit volume is given by

$$U = K_u(\cos^2\theta_M - \tfrac{1}{3}) + \langle B(i)\rangle(\cos^2\theta_M - \tfrac{1}{3})\epsilon + (\tfrac{3}{2})G\epsilon^2, \tag{7}$$

where G is the shear elastic modulus. The strain is given from Eq. (7) as the value of ϵ that minimizes U. The saturation magnetostriction λ_s is the difference between the strain for $\theta_M = 0$ and that for $\theta_M = \pi/2$: that is

$$\lambda_s = \langle B(i)\rangle/3G. \tag{8}$$

To calculate the magnetoelastic coupling constant (6) it is convenient to treat contributions of the change of R and the change of θ separately as

$$B(i) = \sum_j \left(\frac{\partial R_{ij}}{\partial\epsilon}\right)\left(\frac{\partial K_u(i)}{\partial R_{ij}}\right) + \left(\frac{\partial\theta_{ij}}{\partial\epsilon}\right)\left(\frac{\partial K_u(i)}{\partial\theta_{ij}}\right). \tag{9}$$

 0021-8979/88/083633-03$02.40 © 1988 American Institute of Physics

Using the equations

$$\frac{\partial R_{ij}}{\partial \epsilon} = \frac{R_{ij}(3\cos^2\theta_{ij} - 1)}{2},$$
$$\frac{\partial \theta_{ij}}{\partial \epsilon} = \frac{-3\sin\theta_{ij}\cos\theta_{ij}}{2}, \tag{10}$$

Eq. (9) can be transformed into

$$B(i) = -An\sum_j \left(\frac{3}{2}\right) q_j [(3\cos^2\theta_{ij} - 1)^2 - 6(\sin\theta_{ij}\cos\theta_{ij})^2]/R_{ij}^3. \tag{11}$$

The first term in the parentheses represents the effect of the change in the distance of the nearest-neighbor ion R_{ij}, and the second term the effect of the change in the orientation of them θ_{ij}. We call the former the ΔR effect and the latter the $\Delta\theta$ effect. Those terms are plotted in Fig. 1 as a function of $\cos\theta$. The $\Delta\theta$ effect and the ΔR effect have opposite contribution to the magnetoelastic coupling constant.[5] The nearest-neighbor ions around the z axis and in the xy plane contribute to $B(i)$ mainly through the ΔR effect, while those in the intermediate direction contribute mainly through the $\Delta\theta$ effect.

In an amorphous structure, distribution of the nearest neighbors is isotropic. Therefore, the angle factor in Eq. (11) can be averaged over a sphere,

$$B = \langle B(i)\rangle \propto \langle (3\cos^2\theta - 1)^2 - 6(\sin\theta\cos\theta)^2\rangle = 0. \tag{12}$$

This means that in pure point charge approximation the magnetoelastic coupling constant is always zero.

The reason why the magnetoelastic coupling becomes zero can be explained more directly with the following argument. The configurational average $\langle B(i)\rangle$ is equivalent to $B(i)$ for a single ion surrounded by a continuous distribution of positive charge defined by the radial distribution function. The distribution of the nearest-neighbor ions can be decomposed into components of spherical shells like the one shown in Fig. 2(a). If the thickness of the shell is sufficiently small, the charge density in the shell can be regarded as uniform. Each spherical shell, by a uniform shear strain (5), turns into an ellipsoidal shell [Fig. 2(b)]. The volume density of charge is unchanged after the deformation because the strain (5) is of a pure shear mode. It is known[8] that the electrostatic potential inside an ellipsoid uniformly changed by ρ is

$$\phi = \text{const.} - \rho(N_x X^2 + N_y Y^2 + N_z Z^2)/2, \tag{13}$$

where N_x, N_y, and N_z are the same as the demagnetization factors for the ellipsoid. Since an ellipsoidal shell can be regarded as a superposition of two similar ellipsoids charged by ρ and $-\rho$, the electric field, being the superposition of the fields created by those two ellipsoids, is zero inside the shell. Thus the charge distributed on this shell has no contribution to magnetoelastic coupling.

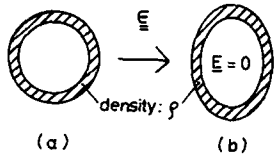


FIG. 2. Mechanism of zero-magnetostriction in a pure point charge model. Distribution of the nearest-neighbor ions can be decomposed into components of uniformly charged spherical shells (a). Each shell, by uniform shear strain, turns into a uniformly charged ellipsoidal shell (b), inside which the electric field is zero.

Magnetostriction is generally nonzero for actual amorphous ferromagnets in contrast to the above analysis. This is because we employed the following approximations: (1) a uniform strain assumption [Eq. (5)]; (2) the screening of electric field by conduction electrons is ignored; (3) the magnetic moments at rare earth sites were assumed to be aligned parallel to the bulk magnetization, while they are actually oriented closer to the local easy axis.[9] Among them, the second seems to be the main cause for the nonzero value of magnetostriction.

In general, the potential $1/R^3$ in Eq. (1) have to be replaced with a screened potential $g(R)/R^3$ with a screening factor $g(R)$. Then the magnetoelastic coupling constant B [$= \langle B(i)\rangle$] can be calculated, from Eq. (9), as

$$B = \left\langle An\sum_j \left(\frac{1}{2}\right) q_j g'(R_{ij}) \frac{(3\cos^2\theta_{ij} - 1)^2}{R_{ij}^3} \right\rangle$$
$$= \left(\tfrac{2}{5}\right) AnqN_c g'(a)/a^2, \tag{14}$$

where N_c is the coordination number and a is the average nearest-neighbor distance. The magnetostriction can now be written in the following form[10]:

$$\lambda_s = \tfrac{1}{10}\alpha(J^2 - J/2)(qe\langle r^2\rangle N_c/a^3)nG^{-1}ag'(a). \tag{15}$$

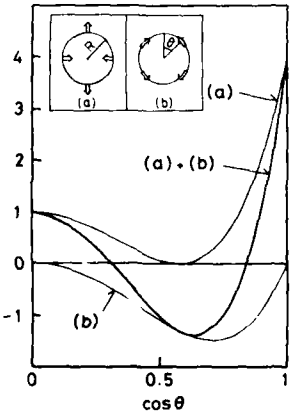


FIG. 1. The ΔR effect (a), and the $\Delta\theta$ effect (b) on magnetoelastic coupling plotted against the orientation of the nearest-neighbor ions.

III. COMPARISON WITH EXPERIMENT

Figure 3 is the magnetostriction λ_s in rf sputter deposited $(Gd_{0.75}R_{0.25})_{19}Co_{81}$ films.[4] Perpendicular magnetic anisotropy K_u was measured for the films before and after removal of the substrate. The difference ΔK_u between those two values is the part of K_u due to inverse magnetostriction mechanism. The saturation magnetostriction λ_s can be calculated using the relationship[3] $\Delta K_u = -(\tfrac{3}{2})\lambda_s\sigma$, where σ is the in-plane stress in the film. The stress $\sigma(= -4\times10^9$

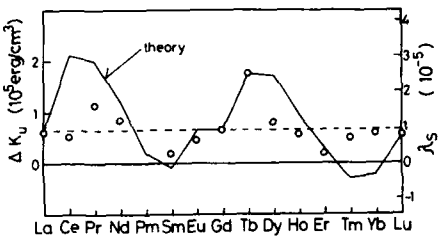


FIG. 3. The magnetostrictive part of uniaxial anisotropy obtained as the difference between K_u before and after removal of the substrate in sputter deposited $(Gd_{0.75}R_{0.25})_{19}Co_{81}$ films for various substitutional rare earth elements R (Ref. 4). The vertical scale to the right indicates the corresponding values of saturation magnetostriction.

dyne/cm^2) was determined from the bending of a silicon wafer on which $Gd_{19}Co_{81}$ film was deposited. Since Gd atoms have no single ion anisotropy, the value of λ_s for $Gd_{19}Co_{81}$ was taken as a basis (broken line in Fig. 3), and the effect of each rare earth element R was measured as the difference from this base line. By substituting into Eq. (15) the observed difference in λ_s between $(Gd_{0.75}Tb_{0.25})_{19}Co_{81}$ and $Gd_{19}Co_{81}$ films (1.9×10^{-5}), with shear modulus $G=5\times10^{11}$ dyne/cm^2, $q=|e|$ and other parameters as described in Ref. 4, we obtained the screening factor $ag'(a)=-7.2\times10^{-2}$. A negative sign is what we expect of an ordinary screening function. The magnetostriction λ_s calculated using this screening factor (solid line in Fig. 3), is within a reasonable agreement with the observation.

IV. CONCLUSION

Magnetostriction in rare-earth–transition-metal amorphous films was analyzed based on a single ion anisotropy model of rare-earth elements using a point charge approximation with screening. The dependence of the observed magnetostriction in $(Gd_{0.75}R_{0.25})_{19}Co_{81}$ films on the substitutional rare earth element R is in reasonable agreement with the theory. The screening function which was determined to fit the observed magnetostriction is of the type in which an electric field decreases more rapidly on increasing the distance than a Coulombic interaction.

[1] H. Takagi, S. Tsunashima, S. Uchiyama, and T. Fujii, J. Appl. Phys. **50**, 1642 (1979).
[2] S. Tsunashima, H. Takagi, K. Kamegaki, T. Fujii, and S. Uchiyama, IEEE Trans. Magn. **MAG-14**, 844 (1978).
[3] S. Yoshino, H. Takagi, S. Tsunashima, M. Masuda, and S. Uchiyama, Jpn. J. Appl. Phys. **23**, 188 (1984).
[4] Y. Suzuki, S. Takayama, F. Kirino, and N. Ohta, IEEE Trans. Magn. (to be published).
[5] Y. Suzuki and T. Egami, J. Magn. Magn. Mater. **31-34**, 1549 (1983).
[6] M. T. Hutchings, *Solid State Physics*, edited by F. Seitz and D. Turnbull (Academic, New York, 1964), Vol. 16, p. 227.
[7] K. W. H. Stevens, Proc. Phys. Soc. **A65**, 209 (1952).
[8] E. C. Stoner, Philos. Mag. **36**, 803 (1945).
[9] J. M. K. Coey and D. H. Ryan, IEEE Trans. Magn. **MAG-20**, 1278 (1984).
[10] The corresponding equation in Ref. 4 is wrong by a factor of $\sqrt{8\pi}/3$. A negative sign in its Eq. (7) should also be removed.

Magneto-optical properties of PtMnSb films prepared by facing targets sputtering

M. Naoe and N. Kitamura
Department of Physical Electronics, Faculty of Engineering, Tokyo Institute of Technology, 2-12-1 Oh-okayama, Meguro-ku, Tokyo 152, Japan

M. Shoji and A. Nagai
Advanced Material Systems Laboratories, Kureha Chemical Industry Co., Ltd., 3-25-1 Hyakunin-cho, Shinjuku-ku, Tokyo 160, Japan

The magneto-optical properties of PtMnSb Heusler alloy films prepared by a facing targets sputtering (FTS) system have been studied. The specimen films were deposited onto glass substrates heated between 20 and 350 °C. The films exhibiting diffraction peaks of Clb-PtMnSb Heusler alloy were obtained at temperatures above 150 °C. The saturation magnetization $4\pi M_s$ increased with increasing substrate temperature and the maximum value of magnetization was 5.8 kG, which is lower than PtMnSb bulk magnetization. The polar Kerr rotation measured with a He-Ne laser was evaluated at 1.9° on the glass side when an external dc magnetic field of 7 kOe was applied in a perpendicular direction.

I. INTRODUCTION

As the PtMnSb Heusler alloy with Clb phase has an extremely large Kerr effect,[1] the preparation of PtMnSb films attracts much interest for the magneto-optical recording application. Recently, several works have been carried out on PtMnSb thin films fabricated by sputtering and vacuum evaporation techniques and the preparation conditions to obtain a large polar Kerr rotation were studied.[2–4]

Generally, it is said that the magnetic and crystallographic properties of sputtered films can be changed by the plasma conditions, substrate temperature, incidence energy of sputtered particles, and deposition rate. In the facing targets sputtering (FTS) system, the plasma is confined by means of a magnetic field in a space between two targets that are facing each other and the substrates are placed outside this region (plasma-free region). As the irradiation by γ electron, Ar atoms, and negative transition metal ions to the growing film surface is greatly reduced, nondamaged deposition of the growing film surface can be achieved.[5]

In this work, PtMnSb Heusler alloy thin films have been prepared using the FTS apparatus and their crystallographic, magnetic, and magneto-optical properties will be described.

II. EXPERIMENT

The FTS apparatus used in this study is schematically shown in Fig. 1. For the plasma confinement, a magnetic field of 180 G was applied normal to each target plane. The substrate was in the "plasma free" region. The specimen films were deposited onto glass substrate (Corning 7059) heated between 20 and 350 °C.

In this study, a Mn plate (100 mmϕ × 5 mm^t) was used as the upper side facing target. A Sb/Pt composite target consisting of a Sb plate (100 mmϕ × 5 mm^t) and Pt chips (10 × 10 mm^2) was used as the lower side facing target. The composition of films was controlled by altering the number of Pt chips on the Sb target.

In the preliminary experiment, the surface color of the Sb target changed to black from metallic. By means of SEM observation and EPMA (Electron-Probe Microanalysis), many fine Sb prominences were detected on the Sb target surface whose color changed to black. This phenomenon is well known to occur under condition that the temperature of the Sb target surface is higher than the critical temperature,[6–8] which causes the compositional change of Sb in PtMnSb films. For preventing the change of the Sb target surface, the Sb target was sufficiently cooled by bonding to target holder.

The sputtering was carried out under argon pressure P_{Ar} in the range of 0.7–6 mTorr and the deposition rate was 250–630 Å/min. The deposition rate of the sputtered PtMnSb thin film decreased with increasing number of Pt chips on the Sb target and was proportional to discharge current.

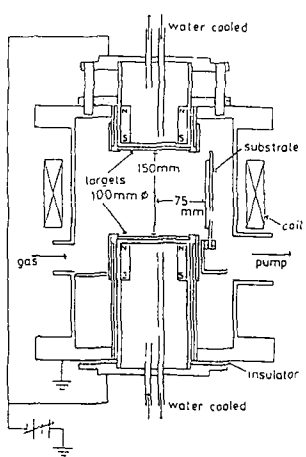


FIG. 1. Schematic diagram of FTS apparatus used in this study.

 0021-8979/88/083636-03$02.40 © 1988 American Institute of Physics

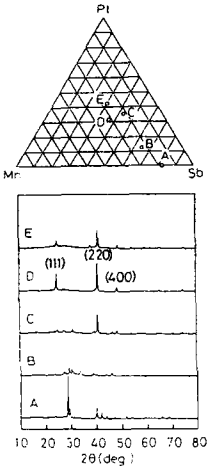


FIG. 2. X-ray diffraction patterns for various compositions: (a) compositional diagram, (b) diffraction pattern.

In this experiment, using the FTS system consisting of two facing targets of different composition (the upper target is pure Mn and the lower is a Pt/Sb mosaic target), it is unavoidable that a compositional change in the sputtered films occurs along the direction normal to the facing target plane. The specimen films were therefore cut at the center of glass substrate for the measurement.

The film composition was determined by EPMA. The crystalline structure of specimen film was determined by x-ray diffraction method with Cu$K\alpha$. Polar Kerr hysteresis loops were measured at normal incidence using a He-Ne laser source (633 nm) under external magnetic field up to 7 kOe. Magnetization of specimen was estimated by a VSM system.

III. RESULTS AND DISCUSSION

A. Crystallographic properties

Figure 2 shows the compositional diagram and the x-ray diffraction patterns of PtMnSb films of five different compositions (A)–(E). The specimen films were prepared under the argon pressure $P_{Ar} = 1.0$ mTorr, deposition rate 250 Å/min, and substrate temperature $T_s = 200$ °C. The thickness of each specimen was 2500 Å. Sample (A), not containing Pt, exhibited Sb and MnSb diffraction peaks, which is expected from the composition of 80 at. % Sb in the Mn-Sb

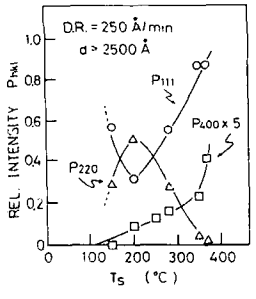


FIG. 3. Dependence of relative peak intensity on substrate temperature (D.R.: deposition rate; d: film thickness).

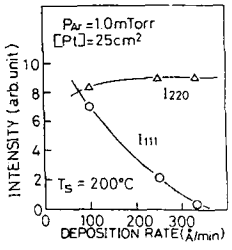


FIG. 4. Diffraction peak intensity as function of deposition rate at argon pressure $P_{Ar} = 1.0$ mTorr (Pt: area of Pt chips).

binary alloy system. With increase of Pt content from sample (A), the diffraction peaks once became weak in sample (B), but with further increase of Pt content, intense diffraction peaks of Clb phase PtMnSb (220) were observed in samples (C)–(E). The compositions of samples (C)–(E) were different from the stoichiometric composition (Pt:Mn:Sb = 1:1:1). It is therefore considered that the compositional range making Clb phase PtMnSb spreads around the stoichiometric composition.

Figure 3 shows the substrate temperature dependence of x-ray diffraction peak intensities for the films prepared at $P_{Ar} = 1.0$ mTorr and deposition rate 250 Å/min. The films prepared with substrate temperatures below 100 °C were amorphous. The crystallization of films prepared by the FTS system was achieved at substrate temperatures above 150 °C, which was higher than with the films prepared by magnetron sputtering.[4] The relative peak intensities P_{hkl} is given by

$$P_{hkl} = I_{hkl}/(I_{111} + I_{220} + I_{311} + I_{400} + I_{331} + I_{422}),$$

where I_{hkl} is the diffraction peak intensities at (hkl) reflection of Clb-PtMnSb. Figure 3 indicates that the orientation of the PtMnSb films was changed by altering substrate temperature and it is the same tendency as with the films prepared by evaporation technique.

Figure 4 shows the change of diffraction peak intensities with the deposition rate at the substrate temperature of 200 °C and the argon pressure $P_{Ar} = 1.0$ mTorr. I_{220} was almost constant with deposition rate but I_{111} decreased with an increase of deposition rate.

ClB-PtMnSb has a cubic symmetry. As sputtered films may have large stress and a lattice strain may be caused by the large stress in sputtered film, the lattice strain in PtMnSb sputtered films was examined. Figure 5 shows the lattice strain of PtMnSb films as the function of the Pt chip area on the Sb target. The lattice strain was given by

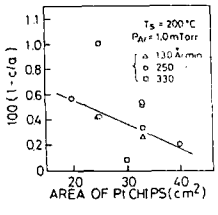


FIG. 5. Lattice strain vs area of Pt chips in PtMnSb films for various deposition rates.

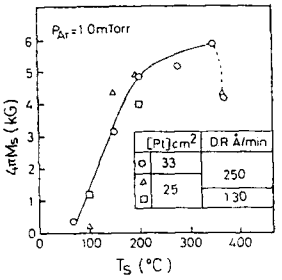


FIG. 6. Change of saturation magnetization with substrate temperature for various areas of Pt chips on Sb and deposition rates (Pt: area of Pt chips; D.R.: deposition rate).

$$c/a = 1/\sqrt{8(d_{220}/d_{111})^2 - 2},$$

where c/a is the ratio of a axis and c axis lattice constants for the tetragonal system, and d_{220} and d_{111} are lattice plane spacings (d spacings) of PtMnSb films which are calculated from the diffraction data. If the lattices of PtMnSb films prepared by the FTS system have no strain, the c/a value should be equal to unity. As it is smaller than 1, the PtMnSb lattices appear to be compressed in the direction of the c axis.

B. Magnetic properties

Figure 6 shows the dependence of the saturation magnetization on the substrate temperature. The saturation magnetization $4\pi M_s$ increased with increasing substrate temperature and had maximum value of 5.8 kG, which is lower than the PtMnSb bulk magnetization of 6.9 kG. The increase of $4\pi M_s$ was caused by the crystallization of Clb–PtMnSb. The crystallization of films was still incomplete because the maximum value of $4\pi M_s$ was lower than that of bulk PtMnSb.

H_c increased from 50 to 120 Oe with increasing substrate temperature (from 100 to 350 °C) when an external magnetic field was applied parallel to the film plane but H_c decreased from 240 to 60 Oe when a magnetic field was applied normal to the film plane.

C. Magneto-optical properties

Figures 7(a) and 7(b) show the dependence of the polar Kerr rotation angle θ_k on substrate temperature for PtMnSb films. The angles were measured from the film side and the substrate side. The Kerr rotation angles increased with an increase of substrate temperature. The maximum value of θ_k on the film side was 1.2° at $T_s = 350$ °C and that on the substrate side was 1.9° at 300 °C.

In these films, the θ_k measured from the film side and substrate side showed different dependencies upon substrate temperature as shown in Fig. 7. Furthermore, the behavior of the saturation magnetization and the polar Kerr rotation angles with substrate temperature was not similar, as is shown in Figs. 6 and 7(a). These differences are probably

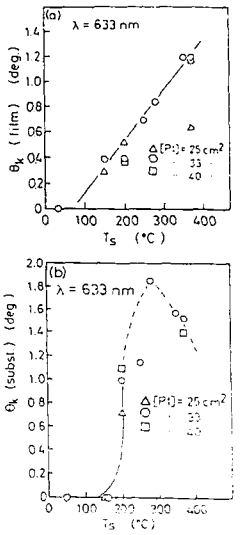


FIG. 7. Dependence of polar Kerr rotation on substrate temperature measured at 633 nm: (a) film side, (b) substrate side (Pt: area of Pt chips).

because the measured specimens may have different magnetic and magneto-optical properties on the film side and the substrate side, which are influenced by crystallographic properties, compositions, and the smoothness of each sides surface.

IV. CONCLUSIONS

PtMnSb Heusler alloy films have been prepared on glass substrates heated between 20 and 350 °C by the facing targets sputtering (FTS) system. Their crystallograhpic, magnetic, and magneto-optical properties were studied. The films with diffraction peaks of Clb-PtMnSb Heusler alloy were obtained at temperatures above 150 °C. The saturation magnetization $4\pi M_s$ increased with increasing substrate temperature and the maximum value of magnetization was 5.8 kG, which is lower than PtMnSb bulk magnetization. Polar Kerr rotation measured with a He-Ne laser was evaluated at 1.9° on the glass side when an external dc magnetic field of 7 kOe was applied in a perpendicular direction.

[1] P. G. van Engen, K. H. J. Bushchow, R. Jongebreur, and M. Erman, Appl. Phys. Lett. **42**, 202 (1983).
[2] R. Ohyama, J. Abe, and K. Matsubara, J. Magn. Soc. Jpn. **9**, 145 (1985).
[3] T. Inukai, M. Matsuoka, and K. Ono, Appl. Phys. Lett. **49**, 52 (1986).
[4] M. Shoji, A. Nagai, N. Murayama, Y. Obi, and H. Fujimori, J. Magn. Soc. Jpn. **10**, 191 (1986).
[5] M. Naoe, S. Yamanaka. and Y. Hoshi, IEEE Trans. Magn. **MAG-16**, 646 (1986).
[6] S. Ashida, T. Yoshida, and K. Akashi, J. Vac. Sci. Technol. A **4**, 2388 (1986).
[7] R. S Robinson and M. Rossnagel, J. Vac. Sci. Technol. **21**, 79 (1982).
[8] O. Auchiello, J. Vac. Sci. Technol. **19**, 841 (1981).

Microstructure of sputtered garnet films for magneto-optical recording media

K. Shono, H. Kano, N. Koshino, and S. Ogawa
Fujitsu Laboratories Ltd., Morinosato-Wakamiya, Atsugi, Kanagawa, Japan

Sputtered garnet films have a high potential for use as a magneto-optical recording medium. However, the medium noise is thought to be large because of its crystal boundaries. We investigated the microstructure of films on GGG substrate, using TEM and SEM. The film crystallized by postannealing shows a rectangular hysteresis loop with high coercivity, and has an uneven surface. This is because the direction and size of each crystallite is not uniform. However, the film crystallized during deposition has quite a smooth surface, but does not have magnetic properties suitable for use in magneto-optical recording. This film has a mosaiclike structure, in which all crystallites are uniformly oriented. We found that ion implantation of Ne^+ and successive annealing of the film crystallized during deposition improved the magnetic properties without roughening the surface.

I. INTRODUCTION

Sputtered garnet film is very promising for use with applications such as magneto-optical recording because of its large magneto-optical figure of merit.[1,2] We have already reported that it has a high C/N value at the Ar laser wavelength (52 dB for a GGG substrate and 45 dB for a glass substrate).[3] Furthermore, we found that recording using a laser diode was possible in spite of the transparency at the laser diode wavelength, if the film was coated with Cr.[4]

However, noise induced by this medium is thought to be much larger than that of amorphous rare-earth transition metals because this material is crystalline. However, no definite relationship has been developed between the medium-induced noise and the crystalline nature of the medium. In addition, there are two methods of preparing a sputtered garnet film on a single-crystal substrate such as GGG. One crystallizes an amorphous film by postannealing. The other makes a crystallized film during deposition.[2] Both films are found to be epitaxially grown, when observed using x-ray diffraction, but there are great differences in surface smoothness and in magnetic properties.

We investigated the microstructures of these films to clarify the source of the medium-induced noise, using a transmission electron microscope (TEM), reflection of high-energy electron diffraction (RHEED) equipment, and a scanning electron microscope (SEM).

II. FILM PREPARATION

Films were prepared on a (111) GGG substrate by rf diode sputtering, using the ceramic target shown in Table I. Films were crystallized during deposition when the substrate temperature was 530 °C (as-deposited crystallized film). Films deposited with the substrate temperature of 350 °C were crystallized by annealing at 700 °C (postannealed film). The film compositions are given in Table I. These results were determined by x-ray microanalysis, presupposing that the sum of cations was 8. The deviation from the target composition is slightly smaller in the as-deposited crystallized film than in the postannealed film.

TABLE I. Target and film composition.

	Composition				
	Bi	Y	Ga	Fe	O
Sputtering target	2.0	1.0	1.0	4.0	12.0
As-deposited crystallized film	1.5	1.3	1.0	4.2	12.0
Postannealed film	1.4	1.2	1.1	4.3	12.0

III. CRYSTALLOGRAPHIC PROPERTIES

The x-ray diffraction pattern showed only a (444) peak of garnet phase in the as-deposited crystallized film. No impurity phase was observed in spite of the large deviation from the stoichiometric value. The lattice mismatch was about 1%. Figure 1 shows the RHEED pattern of the as-deposited crystallized film. The direction of incident electron beam is parallel with $\langle\bar{1}10\rangle$ direction of the substrate. The diffraction pattern is not streaky, but forms clear spots. From this result, we could assume that the film is similar to a single crystal. The results of x-ray diffraction and RHEED for the postannealed film were almost the same.

IV. SURFACE MORPHOLOGY

Figure 2 shows the SEM images of the as-deposited crystallized film and the postannealed film, which are Y axis modulated to amplify any roughness.

The surface of the as-deposited crystallized film is very smooth, although there are some small wrinkles. The surface

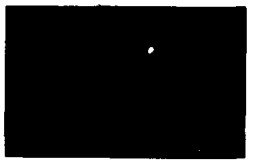


FIG. 1. RHEED pattern of the as-deposited crystallized film.

 0021-8979/88/083639-03$02.40 © 1988 American Institute of Physics

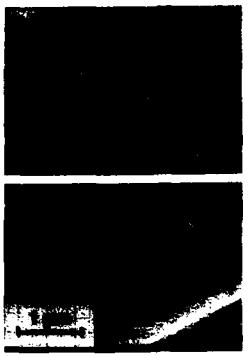


FIG. 2. SEM image of the as-deposited crystallized film (a), and of the postannealed film (b).

of the postannealed film is uneven. It seems that 70-nm particles are dispersed.

Using a precise surface analyzer, we obtained an average surface roughness value of 2 nm for the postannealed film, but the roughness of the as-deposited crystallized film was below the instrument resolution.

V. MICROSTRUCTURE

We analyzed the structure using TEM, removing the substrate, by mechanical polishing and ion milling.

Figure 3 shows the TEM image of the as-deposited crystallized film. The microcrystallites, each about 70 nm long, are arranged in a mosaic structure. The diffraction pattern is quite regular, like that of a single crystal.

The microstructure changes with film thickness in the postannealed film. The same mosaic structure as that in Fig. 3 was observed near the interface with the substrate. As the film becomes thicker, the uniformity in crystallite size becomes worse. Figure 4 shows the TEM images of the inner region and the surface region. The microcrystallites, with average size of 30 nm, are randomly placed in the inner region. However, larger particles, with average size of about 70 nm, are observed in the surface region. It seems that these particles are composed of several crystallites. This corresponds to the result of SEM. From the diffraction patterns, we find that the direction of each crystallite is generally in line in the postannealed film. We think that this change with

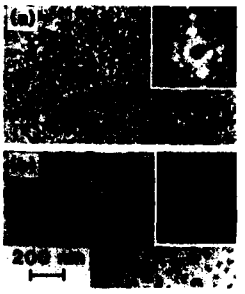


FIG. 4. TEM images of the postannealed film: (a) inner region, (b) surface region.

thickness is caused by random nuclear generation at crystallization. Figure 5 shows the TEM image of the cross section for the as-deposited crystallized film. The columnar structure is observed very clearly, and the width of column almost corresponds with the size of crystallite. We can see dislocations at the interface with the substrate, which may be caused by the lattice mismatch.

The result of cross section for the post-annealed film is the same as Fig. 4(a).

VI. ION IMPLANTATION

Figure 6 shows the Faraday loops of the as-deposited crystallized film and the postannealed film. The as-deposited crystallized film has small coercivity and small squareness ratio, while the postannealed film shows a rectangular loop with high coercivity. The magnetic property of as-deposited crystallized film is not suitable for magneto-optical recording.

We performed ion implantation in the as-deposited crystallized film to improve the magnetic property. Ne^+ was implanted in the 0.25-μm film with 100 keV and 1×10^{15} ions/cm^2. The as-implanted film did not show Faraday rotation because of crystal destruction, but the crystal recovered after annealing at 600 °C. Figure 7 shows the Faraday loop after the annealing. A squareness ratio of 1 and a coercive force of 850 Oe are obtained. We examined the microstructure after the ion implantation and the annealing. No change was recognized in the surface, when compared with the as-deposited crystallized film. However, using TEM we found that the mosaic structure was distorted by ion implantation.

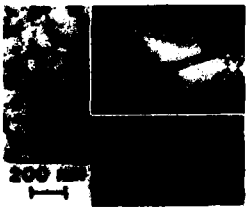


FIG. 3. TEM image of the as-deposited crystallized film.



FIG. 5. Cross-section TEM image of the as-deposited crystallized film.

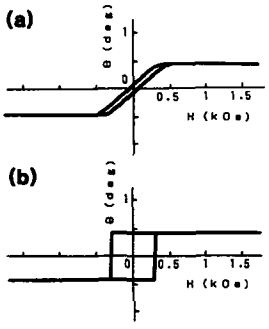


FIG. 6. Faraday loop of the as-deposited crystallized film (a) and of the postannealed film (b).

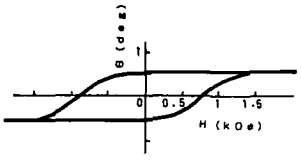


FIG. 7. Improved Faraday loop of the as-deposited crystallized film by ion implantation and successive annealing.

VII. CONCLUSION

The microstructures of sputtered garnet films on GGG substrate were clarified. The film crystallized during deposition is superior in surface smoothness and crystal orientation to the film crystallized by postannealing. Ion implantation improves the magnetic property without roughening the surface. A higher C/N value can be obtained by the combination of crystallization during deposition and ion implantation.

ACKNOWLEDGMENTS

The authors would like to express their sincere thanks to Hanami for the TEM observations, and Yamazaki and Udo for the x-ray microanalysis.

[1] M. Gomi, K. Utsugi, and M. Abe, IEEE Trans. Magn. **MAG-22**, 1233 (1986).
[2] J. P. Krumme, V. Doorman, B. Strocka, and P. Willich, J. Appl. Phys. **60**, 2066 (1986).
[3] H. Kano, S. Shono, N. Koshino, and S. Ogawa, *Digest of the Tenth Annual Conference on Magnetics in Japan* (1986) (in Japanese), p. 32.
[4] K. Shono, H. Kano, N. Koshino, and S. Ogawa, IEEE Trans. Magn. **MAG-23**, 2970 (1987).

Improvement in optical and magnetic properties of Bi-substituted garnet sputtered films for magneto-optical recording

M. Gomi, K. Satoh, and M. Abe
Department of Physical Electronics, Tokyo Institute of Technology, Ookayama, Meguro-ku, Tokyo 152, Japan

We have investigated the effect on the optical and magnetic properties of adding W or Co to Bi-substituted garnet films sputtered on glass substrates. Adding a small amount (< 1.2 at. %) of W makes the film optically homogeneous. It also increases coercivity more than three times, probably due to wall pinning by W atoms. Adding Co reduces coercivity. On the thin film with added W, we have successfully performed a dynamic thermomagnetic writing with a regular bit shape. This promotes development of magneto-optical memory using garnet sputtered film.

I. INTRODUCTION

Sputtered films of Bi-substituted iron garnet on glass substrates are promising media for magneto-optical memory applications.[1–6] For practical use, however, we must overcome the following serious problem inherent in polycrystalline films: Crystal grain boundaries (1) reduce optical homogeneity of the film due to concentration of defects around the boundaries and (2) make recorded domains irregular in shape, causing media noise.[5] Problem (2) becomes more serious when domain wall coercivity is low inside the grains.

We have successfully improved (1) by intentionally making oxygen defects inside the grains[2] or by relaxing segregation of the defects around the boundaries.[3] However, (2) has not yet been improved, which is the subject of this study.

We describe in this paper how the recorded domain shape is improved by adding impurity ions into the film. The improvement is demonstrated by the domain shape recorded dynamically.

II. FILM PREPARATION

The films were prepared on glass substrates (Corning No. 0317) by the following two steps; (a) deposition of amorphous films by rf-diode sputtering in Ar and (b) post-annealing for crystallization at $T_A = 550$–600 °C for 3 h in air. The sputter deposition was performed under these conditions: rf power density $= 8.8$ W/cm^2, deposition rate $= 10$ nm/min, and substrate temperature $T_S = 400$–480 °C. As a target, we used a ceramic disk of composition $Bi_{2.7}Dy_{0.9}Fe_{3.6}Ga_{0.9}O_{12}$, on which metal chips of W or Co were placed at 0–0.13 area % as the additive. The substrate was rotated to get uniformity in film composition and thickness.

III. RESULTS AND DISCUSSION

A. Film composition and quality

Table I gives the chemical compositions of the thin films with W additive which has been measured by induction-coupled plasma (ICP) method. The composition does not appreciably change with the W content. Bismuth is slightly overdosed in these garnet films. X-ray diffraction measurement has shown that these films are of polycrystalline garnet structure having impurity phases of $Bi_2Fe_4O_9$ and/or $Bi_{46}Fe_2O_{72}$, which do not contain W.

Figure 1 compares surface morphology between the films with and without the W additive; adding W improves smoothness in the surface. Furthermore, we have found that adding W makes the film optically homogeneous (the grain boundaries are undiscernible), and makes reproducibility in film preparation good.

Similar results were obtained for the Co additive.

B. Magnetic and magneto-optic properties

All the films had magnetization of ~ 3 emu/cm^3, Curie temperature of 160 °C, and uniaxial magnetic anisotropy K_u (perpendicular to the film plane) of 3×10^4 erg/cm^3, nearly independent of the content of the W or Co additive. However, coercive force strongly changes by adding W or Co as below.

Figure 2 shows typical Faraday hysteresis loops of the films added W (1 at. %) or Co (0.09 area % per target) compared to that of a film with no additive. The squareness of the loop is not changed by the additives. The remanence ratio of all the loops is unity, which is an important factor required for magneto-optical memory media. The coercive force H_c decreases by adding Co, but increases by adding W. Since increasing H_c improves shape of thermomagnetically written bit, we hereafter focus our interest only on the films added with W. Figure 3 shows H_c and Faraday rotation F of the films (~ 0.3 μm thick, $T_A = 580$ °C) plotted as a function of the W content. Here, H_c for the films annealed at 570 °C are also shown for comparison. The H_c increases with increasing W content, reaching about 3.5 kOe at W = 1

TABLE I. Chemical compositions of the films sputtered at $T_S = 480$ °C.

Area of W chips on a target (area %)	Bi (at. %)	Fe (at.%)	Ga (at.%)	Dy (at.%)	W (at.%)
0	34.1	41.5	12.3	12.1	0
0.08	34.0	41.0	12.3	12.0	0.6
0.10	36.2	39.4	11.8	11.6	1.0
0.12	35.4	39.9	11.9	11.7	1.2

 0021-8979/88/083642-03$02.40 © 1988 American Institute of Physics

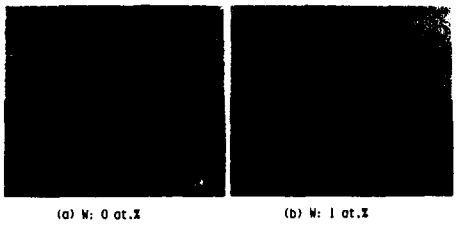


FIG. 1. SEM micrographs of film surfaces.

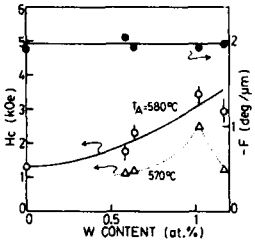


FIG. 3. Coercive force H_c and Faraday rotation F of ~0.3-μm-thick films plotted as a function of W content. The annealing temperature T_A is the parameter.

at. % for the film annealed at 580 °C. The value is three times larger than that (1.3 kOe) in the film without the additive. Since magnetization in garnet films is reversed by wall motion,[7,8] H_c may be increased by increasing W atoms which act as wall pinning sites.

On the other hand, the Faraday rotation is independent of the W content, having a value of 2°/μm. Faraday rotation spectra measured in the wavelength range of 480–800 nm showed no marked change with the W addition, as seen in Fig. 4.

Figure 5 shows temperature dependencies of H_c and F of the films with and without the addition of W. The H_c of the film with added W reduces more rapidly, with elevating temperature, than that without W. This may be a feature of the coercivity caused by wall pinning. The Faraday rotation monotonously decreases with temperature increase, independent of the W content.

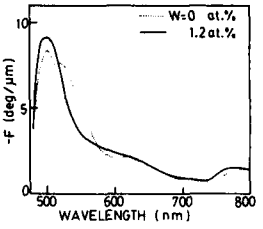


FIG. 4. Faraday rotation spectra of 0.3-μm-thick films.

C. Recording performance

To estimate the effect of W addition on domain shape, we have performed a dynamical thermomagnetic writing. Figure 6 illustrates the bit shape of the thin films (~0.3 μm

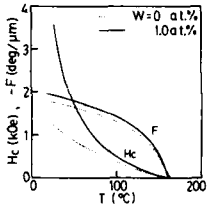


FIG. 5. Temperature dependencies of H_c and F of the films with and without the addition of W.

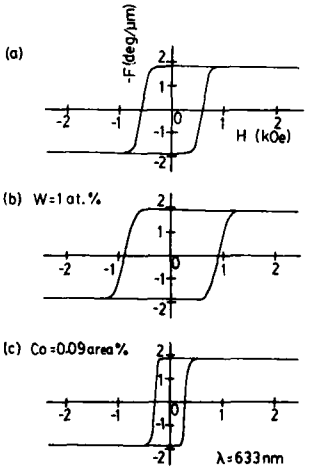


FIG. 2. Typical Faraday hysteresis loops of films at room temperature.

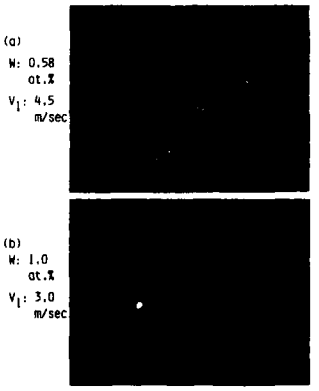


FIG. 6. Dynamically recorded bits in ~0.3-μm-thick garnet films with W content = (a) 0.58 at. % and (b) 1 at. %.

thick) with W content = (a) 0.58 at. % and (b) 1 at. %. Both films were coated with a 0.1-μm-thick Cr reflective layer which works as a heat absorber. The writing experiments were performed using He–Ne laser ($\lambda = 633$ nm, power at film surface = 3.8 mW, spot size = 3 μm) at linear velocity of 3–4.5 m/s and recording frequency of 500 kHz (duty ratio: 50%) under bias field of 50 Oe. The recorded bits are 1×3 μm in size, which are regular in shape for the film (b), while some of them are remarkably diffuse for the film (a). Thus the addition of W effectively improves the regularity in shape of the written bit.

IV. CONCLUSIONS

We have improved the magnetic and optical properties of Bi-substituted garnet thin film by adding a small amount of W less than 1.2 at. %. The addition of W makes the optical quality homogeneous and increases the coercive force up to three times, which prevents the domain shape from being diffused. Using the thin film with W additive, we have successfully performed a dynamic thermomagnetic writing with a regular shape in domains. This promotes development of magneto-optical memory using garnet sputtered film.

ACKNOWLEDGMENTS

The authors would like to thank S. Katayama of Tsukuba Research Laboratory, Nippon Sheet Glass Co., Ltd. for the chemical analysis of the films. This work was partly financed by Grant-in-Aid for Scientific Research from the Ministry of Education, Science, and Culture of Japan.

[1] M. Gomi, T. Tanida, and M. Abe, J. Appl. Phys. **57**, 3888 (1985).
[2] M. Gomi, K. Utsugi, and M. Abe, IEEE Trans. Magn. **MAG-22**, 1233 (1986).
[3] M. Gomi, T. Okazaki, and M. Abe, IEEE Trans. Magn. **MAG-23**, 2967 (1987).
[4] K. Shono, H. Kano, N. Koshino, and S. Ogawa, IEEE Trans. Magn. **MAG-23**, 2970 (1987).
[5] M. Abe and M. Gomi, J. Magn. Soc. Jpn. **11**, Supplement No. S1, 299 (1987).
[6] J.-P. Krumme, V. Doormann, and P. Willich, J. Appl. Phys. **57**, 3885 (1987).
[7] O. Voegeli and F. J. Friedlaender, IEEE Trans. Magn. **MAG-7**, 711 (1971).
[8] W. D. Doyle, G. K. Goldberg, and W. E. Flannery, IEEE Trans. Magn. **MAG-6**, 548 (1970).

Magnetic anisotropy in TbFe thin films prepared at oblique incidence

Sung-Chul Shin and Ashok K. Agarwala
Diversified Technologies Group Research Laboratories, Eastman Kodak Company, Rochester, New York 14650

Effects of the incident vapor-beam orientation on magnetic anisotropy of TbFe thin films were investigated. By coevaporation of Tb and Fe on tilted substrates, the angle of incident vapor beam was made to vary from 0° to 60° with respect to each substrate normal. The magnetic measurements were carried out using a vibrating sample magnetometer and a torque magnetometer in applied fields of 15 and 20 kOe, respectively. Assuming an intrinsic anisotropy with a single easy axis, the easy axis orientation and the intrinsic anisotropy energy were estimated. It was found that perpendicular magnetic anisotropy did not deteriorate until the angle of incidence reached 30°. However, the easy axis became tilted from the film normal for angles of incidence larger than 30°; finally, at an incident angle of 60°, it was in the film plane. A rapid increase in the shape anisotropy energy and a simultaneous decrease in the intrinsic anisotropy energy with the angle of incidence are believed to be causes for the loss of perpendicularity in the film.

I. INTRODUCTION

Amorphous rare-earth (RE) transition-metal (TM) alloy films with perpendicular magnetic anisotropy have attracted wide attention as promising materials for achieving erasable high-density data recording. Perpendicular magnetic anisotropy for magneto-optical recording is essential, because the polar Kerr rotation is utilized in the data reading. Perpendicular magnetic anisotropy of RE-TM alloy films seems to be sensitive to the preparation conditions as well as the composition. In this paper, we report the dependence of magnetic anisotropy on the angle of incidence in amorphous TbFe films prepared by evaporation.

II. EXPERIMENT

Details of the sample preparation technique have been reported elsewhere.[1] Briefly, samples were prepared by thermal coevaporation of Tb and Fe on Kodak Estar base substrates (for magnetic measurements) and Si wafer substrates (for structural studies) in a vacuum system maintained at $\sim 1\times10^{-6}$ Torr during deposition. The oblique incidence was achieved by depositing evaporants on substrates mounted on tilted substrate holders. It should be emphasized that a series of samples with different angles of incident vapor beams was prepared in the same run. Hence, possible variations in preparation conditions between different runs, excepting the angle of incidence, were minimized.

The film compositions were determined by inductively coupled plasma (ICP) atomic emission spectrometry, and the film structures were investigated by θ-2θ x-ray diffractometry and microfractography.

Torque curves were measured by a torque magnetometer in an applied magnetic field of 20 kOe. They were measured in the incident vapor-beam plane, defined by the film normal and the incident vapor-beam orientation. M-H hysteresis loops were measured by a vibrating sample magnetometer, while a magnetic field up to 15 kOe was applied both in the film plane and normal to the film plane.

III. RESULTS AND DISCUSSION

In Table I, we list the characteristic structural and magnetic parameters of the TbFe films in this study. All films in this study showed amorphous phase and had columnar structure, irrespective of the angle of incidence. The growth orientation of columns measured from cross-sectional scanning electron micrographs generally followed the empirical relationship[2] $\tan\beta = 1/2 \tan\alpha$, as reported in Ref. 1. Here, α and β are inclined angles of incident vapor beam and columnar growth orientation from the substrate normal, respectively.

Figure 1 shows torque curves measured in the incident vapor beam plane for TbFe films prepared at different angles of incidence. Here, ϕ denotes the angle that an applied field makes from the film normal as shown in Fig. 2. As seen in Fig. 1, the shape of torque curve is essentially not changed up to a 30° angle of incidence, where the columns are tilted by 15° from the film normal. A noticeable change is seen in the torque curve at $\alpha = 40°$, and the torque curve at $\alpha = 60°$ indicates that the easy axis is placed in the film plane.

To estimate the intrinsic anisotropy energy and the easy axis orientation, torque curves were analyzed by a simple model described as follows. We assume that a film has a

TABLE I. Some structural and magnetic parameters of TbFe films prepared at oblique incidence. Each parameter is denoted as follows: α is the angle of incidence, β is the columnar growth orientation, τ_p is the peak torque value, ϕ_0 is the angle where the torque is zero in the first quadrant of ϕ, and M_s is the saturation magnetization.

Sample code	α (°)	β (°)	τ_p (10^5 dyne cm/cm^3)	ϕ_0 (°)	M_s (emu/cm^3)
TbFe-71	0	0	−6.9	0	127
TbFe-72	20	6	−6.5	10	133
TbFe-73	30	15	−7.2	3	166
TbFe-74	40	23	9.3	78	369
TbFe-75	60	40	31.6	90	702

 0021-8979/88/083645-03$02.40 © 1988 American Institute of Physics

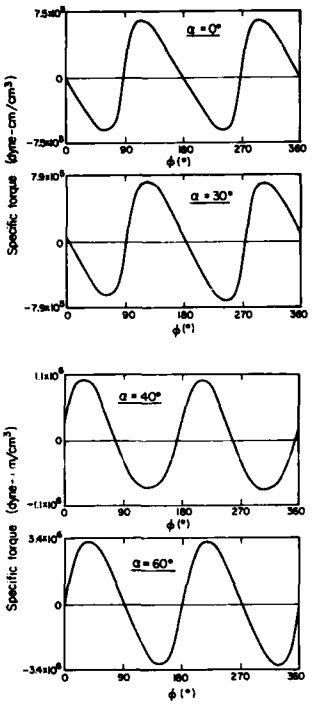


FIG. 1. Torque curves of TbFe films prepared at different angles of incidence.

uniaxial anisotropy with a single easy axis making an angle δ from the film normal (Fig. 2). We consider only the first-order anisotropy energy constant K_u and ignore any higher-order terms. Assuming a continuous film of the bulk magnetization M_s, we consider a shape anisotropy energy K_s of $2\pi M_s^2$ present in the film plane. Then, the total magnetostatic energy E of the system may be expressed by

$$E = K_u \sin^2(\theta - \delta) + K_s \cos^2\theta - M_s H \cos(\phi - \theta), \tag{1}$$

where θ and ϕ indicate the magnetization direction and the direction of applied magnetic field, respectively, measured from the film normal as defined in Fig. 2. Then, the torque τ at equilibrium is given by

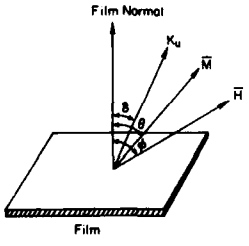


FIG. 2. Illustration of coordinates in the torque magnetometry.

$$\tau = -M_s H \sin(\phi - \theta)$$
$$= K_s \sin 2\theta - K_u \sin 2(\theta - \delta). \tag{2}$$

From Eq. (2), using the peak value τ_p in the measured torque curve and the angle ϕ_0 where the torque is zero, one can derive explicit analytical expressions[3] for K_u and δ as given in Eqs. (3) and (4), respectively:

$$K_u = (K_s^2 + \tau_p^2 \pm 2K_s\tau_p \cos 2\phi_0)^{1/2} \tag{3}$$

$$\delta = \phi_0 - \frac{1}{2}\arctan\left(\frac{K_s \sin 2\phi_0}{K_s \cos 2\phi_0 \pm \tau_p}\right), \tag{4}$$

where the positive sign is taken when $\pi/4 \leqslant \phi_0 \leqslant \pi/2$ and the negative sign is taken when $0 \leqslant \phi_0 < \pi/4$. Then, putting the values of K_u and δ into Eq. (2), the torque curve can be numerically generated. We confirmed that our experimental torque curves matched well to the theoretical ones within 10% accuracy.

The intrinsic anisotropy energy K_u of our TbFe films calculated from Eq. (3) is plotted with respect to the angle of incidence in Fig. 3(a), in conjunction with the shape anisotropy energy K_s. In Fig. 3(b), we plot the easy axis orientation δ estimated from Eq. (4) and the "perpendicularity" defined by a Q value of $K_u \cos\delta/K_s$. As seen in these figures, for incident angles of up to 30° the intrinsic anisotropy energy of the film maintains similar values that average about 8×10^5 erg/cm^3, without much deterioration of the perpendicular magnetic anisotropy. However, for angles of incidence larger than 30°, K_u decreases with the angle of incidence, and the easy axis shifts from the film normal to in

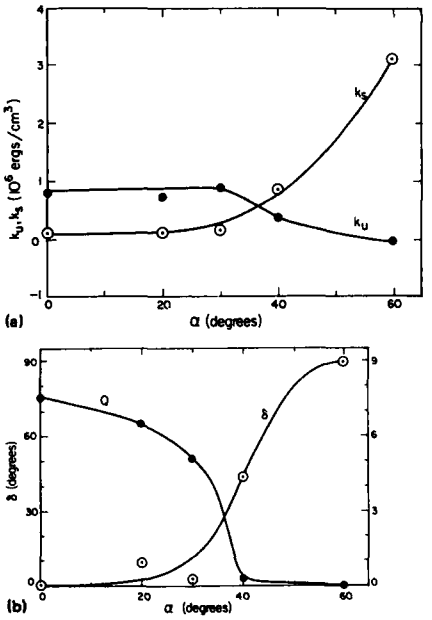


FIG. 3. (a) Dependence of the intrinsic anisotropy energy K_u and the shape anisotropy energy K_s on the angle of incidence. (b) Dependence of the easy axis orientation δ and the perpendicularity Q on the angle of incidence.

plane. In particular, the easy axis is completely in the plane at the incident angle of 60°. Therefore, the easy axis orientation in our obliquely deposited TbFe film is generally not along the incidence beam, in contrast to HoCo system reported by Heiman *et al.*[4]

It is interesting to note that the shape anisotropy energy is drastically increased with the angle of incidence, in particular for angles greater than 30°. We believe that a rapid increase of the shape anisotropy energy with the angle of incidence is mainly ascribed to a change of the "effective" Tb concentration, presumably due to a preferential oxidation of Tb. (We define the "effective" Tb concentration as the amount of Tb which is magnetically active.) As reported in Ref. 1, the density of a TbFe film decreases with increasing angle of incidence, which indicates that more voids are expected to exist in a film deposited at a higher angle of incidence. For instance, the density of a TbFe film prepared at $\alpha = 60°$ was 15% smaller than that prepared at $\alpha = 0°$. Therefore, the amount of Tb oxidation becomes enhanced for a higher angle of incidence. Considering the fact that the magnetization of TbFe film rapidly increases as Tb concentration departs from the compensation composition,[5] an increase in the shape anisotropy energy with increasing angle of incidence is not unexpected.

There has been much controversy on the contribution of the internal stress of TbFe film to the intrinsic anisotropy. Kobayashi *et al.*[6] and van Dover *et al.*[7] have observed that the magnetostrictive energy due to the stress was negligible in their films, while Takagi *et al.*[8] have reported a predominant role of the stress in the perpendicular magnetic anisotropy. Our films showed tensile stress of about 1×10^8 dyne/cm^2, relatively independent of the incident angle. The magnetostrictive energy K_m due to the stress is given by $K_m = -3\lambda\sigma/2$,[8] where λ is the magnetostrictive coefficient and σ is the stress in a film. Taking the value of $\lambda \approx 5\times10^{-5}$ at $Tb_{23}Fe_{77}$ from Ref. 9, the magnetostrictive energy of our films is estimated by 7.5×10^3 ergs/cm^3. Therefore, the stress contribution to the magnetic anisotropy in our films is thought to be less than 5%.

IV. CONCLUSIONS

We have studied the effects of the incident vapor-beam angle on magnetic anisotropy of TbFe thin films. Perpendicular magnetic anisotropy was not destroyed until the angle of incidence α was tilted about 30° from the substrate normal. However, the easy axis became shifted from the film normal for α larger than 30° and, finally, the film prepared at $\alpha = 60°$ had completely in-plane anisotropy. A rapid increase of the shape anisotropy and a simultaneous decrease of the intrinsic anisotropy with the angle of incidence are believed to be the causes for a loss of the perpendicularity in the film.

ACKNOWLEDGMENTS

We are grateful to D. Bono and M. Regelsberger for their measurements of torque and vibrating sample magnetometers.

[1] S. C. Shin, J. Appl. Phys. **61**, 3340 (1987).
[2] A. G. Dirks and H. J. Leamy, Thin Solid Films **47**, 219 (1977).
[3] Details will be reported elsewhere.
[4] N. Heiman, A. Onton, D. F. Kyser, K. Lee, and C. R. Guarnieri, AIP Conf. Proc. **24**, 573 (1975).
[5] Y. Mimura and N. Imamura, Appl. Phys. Lett. **28**, 746 (1976).
[6] H. Kobayashi, T. Ono, and A. Tsushima, Appl. Phys. Lett. **43**, 389 (1983).
[7] R. B. van Dover, M. Hong, E. M. Gyorgy, J. F. Dillon, Jr., and S. D. Albiston, J. Appl. Phys. **57**, 3897 (1985).
[8] H. Takagi, S. Tsunashima, and S. Uchiyama, J. Appl. Phys. **50**, 1642 (1979).
[9] D. W. Forester, C. Vittoria, J. Schelleng, and P. Lubitz, J. Appl. Phys. **49**, 1966 (1978).

Materials for magneto-optic data storage (invited) (abstract)

Alan E. Bell
IBM Research Division, Almaden Research Center, 650 Harry Road, San Jose, California 95120

The optimization of magneto-optic media for data storage applications involves a detailed consideration of the impact of material properties on the overall performance and reliability characteristics of the complete media design, which includes both the active layer structure and the substrate material. Currently, the most highly developed materials for the active layer are the amorphous rare earth-transition metal (RE-TM) alloys. The RE-TM composition determines both the Curie temperature and the compensation temperature, both of which parameters affect the sensitivity, and therefore the data rate which can be achieved using currently available diode lasers. The thermal and optical characteristics of the active layer thin-film structure affect the sensitivity, and also determine the degree of enhancement of the shot-noise-limited SNR during playback. Reliability of magneto-optic media is affected by uniform surface oxidation of RE-TM alloys, which leads to reduced Kerr rotation through the formation of an absorptive surface layer with only in-plane anisotropy. The proper choice of dielectric passivation layers and deposition process can significantly limit this and other degradation mechanisms. The choice of substrate material must be compatible with the coating process for the active layer structure, provide a stable mechanical interface to the drive mechanisms, and also possess good optical properties, most notably low birefringence. This talk will review the current directions in materials research on magneto-optic media, and relate the physical characteristics of the materials involved to the major requirements of the data storage application.

 0021-8979/88/083648-01$02.40 © 1988 American Institute of Physics



Long-range magnetic reconstruction of ferromagnetic films with diffused interfaces

J. R. Cullen and K. B. Hathaway
Naval Surface Warfare Center, Silver Spring, Maryland 20910

J. M. D. Coey
Physics Department, Trinity College, Dublin, 2, Ireland

Two models of the magnetic structure of a ferromagnetic film deposited on a substrate are developed, with a view to explaining the reduced moment of Fe on GaAs. In the first, spin canting induced by antiferromagnetic exchange in the interface layer falls off rapidly in the interior of the ferromagnet, the characteristic distance being the size of the reconstructed magnetic unit cell in the interface. In the second, random anisotropy in the interface layer induces weakly pinned fluctuations of the magnetization which penetrate to a distance of order the domain wall width, approximately 100 Å.

I. INTRODUCTION

It has been recently demonstrated that bcc Fe and Co can be grown epitaxially on GaAs substrates.[1,2] The magnetic properties of the resulting single-crystal films have been studied as a function of film thickness. In the particular case of Fe it was found that there is an anomalous decrease in the magnetization with decreasing film thickness.[3] The original FMR measurements inferring the magnetization decrease were confirmed by magnetometry results.[4] Further, the dependence of magnetization on thickness is found to deviate significantly from inverse proportionality: this observation can be explained by a spatially varying magnetization in the bulk of the Fe films. Other evidence for a magnetization decrease near the film-substrate interface comes from a comparison of the measured surface spin waves with a theory which includes spatial variation in the magnetic parameters.[5] A penetration depth for the magnetization defect of 50 Å was inferred from the data.

These variations in the magnetic parameters of films grown on nonmagnetic substrates are certainly due to the interaction of the substrate atoms with those of the magnetic film. It had earlier been suggested that lattice mismatch and consequent stress relief was the mechanism. Estimates of the change in magnetization due to strain prove this not to be so.[6] Two more promising mechanisms come from the exchange and anisotropy fluctuations experienced by Fe atoms in the interfacial layers due to bonding with interdiffused As atoms. Analysis of core level shifts in photoemission spectra of this interface indicates that actual interdiffusion occurs over at most 5–10 Å, significantly less than the distance over which the magnetization is reduced. In the present work we consider first the implications of a surface antiferromagnetic coupling on the magnetic properties of a model ferromagnetic material. We find that, if the interface layers are modeled as an ordered Fe-As compound with antiferromagnetic coupling, there is a magnetic surface reconstruction, leading to a reduced magnetization. This reduction, however, essentially disappears in the first one or two layers of the bulk ferromagnet. This does not agree with the penetration depths inferred from experiment. The result is not altered dramatically when exchange fluctuations in the surface layer are taken into account.

We then augment the model by subjecting surface spins to uniaxial anisotropy whose axes are randomly distributed on the surface. We show that the resulting magnetization reduction extends deeply into the bulk; in the simplest form of this model the penetration length, κ^{-1}, is proportional to (Ja^2/K) where J is the ferromagnetic coupling strength, K is the bulk anisotropy and a is the lattice parameter. We estimate this quantity to be 100 Å for bcc Fe, which is in good agreement with penetration depths obtained experimentally. We conclude that magnetic surface reconstruction due to anisotropy of a random kind offers a simple, plausible explanation of the observations of spatial variation of magnetic properties of Fe films grown on GaAs.

In the next section we describe the model and its consequences, including a comparison of the results for average magnetization versus thickness with existing experimental results. We discuss the implication of the theory for other types of interfaces in the last section.

II. MAGNETIC SURFACE RECONSTRUCTION

We consider semi-infinite bcc Fe with a (110) surface layer consisting of randomly distributed As atoms substituting on Fe sites. The problem of ordered surface arrays with competing ferromagnetic and antiferromagnetic coupling has been treated in several papers.[6] To set the stage, and motivate our extension to randomly distributed couplings, we first calculate the magnetization of an ordered bcc structure, consisting of a set of Heisenberg spins with nearest-neighbor coupling J between (110) layers and within each (100) layer except the first. In the first (surface) layer half the Fe atoms are replaced by As atoms so that two two-dimensional sublattices, one Fe and one As are formed (see Fig. 1). Those Fe atoms connected by 180° As bonds are taken to be coupled antiferromagnetically with a strength

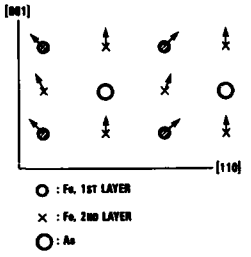


FIG. 1. A picture of the model (110) interface showing the Fe and As positions. As is assumed to have replaced the body-centered Fe atoms on the first layer only. The directions of the a- and b-sublattice spins are shown schematically.

J_a. All other bonds in the first layer are taken as zero. (There are no other nearest-neighbor bonds.) The spins are assumed to lie in the (110) plane. The Hamiltonian is

$$H = J_a \sum_{i,j} \cos(\theta_{i,1} - \theta_{j,1}) - J \sum_{ijll'} (1 - \delta_{l,1}\delta_{l',1}) \cos(\theta_{il} - \theta_{jl'}) + H_b. \quad (1)$$

The sums are over near neighbors. i and j refer to sites in the plane, whereas l distinguishes planes. δ is Kronecker's delta symbol. H_b is the crystalline anisotropy energy. We first solve for the $\theta_{i,l}$ in the mean-field approximation, allowing for a spin-canted solution:

$$\Theta_{i,l} = \Theta_i \text{ if } i \text{ refers to an "}a\text{" site}$$

and

$$\Theta_{i,l} = -\Theta_i \text{ if } i \text{ refers to a "}b\text{" site.} \quad (2)$$

We choose the sign of the single-ion anisotropy such that [001] is easy, and θ is measured with respect to this direction. As shown in Fig. 2, the ferromagnetic state is lowest in energy for $Ja/J < 0.173$; for larger values of this ratio, there is a canting of the spins. However, the canting practically disappears for $l > 3$. In fact, for the general case of surface spin reconstruction the canting angle falls off as $\exp(-z/b)$ where b is the length of the magnetic unit cell which forms on the surface. It is highly unlikely that regular arrays of As and Fe atoms will form with spacings larger than a few angstroms.

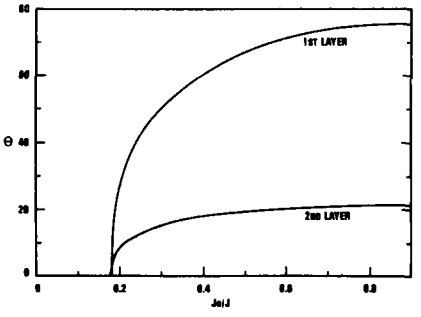


FIG. 2. Results of the mean field calculation for the canting angles in the first two layers as a function of the ratio of anti-to-ferromagnetic coupling. The third layer angle is practically zero. Angles are with respect to [100].

We modeled the more probable case of random arrangements by allowing fluctuation in J_a and J and studied the resulting changes in the $\Theta_{i,l}$. The conclusion as to the disappearance of the canting angle as a function of distance from the interface remains virtually unchanged. It was with this as a background that we were led to consider another consequence of random distributions of As atoms, namely random axial anisotropy.

III. RANDOM SURFACE ANISOTROPY

The surface anisotropy contribution to the Hamiltonian can be written as

$$H_a = -D \sum_i \cos^2(\Theta_{i,1} - \phi_i), \quad (3)$$

where ϕ_i is a random function of the site indices. The J's are assumed to be constants. We look for solutions to the equations

$$\frac{\partial H}{\partial \Theta_i} = 0.$$

For the sake of brevity, we describe the effect of the random anisotropy on the ferromagnetic order, i.e., $Ja/J < 0.173$. The important results are essentially the same but require lengthier description in the spin canted state. We look for solutions for which the differences $\Theta_i - \Theta_j$, where i and j are near-neighbor sites, are small. (The Θ_i themselves are not necessarily small.) In the interior, Eq. (3) becomes, in the continuum approximation,

$$\nabla^2\Theta(x,y,z) = 4K/Ja^2(-\cos^3\Theta\sin\Theta + \tfrac{1}{2}\sin^3\Theta\cos\Theta), \quad (4)$$

where K is the strength of the bulk fourth-order anisotropy. In the surface layer Eq. (3) takes a more complex form, reflecting both the presence of the random anisotropy and the existence of the interface itself. The important terms which remain after using equations (3) and (4) give rise to a boundary condition on Θ:

$$\frac{\partial\Theta}{\partial z}(x,y,0) = (D/Ja)\sin[2\Theta(x,y,0) - (\Phi(x,y)], \quad (5)$$

where Φ is a random function of x and y. (The z axis is perpendicular to the surface, with z increasing in the Fe interior.) This fact will make Θ a random variable as well; however, the scale over which Φ is correlated is much smaller than that over which Θ correlations exist. For this reason the right-hand side of Eq. (5) may be regarded as a known function of Φ whose average over all possible values of Φ is zero. The problem of finding the rms value of Θ, $\overline{\Theta^2}$, as a function of z is manageable deep in the interior where θ can be treated as small. We find

$$\overline{\Theta^2}(z) = \lambda[-Ei(-2\kappa z) + Ei(-2k_0 z)], \quad (6)$$

where $-Ei(-x) \equiv \int_x^\infty (dy/y)e^{-y}$, κ is the reciprocal of the familiar domain-wall width, and

$$\lambda = (D/J)^2$$

while k_0 is a wave-number cutoff of the order of a^{-1} which accounts for the neglect of the second derivative term in the

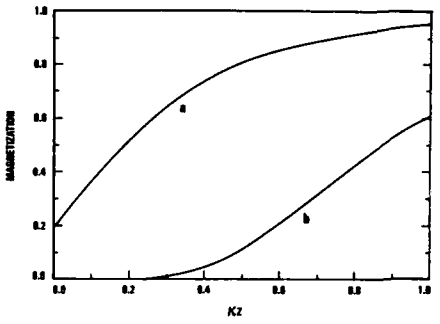


FIG. 3. The magnetization relative to the bulk as a function of the dimensionless variable κz. Two cases, (a) one for weak and (b) one for strong random surface anisotropy, are indicated.

boundary condition, Eq. (5). The magnetization can be obtained from $\overline{\Theta^2}$ by exponentiation:

$$M(z)/M_0 = \exp - (\overline{\Theta^2}/4) .$$

Curves of $M(z)$ for two values of λ are plotted in Fig. 3. For large z we obtain

$$M(z)/M_0 = 1 - (\pi\lambda/\kappa z)\exp(-\kappa z),$$

which shows that the penetration depth for the reconstruction is equal to that of the domain wall width, approximately 100 Å for Fe. To compare the theory with experiment, we calculate

$$\bar{M}(L) = L^{-1}\int_0^L M(z)\,dz,$$

where L is the film thickness.

Comparing our $M(L)$ vs $1/L$ results for large L with "thick" (1000–4800 Å) film experiments, we find the "coherence length" $\lambda\kappa^{-1}$ to be in the range 100–200 Å; the uncertainty is due to the variation in the different sets of data available to us. The main point we wish to emphasize is that this range is well beyond the 5–10-Å interfacial diffusion lengths obtained from photoemission spectra.

IV. CONCLUSIONS

The model of random surface anisotropy introduced here gives a satisfactory explanation of the magnetic properties of the GaAs/Fe (110) interface, in particular, the variation of the magnetization as a function of film thickness. More generally, we expect the mixing of substrate and ferromagnetic atoms at an interface to have a nonlocal effect on magnetic properties whenever such mixing produces anisotropic spin coupling.

[1]G. A. Prinz and J. J. Krebs, Appl. Phys. Lett. **39**, 397 (1981).
[2]G. A. Prinz, Phys. Rev. Lett. **54**, 1051 (1985).
[3]C. Vittoria, F. J. Rachford, J. J. Krebs, and G. A. Prinz, Phys. Rev. B **30**, 3903 (1984).
[4]T. R. McGuire, J. J. Krebs, and G. A. Prinz, J. Appl. Phys. **55**, 2505 (1984).
[5]M. W. Ruckman, J. J. Joyce, and J. H. Weaver, Phy. Rev. B **33**, 7029 (1986).
[6]K. B. Hathaway, H. J. F. Jansen, and A. J. Freeman, Phys. Rev. B **31**, 7603 (1985).
[7]See, for example, C. Demangeat and D. L. Mills, Phys. Rev. B **14**, 4997 (1976) and references therein.

Monolayer ferromagnetism of Fe(110) on W(110) studied by Mössbauer spectroscopy

M. Przybylski[a] and U. Gradmann
Physikalisches Institut, Technische Universität Clausthal, D-3392 Clausthal-Zellerfeld, Federal Republic of Germany

Fe(110) films in the monolayer regime were prepared at 300 K in UHV on W(110). Pseudomorphic structure and layer-by-layer growth were established using LEED, AES, and conversion electron Mössbauer spectroscopy (CEMS). For the pseudomorphic monolayer, ferromagnetic order was established using CEMS below a monolayer Curie temperature $T_C(1) = (210 \pm 10)$ K $= 0.20 T_C(\infty)$ for a free monolayer and $T_C(1) = (296 \pm 1)$ K $= 0.28 T_C(\infty)$ for a Ag-coated monolayer, respectively. Magnetic hyperfine fields $B_{hf}(T)$ could be measured for $T > 90$ K. Ground-state values could be determined by extrapolation to $B_{hf}(0) = (10 \pm 1)$ T for the free and $B_{hf}(0) = (11.9 \pm 0.3)$ T for the Ag-coated monolayer, respectively. A critical region $270 < T < 300$ K was analyzed to some detail for the Ag-coated monolayer. In this region, the CEMS spectrum contains a magnetic and a nonmagnetic component. Transition to the paramagnetic phase occurs by transition of intensity from the magnetic to the nonmagnetic line, whereas B_{hf} of the magnetic component remains finite with approach to T_C. Beyond the true monolayer, double layer and monolayer components can be distinguished in the CEMS spectra.

I. INTRODUCTION

The problem of ferromagnetic order in a monolayer was raised by Bloch,[1] who stated its absence for an isotropic Heisenberg model. However, it became clear through the work of Döring[2] how magnetic order can be triggered by magnetic anisotropies. As strong, surface-type anisotropies are working in the monolayer regime,[3] it was reasonable that monolayer ferromagnetism could be established then for the case of monolayers of NiFe and of Co, both in Cu(111) matrices,[4] with Curie temperatures of 0.2 and 0.3 times the bulk value, respectively. Recent interest in the ferromagnetic monolayer was raised by strong general interest in two-dimensional ordering phenomena near surfaces, by extended band calculations of ultrathin films in the ground state,[5] by theoretical work on the role of shape anisotropy in monolayer magnetism[6] and by recent experimental detection of monolayer ferromagnetism for fcc Co and fcc γ-Fe, using spin-polarized photoemission.[7,8] Strong indications on monolayer ferromagnetism in Gd on W(110), with a surprisingly high Curie temperature, only slightly below that of bulk material, have been obtained recently using electron spin resonance.[9]

For the case of bcc α-Fe, ferromagnetic order at room temperature was reported recently for a Fe(110) monolayer on W(110), using spin-polarized photoelectrons.[10] It is just this case of Fe, for which Mössbauer spectroscopy provides a unique tool of microscopic, local analysis of magnetic order. New insight in the nature of two-dimensional ordering phenomena seemed to be expected from its application to the analysis of magnetic order in Fe monolayers. We therefore recently performed an experimental study of magnetism in a Fe(110) monolayer on W(110),[11] using conversion electron Mössbauer spectroscopy (CEMS) in UHV,[12,13] which we report in the present paper.

[a] Permanent address: Department of Solid State Physics, Academy of Mining and Metallurgy, Krakow.

II. EXPERIMENTAL METHOD

Experiments were performed in a UHV system,[12,13] equipped for molecular beam epitaxy, LEED, AES, and magnetic analysis *in situ* by CEMS for $T > 90$ K. Pure Fe-57(110) films were prepared at $T_P = 300$ K on clean W(110) surfaces. Film thickness was measured using a quartz crystal monitor with an accuracy on 4% of one monolayer. In agreement with previous work,[14] the first two monolayers were pseudomorphic on W(110), thus containing each the material of 0.82 monolayers of bulk Fe(110) ($a_{Fe} = 2.866$ Å, $a_W = 3.165$ Å, $f_{FeW} = -9.4\%$). For the following analysis, it is crucial to know whether the first monolayer is completed before the second one starts to grow. It has been shown recently by CEMS (Ref. 15) that this ideal layer-by-layer growth mode is realized for Fe(110) on W(110) at the present preparation temperature $T_P = 300$ K, for $D < 3$. Both Ag-coated and free films of pure Fe-57 on W(110) were prepared for CEMS analysis. Samples were characterized by the following notation: W(110)/D/Ag and W(110)/D/ – represent pure Fe-57 films on W(110), containing the material of D bulk monolayers, coated by Ag, or with free surface, respectively. Because of pseudomorphism, the true monolayer is given by W(110)/0.82/Ag or W(110)/0.82/ –, respectively.

III. THE Ag-COATED MONOLAYER

Extended measurements between 90 and 400 K were performed with the Ag-coated monolayer, W(110)/0.82/Ag, which is stable with respect to residual gas adsorptions. For $T < 263$ K, magnetic Mössbauer spectra were measured, which could be fitted with one single Zeeman sextet, with relative intensities of the six lines very near that to be expected for the given geometry. For $T > 300$ K, a nonmagnetic single line was observed. In a critical region $270 < T < 300$ K,

 0021-8979/88/083652-03$02.40 © 1988 American Institute of Physics

the spectra were more complicated. They could be fitted by the superposition of one magnetic sixline component and one nonmagnetic single line. In Fig. 1, we show, versus temperature, the magnetic hyperfine field B_{hf} of the magnetic component (○), the relative contribution of the single line (×), and B_{hf}, the mean hyperfine field of the sample (●). Ferromagnetism disappears at a well-defined critical temperature $T_C(1) = (296 \pm 1)$ K $= 0.28 T_C(\infty)$, in qualitative agreement with an estimate from a high-temperature series expansion[16] which predicts $T_C(1) = 0.46\, T_C(\infty)$ for $S = 2$, and with the experience from 48Ni/52Fe(111) in Cu(111), $T_C(1) = 0.21 T_C(\infty)$, and Co in Cu(111), $T_C(1) = 0.30 T_C(\infty)$.[4] A remarkable good coincidence appears with simple mean field arguments,[17] which tells us that T_C should be proportional to the number of nearest neighbors, resulting in $T_C(1) = 0.50 T_C(\infty)$.

It is now generally accepted that the dependence of B_{hf} on temperature reflects that of spontaneous magnetization J_s. Surprisingly, we observe roughly the same dependence as in bulk material. Extrapolation to $T = 0$ K is problematic. A tentative $T^{3/2}$ extrapolation, in the spirit of that bulklike gross behavior, is used in Fig. 1. Considering for this uncertain extrapolation, we take $B_{hf}(0) = (11.9 \pm 0.3)$ T as a reliable result for the Ag-coated monolayer. A most interesting result concerns the microscopic behavior of the phase transition, which apparently can be only analyzed by the present method: Phase transition to the paramagnetic state takes place not by disappearance of B_{hf}, which contrarily remains finite with approach to $T_C(1)$, but by a transition of intensity from the magnetic sextet to the nonmagnetic single line. This might be connected with a nucleation from surface steps.[11] In our opinion, a superparamagnetic interpretation of the transition is improbable. Magnetometric measurements for final decision are in preparation.

Some experiments were done for films a little bit thicker than the pseudomorphic monolayer, $D > 0.82$. For $0.82 < D < 1.64$, a sample contains monolayer and double layer patches. The microscopic, local character of CEMS allows to see them separately, as can be seen in Fig. 2 for the

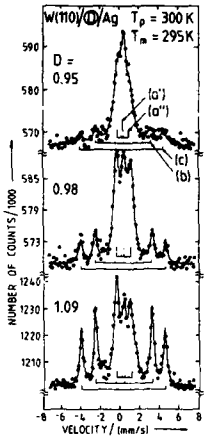


FIG. 2. CEMS spectra, taken at room temperature, for Ag-coated samples W(110)/D/Ag just above the monolayer ($D = 0.95, 0.98, 1.09$, respectively). Components (a), (b), and (c) represent monolayer patches, W and Ag side of double-layer patches, respectively. (a) contains a nonmagnetic and a magnetic subcomponent, (a') and (a''), respectively.

room-temperature spectra for $D = 0.95$, 0.98, and 1.09. Spectra are composed of the nonmagnetic and magnetic monolayer components (a') and (a''), respectively, known from the critical region of the true monolayer, and double-layer components (b) and (c), belonging to the W and Ag side of the double layer, respectively. Magnetic hyperfine fields B_{hf}, and relative contributions p of the components are shown in Fig. 3, as a function of D. Predictions of a layer-by-layer growth model for $P_a = P_{a'} + P_{a''}$ are given for comparison. Excellent agreement is observed. Further, p_b equals p_c, as expected. Note the weak dependence of $B_{hf,a''}$, the magnetic hyperfine field of the magnetic monolayer component (a''), on D. Apparently, the presence of double-layer patches influences the distribution only on subcomponents (a') and (a''), not the magnitude of $B_{hf,a''}$. Preliminary experiments indicate that also the Curie temperature of the monolayer component depends only weakly on D.

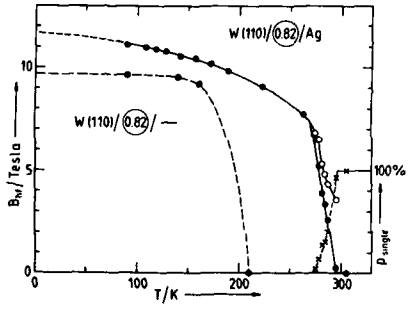


FIG. 1. Magnetic hyperfine fields in Fe(110) monolayers on W(110), as a function of temperature T. Hyperfine field B_{hf} of the magnetic component (○), mean hyperfine field B_{hf} (●), and relative contribution p_{single} of the single line (×), all for the Ag-coated monolayer, W(110)/0.82/Ag. For the case of the uncoated monolayer, W(110)/0.82/—, B_{hf} (⊗) is given for three temperatures, from Fig. 4, below, and $T_C(1)$ from thermal scanning.

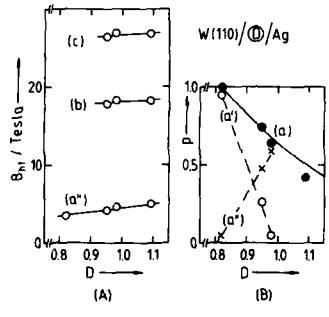


FIG. 3. Parameters of room-temperature spectra for Ag-coated samples W(110)/D/Ag, just above the monolayer, $D > 0.82$. (a) Hyperfine fields B_{hf} vs D, for the magnetic monolayer component (a'') and for two components, of the double layer, (b) and (c), respectively. (b) Relative contributions p of the monolayer (a) and of its nonmagnetic (a') and magnetic (a'') subcomponent, respectively. For $P_a = P_{a'} + P_{a''}$, model prediction are given for comparison (full line). Dotted lines to guide the eye for $P_{a'}$, $P_{a''}$.

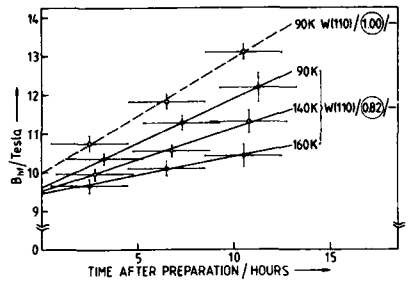


FIG. 4. Evolution of B_{hf} with time after preparation, for the uncoated monolayer, W(110)/0.82/ − , at $T = 90$, 140, and 160 K, respectively. Data for the monolayer component in a sample W(110)/1.00/ − , at $T = 90$ K, are given for comparison.

IV. THE UNCOATED MONOLAYER

Because of residual gas adsorption, the analysis of the free monolayer had to be done in a more complicated manner, which has been developed previously[12] for the free surface of thick Fe(110) films. As shown in Fig. 4, the evolution of B_{hf} with time after preparation was observed and its value for the free surface was determined by extrapolation. Results are included in Fig. 1. One special monolayer had to be prepared for each temperature. Only three of these time-consuming experiments were performed for the true monolayer. In addition, $T_C(1) = 210$ K was determined using thermal scanning at $v = \pm 0.15$ mm/s.[11] Again, this Curie temperature of the monolayer component seems to depend only weekly on coexisting double layer patches in samples with $D > 0.82$: A sample W(110)/1.00/ − , which is shown in Fig. 4 for comparison, showed a value of T_C which was only slightly shifted to 214 K. Results for the ground state, a rough estimate only is possible of $B_{hf}(0) = (10 \pm 1)$ T.

The question remains why Kurzawa *et al.*[10] reported ferromagnetism at room temperature for the free Fe(110) monolayer on W(110), in apparent contradiction to our results. We suppose the following answer: Their statement applies to a film of "(2.0 ± 0.2) Å." 2.2 Å equals $D = 1.1$, corresponding to 1.34 pseudomorphic layers, roughly the situation of the lowest spectrum in Fig. 2; half of the atoms in such a sample are included in double-layer patches, which, of course, are ferromagnetic at room temperature.

V. CONCLUSIONS

The unique possibilities of the Fe(110) monolayers on W(110) for the analysis of monolayer ferromagnetism are given first by its two-dimensional translational symmetry (pseudomorphism) and secondly by the applicability of Mössbauer spectroscopy, which enabled this work. However, a full experimental analysis should include the application of other methods like magnetometry and spin polarized electron diffraction, which are in preparation.

ACKNOWLEDGMENT

This work was supported by the Stiftung Volkswagenwerk.

[1] F. Bloch, Z. Phys. **49**, 619 (1928).
[2] W. Döring, Z. Phys. **16a**, 1008 (1961).
[3] U. Gradmann, J. Magn. Magn. Mater. **54-57**, 733 (1986).
[4] U. Gradmann, Appl. Phys. **3**, 161 (1974).
[5] C. L. Fu, A. J. Freeman, and T. Oguchi, Phys. Rev. Lett. **54**, 2700 (1985).
[6] Y. Yafet, J. Kwo, and E. M. Gyorgy, Phys. Rev. B **33**, 6519 (1986).
[7] D. Pescia, G. Zampieri, M. Stampanoni, G. L. Bona, R. F. Willis, and F. Meier, Phys. Rev. Lett. **58**, 933 (1987).
[8] D. Pescia, M. Stampanoni, G. L. Bona, A. Vaterlaus, R. F. Willis, and F. Meier, Phys. Rev. Lett. **58**, 2126 (1987).
[9] M. Farle and K. Baberschke, Phys. Rev. Lett. **58**, 511 (1987).
[10] R. Kurzawa, K. P. Kämper, W. Schmitt, and G. Güntherodt, Solid State Commun. **60**, 777 (1986).
[11] M. Przybylski and U. Gradmann, Phys. Rev. Lett. **59**, 1152 (1987).
[12] J. Korecki and U. Gradmann, Phys. Rev. Lett. **55**, 2491 (1985).
[13] J. Korecki and U. Gradmann, Hyperfine Interactions **28**, 931 (1986).
[14] U. Gradmann and G. Waller, Surf. Sci. **116**, 539 (1982).
[15] M. Przybylski and U. Gradmann, Surf. Sci. (to be published).
[16] H. E. Stanley and F. A. Kaplan, Phys. Rev. Lett. **17**, 913 (1966).
[17] I. Valenta, Phys. Status Solidi **2**, 112 (1962).

Structural and magnetic properties of Au/Pd/Au sandwiches: A total energy all-electron approach

Soon C. Hong and C. L. Fu
Physics Department, Northwestern University, Evanston, Illinois 60201
A. J. Freeman
Physics Department, Northwestern University, Evanston, Illinois 60201
and Materials Science Division, Argonne National Laboratory, Argonne, Illinois 60439

The possibility of magnetism induced in Pd when sandwiched between Au layers, first proposed and studied experimentally by Brodsky and Freeman, is investigated by means of highly precise all-electron total energy local spin-density calculations employing the thin-film full-potential linearized augmented plane wave (FLAPW) method. Total energy local density calculations are employed on a Au/Pd/Au sandwich with three Pd layers to obtain the structural properties and five Pd layers to obtain the magnetic properties of an Au/Pd/Au sandwich. Detailed results are obtained with spin polarized calculations for the Pd lattice constant stretched taking into account (i) the misfit between the lattice constants of Au and Pd and (ii) proximity effects in a self-consistent way. The magnetic moment of the center Pd layer is found to be $0.02\mu_B$ which is consistent with the experiment of Brodsky. A negligible magnetic moment for the interface Pd layers is obtained.

I. INTRODUCTION

Pd metal shows exotic properties due to its large spin fluctuations, the strongest among the pure metals. The spin fluctuations, which are not large enough to induce ferromagnetism, depress the usual *s*-wave pairing superconductivity and instead are thought to make Pd a most likely candidate for *p*-wave pairing superconductivity. However, *p*-wave superconductivity was not observed down to 1.7 mK for very pure Pd.[1] Some theoretical studies[2] also yield very doubtful results for the existence of observable *p*-wave superconductivity.

Now, negative pressure on Pd metal has been shown to enhance the density of states (DOS) at the Fermi energy.[3] Since the enhanced DOS at E_F may lead to an enhanced Stoner factor and hence to a detectable transition temperature for either magnetism or *p*-wave superconductivity, Brodsky and Freeman[4] made thin films of Pd sandwiched between Au layers. Their measurements yielded very large Stoner factors (350–25 000) for these sandwiches. With these large Stoner factors, the modified paramagnon model for superfluid ^{3}He leads to appreciable T_c from *p*-wave pairing superconductivity in the absence of magnetic ordering.[5] Further, in another analysis of the earlier results,[4] Brodsky found evidence for ferromagnetism, with a very small induced magnetic moment. Thus, an interesting question is whether a Au/Pd/Au sandwich is ferromagnetic or a likely *p*-wave pairing superconductor.

In this paper, we present a theoretical determination of the structural, electronic and magnetic properties of Au/Pd/Au sandwiches using the highly precise local spin-density functional total energy full potential linearized augmented plane wave (FLAPW) method for thin film.[6]

II. METHOD

To investigate the structural properties we use three-layer Pd sandwiched between Au layers (Au/3Pd/Au). To investigate the magnetic properties we expand the number of layers up to five (Au/5Pd/Au).

The local density equations[7] are solved self-consistently by use of the FLAPW method.[6] In this method, no shape approximations are made to the potential or charge density in solving Poisson's equation for a general potential and all matrix elements corresponding to this general potential are rigorously taken into account in all parts of space. A total of about 2×300 augmented plane waves are used as a variational basis set. The charge density and potential are expanded in lattice harmonics with angular momentum components $l\leq 8$. A total number of 21-k points in the irreducible wedge of 2D Brillouin zone is used to converge the total energy and spin density.

III. RESULTS

A. Structural properties

We first investigate the structural properties in the ground state by calculating the total energy of Au/3Pd/Au. We have four variables, the 2D lattice constant and the three Au-Au, Au-Pd, and Pd-Pd interlayer spacings. Now, it is reasonable to take the value of Au-Pd as the average of the interlayer spacings of Au-Au and Pd-Pd and to assume that there is a relationship between the 2D lattice constant and the interlayer spacings. Thus, to investigate how the unit cell volume varies with the change in the 2D lattice constant, we calculate, at each 2D lattice constant, the total energy for three assumed values of interlayer spacing: (1) the same as their bulk interlayer spacing regardless of the variations in the 2D lattice constant; (2) a spacing corresponding to the tetragonal distortion which gives a constant area per atom in the *xz* (or *yz*) plane; and (3) a spacing which yields constant volume per atom (i.e., the same as their respective bulk unit cell volume).

We find that condition (2) gives the smallest total ener-

 0021-8979/88/083655-02$02.40 © 1988 American Institute of Physics

gy at any 2D lattice constant. There is a flat minimum in the E_{tot} over the range between the bulk Pd lattice constant (a_{Pd}) and the average of a_{Pd} and the bulk Au lattice constant (a_{Au}). The flatness in the total energy is seen from the fact that over this range, E_{tot} is almost the same within 0.5 mRy. Hence, it is difficult to determine the stablest structure from our calculations despite their high precision. This small total energy difference may explain the experimental result which indicates that the lattice constants of Au/Pd/Au sandwiches also lie between a_{Pd} and $\frac{1}{2}(a_{Pd} + a_{Au})$.

B. Charge density, spin density, and magnetism

The charge density and spin density, which has direct physical significance as obtained from LSD theory, gives some insights for the formation of the surface and interface.

Figure 1 shows the charge density and spin density of a Au/5Pd/Au sandwich whose lattice constant is $\frac{1}{4}(3a_{Pd} + a_{Au})$ (which we consider to be a conservative choice). Here the interlayer spacings are determined by the condition which gives the minimum total energy. The orbital decomposition of the charge density indicates that the charge density of Pd atoms just one layer below the interface is almost the same as that of the bulklike center-layer Pd. This means that the screening length for charge density is of the order of one atomic layer. The p-like charge of the surface Au layer spills out into vacuum to cure the abruptness of the surface and forms the dipole layer which determines the work function. The spin density in Fig. 1(b) displays the result that Pd atoms are positively polarized and are separated by interstitial regions that are negatively polarized. The negative polarization of the interstitial is well known from studies on the $3d$ transition metals.

The calculated magnetic moments of the Pd layers are <0.01, 0.015, and $0.02\mu_B$ at the interface, sub-interface, and center layer Pd, respectively. These values are quite consistent with the experimental value found by Brodsky.[8] The charge transfer from Au to Pd seems to lower the magnetic moment of the Pd layer adjacent to Au atoms by filling the minority spin states. Assuming a conservative value for the lattice spacing (a 1.2% expansion for Pd), the difference in the calculated total energy between the paramagnetic and ferromagnetic states is quite small (<0.5 mRy/unit cell) and it is hard to determine from the total energy calculations which state is more stable. We can conclude, however, that if magnetic the Pd in Au/Pd/Au sandwich is weakly ferromagnetic with a small moment, the interstitial region is negatively polarized (as in the magnetic transition metals) and the magnetic moment of the center layer is larger than those of the other layers.

IV. CONCLUSION

We have investigated the structural and magnetic properties of Au/Pd/Au sandwiches. The two-dimensional lattice constant of Pd is found from total energy calculations to be expanded between 0.0% and 2.4%. The spin-polarized calculations for a Pd expansion of 1.2% show that the Pd thin films sandwiched between Au layers may be weakly ferromagnetic. The center-layer Pd has a magnetic moment of 0.02 μ_B which is quite consistent with an experimental value.[8] The magnetic moment of the interlayer Pd is reduced to $<0.01\ \mu_B$ by charge transfer and d-band hydridization.

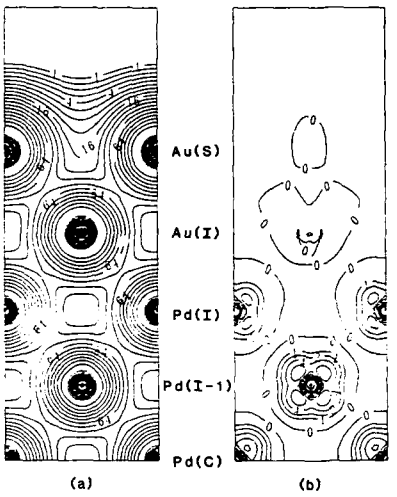


FIG. 1. The charge and spin-density contour map for Au/5Pd/Au.

ACKNOWLEDGMENTS

This work was supported at Northwestern University by the Naticnal Science Foundation (DMR Grant No. 85-18607 and by a computing grant from its Division of Advanced Scientific Computing at the National Center for Supercomputer Applications, University of Illinois, Urbana, Illinois), and at Argonne by the Department of Energy (Grant No. W-31-109 ENG-38). We are grateful to M. B. Brodsky for informative discussions.

[1] P. A. Webb, J. B. Ketterson, W. P. Halperin, J. J. Vuillemin, and N. B. Sandesara, J. Low. Temp. Phys. **32**, 659 (1978).
[2] D. Fay and J. Appel, Phys. Rev. B **16**, 2325 (1977); F.J. Pinski, P. B. Allen, and W. H. Butler, Phys. Rev. Lett. **41**, 431 (1978).
[3] S. G. Das, D. D. Koelling, and F. M. Mueller, Solid State Commun. **12**, 89 (1973).
[4] M. B. Brodsky and A. J. Freeman, Phys. Rev. Lett. **45**, 133 (1980).
[5] K. Levin and O. T. Valls, Phys. Rev. B **17**, 191 (1978).
[6] E. Wimmer, H. Krakauer, M. Weinert, and A. J. Freeman, Phys. Rev. B **24**, 864 (1981), and the references therein.
[7] P. Hohenberg and W. Kohn, Phys. Rev. **126**, B864 (1964); W. Kohn and L. J. Sham, *ibid.* **140**, A1133 (1965).
[8] M. B. Brodsky, J. Phys. (Paris) C5, 349 (1984).

Magnetic proximity effects for Fe films across a thin Ag barrier

Z. Q. Qiu, H. Tang, Y. W. Du, G. P. Stern, and J. C. Walker
Johns Hopkins University, Baltimore, Maryland 21218

Multilayer (^{56}Fe/^{57}Fe/Ag/^{56}Fe) films were prepared by a high vacuum evaporation technique. Magnetic proximity effects for Fe films across a thin Ag barrier were studied by Mössbauer spectroscopy using ^{57}Fe as a probe. The hyperfine field of ^{57}Fe increases with the increase in thickness of the Ag barrier layer. We believe the proximity effects result from the RKKY interaction, mediated by the *s-p* electrons of Ag.

INTRODUCTION

Great interest has been given to magnetic thin films epitaxially deposited on single-crystal substrates from the standpoint of basic research in low dimensional magnetic systems and because of the potential importance for applications. Thin films also serve as the basic unit to build superlattices and other heterostructures. The different magnetic behavior of thin films compared with bulk materials comes primarily from the surface of the film. For this reason, the subject of surface magnetism has generated a great deal of interest both experimentally and theoretically. On the experimental side, the techniques of epitaxy for preparation of flat, single crystal surfaces has led to the control of the growth of films on a layer-by-layer basis.

We have studied the properties of the surface of epitaxial Fe films covered by various materials for some time using Mössbauer spectroscopy. The hyperfine field, which is believed to be proportional to the magnetic moment, is generally different at the surface from that of bulk iron. The temperature dependence of the hyperfine field at the surface, which is related to the collective magnetic excitations (for example, spin waves) critically depends on the covering material. For instance, when the Fe film is covered by Ag, it gives a $T^{3/2}$ temperature dependence of the H_{hf} but with the coefficient 3.5 times the value of bulk.

In this work, we focus our attention on the Fe-Ag system and study the Fe-Fe interaction through an Ag barrier. This is important not only for studying surface effects but also for producing the Fe-Ag superlattices.

EXPERIMENT AND DISCUSSION

Our films were grown in a vacuum chamber at about 10^{-9} Torr. 1000 Å of Ag were first deposited onto a mica substrate to supply a flat surface for additional deposition. The substrate was kept at room temperature during deposition. X-ray diffraction shows that only a (111) Ag diffraction peak exists with the coherence length corresponding to the thickness of the Ag film. Therefore, we expect that a single orientation Ag film is formed with the horizontal grain size larger than 1000 Å and probably on the order of microns, which is "infinite" for Mossbauer spectroscopy. In order to measure the hyperfine field at the interface, the bulk of the Fe film is made of isotopically pure ^{56}Fe, usually grown to a thickness of about 50 layers. Probe layers of ^{57}Fe are then grown on the ^{56}Fe. All Fe films are oriented in the (110) direction. The (111) Ag barrier layer is deposited on top of the ^{57}Fe and then about 50 layers of ^{56}Fe is grown on the Ag. In order to protect the film from oxidation, a 1000-Å Ag layer is grown on top of the ^{56}Fe. The configuration of the film is shown in Fig. 1. During the deposition, the vacuum is about 10^{-9} Torr. We made three samples with Ag thicknesses of the 3, 10, and > 1000 layers.

Transmission Mössbauer spectroscopy was used to investigate the magnetic properties of the samples. The source used was ^{57}Co in a Rh matrix, with an intensity of about 100 mCi. The spectra were taken at 4.2 K, 77 K, and room temperature and were fitted by a least-squares method.

The spectra exhibit a six-Lorentzian absorption line with the intensity ratio about 2:4:1 (Fig. 2), indicating that the magnetic moments lie in the plane of the interface. The hyperfine fields of the three samples at different temperatures are listed in Table I.

From the table we can see that at 4.2 K the hyperfine field becomes smaller as the Ag barrier layer gets thinner, finally approaching the bulk value of 340 kG, which demonstrates that there must exist coupling between the two Fe films across the Ag barrier. This result is very reasonable if one considers the following: the Ag barrier is more like a perturbation introduced to a bulk Fe in which a few layers of Fe atoms are replaced by Ag atoms. Thus, the thicker the Ag layer, the more the perturbation and the greater the change of hyperfine field. It should be pointed out that Ag can grow

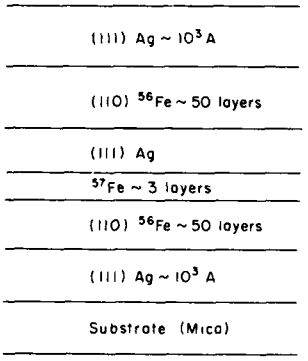


FIG. 1. The configuration of multilayer (Fe/Ag) film at different temperatures.

 0021-8979/88/083657-02$02.40 © 1988 American Institute of Physics

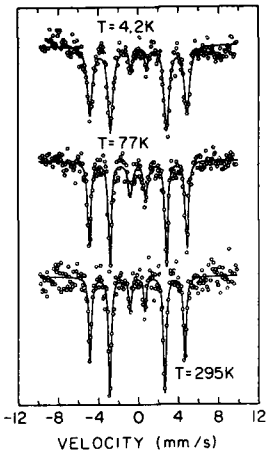


FIG. 2. Mössbauer spectra of (Fe/3-layers Ag) film at 4.2, 77, and 295 K temperature.

very flat on Fe and there is little interdiffusion between the Fe and Ag. Therefore, there is only a slight possibility for the Ag interlayer to form holes through which the two Fe films can contact.

When an Fe surface is coated with Ag, the surface states that give rise to the increased surface magnetism are still present, but are not as localized as they are for a free surface. This means the Ag delocalizes the Fe surface state making the Fe electrons more itinerant. Hence, the increase of surface magnetization is less pronounced than at the clean surface.[1] In this way, the delocalization of the surface state decreases the surface magnetism. We noticed that the small shifts of the majority and minority densities may result in only small changes in the total charge densities, but they can cause a large change of spin density. Therefore, although the density of the Fe at the interface is bulk-like, due to the presence of the Ag atoms the spin density is not. When the Ag layer is coated by other thicker Fe films, the interaction between the two Fe films across the Ag layer does not seem to change the charge density greatly, but may result in a large change of spin density, since the noble metal *s-p* electrons act as an electron gas and can couple with the Fe *d*-moment, giving rise to a RKKY interaction.

The hyperfine field is mainly due to the Fermi contact term which is proportional to the spin density at the nucleus, involving only *s* electrons. The large negative polarization of the core *s* electrons due to the *d* moment contributes to the hyperfine field about -130 kG/unpaired spin and this value is almost independent of the local environment.[1] However, the valence contribution from the valence *s*-like electrons strongly depends on the Fe-Ag and Fe-Fe interactions. When the Ag barrier layer is thick the hyperfine field has the largest value. When the Ag barrier becomes thinner, the coupling between the two Fe films through RKKY interaction becomes stronger. This will result in a change of the spin density of the Fe conduction electrons at the interface, and brings the hyperfine field closer to the bulk value.

TABLE I. Hyperfine field of multilayer (Fe/Ag) film at different temperatures.

Thickness of the Ag barrier layer	Hyperfine field (kG)		
	4.2 K	77 K	295 K
3 layers	341.8	340.9	330.8
10	346.7	344.1	331.0
∞	349.4	346.5	327.6

We now turn our attention to the thermal excitations. For a free surface, the surface magnetism obeys the Bloch law:

$$M(T)/M(0) = (1 - B_s T^{3/2}).$$

B_s is twice as large as the bulk value B_b.[2] For our sample with Ag covering, B_s is almost 3.5 times greater than the bulk value.[3] After the Ag layer is coated by another Fe film, the surface spins of Fe atoms should get more rigid due to the coupling between the two Fe films. After we have completed our measurement of the hyperfine field as a function of temperature, we will have more information about the interaction between the two Fe films. We intend to use more samples with different Ag barrier thicknesses.

CONCLUSION

We have used Mössbauer spectroscopy to investigate the effect of a (111) Ag barrier layer, which is sandwiched between two thick Fe films, on the hyperfine field of Fe at the Ag-Fe interface. We have found that there exists coupling between the two Fe films. This coupling, which we believe is through the RKKY interaction, mediated by the *s-p* electrons of the Ag, changes the thermal excitation and the conduction electron spin density of the atoms at the interface, resulting in a change of the hyperfine field.

[1] S. Ohnishi, M. Weinert, and A. J. Freeman, Phys. Rev. B **30**, 36 (1984).
[2] D. L. Mills and A. A. Muradudin, J. Phys. Chem. Solids **28**, 1855 (1967).
[3] J. C. Walker, R. Droste, G. Stern, and J. Tyson, J. Phys. (Paris) Colloq. **45**, C5-357 (1984).

Effects of magnetic surface anisotropy near the (110) Fe/MnF_2 interface

H. Tang, Z. Q. Qiu, Y. W. Du, G. P. Stern, and J. C. Walker
The Johns Hopkins University, Baltimore, Maryland 21218

Epitaxial (110) ^{56}Fe samples have been grown on (111) Ag and then covered with MnF_2 in ultrahigh vacuum. Three ^{57}Fe layers have been placed at various depths from the Fe/MnF_2 interface to permit Mössbauer spectroscopy. A linear temperature dependence of the hyperfine field for ^{57}Fe layers up to at least 10 layers into the sample is observed. This persistence of surface magnetic effects into the deep layers of the (110) Fe sample can be understood within the framework of a classical spin-wave calculation by Rado.

In recent years it has been possible to characterize, both theoretically and experimentally, the collective magnetic behavior at the surface of a ferromagnet. We have probed the surface regions of Fe at an MnF_2 interface to determine whether the Mn moment can interact with surface Fe moments to produce a magnetically changed Fe surface.

For some time theoretical investigations[1-3] have also been made of the collective magnetic excitation at the surface of a ferromagnet. The excitations are different from bulk because of differences in the exchange interaction for surface spins as well as different longer range interactions and specific surface anisotropies. Experimental studies have been few because of the difficulty of separating surface behavior from bulk. In the case of Fe metal, we have demonstrated that there are large collective spin deviations specific to the surface which are not detectable beyond three or four layers from the surface. In the work described here these surface specific spin deviations are thermally excited rather than being driven by a resonance method. From the temperature dependence of the magnetic hyperfine fields information can be obtained about the nature of the surface magnetic anisotropies.

Because Fe surfaces are very reactive, our experiments have been carried out on epitaxially grown Fe samples covered with nondiffusing, nonalloying materials which prevent the deterioration of the Fe surface. In the work discussed here these include Ag, MgO, and MnF_2.

The basic methods for sample production have been described in detail elsewhere.[4] The samples are grown on a (111) Ag surface which has been prepared in vacuum by vapor deposition of about 500 layers of Ag on Fe-free synthetic mica. Reflection electron diffraction has shown that this produces an excellent, flat, single-crystal surface. The Fe is then vapor deposited on a heated Ag surface and grows epitaxially with the (110) surface exposed. This particular system has been well studied and a high degree of epitaxy results. Because we are only interested in the Fe surface behavior and because the initial growth of Fe on Ag may not be completely smooth, our samples are at least 50 Fe layers thick. To probe the temperature dependence of the spin deviations in the surface layers we take advantage of Mössbauer spectroscopy. Most of the 50-layer (110) Fe samples are grown from isotopically pure ^{56}Fe which shows no Mössbauer effect. Only the relevant layer or layers (at or near the surface) which we wish to study are "labeled" by being made of ^{57}Fe. Quartz oscillator deposition monitors and appropriate shutters permit very accurate construction of the samples. At temperatures up to 600 K the diffusion of Fe into Ag and the interdiffusion of ^{57}Fe and ^{56}Fe are completely negligible. The very high count rate makes it possible to obtain good Mossbauer spectra of the thinnest ^{57}Fe layers in 2 days. While the magnetization and hyperfine fields may not have the same relationship at the surface as in bulk,[5] we can assume quite similar temperature dependencies. Thus we can equate $H_{hf}(T)/H_{hf}(0)$ to $M(T)/M(0)$ for each Fe layer of the sample.

The results of measurements of the temperature dependence of the surface magnetism of Fe at an Ag interface are shown in Fig. 1. The results fit a $T^{3/2}$ dependence but the value of B_s obtained is 3.5 times the bulk value, not the fact of 2 predicted in the model calculations,[1,2] where

$$M(T) \simeq M(0)(1 - B_s T^{3/2}).$$

It is interesting to note that recent measurements by Pierce *et al.*[6] using polarized electron scattering from a free surface of

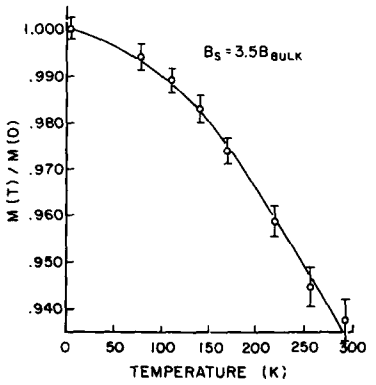


FIG. 1. Plot of $M_s(T)/M_s(0)$ for the two surface layers of a 50-layer (110) sample with an Ag interface. The curve is fit to $M_s(T)/M_s(0) = 1 - B_s T^{3/2}$ with $B_s = 3.5B_{bulk}$.

 0021-8979/88/083659-03$02.40 © 1988 American Institute of Physics

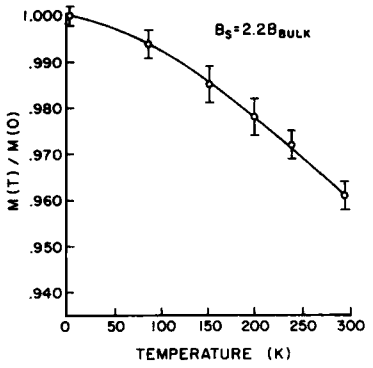


FIG. 2. Plot of $M_s(T)/M_s(0)$ for the top three surface Fe layers of a 50-layer (110) sample with an MgO interface. Here the fit curve gives a $T^{3/2}$ dependence with $B_s = 2.2B_{bulk}$.

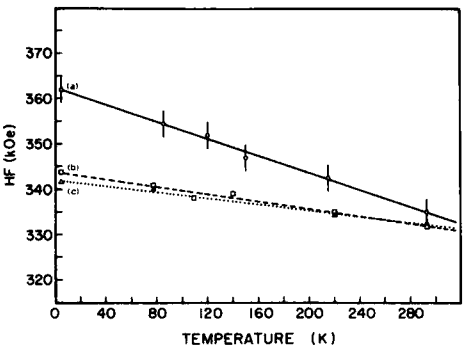


FIG. 3. Plot of hyperfine field for (a) and (b), the first two layers and the first three layers of a 50-layer Fe sample with an MnF_2 interface. (c) shows the situation for a two-layer ^{57}Fe probe placed five layers below the interface.

an amorphous ferromagnet $Fe_{80}B_{20}$ also shows a $T^{3/2}$ dependence with $B_s = 3.4B_{bulk}$.

The result for the temperature dependence of the surface magnetism of Fe at an interface with MgO is shown in Fig. 2. It can be seen that the data also fit to a $T^{3/2}$ temperature dependence. In this case, however, the B_s is 2.2 times the bulk value. This is much closer to the value of 2 predicted by Mills and Maradudin.[2] The choice of MgO as an interface material was dictated by the result of spin-wave resonance experiments[7] on a thick single Ni film with MgO interfaces. In these experiments no spin-wave resonances were observed other than the uniform mode, strongly implying that there was no spinning at the Ni-MgO interfaces. We interpreted this as implying that magnetic anisotropy is very weak at this interface. The fact that we observe a value of B_s consistent with the model calculations for a completely free surface lends support to this conjecture for Fe-MgO as well.

The most interesting result of all was obtained for the Fe surface at an interface with MnF (Fig. 3). The variation of hyperfine field with temperature is clearly linear instead of the $T^{3/2}$ dependence seen with the other interfacial materials and predicted by the previously mentioned theoretical models. Although some theoretical models have predicted a quasilinear temperature dependence for the magnetization of ultrathin ferromagnetic films with thicknesses of a few layers, no general theoretical model predicts this behavior for thick samples at temperatures much less than T_c.

Rado[8] has recently shown that a special value of the ratio of the two surface anisotropy constants characterizing the (110) Fe surface could result in a quasilinear temperature dependence for the surface magnetization. The model used is the semiclassical model first suggested by Landau. A unique feature of this present model is a description of the magnetic anisotropy in terms of *two* constants K_s and K_{ss}. The first constant is familiar from early work of Néel. The latter constant is new and is needed for a full parametric description of surface anisotropy. In Rado's model the relative values and signs of K_s and K_{ss} can determine the overall behavior of the collective magnetic excitation. For $K_s = K_{ss} = 0$ the model predicts a $T^{3/2}$ temperature dependence for the magnetization of the surface spins with $B_s = 2B$ as previously discussed. For small positive or negative values of K_s and K_{ss}, a $T^{3/2}$ behavior still occurs but B_s may be greater than $2B$. It is possible, for selected values of K_s and K_{ss}, to see *surface* spin waves which may dominate the bulk spin waves in the surface region. These surface waves decrease in amplitude experimentally as one moves into the material and lead to a quasilinear temperature dependence of the surface magnetism. The linear dependence only occurs if the perpendicular anisotropy K_{ss} is positive and the bulk anisotropy K_s is much smaller. The resulting relationship is

$$\frac{\Delta M(T)}{M_0} = \frac{K_{ss} k_B T e^{-2K_{ss}/g}}{4\pi A^2} \times \ln\left\{1 - \exp\left[\frac{-8t_2}{k_B T^1}\left(H_k - \frac{2K_{ss}^2}{M_0 A}\right)\right]\right\}.$$

In this relation g is the depth into the ferromagnetic film in numbers of layers and A is the parameter describing the magnetic exchange strength.

In Fig. 3 we see results for an Fe surface in contact with an MnF_2 interface. Because of possible interaction between the Fe and Mn moments, we expect a significant change in the magnetic anisotropy in the Fe interface layers. Whether we attribute this to a modified perpendicular exchange interaction or simply call it a change in K_{ss}, we can still apply Rado's model. The measurements made for an ^{57}Fe probe layer five layers in from the interface indeed shows the decay in slope compared with measurements made at the interface itself, in good agreement with the model. By examining the data shown in Fig. 3, we can see that the change in slope from (b) to (c) implies, assuming a standard value for A, a value of 5.9 ergs/cm^2 for K_{ss}.

This work was supported by NSF Grant No. DMR-8500889 and the Chinese APS Program.

[1]G. T. Rado, Bull. Am. Phys. Soc. **2**, 127 (1957).
[2]D. L. Mills and A. A. Maradudin, J. Phys. Chem. Solids **28**, 1855 (1967).
[3]J. Mathon, Phys. Rev. B **24**, 6588 (1981).
[4]Papers dealing with our work on the surface magnetism of (110) Fe include S. Duncan *et al.*, Hyperfine Interactions **4**, 886 (1978); J. Tyson *et al.*, J. Appl. Phys. **52**, 2487 (1981); J. Tyson *et al.*, J. Magn. Magn. Mater. **35**, 126 (1983); J. Walker *et al.*, J. Appl. Phys. **55**, 2500 (1984).
[5]S. Ohnishi, M. Weinert, and A. J. Freeman, Phys. Rev. B **30**, 36 (1984).
[6]D. J. Pierce, R. J. Celotta, and J. Unguris, J. Magn. Magn. Mater. **38**, 28 (1983).
[7]A. A. Hussain and J. S. S. Whiting, J. Magn. Magn. Mater. **35**, 59 (1983).
[8]G. T. Rado, J. Appl. Phys. **55**, 2505 (1984).

Magnetic properties of molecular-beam epitaxial grown (100) iron films

D. K. Lottis, J. Florczak, and E. Dan Dahlberg
School of Physics and Astronomy, University of Minnesota, Minneapolis, Minnesota 55455

S. Batra, A. M. Wowchak, and P. I. Cohen
Department of Electrical Engineering, University of Minnesota, Minneapolis, Minnesota 55455

The magnetic properties of epitaxial iron films have been studied. The iron films were grown on {100} GaAs and GaInAs substrates. Both the magnitude of the anisotropy energies and direction of the easy axes were studied using a SQUID magnetometer. In particular, measurements were made of the magnetization in the plane of the film along the ⟨100⟩ and ⟨110⟩ directions. From these measurements the magnitude of the anisotropy energy and the direction of the easy axis were determined. Also measurements of the coercivity of the films were made using a magneto-optic Kerr effect system. These results are compared with those determined previously for iron films grown on GaAs.

INTRODUCTION

Recently iron films have been grown by molecular-beam epitaxy (MBE) on both the {110} surface[1] and {100} surface[2] of GaAs and on the {100} surface of ZnSe.[3] The GaAs substrates were prepared by chemical polishing and annealing in the MBE system whereas the ZnSe substrates had been grown by MBE. In the study of the films grown on GaAs the coercivities were on the order of 50 Oe whereas those grown on ZnSe were on the order of 2 Oe. Both determinations of the coercivities were made utilizing a vibrating sample magnetometer (VSM). It was not clear why there was a large difference in the two coercivities but possible reasons include the effect of substrate preparation prior to deposition of the iron films, a difference in the growth of the iron films due to the slightly different lattice constant of the substrates and the possibility of chemical reactions or lack thereof between the iron and the various substrate materials. Qualitatively the films grown on the two substrate materials were similar in that the thinner of the films grown on either type of substrate possessed anisotropy energies which differed from bulk iron.

In order to better understand the differences and similarities of the iron films grown on the two different types of substrates, we have studied iron films grown on the {100} surface of GaAs and $Ga_{0.81}In_{0.19}As$ (GaInAs) substrates. One GaAs substrate was prepared in a manner to approximate the preparation technique of the GaAs substrates used in the earlier study and another to approximate the ZnSe prepared substrate. The GaInAs substrate provided a growth plane with a lattice constant very close to that of bulk iron. In the next section we will discuss the experimental procedures used for the growth of the films and the magnetic measurements. This will be followed by a description of the experimental results. The last section contains a discussion of the experimental results and conclusions.

EXPERIMENTAL PROCEDURES

All three films used in this study were prepared by MBE. The GaAs substrate to be used for comparison with the earlier chemically polished and vacuum annealed GaAs substrate studies was prepared by etching in a sulfuric acid, hydrogen peroxide, and water solution. After the etch, the wafer was inserted in the MBE system and heated to 600 °C in the presence of As to remove the remaining oxide and to anneal the surface. An iron film approximately 25 nm in thickness (FE1) was then grown on this substrate. For these substrates, the ones used in Refs. 1 and 2 and FE1, the surfaces will be relatively rough. For the comparison with the ZnSe prepared substrates a buffer layer of 140 nm of GaAs was grown on the second GaAs wafer prior to the growth of an iron film of 11 nm in thickness (FE3). The GaAs buffer layer used for FE3 showed reflection high-energy electron diffraction (RHEED) oscillations indicating the surface prior to the iron deposition was smooth to a few atomic layers. This smooth surface will be important in a comparison of the magnetic properties of this sample to the other samples grown on rough surfaces. The third substrate had a GaInAs buffer layer grown on it of 1.5 μm in thickness. Next a 30-nm iron film (FE4) was grown over this lattice-matched layer. From a comparison point of view, one might expect this sample to provide the best iron data since the substrate should be smoother than the chemically polished substrates (although not as smooth as the substrate of FE3) and the iron film should not be strained. The thicknesses of the above iron films were determined by calibration of the evaporation source rate by the RHEED oscillations of iron grown on an iron whisker.

A commercial SQUID susceptometer[4] equipped with a 50 kOe superconducting magnet was used to measure both the anisotropy energies and the coercivities of the samples. Most of the data taken on the Fe films with the SQUID system required relatively long periods of time for the data accumulation and in addition the data were taken at discrete values of applied magnetic field and not continuously. For example, a sweep from + 10 to − 10 Oe with 21 points would take roughly an hour which corresponds to an effective field sweep rate on the order of 5 mOe/s. This system was used to measure the field-dependent magnetization on all samples with the field applied along the ⟨110⟩ and ⟨100⟩ directions. In each case the easy axis was found to lie along the ⟨100⟩ direction, as evidenced by plots like Fig. 1. The anisotropy energies were determined from the area between the *M-H* loops along the two directions.[5] The diamagnetic

 0021-8979/88/083662-02$02.40 © 1988 American Institute of Physics

contribution from the substrates was subtracted by examining the linear behavior of the moment observed at fields greater than about 800 G. All of the data shown in this paper were accumulated at 300 K.

A Kerr magneto-optic system was also used to study the coercivities of the MBE films. The Kerr system was operated with the applied magnetic field in the plane of the film and perpendicular to the plane of incidence. The magnetic field could be swept by a computer at various rates from 90 to 0.33 Oe/s. Once a sample was mounted in the system it was saturated magnetically in an applied field of 600 Oe. By sweeping the magnetic field while measuring the Kerr signal the coercivities of the Fe films could be measured.

EXPERIMENTAL RESULTS AND DISCUSSION

First we will present the results of the measurements of the anisotropy energies of the films. An example of the data used in the determination of the anisotropy energies of the films is exhibited in Fig. 1. The data in this figure are the magnetization data of FE1 with the magnetic field applied parallel to the ⟨110⟩ and ⟨100⟩ directions in the plane of the film. As shown in Table I. the two thicker films have fourth-order anisotropy energies which are essentially the same as bulk iron. The thinner film (FE3), however, has an anisotropy energy which is roughly one-half that of bulk iron. The experimental error in these figures is roughly 15% and is due to the uncertainties in the thickness of the films. From this study it would appear that iron films grown on the {100} surface of GaAs have an interfacial anisotropy energy which tends to make the ⟨110⟩ axis the easy axis. This is the same result as was obtained in Refs. 1 and 2. The anisotropy energy for FE3 compares favorably with the energy of films of a similar thickness measured in the other studies. The film FE3 was grown on a smooth GaAs substrate, i.e., a buffer layer of GaAs had been first grown to minimize the disorder in the surface. This would tend to indicate that the surface anisotropies on GaAs are not a manifestation of surface morphology.

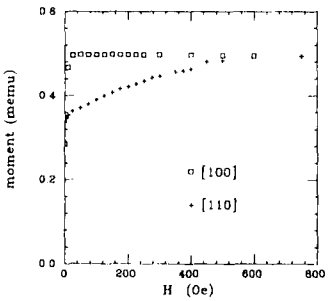


FIG. 1. Magnetization of the 25-nm-thick sample (FE1) as a function of magnetic field applied along the ⟨110⟩ (+) and the ⟨100⟩ (□) directions. The anisotropy energy is determined by integrating the area between the two curves.

TABLE I. Measured properties of the MBE grown magnetic films. The ansiotropy energies were determined by studies of the M-H loops produced with a SQUID susceptometer. The coercivities were measured with the aid of a magneto-optic Kerr system.

Sample	K_1 (10^3 ergs/cm^3)	Thickness (nm)	Coercivity (Oe)
FE1	4.5	25	40
FE3	2.4	10	10
FE4	4.7	28	20

The results of the magneto-optic determination of the coercivities are also displayed in Table I. Possibly the most important feature in these results is that the lowest coercivity came from the sample with the most perfect surface. The chemically polished substrate sample (FE1) and the lattice matched sample (FE4) both had coercivities larger than FE3. In the previous studies the chemically polished GaAs samples had coercivities comparable to the one here but the smooth ZnSe samples had a coercivity of only a few Oe. The previous results and the results reported here suggest that the dominant factor affecting the coercivity is the smoothness of the substrate and not the lattice match. The one caveat is that the reduced anisotropy energy of sample FE3 may also be relevant.

CONCLUSIONS

The experiments reported here involve a study of the anisotropy energies and coercivities of three MBE iron films grown on differently prepared substrates of GaAs. The parameters varied in the experimental procedure included the smoothness of the substrate, and the degree of lattice match to the iron films. In a comparison of the results presented here and previous results it would appear that independent of substrate orientation, surface smoothness, and chemical composition (at least with respect to ZnSe and GaAs) the iron films all possess surface anisotropy energies resulting from the iron/semiconductor interface. For the iron films grown on GaAs the surface anisotropy tends to make the ⟨110⟩ direction the easy direction of the magnetization. The coercivities measured in these films indicate the surface morphology plays a dominant role. An investigation focusing on the coercivities of similarly prepared films is currently in progress.

ACKNOWLEDGMENTS

This research was supported by the AFOSR (under Grant No. AFOSR-86-0201) and the Control Data Corp. (under Grant No. 86M101).

[1] J. J. Krebs, F. J. Rachford, P. Lubitz, and G. A. Prinz, J. Appl. Phys. **53**, 8058 (1982).
[2] J. J. Krebs, B. T. Jonker, and G. A. Prinz, J. Appl. Phys. **61**, 2596 (1987).
[3] G. A. Prinz, B. T. Jonker, J. J. Krebs, J. M. Ferrari, and F. Kovanic, Appl. Phys. Lett. **48**, 1756 (1986).
[4] Quantum Design Inc., San Diego, CA.
[5] B. D. Cullity, *Introduction to Magnetic Materials* (Addison-Wesley, Reading, MA, 1972), pp. 229–233.

Surface magnetism of oxygen and hydrogen adsorption on Ni(111)

H. J. Elmers and U. Gradmann
Physikalisches Institut, Technische Universität Clausthal, D-3392 Clausthal-Zellerfeld, Federal Republic of Germany[a]

The changes of surface magnetization and of surface anisotropies of Ni(111) surfaces during adsorption of oxygen and hydrogen were measured at room temperature using torsion oscillation magnetometry *in situ* in UHV (UTOM) of ultrathin epitaxial Ni(111) films on Re(0001). In the case of oxygen, a rapid chemisorption process is connected with an initial change in magnetic moment per O atom, $\Delta\mu_{ox} = -4.5\mu_{Ni}$ (bulk Ni moment μ_{Ni}), which is reduced to $-3.8\mu_{Ni}$ in the saturated chemisorption state ($\theta = \frac{1}{2}$). This chemisorption is followed by a slow oxidation up to three layers of epitaxial NiO, connected with a change of the film moment $\Delta m = -2.7 m_{ML}$ (moment m_{ML} of bulk Ni monolayer). Surface anisotropy fields are reduced from (10 ± 1) T (free surface) to (0 ± 1) T both for chemisorbed and oxidized surfaces. For the case of hydrogen, saturation adsorption at room temperature ($\theta = \frac{1}{2}$) results in $\Delta\mu_H = -1.6\mu_{Ni}$ and a reduction of the surface anisotropy field to (3 ± 1) T.

I. INTRODUCTION

During the last years, the main interest in surface magnetism was concentrated on clean surfaces and metal-metal interfaces.[1] Little is known on the influence of gas adsorption on magnetic surface properties. For the case of small particle systems only, the influence of adsorption has been analyzed to some extent by magnetometry, with the main emphasis on changes in surface magnetization.[2] In the case of single crystal surfaces, first experimental informations on the surface magnetism of surface reactions were obtained by spin polarized electron techniques. In the case of Ni, a reduction of polarization was observed as a result of oxygen-adsorption on Ni(110) by spin-polarized photoemission,[3] spin-polarized inverse photoemission,[4] and spin-polarized secondary emission.[5] For the adsorption of H_2 on Ni(111), similar observations were done by electron capture spectroscopy.[6] These reductions in polarization indicate a reduction of surface magnetization without giving quantitative values for it. Magnetic surface anisotropies,[7] which are important for applications because they determine magnetic reversal properties of thin film devices, cannot be followed by these spin polarized electron techniques. A most direct method to follow both surface magnetization and magnetic surface anisotropies during adsorption processes is given by torsion oscillation magnetometry of ultrathin epitaxial films[8] *in situ* in UHV (Ref. 9) (UTOM). As a first application of the method, changes in the magnetic properties of Ni(111) surfaces were observed, caused by Cu coatings.[10]

In the present paper, we report on the first magnetometric analysis of gas adsorption processes on magnetic single-crystal surfaces, in the case of the adsorption of H_2 and O_2 on Ni(111). The experimental method is described in Sec. II. Experiments with H_2 on Ni(111) are discussed in Sec. III, a more extended study of O_2 on Ni(111) (Ref. 11) is reported in Sec. IV. Some concluding remarks are given in Sec. V.

II. EXPERIMENTAL METHOD

Experiments were performed using a previously described vacuum system,[9] equipped for epitaxial growth of metal films, for testing by LEED and AES, and for magnetometry using a torsion oscillation magnetometer working *in situ* in UHV (UTOM). Clean Ni(111) films with smooth surfaces were prepared by epitaxy on Re(0001), as described previously.[9] Adsorption of O_2 and H_2 was followed continuously by UTOM. The working principle of TOM is simple. For a sample, suspended on a torsion filament, we measure the period T of torsion oscillations near equilibrium, as a function of an applied magnetic field, H. From T, we easily calculate the magnetic directional moment R. For a ferromagnetic film, R is determined by the magnetic moment $m = J_s V$, and by the magnetic anisotropy energy $E = LV\cos^2\vartheta$ (anisotropy constant L, angle ϑ between J_s, and surface normal). In the case of magnetic saturation, R is connected with $J_s V$ and LV by

$$1/R = 1/(J_s VH) + 1/2LV. \tag{1}$$

Using an anisotropy field $H_L = 2L/J_s$, this can be written as

$$R = J_s VH/(1 + H/H_L). \tag{2}$$

Two modes of analysis can be performed: In a complete analysis, using a series of external fields, we plot $1/R$ vs $1/H$ and get, independently, $J_s V$ from the slope and LV from the axial section. For an example, compare Fig. 1(b) below. As this complete analysis takes about 15 min for a given state of the surface, it is not convenient for following adsorption processes continuously. In this case, we use an approximate analysis at constant field $H \ll H_L$. The magnetic moment only can then be determined by $J_s V \simeq R/H$, compare Eq. (2). This constant field mode was used for continuous registration of adsorption processes, compare Figs. 1(a) and 2(a) below.

III. HYDROGEN ON NI(111)

For the adsorption of hydrogen, the following picture has evolved during the last years[12,13]: On smooth Ni(111) surfaces, H_2 adsorbs atomically and activated in two states, β_1 and β_2, which desorb in thermal desorption (10 K/s) with desorption peaks at 346 and 384 K, respectively.[13] The atoms in β_2 form an overlayer of graphitic structure up to

[a] Sonderforschungsbereich 126 of the Deutsche Forschungsgemeinschaft.

 0021-8979/88/083664-03$02.40 © 1988 American Institute of Physics

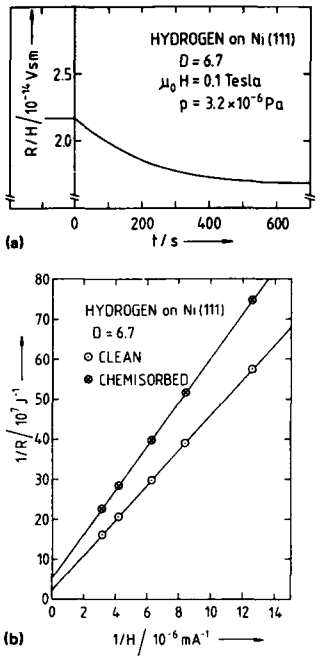


FIG. 1. Magnetometric analysis of H adsorption on Ni(111), at room temperature, for a Ni(111) film of $D = 6.7$ atomic layers. (a) Continuous record in the constant field mode ($\mu_0 H = 0.1$ T) of R/H vs time t after H_2 inlet at $p = 3.2\times10^{-6}$ Pa. (b) Complete analysis $1/R$ vs $1/H$ for the clean film (⊙) and for saturation chemisorption (⊗).

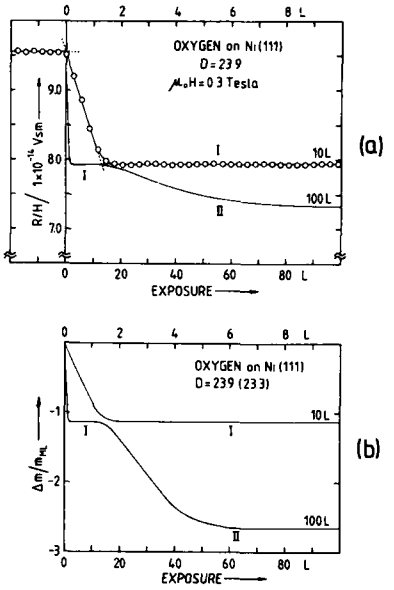


FIG. 2. Magnetometric analysis of O adsorption on Ni(111), at room temperature. (a) Continuous record at constant field ($\mu_0 H = 0.3$ T) of R/H vs O_2 exposure, for a Ni(111) film of $D = 23.9$ atomic layers. (b) Change of magnetic moment from complete analysis; m/m_{ML} vs O_2 exposure [moment m_{ML} of a bulk monolayer Ni(111)]. Note the different exposure scales for the initial part and for the total process, respectively.

$\theta = 0.5$,[12] which does not desorb at room temperature. On a perfect surface, the initial sticking probability for β_2 is $S_0 = 0.02$ (Ref. 13); the sticking probability for β_1 is roughly two orders of magnitude lower. Surface defects of low concentration open a nonactivated channel for adsorption and therefore sensitively increase the sticking probability. By highly concentrated defects, both desorption peaks are shifted downward in temperature, and desorption from β_2 is enabled even at room temperature.

In Fig. 1, the magnetometric analysis is shown for adsorption of hydrogen on a Ni(111) film, consisting of $D = 6.7$ atomic layers, at room temperature, $p = 3.2\times10^{-6}$ Pa (base pressure $< 10^{-8}$ Pa). Figure 1(a) shows a continuous record of $R/H \approx J_s V$ versus time t after H_2 inlet, in the constant field mode ($\mu_0 H = 0.1$ T). R/H saturates at $t \approx 600$ s $\hat{=}$ 14 L (1 L = 10^{-6} Torr s). For $t > 600$ s, R/H was stable, even after pumping off the H_2. Obviously, saturation corresponds to the saturated β_2 state, $\theta = \frac{1}{2}$. Its stability at room temperature reflects a low defect concentration. Using the assumption that the decrease of magnetic moment per adsorbed H atom, $\Delta\mu_H$, is constant, an initial sticking probability $S_0 = 0.06$ can be derived, which again indicates a low concentration of surface defects.[13] Figure 1(b) shows a complete analysis ($1/R$ vs $1/H$) for the clean surface and for saturation adsorption, respectively. The excellent linearity indicates excellent ferromagnetic behavior. From the change in slope induced by H adsorption, we take the change in magnetic moment, $\Delta m = -4.0\times10^{-15}$ V s m $= -0.68 m_{ML}$ [$m_{ML} = 5.9\times10^{-15}$ V s m = magnetic moment of a (bulk) monolayer]. Using $\theta = \frac{1}{2}$, this results in $\Delta\mu_H = -1.80\ \mu_{Ni}$ [moment μ_{Ni} per (bulk) Ni atom]. From the change in axial sections, we take the change in surface anisotropy field, $\Delta(\mu_0 H_s) = -6.9$ T. A similar analysis with a film of $D = 13$ layers resulted in $\Delta\mu_H = -1.36\mu_{Ni}$ and $\Delta(\mu_0 H_s) = -6.9$ T. The excellent agreement of $\Delta(\mu_0 H_s)$ clearly confirms the surface character of the phenomenon. The reduction of $\mu_0 H_s$ from 9.9 T for the free Ni(111) surface[7] to 3.0 T after H adsorption agrees with the previous experience that $\mu_0 H_s$ is lowered to 4 T when Ni(111) is coated by nonmagnetic metals.[7] The cause for the difference in $\Delta\mu_H$ is not clear, at present; further experiments are required. For the present our result is $\Delta\mu_H = -(1.6 \pm 0.3)\mu_{Ni} = (0.93 \pm 0.2)\mu_B$. Selwood[2] found $\Delta\mu_H = -1.16\mu_{Ni}$ for polycrystalline samples and, neglecting the small difference from -1, proposed a pair-bonding model. Our result $\Delta\mu_H \approx 1\mu_B$ rather suggests a model in which one electron from the H-atom fills one minority hole.

IV. OXYGEN ON Ni(111)

For the adsorption of oxygen on Ni(111), the following picture is now generally accepted[14]: A fast initial dissociative chemisorption up to $\theta = \frac{1}{3}$ is followed by a state of very low sticking probability, which, finally, above 10 L, is followed

by slow oxidation up to roughly three layers of epitaxial NiO(111), which are formed by lateral growth of three layers high nuclei. This behavior is clearly confirmed in the magnetometric analysis at constant field ($\mu_0 H = 0.3$ T), which is shown in Fig. 2(a) for film of $D = 23.9$ atomic layers. One clearly observes the sequence of rapid chemisorption up to 1.2 L (extended exposure scale), followed by a completely flat chemisorption plateau (I) ($S \approx 0.005$), and then by a slow oxidation from 11 L up to the oxidation plateau (II) above ≈ 90 L. A special type of analysis was done using two films of nearly equal thickness [$D = 23.9$ (23.3)], and fixed field analysis for different fields of $\mu_0 H = 0.3$ T (0.1 T), followed by a complete analysis for changes of moment and anisotropy using Eq. (1). The result for Δm is shown in Fig. 2(b); it agrees qualitatively with Fig. 2(a); the need for the complete analysis for obtaining quantitative results is clearly seen. The surface character of the observed Δm was checked by a complete analysis [like that in Fig. 1(b)] in both plateaus (I) and (II), for a series of films with different D. For $15 < D < 52$, Δm was independent of D, thus clearly confirming the surface nature of Δm. The final result then is a moment reduction $\Delta\mu_{ox}$ per adsorbed oxygen atom. We found $\Delta\mu_{ox} = -4.5\mu_{Ni}$ for the initial chemisorption. It is reduced to $\Delta\mu_{ox} = -3.8\,\mu_{Ni}$ for the chemisorption plateau (I). The surprisingly high magnitude excludes a pair-bonding model. The negative sign agrees qualitatively with previous evidence from spin polarized electron experiments.[3-5] It indicates a homopolar character of this chemisorption bond, which remains to be analyzed in theory. For the oxidation plateau (II), we found $\Delta m = -2.7 m_{ML}$, corresponding to three monolayers of antiferromagnetic NiO.[11]

Complete analysis before adsorption and in both plateaus further resulted in the change of total anisotropy field, H_L. The surface character of this change was checked in the usual way[7,10] by plotting $\mu_0 H_L$ vs $1/D$. Linear dependence, which was found, confirmed the surface character of changes in $\mu_0 H_L$.[11] Resulting surface anisotropy fields are given by $\mu_0 H_s^{Ni/O} = (+0.7 \pm 1)$ T for the chemisorbed surface [plateau (I) and $\mu_0 H_s^{Ni/NiO} = (-0.5 \pm 1)$ T for the oxidized surface [plateau (II)], respectively. They must be compared with $\mu_0 H_s^{Ni/UHV} = (+9.9 \pm 1)$ T for the free surface. In both plateaus, the surfaces are nearly isotropic, magnetically.

V. CONCLUSIONS

We have shown that magnetometry of ultrathin films *in situ* provides an excellent tool to follow the magnetic aspects of surface reactions. For the chemisorption of H and O on Ni(111), the magnitude of the magnetic moment reduction favours a nonlocal model of the chemisorptive bond. The previous experience that the magnetic surface anisotropy of Ni(111) is lowered by a metallic coating is confirmed for gaseous chemisorption, which strongly diminishes surface anisotropies (for the case of H), or even virtually extinguishes them (for the case of O).

[1] A. J. Freeman and C. L. Fu, in *Magnetic Properties of Low-Dimensional Systems*, edited by L. M. Falicov and J. L. Moran-López (Springer, Berlin, 1986).
[2] P. W. Selwood, *Chemisorption and Magnetization* (Academic, New York, 1975).
[3] W. Schmitt, H. Hopster, and G. Güntherodt, Phys. Rev. B **31**, 4035 (1985).
[4] A. Seiler, C. S. Feigerle, J. L. Pena, R. J. Celotta, and D. J. Pierce, Phys. Rev. B **32**, 7776 (1985).
[5] D. L. Abraham and H. Hopster, Phys. Rev. Lett. **58**, 1352 (1987).
[6] S. Eichner, C. Rau, and R. Sizmann, J. Magn. Magn. Mater. **6**, 208 (1977).
[7] U. Gradmann, J. Magn. Magn. Mater. **54-57**, 733 (1986).
[8] U. Gradmann, Appl. Phys. **3**, 161 (1974).
[9] U. Gradmann, R. Bergholz, and E. Bergter, IEEE Trans. Magn. **MAG-20**, 1840 (1984).
[10] E. Bergter, U. Gradmann, and R. Bergholz, Solid State Commun. **53**, 565 (1985).
[11] H. J. Elmers and U. Gradmann, Surf. Sci. **193**, 94 (1988).
[12] K. Christmann, R. J. Behm, G. Ertl, M. A. van Hove, and W. H. Weinberg, J. Chem. Phys. **70**, 4168 (1979).
[13] K. D. Rendulic, A. Winkler, and H. P. Steinrück, Surf. Sci. **185**, 469 (1987).
[14] P. H. Holloway, J. Vac. Sci. Technol. **18**, 653 (1981).

Ferromagnetic order at Tb surfaces above the bulk Curie temperature

C. Rau and C. Jin
Physics Department, Rice University, Houston, Texas 77251

M. Robert
Department of Chemical Engineering, Rice University, Houston, Texas 77251

The magnetic order at surfaces of the 4*f* rare-earth metal terbium is investigated using electron capture spectroscopy (ECS), which probes the electron spin polarization (ESP) of the *topmost* surface layer. In ECS, the capture of spin-polarized electrons during grazing-angle ion-surface interaction is used to determine the ESP due to long- and short-ranged surface magnetic order. It is found that long-ranged ferromagnetic order exists far above the bulk Curie temperature, measured to be $T_{Cb} = 220$ K. At 140 K, the long-ranged ESP amounts to 24%. With increasing temperature, the ESP first decreases montonically up to the bulk Néel temperature $T_{Nb} = 228$ K, then exhibits a pronounced maximum at $T = 238$ K, and ultimately vanishes at the surface Curie temperature $T_{Cs} = 248$ K. These striking results on enhanced magnetic order at Tb surfaces suggest the presence of very large surface anisotropies.

INTRODUCTION

Recent studies have shown that the magnetic properties of surfaces may differ strongly from those of the bulk.[1-3] For sufficient enhancement of the interactions between the surface spins, an ordered surface phase is expected to coexist with a disordered bulk phase.[4] This remarkable phenomenon was first observed in Gd.[5,6]

The magnetic order at the *topmost* surface layer of a sample is conveniently studied with electron capture spectroscopy (ECS).[7] For Gd, ECS was used to investigate the temperature dependence of the surface magnetic order. Over the whole investigated temperature region, which ranged from well below the bulk Curie temperature to well above the surface Curie temperature, the surface magnetization was found to decrease monotonically with increasing temperature.[5,8]

In this work, we have studied the surface magnetization of another rare-earth, Tb, which, for reasons described below, is expected to behave differently from Gd.

In the bulk, Tb is ferromagnetic at low temperatures, up to the bulk Curie temperature $T_{Cb} = 220$ K, at which it undergoes an antiferromagnetic transition with helical spin structure. The antiferromagnetic (helical) order disappears at the bulk Néel temperature T_{Nb}, above which bulk Tb is paramagnetic.[9]

Contrary to Gd, which has zero total orbital angular momentum, Tb has eight electrons in the 4*f* shell, so that its total orbital angular momentum is equal to 3. This very high anisotropy is expected to strongly affect the temperature dependence and variation of the magnetic ordering at the topmost surface layer of Tb samples.

These expectations are confirmed by the present study: We first find that ferromagnetic order exists at the topmost surface layer of Tb *far above* the bulk Curie temperature $T_{Cb} = 220$ K. With increasing temperature, starting well below T_{Cb}, the electron spin polarization first decreases monotonically up to the bulk Néel temperature $T_{Nb} = 228$ K; it then exhibits a very sharp maximum at $T = 238$ K, which is almost independent of the applied magnetizing field, then decreases steeply and ultimately vanishes at and above the surface Curie temperature $T_{Cs} = 248$ K. This T dependence of the electron spin polarization of the topmost layer of Tb contrasts sharply with that found for Gd in which the electron spin polarization is a monotonic function of temperature from T well below T_{Cb} up to T well above the surface Curie temperature T_{Cs}.

EXPERIMENT

The basic process in electron capture spectroscopy (ECS) is the capture of spin-polarized electrons during small-angle surface reflection of deuterons D^+. For an angle of incidence of 0.3°, the distance of closest approach of the deuterons to the surface is about 0.8–1.5 Å. Therefore, the deuterons probe the spin-polarized local electron densities of state of the topmost surface layer of the sample.[7]

Typically, a well-collimated beam of 150-keV D^+ ions is reflected at grazing angle on the target, which is magnetized parallel to the surface plane and perpendicular to the incoming beam. Next, specularly reflected particles enter a transverse electric field, which separates the remaining D^+ from the neutral D^0 and ionic D^- created in one- and two-electron capture processes, respectively. Finally, the D^0 atoms then hit a tritium(^{3}H) target inducing the nuclear reaction $^3H(d,n)^4He$ ($D^0 + {}^3H = n + {}^4He$). The emitted ^{4}He particles are detected using two perpendicular surface barrier solid-state detectors.

One-electron capture processes at ferromagnetic surfaces yield D^0 atoms with polarized electron shells. A nuclear polarization of the D^0 atoms is then induced by hyperfine interaction and is measured by the asymmetry in the angular distribution of the ^{4}He particles emitted in the nuclear reaction described above. Nuclear polarization is a direct measure of the electron spin polarization of the captured electrons.

A target magnetizing field is applied to align otherwise randomly oriented Weiss domains, thereby producing a

 0021-8979/88/083667-02$02.40 © 1988 American Institute of Physics

macroscopic magnetization along which the sign and magnitude of the ESP can be measured. With P the ESP along the target magnetizing field, we have $P=(n^+-n^-)/(n^+ + n^-)$, where n^+ and n^- are the fractional numbers of electrons with spin moment antiparallel (majority-spin electrons) and parallel (minority-spin electrons), respectively, to the target magnetizing field.

Many experimental difficulties must be overcome in order to maintain clean surfaces during multiple heating and cooling cycles. At all temperatures, before and after each measurement, the residual surface contaminations C, S, and O were shown, using a cylindrical mirror analyzer for Auger electron spectroscopy, to be less than 0.01 monolayer. The ESP measurements are performed at working pressures of about 5×10^{-11} mbar. Further details on our experimental procedures can be found in Ref. 7.

The bulk Curie temperature was determined by two independent methods, ferromagnetic induction and the magneto-optical Kerr effect. Details are given in Ref. 10.

RESULTS AND DISCUSSION

The main results are shown in Fig. 1, which illustrates the temperature dependence of the electron spin polarization of the topmost surface layer of a 1-mm-thick Tb sample. The experimental temperatures ranged from 140 to 300 K, respectively, well below and above the bulk Curie and Néel temperatures. The applied magnetic field was varied between $H=30$ and $H=600$ Oe. The ESP data shown in Fig. 1 correspond to $H=60$ Oe.

As the temperature increases from low values, the ESP is found to initially decrease monotonically. The same behavior was found in our earlier studies of Gd. Moreover, as in Gd, the ESP of the surface does not vanish at T_{Cb}. But, whereas for Gd the ESP always decreases monotonically up to the surface Curie temperature at which it vanishes, the ESP of the topmost layer of Tb exhibits a very pronounced nonzero minimum at, or at least very close to, T_{Nb}, beyond which it steeply increases within the next 10° to ultimately suddenly drop to zero at a surface Curie temperature T_{Cs} = 248 K, remaining zero at higher temperatures.

It is tempting to account for such remarkable behavior of the ESP of the topmost layer by invoking the change of the effective coupling of the latter to the bulk, and assuming that the latter is antiferromagnetically, or at least helically, coupled to the second and deeper surface layers. This assumption is consistent with the observation that the ferromagnetic order, which sets in as temperature is lowered below T_{Cs}, decreases in the neighborhood of T_{Nb}, where antiferromagnetic or helical order appears in the bulk. A similar argument applies to the subsequent increase of the ESP below T_{Nb}, as helical order gradually gives way to ferromagnetic order. Clearly, the validity of this argument relies upon sufficiently strong interlayer couplings. Similar arguments were advanced in Refs. 6 and 11–13.

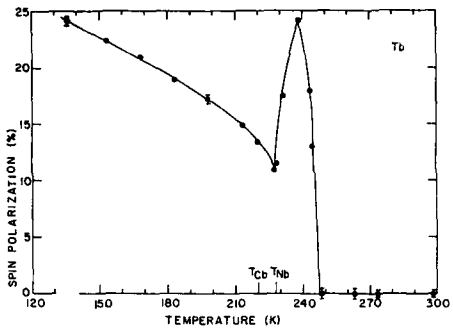


FIG. 1. Electron spin polarization of the topmost surface layer of 1 mm-thick Tb samples as function of temperature. T_{Cb} denotes the bulk Curie temperature as determined using ferromagnetic induction and the magneto-optical Kerr effect. T_{Nb} denotes the bulk Néel temperature of Tb.

It may finally be mentioned that recent work in our group on single crystalline Tb indicates that the behavior observed here is not due to the polycrystalline nature of the present Tb samples.

ACKNOWLEDGMENTS

This work was supported by the National Science Foundation, the Robert A. Welch Foundation, and by the Petroleum Research Fund.

[1] A. J. Freeman and C. L. Fu, in *Magnetic Properties of Low-Dimensional Systems*, Vol. 14 of *Springer Proceedings in Physics*, edited by L. M. Falicov and J. L. Morán-López (Springer, Berlin, 1986).
[2] G. Allan, in *Magnetic Properties of Low-Dimensional Systems*, Vol. 14 of *Springer Proceedings in Physics*, edited by L. M. Falicov and J. L. Morán-López (Springer, Berlin, 1986).
[3] H. W. Diehl, in *Phase Transitions and Critical Phenomena*, edited by C. Domb and J. L. Lebowitz (Academic, London, 1986), Vol. 10.
[4] D. L. Mills, Phys. Rev. B **3**, 3887 (1971).
[5] C. Rau and S. Eichner, in *Nuclear Methods in Materials Research*, edited by H. Bethge, H. Baumann, H. Jex, and F. Rauch (Vieweg, Braunschweig, 1980), p. 354.
[6] D. Weller, S. F. Alvarado, W. Gudat, K. Schröder, and M. Campagna, Phys. Rev. Lett. **54**, 1555 (1985).
[7] C. Rau, J. Magn. Magn. Mater. 30, 141 (1982).
[8] C. Rau and S. Eichner, Phys. Rev. B **34**, 6347 (1986).
[9] See, for example, R. D. Greenough and N. F. Hettiarachchi, J. Magn. Magn. Mater. **31-34**, 178 (1983).
[10] C. Rau, C. Jin, and C. Liu, to appear in Proceedings of the International Symposium on Applications of Ion Beams produced by Small Accelerators, Jinan, People's Republic of China, 1987.
[11] F. Aguilera-Granja and J. L. Morán-López, Phys. Rev. B **31**, 7146 (1985).
[12] E. F. Sarmento and C. Tsallis, J. Phys. **47**, 1115 (1986).
[13] C. Rau and M. Robert, Phys. Rev. Lett. **58**, 2714 (1987).

Magnetization depth profiling with low-energy electron spectroscopy and MOKE

J. Woods, A. Ushioda,[a] M.M. Donovan, S. W. Sun, M. Tobise,[b] and R. C. O'Handley
Department of Materials Science and Engineering, Massachusetts Institute of Technology, Cambridge, Massachusetts 02139

Low-energy electron spectroscopy with (spin) polarization analysis (LEESPA) is described. The power of this new technique, especially in combination with magneto-optic Kerr effect (MOKE), for studying the important effects of surface magnetism are illustrated with the first results on low magnetostriction amorphous Co-Fe-B ribbons.

I. INTRODUCTION

Saturation moments of magnetic materials depart from their bulk values near a surface because of reduced symmetry and altered charge distributions (variations over a few Angstroms in metals) as well as due to surface stresses and/or surface segregation (variations over several tens of Angstroms). Surface magnetic effects are evident in studies of thin magnetic films and multilayers and can be measured to an extent using surface sensitive techniques such as conversion electron Mössbauer spectroscopy[1] or magneto-optic Kerr effect (MOKE).[2] With growing interest in surface magnetism motivated by extensive calculations showing enhanced surface moments[3] and by the drive to higher-density magnetic recording, new, more versatile surface probes are needed. Low-energy secondary electrons are known to bear information about the valence-band magnetization of their source[4] and the depth from which they are emitted can be inferred from the dependence of their mean free path on kinetic energy.[5] Typically the true secondaries ($E_K < 70$ eV) come from the outermost 50 Å of a metal. Thus low-energy electron spectroscopy with (spin) polarization analysis (LEESPA) appears to be a powerful technique for magnetic surface depth profiling[6] especially when combined with techniques such as MOKE,[7] which probes to a few hundred Angstroms, and with bulk magnetic measurements. Some controversy remains over the depth probed by low-energy secondaries.[8]

We describe a LEESPA/MOKE system which has been built to study surface variations of magnetization and anisotropy using the concepts employed by Landolt's group on $Fe_{83}B_{17}$ amorphous ribbons[6] and Fe single crystals.[7] However, our system makes use of a thin-film spin polarimeter[9] for secondary electron polarization analysis. The components of the system are described and its capabilities demonstrated with the first results on low magnetostriction amorphous cobalt-iron boron ribbons.

II. EXPERIMENT

The NBS group has designed a thin-film spin polarimeter and used it in a variety of magnetic surface studies.[7] Our polarimeter is based on their design. Secondary electrons with energies of 50 eV or less emitted from the sample of interest are accelerated to approximately 150 eV and backscattered from a polycrystalline gold film. An appreciable spin-orbit contribution to the scattering potential causes an asymmetry in the scattered intensity for electrons. The scattering asymmetry is proportional to the polarization of the secondary electron beam incident on the gold target, and the proportionality constant is the "effective Sherman function."[11] We have not yet calibrated our spectrometer with a beam of known polarization, so we display our raw asymmetry data. This scattering asymmetry is detected on a channel plate [CP, Fig. 1(a)] detector[12] whose anode is divided into four quadrants. Thus P_x is proportional to the intensity ratio $(I_1 - I_3)/(I_1 + I_3)$ where $I_i (i = 1,2,3,4)$ are the count intensities in the four quadrants labeled clockwise from the top. Similarly P_y is proportional to $(I_2 - I_4)/(I_2 + I_4)$.

The thin-film spin polarimeter is mounted in a UHV Auger chamber in the geometry shown in Fig. 1. The Auger electron gun in the cylindrical mirror analyzer (CMA) is the source of primary electrons (20 μA at the sample at 2 keV). The primary electron (PE) beam is focussed to a spot approximately 1 mm in diameter on a sample (S). The secondary electrons excited from the sample pass through a

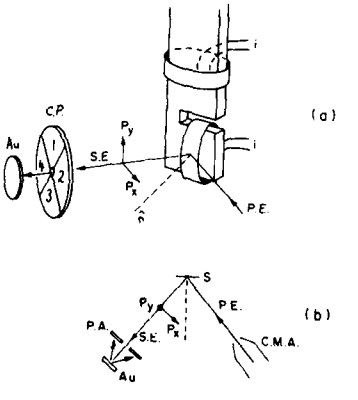


FIG. 1. Sketch of LEESPA magnetic sample holder (a) and scattering geometry (b). PE and SE indicate primary and secondary electrons, respectively. Au is the gold film and CP is the channel plate detector of the polarization analyzer (PA).

[a] Graduate fellowship supported by Fujitsu Corp.
[b] Permanent address: Hitachi Metals, Kumagaya, Japan.

0021-8979/88/083669-03$02.40
© 1988 American Institute of Physics

grid before entering the polarization analyzer (PA). A current of 5 nA is measured at the gold film. The PA is configured to measure components of electron polarization P_x and P_y in two orthogonal axes normal to the secondary electron beam incident upon it.

Details of the sample configuration are shown in Fig. 1(a). Two ribbons of low magnetostriction Co-Fe-B amorphous alloy are held in closed loops and magnetized by five turns of electrical windings in back. The sample holder is made of OFHC copper and is mounted on a Varian *X-Y-Z-θ* manipulator.

Our MOKE system is based on a design by Mansuripur *et al.*[13] It uses a He-Ne laser incident at 45° on a sample in either a perpendicular or in-plane field ($H < 6$ kOe). Details of its operation will appear in a forthcoming paper.[14]

III. RESULTS AND DISCUSSION

A. Surface *M-H* loops

The initial experiment to test the polarimeter was to illuminate the surface of a soft ferromagnetic amorphous ribbon with the Auger electron gun and measure the spin of the secondary electrons as a function of the magnetizing field. We have used a low-magnetostriction ($\lambda \lesssim 0$) Co-Fe-B amorphous ribbon from Hitachi Metals.

The initial hysteresis loops were obtained from a relatively dirty sample ($p = 10^{-7}$ Torr in the unbaked chamber); the Auger spectrum showed only carbon and oxygen at the surface. (The mean free path of Auger electrons with kinetic energies of a few hundred eV is approximately 10 Å. Thus the Auger signal is extremely surface sensitive.) The kinetic energy of the incident electron beam is 2 keV and initially secondaries of all energies are measured at the polarimeter. Thus the LEESPA signal measures the spin polarization averaged over approximately the outermost 50 Å of the sample,[5–8,15] which is much deeper than the Auger electrons probe.

One of our initial LEESPA *M-H* loops is shown in Fig. 2(a). The data are taken from the lower magnetic sample in Fig. 1. The LR (left right) gold scattering asymmetry detected in the PA is proportional to the polarization P_y of the electrons parallel to H (which lies along the ribbon length). The PA is sensitive to less than 0.1% change in the scattering asymmetry. Note that the surface *M-H* loop is not very square for this closed-loop specimen (no end effects) suggesting that at $H = 0$ the magnetization does not lie fully in the y direction. This may be due to a transverse anisotropy at the front surface of the sample induced by its bending stress and the fact that $\lambda < 0$. It may also reflect an intrinsic surface anisotropy orthogonal to y.[16]

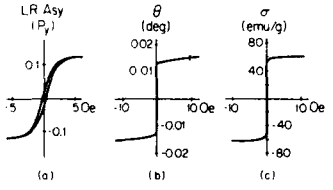


FIG. 2(a). Left right asymmetry (P_y) vs magnetizing field for a closed loop of low magnetostriction Co-Fe-B amorphous ribbon taken by LEESPA. (b) Planar Kerr *M-H* loop for a short sample of the same material as in (a). (c) Bulk vibrating sample magnetometer *M-H* loop for a short sample of the same material as in (a). The loops in (b) and (c) have been corrected for demagnetization.

B. Energy dependence of polarization

A simple energy analyzer in the form of a single retarding grid is positioned between the channel plate and the sample. The retarding grid was held at $V_G = 0$ V in the data displayed in Fig. 2(a), and all electrons passed the grid. The secondary electron yield drops significantly above a kinetic energy of 50 eV. Thus, from the "master curve" (see insert of Fig. 3),[5] data taken with $V_G = 0$ integrate information coming from approximately 50 Å closest to the surface. In Fig. 3 the asymmetry at $H = 6$ Oe [Fig. 2(a)] is plotted as a function of the retarding grid voltage. These data resemble that taken by Mauri *et al.*[6] on amorphous $Fe_{83}B_{17}$ out to secondary electron energies of 40 eV. The curve (Fig. 3) reflects the combined effects of primary electron penetration and secondary electron mean free path (escape depth). It is complicated further by the plateau at 40–60 eV due to polarization of the $M_{23}M_{45}M_{45}$ Auger electrons of cobalt and iron which reflect valence-band magnetization. Given that the energy of our primary electrons exceeds the critical E_P beyond which secondary electron yield is relatively constant[7] the overall variation in polarization with $|V_G|$ (secondary E_K) represents an effective magnetization depth profile.[15] At low $|V_G|$ the asymmetry is a measure of magnetization closer to that of the bulk; at high grid voltages the asymmetry is more a measure of surface magnetization. The magnetization of this Co-Fe-B ribbon decreases significantly over the 50 Å closest to the surface.

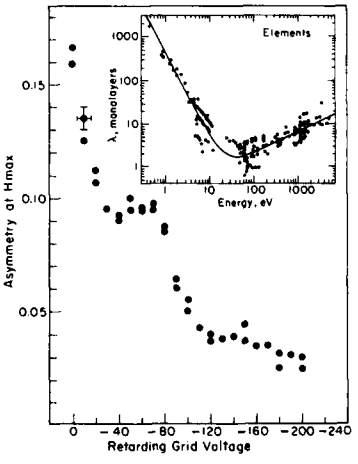


FIG. 3. LEESPA data: Scattering asymmetry vs retarding grid voltage represents a magnetization depth profile. Insert: Electron mean free path vs kinetic energy (from Ref. 5).

C. MOKE

The MOKE system probes the surface to a depth of approximately 250 Å and is therefore less surface sensitive than LEESPA. Figure 2(b) shows a planar Kerr *M-H* loop taken on a short sample magnetized in plane with an external field. The shape of the MOKE loop on Co-Fe-B is essentially square (it has been corrected for demagnetization) unlike the LEESPA loop [Fig. 2(a)]. A bulk VSM measurement on the same short specimen [Fig. 2(c)] also shows the same general features observed by MOKE. In either case [Figs. 2(b) and 2(c)] it was not possible to measure any coercivity. These data (Fig. 2) support the inference made above that the rounded *M-H* loop obtained by LEESPA [Fig. 2(a)] reflects a surface component of magnetization orthogonal to the applied field. Allenspach *et al.*[7] have seen a similar rounding of the *M-H* loop of crystalline (100) Fe for LEESPA probe depths of 5 Å or less.

If the surface magnetization perpendicular to y inferred by the LEESPA data were due to bending stress, it would have been seen also in the MOKE signal. Thus it is probably due to an intrinsic surface anisotropy. For the magnetization to have an appreciable component orthogonal to *y only* in its outer 50 Å implies a variation of M over a much shorter distance than dictated by balancing bulk exchange and anisotropy energies (domain wall width δ is a few thousand Angstroms). Some other anisotropy must force the magnetization back into the field direction once the surface anisotropy is no longer effective. The simplest mechanism to invoke is demagnetization. Thus the surface component of magnetization orthogonal to the applied field [y axis in Fig. 1(a)] is *out of the ribbon plane* [along $\hat{n}$ in Fig. 1(a)]. Within a surface layer less than or equal to 50 Å, the perpendicular volume anisotropy K_s in the surface region must be greater than the demagnetization anisotropy K_D which tends to keep the magnetization in the ribbon plane: $K_s > K_D = M_s H_D/2 = 6\times 10^6$ erg/cm^3. (We express the anisotropy near the surface as energy per unit volume because of the uncertainty of the depth over which it is effective.)

IV. OUTLOOK

LEESPA appears to be a powerful probe of surface magnetism especially in consort with MOKE (which is more widely practiced and less surface sensitive) and with bulk magnetometry. Surface anisotropy and reversal domain nucleation may be well studied by the *M-H* loops generated by this technique. Magnetization depth profiling by LEESPA may reveal further aspects of surface anisotropy, surface magnetochemistry, and fundamental surface magnetic phenomena. An ambitious agenda lies ahead.

ACKNOWLEDGMENTS

The facilities and research described herein are part of a larger Magnetic Surface Characterization Facility (MSCF) which was established with an initial capital equipment grant from the U.S. Army Research Office and the Office of Naval Research. Ongoing support for various aspects of the research within MSCF come from ONR grant No. N00014-86-K-0257 and support from 3M Company, Digital Equipment Corporation, TDK, AT&T Bell Labs, SOHIO, and Hitachi Metals. This generous support is deeply appreciated.

[1] J. C. Walker, R. Droste, G. Stern, and J. Tyson, J. Appl. Phys. **52**, 2500 (1984), M. Przybylski and U. Gradmann, Phys. Rev. Lett. **59**, 1152 (1987).
[2] S. Bader, E. R. Moog, and P. Grunberg, J. Magn. Magn. Mater. **53**, L295 (1986).
[3] A. J. Freeman, C. L. Fu, S. Onishi, and M. Weinert, in *Polarized Electrons in Surface Physics*, edited by R. Feder (World Scientific, Singapore, 1985), p. 1.
[4] G. Chrobok and M. Hoffman, Phys. Lett. **57A**, 257 (1976); J. Unguris, D. T. Pierce, A. Galejs, and R. J. Celotta, Phys. Rev. Lett. **49**, 172 (1982).
[5] M. P. Seah and W. A. Dench, Surf. Interface Anal. **1**, 2 (1979).
[6] D. Mauri, R. Allenspach, and M. Landolt, J. Appl. Phys. **58**, 906 (1985).
[7] R. Allenspach, M. Taborelli, M. Landolt, and D. Mauri, Phys. Rev. Lett. **56**, 953 (1986).
[8] D. L. Abraham and H. Hopster, Phys. Rev. Lett. **58**, 1352 (1987).
[9] J. Unguris, D. T. Pierce, and R. J. Celotta, Rev. Sci. Instrum. **57**, 1314 (1986).
[10] R. J. Celotta and D. T. Pierce, Science **234**, 333 (1986).
[11] J. Kessler, *Polarized Electrons* (Springer, Berlin, 1976), pp. 77–79.
[12] Galileo ElectroOptics, Galileo Park, Sturbridge, MA 01518.
[13] P. Wolniansky, S. Chase, R. Rosenvald, M. Ruane, and M. Mansuripur, J. Appl. Phys. **60**, 346 (1986).
[14] A. Ushioda, A. Fukuno, J. Woods, and R. C. O'Handley (unpublished).
[15] M. Landolt, in *Polarized Electrons in Surface Physics*, edited by R. Feder (World Scientific, Singapore, 1985), p. 385.
[16] B. T. Jonker, K-H. Walker, E. Kisker, G. A. Prinz, and C. Carbone, Phys. Rev. Lett. **57**, 142 (1986); B. Heinrich, K. B. Urquhart, A. S. Arrott, J. F. Cochran, K. Myrtle, and S. T. Purcell, Phys. Rev. Lett. **59**, 1756 (1987).

Substrate modified growth of epitaxial Fe films (abstract)[a)]

S. Batra, A. M. Wowchak, and P. I. Cohen
Department of Electrical Engineering, University of Minnesota, Minneapolis, Minnesota 55455
D. K. Lottis and E. D. Dahlberg
Department of Physics, University of Minnesota, Minnesota 55455

It is now clear that both the atomic and magnetic properties of epitaxial Fe films can be controlled by the precise nature of the substrate which acts as the template for the growth. We have investigated the role of defects and strain arising from lattice mismatch on the growth and the magnetic properties of the Fe films. The films were grown by molecular-beam epitaxy (MBE) on three different well characterized surfaces: GaAs(100), $In_{0.2}Ga_{0.8}As$(100), and Fe(100). The first two surfaces were also prepared by MBE. This mole fraction of In was chosen to match the lattice constant of bulk α-Fe. The growth of the Fe film was characterized by using reflection high-energy electron diffraction (RHEED) and the results indicate that the morphology of the Fe films is smoother on the InGaAs surface than on the GaAs surface. Yet is is still much rougher than the growth on Fe(100) substrate. The magnetic properties were measured by using a SQUID magnetometer and coercivity values are comparable to that of the films grown on ZnSe.[1]

[a)] Work supported by AFOSR 86-0201, CDC, and Honeywell.

[1] J. J. Krebs, B. T. Jonker, and G. A. Prinz, J. Appl. Phys. **61**, 3744 (1987).

 0021-8979/88/083672-01$02.40 © 1988 American Institute of Physics

Collective density fluctuations in heavy-fermion systems (invited)

P. Fulde and K. W. Becker
Max-Planck-Institut für Festkörperforschung, 7000 Stuttgart 80, Federal Republic of Germany

Density fluctuations in heavy-fermion systems are discussed. Particular attention is paid to the hydrodynamic modes and it is pointed out how they differ from those of ordinary metals. A large Landau–Placzek ratio should help to make the quasiparticle diffusion mode observable. The role of the Coulomb interaction is discussed and it is shown that a low-lying optical plasmon should exist. The latter can be overdamped. It compliments the acoustic plasmon (or zero sound) mode into which the quasiparticle diffusion mode goes over for q values outside the hydrodynamic regime. In a recent experiment quasielastic light scattering due to density fluctuations has been observed in UPt_3. Furthermore, it is shown that the attenuation mechanism of longitudinal ultrasound in heavy-fermion systems is very different from that of ordinary metals.

I. INTRODUCTION

Heavy-fermion systems are characterized by a large effective mass m^* of the quasiparticles at low temperatures. It results from the formation of singlet states at the sites of the magnetic ions (in most cases Ce or U ions). Since it takes only a small energy $k_B T^*$ to break up a singlet (T^* is typically of order of several tens of degrees) there are an enormous number of low-lying excitations which lead to the observed large linear specific heat. Since the singlet formation involves mainly spin degrees of freedom, m^* is always associated with spin fluctuations.[1,2] Due to that, the investigation of density fluctuations in heavy-fermion systems have been unduly neglected for a long time. As we shall see they show a number of novel features. Their treatment is particularly facilitated in the small frequency and long-wavelength regime for which a hydrodynamic description can be given.[3] Of particular interest is thereby the effect of the long-range Coulomb interaction. It is well known that it has a strong influence on the density-fluctuation spectrum and the question is to what extent it leads to new observable effects.[4]

II. HYDRODYNAMIC THEORY

We are interested in determining the ion displacement function

$$\chi_{\psi\psi}(\mathbf{q},\omega) = -i\int_0^\infty dt\, e^{i\omega t}\langle[\psi_{-\mathbf{q}}(t),\psi_{\mathbf{q}}]\rangle \qquad (1)$$

in the hydrodynamic regime[3] for which $\omega\tau \ll 1$, $l_{\mathbf{q}} \ll 1$. Here τ and l are the mean-free time and mean-free paths of the quasiparticles, respectively. The longitudinal displacement operator $\psi_{\mathbf{q}}$ of the ions has the form

$$\psi_{\mathbf{q}} = (1/\sqrt{2M\omega_{\mathbf{q}}})\,(b_{\mathbf{q}}^+ + b_{-\mathbf{q}})\,, \qquad (2)$$

where $b_{\mathbf{q}}^+$, $b_{\mathbf{q}}$ are phonon creation and annihilation operators. Furthermore, M is the ion mass and $\omega_{\mathbf{q}}$ denotes the phonon energy dispersion.

The spectral density $\mathrm{Im}[\chi_{\psi\psi}(\mathbf{q},\omega)/\omega]$ is directly related to light scattering and neutron scattering cross sections. From the poles of $\chi_{\psi\psi}(\mathbf{q},\omega)$ one can also extract information about the velocity and attenuation of longitudinal ultrasound.

The advantage of hydrodynamic theory is that it is general and does not require specifying the Hamiltonian. Instead, it relates quantities such as the sound velocity and attenuation to (i) static thermodynamic functions (e.g., specific heat, thermal expansion, etc.) and (ii) Onsager coefficients (e.g., electrical or heat conduction).

The function $\chi_{\psi\psi}(\mathbf{q},\omega)$ is evaluated by applying the projection technique of Mori and Zwanzig.[5] Thereby it is important to select those variables, which must be treated explicitly and cannot be included in internal friction coefficients. In addition to $\psi_{\mathbf{q}}$ we choose for them the Fourier components of the total energy and electron number operators $h_{\mathbf{q}}$ and $\rho_{\mathbf{q}}$, and the phonon momentum operator $i\Psi_{\mathbf{q}}$. While $\psi_{\mathbf{q}}$ relates to the broken (continuous) translational symmetry in a lattice, the other three dynamic variables relate to conserved quantities. This is in accordance with a general theorem[6] which states that the number of hydrodynamic modes equals the number of conserved quantities plus the number of broken continuous symmetries. This rule is modified if long-range Coulomb interactions are present. The details of the calculations are straightforward when the projection method is used. We refer for them to the original literature[3] and state here merely the results.

The displacement correlation function has the general form

$$\chi_{\psi\psi}(\mathbf{q},\omega) = -1/[\omega^2 - (v_T q)^2 + i\omega q^2 D(\mathbf{q},\omega)]\,, \qquad (3)$$

where v_T is the isothermal sound velocity. $D(\mathbf{q},\omega)$ contains contributions from coupling to the energy and electron density operators and an internal friction contribution D_R. Thereby D_R incorporates all those degrees of freedom, which are not treated explicitly by the above variables. One finds

 0021-8979/88/083673-03$02.40 © 1988 American Institute of Physics

$$D(\mathbf{q},\omega) = D_R + i\,[A/(\omega + iD_E q^2)] + i\,[B/(\omega + iD_T q^2)]\,. \tag{4}$$

Here D_E and D_T are the quasiparticle energy and density diffusion constants. It is $D_E = \kappa/C_V$ and $D_T = \sigma/(e^2\chi_c)$, where κ and σ are the thermal and electrical conductivities. More precisely, σ is the heavy quasiparticle contribution to the electrical conductivity. C_v is the specific heat at constant volume and χ_c is the electronic density susceptibility. The prefactors A and B contain static thermodynamic functions. We show in Fig. 1 the different hydrodynamic modes due to density fluctuations. One notices two Rayleigh peaks (i.e., overdamped modes). It can be shown that the width of the particle diffusion mode $D_T q^2$ is by a factor m^*/m larger than that due to energy diffusion (i.e., $D_T = D_E m^*/m$). This is due to the fact that χ_c is *not* enhanced in heavy-fermion systems.

The Landau–Placzek ratio, i.e., the relative intensity between the quasielastic peaks and the two Brillouin peaks is by a factor of order 10^5–10^6 larger than in ordinary metals.[3] This opens up the possibility of observing quasielastic light scattering due to density fluctuations in a metal. In a pioneering experiment of Mock *et al.*[7] such scattering has been observed in UPt_3 but not in UBe_{13}. In these experiments Brillouin scattering is observed and the Brillouin scattering intensity is directly related to $\mathrm{Im}\,\omega^{-1}\chi_{\psi\psi}(\mathbf{q},\omega)$. Since the wave vector $\mathbf{q}$ could not be varied it is at present still open whether or not it is the hydrodynamic quasiparticle diffusion mode which is seen in that experiment.

III. ROLE OF LONG-RANGE COULOMB INTERACTION

In the preceding section the hydrodynamic modes have been discussed which appear in the displacement correlation function. Their common feature is that the excitation energies vanish in the long-wavelength limit $q \to 0$. We want to discuss in the following electronic density modes, which are either outside the hydrodynamic regime $ql \ll 1$, $\omega\tau \ll 1$, or which fall into the hydrodynamic regime but have finite excitation energies, even as $q \to 0$ (nonhydrodynamic modes).[8] A crucial part is thereby played by the long-ranged Coulomb interactions. Until now we have incorporated only the short-range part of the electron interactions by an on-site Hubbard U interaction term. But it is known that generally the long-range part converts a hydrodynamic mode into a plasma oscillation. Therefore, one has to show that the calculated hydrodynamic modes remain correct even when the long-range part of the Coulomb interaction is included. In order to do this one must start from a realistic Hamiltonian. It consists of two (or more) quasiparticle bands which are intersected by the Fermi energy E_F. We believe that this model better describes actual heavy-fermion systems than one with one quasiparticle band and a hybridization gap just above E_F. The quasiparticle Hamiltonian can be obtained by a "downfolding" procedure when one starts from a LMTO type of calculation.[9] Assuming that two quasiparticle bands are intersected by E_F implies that two quasiparticle numbers are conserved, i.e., one for each band. This assumes that the short-range part of the quasiparticle interaction does not appreciably mix the different quasiparticle bands. Therefore the two partial densities must be included in the set of variables which are treated explicitly, as well as the interband transition operator between the two bands. Added to this Hamiltonian is the long-ranged part of the Coulomb-interaction Hamiltonian.

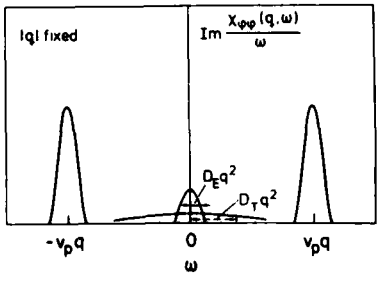


FIG. 1. Spectral density of the ion-displacement correlation function in the hydrodynamic regime. For the different symbols see the text (from Ref. 3).

When one computes the density modes of the system one may neglect their weak coupling to the energy-density fluctuations. In the hydrodynamic regime the following modes are found to be present:

$$\omega_{1,2}(\mathbf{q}) = \begin{cases} -iD_T q^2 \\ -i/\tau_1, \end{cases}$$

$$q < 1/2v_{\mathrm{apl}}\tau_1\,. \tag{5}$$

Here $v_{\mathrm{apl}} = v_F^*[m^*/(3m)]^{1/2}$ is the velocity of acoustic plasmons (see below) and τ_1 is a particle-current relaxation time. The latter is the mean free time of the heavy quasiparticles which enters into their contribution to the resistivity. The term $-iD_T q^2$ can be also rewritten as $-iv_{\mathrm{apl}}^2\tau_1 q^2$. For $q > (2v_{\mathrm{apl}}\tau)^{-1}$ the two modes go over into propagating modes

$$\omega_{1,2}(\mathbf{q}) = \pm v_{\mathrm{apl}} q - i/2\tau_1\,. \tag{6}$$

These are acoustic plasmon or zero-sound modes. For details of this crossover we refer to Refs. 3 and 8. Acoustic plasmons have been considered before for transition metals.[10] There is one interesting difference, though to the present case. In the theory put forward for transition metals the (heavy) d electrons are screened by the (light) s electrons and that reduces the large density susceptibility of the d electrons. In the heavy-fermion systems the density susceptibility of the heavy quasiparticles is small from the beginning because of the large Landau parameter $F_0^s \simeq m^*/m$ (for more details see, e.g., Ref. 9). Therefore, screening has no dramatic effect on the static density susceptibility.

Outside the hydrodynamic regime four propagating modes are found:

$$\omega = \pm\omega_{\mathrm{pl}}^* - i/2\tau_1\,,$$
$$\omega = \pm\omega_{\mathrm{pl}} - i/2\tau_1\,. \tag{7}$$

Here $\omega_{\mathrm{pl}}^* = \sqrt{6}k_B T^*$ is a low-lying optical plasmon[8,11] while

$\omega_{pl} = (n_c e^2/m)^{1/2}$ (n_c is the conduction electron density) is the conventional plasmon frequency. When $(\omega_{pl}^* \tau_l)^2 \ll 1$ the low-lying plasmon is overdamped and $\omega = -i\tau_l (\omega_{pl}^*)^2$. [Note that in this model there is no plasmon mode with an energy $(n_c e^2/m^*)^{1/2}$, i.e., with the electron mass replaced by the large mass m^*.] As long as the q dependence of the quasielastic light scattering observed in Ref. 7 is not known, it is also possible that it is an overdamped optical plasmon which is seen in that experiment.

IV. ULTRASOUND ATTENUATION

For sound frequencies in the MHz regime and electron mean-free paths of order 10^{-6} cm one finds that $D_T q^2 \ll v_T q$. Therefore one is in the "isolated" regime with a sound velocity v_p. An interesting result, which follows from $\chi_{\psi\psi}(\mathbf{q},\omega)$ is the attenuation of ultrasound. It turns out that the dominant attenuation mechanism is very different from the one in ordinary metals, which has been worked out by Pippard.[12] In heavy-fermion systems it is the effect of the quasiparticle diffusion which dominates the temperature dependence of the longitudinal sound attenuation α_l. One finds[3]

$$\alpha_l = \frac{q^2\Omega^2}{v_p M}\left(\frac{\partial\mu}{\partial\Omega}\right)^2_{T,N_e} \frac{\sigma}{e^2 v_p^2}. \tag{8}$$

Here $(\partial\mu/\partial\Omega)_{T,N_e}$ denotes the change of the chemical potential with volume when the electron numer and temperature are kept fixed, and M is the ionic mass. Compared with this damping mechanism the other two contributions which result from internal friction and from the heat conduction pole of $\chi_{\psi\psi}(\mathbf{q},\omega)$ are small (see, e.g., Ref. 8). Since $(\partial\mu/\partial\Omega)_{T,N_e}$ is not known experimentally one must try to compute it from an Anderson lattice model-Hamiltonian. One finds[3] that

$$\left(\frac{\partial\mu}{\partial\Omega}\right)_{T,N_e} = \frac{1}{\Omega}\left\{1 + \frac{\eta}{2N(0)}\frac{\pi T^*}{\Gamma} \times\left[\mu + \frac{\pi^2}{3}\left(\frac{T}{T^*}\right)^2 + \cdots\right]\right\}, \tag{9}$$

where η is an electronic Grüneisen parameter, $N(0)$ is the (small) density of states of the conduction electrons, T^* is the analog of the Kondo temperature for a lattice, and $\Gamma = \pi N(0) V^2$ (V is the hybridization matrix element between the f and conduction electrons). By using Eq. (9) one finds that the $(T/T^*)^2$ dependent contribution has a prefactor of the observed size.[13] Note that the attenuation due to quasiparticle diffusion is crucial to account for the strong T dependence observed for α_l.

V. SUMMARY AND CONCLUSIONS

Hydrodynamic theory for density fluctuations in heavy-fermion systems leads to two new physical effects. One is the possibility of observing in a metal quasielastic scattering due to density fluctuations. This is due to an enhancement of the Landau–Placzek ratio by 5–6 orders of magnitude as compared with conventional metals. Indeed, in recent experiments by Mock *et al.*[7] quasielastic Brillouin scattering has been seen for the first time in the heavy-fermion metal UPt_3. At present it is still open whether it is due to a hydrodynamic diffusion mode or a nonhydrodynamic mode, because the momentum transfer q cannot be varied in the experiment. The second physical effect is a new damping mechanism for longitudinal ultrasound. It yields a larger T dependent sound absorption than the one due to internal friction or heat conduction.

In addition to the hydrodynamic modes a new low-lying optical plasmon mode is found due to the long-range part of the Coulomb interaction. Whether or not it is overdamped in UPt_3 is not clear at present.

[1] C. Varma, in *Theory of Heavy Fermions and Valence Fluctuations*, Vol. 62 of Springer Series in Solid State Sciences, edited by T. Kasuya and T. Saso (Springer, New York, 1985).
[2] G. Lonzarich, lectures given at the workshop on Magnetism in Transition Metals, Kuparovice (1986).
[3] K. Becker and P. Fulde, Z. Phys. B **65**, 313 (1987); see also Europhys. Lett. **1**, 669 (1986).
[4] See e. g., F. Marabelli, P. Wachter, and J. J. M. Franse, J. Magn. Magn. Mater. **62**, 387 (1986).
[5] See, e.g., D. Forster, *Hydrodynamic Fluctuations, Broken Symmetry, and Correlation Functions* (Benjamin, Reading, MA, 1975).
[6] P. C. Martin, in *Problème à N corps*, edited by C. DeWitt and R. Balian (Gordon and Breach, New York, 1986).
[7] R. Mock, B. Hillebrands, P. Baumgart, and G. Güntherodt, Verh. Dtsch. Phys. Ges. **1**, AM-8.9 (1987).
[8] K. Becker and P. Fulde, Z. Phys. B **67**, 35 (1987).
[9] P. Fulde, J. Keller, and G. Zwicknagl, in *Solid State Physics*, Vol. 41, edited by D. Turnbull and H. Ehrenreich (in press).
[10] See, e.g., H. Gutfreund and Y. Unna, J. Chem. Phys. Solids **34**, 1523 (1973).
[11] A. J. Millis, M. Lavagna, and P. A. Lee, Phys. Rev. **36**, 864 (1987).
[12] A. B. Pippard, in *Low Temperature Physics*, edited by C. DeWitt, B. Dreyfus, and P. G. DeGennes (Gordon and Breach, New York, 1962).
[13] V. Müller, D. Maurer, K. de Groot, E. Bucher, and H. E. Bömmel, Phys. Rev. Lett. **56**, 248 (1986).

Electronic structure of the light actinide oxides from electron spectroscopy (Invited)

O. Gunnarsson
Max-Planck Institut für Festkörperforschung, D-7000 Stuttgart 80, West Germany

D. D. Sarma[a] and F. U. Hillebrecht[b]
Institut für Festkörperforschung der Kernforschungsanlage Jülich, D-5170 Jülich, West Germany

K. Schönhammer
Institut für Theoretische Physik, Universität Göttingen, D-3400 Göttingen, West Germany

The $4f$ core level spectra of ThO_2, UO_2, and NpO_2 are shown to be well described in the Anderson impurity model. The $O(2p)$-actinide ($5f$) hybridization is found to be very large. This leads to a new interpretation of the 7-eV satellite in the $4f$ spectrum, which corresponds to an antibonding $5f^n - 5f^{n+1}$ final state, where $n = 0,2$, and 3 for ThO_2, UO_2, and NpO_2, respectively. The resonance photoemission $4f$ spectrum is studied, and it is found that interference between different intermediate states is crucial for its interpretation. In particular, the photon energy dependence (CIS spectrum) is strongly influenced by these interference effects. In the $5f$ valence spectrum of UO_2 the theory gives a satellite, which is due to a split-off state caused by the large hybridization.

I. INTRODUCTION

Core level x-ray photoemission spectroscopy (XPS) together with the Anderson impurity model has provided a microscopic understanding of the electronic structure of light rare-earth compounds.[1] In particular, it was possible to use the core XPS spectrum to deduce the parameters of the Anderson model. From these parameters other electron spectra as well as "low-energy" properties, such as the static susceptibility, were calculated.[1] In this way it was possible to obtain a description of Ce compounds using one set of parameters for each system. Apart from a study of the $5f^0$ Th compounds[2] and some recent work on U compounds,[3] this approach has not been applied to the actinides. It is therefore an interesting question as to what extent the Anderson impurity model can describe actinide compounds. We demonstrate that this model gives a good description of the core spectra of the light actinide (Th, U, and Np) oxides, and we resolve a longstanding controversy about the importance of the p-f hybridization for these systems. We further analyze the UO_2 $4f$ resonance photoemission spectra. We find that interference between different intermediate states plays a crucial role for the photon energy dependence, and we reconcile the apparent contradiction between this dependence and our interpretation of the $4f$ satellite. Finally we have studied the $5f$ photoemission spectrum. Due to the large hybridization, deduced from the $4f$ core spectrum, the theory predicts a satellite below the O $2p$ band, which has been observed experimentally.

There has recently been a great interest in the electronic structure of metal oxides, for instance the transition-metal oxide NiO (Refs. 4 and 5) and the rare-earth oxide CeO_2.[6] Among the actinide oxides, UO_2 is by far the most studied system.[7] There is, however, no agreement about the electronic structure of UO_2, in general, and about the strength of the hybridization between the oxygen $2p$ and uranium $5f$ states, in particular. One-particle calculations indicate a strong hybridization.[8,9] To obtain an insulator, the f electrons, nevertheless, have to be treated as localized (corelike) in a band calculation.[8] The valence spectra have usually been explained in a localized picture, where the p-f hybridization is neglected,[7] but there is also evidence that this hybridization is of importance.[10–12] The valence spectrum shows a satellite just below the O $2p$ band.[10–12] Resonance photoemission strongly suggests that the satellite has $5f$ character,[12] but its origin is otherwise unknown. The $4f$ core level spectra of UO_2 has a satellite at 7 eV below the main peak. This satellite has been assigned to a $O(2p) \rightarrow U(5f)$ (Refs. 9,13–15) or a $O(2p) \rightarrow U(6d)$ (Ref. 16) shake-up excitation. The main peak has also been interpreted as a "shake-down" satellite related to a $6d$ (Ref. 17) or a $5f$ (Ref. 18) screening orbital, i.e., the assignments of the main peak and the satellite are reversed relative to the two shake-up interpretations. The assignment of the satellite to a $5f^1$ state has also been discussed.[7]

II. CORE LEVEL XPS SPECTRUM

The calculations of the spectra are performed in the Anderson impurity model. The $5f^n$, $5f^{n+1}$, and $5f^{n+2}$ configurations are taken into account in the core level XPS and the Bremsstrahlung isochromat spectroscopy (BIS) calculations and the $5f^{n-1}$, $5f^n$, and $5f^{n+1}$ configurations in the

[a] S.S.C.U., Indian Institute of Science, Bangalore 560012, India.
[b] Max-Planck Institut für Festkörperforschung, D-7000 Stuttgart 80, West Germany.

 0021-8979/88/083676-04$02.40 © 1988 American Institute of Physics

$5f$ XPS calculation, where $n = 0,2$, and 3 for Th, U, and Np, respectively. The hybridization to the O $2p$ band, the Coulomb interaction U between two $5f$ electrons and the interaction U_{fc} between a core electron and a $5f$ electron are included. All multiplet effects are neglected. BIS measurements suggest that the multiplet splitting is of the order a few eV. Considering the large hybridization ($N_f\Delta_{av} \sim 11$ eV) found below, the neglect of the multiplet splitting appears reasonable for the oxides, although we do not expect this to be generally true for the actinide compounds. With these assumptions, we can apply the theory developed earlier for Ce,[1] provided that the energy ϵ_f of the f level is renormalized.[19] The main parameters in the model are ϵ_f, U, U_{fc}, and the strength Δ_{av} of the p-f hybridization. The relative energies of the $5f^{n-1}$, $5f^n$, and $5f^{n+1}$ configurations were adjusted so that the theoretical spectra reproduced the centers of the peaks in the $5f$ XPS and BIS spectra.[20–22] Then we have $\epsilon_f = E(f^{n+1}) - E(f^n)$ and $U = E(f^{n+1}) + E(f^{n-1}) - 2E(f^n)$. For ThO_2 we used the same value of $U = 7.7$ eV as for UO_2 and NpO_2, since $n = 0$ for ThO_2 and the method above cannot be used. To take the $4f$ spin-orbit splitting into account in the $4f$ core spectrum, two spectra separated by the experimental splitting were superimposed. The parameters $U_{fc} = 7.2$ eV and $\Delta_{av} = 0.76$ eV were adjusted so that the UO_2 $4f$ spectrum was well reproduced.

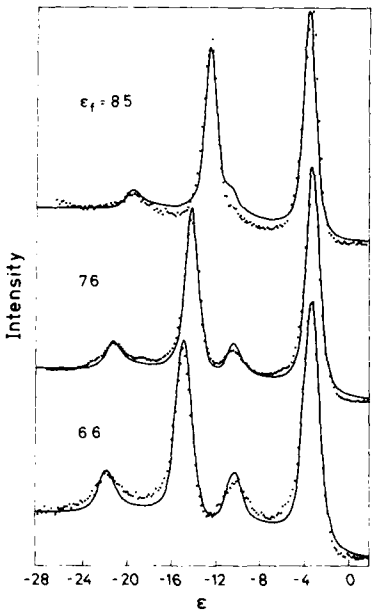


FIG. 1. Theoretical (full line) and experimental (dots) $4f$ core level spectra. The energy zero is arbitrary. The experimental results were obtained from Ref. 20 (ThO_2 top curve), Ref. 21 (UO_2 middle curve), and Ref. 22 (Np_2O_5 bottom curve). The spectra have a $4f_{7/2}$ and a $4f_{5/2}$ component, and each component has a main peak and a satellite, corresponding to a bonding and an antibonding $5f^n$-$5f^{n-1}$ state, respectively.

These parameters were then kept fixed for ThO_2 and NpO_2 and there are no adjustable parameters for these systems. The results are shown in Fig. 1. Both the relative energies and weights of the structures in the calculated spectra agree well with experiment, and the agreement would further improve if slightly different values of U_{fc} and Δ_{av} were allowed for the different systems. The increase in the weight of the satellite in going from ThO_2 to NpO_2 is due to the lowering of the $5f$ level energy (ϵ_f). The model therefore directly relates the lowering of the $5f$ BIS spectrum to the increased weight of the satellite in the $4f$ core spectrum. In the presence of a core hole, the lowest $5f^{n+1}$ configuration is almost degenerate with the $5f^n$ configuration. The leading peak and the satellite therefore correspond to final states which are strong mixtures of these two configurations. The large separation (~ 7 eV) of the main peak and the satellite is therefore not primarily due to the separation of the two configurations ($\leqslant 1$ eV) but due to the strong hybridization, which gives final states of primarily bonding and antibonding character with a large separation. This differs from *all* the interpretations given above, which assume that the peaks can be assigned to essentially "pure" configurations and that the peak separation is close to the energy difference of these configurations. We note that these spectra cannot even be described qualitatively with a small Δ_{av}, unless we make the unphysical assumption that $U_{fc} \sim 0$. $\Delta_{av} \sim 0$ would require that the leading peak in the core spectrum has $5f^n$ character and the separation between the f^n and f^{n-1} configurations would then have to be close to the value in the initial state.

III. RESONANCE PHOTOEMISSION

Cox *et al.*[15] have studied the $4f$ core spectrum of UO_2 for photon energies $h\nu$ close to the resonance due to the $3d \rightarrow 5f$ transition. They found a small change in the satellite intensity when $h\nu$ was increased to 10 eV above resonance. The resonance process involves the transition

$$3d^{10}4f^{14}5f^2 \rightarrow 3d^9 4f^{14}5f^3 \rightarrow 3d^{10}4f^{13}5f^2\epsilon g,$$

where ϵg refers to a continuum electron. It is then natural to assume that a peak is enhanced at resonance if it corresponds to a final state with some $5f^2$ character.[15] Cox *et al.* therefore assigned the main peak to a $5f^2$ state and the satellite to a $5f^3$ state, in contrast to our conclusion that both structures contain a substantial $5f^2$ character. To understand this apparent contradiction, we have performed resonance photoemission calculations, using a theory presented elsewhere.[23] The parameters were the same as in the calculation of the XPS spectrum, except that U was reduced to 4 eV. Figure 2 shows results for the constant initial state (CIS) spectrum for the main peak and the satellite of the $4f$ spectrum. The results are in fair agreement with experiment.[24] In particular, the satellite intensity at resonance ($h\nu_{res}$) is not much larger than at $h\nu + 10$ eV, in good agreement with experiment.[15,24] To understand these results it is important to notice that the $5f^4$ configuration is only about 4 eV above the $5f^3$ configuration in the presence of the $3d$ hole. Because of the strong hybridization ($N_f\Delta_{av} \sim 11$ eV) there is therefore a mixing of these configurations, and the $5f^4$ configuration has a finite amplitude in the intermediate state, even if the $5f^3$ amplitude

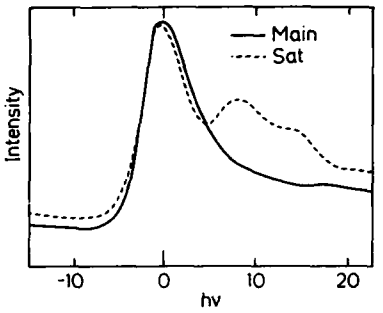


FIG. 2. Theoretical CIS spectrum (photon energy dependence) of the main peak (full curve) and the satellite (dashed curve) for the $4f$ spectrum of UO_2. The energy zero for $h\nu$ (in eV) is at resonance. The curves are normalized to their maximum values.

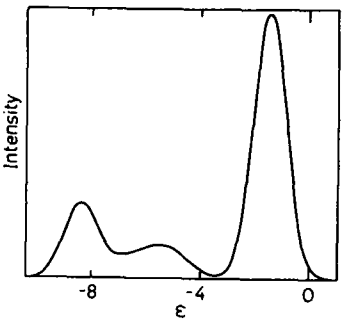


FIG. 3. Theoretical $5f$ photoemission spectrum of UO_2.

in the initial state is assumed to be zero. The following Auger process therefore creates both $5f^2$ and $5f^3$ configurations. The relative phase of these configurations is crucial, since the leading peak and the satellite correspond to bonding and antibonding linear combinations of these configurations. At resonance the phase favors the main peak while the satellite is somewhat suppressed. As the photon energy is increased to the resonance energy of the $5f^4$ configuration, the relative phase of the two configurations in the intermediate state changes. At this value of $h\nu$ the satellite tends to be favored while the main peak is suppressed. This behavior is superimposed on the decreasing Fano line shape, leading to a large reduction of the main peak but only a small reduction for the satellite as $h\nu$ is increased. The three structures in the satellite CIS curve reflects the three intermediate states formed by the $5f^3$, $5f^4$, and $5f^5$ configurations. The splitting of these is somewhat too large in the calculation.

IV. VALENCE SPECTRUM

We have finally calculated the $5f$ photoemission spectrum, which is shown in Fig. 3. The same parameters as in the calculation of the XPS core spectrum were used. Due to the strong hybridization, a bound state is split off below the O $2p$ band (extending between -4 and -8 eV). Such a split-off state is not observed in band calculations.[8] The reason is that manybody effects effectively enhances the coupling strength by a factor N_f relative to a one-particle calculation ($N_f\Delta_{av}$ instead of Δ_{av}).[1] This split-off state leads to a satellite in the $4f$ spectrum, which has been observed experimentally, although the experimental results appears to depend on the sample preparation.[10-12] The calculated apparent weight is somewhat larger than the experimental weight. This may be due to the neglect of lifetime broadening effects and interference[1] between $5f$ and O $2p$ emission. The f spectrum also has weight in the energy range -4 to -8 eV, explaining the weak resonance behavior observed experimentally for the O $2p$ band.[11,12]

The strong O($2p$)-actinide ($5f$) hybridization ($\Delta_{av} = 0.76$ eV) may seem surprising in view of the values in the range 0.1–0.2 eV obtained for the Th and U intermetallics.[2,3] The value[6] ($\Delta_{av} = 0.4$ eV) obtained for CeO_2 is, however, also much larger than for the Ce intermetallics.[1] Since the $5f$ orbital of Th is more extended than the $4f$ orbital of Ce, it is also natural that Δ_{av} is larger for ThO_2 than for CeO_2. In spite of the large value of Δ_{av}, our parameters are consistent with the fact that ThO_2-NpO_2 are insulators. Applying the arguments and notations of Zaanen *et al.*[5] and using the normal interpretation of the BIS spectrum,[14] these systems can be characterized as having a finite gap of a $5f$-"$6d$" character.

V. SUMMARY

In conclusion, we have studied ThO_2, UO_2, and NpO_2 and found that the $4f$ core spectrum, its photon energy dependence (for UO_2), and the $5f$ BIS and PES spectra can be described within the Anderson impurity model using the same parameters for a given compound and only changing ϵ_f in going across the series. The analysis of the core spectrum shows that the p-f hybridization is very strong ($\Delta_{av} = 0.76$ eV). The main peak and the 7-eV satellite in the $4f$ spectra are therefore strong mixtures of $5f^2$ and $5f^3$ configurations with bonding and antibonding character, respectively. Due to the strong hybridization, the theoretical $5f$ spectrum of UO_2 has a split-off satellite below the O $2p$ band at an energy where a $5f$ satellite is observed experimentally. The resonance photoemission $4f$ spectrum has been studied. We find that the photon energy dependence for the main peak and the satellite does not show directly the amount of $5f^2$ character in these features. Instead the different photon energy dependence can be explained from the interference of different intermediate states. This effect should be important for resonance photoemission of other systems as well.

ACKNOWLEDGMENTS

We want to thank J. W. Allen and J. Zaanen for useful discussions and J. W. Allen for making unpublished material available.

[1]O. Gunnarsson and K. Schönhammer, Phys. Rev. Lett. **50**, 604 (1983); Phys. Rev. B **28**, 4315 (1983); *ibid.* **31**, 4815 (1985); in *Handbook on the Physics and Chemistry of Rare Earths*, edited by K. A. Gschneider, L. Eyring, and S. Hüfner (North-Holland, Amsterdam, 1988), Vol. 10; J. W. Allen, S.-J. Oh. O. Gunnarsson, K. Schönhammer, M. B. Maple, M. S. Torikachvili, and I. Lindau, Adv. Phys. **35**, 275 (1986).

[2]O. Gunnarsson, K. Schönhammer, D. D. Sarma, F. U. Hillebrecht, and M. Campagna, Phys. Rev. B **32**, 5499 (1985); D. D. Sarma, F. U. Hillebrecht, O. Gunnarsson, and K. Schönhammer, Z. Phys. B **63**, 305 (1986).

[3]D. D. Sarma, F. U. Hillebrecht, and M. S. S. Brooks, J. Magn. Magn. Mater. **63–64**, 509 (1987).

[4]K. Terakura, A. R. Williams, T. Oguchi, and J. Kübler, Phys. Rev. Lett. **52**, 1830 (1984).

[5]A. Fujimori and F. Minami, Phys. Rev. B **30**, 957 (1984); G. A. Sawatzky and J. W. Allen, Phys. Rev. Lett. **53**, 2239 (1984); J. Zaanen, G. A. Sawatzky, and J. W. Allen, Phys. Rev. Lett. **55**, 418 (1985); J. Magn. Magn. Mater. **54–57**, 607 (1986).

[6]A. Fujimori, Phys. Rev. B **28**, 2281 (1983); Phys. Rev. Lett. **53**, 2518 (1984); E. Wuilloud, B. Delley, W.-D. Schneider, and Y. Baer, Phys. Rev. Lett. **53**, 202 (1984); *ibid.* **53**, 2519 (1984).

[7]Y. Baer, in *Handbook on the Physics and Chemistry of the Actinides*, edited by A. J. Freeman and G. H. Lander (North-Holland, Amsterdam, 1984), p. 271.

[8]P. J. Kelley and M.S.S. Brooks, Physica **102B**, 81 (1980).

[9]J. Weber and V. A. Gubanov, J. Inorg. Nucl. Chem. **41**, 693 (1979).

[10]L. E. Cox, J. Electron Spectrosc. **26**, 167 (1982).

[11]A. J. Arko, D. D. Koelling, A. M. Boring, W. P. Ellis, and L. E. Cox, J. Less-Common Metals **122**, 95 (1986).

[12]L. E. Cox, W. P. Ellis, R. D. Cowan, J. W. Allen, S.-J. Oh, I. Lindau, B. B. Pate, and A. J. Arko, Phys. Rev. B **35**, 5761 (1987).

[13]N. Beatham, A. F. Orchard, and G. Thornton, J. Electron Spectrosc. **19**, 205 (1980).

[14]Y. Baer, Physica **102B**, 104 980).

[15]L. E. Cox, W. P. Ellis, R. D. Covan, J. W. Allen, and S.-J. Oh, Phys. Rev. B **31**, 2467 (1985).

[16]J. J. Pireaux, J. Riga, E. Thibaut, C. Tenret-Noël, R. Caudano, and J. J. Verbist, Chem. Phys. **22**, 113 (1977).

[17]J. R. Naegele, J. Ghijsen, and L. Manes, in *Structure and Bonding* (Springer, Heidelberg, 1985), p. 197.

[18]W.-D. Schneider and C. Laubschat, Phys. Rev. Lett. **46**, 1023 (1981).

[19]The energy of a configuration with n_f f electrons is given by $E(n_f) = n_f\epsilon_f^0 + \frac{1}{2}Un_f(n_f - 1)$. We introduce $\Delta n_f = n_f - n$ and $\epsilon_f = \epsilon_f^0 + nU$. Then we have $E(\Delta n_f) = \Delta n_f\epsilon_f + \frac{1}{2}U\Delta n_f(\Delta n_f - 1) + E_0$, where E_0 is independent of Δn_f and $\Delta n_f = 0, 1$ or 2. The theory for Ce can then be used with a rescaled ϵ_f. This approach neglects that the hopping matrix elements have an n dependence. The restriction to three different configurations is less justified for the actinides than for Ce due to the smaller value of U for the actinides. The calculations are performed to lowest order term in $1/N_f$, where N_f is the $5f$ level degeneracy, which is less well justified for $n = 2$ or 3. The $1/N_f$ expansion should nevertheless converge rapidly for an insulator, such as UO_2 or NpO_2.

[20]D. D. Sarma (unpublished).

[21]Y. Baer and J. Schönes, Solid State Commun. **33**, 885 (1980).

[22]S. Krummacher, D. D. Sarma, M. Campagna, and J. Naegele (unpublished).

[23]O. Gunnarsson and K. Schönhammer, in *Giant Resonances in Atoms, Molecules and Solids*, edited by J. P. Connerade, J.-M. Esteva, and R. C. Karnatak (Plenum, New York, 1987), p. 405; O. Gunnarsson and T. C. Li, Phys. Rev. B **36**, 9488 (1987).

[24]J. W. Allen (private communication).

Photoemission study of 5*f* localization in $UPd_{3-x}(Pt,Rh)_x$

A. J. Arko
Los Alamos National Laboratory, Los Alamos, New Mexico 87545

D. D. Koelling, B. D. Dunlap, and A. W. Mitchell
Argonne National Laboratory, Argonne, Illinois 60439

C. Capasso and M. del Giudice
Department of Chemical Engineering and Materials Science, University of Minnesota, Minneapolis, Minnesota 55455

Photoemission measurements in the two systems $UPd_{3-x}(Pt,Rh)_x$ show that the 5*f* spectra are consistent with localized 5*f* electrons (peak in spectral weight is below E_F for all x within the double hexagonal DO_{24} phase) while at both phase transitions the 5*f* peaks lock in at E_F consistent with intinerancy. A satellite 5*f* peak which we attribute to *d* screening is observed in both localized and itinerant systems.

UPd_3 is the only uranium-based intermetallic compound in which the 5*f* electrons are known to be localized, as determined from neutron diffraction[1] and heat capacity[2] measurements. The compound crystallizes in the double hexagonal DO_{24} structure, with the 5*f* electrons in the f^2 singlet ground state. The isoelectronic compound UPt_3, on the other hand, is an itinerant heavy fermion system[3] which crystallizes in the simple hexagonal DO_{19} structure. Why it is that only UPd_3 among the uranium intermetallic compounds displays localized 5*f* behavior is still open to speculation. It has been suggested[4] that it is the unique feature of the Pd electronic structure which prevents 5*f*-4*d* overlap. It is also true however that $AnPd_3$ compounds (An = Th, U, Np) tend to crystallize in the DO_{24} structure. While both phenomena may be driven by the same set of circumstances, we will show in this paper that localized 5*f* behavior in the $UPd_{3-x}(Pt,Rh)_x$ systems is tied to the DO_{24} crystal structure.

We report results of photoemission measurements on a series of compounds in the systems $UPd_{3-x}Pt_x$ and $UPd_{3-x}Rh_x$. Previous photoemission measurements[5,6] in UPd_3 have shown that the peak of the 5*f* spectral density occurs *not* at E_F, but rather at ≈ -1 eV, consistent with localization. In itinerant systems like UPt_3, on the other hand, the centroid of the 5*f* peak is always observed precisely at E_F to within experimental resolution.[7] This observation has been utilized[5] as a "fingerprint" of localized versus itinerant behavior. In the compounds reported here we also utilize this "fingerprint" since it has been determined to be consistent with[2,8,9] specific heat, resistivity, and susceptibility measurements.

There are several interesting features of the data shown below, which, because of length requirements, will be the subject of future papers. We point out here that one of the previously puzzling features of the UPd_3 5*f* spectrum has been its large width[6] (≈ 1.5 eV full width at half maximum or FWHM) and non-Lorentzian shape. Following our own suggestion[10,11] that one should expect satellite structure in nearly localized or localized 5*f* compounds we reanalyzed the UPd_3 spectrum and found that indeed it consists of two peaks which account for the width and the line shape. The exact position in energy of these peak depends somewhat on analysis, but they are approximately at -0.8 and -1.5 eV. An interesting side benefit of the present experiment then has been the ability to follow the progression of the satellite through the phase transitions and to show that indeed it exists even for the narrow-band-like systems.

The $UPd_{3-x}(Pt,Rh)_x$ specimens were made by arc melting the constituent materials, annealing the resulting buttons at ≈ 1000 °C for 24 h, and checking for the correct phase and lattice parameter with x-ray powder pattern techniques. Only those buttons determined to be single phase were used in the experiments. Samples of $\approx 3\times 3\times 10$ mm^3 were cut from the buttons and cleaved *in situ* in the UHV system just prior to making measurements in order to expose a clean surface. The surface purity was monitored via the oxygen 2*p* peak at -6 eV. For all these materials the freshly exposed surface remained oxygen free for several hours after cleaving.

Measurements were made at the U2 beamline of the National Synchrotron Light Source in Brookhaven. While spectra were taken at several photon energies from 40 to 124 eV, we present here only the 108 eV data ($5d_{3/2}$ resonance)[12] where the 5*f* signal is strongest. We do not show the 92 eV data although these were used to make an accurate determination of E_F. This was needed since there was some ambiguity about the exact location in E_F whenever a strong 5*f* signal centered below E_F drowned out the ligand *d*-like Fermi edge. Our overall instrument resolution was generally ≈ 0.25 eV as determined from the Fermi edges of the 92 eV spectra. It was never worse than 0.3 eV. In all spectra we have subtracted out the background in the usual fashion by assuming that the secondary electron photocurrent at each binding energy is proportional to the total integrated photocurrent at lower binding energies.

The data taken at $h\nu = 108$ eV are shown in Fig. 1 for several of the $UPd_{3-x}Pt_x$ alloys studied, with x ranging from 0 to 3. For $x = 0$, 1.5, and 3, the alloys are ordered. X-ray data show that the DO_{24} structure is maintained up to $x = 2.4$ with DO_{19} continuing up to $x = 3$. Near $x = 1.5$ one obtains[13] very weak superlattice lines in the x-ray patterns superimposed on the DO_{24} structure, indicating some addi-

 0021-8979/88/083680-03$02.40 © 1988 American Institute of Physics

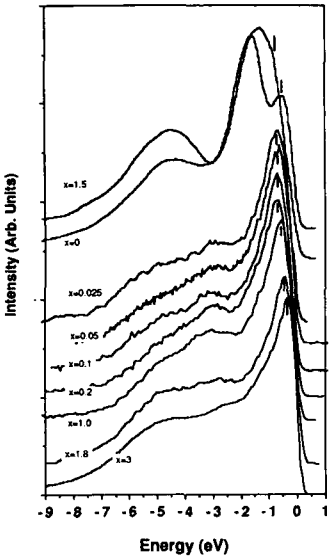


FIG. 1. Photoemission spectra at $h\nu = 108$ eV for the system $UPd_{3-x}Pt_x$ for the x values as shown. The background has been subtracted. Tic marks show the position of the well-screened peak. Note that for $x = 0$ and 1.5 the d-like intensity is dramatically different from the remaining alloys.

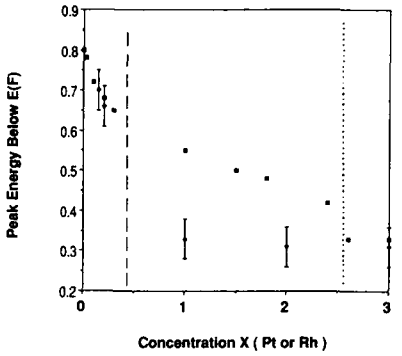


FIG. 2. $5f$ spectrum for $UPd_{1.2}Pt_{1.8}$ as obtained at the 108 eV resonance (i.e., 108 eV spectrum minus 92 eV spectrum) decomposed into two symmetric components. The lower intensity component (at -1.2 eV) is simply a scaled version of the peak in $UPd_{1.5}Pt_{1.5}$.

tional, thus far unknown, periodicity for a narrow range of compositions. We point this out because it is clear that for $x = 0$ and 1.5 the $5f$ peaks (the large intense peaks between E_F and ≈ -2 eV) are dramatically different from the disordered alloys. For $x = 1.5$ one can clearly distinguish two $5f$ peaks in the spectra, at -0.5 and 1.5 eV. Similarly one can distinguish two peaks for UPd_3 if it is noticed that the lower binding energy peak is now at ≈ -0.8 eV and the higher binding energy peak remaining at ≈ -1.5 eV. It is of course common for corelike levels to display satellite structure in photoemission spectra[14] so that the observation of two peaks in UPd_3 is indeed satisfying. In general, one interprets[15,16] the higher binding energy peak as being due to poor screening (d-like in our case) while the lower binding energy peak as resulting from good screening (f-like). We will use this interpretation as well.

The surprising result to be noted in Fig. 1 is that the addition of even $\approx 1\%$ UPt_3 to UPd_3 (i.e., $x = 0.025$) results in a dramatic reduction of the d-screened peak and a slight shifting toward E_F (to ≈ -1.2 eV). This is shown more clearly in Fig. 2 where we display a spectrum for $x = 0.05$, representative of $5f$ emission only, and decomposed into two symmetric peaks. The $5f$ spectrum is obtained by subtracting the off-resonance curve ($h\nu = 92$ eV) from the spectrum at $h\nu = 108$ eV. The asymmetry of the $5f$ line shape is more obvious when displayed in this fashion. While the decomposition is not done in a self-consistent fashion (the FWHM of the d-screened peak was simply chosen to correspond to that of $x = 1.5$), it is nonetheless obvious that the asymmetric line shape of the $5f$ spectrum can result from the addition of the two symmetric peaks separated by ≈ 0.6 eV as shown in the figure.

Returning to Fig. 1, one can see that the gross features of the asymmetric $5f$ spectrum remain more or less unchanged right up to $x = 3$ (except for $x = 1.5$, of course). In all cases, then, it is a composite of two peaks. In particular, it remains unchanged past the phase transition and into the itinerant heavy fermion systems. The only thing that changes with x is the position of the well-screened peak which is marked by tic marks in Fig. 1. It continues to shift with x slightly toward E_F. This is shown more clearly in Fig. 3 where the well-screened peak positions from the raw data in Fig. 1 are plotted versus concentration x. (A complete decomposition of the $5f$ peaks as done in Fig. 2 would result in ≈ 0.1 eV shift of the well-screened peak toward E_F, but the physics would be unchanged.) In Fig. 3 we also superimpose the peak positions for the $UPd_{3-x}Rh_x$ series on the same plot and note that small additions of URh_3 to UPd_3 yield results identical to those obtained for UPt_3 addition. (Error bars indicate the approximate uncertainty in peak position.) The interesting feature to note is that at the phase transitions (into the DO_{19} phase at $x = 2.4$ for UPt_3 addition and into the $L1_2$ phase at $x \approx 0.5$ for URh_3 addition) the well-screened peak suddenly locks in at E_F to within experimental resolution (remember that experimentally the peak still appears below E_F due to the finite resolution) and remains locked at E_F up to $x = 3$.

We interpret the locking in of the $5f$ peak at E_F as indicative of the localization-delocalization transition which for both alloy systems occurs, as stated above, at the crystalline phase transition. The necessary conclusion is that the localized nature of the $5f$ electrons in UPd_3 is at least partially a consequence of the crystal structure.

The sudden drop in amplitude of the satellite peak (or conversely the sudden increase at $x = 0$ and 1.5) is not fully understood. It has been considered that in fact the lower peak is not a satellite but rather that the two $5f$ peaks are related to the two unique sites (cubic and hexagonal) of the uranium atoms in the DO_{24} structure. They thus represent

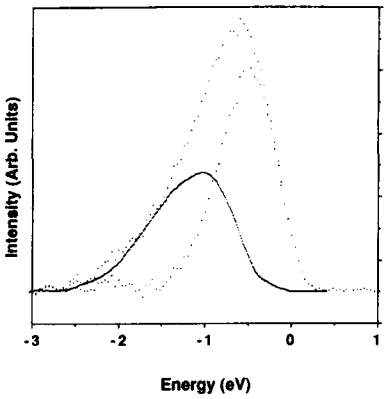


FIG. 3. Positions in energy of the well-screened peak (taken from the raw data) vs composition for the systems $UPd_{3-x}Pt_x$ and $UPd_{3-x}Rh_x$. Note the locking-in at E_F (actually -0.3 eV due to finite resolution) above the phase transitions shown by the dashed lines for Rh addition and dotted line for Pt addition.

two separate $5f$ levels. This argument overlooks the fact that the "satellite" peak is observed in the DO_{19} and the $L1_2$ structures as well, albeit much diminished from UPd_3. Moreover, it does not explain the large, sudden drop in intensity with minute additions of Pt or Rh since the site symmetry remains undisturbed. We conjecture that the explanation for the satellite *intensity* lies in the position in energy of the uranium $6d$ electrons. It is known from resonance work (the $6p$-$6d$ fano resonance at $h\nu = 19$ eV) on single crystals[17] that in UPt_3 the $6d$ electrons along the Γ-M direction are situated at ≈ -1 eV while similar experiments on UPd_3 place them at -3.6 eV. Substitutions of Pt for Pd then may result in the shifting of some U-$6d$ density toward E_F where the greater f-d overlap favors the f-screening channel (refilling of the f hole). This is also consistent with the $h\nu = 92$ eV antiresonance spectra (here the spectrum is heavily weighted in favor of ligand d intensity) which show a sudden shifting of the ligand d-DOS toward E_F with small Pt addition. The U-$6d$ DOS will generally mimic the ligand d-DOS. For the ordered compound $UPd_{1.5}Pt_{1.5}$, however, the ligand d-DOS is found centered at -4.5 eV. This may explain the greater tendency toward d-screening in the middle of the composition range but leaves us with the puzzling question of why the sudden d-shift occurs in the first place.

Finally we wish to point out that the spectra for $x = 1.8$ and $x = 3$ are nearly identical, except that the peak position for $x = 1.8$ is shifted away from E_F by ≈ 0.2 eV toward higher binding energy. This is as expected[5] for localized $5f$ electrons. It is reasonable to conclude, then, that if a satellite exists for $x = 1.8$, it exists for UPt_3 as well, as we have suggested earlier.[10,11] Indeed, the satellite in UPt_3 is clearly seen as a shoulder in the spectrum (Fig. 1) at ≈ -1 eV. It is easily observable because the main peak is narrower for the itinerant case than for the localized case, is situated at E_F, and is thus somewhat farther removed from the satellite than for $x = 1.8$.

Research at Los Alamos National Laboratory and Argonne National Laboratory was performed under the auspices of the U.S. Department of Energy. The Dept. of Chemical Engineering and Materials Science, University of Minnesota, is supported by the National Science Foundation under Contract No. NSF DMR-88-10837.

[1] A. F. Murray and W. J. L. Buyers, in *Crystalline Electric Field and Structural Effects in f-Electron Systems*, edited by J. E. Crow, R. P. Guertin, and T. W. Mihalisin (Plenum, New York, 1980), p. 257.
[2] K. Andres, D. Davidov, P. Dernier, F. Hsu, W. A. Reed, and G. J. Nieuwenhuys, Solid State Commun. **28**, 405 (1978).
[3] For an experimental review of heavy electron systems, see G. R. Stewart, Rev. Mod. Phys. **56** 755 (1984) and reference therein.
[4] B. Johansson and O. Eriksson, J. Less Common Metals **133**, 25 (1987).
[5] Y. Baer, H. R. Ott, and K. Andres, Solid State Commun. **36**, 387 (1987).
[6] B. Reihl, N. Martensson, D. E. Eastman, A. J. Arko, and O. Vogt, Phys. Rev. B **26**, 1842 (1982).
[7] A. J. Arko, C. G. Olson, D. M. Wieliczka, Z. Fisk, and J. L. Smith, Phys. Rev. Lett. **53**, 2050 (1984).
[8] B. D. Dunlap, H. A. Kierstead, S. K. Malik, D. J. Lam, and A. W. Mitchell, Bull. Am. Phys. Soc. **31**, 444 (1980); F. J. Litterst, S. K. Malik, B. D. Dunlap, H. A. Kierstead, D. J. Lam, A. W. Mitchell, and D. Niarchos, Bull. Am. Phys. Soc. **31**, 446 (1986).
[9] A. deVisser, J. C. P. Klaasse, M. van Sprang, J. J. M. Franse, A. Menovsky, and T. T. M. Palstra, J. Magn. Magn. Mater. **54–57**, 375 (1986); A. deVisser, J. C. P. Klaasse, M. van Sprang, J. J. M. Franse, A. Menovsky, T. T. M. Palstra, and A. J. Dirkmaat, Phys. Lett. **113**, 489 (1986).
[10] A. J. Arko, B. W. Yates, B. D. Dunlap, D. D. Koelling, A. W. Mitchell, D. J. Lam, Z. Zolnierek, C. G. Olson, Z. Fisk, J. L. Smith, and M. del Giudice, J. Less Common Metals **133**, 87 (1987).
[11] A. J. Arko, B. W. Yates, B. D. Dunlap, D. D. Koelling, A. W. Mitchell, D. J. Lam, Z. Zolnierek, C. G. Olson, Z. Fisk, J. L. Smith, M. del Giudice, in Proceedings of the 5th International Conference on Valence Fluctuations, Bangalore, India, January 5–9, 1987.
[12] For a discussion of resonant photoemission, see U. Fano, Phys. Rev. **124**, 1886 (1961), and also Ref. 6 for resonant photoemission in UPd_3.
[13] G. H. Lander (private communication).
[14] L. C. Davis and L. A. Feldkamp, Phys. Rev. B **23**, 6239 (1981) and references therein.
[15] B. W. Veal and A. P. Paulikas, Phys. Rev. B **31**, 5399 (1985).
[16] M. R. Norman, D. D. Koelling, and A. J. Freeman, Phys. Rev. B **31**, 6251 (1985).
[17] A. J. Arko (unpublished).

Basis of strong change of hybridization-induced magnetic ordering between CeSb and CeTe

N. Kioussis[a] and B. R. Cooper
Department of Physics, West Virginia University Morgantown, West Virginia 26506
J. M. Wills
Los Alamos National Laboratory, Los Alamos, New Mexico 87545

A sharp change in the nature of the magnetic ordering has been observed on going from CeSb to CeTe, both of which have NaCl structures with a small decrease in lattice parameter. This is an interesting example of the way in which hybridization of partially delocalized f electrons with band electrons gives rise to highly unusual magnetic properties which show great chemical sensitivity. In the present paper we apply our previous *ab initio* treatment of hybridization-induced effects to investigate this striking change in magnetic behavior. We have performed self-consistent warped muffin-tin LMTO band calculations treating the Ce $4f$ states as resonance states that are constrained to be localized. Compared to CeSb, the anion-derived p bands in CeTe sink well below the Fermi energy, thus strongly changing the band-f hybridization. We have calculated the hybridization dressing of the crystal-field levels and the anisotropic two-ion exchange interaction and compared them with those calculated for CeSb and with experiment. A strong decrease in the two-ion interaction explains the drastic change in observed magnetic behavior between CeSb and CeTe.

I. INTRODUCTION

Among the NaCl-structure monopnictides and monochalcogenides of cerium, CeSb exhibits the most unusual magnetic behavior.[1] The most striking feature of its low-field phase diagram is the occurrence of high-temperature ($8.5 < T < T_N \simeq 16.2$ K) phases consisting of a periodic sequence of nonmagnetic and magnetically ordered (001) planes with up or down moments along the [001] cube edge and close to saturation ($\sim 2.1\mu_B$). The nonmagnetic planes, which are actually paramagnetic in nature,[1] disappear below 8.5 K yielding a type-IA antiferromagnetic structure.

The unique magnetic properties of CeSb are very sensitive to any perturbation such as pressure,[1] the dilution[2] of cerium by nonmagnetic Y or La, or the substitution of antimony by another pnictogen[3] (Bi, As), or by tellurium.[1,4] In particular, magnetization[1,4] and neutron scattering[1] experiments on $CeSb_{1-x}Te_x$ have shown that for a Te concentration as small as $x = 0.02$, the Néel temperature drops abruptly from 16 K to less than 4 K, and the nonmagnetic planes are supressed. Moreover, the crystal-field (CF) splitting between the ground-state Γ_7 doublet and the Γ_8 quartet of the $4f_{5/2}$ multiplet, which is about 37 K in CeSb, increases with tellurium concentration, reaching its maximum value of about 105 K at $x = 0.5$, and the decreases monotonically with further increase of x to the value of about 32 K in[1] CeTe. CeTe orders at[5,6] $T_N \simeq 2.2$ K into a type-IA antiferromagnetic structure, with a Ce^{3+} local moment of only $0.2\mu_B$ aligned along the ⟨111⟩ direction, in sharp contrast with CeSb. This dramatic change in magnetic behavior on going from CeSb to CeTe with little change in the lattice constant, and where the only obvious change is the addition of an anion p electron, clearly demonstrates the sensitivity of the hybridization-mediated exchange interactions to chemical environment.

The large cube-edge anisotropy and consequent unusual magnetic behavior of the heavier cerium monopnictides (CeSb and CeBi) have been successfully explained[7-9] on the basis of an anisotropic hybridization-mediated two-ion interaction. This interaction arises through cooperative hybridization between moderately delocalized f electrons of the Ce^{3+} lattice and band electrons of non-f atomic parentage. However, until recently, the basic parameters entering the theory, namely, the anisotropic two-ion exchange interactions and the CF splitting, had been taken as phenomenological input to match the experimentally observed Néel temperature, low-temperature moment, and CF splitting. Recently, Wills and Cooper[10] have presented a first-principles calculation of the model parameters for the cerium monopnictides, based on self-consistent, warped muffin-tin, LMTO band structures calculated for these compounds. The purpose of this paper is to evaluate from first principles the model parameters for CeTe in order to understand quantitatively the origins of the variation of the hybridization-induced anisotropies on going from a weakly hybridizing system such as CeSb to the presumably more strongly hybridizing CeTe system, which being at the border between a magnetic and a nonmagnetic state has sometimes been referred to[1] as a dense Kondo system.

II. THE METHOD

The first step is the generation of a self-consistent one-electron potential describing the band structure of CeTe. This is obtained from a warped muffin-tin LMTO band-structure calculation, without recourse to the atomic sphere approximation,[11] i.e., using a nonzero tail parameter as a variational parameter. The full interstitial potential is used,

[a] Present address: Department of Physics, California State University at Northridge, Northridge, CA 91330.

 0021-8979/88/083683-03$02.40 © 1988 American Institute of Physics

and the only shape approximation to the potential is a spherical averaging in nonoverlapping muffin-tin spheres surrounding the Ce and Te sites. The potential is evaluated at the experimental volume, and the radii of the muffin-tin spheres are chosen to make the potential continuous where spheres touch.

The core states are included self-consistently and are obtained from the Dirac equation for the spherically averaged potential at each site. The Ce f electrons are treated as localized rather than itinerant states and thus they are included self-consistently as core states at each iteration, not being allowed to hybridize with band states. Thus as each iteration these $4f$ states are treated as resonant states that are constrained to be localized.[10] The radial basis functions for the (non-f) bands within the muffin-tin spheres are solutions of the scalar relativistic radial equation.[12] Spin-orbit coupling is included self-consistently. The band structure is divided into three energy windows: the semicore Ce $5p$ and Te $5s$ bands are calculated with an imaginary LMTO tail parameter κ, with κ^2 equal to -0.9 and -0.3 Ryd, respectively; and the Ce valence $6s$, $6p$, and $5d$ states and Te valence $5p$ states are calculated with a $\kappa^2 = 0.23$ Ryd, which is the average energy over occupied states in the interstitial.

We next calculate the basic model parameters entering the Anderson (Coqblin–Schrieffer) model Hamiltonian.[13] These are the band energies, ϵ_{nk}; the band f hybridization matrix element, $V_{nk,m}$ of the Hamiltonian for a single-particle potential surrounding the Ce site between the band state $|n,\mathbf{k}\rangle$ and the Ce$|5/2,m\rangle$ state; the f-state energy, E_f, with respect to the band Fermi energy E_F; and finally the intra-atomic f-f correlation energy U. Because accurate determination of these quantities requires a highly accurate representation of the bands around the resonant f-state energy, we perform a final band calculation, after the self-consistency process, with the tail parameter of the highest-energy window set equal to the resonant f-state energy.

Identifying the Ce $4f_{5/2}$ state wit the $l = 3, j = 5/2$ resonance in the local potential within a Ce muffin tin and projecting band-f overlap out of the matrix element to correct for band-f nonorthogonality, the hybridization potential matrix elements $V_{nk,m}$ have been shown[10] to be the product of two quantities. The first of these is the hybridization potential, which is proportional to the resonance width Γ, and which provides an overall scale. The second of these is proportional to the product of the KKR structure function and the LMTO eigenvectors, and describes the details of the band structure. The energy necessary to place the Ce f electron in a band state at the Fermi level, $E_F - E_f$, and the energy required to change from an f^1 configuration to an f^2 configuration, $E_f + U - E_F$, are obtained from self-consistent local-density supercell calculations, in which one considers eight atoms per unit cell as opposed to two for the ground-state calculation. These energies are obtained by removing (adding) an f electron to the central Ce site and allowing the system to relax, resulting in a d screening (antiscreening) of the f hole (electron).[14] We find that $E_F - E_f = 3$ eV, in good agreement with the value of 2.6 ± 0.1 eV found in x-ray photoemission experiments,[15] and $U = 6.3$ eV.

The hybridization-induced shift in the crystal-field energy levels, ΔE_M, in the paramagnetic phase is calculated by applying the Schrieffer–Wolff[16] transformation to the CS Hamiltonian to order $(V_{nk,m})^2$; and the hybridization-mediated two-ion interactions are determined[10] by applying the Schrieffer–Wolff transformation to order $(V_{nk,m})^4$ and treating the exchange scattering Hamiltonian in second-order perturbation theory on band states. There are two contributions to ΔE_M: a negative contribution resulting from hybridization of band states above E_F with the Ce f^1 state below E_F, and a second positive contribution (which is, however, smaller by a factor of $1/U$ relative to the first one) resulting from hybridization of band states below E_F with the Ce f^2 state above E_F.

III. NUMERICAL RESULTS AND DISCUSSION

The band structure of CeTe is plotted in Fig. 1. The energy of the corelike Ce $4f_{5/2}$ state lies 78 mRyd below the Fermi energy. At Γ, the Te p-derived bands have $\Gamma_8^{(-)}$ symmetry while the Ce d-derived bands are the bases for three representations, one with $\Gamma_7^{(+)}$ and two with $\Gamma_8^{(+)}$ symmetry. It is important to note that on going from CeSb to CeTe, the addition of an anion p electron has caused the p-derived bands to sink far below the Fermi level, so that the bands dominating the hybridization-induced properties in CeTe in the vicinity of Γ are largely derived from the Ce $5d$ states.

The total density of states (solid curve) corresponding to the band structure in Fig. 1 is shown in Fig. 2. Also plotted in the same figure are the partial density of states for the Ce d-derived (short-dashed curve) and the Te p-derived (long-dashed curve) bands, respectively. The Fermi energy and the density of states at the Fermi energy in CeTe are 0.475 Ryd and 15.6 states/Ryd, respectively, compared to the corresponding values of 0.374 Ryd and 4.4 states/Ryd in CeSb, indicating the metallic and semimetallic character of these compounds, respectively. However, aside from the location of E_F and the consequent density of states at E_F, and the opening of a gap in the density of states in CeTe below E_F between 0.325 and 0.375 Ryd, the density of states for the two compounds are qualitatively similar.

In both compounds, the hybridization-induced shift,

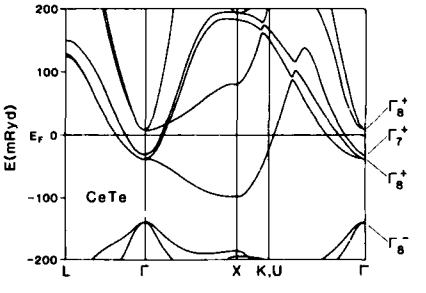


FIG. 1. Warped-muffin-tin LMTO band structure of CeTe along symmetry lines of the fcc Brillouin zone with the Ce $4f$ states treated as localized (see text). Energies are relative to the Fermi energy.

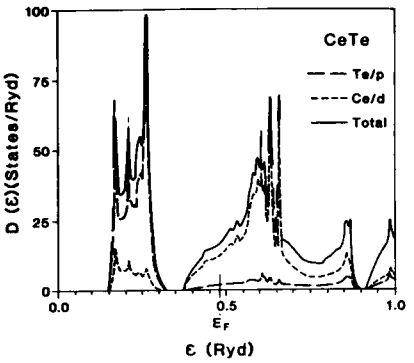


FIG. 2. Total density of states (solid curve) of the LMTO band structure of CeTe corresponding to the band structure in Fig. 1. Also shown are the partial density of states for the Ce d-derived (short-dashed curve) and Te p-derived (long-dashed curve) bands, respectively. The Fermi energy is at 0.475 Ryd.

δE_{Γ_8}, in the bare crystal-field energy level of the Γ_8 quartet is found to be larger than the corresponding shift, δE_{Γ_7}, of the Γ_7 doublet, by approximately a factor of 2. This results[10] from the fact that the set of degenerate bands belonging to the star of a general point in the irreducible wedge of the Brillouin zone form a basis for a representation of the cubic group that contains the Γ_7 representation twice and the Γ_8 representation four times. Importantly, the positive contributions to δE_{Γ_7} and δE_{Γ_8} resulting from hybridization of band states below the Fermi with the f^2 state are about the same in both CeTe and CeSb. On the other hand, the negative dominant contribution to δE_{Γ_7} and δE_{Γ_8} resulting from hybridization of band states above the Fermi energy with the f^1 state decreases by about a factor of 2 on going from CeSb to CeTe. This arises from the fact that the hole band states in CeSb in the vicinity of its Fermi energy, which were yielding the largest negative contribution to δE, become occupied on going to CeTe, thus giving a positive contribution, which, however, is reduced by a factor of $1/U$. Furthermore, the large cancellation between the positive and negative term, which are of comparable magnitude, results in a net shift, $\delta E_{CF} = \delta E_{\Gamma_8} - \delta E_{\Gamma_7}$, of 45 K in CeTe compared to the corresponding value of 194 K in CeSb. However, in the absence as yet of a value for the "bare" (without hybridization dressing) CF splitting for CeTe, it is rather difficult to make a direct comparison of theory and experiment as in the case of CeSb, where the agreement was found to be excellent.[10]

Finally, of most immediate interest, we have calculated the hybridization-mediated exchange interactions,[7,8] $E_n^{mm'}$, between two nth nearest-neighbor Ce^{3+} ions (where m and m' denote the components of the angular momentum quantized along the interionic axis) which are pertinent to the dramatic change in magnetic behavior on going from CeSb to CeTe. We find that as in the case of[10] CeSb, the dominant matrix elements involve the $m,m = \pm 1/2$ states, which correspond to the piling up of charge along the interionic axis. In particular, for $m,m' = \pm 1/2$ we find that E_1, which in the phenomenological treatment[7-9] is chosen to match the Néel temperature, decreases from 0.84 K in CeSb to 0.15 K in CeTe, yielding a ratio of about 5.7, in good agreement with the value of 7 for the ratio of the experimentally observed Néel temperatures. Moreover, for $m,m' = \pm 1/2$ we find that $E_2 = 3.1E_2$ (ferromagnetic) in CeSb compared to $0.42E_1$ (antiferromagnetic) in CeTe; and $E_3 = -0.02E_1$ in CeSb compared to $0.17E_1$ in CeTe. This occurrence of ferromagnetic and antiferromagnetic interactions of comparable strength, and the consequent need for "compromise" might be responsible for the low moment value in CeTe rather than a "Kondo effect," and also for the change in magnetic structure compared to that of CeSb. The inclusion of all the transition channels of the range function matrix in the phenomenological theory to treat in detail the magnetic ordering in these compounds is currently under investigation.

ACKNOWLEDGMENTS

The research at West Virginia University was supported through the National Science Foundation under grant No. DMR-85-04449. The research at Los Alamos National Laboratory was supported by the U.S. Department of Energy.

[1] J. Rossat-Mignod, J. M. Effantin, P. Burlet, T. Chattopadhyay, L. P. Regnault, H. Bartholin, C. Vettier, O. Vogt, D. Ravot, and J. C. Achart, J. Magn. Magn. Mater. **52**, 111 (1985).
[2] B. R. Cooper and O. Vogt, J. Phys. (Paris) **32**, C1-1026 (1971).
[3] H. Bartholin, O. Vogt, and J. P. Senateur, J. Magn. Magn. Mater. **15–18**, 1247 (1980).
[4] D. Ravot, A. Mauger, J. C. Achard, M. Bartholin, and J. Rossat-Mignod, Phys. Rev. B **28**, 4558 (1983).
[5] F. Hulliger, B. Natterer, and H. R. Ott, J. Magn. Magn. Mater. **8**, 87 (1978); H. R. Ott, J. K. Kjems, and F. Hulliger, Phys. Rev. Lett. **42**, 1378 (1979).
[6] D. Ravot, P. Burlet, J. Rossat-Mignod, and J. L. Tholence, J. Phys. (Paris) **41**, 1117 (1980).
[7] R. Siemann and B. R. Cooper, Phys. Rev. Lett. **44**, 1015 (1980).
[8] B. R. Cooper, R. Siemann, D. Yang, P. Thayamballi, and A. Banerjea, in *The Handbook of the Physics and Chemistry of the Actinides*, edited by A. J. Freeman and G. G. Lander (North-Holland, Amsterdam, 1985), Vol. 2, Chap. 6, pp. 435–500.
[9] N. Kioussis, B. R. Cooper, and A. Banerjea, J. Appl. Phys. **61**, 3388 (1987).
[10] J. M. Wills and B. R. Cooper, Phys. Rev. **36**, 3809 (1987).
[11] H. L. Skriver, *The LMTO Method* (Springer, Berlin, 1984).
[12] D. D. Koelling and B. N. Harmon, J. Phys. C **10**, 3107 (1977).
[13] B. Coqblin and J. R. Schrieffer, Phys. Rev. **185**, 847 (1969).
[14] M. R. Norman, D. D. Koelling, A. J. Freeman, H. J. F. Jansen, B. I. Min, T. Oguchi, and L. Ye, Phys Rev. Lett. **53**, 1673 (1984).
[15] W. Gudat, M. Campagna, R. Rosei, J. H. Weaver, W. Eberhardt, F. Hulliger, and E. Kaldis, J. Appl. Phys. **52**, 2123 (1981).
[16] J. R. Schrieffer and P. A. Wolff, Phys, Rev. **149**, 491 (1966).

Shift in maximum of sound attenuation with magnetic field in UPt_3

H.-P. Baum and M.-F. Xu
Physics Department, University of Wisconsin-Milwaukee, Milwaukee, Wisconsin 53201

Y. J. Qian[a)]
Physics Department, University of Wisconsin-Milwaukee, Milwaukee, Wisconsin 53201 and Department of Physics, Northwestern University, Evanston, Illinois 60201

A. Schenstrom
Physics Department, University of Wisconsin-Milwaukee, Milwaukee, Wisconsin 53201

J. B. Ketterson
Department of Physics, Northwestern University, Evanston, Illinois 60201

D. H. Hinks
Materials Science and Technology, Argonne National Laboratory, Argonne, Illinois 60439

M. Levy and B. K. Sarma
Physics Department, University of Wisconsin-Milwaukee, Milwaukee, Wisconsin 53201

We have measured ultrasonic attenuation and ac susceptibility simultaneously on a UPt_3 single crystal, in various constant magnetic fields at 293 MHz, and in zero field at several frequencies. The temperature of the attenuation maximum $T_{m\alpha}$ appears lower than (or very close to) the susceptibility transition temperature $T_{c\chi}$. A breakpoint is defined, which occurs always at a lower temperature T_{bp} than $T_{m\alpha}$. The shift of this breakpoint, $T_{c\chi} - T_{bp}$, exhibits a small frequency dependence.

INTRODUCTION

Ultrasonic attenuation measurements in UPt_3 have previously shown that the temperature $T_{m\alpha}$, at which the attenuation α is maximum, is lower than the superconducting transition temperature $T_{c\chi}$ associated with ac susceptibility $T_{c\chi}$ measurements.[1-3] In this paper, we present our results of simultaneous measurements of the ultrasonic attenuation α and ac susceptibility χ as a function of temperature T, at 293 MHz in various constant magnetic fields, and at several frequencies in zero field.

The results will be discussed in terms of the shift $T_{c\chi} - T_{m\alpha}$ and of another shift $T_{c\chi} - T_{bp}$, where T_{bp} is the temperature corresponding to the occurrence of a "breakpoint" in the α-vs-T curve, which will be defined shortly. This second definition of a temperature shift exhibits a small frequency dependence. Furthermore, the temperature T_{bp} is always lower than the temperature $T_{c\chi}$; however, T_{bp} rapidly approaches $T_{c\chi}$ as the field is increased.

EXPERIMENTAL DETAILS

We have investigated a single crystal of UPt_3 in a dilution refrigerator between 50 mK and 0.8 K. A quartz transducer of 26 MHz fundamental frequency was used to produce longitudinal ultrasonic waves up to 565 MHz. A superconducting magnet provided a stable and homogeneous (0.01% in 1 cm dsv) magnetic field between 0 and 1.4 T (at $T = 0$ K, $H_{c2} \simeq 2.01$ T) parallel to the wave propagation which was also the crystal c axis. At zero field, temperatures were measured with a germanium resistance thermometer (GRT). For thermometry in the presence of fields, a Matsushita carbon resistance thermometer (CRT, calibrated against the GRT at zero field) was used. Both thermometers were bonded to the copper slug with GE 7031 varnish, within a few mm of the sample.[4] The frequency generator was part of the MATEC system used for the production and detection of the ultrasonic waves.

A typical graph of the temperature dependence of the attenuation and susceptibility is depicted in Fig. 1, which also illustrates how the three temperatures discussed in this paper were determined. The critical temperature $T_{c\chi}$ is measured on the susceptibility curve (b) at the midpoint of the transition step, marked by a star and an arrow. On the attenuation curve, the temperature $T_{m\alpha}$ corresponding to the maximum in attenuation is the highest point of the smooth curve passing through the raw data curve, and is indicated by the arrow on the right above curve (a). The breakpoint is defined as the intersection of the extrapolations of the "asymptotic" behavior of the attenuation on each side of the maximum, and is indicated by the arrow on the left above curve (a); its corresponding temperature is T_{bp}.

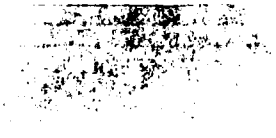
The determination of $T_{c\chi}$ was relatively unambiguous and generally better than ± 2 mK on the graph. For $T_{m\alpha}$ and T_{bp} we report only those results resolved to better than ± 8 mK; however, the resolution was typically a few mK.

DISCUSSION

Figure 2 shows a plot of $T_{c\chi} - T_{m\alpha}$ vs $T_{c\chi}$ at the eleventh harmonic, 293 MHz, a high frequency at which the

[a)] Permanent address: Physics Department, Fudan University, Shanghai, People's Republic of China.

 0021-8979/88/083686-03$02.40 © 1988 American Institute of Physics



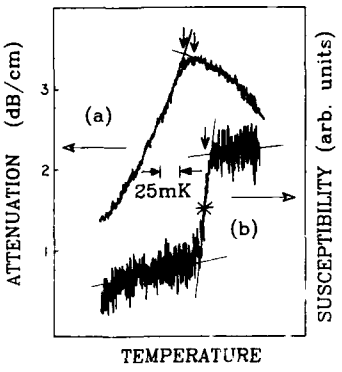


FIG. 1. Raw data and definitions: curve (a) shows attenuation with temperatures of the maximum $T_{m\alpha}$ (indicated by the right vertical arrow above the curve) and of the breakpoint T_{bp} (left vertical arrow); curve (b) is ac susceptibility with critical temperature $T_{c\chi}$ at the transition midpoint (star and vertical arrow above curve).

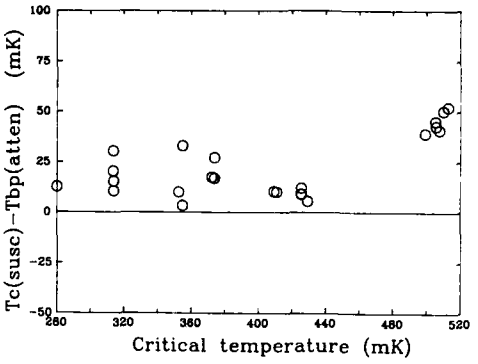


FIG. 3. Shift of the breakpoint temperature T_{bp} as a function of $T_{c\chi}$ at 293 MHz.

signal was reasonably strong. From this figure, it appears that the maximum occurs at about 35 mK below the superconducting transition temperature as defined from the susceptibility measurement. However, in magnetic fields large enough to shift the transition temperatures to lower than 430 mK, the temperature $T_{m\alpha}$ of the maximum appears to move above $T_{c\chi}$, although when considering the uncertainty in the measurements, the positions of the maximum and the midpoint of the susceptibility transition may well coincide. A similar analysis of the position of the breakpoint (illustrated in Fig. 3) indicates a small increase in the shift $T_{c\chi} - T_{bp}$ as compared to the shift $T_{c\chi} - T_{m\alpha}$, implying that the temperature corresponding to the breakpoint is always lower than both the temperatures $T_{m\alpha}$ and $T_{c\chi}$.

Figure 4 shows a plot of $T_{c\chi} - T_{bp}$ as a function of frequency at zero magnetic field. Each point in this figure was obtained by calculating the average of the results for $T_{c\chi} - T_{bp}$ for all runs at the same frequency. The straight line is a least-squares fit of the points obtained as explained above. This line shows that there seems to be a weak dependence of the position of the break point with respect to frequency. From our data, a dependence on frequency of the position of the maximum could however not be resolved.

As yet there are no theoretical models for the fact that in zero magnetic field the attenuation maximum appears below the temperature at which the susceptibility indicates a superconducting transition. We would like to postulate a possible explanation for the results that have been observed in Figs. 2, 3, and 4.

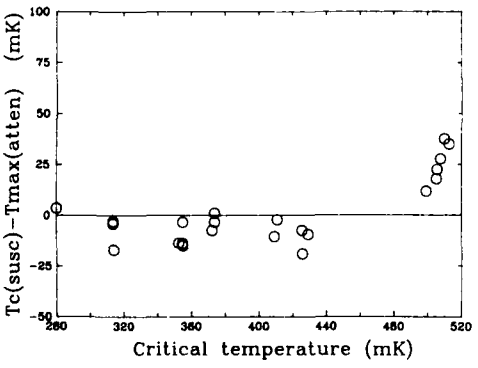


FIG. 2. Shift of the temperature $T_{m\alpha}$ of the attenuation maximum as a function of $T_{c\chi}$ at 293 MHz.

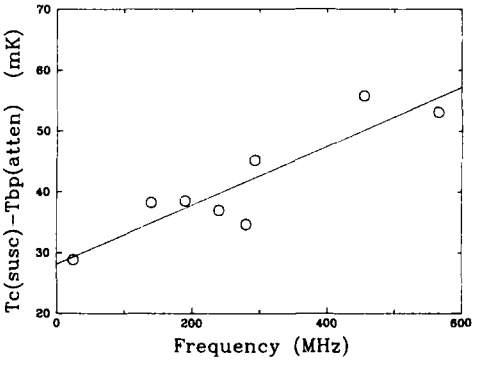


FIG. 4. Shift of the attenuation breakpoint temperature T_{bp} as a function of frequency in zero magnetic field. Each point represents the average of all results at that frequency; the straight line is a least-squares fit of those points.

If it is assumed that this heavy fermion superconductor possesses an anisotropic energy gap[5] which vanishes at several places on the Fermi surface, then it is natural to ask what might be the effect of pair breaking impurity scattering. It is possible that the node line or points expand into local regions or bands which have zero gap. Near the transition temperature these zero gap regions may extend over substantial portions of the Fermi surface. The attenuation may then begin to change only slightly on passing through the transition temperature and not decrease significantly until a substantial portion of the Fermi surface has a local gap $\Delta(\hat{k}) > \hbar\omega_s/2$. At higher frequencies, one has to go lower in temperature to achieve this condition, i.e., T_{bp} or $T_{m\alpha}$ should move lower relative to $T_{c\chi}$. Note that in Fig. 4 the zero frequency extrapolation of the shift is finite, supporting the idea of an extended region of gaplessness over the Fermi surface. In the presence of a magnetic field, the alignment of the nodal structure may shift, which can in turn affect the interaction with the sound waves.

CONCLUSION

We have simultaneously measured the ultrasonic attenuation α and the ac susceptibility χ of a single crystal of UPt_3 as a function of temperature, at 293 MHz in several constant magnetic fields, and also at zero field for several frequencies. The analysis of the field-dependent data shows that the temperature $T_{m\alpha}$ of the maximum in attenuation is always lower than, or almost coincident with, the transition temperature $T_{c\chi}$ from ac susceptibility. We defined a break point in the attenuation curve, and its corresponding temperature T_{bp} is always lower than $T_{m\alpha}$. The studies as a function of frequency show that the shift $T_{c\chi} - T_{bp}$ increases with frequency. We postulate that an explanation for these results might be found in the anisotropic nature of the energy gap, which in the presence of impurity scattering may even vanish over a region of finite area in the vicinity of lines or points. Lowering the temperature would reduce the gapless fraction of the Fermi surface. A magnetic field, while lowering $T_{c\chi}$, could realign the gap anisotropies, thereby changing the effective interaction of the sound waves with the quasi particles.

ACKNOWLEDGMENT

This research was partially supported by AFOSR grant No. AFOSR 84-0350.

[1] V. Muller, D. Maurer, E. W. Scheidt, Ch. Roth, K. Luders, E. Bucher, and H. E. Bommel, Solid State Commun. **57**, 319 (1986).

[2] D. J. Bishop, C. M. Varma, B. Batlogg, E. Bucher, Z. Fisk, and J. L. Smith, Phys. Rev. Lett. **53**, 1009 (1984).

[3] Y. J. Qian, M-F. Xu, A. Schenstrom, H-P. Baum, J. B. Ketterson, D. Hinks, M. Levy, and Bimal K. Sarma, Solid State Commun. **63**, 599 (1987).

[4] H-P. Baum, Y. J. Qian, M-F. Xu, A. Schenstrom, M. Levy, and Bimal K. Sarma, Proceedings of the 18th Conference on Low Temperature Physics, Kyoto, 1987, Jpn. J. Appl. Phys. **26-3**, 1731 (1987).

[5] J. R. Rodriguez, Phys. Rev. Lett. **55**, 250 (1985); C. M. Varma, Comm. Solid State Phys. **11**, 221 (1985); E. Bucher, B. Batlogg, D. J. Bishop, C. M. Varma, Z. Fisk, and J. L. Smith, J. Appl. Phys. **57**, 3060 (1985).

Magnetization measurements on (Ce,Gd)Al_3

A. S. Edelstein and R. L. Holtz
Naval Research Laboratory, Washington, DC 20375

$Ce_{1-x}Gd_xAl_3$ exhibits an interesting interplay of heavy-fermion, spin-glass, and antiferromagnetic behavior. Magnetization measurements were undertaken to further our understanding of this system and to estimate the fraction of the magnetization involved in the spin-glass and antiferromagnetic transitions. By making a linear extrapolation of the magnetization data to $H = 0$, one defines the spontaneous magnetization, M_s. At $T = 2$ K, we find that M_s is approximately proportional to x for $x \leqslant 0.4$ and equal to approximately 10% of the maximum possible contribution from just the Gd moments. M_s increases at a much faster rate between $x = 0.40$ and 0.50, but then decreases to zero at $x = 0.635$ where the system is antiferromagnetic. For $x = 0.635$ and $T = 1.5$ K, the magnetization is proportional to H for $H \leqslant 80$ kOe. Using this linearity, we suggest that nearly all the spins are correlated at low temperatures for $x \geqslant 0.635$.

I. INTRODUCTION

Previous specific heat, susceptibility, and resistivity measurements[1,2] on $Ce_{1-x}Gd_xAl_3$ have established that this system exhibits an interesting interplay of heavy-fermion, spin-glass, and antiferromagnetic behavior. For $0.08 \leqslant x \leqslant 0.9$ there is a susceptibility cusp similar to the one found in spin-glass systems. The temperatures T_m at which these anomalies occur, e.g., 100 K for $x = 0.5$, are surprisingly high. None of the ordering temperatures of the trialuminides[3] are higher than 25 K. Modeling of the specific heat and susceptibility data on samples having $x \leqslant 0.23$ suggests[2] that for temperatures less than approximately 5 K the spin-glass and heavy-fermion states coexist.

The nature of the transition, which resembles a spin-glass transition, is drastically modified at high concentrations. This modification occurs for $x > x_c$ where x_c is the critical concentration or percolation threshold above which the system is antiferromagnetic. Susceptibility measurements[1,2] have determined that $0.5 < x_c < 0.635$. The specific changes that occur for $x > x_c$ are: (1) the amplitude of the susceptibility anomaly at T_m decreases by more than two orders of magnitude as one increases x from 0.5 to 0.56, and (2) a resistivity anomaly appears at T_m. We have performed magnetization measurements to further investigate the nature of the magnetism above and below x_c. These magnetization measurements provide further evidence that the magnetism is very different in these two concentration regimes. Specifically, it appears that there is a rapid change from a situation where ferromagnetic interactions dominate below x_c to one where antiferromagnetic interactions dominate above x_c.

II. EXPERIMENT

X-ray diffraction measurements at 10 concentrations show that the lattice parameters a and c of the hexagonal DO_{19} strucure of the system vary approximately linearly as a function of x. This linearity implies that the unusual behavior described above is not associated with any valence instability or structural transformation. We have investigated[4] samples with $x = 0.05$, 0.20, 0.40, 0.50, and 0.635. The samples with $x \geqslant 0.4$ are the same samples that were employed in the earlier[1,2] susceptibility measurements. The measurements for $x \leqslant 0.2$ were made using a vibrating sample magnetometer while for $x > 0.2$ we employed a SQUID system.

Figure 1 is a plot of the magnetization M versus the applied field for the $x = 0.50$ sample at several temperatures. Though there is a rapid rise in M at low fields for $T \leqslant 90$ K, M does not saturate at high fields as it would for a simple ferromagnet. By making a linear extrapolation of this data to $H = 0$, as illustrated in Fig. 1, one defines the spontaneous magnetization M_s. A plot of M_s vs T for $x = 0.50$ is shown in Fig. 2. The temperature T_m of the cusp in the susceptibility at this composition is 100 K. The temperature at which M_s extrapolates to zero is somewhat above T_m. This is not surprising, since the magnetic field has a tendency to align the moments and shift the transition. Our magnetization data for the $x = 0.05$, 0.02, and 0.40 samples are qualitatively similar but the values of M_s are much smaller. The magnetization for $x = 0.635$ for several temperatures is shown in Fig. 3. The system is antiferromagnetic at this composition at 10 K. One sees that there is no spontaneous magnetization and that the magnetization is a linear function of the applied field. The ratio of M/H for a fixed temperature is constant to

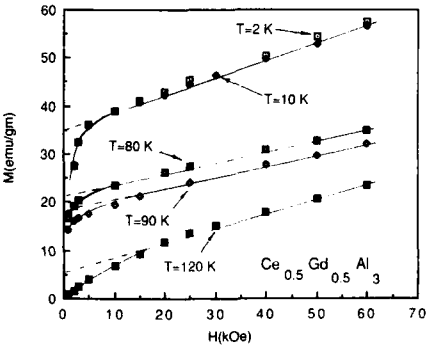


FIG. 1. Magnetization of $Ce_{0.50}Gd_{0.50}Al_3$ vs H for several temperatures.

 0021-8979/88/083689-03$02.40 © 1988 American Institute of Physics

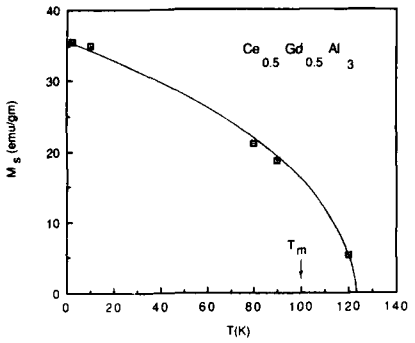


FIG. 2. Spontaneous magnetization M_s of $Ce_{0.5}Gd_{0.5}Al_3$ vs temperature.

within a few percent. Clearly the magnetization changes dramatically between $x = 0.50$ and $x = 0.635$.

III. DISCUSSION

One way of investigating this change is to consider the spontaneous magnetization. It is reasonable to compare this value with the maximum value one could obtain if only the Gd were contributing, $M_{s,Gd}$. Tabulated in Table I is the spontaneous magnetization M_s at 2 K, the ratio $M_s/M_{s,Gd}$ at 2 K, and x. One sees that the ratio $M_s/M_{s,Gd}$ stays constant at approximately 0.1 for $x \leqslant 0.4$ but that it is much larger at $x = 0.5$. This approximate scaling of M_s with x for $x \leqslant 0.4$ suggest that interacting Gd moments are responsible for the spin-glass transition. The fact that the ratio $M_s/M_{s,Gd}$ is approximately 0.4 for $x = 0.50$ suggests that the number of ferromagnetic interactions increases rapidly between 0.40 and 0.50, i.e., as one approaches x_c from below. The large decrease in the susceptibility at T_m above x_c and the absence of any spontaneous magnetization indicates that there is a rapid change in the magnetic character of the system. It may be that antiferromagnetic interactions dominant for $x > x_c$ even at temperatures as high as 100 K. Since the $x = 0.635$ sample is antiferromagnetic at $T = 10$ K, one expects that antiferromagnetic interactions will be important, but it is not

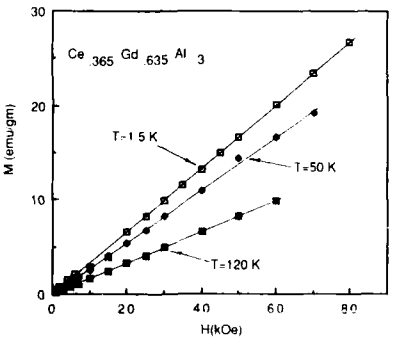


FIG. 3. Magnetization of $Ce_{0.365}Gd_{0.635}Al_3$ vs H for several temperatures.

TABLE I. Spontaneous magnetization M_s at 2 K.

x	M_s (emu/g)	$M_s/M_{s,Gd}$
0.05	1	0.1
0.20	4.5	0.13
0.4	10	0.15
0.50	36	0.42
0.635	0.0	0.0

obvious that antiferromagnetic interactions should dominate at much higher temperatures.

One can use the magnetization to investigate whether the spins are correlated. Consider the magnetization data for the $x = 0.635$ sample at $T = 1.5$ K. The contribution of the Ce is less than it is in $CeAl_3$. This follows from fact that, if one scales the $CeAl_3$ magnetization[5] at $T = 1.4$ K by 0.365, then the resulting magnetization is larger than the magnetization for the $x = 0.635$ sample. Further, since the magnetization of $CeAl_3$ shows considerable curvature as a function of H at 1.4 K, one might expect that the slope of the magnetization curve for the $x = 0.635$ sample as a function of H should decrease at high fields. Instead of the anticipated decrease in slope in going from 0 Oe to 6 T, we have observed a 1% increase in slope for $x = 0.635$ at $T = 1.5$ K. We use these results to suggest that both the Ce and Gd spins are correlated for $x > x_c$. Figure 4 shows a plot of $M_s/M_{s,Gd}$ vs x at 2 K and the one point representing the fraction of the spins that are correlated at $x = 0.635$, $T = 1.5$ K. The dashed curves in Fig. 4 are used only to illustrate likely trends. The curve for the number of spins which are correlated may be either above or below the curve for $M_s/M_{s,Gd}$ near $x = 0.5$. Nevertheless, Fig. 4 illustrates that there is a dramatic change in the character of the system at $x > 0.5$. If nearly all the spins are correlated for $x > x_c$, then one might expect a resistivity anomaly for $x > x_c$. It is surprising that this anomaly does not occur at the Néel temperature, of order 10 K,

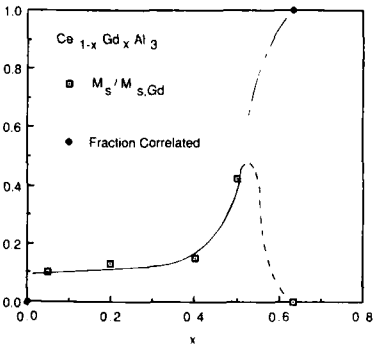


FIG. 4. Plot showing (i) the fraction of the spins that are correlated at the point $x = 0.635$ and 1.5 K and (ii) the ratio of the spontaneous magnetization at 2 K to the maximum theoretical moment from just the Gd, $M_s/M_{s,Gd}$, as a function of Gd concentration x. The dashed lines are used to suggest likely trends.

but instead occurs[1] at the much higher temperature T_m, of order 100 K. This result leads one to suspect that many of the spins are correlated at high temperatures. The magnetization data and resistivity data are consistent with the idea that a large fraction of the spins become correlated for $x > x_c$ and $T < T_m$.

In general, we find that the magnetization of $(Ce,Gd)Al_3$ is consistent with the behavior determined by our earlier[1,2] measurements. The magnetization measurements permit us to infer that a large fraction of the Gd spins are involved in spin-glass transition as one approaches x_c from below and that a large fraction of both the Ce and Gd spins are probably involved in the antiferromagnetic transition for $x \geqslant x_c$.

[1]A. S. Edelstein, R. L. Holtz, D. J. Gillespie, R. A. Fisher, and N. E. Phillips, J. Magn. Magn. Mater. **63 & 64**, 335 (1987).
[2]A. S. Edelstein, R. L. Holtz, D. J. Gillespie, M. Rubinstein, J. Tyson, R. A. Fisher, and Norman E. Phillips, Phys. Rev. (to be published).
[3]K. H. J. Buschow and J. F. Fast, Z. Phys. Chem. (Frankfurt) **50**, 1 (196€).
[4]For $x = 0.05$ and 0.20, magnetization data have been presented earlier [A. S. Edelstein and N. C. Koon, J. Appl. Phys. **55**, 1984 (1984)].
[5]F. R. de Boer, J. Klaasse, J. Aarts, C. D. Bredl, W. Lieke, U. Rauchschwalbe, F. Steglich, R. Felten, U. Umhofer, and G. Weber, J. Magn. Mater. **47 & 48**, 60 (1985).

Unstable valence rare earths ion implanted into transition metals: Valence variation studies

F. Lu, S. Gunapala, and M. Croft
Rutgers University, Piscataway, New Jersey 08855-0849

N. G. Stoffel
Bell Communications Research, Navasink, New Jersey 07752

M. L. den Boer
Hunter College/CUNY, New York, New York 10021

The technique of ion implantation is applied to study the problem of valence instabilities of Ce and Eu in transition-metal hosts. L_3 x-ray absorption spectroscopy measurements are used to probe the rare-earth valence state in these materials. Typical extreme valence variations are illustrated with Y, Ti, and Pd hosts. The important question of identifying extrinsic oxidation of the rare-earth implant is addressed in detail. The signatures of rare earth oxidation in the x-ray spectra of both bulk compound and implanted materials are discussed using specific examples.

Ion implantation has become a standard tool for preparing precise near-surface semiconductor alloys.[1] In many cases, this technique allows the metastable preparation of atomically dispersed alloys which, under equilibrium conditions, simply cannot be formed. The flexibility in implant and of host afforded by this technique makes it an attractive new route to study long-standing questions regarding valence and magnetic moment instabilities in solids. These questions address the often subtle interactions of the impurity orbitals with the host band states, which determine the stability of the impurities valence state and magnetic moment.[2]

In this paper, we will discuss x-ray absorption spectroscopy (XAS) measurements to determine the average valence state of Ce and Eu atoms implanted into selected transition-metal (T) hosts. Transition-metal hosts chosen to illustrate the extrema of the valence variation of these implanted valence fluctuators are discussed. We will also address the important experimental issue of the identification of oxidation effects in unstable valence materials.

The samples discussed here were prepared by implanting 100-keV Ce or 150-keV Eu ions into transition-metal foils. Implant profiles varied from sample to sample, however, typically the concentration of rare earths was about 1% or 3% for Ce, and 3% or 10% for Eu in the top 100–300-Å range of the foils. RBS measurements on and computer simulation of the implanted materials were made to determine the implantation profile. The XAS measurements were made at the Cornell High Energy Synchrotron Source with the implanted materials being measured in the total electron yield mode[3] and with the powdered $CePb_3$ and CeO_2 samples being measured in the standard transmission mode.

The phenomenon of valence mixing entails the quantum tunneling (on a time scale of 10^{-13} s) of a rare-earth atom between two nearly degenerate valence $4f$ occupancy states (e.g., $Ce^{3+}4f^1 \leftrightarrow Ce^{4+}4f^0$ or $Eu^{2+}4f^7 \leftrightarrow Eu^{3+}4f^6$).[4] In the mixed valent state the valence and $4f$ occupancy are nonintegral and lie between the mixing and endpoint states.[5] L_3-XAS provides a sensitive probe of rare-earth valence by virtue of the 7–10 eV shift in the $2p$ binding energy that accompanies an integral valence change. Moreover, the 10^{-17} s time scale for XAS places it in the "fast" or "snapshot" regime among valence probing techniques.[4–6] Thus, the L_3-XAS spectrum of a mixed valence substance consists of a superposition of two integral valent edge features displaced by 7–10 eV with the relative weight of the features being related to the average valence.[4] The two integral valent contributions used to model our Ce in Pd spectrum are shown in Fig. 1. A more detailed discussion of the fitting procedures used to determine the L_3-valence estimates have been discussed elsewhere.[4]

We have discussed the propensity of transition-metal-based compounds to stabilize the highest valence state of unstable valence rare earths in a number of previous papers.[4–6] This behavior is traceable in part to the strong variation in the T-d orbital energy with varying d occupancy.

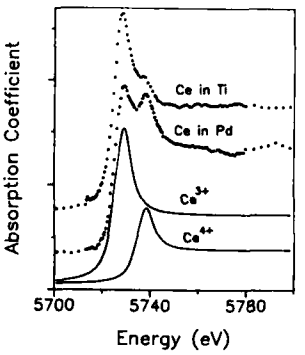


FIG. 1. Ce-L_3 spectra for Ce implanted in Ti and Pd (dots). The solid lines represent the separate Ce^{3+} and Ce^{4+} components used to model the Ce in Pd spectrum. The average Ce-L_3 valence in the Ti and Pd hosts were 3.14 and 3.33, respectively.

 0021-8979/88/083692-03$02.40 © 1988 American Institute of Physics

Specifically, a healthy depression of the d-orbital energy occurs (i) at high values of the d occupancy (n_d), due to the large unscreened core charge, and (ii) when the d-band (or correlated subband) is half filled, due to the d-bonding energy. The response of the valence of an unstable valence rare earth chemically combined with transition-metal-based materials appears to track these d-band energy variations.[4,7,8]

Whereas intermetallic compounds offer only a restricted set of systems in which to study the rare-earth valence state to transition-metal coupling, ion-implanted metastable alloys open all of the transition metals for study. The strong valence state to transition metal coupling is illustrated in Figs. 1 and 2 where the L_3 spectra for Ce in Ti and Pd, and Eu in Y and Pd are shown. Both Ti and Y represent low-d band occupancy transition metals with low unscreened core charges and hence not too deeply bound d orbitals. Pd, on the other hand, has a very high d-band occupancy (i.e., large effective core charge) and also possesses substantial d-band bonding. Ce and Eu implanted in Pd assume their highest possible valence state. The valence state of Eu implanted in Pd is pure Eu^{3+} with the L_3 spectrum showing essentially no intensity in the lower-energy Eu^{2+}-edge range. The L_3 spectrum of Ce in Pd shows clearly resolved Ce^{3+} and Ce^{4+} contributions with the L_3 valence obtained from their respective weights being about 3.3. This Ce-L_3 valence of 3.3 is known to represent the highest Ce-valence state in metals, however, the full interpretation in terms of the equivalent chemical valences is still an open question.[9]

By contrast the L_3 spectra for Ce in Ti and Eu in Y evidence much lower valences (than in Pd). The Eu^{2+} component in the Eu in Y spectra is clearly dominant, with the average valence being $v = 2.3$. Indeed, concentrated materials [like $Eu(Pd, Au)_2Si_2$] with Eu valences near 2.3 are close enough to the magnetic Eu^{2+} valence state to support magnetically ordered ground states.[10] The Ce in Ti L_3 spectrum is typical of a Ce system on the border line between a mixed valent and a Kondo regime with a Ce-L_3 valence of 3.14.[8]

The rare earths (especially Ce and Eu) are well known for their tendency to react strongly with oxygen. This reactivity is sometimes (but not always) inhibited in compounds and alloys. The occurrence of oxidation on the bulk compound $CePb_3$ is illustrated in Fig. 3. The solid line in the figure is the Ce-L_3 spectrum of a $CePb_3$ sample sealed in an inert Ar atomosphere ($CePb_3$). The vertically displaced dashed spectrum is that of CeO_2, the highest oxide of Ce. The dotted spectrum superimposed on the $CePb_3$ spectrum is that of the sample after being exposed to air for roughly 60 min (in fact, much shorter exposures achieve the same effect). Clearly, the oxidized spectrum [$CePb_3(ox)$] consists of a superposition of some sites which are oxidized to CeO_2 and some which remain $CePb_3$ like.

Using this case as an example, we wish to note several spectral features which accompany the Ce-oxidation process. First, since the oxidation drives Ce sites to their highest valence state, the Ce^{4+} feature in the spectra gains intensity. Second, CeO_2 exhibits a strong chemical shift to higher energy (roughly 4 eV) relative to metallic Ce compounds of any valence. The first (Ce^{3+}-related) feature in a partially oxidized material is therefore strongly broadened consisting of unresolved Ce^{3+} metallic and Ce^{3+} oxidized features. Also, of course, the Ce^{4+} oxidized feature is shifted to higher energy.

Third, and finally, we wish to note that there is a strong "continuum resonance" feature in the CeO_2 spectra occurring roughly 38 eV beyond the Ce^{3+} feature. Such a "continuum resonance" is caused by the multiple scattering of the outgoing photoelectron by the nearest neighbor shell of ligand oxygen atoms.[11] The strength and energy of this continuum resonance is related to the size and coordination (eightfold for CeO_2) of this oxygen shell.[11] Typical metallic environments, where the neighbors are not strongly electronegative, show much weaker structures in this energy range. Thus, we also associate the appearance of this strong continuum resonance feature with oxidation. The reader should note that this effect and those noted in the proceeding paragraph involve atomic or nearest-neighbor shell effects and

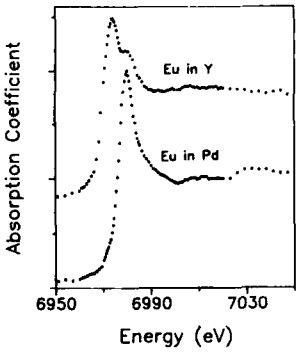


FIG. 2. Eu-L_3 spectra for Eu implanted in Y (average valence 2.2) and Pd (average valence 3.0).

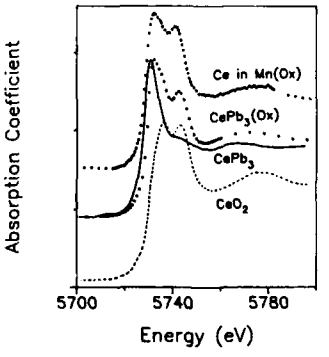


FIG. 3. Ce-L_3 spectra for: $CePb_3$ (solid line), partially oxidized $CePb_3$-[$CePb_3(ox)$]; CeO_2 (dashed line); and Ce implanted in Mn which exhibits oxidation effects.

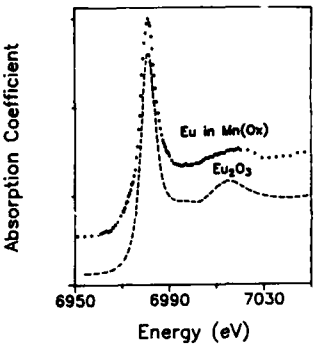


FIG. 4. Eu-L_3 spectrum of Eu_2O_3 and Eu implanted in Mn which exhibits oxidation effects.

hence could reflect oxidation at individual sites long before any oxide precipitant would be visible.

In Fig. 3 we show the Ce-L_3 spectrum for Ce implanted at the 3% level in Mn. The chemical shift of this spectrum, the strong Ce^{4+} feature, and the strong indication of a continuum resonance all support the conclusion that Ce in Mn is strongly oxidized. Indeed, elemental Mn is well known to be prone to oxygen incorporation and penetration. In contrast, the Ce in Pd spectra shown above showed no evidence of oxidation and represents an example of high valence Ce in a metallic system.

In the case of Eu the stable oxide is trivalent Eu_2O_3. An Eu_2O_3 spectrum is shown below that of Eu implanted in Mn in Fig. 4. The strength and position of the continuum resonance for the Eu in Mn spectrum again evidences oxidation. By contrast, the Eu^{3+} character of Eu in Pd noted above appears to be consistent with the intrinsic metallic-Pd environment.

Summarizing, it appears that ion implantation provides a promising tool with which to introduce unstable valence rare-earth atoms into a large number of hosts. Moreover, L_3-XAS measurements appear to be a useful first step in studying these materials both to gain insight into the rare-earth valence state and to identify potential oxidation effects in the near surface alloys.

This work was supported by SNJCST 86-240040-13, SNJCST 87-240090-13, and DE-F605-84 ER45081. We are grateful to the CHESS staff at Cornell, where the x-ray absorption measurements were carried out.

[1]S. Namba, Nucl. Instrum. Methods **189**, 175 (1981).
[2]J. M. Robinson, Phys. Rep. **51**, 1 (1979).
[3]T. Guo and M. L. den Boer, Phys. Rev. B **31**, 6233 (1985).
[4]M. Croft, R. Neifeld, C. U. Segre, S. Raeen, and R. D. Parks, Phys. Rev. B **30**, 4146 (1984).
[5]See J. M. Lawrence, P. R. Riseborough, and R. D. Parks, Rep. Prog. Phys. **44**, 1 (1981), and references therein.
[6]M. Croft, R. Neifeld, B. Qi, G. Liang, I. Perez, S. Gunapala, F. Lu, S. A. Shaheen, E. G. Spencer, N. Stoffel, and M. den Boer in *Proceedings of the International Conference on Valence Fluctuations*, Bangalore, India, edited by S. K. Malik and L. C. Gupta (Plenum, New York) (to be published).
[7]R. Neifeld, M. Croft, T. Mihalisin, C. U. Segre, M. Madigan, M. Torikachvil, M. B. Maple, and L. E. DeLong, Phys. Rev. B **33**, 5950 (1986).
[8]F. Lu, N. Stoffel, R. A. Neifeld, S. Gunapala, M. Croft, and M. L. den Boer (to be published).
[9]See papers in *Proceedings of the International Conference on Valence Fluctuations*, Bangalore, India, edited by S. K. Malik and L. C. Gupta (Plenum, New York) (to be published).
[10]C. U. Segre, M. Croft, J. A. Hodges, V. Murgai, L. C. Gupta, and R. D. Parks, Phys. Rev. Lett. **49**, 1947 (1982).
[11]See Y. Jeon, F. Lu, H. Jhans, S. A. Shaheen, M. Croft, and P. Ansari (these proceedings).

Photoemission and BIS spectra of narrow-band uranium systems (abstract)

P. S. Riseborough
Physics Department, Polytechnic University, Brooklyn, New York 11201

The joint photoemission and inverse photoemission spectra should yield the density of states for removing or adding an electron to the system. In the heavy fermion systems there is a large discrepancy between the experimentally measured density of states and the density of states obtained from local density functional band structure calculations. This discrepancy is clearly indicative of manybody effects. Arko and collaborators[1] have recently discovered that similar manybody anomalies can be found in the narrow-band uranium systems. In a systematic series of studies on uranium compounds and alloys, it was observed that for the systems in which the f bands are expected to be more localized, the one-electron spectra were found to be broader. We have performed calculations using an N-fold degenerate Hubbard model, utilizing an expansion in the Coulomb interaction. The infinite set of diagrams containing independent single loops have been evaluated. This approximation should be exact in the limit $N \to \infty$. We obtain a qualitative agreement with the experimental findings.

[1]A.J. Arko, B. W. Yates, D. D. Koelling, B. P. Dunlap, Z. Zolnierek, A. W. Mitchell, D. J. Lam, C. G. Olson, and M. del Giudice (preprint).

 0021-8979/88/083695-01$02.40 © 1988 American Institute of Physics

The magnetic properties of Sm-Ti-Fe and Nd-Ti-Fe hard and soft sputtered phases

N. Kamprath, L. Wickramasekara, H. Hegde, N. C. Liu, J. K. D. Jayanetti, and F. J. Cadieu
Physics Department, Queens College of CUNY, Flushing, New York 11367

A series of Sm-Ti-Fe and Nd-Ti-Fe film samples have been synthesized by rf diode sputtering for Fe-rich compositions. Samples have been directly crystallized onto heated substrates as well as first deposited amorphous and then subsequently crystallized. In the film plane magnetic fields have been applied during the deposition and during the crystallization to induce in-the-film-plane anisotropies into the films. A phase that contained only Sm, Ti, and Fe has been synthesized in film form that exhibited an in-plane intrinsic coercive force, ${}_iH_c$, of 31 kOe at room temperature and 58 kOe at 5 K. Tetragonal lattice parameters with $a = 8.391$ Å and $c = 12.297$ Å have been assigned to the high ${}_iH_c$ phase by a fitting to 12 diffraction lines. The Nd-Ti-Fe and the Sm-Ti-Fe systems also exhibited a soft magnetic phase of the $ThMn_{12}$-type at a nominal composition of $Nd(TiFe_{11})$.

INTRODUCTION

In this paper we report on the magnetic properties of several ferromagnetic phases that have been synthesized in sputtered films of Fe-rich Sm-Ti-Fe and Nd-Ti-Fe. For both of these systems a soft magnetic phase has been observed which has been identified to be of the $ThMn_{12}$-type structure. Some of the x-ray properties of this phase have been reported separately.[1] This phase had the approximate composition $R(TiFe_{11})$ where R = Nd or Sm. The x-ray structure of this phase has been fitted to a tetragonal $ThMn_{12}$-type structure with $a = 8.579$ Å and $c = 4.799$ Å for the case of $Sm(TiFe_{11})$.[1]

Previously we have reported on the stabilization of a $(Sm + A)Fe_5$ phase where A = Ti or O.[2] In addition, R_2Fe_{17} phases have been synthesized in film form for R = Nd and Sm. The phases observed in the sputtered films have been a sensitive function of the sputtering mode employed. Films have been directly crystallized onto heated substrates as well as first deposited in an amorphous form and then subsequently crystallized. Normally, a magnetic field that we call H_s has been applied during the sputter deposition and or crystallization to induce in-the-film-plane anisotropies into the growing films. The expected effects of such a field have been reported elsewhere.[3] It has been possible to synthesize Sm-Ti-Fe films that have exhibited in-the-film-plane anisotropy constants of 10^7 erg/cm^3 for magnetizing the films in-plane parallel versus perpendicular to the direction of the field H_s.[3] For the Sm-Ti-Fe system only, a hard magnetic phase has been observed for films that were subsequently crystallized from amorphous deposits. We have previously reported in-plane ${}_iH_c$ values of 24 kOe at room temperature.[4]

In this paper we wish to report new measurements on this high ${}_iH_c$ Sm-Ti-Fe phase. Room temperature in-plane ${}_iH_c$ values of 31 kOe have now been reported for this phase. The in-plane ${}_iH_c$ value measured at 5 K was 58 kOe for the same sample. Films of Sm-Ti-Fe have been synthesized for which the hard phase was estimated to occupy 95% of the film volume. No corresponding hard phase has been observed for the Nd-Ti-Fe system.

EXPERIMENTAL PROCEDURE

Samples have been rf diode sputtered in a stainless-steel system with a base pressure in the 10^{-9} Torr range. Samples have been directly crystallized onto heated substrates or first made amorphous onto water cooled substrates and then subsequently crystallized. A magnetic field, $H_s = 2.5$ kOe, was applied in the substrate plane during the depositions to induce in-the-film-plane anisotropies. The sputtering gas used was Ar at pressures from 100 to 120 mTorr. These pressures were high enough to thermalize the sputtered atoms before their arrival at the substrates. Arc-melted buttons with compositions 8.3 at. % Nd, 8.3 at. % Ti, 83.3 at. % Fe and 11.2 at. % Sm, 5.5 at. % Ti, 87.3 at. % Fe were used as targets for sputtering the Nd and Sm films, respectively. For these studies polished polycrystalline Al_2O_3 substrates were used. The film thicknesses studied ranged from 1 to 20 μm. Little substrate specific effects are expected for films of these relatively large thicknesses. At this time substrate specific effects have not been studied. Magnetic measurements to 20 kOe were made using a PAR vibrating magnetometer at room temperature. High field measurements were made using a Janis Research Varitemp 9-T superconducting magnet system. X-ray diffraction data was collected using a Si(Li) solid state detector to provide discrimination of Fe fluorescence events. This allowed a high signal to noise ratio to be obtained for Cu radiation.

 0021-8979/88/083696-03$02.40 © 1988 American Institute of Physics

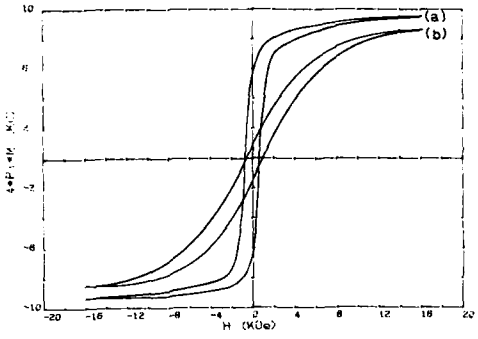


FIG. 1. Room-temperature hysteresis loops for Nd-Ti-Fe film that exhibited the $ThMn_{12}$-type structure (a) in the film plane and (b) perpendicular to the film plane.

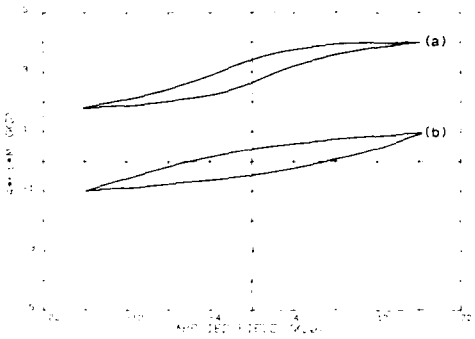


FIG. 3. Room-temperature hysteresis loop for Sm-Ti-Fe (0.112:0.055:0.873) sample first sputtered amorphous and then crystallized at < 400 °C. (a) In-plane parallel to H_s, (b) In-plane perpendicular to H_s.

RESULTS

Figure 1 shows hysteresis loops measured at room temperature for a Nd-Ti-Fe sample that exhibited the $ThMn_{12}$-type structure. Samples of this structure could be synthesized for both the Nd-Ti-Fe and Sm-Ti-Fe systems in both bulk and film form. For the Nd-Ti-Fe films made at substrate temperatures less than 500 °C this structure was the dominant phase. Samples made onto substrates at temperatures of 500 °C exhibited a simpler x-ray pattern corresponding to the Nd_2Fe_{17} phase. It was possible to directly crystallize such films so that a dominant (300) texture was evidenced.[1] Figure 2 shows hysteresis loop measured for a Nd-Ti-Fe film sample at room temperature. This film was sputtered onto a substrate at 500 °C with an in-plane field of 2.5 kOe. This film exhibited a Nd_2Fe_{17} structure with a predominant (300) texture. The coercive force measured in the film plane was < 2 kOe. The measured saturation value of $4\pi M$ was 13.6 kG.

In Fig. 3 hysteresis loops measured at room-temperature in-plane parallel and perpendicular to H_s for a Sm-Ti-Fe film are shown. This film sample was sputtered amorphous in an in-plane field of 2.5 kOe and then crystallized at 475 °C in the same field. The coercive force measured in the film plane was > 21 kOe as deduced from the minor loop. At 16-kOe magnetizing field in the film plane, $4\pi M$ was 3.9 kG. Although this sample contained both a hard and soft magnetic phases, it was estimated from magnetic data that 95% by volume was of the hard magnetic phase. The in-the-film-plane anisotropy was exhibited in this sample because of the in-plane field that had been applied during the crystallization. A model was developed[3] that showed the crystallization temperature must be below the Curie temperature and that the size of the crystallites should be greater than a limit value as well to exhibit this in-the-film-plane anisotropy.

In Fig. 4 a hysteresis loop measured in-plane and parallel to H_s for a high $_iH_c$ Sm-Ti-Fe sample measured at 293 K is shown. The in-plane $_iH_c$ measured parallel to H_s was 31 kOe. The magnetization has not been fully saturated by the highest field available of 90 kOe. This sample was amorphous as sputtered and then crystallized *in situ* at $\lesssim 400$ °C. The film surface was specular reflecting with an SEM measured grain size of 500–600 Å diam. In Fig. 5 is shown the second quadrant hysteresis loop for the same sample as Fig. 4 measured at 5 K. The measured coercivity, $_iH_c$, was 58 kOe.

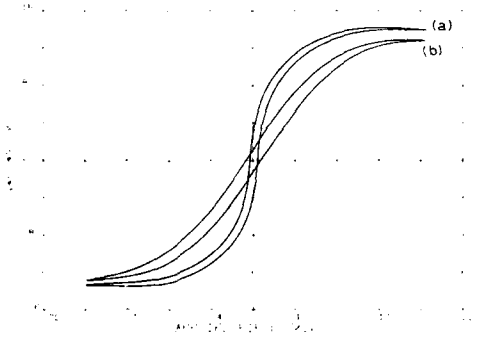


FIG. 2. Room-temperature hysteresis loop for a Nd-Ti-Fe crystalline composition that exhibited a R_2Fe_{17} structure with a highly dominant (300) texture (a) in the film plane and (b) perpendicular to the film plane.

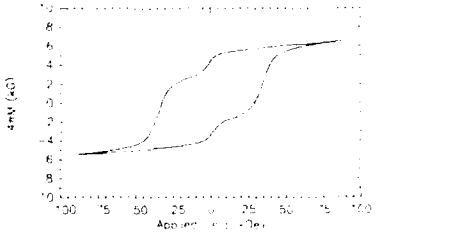


FIG. 4. In the film plane hysteresis loop measured at 293 K parallel to H_s for a Sm-Ti-Fe(0.112:0.055:0.873) sample first sputtered amorphous and then crystallized.

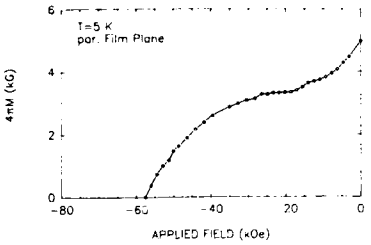


FIG. 5. Second quadrant in-plane hysteresis loop measured at 5 K parallel to H_a for Sm-Ti-Fe(0.112:0.055:.873) sample first sputtered amorphous and then crystallized.

The high $_iH_c$ Sm-Ti-Fe sample hysteresis loops exhibited a drop in the magnetization as the second quadrant was entered. This drop in magnetization and the x-ray patterns supported the hypothesis that the samples contained an admixture of a soft phase. If the hysteresis loop of Fig. 4 was decomposed into hard and soft phase hysteresis loops, it was estimated that this sample consisted of approximately 92% by volume the hard phase. The estimated $_iH_c$ value for the hard phase was then 33 ± 2 kOe. The x-ray diffraction pattern of the high $_iH_c$ Sm-Ti-Fe was fitted to tetragonal lattice parameters for 12 relatively intense diffraction lines that were assigned to the hard phase. The results of this fitting gave $a = 8.391 \pm 0.002$ Å and $c = 12.297 \pm 0.004$ Å for a tetragonal cell. No specific tetragonal structure type has been assigned to this hard phase.

CONCLUSIONS

We have observed four different magnetic phases in Fe rich Sm-Ti-Fe sputtered films prepared under different sets of sputtering conditions. They were Sm_2Fe_{17}, $(Sm + Ti)Fe_5$, $Sm(Ti,Fe)_{12}$, and the high $_iH_c$ Sm-Ti-Fe phase. The new magnetic properties reported in this paper were magnetic measurements for the $Sm(TiFe_{11})$ $ThMn_{12}$-type structure and the high $_iH_c$ Sm-Ti-Fe phase that we have previously observed. In-plane $_iH_c$ values of 31 kOe at 293 K and 58 kOe at 5 K have been observed. This high $_iH_c$ Sm-Ti-Fe phase has only been observed in samples that were first deposited in an amorphous form and then subsequently crystallized within a certain temperature range. By fitting to a tetragonal cell $a = 8.391$ Å and $c = 12.297$ Å parameters have been assigned for this phase. A corresponding high $_iH_c$ phase has not been observed for Nd-Ti-Fe films. Two low $_iH_c$ phases were observed for Nd-Ti-Fe films, a $Nd(TiFe_{11})$ $ThMn_{12}$-type structure and a Nd_2Fe_{17}-type structure. The Nd_2Fe_{17} phase was dominant for higher substrate temperatures for films that were directly crystallized. Directly crystallized films made at higher substrate temperatures exhibited the Nd_2Fe_{17} phase with a predominant (300) crystal texture.

ACKNOWLEDGMENT

This work was supported by the U. S. Department of Energy and the Professional Staff Congress–Board of Higher Education Faculty Research Award Program of the City University of New York.

[1]N. C. Liu, N. Kamprath, L. Wickramasekara, and F. J. Cadieu, these proceedings.
[2]F. J. Cadieu, T. D. Cheung, L. Wickramasekara, and S. H. Aly, J. Appl. Phys. **55**, 2611 (1984).
[3]F. J. Cadieu, T. D. Cheung, L. Wickramasekara, N. Kamprath, H. Hegde, and N. C. Liu, J. Appl. Phys. **62**, 3866 (1987).
[4]T. D. Cheung, L. Wickramasekara, and F. J. Cadieu, J. Magn. Magn. Mater. **54-57**, 1641 (1986).

Magnetic properties of rapidly quenched and annealed $Fe_{10}RTi$ and related alloys

Z. R. Zhao, Y. G. Ren, K. D. Aylesworth, and D. J. Sellmyer
Behlen Laboratory of Physics, University of Nebraska, Lincoln, Nebraska 68588-0111

E. Singleton, J. Strzeszewski, and G. C. Hadjipanayis
Department of Physics, Kansas State University, Manhattan, Kansas 66506

Magnetic measurements are reported for iron-rich ternary alloys with the following compositions: $Fe_{10}Nd_xDy_{1-x}Ti$ ($0 \leqslant x \leqslant 1$), $Fe_{10}SmM$ (M = Ti, V, and Mo), and $Fe_{10}RV$ (R = Y, Gd, and Dy). The samples were prepared by splat cooling or melt spinning and selected samples were heat treated. The results of x-ray diffraction, electron microscopy, and thermomagnetic measurements on the $Fe_{10}Nd_xDy_{1-x}Ti$ series are presented and indicate that the rapidly quenched alloys are nearly single phase and become multiphase upon heating. Magnetic measurements on the other two series show that the substitution of V for Ti increases the saturation magnetization.

I. INTRODUCTION

The search for novel permanent magnet materials has recently focused on ternary alloys containing iron, a rare earth, and a transition metal. Interest in these materials was sparked by the discovery of $Fe_{14}Nd_2B$ several years ago.[1] Alloys of the 14:2:1 type have relatively large coercivities (though not larger than Sm-Co based magnets) and large energy products.

Recently Ohashi *et al.*[2] discovered another iron-rich compound, $Fe_{10}SmTi$, with an anisotropic structure. Their results indicate that single-phase alloys with this 10:1:1 stoichiometry can only be produced with heavy rare earths. If a light rare earth is used the alloy becomes a phase mixture of the 10:1:1 phase with α-Fe and Fe_2R, or Fe_3R.

In this work we investigate the use of rapid-quenching techniques in the production of single-phase 10:1:1 alloys, and the possibility that these techniques could be used to stabilize single-phase alloys containing light rare earths. In addition, the effects of substituting V and Mo for Ti were studied.

II. EXPERIMENTAL METHODS

Rapidly quenched samples of $Fe_{10}Nd_xDy_{1-x}Ti$ ($x = 0.0, 0.33, 0.60, 1.0$), $Fe_{10}SmM$ (M = Ti, V, and Mo), and $Fe_{10}RV$ (R = Y, Gd, and Dy) were prepared by splat-cooling or melt-spinning mixtures containing the appropriate weight of each element.

Measurements were made on the rapidly quenched alloys and selected samples were subjected to a heat treatment at 800 °C for 1 h in a pure argon atmosphere.

The crystal structure of the $Fe_{10}Nd_xDy_{1-x}Ti$ series was investigated by Cu$K\alpha$ x-ray diffraction and by electron microscopy with a transmission-electron microscope (TEM), and thermomagnetic data on this series were obtained with a high-temperature vibrating-sample magnetometer (VSM). The moment of each sample was measured in a constant 1.3-kOe field while the temperature was slowly raised to 650 °C, held constant for 20 min, and then slowly lowered to room temperature.

This VSM was also used to obtain room-temperature hysteresis loops to 8 kOe for each series. Some additional measurements to 80 kOe at 100 K were made in a low-temperature VSM.

III. RESULTS AND DISCUSSION

Representative results of the x-ray diffraction, electron microscopy, and thermomagnetic measurements for the $Fe_{10}Nd_xDy_{1-x}Ti$ series are shown in Figs. 1, 2, and 3, respectively. The top half of Fig. 1 shows x-ray diffraction data for an as-quenched sample with $x = 0.0$. All of the lines can be indexed according to the tetragonal structure proposed by Ohashi *et al.*[2] However, electron diffraction patterns (Fig. 2) in several grains of an annealed $Fe_{10}DyTi$ sample are inconsistent with this structure; rather, they are generally consistent with a $ThMn_{12}$ structure with $c = 4.8$ Å, $a = 8.3$ Å ($c/a = 0.58$). The x-ray data can also be indexed successfully with this latter structure. In addition, Fig. 2(b) shows satellites that suggest a structural modulation along the c

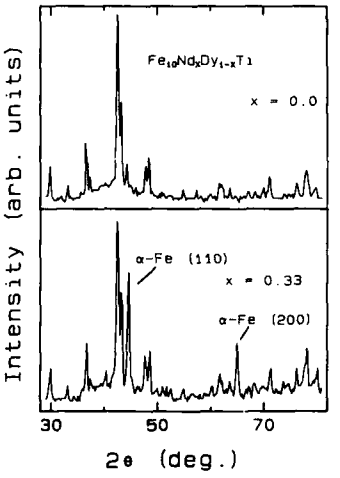


FIG. 1. X-ray diffraction patterns for $x = 0.0$ and 0.33 (Cu$K\alpha$ radiation).

 0021-8979/88/083699-03$02.40 © 1988 American Institute of Physics



(a)



(b)

FIG. 2. Electron diffraction data for heat-treated $Fe_{10}DyTi$. (a) shows fourfold rotation symmetry about $[00\bar{1}]$. In (b) the beam is along [100], and a modulation of about 12 Å along the c direction is seen.

axis with a period of about 12 Å. Thus, it is possible that the rapidly quenched material has a relatively simple tetragonal structure and that annealing produces a rather complex structure. Further work is necessary to determine whether the as-quenched material also has this structural modulation.

The absence of α-Fe peaks in the x-ray pattern for $x = 0.0$ indicate that the sample is single phase in the as-quenched state. Preliminary x-ray data (not presented here) for as-quenched $Fe_{10}NdTi$ suggest that it too is single-phase.

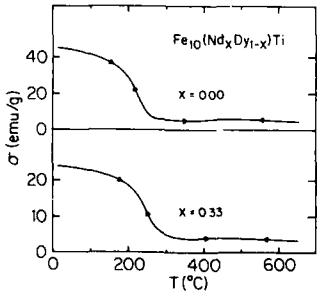


FIG. 3. Thermomagnetic data at $H = 1.3$ kOe for $x = 0.0$ and 0.33.

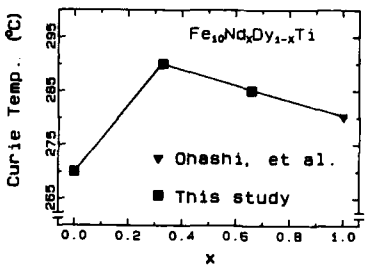


FIG. 4. Curie temperature vs composition for the $Fe_{10}Nd_xDy_{1-x}Ti$ series.

The bottom half of Fig. 1 shows diffraction data for the heat-treated sample with $x = 0.33$. As indicated in the figure, the material contains a substantial amount of α-Fe. All of the heat-treated samples studied (including $x = 0.0$) show this iron precipitation upon annealing.

The thermomagnetic data in Fig. 3 indicate the presence of a high-temperature magnetic phase above the Curie point of the tetragonal phase. The x-ray data indicate that this secondary phase is α-Fe.

Magnetization data at $H = 8$ kOe for this series are summarized in Figs. 4 and 5. Figure 4 shows that the Curie temperature T_c for the heat-treated samples rises from 270 °C for $x = 0.0$ to 290 °C for $x = 0.33$ and then diminishes with increasing x.

The hysteresis measurements for this series indicate that the largest room-temperature coercivity is 630 Oe and occurs in samples with $x = 0.0$. There was no significant difference between the hysteresis loops for as-quenched and heat-treated samples. TEM measurements indicate that the typical grain size for the $x = 0.0$ sample is about 4000 Å. This indicates that despite the rapid quenching, the grain size is so large that there is little magnetic hardening due to microstructure.

Measurements to 80 kOe show that for $x = 0.0$ the average moment per iron is about $1.8\,\mu_B$, assuming the structure is ferrimagnetic, i.e., the Dy moment opposes the Fe moment. Similar results are found for $x = 1.0$ assuming a ferromagnetic structure for the Nd.

Table I summarizes the results of the magnetic measurements. These data indicate that $Fe_{10}SmV$ has the largest magnetization of the $Fe_{10}SmM$ materials studied. Hystere-

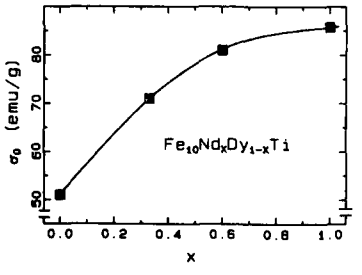


FIG. 5. Magnetization at $H = 8$ kOe vs composition for the $Fe_{10}Nd_xDy_{1-x}Ti$ series.

TABLE I. Magnetization at 8 kOe for the $Fe_{10}SmM$ and $Fe_{10}RV$ series.

Sample	σ_0 (emu/g)
$Fe_{10}SmV$	98.6
$Fe_{10}YV$	94.8
$Fe_{10}SmTi$	86.6
$Fe_{10}GdV$	70.0
$Fe_{10}SmMo$	68.3
$Fe_{10}DyV$	64.2

sis measurements show that $Fe_{10}GdV$ has the highest coercivity of all the samples studied, 1.2 kOe.

Preliminary x-ray data on the series indicate that the as-quenched $Fe_{10}SmM$ and $Fe_{10}RV$ series are single phase. The precipitation of α-Fe upon heat treatment has also been observed in these series.

IV. CONCLUSION

This study indicates that rapidly quenched $Fe_{10}RM$ alloys have structures that are generally consistent with the $ThMn_{12}$ structure. However, some evidence has been obtained for a modulation of about 12 Å along the c axis, which requires further study. Annealing these samples at 800 °C produced multiphased mixtures containing α-Fe. TEM measurements indicate that despite rapid quenching the alloys are rather coarse grained. This may explain the small coercivities observed for both as-quenched and annealed samples.

ACKNOWLEDGMENTS

We thank J. Steele for assistance in gathering data. For financial support we are indebted to the U.S. Department of Energy under Grants Nos. DE-FGO2-86ER45262 and DE-FGO2-86ER45263.

[1]See K. H. J. Bushow, Mater. Sci. Rep. 1, 1 (1986), and references therein.
[2]K. Ohashi, T. Yokogama, R. Osugi, and Y. Tawara (unpublished).

Intrinsic magnetic properties of $SmTiFe_{10}$

Ying-chang Yang, Lin-shu Kong, Shu-he Sun, and Dong-mei Gu
Department of Physics, Peking University, Beijing, China

Ben-pei Cheng
Institute of Solid State Physics, Academia Sinica, Hefei, China

The rare-earth–iron intermetallic compounds $SmTiFe_x$, with x ranging between 8 and 10, have been synthesized by an arc-melting technique. We found that they crystallize in the $ThMn_{12}$-type tetragonal structure, $I4/mmm$. Unusual uniaxial magnetocrystalline anisotropies have been observed. The c axis is the easy magnetization direction. Curie temperature is 610 K. After the discovery of the $R_2Fe_{14}B$ compounds, we have other ternary rare-earth–iron intermetallic compounds with strong uniaxial anisotropy.

I. INTRODUCTION

The permanent magnets based on the $Nd_2Fe_{14}B$ compounds exhibit the highest-energy product. However, the poor temperature stability limits their applications. The aim of this work is to search for rare-earth–iron intermetallic compounds with high magnetocrystalline anisotropy. We were particularly interested in $ThMn_{12}$-type derivatives with high iron concentrations.[1–4] Strong uniaxial magnetocrystalline anisotropies have been observed in the compounds with a composition of $SmTiFe_x$, with x ranging between 8 and 10. In this investigation we report on the crystallographic structure and magnetic properties of the new compounds.

TABLE I. X-ray powder pattern of $ThMn_{12}$-type tetragonal $SmTiFe_{10}$ obtained with $CuK\alpha$ radiation.

$h\,k\,l$	d (Å) (obs)	d (Å) (calc)	I% (obs)
2 1 1	2.9894	2.9890	28
3 1 0	2.7037	2.7058	14
3 0 1	2.4494	2.4511	42
0 0 2	2.3921	2.3955	22
4 0 0	2.1405	2.1401	78
3 2 1	2.1263	2.1275	100
2 0 2	2.0918	2.0908	69
4 2 0	1.9157	1.9145	15
4 1 1	1.9066	1.9055	15
2 2 2	1.8788	1.8790	29
3 1 2	1.7957	1.7947	8
5 1 0	1.6799	1.6795	8
5 0 1	1.6119	1.6130	5
3 3 2	1.5443	1.5442	9
4 4 0	1.5135	1.5141	23
5 2 1	1.5095	1.5096	16
4 2 2	1.4976	1.4964	12
5 3 0	1.4698	1.4690	14
3 0 3	1.3952	1.3948	6
5 1 2	1.3761	1.3760	7
6 1 1	1.3524	1.3512	11
3 2 3	1.3267	1.3263	19
5 3 2	1.2532	1.2530	15
6 3 1	1.2346	1.2342	23
6 0 2	1.2264	1.2269	35
5 5 0	1.2115	1.2119	5
0 0 4	1.1986	1.1991	34
6 2 2	1.1796	1.1795	5
7 2 1	1.1420	1.1430	9

II. EXPERIMENT

The samples were prepared by arc melting of 99.9% pure primary materials in a purified argon atmosphere. X-ray diffraction experiments with $CuK\alpha_1$ radiation were made to determine the crystallographic structure. In addition to the x-ray patterns, electron microscope observation and thermomagnetic analysis were used to identify the single phase.

Magnetization curves along the easy and hard directions were measured on aligned samples with a field of up to 70 kOe in a temperature range between 1.5 and 300 K. Besides the magnetic measurements, x-ray diffraction experiments performed on powder samples aligned in a field were made in order to investigate the easy magnetization direction. Curie temperatures were measured by using a vibrating-specimen magnetometer in a temperature range between 300 and 1000 K.

III. RESULTS

A. Crystallographic structure

On the basis of x-ray diffraction experiments, we found that the $SmTiFe_x$ compounds, with x ranging between 8 and 10, crystallize in the $ThMn_{12}$-type tetragonal structure, $I4/mmm$. For $SmTiFe_{10}$, $a = 8.575$ Å, $c = 4.800$ Å. The powder pattern is shown in Table I. However, second phases as $SmFe_2$ and $TiFe_2$ appear with the $SmTiFe_x$ compounds, when $x > 8$.

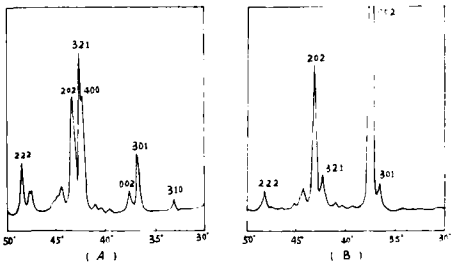


FIG. 1. X-ray diffraction patterns of $SmTiFe_{10}$. (a) Nonaligned powder sample; (b) aligned powder sample.

 0021-8979/88/083702-02$02.40 © 1988 American Institute of Physics

TABLE II. Magnetic data of $SmTiFe_{10}$.

Magnetization				Magnetocrystalline anisotropy				Curie temperature
σ (emu/g)		σ (μ_B/u.f.)		H_A (kOe)		K_1 ($\times 10^7$ erg/cm^3)		T_C (K)
$T = 1.5$ K	$T = 300$ K	$T = 1.5$ K	$T = 300$ K	$T = 1.5$ K	$T = 300$ K	$T = 1.5$ K	$T = 300$ K	
135.2	123.0	15.6	14.1	268.1	104.5	12.1	4.27	610

B. Magnetocrystalline anisotropy

Strong uniaxial anisotropies were observed in $SmTiFe_8$ and $SmTiFe_{10}$ compounds. Figure 1 shows the x-ray diffraction patterns performed on an aligned powder sample [Fig. 1(b)] in comparison with that of a nonaligned sample. In the experiments, the orientation of the grains lies in the plane of the incident and reflected x-ray beam. A strong increase of the (0, 0, 1) reflections and a diminution of the (h, k, 0) lines in Fig. 1(b) shows that the c axis is the easy axis for these compounds.

The anisotropy field H_A is estimated by measuring magnetization curves. Figure 2 shows magnetization curves at 1.5 and 300 K, respectively, measured on the easy and hard directions. In order to estimate the anisotropy constant, magnetization curves were corrected for the misalignment of some grains and demagnetization effects.

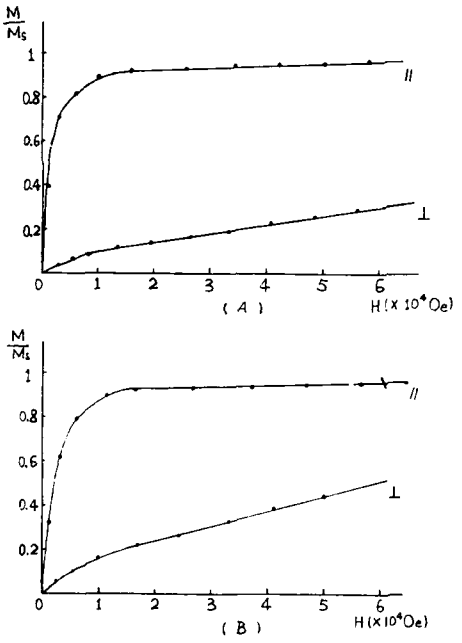


FIG. 2. Magnetization curves of $SmTiFe_{10}$ in easy and hard directions. (a) $T = 1.5$ K; (b) $T = 300$ K.

C. Magnetic data

A single phase is identified with the sample of $SmTiFe_8$. Magnetic data of $SmTiFe_8$ are summarized in Table II.

IV. DISCUSSION

(1) In the $ThMn_{12}$-type tetragonal structure, the Mn atoms are distributed on three nonequivalent crystallographic sites which are designed as 8i, 8j, and 8f. According to previous work,[2] the neutron diffraction studies on $Y(Mn_{1-x}Fe_x)_{12}$ give evidence of the reluctance of Fe atoms to occupy the 8i sites. For the $SmTiFe_x$ compounds with $ThMn_{12}$-type tetragonal structure, the occupation by the Fe atoms of $\frac{2}{3}$ of the available sites would correspond to a stoichiometry of $SmTiFe_8$. The reluctance of Fe atoms to occupy the 8i sites is consistent with the fact that second phases are associated with $SmTiFe_x$ compounds, when $x > 8$.

(2) On the basis of unusual aniaxial anisotropies of $SmTiFe_8$ and $SmTiFe_{10}$, a high coercivity with these compounds would be expected. The estimated potential maximum energy product is 38 MGOe. In order to increase the magnetization of these compounds, continuous investigations are in progress.

[1] Yang Ying-chang, Acta Metall. Sinica **17**, 355 (1981).
[2] Y. C. Yang, B. Kebe, J. James, J. Deports, and W. Yelon, J. Appl. Phys. **52**, 2077 (1981).
[3] Y. C. Yang, G. J. Long, W. J. James, and R. Yeh, J. Appl. Phys. **53**, 1958 (1982).
[4] Y. C. Yang, G. J. Long, B. Kebe, W. J. James, and J. Deportes, *The Rare Earths in Modern Science and Technology* (Plenum, New York, 1982), Vol. 3, p. 403.

Magnetic properties of rare-earth transition-metal borides

S. H. Aly, E. Singleton, and G. C. Hadjipanayis
Department of Physics, Kansas State University, Manhattan, Kansas 66506

D. J. Sellmyer and Z. R. Zhao
Department of Physics and Astronomy, University of Nebraska, Lincoln, Nebraska 68588-0111

The magnetic and structural properties of quaternary $RCo_{4-x}Fe_xB$ alloys with R = Nd, Sm, Er have been examined with magnetometry and x-ray diffraction. The $CeCo_4B$-type phase is found for all x in Er, for $x \leq 3$ in Sm, and for $x = 0$, 1, and 2 in Nd. Maximum coercivities have been obtained in a crystallized $SmFe_2Co_2B$ sample with $H_c > 17$ kOe at room temperature.

INTRODUCTION

The magnetic and structural properties of as-cast[1-3] and melt-spun[4] RT_4B alloys, where B and T denote rare-earth and transition-metal, respectively, have been recently studied. It was found that for Co-containing alloys the hexagonal $CeCo_4B$-type phase is formed with all R except Eu and Yb. For the Fe alloys the phase is formed only in Er-Fe-B.

In the present study we investigate the magnetic properties of quaternary $RCo_{4-x}Fe_xB$ alloys in the as-cast and melt-spun state. The idea was to partially substitute Co with Fe in an attempt to stabilize the 1:4:1 phase in the Fe-containing alloys and study its magnetic properties.

EXPERIMENT

Alloys with composition $RCo_{4-x}Fe_xB$ where R = Nd, Sm, Er were prepared by arc-melting the pure constituents under argon atmosphere. Ribbon samples were made by melt-spinning small pieces from the as-cast alloy. For the Nd-Fe-B system, splat-cooled samples were also made using the piston and anvil technique. The ribbons and splat-cooled samples were heat-treated at a temperature of about 600 °C for optimum magnetic hardening.

The crystal structure of the alloys was determined by x-ray diffraction using Co$K\alpha$ radiation. The magnetic properties were measured with a vibrating-sample magnetometer in magnetic fields up to 80 kOe and in the temperature range of 4.2–700 K. Thermomagnetic data (M_H vs T) were obtained by measuring the magnetization in a small constant field H as a function of temperature.

RESULTS AND DISCUSSION

$NdCo_{4-x}Fe_xB$

The x-ray diffraction patterns showed that the samples generally have a two-phase structure with the $CeCo_4B$ structure as the majority phase in the $x = 0,1,2$ alloys. The Curie temperature of the phase increased from 200 °C in $NdCo_4B$ to 380 °C in $NdCo_2Fe_2B$. Diffraction lines not fitting the $CeCo_4B$-type phase could be indexed with an $(Fe,Co)_2B$ phase. This is also consistent with M-vs-T data which showed a Curie temperature of about 740 °C for this phase. There is no diffraction evidence for a 2:14:1 phase.

The two-phase microstructure of the samples resulted in constricted hysteresis loops. Figure 1 shows the hysteresis loops of a splat-cooled and subsequently heat-treated $NdFe_2Co_2B$ sample parallel and perpendicular to the plane of the foil. The sample is strongly anisotropic with an easy axis along the plane of the foil. The coercivity of the sample after crystallization is much larger than 8 kOe. Low-temperature hysteresis loop measurements (Fig. 2) showed an H_c value of 16 kOe at 200 K, which is decreased upon cooling to 4.2 K. The anomalous structure of the hysteresis loop could be attributed to the presence of the $(Fe,Co)_2B$ phase

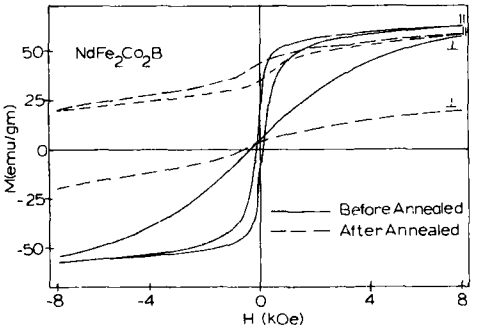


FIG. 1. Hysteresis loops of a splat-cooled and heat-treated Nd-Fe-Co-B sample along and perpendicular to the sample plane.

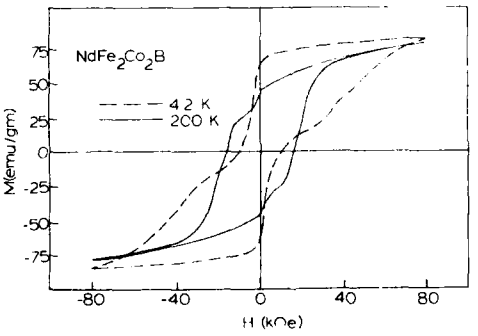


FIG. 2. Temperature dependence of hysteresis in $NdFe_2Co_2B$.

 0021-8979/88/083704-03$02.40 © 1988 American Institute of Physics

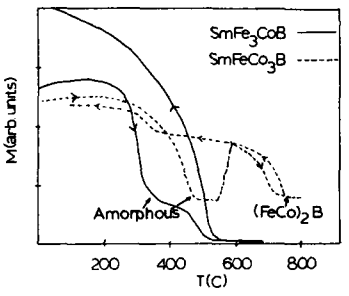


FIG. 3. Thermomagnetic data in $SmFeCo_3B$ and $SmFe_3CoB$ melt-spun samples.

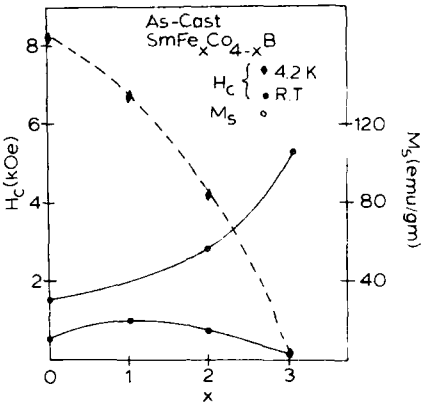


FIG. 5. Coercivity and saturation magnetization in $SmFe_xCo_{4-x}B$ alloys.

or to a spin reorientation of the 1:4:1 phase. The coercivity of a fine $NdCo_2Fe_2B$ powder was also measured and a value of 2 kOe was found. Magnetization curves obtained parallel and perpendicular to the alignment direction showed an anisotropy field of about 80 kOe. The coercivity of crystallized $NdCo_4B$ ribbons was below 1 kOe. This result was unexpected since the coercivity of crystallized ribbons of anisotropic rare-earth alloys is much higher.[5] It could be that the crystallization temperature of these alloys is higher than 600 °C and therefore a heat treatment at higher temperatures is required to fully crystallize the sample.

$SmCo_{4-x}Fe_xB$

For this system the 1:4:1 phase is found to form over a wider range of compositions, up to $x = 3$ (Fig. 3). The Curie temperature of the Fe-substituted alloys is also found to increase with Fe content (Fig. 4). This is in contrast to the 2:14:1 compounds where T_c decreases with Fe content.[6] The Fe_2B-type phase was strongly present in the $x = 1$ alloy after crystallization (Fig. 3).

Figure 5 shows the magnetic properties of as-cast samples. Maximum coercivity was obtained in the $x = 0$ sample. As the Fe content is increased, the magnetization increases but the coercivity is reduced, as expected. However, in crystallized ribbons the maximum coercivity was obtained for the $x = 2$ alloy (Fig. 6). The room-temperature coercivity was much higher than 17 kOe, but it dropped to below 10 kOe at 4.2 K. At 4.2 K a magnetic field of 80 kOe was not sufficient to saturate the sample. This is because the true H_c is much higher at cryogenic temperatures and therefore much higher fields are needed to saturate the magnetic moments; this behavior results in an "apparent" smaller H_c. The anisotropy field for these alloys was estimated[3] to be around 400 kOe. High coercivities were also obtained in fine powders (Fig. 7). The size corresponding to the highest H_c was found to be in the range 1.5–4.5 μm.

$ErCo_{4-x}Fe_xB$

The 1:4:1 phase was found in all alloys studied. The Curie temperature of the Co-containing alloys (Fig. 4) is

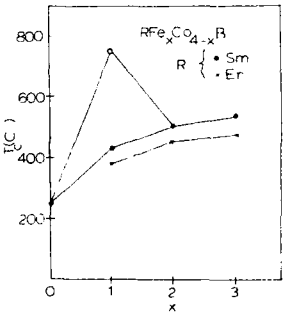


FIG. 4. Curie temperatures in $RFeCo_{4-x}B$ alloys. The O point is believed to be the Curie temperature of the Fe_2B-type phase.

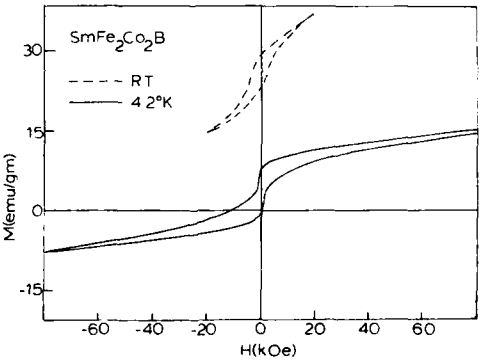


FIG. 6. Hysteresis loops in a crystallized $SmFe_2Co_2B$ sample.

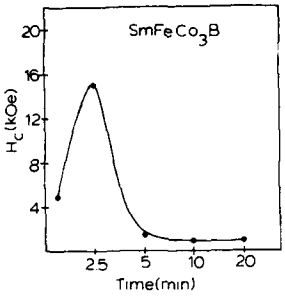


FIG. 7. Coercivity as a function of milling time in $SmFe_2Co_2B$.

higher than the Curie temperature reported[7] for $ErFe_4B$. However, H_c of the former samples is much lower. A coercivity of 6 kOe has been reported[4] for $ErFe_4B$. Relatively high coercivities (2–5 kOe) were also obtained in fine powders. The anisotropy fields found from magnetization measurements on aligned powders are shown in Table I.

The magnetic phase diagram of all alloys studied is presently being examined with ac susceptibility. These data together with microstructure studies are required to understand the results of coercivity in these systems.

TABLE I. Anisotropy fields of $ErCo_{4-x}Fe_xB$ alloys.

x	M_s (emu/g)	H_a (kOe)
0	30	47
2	30	40
3	38	38

ACKNOWLEDGMENTS

This work was supported by the Department of Energy under Grants Nos. DE-FG02-86ER45262 and DE-FG02-86ER45263. We are grateful to Y. G. Ren for his assistance with the measurements.

[1]H. M. Van Noort, D. B. deMooij, and K. H. J. Buschow, J. Less-Common Met. **111**, 87 (1985).
[2]P. P. Vaishnava, C. W. Kimball, A. M. Umarji, S. K. Malik, and G. K. Shenoy, J. Magn. Magn. Mater. **49**, 186 (1985).
[3]H. Oesterreicher, F. Spada, and C. Abache, Mater. Res. Bul. **19**, 1069 (1984).
[4]S. Aly and G. C. Hadjipanayis, J. Appl. Phys. **61**, 3757 (1987).
[5]G. C. Hadjipanayis, R. C. Hazelton, and K. R. Lawless, Appl. Phys. Lett. **43**, 797 (1983).
[6]K. H. J. Buschow, D. B. deMooij, S. Sinnema, R. J. Radwanskii, and J. J. M. Franse, J. Magn. Magn. Mater. **51**, 211 (1985).

The enhancement of the magnetic properties of Fe-Cr-Co-Mo polycrystalline permanent magnet alloys by cold rolling and annealing

S. Sugimoto, M. Okada, and M. Homma
Department of Materials Science, Faculty of Engineering, Tohoku University, Sendai 980, Japan

Present works describe the development of Fe-Cr-Co-Mo alloys with favorable {110}⟨100⟩ texture, which will lie along the transverse direction (TD) of the rolled strips. The studied alloy composition is Fe-30 wt. % Cr-15 wt. %Co-3 wt. % Mo-0.1 wt. % Mn-0.05 wt. % S. The magnetic properties of the alloys have been enhanced along the TD and the best magnetic properties obtained with TD alloys are $B_r = 1.2$ T (12.0 kG), $_iH_c = 82$ kA m^{-1} (1025 Oe), and $BH_{max} = 56$ kJ m^{-3} (7.0 MGOe). The favorable texture is developed by secondary recrystallization, caused by a mixture of rolling and annealing. It can be considered that the process adopted in this investigation is useful for mass production of Fe-Cr-Co alloys with high energy products, without forming a columnar structure or a single crystal.

INTRODUCTION

Fe-Cr-Co permanent magnets produce good magnetic properties with the advantage of cold formability.[1-11] Fe-Cr-Co alloys can provide expanded applications for high-performance small magnet circuits, which are difficult to make with Alnico and ferrite magnets.[6,7]

The magnetic hardening of this alloy is performed by the heat-treating within the miscibility gap after the solution treatment, producing modulated structures consisting of two phases: an FeCo-rich phase (α_1) and a Cr-rich phase (α_2).[12-14] It is noted that the addition of Mo to this alloy increases the coercive force because of the enhancement of the anisotropic decomposition along the ⟨100⟩ directions.[1,15] Good magnetic properties can be expected utilizing the anisotropic decomposition to more efficiently elongate and align the α_1 phase along the applied field direction in ⟨100⟩ texture samples. This was done with a Fe-24%Cr-15%Co-3%Mo alloy in developing the ⟨100⟩ columnar structure[11] or with a ⟨100⟩ ridge single-crystal Fe-22%Cr-18.5%Co-3%Mo alloy.[3,10] But it needs a large outlay to produce a columnar structure or a single crystal.

It is known that the (110)[001] texture is well developed in silicon steels.[16] The (110)[001] texture in silicon steels is formed as follows: a properly prepared cold-rolled strip is annealed at about 800 °C, and primary recrystallization occurs. As the temperature is raised, some grains grow at the expense of the many grains by secondary recrystallization.[17] The strong texture is developed by this secondary recrystallization.[18]

Since Fe-Cr-Co alloys have good ductilities, it can be expected to form a favorable texture by the same method. The purpose of this work is to find a possible annealing method to cause secondary recrystallization which gives the favorable texture including ⟨100⟩ axes.

EXPERIMENTAL PROCEDURE

The experimental procedure is shown in Fig. 1. The nominal composition of the studied alloys was Fe-30 wt. % Cr-15 wt. % Co-3 wt. % Mo-0.1 wt. % Mn-0.05 wt. % S. The alloys were induction-melted in Ar atmosphere and cast into a cylindrical specimen in a mold with an inside diameter of 25 mm. Chemical composition of the alloys was verified as Fe-29.7 wt. % Cr-15.0 wt. % Co-3.05 wt. % Mo-0.053 wt. % Mn-0.0660 wt. % S-0.0747 wt. % O-0.0119 wt. % N-0.0145 wt. % C. The ingots were hot-forged to a bar of approximately 18 × 18 mm in cross section. The bars were solution-treated at 1300 °C for 30 min and then hot-rolled to strips in thickness of 2 mm at 1200 °C. In order to prevent the precipitation of brittle σ phase, the strips were reheated to 1200 °C after every pass. The hot-rolled strips were cold-worked to strips of 0.4 mm in thickness in two steps, after the heat-treatment at 1250 °C for 10 min. The specimens were cut along the rolling direction (RD) and transverse direction (TD), respectively, from the final cold-rolled strips.

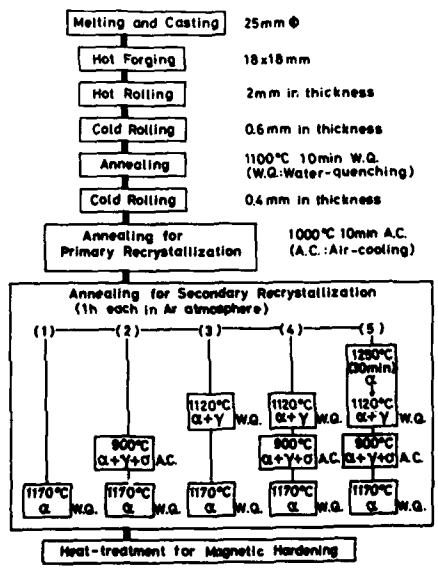


FIG. 1. The alloy preparations.

 0021-8979/88/083707-03$02.40 © 1988 American Institute of Physics

After the final cold-rolling, the alloys were annealed at 1000 °C for 10 min for primary recrystallization.

It is reported that the phase transformation among three different $\alpha+\gamma+\sigma$, $\alpha+\gamma$, and α phase regions, is utilized for secondary recrystallization in the preparation of Fe-Cr-Co single crystals.[3,10] In order to find the possible annealing method which easily causes secondary recrystallization and gives favorable texture, five different annealing methods shown in Fig. 1 were adopted in this investigation.

The alloys were heat-treated for magnetic hardening after the five different annealing methods. The heat treatment is as follows: After the solution treatment at 1200 °C for 1 h, the alloys were aged at 635 °C for 20 min (TMT-1) and were aged at 615 °C for 4 h (TMT-2) in a magnetic field of 160 kAm^{-3} (2 kOe). The alloys were then held at 610 °C for 2 h, followed by the controlled cooling at a rate of 4 °C/h and held at 500 °C for 10 h. Details are described elsewhere.[19]

The magnetic properties were measured with automatic fluxmeter. Textures were determined by x-ray diffractions and the shape of etching pits.[20]

RESULTS AND DISCUSSION

Figure 2 shows the magnetic properties of Fe-30%Cr-15%Co-3%Mo-0.1%Mn-0.05%S alloys versus the five annealing methods. The magnetic properties of TD alloys increase with changing the annealing methods from the first to the fifth method. As a result, the difference of magnetic properties between TD and RD alloys increases. The best magnetic properties of this compositional alloys are ${}_iH_c = 82$ kA m^{-1} (1025 Oe), and $(BH)_{max} = 56$ kJ m^{-3} (7.0 MGOe), obtained by the fifth method with TD alloys.

Figure 3 shows x-ray diffractions of the alloys after the first, the third and the fifth annealing methods. The {200}, {211}, and {222} diffractions can be seen in the alloys after the first and the third methods. In the alloys after the fifth

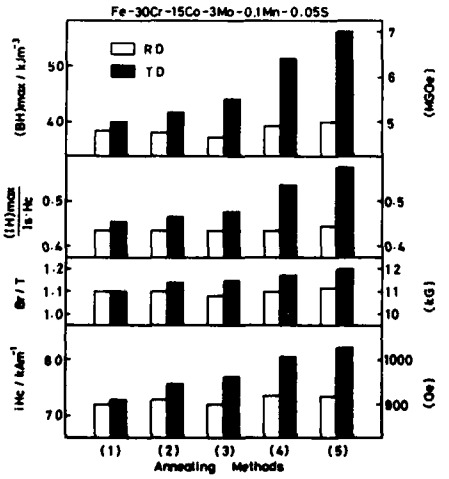


FIG. 2. The magnetic properties of Fe-30% Cr-15% Co-3% Mo-0.1% Mn-0.05% S alloy vs the five different annealing methods.

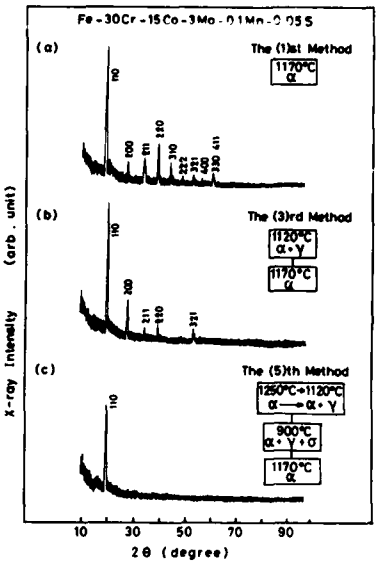


FIG. 3. The x-ray diffractions of the alloys after the (a) first, the (b) third, and the (c) fifth annealing methods.

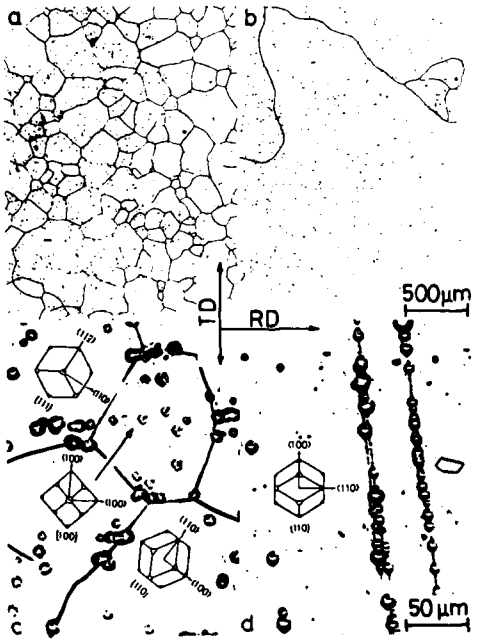


FIG. 4. The optical microstructures and the etching pits taken from the alloys annealed by the [(a) and (c)] first and the [(b) and (d)] fifth annealing method.

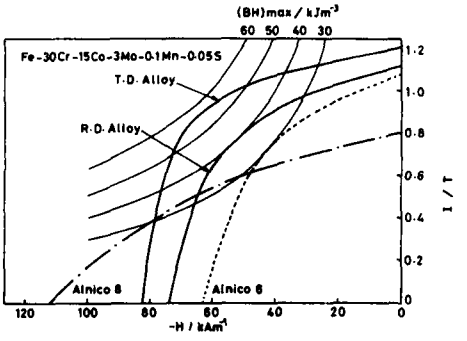


FIG. 5. The demagnetization curves of Fe-30% Cr-15% Co-3% Mo-0.1% Mn-0.05% S alloy measured along RD and TD with those of Alnico 6 and 8.

method, all diffractions are weak but only {110} diffraction can be detected.

Figure 4 shows the optical microstructures and the etching pits taken from the alloys after the first and the fifth annealing methods. Although the average grain size of the alloy annealed by the first method is 120 μm, that by the fifth method is 2.6 mm. The grains obtained by the fifth method are larger than those by the first method. It can be considered that secondary recrystallization occurs efficiently in the alloys annealed by the fifth method.

From the etching pits shown in Fig. 4(c), the grains of the alloys annealed by the first method have the {111} and {100} components. It results from the fact that the ⟨100⟩ directions exist randomly in the alloys. But the grains grown by the fifth method have the {110} components with ⟨110⟩ directions along RD shown in Fig. 4(d). It can be considered that the texture mainly composed of {110}⟨110⟩ are obtained by the fifth method from Figs. 3(c) and 4(d). In this texture, the ⟨100⟩ directions exist along TD and good magnetic properties can be obtained with TD alloys.

The demagnetization curves of RD and TD alloys are shown in Fig. 5, and compared with those of Alnico 6 and Alnico 8. TD alloy has good magnetic properties higher than those of RD alloy and Alnico 6. Although the coercivity of TD alloy is lower than that of Alnico 8, the alloy has good formability.

In regard to the present processing, the process takes short time to produce the favorable texture than that used in silicon steels. It can be considered that this process is useful for the mass-production of Fe-Cr-Co with high-energy products comparable to Alnico 8.

ACKNOWLEDGMENT

We express thanks to Dr. N. Ikuta for his suggestions.

[1]H. Kaneko, M. Homma, and K. Nakamura, AIP Conf. Proc. **5**, 1088 (1971).
[2]H. Kaneko, M. Homma, K. Nakamura, and M. Miura, IEEE Trans. Magn. **MAG-18**, 347 (1973).
[3]H. Kaneko, M. Homma, M. Okada, S. Nakamura, and N.Ikuta, AIP Conf. Proc. **29**, 620 (1975).
[4]H. Kaneko, M. Homma, T. Fukunaga, and M. Okada, IEEE Trans. Magn. **MAG-11**, 1440 (1975).
[5]H. Kaneko, M. Homma, and T. Minowa, IEEE Trans. Magn. **MAG-12**, 977 (1976).
[6]G. Y. Chin, J. T. Plewes, and B. C. Wonsiewicz, J. Appl. Phys. **49**, 2046 (1978).
[7]S. Jin, G. Y. Chin, and B. C. Wonsiewicz, IEEE Trans. Magn. **MAG-16**, 139 (1980).
[8]T. Minowa, M. Okada, and M. Homma, IEEE Trans. Magn. **MAG-16**, 529 (1980).
[9]M. Homma, M. Okada, T. Minowa, and E. Horikoshi, IEEE Trans. Magn. **MAG-17**, 3473 (1981).
[10]N. Ikuta, M. Okada, M. Homma, and T. Minowa, J. Appl. Phys. **54**, 5400 (1983).
[11]M. Homma, E. Horikoshi, T. Minowa, and M. Okada, Appl. Phys. Lett. **37**, 92 (1980).
[12]M. Okada, G. Thomas, M. Homma, and H. Kaneko, IEEE Trans. Magn. **MAG-14**, 245 (1978).
[13]Y. Belli, M. Okada, G. Thomas, M. Homma, and H. Kaneko, J. Appl. Phys. **49**, 2049 (1978).
[14]S. Mahajan, E. M. Gyorgy, R. C. Sherwood, S. Jin, D. Brasen, S. Nakahara, and M. Eibschutz, Appl. Phys. Lett. **32**, 688 (1978).
[15]R. Cremer and I. Pfeiffer, Physica (Utrecht) **80B**, 164 (1975).
[16]N. P. Goss, U. S. Patent No. 1965559.
[17]W. G. Burgers, *Handbuch der Metallphysik* (Metallphisik, Leipzig, 1941), Vol. 3.
[18]J. E. May, and D. Turnbull, Trans. Met. Sci. AIME **212**, 769 (1958).
[19]S. Sugimoto, J. Honda, Y. Ohtani, M. Okada, and M. Homma, IEEE Trans. Magn. **MAG-23**, 3193 (1987).
[20]B. Chalmers, Proc. R. Soc. London **47**, 733 (1935).

The effect of Ga substitution on the magnetic properties of $Nd_2Fe_{14}B$, $Pr_2Fe_{14}B$, and $PrCo_5$

A. T. Pedziwiatr,[a] S. G. Sankar, and W. E. Wallace
Mellon Institute and Metallurgical Engineering and Materials Science Department, Carnegie Mellon University, Pittsburgh, Pennsylvania 15213

$R_2Fe_{14-x}Ga_xB$ (R = Pr and Nd) and $PrCo_{5-x}Ga_x$ alloys were synthesized and examined by powder x-ray diffraction at room temperature and by magnetometry in the temperature range 4.2–1100 K. Lattice parameters, Curie temperature, spin-reorientation temperatures, anisotropy fields, and saturation magnetizations were determined. Phase analysis revealed that single-phase materials exist only for $x<1$ in the case of 2:14:1 alloys and for $x<2$ for 1:5 alloys. An increase in lattice parameters is observed upon Ga substitution in all cases. About 20 K increase in the Curie temperature is observed for 2:14:1 alloys, whereas there is a dramatic decrease in 1:5 alloys. Saturation magnetization values decrease upon Ga substitution. The anisotropy field is slightly enhanced by Ga addition in the $Nd_2Fe_{14-x}Ga_xB$ system. Spin-reorientation phenomena in $Nd_2Fe_{14-x}Ga_xB$ and $PrCo_{5-x}Ga_x$ are strongly affected by Ga addition. The observed behavior is discussed in terms of preferential substitution of Ga atoms into the $Nd_2Fe_{14}B$-type crystal structure and random substitution into the $CaCu_5$-type crystal structure.

INTRODUCTION

The rare-earth–3*d* metal compounds which are used for permanent magnet applications are those belonging to the 1:5 and 2:17 compositions, based on Co, and the 2:14:1 composition, based on Fe. Numerous attempts have been made recently to improve the overall properties of these materials by substituting various elements in place of rare earth or 3*d* metal.[1–13] Some substituents give rise to small improvements in certain properties but usually there is a tradeoff, i.e., an improvement in one property but loss in another.

Recent studies revealed that gallium markedly increases the stability of the 1:5 phase.[14,15] It was also found that gallium addition improves coercivity in Nd-Fe-Co-B sintered magnets.[16] The goal of the present work was to determine the effect of Ga substitution on intrinsic magnetic properties of $Nd_2Fe_{14}B$, $Pr_2Fe_{14}B$, and $PrCo_5$, all of which are used to fabricate permanent magnets. Our attention focused also on the effect of Ga on spin-reorientation phenomena which occur in $Nd_2Fe_{14}B$ and $PrCo_5$.

EXPERIMENT

Samples were prepared from 99.9% (or better) purity starting elements which were alloyed by means of induction heating in a purified argon atmosphere. As-cast ingots were wrapped in Ta foil, sealed into quartz tubes filled with argon, and heat treated. $R_2Fe_{14-x}Ga_xB$ alloys were annealed at 900 °C for two weeks and then rapidly cooled. $PrCo_{5-x}Ga_x$ alloys were annealed for 2 h at 1050 °C and quenched in water. X-ray diffraction, thermomagnetic analysis (TMA), and metallographical microscopy were employed to analyze the materials for single-phase character. X-ray diffraction analysis was performed at room temperature on randomly oriented powdered samples with the use of a Rigaku diffractometer and Cr$K\alpha$ radiation. Aligned (in a 20-kOe field) powders of selected samples were also studied by x-ray diffraction in order to draw conclusions as to their anisotropy. Lattice parameter refinement was conducted by a computer procedure based on Cohen's method. TMA was performed by recording magnetization versus temperature, M vs T, curves at low external magnetic field in the temperature range 295–1100 K, with the use of a Faraday-type magnetic balance. The Curie temperatures T_c were also determined from these measurements. The magnetic measurements at 295 and 77 K were made on a PAR vibrating sample magnetometer in external fields up to 20 kOe. For low-temperature measurements (4.2–295 K), a Faraday-type magnetic balance was employed. The saturation magnetizations M_s were obtained from magnetic isotherms using Honda plots. The anisotropy fields H_A were obtained at 295 and 77 K for powders ($<37\ \mu$m) aligned in wax by measuring the M-vs-H curves in the easy and hard directions. H_A was taken as the extrapolated intersection of these curves. The $Nd_2Fe_{14-x}Ga_xB$ and $PrCo_{5-x}Ga_x$ materials were studied for spin-reorientation appearance in the temperature region 4.2–295 K by recording M-vs-T curves at low external field for rough chunks of the samples. The spin-reorientation temperatures T_{SR} were determined from these measurements.

RESULTS AND DISCUSSION

$R_2Fe_{14-x}Ga_xB$ compounds were prepared for R = Pr and Nd with x = 0.0, 1.0, 1.5, 2.0, and 3.0. X-ray and TMA analyses showed, however, that single-phase compounds, crystallizing in the tetragonal $Nd_2Fe_{14}B$-type[17] crystal structure, form only for $x = 0$ and 1.0. $PrCo_{5-x}Ga_x$ compounds were prepared for $x = 0.0$, 0.5, 1.0, 1.5, 2.0, 2.5, and 3.0. Single-phase compounds, crystallizing in the hexagonal $CaCu_5$-type crystal structure, form in this system only for $x<2.0$. The lattice parameters increase upon gallium substi-

[a] On leave from Institute of Physics, Jagiellonian University, 30-059 Cracow, Poland.

 0021-8979/88/083710-03$02.40 © 1988 American Institute of Physics

TABLE I. Crystallographic and magnetic data obtained for $R_2Fe_{14-x}Ga_xB$ and $PrCo_{5-x}Ga_x$ systems.

Composition	a (Å)	c (Å)	T_c (K)	T_{SR} (K)	M_s (μ_B/f.u.) 295 K	M_s (μ_B/f.u.) 77 K	M_s (μ_B/f.u.) 4.2 K	H_A*(kOe) 295 K	H_A*(kOe) 77 K
R = Pr									
$x=0$	8.814	12.253	566	···	31.0	34.8	36.3	80	170
$x=1$	8.813	12.265	586	···	27.5	30.1	32.8	78	120
R = Nd									
$x=0$	8.792	12.201	589	134	32.2	36.4	38.2	71	cone
$x=1$	8.789	12.272	603	110	29.2	32.1	33.0	83	cone
$PrCo_{5-x}Ga_x$									
$x=0$	5.020	3.970	894	100	9.3	10.4	10.7	145	cone
$x=0.5$	5.038	4.004	703	149	6.8	8.3	8.3	100	cone
$x=1.0$	5.066	4.011	466	214	4.2	6.1	6.2	30	cone
$x=1.5$	5.115	4.040	210	···	···	3.6	4.2	···	···
$x=2.0$	5.170	4.049	60	···	···	···	2.0	···	···

*Some of the H_A values are too high to be accurately measured with our present technique; therefore, they should be treated as approximate values.

tution for all single-phase materials (see Table I; Fig. 1).

For $R_2Fe_{14-x}Ga_xB$ systems (R = Pr,Nd) there is a small increase in the T_c observed (Table I) when Ga substitutes for Fe. Superficially it may seem surprising that the replacement of a magnetic atom with a nonmagnetic one can cause an increase in T_c. However, we observed the same effect for Si substitution in $R_2Fe_{14-x}Si_xB$ systems (R = Pr,Nd,Er,Y) which we explained in detail by assuming a preferential substitution of Si into the Fe sites involved in antiferromagnetic interactions.[12,18] By reducing a fraction of the negative exchange interactions, the overall exchange becomes stronger, thus enhancing the T_c. The average T_c increase in the $R_2Fe_{14-x}Si_xB$ systems was ~17 K per one substituted atom, which is almost the same as in the case of Ga substitution. Therefore, we assume that the same mode of preferential substitution may take place in the cases of Ga and Si additions. Neutron and Mössbauer studies on $Nd_2Fe_{14-x}Co_xB$ revealed indeed a preferential substitution of Co in place of Fe.[19–21]

In the $PrCo_{5-x}Ga_x$ system, the T_c sharply decreases with composition (see Table I; Fig. 2). Since the Co-Co interactions determine the value of T_c in this system, we assume that the decrease of T_c is due to dilution of the Co sublattice. It is most probable that Ga substitutes for Co in a random way in $PrCo_{5-x}Ga_x$.

A sharp decrease in saturation magnetization is observed with Ga substitution for both 2:14:1 alloys as well as for 1:5 alloys (see Table I; Fig. 3). The reduction of the magnetic moment is most probably due to the dilution of the 3*d* metal sublattices with nonmagnetic gallium.

The anisotropy field is enhanced by Ga addition in $Nd_2Fe_{14-x}Ga_xB$, but it decreases in $Pr_2Fe_{14-x}Ga_xB$ (Table I). Such a different behavior may be connected with the fact that in $Nd_2Fe_{14}B$ there is a cone-to-axis spin reorientation at ~135 K, whereas $Pr_2Fe_{14}B$ remains axial down to 4.2 K. Addition of Ga decreases the spin-reorientation temperature in $Nd_2Fe_{14-x}Ga_xB$ and increases T_c (see Table I); therefore, the temperature range of axial anisotropy becomes wider, which is the result of enhanced axial anisotropy. In $Pr_2Fe_{14-x}Ga_xB$ the anisotropy field decreases, especially at 77 K. Apparently the dilution of the Fe sublattice

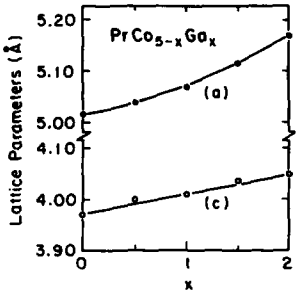


FIG. 1. Composition dependence of lattice parameters for $PrCo_{5-x}Ga_x$.

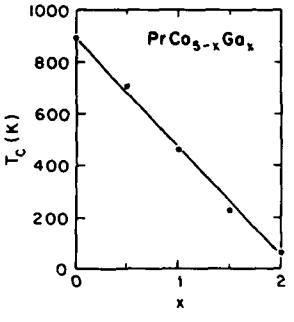


FIG. 2. Composition dependence of the Curie temperature for $PrCo_{5-x}Ga_x$.

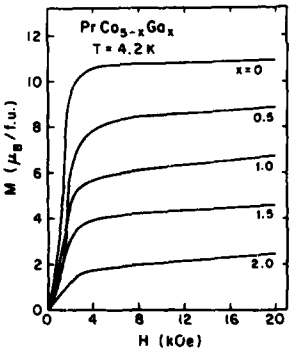


FIG. 3. Magnetic isotherms for $PrCo_{5-x}Ga_x$.

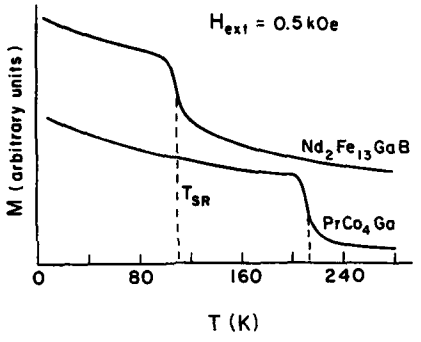


FIG. 4. Magnetization vs temperature curves obtained for rough chunks of materials.

weakens axial anisotropy in this system.

In contrast to $Nd_2Fe_{14-x}Ga_xB$, the spin-reorientation temperature increases for $PrCo_{5-x}Ga_x$. Simultaneously, the Curie temperature decreases in the latter case. Therefore, the temperature range of the axial anisotropy becomes narrower and the anisotropy field sharply decreases with Ga additions (see Table I). The spin-reorientation phenomena observed in $Nd_2Fe_{14-x}Ga_xB$ and $PrCo_{5-x}Ga_x$ appear to be of the same type, i.e., they are of cone-to-axis transitions with increasing temperatures. This conclusion is drawn on the basis of the similarity of the shapes of M-vs-T curves experimentally observed by us in the cases of $Nd_2Fe_{13}GaB$ and $PrCo_4Ga$ (see Fig. 4). Further evidence in support of this conclusion is offered by the computer simulations of spin reorientation in polycrystalline materials reported by Boltich *et al.*[22] and by the experimental work published by Pedziwiatr and Wallace[23,24] on other related intermetallic compounds.

ACKNOWLEDGMENTS

This work was supported by a contract with the Lawrence Livermore National Laboratory and the Materials Research Division of the National Science Foundation Under Grant No. DMR-8613386.

[1]M. Sagawa, S. Fujimura, H. Yamamoto, Y. Matsuura, and K. Hiraga, IEEE Trans. Magn. **MAG-20**, 1584 (1984).
[2]W. E. Wallace, A. T. Pedziwiatr, E. B. Boltich, H. Kevin Smith, S. Y. Jiang, S. G. Sankar, and E. Oswald, in *Proceedings of the Materials Research Society Conference*, edited by S. G. Sankar, J. F. Herbst, and N. C. Koon (Materials Research Society, Pittsburgh, PA 1987), p. 17.
[3]Z. Maocai, M. Dequing, J. Xiuling, and L. Shigiang, *ibid.*, p. 541.
[4]H. H. Staidmeier and A. El Masry, *ibid.*, p. 613.
[5]G. C. Hadjipanayis, K. R. Lawless, and R. C. Dickerson, J. Appl. Phys. **57**, 4097 (1985).
[6]M. Q. Huang, E. B. Boltich, W. E. Wallace, and E. Oswald, J. Magn. Magn. Mater. **60**, 270 (1986).
[7]C. Abache and H. Oesterreicher, J. Appl. Phys. **57**, 6112 (1985).
[8]W. E. Wallace, Prog. Solid State Chem. **16**, 127 (1985).
[9]K. H. J. Buschow, Mater. Sci. Rep. **1**, 1 (1986).
[10]J. M. D. Coey, J. Less-Common Metals **126**, 21 (1986).
[11]A. T. Pedziwiatr and W. E. Wallace, J. Less-Common Metals **126**, 41 (1986).
[12]A. T. Pedziwiatr, E. Burzo, and W. E. Wallace, IEEE Trans. Magn. **MAG-23**, 1775 (1987).
[13]A. T. Pedziwiatr and W. E. Wallace, J. Appl. Phys. **61**, 3439 (1987).
[14]Y. C. Chuang, C. H. Wu, and H. B. Chen, J. Less-Common Metals. **106**, 41 (1985).
[15]Y. C. Chuang, C. H. Wu, and H. B. Chen, *ibid.*, 219 (1985).
[16]M. Endoh, M. Tokunaga, and H. Harada, IEEE Trans. Magn. **MAG-23**, 2290 (1987).
[17]J. F. Herbst, J. J. Croat, F. E. Pinkerton, and W. B. Yelon, Phys. Rev. B **29**, 4176 (1984).
[18]A. T. Pedziwiatr, W. E. Wallace, E. Burzo, and V. Pop, Solid State Commun. **61**, 61 (1987).
[19]H. M. van Noort and K. H. J. Buschow, J. Less-Common Metals **113**, L9 (1985).
[20]J. F. Herbst and W. B. Yelon, J. Appl. Phys. **60**, 4224 (1986).
[21]D. E. Tharp, Y.-ch. Yang, O. A. Pringle, G. J. Long, and W. J. James, J. Appl. Phys. **61**, 4334 (1987).
[22]E. B. Boltich, A. T. Pedziwiatr, and W. E. Wallace, J. Magn. Magn. Mater. **66**, 317 (1987).
[23]A. T. Pedziwiatr and W. E. Wallace, Solid State. Commun. **60**, 653 (1986).
[24]A. T. Pedziwiatr and W. E. Wallace, J. Magn. Magn. Mater. **65**, 139 (1987).

Analysis of high-field magnetization measurements on $R_2Fe_{14}B$ single crystals (R = Tb, Dy, Ho, Er, and Tm)

D. Givord and H. S. Li
Laboratoire Louis Néel, C.N.R.S., B.P. 166X,38042 Grenoble, France

J. M. Cadogan, J. M. D. Coey, and J. P. Gavigan
Department of Physics, Trinity College, Dublin, Ireland

O. Yamada and H. Maruyama
Department of Physics, Okayama University, 3-1-1 Tsushima Naka, Okayama 700, Japan

M. Sagawa and S. Hirosawa
Sumitomo Special Metals Co. Ltd., Egawa, Shimamato-cho, Mishima-gun, Osaka 618, Japan

Single crystals of the compounds $R_2Fe_{14}B$ some 1–4 mm in size have been grown for a study of the anisotropy of the magnetization curves. These curves for crystals with R = Tb, Dy, Ho, Er, and Tm were measured at the Service National des Champs Intenses, Grenoble, between 4.2 and 275 K, with fields of 0–18 T being applied along the [100], [110], and [001] directions. Magnetization curves for all five compounds are analyzed in terms of the exchange and crystal field interactions (including terms up to sixth order, which may differ at 4*f* and 4*g* sites) following the analysis previously developed for $Nd_2Fe_{14}B$. Molecular field coefficients representing the exchange interactions between R and Fe spins decrease from light to heavy R compounds as previously deduced from analysis of Curie temperatures. The CEF parameters are approximately the same across the series. In particular, the A_{20} terms are constant to within 10%.

INTRODUCTION

The complicated interplay of exchange and crystal field (CEF) interactions in the $R_2Fe_{14}B$ series of compounds (R = rare earth) gives rise to interesting magnetic behavior, as evidenced by numerous single-crystal studies. For instance, a field-induced, first-order magnetization process (type 1 FOMP[1]) has been observed in $Nd_2Fe_{14}B$ with **B** applied parallel to the [100] direction.[2] Recently, type 2 FOMP's[1] have been observed in $Pr_2Fe_{14}B$ (Ref. 3) for **B** applied parallel to both [100] and [110]. In $Nd_2Fe_{14}B$ (Ref. 4) and $Ho_2Fe_{14}B$ (Ref. 5) low-temperature spin tilting away from the easy **c** axis is known to occur. Plane-to-axis spin reorientations have been found in $Er_2Fe_{14}B$,[6] $Tm_2Fe_{14}B$,[6] and $Yb_2Fe_{14}B$ (Ref. 7) (polycrystalline).

The key to understanding the complex magnetic behavior of the $R_2Fe_{14}B$ series lies in a quantitative analysis of the exchange and CEF interactions. In two previous papers,[8,9] we presented a molecular field analysis of R-Fe exchange in $R_2Fe_{14}B$ with which we deduced values of the molecular field coefficients $n_{R\text{-}Fe}$ from measured Curie temperatures. In particular, a substantial enhancement of R-Fe exchange for light R relative to heavy R was reported. From a recent detailed analysis of single-crystal high-field magnetization curves of $Nd_2Fe_{14}B$,[10] both CEF and exchange parameters were deduced which gave a very good description of the complex magnetic behavior of this compound.

The purpose of this present paper is to extend the quantitative analysis of single-crystal, high-field magnetization curves to $R_2Fe_{14}B$ compounds with R = Tb, Dy, Ho, Er, and Tm. The systematic variation of exchange and CEF interactions in the $R_2Fe_{14}B$ series is deduced.

EXPERIMENTAL DETAILS

Single crystals of $R_2Fe_{14}B$ (R = Tb, Dy, Ho, Er, and Tm) were prepared both by the Czochralski and floating-zone melting techniques. Magnetization curves along the three principal directions [001], [100], and [110] were measured over the temperature range 4.2–275 K in applied magnetic fields up to 18 T at the Service National des Champs Intenses in Grenoble. These data were analyzed according to the method previously outlined.[10,11] This analysis takes into account the different CEF's at the R *f* and *g* sites (site notation as in Ref. 12).

RESULTS AND DISCUSSION

In Fig. 1 we show the experimental and calculated temperature variation of the spontaneous magnetization

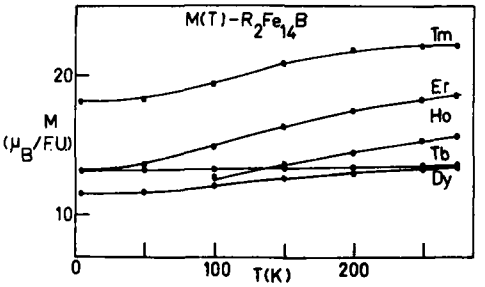


FIG. 1. Experimental (●) and calculated (full lines) thermal variations of the spontaneous magnetization in $R_2Fe_{14}B$.

 0021-8979/88/083713-03$02.40 © 1988 American Institute of Physics

TABLE I. Crystalline electric field parameters (A_{nm}) and molecular field coefficients in $R_2Fe_{14}B$ (R = Tb, Dy, Ho, Er, and Tm). (N.B. Rare-earth site notation f and g as in Ref. 12).

	Tb[a]		Dy		Ho		Er		Tm	
$A_{nm}(Ka_B^{-n})$	f	g	f	g	f	g	f	g	f	g
A_{20}	303.7	308.2	291.6	295.9	297.6	302.0	291.5	295.8	258.1	261.9
A_{22}^{c}	− 200.4	604.9	− 192.4	580.7	− 196.4	592.8	− 221.6	688.9	− 204.5	617.0
A_{40}	− 14.5	− 12.7	− 13.9	− 12.2	− 8.7	− 7.6	− 16.0	− 14.0	− 12.3	− 10.8
A_{44}^{c}	43.4	− 40.6	41.7	− 39.0	26.0	− 24.4	36.7	− 38.6	34.7	− 32.5
A_{60}	− 2.2	− 2.2	− 1.3	− 1.3	− 1.3	− 1.3	− 1.2	− 1.2	− 1.75	− 1.7
A_{64}^{c}	− 33.2	− 12.6	− 19.9	− 7.6	− 18.9	− 7.2	− 5.7	− 2.6	− 26.5	− 10.1
$n_{R\text{-}Fe}(\mu_0)$	158		162		136		137		135	

[a] Note that the CEF parameters listed for Tb are the same as those we reported for the Nd compound in Ref. 10.

[M(T)] for each of the compounds studies. These variations are essentially determined by the strength of the R-Fe exchange. Excellent agreement between experiment and theory is found, the calculations yielding values of the R-Fe molecular field coefficients $n_{R\text{-}Fe}$ (in units of μ_0) listed in Table I. The values of $n_{R\text{-}Fe}$ for the five compounds are approximately half the value of $n_{R\text{-}Fe}$ deduced in a similar manner for the $Nd_2Fe_{14}B$ (Ref. 10) compound ($= 307\mu_0$). This variation of $n_{R\text{-}Fe}$ through the $R_2Fe_{14}B$ series is in excellent agreement with that deduced from T_c values using a simple molecular field analysis.[8,9]

Measured and calculated curves of $Tb_2Fe_{14}B$ and $Dy_2Fe_{14}B$ at 4.2 K are presented in Fig. 2. For the two corresponding R ions the Stevens α_J coefficient is large and negative. Both compounds are characterized by very strong axial anisotropy leading to an easy [001] direction over the entire magnetically ordered temperature range. The measured curves also reveal negligible in-plane anisotropy. The CEF and exchange parameters presented in Table I for these two compounds reproduce these magnetization curves thus accounting for both the small in-plane anisotropy and the large axial anisotropy and its temperature dependence. Specifically the lack of in-plane anisotropy here is due to the A_{44}^{c} terms being almost equal in magnitude but opposite in sign at the f and g sites.

Fitted magnetization curves for $Ho_2Fe_{14}B$ at 4.2 K are shown in Fig. 3. The measurements reveal that above 57 K this compound has easy [001] axis anisotropy but below this temperature the net magnetization is tilted away from [001] the tilt angle θ_c reaching 23° at 4.2 K, in agreement with Ref. 5. This tilting, as in $Nd_2Fe_{14}B$, is due mainly to competition between the second- and fourth-order CEF interactions on the Ho^{3+} ion.[3] The parameters presented in Table I reproduce very well this spin tilt transition ($T_{SR}^{cal} = 58$ K) together with the temperature dependence of the canting angle [$(\theta_c^{cal}$ (4.2 K) = 23°)]. A further similarity to the $Nd_2Fe_{14}B$ compound is the presence of significant in-plane anisotropy between [100] and [110], the latter being easier.

In Fig. 4 we show the fitted magnetization curves of $Er_2Fe_{14}B$ and $Tm_2Fe_{14}B$ at 4.2 K. The Stevens α_J coefficients of the Er and Tm ions are positive and the net magneti-

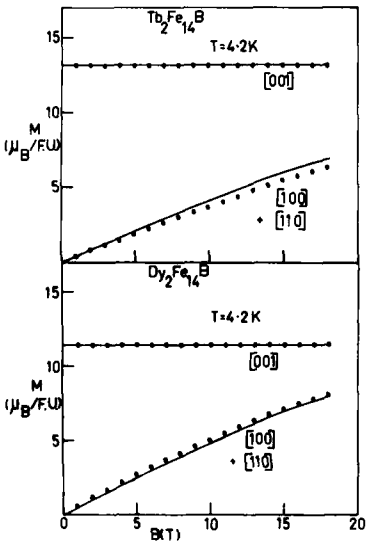


FIG. 2. Experimental (●) and calculated (full lines) single-crystal magnetization curves at $T = 4.2$ K for $Tb_2Fe_{14}B$ and $Dy_2Fe_{14}B$.

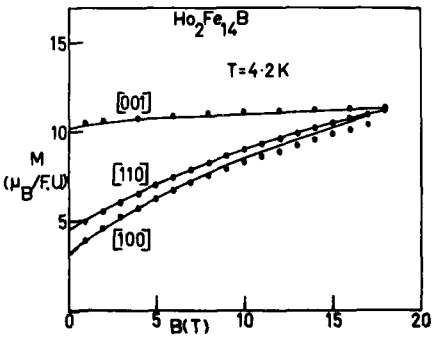


FIG. 3. Experimental (●) and calculated (full lines) single-crystal magnetization curves at 4.2 K for $Ho_2Fe_{14}B$.

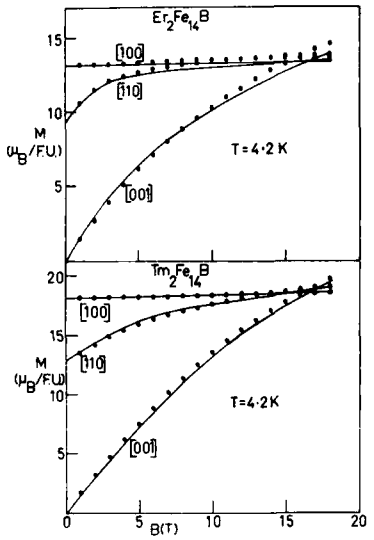


FIG. 4. Experimental (●) and calculated (full lines) single-crystal magnetization curves at 4.2 K for $Er_2Fe_{14}B$ and $Tm_2Fe_{14}B$.

zation at low temperatures lies along [100] in both compounds. As the temperature is increased, spin reorientations occur at the point where the Fe anisotropy, which favors [001], becomes dominant. We have calculated the spin reorientations in these compounds to be $T_{SR}(\mathrm{Er}) = 324$ K and $T_{SR}(\mathrm{Tm}) = 313$ K, which are in excellent agreement with experiment (325 and 315 K, respectively[6]). The crystal field and exchange parameters also account for the experimentally observed easy-plane and in-plane anisotropies as can be seen in Fig. 4. Our calculations in zero field at low temperatures indicate a canted basal-plane magnetic structure in both compounds with canting angles $|\phi^f(\mathrm{Er})| = 7°$, $|\phi^g(\mathrm{Er})| = 13.7°$, $|\phi^f(\mathrm{Tm})| = 17.4°$, and $|\phi^g(\mathrm{Tm})| = 28.8°$, with respect to [100].

In conclusion, our analysis of the magnetization curves of several $R_2Fe_{14}B$ compounds (R = Tb, Dy, Ho, Er, and Tm) from $T = 4.2$ K to room temperature has yielded as set of CEF parameters (A_{nm}) and molecular field coefficients $n_{R\text{-}Fe}$ for each R which reproduce the observed magnetic behavior. All these parameters are presented in Table I including CEF parameters for both the f and g sites.[12] It is remarkable that the parameters obtained have similar values for all compounds. In particular, the second-order CEF parameters are constant to within 10%.

[1]G. Asti and F. Bolzoni, J. Magn. Magn. Mater. **20**, 29 (1980).
[2]L. Pareti, F. Bolzoni, and O. Moze, Phys. Rev. B **32**, 7604 (1985).
[3]H. Hiroyoshi, H. Kato, M. Yamada, N. Saito, Y. Nagawa, S. Hirosawa, and M. Sagawa, Solid State Commun. **62**, 475 (1987).
[4]D. Givord, H. S. Li, and R. Perrier de la Bâthie, Solid State Commun. **51**, 857 (1984).
[5]H. Yamauchi, M. Yamada, Y. Yamaguchi, H. Yamamoto, S. Hirosawa, and M. Sagawa, J. Magn. Magn. Mater. **54–57**, 575 (1986).
[6]S. Hirosawa and M. Sagawa, Solid State Commun. **54**, 335 (1985).
[7]P. Burlet, J. M. D. Coey, J. P. Gavigan, D. Givord, and C. Meyer, Solid State Commun. **60**, 723 (1986).
[8]E. Belorizky, M. A. Fremy, J. P. Gavigan, D. Givord, and H. S. Li, J. Appl. Phys. **61**, 3971 (1987).
[9]J. M. Cadogan, J. M. D. Coey, J. P. Gavigan, D. Givord, and H. S. Li, J. Appl. Phys. **61**, 3974 (1987).
[10]J. M. Cadogan, J. P. Gavigan, D. Givord, and H. S. Li J. Phys. F. (to be published).
[11]J. P. Gavigan, D. Givord, H. S. Li, O. Yamada, H. Maruyama, M. Sagawa, and S. Hirosawa, J. Magn. Magn. Mater. **70**, 416 (1987).
[12]D. Givord, H. S. Li, and J. M. Moreau, Solid State Commun. **50**, 497 (1984).

Electronic structure and spin density of $Gd_2Fe_{14}B$

W. Y. Ching and Zong-Quan Gu[a)]
Department of Physics, University of Missouri-Kansas City, Kansas City, Missouri 64110

The electronic structure of $Gd_2Fe_{14}B$ has been calculated using the spin-polarized orthogonalized linear combination of atomic orbitals method. The use of the band approach to study the magnetic properties of the rare-earth iron-boron compounds should be more valid in the case of $Gd_2Fe_{14}B$ because of the exactly half-filled f shell of the Gd atom, which has a zero orbital angular momentum. The calculated total spin magnetic moment of 18.41 μ_B per formula unit is in good agreement with experiment, and the site-decomposed Fe moments show that the j_2 site has the highest and the e site has the smallest moment. Other results presented include total and partial density of states and the spin density distributions on the basal and [110] plane. The positive spin density from the Fe sites shows a network type of structure parallel to the c axis. These and other results are compared with those calculated for $Nd_2Fe_{14}B$.

I. INTRODUCTION

The high-performance permanent magnetic alloy $Nd_2Fe_{14}B$ and its substitutional derivatives have been the center of attention for research in magnetic materials. Various experimental measurements on the properties of $Nd_2Fe_{14}B$ and similar substituted alloys have been reported. We have studied the electronic structure of this class of materials by means of first principles spin-polarized calculations of band structures.[1-4] Recently, we have made a detailed comparative study of the electronic and magnetic structures in $Y_2F_{14}B$, $Nd_2Fe_{14}B$, $Y_2Co_{14}B$, and $Nd_2Co_{14}B$ crystals.[4] In this paper, we report a similar calculation for $Gd_2Fe_{14}B$ crystal. The use of the band approach to study the magnetic properties of the rare-earth iron-boron compounds should be more valid in the case of $Gd_2Fe_{14}B$ than in $Nd_2Fe_{14}B$ because of the exactly half-filled f shell of the Gd atom which has a zero orbital angular momentum. We used the first-principles orthogonalized linear combination of atomic orbital (OLCAO) method to calculate the band structure of $Gd_2Fe_{14}B$. This method is highly effective for systems with very complex structures. Since this method has been discussed in considerable detail in the previous work,[4] and in the references cited therein, we will not repeat it here. The basis and potential functions for each type of atom were prepared first. For Fe and B we used the same potentials and wave functions as those employed in the $Y_2Fe_{14}B$ and $Nd_2Fe_{14}B$ calculations. The basis and the potential for Gd were separately prepared such that when they were used in the band-structure calculation of Gd metal with the same OLCAO method, good results were obtained. The band structures of Gd along the symmetry lines of the hcp Brillouin zone for the spin-up and spin-down cases are shown in Figs. 1(a) and 1(b), respectively. These band structures for hcp Gd are in good agreement with the self-consistent calculation of Harmon.[5] Both calculations show that the narrow f band lies near the bottom of the s-p band in the spin-up case and slightly above the Fermi level in the spin-down case. Since the Fe moment usually couples ferrimagnetically with the moment of heavy rare earths such as Gd, we used the spin-up potential of Fe with the spin-down potential of Gd and vice versa in our spin-polarized calculation for $Gd_2Fe_{14}B$. The energy eigenvalues and eigenvectors were obtained by diagonalizing the secular equation at the six high symmetry points of the irreducible part of the tetragonal Brillouin zone. The state densities, the charge densities, and the spin densities of $Gd_2Fe_{14}B$ were calculated based on the wave functions at these six-high symmetry points.

II. RESULTS AND DISCUSSION

The calculated total density of state (DOS) for $Gd_2Fe_{14}B$ is shown in Fig. 2(a) and the projected partial

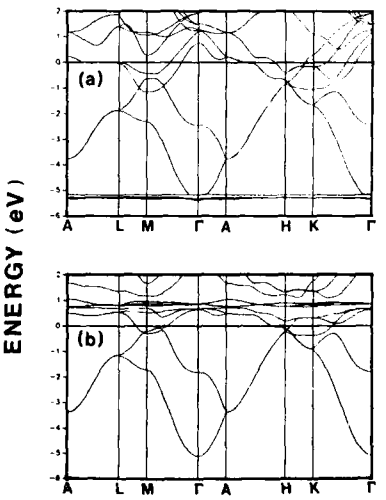


FIG. 1. Spin-polarized band structure of hcp Gd calculated by the minimal-basis OLCAO method. (a) Majority-spin band; (b) minority-spin band.

[a)] Permanent Address: Institute of Semiconductors, Chinese Academy of Sciences, Beijing, China.

 0021-8979/88/083716-03$02.40 © 1988 American Institute of Physics

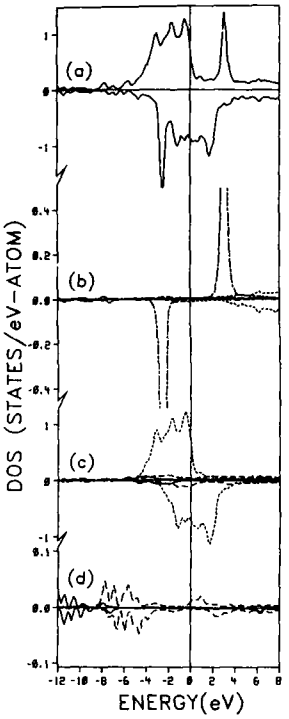


FIG. 2. Total and partial DOS of $Gd_2Fe_{14}B$: (a) Total: (b) Solid line—Gd 6*s*; dashed line—Gd 6*p*; dotted line—Gd 5*d*, dash-dot line—Gd 4*f*; (c) Solid line—Fe 4*s*; dashed line—Fe 4*p*; dotted line—Fe 3*d*; (d) Solid line—B 2*s*; dashed line—B 2*p*.

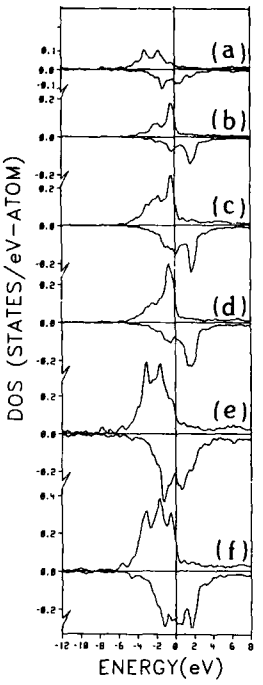


FIG. 3. Partial DOS at different Fe sites in $Gd_2Fe_{14}B$: (a) 4*e*; (b) 4*c*; (c) 8 j_1; (d) 8 j_2; (e) 16 k_1; (f) 16 k_2.

DOS (PDOS) for Gd, Fe, and B atoms and their orbital components are shown in Figs. 2(b), 2(c), and 2(d), respectively. The Gd and Fe moments are ferrimagnetically ordered as observed experimentally. The occupied Gd *f* level is at -2.5 eV and the empty *f* orbitals is at about 3.1 eV. In pure Gd, the same two peaks are at -5.2 and $+0.7$ eV with respect to the Fermi level. Thus the interaction with iron *d* band has shifted the *f* levels of Gd upward. The majority Fe 3*d* band has three well-resolved structures at -0.5, -1.7, and -3.1 eV, respectively, which are to be compared with the same three structures in $Nd_2Fe_{14}B$ at -1.0, -1.9, and -3.3 eV, respectively.[4] This indicates the effects of Gd and Nd on the Fe *d* band are slightly different. The majority Fe 3*d* band is pushed closer to the Fermi level which accounts for a much reduced spin magnetic moment. Our calculated total spin magnetic moment is 18.41 μ_B per formula unit (F.U.) which is in very good agreement of the measured value of 18.02 (μ_B/F.U.).[6] This corresponds to an average Fe moment of 2.30 μ_B. The calculated total magnetic moments in $Y_2Fe_{14}B$ and $Nd_2Fe_{14}B$ are 32.50 and 34.63 μ_B/F.U., respectively.[4] The site-decomposed PDOS for each Fe atom is shown in Fig. 3. These spectra are quite similar to those in $Nd_2Fe_{14}B$ except for the *c* site and the j_1 site which show slight deviation. This is because these two sites are more influenced by the nearby rare-earth atoms. From the site-decomposed PDOS, the spin magnetic moments M_s at each of the Fe sites were obtained. We obtained M_s values of 1.61, 2.96, 2.60, 3.11, 1.90, 2.15 μ_B for the *e*, *c*, j_1, j_2, k_1, and k_2 sites, respectively. These numbers are to be compared with experimental values of 1.94, 2.34, 2.30, 2.67, 2.25, 2.40 μ_B, respectively, deduced from a combination of Mössbauer spectroscopy and nuclear magnetic resonance measurements.[7] The agreement between the theoretical calculation and experimental values is moderate, and is of the same quality as in the $Nd_2Fe_{14}B$ case.[4] Nevertheless, our calculation correctly predicts that the j_2 site should have the highest moment and the *e* site should have the smallest. It is highly desirable to have neutron scattering data on single-crystal $Gd_2Fe_{14}B$ in order to make a more quantitative comparison between theory and experiment.

We used the eigenfunctions at the six high-symmetry *k* points from the band calculation, to evaluate the charge density $\rho\uparrow(r)+\rho\downarrow(r)$ and the spin-density $\rho\uparrow(r)-\rho\downarrow(r)$ on the two important crystallographic planes. These are shown in Fig. 4 for the cases of basal plane $z=0$ (right panel) and the [110] plane (left panel). The basal plane contains both the Gd(*g*) and Gd(*f*) sites as well as Fe(*c*) and B sites. The [110] plane contains not only the two Gd and one B site, but also Fe(*e*), Fe(j_1), Fe(j_2) sites. The labelling of the different atomic sites in Fig. 4 is similar to that of Fig. 6 in Ref. 4. The charge density plot of Fig. 4(a) is to be compared with the charge density distribution of $Nd_2Fe_{14}B$ in the same plane. Two facts merit some comment: First, the charge density due to the *f* electrons in Gd in $Gd_2Fe_{14}B$ is much more tightly bonded than the *f* electrons in Nd atoms in $Nd_2Fe_{14}B$; second, the charge distribution around the two Gd sites,

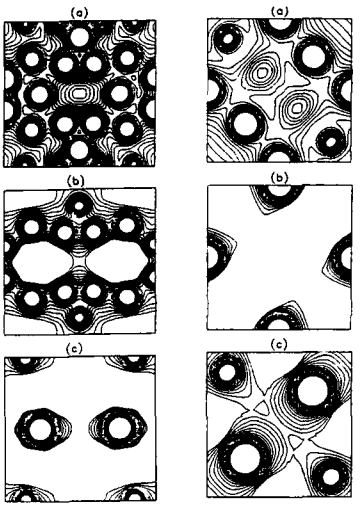


FIG. 4. (a) Charge density, (b) positive spin density and (c) the negative spin density in $Gd_2Fe_{14}B$. The left panel is for [110] plane and the right panel is for the basal plane. The atomic positions were the same as in Fig. 6 in Ref. 4.

Gd(g) and Gd(f), are quite different, which is consistent with experiment. Buschow *et al.*, using ^{155}Gd Mössbauer spectroscopy, found that the two Gd sites experience different types of crystal fields due to the occurrence of quadrupole splitting of unequal sign for the two Gd sites.[8] From a Mulliken analysis of the wave functions, we found effective charges of 8.21 and 8.05 electrons for Gd(g) and Gd(f), respectively. Therefore, approximately two electrons per Gd atom are transferred to the Fe sites. Because of the ferrimagnetic ordering between Gd and Fe moments in $Gd_2Fe_{14}B$, it is necessary to present both the positive part and the negative part of the spin densities on the [110] and the basal plane separately which are shown in Figs. 4(b) and 4(c), respectively. The positive spin-density maps are quite similar to those of $Nd_2Fe_{14}B$: both show an infinite array of network type of structure linking all the Fe sites in the [110] plane. The negative spin densities are all due to the Gd f electrons. The disparity between the Gd(f) and Gd(g) sites is even more prominent in the spin-density map in the basal plane shown in Fig. 4(c). From these spin-density maps, it appears that in $Gd_2Fe_{14}B$, the Fe moments prefer the c direction while the Gd ions may have their moments lie in the basal plane.

ACKNOWLEDGMENT

Work supported by the Weldon Spring Endowment Fund of the University of Missouri and in part by DOE Grant No. DE-FG02-84ER45170.

[1]Z.-Q. Gu and W. Y. Ching, J. Magn. Magn. Mater. **54–57**, 525 (1986); Phys. Rev. B **33**, 2868 (1986).
[2]W. Y. Ching and Z.-Q. Gu, J. Appl. Phys. **61**, 3718 (1987).
[3]Z.-Q. Gu and W. Y. Ching, J. Appl. Phys. **61**, 3977 (1987).
[4]Z.-Q. Gu and W. Y. Ching, Phys. Rev. B **36**, 8530 (1987).
[5]B. N. Harmon, J. Phys. (Paris) Colloq. **5**, C5-65 (1979).
[6]M. Boge', J. M. D. Coey, G. Czjzek, D. Givord, C. Jeandey, H. S. Li, and J. L. Oddon, Solid State Commun. **55**, 295 (1985).
[7]M. Rosenberg, P. Deppe, K. Erdmann, M. Sostarich, and H. Stadelmaier, J. Magn. Magn. Mater. **54–57**, 599 (1986).
[8]K. H. J. Buschow, J. W. C. de Vries, and R. C. Thiel, J. Phys. F **15**, L93 (1985).

An NMR study of tetragonal $Nd_2Fe_{14}B$ and $Nd_2Fe_{14-x}Co_xB$

Y. D. Zhang[a] and J. I. Budnick
Department of Physics and Institute of Materials Science, University of Connecticut, Storrs, Connecticut 06268

E. Potenziani II
US Army Electronics Technology and Devices Laboratory (LABCOM), Fort Monmouth, New Jersey 07703-5000

A. T. Pedziwiatr and W. E. Wallace
MEMS Department and Magnetic Technology Center, Carnegie-Mellon University, Pittsburgh, Pennsylvania 15213

P. Panissod
L.M.S.E.S. (La au CNRS no. 306), Institute Le Bel, Université L. Pasteur, 4, rue Blaise-Pascal, F-67070 Strasbourg Cedex, France

^{10}B, ^{11}B, ^{57}Fe, and ^{59}Co spin-echo NMR experiments have been performed for naturally abundant and ^{10}B-enriched $Nd_2Fe_{14}B$ and $Nd_2Fe_{14-x}Co_xB$ ($x \leqslant 0.7$) at 1.3 and 4.2 K for frequencies from 10 to 300 MHz. The Fe hyperfine field (HF) values in the $Nd_2Fe_{14}B$ compound and their assignment to the six iron sites are the following: 302(e) 320(c) 325(k_1), 334(j_1), 352(k_2), and 378(j_2) kOe. The substitution of Co for Fe decreases the HF at the Fe nuclei at j_2, k_2, j_1, k_1, and c sites while no obvious change in the HF at the e site nor at the B nuclei has been found. The spin-echo amplitude corresponding to the Fe(k_2) site line decreases with increasing Co content. A complex ^{59}Co spectrum is found in the frequencies between 150 and 260 MHz with a strong peak around 250 MHz. These results confirm that Co atoms have a strong preference to enter the k_2 site.

I. INTRODUCTION

In order to understand the details of the magnetic properties of the Nd-Fe-B permanent magnets on an atomic scale, a large number of hyperfine interaction studies concentrated on the tetragonal $Nd_2Fe_{14}B$ compound since the discovery of this new permanent magnet.[1-8] Several Mössbauer studies were devoted to determining the hyperfine fields (HF) at the six nonequivalent Fe sites (4e, 4c, 8j_1, 16k_1, 16k_2). However, the reported results are quite divergent owing to the difficulty in uniquely assigning the six superposed sextet spectra of this phase.[8] NMR studies on this compound also have problem due to a very strong ^{11}B spin-echo which overlapped the ^{57}Fe lines between 41 and 46 MHz. This difficulty was removed by isotopic substitution of ^{10}B in the starting materials and a clear and reliable NMR spectrum has been obtained, which very well shows the six distinct peaks. It was, however, still not easy to assign them to the six Fe sites by looking at the NMR spectrum alone. In considering that a substitution of Co for Fe will vary the Fe HF of these sites and that their changes must follow in a continuous way and correspond with the crystalline environments of the idividual sites, we performed a systematic investigation on the $Nd_{15}Fe_{77-x}Co_xB_8$ alloys.[8]

In addition to helping the assignment, the study of $Nd_2Fe_{14-x}Co_xB$ compounds itself is very important as the addition of Co atoms improves the Curie temperature as well as, within a certain replacement range, the saturation magnetization.[9,10] It is therefore important to know where the Co atoms go. The Mössbauer and neutron experiments give somewhat conflicting conclusions.[11-13] Our previous ^{57}Fe NMR measurements support the idea that the Co has a strong selectivity in occupying the k_2 site.[8] Obviously, the most direct way is to measure the ^{59}Co NMR spectrum in the $Nd_2Fe_{14-x}Co_xB$. In the present work we present the results of the Co NMR experiments in the $Nd_2Fe_{14-x}Co_xB$ phase. These results confirm the preference of Co atoms to enter the k_2 site.

II. SAMPLES AND EXPERIMENTS

In the present work all samples were prepared by arc melting. Two $Nd_2Fe_{14}B$ samples were made using naturally abundant and 98% ^{10}B-enriched boron, respectively. The Co substituted samples were made also using the ^{10}B-enriched boron. A preliminary NMR investigation of the $Nd_2Fe_{14-x}Co_xB$ system found that these samples often contained some amount of Fe and Co precipitates. For instance, the NMR measurements on the $Nd_2Fe_{13.3}Co_{0.7}B$ and $Nd_2Fe_{12.6}Co_{1.4}B$ recorded two strong peaks around 46.7 and 290 MHz. The latter indicates a presence of Co atoms in bcc α-Fe.[14] To avoid the interference of these signals in the NMR spectrun of the tetragonal phase in low Co content range, sample $Nd_{15}Fe_{76}Co_1B_8$ was used whose main phase, responsible for NMR, is close to $Nd_2Fe_{13.8}Co_{0.2}B$. These samples were checked by a Cu$K\alpha_1$ x-ray diffraction using a Norelco diffractometer, and the tetragonal phase was identified for all these samples with the measured lattice parameters found to be very close to the published values.

The spin-echo NMR measurements were made at 1.3 and 4.2 K for frequencies raning from 10 to 300 MHz by employing a variable-frequency spin-echo NMR apparatus. Considering the difference in the relaxation time T_2 for the different lines, a correction $\exp(-t/T_2)$ has been taken into account for each NMR peak when plotting the NMR spec-

[a] Permanent address: Dept. of Physics and Institute of Magnetic Materials, Lanzhou Univ. Gansu, People's Republic of China.

 0021-8979/88/083719-03$02.40 © 1988 American Institute of Physics

tra, where t is the separation between the two pulses. Most experiments were carried out in zero magnetic field, while some measurements were performed in an external magnetic field up to 9 kOe.

III. RESULTS AND DISCUSSION

For the $Nd_2Fe_{14}B$ compound made by naturally abundant B powder, a very strong ^{11}B spin echo was observed centered at 42.4 MHz at 1.3 K which overlaps the ^{57}Fe resonance lines between 41 and 46 MHz. For the ^{10}B-enriched $Nd_2Fe_{14}B$, the spin echo at around 42.4 MHz was almost removed. Instead, a strong ^{10}B resonance occurs at 14.2 MHz. It was found that the ^{10}B NMR frequency of $Nd_2Fe_{14-x}Co_xB$ does not strongly vary with the substitution of Co for Fe. A detailed ^{10}B and ^{11}B NMR measurement on the $Nd_2Fe_{14}B$ and $Nd_{15}Fe_{77-x}Co_xB_8$ will be published elsewhere.[8,15]

In Fig. 1(a) is shown the zero-field ^{57}Fe NMR spectrum of the ^{10}B-enriched $Nd_2Fe_{14}B$ compound. Since the ^{10}B resonance frequency is far away from the Fe resonance, the ^{57}Fe NMR peaks were very well discerned at 41.5, 44.0, 44.7, 46.0, 48.5, 52.0, and 53.0 MHz. An external magnetic field H_0 of 5 kOe removed the 53.0-MHz lines but other peaks remained with very small frequency shifts being accounted for by the addition of the external field. This enables us to suggest that the 52.0 and 53.0 MHz resonances come from the Fe atoms of same site; the 52.0-MHz line originates from the domain wall edge whereas the 53.0-MHz line is from the domain wall center. The strongest peak, namely the 48.5-MHz line, was checked in an external field up to 9 kOe. Only a small decrease of the NMR frequency has been found and can be accounted for by $\gamma(^{57}Fe)H_0$. This implies that the domain and the domain wall have almost the same HF for this system; it enables us to compare the present NMR results with the Mössbauer experiments.

Figure 1(b) gives the NMR spectrum of $Nd_2Fe_{13.3}Co_{0.7}B$. Again six peaks were observed but located at 41.5, 43.3, 44.0, 45.5, 48.0, and 51.0 MHz, showing that the NMR frequencies of the corresponding lines decreased with the Co substitution for all these lines except the 41.5 MHz resonance. The intensity ratio of the 48.0-MHz line to that of the 51.0 MHz one for $Nd_2Fe_{13.3}Co_{0.7}B$ is smaller than the intensity ratio of the 48.5-MHz line to that of the 52.0 MHz one for the $Nd_2Fe_{14}B$. A similar study of $Nd_{15}Fe_{77-x}Co_xB_8$ ($x<12$) also demonstrates that the more the Co content, the less intense this peak will be.[8]

The six Fe NMR peaks [taking the 52.0 and 53.0 MHz resonances shown in Fig. 1(a) as one line as mentioned above, and hereafter taking 52.0 MHz as the frequency of this line] shown in Fig. 1(a) must correspond to the six nonequivalent Fe sites. It turns out from these spectra that the HF at the different Fe sites are very different and sensitive to the Co replacement. Up to now there were several reports of the assignment of these six Fe HF values to the six Fe sites. As pointed in Refs. 5 and 8, they are, however, somewhat at variance. The above ^{11}B and ^{57}Fe NMR results can be used in the assignment.

(1) Although the relative intensities of the six Fe lines shown in Fig. 1(a) for the $Nd_2Fe_{14}B$ compound do not exactly follow the site population ratio 1:1:2:2:4:4, rather large differences in intensity between the individual lines were observed, and this enables us to attribute the two largest peaks, centered respectively at 44.7 and 48.5 MHz, to be from k-type site Fe atoms, while the two smallest lines, at 41.5 and 44.0 MHz, are from the Fe atoms at the e or c sites, and those at 44.7 and 52.0 MHz from the Fe atoms at the two j-type sites.

(2) In the tetragonal $Nd_2Fe_{14}B$ phase, a boron atom is located at the center of a trigonal prism formed by two Fe (e) and four Fe(k_1) atoms. The fact that the ^{10}B NMR frequency does not obviously change with the Co substitution leads to the conclusion that the Co atoms do not preferentially replace the Fe atoms at the e and k_1 sites.

(3) The fact that the relative intensity of the 48-MHz echo decreased with the substitution of Co for Fe suggests that the Co atoms enter preferentially into this site, which must be the k_2 site as we know that the Co atoms do not preferentially enter the k_1 site. Thus, the 44.7-MHz line is assigned to the k_1 Fe site.

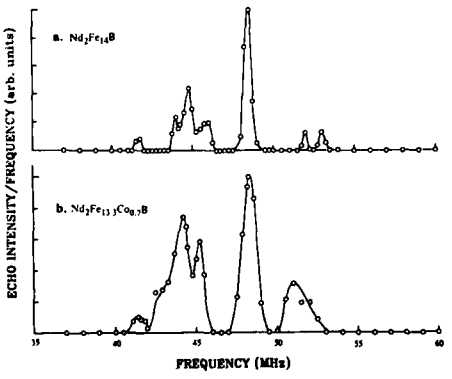


FIG. 1. ^{57}Fe spin-echo amplitude divided by frequency in arbitrary units vs frequency in MHz at 1.3 K for (a) $Nd_2Fe_{14}B$ and (b) $Nd_2Fe_{13.3}Co_{0.7}B$.

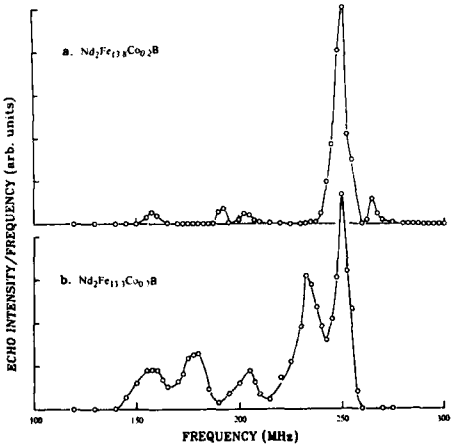


FIG. 2. ^{59}Co spin-echo amplitude divided by frequency in arbitrary units vs frequency in MHz at 4.2 K for (a) $Nd_2Fe_{13.8}Co_{0.2}B$ and (b) $Nd_2Fe_{13.3}Co_{0.7}B$.

(4) The Fe atoms at the $4e$, $4c$, $8j_1$, $8j_2$, $16k_1$, and $16k_2$ sites have, respectively, 0, 4, 3, 2, 3, and 4 Fe(k_2) atoms in their nearest-neighbor shell.[16] With a substitution of the Fe(k_2) by Co, the ^{57}Fe NMR frequencies corresponding to these lines will vary, depending on how many Fe(k_2) atoms are replaced by Co, in their nearest-neighbor shell. It was found, by comparing the corresponding NMR peaks between $Nd_2Fe_{14}B$ and $Nd_2Fe_{13.3}Co_{0.7}B$ shown in Fig. 2, that the Co substitution for Fe produced NMR frequency shifts of 0, 0.7, 0.7, 0.5, 0.5, and 1.0 MHz in order of increasing frequency. Therefore, to assign the 41.5-MHz echo to the e site is consistent with the fact that there is no Fe(k_2) in the nearest neighbor of this site Fe; then the 44.0-MHz echo is attributed to originate from the Fe(c) atoms. As mentioned in Ref. 5, the most reliable result obtained so far from Mössbauer data is that the Fe(j_2) atoms have the largest HF among these six Fe sites. The present NMR results are very consistent with this conclusion in that the 52.0 MHz resonance experienced the largest shift when some amount of the Fe was replaced by Co since the Fe(j_2) has the largest number of the Fe(k_2) neighbors. The 46.0 MHz resonance is then assigned to the Fe in the j_1 site. In the present assignment, the NMR frequency of the j_1 site Fe is higher than that of Fe(k_1). This seems reasonable if we consider the following facts: (1) the Fe(k_1) atoms have one B in its nearest-neighbor shell, whereas the Fe(j_1) atoms do not. In a majority of cases the B tends to decrease its near-neighbor Fe HF. (2) The Fe(j_1) and Fe(k_1) atoms have identical, nine nearest Fe neighbors, but the average distance between the Fe(j_1) atom and their nearest Fe neighbors is smaller than that between the Fe(k_1) atom and its nearest Fe neighbors. This may favor a larger THF contribution to the Fe(j_1) nuclei.

Thus the assignment of the six Fe HF to the six Fe sites is the following: 302(e), 320(c), 325(k_1), 334(j_1), 352(k_2), and 378(j_2) kOe. These values are very close, about 3%, to those obtained from a Mössbauer experiment by Onodera *et al.*,[7] and the assignments of the HF values to the e, c, j_2, k_2 Fe sites by our NMR and by the Mössbauer experiments[7] are coincident with each other as well.

Figure 2 gives the ^{59}Co NMR spectra of the tetragonal $Nd_2Fe_{14-x}Co_xB$ phase with $x = 0.2$ and 0.7. For the low Co content sample, five peaks are clearly shown centered at 160, 192.5, 205, 250, and 265 MHz. The 250-MHz line is over 10 times stronger than the other peaks. This is a direct evidence of the selectivity of Co atoms in this system. From the above discussion of the NMR spectra it appears that this strong line must originate from the Co atoms in the k_2 site of the tetragonal phase. For the composition with $x = 0.7$, the spectrum shown in Fig. 2(b) consists of the peaks at 160, 180, 205, 235, and 250 MHz. Further measurements on the samples containing higher Co content showed that the overall spectra of the samples are similar to that shown in Fig. 2(b), but the relative intensity of the 235 MHz resonance increased with increasing Co content.

It is well known that the ^{59}Co NMR frequency is very sensitive to the local atomic environment as the transferred HF contributes a large amount to the total HF. Since the Co atom carries a small atomic moment, 1.4 μ_B (Ref. 17), in comparison with the Fe moment of 2.2 μ_B in the tetragonal $Nd_2Fe_{14}B$ phase, the Co(k_2) atom surrounded by one Co atom will have a rather smaller HF than that having no Co atom in its nearest-neighbor shell. Thus it is reasonable to assume that the 235 MHz resonance is a satellite caused by the Co(k_2) having one Co atom as its nearest neighbor. If one assumes that all Co atoms enter the k_2 site, the probability for a Co atom in $Nd_2Fe_{14-x}Co_xB$ to have m Co atoms as its nearest neighbors among n possible k_2-site Co atoms is given by

$$(m) = [n!/m!(n-m)!]C^m(1-C)^{(n-m)},$$

where $C = (x/14)/16$ is the fractional Co concentration in the k_2 site and $n = 3$ for the k_2 site. For $x = 0.2$, we obtained $P_3(0) = 0.87$ and $P_3(1) = 0.11$, respectively; for $x = 0.7$, they are correspondingly 0.56 and 0.36. These results seem compatible with the experimental spectra shown in Figs. 2(a) and 2(b). A systematic ^{59}Co NMR study of this system, including site assignment of the Co HF, is in progress.

ACKNOWLEDGMENTS

The authors are grateful to Dr. M. Sagawa for providing a $Nd_2Fe_{14}B$ sample and Dr. W. A. Hines, D. P. Yang, and J. C. Ford for many useful discussions.

[1] H. Onodera, Y. Yamaguchi, H. Yamamoto, M. Sagawa, Y. Matsuura, and H. Yamamoto, J. Magn. Magn. Mater. **46**, 151 (1984).
[2] R. Fruchart, P. L'Heritier, P. Dalmas de Reotier, D. Fruchart, P. Wolfers, J. M. D. Coey, L. P. Ferreira, R. Guillen, P. Vulliet, and A. Yaouanc, J. Phys. F **17**, 483 (1987).
[3] M. Rosenberg, P. Deppe, M. Wojcik, and H. Stadelmeier, J. Appl. Phys. **57**, 4124 (1985).
[4] R. Kamal and Y. Andersson, Phys. Rev. B **32**, 1756 (1985).
[5] H. Onodera, A. Fujita, H. Yamamoto, M. Sagawa, and S. Hirosawa, J. Magn. Magn. Mater. **68**, 6 (1987).
[6] F. E. Pinkerton and W. R. Dunhan, Appl. Phys. Lett. **45**, 1248 (1984).
[7] H. Onodera, H. Yamauchi, M. Yamada, H. Yamamoto, M. Sagawa, and S. Hirosawa, J. Magn. Magn. Mater. **68**, 15 (1987).
[8] Y. D. Zhang, J. I. Budnick, E. Potenziani II, A. T. Pedziwiatr, and W. E. Wallace, Phys. Rev. (to be published).
[9] Y. Matsuura, S. Hirosawa, H. Yamada, S. Fujimura, and M. Sagawa, Appl. Phys. Lett. **46**, 308 (1986).
[10] M. Q. Huang, E. B. Boltich, W. E. Wallace, and E. Oswald, J. Magn. Magn. Mater. **60**, 270 (1987).
[11] H. M. Van Noort and K. H. J. Buschow, J. Less-Common Metals **113**, L9 (1985).
[12] J. F. Herbst and W. B. Yelon, J. Appl. Phys. **60**, 4224 (1986).
[13] D. E. Tharp, Y. C. Yang, O. A. Pringle, G. J. Long, and W. J. James, J. Appl. Phys. **61**, 4334 (1987).
[14] R. F. Jackson, R. G. Scurlock, D. B. Utton, and T. H. Wilmshurst, Phys. Lett. **12**, 168 (1964).
[15] Y. D. Zhang, J. I. Budnick, E. Potenziani II, A. T. Pedziwiatr, and W. E. Wallace (to be published).
[16] J. F. Herbst, J. J. Croat, F. E. Pinkerton, and W. B. Yelon, Phys. Rev. B **29**, 4176 (1984).
[17] K. H. J. Buschow, D. B. de Mooij, S. Sinnema, R. J. Radwanski, and J. J. M. Franse, J. Magn. Magn. Mater. **51**, 211 (1985).

Mössbauer study of the permanent-magnet material $Nd_2(Fe_{1-x}Ni_x)_{14}B$

S. Dai,[a] A. H. Morrish, and X. Z. Zhou[b]
Department of Physics, University of Manitoba, Winnipeg MB R3T 2N2, Canada

B. P. Hu and S. G. Zhang
Institute of Physics, Academica Sinica, Beijing, China

Samples of $Nd_2(Fe_{1-x}Ni_x)_{14}B$, $0 \leqslant x \leqslant 0.20$, with good phase homogeneity have been made by heating under vacuum for 300 h. ^{57}Fe Mössbauer parameters have been determined for all six different iron crystallographic sites at room temperature. The nickel atoms preferentially substitute for iron atoms on the $16k_2$ and $8j_2$ sites. The nickel atoms seem to alter the hyperfine parameters of the ^{57}Fe nuclei via localized interactions.

I. INTRODUCTION

Ever since the first reports in 1984,[1-3] the alloy $Nd_2Fe_{14}B$ has been investigated extensively as a superior, but relatively inexpensive, permanent-magnet material. These studies include magnetic measurements,[4] neutron diffraction,[5] NMR,[6,7] and Mössbauer spectroscopy.[7-12] The neutron-diffraction spectra, after analysis by the Rietveld method,[5] show that the structure is tetragonal with iron ions on six sites, $16k_1$, $16k_2$, $8j_1$, $8j_2$, $4e$, and $4c$, neodymium ions on two sites, $4f$ and $4g$, and boron ions also on $4g$. The cardinal number prefixes indicate the number of each site occupied per four formula units. One productive way to explore the origin of the magnetic properties is to study the influence of cation substitutions. In this work, samples of $Nd_2(Fe_{1-x}Ni_x)_{14}B$ with $x = 0.00, 0.05, 0.10, 0.15$, and 0.20 were made and investigated by Mössbauer spectroscopy. First, the hyperfine fields at the ^{57}Fe nuclei on the various iron sites are identified for the end member, $x = 0$. Next, the location of the nickel ions is inferred from the relative areas of the subpatterns. Then the variation of the ^{57}Fe hyperfine parameters with nickel concentration is deduced for each site. Finally, the data and some of their implications are discussed.

II. EXPERIMENT

The elements Nd, Fe, Ni, and B, all 99.9% purity, were mixed in the desired proportions and melted in a vacuum arc furnace with an argon atmosphere. The products were remelted 4–5 times in order to obtain a homogeneous alloy. The ingots were sealed in an evacuated quartz tube, annealed at 1000 °C for 300 h, and then quenched rapidly to room temperature. X-ray diffraction indicated the samples had the tetragonal crystal structure with a good phase homogeneity; however, a small amount of a second phase was also detected.

^{57}Fe Mössbauer spectra were collected with a triangular drive at room temperature. The data were folded and calibrated with an α-Fe spectrum. The spectra were fitted with six sextet and one doublet subpatterns associated with the tetragonal and impurity phases, respectively.

III. RESULTS AND DISCUSSION

A. $Nd_2Fe_{14}B$

The ^{57}Fe Mössbauer spectrum of $Nd_2Fe_{14}B$ is shown at the top of Fig. 1 as dots. If any difference between the recoil-

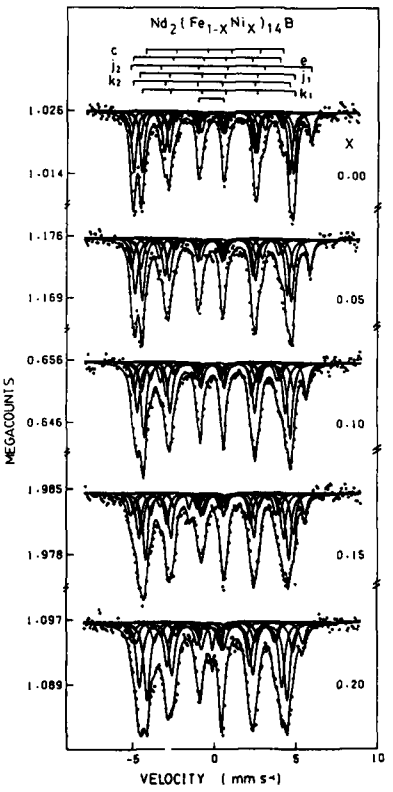


FIG. 1. Room-temperature Mössbauer spectra of $Nd_2(Fe_{1-x}Ni_x)_{14}B$ for $0.0 \leqslant x \leqslant 0.20$. The experimental data are shown as dots; the six-line subpatterns for ^{57}Fe nuclei in the six sites, the doublet for an impurity phase, and their sum are drawn as solid curves. In addition, the peak locations for these seven subpatterns are indicated by the bars for $x = 0.00$.

[a] Now at Institute of Physics, Academica Sinica, Beijing, China.
[b] On leave from Southwest Institute of Applied Magnetics, Mianyang, Sichuan, China.

 0021-8979/88/083722-03$02.40 © 1988 American Institute of Physics

TABLE I. Room-temperature Mössbauer parameters for six iron lattice positions in $Nd_2Fe_{14}B$. The hyperfine field, H_{hf}, quadrupole splitting, $\epsilon = \frac{1}{4}eQV_{zz}$, and isomer shift, δ, associated with each site are given.

Site	H_{hf} (kOe)	ϵ (mm s^{-1})	δ (mm s^{-1})
$16k_1$	288(2)	0.27(5)	0.05(3)
$16k_2$	296	0.13	−0.24
$8j_1$	294	0.24	0.05
$8j_2$	343	0.51	0.14
$4e$	283	−0.73	−0.08
$4c$	261	0.07	−0.05

less fraction at each site is neglected, then the area ratios of the six sextets should be equal to the ratio of the numbers of iron atoms on each site. Therefore, the areas of the subpatterns associated with the k_1, k_2, j_1, j_2, e, and c sites were constrained to be in the ratios 16:16:8:8:4:4, respectively. Then a good fit was obtained when the hyperfine fields in descending order corresponded to the $8j_2$, $16k_2$, $8j_1$, $16k_1$, $4e$, and 4c sites, respectively. The computer fits are shown as solid curves in Fig. 1 and the hyperfine parameters are listed in Table I.

These assignments are in reasonable agreement with those of Pinkerton and Dunham[8] and of van Noort *et al.*,[10] but disagree with the others.[7,9,11,12] The j_2 site, which has the largest hyperfine field, also has the largest number (12) of iron nearest neighbors. The e and c sites have nine and eight iron nearest neighbors, respectively; hence their associated hyperfine fields may be expected to be smaller than that for the k_1 site, which has 10 iron nearest neighbors. Finally, the $4e$ sites have four Fe ions nearly in the same plane, four above this plane and one below. This large asymmetry may be expected to lead to a large electric-field gradient, and therefore a large quadrupole splitting, as observed.

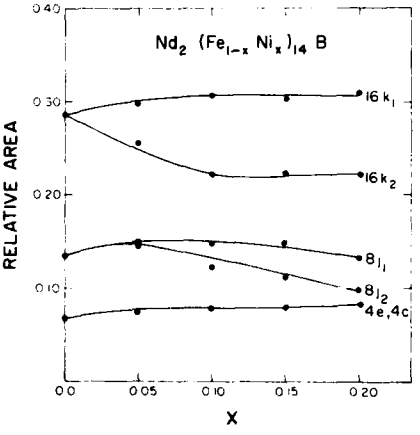


FIG. 2. Relative areas of the six subpatterns associated with the $Nd_2(Fe_{1-x}Ni_x)_{14}B$ phase as a function of the nickel concentration. The relative area for the impurity phase is not shown, but it is included in the total area.

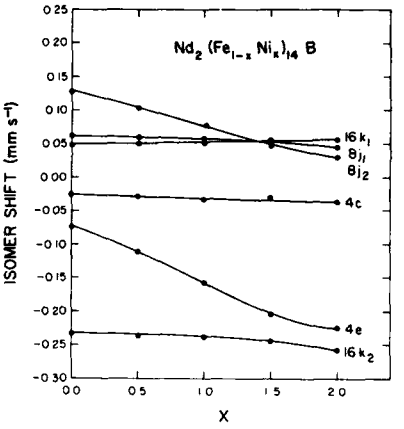


FIG. 3. Isomer shifts for the six iron sites of $Nd_2(Fe_{1-x}Ni_x)_{14}B$ as a function of the nickel content.

B. $Nd_2(Fe_{1-x}Ni_x)_{14}B$

The room-temperature Mössbauer spectra for $Nd_2(Fe_{1-x}Ni_x)_{14}B$ ($x = 0.05, 0.10, 0.15$, and 0.20) are also shown as dots in Fig. 1. The parameters obtained when $x = 0$ were helpful in fitting the subpatterns to the data, since the site occupancies of the nickel were unknown area constraints could not be applied. The fits obtained are also shown by the solid curves in Fig. 1.

The areas of the six sextets as compared to the total absorption area, including the doublet for the impurity phase, are plotted in Fig. 2 as a function of nickel concentration. A substantial decrease in area occurs for the subpatterns associated with the $16k_2$ and $8j_2$ sites. Since it seems unlikely that recoilless fraction differences could account for these decreases, it follows that nickel ions preferentially substitute for iron ions on the $16k_2$ and $8j_2$ sites. At the largest x

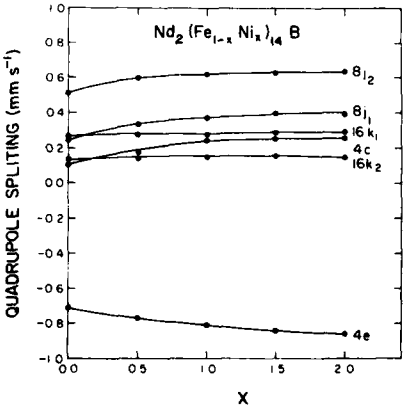


FIG. 4. ^{57}Fe quadrupole splitting versus nickel substitution of iron atoms.

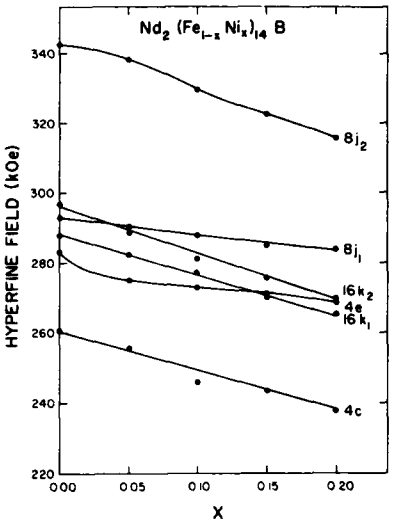


FIG. 5. Hyperfine fields at ^{57}Fe nuclei located at the six crystallographic sites for various x values.

values, the data also suggest that some nickel may enter other sites, particularly the $8j_1$ site. In view of the fitting uncertainties, it is imprudent to make these statements more quantitative.

The isomer shifts, quadrupole splittings, and hyperfine fields identified with each site are plotted as a function of x in Figs. 3, 4, and 5. Clearly the nickel affects the parameters at some sites more than at others.

The largest changes in the isomer shifts occur for the $8j_2$ and $4e$ sites, where the decrease implies an increase in the charge density at the nucleus with increasing nickel content. Since a j_2 site has four nearest-neighbor k_2 sites, and a $4e$ site has two nearest-neighbor j_2 sites, it seems that the nickel on these nearby sites is responsible.

The changes in the quadrupole shift are relatively small. However, the hyperfine fields decrease at all sites; clearly when nickel is present the transferred hyperfine field is reduced.

IV. CONCLUSIONS

Nickel atoms prefer to substitute for iron atoms on the $16k_2$ and $8j_2$ sites of $Nd_2Fe_{14}B$; this result is quite different than that observed for yttrium which substitutes randomly for Nd ions on the $4f$ and $4g$ sites.[13] The variety in the changes of the hyperfine parameters suggests that the nickel interactions are localized, that is, confined to nearest neighbors.

ACKNOWLEDGMENT

This research was partially financed by the Natural Sciences and Engineering Research Council of Canada.

[1]M. Sagawa, S. Fujimura, N. Togawa, H. Yamamoto, and Y. Matsuura, J. Appl. Phys. **55**, 2083 (1984).
[2]J. J. Croat, J. F. Herbst, R. W. Lee, and F. E. Pinkerton, J. Appl. Phys. **55**, 2078 (1984).
[3]G. C. Hadjipanayis, R. C. Hazelton, and K. R. Lawless, J. Appl. Phys. **55**, 2073 (1984).
[4]S. Hirosawa, Y. Matsuura, H. Yamamoto, S. Fujimura, M. Sagawa, and H. Yamauchi, J. Appl. Phys. **59**, 873 (1986).
[5]J. F. Herbst, J. J. Croat, F. E. Pinkerton, and W. B. Yelon, Phys. Rev. B **29**, 4176 (1984).
[6]Cz. Kapusta, Z. Kakol, H. Figiel, and R. Radowanski, J. Magn. Magn. Mater. **39**, 169 (1986).
[7]M. Rosenberg, P. Deppe, and M. Wojcik, J. Appl. Phys. **57**, 4124 (1985).
[8]F. E. Pinkerton and W. R. Dunham, Appl. Phys. Lett. **45**, 1248 (1984).
[9]H. Onodera, Y. Yamaguchi, H. Yamamoto, M. Sagawa, Y. Matsuura, and H. Yamamoto, J. Magn. Magn. Mater. **46**, 151 (1984).
[10]H. M. van Noort, D. B. de Mooij, and K. H. J. Buschow, J. Appl. Phys. **57**, 5414 (1985).
[11]Q. Ling, J. M. Cadogan, and J. M. D. Coey, Hyperfine Interact. **28**, 655 (1986).
[12]R. Fruchart, P. L'Heritier, P. D. de Réotier, D. Fruchart, P. Wolfers, J. M. D. Coey, L. P. Ferreira, R. Guillen, P. Vulliet, and A. Yaouanc, J. Phys. F **17**, 483 (1987).
[13]S. Dai, A. H. Morrish, X. Z. Zhou, B. P. Hu, and S. G. Zhang, Hyperfine Interact. (in press).

Neutron determination of the magnetic order and site preference in $Er_2(Co_xFe_{1-x})_{17}$

R. Kumar and W. B. Yelon
University of Missouri, Research Reactor, Columbia, Missouri 65211
C. D. Fuerst
Physics Department, General Motors Research Laboratories, Warren, Michigan 48090

Neutron powder diffraction has been used to characterize the magnetic ordering and crystallographic behavior of $Er_2(Co_{0.55}Fe_{0.45})_{17}$ which crystallizes in the hexagonal form (Th_2Ni_{17}). The *f* site, which is the dumbbell site, analogous to the *c* site in the rhombohedral 2-17 phase (Th_2Zn_{17}) and to the j_2 site in the 2-14-1 phase, is characterized by long TM–TM bonds (>2.55 Å) and a large number of TM near neighbors, and like its analogues, is strongly preferred by the Fe. The other three sites are slightly cobalt rich, compensating for the Co deficiency on *f*. The magnetic structure at 293 and 580 K is axial with erbium moments antiparallel to the transition-metal moments as expected. At 8.7 K, basal plane components develop in addition to the axial moments on the erbium sites. Further studies will investigate the spin reorientation as a function of temperature and composition across the entire composition diagram.

INTRODUCTION

Rare-earth transition-metal compounds of the type $Er_2(Co_xFe_{1-x})_{17}$ crystallize in an hexagonal structure (Th_2Ni_{17}) having two crystallographically inequivalent rare-earth sites (2*b*, 2*d*) and four transition-metal sites (12*k*, 12*j*, 6*g*, 4*f*). While this and the rhombohedral 2-17 phase are compositionally equally close to the recently discovered $RE_2TM_{14}B$ structure, the presence of two rare-earth sites makes the hexagonal phase most similar to the 2-14-1 phase[1] and consequently of great interest. It is possible that selective substitution of RE and TM constituents would allow the development of new magnetic materials of high intrinsic anisotropy, exploiting at the same time the high M_s and high T_c found in the RE_2TM_{17} phase. For example, there is a change from axial to basal magnetic structure in $Y_2(Co_xFe_{1-x})_{17}$ pseudobinary compounds[2] as a function of Co content which can be related to the intrinsic anisotropy. Several workers[2–4] have attempted to model this by measuring anisotropy constants of various order (mostly K_1 and/or K_2) as a function of temperature and composition in order to understand how the coercivity can be controlled through anisotropy change. Unfortunately, their interpretation is not unambiguous because higher-order contributions to the anisotropy cannot be neglected.[4] Moreover, inclusion of these terms can change the theoretical nature of magnetic ordering.[3] A particularly interesting question is posed by these compounds: Why is the TM sublattice anisotropy in $RE_2TM_{14}B$ (Ref. 5) (and we believe in RE_2TM_{17} compounds too) an order of magnitude less than in the $RETM_5$ compounds, although both the RE_2TM_{17} and $RE_2TM_{14}B$ compounds are only slightly modified stacking sequences of the $RETM_5$ units? Furthermore, why is the first change in the sign of K_1 at 4% Fe temperature independent and the second change in sign of K_1 occurring at ~55% Fe temperature dependent?[2] There is no unanimity as to the causes of the interesting, though complicated, anisotropy behavior observed in rare-earth transition-metal compounds. We hope to answer some of these questions by looking into site-specific magnetic ordering and crystallographic preferences of constituents through a detailed elastic neutron diffraction experiment on the $RE_xRE'_{2-x}(TM_xTM'_{1-x})_{17}$ compounds. We believe the composition and temperature dependence can be very accurately characterized by identifying the spin reorientation transition temperature in each case as measured by our neutron experiments. As part of this program, we report here the site preferences and moment structure found in $Er_2(Cr_{0.55}Fe_{0.45})_{17}$ at two temperatures, 8.7 and 293 K.

EXPERIMENT

The sample of nominal stoichiometry $Er_2(Cr_{0.55}Fe_{0.45})_{17}$ was prepared by arc melting the 99.9% pure constituents in the composition $Er_{2.02}Co_{9.35}Fe_{7.65}$ at General Motors Research Laboratory, Michigan. The 2-at. % extra erbium was added to compensate for boil-off due

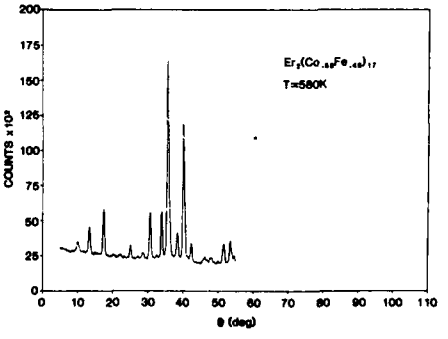


FIG. 1. Measured and calculated intensities at $T=293$ K for $Er_2(Fe_{0.45}Cr_{0.55})_{17}$.

 0021-8979/88/083725-03$02.40 © 1988 American Institute of Physics

TABLE I. Fractional coordinates, occupancies, and moments determined by profile fitting at $T = 293$ K. Moment per f.u. = 30.29 μ_B; $S = 5.20 = (R_{wp}/R_{exp})^2$. R(expected) = 5.55%; R(nuclear) = 7.20%; R(magnetic) = 7.60%. $a = 8.3796$ Å, $c = 8.2502$ Å, V(cell) = 501.7 Å^3.

Crystallographic site		Fractional coordinates			Occupancies		K_z moments (μ_B)
		x	y	z	Constrained	Unconstrained	
Er	2b	0	0	1/4	2.00	2.00	−3.44(18)
Er	2d	1/3	2/3	3/4	2.00	2.00	−4.67(15)
Co	12k	0.1656(4)	0.3312(7)	−0.1670(4)	7.12(10)	5.84(22)	2.54(8)
Co	12j	0.3292(8)	−0.0361(6)	1/4	7.02(10)	5.65(23)	2.20(10)
Co	6g	1/2	0	0	3.59(10)	3.05(14)	1.79(9)
Co	4f	1/3	2/3	0.1079	0.96(6)	0.52(10)	2.32(9)

to its higher vapor pressure. This unannealed ingot was crushed and ground in an acetone bath until the powder could pass through a 45-μm sieve. X-ray diffraction, thermal analysis and magnetization measurements were used to identify and characterize the RE_2TM_{17} hexagonal phase. About 3 g of the powdered sample were encased in a 1/8-in. vanadium can and the powder pattern was measured with the Position-Sensitive Neutron Diffractometer at the University of Missouri Research Reactor.[6] Data was collected in spans of $2\theta = 25°$ for four such intervals with a resolution of 0.1° for approximately 24 h at each temperature. However, a partial powder diagram was measured at $T = 580$ K consisting of only two arm positions of the detector ($5° < 2\theta < 55°$). The sample was heated to high temperature (580 K) using a furnace and a closed-cycle refrigerator was used during low-temperature ($T = 8.7$ K) data collection.

REFINEMENT OF DIFFRACTION DATA

The MURR-modified Rietveld computer code was used to find the best fit between the calculated and measured powder diagram. For $Er_2(Cr_{0.55}Fe_{0.45})_{17}$, this meant an interplay of 26–28 fitting parameters. Approximately 210 Bragg reflections were used in the $2\theta = 100°$ range for preparing the powder profile. The refinement strategy consisted of iterating the first with overall scale and temperature parameter. Then refinement was carried out on cell constants, half-width parameters (U, V, W only) and counter zero point. Once good starting values were obtained for the above eight parameters, the atomic position parameters were varied along with the population factors constrained according to stoichiometry (55% Co, 45% Fe) used in preparing the sample. Finally, the two rare-earth and the four transition-metal moments were varied to minimize the R factors. It is to be noted that only average TM moments were refined for each site because Co and Fe moments are very highly correlated. At this stage, the Voigt parameter was introduced into the refinement process to correct the half-widths for particle-size effects. During the process, the background correction to the total powder diagram was constantly adjusted to follow a smooth curve. Our fit indices were further reduced by iterating with several fixed values of the overall temperature factor (β) by trial and error. As a consistency check, occupancies were finally refined unconstrained as a result of which the Co population decreased somewhat toward an ($Fe_{0.5}Co_{0.5}$) stoichiometry. Other results remained essentially unchanged. The final refined powder diagram at $T = 293$ K is shown in Fig. 1.

RESULTS

The refined nuclear positions, site occupancies and site moments for $T = 293$ and 8.7 K are given in Tables I and II, respectively. As has been observed in other systems, the Er

TABLE II. Fractional coordinates, occupancies, and moments determined by profile fitting at $T = 8.7$ K.

Crystallographic site		Fractional coordinates			Occupancies		Moments	
		x	y	z	Constrained	Unconstrained	K_y	K_z
Er	2b	0	0	1/4	2.00	2.00	−3.43(13)	−6.87(13)
Er	2d	1/3	2/3	3/4	2.00	2.00	−4.32(14)	−8.67(14)
Co	12k	0.1665(6)	0.3330(11)	−0.0177(5)	6.91(14)	6.07(36)		3.55(8)
Co	12j	0.3279(10)	−0.0378(7)	1/4	6.71(13)	5.79(36)		3.04(9)
Co	6g	1/2	0	0	3.68(14)	3.29(20)		3.27(11)
Co	4f	1/3	2/3	0.1078(9)	1.39(9)	1.08(14)		2.73(9)

Goodness-of-fit values for canted model

$S = (R_{wp}/R_{exp})^2 = 6.85$; R(expected) = 5.20%; R(nuclear) = 9.00%; R(magnetic) = 7.10%.
Moment per f.u. = 37.45 μ_B;
$A = 8.3518$ Å, $c = 8.2275$ Å, V(cell) = 497 Å^3.

Goodness-of-fit values for axial model

$S = (R_{wp}/R_{exp})^2 = 7.10$; R(expected) = 5.10%; R(nuclear) = 9.50%; R(magnetic) = 7.39%.

site moments are unequal and at $T = 8.7$ K the Er b site moment is still significantly less than the theoretical effective moment of a $4I_{15/2}$ ion, 9.58 μ_B and less than the paramagnetic moment of Er metal 9.5, presumably due to the effects of local crystal fields. The transition-metal moments are reasonable, although the low-temperature values are slightly large, a feature often noted in Rietveld refinements. At all temperatures, the transition moments are axial, but at 8.7 K there is clear evidence for canting of the Er moments. The axial components of the Er moments are, as usual, antiparallel to the transition-metal moments. At room temperature there is weak evidence for canting but the change in agreement factors for a canted model is very small and not definitive. The structure at high temperature (580 K) is apparently unchanged (Fig. 2).

The most notable result of the refinement is the strong preference of Fe for the f site. This site is analogous to the c site in the rhombohedral 2-17 phase and to the j_2 site in $Nd_2Fe_{14}B$; in each case the site has no rare-earth near neighbors, 12 long TM–TM bonds (2.57–2.7 Å), and in the two RE_2TM_{17} phases a short dumbbell bond ($\sim$2.4 Å). In all three cases, a strong Fe preference is observed for this site. However, in $Nd_2(Co/Fe)_{14}B$ and $Nd_2(Co/Fe)_{17}$, the Fe moment on these sites is large while in the present compound it is relatively small. This difference is presumably due to the cooperation of the Nd and Fe anisotropies in the former two compounds compared to the (presumably) antagonistic anisotropy effects in the present compound. This further emphasizes the importance of these sites in the magnetic properties of the respective phases. The slight decrease in overall Co content from nominal seen in the unconstrained refinement may be due to segregation in the melt. It was observed that the cast ingot consisted of a brittle core and a more ductile skin. Data will be taken to see if the skin is enriched in Co to account for the refined stoichiometry.

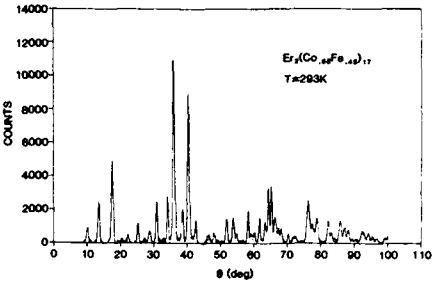


FIG. 2. Partial neutron powder diagram at $T = 580$ K

The observation of site preference for the transition metals and the apparent differences of the two Er sites encourages thinking about the possibility of more complete substitutions: multiple rare earths and transition metals. Little is known, however, about the phase stability or the effects on magnetic properties and these will be the subject of more detailed investigations in the future.

[1] J. F. Herbst, J. J. Croat, F. E. Pinkerton, and W. B. Yelon, Phys. Rev. B **29**, 4176 (1984).
[2] R. S. Perkins and H. Nagel, Physica **80B**, 143 (1975).
[3] D. Melville, W. I. Khan, and S. Rinaldi, IEEE Trans. Magn. **MAG-12**, 1012 (1976).
[4] K. S. V. L. Narasimhan and W. E. Wallace, IEEE Trans. Magn. **MAG-13**, 1333 (1977).
[5] D. Givord, H. S. Li, and R. Perrier de la Bathie, Solid State Commun. **51**, 857 (1984).
[6] C. W. Tompson, D. F. R. Mildner, M. Mehregany, J. Sudol, R. Berliner, and W. B. Yelon, J. Appl. Crystallog. **17**, 385 (1984).
[7] J. F. Herbst, J. J. Croat, R. W. Lee, and W. B. Yelon, J. Appl. Phys. **53**, 250 (1982).

Sublattice magnetization and spin reorientation in $Nd_2Fe_{14}B$ (abstract)[a)]

K. Muraleedharan, G. Kaindl, G. Wortmann, and B. Perscheid
Freie Universität Berlin, D-1000 Berlin 33, West Germany

N. C. Koon
Naval Research Laboratory, Washington, DC 20375

Considerable efforts have recently been made in understanding the magnetic behavior of the rare-earth transition-metal compound $Nd_2Fe_{14}B$, which orders ferromagnetically at $T_c = 600$ K and exhibits a spin-reorientation transition at $T_{SR} = 135$ K. In an effort to obtain direct information on the spin configuration and magnetic ordering in this technologically important compound, we have performed a Nd-145 Mössbauer study on a single crystal of $Nd_2Fe_{14}B$ using the 72.5-keV nuclear gamma resonance of Nd-145. The results clearly show that the temperature dependence of the Nd-sublattice magnetization is totally different from that of the macroscopic magnetization, i.e., dropping off far below T_c. The results suggest that the spin-reorientation transition in $Nd_2Fe_{14}B$ is driven by an ordering of the Nd sublattice below T_{SR}.

a) Supported by the BMFT, project No. 05 313AX B2/TP4.

 0021-8979/88/083728-01$02.40 © 1988 American Institute of Physics



Magnetic-wave-like excitations and cluster modes in randomly disordered $Rb_2Mn_xCr_{1-x}Cl_4$ (invited)

D. Sieger, H. Tietze, and R. Geick
Physikalisches Institut, Am Hubland, 8700 Würzburg, Federal Republic of Germany

P. Schweiss and G. Heger
INFP, Kernforschungszentrum Karlsruhe, 7500 Karlsruhe, Federal Republic of Germany

W. Treutmann
Institut für Mineralogie, Lahnberge, 3550 Marburg, Federal Republic of Germany

The randomly disordered magnetic system $Rb_2Mn_xCr_{1-x}Cl_4$ with competing exchange interactions and with competing anisotropies has been studied by means of inelastic neutron scattering. We have investigated three samples of different concentrations ($x = 0.70, 0.25, 0.59$) at various temperatures ($4.2\ \mathrm{K} < T < 50\ \mathrm{K}$). In the samples with ferromagnetic order ($x = 0.25$) and with antiferromagnetic order ($x = 0.70$), a well-defined spin-wave branch has been found coexisting with a number of well-defined dispersionless excitations in the same frequency range of $0.8\ \mathrm{THz} \leqslant \nu \leqslant 2.5\ \mathrm{THz}$. Of particular interest are the excitations in the sample with $x = 0.59$ which shows no long-range order but spin-glass behavior with a freezing temperature of $T_f = 11$ K. For $T < T_f$, two-dimensional ferro- and antiferromagnetic correlations are observed with the same correlation length $\xi = 15$ Å. The excitation spectrum of this sample gives evidence for a variety of cluster modes and for two types of spin waves, namely antiferromagnetic and ferromagnetic ones, for wavelengths smaller than the correlation length. Such an excitation spectrum as that observed for our sample with $x = 0.59$ has not yet been reported for any other spin glass.

I. INTRODUCTION

Competing interactions are very often the cause for some kind of disorder in solids. In mixed antiferromagnets, for example, competing anisotropies lead usually to an intermediate or oblique antiferromagnetic phase combined with some disorder phenomena for certain values of the composition of the mixture, in the quasi-two-dimensional systems[1,2] $K_2Co_xFe_{1-x}F_4$ for $0.2 \leqslant x \leqslant 0.3$ and in $K_2Mn_xFe_{1-x}F_4$ for $0.02 \leqslant x \leqslant 0.03$. Competing exchange interactions, on the other hand, usually destroy a long-range magnetic order, and the system exhibits spin-glass behavior for certain concentrations. Disregarding, in our context, conducting materials and considering only insulating mixed magnetic systems, examples of this kind are $Eu_xSr_{1-x}S$ with predominantly Heisenberg-type interactions[3] and $Fe_xMg_{1-x}Cl_2$ with mainly Ising-type interactions,[4] where both are three-dimensional magnets. Our main concern is the following question: what are the collective excitations of such systems, especially those with a high degree of disorder, namely, the spin glasses. In mixed antiferromagnets, the spectrum of magnetic excitations usually shows two spin-wave branches corresponding more or less to those of the two constituents,[5,6] even for mixed antiferromagnets with competing anisotropies,[1,7] e.g. $K_2Co_xFe_{1-x}F_4$. For Heisenberg spin glasses like $Eu_xSr_{1-x}S$ solid solutions,[8] neutron inelastic scattering has revealed some structures but not well-defined spin waves. For the three-dimensional Ising spin glass $Fe_{0.4}Mg_{0.6}Cl_2$ with a strong uniaxial anisotropy,[9] on the other hand, spin waves have been observed with wavelengths smaller than the correlation length similar to the excitations in other diluted magnetic systems. But also long-wavelength spin waves have been found with considerably lower frequency, which are explained as being due to the precession of spin clusters around the easy axis.

With respect to the excitations in magnetic systems with randomness, the conjecture of "fractons" has recently been applied to this problem, especially to diluted ferromagnets[10] and antiferromagnets.[11] The essential result of these theoretical considerations is that the excitations are well-defined spin waves below a certain frequency ω_c or wave vector q_c, while above these values the spin waves become overdamped and are then considered as localized or quasi-localized excitations. Such a crossover from spin waves to quasi-localized excitations has been observed[12] experimentally in the diluted antiferromagnet $Mn_{0.5}Zn_{0.5}F_2$.

By means of neutron inelastic scattering, we have studied the collective magnetic excitations of the mixed system $Rb_2Mn_xCr_{1-x}Cl_4$ which is a quasi-two-dimensional model system with both competing anisotropies and competing exchange interactions.[13] Pure Rb_2MnCl_4 is an antiferromagnet with the c axis as the easy axis ($T_N = 54.8$ K). Pure Rb_2CrCl_4 orders ferromagnetically below $T_C = 52.4$ K with the preferred spin direction perpendicular to the c axis. Both types of competing interactions cause the magnetic proper-

 0021-8979/88/083729-06$02.40 © 1988 American Institute of Physics

ties of the mixed crystals to depend strongly on the concentration parameter x. Over the whole concentration range ($0 \leqslant x \leqslant 1$), several antiferromagnetic and ferromagnetic phases have been found as well as spin-glass behavior[14] in the intermediate range $x \approx 0.5$ by means of neutron diffraction and by means of magnetic resonance measurements combined with average model calculations.[15]

The ground state of the system (e.g., magnetic order outside the spin-glass range) turns out to be not well defined for reasons of the competing exchange interactions. For the range $0.13 \leqslant x \leqslant 0.86$, the average model calculations yield canted spin structures with ferro- and antiferromagnetic components. For some concentrations x, this ground state is shown in Fig. 1. For all selected values of x the spins are confined to the c plane and the arrows in Fig. 1 indicate the orientation of the spins with respect to the crystallographic a axis. There are four arrows for each concentration in Fig. 1 corresponding to the four sublattices within the average model. The arrows are unit vectors and do not represent the actual value of the sublattice magnetization for the concentration x under consideration. In addition to $x = 0.25$, 0.59, and 0.70 which are the concentrations of the samples in our investigation, the limiting cases $x = 0.05$ (easy-plane ferromagnet) and $x = 0.90$ (easy-plane antiferromagnet) are shown. The data in Fig. 1 may possibly represent the average spin orientation, but there will be a high degree of disorder causing deviations from the average, especially for $x = 0.59$. The spin-glass behavior at this concentration cannot be described by the average model, which at present provides the only information about the ground state.

According to the information discussed above and in agreement with our own characterisation, the three samples

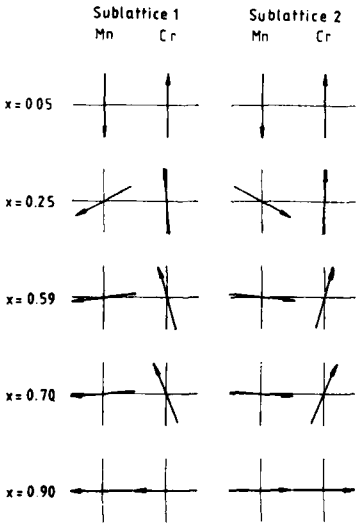


FIG. 1. Ground-state configuration of $Rb_2Mn_xCr_{1-x}Cl_4$ for various concentrations x as calculated by means of a four-sublattice virtual crystal or average model. For the considered concentrations, the spins are confined to the c plane and the arrows show their orientation with respect to the a axis.

studied here exhibit ferromagnetic order ($x = 0.25$, Cr-rich side; see Fig. 1), antiferromagnetic order ($x = 0.70$, Mn-rich side; see Fig. 1), and spin-glass behavior ($x = 0.59$). For the sample with $x = 0.70$, first results[13] yielded one spin-wave branch coexisting in the same frequency range with a number of excitations with practically no dispersion over a wide wave-vector range. This result is in contrast to the results mentioned above for mixed antiferromagnets.[5–7] The analysis of the energies of the dispersionless excitations in our data has lead us to the conclusion that they can be identified as Ising cluster modes. Such modes nearly independent of q have been found before, but without a distinct spin-wave branch, in diluted systems with mainly Ising interactions,[16] such as $Rb_2Co_{1-x}Mg_xF_4$. In systems with more Heisenberg-like interactions[17] like $Rb_2Mn_{1-x}Mg_xF_4$, a single spin-wave branch is observed which broadens and shows an Ising cluster mode structure towards the edge of the Brillouin zone. By applying an external magnetic field to these diluted systems, they show random field effects[18] and disorder phenomena. The above-mentioned coexistence of wavelike magnons with dispersionless Ising cluster modes is also to be considered as a disorder phenomenon caused by the competing exchange interactions and the resulting frustration effects. In other words, the wave vector q is not a good quantum number with respect to the magnetic excitations in our randomly mixed system. And the question to be answered by our study is what is the excitation spectrum of $Rb_2Mn_xCr_{1-x}Cl_4$ samples with magnetic order and especially that of a sample with spin-glass behavior ($x = 0.59$). The latter sample represents a close approximation to the ideal two-dimensional spin-glass model of the easy-plane type (XY-like!), i.e., the spins are confined to the c plane by a strong anisotropy field.[13,15] Our results below will show that spin waves and other excitations are also found in this case.

II. EXPERIMENT

Three different samples of $Rb_2Mn_xCr_{1-x}Cl_4$ mixed crystals have been grown at Marburg University by the Bridgman–Stockbarger method. The final concentrations have been determined to $x = 0.25$, 0.59, and 0.70 by lattice constant refinement. All samples have been characterised and oriented to the (001)-scattering plane on a four-circle neutron diffractometer. Neutron scattering investigations have been performed on the TASKO and IN8 triple-axis spectrometers at the LLB in Saclay and the ILL in Grenoble, respectively, with an integral energy resolution of $\Delta\nu \approx 0.25$ THz and momentum resolution of $\Delta q \approx 0.02$ reduced units. Some additional data have been obtained with the 4F1 triple-axis spectrometer viewing the cold source at Saclay. Further experimental details have been published elsewhere.[19]

According to the expected range of excitations, the energy transfer varied from zero through $\nu = 3.0$ THz for the samples with $x = 0.59$ and 0.70, and from zero through $\nu = 5.5$ THz for the one with $x = 0.25$, respectively. The momentum transfer Q ranged from $(\frac{1}{2},\frac{1}{2},0)$ through $(\frac{3}{2},\frac{3}{2},0)$ in units of the chemical Brillouin zone of $Rb_2Mn_xCr_{1-x}Cl_4$

(see below) with longitudinal polarization of q only. In this region of interest constant-Q scans have been taken predominantly and additionally some significant constant-energy scans at low q.

The different types of magnetic ordering in $Rb_2Mn_xCr_{1-x}Cl_4$ require some remarks on magnetic Brillouin zones. In our results for samples with different magnetic order, we have chosen the reduced wave vector ξ in a unique way: starting from $\xi = 0$ at (1,1,0) and ending with $\xi = 0.5$ at $(\frac{1}{2},\frac{1}{2},0)$. This means that spin waves in a ferromagnetic sample range from $\xi = 0$ to $\xi = 0.5$ while those in an antiferromagnetic one range from $\xi = 0.5$ to $\xi = 0.25$. The actual wave-vector tansfer is $Q = (1 \pm \xi, 1 \pm \xi, 0)$. For reasons of clarity, all values of Q are indexed in terms of the paramagnetic (chemical) unit cell of the Rb_2MnCl_4 (K_2NiF_4) structure throughout this paper. The choice of $(\frac{1}{2},\frac{1}{2},0)$ and (1,1,0) as the centers of the antiferromagnetic and the ferromagnetic Brillouin zones, respectively, is closely related to our experimental scattering conditions. It has been clarified carefully that in the region of interest all coherent inelastic scattering intensity at low temperatures is of magnetic origin and not obscured by phonon scattering. Furthermore, incoherent background scattering was determined seperately and independently from appropriate offset scans.

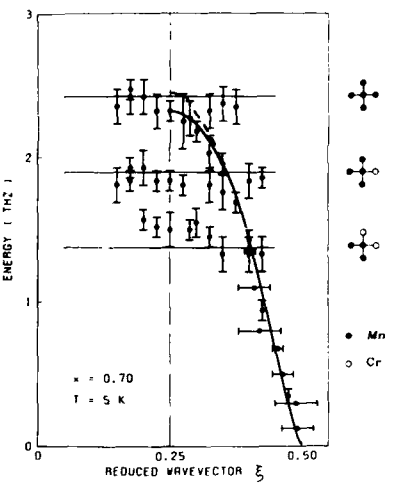


FIG. 2. Frequency vs wave vector relation of the magnetic excitations for an antiferromagnetic $Rb_2Mn_{0.70}Cr_{0.30}Cl_4$ sample: experimental data (●) and their width (⊢⊣). The excitations consist of a spin-wave branch (solid line: guide to the eye; broken line: spin waves of pure Rb_2MnCl_4) and of dispersionless cluster modes (nearest-neighbor configurations to the right). For further explanations see text.

III. RESULTS

We start presenting the experimental results with those of the sample $Rb_2Mn_{0.70}Cr_{0.30}Cl_4$ which shows antiferromagnetic order below $T_N = 40$ K. This is the sample which has been studied first.[13] The experimental data of the inelastic scattering cross section show for a constant-Q scan not only one peak as for an ordinary magnon but several peaks and shoulders extending over a relatively wide frequency range (see Fig. 2 of Ref. 13). From the observed intensities, we have subtracted the incoherent background and extracted the frequencies of the various peaks and shoulders and the corresponding widths. The resulting data, i. e., peak frequencies (full circles) and widths (bars), are shown as a frequency versus wave vector relation in Fig. 2 using the unified wave-vector scale as explained in Sec. II. Vertical bars in Fig. 2 refer to constant-Q scans and horizontal bars to constant-energy scans. These experimental data show a series of points which follow closely the spin-wave branch of pure Rb_2MnCl_4, except for the edge of the Brillouin zone, and which are therefore considered as a magnon branch in the mixed crystal. For $\xi < 0.40$, we observed three additional series of points in Fig. 2 which show practically no dispersion. These dispersionless modes compare well to the excitations observed in the diluted system $Rb_2Co_xMg_{1-x}F_4$ where they have been described as Ising cluster modes.[16] Therefore, we identify such modes as Ising cluster modes. In $Rb_2Co_xMg_{1-x}F_4$, it is easy to find Co^{2+} ions with 1, 2, 3, or 4 Co^{2+} neighbors. In $Rb_2Mn_xCr_{1-x}Cl_4$, the clusters are assumed to originate from frustration effects. Our identification of these excitations as cluster modes is supported by the fact that their energies agree well with those calculated by means of a modified Ising cluster model[5,13] (horizontal solid lines in Fig. 2). It should be noted that the dispersionless cluster modes extend into the range $0.1 \leqslant \xi \leqslant 0.25$ where the magnon is not observed. The three cluster modes in Fig. 2 are those with the highest probability of occurrence as shown in Ref. 13. Our modified Ising cluster model is based on the average model calculations[15] which are related to magnetic resonance experimental data. That means there is no parameter adjustable to the present experimental data.

The sample $Rb_2Mn_{0.25}Cr_{0.75}Cl_4$ shows ferromagnetic order below $T_c \simeq 35$ K. The excitation spectrum exhibits again wavelike magnon excitations in coexistence with dispersionless cluster modes as in the antiferromagnetic sample. Inelastic neutron scattering experiments have been performed on this sample at $T = 13$ K in Saclay (TASCO) and at $T = 5$ K in grenoble (IN 8). Some typical examples of the intensity observed in constant-Q scans are shown in Fig. 3. As for the antiferromagnetic sample, there are several peaks and shoulders in the intensity curves from which we have extracted the peak frequencies and the widths which are shown versus the wave vector for the magnetic Brillouin zone ($0 \leqslant \xi \leqslant 0.5$) in Fig. 4. There is also a series of experimental data points which follows closely the magnon dispersion curve of pure Rb_2CrCl_4, except for $0.4 \leqslant \xi \leqslant 0.5$, and which is identified as a magnon branch. It reaches a maximum frequency $\nu_{max} = 4.8$ THz at the ferromagnetic zone boundary ($\xi = 0.5$). At the Γ point, in-plane anisotropies are responsible for an energy gap of approximately $\Delta\nu \simeq 0.05$ THz (magnetic resonance experiments[15]). In addition to the magnon branch, there are four series of data points in Fig. 4 which show no dispersion and which are again identified as Ising cluster modes. These cluster modes have been observed for $0.1 \leqslant \xi \leqslant 0.5$ but were not found for $\xi < 0.1$.

The most striking feature in our experimental results is

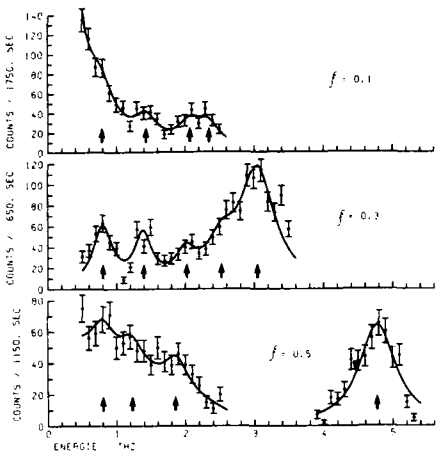


FIG. 3. Inelastic neutron scattering intensity of constant-Q scans on $Rb_2Mn_{0.25}Cr_{0.75}Cl_4$ vs frequency. The bars at the experimental points denote the statistical error of the counting rate. The curves are obtained with a fit and the arrows show the obtained peak frequency of the excitation.

that the wavelike magnon branch has been observed not only in the frequency range of the four dispersionless cluster modes, but also above and below that frequency range. The horizontal solid lines in Fig. 4 are again the results of calculations by means of the modified Ising cluster model based on the average model ground state for $x = 0.25$ (see Fig. 1). The observed cluster configurations are those expected in a sample with $x = 0.25$ from the probabilities of their occurrence. The difference of the frequencies of the spin waves between the mixed crystal with $x = 0.25$ and pure Rb_2CrCl_4 (see Fig. 4) can be understood as a consequence of spin canting in the mixed crystal system and is, hence, much more pronounced towards the zone boundary. A very similar behavior has been observed in the antiferromagnetic sample (see Fig. 2), also explained in terms of the spin canting[13] (see Fig. 1).

In addition to inelastic measurements, the spin-glass sample $Rb_2Mn_{0.59}Cr_{0.41}Cl_4$ has been studied by quasi-elastic neutron scattering (see Fig. 5) which revealed the spin-glass behavior of this sample below $T_f = 11$ K. No magnetic Bragg scattering at either antiferromagnetic or ferromagnetic peak positions has been observed down to temperatures of about 3.3 K. Diffuse magnetic scattering with scans through the rods $(1,1,\zeta)$ and $(\frac{1}{2},\frac{1}{2},\zeta)$ give evidence for the existence of two-dimensional ferromagnetic as well as antiferromagnetic correlations (short-range order). A full account of this investigation will be published elsewhere.[20] The inverse correlation length κ and the energy width ΔE derived from the experimental data are shown in Fig. 5 as a function of temperature. Within the limits of experimental error, κ has the same value for antiferromagnetic correlations and ferromagnetic ones. Below 15 K, κ remains constant well above the instrumental resolution, whereas the energy widths of the two-dimensional rods reach instrumental resolution of $\Delta\nu = 0.03$ THz at $T_f = 11$ K. All this is characteristic of spin-glass behavior.

The inelastic scattering results obtained from the spin-glass sample at $T = 5$ K show again a detailed structure with peaks and shoulders. Also from these data we have extracted peak frequencies and widths (see Fig. 6) as described in more detail above. In general, the scattering intensities are rather weak, the widths (horizontal bar for constant energy

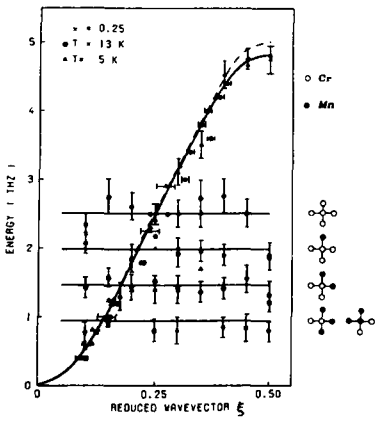


FIG. 4. Frequency vs wave vector relation of the magnetic excitations for a ferromagnetic $Rb_2Mn_{0.25}Cr_{0.75}Cl_4$ sample: experimental data (●) and their width (⊢⊣). The excitations consist of a spin-wave branch (solid line: guide to the eye; broken line: spin waves of pure Rb_2CrCl_4) and of dispersionless cluster modes (nearest-neighbor configurations to the right). For further explanations see text.

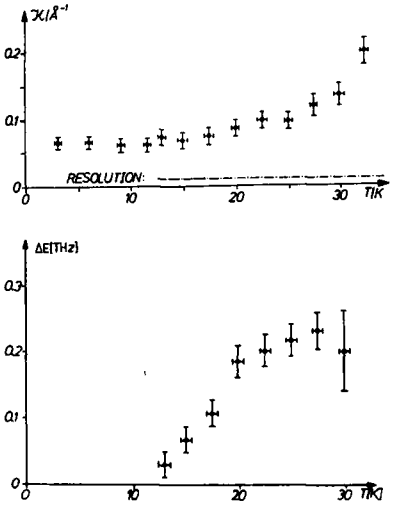


FIG. 5. Inverse correlation length κ and energy width ΔE as a function of temperature as obtained from rod scans $(\frac{1}{2} \pm q,\frac{1}{2} \pm q,\frac{1}{2})$ with a triple-axis spectrometer for the $Rb_2Mn_{0.59}Cr_{0.41}Cl_4$ spin-glass sample.

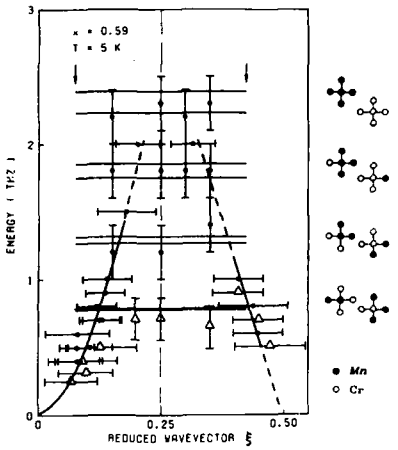


FIG. 6. Frequency vs wave vector relation of the magnetic excitations for a $Rb_2Mn_{0.59}Cr_{0.41}Cl_4$ spin-glass sample: experimental data (● and Δ) and their width (⊢⊣). The excitations consist of "ferromagnetic" and "antiferromagnetic" spin waves (solid and broken lines: guide to the eye) and of dispersionless cluster modes (nearest-neighbor configurations to the right). For further explanations see text.

and vertical for constant-Q scan) are larger than for the antiferro- and ferromagnetic sample and the statistics are poorer here due to the high degree of disorder. The resulting dispersion relations in Fig. 6 (● for data obtained with the IN 8 in Grenoble and Δ for data obtained with the triple-axis spectrometer at the cold source in Saclay) show four dispersionless excitations which again are identified as cluster modes. They gain maximum intensity around reduced wave vector $\xi = 0.25$ but broaden and diminish towards the values $\xi = 0$ and $\xi = 0.5$. Again, the excitation frequencies of the cluster modes (horizontal solid lines) have been calculated by means of the modified Ising cluster model. Here, for $x = 0.59$, all possible eight clusters probably contribute to the cluster modes as shown in Fig. 6, but not all with the same probability of occurrence. An unexpected but very prominant result is the observation of wavelike excitations at energies below and somewhat into the cluster mode regime. They lose their intensities at frequencies above 2.2 THz. The two spin-wave branches, observed for $0 < \xi < 0.2$ and for $0.3 < \xi < 0.5$, are similar to the magnon dispersion curves of the ferromagnet Rb_2CrCl_4 and of the antiferromagnet Rb_2MnCl_4 and thus are identified as ferromagnetic and antiferromagnetic spin waves, respectively. In Fig. 6, the arrows indicate the reduced q values where the wavelength of the excitation is equal to $\kappa^{-1} \approx 15$ Å (see Fig. 4) counted from both zone centers, namely from $\xi = 0$ and from $\xi = 0.5$. Most of our results in Fig. 6 have been obtained between these limits. Due to the large widths of the constant-energy scans at low frequencies (see horizontal bars in Fig. 6) we cannot claim with sufficient certainty that some excitations have also been observed for wavelengths larger than the correlation length.

IV. DISCUSSION

Typical and unique for the collective magnetic excitations in $Rb_2Mn_xCr_{1-x}Cl_4$ mixed crystals is the coexistance of wavelike magnon branches and dispersionless Ising cluster modes in the same frequency range. This has been well established for an antiferromagnetic, a ferromagnetic, and a spin-glass sample in our investigation. Of course, spin waves alone have been observed in every magnetically ordered system and dispersionless cluster modes alone in diluted Co compounds. The coexistence of both types in our sample is the essential new result.

Though we can imagine that our randomly disordered samples with competing exchange interaction could also be described in terms of fractal structures, our experimental results are not in accord with the theoretical predictions for fractons which, admittedly, have been derived for diluted systems. In our ferromagnetic sample, the spin waves were observed above and below the Ising cluster modes. In our other samples, spin waves and cluster modes penetrate each other. On the basis of our experimental results, we find it difficult to define a critical frequency ω_c below which the excitations are wavelike and above which they are localized or quasi-localized.[21] But future theoretical considerations adapted to our magnetic mixed system may yield results which are in accordance with our experimental data.

Very interesting results of our present study are the experimental data for $Rb_2Mn_{0.59}Cr_{0.41}Cl_4$ which is a close approximation to a two-dimensional spin-glass model with predominantly XY interactions. This sample exhibits an excitation spectrum very similar to that of $Rb_2Mn_{0.70}Cr_{0.30}Cl_4$ with antiferromagnetic order and that of $Rb_2Mn_{0.25}Cr_{0.75}Cl_4$ with ferromagnetic order. In no other spin glass has such a complicated spectrum of excitations been observed so far, with two types of spin waves and coexisting cluster modes. These excitations, however, have mostly been observed for wavelengths shorter than the two-dimensional correlation length, measured from either the ferromagnetic ($\xi = 0$) or the antiferromagnetic Γ point ($\xi = 0.5$). This means that our data in Fig. 6 resemble a correspondence to the short-wavelength spectrum of $Fe_{0.4}Mg_{0.6}Cl_2$, an Ising spin glass.[9]

Our explanation for the similarity of the excitation spectrum of the spin-glass sample with that of the ordered samples is that the random disorder is already quite large in the latter as a result of the competing exchange interaction which cause frustration and similar effects additionally to the magnetic order. Therefore, it is possibly a small step from the other samples to the spin-glass sample. For both cases, the ground state is not well defined and more realistic information about it can only be obtained by a computer simulation which will reveal a great amount of randomness in the spin orientations not only in the spin-glass sample but also in the other ones.

As mentioned in Sec. III, the frequencies of the dispersionless modes can be calculated by means of the Ising cluster model developed by Cowley and Buyers.[5] It was modified[13,19] to take into account the ground state as derived from average model calculations.[15] The excitation energies depend on the type of central ion ($Mn^{2+} = M$ or $Cr^{2+} = C$) of

the cluster and on the neighborhood configuration [r Mn^{2+} neighbors and $(4-r)$ Cr^{2+} neighbors] and on the exchange interaction. We have neglected here the anisotropy fields which would contribute only small corrections in our case. The excitation energies for our cluster model are

$$E_{Mn} = 2rJ_{MM}S_M \cos\delta_{MM} + 2(4-r)J_{MC}S_C \cos\delta_{MC} ,$$

$$E_{Cr} = 2rJ_{MC}S_C \cos\delta_{MC} + 2(4-r)J_{CC}S_C \cos\delta_{CC} .$$

The values of the exchange constants[13,15,19] are $J_{MM} = -121.9$ GHz, $J_{MC} = -45.0$ GHz, and $J_{CC} = +157.5$ GHz. The spin values are $S_M = \frac{5}{2}$ and $S_C = 2$. The angles δ_{MM}, δ_{MC}, and δ_{CC} measure the differences between the equilibrum spin directions in the c plane between a pair Mn^{2+}-Mn^{2+}, Mn^{2+}-Cr^{2+}, and Cr^{2+}-Cr^{2+} neighbors. In the average model, they are the difference between the orientation of Mn^{2+} in sublattice 1 and Mn^{2+} in sublattice 2, Mn^{2+} in sublattice 1 and Cr^{2+} in sublattice 2, etc. (see Fig. 1), and are a function of the concentration parameter x. It is very surprising that the equidistant series of cluster excitation frequncies agrees so well with the experimental data (see Figs. 2, 4, and 6) although the average model is only a coarse approximation to the actual ground state.

A detail of our results is that the magnon branches in the two ordered samples ($x = 0.70$, see Fig. 2, and $x = 0.25$, see Fig. 4) are almost identical with those of the pure end members except for the range of maximum frequency close to the zone boundary. The energy of the magnon may be influenced by the degree of disorder in the following way: In this more or less randomly disordered system of canted spins, only those with the time-dependent mean average aligned to the direction appropriate for the magnon excitation will contribute to the coherent inelastic magnetic scattering, which in fact resembles the same excitation frequencies and/or dispersion as in pure Rb_2MnCl_4 or Rb_2CrCl_4 but with less intensity, of course. Only close to the zone boundary, where the magnon wavelength refers close to twice the lattice constant or spin distance, the canting angle between neighboring spins becomes dominant and, hence, the effective exchange value is being lowered.

ACKNOWLEDGMENT

This work has been funded by the German Federal Minister for Research and Technology (BMFT) under the Contract No. 03-Ge1Wue-6.

[1] W. A. H. M. Vlak, E. Frikkee, A.F.M. Arts, and H. W. de Wijn, Phys. Rev. B **33**, 6470 (1986); S. A. Higgins, W. A. H. M. Vlak, M. Hagen, R. A. Cowley, A. F. M. Arts, and H. W. de Wijn, J. Phys. C **20**, 833 (1987).
[2] L. Bevaart, E. Frikkee, J. V. Lebesque, and L. J. de Jongh, Phys. Rev. B **18**, 3376 (1978).
[3] H. Maletta, W. Felsch, H. Scheuer, and H. Pink, J. Magn. Magn. Mater. **15–18**, 167 (1980); H. Maletta and W. Felsch, Z. Phys. B **37**, 55 (1980); H. Maletta, J. Appl. Phys. **53**, 2185 (1982); H. Maletta, G. Aeppli, and S. M. Shapiro, Phys. Rev. Lett. **48**, 1490 (1982).
[4] D. Bertrand, F. Bensamka, A. R. Fert, J. Gerlard, J. R. Redoules, and S. Legrand, J. Phys. C **17**, 1725 (1984); Po-zen Wong, S. von Molnar, T. T. M. Palstra, J. A. Mydosh, S. M. Shapiro, and A. Ito, Phys. Rev. Lett. **55**, 2043 (1985); Po-zen Wong, H. Yoshizawa, and S. M. Shapiro, J. Appl. Phys. **57**, 3462 (1985).
[5] R. A. Cowley and W. J. L. Buyers, Rev. Mod. Phys. **44**, 406 (1972).
[6] R. A. Cowley, AIP Conf. Proc. **29**, 243 (1976).
[7] S. A. Higgins, R. A. Cowley, M. Hagen, J. K. Kjems, U. Dürr, and K. Fendler, J. Phys. C **17**, 3235 (1984).
[8] H. Maletta, W. Zinn, H. Scheuer, and S. M. Shapiro, J. Appl. Phys. **52**, 1735 (1981).
[9] Po-zen Wong, H. Yoshizawa, S. M. Shapiro, J. A. Mydosh, J. van den Berg, and T. T. M. Palstra, Phys. Rev. Lett. **58**, 1276 (1987).
[10] Kin Wah Yu, Phys. Rev. B **29**, 4065 (1984).
[11] Kin Wah Yu and R. Orbach, Phys. Rev. B **30**, 2760 (1984).
[12] Y. J. Uemura and R. J. Birgeneau, Phys. Rev. Lett. **57**, 1947 (1986).
[13] D. Sieger, H. Tietze, R. Geick, S. Bates, R. A. Cowley, W. Treutmann, and U. Steigenberger, Solid State Commun. **60**, 847 (1986).
[14] N. Kohles, H. Theuerkaufer, K. Strobel, R. Geick, and W. Treutmann, J. Phys. C **15**, L137 (1982); K. Katsumata, T. Nire, M. Tanimoto, and H. Yoshizawa, Phys. Rev. B **25**, 428 (1982).
[15] T. Grieb, K. Strobel, and R. Geick, Solid State Commun. **51**, 923 (1984); T. Grieb and R. Geick, Solid State Commun. **53**, 919 (1985).
[16] H. Ikeda and G. Shirane, J. Phys. Soc. Jpn. **46**, 30 (1979); R. A. Cowley, R. J. Birgeneau, G. Shirane, H. J. Guggenheim, and H. Ikeda, Phys. Rev. B **21**, 4038 (1980).
[17] R. A. Cowley, G. Shirane, R. J. Birgeneau, and H. J. Guggenheim, Phys. Rev. B **15**, 4292 (1977).
[18] For recent reviews with respect to experiment and theory, see A. R. King and D. P. Belanger, J. Magn. Magn. Mater. **54–57**, 19 (1986); A. Aharony, J. Magn. Magn. Mater. **54–57**, 27 (1986).
[19] D. Sieger, H. Tietze, R. Geick, P. Schweiss, W. Treutmann, and P. Frings, Solid State Commun. **64**, 1413 (1987).
[20] P. Schweiss, W. Treutmann, and G. Heger (to be published).
[21] R. Orbach, Science **231**, 814 (1986).

Spin-glass transition in the random anisotropy axis model

Amitabha Chakrabarti
School of Physics and Astronomy, University of Minnesota, Minneapolis, Minnesota 55455
and Department of Physics, Temple University, Philadelphia, Pennsylvania 19122[a)]

The critical behavior of the Random Anisotropy Axis model (RAM) is studied by the Monte Carlo simulation method in the limit of infinite anisotropy. Finite size scaling analysis of the data for equilibrium averages strongly suggests a zero temperature critical point in two dimensions and a finite temperature phase transition in three dimensions. The values of the critical exponents in both two and three dimensions indicate that RAM belongs to the same universality class as that of short-range Ising spin-glass models.

The unusual magnetic behavior of amorphous intermetallic compounds of rare earths has drawn considerable attention in recent years.[1] Recent experiments[2] on these materials indicate a spin-glass-type phase transition, whereas theoretical arguments concerning such a transition are still controversial. Theoretical studies of these systems are mostly confined to the random anisotropy axis model (RAM) introduced by Harris, Plischke, and Zuckerman.[3] The Hamiltonian for this model is given by

$$H = -J\sum_{\langle ij\rangle} \mathbf{S}_i\cdot\mathbf{S}_j - D\sum_i (\hat{n}_i\cdot\mathbf{S}_i)^2 , \tag{1}$$

where J is a ferromagnetic exchange interaction between classical m-component spins $\mathbf{S}_i$ of unit length and the local axes of uniaxial anisotropy $\hat{n}_i$ are m-component unit vectors randomly distributed over the surface of an m-dimensional hypersphere. Renormalization-group investigations[4,5] of RAM indicate that long-range ferromagnetic order is not possible for $d<4$. Chen and Lubensky[6] used the replica method and predicted a spin-glass behavior when ferromagnetism is absent. Very recent calculations of Harris, Caflisch, and Banavar[7] suggest that in the limit of infinite anisotropy, the lower critical dimension is probably 4 and ferromagnetic (spin-glass) order is possible at low temperatures when the coordination number z is $\gtrsim m$ ($\lesssim m$).

Computer simulation techniques are also employed in the RAM but they could not lead to a definitive conclusion.[8–11] However, recent numerical studies of Bray and Moore[12] in the limit of $D\to\infty$ and $d=2$ suggest that RAM exhibits a zero temperature phase transition to a nonferromagnetic ground state quite similar to the $d=2$ Ising spin-glass model.

In this paper, I report some results of a detailed numerical study of the thermodynamics of model (1) in both two and three dimensions with $m=3$ and $D\to\infty$. In the limit of $D\to\infty$ each spin is constrained to be parallel or antiparallel to its local anisotropy axes. Writing $\mathbf{S}_i = \hat{n}_i\sigma_i$, with $\sigma_i = \pm 1$, we obtain an effective Hamiltonian as

$$H_{\text{eff}} = -\sum_{\langle ij\rangle} J_{ij}\sigma_i\sigma_j , \tag{2}$$

where

$$J_{ij} = J\hat{n}_i\hat{n}_j . \tag{3}$$

In the computer simulation of model (2) I considered lattice size up to 40^2 in two dimensions and 12^3 in three dimensions. The vectors $\hat{n}_i$ are chosen randomly from a hemisphere at each site, since model (2) is invariant under $\hat{n}_j\to-\hat{n}_j$, $\sigma_i\to-\sigma_i$. I used the standard Metropolis algorithm and used up to 1.2×10^5 Monte Carlo steps/spin to calculate thermodynamic averages of various quantities.

No ferromagnetism was detected in either two or three dimensions and the magnetization is always zero $[0(1/\sqrt{N})]$ for all sample sizes in the temperature range considered. In order to study the presence of spin-glass order if it exists, I considered the single-spin autocorrelation function defined as[13]

$$q(t) = \frac{1}{N}\sum_{i=1}^{N} \langle\langle\sigma_i(0)\epsilon(t)\sigma_j\rangle\rangle_c , \tag{4}$$

where

$$\epsilon(t) = \text{Sign}\left(N^{-1}\sum_{i=1}^{N}\sigma_i(0)\sigma_i(t)\right), \tag{5}$$

N is the number of spins, $\langle\ \rangle$ is the thermodynamic (Monte Carlo) average, and $\langle\ \rangle_c$ is the configurational average for different realizations of the interaction. Then the spin-glass-order parameter q is given by

$$q = \lim_{t\to\infty} q(t) . \tag{6}$$

I also computed the two-spin time correlation function

$$q^{(2)}(t) = \left\langle \frac{1}{N^2}\sum_{i,j}^{N} \langle[\sigma_i(0)\sigma_j(0)] \times [\sigma_i(t)\sigma_j(t)]\rangle \right\rangle_c , \tag{7}$$

and the probability distribution function for q given by

$$P(q) = \frac{1}{t_0}\sum_{t=\tau}^{t_0+\tau} \langle\delta[q-q(t)]\rangle_c , \tag{8}$$

where τ is the equilibration time and t_0 is $\sim 3\tau$. I also calculated the quantity

$$\rho = \tfrac{1}{2}[3 - (\langle q^4\rangle_{\text{av}}/\langle q^2\rangle_{\text{av}}^2)] , \tag{9}$$

where $\langle\ \rangle_{\text{av}}$ represents an average over $P(q)$. This quantity is expected to have a scaling form[14,15]

$$\rho = \tilde{\rho}[L^{1/\nu}(T-T_c)] . \tag{10}$$

[a)] Present address.

 0021-8979/88/083735-03$02.40 © 1988 American Institute of Physics

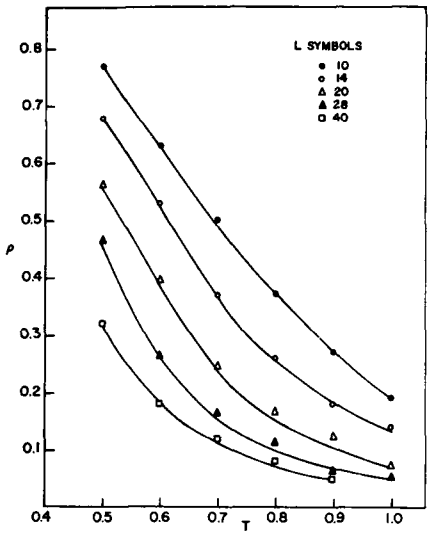


FIG. 1. Plot of ρ (defined in text) vs temperature T in units of J/k_B for various system sizes in two dimensions. Solid lines here and in other figures are guides to the eye.

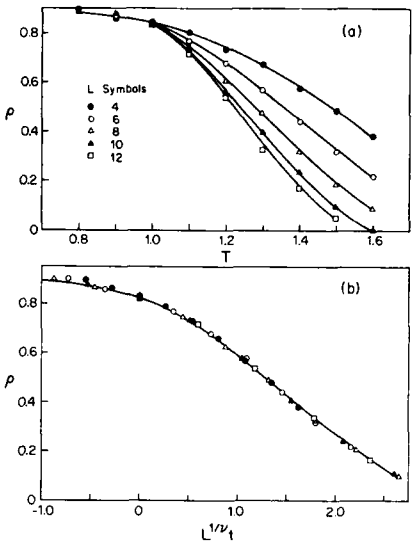


FIG. 2. (a) Same as Fig. 1 except that $d = 3$ in this case. (b) Finite size scaling curve for ρ according to Eq. (10) with $\nu = 1.4$ and $t = (T - T_c)/T_c$.

Thus, if the system exhibits a second-order phase transition at $T = T_c$, then curves of ρ vs T for various system size L should intersect at T_c, since ρ will be independent of L at $T = T_c$. The ρ-vs-T curves in two and three dimensions are shown in Figs. 1 and 2(a), respectively. In two dimensions the curves do not intersect each other at any point and hence indicate that no phase transition takes place for $T \geq 0.5 J/k_B$. This leads one to consider the possibility that $T_c = 0$ in two dimensions. For a zero temperature critical point in two dimensions $\eta = 0$ and $\gamma = 2\nu$. Then finite-size scaling[16] predicts that

$$\rho \simeq \tilde{\rho}(L^{1/\nu}T)\,, \tag{11}$$

$$q \simeq \tilde{q}(L^{1/\nu}T)\,, \tag{12}$$

and

$$q^{(2)} \simeq \tilde{q}^{(2)}(L^{1/\nu}T)\,, \tag{13}$$

where

$$q^{(2)} = q^{(2)}(t \to \infty)\,. \tag{14}$$

Actually ρ, q, and $q^{(2)}$ scale well with $T_c = 0$ and $\nu \sim 2.5$. This implies that $\gamma \sim 5$ in two dimensions. This value of γ is consistent with those found for 2D short-range Ising spin-glass models[17,18] but is lower than that found by Bray and Moore for both 2D RAM[12] and 2D Ising spin glass.[19]

The situation is dramatically different in three dimensions as depicted in Fig. 2(a). From the high-temperature phase the ρ-vs-T curves for different system sizes come together at around $T = 1.0$, measured in units of J/k_B. This indicates a phase transition at a temperature $T_c = 1.0 \pm 0.1$ in three dimensions. The ρ values for $T > 1.0$ scale well according to Eq. (10) with $T_c = 1.0$ and $\nu = 1.4 \pm 0.3$ as shown in Fig. 2(b), whereas systematic departures from scaling are observed for $T < 1.0$. To estimate other critical exponents I considered the expected finite size scaling form of q and $q^{(2)}$ as

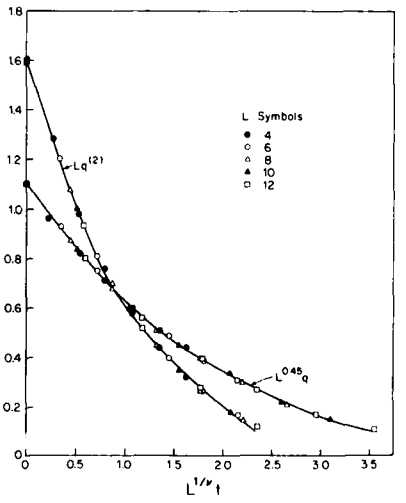


FIG. 3. Finite size scaling plots for q and $q^{(2)}$ according to Eqs. (15) and (16) with $\gamma/\nu = 2.0$ and $\beta/\nu = 0.45$.

$$L^{\beta/\nu}q \simeq f(L^{1/\nu}|t|) \tag{15}$$

and

$$L^{3-\gamma/\nu}q^{(2)} \simeq g(L^{1/\nu}|t|)\,, \tag{16}$$

where $t=(T-T_c)/T_c$. Figure 3 shows that the data of q and $q^{(2)}$ for $T>1.0$ scale nicely according to Eqs. (15) and (16) with $\gamma=2.8\pm0.4$ and $\beta=0.6\pm0.2$ and the previously found values of T_c and ν. These exponents are quite similar, within error bars, to those found[14,17,20] for a short-range Ising spin glass in three dimensions.

In summary, I conclude that these results are consistent with the arguments predicting an absence of ferromagnetic order for $d<4$ and give strong support to the suggestion of Chen and Lubensky that the Ising spin-glass behavior should be expected when ferromagnetism is absent. They also provide strong evidence that RAM actually belongs to the same universality class of short-range Ising spin glass.

It is a pleasure for me to thank Dr. Chandan Dasgupta for many useful suggestions. I am grateful to the University of Minnesota Supercomputer Institute for a grant of computer time on their Cray-2 computer.

[1]For review, see K. Moorjani and J. M. D. Coey, *Magnetic Glasses* (Elsevier, New York, 1984).
[2]D. J. Sellmyer and S. Nafis, Phys. Rev. Lett. **57**, 1173 (1986); B. Dieny and B. Barbara, Phys. Rev. Lett. **57**, 1169 (1986).
[3]R. Harris, M. Plischke, and M. J. Zuckerman, Phys. Rev. Lett. **31**, 160 (1973).
[4]A. Aharony, Phys. Rev. B **12**, 1038 (1975).
[5]R. A. Pelcovits, E. Pytte, and J. Rudnick, Phys. Rev. Lett. **40**, 476 (1978).
[6]J. H. Chen and T. C. Lubensky, Phys. Rev. B **16**, 2106 (1977).
[7]A. B. Harris, R. G. Caflisch, and J. R. Banavar, Phys. Rev. B **35**, 4929 (1987).
[8]M. C. Chi and R. Alben, J. Appl. Phys. **48**, 2987 (1977).
[9]M. C. Chi and T. Egami, J. Appl. Phys. **50**, 1651 (1979).
[10]R. Harris and S. H. Sung, J. Phys. F **8**, L299 (1978).
[11]C. Jayaprakash and S. Kirkpatrick, Phys. Rev. B **21**, 4072 (1980).
[12]A. J. Bray and M. A. Moore, J. Phys. C **18**, L139 (1985).
[13]N. D. Mackenzie and A. P. Young, J. Phys. C **16**, 5321 (1983); Phys. Rev. Lett. **47**, 935 (1981).
[14]R. N. Bhatt and A. P. Young, Phys. Rev. Lett. **54**, 924 (1985).
[15]K. Binder, Z. Phys. B **43**, 119 (1981).
[16]M. N. Barber, in *Phase Transitions and Critical Phenomena*, edited by C. Domb and J. Lebowitz (Academic, New York, 1983), Vol. 8.
[17]R. R. P. Singh and S. Chakravarty, Phys. Rev. Lett. **57**, 245 (1986).
[18]R. H. Swendsen and J. S. Wang, Phys. Rev. Lett. **57**, 2607 (1986).
[19]A. J. Bray and M. A. Moore, J. Phys. C **17**, L463 (19 4).
[20]A. T. Ogielski and I. Morgenstern, Phys. Rev. Lett. **54**, 928 (1985).

Critical behavior of weakly diluted frustrated antiferromagnets

Julio F. Fernandez
Centro de Física, IVIC, Apartado 21827, Caracas 1020A, Venezuela

We study the effect of small amounts of bond or site dilution on some *frustrated* antiferromagnets (AF) in *zero* external field. We argue that random field (RF) like effects are generated by any small amounts of dilution in a large class of Ising AFs, and that these effects (1) are not covered by the criterion of Harris, (2) obliterate AF order in these systems for $d<2$ (and for $d=2$ quite likely), and (3) produce a reduced crossover temperature to impure critical behavior given by the $t_c \sim (\delta J)^{2/\phi}$ and $\phi \approx \gamma$ (instead of $\phi = \alpha$ prescribed by the criterion of Harris for random ferromagnets) for all fcc AF and some bcc AF. Our transfer matrix results for long strips support our arguments.

Disordered magnetic systems with small amounts of uncorrelated nonmagnetic impurities (which excludes random fields,[1] but allows site dilution and random spatial variations of the exchange bonds) are supposed to follow the criterion of Harris[2]: Critical indexes are unaffected by these impurities if the specific heat critical exponent (α) fulfills $\alpha<0$. For $\alpha>0$, the reduced crossover temperature into the impure regime fulfills[2] $t_{cr} \sim (\delta J)^{2/\alpha}$.

The purpose of this paper is to point out that there exists a wide class of frustrated random antiferromagnets (FREA) which are not covered by the criterion of Harris. Any small amount of impurities obliterates the ordered state for $d<2$ in these systems; for $d=3$, the antiferromagnetic order is stable, but we argue that the reduced crossover temperature fulfills $t_{cr} \sim (\delta J)^{2/\phi}$ and $\phi \approx \gamma$, where γ is the susceptibility exponent.

We shall only consider Ising models in this paper, and shall only discuss in any detail an Ising model on a square lattice with *second*-nearest-neighbor exchange $J_2<0$ and first-neighbor exchange J_1 such that $2|J_1|<|J_2|$. It is a frustrated[3] system, since half the J_1 bonds are broken in the ground state. For $J_1=0$, the system breaks up into two noninteracting systems on interpenetrating square sublattices. Even for $J_1 \neq 0$ (but $2|J_1|<|J_2|$), reversal of all spins on one sublattice leaves the ground-state energy invariant. Removal of a J_1 bond clearly breaks this degeneracy. Removal of a horizontal bond picks one ground state whereas removal of a vertical bond picks the other ground state.

Now consider random removal of a fraction x of J_1 bonds. In any region R of linear size l there will be an unbalanced number $\delta n = l^{d/2}|x(1-x)|^{1/2}$ of vertical and horizontal bonds, and a corresponding energy bias $\epsilon_b \sim J_1 \delta n$. Following Imry and Ma,[4] consider making a domain by reversing all spins within R on one of the two sublattices. It will cost a wall energy $\epsilon_w \sim J_2 l^{d-1}$. Clearly a domain will be formed if $l > \xi$, where

$$\xi \sim (J_2/J_1)^{2/(2-d)}|x(1-x)|^{-\nu} \tag{1}$$

for $d<2$ and $\nu = 1/(2-d)$. For $d=2$, we expect by analogy with the random field ferromagnet[5] $\xi \sim \exp|J_2^2/J_1^2 x(1-x)|$.

In order to check the validity of our arguments thus far we use the transfer matrix method[6] to compute for strips,

$$S = 2N^{-1}\langle |\Sigma_1 S_i e^{iQ\cdot R_i}|^2 + |\Sigma_2 S_i e^{iQ\cdot R_i}|^2 \rangle, \tag{2}$$

where $S_i = \pm 1$ is the spin on the ith site, and Σ_1 and Σ_2 stand for sums over all i on the first and second sublattice, respectively.

We perform our calculations on strips of W spins (for $W=2,4,6$, and 8) across by l spins for $k_B T = 0.2 J_2$, for values of x such that $\xi \gg W$. We deal with essentially infinitely long strips by letting $l \gg \xi$. Clearly, then $S \approx 2W\xi$, and since $\epsilon_w \sim J_2 W$ and $\epsilon_b \sim J_1|x(1-x)|^{1/2}$, it follows that

$$S \sim (J_2/J_1)^2 W^2/|x(1-x)|. \tag{3}$$

The results obtained, averaged over 40 realizations of missing bonds in every case, are shown in Fig. 1. There is reasonably good agreement with Eq. (3), which supports our arguments.

Some results obtained by Monte Carlo simulations for $k_B T = 1.5 J_2$ (the transition temperature for $J_2 = J_1 < 0$ is

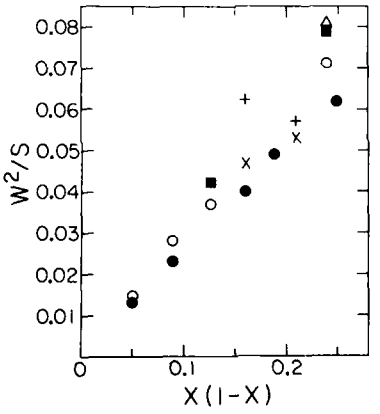


FIG. 1. W^2/S is shown vs $x(1-x)$ for $k_B T = 0.2|J_2|$ and $J_1 = J_2 < 0$. ●, ○, ■, and Δ stand for transfer matrix results for $W = 2$, 4, 6, and 8, respectively, and represent averages over at least 40 realizations in all cases. × and + stand for Monte Carlo results for $W = 8$ and 12, respectively, averages over 10 realizations in both cases.

 0021-8979/88/083738-02$02.40 © 1988 American Institute of Physics

$2.1|J_2|$) are also shown in Fig. 1. They correspond to averages over 10 configurations of missing bonds.

For site dilution, note that one missing spin removes all four J_1 bonds and does not lift the degeneracy. A little thought shows that *pairs* of missing spins lift the degeneracy, and consequently ν is twice as large for site dilution as for bond dilution.

Consider now three-dimensional systems. For bcc lattices, and $J_2<0$, $|J_2|>2|J_1|/3$, there are two interpenetrating simple cubic antiferromagnets. Just as for the two-dimensional case, half of the J_1 bonds are broken, and random-field-like effects are generated by random removal of J_1 bonds (as well as by site dilution). For $d=3$, $\epsilon_w > \xi_b$ for small x, and antiferromagnetic order is indeed stable to dilution in this case. For $|J|_2<2|J_1|/3$, there is no frustration, no degeneracy, and no special effects occur. It is straightforward to show that random-field-like effects are generated by dilution in all three types of antiferromagnets on fcc lattices.

We now compare the crossover exponents for random exchange ferromagnets (REF), for which the Harris[2] criterion holds, and for the frustrated random exchange antiferromagnets (FREA) under consideration. For REF the predicted[2] behavior is $t_c \sim (J_1^2 x)^{1/\phi}$ for $\alpha>0$ and $x \ll 1$. (Experiments[7] do not, however, seem to follow this prediction.) We expect for FREA,

$$t_c \sim (J_1^2 x)^{1/\phi}, \quad \phi \approx \gamma, \tag{4}$$

where γ is the susceptibility exponent, on the basis of the simple minded argument and numerical results that follow. Consider a thermal fluctuation at a reduced temperature t above T_c, of linear size ξ. It costs a free energy $\sim k_B T_c$ in the pure system. Randomness sets in if the random energy ϵ_R in the diluted system fulfills $\epsilon_R \gtrsim k_B T$. To get an expression for ϵ_R, let the effective number of spins within ξ^d be $n=\Sigma_i \langle S_0 S_i\rangle$. Then $\epsilon_R \sim J_1 (nx)^{1/2}$ for $x \ll 1$. Now, if $\Sigma_i \langle S_0 S_i\rangle \sim t^{-\gamma}$ above T_c, then setting $\epsilon_R = k_B T$ yields Eq. (4).

Some support for the above argument is provided by the calculation we describe next. Using the transfer matrix technique, we have calculated S as a function of both T and x for long ($l \gg \xi$) strips for $W=2$. In this one-dimensional-like system, $S \sim e^{4/T}$ (not $t^{-\gamma}$) for the pure case ($x=0$) and $T \ll 4$ (T is in units of $|J_2|/k_B$), and Eq. (4) must be modified to $t_c \sim -4/\log x$ in this case. Finite scaling leads us to expect

$$S \sim e^{4/T} f(e^{-4/T}/x). \tag{5}$$

Our numerical results, shown in Fig. 2, agree well with this prediction. Note that for $e^{-4/T} \ll x$, $S \sim x^{-1}$ as expected from Eq. (3), while for $e^{-4/T} \gg x$, $S \to e^{4/T}$, also as expected. All points shown correspond to $0.3 \lesssim T \lesssim 1.5$.

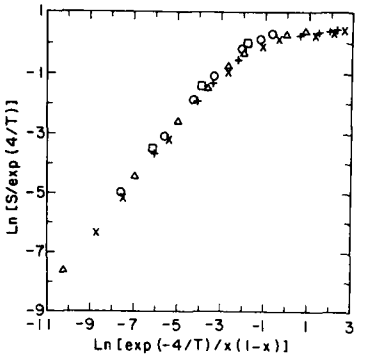


FIG. 2. Data obtained by the transfer matrix methods is shown for S, defined in Eq. (2), appropriately scaled, is shown. × is the fraction unoccupied sites. ×, +, Δ, O, and □ stand for $x=0.01$, 0.02, 0.05, 0.1, and 0.2, respectively.

These results for narrow strips provide a clear example of a system not covered by the criterion of Harris. Indeed, according to the latter criterion, if $\xi > t^{-2/d}$ as $T \to T_c$ (clearly fulfilled by our strips) impurities should be irrelevant, which is contrary to our results.

Finally, the following idea [related to the unexpectedly high crossover temperature (t_c) into the impure behavior[7] in $Fe_{1-x}Zn_xF_2$, which is of bcc AF type] may be worth looking into. Let the multicritical point (MP) where the AFI, AFII, and paramagnetic phases meet be at $J_2 = J_2^{MP}(|J_2^{MP}| \approx 2|J_1|/3)$, and let $y=(J_2 - J_2^{MP})/|J_1|$. Now, for $y>0$ and $t \gtrsim y^{1/\psi}$ the MP behavior will dominate. Thus, for $X^{1/\phi} \gtrsim y^{1/\psi}$ the crossover into the impure regime will be dominated by the effect put forth in this paper (not by the Harris mechanism).

[1] See for instance, A. Aharony, J. Appl. Phys. **54**, 27 (1986).
[2] M. E. Fisher, Phys. Rev. **176**, 257 (1968); A. B. Harris, J. Phys. **7**, 1671 (1974); D. Andelmun and A. Aharony, Phys. Rev. B **31**, 1305 (1985).
[3] G. Toulouse, Commun. Math. Phys. **2**, 115 (1977).
[4] Y. Imry and S. K. Ma, Phys. Rev. Lett. **35**, 1399 (1975).
[5] G.Grinstein and S. K. Ma, Phys. Rev. B **28**, 2588 (1983); J. Villain, J. Phys. (Paris) **43**, 1551 (1982).
[6] J. F. Fernández, J. Phys. C **13**, L555 (1980); J. F. Fernández, Phys. Rev. B **25**, 417 (1982).
[7] See H. Barrett, Phys. Rev. B **34**, 3513 (1986) and references therein.
[8] P. Nightingale, J. Appl. Phys. **53**, 7927 (1982).

Transition behavior in Gd-Co based alloys with strong anisotropy

K. M. Lee and M. J. O'Shea
Cardwell Hall, Department of Physics, Kansas State University, Manhattan, Kansas 66506

We have studied the effect of random magnetic anisotropy (RMA) on transition behavior in Gd-Co glasses. The large RMA induced by alloying with anisotropic rare-earth elements produces standard speromagnetic behavior which includes nonsaturation of magnetization at large enough concentrations at 4.2 K and high fields in all the alloys except the most concentrated Tb alloys. Although these latter alloys have the largest coercivity and the strongest RMA they appear to be closer to saturation at high fields than intermediate concentration Tb alloys. We discuss a mechanism by which this saturation may be produced by short-range correlations in the anisotropy axis.

In this work we will discuss the transition behavior observed in Gd-Co based glasses as a function of random magnetic anisotropy (RMA) of strength D. RMA is induced in a controlled fashion by alloying with anisotropic rare earths (R) Tb and Dy. The glasses studied have a composition $Gd_{65-x}R_xCo_{35}$. We have shown that alloying with these elements produces a crossover from a paramagnetic (PM)–ferrimagnetic (FM) sequence of transitions with decreasing temperature to a PM–speromagnetic (SM) sequence of transitions due to the strong RMA produced on alloying.[1,2] In the SM state the spins are frozen in random directions much like a spin glass due to the presence of RMA.[3] We have also shown that alloying with Er induces the smallest RMA for a given concentration of all the anisotropic rare earths. In these alloys double transitions are present for small Er concentration. For larger Er concentrations where the RMA is stronger the double-transition behavior crosses over to PM–SM behavior. The most recent reviews of the magnetic behavior of RMA systems are given in Ref. 4. In this work we shall discuss some anomalies in the behavior of Tb-rich alloys where the RMA is strong and discuss possible explanations in terms of a quasi-random axes model.

$Gd_{65}Co_{35}$ is a ferrimagnet at low temperatures with a Gd spin of 7.5 μ_B/ion and although there is not general agreement as to the value of the Co spin the most recent work suggests it is about 0.6 μ_B/ion.[5] We choose to study the anisotropy effects in this system for three reasons. The exchange fluctuations present in this system are not large enough to produce SG behavior since it remains collinearly ordered down to low temperatures. The similarity between Gd and the other rare-earth elements allows this system to be alloyed with anisotropic rare earths while maintaining a homogeneous amorphous structure. Finally the RMA strength may be varied over a large range by a judicious choice of the rare-earth R and composition x as we have shown previously.[1]

The glassy alloys were prepared by splat cooling yielding circular foils about 2.5 cm in diameter and 50 μm thick. The composition was determined from the starting constituents and estimated to be accurate to about 0.2 at. % by weighing after melting. X rays were used to check the amorphous nature of the samples. The samples for magnetic measurements were in the form of sandwiches of about eight strips 1.5 cm long (and 0.15 cm wide) aligned parallel to the applied field in both ac susceptibility and magnetization experiments to minimize demagnetization effects. ac susceptibility measurements were made with an RMS field of 1 Oe at a frequency of 280 Hz. Magnetization measurements were made using both low-field (up to 800 Oe) and high-field (up to 75 kOe) vibrating sample magnetometers.

The in-phase ac susceptibility (χ) for the R = Dy system is shown in Fig. 1, and χ for the Tb system has already been presented.[1] The $x = 0$ alloy shows a FM transition with χ showing a small decrease below the transition presumably due to the onset of weak hysteresis in the ferromagnetic phase. As x is increased there is a rapid reduction in peak height of χ for the Dy alloys and the system crosses over to PM–SM transition behavior due to the increase in anisotropy strength. We have also studied the anisotropic rare-earth systems R = Pr, Nd, Sm, Tb, Ho, and Yb and a smooth crossover from PM–FM to PM–SM transition behavior is observed in all of these systems with increasing x.[6] We find that the transition temperatures as a function of composition x decrease approximately linearly with the largest decrease being produced by the alloying rare earth R with smallest spin. Figure 2 shows examples for the Tb and Dy alloys where s is 3 and 5/2, respectively, compared to an s of 7/2 for trivalent Gd ions. Such behavior has been seen in other rare-

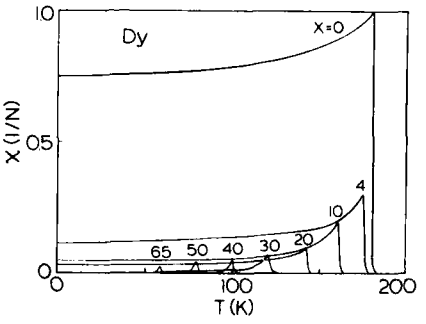


FIG. 1. ac susceptibility for alloys with composition $Gd_{65-x}Dy_xCo_{35}$.

 0021-8979/88/083740-03$02.40 © 1988 American Institute of Physics

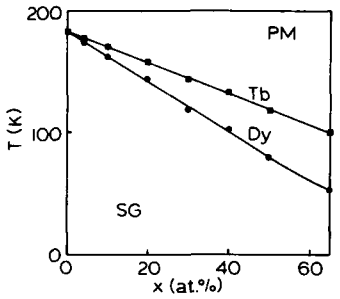


FIG. 2. Magnetic phase diagram for the Tb and Dy alloys as deduced from the peak position of the ac susceptibility.

earth systems including intra-rare-earth alloys[7] and can be rationalized in terms of an exchange related to the weighed average of the contributions from Gd and the anisotropic rare earth R. The height of the ac susceptibility curve decreases with increasing RMA strength as expected. The value of D/J for $Tb_{65}Co_{35}$ is 0.40 ± 0.06. For these alloys the value of D was determined from the magnetization-area method[8] and the value of zJ was determined from the transition temperature.[1] The number of nearest neighbors z was assumed to be 8, which is close to the expected value for a close-packed solid. In the case of the $Dy_{65}Co_{35}$ alloy the magnetization-area method may not be applied with any confidence since the alloy does not come close to saturation. In the SM state hysteresis is present and a time dependence of the magnetization is observed.

The saturation magnetization and coercivity were measured for the Tb and Dy alloys at 4.2 K after cycling the field to 75 kOe, and these results are shown in Figs. 3 and 4, respectively. The coercivity increases rapidly with Dy or Tb content x due to the strong RMA. Also the magnetization decreases rapidly with increasing Dy content due to the presence of the strong RMA which prevents saturation of the

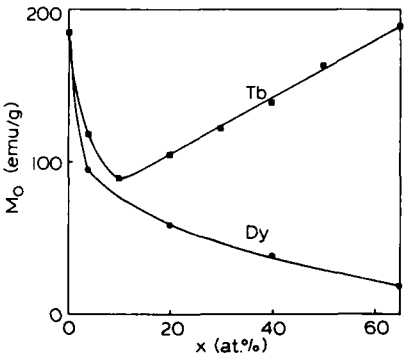


FIG. 3. Saturation magnetization at 75 kOe and 4.2 K for selected alloys from the Tb and Dy systems.

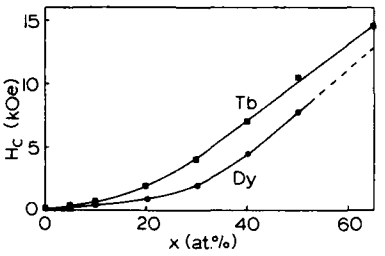


FIG. 4. Coercivity as a function of composition x for the Tb and Dy alloys at 4.2 K.

alloys. All of the other anisotropic rare earths except Tb show similar behavior. The expected saturation for ferrimagnetic $Tb_{65}Co_{35}$ and $Dy_{65}Co_{35}$ are 253 and 282 emu/g assuming a Tb, Dy, and Co moment of 9, 10, and $0.6\mu_B$, respectively. In the case of the Tb alloys this curve shows a minimum at about $x = 10$ at. % with the magnetization being about half of its saturated value before the magnetization rises to within about 20% of its saturation value for $x = 65$ at. % ($Tb_{65}Co_{35}$). The monotonic increase in coercivity is the result of the monotonic increase in RMA strength and as discussed previously[1] the Tb alloys have the highest coercivity and RMA strength of all the anisotropic rare earths studied for a given composition. Although coercivity increases with RMA strength, it does not yield a direct measure of D except at the largest anisotropy values. Since the RMA strength and resulting coercivity increase monotonically with increasing Tb concentration the lack of saturation of intermediate concentration Tb alloys while higher concentration alloys are more easily saturated is rather surprising. The magnetization of the 10 at. % Tb alloy is approximately that expected from a hemispherical fan of Gd and Tb moments and antiparallel Co moments suggesting that at small Tb concentrations the RMA dominates the behavior of the rare-earth ions.

We have considered the possibility of chemical inhomogeniety explanations such as a microscopic phase separation for the rise in saturation magnetization of Tb alloys occurring but consider these unlikely because of the chemical similarity of the rare earths, especially the heavy rare earths Tb and Dy studied here.

The above results show that it is possible to induce ferromagnetic order at high fields in high concentration Tb alloys but not in intermediate Tb concentration alloys. At low fields no anomalies are observed with both the transition temperature as determined from ac susceptibility, and the ac susceptibility height both decreasing monotonically with increasing RMA strength as the Tb concentration increases. A result which we believe to be closely related to this work is the scaling analyses done in a $Gd_{15}Tb_{50}Co_{35}$ alloys.[2] In this work it was shown that although the RMA in this alloy was strong it was possible to achieve excellent ferromagnetic scaling at high magnetic fields (1–80 kOe). Below 1 kOe large deviations from scaling occurred, and below about 700 Oe it was found that a nonlinear or spin-glass scaling equa-

tion of state fitted the results. Demagnetization effects do not become important in these alloys unless the applied field is less than 50 Oe. This result shows that a crossover from a low-field regime where spin-glass-like or SM behavior is present to a high-field regime where ferromagnetic behavior is present occurs.

There are two possible factors that may produce a more ferromagnetic alloy at high Tb concentrations than at intermediate concentrations. The first factor is a strong Tb-Tb exchange. We consider this effect by itself unlikely to produce the above result for the following reason. The overall exchange, as determined from the transition temperature, is strongest for the Tb alloys of all the rare earths studied for a given concentration, however, the Tb-Tb exchange is likely to be weaker than the Gd-Gd exchange since the spin on the trivalent Tb ion is smaller than that on the Gd ion. The second factor concerns the RMA. In most models of RMA systems the anisotropy direction is assumed to vary at random in direction from site to site. A more reasonable assumption and one that has been made in some of the more recent models is that due to the presence of short-range order (which is present in all metallic amorphous systems) the random axes are correlated over short distances.[9,10] This implies that in alloys containing small amounts of Tb and with the short-range order extending a few interatomic spacings there will be no correlation of anisotropy axes because the Tb ions are well separated. At high Tb concentrations where more nearest-neighbor and next-nearest-neighbor Tb pairs exist the short-range order will be important in producing short-range correlations in the anisotropy axes. The result will be a strongly ferromagnetic block of spins which interacts with neighboring blocks via exchange and anisotropy interactions.

We note that although there may be a short-range correlation in anisotropy axes in our Tb-rich alloys there is no correlation on a macroscopic scale (i.e., no coherent anisotropy). We have shown this via torque measurements where we find that the same torque curve is obtained for any field cooling direction. We shall discuss these results in more detail elsewhere.[11] The large discontinuities in the hysteresis loops for Tb-rich alloys at 4.2 K are evidence of the highly cooperative effects in magnetization reversal in these alloys. We suggest that the rise in saturation magnetization at 75 kOe and 4.2 K in the Tb-rich alloys occurs when the correlation length for the anisotropy axes spans more than a single Tb ion. Similar short-range order will be present in other rare-earth alloys such as the Dy system discussed above since the rare earths are chemically very similar and have similar ionic radii. The exchange is weaker in all the other rare-earth alloys including Dy as discussed above so that if ferromagnetic blocks of spins do form they will be more weakly coupled with neighboring block spins than in Tb alloys. Also no evidence for strong cooperative phenomena such as discontinuities in magnetization reversal are present in Dy alloys.

In summary, we have shown that the Tb alloys of this work show a tendency towards collinear order at high Tb concentrations in an applied field and strong speromagnetic effects such as nonsaturation of magnetization at intermediate concentrations of Tb in an applied field. We have proposed an explanation in which short-range structural order induces short-range correlations in the anisotropy axis. When the concentration of Tb ions is large enough that their average spacing is less than the anisotropy axis correlation length, the system crosses over to a behavior where strong cooperative phenomena become important due to the formation of block spins.

We are grateful to D. J. Sellmyer for useful discussions during the course of this work.

[1]M. J. O'Shea, K. M. Lee, and F. Othman, Phys. Rev. B **34**, 4944 (1986).
[2]K. M. Lee, M. J. O'Shea, and D. J. Sellmyer, J. Appl. Phys. **61**, 3616 (1987).
[3]J. M. D. Coey, J. Appl. Phys. **49**, 1646 (1978).
[4]D. J. Sellmyer, to be published in the Proceedings of the Symposium on Magnetic Properties of Amorphous Metals, Spain, 1987; D. J. Sellmyer, S. Nafis, and M. J. O'Shea, these proceedings.
[5]K. Fukamichi, T. Goto, T. Sakakibara, S. Todo, K. Aoki, and T. Masumoto, J. Magn. Magn. Mater. **54**, 239 (1986).
[6]K. M. Lee, N. Singh, and M. J. O'Shea (to be published).
[7]S. Legvold, in *Ferromagnetic Materials*, edited by E. P. Wohlfarth (North-Holland, Amsterdam, 1980), Vol. 1, p. 78.
[8]G. Hadjipanayis, D. J. Sellmyer, and B. Brandt, Phys. Rev. B **23**, 3349 (1981).
[9]E. M. Chudnovsky, W. M. Saslow, and R. A. Serota, Phys. Rev. B **33**, 251 (1986).
[10]W. M. Saslow, Phys. Rev. B **35**, 3454 (1987).
[11]A. Fert and M. J. O'Shea (to be published).

Magnetic transitions and phases in random-anisotropy magnets

D. J. Sellmyer and S. Nafis
Behlen Laboratory of Physics, University of Nebraska, Lincoln, Nebraska 68588
M. J. O'Shea
Department of Physics, Kansas State University, Manhattan, Kansas 66506

The generality and universality of the Ising spin-glass-like phase transitions observed in several rare-earth, random-anisotropy magnets are discussed. Some uncertainties and practical problems in determining critical exponents are considered, and a comparison is made to insulating spin glasses and crystalline spin glasses where an apparent anisotropy-induced crossover from Heisenberg to Ising-like behavior is seen. The observation of a reentrant transition in a weak anisotropy system and its correlation with the theory of Chudnovsky, Saslow, and Serota [Phys. Rev. B **33**, 251 (1986)] for the correlated spin glass is discussed.

INTRODUCTION

The development of a theoretical understanding of phase transitions and glass transformations in disordered media maintains a high level of interest and activity. Disordered magnetic materials with random interactions, for example, spin glasses (SG), random-anisotropy magnets (RAM), and random-field magnets, all have seen significant experimental and theoretical advances in recent years. However, there remain several aspects which have resisted clear interpretations and which, therefore, remain controversial. In this paper we report on extensions of our recent work in which we successfully analyzed magnetic transitions in several strong random-anisotropy systems in terms of a scaling theory developed for Ising SG transitions.[1,2] In addition we make contact with recent theoretical results for the RAM problem and also with phase transitions in Heisenberg spin glasses in which anisotropy plays a role.

RESULTS AND DISCUSSION

A major concern in the quest for developing a consistent phase-transition picture for the transitions observed in random-anisotropy systems is the universality (or lack thereof) in the critical exponents observed from one system to the next. In Table I we have collected most of the exponents measured for RAM glasses. In addition we included several insulating spin glasses and an estimate of the maximum reduced temperature range, $t = (T - T_c)/T_c$, over which the scaling analysis was performed. The three exponents are not independent and the scaling relation $\delta = 1 + \gamma/\beta$ was used to determine one of the exponents. Both ac susceptibility and dc magnetization results are included. With a few exceptions the exponents cluster around the values $\bar{\gamma} = 3.6$, $\bar{\beta} = 1.3$, $\bar{\delta} = 3.7$. However, many of the individual values, at least with their quoted errors, are inconsistent with these average values. The natural questions that arise include: (1) Are these differences significant? (2) Is there evidence for a well-defined Ising-type transition, within a single universality class, in these strong anisotropy systems? (3) Can the insulating SG systems also be regarded as anisotropy-induced Ising-type spin glasses?

There are two points to be made in considering these questions. The first is that the error estimates in scaling analyses tend to be based only on the sensitivity of the quality of scaling to small changes in the exponents (say ± 0.1). These estimates do not account for systematic errors and our recent experience indicates, particularly for dc scaling analyses, that the exponent uncertainties probably should be several times the often-quoted values of ± 0.1. A second point is that in these scaling analyses of nonlinear susceptibility, as well as in standard ferromagnetic scaling analyses, the maximum temperature range of the analysis should be limited. Fähnle, Kellner, and Kronmuller[9] have shown this for ferromagnetic transitions and also have shown, for a $\pm J$ Ising SG, that the effective Edwards–Anderson susceptibility exponent increases from about 2.9 at $t = 0$ to a maximum of about 3.7 at $t = 0.4$ before decreasing again.[10] These results suggest that scaling analyses obtained with data above $t = 0.1$ are likely to contain some sort of averaged $\gamma(T)$ value rather than the true critical value for $t \to 0$. These considerations suggests that there *may* be universal behavior of the exponents based on uncertainties considerably larger than those quoted in the table.

A related point concerns the field dependence of the singular susceptibility, $\chi_s(H) \equiv \chi(H = 0) - M(H)/H$. Namely, it has been observed in several of the RAM systems of Table I that near $t = 0$ there generally is a "kink" in $\chi_s(H)$. An example for DyFeB is shown in Fig. 1. This also has been seen often in SG systems such as Cu(Mn) and others. Given that $\chi_s \propto H^{2/\delta}$ at $t = 0$, the question arises as to the possible existence of high- and low-field values of δ and the problem of which one is relevant to the assumed phase transition. de Courtenay *et al.*[11] have considered this problem for Heisenberg SG systems such as Cu(Mn) and Ag(Mn). Briefly, these systems possess an anisotropy-induced crossover from a Heisenberg to an Ising critical behavior. The low-field, low-temperature region ($t < d^{\phi_4}$) is the Ising regime and the high-field, high-temperature region

 0021-8979/88/083743-03$02.40 © 1988 American Institute of Physics

TABLE I. Compilation of critical exponents for RAM and insulating SG systems.

Material	γ	β	δ	t_{max}	Reference (method)
a-TbFeGa	3.7 ± 0.1	1.7 ± 0.1	3.2 ± 0.2	0.1	1 (ac)
a-DyFeB	3.7 ± 0.1	1.5 ± 0.1	3.5 ± 0.2	0.1	3 (ac)
a-DyFeB	3.5 ± 0.1	1.4 ± 0.1	3.5 ± 0.2	0.1	3 (dc)
a-TbGdCo	3.7 ± 0.2	1.3 ± 0.1	3.8 ± 0.3	0.04	4 (dc)
a-NdGa[a]	5.5 ± 0.4	1.4 ± 0.1	4.9 ± 0.4	0.1	5 (dc)
a-DyNi	2.0 ± 0.1	1.2 ± 0.1	2.7 ± 0.1	0.25	6 (dc)
a-MnAlSiO	3.4 ± 0.1	1.4 ± 0.1	3.4 ± 0.2	0.4	7 (ac,dc)
CsNiFeF	3.0 ± 0.5	1.2 ± 0.1	3.5 ± 0.5	0.1	8 (dc)
a-MnFP	3.6 ± 0.2	0.8 ± 0.1	5.2 ± 0.3	0.2	7 (dc)

[a] Preliminary results.

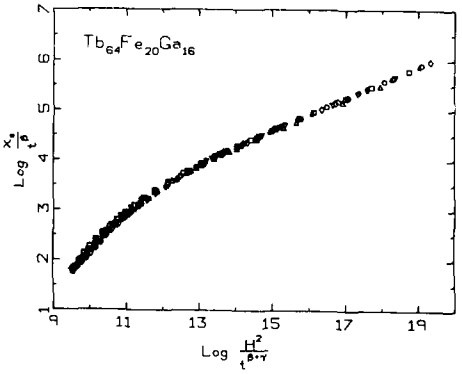


FIG. 2. Scaling of χ_r/t^{β} as a function of $H^2/t^{\beta+\gamma}$ for *a*-TbFeGa. The fields are as follows: (inverted triangles) 40 Oe; (triangles) 78 Oe; (squares) 120 Oe; (circles) 180 Oe; (lozenges) 240 Oe; (stars) 288 Oe.

$(t > d^{\phi_A})$ corresponds to a Heisenberg type of critical behavior. Here d is the ratio of anisotropy to exchange strength and ϕ_A is the anisotropy crossover exponent [~ 0.8 for Cu(Mn)]. The high-field/low-field transition seen in Fig. 1 and also in the scaling plot of Fig. 2 for TbFeGa appears to have nothing to do with this type of crossover. The scaling plot of Fig. 2 was obtained with a single set of exponents over the whole field and temperature region for which $t < 0.1$ so that $t \ll d \cong 5$. Thus this would correspond to the Ising regime of de Courtenay *et al.* An additional point of interest is that for the alloys considered by de Courtenay *et al.* d ranges from about 0.03 to 0.8. If $\phi_A \simeq 1$ and $d > 0.1$, it would appear from our previous discussion on limiting scaling analyses to $t < 0.1$ that no meaningful scaling analysis and critical-exponent determination can be performed in the Heisenberg regime. Thus the effective conversion of Heisenberg spin glasses to Ising spin glasses by anisotropy is a well-defined phenomenon, but the meaning of any "high-temperature" Heisenberg critical phenomena remains to be clarified.

Our final point concerns the likely observation of the "correlated spin-glass" (CSG) state first discussed theoretically by Chudnovsky, Saslow, and Serota.[12] The CSG state refers to the weak anisotropy case of a random-anisotropy magnet where in zero field there is no net moment and a smooth stochastic rotation of the magnetization (with no domain walls). The theory predicts that if α, β_r, and β_c represent exchange, random-, and coherent-anisotropy strengths, respectively, then the condition for the existence of the CSG is

$$\Lambda_c^{1/4} \ll \Lambda_r/4 \ll 1, \tag{1}$$

where $\Lambda_r = \beta_r(\alpha/J^2)^{-1}R_c$ and a similar relation exists between Λ_c and β_c. Here J is the magnitude of the angular momentum and R_c is the correlation length of the anisotropy axes. The theory also predicts in the CSG state that the

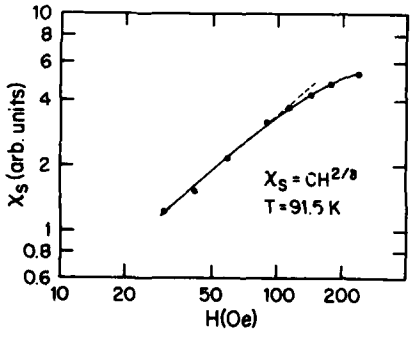


FIG. 1. Field dependence of singular part of the susceptibility for *a*-DyFeB. A change in slope is seen at about 100 Oe.

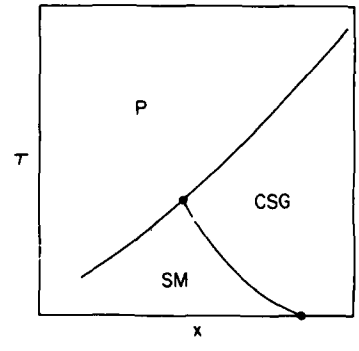


FIG. 3. Magnetic phase diagram shown paramagnetic (P), speromagnetic (SM), and correlated spin-glass phases (after Ref. 12). X is magnetic moment concentration.

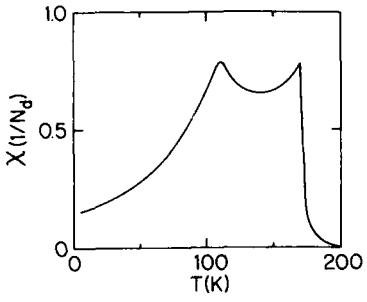


FIG. 4. ac susceptibility of a-$Er_4Gd_{61}Co_{35}$ as a function of temperature. N_d is the demagnetization factor.

susceptibility is large, but finite, and is given by

$$\chi_{CSG} = \frac{1}{2\beta_r}\left(\frac{15}{4}\frac{\alpha}{\beta_r R_c^2}\right)^3. \quad (2)$$

Figure 3 shows a schematic phase diagram for a RAM with a varying concentration of anisotropic moments. This is based on the theory of Chudnovsky and co-workers which considers the concentration dependence of the exchange and the temperature dependence of the anisotropy $[\beta_r(T) \sim M(T)]$. Our results for a-$Er_4Gd_{61}Co_{35}$ are shown in Fig. 4. a-$Gd_{65}Co_{35}$ is a collinear ferrimagnet and for large concentrations of Er substitutions for Gd, a speromagnet is obtained.[13] Figure 4 shows an apparent double transition from paramagnetism to CSG to speromagnet. Estimates of $\alpha(8\times10^{-7}$ erg/cm) and $R_c(\sim 4$ Å) lead with Eq. (2) to $\beta_r = 5\times10^6$ erg/cm^3 and $\Lambda_r \simeq 0.5$. Thus $\Lambda_r/4 \simeq 0.1$ which does satisfy Eq. (1), the condition for the existence of the CSG. Moreover, we expect β_c to be less than about 10^4 erg/cm^3 (no bulk or coherent anisotropy is observable) so that the other condition $\Lambda_c^{1/4} \ll \Lambda_r/4$ also can be shown to be satisfied. These results then constitute a fairly clear observation of the CSG and an associated reentrant transition as predicted by the theory.

CONCLUSIONS

We have considered the universality of the apparent phase transitions observed in a number of RAM systems, and suggest that scaling analyses with higher precision and with smaller maximum reduced temperature are needed to confirm a true universality with consistent critical exponents. The relationship between the field dependence of the nonlinear susceptibility seen in RAM's and Heisenberg SG's was discussed, and a difficulty pointed out in determining Heisenberg exponents for small enough t to be in the critical region. Finally, the observation of a reentrant transition involving the correlated spin-glass phase as predicted by theory was discussed.

ACKNOWLEDGMENTS

We are grateful for financial support to the Solid State Physics Program of National Science Foundation under Grant No. DMR 8605367. We thank Professor Wayne Saslow for informative discussions on the theory.

[1]D. J. Sellmyer and S. Nafis, Phys. Rev. Lett. **57**, 1173 (1986).
[2]D. J. Sellmyer, in *Proceedings of the Symposium on Magnetic Properties of Amorphous Metals*, Malaga, Spain, 1987 (North-Holland, Amsterdam) (in press).
[3]S. Nafis and D. J. Sellmyer (to be published).
[4]K. M. Lee, M. J. O'Shea, and D. J. Sellmyer, J. Appl. Phys. **61**, 3616 (1987).
[5]M. J. O'Shea and D. J. Sellmyer (to be published).
[6]B. Dieny and B. Barbara, Phys. Rev. Lett. **57**, 1169 (1986).
[7]P. Beauvillain, C. Chappert, J. P. Renard, and J. Seiden, J. Magn. Magn. Mater. **54–57**, 127(1986).
[8]C. Pappa and J. Hammann, J. Phys. (Paris) **46**, 637 (1985).
[9]M. Fahnle, W. U. Kellner, and H. Kronmuller, Phys. Rev. B **35**, 3640 (1987).
[10]R. P. Singh and M. Fahnle (private communication).
[11]N. de Courtenary, H. Bouchiat, H. Hurdequint, and A. Fert, J. Phys (Paris) **47**, 1507 (1986).
[12]E. M. Chudnovsky, W. M. Saslow, and R. A. Serota, Phys. Rev. B **33**, 251 (1986), and references therein.
[13]M. J. O'Shea, K. M. Lee, and F. Othman, Phys. Rev. B **34**, 4944 (1986).

Random-anisotropy ferromagnetism in amorphous $U_{27}Fe_{73}$ films

P. P. Freitas,[a] T. S. Plaskett, and T. R. McGuire
IBM T. J. Watson Research Center, Yorktown Heights, New York 10598

We measured magnetic and transport properties of amorphous $U_{27}Fe_{73}$ films deposited by magnetron sputtering. The films show a magnetic ordering temperature $T_f = 32$ K, and a spin-glass regime below a temperature $T_{irr}(H)$. The Arrott plot shows a characteristic change in concavity at the transition, as predicted by Aharony and Pytte (A-P) for random-anisotropy systems with $D \ll J$. Although we find a finite susceptibility below T_f, with $\chi_0 = 0.66$ in units of the inverse of the demagnetizing factor, the critical exponents δ_1 and δ_2 are close to the values predicted by the A-P model. The electrical resistivity has a minimum at 31 K, resulting from the competition between exchange scattering and inelastic spin-flip processes. For $T > 200$ K a linear regime with negative $d\rho/dT$ is found, characteristic of phonon scattering in amorphous materials. The isotropic magnetoresistance is positive and levels off below T_f reflecting freezing of spin correlations at this temperature. This behavior can be explained by the existence of small Imry and Ma domains and partial local magnetic order below T_f.

INTRODUCTION

Noncollinear magnetic structures are common in amorphous metallic alloys.[1] The topological magnetic disorder, existing in random systems, results from the interplay between local anisotropy and exchange interactions, and determines their magnetic and transport properties. A simple Hamiltonian to describe these competing effects was introduced by Harris, Plischke and Zuckerman[2]:

$$\mathcal{H} = -\sum_i D_i S_{i_z}^2 - \sum_{ij} J(R_{ij})\mathbf{S}_i \cdot \mathbf{S}_j .$$

Two main extreme cases can be considered. First, random-exchange-dominated materials ($J > D$), such as most spin glasses described in terms of the Edwards–Anderson model, where there is a distribution of the exchange interaction around an average value J_0 that can be zero or positive. Second, random-anisotropy-dominated systems like non-S-state rare-earth amorphous alloys, where the local anisotropy fields from the magnetic ions dominate over the average exchange field ($D > J$).[3,4] Common features of both types of materials are a finite high-field susceptibility caused by the alignment of randomly oriented spins into the field direction, a reduced average moment in the ordered regime when compared with the atomic paramagnetic moment, and the onset of spin-glass-like behavior below a certain temperature T_{irr}. Differences can occur however in the critical behavior and should show up in the low-field initial susceptibility, Arrott plots and transport properties. In the critical region, and for low anisotropy values, Aharony and Pytte[5,6] (A-P) have shown that the susceptibility of a random-anisotropy system should obey $\chi \simeq \xi^2 = (J/D)^4$ in three dimensions, implying infinite susceptibility only for vanishingly small anisotropy. In the latter case, the isotherms go as $H \simeq M^{\delta_1}$ at $T = T_f$ and $H \simeq M^{\delta_2}$ at $T < T_f$. In an Arrott plot, a change in the concavity of the isotherms is observed at T_f, and all isotherms will approach the origin without intersecting the M^2 axis (no spontaneous moment). In the random-exchange case, there is no change in the curvature of the isotherms in the Arrott plot, and all lines intersect the H/M axis away from the origin due to a finite susceptibility for all $T > 0$. While magnetization measurements provide a way to measure the average magnetic moment, transport properties give information about the spin correlations at the atomic level as the electron mean free path in amorphous materials does not exceed 1–2 atomic distances. Theories[7–10] based on coherent exchange scattering by localized spins predict a change in sign of the magnetic resistivity and of the magnetoresistance as the interatomic exchange changes from ferromagnetic to antiferromagnetic. Furthermore, inelastic spin-flip processes are important above T_f and when $k_B T \gg DS$.[2] This is not the case in crystalline materials where the paramagnetic spin-disorder resistivity is temperature independent. The amorphous U-Fe system is one in which we can change from collinear ferromagnetism ($U_{10}Fe_{90}$) to random ferromagnetism ($U_{35}Fe_{65}$). *A priori*, it could be thought to be similar to the Y-Fe system dominated by random exchange. As we will show, the intermediate $U_{27}Fe_{73}$ seems rather to be characterized by a weak random anisotropy of the type found in the A-P model.

EXPERIMENTAL METHOD

$U_{27}Fe_{73}$ films were deposited by magnetron sputtering from U and Fe targets on rotating glass and Si substrates held at room temperature, at a rate of 2–3 Å/s. The films were 2000 Å thick and overcoated by 400 Å of SiO_2 to prevent oxidation. The pressure in the sputtering chamber before backfilling with Ar was 10^{-8} Torr. Measurements of the paramagnetic moment were done on a 1-μm-thick film deposited on Si, using a SHE SQUID magnetometer with a

[a] Present address: INESC, R. Alves Redol No. 9-2, 1000 Lisbon, Portugal.

 0021-8979/88/083746-03$02.40 © 1988 American Institute of Physics



resolution of $2-5\times10^{-7}$ emu. Four-probe dc resistivity measurements with a resolution of 2 parts in 10^5 were made in fields up to 2 T. Sample composition was obtained by wet chemical analysis, and the amorphous character checked by x-ray diffraction.

EXPERIMENTAL RESULTS AND DISCUSSION

In Fig. 1 we show the Arrott plot obtained from magnetization measurements in the reversible regime for $T>25$ K. $M(T)$ was measured at decreasing temperatures between 37 and 27 K, under a constant magnetic field ($5<H<200$ Oe) applied in the plane of the sample. The general features of the Arrott plot are similar to those predicted by A-P[6] for a random-anisotropy ferromagnet with $D<<J$. The curvature of the isotherms changes sign between 32 and 33 K, showing that the phase transition occurs between these temperatures. Also, the isotherms do not seem to intercept the M^2 axis below T_f. In the insert, we show magnetization measurements at $H=10$ Oe for a sample cooled in a 0.5-Oe field. These results show that the ground state of this system is a spin glass[5] with T_{irr} $(H=10\text{ Oe})=20$ K.

In addition, the low-field susceptibility χ_0 was measured with the field perpendicular to the plane of the sample. At the transition, we find $\chi_0=0.66$ in units of $1/N$, where N is the demagnetizing factor ($N\simeq1$). This shows that there is no spontaneous moment, the susceptibility does not diverge, and it does not reach the demagnetizing limit. Using $\chi_0\simeq(J/D)^4$, we estimate $D/J\simeq0.06$. For H equal to the demagnetizing field H_d, we find $M_d=0.24\,M_s$, where M_s is the saturation magnetization and M_d the magnetization value for $H=H_d$. This means that this system cannot be simply described as an asperomagnet[1] for which $M_d=0.5M_s$. Note also that $M_{ii}=M_s$ for a collinear ferromagnet. A small random-exchange contribution can be responsible for the low value of M_d/M_s. From the isothermal lines, we obtain the critical exponents $\delta_1=2.95\pm0.03$, $\delta_2=5.26\pm0.01$, and $\gamma=1.41\pm0.03$. We take $T_f=32.6$ K, as obtained from a plot of χ_0^{-1} vs T. The values of δ_1 and δ_2 can be compared with the mean-field values predicted by the A-P model, respectively, 7/3 and 5. The value found for γ is close to that observed in most amorphous magnets. The paramagnetic moment was also measured and found to be $2.6\,\mu_B$ per formula unit, probably indicating that all the moment is carried by the Fe atoms. The moment increase, as compared with 2.2 μ_B for bcc Fe, can be due to polarization of conduction-band electrons. At 4.2 K and in a 4 T field, we find a moment of $0.45\,\mu_B$ per formula unit. As the average exchange interaction is positive, with a Curie–Weiss temperature of $\theta_p=32$ K, this is also an indication of noncollinear structure. The T_f value for amorphous $U_{27}Fe_{73}$ is much lower than the 160 K Curie temperature found in the crystalline Laves-phase compound UFe_2,[11] where most of the moment is also carried by the Fe atoms. The reduction in T_f may denote a decrease of the exchange constant in the amorphous alloy, probably due to RKKY interactions between the Fe atoms.

In Fig. 2 we show the temperature dependence of the resistivity. For $T>200$ K, we observe a linear dependence with a negative $d\rho/dT$, characteristic of phonon scattering in amorphous materials.[12,13] A progressive deviation from this linear regime occurs below 200 K and the resistivity reaches a minimum at 31 K, just below the ordering temperature. For $T<T_f$, the resistivity increases sharply, as is the case in various amorphous ferromagnets or random ferromagnets. Using Matthiessen's rule, we write $\rho=\rho_0+\rho_{ph}+\rho_m$ where ρ_0 is the temperature-independent residual resistivity, ρ_{ph} the phonon resistivity usually linear in T for amorphous materials and ρ_m the magnetic resistivity. To seperate the magnetic-scattering contributution to the resistivity we show in the insert the resistivity of a nonmagnetic analog of nominal composition $U_{30}Ni_{70}$. The region of constant negative $d\rho/dT$ extends down to 50 K. Comparing the curves, we can say that magnetic-scattering processes are responsible for the deviations from the linear regime observed in $U_{27}Fe_{73}$ below 200 K. The magnetic resistivity involves both elastic

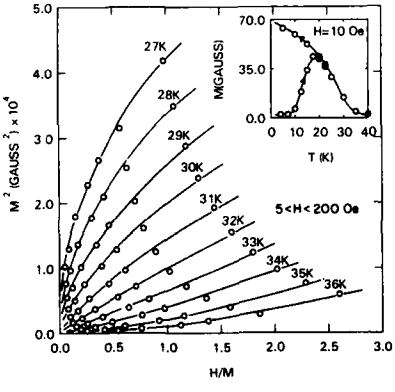


FIG. 1. Arrott plot and spin-glass regime in $U_{27}Fe_{73}$.

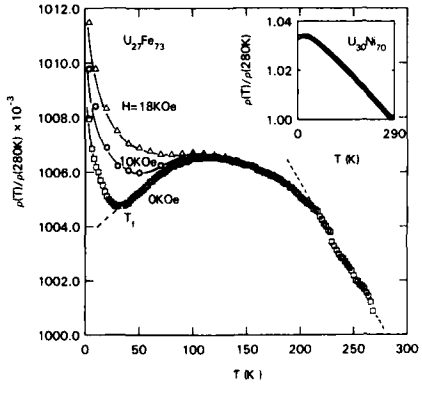


FIG. 2. Resistivity vs temperature for various magnetic fields. The insert shows the behavior of a nonmagnetic U-Ni film.

spin-conserving processes[14] as well as inelastic spin-flip processes.[15] The latter should give a decreasing resistivity for decreasing temperature, as spin-flip processes freeze out, either when $k_B T$ becomes comparable to DS^2 or when magnetic order sets in. A magnetic field will have a similar effect. In our case this term seems to exist down to T_f (Fig. 2), and therefore spin-flip processes are frozen by magnetic order. This suggests $DS^2 \ll k_B T$ in the temperature range studied.

Let us now discuss the origin of the minimum at T_f. The strong field dependence eliminates the possiblity of structural effects as observed in two level systems. Also, a Kondo-like anomaly is excluded because it should be associated with negative magnetoresistance. We are left with coherent exchange scattering as found in rare-earth amorphous magnets.[7,10] The minimum at T_f is then caused by the competition between elastic exchange scattering and inelastic spin-flip collisions. The behavior of the magnetic resistivity, as well as the sign of the magnetoresistance, qualitatively agree with the calculations of Borchi, Poli, and De Gennaro[9] for the magnetic resistivity of random ferromagnets. That should be compared with a calculation by Coqblin[8] where spin-flip processes were ignored. In that case, the sharp increase in resistivity below T_f is still observed, but the magnetic resistivity becomes constant above T_f, although still reflecting short-range order effects on the local moment.

In Fig. 3 we show the isotropic and anisotropic contributions to the magnetoresistance in several fields. The anisotropic part is obtained the usual way by a linear extrapolation of $\rho(H)$ to $B=0$. The observed small value is characteristic of spin-glass like materials presenting a small exchange gap. This gives rise to similar densities of state at the Fermi level for the spin-up and spin-down bands, and therefore to small anisotropic magnetoresistance.[16] The isotropic magnetoresistance, $\Delta\rho/\rho = [\rho(H) - \rho(0)]/\rho(0)$, in contrast to the anisotropic part is large. In the exchange-scattering model, it is proportional to the two-spin correlation function, and $\Delta\rho/\rho \propto \langle \mathbf{S}_i \cdot \mathbf{S}_j \rangle = \mu_1^2 S^2$, where μ_1 is a parameter describing local magnetic order.[7] The field dependence of the magnetoresistance is shown in the insert. Above T_f, we observe that $\Delta\rho/\rho \propto H^2$, as expected because $\mu_1 \propto H/(T-\theta_p)$. For $T < T_f$, the magnetoresistance is linear in field, indicating that $\langle \mathbf{S}_i \cdot \mathbf{S}_j \rangle = \mu_1^2 S^2 \propto H$ and $\mu_1 \propto H^{1/2}$. The fact that $\Delta\rho/\rho$ is strongly field dependent below T_f indicates that $\mu_1 < 1$, and also that a small Imry and Ma domain size is exists.[17] If $J \gg D$, large domains are expected with size proportional to $(J/D)^2$, leading to $\mu_1 = 1$ and therefore to very weak or null magnetoresistance. Our results indicate an intermediate situation between $J \gg D$ and $J = D$. Note that, in low fields, the magnetoresistance levels off at T_f, reflecting the freezing of spin correlations below this temperature. At high fields, spin realignment takes place inside the small domains, giving rise to an increase of μ_1 and of the magnetoresistance. This behavior is different from that observed in most random ferromagnets, where a peak is observed in the magnetoresistance at T_f. We can obtain this regime by increasing the amount of Fe, therefore increasing the exchange and reducing the degree of randomness. The positive magnetoresistance found above T_f means that the positive contribution coming from the exchange-scattering term and induced short-range order dominates over the negative contribution coming from suppression of spin-flip processes.

In conclusion, the magnetic and transport properties of $U_{27}Fe_{73}$ films suggest that we have a random-anisotropy ferromagnet rather than a random-exchange system. The isotropic magnetoresistance, however, does not show the characteristic peak at T_f as usually found or predicted for random ferromagnets. This probably indicates that mean-field theories, not taking into account the existence of Imry and Ma domains, cannot properly account for the transport properties in the magnetically ordered region. A more complete account of the research, involving a whole series of compositions, is now being prepared.

We acknowledge discussions with E. Pytte concerning the behavior of random systems.

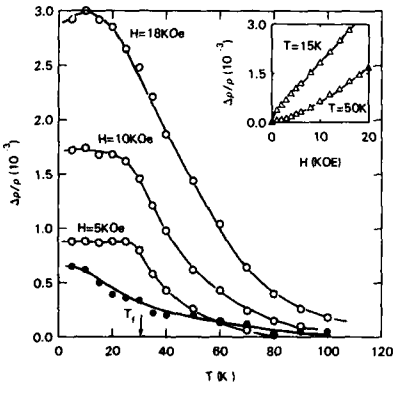


FIG. 3. Isotropic part (open circles) and anisotropic part (solid circles) of the magnetoresistance. The insert shows the field dependence of the isotropic part above and below T_f.

[1] J. M. D. Coey, J. Appl. Phys. **49**, 1646 (1978).
[2] R. Harris, M. Plischke, and M. J. Zuckermann, Phys. Rev. Lett. **31**, 160 (1972).
[3] S. von Molnar, T. R. McGuire, R. J. Gambino, and B. Barbara, J. Appl. Phys. **53**, 7666 (1982).
[4] B. Dieny and B. Barbara, J. Phys. (Paris) **46**, 293 (1985).
[5] A. Aharony and E. Pytte, Phys. Rev. B **27**, 5872 (1983).
[6] A. Aharony and E. Pytte, Phys. Rev. Lett. **45**, 1583 (1980).
[7] R. Asomoza, I. A. Campell, A. Fert, A. Lienard, and J. P. Rebouillat, J. Phys. F **9**, 349 (1979).
[8] A. K. Bhattacharjee and B. Coqblin, J. Phys. F **8** L 221 (1978).
[9] G. Borchi, M. Poli, and S. De Gennaro, J. Magn. Magn. Mater. **27**, 127 (1982).
[10] A. Fert and R. Asomoza, J. Appl. Phys. **50**, 1886 (1979).
[11] A. T. Aldred, J. Magn. Magn. Mater. **10**, 42 (1979).
[12] S. R. Nagel, Phys. Rev. B **16**, 1694 (1977).
[13] C. C. Tsuei, Phys. Rev. Lett. **57**, 1943 (1986).
[14] P. G. de Gennes and J. Friedel, J. Phys. Chem. Solids **4**, 71 (1958).
[15] T. van Peski-Tinbergen and A. J. Dekker, Physica **29**, 917 (1963).
[16] P. P. Freitas and L. Berger, J. Magn. Magn. Mater. **54–57**, 1515 (1986).
[17] Y. Imry and S. Ma, Phys. Rev. Lett. **35**, 1399 (1975).

Low-temperature spin waves in amorphous $Fe_{90-x}Ni_xZr_{10}$

J. A. Fernandez-Baca
Solid State Division, Oak Ridge National Laboratory, Oak Ridge, Tennessee 37831 and Center of Materials Science, National Bureau of Standards, Gaithersburg, Maryland 20899

J. W. Lynn
Department of Physics, University of Maryland, College Park, Maryland 20742 and Center of Materials Science, National Bureau of Standards, Gaithersburg, Maryland 20899

J. J. Rhyne
Center of Materials Science, National Bureau of Standards, Gaithersburg, Maryland 20899

G. E. Fish
Allied Signal, Inc., Morristown, New Jersey 07960

Inelastic neutron scattering measurements have been performed on rapid-quenched ribbons of $Fe_{90-x}Ni_xZr_{10}$ ($x = 1,5,10$) to measure the small wave-vector spin-wave spectrum. At all three concentrations a quadratic dispersion relation typical of an isotropic ferromagnet is observed, but with anomalous properties at low temperatures. For $x = 5$ and 10 the excitations are found to broaden considerably for temperatures $\lesssim 0.3\ T_c$. For $x = 1$ the spin waves not only broaden for $T \lesssim 0.5 T_c$, but the spin-wave energies decrease monotonically with decreasing temperature while a resolution-limited quasielastic component of the scattering develops. These results are consistent with a picture of competing ferromagnetic and antiferromagnetic interactions, with reentrant spin-glass behavior evident if the frustration is sufficiently strong.

The unusual compositional dependence of the magnetic properties of the amorphous Invar $Fe_{90-x}Ni_xZr_{10}$ system is of considerable interest. Bulk magnetization and susceptibility measurements show a paramagnetic to "ferromagnetic" transition at a temperature T_c that *decreases* with decreasing Ni content.[1] Furthermore, small-angle neutron scattering measurements have shown[2] that in the iron-rich limit the spin fluctuations are correlated over relatively short ranges of about 100 Å, but static domains also exist which are approximately five times larger. These results indicate that the phase below T_c is not a true ferromagnetic state. The appearance of an irreversible susceptibility below $T_F \simeq 80$ K has been interpreted as a transition to a spin-glass-like phase[1] and the low-temperature magnetization fails to saturate in fields as large as 19 T.[3] These observations have suggested the description of amorphous $Fe_{90}Zr_{10}$ as a "wandering axis ferromagnet" with a low-temperature asperomagnetic phase.[3] This unusual magnetic ordering would be a consequence of strong competition between ferromagnetic and antiferromagnetic exchange interactions originating from a distribution of Fe-Fe nearest-neighbor distances.[1-3]

The partial substitution of Fe by Ni modifies this distribution, which can result in drastic changes of the magnetic properties, and favors long-range ferromagnetic order. To obtain a better understanding of how this transition to conventional ferromagnetism occurs we have undertaken a program to study the spin dynamics of $Fe_{90-x}Ni_xZr_{10}$ for various Ni concentrations x. For $x = 5$, 10, 20, we have reported[4] the existence of well-defined spin waves with a quadratic dispersion relation of the form

$$E_q = D(T)q^2 + \Delta. \tag{1}$$

In this equation D is the spin-wave stiffness parameter and Δ is a small effective gap in the spectrum originating from dipolar interactions. The stiffness parameter D renormalizes with temperature as

$$D(T) = D(0)[1 - A(T/T_c)^{5/2}], \tag{2}$$

as predicted by the magnon-magnon interaction theory of a Heisenberg ferromagnet. The value $D(0)$ increases with increasing Ni content x. In addition, $D(0)$ is consistently higher than the value estimated from bulk magnetization measurements, as found in other Invar alloys. The temperature dependence of the spin-wave intrinsic linewidths was found to be in disagreement with the T^2 form predicted from the two-magnon interaction theory.[5] Instead the linewidths were found to be independent of T in the range $0.55 \lesssim T/T_c \lesssim 0.90$, indicating that there are relevant spin-wave broadening mechanisms other than two-magnon interactions.

In this paper we report new results obtained at lower temperatures for $x = 5$, 10, as well as results for a new sample with $x = 1$.

RESULTS AND DISCUSSION

The samples used in our experiments were amorphous ribbons of $Fe_{90-x}Ni_xZr_{10}$ ($x = 1$, 5, 10) prepared by the flow casting technique in vacuum. The ribbons, approximately 25 μm thick and 0.5 cm wide, were loosely wound between two aluminum posts to produce flat platelike samples. The samples were then placed in a Displex closed-cycle refrigerator. The neutron scattering experiments were performed on the BT-4 triple axis spectrometer at the National Bureau of Standards Reactor, with pyrolytic graphite (PG 002) crystals used as monochromator and analyzer. The neutron incident energy was fixed at 3.7, 4.9, or 13.5 meV for $x = 1$, 5, and 10, respectively. In order to suppress higher-order wavelength contaminations a filter (cooled beryllium for $E_i = 3.7$ and 4.9 meV, and PG for $E_i = 13.5$ meV) was

 0021-8979/88/083749-03$02.40 © 1988 American Institute of Physics

placed in the incident beam. Suitable Söller slit horizontal collimators were chosen to produce energy resolutions ΔE (FWHM) of 0.065 meV ($E_i = 3.7$ meV), 0.089 meV ($E_i = 4.9$ meV), or 0.40 meV ($E_i = 13.5$ meV).

In analyzing the spin-wave data, excitation energies and linewidth information were obtained by least-squares fitting the inelastic scattering spectra to a parametrized theoretical cross section convoluted with the instrumental resolution function. Two forms of the spectral weight function were used in this analysis: Double-lorentzian and damped harmonic oscillator. Both forms of the spectral weight function yielded qualitatively similar results and in this paper we make reference only to the results corresponding to the double lorentzian-type cross section.

(a) $Fe_{89}Ni_1Zr_{10}$ ($T_c = 248$ K)

Constant-q scans for wave vectors 0.04 Å$^{-1} \leq q \leq 0.10$ Å^{-1} at temperatures 0.04 $T_c < T \leq 0.91$ T_c were taken for $Fe_{89}Ni_1Zr_{10}$. Figure 1 shows the constant-q spectra obtained for $q = 0.08$ Å^{-1} at $T = 10, 30, 50, 75$, and 125 K. The peaks for energy gain ($E < 0$) and energy loss ($E > 0$) correspond to annihilation and creation of spin-wave excitations, and the (resolution-limited) peak at $E = 0$ corresponds to elastic and quasielastic scattering from the sample and environment. Due to resolution effects and the fact that our measurements were performed with fixed incident energy, the peaks on the energy-gain side of the spectra appear larger than the peaks on the energy-loss side. The solid lines shown in the figure are the result of the least-squares fits.

In the analysis of the inelastic scattering data for this concentration, we have identified three different temperature regions, corresponding to $T = 125$–225 K ($0.5T_c$–$0.91T_c$), 50–125 K ($0.2T_c$–$0.5T_c$), and 10–50 K ($0.04T_c$–$0.2T_c$). In the $T = 125$–225 K region, well-defined excitations that are consistent with the dispersion relation of Eq. (1) are observed. In addition, the temperature dependence of the stiffness parameter D is consistent with Eq. (2), with $D(0) = (24.57 \pm 0.72)$ meV Å^2. However, in this region the spin-wave intrinsic linewidths appear to be temperature independent.

In the $T = 50$–125 K region well-defined excitations which are consistent with Eq. (1) are also observed. However, the stiffness parameter D decreases with decreasing temperature with a concomitant increase in the damping of the excitations, while the intensity of the resolution-limited peak at $E = 0$ increases considerably. This increase of the quasielastic scattering intensity is associated with the development of a spin-glass-order parameter.[6] Hence we find in this region a coexistence of spin-wave excitations and spin freezing phenomena, similar to that found in other "reentrant spin-glass" systems.[7]

Below $T = 50$ K no well-defined excitations can be identified. In this region the inelastic scattering spectra can be well described either by overdamped spin waves with energies that continue to decrease with the decreasing temperature and collapse at $T = 10$ K, or by a spin diffusion cross section with no propagating features. In both cases the inelastic scattering coexists with the intense resolution-limited peak at $E = 0$, which continues to increase with the decreasing temperature.

(b) $Fe_{85}Ni_5Zr_{10}$ ($T_c = 306$ K)

Constant-q scans for wave vectors 0.04 Å$^{-1} \leq q \leq 0.10$ Å^{-1} in the temperature range $0.07\ T_c < T \leq 0.33 T_c$ were taken for this sample. Figure 2 shows the spectra obtained at $q = 0.08$ Å^{-1} for $T = 20, 40, 60, 100$ K. At all temperatures under study well-defined spin waves were identified that are consistent with Eq. (1). Unlike the case for $x = 1$ no indication of softening of the spin-wave modes at low temperatures

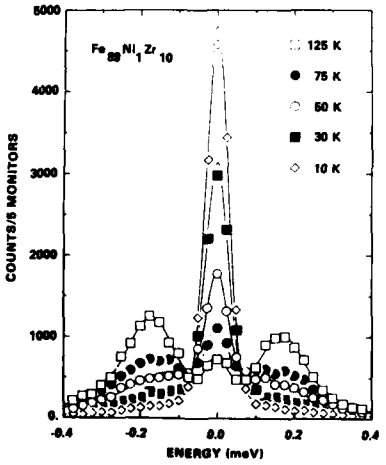


FIG. 1. Constant-q scans at $q = 0.08$ Å^{-1} for several temperatures for amorphous $Fe_{89}Ni_1Zr_{10}$. The intensities have been normalized to 5 monitor counts ($\approx$5 min). The solid lines are the result of the least-squares fit to a double lorentzian-type cross section convoluted with the instrumental resolution, as explained in the text.

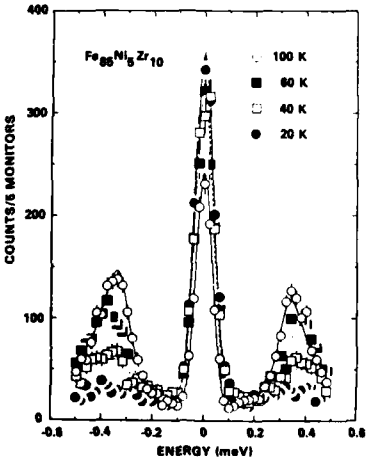


FIG. 2. Constant-q scans at $q = 0.08$ Å^{-1} for amorphous $Fe_{85}Ni_5Zr_{10}$. The solid lines are from the fits.

was observed, and the temperature dependence of the stiffness parameter D was consistent with Eq. (2) with $D(0) = (46.90 \pm 0.72)$ meV Å^2. In addition, the resolution-limited peak at $E = 0$ showed no significant temperature dependence, unlike the findings for $x = 1$. The lower-temperature excitations, however, are considerably broadened and this broadening is strongly q dependent. This low-temperature broadening causes the apparent increase of the elastic peak intensity with decreasing temperature evident in Fig. 2.

(c) $Fe_{80}Ni_{10}Zr_{10}$ ($T_c = 359$ K)

Constant-q scans for wave vectors 0.06 Å$^{-1} \leqslant q \leqslant 0.09$ Å^{-1} and temperatures $0.06T_c < T < 0.28T_c$ were taken for this sample. At the lowest temperature studied ($T = 20$ K) no excitations could be identified due to the coarse resolution of these measurements ($\Delta E = 0.40$ meV) and the small thermal population factor in the spin-wave cross section. For all the other temperatures the results are qualitatively similar to those for the $x = 5$ sample. Above 40 K well-defined spin waves were identified, with no indication of softening at low temperatures. The spin-wave stiffness parameter D renormalized with temperature according to Eq. (2), with $D(0) = (74.2 \pm 1.3)$ meV Å^2. No indications of a low-temperature elastic (or resolution-limited quasielastic) component of the magnetic scattering were found, but the spin-wave excitations broadened considerably at lower temperatures.

In order to illustrate the enhancement of ferromagnetic ordering by the partial substitution of Fe by Ni in $Fe_{90-x}Ni_xZr_{10}$, we have plotted in Fig. 3 the ratio D/kT_c vs T/T_c for $x = 1, 5, 10, 20$. The higher-temperature values of D/kT_c for $x = 5, 10, 20$ have been taken from our previous measurements. The solid lines are the result of least-squares fits to the two-magnon interaction form of renormalization of the stiffness parameter [Eq. (2)]. The ratio D/kT_c is directly related to the mean-square range of the exchange interaction, and clearly decreases with decreasing x. The substitution of Fe by Ni increases the average Fe-Fe distance and thereby decreases the competition between ferromagnetic and antiferromagnetic interactions. A similar enhancement of ferromagnetism has also been obtained by partial substitution of Fe by Co and by hydrogenation.[1,3]

The onset of the low-temperature softening of the spin-wave energies for $x = 1$ occurs at a temperature ($T \approx 125$ K) considerably higher than the reported temperature where $Fe_{90}Zr_{10}$ (no Ni) enters a asperomagnetic phase ($T_F \approx 40$ K).[3] The lack of low-temperature spin-wave softening for $x = 5$ and 10 would indicate that, at these Ni concentrations, the short-range asperomagnetic phase is gradually replaced by a more aligned structure. The low-temperature broadening of the spin waves at these concentrations, however, would indicate that there remains some noncollinearity of the spins in the ground state. The origin of this broadening might be the superimposition of spin waves and a diffusive component, such as the elementary excitations of the noncollinear configuration of spins suggested by Continentino and Rivier.[8] These additional modes would cause an additional $T^{3/2}$ decrease of the magnetization and would explain the discrepancy between the stiffness parameter $D(0)$ obtained from neutron scattering and magnetization measurements.

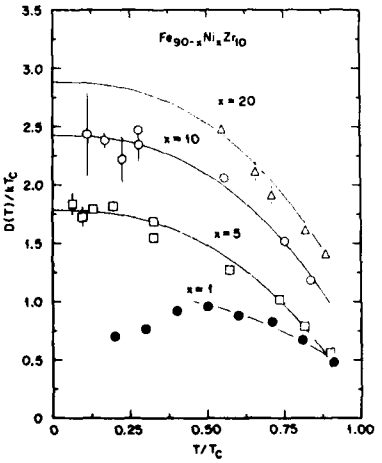


FIG. 3. Plot of D/kT_c vs T/T_c for $Fe_{90-x}Ni_xZr_{10}$ for $x = 1, 5, 10, 20$. The decrease of D/kT_c with decreasing Ni content is indicative of strong competition between ferromagnetic and antiferromagnetic interactions.

ACKNOWLEDGMENTS

The work at ORNL was supported by the U. S. Department of Energy under contract No. DE-AC05-840R21400 with Martin Marietta Energy Systems, Inc. The work at the University of Maryland was supported by the National Science Foundation, grant No. DMR 86-20269.

[1] K. Shirakawa, S. Ohnuma, M. Nose, and T. Masumoto, IEEE Trans. Magn. MAG-16, 910 (1980); *ibid.* 1129 (1980).

[2] J. J. Rhyne, R. W. Erwin, J. A. Fernandez-Baca, and G. E. Fish (these proceedings).

[3] D. H. Ryan, J. M. D. Coey, E. Batalla, Z. Altounian, and J. O. Strom-Olsen, Phys. Rev. B 35, 8630 (1987), and references therein.

[4] J. A. Fernandez-Baca, J. W. Lynn, J. J. Rhyne, and G. E. Fish, J. Appl. Phys. 61, 3406 (1987); J. A. Fernandez-Baca, J. J. Rhyne, and G. E. Fish, J. Magn. Magn. Mater. 54-57, 289 (1986).

[5] A. B. Harris, Phys. Rev. 175, 674 (1968); 184, 606 (1969).

[6] J. W. Lynn, R. W Erwin, H. S. Chen, and J. J. Rhyne, Solid State Commun. 46, 317 (1983).

[7] For a review see J. W. Lynn and J. J. Rhyne, in *Spin Waves and Magnetic Excitations*, edited by A. S. Borovik-Romanov and S. K. Sinha (North-Holland, Amsterdam, 1988), Part II, Chap. 4; S. M. Shapiro, *ibid.*, Part II, Chap. 5.

[8] M. A. Continentino and N. Rivier, J. Phys. F 9, L145 (1979); J. Magn. Magn. Mater. 15-18, 1419 (1980).

Small-angle neutron scattering from amorphous $ErFe_2$ and $HoFe_2$ alloys

M. L. Spano
Naval Surface Weapons Center, Silver Spring, Maryland 20903 and National Bureau of Standards, Gaithersburg, Maryland 20899

J. J. Rhyne
National Bureau of Standards, Gaithersburg, Maryland 20899

Small-angle neutron scattering measurements (SANS) have been made an amorphous $ErFe_2$ and $HoFe_2$ alloys as a function of temperature. These alloys show strong "subcritical" scattering as the temperature is lowered below their SANS-determined transition temperatures (T_f's) of 105 K ($\pm$ 1 K) and 185 K ($\pm$ 5 K), respectively. The SANS line shapes are Lorentzian above T_f, but become increasingly non-Lorentzian below T_f and are consistent with a Lorentzian plus Lorentzian-squared cross section which is appropriate for these random anisotropy systems. The correlation lengths for $ErFe_2$ and $HoFe_2$ at low T are in the range of 60–70 Å. Near T_f $ErFe_2$ shows a sharp peak, while for $HoFe_2$ ξ is resolution limited over a range of 25 K below T_f.

I. INTRODUCTION

The effects of the interplay of random anisotropy and random exchange fields have been well documented in the Tb_xFe_{1-x} system of amorphous alloys,[1-4] where the relative proportions of the terbium and the iron have been varied from 2% Tb to 75% Tb. In this collateral study we are examining the effect of varying the type of rare-earth material while keeping the rare earth to iron ratio constant. It is expected that, by keeping the amount of iron constant, we will be able to separate out the effect of the random anisotropy in these materials. Previous *neutron* scattering work on the RFe_2 alloys has been carried out on $NdFe_2$ (Ref. 5) as well as $TbFe_2$.[1] The present paper presents results on the two alloys $HoFe_2$ and $ErFe_2$.

The large values of magnetic anisotropy characteristic of rare-earth atoms, coupled with the amorphous structure, have a very strong effect on the magnetism. Specifically, Aharony and Pytte[6] show that in three dimensions ferromagnetic ordering of the spins in a system with random anisotropy fields cannot occur at any temperature. Further, they predict that the magnetic correlation length ξ will be proportional to $(I/D)^2$, where I is the average value of the random exchange and D is the leading term in the expression for the random anisotropy. Therefore, a true second-order phase transition is possible only in the limit of vanishingly small anisotropies, which can be approximated by Gd-based alloys. Although bulk magnetization measurements may give the appearance of ferromagnetic behavior in these alloys, this is generally due to either the use of finite magnetic fields in these measurements or the fact that ξ, while not divergent, may still become quite large.

II. SANS RESULTS

Small-angle neutron scattering (SANS) measurements are presented from the area-detector SANS instrument at the NBS reactor. Since these materials are structurally amorphous, coherent phenomena may only be studied in the small scattering angle regime. Neutron wavelengths of 5.5 Å ($HoFe_2$) and 6.0 Å ($ErFe_2$) were used, giving a minimum usable wave-vector transfer of about $q = 0.017$ Å^{-1}.

Above the transition temperature T_c for a conventional ferromagnet, the neutron scattering cross section (in the static approximation) is a Lorentzian:

$$I(q) = A/(q^2 + \kappa^2), \tag{1}$$

where $\kappa = \xi^{-1}$ is the inverse spin correlation length. Approaching T_c from above one normally expects that κ will tend to zero. Below T_c, κ should consist of a transverse part κ_t and a longitudinal part κ_l. κ_l becomes large and the longitudinal term contributes very little to the observed scattering. On the other hand, κ_t is zero and leads to spin-wave scattering with a q^{-2} dependence and an amplitude which decreases with decreasing T.

Aharony and Pytte[6] have shown that the scattering cross section appropriate for a random anisotropy system has the form

$$I(q) = \frac{A}{q^2 + \kappa^2} + \frac{B}{(q^2 + \kappa^2)^2}. \tag{2}$$

Here κ is again the inverse correlation length and is the same for both the conventional Lorentzian term and for the Lorentzian-squared term. As will be seen in the following sections, Eq. (1) is not a good description for these alloys below the transition temperature, whereas Eq. (2) provides an adequate fit of the data and yields finite low T values of κ. This, along with previous results, indicates that the amorphous RFe_2 alloys are not "normal" ferromagnets, but are more properly thought of as "correlated" spin glasses[7] for $T < T_f$.

A. $ErFe_2$

In Fig. 1 we plot the inverse intensity $I(q)$ as a function of q^2 for several T's both above and below the transition temperature for $ErFe_2$. Note that the lower-temperature curves are not straight lines, as expected from Eq. (1), but are consistent with the cross section of Eq. (2) shown by the solid lines in the figure. From these fits we have derived the coefficients A, B and $\kappa(=\xi^{-1})$. Figure 2 displays ξ as a

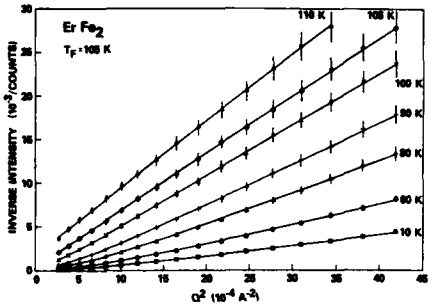


FIG. 1. Inverse intensity vs q^2 at several temperatures for $ErFe_2$. Note that the transition temperature $T_f = 105$ K. The solid lines are fits of the data to Eq. (2).

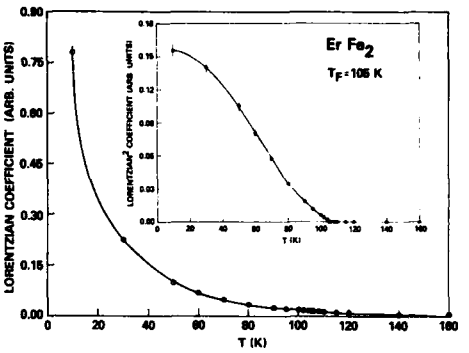


FIG. 3. Lorentzian and Lorentzian-squared (inset) coefficients as a function of temperature for $ErFe_2$. Both quantities are presented in relative units.

function of T for $ErFe_2$. As T is lowered the correlation length rises to a sharp feature ($\xi = 145$ Å) at $T_f = 105$ K (± 1 K) and then decreases to a plateau of about 70 Å at low T. This value of T_f is in agreement with the magnetization determined value of 105 K.[8] The sharp peak at T_f suggests that long range correlations appear and are quenched at lower T by the random anisotropy.

Figure 3 shows the Lorentzian and Lorentzian-squared coefficients plotted versus T. The Lorentzian coefficient behaves in an unconventional manner and increases slowly as T is lowered through T_f. As $T \to 0$ it begins to rise more sharply. The Lorentzian-squared coefficient increases sharply as T falls below T_f and begins to level off at lower T. This coefficient divided by κ is proportional to the square of an order parameter.

B. $HoFe_2$

The SANS data for $HoFe_2$ are qualitatively similar to those of $ErFe_2$ and have been fit to Eq. (2). The correlation length ξ increases as T is lowered toward $T_f = 185$ K (± 5 K). However, ξ becomes extremely large at T_f, exceeding the resolution of the experiment ($\sim$350–400 Å). It remains at this "experimental infinity" until about 160 K, where it has a value of 330 Å. Finally it decreases to a value of 75 Å at the lowest T measured. Because of this divergence it is more instructive to plot the inverse correlation length κ, as is shown in Fig. 4. Again we find that the SANS value for T_f is in agreement with the value of 195 K as found from the magnetization data.[8]

III. COMPARISON WITH OTHER RFe_2 ALLOYS

There are many features of the magnetic scattering which are common to all the RFe_2 alloys studied, in particular the transition from the Lorentzian to the Lorentzian plus Lorentzian-squared cross section below T_f and the finite low T values of ξ. For $TbFe_2$ (Ref. 1) the correlation length rose to a cusp of 130 Å at T_f and upon further cooling decreased to about 55 Å at low T. Later studies of the Tb_xFe_{1-x} system[2–4] discovered that, while the behavior of ξ near the critical region was strongly dependent upon the amount of rare earth present, the correlation length always decreased to a plateau at lower T. In all four of the Tb alloys studied to date the value of ξ at low T is essentially the same: $55 + 5$ Å.[4]

In $NdFe_2$ (Ref. 5) the correlation length rises to a broad maximum as T is lowered toward T_f. The height of this maximum is 170 Å. As in the other three samples ξ decreases to a plateau at lower T (here about 80 Å).

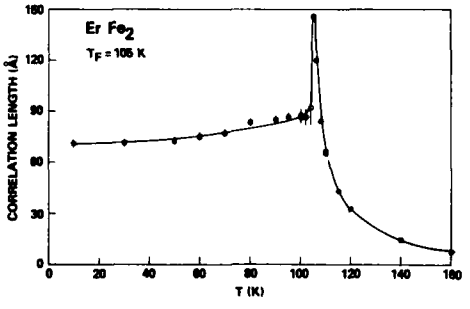


FIG. 2. Correlation length vs temperature for $ErFe_2$. Note the sharp feature near T_f.

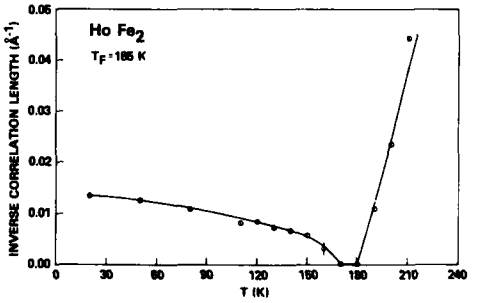


FIG. 4. Inverse correlation length vs temperature for amorphous $HoFe_2$.

TABLE I. Transition temperatures and values of the low-temperature correlation length for several different RFe_2 alloys. The T_f's for the magnetization data were taken from Ref. 10.

Rare earth	T_f^{neut} (K)	T_f^{mag} (K)	ξ_p (Å)
Tb	393	383	55
Nd	330	360	80
Ho	185	195	75
Er	105	105	70
Tm	···	<50	20

SANS measurements have also been made on $TmFe_2$.[9] As in the other alloys Eq. (2) was required to fit the data at low T. The low T value of ξ is about 20 Å.

There are several features that are common to all of the systems studied so far. All (except $TmFe_2$ which has not been measured near T_f) exhibit maxima in $\xi(T)$ near the transition temperature. At the lowest temperatures the value of ξ levels off to a "plateau" which we denote as ξ_p. The magnitude of ξ_p seems to be somewhat dependent on the rare earth species present and to be independent of the rare earth–iron ratio. These values, along with the values for T_f, are tabulated in Table I.

ACKNOWLEDGMENTS

The work at NSWC was supported by the Office of Naval Research and the NAVSWC Independent Research Fund.

[1] J. J. Rhyne, Physica **130B**, 253 (1985).
[2] M. L. Spano and J. J. Rhyne, J. Appl. Phys. **57**, 3303 (1985).
[3] M. L. Spano and J. J. Rhyne, J. Magn. Magn. Mater. **54–57**, 300 (1986).
[4] M. L. Spano and J. J. Rhyne, J. Appl. Phys. **61**, 4100 (1987).
[5] M. L. Spano, H. A. Alperin, J. J. Rhyne, S. J. Pickart, S. Hasanain, and D. Andrauskas, J. Appl. Phys. **57**, 3432 (1985).
[6] A. Aharony and E. Pytte, Phys. Rev. B **27**, 5872 (1983).
[7] E. M. Chudnovsky, W. M. Saslow, and R. A. Serota, Phys. Rev. B **33**, 251 (1986).
[8] J. J. Rhyne, AIP Conf. Proc. **29**, 182 (1976).
[9] M. L. Spano and J. J. Rhyne (unpublished).
[10] J. J. Rhyne, *Handbook on the Physics and Chemistry of Rare Earths*, edited by K. A. Gschneidner and L. Eyring (North-Holland, Amsterdam, 1979), Vol. 2, p. 282.

Evidence for a spin-glass behavior in the diluted antiferromagnet $Fe_xZn_{1-x}F_2$

F. C. Montenegro,[a] S. M. Rezende, and M. D. Coutinho-Filho
Universidade Federal de Pernambuco, Departamento de Física, 50.000 Recife, PE, Brazil

We report dc susceptibility (χ) measurements in the diluted antiferromagnet $Fe_xZn_{1-x}F_2$ with concentrations $x = 0.10$, 0.25, 0.31, and 0.46. The field and temperature dependencies of χ in the $x = 0.10$ and 0.25 samples reveal that a spin-glass (SG) phase appears at low temperatures. For $x = 0.31$, which is slightly above the percolation limit ($x_p = 0.24$), the SG phase is also present at low temperatures, but there is a clear indication of long-range antiferromagnetic (AF) ordering at intermediate temperatures. Finally, in the sample with $x = 0.46$, AF ordering with random-field effects determines the characteristic behavior. These studies will help in the understanding of the crossover from random field to SG behavior in dilute antiferromagnets.

The random-field problem[1,2] continues to attract a great deal of attention both theoretically and experimentally. Very recently, de Almeida and Bruinsma[3] showed that a diluted Ising antiferromagnet (AF) with large dimensionality in a field can be mapped on an AF with gaussian randomness, and that a true glassy phase can occupy a substantial part of the (H,T) phase diagram, particularly for large effective random fields. In this paper we report investigations of this effect in the virtually unexplored high dilution region of the randomly diluted, highly anisotropic, rutile compound $Fe_xZn_{1-x}F_2$. At intermediate concentrations ($x > 0.4$), under an external field, this system has been recognized as an ideal experimental realization of a $d = 3$ random-field Ising model (RFIM) system.[4]

We have performed dc susceptibility (χ) measurements in samples with concentrations $x = 0.10$, 0.25, 0.31, and 0.46. The experiments were carried out with a vibrating sample magnetometer in magnetic fields in the range $0 < H < 65$ kOe. The temperature was measured with a carbon glass thermometer and controlled to within 1 mK in the range $4.2 < T < 60$ K.

The field and temperature dependencies of χ in the $x = 0.10$ and 0.25 samples reveal that a spin-glass (SG) phase appears below the de Almeida–Thouless[5] (AT) transition lines in the (H,T) phase diagram. This is characterized by nonexponential relaxation times, remanence, strong history dependence, and critical behavior of the nonlinear susceptibility. For $x = 0.31$, which is slightly above the percolation limit ($x_p = 0.24$), the SG phase is also present at low temperatures, but there is a clear indication of long-range AF ordering at intermediate temperatures. Finally, in the sample with $x = 0.46$, AF long-range order with random-field effects determines the characteristic behavior.

The temperature dependence of the susceptibility, $\chi = M/H$, of the $x = 0.25$ sample, after zero-field-cooling (ZFC) and field-cooling (FC) procedures, for H parallel to the easy axis, is shown in Fig. 1 for various applied magnetic fields. The "FC-ZFC" irreversibilities are clearly evidenced at low temperatures, notably for low applied fields, as usual in spin glasses. The susceptibility data were taken in successive temperature steps after the sample had been ZFC for the lowest temperature in the range of measurement and the field increased to the indicated value. The susceptibility measured on heating shows a cusp, which rounds as H increases, but is time dependent and irreversible below an irreversibility temperature $T_i(H)$. In contrast to the RFIM behavior,[6] the data obtained on cooling (FC) are reversible and do not show noticeable time dependence. The departure of the ZFC and FC curves defines the onset of the irreversibility line $T_i(H)$. A log-log plot of T_i shows that this line can be fitted by $t(H) = -AH^{2/\phi}$, where $t = [T_i(H) - T_i(0)]/T_i(0)$ is the reduced temperature and ϕ is a crossover exponent. The measurements yield $T_i(0) = 11.2 \pm 0.2$ K and $\phi = 3.4 \pm 0.2$. This value of ϕ is similar to that obtained in other spin glass systems[7] and it is also compatible with the $H^{2/3}$ dependence of the AT mean-field

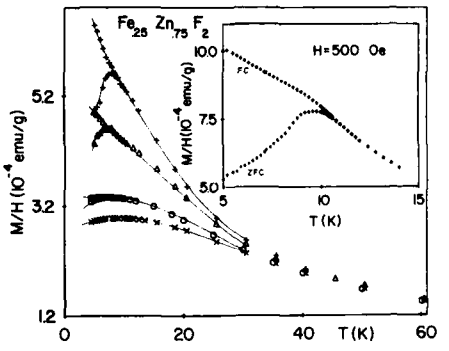


FIG. 1. Temperature dependence of the dc susceptibility M/H for zero-field-cooled (χ_{ZFC}) and field-cooled (χ_{FC}) $Fe_{0.25}Zn_{0.75}F_2$ with applied magnetic field $H = 10$ kOe(+); $H = 20$ kOe(Δ); $H = 40$ kOe(O); $H = 60$ kOe(×). Inset shows χ_{ZFC} and χ_{FC} for H = 500 Oe. The solid lines are guides to the eye.

[a] On leave from Departamento de Física, Universidade Federal da Paraíba, 58.100 Campina Grande, PB, Brazil.

 0021-8979/88/083755-03$02.40 © 1988 American Institute of Physics

(MF) instability line for a short-range Ising spin-glass model.[5]

A salient feature of the curves in Fig. 1 is the fact that $T_i(H)$ is slightly larger than the temperature of the maximum of the ZFC susceptibility (χ_{ZFC}) (see inset). The coincidence of these two temperatures has indeed been found both in metallic[8] and insulating[9] spin glasses, but there are systems in which this does not occur.[7] Also, evidence was produced that remanence exists above the spin-glass freezing temperature T_f,[10] but it was suggested[11] that this is a result of inhomogeneities and should not occur with proper annealing of the sample. This fact reflects also in the temperature dependence of the initial susceptibility $\chi_0 = (dM/dH)_{H\to 0}$. As is well known, χ_0 presents a maximum at the freezing temperature T_f, identical to that of the ac susceptibility.[12] For $Fe_{0.25}Zn_{0.75}F_2$, χ_0 indeed presents a maximum around $T_f = 10.2 \pm 0.2$ K, as shown in Fig. 2, but this temperature is different from the irreversibility temperature at $H = 0$, $T_i(0) = 11.2 \pm 0.2$ K. Figure 1 also shows a nonlinear susceptibility region, which emerges for $T \lesssim 30$ K, where the M/H curves begin to be notably field dependent. This is the region where presumably cluster formation initiates, before the SG state sets in at the AT transition line. In addition, we briefly mention studies of a scaling analysis of the critical phenomena, made for the sample with $x = 0.25$, which will be reported in detail elsewhere.[13] We used the following scaling form for the nonlinear susceptibility: $\chi_{NL} = H^{2/\delta} f_+(t/H^{2/\phi})$. Here $t = (T - T_f)/T_f$ is the reduced temperature, δ and ϕ are scaling exponents, and $f_+(x)$ is a scaling function which approaches a constant as $x \to 0$ and $x^{-\gamma}$ as $x \to \infty$ with the scaling relations $\gamma = \phi(\delta - 1)/\delta$ and $\phi = \beta\delta = \gamma + \beta$. The exponent δ was determined by the initial slope (H up to 20 kOe) of a log-log plot of the nonlinear susceptibility $\chi_{NL} = \chi_0 - M/H$ versus magnetic field at $t = 0$, where $\chi_{NL} \sim H^{2/\delta}$ (for higher fields we find deviations towards higher values of δ) whereas ϕ was obtained from the AT transition line. Scaling was tested for 20 different temperatures between T_f and $2T_f$ and H up to 20 kOe, with $\delta = 3.3 \pm 0.2$ and $\phi = 3.4 \pm 0.2$. Our data collapse on a curve giving clear indication that the system satisfies scaling in the critical region above T_f. The values of the exponents are in close agreement with those found by Bouchiat[8] in AgMn metallic spin glasses for various concentrations of Mn. This result suggests the existence of universality in the critical behavior of Ising SGs regardless of their metallic or insulating natures.

The temperature dependence of χ of the sample $Fe_{0.10}Zn_{0.90}F_2$ is presented in Fig. 3. As in the case of $x = 0.25$, SG behavior is found below an irreversibility line $T_i(H)$, where field hysteresis loops, and remanence and temporal dependence of the isothermal remanent magnetization (IRM), thermoremanent magnetization (TRM), and χ_{ZFC} are seen. We note, however, that this occurs in a temperature region lower than that for $x = 0.25$. The onset of the nonlinear susceptibility region also moved, in this case, for $T \lesssim 20$ K.

Figure 4 shows the temperature dependence of the susceptibility of $Fe_{0.31}Zn_{0.69}F_2$. In this case, the maximum in χ_{ZFC} is clearly reversible in high fields whereas in low fields the onset of irreversibility $T_i(H)$ coincides with the susceptibility peak. We believe that the temperature $T_M(H)$ of the maximum of the susceptibility (which is close enough to the maximum of $d\chi/dT$) corresponds to the P-AF transition. On the other hand, the irreversibility temperature $T_i(H)$ corresponds to the SG transition. For temperatures below $T_i(H)$, χ_{ZFC} shows temporal dependence as expected in spin glasses. The interesting feature here is the fact that χ_{FC} exhibits a dip at low fields. The increase of χ_{FC} with decreasing T, starting around $T_m(H)$, seems to indicate that long-range AF order has been suppressed in favor of the SG phase, the latter emerging from a region of coexistence in which the AF ordering predominates. We found that the field-hysteresis loops are quite narrow in the coexistence region and become wider below $T_m(H)$, where the SG phase is now well established. The coexistence of SG and AF orderings has recently been observed in $Fe_{0.55}Mg_{0.45}Cl_2$ (Ref. 14)

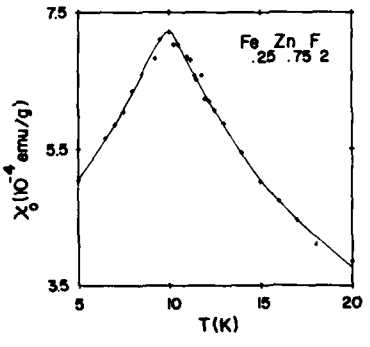


FIG. 2. Temperature dependence of initial susceptibility $\chi_0 = (dM/dH)_{H\to 0}$ of $Fe_{0.25}Zn_{0.75}F_2$ for H parallel to the easy axis.

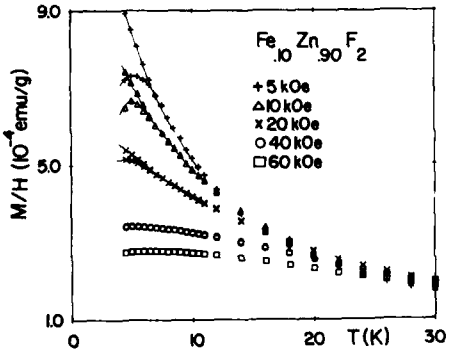


FIG. 3. ZFC and FC susceptibilities M/H vs temperature of $Fe_{0.10}Zn_{0.90}F_2$ for several applied magnetic fields.

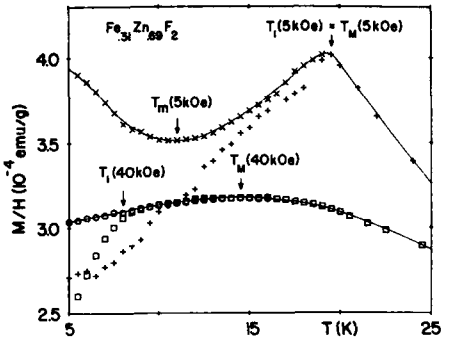


FIG.4. ZFC and FC susceptibility M/H of $Fe_{0.31}Zn_{0.69}F_2$ plotted against temperature for two values of the applied field. Full curves for the FC procedure are guides to the eye.

using specific-heat, ac-susceptibility, and neutron-scattering techniques.

The measurements presented here provide clear indication that the dilute Ising antiferromagnet $Fe_xZn_{1-x}F_2$ with low magnetic concentrations ($x<0.30$) has a spin-glass phase at low temperatures. These properties contrast with the random-field effects that this system exhibits in the presence of a uniform field at larger concentrations ($x>0.4$). The origin of the spin-glass phase in this compound probably lies in the presence of competing short-range interactions. Pure FeF_2 has the rutile crystal structure with an intersublattice AF exchange coupling ($J_2 = -3.64\,\mathrm{cm}^{-1}$) between the neighboring Fe ions at the corner and body center of the rutile unit cell. The interaction between the two neighboring ions of the same sublattice along the c axis is small and ferromagnetic ($J_1 = +0.048\,\mathrm{cm}^{-1}$), favoring a two-sublattice AF long-range order. However, the intrasublattice interaction between the neighboring ions in the a plane is antiferromagnetic[15] ($J_3 = -0.19\,\mathrm{cm}^{-1}$), so it is frustrated when the spins in the same sublattice are parallel. With dilution, the magnitude as well as the balance of these exchange forces may be altered, leading to a SG phase. Another possible mechanism is the competition between cluster interactions and the random field originating in the diluted antiferromagnet in a uniform field,[2] since evidence is given (see Fig. 4) that a true glassy phase can occupy a substancial part of the (H,T) phase diagram,[3] even for concentrations above the percolation threshold. The coexistence of AF ordering with random field and SG behavior is a new feature in this class of system and deserves further investigation.

ACKNOWLEDGMENTS

The authors acknowledge Professor M. Continentino for fruitful discussions, Professor C. Magon and Fernando Rocha for building the temperature control used in the experiments, Antonio Nascimento and Severino Ramos for technical assistance, and Professor V. Jaccarino for providing the $Fe_xZn_{1-x}F_2$ crystals. The crystals were grown at University of California at Santa Barbara (UCSB) under the National Science Foundation grant No. DMR 85-16786. The work at UFPE was supported by FINEP, CNPq, and CAPES (Brazilian Agencies).

[1] Y. Imry and S.-K. Ma, Phys. Rev. Lett. **35**, 1399 (1975).
[2] S. Fishman and A. Aharony, J. Phys. C **12**, L729 (1979).
[3] J. R. L. de Almeida and R. Bruinsma, Phys. Rev. B **35**, 7267 (1987).
[4] A. R. King and D. P. Belanger, J. Magn. Magn. Mater. **54–57**, 19 (1986); D. P. Belanger, A. R. King, and V. Jaccarino, J. Appl. Phys. **55**, 2383 (1984).
[5] J. R. L. de Almeida and D. J. Thouless, J. Phys. A **11**, 983 (1978).
[6] A. R. King, V. Jaccarino, D. P. Belanger, and S. M. Rezende, Phys. Rev. B **32**, 503 (1985).
[7] A. P. Malozemoff, S. E. Barnes, and B. Barbara, Phys. Rev. Lett. **51**, 1704 (1983).
[8] H. Bouchiat, J. Phys. (Paris) **47**, 71 (1986); N. de Courtenay, H. Bouchiat, H. Hurdequint, and A. Fert, J. Appl. Phys. **61**, 4097 (1987).
[9] N. Bontemps, J. Rajchenbach, R. V. Chamberlin, and R. Orbach, J. Magn. Magn. Mater. **54**, 1 (1986).
[10] C. N. Guy, J. Appl. Phys. **50**, 7308 (1979).
[11] R. V. Chamberlin, M. Hardiman, and R. Orbach, J. Appl. Phys. **52**, 1771 (1981).
[12] J. L. Tholence and R. Tournier, J. Phys. (Paris) Colloq. **C4**, 229 (1974).
[13] F. C. Montenegro, M. D. Coutinho-Filho, and S. M. Rezende (to be published).
[14] P. -z. Wong, S. von Molnar, T. T. M. Palstra, J. A. Mydosh, H. Yoshizawa, S. M. Shapiro, and A. Ito, Phys. Rev. Lett. **55**, 2043 (1985).
[15] M. T. Hutchings, B. D. Rainford, and H. J. Guggenheim, J. Phys. C **3**, 307 (1970).

Tricritical point in dilute Ising antiferromagnets in magnetic field

P. Azaria and H. T. Diep
Laboratoire de Magnétisme des Surfaces, Université Paris 7, 75251 Paris Cedex 05, France

Serge Galam
Département de Recherches Physiques, T22-E3, Université Pierre et Marie Curie, 75252 Paris Cedex 05, France

We show by Monte Carlo simulation that the inclusion of next-nearest-neighbor (nnn) interactions, which are always present in real systems, results in the existence of a tricritical point in the temperature-field plane. The location of this point depends on the dilution concentration p and on the nnn interaction strength. These results are discussed.

I. INTRODUCTION

Random field Ising model (RFIM) has been subject to extensive studies during the last decade. It is now known by an exact proof[1] that the lower critical dimensionality is 2. The nature of the phase transitions in three dimensions remains, however, an open question. Mean field theories[2,3] predicted that the existence of a tricritical point depends on the random field distribution, in particular, a bimodal distribution ($\pm H$) yields a tricritical point while a Gaussian one does not.[2] In contrast Monte Carlo (MC) results of RFIM with a bimodal distribution have been inconclusive: some were interpreted in support of a first-order transition at finite low temperature,[4] others favored a continuous transition.[5] It is noted that MC results of Ref. 4 have been also interpreted[6] as consistent with a second-order transition provided dynamical effects are included. Experimentally random field systems are obtained by dilution of antiferromagnets (AF) in a uniform magnetic field.[7,8] It is not known to what extent dilute AF in a field is equivalent to RFIM. Qualitatively when dilution is important the uniform AF order can be broken into domains of AF order making the action of a uniform field site-dependent. MC simulations performed for the dilute AF in a field[9] suggested a second-order transition even for strong fields at vacant site concentration $p = 0.3$. By including nnn interactions we have found a tricritical point by MC simulations at $p = 0.2$ for the ratio $\alpha = -0.5$ of nnn to nn interaction strengths.[10]

In this paper we extend our previous simulations[10] to different values of p and α. The dependence of the location of the tricritical point on p and α is shown and discussed. Finally a comparaison with a recent probabilistic mean field calculation[11] and some earlier mean field prediction[12] is briefly presented.

II. PHASE DIAGRAM

We consider the following Hamiltonian:

$$\mathcal{H} = J \sum_{\langle i,j \rangle} S_i S_j + \alpha J \sum_{\langle i,k \rangle} S_i S_k - H \sum_i S_i, \qquad (1)$$

where $J > 0$ is taken as unit of energy in the following. The coefficient α is the ratio of nnn to nn interactions and H is the applied uniform magnetic field. The Ising spins S_i take the values ± 1 except at a concentration p of lattice sites where they are zero. These vacant sites are chosen at random. The first two terms in Eq. (1) are performed over all nn and nnn pairs respectively while the last one over all occupied lattice sites.

We have carried out extensive MC simulations with different simple cubic lattice samples of size $N = 20^3$. Finite size effects have been studied for one case ($p = 0.2$, $\alpha = -0.5$).[10] The periodic boundary conditions have been imposed throughout. The MC technique used here is the single-spin flipping procedure where in each run we discard a sufficient number of MC steps (MCS) per spin to equilibrate the system before averaging physical quantities over a number of MCS/spin. The two following procedures have been used in our simulations: (i) applying H on the antiferromagnetic (AF) and ferromagnetic (F) initial spin configurations at a given temperature T; (ii) heating or cooling the system at a given field H. The choice of the former or the latter procedure depends on the trajectory followed in the simulation with respect to the critical line in the (T,H) plane. The first procedure is convenient at high values of H while the second one is more suitable at low values of H. The use of AF and F configurations as initial conditions helps to stabilize the system more rapidly than the use of random initial configurations. The AF is one of the ground states of the system when H does not exceed the critical value $H_c(p)$ given by $H_c(p) = (1-p)H_0$, where $H_0 = 6$ for simple cubic structures. The F state, on the other hand, is the stable configuration at high temperatures. Besides, at each concentration p we used different samples to make sure that the results are independent of vacant site distributions.

A full account of this work will be published elsewhere.[11] We recall briefly here that the order of the transition is determined by examining the staggered magnetization m_{st}, internal energy U, specific heat c_v and staggered susceptibility χ. The existence of a hysteresis in m_{st} and in U means a first-order transition, otherwise it is a continuous transition. The system equilibrium is verified by looking at the time-dependence of the local Edwards–Anderson order parameter as well as of other physical quantities. For p up to 0.3 we used 20.000 MC steps/spin, half of which were discarded for equilibrating. For p larger than 0.3 longer runs are needed. For a given p we look for the critical points at var-

 0021-8979/88/083758-02$02.40 © 1988 American Institute of Physics

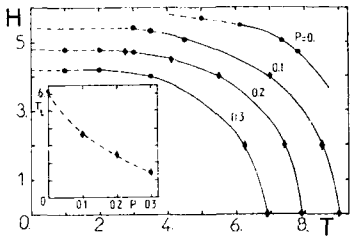


FIG. 1. Phase diagram in the (T,H) plane for $\alpha = -0.5$ at various values of p. Results of runs with fixed H are denoted by solid circles and those with fixed T by diamonds. First- and second-order critical lines are shown, respectively, by discontinued and solid lines. Results at $p = 0$ are taken from Ref. 13. The inset shows the tricritical temperature as a function of p.

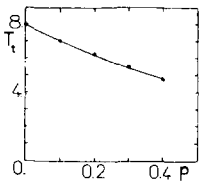


FIG. 2. The tricritical temperature obtained by the probabilistic mean field equations is shown as a function of p at $\alpha = -0.5$.

ious values of H and T. In the first-order region we measure the hysteresis width and the tricritical point is taken where this width goes to zero by extrapolating. An example at $p = 0.2$ has been shown in Ref. 10. The resulting phase diagram at $p = 0.1, 0.2$, and 0.3 for $\alpha = -0.5$ is shown in Fig. 1 where results of Landau[13] for $p = 0$ are also presented. In the inset of Fig. 1 we show the tricritical temperature T_t as a function of p. It is observed that T_t decreases strongly with increasing p. This suggests that there exists a threshold p_c at which the tricritical point disappears.

We note that at $p = 0.3$ the full AF order is often broken into domains of AF order. This is seen in runs with high-temperature F initial spin configurations: below the transition the staggered magnetization obtained upon cooling can be smaller than that obtained by heating from AF initial configurations. This effect is not due to metastability since the local Edwards-Anderson order parameter in runs with F and AF initial conditions are identical within statistical errors.

We have also obtained the phase diagram at $\alpha = -0.6$ for $p = 0.2$. The critical point at $H = 0$ is $T_c = 8.75 \pm 0.05$ and the tricritical point is located at $T_t = 3.0 \pm 0.2$, $H_t \cong 4.8$. This is to be compared with the case $\alpha = -0.5$ and $p = 0.2$ where $T_t = 2.5 \pm 0.1$, $H_t \cong 4.8$. The full phase diagram in the space (H,T,α) which requires an enormous computer time is left for future work.

III. MEAN FIELD MODEL

We present now the results of a probabilistic mean field model. Details will be given elsewhere.[11] Since mean field theory is a one-site approach, once dilution is introduced the various one-site configurations of the dilute problem should be included. There exist three types of situation: both nn and nnn interactions, only nn, or only nnn are present. We define these configurations through the variables γ_i and δ_i with a probability p_i as

$$\gamma_1 = cJ + \alpha zJ, \quad \delta_1 = cJ + \alpha zJ, \quad p_1 = (1-p)^2, \tag{2a}$$

$$\gamma_2 = cJ, \quad \delta_2 = cJ, \quad p_2 = p(1-p), \tag{2b}$$

$$\gamma_3 = \alpha cJ, \quad \delta_3 = -\alpha zJ, \quad p_3 = p(1-p), \tag{2c}$$

where c is the number of nn and z the number of nnn. The equations of state become averages of equations of state over the various configurations (2). We obtain for uniform and staggered magnetizations

$$m = \sum_{i=1}^{3} p_i m(\beta,H,m,m_s,\gamma_i,\delta_i) \tag{3}$$

and

$$m_s = \sum_{i=1}^{3} p_i m_s(\beta,H,m,m_s,\gamma_i,\delta_i), \tag{4}$$

where the expressions of m and m_s are identical to those of the pure case when $\gamma_i = \gamma_1$ and $\delta_i = \delta_1$.[14] Using Eqs. (3) and (4) we calculated the location of tricritical point for $\alpha = -0.5$ at various values of p. The results are shown in Fig. 2. The p dependence of the location of the tricritical point justifies an earlier mean field treatment.[12] A qualitative agreement with the MC results shown in the inset of Fig. 1 is observed.

IV. CONCLUSION

To summarize we would like to emphasize that both nnn interactions and dilution can change the nature of the phase diagram. Therefore, experiments on different systems may give different phase diagrams. Experimental results should thus be interpreted with caution.

ACKNOWLEDGMENT

The simulations have been carried out on the computer FPS-164 of GRECO "Expérimentation Numérique" at the Ecole Normale Supérieure.

[1] J. Imbrie, Phys. Rev. Lett. **35**, 1747 (1984); Y. Imry and S. Ma, *ibid.* **35**, 1399 (1975).
[2] A. Aharony Phys. Rev. B **18**, 3318 (1978).
[3] S. Galam and J. L. Birman, Phys. Rev. B **28**, 5322 (1983); D. Andelman, *ibid.* **27**, 3079 (1983).
[4] A. P. Young and M. Nauenberg, Phys. Rev. Lett. **54**, 2429 (1985).
[5] J.C. d'Angles d'Auriac, Ph.D. Thesis, Grenoble (1986).
[6] D. S. Fisher, Phys. Rev. Lett. **56**, 416 (1986).
[7] S. Fishman and A. Aharony, J. Phys. C **12**, L729 (1979).
[8] P. z. Wong, S. Von Molnar, and P. Dimon, J. Appl. Phys. **53**, 7954 (1982); Solid State Commun. **48**, 573 (1983).
[9] A.T. Ogielski and D.A. Huse, Phys. Rev. Lett. **56**, 1298 (1986).
[10] H.T. Diep, S. Galam, and P. Azaria, Europhys. Lett. **4**, 1067 (1987).
[11] S. Galam, P. Azaria, and H.T. Diep (unpublished).
[12] S. Galam, Phys. Lett. A **121**, 459 (1987).
[13] D. P. Landau, Phys. Rev. B **14**, 4054 (1976).
[14] J.M. Kincaid and E.G.D. Cohen, Phys. Rep. **22**, 57 (1975).

Reorientations, freezing, and plastic phase

Serge Galam
Departement de Recherches Physiques, T22-E3, Universite Pierre et Marie Curie, 75252 Paris Cedex 05, France

A physical mechanism for the production of random fields in plastic molecular crystals is proposed. To account for the reorientating processes, a rotational state is introduced in addition to the set of equivalent allowed orientations. Molecules in the rotational state act as static impurities which in turn generate random fields. A magneticlike Hamiltonian is presented. Experimental implications of the rotational state are discussed.

I. INTRODUCTION

A growing interest has been devoted recently to the study of plastic crystals.[1-5] Plastic crystals exhibit an intermediate thermodynamically stable phase, the plastic phase, between the solid and the liquid phases. In this intermediate phase, the centers of mass of the molecules form a regular lattice whereas their orientations are disordered. Plastic crystals can be either of the molecular kind, like $C(CH_3)_4$,[2] or of the ionic kind, like NaCN.[3,4]

In the plastic phase the nature of rotational disorder is rather complicated.[5] There exists a static orientational disorder distributed among a discrete set of equivalent directions, which usually results from the interplay of symmetries both of the site and the molecule. Large amplitude librations occur around each direction together with jumps from one direction into another. Using some hints from molecular dynamics,[3,6] it appears that rotational jumps may proceed through some free rotation of the molecule, i.e., rotations larger than 2π. Moreover, the coexistence of rotational disorder with translational long-range order is mediated by steric hindrace, which makes the translation-rotation coupling of central importance.[7]

In Sec. II we propose to account for part of the dynamics of reorientations by introducing a rotational state which makes the problem static on short timescales. On this basis, a magnetic like model is presented in Sec. III. Two different phase transitions are obtained from the same Hamiltonian to describe the solid-plastic and the plastic-liquid transitions. In the plastic phase the rotational degrees of freedom are found to be frozen. Finally the rotational state hypothesis is discussed in the Sec. IV with respect to a recent neutron experiment on neopentane.[8] Concluding remarks are contained in the last part.

II. DYNAMICAL VERSUS STATIC DISORDER: THE ROTATIONAL STATE HYPOTHESIS

Because reorientation processes exist which involve rotations larger than 2π, the corresponding typical reorientation time τ should allow some relaxation of translational degrees of freedom. This very fact suggests that one consider a molecule in the reorientating process as being in an "excited state." For every plastic crystal a new state may therefore be introduced, in addition to the set of discrete orientations allowed by symmetry. The excited state is thus surrounded by a local deformation of the lattice. To account for such a phenomenon it is appealing to consider the excited state plus the local deformation as equivalent to some virtual static impurity. This equivalence simplifies much the complicated dynamics of the plastic crystal by dividing it into two problems:

(i) a static problem which is the study of a plastic crystal diluted with impurities;

(ii) a dynamical problem which is the study of the dynamics of the virtual impurities.

From now on we concentrate on point (i) assuming that we are dealing with times of order τ.

Using the rotational state hypothesis, a mapping can be established between the plastic crystal with reorientations and a dilute plastic crystal with no reorientations larger than 2π. Results obtained recently in the study of $M(CN)_{1-x}X_x$ mixed crystals,[9] with orientational disorder, may be relevant to study the plastic phase. In these systems M is an alkali metal with M = Na, K, and Rb and X is halogen ion with spherical symmetry. It was suggested that substitutional halogens x generate random strains which in turn couple to the rotational degrees of freedom of the CN.[9] These static strains appear to be quenched with a zero configurational average which causes the problem to belong to the class of random field systems. In our problem, X stands for the virtual impurities, i.e., the large angle reorientating molecules. We therefore argue that, in plastic crystals at timescales of order τ, there exist random fields which couple to the rotational degrees of freedom.

III. A NEW MAGNETICLIKE MODEL FOR PLASTIC CRYSTALS

On this basis a magneticlike model can be defined as follows for timescales of order τ. To each molecule i we associate a variable $T_i = \pm 1$ to represent translational degrees of freedom and a variable $R_i = \pm 1$ to account for the discrete rotational degrees of freedom. At this stage a crude but physically meaningful way to account for reorientating processes is to include a random field $H_i = \pm H$ which couples to R_i. Molecules in the excited state do not appear explicitly. Only their effects are included via the $\{H_i\}$. Such an approximation holds only for a very low concentration of reorientating molecules. From some experiments it seems that the concentration is indeed rather low.[8]

Taking ferromagnetic couplings between nearest neighbors for both the $\{T_i\}$ and the $\{R_i\}$ together with a local linear coupling, leads to Hamiltonian of the form[10]

 0021-8979/88/083760-02$02.40 © 1988 American Institute of Physics

$$\mathcal{H} = -J_T \sum_{\langle i,j \rangle} T_i T_j - J_R \sum_{\langle i,j \rangle} R_i R_j - \sum_i (H_i + \lambda T_i) R_i. \quad (1)$$

The global phase diagram of plastic crystals can be described qualitatively using Hamiltonian (1). Taking $J_T \gg J_R$ produces two regimes for the Hamiltonian (1).

There is a low-temperature regime in which the $\{T_i\}$ are ordered and behave as a uniform field $T = \langle T_i \rangle$. The $\{R_i\}$ are the critical variables and the effective Hamiltonian is

$$\mathcal{H}_1 = -J_R \sum_{\langle i,j \rangle} R_i R_j - \sum_i (H_i + \lambda T) R_i. \quad (2)$$

The solid-plastic transition is thus described by the transition of a ferromagnet in competing uniform and random fields.[11] The plastic phase appears as an orientational glass-like system for times of order τ since $\{\langle R_i \rangle\}_{av} = 0$ while $\{\langle R_i \rangle^2\}_{av} = 0$ (av denotes configurational average). The $\{R_i\}$ are frozen by their local random fields $\{H_i\}$.

At higher temperatures a second regime takes place described by the effective Hamiltonian

$$\mathcal{H}_2 = -J_T \sum_{\langle i,j \rangle} T_i T_j - \sum_i L_i T_i, \quad (3)$$

where $L_i = \lambda R_i = \pm \lambda$ is a quenched random field. The order parameter is now defined by the $\{T_i\}$. A transition of a ferromagnet in random fields thus describes the plastic-liquid transition.

It is worth stressing that the random field intensity λ relevant to the plastic-liquid transition is different from the random field intensity H which drive the solid-plastic transition. In the last case the random fields $\{H_i\}$ are generated by the reorientating processes whereas in the former case the $\{L_i\}$ result from the translation-rotation linear coupling.

IV. THE ROTATIONAL STATE HYPOTHESIS AND EXPERIMENTS

Recent neutron experiments on deuterated neopentane showed that orientational disorder was much weaker than expected.[8,12] Indeed, no isotropic contribution to the elastic structure factor could be detected. This result justifies the approximation of low concentration for reorientating molecules. Simultaneously the translational disorder associated with the molecular centers of mass was found to be very large and strongly temperature dependent: the translational Debye–Waller factor exhibits a strikingly rapid increase with temperature.[12]

It was found[13] that this thermal behavior can be understood using the rotational state hypothesis by taking into account the increase in the number of rotational states with temperature; this number, however, always being of the order of a few percent.

V. CONCLUSION

We have presented a Hamiltonian which yields the global phase diagram found for plastic crystals. The main assumption of the model sketched above is the existence of local excited states which in turn generate random fields. At this stage more experiments are needed to check the rotational state hypothesis.

ACKNOWLEDGMENTS

I would like to thank Ph. Depondt and R. M. Pick for stimulating discussions.

[1] S. Galam, O.D.I.C. Newslett. **6**, 1 (1987).
[2] W. Breymann, Ph. D. thesis, Paris (1987).
[3] M. H. Ambard, Ph. D. thesis, Paris (1987).
[4] Ph. Buchet and R. M. Pick, Europhys. Lett. **2**, 709 (1986).
[5] M. T. Dove, O.D.I.C. Newslett. **6**, 6 (1987).
[6] M. Yvinec, Mol. Cryst. Liq. Cryst. **89**, 359 (1982).
[7] K. H. Michel and J. Naudts, Phys. Rev. Lett. **39**, 212 (1977).
[8] Ph. Depondt and M. Debeau, J. Phys. (Paris) **48**, 1513 (1987).
[9] K. H. Michel, Phys. Rev. Lett. **57**, 2188 (1986).
[10] S. Galam, Phys. Lett. A **122**, 271 (1987).
[11] S. Galam, J. Phys. C **15**, 529 (1982).
[12] B. Denise, Ph. Depondt, M. Debeau, and P. Schweiss, J. Phys. (Paris) **48**, 612 (1986).
[13] S. Galam and Ph. Depondt, Europhys. Lett. **5**, 43 (1988).

Effect of demagnetizing fields on Kerr effect in ferrites

Prabhat K. Singh, P. K. Singh,[a] and S. Prasad[b]
Department of Physics and Astrophysics, University of Delhi, Delhi-10007, India

The analysis of experimental data of magnetomicrowave Kerr effect in MgMn ferrite samples at 9.442 GHz has been carried out using external permeability tensor components which take care of demagnetizing fields more accurately in the theory and is based on the guided wave propagation of the microwave inside the sample. The present analysis gives a better agreement with the experimental data in comparison to our earlier analysis which was based on the free-wave propagation of the microwave. The importance of the image effect in the demagnetizing factor is also discussed.

INTRODUCTION

The study of microwave behavior of ferrites has always been a subject of great interest as this combines both interesting physics and technical importance. The transmission of microwaves from magnetized ferrites placed in a waveguide has been studied earlier by many workers.[1] However, it was noticed recently that the microwave reflection from magnetized ferrites, called the magnetomicrowave Kerr effect, could also be very interesting, particularly in disk-shaped samples.[2] In this effect the sample may be kept both inside and outside a circular waveguide (generally backed by a metallic plate in order to account the multiple reflection[2] easily). The sample can be magnetized either along the direction of microwave propagation (i.e., Faraday configuration) or perpendicular (i.e., Voigt configuration) to it. We have recently published quite a bit of work on the study of microwave reflection from the magnetized ferrite sample in the Faraday configuration.[2–4] The reflected waves were analyzed in terms of R, the amplitude ratio of two orthogonal linearly polarized components of the reflected wave and δ, the phase difference between them. Experimentally, various extremes in the value of R as a function of magetic field were observed, most of which could be attributed to dimensional resonance phenomenon.[2–4] Most of the time, the theoretical analysis of the results reproduced the peak structure quite accurately. In the theoretical interpretation of the experimenatal data, however, we mainly faced two problems. First, the theoretical peak positions were found to be off sometimes by more than 1 kOe from the corresponding experimental peaks, and second, the damping parameter (α), introduced in order to account for magnetic losses in the material, was found to be rather larger than the one expected from independent effective linewidth measurements.[5] One of the possible reasons for this discrepancy was thought to be the improper accounting of the demagnetizing field in the disk-shaped samples. In this paper we report our experimental results on MgMn ferrite samples at X-band frequency. These results are analyzed using a more refined theory reported in this paper which takes care of the demagnetizing field more accurately than reported earlier. Our analysis also takes account of the guided wave nature of microwave propagation inside the sample.[6]

EXPERIMENTAL PROCEDURE

The experiments were performed using a double microwave bridge originally envisaged by Brodwin and Vernon[7] for a similar study in semiconductors. The details of the interferometer and modification needed for its use in magnetic materials have already been reported in an earlier publication.[3] The details of the sample preparation and the parameters are given in Ref. 3.

THEORETICAL BACKGROUND

The experimentally measured parameter R depends theoretically on the reflection coefficient of negative and positive circularly polarized components of the incident microwaves from the magnetized ferrite. These reflection coefficients are related to the permeability tensor components of the ferrites and the damping parameter. The expressions of permeabilty tensor components for the unsaturated and saturated states of magnetization are different. However, in this paper we have considered only the case of the saturated state of magnetization. This is because in the unsaturated state of magnetization the expressions of the permeability tensor elements are not exact and contain adjustable fitting parameters[8] which can alter the positions of the peaks in the R-vs-H curve. It is, therefore, difficult to see the effect of demagnetizing fields separately. Moreover, in this state of magnetization, additional losses may occur due to the motion of domain walls. In our earlier analysis we made the following assumptions for calculation of permeability tensor components at different externally applied dc magnetic fields.

[a] Also at Division of Materials, National Physical Laboratory, Dr. K. S. Krishnan Road, New Delhi-110012, India.
[b] Also at Department of Physics, Indian Institute of Technology, Powai, Bombay-400076, India.

 0021-8979/88/083762-03$02.40 © 1988 American Institute of Physics

(a) The demagnetizing fields in the sample are uniform and can be accounted by a position-independent demagnetizating factor along the x, y, and z directions, e.g., N_x, N_y, and N_z.

(b) The originally derived Polder's internal permeability tensor components are valid in our case except that the internal field H_{int} is given in terms of externally applied magnetic field H by the following equation:

$$H_{int} = H - N_z 4\pi M_s, \tag{1}$$

where $4\pi M_s$ is the saturation magnetization of the sample.

It was discussed earlier[3] that assumption (a) could be valid if the ferrite sample is thin and has a larger dimension in comparison to the waveguide diameter. This is because the first-order demagnetizing factor varies significantly as a function of position only near the sample edges.[10] In the present work it was, therefore, decided to use external permeability tensor components instead of internal permeability tensor components. The expressions of permeability tensor components used in our analysis are taken from Ref. 1 [expression (4.29) of Ref. 1, however, contains a printing error which has been corrected in the present calculation] which includes the loss, i.e., the damping term and demagnetizing factors. In our earlier analysis of the data of the saturated state of magnetization, the contribution of the demagnetizing factor was not considered. In the present text the theoretical results obtained by the earlier theory is referred to as the free-wave (FW) theory and the theoretical results based on the present theory are referred to as the modified theory. For the calculation of the demagnetizing factor we have used Sawado's[9] and Joseph and Schlömann's[10] expression. In the former the image effect has been considered while in the latter spatial variation of the demagnetizing field is considered.

RESULTS AND DISCUSSION

The analysis of Faraday configuration Kerr effect data in terms of the parameter R as a function of applied dc magnetic field has been carried out using the theory discussed in the earlier section. The results have been compared with the theoretical results based on the FW model. The results of two representative samples have been shown in Figs. 1 and 2.

The experimental curve of R as a function of externally applied dc magnetic field in the saturated state of magnetization for the sample MgMn2000 is shown in Fig. 1. In this sample the experimental minima and maxima are observed at fields of 1.90 and 2.23 kOe, respectively, in the value of R which is followed by a plateau between 2.7 and 4.0 kOe. The calculations of R have been carried out by using the free-wave model as well as the present modified theory and the curves are plotted in the same figure by broken and continuous curves, respectively. The calculations from both models reproduced the maxima in the R-vs-H curve as observed experimentally. The maximum was due to dimensional resonance. The theoretical maxima by the FW model was at 2.60 kOe, corresponding to an experimental maximum at 2.23 kOe. On the other hand, the present theory gives the peak (at 2.23 kOe) exactly at the same field where the experimental peak is observed. Thus, the use of the present theory improves the agreement between the theory and experiment, particularly in regards to the position of the peaks.

Figure 2 illustrates the R-vs-H experimental curve for MgMn1750. The theoretical curves calculated with the help of the present theory and FW model are also shown in the same figure, the former being represented by a continuous curve. In this sample also the results obtained by the present theory improve the agreement between theory and experiment. In fact, the matching is almost perfect.

Similar calculations were also carried out for other samples reported in our earlier publications.[3] It is found that, in general, in all the cases where agreement between theory and experiment was not so good from the FW theory, a tremendous improvement was observed by using the modified theo-

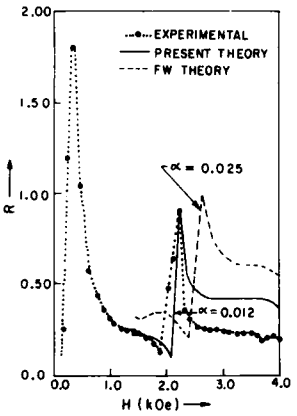


FIG. 1. Theoretical (using present theory and FW theory) and experimental R-H curves for MgMn2000 The theoretical curve in the partially magnetized state has not been plotted.

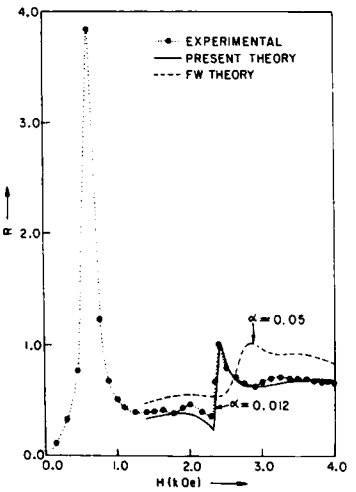


FIG. 2. Theoretical (only for the saturated state of magnetization) and experimental variation of R as a function of applied dc magnetic field for MgMn1750.

ry so far as the positions of the peaks are concerned. In the theoretical curves plotted in Figs. 1 and 2, the demagnetizing factor was evaluated by using Sawado's expression. The results obtained by the first-order theory of the demagnetization factor after Joseph and Schlömann did not give better results than Sawado's expression. The possibility of an agreement with Joseph and Schlömann's data cannot be rule out if their second-order correction to the demagnetization factor (which is sometimes as large as 20% of the first-order contribution but difficult to evaluate) could be properly accounted in the theory. The better agreement with Sawado's expression clearly brings out a fact that it is important to take into account the image effect in the theory. This is because the basic difference between Sawado and the first-order theory of Joseph and Schlömann is that in the former the image effect is included in the expression of the demagnetization factor while in the latter it was not considered.

The slight discrepancy still remained in some cases, particularly in regard to the magnitude of R in the regions away from the maxima which may be due to two reasons: First, for an exact evaluation of magnetic field inside the sample, the solution of the electromagnetic boundary value problem is needed and impedance matching at the waveguide-sample interface is required. The calculations are quite complicated and tedious but in the case of a finite sample, particularly when its dimensions are of the order of wavelength of the incident radiation, the microwave field inside the sample can be considered almost uniform for the first order of approximation (as considered in the present theory). However, due to the small normalized electrical length of the sample thickness, high-order evanescent modes generated at the waveguide-sample interface may not die out significantly before their reflection from the other surface of the sample. These modes have a complicated distribution of the microwave field inside the sample. This may lead to a difference in the magnitude of R and also to a slight shift in the experimental and theoretical peak positions.

Second, the anisotropy shifts the resonant frequency. The phenomenon is well known in single-crystalline materials.[1] As the polycrystalline samples consist of randomly oriented crystallite separated by grain boundaries, the angle between applied field and the crystal axis varies through all values. The demagnetizing field at voids, grain boundary, and inhomogeneous regions in the sample may also vary from grain to grain. Thus, the demagnetizing field calculated in terms of N_x, N_y, and N_z by considering an idealized model may also differ from the actual values. All these effects may result in a broadening of the dimensional resonance peak and a shift in the positions of the theoretical and experimental peaks by different amounts.

[1] B. Lax and K. J. Button, *Microwave Ferrites and Ferrimagnetics* (McGraw-Hill, New York, 1962).
[2] S. Prasad and R. M. Mehra, J. Phys. Chem. Solids **39**, 353 (1978).
[3] P. K. Singh, S. Prasad, P. K. Singh, and S. B. Singh, J. Appl. Phys. **53**, 9180 (1982).
[4] P. K. Singh, P. K. Singh, and S. Prasad, J. Phys. C **18**, 2305 (1985).
[5] Q. H. F. Vrehen, A. B. VonGroenou, and J. G. M. deLau, Phys. Rev. B **1**, 2332 (1970).
[6] P. K. Singh and S. Prasad, IEEE Trans. Magn. **MAG-18**, 1633 (1982).
[7] M. E. Brodwin and R. J. Vernon, Rev. Sci. Instrum. **34**, 1129 (1963).
[8] F. Sandy, Raytheon Technical Memo No. T 815 (1969).
[9] E. Sawado, J. Appl. Phys. **40**, 1860 (1969).
[10] R. I. Joseph and E. Schlömann, J. Appl. Phys. **36**, 1579 (1965).

Generalization of Snoek's limit for modeling initial permeability of magnetic materials

Gary G. Bush
Research and Development Division, Lockheed Missiles and Space Company, Inc., Palo Alto, California, 94304

Permeability relates the magnetic field intensity in a magnetic material to the resulting flux density. The initial part of the permeability extending from dc fields to the radio-frequency fields of a few hundred megahertz is due to domain wall displacement. A spin resonance occurs due to the presence of an anisotropy field, with the result that the permeability drops rapidly at frequencies above this resonance. It has been observed experimentally that the variation of the ratio of the magnetic oxides in a given ferrite crystal structure changes the initial permeability and the resonance frequency. The product of the resonance frequency and the initial permeability is approximately constant, i.e., Snoek's limit. Thus, if the resonance frequency increases, the initial permeability decreases in inverse proportion. Experimental results in the literature confirm the variation of the initial permeability with composition. A modification of the equations for Snoek's limit suggest that a variable quasistatic magnetic field would have the same effect on initial permeability as a variation in composition. This effect has been verified experimentally for magnesium-zinc ferrite samples in a brass coaxial transmission line with an applied dc magnetic field of 0–500 Oe. The initial permeability of many magnetic materials can thus be modified in the VHF range by the application of an externally applied magnetic field.

INTRODUCTION

The ability to dynamically change the electromagnetic constitutive properties of a material by the application of a quasistatic field is very useful. Among the electromagnetic properties that can be varied by the application of an electric field are the conductivity of semiconductors and the permittivity and permeability of ferroelectric materials. The magnitude of electric field required to produce significant changes, and the simultaneous change of permeability and permittivity with electric field, have limited the applications for ferroelectric materials.

The permeability of ferrimagnetic materials, such as ferrites that exhibit Snoek's limit,[1] can be controlled by a quasistatic magnetic field without incurring significant changes in permittivity. These materials have found application in cyclotrons, linear accelerators,[2,3] and radio-frequency (rf) generators. The change in permeability with applied field can be independent of frequency also. These materials are the subject of this paper.

INITIAL PERMEABILITY

The initial permeability spectrum is that part of the permeability spectrum as a function of frequency that is due to domain wall motion. As the frequency of rf excitation increases, the material reaches a point beyond which the spins cannot fully respond to the excitation. The magnetization no longer moves in phase with the excitation and losses occur. The real part of the permeability μ' decreases with increased frequency and the imaginary part of the permeability μ'' goes through a broad resonance. Figure 1 describes this behavior of the real part of permeability of the ferrite $Ni_\delta Zn_{1-\delta}Fe_2O_4$. The concentration of nickel is the parameter for the family of curves. The dashed line represents a bound for this family of curves and is called Snoek's limit.

SNOEK'S LIMIT

The boundary defined by Snoek's limit[4–7] can be found by taking the product of μ' and the angular resonance frequency for domain wall motion ω. The resonance frequency can be expressed as a function of the gyromagnetic ratio γ and the total applied quasistatic magnetic field,

$$\omega = \gamma(H_a + H_0), \tag{1}$$

where H_a is the cubic anisotropy equivalent field and H_0 is the externally applied field. The real part of the permeability μ' can be expressed as a function of the saturation magnetization M_s and the cubic anisotropy constant K_1,

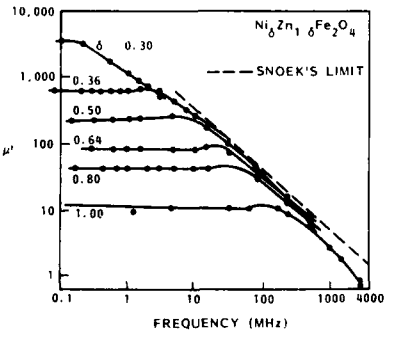


FIG. 1. Real part of the permeability of $Ni_\delta Zn_{1-\delta}Fe_2O_4$ as a function of frequency for various fraction δ of nickel (Refs. 4 and 8).

 0021-8979/88/083765-03$02.40 © 1988 American Institute of Physics

$$\mu' = M_s^2/3K_1. \tag{2}$$

Before forming the product of $\omega\mu'$ to define the bound, the effect of an external field on the resonance frequency must be taken into account. Due to symmetry, the applied field adds to the cubic anisotropy field. Thus, an effective cubic anisotropy constant can be defined as

$$K_1^{\text{eff}} = (M_s/2)\,(H_0 + H_a). \tag{3}$$

The product of ω and μ' is therefore

$$\omega\mu' = \gamma \frac{2K_1^{\text{eff}}}{M_s} \frac{M_s^2}{3K_1^{\text{eff}}} = \frac{2\gamma M_s}{3}. \tag{4}$$

The product $\omega\mu'$ is independent of the cubic anisotropy field and the externally applied field. If the applied field increases, Eq. (1) indicates that the resonant frequency will increase, and Eq. (4) predicts a corresponding decrease in μ'. If the frequency of operation is below the resonance frequency corresponding to the applied field, the resulting μ' should be *independent of frequency*.

EXPERIMENTS

The objective of this work was to investigate the control of permeability by an applied magnetic field. To measure the magnitude of the effect, a coaxial transmission line test fixture was designed (Fig. 2). The control field, H_0, is produced by a concentric coil of 1940 turns wound on the outside of a section of rigid coaxial transmission line. A current of 2.5 A in the coil produced a maximum field of 675 Oe in the transmission line. The rf magnetic field is concentric with the center conductor and perpendicular to the applied dc magnetic control field, H_0. The ferrite sample completely fills the gap between the center conductor and the outer conductor.

Figures 3(a) and 3(b) are idealized permeability curves intended to explain the link between the initial permeability curves such as Fig. 1 and the measured permeability curves in Figs. 4 and 5. The same data is plotted in Figs. 3(a) and 3(b) with the applied field H_0 as the parameter for the family of curves in Fig. 3(a) and the frequency as the parameter in Fig. 3(b). In Fig. 3(a), the square icons at frequency f_1, points 1 and 2, represent the sweeping of the nonlinear leading edge of the resonance past frequency f_1 as H_0 increases. These two points correspond to the square icons labeled 1

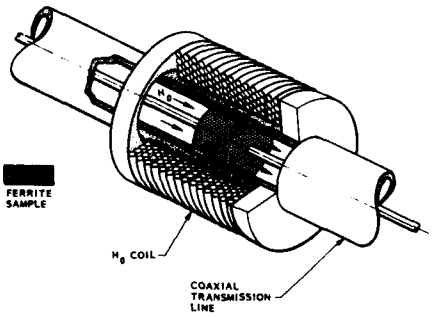


FIG. 2. Transmission-line sample holder.

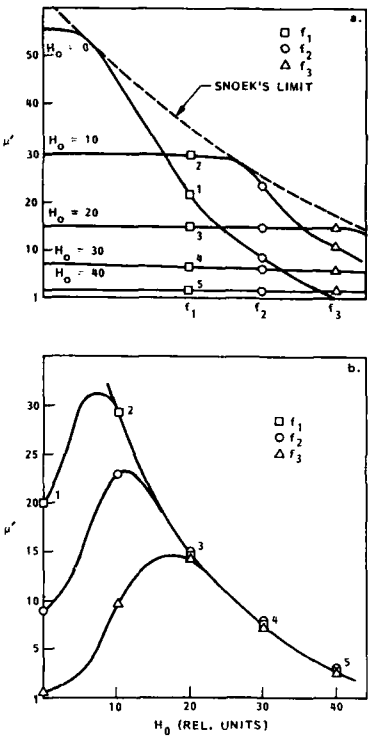


FIG. 3. Idealized relationship of μ', f, and H_0.

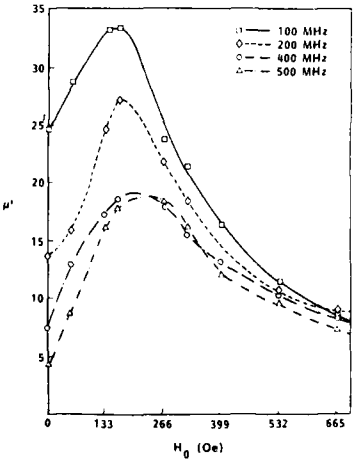


FIG. 4. Real part of the permeability μ' of $Mg_{0.35}Zn_{0.65}Fe_2O_4$ vs H_0 for frequencies between 100 and 500 MHz.

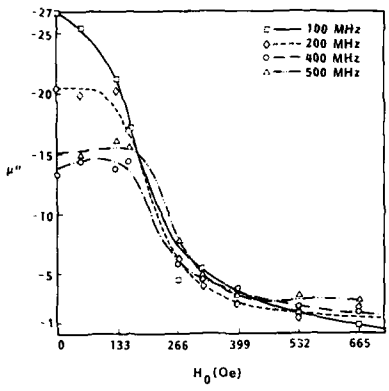


FIG. 5. Imaginary part of the permeability μ'' of $Mg_{0.35}Zn_{0.65}Fe_2O_4$ vs H_0 for frequencies between 100 and 500 MHz.

and 2 in Fig. 3(b). As the resonance passes frequency f_1 and μ' becomes constant for frequencies below the resonance, an increase in H_0 moves μ' from point 3 to point 5. As shown in Fig. 3(b), the expected change in μ' with frequency is a smooth curve proportional the relative spacing between the curves at f_1 in Fig. 3(a). Equation (2) indicates an inverse relationship between μ' and H_0 that is independent of frequency below the resonance at points 3, 4, and 5 and strongly frequency dependent above the resonant frequency, points 1 and 2.

The measured data shown in Figs. 5 and 6 are for a magnesium zinc ferrite, $Mg_{0.35}Zn_{0.65}Fe_2O_4$, with the spinel crystal structure. The real part of the permeability is shown in Fig. 4 and the corresponding imaginary part of the permeability is shown in Fig. 5. In Fig. 4, the curves for frequencies between 100 and 500 MHz are frequency dependent below a field of $H_0 = 266$ Oe. Above this field, the curves come together and are relatively frequency independent, as suggested by Eq. (2) and Fig. 3(b). Approximately the same behavior is seen in Fig. 5 for μ'' above a field of $H_0 = 200$ Oe. After each data point was measured, the sample was subjected to a diminishing ac degaussing field to reduce hysteresis effects. All measurements were made at room temperature.

CONCLUSIONS

Snoek's limit describes a general bound for the family of initial permeability curves for various compositions of ferrites possessing cubic anisotropy. The effect of an external field on the permeability of ferrites has been investigated in the VHF frequency range in light of this theory. The theory indicated that a frequency-dependent and a frequency-independent control field range for μ' and μ'' should exist. Measurements of $Mg_{0.35}Zn_{0.65}Fe_2O_4$ in the frequency range of 100–500 MHz confirm this behavior. These results should be useful for the molecular engineering of ferrite materials.

ACKNOWLEDGMENTS

The author is greatly indebted to L. C. Eisaman for constructing the experimental test fixtures and taking the data reported in this paper and to Dr. Russ West of Trans-Tech Corporation for invaluable discussions and providing the materials tested.

[1] J. L. Snoek, Physica **14**, 207 (1948).
[2] L. M. Earley, IEEE Trans. Nucl. Sci. **NS-30**, 3460 (1983).
[3] L. M. Earley, G. P. Lawrence, and J. M. Potter, IEEE Trans. Nucl. Sci. **NS-30**, 3511 (1983).
[4] S. Chikazumi, *Physics of Magnetism* (Krieger, Malabar, FL, 1964), pp. 328–332.
[5] J. Smit and H. P. J. Wijn, *Ferrites* (Wiley, New York, 1959), pp. 260–276.
[6] A. H. Morrish, *The Physical Principles of Magnetism* (Krieger, Malabar, FL, 1983), pp. 593–599.
[7] C. Kittel, Phys. Rev. **73**, 155 (1948).
[8] E. W. Gorter, Proc. IRE **43**, 1945 (1955).

Validation of mixture equations for dielectric-magnetic composites

H. M. Musal, Jr., H. T. Hahn, and G. G. Bush
Research and Development Division, Lockheed Missiles and Space Company, Inc., Palo Alto, California 94304

Mixture equations relate the effective macroscopic electromagnetic properties (dielectric constant and magnetic permeability) of a composite material to the intrinsic microscopic electromagnetic properties of its constituents. The predictions of mixture equations in popular use generally agree with each other when particles are widely separated (small volume fraction), but begin to diverge when the volume fraction of particles in the composite is greater than 10%. This paper reviews the assumptions and characteristics of different representative mixture equations. The validity of these mixture equations for application to magnetic composites was tested by comparing their predictions of macroscopic electromagnetic properties to VHF and UHF measurements of these properties for a series of well-characterized dielectric-magnetic composite samples comprised of ferrite particles in an epoxy binder. The investigation emphasized the parameter regimes where large disparities between the predictions of the various equations exist, namely, large volume fraction of particles, complex dielectric constant and magnetic permeability (lossy material), and large contrast ratio between particle and binder properties. Correlation and lack of correlation between the mixture equation predictions and experimental data are shown.

INTRODUCTION

Mixture theories and their resultant mixture equations have been applied with some success to predict the effective macroscopic electromagnetic properties of artificial dielectrics and dielectric composites. The objective of the work reported here was to evaluate the predictive accuracy of various mixture equations when applied to magnetic composites, particularly in the stressful parameter regimes of large contrast ratio between constituent properties, large volume fraction of particles, and highly lossy constituent materials.

In the usual composite consisting of particles in a binder, the binder material "wets" the particles. Thus, the particles are isolated from each other by the contiguous binder. However, when the volume fraction of particles in the mixture becomes large, or there is magnetic attraction between particles, complete wetting may be frustrated, and agglomeration of particles produces regions where the particle material forms a semicontiguous geometry. In the limit of all particle material, the particle material must be completely contiguous. This microgeometry transition from contiguous binder material to contiguous particle material, as the volume fraction of particles is increased, is an important aspect of composite modeling.

MIXTURE EQUATIONS

Most commonly used mixture theories are based on an equivalent dipole representation of the mixture. The effective macroscopic electromagnetic properties of the mixture are modeled as an effective dipole moment per unit volume, determined from the intrinsic dipole moments per unit volume, or per particle, of the constituents, and their relative volume fractions within the mixture. This approach divides the calculation into two parts. First, the electric and magnetic intrinsic dipole moments for isolated particles are calculated. Then, these dipole moments are combined with the electric and magnetic intrinsic dipole moments per unit volume of the binder material by use of the mixture equation. In the static (or quasistatic) regime, the electric or magnetic dipole moments of particles depend only on the dielectric or magnetic properties, respectively, of the particle materials. In this regime, Aspnes[1] has shown that the general form of the mixture equation for solid spherical particles is

$$\frac{K-K_h}{K+2K_h}=f_a\frac{K_a-K_h}{K_a+2K_h}+f_b\frac{K_b-K_h}{K_b+2K_h}, \qquad (1)$$

where K is the effective macroscopic dielectric constant or magnetic permeability of the mixture; K_h, K_a, and K_b are the intrinsic dielectric constants or magnetic permeabilities of a contiguous host (binder) and isolated particle materials; and f_a and f_b are the volume fractions of particles a and b materials within the mixture. The mixture equation is written in this form to facilitate display of how the choice of the host material leads to the various well-known mixture equations.

If the host material is chosen to be either a or b material ($K_h=K_a$ or K_b), and $f_a+f_b=1$, then there are isolated b or a particles in a contiguous a or b binder. This gives the Maxwell Garnett[2] (MGa or MGb) mixture equation. The computed value of K for a given volume fraction of particles is different using MGa vs MGb. Because the host is contiguous, its properties dominate until the isolated particle volume fraction closely approaches unity.

Alternatively, the host material can be chosen to be free space ($K_h=1$) and $f_a+f_b\leqslant 1$. Then there are isolated a and b particles in a contiguous free-space background. This gives the Lorentz–Lorenz,[3,4] or Clausius–Mossotti,[5,6] mixture equation. Even if $f_a+f_b=1$ (no free-space volume), the behavior of K is as though the particles are always isolated (neither acts as a contiguous material).

Finally, the host material can be chosen to be the mixture itself ($K_h=K$) and $f_a+f_b=1$. Then Eq. (1) reduces to

 0021-8979/88/083768-03$02.40 © 1988 American Institute of Physics



$$0 = f_a \frac{K_a - K}{K_a + 2K} + f_b \frac{K_b - K}{K_b + 2K}. \quad (2)$$

This is the Bruggeman[7] (B), or effective-medium, mixture equation, which is to be solved for K. Neither a nor b materials are treated as contiguous constituents.

The microstructure of a composite may change as the volume fractions of its constituents are varied from one extreme to another. Therefore, a mixture equation based on a single simple model of the microstructure may be inadequate to predict the effective macroscopic electromagnetic properties over the full range of possible compositions. Sheng[8] has proposed a two-phase binary-mixture model in which the volume fractions occupied by the two different phases change with the relative volume fractions of the two constituents of the mixture. The electromagnetic properties of the two different phases are calculated using the MGa and MGb mixture equations, and the effective macroscopic electromagnetic properties of the entire composite are calculated using the Bruggeman mixture equation. The latter step imposes the assumption that at all volume fractions, other than zero or unity, there is no contiguous material in the composite.

In the dielectric-magnetic composites under study here, the binder material that holds the ferrite particles together is a contiguous host material. However, there are regions of localized agglomeration of the ferrite particles, which increase as the volume fraction of ferrite is increased. It therefore was proposed that a two-phase binary-mixture model would be appropriate, with the two different phase properties calculated via MGa and MGb. In order to preserve the identity of the contiguous binder material even at very large volume fractions of ferrite, the effective macroscopic properties of the entire composite are also calculated using the MG mixture equation with the two different phases as constituents. Explicitly, the mixture equation used is

$$K = K_h \left[1 + 3 \left(\frac{(K_p + 2K_h)}{F_p (K_p - K_h)} - 1 \right)^{-1} \right]. \quad (3)$$

To calculate the properties of the isolated ferrite particle phase (K_I), which will become the contiguous host phase of the entire composite, K_h is taken to be that of the binder (K_b), K_p is taken to be that of the ferrite (K_f), and F_p is taken to be the volume fraction of ferrite (F_f). To calculate the properties of the agglomerated ferrite particle phase (K_A), $K_h = K_f$, $K_p = K_b$, and $F_p = (1 - F_f)$. Finally, to calculate the properties of the entire composite, $K_h = K_I$, $K_p = K_A$, and F_p is the phase transition function. For the numerical results presented here, the phase transition function was simply taken to be F_f^n. This mixture equation is designated $MU(n)$.

COMPOSITE SAMPLES AND MEASUREMENTS

A nickel-zinc ferrite material (designated X-1) was chosen for composite sample fabrication. The electrical conductivity of this ferrite is very low, which ensures that eddy currents within the particles will not contribute to the particle dipole moments[9] and thus invalidate the quasistatic assumption inherent in the derivation of the mixture equations examined here. A necessary input to the mixture equations is the intrinsic electromagnetic properties of the particles, i.e., the properties at a volume fraction of unity. This was obtained by measuring the dielectric constant and magnetic permeability of a solid ferrite tile. The tile was then fractured into small particles (of the order of 100-μm average size) to be used in fabricating the composite samples. Using these particles in an epoxy binder, different volume fraction composite samples were cast into sections of rigid circular coaxial transmission line. These were mounted in a fixture connected to an automatic network analyzer, where their reflection and transmission coefficients (S-parameters) were measured. Computerized data-reduction procedures used these data to calculate the effective dielectric constant and magnetic permeability of the composites.

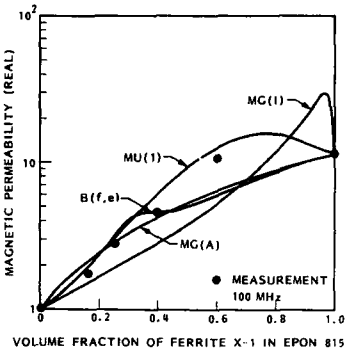


FIG. 1. Magnetic permeability (real part) of composite at 100 MHz.

CORRELATIONS

Validation of a mixture equation for application to a type of composite is based on achieving good correlation

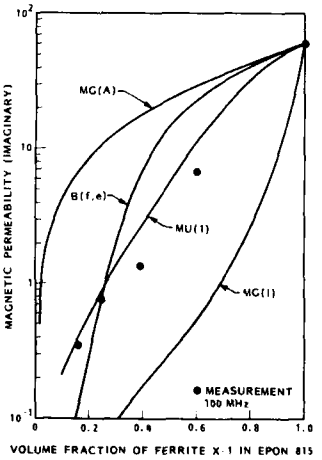


FIG. 2. Magnetic permeability (imaginary part) of composite at 100 MHz.

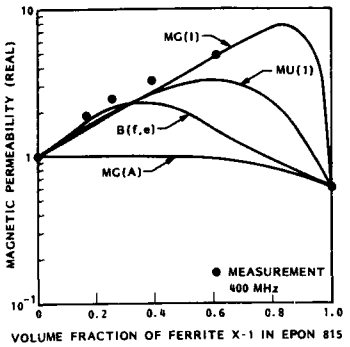


FIG. 3. Magnetic permeability (real part) of composite at 400 MHz.

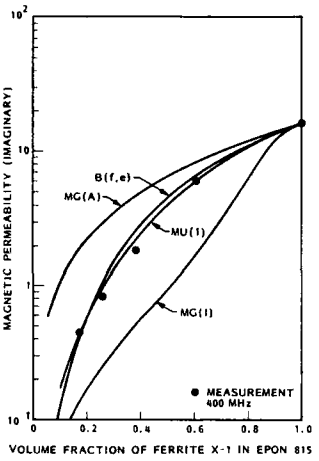


FIG. 4. Magnetic permeability (imaginary part) of composite at 400 MHz.

between the predictions of the equation and experimental data from typical samples of that type of composite, consistently for both real and imaginary parts of both dielectric constant and magnetic permeability over the entire range of volume fraction and frequency. Figures 1–4 show comparisons between mixture equation predictions and experimental data for the magnetic permeability of the composite at frequencies of 100 and 400 MHz. The data points were obtained from six different ferrite volume fractions: zero (pure epoxy); 16.4%, 25.6%, 39.0%, and 60.5% (ferrite composites); and unity (solid ferrite tile).

The end points of the theoretical and experimental results (at zero and unity volume fractions) correlate perfectly, as they should, because the experimental data of these two points are inputs to the mixture equation calculation. The predicted results of the various mixture equations are identified as follows: MG(I) and MG(A) are Maxwell Garnett results for isolated and agglomerated ferrite particle phases, respectively; B(f,e) are Bruggeman results with ferrite and epoxy as the two constituents; and $MU(1)$ are results of the two-phase binary-mixture equation defined earlier, with $n = 1$.

The imaginary part of the predicted magnetic permeability is much more sensitive to the mixture equation that is used in the calculation than is the real part. Overall, the two-phase binary-mixture equation appears to best represent the behavior of the magnetic permeability over the ranges of volume fraction and frequency that are covered. These results suggest that the mixture equation approach to predicting the effective macroscopic electromagnetic properties of dielectric-magnetic composites is valid, provided that the microgeometry of the composite structure is considered when selecting the mixture equations to be used.

[1]D. E. Aspnes, Am. J. Phys. **50**, 704 (1982).
[2]J. C. Maxwell Garnett, Philos. Trans. R. Soc. London **203**, 385 (1904); **205**, 237 (1906).
[3]H. A. Lorentz, Wiedem. Ann. **9**, 641 (1880).
[4]L. Lorenz, Wiedem. Ann. **11**, 70 (1881).
[5]R. Clausius, *Mechanische Warmetheori*, 2nd ed. (Vieweg, Braunschweig), Vol. 2, p. 62.
[6]O. F. Mossotti, Mem. Soc. Sci. Modena **14**, 49 (1880).
[7]D. A. G. Bruggeman, Ann. Phys. (Leipzig) **24**, 636 (1935).
[8]P. Sheng, Phys. Rev. Lett. **45**, 60 (1980).
[9]D. Stroud and F. P. Pan, Phys. Rev. B **17**, 17 (1978).

Microwave susceptibility and effective linewidth of iron-carbonyl powders

G. A. Naziripour, C. E. Patton, and M. V. Kogekar
Department of Physics, Colorado State University, Fort Collins, Colorado 80523

The effective linewidth technique has been applied to study the microwave response and effective linewidth of iron carbonyl powders. The frequency and Q of a high-Q microwave cavity containing small powder samples was measured over a field range of 0–12 kOe at 10 GHz. The frequency data for high field (9–12 kOe) were used in conjunction with magnetization data and theory to calibrate the microwave system. The calibration parameters were then used in conjunction with the Q data to determine the negative imaginary part of the powder microwave permeability μ'' vs field. The μ'' results at high field were then fitted to theory to estimate the operational effective linewidth parameter for the powders. The procedure provided clear microwave evidence for (1) magnetic saturation of the powders in the expected field range of 7–8 kOe, (2) the operational validity of a model which treats the powder particles as noninteracting spheres, and (3) an off-resonance effective linewidth of about 500 Oe at 10 GHz.

The objective of this study was to perform off-resonance microwave permeability measurements and effective linewidth analyses on a series of iron-carbonyl powders. This technique has proved useful for the separation of resonance losses from off-resonance losses and the determination of intrinsic linewidth parameters under conditions for which direct FMR measurements are not possible.[1,2]

The effective linewidth technique is discussed at length in the references cited above. The basic idea is that cavity Q and frequency data can be used in conjunction with microwave perturbation theory and an analysis of the dynamic magnetic response to obtain the field dependence of the negative imaginary part of the microwave permeability for the material of interest. Based on various models for the microwave response, one can use the high-field permeability data to determine an operational "effective linewidth" for the material.

The complex microwave permeability μ for spherical, nonconducting particles magnetized to saturation by an applied static magnetic field H_0 may be written as

$$\mu - 1 = \omega_m(\omega_0 + i\eta_0)/[(\omega_0 + i\eta_0)^2 - \omega^2]. \quad (1)$$

The parameters $\omega_m = \gamma 4\pi M_s$ and $\omega_0 = \gamma H_0$ express the saturation induction $4\pi M_s$ and the static applied field H_0 in frequency units [γ is the (positive) gyromagnetic ratio, approximately 2.9 GHz/kOe for iron], ω is the microwave frequency, and η_0 denotes the relaxation rate. The "effective linewidth" for a material with the above response is given by $\Delta H_{\text{eff}} = 2\eta_0/\gamma$. This ΔH_{eff} parameter simply expresses the off-resonance relaxation rate in linewidth units for convenient comparison with the conventional half-power ferromagnetic resonance linewidths for saturated materials.

The microwave premeability is related to the microwave cavity Q and resonance frequency ω through perturbation theory.[2] With the usual definition of μ in terms of its positive real and negative imaginary parts, $\mu = \mu' - i\mu''$, the connections with Q and ω are given by

$$\mu' - 1 = -2K[(\omega - \omega_\infty)/\omega] \quad (2)$$

and

$$\mu'' = K(1/Q - 1/Q_\infty). \quad (3)$$

The ω_∞ and Q_∞ parameters correspond to the cavity resonance frequency and Q extrapolations at infinite field. From the response in Eq. (1), the infinite field frequency ω_∞ can be obtained from plots of ω vs a "$1/H$" parameter p given by

$$p = (\omega/\omega_0)/[1 - (\omega/\omega_0)^2]. \quad (4)$$

Such plots (essentially ω vs $1/H_0$) are linear at high field [as one would expect from Eqs. (1) and (2)] and extrapolate to ω_∞ at $p = 0$ (or $H_0 = \infty$). Similarly, Q_∞ is obtained from plots of Q vs a "$1/H^2$" parameter q given by

$$q = \frac{1}{2}\left(\frac{\gamma^2}{\omega_0^2}\right)\frac{[1 + (\omega/\omega_0)^2]}{[1 - (\omega/\omega_0)^2]^2}. \quad (5)$$

Such plots (essentially Q vs $1/H_0^2$) are linear at high field and extrapolate to Q_∞ at $q = 0$ (or $H_0 = \infty$). These extrapolation procedures were carried out for fields in the range 10–15 kOe.

The coefficient K in Eqs. (2) and (3) may be obtained empirically or directly from perturbation theory. The empirical approach was used here. This approach uses the fact that μ' at high field is relatively insensitive to the parameter η_0 and depends only on γ, $4\pi M_s$, H_0, and ω. Calculated values of μ' vs field were used in conjunction with measurements of the cavity frequency versus field and Eq. (2) to determine K for a given powder sample/cavity combination. This value of K was used to convert Q versus field data to values of μ'' versus field. The imaginary part of Eq. (1) was then fitted to the empirical μ'' vs H_0 results to determine η_0 and ΔH_{eff}. Values of K from perturbation theory were found to be almost a factor of 2 smaller than indicated by the empirical approach. These errors are attributed to problems in accurately estimating sample volumes, cavity loading effects for the metallic powder specimens, and modifications in μ due to particle interactions.

The basic experimental procedure was to load a small, loosely compacted powder sample in a high-Q TE011 cylindrical 9.9-GHz microwave cavity, use the technique of Refs. 1 and 2 to measure the cavity frequency and Q as a function of applied field, use the analysis described above to calibrate

 0021-8979/88/083771-03$02.40 © 1988 American Institute of Physics

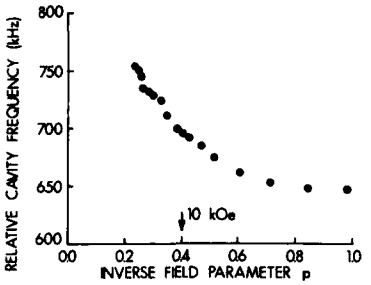


FIG. 1. Cavity frequency, relative to a reference frequency of 9.966 GHz, as a function of the "$1/H$" inverse field parameter p defined in the text.

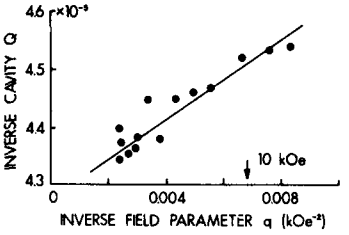


FIG. 2. Inverse cavity Q as a function of the "$1/H^2$" inverse field parameter q defined in the text.

the system response, and then determine μ'' versus field and the effective linewidth at high field.

Data were obtained on iron-carbonyl powder materials with 0.6–0.8 wt. % carbon, 0.6–0.8 wt. % nitrogen, nominal particle sizes of 1.5–2.5 μm, and nominal saturation inductions ($4\pi M_s$) of 17–19 kG. The $4\pi M_s$ values were obtained by standard vibrating sample magnetometry (VSM) techniques. Magnetic saturation required fields in excess of about 10 kOe, as expected for iron-based powders consisting of irregular but roughly spherical particles.[3] The measurements were made on 0.5–0.6-mg powder samples compacted and sealed in 1-mm-diam cups in small microwave dielectric sample holders.

Data on cavity frequency versus the dimensionless "$1/H$" parameter p are shown in Fig. 1. The frequency values on the vertical axis indicate the cavity frequency shift, in kHz, relative to 9.966 GHz. The 700-kHz point, for example, corresponds to a cavity frequency of 9.966 700 GHz. The measured cavity frequency increases as the "p" parameter decreases. There is a more-or-less linear region for $p < 0.4$ and a more gradual, somewhat rounded response for higher values of p. The $p = 0.4$ point corresponds to an applied static field H_0 of 10 kOe. As mentioned above, the VSM data showed that fields above about 10 kOe are necessary to magnetically saturate the powders, a necessary condition for the above microwave response equations to be applicable. The data for $p < 0.4$ were used, therefore, for the extrapolation to obtain ω_∞.

Figure 2 shows the corresponding results on inverse cavity Q vs the "$1/H^2$" parameter q. Here, the high field data region corresponding to magnetic saturation ($H_0 > 10$ kOe is for $q < 0.007$ kOe^{-2}). The changes in cavity Q at high field, however, are so small that the scatter in the data makes it difficult to separate the character of the $1/Q$ vs q response into saturated and unsaturated regions. Nevertheless, only the data for $q < 0.007$ kOe^{-2} were used for the $q = 0$ ($H_0 = \infty$) extrapolation to obtain Q_∞.

Figure 3 shows two theoretical curves and two sets of data points for the reduced real part of the permeability ($\mu' - 1$) vs static field H_0. The theoretical curves are based on Eq. (1) for two different values for ΔH_{eff}, 500 Oe [curve (a)] and 4000 Oe [curve (b)]. These curves show that ($\mu' - 1$) is relatively insensitive to the choice of the ΔH_{eff} parameter for fields above 10–12 kOe.

The open circle data points in Fig. 3 represent values of ($\mu' - 1$) which were obtained directly from perturbation theory, based on the theoretical empty-cavity unperturbed TE011 mode, a sample volume inferred from measured sample mass and density values, and the frequency data discussed above. It is evident from the figure that these points lie well *below* the theoretical curves. The discrepancy at the highest fields shown is almost a factor of 2. This discrepancy is attributed to cavity loading effects and the lack of a well-defined powder volume parameter for the metallic powders. The approach used here was to adjust empirically the perturbation theory coefficient K in Eq. (2) [and in Eq. (3)] to "force" a fit of the ($\mu' - 1$) data to the theoretical curves at very high field, $H_0 > 14$ kOe. This "empirical" K value was then used for the μ'' versus field and effective linewidth analysis (discussed below). The result of this procedure for ($\mu' - 1$) is shown by the *solid* circle data points in Fig. 3. These points track the theoretical curve for $\Delta H_{\text{eff}} = 500$ Oe rather well for fields above 9 kOe and fall below this curve at lower fields. This fall-off is attributed to the lack of magnetic saturation for fields below 10 kOe.

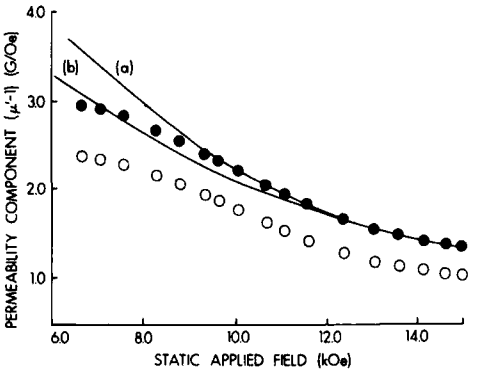


FIG. 3. Real part ($\mu' - 1$) of the reduced microwave permeability as a function of applied static field. The solid lines represent theoretical curves for $\Delta H_{\text{eff}} = 500$ Oe [curve (a)] and $\Delta H_{\text{eff}} = 4000$ Oe [curve (b)]. The open circles represent the experimental results based on the frequency data and cavity perturbation theory. The solid circles represent the experimental results adjusted to fit the theoretical curves at high field.

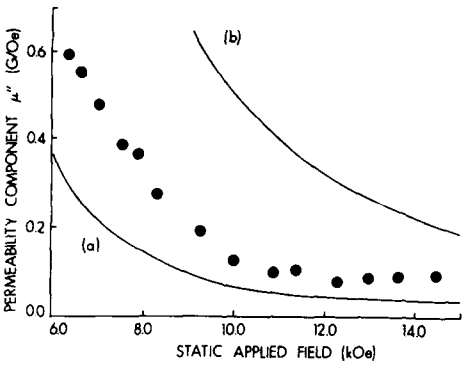


FIG. 4. Negative imaginary part μ'' of the reduced microwave permeability as a function of applied static field. The solid lines represent theoretical curves for $\Delta H_{\text{eff}} = 500$ Oe [curve (a)] and $\Delta H_{\text{eff}} = 4000$ Oe [curve (b)]. The solid circles represent the experimental results based on the empirical cavity calibration procedure discussed in the text.

Before considering the μ'' results, it is worthwhile to point out that the curves and fits in Fig. 3 for $(\mu' - 1)$ already give a rough indication of the operational ΔH_{eff} value for the powder. The theoretical curve for $\Delta H_{\text{eff}} = 500$ Oe tracks the solid data points down to somewhat lower fields than does the $\Delta H_{\text{eff}} = 4000$ Oe curve. This better tracking provides a preliminary indication that the operational powder effective linewidth is in the "hundreds of Oe" rather than the "thousands of Oe" range.

Figure 4 shows the corresponding theoretical curves and adjusted data points for μ'' vs H_0. The two curves are based on the same parameters as in Fig. 3, with ΔH_{eff} values of 500 Oe (lower curve) and 4000 Oe (upper curve). The data points (solid circles) were obtained from the Q vs H_0 data and the empirical K parameter from the $(\mu' - 1)$ fit discussed above. The theoretical μ'' vs H_0 curves for $\Delta H_{\text{eff}} = 500$ Oe and $\Delta H_{\text{eff}} = 4000$ Oe are quite different. As is evident from Eq. (1), the theoretical expression for μ'' contains η_0 (and hence ΔH_{eff}) as a multiplying factor. It is precisely this sensitivity of μ'' to ΔH_{eff} that makes it possible to use the μ'' versus field data to determine high-field effective linewidths. The data points in Fig. 4 lie slightly above the theoretical curve for $\Delta H_{\text{eff}} = 500$ Oe and track this curve fairly closely down to $H_0 = 10$ kOe. This high-field fit indicates an intrinsic X-band effective linewidth slightly higher than 500 Oe. The slight upturn in the data points at fields above 13 kOe is an artifact of the technique at high fields when μ'' becomes small.

For fields below 10 kOe, the data points move above the theoretical curve for $\Delta H_{\text{eff}} = 500$ Oe. As the powder becomes unsaturated, the microwave losses increase and the measured μ'' values become larger than expected on the basis of Eq. (1). It should be possible to use μ'' data for the entire range of fields below saturation, $0 < H_0 < 10$ kOe, to model the powder microwave properties for the partially magnetized and demagnetized states.

An alternative procedure to determine ΔH_{eff} should be mentioned. This procedure is based on the fact that the *slope* of the $1/Q$ vs q response at high field (Fig. 2) is proportional to η_0, and hence to ΔH_{eff} as well. The straight line in Fig. 2 corresponds to $\Delta H_{\text{eff}} = 500$ Oe, based on the empirical calibration parameter K discussed above.

The authors are grateful to Dr. I. B. Goldberg of the Rockwell International Science Center, Thousand Oaks, California, for supplying the samples, and to Dr. Gopalan Srinivasan for assistance with the measurements and analyses.

[1]C. E. Patton and H. Schmidt, IEEE Trans. Magn. **MAG-14**, 880 (1978).
[2]C. E. Patton and T. Kohane, Rev. Sci. Instrum. **43**, 76 (1972).
[3]See the brief but useful article, C. P. Bean and I. S. Jacobs, J. Appl. Phys. **31**, 1228 (1960), for a discussion of magnetization processes and magnetic saturation in iron powders.

Ferrite-organic multilayer film for microwave monolithic integrate circuits prepared by ferrite plating based on the spray-spin-coating method

M. Abe,[a] T. Itoh,[a] Y. Tamaura,[b] and M. Gomi[a]
Tokyo Institute of Technology, Ookayama, Meguro-ku, Tokyo 152, Japan

We have made multilayer films in which NiZn-ferrite ($Fe_{2.70\pm0.04}$-$Ni_{0.14\pm0.03}Zn_{0.14\pm0.03}O_4$) layers (2000–8000 Å thick) and dextran [$(C_6H_{10}O_5)_{1200\text{-}1800}$] buffer layers (100 Å thick) are laminated alternately on a glass substrate. The ferrite layers were formed by ferrite plating based on the spray-spin-coating method at 80 °C, compatible with the low heat resistance (~300 °C) of GaAs microwave monolithic integrated circuits. To enhance the adhesive power of the multilayer film, thin (~300 Å) magnetite layers were deposited intermediate between the NiZn-ferrite and dextran and also between the NiZn-ferrite and the substrate. The grain growth in the ferrite layers is interrupted at the dextran buffer layers, which release the stress induced in the ferrite layers. Thus the multilayer film can grow much thicker (i.e., up to ~5 μm) than a NiZn-ferrite monolayer film which peels off at ~1.5 μm thickness due to the stress. In the multilayer films, the ferrite layers are of polycrystalline spinel structure having no preferred orientation. The magnetization does not exhibit an anisotropy, lying in the plane of film.

I. INTRODUCTION

Ferrite plating facilitates formation of crystalline spinel films at low temperature (<90 °C) in an aqueous solution.[1–9] This enables us to use non-heat-resisting materials, such as plastics, as a substrate. Thus the ferrite plating has opened the door to new ferrite-film devices using a substrate made of non-heat-resisting materials. The first practical application of the ferrite plating is a magnetic capsule toner and carrier for zerography and magnetography, in which organic polymer particles are coated with a magnetic layer by ferrite plating.[9] We hope the second application of the ferrite plating to be nonreciprocal ferrite components on a microwave monolithic integrated circuit (MMIC) based on GaAs.[8] The ferrite plating is considered to be the only technique available at present to form a continuous ferrite layer of good quality on GaAs IC chips which have a low deterioration temperature of ~300 °C.[8] Conventional ferrite film preparation techniques, such as sputtering, pyrolysis, paste method, etc., require substrate heating above several hundred °C to get the ferrite crystallized.

We have reported in a previous paper that the ferrite-plating film can be formed on GaAs in various ways.[8] The best way among them was to form the ferrite film by the spray-spin-coating method on a SiO_2 intermediate layer formed on the surface of the GaAs surface. The intermediate layer enhances adhesion of the film onto the substrate surface. Using a NiZn-ferrite film made in the best way, we have fabricated a junction-type circulator, on which nonreciprocal isolator action has been observed. However, a serious problem has arisen in that the ferrite film lost its mirror luster when its thickness exceeded ~1 μm, and it peeled off when it exceeded ~1.5 μm. This may be because stress is induced in the film, which becomes strong as columnar-shaped grain[7,8] grows with an increase of thickness.

We may be able to overcome this defect by laminating alternately the ferrite films and buffer layers which release the stress. Candidates for the buffer layer material are polymers (such as saccharides) having OH groups and polymers (such as silylation reagents) having function groups. The OH and the function groups can chemically couple with Fe ions of the ferrite film.[3,4] In this study we have made on trial the laminated films, using as the buffer layer material saccharides such as D-glucose [$C_6H_{12}O_6$], soluble starch [$(C_6H_{10}O_5)_6$], and dextran [$(C_6H_{10}O_5)_n$, $n=1200$–1800], and silylation reagents such as 3-aminopropyl-ethoxysilane and 3-mercaptopropyltrimethoxysilane. Since good results were obtained only for dextran, we concern ourselves with only the multilayer films of the dextran buffer layers in the following sections. We describe the preparation of the multilayer films, and present structural and magnetic properties of the films.

II. EXPERIMENTAL AND RESULT

On glass substrates (3 cm×3 cm×0.5 mm) we have formed the multilayer films of the structure shown in Fig. 1, laminating the NiZn-ferrite and dextran layers. The initial NiZn-ferrite layer was intermediated by a thin (~300 Å)

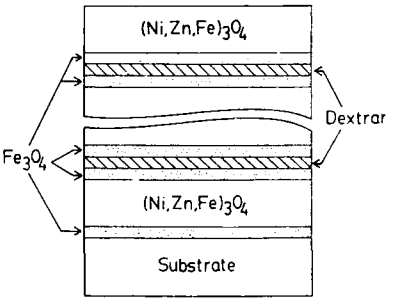


FIG. 1. Structure of ferrite-organic multilayer film.

[a] Department of Physical Electronics.
[b] Department of Chemistry.

 0021-8979/88/083774-03$02.40 © 1988 American Institute of Physics

magnetite layer, and the dextran layers were sandwiched by similar magnetite layers. This was required to enhance the adhesion of the NiZn-ferrite films onto the surfaces of the substrate and the dextran layers.

We have formed the NiZn-ferrite and the magnetite layers by the "improved spray-spin-coating" method.[10] Reaction and oxidizing solutions given in Table I were simultaneously sprayed onto the substrate, which was kept at 80 °C and rotated at 300 rpm. For the dextran layer we sprayed a dextran solution (1 g/l concentration) for 2 min, after which we sprayed water to wash off the dextran which did not react into the layer.

We have made multilayer films of three types, F-5, F-10, and F-20, in which each NiZn-ferrite layer was plated for 5, 10, and 20 min, respectively, ~2000, ~4000, and ~8000 Å in thickness. The deposition rate in the ferrite plating was 400 Å/min. The films of types F-5, F-10, and F-20 peeled off when the thickness of the multilayer film exceeded ~5.5, ~4, and ~3 μm, respectively. The thinner the NiZn-ferrite layer, the thicker the multilayer film can grow. The thickest multilayer films obtained for the respective types, together with a monolayer film for comparison, are listed in Table II.

The chemical composition of the films has been analyzed by the atomic absorption method. The compositions of all the multilayer films (averaged over the NiZn and Fe_3O_4 ferrites) were expressed as $Fe_{2.70\pm0.04}Ni_{0.14\pm0.03}Zn_{0.14\pm0.03}O_4$ with which that of the monolayer film (composed only of NiZn-ferrite) agreed. The composition difference between the multilayer and the monolayer films due to the Fe_3O_4 layers was masked by the error in the analysis.

Figure 2 shows cross sections of the multilayer films observed by SEM. The columnar structure is interrupted by the dextran buffer layers. The grain stops growing and starts growing again at the buffer layers. This releases the stress due to the grain growth, so that the multilayer film can grow without peeling off above the limit for the monolayer. The dextran layer was hardly recognized by SEM, indicating that its thickness is less than ~100 Å. This implies that the dextran layer is of a monomolecular type, since dextran is about 100 Å in size.

The multilayer films have given x-ray (Cu $K\alpha$) diffraction diagrams composed only of peaks ascribable to spinel structure, exhibiting no preferred orientation.

Measurement by a VSM has shown that the magnetization in the multilayer films does not show an anisotropy, lying in the plane of film, similar to the monolayer film. As one can see in Table II, the saturation magnetization does not change appreciably for F-5, F-10, F-20, and the monolayer, but coercive force reduces in this order, from 77 Oe in F-5 to 31 Oe in the monolayer film.

Figure 3 shows ferromagnetic resonance (FMR) traces obtained for the multilayer film F-5 together with a monolayer film (~1 μm thick) for comparison. They were taken at 8.941 GHz with the magnetic field perpendicular to the film plane. The multilayer film exhibits a resonance centered at $H = 7.5$ kOe with a width $\Delta H = 366$ Oe, while the monolayer film exhibits that at $H = 7.6$ kOe with $\Delta H = 175$ Oe. The ΔH in the multilayer film is twice as wide as that in the monolayer film.

TABLE I. Aqueous solutions used in ferrite plating.

	pH	Chemical	Content (g/l)
Reaction solution	5.2	$FeCl_2\,3.5H_2O$	3.0
		$NiCl_2\,6H_2O$	1.5[a]
		$ZnCl_2$	0.02[a]
Oxidizing solution	6.9	$NaNO_2$	0.5
		CH_3COONH_4	5.0

[a] 0 g/l for plating Fe_3O_4 layer.

TABLE II. Parameters for multilayer films (F-5, F-10, F-20) and monolayer film.

Type of film	NiZn-ferrite layer: Plating time (min)	NiZn-ferrite layer: Number	Total thickness[a] (μm)	Magnetization (emu/g)	Coercive force (Oe)
F-5	5	20	5.2[b]	92[b]	79[b]
F-10	10	10	3.7[b]	93[b]	67[b]
F-20	20	4	3.0[b]	90[b]	56[b]
Monolayer	30	1	0.8	81	31

[a] Determined by chemical analysis based on atomic absorption method, assuming that the film density is equal to that for Fe_3O_4.
[b] Averaged over NiZn-ferrite and Fe_3O_4 layers.

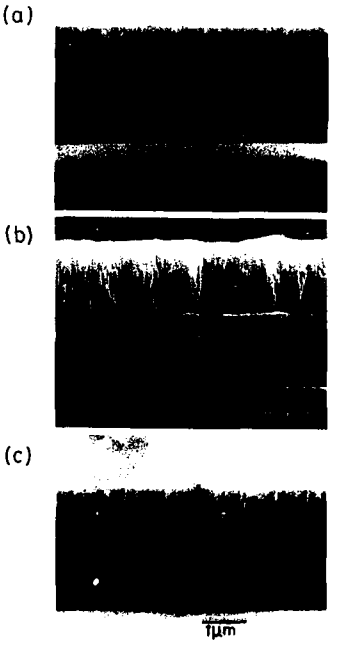


FIG. 2. SEM observation on a cross section of multilayer films of (a) F-5, (b) F-10, and (c) F-20, given in Table II.

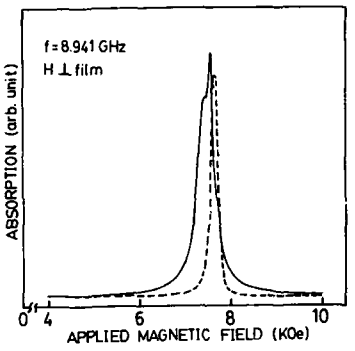


FIG. 3. FMR traces for multilayer film F-5 (solid curve) and monolayer film (dotted curve).

We have encountered a serious problem where the multilayer films peels off when they are heated above ~100 °C, though the monolayer film (which is thin, i.e., ~0.8 μm) does not. We could not, therefore, make microstrip lines of Au on the multilayer film in order to fabricate a junction-type circulator. Making the strip lines, the film is heated above ~100 °C during sputtering of Au or making a photoresist coating. Then, we have constructed the circulator by pressing microstrip lines which were formed on a glass plate onto the multilayer film of type F-5. Its circulator performance at 3–5 GHz was similar to that obtained on the NiZn-ferrite monolayer film.[8] Details will be reported elsewhere.

III. CONCLUDING REMARKS

Our main results are summarized as follows:

(1) By the improved spray-spin-coating method we have made multilayer films composed of NiZn-ferrite layers and dextran buffer layers (~100 Å in thickness). The dextran layers were sandwiched by thin (~300 Å) intermediate Fe_3O_4 layers, and the initial NiZn-ferrite layer was intermediated by a similar Fe_3O_4 layer in order to enhance the adhesive power of the NiZn-ferrite films.

(2) In the multilayer films the columnar structure and grain growth in the NiZn-ferrite layers are interrupted at the buffer layers. This releases the stress which is induced in the NiZn-ferrite layers as the grain grows. Thus the multilayer film can grow much thicker (i.e., ~5 μm) than the monolayer film which peels off above ~1.5 μm thickness due to the stress. A multilayer film having thinner NiZn-ferrite layers can grow thicker than that having thicker NiZn-ferrite layers, because the stress is released more in the former than the latter.

(3) The multilayer film exhibits a wider ΔH of the FMR curve than the monolayer film, probably due to the Fe^{2+} ions in the Fe_3O_4 intermediate layers.

(4) The multilayer films peel off when heated above ~100 °C. To overcome defects (3) and (4), we must dispense with the Fe_3O_4 intermediate layer. For this we must find a buffer layer material which has a strong adhesion onto the NiZn ferrite as well as a higher heat resistance than dextran.

The authors are thankful to Professor Y. Gondo of Yokohama National University for allowing us to perform the FMR measurement at his laboratory.

[1] M. Abe and Y. Tamaura, Jpn. J. Appl. Phys. **22**, L511 (1983).
[2] M. Abe and Y. Tamaura, J. Appl. Phys. **55**, 2614 (1984).
[3] M. Abe, Y. Tanno, and Y. Tamaura, J. Appl. Phys. **57**, 3795 (1985).
[4] Y. Tamaura, Y. Tanno, and M. Abe, Bull. Chem. Soc. Jpn. **58**, 1500 (1985).
[5] M. Abe and Y. Tamaura, Adv. Ceram. **15**, 639 (1985).
[6] M. Abe, Y. Tamaura, Y. Goto, N. Kitamura, and M. Gomi, J. Appl. Phys. **61**, 3211 (1987).
[7] M. Abe, Y. Tamaura, M. Ohishi, T. Saitoh, and M. Gomi, IEEE Trans. Magn. (to be published).
[8] M. Abe, T. Itoh, Y. Tamaura, Y. Goto, and M. Gomi, IEEE Trans. Magn. **MAG-23**, 3736 (1987).
[9] K. Ishikawa, M. Ohishi, T. Saitoh, M. Abe, and Y. Tamaura, Digests of Intermag '87, EB-04.
[10] In this method the reaction solution has a low pH value (i.e., 5.2), which prevents Fe^{2+} ions in the solution from being oxidized to Fe^{3+} before the solution is sprayed and mixed with the oxidizing solution. Thus we do not need to use oxygen-free water which was used in the previous spray-spin-coating method to inhibit the oxidization. This saves labor in the experiment. Details will be reported elsewhere.

Molecular-field coefficients of $MnFe_2O_4$ and $NiFe_2O_4$ spinel ferrite systems

Gerald F. Dionne
Lincoln Laboratory, Massachusetts Institute of Technology, Lexington, Massachusetts 02173

Calculated thermomagnetization curves for $MnFe_2O_4$ and $NiFe_2O_4$ have been matched to reported experimental results. Since both Mn^{2+} and Ni^{2+} ions are also strongly exchange coupled to the Fe^{3+} ions, separate sets of molecular-field coefficients were determined for each of these interactions and then averaged into the basic two-sublattice solution. For the usual case with 80% of the manganese in tetrahedral (A) sites, the ratios of coefficients determined from the fit to experiment agree closely with the values found from high-temperature susceptibility measurements, with $|N_{AA}/N_{AB}| = 0.840$ and $|N_{BB}/N_{AB}| = 0.295$. For Ni ferrite, these ratios exceed those determined from magnetic susceptibilty measurements, suggesting an intrasublattice exchange for nickel that is stronger than previously considered. Calculations of magnetic dilution effects in both the manganese and nickel families show good accuracy for a practical range of Zn^{2+} substitutions in A sites.

I. INTRODUCTION

The phenomenological theory of ferrimagnetism has been successfully extended to multication oxide systems through the use of semiempirical relations between molecular-field coefficients and magnetic ion concentrations. In particular, thermomagnetization curves for a wide range of rare-earth magnetic garnets[1,2] and spinel ferrites[3] have been computed with high accuracy. In the work reported to date for the spinels, however, the analyses have been restricted to systems in which Fe^{3+} is the only magnetic ion. Unlike the garnet system where the magnetic rare earths occupy their own separate sublattice of dodecahedral sites, strongly magnetic Mn^{2+} and Ni^{2+} ions of the important manganese and nickel ferrites share the tetrahedral (A) and octahedral (B) sites with the principal Fe^{3+} magnetic constituent.

To adapt the conventional molecular-field approach to Mn and Ni ferrites, individual coefficients for Mn^{2+} and Ni^{2+} among themselves and with the Fe^{3+} ions that share the two sublattices must be determined. In this paper, the exchange effects between the different magnetic ions/sublattices are represented by effective values for the N_{AA}, N_{BB}, and N_{AB} coefficients found by a weighted averaging procedure. The results of this model are then presented in the form of thermomagnetization curves of $MnFe_2O_4$ and $NiFe_2O_4$ that include Zn^{2+} A-sublattice dilutions of up to 40%.

II. THEORY

The basic model and notation to be applied here has been detailed in earlier work[3] and will be followed in every respect. For the case where more than one type of magnetic ion shares the i and j sublattices, the effective values of the spin S_i, the spectroscopic splitting factor g_i, and the molecular-field coefficients N_{ij} will be determined as mean values of the individual ion contributions, weighted by the respective fractional concentrations. To keep track of the second magnetic cation and its distribution over the two sublattices, the following notation will be adopted. The generic spinel chemical formula $A[B_2]O_4$ will be written as $Fe_{af}M_{am}[Fe_{bf}M_{bm}]O_4$, where $af + am = 1$, and $bf + bm = 2$. With these definitions, the weighted average values of the relevant variables may now be listed according to

$$S_A = S_f p_{af} + S_m p_{am} , \quad (1)$$
$$S_B = S_f p_{bf} + S_m p_{bm} ,$$

$$g_A = g_f p_{af} + g_m p_{am} , \quad (2)$$
$$g_B = g_f p_{bf} + g_m p_{bm} ,$$

$$N_{AA} = N_{aaff} p_{af}^2 + N_{aamm} p_{am}^2 + 2N_{aafm} p_{af} p_{am} , \quad (3)$$
$$N_{BB} = N_{bbff} p_{bf}^2 + N_{bbmm} p_{bm}^2 + 2N_{bbfm} p_{bf} p_{bm} ,$$
$$N_{AB} = N_{abff} p_{af} p_{bf} + N_{abmm} p_{am} p_{bm} + N_{abfm} (p_{af} p_{bm} + p_{bf} p_{am}) ,$$

where the N_{ijkl} coefficients represent the average exchange interactions between the various combinations of sublattices and ions as indicated by the respective subscripts, and the weighting fractions (probabilities) are given by

$$p_{af} = af/(af + am), \quad p_{am} = am/(af + am) , \quad (4)$$

TABLE I. N_{ijkl} coefficients of $MnFe_2O_4$ and $NiFe_2O_4$.

	ff (cm^3/mole)	*mm* (Mn) (cm^3/mole)	*fm* (Mn) (cm^3/mole)	*mm* (Ni) (cm^3/mole)	*fm* (Ni) (cm^3/mole)
N_{AA}	− 200	− 160	− 180	...	...
N_{BB}	− 60	− 58	− 59	− 60	− 60
N_{AB}	312	62	187	240	276

 0021-8979/88/083777-03$02.40 © 1988 American Institute of Physics

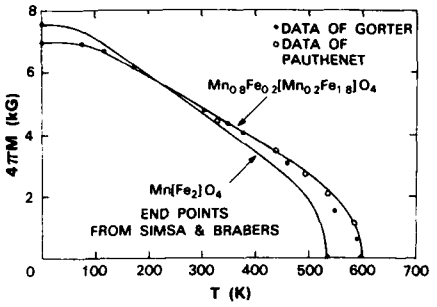


FIG. 1. $Mn_{0.8}Fe_{0.2}[Mn_{0.2}Fe_{1.8}]O_4$ and $Mn[Fe_2]O_4$ computed thermomagnetization curves, compared with published data (Refs. 6–8).

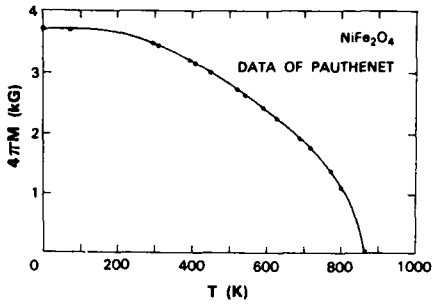


FIG. 3. $Fe[NiFe]O_4$ thermomagnetization curve, compared with data (Ref. 8).

$$p_{bf} = bf/(bf + bm), \quad p_{bm} = bm/(bf + bm) .$$

A final relation based on reported experiments will be required:

$$N_{ijfm} \approx (1/2)(N_{ijff} + N_{ijmm}) . \tag{5}$$

III. DETERMINATION OF MOLECULAR-FIELD COEFFICIENTS

Of the two basic systems studied in this work, manganese ferrite is more complex, principally because the Mn^{2+} ion can occupy either sublattice. In addition, severe spin canting of the Mn in the B sublattice must be taken into account by a factor ($\cos 53° = \frac{3}{5}$) multiplying the Mn contribution to the B-sublattice magnetic moment.[6]

The nine individual coefficients of Eq. (3) listed in Table I were determined from data for two Mn site distributions: (i) partially inverted $Mn_{0.8}Fe_{0.2}[Mn_{0.2}Fe_{1.8}]O_4$,[7,8] with $af = 0.2$, $am = 0.8$, $bf = 1.8$, and $bm = 0.2$, and normal $Mn[Fe_2]O_4$[4,6] with $af = 0$, $am = 1$, $bf = 2$, and $bm = 0$. The procedure was as follows:

(1) N_{aaff}, N_{bbff}, and N_{abff} of the Fe^{3+}–O^{2-}–Fe^{3+} couplings were taken from previously reported work.[9]

(2) The remaining six coefficients in Eq. (3) were then reduced to three by means of Eq. (5).

(3) A computed thermomagnetization curve of the well-documented $Mn_{0.8}Fe_{0.2}[Mn_{0.2}Fe_{1.8}]O_4$ (see Fig. 1) was carefully fitted to the data, and the resulting values of N_{AA}, N_{BB}, and N_{AB} were used in Eq. (3) to determine the remaining three [six with the aid of Eq. (5)] individual coefficients listed in Table I.

(4) The coefficient values determined above were then verified with a computed thermomagnetization curve of normal $Mn[Fe_2]O_4$ (see Fig. 1) that was plotted to fit the Curie temperature and the data point at $T = 0$.

With these coefficients, thermomagnetization curves for the complete range of Mn site distributions in the system $Mn_{1-y}Fe_y[Mn_yFe_{2-y}]O_4$ from $y = 0$ (normal) to $y = 1$ (inverted) were computed and are presented in Fig. 2.

To determine the coefficients for nickel ferrite, the same trial-and-error technique was employed. The case for $Fe[NiFe]O_4$ is less complicated than Mn^{2+} because the Ni^{2+} ions occupy only the B sublattice, which means that all quantities identified by the subscript am are zero (including N_{aamm} and N_{aafm}). In addition, $S_m = 1$, $g_m \approx 2.3$, and the B-sublattice canting factor is unity.

The computed thermomagnetization curve for nickel ferrite is plotted in Fig. 3 and compared with the experimental results,[8] with the resulting coefficients listed in Table I.

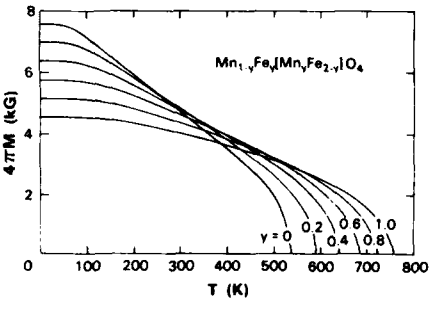


FIG. 2. Thermomagnetization curves for $Mn_{1-y}Fe_y[Mn_yFe_{2-y}]O_4$.

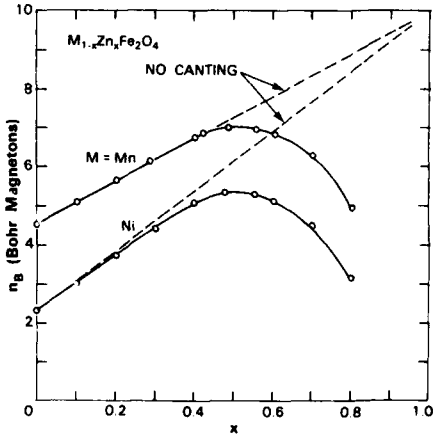


FIG. 4. B-sublattice canting effects on the resultant n_B per formula unit as a function of A-sublattice dilution for Mn and Ni ferrite.

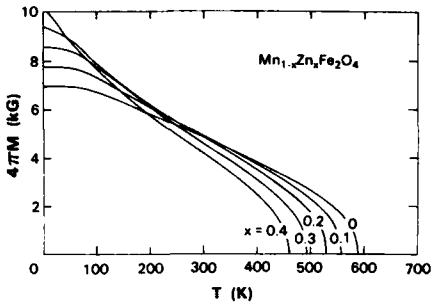


FIG. 5. $Mn_{0.8(1-x)}Fe_{0.2(1-x)}Zn_x[Mn_{0.2(1-x)}Fe_{1.8+0.2x}]O_4$ thermomagnetization curves. Theory compares favorably with the limited published data (Ref. 12).

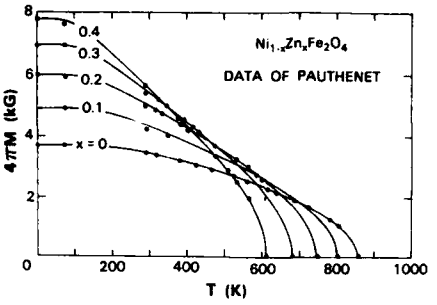


FIG. 6. $Fe_{1-x}Zn_x[Ni_{1-x}Fe_{1+x}]O_4$ thermomagnetization curves, compared with data (Ref. 8).

IV. MAGNETIC DILUTION WITH ZINC

Mn and Ni ferrites are also important technological compositions with Zn^{2+} substitutions into the A sublattice. To dilute the A sublattice of these systems, the effects of B-sublattice canting as a function of dilutant concentration must be introduced.

In Fig. 4,[10] it is seen that for $x \leq 0.4$ there is no departure from the collinear model for Mn ferrite. For Ni ferrite, however, an empirical factor $(1 - 0.4x^2)$ must be applied to the resultant B-sublattice magnetization. For Li ferrite, this factor was determined to be $(1 - 0.8x^2)$.[3] In addition, the N_{ij} correction factors for dilution of LiZnTi ferrite[11] must also be applied in these systems.

For the MnZn ferrite curves plotted in Fig. 5, it was assumed that Mn maintained the 4:1 distribution between the A and B sites through the entire series, according to $Mn_{0.8(1-x)}Fe_{0.2(1-x)}Zn_x[Mn_{0.2(1-x)}Fe_{1.8+0.2x}]O_4$. In Fig. 6, curves are presented for the NiZn ferrite family, following the simpler formula $Fe_{1-x}Zn_x[Ni_{1-x}Fe_{1+x}]O_4$. In both cases, good agreement with experiment[8,12] was obtained over the range of $x \leq 0.4$.

V. CONCLUSIONS

For the usual case with 80% of the manganese in tetrahedral (A) sites, the coefficients determined from the fit to experiment agree closely with the values found from high-temperature susceptibility measurements, with $|N_{AA}/N_{AB}| = 168/200 = 0.840$ and $|N_{BB}/N_{AB}| = 59/200 = 0.295$. The corresponding ratios determined from susceptibility measurements are 0.82 and 0.28, respectively.[13] With coefficients available for Mn^{2+} on both A and B sites, predictions of thermomagnetization curves made for various Mn^{2+} site distributions suggest that the B-sublattice spin canting effects remain a dominant factor in limiting the maximum magnetization and Curie temperature values. As a consequence, magnetization values much above 5000 G that were discussed in recent work[9] appear unlikely in this system.

For Ni ferrite, $|N_{AA}/N_{AB}| = 200/294 = 0.680$ and $|N_{BB}/N_{AB}| = 60/294 = 0.204$, exceeding those determined from magnetic susceptibilty measurements 0.20 and 0.15, respectively,[14] to suggest an intrasublattice exchange for nickel stronger than previously considered.

Calculations of magnetic dilution effects in both the manganese and nickel families show good accuracy for up to 40% of Zn^{2+} substitution in A sites.

ACKNOWLEDGMENTS

The author is grateful to Gary A. Allen for invaluable assistance in computer programming and computation. This work was sponsored by the Department of the Army.

[1] G. F. Dionne, J. Appl. Phys. **41**, 4874 (1970).
[2] G. F. Dionne and P. F. Tumelty, J. Appl. Phys. **50**, 8257 (1979).
[3] G. F. Dionne, J. Appl. Phys. **45**, 3621 (1974).
[4] F. K. Lotgering, Philips Res. Rep. **20**, 320 (1965).
[5] A. Broese van Groenou, P. F. Bongers, and A. L. Stuijts, Mater. Sci. Eng. **3**, 317 (1968).
[6] Z. Simsa and V. A. M. Brahers, IEEE Trans. Magn. **MAG-11**, 1303 (1975).
[7] E. W. Gorter, Philips Res. Rev. **9**, 295 (1954).
[8] R. Pauthenet, Ann. Phys. **7**, 710 (1952).
[9] G. F. Dionne, J. Appl. Phys. **61**, 3865 (1987).
[10] J. Smit and H. P. J. Wijn, *Ferrites* (Wiley, New York, 1959), p. 151.
[11] In previous work (Ref. 9), two dilution factors were adopted for the A sublattice, $x = k'_A$ and/or k'_A. For the systems studied here, k'_A was used for Mn ferrite and $x = k'_A$ for Ni ferrite.
[12] C. Guillaud and H. Creveaux, C. R. Acad. Sci. **230**, 1458 (1950).
[13] C. A. Clark and W. Sucksmith, Proc. R. Soc. London Ser. A **225**, 147 (1954).
[14] L. Néel and P. Brochet, C. R. Acad. Sci. **230**, 280 (1950).

Dielectric and magnetic properties of polycrystalline cobalt-substituted LiTi ferrites

B. K. Kuanr
Department of Electronic Science, University of Delhi, Delhi-110021, India

P. K. Singh
National Physical Laboratory, New Delhi-110012, India

P. Kishan and N. Kumar
Solid State Physics Laboratory, Delhi-110007, India

S. L. N. Rao
Department of Electronic Science, University of Delhi, Delhi-110021, India

Prabhat K. Singh
Physics Department, University of Delhi, Delhi-110007, India

G. P. Srivastava
Department of Electronic Science, University of Delhi, Delhi-110021, India

The electric, dielectric permittivity, loss tangent, microwave power absorption, and hysteresis loop parameters were studied on a series of cobalt-substituted lithium titanium ferrites. The experimental results indicate that cobalt substitution affect all these parameters. The observed dispersion in conductivity and dielectric permittivity with frequency and temperature are in accordance with Maxwell–Wagner model while the microwave and hysteresis loop properties can be interpreted with the help of Dionne's exchange isolation model.

INTRODUCTION

In some microwave device applications the nonlinearities impair the performance of ferrites at high-power levels. The general practice adopted to overcome this difficulty is (i) by incorporating some fast relaxing ions in the composition and (ii) by inhibiting the grain growth during the processing of the material to achieve fine grain material. In the former case, small concentrations of divalent cobalt (Co^{2+}) in spinel ferrites has been found to be quite effective. The effect of Co^{2+} ions on magnetocrystalline anisotropy and relaxation processes has been successfully exploited in engineering the materials for high-power applications.

The present work is confined to the studies carried out in a composition of lithium titanium ferrite suitably substituted with small contents of zinc and manganese to obtain material with rectangular loop characteristics for employment in latching devices. The cobalt substituted compositions have been prepared and studied for its various magnetic and electrical properties.

The purpose of the present work was to study the electrical properties such as resistivity, dielectric constant, and the loss factor as a function of frequency and temperature in the series of Co^{2+} substituted composition of Li ferrite. The microwave properties such as resonance linewidth ΔH, spin-wave linewidth ΔH_k, and hysteresis loop parameters, namely remanence ratio R and coercive field H_c are also studied. To the best of our knowledge such an extensive experimental study of all these parameters has not been reported so far, although the microwave behavior in Co-substituted ferrites has been reported by others.[1–3]

MATERIALS AND METHODS

The ferrite composition chosen for the present studies have a generic formula $Li_{0.68-x/2}Zn_{0.1}Mn_{0.1}Ti_{0.46}Co_xFe_{1.66-x/2}O_4$. The room-temperature saturation magnetization ($4\pi M_s$) and Curie temperature (T_c) of the sample having no cobalt substitution (i.e., $x = 0$) is 1550 G and 350 °C, respectively. No appreciable variation in the $4\pi M_s$ and T_c with cobalt substitution up to a level of $x = 0.04$ was noticed. The spinel phase formation was confirmed by x-ray diffraction study. The samples were annealed prior to the measurements to remove deleterious effects.

The FMR linewidth measurements on spherical samples were carried out at X band. ΔH_k at high-power level was determined using a magnetron (80 kW peak power, 4 μs pulsewidth at 9.4 GHz) as a microwave source. The coercive field and remanence magnetization were measured on toroidal samples with the help of a 50- Hz hysteresis loop tracer. The measurements of ac conductivity (σ_{ac}), dielectric con-

TABLE I. Sample parameters.

Sample	x	ΔH (Oe)	ΔH_k (Oe)	H_c (Oe)	R
S1	0.000	350	1.5	1.3	0.9
S2	0.005	350	3.1	1.15	0.84
S3	0.010	365	5.5	1.25	0.77
S4	0.020	380	11.4	1.3	0.6
S5	0.040	390	14.2	2.0	0.42

 0021-8979/88/083780-03$02.40 © 1988 American Institute of Physics

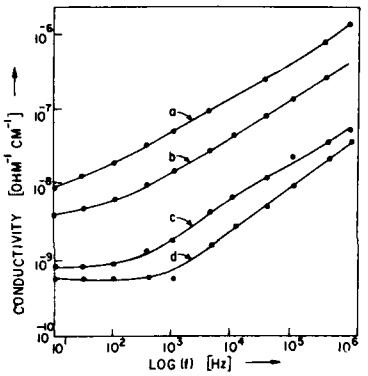


FIG. 1. Experimental ac conductivity vs frequency curve at room temperature for different cobalt substitution. Curves a, b, c, and d are for $x = 0.0$, 0.005, 0.01, and 0.04 ions/formula units, respectively, in LiTi ferrites.

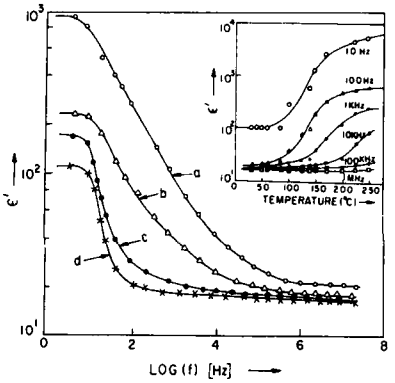


FIG. 3. Experimental variation of dielectric permittivity as a function of frequency at room temperature for different cobalt substitution. Curves a, b, c, and d are for $x = 0.0$, 0.005, 0.01, and 0.04 ions/formula units in LiTi ferrites, respectively. The insert shows the variation of ϵ' with temperature at different frequencies for the sample S3.

stant (ϵ'), and loss tangent ($\tan\delta$) were carried by using a HP 4192A LF Impedence Analyzer as a function of frequency from 5 Hz to 10 MHz and temperature.

RESULTS AND DISCUSSION

Figure 1 depicts the ac conductivity as a function of frequency for the samples of different cobalt concentrations. It is observed that for the samples having smaller Co^{+2} concentration (i.e., $x = 0.00$ and 0.005), ac conductivity varies rapidly with the increase in the frequency while for large Co^{+2} percentage samples (see sample S5) σ_{ac} becomes almost frequency independent at low frequencies and after a certain frequency its value increase rapidly. In the intermediate Co^{+2} concentration samples σ_{ac} increases slowly at lower frequencies while its value increases sharply at higher frequencies (for $x = 0.01$).

Figure 2 illustrates the variation of σ_{ac} with temperature at different frequencies for sample S3. It was observed that at higher temperature the conductivity is high and as the temperature is decreased the conductivity also decreases but a marked difference is found in this variation at low and high frequencies. At low frequencies (for example, at 10 Hz) σ_{ac} decreases monotonically with the decrease in T while at higher frequencies (> 10 kHz) the conductivity decreases sharply up to a certain temperature and thereafter the rate of decrease reduces significantly with the reduction in the temperature. It was noted that the value of conductivity increases with the increase in the frequency at all temperatures but at lower temperatures this difference is more prominent. The activation energy (E_a) decreases with the increase in the frequency as determined in the high-temperature region (> 300 K) and is shown in the insert of Fig. 2.

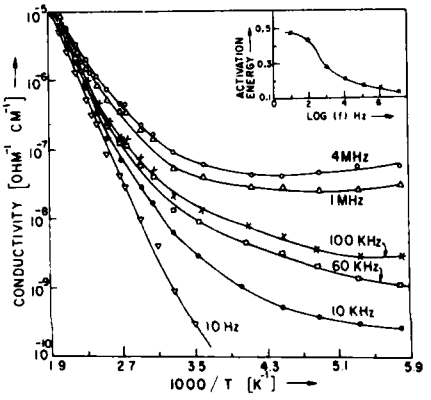


FIG. 2. Experimental variation of conductivity as a function of temperature at various frequencies for the samples S3. The insert shows the activation energy as a function of frequency for the same sample.

Figure 3 illustrates the experimental dielectric permittivity data for the samples having various cobalt concentrations as functions of frequency, and the insert shows its temperature dependence in the range of 0–250 °C for the sample S3 at various frequencies. The permittivity shows a dispersion with frequency for all the samples having different Co^{2+} concentration. In low-frequencies region, the value of ϵ' is very high and its value decreases with the increase in the cobalt concentration. On the other hand, the value of ϵ' at the higher frequencies is small and is nearly frequency independent. Moreover, its value is not as sensitive to cobalt concentrations as observed at lower frequencies. The temperature dependence of ϵ' shows that at high frequencies the permittivity is almost temperature independent but as the frequency decreases its value becomes more temperature sensitive particularly in the intermediate temperature range (i.e., between 100 and 200 °C) where the temperature coefficient is positive. Moreover, the dispersion region shifts towards high frequencies as T is increased.

The observed dispersion in the ac conductivity and permittivity can be explained on the basis of Maxwell and Wagner model[4] in which the solid is assumed as composed of well conducting grains (thickness d_1, conductivity σ_1, permittivity ϵ_1) separated from the poorly conducting grain boundary (thickness d_2, conductivity σ_2, permittivity ϵ_2). Follow-

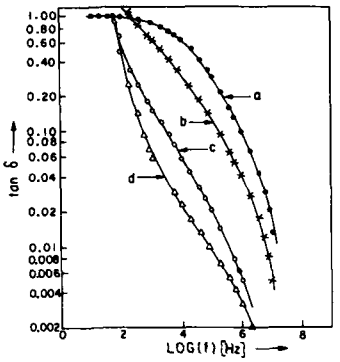


FIG. 4. Loss tangent vs frequency curves at room temperature for LiTi ferrites at different cobalt substitution. Curves a, b, c, and d are for $x = 0.0$, 0.005, 0.01, and 0.04 ions/formula units, respectively.

ing this model the frequency (ω) dependence of σ and ϵ' can be written as[4]

$$\sigma(\omega) = \frac{\sigma_s + \sigma_\infty (\omega\tau)^2}{1 + (\omega\tau)^2}, \tag{1}$$

$$\epsilon(\omega) = \frac{\epsilon_s + \epsilon_\infty (\omega\tau)^2}{1 + (\omega\tau)^2}. \tag{2}$$

In Eqs. (1) and (2) τ is the relaxation time, $\epsilon_1 = \epsilon_2 = \epsilon$ (assumed) $\epsilon_s = \alpha\epsilon$, $\epsilon_\infty = \epsilon$, $\sigma_s = \alpha\sigma_1$, and $\sigma_\infty = \beta\sigma_2$ where $\alpha = d_2/(d_1 + d_2)$ and $\beta = (d_1 + d_2)/d_1$. The temperature dependence in σ and ϵ' can be introduced in Eqs. (1) and (2) if [5]

$$\sigma_i = \sigma_{i\infty} e^{-E_{ai}/kT}, \tag{3}$$

where $i = 1$ and 2. $\sigma_{i\infty}$ and E_{ai} are specific properties of the material.

The calculations carried out by using Eqs. (1) and (2) in conjunction with Eq. (3) reproduced qualitatively the observed dispersion in σ_{ac} and ϵ' as a function of frequency and temperature. For example, Eq. (2) gives a shift in the dispersion region towards higher frequency as the temperature is increased as observed experimentally (Fig. 2). It is important to point out that the observed behavior of ϵ' with T can be explained only if we assume the activation energies of the two regions same. If different values of activation energies for the two regions are used in Eq. (2) then it gives a dispersion curve which has a negative temperature coefficent (a behavior opposite from the observed one). The details of the theoretical analysis of the data will be reported elsewhere.

Figure 4 depicts tan δ as a function of frequency for different Co^{2+} concentrations. This parameter decreases with both in the increase in the frequency and cobalt concentration. It is to be noted that the sample with $x = 0$ shows a weak frequency dependence at lower frequencies while the cobalt inclusion makes the sample more sensitive to the frequency. An interesting feature noted is that the value of tan δ decreases with the increase in frequency near room temperature while its value initially increases with the increase in frequency and after a certain frequency, the value of tan δ starts decreasing with the further increase in the frequency at higher temperatures. The peak observed in this variation shifts towards higher frequencies as the temperature is increased.

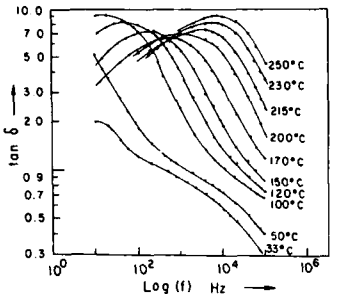


FIG. 5. Experimental variation of tan δ as a function of frequency at different temperatures for the sample SI.

It is observed that the ΔH_k value increases almost linearly by more than an order of magnitude for the Co^{2+} concentration varying from zero to 0.04 ions per formula units (see Table I). Similar results have been reported earlier.[2,3] The FMR linewidth ΔH, however, does not show a large change with x. The results of ΔH are also consistent with the observation reported by others.[3]

It is noted that the value of the R is adversely affected by the addition Co^{2+} content and decreases with the increase in the Co^{+2} percentage in the sample. On the other hand, H_c shows an opposite behavior with the cobalt concentration except for $x = 0.005$. Dionne[3] had reported a gradual increase of H_c with increasing x throughout the range of study. The behavior of H_c shows that the Co^{+2} ions known for their high positive anisotropy, however, provide an indication of its effectiveness in lowering the H_c value for small concentrations of Co^{+2}.

The increase in ΔH_k arises due to the fast relaxation effect of Co^{2+} ions in octahedral sites, which is based on their crystal field stabilization energy. The higher charge Ti^{4+} ions on neighboring octahedral sites and low charge Li ions on adjacent tetrahedral sites help in the stabilization of Co^{2+} in octahedral sites. The clustering effect of Ti^{4+} ions around octahedral sites, if any, is expected even in the absence of Co^{2+} ions and is not going to affect the material behavior on addition of the fast relaxing Co^{2+} ions. The observed data can be explained by considering the effect of Co^{2+} on the anisotropy of the material and the enhancement of spin-lattice relations rates leading to a larger value of ΔH_k. It has been pointed out that Co^{2+} additions in the presence of Ti^{4+} ions in lithium ferrites do not produce the expected compensation point in magnetocrystalline anisotropy. The absence of a dip in the ΔH data lends support to the exchange isolation model. The small increase in microwave resonance linewidth with Co^{2+} content is caused by the fast relaxing mechanism of Co^{2+} ions.

[1] J. J. Green and H. J. van Hook, IEEE Trans. Microwave Theory Tech. MTT-25, 155 (1977).
[2] H. J. Van Hook and G. F. Dionne, AIP Conf. Proc. 24, 487 (1975).
[3] G. F. Dionne, J. Appl. Phys. 57, 3727 (1985).
[4] J. Volger, Progr. Semicond. 4, 207 (1960).
[5] F. Haberey and H. P. J. Wijn, Phys. Status Solidi 26, 231 (1968).

Charge transport in Li-Ni ferrospinels

P. Venugopal Reddy
University College of Technology, Osmania University, Hyderabad-500007, India

The electrical conductivity (σ) and thermopower (Q) of Li-Ni mixed ferrites have been studied as a function of composition and temperature. The conduction mechanism in these ferrites has been explained with the help of carrier concentration (n) and charge carrier mobility (μ) calculated from the measured experimental values. The composition and frequency dependence of dielectric constant (ϵ') and dielectric loss tangent ($\tan\delta$) have also been studied at low frequencies. A relationship between dielectric constant (ϵ') and electrical resistivity (ρ) has been arrived at. A qualitative explanation for observing a maximum in the plots of dielectric loss tangent and frequency has also been given.

Lithium ferrite has attracted considerable attention because of the squareness of the hysteresis loop coupled with a superior temperature performance. The squareness of the hysteresis loop can be considerably improved by adopting a suitable fabrication process, e.g., by controlling the grain growth, loss of lithia, etc. It has also been demonstrated that the squareness of the hysteresis loop can be improved by small additions of nickel or nickel plus zinc. As such, four Li-Ni mixed ferrites having different compositions have been prepared. Although several researchers reported the electrical, magnetic, and mechanical properties of lithium ferrites, no work has been reported for Li-Ni mixed ferrites. Therefore, a study of electrical transport properties of Li-Ni mixed ferrites as a function of composition and temperature has been undertaken and the results of such a study are presented in this paper.

Polycrystalline lithium-nickel ferrites having the compositional formula $(Li_{0.5}Fe_{0.5})_{1-x}Ni_xFe_2O_4$, where $x = 0$, 0.3, 0.6, and 0.9 were prepared by the well-known double-sintering process. The ferrites were sintered at 1100 °C in an atmosphere of oxygen. The details of method of preparation are given in an earlier publication.[1] X-ray diffraction studies of all the specimens confirm the formation of a single spinel phase.

The electrical conductivity measurements were carried out on polycrystalline ferrite samples of about 3–4 mm^2 and 1–2-mm thickness using a two-probe method.[2] Thermopower measurements were carried out by an integral method. In this method a point contact probe is used. The details of the technique are given elsewhere.[3] The dielectric constant (ϵ') and the loss tangent, $\tan\delta$, were also measured at room temperature using a capacitance bridge (General Radio Type 1615A).

Thermopower measurements were carried out from room temperature to 550 K. The values of Seebeck coefficient (Q) obtained from the values of thermo emf are given in Table I. It can be seen from the table that the values of Q are continuously decreasing with increasing nickel content. Based on the negative sign of the Seebeck coefficients observed for all the four Li-Ni mixed ferrites under study it can be understood that the predominant conduction mechanism is the hopping of electrons between neighboring Fe^{2+} and Fe^{3+} ions on the octahedral sites leading to n-type conduction. The Seebeck coefficient has been found to decrease continuously with increasing temperature in all the ferrites.

The values of electrical conductivity (σ) obtained at room temperature for all the four ferrites under study are given in Table I. It can be seen from the table that the conductivity is decreasing continuously with increasing nickel content.

The electrical conductivity of Li-Ni mixed ferrites was measured over a temperature range 300–950 K. Plots of $\log \sigma T$ vs $10^3/T$ are shown in Figs. 1–3. They are almost linear and indicate a transition near the Curie temperature with a change of slope of the curve with further increase in temperature. Similar transition were observed earlier near the Curie temperature for Mn-Mg (Ref. 2) mixed ferrites. Activation energies in the ferrimagnetic and paramagnetic regions for all the ferrites have been obtained from the plots of $\log \sigma T$ and temperature and are given in Table II. The activation energies of the ferrimagnetic region are less than those of the paramagnetic region.

TABLE I. Experimental data of Li-Ni mixed ferrites at room temperature.

Sample No.	Ferrite	Sample No.	Bulk density (g/cm^3)	Q ($\mu V/K$)	σ ($\Omega^{-1}cm^{-1}$)	ϵ'	$\tan\delta$
1.	$Li_{0.5}Fe_{2.5}O_4$	LN-I	3.98	−1095	7.20×10^{-6}	935	3.05
2.	$Li_{0.15}Ni_{0.1}Fe_{2.15}O_4$	LN-II	4.15	−674	2.16×10^{-6}	438	0.78
3.	$Li_{0.2}Ni_{0.6}Fe_{2.2}O_4$	LN-III	4.28	−639	3.00×10^{-7}	112	0.64
4.	$Li_{0.05}Ni_{0.9}Fe_{2.05}O_4$	LN-IV	4.50	−604	1.30×10^{-8}	42	0.22

 0021-8979/88/083783-03$02.40 © 1988 American Institute of Physics

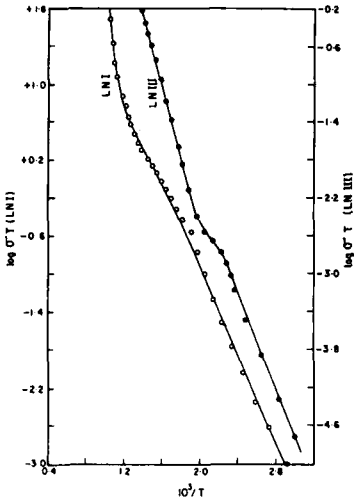


FIG. 1. Conductivity (log σT) vs temperature ($10^3/T$) for samples LN-I and LN-III.

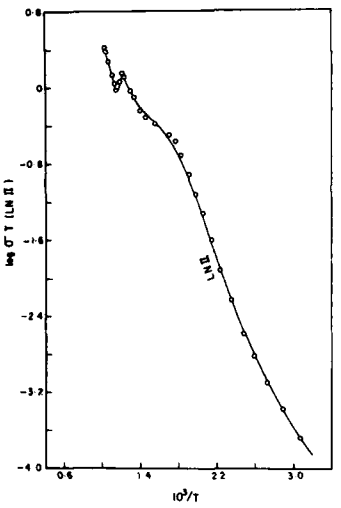


FIG. 2. Conductivity (log σT) vs temperature ($10^3/T$) for sample LN-II.

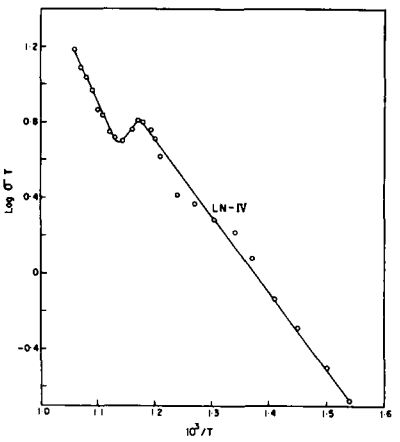


FIG. 3. Temperature variation of electrical conductivity of sample LN-IV.

The absolute thermoelectric power (Q) of the small polaron charge carriers is given by[4]

$$Q=\left(\frac{K}{e}\right)\left(\ln\frac{N}{n}+\frac{S_T}{K}\right), \tag{1}$$

where N is the density of states or concentration of the electronic levels involved in the conduction process, n the carrier concentration, K the Boltzmann constant, e the charge of an electron and S_T is the entropy transport by the charge carriers and is generally small in oxides/ferrites and it contributes less than $10\,\mu$ V/K,[4] so that the equation can be written as

$$Q=(K/e)[\ln(N/n)],$$

which reduces to

$$n=N\exp[(-Qe/K)]. \tag{2}$$

In the case of low mobility semiconductors like ferrites having exceedingly narrow bands or localized levels, the value of N,[5,6] the density of states, can be taken as 10^{22} cm^{-3}. Equation (2) was used by Morin and Geballe[5] to calculate the concentration of charge carriers in the case of $Ni_{0.8}Fe_{2.2}O_4$. The same equation was also used by the author of the present investigation to calculate the carrier concentration (n) of Mn-Mg ferrites.[7] The computed values of n are given in Table II.

If the conduction in ferrite semiconductors under study

TABLE II. Experimental data of Li-Ni mixed ferrites at room temperature.

Sample No.	Carrier concentration (n) (10^{18} cm^{-3})	Mobility (μ_r) (cm^2/V s)	Activation energies (in eV)		$\rho^{1/2}$	ϵ'
			Ferrimagnetic region	Paramagnetic region		
LN-I	0.68	6.61×10^{-5}	0.46	1.34	373	935
LN-II	4.04	3.34×10^{-6}	0.49	0.69	680	438
LN-III	6.06	3.09×10^{-8}	0.50	0.74	1825	112
LN-IV	9.09	8.94×10^{-9}	0.83	1.43	8513	42

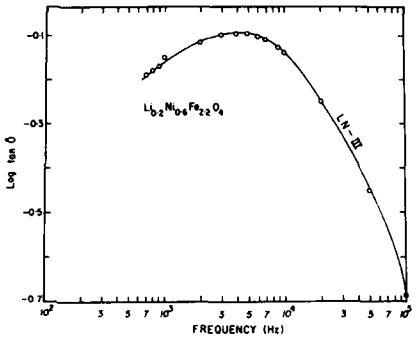


FIG. 4. Plot of log tan δ vs frequency for LN-III.

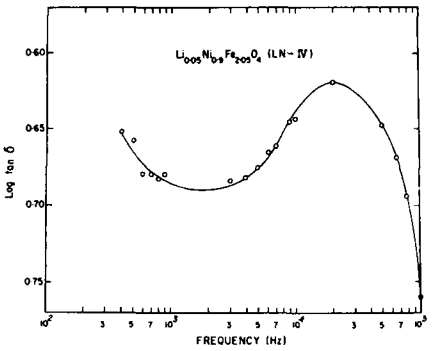


FIG. 5. Plot of log tan δ vs frequency for LN-IV.

is predominantly due to only one type of charge carriers, i.e., electrons, the mobility of charge carriers (μ_e) is given by the well-known relation

$$\sigma = ne\mu_e \quad (\mu_e \gg \mu_h). \tag{3}$$

The values of charge carrier mobility have been calculated using Eq. (3) making use of the experimental values of σ and n, and are included in Table II. It can be seen from the table that the value of charge carrier mobility has decreased from 6.61×10^{-5} cm^2/V s for LN-I to 8.94×10^{-9} cm^2/V s for LN-IV. A careful observation of Table II shows that a continuous decrease in the values of conductivity with increasing nickel content may be due to the decrease in the values of charge carrier mobility rather than due to the carrier concentration.

Rezlescu and Rezlescu[8] have studied the composition, frequency, and temperature of copper containing mixed ferrites such as $Cu_xMn_{1-x}Fe_2O_4$ and $Cu_xZn_{1-x}Fe_2O_4$. These workers explained that the composition dependence of the dielectric constant by using the assumption[9] that the mechanism is similar to that of conduction. They observed that the electron exchange interaction $Fe^{2+} \rightleftarrows Fe^{3+}$ results in a local displacement of electrons in the direction of the electric field which determines the polarization of the ferrites.

A similar explanation is proposed for the composition dependence of the dielectric constant of mixed Li-Ni ferrites. Thus for the sample LN-I, the dielectric constant is more because more numbers of Fe^{2+} ions which take part in the electron exchange interaction, $Fe^{2+} \rightleftarrows Fe^{3+}$, and hence are responsible for the polarization is maximum. Similarly the dielectric constant is continuously decreasing with increasing nickel content indicates that number of ferrous ions on the octahedral sites which are available for polarization are decreasing, resulting in a continuous decrease in the values of dielectric constant. Thus it is clear that the mechanism for both the phenomena, i.e., conductivity and dielectric phenomenon in the case of Li-Ni mixed ferrites, is same.

The values of the dielectric constant ϵ' and $\rho^{1/2}$ for four Li-Ni ferrites under study are given in Table II. It can be seen from the table that ϵ' is roughly inversely proportional to $\rho^{1/2}$. A similar relationship between ϵ' and $\rho^{1/2}$ has been found[10] for $Ni_{0.4}Zn_{0.6}Fe_2O_4$ samples fired in various atmospheres.

It has been observed that log tan δ varies linearly with frequency for the ferrites LN-I and LN-II while the dielectric loss tangent versus frequency curves for the samples LN-III and LN-IV show maxima at frequencies of 5 and 20 kHz, respectively. These results suggest that the frequency at which the maximum occurs decreases with decreasing nickel content. Thus it can be assumed that, though a linear variation of dielectric loss tangent with frequency is observed in the present investigation for the samples LN-I and LN-II, a maxima may occur for these samples also like the one observed for the samples LN-III and LN-IV, provided the measurements are made at still lower frequencies.

A qualitative explanation can be given for the occurrence of the maxima in the log tan δ versus frequency curves for LN-III and LN-IV. As pointed out by Iwauchi[11] the maximum in the dielectric loss is observed when the jumping or hopping frequency is approximately equal to that of the external electric field.[12] Therefore, it can be justifiably assumed that the hopping frequencies for LN-III and LN-IV are such that a maximum in the dielectric loss is observed near applied frequencies of 5 and 20 kHz, respectively.

[1] P. Venugopal Reddy and T. Seshagiri Rao, J. Less-Common Metals **75**, 255 (1980).
[2] P. Venugopal Reddy, T. Seshagiri Rao, and S. M. D. Rao, J. Less-Common Metals **79**, 1 (1981).
[3] P. Venugopal Reddy and T. Seshagiri Rao, Phys. Status Solidi A **77**, K63 (1983).
[4] J. B. Goodenough, Prog. Solid State Chem. **5**, 145 (1971).
[5] F. J. Morin and T. G. Geballe, Phys. Rev. **99**, 467 (1955).
[6] F. J. Morin, Phys. Rev. **93**, 1195 (1953).
[7] P. Venugopal Reddy, Phys. Status Solidi A **102**, 797 (1987).
[8] N. Rezlescu and E. Rezlescu, Phys. Status Solidi A **23**, 575 (1974).
[9] L. I. Rabinkin and Z. I. Nouikoua, *Ferrites* (Minsk, 1960), p. 146.
[10] J. Smit and H. P. J. Wijn, *Ferrites* (N. V. Philips Gloeilampenfabrieken, Eindhoven, 1959).
[11] K. Iwauchi, Jpn. J. Appl. Phys. **10**, 1520 (1971).
[12] V. R. K. Murthy and J. Sobhanadri, Phys. Status Solidi A **36**, K133 (1976).

A novel low-temperature preparation of Ni-Zn ferrite and the properties of the ultrafine particles formed

C. J. Chen, K. Bridger, S. R. Winzer, and V. PaiVerneker
Martin Marietta Laboratory, Baltimore, Maryland 21227

Ultrafine particles of nickel-zinc ferrite have been formed from solutions of metal nitrates by coprecipitation with hydrazine, followed by aging at 90 °C. The crystallites either aggregate into much larger clusters or form single particles, depending upon the preparation conditions, and vary in size from 30 to ≈300 Å. Saturation magnetizations (M_s) of the ferrites varied from 40 to 65 emu/g and the coercivities from 1 to ≈100 Oe. Increasing hydrazine concentrations tended to produce particles with lower M_s. However, for hydrazine/metal ratios below unity, decreasing the hydrazine concentration dramatically lowered the M_s value. Particles formed without hydrazine (e.g., by aging hydroxides precipitated with potassium hydroxide) did not appear to be magnetic. Variations of the magnetic properties and lattice parameters as a function of preparation conditions will be discussed.

I. INTRODUCTION

Ferrites are mostly produced using a conventional ceramic process involving high-temperature (>800 °C), solid-state reactions of α-Fe_2O_3 and the constituent divalent metal oxides.[1] Recently, chemical methods have been used with some success to prepare homogeneous, fine, reproducible ferrite powders[2–4] using aqueous salt solutions of the constituent ions.[5,6] The chemically prepared precursors provide greater reactivity and homogeneity, so that ferrites form at lower temperatures (<600 °C) than in the ceramic process and without crystal growth, yielding small particles that have a large surface area and good sinterability. However, relatively high-temperature annealing (>400 °C) is usually necessary to optimize magnetic properties.

Studies show that hydrazine and related compounds can form complexes with many metal salts.[7–9] These complexes may be ideal as chemical precursors for low-temperature synthesis of metal oxides. In this study, the important nickel-zinc ferrites ($Ni_xZn_{1-x}Fe_2O_4$, $x = 0.5$, 0.65) are prepared through this novel precursor route using hydrazine-hydrate ($N_2H_4 \cdot H_2O$) as the complexing agent in aqueous solutions of metal nitrates. The ferrites thus prepared do not require high-temperature annealing to achieve high-M_s values.

II. EXPERIMENT

The solutions used in the preparations were made up from Baker-analyzed reagents without further purification. Stock solutions of ferric nitrate (2.5M), nickel nitrate (1.25M), and zinc nitrate (1.25M) were made up with deionized water. A 4M hydrazine stock solution prepared by dilution of $N_2H_4 \cdot H_2O$ (Baker) was stored under nitrogen.

Immediately prior to the reaction, aliquots of the three metal stock solutions were premixed in the appropriate ratio and then diluted with deionized water until the total metal ion concentration was 0.75M. This solution was added to a 50-ml Pyrex glass tube, followed by 4M N_2H_4, and 1M KOH. The addition of the N_2H_4 to the metal ion solution resulted in the formation of light to dark brown, gelatinous precipitates. Deionized water was then added to the mixture to reach a total volume of 30 ml. The initial pH of the suspensions was measured after dilution. The reaction vessels containing the coprecipitated precursors were immersed in a constant-temperature oil bath preheated to 90 ± 2 °C. The Teflon-lined plastic caps of the Pyrex tubes were then screwed on. The solutions were typically aged at 90 ± 2 °C for 1 h, then air cooled. During aging, the precipitates gradually settled and darkened. After aging, the solids were filtered and washed, using 0.45-μm Millipore membranes, then air-dried overnight, followed by 1 h of vacuum drying at 50 °C. Some of the dried solids were further heated to 150 °C for 10 min. During this time, some of the dried solids may have ignited, especially when the initial reaction mixture had a high N_2H_4 content.

Transmission electron microscopy (TEM), x-ray diffraction (XRD), and conventional wet-chemical analyses were used for powder characterization. Nickel, zinc, and iron contents were determined by inductively-coupled plasma spectroscopy (ICP). Magnetic properties were recorded on a vibrating sample magnetometer (VSM). Crystallite sizes t of ferrite products were estimated from the linewidth of the 311 peak in the XRD pattern using Sherrer's equation:

$$t = 0.9\lambda / (B \cos \theta_B), \quad (1)$$

where B is the line broadening and θ_B is the Bragg angle.

III. RESULTS

Figures 1 and 2 show TEMs of the ferrite particles. In all cases, the particles are very fine, typically <0.1 μm. Figure 1 shows that increasing the $[N_2H_4]/[Me]_{tot}$ slightly lowered the particulate size, while maintaining quasicubic morphology. Figure 2 shows that raising the pH with a noncomplexing, nonreducing reagent (KOH) resulted in smaller particles (≈100–150 Å) with a more spherical morphology. These ultrafine particles may be very useful for sintering at low temperatures if acceptable magnetic properties can be achieved without high-temperature annealing.

Figure 3 shows M_s for the ferrite particles plotted as a function of $[N_2H_4]/[Me]_{tot}$. Unless stated otherwise, all particles have been annealed at 150 °C. Relatively high magnetizations can be achieved at this low temperature, e.g., >60 emu/g can be readily obtained. When samples were heated to 1000 °C, values of ~76 emu/g were obtained, which compares favorably to the M_s of commercial

 0021-8979/88/083786-03$02.40 © 1988 American Institute of Physics



FIG. 1. TEM of ferrites formed from solutions with $[Me]_{tot} = 0.25M$ and $[N_2H_4]/[Me]_{tot} = 1.33$ (a) and 5.33 (b).

$Ni_xZn_{1-x}Fe_2O_4$ (TT2-111, ex Transtech) at 78 emu/g (M_s^0). Thus, the maximum value of 65 emu/g (shown in Fig. 3) represents 83% of the value for a fully fired sample. The maximum value shown in Fig. 3 occurs around $[N_2H_4]/[Me]_{tot} = 2$, and the equivalence point for the mixture falls between $[N_2H_4]/[Me]_{tot} = 2$–3. Thus, on the low $[N_2H_4]$ side of the maximum, the yield of precipitate tends to be low, indicating that the iron may be in the Fe^{3+} state. On the high $[N_2H_4]$ side of the maximum, the N_2H_4 is in excess over equivalence, and the yield of precipitate is high ($[Me]_{tot} < 5$ ppm remains in solution after the reaction) but the iron might be expected to be in the Fe^{2+} state. The decrease in M_s with increasing $[N_2H_4]/[Me]_{tot}$ might, therefore, be due to increasing amounts of FeO impurities. We will attempt to demonstrate this by Mössbauer spectroscopy in future work. Figure 4 shows the variation of other physical parameters with $[N_2H_4]/[Me]_{tot}$. With the exception of H_c, the values level off after $[N_2H_4]/[Me]_{tot} = 2$.

Figure 5 shows the variation of material and magnetic properties for the particles as a function of $[KOH]/[N_2H_4]$. The results appear fairly scattered, with $40 < M_s < 65$ emu/g and $8.3 < a_0 < 8.4$ Å. Figure 6 shows that the initial pH and particle composition vary with $[KOH]/[N_2H_4]$. Particles prepared from reaction conditions with a pH below equivalence (6–8) become increasingly deficient in nickel as the pH decreases, whereas particles prepared from reaction conditions close to equivalence and at a higher pH have values convergent with the dashed lines, indicating the near stoichiometry of $Ni_xZn_{1-x}Fe_2O_4 (x = 0.65)$. This evidence, combined with the results showing values for a_0 lying close to 8.40 Å indi-



FIG. 2. TEM of ferrite formed from solution with $[Me]_{tot} = 0.25M$, $[N_2H_4]/[Me]_{tot} = 1.33$, and $[KOH]/[N_2H_4] = 0.2$

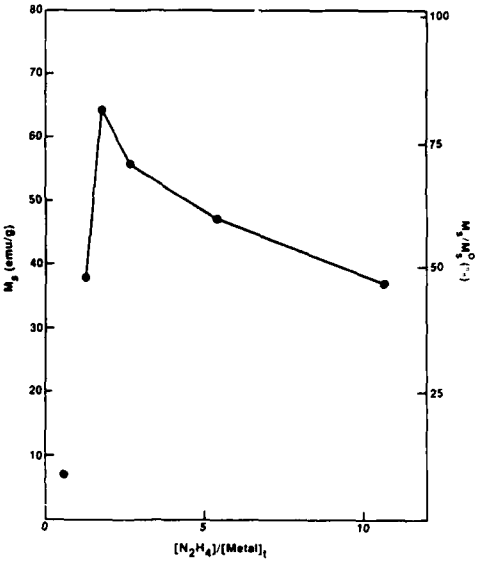


FIG. 3. Dependence of M_s on $[N_2H_4]/[Me]_{tot}$ for $[Me]_{tot} = 0.25M$.

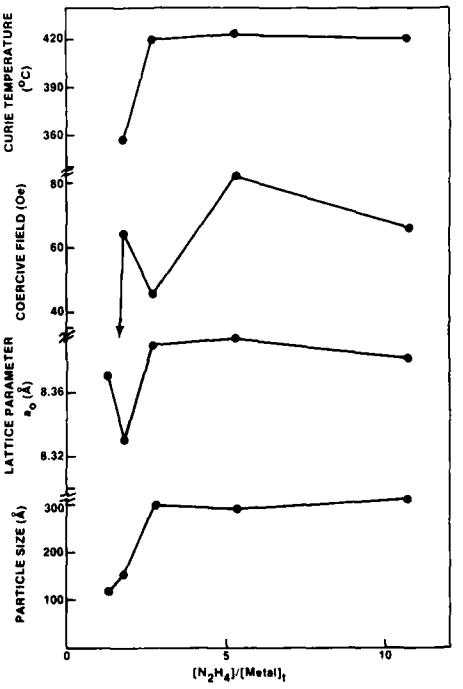


FIG. 4. Variation of crystallite size, lattice parameter (a_0), coercivity, and Curie temperature with $[N_2H_4]/[Me]_{tot}$.

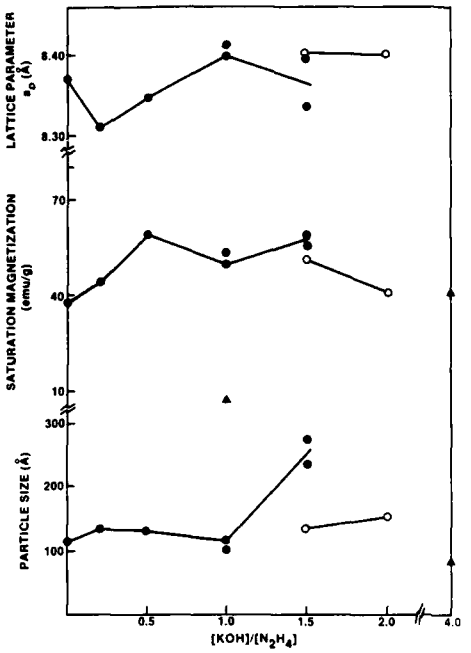


FIG. 5. Variation of crystallite size M_s and lattice parameter with $[KOH]/[N_2H_4]$ for $[Me]_{tot} = 0.25M$ and $[N_2H_4]/[Me]_{tot} = 0.53$ (▲), 1.07 (○), 1.33 (●).

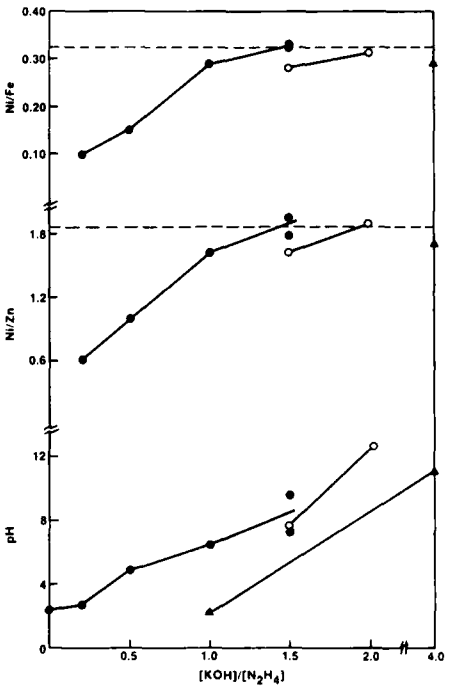


FIG. 6. Variation of initial pH and particle composition with $[KOH]/[N_2H_4]$ for $[Me]_{tot} = 0.25M$ and $[N_2H_4]/[Me]_{tot} = 0.53$ (▲), 1.07 (○), 1.33 (●).

cate that we are forming the desired phase. Note that for $NiFe_2O_4$ and $ZnFe_2O_4$ the values for a_0 are 8.34 and 8.44 Å, respectively.

The above discussion indicates that N_2H_4 did not simply act as a base. Replacing N_2H_4 with KOH did not necessarily lead to the formation of the correct phase, although pH plays an important role in the reaction. In general, we found that too low a $[N_2H_4]/[Me]_{tot}$ ratio tends to give nickel deficient and, in extreme cases, amorphous phases, both of which have low values of M_s. Tamura and Matijevic demonstrated the formation of colloidal $NiFe_2O_4$ by aging hydroxides precipitated with base alone,[10] but to our knowledge have not reported $Ni_xZn_{1-x}Fe_2O_4$.

In conclusion, we have formed $Ni_xZn_{1-x}Fe_2O_4$ at a low temperature and achieved magnetizations as high as 83% of the fully fired material by annealing at only 150 °C. The particles formed are ultrafine, which may make them useful for forming films or sintering at relatively low temperatures. It is also possible that this method may be extended to producing new materials that are not accessible through solid-state reactions.

[1] E. C. Snelling, *Soft Ferrites, Properties and Applications* (CRC Press, Cleveland, Ohio, 1969).
[2] T. Takada and M. Kiyama, in *Proceedings of the First International Conference on Ferrites*, edited by Y. Hoshino, S. Iida, and M. Sugimoto (University Park, Tokyo, Japan, 1971), p. 69.
[3] B. F. B. Yu and A. Goldman, in *Proceedings of the Third International Conference on Ferrites*, edited by S. Iida and M. Sugimoto (University Park, Tokyo, Japan, 1980), p. 68.
[4] A. I. Busev, N. V. Kobrya, P. D. Korostelev, and G. K. Mikhailov, Inorg. Mater. **16**, 1259 (1980).
[5] T. Sato, C. Kurodo, M. Saito, and M. Sugihara, in Ref. 6, p. 72.
[6] B. K. Das, *Preparation and Characterization of Materials*, edited by J. M. Honig and C. N. R. Rao (Academic, New York, 1981), p. 75.
[7] H. Franzen and O. VanMayer, Z. Anorg. Chem. **60**, 247 (1908).
[8] A. Braibanti, F. Dallavalle, M. A. Pellinghelli, and E. Leporati, Inorg. Chem. **7**, 1430 (1968).
[9] A. Braibanti, A. M. ManottiLanfredi, and A. Tiripicchio, Z. Kristallogr. Kristallgeom. Kristallphys. Kristallchem. **124**, 335 (1967).
[10] H. Tamura and E. Matijevic, J. Colloid Interface Sci. **90**, 100 (1982).

Studies on high-density nickel zinc ferrites and its magnetic properties using novel hydrazine precursors

T. T. Srinivasan, P. Ravindranathan, L. E. Cross, R. Roy, and R. E. Newnham
Materials Research Laboratory, The Pennsylvania State University, University Park, Pennsylvania 16802

S. G. Sankar
Mellon Institute, Carnegie-Mellon University, Pittsburgh, Pennsylvania 15213

K. C. Patil
Inorganic and Physical Chemistry Department, Indian Institute of Science, Bangalore, India

Nickel zinc ferrites have been very widely used in the high-frequency applications. In our present study we have prepared $Ni_{1-x}Zn_xFe_2O_4$ ($0<x<1$) using novel hydrazinium metal hydrazinecarboxylate precursors. High densities ($\sim$99%) have been obtained for all the ferrites sintered at relatively low temperatures, 1100 °C, in comparison with the conventional method (>1200 °C). The variation of magnetic properties like magnetic moment, Curie temperature, and permeability with zinc concentration have been studied.

INTRODUCTION

Nickel zinc ferrites, $Ni_{1-x}Zn_xFe_2O_4$, have been commercially used for many years as high-frequency ferrites for radio frequency coils, transformer cores, and rod antennas.[1] There is a specialized application of Ni-Zn ferrites requiring low porosity and controlled microstructure in the magnetic cores of read write heads for high-speed digital tape or disk recording.[2,3] The high density also gives good wear properties against the rapidly moving tapes with their abrasive coating of iron oxide.[4] The conventional ceramic method for the preparation of ferrites involving high temperature can result in the loss of their fine particle nature. Wet chemical methods such as co-precipitation, hydrothermal oxidation, spray drying, and freeze drying are reported[5,6] to yield ferrite particles ranging from 10 to 100 nm. However, these methods do suffer from certain disadvantages like segregation, and the powders obtained do not compact easily to high density. The use of the solid solution precursor technique[7] appears to hold considerable promise. Since solid solutions of hydrazinium metal hydrazinecarboxylate hydrate precursors yield ultrafine ferrites[8] which sinter at low temperatures to give high-density materials, it was considered interesting to extend this technique to prepare ultrafine Ni-Zn ferrites which could be sintered at much lower temperatures to yield high-density materials (>99% theoretical density) and study the magnetic properties.

EXPERIMENT

(a) Preparation of hydrazinium metal hydrazinecarboxylate precursors $(N_2H_5)_3Ni_{1-x}Zn_xFe_2(N_2H_3COO)_9\cdot 3H_2O$, $0<x<1$. Aqueous solutions of metal sulphates of nickel zinc and iron (II) in the required ratio were mixed and a solution of N_2H_3COOH in $N_2H_4\cdot H_2O$ was added until the precipitate dissolves.[8] Crystalline solids separate out from the solution in a couple of days. The crystals were washed with alcohol, ether, and dried over P_2O_5 in a vacuum desiccator. The composition of the crystals were fixed to be $(N_2H_5)_3Ni_{1-x}Zn_xFe_2(N_2H_3COO)_9\cdot 3H_2O$ where $x = 0.0$, 0.25, 0.5, and 0.75 by chemical analysis. Hydrazine content was determined volumetrically using 0.025-M KIO_3 solution under Andrews Conditions.[9]

(b) Preparation of nickel zinc ferrites, $Ni_{1-x}Zn_xFe_2O_4$ ($0<x<1$). The precursors of Ni-Zn ferrites have been decomposed at 250 °C in an oxygen atmosphere for 1 h as the thermal decomposition studies of the precursors show that all the complexes decompose exothermally in a single step in the temperature range 120–200 °C. The formation of a single-phase spinel ferrites has been confirmed through x-ray powder diffraction patterns. The green ferrites were pelletized using polyvinyl alcohol (5%) as a binder and pellets were sintered at various temperatures and soaking times.

(c) The powder x-ray diffraction patterns for the green ferrites and the sintered pellets were taken using a Philips PW 1050/70 diffractometer. The particle size analysis of the green ferrite powder and the grain size of the sintered pellets were examined using transmission electron microscopy (TEM) and scanning electron microscopy (SEM), respectively.

RESULTS AND DISCUSSION

X-ray powder diffraction shows a very broad line indicating the fine particle nature of the ferrite. A typical x-ray

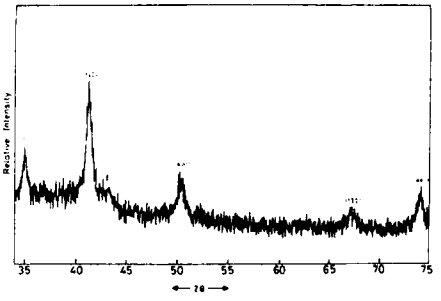


FIG. 1. X-ray powder diffraction pattern of green $Ni_{0.5}Zn_{0.5}Fe_2O_4$.

 0021-8979/88/083789-03$02.40 © 1988 American Institute of Physics

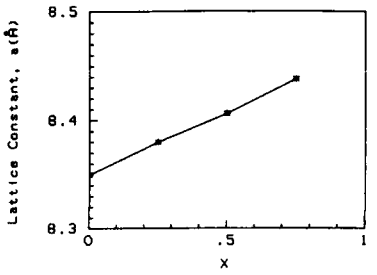


FIG. 2. Variation of lattice constant a as a function of x in $Ni_{1-x}Zn_xFe_2O_4$.

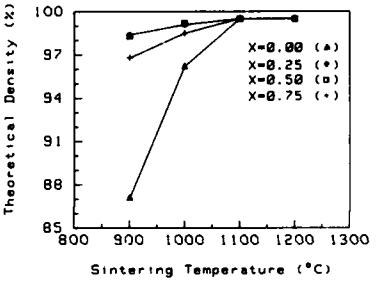


FIG. 4. Density of $Ni_{1-x}Zn_xFe_2O_4$ as a function of sintering temperature.

powder diffraction pattern of green ferrite $Ni_{0.5}Zn_{0.5}Fe_2O_4$ is shown in Fig. 1. The lattice constant a of Ni-Zn ferrites increases linearly with zinc concentration (Fig. 2). The average crystallite sizes of $Ni_{1-x}Zn_xFe_2O_4$ calculated from x-ray line broadening[10] are found to be in the range of 10–20 nm. Transmission electron micrographs of the powders confirm the fine particle nature of the ferrites. Typical TEM picture of $Ni_{0.5}Zn_{0.5}Fe_2O_4$ prepared at 250 °C is shown in Fig. 3. The particle size calculated from the TEM is ~60 nm.

Fine particle Ni-Zn ferrites have been sintered at 900, 1000, 1100, and 1200 °C for 24 h. Densities greater than 98% of the theoretical density were obtained for all the samples sintered above 1000 °C. Density versus firing temperature has been given in Fig. 4. Increased reactivity of the fine particles is responsible for achieving almost theoretical density ferrites at low temperatures compared to those normally employed (> 1200 °C).

The magnetization curves of the green Ni-Zn ferrites at room temperature showed no hysteresis indicating that the ferrites are superparamagnetic in nature.[11] The green ferrites prepared at 250 °C does not attain saturation magnetization even at 18 kOe. The green Ni-Zn ferrites were pelletized and heated for 24 h at 1100 °C to increase the particle size thus rendering them suitable for saturation magnetization measurements. The variation of magnetic moment with zinc concentration (Fig. 5) can be explained on the basis of

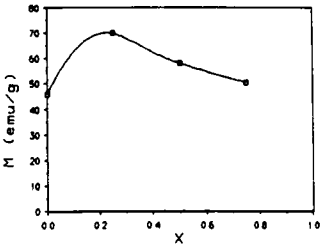


FIG. 5. Variation of saturation magnetization (M_s) as a function of x in $Ni_{1-x}Zn_xFe_2O_4$.

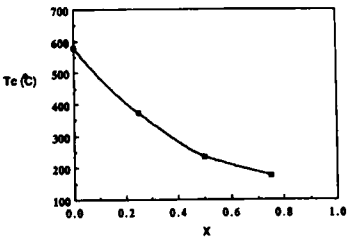


FIG. 6. Plot of Curie temperature (T_c) vs x in $Ni_{1-x}Zn_xFe_2O_4$.

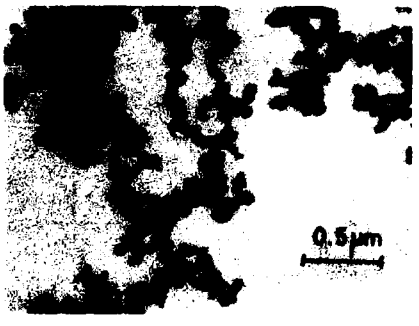


FIG. 3. Transmission electron micrograph of $Ni_{0.5}Zn_{0.5}Fe_2O_4$ prepared at 250 °C.

TABLE I. The variation of the permeability μ' with the firing temperature and frequency for the typical composition, $Ni_{0.75}Zn_{0.25}Fe_2O_4$.

Sintering temperature (°C)	Density (% theor.)	Permeability μ' as a function of frequency				Grain size (μm)
		1 kHz	10 kHz	1 MHz	10 MHz	
900	98.4	23.72	48.85	49.31	49.77	< 1
1100	99.5	50.89	70.43	69.07	73.16	2
1100	99.5	138.84	140.67	129.66	121.71	4



FIG. 7. Scanning electron micrograph of the fracture surface of $Ni_{0.75}Zn_{0.25}Fe_2O_4$ sintered at 1200 °C, 24 h.

Yafet–Kittel type of spin arrangement.[12] With the increase in zinc concentration, the Fe^{3+} ions will have no magnetic neighbors and hence the spins become uncoupled.[13] The Curie temperature decreases with zinc concentration (Fig. 6) and is in agreement with the literature values.

Permeability measurements have been made on all the ferrites sintered at 900, 1000, and 1100 °C in the frequency range of 1 kHz–10 MHz. The values of μ' increase with the increase in firing temperature for the corresponding composition. The variation of the permeability (μ') with the firing temperature and the frequency is given in Table I for the typical composition, $Ni_{0.75}Zn_{0.25}Fe_2O_4$. It is clear from the table that the density does not change very much with the firing temperature but the value of μ' increases with the increase in sintering temperature. This could be attributed due to the variation in grain size of the ferrite. Typical photomicrograph of $Ni_{0.75}Zn_{0.25}Fe_2O_4$ is shown in Fig. 7. The grain size was found to be 3–4 μm.

CONCLUSIONS

From this study, it is seen very clearly that the novel precursor technique leads to fine particle ferrite formation at very low temperature (120–200 °C). Because of the fine ferrite particle (~60 nm), close to theoretical densities (>99%) have been achieved at relatively low temperature (1100 °C). As we can obtain high-density ferrite using this method, hot-pressing techniques could be avoided. The magnetic properties have been studied and match well with the literature values. It has been observed that the value of μ' increases with the firing temperature, though the value of density remains more or less same.

[1] E. E. Riches, in *Ferrites, A Review of Materials and Applications*, edited by J. Gordon Cook (Mills and Boons, London, 1972), p. 17.
[2] J. Kulikowski and A. Lesniewski, J. Magn. Magn. Mater. **19**, 117 (1980).
[3] H. Igarashi and K. Okazaki, J. Am. Ceram. Soc. **60**, 51 (1977).
[4] A. Goldman, Bull. Am. Ceram. Soc. **63**, 582 (1984).
[5] T. Sato, C. Kurodo, M. Saito, and M. Sugihara, in *Ferrites, Proceedings of the International Conference on Ferrites*, edited by Y. Hoshino, S. Iida, and M. Sugimoto (University Park Press, Baltimore, MD, 1971), p. 72.
[6] B. K. Das, in *Preparation and Characterization of Materials*, edited by J. M. Honig and C. N. R. Rao (Academic, New York, 1981), p. 75.
[7] J. M. Longs, H. S. Horowitz, and L. R. Clavenna, in *Solid State Chemistry: A Contemporary Overview*, edited by S. L. Holt, J. B. Milstein and M. Robbins (American Chemical Society, Washington, DC, 1980), p. 139.
[8] P. Ravindranathan and K. C. Patil, Bull. Am. Ceram. Soc. **66**, 688 (1987).
[9] A. I. Vogel, *A Text Book of Quantitative Inorganic Analysis* (Longman Group, London, 1975).
[10] H. P. Klug and L. E. Alexander, *X-ray Diffraction Procedures* (Wiley, New York, 1954), p. 504.
[11] D. W. Collins, J. T. Dehn, and L. N. Mulay, in *Mossbauer Methodology*, edited by I. J. Gruvermann (Plenum, New York, 1967), Vol. 3, p. 103.
[12] N. S. Satya Murthy, M. G. Natera, S. I. Youssef, R. J. Begum, and C. M. Srivastava, Phys. Rev. **181**, 969 (1969).
[13] A. Brooese van Groenou, P. F. Bongens, and A. L. Stuijts, Mater. Sci. Eng. **3**, 317 (1968–69).

New routes for the synthesis of iron oxide based magnetic materials

Sushama Joshi, D. M. Phase, S. M. Kanetkar, and S. B. Ogale
Department of Physics, University of Poona, Pune- 411 007, India

New routes using laser and ion beam techniques are developed to synthesize iron oxide based magnetic materials. The first method, pulsed ruby laser treatment (pulse duration 30 ns, $\lambda = 0.694\ \mu$m) of thermally grown iron oxide (α-Fe_2O_3) under water, is shown to lead to the formation of FeO and Fe_3O_4 phases depending upon the choice of the treatment parameters. The other method, ion beam mixing to atomically mix a deposited overlayer of cobalt (400 Å thick) on an α-Fe_2O_3 substrate with 100-keV Ar^+ at a dose higher than 1×10^{16} ions/cm^2, leads to ferrite formation. The surface layer sensitive technique of conversion electron Mössbauer spectroscopy (CEMS) was employed for characterization.

INTRODUCTION

Among the transition metal oxides, oxides of iron have a special importance in view of their interesting physical, chemical, and magnetic properties. These oxides are normally prepared by chemical processing followed by suitable physical treatments such as thermal annealing under specific ambient conditions.[1–3] Such processing methodologies, though of immense value for gross material synthesis, are hardly suitable for device miniaturization and integration. Recently, there has been considerable emphasis on the use of newer methods, such as ion implantation and laser treatments for processing of materials,[4] because these methods offer unique possibilities such as region selectivity, operational efficiency and process control refinement. In this work we report on two methods based on radiation processing for the synthesis and modification of iron oxide based thin-film systems.

In the first case we have pulsed laser treated the surface of α-Fe_2O_3 in air and under water[5,6] at different energy densities while in the second case we have used the well-established technique of ion beam mixing[7,8] to impart controlled modifications to the region of the interface between a metal film (Co in the present case) and an oxide substrate (α-Fe_2O_3 in the present case).

EXPERIMENT

The iron foils used in both the experiments were 99.99% pure and were obtained from Good Fellow metals. Microetching and cleaning were carried out prior to their use in the experiments. In the first experiment, iron foils were heated to 450 °C for four hours to form a thick layer of iron oxide. Conversion electron Mössbauer spectroscopy (CEMS) (Ref. 9) revealed that the thickness of the oxide was greater than 3000 Å. High-power Q-switched ruby laser pulses (30-ns pulse width) were used to modify the iron oxide surface at different energy densities. The specifications of the samples studied are given in Table I.

In the second experiment, iron substrates were coated with thick layer of iron (1000 Å), enriched to 33% ^{57}Fe, by vacuum evaporation in a Varian ultrahigh vacuum system. These samples were oxidized at 400 °C for 2 h in air to form a thick layer of α-Fe_2O_3. The oxide formation was confirmed by CEMS measurements. These substrates were then overcoated with a 400-Å-thick layer of cobalt by vacuum evaporation at a background pressure of 10^{-7} Torr. A number of such freshly prepared composites were subjected to Ar^+ ion bombardment (energy = 100 keV; dose in the range between 5×10^{15} and 3×10^{16} ions/cm^2) to induce atomic mixing at the interface. In both the experiments samples were studied by CEMS. CEMS spectra of the samples were recorded at room temperature using constant acceleration Mössbauer spectrometer with a Co^{57}:Rh source. To obtain the best fit values of hyperfine interaction parameters, computer analysis of the spectra was carried out using the standard MOSFIT program.[10]

RESULTS AND DISCUSSION

The CEMS spectra of the samples studied in the first experiment are shown in Fig. 1, and those in the second experiment in Fig. 2.

Figure 1(a) shows the CEMS spectrum of the sample no. 1. The spectrum shows only a single sextet contribution corresponding to an α-Fe_2O_3 phase. The spectrum in Fig. 1(b) represents the state of the sample laser treated under water (sample no. 2) and it can be fitted with one singlet, two doublets and two sextets. The values of the corresponding hyperfine interaction parameters are as follows (IS = isomer shift, QS = quadrupole splitting, IMF = internal magnetic field).

Singlet: IS = 0.47 mm/s;
Doublet 1: IS = 1.09 mm/s,
QS = 0.46 mm/s;
Doublet 2: IS = 0.60 mm/s,
QS = 1.03 mm/s;

TABLE I. Sample specifications.

Sample no.	Specification
1	Iron foil oxidized at 450 °C for 4 h
2	Sample no. 1 laser treated under water Energy density = 10 J/cm^2
3	Annealing of sample no. 2 at 300 °C for 1 h

 0021-8979/88/083792-03$02.40 © 1988 American Institute of Physics

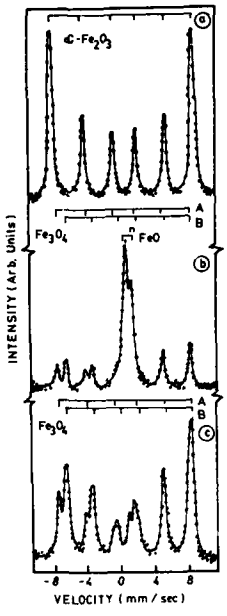


FIG. 1. The CEMS spectra of (a) sample no. 1, (b) sample no. 2, and (c) sample no. 3.

Sextet 1: IS = 0.14 mm/s,

IMF = 482 kOe;

Sextet 2: IS = 0.72 mm/s, IMF = 456 kOe.

The singlet and two doublets together correspond to an FeO (Ref. 11) phase and the remaining two sextets together correspond to a spinel Fe_3O_4 phase.[12] There is no trace of an α-Fe_2O_3 phase. When sample no. 2 was annealed at a temperature of 300 °C for 1 h in vacuum, the corresponding Mössbauer spectrum [Fig. 1(c)] could be fitted primarily with the Fe_3O_4 phase. The contribution of an FeO phase in this spectrum was found to be very small. These results are consistent with the decay scheme for a nonstoichiometric FeO phase.[13] A comparison was made between treatment in water and in air. When the α-Fe_2O_3 sample was laser treated in air at the same energy density as that used in the case of sample no. 2, the Mössbauer spectrum (not shown) indicated that about 6% of FeO is present in the sample. Most of the surface layer is transformed into the Fe_3O_4 phase.

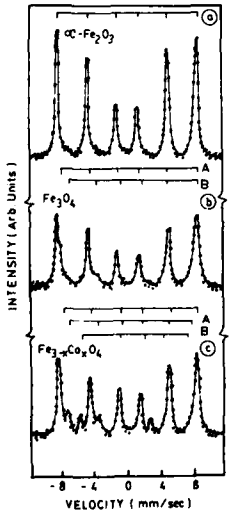


FIG. 2. The CEMS spectra of sample (a) oxidized at 400 °C for 2 h, (b) deposited with 400-Å Co overlayer, and (c) ion beam mixed using 100-keV Kr^+ ions at a dose of 1×10^{16} ions/cm^2.

DISCUSSION

Since the water overlayer is transparent to the ruby laser wavelength of 0.694 μm, the laser energy density is absorbed primarily by the oxide overlayer and the underlying iron. The energy density of 10 J/cm^2 can raise the surface temperature of the sample above the decomposition temperature of α-Fe_2O_3 and can lead to escape of oxygen atoms. At the same time, the water layer near the surface can vaporize in nanoseconds to form a supersaturated vapor of neutral and ionic radicals near the surface. It is possible that the hydrogen released in this process enhances the oxygen desorption via a reduction reaction leading to a significant quantity of the low-oxygen FeO-like phase in the surface layer. The role of hydrogen seems important in controlling the surface stoichiometry of the resulting oxide phase. Of course, it is important to mention that when pure iron is treated with a pulsed laser under water one obtains an oxide of iron, viz., FeO.[5,6] Thus, whether the effective process is an oxidizing or reducing reaction should depend on the chemical driving forces in the system. Also the possibility of a partial laser induced alloying of the underlying Fe into the oxide overlayer cannot be ruled out.

In the above we have demonstrated that pulsed laser beam can be used to modify the surface layer properties of oxides and to synthesize metastable oxide phases. Although such forms of iron oxides can be used in certain applications, the scope of their applicability can be considerably enhanced if these are doped with impurities, such as Co or Ni, at reasonable concentrations, thereby modifying their magnetic properties. Laser processing itself can be used to achieve this objective, however, this method often introduces inhomogeneities in doping patterns and correspondingly undesired microstructures due to the intrinsic character of the associated transient thermal processing. Ion beam based methods, on the other hand, offer better control over the dopant profiles and their concentrations and can be used more effectively to achieve controlled doping. We have demonstrated the use of one such method, ion beam mixing, to achieve synthesis of a ferrite. This was done in the second experiment, discussed below.

As stated earlier, the second experiment involved iron substrates coated with Fe + Fe^{57} before oxidation at 400 °C for 2 h. The CEMS spectrum of such an oxidized sample appears in Fig. 2(a) and it shows the presence of the α-Fe_2O_3 phase in the top 0.3-μm layer accessed by the CEMS technique. The CEMS spectrum corresponding to the cobalt deposited sample is shown in Fig. 2(b). This spectrum shows a significant difference as compared to the case of the as-oxi-

dized sample represented by the spectrum of Fig. 2(a). The spectrum of Fig. 2(b) can be fitted with four magnetic components having hyperfine parameters as stated below:

(i) IMF = 519 kOe; IS = 0.29 mm/s,
(ii) IMF = 492 kOe; IS = 0.27 mm/s,
(iii) IMF = 455 kOe; IS = 0.54 mm/s,
(iv) IMF = 330 kOe; IS = 0.03 mm/s.

The sextet having hyperfine field of 519 kOe once again corresponds to α-Fe_2O_3 phase, while the one having 330 kOe represents α-Fe. The other two sextets together correspond to an Fe_3O_4 phase. Formation of some quantity of Fe_3O_4 in the Co-deposited sample is surprising and needs explanation. Under the ambient of atmospheric pressure, α-Fe_2O_3 is known to be a thermodynamically stable phase on the iron surface. However, when this form of oxide is in a vacuum of 10^{-7} Torr it undergoes a degree of reduction in the surface layers leading to formation of Fe_3O_4 phase over a thickness scale of at least a few hundred Å.[14] If this oxide is again transported to atmospheric condition it would return to α-Fe_2O_3 state. However, in our case we deposit a layer of cobalt on the oxide surface prior to removal from the vacuum environment. This freezes the underlying Fe_3O_4 by encapsulation leading to a degree of structural metastability in the sample.

Figure 1(c) represents the state of the sample implanted at an ion dose of 1×10^{16} ions/cm^2. This spectrum can be fitted with five magnetic contributions to the hyperfine parameters below:

(i) IMF = 512 kOe; IS = 0.23 mm/s,
(ii) IMF = 465 kOe; IS = 0.55 mm/s,
(iii) IMF = 421 kOe; IS = 0.54 mm/s,
(iv) IMF = 325 kOe; IS = 0.022 mm/s,
(v) IMF = 515 kOe; IS = 0.28 mm/s.

Three of these [(i)–(iii)] components together correspond to cobalt ferrite phase,[15] while the other two [(iv) and (v)] are due to α-Fe and α-Fe_2O_3 phases as stated earlier. Similar results are also obtained for implantation at higher dose values, although the relative proportions of the phases are modified to some extent.

CONCLUSIONS

We have demonstrated that the nonequilibrium technique of pulsed laser treatment can be used to impart significant and interesting modifications to the surface of iron oxide depending upon the choice of the ambient. We have also shown that ion beam induced atomic mixing at the interface between a deposited over layer (Co in the present case) and iron oxide can be used to synthesize complex forms of oxides such as ferrite.

ACKNOWLEDGMENTS

The financial support to this work to one of us (S.J.) by Department of Atomic energy (India) is gratefully acknowledged. One of us (SBO) is thankful to the Indian National Science Academy, India for financial support.

[1] J. W. Matens and W. L. Peeters, SPIE Proc. **3220**, 2231 (1983).
[2] R. D. Vanderbezghe, R. Vanlerberghe, and C. G. Robbrecht, Stud. Inorg. Chem. **3**, 395 (1983).
[3] J. W. D. Matens and A. B. Voermans, IEEE Trans. Magn. **MAG-20**, 1007 (1984).
[4] J. M. Poate, G. Foti, and D. C. Jacobson, Eds., *Surface Modifications and Alloying by Laser, Ion and Electron Beams* (Plenum, New York, 1983).
[5] P. P. Patil, D. M. Phase, S. A. Kulkarni, S. V. Ghaisas, S. K. Kulkarni, S. M. Kanetkar, S. B. Ogale, and V. G. Bhide, Phys. Rev. Lett. **58**, 238 (1987).
[6] S. B. Ogale, P. P. Patil, D. M. Phase, Y. V. Bhandarkar, S. K. Kulkarni, Smita Kulkarni, S. V. Ghaisas, S. M. Kanetkar, V. G. Bhide, and S. Guha, Phys. Rev. B **36**, 16 (1987).
[7] B. Y. Tsaur, Z. L. Liau, and J. W. Mayer, Phys. Lett. **71A**, 2270 (1979).
[8] S. B. Ogale, D. M. Phase, S. M. Chaudhari, S. M. Kanetkar, S. V. Ghaisas, P. P. Patil, V. G. Bhide, and S. K. Date, Phys. Rev. B **35**, 1593 (1987).
[9] B. D. Sawika and J. A. Sawiki, in *Mössbauer Spectroscopy-II*, edited by U. Gonser (Springer, Berlin, 1981).
[10] This MOSFIT program was originally written by E. Kreber of the University des Saarlandes, Saarbruken, and was adopted for an ICL 1904S computer by S. K. Date from the National Chemical Laboratory, Pune, India.
[11] D. J. Elias and J. W. Linett, Trans. Faraday Soc. **65**, 2673 (1969).
[12] N. N. Greenwood and T. C. Gibb, *Mössbauer Spectroscopy* (Chapman and Hall Ltd., London, 1971).
[13] M. Shechter, P. Hillman, and M. Ron, J. Appl. Phys. **37**, 3043 (1966).
[14] T. Tachibana and T. Ohya, Bull. Chem. Soc. Jpn. **42**, 2180 (1969).
[15] H. Franke and M. Rosenberg, J. Magn. Magn. Mater. **4**, 186 (1977).

^{57}Fe-YIG: Narrow x-ray linewidth epitaxial layers on $Gd_3Ga_5O_{12}$

D. M. Gualtieri
Electronic Materials and Devices Laboratory, Allied-Signal Incorporated, P. O. Box 1021-R, Morristown, New Jersey 07960

W. Lavender and S. L. Ruby
Stanford Synchrotron Radiation Laboratory, Stanford Linear Accelerator Center, P. O. Box 4349, Stanford, California 94305

Epitaxial layers of 81% ^{57}Fe-enriched $Y_3Fe_5O_{12}$ were grown on thick, (100)-oriented substrates of $Gd_3Ga_5O_{12}$ for experiments in resonant nuclear diffraction. Layers up to 10 μm thick were grown on each side of 32-mm-diam, 5-mm-thick wafers using techniques common for the growth of magnetic bubble materials, but with the use of a PbO-V_2O_5 flux in place of the usual PbO-B_2O_3 flux. The PbO-V_2O_5 flux offers a lower solubility of YIG which allows a reduction in the amount of ^{57}Fe oxide required for layer growth. Thick substrates were used to reduce possible bowing from lattice constant mismatch. Lead incorporation onto yttrium lattice sites was controlled by adjusting the growth temperature, and this allowed a close lattice constant match between the layers and the substrate. Layer thickness was essentially uniform across the layer diameter with the edges 5% thicker than the center. Curie temperature and Faraday rotation measurements of the equivalent (111)-oriented material indicate as a formula unit $(Y_{2.96}Pb_{0.04})Fe_3(Fe_{1.94}Y_{0.06})O_{12}$. YIG/YIG double-crystal diffraction by tungsten L-γ_1 irradiation of a 5×7-mm rectangular area of the first crystal gave a composite linewidth of 13 arcsec for the {400} reflection. This same linewidth was observed in synchrotron illumination of the central 80% of the area of the first layer. The possibility of linewidth reduction in this material is discussed.

INTRODUCTION

Resonant nuclear diffraction of synchrotron radiation can produce brilliant, monochromatic x rays.[1] Calculations have shown that the {200} reflection of $Y_3Fe_5O_{12}$ (YIG) can utilize the nuclei of the tetrahedral ^{57}Fe atoms as a nuclear Bragg diffraction (NBD) monochrometer.[2] A double-crystal monochrometer made by Gerdau and co-workers from two 15-μm-thick layers of ^{57}Fe-enriched YIG on 30-mm-diam (100)-oriented substrates of $Gd_3Ga_5O_{12}$ confirmed the utility of YIG in NBD experiments.[3]

Layers of $Y_3Fe_5O_{12}$ on $Gd_3Ga_5O_{12}$ have been grown for many years by liquid-phase epitaxy from PbO-B_2O_3 fluxes. The high quality of these YIG layers and their substrates is due essentially to the development of magnetic bubble memory (MBM) devices, which require similar garnet layers. However, in this study we have made several modifications to the liquid-phase epitaxial process for MBM layers in our growth of NBD-YIG layers. First, the substrates for magnetic bubble layers are (111) oriented, and a (100) orientation is desired for the NBD crystals. The growth characteristics of these two orientations fortunately are similar.[4] Second, the usual 0.5-mm-thick substrates of MBM layers can bow as a result of the lattice constant mismatch between the YIG layer and the substrate. Thick substrates are preferred for this reason, and 5-mm-thick substrates were used for growth of NBD-YIG layers. Third, the solubility of YIG is high in the typical PbO-B_2O_3 fluxed melts used for the growth of MBM layers, so that a large quantity of ^{57}Fe would be required for the growth of NBD-YIG layers. For this reason a PbO-V_2O_5 flux with about half the solubility of YIG[5] was used for the growth of NBD-YIG layers.

YIG LAYER GROWTH

Layers of $Y_3Fe_5O_{12}$ (natural isotope ratios) were grown from a PbO-V_2O_5 flux on (111)-oriented 0.5-mm-thick $Gd_3Ga_5O_{12}$ substrates for initial lattice contant matching and magnetic studies. The growth solution was formulated from the oxides in the following molar ratios:

$$Fe_2O_3/Y_2O_3 = 26,$$

$$PbO/2V_2O_5 = 10,$$

and

$$[(Y_2O_3 + Fe_2O_3)/(Y_2O_3 + Fe_2O_3 + V_2O_5 + \tfrac{1}{2}PbO)] = 0.14.$$

Depletion of the YIG solute by repeated growth of thick layers allowed variation of the melt saturation and growth temperatures over the range 895.9–947.4 °C. Layer growth was by the horizontal dipping technique,[6] as used in the growth of MBM materials, with a unidirectional rotation rate of 200 rev/min. X-ray diffraction measurements indicate an expansion of the lattice constant at lower growth temperatures (Fig. 1) which is caused by incorporation of lead from the flux.[7] Lattice constant match to the substrate occurs near 895 °C. A layer grown at 894.4 °C with front and back total thickness of 28 μm had a Curie temperature of 549.2 K and Faraday rotations of 0.080 and 0.025 deg/μm at 546.1 and 632.8 nm, respectively. The Curie temperature is close to that for layers grown at the same temperature from PbO-B_2O_3 fluxes, but roughly 10 K lower than that for ceramic specimens synthesized at high temperature. This indicates an incorporation of Y on octahedral Fe lattice sites of about 0.06 atoms/f.u. (Refs. 8 and 9). The Faraday rota-

 0021-8979/88/083795-03$02.40 © 1988 American Institute of Physics

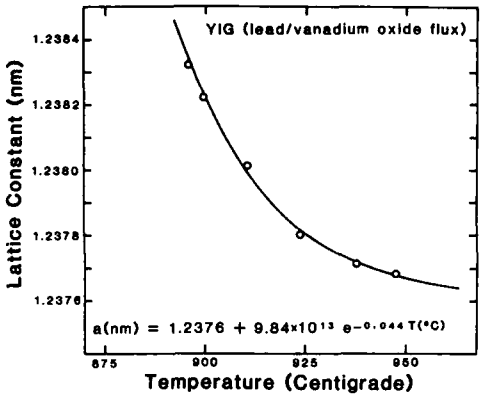


FIG. 1. Variation of YIG layer lattice constant with growth temperature. The lattice constant, measured at the (888) reflection, was corrected for strain using a Poisson ratio of 0.30. Strain-free layers on GGG substrates (1.2384 nm) can be grown from lead oxide-vanadium oxide fluxes at about 890 °C.

tion[10] and lattice constant data indicate a substitution of 0.04 atoms of lead for yttrium on the dodecahedral lattice sites. The formula unit for these layers, consistent with the magnetic and lattice constant data, is

$$(Y_{2.96}Pb_{0.04})Fe_3(Fe_{1.94}Y_{0.06})O_{12}.$$

(100)-oriented wafers of $Gd_3Ga_5O_{12}$, 32 mm diam by 5 mm thickness, were cut from a Czochralski crystal grown by Synthetic Crystal Products (P.O. Box 31428, Charlotte, NC 28231). Cutting and double-sided polishing were performed by IMP (7007 Realm Drive, San Jose, CA 95119) using techniques common in the fabrication of substrates for MBM layers.

The solution for growth of the ^{57}Fe-YIG layers on these thick substrates was formulated from 99.999% pure materials, as listed in Table I. The isotopic analysis of the iron oxide, obtained from Oak Ridge National Laboratory, is as follows: ^{54}Fe, 0.79%; ^{56}Fe, 18.24%; ^{57}Fe, 80.97% ^{58}Fe, 0.0%. These oxides were melted in a platinum crucible 75 mm high by 45 mm diam, the liquid height being about 30 mm. This crucible was placed in an outer concentric crucible to capture any leaking materials. Temperature was measured by a platinum thermocouple placed in contact with the outer wall of the growth crucible at the midpoint of the solution height.

The saturation temperature of the growth solution was found to be 905 °C, and growth was planned at 890 °C and an approximate supercooling of 15 °C. These (100)-oriented layers were grown by the same technique as the (111)-oriented layers above. Growth rate was about $\frac{1}{4}$ to $\frac{1}{2}$ μm per minute at the substrate rotation rate of 200 rev/min. The substrates were not rotated during insertion or removal, and the growth time was measured as the time at rotation. Most residual flux was removed from the crystals after growth by holding them just above the melt and linearly increasing the rotation rate from 0–500 rev/min in 30 s, and then holding at 500 rev/min for 30 s. The remaining flux was removed in a 70% solution of nitric acid at 90 °C.

The 5-mm-thick substrates required a slow rate of insertion into, and withdrawal from, the growth furnace to prevent cracking. An insertion time of 1.5 h and a withdrawal time of 3.0 h was used to move the crystals through the approximately linear 900 °C temperature gradient from the space just above the crucible to room temperature. One effect of these slow rates is an etching of substrate and layer defects, mostly dislocations, by the PbO vapors in the furnace. This involves much less than 1% of the area of the layer and apparently has little effect on the diffracting properties of the layers.

Table II shows the growth conditions of the six layers of ^{57}Fe-YIG on 5-mm-thick substrates in this study. Layer thickness was calculated from weight using a density of 5.168 g/cc, the density of pure $Y_3Fe_5O_{12}$. The layers had one centered, circular fringe under sodium lamp (588-nm) illumination over the central 80% of area of the "epi" side (downward facing in melt). This is the interference pattern caused by the layer-substrate interface, and it reveals a thickness variation of the layer of about 0.15 μm, the edges being slightly thicker than the center. The other side had roughly five times this variation.

X-RAY DIFFRACTION MEASUREMENTS

The x-ray diffraction linewidths of the YIG layers were measured in a double-crystal diffractometer built from Huber model 410 motorized goniometers with 4000-step/deg resolution. The irradiated area of the first crystal was a 5×7 mm rectangle, and calibrations with Si(111)/Si(111) diffraction of Cu$K\beta$ radiation gave a 9 arcsec linewidth. Care was taken in mounting the thick crystals, which are heavier than typical diffraction specimens. A 13 arcsec linewidth for the {400} reflection of a bare $Gd_3Ga_5O_{12}$ substrate was obtained using a Si(111) monochrometer crystal

TABLE I. Solution composition for the growth of YIG layers. The molar ratios are $Fe_2O_3/Y_2O_3 = 15$, $PbO/2V_2O_5 = 10$, and $(Y_2O_3 + Fe_2O_3)/(Y_2O_3 + Fe_2O_3 + V_2O_5 + \frac{1}{2}PbO) = 0.10$.

Oxide	Moles	Mole fraction	Grams
PbO	1.650 88	0.9000	368.459
Fe_2O_3	0.094 58	0.0516	15.104
V_2O_5	0.082 54	0.0450	15.013
Y_2O_3	0.006 31	0.0034	1.424

TABLE II. Growth conditions for the (100)-oriented epitaxial YIG layers grown from the solution in Table I.

Layer	Thickness (μm)	Growth time (s)	Growth rate (μm/min)	Growth temperature (°C)
57-1	9.5	900	0.63	892.5
57-2	6.7	900	0.45	890.0
57-3	2.7	450	0.36	893.0
57-4	4.0	450	0.53	890.2
57-5	3.3	550	0.36	891.5
57-6	4.7	800	0.35	890.5

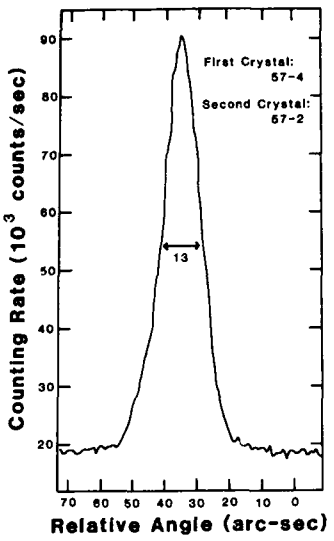


FIG. 2. Double-crystal diffraction of $W\text{-}L\gamma_1$ radiation by ^{57}Fe-enriched YIG layers. Layer 57-4 was the first (monochrometer) crystal, and layer 57-2 was the second (rocking) crystal. Full width at half maximum is 13 arcsec.

and Cu $K\beta$ radiation. The narrowest observed linewidth was 10 arcsec for layer 57-1 using a bare substrate as the first crystal and 14.4-keV radiation.

Several combinations of layers were tried in YIG(400)/YIG(400) double-crystal diffraction. The narrowest observed linewidth was for 57-4 as the first crystal and 57-2 as the rocking crystal, giving a linewidth of 13 arcsec for $W\text{-}L\gamma_1$ radiation (Fig. 2). Translation of the crystals showed that the variation of lattice constant across diameters is smooth, and that there is about three linewidths peak shifting across full diameters. This was confirmed by the double diffraction of white synchrotron radiation from YIG layer pairs, which gave about 35% of the theoretical luminance of ideal crystal pairs.

DISCUSSION

The diffraction linewidths of ideal crystals (2.8s) are 7 arcsec for silicon, 6.7 arcsec for $Gd_3Ga_5O_{12}$, and 4.5 arcsec for YIG. The measured linewidth of silicon was only slightly larger than the ideal case, but the linewidths of the substrates and the YIG layers are considerably larger than ideal. The diffraction peak shifting observed in translating the crystals across diameters indicates that much of the linewidth broadening is the result of lattice constant variation. Incorporation of Pb from the growth solution may be a cause of some of the excess x-ray linewidth in the YIG layers. As discussed above, lead atoms substitute for yttrium atoms in the crystal, causing an increase in the lattice constant. Differentiating the function which fits the data in Fig. 1 gives a variation of lattice constant with growth temperature of 4×10^{-5} nm/deg at 890 °C. The variation of growth rate with temperature is about 0.05 μm/min/deg, so that a growth rate variation arising from a temperature change will lead to a variation of lattice constant with growth rate of about 8×10^{-4} nm/μm/min. Since the fringe pattern reveals a variation of growth rate of the layer across the diameter of the central 80% of area of about 2.5%, or 0.01 μm/min, there can be as much as a 0.000 08 nm variation of lattice constant across the diameter if the growth rate variation is from a temperature gradient alone.

This lattice constant variation arising from variable lead incorporation can be eliminated through the use of a lead-free flux, or growth at high temperature. However, the lattice constant matching to the substrate offered by the lead would be absent. Lithium molybdate-yttrium molybdate fluxes have been used in the growth of YIG. These fluxes have the advantage of an extremely low solubility of YIG,[11,12] allowing considerable conservation of ^{57}Fe.

CONCLUSIONS

Lattice constant matched layers of $Y_3Fe_5O_{12}$ on $Gd_3Ga_5O_{12}$ can be grown from a $PbO\text{-}V_2O_5$ flux by using lead incorporation from the flux as a lattice constant expander. Radial variation in lead incorporation, however, broadens x-ray linewidth by lattice constant spread. Lead-free fluxes, such as lithium molybdate-yttrium molybdate, would be more suitable if lattice constant match to the substrate can be achieved in some other way.

ACKNOWLEDGMENTS

The Curie temperature and Faraday rotation measurements were done by K. P. Dimitrov-Kuhl and P. F. Tumelty.

[1]S. L. Ruby, J. Phys. (Paris) Colloq. **35**, C6-209 (1974).
[2]H. Winkler, R. Eisberg, E. Alp, R. Rüffer, E. Gerdau, S. Lauer, A. X. Trautwein, M. Grodzicki, and A. Vera, Z. Phys. B **49**, 331 (1983).
[3]E. Gerdau, R. Rüffer, H. Winkler, W. Tolksdorf, C. P. Klages, and J. P. Hannon, Phys. Rev. Lett. **54**, 835 (1985).
[4]W. van Erk, H. J. G. J. van Hoek-Martens, and G. Bartels, J. Cryst. Growth **48**, 621 (1980).
[5]G. W. Berkstresser and S. L. Blank, J. Appl. Phys. **52**, 2332 (1981).
[6]H. J. Levinstein, S. Licht, R. W. Landorf, and S. L. Blank, Appl. Phys. Lett. **19**, 486 (1971).
[7]S. L. Blank, B. S. Hewitt, L. K. Shick, and J. W. Nielsen, AIP Conf. Proc. **18**, 256 (1972).
[8]M. A. Gilleo, J. Phys. Chem. Solids **13**, 33 (1960).
[9]D. M. Gualtieri, P. F. Tumelty, and M. A. Gilleo, J. Appl. Phys. **52**, 2335 (1981).
[10]P. Hansen, K. Witter, and W. Tolksdorf, Phys. Rev. B **27**, 6608 (1983).
[11]W. A. Bonner, Mater. Res. Bull. **12**, 289 (1977).
[12]R. Korenstein and C. A. Castro, J. Appl. Phys. **50**, 7830 (1979).

Simplified Mie series calculation of dipole moments for artificial dielectric constituents

Gary G. Bush
Research & Development Division, Lockheed Missiles & Space Company, Incorporated, Palo Alto, California 94304

Artificial dielectrics are composed of particles embedded in a binding material that fills all of the space between the particles. They have homogeneous macroscopic constitutive parameters but significantly inhomogeneous microscopic properties. The macroscopic electric and magnetic polarizations of such a composite material can often be expressed in terms of the effective dipole moments of its constituents. The dipole moments of spherical multilayered particles can be calculated exactly in terms of Mie series. Except for very simple cases, the calculation of dipole moments by Mie series requires the use of significant computer resources to evaluate complex argument special functions. To alleviate this situation, closed-form solutions for spherical particles have been derived in terms of elementary functions for the case of a semiconductive or reactive coating on a dielectric core. If k is the propagation constant and r is the radius of curvature, the product kr must be greater than 10 for the coating and less than $\frac{1}{4}$ for the core and surrounding media. These solutions treat the important case of a coating which does not fully shield the core, such that the core properties must be included. The dipole moments calculated by these equations show very close agreement with exhaustive Mie series results. These equations have also proven useful in evaluating Mie series of large complex arguments. The equations are very easily implemented on a desktop computer and facilitate investigation of the mutual coupling between the imposed electric and magnetic fields and the resulting electric and magnetic dipole moments.

INTRODUCTION

The simplest models of artificial dielectric materials require the ability to calculate dipole moments of spheres.[1] The Mie series can be used for such calculations,[2] but the effort required to program a full Mie series with the corresponding special function is quite significant. The objective of this work was to derive an approximate set of equations for the magnetic and electric dipole moments of a nonperfectly conducting or hollow sphere. In the limit of perfectly conducting or pure dielectric materials, the dipole moments are easily calculated; however, these cases are not usually representative of experimentally encountered conditions. The equations presented here are intended to bridge the gap between simple, idealized models and more realistic complex Mie calculations.

Models of artificial dielectric materials will be discussed in the following sections. The relationship between the dipole moments and electromagnetic constitutive parameters will be formulated. The Mie solution will be introduced as a general method for calculating multipole moments of spheres. An approximation for the Mie coefficients will then be introduced and a comparison of the values calculated by the simplified equations and by the full Mie series will be given.

ARTIFICIAL DIELECTRIC MATERIALS

Artificial dielectric materials are composed of individual particles imbedded in a medium that completely fills the space between the particles. These materials are microscopically inhomogeneous and macroscopically homogeneous. Artificial dielectric materials can be designed to exhibit specific electromagnetic properties such as diamagnetism. The constitutive parameters of artificial dielectrics can be modeled by first calculating the magnetic and electric dipole moments of an isolated particle. The interaction between particles is taken into account by a mixture equation that calculates the effective constitutive parameters for the artificial dielectric from the dipole moments and the volume fraction occupied by the particles.

Series and integral solutions exist for the dipole moments of multilayer spheres and, in the long wavelength approximation, for the ellipsoids. The expression for the dipole moments of the multilayered sphere is in the form of a Mie series. The terms in the Mie series include spherical Hankel and Bessel functions. To initiate work in this area required finding the dipole moments of particles by the Mie series and thus the complex task of devising and programming robust spherical Hankel and Bessel function algorithms.[3,4] The search for an alternative method for the calculation of the Mie coefficients that does not involve special functions lead to the expressions presented in this paper.

DIPOLE MOMENTS

The total electric flux density $\mathbf{D}$ is given as the sum of the free-space flux density and the material-induced flux density $\mathbf{P}$:

$$\mathbf{D} = \epsilon_0 \mathbf{E} + \mathbf{P} \quad \text{or} \quad \mathbf{D} = \epsilon \mathbf{E},$$
$$P = \epsilon_0 \chi_e E, \quad \epsilon = \epsilon_0 (1 + \chi_e), \tag{1}$$

 0021-8979/88/083798-03$02.40 © 1988 American Institute of Physics

where ϵ is the permittivity and χ_e is the electric susceptibility.

The macroscopic polarization P is equal to the sum of the microscopic dipole moments of the individual particles p. Thus, $P = Np$ where N is the number of polarizable particles per unit volume.

The microscopic dipole moments of the artificial dielectric are induced by the local electric field E_L. The resulting microscopic polarizability α_e is given by

$$\alpha_e = p/(\epsilon_0 E_L)\,. \tag{2}$$

If the particles occupy rectangular lattice sites with spacing e, f, and g in the three lattice dimensions, the local electric field E_L is given by the sum of the applied field E and an interaction field E_i (Ref. 1):

$$E_i = pd/\epsilon_0\,, \tag{3}$$

where

$$d = \frac{1.201}{\pi f^3} - \frac{8\pi}{f^3}\left[J_0\left(\frac{2\pi g}{f}\right) + J_0\left(\frac{2\pi e}{f}\right)\right],$$

and J_0 is the zeroth-order Bessel function.

For a cubic lattice $e = f = g$ and $d \sim (3e^3)^{-1}$. The resulting relative permittivity is given by[1]

$$\epsilon = \epsilon_0[(1 + N\alpha_e)/(1 - \alpha_e d)] \tag{4}$$

and, by a similar analysis, the permeability is given by

$$\mu = \mu_0[(1 + N\alpha_m)/(1 - \alpha_m d)]\,, \tag{5}$$

where α_e is the electric polarizability and α_m is the magnetic polarizability.

The dipole moment of a multilayer sphere can be found by solving the related problem of electromagnetic scattering from a sphere.[1,2] The scattered field is the multipole response of the sphere to an external field. All that remains is to identify the electric and magnetic dipole terms in the series and compute the effective permittivity and permeability of the artificial dielectric using Eqs. (4) and (5). The full expressions for the Mie series are given in Ref. 2.

The polarizability, in terms of the Mie series coefficient, is

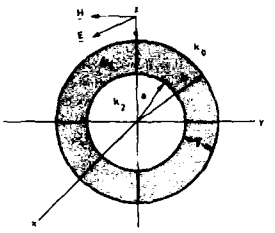


FIG. 1. Geometry of the coated sphere.

$$\alpha_{e,m} = 4\pi f_{e,m}/k_0^3\,, \tag{6}$$

where

$$k_0 = \omega\sqrt{\mu_0\epsilon_0}\,,$$

$$f_e = -j(B_1 + \tfrac{3}{2}A_2 - \tfrac{1}{2}B_3 + \tfrac{15}{2}A_4 - \tfrac{15}{8}B_5 + \cdots)\,,$$

$$f_m = (A_1 + \tfrac{3}{2}A_3 + \tfrac{15}{8}A_5 + \cdots)\,,$$

and A_i and B_i are the Mie series coefficients corresponding to the magnetic and electric dipole terms, respectively.

The Mie coefficients are functions of the propagation constants in each region and the dimensions of the coated sphere. Figure 1 shows the geometry of the problem. The following approximation was derived for the case of a reactive shell ($k_1 a > 10$) and a less-reactive core and surrounding media ($k_0 b < \frac{1}{4}$ and $k_2 a < \frac{1}{4}$). This case is very useful for evaluating artificial dielectric materials composed of thin conductive hollow spheres and ferrite-coated hollow or dielectric core spheres.

APPROXIMATION

If $k_1 a$ is greater than 10, it has been observed that the Mie series can be truncated after the A_1 and B_1 terms with very little error. The Hankel and Bessel functions can be replaced by their asymptotic forms[3,4] for arguments greater than 10. After considerable algebraic manipulation, the following approximations were found for A_1 and B_1:

$$A_1 = \frac{-(k_0 b)^3}{2}\left(\frac{\dfrac{-1}{\mu_1} - \dfrac{2j}{\mu_0 k_1 b} + \dfrac{2j}{\mu_2 k_1 a} - \dfrac{4\mu_1}{\mu_0\mu_2 k_1 b k_1 a} + e^{-j2k_1 T}\left(\dfrac{1}{\mu_1} + \dfrac{2j}{\mu_2 k_1 a} - \dfrac{2j}{\mu_0 k_1 b} + \dfrac{4\mu_1}{\mu_0\mu_2 k_1 b k_1 a}\right)}{\dfrac{-1}{\mu_1} + \dfrac{j}{\mu_0 k_1 b} + \dfrac{2j}{\mu_2 k_1 a} + \dfrac{2\mu_1}{\mu_0\mu_2 k_1 b k_1 a} + e^{-j2k_1 T}\left(\dfrac{1}{\mu_1} + \dfrac{2j}{\mu_2 k_1 a} + \dfrac{j}{\mu_0 k_1 b} - \dfrac{2\mu_1}{\mu_0\mu_2 k_1 b k_1 a}\right)}\right), \tag{7}$$

$$B_1 = \frac{-(k_0 b)^3}{2j}\left(\frac{\dfrac{2k_0^2 j}{3\mu_0\mu_1 k_2 k_1} - \dfrac{4}{3\mu_1^2 k_2 b} - \dfrac{k_0^2 k_2 a}{3\mu_0\mu_2 k_1^2} - \dfrac{2jk_2 a}{3\mu_1\mu_2 k_1 b} + e^{-j2k_1 T}\left(\dfrac{4}{3\mu_1^2 k_2 b} - \dfrac{2jk_2 a}{3\mu_1\mu_2 k_1 b} + \dfrac{2k_0^2 j}{3\mu_0\mu_1 k_2 k_1} + \dfrac{k_0^2 k_2 a}{3\mu_0\mu_2 k_1^2}\right)}{\dfrac{2k_0^2 j}{3\mu_0\mu_1 k_2 k_1} + \dfrac{2}{3\mu_1^2 k_2 b} - \dfrac{k_0^2 k_2 a}{3\mu_0\mu_2 k_1^2} + \dfrac{jk_2 a}{3\mu_1\mu_2 k_1 b} + e^{-j2k_1 T}\left(\dfrac{-2}{3\mu_1^2 k_2 b} + \dfrac{jk_2 a}{3\mu_1\mu_2 k_1 b} + \dfrac{2k_0^2 j}{3\mu_0\mu_1 k_2 k_1} + \dfrac{k_0^2 k_2 a}{3\mu_0\mu_2 k_1^2}\right)}\right). \tag{8}$$

This pair of relations has proven quite useful in analytic modeling of artificial dielectrics. It is not necessary to assume perfectly conducting or lossless dielectric materials for the sphere or to assume that the sphere is a homogeneous solid. These equations reduce to the expected asymptotic formulas. For the case of a solid sphere (no shell)[5]

$$A_1 = (k_0 a)^3[(\mu_2 - 1)/(\mu_2 + 2)]\,,$$

$$B_1 = j(k_0 a)^3[(\epsilon_2 - 1)/(\epsilon_2 + 2)]\,. \tag{9}$$

For the perfectly conducting solid sphere

$$A_1 = -\tfrac{1}{2}(k_0 a)^3\,,$$

$$B_1 = j(k_0 a)^3\,. \tag{10}$$

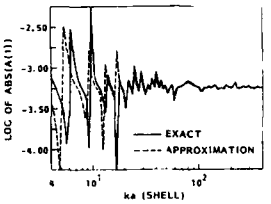


FIG. 2. Comparison of the approximate and exact solutions for Mie coefficient A_1 with $k_2a = 0.021$ at a frequency of 100 MHz.

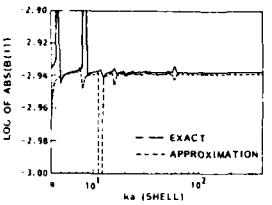


FIG. 3. Comparison of the approximate and exact solutions for Mie coefficient B_1 with $k_2a = 0.021$ at a frequency of 100 MHz.

If the sphere is homogeneous and has the same constitutive parameters as the media, A_1 and B_1 are zero.

To compare the values of A_1 and B_1 calculated by Eqs. (7) and (8) to the values computed by a full implementation of the Mie series, A_1 and B_1 were calculated for k_1a between 4 and 200 at a frequency of 100 MHz. Figures 2 and 3 show the results of this comparison for A_1 and B_1, respectively. When k_1a exceeds 10, the approximation is quite good.

The approximate expressions for A_1 and B_1 are useful as benchmarks to validate the results of robust implementations of the full Mie series.

CONCLUSIONS

An approximation to the Mie series coefficients needed to calculate dipole moments of a single-shell sphere has been presented. The approximation has proven useful for analytic modeling of artificial dielectrics. The program to implement the full Mie calculation required 1500 lines of Fortran 77, while the approximation was implemented in 25 lines. This work should be useful to those modeling artificial dielectric materials with the parameters of actual materials rather than idealized parameters.

ACKNOWLEDGMENT

The author wishes to thank M. V. Smith for her development and programming of the robust Mie series code with which this work was compared.

[1] R. E. Collin, *Field Theory of Guided Waves* (McGraw-Hill, New York, 1960), pp. 509–551.
[2] J. A. Stratton, *Electromagnetic Theory* (McGraw-Hill, New York, 1941), pp. 414–416.
[3] E. W. Hobson, *The Theory of Spherical and Ellipsoidal Harmonics* (Chelsea, New York, 1955), pp. 178–292.
[4] M. Abramowitz and I. A. Stegun, *Handbook of Mathematical Functions* (U.S. Government Printing Office, Washington, D.C., 1970), pp. 355–478.
[5] R. F. Harrington, *Time-Harmonic Electromagnetic Fields* (McGraw-Hill, New York, 1961), pp. 292–298.

Missing magnetic moment in spinel iron oxide films (abstract)

C. Ortiz
IBM Almaden Research Center, San Jose, California 95120

G. Vurens
Center for Advanced Materials, Lawrence Berkeley Laboratory, Berkeley, California 94720

M. M. Chen
IBM Almaden Research Center, San Jose, California 95120

M. Salmeron
Center for Advanced Materials, Lawrence Berkeley Laboratory, Berkeley, California 94720

This work studies the influence of oxygen flow and substrate temperature on the physical properties of reactive sputtered thin films of iron oxide spinels. We have focused on the variations of the magnetic moment, which can be as low as 20% of the bulk value, for certain experimental conditions. We present a model which attributes the missing moment to a mispopulation of Fe moments on the A and B sites. Direct experimental evidence to prove this model is obtained from conversion electron Mössbauer spectroscopic experiments, which correlate the missing moment with increased A-site population compared with the "textbook" population (only 8 A sites out of 64 are filled). For example, samples deposited at room temperature have always a low moment and are found to have a large A-site population. When the samples are annealed in vacuum under specific conditions to maintain the oxygen ratio and to give kinetic energy to the atoms to reach their spinel positions, an increase of the magnetic moment is observed.

 0021-8979/88/083801-01$02.40 © 1988 American Institute of Physics

Magnetic resonance experiments on ion beam sputtered {100} Fe films

S. A. Oliver and C. Vittoria
Center for Electromagnetics Research, Northeastern University, Boston, Massachusetts 02115
E. Schloemann, H. J. Van Hook, and R. W. Tustison
Raytheon Research Division, Lexington, Massachusetts 02173

Ferromagnetic resonance (FMR) measurements have been performed on single-crystal Fe films, produced by ion beam sputtering techniques on GaAs substrates. In-plane FMR results over the frequency range 0.1–20.0 GHz were obtained by a slot line technique. The magnetic parameters deduced from these measurements are comparable to bulk Fe. In-plane angular variation reveals a negligible uniaxial anisotropy contribution to the magnetic anisotropy energy. Spin-wave excitations were observed in 9.5-GHz cavity measurements, and are found to obey the n^2 law. The exchange stiffness constant is found to be somewhat larger than seen in other epitaxial Fe films. These results show that epitaxial Fe/GaAs films possessing good magnetic properties may be produced by ion beam sputtering techniques.

INTRODUCTION

In the past few years, magnetic resonance techniques have been heavily used in studying the magnetic properties of single-crystal Fe films grown on semiconductor substrates.[1–5] These measurements have shown that high-quality magnetic films can be produced by means of molecular-beam epitaxy (MBE). Recently, a new technique for producing epitaxial iron films has been developed, that of ion beam sputtering (IBS).[6] We present results for the magnetic properties of a pair of IBS produced iron films on gallium arsenide substrates, measured by ferromagnetic resonance techniques. We find these films to be of high quality, comparable to those produced by the MBE technique.

EXPERIMENT

The Fe films were epitaxially grown on (100) GaAs substrates by ion beam sputtering. The growth conditions, structural characterization, and results from vibrating-sample magnetometer (VSM) measurements on these films have recently been reported by Tustison *et al.*[6] The two films measured had differing thickness calibrations. Thickness of the thinner film was determined by scanning electron microscopy (SEM) photographs. The thicker film, produced at a later date, was measured repeatedly by a "Dec-Tac" thickness profilometer. The nominal thickness of the two films were found to be 700 and 2440 Å, with thickness accuracy of 10% and 5%, respectively.

Ferromagnetic resonance (FMR) measurements were performed using two different experimental techniques. Spin-wave resonance (SWR) measurements were obtained using the traditional magnetic field swept cavity technique. The sample is mounted in a Varian 9.5-GHz cavity, with the film plane oriented perpendicular to the external magnetic field H. Further FMR results were obtained using a terminated slot line technique.[7] This experimental technique is analogous to traditional FMR, except a planar device is used instead of a microwave cavity. The slot line is mounted between the poles of a bearing mounted 5-kOe magnet, which can be rotated 360°. Microwave energy is transmitted to the slot line through coaxial lines from a Hewlett–Packard 0.01–20.0-GHz sweeper source. Resonance results were obtained with H angularly varying in the plane of the film, and also with H parallel to the ⟨100⟩ or ⟨110⟩ crystallographic axis of the films.

RESULTS AND DISCUSSION

In-plane FMR measurements, using the slot line technique, were used in obtaining values for the effective magnetization and anisotropy fields in the films. Resonant field data taken on the thicker film as a function of angle at fixed frequency (17.1 GHz) is displayed in Fig. 1. Figure 2 shows

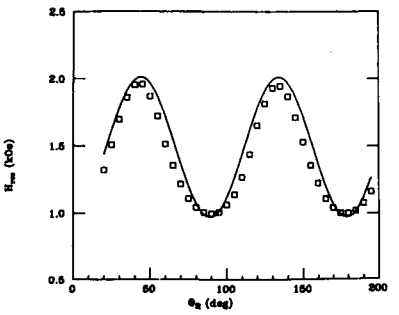


FIG. 1. Resonant field as a function of in plane angular variation for the 2440-Å Fe/GaAs film using the slot line technique. Solid line is the calculated fit using the parameters from Table I.

 0021-8979/88/083802-03$02.40 © 1988 American Institute of Physics

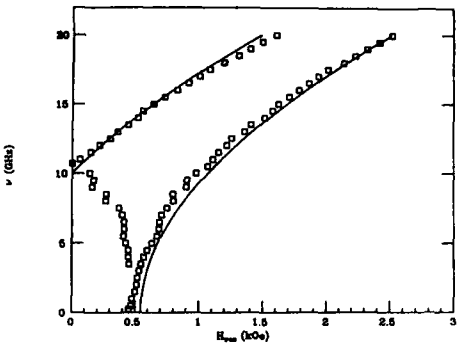


FIG. 2. Resonant field as a function of frequency for the 2440-Å Fe/GaAs film using the slot line technique with H parallel to the ⟨100⟩ or ⟨110⟩ axis. Solid line is the calculated fit to the data using the parameters from Table I.

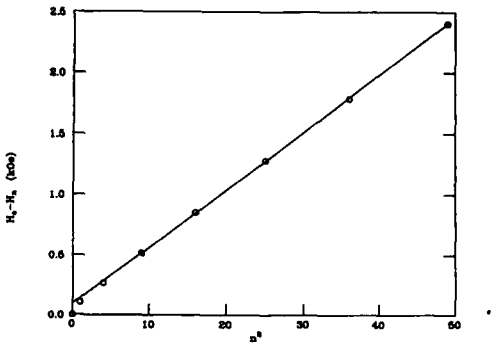


FIG. 3. Spin-wave resonance data for the 2440-Å Fe/GaAs film from perpendicular FMR measurements taken at 9.53 GHz.

resonance results, taken on the same film, where H is parallel to either the crystallographic ⟨100⟩ or ⟨110⟩ axis, performed at a series of frequencies between 0.2 and 20.0 GHz. It should be noted that the error bars for the resonant field in both of these figures are large, being of the order of the plotted block width ($\Delta H_{res} = 80$ Oe). This is due to uncertainty in determination of the resonance position, as the resonance curves obtained by this technique do not necessarily possess the classical Lorentzian lineshape.

We deduce values for the magnetic parameters of these films by means of a least squares fitting routines to the resonance equations. The general resonance equation is obtained by the method of Suhl,[8] starting with the expression for the energy density of a (100) film with magnetization M in an external field H given by

$$E = -\mathbf{M}\cdot\mathbf{H} + (2\pi M^2 + K_u^{\perp})\cos^2\theta + K_1(\alpha_1^2\alpha_2^2 + \alpha_1^2\alpha_3^2 + \alpha_2^2\alpha_3^2) + K_u \sin^2\theta\cos^2(\phi - \phi_u).$$

In addition to terms for the demagnetizing field ($4\pi M$) and the normal first-order cubic anisotropy field (K_1), a pair of uniaxial fields are also present in the free energy. Coefficients $K_u^{\perp}$ and K_u are included for uniaxial fields both normal to and in the plane of the film.[4] The directional cosines α_i are the angles between the magnetization and the cubic axes, and ϕ_u is the angle corresponding to the in-plane uniaxial field. The resonance equation is given by[4]

$$(\omega/\gamma)^2 = (H+\alpha)(H+\beta),$$
$$\alpha = 4\pi M_{eff} + (K_1/M)(2 - \sin^2 2\phi) - (2K_u/M)\cos^2(\phi - \phi_u),$$
$$\beta = (2K_1/M)\cos 4\phi - (2K_u/M)\cos 2(\phi - \phi_u),$$

TABLE I. Summary of magnetic parameters on IBS iron films.

t (Å)	$4\pi M_{eff}$ (kOe)	$2K_1/M$ (kOe)	H_0 (kOe)	ΔH (Oe)
700	20.6	0.50	23.367	20
2440	21.0	0.55	23.705	91

with effective magnetization $4\pi M_{eff} = 4\pi M + 2K_u^{\perp}/M$ and $\gamma = ge/2mc$. Values for $4\pi M_{eff}$ and K_1/M deduced from the fits for both films are listed in Table I. We have taken g to be equal to 2.09 for all experimental fits. We estimate these results to be accurate within 5%. Both sets of values agree well with bulk Fe.[4] The value of the in plane uniaxial term is found to be very small ($K_u/M < 10$ Oe), exhibited by the near perfect cubic symmetry shown by the angular variation curve (Fig. 1), and in agreement with vibrating-sample magnetometer results.[6] Calculated behavior for the magnetic resonances using the deduced parameters from Table I, in the case where the magnetization is saturated, is plotted as solid lines in Fig. 1 and 2. These follow the general trend of the experimental data for both the angular and frequency varied results.

Both ion beam sputtered Fe films displayed distinct spin-wave resonances (SWR) for perpendicular FMR measurements. We were able to resolve all SWR modes above saturation ($H > 4\pi M_{eff}$). The resonance equation in this orientation is given by

$$\omega/\gamma = H' - 4\pi M_{eff} + 2K_1/M,$$
$$H' = H_0 - (2A/M)(\pi^2/t^2)n^2,$$

with t the film thickness, A the exchange stiffness constant, H_0 the main line resonance field at excitation frequency $f = \omega/2\pi = 9.53$ GHz, and n the mode number of the spin-wave excitation. High-order n SWR observed in the thicker film show excellent agreement to this n^2 law (Fig. 3). Deviations from n^2 are seen at low n for the thicker film. Low-n deviations have been noted for other Fe films and are attributed to variation in either the magnetization or uniaxial anisotropy field $K_u^{\perp}/M$ at the film interface.[3] The exchange stiffness constant ($A = 2.37\times10^{-6}$ erg/cm) for the thicker film was found using the measured thickness and $4\pi M_s = 21\,000$ G.[6] This value for the exchange stiffness constant is somewhat higher than those found in the literature,[3] and may be due to uncertainty in the film thickness. Only the first two SWR modes are observable for the thinner film. As these modes also deviate from n^2, we are unable to obtain A for this film.

Table I also lists values for H_0 and the linewidth of the

main line resonance (ΔH) at 9.53 GHz. Line widths of the IBS films are narrow, being comparable to those of films deposited by MBE.[3] This is a strong indicator of the quality of these films. In addition, we find no indication for magnetic resonances above that of the main line. These have been noted in MBE produced films, and described as the result of surface modes.[5] The lack of surface modes indicates that the interfacial structure in IBS produced films is different from that of MBE grown films.

SUMMARY

The ion beam sputtered epitaxial films are found to have magnetic properties comparable to those grown by molecular beam epitaxial techniques. Deduced parameters for the effective magnetization ($4\pi M_{\text{eff}}$), and cubic anisotropy (K_1/M), are close to bulk iron,while the in-plane uniaxial field (K_u/M) is found to be negligible. Spin-wave resonance data on the thicker film displays n^2 behavior for higher n modes, but yields a larger value for the exchange stiffness constant (A) than found in other epitaxial iron films. The resonance linewidths are seen to be small, with no indication of surface modes in the FMR results.

ACKNOWLEDGMENT

The work of S. A. O. and C. V. was supported in part by the National Science Foundation under Grant No. ECS-8601661.

[1] G. A. Prinz, G. T. Rado, and J. J. Krebs, J. Appl. Phys. **53**, 2087 (1982).
[2] J. J. Krebs, F. J. Rachford, P. Lubitz, and G. A. Prinz, J. Appl. Phys. **53**, 8058 (1982).
[3] C. Vittoria, J. J. Krebs, and G. A. Prinz, J. Magn. Magn. Mater. **37**, L111 (1983).
[4] J. J. Krebs, B. T. Jonker, and G. A. Prinz, J. Appl. Phys. **61**, 2596 (1987).
[5] C. Vittoria, F. J. Rachford, J. J. Krebs, and G. A. Prinz, Phys. Rev. B **30**, 3903 (1984).
[6] W. Tustison, T. Varitimos, J. Van Hook, and E. F. Schloemann, Appl. Phys. Lett. **51**, 285 (1987).
[7] H. Dötsch, P. Röschmann, and W. Schilz, Appl. Phys. **15**, 167 (1978).
[8] H. Suhl, Phys. Rev. **97**, 555 (1955).

Spin-wave resonance in FeNiBSi films

J. Xia, J. S. Ryu, and C. Vittoria
Center for Electromagnetic Research, Electrical and Computer Engineering Department, Northeastern University, Boston, Massachusetts 02115

Ferromagnetic resonance (FMR) measurements have been performed on thin films of $Fe_{80-x}Ni_xB_{15}Si_5$ alloys ($x = 5$, 40, and 60). The effective magnetization ($4\pi M_{eff}$), magnetic anisotropy field (H_A), and g factor were measured. The values of g for all the films ranged between $1.90 < g < 2.11$. Spin-wave resonance (SWR) excitations were observed for H, the magnetic field, applied perpendicular to the film plane. SWR fields were found to obey the n^2 law and yielded exchange constants in the range of $A = 0.2$–1.9×10^{-6} ergs/cm. The nearest-neighbor exchange parameter J was deduced from A and implies that J varies within a factor of 2 as the value of x changes. In one of the nickel-rich samples, the SWR fields appear to be linear with n implying nonuniform distribution of magnetization in the film.

I. INTRODUCTION

Thermal, magnetic, and magnetomechanical properties of amorphous ribbons of $Fe_{80-x}Ni_xB_{15}Si_5$ have been studied.[1] This system of materials exhibited ferromagnetic ordering with high effective magnetization and relative low magnetic anisotropy field (in the order of 1–10 Oe). In this paper we explore this system in a thin-film configuration. In particular, the ferromagnetic resonance (FMR) and vibrating sample magnetometer (VSM) measurements are reported on $Fe_{80-x}Ni_xB_{15}Si_5$ ($x = 5$,40, and 60) and $Fe_{20}Ni_{80}$. The thin films were prepared with an ion beam sputtering technique. The effective magnetization, magnetic anisotropy field, and g factor were measured as a function of x. In addition, spin-wave resonance (SWR) has been observed so that the exchange stiffness constant was determined.

In our experimental results, the values of g for all samples were in the range of $1.90 < g < 2.11$. The SWR fields were found to obey the n^2 law and the exchange constants were in the range of $A = 0.2$–1.9×10^{-6} ergs/cm. The exchange integral parameter J varies within a factor of 2 as the value of x varies from 5 to 60. In addition, the SWR linewidth increased as the spin-wave mode number n increased.

II. EXPERIMENT

We fabricated thin films of $Fe_{80-x}Ni_xB_{15}Si_5$ with an ion beam sputtering technique. The composition x was varied from 5 to 60 at. %. The thickness ranged from 2160 to 3690 Å. All films were annealed at 275 °C in order to improve the FMR linewidth. Before annealing the FMR linewidth was approximately 100 Oe. But after annealing the linewidth ranged between 30 and 50 Oe in all tested samples.[2]

The FMR experiments were performed in a microwave cavity which is connected to a 9.5-GHz klystron. The sample was put in the center of the TE_{102} cavity with a teflon sample holder which was rotated in the cavity. Conventional FMR techniques were used to measure the derivative absorption of the sample versus the dc magnetic field on a X-Y recorder. The dc magnetic field was applied in the film plane and normal to it.

From the FMR derivative absorption versus the dc magnetic field curve we obtained the resonant fields of the films. We define $H_\parallel$ (film plane parallel to the dc field) and $H_\perp$ (film plane perpendicular to the dc field). The FMR linewidth, ΔH, was also obtained directly from the resonance curve. The FMR conditions are given below:

$$(f/\gamma)^2 = (H_\parallel + 4\pi M_{eff})H_\parallel , \quad (1)$$

$$f/\gamma = H_\perp - 4\pi M_{eff} , \quad (2)$$

$$4\pi M_{eff} = 4\pi M_s - H_A , \quad (3)$$

where M_s is the saturation magnetization measured in VSM apparatus and H_A is the magnetic uniaxial anisotropy field. H_A may be deduced from VSM and FMR experiments. The VSM measurement measures $4\pi M_s$ in a saturated magnetic field condition. Thus, by subtracting $4\pi M_s$ from $4\pi M_{eff}$, H_A is deduced. If H_A is greater than zero, it implies that the easy axis of magnetization is normal to the film plane. If H_A is smaller than zero, the easy axis is in the film plane. γ is the gyromagnetic ratio. f is the frequency of rf field.

$H_\parallel$ and $H_\perp$ were determined by changing the film orientation to minimize and maximize the FMR field near the parallel and perpendicular sample positions, respectively. The g factor as well as $4\pi M_{eff}$ are obtained from Eqs. (1) and (2).

The spin-wave resonance absorption spectra was measured for H perpendicular to film plane. The SWR fields and linewidths were measured as functions of n, the spin-wave mode number.

TABLE I. Experimental results of $Fe_{80-x}Ni_xB_{15}Si_5$ thin films.

Sample no.	x	d (Å)	g	$4\pi M_{eff}$ (kG)	$4\pi M_s$ (kG)	$-H_A$ (kG)	A (10^{-6} ergs/cm)
1	5	2400	1.92	15.9	12.5	3.4	1.37
2	5	2700	2.09	15.8	11.7	4.1	1.87
3	40	2160	2.10	10.7	7.9	2.8	0.68
4	40	2400	2.10	10.8	9.1	1.7	0.80
5	60	2230	1.91	6.0	5.4	0.6	0.70
6	60	3690	2.01	6.1	4.6	1.5	0.20
7	60	2700	1.97	6.5	4.8	1.7	···

 0021-8979/88/083805-03$02.40 © 1988 American Institute of Physics

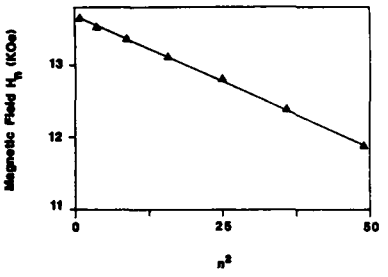


FIG. 1. SWR field H_n in a $Fe_{40}Ni_{40}B_{15}Si_5$ film vs SWR mode number square, n^2.

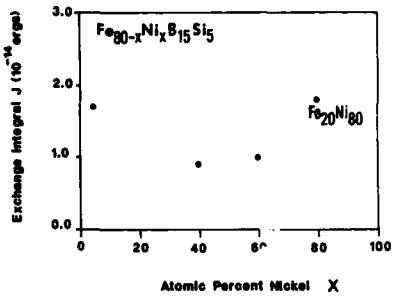


FIG. 2. Exchange integral J of $Fe_{80-x}Ni_xB_{15}Si_5$ and $Fe_{20}Ni_{80}$ thin films vs atomic percent nickel, x.

The SWR data was fitted with the following spin-wave dispersion relation:

$$f=\gamma[H_n-4\pi M_{\text{eff}}+(2A/M_s)(n\pi/d)^2], \quad (4)$$

where d is the thickness and H_n is the SWR resonant field for the nth spin-wave mode, $n=1,2,3,\ldots$. $n=1$ was assigned to the very first spin-wave resonance next to the main ferromagnetic resonance. By plotting H_n vs n^2 we verified the n^2 law[3] of the SWR spectra and calculated the exchange constant A of the ferromagnetic film from the slope of the curve.

In analyzing the data for A, we assumed that the *local* structure of the amorphous film is bcc for $x<20$ and fcc for $x>20$.[4] Clearly, it is meaningless to describe amorphous films in terms of a crystal structure. However, the coherent or coordination length in amorphous films is about 15 Å which is greater than the basic unit cell or local structure. We are saying that this local coordination within that one or two unit cells is bcc or fcc. The exchange interaction is of short range; we, therefore, believe that it is meaningful to explain our data in terms of an exchange parameter. The nearest-neighbor exchange integral J was obtained from

$$A=2JS^2/a \quad \text{(bcc structure)} \quad (5)$$

and

$$A=4JS^2/a \quad \text{(fcc structure)}, \quad (6)$$

where S is the spin quantum number and a is the lattice constant.

III. RESULTS AND DISCUSSION

Table I summarizes the FMR and VSM results for our films. The exchange constant A, g factor, $4\pi M_{\text{eff}}$, $4\pi M_s$, thickness d, and the composition x are listed in Table I. For most samples the n^2 law was obeyed very well and the exchange constants are in the range of $A=0.2$–1.9×10^{-6} ergs/cm. The g factors for all the samples lie in the range $1.90<g<2.11$ which is close to published values for permalloy films.[5] For the samples which have the same value of x, A varied a little for different thicknesses. This is due to experimental error.

TABLE II. Spin-wave resonance data of a $Fe_{40}Ni_{40}B_{15}Si_5$ film at 9.5 GHz. n is the spin-wave mode number, ΔH_n is the SWR linewidth, I_n is the intensity of the nth SWR derivative absorption, I_0 is the intensity of the main resonance, i.e., the FMR, and H_n is the magnetic field at the nth SWR.

n	1	2	3	4	5	6	7
ΔH_n (Oe)	31.6	36.0	44.3	47.5	63.3	79.1	126.6
I_n/I_0 (%)	24	3.2	0.32	0.53	0.27	0.056	0.019
H_n (kOe)	13.7	13.5	13.4	13.1	12.8	12.4	11.9

The SWR fields versus the SWR mode number square, n^2, curve is shown in Fig. 1. The SWR linewidth increases and the SWR intensity decreases as the spin-wave mode number n increases. This is shown in Table II.

Figure 2 shows that the exchange integral J varies within a relative small range of $J=0.97$–1.70×10^{-14} ergs as the value of x changes from 5 to 60. This is understandable in view of the fact that the exchange integral J describes the interaction between two nearest neighbor ions in the material. Hence, it is affected only by the local coordination. The point here is that although the films are amorphous, the local coordination is maintained such that ferromagnetic exchange is possible.

For one nickel-rich film H_n scales linearly with n instead of n^2. The exchange constant A cannot be obtained by using Eq. (4). It is well known that this type of scaling can be explained in terms of nonuniform distribution of magnetization within the film.[6] There are many suggestions which imply that the nonuniformity in magnetization may be due to clusters being formed in the film. At this stage in time it is not clear what the source of the nonuniformity is. The sample number of this film is 7 shown in the Table I.

In summary, we studied thin films of $Fe_{80-x}Ni_xB_{15}Si_5$ ($x=5$,40, and 60) by FMR and VSM techniques. The effective magnetization, g factor, anistropy field H_A, the exchange constant A and exchange integral J were obtained from the experimental results. The spinwave excitations obey the n^2 law and the FMR conditions are explained in terms of the well-known Kittel relations. In conclusion, although the films are amorphous, it is still meaningful to introduce parameters, such as exchange constant, which are related to short-range interactions.

[1]L. T. Kabacoff, M. Wun-Fogle, and F. Bucholtz, IEEE Trans. Magn. MAG-21, 2014 (1985).
[2]C. Vittoria and P. Lubitz, J. Appl. Phys. 49, 4908 (1978).
[3]R. F. Soohoo, *Microwave Magnetics* (Harper & Row, New York, 1985), p. 178.
[4]R. M. Bozorth, *Ferromagnetism* (Van Nostrand, New York, 1951), p. 104.
[5]G. C. Bailey and C. Vittoria, Phys. Rev. B 8, 3247 (1973).
[6]A. M. Portis, Appl. Phys. Lett. 2, 69 (1963).

Spin-wave FMR in annealed NiFe/FeMn thin films

A. Layadi, J.-W. Lee, and J. O. Artman
Magnetics Technology Center, Carnegie Mellon University, Pittsburgh, Pennsylvania 15213-3890

Ferromagnetic resonance (FMR) investigations have been made at 33 GHz on as-deposited and on annealed bilayer NiFe/FeMn thin films. Supplemental investigations were made at 9 GHz. Following a 350 °C anneal, for 1 h or longer in duration, the NiFe FMR spectrum was found to be characterized by a sequence of spin-wave resonance (SWR) modes. The behavior of the SWR modes is in accord with the presence of a thin ferromagnetic layer at the NiFe/FeMn interface with magnetization different from the bulk. Transmission electron microscopy (TEM) examinations indicate that annealing promotes formation of an interdiffused layer at the NiFe/FeMn interface and favors NiFe grain growth. Magnetic field limitations precluded FMR at 0° (perpendicular) field orientation. At various field orientations below the critical angle, the resonant fields, H_n, were found to vary with mode number n as n^2. Also, for $n>1$, the FMR-SWR linewidth ΔH_n has a component varying as n^2. From the 33-GHz 16° orientation data, the exchange constant A is computed to be $(1.03\pm0.15)\times10^{-6}$ erg/cm. The application of an in-plane magnetic field during anneal produces a reduction of the SWR mode intensities and a broadening of the principal peak. A perpendicular magnetic field had little effect.

I. INTRODUCTION

We report here on the spin-wave resonance (SWR) modes seen in the ferromagnetic resonance (FMR) spectrum of NiFe/FeMn. Such modes were not seen in as-deposited samples.[1] However, SWR modes did appear after the proper annealing process. From FMR-SWR data we derive the exchange constant A, the effective anisotropy field $H_{K\,\mathrm{eff}}$, and the magnetogyric ratio $\gamma/2\pi$. We start with a brief theoretical treatment; we then outline the experimental procedure and numerical analysis. The findings are correlated with transmission electron microscopy (TEM) cross-section studies.

II. THEORY

The equation of motion of the magnetization, including spin waves, is given by

$$\frac{d\mathbf{M}}{dt}=\gamma\mathbf{M}\times\mathbf{H}_{\mathrm{equ}}+\gamma 2A\,(\mathbf{M}/M^2)\times\nabla^2\mathbf{M}, \tag{1}$$

where $\mathbf{M}$ is the magnetization, γ is the magnetogyric ratio, A is the exchange constant of the ferromagnet, and $\mathbf{H}_{\mathrm{equ}}$ is an "equivalent" magnetic field which includes the applied and anisotropy fields. Moreover, $\mathbf{M}\times\mathbf{H}_{\mathrm{equ}}=-\mathbf{M}/M\times\nabla E$, where E is the total free energy of the system, including Zeeman and anisotropy contributions:

$$E=K\sin^2\theta-2\pi M_s^2\sin^2\theta-M_sH\cos(\alpha-\theta). \tag{2}$$

The z axis is taken as the normal to the film. Then θ and α are the angles measured from the normal to the film to, respectively, the magnetization $\mathbf{M}$ and the applied field $\mathbf{H}$. Also $K\sin^2\theta$ is the magnetocrystalline anisotropy energy for a film of uniaxial symmetry, $-2\pi M_s^2\sin^2\theta$ is the demagnetizing (anisotropy) energy and $-M_sH\cos(\alpha-\theta)$ is the Zeeman energy term.

The FMR relation, including spin waves, is obtained from the solution of Eq. (1). It can be written in the final form[2]:

$$(\omega/\gamma)^2=[H\cos(\alpha-\theta)+H_{K\,\mathrm{eff}}\cos^2\theta+2Ak^2/M_s]\times[H\cos(\alpha-\theta)+H_{K\,\mathrm{eff}}\cos 2\theta+2Ak^2/M_s], \tag{3}$$

where ω is the microwave frequency, k is the spin-wave propagation constant and $H_{K\,\mathrm{eff}}=2K/M_s-4\pi M_s$ is the effective anisotropy field. The idealized boundary conditions correspond to $k=n\pi/d$ where d is the thickness of the film and n is an integer (the mode number). The tilt θ of the magnetization is found from

$$H\sin(\alpha-\theta)=H_{K\,\mathrm{eff}}\sin\theta\cos\theta. \tag{4}$$

III. EXPERIMENTAL PROCEDURE

The samples were prepared by rf sputtering onto glass substrates in the presence of a magnetic field. The nominal thickness of the FeMn overlay was kept constant at about 80 nm. Most of the experiments were done on three particular samples, each with a different NiFe thickness; these were designated as sample nos. 1, 2, and 3 with respective thicknesses of 160, 108, and 60 nm. The annealing of the samples was done with a quartz halogen lamp at temperatures up to 350 °C. The vacuum was maintained at 10^{-6} Torr. Magnetic fields up to 5 kOe were applied during some of the anneals.[3]

The magnetic properties were measured in a 33-GHz resonant cavity FMR spectrometer with internal field modulation at 50 kHz. The cylindrical cavity was operated in the TE_{011} mode. The external field could reach 19 kOe. Supplementary FMR observations were made with a 9-GHz–10-kOe FMR spectrometer. TEM cross-section analysis was performed on various samples.

IV. RESULTS AND DISCUSSION

The FMR spectra of the as-deposited NiFe/FeMn films were characterized by a single resonance.[1] The $\gamma/2\pi$ and $H_{K\,\mathrm{eff}}$ values were 2.91 GHz/kOe and -10.3 kOe, respectively. The variations in these parameters following anneal-

 0021-8979/88/083808-03$02.40 © 1988 American Institute of Physics

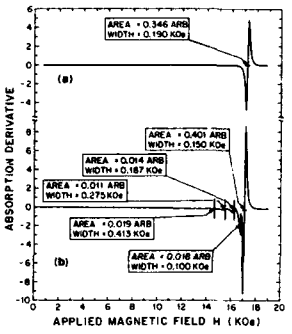


FIG. 1. FMR spectra of a 160-nm-thick NiFe/FeMn sample (specimen no. 1): (a) before and (b) after anneal for one hour at 350 °C. $f = 33.4$ GHz, $\alpha = 20°$.

ing were no more than 4% or so. Since the "average" magnetocrystalline anisotropy in these samples presumably is zero, $H_{K\,\mathrm{eff}}$ is a measure of $-4\pi M_s$. No changes in the essential features of the spectrum were noted following a 1-h 200 °C anneal; however, after a 1-h 350 °C anneal, spin-wave modes appeared. Because of magnetic field limitations, we were not able to see FMR in the perpendicular external field configuration; however up to 6 modes besides the principal (first) one were observed at an angle of 15° from the normal. Examples of FMR spectra taken before and after anneal are shown in Fig. 1. As the magnetic field is rotated away from the normal, the relative intensity of the modes (as compared to the principal mode) decreases monotonically; for angles greater than 30° only the principal mode was seen. The thicker the sample, the larger the number of modes; no spin waves were observed in sample no. 3, the thinnest one.

For all the angles at which the spin waves were seen it was observed that the resonant field H_n of the nth mode varied linearly with n^2, where we assign $n = 1$ to the principal mode; see Fig. 2. The slope of the H_n vs n^2 plot enables us to compute the exchange constant A. In the perpendicular configuration ($\alpha = 0$) it follows from Eqs. (2) and (3) that

$$H_n = -2A\pi^2 n^2/(M_s d^2) + \omega/\gamma - H_{K\,\mathrm{eff}}. \tag{5}$$

The derivation of A from experimental data is obvious here. However, the appropriate procedure to be used when H is oriented arbitrarily is not immediately apparent. But starting from the general relation [Eq. (3)], one can solve for $H_n \Rightarrow H_n = f(\alpha, n, M_s, \cdots)$. After making some reasonable approximations, one finds

$$H_n = an^2 + b. \tag{6}$$

Here the slope a is given by

$$a = -[2A\pi^2/(M_s d^2)][\cos(\theta - \alpha) - C/D]; \tag{7}$$

the intercept b is given by

$$2b = -H_{K\,\mathrm{eff}}\{[\cos(\theta + \alpha) + \cos\theta\cos\alpha] + D\}, \tag{8}$$

with

$$C = \cos(\theta - \alpha)[\cos(\theta + \alpha) + \cos\theta\cos\alpha] + 1 - 3\cos^2\theta \tag{9}$$

and

$$D^2 = [\cos(\theta + \alpha) + \cos\theta\cos\alpha]^2 - 4\cos^2\theta + [2\omega/(\gamma H_{K\,\mathrm{eff}})]^2. \tag{10}$$

[For $\alpha = 0$, Eqs. (6)–(10) reduce to Eq. (4), as expected.]

We derive $H_{K\,\mathrm{eff}}$ and $\gamma/2\pi$ from FMR done at a number of different α values. Then, using Eqs. (4), (7), (9), and (10) and H_n data taken at a particular α, one finds the exchange constant A. In this manner, from sample no. 1 ($d = 160$ nm) H_n data taken at $\alpha = 16°$, we found A to be $(1.03 \pm 0.15) \times 10^6$ erg/cm.

Our spectrometers yields *differentiated* absorption curves, which superficially have a dispersion-type appearance. We define the linewidth ΔH as the magnetic field interval between the derivative peaks. We define the intensity as corresponding to the *absorption* curve area; in practice we compute the FMR signal amplitude times $(\Delta H)^2$ for this purpose. At any particular angle α the linewidth ΔH_n of the nth mode was found for $n > 2$ to vary as n^2, i.e., $\Delta H_n = n^2\delta H' + \delta H''$. The presence of this type of linewidth variation,[4] along with the disappearance of spin waves at a particular $\alpha(\alpha_{\mathrm{crit}})$,[5] suggests that the spin waves are associated with dynamic "pinning." The linewidth of the principal ($n = 1$) mode increased following the annealing process. For the annealed specimens, the plot of ΔH_1 vs α reached a maximum at α_{crit} and then decreased to a minimum at $\alpha = 90°$. The critical angles were determined to be 30° and 10° from observations made on specimen no. 1 at, respectively, 33 and 9 GHz. These experimental α_{crit} values agreed reasonably well with the theoretical values, determined by using Eqs. (3) and (4) to find those α values satisfying the constraint[5] $(dH/dM)_{\omega,\alpha} = 0$.

In specimen no. 1 the intensities of the $n > 2$ modes relative to the principal $n = 1$ mode decreased sharply as the applied field was rotated in direction away from the normal. The $n = 2$ mode decreased in intensity more rapidly than the $n = 3$ mode which eventually becomes the stronger. With the annealing temperature fixed at 350 °C, the relative SWR mode intensities were found at first to decrease with annealing time; the intensities then remained almost constant for longer anneals. As an example, in specimen no. 1 at $\alpha = 16°$ the intensity of the $n = 2$ mode decreased from 10.5% to 3.2% when going from a 1- to a 3-h anneal; correspondingly, the $n = 3$ mode dropped from 5.2% only to 4.7%. This is a particular example of a general tendency at all α for the even-numbered modes to become less intense than the odd-numbered ones following the anneal.

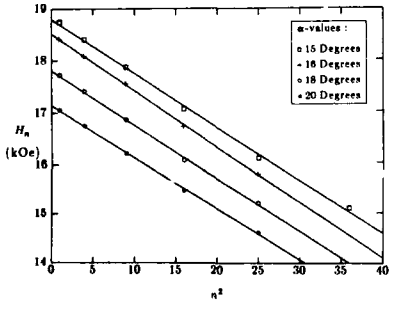


FIG. 2. SWR mode position H_n vs n^2 for the specimen of Fig. 1 at field orientation angles, α, of 15°, 16°, 18°, and 20°.



FIG. 3. TEM micrographs of NiFe/FeMn specimen no. 1: (a) bright field (BF) image of as-deposited film, and (b) BF image and (c) dark field image following anneal for one hour at 350 °C. NiFe and FeMn layers are denoted by numbers 1 and 2, respectively.

A magnetic field of 5 kOe was applied either in-plane or normal to the film during a 350 °C 1-h anneal. For in-plane magnetic anneal, the linewidth, ΔH_1, of the principal mode and the intensities of the secondary SWR modes were particularly affected. As an example, for specimen no. 2, observed at $\alpha = 60°$, $\Delta H_1 = 141$, 178, 259, and 188 Oe, respectively, for as-deposited, straight-annealed, in-plane magnetically annealed, and perpendicular magnetically annealed samples. The increase in linewidth associated with annealing was more pronounced for this thinner specimen than for specimen no. 1. After in-plane magnetic annealing the secondary SWR modes were less intense than after the straight anneal. However, when the magnetic field was applied normal to the film, no reduction in secondary mode intensity was observed.

TEM examination of the as-deposited sample reveals a well-defined interface between the NiFe and FeMn with both layers growing in columnar form; see Fig. 3(a). TEM views of the annealed sample are shown in Figs. 3(b) and 3(c). Here interdiffusion at the interface is seen; furthermore, the NiFe grains grew in diameter but the FeMn grains became equiaxed.

V. CONCLUSIONS

Interdiffusion between the NiFe-FeMn layers associated with anneal was insufficient to create a *distinct* observable region at the interface. (Such an interdiffused region had been detected by us in NiFe/α-Fe_2O_3.[1]) However, we conjecture that the NiFe magnetization was modified slightly at the interface. This, in appropriately annealed specimens, evidently produced sufficient "dynamic" pinning to permit generation of spin-wave modes. At 33 GHz the spin-wave modes disappear at a critical angle of about 30°. Both the resonant field H_n and the linewidth ΔH_n of the secondary modes were found to vary as n^2 (with $n = 1$ being assigned to the *principal* mode). We conjecture that the increase in ΔH_1 after anneal is associated with a growth in grain size; thus, we infer that grain size increases with anneal and even more so for a magnetic anneal. This seems to be in accord with the TEM data. The duration of the anneal seems to be progressively effective up to a particular limit, 3 h in our case. Beyond that no large changes were observed in either the mode intensities or relative line widths. Application of an in-plane magnetic field during anneal led to a reduction in intensity of the secondary modes and to a broadening of the primary peak. Application of a perpendicular magnetic field during anneal produced little effect.

ACKNOWLEDGMENTS

We thank W. C. Cain of the Magnetics Technology Center for the sputtering of the film specimens. This work was partially supported by the Magnetic Research Group through the Division of Materials Research, National Science Foundation under Grant No. DMR-8613386. The work of A.L. was supported by the Ministère de l'Enseignement Supérieur of Algeria.

[1] A. Layadi, W. C. Cain, J.-W. Lee, and J. O. Artman, IEEE Trans. Magn. MAG-23, 2993 (1987).
[2] R. F. Soohoo, *Magnetic Thin Films* (Harper and Row, New York, 1965), Chap. 11, p. 227.
[3] K. R. Mountfield, P. V. Mitchell, and J. O. Artman (unpublished); P. V. Mitchell, Ph.D. Dissertation, Dept. of Physics, Carnegie Mellon University, February (1987).
[4] I. G. Cullis and M. Heath, J. Phys. F 10, 309 (1980).
[5] P. E. Wigen, C. F. Kooi, M. R. Shanabarger, and T. D. Rossing, Phys. Rev. Lett. 9, 206 (1962).

Ferromagnetic antiresonance transmission through pure iron at 73 GHz

J. M. Rudd, J. F. Cochran, K. B. Urquhart, K. Myrtle, and B. Heinrich
Department of Physics, Simon Fraser University, Burnaby, B.C. V5A 1S6, Canada

The magnetic damping in pure iron has been studied over the temperature range 140–300 K using a single-crystal slab 15 μm thick. The results at room temperature are consistent with the accepted value of the damping parameter for iron of $G = 0.7 \times 10^8$ Hz. The damping increases as the temperature is reduced and reaches a value of approximately 1.4×10^8 Hz at 140 K.

The intrinsic magnetic damping in a ferromagnetic metal is dominated by electron-magnon scattering processes in which the electron spin may, or may not, be flipped[1-4]. These electron scattering processes are mediated by spin-orbit coupling and result in a damping which has the Landau–Lifshitz, or Gilbert, form; i.e., the damping is proportional to frequency. Contributions from the intraband processes in which the electron spin is not flipped are expected to reach a maximum at low temperatures for which $ql \gg 1$, where q is the magnon wave vector and l is the electron mean free path. In the limit $ql \gg 1$ the contributions of the intraband processes to magnetic damping become independent of electron mean free path, and reflect the details of the Fermi surface geometry.[3,4] The spin-flip, or interband, contribution to the magnetic damping depends upon the distribution of exchange gaps between spin-up and spin-down electron energy bands. The temperature dependence of spin-flip scattering is expected to reach a maximum at a temperature such that kT is approximately equal to the exchange gap if the splitting between spin-up and spin-down bands is dominated by a single exchange gap.[1] It is therefore of interest to measure the temperature dependence of the damping parameter G for eventual comparison with detailed band structure calculations. The temperature dependence of the damping in nickel has been studied over a wide range using a combination of ferromagnetic resonance (FMR) experiments[5,6] and ferromagnetic antiresonance (FMAR) transmission experiments.[7,8] The damping parameter in iron has not been measured precisely at any temperature, and its temperature dependence is uncertain. The FMR linewidth in iron is dominated by exchange conductivity broadening for frequencies up to several hundred GHz, and FMAR measurements have not been carried out at frequencies sufficiently high to satisfy the requirement[9] $\omega/\gamma > 4\pi M_s$. In this paper we give a preliminary report of FMAR experiments on iron which have been carried out at 73 GHz ($4\pi M_s = 22$ kOe corresponds to 64 GHz for iron). Our goal is to use the transmission technique to study the damping parameter for iron over the temperature range from 0 to 700 K.

The principle of the FMAR transmission method has been described by Heinrich and Mescheryakov[10] as well as by other authors.[9,11] Information about the magnetic properties of a material can be obtained by fitting the experimental transmission line shape, or by measuring the maximum transmitted amplitude. The amplitude varies exponentially with the damping parameter and so provides a very sensitive measure of the strength of the damping.

The 73-GHz apparatus was very similar to the 24-GHz homodyne system described by Cochran, Heinrich, and Dewar.[12] The sample, in the form of a thin disk, was clamped between two cavities and functioned as common endwall for each. The dc magnetic field was oriented to lie parallel with the plane of the specimen and to be perpendicular to the rf magnetic field.

Since the transmission amplitude decreases with increasing conductivity we needed a thin sample to observe the transmission at low temperatures. Our starting material was a single-crystal slab, approximately 0.5 mm thick, whose normal was within 2° of a [100] axis. A 7.5-mm disk was spark cut from the slab. This disk was ground with 600-grit silicon carbide paper to reduce the thickness then polished with 9-μm diamond polish to a thickness of 84 μm. The layer damaged by mechanical polishing was removed by chemically polishing[13] each side for 2 min to obtain the final thickness. The sample was given no further treatment. The average thickness was found to be 15 μm from the weight and area of the disk. The sample was tapered: we estimate the taper to be approximately 1 μm/mm. To reduce the effect of the

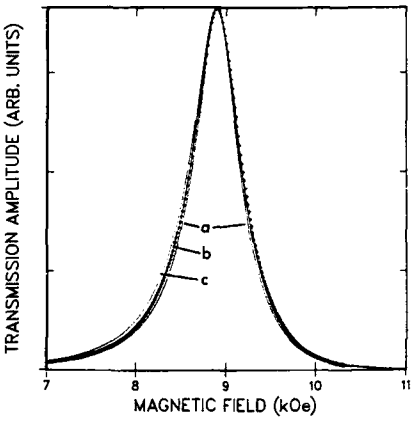


FIG. 1. Transmitted amplitude as a function of magnetic field for Metglas $Fe_{82}B_{12}Si_6$ at room temperature. The experimental data points are shown as crosses (+). The solid lines have been calculated assuming: (a) $G = 0.9 \times 10^8$ Hz, (b) $G = 1.1 \times 10^8$ Hz, (c) $G = 1.3 \times 10^8$ Hz. Other parameters used in the calculations were: saturation magnetization 16.053 kOe, resistivity 124×10^{-6} Ω cm, thickness 37 μm, frequency 72.95 GHz, g factor 2.09. The calculated curves have been scaled to the same peak amplitude.

 0021-8979/88/083811-03$02.40 © 1988 American Institute of Physics

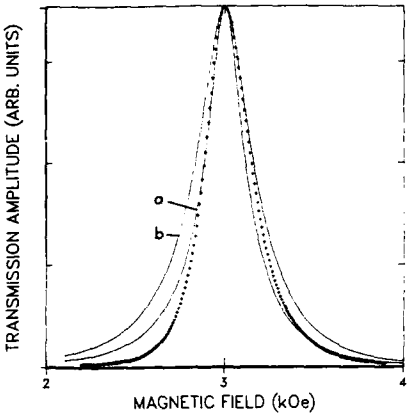


FIG. 2. Transmitted amplitude as a function of magnetic field for pure iron at room temperature. The experimental data points are shown as crosses (+). The dc magnetic field was parallel to the plane of the sample and oriented along a [100] direction. The solid lines have been calculated assuming (a) $G = 0.1 \times 10^8$ Hz, (b) $G = 0.7 \times 10^8$ Hz. Other parameters used in the calculations were: saturation magnetization 21.55 kOe, resistivity 9.8×10^{-6} Ω cm, thickness 15 μm, frequency 73 GHz, g factor 2.09, exchange parameter 2.0×10^{-6} erg/cm, anisotropy 3.5×10^5 erg/cm^3. The calculated curves have been scaled to the same peak amplitude.

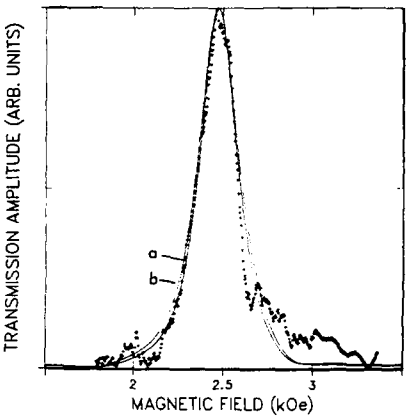


FIG. 4. Transmitted amplitude as a function of magnetic field for pure iron at 140 K. The experimental data points are shown as crosses (+). The dc magnetic field was parallel to the plane of the sample and oriented along a [100] direction. The solid lines have been calculated assuming (a) $G = 1.3 \times 10^8$ Hz, (b) $G = 1.5 \times 10^8$ Hz. Other parameters used in the calculations were: saturation magnetization 21.946 kOe, resistivity 2.69×10^{-6} Ω cm, thickness 15 μm, frequency 73 GHz, g factor 2.09, exchange parameter 2.0×10^{-6} erg/cm, anisotropy 4.5×10^5 erg/cm^3. The curves have been scaled to the same peak amplitude.

taper on the transmission line shape the sample was copper plated on one side over all but a central area 2 mm in diameter. An indium seal was used between the sample and the receiver cavity to reduce microwave leakage around the sample.

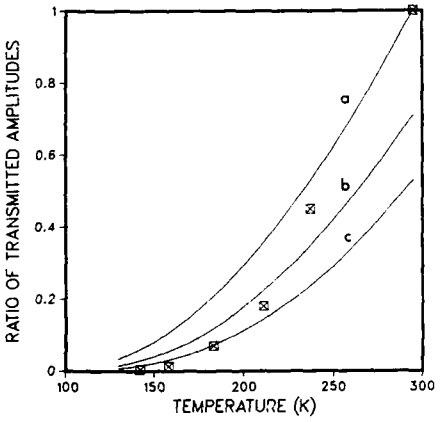


FIG. 3. Solid lines show the ratio of the maximum transmitted amplitude at temperature T calculated for a particular value of the damping parameter G to the maximum transmitted amplitude at 300 K calculated using $G = 0.7 \times 10^8$ Hz. Curve (a) calculated for a temperature independent damping parameter $G = 0.7 \times 10^8$ Hz, (b) calculated for $G = 1.0 \times 10^8$ Hz, (c) calculated for $G = 1.3 \times 10^8$ Hz. The symbols show the experimentally observed values for the ratio of the maximum transmitted amplitude at temperature T to the maximum transmitted amplitude at 300 K. The data include a correction (less than 50%) for the temperature dependence of the sensitivity of the transmission system.

The transmission line shape is very sensitive to the value of the damping parameter for materials in which the FMR linewidth is dominated by the intrinsic damping. For example, we show in Fig. 1 a comparison of the experimental and calculated transmission line shapes for the amorphous Metglas $Fe_{82}B_{12}Si_6$. The solid lines in the figure have been calculated for three values of the damping parameter. These curves have been scaled to the same peak amplitude. Values of the parameters used in the calculations are listed in the figure caption. It is clear from the figure that the best fit to the data is obtained for $G = 1.1 \times 10^8$ Hz and that a change in the damping parameter of 0.1×10^8 Hz gives a noticeably poorer fit. We have chosen this Metglas as a reference material to calibrate the sensitivity of the transmission system because its properties vary little with temperature and because it gives a large transmission signal over the temperature range of interest.

The results of FMAR transmission measurements on the iron single crystal at room temperature are shown in Fig. 2. The solid lines in Fig. 2 have been calculated for a uniformly thick slab 15 μm thick. Unfortunately the experimental lineshape is not well described by the theory. The damping parameter which is required to fit the data lies between 0.1 and 0.7×10^8 Hz. Quoted values for the room temperature damping parameter range from 0.4 to 1.3×10^8 Hz obtained from FMR linewidths.[6,14–18] The commonly accepted value is $G = 0.7 \times 10^8$ Hz. The discrepancy between the calculated and observed line shapes is larger than can be explained by the nonuniform thickness of the specimen. Moreover, the FMR linewidth measured at 73 GHz was found to

be 280 Oe. Very good specimens of iron single crystals exhibit linewidths at 73 GHz which are as small as 170–180 Oe, although linewidths up to 250 Oe are not uncommon.[14,15] We think that the peculiar transmission line shape exhibited by this crystal is connected with the large FMR linewidth but we do not understand its origin.

The variation with temperature of the ratio of the transmission amplitude at temperature T to the transmission amplitude at 300 K is shown in Fig. 3. The transmission lineshape at 140 K is shown in Fig. 4. On the basis of the change in amplitude of the transmission signal, and assuming a room-temperature value of $G = 0.7 \times 10^8$ Hz, we conclude that the damping in iron increases with decreasing temperature and reaches a value of approximately 1.4×10^8 Hz at 140 K. This value of damping is consistent with the line shape observed at 140 K (see Fig. 4).

Experiments will be continued using specimens having narrower FMR linewidths, and we shall attempt to use comparison of transmission amplitudes with a reference material such as Metglas $Fe_{82}B_{12}Si_6$ to measure the damping parameter, and its temperature dependence, for pure iron.

The authors would like to thank the Natural Sciences and Engineering Research Council of Canada for the grants which supported this work.

[1]B. Heinrich, D. Fraitova, and V. Kambersky, Phys. Status Solidi **23**, 501 (1967).
[2]V. Kambersky, Can. J. Phys. **48**, 2906 (1970); Czech. J. Phys. B **26**, 1366 (1976).
[3]V. Korenman and R. E. Prange, Phys. Rev. B **6**, 2769 (1972).
[4]L. Berger, J. Phys. Chem. Solids **38**, 1321 (1978).
[5]D. Rodbell, Physics **1**, 279 (1965).
[6]S. M. Bhagat and P. Lubitz, Phys. Rev. B **10**, 179 (1974).
[7]G. Dewar, B. Heinrich, and J. F. Cochran, Can. J. Phys. **55**, 821 (1977).
[8]B. Heinrich, D. J. Meredith, and J. F. Cochran, J. Appl. Phys. **50**, 7726 (1979).
[9]J. F. Cochran and B. Heinrich, IEEE Trans. Magn. **MAG-16**, 660 (1980).
[10]B. Heinrich and V. F. Mescheryakov, Sov. Phys. JETP **32**, 232 (1970).
[11]J. F. Cochran, B. Heinrich, and G. Dewar, Can. J. Phys. **55**, 787 (1977).
[12]J. F. Cochran, B. Heinrich, and G. Dewar, Can. J. Phys. **55**, 834 (1977).
[13]S. Kadeckova and K. Volenik, Czech. J. Phys. B **17**, 649 (1967).
[14]V. Kambersky, Can. J. Phys. **48**, 1103 (1970).
[15]Z. Frait, D. Fraitova, M. Kotrbova, and Z. Hauptmann, Czech. J. Phys. B **16**, 837 (1966).
[16]S. M. Bhagat, J. R. Anderson, and Ning Wu, Phys. Rev. **155**, 510 (1967).
[17]B. Heinrich and Z. Frait, Phys. Status Solidi **16**, K11 (1966).
[18]S. M. Bhagat and M. S. Rothstein, Solid State Commun. **11**, 1535 (1972).

Light scattering from thermal magnons in thin metallic ferromagnetic films

J. F. Cochran and J. R. Dutcher
Department of Physics, Simon Fraser University, Burnaby, B. C., V5A 1S6, Canada

A computer program has been written with which the complex resonant frequency can be calculated for a thin ferromagnetic metal film sandwiched between a nonmagnetic metallic substrate and a nonmagnetic metallic overlayer. The calculation includes exchange and magnetic damping having the Gilbert form. The program has been used to investigate the sensitivity of thin-film resonant frequencies to the resistivities of the overlayer, the substrate, and the magnetic film. It is concluded that the presence of an overlayer and of a substrate are unimportant for the analysis of Brillouin scattering data from films less than 100 Å thick: uncertainties in the absolute value of the frequency shift of the scattered light—typically 1:200—are greater than, or comparable with, the frequency shifts caused by an overlayer or a substrate.

In this paper we make a quantitative assessment of the effect of a metallic substrate and of a thin metallic overlayer on thin film magnon frequencies. Experiments using Brillouin scattering[1–8] have shown that boundary effects are small, but it has yet to be shown that they are negligible if accurate magnetic parameters are to be obtained from Brillouin scattering data.[8,9]

The theory of Brillouin scattering for thin, unsupported, nonmetallic films has been carried through by Camley, Rahman, and Mills[10] using an application of the fluctuation-dissipation theorem from statistical mechanics. We have chosen to attack this problem using the approach of Wolfram and DeWames[11] in which Maxwell's equations and the Landau–Lifshitz equations for the magnetization are used to calculate the normal modes of the system. We consider a system composed of a magnetic film backed by a nonmagnetic metallic substrate and covered by a nonmagnetic metal overlayer. The x, y axes are in the plane of the film; z is directed into the substrate and is parallel with the film normal. The external magnetic field is directed along x, and the in-plane component of the magnon wave vector is directed along y (only magnetic excitations which propagate normal to the applied magnetic field are considered). The ground state of the system is assumed to be uniformly magnetized. The surfaces of the magnetic film are taken to be at $z=0$ and at $z=d$. The front surface of the overlayer is located at $z=-d_1$.

For this geometry, Maxwell's equations for the magnetically active modes become

$$\frac{\partial e_x}{\partial z} = -\frac{1}{c}\frac{\partial}{\partial t}(h_y + 4\pi m_y)\,, \tag{1a}$$

$$\frac{\partial e_x}{\partial y} = \frac{1}{c}\frac{\partial}{\partial t}(h_z + 4\pi m_z)\,, \tag{1b}$$

$$\frac{\partial h_z}{\partial y} - \frac{\partial h_y}{\partial z} = \frac{4\pi\sigma}{c}\,e_x\,. \tag{1c}$$

The displacement current density has been neglected in (1c) because at microwave frequencies it is very small compared with the conduction current density. Similar equations describe the fields in the nonmagnetic metals except that $m_y = m_z = 0$.

Solutions of Maxwell's equations are sought which are proportional to the factor $e^{i(qy-\omega t)}$. The disturbances in the vacuum, overlayer, and substrate must all be proportional to this same factor in order that the tangential components of e_x and h_y may be continuous everywhere across the interfaces at $z=-d_1$, $z=0$, and $z=d$. The wave vector q is real, and in a Brillouin scattering experiment it is determined by the wavelength and the angle of incidence of the incident laser light.[8] From the outset the frequency f, where $\omega = 2\pi f$, is taken to be a complex quantity. The real part of the frequency is, of course, the resonant frequency of a normal mode; the imaginary part of f must necessarily be negative since the amplitude of a normal mode which has been stimulated by an impulse must die away with time due to magnetic dissipation and eddy current damping. Solutions of Maxwell's equations are sought which have a z dependence $\sim e^{ikz}$ where, by definition, the imaginary part of k is taken to be positive. In the nonmagnetic metals, Eqs. (1) fully specify the dependence of the wave vector k upon frequency. For example, in the metallic overlayer, the wave vector k_1 is given by[12] $k_1^2 = -q^2 + (i/\delta_1^2)$, where $\delta_1^2 = c^2/4\pi\omega\sigma_1$ and σ_1 is the conductivity of the metal in esu. In the vacuum the conductivity is, of course, zero and one must include the displacement current density in Maxwell's equations.

In the magnetic metal Maxwell's equations alone do not determine the allowed values of the wave vector; they serve only to provide one set of relationships between the components of the magnetization and the magnetic fields. From Eqs. (1) one finds

$$4\pi m_y = -(1+i\delta^2 k^2)h_y + i\delta^2 qkh_z\,, \tag{2a}$$

$$4\pi m_z = i\delta^2 qkh_y - (1+i\delta^2 q^2)h_z\,. \tag{2b}$$

A second set of relationships is provided by the Landau–Lifshitz equations of motion for the magnetization which, when linearized, can be written in component form as[13]

$$\frac{2A}{M_s}\left(\frac{\partial^2 m_y}{\partial z^2}\right) - H_z m_y - \left(\frac{i\omega}{\gamma}\right)m_z = -M_s h_y\,, \tag{3a}$$

$$\frac{2A}{M_s}\left(\frac{\partial^2 m_z}{\partial z^2}\right) - H_y m_z + \left(\frac{i\omega}{\gamma}\right)m_y = -M_s h_z\,. \tag{3b}$$

In these equations A is the exchange stiffness parameter and the magnetomechanical ratio, γ, is positive and is given by $g(e/2mc)$. The effective fields H_y and H_z are

 0021-8979/88/083814-03$02.40 © 1988 American Institute of Physics

$$H_y = H + \frac{2Aq^2}{M_s} - i\left(\frac{\omega}{\gamma}\right)\left(\frac{G}{\gamma M_s}\right) + \alpha_y\,, \tag{4a}$$

$$H_z = H + \frac{2Aq^2}{M_s} - i\left(\frac{\omega}{\gamma}\right)\left(\frac{G}{\gamma M_s}\right) + \alpha_z\,, \tag{4b}$$

where H is the externally applied dc field and G is the Gilbert magnetic damping parameter. The terms α_y, α_z represent effective fields due to magnetocrystalline anisotropy. Equations (2) can be used together with Eqs. (3) to obtain two homogeneous equations for the magnetic field components h_y, h_z. The requirement that these equations have a nontrivial solution leads to a secular equation which is cubic in k^2:

$$P_1(k\delta)^6 + P_2(k\delta)^4 + P_3(k\delta)^2 + P_4 = 0\,, \tag{5}$$

where

$$\begin{aligned}
P_1 &= i(2A/M_s\delta^2)^2\,,\\
P_2 &= (2A/M_s\delta^2)^2[1 + i\delta^2q^2]\\
&\quad + i(2A/M_s\delta^2)(H_y + H_z + 4\pi M_s)\,,\\
P_3 &= i(2A/M_s\delta^2)(q^2\delta^2)(H_y + H_z + 4\pi M_s)\\
&\quad + (2A/M_s\delta^2)(H_y + H_z + 8\pi M_s)\\
&\quad + i[B_yH_z - (\omega/\gamma)^2]\,,\\
P_4 &= i\delta^2q^2[B_zH_y - (\omega/\gamma)^2] + [B_yB_z - (\omega/\gamma)^2]\,.
\end{aligned}$$

In the above expressions $B_y = H_y + 4\pi M_s$, $B_z = H_z + 4\pi M_s$, and $\delta^2 = c^2/4\pi\omega\sigma$, where σ is the conductivity in esu of the magnetic metal. The general solution of the combined Maxwell's equations and Landau–Lifshitz equations is specified by six independent wave amplitudes[14]: a forward propagating and a reverse propagating wave for each of the three wave vectors k_1, k_2, k_3 which satisfy Eq. (6). The six wave amplitudes in the magnetic slab must be chosen so as to satisfy six boundary conditions. These are, explicitly, at $z = 0$:

$$\text{(i)}\quad \left.\frac{e_x}{h_y}\right|_0 = \left(\frac{\omega}{ck_1}\right)\left(\frac{1+\alpha}{1-\alpha}\right),$$

where

$$\alpha = \frac{[(k_1/k_0)+1]}{[(k_1/k_0)-1]}\,e^{-2ik_1d_1}\,,$$

and $k_0^2 = -q^2 + (\omega/c)^2$, $Im\ k_0 > 0$;

$$\text{(ii)}\quad \left.A\frac{\partial m_y}{\partial z}\right|_0 = K_y^F m_y(0);$$

$$\text{(iii)}\quad \left.A\frac{\partial m_z}{\partial z}\right|_0 = K_z^F m_z(0);$$

and at $z = d$:

$$\text{(iv)}\quad \left.\frac{e_x}{h_y}\right|_d = \left(\frac{\omega}{ck_b}\right),$$

where $k_b^2 = -q^2 + (i/\delta_b^2)$ and $\mathrm{Im}\,(k_b) > 0$;

$$\text{(v)}\quad \left.A\frac{\partial m_y}{\partial z}\right|_d = -K_y^R m_y(d);$$

$$\text{(vi)}\quad \left.A\frac{\partial m_z}{\partial z}\right|_d = -K_z^R m_z(d).$$

Conditions (i) and (iv) are required to ensure continuity of e_x, h_y across the slab surfaces. Conditions (ii), (iii), (v), and (vi) are Rado–Weertman[15] pinning conditions derived from a surface pinning energy density having the form $E_s = K_y(m_y/M_s)^2 + K_z(m_z/M_s)^2$. The complex frequency ω must be chosen so that the determinant of the coefficients of the six homogeneous equations for the six field amplitudes formed from (i)–(vi) vanishes. This is a very difficult program to carry through algebraically, but one which presents a relatively uncomplicated numerical problem.

Having calculated a normal mode frequency it is a complicated but straightforward matter to calculate the fraction of the incident optical energy which is scattered into a particular direction, and to calculate the frequency distribution of the scattered light.[8,16,17] The frequency of the scattered light is shifted from the frequency of the incident light by $\pm f_R$, where f_R is the real part of the magnetic normal mode frequency. If the normal mode is lightly damped the frequency spectrum of the scattered light is a Lorentzian distribution whose half-power frequency width is $\Delta f = 2/\tau$ where $-1/\tau$ is the imaginary part of the normal mode complex frequency.[8]

The frequencies of the lowest modes have been listed in Table I for an isotropic film having the magnetic properties of iron,[18] for an applied in-plane magnetic field of 1 kOe, and for in-plane wave vectors typical of a backscattering experiment using 5145-Å laser light. For the sake of completeness we have also included a calculation of the frequency using the Damon–Esbach theory[19] for a magnetic insulator without exchange and having no losses, as well as a calculation for a metallic magnetic material having magnetic losses but no exchange torques. The no-exchange frequencies lie remarkably close to the Damon–Eshbach frequencies. The discrepancy decreases with increasing q and increasing magnetic field, but increases with increasing thickness, rising from approximately 1:5000 for a 10-Å-thick film to 1:300 for a 1000-Å-thick film. Even with the inclusion of exchange, the resonant frequencies for the 10-Å-thick film are within a few percent of those calculated using Damon–Eshbach theory. Of course, as is to be expected, exchange becomes more important as the wave number of the excitation and the thickness of the film increases.

The frequencies calculated for the "Normal Case" (a silver substrate and a 40-Å gold overlayer) are compared in Table I with the frequencies calculated for no overlayer but a silver substrate (column 5), and for a 40-Å overlayer and a substrate both of which have the very large resistivity value of 100 Ω cm (column 6). Changing the resistivities of the overlayer and substrate produces a change of approximately 1:500 for the 100-Å film and for the smallest value of q. The difference decreases for larger magnetic fields and for larger values of the in-plane wave vector. The resonant frequency is very insensitive to the resistivity of the magnetic film. The

TABLE I. A comparison of the resonant frequencies, f (in GHz), of a system composed of a metallic magnetic film of thickness d covered by a 40-Å layer of gold (resistivity $= 2.44\times10^{-6}$ Ω cm) and mounted upon a silver substrate (resistivity $= 1.59\times10^{-6}$ Ω cm) for an applied magnetic field of 1.0 kOe. The wave-vector component of the excitation parallel to the film surface and perpendicular to the magnetic field corresponds to that for backscattered 5145-Å wavelength light incident at $\theta = 10°$ ($q = 42\,413\ \text{cm}^{-1}$) and at 45° ($q = 17\,2707\ \text{cm}^{-1}$). The properties of the magnetic film are taken to be those of iron having no magnetocrystalline anisotropy: saturation magnetization, $4\pi M_s = 21.55$ kOe; exchange parameter, $A = 2.0\times10^{-6}$ erg/cm; $g = 2.09$; Gilbert damping parameter, $G = 7.0\times10^{7}$ Hz; resistivity $= 1.0\times10^{-5}$ Ω cm. Frequencies for the 100-Å-thick magnetic film are listed for the lowest normal mode (the uniform mode) and for the first exchange mode whose wavelength is $\lambda = 2d$. It has been assumed that the magnetization is unpinned at the film surfaces. (a) An iron film (except that $A = 0$) sandwiched between a 40-Å gold overlayer and a silver substrate. (b) An iron film mounted on a silver substrate and covered with a 40-Å-thick layer of gold. (c) An iron film mounted on a silver substrate but having no overlayer. (d) An iron film mounted on a substrate whose resistivity is 100 Ω cm and covered by a 40-Å-thick layer of a material whose resistivity is 100 Ω cm. (e) A magnetic film having the magnetic properties of iron but its resistivity has been increased to 10^{-3} Ω cm, mounted on a silver substrate and covered by a 40-Å-thick overlayer of gold.

Thickness angle	Damon–Eshbach frequency (GHz)	No-exchange metal film[a] frequency (GHz)	Normal case[b] frequency (GHz)	Exchange, no overlayer[c] frequency (GHz)	High resistivity overlayer and substrate[d] frequency (GHz)	Increased resistivity of magnetic metal[e] frequency (GHz)
$d = 10$ Å	14.1896	14.1926	14.2226	14.2227	14.2194	14.2226
$\theta = 10°$		$-i$ 0.0953	$-i$ 0.0953	$-i$ 0.0943	$-i$ 0.0765	$-i$ 0.0953
$d = 10$ Å	15.0560	15.0558	15.5188	15.5188	15.5188	15.5188
$\theta = 45°$		$-i$ 0.0818	$-i$ 0.0822	$-i$ 0.0812	$-i$ 0.0770	$-i$ 0.0822
$d = 100$ Å	16.5453	16.5773	16.6112	16.6125	16.5790	16.6113
$\theta = 10°$		$-i$ 0.2373	$-i$ 0.2371	$-i$ 0.2270	$-i$ 0.0781	$-i$ 0.2358
			96.7929	96.7929	96.7929	96.7929
			$-i$ 0.2294	$-i$ 0.2294	$-i$ 0.2294	$-i$ 0.2261
$d = 100$ Å	21.9798	21.9799	22.3769	22.3770	22.3765	22.3769
$\theta = 45°$		$-i$ 0.1109	$-i$ 0.1110	$-i$ 0.1019	$-i$ 0.0784	$-i$ 0.1114
			96.9833	96.9833	96.9833	96.9833
			$-i$ 0.2298	$-i$ 0.2297	$-i$ 0.2297	$-i$ 0.2269

frequencies listed in the last column have been calculated for a magnetic film whose resistivity has been increased two orders of magnitude (from 10^{-5} to 10^{-3} Ω cm). The resulting frequency shifts are less than 1:10^5.

The authors would like to thank the Natural Sciences and Engineering Research Council of Canada for grants and a scholarship (J.R.D.) which supported this work.

[1]B. Heinrich, K. B. Urquhart, J. R. Dutcher, J. F. Cochran, A. S. Arrott, D. A. Steigerwald, and W. F. Egelhoff (these proceedings).
[2]A. P. Malozemoff, M. Grimsditch, J. Aboaf, and A. Brunsch, J. Appl. Phys. **50**, 5885 (1979).
[3]R. E. Camley and M. Grimsditch, Phys. Rev. B **22**, 5420 (1980).
[4]P. Grünberg, M. G. Cottam, W. Vach, C. Mayr, and R. E. Camley, J. Appl. Phys. **53**, 2078 (1982).
[5]P. Kabos, W. D. Wilber, C. E. Patton, and P. Grünberg, Phys. Rev. B **29**, 6396 (1984).
[6]P. Kabos, C. E. Patton, and W. D. Wilber, Phys. Rev. Lett. **53**, 1962 (1984).
[7]G. Srinivasan and C. E. Patton, J. Appl. Phys. **61**, 4120 (1987).
[8]J. R. Sandercock, in *Light Scattering in Solids III*, edited by M. Cardona and G. Güntherodt (Springer, Berlin, 1982), Chap. 6.
[9]Carl E. Patton, Phys. Rep. **103**, 251 (1984).
[10]R. E. Camley, Talat S. Rahman, and D. L. Mills, Phys. Rev. B **23**, 1226 (1981).
[11]T. Wolfram and R. E. DeWames, Phys. Rev. B **4**, 3125 (1971).
[12]In the program which we wrote, the displacement current was included in Eq. (1c) for the substrate and overlayer in order to be able to approach an insulator limit.
[13]William Fuller Brown, Jr., *Micromagnetics* (Krieger, Huntington, New York, 1978), Chap. 3.
[14]W. S. Ament and G. T. Rado, Phys. Rev. **97**, 1558 (1955).
[15]G. T. Rado and J. R. Weertman, J. Phys. Chem. Solids **11**, 315 (1959).
[16]W. Wettling, M. G. Cottam, and J. R. Sandercock, J. Phys. C **8**, 211 (1975).
[17]L. D. Landau and E. M. Lifshitz, *Electrodynamics of Continuous Media* (Pergamon, Oxford, 1960), Chap. XIV.
[18]Anisotropy was ignored in the calculations for Table I because it has no direct effect on the frequency shifts caused by the electrical properties of an overlayer or substrate or on shifts due to the conductivity of the magnetic layer. Such anisotropies do have a profound effect on the resonant frequencies themselves, but that will be the subject for further work.
[19]R. W. Damon and J. R. Eshbach, J. Phys. Chem. Solids **19**, 308 (1961).

Optical observation of evanescent surface magnons in thin magnetic films

G. Srinivasan
Department of Physics, Colorado State University, Fort Collins, Colorado 80523

P. R. Emtage
Research and Development Center, Westinghouse Electric Corporation, Pittsburgh, Pennsylvania 15235

J. G. Booth and C. E. Patton
Department of Physics, Colorado State University, Fort Collins, Colorado 80523

A new type of nonpropagating surface-wave-like magnon has been detected in yttrium iron garnet films (YIG) in a magnetostatic wave (MSW) device structure using Brillouin light scattering. The measurements were carried out on a YIG film stripline device operated at 2–4 GHz. With an applied magnetic field parallel to the stripline, magnon signals were observed at fields above the surface wave band edge. Theory shows that highly localized, evanescent surface modes can exist at such fields, but only when a ground plane is present; the bandwidth in field or frequency is inversely proportional to the separation between the film and the ground plane. The observed evanescent wave band limits are in good agreement with the theoretical values.

I. INTRODUCTION

In the course of Brillouin light scattering (BLS) measurements on magnetostatic wave (MSW) devices utilizing yttrium iron garnet (YIG) films, a new type of spin-wave excitation was recently observed for fields above the magnetostatic surface wave (MSSW) band edge.[1,2] These modes have now been investigated in detail, both experimentally and theoretically. The excitations consist of highly localized evanescent surface wave (EVSW) modes with a complex wave number. The theory shows that these modes are possibly excited only in the presence of a ground plane and that the bandwidth in field for EVSW excitations is inversely proportional to the separation between the ground plane and the YIG film.

The Brillouin light scattering measurements were performed on a signal-to-noise enhancer (SNE) MSW device structure consisting of a 30-μm-wide stripline in contact with a 26.6-μm-thick YIG film.[3,4] The stripline was on a 625-μm-thick alumina substrate backed by a conducting copper ground plane. The incident laser light was focused onto the YIG film through a small hole in the substrate which was drilled in close proximity to the stripline. Interactions between the incident light and magnetic excitations within the YIG film result in a frequency shift for the scattered light. Direct detection of magnons in the YIG film was accomplished by measuring the intensity versus frequency shift profile for the forward scattered light through the film with a high contrast Fabry–Perot interferometer. Details of the measurement technique are given elsewere.[1,2,5]

The basic evidence for the new EVSW modes is shown in the Brillouin spectrum of Fig. 1. This spectrum was obtained for an in-plane bias field of 600 Oe parallel to the stripline and a YIG film-ground plane separation of 625 μm. Despite the fact that the bias field is well above the surface wave band edge of 492 Oe, one observes pronounced scattering peaks at $\pm$ 3 GHz. These peaks disappear when the ground plane is absent.

Intensity profiles and microwave attenuation versus field data are shown in Fig. 2. The YIG-ground plane separation was 625 μm, as for Fig. 1. The data on the intensity of magnon scattered light versus bias field in Fig. 2(a) show the expected scattering due to MSSW excitations within the surface wave region, 150–492 Oe. Strong scattering is also observed *above* the MSSW band edge, up to a field of 625 Oe. The microwave response profile of attenuation in stripline power versus field in Fig. 2(b) shows essentially no power loss above the MSSW band edge, except for a small region of microwave power loss, just above the MSSW band edge, which is due to nonlinear effects associated with the generation of magnons at one half the pump frequency. These results suggest that the observed Brillouin signal above the band edge is due to highly localized evanescent surface-wave-like (EVSW) modes. Such localized modes carry very little microwave power away from the stripline and are not evident in microwave loss measurements.

II. THEORY

This section deals with the theory for the evanescent surface waves. It is found that EVSW modes exist when a

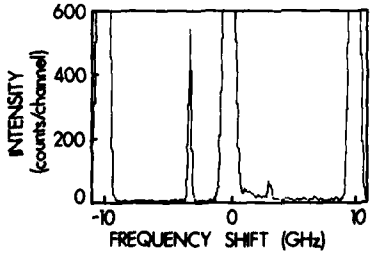


FIG. 1. Brillouin light scattering spectrum for magnetostatic wave signals at 3 GHz in a yttrium iron garnet (YIG) film in a signal-to-noise enhancer (SNE) device structure with a static magnetic field of 600 Oe applied parallel to the stripline in the device. The input power was 40 mW.

 0021-8979/88/083817-03$02.40 © 1988 American Institute of Physics

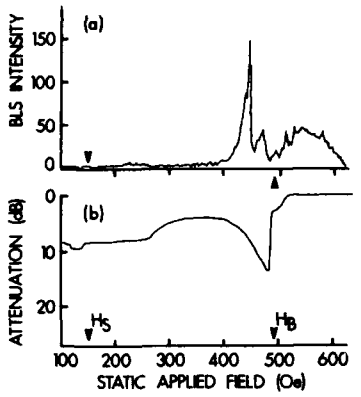


FIG. 2. (a) Profile of scattered intensity vs applied field for MSW signals at 3 GHz in the YIG film in the SNE device. The input power was 40 mW. The arrows indicate the field limits H_S and H_B for magnetostatic surface waves (MSSW) in the YIG film. (b) Data on attenuation in stripline power vs applied field at 3 GHz for the SNE device and an input power of 10 mW.

ground plane is present and that such modes can be supported above the MSSW band edge. The range of fields over which such modes exist is inversely proportional to the separation between the ground plane and the YIG film.

The system under consideration is an in-plane magnetized film of thickness d at a distance l from a metallic ground plane, as shown in Fig. 3. The theory is for magnetostatic waves with a complex in-plane wave number, $\kappa = \kappa' + i\kappa''$, with propagation perpendicular to the in-plane field. The analysis is based on the usual magnetostatic mode formalism.[6] The magnon dispersion has the form

$$f^2 - f_H^2 - f_H f_M - \zeta = 0, \tag{1}$$

where f is the magnon frequency. The parameters $f_H = \gamma H$ and $f_M = \gamma 4\pi M$ express the magnetic field H and the saturation magnetization M in frequency units; γ is a reduced gyromagnetic ratio. The ζ parameter in Eq. (1) is given by

$$\zeta = (f_M^2/4)(1 - e^{-2(\kappa' + i\kappa'')d})(1 + Ae^{-2(\kappa' + i\kappa'')l}) \tag{2}$$

and

$$A = 1 + 2(f + f_H)/f_M.$$

For the case $\kappa'' = 0$, Eq. (1) reduces to the usual dispersion relation for MSSW excitations in the presence of a ground plane. In the absence of a ground plane, i.e., $l \to \infty$, this dispersion reduces to the Damon–Eshbach MSSW dispersion relation.[6] The presence of the ground plane results in an additional set of solutions for which κ'', as well as κ', is nonzero. These solutions correspond to the EVSW modes observed by light scattering.

The complex wave-number solutions for the EVSW modes can be determined from Eqs. (1) and (2). Solutions for κ'' occur near $2\kappa'' l \simeq \pi$ (one can also find more severely localized modes with $2\kappa'' l \simeq 3\pi$, 5π, etc.). Upon setting $2\kappa'' l = \pi + \epsilon$ and assuming the condition $d \ll l$, the ζ parameter can be expressed as

$$\zeta = (df_M^2/4l)[2\kappa' l + i(\pi + \epsilon)] \times \{1 - A[\cos(\epsilon) - i\sin(\epsilon)]e^{-2\kappa' l}\}. \tag{3}$$

Equation (1) then reduces to two coupled equations in κ' and ϵ:

$$2\kappa' l[1 - Ae^{-2\kappa' l}\cos(\epsilon)] - (\pi + \epsilon)Ae^{-2\kappa' l}\sin(\epsilon) - B = 0, \tag{4}$$

$$(\pi + \epsilon)[1 - Ae^{-2\kappa' l}\cos(\epsilon)] + 2\kappa' lAe^{-2\kappa'}\sin(\epsilon) = 0, \tag{5}$$

$$B = (4l/d)(f^2 - f_m f_H - f_H^2)/f_m^2. \tag{6}$$

The complex wave number for the EVSW modes as a function of applied field can be determined by solving Eqs. (4) and (5) for κ' and ϵ.

III. RESULTS

The calculated variation of κ' and κ'' as a function of field for the EVSW modes at 3 GHz are shown in Fig. 4. Results on κ' versus field for the MSSW mode are also shown. Two cases are considered. Figure 4(a) is for $l = 1$ cm, that is, a very large film-ground plane separation. In this case the MSSW band extends between field limits H_S and

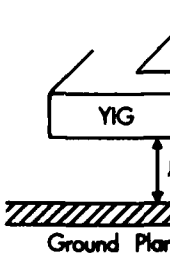


FIG. 3. Schematic diagram of the structure and excitation geometry for surface waves in an in-plane magnetized thin film of thickness d at a distance l from a ground plane.

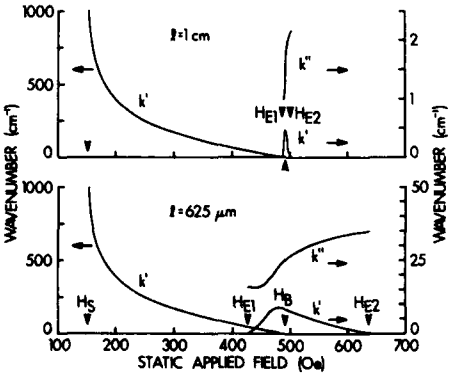


FIG. 4. Calculated variation of the surface magnon wavenumber and the real and imaginary parts of the evanescent wave wavenumber with bias field at 3 GHz in a 26.6-μm-thick YIG film and at a distance (a) 1 cm and (b) 625 μm from a ground plane. The fields H_{E1} and H_{E2} indicate the field limits for the evanescent waves. The field limits for the surface waves are indicated by H_S and H_B.

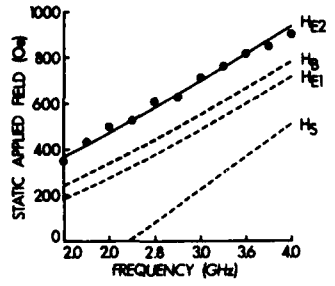


FIG. 5. Variation of the upper cutoff field H_{E2} vs excitation frequency for evanescent waves in the YIG film SNE device. The solid points denote the BLS data and the solid line represents the theory. The dotted lines show the frequency variation of the MSSW band edge, H_S and H_B, and the evanescent wave low-field band edge H_{E1}.

H_B which are very close to the usual Damon–Eshbach values. The EVSW mode solution region is very narrow in this case, and is limited to fields very close to H_B. Figure 4(b) is for a smaller l value of 625 μm which corresponds to the present experimental situation. The essential effect of moving the ground plane closer to the YIG film is to *expand* the interval for EVSW solutions. The low-field EVSW band edge H_{E1} moves well below H_B and the high-field band edge H_{E2} moves well above H_B. For the situation in Fig. 4(b), the band width in field is 209 Oe and the band extends some 145 Oe above the upper MSSW band edge.

One convenient test of the theory is to compare the calculated frequency dependence of the upper EVSW band edge, H_{E2}, with the BLS band-edge measurements at different frequencies. Brillouin light scattering profiles similar to the one in Fig. 2(a) were obtained over the frequency range 2–4 GHz. The resulting experimental EVSW H_{E2} band-edge determinations are shown in Fig. 5, along with the results from the theory. The field limits H_S, H_{E1}, and H_B are shown for reference. Figure 5 shows excellent agreement between data and theory for the upper EVSW band-edge value versus frequency.

In conclusion, a new type of magnetic excitation in thin YIG films has been identified by Brillouin scattering and investigated theoretically; the excitation is an evanescent surface-wave-like (EVSW) mode which can be supported only in the presence of a ground plane. These EVSW modes can transport no power and cannot be observed with microwave loss measurements. The observed cutoff field for such modes agrees well with the theoretical analysis.

ACKNOWLEDGMENTS

The MSW device structure used in these experiments was provided by Dr. J. D. Adam, Westinghouse Research and Development Center, Pittsburgh, Pennsylvania. This work was supported by the Electromagnetics Directorate of the Rome Air Development Center, Hanscom Air Force Base, Massachusetts, Contract No. F19628-85-K-0002. Dr. Booth is with the Department of Pure and Applied Physics, University of Salford, Salford M5 4WT, UK. This work was performed, in part, while Dr. Booth was a Visiting Professor at Colorado State University.

[1]G. Srinivasan and C. E. Patton, Appl. Phys. Lett. **47**, 761 (1985).
[2]G. Srinivasan, C. E. Patton, and P. R. Emtage, J. Appl. Phys. **61**, 2318 (1987).
[3]J. D. Adam, IEEE Trans. Magn. **MAG-16**, 1068 (1980).
[4]J. D. Adam and S. N. Stitzer, Appl. Phys. Lett. **36**, 485 (1980).
[5]G. Srinivasan and C. E. Patton, IEEE Trans. Magn. **MAG-21**, 1797 (1985).
[6]R. W. Damon and J. R. Eshbach, J. Phys. Chem. Solids **19**, 308 (1961).

The dynamics of longitudinal spin fluctuations

U. Balucani and R. Vaia
Istituto di Elettronica Quantistica CNR, 50127 Firenze, Italy

A. Federighi and V. Tognetti
Dipartimento di Fisica dell'Università and CISM-GNSM, 50125 Firenze, Italy

The dynamical processes underlying the longitudinal spin fluctuation spectra in Heisenberg systems are investigated in two distinct physical regimes. Very recent polarized-neutron data in the one-dimensional ferromagnet $CsNiF_3$ have supported our previous prediction of a regime in which longitudinal spectra are dominated by a coupling between spin and exchange energy densities. A quantum-mechanical analysis is found to give results in good quantitative agreement with the experimental line shapes. The second regime investigated deals with much smaller (and less easily accessible) wave vectors. Here, a new hydrodynamic mode ("second magnon") may in principle be supported at not too high temperatures. The observability of this feature in real systems (in particular, EuO) is examined.

The conventional picture of the spin dynamics in Heisenberg systems at low temperatures is framed in terms of magnons, i.e., of excitations probing the dynamics in a direction transverse with respect to the spin ordering, or to an external magnetic field. Comparatively, much less attention has been devoted to the dynamics associated with longitudinal spin fluctuations $\hat{S}^z_k(t)$ (here, k denotes the wave vector, z the direction of spin ordering, and $\hat{A}(t) = A(t) - \langle A \rangle$). As a matter of fact, the longitudinal dynamic correlations $\langle \hat{S}^z_{-k}(0)\hat{S}^z_k(t)\rangle$ are certainly more involved than the transverse ones and, even more important, the corresponding longitudinal intensity turns out to be small at low temperatures, making observation with the conventional neutron spectrometers difficult. However, the recent progress in the techniques using polarized neutrons stimulate a new interest in the field, making future perspectives more optimistic. It is the purpose of this contribution to discuss two physical situations in which the longitudinal spectra exhibit rather unusual features, some of which have actually been observed in very recent neutron experiments.

Starting from the Hamiltonian

$$\mathcal{H} = -\frac{1}{2}\sum_{i\neq j} J_{ij}\mathbf{S}_i\cdot\mathbf{S}_j - g\mu_B H\sum_j S^z_j,$$

where the leading exchange integrals are assumed to favor a ferromagnetic alignment, we shall perform the usual Dyson–Maleev transformation to Bose operators $a, a^\dagger$. The longitudinal spectrum $S^{zz}(k,\omega)$ is the time Fourier transform of $\langle \hat{S}^z_{-k}(0)\hat{S}^z_k(t)\rangle$, where

$$\hat{S}^z_k(t) = -(S\sqrt{N})^{-1}\sum_q a^\dagger_{k+q}a_q. \tag{1}$$

Introducing the Zubarev Green's function $g_k(E) = \langle\langle \hat{S}^z_k; \hat{S}^z_{-k}\rangle\rangle_E$ defined in the usual way, the spectral theorem

$$S^{zz}(k,\omega) = -2\hbar(1-e^{-\beta\hbar\omega})^{-1} \times \operatorname{Im} g_k(E=\hbar\omega+i0^+) \tag{2}$$

reduces the problem to the study of $g_k(E)$. At the lowest level only the part of $\mathcal{H}$ quadratic in the Bose operators is retained, giving for $g_k(E)$ the free-magnon approximation

$$g^{(0)}_k(E) = N^{-1}\sum_q f_{k,q}(E),$$

where

$$f_{k,q}(E) = (2\pi)^{-1}(n_{k+q}-n_q) \times (E+\hbar\Omega_{k+q}-\hbar\Omega_q)^{-1}. \tag{3}$$

Here n_q is the magnon thermal number and $\hbar\Omega_q = (J_0 - J_q)S + g\mu_B H$ is the bare magnon energy ($J_q = \Sigma_j J_{ij}\cos\mathbf{q}\cdot\mathbf{r}_{ij}$). When inserted into Eq. (2), result (3) gives rise to a broad band. Although this unperturbed spectrum presents some noteworthy features [e.g., a square-root singularity at the band edge for $d = 1$ (Ref. 1), both for quantum and classical spins], the physically interesting cases arise from situations where the role of magnon interactions is important. At moderate temperatures the latter can approximately be treated by a Hartree–Fock termination. All the magnon energies become temperature-dependent, $J_q \to \alpha J_q$ where

$$\alpha = 1 - (NS)^{-1}\sum_p\left[1-\left(\frac{J_p}{J_0}\right)\right]n_p.$$

In particular, for $d = 1$ and nearest-neighbor exchange J we obtain[1,2]

$$g_k(E) = \frac{g^{(0)}_k(E) + 4\pi J\{[g^{(0)}_k(E)]^2 - [h^{(0)}_k(E)]^2 - [t^{(0)}_k(E)]^2\}}{1 + 4\pi J\{(1+\cos k)[g^{(0)}_k(E) - h^{(0)}_k(E)]\sin k t^{(0)}_k(E)\}}, \tag{4}$$

where, in lattice units,

$$h^{(0)}_k(E) = \left(\frac{1}{N}\right)\sum_q \cos q f_{k,q}(E)$$

and

$$t^{(0)}_k(E) = \left(\frac{1}{N}\right)\sum_q \sin q f_{k,q}(E).$$

 0021-8979/88/083820-03$02.40 © 1988 American Institute of Physics

In Refs. 1 and 2 result (4) was found to give an excellent account for the data obtained by simulation experiments for $S^{zz}(k,\omega)$ in a *classical chain*. It is interesting to note that the curly-bracketed term in the denominator of Eq. (4) is proportional to the spin-energy coupling $\langle\langle \hat{E}_k;\hat{S}^z_{-k}\rangle\rangle_E$, where $\hat{E}_k$ is the Fourier transform of the fluctuation in exchange energy density. More precisely, at the lowest level,[2]

$$\hat{E}_k \simeq -\left(\frac{JS}{\sqrt{N}}\right)\sum_q [1+\cos k-\cos q-\cos(k+q)] \times a^\dagger_{k+q}a_q. \tag{5}$$

Quite recently, Kakurai *et al.*[3] have measured separately both the transverse and the longitudinal responses in the $d=1$ ferromagnet $CsNiF_3$ by the polarized neutrons techniques. On the basis of the classical results of Ref. 1, these authors invoked spin-energy coupling as the possible mechanism determining the shape of the longitudinal spectrum. However, *a priori* such a transposition of results obtained for classical Heisenberg chains to a "real" easy-plane quantum system seems doubtful. One objection is easily removed: the temperature at which the experiment was performed, $T=25$ K, is sufficiently high that the easy-plane anisotropy of $CsNiF_3$ may be neglected. However, a *quantum treatment* is still *essential*: in particular, a purely classical evaluation would lead to huge renormalization effects ($\alpha\simeq 0.58$) in the transverse part and to a severe shrinkage of the longitudinal bandwidth. Instead, the inclusion of the proper quantum statistics in the magnon numbers is found to account quite well both for the transverse contribution ($\alpha \lesssim 0.9$) and for the longitudinal line shape. The latter, evaluated numerically from Eq. (4), is compared in Fig. 1 with the experimental data; no fitting parameters are used. The relevance of the nonperturbative character of Eq. (4) is evident: in particular, at the band edge the singularity of the unperturbed spectrum [Eq. (3)] is washed out. Whereas this aspect is true both classically and quantum mechanically, Fig. 1 clearly shows that in the experimental situation the classical treatment breaks down completely. In contrast, the good agreement between the quantum results and the data demonstrates in a conclusive way the effects of spin-energy coupling even in this "realistic" system.

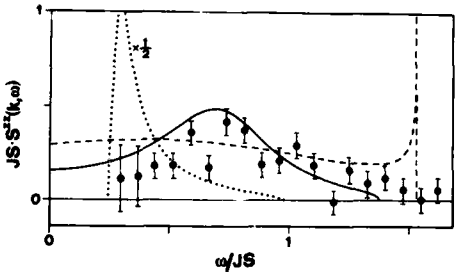


FIG. 1. Longitudinal spectra $S^{zz}(k,\omega)$ for the $d=1$ case at the wave vector $ka=\pi/4$ (a is the lattice spacing). The dotted line is the spectrum evaluated from Eq. (4) using classical statistics. The dashed line is the free-magnon quantum spectrum, and the solid line is our full theoretical based on Eq. (4) and quantum statistics. For all lines, the parameters $h=g\mu_B H/JS=0.48$ and $T^*=k_BT/JS=1.06$ correspond to $H=70$ kG, $T=25$ K, $g=2.4$, $J=23.6$ K, and $S=1$, i.e., to the situation probed by the experimental data of Ref. 3 in $CsNiF_3$ (closed circles). Strictly speaking, for these parameters the classical renormalization effect is so large that no self-consistent solution can be found for α; for illustrative purposes, here we have reported the spectrum obtained with the perturbative value of $\alpha=0.58$.

The situation illustrated so far concerns "microscopic" wave vectors; it is interesting to ask whether this picture is qualitatively changed as $k\to 0$, where *a priori* one expects to approach a quasi-hydrodynamic regime with diffusive peaks centered around $\omega=0$. Even if, in principle, the transition to this regime can be described by the microscopic approach adopted so far, the relevance of anharmonic interactions (magnon "collisions") in a diffusive situation is so great that the Hartree–Fock scheme is no longer sufficient. Proceeding one step further in the Green's function hierarchy, one automatically includes magnon damping. In addition, as far as the longitudinal part is concerned, new, nonperturbative contributions arise which are not interpretable in terms of one-magnon dynamics and yet are essential to establish even simple hydrodynamic results as the proportionality of the spectral width to k^2.

Because of these complications, we preferred to adopt a more heuristic approach, in which the characterization of the hydrodynamic regime in terms of a set of few, quasi-conserved collective variables is exploited from the very start, rather than deduced. For $S^{zz}(k,\omega)$ two such variables have already been introduced, $\hat{S}^z_k$ and $\hat{E}_k$. These are sufficient to treat spin diffusion at high temperatures, but as T is reduced Umklapp processes become progressively frozen, making "quasi-momentum":

$$\mathbf{P}_k=(S\sqrt{N})^{-1}\sum_q \mathbf{q}a^\dagger_{q+\frac{1}{2}k}a_{q-\frac{1}{2}k} \tag{6}$$

also approximately conserved. The inclusion of $\mathbf{P}_k(t)$ in the set of slowly varying collective variables makes the situation formally analogous to the one met in ordinary fluids at the Navier–Stokes level. In order to derive a set of coupled hydrodynamic equations we have adopted the usual Mori–Zwanzig technique, with projection operators over the variables $\hat{S}^z_k$, $\hat{E}_k$ and the "longitudinal current" $\hat{k}\cdot\mathbf{P}_k$ (here $\hat{k}=\mathbf{k}/k$). Denoting by the column vector A_k the set of these three quasi-conserved variables, the corresponding generalized Langevin equation formally reads

$$\dot{A}_k(t)=i\Omega(k)A_k(t) - \int_0^t d\tau\,\Gamma(k,t-\tau)A_k(\tau)+F_k(t). \tag{7}$$

Let us briefly recall the "hydrodynamic" approximations[4] on Eq. (7). First, the frequency matrix $\Omega(k)$ is proportional to static correlations involving $A_k(0)$; since in the limit $k\to 0$ the set A_k is made of quasi-conserved variables, the nonzero elements of $\Omega(k)$ are at least proportional to k. On the other hand, the "memory matrix" $\Gamma(k,t)$ is proportional to a correlation between the fluctuating forces F_k, which in turn involve the parts of $\dot{A}_k$ orthogonal to the set A_k. Thus, $\Gamma(k,t)$ is at least proportional to k^2; moreover, since it evolves in a "fast" subspace orthogonal to the one spanned by the slowly varying set A_k, the customary hydrodynamic

ansatz is to make a Markovian approximation, $\Gamma(k,t) \propto k^2\delta(t)$. It is then straightforward to arrive, in our case, to a three-peaked line shape for $S^{zz}(k,\omega)$, made of three Lorentzians like the familiar Rayleigh–Brillouin spectrum in ordinary fluids. In particular, as $k \to 0$, in addition to a diffusive peak at $\omega = 0$, $S^{zz}(k,\omega)$ exhibits an inelastic peak ("second magnon") with a linear dispersion law $\omega_{SM} = vk$, and width $\Gamma = D_l k^2$, the last result being valid provided that Umklapp processes are really negligible.

This "new" excitation—actually predicted several years ago in quantum $d = 3$ ferromagnets[5]—has still to be observed in a real experiment. More recently, a clear evidence for it has been found only by simulation experiments in classical spin chains ($d = 1$).[6] As before, in our analysis we have considered the general case of a d-dimensional system with either classical or quantum "spins." In the *classical $d=1$ case*, the calculated second magnon frequencies agree with those reported in the simulation data; the latter indicate that the feature virtually disappears for reduced wavevectors $k > 0.06\pi$, where the simpler Hartree–Fock analysis of Eq. (4) becomes valid. Within our perturbative calculations the width for $d = 1$ has an unphysical singularity; as in the case of magnon damping,[7] this feature is likely to be removed by including magnon bound states.

In the *quantum, d-dimensional "cubic" lattices* the second magnon velocity turns out to be

$$v = v_\infty(T^*)\left[F_{\frac{1}{2}d+1}(g\mu_B H/k_B T)/F_{\frac{1}{2}d}(g\mu_B H/k_B T)\right]^{1/2}. \quad (8)$$

Here

$$v_\infty(T^*) = (JS/\hbar)[2(2+d)T^*/d]^{1/2} \quad (9)$$

and $T^* = k_B T/JS$. In the general case with exchange integrals with extended range, J is defined by the relation

$$\lim_{q\to 0}(J_0 - J_q) = J(qa)^2,$$

where a is the lattice parameter of the generalized cubic cell. Finally, the quantity $F_\alpha(x)$ is a generalization of the Riemann zeta function $\zeta(\alpha)$:

$$F_\alpha(x) = [\Gamma(\alpha)]^{-1}\int_0^\infty dy\,\frac{y^{\alpha-1}}{e^{x+y}-1} = e^{-x}f_\alpha(x). \quad (10)$$

In particular, $F_{(\alpha)}(0) = \zeta(\alpha)$, whereas for $x \gg 1$, $f_\alpha(x) \simeq 1 + O(e^{-x})$. As $g\mu_B H$ becomes larger than $k_B T$, v rapidly approaches its infinite-field asymptotic value $v_\infty(T^*)$. It is also possible to evaluate both the elastic to inelastic intensity ratio ("Landau–Placzek ratio") and the widths, but the expressions are rather complicated and will not be reported here. It is instead worthwhile to report the expression for the total intensity of the longitudinal spectrum (parallel susceptibility). For $d = 3$

$$\chi_\parallel \simeq (1/S^2)(4\pi)^{-3/2}F_{1/2}(g\mu_B H/k_B T)(T^*)^{3/2} \quad (11)$$

to be compared with the transverse susceptibility which in this regime turns out be be

$$\chi_\perp \simeq (2S)^{-1}\,\mathrm{cotanh}(\tfrac{1}{2}g\mu_B H/k_B T).$$

To explore the observability of the effect in real systems we have considered EuO, a $d = 3$ fcc ferromagnet with two important exchange constants, J_1 and J_2, cube edge $a = 5.12$ Å and $S = 7/2$. At low temperatures and/or high fields the second magnon velocity is found to be $v_\infty = 6.4\times 10^4\sqrt{T^*}$ cm s^{-1}, where $T^* = k_B T/JS$ and $J = J_1 + J_2 = 1.5$ K in EuO. In this $d = 3$ case the width $D_l k^2$ is perfectly defined, and is much smaller than ω_{SM}: in practice, one has to allow for the small residual Umklapp decay of $\mathbf{P}_k(t)$. The energies and the wave vectors involved are obviously small (e.g., $\omega_{SM} \simeq 0.12$ meV for $ka = 0.20$ and $T = 2.5$ K in EuO), but the major difficulty is the low longitudinal intensity, of the order 10^{-2} of the corresponding transverse one. This fact precludes any measurement by conventional neutron spectrometry, where the two contributions are in general superimposed. In this respect, an extension of the previously mentioned polarized-neutron experiments appears to be essential to throw some light on this interesting (albeit rather elusive) feature of the spin dynamics.

[1] U. Balucani, A. Rettori, and V. Tognetti, Phys. Rev. Lett. **48**, 703 (1982); U. Balucani, M. G. Pini, V. Tognetti, and A. Rettori, Phys. Rev. B **26**, 4974 (1982).
[2] V. Tognetti, A. Rettori, M. G. Pini, J. M. Loveluck, U. Balucani, and E. Balcar, J. Phys. C **16**, 5641 (1983).
[3] K. Kakurai, R. Pynn, M. Steiner, and B. Dorner, Phys. Rev. Lett. **59**, 708 (1987).
[4] See, e.g., B. J. Berne, Ed., *Statistical Mechanics*, Part B (Plenum, New York, 1977), pp. 233–257.
[5] G. Reiter, Phys. Rev. **175**, 631 (1968); F. Schwabl and K. H. Michel, Phys. Rev. B **2**, 189 (1970).
[6] T. Schneider and H. R. Jauslin, Phys. Rev. B **27**, 1919 (1983).
[7] U. Balucani, M. G. Pini, and V. Tognetti, J. Phys. C **17**, 6819 (1984).

Zero point motion and magnetic field effects on the spin configuration in a Heisenberg rhombohedral antiferromagnet. Application to solid oxygen

E. Rastelli and A. Tassi
Dipartimento di Fisica dell'Universita', 43100 Parma, Italy

The ground state of the Heisenberg rhombohedral antiferromagnet in classical approximation exhibits infinite degeneracy corresponding to infinite unequivalent helices. We call degenerate helix (DH) such a spin configuration. In absence of anisotropy long-range order (LRO) is lost even in 3D with a possible algebraic decay of the correlation function due to a low-energy catastrophe related to "soft lines" of the magnon energy which vanishes for all wave vectors falling on the "degeneration line" $\mathscr{L}_{\mathbf{Q}}$, the locus of the $\mathbf{Q}$ wave vectors characterizing the infinite helixes of the ground state. We have studied the effect of the zero point motion which removes the infinite degeneracy of the ground state so that quantum disorder sets up LRO. We have also studied the effect of an external magnetic field. We find that in classical approximation a magnetic field parallel to the c axis does not remove the infinite degeneracy of the ground state but it affects the spin-wave energy spectrum what could be observed in an inelastic scattering experiment. On the contrary, dramatic changes are expected when a magnetic field is applied perpendicular to the c axis because competition arises with the zero point motion effect so that the magnetic field in this configuration should act as a device to tune the DH phase. Possible application to solid oxygen is briefly analyzed.

The classical Heisenberg rhombohedral antiferromagnet (RAF)[1] with nearest-neighbor (NN) in-plane interaction $J<0$ and NN out-of-plane interaction J' has a ground state infinitely degenerate corresponding to infinite unequivalent helixes characterized by $\mathbf{Q}$ wave vectors belonging to lines $\mathscr{L}_{\mathbf{Q}}$ in the reciprocal space we call degeneration lines. The appearance of infinite isoenergetic spin configurations has to be considered as a surprising event: we notice indeed that the hamiltonian symmetry cannot be invoked as a possible source of this striking phenomenon because further spin-spin coupling in addition to J and J' can pick a single helix out of the $\mathscr{L}_{\mathbf{Q}}$ manifold.[2] In absence of anisotropy the magnon spectrum shows "soft lines" due to vanishing of the energy for all wave vectors $\mathbf{k}$ falling on $\mathscr{L}_{\mathbf{Q}}$. This fact destroys LRO in 3D at any finite temperature with possible algebraic decay of the correlation because of a low-energy catastrophe related to a divergent occupation number in correspondence of those wave vectors where soft lines occur. This unorthodox helix was called degenerate helix (DH).[1] LRO is marginally restored by some small interactions like single ion planar anisotropy D_A (Ref. 1) or next-nearest neighbor (NNN) in-plane coupling J_2.[2] D_A does not remove the infinite degeneracy of the ground state but only lifts the soft lines of the magnon spectrum. On the contrary J_2 selects a single helix of the manifold $\mathscr{L}_{\mathbf{Q}}$ and enters a ripple along $\mathscr{L}_{\mathbf{Q}}$ in the magnon spectrum.[3] For planar anisotropy small enough to leave magnon spectrum reminiscent of the soft lines,[4] a sequence of three phases is expected at increasing temperature: a low-temperature degenerate helix with LRO, an unorthodox phase with possible algebraic decay of the spin correlation function at intermediate temperature followed by the usual paramagnetic phase at higher temperature.

We notice that the elastic neutron scattering cross section by a RAF sample in presence of planar anisotropy should provide Bragg lines when the scattering wave vector falls on $\mathscr{L}_{\mathbf{Q}}$ instead of the usual peaks that characterize a conventional helix.[4] Even if further exchange interactions such as J_2 destroy the infinite degeneracy of the ground state, a DH-like scenario could be restored at intermediate temperature by thermal fluctuations which produce heavier renormalization on the further NN coupling constants.[5] Anyway, a detailed knowledge of the actual finite temperature phenomenology of the RAF model requires further theoretical investigation.

Here we consider only the effects produced by the zero point motion and by an external applied magnetic field. The hamiltonian we consider reads

$$H_0 = -\sum_{\alpha} J_{\alpha} \sum_{\delta_{\alpha}} \mathbf{S}_i \cdot \mathbf{S}_{i+\delta_{\alpha}} + D_A \sum_i (S_i^z)^2, \tag{1}$$

where α runs over 1,2: $J_1 = J$ is the in-plane NN antiferromagnetic coupling, $J_2 = J'$ is the out-of-plane NN coupling. i labels the sites of a rhombohedral lattice. δ_{α} is a vector joining the site i with its neighbors of the α shell. D_A is the planar single ion anisotropy strength. The x axis of our reference frame is along an in-plane NNN row and z axis is along the c axis. Looking for helical configurations, the simple spin-wave analysis of hamiltonian (1) leads to the following ground-state energy

$$E_0(\mathbf{Q}) = E_{\mathrm{cl}}(\mathbf{Q})(1 + 1/S) + \Delta, \tag{2}$$

where

$$E_{\mathrm{cl}}(\mathbf{Q}) = -\sum_{\alpha} J_{\alpha} S^2 N \sum_{\delta_{\alpha}} \cos(\mathbf{Q} \cdot \delta_{\alpha}), \tag{3}$$

$$\Delta = \frac{1}{2} \sum_k E_k(\mathbf{Q}). \tag{4}$$

$E_k(\mathbf{Q})$ is the spin-wave energy spectrum given by

$$E_k(\mathbf{Q}) = [S_k(\mathbf{Q}) D_k(\mathbf{Q})]^{1/2}, \tag{5}$$

with

 0021-8979/88/083823-03$02.40 © 1988 American Institute of Physics

$$S_k(\mathbf{Q}) = \sum_\alpha 2J_\alpha S \sum_{\delta_\alpha} (\cos \mathbf{Q}\cdot\delta_\alpha - \cos \mathbf{k}\cdot\delta_\alpha) + D_A(2S-1), \quad (6)$$

$$D_k(\mathbf{Q}) = \sum_\alpha 2J_\alpha S \sum_{\delta_\alpha} \cos \mathbf{Q}\cdot\delta_\alpha (1 - \cos \mathbf{k}\cdot\delta_\alpha). \quad (7)$$

From now on we confine ourselves to accounting for small interplane coupling ($|J'| \ll |J|$). For convenience we remember that in the classical limit ($S \to \infty$) one has $E_0(\mathbf{Q}) = E_{cl}(\mathbf{Q})$, so that minimization of $E_{cl}(\mathbf{Q})$ with respect to $\mathbf{Q}$ provides the wave vector of the stable helix configuration which corresponds in this case to the aforementioned DH.[1] For small interplane coupling the minimum equations reduce to

$$x_0 = -j \sin z_0 + (j^2/6)\sin 2z_0 - (j^3/9)\sin z_0 + \ldots,$$
$$y_0 = 2\pi/3 + (j/\sqrt{3})\cos z_0 + [j^2/(6\sqrt{3})]\cos 2z_0 + [j^3/(9\sqrt{3})]\cos z_0 + \ldots, \quad (8)$$

z_0 arbitrary, where

$$x_0 = \sqrt{3}aQ_x/2, \quad y_0 = aQ_y/2, \quad z_0 = cQ_z/3, \quad j = J'/J, \quad (9)$$

a and c being the NN in-plane and three times the NN out-of-plane distance. Moving along the line $\mathcal{L}_\mathbf{Q}$ given by (8) one can see that $E_k(\mathbf{Q})$ is weakly $\mathbf{Q}$ dependent. This dependence on $\mathbf{Q}$ implies that also the zero point motion energy Δ is $\mathbf{Q}$ dependent so that, possibly, order may be produced by quantum disorder. We have evaluated numerically Δ along $\mathcal{L}_\mathbf{Q}$ (Ref. 6) for antiferromagnetic interplane coupling ($J' < 0$) and we have found that quantum fluctuations select a particular helix. However, the numerical accuracy becomes poorer as one approaches the physically interesting range of small j. Here we have worked out an analytic expansion of Δ in powers of j and we have found

$$\Delta = 2|J|NS[1.211 + 0.559j^2 - (0.088 + 0.034\cos 3z_0)j^3 + \ldots]. \quad (10)$$

In Eq. (10) we have chosen $D_A(2S-1)/(4|J|S) = 0.05$ a suitable value for β-oxygen.[7] The explicit analysis is too cumbersome to be quoted here. As one can see from Eq. (10) quantum fluctuations select the helixes

$$Q_x = -2j/(\sqrt{3}a)\sin(2n\pi/3) + \ldots,$$
$$Q_y = 4\pi/(3a)[1 + \sqrt{3}j/(2\pi)\cos(2n\pi/3) + \ldots],$$
$$Q_z = 2n\pi/c, \quad (11)$$

for $j > 0$, and

$$Q_x = -2j/(\sqrt{3}a)\sin[(2n+1)\pi/3] + \ldots,$$
$$Q_y = 4\pi/(3a)\{1 + \sqrt{3}j/(2\pi) \times \cos[(2n+1)\pi/3] + \ldots\},$$
$$Q_z = (2n+1)\pi/c, \quad (12)$$

for $j > 0$; n is an integer number.

A conventional helix is restored by quantum disorder. However, an interesting point is to investigate what happens at intermediate temperature where thermal fluctuations could overcome quantum fluctuations. Indeed it is possible that the DH scenario appears again when the DH states become populated and clusters of different $\mathbf{Q} \in \mathcal{L}_\mathbf{Q}$ nucleate. We remember that also in a conventional helimagnet such as $NiBr_2$ elastic neutron scattering measurements[8] prove the simultaneous presence of domains characterized by all $\mathbf{Q}$ belonging to the star in spite of the finite energy cost of a domain wall.

Let us consider the effect of a magnetic field applied either parallel or perpendicular to the c axis. The effect of a magnetic field on a DH system is of particular interest because it could be able to remove the degeneration of the ground state playing an important role in testing the existence of the degenerate helix. In addition, an interesting question to clarify is about the interplay between zero point motion and magnetic field effect. We just consider the first order contribution in $1/S$ with respect to the leading (classical) term proportional to S^2.

If a magnetic field is applied along the c axis, a term like

$$-g\mu_B H \sum_i S_i^z \quad (13)$$

has to be added to hamiltonian (1). In Eq. (13) g is the Lande' g factor and μ_B is the Bohr magneton.

We look for cone structure whose axis is parallel to the c axis and call θ the apex angle. $\mathbf{Q}$ is the wave vector of the helix according to which the spins are spiraling on the cone surface. The ground-state energy obtained by the simple spin-wave aproximation that retains all terms of order S^2 reads

$$E_0(\mathbf{Q},\theta) = E_{cl}(\mathbf{Q}) + \cos^2\theta\,[E_{cl}(0) - E_{cl}(\mathbf{Q})] + D_A S^2(1 - 1/2S)N\cos^2\theta + D_A SN/2 - g\mu_B HSN\cos\theta. \quad (14)$$

Minimization of $E_0(\mathbf{Q},\theta)$ with respect to θ gives the cone apex angle of the ground-state configuration

$$\cos\theta = H/H_0 \quad \text{for} \quad H < H_0, \quad (15)$$

where

$$g\mu_B H_0 = D_A(2S-1) + 2[E_{cl}(0) - E_{cl}(\mathbf{Q})]/NS \quad (16)$$

and

$$\theta = 0 \quad \text{for} \quad H > H_0. \quad (17)$$

The cone structure reduces continuously to the ferromagnetic phase for $H \to H_0$.

Minimization of $E_0(\mathbf{Q},\theta)$ with respect to $\mathbf{Q}$ gives the same $\mathbf{Q} \in \mathcal{L}_\mathbf{Q}$ as one obtains for zero magnetic field so that the infinite degeneracy remains. Notice that the cone apex angle does not depend on $\mathbf{Q}$ for $\mathbf{Q} \in \mathcal{L}_\mathbf{Q}$ because

$$E_{cl}(\mathbf{Q}) = -6|J|S^2N(1/2 + j^2/6). \quad (18)$$

We conclude that a magnetic field parallel to the c axis is not a promising tool in order to select particular helix wave vectors. On the other hand, the spin wave spectrum is affected by the applied field: in particular, it is no longer symmetric under the change of sign of the wave vector $\mathbf{k}$. This is a well-known effect in "conventional" helixes.[9,10]

Let us now consider a magnetic field applied in the c plane. To this end we add to hamiltonian (1) a term like

$$-g\mu_B H\sum_i S_i^y. \quad (19)$$

The main contribution in $1/S$ reads

$$-g\mu_B H(2SN)^{1/2}/4i(a_Q + a_{-Q} - a_Q^+ - a_{-Q}^+). \quad (20)$$

We treat (20) as a perturbation with respect to hamiltonian (1) treated in the simple spin-wave approximation. The first-order contribution is obviously zero while the second-order one affects the ground-state energy as follows:

$$E(H,\mathbf{Q}) = E_0(\mathbf{Q}) - (g\mu_B H)^2 SN/[4D_Q(\mathbf{Q})], \quad (21)$$

where E_0 is given by (2) and $D_Q(\mathbf{Q})$ is obtained by (7) putting $\mathbf{k} = \mathbf{Q}$. For small j Eq. (21) reads

$$E(H,\mathbf{Q}) = 6|J|S^2N[a(j,h) + j^2 b(j,h)\cos 3z_0 + \ldots], \quad (22)$$

where

$$\begin{aligned} a(j,h) = &-(1/2 + j^2/6)(1 + 1/S) \\ &- 2h^2/3(1 - 2j/3 - 2j^2/9 + 10j^3/27) \\ &+ (1.211 - 0.559j^2 - 0.088j^3)/3S \end{aligned} \quad (23)$$

and

$$b(j,h) = 8h^2/27(1 - j/3) - 0.034j/3S, \quad (24)$$

with $h = g\mu_B H/(12|J|S)$ and $j = J'/J$.

Notice that for $j > 0$, $b(j,h)$ undergoes a change of sign for

$$h = h_0 = 3/2\{0.034j/[2S(1 - j/3)]\}^{1/2}. \quad (25)$$

This means that the stable configuration corresponds to $z_0 = 2n\pi/3$ [see Eq. (11)] for $h < h_0$ and to $z_0 = (2n + 1)\pi/3$ [see Eq. (12)] for $h > h_0$ so that a change in the position of the elastic neutron scattering peaks should be seen when the magnetic field reaches its "critical" value (25). For $h = h_0$ any dependence on $\mathbf{Q}$ in Eq. (22) is lost and the DH configuration appears again.

The previous result points out that an in-plane magnetic field could be a useful and handy device to pilot the RAF model through the DH phase. This fact seems to support the whole DH phenomenology, which could appear, otherwise, an artefact of the classical approximation.

In conclusion, we have shown that quantum fluctuations destroy the degenerate helix at zero temperature but we expect that a DH scenario could be recovered at intermediate temperature even if this conjecture has to be supported by further studies. We have also found that a magnetic field applied in the c plane competes with the zero point motion so that the degenerate helix can be restored even at zero temperature.

The picture we have given could be useful to get a better insight on the magnetic behavior of solid oxygen in the β phase. Solid oxygen is a widely studied molecular system[11] where spins lie in the c plane and interact via direct exchange. The lattice structure in the range 24–44 K is just a rhombohedral one. As yet monocrystals have not been grown but detailed neutron scattering experiments have been performed on polycrystalline samples.[7] The large peak around a scattering wave vector of magnitude close to that corresponding to a 120°-three sublattice configuration was ascribed to a 2D short-range order. However, the broad peak at zero energy transfer observed in the neutron cross section shows an intensity of the same order of the surely elastic peaks observed in the α-oxygen, the monoclinic ordered phase of solid oxygen in the range 0–24 K. For this reason we suggest to study the magnetic field effect on the neutron scattering experiment in β-oxygen because a narrowing of the peak in presence of magnetic field should be valuable support to the existence of LRO in β phase, the broad peak width being in this case related to the existence of a DH configuration restored by thermal fluctuations instead of a proof of absence of LRO.

The authors thank Dr. P. Stephens of the State University of New York at Stony Brook for having suggested to study the RAF model in presence of a magnetic field.

[1]E. Rastelli and A. Tassi, J. Phys. C **19**, L423 (1986).
[2]A. P. J. Jansen, Phys. Rev. B **33**, 6352 (1986).
[3]E. Rastelli, L. Reatto, and A. Tassi, *Magnetic Excitations and Fluctuations: Springer Series in Solid-State Sciences* (Springer, Berlin, 1984), Vol. 54, p. 195.
[4]E. Rastelli and A. Tassi, J. Appl. Phys. **61**, 4117 (1987).
[5]E. Rastelli and A. Tassi, J. Phys. C **19**, 1993 (1986).
[6]E. Rastelli and A. Tassi, J. Phys. C **20**, L303 (1987).
[7]P. W. Stephens and C. F. Majkrzak, Phys. Rev. B **33**, 1 (1986).
[8]A. Adam, D. Billery, C. Terrier, R. Mainard, L P. Regnault, J. Rossat-Mignod, and P. Meriel, Solid State Commun. **35**, 1 (1980).
[9]T. Nagamiya, Solid State Phys. **20**, 305 (1967).
[10]B. R. Cooper, Solid State Phys. **21**, 393 (1968).
[11]G. C. De Fotis, Phys. Rev. B **23**, 4714 (1981).

Dynamic susceptibility and damping rate of magnetic excitations in hybridizing cerium systems

Gong-Jia Hu and Bernard R. Cooper
Department of Physics, West Virginia University, Morgantown, West Virginia 26506

There has been much interest in the magnetic excitation behavior of cerium and light actinide systems with partially delocalized f electrons. Both the dispersion and the damping show unusual characteristics. Previously we have had considerable success in dealing with the dispersion, and have now developed a theory of the dynamic susceptibility and damping rate of excitations in magnetically ordered cerium systems where the damping is due to the hybridization between the f electrons and the non-f-band electrons. We include in our calculations both the two-ion interaction, which causes anisotropic magnetic ordering, and the hybridization-dressed crystal-field effects. We have applied the theory to CeSb and CeBi and obtained very large renormalization of the single-ion spectrum. The temperature dependence of location and broadening of energy transfer peaks are in excellent agreement with experiment.

I. INTRODUCTION AND FORMALISM

Recently, the unusual magnetic behavior of moderately delocalized cerium compounds, especially the heavier monopnictides CeSb and CeBi, has been studied extensively (see Refs. 1–8 and further references therein). After extending the treatment of f-band electron hybridization (previously developed by Coqblin and Schrieffer[9] using a Schrieffer–Wolff[10] transformation for Ce^{3+} systems) to obtain a hybridization-mediated anisotropic two-ion interaction, Cooper *et al.*[1–6] have successfully explained the main features of the anisotropic magnetic behavior of CeSb and CeBi, namely, very large magnetic anisotropy favoring the cube-edge direction of the NaCl structure,[1–3] complex magnetic phase diagrams,[1,2,4] very small crystal-field splitting,[3] and other anomalous properties such as the static susceptibility and electrical resistivity.[5] Success has also been achieved in explaining the unusual, relatively dispersionless, magnetic excitation spectra.[6]

In this paper we present a theory for understanding another aspect of the magnetic excitation behavior, the damping and shifts of excitations as temperature varies, in magnetically ordered partially delocalized cerium compounds. We show that the damping and temperature shifts again can be understood on the basis of the hybridization between the f electrons and the non-f-band electrons. We include in our calculations both the hybridization-dressed crystal field[2,3] (with Γ_7 ground state and small Γ_7-Γ_8 splitting) and the anisotropic two-ion interaction,[1–3] which causes splitting within and mixing between the Γ_7 and Γ_8 multiplets, and yields anisotropic magnetic ordering. The two-ion interaction is treated in the mean-field approximation.

Our theory is based on a projection-operator method developed by Mori and others.[11] The starting point is the hamiltonian

$$\mathscr{H} = \mathscr{H}_0 + \mathscr{H}' , \tag{1}$$

where $\mathscr{H}_0$ consists of the electron band energies, a configuration energy for the Ce^{3+} ion, a Coulomb energy to take account of correlation effects associated with addition of an electron to this configuration, a crystal-field interaction energy dressed by the hybridization, and a mean-field energy induced by the hybridization-mediated anisotropic two-ion interaction. We characterize $\mathscr{H}_0$ by its eigenstates and eigenvalues as given by $\mathscr{H}_0|m\rangle = \epsilon_m|m\rangle$. For magnetically ordered Ce^{3+} systems, six eigenstates $|m\rangle$ can be determined by the mean-field theory as previously discussed.[1,2,4–6] The perturbation term $\mathscr{H}'$ is the hybridization interaction giving the mixing of f and band electrons.

Next we define a Liouville operator $\mathscr{L}$ which acts on an operator A as $\mathscr{L}A \equiv i[\mathscr{H},A]$. Then the susceptibility can be written as

$$\chi(z) = \beta \langle J | \mathscr{L}(\mathscr{L} - z)J \rangle , \tag{2}$$

where $z = \omega + i\eta$, $\beta = 1/k_B T$, and J is the total angular momentum operator.

After introducing the projection operator

$$Q = 1 - |A\rangle\langle A|A\rangle^{-1}\langle A| \equiv 1 - p \tag{3}$$

for a dynamic variable A and following the method developed by Forster,[11] the damping rate for a transition operator $L_{mn} = |m\rangle\langle n|$, giving a magnetic excitation, is given by the imaginary part of Ω_{mn} with

$$\Omega_{mn}(z) = \langle \dot{L}_{mn}|Q\,[1/(Z - Q\mathscr{L}Q)]Q|\dot{L}_{mn}\rangle \times \langle L_{mn}|L_{mn}\rangle^{-1} , \tag{4}$$

where the dot denotes the time derivative; the spectral line shift is given by the sum of the real part of Ω_{mn} and $\langle \dot{L}_{mn}|L_{mn}\rangle$. (The contribution of $\langle \dot{L}_{mn}|L_{mn}\rangle$, however, is negligible.) Here m, n label the mean-field eigenstates of $\mathscr{H}_0$.

II. RESULTS AND DISCUSSION

The dynamic susceptibilities of Ce^{3+} ions in magnetically ordered CeBi and CeSb exhibit unusual characteristics. For neutron inelastic scattering studies on polycrystalline samples, Heer *et al.*[7] reported that there is only one well-separated inelastic peak observed for both CeBi and CeSb. At low temperatures ($\lesssim 4$ K), the position of the peak is 5.2 meV for CeBi and 4.1 meV for CeSb; and the width of the peak is 1.2 meV for CeBi and 1.0 meV for CeSb. A shift of the

 0021-8979/88/083826-03$02.40 © 1988 American Institute of Physics

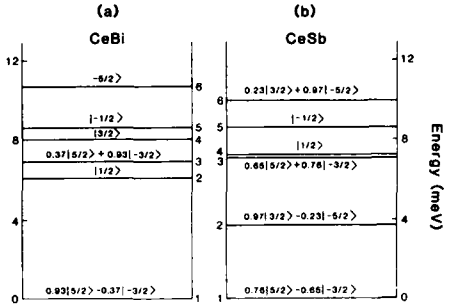


FIG. 1. Calculated Ce^{3+} mean-field states and energy levels: (a) for antiferromagnetic type I (AF-I) CeBi at 5 K with $E_2/E_1 = 0.5$, $E_3/E_1 = -0.3$, $60B_4/E_1 = 0.1$. ($E_1 = 16.2$ K to match $T_N = 25$ K.) See text for discussion of parameter values; (b) for AF-I CeSb at 4.6 K with $E_2/E_1 = 0.4$, $E_3/E_1 = -0.28$, $60B_4/E_1 = 0.6$. ($E_1 = 15.4$ K to match $T_N = 16$ K.)

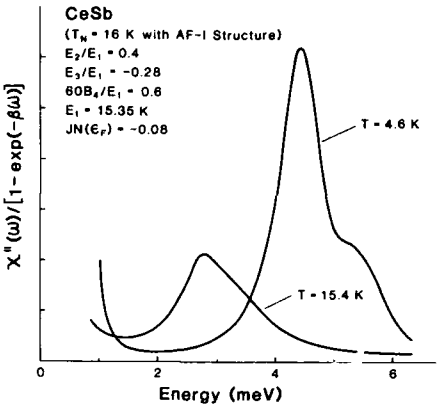


FIG. 2. Imaginary part of the dynamic susceptibility $[\chi''(\omega)]$ for $q = 0$ vs energy $(\hbar\omega)$ for CeSb. $\coth(\beta\omega/2)$ is the normalization factor to keep the area under the curve constant for varying temperature. The E_n and B_4 parameters are the same as in Fig. 1. $\mathcal{J}N(\epsilon_F) = -0.08$, chosen as described in text.

energy transfer peak toward lower energy and a broadening of the peak were observed for both systems with increasing temperature. Later Rossat-Mignod *et al.*[8] reported that the energy gap in the excitation spectrum at $\mathbf{q} = 0$ should be about 4.1 ± 0.1 meV for both CeBi and CeSb. This close similarity for CeBi and CeSb found in Ref. 8 is quite surprising because the crystal-field splitting (45 K in CeSb and 8 K in CeBi) and the ordering temperature ($T_N = 16$ K in CeSb and 25 K in CeBi) are quite different.

In order to understand the unusual damping and line shift behavior of CeBi and CeSb, we have carried out detailed calculations based on the f-band hybridization mechanism. Figure 1 shows the mean-field states and energy levels. These are not pure Γ_7 doublet and Γ_8 quartet, but mixtures because of the two-ion interaction. Here the parameters[1-6] E_1, E_2, E_3 give the two-ion anisotropic exchange interaction strength to first, second, and third neighbor Ce^{3+} ions, respectively; and B_4 gives the crystal-field splitting ($\Delta_{CF} = 360B_4$ for pure Γ_7 and Γ_8 states), which we take from the experimental value at high temperature in the paramagnetic regime. For CeSb, the E_n have been taken as the values Kioussis *et al.*[4] use to obtain the unusual magnetic structural behavior. For CeBi, the scale of the E_n is chosen as previously[1,2,3-6] to fit the experimental T_N, but the ratios E_2/E_1, E_3/E_1 differ slightly from those used previously[6] to obtain the dispersion.

On examining Fig. 1, we can see that from considering the energy level scheme we might expect two energy transfer peaks at low temperature rather than the experimentally observed single peak. These correspond to a longitudinal transition operator (L_{13} for both CeBi and CeSb) and a transverse transition operator (L_{14} for CeBi and L_{12} for CeSb). As shown in Figs. 2 and 3, using the formalism described in Sec. I, we have calculated the imaginary part of the dynamic susceptibility (giving the energy loss as a function of frequency) for $q = 0$ for varying temperature. Besides the E_n and B_4 parameters, the calculation also uses the value of the product of the single-site hybridization strength parameter ($\mathcal{J}$) times the band density of states at the Fermi energy $[N(\epsilon_F)]$. The values used for $\mathcal{J}N(\epsilon_F)$ differ slightly from those calculated by Wills and Cooper[4] (about -0.07 for both compounds).

As can be seen in Fig. 2, in fact, the CeSb we obtain a single peak as experimentally observed.[7] This is because level 2 is at sufficiently low energy that the peak that would correspond to the transverse transition has merged into the central peak, i.e., according to the theory the observed peak should be of wholly longitudinal polarization for CeSb. For CeBi, E_2/E_1 and E_3/E_1 have been adjusted from the previously used values[6] in order to bring levels 3 and 4 sufficiently close together to obtain a single peak of mixed transverse and longitudinal character while still obtaining a type I

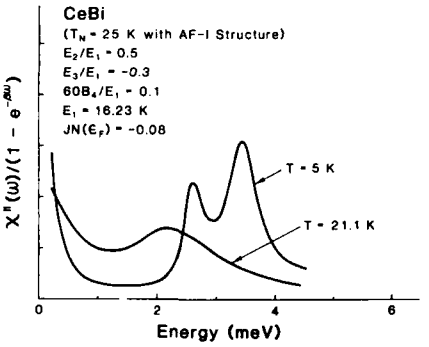


FIG. 3. Imaginary part of the dynamic susceptibility ($q = 0$) vs energy for CeBi. The E_n and B_4 parameters are the same as in Fig. 1. $\mathcal{J}N(\epsilon_F) = -0.08$, chosen as described in text.

antiferromagnetic structure. For both CeSb and CeBi the value of $\mathcal{J}N(\epsilon_F)$ has been increased slightly from the first-principles calculated value of Wills and Cooper[3] in order to match the experimental linewidth at low temperature.

For CeSb, as seen in Fig. 2, at 4.6 K the peak is at 3.7 meV with a width of 0.9 meV. The peak energy decreases (softens) on approaching T_N and the width broadens to 1.5 meV at 15.4 K. This is in excellent agreement with experiment.[7,8] [Note that our only adjustment was to $\mathcal{J}N(\epsilon_F)$ to match the low-temperature width.] For CeBi as seen in Fig. 3, at 5 K the peak is at 4.3 meV, and again the peak shifts to lower energy with increasing temperature. The width is about 1.3 eV at 5 K and has little change as temperature increases.

In conclusion, we have found that upon including the crystal-field splitting and the hybridization-mediated two-ion interaction in the hamiltonian and treating the hybridization between the f electrons and the non-f-band electrons as the main damping mechanism, the unusual dynamic susceptibilities (neutron inelastic spectra) in CeSb and CeBi can be understood. In quantitative agreement with experiment,[7,8] the inelastic peak locations calculated at low temperature are 3.7 meV for CeSb and 4.3 meV for CeBi, while the widths match experiment with slight adjustment to the first principles calculated values for $\mathcal{J}N(\epsilon_F)$. Notice that the lineshifts from the mean-field results are very large. This large renormalization of the single-ion spectra comes from two sources: dispersion and broadening. (Note that the papers cited under Ref. 6 deal only with dispersion.) It is interesting that the theory attributes quite different character to the energy transfer peaks in CeSb and CeBi, despite the peak locations being quite similar at low temperature. For CeSb, the transitions giving the peak are longitudinal, and the calculated width increases significantly with temperature. For CeBi, the peak has mixed longitudinal and transverse character, and the calculated width is almost temperature independent. Detailed experiments investigating this predicted behavior would be valuable.

ACKNOWLEDGMENTS

We have benefited from valuable discussions with G. N. Kioussis and J. M. Wills. This research has been supported by the National Science Foundation through Grant No. DMR-85-04449.

[1] B. R. Cooper and R. Siemann, J. Appl. Phys. **50**, 1991 (1979); R. Siemann and B. R. Cooper, Phys. Rev. Lett. **44**, 1015 (1980).
[2] B. R. Cooper, R. Siemann, D. Yang, P. Thayamballi, and A. Banerjea, *Handbook on the Physics and Chemistry of the Actinides*, edited by A. J. Freeman and G. H. Lander (North-Hollard, Amsterdam, 1985), Chap. 6, pp. 435–500.
[3] J. M. Wills and B. R. Cooper Phys. Rev. B **36**, 3809 (1987).
[4] N. Koussis, B. R. Cooper, and A. Banerjea, J. Appl. Phys. **61**, 3388 (1987); (to be published).
[5] G.-J. Hu and B. R. Cooper (to be published).
[6] P. Thayamballi, D. Yang, and B. R. Cooper, Phys. Rev. B **29**, 4049 (1984); P. Thayamballi and B. R. Cooper, Phys. Rev. B **31**, 5911 (1985).
[7] H. Heer, A. Furrer, W. Halg, and O. Vogt, J. Phys. C **12**, 5207 (1979).
[8] J. Rossat-Mignod, J. M. Effantin, P. Burlet, T. Chattopadhyay, L. P. Regnault, H. Bartholin, C. Vettier, O. Vogt, D. Ravot, and J. C. Achart, J. Magn. Magn. Mater. **52**, 111 (1985).
[9] B. Coqblin and J. R. Schrieffer, Phys. Rev. **185**, 847 (1969).
[10] J. R. Schrieffer and P. A. Wolff, Phys. Rev. **149**, 491 (1966).
[11] H. Mori, Prog. Theor. Phys. (Kyoto) **33**, 423 (1965); D. Forster, *Hydrodynamic Fluctuations, Broken Symmetry and Correlation Functions* (Benjamin, Reading, MA, 1975), Chap. 5.

Ferromagnetic and spin-wave resonance in multilayer films (abstract)

R. F. Soohoo
Department of Electrical and Computer Engineering, University of California, at Davis, Davis, California 95616

Whereas ferromagnetic and spin-wave resonance in single-layered films has been studied for a number of years,[1] the study of such resonances in multilayer films is still at its infancy. Before the multilayer films can be used in possible applications, it is necessary to understand their superlattice properties. We have used FMR techniques to determine the basic parameters of these films, both theoretically and experimentally. Theoretically, we have calculated the FMR spectra for superlattices of single-crystal, polycrystal, and amorphous samples. Experimentally, we have studied ferromagnetic and spin-wave resonances in $Fe/SiO_2/Fe/SiO_2\ldots$, Fe/Co/Fe/Co . . . , $NiFe/SiO_2/NiFe/SiO_2\ldots$, and NiFe/Co/NiFe/Co . . . samples. It was found theoretically and experimentally that for applied fields parallel and perpendicular to the film plane, the internal fields in various layers may differ. This could result in widely separated resonances for the various layers. In the case of ferromagnet/insulator multilayered samples, the FMR spectra depended critically on the insulator thickness and its degree of perfection. Diffusion of ferromagnetic atoms through pinholes in the insulating layer provided exchange coupling between ferromagnetic layers and the FMR spectra appeared similar to samples without insulating layers.

[1]R. F. Soohoo, *Magnetic Thin Films* (Harper and Row, New York, 1965), Chaps. 10 and 11.

Ferromagnetic resonance measurements on epitaxial iron and cobalt films of ZnSe/GaAs substrates (abstract)

S. A. Oliver and C. Vittoria
Center for Electromagnetics Research, Northeastern University, Boston, Massachusetts 02115[a]

J. J. Krebs and G. A. Prinz
Naval Research Laboratory, Washington, DC 20375[b]

Ferromagnetic resonance (FMR) measurements have been performed on single-crystal epitaxial Fe and Co films deposited by molecular-beam epitaxy onto {100} and {110} ZnSe/GaAs substrates. In-plane FMR results as a function of magnetic field H were obtained over the frequency range $0.01 < f < 20.0$ GHz by means of a slot line technique. Additional in-plane measurements and measurements with H perpendicular to the plane of the film were performed using a 9.5-GHz microwave cavity. Zero-field results, as well as frequency versus magnetic field dispersions, were obtained with H in the field plane parallel to the ⟨100⟩ and ⟨110⟩ axes. The following parameters were deduced from the results on the {100} films: effective magnetization (Fe: 21.6 kOe; Co: 18.1 kOe), gyromagnetic ratio (Fe: 2.11; Co: 2.17), and cubic anisotropy field (K_1/M) (Fe: 0.29 kOe; Co: 0.32 kOe). Higher-order terms in the anisotropy field were found to give a negligible contribution. No terms for uniaxial anisotropy energies were included in the fitting equations. These results are in reasonable agreement with published values. Spin-wave excitations were observed in iron films on both substrate orientations, and are found to obey the n^2 law. The experimental exchange constant for the iron films was found to be $A = (1.9 \pm 0.1) \times 10^{-6}$ erg/cm. Spin waves were excited in the {100} Co film, but not in the {110} Co film.

[a]Supported in part by NSF grant ECS-8601661.
[b]Supported by the Office of Naval Research.

 0021-8979/88/083829-01$02.40 © 1988 American Institute of Physics

Spin-wave energies in ferromagnetic nickel alloys (abstract)

R. Bechara Muniz[a] and J. d'Albuquerque e Castro[a]
Instituto de Física, Universidade Federal Fluminense, Niterói, RJ-24.210, Brazil

D. M. Edwards
Department of Mathematics, Imperial College, London, SW7 2BZ, United Kingdom

An expression is derived for the spin-wave stiffness constant D in a ferromagnetic metallic alloy. The formalism is based on a multiorbital tight-binding model and the Hartree–Fock approximation. Both diagonal and off-diagonal disorder are taken into account. Results for Ni-Fe, Ni-Co, and Ni-Cu alloys are obtained within the coherent potential approximation (CPA) and compared with previous calculations and experimental data.

---

[a] CNPq Research Fellow.

 0021-8979/88/083830-01$02.40 © 1988 American Institute of Physics

Magnetization reversal dynamics in magneto-optic media (invited)

M. Mansuripur
College of Engineering, Boston University, Boston, Massachusetts 02215
T. W. McDaniel
IBM Corp., General Products Division, Tucson, Arizona 85744

Dynamics of magnetization reversal in thin films of amorphous rare earth-transition metal alloys are investigated. Using computer simulations for a two-dimensional square lattice of dipoles with nearest-neighbor exchange interaction and random axis anisotropy, the Landau–Lifshitz–Gilbert equation is numerically integrated to yield the static wall structure and its motion under an applied field. The simulated results show excellent agreement with theory in the special cases where analytic solutions exist.

I. INTRODUCTION

The process of magnetization reversal in thin films of amorphous rare earth-transition metal alloys is of considerable importance in erasable optical data storage. The amorphous nature of the media and the presence of random axis anisotropy in alloys containing non-*S*-state magnetic ions (such as Tb and Dy) add a new dimension of complexity to the study of magnetization reversal in these materials. Understanding the nucleation process and the structure and the dynamics of domain walls will enable the experimentalist to better control the position, shape, and size of written domains, uniformity of magnetization distribution within the reversed region, smoothness of the boundary, and stability of recorded domains under external fields and temperature gradients; it will also enhance his ability to fully erase or even overwrite an existing domain.[1]

In an effort to better understand the dynamics of magnetization reversal in amorphous RE-TM thin films, we have developed a computer simulation based on the Landau–Lifshitz–Gilbert equation.[2–4] The model incorporates random spatial variations in magnetic parameters of the media including random axis anisotropy. Like all simulations of physical systems with near-neighbor interactions our model is particularly suited for highly parallel computers (such as the Connection Machine[5]). The inadequacy of ordinary computers is particularly severe when demagnetizing effects have to be incorporated. The small-scale simulations presented in this paper have been obtained with a VAX 11/780 machine and, of necessity, ignore the demagnetizing fields. The goal of the paper then is to introduce the algorithm, show its convergence, and examine the wall structure and dynamics in the limit of negligible demagnetizing effects. We emphasize, however, that the algorithm is quite general and can be employed without restrictions in large-scale simulations on supercomputers or parallel machines.

II. THE LANDAU–LIFSHITZ–GILBERT EQUATION

The fundamental law governing magnetization dynamics is the mechanical law relating the applied torque to the time-rate of angular momentum change. The torque on a dipole moment $\mathbf{m}$ arising from an effective field $\mathbf{H}$ is $\mathbf{m}\times\mathbf{H}$, while the angular momentum is $\mathbf{m}/\gamma$ with γ being the effective gyromagnetic ratio. Thus

$$\dot{\mathbf{m}} = \gamma \mathbf{m}\times\mathbf{H}^{(\mathrm{eff})}. \tag{1a}$$

The effective field has contributions from external, anisotropy, exchange, and demagnetizing sources. In addition, it has a phenomenological term that represents the effect of dissipative phenomena. This term is proportional to the time-rate of change of the unit vector $\mathbf{m}/|\mathbf{m}|$ and, for dimensional reasons, its proportionality constant has been defined as α/γ where α is the dimensionless viscous damping parameter.[2] Therefore,

$$\mathbf{H}^{(\mathrm{eff})} = \mathbf{H}^{(\mathrm{ext})} + \mathbf{H}^{(\mathrm{ans})} + \sum_{\mathrm{n.n.}} \mathbf{H}^{(\mathrm{xhg})} + \sum_{i,j} \mathbf{H}^{(\mathrm{dmag})} + \frac{\alpha \dot{\mathbf{m}}}{\gamma|\mathbf{m}|}. \tag{1b}$$

Combining Eqs. (1a) and (1b) we obtain:

$$\dot{\theta} = -[\alpha\gamma/(1+\alpha^2)]H_\theta - [\gamma/(1+\alpha^2)]H_\phi, \tag{2a}$$

$$\dot{\phi}\sin\theta = [\gamma/(1+\alpha^2)]H_\theta - [\alpha\gamma/(1+\alpha^2)]H_\phi. \tag{2b}$$

In these equations θ and ϕ are the spherical coordinates of $\mathbf{m}$, while H_θ and H_ϕ are the components of the net field from external, anisotropy, exchange, and demagnetizing sources; the derivative with respect to time is indicated by a dot. Equations (2) are the basis of our simulations in which the magnetic film is represented by a two-dimensional square lattice of magnetic dipoles $\mathbf{m}_{ij}$. Each dipole corresponds to a $d\times d$ square section of the film, and is coupled to its four nearest neighbors by an exchange field with macroscopic stiffness coefficient A_x. The anisotropy at each lattice site is uniaxial with strength K_u and direction (θ_0,ϕ_0). For simplicity's sake, θ_0 and ϕ_0 for each site are chosen randomly and independently from the intervals $(0,\theta_0^{\max})$ and $(0,2\pi)$, respectively. The effective field components needed in Eqs. (2) are determined from energy considerations using a variational approach.[6] Finally, the equations are integrated by

 0021-8979/88/083831-04$02.40 © 1988 American Institute of Physics

the fourth-order Runge–Kutta technique and the time steps Δt are chosen to keep rotation angles of $\mathbf{m}$ during each iteration below 2°.

In the next section we describe some of the simulation results. The pattern of magnetization is displayed using the following convention: each moment is represented by its projections on the plane of the lattice ($\parallel$ component) and perpendicular to that plane ($\perp$ component). The perpendicular component will have an arrowhead pointing either up or down depending on whether the moment is above or below the plane. The size of the arrowhead will be proportional to the magnitude of the $\perp$ component itself, so in case of ambiguity one should be guided by this bit of information. To give an example, $\mathbf{\nu}$ is a moment above the plane with the perpendicular component equal to the arrow, and the in-plane component along the appendage to the arrow, pointing towards the upper right corner of the plane. The origin is the point where the two components join and as such the direction of the in-plane component is uniquely identifiable without the need for another arrowhead.

III. RESULTS AND DISCUSSION

The results presented here are based on the following set of parameters: $M_s = 100$ emu/cm^3, $A_x = 10^{-7}$ erg/cm, $K_u = 10^6$ erg/cm^3, $\gamma = -10^7$ Oe^{-1} s^{-1}, $d = 10$ Å, $\alpha = 0.5$. According to the standard theory of domain walls this set corresponds to the following values of domain wall thickness and energy density:

$$\pi\Delta_0 = \pi\sqrt{A_x/K_u} = 99.4 \text{ Å}, \tag{3a}$$

$$\sigma_w = 4\sqrt{A_x K_u} = 1.26 \text{ erg/cm}^2. \tag{3b}$$

Moreover, contributions of exchange and anisotropy to the wall energy must be equal. Now consider the results in Fig. 1. The simulated array is 30×30 and initially the ten columns on the left had their magnetization vector pointing up while the remaining 20 columns were pointing down. The cells in the rightmost and leftmost columns are frozen in their initial orientations while periodic boundary conditions apply to the top and bottom rows. The random spatial variations of parameters and random axis anisotropy are not included here, as would be the case for the simulation of a uniform film with perfect perpendicular anisotropy. Figure 1(a) shows the state of the lattice after 1000 iterations. Clearly, the abrupt transition from up to down magnetization has relaxed into a wall of approximate thickness 100 Å, in close agreement with Eq. (3a). Note that the in-plane components of magnetization are parallel to each other throughout the wall. For this simulation the external field was absent and effects of demagnetization were ignored, leaving exchange and anisotropy as the only driving forces in the Landau–Lifshitz–Gilbert equation.

Figure 1(b) shows exchange, anisotropy, and total energies of the system during the above relaxation process. It is observed that for the first 10 ps, the system moves, albeit very slowly, away from the initial configuration which is an unstable, maximum-energy state. After this period the torques become strong enough to swiftly bring the system to a state of minimum energy. After a few oscillations the wall assumes its final configuration and the energy terms reach a stable value. Note that the final value of exchange energy is only slightly above the anisotropy energy. The total energy, when divided by the length of the wall (300 Å), gives a value of $\sigma_w = 1.28$ erg/cm^2 in good agreement with Eq. (3b).

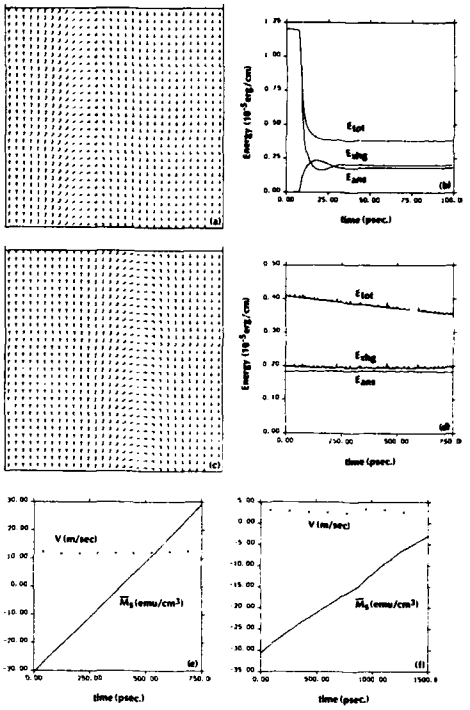


FIG. 1. Domain wall structure and dynamics for a medium with $M_s = 100$ emu/cm^3, $K_u = 10^6$ erg/cm^3, $A_x = 10^{-7}$ erg/cm, $d = 10$ Å, $\gamma = -10^7$ Oe^{-1} s^{-1}, and $\alpha = 0.5$. It is assumed that the medium has perfect uniaxial anisotropy in the perpendicular direction. (a) Straight wall created from an initial condition with ten columns on the left pointing up and the remaining 20 columns pointing down. The pattern is obtained after 1000 iterations, corresponding to $t \simeq 163$ ps. (b) Exchange energy, anisotropy energy, and total energy of the magnetic system during the relaxation process that starts with the unstable initial configuration and ends with the stable wall structure in (a). (c) Under an applied field $H_{ext} = 1$ kOe the wall in (a) moves to the right. The pattern is obtained after 4000 iterations corresponding to $t = 658$ ps. (d) Exchange energy, anisotropy energy, and total energy of the magnetic system under the applied field $H_{ext} = 1$ kOe. While the wall energy consisting of exchange and anisotropy contributions remains constant, the external field energy decreases linearly with time. (e) Average lattice magnetization vs time under the applied field $H_{ext} = 1$ kOe. The initial state of the lattice is shown in (a). The linear increase of the average magnetization with time corresponds to a constant wall velocity of 12.8 m/s, obtained from the average slope of the curve during several time intervals as indicated by the symbols x. (f) Same as (e) except that $H_{ext} = 250$ Oe. The average wall velocity is 2.8 m/s.

When a perpendicular field $H_{ext} = 1$ kOe is applied to the lattice of Fig. 1(a) the wall moves to the right with a constant velocity. The shape of the wall remains the same at all times as shown in Fig. 1(c) but the in-plane component precesses around the field. The exchange and anisotropy energies of the moving wall do not change from their static

values [see Fig. 1(d)] but the average magnetization of the lattice increases with time, as shown in Fig. 1(e). The linear increase of magnetization with time corresponds to a wall velocity of 12.8 m/s. The theoretical formula for wall mobility in the absence of demagnetization[6] is

$$\mu = (\alpha|\gamma|\Delta_0)/(1+\alpha^2), \tag{4}$$

where Δ_0 is the wall thickness parameter given by Eq. (3a). For the parameter values used here, Eq. (4) predicts a mobility of 12.65×10^{-3} m/(s Oe), which is in good agreement with our result. Figure 1(f) shows that under an applied field $H_{ext} = 250$ Oe the velocity drops to 2.8 m/s. Although this velocity is not quite the same as the theoretical value of $V = 3.16$ m/s, the error is only about 10%. The reason for the reduced accuracy is probably the increased significance of numerical errors in relation to the external field. In any event, the preceding example shows that the simulation results are reliable and can yield reasonable estimates of the various media characteristics.

Next, we consider the effect of random axis anisotropy on wall structure and motion. By assuming a uniform distribution of anisotropy axes with $\theta_0 \in (0,\pi/4)$ and $\phi_0 \in (0,2\pi)$ we obtain the wall structure of Fig. 2(a), which contains a 2π Bloch line. (The abrupt transition in this case was initially placed at column 20.) Figure 2(b) shows exchange, anisotropy, and total energies of the system while relaxing from the initial state. Note in comparison with Fig. 1 that the total energy is now greater, in part due to the presence of the Bloch line within the wall. When the field $H_{ext} = -1$ kOe is applied to the lattice of Fig. 2(a), Fig. 2(c) is obtained after 3000 iterations; note that the wall has moved to the left and the line has moved up. The energy versus time curves of Fig. 2(d) confirm that the wall structure during motion has remained intact.

The behavior of average magnetization during wall mo-

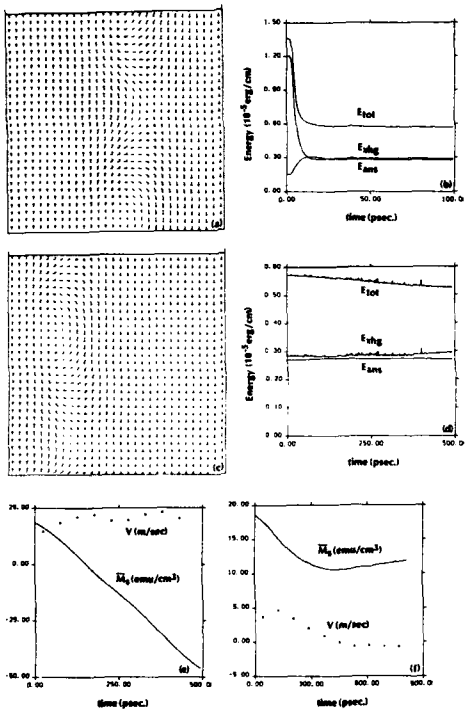


FIG. 2. Domain wall structure and dynamics for a medium with $M_s = 100$ emu/cm^3, $K_u = 10^6$ erg/cm^3, $A_x = 10^{-7}$ erg/cm, $d = 10$ Å, $\gamma = -10^7$ Oe^{-1} s^{-1}, and $\alpha = 0.5$. It is assumed that the medium has random axis anisotropy with $\theta_0^{max} = \pi/4$. (a) Straight wall created from an initial condition with 20 columns on the left pointing up and the remaining ten columns pointing down. The pattern is obtained after 17 000 iterations, corresponding to $t = 2740$ ps. (b) Exchange energy, anisotropy energy, and total energy of the magnetic system during the relaxation process that starts with the unstable initial configuration and ends with the stable wall structure in (a). (c) Under an applied field $H_{ext} = -1$ kOe the wall in (a) moves to the left. The pattern is obtained after 3000 iterations corresponding to $t = 495$ ps. (d) Exchange energy, anisotropy energy, and total energy of the magnetic system under the applied field $H_{ext} = -1$ kOe. While the wall energy consisting of exchange and anisotropy contributions remains constant, the external field energy decreases with time. (e) Average magnetization vs time under the applied field $H_{ext} = -1$ kOe. The initial state of the lattice is shown in (a). The decreasing magnetization vs time curve represents a variable wall velocity as indicated by the symbols x. The average velocity is 19.7 m/s. (f) Same as (e) except that $H_{ext} = -250$ Oe. The applied field is not large enough to overcome the barriers to wall motion created by the random axis anisotropy.

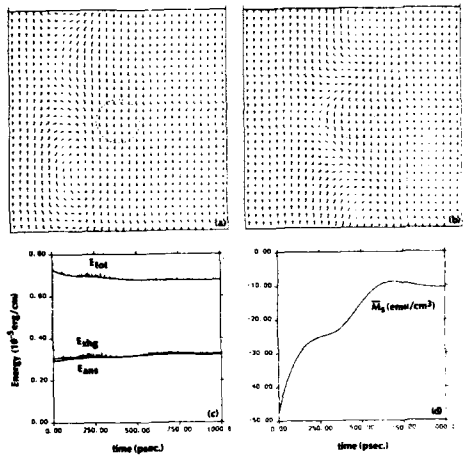


FIG. 3. Domain wall structure and dynamics for a medium with $M_s = 100$ emu/cm^3, $K_u = 10^6$ erg/cm^3, $A_x = 10^{-7}$ erg/cm, $d = 10$ Å, $\gamma = -10^7$ Oe^{-1} s^{-1}, and $\alpha = 0.5$. It is assumed that the medium has random axis anisotropy with $\theta_0^{max} = \pi/4$ Also the central region has a K_u ten times larger than the rest of the lattice. (a) Straight wall created from an initial condition with ten columns on the left pointing up and the remaining 20 columns pointing down. The pattern is obtained after 5000 iterations, corresponding to $t = 731$ ps. (b) Under an applied field $H_{ext} = 3$ kOe the wall bends around the central high-anisotropy region. The pattern is obtained after 7000 iterations corresponding to $t = 979$ ps. (c) Exchange energy, anisotropy energy, and total energy of the magnetic system under the applied field $H_{ext} = 3$ kOe. While the wall energy consisting of exchange and anisotropy contributions increases, the total energy decreases with time. (d) Average lattice magnetization vs time under the applied field $H_{ext} = 3$ kOe. The initial state of the lattice is shown in (a).

tion as depicted in Fig. 2(e) shows a slight nonuniformity, which is expected since the wall has to traverse a region with random distribution of anisotropy axes. The average wall velocity in the 500-ps time interval elapsed between Figs. 2(a) and 2(c) is 19.7 m/s, which is significantly higher than the 12.8-m/s velocity in Fig. 1(e). This difference can be attributed to the gyration of the in-plane component of the wall magnetization: whereas the wall of Fig. 1 can freely gyrate in the plane of the lattice and thereby cause a reduction of the translational velocity, the in-plane component in Fig. 2 is constrained by the local orientations of the axes of anisotropy and its gyration is reduced, causing an increase in the translational velocity. (Of course, the addition of demagnetizing fields with the constraints that they impose on the in-plane gyration will further change the picture.) Figure 2(f) shows the average magnetization versus time when the wall of Fig. 2(a) is subjected to an external field $H_{ext} = -250$ Oe. The wall initially moves to the left, but then it encounters an insurmountable barrier, retreats to the right, and comes to rest near its initial location. One can associate this behavior with wall coercivity.

Finally, Fig. 3 shows the effect of spatial variations in magnetic parameters of the film. A small circular region (radius $= 3d$) at the center of the lattice is assigned a value of $K_u = 10^7$ erg/cm^3; all other parameter assignments are identical to Fig. 2. An abrupt transition placed at column 10 relaxes into the wall (with a 2π Bloch line) shown in Fig. 3(a). Application of the external field $H_{ext} = 3$ kOe results in a bent wall around the central region as shown in Fig. 3(b). While the exchange and anisotropy energies of the system increase in the process of bending, the total energy decreases due to the reduction in the external field energy [see Fig. 3(c)]. The average magnetization versus time is shown in Fig. 3(d), indicating a nonuniform approach to equilibrium. When the field was raised to 8 kOe the wall overcame the barrier and moved to the other side. This example, in addition to identifying a possible source of coercivity, demonstrates that dynamic behavior near a "defect" can be quite complex and, therefore, deserves further attention. Detailed studies are now underway to quantify the effects of this and other random spatial variations of magnetic parameters on the static and dynamic properties of domain walls.

[1]H-P. D. Shieh and M. H. Kryder, J. Appl. Phys. **61**, 1108 (1987).
[2]A. P. Malozemoff and J. C. Slonczewski, *Magnetic Domain Walls in Bubble Materials* (Academic, New York, 1979).
[3]S. Shiomi and C. C. Shir, J. Appl. Phys. **54**, 6847 (1983).
[4]Y. Nakatani and N. Hayashi, IEEE Trans. Magn. **MAG-23**, 2179 (1987).
[5]W. D. Hillis, Sci. Am. **256**, 108 (1987).
[6]M. Mansuripur, J. Appl. Phys. (to be published).

Micromagnetics of magnetization reversal in amorphous Tb-Fe films by Lorentz microscopy

C.-J. Lin, J. C. Suit, and R. H. Geiss
IBM Research Division, Alamden Research Center, 650 Harry Road, San Jose, California 95120-6099

Lorentz electron microscopy has been used to investigate the micromagnetic mechanism of *M-H* hysteresis loop behavior of thin amorphous TbFe films with perpendicular easy-axis magnetic anisotropy. Detailed nucleation and growth behavior of reverse domains was observed while an applied field provided by the microscope objective lens along the film normal was slowly changed. Very different results between $Tb_{19}Fe_{81}$ and $Tb_{32}Fe_{68}$ films have been observed. The reverse domain grew more or less radially in the former case, while a dendritelike domain pattern was observed for the latter case.

I. INTRODUCTION

In the emerging reversible magneto-optical storage technology, information is stored via micron or even submicron-sized vertical magnetic domains on amorphous rare-earth transition-metal (RE-TM) alloy films. Such small thermomagnetically written domains have to be uniform both in size and shape to minimize the read-back modulation noise. There is, therefore, a need to fully understand the detailed thermomagnetic recording process in RE-TM films. The temperature dependence of coercivity obtained from *M-H* and Θ_k-*H* hysteresis loops is traditionally used to discuss the thermomagnetic recording process. However, to fully undertand the formation of micron or submicron-sized domains, one need to investigate the magnetization reversal process at the corresponding spatial scale. Conventional VSM and Kerr loops do not provide such micromagnetic information of the magnetization reversal process, since their signals represent the average magnetization over a large area.

It has been noted that magnetization reversal in amorphous RE-TM films having a strong perpendicular anisotropy occurs by nucleation and growth of reverse domains.[1-5] Some observations of the magnetization reversal process in RE-TM films have been carried out previously using optical microscopy.[1,2,6,7] The limitation of optical resolution, however, precluded clear observation of detailed submicron features. In this paper we present the detailed magnetization reversal process in TbFe films at room temperature observed by Lorentz electron microscopy, which has allowed observation of submicron vertical magnetic domains on TbFe films.[8-10]

II. EXPERIMENT

A. Film preparation

TbFe films of 50 nm thickness were deposited at an average rate of 0.1 nm/s by dc magnetron cosputtering. The base pressure was 8×10^{-8} Torr. Film compositions were determined by x-ray fluorescence. Typical values of magnetic anisotropy energy constant K_u, measured with a 16-kOe torque magnetometer, were in the range of $2\text{–}3\times10^6$ ergs/cm. Samples for transmission electron microscopy were prepared by floating films off carbon-coated mica substrates in deionized water. To avoid the formation of oxidized surface layers, which show in-plane magnetization[11] and can easily obscure the observation of vertical magnetization patterns[8] in Lorentz microscopy, 10-nm SiO_2 was deposited both before and after the deposition of the TbFe layer.

B. Lorentz imaging along *M-H* hysteresis loops

The Fresnel mode of Lorentz electron microscopy[12,13] was carried out in a Philips EM 301. We have found that vertically magnetized TbFe films generally need to be tilted 10°–30° to obtain good contrast Lorentz images.[8] The perpendicular applied field, provided by the objective lens of the microscope, was continuously variable from -10 to $+10$ kOe. First, a film was brought to saturation at 10 kOe, where the Lorentz image appeared featureless. The field was then gradually decreased toward zero, reversed and increased in the opposite direction. We carefully followed the nucleation and growth of reverse magnetic domains. This growth process of reverse domains was investigated at either constant or slowly increasing applied field.

III. RESULTS AND DISCUSSION

Different TbFe compositions and several other RE-TM films have been investigated. Here we concentrate on results from $Tb_{19}Fe_{81}$ and $Tb_{32}FE_{68}$, since they represent two general types of magnetization reversal behavior. Figure 1(a) shows that for $Tb_{32}Fe_{68}$ the difference between the applied field at which magnetization reversal starts (S_1, referred to as the nucleation field) and the applied field required for complete magnetization reversal (S_5, referred to as the saturation field) is large, leading to a nonsquare hysteresis loop.

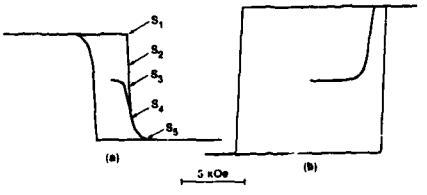


FIG. 1. Θ_k-*H* hysteresis loops for $Tb_{32}Fe_{68}$ (a) and $Tb_{19}Fe_{81}$ (b).

 0021-8979/88/083835-03$02.40 © 1988 American Institute of Physics

Note that the portion of hysteresis loop from S_4 to S_5 is the same whether it is started from a demagnetized or saturated state. On the other hand, for $Tb_{19}Fe_{81}$ as shown in Fig. 1(b), the difference between the saturation field and the nucleation field is small and the hysteresis loop is square. Note that if the loop is started from a demagnetized state, the magnetization starts to change at a field significantly less than the nucleation field and appears to saturate at a field also significantly less than that when nucleation is required.

A. $Tb_{32}Fe_{68}$

Figure 2(a) shows a Lorentz micrograph at the initial stage of magnetization reversal at a field of 0.95 kOe. The reason this field is smaller than the field 1.21 kOe at S_1 in Fig. 1(a) is because the loops in Fig. 1 were obtained at a rather high sweeping rate of about 17 kOe/min. To catch the initial stage of magnetization reversal, we found it was easier if the film was kept at a smaller field. Occasionally defects could be identified as preferred nucleation sites. However, reversal also started at positions where no obvious defects could be identified. The reverse domains grew in an interesting way as shown from Figs. 2(a)–2(f). They could grow with time at a constant applied field of 0.95 kOe [Figs. 2(a)–2(c)], indicating a thermally activated process.[2] This is in good agreement with Θ_k-H hysteresis loop from from S_1 to S_2 [Fig. 1(a)]. During this stage, the observed increase of reverse magnetization along the hysteresis loop occurred microscopically by gradually filling out the entire film with submicron-wide multiple-branch dendritelike reverse domains. The fact that these complicated dendritelike domains, rather than simpler, more or less circular domains occurred, suggests that by choosing this dendrite shape the reduction in the demagnetizing energy was larger than the increase in the domain wall energy. This is understandable since immediately before the start of magnetization reversal, the demagnetizing fields is 3.14 kOe for the M_s of 250 emu/cm^3, and is much larger than the applied field of 0.95 kOe used in Figs. 2(a)–2(c). Once the reversal started, the demagnetizing field at the domain wall of the reverse stripes quickly diminished and eventually would reverse in direction if the width of reverse stripes kept increasing. When the width reached a dimension greater than 5–8 times the film thickness [Figs. 2(a)–2(c)], the domain wall could no longer move because the total field acting on it became too small, and further widening of the reverse stripes could proceed only at larger applied fields as indicated in Fig. 1(a) from S_3 to S_5.

Figures 2(d)–2(f) show how the increasing applied fields from 1.45 to 2.75 kOe expanded the reverse stripes by squeezing the unreversed regions in between. As the width of the unreversed area gets squeezed narrower, stronger applied field is in turn required to cancel the stronger demagnetizing field which is in a direction against the reversal. Given the thickness of a domain wall on the order of 10 nm,[9] the width of narrowest unreversed stripe is expected to be at least 2–3 times the wall thickness, and the corresponding demagnetizing field at the domain walls is at most on the order of $2\pi M_s$, against reversal. This might be why an apparent saturation can be achieved at an applied field of only about 2.8 kOe, instead of a field equal to the sum of wall coercivity and $4\pi M_s$.

Following the above discussion, a magnetization reversal process similar to that of $Tb_{32}Fe_{68}$ is expected for those films having both a nonsquare hysteresis loop and a large magnetization such that $4\pi M_s$ is on the same order of the nucleation field or larger.

Note that the domain walls in Figs. 2(a)–2(c) appeared to be rather ragged, as compared with the smoother domain walls at higher fields [Figs. 2(e) and 2(f)]. The raggedness of domain walls in Figs. 2(a)–2(c) can be attributed to local variation of the wall coercivity. It is expected as the width of unreversed stripes gets narrower, the demagnetizing field becomes more sensitive to the stripe width, the local coercivity variation in comparison becomes less important, and domain walls become less ragged.

Figures 3(a) and 3(b) show a more detailed process of domain growth. During the exposure of this pair of consecu-

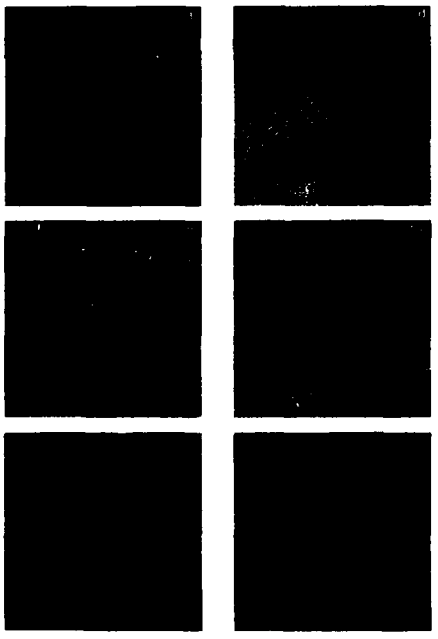


FIG. 2. Growth of reverse domains in $Tb_{32}Fe_{68}$. Micrographs were taken at zero applied field after being at (a) 0.95 kOe for 10 s, (b) 0.95 kOe for 90 s, (c) 0.95 kOe for 390 s, (d) 1.45 kOe for 10 s, (e) 2.10 kOe for 10 s, and (f) 2.76 kOe for 10 s.

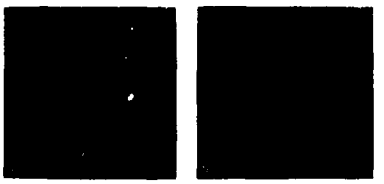


FIG. 3. Growth of reverse domains in $Tb_{32}Fe_{68}$. Micrographs were taken at an applied field of 0.97 kOe. The area indicated by g in (a) shows weaker contrast than the corresponding area in (b).

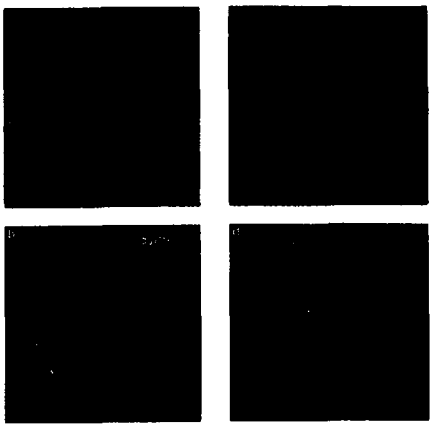


FIG. 4. Growth of reverse domains in $Tb_{19}Fe_{81}$. Micrographs were taken at zero applied field after being at 4.2 kOe (a) for 5 s, (b) for 35 s, (c) for 65 s, and (d) for 125 s.

tive pictures, a field of 0.97 kOe was left on. Some growth proceeded while the micrographs were being taken, and the added reverse area shows weaker contrast, e.g., the area indicated by *g* in Fig. 3(a) compared to the same area in Fig. 3(b). Such *in situ* observation of the magnetization reversal process, and the investigation of the resultant domain geometry indicates that it is a growth process by the advance of an existing domain wall, rather than a process in which a new small domain nucleates adjacent to the existing domain wall and later coalesces into the existing domain. This can also be inferred from the fact that adjacent reverse stripes do not coalesce at this stage.

B. $Tb_{19}Fe_{81}$

Figures 4(a)–4(d) show the growth of a reverse domain with time at a constant applied field, again indicating a thermally activated wall motion process. As shown in Fig. 1(b) the applied field needed to move an existing domain wall is significantly less than that for a reverse domain to nucleate from a saturated state. When the reverse domain nucleates at the nucleation field the domain wall velocity at this applied field is already too high for anyone to visually follow the growth process. Therefore, a field ramping up continuously does not allow observation of the nucleation and growth process of reverse domains. We circumvented this difficulty by using a pulsed field to create a starting domain like the one shown in Fig. 4(a). Note that this reverse domain appears to start from a defect.

Figures 4(a)–4(d) show, in strong contrast to the case of $Tb_{32}Fe_{68}$ film, that the reverse domain in $Tb_{19}Fe_{81}$ film grew radially. This indicates that the effect of demagnetizing field is not as important here and that wall energy factors are dominant. Indeed, the measured M_s of this film is 109 emu/cm^3 and $4\pi M_s$ is not very large compared to the applied field used in Fig. 4. The domain wall, however, is very ragged, presumably due to local variation of the wall coercivity. As shown in Figs. 4(b)–4(d), as the existing domain wall grew outward radially but nonuniformly, occasionally different portions of the wall coalesced and left behind isolated unreversed domains inside the larger reverse domain.

IV. SUMMARY

Lorentz electron microscopy has allowed us to investigate in great detail the nucleation and growth process of reverse domains in amorphous TbFe films having perpendicular easy axis anisotropy. Very different observations were made between $Tb_{19}Fe_{81}$ and $Tb_{32}Fe_{68}$. We believe that the major distinguishing factor between these two examples lies in the relative magnitude of the demagnetizing fields, as compared to the nucleation field.

ACKNOWLEDGMENTS

The authors wish to thank Lois Bynum for the film deposition, and Alan Bell for discussion.

[1] Y. Mimura, N. Imamura, T. Kobayashi, A. Okada, and Y. Kushiro, J. Appl. Phys. **49**, 1208 (1978).
[2] K. Ohashi, H. Tsuji, S. Tsunashima, and S. Uchiyama, Jpn. Appl. Phys. **19**, 1333 (1980).
[3] G. A. N. Connell and R. Allen, Proceedings of the 4th International Conference on Rapidly Quenched Metals, Sendai, 1981, p. 981.
[4] M. Mansuripur, J. F. Ruane, and M. N. Horenstein, Proc. Soc. Photo-Opt. Instrum. Eng. **529**, 25 (1985).
[5] M. Mansuripur, J. Appl. Phys. **61**, 1580 (1987).
[6] Y. Mimura and N. Imamura, Appl. Phys. Lett **28**, 746 (1976).
[7] Y. Takeno, M. Suwabi, T. Sakurai, and K. Goto, Jpn. J. Appl. Phys. **25**, L 657 (1986).
[8] J. C. Suits, R. H. Geiss, C.-J. Lin, D. Rugar, and A. E. Bell, Appl. Phys. Lett. **49**, 419 (1986).
[9] J. C. Suits, R. H. Geiss, C.-J. Lin, D. Rugar, and A. E. Bell, J. Appl. Phys. **61**, 3509 (1987).
[10] D. Rugar, C.-J. Lin, and R. Geiss, IEEE Trans. Magn. MAG-**23**, 2263 (1987).
[11] R. B. van Dover, E. M. Gyorgy, R. P. Frankenthal, M. Hong, and J. Siconolfi, J. Appl. Phys. **59**, 1291 (1986).
[12] M. S. Cohen, IEEE Trans. Magn. MAG-**1**, 156 (1965).
[13] P. J. Grundy and R. S. Tebble, Adv. Phys. **17**, 153 (1968).

Numerical simulation of recorded domain shapes on a rotating magneto-optical disk

Masahiko Takahashi, Hirofumi Sukeda, Masahiro Ojima, and Norio Ohta
Central Research Laboratory, Hitachi Ltd., Kokubunji, Tokyo 185, Japan

For realizing a very high density magneto-optical recording such as a domain-edge recording, the way to control domain shapes and sizes precisely was studied by comparing a numerical simulation with an optical observation of recorded domains on a high-speed rotating disk. The numerical simulation based on a heat flow analysis was applied to a multilayer structure disk. A teardroplike domain shape was analyzed by this simulation, which causes a timing error of edge detection. This shape could be corrected to a symmetrical shape by using a modulated laser pulse. Moreover, it was found that a distance between two domains was affected by a thermal correlation of two laser pulses. This effect is remarkable when the time interval between two pulses is short.

I. INTRODUCTION

In order to realize magneto-optical disks that are competitive with magnetic recording disks and tapes, much attention should be paid to increasing the linear bit density along with the track density. A domain-edge recording, for which information is stored at both side edges of one domain, gives about twice as large a linear density as that of a conventional domain-position recording. However, it requires more precise control of the domain width, length, and shape. For this purpose, it is necessary to make clear the relationship between recorded domains and recording conditions quantitatively. In this paper, we report a numerical simulation of domain sizes and shapes, and compare them with the observation results of domains recorded with various recording conditions on a rotating 5-in. TbFeCo disk.

II. EXPERIMENT

A TbFeCo film with 100-nm thickness was prepared by an in-line–type rf magnetron sputtering apparatus. This film was sandwiched between two dielectric nitride layers. A photopolymelized (2P) pregrooved glass disk with a 130 mm diam was used as a substrate.

The coercive force H_c and Kerr rotation angle θ_K were measured using a Kerr hysteresis loop measurement. Saturation magnetization M_s was obtained with a vibrating sample magnetometer.

The domains were recorded on a nongrooved flat area of the disk using a standard magneto-optical drive,[1] whose objective lens had a numerical aperture of 0.6. A 30-mW laser with a wavelength of 830 nm was used. The recorded domains were observed optically from the overcoating layer side using a TV camera mounted on a high-resolution polarized microscope. The magnification was $80\times2\times10$, and the relative resolution was $\pm0.1\,\mu$m.

III. RESULTS AND DISCUSSION

A. Simulation of recorded domain shapes

Recently we have selected suitable magnetic properties of TbFeCo films for domain-edge recording, for which the formation of the domain is stable against fluctuations of the external field.[2] As one example, for $Tb_{27}Fe_{61}Co_{12}$ film, which has a compensation temperature of 90 °C and Curie temperature of 200 °C, both the domain width and length are almost independent of the external field. The temperature dependencies of M_s, H_c, and θ_K of this film are shown in Fig. 1. In this study, this film was used as a recording layer and the magnetic properties in Fig. 1 were used in the simulation.

On the basis of a simple domain formation model, the domain shape can be identified with an isothermal line of the temperature T_w which satisfies

$$H_{ext} + H_d(T_w) + H_w(T_w) = H_c(T_w) \qquad (1)$$

at the distribution of maximum temperature at each point, where H_{ext} is the external field, and H_d the demagnetizing field. H_w is an effective field due to a wall energy term. The distribution of $H_d(T)$ can be calculated on the basis of a temperature dependence of M_s in Fig. 1. For simplicity, H_w is assumed to be small and constant.

The maximum temperature induced by a high-speed laser was calculated. The model for the calculation consists of

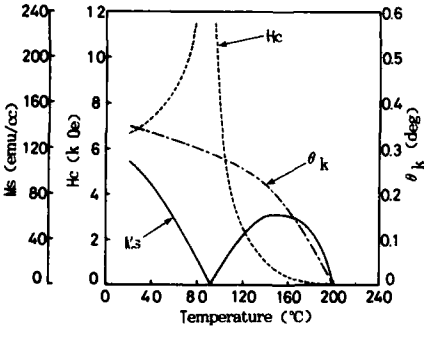


FIG. 1. Dependence of saturation magnetization M_s, coercive force H_c, and Kerr rotation angle θ_K on temperature for $Tb_{27}Fe_{61}Co_{12}$ film.

 0021-8979/88/083838-03$02.40 © 1988 American Institute of Physics

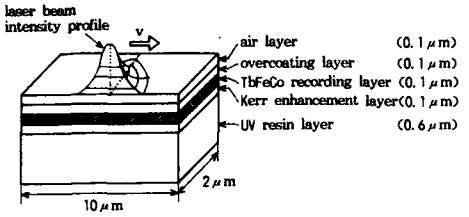


FIG. 2. Five-layer model for heat-transfer simulation.

five layers: resin plastic layer/nitride enhancement layer/TbFeCo recording layer/nitride overcoating layer/air layer, as shown in Fig. 2. Each meshed cell was $0.2\times0.1\times0.025\ \mu m^3$ and the total number was 25 000. The heat-diffusion equation at each mesh point for a gaussian laser beam running at constant velocity was calculated every 10 ns with a DEQSOL (Differential Equation Solver Language)[3] program. The thermal conductivity of the TbFeCo film was estimated to be 0.4 J/cm °C s from a measurement of the decrease of Kerr rotation angle θ_K due to the increase in temperature under a continuous irradiation. Consequently, the maximum temperature at each mesh point was calculated as shown in Fig. 3 by isothermal lines, for which the laser power was 8 mW, the pulse widths 100 and 300 ns, and the linear velocity 9 m/s. In this figure, the laser pulse starts at the point (0,0). From this temperature distribution, the distribution of H_c and H_d was mapped and T_w was estimated from Eq. (1) to be 170 °C for H_{ext} of 400 Oe. A recorded domain shape for H_{ext} of 400 Oe was shown by the hatched region in Fig. 3. This domain shape explains an observed figure very well, as shown in the photograph in this figure.

B. Teardroplike domain shape

For domain-edge recording, the domain shape must be symmetrical. However, both the calculated and observed

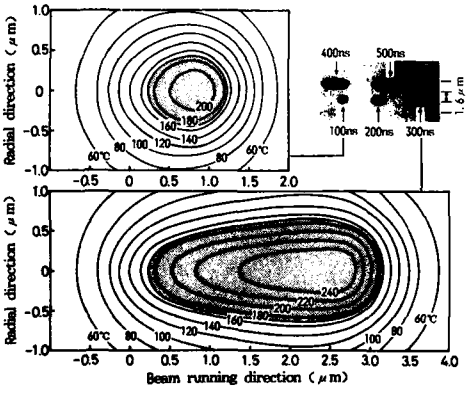


FIG. 3. Calculated distribution of maximum temperature (isothermal line) and a domain shape (hatched region). Laser power is 8 mW, pulse width 300 ns, and linear velocity 9 m/s.

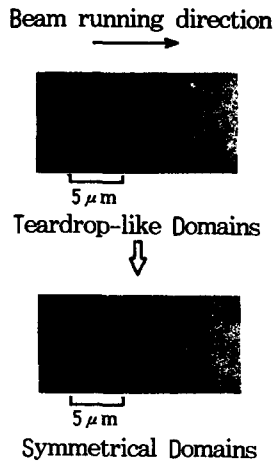


FIG. 4. Teardroplike shaped domains and symmetrical domains recorded with a modified pulse.

domain shapes are teardroplike whose front is sharp, as shown in Figs. 3 and 4. This nonsymmetrical shape causes an unexpected timing shift of edge detection because of the different signal amplitude of each side edge of one domain. Moreover, it was found that the domain width decreases with decreasing pulse width, as shown by the solid circles in Fig. 5. This characteristic also causes a drastic change in read-out signal amplitude and finally causes a timing shift of edge detection at a constant detection threshold.

Based on such a calculation, it was understood that the teardroplike domain shape is caused by the teardroplike temperature distribution. At the start of the laser pulse the temperature does not increase enough owing to a heat diffusion to the surrounding area, while near the end of a pulse the temperature becomes higher owing to a heat transfer from the front. Moreover, in the short-pulse case, laser irradiation stops before the temperature is raised enough, and then small domains are formed. The calculated dependence of the domain width on the pulse width is shown by a broken line in Fig. 5, which explains a behavior of experimental points very well.

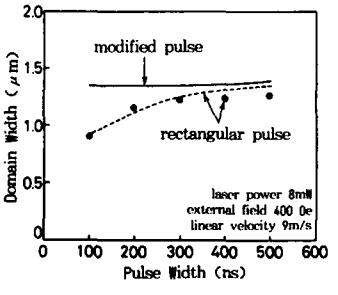


FIG. 5. Filled circles are observed domain width, and broken line is the calculated one recorded with a rectangular pulse. The solid line is a calculated result for the modified pulse case.

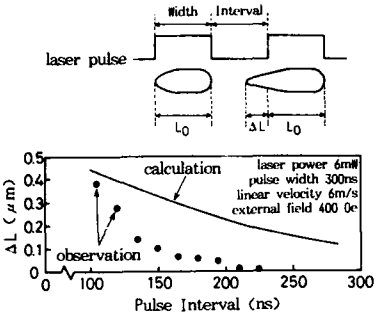


FIG. 6. Difference between the first domain length L_0 and the second one ΔL as a function of pulse interval: filled circles are observed values and the solid line is the calculated result.

These characteristics can be corrected by changing a temperature distribution in a film. For this purpose, the modified laser pulse whose front intensity is higher than that of the rear was used. As a result, the teardroplike shape was corrected to the symmetrical one, as shown in Fig. 4. Moreover, in this case, the calculated domain widths are almost constant for any pulse width, as shown by a thick line in Fig. 5. Therefore, by using this technique, an arbitrary domain shape can be corrected to the suitable shape favorable to the domain-edge recording.

C. Domain length change due to a thermal correlation

In an actual operating case, the recording is done by successive laser pulses. When the time interval between two pulses is short, the second domain is affected by a heat flow from the first heat pulse. This leads to an increase in the second domain length. Figure 6 shows the difference between the length of the first domain L_0 and second domain ΔL plotted against the pulse interval. In this figure, filled circles show observed values, and a solid line shows calculated results, respectively. In this case, increase of the domain length with the pulse interval causes a timing shift of edge detection. This characteristic depends upon a large thermal conductivity of the TbFeCo film.

IV. CONCLUSIONS

Shapes and sizes of recorded domains were simulated by a domain formation model using a heat-transfer calculation for establishing high-density domain-edge recording. By applying this analysis to an actual disk, a teardroplike domain shape could be analyzed, which sometimes causes a timing shift of edge detection. This shape is made to be symmetric by using a modified laser pulse. After this correction, the domain width becomes independent of the laser pulse width. It was also found that, in the successive pulse case, the nucleation of a second domain was affected by a heat flow from the first heat pulse. Such a simulation is very useful for investigating a control method of recorded domains.

ACKNOWLEDGMENTS

The authors would like to thank Professor S. Chikazumi, Keio University, and Dr. Y. Sugita, Hitachi Ltd., for fruitful discussions.

[1] M. Ojima, A. Saito, T. Kaku, and Y. Tsunoda, Soc. Photo-Opt. Instrum. Eng. Proc. **529**, 12 (1986).
[2] M. Takahashi, T. Niihara, H. Sukeda, T. Maeda, and N. Ohta, in Intermag'87 (BB-03) (to be published).
[3] C. Konno, M. Saji, N. Sagawa, and Y. Umetani, Proceedings of the Fall Joint Computer Conference, November 2–8, 1986.

A study of the thermal switching behavior in GdTbFe magneto-optic films using two laser beams

F. J. A. M. Greidanus, W. F. Godlieb, and P. M. L. O. Scholte
Philips Research Laboratories, P. O. Box 80000, 5600 JA Eindhoven, The Netherlands

An understanding of the thermal switching behavior of thin magneto-optic films is of primary importance for memory applications. We studied the formation of large domains induced by locally heating a GdTbFe layer with a krypton laser (753 nm) in a static magnetic field. The switching of the perpendicular magnetization was monitored in a small area of the larger krypton-laser-irradiated area by measuring the change in Kerr effect with a semiconductor laser (820 nm). It is observed that the switching is delayed with respect to the start of the heating pulse. There are strong indications that the delayed magnetization reversal starts simultaneously over the entire area of the heated spot and is followed by a small domain expansion.

I. INTRODUCTION

At present amorphous rare-earth (RE) transition-metal (TM) alloys are considered as most promising for applications in magneto-optic (MO) recording. Although their feasibility for MO recording has been shown (see, for example, Ref. 1), problems related to corrosion and structural relaxation, which lead to long-term instability, have not yet been completely solved. In these layers information is written by locally heating a small area (typically 1 μm^2) with a semiconductor laser, and switching the perpendicular magnetization by means of an external magnetic field. Micromagnetic theories in which this switching behavior is described have been given by various authors.[2–4] Experimental studies, however, are greatly hampered by the small spatial areas and short time scales involved. Recently Shieh *et al.*[5] were able to study domain growth in amorphous MO films using a high-speed magneto-optic sampling camera.

The present paper describes an apparatus used to study the formation of large domains in MO layers by means of two lasers. A high-power krypton laser spot ($\lambda_1 = 753$ nm, e^{-1} radius approximately 7 μm) is used to locally heat the magnetic layer in an external magnetic field. The response of the magnetization to changes in temperature and external field is monitored by measuring the Kerr effect in a smaller spot ($\lambda_2 = 820$ nm, e^{-1} radius approximately 0.6 μm) inside the larger heated area with a semiconductor laser.

II. EXPERIMENT

Figure 1 gives an outline of the experimental apparatus. It is a modification of an apparatus designed by van der Poel[6] for the study of rapid crystallization of thin solid films. A collimated beam of light (krypton laser λ_1) controlled by means of an acousto-optic modulator is focused onto the sample, which is heated by the partially absorbed light. A second beam (semiconductor laser λ_2) is focused into a small spot inside the larger heated area on the sample. This laser is always operated at a very low light level to avoid any influence on the measurements. Due to the Kerr effect in the MO layer, the polarization of the semiconductor laser light is rotated. The rotation has an offset of 2.6° because of a Faraday rotator placed in front of the objective lens. The rotated component is deflected by a polarizing beam splitter (PBS_1), while the remaining light is used for focusing and observation of the laser spots. To separate the light reflected from the probe laser and the heating laser, a wave plate is inserted in the light path which rotates the probe-laser light by 90°, keeping the polarization of the heating-laser light unaffected since it is rotated 180°. A second polarizing beam splitter (PBS_2) deflects the heating-laser light so that only light from the probe laser reaches the photomultiplier. Here, the rotated component, which is a measure of the magnitude of the local Kerr effect, is detected. The final separation between the heating beam and probe beam is achieved by means of interference filters. The relative positions of the two spots can be monitored with a camera and the objective lens–MO film distance is kept constant within the depth of focus of the probe spot by means of a Foucault knife edge method.

The sample studied is a GdTbFe layer made by magnetron sputtering on a glass substrate. The MO layer has a thickness of 44 nm and is covered with a 30-nm aluminum

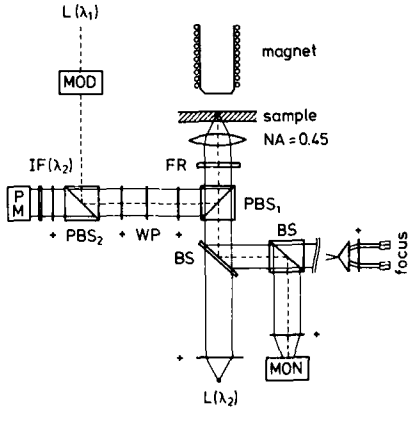


FIG. 1. Schematic drawing of the experimental setup. $L(\lambda_1)$:Laser emitting at 753 nm. $L(\lambda_2)$:Laser emitting at 820 nm. PM:Photomultiplier (RCA C31034). $IF(\lambda_2)$:Interference filter transmitting at 820 nm. BS:Beam splitter. PBS:Polarizing beam splitter. Mon:Monitor. Mod:Acousto-optic modulator. WP:Waveplate ($n\lambda$ for 753 nm, m $1/2\lambda$ for 820 nm). FR:Faraday rotator ($2\theta_f = 2.6°$).

 0021-8979/88/083841-03$02.40 © 1988 American Institute of Physics

protection/reflection layer. The GdTbFe layer has a perpendicular anisotropy and a compensation point below room temperature.

In Ref. 6 a simple model for the thermal behavior of a thin layer on a substrate subject to a laser pulse is discussed. It is shown that the temperature increase in the center of the heating spot, measured from the beginning of the heating pulse, is given by

$$\Delta T = (\alpha P/\pi^{3/2}\lambda\rho_0)\arctan\sqrt{4Dt/\rho_0^2}. \quad (1)$$

Here ρ_0 is the e^{-1} radius of the pulsed Gaussian heat source, and λ and D are the heat conductivity and coefficient of heat diffusion of the substrate, respectively. α is the absorbed fraction of the power, P, incident on the film. Only diffusion in the substrate is taken into account. Radial diffusion effects in the metallic layer are neglected. In our experiment the appropriate values are $\rho_0 = 7.0\ \mu$m, $D = 4.8\times10^{-7}$ m^2/s, $\lambda = 1.10$ W/mK, and $\alpha = 0.54$. Half of the temperature rise is realized in a time $t_1 = \rho_0^2/4D$, which amounts to $t_1 = 26\ \mu$s in our case. In about $5t_1$, which would amount to 130 μs, the temperature has risen to about 75% of its final value. By monitoring the change of the magnitude of the Kerr effect, as measured by the probe beam after the start of a heating pulse, it is found that the temperature rise slows down in times of about 100–300 μs. We regard this to be a satisfactory agreement in view of the simple model.

III. MEASUREMENTS

Figure 2 shows a series of hysteresis loops, measured with the setup described. The external magnetic field was varied slowly while the spot area was kept at an equilibrium temperature determined by the power of the heating beam. The Kerr effect was simultaneously measured with the probe spot. The squareness of the hysteresis loops indicates a perpendicular anisotropy at all temperatures. At the highest laser powers of the heating beam the Curie temperature is approached. In Fig. 3 the coercive field obtained from the hysteresis loops in Fig. 2 is shown as a function of heating-laser power. The rapid decrease at higher temperatures is clearly observed. The functional dependence, however, proved to be somewhat dependent on the position on the sample, which may be due for instance to compositional variations.

In a second set of experiments we studied the switching

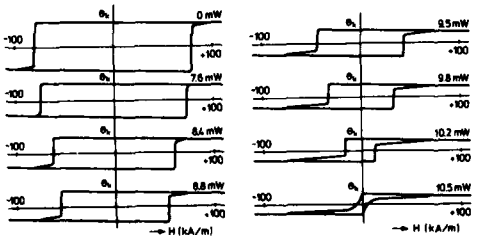


FIG. 2. Kerr rotation as a function of external magnetic field, measured at $\lambda_2 = 820$ nm, for various values of the excitation power ($\lambda_1 = 753$ nm).

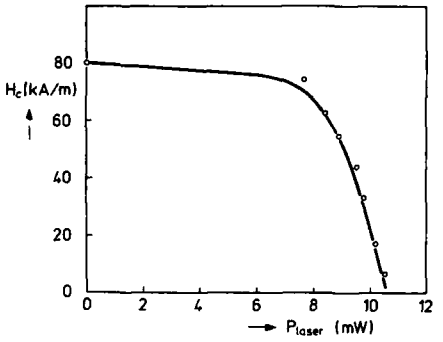


FIG. 3. Coercive field, obtained form the hysteresis loops shown in Fig. 2, as a function of laser power. The drawn line is a guide to the eye.

behavior around the coercive field. At a time t_i the heating laser is switched on while the Kerr rotation is monitored with the probe laser. Due to the heating induced by the absorbed power, the magnitude of the Kerr effect decreases. After a certain delay time t_d the Kerr effect changes sign due to a magnetization reversal in the small spot. At a time t_f the heating power is switched off and the magnitude of the Kerr effect increases by the same magnitude as at time t_i. Surprisingly the delay times t_d varied strongly as a function of applied field and heating-laser power. Delay times, measured at the same position on the sample as the hysteresis loops of Fig. 2, are shown in Fig. 4 as a function of field for various powers of the heating laser. Every data point shown is an average of 10 measurements. Under these conditions the delay times t_d vary from 200 μs to 2 s. Like the hysteresis measurements these data also depend somewhat on the posi-

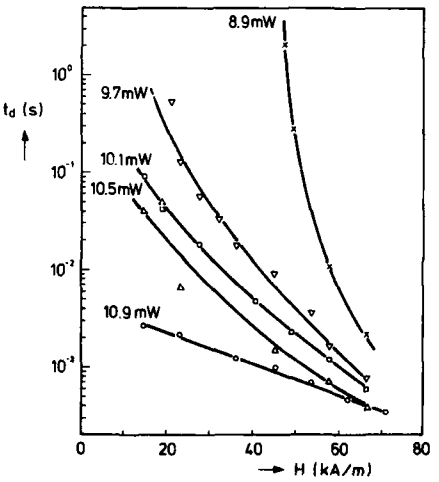


FIG. 4. Delay times as a function of the external field, measured for various powers of the pump beam. Drawn lines are guides to the eye.

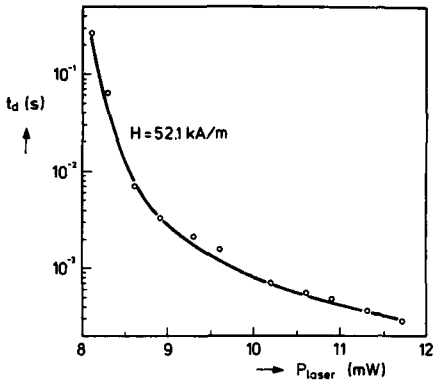


FIG. 5. Delay times as a function of power of the large pump laser beam, for a fixed value of the external field. The drawn line is a guide to the eye.

tion of the heating spot on the sample. At some positions, much shorter delay times could be obtained. Finally, in Fig. 5, delay times as a function of heating laser power at a fixed value of the external field are shown.

IV. DISCUSSION AND CONCLUSIONS

From the measurements discussed in Sec. III it appears that magnetization reversal within the area of the probe spot takes place after a time t_d, which, under specific conditions (low field, low heating-laser power), may range up to seconds. However, it cannot be inferred from the data whether nucleation starts at an earlier moment in the heated region outside the probe spot. The observed magnetization reversal would then correspond to a domain wall passing under the small laser spot. To investigate this we performed a number of experiments in which the heating beam was switched off just before the observation of magnetization reversal with the probe laser was expected to occur. Subsequently the heated area was investigated with a polarization microscope. No sign of domain nucleation inside the heated area was ever found. In a second experiment the probe spot was slowly moved towards the edge of the heated area while the delay time measurements were repeated. No significant changes in delay times were found until the edge was reached. Switching always occurred instantaneously on the time scale of the experiments. When the edge was reached the delay time increased and switching no longer occurred instantaneously, indicating a domain wall passing slowly through the spot. Although both experiments described above may not be conclusive, they strongly support a picture in which magnetization reversal starts in an area of the size of the heating-laser spot, followed by a small expansion of the domain created.

From Eq. (1) it is clear that the temperature slowly approaches its equilibrium value. To investigate whether this could be the origin of the delayed switching we did the following: At relatively long times compared to t_1, Eq. (1) can be approximated and a linear expression for $1/P$ as a function of $1/\sqrt{t}$ is found. The slope of the function is given by

$$\frac{\Delta(1/P)}{\Delta(1/\sqrt{t})} = \frac{-\alpha/\Delta T}{2\lambda D^{1/2}\pi^{3/2}}. \tag{2}$$

It can be shown[7] that this expression is more generally valid than Eq. (1). By plotting values of $1/P$ vs $1/\sqrt{t}$ as obtained from Fig. 5 and by adopting values of the constants given in Sec. II, we calculate a temperature rise of $\Delta T = 93 \pm 10$ K. This value is in reasonable agreement with the switching temperature for this measurement estimated form Fig. 3. This agreement indicates that an important contribution to the observed delay times comes from thermal effects: It takes a finite time, which depends on the heating power, to reach the switching temperature. However, other effects may contribute as well. When measuring hysteresis curves like shown in Fig. 2 we observed time-dependent effects, indicating that magnetic processes may also be of importance. With respect to delayed switching it may be remarked that similar phenomena have been observed by Verhulst *et al.*[8] in photomagnetic garnets. They also observed a delayed switching, which they characterized with a so-called breakfree time t_{bf}. A possible mechanism may be that after nucleation the domain wall moves with a low velocity. After a certain time this velocity becomes unstable and the domain wall moves much faster, immediately leading to the observed magnetization reversal.

The effects discussed in this paper are of importance for the understanding of the behavior of RE-TM layers used for MO recording.

ACKNOWLEDGMENTS

We thank B. A. J. Jacobs and A. H. M. Holtslag for stimulating discussions and are much indebted to U. Enz for useful suggestions and clarifying remarks. The sample was kindly prepared by H. J. H. Wilting of Philips and DuPont Optical Company.

[1] M. Hartmann, J. Braat, and B. Jacobs, IEEE Trans. Magn. MAG-20, 1013 (1984).
[2] B. G. Huth, IBM J. Res. Develop. 18, 100 (1974).
[3] M. Mansuripur and G. A. N. Connell, J. Appl. Phys. 55, 3049 (1984).
[4] P. Hansen, J. Appl. Phys. 62, 216 (1987).
[5] H.-P. D. Shieh and M. H. Kryder, J. Appl. Phys. 61, 1108 (1987).
[6] C. J. v.d. Poel, J. Mater. Res. (to be published).
[7] A. H. M. Holtslag (private communication).
[8] A. G. H. Verhulst, T. Holtwijk, W. Lems, and U. Enz, IEEE Trans. Magn. MAG-7, 729 (1971).

Performance of magneto-optical recording media with direct overwrite capability

M. D. Schultz, H-P. D. Shieh, and M. H. Kryder
Department of Electrical and Computer Engineering, Carnegie Mellon University, Pittsburgh, Pennsylvania 15213

The feasibility of directly overwriting certain magneto-optical recording materials without the use of an external magnetic field has recently been demonstrated in our laboratory. In this report experiments to evaluate the beam positioning accuracy necessary for successful direct overwrite, the effects of static bias fields on the direct overwrite process, and the possibility of writing and erasing domains of arbitrary length on direct-overwrite materials are discussed. The data show that an error in beam positioning of at least 75% of the nominal domain diameter is tolerable for complete erasure without an external applied field. Application of particular values of dc bias field is shown to decrease the pulse width required to write while only slightly narrowing the allowed margin of erase pulse width, thus raising the allowed data rate.

I. INTRODUCTION

Magneto-optical (MO) recording is a promising alternative technology to conventional magnetic recording for data storage applications. It offers several advantages, the most prominent of which are very high density (500 Mbytes/side on a 5-in. disk) and noncontact high-reliability operation. Some of the most promising materials for MO recording are the direct-overwrite rare-earth–transition-metal (RE-TM) thin films.[1] Conventional MO materials require the application of an external bias field to write the material and a reversed bias field to erase the material. The result is a medium that is difficult to overwrite at high data rates due to the constraints that the field requirements impose on the system designers. We have found that RE-TM thin films with compensation temperature a few tens of degrees higher than room temperature have direct overwrite capability. Magnetic domains of μm size can be written and erased without the presence of an external magnetic field in MO media such as TbCo, TbGdCo, TbFeCo, and GdTbFeCo thin films. A properly focused laser pulse with a duration of 100 ns at 10–15 mW of power amplitude will create stable magnetic domains in these materials. The erasing of the domains is achieved by pulsing the laser at the same power amplitude but with a shorter pulse duration, typically only one-half of that used for writing. Alternatively, the same pulse duration may be used with a lower power amplitude. Therefore, a 10-MHz data rate on a single channel is achievable. Previous reports on these materials described the operating margins with respect to pulse width, power amplitude, and ambient temperature.[2] The experimental results have been subsequently predicted theoretically by Hansen.[3,4] In this report, studies of the effects of beam position accuracy and static bias fields on the materials are described. The ability to write and erase domains of arbitrary length is discussed as well.

II. EXPERIMENTS AND DISCUSSION

A. Erase accuracy

One area of concern for direct-overwrite media is the accuracy requirement for the erase laser beam. Erasure of a written domain requires that the laser be fired again (with a lower total energy) into the center of the written domain. An experiment was designed to determine just what exactly "into the center" meant in terms of what the allowed "miss" or off-center distance would be. The apparatus used to conduct this experiment is shown in Fig. 1. A mercury arc lamp is used to illuminate the sample, with the writing laser beam superimposed with the use of a dielectric mirror tuned to the wavelength of the laser beam (790 nm).[5] While the mercury arc lamp is projected onto a large area, a series of lenses terminating in a 100×, 0.90 numerical aperture lens is used to focus the laser beam to a spot approximately 1 μm in

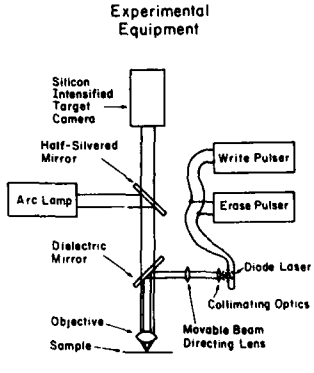


FIG. 1. Experimental setup for measuring beam positioning error.

 0021-8979/88/083844-03$02.40 © 1988 American Institute of Physics

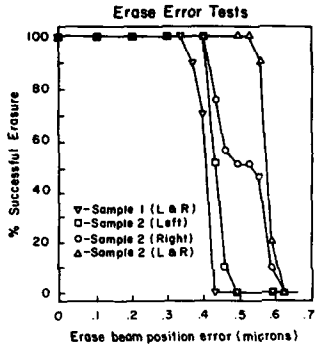


FIG. 2. Plot of percentage successful erasure vs beam positioning error.

diameter when the sample is in focus for observation. The movable beam-directing lens allowed positioning of the beam spot on the media to an accuracy of $\frac{1}{10}$ μm with little distortion of the beam.

The experiment was conducted by writing a domain, moving the beam spot to the left a measured amount, and then attempting to erase the domain. Upon successful erasure, a domain was then written at the new position. The spot was then moved to the right the same measured amount and erasure again was attempted. This cycle was completed at least 10 times for each measurement of beam motion. The resulting data for a GdTbFeCo and a TbCo sample, whose magnetic properties have been described elsewhere,[2] is shown in Fig. 2. The percentage of trials that produced successful erasure is plotted versus the distance between the center of the erase beam spot and the center of the write beam spot (erase position error). Successful erasure was determined visually, with any visible remnants of the domain constituting unsuccessful erasure. Sample 1 (GdTbFeCo) and sample 2 (TbCo) had nominal domain diameters of 0.8 and 1 μm, respectively.

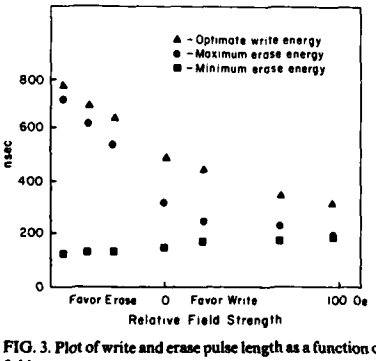


FIG. 3. Plot of write and erase pulse length as a function of dc bias magnetic field.

The data show that if the beam was 0.35 μm or less from the center of the domain in sample 1, erasure occurred 100% of the time. For sample 2, the tolerable error in positioning depended upon whether the beam was being moved to the left of center or to the right of center. To the right, erasure began to fail at 0.43 μm, while to the left, erasure began to fail at 0.57 μm. This asymmetry is not due to material imperfection, as it was independent of location on the sample. We hypothesize that it is due to an asymmetry in the profile of the laser beam. If the intensity profile of the laser beam is not concentric and the most intense point is off center to the right, this asymmetry could occur. Assuming the domain nucleates first at the most intense spot, but grows to fill a region encircled by a specific constant intensity contour, the domain would always be centered to the left of the most intense spot in the laser beam. Thus, assuming it is necessary to nucleate a second domain within the first to cause erasure, the margin for error to the right would be less than the margin for error to the left. Sample 1 showed no such asymmetry, but this could be due to the smaller nominal domain diameter.

The steep slope of the error probability versus beam position curves during the transition from 100% to 0% erasure provides further information. Such a steep slope indicates that the written domain is very consistent in size and position from one repetition to the next, since errors in domain-wall position would produce a shallow slope in the error probability curve. The steep slope of the data allows us to confidently say that even if the worst-case error is taken as being the maximum tolerable, a beam position error in excess of 75% of the nominal written domain radius is acceptable in these films.

B. Bias-field effects

The effects of bias fields on the direct overwrite process in these materials were studied. These fields were dc bias, unchanging for write or erase, and thus do not greatly complicate system design. Direct overwrite materials normally require a smaller laser energy for erase than for write. We hypothesized that by applying a bias field it might be possible to write and erase with the same laser pulse energy. The data for the experiment are shown in Fig. 3. The maximum field applied in the test was approximately 100 Oe.

As the data show, it is possible to bring the erase energy requirement very close to the write energy requirement with a bias field that favors the erase process, but only at the expense of an increased write energy. Such an increase in write energy lowers the data rate significantly and thus is unacceptable in a system. On the other hand, we found that fields which favored the writing of the domain significantly reduced the amount of energy required to write the domain, but narrowed the margin of allowed erase energy. Depending on the system requirements, such a narrowing might be tolerable when matched against the increased data rates gained by a lower write energy requirement. One other benefit of a small field to assist writing might be a reduction in domain irregularity and the associated readout noise.[6]

C. Variable length domains

Early reports on these direct-overwrite materials described only circular or near circular domains. If only circular domains may be used, the bit density and allowed coding and error correction schemes are more limited than those allowed in conventional magnetic recording. We have demonstrated that by using a rapidly pulsed (200-ns pulses) laser on a slowly moving sample, domains of arbitrary length can be written and erased without an external bias field. Selective erasure of portions of a long domain has been successfully accomplished at a reduced energy level as well. These experiments demonstrate the feasibility of using pulse-length modulated codes while still retaining direct-overwrite capability without an ac field.

III. CONCLUSION

The experiments described above show the feasibility of achieving direct overwrite in RE-TM magneto-optical thin films. The data demonstrate that an error in beam positioning of at least 75% of the nominal domain diameter is tolerable for successful erasure without an external field. The reduction of write pulse duration can be achieved by applying a dc field, with the effect on the erase laser pulse duration margin still allowing successful erasure. The demonstration of the writing and erasing of long stripe domains with no magnetic field indicates that the use of codes involving pulse width modulation may be possible.

Proof of the practicality of this scheme, however, is still difficult to develop using only static experiments on small samples of media. Thus work is currently underway to develop a disk tester which can write, read, and overwrite data on a moving disc. The data which will be collected using this system will be very useful in furthering the knowledge of direct overwrite in magneto-optical materials and systems.

ACKNOWLEDGMENT

One of us (H-P.D.S.) would like to acknowledge the support of an IBM Postdoctoral Fellowship.

[1]H-P. D. Shieh and M. H. Kryder, Appl. Phys. Lett. **49**, 473 (1986).
[2]H-P. D. Shieh and M. H. Kryder, IEEE Trans. Magn. MAG-23, 171 (1987).
[3]P. Hansen, Appl. Phys. Lett. **50**, 356 (1987).
[4]P. Hansen, J. Appl. Phys. **62**, 216 (1987).
[5]M. H. Kryder, W. H. Meiklejohn, and R. E. Skoda, Proc. Soc. Photo-Opt. Instrum. Eng. Conf. Opt. Storage Media **420**, 236 (1983).
[6]S. Takayama, T. Niihara, K. Kaneko, Y. Sugita, and M. Ojima, J. Appl. Phys. **61**, 2610 (1987).

Design and performance of magnetic heads for magneto-optic recording with magnetic field modulation

J. J. M. Ruigrok, F. J. A. M. Greidanus, W. F. Godlieb, and J. H. M. Spruit
Philips Research Laboratories, P. O. Box 80000, 5600 JA Eindhoven, The Netherlands

In magneto-optic recording, the most direct way to overwrite stored information is to switch the magnetization in a laser-heated region of the magneto-optic layer by means of an alternating magnetic field generated by a magnetic head. The heat dissipation in the head and the necessary voltage and current amplitude associated with fast switching, the desired high field, and a large head-to-medium distance make high demands upon the head design and the current source, respectively. Design criteria and numerical and experimental results for some circularly symmetric head configurations are presented.

I. INTRODUCTION

In conventional magneto-optic (MO) recording data are written by locally switching the magnetization with a modulated laser beam. Erasure of complete sectors on the disk, by switching the magnetization into the initial direction, is necessary before new data can be recorded. Several methods to overcome this drawback have been suggested.[1–3] A direct approach is to modulate the magnetic field instead of the laser. It is the purpose of the present paper to discuss the design of magnetic heads for this type of MO recording (MOH'S).

II. THEORETICAL CONSIDERATIONS

A. Basic principles and theoretical considerations

Although fast switching times can in principle be achieved by means of an air coil, cf. Figs. 1(a) and 1(f), it is clear that in order to achieve high fields at a certain distance from the head, it is necessary to use soft magnetic material. For the filamentary one-turn coil placed at the surface of a soft magnetic block [see Fig. 1(b)] the field at a certain distance from the block increases by a factor of 2 compared to the air coil. This follows easily from $\oint \mathbf{H}\cdot d\mathbf{r} = NI$ and $\mathbf{H} \to \mathbf{0}$ in the magnetic material and the fact that the shape of the field lines above the magnetic block is unaffected by the presence of the soft magnetic block. For a coil embedded in a soft magnetic block, as shown in Fig. 1(c), this factor will be larger.

The flux density $\mathbf{B}$ just above the soft magnetic block at the center of the coil is maximal when the magnetic reluctance for the return flux is minimal, because the potential drop $\int \mathbf{H}\cdot d\mathbf{r}$ over the return path is then evidently minimal. This situation is obtained for a circular symmetric structure.

The field above the center of the coil decreases more than proportionally with the distance h to the coil/soft-magnetic-block surface, when h exceeds one to two times the radius, r_c, of the cross-sectional area enclosed by the coil. This indicates that h must not be chosen larger than $2r_c$.

It is readily derived for an air coil that a maximum field is obtained (with a given number of ampere turns), when $r_{ci} = h_i\sqrt{2}$ for each turn i. This implies that the air coil is coniform (apex angle 109.5°) and the maximum field is located in the (virtual) apex of the cone. From our numerical calculations it followed that this is not true for coils containing soft magnetic material. The criterion of the minimal number of ampere turns is not the only one. Equally important is the necessary voltage (see Sec. II B) which, for a pure inductance, is inversely proportional to the switching time τ according to $\hat{V} = 2L\hat{I}/\tau$ ($V = -N\,d\Phi/dt \equiv L\,dI/dt$) where Φ is the average flux linked by the windings of the coil, L the self-inductance of the coil, and $2\hat{I}$ the jump in the trapezoidal current of Fig. 2.

B. Design criteria

The demands on the current source needed to drive the MOH are mainly determined by the product $\hat{V}\hat{I}$ (the ratio $\hat{V}/\hat{I}$ is controlled by a transformer), while the operation of the MOH itself is mainly limited by the power dissipation $P = \langle VI\rangle$ ($\langle\ \rangle$ means average) in the head. It is readily derived in the case of a sinusoidal current that

$$\hat{V}\hat{I}\,2\pi\hat{I}^2L/T, \tag{1}$$

$$P = \hat{V}\hat{I}/(2Q) = \pi f\hat{I}^2L/Q, \tag{2}$$

where $T \equiv 1/f$ is the peroid and $Q \equiv 2\pi fL/R$ the quality factor of the head at the frequency f. The resistance $R = R_{cu} + R_{\mu''}$ of the MOH accounts for copper losses in the coil (including eddy-current losses) and dissipation in the core (corresponding to a nonzero imaginary part in the complex permeability $\mu = \mu' - j\mu''$).

For the trapezoidal current,

$$\hat{V}\hat{I} = 2\hat{I}^2L/\tau. \tag{3}$$

For a triangular ($\tau = T/2$) current with $f = 2.5$ MHz or, more generally, a trapezoidal current with $\tau = 200$ ns, as well as a sinusoidal current with $f = 1.59$ MHz, we have equal $\hat{V}\hat{I}$ because of Eqs. (1) and (3).

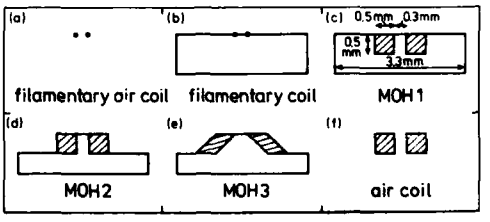


FIG. 1. Cross sections of the circular symmetric MOH's.

 0021-8979/88/083847-03$02.40 © 1988 American Institute of Physics

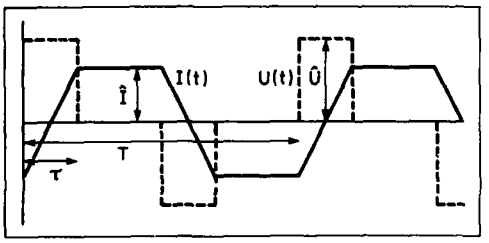


FIG. 2. Trapezoidal drive current and resulting induction voltage.

From Eq. (2) and some formulas from Fourier analysis, general expressions follow for the (average) power losses in the case of periodic and aperiodic currents. Omitting a possible dc power content, one obtains

$$P = \pi \sum_{n=1}^{\infty} f_n \hat{I}_n^2 L(f_n)/Q(f_n) \tag{4a}$$

or

$$P = \pi \int_0^{\infty} f |I'(f)|^2 [L(f)/Q(f)]\, df, \tag{4b}$$

where $\hat{I}_n$ is the amplitude of the nth harmonic component of the periodic current and

$$I'(f) \equiv (2/\sqrt{t_2 - t_1}) \int_{t_1}^{t_2} I(t) \exp(-j2\pi f t) dt .$$

Since L is almost constant [as was implicitly assumed in Eq. (3)] and since Q usually decreases with f [except at lower frequencies, because of $R_{cu}(f) = \text{const}$] and because of the factor f or $1/\tau$ in the equations, the dissipation in the MOH and the demands on the current source increase rapidly with the frequency (or higher harmonic content) of the current.

C. Scaling laws

In Sec. III we will present results of numerical calculations on some actual head designs. All numerical calculations will be carried out for $h = 0.1$ mm. When the dimensions of the head and mounting plate scale up with the distance from the medium to the MOH surface, h, then it is easily derived (eddy-current effects neglected) that

$$L \sim h, \tag{5a}$$

$$R_{cu} \sim 1/h, \tag{5b}$$

$$R_{\mu^-} \sim h, \tag{5c}$$

$$\hat{V}\hat{I} \sim f h^3 H^2, \tag{5d}$$

$$\Delta T \sim P/h^2 \sim f h H^2/Q(f), \tag{5e}$$

where ΔT is the rise in temperature of the MOH (disregarding radiation and convection). It is not necessary to scale up the mounting plate, when it is large compared to the MOH. The proportionality constants follow from our numerical results in Sec. III and/or experimental results in Sec. IV and can also be roughly estimated from simplified models for MOHs.

For a filamentary one-turn air coil $r_c = h$ for minimal $\hat{V}\hat{I}$ and $r_c = h\sqrt{5}$ for minimal ΔT (changes in Q neglected). From Eqs. (5d) and (5e) it is clear that one would like to operate the MOH as near to the MO layer as possible.

III. NUMERICAL CALCULATIONS

In this section we will present the results of two-dimensional magnetostatic calculations based on the finite-element package MAGGY2.[4] Self-inductance values are obtained by post-processing. For the calculations we took the inner coil radius $r_c = \frac{3}{2}h$. In Fig. 1, three MOH's are shown. Calculated values of the self-inductance per turn, L/N^2, and the number of ampere turns, NI, necessary to create a field of 20 kA/m at a distance of $h = 0.1$ mm for these geometries, are listed in Table I. For comparison the same parameters for the coil without any magnetic material (also shown in Fig. 1) are listed. Although the self-inductance of such an air coil is of course much lower, the number of ampere turns necessary to create a field of 20 kA/m is much larger than that for the heads containing magnetic material; hence $\hat{V}\hat{I}$ (also listed, for $\tau = 200$ ns, in Table I) is larger, in accordance with the discussion in Sec. II A. From the numbers we can conclude that the heads MOH1 and MOH2 in Fig. 1 offer fairly optimal designs. We could not find an improvement by varying the shape of the central pole and the yoke. On the contrary, this resulted in a deterioration of the performance, as illustrated by the calculation for the head MOH3. Finally Fig. 3(a) shows the flux and equifield lines generated by the head MOH1. An advantage of choosing $h = r_c$ to $2r_c$ is that H_z is almost independent of r. For this calculation, as well as for all the other calculations discussed in this section, we took a relative permeability of $\mu = 800$, but any μ larger than 100 gives approximately the same results.

IV. EXPERIMENTAL RESULTS

To study the actual performance of MOH's we constructed several heads of the type MOH1 and MOH2 from MnZn-ferrite single crystals. Measured values of L/N^2 ($N = 100$ for MOH1, $N = 56$ for MOH2), Q and NI (necessary to generate a field of 20 kA/m at a distance of 0.1 mm) and the resulting $\hat{V}\hat{I}$ are indicated by an asterisk in Table I. L and R were measured with a Hewlett Packard LF4192A impedance bridge. The above-mentioned NI was obtained by measuring the magnetic field strength by means of a homemade magnetoresistance probe. The small discrepancies between the results of the calculations and measurements mainly originate from deviations in the actual design.

TABLE I. Calculations and measurements (*) on MOH's. NI and $\hat{V}\hat{I}$ are the values necessary to generate a field of 20 kA/m at 0.1 mm. L and Q are measured at 1 MHz.

	L/N^2 (nH)	Q	NI (A turns)	$\hat{V}\hat{I}$ (VA)
MOH1	1.69	···	7.86	1.04
	2.11*	20.3*	(7.35 ± 0.5)*	(1.14 ± 0.16)*
MOH2	1.60	···	7.92	1.00
	1.78*	15.3*	(7.10 ± 0.5)*	(0.90 ± 0.14)*
MOH3	2.35	···	9.74	2.23
Aircoil	0.41	···	36.1	5.39

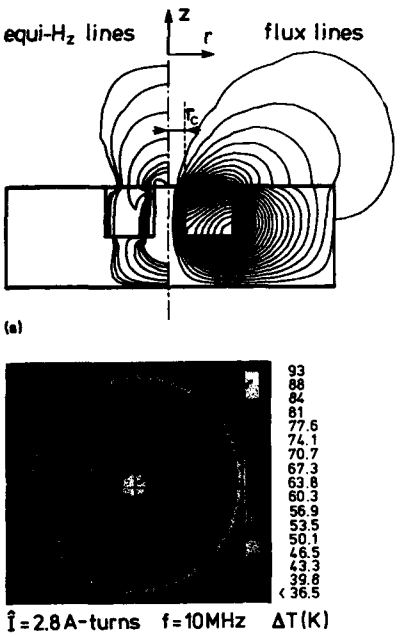


FIG. 3. (a) Equifield lines and flux lines of MOH1. The lines correspond to H_z = 3.5, 2, 1.6, 1.2, 0.8, 0.4, 0.16, 0.08, and 0.04 kA/m, respectively, per ampere turn. (b) Infrared picture of MOH1.

The temperature rise in the MOH is of great importance in practice. Temperature profiles as a function of current and frequency were determined by means of high-resolution infrared photography. A representative example is shown in Fig. 3(b). Here it can be seen that the strongest temperature rise ΔT is present in the central pole, where the core losses are maximal. In Fig. 4, ΔT in the central pole is plotted as a function of current and frequency. The approximately quadratic increase with I (i.e., H) and increase with f are as expected from Eq. (5e). At an amplitude of 8 ampere turns and a frequency of 1 MHz a temperature rise of approximately $\Delta T = 20$ K is measured. This is in every respect satisfactory for practical applications.

To demonstrate the performance of these types of MOH's and of MO recording with magnetic field modulation, we measured carrier-to-noise ratios (CNR) on a GdTbFe MO layer at a carrier frequency of 750 kHz, a resolution bandwidth RBW of 10 kHz, and a disk speed of 1.4 m/s. The noise was measured at some distance on both sides of the carrier. Writing was performed as a function of current using a laser power of 5.0 mW. The results are also shown in Fig. 4. It can be seen that the CNR reaches its maximum at 5.7 ampere turns, which, according to the calculations corresponds to a field of about 15 kA/m. Under the common conditions, i.e., a carrier frequency of 1 MHZ, a RBW of 30 kHz, and a disk speed of 5.0 m/s, a CNR of over 50 dB is obtained.

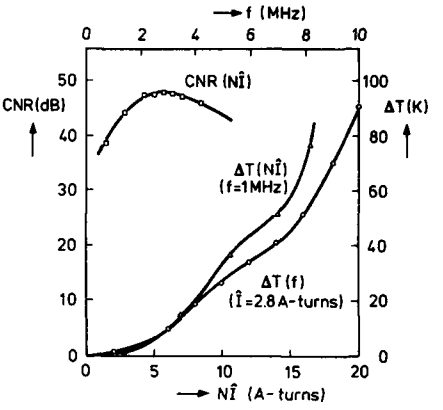


FIG. 4. Temperature rise at the surface of the central pole as a function of the frequency (upper scale) and the number of ampere turns, (lower scale), and the carrier-to-noise ratio at varying ampere turns.

V. SUMMARY AND CONCLUSIONS

In this paper we have discussed some requirements for MOH's. As a criterion for the best MOH, the one with the minimal $\hat{V}\hat{I}$ is used. Scaling laws are given for heads operating at different distances. Following the design rules, MOH's that meet the requirements have been constructed for operation at a small distance from the MO layer. Measurements on these MOH's confirm the numerically obtained results. Finally, it was shown that recording can satisfactorily be performed with the present MOH.

The change of $Q(f)$ with the material properties, head dimensions, and coil design and the consequences for the MOH will be the subject of a future paper.

ACKNOWLEDGMENTS

We thank B. Munneke for taking infrared pictures of the MOH's and H. J. F. Maas for his contribution to the hardware. Stimulating discussions with P. F. Bongers, U. Enz, and B. A. J. Jacobs are gratefully acknowledged.

[1] H. P. D. Shieh and M. H. Kryder, Appl. Phys. Lett. **49**, 473 (1986).
[2] M. Hartmann, J. Braat, and B. Jacobs, IEEE Trans. Magn. **MAG-20**, 1013 (1984).
[3] J. Saito, M. Sato, H. Matsumoto, and H. Akasaka, Jpn. Appl. Phys. **26**, Suppl. 26-4, 155 (1987).
[4] S. J. Polak, A. de Beer, A. Wachters, and J. S. van Welij, Int. J. Num. Methods Eng. **15**, 113 (1980).

Improvement of the *C/N* ratio and corrosivity of TbFeCo amorphous films by controlling their microstructure

M. Naoe and N. Kitamura
Department of Electrical and Electronic Engineering, Tokyo Institute of Technology, 2-12-1 O-okayama, Meguro-ku, Tokyo 152, Japan

H. Ito
Electronic Engineering Research Laboratory, Pioneer Electronic Corporation, 2610 4-chome Tokorozawa-shi, Saitama 359, Japan

The dependence of structural and magneto-optical (MO) properties of TbFeCo films on Ar pressure, deposition rate, and magnetic field have been investigated by using the facing-target sputtering (FTS) system. The films prepared at high deposition rate and/or with the plasma-free substrate did not have any appreciable columnar structure. The Kerr rotation angle of the films was as high as 0.37°. No significant change in the magneto-optical properties of the films was observed after exposing them to air for 250 days. MO disks fabricated by the FTS system had a high *C/N* ratio of 57 dB at a bit length of 5 μm.

I. INTRODUCTION

Rare-earth(RE)–transition-metal(TM) amorphous films are prominent candidates for erasable magneto-optical (MO) recording media. However, since their *C/N* ratio and corrosivity are still not satisfactory for practical application, improvements such as the addition of other elements[1-3] and coating of protective layers[4,5] have been attempted. Furthermore, the relationship[6-10] between microstructure and chemical, magnetic, and magneto-optical properties of the RE-TM films has been investigated.

It is difficult to prepare uniform, dense, and stable TbFeCo films by the conventional dc and rf magnetron sputtering (CMS) system. In the CMS system as shown in Fig. 1(a), the growing films can easily be damaged by bombardment of negative transition-metal ions and the elevated substrate temperature due to irradiation of high-energy γ electrons from targets.

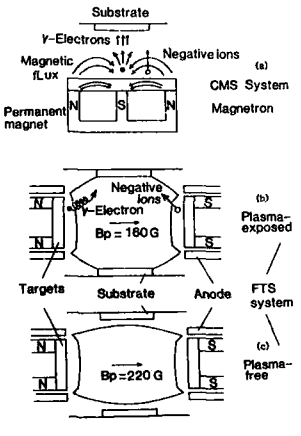


FIG. 1. Schematic diagrams of various sputtering systems: (a) CMS (magnetron), (b) plasma-exposed FTS, and (c) plasma-free FTS.

On the other hand, in the facing-targets sputtering (FTS) system, the bombardment of such ions and γ electrons to the growing films are suppressed by the effective plasma confinement. In this way, plasma-free sputtering with low substrate temperature and high deposition rate can be achieved. It was reported in previous papers[11,12] that the TbFeCo films prepared by the FTS system had a uniform and dense columnar structure and exhibited magnetization perpendicular to the film plane even at a deposition rate of up to 300 nm/min.

The state of the plasma confinement in the FTS system can be easily controlled by adjusting the magnetic field as shown in Figs. 1(b) and 1(c). The proper plasma confinement makes it possible to deposit uniform and stable TbFeCo films without apparent columnar structure on the plasma-free substrate.

In this study the microstructural and magneto-optical properties of the TbFeCo films prepared by using the FTS system at various deposition rates and magnetic fields have been investigated. In addition, the aging test of the TbFeCo films and estimation of read-write characteristics on the MO disks have been made.

II. EXPERIMENT

The FTS system used in this study had been already described in the previous papers.[11-13] The sputtering conditions are listed in Table I. Each of the facing targets consists of an $Fe_{90}Co_{10}$ alloy plate and pure Tb chips (composite

TABLE I. Sputtering conditions of TbFeCo amorphous films.

Residual gas pressure P_B	7×10^{-7} Torr
Argon gas pressure P_{Ar}	3.6 mTorr
Applied voltage	280–430 V
Discharge current	1.4–2.7 A
Deposition rate R_d	50–100 nm/min

 0021-8979/88/083850-03$02.40 © 1988 American Institute of Physics

target). For plasma confinement, the magnetic fields B_p of 160 and 220 G at the central position between the targets are applied normal to each target plane. The substrate holder is at a floating potential. Pyrex glass plate and pregrooved (12-in. diam) glass disks are used.

The film composition $Tb_x(Fe_{100-y}Co_y)_{100-x}$ was determined by x-ray fluorescence analysis. Transmission electron micrographs (TEM) and selected-area electron diffraction (SAED) patterns were observed by a JEM-2000FX microscope under an accelerated voltage of 200 kV and a resolution of 0.14 nm. SAED patterns are converted to a standard x-y format by a microdensitometer. The reflectivity, Kerr rotation angle, and coercivity were determined at a wavelength of 830 nm in an external magnetic field of up to 15 kOe at room temperature. The aging test was made by exposing the films in air for 250 days. In addition, the read-write characteristics of the MO disk using the TbFeCo film are estimated at the same wavelength of 830 nm.

III. RESULTS AND DISCUSSION

A. Microstructure

Figures 2, 3, and 4 show bright-field TEM micrographs, cross-sectional TEM micrographs, and selected-area electron diffraction (SAED) patterns, respectively. Panels (a), (b), and (c) in these figures correspond to the films prepared by CMS, plasma-exposed FTS, and plasma-free FTS systems, respectively. The sputtering conditions of these films are listed in Table II.



FIG. 2. Bright-field TEM micrographs of TbFeCo films: (a) CMS, (b) plasma-exposed FTS, and (c) plasma-free FTS.

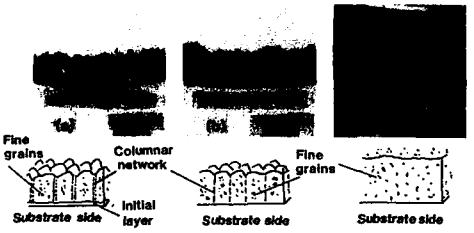


FIG. 3. Cross-sectional TEM micrographs and their schematic diagrams: (a) CMS, (b) plasma-exposed FTS, and (c) plasma-free FTS.



FIG. 4. Selected-area electron diffraction(SAED) patterns for films: (a) CMS, (b) plasma-exposed FTS, and (c) plasma-free FTS.

TABLE II. Sputtering conditions of films used for TEM observations.

Systems	CMS	FTS	
		Plasma exposed	Plasma free
P_B(Torr)	1×10^{-7}	1×10^{-6}	7×10^{-7}
P_{Ar}(mTorr)	6	5	3.6
R_d(nm/min)	50	50	100
B_p(G)	···	160	220
Targets	dual	composite	composite

As seen in Figs. 2 and 3, the film prepared by the CMS system consisted of an initial layer, a columnar network, and fine grains, the size of which is large and inhomogeneous. The film prepared by the plasma-exposed FTS system consisted of a columnar network and fine grains but did not have any initial layer. On the other hand, the film prepared by the plasma-free FTS system did not even have an appreciable columnar network and consisted of only very fine and nearly uniform grains. The schematic drawing in Fig. 3 illustrates the difference of microstructure among the three types of films.

The SAED patterns in Fig. 4 indicate that all specimen films are amorphous. In order to understand the SAED patterns, they were traced by the microdensitometer. The results are shown in Fig. 5. These tracings may be decomposed into the broad peaks as shown in Fig.6, corresponding to the drawing in Fig.3.

B. Aging test

The 170-nm-thick films with the composition of $Tb_{19.1}(Fe_{90.3}Co_{9.7})_{8.9}$ deposited on the glass substrate by the FTS system at P_{Ar} of 3.6 mTorr, R_d of 100 nm/min, and B_p of 160 G were used for the aging test. They were exposed in air for 250 days. The reflectivity R of the film decreased slightly to the extent of 4% but the Kerr rotation angle θ_K of about 0.28° and the coercivity H_c of greater than 12 kOe remained constant. In addition, an aging test of the films exposed at

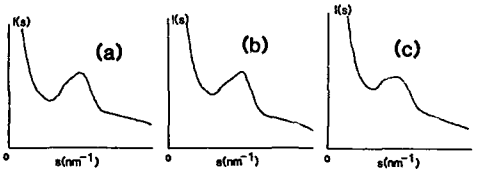


FIG. 5. Microdensitometer tracings of SAED patterns: (a) CMS, (b) plasma-exposed FTS, and (c) plasma-free FTS.

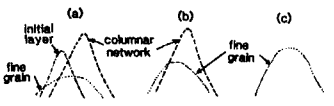


FIG. 6. Schematic decomposition of tracings.

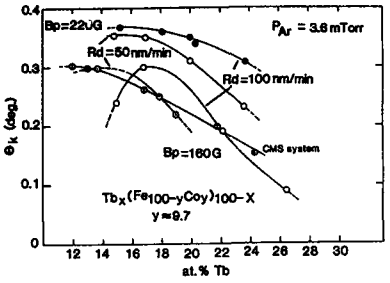


FIG. 7. Dependence of Kerr rotation angle on the Tb concentration: (a) CMS, (b) $B_p = 160$ G, plasma-exposed FTS, and (c) $B_p = 220$ G, plasma-free FTS systems.

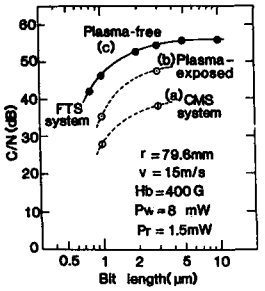


FIG. 8. Relationship between C/N ratio and bit length in MO disks: (a) CMS, (b) plasma-exposed FTS, and (c) plasma-free FTS systems.

50 °C in 90% relative humidity for 150 min was performed. The gradual decrease of reflectivity indicated that the films are strongly influenced by atmospheric water vapor and oxygen under the above-mentioned conditions.

C. Magneto-optical properties

Figure 7 shows the dependence of the Kerr rotation angle θ_K on Tb content. The films with composition of $Tb_x(Fe_{100-y}Co_y)_{100-x}$ were prepared by the FTS system at P_{Ar} of 3.6 mTorr by changing the deposition rate R_d and magnetic field B_p in 50–100 nm/min and 160–220 G, respectively. The θ_K in both films with deposition rates of 50 and 100 nm/min increases significantly with increasing magnetic field. This suggests that preparation of the films on the plasma-free substrate is essential to obtain large θ_K. As illustrated in Fig. 1, the films prepared at B_p of 160 G were exposed to bombardments of negative transition-metal ions and high-energy γ electrons (plasma-exposed). On the other hand, the films prepared at B_p of 220 G were free from such bombardments owing to the proper plasma confinement (plasma-free).

The films prepared at R_d of 100 nm/min on the plasma-free substrate show a large θ_K of 0.37°. The θ_K of these films decreases gradually with increasing Tb content, compared to that of the films prepared at R_d of 50 nm/min on the same plasma-free substrate.

D. Read-write characteristics

The C/N ratio was measured at a radius of 79.6 mm and velocity of 15 m/s with a readout power of 1.5 mW, with the writing power P_w, bit length l_b, and external field H_w, being 8.0 mW, 0.8–10 μm, and 400 G, respectively.

The dependence of the C/N ratio on the bit length in the MO disks (a), (b), and (c) is shown in Fig. 8. The MO disks (b) and (c) prepared by the FTS systems show a higher C/N ratio than that of the MO disk (a) prepared by the CMS system. Especially, the MO disk (c) prepared on the plasma-free substrate shows a high C/N ratio of 57 dB at a bit length of 5 μm. This C/N ratio is about 8 dB higher than that of the MO disk (b) prepared on the plasma-exposed substrate. This agrees with the remarkable increase of the Kerr rotation angle found in the plasma-free FTS system as shown in Fig. 7. Thus, it is necessary to prepare the TbFeCo films on the plasma-free substrate, in order to improve the C/N ratio of the MO disk.

IV. CONCLUSION

The TbFeCo amorphous films have been prepared by the FTS system under an Ar pressure of 3.6 mTorr, deposition rate R_d of 50–100 nm/min, and magnetic field B_p of 160–220 G. It was found from TEM observations that columnar structure was apparent in films prepared at a R_d as low as 50 nm/min, but was not observed in the films prepared at a R_d as high as 100 nm/min. After the TbFeCo film was exposed in air for 250 days, the film did not show a significant change in the reflectivity, Kerr rotation angle, and coercivity. The films prepared at a R_d of 100 nm/min on the plasma-free substrate ($B_p = 220$ G) exhibited a large Kerr rotation angle of 0.37°. The MO disk formed by the TbFeCo film had a high C/N ratio of 57 dB at a bit length of 5 μm. Consequently, it has been found that the TbFeCo films without any appreciable columnar structure prepared at a high deposition rate on the plasma-free substrate had a high C/N ratio and good corrosivity.

[1] N. Imamura, S. Tanaka, F. Tanaka, and Y. Nagao, IEEE Trans. Magn. MAG-21, 1607 (1985).
[2] K. Aratani, T. Kobayashi, S. Tsunashima, and S. Uchiyama, J. Appl. Phys. 57, 3903 (1985).
[3] T. Iijima, Appl. Phys. Lett. 50, 1835 (1987).
[4] T. K. Hatwar, S. L. Shin, and D. G. Stinson, IEEE Trans. Magn. MAG-22, 946 (1986).
[5] M. Miyazaki, I. Shibata, S. Okada, K. Ito, and S. Ogawa, J. Appl. Phys. 61, 3326 (1987).
[6] M. Ohkoshi, M. Harada, T. Tokunaga, S. Honda, and T. Kusuda, IEEE Trans. Magn. MAG-21, 1635 (1985).
[7] T. Kusuda, S. Honda, and M. Ohkoshi, J. Appl. Phys. 53, 2338(1982).
[8] T. Suzuki, Jpn. J. Appl. Phys. 24, L199 (1979).
[9] H. J. Leamy and A G. Dirks, J. Appl. Phys. 50, 2871 (1979).
[10] M. Hong, E. M. Gyorgy, R. B. van Dover, S. Nakahara, D. B. Bacon, and P. K. Gallagher, J. Appl. Phys. 59, 551 (1986).
[11] M. Naoe, N. Kitamura, and T. Hirata, J. Appl. Phys. 61, 3337 (1987).
[12] H. Ito, T. Hirata, N. Kitamura, and M. Naoe, *Advances in Magneto-Optics*, Proc. Int. Symp. Magneto-Optics, J. Magn. Soc. Jpn. 11, Supplement S1, 225 (1987).
[13] M. Naoe, S. I. Yamanaka, and Y. Hoshi, IEEE Trans. Magn. MAG-16, 646 (1980).

Corrosion-resistant-rare-earth–transition-metal amorphous films with high recording sensitivity for magneto-optical disks

A. Kawamoto, K. Nagato, R. Kuzuo, and T. Yorozu
Central Research Laboratory, Sumitomo Metal Mining, Ichikawa, Chiba, Japan

This study provides a method for improving the corrosion resistance of rare-earth–transition-metal films used for magneto-optical recording without depressing the recording sensitivity. This was attained by increasing Co content and substituting Dy for Tb and TbFeCo amorphous films. Potentiostatic polarization measurements indicate that the pitting potential of the film increases with the increase of Co content up to $y = 0.17$ for $(Tb_{0.5}Dy_{0.5})_{0.21}Fe_{0.79-y}Co_y$. Attempts are made to explain the results using Auger electron spectroscopy and x-ray photoelectron spectroscopy. For the above-noted composition, both the Kerr rotation angle and coercivity observed through the substrate retain their initial values after the accelerated aging test. Results indicate that the $(Tb_{0.5}Dy_{0.5})_{0.21}Fe_{0.62}Co_{0.17}$ film offers superior characteristics for corrosion resistance without disturbing the magnetic properties.

INTRODUCTION

For high-density magneto-optical recording, amorphous rare-earth–transition-metal (RE-TM) films have achieved appropriate properties regarding carrier-to-noise ratios (CNR). RE-TM films, however, trade off their intrinsic material properties for their chemical instability. In general, two methods are proposed to protect these films from corrosion. One is to improve the corrosion resistance of the films themselves. The other is to coat them with protective layers, usually metals or inorganic materials.

In this study, improvement of the corrosion resistance in TbFeCo amorphous films is achieved by increasing Co content and substituting Dy for Tb. As reported before, the Curie temperature (T_C) and coercivity (H_c) decreases as Tb is substituted by Dy without suppressing the Kerr rotation angle.[1] This enables us to design disks with desirable recording-power sensitivity and superior corrosion resistance.

EXPERIMENT

TbFeCo and TbDyFeCo amorphous films for static measurements on magneto-optical properties and for potentiostatic measurements were prepared by conventional rf sputtering onto water-cooled and rotating glass substrates. The thickness of the films was about 1200 Å, without protective coatings. The preparation method of the samples for dynamic testing and the testing conditions are described elsewhere.[2]

The potentiostatic polarization of the films was measured in a 0.1 N $NaClO_4$ aqueous solution. Kerr hysteresis loops were measured before and after exposing the films at 60 °C, 80% relative humidity for 120 h. Auger electron spectroscopy (AES) and x-ray photoelectron spectroscopy (XPS) measurements were done for samples on glass substrates by the same procedures as described before.[3] Since Tb and Dy have similar signatures in AES as well as XPS, a peak separation between Tb and Dy was not performed.

RESULTS AND DISCUSSIONS

Potentiostatic polarization curves of $(Tb_{0.5}Dy_{0.5})_{0.21}Fe_{0.62}Co_{0.17}$ and $(Tb_{0.75}Dy_{0.25})_{0.21}Fe_{0.74}Co_{0.05}$ are shown in Fig. 1. In both cases passivation occurs without having an active state, which indicates that spontaneous passivation takes place in these amorphous RE-TM alloys. The pitting potential of the former alloy is somewhat larger than the latter case. This means that films with higher Dy and Co contents are more stable in an oxidative environment. Changes in the pitting potential for various contents of Dy and Co are depicted in Fig. 2. Pitting potentials have tendencies to increase as Dy and Co contents increase, except for the Co content of 17 at. %.

In order to investigate the mechanism of corrosion, AES and XPS analyses were performed to identify the chemical properties of the passivation state. A typical AES depth profile of a TbDyFeCo film after exposure to 60 °C, 80% relative humidity for 120 h is shown in Fig. 3. In general, the oxide layer consists of three different regions. Both AES and XPS analyses confirm that oxidized Fe is the main component at the outermost surface (0–50 Å, region I). Beneath this region, Tb and Dy oxides tend to increase whereas Fe

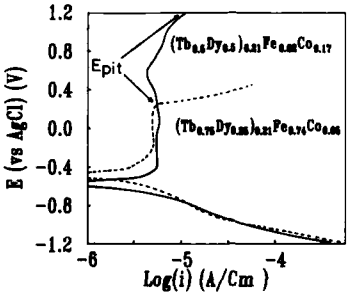


FIG. 1. Potentiostatic polarization curves of TbDyFeCo amorphous films. Pitting potentials are indicated as E_{pit} in the figure.

 0021-8979/88/083853-03$02.40 © 1988 American Institute of Physics

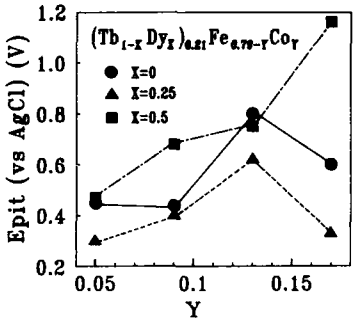


FIG. 2. Compositional dependence of pitting potentials in RE-TM amorphous films.

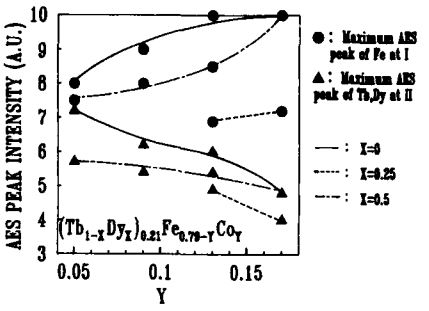


FIG. 4. Compositional dependence of AES peak intensities of Fe in region I and RE in region II after the accelerated aging test.

oxides disappear and are replaced with metallic Fe instead (50–120 Å, region II). In the third region, however, the amount of Tb and Dy oxides decreases and becomes less than that of metallic Fe (120–400 Å, region III). Similar results re obtained for TbFe alloys by van Dover *et al.*[4] On the other hand, both metallic Co and a small amount of oxidized Co are observed at the outermost surface, and only the Co metal increases in the inner layer.

The structure of the passivation state as mentioned above is responsible for the corrosion resistance. AES peak intensities of Fe in region I and RE in region II for various compositions in TbDyFeCo amorphous films are illustrated in Fig. 4. The peak intensity of Fe in region I increases with the increase of Co content, which implies the condensation of oxidized Fe at the outermost surface is conspicuous for high Co content. The peak intensities of RE, existing as oxides in region II, however, decrease as the Co content increases. In the case of Tb:Dy = 75:25, the contents of both Fe and RE show low values. Accordingly, results in Figs. 2–4 indicate that films with superior corrosion resistance are those that have oxidized Fe at the outermost surface layer. In this case surface oxides of Fe act as the passivation state of the film.

The degree of surface oxidation for Fe in TbFeCo alloys with a Co content of 17 at. % is comparable to that of Tb:Dy = 50:50, as shown in Fig. 4. Nevertheless, it has lower values of the pitting potential. The results are interpreted by the behavior of Co metal at the surface layer. AES peak intensities of Co metal at about 30 Å from the film surface are depicted in Fig. 5. With high-Co-content alloys, the amount of Co metal is the lowest for Tb:Dy = 50:50. This together with the facts mentioned above suggests that corrosion resistance is disturbed by the presence of Co metal in the passivation state of oxidized Fe, and this disturbance can be prevented by substituting Dy for Tb up to 50%.

Consequently, as for the corrosion resistance of RE-TM amorphous films, superior characteristics are observed for alloys containing high Co content. In such compositions, Fe tends to segregate at the outermost surface, existing as oxides. However, the amount of Co metal which turns up in the surface will increase proportionally and thus disturbs the passivity of the oxide state. This increase of Co metal in the passivation state can be avoided by using alloys where Dy is substituted for Tb up to 50%.

Changes in the Kerr rotation angle (θ_K) and coercivity (H_c) after exposing the samples at 60 °C, 80% relative humidity for 120 h are illustrated in Fig. 6. The compositions of the films were $(Tb_{0.5}Dy_{0.5})_{0.21}Fe_{0.79-y}Co_y$. Both θ_K and H_c observed through the substrate maintained their initial values regardless of Co content. H_c values observed from the

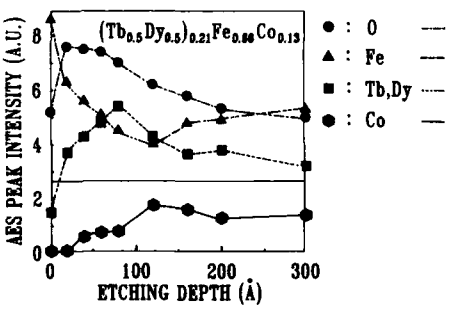


FIG. 3. AES depth profile of the surface layer in amorphous RE-TM films after the accelerated aging test (60 °C, 80% relative humidity 120 h).

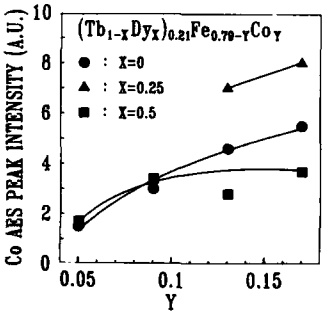


FIG. 5. Compositional dependence of Co AES peak intensities at about 30 Å from the film surface after the accelerated aging test.

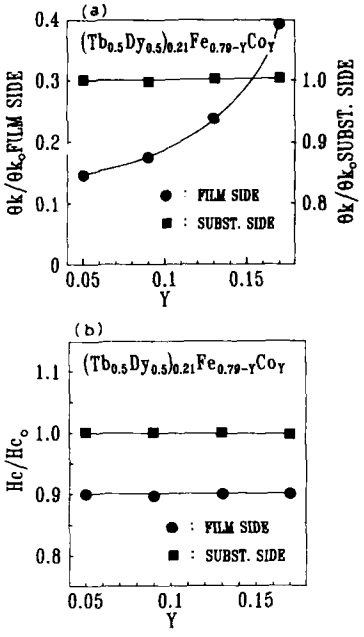


FIG. 6. Changes in (a) Kerr rotation angle θ_K and (b) coercivity H_c for TbDyFeCo films after the accelerated aging test. ● stand for the vlaues observed from the film side and ■ for those observed through the substrate. θ_{K_0} and H_{c_0} represent values observed before the aging test.

film side drop to about 90% of the initial values for all the compositions studied in Fig. 6. On the other hand, changes of θ_K from the initial values decrease with the increase of Co content. When the Co content is increased, the segregation of RE oxides in region II is suppressed at the expense of the increase of Fe metal as shown in Fig. 4. Since θ_K originates from the TM component of the RE-TM alloys, the decrease of θ_K from its initial value will be prevented due to the increase of metallic Fe in region II.

The dynamic characteristics for the disks having the composition $(Tb_{0.5}Dy_{0.5})_{0.21}Fe_{0.62}Co_{0.17}$ indicate a CNR of 50 dB under the conditions of CLV (4 m/s), a 1-MHz carrier signal, a 500-Oe bias field, and an optimum recording power of 2.5 mW. The initial characteristics are maintained after exposure of more than 1000 h at 60 °C, 80% relative humidity.

[1]M. Akihiro, T. Sato, J. Tada, and T. Satoh, IEEE Trans. Magn. **MAG-22**, 928 (1986).
[2]K. Nagato, A. Kawamoto, T. Sato, and T. Yorozu, these proceedings, paper FA-10.
[3]T. Yorozu, M. Hirano, K. Oka, and T. Satoh, IEEE Trans. Magn. **MAG-22**, 1218 (1986).
[4]R. B. van Dover, E. M. Gyorgy, R. P. Frankenthal, M. Hong, and D.J. Siconolfi, J. Appl. Phys. **59**, 1291 (1986).

Compositional dependence of recording noise in amorphous rare-earth–transition-metal magneto-optical disks

K. Nagato, A. Kawamoto, T. Sato, and T. Yorozu
Central Research Laboratory, Sumitomo Metal Mining, Ichikawa, Chiba, Japan

The compositional dependence of recording-power sensitivity and recording-noise characteristics of TbFeCo and TbDyFeCo films have been studied systematically. The sensitivity depends on the compositional ratio of rare earth (RE) and transition metal (TM) rather than on Co content. This is explained by the fact that the temperature at which the coercive force (H_c) coincides with the bias magnetic field of 500 Oe, hereafter denoted as T', varies drastically by altering the RE-to-TM ratio. High recording noise is observed for compositions having T_{comp} close to T_C. When $T_C - T_{comp} \gtrsim 70$ °C, optimal carrier-to-noise ratios are obtained. These results are explained qualitatively by the behavior of domain-wall motion in the vicinity of the magnetically reversed domain.

I. INTRODUCTION

Magneto-optical recording has become an attractive choice for erasable high-density information storage of the next generation. Recent experiments have shown that recording characteristics such as recording-power sensitivity, domain size, domain regularity, etc., are controlled by the laser-induced temperature profile, radial and time dependence of the magnetic properties, domain nucleation, and domain-wall mobility.[1–5]

This study deals primarily with the compositional dependence of recording-power sensitivity in TbFeCo and TbDyFeCo films, namely the correlation between the temperature dependence of coercive force and/or demagnetizing field and the recording laser power at which the second harmonic of the carrier-to-noise ratio becomes minimum. Second, in the course of our study, compositions with high recording noise were observed when compensation temperatures (T_{comp}) were close to Curie temperatures (T_C). Attempts are made to explain the results by applying a quasistatic force balance model relevant to the domain size and shape irregularity for these particular cases.

II. EXPERIMENT

Amorphous TbFeCo and TbDyFeCo films were prepared by nonbiased, dc magnetron co-sputtering of Tb or TbDy and FeCo alloys. Trilayer structures were fabricated on polycarbonate substrates [(polycarbonate substrate)/(oxide layer)/(TbFeCo or TbDyFeCo)/(oxide layer)]. Film thicknesses were 700–1000 Å. The temperature dependence of the saturation magnetization M_s was measured using a vibrating-sample magnetometer (VSM). The coercive force and its temperature dependence were determined by Kerr hysteresis loops observed through the substrate using a diode laser (830 nm) with fields up to ~12 kOe. Film compositions were determined by EPMA (electron probe microanalysis) within an accuracy of ± 1 at. %.

The evaluation of magneto-optical recording characteristics were made on 130-mm-diam polycarbonate disks. The reflected beam from the media was analyzed by a differential detection method using *p-i-n* photodiodes. The dynamic measurements were carried out with test conditions of CLV (constant linear velocity, 4 m/s), 0.5-MHz carrier frequency, 30-kHz resolution bandwidth, and 500-Oe bias magnetic field.

III. RESULTS AND DISCUSSION

A. Recording-power sensitivity

As mentioned in the Introduction, we define optimum recording power at which the second harmonic of the carrier-to-noise ratio becomes minimum as the standard of recording-power sensitivity. The compositional dependencies of optimum recording powers for TbFeCo and TbDyFeCo alloys are illustrated in Fig. 1. Optimum power depends on the compositional ratio of RE to TM rather than on T_C. The results are interpreted qualitatively by the temperature dependence of H_c and M_s. For a simple approximation model, the temperature, denoted as T'', at which H_c is lower than the sum of bias magnetic field, H_{ext}, and demagnetizing field of $4\pi M_s$, correlates to the relative size of the reversed domain.[4,5] Accordingly, the domain size becomes large when T'' is low, namely, the media become sensitive when T'' is low. T'' is lower than T', the temperature at which H_c coincides with only the bias magnetic field, when M_s has a large value as in the case for TM-rich compositions. However, T'' nearly equals T' for RE-rich compositions due to the small contribution of the demagnetizing field.

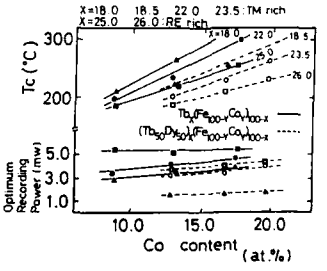


FIG. 1. Compositional dependence of Curie temperature T_C and optimum recording power. Solid lines stand for TbFeCo and dashed lines for TbDyFeCo films.

 0021-8979/88/083856-03$02.40 © 1988 American Institute of Physics

First, let us consider the case for compositions having constant Co content with different RE-to-TM ratio. As illustrated in Fig. 1, T_C increases as the composition is varied from RE-rich to TM-rich side. In spite of this increase in T_C, for example in $Tb_xFe_{87.3-x}Co_{12.7}$ as depicted in Fig. 2(a), T' decreases with the decrease of Tb concentration. This is due to the fact that for RE-rich compositions, H_c increases rapidly in the higher temperature region from T_C towards T_{comp} (above room temperature) and has a larger slope of H_c versus temperature than that for TM-rich compositions in the vicinity of T_C as depicted in the figure. Similar results, i.e., the decrease of T' in TM-rich side, were observed for other compositions shown in Fig. 1 having constant Co content with different RE-to-TM ratios. As mentioned earlier, the demagnetizing field in the elevated temperature range is sufficiently large for the TM-rich side. Consequently, T'' decreases to a larger extent for the TM-rich composition compared to the RE-rich side. This implies that the reversed domain formation occurs with low optimum recording power for the TM-rich side.

On the other hand, the optimum recording-power dependency on Co content with an identical RE-to-TM ratio is rather small. Typical examples of the temperature dependences of H_c and the demagnetizing field, $4\pi M_s$, for $Tb_{25}Fe_{75-y}Co_y$, i.e., compositions having identical RE-to-TM ratios with different Co content are illustrated in Fig. 2(b). Although T_C is different, similar values for T' are obtained. The contributions of the demagnetizing field are about the same in this case. Therefore, comparable values for T'' are obtained as well, resulting in a similar optimum power for compositions indicated in Fig. 2(b).

In the case of TbDyFeCo films, as shown in Fig. 3, substitution of Dy for Tb results in the decrease of T_C compared with TbFeCo having identical Co content. In addition, H_c is smaller than H_c for TbFeCo throughout the temperature range that has been measured. Since the contributions of the demagnetizing field are similar to TbFeCo [see Fig. 2(a)], T' and T'' decrease to a larger extent compared to TbFeCo, which gives rise to higher sensitivity. Thus, disks with highly sensitive media are achieved using TM-rich TbDyFeCo films.

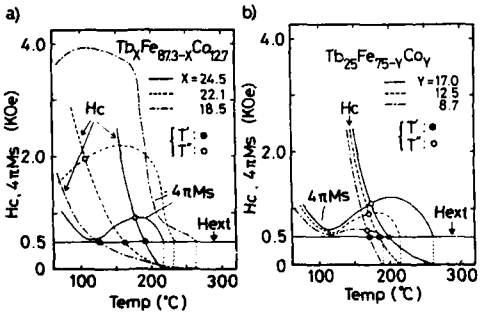


FIG. 2. Temperature dependence of coercive force H_c and demagnetizing field $4\pi M_s$ for (a) $Tb_xFe_{87.3-x}Co_{12.7}$ and (b) $Tb_{25}Fe_{75-y}Co_y$.

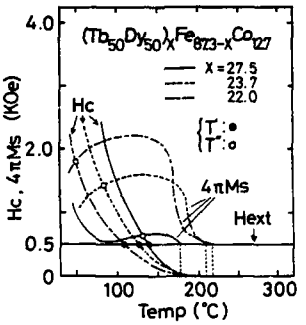


FIG. 3. Temperature dependence of coercive force H_c and demagnetizing field $4\pi M_s$ for TbDyFeCo films.

B. Recording-noise characteristics

Recording noise increases drastically for certain compositions in both TbFeCo and TbDyFeCo alloys as illustrated in Fig. 4. As is observed from Fig. 5, these compositions correspond to the region where the temperature difference between T_C and T_{comp} is below ~ 70 °C. In order to explain these results, we adopted a force balance model analogous to the stability condition of a bubble domain.

A Gaussian temperature profile is assumed in the locally heated area. The temperature distribution is calculated via a finite-difference method.[6] The radial distributions of $M_s(R)$ and $H_c(R)$ are derived by combining this temperature profile with the measured temperature dependence of M_s and H_c. The stability condition of the reversed domain in the writing process is expressed as follows[1,3]:

$$|F| = 4\pi h^2 \left| \left[\frac{\sigma_w(R)}{2h} + \frac{R}{2h} \frac{\partial \sigma_w(R)}{\partial R} - M_s(R) \frac{R}{h} \left(H_{ext} + \frac{4\pi \overline{M_s(R)}}{1+3R/2h} \right) \right] \right| < 2|M_s(R) H_c(R) 2\pi R h| = |F_u|, \quad (1)$$

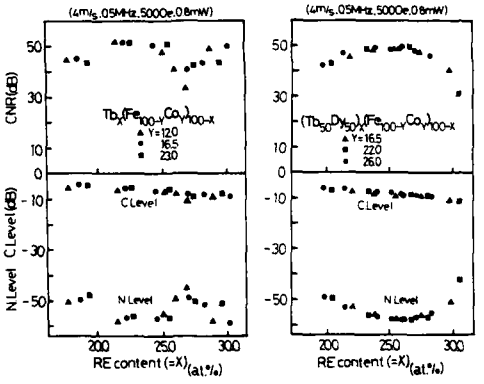


FIG. 4. Compositional dependence of carrier-to-noise ratio for TbFeCo and TbDyFeCo films. Carrier and noise levels are also shown separately below.

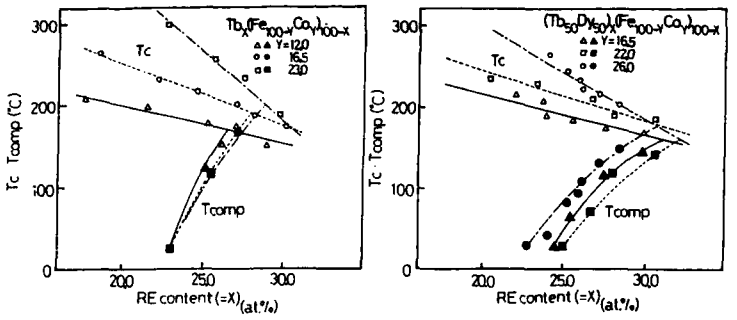


FIG. 5. Compositional dependence of Curie temperature T_C and compensation temperature T_{comp} for TbFeCo and TbDyFeCo films.

where $\sigma_w(R)$ is the domain-wall energy per unit area and H_{ext} is the bias magnetic field. R and h represent the radius of the cylindrical reversed domain and the film thickness, respectively. $\overline{M_s(R)}$ represents the average M_s value in the range $0<r<R$. The temperature dependence of σ_w is calculated using the mean-field model as has been described elsewhere.[1]

Radial profiles of F in Eq. (1) are shown in Fig. 6. Figure 6(a) indicates the situation where T_{comp} is well below T_C, whereas 6(b) indicates the situation where T_{comp} is close to T_C. $F>0$ represents a contracting force that attempts to shrink the reversed domain and $F<0$ represents an expanding force on the domain wall. T_{max} indicates the temperature at the center of the laser beam. It reaches ~ 250 °C at the end of the pulse. A domain wall originates only when F has a negative value at the center of the beam. Once originated, the wall moves from the center toward R_{H_c}, beyond which the inequality of Eq. (1) is satisfied, along the negative curve of F. Thus a reversed domain is observed in the region between R_{T_C} and R_{H_c}. It should be noticed that, except in the early stage, F is negative for radii greater than R_{T_C} during the temperature rise process in Fig. 6(a). In Fig. 6(b), however, F has a large positive value just above R_{T_C}. Furthermore, the reversed domain collapses when T_{max} rises from 208 °C to 209 °C. This is due to the fact that if the domain wall remains at the same position at 209 °C as it was at 208 °C, the F value at R_{H_c} becomes positive and deviates from the inequality of Eq. (1).

It is reasonable to assume that compositional fluctuations over submicron areas exist in the sputtered films. This will be reflected to the fluctuations of F and F_w, resulting in the fluctuations of R_{H_c}. When films with compositions having T_{comp} close to T_C are considered, shrinkage to the small reversed domain as mentioned above occurs nonuniformly because of these fluctuations existing in the heated area. Furthermore, numerical values of F indicated in Figs. 6(a) and 6(b) are distinctly different ($\sim 10^{-4}$ and $\sim 10^{-6}$ dyn, respectively). This implies that the wall velocity of Fig. 6(b) is conspicuously smaller than that of Fig. 6(a). On the other hand, the expanding velocity of R_{H_c} determined by the radial heat diffusion is larger for Fig. 6(b), i.e., R_{H_c} increases drastically with a slight temperature increase. These results suggest that the time needed for the wall mobility of Fig. 6(b) to produce the domain radius of R_{H_c} is too short, since the wall may not be able to catch up with the expanding velocity of R_{H_c}. Therefore, if compositional fluctuations exist, this will also be reflected in the strong variations in the domain radius.[1] These may be some of the reasons for the irregularity and/or collapse of the reversed domain, which results in an increase of recording-noise in Fig. 6(b).

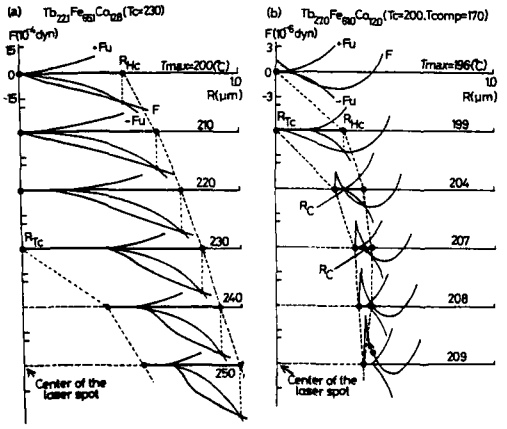


FIG. 6. Radial distribution of the force F and F_w in the heated area. (a) compensation temperature T_{comp} is well below Curie temperature T_C, and (b) T_{comp} is near T_C.

[1] P. Hansen, J. Appl. Phys. **62**, 216 (1987).
[2] H. D. Shieh and M. H. Kryder, J. Appl. Phys. **61**, 1108 (1987).
[3] B. G. Huth, IBM J. Res. Dev. **18**, 100 (1974).
[4] S. Takayama, T. Niihara, K. Kaneko, Y. Sugita, and M. Ojima, J. Appl. Phys. **61**, 2610 (1987).
[5] M. Takahashi, N. Ohta, S. Takayama, Y. Sugita, M. Yoshihiro, and K. Shigematsu, IEEE Trans. Magn. **MAG-22**, 931 (1986).
[6] S. C. Shin, J. Magn. Magn. Mater. **61**, 301 (1986).

Simulation of bit jitter in magneto-optic recording

T. W. McDaniel
IBM Corporation, General Products Division, Tucson, Arizona 85744

The interplay of several writing and reading phenomena that influence bit-position accuracy has been analyzed with a computer model of the magneto-optic (MO) recording process. A micromagnetics simulation determines a minimum energy magnetization state of a MO storage film following local laser heating in an externally applied bias magnetic field. Bit jitter is assessed by measuring the length, width, and position of written domains, and by analyzing the modeled readout signal and its derivative. The influence of variation in the magnetization, anisotropy, and exchange in an amorphous rare-earth–transition-metal film on the position and size of recorded marks has been simulated by specifying random variations of a film's magnetic properties in the thermomagnetic writing step. Variations in medium thermal sensitivity and the reading laser spot size were also considered. Histograms showing the effects of write-read imperfections on bit-position accuracy in MO recording were developed. Comparisons with experiment and separation of other system noise effects have enabled model validation.

INTRODUCTION

Computer simulations of the processes of thermomagnetic writing and magneto-optic (MO) reading are useful supplements to experimental analysis in the development of erasable MO data storage devices. Previously, a method for modeling thermomagnetic writing in amorphous rare-earth–transition-metal (RE-TM) alloy films over a two-dimensional mesh of interacting elements was reported.[1–3] The Monte Carlo model of Ref. 3 was used to examine three mechanisms contributing to bit jitter in MO readout. High-level descriptors of system variance were used because detailed experimental knowledge about jitter sources is lacking. Nevertheless, simulations of this type provide, among other benefits, a quantitative tool for determining a suitable operating point for a chosen combination of optical head and storage film.

As detailed in Ref. 3, the simulation examines for all film elements $\Delta E_{\rm tot} = \Delta E_d + \Delta E_w + \Delta E_b$, the change in total magnetic energy of a single hexagonal cell when its perpendicular magnetization **M** is reversed (the **M** of all other cells being held fixed). The subscripts d, w, and b denote that demagnetizing, domain-wall, and bias-field energy are considered. The switching probability of cell i is $\exp(-\Delta E_{{\rm tot},i}/kT)$, where kT is the Boltzmann energy. Thus, magnetization switching in this model is effected by a nucleation-type reversal, and subsequent domain growth represented by cascading cell reversals, all driven by a lowering of the film magnetic energy.

WRITING, READING, AND ERASING

Figure 1 shows a complete time sequence in the thermomagnetic writing of a short mark symbol (length 0.98 μm, width 0.91 μm). A mesh of hexagonal cells of edge length $a = 0.025$ μm and height $h = 0.07$ μm compose the film throughout this work. The film modeled is a RE-TM alloy, whose compensation temperature $T_{\rm comp}$ and Curie temperature T_C are approximately 300 and 450 K, respectively. No magnetic parameter variation is imposed in this section. The initial state of the film magnetization at ambient temperature is taken to be uniformly down (minus sign). The laser power profile for the writing of Fig. 1 commences at $t = 0$ ns, 9 ns before the time of the first frame of the figure. The peak temperature rise above ambient (300 K) at $t = 0$ ns was already 44 K because the laser was in a quiescent state of output power equal to 2 mW between mark-writing events.

In Fig. 1, the white spot that moves through the film is the central hot spot of the laser beam that raises the temperature above T_C (M goes to zero). Note that the applied bias field $H_b = -300$ Oe helps form the newly written mark as a halo around the region heated above T_C. As the laser spot moves to the right, the trailing edge of the irradiated region cools, freezing in the reversed magnetization and forming the written domain (mark). The last five frames of Fig. 1 show that after the peak temperature of the film has fallen below T_C, the domain boundary has essentially become fro-

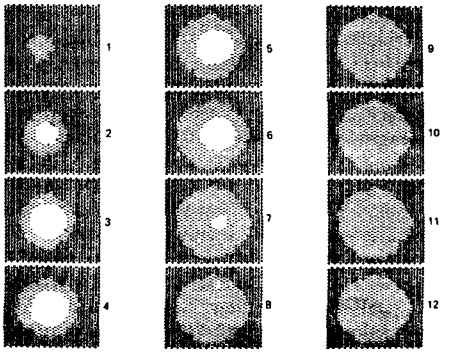


FIG. 1. Time sequence for writing a short mark. $H_b = -300$ Oe. Read frames sequentially down the columns. Frame times shown are 9,12,15,18, ... ,42 ns, and the peak temperature rise above ambient ($T_{\rm amb} \approx T_{\rm comp}$) for each frame is 141, 164, 178, 178, 174, 170, 154, 134, 122, 111, 103, and 96 °C. Plus and minus signs denote up and down magnetization. Blank areas show $|M| < 1$ emu/cm^3. Final mark length and width are 0.98 and 0.91 μm, respectively.

 0021-8979/88/083859-03$02.40 © 1988 American Institute of Physics

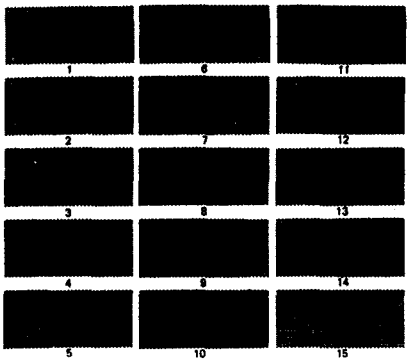


FIG. 2. Time sequence of erasure of a long mark. Time steps are -100, 27, 45, 63, 81, 99, 117, 135, 153, 171, 189, 207, 225, 243, and 1000 ns; ΔT_{max} = 0, 49, 105, 148, 151, 153, 151, 151, 152, 151, 152, 151, 146, 117, and 0 °C. Erasure is incomplete. Initial mark length and width are 2.36 and 0.95 μm, respectively.

zen. The writing laser pulse ended between frames 6 and 7 (24 ns $< t <$ 27 ns).

Some mark boundary irregularity beyond the mesh quantization is evident in Fig. 1. In the simulation, two effects can contribute to this: (1) random variance in the cell's magnetic parameters imposed by the modeler if a noisy film is simulated, and (2) natural randomness in the implementation of the Boltzmann probability of cell switching with the Metropolis rule.[1] The latter reflects the competition among the magnetic energies near the domain wall, and the outcome depends largely on the relative magnitudes and temperature variations of the contributing energies.

Figure 2 illustrates thermomagnetic erasure of a long mark with a continuous-wave laser spot. In this simulation, the erase spot was started and stopped about 1 μm beyond the left and right edges of the modeled film. Two complete, random scans of the film cells were made at each time step to ensure that equilibrium was achieved. As in writing, we can see the effect of the erasing beam elevating the film temperature above T_{comp}, causing the sign of the net magnetization to change (frames 2–14 in Fig. 2). This is not magnetization reversal induced by the applied field. The true reversal effects corresponding to erasure are seen in frames 4–11 in Fig. 2. The erase power was inadequate to achieve a clean erasure, leaving the top and bottom edges of the mark. Increasing the erasing power by 1 mW produced a complete erasure.

The readout signals associated with the marks of Figs. 1 and 2 are shown in Figs. 3(a) and 3(b). These were generated by numerically evaluating the overlap of a Gaussian laser spot of full width at half maximum (FWHM) equal to 0.90 μm with the written marks of Figs. 1 and 2. The signal so computed corresponds to an unequalized readout in arbitrary units. The relative values of the peak signal amplitudes in Fig. 3 can be directly related to the mark sizes of Figs. 1 and 2. The derivative peaks are symmetric for both the short and long marks, reflecting the apparent symmetry of the mark edges.

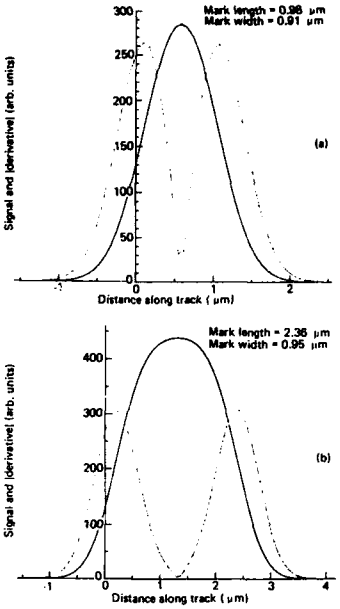


FIG. 3. Read-back signal and magnitude of the signal derivative corresponding to the written marks of (a) Fig. 1 and (b) Fig. 2. Derivative peak amplitude and width asymmetry are less that 1% in each case. Amplitude and width of the signal waveform reflect physical mark sizes of Figs. 1 and 2 as indicated.

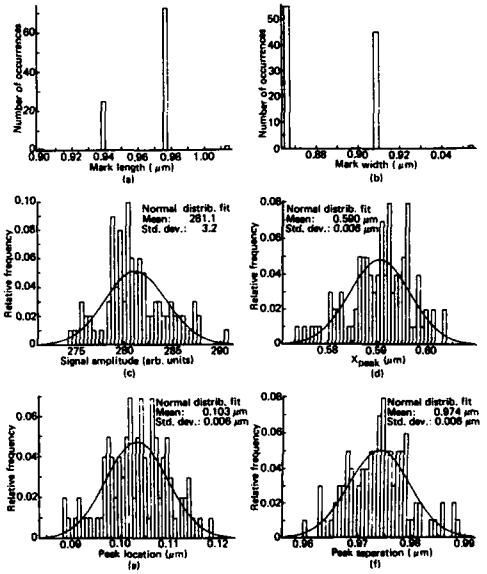


FIG. 4. Jitter statistics for random variation of cell magnetization and wall energy. Uniform distribution; $\pm$ 25% range; 101 trials. (a) and (b) physical mark length and width distribution; (c) distribution of peak signal amplitude; (d) signal peak location; (e) left derivative peak location; (f) derivative peak separation.

TABLE I. Summary of jitter analysis (1σ entries go with preceding column).

Jitter mechanism	No. of trials	Mean mark length (μm)	1σ (μm)	Mean mark width (μm)	1σ (μm)	Mean peak ampl. (arb.units)	1σ (arb. units)	Mean x (left deriv) (μm)	1σ (μm)	Mean Δx (der. pk.sep.) (μm)	1σ (μm)
$(1+\epsilon)\Delta T(x,y)$, $\sigma = 0.02$	24	0.944	0.035	0.879	0.026	281.1	10.25	0.102	0.008	0.971	0.012
ΔFWHM (read)	1100	0.975	0	0.866	0	279.95	7.85	0.102	0.005	0.978	0.01
Normal dist., $\sigma = 0.02$											
ΔFWHM (read)	1100	0.975	0	0.866	0	279.47	2.19	0.102	0.002	0.978	0.005
Unif. dist., width = 0.04											
ΔM, $\Delta\sigma_w$	101	0.966	0.019	0.886	0.022	281.14	3.2	0.104	0.006	0.974	0.006
Unif. dist., width = 0.50											
ΔM, $\Delta\sigma_w$	50	0.948	0.025	0.875	0.017	281.45	3.44	0.1	0.006	0.972	0.005
Normal dist., $\sigma = 0.083$											
No parameter variation	34	0.933	0.022	0.867	0.007	280.36	2.06	0.102	0.007	0.969	0.004

JITTER SIMULATIONS

This section illustrates a modeling capability rather than describing all relevant jitter effects in MO recording. Results are restricted to single values of the following parameters for a single modeled film: bias field (-300 Oe), write power-time profile, laser write spot size (FWHM of 0.90 μm), film velocity, and mark length (short). We chose the short mark to increase computing throughput, although we expect that this choice reduces the sensitivity of detection of jitter effects in readout due to the nature of the correlation (overlap) integral of the spot and mark of comparable size involved in generating the read-back waveform.

The following describes the parameter variations for the three sources of jitter. The temperature rise above ambient in the film $\Delta T(x,y)$ from a finite-element model was modified to $(1+\epsilon)\Delta T(x,y)$, where ϵ is a random number chosen from a normal distribution having mean value zero and $1\sigma = 0.02$. The FWHM of the Gaussian read spot was modified according to $(1+\epsilon)$ (0.90 μm), and ϵ was chosen randomly from either a uniform or normal distribution. For the normal distribution, $1\sigma = 0.02$, while for the uniform distribution, the half-width was 0.02. The third bit jitter source considered is the effect of random variation in the magnetic properties of the MO film on a length scale of the cell size. Cell magnetization and domain-wall energy involved in the evaluation of $\Delta E_{tot,i}$ were each modified by a factor of $1+\epsilon$ (uncorrelated ϵ's for M and θ_w), where ϵ was chosen from both normal ($1\sigma = 0.083$) and uniform (half-width of 0.25) distributions. At this time, the nature of these distributions must be justified simply on the basis of computational convenience and the reasonableness of the results. Nevertheless, it is widely accepted that amorphous alloys are characterized by randomness in physical parameters on a submicrometer scale. T_C and T_{comp} were not varied.

Figures 4(a)–4(f) show representative results, this case being jitter enhanced by random variation of the cell's magnetic properties using a uniform distribution. Note in Figs. 4(a) and 4(b) the mesh element quantization. The histograms of Figs. 4(c)–4(f) suggest that more trials would be desirable for establishing reliable statistics. This condition must be weighed agains the availability of computing resource. Each write trial for the thermal variation study on short marks involved a mesh of 850 cells scanned in 15 time steps. Each cell analysis included examining six nearest neighbors to compute ΔE_w and eight near-neighbor shells of elements (about 80 elements) for calculating ΔE_d. Typically, a single write trial required 3.5 processing minutes on an IBM 3081 processor. Analysis of larger marks requires proportionally greater resource unless temporal and spatial resolution can be sacrificed.

Table I summarizes our analysis of jitter. Jitter analysis on longer marks would be expected to exhibit somewhat larger variances in the output. Nevertheless, comparing the mark sizes for the various cases shows that random variation of input parameters is reflected in the model output. The variation present in the case of "no parameter variation" is just that due to the Monte Carlo minimization of energy via the Boltzmann switching probability.

SUMMARY

We have demonstrated an application of a thermomagnetic write and erase simulation with optical-readout capability to the assessment of bit jitter. Several mechanisms that contribute to bit jitter are considered: variances in medium thermal sensitivity, optical spot size, and the magnetic properties of the storage film. While the methodology presented is computationally intensive, the analysis tool appears to incorporate accurately the essential physics of thermomagnetic recording processes.

[1]M. Mansuripur, J. Appl. Phys. **61**, 1580 (1987).
[2]M. Mansuripur, J. Appl. Phys. **61**, 3334 (1987).
[3]T. W. McDaniel and M. Mansuripur, IEEE Trans. Magn. MAG-23, 2943 (1987).



Domain shapes of field modulation recorded TbFeCo and GbTbFeCo magneto-optical disks (abstract)

Shigenori Okamine, Takeshi Nakao, Takeshi Maeda, Masahiko Takahashi, and Norio Ohta
Central Research Laboratory, Hitachi, Ltd., Kokubunji, Tokyo 185, Japan

Magneto-optical recording by magnetic field modulation is of particular interest, since direct overwriting of information can be performed as in conventional magnetic recording.[1,2] We used a floating magnetic head to apply a modulated magnetic field ($\pm$ 100– $\pm$ 600 Oe) at 5 MHz. We report here the shape of the recorded domains by this technique on TbFeCo and GdTbFeCo 5¼ in. disks rotating at 1800 rpm. Both TbFeCo and GdTbFeCo films had a Curie temperature of 200 °C and a compensation temperature of 60 °C. The written domains were observed by a polarized microscope. For TbFeCo disks, regular chevron-type domains were formed according to a cooling tail of a continuous laser beam. However, irregular shape domains were observed in GdTbFeCo disks, that is, the outline of a domain was not smooth, which caused a large recording noise and decreased a signal-to-noise ratio. We discuss the relation between domain regularity and magnetic parameters (anisotropy, wall energy, etc.).

---

[1]F. Tanaka *et al.*, Digest of the 10th Annual Conference on Magnetics in Japan, 6pB-4 (1986), p. 229 (in Japanese).
[2]T. Nakao *et al.*, International Symposium on Optical Memory 1987, Tokyo (to be published).

 0021-8979/88/083862-01$02.40 © 1988 American Institute of Physics

Large surface anisotropies in ultrathin films of bcc and fcc Fe(001) (invited)

B. Heinrich, K. B. Urquhart, J. R. Dutcher, S. T. Purcell, J. F. Cochran, and A. S. Arrott
Surface Physics Laboratory, Department of Physics, Simon Fraser University, Burnaby, British Columbia V5A 1S6, Canada

D. A. Steigerwald and W. F. Egelhoff, Jr.
Surface Science Division, National Bureau of Standards, Gaithersburg, Maryland 20899

Large uniaxial anisotropies associated with interfaces are observed for ultrathin films (3-28 ML) of bcc Fe(001) grown epitaxially on Ag(001) single-crystal substrates and for epitaxial sandwiches of fcc Fe(001) grown with three layers of Fe using Cu as substrate and coverlayers. The uniaxial anisotropy is well described by a pseudosurface anisotropy term as theoretically predicted, yet that theory also predicts large in-plane anisotropies that are not observed. Adequate treatment of spin-orbit coupling in magnetic theories remains a challenge. Comparisons of ultrathin films of bcc Fe(001) on Ag(001) with different coverlayers of Ag or Au show subtle differences in magnetic behavior as studied by ferromagnetic resonance (FMR) and Brillouin light scattering (BLS). The FMR measurements were carried out at 9.6, 36.6, and 73 GHz microwave frequencies. The BLS measurements were performed using a six-pass Fabry–Perot interferometer. The power of the techniques of molecular-beam epitaxy (MBE) for producing well-characterized interfaces is stressed. Growths at 140 K are compared with those at 300 K to show the limited role of interdiffusion. Oscillations in the intensity of reflection high-energy electron diffraction (RHEED) are exploited in the characterization of growth. Comparison of the properties of films grown on perfect iron whisker surfaces with results for mosaic single-crystal substrates show that, while the former are much to be preferred for growth studies, the latter are really adequate for magnetic studies.

I. INTRODUCTION

Theoretical calculations by Gay and Richter[1] have predicted that an unsupported Fe(001) monolayer should possess a large uniaxial anisotropy with the easy axis oriented normal to the sample surface. This has been indirectly supported by the spin-polarization experiments of Jonker *et al.*[2] Work by our group[3] has shown that 3–28-ML-thick Fe films in Au/Fe/Ag sandwiches exhibited a strong uniaxial anisotropy as the Fe film thickness was decreased.

Subsequent calculations by Gay and Richter[4] for a Fe(001) monolayer supported by a Ag(001) substrate indicate that even a weak hybridization of Ag and Fe bands results in a substantial decrease in the uniaxial anisotropy. Since the details of the magnetic/nonmagnetic metal interface seem to strongly influence the behavior of uniaxial anisotropy, we have extended our work by replacing the 30-ML Au layer used to cover our ultrathin Fe(001) films with a 30-ML Ag layer. This has allowed us to both simplify our growth structures and examine the role of Au/Fe and Ag/Fe interfaces on observed uniaxial anisotropies.

Since Fe atoms in ultrathin films are located mostly in the interface region, and the uniaxial anisotropy is a near surface effect, one expects that the sharpness of the magnetic/nonmagnetic interface and quality of the epitaxial growth would play significant roles in magnetic properties of the bcc Fe(001) films.

We must emphasize that investigations of this type would not be possible without molecular-beam-epitaxy (MBE) techniques. Well-controlled ultrapure atomic beams, angular resolved x-ray photoemission spectroscopy (XPS), Auger electron spectroscopy (AES), and observation of RHEED patterns during growth are necessary prerequisites for the successful development of well-defined, reproducible, magnetic structures.

The perfect surfaces of Fe(001) whiskers exhibit almost flawless RHEED patterns. Intensity oscillations during growth of Ag/Fe/Ag sandwiches on them allowed us to identify those RHEED features which are essential in the characterization of crystal growth.

Magnetic properties of grown Ag/Fe/Ag sandwiches were measured by ferromagnetic resonance (FMR) at 9.6, 36.6, and 73.0 GHz and Brillouin light scattering (BLS) covering the 10–40-GHz range. The most interesting result was that a Au/Fe(3 ML)/Ag sandwich grown on an Fe whisker possessed a uniaxial anisotropy field large enough to pull the saturation magnetization M_s normal to the specimen surface at room temperature (300 K).

Results of FMR and BLS measurements carried out on 3-ML-thick metastable fcc Fe(001) films grown on Cu(001) by the NBS group are presented in Sec. VI. The uniaxial anisotropy field in fcc Fe films also strongly holds the saturation magnetization normal to the specimen surface at 300 K.

Uniaxial anisotropy in bcc Fe is well described by a pseudosurface anisotropy term as predicted by Gay and Richter.[4] However, major disagreements between theory and experiment remain. In particular, their predicted large in-plane anisotropies are not observed.

II. GROWTH OF bcc Fe(001) FILMS

Three nearly identical [30-ML Ag(001)/3-ML bcc Fe(001)/bulk Ag(001) substrate] sandwiches were grown at 300 K. Two [30-ML Ag(001)/3.4-ML bcc Fe(001)/bulk Ag(001) substrate] sandwiches were grown at 140 K. One of the two Fe(001) films was annealed by warm-

 0021-8979/88/083863-06$02.40 © 1988 American Institute of Physics

ing to room temperature before recooling to 140 K for deposition of the 30-ML Ag(001) cover layer. Two special structures consisting of [30-ML Ag(001) or 30-ML Au(001)/3-ML bcc Fe(001)/12-ML Ag(001)/Fe(001) whisker] were grown at 140 and 300 K, respectively, to investigate growth of Fe(001) films on essentially perfect Ag(001) substrates (see Sec. III).

The growths at 140 K were accomplished by tightly grasping the molybdenum substrate holder between a pair of liquid-nitrogen-cooled, copper-tipped jaws which had been recently installed in the growth chamber of our PHI 400 MBE machine.

Preparation of the bulk Ag(001) substrates for growth has been described elsewhere.[3] Preparation of the Fe(001) whisker was straightforward. The 15-mm-long Fe whisker, grown by chemical vapor deposition, was clamped at one end to the substrate holder. The whisker was sputtered at 2 keV for 30 min at 750 °C using Ar^+ ions, left to anneal for 20 min, resputtered for 5 min, and left to sit for 5 min more before the substrate heater was shut off and the whisker allowed to cool to room temperature.

AES and XPS studies revealed that both the bulk Ag(001) substrates and the Fe(001) whisker were quite free from contamination after sputtering and annealing. The strong RHEED patterns of a Ag(001) substrate and the Fe whisker are shown in Fig. 1.

During deposition, the vacuum in the growth chamber was held in the low 10^{-10} Torr range. The deposition rate was approximately 1 ML/min for both Fe and Ag. Evaporation rates were monitored using a Phillips quartz crystal monitor, RHEED specular spot intensity oscillations, and Auger peak intensities.

Since interface atomic mixing is almost nil for the 140 K growths of the Fe(001) on Ag(001), the thickness monitor readings could be used to calibrate the Auger electron inelastic mean free path which is then used to calculate the apparent film thickness. Applying these results to our 300 K growths of 3-ML Fe(001) on Ag(001) revealed that the apparent thickness was 15% lower at 300 K than that given by the thickness monitor. A simple model calculation for a 3-ML-thick film, which included 1-ML interface atomic mixing at the Fe/Ag interface, showed that the apparent thickness should be 17% lower than that given by the thickness monitor. Hence, atomic intermixing at Ag/Fe interfaces seems to be limited to less than one monolayer for room-temperature growths. This is far less serious than the intermixing observed in fcc Fe(001) grown on Cu(001) substrates at 300 K where Cu and Fe atoms intermixed.[5,6]

III. GROWTH CHARACTERIZATION BY RHEED

RHEED patterns of typical substrates are shown in Fig. 1. Notice a dramatic difference in the RHEED patterns of the bulk Ag(001) substrates and the Fe(001) whisker. Intensity variations along the RHEED streaks of the bulk Ag(001) reflect the presence of steps and variable length terraces. The broad specular spot is the result of a short sample coherence length related to the Ag substrate's mosaic

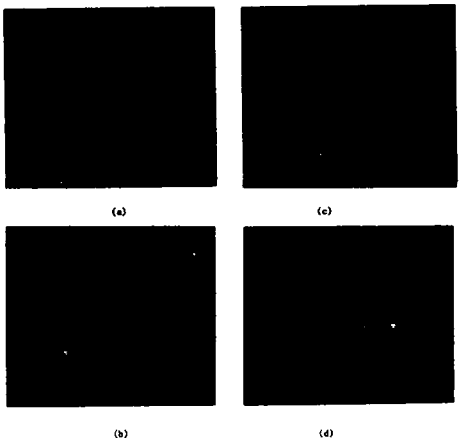


FIG. 1. RHEED patterns at room temperature: (a) bulk Ag(001) substrate, [110] azimuth, (b) 3-ML-thick Fe(001) overlayer grown at room temperature on bulk Ag(001), [110] azimuth, (c) Fe(001) whisker facet, [100] azimuth, (d) Fe(001) whisker facet, [110] azimuth. This photogragh was deliberately overexposed to emphasize Kikuchi patterns.

structure [Fig. 1(a)]. In contrast, the Fe whisker exhibits nearly perfect diffraction patterns [Figs. 1(c) and 1(d)]. The Ewald sphere intersects the 2D rods in well-defined spots (Ewald sphere spots) with very little streaking.

While RHEED oscillations were readily observed in all our samples at room temperature,[7] we were surprised to find very pronounced RHEED oscillations for 140 K growths carried out on the Fe whisker (see Fig. 2). The absence of interface mixing at 140 K, coupled with the ability to grow epitaxially at this temperature, led us to investigate in detail the growth of a Ag/Fe/Ag sandwich on the essentially perfect surface of the Fe(001) whisker.

The RHEED oscillations observed during the 140 K growths on the Fe whisker are shown in Fig. 2. The Ag(001) film used to cover the Fe whisker was terminated after 12 ML [Fig. 2(a)]. Although not shown on Fig. 2(a), we found that when the Ag furnace was closed, the Ag RHEED intensity decreased with time, reaching an equilibrium value below that corresponding to a half-covered surface; usually after growth, the specular spot intensity either remains constant or increases because of post-growth annealing. Upon reopening the shutter, the spot intensity quickly recovered. Clearly, surface diffusion is still taking place at 140 K.

Subsequent deposition of the 3-ML Fe(001) film also exhibited well-defined oscillations [Fig. 2(b)]. The RHEED patterns of grown Fe and Ag layers preserve their Ewald sphere spots but are now accompanied by short and very narrow streaks. Wide diffuse bands perpendicular to the RHEED streaks are also visible, indicating that the growth at low temperature is accompanied by numerous defects.[8] The 30-ML Ag(001) cover layer exhibits at least six well-defined RHEED oscillations [Fig. 2(c)]. With increasing thickness, a dark Kikuchi band splits the RHEED streaks into two well defined and intense spots. The spots broaden with further increase in the silver cover layer thick-

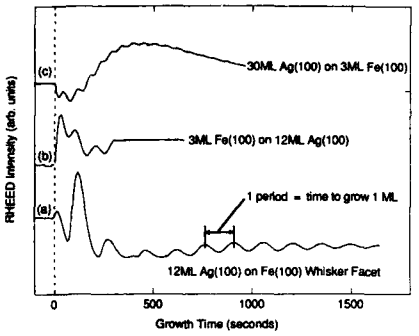


FIG. 2. RHEED pattern oscillations for growth at 140 K. The intensity of the specular spot is plotted against growth time. (a) 12-ML Ag grown on the Fe(001) whisker. (b) Subsequent growth of 3-ML Fe on the 12-ML Ag film. (c) Growth of the 30-ML coverlayer of Ag on the 3-ML Fe film.

ness and eventually changed into chevrons indicate the onset of surface faceting. Annealing the Ag coverlayer at room temperature removed the faceting, leaving the Ag RHEED streaks long and very narrow. The Ag cover layer surface is flat with its terraces significantly larger than those observed in well annealed (>400 °C) bulk Ag substrates.

The bright Ewald sphere spots are visible even when facets are present. Hence the presence of Ewald sphere spots reflects a long-range coherence on the sample surface. It is the rest of the RHEED pattern that indicates growth perfection. Specifically, the absence of any RHEED features other than Ewald sphere spots indicates an almost perfect surface. The appearance of narrow streaks shows the presence of surface steps and large terraces, ~ 100 Å long. The intensity modulation along RHEED streaks reflects a tendency for 3D surface roughening. The wide bands perpendicular to the RHEED streaks are a consequence of numerous defects on a very short lateral scale.

IV. DETERMINATION OF MAGNETIC PROPERTIES OF Fe FILMS

FMR is a powerful tool for the study of magnetic materials. For the Fe(001) surface orientation and the parallel FMR configuration (applied dc field H and microwave field h are orthogonal and in the plane) the equations of motion in the ultrathin film limit [film thickness $d \ll (A_{ex})^{1/2}/M_s$, where A_{ex} is the continuum exchange stiffness constant and M_s is the spontaneous magnetization] are

$$i\frac{\omega}{\gamma} m_{\parallel} + \left(H + 4\pi D_{\perp} M_s - H_s + \frac{K_1}{2M_s}(3 + \cos 4\varphi) + i\frac{\omega}{\gamma}\frac{G}{\gamma M_s}\right) m_{\perp} = 0 ,$$

$$\left(H + \frac{2K_1}{M_s}\cos 4\varphi + i\frac{\omega}{\gamma}\frac{G}{\gamma M_s}\right) m_{\parallel} - i\frac{\omega}{\gamma} m_{\perp} = h M_s , \quad (1)$$

where $m_{\parallel}$ and $m_{\perp}$ are the rf magnetization components parallel and perpendicular to the sample surface, $2K_1/M_s$ is the effective cubic anisotropy field, and H_s is an additional uniaxial anisotropy field which could be represented[9] by $H_s = 2K_s/(M_s d)$ if the effective field were due to a surface anisotropy energy $E_s = -K_s\alpha^2$ with its uniaxial symmetry axis normal to the sample film. G is the Gilbert damping parameter, $\omega = 2\pi f$ where f is the microwave frequency, $\gamma = g|e|/(2m_e c)$ is the spectroscopic splitting factor, g is the g-factor, and φ is the angle between M_s and the [001] direction. A time variation $\exp(-i\omega t)$ has been assumed.

The uniaxial surface anisotropy normal to the surface can be thought of as an effective field contributing to the demagnetizing field

$$(4\pi D_{\perp} M_s)_{\text{eff}} = 4\pi D_{\perp} M_s - 2K_s/(M_s d) , \quad (2)$$

where $4\pi D_{\perp} M_s$ is the demagnetizing field perpendicular to the sample surface. For ultrathin films, $D_{\perp}$ is thickness dependent (see Table I). The FMR resonance field measures the effective demagnetizing field $(4\pi D_{\perp} M_s)_{\text{eff}}$, whereas the strength of the microwave absorption is proportional to the value of the true saturation magnetization M_s. The FMR peak-to-peak amplitude I of the magnetic field derivative of the microwave power absorption is given by

$$I \sim \frac{4\pi M_s}{(\Delta H)^2} d \frac{[H + (4\pi D_{\perp} M_s)_{\text{eff}}]}{[2H + (4\pi D_{\perp} M_s)_{\text{eff}}]} . \quad (3)$$

The experimental FMR linewidth $\Delta H(\omega)$ is related to the intrinsic Gilbert damping constant G and the inhomogeneous line broadening $\Delta H(0)$ by

$$\Delta H(\omega) = 1.16(\omega/\gamma)[G/(\gamma M_s)] + \Delta H(0) . \quad (4)$$

To determine both $(4\pi D_{\perp} M_s)_{\text{eff}}$ and g, for a given specimen we carried out FMR at 9.6, 36.6, and 73 GHz. More detailed studies, over the narrower frequency range of 10–40 GHz, were done using Brillouin light scattering[10] (BLS) with a six-pass Fabry–Perot interferometer. Both techniques provide signals with excellent signal-to-noise ratios for the ultrathin films. The electron-spin-resonance (ESR) peak intensity of the paramagnetic free radical DPPH was used to provide an absolute calibration of the FMR intensity. Comparisons of the saturation magnetization M_s in different samples were then carried out using Eq. (3).

V. MAGNETIC MEASUREMENTS ON bcc Fe(001) FILMS

We summarize the results of our FMR measurements in Table I. For completeness, we have included our previous FMR results[3] for Au/Fe/Ag sandwiches. The fifth entry in Table I is representative of the results obtained for the three 3-ML Fe(001) films grown in Ag/Fe/Ag sandwiches at 300 K. The last two table entries are for one of the two 3.4-ML-thick Fe(001) films grown at 140 K. The other 3.4-ML Fe(001) film grown at 140 K (the one allowed to anneal to room temperature before being recooled and covered with Ag) was not included in Table I because its FMR line split during cooling to 77 K. This rendered it unsuitable for a complete FMR study. The Ag/Fe/Ag and Au/Fe/Ag sandwiches grown on the Fe whiskers were studied using Brillouin light scattering.

As seen in Table I, the static magnetic properties of Ag/Fe/Ag films grown at room temperature [and hereafter referred to as $(\text{Ag/Fe/Ag})_{300}$ films] do not differ signifi-

TABLE I. FMR results for ultrathin Fe(001) films on Ag(001) substrates assuming $A_{xx} = 1 \times 10^{-6}$.

d (ML)	T (K)	Cover metal	$4\pi M_s$ (kG)	$(4\pi D_\perp M_s)_{eff}$ (kG)	g	K_1(36 GHz) (ergs/cm^3)	$D_\perp$	K_s (ergs/cm^2)	G (s)$^{-1}$	$\Delta H(0)$ (Oe)	Frequency (GHz)	
28	300	Au	21.55	18.034	(2.09)[a]	⋯	0.984	0.943	$(0.66\times10^8$)[a]	50.0	73.00	⋯
17	300	Au	21.55	16.553	2.08	4.1×10^5	0.973	0.825	0.65×10^8	69.9	72.91	36.50
4.9	300	Au	21.55	6.817	2.09	1.1×10^5	0.908	0.568	2.3×10^8	97.2	72.79	36.54
2.8	300	Au	14.00	0.562	2.09	0.0	0.846	0.253	5.7×10^8	209.0	72.90	36.50
3.0	300	Ag	14.00	0.320	2.00	0.0	0.846	0.277	1.0×10^9	640.0	36.60	9.54
(3.4)[b]	300	Ag	7.00	−0.023	2.02	0.0	0.879	0.084	2.0×10^8	115.0	36.62	9.54
(3.4)[b]	77	Ag	20.00	−3.025	2.00	0.0	0.879	0.894	2.1×10^8	480.0	36.75	9.56

[a] Assumed same as that for bulk Fe.
[b] This substrate was grown at 140 K, but all others were grown at 300 K.

cantly from our previously studied $(Au/Fe/Ag)_{300}$ samples.[3] The effective $(4\pi D_\perp M_s)_{eff}$ is very close to that of the $(Au/Fe/Ag)_{300}$ structures of equivalent thickness. Thus, at ambient temperature Au and Ag contribute to the pseudo-surface anisotropy almost equally. Noticeable differences occur at low temperature, though. All 3-ML-thick (Ag/Fe/Ag) samples show a negative value of $(4\pi D_\perp M_s)_{eff}$ at 77 K while all of the 3-ML-thick $(Au/Fe/Ag)_{300}$ films still have a positive $(4\pi D_\perp M_s)_{eff}$.

The saturation magnetization M_s is independent of the choice of an Au or Ag cover layer for 300 K growths. Recent SQUID magnetometer measurements indicate[11] that our 3-ML samples with Au cover layers have somewhat lower saturation magnetizations than bulk Fe [$4\pi M_s$(3-ML Fe) ≈ 14 kG compared to $4\pi M_s$(bulk Fe) $= 21.55$ kG]. However, comparisons of FMR signals with thick Fe films show that the bulk saturation magnetization is already recovered in 5-ML-thick samples.

There are still noticeable differences in the dynamic magnetic behavior between $(Au/Fe/Ag)_{300}$ and $(Ag/Fe/Ag)_{300}$ films. A spectroscopic splitting factor of $\gamma = 1.7588\times10^7\ G^{-1}\ s^{-1}$, and hence a g factor of $g \approx 2.00$ was observed in *all* our Ag/Fe/Ag samples. In contrast, all of the $(Au/Fe/Ag)_{300}$ samples maintained the bulk Fe g factor of $g = 2.09$. Fits of Brillouin light scattering spectra obtained on the same specimens agree with the FMR results proving that the g factor in Ag/Fe/Ag samples is close to the free-electron value (see Fig. 3). This is a rather surprising result. We could argue[3] that the absence of in-plane anisotropy is due to the in-plane anisotropy changing its sign as the 2D limit is approached. This argument is invalid in this case because the g factor is quadratically dependent on the spin-orbit-induced orbital moment.[12] The decreased value of the g factor is either due to the absence of spin-orbit coupling in our Ag/Fe/Ag samples or is a result of dynamic interactions which increase the energy of the measured resonance mode. The absence of the spin-orbit interaction in our Ag/Fe/Ag samples is not likely because the uniaxial anisotropy is essentially the same as for the Au/Fe/Ag samples. On the other hand, if we assume a complex-valued Gilbert damping coefficient, $G = G_R + iG_I$, then G_I would shift the energy of the resonant mode proportionally with the microwave frequency ω and hence renormalize the g factor. The g factor is likely shifted by dynamic interactions.

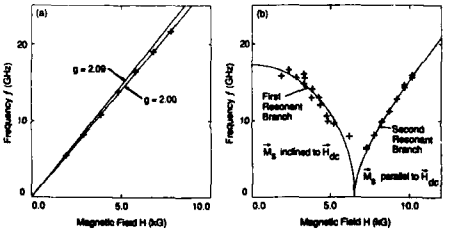


FIG. 3. Spectra obtained by Brillouin light scattering measurements. (a) [30-ML Ag(001)/3 ML bcc Fe(001)/Ag(001) bulk substrate], $(4\pi D_\perp M_s)_{eff} \approx 0$. (b) [100-ML Cu(001)/3-ML fcc Fe(001)/Cu(001) bulk substrate], $(4\pi D_\perp M_s)_{eff} = -6.5$ kG, $\gamma = 1.618\times10^7$ (Oe s)$^{-1}$, $H_{x2} = 0.23$ kOe.

It is interesting to note that the $(Ag/Fe/Ag)_{300}$ samples exhibit much higher values of $\Delta H(0)$ than those observed in Au/Fe/Ag samples while at the same time the Gilbert damping coefficient G decreases substantially from $G = 5.7\times10^8\ s^{-1}$ in the Au/Fe/Ag samples to $G = 1.0\times10^8\ s^{-1}$ in the Ag/Fe/Ag samples of comparable thickness (see Table I). The frequency-independent part of the FMR linewidth, $\Delta H(0)$, is caused by magnetic inhomogeneities. Variations of sample thickness result in appreciable variations of the surface anisotropy fields since $H_s \sim 1/d$. However, inhomogeneities contribute to FMR linebroadening only if their lateral extent is larger than the exchange length (~ 100 Å in Fe). Fast variations related to small terraces are averaged out by strong exchange fields. It is likely that long-range imperfections in our Fe films are due to the pronounced "lemon peel" surfaces of the bulk Ag substrates.

The growth of the [30-ML Ag(001)/3.4-ML bcc Fe(001)/Ag(001) substrate] sandwich at 140 K [hereafter referred to as $(Ag/Fe/Ag)_{140}$] resulted in a substantial decrease in the room-temperature value of the saturation magnetization to $4\pi M_s \approx 7$ kG as obtained from Eq. (3). However, its value of $4\pi M_s$ recovers to ~ 20 kG when $(Ag/Fe/Ag)_{140}$ was cooled to liquid-nitrogen temperatures. The same increase of $4\pi M_s$ with decreasing temperature was observed at 9.6 and 36.6 GHz microwave frequencies with corresponding FMR field values of 3.4 and 13.0 kOe, respectively. The rapid increase of the saturation magnetization upon cooling indicates that the critical temperature T_c of the $(Ag/Fe/Ag)_{140}$ sample was $T_c \approx 420$ K (assuming a linear dependence of M_s upon temperature T). The increase in M_s with decreasing temperature, independent of the dc magnetic field, implies that superparamagnetic fluctuations *is not* the mechanism responsible for the decrease in

T_c. The wide bands observed in RHEED patterns of the Ag/Fe/Ag samples show the presence of numerous defects which lead to the exposure of the inner Fe layers to surrounding Ag atoms. This results in a decrease of the exchange coupling and therefore a decrease in the critical temperature T_c. This interpretation seems to be confirmed by results obtained with the Ag/Fe/Ag sample whose Fe film was grown at 140 K and then allowed to anneal by warming slowly to room temperature before recooling for growth of the Ag cover layer. The saturation magnetization M_s in this annealed sample was close to that measured in the $(Ag/Fe/Ag)_{300}$ samples. The annealing process recovers atomic surface homogeneity and results in the increase of T_c. Note that for the $(Ag/Fe/Ag)_{140}$ specimen the saturation magnetization M_s increased by a factor of 3 in going from room to liquid-nitrogen temperature [$4\pi M_s(300\ \mathrm{K}) \approx 7$ kG, $4\pi M_s(77\ \mathrm{K}) \approx 20$ kG]. At the same time, $(4\pi D_\perp M_s)_{\mathrm{eff}}$ changed from 0 to -3 kG corresponding to a change in H_s by a factor of 3 (from 7 to 23 kOe). Hence, H_s scales approximately as M_s and the uniaxial anisotropy energy, $-K_s\alpha^2$, scales as M_s^2.This result is acceptable since close to T_c the magnetic energies scale according to the powers of α.[13,14] The fact that H_s scales with M_s gives $\Delta H(0)$ its strong temperature dependence. $\Delta H(0) = 115$ G at 300 K and $\Delta H(0) = 480$ G at 77 K. This is consistent with inhomogeneity linebroadening, for which $\Delta H(0) \sim (\delta H_s)^2 \sim M_s^2$.

Brillouin light scattering measurements carried out on the [30-ML Au(001)/3-ML bcc Fe(001)/12-ML Ag(001)/Fe(001) whisker facet] sandwich grown at room temperature showed that the uniaxial anisotropy is close to that observed in the samples grown on bulk Ag substrates. However, the uniaxial anisotropy of the Au/Fe/Ag sandwich grown on an Fe whisker was increased by 2.5 kOe resulting in a negative value of $(4\pi D_\perp M_s)_{\mathrm{eff}} = -2.5$ kOe. M_s of this sample is perpendicular to the sample surface at room temperature (300 K) and below.

VI. MAGNETIC MEASUREMENTS ON fcc Fe(001) FILMS

The higher melting point and almost identical atomic size of Fe compared to those of Cu create favorable thermodynamic conditions for Fe agglomeration and atomic mixing due to Cu surface segregation onto Fe. The Cu/Fe interface behavior was extensively studied by the NBS group.[5] 1-, 2-, and 3-ML-thick Fe overlayers were grown on Cu substrates held at 100 K. At that temperature, the atomic intermixing was completely supressed. Samples were then gradually brought to 350 K while the intensity of the Cu $2p$ XPS peak was continuously monitored. It was found that in 1-ML-thick films the Fe started to agglomerate around 200 K and Cu surface segregation began around 300 K. However, 3-ML-thick samples do not show any signs of Fe agglomeration or Cu surface segregation at 325 K and hence provide a well-defined structure suitable for magnetic studies. These conclusions were further checked and supported by CO titration and Cu, Fe XPS angular resolved studies.[6]

Magnetic studies using FMR and Brillouin light scattering were carried out on 3-ML-thick fcc Fe(001) films grown on Cu(001) substrates held at 100 K. The films were then annealed at 325 K and subsequently covered at ambient temperature by a 100-ML-thick Cu(001) coverlayer.

The FMR resonance field at 9.54 GHz is 7.9 kOe, approximately 4.5 kOe above the effective field of $\omega/\gamma \sim 3.4$ kOe. This result, and the absence of any in-plane anisotropy, show that measured samples have a large uniaxial anisotropy which results in $(4\pi D_\perp M_s)_{\mathrm{eff}} \approx -6.5$ kG. The Brillouin light scattering spectra show two distinct resonance branches [Fig. 3(b)], proving unambiguously that the substrate magnetization M_s is perpendicular to the sample surface in the absence of a dc magnetic field. The first branch corresponds to resonance modes with the saturation magnetization inclined with respect to the sample surface. The second branch represents resonance modes with the saturation magnetization M_s in the plane of the specimen and parallel to the applied dc magnetic field.

Detailed fits reveal that a fourth-order anisotropy term, $-K_{s2}\alpha^4$, is needed along with the second-order uniaxial anisotropy, $-K_{s1}\alpha^2$, to increase the calculated resonant frequencies of the first branch [Fig. 3(b)]. The angle of inclination of the saturation magnetization is given by

$$[M_s H + (4\pi D_\perp M_s)_{\mathrm{eff}} M_s \cos\varphi - 4K_{s2}\sin^2\varphi\cos\varphi]\sin\varphi = 0\,, \tag{5}$$

where φ is the angle between M_s and the specimen plane. The corresponding resonance modes are then found by solving the Landau–Lifshitz equations of motion.[10]

Note that the effective field caused by the fourth-order term $H_{s2} = 0.23$ kOe is much smaller than the effective demagnetizating field $|4\pi D_\perp M_s|_{\mathrm{eff}} = 4.5$ kG. This is contrary to Brillouin light scattering experiments[10] carried out on Cu/Fe superlattices which show $H_{s2} \approx |4\pi D_\perp M_s|_{\mathrm{eff}}$.

The FMR linewidth increases rapidly with decreasing temperature, resulting in a virtual absence of a FMR signal at liquid-nitrogen temperature (77 K). Therefore, no estimate of the critical temperature T_c could be made for the 3-ML-thick fcc Fe specimens.

VII. SUMMARY AND DISCUSSION

We have successfully grown ultrathin bcc Fe(001) films surrounded by Ag or Ag and Au layers at room temperature. The presence of a uniaxial anisotropy field with easy axis perpendicular to the sample surface was firmly established. The uniaxial anisotropy is mainly confined to the surface region,[4] hence the use of the term "pseudosurface" anisotropy to describe it.

This slow variation of K_s with d is in agreement with recent calculations by Gay and Richter.[1] Using the spin-orbit interaction in their SCLO band calculations they found the uniaxial surface anisotropy decreases with the number of atomic layers of Fe. For example, calculations carried out for a 5-ML-thick iron film show that the uniaxial energy decreases 1.7 times from that in the thick film limit which compares well with our decrease of K_s by a factor of ~ 1.7.

Ag and Au contribute almost equally to the pseudosurface anisotropy energy K_s at ambient temperature. However, at low temperatures, the Fe/Ag interface contribution to K_s is somewhat larger than that of the Fe/Au interface

and results in a negative $(4\pi D_1 M_s)_{\text{eff}} \approx -3$ kOe at liquid N_2 temperatures (77 K). It should be pointed out that Ag(001) and Fe(001) lattices are well matched *only* in the (001) plane. There is an appreciable vertical mismatch due to the large tetragonal distortion between fcc and bcc lattices. It follows that the presence of steps might affect the growth of Fe on bulk Ag(001). A significantly smaller density of steps on the Fe whisker substrates may be a reason why we observed an increased uniaxial anisotropy of the Au/Fe(3 ML)/Ag sandwiches grown on Fe whiskers compared to those sandwiches grown on bulk Ag(001). In the [30-ML Au/3-ML Fe/12-ML Ag/Fe whisker] specimens, $(4\pi D_1 M_s)_{\text{eff}} \approx -2.5$ kOe at room temperature (300 K). Note, however, that the overall uniaxial anisotropy field is not significantly changed by the quality of the substrate surface.

We have grown Ag/Fe/Ag sandwiches at 140 K. RHEED patterns and intensity oscillations clearly show that epitaxial growth can be achieved at low temperatures. The growth at 140 K is epitaxial but results in numerous defects and short terraces causing a substantial decrease in the critical temperature T_c.

The 3-ML-thick fcc Fe(001) layers grown on bulk Cu(001) substrates show a strong uniaxial anisotropy field, $(4\pi D_1 M_s)_{\text{eff}} = -6.5$ kG, with the easy axis perpendicular to the sample surface. Note the significant difference between the values of $(4\pi D_1 M_s)_{\text{eff}}$ in the 3-ML fcc and bcc Fe(001) films. While $(4\pi D_1 M_s)_{\text{eff}}$ was nearly zero in the bcc Fe films grown on bulk Ag(001) substrates at 300 K, increasing negatively with decreasing temperature, $(4\pi D_1 M_s)_{\text{eff}}$ was already -6.5 kG at room temperature for the fcc Fe(001) films. The two resonance branches observed in the Brillouin light scattering experiments prove that the fcc Fe(001) samples are magnetized perpendicularly to their surface in the absence of a dc magnetic field. A very weak fourth-order anisotropy energy, $-K_{s2}\alpha^4$, is present with its easy axis perpendicular to the sample surface. This is contrary to results obtained in Mo/Ni superlattices[15] where the fourth-order term holds the saturation magnetization M_s parallel to the sample surface.

No in-plane anisotropy was observed in any of the 3-ML-thick fcc or bcc Fe(001) samples This differs from the theoretical calculations of Gay and Richter[1,4] who predicted very strong in-plane anisotropies.

It is less well known that the Gilbert damping is primarily due to the spin-orbit interaction.[12] In bcc Fe(001) films, the spin-orbit interactions contribution to Gilbert damping is dramatically changed when the Au coverlayer is replaced with Ag. The Gilbert damping coefficient changes from $G \approx 5.7 \times 10^8\ \text{s}^{-1}$ in [Au(30 ML)/Fe(3 ML)/Ag bulk] samples to $G \approx 1.0 \times 10^8\ \text{s}^{-1}$ in [Ag(30 ML)/Fe(3 ML)/Ag bulk] samples. Gay and Richter have pointed out that moderate changes in the electronic structure can profoundly effect the contribution of the spin-orbit interaction to magnetic anisotropies. Perhaps this should be extended to the intrinsic Gilbert damping as well.

The authors wish to acknowledge the help of K. Myrtle and J. Rudd in this work and funding from the National Science and Engineering Research Council of Canada.

[1]R. Richter, J. G. Gay, and J. R. Smith, Phys. Rev. Lett. **54**, 2704 (1985).
[2]B. T. Jonker, K.-H. Walker, E. Kisker, G. A. Prinz, and C. Carbone, Phys. Rev. Lett. **57**, 142 (1986).
[3]B. Heinrich, K. B. Urquhart, A. S. Arrott, J. F. Cochran, K. Myrtle, and S. T. Purcell, Phys. Rev. Lett. **59**, 1756 (1987).
[4]J. G. Gay and R. Richter, J. Appl. Phys. **61**, 3362 (1987).
[5]D. A. Steigerwald and W. F. Egelhoff, Jr., Surf. Sci. **192**, L887 (1987).
[6]D. A. Steigerwald and W. F. Egelhoff, Jr., Surf. Sci. (to be published).
[7]S. T. Purcell, A. S. Arrott, and B. Heinrich, Proceedings of the 1987 MBE Workshop (to be published).
[8]P. R. Pukite, P. I. Cohen, and S. Batra, 1987 NATO Workshop Proceedings in RHEED and REM (to be published).
[9]J. F. Cochran, B. Heinrich, and A. S. Arrott, Phys. Rev. B **34**, 7788 (1986).
[10]J. R. Dutcher, B. Heinrich, J. F. Cochran, D. A. Steigerwald, and W. F. Egelhoff, Jr. (these proceedings).
[11]Preliminary studies using SQUID magnetonmeter measurements were carried out by J. J. Krebs and G. A. Prinz at the Naval Research Lab.
[12]V. Kambersky, Czech. J. Phys. B **26**, 1366 (1976).
[13]H. B. Callen and E. Callen, J. Phys. Chem. Solids **27**, 1271 (1966).
[14]S. D. Hanham, A. S. Arrott, and B. Heinrich, J. Appl. Phys. **52**, 1941 (1981).
[15]M. Y. Pechan and I. K. Schuller, Phys. Rev. Lett. **59**, 132 (1987).

Hyperfine fields and spin orientations in (Fe^{57}/Ag) superlattices from conversion electron Mössbauer studies (invited)

F. A. Volkening,[a] B. T. Jonker, J. J. Krebs, N. C. Koon, and G. A. Prinz
Naval Research Laboratory, Washington, DC 20375-5000

Conversion electron Mössbauer studies have been carried out as a function of temperature on a series of single-crystal [(100)^{57}Fe/(100)Ag] superlattices grown by MBE on GaAs substrates. The ^{57}Fe layer thickness was varied from approximately 1 to 5.5 ML. From the relative intensity of the Mössbauer lines we show conclusively that the orientation of the magnetic moment for films 2.4 ML and thinner in zero applied field is perpendicular to the film plane at low temperatures. For a 5.5-ML film the spin alignment at room temperature is in the film plane and partially out of the plane at low temperatures. The low-temperature magnetic hyperfine fields are enhanced relative to bulk Fe.

I. INTRODUCTION

The study of magnetism at surfaces, interfaces, and in ultrathin films has emerged in recent years as one of the most active areas of solid-state physics. Experimentally, the application of new thin-film growth technologies to the production of transition-metal single-crystal films, superlattices, and modulated structures has opened the door to the discovery and engineering of new materials with novel properties.[1-3] Equally important, advances in theoretical and computational methods have allowed meaningful comparison of calculated results with experiment and serve as guideposts to advancing the search for new materials which may exhibit unusual properties.[4,5]

Attractive systems to investigate are ultrathin magnetic films grown epitaxially on single-crystal substrates. Such systems are the building blocks of more complicated structures, form a close approximation to ideal 2D magnetic films, and approximate the theoretical model calculations. In particular, epitaxial Fe(100) on Ag(100) has proved to be a very interesting system.[4-10] It can be grown in high-quality single-crystal form with well-defined, flat interfaces. Furthermore, Fe and Ag have very little overlap of their valence electron bands,[4,5] leading to only a small degree of band hybridization and thus permitting the approximate realization of two-dimensional Fe films. Among the properties of this system which are of intense interest are the size of the magnetic moments, theoretically predicted to be enhanced relative to bulk Fe,[4,5] the magnetic anisotropy,[6,7,9] the magnetic hyperfine fields,[10] and the nature of the magnetic ordering process, which may exhibit two-dimensional behavior for the thinner films.[11,12]

The importance of the magnetic surface anisotropy was recently emphasized by the work of Jonker *et al.*[6] who carried out spin polarized photoemission studies of ultrathin epitaxial Fe(100) layers on Ag(100). It was shown that at room temperature there was no in-plane magnetic moment for films thinner than 3 monolayers (ML). It was suggested that this resulted from a perpendicular surface anisotropy strong enough to compete with the demagnetization field ($4\pi M = 21.5$ kG in bulk Fe). The photoemission results stimulated theoretical efforts by Gay and Richter[7,9] to calculate the spin anisotropy of the Fe/Ag(100) system. They found that the out-of-plane configuration is the most energetically favorable for a free-standing Fe(100) monolayer[7] but there results were inconclusive for a monolayer of Fe on Ag(100).[9]

More recently, Heinrich *et al.*[8] carried out FMR studies on 3-, 5-, 17-, and 24-ML-thick Fe(100) films on Ag(100). By extrapolating their results to thinner films they found indications that the magnetization of a bilayer of Fe on Ag (100) should be perpendicular to the film.

Previous Mössbauer studies of polycrystalline films of Fe on Cu and Ag,[13] Fe on Mg,[14] and Fe on MgO (Ref. 15) have shown that for films thinner than 8 Å, the magnetization was predominantly oriented perpendicular to the plane of the film. However, it remained unclear if the properties arose from superparamagnetic clusters or other effects related to the structure of the film.

Also of interest are the sizes of the magnetic moments and the related magnetic hyperfine fields. Layer-by-layer Mössbauer investigations of the Fe(110)/Ag(111) interface show an increase in the ground-state magnetic hyperfine field to 350 kG at the interface in comparison to 340 kG for bulk Fe.[16,17] Recent band-structure calculations[4,5] on both free-standing Fe(100) layers and Fe/Ag(100) interfaces and sandwiches have predicted an enhancement of the Fe moment to the order of $3\mu_B$ or more from the bulk value of $2.2\mu_B$, and wide variations in the magnetic hyperfine field away from the bulk value of 340 kG at low temperatures due to the effect of the *s*-like conduction electron polarization on the magnetic hyperfine field.[10]

It was the aim of the present work to determine via Mössbauer spectroscopy both the orientation of the magnetic moments and the size of the magnetic hyperfine fields in high-quality ultrathin Fe(100)/Ag(100) single-crystal superlattice films as a function of temperature. In a previous paper[18] we presented the first direct evidence for perpendicular anisotropy in the Fe(100)/Ag(100) system; this report represents an expansion of that work. Also appearing in this journal are the results of SQUID magnetometer measurements made on the same samples used in this investigation.[19] These measurements confirm that at low temperatures there is a significant perpendicular remanence M_R in these ultrathin Fe/Ag superlattice films. Furthermore, the strong

[a] Permanent address: Sachs/Freeman Associates, Landover, MD 20785.

 0021-8979/88/083869-05$02.40 © 1988 American Institute of Physics

temperature dependence of M_R and the relaxation behavior observed in the Mössbauer spectra raise interesting questions about the dynamics of these films.

II. SAMPLES AND METHODS

The epitaxial growth of Fe on Ag(100) at room temperature has been shown to proceed in a layer-by-layer fashion through the completion of 3 monolayers, with further deposition accompanied by island formation.[6,20] Since the lattice constants of bcc α-Fe and fcc Ag differ by a factor very near $\sqrt{2}$, there is only a 0.8% mismatch between the α-Fe(100) and Ag(100) surface nets after a rotation of 45° about the surface normal.

The samples used in this experiment were grown in a PHI Model 400 molecular-beam epitaxy system, and characterized *in situ* with Auger electron spectroscopy (AES) and reflection high-energy electron diffraction (RHEED). The Fe/Ag superlattices were grown at room temperature on a Ag(100) film 500 Å thick grown on a 0.2-μm-thick ZnSe(100) epilayer, which was grown in turn on a GaAs(100) substrate to optimize the surface morphology as indicated by sharp, well-defined streaks in the RHEED pattern. The ^{57}Fe and Ag were deposited alternately from shuttered Knudsen cell-type sources at rates of 1–2 and 5–7 ML/min, respectively. Samples were grown with superlattice periods in which the ^{57}Fe/Ag layer thicknesses were 0.9/3.9, 1.8/4.8, 2.4/5.6, and 5.5/7.0 ML (1 ML Fe = 1.43 Å, 1 ML Ag = 2.045 Å), as determined by x-ray resonance fluorescence (XRF) measurements. The number of periods in the superlattices were 45, 30, 20, and 7, respectively. Each growth was terminated with an extra period of Ag, and the sample was finally coated with 75 Å of Al before removal from the MBE system to prevent oxidation or tarnish on exposure to atmosphere.

The single-crystal nature of each layer was verified during growth by RHEED. In an accompanying article,[19] RHEED patterns obtained at various stages during the growth of the 0.9/3.9 ML sample are shown and discussed. In brief, the Ag base layer patterns exhibit well-defined streaks and a low background intensity characteristic of a well-ordered single-crystal surface, and reflect the symmetry of the Ag(100) surface net (assuming simple termination of the bulk Ag lattice). RHEED shows that the Fe layers exhibit a surface net identical to that of the Ag, as expected. The layers exhibit very well-ordered single-crystal surfaces throughout the growth of the superlattice, as evidenced by comparing Fe and Ag RHEED patterns produced by the final period with those of earlier layers and with the Ag base layer.

The conversion electron Mössbauer spectrometer used in this work was of the cylindrical mirror analyzer type. The acceptance angle was 30°–60° and the energy resolution was approximately 4%. The pass energy was set for the 7.3-keV K-shell conversion electrons. The sample was mounted on a Cu block connected via a Cu braid to a closed-cycle refrigerator, the first stage of which was used to cool a radiation shield that also served as a cryopumping surface. The transducer and source were inside of the vacuum chamber eliminating the need for a lengthy drive rod assembly and window. The γ rays were incident normal to the sample plane. With a 40-mCi source (Co in Rh) a statistically meaningful spectra for the 2.4-ML sample (20 repeats = 48 ML ^{57}Fe total) could be obtained in one day.

The fitting procedure was based on using the minimum number of Fe sites needed to obtain a good representation of the data. For the 2.4- and 5.5-ML films the spectra could be fit with a simple two-site model. For the 0.9- and 1.8-ML films additional nonmagnetic components, most likely corresponding to isolated Fe atoms and small Fe clusters, had to be added to fit the inner lines. The criteria used in choosing the fit was that the parameters remain well behaved over a wide temperature range. Although there are two possible low-temperature fits only one fit was chosen due to the inability of the other to fit the room-temperature data without significantly changing the isomer shift and quadrupole splitting obtained at the lower temperatures.

III. RESULTS AND DISCUSSION

A. Anisotropy

Mössbauer spectra for the superlattices containing 5.5-, 2.4-, 1.8-, and 0.9-ML-thick ^{57}Fe layers and measured at 15 K are shown in Fig. 1. For comparison, the spectrum of a 500-Å-thick ^{57}Fe film is also shown. Information concerning the orientation of the magnetization relative to the direction of propagation of the gamma rays is contained in the intensities in lines 2 and 5. The intensity ratio is given by $3{:}x{:}1{:}1{:}x{:}3$, where $x = 4\sin^2\theta/(1+\cos^2\theta)$ and θ is the angle between the incident γ-ray direction and the direction of the magnetic hyperfine field. Normally, thin ferromagnetic films are magnetized in-plane due to the large shape (or demagnetization) anisotropy. This corresponds to the line intensity ratio 3:4:1:1:4:3 which is exactly that observed for the 500-Å-thick sample.

For the 2.4 ML and thinner ^{57}Fe superlattices the intensities in the second and fifth lines are very weak indicating that the magnetization points predominantly out of plane at 15 K. The integrated line intensity ratios for these films are approximately 3:0.5:1:1:0.5:3 which is close to the value 3:0:1:1:0:3 corresponding to having all of the Fe moments oriented perpendicular to the plane. This ratio corresponds to a uniform deviation of the Fe moments from perpendicular of approximately 30° or, alternately, that approximately 20% of the moments lie in the plane and 80% are perpendicular to it. Because of possible domain formation and imperfections in the films, the correct physical picture probably lies in between these two extremes.

At room temperature the hyperfine splitting for the three thinnest films measured has collapsed (Fig. 2) and at intermediate temperatures the spectra exhibit broadening suggestive of a relaxation process. This broadening is still somewhat present in the spectra of the 0.9-ML superlattice measured at 15 K. At all temperatures for which the lines can be resolved the spectra indicate a pronounced perpendicular anisotropy indicating that the relaxation is not due to 3D superparamagnetic clusters.

The 5.5-ML sample exhibits a temperature-dependent orientation of the magnetization as evidenced by comparing the room-temperature spectra shown in Fig. 2 with the spec-

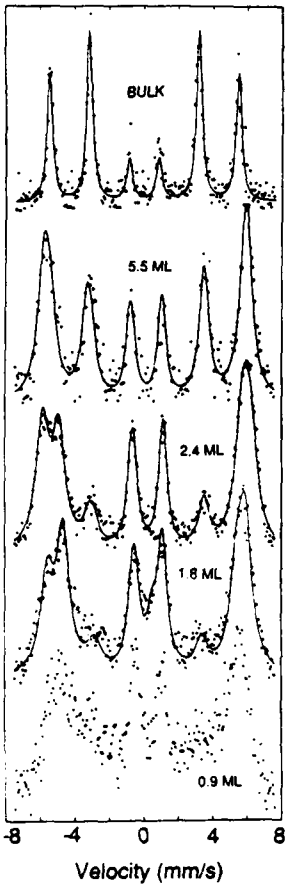


FIG. 1. Conversion-electron Mössbauer spectra taken at 15 K for 0.9-, 1.8-, 2.4-, and 5.5-ML multilayer films of ^{57}Fe(100) on Ag(100). Shown for comparison is the spectra of a thick film of ^{57}Fe($\approx$500 Å).

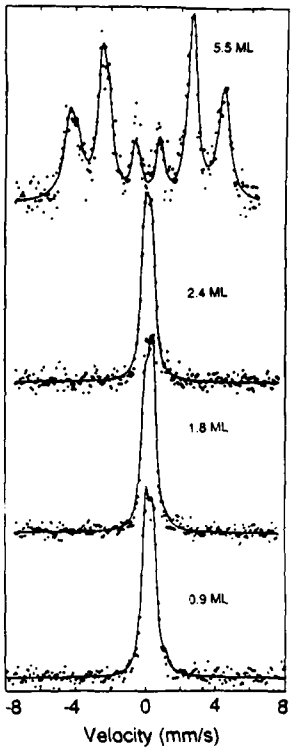


FIG. 2. Conversion-electron Mössbauer spectra taken at room temperature for 0.9-, 1.8-, 2.4-, and 5.5-ML multilayer films of ^{57}Fe(100) on Ag(100).

trum taken at 15 K (Fig. 1). At room temperature the magnetization is in the film plane, corresponding to the observed 3:4:1:1:4:3 intensity ratio. With decreasing temperature the magnetization points increasingly out of the plane until approximately 77 K, below which the line intensity ratio remains close to 3:2:1:1:2:3, which is just that observed for powder samples which have a random orientation of moments.

This suggests that at low temperatures the surface anisotropy of the 5.5-ML film is comparable to the demagnetization field, whereas at room temperature the demagnetization field dominates. This effect may be due in part to the morphology of the film since the RHEED pattern for this film was not as good as that from the thinner films ($d < 3$ ML). This is expected since the growth of Fe on Ag(100) should proceed in a layer-by-layer fashion for the first three monolayers and then exhibit island growth.[6,20]

In comparison the previous investigation by Jonker *et al.*[6] of Fe/Ag(100) films via spin-polarized photoemission revealed a net in-plane spin polarization indicative of long-range ferromagnetic order for a 5.2-ML Fe film at room temperature. However, no in-plane moment was observed for the thinner films (2.5 ML and less) indicating that those films had no remanent magnetization along the [100] axis at room temperature. They interpreted this as either being caused by a surface anisotropy strong enough to force the moments to lie perpendicular to the plane or that T_C for these films had dropped below room temperature. This investigation and the magnetization measurements of Krebs *et al.*[19] (done on the same superlattice films used in this investigation) show that they were correct on both accounts, i.e., 2.4 ML and thinner films do exhibit strong perpendicular anisotropy, however, they also have a magnetic ordering temperature below 300 K.

B. Hyperfine fields

Spectra taken at 15 K for the 5.5-, 2.4-, 1.8-, and 0.9-ML Fe superlattices are shown in Fig. 1. The spectra for the 2.4- and 1.8-ML Fe films exhibit a pronounced left-right asymmetry in both the apparent linewidths and intensities for the outer lines suggestive of a nonzero quadrupole interaction. The observed line broadening indicates some distribution of hyperfine fields and the asymmetry in the spectra requires the presence of at least two crystallographically inequivalent sites as is expected due to the presence of Fe atoms with differing local surroundings of Fe and Ag atoms (e.g., Fe atoms in edge, surface, or interior positions). In order to approximate the distribution and the asymmetry we used a

simple two-component model to fit the spectra. The instrumental linewidth (FWHM) was 0.3 mm/s, the linewidth used in fitting the spectra was 0.8 mm/s for lines 1 and 6. The inner lines exhibit a decreasing linewidth as expected if the excess linewidth is due to a distribution in the magnetic hyperfine field.

The parameters obtained form the fits at 15 K and room temperature are given in Table I. At 15 K the hyperfine fields for the 2.4-ML superlattice film are 358 and 344 kG, each component accounting for approximately 50% of the ^{57}Fe in the sample. The positive isomer shifts of 0.06 and 0.5 mm/s implies a decrease in the *s*-electron density at the nucleus. The hyperfine fields are temperature dependent as shown in Fig. 3, where the average values of the two components are plotted. A linear extrapolation of the fits to $T = 0$ for the 2.4-ML superlattice results in hyperfine fields of 371 and 358 kG. The nonzero quadrupole splitting observed for both components reflects a loss of cubic symmetry as one would expect for Fe atoms at an interface or a step. In comparison the hyperfine properties of bulk Fe are well known with zero quadrupole splitting, zero isomer shift, and a magnetic hyperfine field at 4.2 K of 340 kG.

A similar increase in the $T = 0$ ground-state values of the hyperfine fields for the 1.8-ML superlattice can also be extrapolated from those fits. As shown in the table the two magnetic components have the same values of the quadrupole splitting and isomer shift as for the 2.4-ML superlattice, the only difference being the relative weighting factors of the two components and the additional presence of a small amount of nonmagnetic Fe in this sample (the isomer shift and quadrupole splitting for these nonmagnetic components agrees with data for small Fe clusters and isolated Fe atoms in Ag.[21,22]

Since relaxation effects are still present in the spectra of the 0.9-ML superlattice at 15 K the simple two-component model yielded a slightly poorer fit and is not shown. However, a preliminary fit using a stochastic model suggest that the extrapolated ground-state hyperfine fields for this sample are again similar to those of the 2.4- and 1.8-ML superlattice samples. Also at room temperature where the data was

TABLE I. Hyperfine-field parameters for bulk Fe and for the 0.9-, 1.8-, 2.4-, and 5.5-ML films. The spectra for the 0.9-ML film at 15 K was not fit due to relaxation effects. At room temperature the hyperfine splitting for the 0.9-, 1.8-, and 2.4-ML films has collapsed.

15 K (300 K)	Weighting factor	H_{HF} (kG)	QS (mm/s)	IS (mm/s)
Bulk Fe	1.0	340 (330)	0.0 (0.0)	0.0 (0.0)
0.9 ML	0.47	··· (0)	··· (−0.07)	··· (0.02)
	0.47	··· (0)	··· (0.09)	··· (0.43)
	0.06	··· (0)	··· (0.77)	··· (0.39)
1.8 ML	0.37	341 (0)	−0.11 (−0.07)	0.06 (0.00)
	0.55	323 (0)	0.16 (0.09)	0.49 (0.37)
	0.03	0 (0)	0.77 (0.77)	0.39 (0.39)
	0.05	0 (0)	0.00 (0.00)	0.50 (0.50)
2.4 ML	0.48	358 (0)	−0.11 (−0.09)	0.06 (0.00)
	0.52	344 (0)	0.16 (0.09)	0.49 (0.36)
5.5 ML	0.65	363 (274)	0.00 (0.00)	0.06 (0.06)
	0.35	352 (258)	0.00 (0.00)	0.28 (0.28)

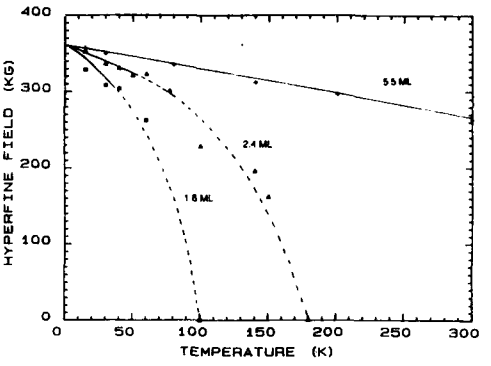


FIG. 3. Average hyperfine field as a function of temperature for 1.8-, 2.4-, and 5.5-ML films of ^{57}Fe(100) on Ag(100). The dotted portion of the curves corresponds to the temperature regime where relaxation effects are present in the spectra.

fit, the parameters are similar to that of the 2.4- and 1.8-ML superlattices. Although a quantitative theory does not yet exist, it seems probable that the relaxation is intimately connected with the 2D nature of these ultrathin films. This will be discussed in greater detail in a later paper.

For the 5.5-ML superlattice the magnetic hyperfine fields H_{HF} at 15 K were slightly larger than the values for the 2.4 ML and thinner films. This is related to the strong temperature dependence of H_{HF} for those films. Extrapolating linearly to $T = 0$ resulted in values of 368 and 353 kG for the two components, which are slightly lower than the values for the 2.4-ML film. The best fit to the data was obtained using zero quadrupole splitting for both components and a smaller isomer shift than the 2.4- and 1.8-ML films for the low-field component. At room temperature there is a substantial decrease (which is much greater than seen for bulk Fe) in H_{HF} suggesting a lower Curie temperature for this film. The weighting factors of 65% and 35% respectively, are exactly what one expects for the amount of interior and surface atoms for a 5.5-ML-thick film if one assumes layer-by-layer growth. This immediately suggest the model of interior and surface atoms as the two different environments.

For the 5.5-ML film the model of interface and interior atoms implies that the interface atoms (352 kG) have a lower hyperfine field than the interior (363 kG). This is in agreement with the theoretical studies of a seven-layer Ag/5Fe/Ag(100) sandwich by Ohnishi, Weinert, and Freeman.[10] Furthermore, it is interesting to note that the magnitude of the extrapolated ground-state hyperfine fields for all of the samples are approximately equal and that there seems to be a trend in the data in that the weighting factor of the low-field component increases with decreasing sample thickness for the 5.5-, 2.4-, and 1.8-ML films. This is suggestive of a model in which these thinner films consist of patches and that the higher hyperfine field component corresponds to interior atoms in the patch. This is inconsistent with the assumption of a layer-by-layer growth mode for Fe(100) on Ag(100) up to 3 ML, with island growth for the thicker films, such as the 5.5-ML film. This conflict may either stem

from the fact that the samples grown as superlattices do not exhibit the same growth habits as single-layer samples, or that the simple two-site fit used here is an oversimplification.

IV. CONCLUSIONS

We have shown conclusively that for well-characterized single-crystal Fe/Ag(100) superlattice films with Fe layers of thicknesses 2.4 ML and thinner that a contribution to the anisotropy from the interface layers results in a magnetic moment at low temperature which points predominantly perpendicular to the plane.

We have also shown that the hyperfine field in these superlattice films is enhanced relative to bulk Fe and it appears that the interface atoms have lower hyperfine fields than the interior atoms, in qualitative agreement with theoretical calculations.

Finally, Mössbauer spectra of superlattice films with Fe layers less than 3 ML thick exhibit broadening suggestive of a relaxation process and a considerable reduction in the critical temperature below which magnetic hyperfine splitting is observed. This is probably due to the two-dimensional nature of these superlattice films. Further studies of the relaxation phenomena clearly are justified to determine the nature of the magnetic ordering process in these systems, which should approach that of ideal two-dimensional Heisenberg ferromagnets with anisotropy.

[1]U. Gradmann, J. Magn. Magn. Mater. **54**, 733 (1986); U. Gradmann, R. Bergholz, and E. Bergter, Thin Solid Films **126**, 107 (1985); U. Gradmann, J. Magn. Magn. Mater. **6**, 173 (1977).

[2]Z. S. Shan, Z. R. Zhao, J. G. Zhao, and D. J. Sellmyer, J. Appl. Phys. **61**, 4320 (1987); N. K. Flevaris, J. B. Ketterson, and J. E. Hilliard, J. Appl. Phys. **53**, 8046 (1982).

[3]A. S. Arrott, B. Heinrich, S. T. Purcell, J. F. Cochran, and K. B. Urquhart, J. Appl. Phys. **61**, 3721 (1987); P. Grunberg, J. Appl. Phys. **61**, 3673 (1987).

[4]R. Richter, J. G. Gay, and J. R. Smith, Phys. Rev. Lett. **54**, 2704 (1985); J. Vac. Sci. Technol. A **3**, 1498 (1985).

[5]C. L. Fu, A. J. Freeman, and T. Oguchi, Phys. Rev. Lett. **54**, 2700 (1985).

[6]B. T. Jonker, K. -H. Walker, E. Kisker, G. A. Prinz, and C. Carbonne, Phys. Rev. Lett. **57**, 142 (1986).

[7]J. G. Gay and Roy Richter, Phys. Rev. Lett. **55**, 2728 (1986).

[8]B. Heinrich, K. B. Urquhart, A. S. Arrott, J. F. Cochran, K. Myrtle, and S. T. Purcell, Phys. Rev. Lett. **59**, 1756 (1987).

[9]J. G. Gay and Roy Richter, J. Appl. Phys. **61**, 3362 (1987).

[10]S. Ohnishi, M. Weinert, and A. J. Freeman, Phys. Rev. B **30**, 36 (1984); A. J. Freeman, C. L. Fu, M. Weinert, and S. Ohnishi, Hyperfine Interactions **33**, 53 (1987); A. J. Freeman and C. L. Fu, J. Appl. Phys. **61**, 3356 (1987).

[11]N. D. Mermin and H. Wagner, Phys. Rev. Lett. **17**, 1173 (1966).

[12]M. E. Lines, J. Appl. Phys. **40**, 1352 (1969).

[13]W. Keune, J. Lauer, U. Gonser, and D. L. Williamson, J. Phys. (Paris) **40**, C2-69 (1979).

[14]K. Kawaguchi, R. Yamamoto, N. Hosoito, T. Shinjo, and T. Takada, J. Phys. Soc. Jpn. **55**, 2375 (1986); T. Shinjo, N. Hosoito, K. Kawaguchi, N. Nakayama, T. Takada, and Y. Endoh, J. Magn. Magn. Mater. **54**, 737 (1986).

[15]T. Shinjo, S. Hine, and T. Takada, J. Phys. (Paris) **40**, C2-86 (1979).

[16]T. Tyson, A. H. Owens, and J. C. Walker, J. Appl. Phys. **52**, 2487 (1981).

[17]J. Korecki and U. Gradmann, Phys. Rev. Lett. **55**, 2491 (1985).

[18]N. C. Koon, B. T. Jonker, F. A. Volkening, J. J. Krebs, and G. A. Prinz, Phys. Rev. Lett. **59**, 2463 (1987).

[19]J. J. Krebs, B. T. Jonker, and G. A. Prinz (these proceedings).

[20]G. C. Smith, G. A. Padmore, and C. Norris, Surf. Sci. **119**, L287 (1982).

[21]G. Longworth, and R. Jain, J. Phys. (Paris) **40**, C2-608 (1979); J. Phys. F **8**, 993 (1978).

[22]E. Kita, K. Kainosho, A. Tasaki, N. Seagusa, and M. Takao, J. Appl. Phys. **59**, 2991 (1986); N. Kataoka, K. Sumiyama, and Y. Nakamura, Trans. Jpn. Inst. Metals (Jpn.) **26**, 703 (1985); C. L. Chien and K. M. Unruh, Phys. Rev. B **28**, 1214 (1983).

Mechanisms of exchange anisotropy (invited)

A. P. Malozemoff
IBM Thomas J. Watson Research Center, Yorktown Heights, New York 10598

Exchange anisotropy refers to a group of phenomena which appear in ferromagnetic-antiferromagnetic sandwiches, particularly to a field offset in the hysteresis loop. After a brief review of experiment and earlier theory, a new theory is described involving a random field at the interface which causes the antiferromagnet to break up into domains, whose size is inversely proportional to the exchange field offset. The theory is extended by considering the temperature dependence and also the topological properties of the domains, in particular nonzero winding numbers which increase the size of the domains and give them added stability. The metastability of such structures provides an explanation of the magnetic "training" effect observed in multiple cycles of the hysteresis loop.

I. INTRODUCTION

This paper compares theories of exchange anisotropy,[1-7] particularly the recent random-field model,[4,5] to experiment.[1,8-15] Several new aspects of the random-field model are introduced, including the topological properties of the domains and a cubic spin anisotropy. These features impact comparison to experiment.

Exchange anisotropy refers to a complex of unusual properties of exchange-coupled ferromagnetic-antiferromagnetic (F-AF) sandwiches.[1-15] Typically these properties appear after the sandwich is cooled through the AF Néel temperature T_N with an applied field which single-domains the ferromagnetic layer. At the operating temperature, which is usually room temperature in typical systems like Co/CoO and FeNi/FeMn, the applied field can then be removed, but the ferromagnet now behaves as if it were subject to some sort of internal "exchange field" acting in the same direction as the previously applied magnetic field. Alternatively the effect may be described as a "unidirectional" anisotropy which breaks time reversal symmetry.

Exchange anisotropy may be observed most simply in the hysteresis loop of the ferromagnet, which is found to be offset from zero on the field axis. The offset or "exchange anisotropy field" H_E can be understood as arising from the antiferromagnetic interface, in particular from an energy difference $\Delta\sigma$, per area of the F-AF interface, between the two principal time-reversed ferromagnetic directions.

Balancing pressures on an assumed domain wall between these two directions, one finds

$$H_E = \Delta\sigma/2M_F t_F, \tag{1}$$

where M_f and t_F are the magnetization and thickness of the ferromagnet, respectively. The inverse t_F dependence has been convincingly verified in experiment,[11,15] confirming the interfacial origin of the effect. The exchange field is also revealed by a sin ψ contribution to the torque curve,[1,8] and to the ferromagnetic and spin-wave resonance,[14,15] where ψ is the rotation angle in the plane.

Other experimental observations calling for theoretical explanation include (1) the relative independence of the exchange field on AF-layer thickness down to a critical thickness of typically a few tens of Angstroms, below which the exchange field drops to zero,[1,13] (2) the approximately linear falloff $(1 - T/T_{crit})$ of the exchange field with temperture to zero at a critical temperature T_{crit} somewhat below the bulk AF Néel temperature[9,11] T_N, (3) a magnetic "training" effect, that is, the gradual reduction in the exchange field and coercivity with the number of hysteresis loop cycles[9,12] at a temperature where interdiffusion and other underlying materials changes are excluded, (4) the appearance of exchange anisotropy in AF films grown *at room temperature* on a single-domained F layer,[8] but with amplitude roughly half the size of that achieved by cooling the AF through T_N, and (5) in FeNi/FeMn layers particularly, the dependence of the effect on order of deposition (F or AF first).

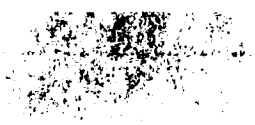
In the next section, some of the previous theories of exchange anisotropy are reviewed, including previous work on the random-field model which is the main topic of this paper. Section III describes a new aspect of the random-field Heisenberg problem: the effect of domain wall topology,[16] which introduces a new twist into the problem, both literally and figuratively. These effects could be important in understanding magnetic training. While the previous theory assumes a uniaxial anisotropy in the antiferromagnet, most systems are cubic. In fact, FeMn has four sublattices with moments pointing along the four different [111] directions.[17] Some implications of the cubic anisotropy are discussed in Sec. IV, along with the conclusions.

II. THEORIES OF EXCHANGE ANISOTROPY

As in many other micromagnetic problems like magnetic domain switching or domain wall dynamics,[16] theories of exchange anisotropy have progressed in complexity from the most simplistic models treating a layer as a single spin, to one-dimensional models treating a layer as a coupled spin chain, to two- and three-dimensional models with the full flexibility of the multidimensional magnetic vector field. The simple models give a qualitative phenomenological picture of the effect but fail quantitatively by a large margin.

In the first model of exchange anisotropy, Meiklejohn and Bean[1] treated both the F and AF layers as single spins, with F subject to applied field ($E \simeq -HM_F$), with AF sub-

 0021-8979/88/083874-06$02.40 © 1988 American Institute of Physics



ject to uniaxial anisotropy ($E \simeq K_A \sin^2 \psi$) and with the two coupled by an interfacial exhange J_i. While this model nicely predicts an exchange field of order J_i/M_F and a sin ψ torque curve, the experimentally fitted value for J_i was found to be a hundred to a thousand times smaller than typical bulk F or AF exchange parameters.[1,7,11]

This is a highly implausible result. If the reduced J is interpreted as that of some relatively uniform but chemically modified interfacial layer, it is hard to understand why the magnetic ordering temperature of that layer would not also be suppressed by a similar ratio (e.g., 500 K/100 = 5 K), making the layer paramagnetic at room temperature and decoupling the F and AF layers. On the other hand, if the reduced J is interpreted in terms of occasional pinholes, it is hard to understand the consistency and reproducibility of the effect. There is also the problem that a very special antiferromagnetic configuration is required to give an offset: the so-called "uncompensated" configuration shown in Fig. 1(b) in which only one of the two AF sublattices happens to adjoin the interface. The more natural "compensated" configuration of Fig. 1(a) gives no effect. The model also cannot explain magnetic training.

A first step towards more theoretical flexibility comes with a one-dimensional chain model, permitting variations perpendicular to the interfacial plane.[6] When the ferromagnetic layer in the uncompensated configuration of Fig. 1(b) is reversed, or alternatively when the AF spins are reversed relative to the F spins, a high interfacial energy is generated in the configuration of Fig. 1(c), but this can be relaxed by the introduction of an interfacial domain wall, as shown schematically in Fig. 1(d). $\Delta\sigma$ in Eq. (1) is now $4\sqrt{A_A K_A}$, where $A_A \simeq J/a$ and K_A are the AF exchange stiffness and uniaxial anisotropy per unit volume, and a is the lattice constant. It is assumed here that the corresponding ferromagnetic A and K are sufficiently larger to keep the domain wall

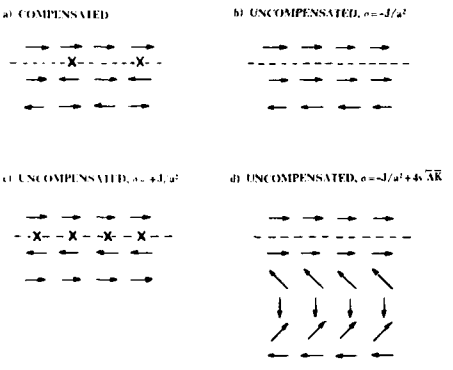


FIG. 1. Schematic side view of possible atomic spin configurations in a ferromagnetic-antiferromagnetic sandwich with a planar ferromagnetically coupled interface indicated by the dashed line. Frustrated bonds are indicated by crosses. The unfavorable configuration of (c) can reduce its energy by forming a planar antiferromagnetic domain wall as in (d). (After Ref. 4.)

primarily in the antiferromagnetic layer, as suggested by the experimental observation[7,12] that the ferromagnetic moment in the two directions differs at most by a very small amount.

With Eq. (1) this model predicts an offset field of $2\sqrt{A_A K_A}/M_F t_F$, which, with typical parameters, is in good agreement with experiment.[4,6] Rather than being concentrated across a single atomic interface, the exchange energy is now spread out over a domain wall width $\simeq \pi\sqrt{A_A/K_A}$, leading to a reduction by a factor of $\pi\sqrt{A_A/K_A}/a \simeq 100$, just what is needed to correct the previous model.

However, the one-dimensional model fails to explain the persistence[1,13] of exchange anisotropy, with no diminution of H_E, down to AF thicknesses of $\simeq 25$ Å, an order of magnitude lower than the characteristic domain wall width. In fact, essentially all published data is on AF layers thinner than the domain wall width, with the possible exception of some thick single-crystal NiO data.[8] In FeMn, for example, a structural transformation from the AF α phase to the nonmagnetic (at room temperature) γ phase occurs in thick films,[11] so that only a thin magnetic layer is likely to remain near the interface. The model also fails to account for magnetic training. And it implausibly assumes a monatomically perfect, uncompensated interface.

Kouvel[2] and Néel[3] first recognized the possibility of obtaining exchange anisotropy with AF domain structures extending along the interface, that is with the AF domain walls standing *perpendicular* to the interface. Néel pointed out how such structures, pinned by coercivity in the AF layer, could account for magnetic training, much as domains give history-dependent phenomena in coercive ferromagnets. However, these early theories could not specify the size of these domains and hence could not predict the exchange field magnitude.

The present author suggested a way to do this[4] by recognizing the likely randomness in exchange interactions at the interface, arising from surface roughness or chemical inhomogeneity on an atomic scale. Following an argument initially made by Imry and Ma,[18] one expects the AF to break up into a domain state as local regions reorient to minimize the interfacial random-field energy.[19] The characteristic size of these domains can be estimated by balancing derivatives of the random-field energy and the opposing AF domain wall energy.

Let $J_i \equiv f_i J \equiv f_i A_A a$ be the magnitude of the atomistic interfacial energy, with the field pointing randomly parallel or antiparallel to an assumed AF and F easy uniaxial anisotropy axis lying in the film plane. According to random statistics, in an interface area L^2 with $N = L^2/a^2$ atoms, the averaged random-field energy per area will be $\simeq -f_i J/a^2\sqrt{N} \simeq -f_i J/aL$. Thus the larger the characteristic domain size, the smaller will be the averaged interfacial energy. A detailed analysis[5] shows that L is of order the domain wall width $\pi\sqrt{A_A/K_A}$; so again, as in the one-dimensional model, the energy is scaled down by a factor of order 100.

In a hysteresis loop, the F magnetization direction is reversed. If coercivity in the AF layer can be assumed to hold the domain walls fixed in position, the domain orientations,

originally favorably aligned along the averaged random interfacial field, become unfavorable and metastable. Thus the interfacial random-field energy term changes sign and $\Delta\sigma$ of Eq. (1) is just twice $f_i J/aL$. Substitution into Eq. (1) leads to an offset field of the form

$$H_E \propto f_i J/2M_F t_F aL \propto f_i\sqrt{A_A K_A}/M_F t_F, \tag{2}$$

which has the correct order of magnitude to explain experimental data,[4] with f_i of order unity.

In the first paper[4] on the random-field model of exchange anisotropy, the AF thickness was assumed infinite. In fact, the energy of such a domain state was positive, giving at best a metastable state. However, for AF layers thinner than a critical value of order the domain wall width, the domain state can be shown[5] to be negative and hence stable. Indeed, essentially all experimental data fall in this limit. The reason for this upper critical thickness is that the relative contribution of wall exchange and anisotropy energy, which opposes the formation of the domains, becomes greater as the AF layer thickness is increased and eventually a longer-range ordered state becomes stable.[5] Kinetic effects[20] may make it difficult to observe this critical thickness experimentally; this is a well-known problem in the extensive studies of bulk disordered antiferromagnets, which have previously been the principal experimental realization of the random-field model.

The predictions of the random-field model seem consistent with a variety of other exchange-anisotropy experiments which probe the ferromagnetic layer and which can be interpreted simply in terms of an interfacial unidirectional pinning anisotropy $K_s = H_E M_F t_F$. In spite of the strong atomistic interfacial exchange, the F layer as a whole is not strongly pinned because of the competition and cancellation of the random exchange directions. Thus there is no contradiction with the recent work of Rave *et al.*[7] who point out that strong interfacial pinning would have a drastic effect on the ferromagnetic reorientation. The FMR and spin-wave linewidths,[14,15] which indicate a variation of the local inhomogeneous fields of about double the average exchange offset field, can also be understood in a natural way. Just as the average Imry–Ma domain size is determined statistically, so the distribution of sizes will, according to Gaussian statistics, be comparable to the average. The FMR linewidth does not "see" the much stronger randomness on shorter length scales L because in this limit the exchange field $2A_F k^2/M_F \simeq 2\pi^2 A_F/M_F L^2$ exceeds the random field $f_i J/M_F t_F aL$ (because $1/L^2$ dominates $1/L$ as $L \to 0$).

The critical lower AF thickness observed in experiment[1,13] can be attributed to the inability of AF coercivity to hold the domain walls in place when the F orientation is reversed. The strength of this coercivity is not known, and so it is difficult to make a quantitative estimate. But as long as that coercivity is a bulk phenomenon, its strength will scale with AF thickness, while the driving force for domain collapse is an interfacial effect, independent of thickness, which arises when the F orientation switches and makes the interfacial energy of the domains unfavorable. Thus below a critical thickness the coercivity will be too weak to hold the domains and they will simply move to new positions with, on average, the same energy (by time reversal symmetry). Then $\Delta\sigma$ in Eq. (1) drops to zero.

While the random field theory can thus explain many experimental aspects of exchange anisotropy, some extension of the theory is required to understand the magnetic training effect and the temperature dependence. These aspects are treated in the following sections.

III. SPIN TOPOLOGY IN THE TWO-DIMENSIONAL HEISENBERG MODEL

A previous paper[5] studied the energy σ per interfacial area of a cylindrical antiferromagnetic domain stabilized by random interfacial energy in a two-dimensional Heisenberg system with uniaxial anisotropy. σ can be written

$$\sigma\left(\frac{a^2\delta_0}{8\pi t_A A_A}\right) = -\frac{\eta}{l} + \frac{1}{l}, \quad l > \delta_0, \tag{3}$$

$$\eta = f_i a\delta_0/4\pi^{3/2} t_A, \tag{4}$$

where l is the normalized domain diameter L/a and δ_0 is the normalized Bloch wall width $\pi\sqrt{A_A/K_A}/a$. The parameter η measures the local interfacial field strength through $f_i \equiv J_i/J$. In Eq. (3), the first term represents the random-field energy and the second the domain wall energy assuming the simple Bloch wall surface energy $4\sqrt{AK}$. Equation (3) is valid only for $l > \delta$ because at lower values, the walls squeeze against each other[5] and the exchange energy goes as $1/l$.[2] It should be recognized that because of the randomness of the interfacial field, the domain geometries can be complex and both polarities of encircled domain moments can occur. The cylindrical domain is a typical, though not the only, geometry because surface tension will round out the wall boundaries.

Actually Eq. (3) implicitly assumes a domain wall structure in which the spin direction in the middle of the wall is everywhere the same, as shown schematically in Fig. 2(a). In this figure the spins represent the staggered magnetization, or equivalently, the spin of a single sublattice. If the

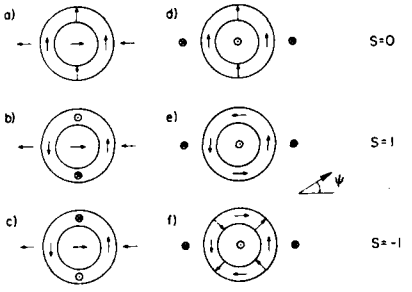


FIG. 2. (a)–(c) show a schematic top view of domain configurations in the antiferromagnetic layer. Arrows represent the staggered spins, or, alternatively, only one of the two sublattices. (d)–(f) show equivalent topological configurations obtained by rotating all spins by 90° around the vertical axis. These configurations are the same as those studied in magnetic bubbles (Ref. 16) and can be characterized by a winding number S.

spin direction in the middle of the wall varies as in Figs. 2(b) or 2(c), an additional exchange term appears.

This problem is in fact closely related to the problem of magnetic bubble domains with different winding numbers.[16] A simple rotation of the spin directions by 90° around the vertical axis of Fig. 2 transforms Figs. 2(a), 2(b), and 2(c) into Figs. 2(d), 2(e), and 2(f). These are the $S=0$, $S=1$, and $S=-1$ bubbles,[16] where S is the winding number defined by the contour integral $(2\pi)^{-1}\int(d\psi/ds)ds$ around the domain perimeter s [Eq. (8.22) of Ref. 16].

One difference with the magnetic bubble case is the absence of demagnetizing fields. In magnetic bubbles, domain wall twists compress into so-called Bloch lines (e.g., see Fig. 8.5 of Ref. 16) under the influence of such fields. In the AF case, the azimuthal angle ψ [see Fig. 2(d)] simply twists linearly as a function of distance s along the domain contour. Then it can be shown [see Eqs. (8.19) and (8.21) of Ref. 16] that the wall surface energy σ and wall width $\Delta\equiv\delta a$ are, respectively,

$$\frac{\sigma}{4\sqrt{A_A K_A}}=\left[1+\left(\frac{a\delta_0\partial\psi}{\pi\partial s}\right)^2\right]^{1/2}=\left[1+\left(\frac{2S\delta_0}{\pi l}\right)^2\right]^{1/2}, \tag{5}$$

$$\frac{\Delta}{\pi\sqrt{A_A/K_A}}=\left[1+\left(\frac{a\delta_0\partial\psi}{\pi\partial s}\right)^2\right]^{-1/2}=\left[1+\left(\frac{2S\delta_0}{\pi l}\right)^2\right]^{-1/2}. \tag{6}$$

Substituting this new energy term into Eq. (2), one obtains an equation of the form

$$\sigma\propto-\frac{\eta}{l}+\frac{1}{l}\left[1+\left(\frac{2S\delta_0}{\pi l}\right)^2\right]^{1/2}. \tag{7}$$

Minimization gives a ferromagnetic state ($l\to\infty$) for $\eta<1$, while for $\eta>1$,

$$l=\frac{2|S|\delta_0}{\pi}\left(\frac{4-\eta^2+\eta(8+\eta^2)^{1/2}}{2(n^2-1)}\right)^{1/2}. \tag{8}$$

This result is valid for $l>\delta$, where $\delta\equiv\Delta/a$ is now given in Eq. (6) and shrinks as the winding number S increases. Equation (8) is plotted in Fig. 3 along with the predicted domain size for the $S=0$ case calculated earlier.[5] The increase in domain diameter can be understood, as in the case of "hard" magnetic bubbles,[16] from the physical picture of the winding acting like a spring compressed inside the domain wall. Only for $S=1$, the size can be smaller than $S=0$ because of the narrowing of the domain wall width. The $S=1$ curve in Fig. 3 ends where $\delta=l=\delta_0\sqrt{1-(4/\pi^2)}$; extending it to higher η requires extension of the theory to the Heisenberg limit. For higher S the Ising limit persists to $l\to0$.

To calculate the offset field H_E from Eq. (1), one needs $\Delta\sigma$. As before, flipping the ferromagnetic orientation and leaving the antiferromagnetic domain wall in place causes the interfacial energy to be reversed in sign: so $\Delta\sigma$ is given by twice the interfacial term in Eq. (3). Thus one finds $H_E=2f_iA_A/\sqrt{\pi}M_F t_F L$. The inverse L dependence, combined with the increased L's shown in Fig. 3, implies that the exchange field is generally *reduced* by the presence of $S\neq0$ winding states.

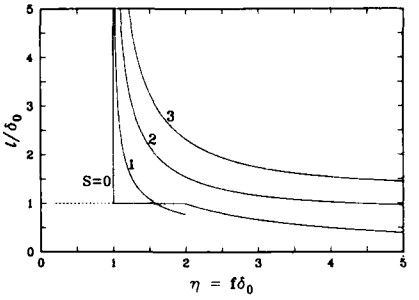


FIG. 3. Equilibrium domain sizes of the two-dimensional random-field Heisenberg model with uniaxial anisotropy, as a function of the random field strength parameter η, for different winding states S of the domain walls. The dashed line for $S=0$ indicates the likely metastable state caused by slow kinetics (Ref. 20).

Since these $S\neq0$ states are higher energy states of the system, the question arises as to why they should be present at all. There are possible thermodynamic as well as kinetic reasons. First it is important to recognize that the $S\neq0$ states have a greater stability against collapse than the $S=0$ state. This effect can be understood with reference to Fig. 4.

In a one-dimensional (1D) system, with Ising (1D) spins, domain walls are point defects, and two such defects can annihilate if bought together [Fig. 4(a)]. In a 1D system with 2D spins [Figs. 4(b) and 4(c)], domain walls consist of spin rotation, and the two possible rotation polarities imply two possibilities for two adjacent walls: Opposite rotations [Fig. 4(b)] can unwind and annihilate, but rotations in the same sense [the "winding" configuration of Fig. 4(c)] have a great stability because as the walls are pushed together their exchange energy diverges. The winding configuration can only be annihilated when the wall centers move to within atomic distances of each other. By contrast, in a 1D system with 3D spins, the rotations of Fig. 4(c) can unwind because the spins can twist out of the plane.

An analogous situation occurs in 2D, as illustrated in Figs. 4(d)–4(f). A finite domain with 1D Ising spins has a wall consisting entirely of an abrupt change in spin orientation across one atomic separation [Fig. 4(d)]. A domain with 2D spins, while supporting wall rotations, is inherently unwinding, as can be seen by following a horizontal cut through the domain in Fig. 4(e). The apparently winding configuration along a horizontal line through the domain of Fig. 4(f) can actually also unwind because such a domain wall must always contain two point singularities of the vector field, which, if brought together, annihilate one of the two senses of rotation within the wall.

The 2D case with 3D spins was already shown in Fig. 2. Here $S\neq0$ states have inherently winding configurations and therefore should be particularly stable.

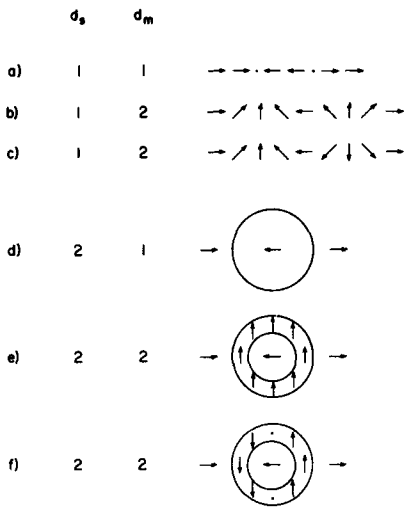


FIG. 4. Domain configurations for various space (d_s) and spin (d_m) dimensionalities. The dots in (a) and the line in (d) represent abrupt atomic reorientations characteristic of the Ising model. Configurations (b) and (c) are called "unwinding" and "winding", respectively. The 2D configurations (e) and (f) are both unwinding, in the latter case because the abrupt wall transitions, indicated by the dots, can move together and annihilate, leaving a configuration equivalent to (e).

This process may be generalized to higher dimensionalities. Stable winding configurations can be achieved only in certain dimensionalities when closed domains are imbedded in a uniform vector field: in particular only when the spin dimensionality d_m is one greater than the space dimensionality d_s. The structures are always unwinding for $d_m \geqslant d_s + 2$ or $d_m < d_s$. Interestingly the critical case $d_m = d_s + 1$ is the one relevant for experimental studies of exchange anisotropy in sufficiently thin AF films because the exchange coupling through the thickness in effect collapses that perpendicular dimension and leaves an essentially two-dimensional problem. It should be noted that vortices are also stable for $d_m = d_s = 2$ (e.g., in the Kosterlitz–Thouless transition), but not in a way consistent with a uniform imbedding vector field.

How then are the different winding states determined? This depends on the process by which exchange anisotropy is "written" into the F-AF sandwich.

The most common technique, as mentioned earlier, is to heat the sandwich through the AF Néel temperature T_N, while applying a field to single domain the ferromagnet with a higher ordering temperature. Near T_N, the AF spins are expected to be "labile," partially disordered by thermal fluctuations. Only below T_N does coercivity "freeze in" the domain structure. Entropy could then lead to a distribution in the winding states, although the predominant state is likely to be the lowest-energy $S = 0$ state.

When the applied field direction is reversed at $T < T_{crit}$, the originally favorable domain alignment becomes unfavorable, and so forces are exerted tending to displace the walls. If coercivity is too weak, the $S = 0$ domains can unwind and annihilate. As they do so, the average domain size increases and H_E is reduced according to Eq. (8). On further field cycles, more and more domains annihilate until the remaining walls are sufficiently far apart to remain stable under field cycling. This process possibly explains the observed magnetic training effect.[9,12]

Another way to induce exchange anisotropy is to grow the AF film *in situ* on the ferromagnet at a temperature well below T_N, for example, by surface oxidation of Co to form CoO or by sputtering of FeMn onto FeNi. In this case the moments of the growing layer, which may initially begin as islands, are likely to adopt random orientations. As the islands merge and the domains form, the wall will be left with random orientations giving a statistical distribution of winding numbers. If the island scale were known, it would be possible to estimate the width of that distribution. Even without this information, a qualitative prediction can be made of a larger average domain size [Eq. (8)], because of more $S \neq 0$ bubbles, leading through Eq. (2) to a lower offset. This trend is observed in experiment, where offset fields are typically half the size of those obtained in the same films by thermal cycling.[11] The stability of $S \neq 0$ winding states implies another experimentally verifiable effect, namely that the lower critical thickness for exchange anisotropy should be smaller for the low-temperature process than for the thermal cycling process.

IV. CUBIC ANISOTROPY AND TEMPERATURE DEPENDENCE

So far the theory has assumed uniaxial AF anisotropy and a simple colinear AF spin structure. In fact both CoO and FeMn are believed to be cubic, and FeMn has a four sublattice structure in which the four sublattice moments point towards along the four [111] directions.[17]

In this case, a variety of different domain types exist, corresponding to the different possible directions of the sublattices. This is a complex topological problem which will not be addressed here. However, it is plausible to imagine that random interfacial fields can also act to stabilize these domains and that different topological structures can arise. The typical wall width $\sqrt{A_A/K_{Ac}}$ is now determined by the cubic anisotropy K_{Ac}. Thus one can anticipate a formula like that of Eq. (2) for the exchange field, but with K_{Ac} substituting for K_A.

Here we focus on one particular consequence of the cubic anisotropy, namely its implications for the temperature dependence of the offset field.[11] The interfacial exchange interaction JS_FS_A is quadratic in spin, but with one F spin and one AF spin. Similarly uniaxial anisotropy is, in simplest approximation, quadratic in the AF spin while cubic anisotropy is fourth order. In mean field $S_A \propto (1 - T/T_N)^{1/2}$, while if the F Curie temperature is much higher than T_N, there is essentially no temperature dependence in S_F in the temperature range around T_N.

Putting these factors together, one predicts an AF wall width parameter independent of temperature for the uniaxial case but going as $(1 - T/T_N)^{-1/2}$ for the cubic case. The latter result implies a divergence in domain width with increasing temperature. Alternatively it means that domains formed in the process of cooling and frozen in by coercivity at a higher temperature will be larger than the equilibrium domain size at lower temperature.

The predicted equilibrium temperature dependence of the offset field is similarly $(1 - T/T_N)^{1/2}$ for uniaxial anisotropy but $(1 - T/T_N)$ for cubic anisotropy. The linear prediction resembles many experimental observations,[9,11] at least near T_N, and is consistent with the expected cubic symmetry of these systems. One must also assume that the thin-film T_N is somewhat reduced from its bulk value. In earlier work[11] it had been suggested that the averaged effect of a T_N distribution could give the linear dependence; certainly this is possible but is no longer necessary in view of the above argument.

In summary, the random-field model of exchange anisotropy appears to resolve certain basic problems in the earlier theoretical approaches. It gives a plausible estimate of the size of the offset field, although a more detailed test of the theory requires a better determination of the relevant materials parameters, particularly the cubic AF anisotropy constant.[6] It treats the interface in a realistic way, taking into account the likely interfacial disorder rather than assuming an artificially perfect interface. The new topological considerations presented in this paper offer a model for the magnetic training effect and for some of the peculiar differences arising from different ways of inducing exchange anisotropy. The temperature dependence of the offset field can also be explained in a natural way.

The richness of this physical model calls for more detailed experimental tests. It would be important, of course, to directly observe the interfacial domain structure, although this is difficult in an AF on a few hundred Angstrom scale. The predicted upper critical thickness should be looked for. The presence of winding topologies would be of interest to test via their unusually high stability. It seems safe to predict that this field of study is just in its infancy.

ACKNOWLEDGMENTS

The author thanks J. C. Slonczewski, G. Grinstein, D. Mauri, Y. Imry, S. S. P. Parkin, V. S. Speriosu, E. Kay, and J. K. Howard for key discussions on exchange anisotropy.

[1] W. H. Meiklejohn and C. P. Bean, Phys. Rev. **102**, 1413 (1956); Phys. Rev. **105**, 904 (1957); W. H. Meiklejohn, J. Appl. Phys. **33**, 1328 (1962).
[2] J. S. Kouvel, J. Phys. Chem. Solids **21**, 57 (1961); **24**, 795 (1963).
[3] L. Néel, Ann. Phys. **2**, 61 (1967).
[4] A. P. Malozemoff, Phys. Rev. B **35**, 3679 (1987).
[5] A. P. Malozemoff, Phys. Rev. B (to be published).
[6] D. Mauri, H. C. Siegmann, P. S. Bagus, and E. Kay, Z. Phys. (to be published).
[7] W. Rave, W. C. Cain, A. Hubert, and M. H. Kryder, IEEE Trans. Magn. (to be published).
[8] A. E. Berkowitz and J. H. Greiner, J. Appl. Phys. **36**, 3330 (1965); J. H. Greiner, J. Appl. Phys. **37**, 1474 (1966).
[9] C. Schlenker and D. Paccard, J. Phys. (Paris) **28**, 611 (1967); C. Schlenker, Phys. Status Solidi **28**, 507 (1968).
[10] R. D. Hempstead, S. Krongelb, and D. A. Thompson, IEEE Trans. Magn. **MAG-14**, 521 (1978).
[11] C. Tsang, N. Heiman, and K. Lee, J. Appl. Phys. **52**, 2471 (1981); C. Tsang and K. Lee, J. Appl. Phys. **53**, 2605 (1982).
[12] C. Schlenker, S. S. P. Parkin, J. C. Scott, and J. K. Howard, J. Magn. Magn. Mater. **54-57**, 801 (1986).
[13] D. Mauri, E. Kay, D. Scholl, and J. K. Howard, Appl. Phys. Lett. (to be published).
[14] J. C. Scott, J. Appl. Phys. **57**, 3681 (1985).
[15] V. S. Speriosu, S. S. P. Parkin, and C. H. Wilts, IEEE Trans. Magn. (to be published).
[16] A. P. Malozemoff and J. C. Slonczewski, *Magnetic Domain Walls in Bubble Materials* (Academic, New York, 1979).
[17] H. Umebayashi and Y. Ishikawa, J. Phys. Soc. Jpn. **21**, 1281 (1966).
[18] Y. Imry and S. K. Ma, Phys. Rev. Lett. **35**, 1399 (1975).
[19] Y. Y. Goldschmidt and A. Aharony, Phys. Rev. B **32**, 264 (1985).
[20] G. Grinstein and J. F. Fernandez, Phys. Rev. B **32**, 264 (1985).



Brillouin scattering from collective spin waves in magnetic superlattices (invited)

B. Hillebrands
Optical Sciences Center, University of Arizona, Tucson, Arizona 85721

A. Boufelfel and C. M. Falco
Department of Physics and Optical Sciences Center, University of Arizona, Tucson, Arizona 85721

P. Baumgart and G. Güntherodt
II. Physikalisches Institut, Universität Köln, 5000 Köln 41, Federal Republic of Germany

E. Zirngiebl and J. D. Thompson
Los Alamos National Laboratory, Los Alamos, New Mexico 87545

We report on the observation and the analysis of collective magnetostatic spin-wave excitations in magnetic superlattices. The influence of interface anisotropies, which can become dominant for small modulation wavelengths, is discussed. For the system Fe/Pd we show that Brillouin spectroscopy experiments in combination with the measurement of the saturation magnetization by a SQUID magnetometer give evidence for a magnetic polarization of the Pd spacer layers, as well as for a small negative out-of-plane interface anisotropy constant of $K_s = -0.15$ erg/cm^2.

Magnetic multilayered structures have gained considerable interest in the past few years due to their unusual magnetic properties. Besides novel static phenomena like the antiphase domains in Gd/Y superlattices[1] and the spin spiral effects in Dy/Y superlattices[2] the so-called collective spin-wave excitations are the first and the only dynamic collective features of superlattices reported so far.[3–10] In most cases they are made up from surface spin waves in each magnetic layer coupled by their dipolar stray fields via the intervening nonmagnetic spacer layers giving rise to a new kind of spin-wave band, which exhibits partially bulk-mode- as well as surface-mode-like behavior. A study of these excitations can reveal information about the magnitude and the direction of the saturation magnetization, about magnetic anisotropies, and about a possible polarization of the spacer material. In particular, Brillouin spectroscopy seems to be best suited to study magnetic interface anisotropies due to the sensitivity of spin waves to the anisotropy fields. It is therefore of crucial importance to consider Brillouin scattering experiments in addition to established methods of magnetic measurements in order to gain more information about the magnetism of multilayered structures.

So far there are only few reports on the observation of spin waves in magnetic superlattices by Brillouin spectroscopy.[6–10] After theoretical predictions of the existence of the collective modes by Camley *et al.*,[3] Grünberg and Mika,[4] and by Emtage and Daniel,[5] first experimental evidence was provided by Brillouin scattering experiments in Mo/Ni superlattices by Grimsditch *et al.*[6] and Kueny *et al.*[7] A first detailed experimental proof of the predicted magnetic properties of the collective spin-wave band including measurements of the band shapes was presented by Hillebrands *et al.* for Fe/Pd and Fe/W superlattices.[8,9]

In this paper we present Brillouin scattering experiments on Fe/Pd superlattices in addition to a brief review of earlier reported results.[8,9] We outline how to fully include interface anisotropies in the calculation of the spin-wave frequencies and reanalyze within the new model the experimental data of the Fe/Pd system. We demonstrate that a previous description[8,9] of the observed spin-wave frequencies by a decrease of the saturation magnetization $4\pi M_s$ for small modulation wavelengths Λ can be improved by the approach of considering a small out-of-plane interface anisotropy assuming a value of $4\pi M_s = 17 \pm 2$ kG independent of Λ. A recently reported strong increase of $4\pi M_s$ for small Λ, as measured by den Broeder *et al.* using a vibrating sample magnetometer,[11] can consistently be described by the assumption of a magnetic polarization of the Pd spacer layers. The interpretation is corroborated by magnetization measurements in magnetic fields parallel and perpendicular to the layers using a SQUID magnetometer.

The Brillouin scattering experiments were performed at room temperature under vacuum in backscattering geometry using a (3 + 3)-pass tandem Fabry–Perot interferometer described elsewhere.[13] A single-mode 5145-Å Ar^+ ion laser was used with an incident power of *p*-polarized light of up to 250 mW. The sampling time per spectrum was typically 5 h. The inelastically scattered light was analyzed depolarized in order to suppress surface phonon signals. The applied magnetic field was oriented parallel to the layer planes and perpendicular to the scattering plane.

The Fe/Pd superlattice samples were prepared on single-crystal sapphire substrates using a sputtering technique described elsewhere.[14] The sample parameters are listed in Ref. 8. The modulation wavelength Λ varies between 33 and 188 Å, and the number of bilayers N varies between 49 and 90. The modulation wavelengths of the samples were determined by x-ray diffraction. As shown by Bragg and wide-film Debye–Scherrer x-ray diffraction the layers grew with a preferred orientation of bcc Fe(110) planes and fcc Pd(111) planes, with no in-plane orientation. The samples exhibited long-range structural coherence of at least 300 Å perpendicular to the layers.

In Figs. 1 and 2 typical Brillouin spectra of magnetic

 0021-8979/88/083880-05$02.40 © 1988 American Institute of Physics

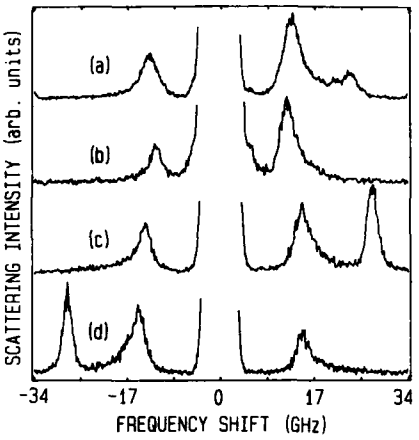


FIG. 1. Room-temperature Brillouin spectra of Fe/Pd superlattices in an applied magnetic field of 1 kG: (a) $d = 21.9$ Å and $d_0 = 24.3$ Å, (b) $d = 41.7$ Å and $d_0 = 138.7$ Å, and (c),(d) $d = 41.0$ Å and $d_0 = 9.1$ Å. In (d) the direction of the applied field has been reversed compared to (c). The angle of incidence of the laser beam is 45°.

superlattices are displayed for an applied magnetic field of 1 kG. Figure 1(a) shows the spectrum of a Fe/Pd superlattice with a modulation wavelength of $\Lambda = 46.2$ Å. The thickness d of the magnetic material is close to that of the nonmagnetic material (d_0). The band of collective spin-wave excitations can clearly be identified in the right-hand part of the spectrum by its specific asymmetric shape. The density of states is largest at small frequency shifts and decreases asymmetrically toward the upper band edge. At the latter discrete spin-wave modes can still be resolved due to the small thickness and the finite number of bilayers.[8,9] Their strong Stokes/anti-Stokes asymmetry identifies them as surface-mode-like spin waves. On the other hand, the modes near the lower edge of the spin-wave band are bulk-mode-like because of their small Stokes/anti-Stokes asymmetry. If we neglect the discrete modes near the upper band edge the shape of the spin-wave excitation band is qualitatively similar to the calculated Brillouin scattering cross section for the semi-infinite superlattice system Mo/Ni.[5]

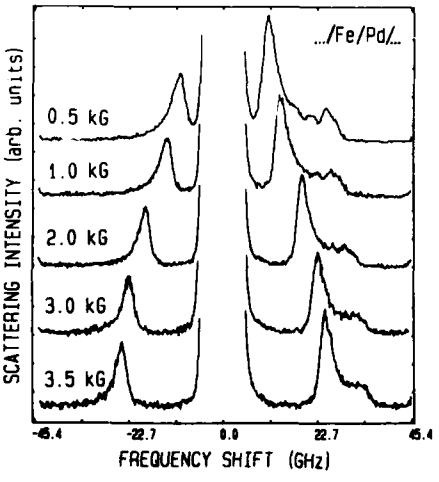


FIG. 2. Room-temperature Brillouin spectra of a Fe/Pd superlattice consisting of 49 bilayers with $d = 89.4$ Å and $d_0 = 99.0$ Å for different applied magnetic fields as indicated in the figure. The angle of incidence of the laser beam is 45°.

In Fig. 1(b) we show the Brillouin spectrum of an Fe/Pd superlattice with $d = 41.7$ Å and a much larger $d_0 = 138.7$ Å. In this case the spin-wave band becomes narrower and no discrete peaks are observable near the upper band edge. A drastically different spectrum is found for the case of d_0 (9.1 Å) much smaller than d (41.0 Å) as shown in Fig. 1(c). In this case a very intense discrete mode is found near 27.7 GHz in the anti-Stokes spectrum. This superlattice surface spin-wave mode, which travels about the total superlattice stack, is allowed to exist besides the collective spin-wave band.[3–5] It would merge with the latter for $d = d_0$.

The effect of inverting the applied magnetic field on the Brillouin cross section is demonstrated in Fig. 1(d). Since the direction of the applied field defines the sense of revolution of each surface spin-wave mode about each magnetic layer, an inverted field exchanges the Stokes and anti-Stokes parts of the spectra.

Figure 2 shows Brillouin spectra of an Fe/Pd superlattice sample with $d = 89.4$ Å and $d_0 = 99.0$ Å for different applied magnetic fields H. With increasing H the spin-wave frequencies increase, accompanied by a bandwidth narrowing.

Since the thickness of each magnetic layer in the superlattices considered here is as low as 16 Å for the smallest modulation wavelength, an influence of interface anisotropies of the spin-wave frequencies cannot generally be excluded. For a single epitaxial layer of Fe(110) on a W(110) substrate prepared in UHV by electron beam evaporation and *in situ* measured by Brillouin scattering an *increase* of the spin-wave frequencies toward smaller Fe thicknesses has been observed for $d < 60$ Å.[15] Using a modified Damon–Eshbach theory, which includes properly the magnetic in-plane and out-of-plane anisotropy contributions, a quantitative description of the observed mode behavior could be achieved. From a fit of the experimental data the anisotropy constants could be determined.[15]

In the following we will describe the theory used in the present work on magnetic superlattices, which includes magnetic interface anisotropy contributions. It is an extension of a theoretical approach described elsewhere,[12] which allows in the magnetostatic limit for the calculation of spin-wave frequencies of superlattices under the inclusion of volume anisotropy contributions described by the volume anisotropy constant K_1 and an uniaxial anisotropy constant K_u. We dropped contributions from the latter, since there is no evidence in the superlattices for uniaxial contributions, which cannot be described more adequately by surface anisotropies. Exchange contributions are neglected.[3–5,10,12]

Since the Fe layers investigated here all have the (110) planes parallel to the interfaces of the superlattice, we restrict ourselves in the following to this case. We will use a spherical coordinate system, where Θ is the azimuthal angle measured against the interface normal and Φ is the polar angle measured with respect to the crystallographic [001] axis in the layer plane. The free-energy density[16–18] of the system consists of (i) the potential energy density f_p of the magnetization M_s in the external field H,

$$f_p = -M_s H \sin\Theta \cos(\Phi_H - \Phi), \tag{1}$$

where Φ_H is the angle between the crystallographic [001] direction in the surface and the external field H, (ii) the free-energy density f_v due to volume anisotropies,

$$f_v = (K_1/4)\{\cos^4\Theta + \sin^4\Theta[\sin^4\Phi + \sin^2(2\Phi)] + \sin^2(2\Theta)[\cos^2\Phi - \tfrac{1}{2}\sin^2\Phi]\}, \tag{2}$$

and (iii) the free-energy density f_i due to interface anisotropies in the homogeneous magnetization approximation,[19]

$$f_i = (2/d)(K_s \cos^2\Theta + K_{s,p} \sin^2\Theta \cos^2\Phi), \tag{3}$$

where d is the thickness of the magnetic layers and the factor of 2 counts the two interfaces. K_s and $K_{s,p}$ are the out-of-plane and the in-plane anisotropy constants, respectively. Since the films considered here are isotropic in plane, we have to average Eqs. (1)–(3) over the in-plane angle Φ:

$$f_p^{\text{iso}} = -M_s H \sin\Theta, \tag{4}$$

$$f_v^{\text{iso}} = (K_1/4)(\tfrac{3}{8}\sin^4\Theta + \cos^2\Theta), \tag{5}$$

$$f_i^{\text{iso}} = (2/d)(K_s \cos^2\Theta + \tfrac{1}{2}K_{s,p} \sin^2\Theta). \tag{6}$$

With the resulting free-energy density f,

$$f = f_p + f_v + f_i, \tag{7}$$

we are now able to determine the components of the dynamic susceptibility tensor χ (Refs. 16–18):

$$\chi_{11} = 4\pi\gamma^2 f_{\Phi\Phi}/\Omega^2 \sin^2\Theta, \tag{8}$$

$$\chi_{12} = (4\pi/\Omega^2)[(\gamma^2 f_{\Theta\Phi}/\sin\Theta) - i\gamma M_s], \tag{9}$$

$$\chi_{21} = (4\pi/\Omega^2)[(\gamma^2 f_{\Theta\Phi}/\sin\Theta) + i\gamma M_s], \tag{10}$$

$$\chi_{22} = 4\pi\gamma^2 f_{\Theta\Theta}/\Omega^2, \tag{11}$$

with

$$\Omega^2 = \omega_0^2 - \omega^2, \tag{12}$$

$$\omega_0 = (\gamma/M_s \sin\Theta)\sqrt{f_{\Theta\Theta} f_{\Phi\Phi} - f_{\Theta\Phi}^2}, \tag{13}$$

where $f_{\mu\nu}$ refer to the second derivatives of f with respect to μ and ν. γ is the gyromagnetic ratio and ω the spin-wave frequency. Since for all superlattices considered in this work the magnetization has no out-of-plane component (see below) we may assume in the following $\Theta = 90°$. The evaluated expressions for $f_{\Theta\Theta}$, $f_{\Phi\Phi}$, and $f_{\Theta\Phi}$ are

$$f_{\Theta\Theta} = M_s H - \tfrac{1}{8}K_1 + (4/d)(K_s - \tfrac{1}{2}K_{s,p}), \tag{14}$$

$$f_{\Phi\Phi} = M_s H, \tag{15}$$

$$f_{\Theta\Phi} = 0. \tag{16}$$

It should be pointed out, that due to the (110) orientation of the crystallites in each magnetic film the anisotropy contributions do not average to zero. However, only a linear combination of the three anisotropy constants enters the calculation, contrary to results of epitaxial films, where the constants enter independently in $f_{\Theta\Theta}$ and $f_{\Phi\Phi}$.[15]

The rest of the calculation is straightforward. Solving Maxwell's equations in the magnetic and nonmagnetic layers and taking the magnetic boundary conditions at each interface into account, the problem of finding solutions for propagating spin waves can be reduced to finding the zeros of the boundary-condition determinant. Since at each interface only magnetic interactions between the adjacent layers have to be considered the boundary-condition determinant can be written in the form of a band matrix. This allows to apply very effective numerical tools in order to efficiently calculate the spin-wave frequencies even for 90 bilayers.

The parallel component of the spin-wave wave vector, $q_\parallel$, is defined by the scattering geometry of the Brillouin scattering experiment. The perpendicular component $q_\perp$ is given in each layer by the relation[12]

$$q_\perp = q_\parallel \sqrt{-[(1 + \chi_{22}\sin^2\alpha)/(1 + \chi_{11})]}, \tag{17}$$

where α is the angle between $q_\parallel$ and $4\pi M_s$. In the absense of surface anisotropies $q_\perp$ is always imaginary, resulting in surface spin-wave modes. However, in particular for small magnetic thicknesses and large positive surface anisotropy contributions, $q_\perp$ can become real and the spin waves have bulklike character in the corresponding layer.

Figures 3 and 4 show results of the calculations. We used the parameters obtained from the fit of the spin-wave frequencies in single epitaxial Fe(110) films on W(110) reported in Ref. 15. The parameters are given in Figs. 3 and 4. Figure 3 shows the obtained spin-wave frequencies for a $N = 10$ superlattice as a function of the Fe layer thickness d, which is equal to the thickness d_0 of the nonmagnetic spacer material. As in the case of single layers the spin-wave frequencies increase for small d. The mode of highest frequency, which is the surface spin-wave mode revolving about the total superlattice stack, shows an overall frequency increase with decreasing d and is well separated from the residual modes. Contrary to the case of vanishing interface anisotro-

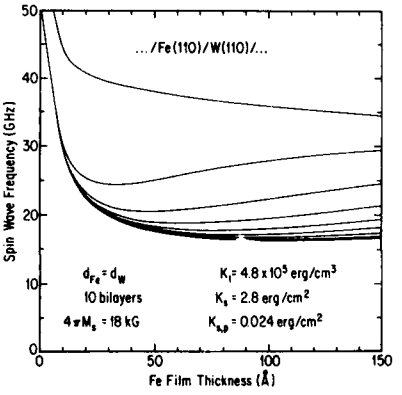


FIG. 3. Calculated spin-wave frequencies as a function of the layer thickness for a $N = 10$ superlattice with equal thicknesses of the magnetic and nonmagnetic layers. The parameters are as indicated in the figure.

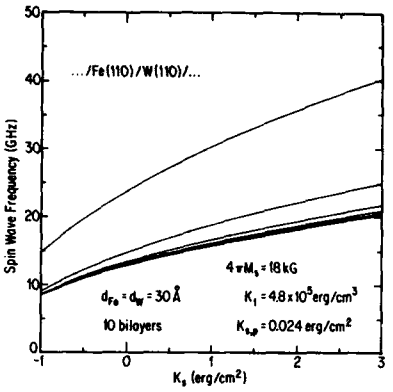


FIG. 4. Calculated spin-wave frequencies as a function of the out-of-plane interface anisotropy constant K_s. The parameters are as indicated in the figure.

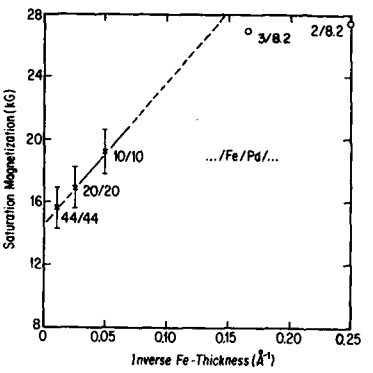


FIG. 5. Values of the saturation magnetization obtained from the SQUID measurements (crosses) and values from Ref. 11 (circles) as a function of the inverse Fe thickness. The solid line is a fit to our data and the dashed line is an extrapolation into the regime of the data of Ref. 11.

pies, this mode cannot be described as a surface spin wave of a magnetic layer of a thickness equal to the total thickness of the superlattice stack,[3–5] since in the latter case the surface anisotropy contribution should be negligible due to the $1/d$ factor. All residual modes are nearly degenerate in frequency for very small d. An analysis of the wave solutions in each layer shows, that due to the dominating interface anisotropy terms the spin waves are bulk-mode-like in each layer, which compared to surface modes have smaller dipolar stray fields in the nonmagnetic spacer layers and are thus less coupled to each other.

Figure 4 shows the spin-wave frequencies of a $N = 10$ superlattice with $d = d_0 = 30$ Å as a function of the surface anisotropy constant K_s. In the plotted range the energy contribution of the surface anisotropy is too small to turn the magnetization out of plane for negative values of K_s. With increasing K_s the spin-wave frequencies increase, whereas for negative values of K_s the spin-wave frequencies are reduced.

In order to test the influence of interface anisotropies in Fe/Pd superlattices as well as to address the above described discrepancies in the reported values of the saturation magnetization,[8,9,11] we have reanalyzed the previously measured Brillouin scattering data using the new model. In order to support the reported increased values of the saturation magnetization for vapor-deposited Fe/Pd superlattices of Fe thicknesses between 2 and 6 Å (Ref. 11) we also measured for some of our samples $4\pi M_s$ and the saturation field (kink field) H_s by means of a SQUID magnetometer for applied magnetic fields H up to 54 kG parallel as well as perpendicular to the layers. The results from the SQUID measurements are listed in Table I together with those from Ref. 11. For all samples we obtained higher values of the saturation magnetization as compared to the Brillouin scattering results reported in Refs. 8 and 9. Figure 5 shows a plot of the saturation magnetization obtained from the SQUID measurements as a function of the inverse Fe thickness $1/d$ including the data from Ref. 11, except sample 1/8.2. The values of $4\pi M_s$ of each superlattice sample have been obtained by dividing the measured magnetic moment by the total Fe volume. The data points lie roughly on a straight line, which can be described by

$$4\pi M_s(d) = 4\pi M_s(d = \infty)(1 - d_s/d), \qquad (18)$$

where d_s is the amount, by which the thickness of the magnetic layers differs from that of the Fe layers. $4\pi M_s(\infty)$ is the intrinsic magnetization of Fe. An extrapolation of this line into the regime of the data of Ref. 11 agrees with the latter, in particular with the sample of largest Fe thickness ($d = 6$ Å). The line is given by $4\pi M_s(\infty) = 14.5 \pm 1.5$ kG and $d_s = -1.5$ Å, assuming a uniform magnetization across the total magnetic thickness. The negative value of d_s implies that the thickness of the magnetically active material is larger than the Fe thickness, i.e., that Pd is magnetically polarized. However, since in the Pd material only the product of $4\pi M_s(\infty)$ of Pd and d_s enters Eq. (18), we cannot determine each of both factors independently.

An intrinsic saturation magnetization, which is independent of Λ, allows for a consistent description of the Brillouin scattering data as well. An increased value of $4\pi M_s$

TABLE I. Parameters and results of the Fe/Pd superlattices investigated by SQUID measurements. n_{Fe} (n_{Pd}): number of atomic Fe (Pd) layers per bilayer; Λ: modulation wavelength; $4\pi M_s$: measured SQUID values of the saturation magnetization: $\mu_0 H_k$: perpendicular saturation field.

n_{Fe}/n_{Pd}	Number of bilayers	Λ (Å)	$4\pi M_s$ (kG)	$\mu_0 H_k$ (kG)
44/44	49	188.4	15.6	20.0
20/20	70	86.8	16.9	17.2
10/10	90	42.2	19.2	14.7
3/8.2[a]	125	26.5	27.0	11.0
2/8.2[a]	136	24.4	27.4	8.5
1/8.2[a]	150	22.2	25.2	4.6

[a] Data from den Broeder *et al.*[11]

would result in increased spin-wave frequencies, which, however, are not observed experimentally. On the other hand, a small increase in d with a corresponding decrease in d_0 modifies the spin-wave frequencies only slightly.

Assuming therefore the saturation magnetization to be independent of the modulation wavelength Λ, magnetic anisotropy effects have to account for the observed decrease of the spin-wave frequencies with decreasing Λ. Since only a linear combination of all anisotropy constants enter the folmula [see Eqs. (14) and (15)] and $K_{s,p}$ is usually much smaller than K_s, we assumed $K_{s,p} = 0$ and for K_1 a literature value of 4.8×10^5 erg/cm^2.[20] A good fit of the experimental data could be achieved within the experimental error by a value of $4\pi M_s = 17 \pm 2$ kG and an out-of-plane anisotropy constant $K_s = -0.15 \pm 0.03$ erg/cm^2. For comparison, an analysis of the saturation field H_s (see Table I) as a function of $1/d$ as determined by the SQUID magnetometer yields a value of $K_s = -0.38 \pm 0.1$ erg/cm^2. The latter value has the same sign as the value obtained from the Brillouin spectroscopy data. The higher absolute value might be due to the contribution of higher-order constants, which may show no influence on the spin-wave frequencies.[21] However, both values are too small to rotate the direction of magnetization out of plane. This is confirmed by the absence of hysteresis effects in the perpendicular-field SQUID measurements.

In conclusion, we have shown that the observation of spin-wave spectra in superlattices by Brillouin spectroscopy reveals important information about the magnetic properties of these artificially layered materials. In particular we have demonstrated the influence of interface anisotropies on the spin-wave frequencies which may become dominant for small modulation wavelengths. Since the spin-wave frequencies are sensitive to the intrinsic saturation magnetization, the combination of Brillouin spectroscopy with magnetometric investigations allows potentially for the determination of dead layers as well as polarization of the nonmagnetic spacer layers at the interfaces. We applied both types of methods to the Fe/Pd superlattice system. From the comparison of the results a consistent description could be found by assuming a saturation magnetization of 17 ± 2 kG, which is independent of the modulation wavelength, a polarization of the Pd layer at each interface and a small negative out-of-plane interface anisotropy of $K_s = -0.15$ erg/cm^2. The obtained value for the saturation magnetization is about 20% smaller than the bulk Fe value of 21 kG, which might be due to the sputtering process. Future investigation on both sputtered and MBE-grown Fe/Pd systems will help to clarify this point. Presently the physical origin of the Pd polarization is not clear. The situation is reminiscent of the formation of giant moments,[22] but the physical conditions, i.e., the Fe concentration and the temperature range, are not comparable. From the Bethe–Slater diagram and the lattice constant mismatch, which causes a stretching of the spacing of nearest-neighbor Pd atoms by 10%, the interface mismatch would not give rise to a magnetic moment in the Pd layer. On the other hand, a hybridization of the Pd(d) states with the Fe(d) states is very likely due to the large density of Pd states at the Fermi level, and might account for the observed behavior. A fully self-consistent band-structure calculation would be most desirable for this case.

We would like to thank G. Rado and G. Stegeman for discussions and support. The work at the University of Arizona was supported by the Air Force Office of Scientific Research/University Research Initiative Program under Contract No. F49620-86-C-0123, and by the Department of Energy-Materials Sciences Division under Contract No. DE-FG02-87-ER45297. The work at the University of Cologne was supported by Deutsche Forschungsgemeinschaft, SFB 125. Work at Los Alamos National Laboratory was performed under the auspicies of the Department of Energy.

[1] C. F. Majkrzak, J. W. Cable, J. Kwo, M. Hong, D. B. McWhan, Y. Yafet, J. V. Waszczak, and C. Vettier, Phys. Rev. Lett. **56**, 2700 (1986).
[2] M. B. Salamon, S. Sinha, J. J. Rhyne, J. E. Cunningham, R. W. Erwin, J. Borchers, and C. P. Flynn, Phys. Rev. Lett. **56**, 259 (1986).
[3] R. E. Camley, T. S. Rahman, and D. L. Mills, Phys. Rev. B **27**, 261 (1983).
[4] P. Grünberg and K. Mika, Phys. Rev. B **27**, 2955 (1983).
[5] P. R. Emtage and M. R. Daniel, Phys. Rev. B **29**, 212 (1984).
[6] M. Grimsditch, M. R. Khan, and I. K. Schuller, Phys. Rev. Lett. **51**, 498 (1983).
[7] A. Kueny, M. R. Khan, I. K. Schuller, and M. Grimsditch, Phys. Rev. B **29**, 2879 (1984).
[8] B. Hillebrands, P. Baumgart, R. Mock, G. Güntherodt, A. Boufelfel, and C. M. Falco, Phys. Rev. B **34**, 9000 (1986).
[9] B. Hillebrands, P. Baumgart, R. Mock, G. Güntherodt, A. Boufelfel, and C. M. Falco, J. Appl. Phys. **61**, 4308 (1987).
[10] G. Rupp, W. Wettling, W. Jantz, and R. Krishnan, Appl. Phys. A **37**, 73 (1985).
[11] F. J. A. den Broeder, H. C. Donkersloot, H. J. G. Draaisma, and W. J. M. de Jonge, J. Appl. Phys. **61**, 4317 (1987).
[12] G. Rupp, W. Wettling, and W. Jantz, Appl. Phys. A **42**, 45 (1987).
[13] R. Mock, B. Hillebrands, and J. R. Sandercock, J. Phys. E **20**, 656 (1987).
[14] C. M. Falco, J. Phys. (Paris) Colloq. **45**, C5-499 (1984).
[15] B. Hillebrands, P. Baumgart, and G. Güntherodt, Phys. Rev. B **36**, 2450 (1987).
[16] G. Rupp, W. Wettling, A. S. Smith, and W. Jantz, J. Magn. Magn. Mater. **45**, 404 (1984).
[17] J. O. Artman, Phys. Rev. **105**, 62 (1957).
[18] E. P. Valstyn, I. P. Hanton, and A. M. Morrish, Phys. Rev. **128**, 2078 (1962).
[19] U. Gradmann, J. Korecki, and G. Waller, Appl. Phys. A **39**, 101 (1986).
[20] E. P. Wohlfarth, in *Ferromagnetic Materials*, edited by E. P. Wohlfarth (North-Holland, Amsterdam, 1980).
[21] M. J. Pechan, and I. K. Schuller, Phys. Rev. Lett. **59**, 132 (1987).
[22] J. Crangle, and W. R. Scott, J. Appl. Phys. **36**, 921 (1965).

Theory of magnetic surface anisotropy and exchange effects in the Brillouin scattering of light by magnetostatic spin waves (invited)

G. T. Rado and R. J. Hicken
Department of Physics and Astronomy, The Johns Hopkins University, Baltimore, Maryland 21218

A new theory of the Brillouin shift in the inelastic scattering of light by magnetostatic spin waves is presented. Contrary to previous work, the present calculations do include exchange effects and treat the magnetic surface anisotropy constants K_s and K_{ss} directly rather than via the stratagem of effective volume anisotropies. The experimental data for {110} Fe on W are explained about as well by the present theory as by previous work. A detailed analysis reveals the previously unnoticed fact that the signs of K_s and K_{ss} for $(\bar{1}10)$ Fe on W are opposite to those for $(\bar{1}10)$ Fe on GaAs. Some new spin-wave modes arising from exchange are predicted and shown to occur outside the frequency range which has been investigated experimentally. A quantitative explanation is proposed for the occasional applicability of a theory based on effective volume anisotropies and zero exchange.

I. INTRODUCTION

Recent light scattering measurements by Hillebrands, Baumgart, and Güntherodt[1] on epitaxially grown Fe (110) films with thicknesses between 8 and 150 Å have shown that for thicknesses below 60 Å the frequency of the Brillouin shift increases with decreasing film thickness by a factor of up to three. These results were attributed[1] to effects of magnetic surface anisotropies. Calculations[1] based on the Damon–Eshbach[2] (DE) magnetostatic surface mode and on the replacement of magnetic surface anisotropies by effective volume anisotropies do, in fact, describe the experimental data reasonably well if fitted values are used for the two surface anisotropy constants and for the magnetization.

Nevertheless, we believe that it is important to determine over what range of film thicknesses the use of effective volume anisotropies is valid and to investigate whether the use of these effective anisotropies adequately accounts for the physical phenomena contained in the Brillouin shift. We present, therefore, a theory of the Brillouin shift in which we completely avoid the replacement of surface anisotropies by effective volume anisotropies. To do this, we introduce the surface anisotropies by means of the general exchange boundary condition of Rado and Weertman[3] and then show that the DE modes must necessarily be replaced by modes involving exchange effects. We further show that the dependence of the Brillouin shift on the film thickness can be calculated from the requirement that a certain 8×8 determinant arising from the boundary conditions must vanish. The Brillouin shifts calculated in this way describe the experimental data about as well as the shifts calculated on the basis of effective volume anisotropies. Moreover, the Brillouin shifts which we calculate are more general and contain more features than those obtained from the DE mode with the use of effective volume anisotropies. Specifically, our calculation of Brillouin shifts includes, for the first time, exchange effects as well as surface anisotropies. The exchange effects lead to Brillouin shifts additional to those predicted previously.

In Sec. II we explain the basis of our theoretical method and contrast it with the previously[1] used method, and in Sec. III we present an outline of our calculations. Section IV contains our numerical results and their comparison with the experimental data.

II. METHOD

The method used by Hillebrands *et al.*[1] in their calculation of the Brillouin shift is based on a modified DE theory. It involves, as does the DE theory, the Maxwell equations of magnetostatics and a simple form of the equation of motion of the magnetization. The solution of the latter was expressed in terms of the magnetic susceptibility tensor which had previously been generalized[4,5] by the inclusion of magnetocrystalline volume anisotropy. Hillebrands *et al.*[1] took even the magnetic surface anisotropy into account by replacing each of its constants, such as K_s, by an effective volume anisotropy constant $K_{\rm eff} = K_s/(2L)$, where $2L$ is the thickness of the ferromagnetic film under investigation. Contrary to a frequently made assumption, we do not believe that such a replacement is generally valid for ultrathin films. Although Gradmann *et al.*[6,7] presented a theoretical argument for the use of $K_{\rm eff}$ in a special static case and Rado[8] proposed specific conditions for the use of $K_{\rm eff}$ in ferromagnetic resonance, a general justification for the use of $K_{\rm eff}$ does not seem to have been obtained so far.

Our method of calculation of the Brillouin shift avoids this problem by not even invoking the concept of $K_{\rm eff}$. Instead, we abandon the DE formalism by introducing the surface anisotropy via appropriate boundary conditions and by including exchange interactions in the theory. We start with the Maxwell equations of magnetostatics,

$$\nabla\times\mathbf{H} = 0, \tag{1}$$

$$\nabla\cdot(\mathbf{H} + 4\pi\mathbf{M}) = 0, \tag{2}$$

and the equation of motion[9] of the magnetization

$$\left(\frac{1}{\gamma}\right)\frac{\partial\mathbf{M}}{\partial t} = \mathbf{M}\times\left[\mathbf{H} - \left(\frac{1}{M}\right)\nabla_M E_{\rm ani} + \left(\frac{2A}{M^2}\right)\nabla^2\mathbf{M}\right], \tag{3}$$

where $\mathbf{H}$ and $\mathbf{M}$ denote the magnetic field and the magnetization, respectively. Here $\gamma = \gamma_e g/2$ is the magnetomechanical ratio, $\gamma_e = 2\pi(2.80)$ MHz/Oe is the value of γ for a free

 0021-8979/88/083885-05$02.40 © 1988 American Institute of Physics

electron, and g is the spectroscopic splitting factor. The parameter A is the exchange stiffness constant, $E_{\rm ani}$ is the volume anisotropy energy density, and ∇_M is the gradient operator in which the differentiation variables are the components of the unit vector $\mathbf{u} = \mathbf{M}/M$. To determine the Brillouin frequency shift $\omega/(2\pi)$ and other aspects of our inelastic light scattering problem, we must solve Eqs. (1), (2), and (3) subject to the magnetostatic boundary conditions and the general exchange boundary condition[3,10]

$$\mathbf{M}\times\left[\nabla_M E_{\rm surf} - \left(\frac{2A}{M}\right)\frac{\partial \mathbf{M}}{\partial n}\right] = 0. \tag{4}$$

Here $E_{\rm surf}$ denotes the surface anisotropy energy density and $\partial/\partial n$ is the partial derivative in the direction of a unit vector $\mathbf{n}$ which is normal to the ferromagnetic film. We recall[10] that at each surface of the film $\mathbf{n}$ points toward the film's interior. It should also be noted that we assume $\mathbf{H}$ and $\mathbf{M}$ to have the form

$$\mathbf{H} = H\mathbf{i}_z + \mathbf{h}, \tag{5}$$

$$\mathbf{M} = M\mathbf{i}_z + \mathbf{m}, \tag{6}$$

where $\mathbf{h}$ and $\mathbf{m}$ are position and time dependent, H and M are constants, and the inequalities

$$|\mathbf{h}|/H \ll 1 \quad \text{and} \quad |\mathbf{m}|/M \ll 1 \tag{7}$$

are both satisfied. The quantity $\mathbf{i}_z$ is a unit vector along the z direction of the x, y, z coordinate system introduced below.

Figure 1 shows the two coordinate systems used in this paper. The axes of the x',y',z' system are parallel, respectively, to the $[100]'$, $[010]'$, and $[001]'$ axes of a cubic crystal. This system is useful for describing the light scattering experiments of Hillebrands *et al.*[1] on monocrystalline films of bcc iron parallel to a $\{110\}'$ plane. The axes of the x,y,z system, on the other hand, are convenient for analyzing the spin waves because the z axis is parallel to the static magnetic field applied along the $[110]'$ axis. It is assumed that the monocrystalline ferromagnetic film is bounded by the planes $x = \pm L$ but unbounded along the y and z axes. A simple calculation shows that the numerical values of certain parameters involved in the experiments[1] (namely H and the quantity K_s^* defined below) are such that for sufficiently small values of the film thickness $2L$ the equilibrium direction of the magnetization is along $[110]'$ rather than along $[001]'$.

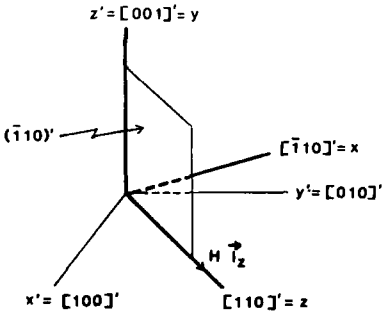


FIG. 1. The x,y,z coordinate system used in the calculations. Also shown are the cubic crystalline axes x',y',z' and the $(\bar{1}10)'$ plane which is parallel to the faces of the monocrystalline ferromagnetic film.

For E_{ani} we use the well-known expression appropriate to cubic crystals

$$E_{\rm ani} = K_1(u_{x'}^2u_{y'}^2 + u_{y'}^2u_{z'}^2 + u_{z'}^2u_{x'}^2), \tag{8}$$

where $u_{x'}$, $u_{y'}$, and $u_{z'}$ are the components of $\mathbf{u}$ along the cubic axes and K_1 is the first-order cubic anisotropy constant. When written in terms of the components of $\mathbf{u}$ along the x,y,z axes, $E_{\rm ani}$ becomes

$$E_{\rm ani} = (K_1/4)(4u_x^4 - 3u_y^4 + 4u_x^2u_y^2 - 4u_x^2 + 2u_y^2), \tag{9}$$

where u_z^2 was eliminated by means of $u_z^2 = 1 - u_x^2 - u_y^2$.

Turning now to $E_{\rm surf}$, we use the two-parameter expression

$$E_{\rm surf} = K_s u_{x'}u_{y'} + K_{ss}u_{z'}^2, \tag{10}$$

introduced by Rado[10] for the $(\bar{1}10)'$ plane. For other planes of the $\{110\}'$ type the form of $E_{\rm surf}$ is given by Rado and Zhang.[11] For the $(110)'$ plane, for example, the sign of K_s in Eq. (10) must be changed, contrary to the impression given by Refs. 6 and 7. More generally, any definition of surface anisotropy constants and their signs must necessarily be accompanied by a specification of the film plane under consideration. Although the surface anisotropy tensor is the same for each of the six $\{110\}'$-type planes, its matrix representation is different for each of these six planes. By writing the $E_{\rm surf}$ of Eq. (10) in terms of the components of $\mathbf{u}$ along the x,y,z axes, we obtain

$$E_{\rm surf} = -K_s u_x^2 - K_s^* u_y^2, \tag{11}$$

where we defined K_s^* by

$$K_s^* = \tfrac{1}{2}K_s - K_{ss}, \tag{12}$$

which should not be confused with the K_s^* introduced in Ref. 10. The terms $-K_s u_x^2$ and $-K_s^* u_y^2$ of Eq. (11) represent, respectively, the out-of-plane and in-plane contributions to the surface anisotropy energy. Analogously, the papers of Gradmann *et al.*[6,7] and Hillebrands *et al.*[1] contain an equation of the form

$$E_{\rm surf} = K_s' u_x^2 + K_{s,p} u_y^2, \tag{13}$$

which may be compared with Eq. (11). The resulting relations

$$K_s' = -K_s, \tag{14a}$$

$$K_{s,p} = -K_s^*, \tag{14b}$$

can be shown to express merely an arbitrary sign convention.

III. CALCULATIONS

We assume that inside the ferromagnetic film $\mathbf{h}$ and $\mathbf{m}$ are proportional to $\exp[i(\omega t - k_y y) - ik_x x]$, and that outside the film (where $\mathbf{h}$ will be called $\mathbf{h}^e$) $\mathbf{h}$ is proportional to $\exp[i(\omega t - k_y y) - k_x^e x]$ and $\mathbf{m}$ is zero. With the use of the relations (5), (6), (7), and (9) we find that inside the film Eqs. (1), (2), and (3) yield the equations

$$k_y h_x - k_x h_y = 0, \tag{15}$$

$$4\pi k_x m_x + 4\pi k_y m_y + k_x h_x + k_y h_y = 0, \tag{16}$$

$$(i\omega/\gamma)m_x - [H_a + (2A/M)P^2]m_y + Mh_y = 0, \quad (17)$$

$$[H_b + (2A/M)P^2]m_x + (i\omega/\gamma)m_y - Mh_x = 0, \quad (18)$$

which contain the abbreviations

$$H_a = H + (K_1/M), \quad (19)$$

$$H_b = H - (2K_1/M), \quad (20)$$

$$P^2 = k_x^2 + k_y^2. \quad (21)$$

Equations (15)–(18) constitute a set of four homogeneous linear equations for m_x, m_y, h_x, and h_y. In order that these equations possess a nonvanishing solution the secular determinant of their coefficients must vanish. This requirement leads to the dispersion relation

$$(2A/M)^2P^6 + (2A/M)(H_a + H_b + 4\pi M)P^4 + [4\pi MH_a + H_aH_b - (\omega/\gamma)^2]P^2 + 4\pi M(H_b - H_a)k_y^2 = 0. \quad (22)$$

Since k_y is a constant determined by the wave number and scattering angle of the incident light beam, as explained in Sec. IV, it is seen that Eq. (22) fully determines the relation between ω and k_x. We shall label the six roots of Eq. (22) by k_{xn}, where $n = 1,2,...,6$ and use $k_{x2} = -k_{x1}$, $k_{x4} = -k_{x3}$, $k_{x6} = -k_{x5}$. The calculation of the k_{xn} values as functions of ω will be performed numerically.

In preparing to formulate the boundary conditions we find it convenient to express each of the six sets of h_{yn}, m_{xn}, and m_{yn} in terms of h_{xn}. This is easily done for h_{yn} by using Eq. (15). For m_{xn} and m_{yn}, on the other hand, we introduce the quantities u_n and v_n which we define by

$$m_{xn} = u_n h_{xn}, \quad (23)$$

$$m_{yn} = v_n h_{xn}, \quad (24)$$

and calculate with the use of Eqs. (17) and (18). Thus we obtain

$$u_n = \frac{M[H_a + (2A/M)P_n^2 - (i\omega/\gamma)(k_y/k_{xn})]}{[H_a + (2A/M)P_n^2][H_b + (2A/M)P_n^2] - (\omega/\gamma)^2}, \quad (25)$$

$$v_n = -\frac{M\{[H_b + (2A/M)P_n^2](k_y/k_{xn}) + (i\omega/\gamma)\}}{[H_a + (2A/M)P_n^2][H_b + (2A/M)P_n^2] - (\omega/\gamma)^2}, \quad (26)$$

where we introduced the abbreviation

$$P_n^2 = k_{xn}^2 + k_y^2. \quad (27)$$

Next we turn to the regions $x > L$ and $x < -L$ which are external to the film. All quantities referring specifically to these regions will be identified by the superscripts $e+$ and $e-$, respectively, rather than merely by the superscript e. From Eqs. (1) and (2) we obtain

$$ik_y h_x^e - k_x^e h_y^e = 0, \quad (28)$$

$$k_x^e h_x^e + ik_y h_y^e = 0, \quad (29)$$

so that a nonvanishing solution h_x^e, h_y^e requires

$$k_x^e = \pm k_y. \quad (30)$$

Upon assuming (without loss of generality) $k_y > 0$ and noting that h_x^e must approach zero as x approaches infinity, we particularize Eq. (30) to give

$$k_x^{e+} = +k_y \quad \text{and} \quad k_x^{e-} = -k_y. \quad (31)$$

The only additional relations needed for the regions external to the film are

$$h_y^{e+} = ih_x^{e+}, \quad (32)$$

$$h_y^{e-} = -ih_x^{e-}, \quad (33)$$

which follow from Eq. (15).

As noted in Sec. II, the boundary conditions we intend to use are the magnetostatic boundary conditions and the general exchange boundary condition of Eq. (4). The former require

$$\text{continuity of } h_y \text{ at } x = \pm L, \quad (34)$$

$$\text{continuity of } h_x + 4\pi m_x \text{ at } x = \pm L, \quad (35)$$

whereas Eq. (4) [supplemented by Eqs. (6), (7), (11) and (12)] requires

$$K_s m_x \mp A\,\partial m_x/\partial x = 0 \quad \text{at } x = \pm L \quad (36)$$

$$K_s^* m_y \mp A\,\partial m_y/\partial x = 0 \quad \text{at } x = \pm L. \quad (37)$$

When expressed in terms of the eight constituents of the field h_x, Eqs. (34)–(37) become

$$\sum_{n=1}^{6}(k_y/k_{xn})h_{xn}\exp(-ik_{xn}L) - ih_x^{e+}\exp(-k_yL) = 0, \quad (38)$$

$$\sum_{n=1}^{6}(k_y/k_{xn})h_{xn}\exp(ik_{xn}L) + ih_x^{e-}\exp(-k_yL) = 0, \quad (39)$$

$$\sum_{n=1}^{6}(1 + 4\pi u_n)h_{xn}\exp(-ik_{xn}L) - h_x^{e+}\exp(-k_yL) = 0, \quad (40)$$

$$\sum_{n=1}^{6}(1 + 4\pi u_n)h_{xn}\exp(ik_{xn}L) - h_x^{e-}\exp(-k_yL) = 0, \quad (41)$$

$$\sum_{n=1}^{6}(K_s + iAk_{xn})u_n h_{xn}\exp(-ik_{xn}L) = 0, \quad (42)$$

$$\sum_{n=1}^{6}(K_s - iAk_{xn})u_n h_{xn}\exp(ik_{xn}L) = 0, \quad (43)$$

$$\sum_{n=1}^{6}(K_s^* + iAk_{xn})v_n h_{xn}\exp(-ik_{xn}L) = 0, \quad (44)$$

$$\sum_{n=1}^{6}(K_s^* - iAk_{xn})v_n h_{xn}\exp(ik_{xn}L) = 0, \quad (45)$$

which are seen to be eight homogeneous linear equations for the eight unknowns h_{x1}, h_{x2}, h_{x3}, h_{x4}, h_{x5}, h_{x6}, h_x^{e+}, and h_x^{e-}. The condition for these equations to have a nonvanishing solution is that the determinant D of their coefficients be zero. Since D has 2580 terms, and since the parameters of the Hillebrands *et al.*[1] experiment do not allow the kind of approximations which would simplify D appreciably, we found it necessary to obtain the value of D from a computer calculation (see Sec. IV). The Brillouin shift is then that value of $\omega/(2\pi)$ which satisfies the equation

$$D = 0. \quad (46)$$

Prior to solving Eq. (46) numerically, we note that in the

limiting case of $A = K_1 = K_s = K_s^* = 0$ the solution of Eq. (46) reduces precisely to the dispersion relation (23) of the DE paper.[2]

IV. RESULTS AND DISCUSSION

The numerical calculation of D requires that we first obtain k_{xn} $(n = 1,2,...,6)$ as functions of ω from the dispersion relation (22). This relation is cubic in P^2 and may thus be solved by well-known methods. As to the parameters occurring in Eq. (22), we use the representative values $A = 2.0\times10^{-6}$ erg/cm, $K_1 = 4.5\times10^5$ erg/cm^3, $g = 2.09$ appropriate for iron at room temperature, and the values $H = 1$ kOe (or $H = 30$ Oe) employed in the experiments.[1] In addition, we adopt the value $4\pi M = 18\times10^3$ emu assumed by Hillebrands *et al.*[1] for fitting their data. For k_y we use the value 1.73×10^5 cm^{-1} given by the momentum conservation condition $k_y = (4\pi/\lambda)\sin\theta$. Here $\lambda = 5.145$ Å is the wavelength of the inelastically scattered light and $\theta = 45°$ is the angle of incidence. The solutions of the dispersion relation (22) obtained in this way are plotted in Fig. 2. Throughout the range shown, k_{x3} and k_{x5}, and hence k_{x4} and k_{x6}, are purely imaginary, thus representing surface modes. On the other hand, k_{x1}, and hence k_{x2}, is entirely real (for all but the smallest values of ω), thus representing volume modes.

Next we calculate ω from Eq. (46) with the use of the parameters listed above and the value $K_s' = +2.8$ erg/cm^2 assumed by Hillebrands *et al.*[1] in fitting their experimental data. Because of Eq. (14a), this K_s' equals $K_s = -2.8$ erg/cm^2. We further note that K_s^*, which equals $-K_{s,p}$ because of Eq. (14b), is essentially known. The reason is that its value, namely $K_s^* = -0.028$ erg/cm^2, can be obtained from a calculation of the critical thickness at which the easy axis of magnetization of a $(\bar{1}10)$ iron film switches from $[001]'$, which is associated with large thicknesses, to $[110]'$, which is associated with very small thicknesses. This switching effect was discovered by Prinz, Rado, and Krebs[12] by means of a ferromagnetic resonance method. Since the numerical value of D is, in general, complex, our solution of Eq. (46) involves the magnitude $|D|$ throughout. By calculating $|D|$ for an array of ordered pairs (ω,L) in the region of interest, we find that a contour plot of $|D|$ immediately reveals likely solutions. Our data array is then used as a starting point for the more accurate solution of Eq. (46) by a midpoint method.

The solutions obtained in this manner consist of plots of $\omega/(2\pi)$ vs $2L$ for $H = 30$ Oe as well as for $H = 1$ kOe and are shown in Fig. 3. Also shown in Fig. 3 are the experimental data of Hillebrands *et al.*[1] It is seen that the agreement between theory and experiment is quite satisfactory, being about as good as that obtained by Hillebrands *et al.*[1] by their method. Attempts at varying the values of M and K_s have not improved this agreement appreciably.

Of particular interest is the previously unnoticed fact that the signs of K_s and K_{ss} (and hence of K_s and K_s^*) in the present situation of uncovered $(\bar{1}10)$ Fe on W are opposite to those[11,10] for Al-covered $(\bar{1}10)$ Fe on GaAs. Stated more physically, this means that the normal to the film plane is a hard axis of Fe in the case of the W substrate but an easy axis of Fe in the case of the GaAs substrate.

Another new result is that our calculated Brillouin shifts contain branches additional to those shown in Fig. 3. These new branches, shown in Fig. 4, occur outside the frequency range which has been investigated in the experiments[1] performed so far. The origins of these branches are certain spin-wave modes which would not exist in the absence of exchange.

It remains to explain the remarkable fact that the replacement of surface anisotropies by effective volume anisotropies and the concurrent neglect of exchange effects does describe the experimental data of Hillebrands *et al.*[1] reasonably well, as mentioned in Sec. I. We begin our explanation by dividing each of the Eqs. (38)–(45) by h_x^{s-}. Since they are, in general, not linearly dependent, we proceed to solve them, by means of Cramer's rule, for the seven variables (h_{xn}/h_x^{s-}) and (h_x^{s+}/h_x^{s-}). We find, in particular, that for $2L < 15$ Å the amplitudes of the fields h_{x1} and h_{x2} are at least an order of magnitude larger than those of the other fields h_{xn}. This is an important fact because Fig. 2 shows that the $|k_{xn}|$ value for $n = 1,2$ is relatively small, being about 10^6

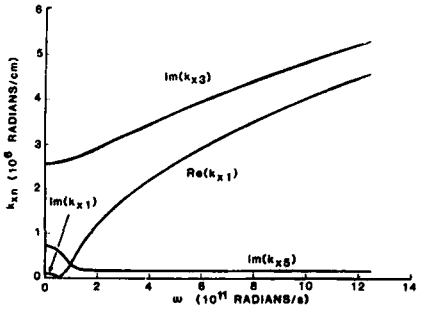


FIG. 2. Dependence of k_{x1}, k_{x3}, and k_{x5} on ω according to the dispersion relation (22). The values of k_{x2}, k_{x4}, and k_{x6} are given by $-k_{x1}$, $-k_{x3}$, and $-k_{x5}$, respectively. The calculations are based on $H = 1$ kOe and on the additional parameters given in text.

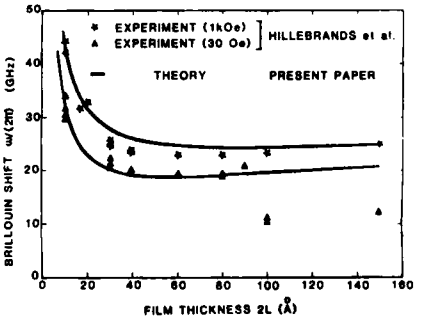


FIG. 3. Dependence of the lowest-lying branch of the Brillouin shift $\omega/(2\pi)$ on the thickness $2L$ of a $\{110\}$ Fe film. The stars ($H = 1$ kOe) and triangles ($H = 30$ Oe) indicate the experimental data of Hillebrands *et al.* (Ref. 1). The curves are based on the theory of the present paper and the parameters given in the text.

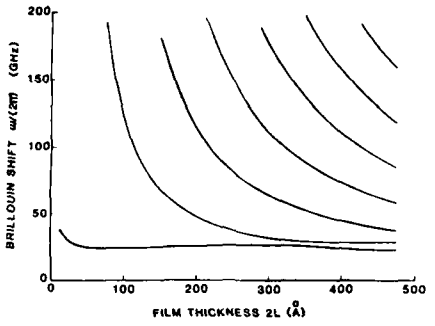


FIG. 4. Dependence of seven branches of the Brillouin shift $\omega/(2\pi)$ on the thickness $2L$ of a {110} Fe film for $H = 1$ kOe. The curves are based on the theory of the present paper and the parameters given in the text. The lowest-lying branch is the same as that shown in Fig. 3, and the other branches would not exist in the absence of exchange.

rad/cm at 25 GHz. Thus we see that for $2L = 15\times10^{-8}$ cm, i.e., for the region which contains the largest changes in ω (see Fig. 3), the most strongly excited fields satisfy the relation

$$|k_{x1}L| \ll 1. \tag{47}$$

This means that π times the film thickness is small compared to the spin wavelength so that the film is more or less uniformly magnetized. Exchange effects are, therefore, essentially negligible and the use of effective volume anisotropies is reasonably justified. We emphasize, however, that this result could not have been available without the extensive calculations of the present paper. A criterion analogous to the inequality (47), derived by Rado[3] for ferromagnetic resonance, also requires detailed calculations before it can be used.

ACKNOWLEDGMENTS

We wish to thank B. Hillebrands for useful discussions and C. Boswell for advice in the early stages of the numerical calculations.

Note added in proof. The exchange dominated modes predicted in the present paper may correspond to the standing spin waves observed in Brillouin scattering experiments by P. A. Grünberg [Prog. Surf. Sci. **18**, 1 (1985)].

[1]B. Hillebrands and G. Güntherodt, J. Appl. Phys. **61**, 3756 (1987); B. Hillebrands, P. Baumgart, and G. Güntherodt, Phys. Rev. B **36**, 2450 (1987).
[2]R. W. Damon and J. R. Eshbach, J. Phys. Chem. Solids **19**, 308 (1961).
[3]G. T. Rado and J. R. Weertman, J. Phys. Chem. Solids **11**, 315 (1959).
[4]G. Rupp, W. Wettling, R. S. Smith, and W. Jantz, J. Magn. Magn. Mater. **45**, 404 (1984).
[5]B. Schneider, Phys. Status Solidi B **51**, 325 (1972).
[6]U. Gradmann, J. Korecki, and G. Waller, Appl. Phys. A **39**, 101 (1986).
[7]U. Gradmann, J. Magn. Magn. Mater. **54–57**, 733 (1986).
[8]G. T. Rado, J. Appl. Phys. **61**, 4262 (1987).
[9]L. Landau and E. Lifshitz, Phys. Z. Sowjetunion **8**, 153 (1935).
[10]G. T. Rado, Phys. Rev. B **26**, 295 (1982); Phys. Rev. B **32**, 6061 (E) (1985).
[11]G. T. Rado and L. Zhang, Phys. Rev. B **33**, 5081 (1986).
[12]G. A. Prinz, G. T. Rado, and J. J. Krebs, J. Appl. Phys. **53**, 2087 (1982).

Observation of high-temperature spin fluctuations in UBe_{13} by nuclear-spin relaxation

W. G. Clark, W. H. Wong, W. A. Hines,[a] and M. D. Lan
Department of Physics and Solid State Science Center, University of California, Los Angeles, California 90024

D. E. MacLaughlin
Department of Physics, University of California, Riverside, California 92521

Z. Fisk and J. L. Smith
Los Alamos National Laboratory, Los Alamos, New Mexico 87545

H. R. Ott
ETH-Hönggerberg, CH-8093 Zurich, Switzerland

We report the extension of measurements of the ^{9}Be spin-lattice relaxation rate in UBe_{13} from 300 up to 1000 K. They reflect the fluctuating local magnetic field at the site of the ^{9}Be nuclei. Above about 100 K, there appears a new contribution in addition to the rate observed at lower temperatures. The high temperature contribution is modeled in terms of the thermal excitation of low-lying states of the U^{3+} ion along lines used by Felton *et al.* to explain their measurements of the specific heat. Our results indicate a splitting of 200 ± 20 K between the ground and excited states of the system, and a lifetime of 8×10^{-14} s for the excited states (width $= 95$ K).

I. INTRODUCTION

The attempt to understand the mechanism that produces "heavy fermions" in actinide and rare-earth intermetallic compounds and alloys has been one of the most actively pursued challenges in condensed-matter physics over the past few years. An important key to this understanding is their magnetic properties. One useful probe of the magnetic behavior is nuclear magnetic resonance (NMR), as it constitutes a *microscopic* probe of both the static and the dynamic behavior of the local magnetic field. In particular, it is known from its large heavy fermion enhancement[1,2] and its behavior in the superconducting state[3] that the ^{9}Be resonance is sensitive measure of the magnetic properties of the heavy fermions in UBe_{13}.

In this paper we describe measurements of the ^{9}Be nuclear spin lattice relaxation rate $1/T_1$ in UBe_{13} at high temperatures and analyze them in terms of a simple phenomenological model. The major result is that a new contribution to $1/T_1$ appears above 100 K. From the magnitude and temperature dependence of $1/T_1$, we infer the existence of low-lying excited states of the system, which are split from the ground state by an energy $\Delta E \approx 200(\pm 20)$ K and have a lifetime $\tau \approx 8\times10^{-14}$ s (i.e., a width ≈ 95 K). These results are in substantial agreement with related observations based upon specific-heat measurements,[4] and show in addition the rapidly fluctuating magnetic moment associated with the states.

II. EXPERIMENTAL DETAILS AND RESULTS

The sample was taken from a nominally pure arc-melted polycrystalline ingot, which was ground to a particle size ≈ 0.2 mm and sealed under He gas in a quartz tube. Standard pulsed NMR methods and apparatus were used for the measurements. The furnace used to obtain the elevated temperatures follows designs described elsewhere.[5] Temperature errors were on the order of 10 K, and uncertainties in the value of T_1 at high temperature approximated $\pm 10\%$.

A graph of $1/T_1$ as a function of T over the range 1–1000 K is shown in Fig. 1. The crosses and $\times$'s refer to measurements made at 9.0 and 18.5 MHz, respectively. Some of the low-temperature data have been published earlier.[6] The solid line is a fit to the data of the model to be discussed below, and the dashed line is a continuation of the trend established by the lower temperature data. From Fig. 1 it can be seen that the data below 40 K follow the solid curve, and that if it were to be extended to higher temperatures without knowledge of the higher-T data, the dashed line would be followed.

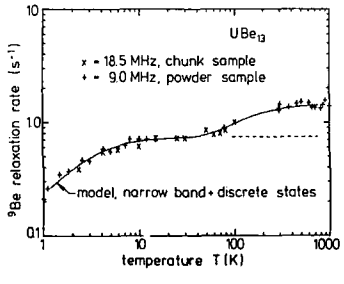


FIG. 1. ^{9}Be relaxation rate in UBe_{13} as a function of temperature. The solid line is the model developed in the text and the dashed line is a continuation of the low temperature behavior. The difference between the solid line and the dashed line at high temperature is attributed to thermal excitation of states 200 K above the ground state and whose spin correlation time is 8×10^{-14} s.

[a] Permanent address: Physics Department, University of Connecticut, Storrs, CT 06268.

 0021-8979/88/083890-03$02.40 © 1988 American Institute of Physics

The interpretation presented below identifies the low-T solid line and its dashed continuation as relaxation of the ^{9}Be nuclei by itinerant electrons, and treats the high-T rise of the solid line as an additional process (called the "additional relaxation") that is thermally excited above 100 K.

III. DISCUSSION

In order to discuss our result, we use a formulation of nuclear relaxation that can be applied to both itinerant and localized electrons. When nuclear magnetic moments are relaxed in a metal by electrons, $1/T_1$ can be written as[7,8]

$$\frac{1}{T_1} \approx \gamma_n^2 \langle \delta H^2 \rangle n_{\text{eff}} J(\omega) \approx \gamma_n^2 \langle \delta H^2 \rangle n_{\text{eff}} \tau, \tag{1}$$

where γ_n is the nuclear gyromagnetic ratio, $\langle \delta H^2 \rangle$ is average of the square of the amplitude of the fluctuating magnetic field at the nucleus associated with one electron, n_{eff} is the (effective) number of electrons (normalized to the unit cell) that contribute to $\langle \delta H^2 \rangle$, $J(\omega) \simeq \tau$ is the spectral density of the fluctuations at the NMR transition frequency ω, and τ is the correlation time for the fluctuations. In Eq. (1), we assume the short correlation time limit $\omega\tau \ll 1$, as discussed below. When dealing with itinerant conduction electrons, $n_{\text{eff}} \approx k_B T/\Delta$ and $\tau \simeq \hbar/\Delta$ (k_B is Boltzmann's constant; $\hbar$ is Planck's constant), and the usual Korringa relaxation rate is obtained.[7,8] For direct relaxation by localized electrons, n_{eff} is the local moment concentration and τ is the lifetime for the z component of the electron spin. The solid line below 40 K and the dashed line extension is the temperature dependence that one calculates using the model of Korringa relaxation, but in a narrow, Lorentzian-shaped band with a half width at half maximum $\Delta = 7.5$ K. The implications of this result will be discussed in a different publication; it is introduced here only to establish the *extra* relaxation that appears above 100 K.

We use the following phenomenological model for the additional relaxation. For the sake of concreteness, the same microscopic picture used to explain the specific heat[4] is adopted: The ground state of the U^{3+} ion, which would otherwise be degenerate, is split by the crystal field into a ground-state doublet (Γ_6) and a low-lying excited quartet (Γ_8). At low T only the Γ_6 states are occupied. As T is increased, there is a thermal population of the Γ_8 states. They have a different $\langle \delta H^2 \rangle$ (and perhaps τ) from the ground state, so that as they become populated, $1/T_1$ changes accordingly. This model is put on a quantitative basis by assuming that there is a splitting ΔE between the ground and first excited states of the system and that the states obey Boltzmann statistics. Then the relaxation rate is a linear combination of the rate R_g associated with the group of ground states and the rate R_e associated with the group of excited states:

$$1/T_1 = R_g P_g + R_e P_e, \tag{2}$$

where P_g and P_e are the probability that the system occupies the ground or the excited states respectively. These probabilities are

$$P_g = \frac{1}{1 + 2e^{-\Delta E/k_B T}}, \quad P_e = \frac{2e^{-\Delta E/k_B T}}{1 + 2e^{-\Delta E/k_B T}}. \tag{3}$$

The solid line on Fig. 1 is then obtained with the assignments $R_g = 0.75(\pm 0.05)$ s^{-1}, $R_e = 1.88(\pm 0.18)$ s^{-1}, and $\Delta E/k_B = 200(\pm 20)$ K.

The model just described provides a good fit to the data, and yields a value $\Delta E/k_B$ that is quite close to the one (180 K) obtained from the specific heat.[4] In addition, from the value of R_e we can estimate τ for the excited states. By using the theory of direct relaxation of a nucleus by a localized electron spin via dipolar coupling[9] we estimate

$$1/T_1 \approx (0.8/r^6)\gamma_n^2 \mu_e^2 \tau, \tag{4}$$

where μ_e is the fluctuating moment associated with the excited states, r is the typical distance from a localized excited state to the Be nucleus, and we have included the fact that each Be nucleus has two near-neighbor U ions. If we use the values $r = 2.8$ Å (a typical U-Be spacing) and $\mu_e = 3.4$ Bohr magnetons (from the high-T susceptibility[10]), Eq. (4) gives $\tau = 8.0 \times 10^{-14}$ s, or $\hbar/k_B\tau = 95$ K. The picture that then emerges from this interpretation is that there is a set of 4 excited states (such as a $U^{3+}\Gamma_8$) 200 K above a doublet ground state (such as a $U^{3+}\Gamma_6$) and the excited state system has a lifetime of 8×10^{-14} s, which corresponds to a width of 95 K. The smallness of τ justifies the use of the short correlation time limit in Eqs. (1) and (4).

The picture obtained from this experiment agrees closely with what was inferred from the specific-heat measurements of Felton *et al.*[4] The main difference compared to their work is that they introduced an additional crystal field splitting (two levels 115 K above the ground state and two levels 270 K above it for an excited state splitting of 155 K) of the excited states to fit the observed width of their Schottky anomaly. On the basis of our work, we identify that width as a lifetime broadening of the levels. The energy scale for the excited state observed in our experiment is also the same as that of a feature seen (but not identified) in the inelastic scattering of neutrons by UBe_{13}.[11] For a further discussion of the neutron results, see Felton *et al.*[4]

There are several aspects of the model we have used that require comment. Implicit in the treatment is the notion that the additional relaxation at high T is due to *orientational* relaxation of a local moment. The microscopic physical situation could as well be dominated by transitions *between* the electronic levels, or a combination of the two. At the present level of understanding, we cannot distinguish among these cases on the basis of the nuclear relaxation rate; all of them would generate a fluctuating magnetic field that would relax the nuclei, and it is reasonable to expect that similar values of ΔE and τ would be obtained. More detailed microscopic calculations are needed to improve this aspect of the interpretation.

A second point is related to the choice of the Γ_6 doublet and Γ_8 quartet suggested by Felton *et al.*[4] The temperature dependence obtained with our nuclear relaxation model is not sensitive to the total number of degenerate states, but rather to the ratio of the degeneracy of the excited state to that of the ground state. We have used a ratio of 2. A similar model in which the ratio is 1 fits the data almost as well and gives similar parameters (we did not try other ratios). From this observation we conclude that the model used is consis-

tent with our experimental results, but that it is not uniquely so.

The final point to be made is that the picture of a purely localized set of spins being responsible for the relaxation is probably too simplified to apply to the real physical situation in UBe_{13}. We expect, instead, that ΔE represents the difference in energy between a many-body ground state and a many-body excited state (or states) for which localized states of the U ion $5f$ electrons play a major role, but that the states responsible for the physical properties cannot be described simply in terms of fully localized ionic states.

IV. CONCLUSIONS

We have reported high-temperature measurements of the ^{9}Be relaxation rate in the heavy fermion intermetallic compound UBe_{13}. An additional relaxation component is observed above 100 K. It is interpreted in terms of dipolar coupling to a localized U^{3+} moment with a doublet ground state and a quartet first excited state. The deduced splitting between the ground and excited states is $200(\pm 20)$ K. The correlation time for the excited states is 8×10^{-14} s (width $= 95$ K).

ACKNOWLEDGMENTS

We thank F. Steglich and K. Baberschke for helpful discussions. This report is based upon work supported by NSF Grant No. DMR-8409390 (UCLA) and NSF Grant No. DMR-8413730 (UC Riverside), the U. S. DoE (Los Alamos), and the SNFWF (Zurich).

[1] M. D. Lan, W. G. Clark, C. Tien, D. E. MacLaughlin, Z. Fisk, J. L. Smith, and H. Ott (unpublished) have measured $1/T_1$ of ^{9}Be in the isostructural, nonheavy fermion material $ThBe_{13}$ in the range 1.5–4.2 K. They find $1/T_1T = 2\times10^{-4}\,s^{-1}\,K^{-1}$, which is three orders of magnitude less than the low-T value seen for UBe_{13} in Fig. 1. This difference demonstrates the importance of the heavy-fermion enhancement for the nuclear relaxation rate.

[2] W. G. Clark, M. D. Lan, G. van Kalkeren, W. H. Wong, C. Tien, D. E. MacLaughlin, J. L. Smith, Z. Fisk, and H. R. Ott, J. Magn. Magn. Mater. **63-64**, 396 (1987).

[3] D. E. MacLaughlin, C. Tien, W. G. Clark, M. D. Lan, Z. Fisk, J. L. Smith, and H. R. Ott, Phys. Rev. Lett. **53**, 1833 (1984).

[4] R. Felten, F. Steglich, G. Weber, H. Reitschel, F. Gompf, B. Renker, and J. Beurs, Europhys. Lett. **2**, 323 (1986).

[5] W. W. Warren, Jr. and W. G. Clark, J. Phys. E **1**, 1019 (1968); A. L. Kerlin, Ph.D. Thesis (University of California at Los Angeles, 1972) (unpublished).

[6] W. G. Clark, Z. Fisk, K. Glover, M. D. Lan, D. E. MacLaughlin, J. L. Smith, and C. Tien, *LT-17 (Contributed Papers)*, edited by U. Eckern, W. Weber, and H. Wühl (Elsevier, Amsterdam, 1984), p. 227.

[7] A. Abragam, *The Principles of Nuclear Magnetism* (Oxford University Press, Oxford, 1961).

[8] D. Pines and C. P. Slichter, Phys. Rev. **100**, 1014 (1955).

[9] A. Abragam, *The Principles of Nuclear Magnetism* (Oxford University Press, Oxford, 1961), p. 380; also D. L. Cox, Phys. Rev. B **35**, 6504 (1987).

[10] See the discussion of the susceptibility in Ref. 4.

[11] A. I. Goldman, S. M. Shapiro, G. Shirane, J. L. Smith, and Z. Fisk, Phys. Rev. B **33**, 1627 (1986).

Magnetic field dependence of the cyclotron effective mass in the Kondo lattice CeB_6

W. Joss[a] and J. M. van Ruitenbeek
Max Planck Institut für Festkörperforschung, Hochfeld Magnetlabor, B. P. 166X, F-38042 Grenoble Cedex, France

G. W. Crabtree[b] and J. L. Tholence
Centre de Recherche sur les Tres Basses Temperatures (CNRS), B. P. 166X, F-38042 Grenoble Cedex, France

A. P. J. van Deursen
Technische Universiteit Eindhoven, P. O. Box 513, 5600 MB Eindhoven, The Netherlands

Z. Fisk
Los Alamos National Laboratory, Los Alamos, New Mexico 87545

We report the first observation of a field-dependent mass in a hybridizing f-electron system. CeB_6 is an ordered moment heavy fermion system with an electronic specific heat coefficient γ of order 225–300 mJ/mole K^2. Using the de Haas–van Alphen effect at temperatures as low as 60 mK in steady magnetic fields as large as 22 T, we observe a cyclotron orbit of frequency 8680 T for fields along the [100] direction. The mass of this orbit was measured at eight fixed fields and found to decrease from $18m_e$ to $8m_e$ as the field increases from 12 to 22 T. The observed Fermi surface is very similar to that of LaB_6, indicating that the f-electrons are largely local rather than itinerant in CeB_6, a picture confirmed by bandstructure calculations. The observed field dependence of the cyclotron mass is consistent with the low-energy scale of the system as measured, for example, by the Kondo temperature. Our results are compared with Fermi surface observations in other heavy fermion systems.

The heavy fermion materials form a major challenge to our understanding of the physics of metals.[1] They are unusual in almost every physical property but the most characteristic one is the high value of the low-temperature specific heat (LTSH). Many of these systems show properties resembling the impurity Kondo effect or intermediate valence behavior and the physics of heavy fermions is closely related to the physics of both the Kondo effect and valence fluctuations. Recently de Haas–van Alphen (dHvA) experiments have provided conclusive microscopic information in a number of these compounds: the very heavy fermion system $CeCu_6$ (Ref. 2) ($\gamma \simeq 1500$ mJ/mole K^2), the heavy fermion superconductor UPt_3 (Ref. 3) ($\gamma = 420$ mJ/mole K^2), the intermediate valence compound $CeSn_3$ (Ref. 4) ($\gamma = 17$ mJ/mole K^2) and the Kondo lattice CeB_6 (Ref. 5) ($\gamma \simeq 260$ mJ/mole K^2). The information obtained in these experiments can be summarized as follows.

(1) At low temperatures the conduction electrons form coherent states and the mean free path is several hundreds of nanometers long.

(2) For UPt_3 and $CeSn_3$ the dHvA frequencies are consistent with bandstructure calculations treating the f electrons as itinerant. The f electrons form a band at the Fermi energy. (CeB_6 will be discussed below.)

(3) The electron mass is very high and one or two orders of magnitude larger than found by conventional bandstructure calculations. Estimates show that the masses found in dHvA experiments explain the large values of the LTSH (with the possible exception of $CeCu_6$).

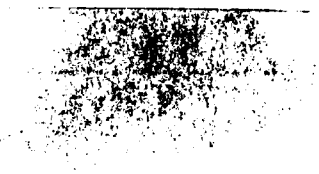
Here we discuss the results for CeB_6 and we show in addition that the electron mass is strongly suppressed in high magnetic fields (see also Ref. 5). This is the first observation of a field-dependent electron mass in this type of compound. It shows that the many body interactions which make the electrons heavy (or in other words slow) are strongly reduced in high fields and the electrons become light again (speed up). At the same time it is observed that the size of the Fermi surface, as measured by the dHvA frequency, is field independent. Thus the *number* of particles is conserved.

CeB_6 is one of the most typical Kondo lattice systems and has therefore received a lot of attention, see, e.g., Kasuya *et al.*[6] The Kondo temperature is very low, only 1–2 K.[7] It is interesting to compare the experimental Fermi surface information to that of LaB_6 and to bandstructure calculations by Norman and Min.[8] The results indicate that the f electron of CeB_6 is localized and can be treated as part of the ion core. This is in sharp contrast to the situation for UPt_3 and $CeSn_3$. We conclude that CeB_6 belongs to a different class of heavy fermion compounds: the hybridization is apparently not strong enough to bring the f electrons to the Fermi level. Yet an electron mass enhancement of roughly a factor 100 is observed.

The dHvA effect measures the oscillatory magnetization in high magnetic fields which arises due to the quantiza-

[a] Also at Laboratorium für Festkörperphysik, Eidgenössische Technische Hochschule, 8093 Zürich, Switzerland.
[b] Permanent address: Argonne National Laboratory, Argonne, Illinois 60439.

 0021-8979/88/083893-03$02.40 © 1988 American Institute of Physics



tion of the electron motion on Landau orbits.[9] The frequency observed when changing the applied field is directly proportional to the cross-sectional area of the Fermi surface. The field and temperature dependence of the oscillation amplitude allow a determination of the mean free path with respect to the effective mass for this orbit. The dHvA effect is usually only observed in high magnetic fields and at low temperatures. These restrictions are the more severe as the mean free path is shorter and the effective mass is larger. In order to obtain these conditions our experiments were carried out in a special dilution refrigerator designed to operate in the 25T polyhelix magnet of the Grenoble high magnetic field facility (SNCI/MPI). A low-frequency large-amplitude modulation technique and phase sensitive detection at the second harmonic of the modulation frequency were used to measure the signals.

The angular dependence of the dHvA frequencies[10] closely resembles that for the isostructural compound LaB_6.[11] The latter is an ordinary metal with a LTSH coefficient[12] $\gamma = 2.6$ mJ/mole K^2. Its Fermi surface consists of spheres centered at the X points of the Brillouin zone which are connected by small necks and contain one electron per cell per spin.[11] In addition, CeB_6 has one f electron. However, the Fermi surface does not seem to be affected very strongly by this extra electron and we conclude that the f electron is localized and sits below the Fermi energy. Strong evidence for this interpretation is also found from the band-structure calculations by Norman and Min.[8] They performed calculations using several approximations first treating the f electron on equal footing with the other valence electrons and next treating it as part of the ion core allowing no hybridization with the conduction electrons. Only for the second approach a satisfactory agreement with the experimental Fermi surface information is found, although an important discrepancy of 10% in size remains to be explained. This conclusion is opposite to the results for UPt_3 (Ref. 3) and $CeSn_3$ (Ref. 4) where the f electrons form a band which clearly intersects the Fermi level.

It is of importance to note that we do not find a double frequency, not even a beating, as would be expected for a spin splitting of the Fermi surface. In the strong fields used here the induced magnetic moment is close to $1\mu_B$/Ce. As a consequence the exchange interaction between the conduction electrons and the local magnetic moments of the f electrons must be very small.

The effective mass study was carried out for the field along [100]. In this field direction and with the present technique one strong frequency is observed of $F = 8680$ T. This frequency is constant with field and temperature to a precision of 0.5% showing that the number of particles is field and temperature independent. The electron mass was determined at different field values by fitting the temperature dependence to the usual Liftshitz–Kosevich theory for the dHvA effect.[9] The resulting masses are plotted as a function of field in Fig. 1. The mass measured in fields above 30 T by van Deursen *et al.*[10] is also included in the figure. A substantial suppression of the electron mass with field is observed. Also, even in high fields, the masses are very high compared to $m^* = 0.61m_e$ for the equivalent orbit in LaB_6. In order to allow a comparison to the specific heat the data in Fig. 1 are presented on a semi logarithmic scale. The LTSH of CeB_6 has been measured to very low temperatures and in fields up to 8 T by Marcenat and by Bredl.[13] There appears to be some sample dependence of the absolute values: the linear term γ in zero field ranges between 225 and 300 mJ/mole K^2. However, the general behavior is the same and it was found that γ initially increases with field toward the transition from the low-field antiferromagnetic phase to the high-field phase II. Then a strong decrease of γ with field is observed. The curve in Fig. 1 represents this field dependence of γ schematically.

The cyclotron mass is an integral of the inverse Fermi velocity $1/v_F$ over the cyclotron orbit. The LTSH coefficient γ, if conventional theory applies, is proportional to the density of electronic states at the Fermi level which in turn is an integral of $1/v_F$ over the entire Fermi surface. The zero field specific heat for CeB_6 $\gamma_{Ce} = 260$ mJ/mole K^2 is enhanced over the value of LaB_6 $\gamma_{La} = 2.6$ mJ/mole K^2. This enhancement corresponds to an enhancement of the electron mass and a reduction of the Fermi velocity. If we assume that the enhancement is nearly isotropic then we can relate the measured γ value for CeB_6 to the cyclotron mass for the present orbit via $m^*_{Ce} = (\gamma_{Ce}/\gamma_{La})m^*_{La}$. The mass for the corresponding orbit in LaB_6 is $m^*_{La} = 0.61m_e$.[11] The relation above is used to adjust the scales in Fig. 1. It shows that the zero field effective mass for this orbit should be roughly $60m_e$. We find from Fig. 1 that there is a fairly good agree-

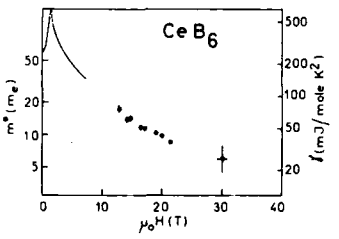


FIG. 1. Field dependence of the effective mass in CeB_6 for the 8680 T orbit with the field along [100]. The data are presented on semi-logarithmic scale in order to allow comparison to the electronic specific heat γ. For the positioning of the scale of γ with respect to that for m^* see text. The curve at low fields represents the specific heat as measured in Ref. 13. The divergence at 2 T is related to the phase transition going from antiferromagnetic to quadrupolar order.

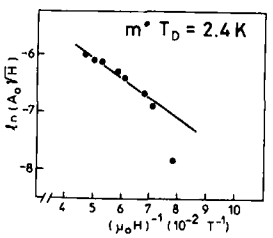


FIG. 2. Field dependence of the zero-temperature dHvA amplitude. After correction for the temperature dependent terms the field dependence of the dHvA amplitude is $(1/B)\exp(-\alpha m^* T_D/B)$ where $\alpha = 14.69$ T/K is a constant. The product $m^* T_D$, which in turn gives the mean free path, is found from the slope of this plot.

ment, though not yet quantitative, between γ and m^* and that these are both enhanced by the same amount.

The mean free path of the electrons on this orbit was determined by analysing the field dependence of the amplitude of the dHvA oscillations. First the temperature dependent factor in the amplitude was eliminated by linear extrapolation to $T = 0$. The field dependence of the resulting zero temperature amplitudes is given in Fig. 2. The straight line gives[14] $m^* T_D = 2.4$ K where T_D is the so-called Dingle temperature which is inversely proportional to the scattering time τ. Now, since m^* is field dependent, so are T_D and τ. A possibly more fundamental property is the mean free path l which is inversely proportional to the product $m^* T_D$. We find no evidence that this product is field dependent although this might be hard to distinguish in a limited field interval. (For a discussion of the 12.7 T point in Fig. 2 see below.) From the quoted value for $m^* T_D$ we calculate a mean free path $l = 0.30\ \mu$m. The circumference of the real space orbit at 10 T is $2\pi r = 2.13\ \mu$m. Thus, we find that the electrons form coherent states which extend over a very large number of unit cells.

Finally, a remarkable effect was observed on thermal cycling of the samples. In three different samples from two different batches the signal after the first cool down was roughly of the same amplitude. Thermal cycling reduced the signal amplitude drastically. After 2 or 3 cycles the signal in all three samples was below noise level. To our knowledge there is no crystalline phase transition below room temperature which would explain this phenomenon. The samples were carefully mounted in cotton wool and no glue or grease was used, in order to avoid stress due to differential thermal contraction on cooling. All data in Figs. 1 and 2 were taken without heating above 1 K, except for the lowest field point. This was taken after one room temperature cycle and $m^* T_D$ for this point appears significantly higher. The field dependence of the cyclotron mass was reproduced in one other sample and found to be consistent with the results presented here.

The most salient feature of the results presented here is the direct observation of a strong suppression of the heavy mass in CeB_6. In order to describe this effect one could start from an impurity Kondo model or, alternatively, from a spin fluctuation model. However, the situation here is complicated by the fact that Kondo effect and magnetic order play an important role and the characteristic temperatures are all small: $T_K = 1$–2 K, $T_N = 2.4$ K. It is due to the smallness of these energy scales that the effect is so clearly observed. In UPt_3 the characteristic temperatures are an order of magnitude higher and up to 15 T no field effects are observed.[3] For $CeCu_6$ the problem is even more interesting: the electronic specific heat is suppressed by a factor 2 or 3 in high fields but in dHvA experiments a search for a field dependence in the electron mass did not show any corresponding effect.

Further, it is observed that the f electron is local and has only minor effects on the Fermi surface. These small effects, however, deserve our full attention and should be studied in more detail. More experiments are under way.

We would like to thank J. Flouquet and P. Wyder for their stimulating support and P. Stamp for helpful discussions. The assistance of M. Caussignac in development and maintenance of the dilution refrigerator is gratefully acknowledged. The work was partially supported by the US-DOE-BES-Materials Sciences under Contract No.W-31-109-ENG-38.

[1] G. R. Stewart, Rev. Mod. Phys. **56**, 755 (1984); P. A. Lee, T. M. Rice, J. W. Serene, L. J. Sham, and J. W. Wilkins, Comments Cond. Mat. Phys. **12**, 99 (1986).
[2] P. H. P. Reinders, M. Springford, P. T. Coleridge, R. Boulet, and D. Ravot, Phys. Rev. Lett. **57**, 1631 (1986).
[3] L. Taillefer, R. Newbury, G. G. Lonzarich, Z. Fisk, and J. L. Smith, J. Magn. Magn. Mater. **63&64**, 372 (1987) and references therein; L. Taillefer and G. G. Lonzarich, Phys. Rev. Lett. (to be published).
[4] W. R. Johanson, G. W. Crabtree, A. S. Edelstein, and O. D. McMasters, Phys. Rev. Lett. **46**, 504 (1981); D. D. Koelling, Solid State Commun. **43**, 247 (1982).
[5] W. Joss, J. M. van Ruitenbeek, G. W. Crabtree, J. L. Tholence, A. P. J. van Deursen, and Z. Fisk, Phys. Rev. Lett. **59**, 1609 (1987).
[6] T. Kasuya, K. Takegahara, Y. Aoki, K. Hanzawa, M. Kasaya, S. Kunii, T. Fujita, N. Sato, H. Kimura, T. Komatsubara, T. Furuno, and J. Rossat-Mignod, in *Valence Fluctuations in Solids*, edited by L. M. Falicov, W. Hanke, and M. B. Maple (North-Holland, Amsterdam, 1981), p. 215.
[7] N. Sato, S. Kunii, I. Oguro, T. Komatsubara, and T. Kasuya, J. Phys. Soc. Jpn. **53** 3967 (1984).
[8] M. R. Norman and B. I. Min, private communication.
[9] For a comprehensive review of the dHvA effect see D. Shoenberg, *Magnetic Oscillations in Metals* (Cambridge University Press, Cambridge, 1984).
[10] A. P. J. van Duersen, R. E. Pols, A. R. de Vroomen, and Z. Fisk, J. Less-Common Met. **111**, 331 (1985). Low-frequency oscillations in the elastic constants of CeB_6 have been observed in lower fields by T. Suzuki, T. Goto, S. Sakatsume, A. Tamaki, S. Kunii, T. Kasuya, and T. Fujimura, in Proceedings of the 18th International Conference on Low Temperature Physics, Kyoto, 1987 and private communication. These oscillations can most probably be attributed to small features related to the neck structure of the Fermi surface in close analogy to LaB_6.
[11] Y. Ishizawa, T. Tanaka, E. Bannai, and S. Kawai, J. Phys. Soc. Jpn. **42**, 122 (1977); A. J. Arko, G. W. Crabtree, D. Karim, F. M. Mueller, L. R. Windmiller, J. B. Ketterson, and Z. Fisk, Phys. Rev. B **13**, 5240 (1976); A. Hasegawa and A. Yanase, J. Phys. F **7**, 1425 (1977).
[12] J. Etourneau, J. P. Mercurio, R. Naslain, and P. Hagenmuller, J. Solid State Chem. **2**, 332 (1970).
[13] C. D. Bredl, J. Magn. Magn. Mater. **63&64**, 355 (1987); C. Marcenat, Ph.D. Thesis (University of Grenoble, 1986); Y. Peysson, C. Ayache, J. Rossat-Mignot, S. Kunii, and T. Kasuya, J. Phys. **47**, 113 (1986).
[14] In fact, this is an upper limit. The sample is rectangular so that the inhomogeneous demagnetizing field contributes some phase smearing.

Hall effect for Kondo systems

P. M. Levy and Wei Guo
Department of Physics, New York University, 4 Washington Place, New York, New York 10003
D. L. Cox
Department of Physics, Ohio State University, 174 West 18th Avenue, Columbus, Ohio 43210

We have calculated the variations with temperature of the skew scattering contribution to the Hall effect for a Kondo-type ion. The conduction electron t matrix is calculated by using the single-ion Anderson model, and the $4f$ electrons' Green's function is evaluated by self-consistently solving a set of integral equations. Except for the asymptotic region $T/T_k \gg 1$, the Hall constant is not proportional to the susceptibility, nor does the constant change sign for realistic values of the parameters entering the theory.

The Hall effect is a fine probe of the details of the scattering of conduction electrons by Kondo-type ions in heavy fermion and mixed valence compounds.[1] The skew scattering contribution to this effect has been calculated at high temperatures $T \gg T_k$ and at $T = 0$ K,[2,3] but little is known about its variation with temperature in between these limits. We have derived an expression for this contribution to the Hall effect based on the single-ion Anderson model; it is valid for all temperatures, especially for strong coupling $T \ll T_k$, and for large fields.[4] Here, we limit ourselves to the linear Hall effect (in field), for which the spin-independent skew scattering contribution to the Hall constant is[4]

$$R_H \equiv \frac{\rho_{xy}}{H} = -\frac{36}{49}\frac{c|V_k|^2}{e^2\hbar H}\sin\eta_2 \int\left[\left(-\frac{\partial f^0}{\partial\epsilon}\right)n(\epsilon)v^2(\epsilon)\mathrm{Im}\left(e^{-i\eta_2}\sum_{m_j} m_j G^{4f}_{m_j}(\epsilon)\right)\Big/\rho_0^2(\epsilon)\right]d\epsilon$$
$$\times\left\{\int\left[\left(-\frac{\partial f^0}{\partial\epsilon}\right)n(\epsilon)v^2(\epsilon)/\rho_0(\epsilon)\right]d\epsilon\right\}^{-2}, \tag{1}$$

where

$$\rho_0(\epsilon) \equiv \sum_{m_j}\rho^{4f}_{m_j}(\epsilon) = -\,\mathrm{Im}\sum_{m_j} G^{4f}_{m_j}(\epsilon),$$

V_k is the parameter describing the mixing of the local ($4f$) and conduction electrons in the Anderson model, c is the concentration of magnetic ions, $n(\epsilon)$ the density of conduction electron states, $v(\epsilon)$ their velocity, and η_2 is the phase shift in the nonresonant $l = 2$ channel.

The matrix elements of the $4f$ electrons' Green's function have been evaluated by self-consistently solving a set of integral equations based on the noncrossing approximation.[5] We used the parameters (in units of the bandwidth D) $\Gamma = \pi N(0)|V_k|^2 = 0.0159$ and $E_f = -0.152$, where E_f is the energy position of the f electron relative to the Fermi level; for these parameters we find the number of electrons in the f orbital at $T = 0$ K is $n_f(0) = 0.86$. In Fig. 1 we present our results for the variation with temperature of the skew scattering contribution to the Hall constant [Eq. (1)] for a $j = \frac{5}{2}$ ($N_f = 6$) level and for $\eta_2 = -0.1$.[3] To ascertain whether our results are proportional to the product of the resistivity and the susceptibility, we form the ratio $R_H/\rho_{\mathrm{iso}}\tilde{\chi}$, where the isotropic resistivity is just the integral appearing in the denominator of R_H [see Eq. (1)], i.e.,

$$\rho_{\mathrm{iso}}^{-1} = \sigma_{\mathrm{iso}} = \frac{2}{3}e^2\frac{\hbar}{c|V_k|^2} \times\int\left[\left(-\frac{\partial f^0}{\partial\epsilon}\right)n(\epsilon)v^2(\epsilon)/\rho_0(\epsilon)\right]d\epsilon, \tag{2}$$

and the susceptibility is[6]

$$\tilde{\chi} = \frac{k_B\chi(T)}{\frac{1}{3}j(j+1)g^2\mu_B^2} = \frac{-3k_B}{j(j+1)g\mu_B}\sum_{m_j} m_j\int\frac{d\epsilon}{\pi}f^0(\epsilon)\frac{\partial\rho^{4f}_{m_j}}{\partial h}(\epsilon,T,h)\Big|_{h=0}. \tag{3}$$

with

$$\tilde{\chi}(T=0) \equiv 1/T_L.$$

The temperature scale T_L is proportional to the Kondo temperature via a j-dependent constant of order unity. For the above-mentioned parameters, the temperature T_L is $3.3\times10^{-3}\,k_B^{-1}$ (in units of the bandwidth D).

At high temperature, the above quantities approach their weak coupling values, which are[3]

$$R_H = -\frac{2}{49}\frac{mc}{\pi N(0)ne^2\hbar}\left(\frac{\Gamma}{E_f}\right)^2 j(j+1)(2j+1) \times\frac{g\mu_B}{k_BT}\sin\eta_2\left(\cos\eta_2 + \frac{2}{2j+1}\frac{|E_f|}{\Gamma}\sin\eta_2\right), \tag{4}$$

$$\rho_{\mathrm{iso}} = \frac{2j+1}{2}\frac{mc}{\pi N(0)ne^2\hbar}\left(\frac{\Gamma}{E_f}\right)^2, \tag{5}$$

$$\tilde{\chi} = 1/T, \tag{6}$$

and

 0021-8979/88/083896-03$02.40 © 1988 American Institute of Physics

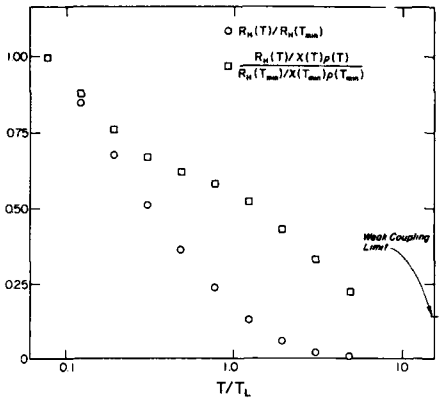


FIG. 1. Skew scattering Hall constant for dilute rare-earth impurity concentrations. All calculations are performed in the low-field limit. The parameter values are $E_f = -0.152D$, $\Gamma = 0.0159D$, $N_f = 6$, and $\eta_2 = -0.1$. The temperature T_{min} is $0.077T_L$.

$$f \equiv \frac{k_B}{g\mu_B}\frac{R_H}{\rho_{iso}\tilde{\chi}} = \frac{-4}{49} j(j+1)\sin\eta_2\left(\cos\eta_2 + \frac{2}{2j+1}\frac{|E_f|}{\Gamma}\sin\eta_2\right), \tag{7}$$

where n is the number of conduction electrons per unit volume and spin direction. In Table I we compare our numerical results at high temperatures ($T = 4.83\ T_L$) with their asymptotic values for $j = \frac{1}{2}$. These are found by placing the parameters cited above in Eqs. (4)–(7). The ratio f is 0.048, while the calculated value at $T/T_L = 4.83$ is 0.068. It is noteworthy that this ratio approaches its weak coupling value much more rapidly than the parts which comprise it, see Table I. The deviations of the individual quantities are not surprising, since corrections to the weak coupling limit are logarithmic in T/T_L. In addition, this approximation sets $(-\partial f^0/\partial\epsilon)$ to a delta function, which is less appropriate when $k_B T \simeq \Gamma, |E_f|$, as we have here.

At low temperatures the calculated values approach their $T = 0$ K values of

TABLE I. Comparison of numerical results with analytic estimates for low and high temperatures. The analytic comparisons are obtained from Eqs. (4)–(11) by using the parameters (in units of the bandwidth D) $\Gamma = 0.0159$, $E_f = -0.152$, $n_f(0) = 0.86$, $\eta_2 = -0.1$, and $T_L = [\tilde{\chi}(0)]^{-1} = 3.3\times10^{-3}\ k_n^{-1}$.

	$\frac{(R_H)_{num}}{(R_H)_{analytic}}$	$\frac{\chi_{num}}{\chi_{analytic}}$	$\frac{(\rho_{iso})_{num}}{(\rho_{iso})_{analytic}}$	$\frac{f_{num}}{f_{analytic}}$
$T \ll T_L$ ($T = 0.077T_L$)	0.85	1.0	0.88	0.97
$T \gg T_L$ ($T = 4.83T_L$)	3.94	0.86	3.24	1.42

$$R_H(0) = \frac{-4}{49} j(j+1)(2j+1) \times \frac{g\mu_B}{\Gamma^*}\frac{mc}{\pi N(0) n e^2\hbar}\sin\eta_2\sin^2\eta_3(0) \times \sin[2\eta_3(0) - \eta_2], \tag{8}$$

$$\rho_{iso}(0) = \frac{(2j+1)}{2}\frac{mc}{\pi N(0) n e^2\hbar}\sin^2\eta_3(0), \tag{9}$$

$$\tilde{\chi}(0) = \frac{(2j+1)\sin^2\eta_3(0)}{\pi\Gamma^*}k_B, \tag{10}$$

and

$$f(0) = \frac{k_B}{g\mu_B}\frac{R_H(0)}{\rho_{iso}(0)\tilde{\chi}(0)} = \frac{-8}{49}\pi\frac{j(j+1)}{2j+1}\sin\eta_2\frac{\sin[2\eta_3(0) - \eta_2]}{\sin^2\eta_3(0)}. \tag{11}$$

From the relation of the reduced susceptibility to T_L [see Eq. (3)] we find

$$\Gamma^* = [(2j+1)\sin^2\eta_3(0)/\pi]k_B T_L. \tag{12}$$

We note that Γ^* reflects a magnetic Kondo resonance scale, namely, the Wilson ratio distinguishes this from the resonance scale of the specific heat. For $j = \frac{1}{2}$, $\eta_2 = -0.1$, and $\eta_3(0) = (n_f\pi/6)$ ($n_f = 0.86$ for $N_f = 6$ and the parameters used in our calculation) the ratio $f(0)$ is 0.332 while the calculated value at $T/T_L = 0.077$ is 0.317. In Table I we compare our numerical results at low temperatures ($T = 0.077T_L$) with the values found by evaluating the above analytic expressions valid at $T = 0$ K. The deviations of the calculated $R_H(T)$ and $\rho_{iso}(T)$ values from their limiting low-temperature forms arise from the well-known pathology in the noncrossing approximation.[7]

From the calculated variation with temperature of the ratio $R_H/\rho_{iso}\tilde{\chi}$ we note that while it approaches its asymptotic values at high and low temperatures, it does so rather gradually at high temperatures. In the vicinity of the Kondo temperature the Hall constant is not proportional to the product of resistivity and susceptibility, neither is it at low temperatures (see Fig. 1). Only at $T = 0$ K can one write it as shown in Eq. (11), and at only *very* high temperatures $T/T_L \gg 1$ does the Hall constant approach Eq. (7). For the case we have considered of a $j = \frac{1}{2}$ level, it would require unrealistically large phase shifts η_2 in the nonresonant channel to drive the Hall constant negative [see Eq. (8)] (remember $\sin\eta_2$ is negative for $-\pi < \eta_2 < 0$). For our parameters, $\eta_2 = -2.24$ is required; this is greater than the phase shift in the resonant channel. Therefore, for a $N_f = 6$ level the skew scattering contribution cannot cause the Hall constant to change sign at low temperatures. From Eq. (8), we see that even for a doublet $N_f = 2$ with $\eta_3(0) = (n_f\pi/2)$ (with, say, $n_f = 0.86$) an unrealistically large value of $\eta_2 \simeq -0.44$ is needed to change the sign of the Hall constant.[2] We note that should η_2 be positive, correponding to an attractive potential, a sign change between high and low temperatures in R_H is possible for $0.86\pi < \eta_2 < 1.86\pi$ if $N_f = 2$, and for $0.29\pi < \eta_2 < 1.29\pi$ if $N_f = 6$. These are still very unrealistically large values for η_2.

To summarize, we have calculated the variation with temperature of the skew scattering contribution to the Hall effect for a Kondo-type ion. Except for the weak coupling region $T/T_L \gg 1$, the Hall constant is not proportional to the susceptibility, nor does the constant change sign for realistic values of the phase shift η_2 in the nonresonant channel.

The work of W. G. was supported by a grant from the New York University Research Challenge Fund. One of us (D. L. C.) acknowledges support from an Ohio State University seed grant and Department of Energy Grant No. DE-FG02-87ER45326.A000. Computation at the San Diego Supercomputer Center was supported by National Science Foundation under Grant No. DMR-85-14195.

[1]T. Penney, J. Stankiewicz, S. Von Molnar, Z. Fisk, J. L. Smith, and H. R. Ott, J. Magn. Magn. Mater. **54–57**, 370 (1986); M. Hadzic-Leroux, A. Hamzic, A. Fert, P. Haen, F. Lapierre, and O. Laborde, Europhys. Lett. **1**, 579 (1986); F. Lapierre, P. Haen, R. Briggs, A. Hamzic, A. Fert, and J. P. Kappler, J. Magn. Magn. Mater. **63–64**, 338 (1987); T. Penney, F. P. Milliken, and F. Holtzberg, in Proceedings of the Conference on Heavy Fermions, Bangalore, 1987.
[2]P. Coleman, P. W. Anderson, and T. V. Ramakrishnan, Phys. Rev. Lett. **55**, 414 (1985).
[3]A. Fert and P. M. Levy, Phys. Rev. B **36**, 1907 (1987).
[4]P. M. Levy and D. L. Cox (unpublished).
[5]D. L. Cox, Ph. D. thesis, Cornell University (1985); N. E. Bickers, D. L. Cox, and J. W. Wilkins, Phys. Rev. B **36**, 2036 (1987).
[6]D. L. Co , Phys. Rev. B **35**, 4561 (1987).
[7]E. Müller-Hartmann, Z. Phys. B **57**, 281 (1984).

Transport properties of $CeAl_3$ under pressure

Ch. Fierz, D. Jaccard, and J. Sierro
DPMC, Université de Genève, CH-1211 Geneva 4, Switzerland

J. Flouquet
CRTBT/CNRS, BP 166 X, F-38042 Grenoble-Cédex, France

Transport experiments on $CeAl_3$ samples under quasihydrostatic pressure up to 1.63 GPa are reported. Magnetoresistivity measurements in magnetic fields up to 7.3 T from 40 mK to 4 K were performed. Resistivity and thermopower were measured from 1.5 to 300 K. Taking the low-temperature resistivity as $\rho = \rho_0 + AT^2$, A increases initially with pressure as expected from the zero pressure thermal dilatation. Above 0.2 GPa, both A and ρ_0 decrease dramatically with pressure. It is, however, noteworthy that a T^2 law of the resistivity can hardly be extracted from the data above 0.2 GPa. The positive low-temperature magnetoresistivity also varies strongly with pressure. At 0.82 GPa the low field bump has disappeared and the magnetoresistivity is still positive up to 2.5 K. The thermopower shows an even more drastic pressure dependence. The negative bump around 3.5 K at zero pressure becomes positive above 0.3 GPa and a complex temperature dependence develops. The temperature variation cannot be scaled by a unique pressure-dependent parameter.

I. INTRODUCTION

The $CeAl_3$ compound is often quoted as the archetype of a heavy fermion (HF) lattice which does not order magnetically (see Ref. 1). Applying an external variable such as pressure (P) changes drastically the strength of the electronic coupling. However, if it is clear that a strong nonlinearity with P occurs in all published experiments, there are contradictions and also spurious effects among the data. Measurements of the specific heat C of $CeAl_3$ under P pointed to a sharp decrease of C/T at $T = 0.4$ K at low pressure[1] while the reported negative thermal expansion predicts an initial increase of $\gamma = C/T$ at very low temperature.[2] Down to 1.5 K, the resistivity ρ under pressure seems to show large hysteresis effects due to the pressure cycles.[3]

To clarify the situation, we have performed new resistivity experiments which were extended down to 40 mK. A magnetic field up to 8 T was also applied since interesting field effects were found in transport and thermodynamic measurements. Above 1.5 K, the thermoelectric power Q under pressure was also measured. The absolute thermopower Q is very sensitive to the energy derivative of the transport integral. Therefore, the temperature dependence of Q reveals often distinct energy scales which are hardly seen in other properties.[4]

We will focus mainly on the low-temperature magnetoresistivity data, notably on the pressure and field dependence of the coefficient A of the low temperature T^2 term of ρ written as $\rho = \rho_0 + AT^2$. This law is generally obeyed at very low temperature reflecting the Fermi liquid property of the ground state.[4] The major role of the local magnetic fluctuation in the formation of the huge effective mass leads to the remarkable feature that $\sqrt{A}$ is roughly proportional to γ, or put in another form, to the inverse of a characteristic temperature T^*.[4,5] If one assumes that $\rho(P)$ scales as a function of $T/T_{HF}(P)$ over a large temperature range (see Ref. 6), the single but not unique parameter T_{HF} can be chosen to be T^*, the temperature up to which a quadratic law is obeyed; at $P = 0$, $T^* \simeq 350$ mK.[4] Another choice commonly used for T_{HF} is the temperature of the resistivity maximum, $T^{\rho}_{max}(P = 0) = 31.4$ K. Special attention will be also given to the field and pressure dependence of ρ_0 with the aim to observe the relation between disorder and lattice properties.

II. EXPERIMENTAL DETAILS

Two samples of $3 \times 0.6 \times 0.55$ mm^3 and $3 \times 1 \times 0.6$ mm^3 were spark cut from the same well characterized batch.

Quasihydrostatic pressures are achieved in a single piston self-clamped cell with a 1:1 mixture of n-pentane and isoamyl alcohol as a pressure transmitting medium. The pressure was inferred to within ± 0.06 GPa from the superconducting transition temperature of tin. The absolute thermopower Q was measured by a differential method using Chromel and Au + 0.07 at. % Fe thermocouples. Neglecting pressure effects on these thermocouples, we estimate the accuracy of Q to $\pm 0.4\,\mu$V K^{-1}.

Both dc and ac techniques were used to measure the resistivity with an accuracy of ± 0.01 and $\pm 0.007\,\mu\Omega$ cm, respectively.

III. RESULTS AND DISCUSSION

Our results are in good qualitative agreement with previously reported data at zero pressure[4,7,8] as well as under pressure at ambient temperature.[9] In zero field, $\Delta\rho(P)/\rho(P = 0)$ at 3.5 K coincides for both samples investigated. Furthermore neither sample showed any hysteresis effects due to the pressure cycles. These facts allow us to compare straightforwardly the results of the two runs. Figure 1 shows the pressure dependence of A. In zero field, $T^* \simeq 350$ mK at zero pressure and $\sqrt{A}/T^*$ is approximately

 0021-8979/88/083899-03$02.40 © 1988 American Institute of Physics

constant below 0.2 GPa. In addition, our zero field results are in accordance with thermal expansion measurements.[2]

Above 0.2 GPa the amplitude of the T^2 term of ρ is drastically reduced. This reduction is accompanied by a similar pressure dependence of the residual resistivity ρ_0 (see inset of Fig. 1). Therefore, we can question the validity of Matthiesen's rule which is assumed in the foregoing. In this context we note the difficulty to extract a clearcut T^2 law from our resistivity data between 0.2 and 1.0 GPa. For comparison purposes, however, we take our A values as reasonable estimates.

Thus, using the zero pressure values in zero field, the proportionality of $\sqrt{A}$ and $1/T^*$ yields $T^* = 1.2$ and 3.2 K compared to the observed values 0.6 and 9 K at 0.82 and 1.63 GPa, respectively.

Another evidence of the impossibility to scale $\rho_P(T)$ by an unique parameter T/T_{HF} is also found if, instead of T^*, T^{ρ}_{max} is chosen for T_{HF}. If the scaling is obeyed, the coefficient α defined as

$$\alpha = \sqrt{A(P)}\,T^{\rho}_{max}(P)/\sqrt{A(0)}\,T^{\rho}_{max}(0)$$

should be of order unity for all pressures. Taking the A values from Fig. 1 and T^{ρ}_{max} as 31.4, 34, 45, and 66.2 K at 0, 0.3, 0.82, and 1.63 GPa, respectively, α is 0.88, 0.40, and 0.23 at 0.3, 0.82, and 1.63 GPa, respectively.

The failure to scale with a single parameter is also exemplified by the pressure dependence of the absolute thermopower Q. In Fig. 2, $Q(T)$ is shown up to 130 K at 0, 0.35, and 1.63 GPa. At zero pressure $Q(T)$ shows a negative peak at 3.5 K followed by a broad positive peak whose maximum lies at $T^{Q}_{max}(P=0) = 53$ K. We also note a change of slope of $Q(T)$ around $T_1 = 30$ K. With pressure, the low-temperature negative contribution to $Q(T)$ disappears as shown in the inset of Fig. 2. As the pressure increases further, Q remains positive. Under pressure, T^{Q}_{max} shifts towards higher temperatures with the same relative pressure variation than T^{ρ}_{max}, i.e., $T^{Q}_{max}/T^{\rho}_{max} = 1.75$. As the corresponding Grüneisen parameter

$$\Omega_{T_{max}} = \frac{-\partial \log T_{max}}{\partial \log V}$$

(V being the molar volume) is still large at high pressure (~ 20 for $P = 16$ kbar), the intermediate valent (IV) regime

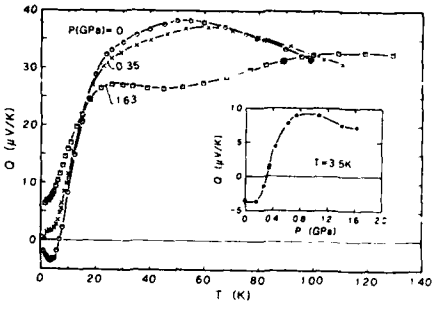


FIG. 2. Absolute thermopower $Q(T)$ at various pressures. Open circles: 0 GPa; crosses: 0.35 GPa; open squares: 1.63 GPa. Inset: $Q(P)$ at 3.5 K.

is far to be achieved with the present applied pressure. It is generally admitted that in the IV domain, the scaling by an unique parameter may be observed as competing phenomena of the heavy fermion compounds like crystal field effects and magnetic correlations have collapsed (see Ref. 4). Here the evidence of the occurence of different couplings is given by the emergence under P of a double structure in $Q(T)$ characterized by the observation of a well resolved peak at T_1 above 1.06 Pa. Such a double peak structure has been observed in $CeCu_2Si_2$ above 2.5 GPa (Ref. 5) or $CeRu_2Si_2$ at $P = 0$.[10] These anomalies will be discussed in a forthcoming paper.

Let us focus now on the magnetoresistivity data. On cooling the initially negative magnetoresistivity becomes positive at some temperature T_x. At zero pressure the field dependence of T_x agrees qualitatively with the one reported by Remenyi *et al.*[8] This field dependence is observed up to 0.3 GPa, T_x increasing with pressure. In Fig. 3 we show the magnetoresistivity $\Delta\rho(B)/\rho(B=0)$ at 450 mK and various pressures. Results around 50 mK are qualitatively similar

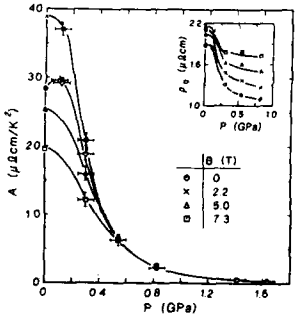


FIG. 1. Pressure dependence of the coefficient $A(P)$ of the T^2 term of ρ at various magnetic fields B. Open circles: 0 T; crosses: 2.2 T; open triangles: 5 T; open squares: 7.3 T. Inset: corresponding curves for the extrapolated residual resistivity ρ_0.

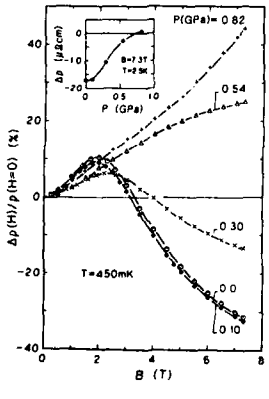


FIG. 3. Magnetoresistivity $\Delta\rho(B)/\rho(B=0)$ at 450 mK and various pressures. Open circles: 0 GPa; open diamonds: 0.1 GPa; crosses: 0.3 GPa; open triangles: 0.54 GPa; straight crosses: 0.82 GPa. Inset: $\Delta\rho = \rho(7.3\text{ T}) - \rho(0\text{ T})$ vs pressure at 2.5 K.

except that $\Delta\rho(B)$ remains positive up to 7.3 T at all pressures.

As can be seen in Fig. 1, at low pressure ($P<0.3$ GPa) $A(B)$ increases initially with B for reaching a maximum at $B_{max}\simeq 2$ T. The amplitude of $A(B_{max})/A(B=0)$ seems to decrease rapidly with P. Up to 0.3 GPa, the temperature T^* up to which at T^2 law is observed does not yield a constant value of $\sqrt{A(B)}/T^*$. That reflects even at very low temperature the occurence of competing coupling ie of a coherent state strongly disturbed by B.

Above 0.3 GPa the peaks of both $\Delta\rho(B)$ and $A(B)$ have disappeared. The magnetoresistivity behavior is not a trivial continuation of the low pressure data. $\Delta\rho(B)$ is still positive at 7.3 T. As it is observed in $CeRu_2Si_2$,[11] it is not precluded that a maximum in $\Delta\rho(B)$ and $A(B)$ will not occur at higher fields. The inset of Fig. 3 shows the pressure dependence of $\Delta\rho=\rho(7.3\text{ T})-\rho(0\text{ T})$ at 2.5 K. Again, the observed change of regime appears at $P\sim 0.3$ GPa. It must also be stressed that no clear B dependence can be observed in the isothermal magnetoresisitvity data. However, at $T=2.5$ K, $\Delta\rho(B)$ shows linear field dependences over large ranges of B.

Finally, an interesting experimental correlation is that $\rho_0(B)_P$ and $\rho_0(P)_B$ behave like $A(B)_P$ and $A(P)_B$, respectively. This result emphasizes again the coupling of the impurities with the lattice. It is thus questionable to assume independent mechanisms for these two terms of the resistivity throughout the investigated pressure and field ranges.

IV. CONCLUSIONS

The discrepancy of the present results with those of the specific heat under pressure is unclear.[1] By contrast, an excellent agreement has been found under pressure between specific heat and other experimental methods for other heavy fermion compounds like $CeCu_6$ or UPt_3 (see Ref. 12). This suggests that the low-pressure phase of $CeAl_3$ has particular properties very sensitive to the experimental conditions.

Our main results are as follows: the impossibility to scale ρ and Q by an unique parameter; the large difference in the transport properties at low and high pressures ($P\lesssim 0.3$ GPa). At $P=0$ recent data of transport measurements on single crystal[13] and of muon experiments on polycrystal[14] suggest that $CeAl_3$ may be magnetically ordered at $T\sim 1.6$ K with a very weak moment. An appealing possibility is a transition under pressure from a long-range magnetically ordered phase to a nonmagnetic ground state whereas in $CeRu_2Si_2$ strong antiferromagnetic correlations persist.[11]

[1] G. E. Brodale, R. A. Fisher, N. E. Phillips, and J. Flouquet, Phys. Rev. Lett. **56**, 390 (1985).
[2] M. Ribault, A. Benoit, J. Flouquet, and J. Palleau, J. Phys. (Paris) **40**, L-413 (1979).
[3] A. Percheron, J .C. Achard, O. Gorochov, B. Cornut, D. Jérome, and B. Coqblin, Solid State Commun. **12**, 1289 (1973).
[4] D. Jaccard and J. Flouquet, Helv. Phys. Acta **60**, 108 (1987).
[5] D. Jaccard, J. M. Mignot, B. Bellarbi, A. Benoit, H. F. Braun, and J. Sierro, J. Magn. Magn. Mater. **47&48**, 23 (1985).
[6] J.D. Thompson, J. Magn. Magn. Mater. **63&64**, 358 (1987).
[7] K. Andres, J. E. Graebner, and H. R. Ott, Phys. Rev. Lett. **35**, 1779 (1975).
[8] G. Remenyi, A. Briggs, J. Flouquet, O. Laborde, and F. Lapierre, J. Magn. Magn. Mater. **31-34**, 407 (1983).
[9] V. Vijayakumar, S. N. Vaidya, E. V. Sampathkumaran, and R. Vijayaraghavan, Solid State Commun. **46**, 549 (1983).
[10] A. Amato and J. Sierro, J. Magn. Magn. Mater. **47&48**, 526 (1985).
[11] P. Haen, J. Flouquet, F. Lapierre, P. Lejay, and G. Remenyi, J. Low Temp. Phys. **67**, 391 (1987).
[12] R.A. Fisher, S. E. Lacy, C. Marcenat, J. A. Olsen, N. E. Phillips, J. Flouquet, A. Amato, and D. Jaccard, Jpn. J. Appl. Phys. **26**, 1257 (1987).
[13] D. Jaccard, R. Cibin, J. L. Jorda, and J. Flouquet, Jpn. J. Appl. Phys. **26**, 517 (1987).
[14] S. Barth, H. R. Ott, F.N. Gygax, B. Hitti, E. Lippelt, A. Schenk, and C. Baines, Jpn. J. Appl. Phys. **26**, 519 (1987).

Magnetic order and superconductivity in heavy fermion systems (invited) (abstract)[a)]

G. Aeppli
AT&T Bell Laboratories, 600 Mountain Avenue, Murray Hill, New Jersey 97974

The neutron scattering technique, which directly probes magnetic correlation functions, has been used to identify the magnetic order in several heavy fermion systems, notably U_2Zn_{17}[1] and $U_{1-x}Th_xPt_3$.[2] Our measurments[3] show that *pure* UPt_3, which is superconducting, is also a weak antiferromagnet with an ordered moment of 0.02 μ_B and a Néel temperature of roughly 5 K. We also find that the onset of superconductivity affects the magnetic correlations in UPt_3. The relation between magnetism and superconductivity in compounds containing copper oxides is compared to that in the heavy fermion systems.

This paper was not proofread by the author; however, it has been proofread by one of the Publication Chairpersons.

[a)] The work reported was partially performed at Brookhaven (under U.S.D.D.E. contract DE-AC02-76CH00016) and Risø (Denmark) National Laboratories.

[1] D. E. Cox *et al.*, Phys. Rev. B 33, 3614 (1986).
[2] A. I. Goldman *et al.*, Phys. Rev. B 34, 6564 (1986).
[3] C. Broholm, J. Kjems, G. Aeppli, and E. Bucher (unpublished).

Two-impurity Kondo problem: Relevance to heavy fermions (invited) (abstract)[a)]

B. A. Jones
LASSP, Clark Hall, Cornell University, Ithaca, New York 14853

We have applied the numerical renormalization group to the problem of two Kondo impurities in an electron gas.[1] This approach allows an analysis of the physics at all temperature scales as a function of the initial (high-temperature) exchange coupling and of the initial RKKY interaction. A new symmetry of the Kondo and Anderson models, which we call the axial charge, provides further details of the important physical states involved in the evolution to the low-temperature (strong-coupling) fixed point. At high temperatures, we calculate the change of the coupling interactions as the temperature is lowered from the free-local-moment fixed point. We identify the relevant lower temperature fixed points, and provide scaling results for the flows in the crossover regions. We evaluate both the range of validity of thermodynamic scaling[2] at high temperatures and the strong influence of the initial interimpurity interaction on the scaling of the effective RKKY interaction. At the strong-coupling fixed point we construct a Fermi-liquid model and calculate the low-temperature specific heat, susceptibility, and staggered susceptibility; and discuss the nonuniversality of the Sommerfeld ratio. In particular, antiferromagnetic correlations produce an increased tendency to Cooper-type pairing, and we discuss these interactions in light of the new axial charge symmetry. Extensions of these pair interactions to the Fermi liquid for a lattice provide a possible description of correlations in heavy fermions.

[a)] This work was supported by DOE-Basic Energy Sciences, Division of Materials Research.

[1] B. A. Jones and C. M. Varma, Phys. Rev. Lett. 58, 843 (1987).
[2] C. Jayaprakash *et al.*, Phys. Rev. Lett. 47, 737 (1981).

 0021-8979/88/083902-01$02.40 © 1988 American Institute of Physics

Spatially dependent correlation functions in the Anderson model (abstract)

Kan Chen and C. Jayaprakash
Physics Department, The Ohio State University, Columbus, Ohio 43210
H. R. Krishnamurthy
Indian Institute of Science, Bangalore, India

We report results from a first principles calculation of spatially dependent correlation functions around a magnetic impurity in metals described by the nondegenerate Anderson model. Our computations are based on a combination of perturbative scaling theory and numerical renormalization group methods. Results for the conduction election charge density around the impurity and correlation functions involving the conduction electron and impurity charge and spin densities will be presented. The behavior in various regimes including the mixed valent regime will be explored.

Solutions of the magnetic Eliashberg equations for heavy fermion superconductors (abstract)

M. R. Norman
Materials Science Division, Argonne National Laboratory, Argonne, Illinois 60439

The Eliashberg equations for magnetic fluctuations are solved for heavy fermion superconductors. The susceptibility is taken from neutron data, and the Fermi surface from band calculations. For the case of UPt_3, mass renormalizations of about 16 are found consistent with de Haas–van Alphen data. A superconducting transition temperature of the order of 0.12 K is calculated, due to the momentum dependence of the susceptibility, with the gap function having lines of zeros in parts of the zone. The transition temperature can be boosted up to experimental values by crude incorporation of interband matrix elements. Extensions of these calculations to other heavy fermion superconductors will be reported.

 0021-8979/88/083903-01$02.40 © 1988 American Institute of Physics

Magnetoelastic effects on antiferromagnetic phase transitions (invited)

W. P. Wolf
Yale University, Applied Physics, Becton Center, P. O. Box 2157, New Haven, Connecticut 06520
C. H. A. Huan
University of Oxford, Clarendon Laboratory, Oxford 0X1 3PU, United Kingdom

The effect of elastic strains on antiferromagnetic phase transitions is considered. For cases in which the magnetic and chemical unit cells coincide, the combination of a strain and an applied field is found to lead to the possibility of a linear magnetoelastic (LME) coupling which may induce antiferromagnetic order, even in the normally paramagnetic phase. Such an effect can, in principle, destroy any second-order phase transition. An order of magnitude estimate shows that the effect is small but not negligible, and that it may explain a number of unusual effects observed in dysprosium aluminum garnet, including anomalous neutron scattering, magnetic hysteresis and magnetostriction. Similar strain-induced effects may be important in many other antiferromagnets, including CoF_2, FeF_2, MnF_2, and αFe_2O_3, as well as in mixed crystals with the same structures. Strain gradients may produce similar effects in other antiferromagnets which are magnetoelectric, including $DyPO_4$, $DyAlO_3$, and Cr_2O_3.

I. INTRODUCTION

It has long been recognized that elastic deformations can affect magnetic phase transitions.[1-5] There are basically two types of effects: strains due to externally applied stresses, and magnetoelastic strains which are the result of the magnetic phase transition itself. The former is generally considered rather trivial, since it merely changes the lattice from one structure to another very similar structure, and one would suppose that a phase transition in one structure would be closely mirrored in the other. The latter effect, on the other hand, has been the subject of much discussion and controversy, and for a time it was believed that magnetoelastic effects could change a second-order transition into a first-order transition.[1-3] Since all crystal lattices are to some extent magnetoelastic, this raised the question whether true second-order magnetic phase transitions could ever be observed in real materials. It was then recognized by Fisher[4] that the effect of an additional variable such as elastic strain would be to shift the actual critical point and modify the critical exponents characterizing the phase transition by a renormalization factor, but not otherwise change the character of the transition. Subsequently, Bergman and Halperin[5] reexamined the renormalization group arguments and concluded that a very weak first-order singularity might, in principle, occur, but in practice, most transitions appear to be close to second order. In any case, neither applied nor spontaneously generated strains are generally thought of as destroying the phase transition in real crystals.

In this paper we wish to draw attention to an important class of exceptions to this general rule. We first encountered the special circumstances in the course of a systematic study of magnetoelastic effects in the metamagnet dysprosium aluminum garnet (DyAlG).[6] However, the same conditions may be found in a wide variety of other magnetic systems, and our finding raises the question whether other phase transitions may not also be affected significantly by elastic effects. In such systems, several new effects should appear *in the presence of an applied magnetic field*. These include the destruction of the phase transition by externally or internally applied stresses, evident as an apparent rounding of the transition, and an anomalous magnetostrictive strain which appears in the ordered state. Other consequences include a dependence of various properties on the field and temperature history of the sample and, in particular, a marked difference between cooling through the transition in zero field (ZFC) and cooling in a finite field (FC).

II. THEORY

A. Symmetry considerations

It is simplest to discuss the effects in terms of a Landau expansion of the free energy, though the conclusions will be more general, since they are based on essential symmetry principles.

Let us consider a magnetic system undergoing a second-order phase transition in which some particular antiferromagnetic order parameter η goes to zero. We shall assume that η has only one component ($n = 1$); for $n > 1$ multiple phase transitions are possible. The corresponding Landau free-energy expansion is

$$F_a = \tfrac{1}{2} A_1 \eta^2 + \tfrac{1}{4} B_1 \eta^4 + \dots , \tag{1}$$

where $A_1(T) \to 0$ as $T \to T_c$. We now include the terms corresponding to an elastic strain ϵ limited for now to a single component. These will have the form

$$F_e + F_{me} = (-\sigma\epsilon + \tfrac{1}{2} C_1 \epsilon^2 + \dots) + (D_1 \eta^2 \epsilon + \tfrac{1}{2} G_1 \eta^2 \epsilon^2 + \dots) , \tag{2}$$

where F_e represents the purely elastic terms and F_{me} the

 0021-8979/88/083904-06$02.40 © 1988 American Institute of Physics

magnetoelastic terms, coupling ϵ to η. Here σ is a possible external stress, which we assume at first to be equal to zero. In the absence of magnetoelastic terms, the strain is then zero. Adding the elastic and magnetoelastic terms to (1) and minimizing with respect to ϵ, we find the induced magnetostrictive strain

$$\epsilon_m = -\frac{D_1\eta^2 + \dots}{C_1 + G_1\eta^2 + \dots}. \tag{3}$$

In the disordered phase, $\eta = 0$ and the strain goes to zero. To this approximation, the onset of order is not affected and still given by $A_1(T_c) = 0$.

On the other hand, if there is a nonzero strain as the result of an external stress σ

$$\epsilon_\sigma = (\sigma/C_1) + \dots, \tag{4}$$

and the effect of the magnetoelastic terms will then be to shift the conditions for the onset of η. The new T_c will be given by

$$A_1(T_c) + 2D_1(T_c)\epsilon_\sigma + G_1(T_c)\epsilon_\sigma^2 + \dots = 0. \tag{5}$$

However, even though ϵ_σ shifts T_c, it will not affect the character of the phase transition which remains second order in this approximation.

If we look back to the form of Eqs. (1) and (2), we note that we had followed the usual convention[7] of choosing to include only terms *even* in powers of η. The reason, of course, is that odd powers of η are excluded by the requirement of time reversal invariance. However, this restriction can be removed if we extend the discussion to include a new variable in the problem, one which is also odd under time reversal.

Specifically, let us consider possible terms involving M, the uniform magnetization. In an antiferromagnet, M is generally zero in the absence of an applied field, but in the presence of a magnetic field, M is not zero. We must then consider additional terms in the free energy. These may include

$$F_M = -HM + \tfrac{1}{2}A_2M^2 + A_3\eta M + \tfrac{1}{2}B_3\eta^2M^2 + \tfrac{1}{4}B_2M^4 + D_2M^2\epsilon + D_3\eta M\epsilon + \dots. \tag{6}$$

Such terms are all consistent with time reversal invariance but they are not necessarily allowed by other symmetry considerations. For a particular term to be allowed, it must transform as the identity representation of the symmetry group of the crystal, including both proper and improper rotations and translations.

The requirement of translational invariance immediately tells us that terms involving odd powers of η, such as the term $D_3\eta M\epsilon$, will be allowed *only if η is itself translationally invariant*, since both M and ϵ are translationally invariant. Not all magnetic states of antiferromagnetic order satisfy this condition, but many do. All that is required is that the magnetic unit cell should be the same as the chemical unit cell. This is the case in many antiferromagnets.

In addition to the condition of translational invariance, it is also necessary for the terms in F_{me} to be invariant under the rotational elements of the symmetry group. This can only be verified by detailed examination of each particular structure. We can illustrate the procedure by examining the specific case of dysprosium aluminum garnet (DyAlG).

The garnets are cubic with space group $Ia\bar{3}d$, and we therefore classify possible translationally invariant order parameters according to the irreducible representations of the cubic point group O_h. The specific order parameter which describes the antiferromagnetic state of DyAlG, η, transforms as A_2^+,[8] while the components M_μ ($\mu = x,y,z$) of M transform as T_1^+. The six components of elastic strain $\epsilon_{pq} = \epsilon_{qp}$ ($p,q = x,y,z$) transform as $(T_1^- \times T_1^-)_s = A_1^+ + E^+ + T_2^+$. Thus we can see that products of the form $\eta M_\mu \epsilon_{pq}$ will transform as

$$T_1^+ \times A_2^+ \times (A_1^+ + E^+ + T_2^+) = A_1^+ + E^+ + 2T_1^+ + 3T_2^+ .$$

The presence of one A_1^+ in this decomposition shows that one invariant exists. Detailed examination[6] shows that the invariant has the form

$$\eta M_z\epsilon_{xy} + \eta M_x\epsilon_{yz} + \eta M_y\epsilon_{zx}, \tag{7}$$

which is just a three-dimensional extension of the last term in Eq. (6).

The consequences of a term of the form of (7) are profound. If any one of the three products $M_z\epsilon_{xy}$, $M_x\epsilon_{yz}$, or $M_y\epsilon_{zx}$ is nonzero by virtue of externally applied fields and stresses, the resulting term will act exactly the same as that for a staggered field, H_s, and it will serve to induce a nonzero value of η for all values of the parameters in F, even above the normal T_c. This implies, therefore, that the previous second-order phase transition *is now destroyed by the combination of an applied field and stress*. The stress producing the ϵ's need not, of course, be applied directly; it may be generated by the mounting of the sample, or by imperfections in the growth of the crystal. Such strains will generally not be uniform but they can extend over length scales which are long compared to correlation lengths and thus effectively macroscopic. Dislocations, impurities, or other "dirt effects" can also set up internal strains and these may be more localized.

One region where this effect may be particularly troublesome is in the vicinity of tricritical points. Here, both the uniform and staggered susceptibilities diverge, and any broadening of the second-order phase transition will be difficult to distinguish from the first-order region, spread in field by demagnetizing effects. It could well be that the marked experimental difficulties which have been reported in connection with high-resolution measurements of tricritical exponents[9] could be the result of accidental strains in the samples.

B. Magnitude of the effect

Microscopic mechanisms responsible for the coupling are discussed elsewhere.[6] They involve strain dependence of the dipole, exchange, and Zeeman interactions and in general they will be quite complicated and difficult to calculate quantitatively. However, all the mechanisms lead to similar order of magnitude estimates, which agree with available magnetoelastic data,[6] and we can discuss these in terms of a simple macroscopic model.

If $-U_M$ is the energy of the antiferromagnetic state at $T = 0$ K, the change in energy produced by a strain ϵ will be $\sim -U_M\epsilon = -H_s\eta_{T=0}$. But U_M can also be expressed in terms of the mean field acting at $T = 0$ K, $H_{T=0}$:

$$-U_M = -\tfrac{1}{2} H_{T=0}\eta_{T=0} . \quad (8)$$

Thus,

$$H_s \sim \epsilon H_{T=0} . \quad (9)$$

Since strains are generally quite small, this shows that the induced staggered field will also be small, relative to the internal fields aligning the spins. However, even a small staggered field will have a significant effect near a phase transition, since the corresponding staggered susceptibility diverges at that point. The effect is similar to that of applying a uniform field to a ferromagnet at its Curie point, but with the difference that there are no demagnetizing effects to reduce the induced moment.

To estimate the order of magnitude of η induced by a given H_s, it is simplest to use a mean field model. For a system with $S = 1/2$, we can write

$$m = \tanh[(h + m)/t] , \quad (10)$$

where m, h, and t are expressed in reduced units, $m = \eta/\eta_{T=0}$, $h = H_s/H_{T=0}$, and $t = T/T_c$. Equation (10) can be solved numerically for m as a function of t for given values of h. The results for $h = 10^{-2}$, 10^{-3}, 10^{-4}, 10^{-5}, and 0 are shown in Fig. 1. It can be seen that even very small values of h can produce quite significant changes in m, especially close to T_c. A simple order of magnitude of the effect can be obtained by considering $t = 1$ when we can expand Eq. (10) to give

$$h = \tfrac{1}{3} m^3 + \ldots . \quad (11)$$

This expression shows quantitatively how even a very small staggered field can lead to a significant induced m. For example, $h = 10^{-5}$ results in $m = 0.03$. In a more accurate theory, the exponent 3 in Eq. (11) would be replaced by $\delta \sim 5$ and the variation with h would be even more rapid.

Since the magnitude of h is comparable to that of ϵ, we see, therefore, that even very small strains can lead to quite sizable induced amounts of antiferromagnetic order in regions where the usual theory predicts zero. At higher temperatures (or applied fields), the value of m becomes smaller quite rapidly, but it will never be identically equal to zero, as long as there is a finite amount of applied strain ($\epsilon_\sigma \neq 0$). Thus, we must conclude that even a small amount of stress, combined with a finite magnetization and a nonzero coupling coefficient D_3, will destroy the phase transition. In some sense, the system is antiferromagnetic everywhere, except in zero field. Of course, in practice, the region over which the strain-induced order will be observable will be quite small, and the usual critical point singularities will be modified only very close to the zero-strain transition. One would normally interpret this as "rounding" due to "experimental imperfections."

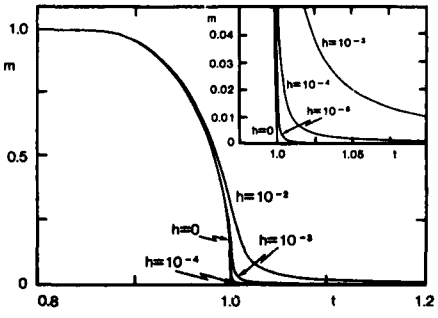


FIG. 1. Numerical solution of Eq. (10) showing the variation of reduced magnetization m as a function of reduced temperature t for various values of applied field h. For an antiferromagnet, m is the reduced order parameter, $\eta/\eta_{T=0}$, and h the reduced staggered field. These results show that even a very small field can induce a significant amount of order close to a phase transition.

In some ways the effect we have found is analogous to the fourth-order term $\eta M_x M_y M_z$ discovered by Alben *et al.*[10] Such a term also induces η when a field is applied, provided only that $M_x M_y M_z \neq 0$. This purely magnetic term vanishes when the field is applied along certain high symmetry directions, such that one or more of the components of M vanishes. The magnetoelastic term (7), on the other hand, does not vanish for any orientation of the applied field, provided only that some of the strains are not zero.

The magnetoelastic terms (7) will also have other consequences. Throughout the antiferromagnetic phase ($\eta \neq 0$), the system will be *piezomagnetic*, that is, an applied stress will produce a uniform magnetic moment. This moment can be thought of as resulting from a strain-induced uniform magnetic field with components $\eta\epsilon_{yz}$, $\eta\epsilon_{zx}$, and $\eta\epsilon_{xy}$. Such an effect has previously been observed in tetragonal and trigonal antiferromagnets,[11] but it does not seem to have been considered for a cubic system such as DyAlG. We shall discuss this further in the following section. Similarly, when M and η are nonzero anomalous shear strains will be produced, proportional to the products ηM_μ. Such strains will go to zero at T_c, as do the regular magnetostrictive strains, which are proportional to η^2 [Eq. (3)]. Shear strains can be especially important in magneto-optical experiments where they will produce additional birefringence effects. They can also affect thermal expansion and magnetostriction measurements which will require careful analysis when linear magnetoelastic terms are allowed by the symmetry.

III. EXPERIMENTS

Experimental evidence for nonzero values of η in regions where we would expect $\eta = 0$ is provided by the thermal neutron scattering experiments on DyAlG (Ref. 10) with fields applied along [001] and [110].[12] For these directions the induced staggered field due to higher-order magnetic terms is zero, but antiferromagnetic Bragg scattering in the paramagnetic phase has been observed nevertheless in both cases. For the case $H//[001]$, one can explain the observation in terms of a second induced order parameter,[8] but for $H//[110]$ there is no such effect. The stress induced staggered field effect would seem to provide a likely explanation. In retrospect, it is really not too surprising that DyAlG should show magnetoelastic effects even in the absence of externally applied stresses, since one can readily expect strains of the order of 10^{-4}–10^{-5} due to differences in thermal expansion between the sample and its mounting, or due

to imperfections introduced during growth. Examining crystals between crossed polarizers often shows patterns which would correspond to strains of such magnitudes. In any case, the idea should be susceptible to a direct test since, by applying varying external stresses in the presence of uniform fields, one should be able to observe neutron scattering corresponding to antiferromagnetic order in regions of field and temperature where the unstrained crystal shows no long-range order.

Another experiment on DyAlG in which evidence for magnetoelastic effects may already have been observed concerns the anomalous low-field susceptibility of polycrystalline samples. It was found, already in the very earliest measurements,[13] that there is a small temperature-dependent ferromagnetic moment below the Néel temperature which is absent in flux-grown single crystals. Recent experiments[14] have confirmed this effect and have found a monotonic correlation with particle size. Initially, it was thought that finite size effects of the sort postulated by Néel[15] might be important, but the particle sizes for which the effect was found appear to be much too large (1–50 μm) and another explanation must be sought.

If we postulate that the particles are elastically strained in the course of preparation, the magnetoelastic coupling discussed above will lead to a weak ferromagnetic moment, which will be proportional to the antiferromagnetic order parameter, as observed experimentally. It should be possible to verify this effect directly by measuring the low-field magnetization as a function of externally applied stress. It must be noted, however, that any quantitative analysis will entail first obtaining a single domain state. This should be possible by cycling the magnetic field through the phase transition or by cooling in a magnetic field. Such annealing procedures may be complicated by nonuniform residual strains, but in a sufficiently strong magnetic field the purely magnetic fourth-order mechanism of Alben *et al.*[10] should differentiate unambiguously between the two time-reversed antiferromagnetic states, A^+ and A^-.

Experiments to study the field dependence of the sign of η in single crystals of DyAlG are currently in progress and will be reported elsewhere.[16] The method being used involves measurements of the transit time of high-frequency ultrasonic shear waves[17] which, as we have shown previously,[6] also contains a term linear in η. Preliminary results indicate large hysteresis effects, as expected.

Further clear evidence for linear magnetoelastic effects in DyAlG has also been obtained by Dillon *et al.*[18] using both optical birefringence and direct magnetostrictive measurements. In particular, they observed linear variations with field through zero field, which are direct consequences of the linear magnetoelastic terms (7). These effects will be discussed further elsewhere.[6,19]

IV. DISCUSSION

We have so far discussed only the metamagnet DyAlG but similar effects should be observable in many other materials. One principal requirement is an antiferromagnetic order parameter which corresponds to zero wave vector. Many common antiferromagnets satisfy this condition. The second major requirement is that the order parameter should be invariant to the inversion operation, if the crystal in fact possesses a center of symmetry. This is evident from the fact that the components of both the field and the strain are invariant under inversion. Thus, all antiferromagnets which are magnetoelectric would appear to be excluded, since for these the order parameter must change sign under inversion.[20] But this still leaves a number of well-known antiferromagnets including MnF_2, CoF_2, FeF_2, and αFe_2O_3, as well as mixed crystals with the same structures.

It is necessary, in principle, to verify that the order parameter in each case transforms under the various rotational elements of the symmetry group in the same way as some combination of $M_\alpha \epsilon_{\beta\gamma}$, where α, β, $\gamma = x$, y, or z, but in practice this is not likely to be a limitation since the 18 possible combinations of α, β, and γ provide a rich variety of terms which transform in different ways. Certainly, for each of the six antiferromagnets listed above, there are at least two invariants: $M_z\epsilon_{xy}$ and $M_x\epsilon_{yz} + M_y\epsilon_{zx}$. Any arbitrary shear strain, together with a field not restricted to one symmetry axis, will therefore couple to the antiferromagnetic order parameter in all these cases.

There is another way to view the mechanism we have been discussing. In antiferromagnets in which a weak ferromagnetic moment is allowed by symmetry[21] (e.g., NiF_2), a uniform magnetic field will clearly couple to the antiferromagnetic order and destroy the phase transition, just as in the case of a simple ferromagnet in a field illustrated above. For weak ferromagnetism to be allowed in an antiferromagnet, the symmetry must be such that the term $A_3\eta M$ in Eq. (6) is not zero. This is a relatively rare occurrence in high symmetry structures and for all of the six examples listed above $A_3 = 0$. However, the application of a shear strain to such a structure will generally lower the symmetry and a term in ηM may then become allowed.

For example, the application of strain ϵ_{xy} to the tetragonal rutile structure of the MF_2 will lower the point group from D_{4h} to an orthorhombic D_{2h}. For such a symmetry, the three components of M transform as B_1^+, B_2^+, and B_3^+, so that any η transforming as a B_i^+ ($i = 1$, 2, or 3) will give a nonzero invariant in Eq. (6), and therefore couple to an applied field. The case of DyAlG can be analyzed similarly as a reduction from O_h to D_{2h} for a strain e_{xy}, and to C_i for a general shear strain with $\epsilon_{xy} \neq \epsilon_{yz} \neq \epsilon_{zx} \neq 0$.

The effects of the magnetoelastic coupling are, of course, not restricted to the region of the phase transition. The phenomenon of *piezomagnetism* has previously been studied in several of the antiferromagnets listed above,[11] and the effect of externally applied stresses on antiferromagnetic domains has been reported for CoF_2 (Ref. 22) and MnF_2.[23] In all of these earlier experiments, evidence of residual internal strains in the absence of applied stresses was in fact noted, but the effect of these strains on the phase transitions to the paramagnetic state does not seem to have been considered before. It is fortunate, in hindsight, that the classic high-resolution measurements of the critical exponent β in MnF_2 (Ref. 24) were made in zero magnetic field, where any residual strains would be less important. Also, since Mn^{2+} is an

S-state ion, the magnitude of the magnetoelastic coupling terms will be much smaller than for ions such as Dy^{3+} or Co^{2+} which have large orbital angular momentum ground states.

One system for which residual elastic strains may play an important and so far unrecognized role is $Fe_xZn_{1-x}F_2$. This system shows a number of striking properties in the presence of applied magnetic fields, which have been interpreted, with much controversy, in terms of the theory for a random Ising antiferromagnet.[25] It is not clear what role residual strains may have played in any of the phenomena which were observed, but significant effects are certainly possible. In particular, the formation of antiferromagnetic domains in the presence of an applied field could be affected by strains in competition with the usually invoked mechanism of statistical imbalance between up and down spins in a randomly diluted system. Strains could also lead to a small ferromagnetic moment, as discussed above, which could then complicate the analysis of low-field ac measurements. Even in absence of residual strains, the anomalous magnetostrictive shear strains induced by a nonzero product ηM_μ could affect the optical birefringence which is observed to sharpen significantly near T_c in the presence of an applied field.

We shall not pursue these possibilities here, as this is clearly a complex matter, but we must note that it is remarkable that the effects of elastic strains, both uniform and local, do not seem to have been considered in the extensive discussion of these interesting systems.

Our treatment so far would suggest that magnetoelastic effects would only be expected in antiferromagnets in which the order parameter is *even* under inversion. This would imply that all magnetoelectric antiferromagnets, in which η changes sign under inversion, will not show any linear magnetoelastic coupling. One may note, however, that a material such as $DyPO_4$ which is magnetoelectric and whose antiferromagnetic order parameter transforms as B_1^- does, in fact, show some quite marked strain-dependent effects, especially near the field-induced phase transition.[26] Also there are some striking hysteresis effects in the magnetoelectric measurements in systems such as $DyPO_4$ (Ref. 27) and $DyAlO_3$ (Ref. 28) which were not expected. To explain such effects we need a more complex mechanism than the one we have discussed so far, one in which the strain still somehow couples to the order parameter.

One possible way of achieving such a coupling is to consider an *inhomogeneous* strain with large local strain gradients $f_{\alpha\beta\gamma} = \partial\epsilon_{\beta\gamma}/\partial\alpha$ ($\alpha,\beta,\gamma = x,y,$ or z). Such gradients will transform as components of a third rank tensor, which will change sign under inversion and thus provide the possibility of forming invariants of the form $\eta M_\mu f_{\alpha\beta\gamma}$. It is not clear whether such a mechanism will, in fact, explain the particular effects observed in $DyPO_4$ and $DyAlO_3$, but it suggests more generally that there is always the possibility of a higher-order combination of factors which may provide a coupling mechanism between elastic strain and the antiferromagnetic order. The only condition which would seem to be essential is that the order parameter must be translationally invariant.

V. CONCLUSION

Our discussion has shown that relatively small strains can lead to significant effects, especially near field-induced phase transitions. It is a complication which will be important only for certain classes of antiferromagnets, those with magnetic unit cells which are the same as the corresponding chemical unit cells, but these include a number of systems which have been studied quite intensively and where this feature has not previously been suspected of producing any observable effects.

It is interesting in this connection to recall a concept introduced by Giauque *et al.* when they introduced the word "pernt" to denote a critical point which has become smeared out by some effect. For many years this idea was not accepted because it was generally believed that long-range order sets in at some specific singular point, and that while elastic effects might shift that point and alter the thermodynamic properties in its vicinity, they would not spread the apparent onset of long-range order over an observable region. Our specific examples have shown that the word "pernt" may indeed describe some real systems if they are accidentally strained.

The presence of linear magnetoelastic terms in the free energy will have significant consequences also in initially unstrained crystals. For these, some anomalous magnetostrictive effects should be observed.

Our discussion here has been restricted to classical Landau theory, but the effects should be evident also in more exact treatments. Other interesting extensions will include consideration of systems with order parameters with $n > 1$, random strains on a microscopic scale, and effects in systems with weakly first-order phase transitions.

In any case, it would appear that linear magnetoelastic effects can add a new dimension to the discussion of antiferromagnetic phase transitions.

ACKNOWLEDGMENTS

We would like to thank J. F. Dillon, Jr., M. E. Fisher, G. A. Gehring, J. F. Gregg, D. Mukamel, and M. R. Wells for encouragement and a number of helpful discussions, and I. D. Morris for help with the figure. This work was supported in part by NSF grant No. DMR-8216222. One of us (C.H.A.H.) would like to acknowledge support from a Magdalen College Senior Mackinnon Scholarship, and one of us (W.P.W.) from a Royal Society Guest Research Fellowship.

[1]O. K. Rice, J. Chem. Phys. **22**, 1535 (1954).
[2]C. Domb, J. Chem. Phys. **25**, 783 (1956).
[3]C. W. Garland and R. Renard, J. Chem. Phys. **44**, 1120 (1966).
[4]M. E. Fisher, Phys. Rev. **176**, 257 (1968).
[5]D. J. Bergman and B. I. Halperin, Phys. Rev. B **13**, 2145 (1976).
[6]W. P. Wolf and C. H. A. Huan, Phys. Rev. B **37**, 2033 (1988).
[7]See, for example. C. Tsallis, J. Phys. (Paris) **32**, 903 (1971).
[8]D. Mukamel and M. Blume, Phys. Rev. B **15**, 4516 (1977).
[9]W. P. Wolf, in *Multicritical Phenomena*, edited by R. Pynn and A. T. Skjeltorp (Plenum, New York, 1984), p. 13, and references therein.
[10]R. Alben, M. Blume, L. M. Corliss, and J. M. Hastings, Phys. Rev. B **11**, 295 (1975).

[11]See, for example, A. S. Borovik-Romanov, Sov. Phys. JETP **11**, 786 (1960), and references therein.
[12]M. Blume, L. M. Corliss, J. M. Hastings, and E. Schiller, Phys. Rev. Lett. **31**, 527 (1973); L. M. Corliss and J. M. Hastings (private communication).
[13]A. F. G. Wyatt, D. Phil. thesis (Oxford University, 1963) (unpublished).
[14]C. P. Tigges, S. Mroczkowski, and W. P. Wolf, Bull. Am. Phys. Soc. **30**, 440 (1985).
[15]See, for example, I. S. Jacobs and C. P. Bean, in *Magnetism*, Vol. III, edited by G. T. Rado and H. Suhl (Academic, New York, 1963), p. 294.
[16]J. F. Gregg, I. D. Morris, M. R. Wells, and W. P. Wolf (to be published).
[17]C. H. A. Huan, J. F. Gregg, M. R. Wells, G. A. D. Briggs, and W. P. Wolf, J. Appl. Phys. **61**, 3193 (1987).
[18]J. F. Dillon, Jr., L. D. Talley, and E. Y. Chen, *Magnetism and Magnetic Materials*, AIP Conf. Proc. **34**, 388 (1976); J. F. Dillon, Jr., E. M. Gyorgy, E. I. Blount, E. Y. Chen, and L. G. Van Uitert, J. Appl. Phys. **49**, 1371 (1978); *ibid.* **50**, 1844 (1979).
[19]J. F. Dillon, Jr., E. Y. Chen, E. M. Gyorgy, and W. P. Wolf (to be published).
[20]See, for example, G. T. Rado and V. J. Folen, J. Appl. Phys. **33**, 1126 (1962) and references therein.
[21]See, for example, T. Moriya, in *Magnetism*, Vol. 1, edited by G. T. Rado and H. Suhl (Academic, New York, 1963), p. 85.
[22]P. Radhakrishna, P. J. Brown, D. Derrmann-Ronzaud, and R. Alben, J. Phys. C **11**, 2851 (1978).
[23]J. Baruchel, M. Schlenker, and B. Barbara, J. Magn. Magn. Mater. **15–18**, 1510 (1980).
[24]P. Heller and G. B. Benedek, Phys. Rev. Lett. **8**, 428 (1962).
[25]See, for example, A. R. King and D. P. Belanger, J. Magn. Magn. Mater. **54–57**, 19 (1986), and references therein; R. A. Cowley, H. Yoshizawa, G. Shirane, and R. J. Birgeneau, Z. Phys. B **58**, 15 (1984), and references therein.
[26]I. R. Jahn, J. Ferré, M. Regis, and Y. Farge, Solid State Commun. **28**, 421 (1978).
[27]G. T. Rado, Phys. Rev. Lett. **23**, 644 (1969); **23**, 946 (E) (1969).
[28]L. M. Holmes, Int. J. Magn. **6**, 111 (1974).
[29]W. F. Giauque, G. E. Brodale, R. A. Fisher, and E. W. Hornung, J. Chem. Phys. **42**, 1 (1965).

Magnetostriction "jumps" in twinned $Tb_{0.3}Dy_{0.7}Fe_{1.9}$

A. E. Clark and J. P. Teter
Naval Surface Weapons Center, Silver Spring, Maryland 20903-5000
O. D. McMasters
Iowa State University, Ames, Iowa 50011

Large "jumps" in the magnetostriction have been observed in twinned single crystals of $Tb_{0.3}Dy_{0.7}Fe_{1.9}$ (Terfenol-D) for magnetic fields parallel to the crystalline $[11\bar{2}]$ direction. The interpretation of these large magnetostriction discontinuities is based upon a model of twinned dendritic Terfenol-D in which the magnetization of one twin jumps between two [111] directions while the magnetization of the remaining twin undergoes a continuous rotation of the magnetization. The field dependence of the magnetization and magnetostriction of cubic single crystals with $\lambda_{111} \gg \lambda_{100}$ was calculated using an expression which included the anisotropy constants K_1 and K_2 and compressive loads along $[11\bar{2}]$. With $K_1 = -0.6\ J/m^3$ and $K_2 = -2.0\ J/m^3$ (values appropriate for Terfenol-D near room temperature), magnetization "jumping" is predicted. For the twinned crystal, the jump in the magnetostriction was calculated to be greater than 1000 ppm. Because of this large magnetostriction, it is possible to configure a device to perform a substantial amount of work by the application of only a triggering magnetic field centered about an optimum bias field.

INTRODUCTION

Recent studies have shown that the highly magnetostrictive alloy $Tb_xDy_{1-x}Fe_{2-y}$, $x = 0.3$, $0 < y < 0.2$ (Terfenol-D) grows preferentially along a crystallographic $[11\bar{2}]$ direction in twinned dendritic sheets.[1] Because the growth direction is a nonprincipal direction and because $\lambda_{111} \gg \lambda_{100}$, magnetostrains along $[11\bar{2}]$ depend upon the magnetization in an unexpected way. In untwinned single crystal Terfenol-D, for example, the maximum magnetostriction does not occur with the magnetization direction parallel to the $[11\bar{2}]$ measurement direction, but with the magnetization directed at some angle between the measurement direction and the nearby $[1\bar{1}1]$ direction.[2] In a twinned crystal, the magnetostriction is even more complex and difficult to analyze. The purpose of this paper is to examine the magnetostriction of twinned single crystalline Terfenol-D over a broad temperature range spanning room temperature. At low temperatures, the nonmagnetostrictive ⟨100⟩ axes are magnetically easy. At high temperatures, the highly magnetostrictive ⟨111⟩ axes are easy and magnetization "jumping" can occur between the perpendicular [111] direction and the $[1\bar{1}1]$ direction close to the $[11\bar{2}]$ measurement axis. Huge changes in sample length accompany these jumps. Internally stored magnetic energy is released abruptly during the jump and can appear as work done against an externally applied stress.

EXPERIMENT

Twinned $[11\bar{2}]$ rods of $Tb_{0.3}Dy_{0.7}Fe_{1.9}$ ($\frac{1}{4}$ in. diam × 6 in. long) were prepared by a free-standing rf zone method (FSZ) using a zoning rate of 20 in/h. The $[11\bar{2}]$ crystal axes are parallel to the rod axes to within 2°. Magnetostriction measurements were made on 2.2-in.-long samples using standard strain gauge techniques employing a Tenney temperature-controlled chamber. The magnetic field was applied quasistatically in 30-ms steps by a solenoid placed around the cylindrical Terfenol sample. A soft iron path provided flux return. In a conventional fashion, the magnetization was calculated from the flux change in a pick-up coil wound around the sample. Measurements were made under static compressive loads (σ) from 0 to 25 MPa at temperatures (T) from −50 to 90 °C.

Figure 1 illustrates the progression in the temperature dependence of the magnetization and magnetostrictive behavior at 13.3 MPa as the sample undergoes the transition from a strong positive anisotropy (⟨100⟩ easy) at low temperature to a strong negative anisotropy (⟨111⟩ easy) at high temperatures. At −50 °C a conventional magnetization curve with a small magnetostriction is observed. The primary magnetization process occurs by 180° wall motion, followed by some magnetization rotation away from the nonmagnetostrictive ⟨100⟩ axes. From −50 to −10 °C the magnetostriction gradually increases until at −10 °C, $K_1 \simeq 0$. At −10 °C with the compressive stress of 13.3 MPa providing a preferential transverse easy direction, the magnetization lies along the magnetostrictive [111] direction for zero applied field. As the field in the solenoid is increased, a relatively minor change in length is observed until at a critical field, H_{cr}, an abrupt change in length occurs with $\Delta l/l > 1000$ ppm. A still further increase in length occurs at greater fields. At 0 °C and above, the ⟨111⟩ directions are sufficiently easy to cause the magnetization to "jump" between two [111] directions as the magnetic field is applied. For $20\ °C < T < 80\ °C$, the break in the curve at H_{cr} is even more distinct. At these higher temperatures, K_1 is more negative and the barrier between the [111] directions is higher. The decreasing value of magnetostriction with increasing temperature for $20\ °C < T < 80\ °C$ is due to the decrease in the saturation magnetostriction. At the higher temperatures

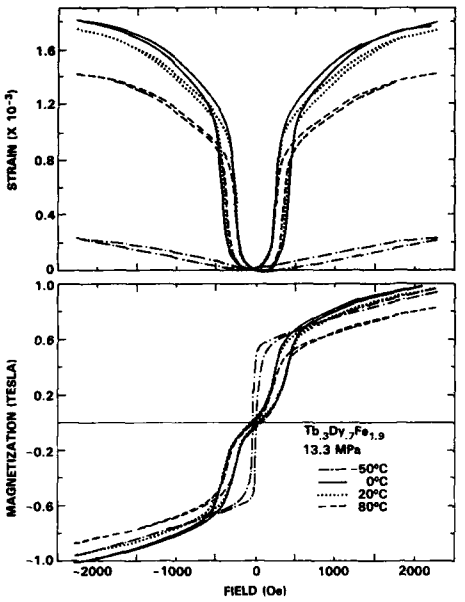


FIG. 1. Magnetostriction and magnetization curves of $Tb_{0.3}Dy_{0.7}Fe_{1.9}$ at 13.3 MPa compressive stress.

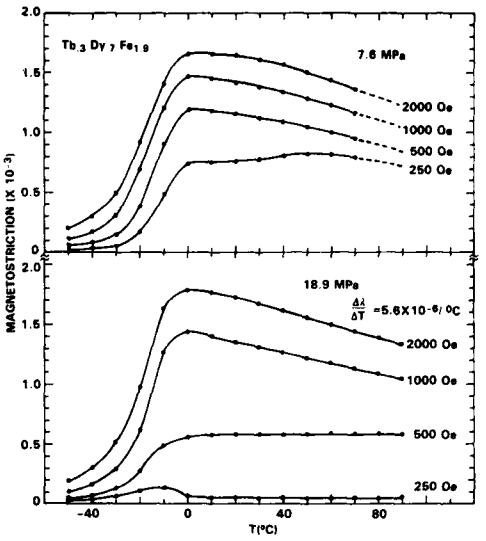


FIG. 3. Magnetostriction of $Tb_{0.3}Dy_{0.7}Fe_{1.9}$ vs temperature for 7.6 and 18.9 MPa.

($T > 0$ °C) both the magnetization and magnetostriction curves consist of three distinct regions: (1) a very-low-field region where there is little magnetization and magnetostriction, (2) a magnetization jumping region in which the magnetic moment jumps between two directions which have widely different magnetostrictions, and (3) a magnetization rotation region where the magnetic moment rotates toward the $[11\bar{2}]$ rod axis. Substantial magnetostriction also occurs in the high-field region.

Similar magnetostriction and magnetization curves are observed at compressive stresses $\sigma > 7.6$ MPa. As the compressive load is increased, however, a larger external field must be applied to produce the greater work done by the expansion against the load. This is illustrated in Fig. 2 for $\sigma = 7.6$ and 18.9 MPa. At very low applied stresses ($\sigma < 5$ MPa), internal stresses developed during the growth process become significant and prevent the $H = 0$ state from being the minimum magnetostriction state (one in which all domains point in the transverse direction). Figure 2 shows that for zero applied stress there is no magnetization "jumping." In this case the magnetization process proceeds by 180° wall motion at low fields, followed by magnetization rotation at high fields. For $\sigma = 0$, only this latter process gives rise to magnetostriction. At 20 °C approximately 5 MPa is required to achieve 70° wall motion and magnetostriction "jumping."

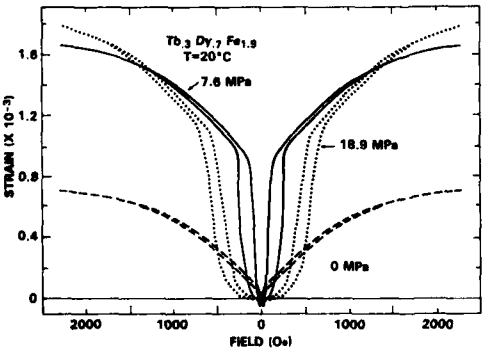


FIG. 2. Magnetostriction of the $Tb_{0.3}Dy_{0.7}Fe_{1.9}$ at 0, 7.6, and 18.9 MPa.

The experimental results are summarized in Fig. 3 for $\sigma = 7.6$ and 18.9 MPa. Here $H = 250$, 500, 1000, and 2000 Oe. The onset of the magnetostrictive state ($\langle 111 \rangle$ easy) occurs between -20 and 0 °C in $Tb_{1-x}Dy_xFe_{1.9}$ with $x = 0.3$. For samples where $x < 0.3$, this onset moves to higher temperatures.[3] The decrease in the saturation magnetostriction (λ_{111}) of Terfenol-D with temperature is also clearly seen in the curves for $H = 1000$ and 2000 Oe. We find $\Delta\lambda_{111}/\Delta T = 5.6 \times 10^{-6}$/°C. The important experimental feature of twinned single-crystal Terfenol-D is the large change in length at low applied fields. Because of magnetization jumping, magnetostrictions $\simeq 800$ ppm exist at 250 Oe for $\sigma = 7.6$ MPa, and $\simeq 600$ ppm at 500 Oe with $\sigma = 13.8$ MPa.

DISCUSSION

Our proposed model of the magnetization process is depicted in Fig. 4. Here at $H = 0$ (and with pressure sufficient to populate only the [111] direction perpendicular to the rod axis), a single domain exists which traverses the den-

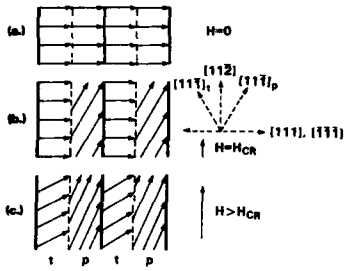


FIG. 4. Model of the magnetization process for [11$\bar{2}$] twinned Terfenol-D single crystal. The cross section of two twinned dendrites is depicted. Twin segments are denoted by p and t.

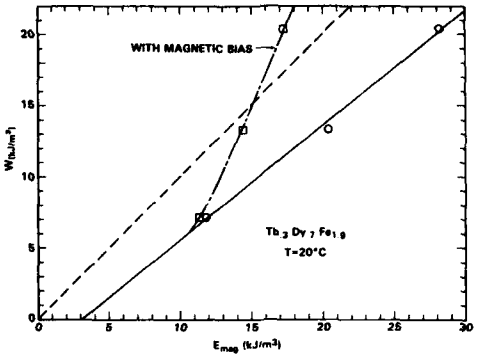


FIG. 5. Magnetic energy (MH) converted to work ($\Delta\lambda\ \sigma$) during the magnetization process. The dotted line represents lossless conversion. The vertical difference between the solid line and dotted line is a measure of the energy stored within the sample.

drites. As the field is first increased the magnetic moments remain close to the perpendicular [111] direction until the Zeeman energy is sufficient to surmount the anisotropy energy barrier and perform the work required against the compressive load. In this region only a small magnetostriction results. At the critical magnetic field, H_{cr}, the magnetization of one twin "jumps" to a new direction close to the [1$\bar{1}$$\bar{1}$] direction 19.5 from the [11$\bar{2}$] rod axis, while the magnetization of the other twin remains clsoe to the perpendicular [111] direction [Fig. 4(b)]. With a further increase in magnetic field, rotation of both twins toward [11$\bar{2}$] occurs [Fig. 4(c)].

The application of this model to the data of Fig. 2 shows that the strain $\Delta\lambda$ that occurs with magnetization jumping is given approximately by $\frac{1}{3}$ of the saturation magnetostriction. For measurements along [11$\bar{2}$] and rotation from [111] to [1$\bar{1}$$\bar{1}$], the saturation magnetostriction is $\frac{2}{3}\lambda_{111}$. Thus we predict the strain in the twinned sample to be $\Delta\lambda = \Delta\lambda_p/2 + \Delta\lambda_t/2 = 0 + \frac{2}{3}\lambda_{111} = 1067$ ppm. Here we assume an equal volume of parent (p) and twin (t) and $\lambda_{111} = 1600$ ppm. The calculated value is very close to the observed value of 1000 ppm. Similarly the magnetization jump (ΔM) is simply given by $(M_s/2)\sin 70.5° \simeq 0.5$ T, where we take the saturation magnetization M_s to be 1.05 T. This is close to the observed value of $\Delta M \simeq 0.58$ T. At higher compressive loads, the magnetostriction and magnetization becomes somewhat smaller since the angle change is less than 70.5°.

Finally, it is important to compare the work done against the compressive load to the magnetic energy supplied through the magnetic field. For pressures of 7.6, 13.3, 18.9, and 24.5 MPa, we measured critical fields H_{cr} of 295, 500, 705, and 1000 Oe, respectively. In Fig. 5 we show the fraction of the magnetic energy (MH) converted to mechanical energy ($\sigma\,\Delta\lambda$) during the magnetization "jumping" process. (The additional work done during the final rotation process is not addressed in the figure.) As the compressive load is increased, a larger fraction of the magnetic energy is converted to work. Because of magnetization jumping, only a moderate triggering magnetic field (superimposed on a static bias field) is required to transfer the energy between the magnetic state and the mechanical state. The size of this field depends upon the magnetic hysteresis. The quality of the single crystal used in this experiment required $\simeq 100$ Oe to trigger the "jump." If a bias magnetic field (H_b) is introduced and the magnetic energy E_{mag} is given by the triggering magnetic energy, $M(H - H_b)$ rather than by MH, the ratio of work to the magnetic energy, W/E_{mag}, can become far greater than unity. Using this phenomenon and samples with low hysteresis, large amounts of energy can be transferred from the internal magnetic state to the external mechanical state by a small applied magnetic field. The strain discontinuities for twinned [11$\bar{2}$] samples are limited to $\simeq 1000$ ppm at room temperature. However in [11$\bar{2}$] untwinned single crystals these discontinuities would be increased to $\simeq 2000$ ppm, and in single crystal $TbFe_2$ strains up to $\simeq 3500$ ppm might be achieved. A proposed application of these magnetostriction jumping alloys is a rapid solid-state mechanical switch in which a large amount of energy is transferred between the magnetic and mechanical states. An "inchworm" or "magnetostriction" motor developed from these materials would require only small external magnetic fields.

[1] A. E. Clark, J. D. Verhoven, O. C. McMasters, and E. D. Gibson, IEEE Trans. Magn. MAG-22, 973 (1986).
[2] J. P. Teter, A. E. Clark, and O. D. McMasters, J. Appl. Phys. 61, 3787 (1987).
[3] A. E. Clark and D. N. Crowder, IEEE Trans. Magn. MAG-21, 1945 (1985).

Magnetoelasticity and magnetovolume of dilute Cr-Si alloys

H. L. Alberts and J. A. J. Lourens
Department of Physics, Rand Afrikaans University, P.O. Box 524, Johannesburg 2000, South Africa

The recently predicted reentrant feature near the triple point on the magnetic phase diagram of the Cr-Si system was not observed in magnetoelastic and magnetovolume measurements. Known itinerant electron theories, which were previously applied successfully to other Cr systems, fail in several aspects when applied to the magnetovolume of Cr-Si alloys.

INTRODUCTION

The previously determined[1,2] magnetic phase diagram of dilute Cr-Si alloys contains a triple point where the paramagnetic (P), commensurate (C) spin-density wave, and incommensurate (I) spin-density wave states coexist. Mizuki *et al.*[3] recently suggested a behavior near the triple point that is more complex than that previously expected. They suggested a sequence of phase changes near the triple point from P to I to C and back to I when cooled below the Néel point (T_N) instead of the sequence P to C to I previously observed. We have studied the effects of magnetic transitions on the magnetoelastic and magnetovolume behavior of dilute Cr-Si alloys in an attempt to gain a better understanding of its complex behavior.

EXPERIMENTAL DETAILS

Dilute Cr-Si alloys containing 0.50, 0.74, 0.90, 1.04, 1.42, 1.79, and 3.43 at. % Si were prepared from 99.999% starting material and concentrations determined as previously described.[4] Bulk moduli in suitably prepared[4] samples were measured using a phase comparison method[5] to determine ultrasonic wave velocities. Thermal expansion measurements were carried out on the same samples using a strain gauge technique.[4] The experimental error in the absolute values of B is estimated to be about 2% while changes in the order of 5 in 10^4 with temperature could be detected easily. Those in $\Delta L/L$ and the thermal expansion coefficient (α) are estimated to be 5% and 10%, respectively.

RESULTS AND DISCUSSIONS

The coefficient of thermal expansion was obtained for each sample by differentiating the $\Delta L/L$-T curves. The α-T curves for alloys containing 0.50, 0.74, 0.90, 1.79 and 3.43 at. % Si display only one anomaly associated with T_N in the temperature range 77 K $< T <$ 400 K. Two separate anomalies were observed for $c = 1.04$ and 1.42 at. % Si. The high temperature one is associated with T_N and the low temperature one with the I-C transition temperature (T_{IC}). The transitions at T_N on the $\Delta L/L$-T curves were observed to be continuous for $c = 0.50$, 0.74, and 0.90 at. % Si while it was distinctively discontinuous for $c = 1.42$ and 1.79 at. % Si and very nearly so for $c = 1.04$ and 3.43 at. % Si. The discontinuities or near discontinuities in the $\Delta L/L$-T curves are associated with C-P transitions which are first order in character.[6] Typical examples of α-T curves are shown in Fig. 1(a) for $c = 0.74$, 1.42 and 3.43 at. % Si.

The α-T curves of samples (0.74, 0.90, 1.04, and 1.42 at. % Si) near the triple point (1.0 at. % Si) reveal only one (I-P for 0.74 and 0.90 at. % Si) or two (I-C and C-P for 1.04 and 1.42 at. % Si) transitions and not three, associated with the P-I-C-I sequence, as suggested by Mizuki *et al.*[3] We conclude that the reentrant feature of the magnetic phase diagram suggested by Mizuki *et al.*[3] is not detected in α-T measurements of polycrystalline Cr-Si alloys. This is in agreement with previous work of Suzuki.[2]

The $\Delta L/L$-T curves of the Cr-Si alloys and of $Cr_{95}V_5$ were used to determine[4,5] the mangetovolume, $\Delta\omega(T)$, for each Cr-Si alloy. Typical examples are shown in Fig. 1(b).

All the samples display large magnetic effects in the bulk modulus, B, when cooled from high temperatures. Very large ultrasonic attenuation was observed in the alloys with 0.90, 1.04, 1.42, 1.79, and 3.43 at. % Si near their Néel temperatures, to such an extent that the ultrasonic echoes were completely lost near T_N so that B could not be measured for these alloys in a certain temperature range near the transition temperature. Typical examples are shown in Fig. 1(c). The B-T curves display anomalies of magnetic origin only at T_N and not at the I-C transition temperature T_{IC}.

Using the equation[7]

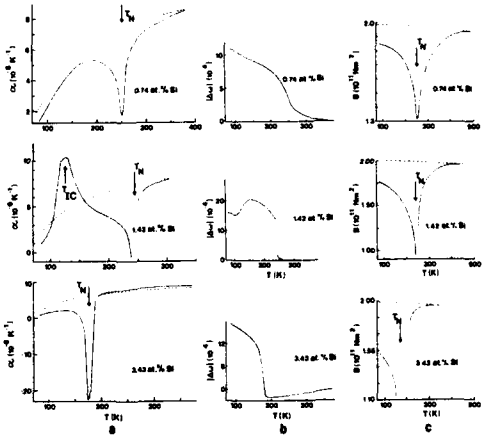


FIG. 1. (a) The variation of the coefficient of thermal expansion (α) with temperature for Cr-Si alloys with 0.74, 1.42 and 3.43 at. % Si. (b) Magnetovolume of Cr + 0.74 at. % Si, Cr + 1.42 at. % Si and Cr + 3.43 at. % Si. (c) Temperature dependence of the bulk modulus of Cr-Si alloys with 0.74, 1.42, and 3.43 at. % Si. The broken lines in (a) and (c) indicate the expected paramagnetic behavior of the Cr-Si alloys assuming (Ref. 4) that the paramagnetic states of Cr-Si and $Cr_{95}V_5$ are identical down to 0 K.

 0021-8979/88/083913-02$02.40 © 1988 American Institute of Physics

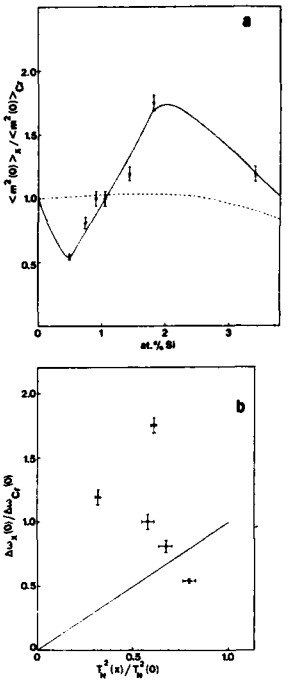


FIG. 2. (a) Comparison of the measured (Ref. 8) and calculated ratios of the mean square moments of the Cr-Si alloys relative to that of pure Cr. The broken line represents the measurements of Costa *et al.* (Ref. 8). (b) Comparison of the measurements with the equation $\Delta\omega_x(0)/\Delta\omega_{Cr}(0) < T_N^2(x)/T_N^2(\mathrm{Cr})$.

$$\Delta\omega(T) = (C/B)\langle m^2(T)\rangle, \tag{1}$$

where C is a magnetoelastic coupling constant and $\langle m^2(T)\rangle$ the mean square moment, we calculated $\langle m^2(0)\rangle_{\text{Cr-Si}}/\langle m^2(0)\rangle_{\text{Cr}}$ for each alloy from the magnetoelastic data on the assumption that C is the same for Cr and its alloys. As shown in Fig. 2(a) the calculated values compare poorly with direct neutron diffraction measurements of Costa *et al.*[8] Many dilute Cr alloys obey the following equation[7,9]:

$$\Delta\omega_x(0)/\Delta\omega_{Cr}(0) < T_N^2(x)/T_N^2(\mathrm{Cr}). \tag{2}$$

Here the $=$ sign applies to ISDW alloys and the $<$ sign to CSDW ones. Comparison between the present results and this equation is shown in Fig. 2(b) for those alloys that do not show *I-C* transitions. The results do not fit Eq. (2). Equations (1) and (2) were previously applied[4,5] successfully to other Cr alloys. Its failure in the case on Cr-Si alloys is probably due to the way in which Si affects the electronic band structure of Cr. Although it has an electron to atom ratio smaller than that of Cr, it acts as an electron donor, through a negative electron reservoir from which electrons are supplied to the magnetic bands,[1] when alloyed with Cr.

dT_N/dp values determined by Jayaraman *et al.*[10] were used to calculate the latent heats associated with the first-order *C-P* transitions from the Clausius–Clapeyron equation. The results are $L = 6.6$ J mol^{-1} and 6.3 J mol^{-1}, respectively, for $c = 1.42$ and 1.79 at. % Si which compare fairly well with direct measurements of Benediktsson *et al.*[6]

[1] Y. Endoh, J. Mizuki, and Y. Ishikawa, J. Phys. Soc. Jpn. **51**, 2826 (1982).
[2] T. Suzuki, J. Phys. Soc. Jpn. **43**, 869 (1977).
[3] J. Mizuki, J. R. D. Copley, Y. Endoh, and Y. Ishikawa, J. Phys. F **16**, L195 (1986).
[4] H. L. Alberts and J. A. J. Lourens, Phys. Rev. B **29**, 5279 (1984).
[5] H. L. Alberts and J. A. J. Lourens, J. Phys. F **15**, 2511 (1985).
[6] G. Benediktsson, L. Hedman, H. U. Åstrom, and K.V. Rao, J. Phys. F **12**, 1439 (1982).
[7] A. B. Kaiser, G. K. White, and E. Fawcett, Phys. Rev. B **11**, 7438 (1985).
[8] M. M. R. Costa, K. R. A. Ziebeck, and P. J. Brown, J. Phys. F **10**, 2793 (1980).
[9] W. C. Koehler, R. M. Moon, A. L. Trego, and A. R. Mackintosh, Phys. Rev. 151, 405 (1966).
[10] A. Jayaraman, R. G. Maines, K. V. Rao, and S. Arajs, Phys. Rev. Lett. **37**, 926 (1976).

Nonlinear magnetization in magnetostrictive amorphous metal ribbons

M. D. Mermelstein[a] and A. Dandridge
Naval Research Laboratory, Washington, DC 20375-5000

Measurements are presented of the quadratic field and stress contributions to the nonlinear magnetization in a field-annealed amorphous metal ribbon. The magnetization process is characterized by the Stoner–Wohlfarth model for a uniaxial single domain with magnetostriction. Parameter values for the model are deduced from the experimental data.

The longitudinal magnetization $M(H,\sigma)$ in a transversely field-annealed magnetostrictive metallic glass ribbon is a nonlinear function of the longitudinal field strength H and longitudinal stress σ. The linear and nonlinear contributions to the field and stress-induced magnetization fluctuations are revealed by a Taylor series expansion about the equilibrium state characterized by $(\bar{H},\bar{\sigma})$. A recent experiment has measured the linear response of the magnetization to an applied field and stress; i.e., the magnetic susceptibility and the piezomagnetic modulus.[1] In this paper, measurements of the magnetization response have been extended into the nonlinear regime to include terms quadratic in field and stress. Data are presented for the longitudinal field dependence to the non-linear susceptibilities given by $(\partial^2 M/\partial H^2)_0$, $(\partial^2 M/\partial H\,\partial\sigma)_0$, and $(\partial^2 M/\partial\sigma^2)_0$ where the zero subscript indicates the equilibrium state. These nonlinear susceptibilities are calculated from the dipole rotation model (Stoner–Wohlfarth model) and are in good agreement with the experimental results. Model parameter values are deduced from the experimental data.

The magnetization process in the transversely field-annealed ribbon is described by the Stoner–Wohlfarth model for a uniaxial single domain with magnetostriction. The domain potential energy density is

$$U = K\sin^2\theta + (3/2)\lambda_s\sigma\cos^2\theta - \mu_0 M_s H\sin\theta, \qquad (1)$$

where K is the crystal-like uniaxial anisotropy energy density, θ is the rotation angle from the easy axis, λ_s is the saturation magnetostriction, M_s is the saturation magnetization, and μ_0 is the permeability of free space. Note that H is the local magnetic field strength. Minimization of Eq. (1) with respect to the rotation angle θ yields the following expression for the longitudinal magnetization, $M = M_s\sin\theta$:

$$M(H,\sigma) = M_s(H/H'_A)[u(H+H'_A) - u(H-H'_A)] - M_s[1 - u(H+H'_A) - u(H-H'_A)], \qquad (2)$$

where the step function $u(x)$ is equal to unity for $x>0$ and equal to zero for $x<0$. The effective anisotropy field H'_A is given by $H'_A = H_A(1-\sigma/\sigma_C)$, where the crystal-like anisotropy field $H_A = 2K/\mu_0 M_s$ and the critical stress $\sigma_C = 2K/3\lambda_s$. Equation (2) demonstrates that $M(H,\sigma)$ is a nonlinear function of the applied field and stress; i.e., it is proportional to H for $|H|<H'_A$ and equal to $\pm M_s$ for $H>H'_A$ and $H<-H'_A$, respectively. Furthermore, the magnetization is inversely proportional to H'_A. The small field response is obtained by expanding $M(H,\sigma)$ about the equilibrium state:

$$M(H,\sigma) = \bar{M} + \left(\frac{\partial M}{\partial H}\right)_0 H + \left(\frac{\partial M}{\partial\sigma}\right)_0\sigma + \frac{1}{2}\left(\frac{\partial^2 M}{\partial H^2}\right)_0 H^2 + \left(\frac{\partial^2 M}{\partial H\,\partial\sigma}\right)_0 H\sigma + \frac{1}{2}\left(\frac{\partial^2 M}{\partial\sigma^2}\right)_0\sigma^2 + \ldots, \qquad (3)$$

where $\bar{M} = M(\bar{H},\bar{\sigma})$. The coefficients of the linear and nonlinear terms in this expansion are determined by evaluating the appropriate partial derivatives of Eq. (2). These susceptibilities are found to be

$$\left(\frac{\partial M}{\partial H}\right)_0 = \left(\frac{M_s}{\bar{H}'_A}\right)[u(\bar{H}+\bar{H}'_A) - u(\bar{H}-\bar{H}'_A)], \qquad (4a)$$

$$\left(\frac{\partial M}{\partial\sigma}\right)_0 = \left(\frac{3\lambda_s\bar{H}}{\mu_0\bar{H}'^2_A}\right)[u(\bar{H}+\bar{H}'_A) - u(\bar{H}-\bar{H}'_A)], \qquad (4b)$$

$$\left(\frac{\partial^2 M}{\partial H^2}\right)_0 = \left(\frac{M_s}{\bar{H}'_A}\right)[\delta(\bar{H}+\bar{H}'_A) - \delta(\bar{H}-\bar{H}'_A)], \qquad (4c)$$

$$\left(\frac{\partial^2 M}{\partial H\,\partial\sigma}\right)_0 = \left(\frac{3\lambda_s}{\mu_0\bar{H}'^2_A}\right)[u(\bar{H}+\bar{H}'_A) - u(\bar{H}-\bar{H}'_A)] - \left(\frac{3\lambda_s}{\mu_0\bar{H}'_A}\right)[\delta(\bar{H}+\bar{H}'_A) + \delta(\bar{H}-\bar{H}'_A)], \qquad (4d)$$

$$\left(\frac{\partial^2 M}{\partial\sigma^2}\right)_0 = \left(\frac{18\lambda_s^2\bar{H}}{\mu_0^2 M_s\bar{H}'^3_A}\right)[u(\bar{H}+\bar{H}'_A) - u(\bar{H}-\bar{H}'_A)] + \left(\frac{9\lambda_s^2}{\mu_0^2 M_s\bar{H}'_A}\right)[\delta(\bar{H}+\bar{H}'_A) - \delta(\bar{H}-\bar{H}'_A)], \qquad (4e)$$

where the Dirac delta function $\delta(x) = du(x)/dx$. Equations (4a) and (4b) define the free magnetic susceptibility χ_0^σ and the piezomagnetic modulus d^H, respectively. The remaining coefficients describe the quadratic contributions of the field and stress to the magnetization fluctuations.

An elliptically shaped sample was cut from Allied Corp. 2605-S2 material and subsequently field annealed for 1 h along the minor axis in a 10^5 A/m field at 400 °C. The sample has major and minor axes of 5.1 and 1.3 cm, respectively, and a thickness of approximately 25 μm. The field- and stress-induced magnetization fluctuations were measured with a centrally located 3-mm-long pick-up coil having N turns as described in Ref. 1. An oscillating field of local amplitude H_0 and frequency ω_H was applied to the ribbon along with an oscillating stress of amplitude σ_0 and frequency ω_σ. The field is supplied by a solenoid and the stress is generated by a resonating piezoelectric plate. The magnetization fluc-

[a] Also at Geo-Centers, Inc., Newton Centre, MA.

 0021-8979/88/083915-03$02.40 © 1988 American Institute of Physics

tuations, as measured by the electromotive force (emf) developed across the pick-up coil, was measured as a function of the applied equilibrium field strength. Each contribution expressed by Eqs. (4a)–(4e) was measured individually by referencing the lock-in amplifier to the appropriate driving frequency. Hence, there are six contributions to the emf:

$$\mathscr{E}(\omega_H) = NA\omega_H\left[1+\left(\frac{\partial M}{\partial H}\right)_0\right]\mu_0 H_0 \sin\omega_H t + NA'\omega_H\mu_0 H_0^{\rm ex}\sin\omega_H t, \tag{5a}$$

$$\mathscr{E}(\omega_\sigma) = \mu_0 NA\omega_\sigma\left(\frac{\partial M}{\partial\sigma}\right)_0\sigma_0\sin\omega_\sigma t, \tag{5b}$$

$$\mathscr{E}(2\omega_H) = \frac{1}{2}NA\omega_H\left(\frac{\partial^2 M}{\partial H^2}\right)_0\mu_0 H_0^2\sin 2\omega_H t, \tag{5c}$$

$$\mathscr{E}(\omega_\sigma\pm\omega_H) = \frac{1}{2}NA(\omega_\sigma\pm\omega_H)\times\left(\frac{\partial^2 M}{\partial\sigma\,\partial H_0}\right)_0\mu_0 H_0\sigma_0\sin(\omega_\sigma\pm\omega_H)t, \tag{5d}$$

$$\mathscr{E}(2\omega_\sigma) = \frac{1}{2}NA\omega_\sigma\left(\frac{\partial^2 M}{\partial\sigma^2}\right)_0\mu_0\sigma_0^2\sin 2\omega_\sigma t, \tag{5e}$$

where $H_0^{\rm ex} = 14$ A/m is the external field amplitude, A is the ribbon cross-sectional area, and A' is the cross-sectional area

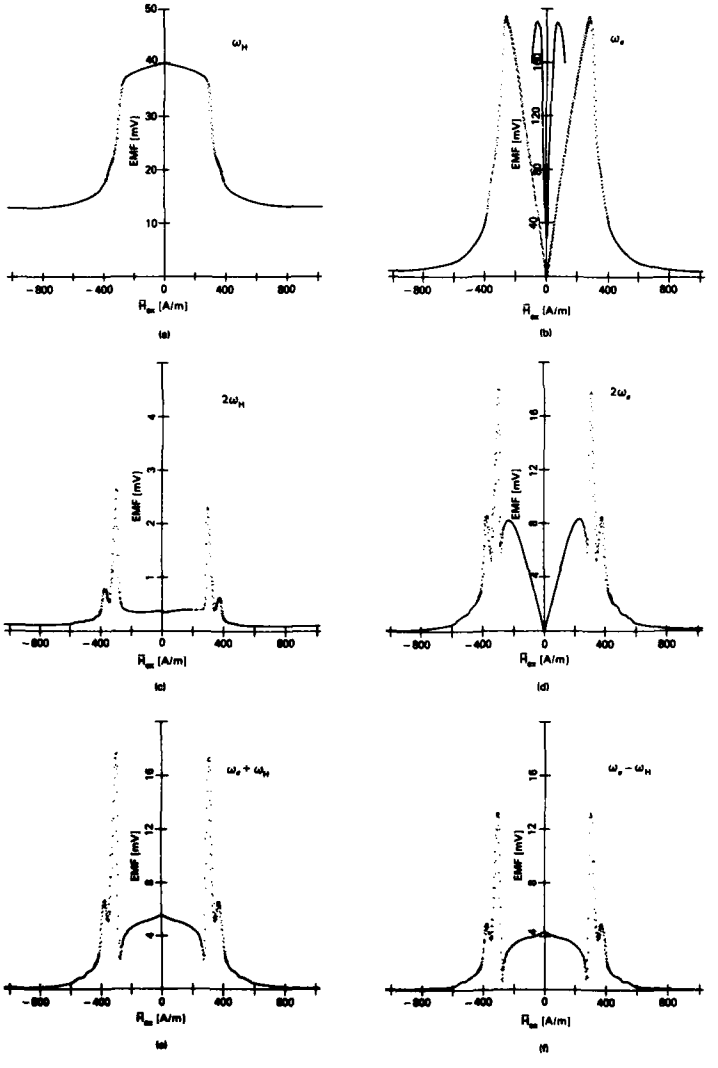


FIG. 1. Digital plots of the emf magnitude generated in the 200-turn pick-up coil in response to linear and quadratic driving of the magnetostrictive ribbon by a longitudinal magnetic field and longitudinal stress. The field frequency $\omega_H/2\pi = 3.0$ kHz and the stress frequency $\omega_\sigma/2\pi = 22$ kHz. (a) Linear response to field driving. (b) Linear response to stress driving. The solid line for the 1.0-mm sample corresponds to 50-mV full scale. (c) Harmonic response to field driving. (d) Harmonic response to stress driving. (e) Nonlinear response at $\omega_\sigma + \omega_H$ to stress and field driving. (f) Nonlinear response at $\omega_\sigma - \omega_H$ to stress and field driving.

of the pick-up coil that is excluded by the ribbon. The results of these experiments are presented in Fig. 1. Shown in Figs. 1(a) and 1(b) are the magnetic susceptibility and piezomagnetic modulus, respectively. The measured susceptibility exhibits the general features presented by Eq. (4a). It is relatively flat for external longitudinal fields approaching an external anisotropy field $[\overline{H}'_A]_{ex} \simeq 270$ A/m and rapidly falls to a nearly constant level for $|\overline{H}| > [\overline{H}'_A]_{ex}$. This offset is due to the flux contained with the excluded area A'. The local field strength is related to the externally applied field strength by $H = n H_{ex}$ where the factor $n < 1.0$ reflects the reduction in local field due to the demagnetization field. The product $n\chi_0^\sigma$ is most easily computed from the ratios of the cross-sectional areas ($A'/A = 880$) and the ratio of the emf generated by the flux in the respective areas: $n\chi_0^\sigma = (\mathscr{E}_A/\mathscr{E}'_A)\ (A'/A)$. It is evaluated to be $n\chi_0^\sigma \simeq 1.9\times 10^3$. Figure 1(b) illustrates the field dependence to the piezomagnetic modulus. It increases in an approximately linearly fashion until it peaks at $\sim$280 A/m. The solid line in Fig. 1(b) is the piezomagnetic modulus of a field-annealed sample of equal length and a 1.0-mm width. This sample exhibits a peak in the piezomagnetic modulus at an applied field of $\sim$60 A/m. It is assumed that the tangential field applied to the narrow sample is essentially continuous in the central 3-mm length enclosed by the pick-up coil. Therefore, the field value corresponding to this peak is taken to be equal to the local anisotropy field; i.e., $\overline{H}'_A \simeq 60$ A/m. A demagnetizing ratio of $n \simeq 0.22$ for the wider sample may be inferred from this measurement. This implies a susceptibility: $\chi_0^\sigma = 8.6\times 10^3$. The harmonic response of the field-driven magnetization oscillations is presented in Fig. 1(c). The dipole rotation analysis predicts that this susceptibility vanishes except for the presence of delta function responses (of opposite sign) occuring at $\pm\overline{H}'_A$. The measured response for $|\overline{H}_{ex}| < [\overline{H}'_A]_{ex}$ is reduced by two orders of magnitude compared to the linear susceptibility and is taken to be essentially zero. The two prominent peaks appearing at $\pm\overline{H}'_A$ verify the presence of the delta functions in the harmonic response. Furthermore, the phase output of the lock-in amplifier demonstrated that these two peaks are of opposite sign. The minor peaks occuring at approximately $\pm\overline{H}'_A$ may be associated with a partial volume exhibiting a slightly larger anisotropy field. Figure 1(d) illustrates the harmonic response of the stress-driven magnetization oscillations. The calculated response is given by Eqs. (4e) and (5e). For $|\overline{H}_{ex}| < [\overline{H}'_A]_{ex}$, the data is proportional to $\overline{H}$ as predicted by the rotation model. The ratio of the stress amplitude to the critical stress may be determined by computing the ratio of the slope $\Delta\mathscr{E}(2\omega_\sigma)/\Delta\overline{H}_{ex}$ to the slope $\Delta\mathscr{E}(\omega_\sigma)/\Delta\overline{H}_{ex}$. This calculation yields a fractional stress amplitude of $\sigma_0/\sigma_C \simeq 0.19$. As the applied field approaches the anisotropy field, the harmonic response rolls off and then displays the delta function responses of opposite sign at $\pm\overline{H}'_A$. Hence, the major features of the stress-driven harmonic response is in agreement with the analysis. Figures 1(e) and 1(f) exhibit the two mixed susceptibilities $(\partial^2 M/\partial H\,\partial\sigma)_0$ appearing at $\omega_\sigma \pm \omega_H$, respectively. Note that the linear susceptibility χ_0^σ is replicated (with a scaling factor) for $|\overline{H}_{ex}| < [\overline{H}'_A]_{ex}$ as predicted by the model. In this case the two delta function responses are of the same sign and opposite to that of the zero field response. This behavior was verified by the lock-in amplifier phase output.

In conclusion, measurements of the magnetization response have been extended to include terms quadratic in the driving field and stress. These response functions, as well as the linear susceptibilities, are adequately characterized by the dipole rotation model for a magnetostrictive domain. Prominent peaks were observed in the nonlinear response functions which corresponds to the discontinuous change in the magnetic susceptibility at the anisotropy field. Ideally, these peaks would be represented by the Dirac delta function. However, the experimental data reveals a distinct linewidth which is attributed to a distribution in the local anisotropy field. (The linewidth may also be due to the inhomogeneous demagnetizing field.) This distribution may be expressed quantitatively by using a Gaussian distribution representation for the delta function:

$$\delta(\overline{H} - \langle H_A\rangle) \simeq \frac{1}{\sqrt{2\pi}}\frac{1}{H_A^{rms}}\exp\left(-\frac{(\overline{H} - \langle H_A\rangle)^2}{2H_A^{rms}}\right), \tag{6}$$

where $\langle H_A\rangle$ is the mean anisotropy field and H_A^{rms} is the standard deviation. This expression is valid for $H_A^{rms} \ll \langle H_A\rangle$. The experimental data indicates a standard deviation for the local anisotropy field of 4.5 A/m. This result is in good agreement with independent measurements on identically prepared samples of the same material.[2] The magnetic susceptibility and anisotropy field measurements imply a saturation magnetization of $M_s = 0.6\times 10^6$ A/m which is approximately half the value ($M_s = 1.2\times 10^6$ A/m) reported by the manufacturer.[3] This discrepancy may reflect the rather large moment distribution occurring in the ribbon at low field strengths.[4]

[1] M. D. Mermelstein, K. Doty, and A. Dandridge IEEE Trans. Magn. MAG-23, 3512 (1987).
[2] F. Bucholtz, K. P. Koo, A. Dandridge, and G. H. Sigel, Jr., J. Magn. Magn. Mater. 54–57, 1607 (1986).
[3] Allied Corporation, Parsippany, NJ.
[4] M. Melamud, L. J. Swartzendruber, L. G. Bennett, J. Cullen, and M. Wun-Fogle, J. Appl. Phys. 61, 3644 (1987).

Improved calculations of magnetoelastic properties in collinear metamagnets

J. A. Tuszyński[a)]
Department of Physics, Memorial University of Newfoundland, St. John's, Newfoundland A1B 3X7, Canada

Metamagnets such as Mn_3GaC, Fe-Rh, $Mn_{2-x}Cr_xSb$, and $Mn_{1-x}Cr_xSb$ exhibit strong magnetoelastic couplings via strain dependence of exchange integrals. The purpose of this paper is to improve the calculations of the relevant elastic and magnetic ensemble averages for model Hamiltonians using some novel non-Gaussian approximations. The results derived are applicable to a wide range of magnetically ordered spin systems placed on anharmonic crystal lattices in the presence of an exchange-striction mechanism. It is found that the commonly invoked polynomial series expansions for the temperature dependence of the displacement and magnetization are valid only at sufficiently low temperatures. At significantly higher temperatures exponential series expansions are found to be more appropriate. Intermediate temperature ranges involve special functions of the parabolic cylinder type.

I. INTRODUCTION

The phenomenon of magnetostriction is a manifestation of the strain component's ϵ dependence on the magnitude and direction of an externally applied magnetic field $\mathbf{h}$.[1] This has been observed in a very large number of magnetically ordered substances including metamagnets. The strength of this effect is measured by the coefficient of magnetostriction $\lambda \equiv [\epsilon(\mathbf{h}) - \epsilon(0)]/\epsilon(0)$, which, through the thermodynamic Maxwell relations, is related to the dependence of bulk magnetization $\mathbf{M}$ on the stress component σ that is conjugate to ϵ: $(\partial \mathbf{M}/\partial\sigma)_{\mathbf{h}} = (\partial\lambda/\partial\mathbf{h})_{\sigma}$. Depending on the substance and the experimental conditions, λ may be positive as well as negative, and is usually a highly anisotropic tensor quantity. By and large, for small $\mathbf{h}$, λ is a nearly linear function of $\mathbf{h}$, becoming nonlinear and reaching saturation values as $\mathbf{h}$ increases. As the stress σ is increased, λ markedly decreases and a similar trend prevails for the temperature variation. It is commonly accepted that for small values of magnetization the magnetoelastic effects are predominantly caused by the strain dependence of magnetocrystalline anisotropy while for $\mathbf{M}$ close to its saturation value, they are caused by the strain dependence of the exchange constants. Exchange striction plays an important role in second-[2] and first-order[3] phase transitions from the ferromagnetic (F) or the antiferromagnetic (A) phase to the paramagnetic (P) phase. For example, rare-earth–Al_2 compounds[4] have both positive (Dy, Ho) and negative (Gd, Tb) strain derivatives of molecular exchange constants close to 0 K. Exchange striction is also at play in a variety of metamagnetic transitions. In Fe-Rh, a temperature-induced A→F transition at $T_M \cong 350$ K has been observed[5] together with a fairly linear uniaxial thermal expansion of the lattice and a jump of $\Delta\epsilon/\epsilon \cong +0.35\%$ at T_M. This has been explained[6] assuming the so-called exchange inversion, which means that the exchange constant is a linear function of strain which goes through 0 at T_M. The $Mn_{2-x}Cr_xSb$ compounds also exhibit a spontaneous A→F transition whose mechanism involves a quadratic dependence of the exchange constant on strain.[7] In Mn_3GaC a spontaneous A→F transition at $T_M \cong 150$ K has been observed[8] together with a uniform quadratic thermal expansion of the lattice and a volume contraction of $\Delta\epsilon/\epsilon \cong -0.45\%$ at T_M. This negative volume jump has recently been explained[9] using a quadratic expansion of the exchange constant in terms of ϵ and an inclusion of thermal fluctuations. The $Mn_{1-x}Cr_xSb$ compounds undergo transitions between noncollinear ferromagnetic (NF) phases and the A phase and the measured[10] λ is positive or negative depending on x. This exchange-striction mechanism still awaits theoretical explanation.

The purpose of this paper is to provide a formalism to describe exchange-striction-originated magnetoelastic effects in a number of magnetically ordered substances (especially collinear metamagnets) over a wide range of temperatures T, applied magnetic fields, and stresses. This model is an extension of earlier ideas on the subject.[6,7,9] Due to space limitations of this publication, only the main results will be presented in this paper.

II. THE MODEL AND THE METHOD

Consider the following mean field Hamiltonian for a two-sublattice spin system with sublattice magnetizations $\mathbf{M}_1$ and $\mathbf{M}_2$, respectively, placed on an anharmonic crystal lattice in the presence of an external magnetic field $\mathbf{h}$ and an applied stress σ,

$$H = H_L + H_M, \tag{1}$$

where the magnetic part of the Hamiltonian is

$$H_M = B_2(M_1^2 + M_2^2) B_4(M_1^4 + M_2^4) A_2 \mathbf{M}_1\cdot\mathbf{M}_2 + A_4(\mathbf{M}_1\cdot\mathbf{M}_2)^2 + \mathbf{M}_1\cdot\mathbf{h} + \mathbf{M}_2\cdot\mathbf{h}, \tag{2}$$

and the lattice part of the Hamiltonian is

$$H_L = T + \sum_{k=2}^{4} C_k \epsilon^k - \sigma\epsilon, \tag{3}$$

[a)] Present address: Department of Physics, University of Alberta, Edmonton, Alberta T6G 2J1, Canada.

 0021-8979/88/083918-03$02.40 © 1988 American Institute of Physics

and T is the classical kinetic energy of the crystal. We further assume that the sublattices are equivalent, i.e., that $M_1 = M_2$ and $\mathbf{M}_1 \cdot \mathbf{M}_2 = M^2 \cos\phi$. Moreover, magnetoelastic couplings are included by expanding the intrasublattice and intersublattice exchange constants in power series as[7,9]

$$B_2 \cong B_{20} + B_{21}\epsilon + B_{22}\epsilon^2 + \cdots$$

and

$$A_2 \cong A_{20} + A_{21}\epsilon + A_{22}\epsilon^2 + \cdots,$$

respectively. It is also assumed that the magnetoelastic part of the Hamiltonian can be considered a small perturbation, so that the method of calculating statistical averages outlined in Ref. 9 can be used in this paper. This yields the following values of the effective stress σ_e and the effective elastic constants of the crystal lattice:

$$\sigma_e = \sigma - \langle M^2 \rangle (A_{21}\langle \cos\phi \rangle + B_{21});$$

$$c_2 = C_2 + \langle M^2 \rangle (A_{22}\langle \cos\phi \rangle + B_{22});$$

$$c_3 = C_3; \quad c_4 = C_4.$$

The effective exchange constants of the spin system are similarly found as

$$a_2 = A_{20} + A_{21}\langle \epsilon \rangle + A_{22}\langle \epsilon^2 \rangle + \cdots;$$

$$b_2 = B_{20} + B_{21}\langle \epsilon \rangle + B_{22}\langle \epsilon^2 \rangle + \cdots.$$

Here $\langle \ldots \rangle$ denotes taking an average of a physical quantity over the corresponding part of the ensemble.[9] The presence of the A_{22} term in a_2 is crucial to the explanation of the long-standing controversy[9] over the possibility of a lattice contraction at T_M. Close to T_M the exchange inversion takes place through $a_2 \cong a(T - T_M)$ and for $a > 0$ the transition is F→A while for $a < 0$ the transition is A→F. In the vicinity of the order-disorder temperature T_t there is also an exchange inversion for the resultant second-order exchange constant $d_2 = b_2 + \langle \cos\phi \rangle a_2 \cong b(T - T_t)$ where $T_t = T_c$ for $a < 0$ and $T_t = T_N$ for $a > 0$. Moreover, if $A_4 > 0$, an NF phase may exist around T_M.

III. THE RESULTS

The model and the method described in Sec. II have been recently applied to collinear metamagnets using the Gaussian approximation as a way of calculating ensemble averages.[9] This approach, however, is adequate only under a restricted set of conditions, in particular, at high temperatures and outside of the immediate vicinity of the transition temperature. Here, we have extended it by using novel non-Gaussian integrals[11] which lead to fast convergence and analytical properties in the entire range of physical parameters. The only limitations left are those due to the mean field approximation (MFA) and the neglect of quantum effects. The average displacement is then found to be

$$\langle \epsilon \rangle \cong -\beta [\mu_2 \sigma_e + (c_3 + \beta^2 \sigma_e^3/6)\mu_4]/ \{1 + \beta^2 \sigma_e [\sigma_e \mu_2 + (c_3 + \beta^2 \sigma_e^3/12)\mu_4]/2\}, \quad (4)$$

and the average of the displacement squared is

$$\langle \epsilon^2 \rangle \cong (\mu_2 + \beta^2 \sigma_e^2 \mu_4/2)/ \{1 + \beta^2 \sigma_e [\sigma_e \mu_2 + (c_3 + \beta^2 \sigma_e^3/12)\mu_4]/2\}, \quad (5)$$

where

$$\mu_2 = D_{-3/2}(x)[6\sqrt{2\beta c_4} D_{-1/2}(x)]^{-1},$$

$$\mu_4 = 3D_{-5/2}(x)[40\beta c_4 D_{-1/2}(x)]^{-1},$$

and $D_{-\nu}$ is the parabolic cylinder function[12] of x where $x = c_2\sqrt{\beta/2c_4}$. For the plot of μ_k $(k = 2,4)$ as a function of x, see Fig. 1. At low temperatures (i.e., for $x \gg 1$), $\mu_k \propto x^{-k/2}$ which leads to a polynomial temperature behavior for both $\langle \epsilon \rangle$ and $\langle \epsilon^2 \rangle$ whose explicit form has been shown in Ref. 9. On the other hand, at high temperatures (i.e., for $x \ll 1$), we find that $\mu_k \propto \exp(-\sqrt{k/2}x)$ which leads to a combination of products of exponential terms with integer and half-integer powers of T for both $\langle \epsilon \rangle$ and $\langle \epsilon^2 \rangle$.

It should also be noted that, through the dependence of c_2 on $\langle \cos\phi \rangle$, the value of x changes rather abruptly as T crosses T_M. For example, since for Mn_3GaC (Refs. 8 and 9). $A_{20} > 0$, $A_{21} > 0$, and $A_{22} < 0$, and $\langle \cos\phi \rangle$ changes from -1 to $+1$ at T_M as the sample is heated up, one sees an increase of σ_e, a decrease of c_2, and increases of μ_2, μ_4, and $\langle \epsilon^2 \rangle$, and eventually a contraction of $\langle \epsilon \rangle$ which agrees with experimental observations. Moreover, it follows that x diminishes in the F phase, making the plot of $\langle \epsilon \rangle$ as a function of T more curved than in the A phase (as a result of x getting closer to the exponential regime of $x \approx 0$).

It is obvious that the external magnetic field affects the value of $\langle \epsilon \rangle$. In the vicinity of T_M, the effect of h on $\langle \epsilon \rangle$ is mainly felt through the reorientation between sublattices, i.e., through the dependence of $\langle \cos\phi \rangle$ on h. This can be further analyzed by replacing the mean value $\langle \cos\phi \rangle$ with the most probable value $\overline{\cos\phi}$ to get the relationship between $\overline{\cos\phi}$ and h as either $\overline{\cos\phi} = 1$ or

$$\Gamma^2 \overline{\cos\phi}^3 + \Gamma(2 + \Gamma)\overline{\cos\phi}^2 + (1 + 2\Gamma)\overline{\cos\phi} = 1 - \Delta,$$

where $\Gamma = 2A_4 M^2/A_2$ and $\Delta = h^2/A_2^2 M^2$. To the lowest order of approximation then, the coefficient of magnetostriction can be calculated to be

$$\lambda \cong (1 + \overline{\cos\phi})/(B_{21}/A_{21} - 1). \quad (6)$$

It is clear that λ virtually vanishes in the A phase for which $\overline{\cos\phi} = -1$. Since in Mn_3GaC, $B_{21} > 0$, $A_{21} > 0$, and $B_{21} > A_{21}$, it can be concluded that λ is positive and increases rapidly to its saturation value in the F phase for $\overline{\cos\phi} = 1$

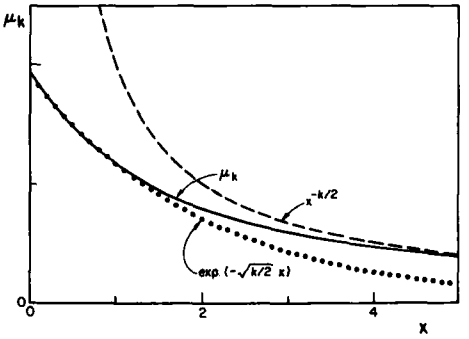


FIG. 1. Plot of μ_k $(k = 2,4)$ as a function of $x = c_2\sqrt{\beta/2c_4}$ and a comparison with the functions $x^{-k/2}$ and $\exp(-\sqrt{k/2}x)$.

during a field-induced A→F transformation in the vicinity of T_M.

Close to T_t, however, both μ_2 and μ_4 depend on h through a strong dependence of $\langle M \rangle$ on h. The latter relationship is rather complicated, but replacing the mean value $\langle M \rangle$ with the most probable value $\bar{M}$, a cubic equation for $\bar{M}$ as a function of h is obtained:

$$d_2\bar{M} + 2d_4\bar{M}^3 = \mathrm{h}\langle\cos(\phi/2)\rangle,$$

where d_2 is defined at the end of Sec. II and $d_4 = B_4 + A_4\langle\cos^2\phi\rangle$. In order to minimize the energy, the direction of h is taken to bisect the angle ϕ. This, again, leads to the insensitivity of M to h in the A phase, resulting in a near-zero value of λ. For low fields and T close to T_c, $\bar{M} \sim \mathrm{h}^{1/\delta}$ where $\delta = 3.0$ within the MFA and, as a result, the dominant behavior of λ is

$$\lambda \sim \mathrm{h}^{2/\delta} \exp(-\alpha \mathrm{h}^{2/\delta}),$$

where α is a temperature-dependent coefficient. As h increases, saturation effects set in and λ tends to a constant value.

Using the same technique we have also calculated the average sublattice magnetization and the average of $\cos\phi$. Preliminary results indicate that for temperatures removed from T_t, $\langle M \rangle$ tends to its maximum at $T = 0$ K according to a $|T - T_t|^{1/2}$ power law and it slowly decays according to a $[T/(T - T_t)]^{1/2}$ power law to zero achieved at a temperature above T_t. In the neighborhood of T_t, $\langle M \rangle$ grows exponentially immediately below T_t and decays exponentially just above T_t. We have found that in the high-temperature regime $\langle\cos\phi\rangle$ has the opposite (correct) sign as compared to the sign of A_2. However, the value of $\langle\cos\phi\rangle$ changes continuously with temperature indicating a lack of perfect compensation between the sublattices in the A phase, in agreement with experimental data.[5–8]

A more detailed presentation of these calculations will be published separately in the near future.

ACKNOWLEDGMENT

This research has been supported by a grant from the Natural Sciences and Engineering Research Council of Canada.

[1] R. M. Bosorth, *Ferromagnetism* (Van Nostrand, New York, 1953).
[2] R. Becker, Z. Phys. **87**, 547 (1934); M. Kornetzki, Z. Phys. **98**, 286 (1936).
[3] D. S. Rodbell and C. P. Bean, J. Appl. Phys. **33**, 1037 (1962).
[4] F. Pourarian, J. Phys. Chem. Solids **41**, 123 (1980).
[5] F. de Bergevin and L. Muldawer, C. R. Acad. Sci. **252**, 1347 (1962).
[6] C. Kittel, Phys. Rev. **120**, 335 (1960).
[7] H. S. Jarrett, Phys. Rev. **134**, A942 (1964).
[8] J. -P. Bouchaud, R. Fruchart, R. Pauthenet, M. Guillot, H. Bartholin, and F. Chaisse, J. Appl. Phys. **37**, 971 (1966).
[9] J. A. Tuszyński and H. Cofta, Physica B **115**, 161 (1983).
[10] N. P. Grazhdankina, Yu S. Bersenyev, and R. I. Zainullina, Zh. Eksp. Teor. Fiz. **87**, 537 (1984).
[11] J. A. Tuszyński, M. J. Clouter, and H. Kiefte, Phys. Rev. B **33**, 3423 (1985).
[12] *Handbook of Mathematical Functions*, edited by M. Abramowitz and I. A. Stegun (Dover, New York, 1965).

Magnetovolume in fcc ferro- and antiferromagnetic 3*d*-metal alloys

M. Acet, H. Zähres, W. Stamm, and E. F. Wassermann
Tieftemperaturphysik, Universität Duisburg, 4100 Duisburg 1, West Germany

Thermal expansion measurements as a function of temperature and magnetic field were carried out on Fe-Ni-Cr and Fe-Ni-Mn alloys. The magnetic contribution to the thermal expansion was determined with respect to the paramagnetic reference samples in the Fe-Ni-Cr and Fe-Ni-Mn series. We observe a general behavior that alloys which order ferromagnetically show a positive magnetovolume effect which persists to temperatures much higher than the Curie temperature, whereas in the case of antiferromagnetic ordering the magnetovolume effect is positive below temperatures slightly higher than the Néel temperature, and negative above it.

I. INTRODUCTION

One major problem in magnetovolume phenomena that still exists is the behavior of antiferromagnetic (AF) systems which have received much less attention both theoretically and experimentally as compared to ferromagnetic (FM) systems. In this study we give attention to both types of systems and compare their magnetovolume behavior. To do this we have measured the thermal expansion, $\Delta l/l$, as a function of temperature and field of the sample systems $Fe_{80-x}Ni_xCr_{20}$ and $Fe_{50}Ni_xMn_{50-x}$ which are FM or AF depending on their composition (mixed magnetic). We have also collected some similar data from literature and presented them along with ours to have a sizable set of results that will enable us to draw some general features of magnetovolume effects in FM and AF 3*d* systems.

II. EXPERIMENT

The alloy ingots were prepared at Mannesmann Forschung and were chemically analyzed. The samples which measured 6 mm in diameter and 7 mm in length had both faces polished and were annealed at 950 °C for 15 min and then cooled in air. $\Delta l/l$ was measured as a function of temperature beween 4.2 and 300 K and as a function of field parallel to the field up to 6 T using a three-terminal capacitance cell in a variable temperature gas-flow cryostat which also incorporated a superconducting magnet. The primary (coarse) temperature control of (± 250 mK) was achieved by using helium gas flow surrounding the encapsulated capacitance cell and the fine control of (± 1 mK) by an exchange gas unit within the encapsulation. The thermal expansion coefficient $\alpha(T)$ was calculated by differentiating with respect to temperature an analytical fit to the experimental $\Delta l/l$-vs-T data.

III. RESULTS AND DISCUSSION

A. The temperature dependence of the thermal expansion coefficient

1. $Fe_{80}Ni_xMn_{80-x}$, $Fe_{65}Ni_xMn_{35-x}$, and $(Fe_{0.5}Mn_{0.5})_{100-x}Co_x$

These systems are shown in Figs. 1, 2, and 3, respectively. The samples that show AF behavior are plotted in parts (a) and those that show FM behavior are plotted in parts (b). In Figs. 1 and 2 the temperature extends to 600 K and in Fig. 3 to 1200 K. The magnetic phase diagrams are shown as insets in part (a) or part (b) where PM and SG represent the paramagnetic and spin-glass states, respectively. The continuous line in each figure represents the experimental paramagnetic reference denoted by (ref) and the arrows mark T_N or T_C whichever appropriate. The method of choosing the reference is given elsewhere.[1] Figure 1 is a combination of our present data ($T<300$ K) and that of Ref. 2 ($T>300$ K). No high-temperature data was available for the $x=10$ at. % sample. The curves in Fig. 2 were calculated from Ref.

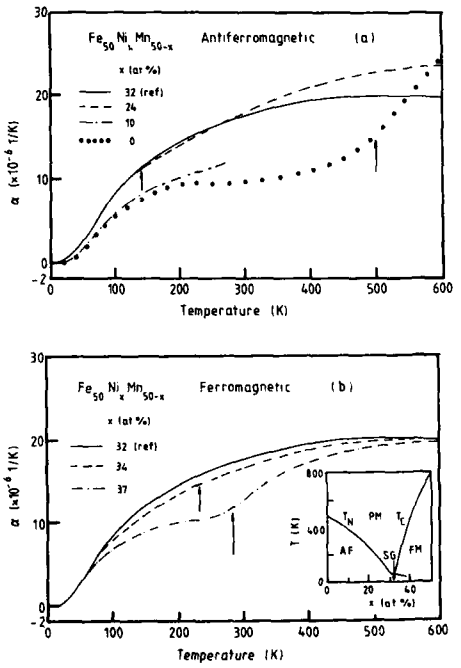


FIG. 1. α vs T for $Fe_{50}Ni_xMn_{50-x}$. (a) FM and (b) AF. Arrows mark critical temperatures. T_N which is not shown for the 10 at. % AF sample in (b) is 400 K.

 0021-8979/88/083921-03$02.40 © 1988 American Institute of Physics

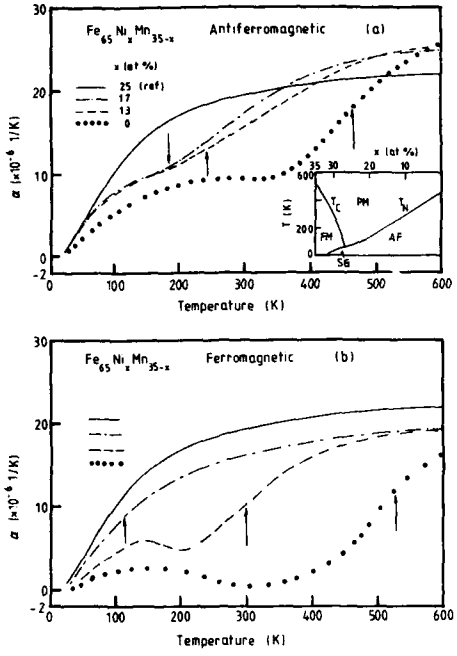


FIG. 2. α vs T for $Fe_{65}Ni_xMn_{35-x}$. (a) FM and (b) AF. Arrows mark critical temperatures.

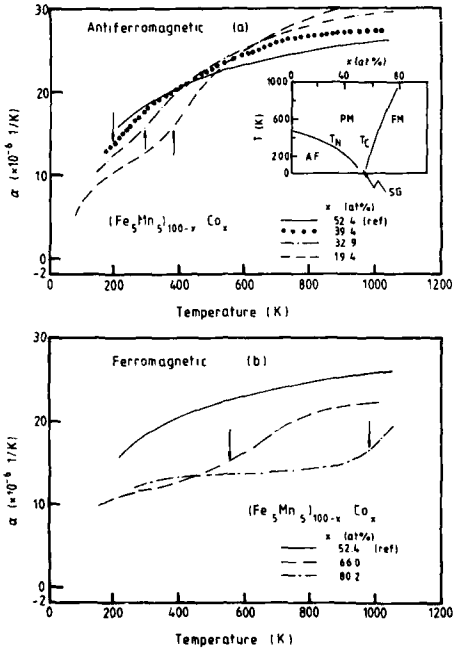


FIG. 3. α vs T for $(Fe_{0.5}Mn_{0.5})_{100-x}Co_x$. (a) FM and (b) AF. Arrows mark critical temperatures.

3 and those of Fig. 3 were obtained from Ref. 2. No low-temperature data was available for the latter.

It is seen that in the case of FM systems $\alpha(T)$ curves always lie below that of the reference both above and below T_C. The area developed between these curves increases as T_C increases. In the case of AF systems the curves lie below the reference and eventually cross it at some temperature $T > T_N$. Below the reference curve, a larger area between the curves is developed as T_N increases.

2. $Fe_{80-x}Ni_xCr_{20}$

The data for this system is seen in Fig. 4 where the vertical scale of parts (a) and (b) have been expanded about twice as that of Figs. 1–3. As seen from the phase diagram in the inset, the T_C's and T_N's of these samples are smaller than the systems presented in Figs. 1–3. Here again the curves for the FM samples lie below the reference curve as seen in part (b). In part (a) we show the data for the $x = 14$ at. % sample plotted along with the reference sample. In this figure the high-temperature data ($T > 300$ K) is from Ref. 4. The other AF samples (not shown) show similar behavior since their T_N's are nearly equal. The low T_N's (~ 20 K), on the other hand, hinder observation of any appreciable magnetovolume effect.

B. The field dependence of $\Delta l/l$ parallel to the applied field

We show in Figs. 5 and 6 the field dependence of $\Delta l/l$ at 5 K for some of the FM $Fe_{80-x}Ni_xCr_{20}$ and $Fe_{50}Ni_xMn_{50-x}$

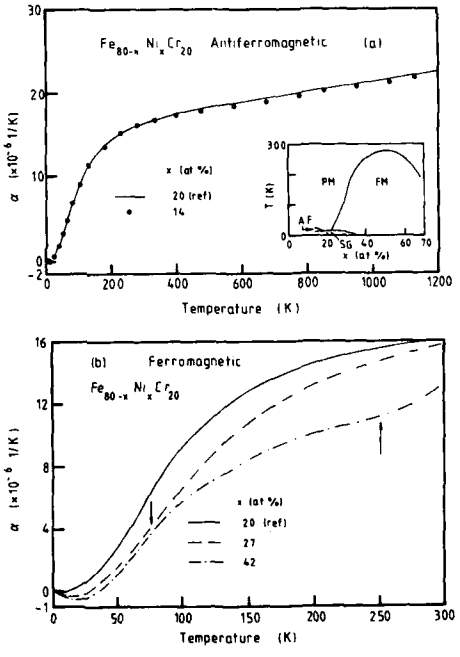


FIG. 4. α vs T for $Fe_{80-x}Ni_xCr_{20}$. (a) FM and (b) AF. Arrows mark T_C in (a).

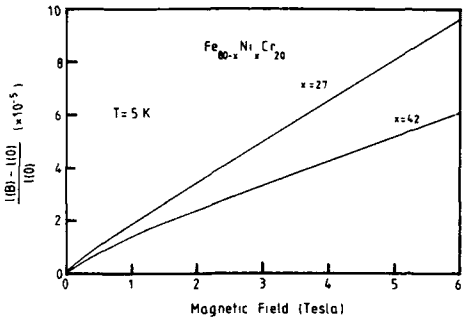


FIG. 5. Field dependence of the relative length change parallel to the field of two FM $Fe_{80-x}Ni_xCr_{20}$ samples.

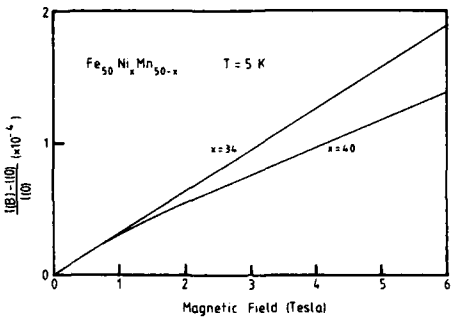


FIG. 6. Field dependence of the relative length change parallel to the field of two FM $Fe_{50}Ni_xMn_{50-x}$ samples.

samples, respectively. Within this field range the AF samples show field dependence that is in the order of 10^3 times smaller than for the FM samples and therefore are not plotted. This is also the case for the AF binary systems $Fe_{100-x}Mn_x$ and $Mn_{92}Cu_8$ which we have also studied and will be reported elsewhere.

IV. CONCLUSION

Among the systems that were measured and those which were taken from literature, three general features can be drawn from the data: (1) $\alpha(T)$ of a 3*d* ferromagnet always lies below the paramagnetic reference curve and shows positive magnetovolume irregardless of the temperature. (2) $\alpha(T)$ of a 3*d* antiferromagnet lies below the paramagnetic reference curve showing positive magnetovolume up to some temperature above T_N where it crosses it and shows negative magnetovolume. (3) $\Delta l/l$ of Af 3*d* systems measured parallel to the field show almost no field dependence as compared to the FM 3*d* systems, the factor being about 10^3 larger.

ACKNOWLEDGMENTS

We would like to thank W. Pepperhoff for his continued interest and his generosity in supplying us the samples. This work was supported by the Deutscheforschungsgemeinschaft (SFB 166).

[1]M. Acet, W. Stamm, H. Zähres, and E. F. Wassermann, J. Magn. Magn. Mater. **68**, 233 (1987).
[2]W. Bendick, H. H. Ettwig, F. Richter, and W. Pepperhoff, Z. Metallkde. **68**, 103 (1977).
[3]M. Hayase, M. Shiga, and Y. Nakamura, J. Phys. Soc. Jpn. **30**, 729 (1971).
[4]F. Richter and W. Pepperhoff, Arch. Eisenhüttenwes. **47**, 45 (1976).

Simulation of the magnetostrictive performance of Terfenol-D in mechanical devices

G. Engdahl
Electrical Power Apparatus and Systems, ASEA, Västerås, Sweden

L. Svensson
Electric Power Research Centre, Royal Institute of Technology, Stockholm, Sweden

A dynamic simulation model has been developed. Registered data from static measurements of the magnetostrictive strain for different magnetizations and mechanical stresses are used as numerical input. Easy examination of differences in dynamic performance between samples of different compositions and manufacturing methods is also possible due to a computer-aided input data handling system. The shape of the imposed magnetization can be a step, impulse, sinusoidal, or an arbitrary function. The mechanical load can be a prescribed force against the magnetostrictive element or an arbitrarily chosen mechanical impedance. The model has been verified against dynamic measurements in an experimental setup for sinusoidal and impulse magnetizations. Comparison between the model and the experimental data reveals that the model is a powerful tool for designing magnetomechanical devices based on giant magnetostrictive materials.

INTRODUCTION

Many potential applications based on giant magnetostrictive materials have been suggested. In order to technically analyze the various applications, a simulation model has been developed.[1] Registered data from static measurements of the magnetostrictive strain for different magnetizations and mechanical stresses are used as numerical input.

THE MODEL

The method of modeling the dynamic behavior of a magnetostrictive rod is based on cutting it mathematically in a finite number of sections where each of them is characterized by the state variables $x_i, \sigma_i, \epsilon_i$, (see Fig. 1). x_i's are the actual coordinates of the boundaries between the sections. σ_i are the mechanical stresses in each section. ϵ_i's are the actual compressions of each section.

The measured magnetostriction and E modulus for different magnetizations and mechanical stresses give, together with one equation for each state variable, a system which is solved by a computer program called SANDYS.

Measured quantities:

$$f = f(H), \tag{1}$$

$$E_i = E_i(H, \sigma_i) \tag{2}$$

Compression:

$$\epsilon_i = f - (x_{i+1} - x_i). \tag{3}$$

Hook's law:

$$\sigma_i = \epsilon_i E_i. \tag{4}$$

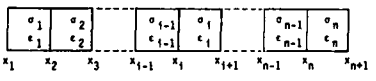


FIG. 1. Magnetostrictive rod cut in a finite number of sections, each with the state variables x_i, σ_i, and ϵ_i.

Newton's second law:

$$\sigma_{i-1} - \sigma_i = \rho d^2 \frac{d^2 x_i}{dt^2} + 2d\sqrt{E_i}\,\rho\xi \frac{dx_i}{dt}. \tag{5}$$

f is the magnetostriction (no load), E_i is the E modulus for

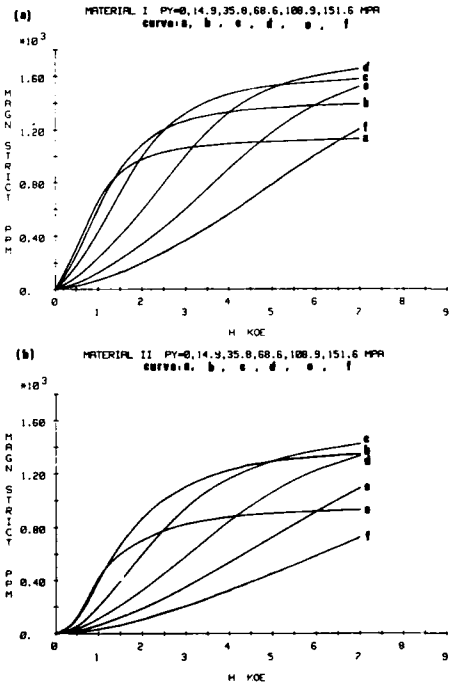


FIG. 2. Magnetostriction curves for material I (a) and material II (b). PY stands for prestress.

 0021-8979/88/083924-03$02.40 © 1988 American Institute of Physics

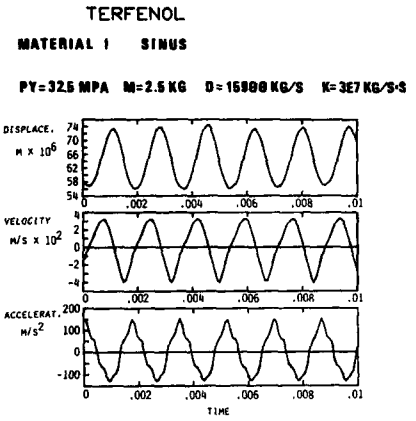


FIG. 3. Registrations of displacement, velocity, and acceleration for a sinusoidally magnetized rod of material I. M, D and K stand for mass load, damping coefficient, and spring coefficient.

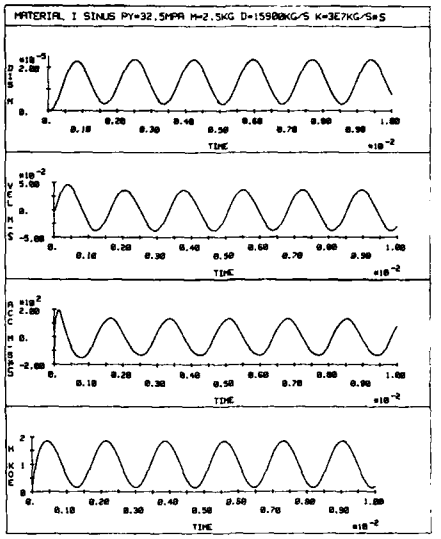


FIG. 4. Displacement, velocity, and acceleration obtained from the simulation model for a sinusoidally magnetized Terfenol-D rod of material I. The bottom curve shows the magnetizing H field.

each section, ρ is the density, d is the section length, ξ is the relative damping coefficient, and H is the magnetizing field. The shape of the imposed magnetization and the mechanical load of the rod can be chosen arbitrarily.

INPUT DATA

The input data can be represented by a set of magnetostriction curves for different mechanical stresses. In Fig. 2 some of such curves are shown for two Terfenol-D rods of different origin. The quality of the rods are not representative for the manufacturers. Instead the two different materials serve as an example of the capability of the input data handling system.

The measurements have been done in a specially designed setup monitoring the magnetostriction for magnetizations up to 7.5 kOe and stresses up to 300 MPa.

VERIFICATION OF THE MODEL

A specially designed setup for dynamic measurements of the magnetostriction of magnetostrictive rods has been used for verification of the model.[2] Figure 3 shows the displacement, velocity, and acceleration registrations for a rod of material I when it is magnetized sinusoidally. The length and diameter of the rod is 76 and 6.5 mm, respectively. Figure 4 shows the corresponding curves obtained from the simulation model for the same mechanical load, size, and magnetization. In Table I the results from the experiments and the simulation model are shown for comparison. The agreement seems to be good.

The model has also been verified when the magnetizing field is a pulse, generated from the discharge current of a capacitor.[2]

COMPARISON BETWEEN DIFFERENT TERFENOL-D RODS

As soon as static registrations of the magnetostriction of magnetostrictive rods are completed according to Fig. 2, a qualitative comparison between different rods is possible for any specific application.

In Fig. 5 the step response for 3-kOe magnetization is shown for materials I and II. In order to illustrate the jumping process between two curves in the static magnetostriction curves the mechanical load has been chosen very near a pure spring load. The viscous damping has been chosen high enough to suppress significant overshots and the mass load is representing the mass of a disk spring. In Fig. 6 a similar comparison is made when the viscous damping has been chosen low enough to allow significant oscillations.

TABLE I. Numerical comparison between displacement, velocity, and acceleration obtained from experiments and the simulation model, respectively.

	$\lvert DIS_{max} - DIS_{min} \rvert$ ($m \times 10^6$)	$\lvert VEL_{max} - VEL_{min} \rvert$ ($m/s \times 10^3$)	$\lvert ACC_{max} - ACC_{min} \rvert$ (m/s^2)
Experiments	18	72	280
Simulation model	20	74	266

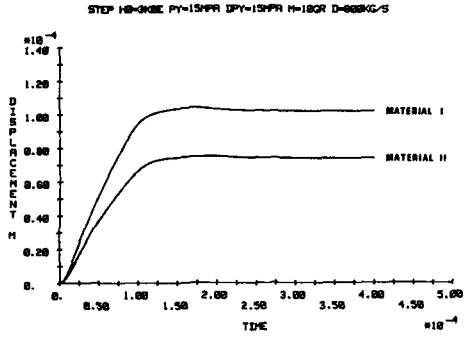


FIG. 5. Step response for 3-kOe magnetization when the damping coefficient is high enough to suppress significant overshots. DPY is the added static stress from the spring when steady state is achieved. The length and diameter of the rod is 100 and 6.5 mm respectively.

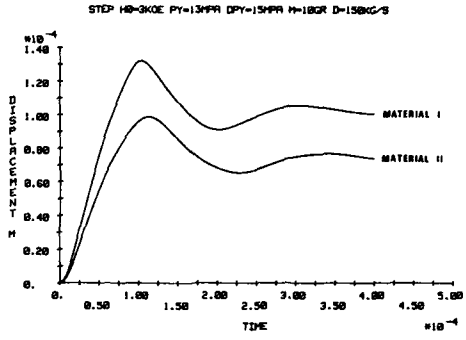


FIG. 6. Step response for 3-kOe magnetization when the damping coefficient is low enough to allow significant oscillations.

CONCLUSIONS

The measurements verify that the model can be used to estimate the performance of a rod of a specific material in different applications. This is possible in all cases where the mechanical load is a prescribed force or can be formulated mathematically. The above combined with the capability of the model to handle an arbitrary time variation of the imposed magnetization makes it a powerful tool for designing magnetomechanical devices based on giant magnetostrictive materials.

[1]G. Engdahl, Proceedings of First International Conference on Giant Magnetostrictive Alloys and Their Impact on Actuator and Sensor Technology (1986), p. 101.
[2]L. Svensson, ASEA Research and Innovation Technical Report KZES 87-010 (in Swedish) (1987).

Magnetoelastic-surface-acoustic-wave attenuation peaks in thin ferromagnetic films

D. Walikainen, R. F. Wiegert, and M. Levy
Department of Physics, University of Wisconsin-Milwaukee, Milwaukee, Wisconsin 53201

We report on the in-plane magnetic field dependence of the attenuation of 600-MHz Rayleigh-mode surface acoustic waves (SAW) propagating through rf-sputtered $Fe_{80}B_{20}$ and $Fe_{78}Si_{10}B_{12}$ and evaporated $FeNi_3$ films. The films vary in thickness from 200 to 2000 Å. The attenuation has narrow (width≈15 Oe) peaks≈25 dB/cm at fields≈30 Oe. This is qualitatively different behavior than previously reported for Ni. Since the hysteresis in these peaks is very small they may be useful in magnetically controlled SAW filters.

I. INTRODUCTION

We shall begin by briefly describing the experimental setup. Figure 1 shows the film-substrate configuration. Here we have an evaporated or sputtered magnetic film≈200 Å deposited between two interdigital transducers upon a single-crystal quartz substrate. A pulsed rf signal is applied to one of the interdigital transducers which produces a surface acoustic wave (SAW) or Rayleigh wave in the quartz substrate through piezoelectric coupling. The wave propagates along the surface where it interacts with the film. The wave is received at the other interdigital transducer where it is converted into an rf signal through piezoelectric coupling and compared with the transmitted signal. Such designs respond to a slowly ramped in-plane dc magnetic field.

There are two potential uses for these magnetically controlled SAW devices. One uses the change in sound velocity[1] accompanying this change in applied field for Doppler tracking of targets. The other uses the large attenuation associated with the field change, which has recently[2] been increased (40 to 70 dB/cm) for a change of 80 Oe in the applied in-plane magnetic field for Ni films. Using this property researchers have made[3] a multichannel filter and a nondispersive delay line with an adjustable bandwidth.

The theory[4] that we have used to understand this attenuation response assumes that the film may be modeled by a magnetization vector in the film plane. The theory uses three ideas. First, the Gilbert equation,

$$\dot{\mathbf{M}} = \gamma(\mathbf{M}\times\mathbf{H}) + G/M(\mathbf{M}\times\mathbf{M}), \tag{1}$$

accounts for the dissipation phenomenologically. Here M is the magnetization, $\dot{M}$ is the change in M with respect to time, G is the Gilbert damping parameter, γ is the magnetomechanical ratio, and H is the field "seen" by M. Second, the SAW's periodic variation of the anisotropy field through magnetoelastic coupling, provides the driving force for M. Specifically, the SAW of frequency ω and wave vector k produces a variation,

$$\Delta H_a M/2\sin^2(\theta-\psi)\exp(i\omega t) \tag{2}$$

in the free energy, where H_a is the anisotropy field and (ψ) θ is the angle (k) M makes with the external field H. Third, to model the hysteresis we used the Stoner–Wohlfarth theory for a single domain, which is represented by the astroid whose equation is (see Fig. 3)

$$h_{\text{e.a.}}^{2/3} + h_{\text{h.a.}}^{2/3} = 1, \tag{3}$$

where the h's are the in-plane field components normalized with respect to the anisotropy field and e.a. (h.a.) represents the easy (hard) axis. Using these we have an expression for the energy dissipation per cycle per unit volume,

$$E_d = \pi H_S MG\,[\Delta H_a/2\sin 2(\theta_0-\psi)]^2 \times[B^2 + H_S^2(1+G^2)]/D, \tag{4}$$

where

$$B = H\sin\theta_0 + 4\pi M, \quad H_S = \omega/\gamma, \quad \Delta H_a = \eta e,$$
$$D = [AB - H_S^2(1+G^2)]^2 + [H_S G(A+B)]^2,$$
$$A = H_a\cos[2(\theta_0-\phi)] + H\sin\theta_0,$$

e is the strain, θ_0 is the equilibrium position for M, ϕ is the angle between H_a and H, and η is the magnetoelastic coupling coefficient.

Our concern in this paper is to discuss the attenuation of rf sputtered $Fe_{80}B_{20}$ and $Fe_{78}Si_{10}B_{12}$ and evaporated $FeNi_3$ films in terms of our single domain model. Here we have varied the thickness of the films from 200 to 2000 Å to determine if there is a sharp drop in the attenuation at a critical thickness as was found for Ni.[5] No critical thickness was found.

II. EXPERIMENT

We have vacuum-evaporated films of $FeNi_3$ from W sources onto ST-cut single-crystal quartz substrates provided with interdigital transducers of 0.27-mm beamwidth to produce and receive 600-MHz Rayleigh waves and with electrical contacts to measure the resistance. The base pressure of the oil diffusion pump vacuum system was about 0.15 μTorr.

A R.D. Mathis SP310 rf sputtering system operating at

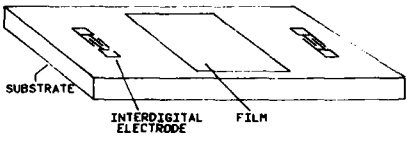


FIG. 1. Schematic of film-substrate configuration with interdigital transducers to produce and receive 600 MHz Rayleigh waves.

 0021-8979/88/083927-03$02.40 © 1988 American Institute of Physics

13.56 MHz was used to deposit thin films of $Fe_{80}B_{20}$ and $Fe_{78}Si_{10}B_{12}$. The 4-cm-diam cast disk target was mounted 10 cm above the substrate and presputtered for 90 min at a dc bias of 3 kV in an argon atmosphere of 10 mTorr.

III. RESULTS AND DISCUSSION

In an attempt to characterize our films we began to measure the magnetoresistance. Such information allows us to determine the easy axis direction, or ϕ in our theoretical expression for the energy dissipation [see Eq. (4)]. For polycrystalline samples of 3*d* ferromagnetic transition metals with low saturating fields[6] the null magnetoresistance curve may be associated with the easy axis which agrees with the hysteresis curves we obtained from our magneto-optical studies.[7] This uniaxial easy axis varied in direction from film to film between 98.5° to 112° with respect to the SAW direction, and the response maxima varied from 14 to 35 dB/cm.

The attenuation vs in-plane dc magnetic field has the same qualitative behavior for SAW propagating along the center of rf sputtered $Fe_{80}B_{20}$ and $Fe_{78}Si_{10}B_{12}$ and evaporated $FeNi_3$ films in the thickness range 200–2000 Å. Thus we need only discuss the attenuation versus in-plane dc magnetic field of one film. I shall choose an rf sputtered 200-Å $Fe_{80}B_{20}$ film as our representative.

Figure 2 shows the attenuation for an in-plane applied dc magnetic field directed 11° with respect to the propagation direction of the SAW. Here we choose such a direction since the response is not symmetric with respect to zero field, a type of behavior not observed in our Ni films. The $\pm$ fields corresponding to the maximum attenuation differ by 1.6 Oe in magnitude. Also, their maximum responses are not equal, differing by 1.6 dB/cm. The higher response corresponding to the lower field maximum, a general trend in all films.

We wish to account for such new behavior using our model. Perhaps as for cast[8] $Fe_{75}Si_{15}B_{10}$ we have high coercivity, hard rods of Fe_2B in a matrix of soft magnetic material. The Fe_2B provides a permanent magnetic layer. The asymmetry in magnitude of the $\pm$ fields corresponding to the maximum attenuation may be due to this permanent magnetic layer directed along the easy axis. Let us discuss this in terms of the single domain model. Figure 3 is the Stoner–Wohlfarth astroid. Here the field values are normalized with respect to the anisotropy field. Drawing a line in Fig. 3 along the direction of the slowly ramped field which has an easy axis component and displacing it with the reduced permanent magnetization value m we may easily verify that the intersection of this displaced line with the astroid corresponds to different switching fields. That is, the magnitude of the distance from the origin to the two intersection points are different, $h_s^- \neq h_s^+$, where s refers to the switching fields. Consider the response 90° with respect to the easy axis or the hard axis. The dotted line in Fig. 3 shows that the switching fields are equal in magnitude, $h_s' = h_s'$. The data verify this conclusion, and we shall discuss this in the next paragraph.

Figure 4 shows the Rayleigh wave attenuation versus field for our 200-Å $Fe_{80}B_{20}$ rf sputtered film. Figure 5 shows the magnetoresistance corresponding to Fig. 4. Here the dotted lines correspond to the field directed 112° with respect to the Rayleigh wave propagation direction. Notice that this is the null magnetoresistance, and thus the easy axis is directed along here. Also, this is the null attenuation direction. The solid lines correspond to a 90° rotation from this easy axis, and thus the hard axis. Figure 4 shows the Rayleigh wave attenuation versus field directed 22° with respect to Rayleigh wave propagation direction for our 200-Å $Fe_{80}B_{20}$ rf sputtered film. Here we see a response with maximum in attenuation of 30 dB/cm at fields of $\pm$ 12 Oe. If we associate the switching field with the field corresponding to the maximum attenuation then as suggested in the last paragraph the switching fields are equal in magnitude: $|12\ \text{Oe}| = |-12\ \text{Oe}|$. Figure 5 shows the corresponding magnetoresistance.

Biasing the sample to the maximum attenuation and

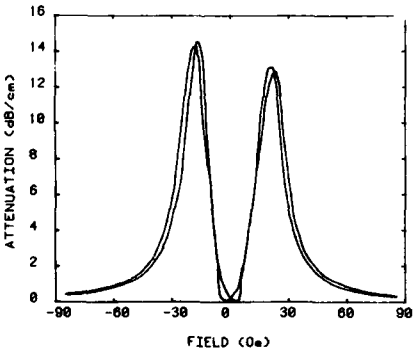


FIG. 2. Rayleigh wave attenuation vs applied field which is directed 11° with respect to the propagation direction for a 200-Å $Fe_{80}B_{20}$ rf sputtered film.

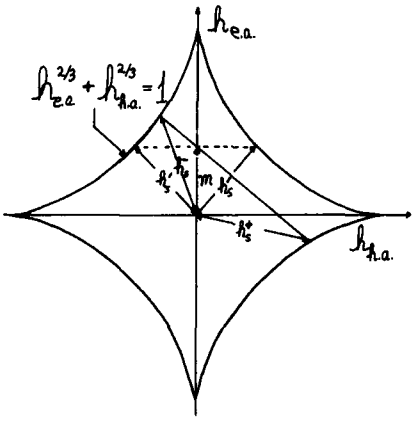


FIG. 3. Stoner–Wohlfarth astroid where the fields are normalized with respect to the anisotropy field. The solid diagonal (dotted) line corresponds to a slowly ramped dc applied magnetic field with (without) an easy axis component. The switching fields are indicated with h_s^- and h_s^+ (h_s). The reduced magnetization m is along the easy axis (e.a.). The hard axis is labeled h.a.

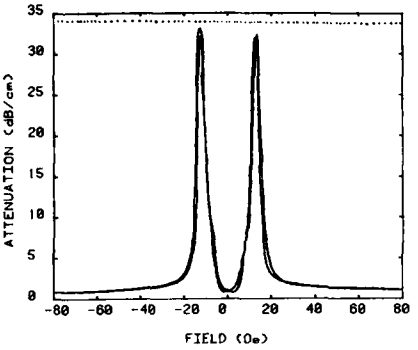


FIG. 4. Rayleigh wave attenuation vs field for an rf-sputtered 200-Å $Fe_{80}B_{20}$ film. The dotted line (solid line) is for the field directed 112° (22°) with respect to Rayleigh wave propagation direction. The dotted (solid) line corresponds to the easy (hard) axis.

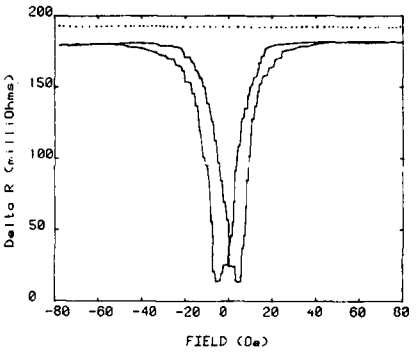


FIG. 5. Magnetoresistance vs field corresponding to Fig. 4. The dotted (solid) line corresponds to the easy (hard) axis.

varying the field $\pm$ 10 Oe we recorded no attenuation. This is important for applications where a low bias field with very little hysteresis is desirable.

We may use our theory to generate attenuation versus in-plane dc magnetic field curves similar to those in Fig. 4. Here we use the magnetoresistance data to determine the easy axis direction $\phi = 89°$, and we choose appropriate values of $G = 0.10$ and $H_a = 12$ Oe.

IV. CONCLUSION

We have provided data showing the attenuation of surface acoustic waves for rf sputtered $Fe_{78}Si_{10}B_{12}$ and $Fe_{80}B_{20}$ and evaporated $FeNi_3$ films versus in-plane dc magnetic field. We were able to account for the response using our single domain model with Gilbert damping. The thicknesses of the films ranged from 200 to 2000 Å. Currently we are annealing the samples to increase their attenuation response.

ACKNOWLEDGMENT

This research was supported by the National Science Foundation under Grant No. ECS-85 19695.

[1]D. C. Webb, D. W. Forester, A. K. Ganguly, and C. Vittoria, IEEE Trans. Magn. MAG-15, 1410 (1979).
[2]R. F. Wiegert and M. Levy, J. Appl. Phys. 61, 4270 (1987).
[3]M. Levy, R. F. Wiegert, B. R. McAvoy, H. L. Salvo, Jr., and D. Bailey, in *1985 Ultrasonics Symposium Proceedings* (85 CH 2209-5), edited by B. R. McAvoy (IEEE, New York, 1985), p. 88.
[4]I. Feng, M. Tachiki, C. Krischer, and M. Levy, J. Appl. Phys. 53, 177 (1982).
[5]R. F. Wiegert, H. Yoshida, K. J. Sun, M. Levy, H. L. Salvo, Jr., and B. R. McAvoy, J. Phys. (Paris) Colloq. C10, 737 (1985).
[6]G. Kneer, IEEE Trans. Magn. MAG-2, 747 (1966).
[7]E. R. Moog, S. D. Bader, R. F. Wiegert, D. Walikainen, and M. Levy (unpublished).
[8]J. D. Livingston, A. E. Berkowitz, and J. L. Walter, IEEE Trans. Magn. MAG-15, 1295 (1979).

A model for the effect of stress on the low-frequency harmonic content of the magnetic induction in ferromagnetic materials

M. J. Sablik, G. L. Burkhardt, and H. Kwun
Southwest Research Institute, P.O. Drawer 28510, San Antonio, Texas 78284

D. C. Jiles
Ames Laboratory, Iowa State University, Ames, Iowa 50011

A simple model used previously by the authors to explain stress variation of magnetic hysteresis is now employed to explain the effect of stress on the amplitudes of the first- and third-order harmonics of the magnetic induction signal resulting from application of an ac magnetic field of low frequency to a steel specimen. An improved expression for the effective field contribution H_σ due to stress has been derived from thermodynamic considerations.

INTRODUCTION

When a ferromagnetic material is excited by a sinusoidal magnetic field H of frequency ν, harmonic frequencies $n\nu$ (where n is an odd integer) are generated in the magnetic induction B. This generation of harmonics results from nonlinearity in the magnetic hysteresis. Even harmonics do not occur because the condition that $B(t + 1/2\nu) = -B(t)$ is not satisfied.

It has been observed[1,2] that in steel samples under uniaxial stress with stress axis parallel to the applied magnetic field, the harmonic amplitudes are generally larger when the applied stress is more positive (tension being positive, compression being negative). Thus, variation of the harmonic amplitudes is generally monotonically increasing if the stress applied to the sample is changed from compressive to tensile. In some samples under tension, however, the amplitudes may reach a maximum and then get reduced slightly as the applied tension is increased.

To account for the above phenomena, we employ a model originally used by Sablik *et al.*[3] to account for the effects of stress on hysteresis. The magnetization $M(H)$ obtained from that model is computed for a sinusoidally varying $H = H_{max} \sin \omega t$. The result is fitted by a least-squares Newton–Raphson technique[4,5] to $M(t) = m_1 \sin(\omega t + \theta_1) + m_3 \sin(3\omega t + \theta_3)$, which is the magnetization expressed in terms of the first and third harmonic components. By this method we get good agreement with the experimentally obtained[1] stress dependence of the harmonics at low frequencies (8 Hz). In other words, the domain wall pinning model[3] for $M(H,\sigma)$ can also account for the *low-frequency* behavior of the harmonic amplitudes.

FORMULATION

In accounting for the effects of stress on magnetic hysteresis, the key addition to the original theory of Jiles and Atherton[6,7] is the inclusion[3] of a stress term H_σ in the effective field contributing to the magnetization. In the paper by Sablik *et al.*,[3] it was pointed out that this field had to change sign with magnetization and hence was an odd power of the magnetization. Models with H_σ proportional to M and to M^3 were tried with reasonable success. At the end of the paper, it was suggested that a linear combination of terms in M and M^3 would be even better. For this paper, we employ

$$H_\sigma = \frac{3}{2}\left(\frac{\sigma}{\mu_0 M_s}\right)\left\{\frac{M}{M_s}\left[\lambda_1 + \frac{3}{2}\lambda_3\left(\frac{M}{M_s}\right)^2\right]\right\}, \tag{1}$$

where σ is the applied stress, M_s the saturation magnetization, μ_0 the permeability of free space, and λ_1 and λ_3 are dimensionless parameters related to the magnetostrictive response of the sample.

We can develop a better appreciation of Eq. (1) by considering

$$G = U - TS + \tfrac{3}{2}\sigma\lambda, \tag{2a}$$

$$A = G + \mu_0 HM, \tag{2b}$$

$$U = \tfrac{1}{2}\kappa M^2, \tag{2c}$$

where G and A are the Gibbs and Helmholtz free energy of the stressed magnetic sample and where T, S, and U refer to the temperature, entropy, and magnetic internal energy. The effective field in the sample is written as

$$H_e = \frac{1}{\mu_0}\left(\frac{\partial A}{\partial M}\right)_T = H + \alpha M + \frac{3}{2}\frac{\sigma}{\mu_0}\left(\frac{\partial \lambda}{\partial M}\right)_T, \tag{3}$$

with effective field constant $\alpha = \kappa/\mu_0$. We identify the stress contribution to the effective field as

$$H_\sigma = \frac{3}{2}\frac{\sigma}{\mu_0}\left(\frac{\partial \lambda}{\partial M}\right)_T, \tag{4}$$

which means that from Eq. (1),

$$\left(\frac{\partial \lambda}{\partial (M/M_s)}\right)_T = \frac{M}{M_s}\left[\lambda_1 + \frac{3}{2}\lambda_3\left(\frac{M}{M_s}\right)^2\right]. \tag{5}$$

Equation (5) is reasonable since the magnetostriction λ should be proportional to an even power of the magnetization.[3] Note that previous authors[8,9] have used $H_\sigma = (3\sigma/2\mu_0)(\lambda_s/M_s)$ as the stress contribution to the effective field, an expression derived on the basis of magnetostriction within a domain. When considering the bulk material, such an expression is not appropriate, since the bulk magnetostriction λ changes from 0 in a demagnetized state to λ_s at magnetic saturation.

Inserting the above expressions into the model previously used by us,[3,7] we obtain

$$M_{an}(H_e) = M_s f(H_e/a), \tag{6a}$$

 0021-8979/88/083930-03$02.40 © 1988 American Institute of Physics

$$\frac{dM_{\rm irr}}{dH} = \frac{M_{\rm an} - M_{\rm irr}}{(k\delta/\mu_0) - (\alpha + \alpha_\sigma^{(1)} + 3\alpha_\sigma^{(3)})(M_{\rm an} - M_{\rm irr})}, \tag{6b}$$

$$M_{\rm tot}(H) = M_{\rm irr} + M_{\rm rev} = M_{\rm irr} + c(M_{\rm an} - M_{\rm irr}), \tag{6c}$$

where

$$\alpha_\sigma^{(1)} = 3\lambda_1\sigma/(2\mu_0 M_s^2), \tag{7a}$$

$$\alpha_\sigma^{(3)} = [9\lambda_3\sigma/(4\mu_0 M_s^2)](M/M_s)^2. \tag{7b}$$

In the above, $f(H_e/a)$ is the Langevin function,[6] k is the domain wall pinning constant,[3,6,7] $\delta = \pm 1$ depending on whether H is increasing or decreasing, and c is the ratio of the initial susceptibilities of the normal ($M_{\rm tot}$) and anhysteretic ($M_{\rm an}$) magnetization. The terms $M_{\rm irr}$ and $M_{\rm rev}$ represent the irreversible and reversible contributions to the magnetization associated with domain wall translation and domain wall bending, respectively.[7]

The expression $M_{\rm tot}(H)$ is next evaluated for a sinusoidally varying magnetic field $H = H_{\max}\sin\omega t$ at successive time increments. The resulting points trace out an initial magnetization curve followed by a hysteresis loop. The points on the loop are fitted, using a least-squares Newton–Raphson fitting procedure,[4] to the expression

$$M(t) = m_1\sin(\omega t + \theta_1) + m_3\sin(3\omega t + \theta_3), \tag{8}$$

where the parameters m_1 and m_3 represent the first and third harmonic amplitudes. Only two of the four parameters m_1, m_3, θ_1, and θ_3 are free to vary in the fit. The other two are fixed by the constraints that $B_{\max} = \mu_0(H_{\max} + M_{\max})$ and that $dM/dt = 0$ for $t = \tau/4, 3\tau/4, 5\tau/4$, etc., where $\tau = 1/\nu$. Thus, the Newton–Raphson fit reduces to a two-parameter fit. The corresponding harmonic amplitudes b_1 and b_3 in B can then be computed from m_1, m_3, θ_1, and θ_3.

RESULTS

We have have compared our model to the experimental data[1] obtained from an AISI 410 stainless-steel specimen having Rockwell C Hardness 42 with a 8-Hz applied magnetic field of amplitude 80 Oe. A fit is shown in Fig. 1 for the stress variation of the harmonic amplitudes of B when $M_s = 1.35\times10^6$ A/m, $a = 2750$ A/m, $k = 1800$, $\alpha = 0.0033$, $c = 0.25$, $\lambda_1 = 0.000\,005$, and $\lambda_3 = 0.000\,014$. In Fig. 1, the harmonic amplitudes are normalized relative to their zero stress value; the normalized experimental first and third harmonic amplitudes are indicated by triangles and crosses, respectively. For positive stress, the theoretical curves are shown as dashed curves. Although these theoretical curves are approximately linear, they characteristically exhibit a greater slope for positive stress than negative stress, which is opposite to experimental behavior. In practice, it is known[10] that λ vs M varies with stress. The solid curves in Fig. 1 are for the case where a stress-dependent λ_1 is used in Eqs. (1) and (5), namely,

$$\lambda_1(\sigma) = \begin{cases} \lambda_1^{(0)}[1 - (\sigma/\sigma_t)^{1/2}], & \sigma > 0 \\ \lambda_1^{(0)}, & \sigma \le 0, \end{cases} \tag{9}$$

where $\lambda_1^{(0)} = 0.000\,005$ and $\sigma_t = 40$ ksi. This is similar to the stress dependence we have previously[3] introduced into the magnetostriction. It is seen that both theory and experiment indicate a roughly linear variation with stress, with the third-order harmonic having the larger slope. This time, however, the theoretical curves for the first and third harmonics exhibit a slightly smaller slope for positive stress than negative stress, as in experimental data, yielding a good fit.

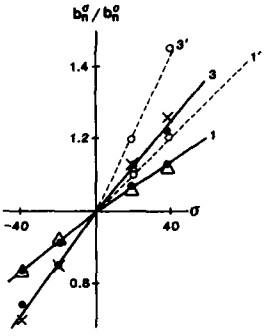


FIG. 1. First (Δ) and third (×) order harmonic amplitudes vs applied stress σ in AISI 410 steel ($R_c = 42$). The amplitudes are normalized with respect to their values at zero stress. A rough straight line to guide the eye is drawn through the solid circles computed by the theory, which uses $\lambda_1(\sigma)$ given by Eq. (9) and constants $\lambda_3 = 0.000\,014$ and $\lambda_1^{(0)} = 0.000\,005$. If $\lambda_1(\sigma)$ is instead replaced by the constant $\lambda_1^{(0)}$ then the open circles and dashed curves are obtained for positive stress, indicating that the stress-dependent $\lambda_1(\sigma)$ gives a better fit.

We have also plotted $M_{\max}/M_s$ vs stress σ in Fig. 2 for both experimental and predicted variation, using Eq. (9) and again normalizing with respect to the zero stress value. A good fit is also seen here as well. This should not be surprising since a fit to the harmonic amplitudes should also yield a fit to the total magnetization amplitude as well.

We have varied parameters a, k, α, c, and M_s and have found that to increase the spread in slopes between the first and third harmonic normalized amplitudes, one must increase α, increase c, decrease k, or decrease a. M_s does not appear to affect the relative spread in slopes.

It is also possible to change the shape of the variation of

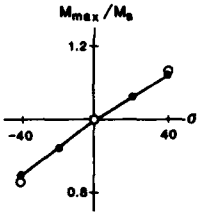


FIG. 2. Maximum value of the magnetization for an 80-Oe applied field vs applied stress σ. The theoretical magnetization values (solid circles) are normalized with respect to their zero stress values. Experimental points (○) for AISI 410 steel ($R_c = 43$) represent similarly normalized magnetic induction values.

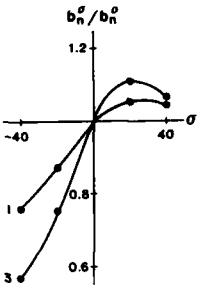


FIG. 3. Theoretical first- and third-order normalized harmonic amplitudes vs stress for $\lambda_3 = 0.000\,005$ and $\lambda_1^{(0)} = 0.000\,014$.

harmonic amplitudes with stress by changing the relative values of the constants $\lambda_1^{(0)}$ and λ_3. Figure 3 shows how it is possible with certain values of $\lambda_1^{(0)}$ and λ_3 to produce a maximum in the normalized amplitudes as tension is increased. The same variation also occurs in the magnetization and is identified with what is called the Villari reversal by Bozorth.[11]

CONCLUSION

We have demonstrated how a simple model can explain the stress variation of both the magnetization and the harmonic amplitudes in ferromagnetic steel. A thermodynamic expression for the stress contribution H_σ to the effective field has also been derived, which can be used to relate the effects of stress to the observed bulk magnetization.

ACKNOWLEDGMENT

We thank B. Howard for assistance in running the computer program.

[1]H. Kwun and G. L. Burkhardt, Proceedings of the 2nd National Seminar on NDE of Ferromagnetic Materials, Houston, TX (March 1986).
[2]H. Kwun and G. L. Burkhardt, NDT Int. **20**, 167 (1987).
[3]M. J. Sablik, H. Kwun, G. L. Burkhardt, and D. C. Jiles, J. Appl. Phys. **61**, 3799 (1987).
[4]D. D. McCracken and W. S. Dorn, *Numerical Methods and Fortran Programming* (Wiley, New York, 1968), p. 133.
[5]M. J. Sablik and Y. L. Wang, Phys. Rev. B **19**, 2729 (1979).
[6]D. C. Jiles and D. L. Atherton, J. Appl. Phys. **55**, 2115 (1984).
[7]D. C. Jiles and D. L. Atherton, J. Magn. Magn. Mater. **61**, 48 (1986).
[8]C. S. Schneider and E. A. Semcken, J. Appl. Phys. **52**, 2425 (1981).
[9]C. S. Schneider and M. Charlesworth, J. Appl. Phys. **57**, 4198 (1985).
[10]B. D. Cullity, *Introduction to Magnetic Materials* (Addison-Wesley, Reading, MA, 1972), Chap. 8.
[11]R. M. Bozorth, *Ferromagnetism* (Van Nostrand, New York, 1951), Chap. 13.

Magnetic field dependence of the elastic constants in Nd_3Se_4[a] (abstract)

H. Fütterer, T. Yohannes, H. Bach, and J. Pelzl
Institut für Experimentalphysik, Ruhr Universität, D-4630 Bochum 1, Federal Republic of Germany
K. Nahm
Department of Physics, Yonsei University, 120 Seoul, Korea

Most of the metallic rare-earth chalcogenides of RE_3X_4 type, where X stands for S, Se, Te, show marked elastic anomalies which appear either in conjunction with a structural transformation or with a magnetic ordering transition. In this contribution we report on results obtained from Nd_3Se_4 where the elastic constants display a particular magnetic field dependence. Single crystals were grown by a Bridgman–Stockbarger method and the three cubic elastic constants were measured by ultrasonic techniques as function of temperature and in an external magnetic field. The occurrence of magnetic ordering was proved independently by susceptibility measurements. Nd_3Se_4 has been found to order ferromagnetically at $T_c = 52$ K. In the absence of an external magnetic field approaching T_c from above, the shear elastic constants $(C_{11} - C_{12})/2$ softens by about 40%. Below T_c the elastic constants harden again where the increment of C_{11} follows the Brillouin function of the magnetization. An external magnetic field parallel to the propagation direction of the sound waves affects the elastic anomalies in the paramagnetic as well as in the ferromagnetic phase. Above T_c the sound velocities exhibit a H^2 field dependence, as is expected from a magnetoelastic coupling mechanism. At temperatures smaller T_c the field-dependent elastic anomalies are related to the hysteresis loop $M(H)$. The change of the elastic constants as a function of the magnetic field is proportional to the field derivative dM/dH. The coupling coefficient has an opposite sign for the C_{44} and $(C_{11} - C_{12})/2$ shear elastic constants.

This paper was not proofread by the author; however, it has been proofread by one of the Publication Chairpersons.

[a] Work supported by the Deutsche Forschungsgemeinschaft, SFB 166.

 0021-8979/88/083933-01$02.40 © 1988 American Institute of Physics

Electron spin injection and detection at a ferromagnetic-paramagnetic interface (invited)

Mark Johnson[a] and R. H. Silsbee
Laboratory of Atomic and Solid State Physics, Cornell University, Ithaca, New York 14853-2501

A new technique for investigating conduction electron magnetization is presented. A coupling between electronic charge and spin transport in ferromagnetic metals follows from generalizing the linear transport equations. In practice, this means that ferromagnetic films act as conduction electron spin polarizers. At an interface between a ferromagnetic and a paramagnetic metal, one can inject and detect nonequilibrium magnetization in the paramagnet, and use sensitive electric measurements to probe spin transport. Application of a small external magnetic field dephases the spins. The result is a new technique for measuring conduction spin relaxation times, which is demonstrated on bulk aluminum samples. Three advantages of the technique make it applicable to a wide range of studies. (1) The measurement can be made in the limit of zero field so that systems with interesting properties which are altered or destroyed by magnetic fields can now be probed (spin glasses, superconductors, metals with g anisotropies). (2) A SQUID voltmeter with picovolt noise floor provides a sensitivity that allows detection of one nonequilibrium spin in a background of 10^{12} equilibrium spins. (3) The experimental geometry utilizes microfabrication techniques and is ideal for application to small-size systems that are inaccessible to conventional electron spin resonance methods. The geometry conveniently needs but one good surface; other sample surfaces are available for alteration *in situ* for the study of surface relaxation effects. Finally, there are obvious applications to the study of ferromagnets and interfaces.

I. INTRODUCTION

The concept that a coupling between conduction electron charge and spin exists at the interface between a ferromagnetic and a paramagnetic metal is introduced, discussed, and demonstrated empirically.[1] An electric current driven from the ferromagnet to the paramagnet is spin polarized, and the resulting current of magnetization, I_M, creates a nonequilibrium magnetization $\tilde{M}$ in the paramagnet. Conversely, $\tilde{M}$ can be detected as an electric current across a paramagnetic-ferromagnetic interface. Using this concept, a new, nonresonance technique to measure conduction electron relaxation time T_2 in the limit of vanishing applied magnetic field is presented.

Figure 1 illustrates a "thought experiment." In the middle is a thin slab of bulk (paramagnetic) metal of thickness L. On the left is a source that drives electrons into the metal. They pass through a spin polarizer, so that some fraction of the injected electrons are spin polarized along some chosen axis. The conduction electrons move diffusively in the paramagnet, and the current is drained to ground at the bottom of the slab. On the right is a second spin polarizer, whose axis of polarization may be experimentally defined. A diffusing electron incident on this polarizer will be transmitted if it is polarized parallel to the axis of the polarizer. A detector counts particles that go through the polarizer. The polarizers, which will be explained in Sec. II, work in the following way. When their axes are aligned, there is a maximum current through the detector. When their axes are antialigned, there is a current of equal magnitude but of opposite sign through the detector. For angles α between maximum and minimum, there is a current proportional to $\cos\alpha$.

We propose several ways to demonstrate this effect. (1) One could measure the detector current as a function of α. Although in practice it is difficult to manipulate the axes of the polarizers, a few examples of this kind of measurement will be given. (2) If the paramagnetic metal contains some scatterers that can destroy (relax) the spin polarized electrons, then the "memory" of the spin orientation is lost after many collisions, and the nonequilibrium magnetization $\tilde{M}$ decreases exponentially from $x = 0$ as $\tilde{M} = \tilde{M}_0 e^{-x/\partial_s}$. Here $\partial_s \equiv \sqrt{2DT_2}$ is the spin depth (D is the diffusion constant), which is the average distance a spin travels in the metal before its spin orientation is randomized. By performing experiments on several samples that are identical except for different thicknesses L, the detector current as a function of L would decrease exponentially. This would demonstrate the polarizers, and the decay constant would be a measure of the spin depth, i.e., of T_2, which is an important property of electronic transport. (3) It is possible experimentally to destroy $\tilde{M}$ by the application of a small transverse field B. The spins, which move diffusively, dephase with increasing field strength, and a measurement of detector current as a function of increasing B will measure the rate at which the spins dephase. Known as the Hanle effect, this is experimentally the easiest technique, and is presented in detail in Sec. III.

[a] Present address: Dept. of Physics, University of California, Berkeley, CA 94720.

 0021-8979/88/083934-06$02.40 © 1988 American Institute of Physics

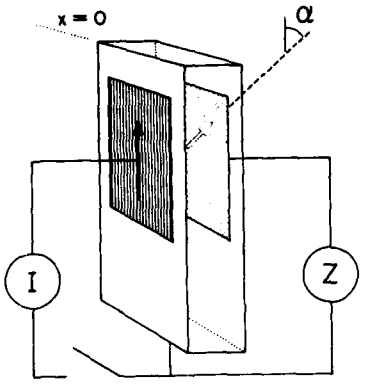


FIG. 1. A "thought experiment" for spin polarized conduction electrons.

II. CHARGE-SPIN COUPLING

In this section, microscopic models of interfacial transport are presented to illustrate the idea of charge-spin coupling. Figure 2 depicts the steady-state processes occurring in the pedagogical model of Fig. 1. The polarizers are thin, ferromagnetic films, each a single domain whose axis of magnetization is confined to lie in the plane but may be chosen along any direction within the plane. The axis of magnetization of the left film is chosen to be up, and we consider the case $\alpha = 0$. Both films are in interfacial contact with a paramagnetic metal of thickness $L < \partial_s$. In steady state, a battery drives a current through the left film, into the slab. On the right, an impedance Z is chosen to connect the second film to the bottom of the slab via an external circuit.

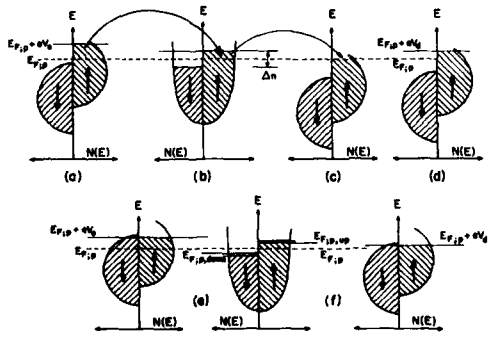


FIG. 2. Microscopic models for the experiment of Fig. 1. (a) Injection, (b) steady-state nonequilibrium magnetization, (c) detection via a low impedance ammeter, and (d) detection via a high impedance voltmeter for oversimplified Stoner ferromagnets. (e) Injection and (f) detection for nonideal ferromagnetic films.

Figure 2(a) depicts the injection process for an overidealized Stoner model of the ferromagnet. The spin subbands are shifted, the majority subband lies entirely below E_F, and a voltage applied across the interface drives a current carried solely by electrons in the minority subband. There is a current of nonequilibrium magnetization[2] associated with the electric current, and if there is no relaxation at the interface, it is trivially given by the number current of carriers times the magnetic moment that each carries, $I_M = \beta I_e/e$, where β is the Bohr magneton.

In the bulk metal [Fig. 2(b)], there is a source of injected magnetization, I_M, and a sink of magnetization, which are the relaxation processes characterized by time T_2. The steady-state magnetization will be a balance between the two processes, given by $\tilde{M} = I_M T_2/\Omega = \beta \Delta n$, where Ω is the volume occupied by the magnetization. Figure 2(c) depicts the detection process. There is no transport across the interface between the spin-down subbands, because there are no states available at or near E_F in the ferromagnet. However, if Z is a low impedance ammeter, there *will* be a current, from the spin-up subband in the paramagnet to the spin-up subband in the ferromagnet, that is proportional to $\tilde{M}$. If Z is a high impedance voltmeter [Fig. 2(d)], then the chemical potential of the ferromagnet will rise to align with that of the spin-up subband of paramagnet, and this difference of voltage will be proportional to $\tilde{M}$. Notice that if the nonequilibrium magnetization were of the opposite sign, then the interfacial current (voltage) would also be of the opposite sign. Thus, the films behave in the manner that was postulated for the polarizers.

The detector voltage V_d can be calculated in a straightforward way. The chemical potential of the detector ferromagnet is the same as that of a subband of the paramagnet, so the calculation is performed in the paramagnet, where free-electron expressions can be used. We have

$$\frac{\tilde{M}}{\chi} = \Delta n = \int_{E_{F,p}}^{E_{F,p} + eV_d} N_\uparrow(E)\,dE, \tag{1}$$

where V_d is assumed small, and $N_\uparrow(E)$ is the single-spin subband density of states in the paramagnet which is approximately constant near E_F. Performing the integral gives $\tilde{M}/\chi = N(E_F)eV_d = (\chi/\beta^2)eV_d$, and solving for V_d yields[3]

$$V_d = (\beta/e)(\tilde{M}/\chi), \tag{2}$$

where χ is the Pauli paramagnetic susceptibility $\chi = \beta^2 N(E_F)$.

We can readily generalize to the nonideal case, where the Fermi level of the ferromagnet cuts, in a nonequivalent way, across both spin subbands. An interfacial conductance for each spin subband s ($\uparrow$ or $\downarrow$) can be defined: $g_s = e^2[N(E_F)\langle v_\perp\rangle\langle t\rangle]_{i,s}$, where $\langle v_\perp\rangle$ is an angular average of the component of the Fermi velocity perpendicular to the interface, $\langle t\rangle$ is an average transmission probability, and index i is either p for the paramagnet or f for the ferromagnet (by detailed balance, one could evaluate the quantities in either one). For the injector, the net currents are from the ferromagnet to the paramagnet [Fig. 2(e)], and $g_\uparrow \neq g_\downarrow$ is a natural consequence of the difference in density of states and Fermi velocity for the two subbands of the ferromagnet. Let

$E_{F,i,s}$ be the Fermi energy of the subband s of the material i, and impose a voltage $-V_0$ across the interface. The magnetization in the ferromagnet remains in equilibrium: $E_{F,f,\uparrow} = E_{F,f,\downarrow} = E_{F,p} + eV_o$, where $E_{F,p}$ is the average Fermi level of the two subbands in the paramagnet, and the chemical potential in the ferromagnet is raised by $(-e)(-V_0)$ relative to that of the paramagnet. Then the electric and magnetic currents from the ferromagnet to the paramagnet are, respectively,

$$J_e = \frac{1}{e}\left[g_\uparrow (E_{F,f,\uparrow} - E_{F,p}) + g_\downarrow (E_{F,f,\downarrow} - E_{F,p})\right]$$

$$= (g_\uparrow + g_\downarrow)V,$$

$$J_M = \frac{\beta}{e}\left[g_\uparrow (E_{F,f,\uparrow} - E_{F,p}) - g_\downarrow (E_{F,f,\downarrow} - E_{F,p})\right]$$

$$= \frac{\beta}{e}(g_\uparrow - g_\downarrow)V.$$

The ratio of J_M to J_e is

$$\frac{J_M}{J_e} = \frac{g_\uparrow - g_\downarrow}{g_\uparrow + g_\downarrow}\frac{\beta}{e} \equiv \eta \frac{\beta}{e}. \tag{3}$$

Notice that if either $g_\uparrow$ or $g_\downarrow \to 0$ (which implies an ideal Stoner ferromagnet), then $|\eta| \to 1$, and we recover the previous result $J_M = \beta J_e/e$. Equation (3) defines the interfacial transport parameter η. Under the assumption of no interfacial spin relaxation:

$$\eta = \frac{J_\uparrow - J_\downarrow}{J_e} = \frac{g_\uparrow - g_\downarrow}{g_\uparrow + g_\downarrow}. \tag{4}$$

For the detector [Fig. 2 (f)], consider first the interfacial currents that flow when a low impedance circuit externally connects the ferromagnet to the bottom of the slab. Nonequilibrium magnetization has caused a different occupation of the subbands, and the subband chemical potential is given by

$$E_{F,p,\uparrow(\downarrow)} = E_{F,p} + (-)\beta\tilde{M}/\chi.$$

The current from the paramagnet to the ferromagnet is

$$J_e = \frac{1}{e}\left[g_\uparrow (E_{F,p,\uparrow} - E_{F,f}) + g_\downarrow (E_{F,p,\downarrow} - E_{F,f})\right]$$

$$= \frac{1}{e}\left((E_{F,p} - E_{F,f})(g_\uparrow + g_\downarrow) + \frac{\beta\tilde{M}}{\chi}(g_\uparrow - g_\downarrow)\right).$$

Note that there is a forward (paramagnet to ferromagnet) current between the spin-"up" subbands, and a back (ferromagnet to paramagnet) current between the spin-"down" subbands. When a high impedance voltmeter is inserted in the external circuit, no current flows ($J_e = 0$) and the result is

$$-\frac{1}{e}(E_{F,p} - E_{F,f}) = \frac{\beta\tilde{M}}{e\chi}\frac{g_\uparrow - g_\downarrow}{g_\uparrow + g_\downarrow}.$$

The left-hand side is identified as V_d and η is identified from Eq. (4), giving

$$V_d = \eta\beta\tilde{M}/e\chi. \tag{5}$$

Thus we learn that, under the assumption of no spin relaxation at the interface, the magnetization transport parameter η is the same for injection as it is for detection. Although microscopic arguments have been presented for a specific model of noninteracting electrons, the physics of spin injection and detection can be quite generally derived from a more fundamental entropy production argument in the formalism of nonequilibrium thermodynamics. In another paper[4] it is shown that the generalized linear transport equations are

$$-I_q = \frac{L_{11}}{T}\Delta V + L_{12}\Delta\left(\frac{1}{T}\right) + \frac{L_{13}}{T}\Delta(-H^*),$$

$$I_Q = \frac{L_{21}}{T}\Delta V + L_{22}\Delta\left(\frac{1}{T}\right) + \frac{L_{23}}{T}\Delta(-H^*),$$

$$-I_M = \frac{L_{31}}{T}\Delta V + L_{32}\Delta\left(\frac{1}{T}\right) + \frac{L_{33}}{T}\Delta(-H^*),$$

where $-H^* \equiv (\tilde{M}/\chi - H)$ is the thermodynamic driving potential for a magnetization current; H is an applied magnetic field; I_q, I_Q, I_M, are the currents through the interface of charge, heat, and magnetization; differences ΔV, $\Delta(1/T)$, and ΔH^* are measured across the interface; and L_{ij} are the kinetic coefficients. If the terms L_{i3}, L_{3j} are omitted, the familiar linear dynamic equations of the thermoelectric effects are recognized. From the full set of terms, the injector relation comes from L_{13} (for an isothermal system), the detector comes from L_{31} and L_{33} [with $I_M = 0$ and $\Delta(1/T) = 0$], and the equivalence of η for injector and detector follows from an Onsager relation.

III. A NEW TECHNIQUE TO MEASURE T_2

In this section we discuss a specific (one-dimensional, random walk) model for how to use spin polarized electrons to measure conduction electron relaxation times. Figure 3 shows the true experimental geometry. A bar of pure bulk metal, about 50 μm thick and 100 μm wide, is coated with an insulating film. Small windows are photolithographically defined and chemically etched to the surface of the metal, ferromagnetic films are evaporated on the windows, and indium wires that lead to an injector and detector are cold welded to these films.

The injection current is returned at one end of the bar and the detector voltage measured with respect to the other end, so that (in the absence of spin injection) there is no voltage across the detector because there is no net current upstream of the injector. In the vicinity of the injector, spin

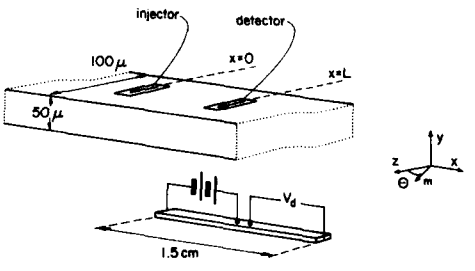


FIG. 3. True experimental geometry.

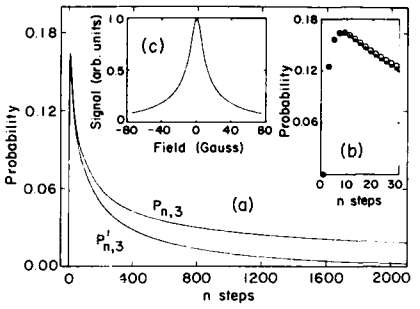


FIG. 4. (a) The unnormalized probability $P_{n,3}$ that a moment took n steps to arrive at the detector located at $L = 3l$, in the absence of relaxation. $P'_{n,3}$ is the reduced probability in the presence of relaxation. (b) A detail of (a) showing the distribution of arrival times. (c) Signal calculated numerically from Eq. (6).

polarized electrons are injected in steady state at $x = 0$ and eventually relax by a T_2 process. We neglect transverse motion and assume that each electron undergoes a random walk along the x axis. Every τ seconds it moves $l = v_F\tau$, where v_F is the Fermi velocity, either forward or backward. Whenever an electron is at $x = L = pl$ it has a small probability of exiting the bar through the detector. For this sample of electrons, the distribution of times spent in the bar is plotted in Fig. 4. Parameters for the results of Fig. 6(a) are $\tau = 9$ ps, $l = 17\,\mu$m, $L = 50\,\mu$m, and $p \sim 3$. In the absence of relaxation, the probability $P_{n,p}$ is just the number of ways to get to $x = pl$ in n steps, i.e., the binomial coefficient ${}_nC_{(n+p)/2}$, divided by 2^n:

$$P_{n,p} = \binom{n}{(n+p)/2} 2^{-n}, \quad n+p \text{ even}$$
$$= 0, \quad n+p \text{ odd}.$$

The peak probability occurs at around nine steps [Fig. 4(b)], as expected for a random walk. There follows a long tail that eventually falls off as $n^{-1/2}$; it takes a long time for electrons to diffuse away from the origin in a one-dimensional bar. In the presence of relaxation there is a probability per step of τ/T_2, which is 0.001 for the data of Fig. 6(a), that a spin gets randomized by its collision and is lost to the system. The probability that a spin polarized electron arrives at the detector after n steps without relaxation is reduced from $P_{n,p}$ by the factor $e^{-n\tau/T_2}$, and is plotted in Fig. 4 as $P'_{n,p}$.

Next consider the effect on the spin polarized electrons of a small, static external field parallel to $\hat{y}$. We suppose that the injected electrons are polarized along $\hat{z}$, and that the axis of the detector is along $\hat{z}$ as well. A moment pointing at angle θ to $\hat{z}$ will register a magnetization proportional to $\cos\theta$. An external field along $\hat{y}$ will cause every spin to precess through a phase angle of $\partial\theta = \gamma B\tau$ in each step, where γ is the spin gyromagnetic ratio. The signal of the analyzer in a static magnetic field B is then the sum of the contributions of all the electrons, weighted by the probability $P'_{n,p}$ that they started from the injector n steps earlier, and multiplied by the precession factor $\cos(\gamma B\tau)$:

$$\text{Signal} \propto \sum e^{-n\tau/T_2}\,{}_nC_{(n+p)/2}\,2^{-n}\cos(\gamma Bn\tau). \qquad (6)$$

The signal as a function of field, calculated numerically from this equation with $p = 3$, is plotted in Fig. 4(c). Note that a field along $\hat{x}$ would generate the same shape signal. However, a field along $\hat{z}$ exerts no torque on the spins; they will not precess, and there will be no quenching of the signal by the applied field. In that case one should see a signal independent of applied field (for small fields).

We have presented this model because there is a clear physical interpretation of the signal: it is the Fourier transform of the probability $P'(t)$ of finding an unrelaxed moment at the detector at time t. An equivalent solution is achieved by analytically solving the Bloch equations with a diffusion term.[5] The solution incorporates three phenomenological fitting factors, each with a direct physical interpretation. The amplitude is largely determined by η, which is the interfacial magnetization transport parameter previously introduced. The width is largely determined by the conduction electron relaxation time T_2. Finally, there is a family of solutions for the Bloch equations, and a particular solution is determined by the angle α between the axes of magnetization of injector and detector. The solution for injector and detector both aligned along $\hat{z}$ has been presented. An independent solution is for the case where injector and detector are at right angles to each other. Then the application of field of one sign brings the spins towards alignment with the detector and a positive signal results, whereas application of a field of the other sign brings the spins towards antialignment with the detector and a negative signal results. The resulting signal is "dispersive" in appearance. In general, for arbitrary angle α between injector and detector, the solution will be a linear combination of these two, and the fraction of the solution with injector and detector aligned is $\cos\alpha$, while the fraction with injector and detector perpendicular is $\sin\alpha$.

IV. EXPERIMENTAL RESULTS

The magnetization of thin ferromagnetic films remains nearly in the plane of the films for fields of any orientation as long as the applied field is small in magnitude compared to the $4\pi M$ of the film. At low temperatures, the film will align as a single domain with an applied field in the plane of the film for field magnitudes larger than some characteristic val-

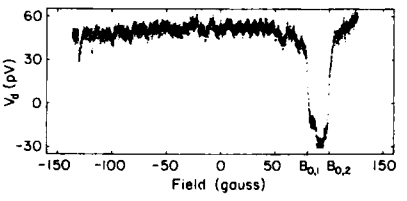


FIG. 5. Magnetic field is swept along the $-\hat{z}$ axis. Between $B_{0,1}$ and $B_{0,2}$ the films are antialigned, and V_d changes signs.

ue B_0, and will stay a single domain until a field B_0 in another direction is applied. The magnitude of B_0 is determined by a number of magnetic anisotropies that may exist within the particular film, or may exist through an interaction with the substrate. High-quality permalloy films on a clean substrate have characteristic fields on the order of 1 G, i.e., an applied field of a gauss in the plane is enough to orient the magnetization of the film.

A demonstration of the effect by manipulating the axis of magnetization of the detector relative to that of the injector may be performed in the following way. Starting with both films aligned, one could apply a field, in the plane of the films, in the opposite direction. Each film should have a slightly different characteristic field because of differring unique anisotropies, so that each will flip orientation for different field values. The detector voltage should change signs when one of them has flipped but the other hasn't, so that they are antialigned. Figure 5 presents data from this kind of experiment. A constant current is driven through the injector, and the detector voltage is rec: -ded as the field is swept along the $\hat{z}$ axis. Starting at negative field, both films are aligned together along $-\hat{z}$. Near $B = 0$ there is no Hanle signal because the field is parallel to the injected spins, so there is no torque to dephase them. In other words, up to $B_{0,1}$ the detector records a voltage due to the magnetization injected into the bar. At $B_{0,1}$ one of the pads has flipped its orientation, the pads are antialigned, and the voltage due to the injected spins is negative. At $B_{0,2}$ the other pad reverses its direction and the original signal is recovered. Notice that the characteristic fields are about a hundred gauss, about a hundred times larger than expected.

Figure 6(a) presents some data which illustrate the Hanle effect, and which correspond to the line shape that was numerically calculated previously for aluminum with $L = 50\ \mu$m. The numerical calculation is equivalent to the following parameter values of our fitting function: $\eta = 0.067$, $T_2 = 9$ ns, and $\alpha = 0°$. Here the injector and detector are aligned, and the field is swept along $\hat{x}$. Recall that the Hanle effect should exist for field sweeps transverse to the orientation of the injected spins. Note that the noise in these data are a couple of picovolts, which is nearly the level of the Johnson noise of the input circuit.

Recall our interpretation of the data in Fig. 5; the films reverse their magnetization at different field values, so that between $B_{0,1}$ and $B_{0,2}$ they should be antialigned. If that's the case, one could halt the $\hat{z}$ field sweep between $B_{0,1}$ and $B_{0,2}$, then sweep field along the $\hat{y}$ direction, which is transverse to the direction of the injected spins, and one should see a Hanle signal similar to Fig. 6(a), but the feature should be a dip rather than a peak. The data in Fig. 6(b) are from just this experiment, and validate our interpretation [the amplitude is less than in Fig. 6(a) because there is less than complete reversal]. As a final example, Fig. 6(c) is a demonstration of a sample wherein the injector and detector were "stuck" nearly perpendicular to each other, and the result is a "dispersive"-shaped signal, as previously described.

The experiment was performed in aluminum, because T_2 has been measured in aluminum by transmission electron spin resonance (TESR). Aluminum is a metal that has a g

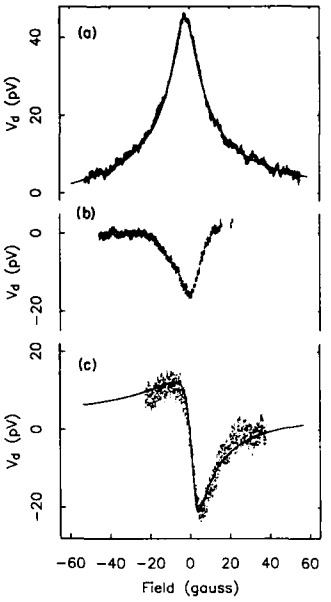


FIG. 6. Examples of data. (a) An $\hat{x}$ sweep for the parameters of Fig. 4. (b) A $\hat{y}$ sweep when the films are antialigned. (c) A "dispersive" shaped signal results when injector and detector are perpendicular. Here they are actually past perpendicular ($\alpha = 124°$), i.e., partially antialigned.

anisotropy. In practice this means that the signal is broadened if it is measured at high frequency in a large field. To minimize the effect of this g anisotropy, we compare our data with the lowest frequency measurement available, which is data from Lubzens and Schultz[6] at 1.3 GHz. Figure 7 shows a comparison of our deduced values of T_2 for one sample at different temperatures, compared with Lubzens' 1.3-GHz results. Contributions to the linewidth come from spin-flip scattering with impurities, sample surfaces, and phonons. The first two account for the residual width at low temperature. This width is subtracted from the higher-temperature values for both samples in order to isolate and compare the

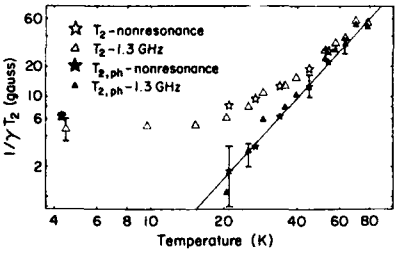


FIG. 7. Comparison of relaxation times between the new, nonresonance method and TESR at 1.3 GHz.

temperature dependence of T_2, which is verified to be independent of technique.

Values of η from 17 data sets, over a temperature range of 4–45 K, with probe separations of 50, 200, and 300 μm, and for sweeps along $\hat{x}$ and $\hat{y}$ varied within $\pm 25\%$ of a mean value of 0.061. The fact that a single set of fitting parameters consistently describes a signal that varies in amplitude by an order of magnitude gives us confidence in the validity of our one-dimensional model.

V. DISCUSSION

The coupling of charge and spin enables the use of highly sensitive electronic measurements to probe magnetic interactions. The technique is experimentally convenient; it requires only one good surface, and can be used on very small samples, such as single crystals. We believe our new technique will be useful for a range of studies. The sensitivity is readily calculated in terms of spin parameters. Recall Eq. (1), and use a free-electron, single spin subband density of states $N\uparrow(E_F) = 3n/4E_F$ to get

$$\Delta n/n = 3eV_d/2\eta E_F.$$

For a sensitivity of a picovolt, $\eta \approx 0.07$, and $E_F \approx 10$ V, we find $\Delta n/n = 10^{-12}$. Said another way, the sensitivity is one nonequilibrium spin in a background of 10^{12} equilibrium spins; so that if there are a trillion up spins and a trillion down spins, and *one* of them is flipped out of equilibrium, it could be detected! The equivalent equilibrium magnetization is $H = M/\chi = \beta\Delta n/\chi$, where χ is the free-electron susceptibility, and is *a few milligauss*. Of course, this equilibrium magnetization would have to be turned into nonequilibrium magnetization for it to be detected in our experiment.

The good sensitivity suggests looking for single spin effects, or quantum fluctuations in magnetic conductance. As a zero field, zero frequency technique it is applicable to systems whose interesting properties are altered by magnetic fields, such as spin glasses and superconductors. Semiconductors whose carriers have adequate mean free paths may be studied, if there exist suitable methods for forming ohmic contacts.

[1] M. Johnson and R. H. Silsbee, Phys. Rev. Lett. **55**, 1790 (1985).
[2] A. G. Aronov, Pis'ma Zh. Eksp. Teor. Fiz. **24**, 37 (1976) [JETP lett. **24**, 32 (1976)].
[3] R. H. Silsbee, Bull. Magn. Reson. **2**, 284 (1980).
[4] M. Johnson and R. H. Silsbee, Phys. Rev. B **35**, 4959 (1987).
[5] M. Johnson and R. H. Silsbee, Phys. Rev. B **37** (1988).
[6] D. Lubzens and S. Schultz, Phys. Rev. Lett. **36**, 1104 (1976).

An alternating-gradient magnetometer (invited)[a)]

P. J. Flanders
Department of Physics and Laboratory for Research on the Structure of Matter, University of Pennsylvania, Philadelphia, Pennsylvania 19104

This paper describes a type of vibrating-sample magnetometer capable of sensitivity exceeding 10^{-8} emu. The instrument is 1000 times more sensitive than a conventional VSM with comparable working space, and is much quicker to use than a SQUID magnetometer, which generates point-by-point data. The magnetic sample is mounted on the end of a cantilevered rod that incorporates a piezoelectric element. The sample is magnetized by a dc field (variable in magnitude), and is simultaneously subjected to a small alternating field gradient. The alternating field gradient exerts an alternating force on the sample, proportional to the magnitude of the field gradient and to the magnetic moment of the sample. The resulting deflection of the cantilever rod is measured by the voltage output of the piezoelectric element. By operating at or near a mechanical resonance frequency of the cantilever, the output signal is greatly amplified. In practice, the operating frequency is 100–1000 Hz, with mechanical Q values of 25–250. Mechanical and acoustic noise in the environment limits the sensitivity. Measurements have been made with a signal-to-noise ratio of about 500 on a 25-μm sphere with a moment of 3.7×10^{-6} emu; this corresponds to a sensitivity of at least 10^{-8} emu. A complete hysteresis loop over $\pm$ 10 kOe can be made in about 100 s. Measurements have been made over a temperature range from 77 to 400 K.

INTRODUCTION

This paper describes a modification of an alternating gradient method[1] to measure magnetic moment. The system uses an alternating field gradient to produce a periodic force on a magnetized sample [Figs. 1(a) and 1(b)]. The sample is mounted on the tip of a vertical extension rod, which is taken to lie along the z axis, and the gradient field is along the x or the y axis. The top end of the sample rod is attached to the bottom end of a piezoelectric element [Fig. 1(c)]. The top end of the piezoelectric element is rigidly clamped. The force of the field gradient on the magnetized sample produces a bending moment on the piezoelectric element, which generates a voltage proportional to the force on the sample. The output from the piezoelectric element is synchronously detected at the frequency of the gradient field. The amplitude of this voltage is proportional to the magnetic moment of the sample, which can be varied by changing an applied dc field H_x which is along x.

The first alternating-gradient force magnetometer was developed by Zijlstra,[1] who detected the vibrational amplitude optically using a microscope. Reeves[2] detected the vibration amplitude with a piezoelectric sensor, but the sensor was not part of the vibrating rod; he also designed a null method for higher stability. Roos *et al.*[3] describe a system basically the same as ours. Our system differs in being more rugged, and allowing for easy change of piezoelectric elements, extensions, and samples. Our system also permits measurements over a wide temperature range (77–400 K has been accomplished) while heating or cooling only the sample and the tip of the extension rod.

A review of ac force magnetometers and a comparison with other methods has been given by Foner.[4]

APPARATUS

The sensing element is composed of two polarized sheets of a metallized piezoelectric which are cemented back to back to either side of a thin brass vane. These form what is referred to as a series-connected bimorph. Generally, we use a PZT-5B ceramic bimorph,[5] coated with silver rather than the usual nickel to avoid the ferromagnetism of nickel. The total thickness of the element, including the brass vane, is $t_b = 0.6$ mm. One end of the bimorph is clamped in a slot in the end of a 5-mm-diam nonmetallic rod. At the clamped end of the bimorph, a pair of electrodes contact the outer metallized surfaces. These contacts are connected to a high-impedance differential preamplifier through light-weight shielded wire intended for use in a phonograph tone arm.

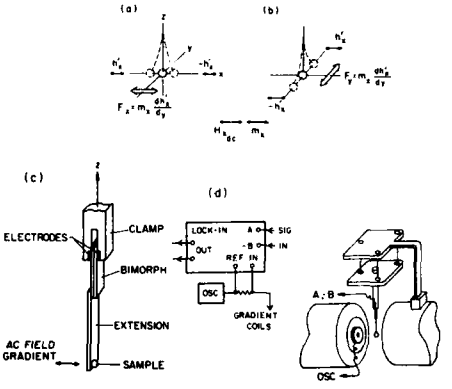


FIG. 1. Configuration of the magnetizing and gradient fields (a) and (b); the bimorph, extension, and sample (c); and the overall system (d).

[a)] This study is dedicated to Mula Shtrikman, Bill Doyle, Chad Graham, and Ami Berkowitz, friends over a period of many years.

 0021-8979/88/083940-06$02.40 © 1988 American Institute of Physics

The preamplifier is the front end of a lock-in amplifier, which automatically tracks the frequency of the ac current in the gradient coils [Fig. 1(d)].

The length, thickness, density, and Young's modulus of the bimorph and extension rod are chosen such that the resonant frequency of the system is in the range 100–1000 Hz. Higher frequencies in this range are less susceptible to background vibration.

The extension rod is cut from a plastic, glass, or metal sheet which has about the same width as the bimorph and is as free as possible from magnetic impurities. A conducting spray on the extension rod helps prevent signals resulting from electrostatic charge. When the extension rod or a bulk sample is highly conducting, eddy currents may interfere with the measurement of very small moments. Eddy current signals are proportional to the dc field and so appear as an excess susceptibilty. The mass of the sample must be small enough so that the resonance frequency is not reduced significantly below 100 Hz.

The ac gradient along the x or y axis can be generated with one of several coil configurations. We define the field h' as an ac field which varies as $h \sin \omega t$.

In the system shown in Fig. 2(a), a pair of split coils $(a, -a')$, 3 mm thick, 4 mm i.d., and 8 mm o.d., containing 250 turns of #36 wire, are spaced 10 mm apart to produce oppositely directed fields along the x axis. With a current of 0.25 A rms, the gradient along x midway between the two coils is about 40 Oe/cm.

In another system,[2] two pairs of offset split coils (a,a') and $(-b,-b')$ are connected so as to have oppositely directed fields. The axis of each pair is parallel to the dc magnetizing field H_x, and the pairs are offset by $\pm y$ [Fig. 2(b)]. The gradient dh'/dy at the center of symmetry where the sample is located is typically 40 Oe/cm (rms).

Another coil arrangement permits the gap of the electromagnet to be reduced to the thickness of a single gradient coil, which can be less than 10 mm. Here, two identical coils, $(a, -a)$ in Fig. 2(c), are offset $\pm y$ from the central axis of the magnet. The field along x from each coil is oppositely directed and the space for the sample between the coils is typically 0.5–1 cm. A gradient of 15–25 Oe/cm is achieved at the sample using coils like those described above.

Gradients an order of magnitude stronger can be generated for all these configurations if higher currents are used in water-cooled coils[6] or if the gap between the coils is decreased.

The interaction of the fields from the ac gradient coils and from the iron-core magnet produces an alternating force on the coils (and on the magnet) at the gradient frequency and proportional to the product of the two fields. This force can produce a motion of the coils which couples to the bimorph, either mechanically through the magnet and bimorph mount, or acoustically through the air, producing an unwanted output signal proportional to H. This signal can be lowered by judiciously reducing the size of the gradient coils, and by minimizing any motion between the coils and the poles. Therefore, the coils must always be rigidly attached to the magnet pole faces.

It is also important to mechanically isolate the magnetometer from the environment. One way to achieve this is to attach the bimorph support to a $60\times60\times7$ mm^3 slab of lead suspended by three rubber cords spaced 55 mm apart [Fig. 1(d)]. The upper end of each cord is attached to a platform, which is positioned with an xyz manipulator clamped to the magnet frame. This type of mechanical isolation is effective because a bimorph mounted vertically responds primarily to horizontal forces. Additional isolation stages can be added for higher sensitivity. Mechanical and acoustical noise from nearby sources should be kept to a minimum. Noise from cooling fans in electronic equipment can be troublesome; we place a power amplifier in the next room and operate it by remote control.

Unlike the vibrating-sample magnetometer, which responds to a voltage that is induced in a coil by a time-varying flux from the sample, the piezoelectric elements are not sensitive to a changing magnetic field. The noise from the bimorph is therefore independent of the magnitude of the magnetizing field and its sweep rate. This is illustrated by the fact that the system can operate at maximum sensitivity even when the magnet supply voltage has a very large ripple, as long as the frequency components of the ripple are not too near the frequency of the gradient coil.

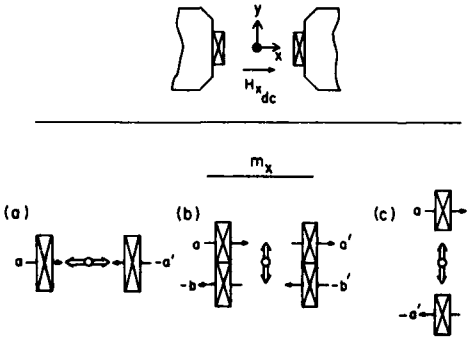


FIG. 2. Gradient coil arrangements for (a) split pair $a, -a'$; (b) two offset split pairs a, a' and $-b, -b'$; (c) offset pair $a, -a'$ in a narrow gap.

THEORY OF OPERATION

The orientation of the bimorph will depend on the direction of the field gradient. In Fig. 2(a), the force along x from the interaction of the gradient and the magnetic moment m_x is

$$F_x = m_x\, dh'_x/dx, \tag{1}$$

while in Figs. 2(b) and 2(c) the force along y is

$$F_y = m_x\, dh'_x/dy. \tag{2}$$

For the cases corresponding to Eqs. (1) and (2), m_x is varied by changing H_x.

For a simple cantilever rod, the fundamental resonance frequency is given by

$$_0f = \frac{1}{2\pi}\frac{t}{l^2}\left(\frac{Y}{\rho}\right)^{1/2} \quad \text{(Hz)}, \tag{3}$$

where t and l are the thickness and length of the cantilever (m), Y is the elastic modulus (Pa), and ρ is the density (kg/m^3). The resonance frequency is lowered by attaching a mass to the end of rod or by adding an extension rod.

Considering only a cantilever of mass W_e with a concentrated sample mass W_s fastened to its end, the combined resonance frequency ${}_0f_{e+s}$ is given by[7]

$$ {}_0f_{e+s} = {}_0f_e[W_e/(W_e + 4.2W_s)]^{1/2} \quad \text{(Hz)}. \tag{4} $$

The resonance for the total cantilever system, ${}_0f_{b+e+s}$, when the bimorph and the extension rod have equal widths, follows the relation

$$ \frac{1}{({}_0f_{b+e+s})^2} = \frac{1}{({}_0f_b)^2} + \frac{1}{({}_0f_{e+s})^2}. \tag{5} $$

From this,

$$ {}_0f_{b+e+s} = \frac{{}_0f_e}{\{({}_0f_e/{}_0f_b)^2 + [(W_e + 4.2W_s)/W_e]\}^{1/2}}. \tag{6} $$

The values for ${}_0f_e$ and ${}_0f_b$ individually can be calculated from Eq. (3). Figure 3(a) gives the resulting lengths when single-element cantilevers with different thickness are designed to resonate at ${}_0f$. In general, the extension length and mass required to achieve an optimum ${}_0f$ are 10–25 mm and 10–30 mg, respectively. When ${}_0f_b \gg {}_0f_e$, we estimate the decrease in resonance frequency as a function of increased sample mass in terms of the ratio ${}_0f_{e+s}/{}_0f_e$, using Eq. (4). Figure 3(b) shows a plot of ${}_0f_{e+s}/{}_0f_e$ against W_s/W_e.

Extensions made from glass (0.16 and 0.21 mm thick), plastic (0.42 and 0.6 mm), and copper (0.12 mm) generally range in length from 10 to 25 mm when operated at the fundamental and from 40 to 70 mm when at an overtone.

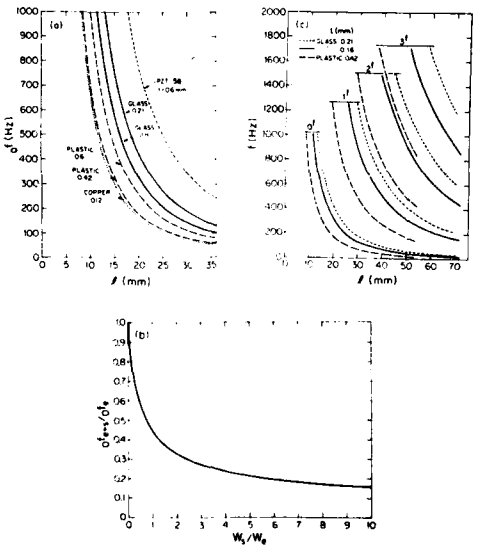


FIG. 3. (a) Fundamental resonance frequency as a function of length, from Eq. (3), for simple cantilevers of PZT-5B, glass, plastic, and copper. (b) Change in the resonant frequency of a cantilever extension as a function of sample mass. (c) Fundamental and first three overtones for glass and plastic cantilevers.

Higher-order mechanical resonances also occur. The first, second, and third overtone frequencies of the cantilever: ${}_1f$, ${}_2f$, and ${}_3f$, are at frequencies[7] 6.26, 17.53, and 34.36 times ${}_0f$, and are generally observed only when the extension rod is longer than 25 mm [Fig. 3(c)].

The bimorph output for each overtone V_n is smaller than the voltage output at the fundamental frequency. Experimentally, the signal decreases as the reciprocal of the resonance frequency. Despite the lower output at the first overtone compared with the fundamental, the signal-to-noise ratio is often higher. This sometimes favors operation at the first overtone when maximum sensitivity is the primary requirement.

From Fig. 3(c) we see that by operating at the first overtone it is possible to significantly increase the length of an extension rod and still work at a high resonant frequency. A greater extension rod length permits the bimorph to be located further from the sample. This is an advantage if the temperature of the sample needs to be raised or lowered. The greater mass of a longer extension also results in a smaller change in the resonant frequency when a sample of fixed mass is attached. A short, thin extension can be added to the end of a longer or thicker one, or the thickness at the end of the rod can be reduced. In addition to raising the resonant frequency, this lowers the magnetic moment of the extension in the region of the gradient field.

When the easy plane of the sample is normal to H, precise alignment of the sample and bimorph plane are required to prevent unwanted signals from the gradient along y.

When a bending force is applied to the end of a bimorph, the output voltage in terms of this force is given by the expression

$$ V/F = 3Gl_b g_{31}(1 - \delta^2/t_b^2)/2w_b t_b, \tag{7} $$

where δ is the thickness of the brass vane in the bimorph.

We consider the factors in this equation: G is a mechanical gain which is unity for a dc field gradient and is equal to a mechanical quality factor Q when the gradient is at the fundamental resonance frequency. The magnitude of Q varies with a number of parameters; in our system, it is generally between 25 and 250. The expressions for G at the overtones and for off-resonance operation are given later in the paper. The quantity g_{31} is the transverse piezoelectric modulus or voltage coefficient. For a bimorph made of PZT-5B, g_{31} is -9.1×10^{-3} V m/N at 20 °C, and decreases about 40% from 77 to 400 K.[5]

When a bending force F is applied to the end of an extension rod, the moment arm of the extension increases the bimorph output by a factor which is equal to $(l_b + l_e)/l_b$, so that

$$ V/F = 3G(l_b + l_e)g_{31}(1 - \delta^2/t_b^2)/2w_b t_b. \tag{8} $$

When Eqs. (1), (2), and (8) are combined, we can predict the output in terms of the magnetic moment m_x for a sample which is located at the tip of the extension rod. When we express the gradient in Oe/cm, the force in dynes (10^5 dyn/N), V/m_x in volts per emu, g_{31} in V m/N, and the linear dimensions in cm,

$$\frac{V}{m_x} = 3G(l_b + l_e)g_{31}\left(1 - \frac{\delta^2}{t_b^2}\right)\frac{(dh_x'/dy)10^{-3}}{2w_b t_b}. \quad (9)$$

The dimensions of l_b, w_b, t_b, and δ of our bimorphs are typically 1, 0.15, 0.06, and 0.001 cm.

With a Q of 100, a field gradient of 40 Oe/cm, and an extension which is 2 cm long, V/m_x at the fundamental resonance frequency is 15 V/emu. A moment of 10^{-8} emu produces a voltage of 0.15 μV, which can be raised to 1.5 μV if the gradient is increased by cooling the coils or by decreasing their spacing.

In terms of V, m_x, and G,

$$V/m_x G = 0.05(l_b + l_e) \quad \text{(V/emu cm)}. \quad (10)$$

To provide an independent calibration of the system in terms of V/m_x with the sample in place, we can generate a magnetic moment by passing a dc current through a coil which surrounds the sample and has its plane normal to the applied field. The magnetic moment m of the coil is

$$m = NIA/10 \quad \text{(emu)}, \quad (11)$$

where N is the number of turns, I is the current, and A is the coil area in cm^2.

A coil of 100 turns of #40 wire, with an area of 0.2 cm^2, will generate a moment of 0.1 emu with a current of 50 mA. This is a moderately large area and mass relative to our system. Ordinary magnet wire used for this coil contains enough ferromagnetic impurity to be easily measurable at high sensitivity. It is not possible to generate a magnetic moment in excess of 1 emu without exceeding the mass limit for a small system. (One emu is a sphere of nickel about 800 μm in diameter.)

The instrument sensitivity can be made independent of changes in many of the system parameters by opening the integrator feedback loop of the lock-in and applying the lock-in output to a coil like that described in the previous paragraph, placed around the sample. This closes the loop and produces a nulling current in the coil which is proportional to the magnetic moment m_x. Comparable sensitivity and response is observed with and without feedback nulling. Feedback operation is useful if there are variations in Y, g_{31}, Q, or ${}_nf$ during the course of an experiment, most commonly because of temperature changes in the bimorph or extension rod.

MEASURING PROCEDURE

The specimen is usually attached to the end of the extension with grease. The isolation support table is positioned with the *xyz* positioner so that the sample is at the center of symmetry of the gradient coils and the magnet. Centering along the gradient axis is particularly important when measuring a material which has a low coercive field, since the net ac field from the gradient coils is only zero at the center and increases with the amount of offset along the gradient axis.

Before making a measurement, the phase of the lock-in amplifier is adjusted so that the in-phase and quadrature output voltages V_0 and V_0^* behave as shown in Fig. 4 when the frequency is varied. The magnetic moment m_x of the sample and the amplitude of the gradient field are held constant as the frequency is slowly varied. The value of Q can be determined from these curves:

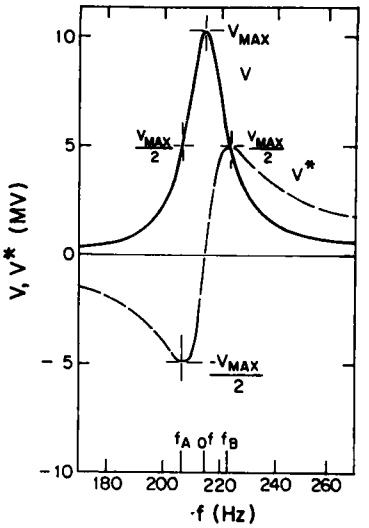


FIG. 4. In-phase and quadrature lock-in output, V and V^*, as a function of the gradient frequency, for a 3-mm^2 γ-Fe_2O_3 recording tape sample at remanence.

$$Q = \frac{{}_0f(V_{max})}{f_B(V_{max}/2) - f_A(V_{max}/2)}, \quad (12)$$

where f_A and f_B are the frequencies at which the in-phase lock-in output drops to half its peak value. These two frequencies also are the frequencies where the out-of-phase signal V_0^* goes through a maximum and a minimum.

The mechanical gains G and G^* for the in-phase and quadrature output vary with frequency as

$$G(f) = {}_0fQ/{}_nf(1 + A^2) \quad (13)$$

and

$$G^*(f) = {}_0fQA/{}_nf(1 + A^2), \quad (14)$$

where

$$A = [(f/{}_nf) - ({}_nf/f)]Q. \quad (15)$$

We see that off resonance the quadrature signal is A times the in-phase signal.

We can choose to operate either on or off resonance, and to measure either the in-phase or the quadrature bimorph output V or V^*, or the associated feedback coil nulling current I_c. Use of a long extension rod permits the sample to be in a furnace or Dewar vessel while the bimorph remains at room temperature. If no feedback coil is used and the sample temperature is varied, it is preferable to measure V^* off resonance from the fundamental so as to minimize any variations in $G^*(T)$. If one operates off resonance, Eqs. (13) and (14) and Fig. 4 show that the gain of the system decreases but the

variations in f, ${}_nf$, or Q. To make the gain of the system independent of changes in temperature, measure I_c rather than V^*.

Figure 5 shows hysteresis loops of a 3-mm^2 sample of γ-Fe_2O_3 recording tape, with the lock-in phase set to 0 and $\pi/2$, for six values of f when ${}_0f$ is 920.4 Hz. Even at a frequency where the output is down by a factor of 100 from the in-phase resonance value, the signal-to-noise ratio is excellent.

CALIBRATION

The numerical value of m_x can be determined to within $\pm$ 10% by using Eq. (9) if dh_x'/dy, g_{31}, t_b, w_b, δ, l_b, l_e, G, and V are known, or the system can be calibrated in terms of V and G by measuring a sample of known magnetic moment or the moment from a dc current through a known coil around the sample [Eq. (11)]. Reproducibility and accuracy are estimated to be within a few percent, depending mainly on the precision to which the sample can be positioned on the extension. Sensitivities better than 10^{-6}, 10^{-7}, and 10^{-8} emu are achieved with lock-in time constant settings of 10^{-2}, 10^{-1}, and 1 s, respectively. The signals are on the order of 100, 10, and 1 μV.

EXAMPLES

The performance of the magnetometer is demonstrated in Fig. 6 for the case where the sample is a 25-μm ferromagnetic sphere with a saturation moment of 3.7×10^{-6} emu.

The magnetization curves in Fig. 7 include a small (a) permalloy film, (b) diamagnetic NaCl crystal, and (c) paramagnetic sample of Ti.

It appears to be almost impossible to make an extension rod of zero susceptibility. One way to cancel out the unwanted susceptibility signal is to insert an ac voltage at the preamp that cancels the signal from the diamagnetic signal.

Figure 8(a) shows magnetization curves at 77 and 110 K of a small superconducting sample of $Ba_2YCu_3O_7$. The temperature was varied by controlling the liquid level below the sample in an open-mouth container, $0.7\times2.5\times3$ cm^3

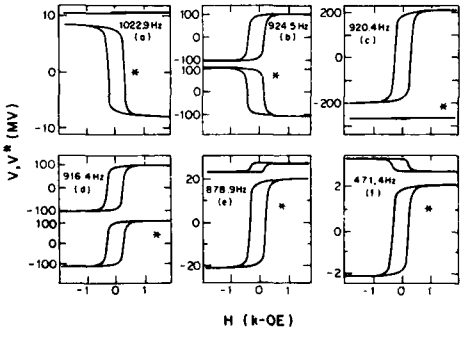


FIG. 5. Hysteresis loops on a 3-mm^2 γ-Fe_2O_3 tape, measured in phase (V) and out of phase (V^*) at six frequencies. Here, ${}_0f$ is 920.4 Hz, Q is 115, the glass extension is $0.16\times1.5\times10$ mm^3, and the offset coil arrangement is shown in Fig. 2(c).

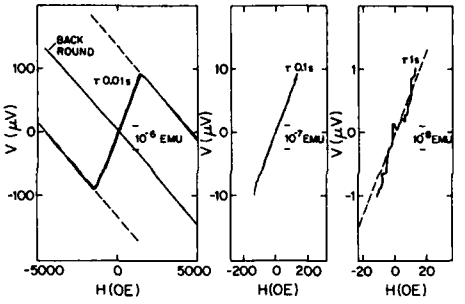


FIG. 6. Signals from a 25-μm-diam amorphous $Fe_{77.5}Co_{0.7.5}Si_{15}B_{10}$ sphere with a saturation moment of 3.7×10^{-6} emu and from the background diamagnetic glass extension tip. Measured at the first overtone ${}_1f = 950$ Hz, $Q = 115$, using the split coil arrangement of Fig. 2(a) but with a 2-mm gap. The compound extension was $1.75\times1.5\times37$ mm^3 plastic with a $0.15\times1.5\times10$ mm^3 glass tip, and the bimorph was $0.6\times1.5\times7$ mm^3.

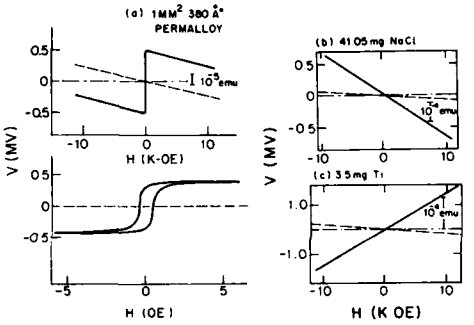


FIG. 7. Magnetization curves of samples having low magnetic moment. These are measured at the first overtone ${}_1f$ using the split coils of Fig. 2(a) with a $0.21\times1.5\times34$ mm^3 glass extension and $0.6\times1.5\times7$ mm^3 bimorph. The background is indicated by the dashed curves. (a) A 1-mm^2, 380-Å permalloy film on a 20-mil Si substrate; ${}_1f = 725$ Hz and $Q_1 = 207$ [offset coils of Fig. 2(b)]. (b) A 41.05-mg diamagnetic crystal of NaCl; $\chi = -0.513\times10^{-6}$ emu/gOe, ${}_1f = 553$ Hz, and $Q_1 = 205$. (c) A 3.5-mg paramagnetic crystal of Ti which contains a ferromagnetic impurity; $\chi = 3.2\times10^{-6}$ emu/gOe, ${}_1f = 678$ Hz, and $Q = 104$.

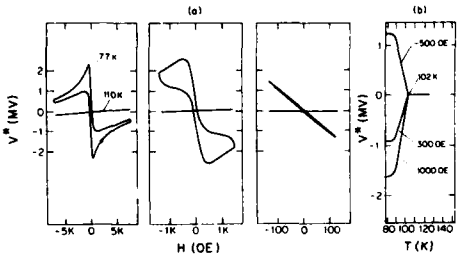


FIG. 8. (a) Magnetization at 77 and 110 K vs field and (b) at 1000, 300, and $-$ 500 Oe vs temperature for an 11-mg $Ba_2YCu_3O_7$ superconductor. A 0.001-cm-diam Cu-constantan thermocouple is glued to the $0.21\times1.5\times34$ mm^3 glass extension rod. V^* is measured at 650 Hz, which is 20 Hz below ${}_1f$.

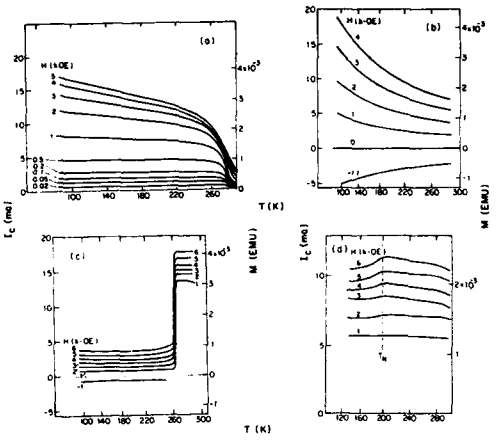


FIG. 9. Feedback coil current against temperature for (a) Gd, 13 μg, (b) $FeCO_3$, 5.5 mg, (c) α-Fe_2O_3, 9.0 mg, and (d) FeO, 1.21 mg.

high, made of 0.08-mm brass sheet. Plots of magnetization against temperature for three different applied fields are shown in Fig. 8(b).

Measurements of magnetization at fixed field with varying temperature are most easily made using a feedback coil and null system. Figure 9 shows plots of coil current, I_c, against thermocouple output at fixed magnetizing field for very small samples of (a) Gd, (b) $FeCO_3$, (c) α-Fe_2O_3, and (d) FeO. Here, we measure the current in a 20-turn, 3.8-mm diam coil of #40 wire which is wound in the plane of a $1\times1.5\times65$ mm^3 plastic extension with $Q=44$ at the first overtone, ${}_1f=349$ Hz with no sample. From Eq. (11), the magnetic moment for this coil is 2.3×10^{-4} emu/mA. The frequency of the gradient field is set ~10 Hz above or below ${}_1f$, and the lock-in phase is set at $\pi/2$. The current I_c, proportional to the magnetic moment, is recorded as the sample warms from 77 to 295 K after being removed from a small container of liquid nitrogen. Each curve in Fig. 9 was traced in a time of about 100 s.

Large magnetic moments can be measured by decreasing the field gradient, or by scaling up the size of the system to accommodate heavier specimens and greater forces. Hysteresis loops have been measured with a $2\times5.25\times15$ mm^3 bimorph and a 6 mm diam $\times$ 40 mm plastic extension rod.

ACKNOWLEDGMENTS

I thank Don Flickinger for suggestions concerning the electronics and mechanics of the instrument, H. Reichard for pointing out the merits of the pendulum-type suspension, R. Josephs and A. E. Berkowitz for supplying test samples with low magnetic moment, and Ron Flowers for winding gradient coils. C. D. Graham, Jr. provided editorial and technical assistance. This work was supported in part by the Office of Naval Research under Contract No. N00014-80-C-0896, and by an equipment grant from the Magnetics Society of IEEE.

[1] H. Zijlstra, Rev. Sci. Instrum. **41**, 1241 (1970).
[2] R. Reeves, J. Phys. E **5**, 547 (1972).
[3] W. Roos, K. A. Hempel, C. Voight, H. Dedericks, and R. Schippan, Rev. Sci. Instrum. **51**, 612 (1980).
[4] S. Foner, IEEE Trans. Magn. **MAG-17**, 3358 (1981).
[5] Vernitron Piezoelectric Div., *232 Forbes Rd., Bedford, OH 44146-5478.*
[6] R. T. Lewis, J. Vac. Sci. Technol. **11**, 404 (1974).
[7] F. S. Tse, I. E. Morse, and R. T. Himble, *Mechanical Vibrations*, 2nd ed. (Allyn and Bacon, Boston, 1978), p. 190.

Integrated on-line instrumentation for simultaneous automated measurement of magnetic field, induction, Barkhausen effect, magnetoacoustic emission, and magnetostriction

D. C. Jiles
Ames Laboratory, Iowa State University, Ames, Iowa 50011

A microcomputer-controlled instrument for simultaneous measurement of magnetic hysteresis, magnetostriction, Barkhausen effect, and magnetoacoustic emission is described. It incorporates custom designed software for control of the magnetic field during operations such as demagnetization, field sweeping, and anhysteretic magnetization, and for data logging and analysis. Results are recorded using a 12-bit analog to digital converter and are then stored on floppy disk. The magnetic hysteresis data are converted into six important magnetic parameters: coercivity, remanence, hysteresis loss, initial permeability, maximum differential permeability, and anhysteretic permeability. These, together with the magnetostriction, Barkhausen, and magnetoacoustic emission, are then related to the microstructure of the material.

I. INTRODUCTION

A multiparameter magnetic inspection system has been developed for measurement of the magnetic properties of soft magnetic materials. Measurements are all made under on-line computer control using a standard IBM PC desk top computer. The magnetic field is controlled using an analog output line from the control and data acquisition system, which operates a bipolar power supply. Results are taken on five analog-to-digital input lines and are stored on floppy disks. Hard copies of results are also generated simultaneously.

The instrument allows rapid and simultaneous measurement of a range of independent parameters which can be used to characterize the magnetic properties of a material. The properties measured by the system are all structure sensitive and consequently the system has been used in studies of the effects of microstructure on magnetic properties.

Each of the magnetic measurements incorporated in the system is widely used in nondestructive evaluation (NDE)[1]; however, we are unaware of any previous attempts to coordinate all five measurements for materials evaluation. The system has consequently proved to be a valuable tool for NDE of the condition of steel specimens.

The various magnetic measurements made by the system generate a range of independent parameters which can be used to quantify the state of the material. The magnetostriction is measured as a function of both field $\lambda(H)$ and induction $\lambda(B)$. Hysteresis curves allow determination of coercivity H_c, remanent induction B_R, hysteresis loss W_H, initial differential permeability μ'_{in}, anhysteretic differential permeability μ'_{an}, and maximum differential permeability μ'_{max}. The Barkhausen effect and magnetoacoustic emission each give count rates dN/dt, total number of pulses $\int N(H)dH$, and the pulse height spectra $N(E)$.

II. BACKGROUND

Microcomputer-controlled systems for measuring the magnetic properties of materials have been described previously.[2] Earlier systems have concentrated mainly on magnetic hysteresis measurements, although a system for simultaneous application of magnetic field H and stress σ has also been reported.[3]

Theiner and co-workers[4,5] have shown that it is advisable to take a number of independent magnetic measurements for nondestructive evaluation. Their system measures the Barkhausen effect, dynamic magnetostriction, and incremental permeability. From these three measurements it is possible to unravel the competing influences of several factors in order to determine levels of stress.[6]

III. PROGRESS TO DATE

The early development of the present system has been described previously by Habermehl and Jiles.[7] It now contains completely integrated instrumentation for measurement of field, induction, magnetostriction, magnetoacoustic emission, and Barkhausen effect (Fig. 1). These five measurements are the most widely used magnetic techniques for evaluation of intrinsic (i.e., non flaw related) magnetic properties of materials.[1]

A. Control functions

The field control functions, which are common to all measurements, are now operated from one of the two digital-to-analog output lines on the Labmaster board.[8] A number of routines have been written to vary the magnetic field in well-defined ways. These include demagnetization, initial magnetization, anhysteretic magnetization, and hysteresis loop algorithms.

The parallel port I/O lines from the Labmaster board are used to operate the instruments directly from the computer. Such operations include zeroing the flux meter when necessary, enabling and disenabling the three x-y recorders, and controlling the pen status on each of the recorders to ensure that hard copy recording of results occurs only when needed.

 0021-8979/88/083946-03$02.40 © 1988 American Institute of Physics

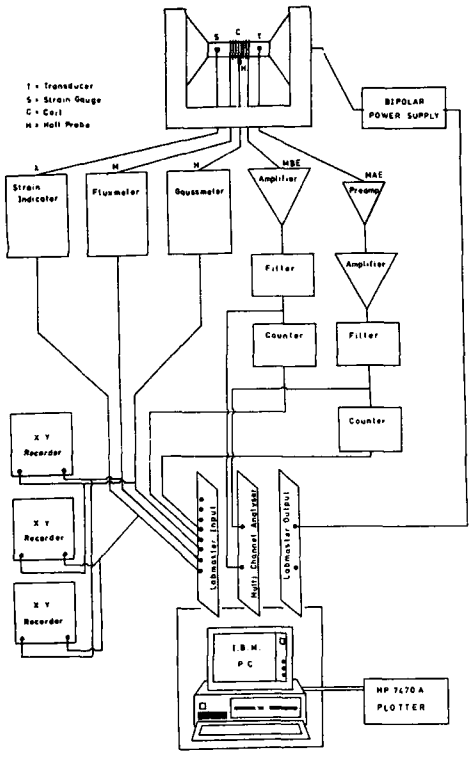


FIG. 1. Schematic diagram of the multiparameter magnetic measuring system.

B. Data acquisition

The data acquisition system used has a 12-bit analog-to-digital converter with eight separate input lines. The programmable gain on the input allows measurement of voltages in the ranges -20 to $+20$ mV up to -10 to $+10$ V, with 4096 incremental steps on each range. Typical operation of the instrument uses an output range of 100 Oe V^{-1} from the H field meter (Walker Scientific, Inc. Model MG-3A), and an input range of -0.1 to $+0.1$ V on the data acquisition system. With 12 bits this gives a field resolution of 0.0048 Oe. Calibration of the Hall probe using a standard field of 2500 Oe indicated an accuracy of 2%. Magnetic induction measurements use a typical output range of 10 kG V^{-1} from the B meter (Walker Scientific, Inc. MF-3A), and with 12-bit resolution on an input range of -0.1 to 0.1 V this corresponds to a resolution of 0.48 G.

Magnetostriction measurements are taken using a commercial strain gauge bridge (Micromeasurements model 3800 wide-range strain indicator). The strain sensitivity is such that 1 mV corresponds to 10^{-6} strain. For typical operation of the system on the range -1.0 to $+1.0$ V with 12-bit resolution this gives a strain resolution of 0.48×10^{-6} and on the range -0.1 to $+0.1$ V this gives a strain resolution of 0.048×10^{-6}.

C. Analysis

A data analysis software package has been written for use with the system. This takes the recorded results from floppy disk in the form of values of H and B, λ and Barkhausen count rate dn/dt at each point. It then calculates magnetization $(B-H)/4\pi$, permeability $\mu = B/H$, differential permeability $\mu' = dB/dH$, magnetostriction, and Barkhausen emissions at each point.

Coercivity H_c and remanence B_R are calculated by interpolation of results close to $B=0$ and $H=0$ on the hysteresis loop to saturation to obtain intercepts on the H and B axes. Hysteresis loss W_H is calculated by integration around the hysteresis loop. Initial and anhysteretic permeabilities μ'_{in} and μ'_{an} are obtained using linear least-squares analysis of data at the origin $H=0$, $B=0$. The maximum differential permeability μ'_{max} is calculated from the slope of the hysteresis loop at $H=H_c$, $B=0$.

A digital plotter (Hewlett Packard HP7470A) has been added to the system to provide hard copy plots of various derived functions which are not recorded on the x-y recorders. A routine in the software analysis package enables plots to be made of magnetization, magnetic induction, permeability, differential permeability, susceptibility or differential susceptibility against magnetic field using either hysteresis loop, initial magnetization curve, or anhysteretic magnetization data.

D. Barkhausen and MAE

The magnetic Barkhausen effect emissions are detected from a search coil wound onto the specimen. The signal is then amplified using a preamplifier (Princeton Applied Research, Model 113A), a filter (Krohn-Hite, Model 3202), and a pulse counter (Hewlett Packard HP5304A). The count rate of Barkhausen pulses above a preset threshold level is then measured. By integration of the signal the total

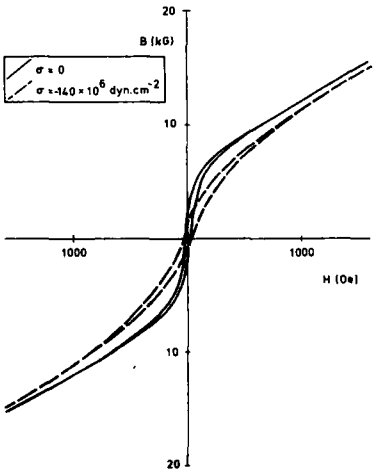


FIG. 2. Hysteresis loops for a specimen of terfenol (Tb-Dy-Fe) under zero stress and under a compressive load of 140×10^6 dyn cm^{-2} (2000 psi).

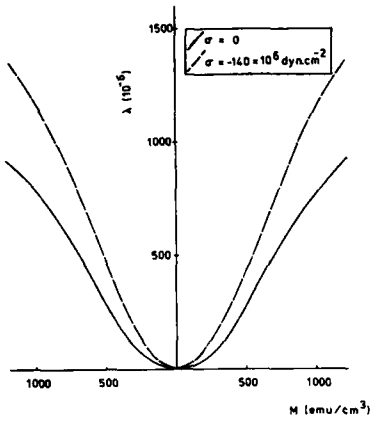


FIG. 3. Variation of magnetostriction λ for the same specimen of terfenol as a function of magnetization under zero stress and under a compressive load of 140×10^6 dyn cm^{-2}.

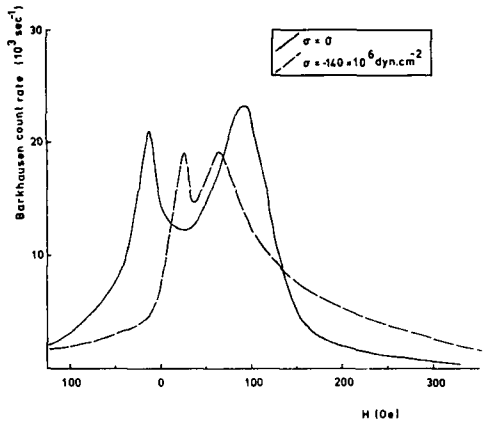


FIG. 4. Magnetic Barkhausen emission count rate as a function of magnetic field for the same specimen of terfenol. The emissions were recorded as the H field was increasing after saturating the magnetization of the specimen in the negative direction.

number of emissions is found. The MAE is detected in a similar way.

IV. RESULTS

Some results taken on a specimen of highly magnetostrictive terfenol are shown in Figs. 2–4 as an example. The measurements were made during two experimental runs during which the specimen was subjected to zero stress and then a compressive load of 140×10^6 dyn cm^{-2} (14×10^6 N m^{-2}, 2000 psi).

The hysteresis curve, Fig. 2, shows the reduction in permeability of the material under compressive loading. The maximum differential permeability was reduced from about 90 G Oe^{-1} under zero stress to about 40 G Oe^{-1} under 140×10^6 dyn cm^{-2}. The magnetostriction as a function of magnetization is shown in Fig. 3. It is seen from this that λ was improved under compressive loading by as much as 50%. Barkhausen emissions as a function of magnetic field are shown for the two stress levels in Fig. 4.

V. PLANS FOR FUTURE DEVELOPMENT

The remaining task is to fully integrate the MAE measurements. For this we use one of the remaining A/D input lines on the Labmaster board. The measurement of MAE will require similar instruments to the Barkhausen effect, so the configuration of these two parts of the system will be almost identical. To investigate the pulse height spectra of the emissions we will use a multichannel analyzer (The Nuclei, Inc. Model PCA-1000)[13] which is a plug-in board for the IBM PC. The pulse height spectra contain additional information which can be related to the microstructure of the material.

ACKNOWLEDGMENT

Ames Laboratory is operated for the U.S. Department of Energy by Iowa State University under Contract No. W-7405-ENG-82.

[1]D. C. Jiles, to be published in NDT Int. (1988).
[2]E. Martin, K. M. Zamarro, and J. Rivas, J. Phys. E **15**, 539 (1982).
[3]D. C. Jiles, D. L. Atherton, H. E. Lassen, D. Noble, J. deVette, and T. Astle, Rev. Sci. Instrum. **55**, 1843 (1984).
[4]W. A. Theiner and P. Deimel, "Nondestructive testing of welds with 3MA analyzer," Twelfth MPA Seminar, October, 1986 (unpublished).
[6]W. A. Theiner and I. Altpeter, in *New Procedures in Nondestructive Testing*, edited by P. Holler (Springer, Berlin, 1983).
[7]S. Habermehl and D. C. Jiles, in *Review of Progress in Quantitative NDE*, edited by D. O. Thompson and D. E. Chimenti (Plenum, New York, 1986), Vol. 5A, p. 843.
[8]Tecmar, Inc. 6225 Cochran Rd., Solon, Cleveland, OH 44139.
[9]D. C. Jiles, to be published in J. Phys. F (1988).
[10]D. C. Jiles, to be published in J. Phys. F (1988).
[11]D. C. Jiles and D. Utrata, to be published in J. NDE (1988).
[12]D. C. Jiles, C. V. Owen, and W. A. Spitzig, to be published in J. NDE (1988).
[13]The Nuclei, Inc., P. O. Box 2561, 761 Emory Valley Rd., Oak Ridge, TN 37830.

Large Barkhausen discontinuities in Co-based amorphous wires with negative magnetostriction

J. Yamasaki
Kyushu Institute of Technology, Tobata, Kitakyushu 804, Japan

F. B. Humphrey
Electrical and Computer Engineering Department, Carnegie-Mellon University, Pittsburgh, Pennsylvania 15213

K. Mohri, H. Kawamura, and H. Takamure
Kyushu Institute of Technology, Tobata, Kitakyushu 804, Japan

R. Mälmhäll
Royal Institute of Technology, S-100 Stockholm, Sweden

Magnetic properties, such as domain patterns and anisotropy, were measured for negative magnetostrictive Co-Si-B amorphous wires exhibiting large Barkhausen discontinuities and the results are compared to those of Fe-Si-B wires with positive magnetostriction. The Co-based wire was found to have a bamboolike domain structure at the wire surface. It was also shown that the amorphous wires prepared by the in-water quenching technique store tensile stress in the radial direction. The magnetostrictive anisotropy due to residual stress will produce an axial component of magnetization in conjunction with the two-dimensional geometry of wires making both Co- and Fe-based wires exhibit large Barkhausen discontinuities along the axis of the wire.

INTRODUCTION

Magnetostrictive amorphous wires prepared by the in-rotating water spinning method exhibit large Barkhausen discontinuities(LBD).[1] This property makes amorphous wires attractive as sensor elements in applications such as rotary encoders and high harmonics generators. We reported earlier that the LBD of Fe-based positive magnetostrictive wires is attributable to the anisotropy caused by interaction between magnetostriction and residual stresses quenched-in during solidification.[2] For a further understanding of the role of the magnetostrictive anisotropy, we measured the magnetic properties, including domain patterns, for in-water quenched Co-Si-B amorphous wires with negative magnetostriction and compared the results with those of Fe-Si-B wires with positive magnetostriction.

EXPERIMENT

The amorphous wire $Co_{72.5}Si_{12.5}B_{15}$ was produced by UNITIKA Co.(Kyoto, Japan) by the in-rotating water quenching method. The wire has a diameter of about 120 μm and a saturation magnetostriction of about -2×10^{-6}. The amorphous phase of the wire was checked by the measurement of the thermomagnetization characteristics. The Curie temperature and crystallization temperature of wire are 320 and 630 °C, respectively. Domain observation was made by the Bitter technique applying a constant 10-Oe field perpendicular to the wire axis.

RESULTS

The *B-H* loops of Co-Si-B wires are shown in Fig. 1 together with those of nonmagnetostrictive (Fe,Co)-Si-B and highly magnetostrictive Fe-Si-B wires. All loops were measured in a 60-Hz sinusoidal field in the wire axis direction. The Co-based wire [Fig. 1(a)] exhibits characteristic properties similar to the Fe-based wire [Fig. 1(c)]. When the amplitude of the drive field is below some threshold, the wire exhibits no irreversible flux change. A LBD takes place when the applied field is equal to or higher than a critical

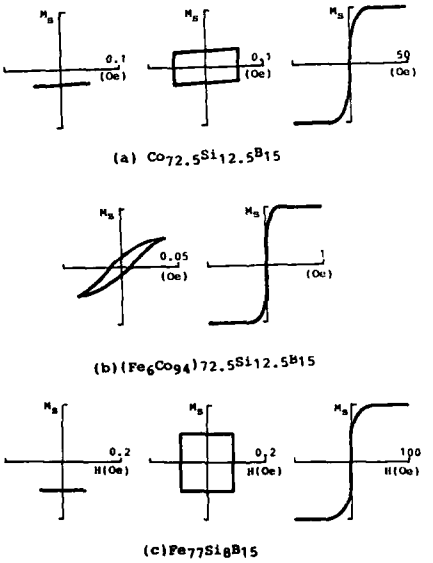


FIG. 1. *B-H* loops of as-quenched (a) Co-Si-B, (b) (Fe,Co)-Si-B, and (c) Fe-Si-B amorphous wires measured at 60 Hz.

 0021-8979/88/083949-03$02.40 © 1988 American Institute of Physics

reverse domain nucleation field H_n. The value of H_n and the fraction of magnetization participating in the LBD of Co-based wire are smaller than those of Fe-based wire. On the other hand, the nonmagnetostrictive Fe-Co-based wire [Fig. 1(b)] shows the very soft magnetic properties without LBD. The coercivity is less than 10 mOe and complete saturation can be achieved with an applied field of about 0.3 Oe. It is clear, by comparing the loops of the three wires, that magnetostriction is important for the occurrence of LBD. In fact, the LBD behavior of Co-based wire was found to disappear after stress relief annealing at 420 °C for 30 min, as shown in Fig. 2. The annealed wire has the soft magnetic properties similar to the nonmagnetostrictive wire.

Bitter patterns of Co- and Fe-based wire are shown in Fig. 3. The pictures show only the top surface of the circular wires, so the actual wire diameter is much larger than the visible width. These domain patterns were observed all along the surface of both wires. The Co-based wire [Fig. 3(a)] has bamboolike straight walls at the surface, while the Fe-based wire [Fig. 3(b)] exhibits the well-known maze domain pattern. The domain width is about 20 μm for Co wire and 4 μm for Fe wire. It was observed that both domain patterns do not change their configuration before and after the LBD in a low applied field. Therefore, both wires must have the component of magnetization along the wire axis in the inner core participating in the LBD.

Figure 4 shows a schematic of the domain structures expected for both wires. From the observed straight walls, the magnetization at the surface of Co-based wire is assumed to align in the circumferential direction [Fig. 4(a)]. The maze domain pattern [Fig. 4(b)] has been previouly discussed for amorphous ribbons.[3] This pattern at the surface of Fe-based wire indicates the presence of domains with magnetization perpendicular to the wire surface. The core domain size can be estimated to be about 70 and 90 μm for Co- and Fe-based wires, respectively, from the ratio of remanence to saturation. The Co-based wire has a single circular domain at the core which is covered with domains with magnetization in the circumferential direction, while Fe-based wire has a circular core covered with a closure domain structure near the surface.

The change of the core domain diameter with wire length for wires exhibiting LBD is shown in Fig. 5 as determined by the remanence-to-saturation ratio. The short-cut wires do not exhibit LBD due to the demagnetizing effect at the wire ends. The critical wire length to have LBD property is about 4 and 8 cm for Co and Fe wires, respectively. The core domain size is a very weak function of wire length,

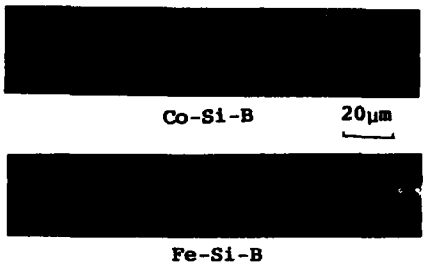


FIG. 3. Bitter patterns of Co-Si-B and Fe-Si-B amorphous wires observed with a constant applied field of 10 Oe perpendicular to the wire axis.

which suggests that the magnetostatic energy is associated for formation of inner core domain.

Figure 6 shows the distribution of the off-wire axis anisotropy in the cross section of wires evaluated from the magnetization curve measured in an applied field of 100 Oe along the wire axis for chemically etched samples. The anisotropy of Co-based wire is smaller by an order in magnitude compared to that of Fe-based wire. This difference can be attributed to the low magnetostriction of Co wire. Both wires have the higher anisotropy near the surface which decreases gradually with decreasing wire diameter.

DISCUSSION

As we have seen (Fig. 1), only the magnetostrictive, as-quenched wires exhibit LBD. This indicates that the magnetostrictive anisotropy quenched-in during solidification plays an essential role for occurrence of LBD. In general, the reverse nucleation field must be much larger than wall coercivity for materials to exhibit LBD. In the classical Sixtus and Tonks's experiment,[4] the tensile stress applied along the wire axis raised the wall energy and increased the nucleation field. The tensile stress produced a wire axis magnetization component participating in LBD, whereas it seems in amorphous wires that the tensile stress in the radial direction contributes to the increase of the nucleation field and produces wire axis magnetization in conjunction with the cylindrical geometry of wires.

The radial tensile stress in amorphous wires originates from the unique solidification process of the in-water quenching technique. When the jet of the molten alloy is ejected into the water, the outer surface first solidifies forming the solid wire diameter, and then solidification proceeds toward the inner core. During this process, the core tends to

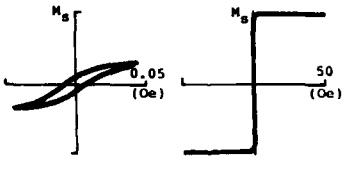


FIG. 2. *B-H* loops of Co-Si-B amorphous wires annealed at 420 °C for 30 min.

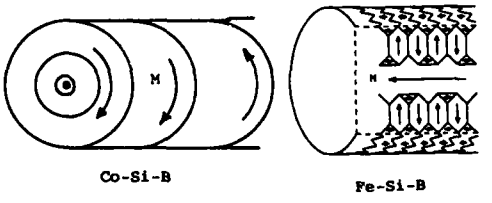


FIG. 4. Schematic domain structures assumed for (a) Co-Si-B and (b) Fe-Si-B amorphous wires.

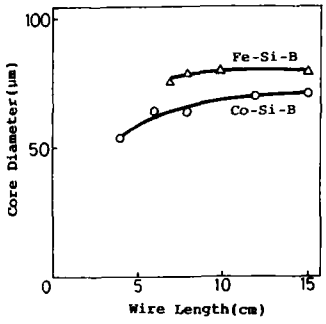


FIG. 5. Core domain size as a function of wire length for Co-Si-B and Fe-Si-B amorphous wires.

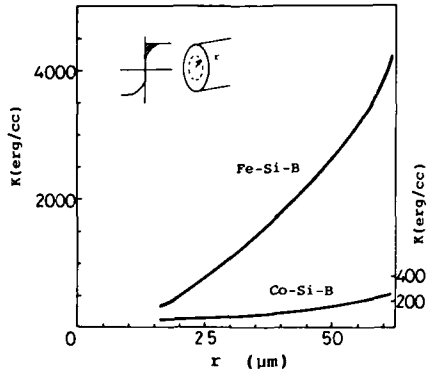


FIG. 6. Anisotropy distribution in wire cross section estimated from magnetization curve for chemically etched Co-Si-B and Fe-Si-B amorphous wires.

shrink against the surface to create tension in the radial direction. The quench rate is higher at the outer surface and decreases gradually toward the inner core. The measured off-wire axis anisotropy shown in Fig. 6 supports this model of the quenching process. Of course, the radial tension must be compensated with the compressive stress in the wire axis direction. These residual stresses would create anisotropy with the two easy axes in the circumferential and wire axis direction for Co-based wire and the anisotropy with the easy axis in the radial direction for Fe-based wire. The Bitter patterns on the wire surface in Fig. 3 are consistent with such magnetostrictive anisotropy. However, the shape effect of wire other than magnetostrictive anisotropy seems to take part for formation of the inner core single domains illustrated in Fig. 4.

In the bamboo domains of the Co-based wire, neighboring magnetic spins change their direction along the circumferential direction to store the exchange energy. The neighboring spins at the inner part make a larger angle compared to the outer spins. It is tempting to construct a model where, for lowering the exchange energy at the inner part, it is preferable for magnetization to align in the wire axis direction in the expense of magnetostatic energy near the wire ends. Thus in Co-based wire, core domain size would be determined mainly by the exchange energy. A simple calculation indicates that the core would be very much smaller than the observed size. Figure 5 shows the core diameter of the Co-based wire as a function of wire length with the Fe-based wire included for comparision. It is clear that the core is large and essentially independent of wire length. Therefore, the stress distribution must be much more complicated than our simple model assumed.

CONCLUSION

The amorphous wires prepared by the in-rotating water quenching technique store tensile stress in the radial direction. The magnetostrictive anisotropy associated with this residual stress gives rise to the wire axis component of magnetization in conjunction with the two-dimensional geometery of wires, and makes wires exhibit large Barkhausen discontinuities regardless of the sign of magnetostriction.

[1]K. Mohri, F. B. Humphrey, J. Yamasaki, and K. Okamura, IEEE Trans. Magn. **MAG-20**, 1409 (1984); K. Mohri, *ibid.*, 942 (1984).
[2]K. Mohri, F. B. Humphrey, J. Yamasaki, and F. Kinoshita, IEEE Trans. Magn. **MAG-21**, 2017 (1985).
[3]H. Kronmüller and B. Gröger, J. Phys. (Paris) **42**, 1285 (1981); H. Kronmüller, R. Schäfer, and G. Schoeder, J. Magn. Magn. Mater. **6**, 61 (1977).
[4]K. J. Sixtus and L. Tonks, Phys. Rev. **47**, 930 (1930).

Training of Barkhausen emission in nickel and iron

H. Weinstock
Air Force Office of Scientific Research, Bolling Air Force Base, D.C. 20332

T. Erber
Department of Physics, Illinois Institute of Technology, Chicago, Illinois 60616

Barkhausen emission from annealed nickel and iron was measured with a SQUID gradiometer that could detect magnetization jumps above a noise level of 3×10^{-8} emu. The equipment was installed in a three-axis 12.7-m-diam Braunbeck coil system at NASA's Goddard Space Flight Center. This arrangement provided an overall cancellation of the geomagnetic field to $\pm10^{-6}$ Oe, and a field homogeneity of 0.001% over a spherical volume of 24.4 m^3. Auxiliary windings in the Braunbeck coils were used to generate uniform magnetizing fields at sweep rates as slow as 0.81 μOe/s. The nickel measurements were carried out in field ranges that interpolated between those used in previous training experiments with iron and gadolinium samples. In all cases, repeated field sweeps eliminated or diminished the Barkhausen signals in a systematic way paralleling the Kaiser effect in acoustic emission. These results can be related to the training behavior predicted by a general hysteresis theory.

I. THREE KINDS OF HYSTERESIS

Hysteresis phenomena in ferromagnets, Ewing arrays, elastic-plastic frameworks, and materials under stress have many similar features that can be described in terms of a unified theory.[1] For instance, the training of Barkhausen emission in ferromagnets is a direct analogy of the Kaiser effect in acoustic emission and the shakedown of complex frames in structural mechanics. In all of these situations, repeated sweeps of a hysteresis or control variable—which might be an external load or a magnetic field—diminish the irreversible response of the systems: In materials this corresponds to a progressive narrowing of the stress-strain hysteresis loops and the fading of acoustic emission; and in ferromagnets to the closure of M-H loops, and the extinction of Barkhausen jumps. Of course, this type of quenching of irreversible behavior by *self-limiting* hysteresis can occur only if either the loads or fields are sufficiently small.

For larger values of the hysteresis variables, the mechanical and magnetic systems generally exhibit a long-term *drifting* hysteresis under repeated cycling. For reasons that will become apparent later, in this intermediate regime neither the drift nor the hysteresis can be eliminated by simple conditioning procedures. Finally, for sufficiently high values of the control variables, the iterative time scales of the hysteresis decrease again. In practice, this means that the hysteresis loops stabilize in a comparatively small number of cycles, and that the mechanical or magnetic response of the systems approaches the steady state of *asymptotic* hysteresis.

These general trends have been observed in a variety of systems. Here, we present some further data concerning the development of Barkhausen emission and magnetic hysteresis loops in field ranges that interpolate between those used in previous training experiments with iron and gadolinium samples.[2,3] We also discuss the widely different reasons for the rapid stabilization of hysteresis at low and high field values.

II. BARKHAUSEN EMISSION AND HYSTERESIS

The nickel measurements were performed with essentially the same equipment that was used in earlier hysteresis studies of iron and is described in detail in Ref. 2. Background fields were minimized by working at NASA's Attitude Control Test Facility at Greenbelt, MD. Measurements were carried out with a 98% pure annealed nickel cylinder, approximately the size of a pill (3.2 mm high and 5.0 mm in diameter). At the beginning of each run, the sample magnetization was reduced to 10^{-5} emu by the anhysteretic demagnetization procedure described in Ref. 2. Highly uniform external magnetizing fields were provided by the auxiliary windings of a Braunbeck coil system. The relative orientation of the external field, samples, and SQUID gradiometer coils is shown on the inset of Fig. 1. The demagnetizing factor in this setup is 3.6; consequently, the internal nickel fields are approximately $0.03H_{ext}$. The power supplies of the previous experiments were modified to permit uni-

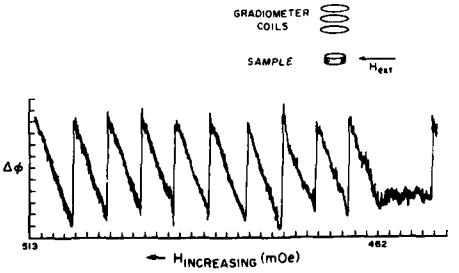


FIG. 1. Strip-chart record of flux variations ($\Delta\Phi$) as a function of external field (H). Each vertical division represents $4.86\times10^{-3}\ \Phi_0$ flux units; each horizontal division is an increment of 1.37 mOe. The vertical lines are due to manual resets. The inset shows the orientation of the external field, sample, and SQUID gradiometer.

 0021-8979/88/083952-03$02.40 © 1988 American Institute of Physics

form, slow field sweeps extending to 650 mOe. As before, both the continuous as well as the discontinuous changes in the magnetization of the nickel sample were measured with an independently calibrated SQUID gradiometer. The limiting slew rate of this instrument was approximately $10^5\Phi_0$/s, where Φ_0 is the flux quantum ($hc/2e \simeq 2.07\times10^{-7}$ G cm^2). This leads to an upper limit of the order of 10^{-5} emu for the magnetic moments of the Barkhausen jumps that could be detected.[2] On the other hand, discontinuous magnetization changes as small as 3×10^{-8} emu could be distinguished from the smooth background variations due to the ramping of the external field.

In a similar setup with iron samples the threshold of Barkhausen emission occurred for external fields in the range 40–100 mOe. In contrast, the onset of Barkhausen noise in nickel has had a long and controversial history.[4–6] Indeed, the present SQUID results show that in nickel, the onset of Barkhausen noise is not as sharply defined as in iron and occurs at field values above 200 mOe. These trends are consistent with earlier observations of Tebble *et al.*[7] Figures 1–3 illustrate the training of Barkhausen emission: Specifically, Fig. 1 shows the response of a previously demagnetized nickel sample to the *first increasing* field sweep from 462 to 513 mOe. In this case, the Barkhausen signals correspond to individual magnetization jumps of the order of 6×10^{-7} emu. Figure 2 is an excerpt from the *first decreasing* field sweep. This record covers the range 480–455 mOe, and evidently most of the Barkhausen emission exceeding a background level of about 10^{-7} emu has been eliminated. This behavior agrees with the training found in gadolinium at higher field values.[3] Finally, Fig. 3 shows the reappearance of Barkhausen noise during the succeeding field sweep which extended up to 564 mOe. The nickel results show that with sufficient resolution, the correlation between hysteresis, Barkhausen noise, and training previously found for iron at lower fields ($\gtrsim\mu$Oe), and gadolinium at higher fields ($\gtrsim$3 Oe), can also be exhibited in the intermediate field range $\gtrsim$0.2 Oe.

During incipient and drifting hysteresis, the *M-H* loops generally do not close, and their areas do not have a simple correspondence to the cumulative irreversible magnetization changes due to Barkhausen jumps.[2,7] However, if repeated field variations over some restricted range reduce or eliminate the Barkhausen emission, then the associated hysteresis loops also narrow and disappear. Such trends have frequently been reported in the literature,[8] but show up in a particularly clear way at low field levels and with very slow sweep rates. This is illustrated in Fig. 4, which shows a virgin

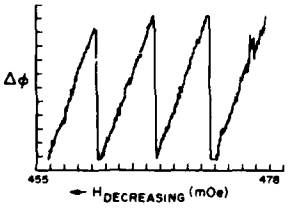


FIG. 2. Suppression of Barkhausen signals in nickel in a decreasing field sweep from 480 to 455 mOe.

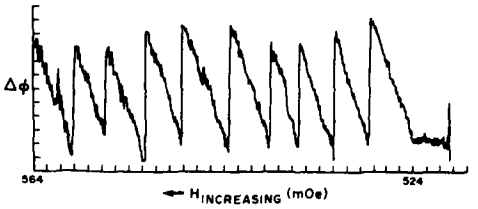


FIG. 3. Reappearance of Barkhausen signals during an increasing field sweep from 525 to 564 mOe.

hysteresis curve for an annealed iron sample. Repeated cycling between the fixed field limits, 0–62 mOe, resulted in a progressive narrowing of the loop, until by the ninth cycle, the loop had closed to within the limit of experimental resolution. This terminal behavior is shown in Fig. 5. The typical quenching of Barkhausen emission that occurs in this field range in iron is displayed in Fig. 3 of Ref. 2.

III. THE STABILIZATION OF HYSTERESIS SYSTEMS

Formally, it is easy to introduce a quantitative measure of the stabilization of hysteresis systems: n_L is said to be the iterative "time" scale of the stabilization if after n_L complete cycles of the hysteresis variable—which could be a mechanical loading or an external magnetic field—there are no

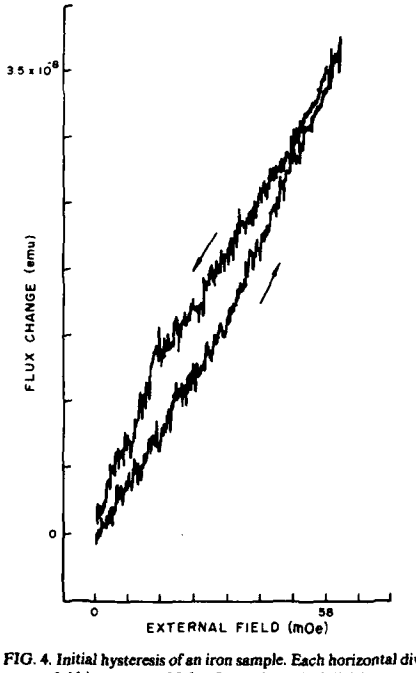


FIG. 4. Initial hysteresis of an iron sample. Each horizontal division represents a field increment of 8.3 mOe; each vertical division corresponds to a flux change of $2.43\times10^{-2}\,\Phi_0$ *units.*

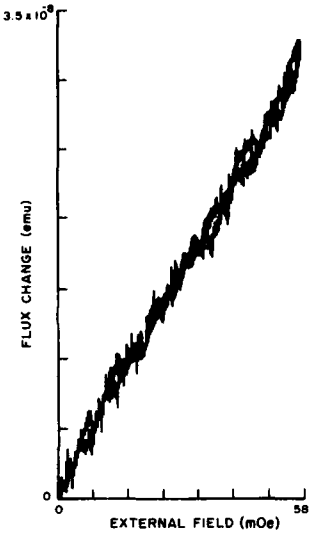


FIG. 5. Closure of the iron hysteresis loop at the ninth cycle.

further changes in the response of the system. In practice this situation is complicated by the fact that the initial conditions have to be specified in some reasonable way so that the magnitude of n_L does not have an arbitrary scale. For instance, in magnetism, anhysteretic demagnetization is an accepted method for establishing a virgin reference state. Another essential complication is that n_L generally is a non-monotonic function of the peak value of the hysteresis variable. For example, in structural shakedown it can be shown explicitly that n_L is small both in the limits of large and small loadings, but in addition there is an intermediate load, W_S, with the property that $n_L(W)$ *diverges* when W_s is approached either from above or below.[9] Qualitatively similar behavior appears in large Ewing arrays and other magnetic systems.

The Barkhausen training effects described in Sec. II and Ref. 2 fit into this picture because $n_L(H)$ in these cases simply denotes the number of cycles required to reach a reversible state. Specifically, if H_t denotes the threshold field for the appearance of the initial Barkhausen jump,[2] then the observations indicate that $n_L(H)$ is an increasing function of the field for $H \gtrsim H_t$. Furthermore, if after $n_L(H_1)$ cycles in the interval $0<H<H_1$, another cycle extending to $H_2 > H_1$ is added, renewed Barkhausen signals will appear in the range above H_1: this is the essence of the magnetic Kaiser effect.[2,3]

The physical processes that result in this behavior can be described with the help of *hysteresis manifolds*. These are basically phase spaces that are spanned by all the magnetic or mechanical variables that are required to specify the states of the systems. Since the effects of hysteresis are multivalued and history dependent, these spaces have extra dimensions for each control variable. The evolution of an arbitrary hysteresis system is then represented by a *unique* path or phase portrait in these extended spaces. In the case of ferromagnetism, this is equivalent to replacing Néel's ensemble of potential wells by a network of stability troughs.[1-3] The training behavior and the Kaiser effect then appear as consequences of a simple geometric feature—the successive troughs of the hysteresis networks are linked by monotonic progressions of instability points. The corresponding iteration index $n_L(H_1)$ is just a measure of how many instability points are traversed before a stable trough in the range $0<H<H_1$ is reached; cf. Fig. 3 of Ref. 1 and Figs. 6 and 7 of Ref. 2.

For large values of field or load, n_L represents the number of cycles required to reach steady-state hysteresis.[10] In particular, for nickel and iron it is well known that $n_L(H) \lesssim 10$ for $H \gtrsim 10$ Oe. Since ferromagnetic hysteresis cycles typically traverse more than 10^9 Barkhausen discontinuities per cm^3 of material[7], the macroscopic stabilization of these loops after only a few cycles reflects the operation of powerful microscopic selection principles. The existence of such sequences of metastable attractor states can also be exhibited in model systems such as Ewing arrays. It is plausible to assume that the stabilization of hysteresis loops is the cumulative result of energy minimization. However, several computer simulations of spin glasses[11] and Ewing arrays[12] have shown that the terminal hysteresis cycles lie on essentially flat energy terraces rather than in valleys. Model studies suggest that in these situations the asymptotic hysteresis cycles are the terminal loops of pseudo-random iterations. It can then be shown that for an N-state system with an average of d discontinuities per hysteresis cycle, the average number of cycles required to reach the terminal loop is of the order of $n_L \sim N^{0.5}/d$. For example, in a 6×6 Ewing array, $N \sim 1200$, $d \sim 10$, and therefore $n_L \sim 3.5$—this estimate agrees with observations.[12] If the trend $\mathcal{O}(N^{0.5}/d) \sim 1$–10 could be confirmed for larger systems, we would have an essentially combinatorial explanation for the rapid approach to asymptotic hysteresis for large field excursions.

ACKNOWLEDGMENT

We thank Dr. M. Nisenoff for his help in all phases of this work.

[1] T. Erber, S. A. Guralnick, and H. G. Latal, Ann. Phys. (N.Y.) **69**, 161 (1972).
[2] H. Weinstock, T. Erber, and M. Nisenoff, Phys. Rev. B **31**, 1535 (1985).
[3] T. Erber, J. L. Porteseil, and P. Molho, Philos. Mag. B **52**, 963 (1985).
[4] A. Koller, Z. Angew. Phys. **23**, 161 (1967).
[5] K. Stierstadt, *Der Magnetische Barkhausen Effekt*, Vol. 40 of *Springer Tracts in Modern Physics* (Springer, Berlin, 1966).
[6] M. Lambeck, *Barkhausen Effekt* (de Gruyter, Berlin, 1971).
[7] R. S. Tebble, I. C. Skidmore, and W. D. Corner, Proc. Phys. Soc. London **63**, 739 (1950).
[8] H. Rogalla and C. Heiden, Phys. Lett. **A63**, 63 (1977).
[9] T. Erber and S. A. Guralnick, Ann. Phys. (N.Y.) (to be published).
[10] In stress-strain hysteresis, steady-state response may be reached for only a subset of the physical variables (Ref. 9).
[11] A. E. Jacobs and C. M. Coram, Phys. Rev. B **36**, 3159 (1987).
[12] T. Erber, T. M. Rynne, W. F. Darsow, and M. J. Frank, J. Comput. Phys. **49**, 394 (1983).

Acoustic emission along the hysteresis loops of various ferro- and ferrimagnets

M. Guyot, T. Merceron, and V. Cagan
Laboratoire de Magnétisme, C.N.R.S., 1, Place A. Briand, 92195 Meudon Bellevue, France

For the first time, the acoustic emission (AE) along a hysteresis loop has been investigated at variable magnetizing field frequency (10^{-2} up to 10^{2} Hz) on three very different magnetic materials: polycrystalline YIG, amorphous FeNiBSi ribbon and mumetal. For all the samples the AE activity is hysteretic; in the very-low-frequency range it shows two sharp minima around the coercive field values $\pm H_c$ and a smooth decrease when approaching the saturation, as we have reported in a previous paper. At increasing frequency, the AE minima at H_c vanish progressively and in some cases are even replaced by broad maxima, as already reported in the literature. Such an effect could be attributed to the complex situation occurring when increasing the frequency, due either to the measurement technique or to physical phenomena such as echoes. However, we cannot exclude the possible influence of dynamical changes of the microprocesses which originate the AE. That leads us to the conclusion that AE is better investigated in quasistatic conditions.

I. INTRODUCTION

Acoustic emission (AE) is a general phenomenon observed in various materials, which involves bursts of stress waves internally generated during a dynamical process.[1] Generally, the origin is not well known; in a few cases a pure mechanical origin has been suggested (dislocation or crack propagation, interparticle movement, fracture, etc.), and various models have been proposed accordingly.[1] In the case of magnetic materials. Lord[2] suggested the possibility of AE during the Barkhausen discontinuities, due to the magnetoelastic coupling. More recently, several authors[3,4] have attributed the origin of AE in ferromagnetic metals or alloys to the irreversible movements of non-180° domain walls (DW). In a recent work on YIG samples,[5] an insulating ferrimagnet, we proposed to associate the AE to the necessary process of DW creation/annihilation along the hysteresis loop: on one hand, Mohammad *et al.*[6,7] have indeed shown on ferroelectrics that AE is due to DW creation/annihilation; on the other hand, we have shown earlier[8,9,10] that the DW creation/annihilation is a dissipative process responsible for the main part of the hysteresis losses.

Our interpretation is mainly backed by the observed linearity between the total AE activity and the hysteresis losses for the loops recorded, for a given sample, at increasing maximum field. In addition, our experimental procedure allows us to clearly show an anticorrelation between the AE and the Barkhausen noise (BN): around the coercive field AE exhibits a sharp minimum, while BN is maximum as classically known. This observation, which is consistent with our interpretation, is in contradiction with the few results reported on AE along hysteresis loops.[1,11,12] In fact, these results, obtained exclusively on metals or alloys generally magnetized at the line frequency (except Ref. 12, where $f = 0.1$ Hz), cannot be directly compared with our measurements performed on insulators at 10^{-2} Hz frequency.

The present paper reports, for various soft magnetic materials, some results on how the magnetizing field frequency affects the AE.

II. EXPERIMENT

The samples are toroid shaped in order to avoid any shape demagnetizing effect. We present here the results from three very different samples: a polycrystalline YIG, an amorphous $Fe_{0.4}Ni_{0.4}B_{0.12}Si_{0.08}$ ribbon[13] 28 μm thick wounded on a plastic ring and a "Mumetal" thin ring.

The magnetizing field is produced by a triangular wave current flowing in the primary winding of the sample through a load resistor. As classicaly, the Barkhausen noise is recorded from the voltage induced in a pick up coil.

For the AE recording, a piezoelectric captor in contact with the surface sample is connected, through a high gain (up to 100 dB) amplification chain, to a digital oscilloscope. By using for the present study a scope with a peak detector function associated with a high sampling rate, we have been able to extend the measuring frequency range from 10^{-2} up to 10^{2} Hz. Using the numerical averaging function of the scope allowed us to smooth the traces when needed.

III. RESULTS

Figures 1–3 present the results obtained on each sample at different frequencies: 10^{-2} up to 10^{2} Hz. The AE and the BN amplitudes versus the applied field are shown on the left-hand side and the right-hand side, respectively. The scaling is indicated in the captions.

Figure 1 is devoted to the YIG sample. The BN shows a more or less discrete series of spikes at 10^{-2} Hz, which shifts progressively to a continuum as the frequency increases. It must be remarked that the BN maximum occurs for a nearly constant field value over the covered frequency range; this value corresponds roughly to the coercive field H_c, as observed on the 10^{2} Hz plotting which includes the hysteresis loop.

 0021-8979/88/083955-03$02.40 © 1988 American Institute of Physics

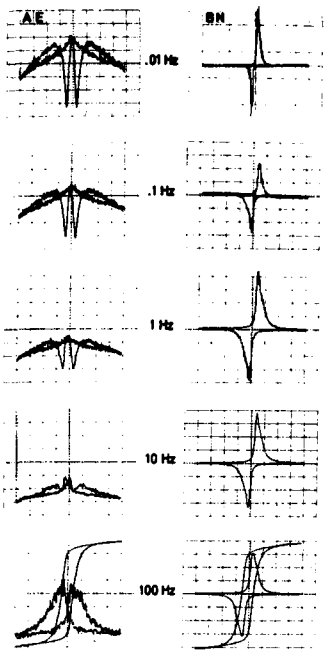


FIG. 1. YIG polycrystalline toroid. Acoustic emission (left-hand side) and Barkhausen noise (right-hand side) vs applied field at different applied field frequencies. All horizontal scales: triangular ac field, 0.6 Oe/div. Vertical scales: (i) for AE, same arbitrary scale for all frequencies, ground level at the screen bottom. (ii) for BN, variable arbitrary scale, ground level at the center line of the screen.

The AE recording at 10^{-2} Hz confirms our previous results: the AE shows a hysteretic behavior with two sharp minima around the coercive field and tends to decrease when approaching the saturation. The same general behavior is roughly conserved up to about 1 Hz although the total amplitude becomes compressed; above this frequency the behavior is seen to change progressively to a completely different one as the frequency increases. At 10^2 Hz the AE now exhibits a clear maximum around H_c.

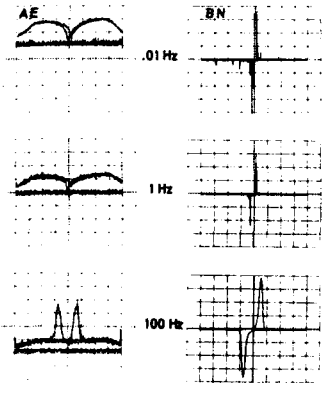


FIG. 2. Amorphous $Fe_{0.4}Ni_{0.4}B_{0.12}Si_{0.08}$ ribbon. Same as Fig. 1, except horizontal field scale: 0.7 Oe/div. Due to the high gain needed for AE, the noise level is different from the ground level.

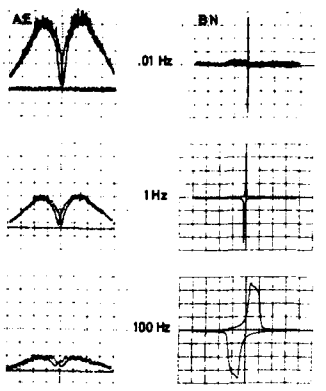


FIG. 3. Mumetal ring. Same as Fig. 1, except horizontal field scale: 0.7 Oe/div. As in Fig. 2, the noise level for AE is recorded.

Figure 2 shows the results obtained on the amorphous ribbon which presents the same general trends as the YIG sample. However, some peculiarities must be emphasized: looking at the BN signal, it is obvious that the coercive field increases with the frequency and that the singularities of AE (minimum or maximum) follow this variation. The AE amplitude is much smaller than for the YIG sample, so we have also recorded the AE noise level with no magnetizing field applied.

Figure 3 is devoted to the Mumetal sample. More than the amorphous ribbon, the coercive field increases with the frequency; the BN shape at 100 Hz allows a deformation of the corresponding hysteresis loop to be foreseen. The AE signal (the residual noise level has also been recorded) shows the same type of evolution as the other samples: however, AE does not exhibit at 10^2 Hz any maximum around H_c. According to its frequency dependence, one should expect the occurence of a maximum at higher frequency.

IV. DISCUSSION

To our knowledge, this is the first study of the AE at variable frequency. We have found both AE and BN to be frequency dependent. Is such a dependence a true physical effect or an artefact related to the measurement method? The only published work[11] concerning measurements along an hysteresis loop cycled at about 50 Hz makes mention of an AE maximum around H_c; that is what we observed for two among the three typical samples reported here and for several others. In addition, the response for the three samples at 10^2 Hz looks different, one of them showing no maximum at all. This is another good reason not to suspect our own equipment by itself compared to other authors. However, as far as the measurements method is concerned, we must remark that most of the works in that field are made by

using the same kind of equipment, namely, a piezoelectric captor set at its resonance frequency and the associated electronics. The response of such a system to a given stress wave is a damped voltage oscillating at the resonance frequency: at very low frequency, such at 10^{-2} Hz, the resulting signal at the output of the amplification chain will correctly represent the AE. On the contrary, at a higher frequency (10^{2} Hz, for example) the time extension of the voltage produced by a single spike will no longer be negligible compared to the measurement period, resulting in a possible alteration of the final signal which will no longer correctly represent the AE.

Another point of interest is the pulse echoes. Taking into account the mean velocity of the sound in our materials ($\approx 5\times 10^{5}$ cm/s), the transit time could typically be about a few μs. Since the attenuation coefficient is quite small (of the order of a few percent), one must expect a great number of echoes taking place after a single spike. At very low measurement frequency such echoes might be generally damped prior the next spike. At higher frequency, say 1 Hz or above, they can overlap and/or even interact with new spikes. Moreover, according to the measurement frequency some echoes could be analyzed as actual direct spikes, resulting obviously in a perturbed final signal. All these different mechanisms combined together lead to a situation more and more complex as the measurement frequency increases, where it could no longer be possible to relate the final signal to the primary ultrasonic spike. An additional evidence of such a complexity is given by the fact that, at high frequencies, the recorded signal needs to be strongly averaged in order to produce relatively smooth curves, while it can be directly reproduced at very low frequencies.

In any event, whatever the physical origin of the AE may be—non-180° DW motion[3,4] or DW creation/annihilation[6,8]—is there any possibility of DW dynamical changes in the observed frequency range? For metal, the answer is positive if looking at the loop changes (refer to Figs. 2 and 3). It is known that in soft ferromagnetic conductors the number of DW increases with the magnetizing frequency.[14] For insulators, although we do not observe any change of the loop parameters as a function of frequency, our results show (refer to Fig. 1, right) that the DW motion is made of successive jumps at very low frequency while it follows as a whole the magnetizing field at higher frequencies. It must be remarked that the AE behavior changes at the same time.

V. CONCLUSION

If we do not reject *a priori* some possible dynamical changes in the microprocesses which originate the AE, we are of the opinion that, when increasing the measurement frequency, some parasitic effects related to the measurement technique and/or to the physics itself (echoes) may affect progressively the quasistatic response and make the results as a function of frequency hard to analyze. To our opinion, it should be better to investigate the origin of the AE by using quasistatic measurements instead of line frequency measurements; this is particularly true for metallic materials which exhibit generally at 50 Hz an hysteresis loop yet affected by the dynamical changes of the number of the DW.

[1] A. E. Lord, in *Physical Acoustic*, edited by Mason (Academic, New York, 1975), Vol. XI, p. 289.
[2] A. E. Lord, Acoustica **18**, 187 (1967).
[3] K. Ono and M. Shibata, in *Advances in Acoustic Emission*, edited by H. Dunegan and W. Hartmann (Dunhart, Knoxille, TN, 1981), pp. 154–174.
[4] H. Kusanagi, H. Kimura, and H. Sasaki, in *Fundamentals of Acoustic Emission*, edited by K. Ono (UCLA School of Engineeering, Los Angeles, 1978), p. 309.
[5] M. Guyot, T. Merceron, and V. Cagan, Phys. Lett. A **120**, 64 (1987).
[6] I. J. Mohamad, L. Zammit-Mangion, E. F. Lambson, and G. A. Saunders, J. Phys. Chem. Solids **43**, 749 (1982).
[7] L. J. Zammit-Mangion and G. A. Saunders, J. Phys. C **17**, 2825 (1984).
[8] M. Guyot and A. Globus, Phys. Status Solidi B **59**, 447 (1973).
[9] M. Guyot, *Ph.D. thése d'Etat* (Paris, 1975).
[10] M. Guyot and A. Globus, J. Phys. C **1**, 157, (1977).
[11] O. A. Bartenev, V. A. Khamitov, and E. A. Gorkunov, Instrum. Exp. Tech. **27**, 205 (1984).
[12] R. Rajan, D. C. Jiles, and P. K. Rastogi, IEEE Trans. Magn. **MAG-22**, 511 (1986).
[13] The authors are in debt to Dr. R. Krishnan who kindly supplied some amorphous ribbon samples.
[14] T. H. Haller and J. J. Kramer, J. Appl. Phys. **41**, 1034 (1970).

Modified magnetic properties in laser welded materials

N. Smith and R. Bird
IBM Corporation, Information Products Division, 1001 W. T. Harris Boulevard West, Charlotte, North Carolina 28257

The magnetic properties of laser welded magnetic materials can be modified by selecting material composition, and by setup parameters. The modification depended upon the original material composition, annealed coercive force, and the size of the weld size. Original grain boundaries were reformed in the silicon iron samples only, which also had the smaller increase in coercive force. The coercive force of cobalt-vanadium iron with a lower initial value was increased more than similar samples with a higher initial coercive force value. Double welds doubled the increase in coercive force of single welds. Magnetic fields of the intensity used in this test were not found to have a large effect upon the changes in coercive force due the laser welding process. In prior tests, stronger alternating magnetic fields reduced coercive force in cobalt-vanadium iron alloys.

I. INTRODUCTION

Prior experiments joined highly permeable, high-saturation level magnetic material to thin, high-strength nickel iron alloy by means of pulsed laser welding (see Table I). The advantages of a filler material as shown by Banas[1] were achieved by tactical relative positioning of the parts in a similar way to that shown by Saifi and Vahaviolos[2] such that excess material from the upper part flowed into the junction, forming fillets, thereby raising the section modulus and thus reducing the induced stresses below the endurance limit of the material in the fused junction.[3] Figure 1 illustrates a cross section of the setup, and Fig. 2 illustrates a cross section of a resulting weld.

Remaining stresses from the welds are primarily tensile, tangential to the weld circle, and as noted by Moses and Thomas[4] are beneficial to the B/H relationship in this region. The resulting detrimental compressive stresses at the center[4] are minimized due to distance from the path of high flux density.

Analysis of our prior laser welding fabrication experiments for minimum coercive force showed, within some welds, the original grain boundaries had been reestablished after the welding. See Fig. 3. Assemblies, held in place by dc magnetic fields at the time of welding, did not function well at high cyclic rates. Conversely, assemblies held in place by high-frequency alternating magnetic fields at the time of welding, performed well.

From the above experience a second matrix of tests were configured to simulate the welds and quantify the changes in the magnetic properties, as functions of (1) materials, (2) material condition, (3) size of welds, and (4) surrounding magnetic fields.

TABLE I. Prior weld junction experiments.

Magnetic field	Magnetic materials	
	CoVFe	SiFe
120 kHz	X	X
10 kHz	X	
1 kHz	X	X
Steady	X	
Earth	X	X

II. METHOD OF TESTING

Four lots of soft magnetic materials of the same shape were tested. From each lot parts were selected for five different magnetic field conditions forming a 4×5 test matrix. Each part was individually identified and measured for coercive force. Each part was laser "welded"[5] in magnetic fields as shown and then remeasured for coercive force. The average change and standard deviation. Parts from each group were sectioned, etched to show grain boundaries, and photographed.

III. DESCRIPTION OF TEST APPARATUS

Samples were welded in a fixture (see Fig. 4) with coil windings, connected as shown below. As the fixture was moved in a circular motion the laser fired downward at the

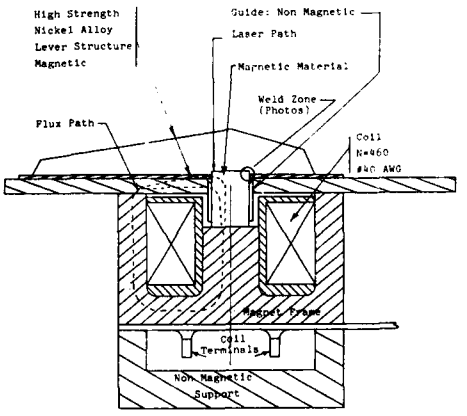


FIG. 1. Cross section of magnetic retention weld setup.

 0021-8979/88/083958-03$02.40 © 1988 American Institute of Physics



FIG. 2. Prior experiment showing typical laser welded junction (100×).

top of the test part forming a ring of overlapping spotwelds (see Fig. 5).

A. Laser I. D. and parameters:

JK Model 702 400 W Neodymium doped: YAG laser.

Pulse duration	0.003 s
Pulse Rate	4.5 Hz
Energy/Pulse	1.0 J
Pulses/Part	54.0
Weld Spot Diameter	0.4 mm

B. Coil power source

1. 100 kHz: 18 V peak to peak
2. 10 kHz: 15.5 V peak to peak
3. 1 kHz: 6.4 V peak to peak
4. dc power source: set at 4 V

IV. DESCRIPTION OF MATERIALS TESTED

Samples were 2.06 mm diam × 3.00 mm length.

Lot No 1: Co (48.75%)V(1.90%)Fe(Balance)

Quenched, machined, and annealed
Initial $H_c = 0.75 - 0.95$ Oe
To be welded around one end only

Lot No. 2: Si(2.50%)Fe(Balance)

Machined and annealed
Initial $H_c = 0.35$–0.55 Oe
To be welded around one end only

Lot No. 3: Same as Lot No. 1 except:

Quenched, machined, and annealed
Initial $H_c = 1.55$–1.75 Oe
To be welded around one end only

Lot No. 4: Same as Lot No. 1 except:



FIG. 3. Prior experiment showing reestablished grain boundaries (200×).

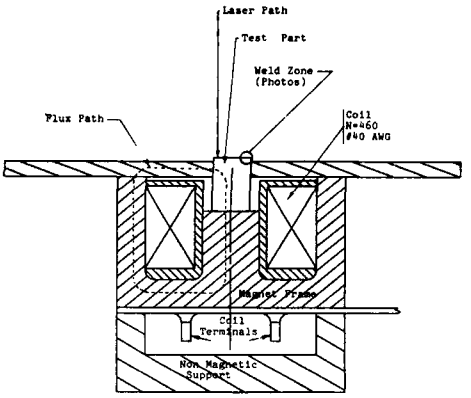


FIG. 4. Cross section of test part weld positioning fixture.

Quenched, machined, and annealed
Initial $H_c = 0.95$–1.15 Oe
To be welded around both ends

V. RESULTS OF TEST

The average increase in coercive force and the corresponding standard deviation for each group of the 4×5 matrix are shown in Table II. All of the parts in Lot No. 2 exhibited the reestablishment of the original grain boundaries within the welds after the welding process. Figure 6 illustrates a typical weld cross section. The increase in coercive force for this lot was smaller than for any of the other three lots.

Figure 7 illustrates a typical weld cross section of Lot No. 1, which was also similar to Lots 3 and 4. None of the parts in these lots exhibited reestablished grain boundaries.

The actual confinement of the detrimental effects of the weld to the proximity of the weld was verified by subsequent experiment in which approximately 0.3 mm of the weld end of the test part was polished away and the part remeasured for coercive force, at which time it was determined that its preweld value had been restored.

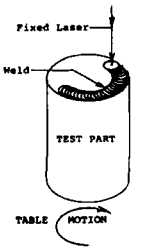


FIG. 5. Circular pattern of overlapping laser spotwelds.

TABLE II. Increase in coercive force (Oe).

Magnetic field		Materials: Lot No. 1 CoVFe $H = 0.85$	Lot No. 2 SiFe $H = 0.45$	Lot No. 3 CoVFe $H = 1.65$	Lot No. 4 CoVFe $H = 1.05$	Ave. for CoVFe
100 kHz	ave.	0.435	0.238	0.362	0.929	0.573
18 V	sigma	0.032	0.041	0.016	0.102	
10 kHz	ave.	0.443	0.237	0.351	0.882	0.558
15.5 V	sigma	0.064	0.031	0.027	0.063	
1 kHz	ave.	0.387	0.271	0.277	0.898	0.520
6.4 V	sigma	0.031	0.025	0.020	0.070	
Steady	ave.	0.422	0.205	0.327	0.935	0.561
4 V	sigma	0.036	0.015	0.044	0.057	
Earth	ave.	0.433	0.228	0.293	0.852	0.526
	sigma	0.040	0.059	0.049	0.096	
Average increase		0.424	0.235	0.322	0.899	
Final value		1.27	0.68	1.97	1.95	



FIG. 6. Weld damage to CoVFe in Oe.

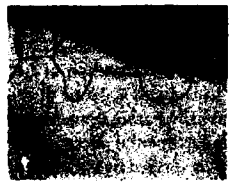


FIG. 7. Lot 2: typical weld section and reestablished grain boundaries (200×).

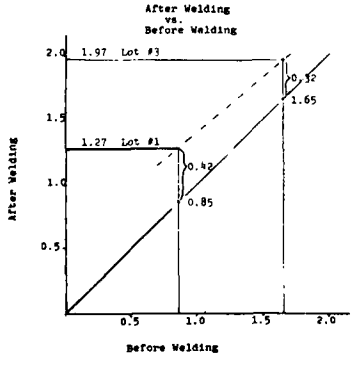


FIG. 8. Lots 1, 3, and 4: typical weld section and interrupted grain boundaries (200×).

VI. DISCUSSION OF RESULTS

Of CoVFe parts Lot No. 3 had a lower increase in coercive force; Lot No. 1 had a lower final final value due to its lower initial value (see Fig. 6). The shorter radius of the laser path[5] resulted in shallower welds traversing only the edge of the flux loop. This, the omitting of the adjoining magnetic structural member and a lower ac drive voltage, reduced the flux density of the weld losing most of the benefits of the alternating magnetic field as compared to the prior set of experiments.

VII. CONCLUSIONS

The same materials with lower coercive forces are degraded more by a given welding process than those with higher coercive forces: In Table II compare Lots 1 and 3; also see Fig. 6. The size of a weld on a given part causes a degradation approximately proportional to its volume: In Table II compare Lots 1 and 4. The reestablishment of grain boundaries within the weld was conditional upon material composition: Fig. 7 versus Fig. 8.

High flux densities within the welds accentuate the differences between the results of dc fields and alternating fields: prior experiments versus Table II. The advantages of alternating fields (over no fields) are not as pronounced as the disadvantages of dc fields: Prior experiments.

VIII. RECOMMENDATIONS

Further experimentation is needed to determine flux level and frequency for maximum magnetic properties.

ACKNOWLEDGMENTS

The authors wish to acknowledge M. A. Elkins, IBM Metallurgist, R. C. Grose, Technician, James M. White, Physicist, for suggestions and comments; and vendor engineers and technicians for laser welding and instrumentation.

[1] M. Banas, Opt. Eng. **17**, 210 (1978).

[2] A. Saifi and S. J. Vahaviolos, IEEE Quantum Electron. **QE-12**, 129 (1976).

[3] The results of this achievement are essential for using high-quality soft magnetic materials together with high strength structural alloys to fabricate high performance electromagnetic devices.

[4] A. J. Moses and B. Thomas, Proc. IEEE **122**, 761 (1975).

[5] The adjoining part was omitted in the test, and the top of the test part was lowered by the thickness of the adjoining part, thus keeping the same step between the top surfaces. The radius of the circular path of the laser was reduced to keep all of the laser heated areas on the top end of the test part.

rf sputtered CoCr for magnetography

D. Jeanniot, J. C. Bouchand, and G. Sache
Bull S. A., Boite Postale 53, 78340 Les Clayes-Sous-Bois, France

In order to improve the resolution in the inking of the dots, vertical anisotropy media configuration is applied to magnetography. The magnetization transition zone length between the dot and the nonmagnetized drum is hoped to be shorter than in the longitudinal configuration. Some preliminary inking tests were successfully carried out on plane samples. A specially designed sputtering group was built for the deposition of CoCr layers. The substrates are full-size drums (diameter = 10 cm, length = 40 cm) and the $Co_{80}Cr_{20}$ target is a cylinder (diameter = 20 cm, length = 50 cm) around the drum. In this paper, the first results obtained with this group are described. The dispersion of the properties of the CoCr layer around the drum is less than 10%. The whole incident power range (up to 15 kW) was scanned. The deposition rate continuously increases with increasing incident power (P_w) up to 9 kW. This rate saturates after 9 kW to a value of 20 Å/s. As in the planar diode sputtering system, the vertical anisotropy of CoCr thin films is improved when high P_w values are used. For these reasons, the optimal incident power was determined as 9 kW. These results show, for the first time, that a dry process could be used for the deposition of a magnetographic medium on a drum.

I. INTRODUCTION

Magnetic printing has been thought of[1] and developed[2] a long time ago. A compact magnetographic printer has been developed since 1980. The working elements of the printer are the magnetic drum and the recording head. Both are shown in Fig. 1. The principle of this technology is roughly the same as in magnetic recording.[2] The main elements of the machine are described in Fig. 2. Some years before, the perpendicular (or vertical) magnetic recording had begun to be developed by many laboratories.[3] The most efficient configuration of the vertical recording on rigid disks was found to be the double recording-layer–single-sided monopole-type head couple. This configuration was adapted to magnetography.[4] On the other hand, the most convenient alloy for the vertical magnetic recording medium was found to be the cobalt-chromium alloy. In this paper are described the first results of a new elaboration method of the drum.

II. PLANAR CONFIGURATION EXPERIMENTS

In order to study the behavior of rf diode CoCr thin films, some depositions were carried out on planar samples (Table I). The evolution of magnetic and structural properties with deposition parameters was studied.[5] The four parameters that were studied were the cathode and the bias voltages (V_k and V_b, respectively), the argon pressure (P_{Ar}) and the thickness of the layer (t_{CoCr}). An example of the resulting variations is given on Fig. 3. The three former parameters were then chosen in order to get the highest vertical magnetic anisotropy. Although the optimal thickness was found to be about 1 μm, the thickness was increased to 10 μm for the magnetographic application. The corresponding hysteresis loops are shown in Fig. 4: the vertical magnetic anisotropy is lowered, but it still remains. Then, some encouraging inking tests were carried out which will not be described here.

III. DEPOSITION APPARATUS, PROCESS, AND PROPERTIES

After this first step, a rf sputtering group was specially designed to deposit CoCr thin films on the real working element of the machine, i.e., the full-size drum. The cathode and the drum are water-cooled and the composition of the target is $Co_{80}Cr_{20}$. The schematics of this new sputtering group is represented on Fig. 5 and the main deposition parameters are summarized in the Table I. A cylindrical and removable shield lies between the cathode and the drum dur-

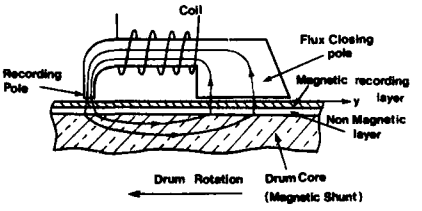


FIG. 1. Head-medium couple for magnetography (Ref. 2).

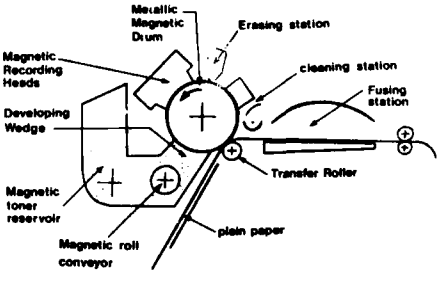


FIG. 2. Magnetographic printer cross section (Ref. 2).

 0021-8979/88/083961-03$02.40 © 1988 American Institute of Physics

TABLE I. Deposition conditions in the planar and cylindrical configurations.

		Planar	Cylindrical
Cathode	shape	disk	cylinder
	diameter (cm)	20	20
	length (cm)	...	50
Substrate	shape	disk	cylinder
	diameter (cm)	13	10
	composition	glass	FeNi/Al
Etching of the cathode	incident power P_w (W/cm^2)	2.31	1.43
	Argon pressure P_{Ar} (mTorr)	11.5	10
	operating time t (min)	30	48
	energy $t \times P_w$ (10^9 erg/cm^2)	41.6	41.6
Etching of the substrate	incident power P_w (W/cm^2)	2.31	0.046 ($t = 0$)
	Argon pressure P_{Ar} (mTorr)	11.5	100
	operating time t (min)	6	70 (ΔP_w)
	energy $t \times P_w$ (10^9 erg/cm^2)	8.3	8.3
CoCr deposition	incident power P_w (W/cm^2)	3.4	2.4
	Argon pressure P_{Ar} (mTorr)	5	10
	deposition rate R (Å/s)	9.26	9.77

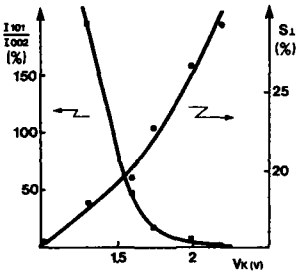


FIG. 3. Perpendicular hysteresis loop squareness ($S_\perp$) and x-ray diffraction ratio I_{101}/I_{002} vs cathode voltage in the planar configuration.

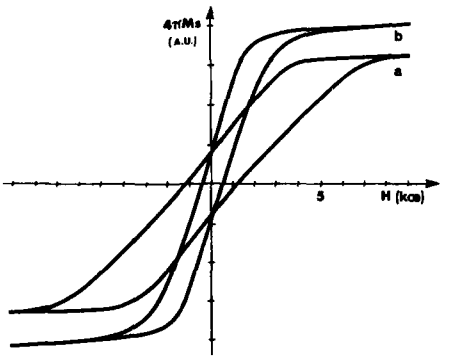


FIG. 4. Perpendicular hysteresis loops of two CoCr layers deposited in the planar configuration with different thicknesses. (a) $t_{CoCr} = 1\ \mu$m and (b) $t_{CoCr} = 9.8\ \mu$m.

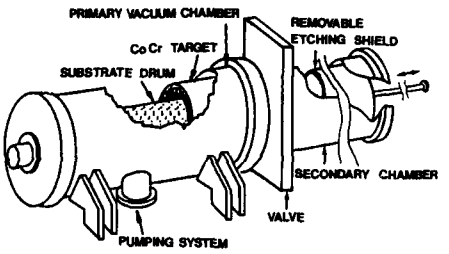


FIG. 5. Scheme of the vacuum chamber for the cylindrical configuration rf sputtering group.

ing the pre-etching of both of them. A rf power supply is used for the pre-etching and the deposition from the cathode and a dc power supply is only used to sputter-etch the drum substrate. Prior to deposition, the vacuum chamber was pumped out until the pressure became lower than 5×10^{-1} Torr. Then the CoCr cathode was pre-etched in the conditions that are described in Table I.

The second step of the process was the dc etching of the drum. The variations of the intensity of the current passing through the plasma when the applied voltage is increased are plotted in Fig. 6 for different P_{Ar}. The variation of the applied power with the etching time is plotted on the Fig. 7. This power obviously stabilizes after 20 min and we think that this time corresponds to the end of the etching of the superficial oxide layer.

The third and last step of the process was the deposition of the CoCr layer. In order to increase the deposition rate (R), we increased the incident power (P_w) from 0 to 15 kW. The relation between these two parameters is represented in Fig. 8. The usual linear relation holds until $P_w = 9$ kW; after

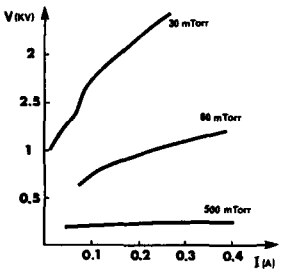


FIG. 6. Variations of the applied voltage (V) vs the current intensity (I) during the pre-etching of the drum for different argon pressures.

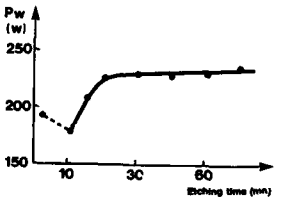


FIG. 7. Evolution of the incident power (P_w) with the etching time of the drum.

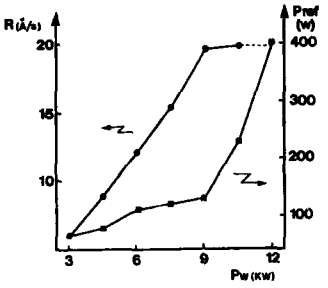


FIG. 8. Deposition rate (R) and reflected power on the drum (P_{ref}) vs incident power (P_w) during the deposition of the CoCr layer.

this value, the deposition rate saturates. Figure 8 also indicates that the reflected power sharply increases after 9 kW; then, thermal losses increase. The optimal value of P_w was chosen as 9 kW.

A typical x-ray diffraction diagram is shown in Fig. 9. Although this layer is structurally well oriented, its magnetic properties do not reveal a vertical orientation. The corresponding vibrating-sample magnetometer (VSM) hysteresis loops are represented in Fig. 10. The fact that those two properties do not fit could be atrributed to the heating of the substrate during the deposition. These results clearly show that the properties of rf sputtered CoCr have to be improved. To complete this first study, some parameters have to be optimized: the optimal CoCr thickness still remains unknown and a bias voltage would improve the properties of the layer.

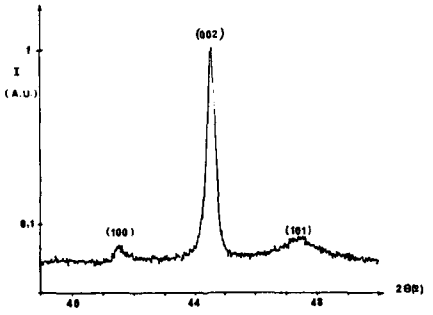


FIG. 9. X-ray diffraction diagram of a CoCr layer deposited in the cylindrical configuration.

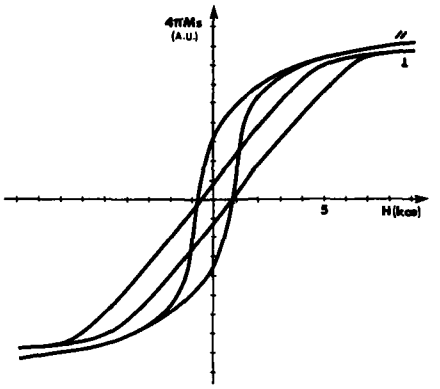


FIG. 10. VSM hysteresis loops of a CoCr layer deposited in the cylindrical configuration.

IV. CONCONCLUSIONS

Based on planar configuration results, a specially designed rf sputtering group has been built for the deposition of thick CoCr layers ($\simeq 10\,\mu$m) on full-size drums for a magnetographic printer. In spite of such large thicknesses, the vertical magnetic anisotropy still exists in the plane films. The crucial point of the deposition process was the pre-etching of the substrate. Then, the incident power was optimized for the deposition of CoCr. The deposited layers are structurally well oriented, but the heating of the substrate during the deposition is thought to be responsible for their weak vertical magnetic anisotropy. The temperature of the drum, bias voltage and thickness of the layer must be optimized for magnetography. This study has shown, for the first time, that a magnetographic drum can be obtained by a dry deposition process.

ACKNOWLEDGMENT

The authors thank J. J. Eltgen for fruitful discussions.

[1]Jones, Mechanics Magazine, 385 (1839).
[2]J. J. Eltgen and J. Magnenet, IEEE Trans. Magn. **MAG-16**, 961 (1980).
[3]S. Iwasaki and Y. Nakumura, IEEE Trans. Magn. **MAG-13**, 1272 (1977).
[4]J. J. Eltgen, J. Am. Chem. Soc., Product R and D, **24**, 196 (1985).
[5]D. Jeanniot and J. Desserre, J. Phys. (Paris) **C6-105**, 446 (1985).

Prediction of magnetic phase diagrams of selected $(R_xR'_{1-x})_2Fe_{14}B$ systems

E. B. Boltich, F. Pourarian, R. T. Obermyer,[a] S. G. Sankar, and W. E. Wallace
MEMS Department and Magnetics Technology Center, Carnegie Mellon University, Pittsburgh, Pennsylvania, 15213

Preliminary experiments on $(Tm_xDy_{1-x})_2Fe_{14}B$ have suggested the presence of axial, conical and planar regions in the magnetic phase diagram. Here we report the magnetic phase diagram for this and other mixed rare-earth systems, as predicted by second-order crystal field theory. The specific systems considered were those containing (Er or Tm) and (Pr, Tb, or Dy). It is shown that in these systems, which contain two rare-earth ions of opposite second-order Stevens coefficients, the occurrence of all three regions can be accounted for by second-order crystal field theory. The shapes of the phase boundaries are discussed in terms of the stabilization energies of the various rare earth ions. In particular, it was found that the relatively strong temperature dependence of the stabilization energies of Pr and Tm is responsible for low-temperature contractions of the planar and axial phases, respectively. This temperature dependence is attributed to the weaker exchange interaction $[(g-1)J<1]$ experienced by these ions.

INTRODUCTION

One of the most technologically important and fundamentally interesting features of the $R_2T_{14}B$ class of compounds is their easy direction of magnetization (see, for example, Ref. 1). It is presently known that these systems exhibit two distinct types of spin reorientations, types 1 and 2. The former, which is an intrinsic characteristic of the rare-earth ion, occurs in Nd and Ho compounds and is a consequence of higher-order crystal field term.[2,3] The latter, with which the present work is concerned, is the result of a competition between the anisotropies of various sublattices (e. g., rare earth and transition metal).[4]

It has previously been shown that many phenomena associated with type 2 spin reorientations can be explained directly by second-order crystal field theory. Among these are the following: (1) the composition dependence of the spin reorientation temperature, T_{sr}, in the systems $(Er_xGd_{1-x})_2Fe_{14}B$, $(Er_xY_{1-x})_2Fe_{14}B$, and $(Er_xPr_{1-x})_2Fe_{14}B$ (Refs. 5–7); (2) the increase in the magnetization of $Er_2Fe_{14}B$ above T_{sr} (Refs. 6 and 8); (3) the rare-earth magnetic structures of $Er_2Fe_{14}B$ and $Tm_2Fe_{14}B$ below T_{sr} (Refs. 6, 7, and 9); and (4) the presence, in the magnetic phase diagram of $(Er_xPr_{1-x})_2Fe_{14}B$, of axial, conical, and planar regions.[7] The presence of this planar phase in the phase diagrams of mixed rare-earth systems has recently been observed in preliminary experiments on the system $(Tm_xDy_{1-x})_2Fe_{14}B$.[10]

The primary objectives of the present work are to predict the magnetic phase diagrams of other mixed rare-earth systems exhibiting type 2 spin reorientations, and to correlate the various features observed with individual ion properties. The particular systems chosen are those of the type $(R_xR'_{1-x})_2Fe_{14}B$, with R = Er and Tm, and R' = Pr, Tb, and Dy.

CALCULATIONAL DETAILS

The multi-ion model employed in the present calculation is described in detail elsewhere.[7] The crystal field coefficients of the various ions considered were scaled from those of Er^{3+}, according to the $\langle r^2\rangle$'s and α's.[11] The resulting ratios are given in Table I, along with the other relevant parameters (taken from Ref. 7).

The same multi-ion model was used to calculate the stabilization energies SE(0) and SE (90), of the various rare-earth sublattices. These stabilization energies are defined as $[E(\theta=0°,\phi=0°)-E(\theta=45°,\phi=0°)]$ and $[E(\theta=90°,\phi=0°)-E(\theta=45°,\phi=0°)]$, respectively, where θ and ϕ are the polar and azimuthal angles specifying the orientation of the exchange field with respect to the c axis and the a-c plane.

RESULTS AND DISCUSSION

The predicted magnetic phase diagrams of $(Tm_xPr_{1-x})_2Fe_{14}B$, $(Er_xDy_{1-x})_2Fe_{14}B$, and $(Tm_xDy_{1-x})_2Fe_{14}B$ are shown in Figs. 1–3. The phase diagrams of the Tb systems are, for all practical purposes, iden-

TABLE I. Parameters employed in calculation of magnetic phase diagrams.

$B_2^0(\mathrm{Er}\,f) = 0.370$ K	$B_2^m(\mathrm{Pr}) = -13.49\,B_2^m(\mathrm{Er})$
$B_2^{2c}(\mathrm{Er}\,f) = -0.165$ K*	$B_2^m(\mathrm{Tb}) = -4.527\,B_2^m(\mathrm{Er})$
$B_2^0(\mathrm{Er}\,g) = 0.344$ K	$B_2^m(\mathrm{Dy}) = -2.725\,B_2^m(\mathrm{Er})$
$B_2^{2c}(\mathrm{Er}\,g) = 0.679$ K*	$B_2^m(\mathrm{Tm}) = 3.822\,B_2^m(\mathrm{Er})$
$2\lvert\mu_B H_{Ex}\rvert = 378$ K	
$K_{1,\mathrm{Fe}}(4.2\ \mathrm{K}) = 7.05\times10^6$ erg/cm^3	
$K_{1,\mathrm{Fe}}(300\ \mathrm{K}) = 10.2\times10^6$ erg/cm^3	

*The signs of the nonaxial terms refer to the basal plane atoms, with the X axis taken along [110].

[a] Permanent address: Physics Department, The Pennsylvania State University, McKeesport, PA 15132.

 0021-8979/88/083964-03$02.40 © 1988 American Institute of Physics

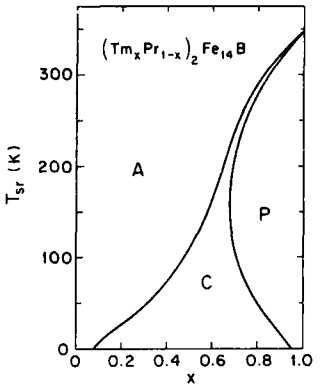


FIG. 1. Predicted magnetic phase diagram of the system $(Tm_xPr_{1-x})_2Fe_{14}B$.

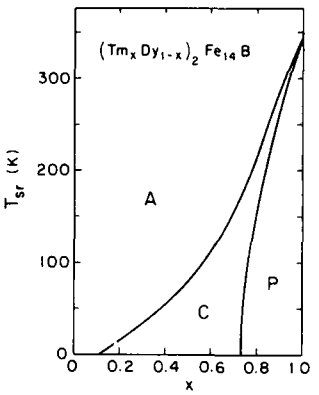


FIG. 3. Predicted magnetic phase diagram of the system $(Tm_xDy_{1-x})_2Fe_{14}B$.

tical to their Dy analogs and are, therefore, not shown. That this should be so, is evidenced by the fact that the stabilization energies, SE(0) and SE(90), of these two ions are not only of similar magnitude, but also possess similar temperature dependencies, as shown in Figs. 4 and 5. The phase diagram of $(Er_xPr_{1-x})_2Fe_{14}B$ is presented in Ref. 6.

Although these calculated phase diagrams should not be considered entirely quantitative, due to the various approximations involved, their qualitative features are consistent with existing experimental data [e.g., the presence of the conical phase in $(Er_xPr_{1-x})_2Fe_{14}B$ and the apparent presence of the planar phase in $(Tm_xDy_{1-x})_2Fe_{14}B$]. Several of the more significant aspects of these diagrams are discussed below.

All of the diagrams show the axial state to be stable at sufficiently high temperatures, throughout the entire composition range. This feature is attributable to the uniaxial anisotropy of the Fe sublattice (as evidenced by $Y_2Fe_{14}B$), which is dominant at high temperatures.[12] Similarly, since Er^{3+} and Tm^{3+} exhibit planar anisotropy in the $Nd_2Fe_{14}B$ structure, compositions sufficiently rich in these elements were found to become planar in the low temperature regime, where the rare-earth anisotropy is dominant. Conversely, compositions rich in the axis seeking rare earths (Pr^{3+}, Tb^{3+}, and Dy^{3+}) remained uniaxial at all temperatures.

As shown in the diagrams, the shapes of the phase boundaries are strongly characteristic of the rare earth species present. As can be inferred from the Figs. 1–3, the shape of the cone-axis phase boundary is correlated with the rare earth ion having the positive Stevens coefficient (Er^{3+} and Tm^{3+}). In the Er containing systems the uniaxial state was predicted to be stable at all temperatures, for compositions with $x < 0.5$. This feature is in agreement with the experiments on both $(Er_xPr_{1-x})_2Fe_{14}B$ and $(Er_xDy_{1-x})_2Fe_{14}B$.[6,13] In contrast, in the Tm systems, the conical state was found to exist for all compositions with $x > 0.1$, in agreement with preliminary measurements on

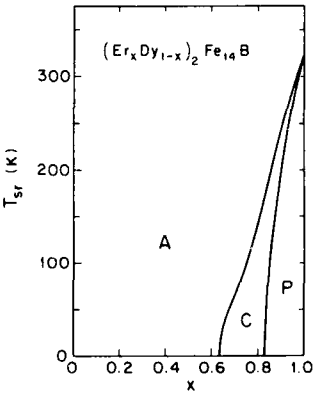


FIG. 2. Predicted magnetic phase diagram of the system $(Er_xDy_{1-x})_2Fe_{14}B$.

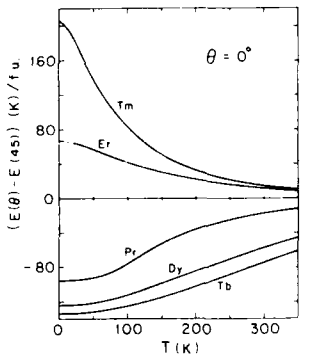


FIG. 4. Stabilization energy, SE(0), of various rare-earth ions in the $Nd_2Fe_{14}B$ structure.

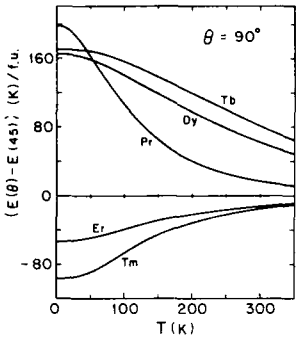


FIG. 5. Stabilization energy, SE(90), of various rare-earth ions in the $Nd_2Fe_{14}B$ structure.

$(Tm_xDy_{1-x})_2Fe_{14}B$.[10] This difference between the Er and Tm systems can be ascribed to the fact that the crystal field interaction is much stronger for Tm^{3+} than for Er^{3+} (see Table I). Furthermore, the pronounced upward concavity of the cone-axis phase boundary in the Tm systems at low temperatures can be inferred to be a consequence of the strong temperature dependence of the stabilization energy, SE(0), as shown in Fig. 4. This temperature dependence is a direct result of the relatively small exchange interaction experienced by Tm^{3+} [$(g-1)J=1$, in comparison to $-\frac{4}{5}$, 3, $\frac{2}{3}$, and $\frac{1}{2}$ for Pr, Tb, Dy, and Er, respectively)].

The shape of the plane-cone boundary, on the other hand, was found to correlate most strongly with the rare earth having the negative Stevens coefficient (Pr^{3+}, Tb^{3+}, and Dy^{3+}). As shown in the figures, the plane-cone spin reorientation temperature was found to decrease monotonically with decreasing x for the Tb and Dy systems. This is, as one would *a priori* expect, when a plane-seeking ion (Er^{3+}, Tm^{3+}) is replaced with an axis seeking one (Tb^{3+}, Dy^{3+}). Significantly more interesting is the case of the Pr systems. In both of these systems, a reentrance of the conical phase was predicted to occur at low temperatures. The explanation of this phenomenon is analogous to the one given above for the upward concavity of the cone-axis boundary in the Tm systems. At low temperatures the uniaxial anisotropy and, hence, the stabilization energy, SE(90), of Pr^{3+} increases dramatically (see Fig. 5), resulting in a destabilization of the planar phase. This low-temperature increase in the uniaxial anisotropy of Pr^{3+}, has been experimentally observed by measurements of the anisotropy field of $Pr_2Fe_{14}B$.[14] As is the case with Tm^{3+}, this behavior is a result of the large crystal field (see Table I) and relatively weak exchange $[(g-1)J=-\frac{4}{5}]$ experienced by Pr^{3+}.

Finally, it should be noted that, according to second-order crystal field theory, the occurrence of an extended conical phase requires the presence of two different rare-earth ions having opposite second-order Stevens coefficients. This is conjectured from similar calculations for the system $(Er_xY_{1-x})_2Fe_{14}B$, which show the conical state to be stable only over a narrow band.

In conclusion, it is noted that second-order crystal field theory predicts the occurrence of axial, conical and planar regions in the magnetic phase diagrams of $(R_xR'_{1-x})_2Fe_{14}B$ systems, where R = Er or Tm and R′ = Pr, Tb, or Dy. Experimental observations on the systems $(Er_xPr_{1-x})_2Fe_{14}B$, $(Er_xDy_{1-x})_2Fe_{14}B$, and $(Tm_xDy_{1-x})_2Fe_{14}B$ tend to support these predictions. However, in the final analysis, detailed single-crystal work is necessary.

ACKNOWLEDGMENTS

The authors wish to acknowledge the assistance of K. Obermyer, in performing the numerical computations. E. B. B. was supported in part by the Magnetic Materials Research Group, through the Division of Materials Research, National Science Foundation, under Grant No. DMR-8613386.

[1]K. J. Strnat, Ed., *Proceedings of the 4th International Symposium on Magnetic Anisotropy and Coercivity in Rare Earth-Transition Metal Alloys* (University of Dayton Press, Dayton, OH, 1985).
[2]E. B. Boltich and W. E. Wallace, Solid State Commun. **55**, 529 (1985).
[3]H. Oesterreicher, Phys. Status Solidi B **131**, K123 (1985).
[4]W. E. Wallace, A. T. Pedziwiatr, E. B. Boltich, F. Pourarian, E. Oswald, and S. Y. Jiang, in *Proceedings of the 3rd International Conference on Physics of Magnetic Materials*, Szczyrk-Bila, Poland, edited by W. Gorzowski, H. Lachowicz, and H. Szymczak (1986), p. 303.
[5]A. Vasquez and J. P. Sanchez, J. Less Common Metals **127**, 71 (1987).
[6]E. B. Boltich, A. T. Pedziwiatr, and W. E. Wallace, *Proceedings of MRS Conference*, edited by S. G. Sankar, J. F. Herbst, and N. ' Koon (Materials Research Society, Pittsburgh, PA, 1987), p. 119
[7]E. B. Boltich, F. Pourarian, R. T. Obermyer, S. G. Sankar, and W. E. Wallace (these proceedings).
[8]S. Hirosawa and M. Sagawa, Solid State Commun. **54**, 355 (1985).
[9]M. Yamada, Y. Yamaguchi, H. Kato, H. Yamamoto, Y. Nakagawa, S. Hirosawa, and M. Sagawa, Solid State Commun. **56**, 663 (1985).
[10]Unpublished bulk magnetization measurements.
[11]W. E. Wallace, S. G. Sankar, and V. U. S. Rao, Structure and Bonding **33**, 1 (1977).
[12]D. Givord, H. S. Li, and R. Perrier de la Bathie, Solid State Commun. **51**, 857 (1984).
[13]D. Niarchos and A. Simopoulos, Solid State Commun. **59**, 669 (1986).
[14]S. Sinnema, J. J. M. Franse, R. J. Radwanski, K. H. J. Bushow, and D. B. de Mooij, J. Phys. (Paris) **46**, C6-301 (1985).

Spin reorientation in $(Y_{1-x}Sm_x)_2Fe_{14}B$

Chin Lin, Zun-Xiao Liu, Yun-Xi Sun, Zheng-Hua Lou, and Bayinqilao
Department of Physics, Peking University, Beijing, People's Republic of China

Magnetization measurements have been made on $(Y_{1-x}Sm_x)_2Fe_{14}B$ compounds with $x \leq 0.1$ over the temperature range from 1.5 K to room temperature. The c axis is the easy magnetization direction for pure $Y_2Fe_{14}B$ at all temperatures, reflecting the anisotropy of the Fe sublattice. X-ray diffraction analyses on aligned powders indicate that all samples studied have easy magnetization direction parallel to the c axis at room temperature. The addition of Sm results in a decrease of anisotropy at room temperature. At low temperatures it induces a spin reorientation in all systems studied. A transition to planar anisotropy is observed for $x = 0.08$ and 0.1.

INTRODUCTION

A spin reorientation has been observed in $Nd_2Fe_{14}B$ at about 135 K. Several models[1–4] have been proposed to explain this behavior. These explanations are not completely convincing and clear. Investigations on $Nd_2(Fe_{1-x}Co_x)_{14}B$[5] showed the effect of 3*d* sublattice anisotropy on the spin reorientation. The spin reorientation observed in $Er_2Fe_{14}B$ and $Tm_2Fe_{14}B$[6] at high temperature is of a different nature and can be completeiy accounted for in terms of rare-earth and transition-metal anisotropy competition.[7] Recently, Koon *et al.*[8] reported the spin reorientation in $Y_{1.8}Er_{0.2}Fe_{14}B$ single crystal. The magnetization begins to rotate slowly away from the c axis near 90 K, and forms a canting angle of 78° from the c axis at 40 K and below.

$Sm_2Fe_{14}B$ has strong planar anisotropy.[9] The [100] direction is the easy magnetization direction. In $Y_2Fe_{14}B$ the easy magnetization direction is parallel to the c axis. The absolute value of anisotropy constant of $Sm_2Fe_{14}B$ is larger than that of $Y_2Fe_{14}B$ by an order of magnitude. When Y is substituted by Sm, small amounts of Sm can affect the anisotropy greatly. With decreasing temperature, the anisotropy of the Fe sublattic decreases slightly, while the anisotropy of Sm increases steeply. The resultant anisotropy of the Sm and Fe sublattices varies significantly with temperature. Spin reorientation were observed in all substituted $(Y_{1-x}Sm_x)_2Fe_{14}B$ samples.

EXPERIMENTAL METHOD

Samples of $(Y_{1-x}Sm_x)_2Fe_{14}B$ with $x \leq 0.1$ were prepared by arc melting under a purified argon atmosphere. The samples were annealed in vacuum for several hours at 900 °C and quenched. X-ray diffraction analyses on powdered samples showed that the samples have the tetragonal $R_2Fe_{14}B$ structure.[10]

Powdered samples were aligned in a magnetic field of 10 kOe at room temperature and fixed in epoxy resin. X-ray diffraction analyses on aligned powders indicate that all samples studied have easy magnetization direction parallel to the c axis of the tetragonal structure at room temperature. Magnetization curves were measured with the measuring field applied parallel ($\sigma_{\parallel}$) and perpendicular ($\sigma_{\perp}$) to the alignment direction over the temperature range from 1.5 to 300 K. The modified Sucksmith–Thomson method[11] was

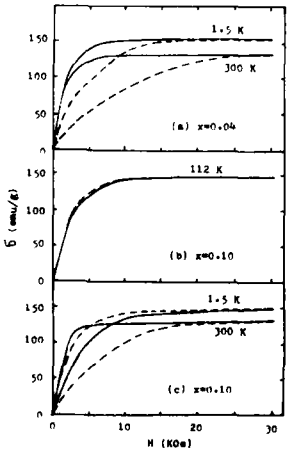


FIG. 1. Magnetization curves parallel ($\sigma_{\parallel}$) and perpendicular ($\sigma_{\perp}$) to the alignment direction at different temperatures for $(Y_{1-x}Sm_x)_2Fe_{14}B$. Solid lines are for $\sigma_{\parallel}$, dashed lines are for $\sigma_{\perp}$. (a) $x = 0.04$; (b) and (c) $x = 0.10$.

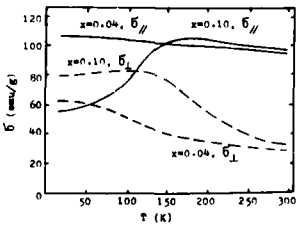


FIG. 2. Temperature dependencies of the magnetization parallel ($\sigma_{\parallel}$) and perpendicular ($\sigma_{\perp}$) to the alignment direction in a field of 2 kOe for $(Y_{1-x}Sm_x)_2Fe_{14}B$ with $x = 0.04$ and 0.10.

 0021-8979/88/083967-02$02.40 © 1988 American Institute of Physics

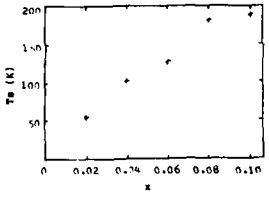


FIG. 3. Composition dependence of the spin reorientation temperature for $(Y_{1-x}Sm_x)_2Fe_{14}B$.

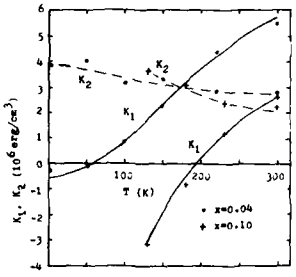


FIG. 5. Temperature dependencies of the magnetocrystalline anisotropy constants K_1 and K_2 for $(Y_{1-x}Sm_x)_2Fe_{14}B$. with $x = 0.04$ and 0.10. Solid lines are for K_1, dashed lines are for K_2.

used to determine the magnetocrystalline anisotropy constants K_1 and K_2. A correction for the nonalignment was carried out in the calculation.

RESULTS AND DISCUSSION

Magnetization curves parallel and perpendicular to the alignment direction at different temperatures for $x = 0.04$ and 0.10 are plotted in Fig. 1. When temperature decreases from 300 to 112 K, the magnetocrystalline anisotropy of the sample with $x = 0.1$ decreases. The sample becomes almost isotropic at 112 K, as shown in Fig. 1(b). The easy magnetization direction rotates to the basal plane at lower temperatures. The anisotropy of the sample with $x = 0.04$ decreases monotonically with decreasing temperature.

Temperature dependencies of the magnetization parallel and perpendicular to the alignment direction in a field of 2 kOe for $x = 0.04$ and 0.1 are shown in Fig. 2. The spin reorientation temperatures T_s were obtained from the inflection points in the (σ_1) curves. Figure 3 shows the composition dependence of the spin reorientation temperature. T_s increases gradually with increasing the Sm content.

Compositio· lependence of the magnetocrystalline anisotropy constants K_1 and K_2 at 300 K are shown in Fig. 4. At 300 K, K_1 and K_2 decrease gradually as the Sm content increases. Temperature dependencies of K_1 and K_2 for $x = 0.04$ and 0.1 are shown in Fig. 5. With decreasing temperature, K_1 becomes negative and a spin reorientation takes place. The canting angle θ between the easy magnetization direction and the c axis was obtained from the relation $\sin\theta = (-K_1/2K_2)^{1/2}$. The canting angle is about 10° at 1.5 K for $x = 0.04$.

With decreasing temperature, the easy magnetization direction remains parallel to the c axis and magnetocrystalline anisotropy decreases slightly for pure $Y_2Fe_{14}B$.[5] This reflects the anisotropy of the Fe sublattice. On the other hand, Sm has strong planar anisotropy. It increases steeply when the temperature decreases. The resultant anisotropy of the sample is determined by the competition between the anisotropies of the Sm and the Fe sublattices. The anisotropy of the Fe sublattice is dominant at room temperature for $x \leqslant 0.1$. The samples exhibit easy c axis. When temperature decreases, the anisotropy of Sm increases steeply and becomes dominant at 1.5 K for $x = 0.08$ and 0.1. These samples exhibit planar anisotropy at 1.5 K. Spin reorientation takes place when temperature decreases from room temperature to 1.5 K. For a smaller amount of Sm, the planar anisotropy of Sm is comparable with c axis anisotropy of the Fe sublattice at 1.5 K, resulting a canting angle between the easy magnetization direction and the c axis.

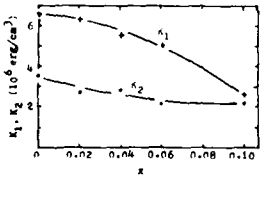


FIG. 4. Composition dependence of the magnetocrystalline anisotropy constants K_1 and K_2 at 300 K for $(Y_{1-x}Sm_x)_2Fe_{14}B$.

ACKNOWLEDGMENT

This work was supported by the National Natural Science Foundation of China.

[1] C. Abache and H. Oesterreicher, J. Appl. Phys. **57**, 4112 (1985).
[2] D. Givord, H. S. Li, J. M. Moreau, and P. Tenaud, J. Magn. Magn. Mater. **54–57**, 445 (1986).
[3] Zhao Tiesong, Jin Hanmin, and Zhu Cheng, Chinese Phys. Lett. **3**, 485 (1986).
[4] S. G. Sankar and K. S. V. L. Narasimhan, J. Magn. Magn. Mater. **54–57**, 530 (1986).
[5] Chin Lin, Zun-Xiao Liu, and Xiao-Feng Xu, IEEE Trans. Magn. (to be published).
[6] S. Hirosawa and M. Sagawa, Solid State Commun. **54**, 335 (1985).
[7] G. Asti, F. Bolzoni, and L. Pareti, IEEE Trans. Magn. (to be published).
[8] N. C. Koon, B. N. Das, and C. M. Williams, J. Magn. Magn. Mater. **54-57**, 523 (1986).
[9] M. Sagawa, S. Fujimura, H. Yamamoto, Y. Matsuura, and S. Hirosawa, J. Appl. Phys. **57**, 4094 (1985).
[10] S. Sinnema, R. J. Radwanski, J. J. M. Franse, D. B. de Mooij, and K. H. J. Buschow, J. Magn. Magn. Mater. **44**, 333 (1984).
[11] U. S. Ram and P. Gaunt, J. Appl. Phys. **54**, 2872 (1983).

Spin reorientation in substituted Nd_2Co_{17} compounds

H. Y. Chen, S. G. Sankar, and W. E. Wallace
Carnegie Mellon University, Mellon Institute and Department of Metallurgical Engineering and Materials Science, Pittsburgh, Pennsylvania 15213

Nd_2Co_{17} alloy exhibits a saturation magnetization about 30% higher than that of Sm_2Co_{17} at room temperature. However, the former is not a useful material for permanent magnet fabrication due to its basal plane anisotropy near room temperature. In this study, an attempt is made to investigate the effect of partial substitution of Nd_2Co_{17} with other elements. In particular, alloys of the compositions $Nd_{2-x}Sm_xCo_{13}Fe_4$ and $Nd_2Co_{13}Fe_{4-x}T_x$ (where T = Zr or Mn) have been examined. The results obtained in this investigation show several interesting trends in the behavior of these alloys. Substitution of ~20% Sm in $Nd_{2-x}Sm_xCo_{13}Fe_4$ decreases the spin-reorientation temperatures from 613 to 224 K. Further, an increase in x up to 1.0 causes only a moderate decrease in the saturation magnetization but results in a considerable enhancement of the anisotropy field. Typical thermomagnetic curves of $Nd_2Co_{13}Fe_{4-x}T_x$ (T = Zr,Mn) exhibit spin-reorientation temperatures. These results are discussed in terms of preferential substitution of Zr or Mn in this system.

I. INTRODUCTION

R_2Co_{17} compounds exhibit higher Curie temperatures than the RCo_5 analogs and for the light rare earths, the former materials possess comparable or slightly greater saturation magnetization.[1] Hence, on the basis of only these considerations, R_2Co_{17} compounds are attractive for the development of permanent magnets. However, a third and equally important criterion for the fabrication of permanent magnets is the magnitude and direction of magnetocrystalline anisotropy. Techniques for the manipulation of magnetocrystalline anisotropy by various substitutions in the rare-earth–transition-metal compounds were developed by, among others, Ray and Strnat[2] and Schaller *et al.*[3]

Specifically, Nd_2Co_{17} exhibits a higher saturation magnetization ($33.5\mu_B$/f.u. at room temperature) in comparison to Sm_2Co_{17} ($23.2\mu_B$/f.u.). However, the easy direction of magnetization for Nd_2Co_{17} prefers the basal plane.[4,5] Attempts were made to modify the anisotropy by partial substitution of cobalt with iron[2] and with aluminum[6]; however, these results were not encouraging. Partial replacement of neodymium with samarium by Lee[7] resulted in the modification of basal plane anisotropy to a more favorable easy c-axis anisotropy. In the present investigation, the intrinsic magnetic properties such as saturation magnetization, anisotropy field, Curie temperature and spin-reorientation temperature were determined for alloys of the compositions $Nd_2Co_{13}Fe_{4-x}T_x$ (where T = Zr or Mn) and $Nd_{2-x}Sm_xCo_{13}Fe_4$. The results show that in the former case, addition of Zr or Mn results in a preferential occupation in the 2:17 structure. In the latter case, for some compositions, the magnetic properties are considerably modified.

II. EXPERIMENT

The alloys were melted in an induction furnace in a water-cooled copper boat under a purified argon atmosphere, followed by annealing at 1000 °C in argon for one week. Powder x-ray diffraction patterns with chromium radiation and thermomagnetic analyses were performed to ensure that these compounds were single phase. The saturation magnetization and the anisotropy field were measured using a PAR vibrating sample magnetometer. For the latter experiments, the aligned samples were prepared by fixing the powders ($<37\ \mu$m) in paraffin wax in an external magnetic field (~20 kOe). The Curie temperature T_C and the spin-reorientation temperature T_{sr} were determined by measuring the temperature dependence of magnetization at low external magnetic field (<0.5 kOe) in the temperature range 4.2–1200 K.

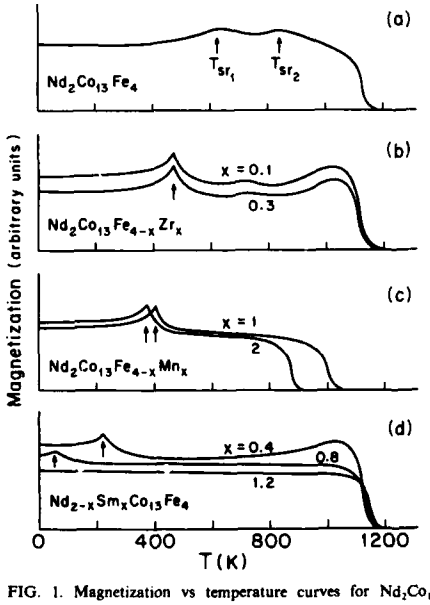


FIG. 1. Magnetization vs temperature curves for $Nd_2Co_{13}Fe_{4-x}T_x$ (T = Zr,Mn) and $Nd_{2-x}Sm_xCo_{13}Fe_4$ systems.

 0021-8979/88/083969-03$02.40 © 1988 American Institute of Physics

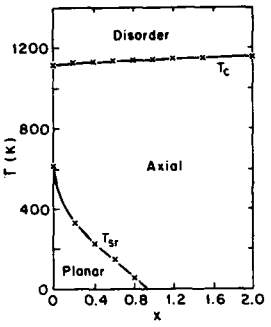


FIG. 2. The magnetic phase diagram of $Nd_{2-x}Sm_xCo_{13}Fe_4$.

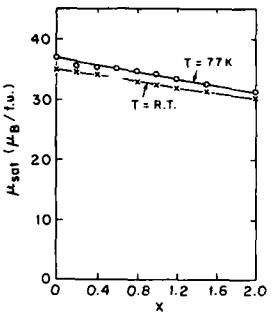


FIG. 3. Variation of saturation magnetization as a function of x for $Nd_{2-x}Sm_xCo_{13}Fe_4$ compounds.

III. RESULTS AND DISCUSSION

A. $Nd_2Co_{13}Fe_{4-x}T_x$ system

Typical thermomagnetic curves of $Nd_2Co_{13}Fe_{4-x}T_x$ (T = Zr or Mn) are illustrated in Figs. 1(a)–1(c). It may be noted that $Nd_2Co_{13}Fe_4$ exhibits two spin reorientations [see Fig. 1(a)]. The anisotropy is planar at temperatures $T < T_{sr_1}$ or $T > T_{sr_2}$. At any temperature between T_{sr_1} and T_{sr_2}, the anisotropy is conical.

Upon partial substitution of Fe with Zr, the spin-reorientation temperature T_{sr_1} shifts towards lower temperatures, but T_{sr_2} is shifted towards higher temperatures [see Fig. 1(b)]. The value of T_{sr_1} is nearly the same for all three Zr-substituted samples ($x = 0.1$, 0.2, and 0.3) investigated in this study. This is perhaps related to the preferential occupation of Zr atoms. It is reported[8] that Zr atoms can be accommodated in the 2:17 structure only at the dumbbell sites (6c) and that too only as zirconium-vacancy pairs. All 6c sites will be occupied by the Zr-vacancy pair when $x > 1$ in $Nd_2Co_{13}Fe_{4-x}Zr_x$. However, at values of $0 < x < 1$, small increases, for example, from 0.1 to 0.3, should have very little effect on T_{sr_1}. This is borne out by experimental observations. It may also be noted that the small spikes between T_{sr_1} and T_{sr_2} in Fig. 1(b) are due to the unsubstituted portions.

Similarly, the spin-reorientation temperature T_{sr_1} is shifted towards lower temperatures when Mn enters the lattice [see Fig. 1(c)]. However, due to the rapid decrease in the Curie temperatures for the concentrations of Mn additions, T_{sr_2} does not occur. The effect of Mn substitution on the decrease of T_{sr_1} can also be explained by its preference for the dumbbell sites. Neutron diffraction experiments reported by Yang[9] lend further support to these conclusions.

B. $Nd_{2-x}Sm_xCo_{13}Fe_4$ system

The magnetic phase diagram of this system is shown in Fig. 2. It may be noted that the spin-reorientation temperature T_{sr_1} decreases monotonically with increasing x. The variation of magnetization as a function of temperature is shown in Figs. 1–3. At $x > 0.4$, the compositions exhibit uniaxial anisotropy at room temperature. The lattice constants, saturation moment, anisotropy field, Curie temperature and spin-reorientation temperature of this series of compositions are given in Table I and are plotted in Figs. 2–4. Several interesting features are worth noting. With increasing samarium content the spin-reorientation temperatures reduce rapidly. While the Curie temperature is substantially unaffected, the anisotropy field increases significantly. The saturation moment is not very much altered.

Thus, it is concluded that samarium substitution is very effective in altering the magnetic properties of $Nd_{2-x}Sm_xCo_{13}Fe_4$ alloys.

In conclusion, it is noted that the spin-reorientation temperature T_{sr_1} cannot be shifted to below room temperature by partial replacement of the transition-metal sublattice

TABLE I. Lattice constants and magnetic properties of $Nd_{2-x}Sm_xCo_{13}Fe_4$.

Composition	Lattice constant		T = 77 K		T = R.T.		T_c	T_{sr}
	a (Å)	c (Å)	μ_{sat} (μ_B/f.u.)	H_A (kOe)	μ_{sat} (μ_B/f.u.)	H_A (kOe)	(K)	(K)
$Nd_2Co_{13}Fe_4$	8.457	12.342	36.99	···	35.00	···	1113	613
$Nd_{1.8}Sm_{0.2}Co_{13}Fe_4$	8.455	12.322	35.29	···	34.36	···	1126	330
$Nd_{1.6}Sm_{0.4}Co_{13}Fe_4$	8.453	12.316	35.08	···	34.15	8.8	1126	224
$Nd_{1.4}Sm_{0.6}Co_{13}Fe_4$	8.446	12.306	35.07	···	33.44	16.3	1132	148
$Nd_{1.2}Sm_{0.8}Co_{13}Fe_4$	8.439	12.314	34.58	···	32.60	25.5	1134	57
$Nd_{1.0}Sm_{1.0}Co_{13}Fe_4$	8.437	12.314	34.13	17.3	32.24	31.2	1137	···
$Nd_{0.8}Sm_{1.2}Co_{13}Fe_4$	8.436	12.310	33.32	37.2	31.59	41.0	1137	···
$Nd_{0.5}Sm_{1.5}Co_{13}Fe_4$	8.434	12.310	32.44	51.9	31.05	49.3	1143	···
$Sm_2Co_{13}Fe_4$	8.416	12.308	30.98	59.9	30.06	53.2	1145	···

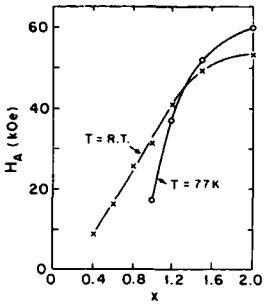


FIG. 4. Variation of anisotropy field for $Nd_{2-x}Sm_xCo_{13}Fe_4$ compounds.

in $Nd_2Co_{14}Fe_{3-x}T_x$, where T = Zr or Mn. However, samarium additions in the $Nd_{2-x}Sm_xCo_{13}Fe_4$ system are very effective in altering the magnetic properties. This is undoubtedly related to the large basal plane anisotropy of the neodymium sublattice in these compositions.[10]

ACKNOWLEDGMENT

This work was assisted by a contract with the U.S. Army Research Office.

[1]K. J. Strnat, IEEE Trans. Magn. **MAG-8**, 511 (1972).
[2]A. E. Ray and K. J. Strnat, IEEE Trans. Magn. **MAG-8**, 518 (1972).
[3]H. J. Schaller, R. S. Craig, and W. E. Wallace, J. Appl. Phys. **43**, 3161 (1972).
[4]R. S. Perkins, S. Strassler, and A. Menth, AIP Conf. Proc. **29**, 610 (1975).
[5]J. E. Greedan and V. U. S. Rao, J. Solid State Chem. **6**, 387 (1973).
[6]K. S. V. L. Narasimhan and W. E. Wallace, IEEE Trans. Magn. **MAG-13**, 1333 (1977).
[7]R. W. Lee, IEEE Trans. Magn. **MAG-15**, 1762 (1979).
[8]A. E. Ray, J. Appl. Phys. **55**, 2094 (1984).
[9]Y. C. Yang, IEEE Trans. Magn. **MAG-21**, 1987 (1985).
[10]W. E. Wallace, S. G. Sankar, and V. U S. Rao, Structure and Bonding **33**, 1 (1977).

Structure and magnetic properties of quaternary $Pr_{2-x}R_xCo_{14}B$ (R=Dy and Er) systems and their hydrides

F. Pourarian, S. Y. Jiang, S. G. Sankar, and W. E. Wallace
Carnegie Mellon University, Mellon Institute and Magnetic Technology Center, Pittsburgh, Pennsylvania 15213

Single-phase materials of quaternary $Pr_{2-x}R_xCo_{14}B$ (R = Dy or Er), which crystallize in the $Nd_2Fe_{14}B$-type tetragonal structure, form for the compositions only up to about $x = 1.5$. Measurements of lattice parameters and the bulk magnetization were carried out on these compounds and their hydrides. Saturation magnetizations M_s, magnetic ordering temperatures T_c, spin-reorientation temperatures T_{sr}, and anisotropy fields were determined. $Pr_2Co_{14}B$ exhibits a transition between uniaxial and planar anisotropy, with increasing temperature. Partial replacement of Dy or Er for Pr in the $Pr_2Co_{14}B$ lattice reduces the observed T_{sr} and H_A values. Substitution with Dy in $Pr_{2-x}R_xCo_{14}B$ has a smaller effect than with Er. This behavior is believed to be a consequence of a stronger crystal field interaction in the Dy-substituted systems. All materials investigated were found to absorb about 3.5 hydrogen atoms per formula unit at an applied pressure of 10 atm. Introduction of hydrogen into the alloy expands the lattice, changes the magnetic moment of the system slightly and reduces T_{sr} and H_A significantly. This effect is found to be stronger in the Dy-substituted compounds. The weakening of the 4*f*-3*d* exchange interactions relative to crystal field interactions of the 4*f* ions is considered to be responsible for lowering the anisotropy fields upon hydrogen absorption. The results obtained for the host and the hydrides are discussed in terms of their proposed magnetic phase diagram.

INTRODUCTION

Single-phase materials of the composition $R_2Co_{14}B$ (where R = a rare earth) in the characteristic $Nd_2Fe_{14}B$ structure can be obtained only for rare earths lighter than Dy.[1,2] This may be a consequence of the small size of the R atoms in these systems. In the quaternary $R_{2-x}R'_xCo_{14}B$, where R' = Pr (or Nd), it is thought that the amount R' needed to stabilize the structure is the largest, the smaller the heavy rare earth.[2]

In the isostructural $R_2Fe_{14}B$ systems the magnetic anisotropy arises from two contributions—the 4*f* sublattice and the 3*d* sublattice anisotropies.[3–5] The 3*d* sublattice favors an axial anisotropy as in $Y_2Fe_{14}B$.[6] At room temperature the 4*f* anisotropy dominates over the 3*d* anisotropy in all cases where the R atoms are magnetic, but the axial anisotropy develops only in the alloys in which the R component has a characteristic negative second-order Stevens coefficient ($\alpha_J < 0$). For $R_2Co_{14}B$ alloys, the 4*f* sublattice (R = Pr to Tb) anisotropy is believed to behave similar to that of $R_2Fe_{14}B$ systems. However, the contribution from the cobalt (3*d*) sublattice gives rise to a planar anisotropy, such as in the case of $Y_2Co_{14}B$.[1,7]

The influence of hydrogen on the magnetic properties of $R_2Co_{14}B$, $R_2Fe_{14}B$ or the quaternary $Pr_2Fe_{14-x}Co_xB$ alloy systems was shown to be remarkable.[8–10] The hydrogen site occupation in the lattice undoubtedly has a strong influence on the exchange interactions and the anisotropy fields of the system.[11]

The research investigation devoted to the studies of the basic magnetic properties of the Pr-based 2:14:1 type materials is crucial for the fabrication of permanent magnets. One objective of the present investigation is to study the influence of partial substitution in $Pr_{2-x}R_xCo_{14}B$ (R = Dy or Er) on the magnetic ordering temperature T_C, the spin reorientation T_{sr}, and magnetic anisotropy field H_A. The work also includes the effect of hydrogen on the magnetic characteristics of these alloys.

EXPERIMENT

The purities of the starting metals are 99.9% for Pr, Dy, and Er, 99.95% for Co and 99.98% for B. $Pr_{2-x}R_xCo_{14}B$ (R = Dy or Er) were prepared by induction melting of the constituent metals in a water-cooled copper boat under a Ti-gettered argon atmosphere. As-cast samples were wrapped in a tantalum foil, sealed in a quartz tube, filled with ½ atmosphere or argon gas and annealed at ~900 °C for 14 days. X-ray diffraction analysis was performed at room temperature on randomly oriented powders with the use of Rigaku diffractometer and Cr$K\alpha$ radiation. Samples with $x \leq 1.5$ were found to be single phase.

The hydrides were obtained by exposing the host materials at room temperature to approximately 60 atm of pure hydrogen. After an induction period of ~2–3 h, the samples absorbed hydrogen and were converted to a fine powder (~20–50 μm). A portion of the sample was used for the lattice constant measurements. The method of hydride preparation for x-ray diffraction work is described elsewhere.[9,12] Lattice parameter refinement was performed using a computer program based on Cohen's method.

The spin-reorientation temperatures T_{sr} were determined from the cusp-shaped part of the magnetization M vs

 0021-8979/88/083972-03$02.40 © 1988 American Institute of Physics

T curves. The Curie temperatures T_C were obtained by plotting M^2 vs T and extrapolating to $M^2 = 0$. Magnetization measurements were carried out at 295 and 77 K with a PAR vibrating sample magnetometer in external fields up to ~20 kOe. Saturation magnetizations M_s were obtained from M vs H isotherms, using Honda (M vs $1/H$) plots. Anisotropy fields H_A were determined at 295 and 77 K for powder with size ~37 μm which were aligned in wax, by measuring the easy and hard directions of magnetization. H_A values were deduced from the extrapolated intersection of these curves.

RESULTS AND DISCUSSION

Structural and intrinsic magnetic data of all alloys of $Pr_{2-x}Dy_xCo_{14}B$ and $Pr_{2-x}Er_xCo_{14}B$ and their hydrides, with $x = 0$, 0.5, 1.0 and 1.5, are studied in detail. Single-phase materials of these quaternary alloys were obtained only for the compositions up to $x = 1.5$. These alloys crystallize in a tetragonal $Nd_2Fe_{14}B$-type structure with the space group $P42/mnm$. Efforts to prepare stoichiometric $Dy_2Co_{14}B$ and $Er_2Co_{14}B$ systems and also the composition, slightly beyond the Co/R ratio≃7 (annealed at 900–1000 °C for a period of 14 days) have proved unsuccessful. In these instances prepared alloys were found to contain between 20% and 30% of the 2:17 material as a second phase. For $Pr_{2-x}Dy_xCo_{14}B$, the lattice parameters a, c, and the unit cell volume V showed a linear behavior with the increase in Dy content, while in Er-substituted systems the corresponding parameters decrease nonlinearly with the increase in Er concentration. This behavior may partly be a consequence of some preferential site occupation of the Er atoms on R ($4f$ or $4g$) lattice sites.

Results of hydrogen absorption revealed that the hydrides retianed the $Nd_2Fe_{15}B$-type structure. The absorbed hydrogen leads to an increase of 2.1% to 3.1% in unit cell volume. The behavior of the dependence of a, c, and V vs R content for the hydrides is found to be similar to their corresponding host alloys.

The magnetic ordering temperatures T_C of the partially substituted alloy system increase linearly, although slightly with the increase in Dy or Er. This is shown in Figs. 1 and 2. In this series the $3d$-$3d$ direct exchange interactions are considered to be strong and mainly determines the high T_C values. The relatively small change in T_C upon partial replacement of Pr by Er or Dy in $Pr_2Co_{14}B$, in fact, is partly attributed to the $4f$-$3d$ exchange interactions. Curie temperatures of the hydrides could not be determined due to their decomposition above ~300 °C.

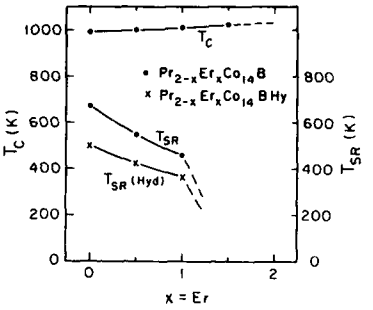


FIG. 2. Magnetic phase diagrams of $Pr_{2-x}Er_xCo_{14}B$ and the hydrides which shows the border between paramagnetic, basal and axial regions.

Measurements of magnetization M versus temperature T for $Pr_{2-x}R_xCo_{14}B$, with $x = 0$, above room temperature exhibited an anomaly at about 668 K. This phenomenon was detected from the spikelike shape in M vs T curves. It is believed that the effect of competing anisotropies of Pr and Co sublattices triggers a spin reorientation T_{sr} above which the system favors planar anisotropy. Illustrative M vs T curves of the partially substituted R elements with $x = 1$, are displayed in Fig. 3. Progressive increase in Dy content in $Pr_{2-x}R_xCo_{14}B$ series results in a decrease in T_{sr}. This reduction is observed to be larger in Er-substituted alloys. This is thought to be a consequence of a weaker crystal field interaction in the Er-containing compounds. Figures 1 and 2 also show the proposed magnetic phase diagrams of $Pr_{2-x}Dy_xCo_{14}B$ and $Pr_{2-x}Er_xCo_{14}B$ systems. As can be seen, T_{sr} is linearly dependent on Dy content up to $x = 1.5$, and it varies almost linearly with Er content only up to $x = 1$. For the latter system, T_{sr} decreases drastically at about $x > 1$ and no effect was observed down to 77 K. A similar linear dependence was also observed in the related partially substituted (Nd,Pr) system.[13]

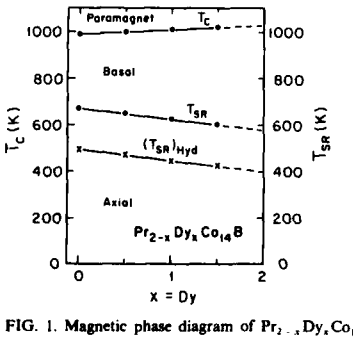


FIG. 1. Magnetic phase diagram of $Pr_{2-x}Dy_xCo_{14}B$ and the hydrides which shows the border between paramagnetic, basal and axial regions.

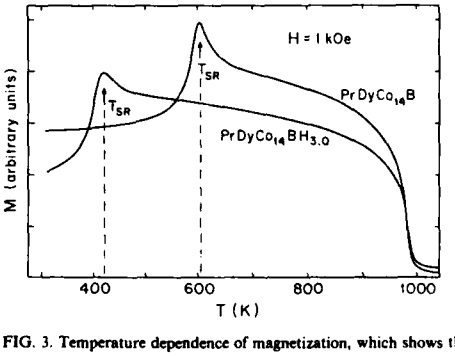


FIG. 3. Temperature dependence of magnetization, which shows the T_{sr} phenomenon in $Pr_{2-x}Dy_xCo_{14}B$ and the hydrides.

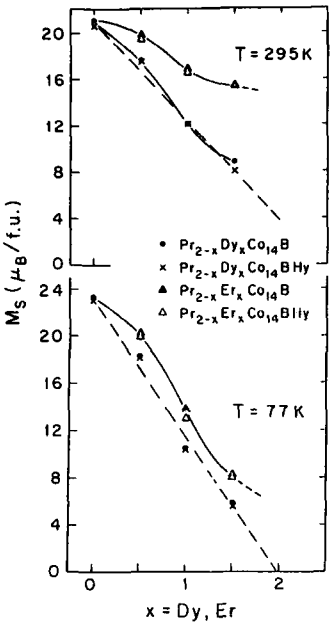


FIG. 4. Dependence of saturation magnetization on R content in $Pr_{2-x}R_xCo_{14}B$ systems and the hydrides. The dotted lines is developed from the collinear magnetic coupling assumption.

The direction of magnetization of the host compounds was found to be sensitive to hydrogenation. In all cases, T_{sr} reduces by hydriding and its behavior with x content is observed to be similar to their corresponding host alloys (see Figs. 1–3).

The composition dependence of M_s for both Dy- and Er-substituted alloy systems is displayed in Fig. 5. Partial substitution of Pr by Dy decreases M_s almost linearly but decreases nonlinearly when Pr is replaced by Er at 295 and 77 K. The average Co moment can be calculated in the series by using the Pr, Dy, and Er moments previously determined in $Pr_2Fe_{14}B$ and $Dy_2Fe_{14}B$ (Ref. 12) and $Er_2Fe_{14}B$ systems.[6] Assuming a constant Pr or R moment along with $Pr_{2-x}R_xCo_{14}B$ series and also assuming a collinear ferro- (and/or ferri-) magnetic coupling between R and the 3*d* moment, the average Co moment is found to be $\sim 1.35\,\mu_B$/Co) at 77 K for all the systems studied. This is in good agreement with those determined in $Y_2Co_{14}B$.[7] The dotted lines in Fig. 5 are derived employing the collinear magnetic coupling assumptions. As shown in Table II, the M_s values at 295 and 77 K are lowered slightly upon hydrogen absorption. This is in contrast to the behavior observed previously in related $R_2Fe_{14}B$ hydrides and the binary RFe_2 hydrides.[9,14] The change in the 3*d* moment upon hydriding is presumably an electronic effect, which is related to the electron transfer from H to the depopulated 3*d* sub-bands of the transition elements in the systems.

The dependence of the magnetic anisotropy field H_A on Dy or Er content in the series is given in Table II for the host and the hydrides. For the $Pr_{2-x}Dy_xCo_{14}B$ series, H_A decreases monotonically with x at 77 K and linearly at 295 K. The decrease in H_A for Er-substituted alloys is rather sharp, relative to the Dy analogs. This behavior is related to the Er atom. In this system Er, with a negative Stevens coefficient, favors a planar anisotropy. Hydrogenation has a marked influence in decreasing the H_A values for a particular composition x. Therefore, in these series, hydrogen has a strong tendency in lowering the axial anisotropy regions. (This reduction is found to be stronger for Pr-rich systems relative to the Dy or Er-rich compounds.) It is clear that both the rare earth and the 3*d* sublattice anisotropies are significantly influenced by the hydriding process.

ACKNOWLEDGMENT

This work was supported by the Lawrence Livermore National Laboratory.

[1]K. H. J. Buschow, D. B. de Mooij, S. Sinnema, R. J. Radwanski, and J. J. M. Franse, J. Magn. Magn. Mater. **51**, 211 (1985).
[2]S. Y. Jiang, F. Pourarian, E. B. Boltich, and W. E. Wallace, presented at Inter. Magn. Conf., Tokyo, Japan, 1987 (to be published).
[3]E. B. Boltich and W. E. Wallace, Solid State Commun. **55**, 529 (1985).
[4]S. G. Sankar and K. S. V. L. Narasimhan, J. Magn. Magn. Mater. **54-57**, 530 (1985).
[5]D. Givord, H. S. Li, J. M. Moreau, and P. Tenaud, J. Magn. Magn. Mater. **54-57**, 445 (1985).
[6]S. Sinnema, R. J. Radwanski, J. J. M. Franse, D. B. de Mooij, and K. H. J. Buschow, J. Magn. Magn. Mater. **54-57**, 333 (1984).
[7]M. Q. Huang, E. B. Boltich, W. E. Wallace, and E. Oswald, J. Magn. Magn. Mater. **60**, 270 (1986).
[8]L. Y. Zhang, F. Pourarian, and W. E. Wallace, Magn. Magn. Mater. (to be published).
[9]F. Pourarian, M. Q. Huang, and W. E. Wallce, J. Less-Common Met. **120**, 63 (1986).
[10]F. Pourarian, S. Y. Jiang, and W. E. Wallace, in *Proceedings of the MRS Conference*, edited by S. G. Sankar, J. F. Herbst, and N. C. Koon (Materials Research Society, Pittsburgh, PA, 1987), p. 231.
[11]J. M. Friedt. A. Vasquez, J. Sanchez, PH. L'Heritier, and R. Fruchart, J. Phys. F **16**, 651 (1986).
[12]F. Pourarian, S. G. Sankar, A. T. Pedziwiatr, E. B. Boltich, and W. E. Wallace, in *Proceedings of the MRS Conference*, edited by S. G. Sankar, J. F. Herbst, and N. C. Koon (Materials Research Society, Pittsburgh, PA, 1987), p. 103.
[13]J. F. Herbst and W. B. Yelon, J. Appl. Phys. **57**, 2343 (1985).
[14]F. Pourarian, W. E. Wallace, and S. K. Malik, J. Magn. Magn. Mater. **25**, 299 (1982).

Magnetic properties of NdDyFeCoAlB alloys

A. S. Kim
I G Technologies, Incorporated, 405 Elm Street, Valparaiso, Indiana 46383

The temperature stability of Nd-Fe-B alloy has been improved by the combined addition of Dy and Co and either Al, Ga, or Nb. However, additions of large amounts of Dy, Al, Ga, and Nb substantially reduce the B_r from that of Nd-Fe-B, and thus reduce overall magnet performance. This study shows that properly combined additions of Dy, Co, and Al to pseudoternary (Nd,Dy)-(Fe,Co,Al)-B compounds improve both temperature stability and energy density. H_{ci} and B_r increase more than in the alloys modified with Dy, Co, or Al alone. The H_{ci} of the alloys increases almost linearly with Dy content at a rate of about 6.8 kOe/at. % Dy, when the alloys contain approximately 5–6 at. % Co, and Al and Dy in a ratio of 1 to 1.2 Al/Dy. The temperature coefficients of B_r and H_{ci}, and the irreversible losses of (Nd,Dy)-(Fe,Co,Al)-B alloys are lower than those of the other alloys tested. When compared to Nd-Dy-Fe-Co-B alloy, the reduced consumption of Dy increases the energy products and reduces the material cost, without sacrificing temperature stability.

INTRODUCTION

Since Nd-Fe-B compounds[1,2] were discovered to produce superior magnetic properties, many efforts have been concentrated on improving their thermal stability.[1–8] It has been shown that combined addition of Dy and either Al or Ga to Nd-Fe-B compounds increase H_{ci} more effectively than single addition of Dy or Al.[3,4] However, it does not increase Curie temperature, or reduce temperature coefficients of B_r and H_{ci}. Studies have also shown that combined addition of Co and Dy to Nd-Fe-B increases Curie temperature and enhances temperature coefficients.[5,6] However, it does not increase H_{ci} efficiently, as it requires large quantities of Dy for high coercivity.[4,5] Combined additions of Ga and/or Nb to Nd-Dy-Fe-Co-B effectively increase both H_{ci} and temperature stability, although they significantly reduce B_r.[4,7,8] Thus, studies were carried out for the purpose of preparing a compound, (Nd,Dy)-(Fe,Co,Al)-B, which would produce both high H_{ci} and B_r with reduced temperature coefficients.

EXPERIMENT

The magnet materials were prepared by the conventional powder metallurgy method described elsewhere.[3] The alloys examined are (Nd-Dy-Fe-B), -Al, -Co, -Co-Al, -Co-Ga, -Co-Nb, -Co-Nb-Al, -Co-Nb-Ga, and -Co-Ga-Al. The permanent magnet properties at different temperatures were measured with hysteresigraph equipped with a KJS Associates' temperature probe fixture (TPF-1). The irreversible losses were measured with a Helmholtz coil and an integrating digital fluxmeter before and after exposure at elevated temperatures for 1.5 h. The microstructures of the samples were examined by a SEM with EDX.

RESULTS AND DISCUSSION

Various Dy, Al, Co, and TRE contents in (Nd,Dy)-(Fe,Co,Al)-B alloys were tested. Figures 1–3 relate the magnetic properties to chemical composition. As shown in Fig. 1, the (Nd,Dy)-(Fe,Co,Al)-B alloy exhibits its maximum coercivity when Co content ranges between 5 and 6.2 at. %. It is observed that B_r is independent of Co content between 3.9 and 7.3 at. %. With this in mind, the (Nd,Dy)-(Fe,Co,Al)-B alloys in the region of 5–6 at. % of Co are

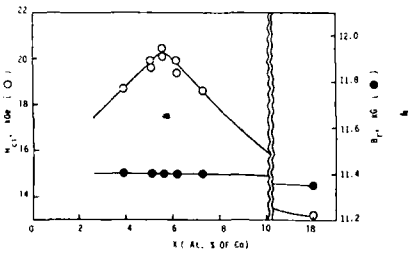


FIG. 1. Variation of magnetic properties, for $Nd_{14.4}Dy_{1.6}Fe_{77.4-x}Co_xAl_{1.6}B_6$ alloys, as a function of Co content.

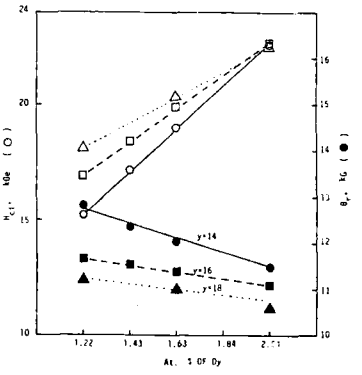


FIG. 2. Variation of magnetic properties, for $(Nd_{1-x}Dy_x)_y(Fe_{91.1}Co_{6.6}Al_{2.3})_{92-y}B_8$ magnets, as a function of Dy and TRE contents.

 0021-8979/88/083975-03$02.40 © 1988 American Institute of Physics

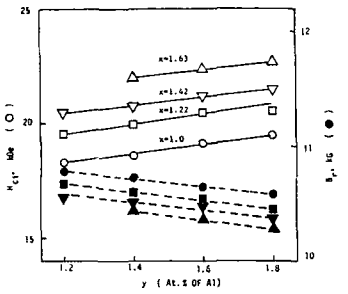


FIG. 3. Variation of magnetic properties, for parallel pressed $Nd_{16-x}Dy_xFe_{77-y}Al_yCo_5B_8$ magnets, as a function of Al and Dy contents.

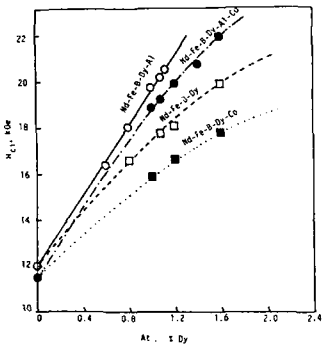


FIG. 4. Comparison of H_{ci} variations of various alloys as a function of Dy content.

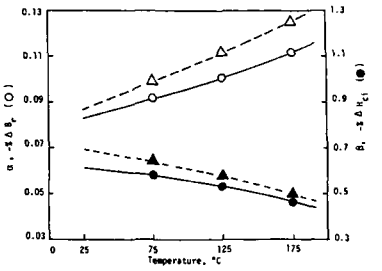


FIG. 5. Variation of temperature coefficients of B_r and H_{ci}, for Nd-Dy-Fe-Al-B and Nd-Dy-Fe-Co-Al-B magnets, depending on temperature (from 0 °C).

examined. The variation of magnetic properties for these alloys is exhibited as a function of total rare earth and Dy contents in Fig. 2. B_r and H_{ci} change almost linearly with Dy content. As Dy or TRE inreases, H_{ci} increases and B_r decreases. Magnetic properties are more sensitive to Dy content when total rare earth is low. Since it is necessary to maintain relatively high TRE or Dy content for high coercivity, high Dy content with lower TRE is desirable for both high B_r and H_{ci}. Figure 3 shows the variation of magnetic properties versus Al and Dy content. As Al and Dy increase, the coercivity increases almost linearly, while B_r decreases. Unlike (Nd,Dy)-(Fe,Al)-B alloy,[3] no optimum composition ratio of Dy to Al, showing a peak coercivity, is observed in (Nd,Dy)-(Fe,Co,Al)-B alloy. However, high coercivity with good squareness is always observed when the Al/Dy ratio slightly exceeds one(1–1.2) in Co bearing alloys.

While maintaining this Al/Dy ratio and 5.1 at. % of Co, $(Nd,Dy)_{16}(Fe,Co,Al)_{76}B_8$ alloys were made with varying Dy content. The rate of H_{ci} increase with Dy for Nd-Dy-Fe-Co-Al-B alloy is compared with those for other alloys as shown in Fig. 4. The rate of H_{ci} increase with Dy for this alloy is much faster than Nd-Dy-Fe-Co-B or Nd-Dy-Fe-B alloy. Thus, a very high coercivity magnet can be made with Nd-Dy-Fe-Co-Al-B by utilizing relatively lower Dy content compared to Nd-Dy-Fe-Co-B or Nd-Dy-Fe-B. Because Dy content is lower, this alloy exhibits B_r higher than that of Nd-Dy-Fe-Co-B alloy at an identical coercivity level. However, Nd-Dy-Fe-Co-Al-B alloy has lower B_r and H_{ci}

TABLE I. Magnetic properties at room temperature and irreversible loss at 200 °C for various Nd-Fe-B magnets.

	B_r (kG)	H_{ci} (kOe)	$(BH)_{max}$ (MGOe)	Irr. loss (%,pc = 2.4)
$(Nd_{0.9}Dy_{0.1})_{15}Fe_{77}B_8$	12.08	20.6	34.4	17.3
$(Nd_{0.9}Dy_{0.1})_{15}Fe_{75.5}Al_{1.5}B_8$	12.60	20.2	38.4	12.3
$(Nd_{0.88}Dy_{0.12})_{15}Fe_{70.2}Co_5Al_{1.8}B_8$	11.90	20.4	34.4	1.6
$(Nd_{0.9}Dy_{0.1})_{15}Fe_{70.3}Co_5Ga_{1.7}B_8$	10.67	14.7	26.6	24.5
$(Nd_{0.9}Dy_{0.1})_{15}Fe_{68.8}Co_5Ga_{1.7}Al_{1.5}B_8$	10.26	20.8	21.6	6.8
$(Nd_{0.9}Dy_{0.1})_{15}Fe_{70.4}Co_5Nb_{1.6}B_8$	11.65	16.0	32.6	7.7
$(Nd_{0.9}Dy_{0.1})_{15}Fe_{68.8}Co_5Nb_{1.6}Al_{1.6}B_8$	10.85	20.3	28.4	4.3
$(Nd_{0.9}Dy_{0.1})_{15}Fe_{68.8}Co_5Nb_{1.6}Ga_{1.6}B_8$	10.55	16.4	26.2	13.9

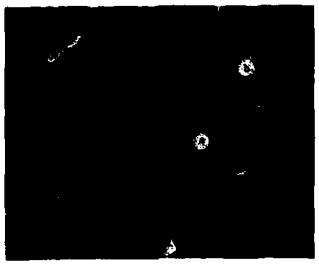


FIG. 6. Backscattered electron image of $Nd_{13.2}Dy_{1.8}Fe_{70.2}Co_{5.0}Al_{1.8}B_8$ magnet (etched by 3% nital).

than Nd-Dy-Fe-Al-B alloy. For the Co bearing alloy, maintaining a high H_{ci} requires high TRE or Dy although high TRE or Dy degrades B_r. In addition, H_{ci} is less sensitive to the Dy when Co is present. Therefore, it is difficult to produce both high B_r and H_{ci} in the (Nd,Dy)-(Fe,Co,Al)-B alloy.

Neverthless, Nd-Dy-Fe-Co-Al-B alloy seems to be more stable than Nd-Dy-Fe-Al-B alloy at elevated temperatures. As shown in Fig. 5, the temperature coefficients of B_r and H_{ci} of the former are lower than those of the latter. The irreversible loss of $(Nd_{0.88}Dy_{0.12})_{15}Fe_{70.2}Co_{5.0}Al_{1.8}B_8$ alloy is 1.6% at 200 °C, while the $(Nd_{0.9}Dy_{0.1})_{15}Fe_{75.5}Al_{1.5}B_8$ alloy is 12.3%. As shown in Table I, the Nd-Dy-Fe-Co-Al-B alloy exhibits the lowest irreversible loss at 200 °C of the alloys tested. Ga or Nb addition to the alloy significantly reduces B_r, while it improves H_{ci}. The irreversible losses of $(Nd_{0.9}Dy_{0.1})_{15}Fe_{70.3}Co_{5.0}Ga_{1.7}B_8$ and $(Nd_{0.9}Dy_{0.1})_{15}Fe_{70.4}Co_{5.0}Nb_{1.6}B_8$ alloys are 24.5% and 7.7% at 200 °C, respectively. This indicates that Ga or Nb addition is probably not as effective method as Al addition for improving temperature stability and performance.

To understand the coercivity mechanism of (Nd,Dy)-(Fe, Co,Al)-B alloy system, the microstructure of the specimen was studied with SEM and EDX. The BSE image of the specimen displays two phases—dark matrix and light phase. as shown in Fig. 6. EDX analysis on these phases indicates that the dark matrix seems to be $(Nd,Dy)_2(Fe,Co_{14})B$ and the light phase $(Nd,Dy)_2(Fe,Co)_7$ as shown in Table II. It is noted that Co is uniformly distributed both in the matrix and the 2nd phase without forming Co-rich phase. It is also noted that Al is hardly detected in the matrix and 2nd phase, but mainly in the triple junctions of the grain boundaries. Therefore, Al is believed to exist in the grain boundary. Unlike (Nd,Dy)-(Fe,Co)-B alloy,[5] Co-rich phase may be replaced by Al-rich phase in the grain boundary, and enter in the matrix. This may account for increases in H_{ci} and T_c with reduction of temperature coefficients.

TABLE II. Quantitative analysis of $Nd_{13.2}Dy_{1.8}Fe_{70.2}Co_{5.0}Al_{1.8}B_8$ sample obtained by EDXA.

	Nd	Dy	Fe	Co	Al	$\frac{Fe+Co}{Nd+Dy}$
Matrix (region a)	11.75	2.15	80.09	5.74	0.0	6.17
Light phase (b)	17.61	3.78	73.02	5.40	0.0	3.66

CONCLUSION

The Nd-Dy-Fe-Co-Al-B alloys containing approximately 5–6 at. % Co, and Al and Dy with about 1–1.2 Al/Dy ratio have turned out to be very promising. They exhibit high H_{ci} with moderately high energy products and relatively low irreversible losses at elevated temperatures.

[1] M. Sagawa, S. Fujimura, N. Togawa, H. Yamamoto, and Y. Matsuura, J. Appl. Phys. **55**, 2083 (1984).
[2] J. Croat, J. Herbst, R. Lee, and F. Pinkerton, J. Appl. Phys. **55**, 2078 (1984).
[3] A. Kim (these proceedings).
[4] M. Tokunaga, H. Kogure, M. Endoh, and H. Harada, in Proceedings of '87 Intermag. Conference, Tokyo, Japan 1987, paper BC-03.
[5] S. Arai, T. Shibata, N. Koshizuka, and M. Nagakura, in Proceedings of '87 Intermag. Conference, Tokyo, Japan 1987, paper BC-07.
[6] S. Fujimura, M. Sagawa, Y. Matsuura, H. Yamamoto, and N. Togawa, European Patent Publication No. 0134304 (08.07.87).
[7] Y. Xiao, K. Strnat, H. Mildrum, and A. Ray, in *Proceedings of the 9th International Workshop on REPM, Bad Soden, Germany,* Aug. 1987, edited by C. Herget and R. Poerschke (DPG-GMBH, HAUPTSTR.), p. 467.
[8] M. Tokunaga, M. Endoh, and H. Harada, in *Proceedings of the 9th International Workshop on REPM, Bad Soden, Germany,* Aug. 1987, edited by C. Herget and R. Poerschke (DPG-GMBH, HAUPTSTR.), p. 477.

Giant intrinsic coercivities in as-cast RFe_2Ni_2B alloys

J. Strzeszewski,[a] A. Nazareth, and G. C. Hadjipanayis
Department of Physics, Kansas State University, Manhattan, Kansas 66506

The origin of high coercivities in as-cast RFe_2Ni_2B alloys is investigated by correlating the magnetic properties with the microstructure. Hysteresis loop measurements showed high coercivities in samples containing Sm and Er. In $SmFe_2Ni_2B$ the coercivities could not be measured in a field of 80 kOe at 4.2 K but they decreased to 56 kOe at 50 K. The coercivities are lower in $ErFe_2Ni_2B$, reaching the value of 38 kOe at 4.2 K. Electron diffraction studies showed a multiphase structure with a majority phase having a crystal structure of $CeCo_4B$ type. In $SmFe_2Ni_2B$, many stacking faults were observed which may explain the high coercivities.

INTRODUCTION

In recent years the magnetic hardness of the homologous series $T_{3n+5}R_{n+1}B_{2n}$ (where T = transition metal and R = rare earth) and disordered $SmCo_{5-x}Ni_x$ alloys has received much attention.[1–3] These compounds exhibit high magnetic anisotropy and crystallographic site disorder. The large coercivities observed, particularly at cryogenic temperatures, have been attributed to domain wall pinning at the atomic scale due to fluctuations in exchange and magnetic anisotropy.[4] However, recent studies[5] on powdered and melt-spun $SmCo_{5-x}Ni_x$ ribbons show a strong size dependence of H_c in addition to the intrinsic effect.[6] The coercivity of the latter samples was much greater than that of as-cast alloys.

In the present work, we extend our studies to other rare-earth systems RFe_2Ni_2B where R = Pr, Nd, Sm, Er, Dy, and Gd. Our objective is to correlate the magnetic properties with the microstructure in order to understand better the mechanism responsible for the giant coercivities observed in these materials.

EXPERIMENT

Bulk samples of the alloys RFe_2Ni_2B (R = Pr, Nd, Sm, Er, Dy and Gd) were prepared by arc-melting high-purity elements (99.9%) in an Ar atmosphere. A Cr$K\alpha$ tube was used for x-ray diffraction analysis. Magnetic measurements were made using a VSM equipped with a superconducting magnet with a maximum field of 80 kOe. Thermomagnetic data were obtained with another VSM using an electromagnet and a homemade furnace assembly capable of handling temperatures up to 800 °C. Microstructure studies and composition analysis were performed with a Jeol/100C scanning transmission electron microscope equipped with an energy dispersive x-ray detector.

RESULTS AND DISCUSSION

X-ray diffraction studies established the presence of the 1:4:1 phase in all the as-cast alloys as the majority phase.

Thermomagnetic data indicate the presence of a major magnetic phase in each alloy with Curie temperatures around 200 °C. Hysteresis loops and initial magnetization curves of RFe_2Ni_2B (R = Er, Nd) taken at 4.2 K and for $SmFe_2Ni_2B$ taken at 100 K are shown in Fig. 1. $NdFe_2Ni_2B$ while being relatively soft, has the largest moment of the alloys studied, as expected because of the ferromagnetic coupling of Nd with Fe. The shape of the initial magnetization curves is indicative of a typical uniform domain wall pinning process. The critical field H_{cr} at which the walls begin to move is approximately equal to the coercivity. At this field, during the initial magnetization process, the magnetization increases almost abruptly. This is consistently evident in all the alloys studied. The highest H_c were obtained for the Sm and Er containing alloys (Table I). In fact, the hysteresis loop for $SmFe_2Ni_2B$ could not be obtained at 4.2 K (Fig. 1). It could be that the second-order Stevens coefficient[7] is negative for Sm and Er compounds only, leading to an easy axis for these two alloys and a planar alignment for the others. This is opposite to $R_2Fe_{14}B$ behavior.[8] The temperature dependence of H_c for $SmFe_2Ni_2B$ and $ErFe_2Ni_2B$ alloys is shown in Fig. 2. The shape of $H_c(T)$ suggests a strongly thermally activated domain wall motion.

The microstructure studies were concentrated on $NdFe_2Ni_2B$ and $SmFe_2Ni_2B$ samples. A multiphase structure has been observed in $NdFe_2Ni_2B$ with 1:4:1 (Fig. 3) as

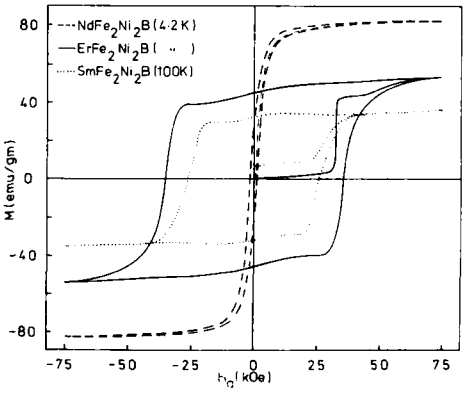


FIG. 1. Hysteresis loops and magnetization curves of RFe_2Ni_2B alloys.

[a] On leave from the Institute of Physics, Warsaw Technical University, Warsaw, Poland.

 0021-8979/88/083978-03$02.40 © 1988 American Institute of Physics

TABLE I. Magnetic properties of RFe_2Ni_2B alloys at 4.2 K.

	H_c (kOe)	M_s (emu/g)
$SmFe_2Ni_2B$	56.00[a]	36.00
$ErFe_2Ni_2B$	38.02	53.28
$NdFe_2Ni_2B$	1.51	81.88
$DyFe_2Ni_2B$	2.81	55.40
$PrFe_2Ni_2B$	2.34	69.86
$GdFe_2Ni_2B$	0.23	47.77

[a]At 51 K.

one of the phases present. The micrograph picture of Fig. 4 revealed some layered morphology with many structural defects. Together with the 1:4:1 structure we often found some smaller grains of the cubic Laves phase $Nd(Fe,Ni)_2$. In addition, relatively large (a few microns) well-developed grains of $(Fe,Ni)_2B$ were also observed. STEM x-ray microanalysis of this phase indicated that it contained much more Fe than Ni. The domain wall contrast in the 1:4:1 phase was rather weak, and it was easy to move the domain walls in the magnetic field of the objective lens ($H \sim 5$ kOe). The most pronounced feature of the $SmFe_2Ni_2B$ microstructure was the existence of large areas (several microns) having a hexagonal structure with $a \simeq 5$ Å and different values of c spacings. The whole area had the same orientation for the c axes but different orientations for the a axes. Among the different values of c spacing found, $c = 6.9$ Å corresponds to the 1:4:1 phase and $c \simeq 12.9$ Å may correspond to the $Sm_2Co_7B_3$ structure.[9] Most of the diffraction patterns taken from the above regions show characteristic streaking in all spots along the c direction which is probably connected with stacking faults existing in these samples (Figs. 5 and 6). Besides these phases very few grains were also observed with a $Sm(FeNi)_2$ phase and a B-rich $Sm(FeNi)_4B_4$ phase having a tetragonal structure with $a = 7.1$ Å and $c = 3.9$ Å.

We believe that the heavily faulted stacking found in $SmFe_2Ni_2B$ grains may lead to domain wall pinning that



FIG. 3. Electron diffraction pattern showing the 1:4:1 phase in $NdFe_2Ni_2B$ (zone-axis 100).



FIG. 4. Microstructure of a $NdFe_2Ni_2B$ sample.



FIG. 5. Electron diffraction pattern showing streaking of diffraction spots along c-axis in $SmFe_2Ni_2B$.

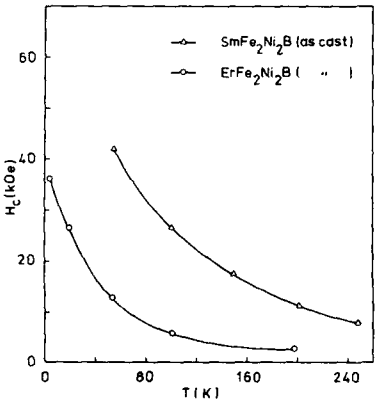


FIG. 2. Temperature dependence of H_c in as-cast RFe_2Ni_2B alloys.

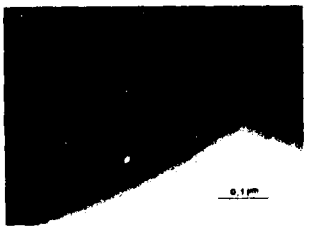


FIG. 6. Stacking faults in a $SmFe_2Ni_2B$ sample.

plays an integral role in the large coercivities measured in these alloys. Careful Lorentz microscope studies are underway to clarify this issue.

ACKNOWLEDGMENT

This work was supported by NSF Grant No. DMR-8607023.

[1]N. A. El-Malsry and H. H. Stadelmaier, J. Appl. Phys. **61**, 3589 (1987).
[2]S. Foner, E. J. McNiff, Jr., H. Oesterreicher, F. T. Parker, and M. Misroch, J. Appl. Phys. **49**, 2061 (1978).
[3]K. H. J. Buschow, M. Brouha, and A. G. Rijnbeck, Solid State Commun. **16**, 31 (1975).
[4]H. Oesterreicher, Appl. Phys. **15**, 341 (1978).
[5]M. T. Mikhov and G. C. Hadjipanayis, Magn. Magn. Mater. **61**, 3460 (1987).
[6]B. Barbara, C. Becke, R. LeMaive, and D. Paccard, J. Phys. Suppl. **32**, 229 (1971).
[7]T. E. Creedon and V. U. S. Rao, J. Solid State Chem. **6**, 387 (1973).
[8]S. Sinnema, R. J. Radwanski, J. J. M. France, D. B. deMooij, and K. H. J. Buschow, J. Magn. Mater. **44**, 333 (1984).
[9]N. A. ElMastry, H. H. Stadelmaier, C. J. Shahwan, and L. T. Jordan, Z. Metallkd. **74**, 33 (1983).

The effect of Lorentz demagnetization field (LDF) on the saturation magnetization of $SmCo_5$ magnets

Shiang-Jiun Heh and Swe-Kai Chen
Materials Research Laboratories, Industrial Technology Research Institute, Chutung, Taiwan 31015 Republic of China

In order to have a further understanding of the cause of the increase in the saturation magnetization, $4\pi M_s$, of $SmCo_5$ magnets in sintering, saturation magnetization as a function of density, phase change and the grain sizes were measured in this study. While Tawara and Senno considered that the increasing in $4\pi M_s$ of the "Ce-Co-Fe-Cu" system was due to the improvement of the magnetization alignment caused by increasing the grain size during the magnet sintering process [Y. Tawara and H. Senno, IEEE Trans. Magn. MAG-8, 560 (1972)], it was shown that the Lorentz demagnetization field (LDF) [S. Chikazumi, *Physics of Magnetism* (Wiley, New York, 1964), Sec. 2-2; B. D. Cullity, *Introduction to Magnetic Materials* (Addison-Wesley, Reading, MA, 1972), Sec. 4-3, p. 132] was the major factor in the $4\pi M_s$ increment after the magnet sintering. As a result of calculation by the use of the LDF in the $SmCo_5$ system, an accuracy of $\pm 3\%$ was readily obtained, while that of Tawara and Senno has an accuracy of 29.6% higher than its normalized (or expected) value in their system. But if LDF was involved in the "Ce-Co-Fe-Cu" system, a value of $+6.5\%$ can be obtained. Finally, it was thought that the phase change occurring in sintering, e.g., Sm_2Co_7 to $SmCo_5$, may be a minor factor in favor of the increasing phenomena in the system by the observation of x-ray diffraction patterns.

INTRODUCTION

It was understood that, owing to the shrinkage of a magnet, the saturation magnetization, $4\pi M_s$, of a magnet increases greatly during its sintering process,[1] i.e., $4\pi M_s$ increases as the density increases during sintering. For rare-earth cobalt magnets, it was shown that the sintered density depends on the various processing factors such as sintering temperature and time, oxygen partial pressure of the sintering chamber used, and positive pressure, negative pressure, or vacuum sintering used, etc.

According to Tawara and Senno,[2] the $4\pi M_s$ values increase not only with the increase in density, but also with grain growth during sintering in their $Ce(Cu,Fe,Co)_5$ system. Accordingly, they got a 29.6% gain in the $4\pi M_s$ of their magnet. They assumed that the gain was due to the improvement of the orientation of the easy axis, caused by the grain growth during sintering. Obviously, their work was done by the use of the normalization of $4\pi M_s$, i.e., $4\pi M_s$ in 100% density, and by comparing the normalized $4\pi M_s$ of the green compacts with that of the sintered bodies.

In this study, the increase of $4\pi M_s$ value of $SmCo_5$ magnets after sintering was checked again by the observation of grain size, phase change, and the measurement of $4\pi M_s$ in green compacts and sintered bodies. It was shown that as the Lorentz demagnetization field (LDF) in pores of the green compacts and sintered bodies was involved in the $4\pi M_s$ normalization process (LDF involved normalization technique), the two normalized $4\pi M_s$ values for both green compact and sintered body of the same specimen are nearly the same within a $\pm 3\%$ tolerance.

EXPERIMENT

Raw Materials was "Reduction-Diffusion" $SmCo_5$ alloy with Sm 35.2 ± 0.5 wt. %. After pulverizing and grinding, the average particle size is about 5 μm under the Fisher Subsieve Sizer test. Green compacts of pellet shape were magnetically die-pressed in a metal mold under a pressure of 3 T/cm^2 with a parallel-to-pressing direction magnetic field strength of 17 kOe. After measuring the dimension of the green compacts directly with a micrometer, it can be estimated that the compacts density are in the range of 63%–65%. The compacts were then sintered in an atmosphere controlled chamber under conventional steps and conditions including different sintering temperatures and times and ageing processes, so as to get sintered magnet bodies with relative densities ranging from about 90% to 99%.

Magnetic properties were performed with a YEW type 3250, dc B-H hysteresis loop tracer, under a maximum magnetic field strength of 15 kOe. Green compacts and sintered bodies with dimensions of r_0 (diameter) $\times$ h_0 (height) and $r_1 \times h_1$, respectively, were tested with the YEW 3250. The $4\pi M_s$ values were taken by the use of different combinations: (r_0,h_0) for green compacts and (r_1,h_1) for sintered bodies. A normalization of a $4\pi M_s$ was obtained as the $4\pi M_s$ was divided by its relative density. If pores in compacts or sintered bodies were assumed to be spherical, and the Lorentz demagnetization field (LDF) was taken into consideration, a modified normalization of $4\pi M_s$ (LDF involved normalization of $4\pi M_s$) would be obtained. In this study, x-ray diffraction patterns were used to check the phase changes after sintering. Sintered bodies were ground,

 0021-8979/88/083981-03$02.40 © 1988 American Institute of Physics

TABLE I. Measured data of saturation magnetization and density for $SmCo_5$ and $Ce(Cu,Fe,Co)_5$. D_0: density of green compact; D_1: density of sintered body; A_0 (r_0,h_0): apparent or measured $4\pi M_s$ of green compact; B_0(r_1,h_1): apparent or measured $4\pi M_s$ of sintered body; Nos. 1–5 for $SmCo_5$; No. 6 for $Ce(Cu,Fe,Co)_5$ (Ref. 1).

Sample No.	D_0 (%)	A_0 (kG)	D_1 (%)	B_0 (kG)
1	64.5	4.5	89.6	7.6
2	64.5	4.8	93.8	8.55
3	63.0	4.7	95.3	8.8
4	65.0	4.8	96.0	8.8
5	65.0	4.9	99.3	9.35
6	65.0	3.5	100.0	7.0

etched with a mixture of nitric acid, acetic acid, pure water, and hydrochloride acid in a ratio of 1:1:1:4.[3] Photos of microstructures were taken by using an Olympus optical microscope at a magnification of 1000 times, and thereafter the average grain sizes were obtained in order to understand the influence of grain growth on the $4\pi M_s$ values.

RESULTS AND DISCUSSION

Table I shows the measured data of saturation magnetization and density of green compacts and sintered bodies for $SmCo_5$ and $Ce(Cu,Fe,Co)_5$.

In view of green and sintered densities in Table I, it can be seen that there are many pores in the green compacts and sintered bodies. According to Chikazumi[4] and Cullity,[5] in magnetic materials, where pores exist, there appear magnetic free poles on the surface of the pores.

The magnetic field induced by these free poles is parallel to the direction of magnetization. Therefore, apparent saturation magnetization = normalized saturation magnetization in materials + magnetic field strength induced by free poles.

If it is assumed that pores in magnets are spherical, one then has the following relation:

$$(4\pi M_s)_{app} = (4\pi M_s)_{theo}(V/V_0) + \tfrac{1}{3}(4\pi M_s)_{theo}(1 - V/V_0), \quad (1)$$

where, $(4\pi M_s)_{theo}(V/V_0)$ is the normalization value of $4\pi M_s$, $\frac{1}{3}(4\pi M_s)_{theo}(1 - V/V_0)$ is the Lorentz demagnetization field at pores in materials, and $(4\pi M_s)_{app}$ is the apparent or measured value of $4\pi M_s$.

From Eq. (1), we can have

$$(4\pi M_s)_{theo} = (4\pi M_s)_{app} \frac{V}{V_0} - \frac{1}{3}\left(1 - \frac{V}{V_0}\right). \quad (2)$$

Here, $(4\pi M_s)_{theo}$ is a normalized saturation magnetization with LDF involved for green compacts and sintered bodies. This LDF-involved-normalized $4\pi M_s$ and the simple-normalized $4\pi M_s$ for green compacts and sintered bodies are compared and listed in Table II.

It is shown in Table II that if LDF is involved in the normalization of $4\pi M_s$, the $4\pi M_s$ increments after sintering range from -1.8% to $+3.2\%$, as compared with that of the simple normalization about volume fraction of the magnets from $+20.7\%$ to 23.5%. It also can be seen, from Table II, that if the same calculation was done with Tawara's data, the increment of $4\pi M_s$ would be $+6.5\%$ as compared with the value, $+29.6\%$, of Tawara's simple normalization.

Figure 1 shows the typical x-ray diffraction patterns of the green compact and the sintered body.[6,7] A second phase of Sm_2Co_7 exists for the green compacts, but only the $SmCo_5$ phase does exist for sintered bodies. This means that there is a phase change during the compacts sintering. Saturation magnetization $4\pi M_s$ values for $SmCo_5$ and Sm_2Co_7 phases[6] are 835 and 550 emu, respectively.[8] Therefore, the positive increment in $4\pi M_s$ shown in Table II was partly contributed by the phase change from Sm_2Co_7 to $SmCo_5$.

TABLE II. Normalized $4\pi M_s$ values for green compacts and sintered bodies of $SmCo_5$ and $Ce(Cu,Fe,Co)_5$ magnets. A_1,A_2 for green bodies; B_1,B_2 for sintered bodies. Remarks: Nos. 1–5 for $SmCo_5$ magnets; No. 6 for Tawara's $Ce(Cu,Fe,Co)_5$ magnets; $A_2 = (4\pi M_s)_{theo}$ of green compact; $B_2 = (4\pi M_s)_{theo}$ of sintered body.

Sample No.	Simple normalized $4\pi M_s$		$4\pi M_s$ increment, Δ_1(%)	LDF-involved normalized $4\pi M_s$		$4\pi M_s$ increment, Δ_2(%)
	A_1 (kG)	B_1 (kG)		A_2 (kG)	B_2 (kG)	
1	6.98	8.48	+21.5	8.54	8.82	+3.2
2	7.44	9.14	+22.9	9.10	9.36	+2.9
3	7.46	9.21	+23.5	9.27	9.37	+1.1
4	7.60	9.17	+20.7	9.46	9.29	−1.8
5	7.54	9.42	+24.9	9.17	9.44	+2.7
6	5.38	7.00	+29.6	6.56	7.00	+6.5

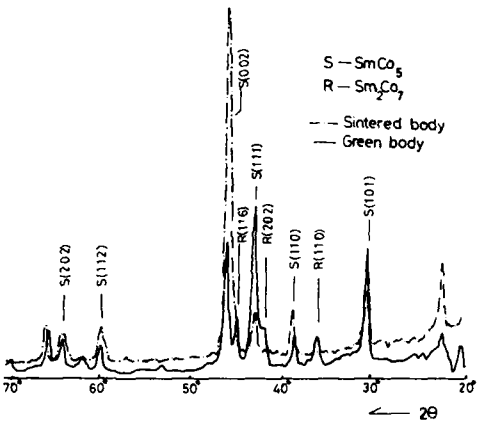


FIG. 1. X-ray diffraction patterns for the sintered and green bodies of the $SmCo_5$ magnets. Note that a second phase of Sm_2Co_7 for the green compact was observed while only the $SmCo_5$ phase for the sintered body. This means that a phase change occurs from Sm_2Co_7 phase for the sintered body. This means that a phase change occurs from Sm_2Co_7 to $SmCo_5$ during the compact sintering.

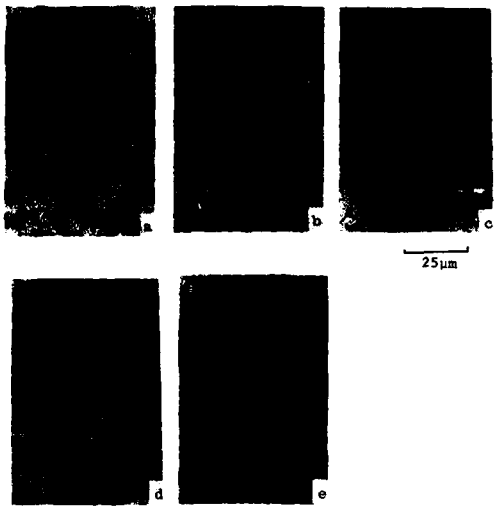


FIG. 2. Microstructures of $SmCo_5$ for different grain sizes and densities. (a)–(e) were the photos taken from Sample Nos. 1–5 correspondingly. (a) 89.6% (11.0 μm), (b) 93.5% (12.7 μm), (c) 95.3% (19.8 μm), (d) 96% (14.0 μm), and (e) 99.3% (35.8 μm).

Figure 2 shows the relation between grain size and density for $SmCo_5$. It is shown that relative densities range from 89.6% to 99.3%, while the corresponding average grain sizes range from 11.0 to 35.8 μm. Figures 2(a)–2(e) are the photos taken from sample Nos. 1 to 5 correspondingly. Although the grain growth increases from approximately 3 to 7 times, and that of Tawara's increases 10 times, the increments shown in Table II have no significant relation with grain size. Therefore, it can be supposed that the increment in $4\pi M_s$ is not a function of grain size for the $SmCo_5$ system.

CONCLUSION

The increase in $4\pi M_s$ for the sintered $SmCo_5$ magnets is principally due to the volume shrinkage of the specimen and thus due to the increase in density, so as to decrease the pores-induced-demagnetization field. By use of the LDF involved normalization technique, the variation of the calculated $4\pi M_s$ value from its measured value is readily obtained within a $\pm$ 3% tolerance. The phase-change-induced-increment of $4\pi M_s$ as can be seen from x-ray diffraction patterns has an important contribution to the variation. In fact, the occurence of a small amount of higher saturation magnetization phase and oxidation during sintering, experimental error, the assumption of the spherical shape of pores in the calculation of demagnetization field, and grain growth are also contributive factors to the variation.

[1]D. L. Martin and M. G. Benz, AIP Conf. Proc. **5**, 970 (1972).
[2]Y. Tawara and H. Senno, IEEE Trans. Magn. **MAG-8**, 560 (1972).
[3]M. G. Benz and D. L. Martin, J. Appl. Phys. **43**, 3165 (1972).
[4]S. Chikazumi, *Physics of Magnetism* (Wiley, New York, 1964), Sec. 2-2.
[5]B. D. Cullity, *Introduction to Magnetic Materials* (Addison-Wesley, Reading, MA, 1972), Sec. 4-3, 132.
[6]C. E. King, I. R. Harris, D. W. A. Murphy, and D. Kennedy, in *Proceedings of the VI International Workshop on Re-Co Magnetism and their Applications*, 1982, edited by J. Fidler (Technical University of Vienna, Vienna, 1982), p. 411.
[7]Yu Chengzhou, Ying Qiming, and Di Xiuxuan, in *Proceedings of the 7th International Workshop on Re-Co Permanent Magnetism and their Applications*, edited by P. Xiaoshuo, H. Wenwang, and Y. Chengzhou (China Academic, Beijing, China, 1983), p. 439.
[8]H. Kronmüller, in *Proceedings of the 7th International Workshop on Re-Co Permanent Magnetism*, 1983, edited by P. Xiaoshuo, H. Wenwang, and Y. Chengzhou (China Academic, Beijing, China, 1983), p. 439.

Thermal stability of five sintered rare-earth–cobalt magnet types

D. Li
Central Iron and Steel Research Institute, Beijing, People's Republic of China
H. F. Mildrum and K. J. Strnat
Magnetics Laboratory, University of Dayton, Dayton, Ohio 45469

Five commercially available magnet types—$SmCo_5$, high- and low-coercivity $Sm_2(Co,Fe,Cu,Zr)_{17}$, $(Sm,Ce)(Co,Cu,Mn)_7$, and $Ce(Co,Cu,Fe)_5$—were systematically studied to obtain a comprehensive overview of the following magnetic properties of interest to the user: reversible and irreversible losses during thermal cycling between 20 °C and 250 °C; open-circuit remanent flux loss during aging at 150 °C and 250 °C up to 2100 h, at permeances of $p = -2.5$ and -0.5. Room-temperature demagnetization curves before and after aging are compared to distinguish recoverable (magnetic) from irrecoverable (structural) aging effects. The $Sm_{0.5}Ce_{0.5}(Co,Cu,Mn)_7$ magnets had the best long-term stability under all test conditions, followed by the high-H_c 2-17 and $SmCo_5$. The low-H_c 2-17 exhibited the greatest absolute flux loss under all conditions, but it stabilized fairly well after 10 h, and the loss was recoverable by remagnetizing. In contrast, for $Ce(Co,Cu,Fe)_5$ the losses continued up to 2100 h without a sign of flux stabilization.

INTRODUCTION

Since their introduction nearly 20 years ago, sintered rare-earth–transition-metal permanent magnets of many different compositions and properties have been developed. Several rare-earth–cobalt compositions have been widely accepted based upon their proven performance in spite of high price and material supply limitations. But applications engineers have difficulties obtaining reliable data on the thermal stability of commercial magnets. Prior stability studies[1–6] often focused on a single material type.

To address this problem, we have compiled a comparative evaluation of several sintered magnet materials, supplementing our own earlier work with additional measurements. In all, five representative commercial magnet materials were selected for this comparison: $SmCo_5$, high- and low-coercivity $Sm_2(Co,Fe,Cu,Zr)_{17}$, $(Sm,Ce)(Co,Cu,Mn)_7$, and $Ce(Co,Cu,Fe)_5$. The scope of the evaluation includes the reversible and irreversible losses during cycling between 20 °C to 250 °C, open-circuit remanent flux loss during aging at elevated temperatures of 150 and 250 °C for approximately 2000 h (unit permeances of $B/H \approx -2.5$ and 0.5), and room-temperature demagnetization curves before and after aging.

SAMPLES AND EXPERIMENTAL METHODS

The test specimens used were axially aligned cylinders ~6.25 mm in diameter with length-to-diameter ratios of 0.83 and 0.20, corresponding to open-circuit operating point at unit permeance of $p = B/H \approx -2.5$ and ≈ -0.5, respectively.

The salient magnetic properties were first characterized using a recording hysteresigraph and found to be within the range of values advertised by the manufacturers.

The reversible temperature coefficients of open-circuit remanent flux were determined on magnets with $p = -2.5$, prestabilized for 5 h at the maximum temperature. This measurement was performed with a pull-coil system and precision integrating digital voltmeter (IDVM). The flux losses during long-term elevated temperature aging were periodically measured at room temperature with an oscillating sample magnetometer (in an open-circuit configuration) or with the pull coil and IDVM. The procedures used have been described elsewhere.[1]

RESULTS AND DISCUSSION

Reversible losses of open-circuit remanent flux as a function of temperature for each magnet type are shown in Fig. 1. Coefficient data at specific points from ambient to the maximum temperature of exposure are reported in Table I. Average values over discrete ranges of temperature are also listed. The reversible losses are lowest (and essentially the same) for the high- and low-H_c 2-17 magnets. Reversible losses for the other compositions increase in this order: $SmCo_5$ (greater by a factor ~1.3), $SmCe(TM)_7$ (~2), and $Ce(TM)_5$ (~3).

Initial irreversible losses and long-term aging losses are shown in Figs. 2 and 3 as a function of time at temperature.

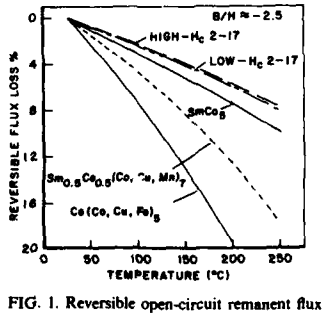


FIG. 1. Reversible open-circuit remanent flux variation as a function of temperature.

 0021-8979/88/083984-03$02.40 © 1988 American Institute of Physics

TABLE I. Reversible temperature coefficients of open-circuit remanent flux for commercial rare-earth–transition-metal magnets, $Bd/Hd \approx -2.5$.

Magnet type	Temperature level (°C)				Over temperature span[b] (− %/°C)		
	+ 20	+ 100	+ 200	+ 250	20–100	20–200	20–250
$SmCo_5$	0.040	0.048	0.060	0.075	0.045	0.047	0.055
$Sm_2(TM)_{17}$[a] (Low $_M H_c$)	0.028	0.030	0.046	0.060	0.028	0.030	0.042
$Sm_2(TM)_{17}$ (High $_M H_c$)	0.029	0.035	0.045	0.054	0.032	0.037	0.040
$SmCe(TM)_7$	0.061	0.068	0.088	0.096	0.062	0.071	0.078
$Ce(TM)_5$	0.090	0.104	0.132	···	0.098	0.111	···

[a] TM is one or several transition metals (Co,Fe,Cu,Zr,Hf,Mn).
[b] Referred to values at 20 °C.

The initial loss depends on the difference between $_M H_c$ at the temperature of exposure and the internal demagnetizing field, and therefore on the sample geometry.[2,7] This is particularly evident for magnets exposed at 250 °C (Fig. 3).

During long-term exposure the $Sm,Ce(TM)_7$ magnets exhibit the best aging behavior. Heating at 250 °C results in a loss of only ~1% at the higher permeance, and only ~4% at the lower operating point. The aging curves in Fig. 2 indicate that the early "prestablization losses" for $SmCo_5$ and high-H_c $Sm_2(TM)_{17}$ at 150 °C are slightly higher than for $SmCe(TM)_7$, but after ~10 h the time rate of loss for all three compositions is approximately the same. At 250 °C (Fig. 3) a similar behavior persists for magnets of higher permeance, but the $p = -0.5$ sample of $SmCo_5$ was inferior after exposure times > 100 hours; the high-H_c $Sm_7(TM)_{17}$ was best. The low-H_c $Sm_2(TM)_{17}$ suffers a severe initial irreversible loss of 10%–12% at 150 °C, but then stabilizes quite well at this reduced flux level. The 1–5 magnets containing cerium as the only rare-earth element continue to lose flux at a much higher rate than the other materials.

Figures 4(a) and 4(b) illustrate the effect of long-term heating on the intrinsic demagnetization curves of two magnet types. For $SmCo_5$ magnets, the remanent induction decreased ~3% and the intrinsic coercivity ~9% after 2000 h. Induction losses are completely recoverable by remagnetizing in a 100 kOe pulsed field, but the loss of coercivity persists. This suggests metallurgical changes in the microstructure at 250 °C.

For low-H_c $Sm_2(TM)_{17}$ magnets, the loss in remanent induction under the same conditions is ~4.5 times greater than for $SmCo_5$, but is recoverable on remagnetizing. $_M H_c$ remains unchanged during the exposure, and recharging has no further effect.

CONCLUSION

Three of the five magnet types evaluated—$Sm_{0.5}Ce_{0.5}(Co,Cu,Mn)_7$, high-$H_c$ $Sm_2(Co,Cu,Fe,Zr)_{17}$,

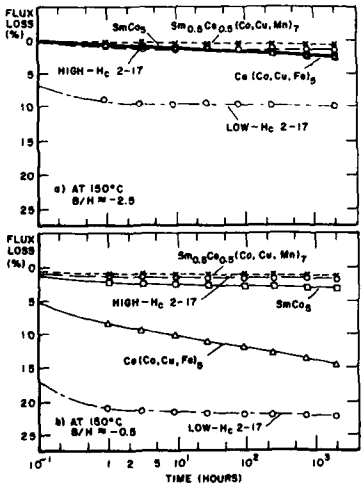


FIG. 2. Initial irreversible loss and long term stability of commercial sintered rare-earth–transition-metal magnets, with unit permeance of ≈ -2.5 and -0.5 for ~2000 h at 150 °C.

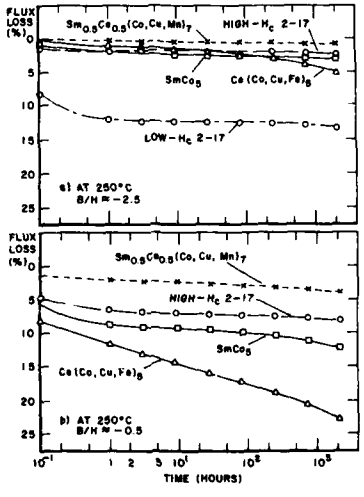


FIG. 3. Initial irreversible loss and long-term stability of commerical sintered rare-earth–transition-metal magnets, with unit permeance of ≈ -2.5 and -0.5 for ~2000 h at 250 °C.

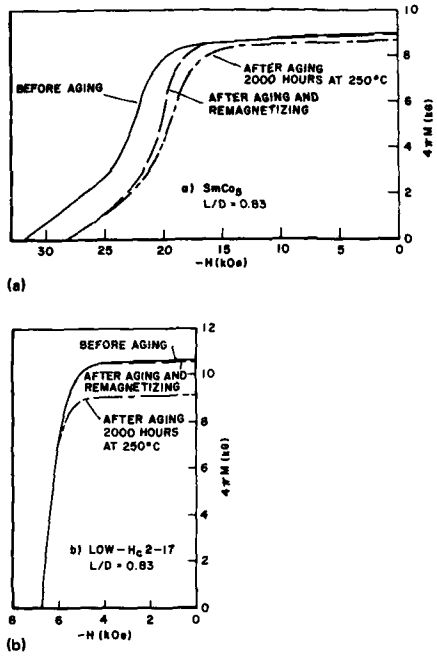


FIG. 4. Variation of intrinsic demagnetization curves of (a) $SmCo_5$, and (b) low-H_c $Sm_2(TM)_{17}$, magnets before and after aging for 2000 h at 250 °C in air, and after remagnetizing.

and $SmCo_5$—exhibit satisfactory thermal stability at temperatures up to 250 °C and at operating permeances $|p|>0.5$, at least to 2000 h. The low-H_c $Sm_2(Co,Cu,Fe,Zr)_{17}$ can only be safely operated at 150 °C and 250 °C if $|p| > 2.0$ and when severe initial irreversible losses can be tolerated.

The $Ce(Co,Cu,Fe)_5$ magnets exhibit severe long-term flux losses at these temperatures. Magnets of this type are limited to operating temperatures less than 150 °C at permeance values $|p| > 2$ when reasonably good temporal flux stability is required.

ACKNOWLEDGMENTS

The magnet samples were obtained from the Shin-Etsu Chemical Company, the TDK Electronics Company, and the Beijing Central Iron and Steel Institute. The work of H. F. Mildrum and K. J. Strnat was supported by the U.S. Army ET&D Laboratory, Ft. Monmouth, New Jersey.

[1]H. F. Mildrum and K. J. Strnat, Technical Report AFML-TR-73-46, March 1973.
[2]K. Bachmann, AIP Conf. Proc. **18**, 1168 (1974).
[3]H. F. Mildrum, K. M. D. Wong, and K. J. Strnat, in *Proceedings of the 2nd Conference on Advances in Magnetic Materials and Applications* (IEE, London, 1976), p. 144.
[4]Z. A. Abdelnour, H. F. Mildrum, and K. J. Strnat, IEEE Trans. Magn. **MAG-16**, 994 (1980).
[5]W. Ervens, in *Proceedings of the 6th International Workshop Rare Earth-Cobalt Permanent Magnets* (Wien, Vienna, Austria, 1982), p. 319.
[6]W. Rodewald, in *Abstract Book, INTERMAG 1984* (IEEE, Hamburg, F.R. of Germany, 1984), p. 13.
[7]D. L. Martin, General Electric Co., R&D Center Techn. Report No. 73CRD071 (1973).

Design applications of magnetic mirrors

H. A. Leupold and E. Potenziani II
U. S. Army Electronics Technology and Devices Laboratory, Fort Monmouth, New Jersey 07703-5000

Recent developments in permanent-magnet materials have made possible several novel high-field sources, with great potential application in mm/microwave/optical technology. However, even the crude approximations to such structures, which are needed to make their manufacture viable, entail as many as 72 pieces with eight distinct shapes. It has recently been shown that simpler equivalents of some of the structures can be made with half a structure, when the effect of the missing half is replaced with that of a reflected anti-image in a ferromagnetic plane. In this manner, the number of parts is decreased to 36. Further reductions are possible by image formation of still smaller segments in perfectly diamagnetic superconducting mirrors. For the ultimate reduction, only nine of the original 72 structural segments are needed. Access to the magnetic field for electrical leads and other conduits is also greatly facilitated. In this paper, we describe and analyze several examples of such design simplification with combinations of superconducting and ferromagnetic mirrors.

DISCUSSION

The recent progress in high-energy product permanent magnets has given rise to the possibility of producing very high magnetic fields ($H > 10$ kOe) with comparatively little magnetic material. Examples are the rings and spheres[1-4] having continously varying magnetization (CVM) which, in principle, can produce arbitrarily large fields in their interior cavities, but which, by practical considerations, are limited to the order of 25 kOe. Two such structures are shown in Figs. 1 and 2. In both instances, the ideal CVM structure must, in practice, be approximated by assembly of uniformly magnetized elements of finite size, i.e., by a structure having a discretely varying magnetization (DVM). Even for rather crude approximations, such DVM structures are quite complex and expensive to manufacture. If, for example, the continuous polar variation in magnetization in the spherical structure is approximated by $\pi/8$ radian increments, 72 segments of nine different types are still necessary for its construction.

Sometimes, if physical and geometrical limitations are not too stringent, the desired field can be produced with a hemisphere of the same geometry resting on a ferromagnetic plane, as shown in Fig. 3.[3] The plane then acts as an antimirror and reproduces the effect of the missing hemisphere. Such a procedure has the advantage of requiring only half as many structural parts, and, also, of providing more convenient access to the field.[3] Magic rings and similar structures may also be reduced by this approach.

A configuration that seems promising for microwave applications is the "pearl-string" TWT shown in Fig. 4.[5] Such a structure can produce nearly square-wave, on-axis fields with amplitudes as high as 15 kOe, as compared to the 5–6 kOe sinusoidal fields that are at or near maximum for present TWT's. Analysis of such configurations shows that their minimum period is about eight times the bore diameter. In many cases, it is desirable to have much smaller ratios—as little as two or less. Figure 5 shows how the pearl-string period-to-bore ratio can be reduced to four by the introduction of ferromagnetic irises each serving as the antimirror for a pair of cobased hemispheres.

It would be advantageous to form a hemispherical TWT stack in the manner of Fig. 4. Easy access to the entire bore would then be available by removal of the mirror. This would greatly simplify repair and adjustment of internal wave structures, magnet-stack "tweaking," placement of electrical and vacuum leads, and the like. Unfortunately, the ferromagnetic antimirror, or perfect paramagnet ($H = 0$) would not accomplish the desired effect. What is needed is a regular mirror that forms an identical image, rather than an anti-image. For this, a perfect diamagnet ($B = 0$) is required. The advent of the high-temperature superconductors may well provide such a material, although, to date, the relevant parameter H_{c1} (the lower critical field) has been disappointingly low. For widespread use of diamagnetic mirrors to be practical, H_{c1} would have to be over 5 kOe at liquid nitrogen temperature.

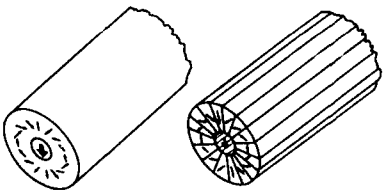


FIG. 1. Ideal continous CVM ring structure with a 16-segment approximation. Small arrows show magnetization direction. Large arrow shows working field.

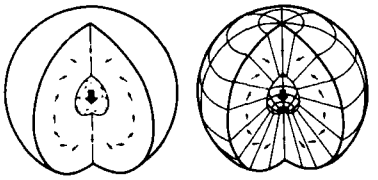


FIG. 2. Ideal CVM structure with a segmented approximation.

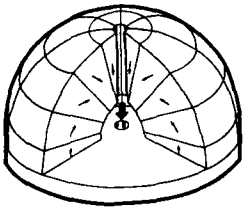


FIG. 3. Hemispherical field source, or "igloo." The ferromagnetic plate at the base reproduces the effect of the missing hemisphere. The axial holes in the iron plate and through the pole of the hemisphere are for access to electrical leads, optical beams, etc.

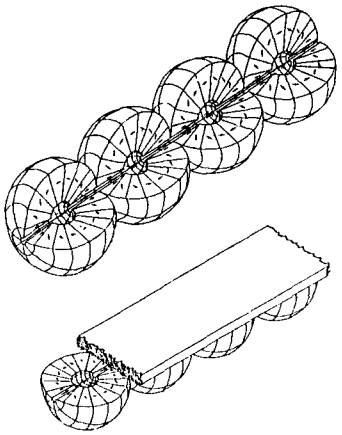


FIG. 4. String of CVM spheres joined end-to-end to form a "pearl string" TWT focussing structure and its hemispherical counterpart formed with diamagnetic mirrors.

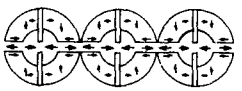


FIG. 5. TWT stack composed of tandem cobased hemispherical sources.

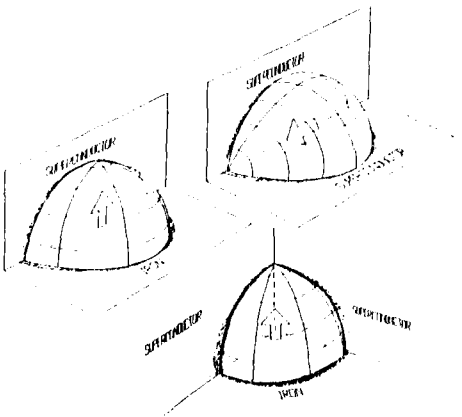


FIG. 6. Various reductions of magic sphere to quarters and eighths. All versions produce the same fields in the interiors.

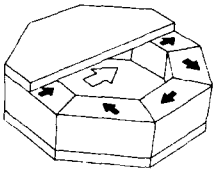


FIG. 7. Ring *pyx*. The diamagnetic mirrors at each end of the ring slice produce the effect of the missing part of the infinite ring. Part of one mirror has been removed for clarity.

With ferromagnetic and diamagnetic mirrors, a number of interesting combinations become possible. If a quarter sphere is bound azimuthally by mutually perpendicular diamagnetic planes, the magnitude of the field in the cavity would be that produced by a whole sphere. If the quarter sphere is further truncated by a cut through the equatorial plane and bound there by a ferromagnetic plate, the field magnitude of a full sphere is reproduced in a spherical octant, with one-eighth the number of magnet pieces found in a full sphere. Combinations of such possibilities are illustrated in Fig. 6.

Similar simplifying truncations of magic rings are also possible, but, perhaps, of even greater value is the reproduction of the field of an infinitely long octagonal magic ring by the bounding of an arbitrarily short section with two diamagnetic plates, as in Fig. 7. Multiple reflections of the ring segment in the diamagnetic mirrors create the infinitely long images needed to supplement the ring slice in producing the effect of a full ring. The resulting *pyx*-like structure of Fig. 7 is of potential use in oratrons, Faraday rotators, wigglers, twisters, and other devices in which high uniform fields are needed in flat, compact geometries.

SUMMARY AND CONCLUSIONS

Potentially useful, but complex, high-field permanent-magnet structures can be simplified greatly through use of perfect ferromagnetic and diamagnetic "mirrors." The former are already practicable to yield fields of up to 20 kOe. At present, the latter are feasible only for the generation of weak fields at low temperatures, because of the insufficiently high H_{c1}'s of the high-temperature superconductors available at this time. Material reported recently by IBM seems most promising in this regard.[6] The reported H_{c1} of 8.0 kOe at 4.2 K translates to an estimate of about 2.0 kOe at liquid nitrogen temperature via the T^2 law. If macroscopic aligned structures of such material could be made, their use would be marginal for oratron structures and possible for light, compact Faraday rotators. It is clear that a substantial rise in H_{c1} would be of enormous benefit to magnetic circuit design.

[1] K. Halbach, in *Proceedings of the Eighth International Workshop on Rare Earth Magnets and Their Applications*, Dayton, OH, 1985, edited by Karl J. Strnat (Univerity of Dayton, School of Engineering, Dayton, OH, 1985), p. 128.

[2] E.Potenziani II and H. A. Leupold, IEEE Trans. Magn. **MAG-22**, 1078 (1986).

[3] H. A. Leupold and E. Potenziani II, IEEE Trans. Magn. **MAG-23**, 3628 (1987).

[4] H. A. Leupold, E. Potenziani II, J. P. Clarke, and D. J. Basarab, Mat. Res. Soc. Symp. Proc. **96**, 279 (1987).

[5] E. Potenziani II and H. A. Leupold, in *Ninth International Workshop on Rare Earth Magnets and Their Applications*, Bad Soden, Federal Republic of Germany, 1987 (Deutsche Physikalische Gesellschaft e.V., D-5340, Bad Honnef, 1, Federal Republic of Germany, 1987), p. 149.

[6] T. R. Dinger, T. K. Worthington, W. J. Gallagher, and R. L. Sandstrom, Phys. Rev. Lett. **58**, p. 2685 (1987).

A magnetostrictive motor

N. Ida and L. E. Roemer
Electrical Engineering Department, The University of Akron, Akron, Ohio 44325

Magnetostriction can be used to effect a linear incremental motion device. Bidirectional incremental motion can be achieved in which the step size is set by the magnetostrictive coil's current. Such a device possesses the variable step width, characteristic of analog devices (unlike salient pole stepper motors). Once the step size is selected by the coil's current, the device behaves as a digital device with incrementally selected steps. Magnetostriction is a nonlinear function, dependent on the material. For the small incremental motion we examined, operation was essentially in the linear portion of the strain versus magnetic field strength curve.

BACKGROUND

Magnetostriction has been used often in analog positioning problems.[1] Electrostrictive motors, too, have been described.[2] Magnetostriction is due to deformations of the crystal structure of the material (typically nickel) in the presence of an imposed magnetic field.[3] The forces associated with crystal deformation are high, but the size of the deformation is small. The magnetostrictive constant is defined by the relation[4]

$$-\Delta l/l = cB^2, \tag{1}$$

where $c = -10^{14}\ \mathrm{m^4/Wb^2}$ for nickel. The magnetostrictive motor (Fig. 1) relies on the length l of magnetized element (shown as the dotted line) constricting until the energy stored,

$$\epsilon_{\text{stored}} = \int_{\text{dotted volume}} d\epsilon = \int \tfrac{1}{2}(\mu)H^2\, d(\text{vol}), \tag{2}$$

is equal to the work available from the device,

$$\epsilon_{\text{available}} = \int F \cdot dl. \tag{3}$$

The force F generated in the metallic structure of the magnetized element relaxes after removal of the magnetic field intensity H. The length dl represents the differential constriction of the moving member. Integration is over the constriction length.

By successively (a) constricting the moving member, (b) releasing one clutch, and (c) deenergizing the coil which causes magnetostriction, motion in one direction can be achieved. It should be noted that the spring constant contributes to an energy term which is linearly proportional to the compression of the bar, whereas the magnetic energy term is affected by the magnetic field intensity, which is proportional to the square of the coil current:

$$\Delta\epsilon_{\text{magnetic}} = \int \tfrac{1}{2}(\mu)H^2\, d(\text{vol}) = \int \tfrac{1}{2}(\mu)H^2 \pi a^2\, dl, \tag{4}$$

where the bar radius is a. This is balanced for a static position by

$$\Delta\epsilon_{\text{mechanical}} = \int k(l_0 - l)dl. \tag{5}$$

The term $k(l_0 - l)$ is the mechanical force of the spring. $(l_0 - l)$ represents the compression from the equilibrium position l_0. The spring constant is k. Sliding friction, which is velocity dependent, contributes to the damping constant, resulting in a displacement which has a sinusoidally damped component.

RESULTS

A motor was constructed in the form of Fig. 1. The step size of the motor was controlled by the magnetostrictive coil's current. The moving element's displacement was measured after 1000 steps. A graph of moving element displacement versus cycles of energizing the coil current (with clutch engagement between coil current pulses) is shown in Fig. 2. A saturation of the magnetostrictive effect was observed at high currents. Low current data were not taken to avoid operation dominated by sticking friction.

The use of a uniform magnetostrictive element allows extended motion in either direction. Alternate configurations which use a region of lower reluctance (and corresponding lower restoring spring constant in the moving element) will behave in a manner similar to the uniform element case. Of course, localizing the region which accounts for device behavior restricts the range of excursion of the moving element.

The moving bar's mass and spring constant system can be described by the well-known second-order differential

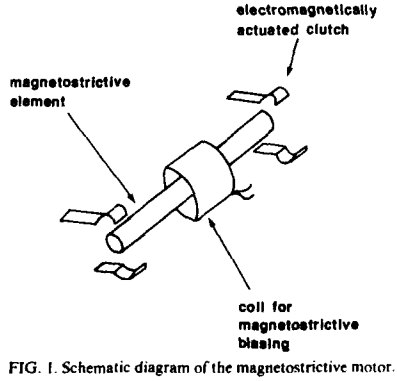


FIG. 1. Schematic diagram of the magnetostrictive motor.

 0021-8979/88/083989-02$02.40 © 1988 American Institute of Physics

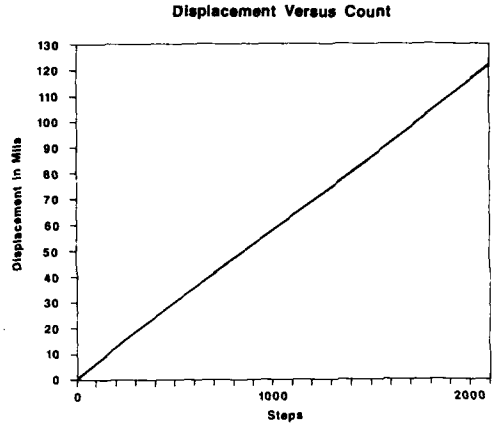


FIG. 2. Moving element displacement vs cycles of coil current energizing, or steps.

equation for damped oscillating systems. The high losses in the metal result in rapid damping of the oscillations within the time for the clutches to restrain bar motion.

The hysteresis and linearity of the device were tested by measuring the cumulative displacement for a fixed number of displacement steps. The device's hysteresis was negligible, affected mainly by nonuniformity in the clutch mechanism.

CONCLUSIONS

The peristoltic motion motor exhibited a repeatable step size. The step size was controllable by the current in the driving coil. Large linear excursions of the moving element, along with small step size, are features of the motor. Simplicity of construction and repeatability of function present attractive features for a motor.

[1] J. Strong, *Procedures in Experimental Physics* (Van Nostrand, New York, 1941).
[2] J. H. Bruning, in *Proceedings of the Fourth Annual Symposium on Incremental Motion Control Systems and Devices*, edited by B. C. Kuo, University of Illinois at Urbana-Champaign, 1975 (Dept. of Electrical Engineering, University of Illinois at Urbana-Champaign, Urbana-Champaign, IL, 1975).
[3] F. Pockels, *Encyklopaedie der mathematischen Wissenschaften* (Teubner, Leipzig, 1906), Vol. V, Part II.
[4] E. C. Jordan, *Reference Data for Engineers*, 7th ed. (Sams, Indianapolis, IN, 1985), pp. 4-28–4-30.

Field enhancement in traveling wave tubes with tapered pole pieces

John P. Clarke and Herbert A. Leupold
U.S. Army Electronics Technology and Devices Laboratory, Fort Monmouth, New Jersey 07703-5000

In many millimeter and microwave devices, the heaviest component is the magnetic focusing structure. Therefore, a decrease in the bulk of this structure can produce a significant reduction in the mass of the entire device. In this paper, we propose a tapered pole piece designed to reduce bulk and/or enhance fields in periodic permanent-magnet focusing structures. To compare these structures with conventional designs, computer calculations have been performed by the finite-element method. The calculations show that the tapered pole piece can offer field enhancement or reduction of mass and bulk of the order of 50%. Finite-element analyses of heat conduction show a favorable comparison of the tapered pole piece with conventional structures in transporting heat away from the working space. The simplicity of form of the tapered pole-piece design, the considerable reduction of bulk it affords, and its adequate heat-handling capabilities make it a promising candidate for widespread traveling wave tube use.

INTRODUCTION

In many millimeter or microwave devices, a magnetic fields is employed to focus an electron beam in an evacuated tube. Traditionally, the magnetic field has been provided by a heavy, bulky electrical solenoid and its accompanying power supply. The demand for airborne and space electronics has increased the need for lighter, less bulky magnetic field sources for beam focusing in traveling wave tubes.

The purpose of this work is to investigate a new pole-piece design that will allow a class of permanent-magnet focusing structures to produce more useful flux and/or reduce the mass and bulk of the structure. Since the heaviest component of millimeter and microwave devices is often the focusing structure, a weight savings here will result in a significant percent reduction in weight of the entire device. For purposes of comparison, calculations have been made of tubes having the same bore diameter of 0.269 cm and period of 1.0 cm. For all magnets, we have assumed that $B_r = H_c = 10.0$ kG.

DISCUSSION

A conventional permanent-magnetic focusing structure is shown in Fig. 1. The structure consists of axially oriented toroidal magnets aligned in opposition and interspersed with iron pole pieces. The pole pieces provide a path to conduct flux into the interior of the stack. They also provide a flux path to the exterior of the magnet structure, which is detrimental to the operation of the structure. Because the permeance of the flux path to the exterior of the structure is greater than the flux-path permeance inside, most of the flux travels to the exterior of the tube and is wasted.

Indentation of the pole pieces from the outer surface of the stack is commonly used to induce more flux to enter the bore, as shown in Fig. 2. When the pole pieces are indented, the length of the exterior flux path between adjacent pole pieces is increased. Lengthening the exterior flux path lowers the exterior permeance and flux leakage. The permeance of the bore is unaffected by pole-piece indentation, but since the reduced exterior permeance increases the mmf between pole pieces, more flux is forced into the bore of the magnet structure.

While indentation of the pole pieces does reduce the permeance of the exterior flux paths, it has the drawback of leaving only about one half of the magnet surfaces in direct contact with the pole pieces. This decreases the effective permeance of the flux path of the bore, to the detriment of the field there. If the pole pieces are shaped with a triangular taper, as shown in Fig. 3, there is no loss of contact between magnet and pole piece.[1] The greater contact between magnet and pole piece favors flux conduction to the working space in the bore of the magnet structure. In addition, the tapered pole piece design offers a slightly greater effective magnet length, with a concomitant increase in the total mmf driving the circuit. Figure 4 shows the effectiveness of this pole-piece design as compared with indented pole pieces.

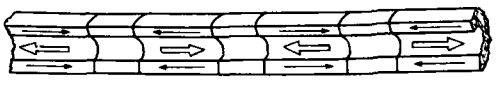


FIG. 1. Conventional permanent-magnet focusing structure.

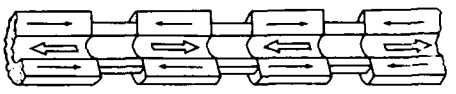


FIG. 2. Permanent-magnet structure with indented pole pieces.

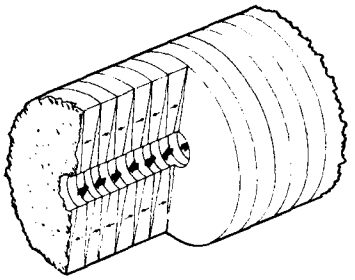


FIG. 3. Permanent-magnet structure employing triangularly tapered pole-pieces.

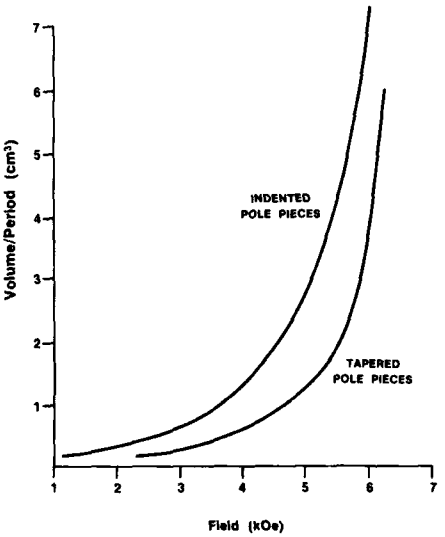


FIG. 4. Bulk volume vs field of a conventional indented pole-piece structure and a triangularly tapered pole-piece structure. At fields greater than 5.0 kOe, the tapered configuration has a volume less than one half that of the conventional configuration.

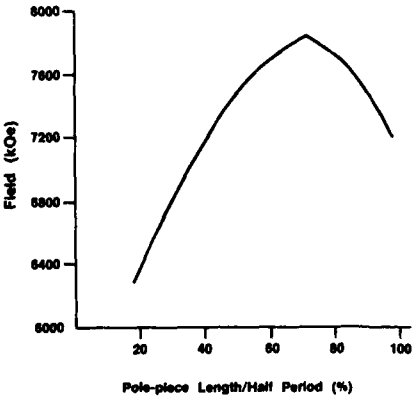


FIG. 5. Field vs base of pole-piece length for a structure with a period of 1 cm and an i.d. of 0.269 cm. A peak field is reached when the base thickness is 35% of the total period.

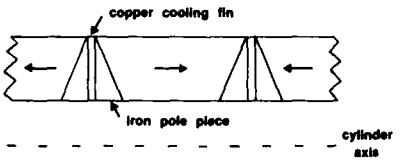


FIG. 6. Tapered pole-piece structure with copper cooling fins.

The performance of the tapered pole-piece structure depends on the width of the inner base of the pole piece. As the base of the pole piece is widened, its flux capacity is increased and the interior flux path is shortened, which results in higher fields in the working space. As the base of the pole pieces increases, the effective magnet length decreases, driving down the mmf generated by the magnets and decreasing the amount of flux in the working space.

The size of the tapered pole piece base must be optimized in order to produce the maximum possible field. Figure 5 shows the effect of pole-piece base width on the field generated in the working space.

The tapered pole-piece is not as efficient as indented pole pieces in conducting heat away from the bore of the magnet structure. Heat conduction in the tapered pole-piece design may be helped by slicing the pole piece in half and inserting copper between the halves, as shown in Fig. 6. The insertion of copper does not have an adverse affect on the field inside the working space, if it remains thin enough, that is, of the order of one-fourth the thickness of a pole-piece base. Indeed, in some cases, it may enhance the field. When the thin strip of copper is inserted between the pole-piece halves, the heat conduction of the tapered pole-piece design compares favorably with those of the conventional pole-piece.

SUMMARY

The pole-piece design, tapered triangularly, shows potential for use in traveling wave tubes; it can also afford a reduction in the mass and bulk of the magnet configuration. The tapered pole-piece configuration is also relatively easy to fabricate. One drawback of this structure is that heat cannot be transported very easily away from the working space of the tube. Incorporation of a copper cooling fin solves the heat transport problem of the configuration without the loss of its magnetic advantages.

[1]H. A. Leupold and J. P. Clarke, IEEE Trans. Electron Devices ED-34, 1868 (1987).

SEM study of the effect of Zr additive on the microstructures of $Sm(Co,Cu,Fe,Zr)_{7.64}$ magnets (abstract)

Ying-Chun Lin, Jiang-Ching Lin, Da-Pun Chiang, Kang-Ming Fan, and Wen Cheng Chang

Materials Research Laboratory, Industrial Technology Research Institute, Hsin-Chu, Taiwan, Republic of China

The effect of Zr on the magnetic properties of $Sm(Co_{0.67-x}Cu_{0.05}Fe_{0.28}Zr_x)_{7.64}$ permanent magnets has been examined by SEM to correlate their initial magnetization curves with microstructures. SEM shows clear network structures which are weaved by 1:5 phase along three directions and embedded in a 2:17 phase matrix. The precipitates cross each other at 120°. The structure is very likely the cellular structures observed by the transmission electron microscope (TEM). The size of network structures corresponds to cellular structures. The Zr controls the density of network structures and its formation of a Zr-rich phase. For Zr content around 1.0 wt. %, low density network structures are observed and low-density Zr-rich phases appear at grain boundaries, and the intrinsic coercivity is only about 800 Oe. For higher Zr content the network structures are more refined; also the density and size of the Zr-rich phase are increased. These may be the reasons why its intrinsic coercivity is exceeding 15 kOe.

 0021-8979/88/083993-01$02.40 © 1988 American Institute of Physics

Short-range Ising spin glasses in general dimensions

Rajiv R. P. Singh[a] and Michael E. Fisher[a]
Baker Laboratory, Cornell University, Ithaca, New York 14853

The equilibrium properties of nearest-neighbor Ising spin glasses on hypercubic lattices are studied as a function of d, the dimensionality. An expansion of $T_c(d)$ to fifth order in inverse powers of d, augmented by high-temperature series estimates for $d = 3$ and 4, yields the critical temperature for all d *and* for general, symmetric distributions of coupling strengths, J_{ij}. By extrapolation of T_c to zero, the lower borderline dimensionality is estimated as $d_l \simeq 2.5$. High-temperature expansions for the spin-glass susceptibility of the $\pm J$ model in powers of $w = \tanh^2(J/k_BT)$ and $u = \tanh^2(H/k_BT)$, where H is the magnetic field, yield estimates of the magnetic field crossover exponent Δ for $d = 3$ to 8.

The role of the dimensionality d in the study of critical phenomena is an important one, as evident from various ϵ expansions about upper and lower critical dimensionalities. However, whereas the dependence of critical exponents on dimensionality is subtle, the dependence on d of the critical temperature itself, in a family of lattices such as the hypercubic lattices, is more direct. Even in classical theories, such as the Bethe–Peierls approximation, the critical point varies with d. Such approximations normally become exact when $d \to \infty$, and, as shown some time ago,[1] it may be possible to expand around this limit in a systematic manner, so as to get improved estimates of the critical temperature. Such expansions in inverse powers of d have been generated for Ising,[1] and general n-vector[2] models (including the spherical model limit, $n \to \infty$). These expansions usually prove to be asymptotic in nature, i.e., they have zero radius of convergence. Nevertheless, the first few terms of the expansions do provide useful information on the location of the critical point and on its variation with parameters like n or the spin-weight distribution.

In recent years the study of spin-glass models has attracted theoretical interest. The existence of a finite temperature transition for Ising spin-glasses in ($d > 3$) dimensions is now well established by numerical calculations.[3–5] Models with various distributions of random couplings, J_{ij}, have been studied for a range of dimensionalities. However, there is no theory beyond mean-field theory that relates the critical points for these different models. Here we report an expansion for the critical temperature, $T_c(d)$, for general symmetric Ising spin glasses on hypercubic lattices in powers of $1/d$ or, more simply, in powers of $1/(2d-1)$.[1] The leading term in the expansions corresponds to the Bethe–Peierls approximation. The corresponding estimates of the critical point for different d can be compared with the critical points obtained by extrapolating high-temperature series for the spin-glass susceptibility. The $1/d$ expansions also provide interesting information regarding the variation of critical temperature with the random coupling distributions. Padé approximants improve the performance of the series as a function of d for $d \lesssim 4$. Furthermore, the value of d for which $T_c = 0$ yields the lower critical dimensionality, d_l.

Finally, we report briefly estimates for the magnetic field crossover exponent Δ for $d = 3,4,\ldots,8$ obtained with the aid of high-temperature general-field expansions of the spin-glass susceptibilities on hypercubic lattices.

Consider the spin-glass susceptibility

$$\chi_{SG} = \sum_j [\langle s_0 s_j \rangle^2]_J, \tag{1}$$

where the angular brackets refer to thermal averaging while the square brackets denote an average over the distribution of nearest-neighbor bond strengths, J_{ij}. Now the susceptibility can be expanded[5] in powers of $w = [\tanh^2(J/k_BT)]_J$ as

$$\chi_{SG} = \sum_l b_l w^l. \tag{2}$$

The critical point may then be defined via the limit,

$$w_c^{-1} = \lim_{l\to\infty} |b_l|^{1/l}. \tag{3}$$

To see that this expression provides a well-defined expansion in powers of d, consider the formal diagrammatic expression

$$[\langle s_i s_j \rangle^2]_J = \{C_{ij}\}[1 + O(d^{-1})] \tag{4}$$

in which $\{C_{ij}\}$ denotes a sum over "doubled-bond" lattice chains stretching from site i to j. To leading order in powers of d, only graphs of l bonds with no closed loops contribute to b_l. If we set

$$\sigma = 2d - 1, \tag{5}$$

the number of such non-self-intersecting chains is[1] σ^l up to

[a] Current address: Institute for Physical Science and Technology, University of Maryland, College Park, Maryland 20742.

 0021-8979/88/083994-03$02.40 © 1988 American Institute of Physics

corrections of relative order $1/\sigma^2$. This is sufficient to show that the Bethe–Peierls approximation, namely $w_c = 1/\sigma$, is, in fact, correct to order $1/\sigma^2$. Graphs containing closed loops yield systematic corrections[1,2] in powers of $1/\sigma$.

An alternative way of generating these series is to obtain a two-variable expression for $1/\chi_{SG}$ in powers of w and d. One may then formally set $1/\chi_{SG} = 0$ and solve in powers of $1/d$ (or $1/\sigma$) for w_c. Since the star graph expansion technique naturally yields $1/\chi_{SG}$, this method proves most efficacious. For the $\pm J$ model we thence obtain the expansion

$$\frac{k_B \tilde{T}_c}{J} = \sqrt{\sigma}\left(1 - \frac{3.5}{\sigma^2} - \frac{10.5}{\sigma^3} - \frac{91.125}{\sigma^4} - \frac{699.416}{\sigma^5} - \cdots\right), \tag{6}$$

where $J/k_B\tilde{T}_c = \sqrt{w_c} = [\tanh^2(J/k_BT_c)]_J^{1/2}$.

The critical point can be estimated by evaluating the series. Since the expansion is at best asymptotic we expect the optimal estimates to come by truncating after the smallest term, which proves to be after roughly d terms of the series. In Table I we show the best estimates obtained from Eq. (6) compared with the estimates from extrapolation of the high-temperature spin-glass susceptibility.[5]

To study the dependence of the critical point on the random bond distributions, note that the expansion for w_c will be a function of the moments

$$\mu_n = [\tanh^{2n}(J/k_BT_c)]_J / [\tanh^2 J/k_BT_c]_J^n, \tag{7}$$

where, of course, the operation $[\cdot]_J$ depends on the bond distribution. Notice that for the $\pm J$ distribution we have $\mu_n = 1$ (all n). For the much-loved Gaussian distribution with $P(J) = (1/\sqrt{2\pi})e^{-J^2/2}$, on the other hand, μ_n depends explicitly on T_c. The first term in the $1/\sigma$ expansion containing a nontrivial moment arises in third order, the general expression being

$$w_c = \frac{1}{\sigma}\left(1 + \frac{7}{\sigma^2} + \frac{24 - 3\mu_2}{\sigma^3} + \cdots\right). \tag{8}$$

In lower orders w_c is the same for all bond distributions. The deviation for a general distribution from the $\pm J$ result can be written as

$$\frac{w_c - w_c^{(\pm J)}}{w_c^{(\pm J)}} = \frac{3(1-\mu_2)}{\sigma^3} + O\left(\frac{1}{\sigma^4}\right). \tag{9}$$

TABLE I. Critical point estimates for $\pm J$ Ising spin glasses: $w_c = [\tanh^2(J/k_BT_c)]_J$.

	high-T series	$1/(2d-1)$ series	
d	w_c	w_c	order
8	0.070 ± 0.001	0.0696	5
7	0.083 ± 0.001	0.0818	5
6	0.102 ± 0.002	0.1002	5
5	0.139 ± 0.002	0.1322	5
4	0.21 ± 0.01	0.2133	5
3	0.48 ± 0.04	0.5036	4

Notice that this is actually an implicit equation since μ_2 depends on T_c; however, it is easily solved numerically.

Now for $d = 3$ the series estimate for the $\pm J$ distribution is[5] $w_c^{(\pm J)} = 0.48 \pm 0.04$ or $T_c^{(\pm J)} = 1.2 \pm 0.1$ (see Table I). For a Gaussian distribution this value of w_c corresponds to $T_c^{(G)} \simeq 0.79 \pm 0.09$. However, on using Eq. (9) to estimate the critical point for a $d = 3$ Gaussian spin-glass one finds that the moment μ_2 increases $T_c^{(G)}$ by about 0.02. This brings the result somewhat closer to the central estimate found in Monte Carlo simulations[6] which yield $T_c^{(G)} \simeq 0.9 \pm 0.1$. For $d = 4$ the series estimate gives[5] $w_c^{(\pm J)} = 0.21 \pm 0.01$ or, $T_c^{(\pm J)} = 2.02 \pm 0.06$. This value of w_c translates, for the Gaussian distribution, into $T_c^{(G)} \simeq 1.74 \pm 0.07$; the μ_2 term brings T_c up to about 1.76, which also compares well with the simulation estimate[6] of $T_c^{(G)} \simeq 1.8$.

Padé approximants may be used to assist in the extrapolation of the critical points from higher dimensions. Since w_c seems most reliably determined for $d = 3$ and, probably, for $d = 4$ by extrapolation of the χ_{SG} high-T series, we have constructed biased approximants which reproduce these estimates at $d = 3$ and 4. We believe that such approximants represent the critical points rather accurately for all $d \gtrsim 3$. We can then ask: "For what, possibly nonintegral, value of d does w_c attain the value 1?" Since $w_c = 1$ implies $T_c = 0$, this represents an estimate for the lower critical dimensionality d_l. We find $d_l \simeq 2.5 \pm 0.2$, which agrees quite well with several real-space renormalization-group calculations.[7]

Finally, we report the calculation of the complete double expansion of χ_{SG} for the $\pm J$ model in a uniform magnetic field H to order 8 in powers of w and $u = [\tanh^2(H/k_BT)]$, and the single-variable series for $(\partial\chi_{SG}/\partial u)_{u=0}$ to order 10. From these we can estimate the crossover or gap exponent governing the field behavior via the usual scaling combination $H/(T - T_c)^{\Delta}$. Since the series are irregular and not so long we extrapolate using the w_c-values obtained from the longer χ_{SG} series and from the $1/\sigma$ expansions. Our tentative estimates for $d = 3$ through 8 are[8]

$$\Delta \simeq 1.7,\ 1.20,\ 1.0,\ 1.00,\ 1.00,\ 1.00. \tag{10}$$

These are consistent with the conclusion that $d = 6$ is the upper critical dimensionality (for leading critical behavior) above which Δ takes the mean-field value unity.[9]

In summary, we have seen that series expansion techniques combined with a study of dependence on dimensionality can yield significant information about "realistic", i.e., finite-dimensional spin-glass models. In the future, we hope to address the role of Griffith's singularities and their temperature analogs in such analyses.

Our work has been supported by the National Science Foundation through the Condensed Matter Theory Program (under Grant No. DMR-87-01223). The interest of Dr. Daniel S. Fisher, Dr. L. Chayes, Dr. J. T. Chayes, and Professor D. J. Thouless has been appreciated.

[1] M. E. Fisher and D. S. Gaunt, Phys. Rev. A 133, 224 (1964).
[2] P. R. Gerber and M. E. Fisher, Phys. Rev. B 10, 4697 (1974).
[3] R. N. Bhatt and A. P. Young, Phys. Rev. Lett. 54, 924 (1985).

[4]A. T. Ogielski and I. Morgenstern, Phys. Rev. Lett. **54**, 928 (1985).
[5]R. R. P. Singh and S. Chakravarty, Phys. Rev. Lett. **57**, 245 (1986); Phys. Rev. B **36**, 546 (1987); **36**, 559 (1987).
[6]R. N. Bhatt and A. P. Young, in *Heidelberg Colloquium on Glassy Dynamics and Optimization*, edited by J. L. Van Hemmen and I. Morgenstern (Springer, Berlin, 1987).
[7]See, e. g., A. J. Bray and M. A. Moore, J. Phys. C **17**, L463 (1984).
[8]Details of the extrapolation procedure will be published elsewhere by R. R. P. Singh and M. E. Fisher. The uncertainties for $d = 5$ are significantly larger than for other values of d and would even allow $\Delta = 1.2$. We believe, however, that $\Delta(d = 5)$ exceeds 1.00, probably having a value close to 1.05. For $d = 4$ and $d > 6$ our uncertainties in Δ amount only to about ± 0.05.
[9]D. S. Fisher and H. Sompolinsky, Phys. Rev. Lett. **54**, 1063 (1984).

Chiral order in a two-dimensional *XY* spin glass

Hikaru Kawamura[a)]
Baker Laboratory, Cornell University, Ithaca, New York 14853

Masaharu Tanemura
Institute of Statistical Mathematics, Minato-ku, Tokyo 106, Japan

Ordering phenomena in the two-dimensional XY ($n = 2$) spin glass have been studied by Monte Carlo simulations with a focus on *chirality*, an Ising-like, multispin variable associated with a broken reflection symmetry. The chiral and $n = 2$ spin-glass orientational degrees of freedom order in a markedly different way: indeed, the chiral susceptibility can be mapped onto the spin-glass susceptibility of a pure Ising ($n = 1$) spin glass.

SUMMARY

The ground state of certain frustrated vector spin systems can display a twofold, Ising-like degeneracy in addition to a continuous orientational degeneracy associated with the original XY spin symmetries. This twofold degree of freedom is called "chirality,"[1] and is closely related to a reflection symmetry of the system. We have studied the nature of chiral ordering in vector spin glasses by employing extensive Monte Carlo simulations for the $\pm J$ XY model on the square lattice,[2] the simplest spin-glass model which can sustain a chiral degree of freedom. The Hamiltonian is given by

$$\mathcal{H} = \sum_{\langle ij \rangle} J_{ij} \cos(\theta_i - \theta_j), \tag{1}$$

where θ_i denotes the orientation of the spin and the sum runs over nearest-neighbor pairs $\langle ij \rangle$. The J_{ij} are independent random variables taking the values $+J$ and $-J$ with equal probability. The local chirality, κ_α at plaquette α, is defined by the scalar

$$\kappa_\alpha = 2^{-3/2} \sum_{\langle ij \rangle}^{\alpha} \mathrm{sgn}(J_{ij}) \sin(\theta_i - \theta_j), \tag{2}$$

where the sum runs over a directed contour, say of clockwise orientation, along the sides of the plaquette. Note that κ_α is invariant under any global rotation of the spins whereas it changes sign under any global reflection $\theta_i \to 2\theta_0 - \theta_i$. The chiral susceptibility for the spin glass is naturally defined by

$$\chi_\kappa = N^{-1} \sum_\alpha \sum_\beta [\langle \kappa_\alpha \kappa_\beta \rangle^2]_J, \tag{3}$$

where N is the total number of spins, $\langle\ \rangle$ denotes a thermal average, while $[\ ]_J$ indicates a configurational average over the bond distribution. The spin-glass susceptibility may be defined in the usual way as

$$\chi_{SG} = N^{-1} \sum_i \sum_j [\langle \mathbf{S}_i \cdot \mathbf{S}_j \rangle^2]_J. \tag{4}$$

In our simulations, we could equilibrate the system for sizes $N = L \times L$ with $L = 10, 14, 20$ in the temperature range $0.25J < T < J$. The chiral degrees of freedom are found to order in a markedly different manner from the XY spins. The data for χ_{SG} can be well fitted by assuming a simple power-law divergence at zero temperature, namely, $\chi_{SG} \propto T^{-\gamma}$ with an exponent $\gamma = 1.9 \pm 0.1$ in agreement with a previous result.[3] On the other hand, the data for χ_κ indicate that the effective exponent $\gamma_\kappa^{\mathrm{eff}} = d(\ln \chi_\kappa)/d(\ln T/J)$ increases with decreasing temperature in the investigated temperature range $T > 0.25J$. In order to make the correspondence with the Ising spin closer, we have defined and computed the reduced chiral susceptibility

$$\tilde{\chi}_\kappa = \chi_\kappa / \langle \kappa^2 \rangle^2, \quad \langle \kappa^2 \rangle = N^{-1} \sum_\alpha [\langle \kappa_\alpha{}^2 \rangle]_J. \tag{5}$$

After subtracting a $T = \infty$ background term, we have found that the net chiral susceptibility $\Delta\tilde{\chi}_\kappa = \tilde{\chi}_\kappa(T) - \tilde{\chi}_\kappa(\infty)$ can be accurately mapped onto the spin-glass susceptibility of a pure *Ising* spin glass[4] with a rescaling of energy/temperature unit, $J_I = (1/4)J$, where J_I is the bond energy of the $\pm J$ Ising spin glass. This result indicates that the chiral component of the two-dimensional XY spin glass behaves essentially like an Ising spin glass. An interesting possibility suggested by this observation is that in three dimensions an XY spin glass might have a phase characterized by a broken reflection symmetry but with orientational symmetry preserved.

The numerical simulations were performed on the M280H computer at the Institute of Statistical Mathematics. This study was carried out under the ISM cooperative Research Program (86-ISM·CRP-24). One of the authors (H.K.) is grateful for partial support to the National Science Foundation through the Condensed Matter Theory Program (under Grant No. DMR 87-01223), and to the Nishina Memorial Foundation for the award of a fellowship. The authors are also grateful to M. E. Fisher for discussions and for reading the manuscript, to D. A. Huse for his useful comments on techniques of data analysis, and to R. H. Swendsen and J. Wang for sending us their numerical data. Discussions with M. A. Moore, C. L. Henley, and R. R. P. Singh are gratefully acknowledged.

[a)] Present address: Institute for Physical Science and Technology, University of Maryland, College Park, Maryland 20742.
Permanent address: Department of Physics, College of General Education, Osaka University, Toyonaka 560, Japan.

[1] J. Villain, J. Phys. C **10**, 4793 (1977).
[2] H. Kawamura and M. Tanemura, Phys. Rev. B **36**, 7177 (1987). See also H. Kawamura and M. Tanemura, J. Phys. Soc. Jpn. **54**, 4479 (1985); **55**, 1805 (1986).
[3] S. Jain and A. P. Young, J. Phys. C **19**, 3913 (1986).
[4] R. H. Swendsen and J. Wang, Phys. Rev. Lett. **57**, 2607 (1986).

 0021-8979/88/083997-01$02.40 © 1988 American Institute of Physics

Introduction of spin disorder by exchange defects

G. Parker and W. M. Saslow
Department of Physics and Center for Theoretical Physics, Texas A&M University, College Station, Texas 77840-4242

Individual negative bonds are introduced in an XY spin system on a square lattice with otherwise nearest-neighbor ferromagnetic interactions. Using a mean-field theory we have found better than 5% agreement between numerical calculations and a continuum theory for this discrete system. In addition, preliminary studies of the interaction of two negative bonds have been made. A continuum theory indicates a dipolelike interaction, some of whose features have been observed in the calculations. Our results are relevant to alloying-induced spin disorder, where defects which individually are not strong enough to disorder the host system can, through a long-range dipolar interaction, interact to produce noncollinearity in the spin system.

INTRODUCTION

In order to model the reentrant spin glass–ferromagnetic transition,[1] we earlier considered XY spins on a square lattice, with nearest-neighbor interactions, treating the system using mean-field theory.[2] In an otherwise ordered array of sites with four ferromagnetic bonds of strength J, we placed sites with two antiferromagnetic bonds. The resulting ground state is as in Fig. 1(a), where the "frustrated" spin points normal to the ferromagnetic background, and its ferromagnetically (antiferromagnetically) coupled neighbors cant toward (away from) its direction. The "frustrated" spin is held in place less strongly than the host spins, thus introducing, in addition to the ferromagnetic energy scale, a second—and weaker—energy scale. In the remainder of Fig. 1, the mean-field solutions are displayed as a function of temperature: the "frustrated" spin "melts" at a lower temperature than do the host spins, leaving a collinear system at temperatures above a noncollinear melting temperature T_{NC}, but below the host Curie temperature T_C. By introducing a finite concentration of these defects, it was possible to produce small (10×10) samples in which reentrance in the magnetization vs temperature could be seen.[2]

To understand the single-site problem better, we rotated and displaced the negative bonds relative to one another. The adjacent-negative-bond configuration (Fig. 2) at $T=0$ gives a more dipolarlike pattern than the opposite-negative-bond configuration [Fig. 1(a)]. Furthermore, when the opposite bonds of Fig. 1(a) are pulled apart, the canting is lessened (Fig. 3). The transverse component "melting" temperature T_{NC} in this configuration is decreased, due to the weaker interactions (Fig. 4). Note that if the negative bonds are not adjacent, then when the transverse components "melt," there still remain longitudinal components.

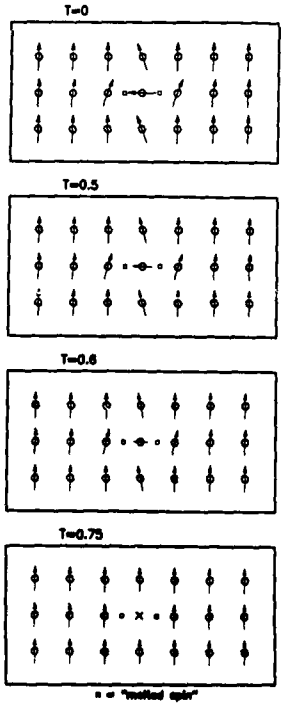


FIG. 1. Mean-field solutions for a spin with two opposite negative bonds in an otherwise ferromagnetic host, for various reduced temperatures (relative to the host Curie temperature). Dots indicate negative bonds of strength $J'=-J$.

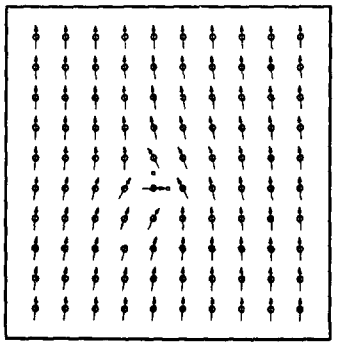


FIG. 2. Zero temperature mean-field solution for a spin with two adjacent negative bonds.

 0021-8979/88/083998-03$02.40 © 1988 American Institute of Physics

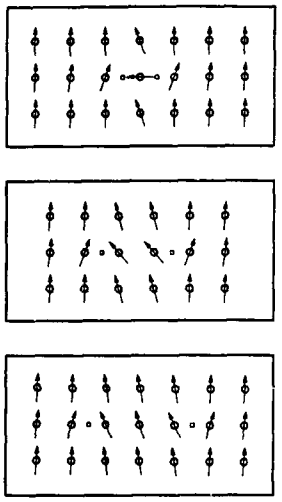


FIG. 3. Zero temperature mean-field solution for a system where two negative bonds are moved apart.

Let us now address the question of how spin disorder is produced by individual bond defects. It is known that if a single bond J' is substituted into the above perfect square lattice, the system is stable so long as $J' > -J$.[3] Thus $J' = -J$, the case studied in the above calculations, is at the edge of stability. The bonds in Figs. 1–3 must somehow yield an instability through an interaction effect.

SINGLE-BOND PROBLEM

Before undertaking study of this interaction effect, it is important to understand the single-bond problem. We have performed studies of this problem, both on the computer and analytically, for a weakly unstable single negative bond. This produces a dipolelike pattern near the bond (Fig. 5), but not

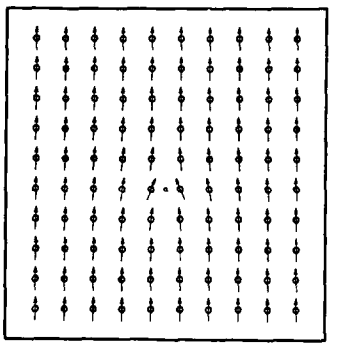


FIG. 5. Zero temperature mean-field solution for a system with a negative bond strength $J' = -1.1J$.

near the edges of the periodically repeated cell. To get agreement with our numerical results, it is necessary to include in the analytic theory (described below) the canting due to sources in other cells. Doing this with the Ewald technique,[4] a fit of analytical and numerical results to the pattern produced by a periodic array of dipoles gave less than 5% disagreement.

To model the single-bond problem analytically, we treated the ferromagnetic host in the continuum limit, obtaining (to lowest order) a Laplace equation, $\nabla^2 S_x = 0$, for the small transverse components S_x of the spins. The negative bond serves as a source (with dipolar symmetry) for the solution to Laplace's equation. One can employ strictly microscopic methods, but it is useful to argue that the strength of the dipole can be obtained by minimizing a Ginzburg–Landau free energy:

$$E = \tfrac{1}{2}a(J' + J)\mu^2 + \tfrac{1}{4}b\mu^4, \tag{1}$$

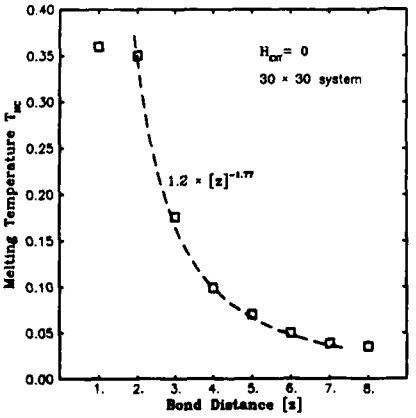


FIG. 4. Temperature T_{NC} at which the transverse components "melt," as a function of negative bond separation.

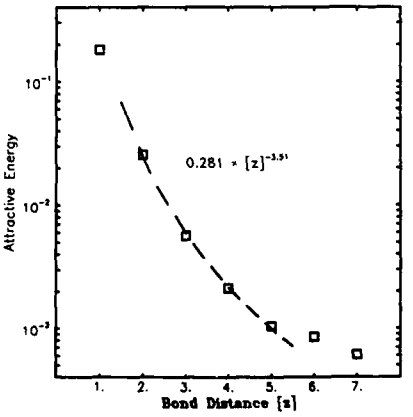


FIG. 6. Energy of interaction as a function of bond separation for a system with two marginally stable ($J' = -J$) bonds which interact with one another through the ferromagnetic host.

where $a,b>0$. The first piece embodies the information that the instability sets in for $J'+J=0$, and the second piece serves to limit the amplitude of the moment. (By considering the microscopic exchange Hamiltonian, one can obtain approximate values for a and b, where the latter comes primarily from nonlinearities in the exchange energy between the two spins connected by J'.) Minimizing E with respect to μ gives

$$\mu = \pm\sqrt{-[a(J'+J)/b]}. \tag{2}$$

The numerical calculations give $a/b \approx -0.77a_0^2/J'$ for $J' = -1.1J$, where a_0 is the lattice constant. When the Ewald sums are performed, the microscopics predict that $a/b \approx -0.70a_0^2/J'$. Moreover, the numerical calculations verify the $\sqrt{J+J'}$ dependence in Eq. (2), for $(J+J') \ll J$.

TWO INTERACTING BONDS

Consider now a system with two negative bonds. Despite the fact that there are only short-range interactions in the microscopic Hamiltonian, the *effective* Hamiltonian for the transverse canting contains long-range (dipolar) interactions. For two dipoles of strength μ_1 and μ_2, induced by negative bonds J', we expect that

$$E = \tfrac{1}{2}a(J'+J)(\mu_1^2+\mu_2^2) + \tfrac{1}{4}b(\mu_1^4+\mu_2^4) + c\mu_1\mu_2, \tag{3}$$

where the interaction term c has the form expected for dipoles in $d=2$:

$$c = A(\hat{\mu}_1\cdot\hat{\mu}_2 - 2\hat{\mu}_1\cdot\hat{r}_{12}\,\hat{\mu}_2\cdot\hat{r}_{12})/r_{12}^2 . \tag{4}$$

As for a and b, the coefficient c can be obtained from the microscopic Hamiltonian; a preliminary calculation yields that the contribution to A from the spins attached to the negative bonds is given by $(88/15)(J-J')$.

By minimizing E, for $c>0$ we find that $\mu_2 = -\mu_1$ and

$$\mu_1 = \pm\sqrt{[-a(J'+J)+c]/b}. \tag{5}$$

Thus, even when $(J'+J)>0$, so that the individual negative bonds are stable, if the system has a strong enough interaction [so that $c>a(J'+J)$], the system can distort. We have verified the prediction of zero interaction when the negative bonds are parallel to one another and at 45° to the vector connecting their centers. Figure 6 gives our numerical results for the case where the negative bonds are parallel to one another and to the vector connecting their centers. They indicate that the effective interaction strength varies as $r^{-1.8}$ for periodic boundary conditions, as opposed to r^{-2} from Eq. (4). We have not yet performed the Ewald sums to obtain the analogous result for the analytic theory. We plan to publish a more complete discussion when this analysis has been performed.

CONCLUSIONS

We conclude the following: (1) A ferromagnetic system which appears collinear at higher temperatures may be noncollinear at lower temperatures, and thus many real-world systems which have appeared to be rather uninteresting may in fact have a much richer behavior than previously thought; (2) Short-range interactions in the Hamiltonian do not imply short-range *effective* interactions[5]; (3) In the alloying process, noncollinearity may set in at a finite concentration, when the exchange defects introduced by alloying are close enough to produce a sufficiently strong interaction. Moreover, chemical clustering may not be necessary for noncollinearity.

ACKNOWLEDGMENT

We would like to acknowledge F. D. M. Haldane for making us aware of the onset of the instability at $J' = -J$.

[1] G. J. Nieuwenhuys, B. H. Verbeek, and J. A. Mydosh, J. Appl. Phys. **50**, 1685 (1979); Y. Yeshurun, M. B. Salamon, K. V. Rao, and H. S. Chen, Phys. Rev. Lett. **45**, 1366 (1980); M. Hennion, I. Mirebeau, B. Hennion, and S. Lequier, Europhys. Lett. **2**, 393 (1986).

[2] W. M. Saslow and G. Parker, Phys. Rev. Lett. **56**, 1074 (1986).

[3] F. D. M. Haldane, C. Jayaprakash, S. Kirkpatrick, and J. Vannimenus, Bull. Am. Phys. Soc. **25**, 209 (1980).

[4] See Appendix B of C. Kittel, *Introduction to Solid State Physics*, 6th ed. (Wiley, New York, 1986).

[5] J. Villain, Z. Phys. B **33**, 31 (1979).

Phase diagram for the Bethe lattice spin glass (abstract)

J. M. Carlson,[a] J. T. Chayes,[b,c] L. Chayes,[c,d] and J. P. Sethna[a]
Laboratory of Atomic and Solid State Physics, Cornell University, Ithaca, New York 14853

D. J. Thouless[e]
Department of Physics, University of Washington, Seattle, Washingon 98195

We present the results of rigorous calculations for the $\pm J$ Ising spin-glass model on the Bethe lattice. The phase diagram for varying temperature and fraction of ferromagnetic bonds is derived near the paramagnetic phase boundary. In addition to the spin-glass and paramagnetic phases, we find a nontrivial ferromagnetic phase and a magnetized spin-glass phase, characterized by diverging Edwards–Anderson susceptibility. The recursion relation for the distribution of single-site magnetizations is studied as a dynamical system on an appropriate function space, the bulk thermodynamics is described by the attractors of the recursion relation, and the phase transitions correspond to bifurcations in the dynamics. Using bifurcation theory, we establish the existence of a stable distribution of single-site magnetizations near the paramagnetic phase boundary. At least in single-site properties, the existence proof precludes chaos, and infinite hierarchy of transitions, and other conceivable bizarre possibilities. While our phase diagram is very similar to the phase diagram for the Sherrington–Kirkpatrick model, the Bethe lattice provides a useful description of the mean-field behavior of spin glasses because the interactions are short range, the analysis is much more straightforward, and the results have been made completely rigorous.

[a] Supported by NSF grant No. DMR-8503544.
[b] Supported by NSF grant No. DMR-8314625.
[c] Supported by DOE grant No. DE-AC02-83ER13044.
[d] Supported by NSF grant No. DMR-8319301.
[e] Current address: Department of Mathematics, UCLA, Los Angeles, CA 90024.

Reentrant ferromagnetism in a two-dimensional Ising model with random nearest-neighbor interactions (abstract)

N. Benayad and A. Benyoussef
Lab. Magnetisme, Faculte des Sciences, Rabat, Morocco

N. Boccara
DPhG/PSRM, CEN Saclay, France and Department of Physics, University of Illinois at Chicago, Chicago, Illinois 60680

Reentrant behavior seems to be characteristic of systems with competing interactions even when no spin-glass phase exists. Using various methods (finite cluster approximation,[1] mean-field renormalization,[2] finite cluster renormalization, etc.) we determined the phase diagram of a two-dimensional square Ising model with random nearest-neighbor interactions J_{ij} distributed according to $P(J_{ij}) = (1-p)\delta(J_{ij}-J) + p\delta(J_{ij}-\alpha J)$, where $J>0$ and $0>\alpha>-1$. Such a model has been considered by Wolff and Zittartz.[3] These authors discussed its qualitative features and argued that a reentrant behavior should be observed. Our calculations agree with this conjecture.

This paper was not proofread by the author; however, it has been proofread by one of the Publication Chairpersons.

[1] N. Boccara, Phys. Lett. 94A, 185 (1979).
[2] J. O. Indekeu, A. Maritan, A. L. Stella J. Phys. A 15, L291 (1982).
[3] W. F. Wolff and J. Zittartz, Z. Phys. B 60, 185 (1985).

 0021-8979/88/084001-01$02.40 © 1988 American Institute of Physics

The antiferromagnetic spin glass with frustrations (abstract)

M. Blazej,[a] S. Krzeminski,[a] and P. Rusek
Department of Physics and Astronomy, Louisiana State University, Baton Rouge, Louisiana 70803-4001

In the antiferromagnetic spin glass (ASG) the distribution of magnetic moment is chaotic but there is an effective antiferromagnetic order in the system. The chaotic distributed positive and negative bonds are source of frustrations. We have studied dynamics of ASG using an effective Lagrangian. The presence of frustrations requires us to introduce additional parameters (gauge fields). The dynamics of frustrations were described with analogy to dynamics of dislocations in crystals. We found spin waves with linear dispersion law in ASG. Due to the frustrations those spin waves are damped and for small frequency they become purely dissipative. The present method can be applied to a description of other magnetic systems with topological solitons.

[a] Permanent address: Institute of Physics, Technical University, 50-370 Wroclaw, Poland.

 0021-8979/88/084002-01$02.40 © 1988 American Institute of Physics

High T_c thin-film superconductivity: Science and technology (invited)

T. H. Geballe
for the Stanford Thin Film Group,[a] *Department of Applied Physics, Stanford University, Stanford, California 94305*

Thin films of high T_c superconducting oxide structures have been synthesized by a number of different methods by Stanford researchers. High-quality films are believed to be yielding intrinsic electrical and optical properties which have scientific and technological implications.

Following the discoveries of Bednorz and Müller[1] and Chu and coworkers,[2] there has been a widespread survey of the normal and superconducting properties of the cuprate perovskite compounds responsible for the unexpectedly high superconductivity. Good superconducting properties as judged by relatively sharp resistive transitions and the substantial expulsion of flux when cycling through the transition in a magnetic field (Meissner Effect) have led to overoptimistic beliefs that further measurements of properties of YBa_2CuO_7, such as J_c, the critical current, would yield intrinsic values. Single-crystal samples and highly oriented thin films are now becoming available which show in fact that much of the optical and electrical data taken until recently on ceramic samples is actually extrinsic and reflects inhomogeneities. It has been well documented that even a small degree of nonstoichiometry causes second phases and weak links.

At Stanford there has been a major effort to produce thin films by vapor deposition. Three methods have been used and all work well: electron-beam,[1] magnetron-sputtering,[2] and MBE.[3] In all cases fluxes of the three metal atoms are simultaneously codeposited on the substrate in the presence of oxygen. It is necessary to subject the samples to a standard post-annealing treatment in oxygen to obtain superconducting films with sharp transitions. Other groups have reported similarly good results,[4] although at present the sputtering is giving the best. The sputtered samples have the lowest resistivities, typically $1.2\,T + 15\,\mu\Omega\,cm$,[5] which is a useful measure of sample quality along with the more usual criteria such as a sharp transition. It is likely that the properties of these samples are more nearly intrinsic and thus can be used to test theories and provide limits for technological purposes. Some of the results so far are summarized below.

Very large critical currents have been measured. Because of the large currents needed and the problems with contacts, it is more convenient to use magnetization curves. In the critical state model of Bean, the hysterisis gives the critical current. We have tested the model by showing ΔM, the difference in magnetization upon field reversal is proportional to the sample radius over macroscopic distances.

The intrinsic properties are essential for sorting out the features of the many microscopic models which have been offered to account for the high T_c's,[6] as well as for setting limits for technologies. A very large surface current of $\sim 3\times 10^8$ A/cm^2 obtained at 4.2 K from magnetization hysterisis measurements with the field applied parallel to the sample is believed to be near to the depairing velocity and sets a limit of $\sim 10^4$ G for the thermodynamic critical field.[7] It is a relevant parameter for estimating minimum hysterisis losses in superconducting power lines.

Optical transmission and reflectance and Raman experiments show, in contrast to previous reports on bulk ceramic samples, no evidence for exciton-like peaks in the region between 0.2 and 1.0 eV.[5] The coherence length parallel to the c-axis evaluated by studying paraconducting fluctuations well above T_c and from the critical field slope below T_c is found in a self-consistent manner to be ~ 2 Å, considerably smaller than previous estimates.[7] This result offers a simple explanation for why the superconductivity in (RE) $Ba_2Cu_3O_{7-\delta}$ is not dependent upon the moment of the rare earth.[4]

The energy gap measured by tunneling has yielded conductance curves[8,9] which suggest a spread of values from 0 (i.e., either shorts through the barrier, or gapless superconductivity) to values so much greater than the BCS value as to reach or exceed the limits of strong coupling theory.[10] The majority of values from many groups are in the strong coupling regime.[11] Iguchi *et al.*[12] found with planar tunnel junctions fabricated on bulk samples that the gap goes to 0 at ~ 50 K which is the T_c for $YBa_2Cu_3O_{6.6}$.[13] Far infrared data in the literature give smaller values for the gap than the tunneling does, but are also variable. Further work is necessary in order to determine reliable behavior.

The available data on films are still not definitive enough to distinguish and study the microscopic mechanism(s) responsible for the high T_c. But the rapid progress in improving film quality leads one to be optimistic that there will be tunneling and optical data of sufficient quality to decide what the important interactions are. It seems likely that the pairing interaction is due primarily to electron-electron correlations rather than the conventional electron-phonon interactions. Since the former can involve higher

[a] Members of the Group are listed in Refs. 1, 2, 3, 5, 8, 9.

 0021-8979/88/084003-02$02.40 © 1988 American Institute of Physics

energies, there is no reason to rule out much higher T_c's, even though there is really no solid evidence for existence of $T_c > 100$ K at this time.

The work at Stanford was supported by the AFOSR and the NSF under the MRL program through Stanford's Center for Materials Research, and the ONR.

[1]M. Naito, R. H. Hammond, B. Oh, M. R. Hahn, J. W. P. Hsu, P. Rosenthal, A. F. Marshall, M. R. Beasley, T. H. Geballe, and A. Kapitulnik (unpublished).
[2]K. Char, A. D. Kent, A. Kapitulnik, M. R. Beasley, and T. H. Geballe (unpublished).
[3]E. S. Hellman, D. G. Schlom, N. Missert, K. Char, J. S. Harris, Jr., M. R. Beasley, A. Kapitulnik, and T. H. Geballe (unpublished).
[4]See, for example, B. Dunlap and M. Slaski, J. Magn. Mater. (in press); H. C. Ku, H. D. Yang, and R. W. McCallum, MRS Proceedings, Anaheim, CA, April 21-25, 1987, and similar results presented by many other groups.
[5]I. Bozovic, D. Kirillov, A. Kapitulnik, K. Char, M. R. Beasley, T. H. Geballe, Y. H. Kim, and A. J. Heeger (unpublished).
[6]T. H. Geballe, in Proceedings of the International Workshop on Novel Mechanisms of Superconductivity, Berkeley, 1987 (Plenum, New York, in press).
[7]A. Kapitulnik, B. Oh, M. Naito, K. Char, A. D. kent, N. Missert, E. Hellman, S. Arnason, J. W. P. Hsu, M. R. Hahn, P. Rosenthal, R. Barton, M. R. Beasley, T. H. Geballe, and R. H. Hammond, in Proceedings of High-T_c Superconductors, ICTP, Trieste, Italy, July 1987 (World Scientific, Singapore, to be published); B. Oh (unpublished).
[8]M. D. Kirk, D. P. E. Smith, D. B. Mitzi, J. Z. Sun, D. J. Webb, K. Char, M. R. Hahn, M. Naito, B. Oh, M. R. Beasley, T. H. Geballe, R. H. Hammond, A. Kapitulnik, and C. F. Quate, Phys. Rev. B **35**, 8850 (1987).
[9]K. W. Ng, S. Pan, A. L. de Lozanne, A. J. Panson, and J. Talvacchio, in *Proceedings of the 18th International Conference on Low Temperature Physics*, Kyoto [Jpn. J. Appl. Phys. **26-3**, 993 (1987)].
[10]V. Z. Kresin, Phys. Rev. Lett. (to be published); J. Blezius and J. P. Carbotte (unpublished).
[11]K. E. Gray, in Proceedings of the International Workshop on Novel Mechanisms of Superconductivity, June 22-26, Berkeley, 1987 (Plenum, New York, in press).
[12]H. Watanabe, Y. Kasai, T. Mochiku, A. Sueishita, I. Iguchi, and E. Yamaka, in Proceedings of the 18th International Conference on Low Temperature Physics, Kyoto [Jpn. J. Appl. Phys. **26-3**, 1201 (1987)].
[13]J. M. Tarascon, L. H. Greene, B. G. Bagley, W. R. McKinnon, P. Barboux, and G. W. Hull, in Proceedings of the International Workshop on Novel Mechanisms of Superconductivity, June 22-26, Berkeley, 1987 (Plenum, New York, in press).

Magnetism and superconductivity in $La_{2-x}Sr_xCuO_{4-y}$ (invited)

D. Jérome and W. Kang
Laboratoire de Physique des Solides (associé au CNRS), Université Paris-Sud, 91405 Orsay, France
S. S. P. Parkin
IBM Almaden Research Center, 650 Harry Road, San Jose, California 95120-6099

We report the results of resistivity and magnetic susceptibility measurements of $La_{2-x}Sr_xCuO_{4-y}$ for $0 \leqslant x \leqslant 0.20$. The various features (superconductivity, spin-density wave state, and localization) are consistent with a model of weakly correlated two-dimensional electrons in which van Hove singularities of the band structure near the Fermi level play a determinant role. We also emphasize that the electron localization observed near half-filling of the conduction band at $x \simeq 0.04$ can be attributed to the effect of correlations boosted by electron Umklapp scattering in a nearly nested two-dimensional Fermi surface. We recall that similar effects have been observed in half-filled band organic conductors and superconductors.

I. INTRODUCTION

The discovery of superconductivity in a new copper-based series of conductors has been of considerable interest for several reasons.[1] First, the $La_{2-x}Sr_xCuO_{4-y}$ family with $T_c \simeq 36$–38 K has been the first material to provide superconductivity above the long-standing critical temperature of 23 K. Second, a major advantage of the $La_{2-x}Sr_xCuO_{4-y}$ series is that its crystal structure is of the well-known K_2NiF_4 type[2] in a wide regime of alkaline-earth substitution with only a single kind of copper oxide plane.[3]

Furthemore, the $La_{2-x}Sr_xCuO_{4-y}$ series exhibit a wealth of interesting features which we shall briefly summarize.

(i) At no alkaline-earth substitution level a small orthorhombic distortion from the tetragonal K_2NiF_4 structure exists at room temperature and vanishes above 533 K.[2]

(ii) Substitution of Sr preserves the distorted orthorhombic structure up to $x \simeq 0.09$ at room temperature[4] and increases the average valence charge of copper ions above the charge 2 + in La_2CuO_4, increasing in turn the net hole concentration available for conduction.

(iii) Superconductivity is observed when x is larger than 0.06 or so and T_c depends on the amount of substitution.[5–7] It passes through a maximum at $\simeq 36$ K for $x \simeq 0.15$.

(iv) These oxides are known to act as sponges for oxygen which can deintercalate and reintercalate easily even at moderate temperature and pressure.[3] Several experiments have recently demonstrated the dominant role played by the oxygen stoichiometry in the existence of the superconducting phenomenon.[8–10] It is thus customary to represent the superconducting lanthanum copper oxide series by the formula $La_{2-x}Sr_xCuO_{4-y}$ where $y \geqslant 0$. An increase in the concentration of oxygen vacancies (with a concomitant decrease in the hole concentration) favors the localization of carriers and suppresses superconductivity.

(v) Finally, these materials exhibit a structure of parallel conducting CuO_2 planes for which electrons travel preferentially in a two-dimensional (2D) network of Cu and O atoms. The atomic levels which contribute to the conduction band are the $d_{x^2-y^2}$ and $2p$ orbitals of copper and oxygen atoms, respectively. In the nearly free-electron limit the conduction is half-filled for La_2CuO_4. The Fermi level lies on or between two logarithmic van Hove singularities for the tetragonal and orthorhombic phases, respectively.

In this paper we summarize some experimental results obtained in the $La_{2-x}Sr_xCuO_{4-y}$ system for $0 \leqslant x \leqslant 0.20$ by electrical resistivity and magnetic susceptibility measurements. We also discuss the dependence of T_c upon Sr substitution within the weak coupling theory of superconductivity and the role of electron-electron repulsion and commensurability on electron localization.

II. EXPERIMENTS

All oxides studied in this work were prepared in the usual way and the oxygen content was determined by the weight loss of the sample under reducing conditions. These experimental procedures are discussed elsewhere.[6] Thermogravimetric analysis shows that the oxygen deficiency is small ($y \simeq 0.01$–0.02) in all Sr-substituted samples for $0 \leqslant x \leqslant 0.15$. This result is in agreement with the early work of Michel *et al.*[3] on oxygen deficiency.

The resistivity data were obtained using a conventional four contact method on small parallelopipedic samples of typical size $0.5 \times 0.5 \times 6$ mm^3. The susceptibility experiments were carried out in a S.H.E. (B.T.I.) VTS SQUID magnetometer.

III. RESULTS

A. The high Sr substitution range ($0.10 < x < 0.20$)

For large Sr substitution the material is a fairly good conductor at room temperature ($\rho < 3$ mΩ cm) with a metal-like resistivity (i.e., $d\rho/dT > 0$) down to the critical temperature for the onset of superconductivity (see Fig. 1). The transition temperature is x dependent with a maximum of the mid-transition temperature at 35 K for $x \simeq 0.15$. It is also at the same substitution level that the narrowest transition is observed ($\Delta T/T_c \simeq 6\%$). Diffraction studies show that the

 0021-8979/88/084005-04$02.40 © 1988 American Institute of Physics

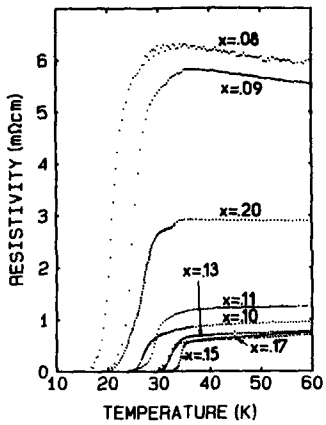


FIG. 1. Temperature dependence of the resistivity of $La_{2-x}Sr_xCuO_{4-y}$ for $x>0.08$.

tetragonal-orthorhombic (T-O) transition is strongly depressed by Sr substitution. The transition occurs at 300 K and 215 K for $x=0.10$ and $x=0.12$, respectively,[4] and it is located above 60 K in a $x=0.15$ sample, according to neutron[11] and x-ray[12] diffraction data. Therefore, the stabilization of the tetragonal phase to zero temperature probably occurs for a Sr substitution level of $x>0.15$. Hence, the maximum in T_c at $x=0.15$, although close to the T-O transition, appears to be an intrinsic property of the orthorhombic phase.

B. The low Sr substitution range ($x<0.10$)

The properties of $La_{2-x}Sr_xCuO_{4-y}$ change drastically below $x\simeq 0.10$. The superconducting state disappears below $x=0.06$, and the temperature dependence of the resistivity reveals a minimum at a temperature which increases with decreasing values of x, as shown in Fig. 2. Many unsubstituted samples display the peculiar behavior shown in Fig. 2 where a sharp drop of the resistance towards a zero value is observed at 35 K after a large increase on cooling. The latter anomaly occurs at a temperature which corresponds to the superconducting transition in a $x=0.15$ sample. The shift of the anomaly under magnetic field (i.e., critical field) is also similar to the data obtained at $x=0.15$. Thus we may conclusively say that La_2CuO_{4-y} exhibits superconductivity at 35 K.[6,13,14] However, it is also clear that only a minor part of the sample volume undergoes the transition. This argument is supported by critical current and Meissner expulsion measurement which both give more than 10^3 times smaller values than those of the $x=0.15$ samples. We have also observed a similar kind of superconducting behavior in samples which have been prepared with a slight lanthanum deficiency, i.e., $La_{2-x}CuO_{4-y}$ $(x>0)$.[15] The magnetic susceptibility data of $x=0$, 0.01, and 0.02 samples are displayed in Fig. 3. A susceptibility cusp is observed in the $x=0$ sample at 240 K. At the same temperature, a resistivity anomaly is also found (see Fig. 2). At lower temperatures the susceptibility becomes strongly dependent on the applied magnetic field. The cusp moves downwards in temperature with Sr substitution and is no longer observed at $x=0.02$. Note that the magnitude of the susceptibility approaches a similar value in all the compounds shown in Fig. 3 at temperatures close to $\simeq$400 K.

IV. DISCUSSION

We shall now proceed to a qualitative discussion of these data with the goal of learning something about the mechanism of superconductivity and the interplay between localization and superconductivity. Within the noninteracting electron picture the Fermi level of the nonsubstituted compound lies at the center of the band formed from antibonding $Cu(d_{x^2-y^2})$ and $O(p)$ states. As shown schematically in Fig. 4 the degeneracy of the van Hove singularities at the center of the band is lifted by the orthorhombic distortion

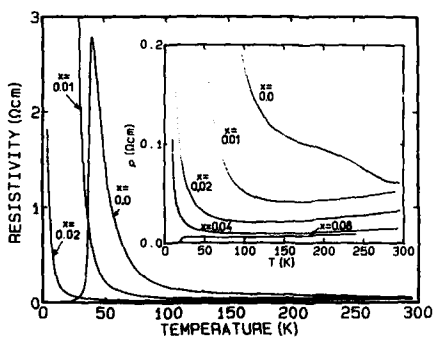


FIG. 2. Temperature dependence of the resistivity of $La_{2-x}Sr_xCuO_{4-y}$ for $0.0<x<0.08$.

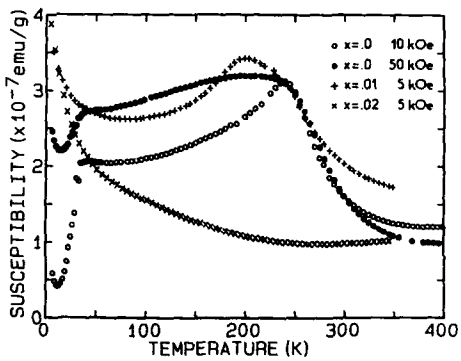


FIG. 3. Magnetic susceptibility vs temperature of $La_{2-x}Sr_xCuO_{4-y}$ for $x=0.0$, 0.01, and 0.02. Data are shown for various magnetic fields as shown in the figure.

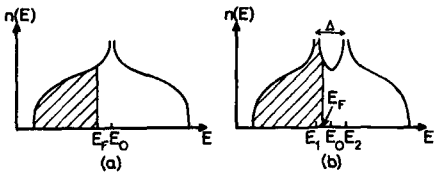


FIG. 4. Schematic band structure of La_2CuO_4: (a) Tetragonal phase, (b) orthorhombic phase.

with a concomitant lowering of the electron energy. The magnitude of the splitting Δ is obtained by balancing the electronic energy gain and the elastic lattice energy loss.[16] One phase or the other is stable at low temperatures according to the concentration of additional holes created by Sr substitution. With reasonable values of parameters for the orthorhombicity, $(b-a)/a = 1\%$,[16] the Slater coefficient of the transfer integral, $q_0 a = 6$,[16] and an overall bandwidth of 6.4 eV,[17] Friedel[18] has estimated that the O-to-T transition should occur at $x \simeq 0.17$ [assuming an average concentration of O vacancies ($y \simeq 0.02$) as indicated by thermogravimetric analysis]. This latter value agrees fairly well with the experimental phase diagram (Fig. 5) and suggests that the maximum in T_c at $x = 0.15$ is indeed an intrinsic property of the orthorhombic state. It is not related to the phase

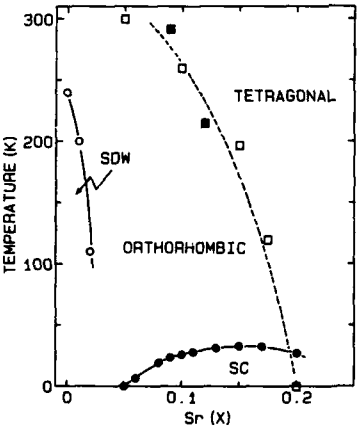


FIG. 5. Phase diagram of $La_{2-x}Sr_xCuO_{4-y}$. Closed circles represent the superconducting transition, open circles the SDW transition, and squares the orthorhombic-tetragonal phase transition (closed squares from Ref. 4 and open squares from Ref. 12). The dashed lines are guidelines for the eye. The superconductivity at $x = 0$ is not indicated on this diagram as it concerns only a small fraction of the sample volume in which the carrier concentration is not that corresponding to "pure" La_2CuO_4.

transformation as one might have speculated from comparison with layer-type superconductors.[19] As a matter of fact, a maximum in T_c at ≈ 40 K can easily be obtained theoretically within the weak coupling limit when the Fermi level passes through the van Hove singularity, E_1.[16,20] This situation corresponds to $x \simeq 0.14$ using the same set of parameters as above to characterize the orthorhombic phase. The drop in T_c observed when $x - 2y$ decreases can be related to the Fermi level shifting away from the singularity E_1 and approaching the middle of the band.

We have already mentioned that superconductivity in pure La_2CuO_4 is derived from a small fraction of the sample volume. Since we have always found for the unsubstituted compounds, values of T_c very close to the maximum observable T_c of substituted samples we are led to believe that the local excess hole concentration in parts of the sample exhibiting superconductivity corresponds to that of about $x = 0.15$ (for Sr doping). Our results on La-deficient samples support a picture in which the superconducting regions arise from the clustering of La vacancies[21] in small conducting domains with a Fermi level near to a van Hove singularity such as E_1. In other words, lanthanum vacancies are not equally distributed but form small domains in which the local concentration is larger than an average concentration of 0.5% or so. The existence of La vacancies in the parent compound La_2NiO_4 is indeed supported from structural considerations.[22]

We turn now to the discussion of the very lightly substituted regime. The $x = 0$ samples exhibit both a resistive anomaly (Fig. 2) and a susceptibility cusp at 240 K (Fig. 3) which can be attributed to the onset of an antiferromagnetic phase revealed in neutron diffraction[23] and Mössbauer studies.[24] As shown in Fig. 3 the susceptibility becomes field dependent at lower temperatures in agreement with the behavior of a spin-density wave (SDW) state under high fields. It is reasonable to ascribe the antiferromagnetic phase to the onset of SDW state which involves the nesting vector $\vec{Q} = (\pm \pi/a, \pm \pi/b)$ of the orthorhombic Fermi surface. The existence of this SDW state is a property of the particular 2D character of the La_2CuO_4 series and is confined to the close vicinity of the half-filled band regime. Model calculations indicate that the SDW state is suppressed very rapidly upon increasing the concentration of holes and consequent destruction of the nesting properties.[16,25] The critical concentration for the destruction of the SDW state $x \simeq 0.01$–0.02, implied by our data is indeed in fair agreement with the computation of the stability criterion using a strength of the electron-electron repulsion U which is of the order of the effective transfer integral between Cu atoms (corresponding to a weak correlation regime).[16]

A minimum in resistance is observed at low temperatures for $x > 0.01$ shifting towards lower temperatures as the substitution level increases (Fig. 2). However, the localization of the carriers at low temperatures is not accompanied by a loss in the spin degree of freedom as shown by the susceptibility data of the $x = 0.02$ sample. This behavior is reminiscent of the localization observed in the one-dimensional conductors of the $(TMTTF)_2X$ series[26] where a correlation-induced localization develops at low temperatures

even for moderate values of the Coulomb repulsion when the Umklapp scattering channel becomes important in a half-filled band.[27] The substitution level around $x \simeq 0.03$ is about the level which is needed to achieve half-filling of the band in the presence of oxygen vacancies. Thus, in the low substitution regime a 3D-ordered SDW state cannot develop because of cation disorder but Umklapp terms with wave vectors $\vec{Q} = (\pm \pi/a, \pm \pi/b)$ result in electron localization.

In summary, the experimental diagram of T_c vs Sr substitution in $La_{2-x}Sr_xCuO_{4-y}$ is consistent with a model based on weakly interacting electrons and van Hove singularities close to the Fermi level. Superconductivity in non-substituted La_2CuO_{4-y} occurs in limited regions of the sample in which the lanthanum concentration is about 1.95 instead of 2. The SDW transition of the 2D nested Fermi surface occurring in the rest of the sample volume is rapidly suppressed when the Fermi level deviates from the center of the band upon Sr substitution. There exists a domain of intermediate substitution level $0.01 < x < 0.06$ in which the low-temperature localization of the charge carriers can be attributed to Umklapp electron scattering terms in a nearly half-filled band with a moderate amplitude ($U/t \simeq 1$) of the Coulomb repulsion.

Our data do not allow any conclusions regarding the mechanism leading to electron pairing (phonon or spin-fluctuation exchange). However, we emphasize that a spin-fluctuation model for the pairing in organic superconductors[28] is supported by the existence of magnetic fluctuations in the normal state[29] and by lines of zeroes of the gap parameter on the Fermi surface.[30] A similar d-type singlet superconductivity model has been proposed for a small U two-dimensional electron gas by Schulz[31] with possible application to $La_{2-x}Sr_xCuO_{4-y}$. This model predicts that the SDW ground state becomes unstable with respect to superconductivity when the Fermi level shifts away from half-filling. However, it also predicts a maximum of T_c at the border between superconductivity and antiferromagnetism which is not observed experimentally. The spin-fluctuation pairing may still be relevant for $La_{2-x}Sr_xCuO_{4-y}$ but our work suggests that Mott–Hubbard or (and) disorder driven localization must also be considered in the interplay between SDW and superconductivity.

ACKNOWLEDGMENTS

We thank G. Collin, Ph. Odier, and J. M. Bassat for their cooperation in sample preparation and characterization and J. Friedel for useful discussions about the physics of high T_c superconductors. W. K. expresses his gratitude to CNRS-PIRMAT for financial support. This work has been partly supported by the DRET Contract No. 86/057.

[1] J. G. Bednorz and K. A. Müller, Z. Phys. B **64**, 189 (1986).
[2] J. Longo and P. M. Raccah, J. Solid State Chem. **6**, 526 (1963).
[3] C. Michel and B. Raveau, Rev. Chim. Miner. **21**, 407 (1984).
[4] R. Moret, J. P. Pouget, and G. Collin, Europhys. Lett. **4**, 365 (1987).
[5] *J. M. Tarascon, L. H. Greene, W. R. McKinnon, G. W. Hull, and T. H. Geballe*, Science **235**, 1373 (1987).
[6] W. Kang, G. Collin, M. Ribault, J. Friedel, D. Jérome, J. M. Bassat, J. P. Coutures, and Ph. Odier, J. Phys. (Paris) **48**, 1181 (1987).
[7] R. B. van Dover, R. J. Cava, B. Batlogg, and E. A. Rietman, Phys. Rev. B **35**, 5337 (1987).
[8] S. Shamoto, S. Hosoya, M. Onoda, and M. Sato, Jpn. J. Appl. Phys. **26**, L493 (1987).
[9] H. Takagi, S. Uchida, K. Kitazawa, and S. Tanaka, Jpn. J. Appl. Phys. **26**, L218 (1987).
[10] R. J. Cava, R. B. van Dover, B. Batlogg, and E. A. Rietman, Phys. Rev. Lett. **58**, 408 (1987).
[11] R. J. Cava, A. Santoro, D. W. Johnson, Jr., and W. W. Rhodes, Phys. Rev. B **35**, 6716 (1987).
[12] R. M. Fleming, B. Batlogg, R. J. Cava, and E. A. Rietman, Phys. Rev. B **35**, 7191 (1987).
[13] J. Beille, R. Cabanel, C. Chaillout, B. Chevallier, G. Demazeau, F. Deslandes, J. Etourneau, P. Lejay, C. Michel, J. Provost, B. Raveau, A. Sulpice, J. L. Tholence, and R. Tournier, C. R. Acad. Sci. (Paris) **304**, 1097 (1987).
[14] P. M. Grant, S. S. P. Parkin, V. Y. Lee, E. M. Engler, M. L. Ramirez, J. E. Vazguez, G. Lim, R. D. Jacowitz, and R. L. Greene, Phys. Rev. Lett. **58**, 2482 (1987).
[15] W. Kang, D. Jérome, J. Arabski, and R. Reich (unpublished).
[16] J. D. Jorgensen, H. B. Schüttler, D. G. Hinks, D. W. Capone II, K. Zhang, M. D. Boorodsky, and J. D. Scalapino, Phys. Rev. Lett. **58**, 1024 (1987).
[17] L. F. Mattheiss, Phys. Rev. Lett. **58**, 1028 (1987); W. Weber, Phys. Rev. Lett. **58**, 1371 (1987).
[18] J. Friedel, J. Phys. (Paris) **48**, 1787 (1987).
[19] R. H. Friend, D. Jérome, R. F. Frindt, A. J. Grant, and A. D. Yoffe, J. Phys. C **10**, 1013 (1977).
[20] J. Labbé and J. Bok, Europhys. Lett. **3**, 1225 (1987).
[21] M. W. Shafer, T. Penney, and B. L. Olson, Phys. Rev. B **36**, 4047 (1987).
[22] J. Choisnet, J. Leblanc, J. M. Bassatt, H. Pilliere, and Ph. Odier (unpublished).
[23] D. Vaknin, S. K. Sinha, D. E. Moncton, D. C. Johnston, J. M. Newsam, C. R. Safinya, and H. E. King, Jr., Phys. Rev. Lett. **58**, 2802 (1987).
[24] Y. Nishihara, M. Tokumoto, K. Murata, and H. Unoki, Jpn. J. Appl. Phys. **26**, L1416 (1987).
[25] Y. Hasegawa and H. Fukuyama, Jpn. J. Appl. Phys. **26**, L322 (1987).
[26] C. Coulon, P. Delhaes, S. Flandrois, R. Lagnier, E. Bonjour, and J. M. Fabre, J. Phys. (Paris) **43**, 1059 (1982).
[27] V. J. Emery, R. Bruinsma, and S. Barisic, Phys. Rev. Lett. **48**, 1039 (1982).
[28] V. J. Emery and C. Bourbonnais, in *Low-Dimensional Conductors and Superconductors*, edited by D. Jérome and L. G. Caron (Plenum, New York, 1987), pp. 103 and 155; D. Jérome and F. Creuzet, in *Novel Superconductivity*, edited by V. Krezin and S. Wolf (Plenum, New York, 1987), p. 103.
[29] C. Bourbonnais, F. Creuzet, D. Jérome, and A. Moradpour, J. Phys. Lett. (Paris) **45**, L755 (1984).
[30] Y. Hasegawa and H. Fukuyama, J. Phys. Soc. Jpn. **56**, 877 (1987); M. Takigawa, H. Yasuoka, and G. Saito, J. Phys. Soc. Jpn. **56**, 873 (1987).
[31] H. Schulz, Europhys. Lett. **4**, 609 (1987).

The effect of lanthanide substitution on the superconductivity in $Ba_2YCu_3O_7$ and $(La,Sr)_2CuO_4$ (invited)

H. Takagi,[a] S. Uchida,[a] H. Eisaki,[a] and S. Tanaka
Department of Applied Physics, Faculty of Engineering, University of Tokyo, Bunkyo-Ku, Tokyo 113, Japan

K. Kishio, K. Kitazawa, and K. Fueki
Department of Industrial Chemistry, Faculty of Engineering, University of Tokyo, Bunkyo-Ku, Tokyo 113, Japan.

The effect of the lanthanide substitution on the superconductivity in $Ba_2YCu_3O_7$ and $(La,Sr)_2CuO_4$ is investigated. The substitution effect is completely different between the two Cu-oxide systems. In $Ba_2YCu_3O_7$, the replacement of Y with lanthanides gives negligible change in the transition temperature, whereas a few percent of lanthanide substitution depresses T_c by about 10 K in the $(La,Sr)_2CuO_4$ system. The depression of T_c in the latter system depends on the atomic number of lanthanides. From the results of the magnetic susceptibility and the relationship between the lattice parameters and T_c, we conclude that the depression of T_c cannot be ascribed to the magnetic effect nor to the volume effect. Possible mechanisms for the depression of T_c are discussed.

I. INTRODUCTION

Until recently, superconducting transition temperature was supposed to have a limit at around 30 K. However, a breakthrough has been brought about by the discovery of the high T_c superconductivity in the series of perovskite-related Cu oxides.

Two types of the superconducting Cu oxides has been found up to now. First, 40 K class superconductivity has been established in the solid solution system $(La,A)_2CuO_{4-y}$ [hereafter denoted as $(La,A)_2CuO_4$, A = Sr, Ba, Ca] having a K_2NiF_4-type structure.[1-5] Shortly after the discovery of 40 K superconductors, high T_c superconductivity above liquid-nitrogen temperature has been achieved in oxygen-deficient perovskite $Ba_2YCu_3O_{7-y}$ with T_c exceeding 90 K. The discovery of $Ba_2YCu_3O_{7-y}$ has stimulated the discovery of a new series of 90 K superconductors, $Ba_2LnCu_3O_{7-y}$ (hereafter denoted as $Ba_2LnCu_3O_7$, Ln = Y, La, Nd, Sm, Eu, Gd, Dy, Ho, Er, Tm, Yb, Tm).[6-11]

The crystal structures of these oxides are characterized by a layered structure. In the 40 K superconductors with a K_2NiF_4 structure, the two-dimensional Cu-O layer is isolated by La-O layers, whereas triple Cu-O layers, the center layer of which is composed of an array of one-dimensional Cu-O chains, are isolated by lanthanides layer in the 90 K superconductors.

The absence of the isotope effect in the 90 K superconductors casts a question about the conventional phonon mediated superconductivity in these systems. Many theoretical models on the mechanism of the superconductivity in the newly discovered Cu-oxide systems have been proposed, such as bipolaron,[12] plasmon,[13] exciton mechanism,[14] and resonating valence bond.[15] It is appropriate now to accumulate the basical experimental data in order to elucidate the mechanism of high T_c superconductivity.

The effect on superconductivity of magnetic ion substitution is expected to provide an insight into the local electronic states, since the magnetic ion can suppress the superconductivity through the exchange coupling without changing the electronic states in the vicinity of the Fermi level. In order to investigate the effect of magnetic lanthanide ion substitution on the superconductivity, we have synthesized $Ba_2LnCu_3O_7$ in which Y is replaced by lanthanides and the solid solution system $[(La,Ln)_{0.925}Sr_{0.075}]_2CuO_4$ with a fixed Sr content of 7.5%.

As has been pointed out in the previous studies,[16-19] the depression of the superconductivity by the lanthanides substitution for the La or Y site is much smaller than that by Cu site substitution, giving an evidence of the two-dimensional nature of the conduction electrons. However, the magnitude of the depression of T_c by lanthanide substitution is strikingly different between 90 and 40 K superconductors, although these Cu oxides possess a similar layered structure. In the 90 K superconductor, the change in T_c by the replacement is negligibly small, whereas a clear depression of T_c is observed with a few percent substitution in the 40 K superconductor. A large part of this paper is devoted to the problem of the origin of the T_c depression in $[(La,Ln),Sr]_2CuO_4$ system.

II. SAMPLE PREPARATION AND EXPERIMENTAL PROCEDURE

The sintered pellets of the $Ba_2LnCu_3O_{7-y}$ (Ln = Y, Eu, Gd, Dy, Ho, Er, Tm, Yb) and $[(La,Ln)_{0.925}Sr_{0.075}]_2CuO_4$ (Ln 3% and 5%, Ln = La, Ce, Pr, Sm, Eu, Gd, Dy, Ho, Er, Tm, Yb, Lu) were prepared as follows.

[a] Also at Engineering Research Institute, Faculty of Engineering, University of Tokyo, Bunkyo-ku, Tokyo 113, Japan

 0021-8979/88/084009-06$02.40 © 1988 American Institute of Physics

A. $Ba_2LnCu_3O_{7-y}$

A prescribed mixture of Ln_2O_3, $BaCo_3$, and CuO was reacted at 900 °C with several intermediate pulvarizations. The obtained powder was pressed into pellets and sintered at 950 °C in continuous O_2 gas flow followed by slowly cooling down to room temperature at 50 °C/h. Room-temperature x-ray powder diffraction showed that most of the obtained samples consist of a single phase of orthorhombic oxygen-deficient perovskite. Only for the Yb-based compound, the presence of a small amount of secondary phase, of the order of 10%, was observed. The lattice parameters systematically decrease with increasing atomic number due to the lanthanide contraction. The results of x-ray powder diffraction are summarized in Table I.

B. $[(La, Ln)_{0.925}, Sr_{0.075}]_2CuO_4$, (Ln 3% and 5%)

A prescribed mixture of Ln_2O_3 (for Ce, Pr, and Tb substitution, CeO_2, Pr_6O_{11}, and Tb_4O_7 were used, respectively.) La_2O_3, $BaCO_3$, and CuO was reacted at 900 °C with several intermediate pulverizations. The obtained powder was pressed into a pellet and sintered at 1050 °C in continuous O_2 gas flow. The obtained pellet was annealed at 500 °C for 24 h for sufficient oxygen incorporation. The room-temperature x-ray powder diffraction shows that the obtained samples consist of a single phase of the tetragonal K_2NiF_4 structure for light lanthanide elements from La to Tb except for Ce. For heavy elements, from Dy to Lu, the presence of the secondary phase was (apparently) observed, suggesting the presence of a solubility limit. Judging from the intensity, the amount of the secondary phase seems to increase with increasing atomic number. The presence of the solubility limit for heavy elements can be clearly seen in Fig. 1, in which the Ln concentration dependence of the lattice parameters up to 20% is plotted. The lattice parameters decrease linearly with lanthanide content for Eu and Gd substitution, whereas the lattice parameters do not change for Er substitution, indicating the presence of the solubility limit for a heavy element as low as a few percent or less.

The transition temperature T_c of the prepared samples was determined by both the resistivity and the magnetic susceptibility measurement. We relied on the Meissner signal data rather than the resistivity data for the determination of T_c, since the former reflects the bulk superconducting properties better than the latter. In order to investigate the nature of the lanthanides, the magnetic susceptibility in the normal state was measured. For the susceptibility measurements, a SQUID magnetometer SHE model 905 was used.

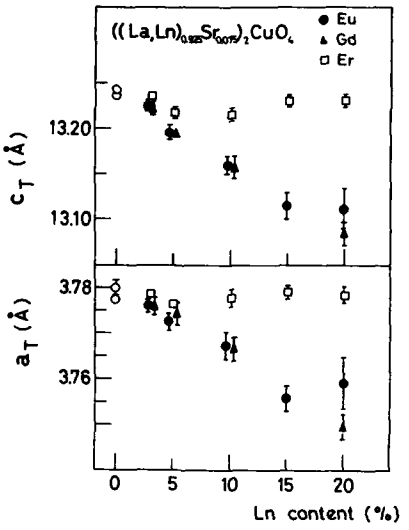


FIG. 1. Lanthanide content dependence of the lattice parameters a and c for $[(La,Ln)_{0.925},Sr_{0.075}]_2CuO_4$ (Ln = Eu, Gd, Er).

III. RESULTS AND DISCUSSIONS

A. $Ba_2YCu_3O_7$ system

First, we describe the superconductivity in $Ba_2LnCu_3O_7$ in which Y is replaced by lanthanides. In Figs. 2 and 3 are shown the temperature dependencies of the resistivity and the Meissner signal for several members of $Ba_2LnCu_3O_7$, respectively. As has been reported by many researchers, T_c

TABLE I. The lattice parameters a, b, and c of the orthorhombic structure, the superconducting transition temperature T_c defined as the onset temperature in the Meissner signal, the effective magnetic moment per Ln atom determined from the slope of the inverse magnetic susceptibility versus temperature curve, and the effective moment expected for free Ln^3 are listed for the various members of $Ba_2LnCu_3O_7$.

Ln	T_c (K)	a (Å)	b (Å)	c (Å)	μ_{exp} (μ_B)	μ_{theory} (μ_B)
Y	92	3.887	3.825	11.67		
Eu	92	3.907	3.854	11.73		
Dy	91	3.906	3.835	11.72	10.3	10.6
Ho	90	3.896	3.828	11.70	10.0	10.6
Er	89	3.896	3.826	11.68	9.0	9.6
Tm	90	3.892	3.817	11.66	7.3	7.6
Yb	89	3.888	3.807	11.67	4.0	4.5

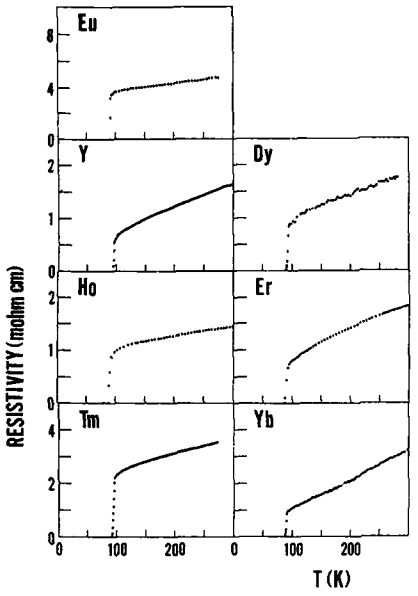


FIG. 2. Temperature dependence of the resistivity for $Ba_2LnCu_3O_7$ (Ln = Y, Eu, Dy, Ho, Er, Tm, Yb).

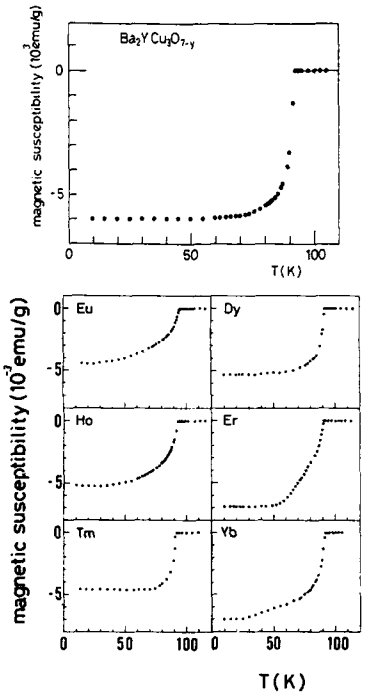


FIG. 3. Temperature dependence of the magnetic susceptibility for $Ba_2LnCu_3O_7$. The measurement was performed by slowly cooling the sample in the constant field of $H = 10$ Oe.

does not change significantly by the replacement.[20,21] All the members shown in Figs. 2 and 3 exhibit superconductivity with T_c of 90 K range. The change in the onset temperature listed in Table I is, at most, as small as 3 K.

The temperature dependence of the inverse magnetic susceptibility in the normal state shown in Fig. 4 indicates that lanthanides take the valence 3 + in the superconducting $Ba_2LnCu_3O_7$. The magnetic susceptibilities of all the members except for Eu obey the Curie–Weiss law. The effective moment per lanthanide atom estimated from the slope of the line coincides well with that of free Ln^{3+} ion, indicating lanthanide atoms are in an almost free Ln^{3+} state. As for Eu, of which the trivalent ion has the nonmagnetic ground state $^7F_0$ ($J = 0$) with the excited states $^7F_1$ almost 40 K above, the experimental curve can be fitted by the calculated one by assuming that Eu is in the trivalent ionic state.

The band calculation indicates that the conduction band is primarily composed of the Cu 3*d* and O 2*p* orbitals and that Y provides a negligibly small contribution to the Fermi level.[22,23] Therefore one can expect that the replacement of Y by the trivalent lanthanides does not change the electronic states in the vicinity of the Fermi level. This is probably one of the reasons why T_c does not change by the replacement. Actually, we did not observe any indication of a change in the electronic states in the various electronic properties such as the resistivity and Hall coefficient. As shown in Fig. 2, all the members show an almost *T*-linear resistivity. No significant differences between $Ba_2YCu_3O_7$ and $Ba_2ErCu_3O_7$ can be seen in the temperature dependence of the Hall coefficient shown in Fig. 5.

As has been pointed out by many groups, another origin of the small change in T_c by the replacement is that the exchange coupling to the magnetic moment of the Ln^{3+} is

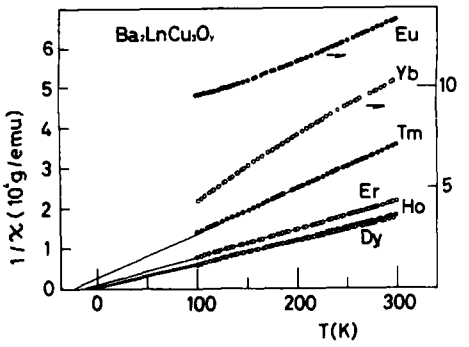


FIG. 4. Temperature dependence of the inverse magnetic susceptibility for $Ba_2LnCu_3O_7$ (Ln = Eu, Dy, Ho, Er, Tm, Yb).

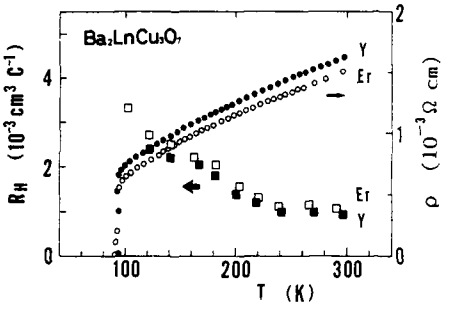


FIG. 5. Hall coefficient of $Ba_2YCu_3O_7$ and $Ba_2ErCu_3O_7$ as a function of the temperature.

weak due to the anisotropic crystal structure in which the Y layer is isolated from the triple Cu-O layers,[21] which is supported by the band-structure calculation. Recently, the antiferromagnetic ordering of the moments on the lanthanide atoms at low temperature was reported for Gd($T_N = 2.2$ K), Dy($T_N = 0.92$ K), Sm($T_N = 0.60$ K), and Er($T_N = 0.59$ K).[24] The observed low Néel temperatures clearly support that the exchange coupling is too weak to compete with the superconductivity.

B. $(La_{0.725}Sr_{0.075})_2CuO_4$

In contrast to the $Ba_2YCu_3O_7$ system, a few percent lanthanide substitution for La degrades the superconductivity. In Fig. 6 is shown the temperature dependence of the Meissner signal for samples with 3% Ln substitution. As can be seen from the figure, T_c clearly decreases with the substitution and the magnitude of the depression depends on the substituted elements. The superconducting transition becomes broad as compared with nonsubstituted sample, probably due to the inhomogeneity introduced by the substitution.

The onset temperatures of the transition seen in the Meissner signal for the sample with Ln 3% and 5% are plotted against the lanthanide elements in Fig. 7. The reduction of T_c obviously depends on the atomic number. T_c for nonsubstituted samples is 38 K. As the atomic number increases, T_c decreases monotonically except for Ce and shows a minimum at Tb where the depression of T_c is 8 and 12 K for 3% and 5% substitutions, respectively. For these light lanthanide elements, the depression of T_c is almost in proportion to the lanthanide concentration. On the other hand, T_c seems to increase for heavy elements from Dy to Lu but in this case the material faces the solubility problem. Due to the presence of the solubility limit, it is not clear whether T_c increases for heavy elements or not. Since the depression of T_c seems to be saturated with increasing the amount of the substitution, the depression of T_c for those heavy elements should probably be larger if the heavy element were soluble.

Then, what is the origin of the depression of T_c in $(La, Sr)_2CuO_4$? First, we can rule out the depression due to the exchange coupling based on the following discussion. The exchange interaction in this system is too weak to cause a large depression of T_c because of the same reason as in the case of $Ba_2LnCu_3O_7$. The depression of T_c due to the exchange coupling is expressed by the Abrikosov–Gorkov formula[25,26]

$$k_B \Delta T_c = (\pi^2/8) C N(0) \Gamma^2 G.$$

Here, C, $N(0)$, Γ, and G denote the concentration of the magnetic impurities, density of states at Fermi level, exchange interaction parameter, and de Gennes factor, respectively. When the depression of T_c is primarily caused by the

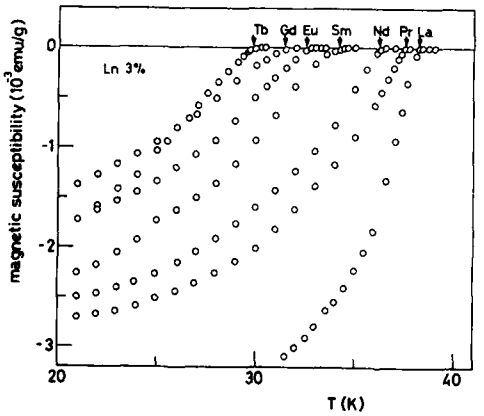


FIG. 6. Temperature dependence of the magnetic susceptibility for $[(La,Ln)_{0.925},Sr_{0.075}]_2CuO_4$ (Ln 3%, Ln = La, Pr, Nd, Sm, Eu, Gd, Tb). The measurement was performed by slowly cooling the sample in the constant field of $H = 10$ Oe.

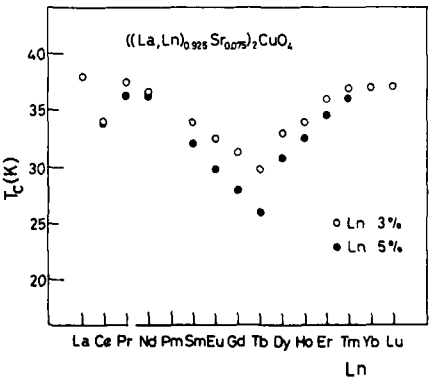


FIG. 7. Onset temperature of the superconducting transition in the Meissner signal for $[(La,Ln)_{0.925},Sr_{0.075}]_2CuO_4$ (Ln 3% and 5%) vs the lanthanide elements.

exchange coupling, the depression is essentially scaled by the de Gennes factor $G = (g-1)^2 J(J+1)$ as far as $N(0)$ and Γ does not change appreciably. Thus, if Ln^{3+} acts as a magnetic impurity, the depression of T_c increases with increasing atomic number from Ce to Gd showing a maximum at Gd and then decreases from Gd to Lu. In the above scenario, Eu should be an exception, since Eu^{3+} has a ground state $^7F_0$, $J = 0$.

On the contrary, the observed depression of T_c for Eu is comparable to the neighboring Sm and Gd. Here, one has to bear in mind that Eu prefers not only the trivalent but also the divalent ionic state. However, as has been pointed out by Tarascon *et al.*,[18] the magnetic susceptibility for Eu in the normal state can be well fitted by the calculated one by assuming that Eu is trivalent as shown in Fig. 8, indicating Eu is certainly in the trivalent ionic state. Therefore, the exchange coupling cannot be the primary origin of the depression of T_c.

It has been reported that the $(La,Sr)_2CuO_4$ has a much larger positive pressure coefficient of the transition temperature dT_c/dp as compared with the $Ba_2YCu_3O_7$ system.[27,28] Now, we discuss the problem from the viewpoint that lanthanide atoms act merely as spacers.

Kishio *et al.* systematically investigated T_c of the solid solution system $[La_{0.9}(Sr,Ba,Ca)_{0.1}]_2CuO_4$ system.[29] They have found that T_c can be scaled well with the lattice parameter a of the tetragonal cell. Based on this finding, they suggested that the Cu-O bond length is of crucial importance in determining T_c. In Fig. 9 the relationship between T_c and the lattice parameters in the $[La,(Sr,Ba,Ca)]_2CuO_4$ solid solution system is reproduced together with the pressure data. The curve for the $\{La,(Sr,Ba,Ca)\}_2CuO_4$ solid solution can be smoothly extrapolated to the high-pressure data. Therefore, the solid solution effect of $[La,(Sr,Ba,Ca)]_2CuO_4$ seems to be essentially the same as the high-pressure effect.

Can the present system be explained on the same line? The relationship between T_c and lattice parameters is also

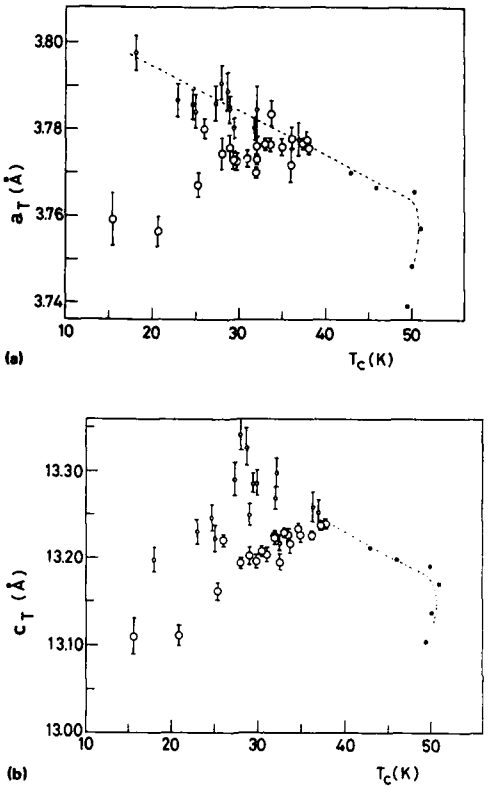


FIG. 9. Relationship between lattice parameters (a) a and (b) c, and T_c in $[(La,Ln)_{0.925},Sr_{0.075}]_2CuO_4$ [large open circles: Ln = La, Pr, Nd, Sm, Eu, Gd, Tb; Ln 3% and 5%; the data for Eu 10%, 15%, 20% and Pr 10% are included], $[La_{0.9},(Sr,Ba,Ca)_{0.1}]_2CuO_4$ reported by Kishio *et al.* (small open circles), and $(Ln_{0.9},Sr_{0.1})_2CuO_4$ with pressure reported by Takahashi *et al.* (small closed circles).

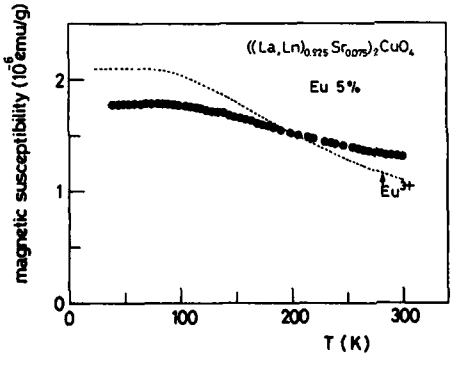


FIG. 8. Temperature dependence of the magnetic susceptibility in the normal state for $[(La_{0.95},Eu_{0.05}),Sr_{0.075}]_2CuO_4$. The dashed curve represents the calculated one assuming that Eu is in the trivalent ionic state.

shown in Fig. 9. The lattice parameters a and c decrease with lanthanide substitution due to the lanthanide contraction, while T_c is always depressed by the substitution. Thus, both T_c vs a and T_c vs c curves have positive slopes. The tendency is in the opposite direction to those of the high-pressure data and $[La,(Sr,Ba,Ca)]_2CuO_4$ solid solution system. Therefore, the depression of T_c cannot be explained simply by the change in the lattice parameters, i.e., volume effect.

The origin of the depression of T_c should be sought in some effects other than the magnetic and the volume effect. An indication of the predominance of the strong modification of local electronic states due to the introduction of lanthanide substitution is observed in the temperature dependence of the resistivity shown in Fig. 10. Whereas nonsubstituted samples show an almost linear temperature dependence, a tendency of the negative temperature coefficient

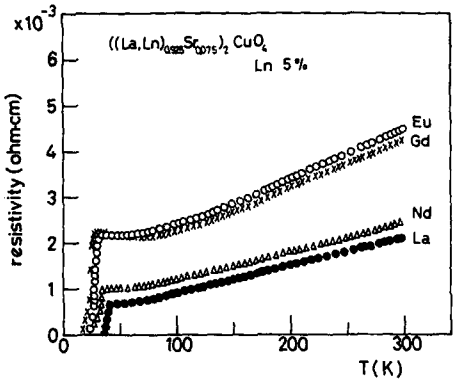


FIG. 10. Temperature dependence of the resistivity for $[(La,Ln),Sr]_2CuO_4$ (Ln 5%; Ln = La, Nd, Gd, Eu).

at low temperature becomes apparent as the atomic number of lanthanide element increases.

We speculate on the following possibilities as the origin of the depression of T_c, although, at the present stage, we cannot draw any firm conclusion.

(1) Local strain introduced due to the difference in ionic radius: In contrast to the Y layer in $Ba_2YCu_3O_7$, there are surrounding oxygens in La layers. Local strain can be transmitted in the Cu-O layer and alter the Cu-O bond length or affect the Cu-O layer by modifying the Jahn–Teller effect. Thus, the local strain may cause the disorder and change the electronic states, resulting in the depression of T_c.

(2) The oxygen vacancy: It has been reported that the electronic properties of $(La,A)_2CuO_4$ (A = Sr,Ba,Ca) system is very sensitive to the oxygen deficiency.[30] A similar temperature dependence of the resistivity has been observed in the oxygen deficient sample.

IV. SUMMARY

A close similarity between $(La,A)_2CuO_4$ (A = Sr, Ba,Ca) and $Ba_2LnCu_3O_7$ has been pointed out in the various physical properties.[31] However, the effect of lanthanide substitution on the superconductivity is quite different between these two Cu-oxide systems. The lanthanide substitution can hardly affect the superconductivity in the former, whereas a clear depression of T_c is observed in the latter. In the latter system, the exchange coupling to the magnetic lanthanide ions cannot primarily cause the depression of T_c due to the anisotropic crystal structure as in the former system. We can rule out the volume effect as the origin of the depression. The presence of the disorder is suggested by the resistivity measurement, which may suggest the presence of the local strain or oxygen deficiency. Possible mechanisms of the depression of T_c are discussed in this context.

ACKNOWLEDGMENTS

The authors would like to thank T. Ito, M. Uota, H. Ishii, H. Sato, N. Kanazawa, and H. Iwabuchi for their help in the experiment.

[1]J. G. Bednorz and K. A. Muller, Z. Phys. B **64**, 189 (1986).
[2]J. G. Bednorz, M. Takashige, and K. A. Muller, Europhys. Lett. **3**, 379 (1987).
[3]S. Uchida, H. Takagi, K. Kitazawa, and S. Tanaka, Jpn. J. Appl. Phys. **26**, L1 (1987).
[4]H. Takagi, S. Uchida, K. Kitazawa, and S. Tanaka, Jpn. J. Appl. Phys. **26**, L123 (1987).
[5]K. Kishio, K. Kitazawa, S. Kanbe, I. Yasuda, N. Sugii, H. Takagi, S. Uchida, K. Fueki, and S. Tanaka, Chem. Lett., 429 (1987).
[6]M. K. Wu, J. R. Ashburn, C. J. Torng, P. H. Hor, R. L. Meng, L. Gao, Z. J. Huang, Y. Q. Wang, and C. W. Chu, Phys. Rev. Lett. **58**, 408 (1987).
[7]R. J. Cava, B. Batlogg, R. B. van Dover, D. W. Murphy, S. Sunshine, T. Siegrist, J. P. Remeika, E. A. Rietman, Z. Zahurak, and G. Epinosa, Phys. Rev. Lett. **58**, 1676 (1987).
[8]S. Hosoya, S. Shamoto, M. Onoda, and M. Sato, Jpn. J. Appl. Phys. **26**, L325 (1987).
[9]K. Kitazawa, K. Kishio, H. Takagi, T. Hasegawa, S. Kanbe, S. Uchida, S. Tanaka, and K. Fueki, Jpn. J. Appl. Phys. **26**, L342 (1987).
[10]H. Takagi, S. Uchida, H. Sato, H. Ishii, K. Kishio, K. Kitazawa, K. Fueki, and K. Kitazawa, Jpn. J. Appl. Phys. **26**, L342 (1987).
[11]K. N. Yang, Y. Dalichaouch, J. M. Ferreira, B. W. Lee, J. J. Neumeier, M. Torikachvili, H. Zhou, M. B. Maple, R. R. Hake, Solid State Commun. (to be published).
[12]H. Kamimura, Jpn. J. Appl. Phys. **26**, L627 (1987).
[13]V. Z. Kresin, Phys. Rev. B **35**, 8716 (1987).
[14]C. M. Varma, S. Schmitt-Rink, and E. Abrahams, Solid State Commun. **62**, 681 (1987).
[15]P. W. Anderson, Science **235**, 1196 (1987).
[16]T. Hasegawa, K. Kishio, M. Aoki, N. Ooba, K. Kitazawa, K. Fueki, S. Uchida, and S. Tanaka, Jpn. J. Appl. Phys. **26**, L337 (1987).
[17]K. Kishio, K. Kitazawa, T. Hasegawa, M. Aoki, K. Fueki, S. Uchida, and S. Tanaka, Jpn. J. Appl. Phys. **26**, L391 (1987).
[18]J. M. Tarascon, L. H. Green, W. R. McKinnon, and G. W. Hull, Solid State Commun. **63**, 499 (1987).
[19]Y. Maeno, T. Nojima, Y. Aoki, M. Kato, K. Hoshino, A. Minami, and T. Fujita, Jpn. J. Appl. Phys. **26**, L774.
[20]Our preliminary results were presented at the APS meeting, New York, March 18, 1987.
[21]S. Tanaka, S. Uchida, H. Takagi, K. Kitazawa, K. Kishio, S. Tajima, and K. Fueki, Proceedings of the MRS Spring meetings, Anaheim (1987); J. M. Tarascon, W. R. McKinnon, L. H. Green, G. W. Hull, and E. M. Vogel, Phys. Rev. B (to be published).
[22]L. F. Mattheiss and D. R. Hamann, Solid State Commun. **63**, 395 (1987).
[23]S. Massida, J. Yu, A. J. Freeman, and D. D. Koelling, Phys. Lett. **122**, 198 (1987).
[24]A. P. Ramirez, L. F. Schneemeyer, and J. V. Waszczak (unpublished).
[25]A. Abrikosov and L. P. Gor'kov, Sov. Phys. JETP **12**, 1243 (1961).
[26]P. G. de Gennes, J. Phys. Rad. **23**, 510 (1962).
[27]H. Takahashi, C. Maruyama, S. Yomo, N. Mori, K. Kishio, K. Kitazawa, and K. Fueki, Jpn. J. Appl. Phys. **26**, L504 (1987).
[28]S. Yomo, C. Maruyama, W. Utsumi, H. Takahashi, T. Yagi, N. Mori, T. Tamegai, A. Watanabe, and Y. Iye, Jpn. J. Appl. Phys. **26**, Suppl. 1107 (1987).
[29]K. Kishio, K. Kitazawa, N. Sugii, S. Kanbe, K. Fueki, H. Takagi, and S. Tanaka, Chem. Lett., 635 (1987).
[30]H. Takagi, S. Uchida, K. Kitazawa, and S. Tanaka, Jpn. J. Appl. Phys. **26**, L218 (1987).
[31]S. Uchida, H. Takagi, K. Kishio, T. Hasegawa, S. Tajima, K. Kitazawa, K. Fueki, and S. Tanaka, to be published in Proceedings of the Workshop on Novel Mechanisms of Superconductivity, Berkeley, June, 1987.

Antiferromagnetism in the high-T_c related compounds (invited)

S. K. Sinha, D. E. Moncton, D. C. Johnston,[a] D. Vaknin[b]
Exxon Research and Engineering Company, Annandale, New Jersey 08801

G. Shirane
Brookhaven National Laboratory, Upton, New York 11973

C. Stassis
Iowa State University, Ames, Iowa 50010

Magnetic susceptibility measurements on La_2CuO_{4-y} have revealed maxima in temperature indicative of antiferromagnetic ordering. Powder diffraction measurements have demonstrated the existence of superlattice peaks at temperatures below those corresponding to the susceptibility maxima, and polarized neutron measurements have confirmed that the peaks are indeed of magnetic origin. The deduced antiferromagnetic structure in the orthorhombic (Cmca) phase of La_2CuO_{4-y} consists of ferromagnetic sheets of Cu atoms in the *b-c* plane which are alternating in sign along the *a* axis [100]. The moment is parallel to the *c* axis. The Neel temperature is extremely sensitive to the oxygen deficiency *y* and decreases rapidly to zero as *y* goes from 0.03 to 0. The saturated moment is $\simeq 0.4\,\mu_B$/Cu atom for samples with the highest T_N (290 K). Antiferromagnetic spin fluctuations have also been observed by polarized neutron scattering in the paramagnetic phase above T_N. Recent results obtained on magnetic ordering in the $YBa_2Cu_3O_{6-y}$ family of compounds are also discussed, together with the possible implications for novel superconductivity mechanisms.

From the basic physics point of view, perhaps the most interesting question regarding the so-called "high-T_c" superconductors is this: Is the mechanism conventional electron-phonon coupling, or is it different from that in all superconductors known so far? In particular, if the mechanism is not due to phonons, could it be associated with spin fluctuations or magnetic interactions in a general sense? The earliest theory advocating the latter point of view for the present group of materials was put forward by Anderson in the form of his resonating valence bond (RVB) theory,[1] and subsequently several different theories have been presented which involve superconductivity arising from the same interactions which produce magnetism, and in some cases, even coexisting with long-range antiferromagnetic order.[1-7] In this paper, we shall describe how antiferromagnetic order is indeed seen by neutron diffraction in this family of compounds, although, as we shall see, the relationship to superconductivity is still unclear at the present time.

We first discuss the case of antiferromagnetism in the "parent" compound La_2CuO_{4-y} of the $A_{2-x}B_xCuO_{4-y}$ family of superconductors, where A = lanthanide and B = Ca, Sr, and Ba. Peaks in the temperature dependence of the measured susceptibility of La_2CuO_{4-y} were found several years ago, indicating some kind of phase transition.[8] Systematic recent studies by Johnston and co-workers[9] indicate a strong sample dependence to the temperature of this transition. The temperatures of the susceptibility maxima are highly sensitive to the value of *y*, increasing from $T_N \simeq 0$ for $y = 0$ to $T_N \simeq 295$ K for $y \gtrsim 0.03$. The anomaly disappears for $La_{2-x}Sr_xCuO_{4-y}$ samples for Sr concentrations $x \gtrsim 0.1$. The susceptibility data for $x \lesssim 0.1$ also indicate a broad *rise* in the susceptibility in the region ~250–600 K, as shown in Fig. 1.

La_2CuO_{4-y} is tetragonal at high temperatures and undergoes an orthorhombic distortion at lower temperature, which doubles the tetragonal unit cell in the basal plane.[10,11] The transition temperature T_0 is highly sensitive to the oxygen vacancy concentration *y* in the material, varying from 450 to 530 K depending on *y*.[9] The orthorhombic space-group is Cmca, where (unlike the tetragonal system) the *a* and *c* axis lie in the basal plane and the *b* axis is along the original tetragonal *c* axis normal to the Cu-O layers.

The La_2CuO_{4-y} powder samples studied were prepared using the normal procedures,[12] and the oxygen vacancy concentration *y* was controlled by final heating either in flowing helium, air or an oxygen-rich atmosphere. The neutron powder diffraction measurements were carried out on neutron spectrometers at the High Flux Brookhaven Reactor, using a neutron wavelength of 2.37 Å and a pyroly-

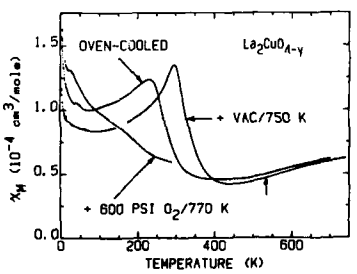


FIG. 1. Magnetic susceptibility X_M vs temperature for three samples of La_2CuO_{4-y}.

[a] Present address: Iowa State University, Ames, Iowa 50010.
[b] Also at the University of Pennsylvania, Philadelphia, Pennsylvania.

 0021-8979/88/084015-04$02.40 © 1988 American Institute of Physics

tic graphite filter to remove $\lambda/2$ contamination to better than 1 part in 10^4.

Figure 2 shows the lattice constants a and c measured as a function of temperature, together with the order parameter η of the orthorhombic distortion $2(c-a)/(c+a)$, as a function of reduced temperature T/T_0 for a sample with $y \simeq 0.03$. T_0 was found to be 505 K. Also shown is the intensity of the (041) orthorhombic nuclear peak (forbidden in the tetragonal phase) whose intensity is proportional to δ^2, where δ is the angle of the octahedral rotation which doubles the unit cell.[11] The data is well fitted by $\eta \sim t^{0.744}$ and $\delta \sim t^{0.476}$ over the whole range of temperatures measured, where $t = |T - T_0|/T_0|$.

Careful searches were made at low temperatures for additional neutron diffraction peaks indicative of antiferromagnetic ordering. Figure 3 shows such a peak which appeared below 220 K at a scattering angle and which could be indexed as (100). [The resolution of the instrument was good enough to differentiate this position from the almost degenerate (010) position, which showed no peak.] The temperature dependence of the peak intensity (measured as peak height above background) is also plotted in Fig. 3. The symmetric peak shape is indicative of three-dimensional ordering, and the peak width (which is not significantly greater than the instrumental resolution width) indicates coherence of the ordered structure for lengths >200 Å. After discovery of the (100) superlattice peak, peaks were searched for and found at the equivalent reciprocal lattice point positions (011), (031), (120), and (300). These are all forbidden by the orthorhombic nuclear structure. Careful

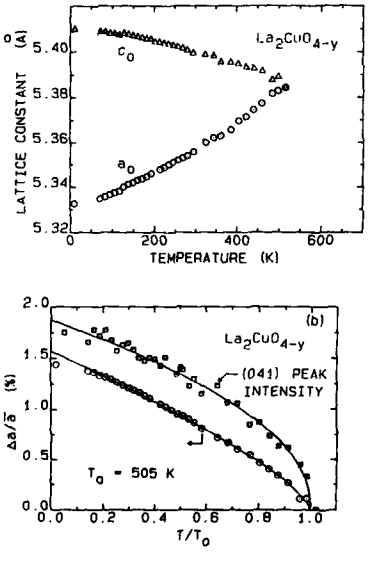


FIG. 2. (a) Orthorhombic lattice constants a and c vs temperature. (b) Orthorhombic distortion η and (041) nuclear reflection intensity (arb. units) vs reduced temperature ($T_0 = 505$ K); the solid curves are power law fits to the data as discussed in the text.

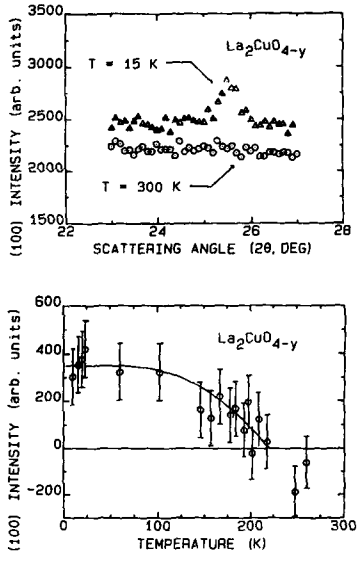


FIG. 3. (a) Intensity vs scattering angle 2θ for neutron powder scans of the (100) peak region at 15 K and at room temperature. (b) (100) peak intensity vs temperature. The solid line is a spin $\frac{1}{2}$ magnetization curve for $T_N = 220$ K, calculated from molecular field theory.

x-ray powder diffraction measurements at these positions yielded no peaks, which suggested that displacive structural transformations or oxygen vacancy ordering as the origin of these peaks was not likely.[13]

In order to confirm that these peaks were indeed of magnetic origin, a polarized neutron diffraction experiment was carried out.[14] These measurements were carried out on a sample with a higher T_N ($\simeq 290$ K). In a polarization analysis experiment, one measures the scattering from the sample which has resulted in a spin-flip of the neutron, both in the configuration where the neutron spin is parallel to Q, the momentum transfer vector (HF configuration) and where it is perpendicular to Q (VF configuration).[15] In this way, all nonmagnetic contributions to the scattering are eliminated, and it can be shown that the magnetic scattering is proportional to twice the difference (HF-VF) intensity. This intensity was observed at the (100) superlattice point and followed a similar temperature dependence to the peaks found earlier, indicating that the peaks are indeed due to magnetic ordering.

From the relative intensities of the various magnetic peaks, and assuming that the magnetic moments are associated with the Cu sites, the antiferromagnetic structure shown in Fig. 4 was deduced, consisting of ferromagnetic sheets of spins in the b-c plane alternating in sign as one moves along the a axis. The moment direction is along the orthorhombic c axis in the basal plane. From the intensities of the magnetic peaks as compared with the nuclear peaks, the low temperature ordered moment was obtained as $0.4 \pm 0.15\ \mu_B$/Cu atom for the sample with $T_N = 220$ K

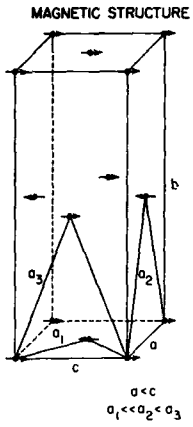


FIG. 4. Proposed spin structure of antiferromagnetic La_2CuO_{4-y}. Only copper sites in the orthorhombic unit cell are shown for clarity.

and $0.43 \pm 0.13\,\mu_B$/Cu atom for the sample with $T_N = 290$ K. The magnetic form factor for the Cu atom can also be obtained from the data and is shown in Fig. 5. Compared with the standard Cu^{2+} form factor, the measured form factor appears to have a shoulder at $Q \simeq 1.26$ Å^{-1}, although the statistical errors in the data are quite large. It is tempting to ascribe these to covalency effects[16] arising from the oxygen atoms. Note that the symmetry of the magnetic structure does not allow the O atoms in the basal planes to have a moment, but the O atoms above and below the basal plane may. It is an interesting fact that recent spin-polarized band-structure calculations by *Harmon et al.*[17] yield a small moment on these oxygen sites and account qualitatively for the shape of the observed form-factor as shown. The magnetic ordering in La_2CuO_{4-y} has also recently been observed in μSR experiments by Uemura *et al.*[18]

The most striking feature of the magnetism in La_2CuO_{4-y} is its extreme sensitivity to oxygen vacancy concentrations, as the ordered state disappears rapidly as y goes to zero. Single-crystal neutron diffraction experiments,[19] carried out by heat treating the crystals in a vacuum to increase y, confirmed this trend. Single crystals with $T_N \simeq 50$ K (ordered Cu moment $= 0.17 \pm 0.05\mu_B$) and

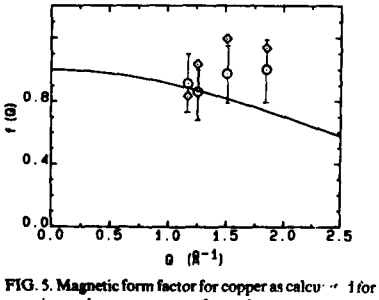


FIG. 5. Magnetic form factor for copper as calcu[illegible] for Cu^{2+} (solid line), experimental measurements from the present [illegible]utron diffraction work (Ref. 13) O, and calculations based on a spin-p[illegible]rized band structure calculation (Ref. 17) ◇.

$T_N \simeq 150$ K (moment $= 0.23 \pm 0.05\mu_B$) were found to show antiferromagnetic ordering. The full ordered amount expected for a Cu^{2+} ion is $\sim 1\,\mu_B$. Zero-point fluctuations can account for some reduction, but not as large as that observed.

We next examined a powder sample of La_2CuO_{4-y} ($y = 0.03$) with $T_N \simeq 250$ K for paramagnetic scattering above T_N at 300 K, using the neutron polarization analysis technique described above. The experiment showed that antiferromagnetic fluctuations exist above T_N around the (100) reciprocal lattice point. Subsequently, measurements on a large single crystal of La_2CuO_{4-y} (Ref. 20) showed that these fluctuations are *two-dimensional*, in the sense of being antiferromagnetic fluctuations within the Cu-O (a-c) basal planes. The existence of rods of scattering passing through the (100) reciprocal lattice point showed that these planes are uncorrelated. It is interesting to note that for the two-dimensional spin structure corresponding to that in the basal plane of the unit cell shown in Fig. 4, the (100) and (001) reciprocal lattice points are equivalent (if there is no unique direction for the spins), and indeed rods of scattering were observed in the single crystal experiment through *both* reciprocal lattice points. In the *three-dimensional* structure, they are not equivalent and the intensity around (001) vanishes. The remarkable features revealed by the single-crystal measurements are that these two-dimensional correlations exist both below and well above the 3D Néel temperature (the anomalous rise in the susceptibility above 250 K is thus presumably due to this effect), and that there is no quasielastic component to the scattering. Rather, the scattering is due to spin excitations which are highly dispersive, corresponding to an extremely large in-plane exchange of the order of 1000 K. They are also gapless. The picture is reminiscent of a 2D analog of the spin excitations in chromium.[21] The in-plane correlation length is of $\sim$100–200 Å, but decreases very rapidly on doping with impurities.

The picture which emerges then is of a strongly exchange-coupled 2D spin system with much weaker interplane coupling (along the b axis), which results in the 3D long-range ordering at T_N. The reason for the weak interplane coupling can be deduced from the spin structure shown in Fig. 4. The spin at $(\frac{1}{2}, 0, \frac{1}{2})$ in the center of the square of the basal plane is coupled (through superexchange interactions via the out-of-plane oxygens) antiferromagnetically to the four nearest spins in the layer above, but these interactions exactly cancel in the undistorted tetragonal structure, leading to frustration. In the distorted orthorhombic phase, a consideration of the relative oxygen displacements shows[22] that the interactions with the pair of spins which favor the observed 3D structure become stronger than those with the pair of spins which oppose it, resulting in the observed 3D spin structure. It thus appears that the interlayer coupling is crucially dependent on the orthorhombic distortion in this structure. What is not clear is why T_N should be so sensitive to oxygen vacancy concentration, and why the 3D structure does not develop the full Cu^{2+} moment at low temperatures. From neutron diffraction data on different La_2CuO_{4-y} samples,[19] it appears that the 3D ordered moment increases monotonically with T_N, as one

might expect for a spin-density wave system rather than a local moment system. However, self-consistent spin-polarized band structure calculations by Wang and Harmon[17] are unable to produce a stable antiferromagnetic structure Since transport measurements in La_2CuO_{4-y} samples indicate the presence of a metal-insulator transition as the oxygen vacancy concentration increases,[9] it is likely that correlation effects beyond the local density functional approximation must be incorporated into the electronic structure to account for the magnetism.

Turning now to the $YBa_2Cu_3O_{7-y}$ family of superconductors, we have carried out neutron powder diffraction scans on samples with $y = 0.01$. An analyzer crystal was used to study only the elastic component, and high resolution (employing 20′-10′-10′-20′ collimation) was used. The intensities of the powder Bragg peaks were consistent with earlier neutron structural determinations for these compounds. The $YBa_2Cu_3O_7$ sample showed no evidence of additional elastic magnetic scattering from room temperature down to 10 K.

In conclusion, from the neutron diffraction experiments one can say that the nonsuperconducting members of the La_2CuO_{4-y} series of compounds show strong magnetic correlations involving spins on both Cu and O sites. In cases where only 2D fluctuations are observed, it is tempting to appeal to the resonating valence bond picture.[1] However, one should remember that 2D isotropic spin systems cannot order on very general principles. Whether the magnetism observed is simply an interesting parallel phenomenon occurring in these compounds, or whether it is intrinsically related to the superconducting mechanism will only become clearer when we find out if magnetic fluctuations exist at all in the superconducting state. Evidence so far indicates that the magnetic correlations disappear very rapidly in the superconducting phase. However, large single crystals of the superconducting materials have not yet been available for study.

The authors wish to thank S. Bhattacharya, A. N. Bloch, M. H. Cohen, B. N. Harmon, A. J. Jacobson, J. Stckes, H. Thomann, and Y. J. Uemura for helpful discussions. Much of this work was also carried out in collaboration with T. Freltoft, J. E. Fischer, J. P. Remeika, A. S. Cooper, D. Harshman, M. S. Alvarez, D. Goshorn, J. Lewandowski, and S. Mitsuda, and we wish to thank them for their invaluable help. The work of G. S. was supported by the U.S. Department of Energy, BES-Materials Sciences under Contract No. DE-AC02-76CH00016. The work of C.S. was supported by the U.S. Department of Energy, BES-Materials Sciences under Contract No. W-7405-ENG-827.

[1] P. W. Anderson, Science **235**, 1196 (1987); P. W. Anderson, G. Baskaran, Z. Zou, and T. Hsu, Phys. Rev. Lett. **58**, 2790 (1987).
[2] J. E. Hirsch, Phys. Rev. B **31**, 4403 (1985); S. Kivelson, D. Rokhsar, and J. Sethna, *ibid.* **35**, 8865 (1987).
[3] V. J. Emery, Phys. Rev. Lett. **58**, 2794 (1987).
[4] H. Fukuyama and K. Yosida, Jpn. J. Appl. Phys. **26**, L371 (1987).
[5] Z. B. Su, Y. Lu, J. M. Dong, and E. Tosatti, ICTP (Trieste) (to be published).
[6] M. Inui, S. Doniach, P. J. Hirschfield, and A. E. Ruckenstein (unpublished).
[7] T. M. Rice (unpublished).
[8] P. Ganguly, S. Kollali, C. N. R. Rao, and S. Kern, Magn. Lett. **1**, 107 (1980); K. K. Singh, P. Ganguly, and J. B. Goodenough, J. Solid State Chem. **52**, 254 (1984); S. Uchida, H. Takagi, H. Yanagisawa, K. Kishio, K. Kitazawa, K. Fueki, and S. Tanaka, Jpn. J. Appl. Phys. **26**, L445 (1987); R. L. Greene, H. Maletta, T. S. Plaskett, J. G. Bednorz, and K. A. Müller, Solid State Commun. (to be published).
[9] D. C. Johnston, J. P. Stokes, D. P. Goshorn, and J. T. Lewandowski, Phys. Rev. B **36**, 4007 (1987).
[10] V. B. Grande, Hk. Müller-Buschbaum, and M. Schweizer, Z. Anorg. Allg. Chem. **429**, 120 (1977).
[11] J. D. Jorgensen, H.-B. Schüttler, D. G. Hinks, D. W. Capone II, K. Zhang, M. B. Brodsky, and D. J. Scalapino, Phys. Rev. Lett. **58**, 1024 (1987).
[12] C. Michel and B. Raveau, Rev. Chim. Miner. **21**, 407 (1984).
[13] D. Vaknin, S. K. Sinha, D. E. Moncton, D. C. Johnston, J. M. Newsam, C. R. Safinya, and H. E. King, Jr., Phys. Rev. Lett. **58**, 2802 (1987).
[14] S. Mitsuda, G. Shirane, S. K. Sinha, D. C. Johnston, M. S. Alvarez, D. Vaknin, and D. E. Moncton, Phys. Rev. B **36**, 822 (1987).
[15] R. M. Moon, T. Riste, and W. C. Koehler, Phys. Rev. **181**, 920 (1969); J. Wicksted, P. Böni, and G. Shirane, *ibid.* **30**, 3659 (1984).
[16] K. Hirakawa and H. Ikeda, Phys. Rev. Lett. **33**, 374 (1974).
[17] S. Wang and B. N. Harmon (private communication).
[18] Y. J. Uemura, W. J. Kossler, X. H. Yu, J. R. Kempton, H. E. Schone, D. Opie, C. E. Stronach, D. C. Johnston, M. S. Alvarez, and D. P. Goshorn, Phys. Rev. Lett. **59**, 1045 (1987).
[19] T. Freltoft, G. Shirane, J. E. Fischer, D. E. Moncton, S. K. Sinha, D. Vaknin, J. P. Rameika, A. S. Cooper, and D. Harshman, Phys. Rev. B **36**, 826 (1987).
[20] G. Shirane, Y. Endoh, R. J. Birgeneau, M. A. Kastner, Y. Hidaka, M. Oda, M. Suzuki, and T. Murakami, Phys. Rev. Lett. **59**, 1613 (1987).
[21] S. K. Sinha, P. R. Kline, C. Stassis, N. Chesser, and N. Wakabayashi, Phys. Rev. B **15**, 1415 (1977).
[22] S. K. Sinha and M. H. Cohen (unpublished).
[23] C. M. Varma, S. Schmitt-Rink, and E. Abrahams, Solid State Commun. **62**, 681 (1987).

Theoretical studies of high T_c superconductors (invited) (abstract)[a)]

D. J. Scalapino
Department of Physics, University of California, Santa Barbara, California 93106

The current theoretical ideas concerning the mechanism responsible for the high transition temperature of the superconducting oxides will be reviewed.

a) Supported in part by the National Science Foundation under grant No. DMR86-15454 and the Department of Energy under grant No. DE-FG03-85ER45197.

 0021-8979/88/084019-01$02.40 © 1988 American Institute of Physics

Laminated CoZr amorphous thin-film recording heads

James L. Su, Mao-Min Chen, Jerry Lo, and Rod E. Lee
IBM Magnetic Recording Institute, IBM Research Division, Almaden Research Center, 650 Harry Road, San Jose, California 95120

Recording heads with four-layer laminated CoZr/Ta films as pole pieces have been fabricated using rf sputter deposition and ion milling techniques. Typical $4\pi M_s$ of 14 000 G were obtained for CoZr amorphous films compared with 10 000 G for Permalloy films. Recording tests performed with this laminated CoZr/Ta film head indicate 8–12 dB better overwrite than with plated Permalloy film heads having an identical structure. However, the former exhibits a 10%–25% lower amplitude than the latter. This may be attributed to the thermal degradation of the initial permeability μ_i of the CoZr film during head-fabrication processes. This CoZr/Ta head also shows poorer amplitude stability than the plated Permalloy head.

I. INTRODUCTION

Interest in CoZr alloy films[1] for recording-head applications stems from the need to develop a high-saturation-magnetization material to satisfy both read and write requirements in high-density recording environments. A thin-film head with CoZr pole pieces has been shown to produce significant improvement in the overwrite performance.[2] However, the magnetostriction λ of the amorphous CoZr film reported was $+2.6\times10^{-6}$, substantially larger than that of sputtered NiFe film heads having $\lambda=(+0.5\text{–}5)\times10^{-7}$, which was reported to cause wiggles in the readback signal.[3] Near-zero λ has been achieved by adding a nonmagnetic element such as Nb to the CoZr alloy film,[4] but usually at the expense of $4\pi M_s$.[5] In this study, we prepared 1-μm-thick and 12-μm-wide unlaminated CoZr and four-layer laminated CoZr/Ta films to examine domain configurations using the Bitter technique. The unlaminated film exhibited distinct closure domains at both edges, while the laminated film did not. This result motivated us to fabricate thin-film inductive heads with four-layer laminated CoZr/Ta pole pieces to assess the read-write performance. This paper reports on the properties and annealing results of the films and on the fabrication and read-write characteristics of laminated CoZr/Ta film heads including the amplitude stability and the peak shift.

II. EXPERIMENT

Single and multiple CoZr/Ta films were deposited from two separate 8-in.-diam targets in a Perkin-Elmer 2400 diode sputtering system. The CoZr target used had a composition of 6.7 at. % Zr. The Ta films served as protection as well as spacer layers and were deposited in the same pump cycle. Thin glass and Al_2O_3-coated ceramic substrates were loaded onto a water-cooled table for deposition. There was no intentional thermal bonding between the substrate and water-cooled table. Thus depending on the power density and substrate bias voltage the substrate temperature increased during deposition. The base pressure of the system was 1×10^{-7} Torr. The magnetic anisotropy of the film was induced by depositing CoZr in a magnetic field of 150 Oe. Typical deposition conditions were 500-W rf forward power, 8-mTorr argon pressure, and -20-V substrate bias voltage. The deposition rate was 225 Å/min. Film thicknesses from 300 Å to 2.2 μm were examined during the course of these studies. For lamination, a nonmagnetic spacer of either conducting or insulating materials can be used. In this experiment, 200-Å-thick Ta was chosen as the spacer material. The deposited films were subsequently annealed up to 280 °C in N_2 or in a vacuum of about 10 mTorr. A top layer of Ta was deposited on the sample to avoid oxidation of CoZr during annealing. The thermal annealing was performed with the following variations: stationary in a magnetic field, rotating (up to 60 rpm) in a magnetic field, and no magnetic field.

The crystal structure of the film was studied using x-ray diffraction techniques. The coercivity (H_c) and anisotropy field (H_k) were evaluated with a B-H looper, while the saturation moment was determined using a vibrating-sample magnetometer. The magnetostriction λ was evaluated by applying a 15-g load at the center line of a 5.0-cm^2 square wafer through a three-point bending scheme.[6] The permeability μ_i was measured with a permeance meter.

III. RESULTS

A. CoZr and CoZr/Ta film deposition and properties

Magnetic properties of the CoZr films were found to depend on the crystal structure of the film. For films deposited in the amorphous phase, low coercivity was obtained. In general, low power density and low substrate bias during deposition play an important role of keeping the substrate temperature from rising too high, thereby preventing the films from forming crystalline phases. Table I shows the properties of amorphous CoZr films, in comparison with plated Permalloy films. Saturation moments of 14 kG, 40% higher than that of Permalloy, were obtained. The permeability was increased drastically by rotating-field annealing (RFA) from as-deposited values of 750 to subsequent values

 0021-8979/88/084020-03$02.40 © 1988 American Institute of Physics

TABLE I. Properties of amorphous CoZr films and plated Permalloy films.

	CoZr		Permalloy	
	As deposited	RFA	As plated	RFA
H_c	<0.2 Oe	<0.2 Oe	0.3–0.4 Oe	0.3–0.4 Oe
H_k	15–20 Oe	2–4 Oe	2.5–3.5 Oe	2–3 Oe
$4\pi M_s$	14 kG	14 kG	10 kG	10 kG
μ_i	750	3500	2600	4200
λ	positive	positive	negative	negative
ρ	77 $\mu\Omega$ cm		21 $\mu\Omega$ cm	
Crystal structure	amorphous		fcc	

of 3500. However, the permeability suffered a loss with subsequent annealing in either a field or the absence of field. Figure 1 shows the degradation in terms of the ratio of H_{k0} (anisotropy field right after rotating field annealing) to H_{ka} (anisotropy field after annealing in the absence of field for 1 h at a given temperature) as a function of annealing temperature. The $4\pi M_s$ of the CoZr film remained unchanged after annealing. The decrease in H_{k0}/H_{ka} indicates that the permeability decreases continuously with increasing temperature. Furthermore, a decrease in the permeability from 3500 to 1200 was observed if one annealed the films in a field aligned with the easy axis of the film at 250 °C for 6 h. This thermal degradation is undesirable, since the film is subjected to similar annealing conditions during the head fabrication.

B. Thin-film inductive head fabrication

Thin-film inductive heads were fabricated for recording characteristics evaluation. The transducer contains a lower pole piece, a polymer insulation layer, a 0.8-μm sputtered Al_2O_3 gap layer, a single-layer 18-turn copper coil, and an upper pole piece. Both NiFe and four-layer laminated CoZr/Ta film heads were fabricated for comparison. The CoZr/Ta pole pieces were rf sputter deposited and then patterned by an ion-beam milling technique through a photoresist mask. Figure 2 shows cross-sectional scanning electron micrographs of a laminated CoZr/Ta head. The Ta spacers are clearly visible in the picture. The plated Permalloy shaping layers on the lower and upper pole pieces as shown in Fig. 2 are without lamination.

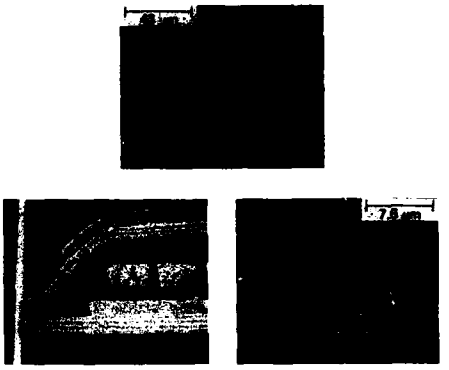


FIG. 2. Cross sections of a four-layer laminated CoZr/Ta film head.

C. Read-write performance

Read-write experiments were carried out with four-layer laminated CoZr/Ta film heads and plated Permalloy film heads flying on a sputtered Co alloy longitudinal thin-film disk which had $H_c = 1100$ Oe, $M_r t = 2\times10^{-3}$ emu/cm^2, and $S^* = 0.85$. All heads had an identical structure and pole-tip geometry with bottom and top pole thicknesses of 2.3 and 1.7 μm, respectively, and a gap length of 0.8 μm. Tests were performed at a flying height of 0.2 μm using a 30-m/s disk velocity.

Figure 3 shows that on thin-film media, the CoZr/Ta head exhibits 9–12 dB better overwrite than the NiFe head for write currents above 80 mA peak to peak. The overwrite was obtained from the ratio of the residual to original fundamental-frequency component of a 250-fc/mm signal after overwriting with a 1000-fc/mm signal. Figure 3 also shows that the CoZr/Ta head produces a peak-to-peak amplitude of 250 compared with 300 μV for the NiFe head. The relatively low amplitude of the CoZr/Ta head may be attributed to the thermal degradation of the initial permeability from 3500 to about 1200 during head-fabrication processes.

Density-roll-off or peak-shift measurements indicate that a typcial − 3-dB density of 900 fc/mm and a corresponding dibit peak shift of 12% have been achieved for the particular head-disk combination. Since the overwrite of the

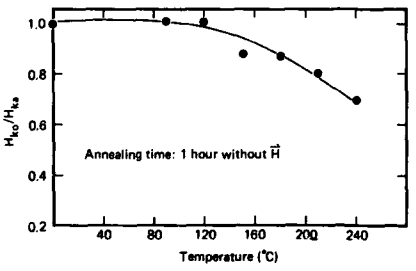


FIG. 1. Temperature dependence of the ratio H_{k0}/H_{ka} during annealing.

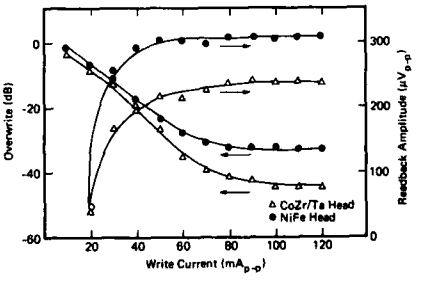


FIG. 3. Write current dependence of overwrite and signal amplitude.

CoZr/Ta head is quite large, the gap length and pole-tip thicknesses can be reduced to enhance the read resolution.

The stability of thin-film heads is associated with the device domain structure.[7,8] One of the methods for evaluating the stability is to measure the amplitude variability by repeatedly writing a track and after each write cycle measuring the peak-to-peak track averaged amplitude.[9] The amplitude variability is defined in this measurement as the ratio of the standard deviation to the mean of the peak-to-peak track averaged amplitude. Figure 4 shows the amplitude variability expressed in percent for two CoZr/Ta heads. Despite four-layer lamination, the CoZr/Ta head exhibits larger amplitude variability than the Permalloy heads which give a typical amplitude variability of less than 1.5% for 12-μm track heads previously reported,[9] as well as the Permalloy heads investigated here. Furthermore, the CoZr/Ta head shows an increase in the amplitude variability as the transition density is increased and the track width is decreased. The CoZr/Ta heads tested here have positive λ of about 3×10^{-6} compared with a small negative λ for the plated Permalloy reference head. If we assume that the same anisotropic stress exists near the air-bearing surface of all heads considered here, then these results suggest that controlling the λ of the pole-piece material is critical for the amplitude stability of the head. This is consistent with findings[3] which reveal wiggles in the readback waveforms of sputtered NiFe film heads with positive magnetorestriction.

IV. CONCLUSIONS

Amorphous CoZr films investigated here exhibit low coercivity and 40% higher saturation magnetization than plated Permalloy films. Rotating-field annealing improves the permeability of the CoZr film from 750 (as deposited) to 3500, but subsequent thermal annealing degrades this value.

Recording heads with four-layer laminated CoZr/Ta films as pole pieces have been fabricated using rf sputter deposition and ion milling techniques. The heads exhibit much better overwrite than plated NiFe heads due to 40% improvement in $4\pi M_s$ for CoZr films. However, the CoZr/Ta heads show a lower signal amplitude and larger amplitude variability than plated Permalloy heads. The results suggest that the CoZr/Ta heads fabricated as described here demonstrated poor amplitude stability, and the use of pole-piece materials with small negative magnetostriction may be required to achieve the desired head stability for narrow-track and high-linear-density applications. The CoZr film head is a good candidate for write head applications.

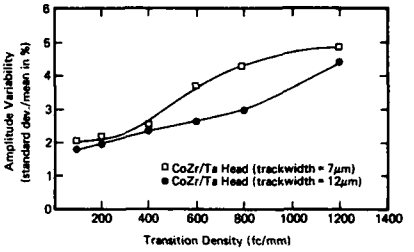


FIG. 4. Readback signal amplitude variability vs transition density.

ACKNOWLEDGMENTS

The authors would like to thank H. H. Zappe, B. H. Schechtman, M. L. Williams, C. J. Spector, and T. J. Beaulieu for technical discussions and T. Huang for x-ray diffraction studies.

[1]Y. Shimada and H. Kojima, J. Appl. Phys. **53**, 3156 (1982).
[2]K. Yamada, T. Maruyama, H. Tanaka, H. Kaneko, I. Kagaya, and S. Ito, J. Appl. Phys. **55**, 2233 (1984).
[3]M. Hanozano *et al.*, J. Appl. Phys. **61**, 4157 (1987).
[4]Y. Shimada and H. Kojima, in Proceedings of 1982 Sendai Symposium on Perpendicular Magnetic Recording, Japan (1982), p. 111.
[5]Y. Shimada and N. Saits, Jpn. J. Appl. Phys. **25**, 419 (1986).
[6]J. Lo, C. Hwang, T. Hwang, and R. Campbell, IEEE Trans. Magn. **MAG-23**, 3065 (1987).
[7]R. E. Jones, IEEE Trans. Magn. **MAG-15**, 1619 (1979).
[8]R. F. Soohoo, IEEE Trans. Magn. **MAG-18**, 1128 (1982).
[9]G. S. Mowry, P. K. George, K. M. Loeffler, and N. R. Belk, IEEE Trans. Magn. **MAG-22**, 671 (1986).

CoZrMo amorphous films as a soft adjacent layer for biasing magnetoresistive elements with a current shunt layer

K. Yamada, T. Maruyama, M. Ohmukai, T. Tatsumi, and H. Urai
Microelectronics Research Laboratories, NEC Corporation, Kawasaki 213, Japan

Sputtered $Co_{94-x}Zr_6Mo_x$ ($4.4<x<17$ at. %) films have been investigated as a soft-adjacent-layer (SAL) material for trilayered magnetoresistive (MR) sensors with a MR element layer, a current shunt layer, and a SAL for biasing layer. The saturation magnetization $4\pi M_s$ linearly decreases from 14 to 3 kG with an increase in Mo content. The magnetic anisotropy field H_k decreases to a low value, equivalent to that for NiFe MR films, as the Mo content is increased. The magnetoresistance ratio $\Delta\rho/\rho$ is negative, but sufficiently small, namely one-hundredth of that for NiFe films, while the electrical resistivity ρ, about 140 $\mu\Omega$ cm, is 5.6 times greater than that for NiFe films. The films also have a small magnetostriction coefficient λ_s on the order of 10^{-7}. A 500-Å-thick CoZrMo film with 12 at. % Mo content is selected as the SAL, because a lesser thickness causes an extreme increase in H_k. Higher Mo content degrades the temperature characteristics of the magnetic properties, due to the lower Curie temperature. Trilayered MR sensors, 100 μm in length and 10 μm in width, are fabricated with a 400-Å-thick NiFe MR layer, a 400-Å-thick Ti layer, and a SAL using this CoZrMo film. An excellent biasing level is achieved with a 15-mA sense current on the MR sensors. CoZrMo amorphous films have a superior capability as a SAL material, especially for the trilayered MR sensors.

I. INTRODUCTION

Magnetoresistive (MR) sensors, which detect magnetic signals through the resistance change in ferromagnetic films, such as NiFe films, have been intensively studied as read elements for use in magnetic recording. For improvement in both MR response linearity and sensitivity, MR sensors have to be appropriately biased.

Trilayered MR sensors[1] with a MR element layer, a current shunt layer, and a soft adjacent layer[2-4] (SAL) for the biasing layer are quite attractive, because of their simple structure and easy fabrication. However, some restrictions exist for this SAL, such as a low magnetic anisotropy field H_k equivalent to that for NiFe films and both a low magnetoresistance ratio $\Delta\rho/\rho$ and high electrical resistivity ρ, compared with NiFe films, in order to achieve a sufficient biasing level.

Amorphous CoZrMo films have been found desirable for use as a SAL for trilayered MR sensors. This paper reports in detail on properties for sputtered CoZrMo amorphous films as a SAL material.

II. EXPERIMENT

Amorphous $Co_{94-x}Zr_6Mo_x$ films were deposited by rf sputtering, using a 100-mm-diam pure Co plate and 5×5-mm^2 pure Zr and Mo chips. After the chamber was evacuated to less than 3×10^{-7} Torr, CoZrMo films were sputtered in 5×10^{-3} Torr Ar atmosphere, where rf power density was 7.5 W/cm^2. The film composition was controlled by changing the number of Mo chips and determined with an electron probe microanalyzer.

Magnetic properties were examined after 1-h annealing at 250 °C in a 480-Oe unidirectional magnetic field for magnetic anisotropy formation, because as-deposited films showed a typical rotatable anisotropy. The saturation magnetization $4\pi M_s$, anisotropy field H_k, coercive force H_c, and Curie temperature T_C were measured by a vibrating-sample magnetometer. The relative permeability μ was measured by an apparatus[5] with a figure-8 coil configuration. The saturation magnetostriction coefficient λ_s was estimated through the H_k change caused by applying stress to the films. The magnetoresistance $\Delta\rho$ and electrical resistivity ρ measurements were performed, using a dc bridge technique and a four-probe method, respectively, for the films ion-etched into a 50-μm-wide and 10-mm-long stripe pattern. The films were confirmed to be amorphous, in the investigated Mo content region, by an x-ray diffraction method.

III. RESULTS AND DISCUSSION

A. $Co_{94-x}Zr_6Mo_x$ film properties

The $4\pi M_s$ at room temperature is shown in Fig. 1 as a function of Mo content. With increasing Mo content, up to 17 at. %, $4\pi M_s$ decreases linearly from 14 to 3 kG, while H_c is almost constant at around 0.02 Oe in the same Mo content range. It is technically important that the $4\pi M_s$ values, cov-

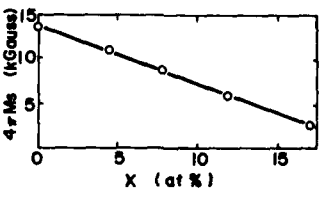


FIG. 1. Saturation magnetization $4\pi M_s$ at room temperature as a function of Mo content for $Co_{94-x}Zr_6Mo_x$ films.

 0021-8979/88/084023-03$02.40 © 1988 American Institute of Physics

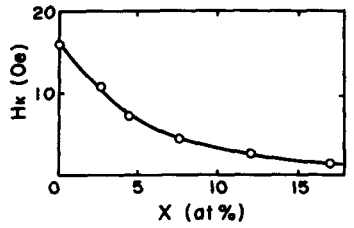


FIG. 2. Magnetic anisotropy field H_k as a function of Mo content for 1-μm-thick $Co_{94-x}Zr_6Mo_x$ films.

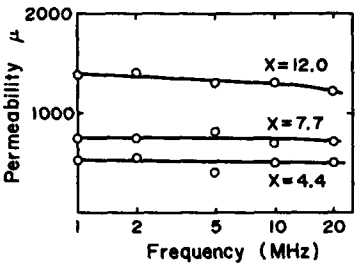


FIG. 4. Frequency characteristics of permeability μ for 1-μm-thick $Co_{94-x}Zr_6Mo_x$ films.

ering a wide range, are easily obtained by pertinent control of the Mo concentration.

Figure 2 illustrates the concentration dependence on Mo content of the H_k for 1-μm-thick films. With an increase in Mo content, H_k decreases. At more than 4.4 at. % Mo content, low H_k values are easily achieved, without weakening their magnetic anisotropy by a rotating magnetic field annealing.

The electrical resistivity ρ is approximately 140 $\mu\Omega$ cm over the investigated Mo content. The total amounts of both Co and Mo are unchanged in $Co_{94-x}Zr_6Mo_x$ system. Bulk Co and Mo have almost the same ρ values, 5.8 and 5.3 $\mu\Omega$ cm, respectively. Thus, it is reasonable that the ρ value for the films remains almost constant, independent of the Mo content. The high ρ value, on the order of 10^2 $\mu\Omega$ cm, is due to the amorphous film structure.

The magnetoresistance ratio $\Delta\rho/\rho$ at room temperature is shown in Fig. 3 as a function of Mo content. $Co_{94-x}Zr_6Mo_x$ films with more than 4.4 at. % Mo content show negative but small $\Delta\rho/\rho$ values, changing from -0.012% to -0.028% with increasing Mo content, whereas non-Mo films, namely $Co_{94}Zr_6$ films, have positive $\Delta\rho/\rho$ values. The negative $\Delta\rho$ is very rare in ferromagnetic films, because most 3*d* ferromagnetic alloys have a positive $\Delta\rho$ value at room temperature.

The permeability-versus-frequency characteristics are adequately flat, up to 20 MHz, as shown in Fig. 4. These flat characteristics are attributed to the decreasing eddy current losses due to the high resistivity for the films. A higher μ value is obtained for films with higher Mo content, because the H_k decrease for these films is greater than the decrease in $4\pi M_s$.

Figure 5 represents the concentration dependence on Mo content of the λ_s. As the Mo content increases to 4.4 at. %, λ_s decreases gradually from $+2.6\times10^{-6}$ to $+4.9\times10^{-7}$. With a further increase in Mo content, λ_s shows a negative but small value, on the order of 10^{-7} after crossing zero at around $x = 7.5$ at. %.

B. CoZrMo film adaptability as a SAL

The SAL material is required to have small $\Delta\rho/\rho$ values and high ρ values, as well as soft magnetic properties equivalent to those for NiFe MR films. $Co_{94-x}Zr_6Mo_x$ films, with more than 4.4 at. % Mo, have sufficiently small $\Delta\rho/\rho$ values, namely one-hundredth that for NiFe films. The ρ value for the films, about 140 $\mu\Omega$ cm, is 5.6 times greater than that for nonmagnetostrictive NiFe films. Using CoZrMo films as a SAL, the current through a SAL is suppressed to a lower value compared with the current through a MR element layer. The MR response from a SAL is neglected due to sufficiently small $\Delta\rho/\rho$ values.

The magnetic properties for films having a low T_C are apt to become worse, due to Joule heating with sense currents. The Curie temperature T_C for films with 17 at. % Mo content is measured as 120 °C, while T_C values higher than 360 °C are obtained for Mo content less than 12 at. %. Therefore, 12-at. % Mo content films, namely $Co_{82}Zr_6Mo_{12}$ films, are selected as SAL material.

Amorphous CoZrMo films 1 μm thick have good soft

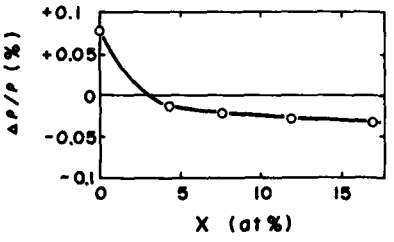


FIG. 3. Anisotropic magnetoresistance ratio $\Delta\rho/\rho$ at room temperature as a function of Mo content for $Co_{94-x}Zr_6Mo_x$ films.

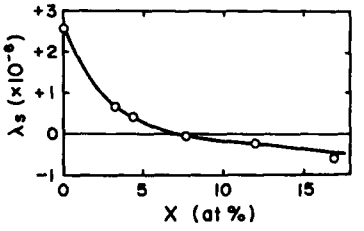


FIG. 5. Saturation magnetostriction coefficient λ_s as a function of Mo content for $Co_{94-x}Zr_6Mo_x$ films.

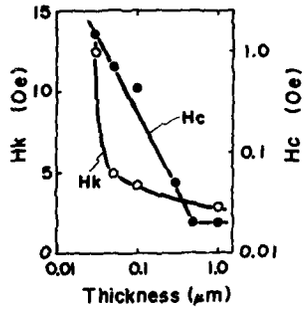


FIG. 6. Thickness dependence of magnetic anisotropy field H_k and coercive force H_c for $Co_{82}Zr_6Mo_{12}$ films.

magnetic properties, such as low H_k and H_c. However, these values are greatly influenced by film thickness. Figure 6 represents the thickness dependence of H_k and H_c values for $Co_{82}Zr_6Mo_{12}$ films. Both values increase rapidly as the film becomes thinner. For 500-Å-thick films, H_c and H_k values are 0.8 and 5 Oe, respectively. These values are almost the same as those for 400-Å-thick NiFe MR films. In addition, a small λ_s value, on the order of 10^{-7}, ensures stability of magnetic properties for films during the fabrication process.

In order to investigate the performance of amorphous CoZrMo films as a SAL, 10-μm-wide and 100-μm-long trilayered MR sensors were fabricated with a 400-Å-thick $Ni_{81}Fe_{19}$ MR element layer, a 400-Å-thick Ti layer, and a SAL using 500-Å-thick $Co_{82}Zr_6Mo_{12}$ films.

Figure 7 shows a typical MR response for the trilayered MR sensors with a 15-mA sense current, where an external field is applied perpendicular to the MR stripe pattern. No Barkhausen noise is observed for the MR characteristics, and a sufficient biasing level is achieved for the MR sensors, where the resistance ratio $\Delta R/R$ for the sensor itself is approximately 1.45%.

The thermal stability of the SAL material anisotropy is an important parameter for the sensor in operation. After a 100-h annealing at 150 °C in a 480-Oe field perpendicular to the easy axis, there is no H_k change for the films preannealed at 250 °C in a 480-Oe unidirectional field. Therefore, CoZrMo films exhibit suitable thermal stability for use as a SAL.

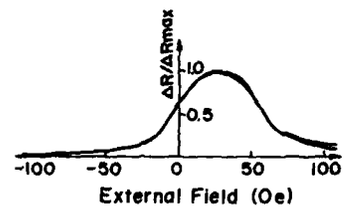


FIG. 7. Typical MR response for trilayered MR sensors using 500-Å-thick $Co_{82}Zr_6Mo_{12}$ films as a SAL.

IV. CONCLUSION

Amorphous $Co_{94-x}Zr_6Mo_x$ films were prepared by rf sputtering. Their properties were examined for use as a soft adjacent layer (SAL) material for trilayered MR sensors. With increasing Mo content, H_k decreases to a value equivalent to that for NiFe films. The films also have both sufficiently small $\Delta\rho/\rho$ value and high ρ value for use as SAL, as well as a small λ_s value.

A 500-Å-thick CoZrMo film with 12 at. % Mo content is preferable as the SAL, because a lesser thickness causes an extreme increase in H_k. Higher Mo content films have lower Curie temperatures T_C.

By using $Co_{82}Zr_6Mo_{12}$ films as a SAL, an excellent biasing level is achieved on the trilayered MR sensors with a 400-Å-thick MR layer, a 400-Å-thick Ti layer, and a 500-Å SAL. It is concluded that sputtered CoZrMo amorphous films have a superior capability for use as a SAL material for trilayered MR sensors.

ACKNOWLEDGMENTS

The authors would like to thank Dr. S. Esho and Mr. S. Ito for their guidance and encouragement. They wish to thank Mr. N. Hayama for useful discussion on MR sensors.

[1]T. Maruyama, K. Yamada, H. Tanaka, S. Ito, H. Urai, and H. Kaneko, IEEE Trans. Magn. MAG-23, 2503 (1987).
[2]D. Voegeli, U. S. Patent No. 3 860 965 (Jan. 1975).
[3]F. Jeffers, J. Freeman, R. Toussaint, N. Smith, D. Wachenschwanz, S. Shtrikman, and W. Doyle, IEEE Trans. Magn. MAG-21, 1563 (1985).
[4]C. Tsang, J. Appl. Phys. 55, 2226 (1982).
[5]P. A. Calcagno and D. A. Thompson, Rev. Sci. Instrum. 46, 904 (1975).

The track-edge bias profile in shunt-biased magnetoresistive heads

D. E. Heim
IBM Magnetic Recording Institute, IBM Corporation, San Jose, California 95193

We present a micromagnetic calculation of the variation in bias angle near the track edge in shunt-biased magnetoresistive heads. This track-edge bias profile shapes the head response at the track edge and hence determines the minimum track spacing based on considerations of adjacent track crosstalk. Our results show that the width of the bias profile at track edge can be substantial and that conditions for minimizing it conflict with those which maximize signal amplitude.

INTRODUCTION

The ideal magnetoresistive MR head for high-track-density applications should have a sensitivity profile which falls to zero as abruptly as possible at the edge of the track. This minimizes adjacent track crosstalk, permitting a minimum spacing between tracks. The sharpness of this profile in real heads, hence the ultimate track resolution, is limited by the magnetics at the track edge. An important part of this is the magnetic state of the MR sensor, and we examine this in a head of shunt-biased type.[1]

The geometry of the head is shown in Fig. 1. The sense current flowing in the MR and shunt films is confined by the leads to an active region defining the track width, the left edge of which is at $z=0$. The structure is placed between two highly permeable shields. The sense current biases the MR element such that the magnetization in the MR film is at an angle $\theta_b(y,z)$ relative to the direction of current flow.

During reading, a transition in the recording medium induces an increment, $\Delta M_y(y,z)$ in the y component of the MR magnetization. The resultant local change in the MR resistivity, from which the sensitivity profile is determined, is[2]

$$\Delta\rho(y,z) = 2\delta\rho \sin\theta_b(y,z)\,[\Delta M_y(y,z)/M_s]\,. \qquad (1)$$

Although other factors also influence the shape of the track profile, e.g., a finite flying height which enters Eq. (1) in via $\Delta M_y(y,z)$, one sees from the proportionality to $\sin\theta_b$ that the distribution of bias angle plays a co-equal role in Eq. (1). As a function of z, $\sin\theta_b(y,z)$ is expected to be zero far outside the active region, where the current is zero, and to increase over some interval near $z=0$ to a final value inside the active region. We present here a calculation of this bias profile.

The bias angle depends in general on both y and z. Previous work in the infinite track width limit[1] shows that at the top and bottom edges of the MR film θ_b increases from zero to the final bias angle with a characteristic length λ. In many applications the stripe height H is sufficiently large relative to λ that the influence of the finite height on the bias angle at the center of the element, $y=H/2$, is small. For these devices the finite stripe height plays no essential role in determining the bias profile at mid-stripe-height, and we may simply consider the infinite stripe-height limit. In the regime of small MR heights, $H<\lambda$, however, the influence of the top and bottom edges is felt over the whole of the element, and the fully three-dimensional situation must be confronted.

INFINITE STRIPE-HEIGHT LIMIT

In the limit of infinite stripe height, θ_b has only a z dependence and represents the bias profile at midheight, $y=H/2$, in Fig. 1(a). The relevant cross-sectional geometry is shown in Fig. 1(b). For high-conductivity leads the current enters the sensor films near $z=0$ in Fig. 1(b). The linear current densities, J_{MR} and J_{SH}, in the two films and the lead current give rise to the applied field biasing the MR element. The distribution of this field is complex near $z=0$ and is highly dependent on the specific geometry of the MR/lead junction. In order to study the basic aspects of track-edge biasing we idealize this field as follows. We assume that the y component of the applied field increases abruptly at $z=0$ from zero to its final value, H_y. The solution of Maxwell's equations for H_y at the center of the MR film is straightforward and yields (mks units)

$$H_y = \frac{J_{MR}(g_1-g_2)+J_{SH}(t_{MR}+2g_1)}{2(t_{MR}+g_1+g_2)}\,. \qquad (2)$$

The z component of the applied field, which is limited to an interval near $z=0$, is neglected. Its effect on our results will be discussed at the end.

To obtain the bias profile $\theta_b(z)$ we resort to a micromagnetic calculation in which the total energy is minimized

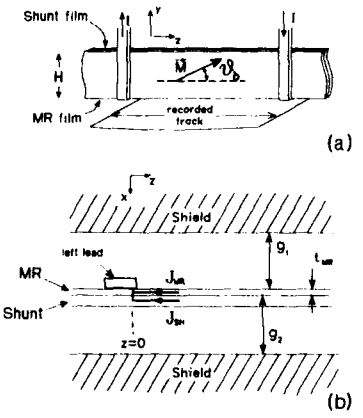


FIG. 1. Geometry of shunt biasing. (a) shows the head positioned over the recorded track with the shields removed. (b) is a cross section in the x-z plane showing the element and shields near the left lead in (a).

 0021-8979/88/084026-03$02.40 © 1988 American Institute of Physics

with respect to variations in $\theta_b(z)$. In our geometry the MR film is tightly coupled magnetostatically to the adjacent shields, similar to the situation considered by Slonczewski in studying domain walls in coupled magnetic films.[3] We simply adapt his theory to the particular circumstances of the MR head.

The total energy density per unit area in the y-z plane takes the following normalized form:

$$E_T(z) = \frac{t_{MR} M_s H_k}{2} \left\{ \sin^2\theta - 2\beta \sin\theta + \left(\frac{d\cos\theta}{ds}\right)^2 + \gamma\left[\left(\frac{d\cos\theta}{ds}\right)^2 + \left(\frac{d\theta}{ds}\right)^2\right]\right\}. \quad (3)$$

M_s, H_k, and t_{MR} are the saturation moment, anisotropy field, and thickness of the MR film. The normalized quantities in Eq. (3) are $s = z/\lambda$ where

$$\lambda = \sqrt{\frac{4\pi M_s t_{MR}}{H_k}\left(\frac{g_1 g_2}{g_1 + g_2}\right)} \quad (4)$$

and

$$\beta = \begin{cases} 0, & z<0 \\ H_y/H_k, & z>0, \end{cases} \quad (5)$$

$$\gamma = 2(A/M_s H_k \lambda^2). \quad (6)$$

The first term in Eq. (3) is the energy associated with a uniaxial anisotropy assumed oriented in the z direction. The second term is the Zeeman energy. The third term is the demagnetization energy arising from the magnetic charge density $\rho = -d(M_s \cos\theta)/dz$ in the MR film. Following Slonczewski, this charge appears as a surface charge density on the outer surfaces of the film as a consequence of a very small canting of the magnetization out of the plane of the film (adding negligibly to the anisotropy energy). The surface charge density is then assumed to be imaged perfectly in the shields, giving rise to a demagnetization field configuration between the MR film and the shields nearly perpendicular to the plane of the structure. The splitting of the charges between the two surfaces of the MR film and resulting expression for the demagnetization energy are derived in the Appendix.

The last term in Eq. (3) is the exchange energy of the MR film. The first contribution to the exchange energy arises from the canting of the magnetization out of the plane of the MR film, while the second is the customary form associated with in-plane rotation. The parameter A appearing in the definition of γ is the exchange constant and equals 1×10^{-6} erg/cm in 80/20 Permalloy.

The length λ is seen to be the same as the flux decay length found in "transmission line models"[4] and appears in discussions of the y dependence of θ_b.[1] Although λ normalizes the z coordinate we will see that it is not necessarily the width of the track-edge bias profile.

THE TRACK-EDGE BIAS PROFILE

$\theta_b(z)$ is the solution of the Euler–Lagrange equation which results from minimizing the total energy $\int dz\, E_T(z)$. In the two domains $z>0$ and $z<0$, it has a first integral which may in turn be integrated subject to the boundary conditions at $s = \pm\infty$. At $s = -\infty$ we set θ and $d\theta/ds$ equal to zero. β is the ratio of the hard-axis field to the MR anisotropy field so that the appropriate condition at $s = +\infty$ is $\sin\theta = \min(\beta, 1)$ and $d\theta/ds = 0$. The solutions for $s<0$ and $s>0$ are matched at $s=0$ by requiring continuity in θ and $d\theta/ds$.

The solution of technological interest is for $\beta<1$, i.e., prior to hard-axis saturation of the MR element. When $\gamma = 0$, it takes the following form in terms of s as a function of $u \equiv \sin\theta$. For $s>0$,

$$s = -\sin^{-1}u + \sin^{-1}(\beta/2) - \beta/(1-\beta^2)^{1/2} \times \ln\left(\frac{\frac{\beta}{2}\left[1-\beta u - \sqrt{(1-\beta^2)(1-u^2)}\right]}{(\beta-u)\left[1-\frac{\beta^2}{2} - \sqrt{(1-\beta^2)\left(1-\frac{\beta^2}{4}\right)}\right]}\right). \quad (7)$$

For $-\sin^{-1}(\beta/2) < s < 0$,

$$u = \sin[s + \sin^{-1}(\beta/2)], \quad (8)$$

while $u = 0$ for $s < -\sin^{-1}(\beta/2)$. The solution obtained numerically for a physically relevant value of $\gamma > 0$ is seen in Fig. 2 to differ inconsequentially from the zero exchange solution.

The solution for the track-edge bias profile is plotted in Fig. 2 with β as a parameter. As expected one sees that the bias is established over an interval at the track edge centered at $s=0$ where the current enters the structure. The quantity $\sin\theta_b$ at the electrical track edge at $s=0$ takes the value $\beta/2$ (for $\beta<1$), one-half the final asymptotic value. Additionally $\sin\theta_b$ goes to zero at $s = -\sin^{-1}\beta/2$ for the zero exchange solution. An important property of the bias profiles in Fig. 2 is that the solutions for the various values of β are not simply versions of universal curve rescaled with β, and indeed one sees a strong dependence on β of the interval at the track edge over which the bias builds to its final value. To quantify this we define the bias edge width, W_E, as the distance over which the bias angle changes from 10% to 90% of its final value. This is plotted, normalized to the scaling length λ, as a function of β in Fig. 3. Remembering that λ is typically greater than 1 μm one sees the possibility of degraded edge widths at the larger values of β.

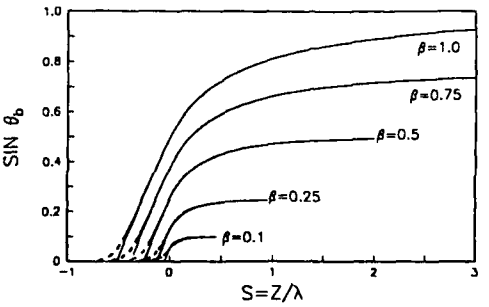


FIG. 2. Track-edge bias profile, $\sin\theta_b$, vs $s = z/\lambda$ with β as a parameter. The solid curves are the zero exchange solution. The dashed curves show the solution for $\gamma = 0.005$ which corresponds to a 200-Å film of 80/20 NiFe and gaps $g_1 = g_2 = 0.5$ μm.

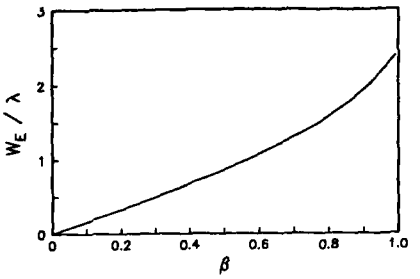


FIG. 3. Edge width W_E vs β for the zero exchange solution. For nonzero exchange W_E approaches a small but finite value at $\beta = 0$. W_E is the distance over which sin θ increases from 10% to 90% of its final value.

The edge width W_E can be minimized by choosing a small value of β. However, since β is the final value of sin θ_b, one sees from Eq. (1) that the signal amplitude is optimized by large values of β, in conflict with the optimum choice of β for track definition. Also, as the track width is reduced, at some point the track-edge bias profiles from the two track edges overlap at the track center, lowering the bias level there and reducing the head sensitivity. This occurs earliest if β is large and is another facet of the trade-off between signal amplitude and track profile.

In addition to the above, the linearity of MR devices depends on bias angle and hence on β. Optimum design from a standpoint of overall performance will therefore include this consideration in the choice of bias level.

The effect of the neglected z component of the applied field, depending on its sign, is to increase or decrease the bias angle at $z = 0$. However, away from $z = 0$ where this component is zero, the bias angle evolves according to the same Euler–Lagrange equation whose solution was just discussed. Thus while we expect the z component to modify the detailed shape of the bias profile, we expect the conclusions obtained above to still hold, i.e., we expect an edge width comparable to that found above with a strong dependence on β and with the same dependencies on the geometrical parameters through λ.

Finally, the finite edge width, W_E, is the result of magnetic charges in the MR film, built up at the track edge with the establishment of the bias, whose sign is such as to generate a z-directed demagnetizing field, suppressing the bias angle. Although discussed here in the context of shunt biasing, the same considerations should apply to the track-edge bias profiles in other MR biasing methods.

ACKNOWLEDGMENT

It is a pleasure to acknowledge discussions with J. C. Slonczewski on his work.

APPENDIX

Denote the demagnetizing field $\mathbf{H}_D$ between the MR film and upper and lower shields by $H_{1,x}(z)$ and $H_{2,x}(z)$, respectively. Following Slonczewski,[3] we assume that it takes a parallel-plate-capacitor configuration. Gauss's law applied to an infinitesimal volume centered on the MR film implies $H_{1,x} - H_{2,x} = 4\pi t_{MR} d(M_s \cos\theta)/dz$. Ampere's law applied around a rectangular contour in the $x - y$ plane going from shield to shield across the gap and linking infinity via the inner shield surfaces gives $g_1 H_{1,x} + g_2 H_{2,x} = 0$. These two conditions determine $H_{1,x}$ and $H_{2,x}$ in terms of θ from which the expression for the demagnetizing energy $E_D = (1/8\pi)\int d^3r |\mathbf{H}_D|^2$, the third term in Eq. (3), may be derived.

[1]F. Shelledy and G. Brock, IEEE Trans. Magn. MAG-11, 1206 (1975).
[2]R. I. Potter, IEEE Trans. Magn. MAG-10, 502 (1975).
[3]J. C. Slonczewski, J. Appl. Phys. 37, 1268 (1966); IBM J. Res. Dev. 10, 377 (1966).
[4]D. A. Thompson, AIP Conf. Proc. 24, 528 (1974).

Behavior of thin-film magnetic recording heads and their application to micromagnetics (invited)

I. R. Walker[a] and A. S. Arrott
Physics Department, Simon Fraser University, Burnaby, British Columbia V5A 1S6, Canada

The ac response at frequencies to 50 MHz of two thin-film magnetic recording heads placed in mirror symmetry with respect to one another is measured as a function of relative position and applied dc fields. One driven head can be used to sense the presence of a second head even when the second head is not driven. An array of wires with current in alternating directions from wire to wire is used to obtain the absolute response of thin-film heads. The efficiency of a head is found to be about 2/3.

INTRODUCTION

The size scale of most interest in the study of the technical aspects of ferromagnetism is from 10 nm to 10 μm, for these are distances over which substantial changes in the direction of magnetization occur. This scale is the domain of the study of micromagnetics. The magnetic recording industry has pursued ever smaller devices to store and retrieve information on magnetic disks at ever higher densities. Thin-film heads are an important element in this pursuit.[1,2] The dimensions of their active pole faces are about 2×20 μm.[2] This enters the range of interest in micromagnetics. The purpose of the research reported here is to explore the possibilities of using commercially produced thin-film-magnetic recording heads for the study of micromagnetics. The thin-film heads were obtained through the courtesy of the Cybernex Corporation and IBM Canada.

The thin-film heads were studied by measuring their response to one another and to especially fabricated arrays of fine current-carrying wires. Phase-sensitive detection and signal averaging techniques were employed to extract the low-level signals in these experiments. Optical interferometry was used to measure the position of the heads.

A schematic presentation of two heads talking to one another is shown in Fig. 1. Conveniently, these devices are manufactured so that each slider has two heads. They can be coupled with mirror symmetry, just as they sit when reading two sides of the same disk. The head in Fig. 1 corresponds to the Cybernex design, containing a center tap on the coil. This helps in the application of heads as susceptometers, described below. The basis problem in using heads is that to be effective they must be close, at least within several micrometers, to whatever is to be measured. This calls for accurate positioning and the avoidance of dust particles.

The flux gathering capacity of the coils is large compared to that of the pole tips. The areas of the coils and the pole tips are in the ratio of 5000 to 1. In micromagnetic applications this can result in weak far fields producing most of the signal unless the tips are sufficiently close to the source of a strong local field. At a 10-μm separation, two heads talk primarily through the coils rather than their pole tips. The experimental arrangement used here permits alignment within 0.1 μm (see below).

[a] Present address: Cavendish Laboratory, University of Cambridge, Madingley Road, Cambridge CB3 0HE, United Kingdom.

APPARATUS

The apparatus used to investigate heads is shown in Figs. 2(a) and 2(b). As pictured, a single head is being used to look at an array of fine Al wires deposited on SiO_2 and Si, mounted on a chip carrier (18). The position of the head is monitored with an interferometer, one element of which is a mirror mounted on the head itself and another is a stationary mirror (15). The head is on the leaf spring suspension (17) designed for disk operation. Because it is relatively free to position itself on the surface of contact, the attitude adjustments can be unsophisticated (16). The lens (13) serves to focus the light from a 1-mW linearly polarized He-Ne laser, leaving the interferometer beam splitter (14), onto a phototransistor mounted some distance from the apparatus.

The head assembly is mounted on a thin walled tube (3) supported by pleated brass diaphragms (10) and attached to small (7.6 cm diam) 30-W loudspeakers (1) with their hermetic seals perforated for stability against atmospheric pressure changes. The loudspeakers are cantilevered (2) far from the pair of magnet coils (4) used for the study of micromagnetics and to investigate the effect of applied dc fields on the heads themselves. A freely suspended head moves about

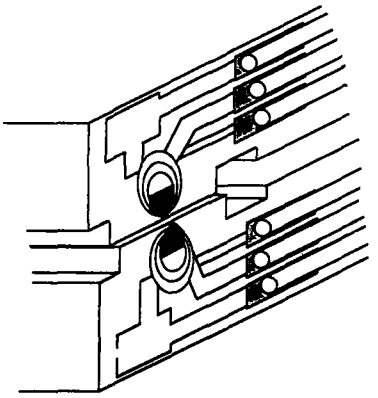


FIG. 1. Two Cybernex heads aligned to measure the cross coupling as a function of the distance between the heads along the direction of the slider (left to right).

 0021-8979/88/084029-04$02.40 © 1988 American Institute of Physics

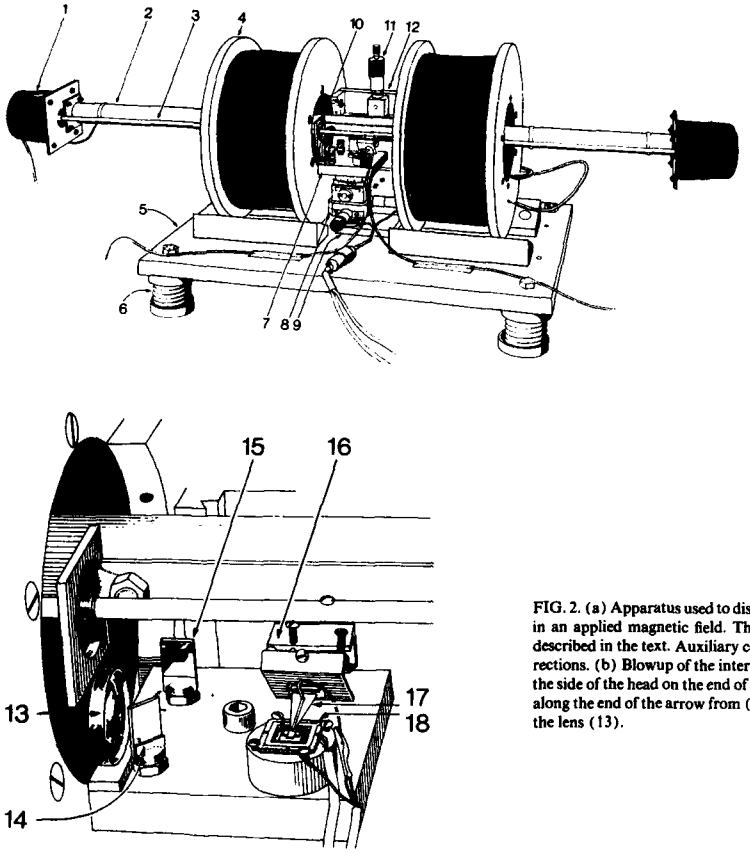


FIG. 2. (a) Apparatus used to displace one head with respect to a test object in an applied magnetic field. The components indicated by numbers are described in the text. Auxiliary coils, not shown, provide fields in other directions. (b) Blowup of the interferometer with a small mirror attached to the side of the head on the end of the leaf spring (17). The laser light enters along the end of the arrow from (14) to the beam splitter and exits through the lens (13).

0.2 μm when the field is ramped from 0 to 80 G. Vibration isolation is obtained by supporting the base plate (5) on springs (6) that give an overall response at 2.8 Hz. The apparatus can be covered to minimize effects of air circulation. The test sample is positioned laterally using the slides on a motor-driven goniometer (8). The sample and interferometer are mounted on a plate (7) attached to the goniometer. Plate (9) supports the assembly which is moved in the vertical by a micrometer (11) attached through plate (12) to the magnet coils.

As the head has considerable freedom with respect to the loudspeakers that drives it, a uniform and low friction lubricant between the head and the test object is important. The low viscosity diester oil, Nye Synthetic Oil 223, manufactured by the William F. Nye Company, worked very well as judged by the very smooth response of the interferometer when the current passing through the loudspeakers was given a linear ramp. The oil was passed through a 0.45-μm filter before leaving the factory. The degree of approach of the thin-film head to an oil-covered substrate was studied using a glass slide with a quartz coating. The head is rocked onto the quartz to squeeze out all but a thin film of the oil. The interference pattern vanishes as the oil leaves, indicating an approach that is within 0.1 μm.

TWO HEADS TALKING

The response of pairs of Cybernex heads slid with respect to one another are shown in Fig. 3. The current was about a 2 mA peak at 10 kHz, producing a signal of 4 μV rms for the Cybernex heads, measured using a PAR 124 lock-in amplifier. The same current at 50 kHz produced 5 μV using the IBM heads. The minima on either side of the peak are separated by 7.9 μm for the Cybernex heads and by 6.6 μm for the IBM heads.

The heads can be run through the sliding response to obtain any particular alignment in the plane. The perpendicular spacing was that given by the oil layer. Most studies of the response of the heads were carried out in the fully aligned position. The second and third harmonic responses were down by at least 50 dB.

The magnetization process in heads is primarily one of rotation from an easy axis in the plane but perpendicular to the flux path.[3–6] If a field is applied vertically, that is, along

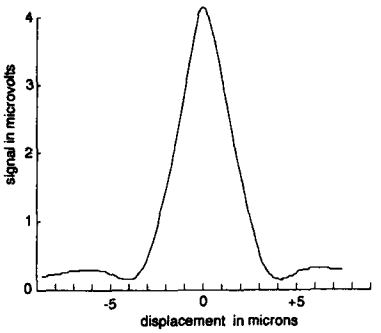


FIG. 3. Voltage induced in the coil of one Cybernex head from an ac signal at 2 mA and 10 kHz in the opposite Cybernex head as illustrated in Fig. 1.

the axis of the flux path, it takes just less than 10 G to drastically reduce the response of the IBM heads and just over 11 G to turn down the response of the Cybernex heads. Figure 4 records how the response of the upper Cybernex head, for an emf of 50 mV rms at 10 kHz applied to the lower head, changes with field applied in the vertical direction using auxiliary coils (not shown in Fig. 1). When the applied field is cycled between $\pm$ 11 G as in Fig. 4, the response differs from cycle to cycle. On a single sweep the coupling between two heads is quite noisy. If the sweep is repeated many times and if the response at each field is averaged over the many sweeps, one finds reproducible features. When averaged over 256 cycles, the structure, as shown in Fig. 4, reproduces precisely from one set of 256 cycles to the next. For small sweeps in field, e.g., $\pm$ 0.5 G, the averaged signal from one set of 256 cycles to the next shows similarities but not true reproducibility. The variations in response are assumed to correspond to Barkhausen-type jumps in closure domain configurations.

A large field (300 G from a hand-held magnet) applied temporarily in the vertical direction produces rather bizarre aftereffects that eventually go away as the head reorganizes itself into a more standard domain configuration.

Very small fields applied in the plane of the thin films and perpendicular to the direction in which it magnetizes by rotation, that is, along the magnetic easy axis, change the response of the head by several percent. Two sets of 512 cycle averages for sweeps between $-$ 12 and $+$ 15 G are shown in Fig. 5. Many, but not all, of the features reproduce. These features do not change appreciably with the frequency of signal coupled between the two heads. These tests were carried out in the range from 10 to 150 kHz.

The response of the heads is primarily by rotation within the domains, but this leads to some wall motion of the closure domains. Presumably the configuration of the closure domains is quite sensitive to the applied fields. For sufficiently large amplitudes for the cycle of applied fields, the closure domains go through essentially the same sequence of configurations. The averaging over many cycles produces an ensemble average of the domain configurations in each field. The variations in any one cycle are greater than or equal to those in the average. From the size of the effects one might judge that about 10% of the ac response depends upon the closure domain configuration.

In previous studies[7] using thin-film heads to measure the fields arising from Fe whiskers, several strange effects were noted. Most of these can be traced to the dependence of the response of the thin-film head to dc bias fields. The thin-film head was successful in mapping out the boundary between the saturated and unsaturated regions of a partially saturated whisker. In that measurement the head was oscillated over the position of the boundary at 50 Hz. It was possible to verify the power law dependence[8] of the size of the saturated region upon the difference of the applied field and the applied field necessary for the onset of saturation.

SUSCEPTOMETER

One Cybernex head was used as a susceptometer to measure the apparent susceptibility of the other head. A 10 MHz current was applied to half of the winding and the voltage at 10 MHz was measured across the other half using a PAR 5202 lock-in amplifier. As this head moved over another

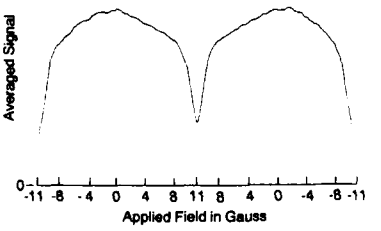


FIG. 4. Turning down the ac coupling between two heads by the application of a field in the plane of the thin films along the axis into which the magnetization rotates. The details of the variations are real and reproducible, corresponding to changes in closure domain wall configurations. This is shown for the Cybernex head. The signal is averaged over 256 field sweeps from $-$ 11 to $+$ 11 to $-$ 11 G.

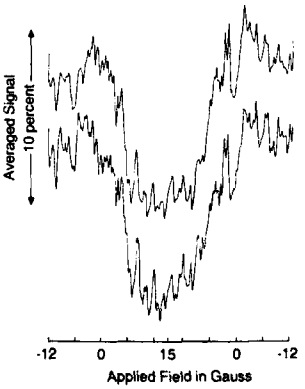


FIG. 5. Effect of an applied field along the easy axis of two Cybernex heads talking to one another. The field is swept 512 times from $-$ 12 to $+$ 15 G. The change in the response is 10% of the total signal. Many details of the response are reproducible from run to run, two of which are shown here.

with no current through its windings, the in-phase voltage decreased by 35%. This demonstrates the possibilities for micromagnetic investigations. Experiments with Fe whiskers have been carried out, but we have yet to see any effects that look like the thin-film head is seeing anything more than the overall susceptibility of the whisker.[9] We would like to be able to interact directly with a domain wall. With two heads one then might transmit a signal along a domain wall from one head to the other.

ABSOLUTE RESPONSE

To obtain some information about the absolute response of the head, we used a grid of wires as illustrated in Fig. 6. Microtel Pacific Research cooperated in the production of the wire grid by plasma etching. The periodicity of the array is 3.97 μm. The wires were 1.77 μm wide and 0.42 μm high. The purpose of the grid is to reduce the effects of far fields coupling directly to the coils. The field from an infinite array of wires conducting in alternating direction from wire to wire falls off exponentially with distance from the wires on the scale of the spacing of the wires. The half period of the variation seen in Fig. 7 matches the spacing of the wires. The background signal is probably the far-field effect from the finite grid used in this measurement. The head slider rides on a layer of quartz deposited beyond the area of the grid. The quartz layer was 1.06 μm thick, measured by a diamond stylus profilometry. The difference of this with respect to the 0.42 μm height of the wire plus the oil film thickness should be the standoff between the pole tips and the grid.

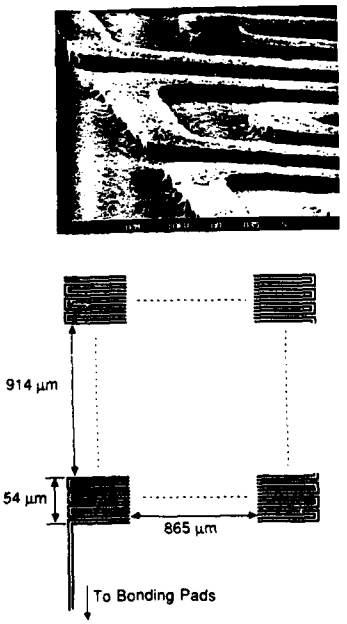


FIG. 6. (a) Schematic of the design of a bifilar grid of fine wires carrying currents in opposite directions in adjacent wires. (A black line represents the wire). (b) SEM picture of a corner of the fabricated array.

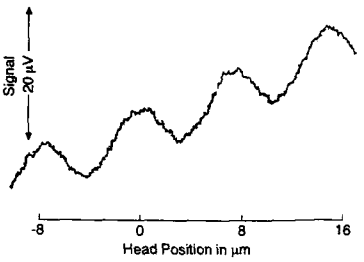


FIG. 7. Voltage generated in a Cybernex head as it moves over the grid of wires, shown in Fig. 6, carrying a current of 1.63 mA rms at 10 kHz. The rising background probably arises from the far fields coupling directly to the detector coils.

This data has been used to measure the efficiency with which flux from the wires can be coupled to the coils of a Cybernex head. We define the efficiency of the head by calculating the unperturbed flux from the source using the dimensions measured by electron microscopy and diamond stylus. The unperturbed flux that would go into one pole face is subtracted from the unperturbed flux that would come out of the other pole face. Half of that value is taken as the next flux intercepted by the head. The fraction of that flux which couples to the coils is measured to be $69 \pm 6\%$. This result matches well the results of Hoyt *et al.*[10-11] on IBM heads.

The original hypothesis of this work was that thin-film heads might prove useful for micromagnetic investigations. The sensitivity of the thin-film head response to small changes in dc fields was not anticipated. This would be a problem if the measurements were made in a changing (in time or in space) field applied over the whole head. A thin-film head may serve as a tool in micromagnetics when used as a susceptometer, where it provides the measuring field itself. A microscopic magnetoresistive probe might be more suitable as a passive measuring device.[12]

[1] F. Jeffers, Proc. IEEE 74, 1540 (1986).
[2] R. W. Wood, Proc. IEEE 74, 1557 (1986).
[3] R. E. Jones, Jr., IEEE Trans. Magn. MAG-15, 1619 (1979).
[4] W. F. Druyvesteyn, L. Postma, and G. Somers, IEEE Trans. Magn. MAG-15, 1613 (1979).
[5] M. E. Re and M. H. Kryder, J. Appl. Phys. 55, 2245 (1984).
[6] B. E. Argyle, B. Petek, and D. A. Herman, Jr., J. Appl. Phys. 61, 4303 (1987).
[7] A. J. van Schyndel, A. Arrott, and T. L. Templeton (unpublished).
[8] T. L. Templeton, A. S. Arrott, and A. Aharoni, J. Appl. Phys. 55, 2189 (1984).
[9] I. R. Walker, MSc. thesis, Simon Fraser University, September 1987.
[10] R. F. Hoyt, J. Appl. Phys. 57, 3947 (1985).
[11] R. F. Hoyt, D. E. Heim, J. S. Best, C. T. Horng, and D. E. Horne, J. Appl. Phys. 55, 2241 (1984).
[12] J. P. J. Groenland and J. H. J. Fluitman, J. Phys. E 14, 503 (1981).

Bloch line influence on wall motion response in thin-film heads

B. E. Argyle, B. Petek, M. E. Re, F. Suits,[a] and D. A. Herman
IBM Research Division, Thomas J. Watson Research Center, Yorktown Heights, New York 10598

We describe a new dynamic response behavior of domain walls in the permalloy of thin-film inductive heads. A laser magneto-optic microscope (LAMOM) which enhances the longitudinal Kerr effect, is used to image Bloch lines (BLs) within the 180° walls by aligning the optical plane of incidence perpendicular to these walls. BLs are visible due to the reversal in the Néel-type surface components of the wall magnetization at the BL position. Current pulses with fast transition times and ac currents within the frequency range of 1–10 MHz are applied to the integrated coil windings. Continuous excitation induces either a continuous flowing of the wall network or a temporary displacement. When individual pulses are applied, displacements of BLs are observed. Correlation of wall displacements with the BL displacements is demonstrated for some pulsed excitations.

INTRODUCTION

The dynamic influence of domain walls on thin film heads has been considered theoretically.[1–4] Due to the complexity of the problem, these theoretical treatments have simplified the real situation; in particular, domain wall structure has not been included in the calculations. Various experimental techniques have been used to observe the domain patterns in thin film heads and the effects these patterns have on the dynamic response of the heads. These include, electron beam[5,6] and optical methods.[7–10] To observe the structure of the Neel-type surface component of the domain walls in the head, Bitter techniques and spin polarized electron analysis[11] have been used. In this paper, the relation of the domain wall response to both pulsed and sinusoidal excitation is correlated with the structure of the domain wall itself in thin-film heads. The experimental results presented here, indicate that complicated wall structure can influence the motion of domain walls in permalloy in thin-film heads.

EXPERIMENT

Our experimental technique involves the laser magneto-optic microscope (LAMOM) (Ref. 8) which provides video detection of longitudinal Kerr magneto-optic contrast and real-time, digital image averaging and subtraction. The optical resolution is limited by the objective numerical aperture (1.0) and the wavelength of light (0.48 μm) from the laser/fiber illuminator.[8(a)]

The wall and Bloch line (BL) displacements were measured starting with a repeatable demagnetized state. Images of displacements are made by digitally subtracting the images made before and after the pulse was applied. Slow rise-time pulses or low-frequency ac excitations produce the well-known rocking motion (not shown) due to the pivoting of the main 180° walls about the center. This is expected from the coil field coupling to the closure domains that terminate the 180° wall at the edge of the yoke and have opposing magnetizations. Rocking and subsequent diminishing of the ac excitation to zero, produces the demagnetized state. In this state the 180° walls usually contain a single BL near the center of the 180° walls.

Responses of the main 180° wall (the one in the yoke area having the greatest length) were investigated in several experimental thin-film heads for various pulse shapes fixed amplitude (40-Oe calculated in-plane field at the yoke center line) and for large amplitude (up to 400 Oe) pulses of 50-ns duration. Results of the 40-Oe pulses are shown in Figs. 1–3. In Fig. 4 a single sharp 50-ns impulse of 320 Oe produced the displacements of three walls present in an apertured yoke region. Response of the main 180° wall was also studied versus frequency and amplitude (Fig. 5) for sinusoidal excitations of 1–10 MHz.

RESULTS AND DISCUSSION

In contrast to the "rocking" motion at slow excitations, we observe different responses to short transition time ("fast") pulses or to high-frequency sinusoidal excitations. The wall network displacement appears to contain little or no rocking or other distortions about the head symmetry axis as exhibited also in the demagnetized state. This wall translation without breaking symmetry is an unexpected effect which allows us to study the possible coupled Bloch-line and wall motion effects and their relation to the head dynamic response.

The responses photographed in Fig. 1 and plotted in Fig. 2 are for consecutive trapezoidal pulses having 300-ns



FIG. 1. LAMOM difference images showing Bloch-line displacements caused by six consecutively applied current pulses. Pulse shape is trapezoidal with 300-ns rise and fall times and 500-ns width producing 40-Oe field at the center line of the head's yoke.

[a] Now at the University of Arizona, Optical Sciences Center, Tucson, AZ.

 0021-8979/88/084033-03$02.40 © 1988 American Institute of Physics

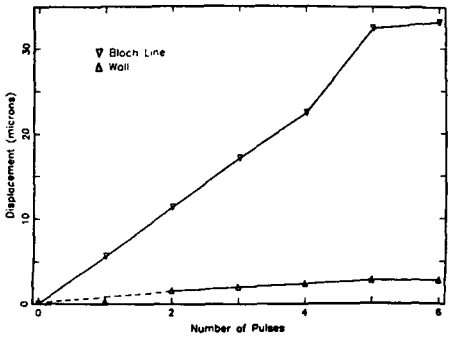


FIG. 2. Bloch line and wall displacements imaged in Fig. 1 after each applied pulse.

transition times, 500-ns width (FWHM), and 40-Oe coil-field amplitude. These results illustrate reproducible displacements of a single BL traveling along a 180° wall. Associated with the net BL motion of 32 μm after six pulses, is a 3-μm displacement of the wall. After six pulses the displacement per pulse decreases, due possibly to an interaction with the nearby intersection with edge closure walls. The bright/dark contrast of the wall (apart from the BL displacement region) photographed in Fig. 1 is explainable by assuming the wall has a surface Néel magnetization component normal to the wall and the wall displacement is approximately the same or slightly less than half a wall width. The area swept out by the BL is the brightest area due to a complete reversal of the Néel component. Reversing the pulse polarity reverses the direction of the BL displacement (not shown), but not (on average) the wall displacement. Thus, the wall displacement direction appears unrelated (in first order) to any residual field acting along the wall as may arise, for example, from some unknown easy axis/coil-field misalignment. Assuming the motion takes place only during the pulse, the average BL velocity is approximately 10 μm/μs in the linear region of Fig. 2. Three times this value has been observed however, under some other pulse conditions. The average

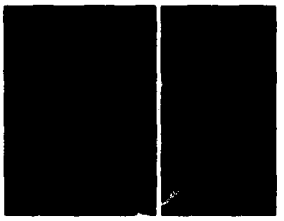


FIG. 4. Difference image showing reference background state (R) and displaced wall positions (D) after a single short pulse (50-ns width, 20-ns transitions) of 320-Oe yoke field is applied. Line scan plot indicates intensity across fixed video scan line as indicated.

cements of a single BL traveling along a 180° wall. Associated with the net BL motion of 32 μm after six pulses, is a 3-μm displacement of the wall. After six pulses the displacement per pulse decreases, due possibly to an interaction with the nearby intersection with edge closure walls. The bright/dark contrast of the wall (apart from the BL displacement region) photographed in Fig. 1 is explainable by assuming the wall has a surface Néel magnetization component normal to the wall and the wall displacement is approximately the same or slightly less than half a wall width. The area swept out by the BL is the brightest area due to a complete reversal of the Néel component. Reversing the pulse polarity reverses the direction of the BL displacement (not shown), but not (on average) the wall displacement. Thus, the wall displacement direction appears unrelated (in first order) to any residual field acting along the wall as may arise, for example, from some unknown easy axis/coil-field misalignment. Assuming the motion takes place only during the pulse, the average BL velocity is approximately 10 μm/μs in the linear region of Fig. 2. Three times this value has been observed however, under some other pulse conditions. The average wall velocity is an order of magnitude smaller. However, no attempt has been made to estimate further the limit on either of these values.

The direction of these dynamic wall displacements is usually away from the pole tip (except for some limited

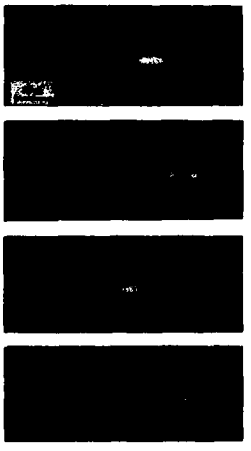


FIG. 3. Wall structure changes occurring for four asymmetric current pulses (fast rise time). Pulse parameters are 20-ns rise time, 300-ns fall time, 300-ns width, and 40-Oe coil field.

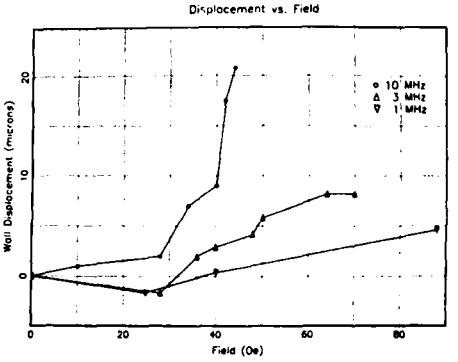


FIG. 5. Displacement of the longest 180° wall in the yoke due to sinusoidal currents at three frequencies plotted vs in-plane field. (Field amplitude has been calculated from the coil turns density and rf current amplitude.)

and Feldkeller[12] and Kusuda *et al.*[13] in unraveling the "wall streaming" and "worming" effects in thin (0.1 μm) permalloy, were also studied. They did not however, improve the statistics for the chaotic process in 3–4 μm-thick films of heads.[14]

Additionally we found that single, "fast" pulses (50-ns duration with 20-ns transition times) of extraordinarily large coil field amplitude (300–400 Oe) and presumably causing an internal field larger than Hk, can produce large displacements of the wall itself, e.g., tens of microns, as shown in Fig. 4. In this figure, there are double images for two of the three walls and a single for the third. The doubly imaged walls (R 1,D 1) and (R 2,D 2) represent their positions before (R = reference) and after (D = displaced) a 300-Oe pulse is applied. The third wall appears as single because it displaced less than twice a wall width. One of the two wall network states (R) is frozen in the background image taken before the pulse is applied; the network arrangement (D) occurring after the pulse has been subtracted, is also visible in the difference image. Thus, the wall position and microstructure (BL position) may both be visible in the difference image whenever either the wall or BL displacements are larger than a wall width or BL width. For the case (not shown) of the largest pulse applied (400 Oe), the displaced wall state was transformed to all, or nearly all, one "color." The opposite color occurred when pulse polarity was reversed. The displacement direction was the same, however. We conclude from the complete color change that the wall structure has undergone a more or less complete transformation. It appears from evidence repeatedly recorded on video tape, that the transformations in wall microstructure are correlated with the large jumps in the wall positions.

The responses shown in Fig. 5 to a spectrum of sinusoidal excitation indicates that the high frequency components are most effective in causing this wall motion. Ten MHz excitation produces tens of microns of wall displacement away from the pole tip region. The low frequency region, at least for low amplitudes, produces motion towards the pole tip. Such contrasting behavior may not be so surprising in view of similar behavior in coupled BL and wall motions as exemplified in the "bubble automotion effect"[15] caused when sinusoidal drive produces bubble translations stemming from coupled circumferential BL and radial wall oscillations.

Unfortunately, there is no complete theory on the wall magnetization microstructure for permalloy films 3–4 μm thick. The computed wall structures of Labonte[16] and of Hubert[17] for 0.1- and 0.1–1.4-μm permalloy, respectively, do, however, possess the Néel-type structure within the surface region (100–200 Å) penetrable with the light waves.

The wall's magnetic structure within the bulk film can only be guessed for thick permalloy at this time. If the computed models scale with thickness, there can be several wall states as in the case of Hubert's stray field free model.[17] The induced motion of "losenge" and "zig-zag" domain walls has been explained by Labrune *et al.*[18] as resulting from increased wall coercivity associated with a mixed phase in the wall during the wall state transition. And similarly, there may in principal exist several types of Bloch line transitions in thick permalloy, each associated with the joining of possible pairs of different internal wall structures. Harrison and Leaver[19] have observed three wall state transitions using transmission electron microscopy on 0.1–0.28-μm-thick films. They presented proposed microstructures for three of the different types of Bloch lines possible. It is certainly premature to imply we may be imaging one or more of these possible cases, although Fig. 3 is quite suggestive.

ACKNOWLEDGMENTS

We are grateful to John Slonczewski, Philip Trouilloud and Al Thiele for valuable discussions.

[1]R. E. Jones, IEEE Trans. Magn. **MAG-15**, 1619 (1979).
[2]R. F. Soohoo, IEEE Trans. Magn. **MAG-18**, 1128 (1982).
[3]M. L. Mallary, J. Appl. Phys. **57**, 3952 (1985).
[4]K. Ohashi, IEEE Trans. Magn. **MAG-21**, 1581 (1985).
[5]P. B. Mee, J. Appl. Phys. **51**, 861 (1980).
[6]O. C. Wells and R. J. Savoy, IEEE Trans. Magn. **MAG-17**, 1253 (1981).
[7]M. E. Re and M. H. Kryder, J. Appl. Phys. **55**, 2245 (1984).
[8]B. E. Argyle, B. Petek, and D. A. Herman, J. Appl. Phys. **61**, 4303 (1987) B. E. Argyle and F. Suits, Digests of 1985 INTERMAG Conference, ab stract No. HC-5.
[9]S. Narishige *et al.*, IEEE Trans. Magn. **MAG-20**, 848 (1984).
[10]P. Kasiraj *et al.*, IEEE Trans. Magn. **MAG-22**, 837 (1986)
[11]H. Matsuyama *et al.*, IEEE Trans. Magn. **MAG-23**, 2173 (1987).
[12]K. U. Stein and E. Feldkeller, J. Appl. Phys. **38**, 4401 (1967).
[13]T. Kusuda, S. Konishi, and Y. Sakurai, IEEE Trans. Magn. **MAG-3**, 286 (1967).
[14]It should be pointed out, however, that the fast pulses of Ref. 12 contained nanosecond transitions whereas in the present case the inductance of film heads limits the transition time to greater than 10–20 ns.
[15]B. E. Argyle and P. Dekker, in International Conference on Magnetic Bubbles, Eindhoven, 1976 (unpublished).
[16]A. E. Labonte, J. Appl. Phys. **40**, 2450 (1969).
[17]A. Hubert, Phys. Status Solidi **32**, 519 (1969).
[18]M. Labrune *et al.*, Magn. Magn. Mater. **58**, 227 (1986).
[19]C. G. Harrison and K. D. Leaver, Phys. Status Solidi **15**, 415 (1973).

Study of field-driven wall-configuration conversions for laminated Permalloy in the easy-axis state

D. A. Herman, Jr., B. E. Argyle, P. L. Trouilloud, B. Petek, L. T. Romankiw, P. C. Andricacos, S. Krongelb, D. L. Rath, D. F. Canaperi, and M. L. Komsa
IBM Research Division, T. J. Watson Research Center, Yorktown Heights, New York 10598

Laminated Permalloy, with edge-curling walls replacing closure domains, has been proposed to increase permeability and reduce wall noise in recording. However, in structures meeting the criteria for Slonczewski's "easy-axis" state, normal walls often coexist with edge-curling walls. We have used our laser magneto-optic microscope to study inductive-head-yoke shaped elements of two and four Permalloy layers separated by nonmagnetic, metallic spacers. In the four-magnetic-layer sample a state with a single wall, terminating at the edge-curling regions and lying along the easy-axis direction, is often observed on the top and bottom layers. Some elements may be driven into an easy-axis state with no observed domain walls. The two-magnetic-layer sample also exhibited simultaneous one-wall structures on the top and bottom layers. The other stable configuration was a no-wall state on the top layer and a two-wall (three-domain) state on the lower layer. These "coupled" states were exceptionally stable in both samples; fields on the order of 300 Oe were required to switch between configurations.

I. INTRODUCTION

Edge-closure domains in thin-film recording devices can lead to wall motion noise, reduced response at high frequencies, and domain configuration instabilities.[1-4] This led some years ago to experiments with laminated soft magnetic films, in which flux closure was expected between the magnetic sheets. Early results were promising—e.g., Feng and Thompson found laminated strips had no closure domains (180° walls were present) and reduced permeability roll off at high frequencies.[4] Lazzari and co-workers produced a thin-film head with laminated legs in 1970.[3] They reported it had no domain walls, and that a two-port consisting of two heads with pole pieces in contact had a 60-MHz bandwidth.

Recently Slonczewski and co-workers presented a theory for laminated, magnetostatically (not exchange) coupled layers (relatively thick-single layers would support Bloch walls).[1] The theory predicts, for certain geometries, an "easy-axis" state. In this state, the magnetization (M) parallels the easy axis in a layer's interior, while flux closure is via a new micromagnetic structure, "the edge-curling wall." Near an edge, M curls both normal to the film planes [for closure in adjacent magnetic layer(s)] and in-plane (to avoid edge poles), leading to the "edge-curling" description. Relating energy to dimensions and material parameters, Slonczewski's theory predicts a given structure will be in this "easy-axis" state, in a "hard-axis" state (M parallels the hard axis), or in a "Bloch-wall" state (walls similar to nonlaminated elements with edge-closure domains).

All three states are seen in practice.[1] However, in the easy-axis case, we have usually observed easy-axis regions separated by 180° walls (without triangular closure domains). Such "domained" easy-axis states are not included in the theory, and this work is an initial experimental effort to understand them. In one sample we have observed what is believed to be a very stable, single-domain, easy-axis state.

II. EXPERIMENT

Samples with two and four layers of near-zero-magnetostriction Permalloy separated by nonmagnetic, metallic spacers were investigated. The two-magnetic-layer sample was plated through a mask with the sputtered seed layer removed by sputter etching in argon. The four-layer elements were shaped by ion milling from a sheet. Magnetic layer thickness was obtained with a Dektak profilometer; spacer thickness was determined from process parameters. Conditions limited accuracy in both cases to about 10%.

Domain-wall configurations and motions were observed with our laser magneto-optic microscope (LAMOM).[5] Samples were observed both on the top surfaces and through their glass substrates. External fields were applied via coils oriented along the x (hard-axis, HA) or y (easy-axis, EA) direction. Digital image processing was performed in real-time (TV frame rate) using a PMI C1966 processor.[5,6]

III. RESULTS AND DISCUSSION

A. Four-magnetic-layer laminate

Results for a four-magnetic-layer element (0.5-μm Permalloy 200-Å spacers) are given in Fig. 1. The images are of wall configurations at zero bias (stable with respect to small perturbing fields). For comparison, the 180° Bloch walls and triangular closure domains typical of an unlaminated yoke are sketched in Fig. 1(a). Two image processing techniques were employed. Figures 1(b) and 1(d) were produced by the Accumulate-Subtract (AS) method. First, with a wall present, 64 frames were added and stored; the element was then driven to single domain. Accumulation was repeated and the difference between summations taken. Remaining figures were obtained by Sequential Subtraction[6] (SS) of

 0021-8979/88/084036-03$02.40 © 1988 American Institute of Physics

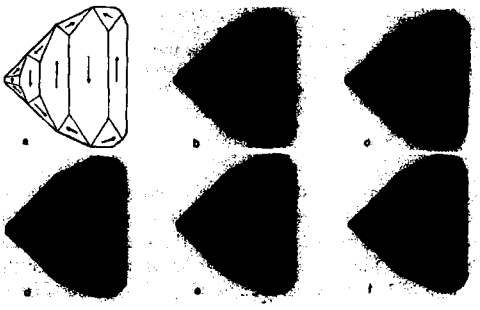


FIG. 1. Wall patterns for an unlaminated element (a) and a four-magnetic-layer laminate (b)–(f). The element's front to back length is approximately 125 μm. The dark line around the border of (e) is charred photoresist residue from ion milling.

frames taken with the wall driven to slightly different locations by a hard-axis (HA) ac external field.

Figures 1(b)–1(e) were obtained from the bottom layer by imaging through the glass substrate. Walls extend from the vicinity of the curling region ($\sim$7 μm wide from theory[1]), with end points and curvature dependent on bias history. Such a "single-wall state" is consistent with the curling region maintaining the same sense of in-plane circulation around the element's edge (opposite in top and bottom layers). Figures 1(c) and 1(d) were obtained in sequence from 1(b) by (twice) applying and removing $\sim$170-Oe HA bias. From 1(b) to 1(d) the wall's center has been displaced $\sim$25 μm. This could be reversed by application of an opposite field of about the same magnitude. Most of the bow seen in 1(b) could be removed without displacing the wall's end points by agitating with an ac HA drive ($\sim$50-Oe peak sufficed). Each of these wall positions was stable in the presence of HA external fields up to $\sim$150 Oe. Here stability means that upon reduction of the perturbing field, the wall's end points remained near their original locations, although wall bow sometimes relaxed. (The pinning of the end points may be due in part to interaction with the edge-curling structure—a topic for future investigation.) The maximum available EA offset field ($\sim$70 Oe) was insufficient to achieve wall displacement in the element shown. Stable wall displacements did result in some other elements on this sample with application of EA offsets of this magnitude. (One such element was checked; its top layer had a number of cracks or scratches. It did not exhibit the coupled no-wall state discussed below.) Figure 1(f) was obtained from the top (film side) layer of the same element when the bottom (interface) layer was in a single-wall state. [The wall in the top layer was sometimes found in the vicinity of the first (left) bend, in which case it often had small triangle closure domains at one or both ends.] Figures 1(b)–1(d) with 1(f) are typical of an indefinite number of coupled (top and bottom layers), locally stable, one-wall states in this element. Wall movements on the top and bottom layers due to EA bias were consistent with a simple symmetric coupling of adjacent layers such as sketched in Fig. 2 (an axial cut through the middle of a sample in an idealized one-wall state).

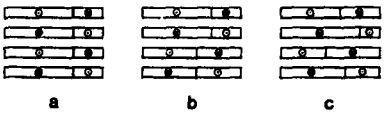


FIG. 2. Domain models for an idealized four-magnetic-layer element in the one-wall coupled state. (a) and (b) show applicable simple layer pairing schemes. (c) derives from (b) with an EA field applied (consistent with observations of the outer layers).

The configuration of Fig. 1(e) was obtained from a one-wall state by applying (and removing) $\sim$300 Oe of HA bias (the top layer also had no visible walls). This structure appears to be mainly a (very stable) single domain; however, it must be cautioned that walls (unobservable by LAMOM) may exist in the sample's inner layers. In a few elements, images obtained by subtracting (AS) no-wall from one-wall states have weak traces, which may indicate the presence of quasi-walls[7] coupled to true walls in inner layers; such traces were not observed in any element exhibiting a coupled no-wall state. (Even if walls do exist on inner layers, devices with walls in only half the magnetic volume may still be attractive from noise and domain stability points of view.) That Fig. 1(e) is an easy-axis state (M vertical) as opposed to a hard-axis state was confirmed by comparing the Kerr-effect signal from (M) rotation in response to EA and HA ac excitation. This no-wall coupled-state remains stable for HA bias fields in excess of 250 Oe and EA fields up to 70 Oe. Transitions between the one- and no-wall states could be consistently effected by applying (and removing) HA 300-Oe fields of opposing polarities. To clarify, note that reapplying the same polarity HA field left the element's state unchanged. In finite samples, paired rotation discontinuities must occur in the curling-edge wall of a no-wall state. Occasional video frames show structure, possibly associated with these discontinuities, near the angles at top and bottom of the elements. This remains to be properly investigated.

Conversion between coupled states was observed in real time (video frame rate). Figure 3 shows several transients seen during the transition from a one-wall to a no-wall state. These interim states (with field applied) show first the penetration of a spear of opposing magnetization in the front domain [Fig. 3(a)], then the linking of walls in a snakelike formation [Fig. 3(b)] reminiscent of that for domain insta-

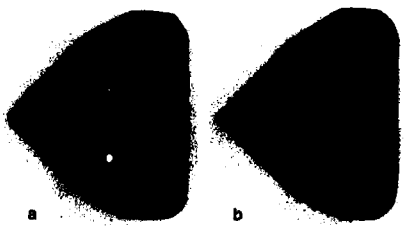


FIG. 3. Transients observed during a one-wall to no-wall state conversion in a four-magnetic-layer element.

bilities in nonlaminated Permalloy yokes.[8] At ~300 Oe, a single domain with strong magnetization vector rotation is seen; upon reduction of the biasing field, rotation disappears and a no-wall state emerges. Application of 300 Oe in the opposite direction yields a single domain with the opposite rotational contrast; upon field reduction, a wall emerges from the back of the yoke, and the one-wall state stabilizes.

In contrast to unlaminated Permalloy samples, in which walls can usually be imaged by displacing them with a few Oe ac drive, laminated walls were rather hard to move. Drive fields (HA ac) of ~50 Oe were required to get movements on the order of a few μm. In general, wall configurations were much more stable in the laminated samples. When wall motion is observed, one is struck by the smooth, fluid nature of the motion in comparison with the rocking action of configurations in unlaminated elements. Some of the elements had rough, apparently cracked top surfaces. Even in these elements, walls seemed to move smoothly over defects without hanging up as seen in unlaminated samples.

B. Two-magnetic-layer laminate

Results for a two-magnetic-layer laminate (1-μm Permalloy, 180-Å spacers) are shown in Fig. 4. The element displays two stable coupled states. When the bottom layer was in a one-wall state [Fig. 4(a)], the upper layer was likewise in a one-wall state. The bottom layer was also stable in a two-wall state [Fig. 4(b)], with a central sliver of magnetization opposing the surrounding domains; this was accompanied by a no-wall state in the top layer. The element could be reliably switched between these coupled states by applying and removing opposing ~300-Oe HA fields.

An explanation for the difference between the coupled states of four-layer elements (Figs. 1 and 2) and those of the two-layer elements (Fig. 4) may lie in the degree of layer thickness and/or composition mismatch. [Some four-layer elements also exhibited two-wall configurations similar to Fig. 4(b).] When not so extreme as to take a laminated element out of the easy-axis state (into a HA or Bloch-wall state), thickness (composition) mismatch could still prevent all flux from a thicker (or higher M_s) layer from being returned through its paired layer, forcing in-plane closure via opposing domains, possibly even requiring triangle closure domains in some areas. (The symmetry of wall patterns at the top and bottom of the yoke along with the difference between layers indicates the effect is probably not due to plating mask misalignment.) Models for the two coupled states deriving from (exaggerated) thickness mismatch are sketched in Fig. 5. The width of the sliver domain in the bottom of the two-layer sample [Fig. 4(b)] undoubtedly relates to the mismatch, but probably not simply, as sufficient wall coercivity is observed to question whether the sample is truly demagnetized. An experiment in which the outer layers could be observed simultaneously (we had to flip our samples over) would be very useful. Top and bottom configurational hysteresis, referenced to the driving field, would clarify the issues.

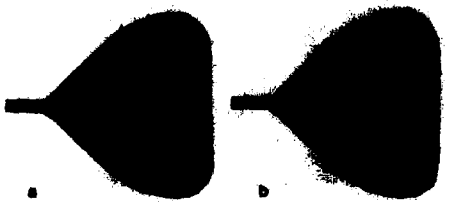


FIG. 4. Wall states in a two-layer laminate.

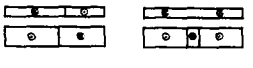


FIG. 5. Domain models for an element with layers of unequal thickness in the (a) one-/one-wall state and (b) the no-/two-wall state.

IV. SUMMARY AND CONCLUSIONS

With zero magnetic field applied a four-magnetic-layer sample exhibited two basic coupled magnetic states. One had a single 180° wall originating near the edge-curling region and paralleling the sample's easy axis. By application of fairly large (about 170 Oe) external fields, this wall could be moved to a number of positions within the yoke. A second state evidenced no walls (at least on the outer layers). Transitions between the one- and no-wall coupled states required application (and removal) of large fields (~300 Oe). Transitions in a given direction (e.g., no-wall to one-wall) could be driven by HA field pulses of only one polarity. A two-magnetic-layer lamination also yielded coupled top and bottom configurations; however, these, probably because of thickness mismatch, did not include a coupled no-wall (single domain) state. In general, these results support the potential of laminated structures for reduced wall-motion noise and increased domain-wall configuration stability in magnetic recording devices.

ACKNOWLEDGMENTS

The authors wish to thank W. J. Fitzpatrick and M. Lilie for their work in automating LAMOM and in developing new image processing algorithms for it.

[1] J. C. Slonczewski, B. Petek, and B. E. Argyle, "Micromagnetics of Laminated Permalloy Films," accepted for publication, IEEE Trans. Magn.
[2] K. Mitsuoka *et al.*, IEEE Trans. Magn. **MAG-23**, 2155 (1987).
[3] J.-P. Lazzari and I. Melnick, IEEE Trans. Magn. **MAG-7**, 146 (1971); D. Augier and J.-P. Lazzari, *ibid.* **MAG-7**, 679 (1971).
[4] J. S. Y. Feng and D. A. Thompson, IEEE Trans. Magn. **MAG-13**, 1521 (1977).
[5] B. E. Argyle, B. Petek, and D. A. Herman, J. Appl. Phys. **61**, 4303 (1987).
[6] D. A. Herman and B. E. Argyle, IEEE Trans. Magn. **MAG-22**, 772 (1986).
[7] J. C. Slonczewski and S. Middlehoek, *Appl. Phys. Lett.* **6**, 139 (1965); J. C. Slonczewski, IBM J. Res. Dev. **10**, 377 (1966).
[8] B. E. Argyle and F. Suits, ICMFS-11 Conf, paper AA-10 (1985).

Measured fields and performance of recording heads

J. A. Brug, H. S. Gill, E. Murdock, S. Naberhuis, and G. Tarnopolsky
Hewlett-Packard Laboratories, Palo Alto, California 94304

R. Simmons
Disc Memory Division, Hewlett–Packard, Boise, Idaho 83714

A method is presented for obtaining the longitudinal magnetic field produced by recording heads. The method entails the use of a microloop to directly measure the perpendicular field H_y across the gap region of the head and the calculation of the longitudinal field H_x using a transform of $H_y(x)$. This method has been applied to the study of narrow-track, thin-film heads. The ability to predict the shape of the readback waveform from a measurement of the head field is demonstrated.

I. INTRODUCTION

The magnetic fields that are produced by recording heads are of interest in magnetic recording because they not only affect the writing process, but they can also be used in conjunction with reciprocity principles and models of media magnetization to derive readback waveforms. Conversely, measurements of head fields and readback waveforms permit studies of the shape of the transitions in the media. Methods for measuring the field distribution in the very small region surrounding the gap of the recording head have been the focus of a number of recent studies.[1–5] We use a microloop to measure the perpendicular magnetic field and demonstrate how the longitudinal field can be obtained from this measurement. An example of the use of reciprocity to relate the head field to the readback waveform is shown for a narrow-track, thin-film head.

II. APPARATUS

The apparatus that is used to directly measure the field distribution is based on a method using a microloop developed by Hoyt *et al.*[1] A very small, lithographically defined conducting loop, shown in Fig. 1, is used to inductively sense the ac field in the vicinity of the pole tips of the head. As the microloop is stepped across the gap region, the voltage induced in the microloop is proportional to the time derivative of the flux that crosses the incremental area defined by the step size and the loop width. Because the plane of the loop is perpendicular to the component of the field in the y direction, only this component is sensed by the microloop.

The apparatus that we have developed was designed to obtain high spatial resolution in the x direction. To achieve this, electron-beam lithography was used in conjunction with ion milling to form the microloop from a 0.18-μm Au/Ti film. A linewidth of 0.3 μm for the sense portion of the microloop was achieved. A quartz wafer with a thickness of 0.5 mm was used for the substrate. The width of the microloop d is proportional to the trackwidth of the head being studied and is typically one-half the track width. The signal induced in the leads during stepping is reduced to a negligible amount by making them parallel to the direction of motion in the region of high field surrounding the gap.

A block diagram of the apparatus is also shown in Fig. 1. The signal induced in the microloop is sensed by a low-noise (1.0 nV/Hz$^{1/2}$) preamp mounted next to the microloop. Movement of the head relative to the microloop is provided by a piezoelectric transducer using step sizes of 0.1 μm. The adjustment of the position of loop relative to the gap before the scan is achieved by an X-Y stage that is driven by stepper motors.

An HP3577A network analyzer provides the current to excite the head and also measures the output of the preamplifier. The gain of the system is calibrated from 1 to 50 MHz with a source of field provided by a coil. The measurement bandwidth is 10 Hz. An HP9836CU microcomputer controls the stepping of the stages and the network analyzer.

III. MEASUREMENT METHOD AND RESULTS

A measurement of the perpendicular field H_y is shown in Fig. 2 for a thin-film head with pole-tip widths as shown in the figure. For longitudinal recording, however, H_x is the component of the field that is coupled to the magnetization in the media. In order to obtain this field from the measured H_y a Hilbert transform[6] is used.

The Hilbert transform requires that the fields be two dimensional with $H_z = 0$. Because of the symmetry of the head across the track this will be valid at the center of the track. The width of the region over which H_z is assumed to

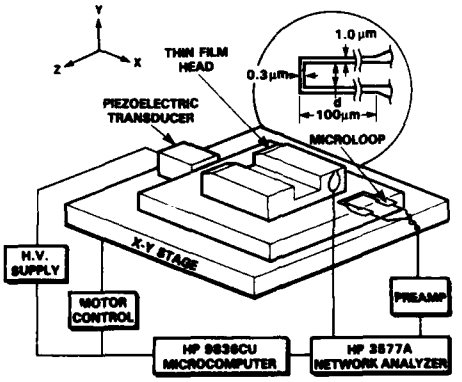


FIG. 1. Diagram of the apparatus used for positioning the recording head and for measuring the field using the microloop. The dimensions of the microloop are shown in the inset to the figure.

 0021-8979/88/084039-03$02.40 © 1988 American Institute of Physics

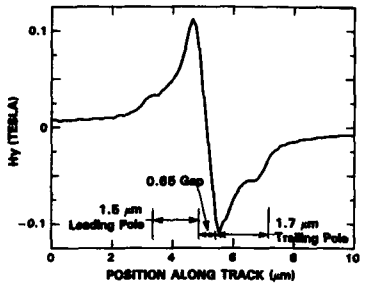


FIG. 2. Example of a measurement of H_y across the gap of a recording head. The widths of the pole tips and the gap are indicated in the figure. The trackwidth is 12 μm and the drive current is 20 mA at 10 MHz.

be negligible is taken to be the region where H_y is not a function of z. For narrow track heads the extent of this region is determined by using a narrow ($d = 2\,\mu$m) microloop that is stepped across the gap at various values of z. An example of a measurement is shown in Fig. 3, where the extent of the region of uniform field in the z direction is 4 μm.

The analytic nature of the magnetic field in the region above the gap allows the Hilbert transform to be used to relate the two components of the field. This relationship is given by

$$H_x(x,y>h) = \frac{1}{\pi}\int_{-\infty}^{+\infty} \frac{(x'-x)H_y(x',y=h)}{(x'-x)^2+(y-h)^2}\,dx', \quad (1)$$

where $H_y(x',y=h)$ is obtained by moving the microloop along the airbearing surface (ABS) of the head and h is the effective height at which the field is measured. This distance is closely approximated by half the thickness of the microloop (0.09 μm) plus any separation of the loop from the ABS. The height of the microloop above the ABS is adjusted by observing the interference fringes between the glass substrate and the ABS. For the measurements presented here, the microloop is kept in contact with the ABS during the

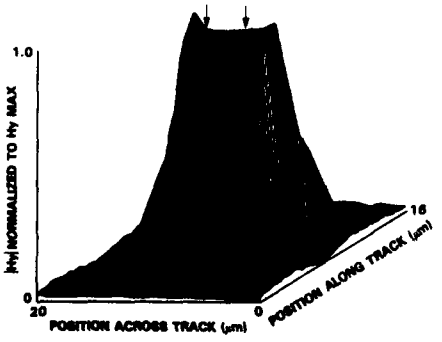


FIG. 3. Example of measurement of H_y along x at various positions across the track. The example shown is for a narrow-track head with a trackwidth of 8 μm and a pole-tip thickness of 3 μm. The arrows indicate the extent of the region of uniform H_y across the track.

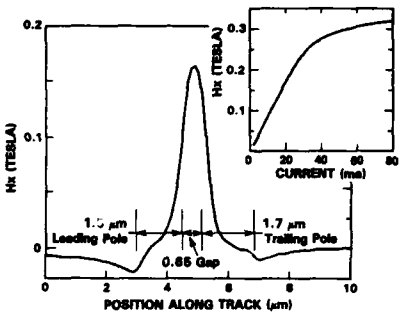


FIG. 4. Variation of H_x along the track at a height of 0.2 μm above the ABS. H_x was calculated using the data shown in Fig. 2 and the procedure in the text. The inset shows the dependence of the field on the excitation current in the head.

scan. It should be noted that H_x can be found at any value of $y > h$ above the ABS from a measurement of $H_y(x)$ at $y = h$. A calculation of H_x at a flying height of 0.2 μm is shown in Fig. 4.

A measurement of $H_x(x)$ permits a detailed study of the recording process by using the principle of reciprocity,[7] which relates the head field, the media magnetization, and the readback waveform by means of a convolution of the head field with the spatial derivative of the magnetization in the media. The expression is

$$V_x(x) = \frac{\mu_0 v w \delta}{i}\int_{-\infty}^{+\infty} \frac{dM_x(x'-x)}{dx'} H_x(x')dx', \quad (2)$$

where $V_x(x)$ is the readback voltage at a position x along the track, μ_0 is the permeability of free space, v is the head velocity, w is the track width, δ is the media thickness, i is the head current, and $M_x(x)$ is the magnetization in the media. The integration along x is over the region for which $H_x(x)$ is nonzero. For simplicity we have taken the field to be constant over the thickness of the media (thickness = 0.075 μm). It should be noted that the efficiency of the head does not enter the expression because the head field is measured directly.

An assumption that is implicit in the use of reciprocity is that the head is a linear device. This implies that there are no regions of the head that are saturating and that hysteretic processes due to domain-wall motion are not occurring. The excitation current for which linear behavior is observed is obtained by measuring the dependence of the field on the current. This is shown in the inset to Fig. 4. The field distribution was measured with an excitation current in the linear region below 25 mA (0 peak).

As an example of the use of reciprocity to study the contribution of the head to the recording process, we derive a readback waveform and compare it with a recording measurement. In order to evaluate Eq. (2) the magnetization in the media is required. This magnetization is, in general, not known. However, the arctangent function is a commonly used approximation for the transition shape[7] and is given by $M(x)/M_s = (2/\pi)\tan^{-1}(x/a)$, where M_s is the saturation magnetization and a is the transition length. The readback

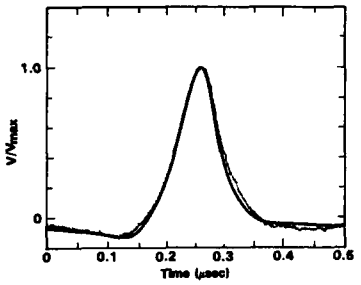


FIG. 5. Example of a comparison between two methods for obtaining the readback voltage. A measured readback voltage, indicated by the data points, is obtained by flying the head over thin-film media with isolated transitions. The solid line is obtained by using the procedure in the text with the measured head field.

waveform $V_x(t)$ is obtained by carrying out the integration in Eq. (2) and converting to the time domain using $t = x/v$.

The frequency response of the head will affect the shape of the readback waveform. To include this effect in the calculation the frequency response of the field is measured with the microloop. For the particular head considered here the magnitude of the frequency response decreases monotonically to 70% of its dc value at 50 MHz. No variation in the frequency response was observed across the thickness of the poles. The readback waveform is modified by calculating the frequency components of $V(t)$ using a Fourier transform and using the frequency response to adjust the amplitude of the components. An inverse Fourier transform is used to obtain the final waveform. This is shown by the solid line in Fig. 5 where an adjustable transition width of 0.2 μm is used to obtain the best fit. Also shown in Fig. 5 is the readback waveform for an isolated transition obtained by flying the head at 18.8 m/s on media with coercivity of 0.1 T. The bandwidth of the tester is 30 MHz.

IV. DISCUSSION

The readback waveform calculated from the measured head field shows good agreement with the measured readback waveform. While further study would be necessary to determine the range of the media for which the arctangent transition is valid, the example presented above demonstrates the ability to separate the head and the media contributions to the readback process. The application of this method to the verification of models of media magnetization is in progress.

ACKNOWLEDGMENTS

This work is part of a collaborative effort with Professor Marcel Muller and Kathy Weismehl of Washington University, whose work is supported in part by National Science Foundation Grant No. ECS 8603580. Vic Hesterman, Tom Anthony, Lee Carlton, and Lung Tran participated at various stages in the development of the microloop tester. Electron beam lithography was done by Paul Rissman and Hua-Yu Liu at Hewlett–Packard Laboratories.

[1]R. F. Hoyt, D. E. Heim, J. S. Best, C. T. Horng, and D. E. Horne, J. Appl. Phys. **55**, 2241 (1984).
[2]Roger F. Hoyt, J. Appl. Phys. **57**, 3947 (1985).
[3]R. S. Omdeck, E. G. Persson, N. Curland, and J. H. Judy, IEEE Trans. Magn. **MAG-23**, 2491 (1987).
[4]O. Watanuki, K. Sueoka, K. J. Ashar, IEEE Trans. Magn. **MAG-23**, 3164 (1987).
[5]Mark E. Re, Romney R. Katti, Stacy L. Zeder, and Mark H. Kryder, IEEE Trans. Magn. **MAG-22**, 840 (1986).
[6]Phillip M. Morse and Herman Feshbach, *Methods of Theoretical Physics* (McGraw-Hill, New York, 1953).
[7]See, for example, C. Dennis Mee and Eric D. Daniel, *Magnetic Recording, Volume I:Technology* (McGraw-Hill, New York, 1987).

Effect of pole tip alignment on magnetic fringing fields from recording heads

P. V. Koeppe, M. E. Re,[a] and M. H. Kryder
Magnetics Technology Center, Department of Electrical and Computer Engineering, Carnegie Mellon University, Pittsburgh, Pennsylvania 15213

The effect of using pole tips of equal width in thin-film recording heads has been studied by examining a head having the track edges of its leading and trailing pole tips virtually aligned on one side and misaligned by 1.5 μm on the other. Magnetic fields produced by this head, as well as by a head whose edges were aligned by ion milling, have been measured. Using a magneto-optic photometer system with spatial resolution of less than 0.5 μm, the response of a thin-film medium spaced 0.25 μm from each head was dynamically monitored at a frequency of 1 MHz as the head was scanned beneath it. Results demonstrate that fringing fields emanate to a larger spatial extent in both dimensions from misaligned edges. These results are correlated with magneto-optic measurements of the dynamic response of the magnetization made directly at the pole tips of the two recording heads. Both a wider written track and broader transitions of magnetization are to be expected in a magnetic storage medium subjected to the fields in the vicinity of misaligned edges. This indicates that to achieve high track densities and to avoid interference from signals recorded on adjacent tracks as well as to minimize distortion during the read process due to a contorted field profile at misaligned edges, it is desirable to use heads with equal top and bottom pole widths.

INTRODUCTION

Magnetic thin-film recording heads have provided high-density digital recording through the utilization of photolithographic thin-film technology for the definition of compact and precise geometrical features. In order to achieve even higher recording densities, track widths are being reduced by narrowing the widths of the pole tips. With this reduction, the spatial offset between the track edges of the leading pole with respect to the those of the trailing pole, which is usually incorporated to allow for photolithographic tolerances, becomes significant. A previous study has examined the effects of misalignment of these edges through measurements made on a large-scale recording model.[1] The effect of this misalignment on the fringing magnetic fields near these edges is demonstrated here through direct microscopic observation of the dynamic response of a thin-film medium placed at a typical flying height above two thin-film recording heads: one having a pair of aligned edges and a pair of misaligned edges, for direct comparison on the same head; the second having edges which were aligned by means of ion milling after deposition.

EXPERIMENTAL PROCEDURES

The techniques used for this study have been presented previously[2] and will only be reviewed and updated here. A scanning magneto-optic photometer system with a measuring spot size of less than 0.5 μm in diameter has been utilized to dynamically monitor the response of a stationary thin film (0.05 μm) of CoNi to thin-film heads scanned beneath it. In preparation for these studies, the CoNi was formed on a thin cover glass by evaporation at an oblique incidence to define magnetic anisotropy in the plane of the film.[3]

An argon laser was used as a light source to a polarizing Leitz microscope, focused by a 125×, 1.30 NA oil immersion objective through the cover glass onto a spot of the CoNi which was oriented such that its hard axis of magnetization lay perpendicular to the gap of the recording head. The dynamic magnetization of this spot was monitored by means of the longitudinal Kerr effect as a head, driven at a frequency of 1 MHz by a typical current used for writing, was two-dimensionally scanned by Klinger stepping motors having a spatial precision of 0.1 μm. A spacing of 0.25 μm, defined interferometrically, was maintained between the CoNi-glass interface and the air-bearing surface of the recording head during the measurements.

The result is a two-dimensional spatial mapping of the magneto-optical signal which represents the root-mean-square (rms) average magnitude of the change in the component of magnetization of the medium in its hard axis. Calibration of this signal to the corresponding field from the head is achieved through the linearity of the response of the magnetization in this axis. The saturation field in this axis was adjusted to a low enough value (approximately 1000 Oe) to ensure that the heads were capable of saturating the medium. Each of Figs. 1 and 2 shows contours of the measured magneto-optic signal on a 0%–100% scale, corresponding to 0–1000 Oe of field.

The dynamic response of the magnetization at the pole tips of the two heads, under the same drive conditions used above, was measured directly in a second set of experiments in order to correlate action in the head to the produced fields. The polar Kerr effect was used to monitor the response of the magnetization perpendicular to the air-bearing surface of the Permalloy pole tips, as each head was scanned in two dimensions under the focused laser beam.[4] The results are displayed in Figs. 3 and 4 using a scheme of grey scales, where darker regions indicate greater switching of magnetization.

[a] Present address: IBM T. J. Watson Research Center, Yorktown Heights, NY 10598.

 0021-8979/88/084042-03$02.40 © 1988 American Institute of Physics

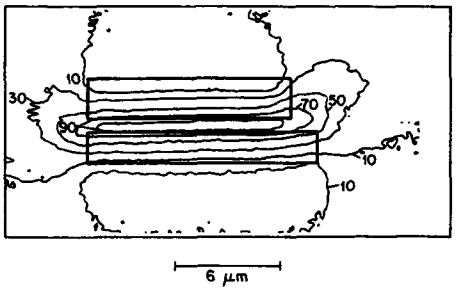


FIG. 1. Contours of magneto-optic signal measured from a thin film of CoNi in response to a thin-film recording head spaced 0.25 μm beneath it. The tips of the poles are outlined, showing both aligned and misaligned (by 1.5 μm) edges.

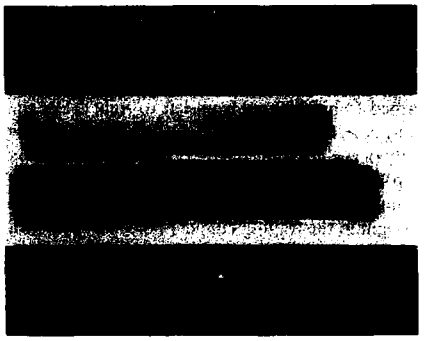


FIG. 3. Magneto-optic response measured directly at the pole tip surface of the recording head measured in Fig. 1. Darker areas indicate greater switching of the magnetization.

RESULTS

Results from the study of the two thin-film recording heads are shown in Figs. 1–4. Figures 1 and 2 show contour plots of the magneto-optic signals measured from the CoNi medium, representing the magnitude of the component of the magnetic field perpendicular to the gap (i.e., along the track) at a spacing of 0.25 $\pm$ 0.05 μm away from the head. The contours in each case are spaced 20% (200 Oe) apart, from 10% to 90%, inclusive. The relative location of the pole tips beneath the medium is outlined. Figures 3 and 4 show magneto-optic images of the dynamic (rms) switching of the normal component of magnetization, measured directly at the air-bearing surfaces of the two heads.

Contours of field from a recording head with poles which are essentially aligned at one edge and misaligned by 1.5 μm at the other are shown in Fig. 1. It is apparent that, whereas the field 0.5 μm away from each edge of the trailing pole is well above 700 Oe, it drops to 500 Oe at a point 1.75 μm away from the aligned edges, while maintaining a value above 500 Oe to 2.2 μm beyond the misaligned edges. Additionally, significant broadening of the contours of field along the track dimension (vertical dimension in the figure) is evident beyond the misaligned edges, in comparison to the aligned edges. The spatial extent of the 500-Oe contour in this dimension is about 1.8 μm at the aligned edges, similar to that above the center of the pole tips, whereas it broadens to 2.3 μm, away from the misaligned edges. Apparently, alignment of the pole tip edges minimizes the extent to which magnetic fields fringe beyond these edges, maintaining a narrow track width, while also minimizing the broadening of the field contours (i.e., the reduction of the field gradient) along the track.

To confirm these results, a second recording head having pole tip edges which were aligned by ion milling was examined. Contours of measured fields from this head are shown in Fig. 2. It is evident that the fields are much more confined to the physical geometry of this head: Field values above 500 Oe extend only 0.5 μm beyond the edges. Virtually no broadening of the contours along the track dimension occurs beyond the edges for fields of 300 Oe and above; for comparison with Fig. 1, the spatial extent of the 500-Oe contour in this dimension in Fig. 2 is a constant 1.6–1.7 μm, whether measured above the center or above the edges of the pole tips.

Images of the dynamic magneto-optic response of the outward normal component of magnetization at the air-bearing surface of the two recording heads under study are shown in Figs. 3 and 4. Darker areas indicate a larger amount of switching of the magnetization. It is evident that more switching occurs near the gap and decreases through

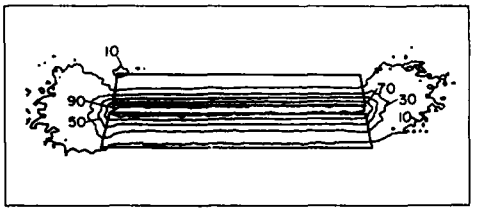


FIG. 2. Similar to Fig. 1, in response to a second thin-film recording head with pole tips aligned by ion milling. The spacing is 0.25 μm.



FIG. 4. Similar to Fig. 3 for the head measured in Fig. 2.

the thickness of the tips away from the gap.[4] In regions away from the gap of the narrower trailing pole of Fig. 3, very little switching of the magnetization is observed near the aligned edges, but increases across the pole as the misaligned edges are approached (white to grey from left to right). For the wider, leading pole, the reverse is true: Less switching occurs in the vicinity of the misaligned edges (both near and away from the gap).

A very uniform switching of magnetization is apparent from left to right in the trailing (upper) pole in Fig. 4, with nearly all of the action near the gap and very little away from it. The wider (tapered) leading pole shows evidence of switching throughout the thickness near the edges, similar to that seen near the aligned edge of Fig. 3, but otherwise uniform response, from left to right, of larger magnitude than that of the trailing pole.

DISCUSSION

The measured fields in Figs. 1 and 2 are readily correlated to the dynamic response of magnetization at the surface of the pole tips in Figs. 3 and 4. Conservation of lines of flux from one pole to the other can qualitatively explain the larger response observed both laterally and longitudiually near the misaligned edge of the trailing pole, as well as the diminished response at the corresponding edge of the leading pole in Fig. 3. The observed spreading of field from the narrower pole to the wider pole in both dimensions, Fig. 1, is a logical consequence. Conversely, very little switching occurs away from the gap in the trailing pole at aligned edges (Figs. 3 and 4). Hence, the magnetic field (Figs. 1 and 2) closes and is confined near the gap of this pole, with little spreading. The switching which occurs through the thickness of the leading pole at the aligned edges and the fact that more switching is detected across the leading pole than the trailing pole, apparent in both Figs. 3 and 4, cannot be explained by such simple magneto-static concepts, but show the results of a complex three-dimensional geometry and of the action of magnetic domains within the structure of the head.

The contours in Fig. 1 demonstrate clearly that misalignment of the edges of the pole tips of a magnetic recording head can result in significant magnetic fields beyond these edges. Comparing the contours at the left and right sides of the figure indicates that the fringing fields from a pair of misaligned poles not only laterally extend the track width, but also result in wider transitions written in these side zones on a medium, since the field gradient is reduced there. These data compare well with results from a three-dimensional computational model,[1] which also demonstrates an increase in the perpendicular component of the head field with misalignment of these edges in the vicinity of the edge of the trailing pole, which agrees well with the increased switching detected there in Fig. 3. Excess media noise at and beyond the track boundaries in metal film disks, has been measured by Yarmchuk[5]; the present results indicate that such noise would likely be diminished if heads with aligned pole tips were used.

The contorted field profile present near the misaligned edges may lead to distortion of the read-back signal, especially for narrow track widths. Distortion during the read process has been examined by Feng and Harper,[6] indicating that transitions are written at the edges of the track *behind* (closer to the rear of the trailing pole than) those in the center of the track. This can be explained by the observed broadening of the field contours near misaligned edges, discussed above. Again, this effect should be minimized by pole tip alignment.

CONCLUSIONS

It has been shown through measurements of magnetic fields above thin-film recording heads that a spatial misalignment of the track edges of the leading and trailing pole tips of a head can lead to significant magnitudes of fields beyond these edges. Images of the distribution of switching of magnetization at the surface of the pole tips aid in the understanding of the measured field profiles. Switching of the magnetization occurs throughout the thickness of the trailing pole at misaligned edges, spreading the magnetic fields in both dimensions beyond the edges. These fringing fields may account for both pulse distortion during read-back and excess media noise detected at and beyond the track edges on recording media. With media of increased coercivity, these effects can be diminished; however, as track widths are further reduced it is desirable to manufacture heads with equal top and bottom pole widths either through the use of tighter photolithographic tolerances or subsequent tailoring such as ion milling.

ACKNOWLEDGMENTS

The authors would like to thank the Data General and Magnex Corporations for supplying the heads used in this study. Special thanks go to W. Eppler and R. Katti for their assistance. This work was supported by the Magnetics Technology Center of Carnegie Mellon University.

[1] D.E. Heim and J.E. Monson, IEEE Trans. Magn. MAG-23, 198 (1987).
[2] M.E. Re, R.R. Katti, S.L. Zeder, and M.H. Kryder, IEEE Trans. Magn. MAG-22, 840 (1986).
[3] S.L. Zeder, J.-F. Silvain, M.E. Re, M.H. Kryder, and C.L. Bauer, J. Appl. Phys. 61, 3804 (1987).
[4] M.E. Re, R.R. Katti, W. Rave, and M.H. Kryder, IEEE Trans. Magn. MAG-23, 3161 (1987).
[5] E.J. Yarmchuk, IEEE Trans. Magn. MAG-22, 877 (1986).
[6] J.S.-Y. Feng and R.D. Harper, IEEE Trans. Magn. MAG-23, 2082 (1987).

Magnetism of metastable phases: Band theory and epitaxy (invited)

P. M. Marcus and V. L. Moruzzi
IBM Research Center, P. O. Box 218, Yorktown Heights, New York 10598

Total-energy band calculations are used to analyze the magnetic phases of metallic elements as functions of volume. The calculations utilize a fixed-spin-moment procedure, which is described and justified as a natural generalization of density-functional theory. This procedure finds the ground-state energies of electronic systems under two constraints, and hence determines the system energy as a function of two variables—volume and magnetic moment. The energy function is used to find the ferromagnetic phases and their ground-state properties, including bulk moduli and magnetic susceptibilities. The systems studied are fcc Fe, fcc Co, bcc Ni, fcc Pd, and bcc Mn, each of which undergoes a phase transition for small changes of the lattice constant from equilibrium (zero-pressure) values.

I. INTRODUCTION

This work uses total-energy band theory to study magnetic phases of various transition elements in certain cubic lattice structures as a function of volume. The systems chosen all have phase transitions between a nonmagnetic state and a ferromagnetic state for a few percent change in lattice parameter from their equilibrium (zero-pressure) values. An essential feature of the analysis is the use of a fixed-spin-moment constraint on the band calculation, as well as the usual constraint of a fixed number of electrons in the given volume, which leads to the energy as a function of two macroscopic variables—volume and magnetic moment—from which the magnetic behavior as a function of volume can be obtained. Thus we can find the phase lines, which give the magnetic moment of each magnetic phase as a function of volume, including the two-phase range of volume and the stability limit of each phase. We prove some theorems about the shapes of phase lines and find the magnetic susceptibility along the nonmagnetic segment of the phase line and follow its approach to singularity as the stability limit of that phase is approached. The calculations exploit the high efficiency of the augmented-spherical-wave (ASW) band method, which makes possible systematic study of the volume dependence of the phases of these elemental systems.

As described in a series of papers,[1–6] this analysis has provided new insight into the nature of the phase transition between magnetic phases. In this paper we put together in compact form the results obtained previously on magnetic systems, supplemented by more careful study of the stability limits of the magnetic phases and by addition of magnetic susceptibility curves in the nonmagnetic phase; we also include additional elemental systems that show such phase transitions. The picture of the phase transition that emerges is essentially a modern version of the phenomenological Stoner theory, in which the *ad hoc* internal field of that theory is replaced by the first-principles mechanism of the spin-polarized exchange-correlation field of modern density-functional theory.

II. TOTAL-ENERGY BAND THEORY

Band calculations which yield the total energy of an electronic system as a function of nuclear coordinates are now a valuable structural tool; such calculations have been applied to find equilibrium bulk lattice dimensions and various deviations from bulk structure at surfaces and defects, etc.[7] The present work illustrates the structural value of total-energy calculations in another way by exploiting the dependence of that energy for bulk crystals on an internal degree of freedom, the spin magnetization or degree of spin polarization, which is strongly coupled to the volume.

These calculations employ the local-density approximation (LDA) for electron-electron interactions, which reduces the calculation for a given nuclear configuration to the self-consistent solution of a set of one-electron equations tied together by a common potential that depends on all occupied one-electron states. In periodic problems the one-electron states form energy bands, but the energy bands are not as significant as the total energy and may be regarded as an intermediate stage in finding the total energy. The structural results are then obtained by minimizing the total energy with respect to the nuclear coordinates (or, alternatively, finding the stress in a given structure). In addition to the LDA, there are computational approximations characteristic of each method of solving the equations and dependent on the representation used for the wave functions and potential. These computational approximations are controlled approximations, which can be improved by increasing the power of the representation (and the amount of computation).

The most favorable case for the LDA, which applies best to states with small changes or slowly varying changes in electron density as a function of position, should be determination of energy changes ΔE when small changes in the nuclear positions of one phase of one material are made and hence small changes in electron density are produced. Determination of such ΔE values is the principal application made here, where we study the volume dependence of the energy of phases of a particular lattice type.

 0021-8979/88/084045-06$02.40 © 1988 American Institute of Physics

III. DOUBLE CONSTRAINTS AND THE FIXED-SPIN-MOMENT CALCULATION

A. Fixed-spin-moment procedure

The detailed study of the magnetic phases of the elements, their transitions, and stability limits, has been made possible by a simple modification of the usual spin-polarized band calculation. This modification holds the magnetic moment M fixed as well as the total number of electrons in a given volume V, leading to the function for the ground-state energy $E(V,M)$. This function can have two or more minima in M at the same V, thereby creating difficulties in the usual spin-polarized calculation in which the value of M is allowed to float until E is minimized at the given V. Then more than one M minimizes E and it is not clear which M or mixture of M values will be found.

Since the fixed-spin-moment procedure is not widely known, we discuss it explicitly as a simple generalization of density-functional theory within the LDA and show that the calculations are in fact doubly constrained ground-state calculations, which introduce two different Fermi levels to describe the electron distribution.[8]

B. Band theory in the LDA with one constraint

We first describe the usual form of self-consistent band theory within the LDA[9] (taking energies in Rydbergs and lengths in atomic units). The total-energy calculation then reduces to the solution of the set of one-particle equations $[-\nabla^2+v_{\rm eff}(n(\mathbf{r}))]\psi_i(\mathbf{r})=\epsilon_i\psi_i(\mathbf{r})$, $i=1,N$, where N is the total number of electrons in the system and the effective potential $v_{\rm eff}(n)$ is an explicitly known function of the total electron density $n(\mathbf{r})$ containing Coulomb interactions and an exchange-correlation term, which is a known function of n (taken from uniform electron-gas theory). The one-particle equations are solved self-consistently for the lowest N states, yielding eigenvalues ϵ_i and normalized wave functions ψ_i, which are assumed to be occupied, so that $n(\mathbf{r})=\sum_{i=1}^{N}|\psi_i(\mathbf{r})|^2$. This equation for $n(\mathbf{r})$ brings in the constraint imposed by the specified value of N, which requires that $\int_V n(\mathbf{r})d^3r=N$, where the integration is over the system volume V. For any set of wave functions ψ_i and the corresponding $n(\mathbf{r})$ the total energy of the system can be evaluated as the sum of a potential energy, which is known explicitly in terms of $n(\mathbf{r})$, and a kinetic energy, which is evaluated indirectly by summing the kinetic energies of the occupied states, $\sum_{i=1}^{N}\int_V\psi_i^*(\mathbf{r})[-\nabla^2\psi_i(\mathbf{r})]d^3r$. When the ψ_i are the solutions of the one-particle equations, the total energy is minimized and we will call it E. We note that the Fermi energy ϵ_F is the energy of the highest occupied state ϵ_N and that E is a ground-state energy, which is a function of the nuclear coordinates and N.

C. Band theory in the LDA with two constraints

This parameterless (hence first-principles) formulation of the ground-state energy of an electronic system can be generalized to allow unequal spin densities at each point, as was done by von Barth and Hedin.[10] Without spin-orbit interaction we can simply describe the electronic state by specifying the separate up- and down-spin densities n_u and n_d at each point, where $n(\mathbf{r})=n_u(\mathbf{r})+n_d(\mathbf{r})$. Then $v_{{\rm eff}\,j}(n_u,n_d)$ depends on two independent variables and requires an index $j=u,d$ since the potentials are different for up and down spins when $n_u\neq n_d$. The solutions of the one-particle wave equations for $\psi_{ij}(\mathbf{r})$ and ϵ_{ij} now also require an index j, and $n_j(\mathbf{r})=\sum_{i=1}^{N_j}|\psi_{ij}|^2$, $N_j=\int_V n_j(\mathbf{r})d^3r$, $j=u,d$, and $N=N_u+N_d$.

The fixed-spin-moment procedure adds one step to the procedure for finding the self-consistent solutions. Instead of just fixing N and letting N_u and N_d vary until the total energy is minimized, this procedure fixes N_u and N_d separately and maintains this double constraint during iteration to self-consistency. Equivalently, we can specify the total number of electrons N and the total (spin) magnetic moment of the system $M=N_u-N_d$ (in Bohr magnetons); for a uniform or periodic system we can specify the average electron density N/V and average magnetization density M/V. The calculation is thus a *doubly* constrained ground-state calculation, rather than a singly constrained one, that finds a ground state at each equilibrium M, and determines a ground-state energy E as a function of the nuclear coordinates and N_u and N_d or N and M.

D. The meaning of two Fermi levels

The description of the spin-polarized system for general M requires two Fermi energies ϵ_{Fu} and ϵ_{Fd}, which are in general unequal. In effect we are dealing with a system in a uniform macroscopic magnetic field H, which maintains the magnetic moment of the system. The difference in Fermi energies corresponds to a difference in magnetic energy $\epsilon_{Fu}-\epsilon_{Fd}=2\mu_B H$, where μ_B is the Bohr magneton (up spins have moments in the field direction). In zero field the usual constancy of the Fermi energy in an equilibrium state is restored. Equivalently, if the electron energies are defined to include the magnetic energy, then a more general Fermi energy $\tilde{\epsilon}_F\equiv\epsilon_F-\boldsymbol{\mu}\cdot\mathbf{H}$ will be constant in the system, i.e., $\tilde{\epsilon}_{Fu}=\epsilon_{Fu}-\mu_B H=\tilde{\epsilon}_{Fd}=\epsilon_{Fd}+\mu_B H$.

IV. MAGNETIC PHASES AND THEIR PROPERTIES FROM $E(V,M)$

A. Thermodynamics of the energy function and phase lines

For a crystal of cubic symmetric (the case considered here) the only geometrical parameter is the volume V; also N is fixed by the atomic number if the system stays neutral. Then the band calculation discussed in Sec. III C yields a function $E(V,M)$. The energy function $E(V,M)$ describes a set of thermodynamic states of the crystal, which can be stable, metastable, or unstable. In general, these states require a magnetic field $H=(\partial E/\partial M)_V$ to maintain them—as noted in Sec. III D. However, the condition $(\partial E/\partial M)_V=0$ defines a locus in the M-V plane along with $H=0$, so that states on that locus, if stable, are sustained without an applied field. Accordingly it is appropriate to call these states magnetic phases and their loci phase lines. We include among the magnetic phases the phase with $M=0$, since such states have been found by a spin-polarized calculation to have a minimum of E at $M=0$. An extremum of E

at $M = 0$ is forced by symmetry, but such a phase can change from stable to unstable where $(\partial^2 E/\partial M^2)_V$ changes sign, i.e., has a stability limit. A paramagnetic calculation, which forced up- and down-spin equality at every point, would not locate such a stability limit.

The general behavior of the magnetic phase lines and of E as a function of M at various V near a phase transition is shown schematically in Fig. 1. (Actual curves of E as a function of M at fixed V are given in Refs. 3 and 4.) The curves on the left-hand side, $E(V_i,M)$, $i = 1,2,3$, show the characteristic behavior at V_1 on the $M = 0$ phase line (with one minimum at $M = 0$), at V_2 in a two-phase range with two minima (for $M>0$), and at V_3 in the ferromagnetic range with one deep minimum (for $M>0$). On the right-hand side the loci along which $(\partial E/\partial M)_V = 0$ are shown, with stable line segments (solid) corresponding to minima of $E(M)$ going continuously into unstable line segments (dashed) corresponding to maxima.

B. Two theorems on phase lines

We note two general properties of the phase lines. (1) The lines terminate in a hook with a vertical tangent.[5] At the termination point a minimum and a maximum of E as a function of M merge to give a horizontal inflection point where $(\partial^2 E/\partial M^2)_V = 0$. Since along the phase line $(\partial E/\partial M)_V = 0$, we have

$$\frac{\partial}{\partial V}\left(\frac{\partial E}{\partial M}\right)_V dV + \frac{\partial}{\partial M}\left(\frac{\partial E}{\partial M}\right)_V dM = 0,$$

and hence the slope of the phase line is

$$\frac{dM}{dV} = -\frac{\partial^2 E}{\partial V\,\partial M}\left(\frac{\partial^2 E}{\partial M^2}\right)_V^{-1},$$

which is in general infinite at the inflection point, since the denominator vanishes there. (2) Two successive stable segments of the phase line must overlap in V, since they are connected by an unstable segment of negative slope. The overlap corresponds to the volume range of the two-phase region of a first-order phase transition. In special cases, the overlap region can shrink to a point and the transition becomes second order. The actual thermodynamic transition point (at constant volume) occurs at the V_0 at which the two minima of $E(V_0,M)$ are equally deep. Since transition from one phase to the other involves only an electronic rearrangement in zero applied field, but no lattice motion, it can be expected to occur readily without hysteresis as V_0 is passed.

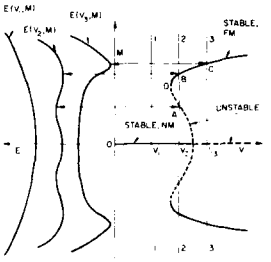


FIG. 1. Schematic plot of magnetic phase lines $(\partial E/\partial M)_{V=0}$ on the M-V plane (right-hand side) linked to corresponding E-vs-M curves (left-hand side) at various values of V. The solid-line segments of the phase line give M values of stable (or metastable) states at minima of E vs M, as at points B and C; these stable segments terminate with a vertical tangent as at D. The dashed-line segments are M values of unstable states at maxima of E as at point A. The ferromagnetic segment is marked FM and the nonmagnetic segment NM. Vertical lines 1, 2, and 3 are at volumes V_1, V_2, and V_3 in the NM, two-phase, and FM volume ranges and correspond to the E-vs-M curves at the left.

C. Additional properties related to phase lines

After finding the phase lines and their stability limits, the E values along that line of minima $E_m(V)$ provide further information about the properties of each phase. We note five basic properties.

(1) The equilibrium lattice constant is determined by $dE_m/dV = 0$. The minimum may occur in a ferromagnetic (FM) phase or a nonmagnetic (NM) phase; examples of both cases will be given.

(2) The hydrostatic stress or pressure $p = -dE_m/dV$, which vanishes at the equilibrium lattice spacing, can be found at any positive or negative volume change from equilibrium; examples will be given.

(3) The bulk modulus $B = V(d^2E_m/dV^2)$ can be found at any V.

(4) A Grüneisen constant

$$\gamma = -1 - \frac{V}{2}\frac{d^3E_m}{dV^3}\left(\frac{d^2E_m}{dV^2}\right)^{-1}$$

can be defined as a dimensionless measure of the deviation of the $E_m(V)$ curve from a harmonic (parabolic) curve. We adopt the definition of Dugdale and MacDonald,[11] which modifies a form due to Slater and fits low-temperature data better.[12] We mention this property for completeness, but do not give any examples here.

(5) The magnetic susceptibility along the phase line can be found from the curvature of E with respect to M at a point on the phase line, $\chi = (\partial M/\partial H)_V = 1/(\partial^2 E/\partial M^2)_V$. Since Pauli paramagnetism corresponds to a susceptibility $\chi_0 = N_d\mu_B^2$, where N_d is the density of states at the Fermi level (including contributions from both spin directions) and μ_B is the Bohr magneton, a susceptibility enhancement ratio can be defined as $\chi/\chi_0 = 1/[\mu_B^2 N_d(\partial^2 E/\partial M^2)_V]$. The values of χ/χ_0 will become much larger than 1 because of the effects of exchange, and will become singular at the stability limit, where, as shown above, $(\partial^2 E/\partial M^2)_V = 0$.

V. THE ASW AND GROUND-STATE PROPERTIES OF FIVE ELEMENTAL SYSTEMS

A. Features of the ASW

The augmented-spherical-wave (ASW) program is a total-energy band-structure program for bulk periodic crystals based on the spin-polarized local-density one-particle equations, which achieves computational efficiency through linearization (of the energy dependence of the matrix elements of the secular equation) and other design features.[13] It is fast enough to explore systematically the volume and magnetization dependence of the total energy with accuracy adequate to find the magnetic phases. It is used here in a nonrel-

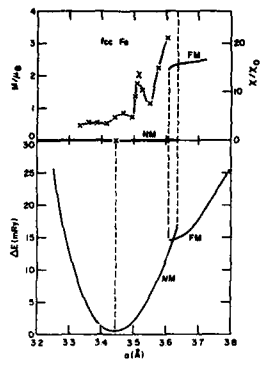


FIG. 2. Ground-state properties of fcc Fe vs cubic lattice constant a in Å. Energy changes per atom in mRy from the minimum along the phase lines are plotted below. The phase lines, which give the magnetic moment per atom in Bohr magnetons vs a, are plotted above and show two segments, a nonmagnetic one (NM) on the $M = 0$ axis and an overlapping ferromagnetic one (FM). The stability limits of these two phases are shown by dashed lines joining both plots, which border the two-phase volume range. The equilibrium lattice spacing at the minimum below is marked with an × above on the NM phase. Also plotted above is the susceptibility enhancement ratio χ/χ_0 (scale on the right-hand side) for the NM phase; calculated points are shown.

ativistic version with the fixed-spin-moment constraints described in Sec. III, and the von Barth–Hedin exchange-correlation dependence on electron and magnetization density[10] as parametrized by Janak.[14] The ASW uses an approximation which spherically averages the charge density and potential inside the equivalent sphere around each atom and hence is best suited to study systems with atoms in cubic environments, as used here.

The accuracy of the ASW for lattice constants and magnetic moments is illustrated in Table I for elements in cubic structures for which experimental values are known. The errors in lattice constants are within 2% in magnitude and the magnetic moments within 3%. Note that the calculated results are all for rigid lattices and do not include the effects of zero-point or thermal motion.

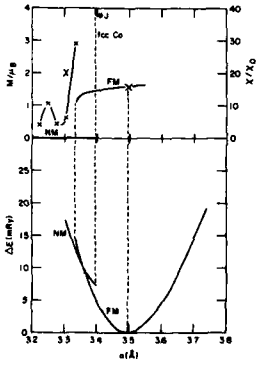


FIG. 3. Same as Fig. 2 for fcc Co. The point marked J is the susceptibility ratio found by Janak (Ref. 17).

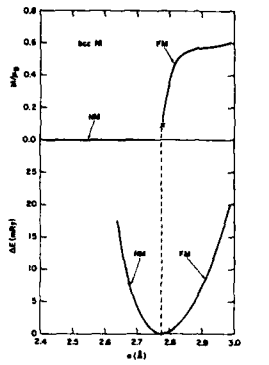


FIG. 4. Same as Fig. 2 for bcc Ni. The two-phase region has not been resolved and is either very small or collapsed.

B. Results for specific systems

We give now in Figs. 2–6 a summary of results obtained on the volume dependence of five elemental crystal lattices which show a magnetic phase transition. Each figure shows three quantities as functions of the cubic lattice constant a in Å: (1) in the lower panel are ΔE_m curves (energy changes along the phase lines in mRy/atom relative to the minimum), (2) in the upper panel are the corresponding magnetic moment curves or phase lines (in Bohr magnetons per atom), and (3) in four cases we show the susceptibility enhancement factor of the nonmagnetic phase. We now discuss features of each of these systems.

1. fcc Fe

Figure 2 shows that fcc Fe, unlike bcc Fe, is nonmagnetic (NM) at its equilibrium lattice spacing $a_0 = 3.44$ Å (marked with a cross on the $M = 0$ axis). However, a 5% stretch of the lattice constant produces a ferromagnetic (FM) phase. The overlap forms a well-developed two-phase region (boundaries marked by vertical dashed lines) within which the energy curves cross. We have also found a third low-moment FM phase, which exists entirely within the two-phase range of the first two phases. It is not shown here, but appears in Ref. 4.

The fcc Fe crystal is particularly interesting because,

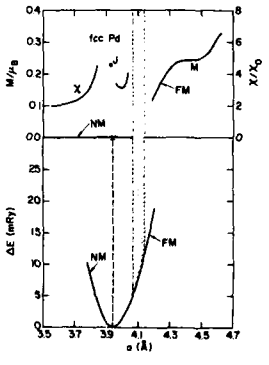


FIG. 5. Same as Fig. 2 for fcc Pd, with point J as in Fig. 3. The shaded region contains the unresolved stability limits and two-phase region; the gap in the susceptibility curve is a range containing wild oscillations that we cannot now fix reliably.

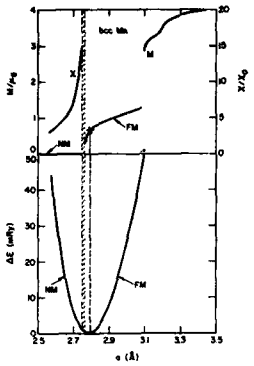


FIG. 6. Same as Fig. 2 for bcc Mn; narrow unresolved two-phase range as in Fig. 5.

although metastable with respect to the bcc crystal by about 15 mRy/atom (up to 140 kbar pressure; above 140 kbar the fcc phase becomes more stable than the bcc phase[4]), it has been grown epitaxially (and pseudomorphically) on Cu for a substantial number of atomic layers.[15] Hence its properties are accessible to measurement—at least at the lattice constant of Cu. We have noted that at the lattice constant of Cu (a 5% stretch) the existence of the relatively unstrained FM phase provides a plausible explanation of the ease of pseudomorphic growth.[6] This epitaxial layer has in fact been shown to be ferromagnetic by spin-polarized photoemission studies.[16]

Also shown in Fig. 2 is the susceptibility enhancement factor χ/χ_0 in the NM phase versus a (scale on the right-hand side) evaluated by the formulas in Sec. IV. The susceptibility is very large and rises rapidly as the stability limit of the NM phase is approached. Oscillatory behavior also appears in χ/χ_0; the oscillation is somewhat uncertain (we show the calculated points used to draw the curve) since accurate evaluation of small values of $(\partial^2 E/\partial M^2)_V$ is difficult, but such oscillations appear also in other cases.

Interesting additional information comes from $E_m(V)$, the energy along the phase lines, using the formulas of Sec. IV. Thus the pressure on NM fcc Fe at the Cu spacing ($a = 3.60$ Å) is -330 kbar (1 Ry/Å^3 = 21.80 kbar); the bulk modulus of NM fcc Fe at the minimum is about 3500 kbar over a small range around the minimum and decreases for larger ranges; the bulk modulus of the FM phase is much smaller—it is about 500 kbar over a range of 0.026 Å above the (extrapolated) minimum at 3.59 Å and increases rapidly for greater ranges.

2. fcc Co

The behavior of fcc Co in Fig. 3 shows an overall similarity to fcc Fe, but now the equilibrium state is FM [as is bcc Co (Ref. 1)] with $a_0 = 3.50$ Å and $B \simeq 2600$ kbar and the transition, two-phase region, and the stability limits occur at reduced lattice constant.[1–4] The transition lattice constant of 3.36 Å corresponds to 4% reduction from equilibrium and a pressure of 420 kbar on the FM phase. Another difference from fcc Fe is that fcc Co is macroscopically stable (although metastable with respect to hcp Co below about 420 °C), so that many of its properties are measured (e.g., the saturation moment in Table I). As for fcc Fe, the susceptibility ratio in the NM phase shows a pronounced oscillation before rising rapidly as the stability limit is approached. We also plot the point found by Janak at one lattice spacing[17] (solid dot marked J) from a paramagnetic band calculation, which shows a large susceptibility ratio, consistent with being near the stability limit (but at 3.41 Å somewhat above our transition range and well below our a_0).

3. bcc Ni

Metastable bcc Ni (with respect to fcc Ni) in Fig. 4 appears to be barely FM at $a_0 = 2.78$ Å, and less than a 1% decrease of a appears to bring it into the NM phase. However, the magnetic moment is so small and the magnetic energy so weak that details of the transition are not resolvable with our accuracy.[3–6] The transition may be a second-order transition or, at most, a first-order transition with a small discontinuity in M and a narrow two-phase region. The average bulk modulus at the minimum is about 2100 kbar for a range of 0.04 Å.

4. fcc Pd

The stable crystal fcc Pd shown in Fig. 5 is NM at equilibrium ($a_0 = 3.94$ Å) with $B \simeq 2000$ kbar, but is well known to be close to FM. Our calculations show that the equilibrium lattice constant is within 4% or 5% of the transition to FM under tension, but, as for bcc Ni, the magnetic energy is so small that we cannot fix the details of the transition, which occurs somewhere in the shaded range in the figure. We also find a range of reduced lattice constant within 1% or 2% of the equilibrium value in which χ/χ_0 shows wildly oscillatory behavior, suggesting the occurrence of further FM ranges under pressure. We cannot fix the behavior with any accuracy, so that range is left blank in the figure. Outside that range the susceptibility behaves more smoothly, decreasing on the left and rising to large values on the right. The point calculated by Janak[17] at $a_0 = 3.92$ Å is now only slightly below our a_0 (unlike fcc Co) within the NM range, and the susceptibility value is consistent with our results.

5. bcc Mn

Mn is another element close to ferromagnetism. Figure 6 shows that in the bcc lattice Mn is FM at equilibrium $a_0 = 2.79$ Å, in agreement with Kübler[18] and Fry *et al.*,[19] but is close to the transition and has a small moment; a 1.4% decrease in a appears to bring it into the NM phase. The bulk modulus at equilibrium is about 2500 kbar. The bcc lattice is metastable with respect to the fcc lattice, whose ground state is not ferromagnetic, but probably antiferromagnetic[18]; high-temperature stable forms of both bcc and fcc Mn exist. The general behavior near the transition is similar to bcc Ni and the small magnetic energy makes details of the transition difficult to resolve; the transitional behavior occurs within the shaded narrow region in Fig. 6. The susceptibility rises smoothly to large values as the transitional range is ap-

proached. There is no comparison with Janak's calculations,[17] since he did not consider bcc Mn (he made a calculation for fcc Mn, which he found NM at equilibrium with a small susceptibility). An unusual feature is the abrupt rise in M values at about 10% expansion of the lattice (3.10 Å), which indicates another phase transition between a low-moment and a high-moment phase (as was found in fcc Fe). Such a high-moment phase was found by Kübler[20] for bcc Mn and by Fry *et al.*[19] The work of Fry *et al.* did not find the transition from the NM to the low-spin FM phase, but found the transition between the low-spin and high-spin FM phases about where we do. However, they show the moment rising steeply but continuously, whereas in our work the transition is first order and discontinuous, thereby illustrating the power of the fixed-spin-moment procedure to resolve details of the transition.

VI. CONCLUSIONS

We conclude from this work that total-energy band theory with the LDA and the fixed-spin-moment procedure provides a good way to study systematically the important volume dependence of metallic magnetic phases. This dependence leads to a greatly enriched magnetic phenomenology and suggests a considerable extension of the number of materials that are ferromagnetic. The volume dependence sensitively controls the relative stabilities of ferromagnetic and nonmagnetic phases leading to phase transitions of a particularly simple kind, i.e., transitions in which the energy is accurately known for all thermodynamic states of the phases involved in the transition. However, the description of these ground-state properties is still largely theoretical and not checked by accurate measurement, since producing sizable changes of lattice dimensions by pressure or epitaxy is limited, and making precise magnetic measurements on materials under high pressure or confined to a few atomic layers is difficult.

ACKNOWLEDGMENTS

We thank F. Meier of the Eidgenossiche Technische Hochschule, Zürich, for preprints of his work and P. C. Pattnaik, IBM Research, for suggesting the study of bcc Mn.

[1] P. M. Marcus and V. L. Moruzzi, Solid State Commun. **55**, 971 (1985).
[2] V. L. Moruzzi, P. M. Marcus, K. Schwarz, and P. Mohn, J. Magn. Magn. Mater. **54-57**, 955 (1986).
[3] P. M. Marcus, V. L. Moruzzi, and K. Schwarz, Mater. Res. Soc. Symp. Proc. **63**, 117 (1986).
[4] V. L. Moruzzi, P. M. Marcus, K. Schwarz, and P. Mohn, Phys. Rev. B **34**, 1784 (1986).
[5] V. L. Moruzzi, Phys. Rev. Lett. **57**, 2211 (1986).
[6] P. M. Marcus, V. L. Moruzzi, Z. Q. Wang, Y. S. Li, and F. Jona, Mater. Res. Soc. Symp. Proc. **83**, 21 (1987).
[7] See, for example, the extensive review by Richard M. Martin, in *Electronic Structure, Dynamic and Quantum Structural Properties of Condensed Matter*, edited by J. T. Devreese (Plenum, New York, 1985), pp. 175–225.
[8] The idea of the fixed-spin-moment procedure is discussed by K. Schwarz and P. Mohn, J. Phys. F **14**, L129 (1984), and applied to a magnetic transition in YCo_2. Extension of density-functional theory to new ground states under general constraints has been discussed by P. H. Dederichs, S. Blügel, R. Zeller, and H. Akai, Phys. Rev. Lett. **53**, 2514 (1984); they focus on charge and moment fluctuations.
[9] We follow the review by W. Kohn and P. Vashishta, in *Theory of the Inhomogeneous Electron Gas*, edited by S. Lundquist and N. H. March (Plenum, New York, 1983).
[10] U. von Barth and L. Hedin, J. Phys. C **5**, 1629 (1972).
[11] J. S. Dugdale and D. K. C. MacDonald, Phys. Rev. **89**, 832 (1953).
[12] V. L. Moruzzi, J. F. Janak, and K. Schwarz, Phys. Rev. B **37**, 790 (1988).
[13] A. R. Williams, J. Kübler, and C. D. Gelatt, Jr., Phys. Rev. B **19**, 6094 (1979).
[14] J. F. Janak, Solid State Commun. **25**, 53 (1978).
[15] U. Gradmann and P. Tillmanns, Phys. Status Solidi A **44**, 539 (1977); P. A. Montano, Y. C. Lee, J. Marcano, and H. Min, Mater. Res. Soc. Symp. Proc. **56**, 183 (1986).
[16] D. Pescia, M. Stampanoni, G. L. Bona, A. Vaterlaus, R. F. Willis, and F. Meier, Phys. Rev. Lett. **58**, 2126 (1987).
[17] J. F. Janak, Phys. Rev. B **16**, 255 (1977).
[19] J. Kübler, in Proceedings of the Institute von Laue–Langevin Workshop on 3*d* Metallic Magnetism, Grenoble, France, 1983, edited by D. Givord and K. Ziebeck (unpublished).
[19] J. L. Fry, Y. Z. Zhao, E. Brener, G. Fuster, and J. Callaway, Phys. Rev. B **36**, 868 (1987).
[20] J. Kübler, J. Magn. Magn. Mater. **20**, 107 (1980).

Ferromagnetism in ultrathin metastable films of fcc Fe, Co, and Ni (invited)

R. F. Willis,[a] J. A. C. Bland, and W. Schwarzacher
Cavendish Laboratory, Department of Physics, University of Cambridge, Cambridge CB3 0HE, United Kingdom

We have applied spin-polarized neutron reflection at a grazing angle of incidence to study the ferromagnetic behavior of thin magnetic films down to the monolayer thickness level. The reflected intensities I^+ and I^- for spin parallel (+) or antiparallel (−) to the sample magnetization are measured near the angle θ_c for total reflection: deviation of the flipping ratio $F = I^+/I^-$ from unity occurs only for ferromagnetic ordering. In general, deviations of F from unity are so small that an accurate determination of the magnetic moment per atom μ is not possible. The success of the present experiments relies on the enhancement ($\sim 500\times$) of the magnetic signal when the film is overcoated with a nonmagnetic layer of thickness sufficient to produce constructive interference in the reflected neutron wave field. With this method, we have determined the magnetic moments in films of the metastable fcc phases of Fe and Co, grown epitaxially on Cu(001) single-crystal substrates. The fcc Fe(001) films have lowered Curie temperatures T_C below 400 K for thicknesses less than 5 monolayers, similar to Ni films. In contrast, the Co(001) films exhibit a constant value of $\mu \approx \mu_{\text{bulk}} = 1.8\mu_B$ down to a single monolayer thickness over the same temperature range. The fcc Fe films exhibit unusual magnetic anisotropy properties which are structure and strain related, as determined by low-energy electron diffraction measurements. The results are discussed in the context of three- to two-dimensional magnetic scaling theories and predictions derived from local-spin-density functional calculations of the magnetic moments per atom as a function of volume strain.

I. INTRODUCTION

We have studied the ferromagnetic behavior of the metastable phases of fcc cobalt and iron by effectively "clamping" the lattice spacing in thin films epitaxially grown on appropriate single-crystal metal substrates. The magnetic moments are predicted to change discontinuously with varying atomic volume and there exist ranges of coexistence of different magnetic phases.[1–4] However, to date there has been very little experimental evidence to corroborate these views, principally due to the difficulties inherent in measuring the magnetic moments in ultrathin epitaxial layers. Recently, we have succeeded in applying spin-polarized neutron reflectance at a grazing angle of incidence to study the ferromagnetic properties of thin magnetic films of Co and Fe down to the monolayer thickness level.[5–7] The technique allows us to determine the magnitude of the magnetic moment per atom μ in ferromagnetically ordered layers, as a function of temperature, thickness, and applied magnetic field.

The results are unusual in that, whereas the fcc Co(001) layers remain ferromagnetic down to a single monolayer with $\mu \approx \mu_{\text{bulk}} \approx 1.8\mu_B$ with no sign of a reduced T_C for temperatures up to 450 K, the fcc Fe(001) films are ferromagnetically ordered only at temperatures below this value, their T_C values being thickness dependent. Similar behavior has been observed with thin Ni films.[8] The fcc Fe(001) films are unique however, in that they exhibit strong magnetic anisotropy effects which are strain related, dependent on the number of layers. Detailed low-energy electron diffraction (LEED) measurements[9,10] have established the degree of strain as a function of film thickness. Perhaps most surprising is the fact that whereas the fcc Co(001) films exhibit spontaneous magnetization within the film plane for all layer thicknesses, the fcc Fe(001) films show in-plane magnetization only for the first monolayer, the succeeding layers up to 7 monolayers showing strong spin anisotropy normal to the interface with remanence strongly dependent on the layer thickness. The 4-monolayer films shows maximum volume expansion and a moment of the order of $\mu = 1$ to $1.5\mu_B$, in agreement with the recently predicted "low-moment" ferromagnetic ground state in the fcc bulk iron phase.[1,3,4]

In Sec. II, we discuss the spin-polarized neutron reflection method; Sec. III, the film thickness and temperature-dependent ferromagnetic behavior; Sec. IV, the strain-related magnetic anisotropy, in relation to LEED measurements; and Sec. V, the ground-state magnetic moment behavior as a function of volume strain. Finally, in Sec. VI, we conclude with some remarks addressing spin-wave finite-temperature properties of these ultrathin metastable magnetic films.

II. SPIN-POLARIZED NEUTRON REFLECTANCE

The possibility of using grazing-incidence neutron reflection as a probe of the magnetization density profile at surfaces was first proposed by Felcher.[11] The method of near-critical reflection of a spin-polarized neutron beam offers a specific advantage for quantitative measurement of magnetic moments. The magnetic scattering cross section gives rise to a spin asymmetry $S(q) \approx P_0^{-1}[F(q) - 1]/[F(q) + 1]$, where the "flipping ratio" $F(q) = R^+/R^-$ is the ratio of the reflected intensities of incident spin-up (R^+) or spin-down (R^-) neutrons for a

[a] Present address: Department of Physics, Pennsylvania State University, University Park, PA 16802.

 0021-8979/88/084051-06$02.40 © 1988 American Institute of Physics

beam spin polarized to a degree P_0, and is a function of the normal component of the incident wave vector, $|q| = \frac{1}{2}|k_i - k_f|$. The q dependence of $S(q)$ provides a measure of the magnetic moment per atom in the ferromagnetic medium.[12] However, $S(q)$ only begins to show any significant deviation from zero for the values of q larger than q_c, the value at the critical angle beyond which the reflected intensity $R(q)$ falls rapidly and the signal-to-noise ratio becomes a limiting factor.[11,12] Thus, the difficulty to date has been one of obtaining sufficient intensity from samples epitaxially grown on flat single-crystal substrates of size typically 1–2 cm^2.

We have overcome this difficulty by overcoating the magnetic thin film with a thicker layer of a nonmagnetic metal, thereby producing interference in the neutron wave field sufficient to enhance the sensitivity of measurements by several orders of magnitude in the statistically relevant range, $q_c < q < 3q_c$, enabling us to determine μ in films down to a single monolayer thickness and surface area 1 cm^2.[5–7]

A simple application of Snell's law of optics illustrates the optical interference of neutrons reflected at grazing incidence from thin metallic films; see Fig. 1. Neutrons of wavelength $\lambda \approx 10$ Å incident at a grazing angle of incidence θ_i on a film of refractive index n_2, characterized by a mean coherent scattering length b and a density of scattering centers per unit volume N, undergo total reflection when θ_i is less or equal to the critical angle, $\theta_c = \lambda(Nb/V)^{1/2}$ with $n_2 = 1 - \theta_c^2/2$ and V the atomic volume. For positive values of b, interference fringes arising from the optical path difference between beams A and B (Fig. 1) are observed for $\theta_i > \theta_c$, dependent on the film thickness t_2. For a magnetized thin-film sample, thickness t_3, b is effectively replaced by $b \pm p$ with $\pm$ signs representing the difference in refractive index for spin-up or spin-down neutron spin states for a magnetic scattering length $p \approx b$. This causes the spin-up (+) and spin-down (−) interference fringes to be displaced relative to each other giving rise to a spin asymmetry enhancement for $q > q_c$.[13]

This is illustrated by the results obtained for ferromagnetically ordered thin films of cobalt, epitaxially grown on Cu(001) single-crystal substrates, Fig. 2. The spin asymmetry S (%) plotted against the normalized quantity

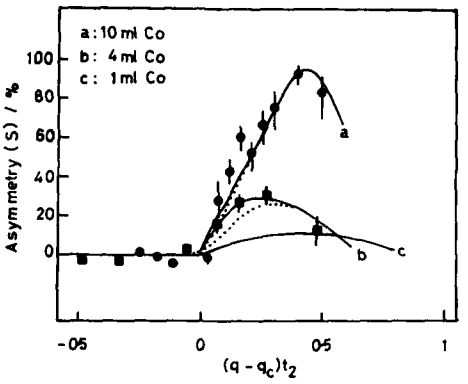


FIG. 2. Spin-asymmetry ratio $S(q)$ for fcc Co(001) films; copper overlayer thickness $t_2 = 42$, 130, and 75 Å for $t_3 = 10$, 4, and 1 monolayer (ml), respectively.

$(q - q_c)t_2$ peaks on the critical region $q \sim 2q_c$, the height of which is a direct measure of the product (μt_3) of the magnetic film. The position of the peak is effectively "tuned" by the thickness t_2 of the Cu(001) epitaxial overlayer.[13] The film thicknesses were controlled by careful atomic-beam evaporation (10^{-10} Torr vacuum), the deposited flux being monitored by Auger signal analysis.[9,10]

III. FILM THICKNESS AND TEMPERATURE DEPENDENCE

A least-squares fit to the cobalt-film data, shown in Fig. 2, gives values for the magnetic moment per Co atom consistent with the ground-state total-energy calculations of Marcus and Moruzzi,[14] who predict a bulk fcc phase moment of $\mu \approx 1.7\mu_B$. We observe $\mu = (1.8 \pm 0.3)\mu_B$ for an 18-Å-thick Co film [10 monolayers (ml)] overcoated with a copper film, 40 ± 5 Å thick. The value rises slightly with reducing film thickness to $\mu = (2.1 \pm 0.3)\mu_B$ for 2 monolayers, as depicted in Fig. 3.

This behavior is compared with results obtained using a

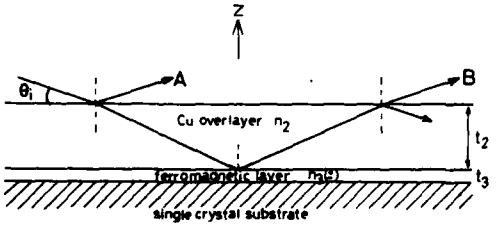


FIG. 1. Illustrating optical interference between neutron rays A and B reflected at grazing incidence from a copper film (thickness t_2, refractive index n_2) deposited on top of a thin ferromagnetic layer (thickness t_3, spin-dependent refractive index $n_3^{\pm}$) epitaxially grown on a single-crystal substrate.

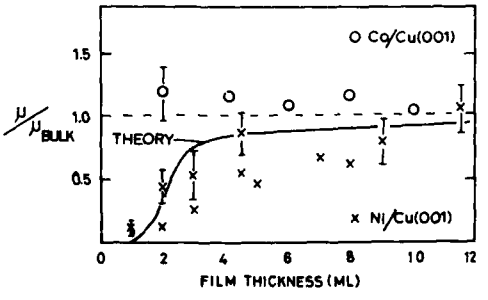


FIG. 3. Magnetization vs film thickness for fcc cobalt (this work) and nickel (Sill *et al.*, Ref. 8) epitaxially grown on Cu(001); theory (Hasegawa, Ref. 19).

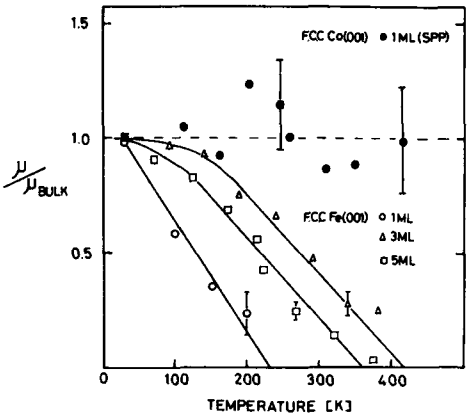


FIG. 4. Magnetization vs temperature for fcc films of Co(001) and Fe(001) epitaxially grown on Cu(001): spin-polarized photoemission (SPP) results (Refs. 20 and 21).

sensitive dc superconducting quantum interference device (SQUID) magnetometer[8] to study nickel films at 4 K prepared by epitaxial growth sandwiched between thicker layers (500 Å) of single crystal Cu(001), shown in Fig. 3. A decrease in the saturation-field moment from that of bulk nickel, $\mu = 0.6\mu_B$, is observed for films of thickness less than 18 Å, falling rapidly to zero for 1 or 2 monolayers thickness. This behavior is in agreement with anomolous Hall-effect measurements[15] on Ni films condensed at 10 K in 10^{-11} Torr vacuum, which indicate that Ni does not develop long-range ferromagnetic order until about 3 ml coverage. The Ni films[8] show a decreasing Curie temperature with decreasing film thickness: T_C = 100, 300, and 400 K for 2, 4.5, and 7 ml, respectively. This behavior has been predicted by various mean-field,[16] spin-wave density,[17] and spin-fluctuation[18] theories. A recent calculation[19] of the finite-temperature ferromagnetic behavior of this itinerant electron system is shown (solid line, Fig. 3). (Signal to noise ratio considerations make it impractical, at the present time, to confirm this behavior of such a low-moment system using the spin-polarized neutron reflectance method.)

Contrary to Ni, the low-temperature anomalous Hall-effect measurements[15] show that Co and Fe develop ferromagnetic order within a single monolayer. This behavior has also been confirmed by spin-polarized photoemission measurements[20] on the *uncoated* magnetic films, which show the fcc cobalt films remaining ferromagnetically ordered down to a single monolayer on a Cu(001) substrate with no evidence for a lowered T_C for temperatures below 450 K, as depicted in Fig. 4. In contrast, the fcc iron[21] and nickel films[8] show reduced T_C behavior as a function of decreasing film thickness, as shown in Figs. 3 and 4.

IV. MAGNETIC ANISOTROPY BEHAVIOR

Spin-polarized photoemission (SPP) measurements in a variable magnetic field applied normal to the surface of fcc iron films epitaxially grown on Cu(001) substrates show

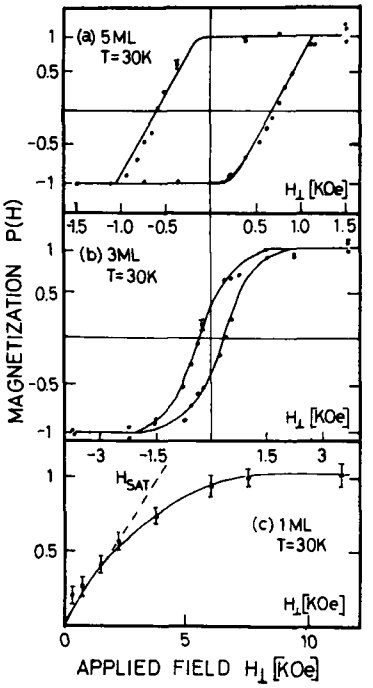


FIG. 5. Magnetization vs applied magnetic field normal to fcc Fe(001) film surfaces, as measured by spin-polarized photoemission (Refs. 20 and 21).

thickness-dependent magnetocrystalline anisotropy effects.[21] Magnetization curves at 30 K for 5-, 3-, and 1-ml films are shown in Fig. 5. In the case of the 5-ml fcc iron film [Fig. 5(a)], the remanence is equal to the full saturation magnetization M_s, i.e., the perpendicular uniaxial anisotropy K_u is sufficient to overcome the in-plane shape anisotropy energy, $K_u > 2\pi M_s^2$, such that the spins align normal to the film plane as the temperature is lowered to 30 K.[22] The 3-ml film also produces a clearly resolved hysteresis, but with reduced coercivity and remanence [Fig. 5(b)]. Although the 1-ml fcc iron film [Fig. 5(c)] does not show any hysteresis, the steep rise of the polarization (magnetization) curve $P(H)$ at $H = 0$ [dashed curve, Fig. 5(c)] is indicative of a strong anisotropy component also perpendicular to the film plane.[20,21] However, it is not sufficient to bring about a nonzero remanence, i.e., $K_u < 2\pi M_s^2$, and the spins align in-plane. The rounding of the $P(H)$ curves [Figs. 5(b) and 5(c)] arises naturally if the easy axis of magnetization (or the direction of uniaxial anisotropy) does not lie exactly along the surface normal but takes some nonzero angle relative to the normal direction.[23] Then saturation is reached only asymptotically for a single-domain thin film.[24]

Magnetization behavior similar to the 1-ml fcc iron film [Fig. 5(c)] is observed for the fcc cobalt films (Fig. 2).[20] With the assumption that the angle between the easy axis of magnetization and the surface normal is negligibly small

(i.e., a true "surface anisotropy" effect), the initial slope of the magnetization curves [dashed curve, Fig. 5(c)] intercepts the saturation magnetization value at $H_{sat} \approx 5$ kOe giving a value of $M_s \approx 1.0$ kOe which translates into a temperature-dependent anisotropy constant $K_u \approx 10$ kOe. The anisotropy field, $H_A = 2k_u/M_s$, amounts to something of the order 20 kOe, giving rise to an anisotropy barrier $U_A = \frac{1}{2}H_A M_s \approx 0.07 \pm 0.01$ meV per atom.[25] This value is 5 times smaller than that calculated by Gay and Richter[26] for the spin anisotropy of a ferromagnetic iron monolayer ($\sim$0.4 meV/atom) arising from the spin-orbit interaction between the eigenstates of a thin slab. However, this anisotropy energy was predicted to dominate the dipole interaction energy (shape anisotropy energy $2\pi M_s^2$) only for film thicknesses of one or two monolayers. In the case of the fcc iron films (Fig. 5) it is the thicker films only which show perpendicular magnetic anisotropy $K_u > 2\pi M_s^2$. Surprisingly, the observed $P(H)$ behavior of the cobalt films[20] and, therefore, also the anisotropy, appears to be independent of the film thickness.

The fact that the fcc iron films prefer to align their spins normal to the surface while the fcc cobalt films remain in-plane magnetized has recently been confirmed by the spin-polarized neutron (SPN) measurements.[27]

The SPN reflection method, illustrated in Fig. 1, measures the spin-dependent reflectivity only when the magnetization M has an in-plane component (either parallel or antiparallel to the neutron spin vector); magnetization normal to the surface gives zero response. However, an applied magnetic field of sufficient strength to pull the spins in-plane gives a positive flipping ratio, $F > 1$, the magnitude of which relates to the in-plane magnetization. This is illustrated by the SPN flipping-ratio curves, shown in Fig. 6, for applied field strengths of 60, 1000, and 4000 Oe in-plane to a 3-ml fcc Fe(001) film sandwiched between Cu(001) media at 4 K. Taking the saturation field value H_s to be between 2 and 5 kOe, the magnitude of the flipping ratio (Fig. 6) gives a value for the mean magnetic moment per atom $1 < |\mu| < 1.5\mu_B$. The SPN results are therefore in substantial agreement with the high remanence curves in Fig. 5.

The anisotropy and magnetization depends on the detailed crystallographic structure of these films, particularly on the lattice strain.[1-4] LEED intensity analysis[9,10] reveals the degree of uniaxial strain to be strikingly different for the Co and Fe films. Whereas the fcc cobalt layers show an overall thickness-independent *contraction* normal to the surface of the order of 3%, similar to the surface lattice relaxation of bulk fcc cobalt, with 2% lateral strain due to the Cu(001) substrate, the fcc iron films exhibit an overall *expansion* normal to the surface, the magnitude of which varies from 1% to 6% over the range 1–7 ml, as shown in Fig. 7. This expansion reaches a maximum value of 6% for the 5-ml-thick fcc iron film, before collapsing back to 1% for 7 ml. The point of interest is that it is the 5-ml-thick film which exhibits the strongest perpendicular magnetic anisotropy; see Fig. 5. The different hysteresis behavior is observed to vary with film thickness in a complimentary manner to the variation in lattice strain as shown in Fig. 7.

These structural variations in the fcc iron films would appear, therefore, to relate directly to the observed magnetic anisotropy. The anisotropy relates to subtle details of the electronic band structure which is critically dependent on the degree of uniaxial strain, particularly in the case of the fcc iron films.

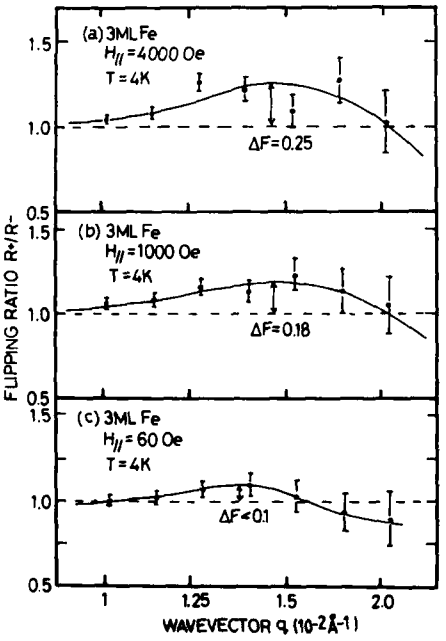


FIG. 6. Spin-polarized neutron reflection flipping ratio (R^+R^-) curves for 3-ml fcc Fe(001) at 4 K showing the decreasing magnitude of $F(q)$ as the in-plane applied magnetic field is reduced: (a) 4000, (b) 1000, and (c) 60 Oe.

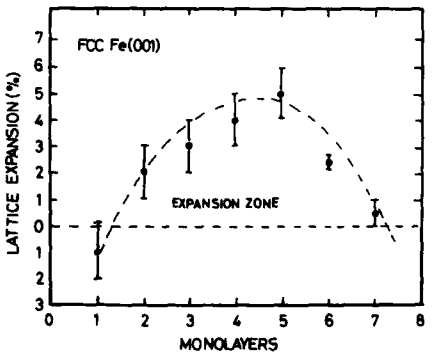


FIG. 7. Plot showing the mean lattice expansion (%) relative to bulk copper lattice spacing as a function of thickness for fcc Fe(001) films, deduced from LEED measurements (Ref. 9).

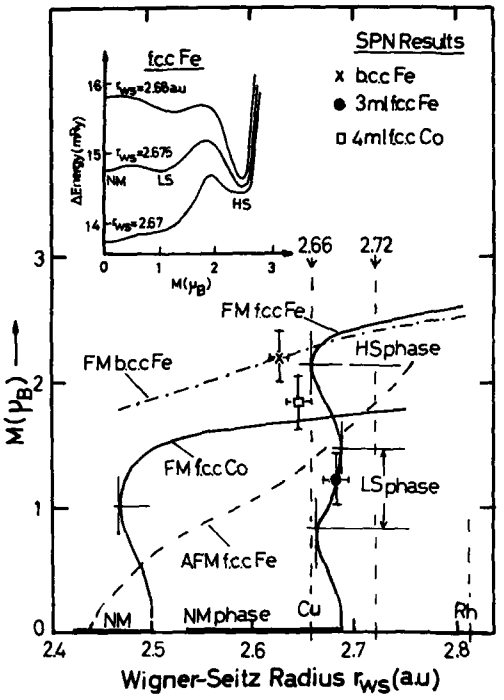


FIG. 8. Magnetization vs Wigner-Seitz radius (r_{ws}), calculated for bcc Fe, fcc Fe, and fcc Co bulk phases (Ref. 1), showing the experimental SPN results: FM—ferromagnetic; AFM—antiferromagnetic (Ref. 4); NM—nonmagnetic. The vertical tangent lines are points at which the susceptibility $(dM/dH)_{H=0}$ is infinite, defining low-spin (LS), high-spin (HS), and zero-spin (NM) moment phases of fcc iron over the range $2.66 < r_{ws} < 2.72$ a.u. (cf. Fig. 7). Inset: total energy (relative to energy minimum) vs magnetization, as a function of r_{ws} in this critical range (Ref. 1).

V. GROUND-STATE MAGNETIC MOMENT BEHAVIOR

The lattice volume expansion of the fcc iron films, expressed by the LEED meaurements in Fig. 7, translates into a change in the Wigner–Seitz radius r_{ws} ($V = 4\pi r^3_{ws}/3$) covering the range $2.66 < r_{ws} < 2.72$ a.u. Over this range, band-structure calculations[2] show a significant change in the d-band occupancy at the Fermi energy. That is, d bands along the zone face of the fcc Brillouin zone change from hole-pocket to filled electron states as r_{ws} is expanded from 2.66 to 2.74 a.u. A detailed analysis of the total-energy surfaces in moment-volume parameter space obtained from energy-band calculations using a local-spin-density approximation[1] indicate that over this range the bulk fcc phase of iron can exist in any of three magnetic phases—a nonmagnetic (NM), a low-spin moment (LS), and a high-spin moment (HS) ferromagnetic phases. This is shown schematically in Fig. 8 (inset diagram). The SPN measurements in Fig. 6 suggest that the 3-ml fcc Fe(001) film with a magnetic moment per atom $\mu \approx (1\text{–}1.5)\mu_B$ is in the LS phase (as indicated in Fig. 8).

However, the complicated hysteresis behavior of the magnetic anisotropy, as shown in Fig. 5, suggests that the coexistence of all three magnetic phases together with finite-temperature effects may be important also. For example, finite-temperature first-principles disordered-local-moment calculations[4] confirm that the magnetic moment collapses as the lattice spacing is reduced but that in the low-moment state, antiferromagnetic order is preferred. The present theoretical situation is compared with our experimental SPN results in Fig. 8.

The important point to realize is that the SPN and SPP measurements cannot detect antiferromagnetism but the results to date confirm ferromagnetic behavior in these fcc Fe(001) and Co(001) thin films. Efforts are in progress to stretch the fcc iron lattice further ($r_{ws} > 2.8$ a.u.) by epitaxial growth on Rh(001) (cf. Fig. 8) to stabilize the predicted high-spin moment phase.[27,28] As shown in Fig. 8, the SPN results confirm the moment of bcc iron, $\mu = 2.15\mu_B$, and fcc cobalt, $\mu \approx 1.8\mu_B$.

VI. DISCUSSION

There are two key elements in theory of ferromagnetic thin films: the first, due to Kittel,[29] predicts that films become single-domain magnetized in a direction parallel to the surface when the thickness falls below approximately 1000 Å; the second, due to Mermin and Wagner,[30] who showed that, for symmetric short-range interactions, there could be no long-range order in strictly one- or two-dimensional (1D or 2D) structures. This predicted instability of ordered structures in low dimensions is so well known that restrictions placed on the original theory are sometimes overlooked. Bloch[31] showed that the result applies only to highly symmetric Heisenberg coupling between spins S, such that the energy $E = J\mathbf{S}\cdot\mathbf{S}$, where J is the exchange constant. He found that the number of thermally excited spin waves increased as $T^{3/2}$ in 3D, but in 2D (or 1D) the number of spin waves diverged at any finite temperature. Since each spin wave represents a decrease in the magnetization of the ferromagnet, an infinite number of spin waves represent a disordered ferromagnet in the low-dimensional limit.

However, these conclusions are not applicable if there exists uniaxial anisotropy in either the magnetic properties (due to the presence of interfaces or crystallographic effects) or in the exchange itself (the case of uniaxial exchange is the Ising model with magnetic interactions of the form $E = J\mathbf{S}_z \times \mathbf{S}_z$). Both the Ising interaction and the magnetic anisotropy introduce an energy gap in the spin-wave spectrum so that the thermal energy kT_C comparable to this gap is required to excite spin-wave disorder. Pinning of spin waves at the interfaces is possible and this "surface anisotropy" effectively increases the energy gap further, yielding a higher T_C.

The much higher T_C threshold for the cobalt films (Fig. 4) would indicate that the spin-wave energy gap is greater than that in the fcc iron films. Given that the magnitudes of their magnetic moments are roughly comparable ($\mu_{Co} \approx 1.8\mu_B$; $\mu_{Fe} \approx 1.5\mu_B$) the results would indicate a strong difference in the anisotropic exchange coupling J. The magnetization behavior of both films suggest a large perpendicular uniaxial magnetic anisotropy,[20,21] which is

not sufficient in the cobalt films to align the spins normal to the surface. With the assumption of a uniformly magnetized, single-domain film, the anisotropy field is estimated to be of the order $H_A \sim 20$ kOe corresponding to an anisotropy barrier to spin rotation of the order $V_A \sim 0.07 \pm 0.01$ meV per atom.[20] The thickness-dependent magnetic anisotropy behavior of the fcc iron films probably derives from the extreme sensitivity of the magnetic moment in the range of volume strain imposed by the Cu(001) sublattice (Fig. 8). Also, the predicted mixed-phase magnetic behavior[1] might account for the rounding observed in the hysteresis loops.[24] It remains to be seen whether this unique behavior of the fcc iron films epitaxially grown on Cu(001) changes when the lattice spacing is expanded by epitaxy to Rh(001) (Ref. 28) to accommodate the more stable high-strain moment magnetic phase predicted to occur for $r_{ws} > 2.7$ a.u.[1] However, it is significant that the bcc Fe ferromagnetic phase curve lies lower in energy than the fcc Fe ferromagnetic phase curve at these larger lattice strains, $r_{ws} > 2.7$ a.u., which could account for the collapse of the fcc films into a disordered (bcc) state for films of thickness greater than 6 ml, as seen in Fig. 7. This would explain the notion of "bcc inclusions" in thicker films of fcc iron.[28]

These general comments ignore electronic interaction (hybridization) between the ferromagnetic film and the nonmagnetic support. Such effects are important in explaining the differences in behavior between Co, Ni, and Fe on various substrates.[32,33] Specifically, besides enhancing or reducing the atomic magnetic moment, the presence of the interface states may affect the direction of any magnetic anisotropy arising from spin-orbit coupling.[26] It is significant, however, that the magnetic hysteresis behavior of these films as measured by the SPP technique on uncoated films (Fig. 5) and the SPN technique on coated films (Fig. 6), is the same. This would suggest that such effects are not important in the present case due to the lack of overlap in energy of the d bands with those of Cu(001).

ACKNOWLEDGMENTS

R. F. W. wishes to acknowledge the hospitality of Professor H. C. Siegmann and F. Meier of the Laboratorium fur Festkorperphysik, Eidgenössische Technische Hochschule, Zurich, where the spin-polarized photoemission measurements were carried out. Likewise, the authors wish to thank the staff of the Institute Laue-Langevin, particularly Dr. O. Schäerpf and Dr. H. Lauter, and the Rutherford-Appleton Laboratory, particularly Dr. J. Penfold, Dr. R. Ward, and Dr. G. Williams, for help with the neutron reflection measurements. Financial support was provided by the Science and Engineering Research Council (U.K.), and a Ministry for Higher Education (Northern Ireland) Studentship to W. S.

[1] V. L. Moruzzi, P. M. Marcus, K. Schwarz, and P. Mohn, Phys. Rev. B **34**, 1784 (1986); P. M. Marcus and V. L. Moruzzi, these proceedings.
[2] D. Bagayoko and J. Callaway, Phys. Rev. B **28**, 5419 (1983).
[3] C. S. Wang, B. M. Klein, and H. Krakauer, Phys. Rev. Lett. **54**, 1852 (1985).
[4] F. J. Pinski, J. Staunton, B. L. Gyorffy, D. D. Johnson, and G. M. Stocks, Phys. Rev. Lett **56**, 2096 (1986).
[5] J. A. C. Bland, D. Pescia, and R. F. Willis, Phys. Scr. **35**, 528 (1987).
[6] J. A. C. Bland, D. Pescia, and R. F. Willis, Phys. Rev. Lett. **58**, 1244 (1987).
[7] D. Pescia, R. F. Willis, and J. A. C. Bland, Surf. Sci. **189/190**, 724 (1987).
[8] L. R. Sill, M. B. Brodsky, S. Bowen, and H. C. Hamaker, J. Appl. Phys. **57**, 3663 (1985).
[9] A. Clarke, G. Jennings, R. F. Willis, P. J. Rous, and J. B. Pendry, Surf. Sci. **187**, 327 (1987).
[10] A. Clarke, P. J. Rous, M. Arnott, G. Jennings, and R. F. Willis (unpublished).
[11] G. P. Felcher, Phys. Rev. B **24**, 1595 (1981); G. P. Felcher, R. T. Kampwirth, K. E. Gray, and R. Felici, Phys. Rev. Lett. **52**, 1539 (1984).
[12] G. P. Felcher, K. E. Gray, R. T. Kampwirth, and M. B. Brodsky, Physica **136B**, 59 (1986).
[13] J. A. C. Bland and R. F. Willis, in *Thin Film Growth Techniques for Low Dimensional Structures*, NATO ASI series, edited by R. Farrow, S. Parkin, P. Dobson, J. Neave, and A. Arrott (Plenum, New York, in press), Vol. 163B.
[14] P. M. Marcus and V. L. Moruzzi, Solid State Commun. **55**, 971 (1985).
[15] G. Bergmann, Phys. Rev. Lett. **41**, 264 (1978).
[16] L. Valenta, Phys. Status Solidi **2**, 112 (1962).
[17] M. Klein and R. S. Smith, Phys. Rev. **109**, 288 (1958).
[18] J. Hubbard, Phys. Rev. B **23**, 5974 (1981).
[19] H. Hasegawa (unpublished).
[20] D. Pescia, G. Zampieri, M. Stampanoni, G. L. Bona, R. F. Willis, and F. Meier, Phys. Rev. Lett. **58**, 933 (1987).
[21] D. Pescia, M. Stampanoni, G. L. Bona, A. Vaterlaus, R. F. Willis, and F. Meier, Phys. Rev. Lett. **58**, 2126 (1987).
[22] The effect of increasing perpendicular anisotropy as the temperature is lowered is seen in a decreasing saturation field H_s (Ref. 21).
[23] C. Kooy and U. Enz, Philips Res. Rep. **15**, 7 (1960).
[24] For a single-domain thin film uniformly magnetized normal to the surface, the magnetization would produce a rectangular hysteresis loop showing a discontinuous jump from M_s to $-M_s$ at an external field $H = -(2K_u/M_s) + 4\pi M_s$, arising from a coherent rotation of the spins. (See Refs. 20, 21, and 23.)
[25] This value is to be compared with the magnetocrystalline anisotropy of bulk iron, $U_A \simeq 4$ μeV/atom, i.e., 100 times less than that of the thin films (Ref. 26).
[26] J. G. Gay and R. Richter, Phys. Rev. Lett. **56**, 2728 (1986).
[27] Previous efforts (Ref. 6) gave zero in-plane ferromagnetic response. However, recent measurements with an increased magnetic field applied in-plane show the fcc Fe films to be ferromagnetic with perpendicular anisotropy [W. Schwarzacher and R. F. Willis (unpublished)].
[28] Preliminary SPN measurements with $H_{\parallel} \simeq 800$ Oe (in-plane applied field) suggest a value for fcc Fe(001) on Rh(001) in the range $1.5 < \mu < 2.0 \mu_B$. However this could be an average of the high-moment (HS) fcc phase and "collapsed lattice" bcc phase inclusions [W. Schwarzacher, J. A. C. Bland, and R. F. Willis (unpublished)].
[29] C. Kittel, Phys. Rev. **70**, 965 (1966).
[30] N. D. Mermin and H. Wagner, Phys. Rev. Lett. **17**, 1133 (1966).
[31] F. Bloch, Z. Phys. **61**, 206 (1930).
[32] J. Tersoff and L. M. Falicov, Phys. Rev. B **26**, 6186 (1982).
[33] A. J. Freeman, J. H. Xu, and T. Jarlborg, J. Magn. Magn. Mater. **31-34**, 909 (1983).

Magnetic structure of bcc and fcc manganese

N. E. Brener, G. Fuster,[a] and J. Callaway
Louisiana State University, Baton Rouge, Louisiana 70803

J. L. Fry and Y. Z. Zhao
The University of Texas at Arlington, Arlington, Texas 76019

Self-consistent band-structure calculations are used to obtain the ferromagnetic moment as a function of lattice constant for bcc and fcc Mn. The ferromagnetic moment of bcc Mn is found to change discontinuously from a small to a large value as the lattice constant increases, while the fcc moment is found to change discontinuously from zero to a large value with increasing atomic volume. In the bcc case, the transition occurs inside a narrow double moment region in which the low spin and high spin states coexist. Information from magnetic susceptibility calculations on bcc and fcc Mn is used to predict whether the ground state is ferromagnetic or antiferromagnetic in certain ranges of lattice constant.

I. INTRODUCTION

The transition metal Mn occurs in a complex body-centered-cubic phase with 29 atoms per unit cell at room temperature and becomes antiferromagnetic below 95 K. At higher temperatures Mn goes into the face-centered-cubic (fcc) phase (1364–1410 K) and then the body-centered-cubic (bcc) phase (1410–1450 K), both of which have one atom per unit cell.[1] Henceforth the term bcc Mn will refer to the one atom per unit cell structure. The question arises as to what magnetic structure Mn would have in the bcc and fcc phases at low temperature if these phases could be stabilized by epitaxial growth on cubic substrates.[2,3]

Previous theoretical work in this area includes that of Kubler,[4] who computed a large ferromagnetic and antiferromagnetic moment for bcc Mn at a single lattice constant, $a = 5.82$ a.u., and found that the ground state is antiferromagnetic at this lattice constant. Bagayoko and Callaway[5] computed the ferromagnetic moment as a function of lattice constant for fcc Fe and found an abrupt low- to high-spin transition with increasing atomic volume. Subsequently Moruzzi *et al.*[6] examined this low-moment to high-moment transition in fcc Fe in more detail and showed that it is actually discontinuous with a narrow overlap region in which the low- and high-spin states coexist. In this paper we use spin-polarized band-structure calculations to obtain the ferromagnetic-moment versus lattice-constant curve for bcc and fcc Mn. Information from magnetic susceptibility calculations is used to predict whether the ground state is ferromagnetic or antiferromagnetic in certain ranges of lattice constant.

II. BAND STRUCTURE AND MAGNETIC MOMENT CALCULATIONS

We have used the linear combination of Gaussian orbitals (LCGO) method to perform local-density, spin-polarized, all-electron calculations of the band structure and ferromagnetic moment of bcc and fcc Mn at a number of different lattice constants. The program BANDPACKAGE[7] (BNDPKG) was employed in these calculations. More details of the band-structure and magnetic-moment calculations are given in Ref. 8.

Table I gives the computed ferromagnetic moment of bcc Mn at a number of lattice constants ranging from 5.2 a.u. (the computed paramagnetic equilibrium value[9]) to 8.0 a.u., where the magnetic moment is close to its maximum possible value of $5\mu_B$, which is the value of the magnetic moment of an isolated Mn atom. As shown by the table, bcc Mn has a small ferromagnetic moment in the lattice constant range $5.2 < a < 6.025$ a.u. and a large moment in the region $a > 5.9$ a.u. The calculations reveal a narrow double-moment region, $5.9 < a < 6.025$ a.u., in which the low-moment and high-moment states coexist, with a discontinuous low-spin to high-spin transition occurring at a point inside this region. Since the total energy was not computed, we cannot determine the precise lattice constant at which the transition occurs; however, this has little effect on the overall behavior of the moment versus lattice-constant curve since the double-moment transition region is very narrow. The results of Table I are displayed graphically in Fig. 1, which shows the moment versus lattice-constant curve for bcc Mn. The double-moment transition region is similar to that found by Moruzzi *et al.*[6] for fcc Fe. Additional calculations on bcc Mn are currently in progress for lattice constants in the region

TABLE I. Lattice constant a and magnetic moment m for bcc Mn. Indices 1 and 2 refer to the low moment and high moment states, respectively.

a (a.u.)	m_1 (μ_B)	m_2 (μ_B)
5.200	0.76	
5.397	0.92	
5.450	0.97	
5.628	1.09	
5.800	1.18	
5.900	1.24	2.40
5.925	1.26	2.93
5.950	1.28	3.12
5.975	1.29	3.40
6.000	1.32	3.49
6.025	1.35	3.53
6.050		3.56
7.000		4.37
8.000		4.93

[a] Permanent address: Universidad Santa Maria, Valparaiso, Chile.

 0021-8979/88/084057-03$02.40 © 1988 American Institute of Physics

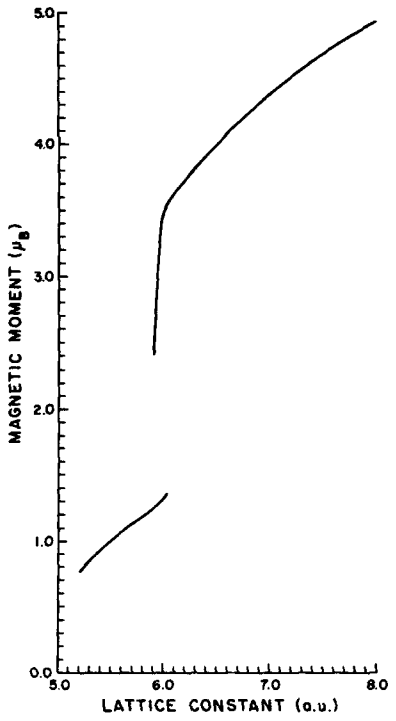


FIG. 1. Ferromagnetic moment of bcc Mn vs lattice constant.

$a < 5.2$ a.u., where the moment is expected to fall to zero at some point.

Table II gives the computed ferromagnetic moment of fcc Mn for a number of lattice constants in the range 6.5–9.0 a.u. As shown by the table, the ferromagnetic moment of fcc Mn is zero in the range $6.5 < a < \sim 7.275$ a.u. and large in the region $a > \sim 7.275$ a.u., with a discontinuous zero-moment to high-moment transition occurring near $a = 7.275$ a.u. In the case of fcc Mn, no double-moment region is found, but rather the transition appears to occur at a single point. The results of Table II are shown graphically in Fig. 2, which gives the moment versus lattice-constant curve for fcc Mn.

In order to facilitate comparisons with bcc Mn, Table II also gives the bcc equal-volume lattice constant (the bcc lattice constant that would yield the same atomic volume). This equal-volume lattice constant is obtained by dividing the fcc lattice constant by $2^{1/3}$, which produces a 21% contraction. Figure 3 shows the high-spin moment versus lattice-constant curve for both bcc and fcc Mn, where the fcc curve is plotted versus the bcc equal-volume lattice constant. The figure shows that as the lattice constant increases, the bcc and fcc curves approach each other closely, indicating that the high-spin ferromagnetic moment in Mn depends primarily on the atomic volume rather than on the lattice structure.

TABLE II. Lattice constant a, bcc equal-volume lattice constant a_{bcc}, and magnetic moment m for fcc Mn. The bcc equal-volume lattice constant is obtained by dividing the fcc lattice constant by $2^{1/3}$.

a (a.u.)	a_{bcc} (a.u.)	m (μ_B)
6.50	5.159	0.00
6.75	5.357	0.00
7.000	5.556	0.00
7.200	5.715	0.00
7.250	5.754	0.00
7.275	5.774	1.71
7.300	6.794	1.88
7.400	5.873	2.82
7.450	5.913	3.20
7.500	5.953	3.42
7.600	6.032	3.55
7.700	6.111	3.63
8.000	6.350	3.84
9.000	7.143	4.44

III. MAGNETIC SUSCEPTIBILITY CALCULATIONS AND PREDICTIONS OF MAGNETIC ORDER

The present version of BNDPKG can consider ferromagnetic and nonmagnetic states but does not permit consideration of a possible antiferromagnetic state. Thus a computed ferromagnetic moment that is greater than zero indicates that the ground state is not nonmagnetic, but the BNDPKG calculations cannot lead to a prediction as to whether the ground state is ferromagnetic or antiferromagnetic. Similarly, a computed ferromagnetic moment of zero indicates that

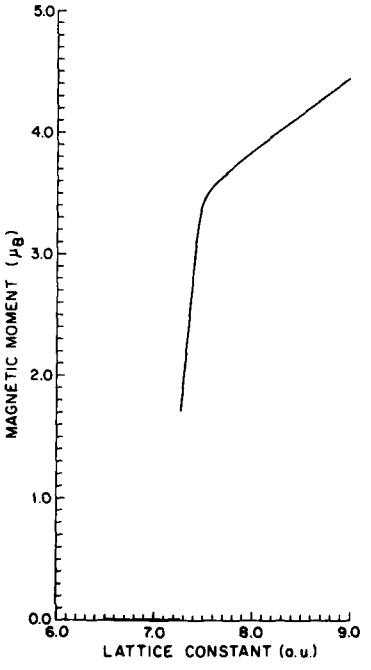


FIG. 2. Ferromagnetic moment of fcc Mn vs lattice constant.

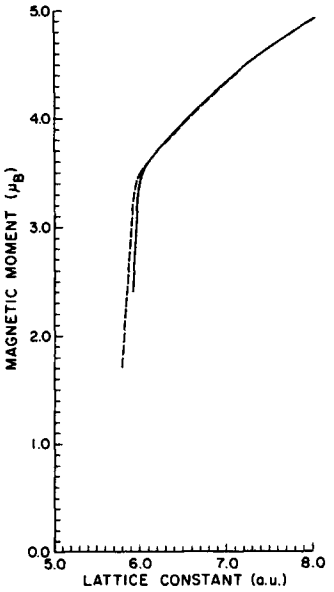


FIG. 3. High-spin ferromagnetic moment vs lattice constant for bcc (solid line) and fcc (dashed line) Mn. The fcc curve is plotted vs the bcc equal-volume lattice constant which is obtained by dividing the fcc lattice constant by $2^{1/3}$.

the ground state is not ferromagnetic, but the band calculations cannot determine whether the ground state is nonmagnetic or antiferromagnetic. Wave-vector-dependent magnetic susceptibility calculations provide the additional information needed to determine whether or not the ground state is antiferromagnetic in certain ranges of lattice constant.

The local-density, local-orbital method of Callaway *et al.*[10] is being used to compute the unenhanced susceptibility χ_0 and the enhanced susceptibility χ for bcc and fcc Mn. Preliminary results of the bcc susceptibility calculations for $a = 5.397$ a.u. are given in Ref. 8. The monotonically decreasing behavior of χ_0 as a function of q and the negative value of χ at $q = 0$ indicate a ferromagnetic ground state. Preliminary results for the susceptibility at $a = 5.2$ a.u., which are not shown here, are very similar to those at $a = 5.397$ a.u. and also indicate a ferromagnetic ground state. Since it is highly unlikely that the ground state would change from ferromagnetic to antiferromagnetic and then back to ferromagnetic as the lattice constant increases from 5.2 to 5.4 a.u., these preliminary calculations suggest that bcc Mn has a ferromagnetic ground state everywhere in the range $5.2 < a < 5.4$ a.u. Preliminary susceptibility calculations for fcc Mn at $a = 6.8$ a.u., which are reported in Ref. 11, indicate an antiferromagnetic ground state at this point. The features of this susceptibility that indicate antiferromagnetism are a maximum in χ_0 at a nonzero value of q and a region of wave vector in which χ is negative. Since in general a tendency toward antiferromagnetism is expected as the lattice constant increases,[12] the fact that the ground state is already antiferromagnetic at $a = 6.8$ a.u. indicates that it will probably remain antiferromagnetic as the lattice constant increases past this point. Thus these preliminary calculations suggest that fcc Mn has an antiferromagnetic ground state everywhere in the region $a > 6.8$ a.u. Further susceptibility calculations on bcc and fcc Mn, which are currently in progress, will be used to check these preliminary results and conclusions and to determine the magnetic order of the bcc ground state for $a > 5.4$ a.u.

ACKNOWLEDGMENTS

This research was supported in part by the National Science Foundation under Grant No. DMR 85-4259. Work at the University of Texas at Arlington was supported by the Robert A. Welch Foundation under Grant No. Y-707. We are indebted to Dr. Paul Marcus (IBM, Yorktown Heights) for useful correspondence regarding the double-moment transition region.

[1] R. J. Weiss and K. J. Tauer, J. Phys. Chem. Solids **4**, 135 (1958).
[2] G. A. Prinz, Phys. Rev. Lett. **54**, 1051 (1985).
[3] B. Heinrich, A. S. Arrott, J. F. Cochran, C. Liu, and K. Myrtle, J. Vac. Sci. Technol. A **4**, 1376 (1986).
[4] J. Kubler, J. Magn. Mater. **20**, 107 (1980).
[5] D. Bagayoko and J. Callaway, Phys. Rev. B **28**, 5419 (1983).
[6] V. L. Moruzzi, P. M. Marcus, K. Schwarz, and P. Mohn, Phys. Rev. B **34**, 1784 (1986).
[7] C. S. Wang and J. Callaway, Comput. Phys. Commun. **14**, 327 (1978).
[8] J. L. Fry, Y. Z. Zhao, N. E. Brener, G. Fuster, and J. Callaway, Phys. Rev. B **36**, 868 (1987).
[9] D. A. Papaconstantopoulos (private communication).
[10] J. Callaway, A. K. Chatterjee, S. P. Singhal, and A. Ziegler, Phys. Rev. B **28**, 3818 (1983).
[11] Y. Z. Zhao, J. L. Fry, P. C. Pattnaik, and K. Schwartzman (these proceedings).
[12] C. Herring, in *Magnetism*, edited by G. Rado and H. Suhl (Academic, New York, 1966), Vol. 2B, p. 1.

Stoner theory of magnetic structure of alternate cubic phases of transition metals

J. L. Fry and Y. Z. Zhao
The University of Texas at Arlington, Arlington, Texas 76019

P. C. Pattnaik and V. L. Moruzzi
IBM Thomas J. Watson Research Center, Yorktown Heights, New York 10598

D. A. Papaconstantopoulos
Naval Research Laboratory, Washington, DC 20375

Epitaxial growth of bcc Co on a (110) GaAs substrate has demonstrated the feasibility of producing thin films of transition metals with structures not usually stable at room temperature and pressure. Thus an entirely new group of magnetic materials may be possible with interesting and perhaps significant magnetic properties. In this paper the simple Stoner theory of ferromagnetism is employed, with exchange-correlation parameters obtained from Janak's work and density of states at the Fermi level determined from self-consistent, paramagnetic energy-band calculations. The theory is applied to each of the 3*d* and 4*d* transition metals in both fcc and bcc phases. Ferromagnetism is obtained for bcc Fe, Co, and Mn and fcc Co and Ni, and strongly enhanced paramagnetism for bcc Sc, Ni, and Y and fcc Sc, Fe, and Pd. Comparisons are made with predictions of total energy and enhanced magnetic susceptibility calculations.

I. INTRODUCTION

Magnetism is conspicuous by its absence throughout most of the Periodic Table of elements at standard conditions of pressure and temperature. In the transition metals ferromagnetism is found in hcp Co, bcc Fe, and fcc Ni, and antiferromagnetism in bcc Cr, but no magnetism has been reported for 4*d* or 5d elements. Considerable excitement was thus produced with the report[1] by Prinz of the stabilization of ferromagnetic bcc Co via epitaxial growth on a GaAs substrate. Perhaps there are more magnetic elements in alternate phases which could be stabilized by the same technique, thus opening up the possibility of new and important magnetic materials. In this short paper the possibility of other magnetic 3*d* and 4*d* elements is investigated theoretically.

II. THEORY

The simplest theory which attempts to account for ferromagnetism is the well known Stoner model[2] based upon an enhanced susceptibility

$$\chi = \chi_0/(1 - I\chi_0)\,, \tag{1}$$

where χ_0 is the unenhanced susceptibility and I is an exchange-correlation enhancement parameter. The condition usually taken for ferromagnetism is a pole of this enhanced susceptibility, which can occur whenever the condition $\chi_0 > 1/I$ is obtained in some elemental metal. Within the random-phase approximation χ_0 is the density of states at the Fermi energy, $D(E_F)$, and the paramagnetic state is unstable if

$$D(E_F) > 1/I\,. \tag{2}$$

Penn[3] considered a q-dependent enhanced susceptibility and a simple s-band model for transition-metal band structures and studied stability regions in the Periodic Table for ferro- and antiferromagnetism. Asano and Yamashita employed the Stoner theory with a fixed parameter I for the 3*d* elements, used self-consistent energy-band results for $D(E_F)$, and considered both bcc and fcc phases. They used a gap equation to study possible antiferromagnetic phases. The most satisfying theoretical work to understand ferromagnetism in the transition metals was reported by Janak.[5] He employed self-consistent paramagnetic band structures[6] at calculated equilibrium lattice constants and a variational form of the enhanced susceptibility[7] which eliminated all adjustable parameters. His study of 32 cubic elements including 3*d* and 4*d* transition metals correctly predicted the occurrence of ferromagnetism in the normal cubic phases.

III. FERROMAGNETISM

Janak's procedure and some of his results are used here to make a quick determination of possible ferromagnetism in the alternate cubic phases of 3*d* and 4*d* transition metals. $D(E_F)$ was calculated for each 3*d* and 4*d* transition metal in a paramagnetic state using an equal-volume lattice constant for the alternate cubic phase. The calculations were done using an augmented-spherical-wave code[8] with Janak's version of the local exchange-correlation potential.[5,6] $D(E_F)$ was also compared with other existing calculations[9,10] where possible, and with rigid-band estimations. Ferromagnetism is expected to occur where $D(E_F)$ is largest, which is in elements whose Fermi energy falls near one of the peaks which naturally occur for fcc or bcc d-electron metals. Near a strong peak care must be taken in calculating both E_F and $D(E_F)$.

In order to use Eq. (1) or (2) it is necessary to compute I. For the first effort this was not done, but the observation made by Janak that I is an atomiclike property, insensitive to crystal structure, was used. This insitivity to crystal structure can be observed by comparing his calculated values of I

 0021-8979/88/084060-03$02.40 © 1988 American Institute of Physics

TABLE I. Stoner criteria for alternate cubic phases of 3*d* and 4*d* transition metals. The alternate structures were chosen to be fcc or bcc, whichever does not occur naturally. Lattice constants were chosen to maintain a cell volume equal to the naturally occurring cell volume. For hexagonal metals the alternate cubic phase was chosen to be the one not computed in Ref. 5 of the text. The columns labeled $ID(A)$ and $ID(N)$ are the products I times $D(E_F)$ for the alternate and normal phases, respectively. Ferromagnetism is possible when the product equals or exceeds unity.

	Element	Structure	a (a.u.)	$D(E_F)$ (Ry^{-1})	I (Ry)	$ID(A)$	$ID(N)$
3*d*	Sc	bcc	6.740	31.6	0.025	0.79	0.83
	Ti	bcc	6.004	26.9	0.025	0.67	0.55
	V	fcc	6.980	22.8	0.026	0.59	0.57
	Cr	fcc	6.678	23.2	0.028	0.65	0.25
	Mn	bcc	5.193	33.1	0.030	0.99	0.63
	Fe	fcc	6.489	22.6	0.034	0.77	1.43
	Co	bcc	5.118	50.3	0.036	1.81	0.97
	Ni	bcc	5.198	19.8	0.037	0.73	2.04
4*d*	Y	bcc	7.326	30.8	0.024	0.74	0.46
	Zr	bcc	6.600	16.1	0.023	0.37	0.39
	Nb	fcc	7.812	21.6	0.022	0.48	0.42
	Mo	fcc	7.420	14.9	0.022	0.33	0.20
	Tc	bcc	5.778	21.0	0.022	0.46	0.37
	Ru	bcc	5.715	27.3	0.022	0.60	0.33
	Rh	bcc	5.746	26.6	0.024	0.64	0.43
	Pd	bcc	5.889	19.4	0.025	0.49	0.78

for bcc and fcc Sc, which were identical,[5] $I = 0.025$ Ry. It is thus assumed in this work that I is the same in the alternate phase of each element, and Janak's values are taken.[5]

Table I contains the results of this study. The column labeled $ID(A)$ provides the test for possible ferromagnetic *alternate cubic phases* using the criterion of Eq. (2). When $ID(E_F)$ exceeds unity the paramagnetic state is unstable with respect to the ferromagnetic phase (it may also be unstable with respect to antiferromagnetic or more complicated order as well). For the alternate cubic phases bcc Co is predicted to be ferromagnetic and bcc Mn almost ferromagnetic. Since the variational theory used to obtain I only ensures that χ in Eq. (1) is the minimum for the assumed form of enhancement,[5,7] it is possible that the tendency for ferromagnetism is underestimated, especially for $ID(E_F)$ near unity. More accurate band calculations, $D(E_F)$ calculations, or determinations of I could result in significantly different predictions for χ. These have been done for fcc Co and predict ferromagnetism.[8] The form of the local exchange-correlation potential used in the self-consistent band-structure calculations may also be a determining factor for these special cases. More complete studies have also been done for bcc and fcc Mn.

For bcc Mn, linear-combination-of-atomic orbitals calculations[10] (LCAO) and augmented-plane-wave[9] (APW) calculations obtained $ID(E_F)$ products which easily exceed unity at the lattice constant used in Table I. A completely different approach[11] to calculating the enhanced susceptibility including the wave-vector dependence has been employed for several transition metals[12] with the conclusion that bcc Mn should be ferromagnetic at this lattice constant. Spin-polarized band calculations using the LCAO method find a stable ferromagnetic moment for bcc Mn,[10] and total-energy calculations as a function of moment and volume confirm this as a stable phase relative to the bcc paramagnetic phase.[13]

Examining Table I for both cubic phases it is seen that only bcc Mn, Fe, and Co and fcc Co and Ni are likely to be ferromagnetic and no 4*d* elements should be ferromagnetic. The latter fact is a consequence of the generally reduced values of $D(E_F)$ and smaller, almost constant values of the integral I in the 4*d* elements. For Fe, Co, and Ni other theoretical predictions have been made through elaborate moment-versus-volume total-energy calculations.[8] At zero temperature, pressure, and applied field these agree with the predictions of Table I and experimental findings. Similar unpublished studies for Mn predict weak ferromagnetism for bcc Mn.[13] Ferromagnetism for bcc Mn has not yet been verified.

Some of the elements exhibit strongly enhanced paramagnetism ($\chi/\chi_0 > 4$) and are likely to display magnetic order at larger lattice constants or upon alloying. These include bcc Sc, Ni, and Y and fcc Sc and Pd.

IV. ANTIFERROMAGNETISM

A simple generalization of Eq. (1) to include a q dependence for χ is possible but this also requires determination of $I(q)$, which is a difficult task. A self-consistent theory for $\chi(q)$ exists and has been applied to some transition metals.[10–12] The many-body enhanced susceptibility is defined by

$$\chi(\mathbf{q}) = \chi_0(\mathbf{q})/[1 - \Lambda\chi_0(\mathbf{q})]\,, \tag{3}$$

where Λ, χ_0, and χ are matrices on a reciprocal-lattice basis. The matrix χ_0 is the random-phase approximation (RPA) *susceptibility tensor*, Λ is a tensor determined by the local exchange-correlation functional, and χ is the enhanced susceptibility. No adjustable parameters appear in these quantities.[10–12]

If the paramagnetic susceptibility of Eq. (3) has a pole at some q, $\chi(q) \to \infty$, then even in the absence of an applied

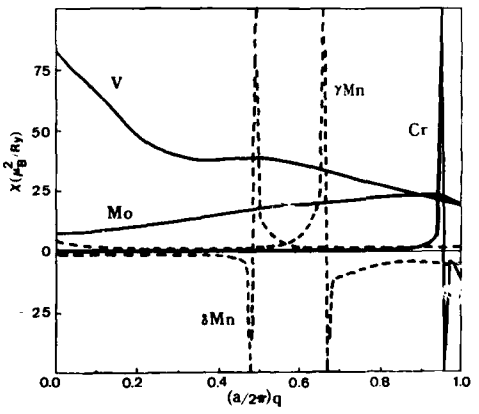


FIG. 1. Exchange-correlation enhanced susceptibility for V, Cr, Mn, and Mo along a cubic axis. For Cr and Mn, χ has been divided by 100 to plot on this scale. δMn is bcc and γMn is fcc.

external field, $H(q)$, $B(q) = \chi(q)H(q)$ may be nonzero, i.e., spontaneous magnetic order may occur. Whether ferromagnetism, antiferromagnetism, or paramagnetism is the stable ground state must be determined experimentally or by total-energy considerations. A simple model[14] relates the change in energy upon magnetic order to the RPA susceptibility χ_0:

$$\Delta E = -K\chi_0(q) \tag{4}$$

with $K > 0$.

Combining Eqs. (3) and (4), a definite prediction of type of magnetic order may be made. For bcc V, Cr, Mn, and Mo and fcc Mn the many-body enhanced susceptibility shown in Fig. 1 predicts that ferromagnetism is possible for bcc Mn, and antiferromagnetism for bcc Cr and fcc Mn. Notably absent is antiferromagnetism in Mo, whose nesting Fermi surface features are identical to Cr. These calculations are very lengthy and are not yet complete for all $3d$ and $4d$ transition metals and will be reported elsewhere.

V. CONCLUSIONS

The Stoner model may be used to predict with relative ease alternate structures which are possibly ferromagnetic and thus stimulate searches for new materials. Alternate ferromagnetic phases predicted in Table I are bcc Mn and Co and fcc Co. Prinz has made ferromagnetic bcc Co.[1]

The generalized Stoner model or $\chi(q)$ is much more expensive to compute, but so far predicts antiferromagnetism for bcc Cr and fcc Mn. The best chance for magnetic order in $4d$ elements should be Mo, but Fig. 1 suggests that it will not occur.

ACKNOWLEDGMENTS

Work at the University of Texas at Arlington was sponsored in part by The Robert A. Welch Foundation and the U.S. Air Force Office of Scientific Research.

[1] G. A. Prinz, Phys. Rev. Lett. **54**, 1051 (1985).
[2] E. C. Stoner, Proc. R. Soc. London Ser. A **169**, 339 (1939).
[3] D. R. Penn, Phys. Rev. **142**, 350 (1966).
[4] S. Asano and J. Yamashita, Prog. Theor. Phys. **49**, 373 (1973).
[5] J. F. Janak, Phys. Rev. B **16**, 255 (1977).
[6] V. L. Moruzzi, J. F. Janak, and A. R. Williams, *Calculated Electronic Properties of Metals* (Pergamon, New York, 1978).
[7] S. H. Vosko and J. P. Perdew, Can. J. Phys. **53**, 1385 (1975).
[8] V. L. Moruzzi, P. M. Marcus, K. Schwarz, and P. Mohn, Phys. Rev. B **34**, 1784 (1986).
[9] D. A. Papaconstantopoulos, *Handbook of the Band Structure of Elemental Solids* (Plenum, New York, 1986).
[10] J. L. Fry, Y. Z. Zhao, N. E. Brener, G. Fuster, and J. Callaway, Phys. Rev. B **36**, 868 (1987).
[11] J. Callaway, A. K. Chatterjee, S. P. Singhal, and A. Ziegler, Phys. Rev. B **28**, 3818 (1983).
[12] Y. Z. Zhao, J. L. Fry, P. C. Pattnaik, and K. Schwartzman (unpublished).
[13] P. C. Pattnaik (private communication).
[14] J. Callaway, *Quantum Theory of the Solid State* (Academic, New York, 1974), p. 799.

Substitutional site preference in a quasicrystal

M. Eibschütz, M. E. Lines, H. S. Chen, and J. V. Waszczak
AT&T Bell Laboratories, Murray Hill, New Jersey 07974

G. Papaefthymiou and R. B. Frankel
Francis Bitter National Magnet Laboratory, Massachusetts Institute of Technology, Cambridge, Massachusetts 02139

Iron has been successfully incorporated in the quasicrystal i-$Al_{74}Si_6Mn_{20-x}Fe_x$ up to a concentration $x = 7$. A combination of magnetic susceptibility and Mössbauer study establishes the fact that there are at least two "classes" in Mn sites and that Fe substitutes for only one of them. High-field Mössbauer measurements at 4.2 K show that the substituted iron carries no local moment, while low-temperature susceptibility data indicate that its presence does not perturb the Curie–Weiss amplitude of the sample. The inference is that both magnetic and nonmagnetic Mn sites must be present in the quasicrystal and that iron can substitute only from among the latter. The simplest interpretation would be in terms of two "classes" on Mn sites (one supporting a local moment, one not), although the possibility of there being more than one class of nonmagnetic site cannot yet be excluded.

Recently there has been great interest in the rapidly quenched Al-rich transition-metal alloys showing icosahedral (or i phase) symmetry incompatible with a periodic lattice.[1] The bulk of this literature has focused on AlMn and AlMnSi alloys for which there is now a growing consensus[2] that the prototypical "building block" is the so-called Mackay icosahedron (MI)[3], formula unit $Mn_{12}(Al/Si)_{42}$, which is found in the crystalline ternary alloy α(AlMnSi).[4] This MI consists of a vacant-centered icosahedron of twelve (defined as α-site) Al/Si inside an equioriented icosahedron of Mn, with the remaining thirty (β-site) Al/Si atoms located at the midpoints of the edges of the Mn icosahedron. No differentiation between Al and Si location (when the latter is present) has yet been made.

The most important uncertainty for these quasicrystals concerns the manner in which orientation-maintaining MI interconnect. Extended x-ray absorption fine-structure (EXAFS) experiments,[5,6] clearly establish that the MI remain practially unchanged on passage from the α phase[7] to the quasicrystalline i phase although their connectivity via Al/Si "glue" atoms is significantly modified. Two kinds of model have been suggested, both involving MI connections along threefold icosahedral directions. One[7–9] places the i-phase MI centers on lattice sites of a 12-fold-vertex[7] three-dimensional Penrose tile (3D PT) lattice, while the other[5,6,10,11] is based on a random-packing procedure.

These models do not contain any precise dual classification of inequivalent Mn (or Al/Si) sites.[12] Nevertheless, a recent combination of NMR spin-echo[13] and magnetic susceptibility[14] experiments has been interpreted in a manner which suggests that two distinct classes of Mn sites can be distinguished both in AlMn and AlMnSi quasicrystals, depending on whether or not they have a localized magnetic moment. Although some skepticism has been voiced[15] concerning this interpretation, we shall establish unequivocally that such a class separation of Mn sites does exist.

We establish experimentally that Fe atoms substituting for Mn in i-$Al_{74}(Mn_{13}Fe_7)Si_6$ do not possess local magnetic moments and also do not influence the total paramagnetic moment of the sample. It follows that both magnetic and nonmagnetic Mn atoms must be present in these i-phase alloys and that Fe selectively substitutes only from among the latter.

Alloys of $Al_{74}Si_6Mn_{20}$ and $Al_{74}Si_6Mn_{13}Fe_7$ were prepared by induction melting of high-purity Al, Si, Mn, and Fe in a boron nitride crucible under argon atmosphere. Ribbon samples of about 1 mm width and 30 μm thickness were obtained by melt-spun technique on a copper wheel $\approx$20 cm in diameter rotating at 2000 rpm. X-ray diffraction measurements confirm 100% i-phase structure in both alloys (see Fig. 1). The Mössbauer abosorption spectra were obtained in a standard transmission with a ^{57}Co in Rh source.

The magnetic susceptibility χ as a function of temperature T is qualitatively similar for both i-phase compositions. In particular, between 20 and 300 K it follows closely a Curie–Weiss dependence of the form

$$\chi = [Np_{\text{eff}}^2/3k(T+\Theta)] + \chi_0 \text{ emu/g},$$

where N is the number of magnetic moments per gram, each of effective moment

$$p_{\text{eff}} = g\mu_B\sqrt{S(S+1)}$$

(in conventional magnetic notation[17]), Θ is the Weiss temperature, and χ_0 is a temperature-independent "Pauli" contribution from unfilled band electrons. The magnetic susceptibility as a function of temperature for i-$Al_{74}Mn_{13}Fe_7Si_6$ is shown in Fig. 2. Computer fitting to the above equation between 20 and 300 K for both the iron-free and iron-containing samples enables us to extract the relevant magnetic parameters Np_{eff}^2, Θ, and χ_0 for each composition. They are shown in Table I.

We note from Table I that both Np_{eff}^2 and Θ are fairly insensitive to iron concentration x. The sign of Θ is antiferromagnetic, suggesting the possibility of spin-glass ordering at low temperatures. The relative constancy of Np_{eff}^2 implies that those iron atoms substituting for Mn in i-$Al_{74}Si_6Mn_{20}$ possess essentially the same magnetic moment as do the Mn which they replace. The Mössbauer experiments described

 0021-8979/88/084063-03$02.40 © 1988 American Institute of Physics



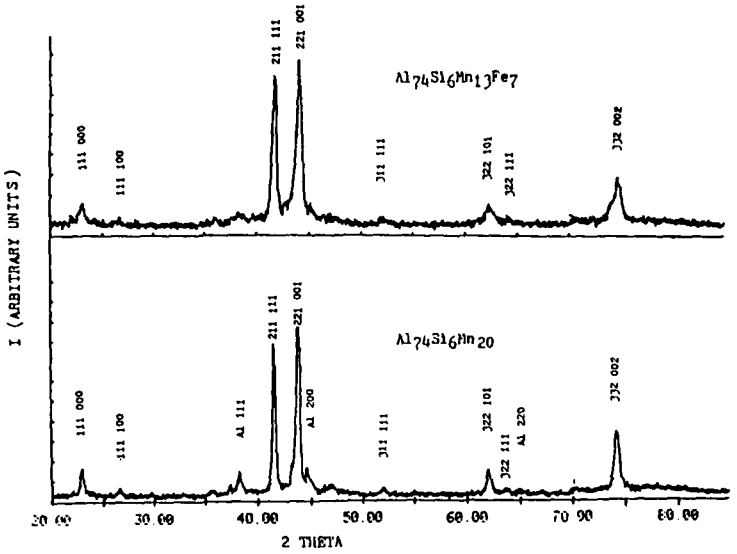


FIG. 1. X-ray diffraction patterns of melt-spun $Al_{76}Mn_{20-x}Fe_xSi_6$ for $x = 0.0$ (bottom) and $x = 7.0$ (top).

below establish beyond question that this moment is zero. It follows, since $p_{\text{eff}} \neq 0$, that there must be two separate classes of Mn in i-(AlMnSi), one possessing a local magnetic moment and one not. For reasons not immediately apparent iron is only able to substitute for the latter. If the concentration $x = 7$ of iron, which is close to the maximum which will still support the i phase, exhausts all of the "nonmagnetic" Mn sites, then the number of Mn sites per gram of i-$Al_{74}Mn_{20}Si_6$ that carry a localized magnetic moment is readily calculated as $N = 12.5N_0/M$, where $N_0 = 6\times10^{23}$ is Avogadro's number, and $M = 3264$ is the molecular weight. Coupling this value of N with the findings for Np_{eff}^2 in Table I now enables us to deduce the effective magnetic moment $p_{\text{eff}} \simeq 1.7$Bohr magnetons per local moment (see Table I).

The 4.2-K zero-field and high-field (80-kOe) Mössbauer spectra for the i-phase composition $Al_{74}Mn_{20}Fe_7Si_6$ are given in Fig. 3. The zero-field spectrum is closely similar in shape to that analyzed in detail for i-$Al_{86}(Mn_{0.98}Fe_{0.02})_{14}$ in Refs. 18 and 19. We record here (Table I) only the isomer shifts (IS) and peak-to-peak quadrupole splitting (QS) of the complete spectra, and note only that the isomer shifts are almost unchanged from the crystalline α phase while the mean electric field gradients (EFG) are somewhat increased (by 40%–50%) from the crystalline counterpart.[20] The high-field (80-kOe) observed spectrum is exactly that expected[21] for a ^{57}Fe nucleus interacting with an essentially sharp magnetic field of 80 kOe (parallel to the γ ray) and subject to a randomly oriented EFG distribution,[22] implying that the iron atoms carry no local moment. Any iron local moment (whether paramagnetic or incipiently spin-glass ordered) in a field of 80 kOe at 4.2 K would severely modify the Mössbauer Zeeman spectrum from its observed form.

Crystalline α(AlMnSi) is, in essence, a bcc arrangement of MI, connected along (all eight) body-centered axes by octahedral chains of Al atoms.[23] In detail, the origin and

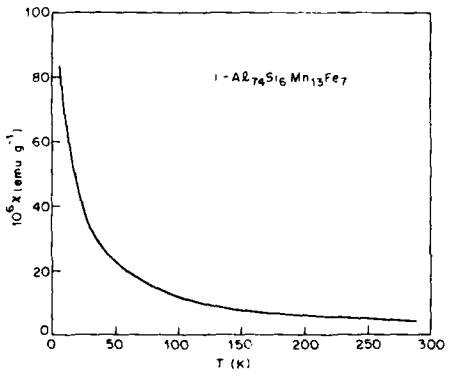


FIG. 2. Temperature dependence of the magnetic susceptibility of the quasicrystal i-$Al_{74}Mn_{13}Fe_7Si_6$.

TABLE I. The Curie "amplitude factor" Np_{eff}^2, Weiss temperature Θ, and Pauli paramagnetic component χ_0 as deduced from measured magnetic susceptibility for quasicrystalline samples i-$Al_{74}Mn_{20-x}Fe_xSi_6$ by fitting to the Curie–Weiss equations between temperatures $T = 20$ K and room temperature (see text). Also shown is the local magnetic moment P_{eff} per *magnetic* Mn atom, and the peak-to-peak quadrupole splitting (QS) and isomer shift (IS) (with respect to iron metal at room temperature) as determined from the $T = 4.2$ K Mössbauer data.

x	Np_{eff}^2 ($10^{21}\mu_B^2$/g)	Θ (K)	χ_0 (10^6 emu/g)	p_{eff} (μ_B)	QS (mm/s)	IS (mm/s)
0.0	6.8	13	0.9	1.7	0.45	0.33
7.0	6.5	10	0.5	1.7	0.41	0.33

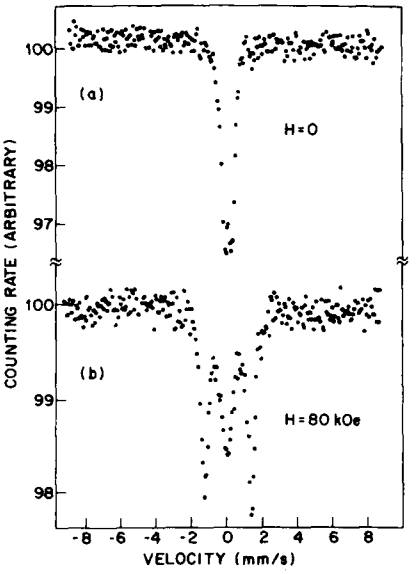


FIG. 3. (a) The 4.2-K field Mössbauer spectrum of quasicrystalline *i*-$Al_{74}Mn_{13}Fe_7Si_6$, and (b) $T = 4.2$ K Mössbauer Zeeman spectrum of the same sample in magnetic field $H = 80$ kOe applied parallel to the direction of γ-ray propagation.

bcc site MI are both slightly distorted from the prototypical configuration but in different ways, giving rise to two inequivalent Mn sites.[4,13] However, both sites, the six (one α-type, five β-type) Al/Si intra-MI nearest neighbors (NN) and either three or four (γ- and β-type) Al/Si inter-MI "glue" NN, contribute a sufficient density of itinerant electron states at a Mn site to suppress local moment formation. Crystalline α(AlMnSi) is, consequently, a Pauli paramagnet.[13,14]

Since Mn is completely nonmagnetic[20] (in the sense of not possessing a local moment) in the fully (eightfold) connected crystalline alloy, we propose that the nonmagnetic sites in the equivalent *i*-phase quasicrystalline alloy are those which are least perturbed on passage to the *i* phase—namely, those which are adjacent to retained threefold icosahedral α-type MI connections. Within the same model it follows that the magnetic Mn sites in the *i* phase must be those adjacent to "broken" MI connections.[22] This picture receives support from the measured modulation of NN pair Mn–Al distributions[24] on passage from the crystalline to *i* phases in both AlMn and AlMnSi alloys,[25] for which the most perturbed bonds (i.e., those adjacent to "broken" MI connections) experience a significant increase in bond length. The resulting expanded Al "cage" would likely give rise to a smaller itinerant electron density at these Mn sites and hence be more likely to favor conditions for the creation of a localized magnetic moment.[26]

Within our model we therefore identify two classes of Mn sites. The first is nonmagnetic, is more compact and less asymmetric as regards its Al NN environment, and, being adjacent to "connected" MI, is only modestly perturbed from its crystalline "parent" site. The second supports a localized magnetic moment, is less compact and more asymmetric in its Al NN environment, is adjacent to a "broken" MI connection, and is very substantially perturbed from its crystalline parent site. This model[21] is consistent with all the experimental findings presented if Fe, which is smaller than Mn, can only substitute for Mn in the smaller, less asymmetric class of sites.[26]

The work by G. Papaefthymiou and R. B. Frankel at the Francis Bitter National Magnet Laboratory was supported by the National Science Foundation.

[1]D. Shechtman, I. Blech, D. Gratias, and J. W. Cahn, Phys. Rev. Lett. **53**, 1951 (1984).
[2]C. L. Henley, Comments Condensed Matter Phys. **13**, 59 (1987).
[3]A. L. Mackay, Acta Crystallogr. **15**, 916 (1962).
[4]M. Cooper and K. Robinson, Acta Crystallogr. **20**, 614 (1966).
[5]E. A. Stern, Y. Ma, K. Bauer, and C. E. Bouldin, J. Phys. (Paris) Colloq. **47**, C3-371 (1986).
[6]Y. Ma, E. A. Stern, and C. E. Bouldin, Phys. Rev. Lett. **57**, 1611 (1986).
[7]C. L. Henley, Phys. Rev. B **34**, 797 (1986).
[8]P. Guyot, M. Audier, and R. Lequette, J. Phys. (Paris) Colloq. **47**, C3-389 (1986).
[9]J.W. Cahn and D. Gratias, *J. Phys. (Paris) Colloq.* **47**, C3-415 (1986).
[10]D. Shechtman and I. Blech, Metall. Trans. **16A**, 1005 (1985).
[11]P. W. Stephens and A. I. Goldman, Phys. Rev. Lett. **56**, 1168 (1986).
[12]V. Elser and C. L. Henley, Phys. Rev. Lett. **55**, 2883 (1985).
[13]W. W. Warren, H. S. Chen, and G. P. Espinosa, Phys. Rev. B **34**, 4902 (1986).
[14]J. J. Hauser, H. S. Chen, and J. V. Waszcak, Phys. Rev. B **33**, 3577 (1986).
[15]L. H. Bennett, M. Rubinstein, G. Xiao, and C. L. Chen, J. Appl. Phys. **61**, 4364 (1987).
[16]C. H. Chen and H. S. Chen, Phys. Rev. B **33**, 2814 (1986).
[17]See, for example, D. C. Mattis, *The Theory of Magnetism* (Harper and Row, New York, 1965).
[18]L. J. Swantzendrubber, D. Shechtman, L. Bendersky, and J. W. Cahn, Phys. Rev. B **32**, 1383 (1985).
[19]M. Eibschütz, H. S. Chen, and J. J. Hauser, Phys. Rev. Lett. **56**, 169 (1986).
[20]M. Eibschütz (unpublished).
[21]M. E. Lines, J. Chem. Phys. Solids **43**, 721 (1982).
[22]M. Eibschütz, M. E. Lines, H. S. Chen, J. V. Waszczak, G. Papefthymiou, and R. B. Frankel, Phys. Rev. Lett. **59**, 2443 (1987).
[23]P. Guyot and M. Audier, Philos. Mag. **52**, L15 (1985).
[24]Here, and henceforth, an Al site implies Al/Si in Si-containing alloys.
[25]J. B. Boyce, J. C. Mikkelsen, F. Bridges, and T. Egami, Phys. Rev. B **33**, 7314 (1986).
[26]P. W. Anderson, Phys. Rev. **124**, 41 (1971); Science **201** 307 (1978).

Epitaxial film growth and metastable phases of single crystal Dy by molecular beam epitaxy

Kai-Yueh Yang and Hitoshi Homma[a)]
Materials Science Division, Argonne National Laboratory, Argonne, Illinois 60439

Ivan K. Schuller
Physics Department, University of California-San Diego, La Jolla, California 92093 and Materials Science Division, Argonne National Laboratory, Argonne, Illinois 60439

We have grown two novel epitaxial phases of dysprosium (Dy) on vanadium (V) by the molecular beam epitaxy technique. Surface structures are studied by *in situ* reflection high-energy electron diffraction, and bulk structures are studied by x-ray diffraction after removal from the growth chamber. The new hcp phases are ~4% expanded uniformly in the (0001) plane and ~9% and ~4% expanded out of plane, along the *c* axes, for noninterrupted and interrupted deposition cases, respectively. We also observed (2×2), (3×3), and (4×4) Dy surface reconstruction patterns and a series of structural changes as the Dy film thickness increases.

INTRODUCTION

Considerable amount of experimental and theoretical effort has been directed towards the study of novel structural, electronic and transport phenomena of surfaces, interfaces, and superlattices.[1,2] Modern technology such as molecular beam epitaxy (MBE) enables the creation of high-quality epitaxial thin films and artificially modulated superlattices. A metastable bcc Co epitaxial film[3] was grown on GaAs showing magnetic properties similar to bcc α-Fe. Rare-earth superlattice systems [(such as Gd/Y (Ref. 4) and Dy/Y (Ref. 5)] have been prepared by MBE to study the propagation of the long-range magnetic order by indirect coupling across nonmagnetic materials. Theoretical predictions of anomalous magnetic behavior have been made in expanded transition metal (TM) films [Ni, Co, V, and Fe (Ref. 6)] and in TM interfaced with normal metals [Fe/Ag, Cr/Au, and V/Ag (Ref. 7)].

The present paper reports on novel epitaxial phases of dysprosium (Dy) on vanadium (V) by MBE. Surface and bulk structures were studied by *in situ* reflection high-energy electron diffraction (RHEED) and x-ray diffraction techniques. The new hcp phases are identified and surface reconstruction patterns of Dy films are also observed for the first time.

EXPERIMENTAL RESULTS AND DISCUSSION

The samples were prepared in a Riber MBE metal deposition system equipped with *in situ* RHEED with a typical base pressure of 4×10^{-11} Torr. The films were deposited from high-purity V (99.99%) and Dy (99.9%) starting materials on temperature-controlled (~900 °C) sapphire $(11\bar{2}0)$ α-Al_2O_3 substrates at a rate of 0.5–1.0 Å, and with a pressure of 5×10^{-10} Torr during evaporation. The film surface structure was monitored by using a 10-keV *in situ* RHEED. Bulk structures were studied further after samples were removed from the growth chamber by a two-axis Rigaku DMAX II x-ray diffractometer equipped with a 2-kW Cu$K\alpha$ tube.

A vanadium film was first deposited on the sapphire substrate as a buffer layer.[8] Under appropriate growth conditions an epitaxial V film (1000 Å) with an atomically smooth surface was grown, as indicated by the streaked RHEED patterns shown in Figs. 1(a) and 1(b), with the electron beam parallel to $\langle111\rangle_V$ and $\langle110\rangle_V$ respectively, and by x-ray diffraction. A Dy film was then evaporated on the V film, either in an interrupted or uninterrupted fashion. A final layer of V(110) (~500 Å) was always evaporated to protect the Dy from oxidation.

Figures 1(c)–1(f) show Dy RHEED pictures at a

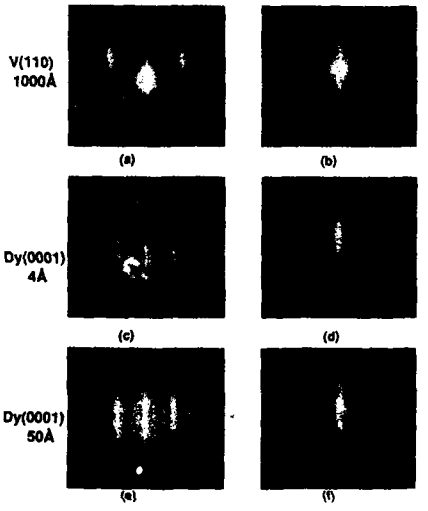


FIG. 1. RHEED patterns at 10 kV from (a) and (b) a 1000-Å-thick V(110) film grown on a sapphire α-Al_2O_3 $(11\bar{2}0)$ substrate at 900 °C, with the electron beam parallel to $\langle111\rangle_V$ and $\langle110\rangle_V$, respectively; (c) and (d) 4-Å-thick Dy(0001) film grown on V(110) in $\langle11\bar{2}0\rangle_{Dy}$ and $\langle10\bar{1}0\rangle_{Dy}$ orientations, respectively; (e) and (f) 50-Å-thick Dy(0001) film in the orientations corresponding to (c) and (d).

[a)] Permanent address: Dept. of Physics, Brooklyn College of C.U.N.Y., Brooklyn, NY 11210.

 0021-8979/88/084066-03$02.40 © 1988 American Institute of Physics

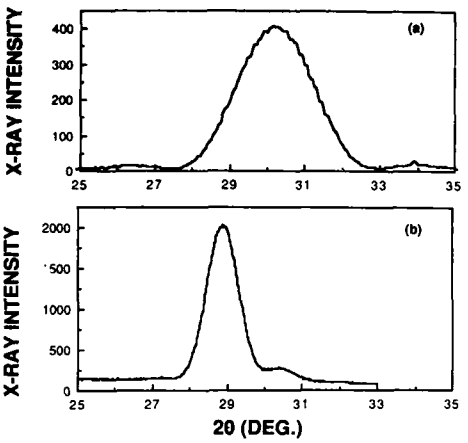


FIG. 2. 2θ–θ x-ray diffraction from a (a) 50-Å Dy(0001) film grown on V(110) in an interrupted fashion, and (b) 50-Å Dy film grown on V(110) in a noninterrupted fashion.

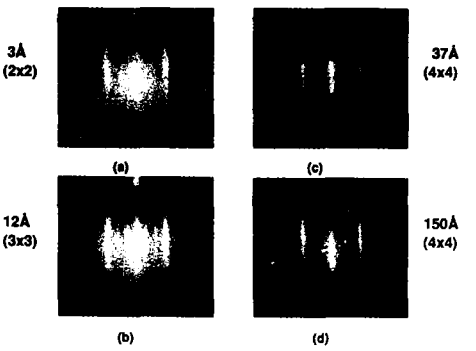


FIG. 3. RHEED patterns at 10 kV from a Dy(0001) film grown on V(110) at (a) 3 Å, (b) 12 Å, (c) 37 Å, and (d) 150 Å, showing (2×2), (3×3), and two (4×4) reconstruction patterns, respectively, indicated by the faint superlattice lines between the main bright diffraction lines.

thickness of 4 Å [1(c) and 1(d)] and 50 Å [1(e) and 1(f)] in two different azimuthal orientations, $\langle 11\bar{2}0\rangle_{Dy}$ and $\langle 10\bar{1}0\rangle_{Dy}$, with respect to the film growth direction. The sharp RHEED streaks are indicative of layer-by-layer growth. The longitudinal θ–2θ x-ray diffraction scan of a 50-Å Dy film along the film normal is shown in Fig. 2(a). The x-ray results imply that the growth direction is $\langle 0001\rangle$, as expected for hcp Dy, with a ~4% expansion ($c_0 = 5.88$ Å) compared to the bulk $c_0^{bulk} = 5.6510$ Å.[9] Note that additional small peaks due to the finite-size effects are observed in both sides of the main broad peak. This fact indicates that both sides of Dy and V interfaces are atomically smooth and chemically sharp. This is possibly due to the fact that the binary phase diagram of Dy and V shows them to be immiscible,[10] so there is no interdiffusion, and because the many interruptions (~2-min stop after 5 Å deposition) may allow the Dy atoms to diffuse laterally and form smooth layers.

The in-plane lattice constant of Dy ($a_0 = 3.72$ Å) obtained from the RHEED streaks in Figs. 1(c)–1(f) is approximately 4% expanded relative to the bulk lattice constant $a_0^{bulk} = 3.5915$ Å.[9] Therefore in the interrupted deposition a new modified hcp phase $a_0 = 3.72$ Å (+4%) and $c_0 = 5.88$ Å (+4%) was grown. It is quite interesting to note that an expansion is observed in both lateral and longitudinal directions, so simple epitaxial geometric arguments combined with Poisson ratios cannot possibly explain these results. If the growth is not interrupted the growth changes considerably. X-ray diffraction from the Dy film shows a larger perpendicular expansion $c_0 = 6.18$ Å (+9.4%) [see Fig. 2(b)] and a thickness dependence ranging from $a_0 = 3.64$ Å (+1%) to $a_0 = 3.79$ Å (+6%) for the in-plane spacing. This observation may relate to the fact that fast deposition (or noninterruption) stabilizes metastable and largely strained structures, an expanded one in this case.

The Dy film surface shows a modified in-plane structure with (2×2), (3×3), and (4×4) reconstruction patterns observed for the first time using the RHEED technique. Figure 3 shows a series of RHEED pictures for increasing Dy film thickness in a noninterrupted deposition.

The in-plane lattice constants obtained for increasing film thicknesses are $a_0 = 3.64$ Å (+1%), 3.72 Å (+4%), and 3.79 Å (+6%) and out-of-plane lattice constants $c_0 = 5.88$ Å (+4%) and 6.18 Å (+9%) with (2×2), (3×3), and (4×4) surface reconstruction patterns, respectively. The $(p\times p)$ reconstruction patterns and the in-plane and out-of-plane crystal structures are clearly correlated; for large p the structures in both lateral and longitudinal directions tend to expand. For the interrupted case (2×2) and (3×3) reconstructions are observed but not the (4×4) pattern. At the present time we have not determined in detail the unit cell of the modulated surface structure. In general the less dense surface structure will accomodate a larger, more complicated unit cell. Obviously the surface reconstruction and the structural changes with film thickness require further study.

The relative epitaxial orientations of Dy(0001) to V(110) was determined from the RHEED measurements (Fig. 1) as well. The $\langle 11\bar{2}0\rangle_{Dy}$ is found to be parallel to $\langle 110\rangle_V$, the well-known Nishiyama–Wassermann orientation[11] in the fcc(111)/bcc(110) system. The same orientation was reported in Gd/Nb,[12] whereas a new orientation was recently found in the Ce/V system.[8] The magnetic properties of this new expanded hcp phase is an interesting subject for further study especially regarding changes in the magnetic structure and phase transitions.

ACKNOWLEDGMENTS

We thank M. Grimsditch for useful conversations. This work was supported by the Office of Naval Research, Contract No. N00014-83-F-0031, and the U. S. Department of Energy, Basic Energy Sciences–Materials Sciences, under Contract No. W-31-109-ENG-38. The work at UCSD supported by DOE Contract No. DE-FGO3-87ER45332.

[1]F. Nizzoli, K. H. Rieder, and R. F. Willis, Editors, *Dynamical Phenomena at Surfaces, Interfaces and Superlattices* (Springer, Berlin, 1985).
[2]J. D. Dow and I. K. Schuller, Editors, *Interfaces, Superlattices and Thin Films* (Materials Research Society, Pittsburgh, 1987).
[3]G. A. Prinz, Phys. Rev. Lett. **54**, 1051 (1985).
[4]C. F. Majkrzak, J. W. Cable, J. Kwo, M. Hong, D. B. McWhan, Y. Yafet, J. V. Waszczak, and C. Vettier, Phys. Rev. Lett. **56**, 2700 (1986).
[5]M. B. Salamon, S. Sinha, J. J. Rhyne, J. E. Cunningham, R. W. Erwin, J. Borchers, and C. P. Flynn, Phys. Rev. Lett. **56**, 259 (1986).
[6]V. L. Moruzzi, Phys. Rev. Lett. **57**, 2211 (1986).
[7]C. L. Fu, A. J. Freeman, and T. Ohuchi, Phys. Rev. Lett. **54**, 2700 (1985).
[8]H. Homma, K.-Y. Yang, and I. K. Schuller, in *Interfaces, Superlattices and Thin Films*, edited by J. D. Dow and I. K. Schuller (Materials Research Society, Pittsburgh, 1987), p. 557; Phys. Rev. B **36**, 9435 (1987).
[9]B. J. Beandry and P. E. Palmer, J. Less-Common Metals **34**, 225 (1974).
[10]R. P. Elliott, *Constitution of Binary Alloys, First Supplement* (McGraw-Hill, New York, 1965).
[11]J. H. van der Merwe, Philos. Mag. A **45**, 159 (1982).
[12]J. Kwo, M. Hong, and S. Nakahara, Appl. Phys. Lett. **49**, 319 (1986).

Spin-polarized electron energy-loss spectroscopy of metastable bcc cobalt films (abstract)[a)]

D. M. Lind,[b)] Y. U. Idzerda,[c)] G. A. Prinz, B. T. Jonker, and J. J. Krebs
Naval Research Laboratory, Washington, DC 20375

Recent developments now allow for the study of the spin dependence of electron energy-loss features for scattering from magnetized ferromagnetic materials. Particular interest in such studies has been focused on Stoner (or spin-flip) excitations[1] because of their fundamental nature as well as their proposed role in the polarization enhancement for low energy secondary electron emission from ferromagnets.[2] We have performed spin-polarized electron energy loss spectroscopy (SPEELS) on thin (~40-Å) metastable bcc Co(110) films which have been grown by *e*-beam evaporation on atomically clean GaAs(110) substrates. Surface order and cleanliness of the substrate and grown film are monitored by LEED and AES. Details of the bcc Co deposition, growth, and characterization have been reported elsewhere.[3] After growth, the thin ferromagnetic films are magnetized to near-saturation remanence magnetization along the in-plane [001] (magnetically easy) direction[3] by placement in the center of a pulsed coil. The spin-polarized primary electron beam is obtained by photoemission from a negative electron affinity GaAs surface excited by circularly polarized light. The direction of polarization of the electron beam is easily reversed without changing the beam intensity or transport characteristics. The degree of polarization of the source is estimated to be 28–30%. The scattering geometry is chosen so that only the energy-loss spectrum of the specularly reflected beam is measured by a hemispherical energy analyzer. We obtain spin dependent loss spectra for specularly reflected electron beams for a range of primary beam energies. Two polarization dependent features are observed in the energy-loss spectra, a shoulder at 1.6 eV and a well-defined peak at 2.8 eV. The data obtained is normalized to the measured elastic peak intensity, which is assumed to be the same for both spin polarization directions. Polarization analysis shows both features to be due almost entirely to inelastic scattering of incident electrons polarized parallel to the spin-down (minority) direction. The FWHM of both features are quite narrow, suggesting a near rigid exchange splitting for the bcc Co bands. The magnetization reversal behavior and the energy dependence of these spin-dependent features are consistant with the behavior of Stoner excitations. We have tentatively identified the feature at 1.6 eV as the primary Stoner excitation which implies the exchange splitting for bcc Co is also 1.6 eV. The higher-energy peak is most likely a second peak in the Stoner density-of-states.[4] Additional theoretical calculations are being performed to verify these identifications.[5]

[a)] Work supported by the Office of Naval Research.
[b)] NRL/ONT fellow (post-doc).
[c)] NRL/NRC fellow (post-doc).

[1] J. Kirschner, Phys. Rev. Lett. **55**, 973 (1985), and references therein.
[2] H. Hopster, Phys. Rev. B **36**, 2325 (1987).
[3] G. A. Prinz, Phys. Rev. Lett. **54**, 1051 (1985).
[4] J. F. Cooke, J. W. Lynn, and H. L. Davis, Phys. Rev. B **21**, 4118 (1980).
[5] Y. U. Idzerda, D. M. Lind, D. A. Papaconstantopoulous, G. A. Prinz, B. T. Jonker, and J. J. Krebs (unpublished).

 0021-8979/88/084069-01$02.40 © 1988 American Institute of Physics



Local structure of $Al_{75}(Mn,Cr,Ru,Re,Si)_{25}$ icosahedral alloys studied by pulsed neutron scattering (abstract)

W. Dmowski and T. Egami
Department of Materials Science and Engineering and Laboratory for Research on the Structure of Matter, University of Pennsylvania, 3231 Walnut Street, Philadelphia, Pennsylvania 19104-6202

P. A. Bancel and P. A. Heiney
Department of Physics and Laboratory for Research on the Structure of Matter, University of Pennsylvania, 3231 Walnut Street, Philadelphia, Pennsylvania 19104-6202

K. Volin
Materials Science Division, Argonne National Laboratory, Argonne, Illinois 60439

The discovery of an icosahedral phase in a rapidly quenched Al-Mn[1] alloy has stimulated intensive research on the structure of these materials. We studied several single-phase icosahedral alloys to address a problem of isomorphous substitution and quasicrystallinity in these solids. The use of neutrons is attractive because the neutron scattering length of Mn is negative and this provides additional diffraction contrast. Since icosahedral solid lacks translational symmetry we used approach based on the pair distribution function (PDF) which gives an averaged distribution of interatomic distances. We observed significant differences in the diffraction pattern (DP) depending on kind of element that substituted Mn. For instance partial substitution by Cr resulted in strong (110000) peak while (100000) remained very weak. After total substitution DP was still different from the x-ray DP for Mn. For Ru the (100000) peak was the strongest whereas for Re (110000). Substitution of Al by 3% of Si caused an increase of (100000) and (110000). The peak positions in PDFs correspond well to distances calculated for the three-dimensional Penrose tiling, suggesting the presence of a quasicrystalline substructure. The observed changes in diffraction patterns and PDFs indicate nonrandom substitution in these alloys, for instance, Ru is found only on vertices. The vertex-vertex distances are predominantly observed in Al-Mn positional correlations. The effect of compositional order on local structure and magnetic properties will be discussed.

[1]D. Shechtman, I. Blech, D. Gratias, and J. W. Cahn, Phys. Rev. Lett. **53**, 1951 (1984).

Specific-heat measurements for the quasi-crystalline, first cubic approximant and hexagonal phase in AlMnSi (abstract)

K. Wang and P. Garoche
Laboratoire de Physique des Solides, Universite Paris-Sud, Bat. 510, 91405 Orsay Cedex, France

Y. Calvayrac
Centre d'Etude de Chimie Metallurgique, CNRS, 15 Rue Georges Urbain, 94407 Vitry Cedex, France

We have investigated the low-temperature specific heat of the quasi-crystalline (Q-C) $Al_{73.2}Mn_{21}Si_{5.8}$ related first approximant and hexagonal crystalline phases. All measurements were performed on small, 2-mg, single-phase crystals. The structure of each phase was carefully analyzed by x-ray diffraction and for the Q-C phase all pics positions were correctly indexed to a "six-dimensional crystal" model.[1] The samples where obtained by planar flow casting and for the hexagonal phase by an adequate annealing of the Q-C phase. The low-temperature specific heat is analyzed in a standard way as the sum of three electronic, magnetic, and phonon contributions. This analysis indicates unambiguously the presence in the Q-C phase of a large magnetic term ($C/T = 11$ mJ/mole K K) that is supposed to be caused by the thermal excitations of a spin-glass-like ordering.[2] Such a large magnetic contribution is observed neither in the hexagonal phase, which has a different local symmetry, nor in the cubic approximant with the same local icosanedral symmetry. Thus it is proposed that the random freezing of the Mn spins observed in the AlMnSi Q-C is not a canonical spin-glass state but a specific property of spins on a quasi-periodic lattice.

[1]J. Cahn, D. Shechtman, and D. Gratias, J. Mater. Res. **1**, 13 (1986).
[2]F. L. A. Machado, W. G. Clark, L. J. Azevedo, D. P. Yang, W. A. Hines, J. J. Budnick, and M. X. Quan, Solid State Commun. **61**, 145 (1987).

 0021-8979/88/084070-01$02.40 © 1988 American Institute of Physics



Magnetic structure and dynamics anomalies in "reentrant" spin glasses (invited)

M. Hennion, B. Hennion, I. Mirebeau, and S. Lequien
Laboratoire Léon Brillouin,[a] *CEN-Saclay, 91191 Gif/Yvette Cédex, France*
F. Hippert
Laboratoire de Physique du Solide, Université d'Orsay, 91405 Orsay Cédex, France

Neutron studies performed at zero field and in applied field on the reentrant spin glasses $Ni_{1-x}Mn_x$ and $(Fe_{1-x}Mn_x)_{75}P_{16}B_6Al_3$ reveal new features both in the static and in the dynamic correlations. The small-angle scattering shows a maximum at a finite q_{max} value in applied field. High-energy resolution measurements show that the stiffness constant of the spin waves has a still more surprising temperature dependence than first expected: as the temperature decreases it goes through a minimum and then increases further in the lowest-temperature range. We report the evolution of these features as a function of field, temperature, and concentration. q_{max} varies linearly with $\sqrt{H}$ with a slope which is related to the stiffness constant D of the spin waves. The dynamic anomalies are also seen in a field which saturates the magnetization.

I. INTRODUCTION

The reentrant spin glasses (RSG) are disordered alloys where exists a competition between ferromagnetic and antiferromagnetic interactions with a dominant ferromagnetism. When lowering the temperature T, the susceptibility[1] and low-field magnetization measurements[2] suggest the existence of two phases below the paramagnetic state: a ferromagnetic phase below T_c and spin-glass properties below a lower-temperature T_G. Actually the observation of these properties (thermal history effects, magnetic viscosity, and hysteresis) does not prove that long-range ferromagnetism is really destroyed and does not even allow to determine a unique temperature T_G. It was even argued in the case of AuFe,[3] that the system continuously evolves with T and does not show any well-defined transition. Actually, the macroscopic measurements which probe a large-scale behavior are insufficient to describe the RSG since they do not inform on the correlations between the spins. The Mössbauer experiments,[4] which probe the "local" magnetization have usually been interpreted by a microscopic change from a collinear state to a noncollinear one either in zero field or in applied field. This would occur at a canting temperature T_K between T_c and T_G, and would consist in a freezing of spin components transverse to the mean magnetization, according to the Gabay and Toulouse theory.[5] We note that the mean-field model predicts below T_K a coexistence of a spin-glass state for transverse components and long-range ferromagnetism for the longitudinal one but its application for a real system is *a priori* questionable. Recent Mössbauer experiments were interpreted by the existence of ferromagnetic correlations between the transverse components.[6] Thus, neutron experiments which allow a straightforward measurement of the spin correlations and the spin dynamics are especially useful. In all RSG the main results in zero applied field are the observation of an intense elastic intensity arising well below T_c in the q range 10^{-2}–10^{-1} Å^{-1} (Ref. 7) and of *strong* anomalies for spin waves. Up to now, the elastic intensity was generally interpreted by a breakdown of long-range ferromagnetic order: the analysis of its asymptotic behavior at large q values yields a finite correlation length K^{-1} at low temperature.[8] This interpretation was supported by the first observations of dynamic anomalies: as T decreases the stiffness constant D of spin waves first increases as in usual ferromagnets and then shows an anomalous decrease.[9] It was thus first concluded that spin waves disappear at low temperature with some intermediate regime where the elastic intensity and the spin waves are observed simultaneously. This picture does not give any role to transverse components but rather emphasizes that of cluster uncorrelated from a percolating network.

In this paper we mainly present neutron experiments in applied field. As we have shown previously in the case of NiMn and a-FeMn,[10] the scattered elastic intensity $I(q)$ exhibits a structure at a finite q_{max} value. Similar results were also observed in FeAl.[11] This very new feature is analyzed here as a function of field, temperature, and concentration; its variation in the q,H plane reveals the major role of transverse components. On the other hand, the spin-wave anomalies are far more surprising than expected: indeed, we have observed a further increase in the $D(T)$ variation below the abnormal decrease.[12] This behavior is studied here as a function of concentration in the a-FeMn system. In the following, we examine successive magnetization, small-angle neutron scattering, and inelastic measurements.

[a] Laboratoire commun CEA-CNRS.

 0021-8979/88/084071-06$02.40 © 1988 American Institute of Physics

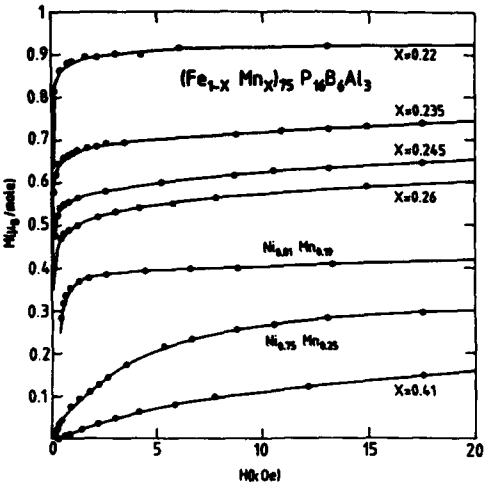


FIG. 1. Magnetization M vs applied field H at 11 K in $(Fe_{1-x}Mn_x)_{75}P_{16}B_6Al_3$ and $Ni_{1-x}Mn_x$.

II. SAMPLE CHARACTERIZATION BY MAGNETIZATION MEASUREMENTS

The systems studied are amorphous $(Fe_{1-x}Mn_x)_{75}P_{16}B_6Al_3$ ($x = 0.22$, 0.235, 0.247, 0.26, 0.41) and poly and single-crystal $Ni_{1-x}Mn_x$ ($x = 0.19$, 0.216, 0.25). All the studied samples have a rather high Curie temperature ($T_c \simeq 200$–300 K) and a low freezing temperature ($T_G \simeq 10$–40 K) except $(Fe_{0.59}Mn_{0.41})_{75}P_{16}B_6Al_3$ which is a true spin glass ($T_G = 35$ K) and $Ni_{0.75}Mn_{0.25}$ which is a RSG close to a spin glass with no well-defined transitions. The transition temperatures are determined as usual by susceptibility measurements $\chi'(T)$: when the temperature T is lowered, χ' shows a sharp increase at T_c then a rounded maximum close to the demagnetization limit and decreases further. T_G is defined here by the inflection point in the downfall of $\chi'(T)$.[13]

Many low-field magnetization measurements have been reported in these systems (see, for instance, Refs. 14 and 15). We would like to point out interesting features of the $M(H)$ curves in higher applied fields ($0.1 < H < 20$ kOe) which are generally not outlined. In this field range (Fig. 1) the most remarkable feature is the existence of a knee between 0.8 and 1.5 kOe which locates a change of regime. It is observed at all temperatures although smeared out in the vicinity of T_c. This behavior looks closely similar to that of an usual ferromagnet where the sharp increase of $M(H)$ between 100 and 800 Oe corresponds to the removal of Bloch walls. By contrast in the true spin glass $(Fe_{0.59}Mn_{0.41})_{75}$PBAl we see no well-defined saturation plateau. In RSG the plateau shows a residual slope which increases with Mn concentration. Magnetoresistance measurements in reentrant AuFe (Ref. 16) show that this slope also increases when T decreases in the lowest-temperature range. These two results suggest an incomplete alignment of the spins in technically saturating fields.

III. SMALL-ANGLE NEUTRON SCATTERING IN APPLIED FIELD

Small-angle neutron scattering measurements were performed in the range of the scattering vector $0.01 < q < 0.15$ Å^{-1}, applied field $0 < H < 12$ kOe, and temperature 10 K $< T <$ 400 K. The results were obtained by using two different techniques. In the diffraction technique, we do not perform any energy analysis, but we can measure the scattered intensity $I(q)$ for several orientations (q,H) simultaneously, with the help of a multidetector. These measurements were made on the spectrometers PAXY at Orphee and D11 at I.L.L. They are only significant at low temperature ($T \simeq 10$ K) when the spin-wave contribution is small. At higher T, elastic measurements (in the direction $q \| H$ only) were carried out on the triple-axis spectrometer 4F2 at Orphee in order to eliminate the spin waves. Data were corrected by subtracting either a high-temperature spectra at $T \simeq 2T_c$ or the environmental background. Details have been given previously.[10]

As already reported, the main result is the occurrence of a maximum of $I(q)$ for $q = q_{max}$ when H is above the knee in the magnetization curve ($H \simeq 1.5$ kOe). This "structure" is seen in all studied samples except in the true spin glass. In the detector plane, it is observed at the same q_{max} value for all angles $\alpha = (q,H)$, while its intensity depends on α (Fig. 2). By analyzing the α dependence of the scattering, we can

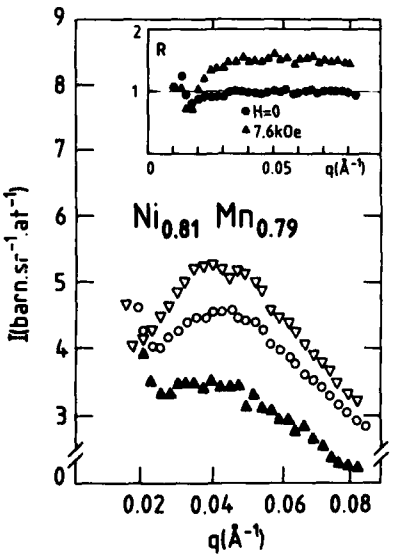


FIG. 2. $Ni_{0.81}Mn_{0.19}$: $I(q)$ intensity at 11 K for $H = 7.6$ kOe and various angles $\alpha = (q,H)$: $\alpha = 0°$, 30°, 90° (▽,○,▲). Insert: anisotropy ratio R vs q: $H = 0$, and 7.6 kOe (○,△). Note that in this figure as in Fig. 3, data points at very small q have been omitted (see, for instance, Lequien *et al.*[10]).

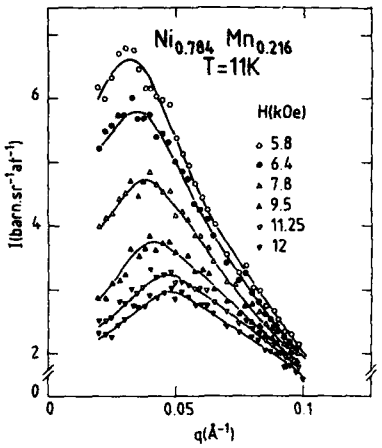


FIG. 3. $Ni_{0.784}Mn_{0.216}$: $I(q)$ intensity ($q \| H$) at 11 K for various applied fields. The lines are guides to the eye.

separate the longitudinal (L) from the transverse (T) correlations, which is obviously meaningful in technically saturating fields. We show that L and T do not depend on α, i.e., are isotropic in the space. The α dependence of the intensity results from the form of the magnetic interaction with the neutron.[10] In this context the anisotropy ratio $R = I_{q\|H}/I_{q\perp H}$ is written as $R = 2T(q)/[L(q) + T(q)]$. R is nearly q independent and equal to 1.55 ± 0.05 (insert Fig. 2), which shows that the transverse correlations represent 80% of the total scattering $L + T$. When H increases, q_{max} increases while the intensity strongly decreases (Fig. 3). As no good fit with simple mathematical law could be found (see Lequien *et al.*[10]), q_{max} was deduced from eye-guide lines. For all the studied samples, we show that q_{max} is proportional to $\sqrt{H}$ once the demagnetization effects are corrected (Fig. 4, see also Ref. 17). This was also shown for FeAl.[11] The slope s of the lines $q_{max} = s\sqrt{H}$ increases with Mn concentration, i.e., when the ferromagnetic character decreases. We can try to be precise about that point by comparing this slope s with the stiffness constant D. A quantitative determination of D is difficult as it is model dependent (see below). This prohibits a precise analysis of the two a-FeMn alloys. However, from a rough comparison between $Ni_{0.784}Mn_{0.216}$ and $(Fe_{0.765}Mn_{0.235})_{75}P_{16}B_6Al_3$ we estimate that D is roughly three times greater in the NiMn than in the a(FeMn) sample. (At 10 K, D ranges respectively from 18 to 20 THz Å^2 and from 7 to 9 THz Å^2.) Very interestingly, the ratio value $s_{FeMn}/s_{NiMn} = 1.7$ is close to the ratio $\sqrt{D_{NiMn}/D_{FeMn}}$, suggesting that q_{max} varies with $\sqrt{H/D}$.

As a remark, in reentrant FeAl, the q_{max} are higher than in the present systems at equal field value.[11] This suggests that FeAl is a soft system with a very low D value in agreement with the fact that spin waves[18] are unobservable at low temperature.

The temperature dependence of the intensity has been studied at several fields and is reported in Fig. 5 for $Ni_{0.784}Mn_{0.216}$ at 5.8 kOe. It shows a continuous decrease when T increases from 10 K and disappears around 120 K, i.e., roughly at the same temperature where the abnormal intensity measured in zero field disappears. We note a small change of q_{max} with T, outlined in the figure, which is slightly different from that observed in other samples.[10] The temperature variation of q_{max} does not reflect the strong anomalies of the D stiffness constant.

Finally, the asymptotical behavior of $I(q)$ for $q \gg q_{max}$, studied at 10 K in zero field and in applied field, is well reproduced by a squared Lorentzian law, whatever the value of H (Fig. 6). Direct comparison between measurements at $H = 0$ and $H \neq 0$ is possible since the isotropy of the in-field experiment is restored by averaging all q directions in the detector plane. The correlation length K^{-1}, deduced from a fit by a law $I = A/(K^2 + q^2)^2$, *decreases* slowly with H while A is independent of H (insert Fig. 6).

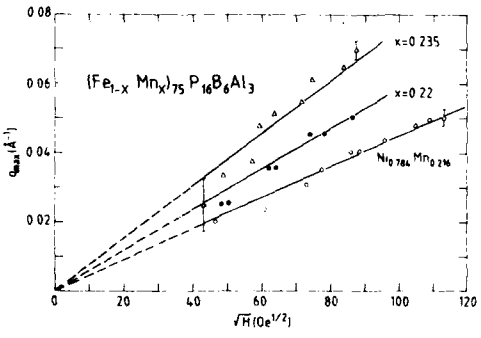


FIG. 4. q_{max} vs $\sqrt{H}$ at 11 K in $Ni_{0.784}Mn_{0.216}$ (○) and $(Fe_{1-x}Mn_x)_{75}P_{16}B_6Al_3$, $x = 0.22, 0.235$ (●,△). The demagnetization effects have been corrected. The full lines are guides to the eye. The dashed lines are extrapolated ones.

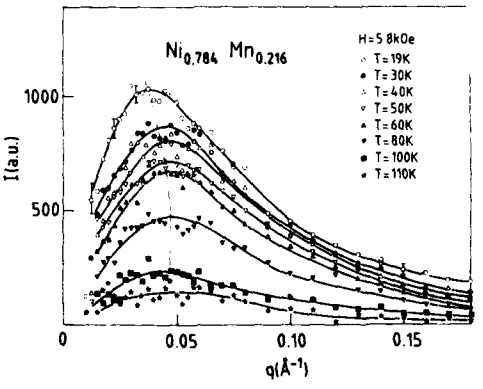


FIG. 5. $Ni_{0.784}Mn_{0.216}$: $I(q)$ intensity ($q \| H$) at 5.8 kOe for various temperatures T. The full lines are guides to the eye. The dashed line shows the variation of q_{max} with temperature. Data have been obtained using a three-axis spectrometer.

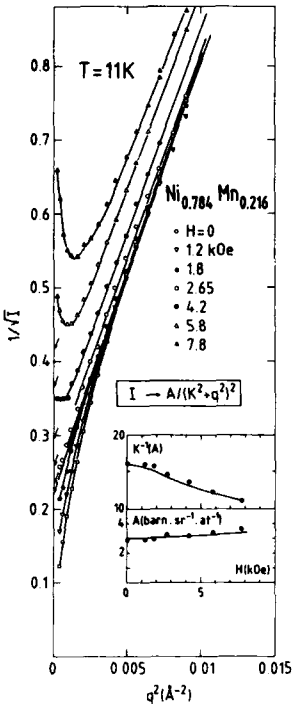


FIG. 6. $Ni_{0.784}Mn_{0.216}$. Asymptotic behavi $^{-1}/\sqrt{I} = f(q^2)$ at 11 K for various applied fields H. The arrow indicates the intercept of the straight lines with the intensity axis. Insert: mean correlation length K^{-1} and A parameter deduced from a fit with a squared Lorentzian law $A/(K^2+q^2)^2$. The $I(q)$ data correspond to an average on all $\alpha = (\mathbf{q},\mathbf{H})$ angles.

V. INELASTIC NEUTRON SCATTERING

In all the studied RSG systems ferromagnetic spin waves appear below T_c. They obey a law $\hbar\omega = \Delta + Dq^2$, where Δ is a small anisotropy gap and D the magnetic stiffness constant. When the temperature is lowered D displays the usual increase below T_c, but then goes through a maximum and starts to decrease while the spin waves become heavily damped and the static transverse susceptibility increases. The final evolution in the temperature range where a spin-glass-like character appears is rather controversial.[23] The first measurements on $Fe_{1-x}Cr_x$ (Ref. 9) concluded to the complete collapse of the spin waves, thus supporting the breakdown of long-range ferromagnetic order. But recent measurements on the same sample with a better resolution[24] ascertain propagative spin waves down to 10 K. This emphasizes the difficulty to get unambiguous results in the lowest-temperature range due to the coexistence of a huge elastic signal and of heavily damped spin waves of small energy. In $Ni_{0.784}Mn_{0.216}$,[12] the relatively large D values made the measurements easier and it was then revealed that after its abnormal decrease, the stiffness constant was increasing again, while the damping exhibited a maximum. The same behavior has been found in a $(Fe_{1-x}Mn_x)_{75}P_{16}B_6Al_3$ for $x = 0.235$, thus excluding the possibility of an artefact in NiMn due to chemical inhomogeneity (local ordering). The characterization of the dynamical behavior in RSG systems is of great importance for the understanding of the microscopic nature of these peculiar systems. We then tried to establish the concentration dependence of the dynamical anomalies in the a-FeMn. Neutron measurements were carried out at the Orphee reactor in Saclay on samples with $x = 0.22$ and $x = 0.247$ to be compared to the previous study for $x = 0.235$. Complete results with detailed experimental conditions will be reported elsewhere but here we may summarize the main conclusions.

In the $x = 0.22$ sample spin waves are easily observed at all temperatures. The stiffness constant display the abnormal decrease, but then it levels off below 30 K. In the $x = 0.247$ sample, lower values of the stiffness constant were expected. In order to facilitate the separation between elastic and inelastic components we have performed a complete set of measurements in an applied field of 3.4 kOe. Indeed, this adds an energy gap of 0.0095 THz to the spin-wave energy and, moreover, strongly reduces the magnetic elastic peak in the low-temperature state. By the way the magnetization was thus kept to its saturation value, which does not exhibit any anomalous decrease at low temperature. Measurements were carried out between $q = 0.035$ and 0.075 Å^{-1} and are illustrated in Fig. 7 where the spectra obtained at $q = 0.050$ Å^{-1} at several temperatures are reported. Here again the minimum of the spin-wave energy is clearly evidenced and the complete data analysis effectively gives a minimum for the stiffness constant simultaneously with a maximum of the damping. In order to check the field effects, measurements as a function of the field (including $H = 0$) were first performed at 12 and 80 K on both sides of the minimum of D. At these temperatures the only differences between measurements without and under field are a slight reduction of the damping and of the intrinsic gap: D was found independent

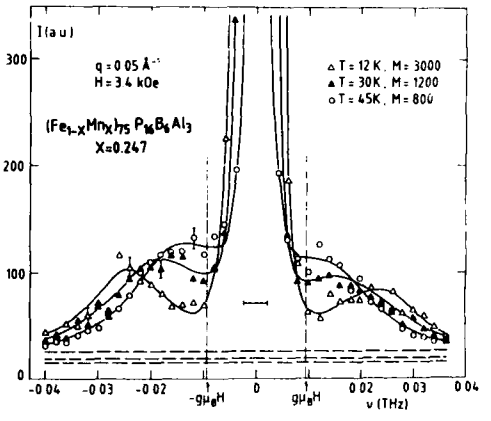


FIG. 7. $(Fe_{0.753}Mn_{0.247})_{75}P_{16}B_6Al_3$: intensity vs frequency at $q = 0.05$ Å^{-1} and $H = 3.4$ kOe for various temperatures. The lines are calculated neutron cross section using the DHO model (see the text).

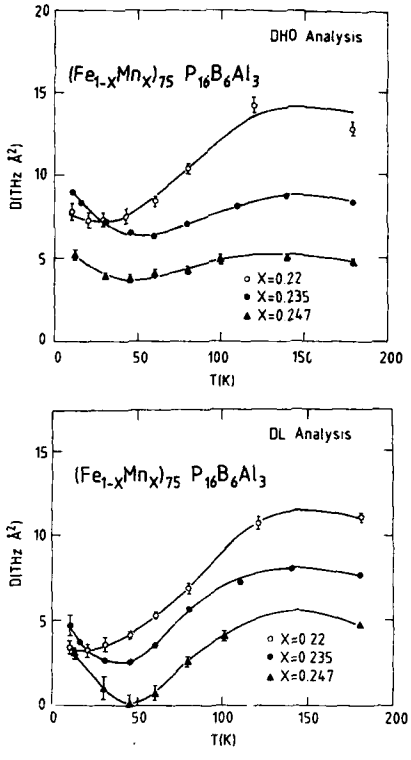


FIG. 8. $(Fe_{1-x}Mn_x)_{75}P_{16}B_6Al_3$. Stiffness constant as a function of temperature for $x = 0.22, 0.235, 0.247$: (a) using the DL model analysis, (b) using the DHO model analysis. Note that measurements corresponding to $x = 0.247$ are performed in a field $H = 3.4$ kOe.

on the field. Then, further investigations with increasing temperatures revealed a measurable field dependence of D mostly in the neighboring of T_c. It corresponds to a strong field dependence of the Curie temperature as already noticed in the Fe_xCr_{1-x}.[9] We evaluated $T_c = 248$ K with $H = 3.4$ kOe to be compared to 221 K without field!

The overall results of the D evolution with temperature for the three concentrations are reported in Figs. 8(a) and 8(b). In the absence of any specific model to describe the dynamics of these systems, the neutron cross section was parametrized with a double Lorentzian (DL) or a damped harmonic oscillator (DHO) form. As emphasized in many previous studies the parameters values are strongly model dependent, so that we cannot argue on their absolute values. But the most striking feature is that regardless of the model the dynamics study reveals a minimum in the stiffness constant variation concurrently with a maximum of the damping. The temperature of the extremum is not sharply defined but it obviously increases when the spin-glass character is enhanced.

VI. DISCUSSION

Here we examine elastic and inelastic neutron results successively. The asymptotical behavior of the SANS intensity in applied field (Fig. 6) is essentially the same as in zero field, with a finite correlation length K^{-1} decreasing with H. Considering that the in-field experiments are performed at "technically" saturated magnetization, this result helps to be precise about the meaning of the K^{-1} parameter: rather than a size of a ferromagnetic domain, it represents a scale of mainly transverse spin fluctuations which coexist with infinite range order.

The main difference between the zero field and the in-field experiment is the observation of a structure once the magnetization is technically saturated. We show that this structure has a dominant transverse character. Thus it seems unlikely to interpret it by a modulation of the spin length as done in Ref. 11 which would mainly concern the longitudinal component. In the same way we cannot be sure that an analogy with the intensity profile found in phase separation of binary alloys (see Ref. ~) is significant. Such an analogy is mostly meaningful for longitudinal correlations where we can establish a direct correspondence between magnetic and chemical scattering lengths. Considering the transverse character of the structure, a possible interpretation would have been to invoke some periodicity in the rotation of transverse components in order to describe some kind of helixes. These helixes should belong to domains of random orientations in order to ensure the existence of a maximum for all q directions which is rather unlikely. An alternative picture has to be found, based on the following considerations. When increasing the field, the strong decrease of the intensity associated with a small increase of q_{max} is strongly suggestive of the evolution of ferromagnetically correlated defects where the intensity is related to the defect's volume and q_{max} to its size. This picture is also supported by the law $q_{max} \sqrt{H/D}$. Similar relationships are used to define the size of magnetic defects like Bloch walls or defects induced by anisotropy.[19,20] Very interestingly, this law is also predicted to determine the transverse correlation length in ferromagnetic systems perturbated by random fields.[21] Since it does not depend on the exact nature of the perturbation, it could be extended to reentrant systems. In the present case, the difficulty is to precise the requirement which could give rise to the observed structure. One could possibly imagine volumes inside which the transverse components M_T perform a 2π rotation. Since the total transverse magnetization is zero inside the volume, the corresponding form factor, related to the Fourier transform of M_T is zero at $q = 0$ and exhibits a maximum at a finite q_{max} value. In absence of any precise model we get a rough estimation of the mean defect size by taking a vorticelike picture as suggested in 2D simulation.[22] It yields a similar form factor with a $q_{max} = \pi/R$, R being the vortice radius. We thus get a mean defect size of about 100 Å to be compared with the "asymptotical" length K^{-1} of about 10 Å. If this interpretation of q_{max} is good, the present observations show that when T decreases below T_K, the defects keep roughly the same size. Therefore, the main effect of the temperature, i.e., the decrease of the intensity can be attributed to the thermal increase of the mean transverse

spin length. This effect could be related to the Gabay–Toulouse model, keeping in mind that in the real systems, the transverse components are strongly correlated. On the other hand, this picture differs from the usual picture of frozen superparamagnetic clusters coexisting with a percolating ferromagnetic network: the defect's size would decrease when the ferromagnetic character increases with concentration, in contradiction with the reported observations.

The inelastic results in zero and applied field show that the final increase of D below its decrease is a real effect: it is confirmed here in a a-FeMn sample for a concentration corresponding to an increase of the spin-glass character compared to the previous study. Also the study of the dynamical parameters with the field as a function of temperature can open new perspectives for studying those systems where experimental difficulties hinder zero-field measurements. Although it cannot be concluded on the universal character of these observations in all RSG (FeAl appears rather different,[18] and the role of Mn or of the metallic character in these systems can also be discussed), the above results allow us some comments.

The abnormal decrease of D after its first increase below T_C is likely related to the occurrence of the noncollinear state: we notice, however, that the central peak is detected at some lower temperature than that of the rounded maximum of D. It was proposed by Continentino[25] that this decrease could result from the interactions of spin waves with two-level states present in the system. But this mechanism could not explain the final increase of D in the lowest-temperature range. The temperature at the minimum of D could characterize a change in the dynamics of the system for the frequency of the neutron technique which could be interestingly compared to the T_G values determined at low frequency. To this respect, the similarities found with anomalies of phonons observed at T_G in molecular glass (minimum of the C_{44} elastic constant, concurrently with a maximum of the damping[26]) are very intriguing. Very recently a theory[27] has been developed to explain these dynamic anomalies which involves interactions between phonons coupled with molecular rotations and static random strain fields. In a very speculative way one can wonder whether an analogy could be found with reentrant spin glasses which would open new perspectives for the understanding of these dynamic anomalies.

ACKNOWLEDGMENTS

We would like to acknowledge A. Brulet and F. Gibert for their help during the experiments on PAXY (Orphée) and Y. Campbell, H. Hurdequint, S. M. Shapiro and W. M. Saslow for enlightening discussions.

[1] B. V. B. Sarkissian, J. Phys. F **11**, 2191 (1981).
[2] Y. Yeshurun, M. B. Salamon, K. V. Rao, and H. S. Chen, Phys. Rev. B **24**, 1536 (1981).
[3] P. A. Beck, Phys. Rev. B **32**, 7255 (1985).
[4] F. Varret, A. Hamzic, and I. A. Campbell, Phys. Rev. B **26**, 5285 (1982).
[5] M. Gabay and G. Toulouse, Phys. Rev. Lett. **47**, 201 (1981).
[6] M. M. Abd Elmeguid, H. Micklitz, R. A. Brand, and W. Keune, Phys. Rev. B **33**, 7833 (1986).
[7] S. K. Burke, R. Cywinski, J. R. Davis, and B. D. Rainford, J. Phys. F **13**, 451 (1983).
[8] G. Aeppli, S. M. Shapiro, R. J. Birgenau, and H. S. Chen, Phys. Rev. B **28**, 5160 (1983); **29**, 2589 (1984).
[9] S. M. Shapiro, C. R. Fincher Jr., A. C. Palumbo, and R. D. Parks, Phys. Rev. B **24**, 6661 (1981).
[10] M. Hennion, I. Mirebeau, F. Hippert, B. Hennion, and J. Bigot, J. Magn. Magn. Mater. **54**, 121 (1986); M. Hennion, I. Mirebeau, B. Hennion, S. Lequien, and F. Hippert, Europhys. Lett. **2**, 393 (1986); S. Lequien, I. Mirebeau, M. Hennion, B. Hennion, F. Hippert, and A. P. Murani, Phys. Rev. B **35**, 7279 (1987).
[11] P. Böni, S. M. Shapiro, and K. Motoya, Solid State Commun. **60**, 881 (1986).
[12] B. Hennion, M. Hennion, F. Hippert, and A. P. Murani, J. Phys. F **14**, 489 (1984); B. Hennion, M. Hennion, I. Mirebeau, and F. Hippert, Physica **136B**, 49 (1986).
[13] R. B. Goldfarb, F. R. Fickett, K. V. Rao, and H. S. Chen, J. Appl. Phys. **53**, 7687 (1982).
[14] W. Abdul Razzac and J. S. Kouvel, Phys. Rev. B **35**, 1764 (1987).
[15] S. Senoussi and Y. Oner, J. Magn. Magn. Mater. **53**, 139 (1985).
[16] A. Hamzic and I. A. Campbell, J. Phys. Lett. **42**, L309 (1981).
[17] I. Mirebeau, M. Hennion, S. Lequien, and F. Hippert (these proceedings).
[18] K. Motoya, S. M. Shapiro, and Y. Muraoka, Phys. Rev. B **28**, 6183 (1983).
[19] G. T. Rado, Phys. Rev. B **26**, 295 (1982).
[20] M. Steiner, K. Kakurai, and J. K. Kjems, Z. Phys. B **53**, 117 (1983).
[21] W. M. Saslow, Phys. Rev. B **35**, 3454 (1987).
[22] H. Kawamura and M. Tanemura, J. Phys. Soc. Jpn. **55**, 1802 (1986).
[23] A. P. Murani, Phys. Rev. B **28**, 432 (1983); J. W. Lynn, R. W. Erwin, J. J. Rhyne, and H. S. Chen, J. Magn. Magn. Mater. **31-34**, 1397 (1983); R. W. Erwin, J. W. Lynn, J. J. Rhyne, and H. S. Chen, J. Appl. Phys. **57**, 3473 (1985).
[24] S. Lequien, B. Hennion, and S. M. Shapiro (to be published in Phys. Rev. B).
[25] M. Continentino, Phys. Rev. B **27**, 4351 (1983).
[26] M. Rowe, J. J. Rush, N. J. Chesser, D. L. Hinks, and S. Sussman, J. Chem. Phys. **68**, 4320 (1978).
[27] K. H. Michel, Phys. Rev. B **33**, 1414 (1987); K. H. Michel, Z. Phys. B (to be published).

Field cooling and demagnetizing field influence on the magnetic structure observed in reentrant spin glasses

I. Mirebeau, M. Hennion, and S. Lequien
Laboratoire Léon Brillouin,[a] *CEN-Saclay, 91191 Gif/Yvette Cédex, France*

F. Hippert
Laboratoire de Physique du Solide, Université d'Orsay, 91405 Orsay, France

In reentrant spin glasses, small-angle neutron scattering measurements performed at low temperature in an applied field show a magnetic structure, i.e., a peak of the scattering $I(q)$ at a finite q_{max} value. This structure has been studied as a function of applied field, cooling conditions, and sample geometry. The q_{max} value is found proportional to $\sqrt{H_{int}}$ where H_{int} is the internal field. In FeMnPBAl, the structure is insensitive to the field applied during the cooling process H_{cool} whereas in NiMn q_{max} increases with H_{cool}. This difference between the two systems is reminiscent of that observed in magnetization measurements which show that the memory effects induced by field cooling are stable in NiMn and unstable in FeMnPBAl.

The reentrant spin glasses (RSG) are characterized by competing ferromagnetic and antiferromagnetic interactions, the frustration arising from chemical disorder. The mean magnetic interaction is nonzero ($\bar{J}>0$ here) instead of null in classical spin glasses. When lowering the temperature, susceptibility and magnetization measurements show a transition from para to ferromagnetism at T_c and below a lower temperature T_G, spin-glass-like properties.[1] Like the usual spin glasses, the RSG below T_G can schematically be classified in two types according to the rigidity of the spin system. In the rigid ones (NiMn,[2] FeZr) field cooling induces a displaced hyteresis cycle. In the nonrigid ones (FeMnPBAl,[3] AuFe) relaxation effects occur: the hysteresis cycle is first of all displaced, but this effect is unstable and easily washed out by the applied field. Despite these analogies with usual spin glasses, other measurements such as inelastic neutron scattering,[4] polarization analysis,[5] and electron microscopy[6] show in the RSG studied here the persistence below T_G of long-range ferromagnetic order associated with spin waves and micronmeter sized domains. As a matter of fact, the magnetization curve $M(H)$ is, except its low field part, similar to that of an ordinary ferromagnet: it exhibits a saturation plateau when the applied field H exceeds 1 or 2 kOe (insert of Fig. 1). In NiMn, FeMnPBAl, and AuFe, we have observed by small-angle neutron scattering (SANS) in an applied field a magnetic structure, i.e., a maximum of the scattering curve $I(q)$ at a finite q_{max} value of the scattering vector q.[7] This structure strongly depends on the field, the temperature, and the concentration. In order to be precise about its field dependence we have studied the influence of the sample geometry (demagnetizing effects) and of the field cooling conditions in $Ni_{0.784}Mn_{0.216}$ and $(Fe_{0.765}Mn_{0.235})_{75}P_{16}B_6Al_3$.

The SANS measurements were performed using the XY multidetector of the ORPHEE reactor at Saclay at temperatures between 9 and 120 K and magnetic fields between 0 and 12 kOe. The scattering vector range was $0.01<q<0.15$ Å^{-1}. The samples were rectangular platelets of a few mm thickness and about 2 cm^2 surface. The field was applied either along the length or along the width of the platelets leading to different values of the demagnetizing field H_d. The scattered intensity was corrected for external background and calibrated in absolute units using a slab of nickel.

The polycrystalline NiMn and amorphous FeMnPBAl samples have very similar characteristic temperatures ($T_c \simeq 250$ K; $T_G \simeq 30$ K). After cooling in zero field, the magnetic structure is observed for $H>1.8$ kOe. Its intensity decreases with T and disappears at a temperature T_K between T_c and T_G ($T_K = 130$ and 90 K, respectively, in these NiMn and FeMnPBAl samples). The study of the scattering anisotropy in the q,H plane ($I_{q\|H}/I_{q\perp H} \simeq 1.55$) shows that the correlations are mostly due to transverse components.[7] The existence of frozen transverse spin components below T_K was also concluded from Mössbauer experiments.[5]

Figure 1 shows the scattered intensity as a function of q for several values of the applied field H and for two orientations of the sample with respect to H in $(Fe_{0.765}Mn_{0.235})_{75}P_{16}B_6Al_3$. When H increases the intensity decreases and q_{max} increases, whereas the magnetization remains almost constant. Clearly the demagnetizing effects are not negligible as the intensity for a given value of H is strongly dependent on the sample orientation. In Fig. 2(a) q_{max} is plotted versus H for the two orientations. The corresponding curves are found similar but translated one from the other by a quantity ΔH of about 550 Oe. ΔH is very close to the difference ΔH_d between the demagnetizing fields evaluated by using magnetization measurements on a piece of the same sample and approximating the platelet by an ellipsoid[8] ($\Delta H_d = 720 - 230 = 490$ Oe). When q_{max} is plotted as a function of H_{int} where $H_{int} = H - H_d$, all the data merge on a single curve. Similar results are found in a $(Fe_{0.78}Mn_{0.22})_{75}P_{16}B_6Al_3$ sample where H_d is much greater ($\Delta H_d = 1350$ Oe) and in $Ni_{0.784}Mn_{0.216}$ [Fig. 3(a)] for which we measured two platelets of different shapes. In all cases q_{max} is found proportional to $\sqrt{H_{int}}$ [Figs. 2(b) and 3(b)] as shown by Böni, Shapiro, and Motoya[9] in FeAl. In $Ni_{0.784}Mn_{0.216}$ measurements up to 12 kOe show unambigu-

[a] Laboratoire commun CEA-CNRS.

 0021-8979/88/084077-03$02.40 © 1988 American Institute of Physics

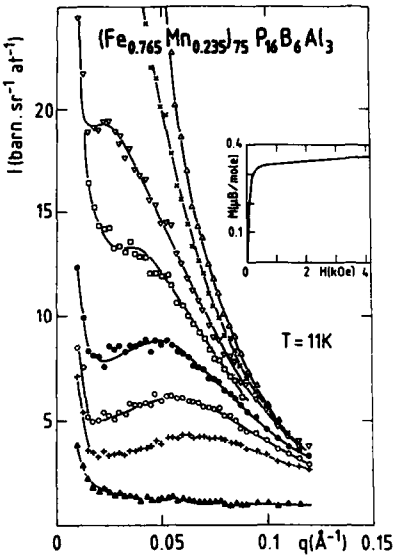


FIG. 1. SANS intensity $I(q)$ $(q\|H)$ in $(Fe_{0.765}Mn_{0.235})_{75}P_{16}B_6Al_3$ at 11 K for various field values: Δ: 0.8, × 1.8; ∇: 2.7; ●: 4.2; O: 5.8, + 7.8 kOe, H being parallel to the sample width; □: 2.7 kOe, H parallel to the sample length; ▲: $T = 443$ K, $H = 8$ kOe. The solid lines are guide to the eye. Insert: Magnetization M vs H at 11 K.

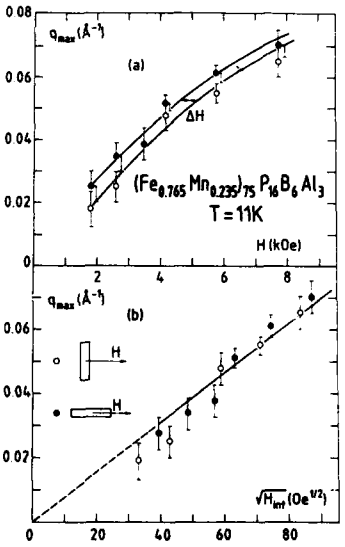


FIG. 2. (a) q_{max} vs H for two orientations of the sample $(Fe_{0.765}Mn_{0.235})_{75}P_{16}B_6Al_3$. O: H parallel to the sample width ($H_d = 720$ Oe); ●: H parallel to the sample length ($H_d = 230$ Oe). The structure remains visible down to 1.8 kOe but the determination of q_{max} becomes then highly uncertain because of another low q scattering (see Fig. 1). (b) q_{max} vs the a square root of the internal field $H_{int} = H - H_d$. The solid lines are a guide to the eye. The dashed lines are extrapolated ones.

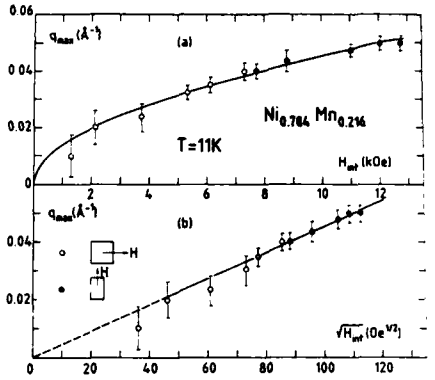


FIG. 3. q_{max} vs H_{int} (a) and $\sqrt{H_{int}}$ (b) in $Ni_{0.784}Mn_{0.216}$ at 11 K. The black and blank dots refer to samples of different shapes ($H_d \simeq 400$ Oe). The solid lines are guides to the eye. The dashed lines are extrapolated ones.

ously that the law $q_{max} \propto \sqrt{H_{int}}$ fits the data better than the law $q_{max} \propto H_{int}$.

We have also cooled the samples from temperatures higher than T_K in a field H_{cool} ($H_{cool} = 1.5$ or 8 kOe) and applied at low temperature (9–11 K) a field H from 0 to 12 kOe. In FeMnPBAl the structure is found identical to that obtained in zero field cooling (ZFC) conditions whereas in NiMn it strongly depends on H_{cool}. As shown in Fig. 4, for a given field H, q_{max} increases with H_{cool}: the increase of q_{max} between $H_{cool} = 8$ kOe and $H_{cool} = 0$ corresponds to an increase of the applied field of about 5 kOe. The structure intensity does not systematically decrease when H_{cool} increases as it does when H increases. Results similar to that of Fig. 4 are obtained whatever the value of H above 2 kOe. In this range the hysteresis loops are closed and the magnetization does not depend on H_{cool} anymore. At lower H values and especially in zero field we see no more structure but the

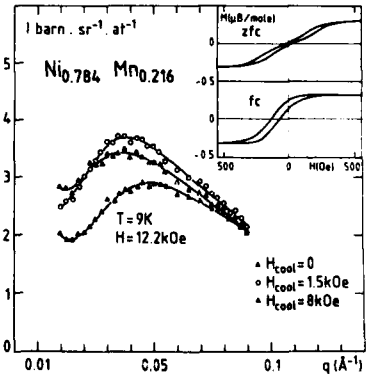


FIG. 4. SANS intensity $I(q)$ $(q//H)$ measured in $Ni_{0.784}Mn_{0.216}$ at 9 K and 12.2 kOe for various field-cooling conditions. The solid lines are guide to the eye. Insert: Magnetization M vs H at 9 K in the z field-cooled (ZFC) state and in the field-cooled (FC) state with $H_{cool} = 1.5$ kOe.

scattered intensity decreases with H_{cool}. Moreover, when $H=0$, the signal which is isotropic after ZFC because of random domain orientations becomes anisotropic ($I_{q\|H} > I_{q\perp H}$) after FC. This is consistent with the existence of an important remanent magnetization.

In conclusion, the study of the structure with several cooling conditions shows qualitatively the same differences between the nonrigid FeMnPBAl and the rigid NiMn as shown by magnetization measurements. Moreover, in NiMn the structure and therefore the transverse correlations are modified by H_{cool}, even in an applied field range ($H>2$ kOe) where the magnetization is found almost insensitive to H_{cool}. We thus observe important modifications of the spin correlations with H and H_{cool} which have a very small effect ($\simeq$%) on the mean magnetization. The study of the structure as a function of applied field and sample geometry shows that q_{max} is proportional to $\sqrt{H_{int}}$ where H_{int} is the internal field. Measurements with several Mn concentrations, which will be reported elsewhere, show that q_{max} varies approximatively with $\sqrt{H_{int}/D}$ where D is the spin-wave stiffness. We note that such a law is expected rather generally when there is a competition between the exchange, the anisotropy, and the external field energies.[10] This result could help to relate q_{max} to a size of magnetic defects defined by the transverse components. This law predicts that the structure would disappear in zero field. Unfortunately, we cannot test the validity of this law down to the zero internal field, as the structure is concealed at low H_{int} values by a low q scattering of many origins both nuclear and magnetic.

It is a pleasure to thank B. Farnoux and A. Brulet for their participation to the SANS experiments and A. Miedan-Gros for his help in performing the magnetization measurements.

[1]B. V. B. Sarkissian, J. Phys. F **11**, 2191 (1981).
[2]J. S. Kouvel and W. Abdul-Razzac, J. Magn. Magn. Mater. **53**, 139 (1985).
[3]S. Senoussi and Y. Oner, J. Phys. (Paris) **46**, 1435 (1985).
[4]B. Hennion, M. Hennion, I. Mirebeau, and F. Hippert, Physica **136B**, 49 (1986).
[5]I. Mirebeau, G. Jehanno, I.A. Campbell, F. Hippert, B. Hennion, and M. Hennion, J. Magn. Magn. Mater. **54**, 99 (1986).
[6]S. Senoussi, S. Hadjoudj, R. Fourmeaux (unpublished).
[7]M. Hennion, I. Mirebeau, B. Hennion, S. Lequien, and F. Hippert, Europhys. Lett. **2**, 393 (1986); S. Lequien, I. Mirebeau, M. Hennion, B. Hennion, F. Hippert, and A. Murani, Phys. Rev. B **35**, 7279 (1987).
[8]J. A. Osborn, Phys. Rev. **67**, 351 (1945).
[9]P. Böni, S. M. Shapiro, and K. Motoya, Solid State Commun. **60**, 881 (1986).
[10]W. M. Saslow, Phys. Rev. B **35**, 3454 (1987).

Magnetic correlations in amorphous Fe-Zr alloys

J. J. Rhyne and R. W. Erwin
Institute for Materials Science and Engineering, National Bureau of Standards, Gaithersburg, Maryland 20899

J. A. Fernandez-Baca
Oak Ridge National Laboratory, Oak Ridge, Tennessee 37831

G. E. Fish
Allied Signal, Inc., Morristown, New Jersey 07960

Results of high-resolution small-angle neutron scattering (SANS) studies on amorphous alloys of composition Fe_xZr_{100-x}, $x = 90, 91, 92$ show that ferromagnetic correlations exist below T_c, but that conventional long-range orde destroyed by competing exchange interactions. The transition temperatures drop with increasing iron concentration ($T_c \approx 226$ K for $Fe_{90}Zr_{10}$ down to $T_c \approx 175$ K for $Fe_{92}Zr_8$). Data taken at very low Q ($0.008\ \text{Å}^{-1} < Q < 0.02\ \text{Å}^{-1}$) provide evidence of relatively large (≈ 200–≈ 400 Å) static spin clusters which do not disorder at T_c. Superposed on this is an ordering with a second shorter length scale which shows a cusp (not divergent) at the bulk T_c. The data were fitted to a combination of a Lorentzian and a power of a Lorentzian, the latter of which represents scattering from clusters with a Maxwellian distribution of sizes.

INTRODUCTION

Alloys of iron and zirconium, Fe_xZr_{100-x}, can be made amorphous by melt spinning over a limited composition range of approximately $88 < x < 93$. In this composition range the metals have extremely unusual magnetic behavior, as first recognized by Hiroyoshi and Fukamichi.[1] Recent complete magnetization and Mössbauer studies of the alloys in this range have been reported by Ryan *et al.*[2] which also confirmed many of the features of previous investigations cited in Ref. 2.

Amorphous Fe_xZr_{100-x} exhibits a relatively low-temperature transition from paramagnetism to an unconventional ordered magnetic state. The temperature varies strongly with composition and is highest for the alloys with lowest iron composition (e.g., $T_c = 265.5$ K for $x = 88$ to $T_c = 163$ K for $x = 93$).[2] The alloys show a very large high-field susceptibility at 4.2 K which increases with x, and the magnetization does not saturate in fields as high as 19 T.[2] The z-component magnetic moments obtained by extrapolating high-field data to $H = 0$ also decrease with x and are several tenths of a Bohr magneton lower than that deduced from the Mössbauer hyperfine fields which are found to be increasing[3] or constant[2] over the full range $0.88 < x < 0.93$. These results, as well as others mentioned later, suggest the presence of competing exchange interactions in these alloys and of a nonconventional ferromagnetic state (described as a "wandering-axis ferromagnet"[2]) below T_c with a lower-temperature "freezing" of transverse spin components based on irreversibilities in the susceptibility.[1]

In this paper we report the results of small-angle neutron scattering (SANS) studies of the magnetic order in alloys of Fe_xZr_{100-x} with $x = 90$, 91, and 92. These experiments were performed at the National Bureau of Standards Reactor SANS instrument using 8-Å neutrons which yielded data down to wave-vector transfers $Q = 0.008$ Å.$^{-1}$ This is considerably higher resolution than was used in the previous neutron experiments[4] on $Fe_{91}Zr_9$ which were made only for $Q > 0.04$ Å^{-1} and has led to a refined interpretation of the magnetic ordering.

EXPERIMENT AND RESULTS

The amorphous alloys were prepared in ribbon form by inside-roll chill-block melt-spinning techniques. About 15 g of sample were wound on an aluminum frame to form a plate geometry for the transmission neutron measurements.

In a conventional ferromagnetic system, the increase in spatial coherence of the spin fluctuations as T approaches T_c gives rise to a Lorentzian cross section form for the neutron scattering:

$$I(Q) = A/(Q^2 + \kappa^2), \tag{1}$$

within the static approximation (integral over all inelastic processes), where κ is the inverse spin correlation length. At the phase transition, κ approaches 0, and below T_c, κ has two components, of which the transverse κ_T remains 0 (spin-wave scattering) and the longitudinal component κ_l rises sharply and thus suppresses the scattering from the longitudinal fluctuations. Below T_c, the Lorentzian coefficient A decreases linearly to zero reflecting the Bose population factor.

The temperature dependence of the scattering from Fe_xZr_{100-x} is highly anomalous as evidenced by a plot of the inverse intensity $I(Q)^{-1}$ vs Q^2 in Fig. 1 for $Fe_{91}Zr_9$ (similar data were obtained for the other two compositions). For temperatures from about 95 K up to above $T_c = 210$ K, the scattering is Lorentzian for Q values larger than approximately 0.03 Å^{-1}. However, at lower Q's the inverse scattering turns down sharply toward the origin for $T > 95$ K and also for temperatures *above* the magnetic ordering tempera-

 0021-8979/88/084080-03$02.40 © 1988 American Institute of Physics

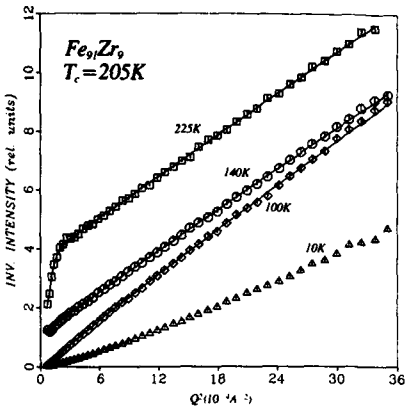


FIG. 1. Inverse intensity vs Q^2 from the SANS data on $Fe_{91}Zr_9$ plotted for several representative temperatures below and above $T_c = 205$ K. The change in curvature with temperature is discussed in the text.

ture. Similar low-Q behavior has been seen in $(Fe_xNi_{100-x})_{80}P_{20}$ alloys[5] and in $Fe_{22}Cr_{78}$.[6]

As will be discussed later, the unusual low-Q dependence suggests the presence of near ferromagnetic clusters which do not disorder at T_c upon which are superposed dynamic spin fluctuations (or alternatively a wandering static disorder) of a shorter length scale. At temperatures below ≈ 95 K where irreversibilities in the susceptibility occur, the scattering (Fig. 1) for the larger Q is observed to depart from Lorentzian and to have a form which can be represented by the sum of a Lorentzian and a Lorentzian squared with the same inverse correlation length:

$$I(Q) = \frac{A}{Q^2 + \kappa^2} + \frac{B}{(Q^2 + \kappa^2)^2}. \tag{2}$$

The Lorentzian squared term is normally ascribed to scattering from static "frozen" spin clusters and its amplitude B is proportional to $(q_{EA} - M^2)\kappa$ where q_{EA} is an Edwards–Anderson "spin-glass" order parameter, and M is a static magnetization (if present).

The functions represented by Eqs. (1) and (2) will yield curves of $1/I$ vs Q^2 which have only positive curvature. It is evident from Fig. 1 that they will thus not represent the higher T data when the low-Q region is included. In particular the abrupt change in curvature at low Q implies a second κ (or length scale) is present in the system. In view of this, we have chosen to evaluate the data using the sum of a Lorentzian and a function representing spin clusters of N spins with a Maxwellian distribution of sizes.[7] For this combination the scattering per unit volume has the following normalized form apart from constant factors:

$$I(Q) = \frac{A}{Q^2 + \kappa^2} + C\frac{(\kappa^2)^{z-1.5}}{(\kappa^2 + Q^2)^z}. \tag{3}$$

C is proportional to $(q_{EA} - m^2)$, and the exponent z reflects the breadth of the distribution. In the limit $z \to \infty$ the real space distribution becomes a delta function (ferromagnetic limit). The Fourier transform $S(\kappa R)$ of the second term of Eq. (3) above is a function only of the dimensionless product κR from which the spin correlation length ξ, for a particular value of κ, can be determined as that value of R which reduces $S(\kappa R)$ to $1/e$ using the calculated (fitted) value of the exponent z. For a Lorentzian squared function ($z = 2$) ξ is simply $1/\kappa$.

Equation (3) is an excellent representation of the scattering data for all three compositions over the full range of T and Q ($0.008\ \text{Å}^{-1} < Q < 0.06\ \text{Å}^{-1}$), as shown by the solid lines in Fig. 1 for $Fe_{91}Zr_9$, for example. At the lowest temperatures where the curves have no low Q inflection (apparent "frozen spin" regime), the upper limit of the Q range was restricted to $Q < 0.03\ \text{Å}^{-1}$ because of calculational difficulties. The power z for $Fe_{91}Zr_9$ ranged from about 2.7 at low T to 4.3 at 160 K, and showed a cusp minimum ($z = 2.6$) at T_c. Above T_c, z increased sharply to 44 at 225 K.

From Eq. (3) two spin correlation lengths can be derived: (a) that represented by the Lorentzian scattering and (b) that given by the power-law Maxwellian distribution. The latter is longer, and shows little awareness of T_c. The persistence of the associated non-Lorentzian (low Q portion in Fig. 1) scattering above T_c reflects definable spin cluster units which remain to temperatures well above T_c. Ryan *et al.*[2] also noted the appearance of "magnetic broadening" in their hyperfine spectra more than 50 K above T_c.

Figure 2 shows the two spin correlation lengths derived

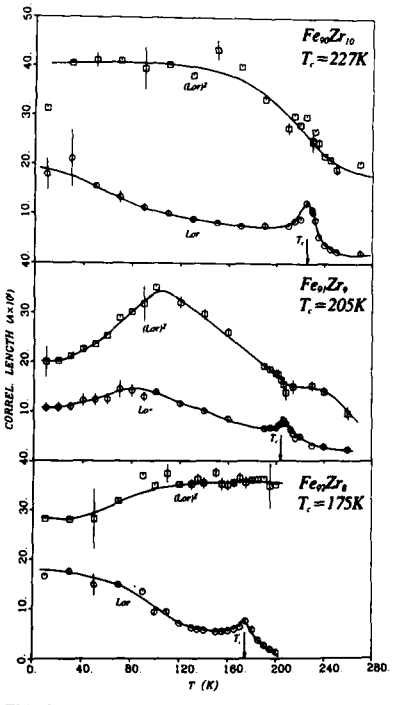


FIG. 2. Temperature dependence of the two length scales (correlation lengths) observed in Fe_xZr_{100-x} alloys. The curves marked Lor and $(Lor)^2$ are the correlation lengths derived from the two terms of Eq. (3).

from the above analysis for each of the three Fe_xZr_{100-x} compositions, $x = 90$, 91, and 92. It is noted that they have similar qualitative features—the longer characteristic length associated with the Maxwellian cluster distribution which is relatively less temperature dependent, and the Lorentzian characteristic length which rises on approach to T_c in a rather conventional fashion, exhibits a cusp, and then decreases to a shallow minimum followed by a small change of curvature at approximately the spin "freezing" temperature. It should be noted that the values of the Lorentzian correlation length are essentially the same as obtained from fits to Eqs. (1) and (2) if the low-Q data (below the inflection point in Fig. 1) are omitted from the analysis. Although the qualitative features are similar, in the $Fe_{91}Zr_9$ alloy the length scale is rather longer than that reported previously.[4] The difference arises from a combination of improved statistics in the SANS data and systematic errors in the resolution corrections required by the large vertical divergence inherent in a triple-axis instrument used for the previous work.

CONCLUSIONS

The broad distribution of exchange fields apparent in amorphous Fe_xZr_{100-x} alloys results in a nonconventional magnetic state, as illustrated by the present SANS results. Initially there are large (order of 200–400 Å) spin clusters (presumably static) which persist to temperatures well beyond the bulk critical temperature as determined by the ac susceptibility or from the coefficient of the Lorentzian term in the neutron scattering [$\chi \propto A/\kappa^2$, Eq. (1) and shown in Fig. 3 (inset)]. Because the background subtraction process removes effects of chemical clustering, these clusters have a magnetic origin, although they may be possibly induced by metallurgical concentration fluctuations. The clusters are relatively abundant in number, as reflected by the intense low-Q SANS. Superposed on this length scale is a second characteristic distance (reflected in the larger Q Lorentzian scattering) which is quite temperature dependent, exhibits a signature at T_c, and remains of order 100 Å below T_c. This latter length may represent a characteristic periodicity in the "wandering axis" ferromagnet or it may reflect a truncation in the range of magnetic excitations. Recent inelastic scattering data[8] taken on $Fe_{91}Zr_9$ with 100-μeV energy resolution show no evidence of discrete propagating spin waves, rather only a broadened "diffusivelike" spectrum which is consistent with strongly damped spin waves having a maximum low-T stiffness $D \approx 15$ meV Å^2.

It should be noted that the Lorentzian scattering observed in the SANS is not of the conventional dynamic form, since the coefficient "A" [Eq. (1)] rises at low temperature as shown in Fig. 3, rather than exhibiting the linear T form characteristic of a normal ferromagnet. This would suggest that the associated scattering is at least in part static in character like the power-law Lorentzian scattering.

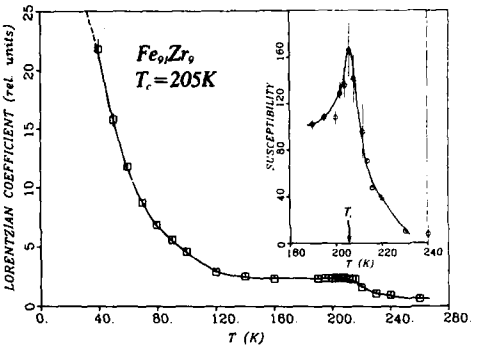


FIG. 3. Temperature dependence of the Lorentzian coefficient A showing its nonconventional sharp increase with decreasing temperature. The inset shows the peak in the susceptibility (A/κ^2) at T_c.

The balance between competing ferromagnetic and antiferromagnetic exchange interactions, presumably responsible for the destruction of long-range order in these alloys, is very sensitive to local environment effects as illustrated (1) by the rapid change in T_c with Fe concentration, and (2) by the near ideal Heisenberg ferromagnetic order induced by the partial substitution of Ni for the Fe [for example, in $Fe_{70}Ni_{20}Zr_{10}$ (Refs. 9 and 10)].

ACKNOWLEDGMENT

Work at Oak Ridge was supported by the U. S. Department of Energy under contract No. DE-AC05-840R21400 with Martin Marietta Energy Systems, Inc.

[1] H. Hiroyoshi and K. Fukamichi, Phys Lett. **85A**, 242 (1981).
[2] D. H. Ryan, J. M. D. Coey, E. Batalla, Z. Altounian, and J. O. Strom-Olsen, Phys Rev. B **35**, 8630 (1987). This reference also contains additional citations to previous work which are omitted here.
[3] K. M. Unruh and C. L. Chien, Phys. Rev. **30**, 4968 (1984).
[4] J. J. Rhyne and G. E. Fish, J. Appl. Phys. **57**, 3407 (1985).
[5] M. B. Salamon and A. P. Murani, J. Appl. Phys. **55**, 1680 (1984).
[6] S. K. Burke, Ph.D. Thesis, Imperial College, 1980 (unpublished).
[7] A. Guinier and G. Fournet, *Small-Angle Scattering of X-Rays* (Wiley, New York, 1955).
[8] (to be published).
[9] R. Krishnan, K. V. Rao, and H. H. Liebermann, J. Appl. Phys. **55**, 1823 (1984).
[10] J. A. Fernandez-Baca, J. J. Rhyne, and G. E. Fish, J. Magn. Magn. Mater. **54-57**, 289 (1986); also these proceedings.

Spin-wave excitations in amorphous $Fe_{78}B_{13}Si_9$

S. C. Yu and J. W. Lynn
Department of Physics, University of Maryland, College Park, Maryland 20742 and National Bureau of Standards, Gaithersburg, Maryland 20899

J. J. Rhyne
National Bureau of Standards, Gaithersburg, Maryland 20899

G. E. Fish
Allied Signal, Inc., Morristown, New Jersey 07969

Inelastic neutron scattering measurements have been used to study the long wavelength spin dynamics of the high T_c amorphous ferromagnetic alloy $Fe_{78}B_{13}Si_9$ (Metglas 2605S2). Spin waves were observed over the accessible wave-vector range of $0.06\ \text{Å}^{-1} < q < 0.12\ \text{Å}^{-1}$, for temperatures between 473 K (0.67 T_c) and 705 K (0.99 T_c). The magnon dispersion curves exhibit the conventional quadratic relationship $E = D(T)q^2 + \Delta$, typical of an isotropic ferromagnet, where the small energy gap $\Delta \approx 0.05$ meV is attributed primarily to the dipole-dipole interaction. An estimate of the $T = 0$ value of $D \approx 156$ meV Å^2 was obtained from a plot of $D(T)$ vs T extrapolated to low temperatures, while the Curie temperature of 710 K was obtained from the extrapolation of $D(T)$ to zero at high temperatures. Spin-wave linewidth data for $T/T_c \approx 0.95$ showed the q^4 wave-vector dependence expected for magnon-magnon interactions.

INTRODUCTION

The magnetic properties of metallic glasses produced by rapid quenching have been the subject of considerable scientific and technological interest. Alloys, of composition near $TM_{80}M_{20}$, can exhibit very low coercive fields, quite high permeability, and have Curie temperatures well above room temperature. Allied Signal has found that the metallic glass having the nominal atomic composition $Fe_{78}B_{13}Si_9$ (Metglas 2605S2) has extremely low core loss at power transformer frequencies and inductions. The Curie temperatures and the crystallization temperatures of this alloy are found to be higher than any of the other Fe-B-Si amorphous systems.[1]

In order to obtain a better understanding of the high T_c amorphous alloys, we have undertaken detailed neutron scattering studies of commercially available $Fe_{78}B_{13}Si_9$ to determine the temperature and wave-vector dependence of the spin-wave excitations. Previous neutron scattering studies on ferromagnetic metallic glass systems showed that conventional spin-wave excitations are found at small wave vectors.[2] The present results confirm the basic conclusion that spin-wave theory is quite successful in describing the long wavelength magnetic excitations in amorphous $Fe_{78}B_{13}Si_9$.

EXPERIMENT

The sample of $Fe_{78}B_{13}Si_9$ used in our measurements was prepared in ribbon form from the melt by rapid quenching techniques in vacuum. Approximately 17 g of the ribbons 20 μm thick and 2.5 cm wide were loosely wound between two aluminum posts to produce a flat platelike sample. This was mounted in a vacuum furnace, and the neutron scattering measurements were taken on a conventional triple-axis spectrometer at the National Bureau of Standards Reactor. The amorphous nature of the system required that measurements be taken near the forward (000) beam position, and precautions were taken to minimize air and sample-container scattering at the small wave-vector (q) transfers required in the experiments. A fixed incident energy of 13.5 meV was used and a pyrolytic graphite (PG) filter was placed after the PG(002) monochromator to suppress high-order wavelength contaminations. Soller slit horizontal collimators of 12′-11′-12′-16′ were used to produce a FWHM (full width at half maximum) energy resolution ΔE of 0.35 meV at the elastic position. The wave-vector transfers examined were in the range $0.06\ \text{Å}^{-1} < q < 0.12\ \text{Å}^{-1}$ and the temperature range was from approximately 473 K (0.67 T_c) to 705 K (0.99 T_c). At lower temperatures the spin-wave energies were too high to measure with these experimental conditions.

RESULTS AND DISCUSSION

Values of the spin-wave energies and linewidths were obtained by convoluting a theoretical cross section with the instrumental resolution and least squares fitting to the observed spectra. Additional experimental details are given in Ref. 3. The spectral weight function used in the convolution was a double Lorentzian-type cross section. Figure 1 shows a set of typical constant-q neutron scans at 0.08 Å^{-1} for 635, 660, and 698 K. The background and elastic scattering which arises principally from the furnace have been subtracted. Spin waves for both neutron energy gain ($E < 0$) and energy loss ($E > 0$) are easily observable and well resolved until they merge into a single central peak close to T_c. The solid lines are the result of the least-squares fits, and the spin-wave positions are indicated by arrows. The actual spin-wave energies occur at an energy which is lower than the observed peak position due to resolution effects.[3] We also observe a broadening of the peaks with increasing temperature.

 0021-8979/88/084083-03$02.40 © 1988 American Institute of Physics

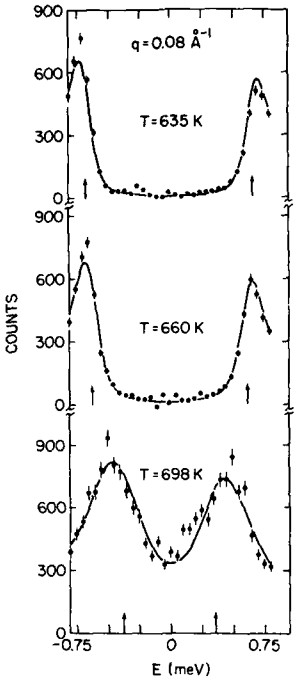


FIG. 1. Temperature dependence of spin-wave excitations in amorphous $Fe_{78}B_{13}Si_9$ at $q = 0.08$ Å^{-1}. The solid lines are the least-squares fits to the convolution of the cross section with the instrumental resolution. Background has already been subtracted.

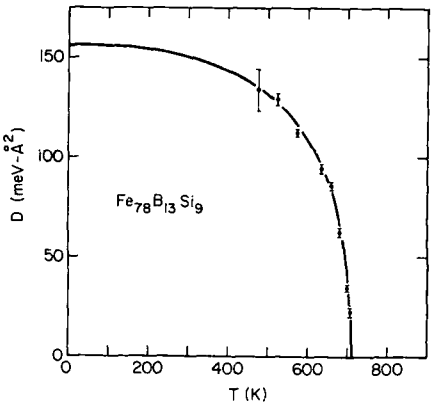


FIG. 2. Temperature dependence of the spin-wave stiffness constant obtained from the slopes of the dispersion relations.

The spin-wave energies obtained from the fits yielded the quadratic dispersion relation expected for an isotropic ferromagnet:

$$E_q = D(T)q^2 + \Delta + \cdots, \quad (1)$$

where $D(T)$ is the spin-wave stiffness constant, q is the magnon wave vector, and Δ is an effective anisotropy gap which originates mainly from the dipolar interactions. We found a gap of $\Delta \approx 0.05$ meV independent of temperature over the range of the measurements. The stiffness constant D obtained from the slopes of the dispersion relation curves is shown in Fig. 2 as a function of temperature. The renormalization of the spin-wave stiffness is typical of isotropic ferromagnetic systems. The Curie temperature of 710 K was obtained from the extrapolation of $D(T)$ to zero at high temperatures, while the estimation of the $T = 0$ value of $D \approx 156$ meV Å^2 was obtained from the plot of $D(T)$ vs T extrapolated to low temperatures. From the extrapolated values $D(0)$ and T_c, the ratio (D/T_c) was determined to be about 0.22 meV Å^2/K, which is quite similar to values found in other amorphous transition metal ferromagnets.[2] In the Heisenberg model this ratio is directly related to the range of the exchange interaction.[4] The values of D obtained in the present measurements are somewhat smaller than the values measured for $Fe_{81}B_{10}Si_9$ and $Fe_{75}B_{10}Si_{15}$ by Minor *et al.*[5]

The observed spin-wave scattering will also have an intrinsic linewidth which can be measured if the instrumental resolution is sufficient. The magnitude of these linewidths can be extracted from the spin-wave data by convoluting the cross section with the instrumental resolution and least-square fitting the energy, linewidth, and scattering strength to the data. Typically, reliable linewidth data can be obtained in this manner when the linewidths Γ_q (FWHM of the Lorentzian spectral weight function) are greater than about 30% of the instrumental energy resolution. As can be seen in Fig. 3, spin-wave linewidth data for $T/T_c \approx 0.95$ (698 K) show the usual q^4 wave-vector dependence expected for thermally induced magnon-magnon interactions. The error bars shown are statistical only.

In summary, the overall results indicate that conventional hydrodynamic spin-wave theory provides an appro-

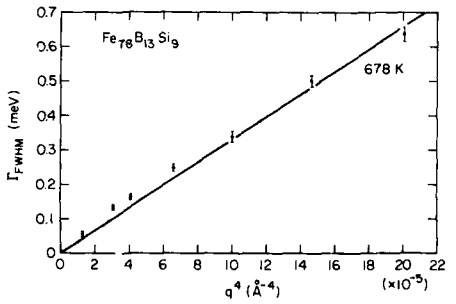


FIG. 3. Intrinsic spin-wave linewidth Γ_q (FWHM of the Lorentzian spectral weight function) vs q^4 for $Fe_{78}B_{13}Si_9$ ($T_c = 710$ K) at $T = 678$ K. The instrumental energy resolution (FWHM) was $\Delta = 0.35$ meV.

priate description of the long wavelength magnetic excitations in the soft amorphous ferromagnetic alloy $Fe_{78}B_{13}Si_9$.

ACKNOWLEDGMENT

The research at the University of Maryland was supported by the National Science Foundation grant No. DMR 86-20269.

[1] A. K. Bhatnagar and N. Ravi, Phys. Rev. B **28**, 359 (1983).
[2] J. W. Lynn and J. J. Rhyne, in *Spin Waves and Magnetic Excitations*, edited by A. S. Borovik Romanov and S. K. Sinha (North-Holland, Amsterdam, 1988), Part II, Chap. 4.
[3] J. A. Fernandez-Baca, J. W. Lynn, J. J. Rhyne, and G. E. Fish, Phys. Rev. B **36**, 8497 (1987).
[4] Further discussion of this point can be found in Ref. 3.
[5] W. Minor, B. Lebech, K. Clausen, and W. Dmowski, *Rapidly Quenched Metals*, edited by S. Steeb and H. Warlimont (Elsevier, New York, 1985), p. 1149.

The domain and the domain wall structures of an $Fe_{90}Zr_{10}$ reentrant alloy

S. Senoussi and S. Hadjoudj
Laboratoire de Physique des Solides, Université Paris-Sud, 91405 Orsay, France
P. Jouret, J. Bilotte, and R. Fourmeaux
Laboratoire d'Optique Electronique du CNRS, 29 Rue Jeanne Marvig, 31055 Toulouse, France

Lorentz electron transmission microscopy investigations of the magnetization structure as a function of temperature ($6\ K \lesssim T \lesssim 290\ K$) in amorphous films of $Fe_{90}Zr_{10}$ are reported. Magnetic domains as large as $\sim 50\ \mu m$ are observed. It is found that the domain configuration stays essentially unchanged upon cooling through the so-called reentrant spin-glass phase. However, direct magnetic measurements on the same sputtered films show that the degree of spin-glass order which sets in below ~ 30 K is rather low, whereas the Curie temperature exceeds 290 K.

During the last few years, considerable attention has been paid, both theoretically[1] and experimentally, to the magnetic alloys which show reentrant spin-glass behaviors. Detailed investigations of the transport and magnetic properties[2–4] of crystalline reentrant alloys $Ni_{1-x}Mn_x$ and $Au_{1-x}Fe_x$ and of amorphous $(Fe_{78}Mn_{22})_{75}P_{16}B_6Al_3$ have led us to the conclusion that both the familiar drops of the zero-field-cooled magnetization $M_{ZFC}(T)$ below T_f and the characteristic shapes of the magnetic cycles of these systems were principally connected with domain pinning and anisotropy effects, whereas the spontaneous magnetization stayed essentially the same during cooling through the reentrant phase. A somewhat similar conclusion was reached by Kouvel and Abdul-Razzaq.[5]

In order to further clarify the nature of the reentrant state we have undertaken a systematic investigation of the magnetic properties of amorphous $Fe_{100-x}Zr_x$, near the composition $x = 10$, both by means of Lorentz electron transmission microscopy (LETM) and by direct magnetic measurements on the same specimens. Here we report preliminary results on sputtered amorphous $Fe_{90}Zr_{10}$ films. We have chosen to begin with this composition which had been extensively investigated recently by various experimental techniques[6–9] and because it seemed that the ferromagnetic correlation length (λ_c) in the amorphous magnetic phase would be as low as 22 Å.

Two TEM were used in this study: the high-voltage electron microscope of the Laboratoire d'Optique Electronique du CNRS à Toulouse (operated at 2 MV) in which the temperature of the specimen could be controlled (within few degrees) from ~ 10 to 290 K and a Philips EM 400 microscope (biased at 120 kV) also equipped with a helium-cooled sample holder, the temperature of which could be varied from ~ 6 to 290 K. To facilitate the interpretation of the magnetic state of the present reentrant alloy, it is interesting to recall briefly how electron-transmission microscopy can allow direct observation of the magnetic structure over a very large spatial scale ($\sim 0.5\ \mu m$–1 mm).[10] Basically, this is because the magnetic flux density $\mathbf{B}(\mathbf{r}) = \mathbf{H}(\mathbf{r}) + 4\pi\mathbf{M}(\mathbf{r})$ at any point $\mathbf{r}$ of the magnetic substance produces a Lorentz force $-(e/c)\mathbf{v}\times(\mathbf{H} + 4\pi\mathbf{M})$ on the travelling electrons and thus a deviation of the transmitted electron beam. Here, e is the charge of the electron, c the velocity of light, $\mathbf{v}$ the velocity of the incident electrons, $\mathbf{H}$ the local magnetic field, and $\mathbf{M}$ the local magnetization. For soft magnetic materials with no external field, $\mathbf{H} = 0$. Then, equating the Lorentz force and the centrifugal force leads (for the transmitted electrons) to an angular deviation $\phi = \langle M_\perp \rangle d(e/2Um)^{1/2}$ where $\langle M_\perp \rangle$ now refers to the component of $\mathbf{M}$ perpendicular to the beam axis (generally the in-plane magnetization) averaged along the trajectory of the electron within the film of thickness d, U is the accelerating potential, and m the electron mass. It can easily be shown[10] that (1) due to the deviation of the electron beam in opposite sense either side of a given domain wall, the latter will be imaged either as a dark line (divergent wall) or as a bright line (convergent wall). (2) A further important property of the ETM technique is that the magnetization $\mathbf{M}$ inside the domains themselves is perpendicular to the magnetic ripples that generally exist in the image and that are due to small spatial fluctuation of $\mathbf{M}$.

The Fe-Zr sputtering targets were prepared by inductively melting together the $Fe_{90}Zr_{10}$ composition. The resulting ingot was then given an appropriate form and subsequently sputtered directly onto a substrate formed by a copper grid covered by a thin (~ 200 Å) carbon layer. The temperature of the substrate during deposition was 115 K. The film thicknesses varied from 500 to ~ 3000 Å and were determined from the weight gain. Both x-ray[8,9] and ETM diffractions indicate that the material was amorphous. The density determined on an identical but thicker ($10\ \mu m$) material[8,9] was equal to the nominal composition within 0.5%.

The domain structures of a 1600-Å-thick $Fe_{90}Zr_{10}$ film at two representative temperatures (54 and 16 K) are shown in Fig. 1. Note that the micrographs at 54 and 16 K correspond to the same area of the specimen but differ in the associated out of focus distances (overfocused, respectively underfocused images). It is well known in Lorentz microscopy that reversing the sign of the out-of-focus distance changes the light trances of the domain walls into dark traces and vice versa.

The most characteristic features of the domain configuration in Fig. 1 are as follows. First, we observe the existence of very large, practically macroscopic, domains and domain walls with quite unusual shapes, that is, instead of the familiar linear walls typical of many crystalline materials, here we have closed and somewhat concentric loops with many

 0021-8979/88/084086-03$02.40 © 1988 American Institute of Physics

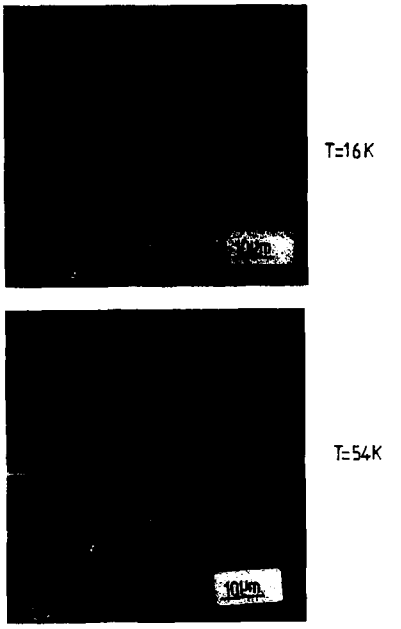


FIG. 1. Domain structures of a sputtered amorphous film (1600 Å thick) of $Fe_{90}Zr_{10}$ at 16 K (a) and at 54 K (b).

branches stretching from the small loops towards the larger ones. The second result of Fig. 1 which is especially interesting for the reentrant problem is the striking similarity between the domain structure at 54 and 16 K. A third important property concerns the presence of a fine magnetization structure or ripples inside the domains themselves.

It is a well-known property[10] of Lorentz microscopy that such striation lines are perpendicular to the local magnetization. This information joined to the fact that a bright line of the domain-wall image corresponds to a counter clockwise wall (viewed from the top side of the microscope) whereas a dark line corresponds to a clockwise wall (i.e., a clockwise rotation of the spontaneous magnetization through the wall) enables us to determine the distribution of the magnetization in the specimen.

Several interesting properties can be deduced from these observations. In particular, we easily observed that the component M_n of the magnetization perpendicular to the wall is continuous (i.e., is conserved) on crossing the wall. This means that no significant amount of magnetic poles and therefore no self-magnetostatic energy are present within the walls. The same is true for the bulk of the domains where we can deduce from a detailed inspection of Figs. 1 that, within a given domain, the flux distribution is linear and uniform in certain area of the domain and circular in certain other areas with a smooth transition between the two regions. This magnetization distribution satisfies the condition $\nabla \mathbf{m} = 0$ (i.e., no magnetic charge in the bulk material) and thus minimizes the magnetostatic energy associated with the intradomain structure. It is to be noticed that the presence of circular flux lines as well as the high curvature of the domain walls both imply that magnetocrystalline anisotropy is negligible within the film as expected for amorphous systems. It is also interesting to note that contrary to crystalline alloys, we find that the angle of the wall (i.e., the angle between the magnetic moments at either sides of the wall) is not constant along a given loop but fluctuates considerably between 0° and 180° varying rather abruptly near the point where several walls come together. The domain patterns displayed in Figs. 2(a) and 2(b) correspond to two different remanent magnetization states and were obtained just after the sample had been submitted (at the indicated temperatures) to a longitudinal field high enough to line up all the inital domains of the demagnetized state. The field was then removed and the subsequent micrographs were recorded few minutes later at the indicated temperatures.

As in Fig. 1 we observe some closed loops, but in addition the domain walls now have a preferred direction which is that of the remanent magnetization. It is also of interest to note the marked difference between the domain structure associated with the remanent magnetization at 54 and 16 K. This difference is probably connected with the onset of some spin-glass freezing and therefore with some increase of the hysteresis effects in the low-temperature state.

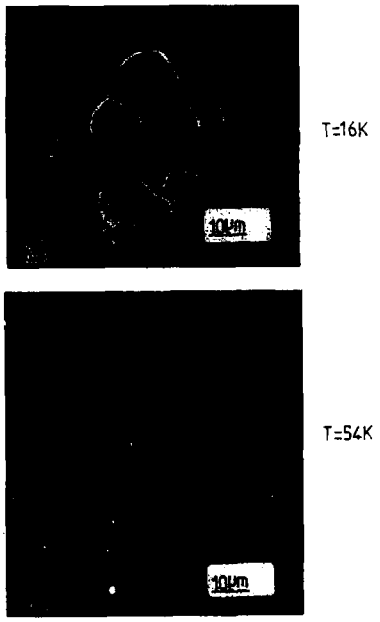


FIG. 2. Domain structures of the same amorphous $Fe_{90}Zr_{10}$ film as in Fig. 1 except that the sample has now a remanent magnetization; (a) $T = 16$ K, (b) $T = 54$ K.

As already mentioned, the reentrant transition is more easily revealed in the temperature variation of the zero-field-cooled magnetization $M_{ZFC}(T)$ in low field. We have measured the $m_{ZFC}(T)$ curves of our film in various constant fields. Due to the lack of space the results will be reported later, together with other measurements on samples with different Zr concentrations. A small but well-defined falloff of $m_{ZFC}(T)$ was clearly seen below $\simeq 30$ K, giving further evidence that a transition towards a spin-glass reentrant state takes place below about 30 K. However, the Curie temperature of the film exceeds 290 K, implying that the degree of spin-glass order in our specimen is very weak compared with that in bulk materials prepared by the melt-spinning technique. The reasons why the degree of ferromagnetic order could be so high in our materials are not clear for us but are discussed in Refs. 8 and 9.

In conclusion, the dimensions of the magnetic domains reported here ($\sim 50\,\mu$m) are more than four orders of magnitude larger than the ones (~ 2.2 nm) deduced from neutron scattering data.[6] We therefore believe that despite the fact that the degree of spin disorder is very weak in our sputtered films, the data are more consistent with our domain anisotropy picture[2,3,4,11] according to which the spontaneous magnetization or, equivalently, long-range ferromagnetic order are little perturbed by the spin-glass reentrant transition, whereas the drop of m_{ZFC} with decreasing T is primarily due to the increase of coercivity and anisotropy effects upon cooling through the reentrant transition.[12] We believe that this conclusion is valuable for many conventional reentrant systems. Nevertheless, in our opinion[4] the transition between the pure ferromagnetic order and the pure spin-glass disorder as a function of concentration is not sharp and the competition between the two types of order would be very severe near the so-called multicritical concentration x_c. It is then possible that near x_c the spontaneous magnetization decreases significantly as the sample is cooled through the reentrant state so that the above conclusions would not hold entirely. This concentration region might be more favorable to check the recent theoretical predictions[1] concerning the structure of the magnetization in reentrant spin glasses and in canted ferromagnets. As in Ref. 4, we tentatively propose that a possible and simple criterion to probe the diminution of the longitudinal (or spontaneous) magnetization below T_f could be given by the drop of the field cooled magnetization $m_{FC}(T)$ (in low H) upon cooling through the reentrant transition.

It is to be emphasized that direct observation of the magnetization structure by Lorentz ETM at very low temperatures is not very usual and this technique is therefore promising and interesting for its own right.

Finally, in order to lower the Curie temperature of our FeZr films and get more reliable information on the reentrant state we are planning to prepare other specimens both by different sputtering technique and by the coevaporation method.

We wish to thank I. A. Campbell, A. Fert, H. Hurdequint, and M. Laridjani for many stimulating discussions concerning this work. We also thank Mrs. Vaures for preparation of the films.

[1] W. M. Saslow, Phys. Rev. B **27**, 6873 (1983); **33**, 7845 (1986).
[2] S. Senoussi, Phys. Rev. Lett. **51**, 2218 (1983); Phys. Rev. B **31**, 6086 (1985).
[3] S. Senoussi and Y. Oner, J. Magn. Magn. Mater. **40**, 12 (1984); J. Appl. Phys. **55**, 1472 (1984).
[4] S. Senoussi and D. Elkhatouri, J. Magn. Magn. Mater. **54–57**, 153 (1986).
[5] J. S. Kouvel and W. Abdul-Razzaq, J. Magn. Magn. Mater. **53**, 139 (1985).
[6] J. J. Rhyne and G. E. Fish, J. Appl. Phys. **57**, 3407 (1985).
[7] D. H. Ryan, J. M. D. Coey, E. Batalla, Z. Altounian, and J. O. Ström-Olsen, Phys. Rev. B **35**, 8630 (1987).
[8] M. Laridjani, B. Krishnan, and P. Rougier, Mod. Phys. Lett. B (in press).
[9] M. Laridjani and J. F. Sadoc, Mod. Phys. Lett. B (in press).
[10] H. W. Fuller and M. E. Hale, J. Appl. Phys. **31**, 238 (1960).
[11] I. Mirebeau, J. Jehanno, I. A. Campbell, F. Hippert, B. Hennion, and M. Hennion, J. Magn. Magn. Mater. **54–57**, 99 (1986).
[12] It is to be emphasized, however, that the present results do not rule out the possibility that some degree of static spin fluctuations exists inside the domaines themselves at very short scale. In fact, previous transport measurements,[4] which probe the degree of magnetic disorder on the scale of the electron near free path (10–50 Å) together with preliminary LETM observations with higher magnification, give evidences that there are static transverse fluctuation[11] with wavelength distribution extending from ~ 10 to about 1000 Å. It could be interesting to see whether these data are consistent with a somewhat different analysis of the neutron data of Refs. 6 and 7.

"Zero" frequency spin relaxation in reentrant magnets

E. M. Jackson, S. M. Bhagat, and S. B. Liao
Department of Physics and Astronomy, University of Maryland, College Park, Maryland 20742
M. A. Manheimer
Laboratory of Physical Sciences, 4928 College Avenue, College Park, Maryland 20740

We present the frequency and concentration dependence of Γ_1, the parameter which characterizes the low-temperature increase in the magnetic resonance linewidth, for several reentrant magnets belonging to the alloy series $(Fe_pNi_{1-p})_{75}G_{25}$ and $(Fe_pNi_{1-p})_{80}G_{20}$. A comparison is made and it is shown that, near the spin-glass-reentrant transition concentration, the low-frequency dependence of Γ_1 is dramatically different for these two apparently similar systems.

In a variety of randomized spin systems, it has been shown[1] that there is an increase in the spin resonance linewidth at low temperatures given by the relation

$$\Delta\Gamma_L = \Gamma_1(T/T_0)\exp(-T/T_0), \qquad (1)$$

where $\Gamma_1(\nu, p)$ and $T_0(\nu, p)$ are empirical parameters, ν being the microwave frequency in GHz. In a recent note, we[2] reported on the frequency dependence of the parameter Γ_1 for a number of reentrant ferromagents belonging to the series a-$(Fe_pNi_{1-p})_{80}G_{20}$ (I) ($p = 0.11$, 0.14, 0.16, 0.19, 0.21, 0.24) and a-$(Fe_pNi_{1-p})_{75}G_{25}$ (II), ($0 = 0.17$, 0.18, 0.20,0.25, 0.30). The percolation concentrations (p_c) are 0.10 and 0.165 for I and II, respectively. It was found that (cf. Fig. 3, Ref. 2) for both I and II, the value of $\Gamma_1(35, p)$ is directly proportional to the number of isolated Fe spins in the system provided that the coordination number is taken to be 12. At the low-frequency end, data were available only for I, and it was shown that $\Gamma_1(0, p)$ varies roughly as the number of large clusters obtained from the scaling hypothesis[3] for p close to p_c. The present experiments, on the frequency dependence of Γ_1 in series II alloys, were undertaken to provide additional evidence for this low-frequency behavior. Indeed, both series of alloys exhibit roughly the same dependence on ν for p values well above p_c. However, for p close to p_c the present data show a totally unexpected rapid rise in $\Gamma_1(\nu, p)$ as ν drops below about 5 GHz. Here, we compare and contrast this low-frequency behavior in series I and II alloys.

The experimental methods have been described elsewhere.[4] Measurements of linewidths were made in the parallel and perpendicular orientations at $\nu = 2$, 2.9, 3.4, 4, 6, 10, 22, and 35 GHz. A typical set of $\Gamma_\parallel$ and $\Gamma_\perp$ values as a function of T are shown in Fig. 1 where we have indicated the "definition" of $\Delta\Gamma_L$ in Eq. (1). Hereafter, we will discuss only the parallel orientation data. Γ_1 is roughly the same in both orientations. Figure 2 shows $\Gamma_1(p, \nu)$ as a function of ν for series II alloys with the p values listed above. For comparison, in Fig. 3 we have reproduced our earlier results in series I alloys. It should be noted that in both cases the lines through the data are guides to the eye. It is clear that for $(p - p_c) \gtrsim 0.08$ the ν dependencies agree remarkably well. However, Γ_1 for series II alloys is roughly twice as large as that for comparable series I materials. The vanishing of $\Gamma_1(0, p)$ at large p in both sets can be taken as support for the previous idea[2] that $\Gamma_1(0, p)$ is controlled by the large clusters in the system.

The surprising feature in Fig. 2 is the rapid increase in Γ_1 below about 5 GHz. Further, it becomes more marked as $p \to p_c^+$. In this connection, it may be useful to note[5] that in the concentrated spin glass $(Fe_{0.16}Ni_{0.84})_{75}G_{25}$, Γ_1 increases rapidly with decreasing ν for $\nu < 4$ GHz. In some sense the present results are disappointing as they fail to provide additional confirmation for the picture proposed in Ref. 2 to understand $\Gamma_1(0, p)$. On the other hand, the interesting question is, can one qualitatively understand the reason for this dramatic difference between the behaviors of two very similar permalloys placed in an amorphous matrix?

It seems reasonable that a larger Γ_1 should be considered symptomatic of greater magnetic inhomogeneity. In this connection, a comparison of the other properties of series I and II alloys yields interesting clues. For instance, (i) for a given Fe concentration it is found[6] that a series I alloy has a T_c roughly 100 K higher than a series II alloy; (ii) the 0

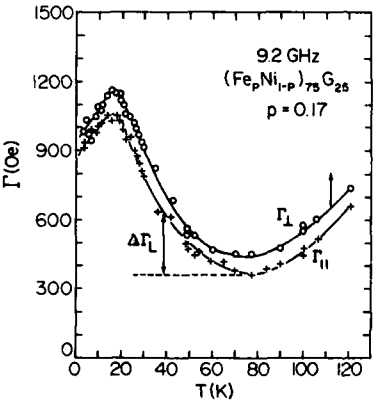


FIG. 1. Linewidths, as a function of temperature in a reentrant magnet.

 0021-8979/88/084069-02$02.40 © 1988 American Institute of Physics

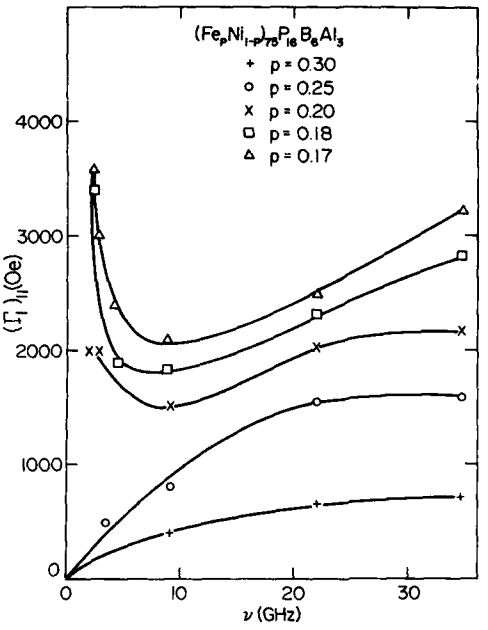


FIG. 2. Dependence of Γ_1 (p, ν) on the microwave frequency for the reentrant alloys, $(Fe_pNi_{1-p})_{75}G_{25}$.

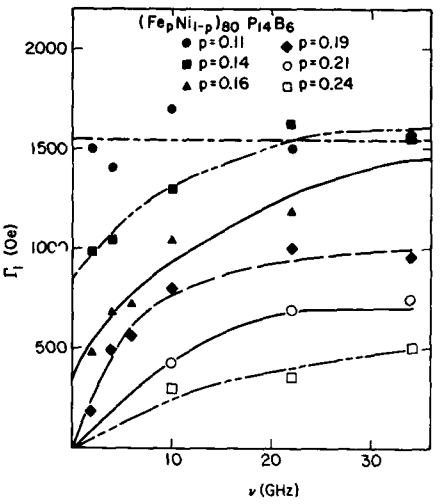


FIG. 3. Same as Fig. 2, for $(Fe_pNi_{1-p})_{80}G_{20}$.

K magnetization in a series I alloy is significantly larger[6] than that for the corresponding material in series II; (iii) the spin resonances in series I alloys are markedly narrower; (iv) p_c is smaller for the series I system[7]; (v) the T_c values of series II alloys are extremely sensitive to small changes in the amorphous matrix.[7] All of the above suggest that, for a given value of $(p - p_c)$, one should expect to observe wider distributions of interaction energies and consequently greater inhomogeneities in series II alloys. Obviously, a thorough understanding must await the development of a microscopic theory of spin resonance linewidths in reentrant magnets.

One of us (S.B.L.) is thankful to the National Science Foundation for support under the U.S./China cooperative program.

[1]S. M. Bhagat and H. A. Sayadian, J. Magn. Magn. Mater. **61**, 151 (1986).
[2]M. A. Manheimer, S. B. Liao, S. M. Bhagat, and K. Moorjani, Solid State Commun. **63**, 21 (1987).
[3]D. Stauffer, Phys. Rep. **54**, 1 (1979).
[4]S. M. Bhagat, D. J. Webb, and M. A. Manheimer, J. Magn. Magn. Mater. **53**, 209 (1985).
[5]S. B. Liao, S. M. Bhagat, M. A. Manheimer, and M. J. Park, Solid State Commun. **63**, 119 (1987).
[6]M. Manheimer, S. M. Bhagat, L. M. Kistler, and K. V. Rao, J. Appl. Phys. **53**, 2220 (1982).
[7]P. Mazumdar and S. M. Bhagat, J. Magn. Magn. Mater. **66**, 263 (1987).

Quenching of ferrimagneticlike ordering in $SrCr_8Fe_4O_{19}$ hexagonal ferrite

X. Obradors, A. Labarta, and J. Tejada
Departament Física Fonamental, Universitat de Barcelona, Diagonal 647, 08028 Barcelona, Spain

M. Pernet
Laboratoire de Cristallographie, CNRS, 166x, 38042 Grenoble, France

J. L. Tholence and M. Saint-Paul
C.R.T.B.T., CNRS, 166x, 38042 Grenoble, France

B. Barbara
Laboratoire Louis Néel, CNRS, 166x, 38042 Grenoble, France

We report here measurements of high field ($H<150$ kOe) isothermal magnetization, dc and ac susceptibility, and Mössbauer spectroscopy of the exchange frustrated insulator $SrCr_8Fe_4O_{19}$. The isothermal magnetization and Mössbauer spectroscopy results are consistent with a ferrimagneticlike transition at $T_C \simeq 250$ K. Low field dc and ac susceptibility measurements reveal a reentrant spin-glass transition at low temperature but they fail to show any anomaly at the nominal Curie temperature T_C. This unusual feature is interpreted as indicative of a transition where long range ferrimagnetic ordering has been replaced by a correlated spin-glass phase with finite spin correlation length.

INTRODUCTION

Crystalline hexagonal ferrites $SrFe_{12-x}Cr_xO_{19}$ ($x<8$) are multisublattice ferrimagnetic compounds evolving from a collinear magnetic ordering ($x=0$) to some kind of noncollinear disordered magnetic structure, as it has been proved from magnetization and Mössbauer spectroscopy measurements.[1,2] The fundamental feature needed to understand the magnetic behavior of this series of insulating compounds is the underlying topological magnetic frustration associated with the Cr ions distributed within the three octahedral sites of the magnetoplumbite structure.[1,3] For instance, we have recently shown that in an isomorphous compound containing only Cr ions, $SrCr_8Ga_4O_{19}$, no magnetic ordering exists down to 4.2 K in spite of the existence of very strong antiferromagnetic interactions.[4] Actually, the topological magnetic frustration of these magnetoplumbite systems is very similar to that existing in octahedral site spinels, such as $ZnCr_{2x}Ga_{2-2x}O_4$, where a complex antiferromagnetic–spin-glass behavior has been detected.[5–7]

In this work we report a magnetic investigation of the end member of the series, $SrCr_8Fe_4O_{19}$, focusing mainly on the ferrimagneticlike ordering observed at $T_C \simeq 250$ K. We conclude from high field magnetization, low field dc and ac susceptibilities and zero field Mössbauer spectroscopy measurements that the transition observed at $T_C \simeq 250$ K is to a correlated spin-glass state with vanishing small spontaneous magnetization. The existence of this intermediate state among spin-glass and true long-range magnetic ordering has been experimentally characterized[8] and clearly detected from measurements of the spin correlation length by means of small angle neutron scattering.[9]

EXPERIMENT

The synthesis procedure and the basic structural characterization of the $SrCr_8Fe_4O_{19}$ oxide has been previously reported together with an investigation of the cation distribution by means of neutron diffraction and Mössbauer spectroscopy.[1] In summary, it has been shown that the octahedral sites of the magnetoplumbite structure contain about 10% of Fe ions while the tetrahedral and five-fold sublattices are fully occupied by Fe ions.

Isothermal high field ($H<150$ kOe) magnetization measurements were carried out in the 4.2 K$<T<$300 K temperature range at the Service National des Champs Intenses, Grenoble. In the same temperature range we performed low field dc ($H=8$ kOe) and ac magnetic susceptibility measurements. The dc magnetization was measured by means of an extraction magnetometer and ac susceptibility was measured with a mutual inductance bridge in a rms field of 10 Oe and a frequency of 110 Hz. Finally, zero field ^{57}Fe Mössbauer spectra were recorded in a conventional constant acceleration spectrometer in the 78 K$<T<$300 K temperature range.

RESULTS AND DISCUSSION

In Fig. 1 we display the temperature dependence of several isothermal magnetization curves where it may be ob-

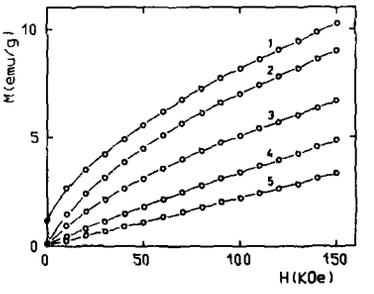


FIG. 1. Isothermal magnetization curves of $SrCr_8Fe_4O_{19}$. (1) $T=4.2$ K, (2) $T=68$ K, (3) $T=151$ K, (4) $T=220$ K, (5) $T=297$ K.

 0021-8979/88/084091-03$02.40 © 1988 American Institute of Physics

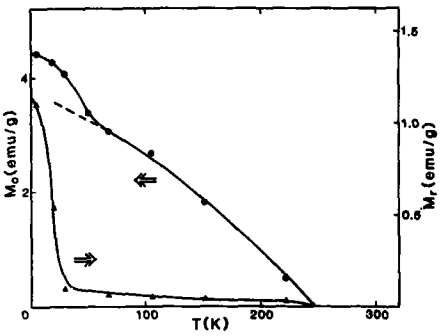


FIG. 2. Temperature dependence of spontaneous magnetization M_0 and magnetic remanence M_r.

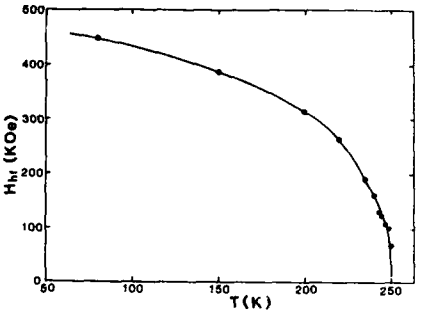


FIG. 4. Temperature dependence of the ^{57}Fe hyperfine field as measured by Mössbauer spectroscopy.

served that the room-temperature curve has a linear M-H relationship, indicative of pure paramagnetic behavior, while in the remaining curves the magnetization is very far from saturation, having a very important differential susceptibility even at the maximum field of 150 kOe. This behavior is consistent with the previous conclusion of a noncollinear spin ordering in the $SrFe_{12-x}Cr_xO_{19}$ series, as indicated by the composition dependence of the 0 K saturation magnetization.[1] In Fig. 2 we plot the temperature dependence of the spontaneous magnetization M_0 while the high field differential susceptibility X, corresponding to the $M(H) = M_0 + XH$ law followed in the high field region is represented in the inset of Fig. 3. In the Fig. 2 we plot as well the temperature dependence of the magnetic remanence M_r measured after the application of the maximum magnetic field of 150 kOe.

From the results reported in Fig. 2 we infer that a ferrimagneticlike ordering is established at $T_C \approx 250$ K with some kind of anomaly or transition occurring at a lower temperature. It is noteworthy that the setting of the low-temperature anomaly in M_0 goes in parallel to a step increase of M_r. We remark as well that the spontaneous magnetization at $T = 0$ K corresponds to about $M_0 \approx 0.9\mu_B$/f.u. which is much smaller than the value expected from a collinear ferrimagnetic ordering ($M_0 \approx 10.8\mu_B$/f.u.), thus indicating a very strongly perturbed ferrimagnetic spin structure.

The existence of a well-defined transition at $T_C \approx 250$ K has been deduced as well from the temperature dependence of the ^{57}Fe hyperfine field measured by means of Mössbauer spectroscopy. A complete report of our Mössbauer investigation will be published elsewhere; however, we would like to look here at the temperature dependence of the mean hyperfine field (Fig. 4) which has a behavior typical of magnetically ordered compounds with a Curie temperature in agreement with the isothermal magnetization study.

All the magnetic characteristics of $SrCr_8Fe_4O_{19}$ reported up to now seem to be consistent with a ferrimagneticlike ordering at $T_C \approx 250$ K and indicate that probably a spin-glass reentrance occurs at a lower temperature. The existence of a spin-glass reentrance at low temperature has been indeed verified from low field susceptibility measurements. As it may be observed in Fig. 3 and 5 the dc susceptibility and the in-phase component of the ac-susceptibility X' display

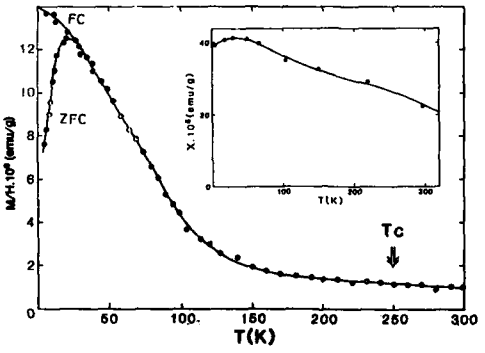


FIG. 3. dc magnetization measured at constant field ($H = 8$ kOe) in field cooled (FC) and zero field cooled (ZFC) processes. Inset: Temperature dependence of the high field differential susceptibility measured in the isothermal magnetization curves.

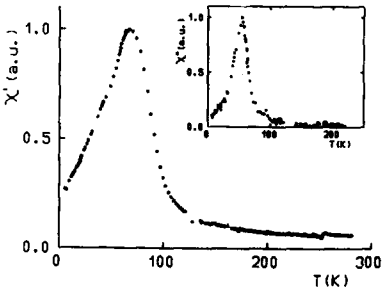


FIG. 5. Temperature dependence of the in-phase ac-susceptibility X'. Inset: Temperature dependence of the out of phase ac-susceptibility X''.

the typical spin-glass cusp at 23 and 68 K, respectively. In the same way, the out of phase component of the ac-susceptibility X'' show a peak at about 55 K, a temperature slightly lower than the cusp in X', as typically occurs in reentrant spin glasses.[9] Furthermore, the dc susceptibility presents the characteristic spin-glass irreversibility among zero field cooled (ZFC) and field cooled (FC) processes.[10] It is clear then that the low-temperature anomaly observed in the spontaneous magnetization corresponds to a phenomenon of spin-glass reentrance.

A full study of the low-temperature spin-glass reentrance in $SrCr_8Fe_4O_{19}$ will be reported elsewhere but we want to remark here that a very strong magnetic field dependence of the dc susceptibility peak temperature has been observed and the $T_g = 68$ K peak temperature of X' corresponds to the zero field limit of the dc susceptibility peaks. This explains then the different peak temperatures observed in Figs. 3 and 5.

However, what is strongly surprising in these low field susceptibility curves is the fact that any anomaly is actually observed at the nominal Curie temperature T_C. This striking anomalous result may only be understood if we assume that the transition observed at T_C is not to a true long-range ferrimagnetic ordering which should display a divergence in the susceptibility at T_C but only a transition to some kind of correlated spin-glass phase have a finite correlation length. In this way if the spin correlation length remains finite and the developed magnetic clusters have vanishing small magnetic moments the divergence of the susceptibility will drop out. Actually, a tendency to this behavior is often observed in reentrant spin glasses where it is found that in the ferromagneticlike transition the ac susceptibilty remains much smaller than that expected from the demagnetizing field limit.[8]

A quenching of the long-range ferromagnetic order has been conclusively observed by Rhyne, in exchange frustrated amorphous systems such as $Fe_{91}Zr_9$, by means of small-angle neutron scattering[9,11] clearly showing that the spin correlation length remains finite and as low as 27 Å.

Characteristic features of this correlated spin-glass phase should be an important spin relaxation, thus leading to a very small magnetic remanence, and a strong polarizibility with external magnetic fields which enhances the apparent ferrimagnetic order. Within this context the low-temperature spin-glass reentrance should mark a further freezing of the magnetic moments below T_g. It remains, however, to be elucidated if the spin freezing occurring at T_g is consistent with a slowing down of the transverse spin components, as predicted by Gabay and Toulouse[12] and experimentally verified by Mössbauer spectroscopy in several systems[13,14] or corresponds mostly to a small clusters blocking phenomena.[15] Actually, our interpretation of the magnetic properties of the exchange frustrated $SrCr_8Fe_4O_{19}$ system in terms of a quenched ferrimagnetic ordering points to the validity of the second model for this system. Further neutron scattering and Mössbauer spectroscopy studies are in progress to clarify this open question.

[1] X. Obradors, A. Isalgué, A. Collomb, M. Pernet, J. Pannetier, J. Rodriguez, J. Tejada, and J. C. Joubert, IEEE Trans. Magn. **MAG-20**, 1636 (1984).
[2] J. A. Pereda, A. Isalgué, J. Tejada, F. J. Litterst, and X. Obradors, Hyperfine Interactions **28**, 569 (1986).
[3] X. Obradors, A. Collomb, M. Pernet, D. Samaras, and J. C. Joubert, J. Solid State Chem. **56**, 171 (1985).
[4] X. Obradors, A. Labarta, A. Isalgué, J. Tejada, J. Rodriguez, and M. Pernet, Solid State Commun. **65**, 189 (1988).
[5] D. Fiorani, S. Viticoli, J. L. Dormann, J. L. Tholence, and A. P. Murani, Phys. Rev. B **30**, 2776 (1984).
[6] J. L. Dormann, A. Saifi, and D. Fiorani, Hyperfine Interactions **28**, 561 (1986).
[7] J. Hamman, D. Fiorani, M. El Yamani, and J. L. Dormann, J. Phys. C **19**, 6635 (1986).
[8] R. B. Goldfarb, K. V. Rao, and H. S. Chen, Solid State Commun. **54**, 799 (1985).
[9] J. J. Rhyne, Physica **136B**, 30 (1985).
[10] K. H. Fischer, Phys. Status Solidi B **116**, 357 (1983); **130**, 13 (1985).
[11] J. J. Rhyne and G. Fish, J. Appl. Phys. **57**, 3407 (1985).
[12] M. Gabay and G. Toulouse, Phys. Rev. Lett. **47**, 201 (1981).
[13] I. A. Campbell, S. Senousi, F. Varret, J. Teillet, and A. Hamzic, Phys. Rev. Lett. **50**, 1615 (1983).
[14] J. L. Dormann, M. El Harfaoui, M. Nogues, and J. Jove, J. Phys. C **20**, L161 (1987).
[15] G. Aeppli, S. M. Shapiro, R. J. Birgeneau, and H. S. Chen, Phys. Rev. B **29**, 2589 (1984).

Magnetic behavior of $CeFe_2$: Effects of ruthenium substitution

S. B. Roy and B. R. Coles
Blackett Laboratory, Imperial College, London SW7 2BZ, United Kingdom

We report ac-susceptibility measurements on the Laves phase compo. ids $Ce(Fe_{1-x}Ru_x)_2$ with $x = 0.02$, 0.04, and 0.06. The results show that the ferromagnetic : lignment of Fe moments seems to be very easily disrupted by substitution of Ru on the 'e sites. All the three compounds, as well as showing the para- to ferromagnetic transition, indicate another transition at lower temperature. In the case of the $x = 0.02$ compound, the character of the susceptibility at the lower transition is similar to that seen in reentrant spin glasses, while in the compounds richer in Ru the suppression of the low-field response is much more drastic.

INTRODUCTION

Of the RFe_2 Laves phase compounds (where R is a rare earth element or Zr or Y), $CeFe_2$ seems to possess idiosyncratic features, since both the moment per iron atom ($1.15\mu_B$) and the Curie temperature (230 K) are very significantly lower than the values of the order of $3.4\mu_B$ and 600 K found in other compounds. Furthermore, neutron scattering studies have been interpreted as showing strong ferromagnetic correlations above the Curie temperature (T_c), persisting even up to $4T_c$.[1] Recent ac-susceptibility and magnetization measurements on $CeFe_2$ with substitutions of Co (Ref. 2) and Al (Refs. 3 and 4) at the iron sites have revealed other interesting aspects of the magnetic behavior of $CeFe_2$. Rastogi and Murani[2] observed a reduction in magnetic moment at low temperature with 4% cobalt substitution and a dramatic loss of magnetic moment at low temperature with ~10% cobalt substitution that suggest a transition to antiferromagnetism. For Al additions, even 2% substitution shows a reentrant spin-glass like behavior at low temperature,[3,4] and at 8% Al long-range ferromagnetic order is no longer found, being replaced by spin-glass-like behavior.[4] All these results raise doubts about the true magnetic character of pure $CeFe_2$ and suggest that its ferromagnetism may be very close to some type of instability. Here we report our ac-susceptibility results on the alloying effects of Ru at the iron sites of $CeFe_2$.

EXPERIMENT

The alloys were prepared by arc melting from metals of at least nominal 99.99% purity and suction chill casting into copper molds to produce square cross-section rods. The alloys were homogenized *in vacuo* at 600 °C for 2 days and then at 700 °C for 5 days. The samples were subjected to metallographic analysis to investigate the possible presence of second phase. Though in some of the alloys a very small amount of second phase was found, this was considered to be negligible for the purposes of our present study. X-ray diffraction examination of the alloy with 4% Ru shows it to have the C15 Laves phase structure of the parent compound $CeFe_2$. ac-susceptibility measurements were performed with a driving frequency of 300 Hz and a driving field of 0.7 G parallel to the axis of samples.

RESULTS AND DISCUSSION

The temperature dependence of the ac susceptibility of the alloys $Ce(Fe_{1-x}Ru_x)_2$ with $x = 0.02$, 0.04, and 0.06 is shown in Fig. 1. The samples were cooled down to the 4.2 K in zero field and the susceptibility χ was measured at different temperatures while warming up slowly. We notice that in addition to a typical para- to ferromagnetic transition at a higher temperature (T_c), there is quite a sharp change in slope in the χ vs T curves at a lower temperature T_f. This behavior is similar to that observed in reentrant spin glasses.[5] The change at low temperature becomes much sharper in the $x = 0.04$ and 0.06 specimens indicating very drastic canting of spins which may even correspond to antiferromagnetism. This is very similar to that observed in $CeFe_2$ with 10% Co substitution where further dc magnetization study showed a rapid reduction of magnetic moment. We have recently performed neutron scattering measurements[6] on $CeFe_2$ with 10% Co. The results indicate a lattice distortion and presence of weak magnetic peaks below the lower transition temperature, hence some sort of antiferromagnetic order. We are planning to do similar neutron measurements on our present alloys as well.

To summarize our results, we can say that the low-temperature anomalies produced by substitutions of 10% of co-

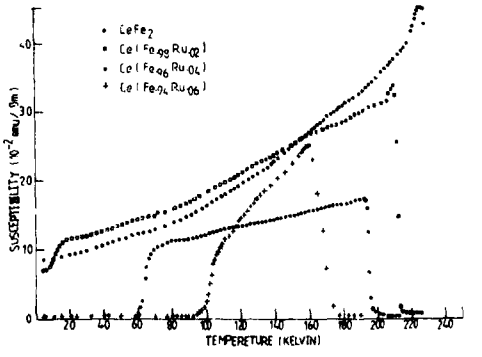


FIG. 1. ac susceptibility of $Ce(Fe_{1-x}Ru_x)_2$ alloys as a function of temperature.

 0021-8979/88/084094-02$02.40 © 1988 American Institute of Physics

balt for Fe in $CeFe_2$ are produced even more rapidly with Ru substitutions. The microscopic origin of these effects is not yet clear. Were the disruption of perfect order in the Fe sublattice to produce competing (antiferromagnetic) interactions, one might expect a reentrant spin-glass type of behavior, as observed in the 2% Ru specimen. The same explanation seems unlikely to hold, however, for the drastic collapse of magnetic response in the more concentrated alloys, especially in the light of the neutron results for the 10% Co alloy.[6] A low-temperature loss of response due to a sharp onset of anisotropy effects that strongly pin domain walls, as suggested for Fe-Ni and Fe-Ni-Mn alloys,[7] would not explain the neutron data, and it should be remembered that competing interactions exist in that system also. Theoretical discussions[8] on the effect of random anisotropies may, however, be relevant, and it is interesting to note that in pure $CeFe_2$ Mössbauer studies[9] show a sharp change in direction at 150 K of the easy axis. It moves in the $(1\bar{1}0)$ plane by 20° with respect to its former [001] direction. If that arises from different temperature dependencies of various Fe-Fe interactions a further development to the point where a ferromagnetic/antiferromagnetic phase change takes place seems possible.

The very general observation of striking effects by substitution on the Fe sites of $CeFe_2$ suggests that the ferromagnetic structure of this phase is rather fragile. It may be important to consider, as a contribution to such effects, the possibility of moments on the Ce atoms, since recent theoretical[10] and experimental[11] work on $ZrFe_2$ and YFe_2 has indicated moments on the Zr and Y sites antiferromagnetically coupled to those of the iron sites.

[1] J. Deportes, D. Givord and K. R. A. Ziebeck, J. Appl. Phys. 52, 2076 (1981).
[2] A. K. Rastogi and A. P. Murani, in *Proceedings of the International Conference on Valence Fluctuations*, Bangalore, 1987, edited by L. C. Gupta (Plenum, New York, 1987).
[3] D. F. Franceschini and S. F. da Cunha, J. Magn. Magn. Mater. 52, 280 (1985).
[4] S. B. Roy and B. R. Coles, J. Phys. F 17, L215 (1987).
[5] B. R. Coles, B. V. B. Sarkissian, and R. H. Taylor, Philos. Mag. B 37, 489 (1978); B. V. B. Sarkissian, J. Phys. F 11, 2191 (1981).
[6] S. B. Roy, S. J. Kennedy, B. R. Coles, and A. P. Murani (unpublished).
[7] T. Miyazaki, Y. Ando, and M. Takahasi, Phys. Rev. B 34, 6334 (1986).
[8] W. M. Saslow, Phys. Rev. B 35, 3454 (1987); Phys. Rev. Lett. 50, 1320 (1983).
[9] U. Atzmony and M. P. Dariel, Phys. Rev. B 10, 2060 (1976).
[10] P. Mohn and K. Schwarz, Physica B 130, 26 (1985).
[11] J. G. M. Armitage, T. Dumelow, R. H. Mitchell, P. C. Riedi, J. S. Abell, P. Mohn, and K. Schwarz, J. Phys. F 16, L141 (1986).

High-pressure study of the magnetic states of disordered Ni-Mn alloys

R. G. Aitken
Department of Physics, University of North Carolina at Charlotte, Charlotte, North Carolina 28223
K. Daneshvar
Department of Electrical Engineering, University of North Carolina at Charlotte, Charlotte, North Carolina 28223

Low-field ac susceptibility measurements have been performed on disordered $Ni_{1-x}Mn_x$, where $x = 0.216$, 0.225, and 0.265, under hydrostatic pressure up to 21 kbar. The measured susceptibility χ_m exhibits transitions from paramagnetic to quasiferromagnetic to spin-glass states on cooling. The pressure dependence indicates a decrease in the magnitude of χ_m and opposite shifts in the temperatures of the two transitions. The nature of the quasiferromagnetic state is discussed.

I. INTRODUCTION

Experimental work on a number of spin-glass alloys has indicated that there exist, within a restricted concentration regime for each, two apparent phase transitions: a paramagnetic → quasiferromagnetic on cooling, and a quasiferromagnetic → spin-glass transition.[1] The temperature T_c for the first transition, and T_{fg} for the second transition to the "reentrant" spin-glass phase, are typically found as a function of composition to merge at a multicritical point; further variation in composition results in a single transition temperature T_g between paramagnetic and spin-glass states. In parallel with this have been theoretical predictions of such behavior for systems exhibiting frustration between competing ferro- and antiferromagnetic interactions.[2] More recent theoretical work by Gabay and Toulouse has predicted an additional "mixed" character to the reentrant state in which it displays a spontaneous ferromagnetic moment.[3] We report on a low-field study of Ni-Mn in which we vary the pressure, rather than the external field.

II. REVIEW OF DATA

We have measured the ac susceptibility χ for $Ni_{1-x}Mn_x$ where $x = 0.216$, 0.225, and 0.265 under hydrostatic pressures up to 21 kbar in an ac driving field of ~1 G peak-peak superimposed on the earth's magnetic field. The alloys were swaged and annealed at 1000 °C for 3 h and water quenched prior to measuring χ with a standard ac inductance bridge operating at 23.3 Hz. Hydrostatic pressure was generated by a self-clamp technique[4]; a 1:1 fluid mixture of *n*-pentane and isoamyl alcohol was used as the pressure medium. The pressure and temperature at low temperatures were determined by a lead manometer situated adjacent to the sample and by a germanium thermometer, respectively.

Ni-Mn is a prototypic spin-glass system. Early work done by Kouvel *et al.* on this system before the discovery of susceptibility cusps demonstrated the spin-glass nature of these alloys by virtue of displaced hysteresis loops upon cooling, magnetic viscosity, etc.[5] Subsequent to this, Goldfarb *et al.* investigated the ac susceptibility and magnetization for atomically disordered and weakly ordered Ni_3Mn and were led to interpret their results in terms of the formation of superparamagnetic clusters and their subsequent blocking. Recent magnetization measurements investigating the unidirectional anisotropy associated with displaced hysteresis loops have been interpreted in terms of a domain model.[7]

The ac susceptibility measurements are summarized in Figs. 1(a)–1(c): the specimen (3×1×1 mm) was in each case mounted with its long axis parallel to the magnetic field; the pick-up coil was mounted directly on the specimen. For $Ni_{0.784}Mn_{0.216}$ and $Ni_{0.775}Mn_{0.225}$ the behavior is qualitatively the same, with a large low-temperature peak in the neighborhood of 35–50 K, and a more demure knee in the vicinity of room temperature. Under hydrostatic pressure, the lower peak height drops in both cases, while it is not clear from this plot whether there is a shift in temperature. The upper knee shifts to lower temperature under pressure, and this is more pronounced for $Ni_{0.775}Mn_{0.225}$. The curve for $Ni_{0.775}Mn_{0.265}$ is substantially different; only a single peak seemingly occurs, in the neighborhood of 80 K.

The same data reveals more when plotted as $1/\chi_m$ versus temperature, as shown in Fig. 2. For $Ni_{0.784}Mn_{0.216}$ and $Ni_{0.775}Mn_{0.225}$ it is seen that in the temperature interval between the lower peak and the upper knee the data may be fitted to a Curie–Weiss form. The negative Curie–Weiss θ's indicated in the figure are not to be taken seriously as the *measured* susceptibility has been used; due to the details of our experimental procedure it was not possible to determine the susceptibility in fundamental units. However, it can be shown that

$$1/\chi_{\text{true}} = 1/\chi_{\text{meas}} - N/\mu_0 \qquad (1)$$

in MKS units, where N is the demagnetization factor of the specimen. The shift will result in higher θ's. The work of Goldfarb *et al.* on $Ni_{0.784}Mn_{0.246}$ indicates similar behavior with $\theta = +117$ K. The interpretation given there involved superparamagnetism among large ($350\mu_B$) clusters whose own ferromagnetic freezing temperatures are taken to be responsible for the upper knee. This interpretation was buttressed by their ability to scale isotherms taken at various temperatures between the peak and the knee to a universal curve, fit by a Langevin function.[8]

The curve for $Ni_{0.735}Mn_{0.265}$, which appears to exhibit a simple peak when plotted directly, indicates a hint of Curie–

 0021-8979/88/084096-03$02.40 © 1988 American Institute of Physics

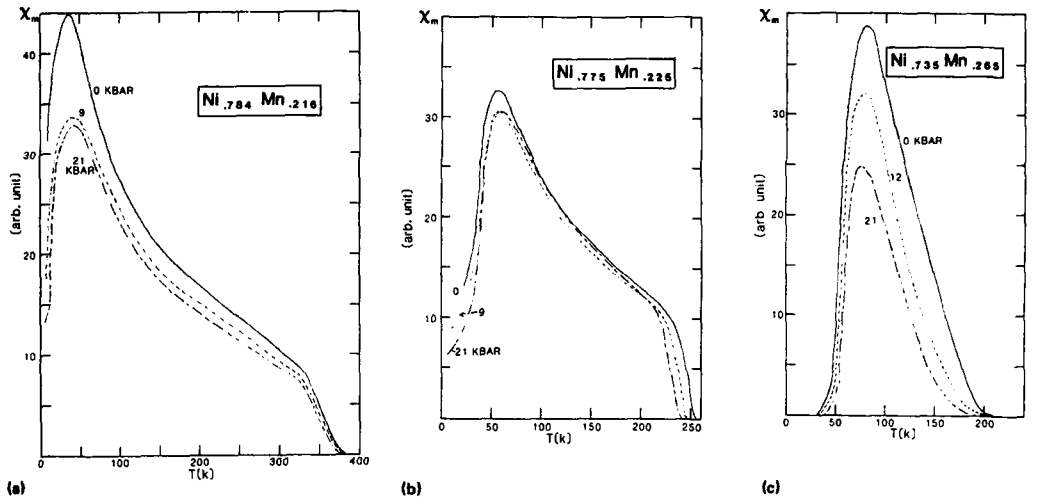


FIG. 1. Temperature dependence of the measured ac susceptibility (χ_m) under hydrostatic pressure up to ~21 kbar for $Ni_{1-x}Mn_x$ where x = (a) 0.216, (b) 0.225, and (c) 0.265.

Weiss behavior over a limited temperature range when plotted as $1/\chi_m$ vs T in Fig. 2(c).

Before discussing these results, it should be pointed out that the magnetic properties of Ni-Mn alloys are sensitive to the degree of atomic short-range order present in the samples and, hence, are dependent on the heat treatment performed. This sensitivity has been demonstrated for other systems such as Au-Fe.[9] Thus, our results for $Ni_{0.775}Mn_{0.225}$ differ in detail with those reported by Goldfarb[10] for $Ni_{0.779}Mn_{0.221}$, and also with those obtained by Hurdequint at Orsay on another $Ni_{0.735}Mn_{0.265}$ specimen.

III. DISCUSSION

The pressure dependencies reported here bear some similarity to those reported by Wu *et al.* on *Pd*-Fe-Mn.[12,13]

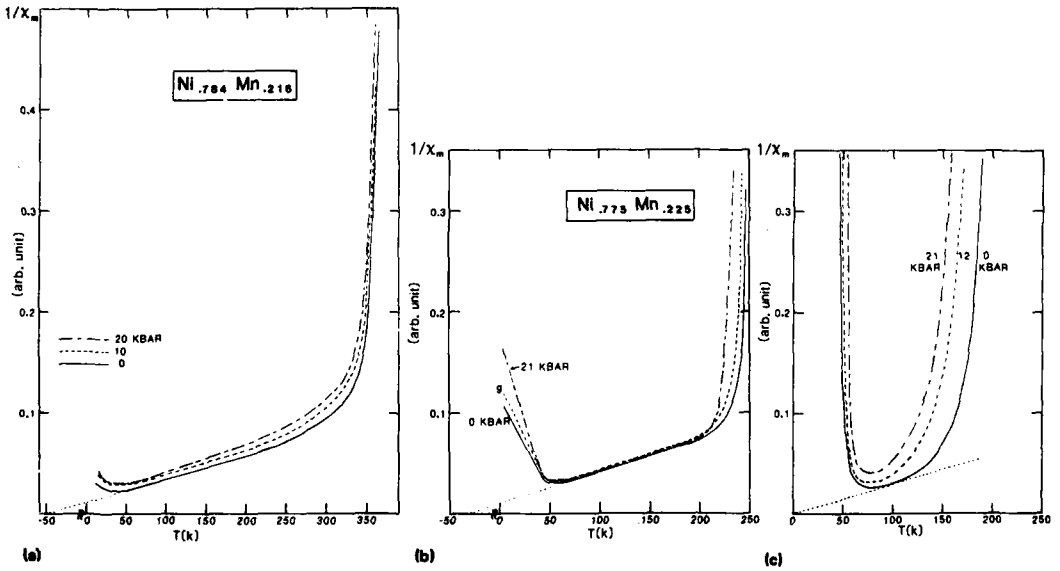


FIG. 2. Temperature dependence of χ_m, plotted as $1/\chi_m$ vs T, under hydrostatic pressure for $Ni_{1-x}Mn_x$ where x = (a) 0.216, (b) 0.225, and (c) 0.265.

The limiting cases of this system are *Pd*-Fe, which is known to exhibit giant moment ferromagnetism,[14] and *Pd*-Mn, which exhibits giant moment ferromagnetism below its ordering temperature only for Mn-concentrations below 3 at. % and spin-glass behavior below a freezing temperature at higher Mn-concentrations. For the 5 at. % Mn specimen studied there, the lower transition temperature, associated with spin-glass freezing, is enhanced under pressure. This effect is presumably caused by an enhancement of nearest-neighbor Mn-Mn antiferromagnetic coupling due to reduced lattice spacing under pressure. Also, the magnitude of the susceptibility is reduced under pressure while still retaining an overall "flat-topped" shape which still gives the appearance of being demagnetization limited.

For Ni-Mn alloys, previous work by Goldfarb *et al.* interpret the high-temperature knee in the susceptibility as the hallmark of ferromagnetic freezing of superparamagnetic clusters. The low-temperature peak in χ_m is taken to indicate the onset of blocking of these clusters. Hysteresis and thermoremanent magnetization measurements also indicate to them the occurrence of another freezing process much stronger than blocking, at a lower temperature yet.[14]

In contrast, the series of magnetization studies referred to earlier (Ref. 7) postulate the existence of weakly antiferromagnetically coupled domains, each containing an internal unidirectional anisotropy field based on Dzyaloshinsky–Moriya interactions. The "mixed" reentrant spin-glass to ferromagnet transition is taken to be a spin-flop-like transition. This sort of model was put forward long ago by Kouvel[15] to explain similar properties observed in *Cu*-Mn and *Ag*-Mn; it is unable, however, to explain the enhancement of unidirectional anisotropy in these systems by small amounts of impurities with strong spin-orbit coupling.[16]

The DM interaction is the leading term in the theoretical treatment of Levy *et al.*,[17] and yields unidirectional anisotropy without hysteresis; it goes as $1/R^3$, R being the distance between Mn or other impurity atoms. Higher order corrections yield uniaxial or other forms of anisotropy, and hysteresis. This can be expected at higher Mn and/or impurity concentrations and at higher temperatures. The hysteresis loss observed by Goldfarb for zero field cooled $Ni_{0.754}Mn_{0.246}$ peaks at just under 50 K and the application of pressure should have a similar effect to variation in concentration in that it will increase nonunidirectional contributions to the anisotropy. This may explain the more rapid dropoff of χ_m below the low- temperature peak under pressure.

[1] R. D. Shull, H. Okamoto, and P. A. Beck, Solid State Commun. **20**, 863 (1976) on Fe-Al; B. H. Verbeck, G. J. Nieuwenhuys, H. Stocker, and J. A. Mydosh, Phys. Rev. Lett. **40**, 586 (1978) on Pd-Fe-Mn; M. D. Wu, R. G. Aitken, and C. W. Chu, J. Appl. Phys. **50**, 7356 (1979) on Pd-Fe-Mn under pressure; H. Meletta and P. Convert, Phys. Rev. Lett. **42**, 108 (1979) on (Eu, Sr)S; M. B. Salamon, K. V. Rao, and H. S. Chen, *ibid.* **44**, 596 (1980) on amorphous $(Fe, Mn)_{75}P_{16}B_6Al_3$; C. R. Fincher, S. M. Shapiro, A. H. Palumbo, and R. D. Parks, *ibid.* **45**, 474 (1980) on Fe-Cr; G. Dublon, Solid State Commun. **33**, 1195 (1980) on amorphous $(Pd, Fe)_{82}Si_{18}$; C. W. Chu, M. K. Wu, B. J. Jin, W. Y. Lai, and H. S. Chen, Phys. Rev. Lett. **46**, 1643 (1981) on amorphous $(Fe,Mn/Ni)_{75}P_{16}B_6Al_3$ under pressure; S. Crane and H. Claus, *ibid.* **46**, 1693 (1981) on Au-Fe.

[2] D. Sherrington and S. Kirkpatrick, Phys. Rev. Lett. **35**, 1792 (1975); S. Kirkpatrick and D. Sherrington, *ibid.* **B17**, 4384 (1978).

[3] M. Gabay and G. Toulouse, Phys. Rev. Lett. **47**, 201 (1981).

[4] C. W. Chu, T. F. Smith, and W. E. Gardner, Phys. Rev. Lett. **20**, 198 (1968).

[5] J. S. Kouvel, C. D. Graham, and I. S. Jacobs, J. Phys. Rad. **20**, 198 (1959); J. S. Kouvel and C. D Graham, J. Phys. Chem. Solids **11**, 220 (1959).

[6] R. B. Goldfarb and C. E. Patton, Phys. Rev. B **24**, 1360 (1981); T. Satoh, R. B. Goldfarb and C. E. Patton, *ibid.* **18**, 3684 (1978); J. Appl. Phys. **49**, 3439 (1978).

[7] R. G. Aitken, T. D. Cheung, J. S. Kouvel and H. Hurdequint, J. Magn. Magn. Mater. **30**, L1 (1982); W. Abdul-Razzaq and J. S. Kouvel, J. Appl. Phys. **55**, 1623 (1984); **57**, 3467 (1985); Kh. Ziq and J. S. Kouvel, *ibid.* **61**, 3625 (1987).

[8] R. B. Goldfarb, Ph. D. thesis, Colorado State University (1979), p. 75.

[9] S. Crane and H. Claus, Phys. Rev. Lett. **26**, 1693 (1981).

[10] R. B. Goldfarb, Ph. D. thesis, Colorado State University (1979), p. 71.

[11] H. Hurdequint, *private communication;* both the specimens reported on in this study plus the one used by Hurdequint were prepared from the same bulk alloys, but heat treated separately, from those used in the magnetization study of Aitken *et al.* [J. Magn. Magn. Mater. **30**, L1 (1982)].

[12] M. K. Wu, R. G. Aitken, C. W. Chu, C. Y. Huang, and C. E. Olsen, J. Appl. Phys. **50**, 7356 (1979).

[13] B. H. Verbeeck, G. J. Nieuwenhuys, H. Stocker, and J. A. Mydosh, Phys. Rev. Lett. **40**, 586 (1978).

[14] G. J. Nieuwenhuys, Adv. Phys. **24**, 515 (1975).

[15] R. B. Goldfarb, Ph. D. thesis, Colorado State University (1979), p. 86.

[16] J. S. Kouvel, J. Phys. Chem. Solids **21**, 57 (1961); J. Appl. Phys. **31**, 142 S (1960).

[17] P. M. Levy, C. Morgan-Pond, and A. Fert, J. Appl. Phys. **53**, 2168 (1982).

Spin dynamics of the reentrant spin-glass system amorphous $(Fe_xCr_{1-x})_{75}P_{15}C_{10}$ (abstract)

P. Mangin, D. Boumazouza, and B. George
Universite Nancy I, 54508 Vandoeuvre, France

R. W. Erwin and J. J. Rhyne
National Bureau of Standards, Gaithersburg, Maryland 20899

Spin-wave excitations have been studied by neutron inelastic scattering in a series of amorphous $(Fe_xCr_{1-x})_{75}P_{15}C_{10}$ alloys with $x = 0.75$, 0.725, and 0.700 and are correlated with small-angle neutron scattering (SANS) results. The Curie temperatures of the three compositions are 212, 181, and 134 K, respectively. These alloys show reentrant spin-glass behavior characterized by a maximum in the spin stiffness parameter D below 0.5 T_c, and an increase in the spin-wave linewidth at low T. This corresponds to the development of a static spin-glass phase as observed by the onset of a Lorentzian-squared component in the SANS. The maximum in D shifts to higher values of T/T_c for smaller Fe concentrations reflecting the increased width of the exchange field distribution. The results for the T dependence of the spin stiffness parameter and the subcritical SANS are remarkably similar to those for crystalline FeCr alloys[1] having the same T_c, although the Fe concentration in the analogous crystalline materials is much lower (e.g., $T_c = 178$ K) for crystalline $Fe_{26}Cr_{74}$ and close to the expected percolation concentration.

[1]S. M. Shapiro, C. R. Fincher, A. C. Palumbo, and R. D. Parks, Phys. Rev. B 26, 6661 (1981).

Double-phase transition in $Au_{82.5}Fe_{17.5}$? (abstract)

L. D. Rakers[a] and Paul A. Beck
Department of Materials Science and Engineering, University of Illinois at Urbana-Champaign, Urbana, Illinoi; 61801

The low steady field susceptibility measured as a function of increasing temperature in a field parallel to the plane of a thin (0.03-mm) disk of $Au_{82.5}Fe_{17.5}$ does not give any indication of magnetic "phase transitions" or for the presence of an intermediate long-range ferromagnetic phase. These findings are in accord with the earlier observation that the temperature of the hyperfine splitting in the ^{57}Fe Mössbauer spectrum is distinctly lower than that of the "critical susceptibility peak"; the latter clearly does not correspond to the onset of long-range ferromagnetism. If measured in a field of 9.6 Oe, the susceptibility has a well-defined maximum at ~100 K, but in a field of 500 Oe the maximum shifts to ~50 K. Showing isothermal remanence as well as magnetothermal history effects up to at least 130 K, the alloy is clearly spin-glass-like well above the temperature of the maximum. The magnetic viscosity increases gradually on cooling and "freezing" takes place in a temperature range extending over 100 K. The susceptibility maximum is a kinematic effect; it does not signify a phase transition. The crossover from the paramagnetic state into the spin-glass state is a very gradual one in $Au_{82.5}Fe_{17.5}$.

[a] Present address: Electro-Optics Division, Honeywell, 2 Forbes Road, Lexington, MA 02173.

 0021-8979/88/084099-01$02.40 © 1988 American Institute of Physics

A Mössbauer study of fine iron particles (invited)

Z. Q. Qiu, Y. W. Du, H. Tang, and J. C. Walker
Department of Physics, Johns Hopkins University, Baltimore, Maryland 21218

Mössbauer spectroscopic measurements have been carried out on uniform-size Fe particles over a size range from approximately 150 to 400 Å. The particles were produced by evaporation into a nitrogen atmosphere. We have discovered that the thin oxide coating on these particles results in a significantly altered surface-phonon spectrum as well as increased coercivity and a larger magnetic hyperfine field for the Fe core. These results correlate well with studies on thin epitaxial films.

I. INTRODUCTION

Between atoms, molecules, and bulk solids there is an intermediate region of fine particles with the linear dimensions of the order of 10 to 10^4 Å. The study of fine particles in this size range is important for both technical applications and for basic research. When the size of the solid is reduced to a value smaller than some characteristic physical length, new phenomena can arise which can be quite different from bulk behavior. There are two primary ways in which these new phenomena arise. The first is through size effects associated with limited boundary conditions. These effects have been associated with properties which differ significantly from bulk forms. Examples are thermodynamic size effects,[1] superparamagnetism,[2] superconductivity,[3] optical size effects,[4] and quantum size effects. A recent review of quantum size effects has been given by Halperin.[5]

A second way new phenomena arise is through surface effects. Fine particles have a large specific surface area. The atoms at the surface have lower symmetry, lower coordination number, and different energy than in the bulk. Therefore, the physical and chemical properties of the surface or interface are generally different. These effects show up as different surface and interfacial magnetism, different phonon spectra, and different surface electronic structure. Compared with thin film, fine particles have some advantages for the study of surface or interfacial properties.[6] The strongest advantage is that they can often be more easily produced. For this reason fine particles have a large potential for applications. Fine iron particles have been used to make high-density magnetic recording media,[7] materials for heterogeneous catalysis, [8,9] ferrofluids,[10] etc.

Among many experimental methods used to study the properties of fine particles, Mössbauer spectroscopy can be used to help to estimate the particle size of small ferromagnetic particles,[11] to study magnetic excitations,[12] surface magnetic structure,[13] the phonon spectrum,[14] and the magnetism of surface and interfaces.

In what follows, we will discuss Mössbauer measurements as a major component in other measurements on fine iron particles in the range from 150 to 400 Å.

II. PREPARATION OF FINE PARTICLES

There are a number of techniques used to prepare fine particles. The main methods are chemical reduction,[16] hydrosols, impregnated porous materials,[18] granular metal films by cosputtering of metals and insulators,[19] and evaporation into an inert gas.[20] Gas evaporation is perhaps the most commonly used method. Particle size can be controlled between 10 and 10^4 Å, depending on the inert-gas pressure, the type of gas, and the temperature of the metal vapor source. Usually, the diameter of the particle is roughly proportional to the pressure of the inert gas and the atomic weight of the gas. When the evaporation temperature is raised, the particle size increases and the distribution of particle size becomes wider. Experimentally, the size distribution of fine particles can be rather well controlled.

We have prepared fine iron particles by evaporation into a nitrogen atmosphere.[21] The nitrogen pressure was in a range 0.3–30 Torr. The average particle diameters determined by the Brunauer, Emmett, and Teller (BET) nitrogen absorption method are listed in Table I. An electron micrograph is shown in Fig. 1. While no histogram of particle sizes was made, a study of the electron micrographs plus consideration of uncertainties in the specific area determination by the gas absorption method leads to the uncertainties in particle diameters quoted in Table I. Particle-size variation is greater for the larger particles than for the finer ones. Before the sample was taken out of the vacuum chamber, nitrogen gas that contained a small amount of oxygen was introduced. The particles were oxidized slowly on their surfaces, and the passivating surface oxide layer prevented the particles from being further oxidized when they were exposed to air. These small iron particles often have a net magnetization

TABLE I. Diameter of the samples.

Samples	N1	N2	N3	N4
Diameter (Å)	164 ± 30	268 ± 37	349 ± 49	404 ± 60

 0021-8979/88/084100-05$02.40 © 1988 American Institute of Physics

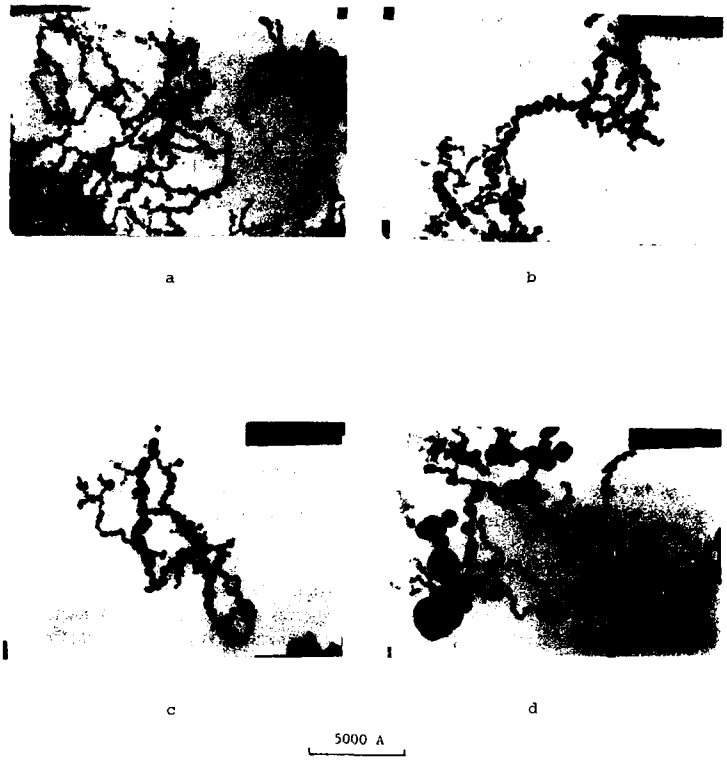


FIG. 1. Electron micrograph for fine iron particles: (a) N1, (b) N2, (c) N3, (4) N4.

as a result of having a very small number of noncanceling magnetic domains. This leads to attraction between adjacent particles.

A well-formed chain-of-spheres-like arrangement due to the static magnetic interaction was observed, particularly in the smaller particle case [Fig. 1(a)]. The single-domain size of the fine iron particles is about 150 Å. When the particle size is much larger than the single-domain size, the particle converts into a multidomain state, and the static magnetic interactions between the iron particles are weaker so that the particles distribute more separately [Fig. 1(d)]. The iron has bcc crystal structure and the particles show truncated rhombic dodecahedral crystal morphology habits.[22]

III. EXPERIMENTS AND DISCUSSION

Pioneering work on fine Fe particles was carried out by von Eynatten and Bömmel.[23] The work here follows closely the work of Picone, Haneda and Morrish,[12] although our samples are different in that they were purposely oxidized on the surface with an oxide layer of about 20–30 Å in thickness, and some of our conclusions are quite different. The Mössbauer spectra are superpositions on an α-Fe spectrum and an iron oxide spectrum. From the nature of the oxide part of the spectrum, we conclude that the iron oxide is composed of γ-Fe_2O_3 or Fe_3O_4.

A. Recoilless fraction or Debye-Waller factor *f*

The recoilless fraction factor f, which determines the amount of Mössbauer absorption, generally reflects the lattice vibrational properties of the absorber. The absorption area of the spectrum is approximately proportional to f. The lattice vibration or phonon spectrum can be characterized by a Debye temperature θ_D which is related to the f factor by the following relation:

$$f^{\text{Debye}} = \exp\left\{-\frac{6E_R}{k\Theta_D}\left[\frac{1}{4}+\left(\frac{T}{\Theta_D}\right)\int_0^{\Theta_D/T}\frac{x\,dx}{e^x-1}\right]\right\}.$$

When the lattice is rigid the Debye temperature has a large value and so does f. The reasons for f to be different in fine particles as compared with bulk materials are as follows:

(1) the cutoff of long-wavelength phonons due to finite-size boundary conditions,

(2) the "softening" of the surface phonons and the large specific surface area for fine particles, and

(3) the macroscopic motion of the fine particles.

Morrish and Picone[24] studied the oxide layer on the iron particles which they produced. From their f measurements they determine the Debye temperature to be about 100 K, which is much less than the bulk value. von Eynatten and Bömmel[23] studied loosely dispersed fine iron particles with different sizes and the particles embedded in different matri-

ces. They suggested that the decrease of the recoilless fraction f is either due to random motions of the microcrystals or surface phonons. They discussed these two effects quantitatively but could not decide which effect was the more important one. These ideas were more systematically developed by Picone, Haneda, and Morrish.[12] In what follows, we use their analysis.

Originally, the f factor comes from the relation

$$f = \exp(-4\pi^2\langle x^2\rangle/\lambda^2).$$

Here x is the displacement of the atom which should include two parts: (1) the macroscopic random motion of the crystallite, and (2) the oscillation of the atom around its equilibrium position. Generally these two parts are independent so $\langle x^2\rangle = \langle x_1^2\rangle + \langle x_2^2\rangle$ and $f = f_1 f_2$. For a macroscopic crystal, the first part can be ignored; $f_1 = 1$ and f is only due to the second part, i.e., the phonons. But for fine particles, the first part may no longer be ignorable. In order to determine this, we made two types of samples: (a) a loose dispersion of fine iron particles, and (b) a highly compressed sample of iron particles in a boron nitride matrix. Thus the only difference between these two types of samples is the possibility of macroscopic motion of particles in the loose structure. The Mössbauer spectra of these two types of samples, for particle samples N1 and N4 (see Table I), at 4.2 K and room temperature are shown in Fig. 2. At 4.2 K, the loose and pressed samples show almost equal absorption areas, indicating that the macroscopic motion of the particle is essentially stopped. At room temperature, however, the absorption areas of these two types of samples are quite different, especially for N1. This suggests that macroscopic motion of the individual particles indeed, plays an important role in the f factor. This is treated very well by Picone, Haneda, and Morrish[12] who show that, for weakly bound particles such as ours (which are at least magnetically bound to each other), we can model their motion by assuming them to be harmonic oscillators of mass M bound to the surrounding medium by face constant q. The oscillation frequency is then $\omega = (8/M)^{1,2}$ and

$$\langle x_1^2\rangle = \frac{\hbar}{2M\omega}\left(\frac{2}{\exp(\hbar\omega/kT)-1}\right) + 1.$$

For $kT \gg \hbar\omega$, we can write $\langle x_1^2\rangle = kT/q$. This implies that $f_1 = \exp(-4\pi^2 kT/q\lambda^2)$. One difficulty in applying this model to our samples is that it *does not* explain the larger difference between the loose and pressed samples for the smaller N_1 particles compared with the larger N_4 particles. This different behavior points more towards a strong role for surface-phonon-mode "softening," as this would be much more apparent in the 160-Å N_1 particles than in the 400-Å N_4 particles. However, this simple model assumes that q, the spring constant, is not dependent on particle size. Since the force between particles is at least partly magnetic, this assumption is probably not valid. We are left then with the feeling that oscillatory motion of the whole particle plays an important role in the overall Mössbauer f for the 160-Å N_1 particles at least.

Because the oxide layer is on the surface and the α-Fe is in the core of the particle, the absorption areas of the oxide iron and the α-Fe spectra can supply some information about the phonon spectrum at the surface and in the core of the particle. For the compressed samples, in which the macroscopic motion of the crystallites is greatly reduced, we see that the absorption areas of the iron oxide spectra decrease more rapidly than that of the α-Fe spectrum as the temperature is raised from 4.2 K to room temperature, indicating that the phonons at the oxide surface are significantly softened, relative to the iron core. The effect remains even when the different Debye temperatures of bulk Fe and bulk oxide are considered. This result is consistent with earlier results of Picone, Haneda, and Morrish, implying a Debye temperature for the oxide surface of about 100 K. The Fe core shows a normal, essentially bulk, Debye temperature.

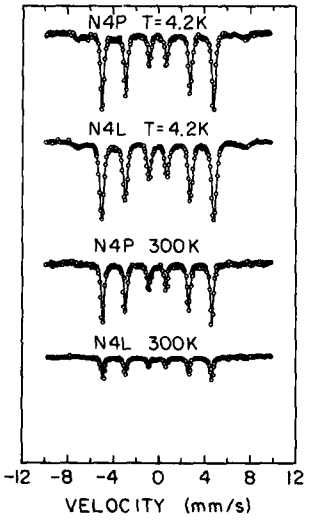


FIG. 2. Mössbauer and spectra at 4.2 and 300 K for (a) sample N1 and (b) sample N4. L and P represent loose and pressed samples, respectively.

B. Thermally induced superparamagnetic relaxation

Superparamagnetic relaxation is generally important for the magnetic behavior of microcrystals. The relaxation time τ can be approximately described as

$$\tau = \tau_0 \exp(KV/kT),$$

where τ_0 is of the order of 10^{-9} s, K is the crystal anisotropy constant, and V is the volume of the fine particle. When τ is less than the characteristic measuring time, superparamagnetic behavior will appear. For Mössbauer spectroscopy, which has the time of measurement of about 10^{-8} s, the condition for superparamagnetic behavior is $V < 2.3kT/K$,[25] which gives the critical diameter for iron particles to be about 70 Å. This value is less than the particle size of our samples, so we are not surprised that we see no superparamagnetic peak in our Mössbauer spectra. But if kT/KV is not too much less than 1, the hyperfine field of the particle divided by the hyperfine field of the bulk materials is propor-

tional to T,[26]

$$H(V,T)/H(V,0) = 1 - kT/2KV.$$

In other words, there should be a linear term in the $H(V,T)$-T curve. This was indeed found in Fe_2O_3 particles.[27] In the work reported here we found no linear term in measurements on our samples. We think the reason is that the magnetic interactions between the fine iron particles create an energy barrier even higher than the normal crystal anisotropy energy, preventing any noticeable superparamagnetic response. Furthermore, a noticeable increase in the coercivity of the particles with decreasing particle size implies a large surface anisotropy at the interface between the α-Fe and the oxide coating. This also serves to effectively increase KV and suppress the linear term.

C. Hyperfine magnetic fields

When the temperature is well below the Curie temperature, thermal excitation of the magnetic moments results in a reduction of the magnetic hyperfine field. This can be described by a spin-wave model with the following formula:

$$H(T) = H_0(1 - BT^{3/2}).$$

We use this formula and obtain a least-squares fit to our data. The results are listed in Table II.

From this table, we can see that both H_0 and B increase as the particle size decreases. The change of the hyperfine field might be interpreted as a demagnetization effect of single crystals and a dipolar field of the neighboring microcrystals. However, it is hard to explain the change of the B value by demagnetization or dipolar mechanisms. As mentioned before, fine particles have large surface to volume ratios. We believe the changes of the H_0 and B are *both* correlated with this increase in the surface of the particles. We think this because, for epitaxial Fe films covered by various materials, the H_0 and B of Fe at the interface is generally different from that of bulk iron, as determined by extensive work in this laboratory. The hyperfine field and the thermal excitations of iron oxide have been investigated for the case of Fe covered by iron oxide.[28,29] As far as we know, however, an investigation of Fe at the interface of iron and iron oxide has not been carried out before. Other work on fine particles[6] suggests that there could exist strong interaction between Fe atoms and the iron oxide atoms at their interface and that such interaction generally will cause a change of H_0 and B. For the fine iron particle case, we consider values H_s and B_s for Fe at the interface. After a few atomic layers, the values of H and B will become constants $H(0)$ and $B(0)$. If we let the distribution function of H and B be f_H and f_B which have value 1 at the interface and 0 at the center of the particle, we may represent average measured values of H and B as

$$H = H(0) + [H_s - H(0)]\frac{1}{V}\int f_H dV,$$

$$B = B(0) + [B_s - B(0)]\frac{1}{V}\int f_B dV.$$

Although we do not know f_H and f_B exactly, we may still obtain information from the relations. For example, H and B will increase as R decreases if $H_s > H(0)$ and $B_s > B(0)$, which is usually the case. We can begin to relate surface phenomena determined from careful thin-film measurements to macroscopic measurements on magnetic fine particles. This can have considerable importance in using fine magnetic particles in magnetic recording.

TABLE II. Parameters of the hyperfine field. H_0 refers to $T = 0$ hyperfine fields.

Samples	N1	N2	N3	N4
H_0 (kG)	344.27 ± 0.15	342.21 ± 0.24	341.19 ± 0.13	340.32 ± 0.33
B ($10^6 K^{-3/2}$)	6.30 ± 0.13	5.45 ± 0.24	5.17 ± 0.13	4.87 ± 0.23

IV. CONCLUSIONS

We made fine iron particles with four different sizes. By using Mössbauer spectroscopy, we found that the center-of-mass motion of the particles plays a very important role in the Debye-Waller factor for the smallest particles, and that the phonons in the surface oxide layer are significantly softened. The static magnetic interaction among the iron particles, as well as strong surface-induced magnetic anisotropy, reduces the thermal relaxation of magnetization of the fine Fe particles so that the variation of hyperfine field with temperature reflects only spin-wave excitations. The changes of H and B as a function of the particle size are explained qualitatively in terms of surface magnetic effects. The increase in magnetic hyperfine fields at $T = 0$ for the N_1 particles compared with N_4 contrasts with the work of Picone, Haneda, and Morrish, where no increases were reported, but is consistent with our own thin-film work where increases in magnetic hyperfine fields at Fe surfaces in contact with both metal and insulating overlayers has been seen for some time.

ACKNOWLEDGMENTS

The authors wish to thank the Institute of Solid State Physics of Nanjing University, People's Republic of China which provided the samples. This work was supported in part by the National Science Foundation, Grant No. DMR-8500889, and the Chinese APS Program.

[1] J. F. Borel, Surf. Sci. **106**, 1 (1981).
[2] C. P. Bean and J. D. Liringeton, J. Appl. Phys. Suppl. **30**, 120S (1959).
[3] E. Mühlschlegel, Surf. Sci. **106**, 350 (1981).
[4] R. Ruppin, Phys. Rev. B **11**, 2871 (1975).
[5] W. P. Halperin, Rev. Mod. Phys. **58**, 533 (1986).
[6] A. H. Morrish and K. Haneda, J. Magn. Magn. Mater. **35**, 105 (1983).
[7] G. Bate, in *FERRITES: Proceedings of the International Conference, Japan, 1980* (Center for Academic Publications, Tokyo, Japan, 1982), p. 509.
[8] B. S. Clausen, S. Mørup, H. Topsoe, R. Candia, E. J. Tensen, A. Baranski, and A. Pattek, J. Phys. (Paris) Colloq. **37**, C6-245 (1976).
[9] I. Dezsi, D. L. Nagy, M. Eszterle, and L. Guczi, . . Phys. **40**, C2-76 (1976).
[10] S. W. Charles and J. Popplewell, IEEE Trans. Magn. **MAG-16**, 172 (1980).
[11] S. Mørup, B. S. Clausen, and H. Topsoe, J. Phys. (Paris) Colloq. **40**, C2-78 (1979).
[12] P. J. Picone, K. Haneda, and A. H. Morrish, J. Phys. C **15**, 317 (1982).
[13] K. Haneda and A. H. Morrish, Surf. Sci. **77**, 584 (1979).
[14] M. Hayashi, I. Tamura, Y. Fukano, S. Kanemak, and Y. Fujio, J. Phys. C **13**, 681 (1980).

[15]J. C. Walker, R. Droste, G. Stern, and J. Tyson, J. Appl. Phys. **55**, 2500 (1984); J. Tyson, A. Owens, and J. C. Walker, J. Magn. Magn. Mater. **35**, 126 (1983); T. Shinjo, N. Hosoito, and T. Takada, *ibid.* **31/34**, 879 (1983).
[16]A. A. van der Glessen, IEEE Trans. Magn. MAG-**9**, 191 (1973).
[17]R. F. Mazke, W. S. Glannsinger, and M. Bayard, Solid State Commun. **18**, 1025 (1976).
[18]R. H. Lindquist, G. Constabaris, W. Kundig, and A. M. Portis, J. Appl. Phys. **39**, 100 (1968).
[19]B. Abeles, Ping Sheng, M. D. Coutto, and Y. Avie, Adv. Phys. **24**, 447 (1975).
[20]U. Yeda, J. Crystal Growth **45**, 485 (1978).
[21]Y. W. Du, Jian Wu, H. X. Lu, T. X. Wang, Z. Q. Qiu, H. Tang, and J. C. Walker, J. Appl. Phys. **61**, 3314 (1987).
[22]T. Hayashi, T. Ohno, S. Yatsuya, and R. Uyeda, Jpn. J. Appl. Phys. **16**, 705 (1977).
[23]A. von Eynatten and H.E. Bömmel, Appl. Phys. **14**, 415 (1977).
[24]A. H. Morrish and P. J. Picone, in *FERRITES: Proceedings of the International Conference, Japan, 1980* (Center for Academic Publications, Tokyo, Japan, 1982), p. 613.
[25]N. Ayoub, M. A. Kobeissi, R. W. Chantrell, K. O'Grady, and J. Popplewell, J. Phys. F **15**, 2229 (1985).
[26]S. Mørup, J. Magn. Magn. Mater. **37**, 39 (1983).
[27]S. Mørup, Appl. Phys. **11**, 63 (1976).
[28]M. Domke, B. Kyvelos, and G. Kaindl, Surf. Sci. **126**, 727 (1983).
[29]M. E. Brett and M. J. Graham, J. Magn. Magn. Mater. **60**, 175 (1986).

Mössbauer investigation of zinc ferrite particles

H. Tang, Y.-W. Du, Z.-Q. Qiu, and J. C. Walker
The Johns Hopkins University, Baltimore, Maryland 21218

Mössbauer spectra of $Zn_{0.2}Fe_{2.3}O_4$ particles at different temperatures have been obtained. They have been analyzed with five components, one due to the *A*-site Fe^{3+} ions, and the others due to the *B*-site Fe^{3+} and Fe^{2+} ions. Magnetic and electronic properties have been discussed with regard to zinc substitution and temperature dependence.

I. INTRODUCTION

Magnetite and related ferrites have long been a subject of great interest both due to their fundamental electric and magnetic properties and their important technological applications.[1] This class of materials possesses the so-called spinel structure and can be represented by the formula $(M)[M_2]O_4$, in which the round and square brackets refer to iron and other metal ions situated in an oxygen tetrahedron and octahedron. In pure magnetite, the tetrahedral (*A*) sites are all occupied by Fe^{3+} ions, and the octahedral (*B*) sites by equal numbers of Fe^{3+} and Fe^{2+} ions. The coexistence of di- and trivalent ions in the *B* sublattice and the dominant antiferromagnetic coupling between the *A*- and *B*-site moments make this class of materials rich in physics. If other metal elements are substituted into magnetite, they generally prefer to occupy *B* sites with zinc as one of the few exceptions. Since Zn^{2+} ions tend to form sp^3 hybrid orbits, they are much more favored to occupy *A* sites.[2] Presence of nonmagnetic Zn^{2+} ions in Zn-substituted magnetite are expected to alter the local magnetic properties as well as electric properties. In this paper, we report our study on $Zn_{0.2}Fe_{2.8}O_4$ ferrite particles with Mössbauer spectroscopy, which is a powerful technique in probing local magnetic properties. The effect of zinc substitution on magnetic and electric properties and other related issues will be discussed.

II. EXPERIMENT

Nearly spherical $Zn_{0.2}Fe_{2.8}O_4$ particles of about 300 Å in diameter were prepared with the chemical coprecipitation method.[3] The Mössbauer target was made by compressing the mixture of 90 mg of the ferrite powders and boron nitride into a thin pellet. Mössbauer spectra at different temperatures were obtained on our Mössbauer spectrometer with a 100-mCi ^{57}Co source embedded in a Rh matrix and a high-count-rate detector. A cryogenic system was employed to provide good temperature control with stability better than 0.5 K. Analysis of the spectra was carried out with a least-squares fit program. All the isomer shifts are given with respect to α-Fe.

III. RESULTS AND DISCUSSION

A room-temperature Mössbauer spectrum of $Zn_{0.2}Fe_{2.8}O_4$ is shown in Fig. 1(a). It clearly consists of several components. In fact, the appearance of multicomponents should be expected and can be justified from the following argument. In $Zn_{0.2}Fe_{2.8}O_4$ the *A* sites are occupied by Zn^{2+} ions as well as Fe^{3+} ions. Therefore an octahedral cation, either Fe^{3+} or Fe^{2+}, may have different numbers of Zn^{2+} and Fe^{3+} ions occupying its six nearest tetrahedral sites. While an Fe^{3+} ion carries a large magnetic moment, a Zn^{2+} ion does not. Consequently, the superexchange interaction of each *B* cation with its six *A* nearest-neighbor cations depends on the population of Zn^{2+} ions among the six *A* cations, which in turn determines the hyperfine field at the nucleus of the *B* cation. In addition, the *s*-electron density at the nucleus of this *B* cation is also likely to be dependent on the composition of the six tetrahedral nearest neighbors. Hence the spectrum must be composite.

The probability of having n Zn^{2+} ions out of six *A* cations is

$$P(n) = \binom{6}{n} x^n (1-x)^{6-n},$$

where x is the occupation percentage of Zn^{2+} ions in the *A* sublattice and the Zn^{2+} ions are assumed to distribute randomly. For our case, $x = 0.2$. Then, the significant configurations for six *A* nearest neighbors are 6Fe, 1Zn5Fe, 2Zn4Fe,

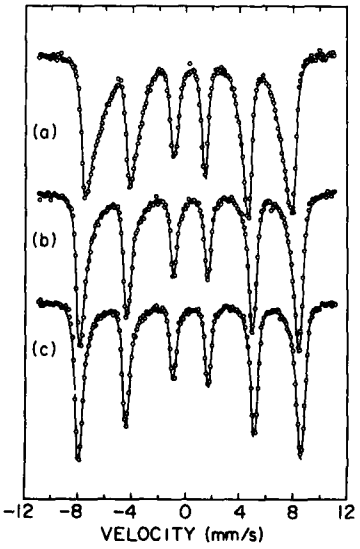


FIG. 1. Mössbauer spectrum of $Zn_{0.2}Fe_{2.8}O_4$ particles at (a) 300 K, (b) 150 K, and (c) 85 K.

 0021-8979/88/084105-03$02.40 © 1988 American Institute of Physics

TABLE I. Mössbauer parameters of $Zn_{0.2}Fe_{2.8}O_4$ at 300, 150, and 85 K, where B_n ($n = 0,1,2,3$) represents the B-site Fe ions with n A-site Zn^{2+} nearest neighbors. QS and IS denote quadrupole splitting and isomer shift, respectively.

T (K)	Crystalline site	H (kOe)	QS (mm/s)	IS (mm/s)	Line intensity
300	A	484(2)	−0.00(1)	0.31(1)	0.40(5)
	B_0	465(2)	−0.01(1)	0.34(1)	0.27(5)
	B_1	441(2)	−0.01(1)	0.40(2)	0.27(5)
	B_2	410(3)	0.00(1)	0.46(2)	0.28(9)
	B_3	369(5)	0.02(2)	0.45(3)	0.17(7)
150	A	506(2)	0.01(1)	0.31(1)	0.40(5)
	B_0	507(2)	0.03(1)	0.53(1)	0.31(5)
	B_1	480(2)	−0.02(1)	0.44(2)	0.35(6)
	B_2	454(3)	−0.02(2)	0.55(2)	0.23(6)
	B_3	405(8)	−0.04(3)	0.61(3)	0.11(5)
85	A	515(2)	0.01(1)	0.33(1)	0.40(5)
	B_0	518(2)	0.02(1)	0.55(1)	0.34(5)
	B_1	496(3)	−0.02(1)	0.44(2)	0.36(5)
	B_2	473(3)	−0.04(2)	0.55(2)	0.18(8)
	B_3	428(8)	−0.09(8)	0.73(3)	0.12(5)

and 3Zn3Fe ions, each with a probability of 0.262, 0.393, 0.246, and 0.080, respectively. Accordingly, we have fitted the spectrum with five components, four from the B iron ions and one from the A iron ions. The excellent quality of the spectrum ensures that such a multicomponent fit with no restrictions on the parameters is justifiable. One can actually see the stepwise feature in line 1, clearly indicating a five-component structure. The obtained Mössbauer parameters are listed in Table I. Based on the line intensity, the hyperfine field, and the isomer shift, each component has been successfully assigned to a specific configuration.

The A component always has the largest hyperfine field at room temperature, and its isomer shift indicates pure trivalent irons. There are more features for the B components. Their isomer shifts correspond neither to divalent nor to trivalent irons. Rather, they represent a mixed-valency state of the B Fe^{3+} and Fe^{2+} ions. This state is associated with a fast electron hopping between neighboring B Fe^{3+} and Fe^{2+} ions.[4] At room temperature, the hopping rate is faster than the Larmor precession frequency of the iron moment, so that the Mössbauer spectrum only displays a time-averaged valency.[5,6] The data of the quadrupole splitting, which show an increasing trend with increasing number of Zn nearest neighbors, are also very informative. The hyperfine field decreases with increasing number of Zn^{2+} ions. A reduction of about 26 kOe is found for each added Zn^{2+} ion from B_0 to B_2. For B_3 the drop is much greater, suggesting that when the number of Zn^{2+} reaches 3, half of the total, the superexchange interaction is greatly reduced. Dobson, Linnett, and Hahman[7] have found that in the system $Zn_xFe_{3-x}O_4$, there is no magnetic ordering for $x>0.8$. Since $x = 0.8$ represents the case that has occupation ratio of Fe^{3+} to Zn^{2+} in the A sublattice just opposite to that of $x = 0.2$, the least number of A-site Fe^{3+} nearest neighbors, 3, for $x = 0.2$ just corresponds to the maximum number for $x = 0.8$. Therefore, the absence of magnetic ordering for $x = 0.8$ may be related to the significant reduction in the hyperfine field for B_3 in the case of $x = 0.2$.

The two Mössbauer spectra (b) and (c) shown in Fig. 1 are taken at 150 and 85 K. Both have been fitted with five components, with their parameters shown in Table I. Many of the characteristics of the room-temperature spectrum remain. For instance, the isomer shifts of the B components still bear a mixed-valency character. However, this should be subjected to question, especially for the 85-K case. At such a low temperature, electron hopping should have significantly slowed down, or even stopped if a Verwey transition exists above 85 K. In either case, the Mössbauer spectrum would distinguish the Fe^{2+} component from the Fe^{3+} one. In this case, the number of Mössbauer components arising from the B-site Fe^{2+} and Fe^{3+} ions should be doubled, namely, 8. Obviously, without a prior knowledge of the eight hyperfine fields, a free fit with so many components can by no means be physically meaningful. At present, our fit with four B components and one A component may be the best one can do.

All the five hyperfine fields increase as temperature decreases. The hyperfine fields of the B components increases faster than that of the A component, a phenomenon that has been observed.[8] This implies that the B-site spin waves are easier to excite. An A Fe^{3+} has twelve B Fe^{3+} or Fe^{2+} nearest neighbors, so that the superexchange interaction is very strong. Thus the tetrahedral spins are more rigid and should be less sensitive to thermal disturbance. At 85 K, the reduction in the hyperfine field as each Zn^{2+} is added from B_0 to B_2 becomes 22.5 kOe, contrasting with the value of 26 kOe at room temperature. This can also be understood from the above argument based on the intensity of superexchange interaction.

In fact, we have done a whole series of low-temperature Mössbauer measurements. The reason for reporting only the 85- and 150-K spectra is twofold. First, together with the room-temperature spectrum, they furnish a complete picture. Secondly, 85 and 150 K sit below and above the Verwey transition temperature, respectively, of magnetite at 119 K,[9] so that we can determine whether a Verwey transition exists in our $Zn_{0.2}Fe_{2.8}O_4$ sample. Because of the small difference between the 85- and 150-K spectra and the difficulty regarding differentiation of the Fe^{2+} component from the Fe^{3+} component as stated above, the question remains unanswered. It is mentioned in Ref. 10 that the Verwey transition is suppressed even for a 2% Zn substitution. This contrasts with the results by Merceron, Djega-Mariadassou, and Dormann,[11] that in the Mg^{2+}- and Li^{2+}-substituted magnetite, the Verwey transition is maintained up to high substitution ratio. Certainly, there is a difference that Zn^{2+} ions substitute into the A sites while Mg^{2+} or Li^{1+} into the B sites. Use of other experimental techniques, such as neutron diffraction, may help determine whether the Verwey transition exists in the $Zn_{0.2}Fe_{2.8}O_4$ system.

It has been reported elsewhere that the B sublattice has a lower Debye temperature than that of the A sublattice.[8] In the $Zn_{0.2}Fe_{2.8}O_4$ ferrite we have examined, however, such an effect has not been observed. The ratio of line intensities of the combined B components to the A component is found to

be 2.50, 2.53, and 2.47 for 300, 150, and 85 K, respectively. Taking into account their uncertainties, these values are in excellent agreement with the population ratio of Fe ions at B and A sites, $n_B/n_A = 2.0/0.8 = 2.5$, implying that the recoilless fractions, therefore the Debye temperatures, for the two sublattices are approximately equal.

IV. CONCLUSIONS

We have performed a series of Mössbauer measurements on zinc-substituted magnetite $Zn_{0.2}Fe_{2.8}O_4$ at various temperatures. From physical consideration it appears that the octahedral Fe ions should give rise to four six-line Mössbauer components, each corresponding to a specific Zn + Fe nearest-neighbor configuration. This is reasonably well verified by careful analysis of the spectra. The magnetic hyperfine field at a B-site Fe nucleus decreases as the number of Zn^{2+} nearest neighbors at the A sites increases, and becomes more sensitive to thermal disturbance as well. These behaviors have been explained in terms of superexchange interactions.

ACKNOWLEDGMENTS

The authors wish to thank the Institute of Solid State Physics of Nanjing University for providing the ferrite samples. This work was supported in part by the National Science Foundation Grant No. DMR-8500889.

[1] J. Smith and H. P. J. Wijn, *Ferrites* (N. V. Philips' Gloeilampenfabrieken, Eindhoven, Holland, 1959).
[2] E. J. W. Verwey and E. L. Hailmann, J. Chem. Phys. **15**, 174 (1947).
[3] Du You-wei, Lu Huan-xian, Wang Ting-xiang, Xue Rong-hua, Cheng Liang, and Hu Hong-quan, Acta Phys. Sin. **35**, 1223 (1986).
[4] E. J. W. Verwey, P. H. Haayman, and F. C. J. Romeijn, J. Chem. Phys. **15**, 181 (1947).
[5] E. Bauminger, S. G. Cohen, A. Marinov, S. Ofer, and E. Segal, Phys. Rev. **122**, 1447 (1961).
[6] W. Kündig and R. S. Hargrove, Solid State Commun. **7**, 223 (1969).
[7] D. C. Dobson, J. W. Linnett, and M. M. Hahman, J. Phys. Chem. Solids **31**, 2727 (1970).
[8] G. A. Sawatzky, F. van der Woude, and A. H. Morrish, Phys. Rev. **187**, 747 (1969).
[9] E. J. W. Verwey and P. W. Haayman, Physica **8**, 979 (1941).
[10] M. Rosenberg and H. Franke, Philos. Mag. B **42**, 419 (1980).
[11] T. Merceron, C. Djega-Mariadassou, and J. L. Dormann, J. Magn. Magn. Mater. **31-34**, 781 (1983); **15-18**, 1435 (1980).

Isomer shift and magnetic properties of EuO under pressure

R. D. Taylor and J. N. Farrell[a)]
Physics Division, MS K764, Los Alamos National Laboratory, Los Alamos, New Mexico 87545

We have measured the Mössbauer effect of ^{151}Eu in EuO at temperatures down to 4 K and pressures to 31 GPa. At ambient pressure EuO becomes ferromagnetic at $T_C = 69$ K; at 31 GPa, $T_C = 105(2)$ K; and a maximum value of T_C in the region 15–25 GPa is inferred. A Brillouin fit of the hyperfine-field-temperature data at 31 GPa gives a reduced magnetic moment compared to ambient although the magnitude of the saturation hyperfine field is not reduced. The isomer shift with pressure weakly supports the expectation of an intermediate-valence change with pressure above 14 GPa.

INTRODUCTION

There has been a widespread interest in the interplay of the magnetic properties of divalent europium compounds and intermediate valence brought about by pressure, temperature, and alloying with selected impurities. Eu ions in EuO are divalent and have a magnetic moment at ambient conditions; the ferromagnetic ordering temperature T_C is 69(1) K. Trivalent Eu ions are nonmagnetic and have an ionic radius about 20% smaller than divalent Eu. It is interesting to speculate that the application of high pressures to EuO would drive the system into an intermediate-valence regime and produce dramatic changes in its physical properties.

A number of experimental studies of EuO under pressure have been reported.[1–7] Nolting and co-workers[6] have considered the coexistence of magnetism and intermediate valence and have made a prediction that T_C for EuO at 30 GPa will be near room temperature.

This is a preliminary report on the pressure-temperature dependence of the isomer shift and the hyperfine field of ^{151}Eu in EuO. The Mössbauer effect is a powerful tool for such studies. The isomer shift is related to the valence, and the hyperfine field is related to the magnetic moment and provides an unambiguous way to measure T_C. The measurements can be carried out in a diamond anvil cell.

EXPERIMENT

The Mössbauer effect of the 21.5-keV level of ^{151}Eu was used to obtain isomer shift and magnetic hyperfine field information of EuO as a function of temperatures down to 4 K and of pressures up to 31 GPa. A 160-mCi $^{151}SmF_3$ source was generally used and was held at the same temperature as the absorber. Stoichiometric, unenriched EuO was contained in a Merrill–Bassett-type diamond anvil cell[9] by a 90-Ta–10-W gasket that also served as a collimator. The sample volume (initially 0.24 mm diam by 0.03 mm thick) contained EuO, ruby chips for measuring the pressure,[9] and a pressurizing medium for obtaining approximately hydrostatic pressures. The 8×10^{-6} -g sample (6 mg/cm^2 of ^{151}Eu) and the 6 mm diameter of the source result in very low counting rates; a datum could be obtained in about one day. No Eu_2O_3 impurity was detected in the samples. The isomer shift of Eu^{2+} is about -12 mm s^{-1} with respect to Eu^{3+}. The source-absorber was held in a furnace cryostat whose temperature could be determined and controlled to about ± 2 K. The Mössbauer spectra were fitted assuming an appropriate Hamiltonian for ^{151}Eu with magnetic hyperfine splitting. The fits yield values of the linewidth (fixed to the room-temperature value), the isomer shift, the intensity, and the internal field.

RESULTS

The isomer shift of ^{151}Eu as a function of V/V_0 (pressure) for two samples of EuO is given in Fig. 1. Sample 1 used silicon oil as a pressurizing medium, and data at room temperature only were taken upon reducing the pressure. Pressure-volume data of Zimmer *et al.*[4] for EuO were used to convert the pressures. The break in slope near 13 GPa is less evident in the data for sample 2, which used argon as the pressurizing medium and a sequence of increasing pressures. Data at room temperature for sample 2 track the 4-K data. At first glance these data suggest a pressure hysteresis for the isomer shift, but that is yet to be proven.

The hyperfine field as a function of temperature for EuO

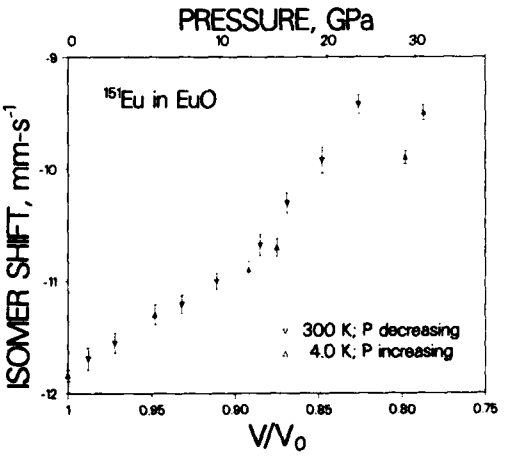


FIG. 1. Isomer shift of ^{151}Eu in EuO as a function of pressure and of reduced volume for two samples (see text). Shifts are referenced to a SmF_3 source at the same temperature.

[a)] Now at Teledyne Brown Engineering, Huntsville, AL 35807.

 0021-8979/88/084108-02$02.40 © 1988 American Institute of Physics

at 31 GPa is shown in Fig. 2. The rapid rise associated with magnetic ordering in the sample provides a sensitive, though laborious, way to determine T_C at pressure. The saturation field at 4 K and 31 GPa is -36.7 T to be compared with -29.0 T at ambient pressure. The ordering temperature at 31 GPa is 105(2) K whereas an onset temperature crudely defined by the long tail above T_C may be as high as 230 K.

DISCUSSION

L_{III} x-ray absorption measurements[7] strongly suggest EuO undergoes a mixed valence transition starting at about 7.0 GPa with the valence reaching 2.38 by 30 GPa. Optical reflection measurements[4] show an insulator-metal transition near 14 GPa, and x-ray structure measurements exhibit a softening near 13 GPa; from these results Zimmer *et al.*[4] conclude that EuO undergoes a continuous valence change starting near 13 GPa. Electrical resistivity measurements[6] have been interpreted to show a semiconductor-to-semiconductor transition near 14 GPa with a gradual approach to metallic behavior by 25 GPa. Mössbauer isomer shift measurments with pressure to 15.3 GPa show[5] a linear behavior with a slope of 0.1 mm s^{-1} GPa^{-1}; they ascribe most of the change to an ordinary volume dependence of the isomer shift and the residual to a valence shift to 2.05 at 15 GPa. Our data give a slope of 0.08 mm s^{-1} GPa^{-1} for the 4-K data with increasing pressure and 0.12 mm s^{-1} GPa^{-1} for the 300-K data above 15 GPa. Extracting a valence change from the Mössbauer isomer shifts with pressure is not straightforward; it depends upon establishing the proper pressure contribution for a Eu^{2+} "system with no valence change." At present we merely comment that the trend shown is in the direction of a valence change toward Eu^{3+}.

The hyperfine field at saturation arises from a number of contributions but is usually taken as a measure of the magnetic moment at the Mössbauer site. Our value at 31 GPa continues the trend found[5] at lower pressures.

The increase of the Curie temperature of EuO with pressure was first studied by McWhan, Souers, and Jura[1] using an ac susceptibility technique. They found that T_C increases nonlinearly with pressure, reaching about 124 K at 8.2 GPa. The slope of T_C with pressure continues to increase according to Moser, Kalvius, and Zinn[5] with T_C reaching 176(3) K at 15.3 GPa. DiMarzio *et al.*[6] associate certain features of the pressure-resistance curves with T_C and find similar trends to 15 GPa but with a saturation value near 200 K in the range 20–25 GPa. Our data (Fig. 2) show T_C to be 105 K at 31 GPa, a value sharply lower than extrapolations of the previous experimental data and in disagreement with the early predictions of $T_C \sim 300$ K at 30 GPa.[8] A refined theory[8] predicts that T_C should have a maximum for EuO-type systems accompanied by a reduced moment. The Brillouin fit of the data shown in Fig. 2 is for a moment of $0.98(1.70)\mu_B$, $g = 2.0$, $T_C = 105(2)$ K, and a saturation field of $-36.7(0.7)$ T. The shape of this curve and a similar

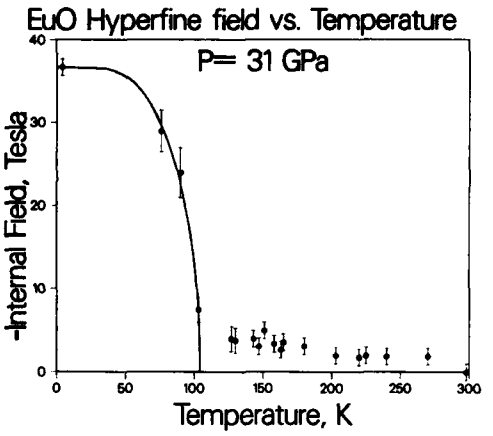


FIG. 2. Internal field in EuO at 31 GPa as a function of temperature. Parameters for the Brillouin fit shown are given in the text. Note the long tail above T_C.

one at 9 GPa indicate a reduced moment compared to the expected value of $\mu = 7\mu_B$ for Eu^{2+}. On the other hand, the monotonically increasing magnitude of the saturation internal field suggests an *increasing* moment with pressure. We note, however, that the internal field arises from a number of contributions; detailed analysis is needed to understand the apparent contradiction. We plan to obtain additional data in the intermediate-pressure regime to help clarify the role of intermediate valence on the ferromagnetic properties of EuO.

ACKNOWLEDGMENTS

We acknowledge the helpful discussions with J. O. Willis, M. Pasternak, and D. Wohlleben. The source was kindly loaned to us by J. G. Mullen. This work was supported by the U. S. Department of Energy, BES-Materials Science.

[1] D. B. McWhan, P. C. Souers, and G. Jura, Phys. Rev. 143, 385 (1965).
[2] A. Jayaraman, A. K. Singh, A. Chatterjee, and S. K. Devi, Phys. Rev. B 9, 2513 (1974).
[3] U. F. Klein, G. Wortmann, and G. M. Kalvius, J. Magn. Magn. Mater. 3, 50 (1976).
[4] H. G. Zimmer, K. Takemura, K. Syassen, and K. Fischer, Phys. Rev. B 29, 2350 (1984).
[5] J. Moser, G. M. Kalvius, and W. Zinn, in Proceedings of the International Conference on the Applications of the Mössbauer Effect, Melbourne, Australia, August 1987 [Hyperfine Interact. (to be published)].
[6] D. DeMarzio, M. Croft, N. Sakai, and M. W. Shafer, Phys. Rev. B 35, 8891 (1987).
[7] J. Rohler, K. Keulerz, E. Dartyge, A. Fontaine, A. Jucha, and D. Sayers, in *EXAFS and Near Edge Structure III*, edited by K. O. Hodgson, B. Hedman, and J. E. Penner-Hahn (Springer-Verlag, Berlin, 1984), p. 385.
[8] W. Nolting, Z. Phys. B 49, 87 (1982); W. Nolting and A. Ramakanth, J. Magn. Magn. Mater. 63 & 64, 548 (1987), and references therein.
[9] A. Jayaraman, Rev. Mod. Phys. 55, 65 (1983).

Probing molecular cages in polymeric gels using paramagnetic ions: Internal motion of cupric ion in a cage

Darbha Suryanarayana
Materials Engineering, Systems Technology Division, IBM Corporation, Endicott, New York 13760

The effect of high-energy irradiation on the aqueous solutions of certain water soluble polymers, namely, poly(vinyl alcohol) and poly(ethylene oxide), brings about physical and chemical changes. The cross links or networks formed in the polymer chains cause gel formation. These gels are considered to be made up of cubic cells or molecular cages with size varying between 0.6 and 1.5 nm. Such cages have been recently probed using the paramagnetic ions of hydrated cupric as well as vanadyl ions and were studied by electron paramagnetic resonance (EPR) and pulsed EPR techniques. The time-dependent EPR spectra of Cu^{2+} ions in the cages are analyzed in this study using specific motional models, employing the modified Bloch equations. Computer simulations show that the spin probe's motion is governed by the segmental motion of the polymer chains.

INTRODUCTION

The paramagnetic spin probes, such as nitroxides[1] and peroxides,[2,3] have been utilized in the past to probe polymers. Recently, this technique has been extended to probe complex systems, such as molecular cages in polymeric gels. A combined study using both electron paramagnetic resonance (EPR) and the pulsed EPR spectroscopic techniques have been used particularly to extract valuable information concerning the motion and coordination of paramagnetic spin probes incorporated in the polymer gels.[4,5]

Gels of water soluble polymers, such as poly(vinyl alcohol) (PVA) and poly(ethylene oxide) (PEO), have been commonly prepared by irradiating the aqueous polymer solutions using high-energy radiation, such as x rays or γ rays.[6] The irradiation process creates transient free radicals in the polymer chains,[7] such as main-chain radical,

$$[-C-\dot{C}-C-]_n$$

and the end-chain radical,

$$[-C-C-]_n-\dot{C}.$$

Bond formation with neighboring chains, resulting in cross linking and formation of networks, is energetically favored by the presence of such radicals. When the number of cross-linking sites increases, the solution viscosity increases, causing gel formation. Highly cross-linked gels are insoluble in water. The structure of polymer gel has been considered to be made up of cubic cells or cages with an average edge $\langle L \rangle$. In PVA gels, the cell dimension has been calculated[8] using the following equation:

$$\langle L \rangle \text{ (nm)} = 0.25[(5.1\times10^8 + 1.37\times10^8 C)/R\,]^{1/2}, \quad (1)$$

where C is the concentration of PVA in H_2O and R is the dose in rads. Thus, by controlling C and R it is possible to prepare PVA gels with various average dimensions. Typical cage sizes can vary between 1.5 and 0.6 nm upon exposure to 10–100 Mrad range.

These cages are large enough to accommodate complex spin probes of transition-metal ions,[4,5] such as hydrated cupric $[Cu^{2+}(H_2O)_6]$ and vanadyl ions $[VO^{2+}(H_2O)_5]$. The results show that the spin probe behaves like a free ion in rather large molecular cages, whereas in small cages the spin probe develops significant bonding with the polymer chains. The nature of chemical bonding between the metal ion and the PVA chains has been determined using the pulsed EPR technique.[4,5] In the case of Cu^{2+}, the proposed structural model is schematically shown in Fig. 1. It is pointed out here that the spin-probe motion is greatly influenced due to its interaction with the polymer chains. Since the polymer exhibits segmental motion along the direction of its chain axis, the spin probe also moves with it. As a result, the EPR spectral line shapes are expected to change when measured as a function of temperature. In this study, the time-dependent EPR spectra of the Cu^{2+} ion are analyzed with specific kinetic models and are presented in this paper.

Figure 2 shows the experimental EPR spectra of

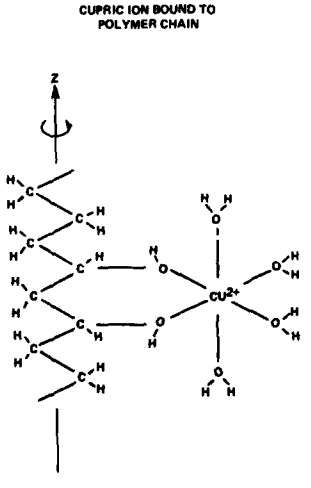


FIG. 1. Schematic representation of the hydrated Cu^{2+} ion bonded to the PVA chains.

 0021-8979/88/084110-03$02.40 © 1988 American Institute of Physics

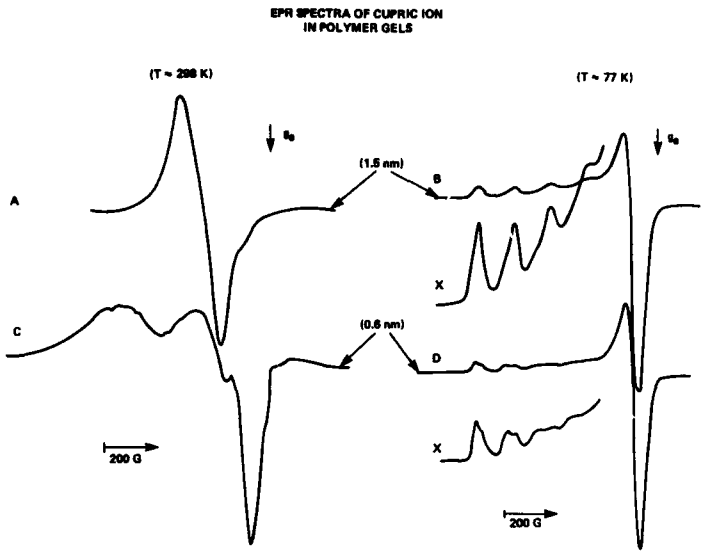


FIG. 2. EPR spectra of Cu^{2+} ions formed in the PVA gels (Ref. 5). Curves A and B refer to the spectra measured in the large cage at 298 and 77 K; C and D were obtained in small cages at 298 and 77 K.

$Cu^{2+}(H_2O)_6$ in the PVA gels having large and small cages.[5] For Cu^{2+} ions in large cages, the room-temperature EPR spectrum (as shown by curve A, Fig. 2) revealed a broad isotropic line, which is due to the rapid internal motion of the spin probe. At liquid-nitrogen temperature, the spin probe's motion is hindered and the EPR spectrum (also shown in Fig. 2, Curve B) revealed the anisotropic parallel and perpendicular features, which are characteristic of Cu^{2+} spectrum. In the small cages also, the EPR spectra (shown in Fig. 2, curves C and D) revealed similar motional effects and the motional time scale was different. In the past, no detailed analysis was pursued. Since these spectra contain all the essential information about the motion of the spin probe, an attempt has been made in this study to simulate the EPR spectra using a theory[2] described below.

THEORY

The spectral dependences as a function of jump rate, τ^{-1}, have been calculated using the formalism of modified Bloch equations. The polycrystalline EPR spectral line shape is written as[2]

$$Y(N,\tau)=\sum_{\theta=0^\circ}^{\pi/2}\sum_{\phi=0^\circ}^{\pi} G(\theta,\phi,\tau,N)\sin\theta. \tag{2}$$

The general solution G for N sites is written as

$$G(\theta,\phi,\tau,N)=i\gamma H_1 M_0 \tau \sum_{s=1}^{N} f_s\left[N\left(1-\sum_{s=1}^{N} f_s\right)\right]^{-1}, \tag{3}$$

with

$$f_s = 1/(N+\alpha_s\tau) \tag{4}$$

and

$$\alpha_s = (T_{2s})^{-1} - i(\omega_s-\omega). \tag{5}$$

In Eq. (3), γ is the gyromagnetic ratio, H_1 is the microwave magnetic field, τ is the mean lifetime of any species in the system, $(T_{2s})^{-1}$ is the average linewidth of species s in the absence of motional effects, M_0 is the magnetization of the species along z, ω is the sweep of the spectrum in frequency units, and ω_s is the resonance frequency of species s. Equation (3) contains both real and imaginary parts,

$$G = G_{\text{real}} + iG_{\text{imag}}. \tag{6}$$

Since the G_{imag} term yields the desired EPR line shape, its explicit form has been derived for the two-jump ($N=2$) case and is given as

$$G_{\text{imag}} = 2[(4+2\tau/T_2)a + \tau b^2 c]/2(a^2+b^2c^2), \tag{7}$$

where

$$a = \tau/T_2^2 + 2/T_2 - \tau\Delta\omega_1\Delta\omega_2, \tag{8}$$

$$b = \Delta\omega_1 + \Delta\omega_2, \tag{9}$$

$$c = 1 + \tau/T_2. \tag{10}$$

In the above equations, it is assumed that $T_{21}=T_{22}=T_2$. For the Cu^{2+} EPR spectrum, one must consider both the g and A (hyperfine) anisotropy. Neglecting the nuclear quadrupole term, one can write the resonance frequency, ω_s, for a single orientation as

$$\omega_s = (l_1,l_2,l_3)\left[\left(\frac{\beta H}{\hbar}\tilde{g}(s) + m_I\tilde{A}(s)\right)\right]\begin{pmatrix} l_1 \\ l_2 \\ l_3 \end{pmatrix}, \tag{11}$$

where m_I has $2I+1$ states with nuclear spin $I=\frac{3}{2}$ for copper. The direction cosines, l_1, l_2, and l_3, are given by

$$l_1 = \sin\theta\cos\phi, \quad l_2 = \sin\theta\sin\phi, \quad l_3 = \cos\theta. \tag{12}$$

SPECTRAL SIMULATIONS

The polycrystalline EPR spectra were computer simulated, using Eqs. (2)–(12). Simulations were performed us-

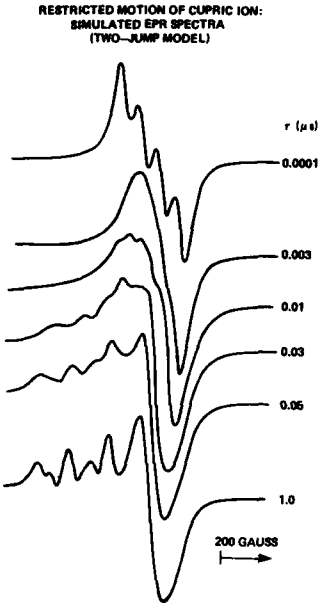


FIG. 3. Simulated EPR spectra of Cu^{2+} motion using the two-jump model.

ing IBM PC AT. The principal g and A values of Cu^{2+} ($g_{\parallel} = 2.40$, $g_{\perp} = 2.04$, $A_{\parallel} = 140$ G, and $A_{\perp} = 10$ G) that correspond to the "rigid" limiting EPR spectrum were used in the simulations. A linewidth of 40 G was also used in the simulations to match the experiment. Since the EPR spectral linewidths are of the order of a few megahertz frequency, the τ value is expected to lie between 1 and 0.0001 μs, and it was varied in appropriate intervals between these extreme limits. Figure 3 shows a few typical simulated EPR spectra obtained for cupric ion motion. The features of the calculated spectra are briefly described in the following.

Using "very fast" interconversion rates ($\tau = 0.0001$ μs), the simulated EPR spectrum yielded an isotropic quartet spectrum, which corresponds to an ideal situation where both the g and A values of cupric ion are fully averaged. Because of motional narrowing, the simulations predict a resolved quartet spectrum, which is characteristic of a freely rotating cupric ion. However, when the interconversion rate is "slow" ($\tau < 0.001$ μs), then the resolved quartet spectrum undergoes line broadening, yielding a broad single-line EPR spectrum. This simulated spectrum matches closely with the experimental EPR spectrum observed at room temperature [see Fig. 2(a)]. For τ values close to 0.1 μs, the simulated spectra revealed the presence of weak hyperfine lines in the low-magnetic-field or high-g-value region, and their features are comparable with the experimental spectra.

DISCUSSION

Since the gel contains a fraction of the solvent, it is considered that the polymer chains experience continuous bombardment from the solvent molecules. The elastic collisons

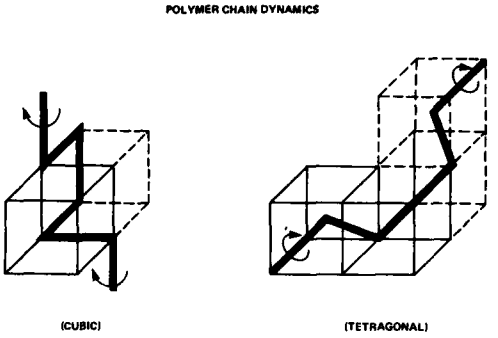


FIG. 4. Schematic models of polymer chain dynamics in cubic and tetrahedral lattices.

can produce whole molecule rotation, segmental motion, or translation motion of the polymer molecule.[9] Assuming that the backbone of the gel surface occupies a lattice structure, the conformational changes correspond to movements on this lattice. If the bond angles are fixed at 90°, we have a cubic lattice. If the angles are 109°24′ apart, then we have a tetrahedral lattice. Thus, rotational isomeric states are possible at 0°, 90°, $-90°$ for a cubic lattice and 120°, 0°, $-120°$ for a tetrahedral lattice. Schematically, these polymer dynamics[9] are shown in Fig. 4. Since the spin probe is bonded to the polymer, its motion is governed by the segmental motion of the polymer chains. In the cubic lattice dynamics model, the spin probe's motion is confined to a rotation in a single plane, which results in only partial averaging of the g and A tensors. However, the tetrahedral polymer lattice dynamics can cause rotation of the spin probe in an arbitrary plane, and it can create a rather complete mixing of both parallel and perpendicular components of the g and A tensors which is needed to produce the desired isotropic spectrum under rapid rotation.

CONCLUSIONS

The time-dependent EPR spectra of Cu^{2+} found in the PVA gels have been simulated using the two-jump model employing the modified Bloch equations. The segmental motion of the polymer chains might play a role in spin-probe motion in the molecular cages.

[1] L. Berliner, Editor, *Spin Labeling: Theory and Application* (Academic, New York, 1976), Vol. 1.
[2] D. Suryanarayana, L. Kevan, and S. Schlick, J. Am. Chem. Soc. **104**, 668 (1982).
[3] D. Suryanarayana and L. Kevan, J. Am. Chem. Soc. **104**, 6251 (1982).
[4] D. Suryanarayana, P. A. Narayana, and L. Kevan, J. Phys. Chem. **86**, 4579 (1982).
[5] D. Suryanarayana, P. A. Narayana, and L. Kevan, Inorg. Chem. **22**, 474 (1982).
[6] M. Dole, J. Macromol. Sci. Chem. **15**, 1403 (1981).
[7] B. Ranby and J. F. Rabek, *ESR Spectroscopy in Polymer Research* (Springer, New York, 1977).
[8] A. Danno, J. Phys. Soc. Jpn. **13**, 609, (1958); **13**, 614 (1958); **13**, 722 (1958).
[9] R. T. Bailey, A. M. North, and R. A. Pethrick, *Molecular Motion in High Polymers* (Clarendon, Oxford, 1981).

A NMR study of $YCo_{12}B_6$ and $GdCo_{12}B_6$ intermetallic compounds

K. Erdmann and M. Rosenberg
Experimentalphysik VI, Ruhr-Universität, PB 102148, 4630 Bochum, West Germany
K. H. J. Buschow
Philips Research Laboratories, 5600 JA Eindhoven, The Netherlands

Spin-echo nuclear magnetic resonance was used to study ^{59}Co hyperfine fields in the intermetallic compounds $RCo_{12}B_6$ with R = Y and Gd. Two groups of signals were obtained and interpreted in terms of anisotropic orbital contributions to the hyperfine field in the domain walls and domains.

INTRODUCTION

The alloys $RCo_{12}B_6$ (R = rare earth) crystallize in the hexagonal $SrNi_{12}B_6$ structure (space group $R\bar{3}m$) with one R site (3*a*), two Co sites (18*g* and 18*h*), and one B site (18*h*). From magnetization measurements it is known[1] that Co atoms have a rather small average magnetic moment μ_{Co} of about $0.44\,\mu_B$ in both alloys. The $GdCo_{12}B_6$ sample with a compensation temperature of 47.8 K has a ferrimagnetic spin structure in which the Co and Gd magnetic moments have opposite directions. The Y atoms can be considered as nonmagnetic, whereas the Gd magnetic moment μ_{Gd} reaches the Gd^{3+} free-ion value of $7\,\mu_B$. Because of differences in the number of R, Co, and B atoms in the environment of the two Co sites, the values of the Co magnetic moments and therefore the hyperfine field (HF) at the Co(18*g*) and Co(18*h*) nuclei could also differ. On the other hand, a nuclear-magnetic-resonance (NMR) study using the spin-echo method can provide evidence of differences in the values of the electronic magnetic moments of Co atoms in domain walls and domains.

EXPERIMENT

The measurements on powdered samples prepared as described in Ref. 1 were carried out in zero external field at 4.2 K using a modified Bruker B-Kr 322s pulse spectrometer. To determine the hyperfine field distribution, nuclear signals were excited by pulses of 1 and 1.4 μs duration with 50 μs delay time between them, the repetition time of the pulse sequence being typically 100 ms. After accumulation of the phase-sensitive detected spin echoes, digital filtering was carried out using a window of $\pm$ 200 kHz. As a measure of the number of nuclei with Larmor frequencies in this window around the spectrometer frequency, the echo amplitude was determined and corrected for both the spectrometer frequency response and the third power of frequency. Further evidence pointing to the quadrupolar nature of the splitting found in the $YCo_{12}B_6$ NMR spectrum was gained by applying the nuclear-double-resonance method[2] with a pulse sequence of 5 μs–8 μs (delay)–5 μs–50 μs (delay)–7 μs, where the first pulse (pumping pulse) was to have a frequency differing from the following spin-echo sequence. This time, because of the small bandwidth of the power amplifier used for determination of the spin-echo spectra, a broadband (1–400-MHz) power amplifier was used.

RESULTS AND DISCUSSION

The frequency-corrected spin-echo spectra of the samples $YCo_{12}B_6$ and $GdCo_{12}B_6$ taken at 4.2 K in the frequency range 10–100 MHz are shown in Figs. 1 and 2, respectively. In the spectrum of $YCo_{12}B_6$ the ^{11}B and ^{10}B signal contributions can be expected only in the lower-frequency range (< 10 MHz) because both the small average Co magnetic moments and the small hyperfine coupling constant for the Co-B interaction[3] shift the transferred HF(B) to low values. This situation seems to be different in the alloy containing Gd. Here the large Gd magnetic moments shift parts of the ^{11}B resonance to values above 10 MHz. Because of the low R concentration in these alloys a significant contribution from ^{89}Y and $^{153}Gd + {}^{155}Gd$ nuclei can be excluded. Therefore, nearly the whole intensity in the spectra has to be ascribed to ^{59}Co signals.

Roughly, the spectra can be divided into two parts. Starting with $YCo_{12}B_6$, one subspectrum, which will be discussed below, consists of seven narrow and equally spaced lines ($\Delta\nu = 1.85$ MHz) and is centered in the high-frequency region at 76.2 MHz corresponding to HF(Co) = 7.55 T. In the lower-frequency range three peaks at 26.7 MHz (2.64 T), 39.4 MHz (3.90 T), and 49.5 MHz (4.90 T) are found. In the sample containing Gd the upper subspectrum is shifted to 80.5 MHz (7.97 T) as the central frequency and has a width of about 13 MHz (1.29 T). The very regular structure found in the Y-containing sample is no longer present. In the lower-frequency range one broad intense peak around 38 MHz (3.76 T) with a width of about 15 MHz (1.49 T) and a comparable low-intensity peak at 20 MHz (1.98 T) are found. The very regular structure in the high-frequency range of the $YCo_{12}B_6$ spectrum provides evidence of a well-defined quadrupolar splitting of the Zeeman line into seven equally spaced components separated by 1.85 MHz due to the ^{59}Co nuclear spin of $\frac{7}{2}$. This was checked by the nuclear-double-resonance technique where the nuclear magnetization at a certain transition (here $\frac{1}{2} \rightleftarrows -\frac{1}{2}$) is measured by a standard spin-echo pulse sequence. A pulse with a frequency differing from the spin-echo pulse frequency is put before the echo sequence. If the frequency difference is equal to the quadrupolar splitting frequency ν_Q, the spin-echo amplitude increases, as shown in Fig. 3.

One is indeed tempted to assign the two subspectra to Co signals arising from nuclei located at the crystallographically different Co sites in the $RCo_{12}B_6$ lattice. The environ-

 0021-8979/88/084113-03$02.40 © 1988 American Institute of Physics

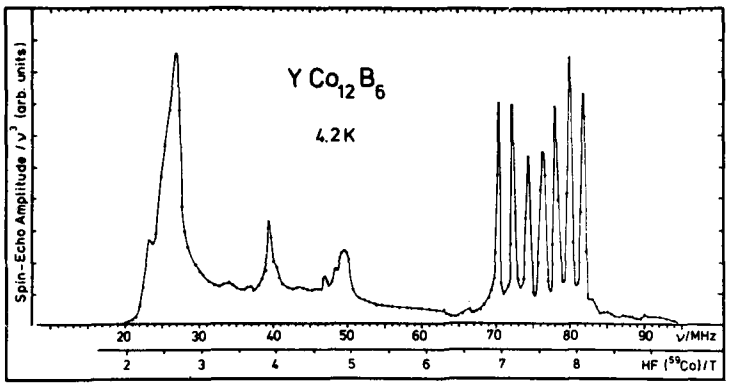


FIG. 1. ^{59}Co spin-echo spectrum of $YCo_{12}B_6$ taken at 4.2 K in zero external field with a pulse separation of $\tau = 50\ \mu s$.

ment of Co(18*g*) atoms consists of three Co(18*g*) neighbors at about 2.53 Å, four Co(18*h*) neighbors at about 2.53 Å, four B neighbors at 2.04 Å. and two R neighbors at 3.24 Å. The total number of neighbors of the Co(18*h*) site is also thirteen, but here one finds only one R neighbor at 3.21 Å, four Co(18*g*) neighbors at about 2.50 Å, five Co(18*h*) neighbors at about 2.50 Å and three B neighbors around 2.03 Å. From NMR measurements in binary Co-B alloys it has been found[4] that μ_{Co} decreases as the number of Co neighbors decrease and the number of B neighbors increases. Applying this result to the alloys investigated one would assign to Co at the 18*h* site a higher magnetic moment and a larger value of the HF. One can try to estimate the magnetic moments at the two crystallographically inequivalent Co sites in the $YCo_{12}B_6$ sample by ignoring an orbital contribution to HF(Co) and taking for both sites the same hyperfine coupling constant of 11 T/μ_B.[4] With average hyperfine fields of 3.3 ± 1 T and 7.55 T for the two sites, one finds values of $(0.30 \pm 0.09)\ \mu_B$ and $0.69\ \mu_B$ for the 18*g* and 18*h* sites and an average value of $(0.50 \pm 0.04)\ \mu_B$, which is close to the one determined from magnetization measurements ($0.44\ \mu_B$).

But a closer analysis of the spectra points to inconsistencies in the interpretation of the two subspectra as derived from the two different Co sites. First of all, the appreciably higher intensity in the low-frequency range does not agree with the equal populations of the two sites. Second, there is no explanation for the large width of the low-frequency subspectrum as compared to the high-frequency one. An analysis of dipolar contributions under the assumption that the magnetization rotates in the hexagonal plane would give rise to shifts of only ± 0.05 T for $YCo_{12}B_6$, which are very small compared with the difference of 1.26 and 1.01 T between the main peaks in the low-frequency subspectrum.

Because of the above-mentioned difficulties another explanation is needed. The basic assumptions in this model will be that the Co spin moments do not differ very much and that the high-frequency subspectrum arises from domains and the low-frequency one from domain walls. We believe that the relatively large difference between the centers of the subspectra of about 4.24 T for both R = Y and Gd arises from a strongly anisotropic orbital moment of the Co atoms. Such effects have been observed in several types of R–Co (Ref. 5) and B-Co (Ref. 6) compounds, giving rise to two or three Co lines differing largely in the hyperfine field. Even small orbital moments can strongly influence the hyperfine

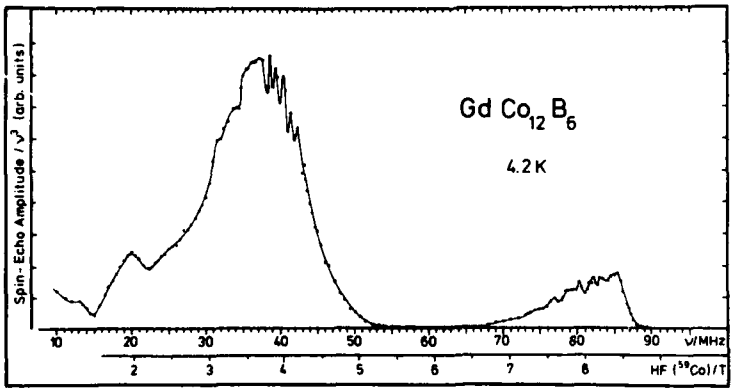


FIG. 2. Spin-echo spectrum of $GdCo_{12}B_6$ taken at 4.2 K in zero external field with a pulse separation of $\tau = 50\ \mu s$. The spectrum mainly reflects the ^{59}Co hyperfine field distribution, but contributions from ^{11}B signals are also present in the frequency range below 20 MHz.

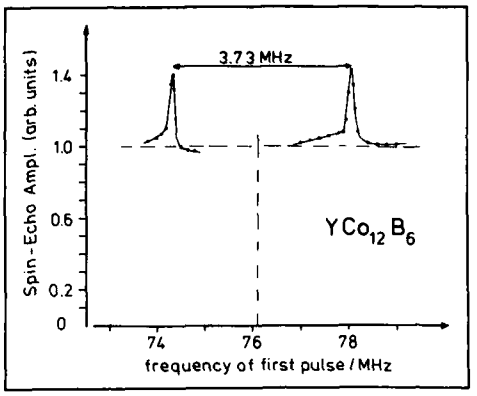


FIG. 3. Results of the nuclear-double-resonance experiment in the sample $YCo_{12}B_6$ at a frequency corresponding to the transition of the central line ($\frac{1}{2} \rightleftarrows -\frac{1}{2}$) of the quadrupolar split septet. The spin-echo amplitude in dependence on the pumping frequency is shown and it is seen that the maxima correspond exactly with the maxima found in the spin-echo spectrum.

field values because of the large orbital hyperfine coupling constant of about 65 T/μ_B,[5] i.e., 5.9 times larger than that for the spin contribution of the Co moment. The orbital HF contribution could show an anisotropic behavior analogous to that of the dipolar field. One can easily see that deviations of the magnetization direction from the hexagonal axis or rotations give rise to up to six groups of magnetically noninequivalent Co atoms, which in the case of an anisotropic orbital contribution would mean three to six different values of the resulting HF when the anisotropic term is added to the one proportional to the spin moment.

In the case of $GdCo_{12}B_6$, dipolar fields created mainly by the Gd magnetic moments give rise to shifts in the range from $+0.2$ to -0.4 T, which can partially explain the smearing of the structure in the NMR spectrum of this compound.

Support for the assumption that the Co moments at the two sites are not too different comes from preliminary Mössbauer measurements of ^{57}Fe-substituted $GdCo_{12}B_6$ made in our laboratory. About 80% of the whole intensity in the Mössbauer spectrum originates from Fe with hyperfine field values between 13 and 15 T.

An argument in favor of the assumption that the high-frequency signals originate from nuclei in domains is provided—besides the smaller intensity—by the above-mentioned Mössbauer experiment, where a ^{57}Fe quadrupolar splitting nearly equivalent to the value of 1.85 MHz obtained from the ^{59}Co NMR experiment has been found. It is obvious that the Mössbauer spectrum is representative for nuclei located in the domains. However, more experimental data on $RCo_{12}B_6$ compounds with different R and NMR measurements in magnetic fields are needed in order to be able to make a definitive choice between the two possibilities presented in this paper.

ACKNOWLEDGMENTS

Financial support received from the Deutsche Forschungsgemeinschaft and the Commission of the European Community in the framework of the research program "Concerted European Action on Magnets" is gratefully acknowledged.

[1] M. Rosenberg, M. Mittag, and K. H. J. Buschow, these proceedings.
[2] M. W. Pieper, H. Lütgemeier, and W. Zinn, Z. Phys. B **63**, 369 (1986).
[3] M. Wojcik, H. Lerchner, P. Deppe, M. Rosenberg, and J. D. Livingston, J. Appl. Phys. **55**, 2288 (1984).
[4] W. Boehner, H. Lütgemeier, and W. Zinn, J. Magn. Magn. Mater. **62**, 152 (1986).
[5] S. Hiroswawa and Y. Nakamura, J. Magn. Magn. Mater. **25**, 284 (1982).
[6] M. Kasaya, T. Hihara, and Y. Koi, J. Phys. Soc. Jpn. **34**, 63 (1973).

A NMR study of $R_2(TM)_{14}B$ compounds with R = Sm, Gd, or Lu and TM = Fe or Co

K. Erdmann and M. Rosenberg
Experimentalphysik VI, Ruhr-Universität, PB 102148, 4630 Bochum, West Germany
K. H. J. Buschow
Philips Research Laboratories, 5600 JA Eindhoven, The Netherlands

Nuclear-magnetic-resonance spectroscopy was used to study hyperfine fields at Fe and B sites in $R_2(TM)_{14}B$ compounds with R = Sm, Gd, or Lu and TM = Fe or Co. The transferred hyperfine fields at B sites reflect changes in the magnetic structure of these compounds and are discussed in terms of dipolar fields

I. INTRODUCTION

In a previous paper[1] we reported results of both Mössbauer and nuclear magnetic resonance (NMR) measurements on $R_2(TM)_{14}B$ alloys , where R was a nonmagnetic element (La, Y, or Th) and TM = Fe or Co. In this paper we extend the NMR investigations to the compounds $Gd_2Fe_{14}B$, $Lu_2Fe_{14}B$, $Sm_2Co_{14}B$, and $Gd_2Co_{14}B$, where all the rare-earth (R) atoms except Lu carry a magnetic moment. In addition to the hyperfine fields (HFs) at Fe nuclei located at six crystallographically different lattice sites $16k_1$, $16k_2$, $8j_1$, $8j_2$, $4e$, and $4c$ in the tetragonal unit cell, we want to study the transferred hyperfine field (THF) at B nuclei located only at $4g$ sites. The investigated compounds show both magnetic anisotropies, being uniaxial for TM = Fe and planar for TM = Co, and small and vanishing R magnetic moments (Sm and Lu) or large R magnetic moments (Gd), respectively, which in the latter case order ferrimagnetically.

II. EXPERIMENT

The alloys were prepared by arc melting in high-purity argon. After vacuum annealing for three weeks the $R_2(TM)_{14}B$ phase was obtained. For NMR measurements the ingots were crushed to powder to reduce eddy currents.

The measurements were carried out at 4.2 K in zero external field in the frequency range 10–100 MHz with a modified Bruker B–Kr 322s pulse spectrometer. Spin echoes were excited with 0.5–τ–0.65 μs pulse sequences at optimal power levels. For each sample we chose a separation τ between the pulses that allowed us to reach the best resolution of the NMR spectrum. The phase-sensitive detected and accumulated spin echoes were digitally filtered with a window of $\pm$ 100 kHz before the echo amplitude was determined. The amplitudes were corrected by the spectrometer response and divided by the third power of frequency.

III. RESULTS AND DISCUSSION

A. $Gd_2Fe_{14}B$ and $Lu_2Fe_{14}B$

In the samples containing Fe a superposition of ^{11}B and ^{57}Fe signals was obtained in the frequency range 35–55 MHz (Figs. 1 and 2). To resolve the ^{57}Fe spectra the pulse distance τ was set to 300 μs and also to 1000 μs for R = Lu. The partial removal of ^{11}B signal contributions due to a faster transverse relaxation than that of ^{57}Fe nuclei can be seen by comparing the ^{11}B-^{57}Fe frequency range with ^{10}B spectra (bottom parts in Figs. 1 and 2), which appear in the lower frequency range 10–23 MHz far away from ^{57}Fe resonances. The ^{10}B spectra were taken at the same values of τ as those for the higher frequency range and also at τ = 20 μs in order to get the "true" B hyperfine field distribution. In the spectrum of $Lu_2Fe_{14}B$ we were able to determine HFs(Fe) of 29.4, 33.0, and 37.1 T at sites $8j_1$, $16k_2$, and $8j_2$, respectively, in good agreement with Mössbauer results, which are indicated by arrows in the figures. The Fe ($16k_1$) signals expected at 30.8 T could not be separated because of the intense ^{11}B signal occurring in the same frequency range. In the Gd-containing sample the HFs(Fe) are shifted to 33.3, 35.9, and 40.1 T for sites $16k_1$, $16k_2$, and $8j_2$, respectively, which, except for the first one, are also in good agreement with Mössbauer results.

The NMR signals arise mainly from domain walls where contributions to HF(Fe) such as dipolar (H_{dip}) and Lorentz fields (H_{Lor}) depend on the position of the nucleus in the wall. This leads to shifts in frequency and broadening of the resonance lines and —besides the small intensity— may explain why no distinct Fe($4e$) and Fe($4c$) lines could be detected. The shift of about 3T found for all Fe sites in $Gd_2Fe_{14}B$ compared to the corresponding sites in $Lu_2Fe_{14}B$ agrees quite well with the increase of the average Fe magnetic moment when Lu is replaced by Gd in $R_2Fe_{14}B$.[2]

The B spectra have maxima at their low-frequency side corresponding to values of the transferred hyperfine field THF(B) of 2.40 and 3.16 T for R = Gd and Lu, respectively. Although B atoms occupy only one site in the $R_2(TM)_{14}B$ structure, the whole range of B signals extends over $\approx$2.6 and $\approx$1.3 T for R = Gd and Lu, respectively. These values can be compared with those determined in $La_2Fe_{14}B$ as a reference, namely THF(B) = 2.81 T for the THF at the maximum intensity and a range of 1.5 T.[3] The large broadening of the B spectra has to be attributed to domain-wall effects, leading, as in the case of the Fe lines, to distributions of both H_{dip} and H_{Lor}, but in the case of B they are amplified because of the larger gyromagnetic ratio of ^{11}B and ^{10}B nuclei.

 0021-8979/88/084116-03$02.40 © 1988 American Institute of Physics

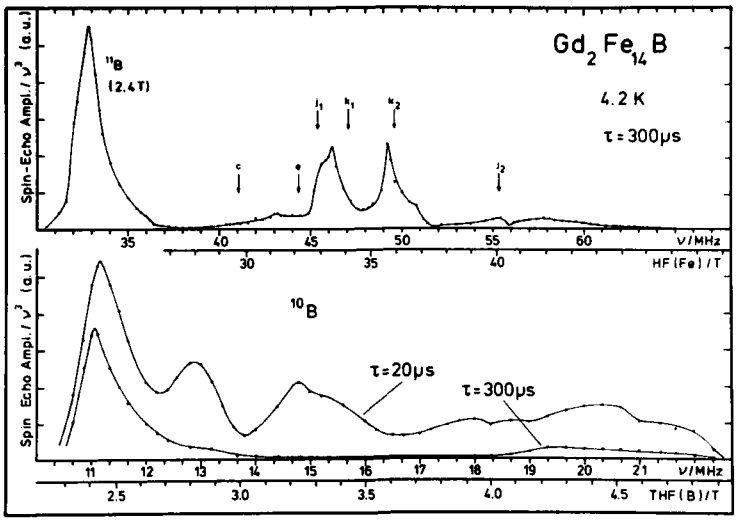


FIG. 1. Frequency-corrected NMR spin-echo spectrum of $Gd_2Fe_{14}B$ taken at 4.2 K in the frequency range 10–66 MHz with pulse separation $\tau = 20$ and 300 μs. Arrows indicate HFs(Fe) evaluated from Mössbauer spectra.

In order to estimate domain-wall effects in the NMR spectra we calculated the local dependence of H_{dip} in 180° walls, choosing a reasonable width of 3 nm and the classical continuum approximation for the magnetization rotation from [001] to [00$\bar{1}$] in the [110] plane because the [110], direction is the easy direction for the spins when turning out of the tetragonal c axis, at least for R = Gd above 110 K.[4] We took spheres of 10 nm radius, an average value for μ_{Fe} of 2.2 μ_B [except $\mu_{Fe}(j_2) = 2.5\mu_B$] and a value for μ_{Gd} of 7μ_B. In the center of the walls the Fe sublattice creates dipolar fields between -0.1 and $+0.1$ T, dependent on the B site in the unit cell where the negative sign denotes a direction opposite to the local magnetization. At the edge of walls and in domains, the dipolar fields reached values of 1.1 and 0.85 T, respectively, where the splitting is negligible. Therefore a difference of about 1.2 T arises between the hyperfine fields at B nuclei located in the center and at the edge of the walls, corresponding to a ^{11}B frequency range of 16 MHz if only Fe magnetic moments contribute to the dipolar field. The range of variation of H_{dip} drastically increased when the Gd sublattice contribution was taken into account. In the vicinity and in the center of the walls H_{dip} was shifted to

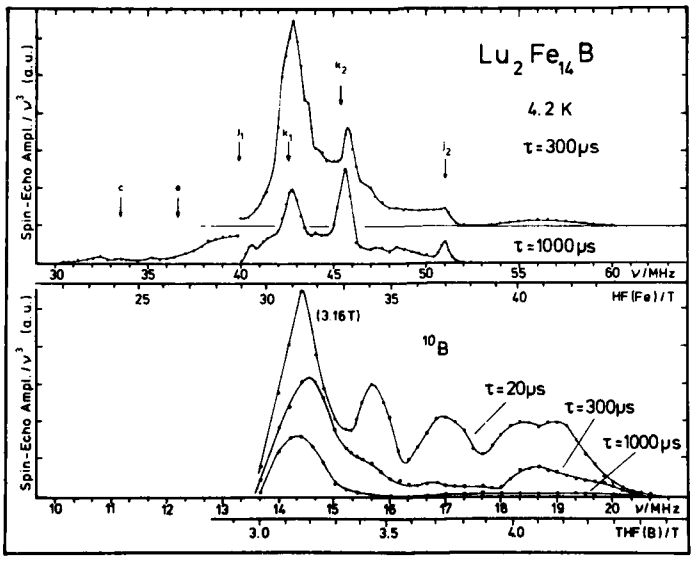


FIG. 2. Frequency-corrected NMR spin-echo spectrum of $Lu_2Fe_{14}B$ taken at 4.2 K in the frequency range 13–61 MHz with pulse separation $\tau = 20$, 300, and 1000 μs. Arrows indicate HFs(Fe) evaluated from Mössbauer spectra. The discontinuity of the amplitudes in the spectrum taken with $\tau = 1000$ μs is due to a multiplication of the amplitudes by a factor of 25.

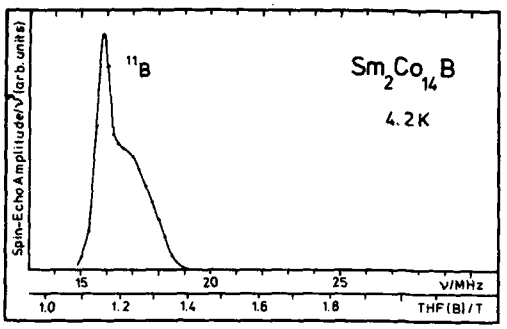


FIG. 3. Frequency-corrected ^{11}B NMR spin-echo spectrum of $Sm_2Co_{14}B$ at 4.2 K taken with $\tau = 100\,\mu s$.

between -0.3 and -0.75 T, whereas at the edge and in the domains it reached 1.65 and 1.5 T, respectively. Evidently the additional dipolar contribution of the Gd sublattice increases the range of values of H_{dip} up to 2.5 T, corresponding to a ^{11}B frequency range of 34 MHz. The values obtained for Fe contributions alone to H_{dip} and that including the Gd contribution are in good agreement with the experimental data for the B spectra in $R_2Fe_{14}B$ with R = La or Lu and in $Gd_2Fe_{14}B$, respectively.

B. $Sm_2Co_{14}B$, and $Gd_2Co_{14}B$

In the Co-containing samples pure ^{11}B spectra were obtained in the frequency 15–28 MHz. ^{59}Co signals were detected only above 70 MHz for R = Sm and above 75 MHz for R = Gd. Both the frequency at the maximum intensity in the ^{11}B spectra and the range of B frequencies are changed when Fe is replaced by Co (Figs. 3 and 4). The values of THF(B) at maximum intensity and the range of B signals are 1.16 and 0.2 T for $Sm_2Co_{14}B$ and 1.49 and 0.5 T for $Gd_2Co_{14}B$. The rather large shift of the B lines to lower frequencies mainly results from the smaller hyperfine coupling constant $a_{Co\text{-}B}$ and the smaller average Co magnetic moment of about 1.4 μ_B.[5] Taking for the average Fe moment in $R_2Fe_{14}B$ a value of 2.2 μ_B and a ratio $a_{Fe\text{-}B}/a_{Co\text{-}B} = 1.8$, which was found in $Co_{3-x}Fe_xB$ alloys with a similar environment of B nuclei,[6,7] we obtain a ratio of 2.8 between THF(B) values in $R_2Fe_{14}B$ and $R_2Co_{14}B$. Preliminary measurements of $Sm_2Fe_{14}B$ with planar anisotropy (as $Sm_2Co_{14}B$) give a value of THF(B) = 4.03 T, which is about 3.5 times the value we find in the latter compound, supporting the expectation of our estimation.

A difficulty arises when one considers the strong reduction of the frequency width of the B spectrum to about 1/6 of its value in the $R_2Fe_{14}B$ compounds with axial anisotropy when Fe is replaced by Co. From the above considerations one would expect reductions of only about 2/3 of the value found in the Fe-containing compounds.

The reason for this discrepancy resides in the circumstance that the investigated Co-containing compounds exhibit planar rather than uniaxial anisotropy. This gives rise to a different magnitude and dependence of dipolar fields on the location of the resonant nuclei in the domain walls.

In the case of planar anisotropy, with the magnetic moments in the walls rotating in the [001] plane, we calculated the variation of the dipolar field taking $\mu_{Co} = 1.4\mu_B$, disregarding the rotation of magnetic moments inside the sphere because of the small anisotropy constant K_3 in the plane. For $\mu_R = 0.3\mu_B$ (Ref. 5) ($Sm_2Co_{14}B$) the dipolar field reached -0.24 T with a splitting of ± 0.08 T around this value when the magnetization is parallel to [110]. In the case of $\mu_R = 7\mu_B$ ($Gd_2Co_{14}B$), H_{dip} reached -0.58 T with a splitting of ± 0.23 T. Both the positive shift of THF(B) (0.34 T) and the increase of the B hyperfine field range (0.3 T) when comparing $Gd_2Co_{14}B$ with $Sm_2Co_{14}B$ are in quite good agreement with the measured B hyperfine field distributions.

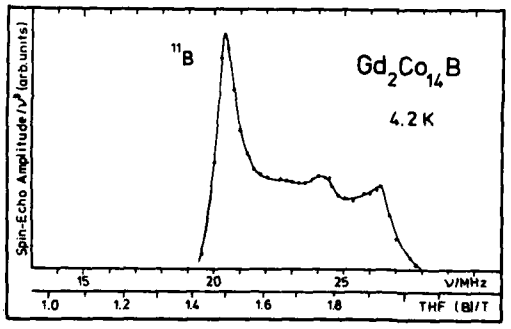


FIG. 4. Frequency-corrected ^{11}B NMR spin-echo spectrum of $Gd_2Co_{14}B$ at 4.2 K taken with $\tau = 150\,\mu s$.

ACKNOWLEDGMENTS

Financial support received from the Deutsche Forschungsgemeinschaft and the Commission of the European Community in the framework of the research program "Concerted European Action on Magnets" is gratefully acknowledged.

[1] K. Erdmann, P. Deppe, M. Rosenberg, and K. H. J. Buschow, J. Appl. Phys. **61**, 4340 (1987).
[2] S. Sinnema, R. J. Radwanski, J. J. M. Franse, D. B. de Mooij, and K. H. J. Buschow, J. Magn. Magn. Mater. **44**, 333 (1984).
[3] M. Rosenberg, P. Deppe, K. Erdmann, M. Sostarich, and H. Stadelmaier, J. Magn. Magn. Mater. **54**, 599 (1986).
[4] W. D. Corner and M. J. Hawton, Meeting of the Concerted European Action on Magnets, Amsterdam, 1986.
[5] K. H. J. Buschow, D. B. de Mooij, S. Sinnema, R. J. Radwanski, and J. J. M. Franse, J. Magn. Magn. Mater. **51**, 211 (1985).
[6] H. Lerchner, K. Erdmann, D. Welz, M. Rosenberg, and F. E. Luborsky, IEEE Trans. Magn. **MAG-17**, 2609 (1981).
[7] M. Wojcik, H. Lerchner, P. Deppe, F. S. Li, M. Rosenberg, and J. D. Livingston, J. Appl. Phys. **55**, 2288 (1984).

NMR spin-echo studies in sputtered Heusler alloy films

K. Le Dang and P. Veillet
Institut d'Electronique Fondamentale, F-91405 Orsay, France

R. Krishnan
Laboratoire de Magnétisme, Centre National de la Recherche Scientifique, F-92195 Meudon Cedex, France

A. Morisako and M. Matsumoto
Faculty of Engineering, Shinshu University, Nagano 380, Japan

M. Naoe
Faculty of Engineering, Tokyo Institute of Technology, Tokyo 152, Japan

We have carried out at 4-K spin-echo studies (of ^{55}Mn, ^{63}Cu) on sputtered Heusler alloy (Cu_2MnAl) films with substrate temperature T_s in the range of 50–300 °C in order to obtain microscopic information on the magnetic structure. For $T_s = 60$ °C a very broad spectrum is obtained, revealing incomplete (disordered) formation of Cu_2MnAl. For $T_s = 158$, 167, 170, and 210 °C, well-defined spectra are observed with Mn at 227 MHz and Cu at 241 and 259 MHz, respectively. Signal intensity studies reveal a maximum for $T_s = 167$ °C in general agreement with the magnetization results of Morisako, Matsumoto, and Naoe. The signal frequencies are also in agreement with those obtained for the bulk alloy. For $T_s = 300$ °C, the spectrum is broadened but the signal frequencies of Mn and Cu remain practically the same. This spectrum is also quantitatively different from that observed for the film with $T_s = 60$ °C, where a low-frequency tail is observed. The effect of post-annealing the films is also presented.

INTRODUCTION

The magnetic properties of sputtered Cu_2MnAl Heusler alloy films were shown to depend very sensitively on the substrate temperature T_s.[1] The saturation magnetization M_s increases monotonously when T_s increases from 50 to 170 °C then decreases drastically for T_s above 210 °C. The x-ray diffraction diagrams showed that the films deposited at T_s of 50 °C were composed of crystallites of Cu_2MnAl. For $T_s = 170$ °C an additional Cu_9Al_4 phase was also formed. For the films deposited at $T_s = 210$ °C the intensity of the diffraction lines corresponding to Cu_2MnAl became weaker. These lines completely disappear with higher T_s of 255 °C. We report here the NMR spin-echo studies of these films in order to obtain information on the magnetic structure of these samples.

EXPERIMENTAL DETAILS

The NMR measurements were done at 4.2 K using a frequency variable spin-echo apparatus. The rf field of the exciting coil was parallel to the film plane. The film thickness was about 1 μm and the surface area 1 cm^2.

RESULTS AND DISCUSSIONS

The NMR spectra in zero external field are shown in Fig. 1. The resonance frequencies corresponding to ^{55}Mn, ^{63}Cu, and ^{65}Cu nuclei are about 227, 241, and 259 MHz, respectively, i.e., the same as in the bulk Cu_2MnAl Heusler alloy. The very broad spectrum for the film with $T_s = 60$ °C clearly shows that its crystalline structure is far from an ordered state. The line shape for the sample with $T_s = 167$ °C is intermediate between those with $T_s = 158$ °C and $T_s = 170$ °C. The line broadening due to atomic disorder in Heusler alloys following cold work was already reported.[2] It was shown in Pd_2MnSn that the Mn moment on the regular Sn site is antiparallel to the lattice magnetization. The Mn-Mn coupling at short distance in Heusler alloys is known to

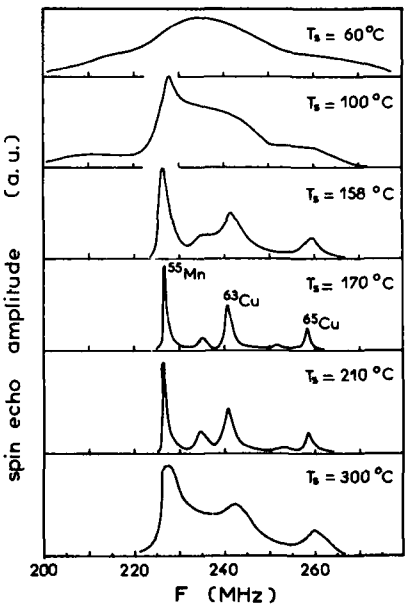


FIG. 1. ^{55}Mn, ^{63}Cu, and ^{65}Cu spin-echo spectra at 4.2 K in sputtered Cu_2MnAl Heusler alloy films deposited at various substrate temperatures T_s. The residual lines between the main lines are due to deviation from exact stoichiometry.

 0021-8979/88/084119-02$02.40 © 1988 American Institute of Physics

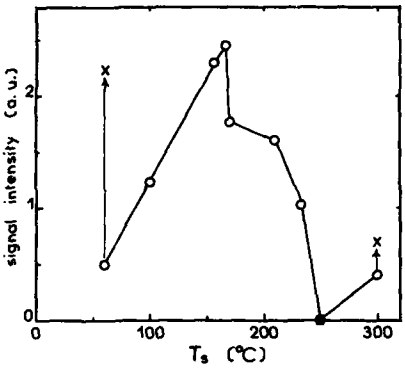


FIG. 2. Integrated signal intensity as a function of the substrate temperature T_s. The × symbols at 60, 250, and 300 °C correspond to samples after annealing at 160 °C for 4 h.

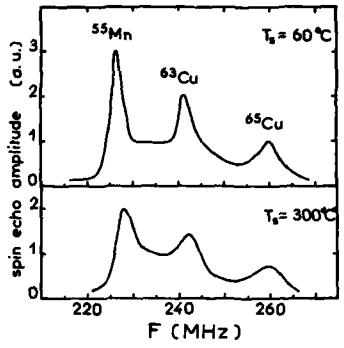


FIG. 3. Spin-echo spectra at 4.2 K for Cu_2MnAl alloy films deposited at T_s = 60 and 300 °C after annealing at 160 °C.

be antiferromagnetic.[3] Consequently the saturation magnetization of a disordered Cu_2MnAl alloy should be reduced. As T_s is raised to 170 °C the resonance lines become sharper, revealing a quasi-ordered structure. For $T_s > 170$ °C the spectrum is again broadened but the main lines remain clearly discernible.

The amount of Cu_2MnAl phase with the $L2_1$ structure is proportional to the integrated signal intensity. Since these films are soft ferromagnetic materials, a dc field of 5 kOe applied parallel to the film plane is enough to obtain practically the same enhancement of the nuclear signal for all the samples. The signal intensity was found to increase with the substrate temperature T_s up to 167 °C (Fig. 2), in agreement with the dependence of the saturation magnetization on T_s. A slight decrease in signal at $T_s = 170$ °C is coherent with the formation of Cu_9Al_4 phase as shown by x-ray diffraction.[1] The absence of Cu_2MnAl phase at $T_s = 255$ °C as revealed by x-ray diffraction is confirmed by the nonobservation of any spin-echo signal in this range of frequencies. Thus the small residual magnetization at this point could be due to some Mn-based alloys among β-Mn and Cu_9Al_4 phase as detected by x-ray diffraction. What is surprising is the reappearance of the spin-echo signal for the film with T_s = 300 °C. We can explain the dependence of the signal intensity on T_s as follows. The optimum temperature for the formation of Cu_2MnAl phase with a well-ordered structure is about 167 °C. When the substrate was maintained near 250 °C the formation of other phases was strongly favored to the detriment of Cu_2MnAl. At higher temperature several phases coexist and none was favored. It should be pointed out that this behavior is much more complex than that of the bulk sample since annealing Cu_2MnIn and Cu_2MnAl powders in the range[2] 200–250 °C for 24 h gives the maximum ordering. The resonance spectrum of the powdered Cu_2MnAl sample is then quite similar to that observed for the film with $T_s = 170$ °C. We wanted to study the effect of thermal annealing on the properties of the films. For this we selected three badly formed films with $T_s = 60$, 250 and 300 °C and annealed them at 160 °C under a vacuum for 4 h. For the sample with $T_s = 250$ °C no spin-echo signal was detected as before. There are changes both in the line shape and in the intensity for the two other films (Fig. 3). However, the annealing effect was much more spectacular for the film with $T_s = 60$ °C with an increase in the signal intensity by a factor of 4 (Fig. 2). Clearly, this annealing results in a better crystallization of Cu_2MnAl alloy. For the samples with $T_s = 250$ and 300 °C phases other than Cu_2MnAl are so stable at 160 °C that annealing has little effect on the crystalline structure of the film.

In conclusion, spin-echo studies of sputtered Cu_2MnAl Heusler alloy films show that a well-ordered Cu_2MnAl structure is obtained when the substrate temperature T_s is maintained in the range 160–210 °C. For the sputtered film prepared with lower T_s, a substantial improvement can be achieved by post-annealing the sample at a higher temperature under a vacuum. On the contrary, annealing has little effect on the films deposited at high temperatures.

[1] A. Morisako, M. Matsumoto, and M. Naoe, International Symposium on Physics of Magnetic Materials, 1987, Sendai, Japan.
[2] J. Schaf, K. Le Dang, P. Veillet, and I. A. Campbell, J. Phys. F 13, 1311 (1983).
[3] K. Le Dang, P. Veillet, and I. A. Campbell, J. Phys. F 8, 1811 (1978).

Magnetic clustering in $LaNi_{5-x}Fe_x$ compounds

M. Escorne, J. Lamlouml,[a] A. Percheron-Guegan, and J. C. Achard
Laboratoire de Chimie Métallurgique des Terres Rares, CNRS, 1 Place A. Briand, 92190 Meudon, France

A. Mauger
Groupe de Physique des Solides, ENS, Université Paris VII, 2 Place Jussieu, 75007 Paris Cédex 05, France

G. Jehanno
DPh.SRM, CEN Saclay, 91191 Gif-sur-Yvette, France

The magnetic phase diagram of $LaNi_{5-x}Fe_x$ ($0<x<1.2$) has recently been investigated down to 20 K. This range has been extended here down to 1.6 K. Magnetic susceptibility curves $\chi(T)$ go through a maximum and then strongly decrease upon cooling below a temperature T_1 which, for all iron concentrations, is smaller than 15 K, i.e., much smaller than the Curie temperature T_c for $x>0.4$ or the spin freezing temperature for $x<0.3$, previously determined. This anomalous behavior is correlated to a sharp decrease of the electrical resistivity at T_1. Mössbauer spectra do not show any anomalous behavior of the hyperfine field upon cooling through T_1. These results, associated to the continuous behavior of the magnetic susceptibility and electrical resistivity versus the iron concentration, suggest that with decreasing temperature there is a progressive freezing of small magnetic clusters which coexists with long-range ferromagnetic ordering for $x>0.4$.

INTRODUCTION

In a previous work[1] we have shown that partial substitution by iron for nickel in the intermetallic compound $LaNi_5$ induces a drastic change of the magnetic properties of this enhanced Pauli paramagnet: in the pseudobinary hexagonal compounds $LaNi_{5-x}Fe_x$ ($0<x<1.2$), Fe ions carry a magnetic moment ranging from 1.23 μ_B for $x<0.5$ to 1.52 μ_B for $x=1.2$. The iron spin freezing has been investigated[2] for the temperature range above 20 K: for $x<0.3$ the observed progressive spin freezing has been related to the 2D character of the magnetic lattice; for $x>0.4$, a long-range ferromagnetic ordering takes place at a temperature T_c rising from 50 K for $x=0.4$ up to 240 K for $x=1.2$. The magnetic phase diagram (Fig. 3 in Ref. 2) shows that for $x<0.3$, the compounds exhibit a spin-glass state whereas for $x>0.4$ a ferromagnetic phase is evidenced.

In the present paper, we complete the magnetic phase diagram in the (x,T) plane at lower temperatures (1.6 K $<T<$ 20 K) from magnetic, electrical resistivity, and Mössbauer measurements. Our results confirm the very progressive spin freezing in these compounds down to lower temperatures.

EXPERIMENT

Polycrystalline samples of different iron concentrations are the same as those described in Refs. 1 and 2. For improving the quality of Mössbauer spectra an enriched ^{57}Fe sample has been prepared for $x=0.4$ in order to get an absorber with 0.1 mg ^{57}Fe per cm^2.

The magnetic measurements have been performed using a SQUID magnetometer in an applied field $H=20$ Oe. The electrical resistivity measurements device has been previously described,[3] as well as the Mössbauer experiment conditions.[1]

RESULTS

The zero-field-cooled (ZFC) magnetic susceptibility is reported in Fig. 1 for typical concentrations ($x=0.1,0.4,0.75$) which illustrate the physical properties of this system on both sides of the critical concentration ($0.3<x_c<0.4$).

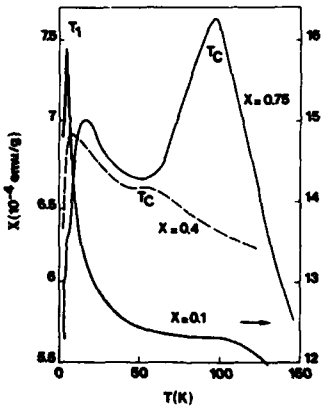


FIG. 1. Zero-field-cooled magnetic susceptibility in a field $H=20$ Oe vs increasing temperature for different iron concentrations. (The samples have been cooled at a rate 20 K per hour.)

[a] Permanent address: ENSET, 5 Avenue Taha Houssein, 1008 Tunis, Tunisia.

 0021-8979/88/084121-03$02.40 © 1988 American Institute of Physics

For $x = 0.4$ and 0.75, the peak at higher temperature, 50 ± 5 and 100 K, respectively, corresponds to the onset of long-range ferromagnetic ordering at T_c. For $x = 0.1$ two ZFC susceptibility cusps have already been reported at $T_g = 160$ K and $T_0 = 100$ K, but no spontaneous magnetization is observed. For all Fe concentrations, we find a new maximum of the ZFC susceptibility at a temperature T_1 much smaller than these characteristic temperatures, namely, $T_1 = 3.5 \pm 0.5$, 8, and 15 K for $x = 0.1$, 0.4, and 0.75, respectively, which gives evidence of another spin freezing.

The resistivity curves $\rho(T)$ are investigated since they probe the temperature dependence of the local spin correlation $\langle S_i S_j \rangle_\lambda$ at the scale of the electron mean free path λ. The results are illustrated in Fig. 2. For all concentrations, a very sharp decrease of ρ upon cooling is observed at a temperature smaller but close to T_1. Actually, T_1 corresponds to a break in the slope of the $\rho(T)$ curve, which suggests the existence of enhanced magnetic fluctuations at this temperature. Such fluctuations are even more apparent at low concentrations x where, like in the $x = 0.1$ sample, $\rho(T)$ goes through a maximum in the close vicinity of T_1. Note that the amplitudes of the susceptibility cusps at T_1 and T_c have the same order of magnitude, because χ is a probe of the bulk magnetic properties and is thus sensitive to the onset of a long-range ferromagnetic ordering. The very small anomaly of $\rho(T)$ at T_c is due to the fact that $\rho(T)$ is only sensitive to the local spin properties and this means that the ferromagnetic phase is very inhomogeneous at the microscopic scale of λ with large local spin fluctuations which freeze at $T \sim T_1$.

To further investigate the nature of this spin freezing, ^{57}FeMössbauer absorption experiments have been carried out on the $LaNi_{4.6}Fe_{0.4}$ compound. This yields a unique quadripolar spectrum ($\Delta E_Q = 1.00$ mm/s) in the paramagnetic region and shows that magnetic ordering appears near $T_c = 50$ K. However, down to 40 K [Fig. 3(a)], the spectrum is made up of a very broad structureless magnetic spectrum and of a residual paramagnetic component which progressively disappears near $T = 35$ K. This can be interpreted as being due to small superparamagnetic clusters fluctuating at frequencies much higher than the nuclear Larmor frequency.

At lower temperatures ($T < 30$ K) six well-defined lines of magnetic spectra are present [(Fig. 3(a)]. We also observe that the shape of the spectra does not change with temperature in the vicinity of $T_1 = 8$ K. This indicates that this temperature is not associated with a transition from a ferromagnetic phase to a reentrant spin-glass state. In particular, down to 1.4 K a quadrupolar interaction is present. This shows that the orientations of the magnetic moments are not randomly distributed with respect to the local principal axis of the electric field gradient (EFG).

Moreover, the measured hyperfine field [Fig. 3(b)] varies smoothly and does not show any discontinuity be-

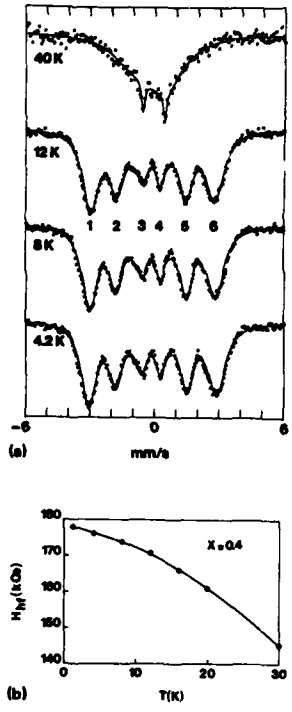


FIG. 3. (a) Mössbauer spectra for $LaNi_{4.6}Fe_{0.4}$ (^{57}Fe enriched) near T_c (40 K) and T_1 (8 K). (b) Hyperfine field vs temperature for $LaNi_{4.6}Fe_{0.4}$ in the vicinity of T_1.

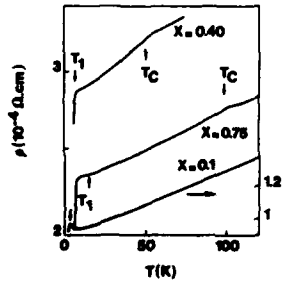


FIG. 2. Resistivity vs temperature for the same iron concentration as in Fig. 1. (The samples have been cooled at a rate 20 K per hour.)

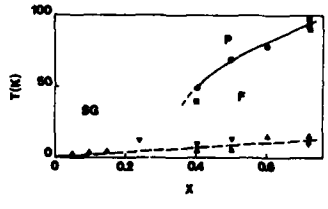


FIG. 4. Magnetic phase diagram of $LaNi_{5-x}Fe_x$ at low temperature. F is the inhomogeneous ferromagnetic phase, P is the paramagnetic phase, and SG the spin glass phase. Experimental determinations of the Curie temperature (full line) have been reported from Ref. 2 using the same symbols completed by the result for $x = 0.6$. Experimental data for T_1 (dashed line) have been deduced from magnetic (▲) and transport (▼) properties as explained in the text.

tween 30 and 1.4 K. This rules out the possibility that collective freezing of transverse spin components occurs as has been observed in other cases.[4,5]

All the magnetic spectra have been fitted in terms of a unique set of hyperfine parameters. The quadrupole interaction was blocked at the value obtained at 77 K ($\Delta E_Q = 1.035$ mm/s) and for all the spectra the same values of θ (the angle between H_{hf} and the principal EFG axis) and η (the EFG asymmetry parameter) have been found, close to 60° and 0.55, respectively.

Finally, we note that for the spectrum at 12 K [Fig. 3(a)], a slight misfit is visible on the left-hand side of line 3. It is weaker at 16 K and 8 K and it disappears at 4.2 and also 20 K. At the present time we do not know how to explain this modification of the shape of the magnetic spectrum which occurs at a temperature slightly higher than T_1.

The set of these results lead to the magnetic phase diagram displayed in Fig. 4. A spin freezing is evidenced in the whole range of iron concentration at a temperature T_1 lower than the Curie temperature T_c for $x \geq 0.4$ and lower than the spin-glass freezing temperature for $x < 0.3$. This result still extends to lower temperatures the outstanding progressive spin freezing observed for $T > 20$ K.[2]

DISCUSSION

Magnetic transport properties and Mössbauer experiments show that the spin freezing at T_1 is most likely attributable to the freezing of local spin fluctuations. This conclusion is sustained by the fact that the x dependence of T_1 is very small. We can, at last, compare this system $LaNi_{5-x}Fe_x$ with other spin glass systems previously described in the literature, considering separately the two parts of the diagram: $x < 0.3$ and $x > 0.4$.

For $x < 0.3$, the anomalous behavior of $\chi(T)$ and $\rho(T)$ can be compared with a spin clustering observed below T_g in insulating spin glass EuSrS.[6] Note, however, that such a behavior can be well explained in insulators where the magnetic interactions are short range, favoring magnetic clustering. In isotropic RKKY spin glasses, however, a much more cooperative behavior is expected since the magnetic interactions are long range. Such a freezing at T_1 may be related to anisotropic magnetic interactions associated to the 2D nature of the magnetic lattice[2] with iron spins almost exclusively located in the plane $z = 1/2$ of the hexagonal structure.

For $x \geq 0.4$ the sharp drop of resistivity at T_1 can be compared to the behavior of another RKKY spin glass, $Sn_{1-x}Mn_xTe$,[7] in which T_1 could be ascribed to the reentrant spin-glass temperature T_r. The decrease of ρ at T_r corresponds to an enhancement of the short-range spin correlation at the expense of the weak long-range ferromagnetic ordering. There is, however, drastic differences between the spin freezing at T_r in $Sn_{1-x}Mn_xTe$ and the spin freezing at T_1 in $LaNi_{5-x}Fe_x$. First, a reentrant spin-glass phase is best evidenced by a cusp in the imaginary part of the ac susceptibility χ''_{ac},[8] while no anomalous behavior of the real part χ'_{ac} is detected (Fig. 1 in Ref. 8). To the contrary, in $LaNi_{5-x}Fe_x$, T_1 corresponds to a cusp of the static susceptibility, i.e., a cusp of χ'_{ac} in the low-frequency limit. Second, a reentrant spin-glass phase can be observed only for spin concentrations large enough to lead to the onset of a long range ferromagnetic order at $T_c > T_r$, with $T_c \sim T_r$ at the magnetic percolation threshold x_c. However, in $LaNi_{5-x}Fe_x$, we observe anomalies of $\rho(T)$ and $\chi(T)$ curves at T_1 in both ranges $x > x_c$ and $x < x_c$. In addition, T_1 is much smaller than T_c in the range $x > x_c$. This additional spin freezing at $T_1 < T_c$ is thus best understood in terms of percolation with finite size clusters coexisting with the infinite ferromagnetic cluster formed at T_c.

ACKNOWLEDGMENT

We are indebted to P. Lethuilier for his assistance in SQUID measurements.

[1] J. Lamloumi, A. Percheron-Guegan, J. C. Achard, G. Jehanno, and D. Givord, J. Phys. (Paris) **45**, 1643 (1984).
[2] M. Escorne, J. Lamloumi, A. Percheron-Guegan, J. C. Achard, and A. Mauger, J. Magn. Magn. Mater. **65**, 63 (1987).
[3] M. Escorne, A. Mauger, D. Ravot, and J. C. Achard, J. Phys. C **14**, 1821 (1981).
[4] I. Mirebeau, G. Jehanno, I. A. Campbell, F. Hippert, B. Hennion, and M. Hennion, J. Magn. Magn. Mater. **54–57**, 99 (1986).
[5] I. A. Campbell, S. Senoussi, F. Varret, J. Teillet, and A. Hamzić, Phys. Rev. Lett. **50**, 1615 (1983).
[6] J. Tholence, J. Appl. Phys. **50**, 7369 (1979).
[7] A. Mauger and M. Escorne, Phys. Rev. B **35**, 1902 (1987).
[8] M. Escorne, M. Godinho, J. L. Tholence, and A. Mauger, J. Appl. Phys. **57**, 3424 (1985).

Local atomic structure in amorphous Fe-P alloys

R. L. McCally, J. S. Morgan, T. J. Kistenmacher, and K. Moorjani
The Johns Hopkins University, Applied Physics Laboratory, Johns Hopkins Road, Laurel, Maryland 20707

Amorphous alloys Fe_xP_{100-x} have been fabricated by rf sputtering in the composition range $50<x<75$. Only a-$Fe_{75}P_{25}$ is ferromagnetic at 293 K, with its Mössbauer spectrum consisting of six broad lines. This simple spectrum differs markedly from that of c-Fe_3P. Similarly, thermogravimetric analysis yielded $T_c = 550$ K for the amorphous phase, a value considerably lower than that of the crystalline phase (700 K). The Mössbauer spectra of the samples having $x<71$ were all similar quadrupole-split doublets. Mean isomer shifts (IS) and $P(H)$ and $P(Q)$ distributions were determined using Window's method. The isomer shift is nearly independent of concentration in the range studied here, but differs significantly from those of the crystalline compounds c-FeP, c-Fe_2P, and c-Fe_3P. The effective quadrupole interaction is also nearly constant for $50<x<71$, indicating a similar local Fe environment. These results contrast sharply with c-Fe_2P and c-FeP, which have different crystal symmetries and whose quadrupole interactions differ substantially both from each other and from their amorphous counterparts.

INTRODUCTION

Although amorphous alloys of Fe with *sp* elements of groups III and IV of the periodic table such as B, C, Si, Ge, and Sn have been studied extensively,[1] it was only recently that comprehensive investigations were begun on the glass-forming elements of group V. In particular, Chien *et al.*[2] recently examined hyperfine interactions and magnetic properties of amorphous Fe-Sb alloys over a wide composition range. Until now, amorphous alloys of Fe with P have been made by electrodeposition[3] or melt spinning,[4,5] and consequently the range of accessible compositions was limited to that near the eutectic $Fe_{80}P_{20}$.

We have used rf sputtering to fabricate films of Fe_xP_{100-x} for $50<x<75$. Our aim was to learn how the local atomic environment of the Fe atoms and ordered magnetic phases varied with composition and how they differed from the crystalline Fe-P compounds in this composition range. Mössbauer spectroscopy is an especially powerful tool for this purpose and has been used here to determine magnetic hyperfine and electric quadrupole field distributions, thereby gaining information on the variation of the magnetic moments of the Fe neighbors and the local symmetry of the Fe environment. Measurements of isomer shift yield information on the charge distribution near the nuclei of the Fe atoms. The Curie temperature of a-$Fe_{75}P_{25}$, the only composition that was ferromagnetic at 293 K, was also measured.

EXPERIMENTAL METHODS

Films were fabricated by rf sputtering in an Ar atmosphere, with the vacuum before sputtering in the 10^{-7} Torr range. The 1.5–4-μm films were prepared on 0.15-mm-thick glass substrates. Because of the undesirable properties of elemental P, sputtering targets were appropriate mixtures of commercially available polycrystalline Fe-P compounds, viz., c-Fe_3P, c-Fe_2P, and c-FeP. All stated compositions are those of the starting mixtures. For compositions with $x<71$, it was essential to cool the substrates with liquid nitrogen. Indeed, failure to bond the glass substrates to the cooled holder with a paste of apiezon-N and Cu powder resulted in polycrystalline films.

The amorphous structure of the samples was verified using a wavelength-dispersive x-ray spectrometer. Mössbauer spectra were obtained at room temperature (293 K) using a conventional constant acceleration spectrometer with a ^{57}Co in Rh source. The hyperfine field distributions $P(H)$ and quadrupole distributions $P(Q)$ were obtained using Window's method[6] with 15 terms in the Fourier series. Isomer shifts (IS) were determined from the centroids of the fitted spectra, and are reported relative to α-Fe.

The Curie temperature of a-$Fe_{75}P_{25}$, the only composition that was ferromagnetic at 293 K, was measured using thermogravimetric analysis. The sample was placed in a commercial thermogravimetric balance (Perkin-Elmer TGS-2) and heated at a constant rate of 40 K/min. An external magnetic field, supplied by a small permanent magnet, exerted a force on the sample which disappeared when the

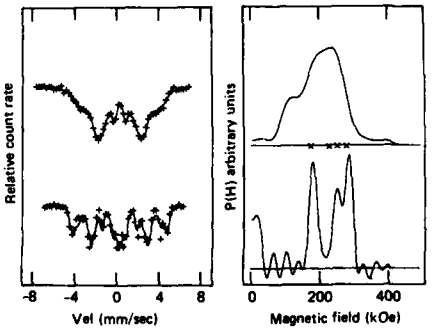


FIG. 1. Mössbauer spectra and $P(H)$ distributions for a-$Fe_{75}P_{25}$ (top) and c-Fe_3P (bottom) at 293 K. The values of the hyperfine field used by Wäppling *et al.* (Ref. 7) to fit the spectrum of c-Fe_3P are indicated by the $\times$'s on the axis of the $P(H)$ distribution for a-$Fe_{75}P_{25}$.

 0021-8979/88/084124-03$02.40 © 1988 American Institute of Physics

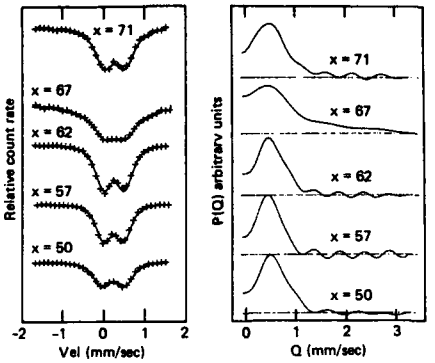


FIG. 2. Mössbauer spectra and $P(Q)$ distributions for the amorphous alloys a-Fe_xP_{100-x} at 293 K.

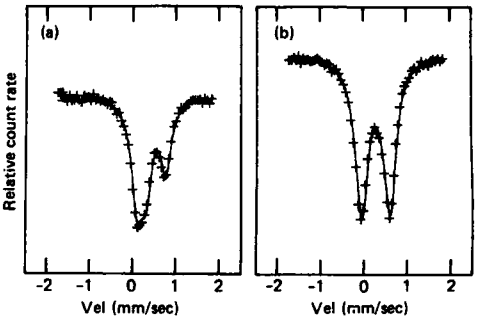


FIG. 3. (a) Mössbauer spectra for c-Fe_2P at 293 K. (b) Mössbauer spectra of c-FeP at 293 K.

Curie temperature was reached, thereby yielding the value of T_c.

RESULTS AND DISCUSSION

The left-hand side of Fig. 1 compares the Mössbauer spectra of a-$Fe_{75}P_{25}$ and c-Fe_3P. The amorphous material's spectrum consists of six broad lines whose relative intensity ratio suggests that the magnetization is largely confined to the plane of the film. The spectrum of c-Fe_3P, similar to that reported earlier,[7] is quite complex, consistent with its tetragonal crystal structure and three distinct Fe sites. Wäppling *et al.*[7] resolved a similar spectrum into four separate six-line spectra, each having different hyperfine fields and isomer shifts. The physical basis for using four spectra to describe three Fe sites is not apparent; nevertheless their values for the hyperfine fields lie well within the bounds of the $P(H)$ distribution for the amorphous sample, as shown on the right-hand side of Fig. 1. We obtained an approximate fit to the spectrum of c-Fe_3P using Window's method[6] by employing 25 terms in the Fourier series. The derived $P(H)$ distribution shows three major peaks. The components at 177 and 287 kOe correspond almost exactly to two of the hyperfine fields used by Wäppling *et al.* to fit their spectrum,[7] while the component at 247 kOe is between the other two hyperfine fields they employed.

We found that the Curie temperature of a-$Fe_{75}P_{25}$ is 553 K. This is close to the value of 550.9 K reported by Logan and Sun[3] for an electrodeposited sample with $x = 74.2$. For comparison, T_c of c-Fe_3P has been reported as 700 K.[8] The suppressed value for the amorphous sample results from a distribution of the magnetic moments as well as exchange interactions arising from many inequivalent sites in the amorphous phase.[1]

Samples with $x<71$ are paramagnetic at 293 K. Their spectra and corresponding $P(Q)$ distributions are shown in Fig. 2, and are similar over the entire range $50<x<71$. Unlike amorphous Fe-Sb,[2] the quadrupole-split spectra are symmetric; i.e., the intensities of the absorption peaks are equal.

For comparison, Fig. 3 displays the spectra for c-Fe_2P and c-FeP. The difference between the spectra of a-$Fe_{67}P_{33}$ (cf. Fig. 2) and c-Fe_2P is especially striking, in both shape and isomer shift. Crystalline Fe_2P has two distinct Fe sites, and following Wäppling *et al.*,[7] we fit its spectrum with two quadrupole-split doublets, each having a different isomer shift. The results [$\delta_1 = 0.438$ mm/s, $\delta_2 = 0.01$ mm/s,

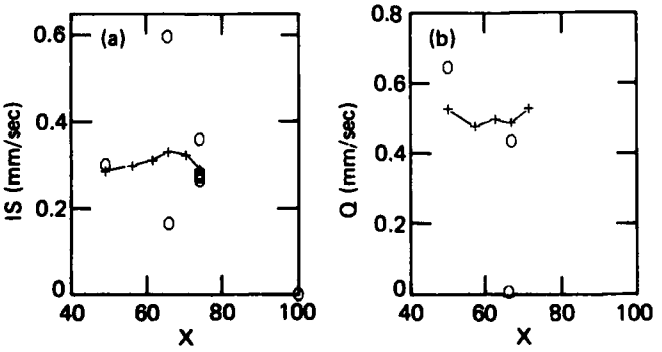


FIG. 4. (a) Isomer shifts (relative to a-Fe) and (b) effective quadrupole interactions for a-Fe_xP_{100-x} alloys and crystalline Fe-P compounds. The quadrupole splittings plotted for the amorphous samples are the positions of the peak in the $P(Q)$ distributions. Symbols + are for amorphous samples and o are for crystalline compounds. The lines connecting the + 's are to guide the eye.

$(IS)_1 = 0.606$ mm/s, and $(IS)_2 = 0.172$ mm/s] are in excellent agreement with those given earlier.[7] Crystalline FeP has a single Fe site, and our values ($\delta = 0.65$ mm/s and IS = 0.31 mm/s) are again close to previously reported values.[7]

The important results of the Mössbauer investigation are compiled in Figs. 4(a) and 4(b). Figure 4(a) shows IS as a function of composition for the amorphous and crystalline samples. The differences for the two phases are striking, especially at $x = 67$. Chein *et al.*[2] found for a-Fe_xSb_{100-x} that the isomer shift was nearly constant, diminishing only slightly below $x \approx 60$, while for $x \gtrsim 60$ it dropped sharply to the value of pure Fe. The present data suggest a similar dependence in a-Fe_xP_{100-x}, except that it is shifted in x. Figure 4(b) displays the composition dependence of the quadrupole interaction. The values given for the amorphous samples are the positions of the peak of the $P(Q)$ distributions. The interactions for c-FeP and c-Fe_2P are substantially different, which reflects the different crystal symmetries for these compounds. On the other hand, the quadrupole interactions for the amorphous samples are nearly constant over this composition range, indicating similar local environments of the Fe atoms in the amorphous phase. However, they differ significantly from the quadrupole interactions of either c-Fe_2P or c-FeP, indicating dissimilar local environments for the two phases.

ACKNOWLEDGMENT

This work was supported by the U.S. Navy under Contract No. N00039-87-C-5301.

[1] K. Moorjani and J. M. D. Coey, *Magnetic Glasses* (Elsevier, Amsterdam, 1984).
[2] C. L. Chein, G. Xiao, and K. M. Unruh, Phys. Rev. B **32**, 5582 (1985).
[3] J. Logan and E. Sun, J. Non-Cryst. Solids **20**, 285 (1978).
[4] M. Eibschütz, M. E. Lines, and H. S. Chen, Phys. Rev. B **28**, 425 (1983).
[5] K. Tanaka, N. Soga, and K. Hirao, J. Appl. Phys. **60**, 728 (1986).
[6] B. Window, J. Phys. E **4**, 401 (1971).
[7] R. Wäppling, L. Häggström, S. Rundqvist, and E. Karlsson, J. Solid State Chem. **3**, 276 (1971).
[8] E. Lisher, C. Wilkenson, T. Ericsson, L. Häggström, L. Lundgren, and R. Wäppling, J. Phys. C **7**, 1344 (1974)

Unusual magnetic and lattice transformation in UNiSn, a possible half-metallic ferromagnetic system

N. Bykovetz and Warren N. Herman
Physics Department, Spring Garden College, Philadelphia, Pennsylvania 19119
T. Yuen, Chan-Soo Jee, C. L. Lin,[a] and J. E. Crow
Physics Department, Temple University, Philadelphia, Pennsylvania 19122

UNiSn, as well as certain other ternary actinide compounds, displays very anomalous behavior in the temperature dependence of the electrical resistivity, $\rho(T)$. In UNiSn this unusual $\rho(T)$ dependence has been attributed to half-metallic behavior with a semiconducting gap in the minority spin band and metallic behavior in the majority spin band with a ferromagnetic transition in the vicinity of 50 K. We have studied UNiSn using ^{119}Sn Mössbauer spectroscopy and observed that annealing procedures influence the microscopic properties of the sample in a profound way. As-cast samples are nonmagnetic. Annealing in the neighbor of 800 °C results in the formation of a magnetic component. The conversion to a magnetic phase is incomplete even after annealing for 210 days at 800 °C. The magnetic component goes through two transformations: (1) a region below approximately 60 K where there is a coexistence and gradual transformation of paramagnetic to magnetically ordered material and (2) a region below 43 K where the magnetic component is completely ordered. In the region between 43 and 60 K, the hyperfine field shows a sequence of first-order transitions. The temperature dependence of the ^{119}Sn hyperfine field for UNiSn is presented and discussed along with measurements of the temperature dependence of the specific heat, electrical resistivity, and the temperature and field dependence of the magnetization.

This paper was not proofread by the author; however, it has been proofread by one of the Publication Chairpersons.

INTRODUCTION

For several years, there has been rapidly growing interest in 5*f*-electron metallic systems with much of the current interest being driven by the anomalous behavior, e.g., heavy-fermion, spin-fluctuation, and Kondo behavior, reported for many of these systems.[1,2] It has long been recognized that a crucial parameter influencing the electronic and magnetic properties of actinide (Ac) alloys and intermetallic compounds is the Ac-Ac spacing, $d_{\text{Ac-Ac}}$. Hill has shown that for $d_{\text{Ac-Ac}} <$ a critical spacing $d_{cr} \simeq 3.4$–3.6 Å, local magnetic moments are quenched due to the increase of intersite *f-f* overlap and that for $d_{\text{Ac-Ac}} > d_{cr}$, *f-spd* hybridization is the dominant factor influencing local moment formation.[3] This fact has attracted interest in systems with large $d_{\text{Ac-Ac}}$ where through alloying or selection of structure, the *f-spd* hybridization can be varied. A very interesting new class of equiatomic ternary UTX compounds, with T being a *d* transition metal and X being a group-III, -IV, or -V element, has been recently reported.[4] These compounds have $d_{\text{Ac-Ac}} \gtrsim d_{cr}$ and display a variety of unusual electronic and magnetic properties. The compounds within this new class having the largest $d_{\text{Ac-Ac}}$ crystallize in a cubic MgAgAs-type structure and display the most unusual properties. Within this subclass, UNiSn is the most interesting. UNiSn has a large $d_{\text{Ac-Ac}} \simeq 4.51$ Å and a pronounced maximum in the temperature dependence of the electrical resistivity $\rho(T)$ followed by an exponential high-temperature resistivity which approximately follows a gap dependence of the form $\rho(T) \propto \exp(\Delta/2kT)$. Recent band-structure calculations suggest that UNiSn is a half-metallic magnet, i.e., a system with a semiconducting gap in the minority spin band and metallic behavior for the majority spin band.[5,6] The unusual properties reported for UNiSn have been attributed to this band structure. As with NiMnSb, a compound isostructural to UNiSn, the splitting of the bands in these systems leads to a 100% spin-polarized state. This feature has been attributed to the lack of inversion symmetry in such a structure. We have measured the temperature dependence of the specific heat $C(T)$ and electrical resistivity $\rho(T)$, along with the temperature and field dependence of the bulk magnetization on UNiSn. At low temperatures, UNiSn orders ferromagnetically and at high temperatures, it is paramagnetic with a paramagnetic moment equal to $(3.31 \pm 0.02)\,\mu_B$ and an antiferromagnetic Curie–Weiss temperature of 66 ± 3 K. In addition, we have measured the temperature dependence of the ^{119}Sn hyperfine field H_{hf} in UNiSn using ^{119}Sn Mössbauer spectroscopy. These results indicate that the heat treatment of this system has a profound influence on the microscopic magnetic properties observed at low temperatures. The transition from the low-temperature ferromagnetic state to the paramagnetic state in the vicinity of 43 K is unusual.

EXPERIMENTAL PROCEDURES AND RESULTS

The samples were prepared by melting stochiometric ratios of the constituents in a conventional inert atmosphere arc furnace. The samples were wrapped in Ta foil and placed in an evacuated quartz tube for annealing. The samples were annealed at a variety of temperatures extending from 500 to 1000 °C and for several different time intervals extending up to 210 days. Powdered x-ray diffraction studies were used to

[a] Present address: Physics Department, Brookhaven National Laboratory, Upton, NY 11973.

 0021-8979/88/084127-03$02.40 © 1988 American Institute of Physics

check the homogeneity and structure of the unannealed and annealed UNiSn samples. For the annealed samples, the x-ray studies showed that the UNiSn crystallized in the cubic MgAgAs-type structure. The indexing of both the positions and intensities of the diffraction lines is consistent with the MgAgAs structure, which is a modified Heusler alloy structure of the type X_2YZ with one X site empty. The Ni ion is at the X site, i.e., (0,0,0), whereas the U and Sn are at the $(\frac{1}{4},\frac{1}{4},\frac{1}{4})$ and $(\frac{3}{4},\frac{3}{4},\frac{3}{4})$ positions, respectively. The room-temperature lattice constant was 6.39 Å. The temperature dependence of $\rho(T)$, $C(T)$, and $\chi(T)$ was measured using a standard four-probe dc method, a quasi-adiabatic heat-pulse method, and a Quantum Design SQUID (superconducting quantum interference device) magnetometer, respectively. The UNiSn Mössbauer specimens were prepared by crushing the sample in a high-purity argon glove box and embedding 600-mesh sieved powder throughout a lucite disk. The absorber thickness was typically 10 mg/cm^2 Sn. A $Ca^{119}SnO_3$ source was used in conjunction with an electromechanical velocity transducer in a triangular velocity mode. The temperature dependence of the Mössbauer spectra was measured from 1.6 to 300 K using a He bath or an adjustable He-flow cryostat.

Shown in Fig. 1 is $\rho(T)$ vs T for UNiSn annealed at 800 °C for 52 days. This behavior is very similar to the $\rho(T)$ data reported by Palstra *et al.*[4] In the vicinity of 300 K, $\rho(T)$ varies approximately as $\exp(\Delta/2kT)$ with $\Delta \simeq 0.07$ eV. The resistivity reaches a value at the maximum which is orders of magnitude larger than anticipated for the unitary limit for a metallic system. According to a recent band-structure calculation, the increase of $\rho(T)$ with decreasing T is due to the semiconducting gap in the electronic structure. At lower temperatures the system orders in a half-metallic magnetic state with the majority spin band becoming metallic.[5]

The temperature at the maximum in $\rho(T)$ does not correspond to features observed in $C(T)$ and $M(T)$. Shown in Figs. 2(a) and 2(b) are $C(T)$ and $M(T)$, respectively, for UNiSn annealed at 800 °C for 52 days. There is a sharp peak in $C(T)$ at $T = 43$ K and this temperature corresponds closely to the break in $M(T)$ vs T. The T dependence of $M(T)$ is very similar to the behavior seen for other ferromagnetic transitions in weakly magnetic systems. Shown in Fig. 2(c) is the temperature derivative of the resistivity

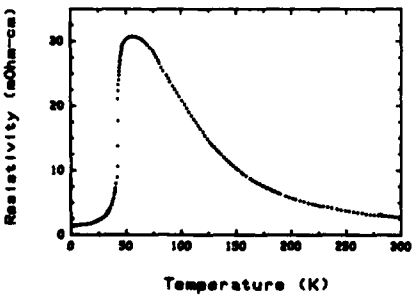


FIG. 1. Temperature variation of the resistivity of a UNiSn sample annealed at 800 °C for 52 days.

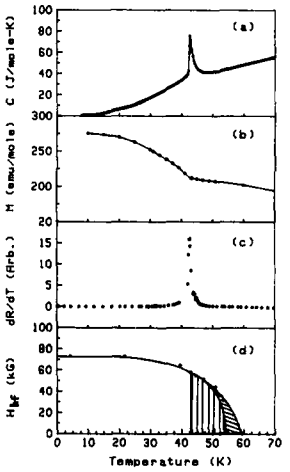


FIG. 2. Specific heat, magnetization, derivative of the resistivity (curve shown in Fig. 1), and the ^{119}Sn hyperfine field as a function of temperature (sample annealed at 800 °C for 52 days).

$d\rho/dT$ vs T. The maximum in $d\rho/dT$ vs T appears to correlate with the features seen in $C(T)$ and $M(T)$. Thus, based on these measurements it would seem that UNiSn has a ferromagnetic-to-paramagnetic transition with a Curie temperature $T = 43$ K. The $\rho(T)$ behavior is qualitatively consistent with the anticipated behavior of a metallic-to-semiconducting transition in the vicinity of T_c.

To more clearly establish the nature of the low-temperature state we have also measured the ^{119}Sn Mössbauer spectra versus T for UNiSn annealed at several temperatures and for several time periods. Shown in Fig. 3 are representative Mössbauer spectra of UNiSn taken at different tempera-

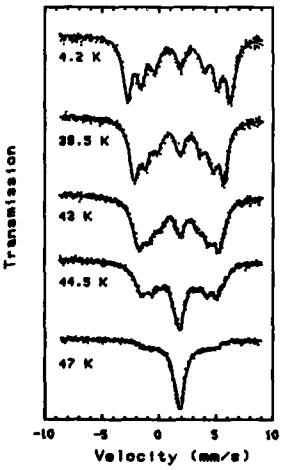


FIG. 3. ^{119}Sn Mössbauer spectra above and below the 43-K macroscopic transition temperature.

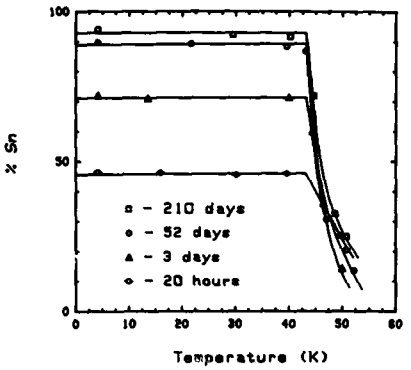


FIG. 4. Percentage of Sn seeing a hyperfine field in UNiSn samples annealed at 800 °C for different time intervals.

tures. At 4.2 K, the spectrum is best fit with approximately 90% of the Sn ions seeing a well-defined $H_{hf} \simeq 7.4$ T and the remaining Sn ions seeing a zero field. The isomer shift of the zero-field Sn is slightly higher than that of the Sn in the magnetic phase. This result indicates the presence of a separate nonmagnetic component. (The amount of the nonmagnetic component decreases for samples annealed for longer times.) As T increases, the fraction of Sn seeing H_{hf} remains constant up to 43 K where a precipitous decrease occurs, as part of the Sn goes into a zero-field state. This is seen in Fig. 3 as an increase in the central dip of the Mössbauer pattern (and is correlated with a corresponding decrease in the field-split area). The temperature dependence of the percentage of Sn nuclei seeing a nonzero H_{hf} is shown in Fig. 4.

Shown in Fig. 2(d) is the temperature dependence of H_{hf} for a sample annealed at 800 °C for 52 days. The H_{hf} as $T \to 0$ is 7.4 T and decreases with increasing T. However, H_{hf} is still at 0.8 of the saturation value at 43 K, the temperature at which anomalies occur in $d\rho/dT$, $M(T)$, and $C(T)$. Because the percentage of Sn nuclei seeing a H_{hf} decreases rapidly above 43 K, it is difficult to trace the decrease of H_{hf} with precision for $T > 50$ K. A smooth extrapolation of H_{hf} vs T as shown in Fig. 2(d) would suggest that H_{hf} would go to zero at or below 60 K, which is much larger than T_C given by the macroscopic measurements.

Certainly the H_{hf}-vs-T behavior obtained, along with the T dependence of $d\rho/dT$, $M(T)$, and $C(T)$, indicates that the transition between the low-temperature half-metallic ferromagnetic state and the paramagnetic semiconductor-like state at $T \geqslant 60$ K is not second order, but instead is better represented by a continuous sequence of first-order transitions. Even though careful hysteresis studies have not been completed, preliminary measurements of $d\rho/dT$ vs T have shown no appreciable hysteresis. The lack of hysteresis may just reflect a small difference in the free energy of the two states. More careful studies are underway to address this issue.

In conclusion, the measurements of $d\rho/dT$, $C(T)$, and $M(T)$ clearly indicate a transition from a paramagnetic state (with antiferromagnetic exchange) at high temperatures, i.e., $T > 60$ K, to a ferromagnetic state at low temperatures. The drop in resistivity, as well as the electronic contribution to the low-temperature specific heat, suggest that the ground state is metallic. The T dependence of $M(T)$ and the presence of a unique hyperfine field indicate that this metallic state is ferromagnetic. The T dependence of H_{hf}, $d\rho/dT$, $M(T)$, and $C(T)$ in the vicinity of T_C point toward a unusual ordering of the $5f$ moments. Even though these studies do not directly indicate that the magnetic state is a half-metallic state, many of the features are consistent with what would be anticipated assuming this new and unusual ground state.

ACKNOWLEDGMENT

This work was supported by the National Science Foundation under Grant No. DMR 8219782.

[1] G. R. Stewart, Rev. Mod. Phys. **56**, 755 (1984).
[2] B. Johansson, O. Eriksson, M. S. S. Brooks, and H. L. Skriver, Phys. Scr. **T13**, 65 (1986).
[3] H. H. Hill, in *Plutonium 1970 and other Actinides*, edited by W. N. Miner (Metallurgical Society of the AIME, New York, 1970), p. 2.
[4] T. T. Palstra, G. J. Nieuwenhuys, R. F. M. Vlastuin, J. van den Berg, J. A. Mydosh, and K. H. J. Buschaw, J. Magn. Magn. Mater. **67**, 331 (1987), and references therein.
[5] R. C. Albers, A. M. Boring, G. H. O. Daalderop, and F. M. Mueller, Phys. Rev. B **36**, 3661 (1987).
[6] R. A. deGroot, F. M. Mueller, P. G. van Engen, and K. H. J. Buschow, Phys. Rev. Lett. **50**, 2024 (1983).

Environmental influence on the nuclear spin-lattice relaxation rate in Cu_xPt_{1-x}

J. Banhart
Institut für Physikalische Chemie, Universität München, Sophienstrasse 11, D-8000 München 2, Federal Republic of Germany

P. Weinberger
Institut für Technische Elektrochemie, Technische Universität Wien, Getreidemarkt 9, A-1060 Wien, Austria

H. Ebert[a] and J. Voitländer
Institut für Physikalische Chemie, Universität München, Sophienstrasse 11, D-8000 München 2, Federal Republic of Germany

The influence of the surrounding atomic configuration on the nuclear spin-lattice relaxation rate of Pt in disordered Cu_xPt_{1-x} alloys has been studied theoretically by calculating the electronic structure of CuPt clusters embedded in a coherent potential approximation medium. The resulting average nuclear spin-lattice relaxation rate is found to be in a very satisfying agreement with experiment.

I. INTRODUCTION

In substitutional alloys the nuclear spin-lattice relaxation rate maps neighborhood-dependent partial local densities of states (DOS) at the Fermi energy. For this reason it offers the possibility to investigate the effects of short-range order and segregation in a rather direct way. Within the framework of multiple scattering theory the relaxation rate can be calculated as a function of configuration and—in the case of binary alloys—its dependence on the number of atoms of one component occupying a particular shell of neighbors or the short-range order parameters, respectively, can be studied. A comparison with the corresponding results for the statistically disordered case allows a quantitative illustration of the validity of the coherent potential approximation (CPA). Furthermore, a comparison with experimental values can be used to interpret data corresponding to one and the same "macroscopical" concentration, however, obtained from samples of different preparational origin and therefore different states of order. In the present paper the theoretical Pt nuclear spin-lattic relaxation rate in Cu_xPt_{1-x} is discussed for a number of concentrations considering all possible configurations of a first-neighbor shell cluster and are compared with available experimental data. For $Cu_{50}Pt_{50}$ also short-range order effects resulting from a shell of second neighbors are taken into account. In addition, experimental order-dependent specific heats are discussed.

II. THEORETICAL FRAMEWORK

The presented calculations were performed using the fully relativistic embedded cluster method (ECM)[1] and are based on results obtained within the framework of the fully relativistic Korringa-Kohn-Rostoker (KKR) CPA method.[2] In terms of the so-called scattering-path operator τ^J the DOS corresponding to a particular site i occupied by species α and cluster configuration J can be obtained from the expression

$$n_i^{\alpha}(E) = -(1/\pi)\,\mathrm{Im\,Tr}\,\mathsf{R}^{\alpha}[\tau^J]_{ii}, \tag{1}$$

where the supermatrix τ^J is defined by its elements

$$[\tau^J]_{ij} = \{(t_{\alpha(i)}^{-1} - t_c^{-1})\delta_{ij} + [\tau^{-1}]_{ij}\}^{-1}. \tag{2}$$

The size of the supermatrix is $N \times 2 \times (l_{\max}+1)^2$, where N is the number of atoms of the cluster and $l_{\max}$ is the maximal angular momentum quantum number used. In Eq. (2) t_α is the single site t matrix of species α and in Eq. (1) R^{α} is a matrix of radial integrals[3]

$$\mathsf{R}^{\alpha}_{QQ'} = \int Z^{\alpha}_{Q}(\mathbf{r}) Z^{\alpha}_{Q'}(\mathbf{r})\, d^3r, \quad Q = (\kappa,\mu). \tag{3}$$

The configuration-dependent DOS can now be used to calculate configuration-dependent nuclear spin-lattic relaxation rates

$$\begin{aligned}(T_1T)^{-1}_{J,\alpha} = 4\pi k_B \hbar \left(\gamma_n \frac{e}{2}\right)^2 \Bigg(&\sum_{\kappa} \frac{2j+1}{6j(j+1)} \\ &\times [n_{\kappa}^{J,\alpha}(E_F)\overline{R}^{\alpha}_{\kappa,\kappa}(E_F)]^2 \\ &+ \sum_{\kappa>0} \frac{1}{3j+1} n_{\kappa}^{J,\alpha}(E_F) n_{-\kappa-1}^{J,\alpha}(E_F) \\ &\times [\overline{R}^{\alpha}_{\kappa,-\kappa-1}(E_F)]^2\Bigg),\end{aligned} \tag{4}$$

where the $\overline{R}^{\alpha}_{\kappa,\kappa'}(E_F)$ are renormalized radial integrals according to Eq. (3.20) of Ref. 4. For further numerical details see Ref. 5.

III. RESULTS AND DISCUSSION

As the number of atoms of a particular species in a first-neighbor shell cluster varies from 0 to 12 for a fcc lattice a total of 144 configurations has to be considered. Going beyond a first shell of neighbors, the number of configurations increases dramatically. For $Cu_{50}Pt_{50}$ it can be argued[6] that

[a] Present address: Siemens AG,ZFETPH11, Paul-Gossen-Str. 100, D-8520 Erlangen, FRG.

 0021-8979/88/084130-03$02.40 © 1988 American Institute of Physics

in accordance with the CuPt structure short-range ordering seems to occur not in the first shell, but in the second shell or beyond. This particular case can easily be handled in the present approach, because by putting "effective" (CPA) atoms at the positions of the first-shell only 10 different second-shell configurations have to be considered. Including the second shell, however, implies that the size of the matrix in Eq. (2) increases from 234 for one shell to 342.

In Fig. 1 one can see that in $Cu_{50}Pt_{50}$ the effects on the Pt nuclear spin-lattice relaxation rate due to changes in the local atomic arrangement are quite pronounced. These effects are found to be large for the first-shell cluster [Fig. 1(a)] as well as for the second-shell cluster [Fig. 1(b)]. As compared to $Cu_{50}Pt_{50}$ the effects in $Cu_{71}Pt_{29}$ on the Pt relaxation rate due to changes of the configuration are much less drastic. This, of course, has to be expected since in $Cu_{71}Pt_{29}$ the Fermi level falls into the onset of the *s* band above the *d* band. It should be noted from Fig. 1 that values to the right of the CPA result are due to "likewise" ordering (segregation), whereas the values to the left incorporate the cases with "antilikewise" ordering (short-range ordering, SRO). In terms of the Warren–Cowley SRO parameters α_r, which are defined for an A atom at the center as

$$\alpha_r = 1 - n_r^B/(c_B n_r), \tag{5}$$

where n_r is the number of all the atoms in the rth shell, n_r^B that of the B atoms, and values to the right of the CPA value correspond to positive α_r and vice versa.

Figure 2 summarizes the results obtained for various "macroscopical" concentrations and compares them to the experimental ones given by Itoh, Asayama, and Kobayashi.[6] From this figure it seems that on the scale of T_1T for Cu-rich Cu_xPt_{1-x} alloys such at $Cu_{71}Pt_{29}$ local arrangement effects are of minor importance. By comparing the theoretical values with the experimental data,[7] it is evident from Fig. 2 that for Cu-rich or Pt-rich Cu_xPt_{1-x} alloys the agreement is excellent. Unfortunately in Ref. 6 no account is given of how the samples were prepared. It is therefore difficult to comment on the fact that for $Cu_{50}Pt_{50}$ the experimental value is considerably below the CPA value in the regime of segregation.

By approximating the DOS for the long-range ordered state in $Cu_{50}Pt_{50}$ by a two-shell cluster corresponding to the occupations in the CuPt structure, one effectively includes also a third shell, since this third shell contains in the ordered structure six atoms of each kind.[5] This situation is well represented by the embedding CPA medium. Together with the DOS for the statistically disordered case (CPA) this approximated DOS for the ordered case can be compared to the experimental values for the linear coefficient of the specific heat γ. The coefficient γ is predicted by the calculations to change from 1.34 to 1.08 mJ/K^2 mol due to ordering. This result is in nice agreement with the experimental findings for disordered[7,8] (1.59 mJ/K mol) and ordered[7] (1.03 mJ/K mol) CuPt alloys.

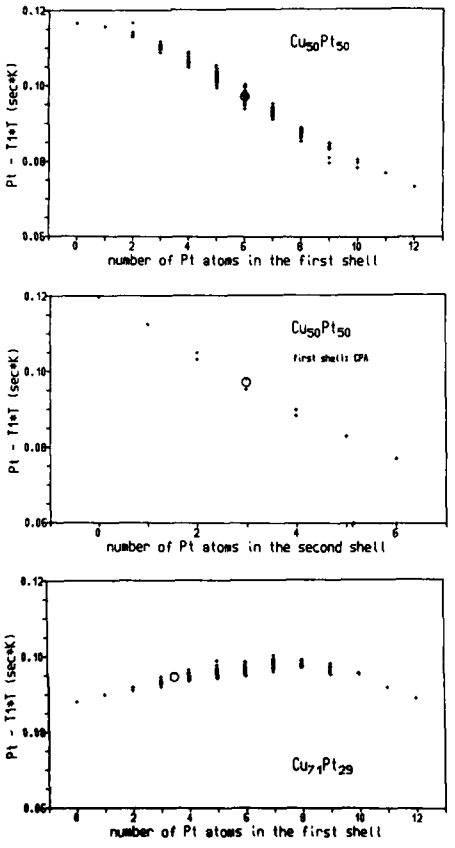


FIG. 1. Pt nuclear spin-lattice relaxation rate in Cu_xPt_{1-x} for various atomic configurations. The crosses represent the possible configurations, while the circles give the CPA results. (a) Pt in $Cu_{50}Pt_{50}$ with the occupation of the first-neighbor shell varied. (b) Pt in $Cu_{50}Pt_{50}$ with the occupation of the second-neighbor shell varied and CPA atoms in the first shell. (c) as for (a) but for $Cu_{71}Pt_{29}$.

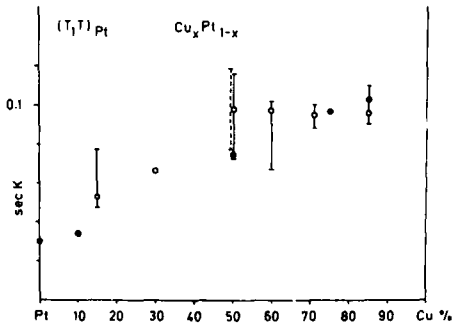


FIG. 2. Pt nuclear spin-lattice relaxation rate in Cu_xPt_{1-x}; solid circles: experiments (Ref. 7); open circles: KKR-CPA results; solid bars: range of variation due to changes of configuration in the first-neighbor shell; dashed bar: range of variation due to changes of configuration in the second-neighbor shell.

ACKNOWLEDGMENT

One of us (J.B.) would like to acknowledge financial support by the Deutsche Forschungsgemeinschaft (DFG).

[1]P. Weinberger, R. Dirl, A. M. Boring, A. Gonis, and A. J. Freeman, Phys. Rev. B 37, 1383 (1988).
[2]J. Staunton, B. L. Gyorffy, and P. Weinberger, J. Phys. F 10, 2665 (1980).
[3]P. Weinberger, J. Staunton, and B. L. Gyorffy, J. Phys. F 12, 2229 (1982).
[4]H. Ebert, P. Weinberger, and J. Voitländer, Phys. Rev. B 31, 7566 (1985).
[5]J. Banhart, P. Weinberger, H. Ebert, and J. Voitländer, Solid State Commun. 65, 693 (1988).
[6]J. Itoh, K. Asayama, and S. Kobayashi, Proc. Coll. Ampere 13, 162 (1964).
[7]D. L. Martin, Phys. Rev. B 17, 1674 (1978).
[8]B. Roessler and J. A. Rayne, Phys. Rev. 136, A1380 (1964).

Crystal/chemical structures and magnetic properties of naturally occurring $Mn_{1.7}Fe_{1.3}O_4$

B. J. Evans, W. R. Dunham, C. Porter, and S. M. Abernathy
Department of Chemistry, University of Michigan, Ann Arbor, Michigan 48109-1055
C. Bluncson
Spelman College, Atlanta, Georgia 30314

An unusually pure $Mn_xFe_{3-x}O_4$ sample ($x \cong 1.3$) from a regionally metamorphosed ore body is expected to exhibit an approach to thermodynamic equilibrium unattainable in synthetic materials. This expectation is confirmed by the observation of (1) a small tetragonal distortion and (2) a complete ordering of Fe on the B sublattice. ^{57}Fe Mössbauer spectra, obtained at 298, 175, 125, and 92 K and in an external field of 30 kG at 92 K, exhibit magnetic hyperfine splitting requiring the fitting of two subspectra, I and II. At 298 K, $H_{eff} = 418$ kOe, $\alpha = 0.36$ mm s^{-1}, and $\epsilon \simeq 0$ for the more intense subspectrum I, whereas for II $H_{eff} = 403$ kOe, $\delta = 0.34$ mm s^{-1}, and $\epsilon \cong -0.15$ mm s^{-1}. The two subspectra are not split by a 30 kG external field. Subspectra I and II correspond to Fe^{3+} ions located on a single magnetic sublattice. Subspectrum II is assigned to Fe^{3+} ions in regions with locally, large tetragonal distortions as a consequence of Mn^{3+} clustering, which has often been invoked to explain the crystal chemistry and physical properties of $Mn_xFe_{3-x}O_4$.

INTRODUCTION

Among the spinel ferrites, the $Mn_xFe_{3-x}O_4$ system, for $1 < x \leq 3$, is perhaps equaled only by Fe_3O_4 (Ref. 1) in the challenges it has presented to the development of a comprehensive description of its structure, properties, and their interrelationships.[2] Thus, notwithstanding the large body of previous works, the crystal chemistry, and electrical and magnetic properties of $Mn_xFe_{3-x}O_4$ are of current interest.[3] The principal obstacle in and between investigations of this system is the difficulty in achieving equilibrium among a number of interrelated processes. For example, the occurrence of the tetragonal distortion is determined not only by the achievement of equilibrium in the cation distribution of the Mn and Fe ions but also by the approach to equilibrium of redox processes among the $+3$ and $+2$ oxidation states of Fe and Mn and by electron transfer processes which can occur at temperatures too low for the concomitant changes in atomic positions necessary for thermodynamic equilibrium. Therefore, the availability of a naturally occurring $Mn_xFe_{3-x}O_4$ sample from a setting suggesting a high degree of thermal equilibration has generated this study as the investigation of this sample might provide a unique opportunity to further our understanding of the $Mn_xFe_{3-x}O_4$ system. This is a report of some of our studies of this mineral which is known as iwakiite.[4]

The close approach of the crystal/chemical structures in this sample to thermodynamic equilibrium is indeed demonstrated by (1) the observation of a tetragonal distortion at a manganese content lower than that for any tetragonally distorted synthetic sample, (2) an ordering of Fe^{3+} exclusively on the B sites, and (3) compelling evidence for Mn^{3+} clustering.

EXPERIMENT

The iwakiite specimen used in this study comes from the Type locality, Gozaisho Mine, near the city of Iwaki, Japan.[4] The iwakiite occurs in a regionally metamorphosed ore deposit in which the mineral assemblage indicates formation temperatures between 675 and 975 K and pressures between 0.4 and 0.8 GPa, conditions appropriate to the medium pressure epidote-amphibolite metamorphic facies.[5] The regional basis of the metamorphism leading to this occurrence of iwakiite indicates heating and cooling rates much lower than those obtainable in a laboratory synthesis, a more facile mass exchange between solid and vapor phases,[4,6] and hence, greater opportunities for attaining equilibrium crystal/chemical structures.

Chemical analysis of iwakiite from the Gozaisho Mine was performed by earlier investigators and the composition was found to be $Mn_{1.644}Fe_{1.278}Mg_{0.035}Al_{0.014}Ti_{0.009}O_4$. As ions other than Fe and Mn are present at less than 0.1 atoms per AB_2O_4 formula unit, the composition of this specimen may be given to a good approximation as $Mn_{1.7}Fe_{1.3}O_4$.

X-ray powder diffraction was performed using Cu$K\alpha$ radiation and a powder diffractometer. After repeated grinding with an agate motor and pestle, ultrasonic dispersal and separation with a hand magnet, a pure iwakiite specimen with a particle size less than 50 μm was mixed with a silicon internal standard and the following lattice constants were determined from the (404) and (440) lines: $a_0 = 0.8514$ nm and $c_0 = 0.8552$ nm ($c/a = 1.004$), in good agreement with previous values.[4]

The techniques for obtaining[7,8] and analyzing the Mössbauer spectra have been reported in detail elsewhere. The only aspect worthy of note here is the higher resolution of the room-temperature spectra (512 data points) relative to the low-temperature spectra (256 data points).

RESULTS AND DISCUSSION

The ^{57}Fe Mössbauer spectra are shown in Figs. 1 and 2. In Fig. 1 the data (points) are shown with the results of a single hyperfine pattern fit (solid line). The inadequacy of

 0021-8979/88/084133-03$02.40 © 1988 American Institute of Physics

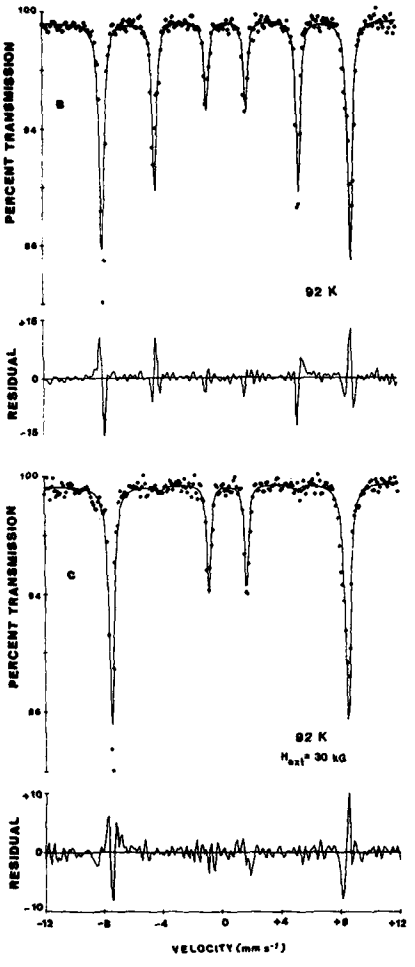


FIG. 1. ^{57}Fe Mössbauer spectra of iwakiite at (a) 92 K and (b) 92 K, and in an externally applied field of 30 kG. The points are the experimental data and the solid line is the fit of a *single* hyperfine pattern to the data. The RESIDUAL is the difference between the data and the fitted pattern. The large amplitude of and considerable structure in the RESIDUAL are to be noted.

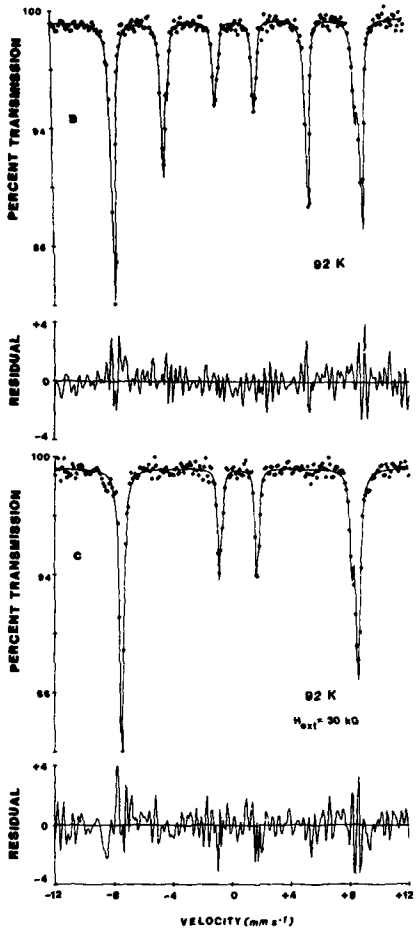


FIG. 2. Same as Fig. 1 except that the solid line now represents a fit of *two* hyperfine patterns to the data. Comparison with Fig. 1 shows a considerable reduction in the amplitudes of the RESIDUAL and a randomization of the structure in the RESIDUAL.

this fitting scheme is clearly evidenced in the pronounced structure in the plots of the difference between the data and the fitted pattern, e.g., the RESIDUAL, and in the maximum excursions in magnitude of the RESIDUAL at individual points which is 4–5 times that expected. Further, the structure in the RESIDUAL indicates the presence of another hyperfine pattern. Therefore, the spectra were fitted to two hyperfine patterns and the results are shown in Fig. 2. The improvement in the fits is clearly evidenced in the close correspondence between the data and fits, especially for the line near $+8$ mm s^{-1}, in the reduction of the magnitude of the RESIDUAL, and in the randomization in the structure of the RESIDUAL. The hyperfine parameters resulting from the two pattern fits are given in Table I.

Irrespective of how the data are fitted, it is clear that the applied, longitudinal magnetic field of 30 kG occasions no additional splitting of the spectrum even though the sample is magnetically saturated [see Figs. 1(c) and 2(c)]. If Fe occupied the A and B sites of the spinel structure, a splitting of the spectrum into two distinct components would be expected.[9] The application of the external field leads to a reduction of H_{eff} for subspectra I and II, and the Fe^{3+} ions are, therefore, located on the B sites.[9] Thus, with respect to the iron cation distribution, this manganese ferrite is highly ordered.

The observation of a bulk tetragonal distortion provides further evidence of the high degree of thermal equilibration

TABLE I. ^{57}Fe Mössbauer parameters of iwakiite at several temperatures and in an applied magnetic field.

Temperature	Subspectrum	H_{eff} (kOe)	ϵ (mm s^{-1})	$\Delta(\delta)^a$ (mm s^{-1})	Integrated intensity
298 K	I	418 (4)[b]	0.03 (2)		85
				003 (1)[c]	
	II	403 (3)	−0.15 (3)		15
175 K	I	480 (1)	0.07 (1)		67
				0.018 (6)	
	II	467 (1)	−0.13 (2)		33
125 K	I	498 (1)	0.06 (1)		67
				−0.004 (4)	
	II	486 (1)	−0.12 (1)		33
92 K	I	507 (1)	0.05 (1)		75
				0.005 (5)	
	II	495 (1)	−0.15 (1)		25
92 K	I	481 (1)	0.05 (1)		75
				−0.002 (3)	
H_{ext} = 30 kG	II	469 (1)	−0.15 (1)		25

[a] $\Delta(\delta) = \delta_{IS}(I) - \delta_{IS}(II)$.
[b] Number in parentheses indicates error in last digit of reported values.
[c] Relative to an iron metal absorber, $\delta(I) = 0.365(1)$ and $\delta(II) = 0.339(8)$ at 298 K.

in this sample. The cubic-tetragonal phase boundary at 300 K had been placed previously at $x \approx 1.9$ in $Mn_xFe_{3-x}O_4$ (Ref. 10) and only noncooperative local distortions were proposed for a synthetic sample with an x value of 1.66.[11] In contrast, the tetragonally distorted iwakiite indicates that the equilibrium, cubic-tetragonal phase boundary is closer to an x value of ~ 1.7.

It now remains to provide some insights into the nature of the iron sites giving rise to subspectra I and II. The difference in δ is not statistically significant and is in all likelihood an artifact of the fitting scheme that treats δ as a free variable. The quadrupole interaction is significant and indicates that the iron species of subspectrum II is subject to a much larger field gradient and presumably larger site distortion than that of subspectrum I. It is proposed that the greater local site distortion results from a clustering of Mn^{3+} ions in the vicinity of the Fe^{3+} species of subspectrum II. The occurrence of an Fe^{3+} ion in a cluster of Mn^{3+} ions would lead to a decrease in the magnitude of H_{eff}[12,13] in good accord with the relative magnitudes of H_{eff} (I) and H_{eff} (II).

CONCLUSION

In comparison with synthetic samples, the expectation of a closer approach to thermodynamic equilibrium of the crystal/chemical structures of a manganese ferrite (iwakiite) occurring under the pressure, temperature, and time conditions of regional metamorphism has been confirmed. The Fe^{3+} ions occur exclusively on the octahedral (B) site. The x value in $Mn_xFe_{3-x}O_4$ at the cubic-tetragonal phase boundary is also lowered to ~ 1.7 in this naturally occurring sample. Convincing evidence for Mn^{3+} clustering is also provided by ^{57}Fe Mössbauer spectroscopy.

[1] R. J. Rasmussen, R. Aragon, and J. M. Honig, J. Appl. Phys. **61**, 4395 (1987) and references therein.
[2] F. K. Lotgering and A. M. van Diepen, J. Phys. Chem. Solids **34**, 1369 (1973) and references therein.
[3] V. A. M. Brabers, Y. G. Proykova, N. Salerno, and T. E. Whall, J. Appl. Phys. **61**, 4390 (1987).
[4] S. Matsubara, A. Kato, and K. Nagashima, Mineral. J. **9**, 383 (1979).
[5] A. Miyashiro, *Metamorphism and Metamorphic Belts* (Halsted, New York, 1973), pp. 61–71, 304–308.
[6] A. Miyashiro, *Metamorphism and Metamorphic Belts* (Halsted, New York, 1973), pp. 22–28.
[7] W. R. Dunham, C. T. Wu, R. M. Polichar, R. H. Sands, and L. J. Harding, Nucl. Instrum. Methods **145**, 537 (1977).
[8] B. J. Evans, F. Grandjean, A. P. Lilot, R. H. Vogel, and A. Gerard, J. Magn. Magn. Mater. **67**, 123 (1987).
[9] B. J. Evans, J. Phys. Chem. Solids **29**, 1573 (1968).
[10] H. M. O'Bryan, Jr. and H. J. Levinstein, J. Phys. Chem. Solids **30**, 1719 (1969).
[11] L. Cervinka, R. Hosemann, and W. Vogel, Acta Crystallogr. A **26**, 277 (1970).
[12] B. J. Evans and L. J. Swartzendruber, Phys. Rev. B **8**, 223 (1972).
[13] F. van der Woude and G. A. Sawatzky, Phys. Rev. B **4**, 3159 (1971).

Microwave solitons in magnetic garnet films (invited)

P. De Gasperis, R. Marcelli, and G. Miccoli
Istituto di Elettronica dello Stato Solido del Consiglio Nazionale delle Ricerche, Via Cineto Romano 42, 00156 Roma, Italy

This work concerns some recent results on the excitation of solitons at microwave frequencies in planar magnetic films. In particular, yttrium iron garnet (YIG) possesses the intrinsic properties of dispersion and nonlinearity required for a system to support such a kind of waves. In this framework, experimental results on a novel nonlinear effect, related to the propagation at about 7 GHz of magnetostatic volume waves in YIG films having thicknesses ranging between a few microns to more than 100 μm, have been interpreted in terms of a solitonic excitation process. By starting from those findings, this paper presents an analysis of the experimental aspects as a function of the various parameters involved (i.e., thickness, frequency, wave vector, and so on) together with a concise discussion with respect to the presently available theoretical approaches.

INTRODUCTION

Formally, a soliton is defined as a traveling solitary wave which preserves its shape and velocity also after a collision with another soliton, the only possible consequence of a mutual interaction being a phase shift.[1] Such a definition does not include dissipation in the medium which, however, in some cases strongly affects the propagation characteristics. In practice, at least a small dissipation effect does exist, but it is negligible when compared to dispersive and nonlinear terms. In fact, a balance between the dissipation and nonlinearity could generate solitary waves but not solitons in the absence of dispersion.[2]

In common practice, it is not always possible to achieve suitable materials that satisfy the condition of a sufficiently low dissipation. For instance, in the case of transparent media, low-loss optical fibers had to be fabricated before the propagation of light solitons could become experimentally feasible.[3] Apart from the interest in the basic research, the above successful result has been the starting point for the development of a wide variety of remarkable applications in optical signal processing, such as the outstanding case of the soliton laser.[4]

In principle, some systems in the field of acoustic and radio-frequency signal transmission also exhibit peculiar features to support soliton excitation. In particular, magnetic films such as yttrium iron garnet (YIG) or some other substituted compositions qualitatively possess properties of nonlinearity, dispersion, and low magnetic damping which appear appropriate to support the propagation of solitons at microwave frequencies through the utilization of magnetostatic waves (MSW's). In fact, as is well established, magnetostatic waves are inherently dispersive slow electromagnetic waves[5] which are generated in a magnetic garnet (or ferrite) chip polarized by an external dc field H_0. Depending on the direction of H_0 with respect to the film plane, three different kinds of MSW's can be excited: (1) forward volume (MSFVW's), (2) backward volume (MSBVW's), and (3) surface waves (MSSW's). They exhibit different properties of dispersion as a function of frequency (for example, "up-chirp" trend for MSFVW's and "down-chirp" trend for MSBVW's) which make them suitable for several applications as delay lines[6] in microwave signal processing. Furthermore, MSW's are also nonlinear, owing to the intrinsic nonlinearity in the motion equation of the microwave magnetization (Landau–Lifschitz approach[7]). However, in the standard derivation of the dispersion relation,[8] the nonlinearity is assumed to be small and hence negligible with respect to the linear terms. For practical purposes, the validity of the above first-order approximation holds until input power levels of about some mW in a continuous-wave (CW) regime for volume magnetostatic waves.[9] Above that, the nonlinear contribution is no longer negligible and, consequently, a severe limitation of the rf pulsed signal starts to take place.

From a theoretical standpoint, owing to the wide spectrum of physical situations in which soliton propagation can be involved, several mathematical models are available to describe the phenomenon. In spite of different starting points, however, common features among them are the balancing between the contribution due to the dispersion, commonly quantified as a second- (or higher-) order derivative of the wave function with respect to the propagation direction, and the contribution due to the nonlinearity, commonly depending on a power expansion of the wave function. For instance, the so-called sine-Gordon equation has been particularly successful in figuring out the behavior of unidimensional magnetic systems.[10]

In the present case, owing to the particular shape of the starting magnetic equations, the approach based on the nonlinear Schrödinger equation (NLSE)[11] seems to be the most appropriate to describe the physical environment. In this

 0021-8979/88/084136-05$02.40 © 1988 American Institute of Physics

way, expected threshold powers for the onset of self-modulation and self-channeling of initial wave forms (pulses), which eventually develop into solitons, can be derived in a dipolar approach.[12]

EXPERIMENT

In the framework of microwave signal propagation, some nonlinear phenomena deduced by analyzing the time envelope of an output pulsed signal have been recently interpreted in terms of multisoliton excitation. In order to experimentally achieve that result, garnet films characterized by comparable dipolar and exchange energies have been exploited. In order to satisfy the conditions of balancing between the nonlinearity and the dispersion, it has been found that the operational frequency had to fall within a discrete number of well-defined regions of the magnetoexchange spectrum, close to the so-called repulsion gaps.[13] In fact, experimentally resolvable gaps can be observed whenever some specific values of spin pinning at the film surfaces are obtained for thicknesses not exceeding 5–6 μm (i.e., the thinner the film, the higher the gap resolution).[14] In the experiment of Kalinikos and co-workers,[13] no soliton excitation has been observed for operational frequencies falling outside the repulsion gaps.

Dissimilarly to the procedures of the above measurements, here the detection and analysis of the output signal envelope in the time domain is not considered a technique capable of achieving unambiguous results. In fact, mainly owing to its limited operational bandwidth, an MSW dispersive delay line (DDL) introduces an amplitude modulation[15] of an rf pulsed signal passing through it. Such a modulation is higher when narrow-band microstrips are adopted to launch and to receive the signal, as is done in the present case. For example, for an MSW device characterized by a passband of about 100–150 MHz at 10 GHz, the presence of several modulation side lobes hinders and confuses the detection of possible satellite peaks peculiar to a multisoliton excitation. Consequently, the time-domain measurement technique has been excluded here and the nonlinear behavior of the MSW DDL has been investigated by looking at its power response, namely, by measuring the peak output power (P_{out}) as a function of the peak input power (P_{in}). Furthermore, films thicker than 6 μm have been utilized to check the possibility of nonlinear wave excitation in the pure dipolar regime, thus avoiding the exchange interaction contribution. A schematic drawing of the experimental apparatus utilized in the present series of measurements is shown in Fig. 1.

Another important step is to avoid the generation of saturated power responses induced by standard nonlinear processes such as the interaction of MSW's with spin-wave manifold (second-order Suhl process)[16]; for this reason, in the present work, only magnetostatic volume waves have been exploited.

To give a deeper insight, a schematic drawing of a simple two-port DDL used to generate MSFVW's is sketched in Fig. 2, where the dc field H_0 is placed normal to both the chip surface and the propagation wave vector. According to standard procedures, two matched microstrips are evaporated

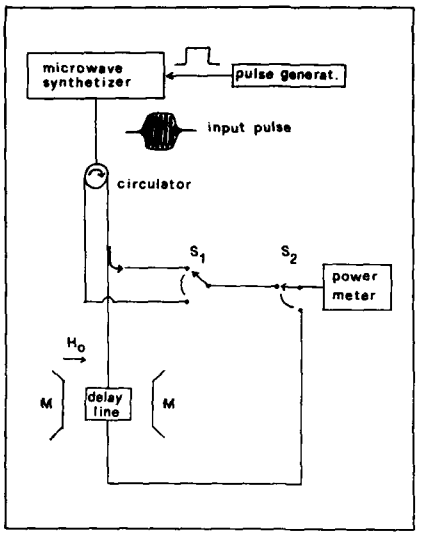


FIG. 1. Experimental setup. In this configuration, well-shaped radio-frequency pulses as short as 20 ns can be launched.

onto a grounded alumina substrate and a rectangular garnet chip is placed on them. One transducer is the launcher and the other one is the receiver of the device. Specifically, 10-mm-distant 50-Ω-matched microstrips, evaporated on a 254-μm-thick alumina substrate, are utilized. As the operational frequency is around 7 GHz, the constant dc field is about 4200 Oe. As mentioned, such a choice is due to the fundamental requirement to cut off any other source of nonlinear effects, especially the interaction with spin-wave manifold. In fact, the work frequency falls definitively outside the region of overlapping between magnetostatic volume waves and half-frequency exchange spin waves (see Fig. 3) where a drastic limitation of the signal[17] output takes place. On the contrary, if the configuration to excite MSSW's is used, signal saturation due to the above mechanism occurs even at a rather low power level (i.e., about -20 dBm),thus masking the possible presence of other nonlinear effects in that power range.

As a preliminary check, the power response to a CW input signal has been analyzed. According to previous analogous measurements,[18] the relative trend is found to be linear

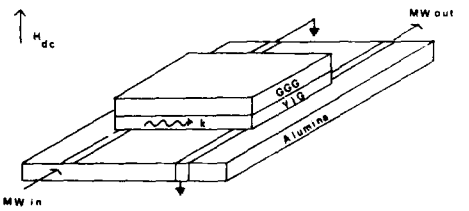


FIG. 2. Schematic drawing of a typical configuration for a dispersive delay line utilizing MSFVW's.

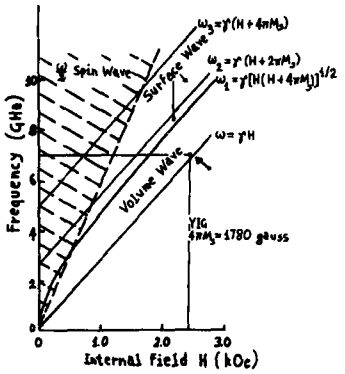


FIG. 3. Graphic representation of the operational internal magnetic field and frequency (black arrow) within the limits of MSW propagation and existence of $\omega/2$ spin waves, as taken from Fig. 1 of Ref. 17.

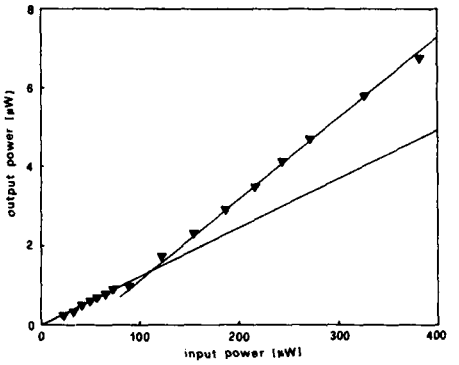


FIG. 4. Typical power response nonlinear above a certain threshold suggesting the existence of microwave soliton. In this specific case, a 32-μm-thick YIG film has been exploited. The operational frequency was 7 GHz (i.e., $H_0 = 4.20$ kOe) and the pulse length $t_p = 30$ ns.

up to input values of the order of 15 mW above which the output signal starts to appear saturated. When pulsed signals are launched, the same linear response is always reobtained whenever the pulse length t_p is of the same order or higher than the characteristic delay time T_d. When pulses shorter than T_d are exploited, the response starts to be nonlinear above a defined threshold power (P_{thr}) of the order of some hundred of μW or less, where the measured output power is found to be *greater* than that expected from the extrapolation of the initial linear trend. Such a peculiar behavior is shown in Fig. 4 for a 32-μm-thick YIG film and for a pulse length of 30 ns ($t_p < T_d = 65$ ns).

The depicted power trend is opposite to what is observed when a signal limitation[17] occurs; thus, standard nonlinear mechanisms such as interaction with spin-wave manifold,[16] multimagnon or multiphonon confluence,[19] can be definitively excluded as origins of the phenomenon.

THEORY AND COMPARISON

The experimental finding of Fig. 4 (and analogous results for different films and pulse lengths), suggests that the loss reduction measured above the threshold power is quantitatively comparable with the intrinsic propagation loss of the material. In fact, the total insertion loss affecting the rf pulsed signal passing through the measurement setup and the device is due to both mismatch and propagation loss. The former one is related to various technical reasons such as matching of transducers, dissipation on cables and connectors, and so on, and it is inherently independent on the nature of the input pulse. On the other hand, the propagation loss is correlated to the intrinsic properties of the exploited film, namely delay time and magnetic damping, according to the simple relation (given in dB):

$$P_L = 10 \log_{10} [\exp(-\gamma \Delta H T_d)] , \qquad (1)$$

where γ is the gyromagnetic ratio (in $\text{Oe}^{-1}\,\text{s}^{-1}$), ΔH is the ferromagnetic resonance (FMR) full linewidth (in Oe), and T_d is the characteristic delay time (in s). In this picture, the observed nonlinear effect can be interpreted in terms of a *decrease* of the propagation loss inside the magnetic film for input power larger than the threshold value P_{thr} by invoking a mechanism of self-induced transparency.[20]

Such an effect was discovered and studied in a resonant medium for a short pulse of coherent optical radiation which, under proper conditions, was found to propagate without attenuation (from that, the use of the term "transparency"). The basic physical concept is that a pulse whose duration t_p is much shorter than the typical relaxation time τ_r of the material does not lose energy as dissipation processes cannot be activated. Above a well-defined threshold, power is absorbed by the medium during the first half of the pulse and given back during the second half.

The above picture is rigorously valid only for $t_p \ll \tau_r$ but, provided that the dissipation be properly accounted for [as in Eq. (3) and related discussion], it maintains its validity up to $t_p \lesssim \tau_r$. For $t_p > \tau_r$, the system loses energy according to the standard linear damping mechanism.

In some previous works, it has been shown that the self-induced transparency effect is related to a soliton formation process. The theoretical treatment has been developed for short electric field pulses by (i) combining the Maxwell and Bloch equations and (ii) noting that the pulse envelope is described by a wave slowly varying with the time and the distance (frequency and wave-vector modulation).

The solutions of the Bloch equations obtained by the above method break into a sequence of solitary waves which have the properties of solitons[21]; these theoretical results have been successively confirmed by experimental findings.[21,22] As is well established, the Bloch equations have the same formalism for the electric[20] and magnetic[23] fields behavior. Thus, the analogous treatment can be straightforwardly exploited for the magnetic-dipole moments as well as for the electric ones.

The relaxation time of a garnet system is evaluated by its resonance full linewidth ΔH and it is defined by $\tau_r = 2/(\gamma \Delta H)$. The linewidth for the utilized samples ranges from 0.3 to 1 Oe, consequently τ_r varies between 114

and 380 ns, well above the pulse durations during the experiment, which do not exceed 60 ns.

The other condition to be satisfied is that t_p must be less than the delay time T_d. If $t_p > T_d$ the soliton cannot be formed, as the spatial length of the pulse is greater than the physical dimensions of the system, and the spins are not relaxed by the second half of the pulse in a time useful to appreciate a propagation loss reduction. In this way, the spin system practically "sees" a CW signal with a consequent linear behavior.

For a given pulse duration t_p and peak power P_{in}, the pulse loses energy from $t = 0$ up to $t = t_p$ owing to the damping contribution related to the fact that $t_p \lesssim \tau_r$. If the remaining part of the pulse area (i.e., the energy available at $t = t_p$) is greater than the required energy threshold, the input pulse generates a soliton which is detected at the output as a decrease of the propagation loss.

Owing to the bidirectionality of the transducers, the delay line configuration shown in Fig. 2 does not allow the creation of one soliton at a time. Hence, we can figure out a "plus" soliton going directly to the output of the device, and a "minus" soliton bouncing on the film end nearest to the launcher. However, the energy of the minus wave is partially recaptured by the input microstrip, thus remaining under the needed threshold value. Eventually, the plus soliton gives the unique effective contribution to the measured loss reduction.

In the assumption that a soliton propagates loss less, the above picture can be quantified as follows. The output power in the linear and nonlinear region is written, respectively,

$$P_{out}^{(L)} = P_{in} \exp\left[-(\Gamma + \gamma \Delta H T_d)\right] \quad \text{for } P < P_{thr},$$

$$P_{out}^{(NL)} = P_{in} \exp\left[-(\Gamma + \gamma \Delta H T_d)\right] \exp(+D) \quad \text{for } P > P_{thr}, \quad (2)$$

where

$$D = \gamma \Delta H (T_d - t_p) \quad (3)$$

is the factor of the reduction of the propagation loss due to the soliton excitation above the threshold, and Γ is the mismatch loss of the device.

To test the assumption that the loss reduction is due to a vanishing (or, at least, a reduction) of the propagation loss, the D values inferred by Eq. (3) by means of experimental determinations of ΔH and T_d have been compared with the slope variations deduced from several plots similar to those of Fig. 4. The rather good agreement[24] found in the comparison of those two sets of D-factor values seems to confirm the validity of the soliton hypothesis. Five pure YIG films having thickness ranging between 9 and 107 μm have been analyzed. They had been grown under different conditions (growth temperatures and melt compositions) and, consequently, are characterized by different FMR full linewidths. Furthermore, their delay response depends on the thickness (besides the bias conditions and the work frequency).[8,25] Due to the above reasons, the (average) D factor varies from 1.04 to 0.36, which is equivalent to an increase of the power output of about 2–4 dB with respect to that expected in the linear regime. In the same time, the measured value of the threshold power (which is also function of the pulse length) ranges from ≈ 400 to $\approx 10\mu$W.

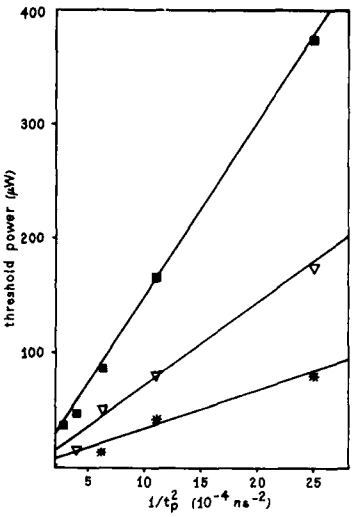


FIG. 5. Experimental values of threshold power (in μW) as a function of the inverse squared pulse length t_p^{-2} for films having thickness of 9 μm (full squares), 32 μm (open triangles), and 107 μm (asterisks), respectively.

Concerning a (possible) analytical description of the motion of magnetostatic solitons, recently the nonlinear Schrödinger equation (NLSE) has been proposed as the most suitable candidate. By starting from the MSW dispersion relation (which implicitly relates the angular frequency ω to the wave vector k), a functional variation on ω and k is introduced to achieve a proper operator to apply to the amplitude of the magnetostatic wave function φ. Physically, φ represents the potential function of the amplitude of the microwave magnetization $\mathbf{m}$ normalized by the saturation magnetization M_s. By standard mathematics, a NLSE is inferred from which the threshold power values can be calculated.[12,26] The development is quite straightforward,[20,21] but a reasonable comparison between theory and experiment can be done only by having a correct evaluation of the fraction of input power which actually enters into the YIG film and by accounting for both boundary effects[27] and beam steering.[27,28] Nevertheless, the theory gives the correct order of magnitude for P_{thr} values and, as verified in a recent work,[24] a linear dependence on t_p^{-2} has been found to fit the experimental trends (see Fig. 5 for film thicknesses of 9, 31, and 107 μm, respectively).

ACKNOWLEDGMENTS

The authors are indebted to A. Paoletti for the encouragement and help. This work has been performed in the framework of a joint cooperation between Consiglio Nazionale Ricerche and Selenia S.p.A. (which has supported the work of R. M.) and also supported by the P. F. "M.A.D.E.S.S."of CNR.

[1]A. C. Scott, F. Y. F. Chu, and D. W. McLaughin, Proc. IEEE **61**, 1443 (1973).
[2]V. I. Karpman, *Nonlinear Waves in Dispersive Media* (Pergamon, New York, 1973).
[3]L. F. Mollenauer, R. H. Stolen, and J. P. Gordon, Phys. Rev. Lett. **45**, 1095 (1980).
[4]L. F. Mollenauer and R. H. Stolen, Opt. Lett. **9**, 13 (1984).
[5]W. S. Ishak and K. W. Chang, Hewlett-Packard J. **2**, 10 (1985).
[6]M. R. Daniel, J. D. Adam, and T. W. O'Keeffe, in Proceedings of the 1979 Ultrasonics Symposium, IEEE Cat. No. CH1472-9/79/0000-806, p. 806.
[7]L. Landau and E. Lifshitz, Phys. Z. Sowjetunion **8**, 153 (1935).
[8]R. W. Damom and J. R. Eshbach, J. Phys. Chem. Solids **19**, 308 (1961).
[9]P. R. Emtage and S. N. Stitzer, IEEE Trans. Microwave Theory Tech. **MTT-25**, 210 (1977).
[10]J. Rubinstein, J. Math. Phys. **11**, 258 (1970).
[11]V. E. Zakharov and A. B. Shabat, Sov. Phys.—JETP **34**, 62 (1972).
[12]A. K. Zvezdin and A. F. Popkov, Sov. Phys.—JETP **57**, 350 (1983).
[13]B. A. Kalinikos, N. G. Kovshikov, and A. N. Slavin, Sov. Phys.—Solid Stat. **27**, 226 (1985); A. Kalinikos, N. G. Kovshikov, and A. N. Slavin, JETP Lett. **38**, 413 (1983).
[14]For a wide review on this subject, see C. Patton, Phys. Rep. **103**, 253 (1984).
[15]See, for example, W. Faber, Electron. Lett. **16**, 452 (1980).
[16]H. Suhl, J. Phys. Chem. Solids **1**, 209 (1957).
[17]J. D. Adam, IEEE Trans. Magn. **MAG-21**, 1794 (1985).
[18]N. D. J. Miller, Electron. Lett. **12**, 467 (1976).
[19]C. W. Haas and H. B. Callen, in *Magnetism I*, edited by G. T. Rado and H. Suhl (Academic, New York, 1963), p. 450.
[20]S. L. McCall and E. L. Hahn, Phys. Rev. Lett. **18**, 908 (1967); Phys. Rev. **183**, 457 (1969).
[21]H. M. Gibbs and R. E. Slusher, Phys. Rev. Lett. **24**, 638 (1970).
[22]C. K. N. Patel and R. E. Slusher, Phys. Rev. Lett. **19**, 1019 (1967).
[23]See, for example, B. Lax and K. J. Button, *Microwave Ferrites and Ferrimagnetics* (McGraw-Hill, New York, 1962), Chap. 4.
[24]P. De Gasperis, R. Marcelli, and G. Miccoli, Phys. Rev. Lett. **59**, 481 (1987).
[25]P. Wahi and Z.Turski, IEEE Trans Microwave Theory Tech. **MTT-30**, 2031 (1982).
[26]P. De Gasperis, R. Marcelli, and G. Miccoli, these proceedings.
[27]R. e. Floyd and J. C. Sethares, J. Appl. Phys. **55**, 2515 (1984).
[28]S. H. Talisa, P. R. Emtage, M. R. Daniel, and J. D. Adam, IEEE Trans. Magn. **MAG-22**, 856 (1986).

One-dimensional Dzyaloshinski–Moriya antiferromagnets in an applied field

Qing Xia and Peter S. Riseborough
Department of Physics, Polytechnic University, 333 Jay Street, Brooklyn, New York 11201

We examine the one-dimensional antiferromagnet, with a small Dzyaloshinski–Moriya component to the exchange, in a symmetry-breaking magnetic field. In the classical, continuum limit, this system is shown to obey a double sine-Gordon field theory which supports nonlinear, soliton excitations as well as linear, spin waves. We examine the dynamic spin-spin correlation function. We find the contributions coming from the nonlinear soliton excitations and the contributions from the quantized linear excitations. The quantized spin waves produce nonlinear contributions to the correlation functions that exhibit qualitative similarities to the soliton contributions.

I. INTRODUCTION

Recently, there has been a growing interest in the dynamics of nonlinear systems. This interest has spurred on investigations of low-dimension magnetic systems, since these provide almost ideal testing grounds of nonlinear field theory. The main advantages of low-dimensional magnets are twofold: The role of the nonlinearities are enhanced at low temperatures, since the low dimensionality favors the occurrence of large amplitude fluctuations yet suppresses long-range ordering. Secondly, magnetic systems are usually well characterized by Hamiltonians that contain only one or two parameters that can be fixed by experiment. This simple description also includes the advantage offered by the possibility of applying a uniform magnetic field, which allows the predictions of the nonlinear field theories to be tested under a variety of experimental conditions.

The one-dimensional easy-plane magnets have been a subject of intensive investigations, since they have an integrable sine-Gordon field theory as their classical continuum limit. In this note we shall investigate such a system, namely a one-dimensional array of spins coupled by an antiferromagnetic Heisenberg exchange interaction and a small Dzyaloshinski–Moriya interaction. The Dzyaloshinski–Moriya interaction produces an easy plane. We then apply a magnetic field to break the spin rotational symmetry within the easy plane. The Hamiltonian of this system is

$$\hat{H} = \sum_i |J|\mathbf{S}_i\cdot\mathbf{S}_{i+1} + \sum_i (-1)^{i+1}\mathbf{D}\cdot(\mathbf{S}_i\wedge\mathbf{S}_{i+1}) - \sum_i g\mu_B\mathbf{H}\cdot\mathbf{S}_i\,.$$

For convenience, we shall take $\mathbf{D}$ to be directed along the z axis. The easy plane is then the x-y plane, and we may choose $\mathbf{H}$ to be aligned with the x axis. There exists some preliminary evidence that the above Hamiltonian may provide an appropriate description for $CuBr_2$ 2DMSO an $S=\frac{1}{2}$ antiferromagnet with $J/K_B = -13.4$ K.

In the next section, we shall show that the above system has as its classical continuum limit a double sine-Gordon field theory. We shall examine the nonlinear excitations and evaluate their contributions to the dynamic correlation function. In Sec. III, we shall show that these linear excitations provide nonlinear contributions to the correlation functions, which resemble those of the classical nonlinear excitations. In Sec. IV we shall discuss our results.

II. THE CLASSICAL CONTINUUM THEORY

We shall describe the spins of the A and B sublattices by classical vectors of length $\tilde{S}$. The polar angles of the spin $\mathbf{S}_i^A$ of the A sublattice are denoted by $(\Theta_i+\theta_i,\ \Phi_i+\varphi_i)$, whereas the spin $\mathbf{S}_i^B$ of the B sublattice are denoted by $(\Theta_i-\theta_i,\ \Phi_i-\varphi_i)$ and the direction of this vector is then reversed.

These classical variables have the Poisson brackets

$$\{\Theta_i;\Phi_i\} = \{\theta_i;\varphi_i\} = -\frac{1}{2\tilde{S}}\frac{\cos\Theta_i\sin\theta_i}{\sin^2\Theta_i-\sin^2\theta_i},$$

$$\{\theta_i;\Phi_i\} = \{\Theta_i;\varphi_i\} = \frac{1}{2\tilde{S}}\frac{\sin\Theta_i\cos\theta_i}{\sin^2\Theta_i-\sin^2\theta_i},$$

and

$$\{\Theta_i;\theta_i\} = \{\Phi_i,\varphi_i\} = 0\,.$$

After forming the equations of motion for the four variables, we Taylor expand and linearize the resulting equations treating $\partial/\partial y$, θ, and φ as quantities of the same order of smallness as $\lambda_d = D/J$ or $\lambda_h = g\mu_B H^x/2J\tilde{S}$.

We shall introduce a dimensionless time $\tau = |J|\tilde{S}t$, so the resulting equations can be written as

$$\frac{\partial\Theta}{\partial\tau} = \left[\left(4\varphi+\frac{\partial\Phi}{\partial y}\right)\sin\Theta - 2\lambda_d\sin\Theta + 2\lambda_h\sin\Phi\right],$$

$$\frac{\partial\Phi}{\partial\tau} = \left(-\frac{4\theta+\partial\Theta/\partial y}{\sin\Theta} + 2\lambda_h\cot\Theta\cos\Phi\right),$$

$$\frac{\partial\theta}{\partial\tau} = -\cos\Theta\left[4\theta\varphi+\theta\frac{\partial\Phi}{\partial y}+2\varphi\frac{\partial\Theta}{\partial y}+\left(\frac{\partial\Theta}{\partial y}\right)\left(\frac{\partial\Phi}{\partial y}\right)\right] - \sin\Theta\left(\frac{\partial\varphi}{\partial y}+\frac{1}{2}\frac{\partial^2\Phi}{\partial y^2}\right)+\lambda_d\cos\Theta\left(2\theta+\frac{\partial\Theta}{\partial y}\right) + \lambda_h\cos\Phi 2\varphi\,,$$

and finally

 0021-8979/88/084141-03$02.40 © 1988 American Institute of Physics

$$\frac{\partial\varphi}{\partial\tau} = -\cos\Theta\frac{1}{2}\left[8\varphi^2 + 4\varphi\frac{\partial\Phi}{\partial y} + \left(\frac{\partial\Phi}{\partial y}\right)^2\right] + \frac{\cos\Theta}{\sin^2\Theta}\left(4\theta^2 + \theta\frac{\partial\Theta}{\partial y}\right) + \frac{1}{\sin\Theta}\left(\frac{\partial\theta}{\partial y} + \frac{1}{2}\frac{\partial^2\Theta}{\partial y^2}\right)$$
$$+ \lambda_d\cos\Theta\left(4\varphi + \frac{\partial\Phi}{\partial y}\right) - \lambda_h\left(\frac{\cos\Phi}{\sin^2\Theta}2\theta + \cot\Theta\sin\Phi\,2\varphi\right).$$

Using these equations, we may eliminate θ and φ to obtain the energy density

$$\frac{H}{J\tilde{S}^2} = \frac{1}{4}\left[\left(\frac{\partial\Theta}{\partial\tau}\right)^2 + \left(\frac{\partial\Theta}{\partial y}\right)^2\right] - (\lambda_d^2 - \lambda_h^2)\sin^2\Theta$$
$$+ \frac{1}{4}\sin^2\Theta\left[\left(\frac{\partial\Phi}{\partial\tau}\right)^2 + \left(\frac{\partial\Phi}{\partial y}\right)^2\right]$$
$$- \lambda_h^2\sin^2\Theta\sin^2\Phi + 2\lambda_h\lambda_d\sin\Theta\sin\Phi.$$

The equations of motion have solutions which are entirely of in plane character, $\Theta = \pi/2$. The in-plane angle must then satisfy the double sine-Gordon equation,

$$\frac{\partial^2\Phi}{\partial\tau^2} - \frac{\partial^2\Phi}{\partial y^2} = 2\lambda_h^2\sin 2\Phi - 4\lambda_h\lambda_d\cos\Phi.$$

This equation possesses many interesting solutions, the most notable of these are the soliton excitations, given by

$$\sin(\Phi) + 1 = \frac{2\,\mathrm{sech}^2\,\eta}{1 - \lambda_h/(\lambda_h + \lambda_d)\tanh^2\eta},$$

where

$$\eta = [2(y - v\tau)]/\sqrt{1 - v^2}\,[\lambda_h(\lambda_h + \lambda_d)]^{1/2}.$$

The soliton has an activation energy of

$$E_s(v) = \frac{4|J|\tilde{S}^2}{\sqrt{1 - v^2}}\left[[\lambda_h(\lambda_d + \lambda_h)]^{1/2} + \frac{\lambda_d}{2}\ln\left(\frac{\lambda_d + 2\lambda_h + 2[\lambda_h(\lambda_h + \lambda_d)]^{1/2}}{\lambda_d}\right)\right].$$

Near $q \simeq 2\pi$, the dominant soliton contribution to the quasielastic portion of the dynamic spin-spin correlation function is given by

$$S^{yy}(q,\omega) = \frac{n_s}{4\pi K_1(\beta E_s(0))}\frac{\exp[-\beta E_s(\omega/q^*c)]}{\sqrt{1 - (\omega/q^*c)^2}q^*c} \times \left(\frac{(\pi\tilde{S}/\lambda_h)\sin\left\{q^*\sqrt{1 - (\omega/q^*c)^2}\ln b/4[\lambda_h(\lambda_h + \lambda_d)]^{1/2}\right\}}{\sinh\left\{(\pi q^*/4)\sqrt{[1 - (\omega/q^*c)^2]/\lambda_h(\lambda_h + \lambda_d)}\right\}}\right)^2,$$

where $c = |J|\tilde{S}$ is the characteristic velocity, $q^* = |2\pi - q|$, and

$$b = \left[1 - \left(\frac{\lambda_h}{\lambda_h + \lambda_d}\right)^{1/2}\right]\left[1 + \left(\frac{\lambda_h}{\lambda_h + \lambda_d}\right)^{1/2}\right]^{-1}.$$

The function $K_1(x)$ is a modified Bessel function. The x-x component is given by a similar expression in which sinh is placed by cosh.

III. THE DISCRETE QUANTUM SYSTEMS

We shall examine the spin-wave dispersion relation of the discrete quantum system, and then evaluate the contributions that these linear excitations make to the dynamic correlation function.

The Hamiltonian is rewritten in terms of the variables S_i^z and φ_i defined by the Villain transformation

$$S_i^+ = e^{i\varphi_i}\sqrt{\tilde{S}^2 - S_i^z(S_i^z + 1)},$$
$$S_i^- = \sqrt{\tilde{S}^2 - S_i^z(S_i^z + 1)}\,e^{-i\varphi_i},$$

where

$$[\varphi_i, S_j^z] = i\delta_{ij}.$$

The angle operator φ_i is then rewritten in terms of its deviation from its equilibrium value through

$$\varphi_i = \psi_i + \frac{\pi}{2}(2i + 1) + (-1)^i\frac{\alpha}{2},$$

where α is the canting angle between neighboring spins. This canting angle is chosen such that the terms linear in ψ_i vanish from the Hamiltonian, that is it is found from the equation

$$\sin\alpha = \lambda_d\cos\alpha - \lambda_h\cos\frac{\alpha}{2}.$$

The Hamiltonian is expanded in powers of the spin deviation operators ψ_i and S_i^z. The terms of higher order than quadratic may be neglected for sufficiently large values of $\tilde{S}$. The quadratic Hamiltonian may be diagonalized for Fourier transforming to k space, and then letting

$$\psi_k = (\alpha_k/\sqrt{2\tilde{S}})(a_k^+ + a_{-k})$$

and

$$S_k^z = (i/\alpha_k)\sqrt{(\tilde{S}/2)}(a_{-k}^+ - a_k),$$

where

$$|\alpha_k|^4 = \frac{\cos\alpha + \lambda_d\sin\alpha + \cos(k/2) + \lambda_h\sin(\alpha/2)}{(\cos\alpha + \lambda_d\sin\alpha)(1 - \cos(k/2)) + \lambda_h\sin(\alpha/2)}.$$

Thus, the harmonic spin-wave Hamiltonian is found to be

$$\hat{H}_0 = \sum_k \frac{\hbar\omega_k}{2}(a_k^\dagger a_k + a_k a_k^\dagger) ,$$

where

$$\hbar\omega_k/2|J|\bar{S} = [(\cos\alpha + \lambda_d \sin\alpha) + \cos(k/2) + \lambda_h \sin(\alpha/2)]^{1/2} \times \{(\cos\alpha + \lambda_d \sin\alpha)[1 - \cos(k/2)] + \lambda_h \sin(\alpha/2)\}^{1/2} .$$

The interactions produce corrections of higher order in $\bar{S}^{-1}$.

An inelastic neutron scattering study of $CuBr_2$ 2DMSO should provide a direct measurement of the spin-spin correlation function and possibly the spin-wave dispersion relation.

In the harmonic approximation, the z-z correlation function consists of two delta functions corresponding to the spin-wave creation and annihilation processes. The in-plane correlation functions can only be evaluated as a power series in $\bar{S}^{-1}$. In addition to the elastic Bragg scattering, and the single spin-wave creation and annihilation processes, there are distinctive nonlinear processes. The lowest nonlinear contributions are of order unity, and these include the two-spin-wave sum and difference processes. The two-spin-wave difference processes form a continuous spectra centered at $\omega = 0$, and its y-y component is given by

$$S^{yy}(q,\omega) = \frac{2\pi\cos^2(\alpha/2)}{4} \sum_k (|\alpha_{q^*/2-k}|^2|\alpha_{q^*/2+k}|^2 + 2 + |\alpha_{q^*/2-k}|^{-2}|\alpha_{q^*/2+k}|^{-2}) \times [1 + N(\omega_{q^*/2-k})]N(\omega_{q^*/2+k})\delta(\omega - \omega_{q^*/2-k} + \omega_{q^*/2+k}) ,$$

where $N(x)$ is the Bose–Einstein distribution function. At low temperatures, the Bose–Einstein function may be approximated by

$$\exp(-\beta\hbar\omega_0)$$

for $q \simeq 2\pi$. Thus, the intensity of this quasielastic peak should show the same type of exponential field and temperature dependence as the soliton central peak near $q \simeq 2\pi$. The corresponding x-x component is given by a three-spin-wave difference process, and like the corresponding soliton contribution is reduced in magnitude from its y-y counterpart. In the next section we shall discuss our results.

IV. DISCUSSION

We have examined the classical, continuum limit of a one-dimensional Dzyaloshinski–Moriya antiferromagnet in an applied magnetic field. We find that in this limit the system may be described by a double sine-Gordon field theory. In addition to the linear excitations, this system possesses nonlinear excitations such as solitons. We have examined the contributions that these solitons make to the dynamic spin-spin correlation functions in the dilue soliton approximation. Near $q \simeq 2\pi$ these solitons show up as a quasielastic peak in the in-plane inelastic neutron scattering cross sections. Closer to $q = 0$ the system also shows a quasielastic peak, but the intensity of this smeared Bragg peak is lower by two powers of λ_d, compared with the q peak. We have shown that the $q \simeq 2\pi$ quasielastic peaks are not unambiguous signatures of solitons, since the in-plane correlation function for noninteracting spin waves also shows similar features.

The solitons would also show up as a small $\omega > 0$, quasielastic peak in the z-z correlation function near $q \simeq 0$. Despite its small predicted intensity, such an observation would be of significance since it is an unambiguous signature of nonlinear excitations and is completely absent from the harmonic spin-wave theory. $CuBr_2$ 2DMSO might prove to be a suitable system for testing the above results.

ACKNOWLEDGMENTS

This work was supported by the U.S. Department of Energy, Office of Basic Energy Sciences under Grant No. DE-FG02-84ER45127.

[1] H. J. Mikeska, J. Phys. C **11**, L29 (1978).
[2] K. M. Leung, D. Hone, D. L. Mills, P. S. Riseborough, and S. E. Trullinger. Phys. Rev. B **21**, 4017 (1980).
[3] H. J. Mikeska, J. Phys. C **13**, 2913 (1980).
[4] A. C. Lamas and C. P. Landee, Solid State Commun. **59**, 441 (1986); also, S. Satija (private communication).
[5] K. M. Leung and D. Huber, Solid State Commun. **32**, 127 (1979).
[6] K. Sasaki, J. Phys. Soc. Jpn. Lett. **53**, 2872 (1984).
[7] J. Villain, J. Phys. (Paris) **35**, 27 (1974).
[8] P. S. Riseborough, Solid State Commun. **48**, 901 (1983).
[9] G. F. Reiter, Phys. Rev. Lett. **46**, 202 (1980).

Two-magnon excitations in quantum spin chains

Jian-Min Liu and Jill C. Bonner
Department of Physics, The University of Rhode Island, Kingston, Rhode Island 02881-0817

Quantum spin chains of higher spin are interesting in the case of both ferromagnets and antiferromagnets. They comprise a wide range of model types—Bethe–Ansatz integrable, nonintegrable, and with limited integrability. It is not well appreciated that the two-magnon (two-body) problems is always solvable, by Bethe–Ansatz and Green's-function techniques, regardless of the integrability character of the entire model, with interesting implications in the context of solitons and bound solitons. Chubukov and Kveschenko have suggested using the two-magnon problem in a test for integrability and claim to find additional classes of integrable spin chains for $s = 1$ and $s = \frac{1}{2}$. Here we investigate this situation.

INTRODUCTION

Recent developments in the area of conformal invariance, and also in the phenomenon of chaos, have focused attention on nonintegrable model systems. Spin clusters and spin chains provide excellent hunting grounds for research into integrable and nonintegrable phenomena. Furthermore, considerable interest has been generated in the critical behavior of Heisenberg-like antiferromagnetic (AFM) spin chains of general spin as a result of a prediction by Haldane that integer spin XXZ chains show radically different $T = 0$ phase behavior from half-integer spin chains. Affleck has generalized Haldane's work, using techniques of conformal invariance to make predictions for the critical behavior of a variety of spin-chain systems of general spin s, including models with spin anisotropy, alternation, and biquadratic exchange. Very recently, Affleck, Kennedy, Lieb, and Tasaki[1] (AKLT) have investigated AFM "valence-bond state" spin chains, inspired by a conjecture of Anderson[2] that resonating valence-bond systems may play a key role in high-temperature superconductivity. AKLT draw upon earlier exact results by Klein.[3]

Integrable and nonintegrable spin chains are fundamental to the study of magnetic solitons. Generally speaking, true solitons are nonlinear excitations of integrable systems. In the case of nonintegrable systems, the nonlinear excitations do not have the stability properties of solitons in integrable systems, and will tend to decay in time. Valence-bond (VB) systems are an interesting intermediate case. We refer to systems where all states can, in principle, be obtained exactly for finite and infinite system size N as "integrable." AKLT have demonstrated that for VB systems, the ground state and ground-state pair correlation functions can be found exactly, but not the excited states. Hence we find it convenient to refer to this new VB class of systems as having "limited integrability." Spin systems with limited integrability character are not new: they occur routinely in models with competing interactions, and have been studied under the names "disorder (order)" points and trajectories, "one-dimensional lines," etc. They reflect a compensation effect where the competing interactions in some sense cancel and hence simplify the model.

Our continuing interest in generalized Heisenberg spin chains with general spin s led us to consider the two-magnon (two-spin deviation) problem. Two-magnon states are, of course, low-lying excited states for the ferromagnetic (FM) problem. As is well known, the one-magnon (single spin deviation) problem is always solvable, and is the basis for simple spin-wave theory. It is less well recognized that the two-magnon problem can also always be solved exactly, for *all spin values s and types of interactions, even when the* complete spin-chain problem is not integrable.

Recently, Chubukov and Kveschenko[4] have studied the two-magnon bound-state problem in generalized spin chains of higher spin, specifically $s = 1$ and $s = \frac{1}{2}$. Their investigations are based on an observation by Haldane[5,6] concerning the behavior of bound n-magnon complexes. For any Hamiltonian of spin s, the n-particle bound-state spectrum has dispersion branches ranging over n consecutive Brillouin zones in an extended zone scheme, for $n < 2s$, while the spectral dispersion curves for $n > 2s$ extend over $2s$ zones. More compactly, bound n-magnon dispersion branches extend over $N = \min(n, 2s)$ Brillouin zones. Haldane investigated both nonintegrable[5] and integrable[5] model spin chains, illustrating his observation for the case of $s = \frac{1}{2}$. For the nonintegrable (Heisenberg) model, the dispersion branches consist of both real and resonant portions, and the various branches are not continuous across the five zones, showing gaps at the zone boundaries attributed to Umklapp processes.[5] However, in the case of an integrable class of general spin-s chains with SU(2) symmetry, first discussed by Takhtajan[7] and Babujian,[8] all branches turn out to be real (i.e., lie outside the two-spin-wave continuum); and the various branches remain continuous through the zone boundaries, showing no gaps. Chubukov and Kveschenko studied just the two-magnon problem, and their major interest was to find generalized spin models having the "zero gap at the zone boundary" integrability criterion conjectured by Haldane.

A simple spin-chain system which displays all the various (non)integrability features noted above is the spin-1 general bilinear-biquadratic model whose Hamiltonian is

$$\frac{H}{J} = \sum_{i=1}^{N} [\mathbf{S}_i \cdot \mathbf{S}_{i+1} + \beta(\mathbf{S}_i \cdot \mathbf{S}_{i+1})^2], \tag{1}$$

 0021-8979/88/084144-03$02.40 © 1988 American Institute of Physics

where $J = -|J|$ for ferromagnets and $|J|$ for antiferromagnets. As the ratio parameter β varies, a number of interesting special cases result.

(i) $\beta = 0$. This gives the regular Heisenberg spin chain for $s = 1$, predicted by Haldane[9] to have a gap between the AFM ground state, which is a nondegenerate singlet associated with exponential decay of the pair correlation function, and the excited-state continuum.

(ii) $\beta = -1$. This is a Bethe-Ansatz integrable model with SU(2) symmetry.[7,8] The ground state is a nondegenerate singlet below an excited-state continuum. There is, therefore, no AFM gap, and the AFM ground-state pair correlation function shows power-law decay.

(iii) $\beta = +1$. This is also a Bethe-Ansatz integrable system, but it has SU$(2s+1)$ symmetry in the case of AFM. This implies SU(3) symmetry in the case of spin 1 and an AFM Brillouin zone extending over $\pm 2\pi/3$ instead of $\pm\pi$.[10]

(iv) $\beta = +\frac{1}{3}$. This model has been discussed in detail by AKLT as an example of a VB system with limited integrability.[1] The AFM excitation spectrum is also under discussion.[11]

(v) $\beta = -\frac{1}{3}$. In this system, the behavior of the FM excited bound states is interesting, reflecting the onset of crossover between the characteristic "single-spin-deviation" behavior and the "two-string" (in Bethe-Ansatz terminology) behavior characteristic of the integrable SU(2) model.[12]

For the two-magnon problem in spin chains, there are two types of excitations. Free or scattering-type excitations produce a two-parameter continuum in the thermodynamic limit which we term the two-spin-wave continuum (2SWC). Other excitations are the single dispersion branches corresponding to bound complexes to two reversed spins. If the expressions for these branches are real, the bound-state dispersion branches lie outside the 2SWC. Otherwise, the branches enter the 2SWC and the states have resonant character. In general, we find that the relation between the 2SWC and the bound-state branches varies as the ratio of the two competing interaction terms in the Hamiltonian varies. At special ratio values, the character of the two-magnon spectra changes qualitatively (for example, a bound-magnon dispersion branch may touch or emerge from the 2SWC continuum).

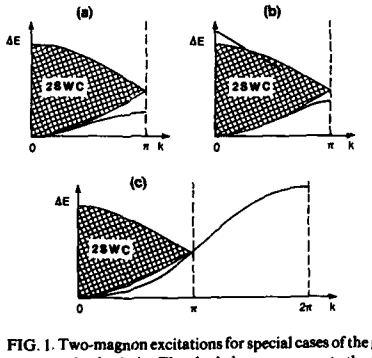


FIG. 1. Two-magnon excitations for special cases of the general spin-1 bilinear-biquadratic chain. The shaded area represents the two-spin-wave continuum (2SWC) and the solid lines represent bound-state dispersion branches. (a) shows the spin-1 Heisenberg antiferromagnet. (b) corresponds to an intermediate case with $\beta = -0.5$, and (c) shows the special behavior of the bound-state branches at the integrable point $\beta = -1$ in an extended zone scheme.

RESULTS

The excitations for several of the above $s = 1$ special models are shown in Fig. 1. Figure 1(a) illustrates the Heisenberg spin chain with $\beta = 0$. The boundaries of the 2SWC are given by

$$\Delta E^{SW}(k) = 2J(1 \pm \cos k/2), \tag{2}$$

where $0 < |k| < \pi$. The 2SWC is indicated by the shaded area in Fig. 1(a). For the Heisenberg FM, a single branch of bound states appears below the 2SWC, degenerate with the FM ground state at $k = 0$.

In Fig. 1(b), corresponding to $\beta = -0.5$, the bound-state dispersion branch below the 2SWC has moved up closer to the continuum, with a smaller gap between continuum and bound-state branch at $k = \pi$. The notable feature, however, is the emergence of a *second* branch of bound states above the continuum at low k (the remainder of the branch disappears into the 2SWC as resonant states). The critical value of β at which this second branch first starts to emerge from the continuum at $k \approx 0$ is given by $\beta = -\frac{1}{3}$.[12,13] This new mode above the band enters the 2SWC at wave vector

$$k = 2\arccos\left(-\frac{1+\beta}{2\beta}\right) \quad \text{for} \quad -\frac{1}{3} \geqslant \beta > -1. \tag{3}$$

The result is that the upper bound-state mode lies entirely above the continuum for $\beta < -1$. Obviously the point at $\beta = -\frac{1}{3}$ is special.

Let us consider the case $\beta = -1$ shown in Fig. 1(c) in an extended zone scheme. The lower and upper bound-state branches coincide with no gap at the zone boundary, $k = \pi$, continuing across the two consecutive Brillouin zones. The situation is reminiscent of the integrable model discussed by Haldane,[6] and the associated discussion. It turns out that the spin-1 bilinear-biquadratic model at the special value $\beta = -1$ is the spin-1 member of the class of SU(2) Bethe-Ansatz integrable models[7,8] whose FM spectral behavior is discussed above.[6] The qualitatively different behavior of the two bound-state branches for $\beta < -1$ and $\beta > -1$ again indicates that here is a special point.

We briefly survey the models with $\beta > 0$. For $0 < \beta < 1$, no upper bound-state branch appears, and the lower bound-state branch shows a progressively decreasing energy gap at $k = \pi$. No special behavior is observed at the point $\beta = +\frac{1}{3}$, corresponding to the $s = 1$ Klein–Affleck VB system with limited integrability, which is therefore qualitatively similar to the Heisenberg FM at $\beta = 0$. However, at the special integrable point $\beta = +1$, the single bound-state branch detaches itself completely from the continuum, lying below even at $k = 0$. This indicates that the aligned "ferromagnetic" ground state, the lowest-lying state of the 2SWC, is no longer the lowest-lying excitation of the system for $\beta > 1$. Hence the SU(3) integrable model is also a special point as far as two-magnon excitations are concerned.

BETHE ANSATZ INTEGRABLE MODELS

The spin-1 models corresponding to $\beta = \pm 1$ of Hamiltonian (1) are special cases of two spin-s classes of integrable models.[7,8,10] Each class of models has a Hamiltonian which takes the form of a power-series expansion of the bilinear term $(\mathbf{S}_i \cdot \mathbf{S}_{i+1})$ up to power $2s$. However, the coefficients differ in the two cases. It is interesting to note that the AKLT class of integer-spin chains with VB ground-state character also possess Hamiltonians of this general form.[1]

The Lai–Sutherland class of integrable models are derived from Hamiltonians based on the spin permutation operator for general s,[10] the Klein–Affleck models are based on spin-pair projection operators,[1] and the SU(2) class were discovered via a systematic procedure using the Yang–Baxter generalized star-triangle relations.[7,8] The question of interest remains: Are there additional classes of spin chains which are fully integrable or have limited integrability which have not yet been discovered?

Chubukov and Kveschenko used a Green's function approach to study the two-magnon problem. Using Haldane's result[6] as a predictor of integrability, they studied models of the general type:

$$H = -J' \sum_{i=1}^{N} [(\mathbf{S}_i \cdot \mathbf{S}_{i+1}) + \gamma (\mathbf{S}_i \cdot \mathbf{S}_{i+1})^2 + \delta (\mathbf{S}_i \cdot \mathbf{S}_{i+1})^3]. \quad (4)$$

In the case of $s = 1$, their Green's-function method yields classes of integrable models whose coefficients are related by the condition

$$\delta = (1 + \gamma). \quad (5)$$

However, it is easy to show that there exists the following spin-1 identity:

$$(\mathbf{S}_i \cdot \mathbf{S}_{i+1})^3 \equiv -2(\mathbf{S}_i \cdot \mathbf{S}_{i+1})^2 + (\mathbf{S}_i \cdot \mathbf{S}_{i+1}) + 2. \quad (6)$$

Substituting (6) into Hamiltonian (4), we obtain the result

$$H = (1 + \delta) J' \sum_{i=1}^{N} [(\mathbf{S}_i \cdot \mathbf{S}_{i+1}) + [(\gamma - 2\delta)/(1 + \delta)](\mathbf{S}_i \cdot \mathbf{S}_{i+1})^2]. \quad (7)$$

This is obviously equivalent to the spin-1 bilinear-biquadratic Hamiltonian (1), with

$$J = (1 + \delta) J' \quad \text{and} \quad \beta = (\gamma - 2\delta)/(1 + \delta). \quad (8)$$

Hence, for spin-1, adding third-order bilinear exchange will not yield anything new. Substituting condition (5) into (7) yields

$$H = -(2 + \gamma) J' \sum_{i} [(\mathbf{S}_i \cdot \mathbf{S}_{i+1}) - (\mathbf{S}_i \cdot \mathbf{S}_{i+1})^2], \quad (9)$$

corresponding to the integrable point $\beta = -1$.

Note, however, that an alternative $s = 1$ special condition found by Chubukov and Kveschenko is given by the relation:

$$\delta = \tfrac{1}{3}(\gamma - 1). \quad (10)$$

Substituting (10) into Hamiltonian (7) gives

$$H = -\tfrac{1}{3}(2 + \gamma) J' \sum_{i} [(\mathbf{S}_i \cdot \mathbf{S}_{i+1}) + (\mathbf{S}_i \cdot \mathbf{S}_{i+1})^2], \quad (11)$$

corresponding to the integrable point $\beta = +1$. Hence the $s = 1$ Chubukov–Kveschenko results yield *both* known $s = 1$ integrable models, but nothing new in addition.

The Chubukov–Kveschenko results for $s = \frac{3}{2}$ may turn out to be more interesting. No identity of the form of (6) exists in the case of $s = \frac{3}{2}$—hence the situation is not obviously trivial. Adding fourth-order terms to Hamiltonian (4) *would* be trivial, since we have the $s = \frac{3}{2}$ identity

$$(\mathbf{S}_i \cdot \mathbf{S}_{i+1})^4 \equiv -5(\mathbf{S}_i \cdot \mathbf{S}_{i+1})^3 + \tfrac{9}{8}(\mathbf{S}_i \cdot \mathbf{S}_{i+1})^2 + \tfrac{423}{16}(\mathbf{S}_i \cdot \mathbf{S}_{i+1}) + \tfrac{4455}{256}. \quad (12)$$

Chubukov and Kveschenko claim the existence of a class of integrable $s = \frac{3}{2}$ spin chains according to the relation:

$$-1 - \tfrac{11}{2}\gamma + \tfrac{17}{16}\delta = 0. \quad (13)$$

Now the Bethe-ansatz integrable SU(2) chain with $s = \frac{3}{2}$ is given by Hamiltonian (4) with coefficient values

$$\gamma = -\tfrac{8}{27}, \quad \delta = -\tfrac{16}{27}. \quad (14)$$

It is easy to see that these special values satisfy relation (13), and hence (4) contains a known $s = \frac{3}{2}$ integrable model as a special case. Whether new $s = \frac{3}{2}$ integrable models occur also cannot be simply ruled out as in the case of $s = 1$, and hence further investigation of such a possibility is proceeding.

ACKNOWLEDGMENTS

We are indebted to Gerhard Müller and John Parkinson for valuable comments and observations. We acknowledge financial support from the National Science Foundation through Grant No. DMR 86-03036 and the Princeton Supercomputer Center.

[1] I. Affleck, T. Kennedy, E. H. Lieb, and H. Tasaki, Phys. Rev. Lett. **59**, 799 (1987).
[2] P. W. Anderson, Science **235**, 1196 (1987).
[3] D. J. Klein, J. Phys. A **15**, 661 (1982).
[4] A. V. Chubukov and D. V. Kveschenko, J. Phys. C **20**, L505 (1987).
[5] F. D. M. Haldane, J. Phys. C **15**, L831 (1982).
[6] F. D. M. Haldane, J. Phys. C **15**, L1309 (1982).
[7] L. A. Takhtajan, Phys. Lett. **87A**, 479 (1982).
[8] H. M. Babujian, Phys Lett. **90A**, 479 (1982).
[9] F. D. M. Haldane, Phys. Lett. **93A**, 464 (1983); Phys. Rev. Lett. **50**, 1153 (1983); and unpublished.
[10] B. Sutherland, Phys. Rev. B **12**, 3795 (1975).
[11] D. P. Arovas, A. Auerbach, and F. D. M. Haldane (unpublished).
[12] J. B. Parkinson and J. C. Bonner, J. Phys. C **19**, 6063 (1986); J. Oitmaa, J. B. Parkinson, and J. C. Bonner, J. Phys. C **19**, L595 (1986).
[13] H. Aghahosseini and J. B. Parkinson, J. Phys. C **11**, 3461 (1978); see also, N. Papanicolaou and G. C. Psaltakis, Phys. Rev. B **35**, 342 (1987).

Spin-wave instabilities and their revival by nonlinear mechanics (invited)

H. Suhl and X. Y. Zhang[a)]
Department of Physics, University of California, San Diego, La Jolla, California 92093

Spin-wave instabilities in high signal power ferromagnetic resonance, first noted more than 30 years ago, have in recent years been reexamined in the light of modern dynamics. Both experiments and computer simulations have demonstrated limit cycles, period doubling, quasiperiodicity, and chaos as the rf power is progressively increased above the original threshold value. A distinctive feature of this problem is the participation of a vast number of spin-wave modes in the original instability, driving the system to a new fixed point with high excitation of an entire manifold. The next instability is a Hopf bifurcation in which a pair of collective modes grows into a limit cycle, and an accompanying spatial correlation pattern. Center manifold theory is used to establish these results. Prospects for some approximate analytic (as distinct from computational) treatment of the succession of higher bifurcations are discussed.

Recent years have seen a revival of activity in a more than 30-year-old subject: the outbreak of stochastic motion of magnetization in high-power ferromagnetic resonance experiments. This renaissance appeared in the wake of recent growing interest in nonlinear mechanics.

An account of the oldest work in this field is given, for example, in Ref. 1. There, it is explained how the uniform precession of the magnetization set up by the microwave rf field begins to parametrically feed certain spin-wave modes, once the rf power exceeds a certain threshold. This happens as the result of nonlinear couplings of the uniform precession to those spin waves whose frequencies stand in the proper (i.e., energy-conserving) relationship to the frequency of the precession. Depending on the experimental situation, one distinguishes two principal regimes: (1) Spin-wave and precession frequencies are equal when two precessional quanta break up into pairs of spin waves with equal and opposite wave vector (to conserve momentum). This happens in the usual ferromagnetic resonance condition. (2) Spin-wave frequency is equal to one-half the precessional frequency, in which case one precessional quantum splits into two spin-wave quanta, again with equal and opposite momenta. This is the case under conditions of so-called "subsidiary absorption," which characteristically sets in only *above* a certain threshold power, in contrast to the usual resonance condition. Under very special experimental conditions there is also a third case: coincidence of subsidiary and main absorption. This case is marked by an especially low onset threshold of the instability. Finally, somewhat distinct from these cases is the instability due to parallel pumping. In that case the rf and dc fields point in the same direction, and a signal quantum breaks into two half-frequency spin-wave quanta directly, without using the uniform precession as intermediary.

These effects were explained in the 1950's on the basis of a mode-mode coupling theory that explained the observations available at the time quite well.[2] Once the instability onset conditions were understood on the basis of a linearized theory, the question immediately presented itself: What does the steady state look like beyond the instability threshold, if indeed there is a steady state? One of the authors (H.S.) was able to answer this question for the case of the subsidiary absorption,[2] which is slightly simpler than the case of the main resonance. In the same Ref. 2, experimental data were presented which confirmed that theory, up to the highest-power level then used. As we known now, that new steady state, in its turn, goes unstable as the power increases beyond a second, higher threshold. In fact, there appears to be a whole cascade of successively higher thresholds ending in chaos. Actually, what now appears to be the second threshold seems to have been observed quite early[3] in the form of what were then called relaxation oscillations. (By now these oscillations have been confirmed by many investigators.) Revival of interest in this subject began in the 1970's and intensified in the early 1980's with a number of theoretical papers.[4,5] These employed the terminology (though not usually the methodology) of nonlinear mechanics. Almost without exception (see, however, Ref. 5) they involved computer simulation of a stripped-down model which coupled the uniform mode to just one pair of spin waves, ignoring the fact that in general a whole manifold of spin waves is eligible for unstable growth. These calculations revealed almost the whole gamut of phenomena associated with increasing "driving" parameter in other nonlinear systems (such as fluid flow between rotating cylinders, or in planar fluid systems subjected to destabilizing temperature gradients). Most of the motivation for the crop of theoretical papers over the past two years or so has come from the beautiful experiments of the Jeffries group at Berkeley,[6] who were able to observe these phenomena in resonance experiments on yttrium iron garnet spheres. Quite a few of their results are as yet unexplained, but a substantial number can be well categorized according to the schemes current in nonlinear dynamics. So it is with the results of other experimental groups, such as N.R.L.[7] and at UC San Diego: each group finds something unexpected and unexplained, in addition to results that are more or less clear.

At some point it becomes necessary to come to grips with the issue of the instability of an entire spin-wave manifold, as distinct from the model restricted to only one pair (or, for that matter, any finite number of pairs, of spin waves). We have been able to do this for signal powers ranging from zero to values slightly above the second threshold.[7] This is done by first of all tracking the fixed points in the

a) Now at Control Data Corporation, 7801 Computer Ave. S., Minneapolis, MN 55435.

 0021-8979/88/084147-04$02.40 © 1988 American Institute of Physics



phase space subtended by the system: (spin waves + uniform precession) as a function of signal power, and then examining the motion of small disturbances around that fixed point. Consider the main ferromagnetic resonance. At very small applied signal, all the spin-wave amplitude coordinates of the fixed point are very small, appropriate to thermal agitation, and the uniform precession coordinate has its usual small-signal value. As the signal is increased, that fixed point begins to move, at first hugging the axis denoting the uniform precession, until the signal attains values very close to the old instability threshold of 30 years ago. From then on it rises sharply into the phase space, but of course does not go to infinity as would be implied by strictly linearized theory. Instead, when the signal power exceeds the threshold by a few thermal energies, the fixed point settles down at a more or less fixed location in phase space, at which all the relevant spin-wave amplitudes now have finite values. Further increases in signal power do not increase the precession angle. The reason for all this is that via the nonlinear coupling terms some small amount of power is being fed parametrically from the uniform precession to the spin waves (even at low signals) in such a sense as to decrease the damping of the spin waves. As the old threshold is approached to within a thermal value, that damping becomes very small, of the order of a thermal field (in appropriate units). The expressions for the amplitudes of spin wave degenerate with the uniform mode will then have the thermal driving field not only in their numerators, but will then have nothing but the magnitude of that driving field in their denominators. So, while their phases are then still random, their magnitudes are finite and nonthermal. In the meantime the damping of the uniform mode is greatly increased due to the loss of power to the spin waves and the uniform mode is thus prevented from growing further with increasing signal. So in a certain sense the old instability theshold doesn't exist at all; what really happens is that the character of the steady state changes rapidly and drastically within a very small range of applied power around critical. Alternatively, if one neglects thermal agitation, this situation can be described by two distinct fixed points, a low-signal one (with all spin-wave amplitudes equal to zero) which goes unstable above the old threshold, and a high-power one that has the same form as the one just described. Taking into account thermal agitation shows how the first fixed point changes continuously into the second fixed point.

There is yet another effect that independently reinforces this movement of the fixed point from position 1 to position 2: The interaction of the degenerate, highly excited spin waves among one another. That interaction renormalizes the coupling constant responsible for the old instability, diminishing that constant progressively more and more as threshold is approached. Its final value is such as to prevent the fixed point from wandering off to infinity; it ultimately sticks at location 2, very nearly the same as the one discussed above. This added effect has, however, an experimental consequence: Detailed calculation shows that this gradual diminution of the renormalized coupling should have a more noticeable effect on the high-power behavior of the main resonance than on that of the subsidiary resonance. In particular, it should cause the imaginary part of the susceptibility at resonance to decline with power more slowly at the main resonance than in the case of coincidence of main resonance with the subsidiary absorption.

However, there is one case in which coupling constant renormalization is of the essence, rather than a mere quantitative improvement: the case of parallel pump instability (PPI). In that case, it is the rf signal field itself that parametrically feeds power into the spin waves directly, without the brokerage of the uniform mode. Therefore (unless there is reason to include the back reaction of the increased absorption on the rf field), there would appear to be nothing to prevent the spin waves from growing indefinitely once threshold is exceeded. In that case the runaway is prevented exclusively by coupling constant renormalization, which, here too, decreases to a value just below threshold value, no matter how hard the system is pumped. The need for such renormalization was already pointed out by Zakharov *et al.*[8]

As the power is increased beyond a further threshold, the system once again becomes unstable due to interactions among the now highly excited spin waves. This is verified by determining the new "normal modes" of the system, that is to say the spectrum of small excitations around the steady state. There are, of course, as many of these as there are spin-wave modes, and below the new threshold they all decay with time. But as that threshold is approached, the real part of the decay rate of one particular pair (with complex conjugate eigenvalues) steadily decreases, eventually crossing zero at the new threshold, but the imaginary part of the decay rate remains finite. This pair has all the characteristics of a collective mode: a superposition of the original spin-wave amplitudes, all of comparable size. (There is actually a second pair of collective modes, which, however, remains stable.) Beyond threshold, then, we have a pair of growing oscillatory modes. (All modes other than this exceptional pair remain stable.) We have shown elsewhere that if the lowest-order nonlinear terms are included in the analysis, the amplitude of the runaway oscillatory pair actually settles down at a finite value, and the steady state is thus a limit cycle. This process is called a Hopf bifurcation. The frequency of the limit cycle turns out to be between tens of kilohertz and 1 or 2 MHz. Associated with this is a characteristic spatial autocorrelation pattern in the magnetization,[5] which oscillates in time with that frequency. At a given time, the autocorrelation decays with distance as $1/r$, times a sinusoidal function of r with a wavelength of the order of a domain wall thickness. This pattern should show up in the structure factor measured in a suitable scattering experiment.

A mathematical technique for establishing this Hopf bifurcation for a system of essentially infinitely many modes is the so-called center manifold theory. This proceeds as follows: close to threshold the interesting few collective modes (for simplicity we shall speak of a single one) decay or grow only slowly with time. Therefore, in the equations of motion of the remaining "single-particle" mode amplitudes, the slow collective mode may be considered constant. The solutions of these equations involve that collective mode, and when these solutions are substituted in the equation of motion for the collective mode, a single equation is obtained for

that mode alone, the so-called center manifold equation.[9] This program must be carried far enough to yield the lowest order nonlinear term of that equation, since the sign of that term will determine if the limit cycle exists or not. The process sounds simple, but frequently requires tedious algebra. The complexity becomes quite prohibitive if one now looks for the next higher threshold; aside from this, one cannot be sure that higher nonlinearities would not have to be taken into acount to discuss that threshold.

We now sketch the formal development of these ideas. The results concerning the fixed point follow directly, and quite simply, from the equations of motion for the slowly varying amplitudes $B_k(t)$ of the spin waves $B_k e^{i\omega_h t}$ (the uniform precession amplitude being denoted by B_0):

$$\dot{B}_k = i\rho_{k0}B_0^2 B^*_{-k} - \eta B_k + i\sum_{k'\neq 0}\rho_{kk'}B_k B_{-k'}B^*_{-k} + ih_k,$$

$$\dot{B}_0 = i\sum_k \rho_{k0}B_k B_{-k}B^* - \eta B_0 - i(h_s - h_0). \tag{1}$$

Here $\rho_{kk'}$ is a coupling constant of spin waves k and k' and η is a damping constant (for simplicity assumed k independent). h_k is the thermal field agitating the k th spin wave, and h_s the signal field (both fields in frequency units). Of course, $h_0 \ll h_s$ and may be neglected. It has been assumed in (1) that $\omega_h = \omega_0 =$ signal frequency. Disregarding for the moment the third term in the first of Eqs. (1), which represents the nonlinear interaction among the $k \neq 0$ spin waves, the steady-state form of Eq. (1) can be written

$$B_k = \eta h_k + i\rho_{k0}B_0^2 h^*_{-k}/\eta^2 - \rho_{k0}^2|B_0|^4, \tag{2a}$$

$$B_0 = ih_s\eta + h_s^*\sum/\eta^2 - \left|\sum\right|^2, \tag{2b}$$

where

$$\sum = \sum \rho_{k0}B_k B_{-k}. \tag{3}$$

In the latter sum, only the nonrandom phase part

$$(B_k B_{-k})_{nr} = 2i|h_k|^2\rho_{k0}\eta B_0^2/(\eta^2 - \rho_{k0}^2|B_0|^4)^2, \tag{4}$$

is retained.

The "sticking" of B_0 close to threshold is seen as follows: Near threshold $|B_0|^2 = \eta/\rho_{k0}$. Assume that

$$|B_0|^2 \simeq (\eta/\rho_{k0}) - (A/\rho_{k0})|h_k|, \tag{5}$$

where A is to be determined. Then from Eq. (2a)

$$B_k \simeq (e^{i\psi_k} + ie^{2i\varphi_0 - \psi_{-k}})/2A, \tag{6}$$

where ψ_k is the (random) phase of h_k, and φ_0 the phase of B_0,

$$\sum \rho_{k0}(B_k B_{-k})_{nr} \simeq \frac{1}{2A^2}\sum \rho_{k0}e^{2i\varphi_0}. \tag{7}$$

From the steady-state equation (2b) for B_0 we then find (noting that $h_s = h_s^* e^{2i\varphi_0}$, and using $|B_0| \simeq |B_0^{crit}| = \sqrt{\eta/\rho_{k0}}$; $h_s^{crit} = \eta^{3/2}/\rho_{k0}^{1/2}$),

$$\left|1 - \frac{y}{\eta}\right| = \frac{h_s}{h_s^{crit}}\frac{\sqrt{1 + y^2/\eta^2}}{1 + y/\eta}, \tag{8}$$

where $y = \Sigma\rho_{k0}/2A^2$. For h_s slightly larger than h_s^{crit}, there is a solution with y small

$$\frac{y}{\eta} = \left|1 - \frac{h_s}{h_s^{crit}}\right| + O\left[\left(1 - \frac{h_s}{h_s^{crit}}\right)^3\right], \tag{9}$$

for which

$$A \simeq \sqrt{\frac{\Sigma\rho_{k_0}}{2\eta}}\left|1 - \frac{h_s}{h_s^{crit}}\right|^{-1/2}. \tag{10}$$

Thus, A is infinite at $h_s = h_s^{crit}$, and B_k would appear to be zero exactly at that point. In actual fact, if the thermal field is retained in the equation for B_0, a more careful analysis at $h_s = h_s^{crit}$ shows that $A \propto 1/\sqrt{|h_{thermal}|}$ there. This means that exactly at h_s^{crit}, B_k still goes like the square root of the thermal field. But beyond h_s^{crit}, B_k acquires a nonthermal value, rising out of the noise as $\sqrt{(h_s/h_s^{crit}) - 1}$.

As already mentioned, when the uniform mode does not provide a "buffer" between the rf drive and the affected spin waves, the steady state comes about somewhat differently. For the case of parallel pumping, the equation of motion is

$$\dot{B}_k = -\eta B_k + ih_s\mu B^*_{-k} + i\sum \rho_{kk'}B_k B_{-k'}B^*_{-k} + h_k, \tag{11}$$

where μ is a dimensionless and (for simplicity) k independent coupling constant. The steady-state solution for B_k with the third term on the right-hand side neglected is found and $\Sigma\rho_{kk'}B_k B_{-k'}$ constructed from the solution. That sum resubstituted in the equation then gives a new coupling constant

$$\mu' = \left(\mu - 2i\eta\sum_{k'}\frac{|h_{k'}|^2\rho_{kk'}\mu}{(\eta^2 - \mu^2 h_s^2)^2}\right). \tag{12}$$

Iterating this process drives μ' to a fixed point given by

$$\mu' = \mu - 2i\mu'\eta\sum\frac{|h_{k'}|^2\rho_{kk'}}{(\eta^2 - |\mu'|^2 h_s^2)^2}, \tag{13}$$

so that

$$|\mu'|^2 = \mu^2\left[1 + 4\eta^2\left(\sum|h_{k'}|^2\rho_{kk'}/(\eta^2 - |\mu'|^2 h_s^2)^2\right)\right]. \tag{14}$$

By graphing both sides of this equation it is seen that $\eta^2 - |\mu'|^2 h_s^2$ never reaches zero. Therefore, the steady-state value of B_μ remains finite. A similar result can be demonstrated for the case of perpendicular pumping at resonance, and acts in addition to the limiting mechanism already discussed.

However, the steady state eventually goes unstable, and the manner in which the instability develops follows from slightly perturbing the equations of motion (1) about the fixed point. The variations δB_0 and δB_k are assumed to vary as $e^{\lambda t}$, and a characteristic equation is obtained for λ. The vast majority of these λ's can be guessed without analysis: it is highly plausible that there are δB_k's that behave almost exactly like the original B_k's, but with decay constants

$$\lambda \simeq -\eta \pm \rho_k|B_0|^2, \tag{15}$$

where ρ_k now stands for the coupling constant (renormalized if necessary). According to our previous discussion, all

these λ are negative since $\rho_k|B_0|^2$ never quite reaches η. By analogy with the electron theory of metals, these excitations may be called "single-particle" modes.

Almost all, but not all the modes belong to this quasiparticle spectrum. Two pairs of modes with complex conjugated λ's split off from this quasicontinuum of negative λ's. The corresponding eigenmodes are superpositions of spin waves.

At a rf field given by

$$(|\bar{B}|^2 N - |B_0|^2 \rho_{k0})/2 = \eta, \tag{16}$$

where

$$|\bar{B}|^2 = \frac{1}{N} \sum |B_k|^2 \rho_k, \tag{17}$$

$$|B_k|^2 = \frac{|h_k|^2(\eta^2 + |\rho_k|^2|B_0|^4)}{\eta^2 - (|\rho_k|^2|B_0|^4)^2}, \tag{18}$$

the real part of one of the two collective pairs of λ's crosses the imaginary axis, at a finite imaginary value approximately equal to $i2\sqrt{2}\eta$. The new instability threshold for the signal field h_s can be estimated from our earlier conclusion that $|B_0|^2$, except in critical places, can be set equal to $\eta/|\rho_k|$, so that

$$|B_k|^2 = 1/2A^2. \tag{19}$$

Using the value of A found earlier, it follows that the new critical field

$$h_s^{\mathrm{crit(II)}} = 4h_s^{\mathrm{crit(I)}} \tag{20}$$

in terms of the critical field of the first instability. [Actually, this is not quite correct, since in solving the equation for A we assumed h_s to be close to $h_s^{\mathrm{crit(I)}}$, but a more accurate result can be found rather easily from Eq. (8).]

Finally, the tedious task of finding the new fixed point, if any, beyond $h_s^{\mathrm{crit(II)}}$ must be undertaken. If it exists it will have the form of a limit cycle in the space of the B_k, with frequency $\mathrm{Im}(\lambda_{\mathrm{coll}}) = 2\sqrt{2}\eta$. The "center manifold" procedure outlined above is carried out on the equations satisfied by δB_k, δB_0, but taken to third order in the increments. The "single-particle" mode amplitudes are eliminated in favor of the unstable collective mode. The detailed calculation is quite complex and is reported in Ref. 10. The result is a differential equation for the amplitude α of the collective mode, which is found to have the form

$$\frac{d\alpha}{dt} = \lambda\alpha - \frac{|\alpha|^2\alpha}{K}, \tag{21}$$

where

$$K = [1 + (3/\sqrt{2})]^{-1}[1 - (\rho_{\mathrm{av}}/\rho_c)], \tag{22}$$

where ρ_c is the value of ρ_{0k} involved in the first threshold, and ρ_{av} is an average of ρ over all the coupling constants implicated in the single-particle modes. This equation shows that any initial α is eventually driven to settle on a limit cycle of squared amplitude

$$|\alpha|^2 = (\mathrm{Re}\,\lambda)K. \tag{23}$$

It is clear that the complexity involved in determining the next higher bifurcation would be prohibitive. One of the needs in this area of investigation is the construction of some kind of iterative map that can, with some degree of credibility, mimic the sequence of bifurcations, including the final one to chaos.

More ambitiously, one may go beyond mode-mode coupling and consider the full partial differential Landau–Lifschitz equation, including dipolar interactions described by $\mathrm{div}\,\mathbf{h} = -4\pi\,\mathrm{div}\,\mathbf{M}$. Such attempts are found mainly in the Russian literature, and some special cases of integrability were found (soliton solutions, etc.). Recently, Zachary and collaborators[11] have established some results for the dimensionality of attractors that the solutions must have. So far, these methods have not yet made much contact with experiment, but the future of the theoretical side of this subject may well be in that direction.

[1] R. W. Damon, in *Magnetism: A Treatise on Modern Theory and Materials*, edited by G. T. Rado and H. Suhl (Academic, New York, 1963), Vol. 1, p. 551.
[2] H. Suhl, J. Phys. Chem. Solids **1**, 209 (1957).
[3] T. S. Hartwick, E. R. Peressini, and M. T. Weiss, Phys. Rev. Lett. **6**, 176 (1961).
[4] K. Nakamura, S. Ohta, and K. Kawasaki, J. Phys. C **15**, L143 (1983); X. Y. Zhang and H. Suhl, Phys. Rev. A **32**, 2530 (1985); F. M. deAguiar and S. M. Rezende, Phys. Rev. Lett. **56**, 1070 (1986).
[5] H. Suhl and X. Y. Zhang, Phys. Rev. Lett. **57**, 1480 (1986).
[6] G. Gibon and C. Jeffries, Phys. Rev. A **29**, 811 (1984).
[7] F. Rachford and L. M. Pecora, Bull. Am. Phys. Soc. **32**, 599 (1987); L. M. Pecora, *ibid.* **32**, 527 (1987).
[8] V. E. Zakharov, V. S. L'vov, and S. S. Starobients, Sov. Phys. Usp. **17**, 896 (1975).
[9] J. Carr, *Applications of Center Manifold Theory*, Vol 35 of *Applied Mathematical Sciences* (Springer, New York, 1981).
[10] X. Y. Zhang and H. Suhl (unpublished).
[11] T. L. Gill and W. W. Zachary, J. Appl. Phys. **61**, 431 (1987); and W. W. Zachary (private communication).

Instabilities of spin waves in parallel-pumped easy plane ferromagnets

S. P. Lim and D. L. Huber
Department of Physics, University of Wisconsin-Madison, Madison, Wisconsin 53706

By applying the *S*-theory formalism of Zakharov *et al.* to a microscopic hamiltonian with uniaxial easy plane anisotropy, we arrive at a set of equations for the system that describe the spin waves and their mutual interactions. The parameters in the theory are related to the various interaction constants of the microscopic hamiltonian. Numerical studies of this system of equations indicate that the stationary states are ones where all spin-wave pair correlation functions have the same phase. The phenomenon of phase locking is universal, independent of the mode of approach to equilibrium. It is found that there is no dependence on the number of modes (up to 100) for the above behavior. This, together with the form of the equations, indicates that a similar result should hold for a macroscopic number of modes. Results for the stationary magnon population are presented. In the phase-locked regime, the approach to a stationary state is governed by a pair of coupled first-order differential equations. Linearizing these equations about the stationary points, we find that the approach to equilibrium involves purely exponential decay just above threshold, and, at higher power levels, we have damped oscillatory decay.

I. INTRODUCTION

Instabilities of spin waves in magnetic materials under both parallel and perpendicular pumping are well-known experimental facts.[1-8] The recent interest in chaos has spurred a renewed interest in this area, and recent studies show such systems to be dynamically rich.

In his pioneering paper, Suhl[9] first gave a theoretical understanding of such instabilities for perpendicularly pumped ferromagnets. Schlöhmann[10] *et al.* and Gottlieb and Suhl[11] followed up with an explanation for the parallel case. Some years later Zakharov *et al.*[12,13] presented a microscopic theory of the parametric excitation of spin waves in parallel pumping experiments. This subsequently became known as the *S* theory, and various authors[1,14,15] have investigated the equations of motion derived in Ref. 12 numerically and obtained period doubling and chaotic behavior. However, such work was done with special, ad hoc choices of parameter values and was limited to a two-mode approximation. An alternative model of instabilities in parallel pumping based on the Landau–Lifshitz equation[6] has been proposed by Waldner *et al.*[16] As for perpendicular pumping, Zhang and Suhl[17,18] and Rezende *et al.*[19] have recently analyzed it from a microscopic viewpoint, and the latter group has also investigated a two-mode model for this case—analogous to that investigated in Refs. 14 and 15.

Although the two-mode models were successful in reproducing some of the features of the parallel pumping experiments, they remain approximations, without basis for the choice of parameters or justification for restricting the number of modes to two. As shown by Suhl and Zhang,[18] in parallel pumping, an entire manifold of spin waves becomes excited above threshold. In this paper we mitigate these two objections. Starting from a microscopic hamiltonian, we obtain explicit expressions for the parameters that appear in the *S* theory for the model of an easy plane ferromagnet with static and oscillating magnetic fields lying in the easy plane. We also go beyond the two-mode approximation. A consideration of the specific solutions to these equations for up to 100 modes leads us to infer the general solution in the neighborhood of the stationary states of a macroscopic ensemble of modes. We also characterize the approach to the stationary states and the range of pumping field strength over which such states are stable.

II. MODEL

We adopt for our study an easy plane ferromagnetic system with static and oscillating magnetic fields perpendicular to the hard (x) axis. The microscopic hamiltonian for such a system is

$$H = -\sum_{i,j}{}' J\mathbf{S}_i\cdot\mathbf{S}_j + \sum_{i,j}{}' DS_i^x S_j^x - g\mu H\sum_j S_j^z + g\mu h\cos(\omega_p t)\sum_j S_j^x, \tag{1}$$

where the prime signifies a sum over nearest neighbors only and both the exchange energy J and anisotropy energy D are positive. H denotes the Zeeman field and h the oscillating field with frequency $\omega_p/2\pi$. In conventional pumping experiments, only magnons near $\mathbf{k}=0$ are excited. On applying the S theory in this long wavelength limit, we obtain the equations of motion[20]

$$\frac{dn_k}{2dt} = n_k\left(-\gamma + V\sin\psi_k + T\sum_{k'}\sin(\psi_k-\psi_{k'})\right), \tag{2}$$

$$\frac{d\psi_k}{2dt} = \Delta\omega + 2T\sum_{k'} n_{k'} + V\cos\psi_k + T\sum_{k'} n_{k'}\cos(\psi_k-\psi_{k'}), \tag{3}$$

and

$$V = (DSz/4)[g\mu H/(g\mu H + DSz)]^{1/2}, \tag{4}$$

$$T = -(Dz/4A)[(2g\mu H + DSz/2)/(g\mu H + DSz)], \tag{5}$$

where A is the number of spins, z is the number of nearest

 0021-8979/88/084151-03$02.40 © 1988 American Institute of Physics

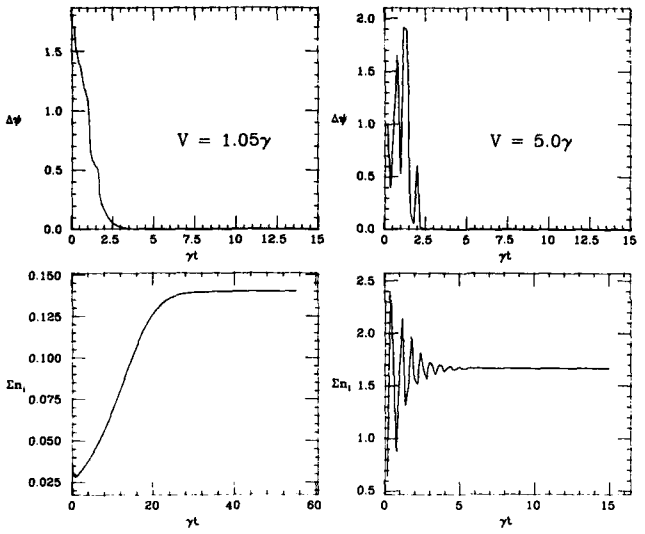


FIG. 1. Upper panels: Variance in ψ, Eq. (8), vs γt for $T=-\gamma$, $\Delta\omega=0.1\gamma$; random initial conditions. Lower panels: Total magnon population vs γt. Same parameters as in upper panel. Note difference in time scales between upper and lower panels of left figures and difference in vertical scales between left and right figures.

neighbors, and $\Delta\omega=[g\mu H(g\mu H+DSz)]^{1/2}-\omega_p/2$. We have assumed that all of the participating modes had the same frequency and decay rate γ. Here, n_k and ψ_k are related to the ensemble averages of the following correlation functions of bose operators c_k and $c_k^\dagger$ that diagonalize the zero-order hamiltonian:

$$<c_k^\dagger(t)c_k(t)>\equiv n_k(t), \tag{6}$$

$$<c_k(t)c_{-k}(t)>\equiv\sigma_k(t)e^{i\omega_p t}=n_k(t)e^{i(\psi_k+\omega_p)t}. \tag{7}$$

We discuss the solutions to (2) and (3) in the following section.

III. FIXED POINTS AND LINEAR STABILITY ANALYSIS

The equations of motion (2) and (3) have been investigated with parameters in the physically relevant ranges, $\Delta\omega>0$ and $T<0$, for a variety of initial conditions for up to one hundred modes. It is found that for $V<\gamma$ the system relaxed to the trivial fixed point where $n_1^0=n_2^0=\ldots=0$. When V exceeded this threshold, the existence of nontrivial (i.e., $\Sigma n_i^0\neq 0$) fixed points become possible. In all of these calculations, we restrict $\Sigma n_i(0)$ to suitably small quantities to comform to physically realistic situations although the results still stand when this requirement is relaxed. Otherwise each $n_i(0)$ was arbitrarily chosen. Without exception it was found that both stable and unstable fixed points were ones of common phase. That is $\psi_1^0=\psi_2^0=\ldots=\psi_0(\mathrm{mod}\,2\pi)$. Furthermore, in the evolution towards the stable fixed points the phases become locked before the fixed point was reached. That is, $\psi_1(t)=\psi_2(t)=\ldots=\psi(t)$ as $\psi(t)\to\psi_0$.

The locking of phases is illustrated in Fig. 1 for different pumping fields with arbitrarily chosen initial conditions above threshold for a hundred-mode system. In the upper panels, we plotted $\Delta\psi(t)$, the variance in the phases, defined by

$$\Delta\psi=\left\{\left(\frac{1}{100}\right)\sum_{i=1}^{100}\left[\psi_i(t)-\left(\sum_{j=1}^{100}\psi_j(t)\right)\Big/100\right]^2\right\}^{1/2}, \tag{8}$$

while in the lower panels, we plotted the total magnon population $N(t)$ defined by

$$N(t)=\sum_{i=1}^{100}n_i(t). \tag{9}$$

A comparison of the upper and lower panels show that phase locking occurs before $N(t)$ reaches its stationary value.

The phase-locked fixed points can be obtained from the equations of motion by setting the left-hand sides to zero and taking $\psi_k\equiv\psi_0$. We then have

$$\sin\psi_0=\gamma/V, \tag{10}$$

$$N_0=\sum_k n_k^0=(-\Delta\omega-V\cos\psi_0)/(3T). \tag{11}$$

Since the physically meaningful states must have $N_0>0$ and as $T<0$ in an easy plane ferromagnet, with $\Delta\omega>0$, one can have stationary states with

$$N_0=[\Delta\omega+(V^2-\gamma^2)^{1/2}]/(3|T|) \tag{12}$$

for all $V>\gamma$. In addition there are also physically accessible stationary states where

$$N_0=[\Delta\omega-(V^2-\gamma^2)^{1/2}]/(3|T|) \tag{13}$$

for $\gamma<V<(\gamma^2+\Delta\omega^2)^{1/2}$. As will be shown below, these latter states are unstable with respect to infinitesimal perturbations whereas the former are stable.

Finally we mention that were $\Delta\omega<0$, one would have physically meaningful stationary states with

$$N_0=[(V^2-\gamma^2)^{1/2}-|\Delta\omega|]/(3|T|) \tag{14}$$

for $V > (\gamma^2 + \Delta\omega^2)^{1/2}$ and like (12) above, they are stable.

The analysis leading to Eqs. (10) and (11) does not provide information on the stability of these fixed points. We can obtain such information by linearizing the equations of motion about the fixed points. In doing this we take phase locking into account explicitly by setting $\psi_k = \psi_{k'} = \psi$. Summing (2) over k and linearizing with respect to $\delta N = N - N_0$ and $\delta\psi = \psi - \psi_0$, we find the solutions for δN and $\delta\psi$ to be sums of two exponential functions with arguments given by

$$S_\pm = -\gamma \pm (\gamma^2 + 12N_0VT\cos\psi_0)^{1/2} . \quad (15)$$

From this, it is quite evident that δN and $\delta\psi$ will decay to zero provided $12N_0VT\cos\psi_0 < 0$. With the physical requirement that $N_0 > 0$ and $T < 0$, the accessible stable stationary states are ones where $V\cos\psi_0 > 0$. That is $V\cos\psi_0 = +(V^2 - \gamma^2)^{1/2}$. Otherwise, for $V\cos\psi_0 = -(V^2 - \gamma^2)^{1/2}$, the states are unstable. Note that for $12N_0VT\cos\psi_0 < -\gamma^2$ the roots $S_\pm$ are complex leading to damped oscillatory decay for $\delta N(t)$ (cf. right half of Fig. 1). On the other hand, when $12N_0VT\cos\psi_0 + \gamma^2 \approx 0$ the two roots become $S_+ \approx 6N_0VT\cos\psi_0/\gamma$ and $S_- \approx -2\gamma$. Hence after a time $\gg \gamma^{-1}$, $\delta N(t)$ decays asymptotically as

$$\delta N(t) = \delta N(0)\exp[-6N_0|T|(V^2/\gamma^2 - 1)^{1/2}t] , \quad (16)$$

which is the behavior displayed in the left half of Fig. 1. This behavior is characterized as the adiabatic limit.[22]

IV. DISCUSSION

The two important points that came out of our investigation are (1) the stationary states are ones of common phase and (2) the phases lock before the system arrives at the final fixed point. The presence of phase locking reduces the macroscopic set of equations (2) and (3) to two:

$$\frac{dN}{dt} = N(-\gamma + V\sin\psi) , \quad (17)$$

$$\frac{d\psi}{dt} = \Delta\omega + 3TN + V\cos\psi . \quad (18)$$

We see that as long as phase locking occurs, the results are the same whether we are investigating two modes, a hundred modes or a macroscopic number of modes. Note that the quantity that is relevant experimentally is N, not the magnitude of each individual occupation number. The fixed point in our result actually resides on an $(A-1)$ dimensional hyperplane since it is the sum of the occupation number that equals a constant, the individual components being dependent on the initial conditions.

The analysis outlined in the preceeding sections characterizes the nonequilibrium stationary states of the system. As discussed in Ref. 8, with increasing power the stationary state in the easy plane ferromagnet $(CH_3NH_3)CuCl_4$ is followed by a regime where the spin-wave population oscillates in time and, ultimately, to a chaotic regime. An extensive analysis of (2) and (3) fails to reveal any periodic or chaotic behavior at high-power levels. The failure to locate any periodic or chaotic behavior appears to invalidate the applicability of the S theory in describing these phenomena on easy plane ferromagnets with dominant single ion or exchange anisotropy.

[1] S. M. Rezende, F. M. deAguiar, and O. F. de alcantara Bonfim, J. Magn. Magn. Mater. **54–57**, 1127 (1986).
[2] G. Gibson and C. Jeffries, Phys. Rev. A **29**, 811 (1984).
[3] F. M. de Aguiar and S. M. Rezende, Phys. Rev. Lett. **56**, 1070 (1986).
[4] M. Mino and H. Yamazaki, J. Phys. Soc. Jpn. **55**, 4168 (1986). See also V. L. Grankin, V. S. L'vov, V. I. Motorin and S. L. Musher, Zh. Eksp. Teor. Fiz. **81**, 757 (1981) [Sov. Phys. JETP **54**, 405 (1981)].
[5] H. Yamazaki, J. Phys. Soc. Jpn. **53**, 1155 (1984).
[6] F. Waldner, R. Badii, D. R. Barberis, G. Broggi, W. Floeder, P. F. Meier, R. Stoop, M. Warden, and H. Yamazaki, J. Magn. Magn. Mater. **54–57**, 1135 (1986).
[7] H. Yamazaki, M. Mino, H. Nagashima, and M. Warden, J. Phys. Soc. Jpn. **56**, 742 (1987).
[8] H. Yamazaki and M. Warden, J. Phys. Soc. Jpn. **55**, 4477 (1986).
[9] H. Suhl, J. Phys. Chem. Solids **1**, 209 (1957).
[10] E. Schlömann, J. J. Green, and U. Milano, J. Appl. Phys. **31**, 386S (1960).
[11] P. Gottlieb and H. Suhl, J. Appl. Phys. **33**, 1508 (1968).
[12] V. E. Zakharov, V. S. L'vov, and S. S. Starobinets, Zh. Eksp. Teor. Fiz. **59**, 1200 (1970) [Sov. Phys. JETP **32**, 656 (1971)].
[13] V. E. Zakharov, V. S. L'vov, and S. S. Starobinets, Usp. Fiz. Nauk. **114**, 609 (1974) [Sov. Phys.-Usp. **17**, 896 (1975)].
[14] K. Nakamura, S. Ohta, and K. Kawasaki, J. Phys. C **15**, L143 (1982).
[15] S. Ohta and K. Nakamura, J. Phys. C **16**, L605 (1983).
[16] F. Waldner, D. R. Barberis, and H. Yamazaki, Phys. Rev. A **31**, 420 (1985). See also G. Broggi, P. F. Meier, R. Stoop, and R. Badii, Phys. Rev. A **35**, 365 (1987).
[17] X. Y. Zhang and H. Suhl, Phys. Rev. A **32**, 2530 (1985).
[18] H. Suhl and X. Y. Zhang, Phys. Rev. Lett. **57**, 1480 (1986).
[19] S. M. Rezende, O. F. de Alcantara Bonfim, and F. M. de Aguiar, Phys. Rev. B **33**, 5153 (1986).
[20] S. P. Lim and D. L. Huber (to be published).
[21] C. Kittel, *Quantum Theory of Solids* (Wiley, New York, 1964), Chap. 4.
[22] V. E. Zakharov, V. S. L'vov, and S. L. Musher, Fiz. Tverd. Tela **14**, 832 (1972) [Sov. Phys.—Solid State **14**, 710 (1972)].

Chaos in spin clusters: Correlation functions and spectral properties

Niraj Srivastava, Charles Kaufman, and Gerhard Müller
Department of Physics, The University of Rhode Island, Kingston, Rhode Island 028801-0817

We investigate dynamic correlation functions for a pair of exchange-coupled classical spins with biaxial exchange and/or single-site anisotropy. This represents a Hamiltonian system with two degrees of freedom for which we have previously established the integrability criteria. We discuss the impact of (non-)integrability on the autocorrelation functions and their spectral properties. We point out the role of long-time anomalies caused by low-flux cantori, which dominate the convergence properties of time averages and determine the long-time asymptotic behavior of autocorrelation functions in nonintegrable cases.

Classical spin dynamics of magnetic insulators, which employs classical counterparts of quantum mechanical exchange Hamiltonians, has proven to be very useful and illuminating in statistical mechanics and magnetic materials research. For a direct connection to experimentally observable quantities and for easy comparison with the results of quantum spin dynamics, it is convenient to focus such classical dynamical studies on the properties of dynamic correlation functions. Nonintegrability effects in spin dynamics have received their due share of attention only fairly recently.[1-5] In fact, spin dynamics lends itself ideally to the study of classical and quantum chaos, which is necessarily numerical in its nature, for the following reasons: The "phase space" of a finite classical spin system is a compact manifold, and the energy is bounded by a finite interval; the Hilbert space of a finite quantum spin system has a finite dimensionality. These special features allow for a numerical analysis with no further truncations or approximations which are likely to introduce artificial effects. The object of the work reported here is to study autocorrelation functions and their spectral properties in integrable and nonintegrable spin clusters.

Consider a system of two localized classical three-component spins $\mathbf{S}_l = (S_l^x, S_l^y, S_l^z)$, $l = 1,2$, specified by an interaction Hamiltonian of the general form

$$H = \sum_{\alpha = xyz} \{ -J_\alpha S_1^\alpha S_2^\alpha + \tfrac{1}{2} A_\alpha [(S_1^\alpha)^2 + (S_2^\alpha)^2] \}, \tag{1}$$

which includes both exchange and single-site anisotropy. Its time evolution is governed by the equation of motion

$$d\mathbf{S}_l/dt = -\mathbf{S}_l \times \partial H/\partial \mathbf{S}_l = \{H, \mathbf{S}_l\}, \quad l = 1,2, \tag{2}$$

where

$$\{S_l^\alpha, S_{l'}^\beta\} = -\delta_{ll'} \sum_\gamma \epsilon^{\alpha\beta\gamma} S_l^\gamma \tag{3}$$

are the Poisson brackets for classical spin variables. Their structure guarantees that the Hamilton equation of motion (2) is consistent with the Heisenberg equation of motion for quantum spin operators. If the classical spins $\mathbf{S}_l$ are expressed in terms of spherical coordinates as

$$\mathbf{S}_l = S(\sin\vartheta_l \cos\varphi_l, \sin\vartheta_l \sin\varphi_l, \cos\vartheta_l)$$

then a set of canonical variables is given by $p_l = S\cos\vartheta_l$, $q_l = \varphi_l$. Hence, the classical two-spin system (1) represents an autonomous Hamiltonian system of two degrees of freedom. It is completely integrable if there exists an independent integral of the motion in addition to H. In a previous study,[3] we have determined the following integrability condition for the two-spin model (1):

$$(A_x - A_y)(A_y - A_z)(A_z - A_x) + \sum_{\alpha\beta\gamma = \text{cycl}(xyz)} J_\alpha^2 (A_\beta - A_\gamma) = 0 \tag{4}$$

and have constructed explicitly the second independent integral of the motion for the integrable cases.

In the present work, we study two types of autocorrelation functions for classical spin clusters:
(i) *autocorrelation function as a time average,*

$$\langle S_l^\alpha(t) S_l^\alpha \rangle_T = \lim_{T\to\infty} \frac{1}{T} \int_0^T dt'\, S_l^\alpha(t+t') S_l^\alpha(t'), \quad l = 1,2; \quad \alpha = x, y, z, \tag{5}$$

where the quantity $S_l^\alpha(t) S_l^\alpha(0)$ is averaged over all points of a single phase-space trajectory. Since the phase flow generated by Hamiltonian (1) is not ergodic on the energy hypersurface even for nonintegrable cases, correlation functions defined as (microcanonical) phase averages are in general different from (5), but no less interesting in the context of our study. Here we focus our discussion of phase averages on canonical ensembles at infinite temperature:
(ii) *autocorrelation function as a phase average,*

$$\langle S_l^\alpha(t) S_l^\alpha \rangle_P = (4\pi)^{-2} \int d\mathbf{S}_1(0) \int d\mathbf{S}_2(0) S_l^\alpha(t) S_l^\alpha(0), \tag{6}$$

where the quantity $S_l^\alpha(t) S_l^\alpha(0)$ is determined as a function of the initial conditions $[\mathbf{S}_1(0), \mathbf{S}_2(0)]$ and then averaged over all initial conditions in phase space. Both types of autocorrelation functions are real and even functions of time.

In integrable cases of the two-spin model (1), the course of any trajectory is confined to an invariant torus, implying that the correlation function $\langle S_l^\alpha(t) S_l^\alpha \rangle_T$ is either periodic, if the two fundamental frequencies of the torus are commensurate, or quasiperiodic, if they are incommensurate. In either case, the intensity spectrum of $\langle S_l^\alpha(t) S_l^\alpha \rangle_T$ as determined by its Fourier transform

 0021-8979/88/084154-03$02.40 © 1988 American Institute of Physics

$$\Phi_{\alpha\alpha}^{(I)}(\omega) = \int_{-\infty}^{+\infty} dt\, e^{i\omega t} \langle S_I^\alpha(t) S_I^\alpha \rangle \tag{7}$$

is discrete, governed by these two frequencies and, unless the time evolution of $S_I^\alpha(t)$ is harmonic, also by their sums and differences.

Quite generally, a continuous frequency spectrum is necessary to produce a correlation function which decays to a constant asymptotically for long times. In integrable two-spin models, this can only be realized in autocorrelation functions of the type $\langle S_I^\alpha(t) S_I^\alpha \rangle_P$, which draw on the combined spectrum of the time evolution for *all* initial conditions. This spectrum is, in general, entirely continuous. For the purpose of illustration, we present here the exact autocorrelation functions $\langle S_I^\alpha(t) S_I^\alpha \rangle_P$ for two integrable cases of (1) for which the analysis is particularly simple.

(I) *"Ising model"* ($J_x = J_y = 0$, $J_z = 2$, $A_x = A_y = A_z = 0$):

$$\langle S_I^x(t) S_I^x \rangle_P = \tfrac{1}{4}[\sin(2t)/2t\,], \tag{8a}$$

$$\Phi_{xx}^{(I)}(\omega)_P = (\pi/6)\Theta(2 - |\omega|). \tag{8b}$$

(II) *Heisenberg model* ($J_x = J_y = J_z = 1$, $A_x = A_y = A_z = 0$):

$$\langle S_I^x(t) S_I^x \rangle_P = \frac{1}{6} + \frac{2}{3}\left(\frac{3}{4t^3}\sin(2t) - \frac{3 + 2t^2}{8t^4} + \frac{3 - 4t^2}{8t^4}\cos(2t)\right), \tag{9a}$$

$$\Phi_{xx}^{(I)}(\omega)_P = \frac{\pi}{3}\delta(\omega) + \frac{\pi}{24}|\omega|(4 - \omega^2)\Theta(2 - |\omega|). \tag{9b}$$

In both models, the correlation functions decay algebraically. The dominant term of the long-time asymptotic decay is determined by the strongest singularity in the continuous part of the intensity spectrum. In case (I), this is a discontinuity at $|\omega| = 2$, which results in the $1/t$ behavior of (8a). In case (II) the linear cusps at $\omega = 0$ and $|\omega| = 2$ give rise to the leading $1/t^2$ terms in (9a). Note that in both models, the intensity spectrum has an upper frequency cutoff. This is so because the time evolution of $S_I^\alpha(t)$ is harmonic for any initial conditions. This property is no longer present in the next simplest integrable case of the general two-spin model (1), the *XY model* ($J_x = J_y = 1$, $J_z = 0, A_x = A_y = A_z = 0$). Here the time evolution is expressible in terms of Jacobi elliptic functions for arbitrary initial conditions,[5] and the intensity spectrum of the autocorrelation functions has no up per frequency bound.

In the nonintegrable cases of the two-spin model (1), i.e., for parameter values which do not satisfy the condition (4), only a subset of the phase-space trajectories is confined to invariant tori. For these regular trajectories, the autocorrelation functions $\langle S_I^\alpha(t) S_I^\alpha \rangle_T$ have the same characteristic properties as in the integrable cases discussed previously: no decay, discrete spectrum, two fundamental frequencies. However, in nonintegrable cases, the set of invariant tori is nowhere dense in phase space, even though it has a nonzero measure. Between any two tori, there is a region in which the phase flow is chaotic. Quite different characteristic features are expected of autocorrelation functions defined as time averages over chaotic trajectories.

For a specific example, we consider the nonintegrable case $J_x = J_y = 1$, $J_z = 0$, $A_x = 2$, $A_y = -1$, $A_z = 0$ of the two-spin model (1). We have evaluated for a particular set of initial conditions the three autocorrelation functions $\langle S_1^\alpha(t) S_1^\alpha \rangle_T$, $\alpha = x, y, z$, via the average over a time interval of length $T = 100\,000$ from the time series of a chaotic trajectory. Figure 1 shows the function $\langle S_1^x(t) S_1^x \rangle_T$ for $0 < t < 250$ and the functions $\langle S_1^y(t) S_1^y \rangle_T$, $\langle S_1^z(t) S_1^z \rangle_T$ for time differences up to $t = 100$. All three correlation functions clearly decay to zero. The rate of decay is slowest in $\langle S_1^z(t) S_1^z \rangle_T$ and fastest in $\langle S_1^x(t) S_1^x \rangle_T$. The *yy*- and *zz*-correlation functions exhibit distinct oscillations unlike the *xx*-correlation function, which decays much more uniformly. The decay of these correlation functions results as a consequence of the chaotic nature of the trajectory and implies that the phase flow in the region sampled by the trajectory has *mixing* character. The oscillations indicate that this mixing flow is superimposed on a quasiperiodic flow which is mostly perpendicular to the x_1 direction. They are signs of quasiperiodicity over short times, i.e., periodicity subject to continued phase slips. The inset to Fig. 1(a) shows $\langle S_1^x(t) S_1^x \rangle_T$ on a log-log scale. For $20 < t < 100$, the curve is

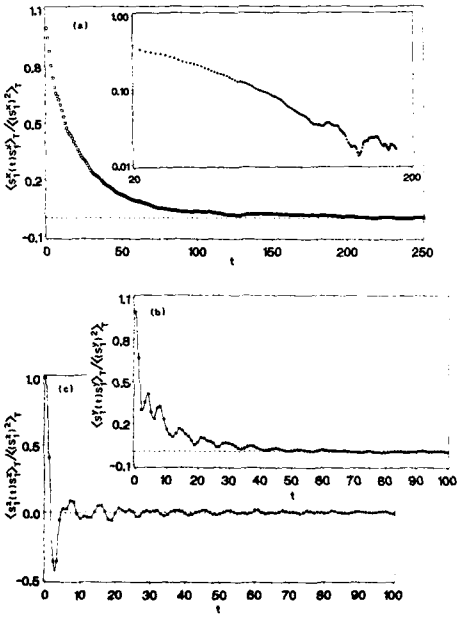


FIG. 1. Normalized autocorrelation function $\langle S_1^\alpha(t) S_1^\alpha \rangle_T / \langle (S_1^\alpha)^2 \rangle_T$, $\alpha = x, y, z$, for the nonintegrable classical two-spin model defined by Hamiltonian (1) with parameter values $J_x = J_y = 1, J_z = 0, A_x = 2, A_y = -1, A_z = 0$. The results are obtained from the chaotic trajectory specified by the initial conditions $\vartheta_1^{(0)} = 1.0$, $\vartheta_2^{(0)} = 2.0$, $\varphi_1^{(0)} = 3.0$, $\varphi_2^{(0)} = 1.29$, and evaluated by a fourth-order Runge–Kutta integration via the time average over an interval of size $T = 100\,000$. The inset to (a) shows the same correlation function $\langle S_1^x(t) S_1^x \rangle_T / \langle (S_1^x)^2 \rangle_T$ in a doubly logarithmic plot for times between $t = 20$ and $t = 200$.

nearly straight, indicating that the xx correlations decay algebraically: $\langle S_1^x(t)S_1^x\rangle_T \sim t^{-1.5}$.

It is interesting to compare our findings with existing results for autocorrelation functions of area-preserving maps. A numerical study of the standard map[6] yielded algebraic decay close to $\sim t^{-1/3}$; a similar study of the quadratic map[7] also found algebraic decay, but the exponent value could be placed only somewhere between 1/2 and 3/2. On the basis of a Markov chain model for transport in the boundary layer of a chaotic region, Hanson, Cary, and Meiss[8] predicted more rapid algebraic decay, $\sim t^{-2.05}$; a considerably slower algebraic decay, $\sim t^{-0.96}$, was predicted by the more elaborate calculation of Meiss and Ott[9] based on a Markov tree model. We can place our result among these others as discussed in the following.

In a previous comprehensive study[5] of time averages in classical two-spin systems, we have already found evidence that the phase flow in chaotic regions is *ergodic*, but also that the convergence of time averages can be extremely slow due to long-time anomalies caused by low-flux cantori via two different mechanisms: (i) In a region of widespread chaos, the dominant mechanism is attributable to the stickiness of its boundaries. They typically consist of layers of cantori separated by Birkhoff chains, in which chaotic trajectories become temporarily trapped. We have found that the slowing down of convergence due to this mechanism is considerable but not alarming. (ii) A different mechanism, which is responsible for much stronger long-time anomalies, occurs in situations where a chaotic region is tessellated by cantori into roughly equal-sized compartments. A characteristic feature of this case is that time averages appear to converge slowly to some mean value, similar to case (i), but then suddenly start to converge toward a different value [again slowly as in case (i)], and that this abrupt change happens repeatedly but irregularly, each change occurring as the trajectory switches compartments through one of the low-flux cantori. The time scales of this process are typically much larger than in process (i). The averages over the trajectory at hand have converged quite well. Thus the series must be long compared to any anomalies encountered, and the time scale for the remaining anomalies to be met must be very long compared to the averaging time used here.

Evidently, these long-time anomalies must play an important role in dynamic correlation functions. In K systems, which are characterized by a special type of mixing flow (a phase flow associated with a positive Kolmogorov entropy production), and where none of the long-time anomalies described above can occur, the autocorrelation functions decay exponentially in time.[10] In the model of Ref. 8, the effect of only one sticky boundary is considered, and fast algebraic decay ensues. In Ref. 9 the effects of a fractal structure of sticky boundaries are included, which results in considerably slower algebraic decay. Since we are, as described previously, in an intermediate region, the intermediate exponent value is to be expected.

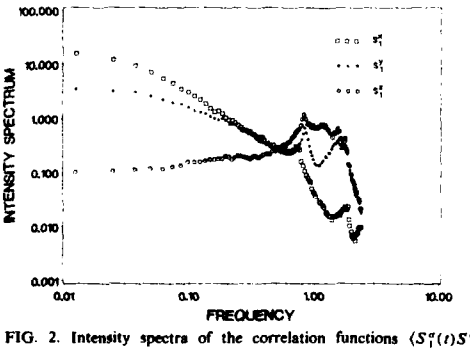


FIG. 2. Intensity spectra of the correlation functions $\langle S_1^\alpha(t)S_1^\alpha\rangle_T$, $\alpha = x, y, z$, shown in Fig. 1, as determined directly from the original time series $S_1^\alpha(t)$ of the chaotic trajectory.

We have also determined the intensity spectra of $\langle S_1^\alpha(t)S_1^\alpha\rangle_T$, $\alpha = x, y, z$, directly from the time series of the chaotic trajectory (see Fig. 2). Each spectrum is continuous, as is characteristic of a chaotic trajectory. We observe marked enhancements at $\omega \simeq 0.8$ and $\omega \simeq 1.3$ in the spectra of S_1^y and S_1^x. These oscillations are, as noted above, apparent in the correlation functions $\langle S_1^y(t)S_1^y\rangle_T$ and $\langle S_1^x(t)S_1^x\rangle_T$ (see Fig. 1). Our results also indicate that none of the spectra diverges in the low-frequency limit $\omega \to 0$, which is consistent with the rapid algebraic decay of the correlation functions.

In summary, we have found that algebraic decay of autocorrelation functions occurs in nonintegrable two-spin systems already for time averages over single (chaotic) trajectories. In integrable two-spin models, by contrast, autocorrelation functions decay only as a result of phase averaging.

A number of interesting questions remain to be answered: What is the role of invariant tori in the correlation functions $\langle S_I^\alpha(t)S_I^\alpha\rangle_P$ in nonintegrable models, given that the tori are nowhere dense in phase space? How do the effects of nonintegrability identified here for classical spin clusters make their appearance in autocorrelation functions of quantum spin systems near the classical limit? A more systematic study of dynamic correlation functions in integrable and nonintegrable classical and quantum spin clusters, which attempts to answer these and other questions, is currently in progress.

We thank H. Thomas and R. Weber for their continued interest in this project. This work was supported by a grant from Research Corporation, by the U. S. National Science Foundation, Grant No. DMR-86-03036 and by Sigma Xi, the Scientific Research Society.

[1] M. Feingold, N. Moiseyev, and A. Peres, Phys. Rev. A **30**, 509 (1984); H. Frahm and H. J. Mikeska, Z. Phys. B **60**, 117 (1985); K. Nakamura and A. R. Bishop, Phys. Rev. B **33**, 1963 (1986).
[2] G. Müller, Phys. Rev. A **34**, 3345 (1986).
[3] E. Magyari, H. Thomas, R. Weber, C. Kaufman, and G. Müller, Z. Phys. B **65**, 363 (1987).
[4] N. Srivastava, C. Kaufman, G. Müller, E. Magyari, R. Weber, and H. Thomas, J. Appl. Phys. **61**, 4438 (1987).
[5] N. Srivastava, C. Kaufman, G. Müller, R. Weber, and H. Thomas, Z. Phys. B (in press).
[6] B. V. Chirikov and D. L. Shepalyansky, Physica **13D**, 395 (1984).
[7] C. F. F. Karney, Physica **8D**, 360 (1983).
[8] J. D. Hanson, J. R. Cary, and J. D. Meiss, J. Stat. Phys. **39**, 327 (1985).
[9] J. D. Meiss and E. Ott, Phys. Rev. Lett. **55**, 2741 (1985); Physica **20D**, 387 (1986).
[10] G. M. Zaslavsky, *Chaos in Dynamic Systems* (Harwood, New York, 1985).

Chaos in magnetic garnet thin films

P. E. Wigen[a)]
The Ohio State University, Columbus, Ohio 43210

H. Doetsch and Y. Ming
University of Osnabrück, Osnabrück, Federal Republic of Germany

L. Baselgia and F. Waldner
University of Zürich, Zürich, Switzerland

Ferromagnetic resonance in thin magnetic garnet films has been studied at excitation frequencies of 10 GHz and from room temperature to 4.2 K. Powers sufficient to drive the magnetization to large precession angles have been studied. Second-order Suhl instabilities of the main resonance have been observed as an onset of auto-oscillations of the magnetization. These oscillations include regular and irregular oscillations, very noisy collective oscillations, as well as spiking. They have been observed in real time and by spectral analysis. In pure yttrium iron garnet (YIG) films the oscillations have been observed in the frequency range from 0.5 to 2 MHz at 300 and 4.2 K. In going from 300 to 4.2 K the threshold power level p_{th} in YIG films is lowered by three orders of magnitude, while the frequency of the regular oscillations are nearly independent of temperature. If p_{th} is connected to the intrinsic damping parameter γ, then γ is temperature dependent, which is in fair agreement with the large number of narrow resonance features observed in the films. Preliminary simulations using a model extending the S theory of Zakharov and Nakamura for large precession angles give time evolutions that are qualitatively similar to the experimental observations. Regular and weekly irregular oscillations are found for one spin-wave mode coupled to a linear resonance circuit, i.e., a phonon mode. More irregularity is found for two coupled spin-wave modes excited to large precession angles.

I. INTRODUCTION

The response of magnetic systems, both ferromagnetic and antiferromagnetic, at high rf powers is known to lead to a chaotic response of the magnetization vector. These investigations have been known for some years for parallel pumped geometries in antiferromagnetic resonance.[1-4]

As these investigations are undertaken in the 10-GHz range the materials are required to have a weak exchange coupling between the magnetic sublattices and, therefore, have a low T_N. Consequently, these experiments have been restricted principally to the antiferromagnetic copper compounds. As a result of these low Néel temperatures, the investigations are limited to temperature ranges near the helium temperature region.

Nonetheless, these successful investigations have stimulated considerable theoretical interest in this process and the field has recently become very active.[5-11]

More recently, experiments have been undertaken in yittrium iron garnet (YIG) spheres using the parallel pump configuration.[12-14] These experiments have been undertaken at the subsidiary resonance, at both liquid helium and room temperatures. In this paper, we report the first observation of the chaotic behavior of the ferromagnetic resonance in the perpendicular orientation in thin YIG films at room temperature and liquid-helium temperature.

II. EXPERIMENTS

Single-crystal YIG films were grown by liquid-phase epitaxy with thicknesses from 0.70 to 1.30 μm. The substrates were cut to 3-mm disks and a pixel of less than 1 mm diameter was etched[15] into the disk. The samples were mounted in the center of a TE 102 cavity of a 10-GHz spectrometer. Both the field and the sample could be rotated about mutually orthogonal axes to assure the perpendicular orientation of the field to the film surface.

The microwave power is supplied by a Varian klystron, having an output power of approximately 300 mW. The power incident to the cavity is controlled by a stepper motor controlled precision attenuator.

A typical linewidth at room temperature was 0.3 G at 10 GHz. At high rf powers, the ferromagnetic resonance goes into the nonlinear regime and the crystal detector output is recorded on a storage scope having 512 channels and from there the data are transferred to a computer for final storage and analysis. At high rf powers the second-order Suhl instabilities of the main resonance are observed and a typical output of the chaotic response detected in the crystal detector is shown in Fig. 1(a). The magnetic field range of the chaotic oscillations is shifted to lower fields with increasing power due to the opening of the magnetization vector. As the power is increased, the system goes from the initial chaotic state into a region of stable oscillations, as shown by the signal in Fig. 1(b). On further increasing the power a bifurcation to a period 2 response as shown in Fig. 1(c) occurs. At still higher powers the system becomes chaotic again.

In the helium temperature region, 4.2 K, the oscillations

[a)] This work was performed while on sabbatical leave to the University of Osnabrück and the University of Zürich 1986–1987.

 0021-8979/88/084157-03$02.40 © 1988 American Institute of Physics

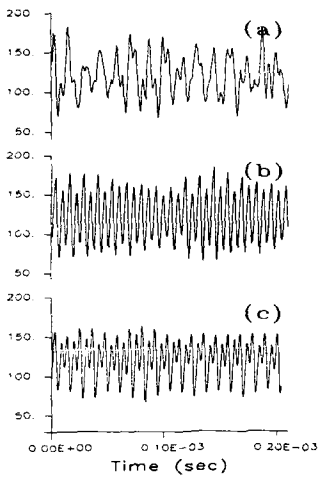


FIG. 1. Room-temperature detector response to the slow oscillations of the precessing magnetic vector in time. (a) A chaotic response at low power. (b) A region of stable oscillations at intermediate power. (c) The bifurcation process at higher powers. At still higher powers the response is again chaotic similar to the pattern shown in (a).

are observed to occur at approximately 30 dB less power than that required at room temperature. The initial response observed at low power is a spiking phenomena in the precessing magnetization vector, as shown in Fig. 2. At higher powers, again periodic bifurcation and a chaotic behavior are observed.

III. RESULTS AND DISCUSSION

A. Room temperature

The amplitude of the rf detector signal is proportional to the number of $k = 0$ magnons excited by the rf field. These

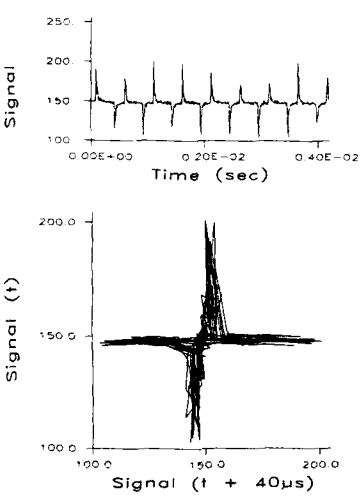


FIG. 2. (a) Spiking observed in the YIG film at 4.2 K. (b) The return map for the spiking process.

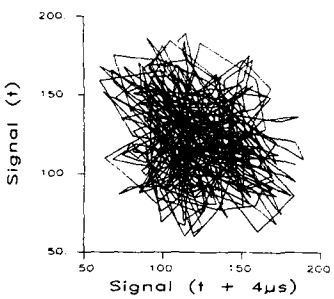


FIG. 3. Return map for the signal shown in Fig. 1(a).

magnons are coupled to other $k \neq 0$ magnons and at sufficiently high rf power auto-oscillations are observed. The experiment has no way of measuring the number of $k \neq 0$ magnons nor their k value.

To analyze the data, the one-dimensional time signal is embedded in a multidimensional phase space by use of the time delay method.[3,4] The voltage is stored in integral units of time τ_0 in the storage scope. An n-dimensional time series is generated in the usual fashion by the sequence of $V(t + n\tau_0)$. In this manner a 2D or 3D phase space portrait can be constructed by plotting $V(t)$, $V(t + \tau)$,..., $V(t + n\tau)$. The 2D phase portrait for the signals in Fig. 1 are shown in Figs. 3–5 for $\tau = 4\,\mu$s. Detailed analysis of these curves and others as functions of power, temperature, and other parameters will allow a comprehensive evaluation of the fractal properties of the system.

B. Liquid-helium temperature

At liquid-helium temperature the distribution of the spiking freuency as a function of the magnetic field for a variety of power levels is shown in Fig. 6. The peak in the frequency and their falling off at either side of the peak frequency is not understood at this time. With a further increase in power, the period and bifurcation of autooscillations are again observed at liquid-helium temperatures though at much lower powers than those observed at room temperature.

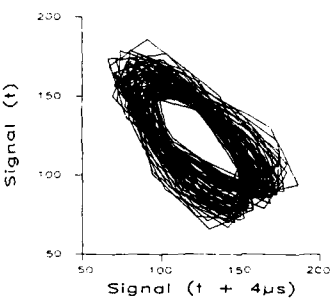


FIG. 4. Return map for the signal shown in Fig. 1(b).

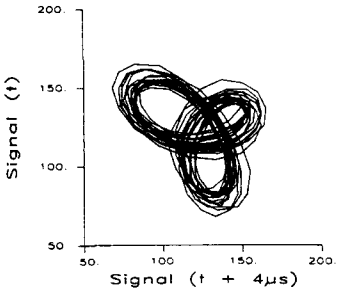


FIG. 5. Return map for the signal shown in Fig. 1(c).

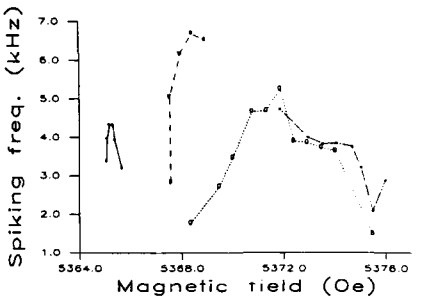


FIG. 6. Dependence of the spiking frequency on magnetic field at different input power levels. The solid curve corresponds to 36 dB; the dashed line, 22 dB; dotted line, 20 dB; and the dot-dashed line, 18 dB.

IV. THE MODEL

Simulations have been obtained using a model extending the S theory of Zakharov–Nakamura[5,6] for large precession angles. The analysis is simplified by employing the "stroboscopic model" (SM) which integrates the spin precession between strobing times analytically. For small polar angles θ of the spin precession, the SM is equivalent to the S theory, which uses the Holstein–Primakoff transformation in the classical limit. Since the stroboscopic model is described in detail elsewhere,[11] only one point is mentioned here.

In the S-theory, standing spin waves interact by a Hamiltonian quadratic in the operators for each mode. Similarly, this interaction is expressed in the SM as components of classical spins, S_k and S_j, also quadratic in the two interacting modes, k and j. After integration over one period between consecutive strobing times, the equations of motion are modified from S-theory as follows:

$$\frac{d\theta_k}{dt} = \text{driving term} + \sin\theta_k \sin^2\theta_j\, b_{kj} \times \sin 2(\phi_k - \phi_j) + \text{damping term},$$

$$\frac{d\phi_k}{dt} = \text{driving term} + \cos\theta_k \sin^2\theta_j\, b_{kj} \times \cos 2(\phi_k - \phi_j) + \text{detuning term}.$$

These equations yield time evolutions of auto-oscillations similar to those in Fig. 1.

As examples, using only two coupled modes, period doubling combined with some irregularity in the amplitudes appeared in the simulations that are similar to those observed in the experiment. At high-power levels, irregular spiking is also seen in the simulations. Moreover, coupling only one spin-wave mode with a linear oscillator representing a phonon mode, resulted in weakly chaotic behavior similar to the experimental conditions performed at parameter settings where magnon-phonon interaction are obvious.

ACKNOWLEDGMENT

The authors wish to thank Mr. A. Brockmeyer for the growing of YIG films, Mr. R. McMichael for assistance with the data, and Dr. M. Warden for his many helpful conversations.

[1]H. Yamazaki, J. Phys. Soc. Jpn. **53**, 1155 (1984).
[2]F. Waldner, D. R. Barberis, and H. Yamazaki, Phys. Rev. A **31**, 420 (1985).
[3]H. Yamazaki and M. Warden, J. Phys. Soc. Jpn **55**, 4477 (1986).
[4]H. Yamazaki, M. Mino, H. Nagashima, and M. Warden, J. Phys. Soc. Jpn. **56**, 742 (1987).
[5]V. E. Zakharov, V. S. L'vov, and S. S. Starobinets, Usp. Fiz. Nauk. **114**, 609 (1974) [Sov. Phys.-Usp. **17**, 896 (1975)].
[6]K. Nakamura, S. Ohta, and K. Kawasaki, J. Phys. C **15**, L143 (1982).
[7]S. Ohta and K. Nakamura, J. Phys. C **16**, L605 (1983).
[8]H. Suhl and X. Y. Zhang, Phys. Rev. Lett. **57**, 1480 (1986).
[9]S. M. Rezende, O. A. Bortim, and F. M. de Aguiar, Phys. Rev. B **33**, 5153 (1986).
[10]A. I. Smirnov, Zh. Eksp. Teor. Fiz. **90**, 385 (1986) [Sov. Phys. JETP **63**, 222 (1986)].
[11]F. Waldner, J. Phys. C (to be published).
[12]G. Gibson and C. Jeffries, Phys. Rev. A **29**, 811 (1984).
[13]F. M. de Aguiar and S. M. Rezende, Phys. Rev. Lett. **56**, 1070 (1986).
[14]P. Bryant, C. Jeffries, and K. Nakamura, Nucl. Phys. B (to be published).
[15]T. S. Stakelon and A. C. Gerhardstein, Rev. Sci. Instrum. **47**, 637 (1976).

Excitation spectra of generalized antiferromagnetic Heisenberg spin chains[a] (abstract)

J. B. Parkinson[b] and J. C. Bonner
Department of Physics, University of Rhode Island, Kingston, Rhode Island 02881

We compare the excitation spectra in the presence of a magnetic field of a number of integrable (exactly solvable) and nonintegrable quantum spin chains of various spin value s. The archetypal Bethe-ansatz integrable model is the $s = \frac{1}{2}$ Heisenberg antiferromagnet (HB AFM). The excitation spectra are characterized by a soft mode which tracks across the Brillouin zone as the field increases to its saturation value. A class of Bethe-ansatz integrable models with SU(2) symmetry and the general spin s display excitation spectra qualitatively similar to the spin-$\frac{1}{2}$ model above, for all s. A second class of Bethe-ansatz integrable models has SU(n) symmetry, where $n = 2s + 1$. Like the SU(2) integrable chains, these models have gapless excitation spectra, but the basic Brillouin zone changes from $k = \pm 2\pi/(2s + 1)a$. Studies show that periodicity of the SU(3) member of the class changes (increases) as the field increases to saturation. For both classes of integrable models, there is a single type of excitation pattern which is generically similar for all s. In the case of the other models, on the other hand, numerical studies show that the excitations divide into at least two distinct classes. In the case of the $s = 1$ HB AFM, at high fields (corresponding to $S^z_T = N, N-1, \ldots, N/2$) the excitations map approximately onto the complete set of excitations for $s = \frac{1}{2}$, whereas at low fields ($S^z_T = N/2, N/2 - 1, \ldots, 0$) the excitations have notable classical character. In the case of the $s = 1$ model with pure biquadratic exchange, one set of excitations, corresponding to S^z_T even ($S^z_T = N, N-2, \ldots, 2, 0$), again shows an approximate mapping to the complete excitation set for $s = \frac{1}{2}$. The second class of excitations, corresponding to S^z_T odd, are very different. They are symmetric about $k = \pm \pi/2a$ *for all* S^z_T, i.e., correspond to a basic Brillouin zone of $\pm \pi/2a$.

[a] Supported by NSF Grant No. DMR86-03036.
[b] Visiting from Dept. of Applied Math., UMIST, Manchester, UK.

Spin-wave instability and "true" foldover in single-crystal YIG films (abstract)[a]

Y. T. Zhang,[b] C. E. Patton, and G. Srinivasan
Department of Physics, Colorado State University, Fort Collins, Colorado 80523

High-power pulsed microwave measurements of ferromagnetic resonance (FMR) in yttrium iron garnet (YIG) films have been extended to include all three in-plane and out-of-plane microwave and static field combinations for FMR. The 5.1-μm-thick films were prepared by liquid phase epitaxy on single-crystal gadolinium gallium garnet substrates and subsequently etched to form 500-μm circles. The FMR spectra were obtained with a 9.18-GHz pulse spectrometer as described in Ref. 1. The results confirm the conclusion of Ref. 1. The pulsed microwave FMR at high-power levels yields line broadening due to spin-wave instability processes, rather than the shifts and distorted profiles which occur due to heating under cw excitation conditions. The key new result is the explicit correlation between the microwave field amplitude for the onset of the line broadening and the FMR pump configuration. In addition to these line broadening effects at high power, a "true" foldover effect is observed for the perpendicular-to-plane static field case: the FMR shoulder shifts down in field at high powers, due to the nonlinear response and the limitations on that response from the spin wave instability processes.

[a] The YIG films were provided by J. D. Adam, Westinghouse Research Laboratory. This work was supported in part by a grant from Verbatim Corporation and Air Force Contract No. F-19628-85-0002.
[b] Visiting scholar from the Shanghai University of Science and Technology, PRC, May, 1985 to April, 1987.

[1] Y. T. Zhang, C. E. Patton, and M. V. Kogekar, IEEE Trans. Magn. MAG-22, 993 (1986).

 0021-8979/88/084160-01$02.40 © 1988 American Institute of Physics



Superconductivity and spin-glass ordering in $RBa_2(Cu_{1-x}Fe_x)_3O_z$: R=Y,Gd; $0 \leqslant x \leqslant 0.12$

K. Moorjani, J. Bohandy, B. F. Kim, and F. J. Adrian
The Milton S. Eisenhower Research Center, The Johns Hopkins University Applied Physics Laboratory, Johns Hopkins Road, Laurel, Maryland 20707

Y. W. Du, H. Tang, Z. Q. Qiu, and J. C. Walker
Department of Physics and Astronomy, The Johns Hopkins University, Baltimore, Maryland 21218

Samples of oxygen deficient perovskites, $YBa_2(Cu_{1-x}Fe_x)_3O_z$ and $GdBa_2(Cu_{1-x}Fe_x)_3O_z$ ($z \simeq 7$) were prepared with up to 12% Fe substituting for Cu. A novel variation of the microwave absorption technique was employed to establish the superconducting transition in these samples and to show that the reduction in the transition temperature with increasing Fe concentration is faster in the Gd samples than in the Y ones. In both series of samples, the room-temperature Mössbauer spectra reveal two distinct Fe sites corresponding to two local oxygen coordinations, and more significantly the spectra at 4.2 K for specimens with $x > 0.03$ show that the Fe moments are magnetically ordered, leading to the coexistence of superconductivity and magnetism.

INTRODUCTION

The superconducting transition temperature T_c of the archetypal oxygen-deficient perovskite,[1] $YBa_2Cu_3O_z$ ($x \simeq 7$, $T_c \simeq 95$), remains essentially unaltered when Y is replaced by a host of magnetic or nonmagnetic rare-earth ions,[2] and the substitution of the isotope[3] O^{18} for O^{16} or replacing one of the oxygens by sulphur[4] also does not alter T_c. However, replacing Cu by almost any other element[5] suppresses T_c. We have previously reported on x-ray structural studies and dc resistivity measurements[6] for the two Fe-substituted perovskite series, $YBa_2(Cu_{1-x}Fe_x)_3O_z$ and $GdBa_2(Cu_{1-x}Fe_x)_3O_z$, with $0 \leqslant x \leqslant 0.15$, and have also reported Mössbauer spectroscopy results[7,8] on materials with $x = 0.06$. On the basis of crystal chemistry and the ionic radii involved, Fe is expected to substitute for Cu and this is borne out by our previous[7,8] and present Mössbauer studies that reveal two Fe sites in agreement with the high-resolution neutron scattering studies[9] on $YBa_2Cu_3O_7$ powders and x-ray diffraction studies[10] on single-crystal $YBa_2Cu_3O_7$, both having established the existence of two Cu sites: a fourfold oxygen-coordinated square planar Cu(1) site between the planes of Ba ions and a fivefold oxygen-coordinated square pyramidal Cu(2) site between Y and Ba planes. The Mössbauer studies also reveal that for samples with $x \gtrsim 0.03$, superconductivity and magnetic ordering coexist at 4.2 K.

In the present study, the suppression of T_c with increasing Fe concentration,[6] is demonstrated by a novel variation of the microwave absorption technique.[11] The details of this technique will be published elsewhere,[12] and here we only point out that the high sensitivity of the technique allows detection of superconductivity in powder samples as small as 1 n.g; since the superconducting transition is recorded as a peak, the technique allows a precise measurement of T_c and easily resolves multiple superconducting phases.[11] The technique is further well suited for studies of superconducting phase transitions since abrupt changes in microwave resistance are recorded only if the changes are magnetic field dependent.

EXPERIMENTAL DETAILS

Samples of $YBa_2(Cu_{1-x}Fe_x)_3O_z$ were obtained by grinding, pressing, and sintering appropriate amounts of Y_2O_3 or Gd_2O_3 with $BaCO_3$, CuO, and Fe_2O_3 in flowing oxygen for 12 h. The process was repeated at least three times so as to complete the solid-state reaction and obtain single-phase materials with high oxygen content ($z = 7$). All samples here investigated by the x-ray diffraction method which revealed the pure samples ($x = 0$) to be orthorhombically distorted with increasing tendency towards the stabilization of the tetragonal phase on increasing the Fe concentration.[6] Conventional ESR (9.3 GHz) and Mössbauer spectrometers were employed to obtain the microwave response and the Mössbauer data.

RESULTS AND DISCUSSION

Figure 1 shows the temperature dependence of the microwave response for five samples from the series $YBa_2(Cu_{1-x}Fe_x)_3O_z$ with $0 < x < 0.12$. Corresponding data for the $GdBa_2(Cu_{1-x}Fe_x)_3O_z$ series with $0 < x < 0.095$ are quite similar resulting in the variation of T_c, with the Fe concentration, shown in Fig. 2 for both series. Within experimental error, the values of T_c and their decrease with increasing x are in good agreement with the values obtained from dc resistance measurements.[6] Additional information is discernible from the detailed temperature dependence of the micro-

 0021-8979/88/084161-03$02.40 © 1988 American Institute of Physics

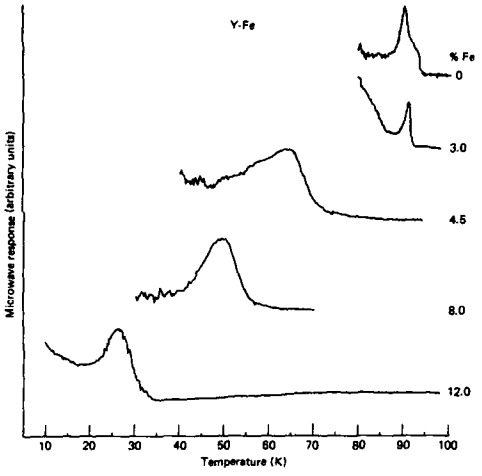


FIG. 1. Temperature dependence of the microwave response for $YBa_2(Cu_{1-x}Fe_x)_3O_z$ for $0 \leqslant x \leqslant 0.12$.

wave response. For example, the spectrum for $x = 0$ in the Y series (Fig. 1) is a superposition of two peaks corresponding to the existence of two distinct superconducting phases with slightly different values of T_c in this particular sample. However, other samples in the series, prepared ostensibly in the same manner, exhibited a single-peak characteristic of a single superconducting phase. The broadening of the peaks in samples with $x > 0.003$ suggests an "inhomogeneous line broadening" due to multiple unresolved superconducting phases. It should be noted that the increase in linewidth with increasing x is nonmonotonic reaching a maximum at Fe concentrations less than 9.5%. Whether this is related to the orthorhombic-tetragonal crystalline transition observed in these series of materials[6] remains to be explored.

The room-temperature Mössbauer spectra for the Y and Gd series are similar and for the former series are shown in Fig. 3. Focusing on the spectrum for the lowest Fe concentration (0.3%), for the moment, it represents the superposition of three pairs of nonsymmetric quadrupole split doublets. Two of the doublets represent approximately 90% of the spectral area while the remaining central doublet shows a much smaller quadrupole splitting and possibly arises from a small number of octahedrally coordinated Fe sites in the grain boundaries of the material. The other two doublets, the pair with the larger splitting ($QS = 1.94$ mm/s in the Y:Fe compound and $QS = 1.97$ mm/s in the Gd:Fe material) is to be associated with the planar Cu(I) site, while the doublet with the smaller splitting ($QS = 1.09$ mm/s for Y:Fe and $QS = 1.05$ mm/s for Gd:Fe) corresponds to the pyramidal Cu(II) site. The slightly different small isomer shifts for the

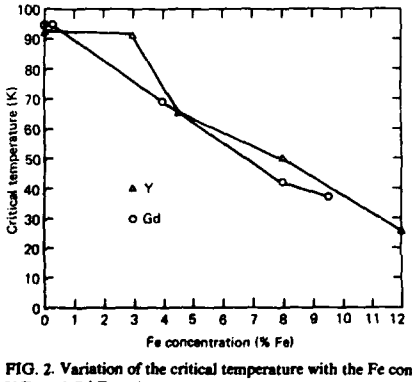


FIG. 2. Variation of the critical temperature with the Fe concentration in Y:Fe and Gd:Fe series.

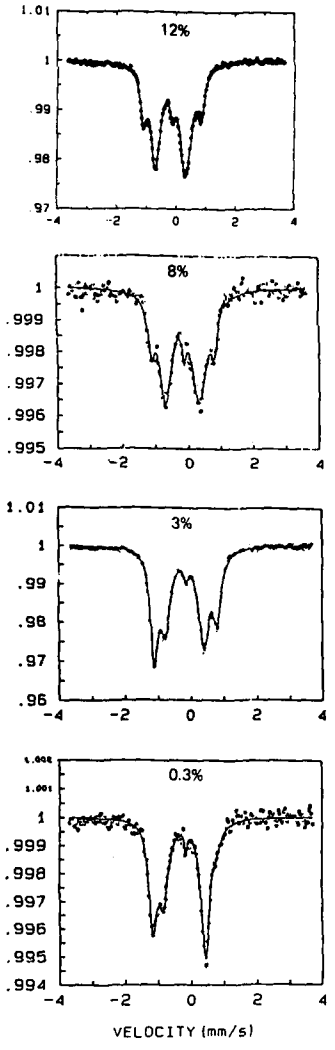


FIG. 3. The room-temperature Mössbauer spectra for Y:Fe series.

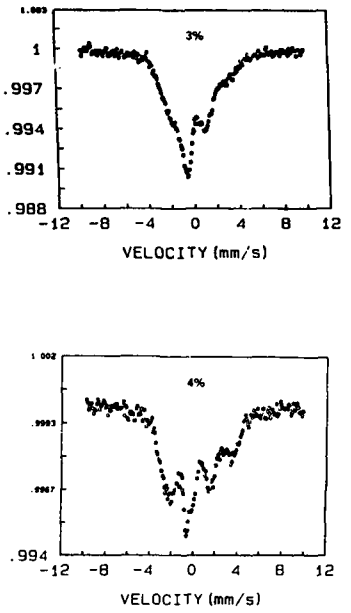


FIG. 4. The Mössbauer spectra at 4.2 K for Y:Fe (top) and Gd:Fe (bottom).

two quadrupole doublets differ from the Fe^{3+} ions in Fe_2O_3 and are in fact closer to metallic Fe suggesting complicated effective valence, like that of Cu in these materials, for Fe ions. The values of isomer shifts and quadrupole splittings are essentially independent of the Fe concentrations. The line intensities and the degree and direction of the asymmetry are, however, clearly dependent on the amount of Fe, but in a manner that does not lend itself to a detailed explanation at present. The intensity ratios for the two doublets would be expected to be in the 2:1 ratio if Fe were to substitute randomly for Cu, and this is indeed occasionally observed. But the ratio depends critically on the formation condition of the compounds and often varies from the 2:1 ratio. Moreover, since the crystal structure goes from orthorhombically distorted to purely tetragonal phase on increasing Fe concentration, one would expect a larger number of sites to be octahedrally coordinated at the high iron concentration as seen, for example, in Fig. 3 with 12% Fe.

Since Fe, for the most part, has clearly substituted into the Cu sites that play a central role in the superconductivity of these materials, it is rather surprising that for concentration of Fe equal to or higher than approximately 3% the Mössbauer spectra reveal magnetic ordering at 4.2 K (Fig. 4). The spectra are complex, show a distribution of magnetic hyperfine fields with a broad range of ~200–400 kOe, and resemble those of spin-glass ordering in the sense that no sharp transition to the ordered state is observed but instead a large broadening in the wings is seen, and the spectra cannot be fit assuming a constant angle between the local magnetization direction and the electric field gradient. The coexistence of the magnetic ordering with large local magnetization and superconductivity implies a robust superconducting mechanism and/or a rather short correlation length for electron-pair formation.

[1]C. W. Chu, P. H. Hor, R. L. Meng, L. Gao, Z. J. Huang, and Y. O. Wang, Phys. Rev. Lett. **58**, 405 (1987).
[2]P. H. Hor, R. L. Meng, Y. O. Wang, L. Gao, Z. J. Huang, J. Bechtold, K. Forster, and C. W. Chu, Phys. Rev. Lett. **58**, 1891 (1987); D. W. Murphy, S. Sunshine, R. B. van Dover, R. J. Cava, B. Batlogg, S. M. Zahurak, and L. F. Schneemeyer, *ibid.* **58**, 1888 (1987).
[3]B. Batlogg, R. J. Cava, A. Jayaraman, R. B. van Dover, G. A. Kourouklis, S. Sunshine, D. W. Murphy, L. W. Rupp, H. S. Chen, A. White, K. T. Short, A. M. Mujsce, and E. A. Rietman, Phys. Rev. Lett. **58**, 2333 (1987); L. C. Bourne, M. F. Crommie, A. Zettl, Hans-Conrad zur Loye, S. W. Keller, K. L. Leary, Angelica M. Stacy, K. J. Chang, Marvin L. Cohen, and D. E. Morris, *ibid.* **58**, 2337 (1987). However, a small isotope effect has recently been reported [K. J. Leary *et al.*, *ibid.* **59**, 1236 1987)].
[4]I. Felner, I. Nowik, and Y. Yeshurun, Phys. Rev. B **36**, 3923 (1987).
[5]G. Xiao, F. H. Streitz, A. Garvin, Y-W. Du, and C. L. Chien, Phys. Rev. B **35**, 8782 (1987).
[6]T. J. Kistenmacher, W. A. Bryden, J. S. Morgan, K. Moorjani, Y-W. Du, Z. Q. Qiu, H. Tang, and J. C. Walker, Phys. Rev. B **36**, 8877 (1987).
[7]H. Tang, Z. Q. Qiu, Y-W. Du, G. Xiao, C. L. Chien, and J. C. Walker, Phys. Rev. B **36**, 4018 (1987).
[8]Z. Q. Qiu, Y-W. Du, H. Tang, J. C. Walker, W. A. Bryden, and K. Moorjani, J. Magn. Magn. Mater. **69**, L221 (1987).
[9]J. E. Greedan, A. H. O'Reilly, and C. V. Stager, Phys. Rev. B **35**, 8770 (1987); F. Beech, S. Miraglia, A. Santoro, and R. S. Roth, *ibid.* **35**, 8778 (1987).
[10]G. Calestani and C. Rizzoli, Nature **328**, 606 (1987).
[11]K. Moorjani, J. Bohandy, F. J. Adrian, B. F. Kim, R. D. Shull, C. K. Chiang, L. J. Swartzendruber, and L. H. Bennet, Phys. Rev. B **36**, 4036 (1987).
[12]B. F. Kim, J. Bohandy, K. Moorjani, and F. J. Adrian, J. Appl. Phys. **63**, 2029 (1988).

Stabilization of the tetragonal phase of $YBa_2Cu_3O_{7-\delta}$ through the addition of Fe impurities

M. T. Causa, S. M. Dutrús, C. Fainstein, H. R. Salva, L. B. Steren, M. Tovar, and R. Zysler

Centro Atómico Bariloche and Instituto Balseiro, Comisión Nacional de Energía Atómica and Universidad Nacional de Cuyo, 8400 Bariloche, Río Negro, Argentina

We report normal and superconducting properties of Fe-doped $YBa_2Cu_3O_{7-\delta}$. Results from x-ray powder diffraction, electrical resistivity, magnetic susceptibility, and ESR measurements are presented. The structural effects of doping are described and their correlation with the change in superconducting properties is discussed. Similarities with the superconducting properties of oxygen deficient $YBa_2Cu_3O_{7-\delta}$ are analyzed. The comparison of the average distance between impurities (or oxygen vacancies) with the coherence length of the material suggests the existence of a nonhomogeneous order parameter in the region of low concentration of defects.

The recent finding of new superconductors[1,2] with high transition temperatures has raised the question of whether the microscopic mechanism leading to superconductivity is the same as in known superconductors. Part of the problem is to determine what is the response of these materials to the presence of magnetic impurities. In the family of compounds $ABa_2Cu_3O_{7-\delta}$ the A atoms may be yttrium or almost any element of the rare-earth group. It has been found so far[3,4] that the superconducting transition temperature, $T_c \simeq 90$ K, is not affected even when the A atoms carry a well-defined magnetic moment such as in the case of Gd, Dy, or Er. This fact is usually explained through the argument that the A atoms occupy sites in the crystal structure isolated from the Cu-O planes where superconductivity is believed to occur. If this is the case, it is an interesting problem to study the effect of magnetic moments associated with atoms located within these superconducting planes. We report results on Fe-doped samples of $YBa_2Cu_3O_{7-\delta}$, assuming that Fe atoms most probably replace Cu ions in the lattice. Preliminary data[5] showed that Fe addition considerably affects the crystal structure of the material. We present a detailed account of the x-ray patterns, electrical resistivity, magnetic susceptibility, and electron spin resonance (ESR) measurements as a function of the Fe concentration.

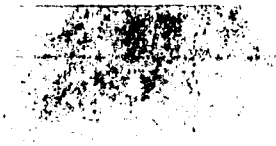
The samples were prepared from $BaCO_3$, Y_2O_3, and a mixture of Cu and Fe oxides coprecipitated from an aqueous solution of the corresponding nitrates. The starting materials were thoroughly mixed in appropriate amounts for the nominal concentration $YBa_2(Cu_{1-x}Fe_x)_3O_{7-\delta}$, pressed into cylindrical shape, and allowed to react in an O_2 atmosphere at 950 °C for 12 h. The samples were then slowly cooled to room temperature, always in an O_2 atmosphere.

X-ray powder diffractograms were made at room temperature and two regions were identified as a function of the Fe concentration. A first region, named I in Fig. 1, was observed for $0 < x < 0.01$ and corresponds to the orthorhombic structure stable at room temperature[6] for the undoped compound. In this region the orthorhombic distortion is slightly reduced with the addition of Fe. A small but monotonous increase of the atomic cell volume with the Fe content was also determined beyond the experimental uncertainty, giving an indication of the incorporation of the Fe atoms into the structure. For Fe concentrations above $x \simeq 0.03$ a tetragonal phase was always observed (region II) with lattice parameters close to those obtained for the tetragonal phase[7] of pure $YBa_2Cu_3O_{7-\delta}$ above 750 °C. Samples with $0.01 < x < 0.03$ formed in either structure without a definite relationship to the nominal Fe concentration. Our samples always showed in their x-ray diffractograms the presence of other phases, which we have identified to be mainly the cubic phase $BaCuO_2$ and the orthorhombic "green phase" Y_2BaCuO_5. Another phase not yet identified was also present in the intermediate region around $x = 0.02$ characterized by a relatively strong peak corresponding to a lattice spacing $d = 2.865(5)$ Å. This peak was also observed in samples with $x > 0.10$. The observed x-ray patterns were compared to a standard sample prepared with a controlled mixture of three major phases present in the samples. As a result we estimate the impurity phases content to be in the range from 0.5 to 6 wt. %.

The electrical resistivity of low Fe concentration samples ($x < 0.003$) showed a metalliclike temperature dependence from room temperature down to 100 K and a sharp superconducting transition, as indicated in Fig. 2. Samples with $x > 0.005$ displayed a semiconductorlike resistivity and a considerable broadening of the superconducting transition. In the case of samples with tetragonal structure the superconducting transition was also shifted to lower temperatures.

Magnetic susceptibility measurements were made using a Faraday balance magnetometer, in the normal state of both "pure" and Fe-doped samples in order to determine their magnetic characteristics. Undoped $YBa_2Cu_3O_{7-\delta}$ samples showed a weak paramagnetic behavior. The temperature-independent component of the susceptibility, measured for two different samples, indicates a Pauli paramagnetic susceptibility $\chi_p = 3.5 \times 10^{-4}$ and 4.8×10^{-4} emu/mole Y, after including corrections for the core diamagnetism but not for the Landau diamagnetism of the conducting electrons. The corresponding values of the parameter γ in a free-electron model are 25 and 34 mJ/mole Y K^2 for the two samples. Although a comparison with other reported mea-

 0021-8979/88/084164-03$02.40 © 1988 American Institute of Physics



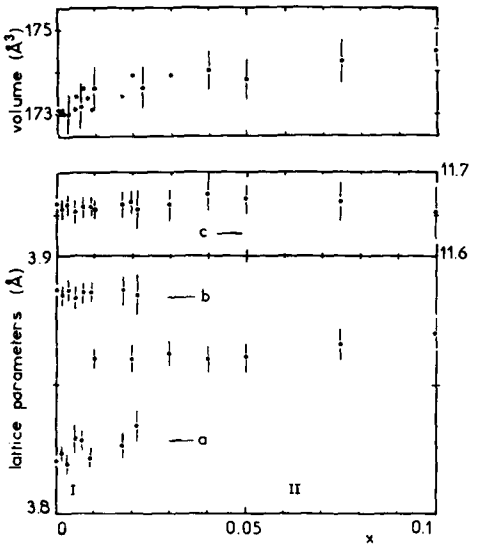


FIG. 1. Lattice parameters and unit-cell volume vs Fe concentration.

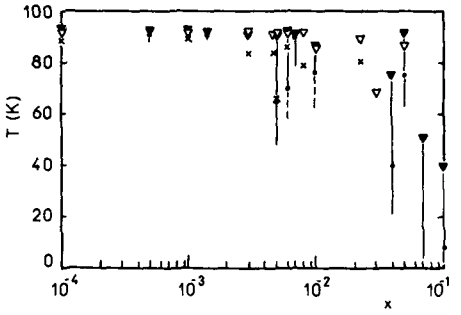


FIG. 2. Characteristic temperatures of the superconducting transition vs Fe concentrations: (▼) onset of the resistive transition, (▽) onset of the magnetic transition, (●) midpoint resistive, (×) 6% Meissner effect.

surements shows that there is considerable scattering of the values of χ_p depending probably on the particular sintering conditions of the material, the values are in reasonable agreement with those derived from the specific-heat anomaly[8,9] at the superconducting transition, assuming a Bardeen–Cooper–Shrieffer (BCS) relation $\Delta C/\gamma T = 1.43$.

A small temperature-dependent component was also observed in the undoped samples. It followed a Curie–Weiss paramagnetic law, and the Curie constants for the two samples measured are consistent with average magnetic moments of $0.26\mu_B$ and $0.44\mu_B$ per Cu ion, respectively. In order to estimate how much of the measured moments is actually associated with the $YBa_2Cu_3O_{7-\delta}$ phase we measured separately the magnetic susceptibility of the other phases known to be present in our samples. We found that both Y_2BaCuO_5 and $BaCuO_2$ are paramagnetic above 55 K (the lowest temperature reached in the measurements) with effective moments of $1.74\mu_B$ and $1.93\mu_B$ per Cu ion, respectively. Y_2BaCuO_5 had an antiferromagnetic Curie–Weiss temperature $\theta = 43$ K and $BaCuO_2$ a ferromagnetic $\theta = 24$ K. From these values and the estimated concentration of these two phases in our samples we conclude, in agreement with other authors,[10,11] that most of the measured magnetic moment is originated in the impurity phases. This fact is important because the Fe-doped samples also showed a Curie–Weiss paramagnetic behavior and the measured Curie constants had to be corrected for the estimated contributions from the impurity phases. An average effective moment $\mu_{\text{eff}} = 5.2(5)\ \mu_B$ per Fe ion was then determined for the samples in region II. For low Fe concentration samples the contribution of impurity phases was comparatively larger and did not allow a precise determination of the magnetic moment.

ESR experiments at room temperature showed in all cases an absorption line at an average g value of 2.09. The g value and line shape observed allowed us to identify this spectrum as arising primarily from the Y_2BaCuO_5 phase (pure $BaCuO_2$ shows no ESR signal for the same sensitivity). The observed ESR intensities correlate with the amount of this impurity phase determined from the x-ray analysis. No other ESR line that could be associated with Fe ions was observed.

The superconducting transitions, as measured by the magnetic susceptibility when cooling in a magnetic field of 50 G, followed the same trend of the resistive transitions. For the samples in region I the onset temperature departed very little from the values of the undoped material, the transitions broadened with the increase in the Fe content, and the diamagnetic susceptibility measured at low temperatures became smaller. Figure 2 shows the measured onset temperatures and also the temperatures where the diamagnetic signal reaches a value of 8×10^{-4} emu/g. This point corresponds to a 6% Meissner effect (for a density of 6 g/cm^3), and it has been taken as an indication of the width of the transition. Tetragonal samples showed also a larger depression of the superconducting transition temperature.

As a conclusion, we can say that Fe doping of $YBa_2Cu_3O_{7-\delta}$ produces changes in the superconducting properties that clearly correlate with structural modifications of the crystal lattice. Low concentrations of Fe ($x \lesssim 0.01$) reduce the orthorhombic distortion of the lattice and large concentrations ($x \gtrsim 0.03$) stabilize a tetragonal structure. Associated with these changes the temperature dependence of the electrical resistivity becomes semiconductorlike and the superconducting transitions broaden and shift to lower temperatures. These effects are not unique of the Fe doping of the samples. The same behavior has been observed[12] for doping with nonmagnetic elements such as Zn, or when the samples are annealed in reducing atmospheres.[13] Similar effects have also been observed when relatively large rare-earth ions occupy the A sites. In this case the lattice parameters correlate with the ionic radii of the rare-earth ion, and there is also a systematic trend of de-

creasing orthorhombic distortions with increasing ionic radii.[5] Associated with this behavior the superconducting transitions of the compounds with light rare earths tend to display broad superconducting transitions.[4]

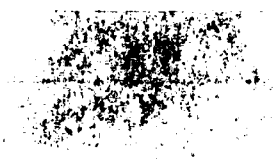
It is interesting to observe the correlation of the impurity concentration regions where structural and superconducting changes occur, with the average distance between impurities, d. Assuming that Fe atoms randomly replace Cu ions in the lattice, we see that the characteristic concentration range where the tetragonal structure appears ($0.01 \lesssim x \lesssim 0.03$) corresponds to a mean separation between Fe atoms from three to five lattice parameters, suggesting that this is the minimum length required for the linear Cu-O chains in order to give rise to a long-range orthorhombic distortion of the lattice. On the other hand, the Fe concentration where the superconducting transition starts to broaden ($x \simeq 0.003$), corresponds to $d \simeq 27$ Å, which is remarkably close to the coherence length $\xi(0) = 34$ Å reported for the undoped material.[14]

Comparison with data on samples with reduced oxygen content[13] shows that there is also a region around $\delta = 0$ where the superconducting transition is not affected by a partial oxygen depopulation of the Cu-O chains. This region extends up to $\delta \simeq 0.16$, corresponding to a mean distance between oxygen vacancies of $\simeq 25$ Å, again of the order of the coherence length.

This interesting behavior of the two systems in the limit of dilute defects may be related to the existence in these oxide superconductors of a nonhomogeneous order parameter as has been suggested[15] to explain magnetic flux penetration experiments. The possibility of observing this kind of behavior is favored in these materials because it is possible to find experimentally a region where the mean distance between defects affecting superconductivity is larger than the coherence length.

We wish to acknowledge helpful discussions with Dr. F. de la Cruz. This work was partially supported by the Consejo Nacional de Investigaciones Cientificas y Técnicas of Argentina.

[1] J. G. Bednorz and K. A. Müller, Z. Phys. B **64**, 189 (1986).
[2] M. K. Wu, J. R. Ashburn, C. J. Torng, P. H. Hor, R. L. Meng, L. Gao, Z. J. Huang, Y. Q. Wang, and C. W. Chu, Phys. Rev. Lett. **58**, 908 (1987).
[3] Z. Fisk, J. D. Thompson, E. Zirngiebl, J. L. Smith, and S. -W. Cheong, Solid State Commun. **62**, 743 (1987).
[4] K. N. Yang, Y. Dalichaouch, J. M. Ferreira, B. W. Lee, J. J. Neumeier, M. S. Torikachvilii, H. Zhou, M. B. Maple, and R. R. Hake, Solid State Commun. **65**, 515 (1987).
[5] M. T. Causa, S. M. Dutrús, C. Fainstein, G. Nieva, H. R. Salva, R. Sánchez, L. B. Steren, M. Tovar, and R. Zysler, in *Proceedings of the Adriatico Research Conference on High Temperature Superconductors, ICTP*, Trieste, Italy, 1987, edited by S. Lundqvist, E. Tosatti, M. P. Tosi, and Yu Lu (World Scientific, Singapore, 1987).
[6] M. A. Beno, L. Soderholm, D. W. Capone II, D. G. Hinks, J. D. Jorgensen, Ivan K. Schuller, C. U. Segre, K. Zhang, and J. D. Grace, Appl. Phys. Lett. **51**, 57 (1987).
[7] Ivan K. Schuller, D. G. Hinks, M. A. Beno, D. W. Capone II, L. Soderholm, J. P. Locquet, Y. Bruynseraede, C. U. Segre, and K. Zhang, Solid State Commun. **63**, 385 (1987).
[8] A. Junod, A. Bezinge, T. Graf, J. L. Jorda, J. Müller, L. Antognazza, D. Cattani, J. Cors, M. Decroux, Ø. Fischer, M. Banovski, P. Genoud, L. Hoffmann, A. A. Manuel, E. Walker, M. François, and K. Yvon, Europhys. Lett. **4**, 247 (1987).
[9] S. E. Inderhees, M. B. Salamon, T. A. Friedman, and D. M. Ginberg, Phys. Rev. B **36**, 2401 (1987).
[10] S.-W. Cheong, S. E. Brown, J. R. Cooper, Z. Fisk, R. S. Kwok, D. E. Peterson, J. D. Thompson, B. L. Wells, E. Zirngiebl, and G. Gruner, Phys. Rev. B **36**, 3913 (1987).
[11] R. J. Cava, B. Batlogg, R. B. van Dover, D. W. Murphy, S. Sunshine, T. Siegrest, J. P. Remeika, E. A. Rietman, S. Zakurak, and G. P. Espinosa, Phys. Rev. Lett. **58**, 1676 (1987).
[12] S. B. Oseroff, D. C. Vier, J. F. Smyth, C. T. Salling, S. Schultz, Y. Dalichaouch, B. W. Lee, M. B. Maple, Z. Fisk, J. D. Thompson, J. L. Smith, and E. Zirngiebl, in *Proceedings of the International Workshop on Novel Mechanisms of Superconductivity*, Berkeley, 1987, edited by S. A. Wolf and V. Z. Kresin (Plenum, New York, 1987).
[13] D. C. Johnston, A. J. Jacobson, J. M. Newsan, J. T. Lewandowski, and D. P. Goshorn, *Proceedings of the Symposium on Inorganic Superconducting Materials*, New Orleans, LA, 1987 (American Chemical Society, Washington, D.C., 1987).
[14] T. K. Worthington, W. J. Gallagher, and T. R. Dinger, Phys. Rev. Lett. **59**, 1160 (1987).
[15] L. Civale, H. Safar, and F. de la Cruz, Solid State Commun. **65**, 129 (1987); F. de la Cruz (private communications).



Magnetic properties of Y-Ba-Cu-O superconductors

T. R. McGuire, F. Holtzberg, D. L. Kaiser, T. M. Shaw, and S. Shinde
IBM Thomas J. Watson Research Center, Yorktown Heights, New York 10598

We report on the superconducting magnetic properties of two polycrystalline $YBa_2Cu_3O_x$ samples which have high densities and show current densities of 7×10^4 A/cm^2. In addition, two single crystals are studied, one of which can support a current density of 3×10^6 A/cm^2. The diamagnetic shielding in these samples in fields of 14 Oe is almost 100%, but the Meissner effect in applied fields above 1000 Oe is less than 1%.

In a recent paper[1] we compared the magnetic properties of some polycrystalline samples of $YBa_2Cu_3O_x$ with that of a single crystal. The present paper represents a continuation of this earlier study. As previously noted, we report on those samples which exhibit some improved or unusual feature of interest.

The samples are listed in Table I. Two of them are polycrystalline and two are single crystals. All compositions have the perovskite-related orthorhombic structure and the single crystals showed a twin structure[2] arising from the distortion due to the tetragonal to orthorhombic phase transition. All four samples were annealed in oxygen[3,4] to optimize the superconducting transition temperature (T_c).

The polycrystalline sample A which has a density $\rho\approx5$ g/cm^3 was prepared by mechanically alloying a powder mixture of Y_2O_3, BaO, and CuO in a mixer mill. The powder was cold pressed at 345 MPa to form a 1.25-cm-diam pellet which was sintered at 950 °C for 40 h in air, then cooled down to 750 °C and held for 20 h in flowing oxygen gas. As a final step the sample was furnace cooled to room temperature at a rate of 100 °C/h. Further details of preparation and properties are reported by Park, McGuire, and Tsuei.[5]

Polycrystalline sample B has a density of $\rho\approx6$ g/cm^3. It was prepared by compacting precalcined $Y_1Ba_2Cu_3O_x$ powders isostatically, at $\sim$150 MPa, and then sintering in flowing O_2 at 950 °C for 72 h. Subsequent annealing in flowing O_2 produced larger grains with very high twin density. Details of sample preparation and microstructure are given by Shinde *et al.*[6]

The single-crystal growth technique is reported by Kaiser *et al.*[2] and Holtzberg *et al.*[7] Essentially, pellets of mixed raw oxides were heated in Pt or Au crucibles until melting occurred. Upon cooling crystals were found within cavities in the solidified melt. Typical size was 1×1 mm in area and 0.01 mm thick. In calculating volumes of single crystals for magnetization data the theoretical density $\rho\approx6.4$ g/cm^3 is used.

The measurements reported are magnetization carried out on a SHE SQUID magnetometer. This instrument has a sensitivity of $\pm10^{-6}$ emu with a temperture range of 4.5 to 300 K in fields up to 40 kOe. A typical set of measurements include a constant-temperature (usually at $T=4.5$ K) moment-field loop extending from 0 to 35 kOe as illustrated in Fig. 1, and in addition a temperature dependence at a low magnetic field (usually about $H=14$ Oe) as shown in Fig. 2. This figure shows the results for the single crystal X-2 with H both parallel and perpendicular to the orthorhombic c axis.

As mentioned, the samples are listed in Table I along with the several measured properties. These properties include the transition temperature as projected from the sharp decrease in magnetic moment as shown in Fig. 2. The sharpness of the transition is given by ΔT_c which is the temperature interval to reach half the value of the low-temperature superconducting moment.

The next two columns of the table list the percent of the sample which is superconducting as extracted from the diamagnetic shielding and from the Meissner effects. These percentages are based on the concept that for a reasonably symmetrically shaped specimen a demagnetizing coefficient (n) can be calculated from which the theoretical susceptibility (χ_{th}) can be obtained as given by $\chi_{th}=1/4\pi(1-n)$. Since the initial slope (dashed line OA in Fig. 1) gives the experimental susceptibility χ_{ex}, then χ_{ex}/χ_{th} is the ratio listed in the table. Similarly, a value of χ^*_{ex} determined for the Meissner effect (point C in Fig. 2) gives a ratio χ^*_{ex}/χ_{th}. However, it is probably more meaningful to list χ^*_{ex}/χ_{ex} which is the ratio of the Meissner effect to the diamagnetic shielding, and this is given in the table.

Critical current densities (J_c) are listed for each sample in Table I. These are obtained using the relation[8] $J_c=30M(\max)/r$, where $M(\max)$ in gauss is the largest val-

TABLE I. $YBa_2Cu_3O_x$.

Sample	Size (mm) h,w,t	T_c (K)	ΔT_c (K)	χ_{ex}/χ_{th} (%)[a]	χ^*_{ex}/χ_{ex} (%)[a]	J_c[b] (A/cm^2) ($\times10^3$)	ρ (g/cm^3)
A	7.6						
	2.2	89	3	58	21	31	5.0
	0.14						
B	4.8						
	2.15	85	12	100	18	75	6.0
	0.65						
X-1 (‖)	1.4	86	10	100	3	1600	6.4
	0.9						
(⊥)	0.04	85	20	100	33	200	
X-2 (‖)	0.6	90	3	100	20	3600	6.4
	0.25						
(⊥)	0.05	89	2.6	100	51	380	

[a] At $H\approx14$ Oe and $T=4.5$ K.
[b] At $H\approx0$ Oe and $T=4.5$ K.

 0021-8979/88/084167-03$02.40 © 1988 American Institute of Physics

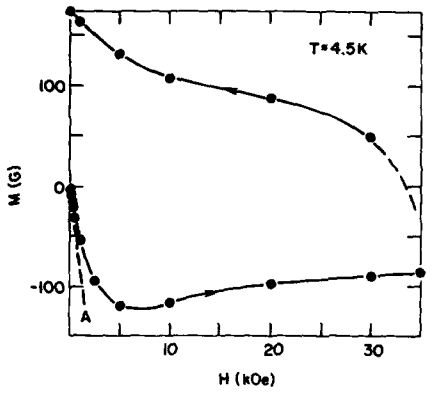


FIG. 1. Magnetization of sample B at 4.5 K. Dashed line OA indicates initial slope from which χ_{in} can be calculated.

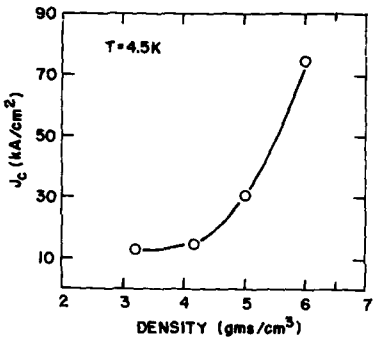


FIG. 3. Critical current in kA per square cm as a function of sample density. The theoretical highest density is 6.4 g/cm^3.

ue obtained in the magnetization loop and r is an estimated radius for the sample in cm. The units of J_c are A/cm^2. If the sample is in the shape of a sphere or cylinder with the applied field along the cylinder axis no problem exists for determining r. If the sample is in the form of a platelet with a cross section 1×0.04 mm it is more difficult to assign a radius. Our general procedure[1] is to calculate an average radius based on one-half the square root of the cross-sectional area of the sample perpendicular to the applied magnetic field. This gives a simple method of comparing J_c in the various samples. The last column of the table lists the densities calculated for the polycrystalline samples and a theoretical density of 6.4 g/cm^3 assigned to the single crystals.

First, consider the current densities. The single crystal X-2 gives a current density $J_c \approx 3.6\times10^6$ A/cm^2, the highest value which we have so far observed. This sample is also quite small and probably subject to the largest error in the determination of r. The larger crystal X-1 has a value of 1.6×10^6 A/cm^2 similar to that found in previous work.[1,9] This large value for J_c is in the Cu plane perpendicular to the c axis of the crystal. Parallel to the c axis the current densities are estimated[1] to be only one-tenth of this value, as listed in Table I. Details of the magnetic measurements on the single crystals are given by Holtzberg *et al.*[10]

One might expect to reach some average value of the single-crystal current density of $J_c \approx 10^6$ A/cm^2 for polycrystalline samples. In Fig. 3 the estimated current density is plotted against sample density for several polycrystalline samples; two from this paper and the two samples reported by us in Ref. 1. Current densities increase with sample density but remain much lower than levels suggested by single-crystal data. The increase of J_c shown in Fig. 3 can be qualitatively accounted for by fewer voids in the high-density sample, but the general low level of J_c makes is appear that another source limiting J_c must be present. It is speculated that nonsuperconducting grain boundary layers are limiting J_c in polycrystalline materials.

A second interesting feature of $YBa_2Cu_3O_x$ superconductors is the small or incomplete Meissner effect. Some comments were made on this condition in our earlier paper.[1] As noted in Table I the ratio χ^*_{ex}/χ_{ex} is less that 50% in fields of 14 Oe. At higher fields the ratio is still smaller. In Fig. 4 χ^*_{ex}/χ_{ex} ratios versus applied field are plotted for samples reported in the present paper. It is noted from the table that the Meissner effect is up to 50% of the diamagnetic shielding

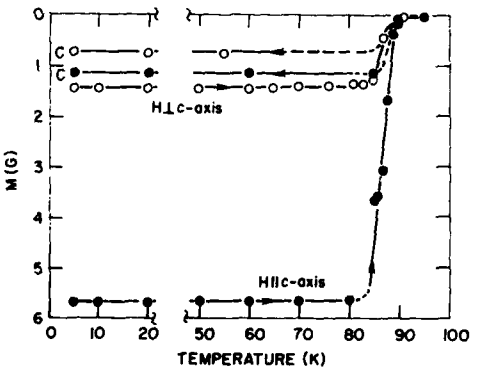


FIG. 2. Temperature dependence of magnetic moment of single crystal X-2. The filled circles are for H parallel to the c axis and the open circles are for H perpendicular to the c axis. The measurements are at $H \approx 14$ Oe. Point C marks the value of the Meissner effect.

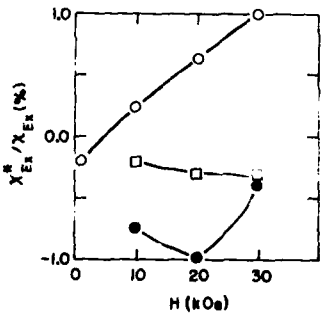


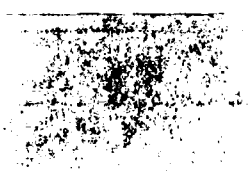
FIG. 4. The Meissner effect as a percentage of the diamagnetic shielding as a function of the applied field. Data points are marked; □, sample B; ○, crystal X-1; and ●, crystal X-2.

at fields of 14 Oe. As seen in Fig. 4 for the higher field the Meissner effect is 1% or less. In the single crystal X-2, which gave the highest values for current density, the ratio of M(Meissner)/M(shielding) is only about 1%. For the single crystal X-1, which has a lower value of J_c, the ratio is positive, i.e., there is frozen in flux rather than an expulsion of flux. The values for the Meissner effect in the ceramic sample B at the higher field is also small.

At this time we do not have a direct comparison of the Meissner effect in $YBa_2Cu_3O_x$ with that found for example in alloys such as Nb_3Sn. It is indicated by Rabinowitz, Garwin, and Frankel,[11] that there is an incomplete Meissner effect in a Nb_3Sn cylinder. Certainly a mixed state must exist in the $YBa_2Cu_3O_x$ crystals where large regions of normal conductivity are adjacent to superconducting regions. The magnetic field in the normal area is not pinned to the crystal in the sense that the measurement gives a large positive moment. Quite possibly the crystals of $YBa_2Cu_3O_x$ have an internal structure due to twinning which enhances the mixed state. The exterior of the crystal which carries superconducting currents of over 10^6 A/cm^2 is not affected by the twinning. At this time we do not know if the small Meissner effect is a fundamental property or depends on crystal imperfection.

We wish to thank S. K. Kang, S. I. Park, and C. C. Tsuei for sample A. We are grateful to H. Lilienthal for his help with magnetic measurements.

[1]T. R. McGuire, T. R. Dinger, P. J. P. Freitas, W. J. Gallagher, T. S. Plaskett, R. L. Sandstrum, and T. M. Shaw, Phys. Rev. B **36**, 4032 (1987).
[2]D. L. Kaiser, F. Holtzberg, B. A. Scott, and T. R. McGuire, Appl. Phys. Lett. **51**, 1040 (1987).
[3]S. B. Qadri, L. E. Toth, M. Osofsky, S. Lawrence, D. U. Gubser, and S. A. Wolf, Phys. Rev. B **35**, 7235 (1987).
[4]P. M. Grant, R. B. Beyers, E. M. Engler, G. Lim, S. S. P. Parkin, M. L. Ramirez, V. Y. Lee, A. Nazzal, J. E. Vazquez, and R. J. Savoy, Phys. Rev. B **35**, 7242 (1987).
[5]S. Park, T. R. McGuire, and C. C. Tsuei (unpublished).
[6]S. Shinde, T. M. Shaw, T. R. McGuire, and D. A. Chance (unpublished).
[7]F. Holtzberg, D. L. Kaiser, B. A. Scott, T. R. McGuire, T. N. Jackson, A. Kleinsasser, and S. Tozer, *Chemistry of High Temperature Superconductors*, American Chemical Society Symposium No. 351, edited by D. L. Nelson, M. S. Whittingham, and T. F. George (American Chemical Society, Washington, DC, 1987), pp. 79–84.
[8]W. A. Fietz and W. W. Webb, Phys. Rev. **178**, 657 (1969).
[9]T. R. Dinger, T. K. Worthington, W. J. Gallagher, and R. L. Sandstrom, Phys. Rev. Lett. **58**, 2687 (1987).
[10]F. Holtzberg, T. R. McGuire, D. L. Kaiser, and B. A. Scott (unpublished).
[11]M. Rabinowitz, E. L. Garwin, and D. J. Frankel, Lett. Nuovo Cimento 7, 1 (1973).



Low-field characterization of $YBa_2Cu_3O_{7-\delta}$ single crystals

H. Claus,[a] G. W. Crabtree, J. Z. Liu, W. K. Kwok,[b] and A. Umezawa[c]
Materials Science Division, Argonne National Laboratory, Argonne, Illinois 60439

Low-field magnetization measurements in fields from 0 to 100 G at temperatures from 4.2 to 100 K on single crystals of $YBa_2Cu_3O_{7-\delta}$ are presented. The crystals have sharp inductive transitions at 91.5 K, occasionally with additional structure suggesting a second phase with a lower T_c. For all crystals in all directions the Meissner effect is a small fraction of the shielding effect. Low-field measurements of H_{c2} within 1 K of T_c show a linear temperature dependence with a slope of 80 G/K, much smaller than observed at higher field.

In this paper we show that low-field magnetization measurements are an effective method for characterizing the magnetic properties of single crystals of the high-T_c superconductor $YBa_2Cu_3O_{7-\delta}$. Our measurements were done in a SQUID magnetometer designed to work at fields of 100 G or less and temperatures between 4.2 K and room temperature. The main feature of this magnetometer is fast field and temperature sweep capability, allowing, for example, for a temperature sweep between 4.2 and 100 K in less than one hour. Since no superconducting shield is used to trap the field, the field can be varied continuously from 0 to 100 G.[1]

The single crystals investigated in this work were grown by the annealing method described earlier.[2] Y_2O_3, $BaCO_3$, and CuO were mixed in stoichiometric ratios, ground with a mortar and pestle, and put into a platinum crucible which was placed in a furnace at approximately 975 °C for 3–5 days. The reaction product contained many small single crystals which were easily removed. Crystals produced by the same method were used in earlier experiments on critical magnetization currents.[3,4] A second method described by Kaiser *et al.*[5] was also used to produce crystals. This method involves growth from the melt near the eutectic point of a mixture of the starting materials. None of the crystals produced by either technique were annealed after growth.

Approximately 20 crystals were investigated in the course of this work. Their sizes varied from 0.1 to 0.5 mm typical dimension. Normally the *c* direction of the crystals was the shorter of the three dimensions, although occasionally crystals of nearly cubic shape could be found. The *ab* plane (i.e., perpendicular to the *c* axis) was easily recognizable by its shiny, metallic appearance, while the other facets were a dull gray. The crystals were visually oriented with an stereo optical microscope so that the applied field was either parallel or perpendicular to the *c* axis. Because of substantial twinning[6] which interchanges the *a* and *b* axes, we made no distinction between various directions in the basal plane.

Figure 1 displays typical magnetization versus temperature curves for several single crystals. Shown are shielding curves obtained by measuring the magnetization with increasing temperature in a field of 10 G along the *c* axis after initially cooling the samples in zero field to 4.2 K. The crystals A, B, and C in Fig. 1 were grown by the annealing method and all have a common temperature of 91.5 K for the onset of superconductivity. Whereas crystal A has a narrow transition typical of a single-phase superconductor, crystals B and C from the same batch show structures below T_c suggesting the presence of a second phase with a different transition temperature. This structure is similar to that observed by Hammann *et al.*[7] in the *ab* plane of crystals grown by a similar method. Crystal D, grown by the second method described above, shows a significantly lower onset of superconductivity and a much broader transition. Considerable improvement in the onset temperature and the transition width can be obtained by oxygen annealing, as shown by Kaiser *et al.*[5] The majority of crystals grown by the annealing method have shielding curves similar to crystals B and C. Only a few can be found of the same quality as crystal A. Measurements like those in Fig. 1 are a convenient method for selecting good crystals for other experiments.

The Meissner effect in all of the crystals is of the order of 5% of the shielding effect. Therefore when a crystal is cooled in a magnetic field, most of the flux is trapped inside the

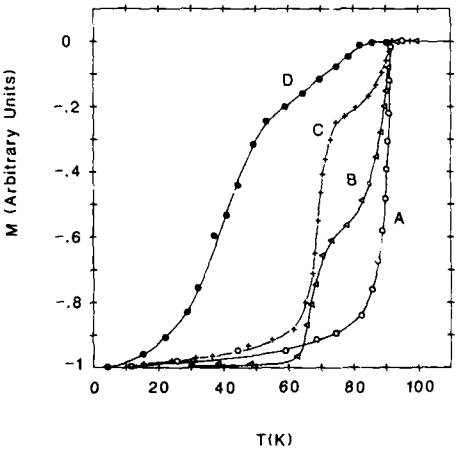


FIG. 1. Shielding curves for various single crystals measured in 10 G. *M* is normalized to 1.0 at 4.2 K. A, B, C, and D refer to different crystals as explained in the text.

[a] Permanent address: Department of Physics, University of Illinois at Chicago, Chicago, IL 60680.
[b] Joint Appointment with Department of Physics, Purdue University, West Lafayette, IN 47907.
[c] Joint Appointment with Department of Physics, University of Alberta, Edmonton, Canada.

 0021-8979/88/084170-03$02.40 © 1988 American Institute of Physics

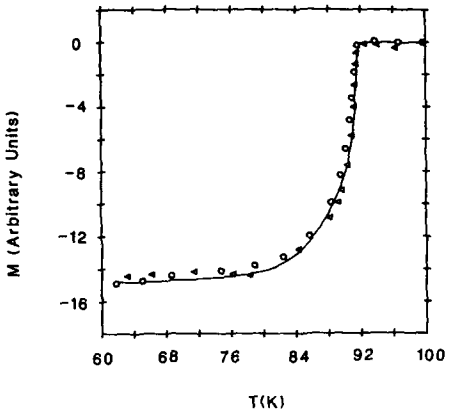


FIG. 2. Shielding curve measured in 10 G after zero-field cooling to 4.2 K (triangles) and inverted flux trapping curve measured in zero field after field cooling in 10 G to 4.2 K (circles).

sample and cannot be expelled. One consequence of this is that if the field is turned off after field cooling to 4.2 K the sample displays a positive magnetization due to the trapped flux. As the temperature is raised in zero field this flux eventually is released from the sample and the positive magnetic moment disappears.

This flux trapping experiment can be compared with the shielding curves as shown in Fig. 2. The sample used for this flux trapping experiment is the one with the sharpest transition in Fig. 1, sample A. For comparison the positive magnetization for the flux trapping experiment has been inverted. The close agreement of the two curves is consistent with the small Meissner effect observed in this sample.

We estimate the shielding at 4.2 K in crystal A to be no

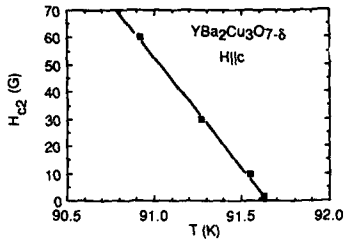


FIG. 4. H_{c2} vs temperature as determined from the shielding curves of Fig. 3.

less than 50% of that expected for an ideal superconductor with the same dimensions ($0.45\times0.38\times0.29\ \text{mm}^3$). A more accurate determination of the magnitude of the shielding is difficult to obtain because of the irregular shape of the sample. When the demagnetizing factor is taken into account, there is no anisotropy observed in the shielding for the field along the c axis or in the ab plane. These results are consistent with earlier measurements on small single crystals.[7]

To determine the variation of H_{c2} with temperature close to $T_c = 91.5$ K for crystal A of Fig. 1, shielding curves were measured in various magnetic fields along the c axis as shown in Fig. 3. The value of T_c for each field was obtained by extrapolation of the linear part of the shielding curves to $M/H = 0$. The uncertainty in this procedure is less than 0.1 K. The shielding susceptibility M/H for the various fields shown in Fig. 3 converge to the same value at low temperature to within 5%. However, near T_c the curves show a wide range of slopes, the smallest slope corresponding to the largest field. This behavior can be explained qualitatively by the temperature dependence of H_{c1}. In an ideal sample, all flux will be shielded for temperatures below that where H_{c1} equals the applied field. Thus the magnetization must

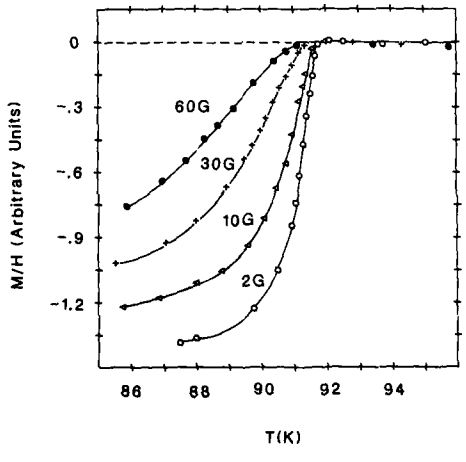


FIG. 3. Shielding curves measured in various magnetic fields: 2 G (open circles), 10 G (triangles), 30 G (crosses), and 60 G (filled circles). The magnetization is normalized by the applied magnetic field.

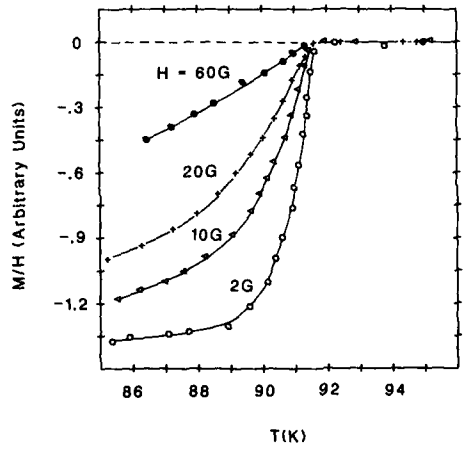


FIG. 5. Inverted flux trapping curves measured in zero field on warming after cooling the sample in various fields to 4.2 K. The magnetization is normalized by the applied cooling field.

change from full shielding at this temperature to zero shielding at T_c. As the applied field is increased, the temperature where the field equals H_{c1} falls and the temperature range over which the shielding falls to zero increases.

The temperature dependence of H_{c2} determined from Fig. 3 is very small as shown in Fig. 4. The relationship between H_{c2} and T is linear with a slope of 80 G/K, about a factor of 100 smaller than the critical field slope observed at higher field.[8,9] This is consistent with the suggestion of upward curvature in the critical field measured resistively on some single-crystal samples.[8] However, it should be pointed out that because of the rounding near T_c of the magnetization curves in Fig. 4 the values we obtain for H_{c2} are not unique. For example, if the onset of diamagnetism is used to determine H_{c2}, its temperature dependence near T_c is considerably larger. Further work relating to this problem is in progress.

Figure 5 demonstrates how the flux trapping curves depend on the magnetic field applied during cooling. After initially cooling the sample in the field shown in Fig. 5 to the lowest temperature the field was turned off. The curves in Fig. 5 were then obtained on warming in zero applied field. Quite similarly to the shielding curves of Fig. 4, the slopes of the flux trapping curves of Fig. 5 near T_c strongly depend on the field applied during cooling. However, because the measuring field is zero, one would expect that the onset of superconductivity should be independent of the cooling field as is indeed observed in Fig. 5.

This work was supported by the U.S. Department of Energy, Basic Energy Science Materials Sciences under Contract No. W-31-109-ENG-38. We thank D. J. Lam for useful conversations.

[1]G. Griffith and H. Claus, J. Magn. Magn. Mater. **54-57**, 151 (1986).
[2]J. Z. Liu, G. W. Crabtree, A. Umezawa, and Li Zongquan, Phys. Lett. **121**, 305 (1987).
[3]G. W. Crabtree, J. Z. Liu, A. Umezawa, W. K. Kwok, C. H. Sowers, S. K. Malik, B. W. Veal, D. J. Lam, M. B. Brodsky, and J. W. Downey, Phys. Rev. B **36**, 4021 (1987).
[4]A. Umezawa, G. W. Crabtree, J. Z. Liu, H. W. Weber, W. K. Kwok, L. H. Nunez, T. J. Moran, C. H. Sowers, and H. Claus, Phys. Rev. B **36**, 7151 (1987).
[5]D. L. Kaiser, F. Holtzberg, M. F. Chisolm, and T. K. Worthington, J. Cryst. Growth **85**, 593 (1987).
[6]Hoydoo You, R. K. McMullan, J. D. Axe, D. E. Cox, J. Z. Liu, G. W. Crabtree, and D. J. Lam, Solid State Commun. (to be published).
[7]J. Hammann, M. Ocio, E. Vincent, A. Bertinotti, D. Luzet, A. Revcolevschi, and J. Jegoudez, in *Proceedings of the Yamada Conference on Superconductivity in Highly Correlated Fermion Systems*, edited by M. Tachiki, Y. Muto, and S. Maekawa (North-Holland, Amsterdam, 1987), p. 325.
[8]Y. Iye, T. Tamegai, H. Takeya, and H. Takei, Jpn. J. Appl. Phys. Lett. **26**, L 1057 (1987).
[9]T. K. Worthington, W. J. Gallagher, and T. R. Dinger, Phys. Rev. Lett. **59**, 1160, (1987).

Flux creep in high T_c superconductors

C. Giovannella
Physique des Solides, Bat. 510, 91405 Orsay, France
and Dipartimento di Fisica, 11 Universitá di Roma, Via O. Raimondo, 00173 Rome, Italy

P. Rouault and I. A. Campbell
Physique des Solides, Bat. 510, 91405 Orsay, France

G. Collin
Université René Descartes, 4 av. de l'Observatoire, 75006 Paris, France

We have performed torque experiments on ceramic samples of the new superconducting perovskites and we studied the flux creep properties of both LaSrCuO and YBaCuO. In addition to its higher T_c, the latter shows stronger flux pinning. Nevertheless, flux pinning in both samples well below T_c is so weak as to be very detrimental to possible high-current applications. Some consequences of our observations on the superconducting "glassy" state are pointed out.

The study of the response of superconductors to an applied magnetic field gives important information for their possible future applications.[1] Moreover, because of the granular nature of these new sintered oxides, interesting signs of a possible "glassy" state are expected.[2]

Following these two main ideas we performed a series of torque measurements on sintered pellets of $La_{1.85}Sr_{0.15}CuO_{4-\delta}$ (LaSrCuO in the following) and $YBa_2Cu_3O_{7-\delta}$ (YBaCuO in the following). Several experimental protocols have been used.

(1) After zero-field cooling (ZFC), the field is raised to a value H_t in the initial direction $\theta = 0$, and is then rotated at a constant rate through 360° and back (about 15 min for a full rotation). The torque signal is monitored permanently.

(2) After ZFC the field is cycled up to our maximum value (8.7 kG) and back to zero before raising the field again to H_t and rotating as in (1).

(3) As in (2) except that after raising the field to H_t it is turned through an angle θ and kept at this angle while the signal relaxation is monitored as a function of time.

(4) The sample is field cooled (FC) in H_a, and after stabilizing at temperature T the field is rotated.

Torque signals are proportional to $\mathbf{M} \wedge \mathbf{H}$ and are expected to be detected only for applied fields H_t greater than the lower critical field for flux penetration, H_{c1}, and smaller than the higher critical field H_{c2}.[3] Once the field has penetrated the sample a magnetization M is created along the field direction; if the flux lines are strongly pinned, following protocols 1, 2, 4, a torque signal proportional to $\sin\theta$ should be observed. No relaxation should be seen following protocol 3. We refer to this as the "rigid" regime. Otherwise, if we are in the weak pinning case, flux lines will lag behind the field when it is turned, with a certain lag angle, and only a constant torque should be detected; we call this the "viscous" regime.

In the LaSrCuO case, depending on the H_t value and the protocol that has been used, we indeed observed both the rigid and the viscous regimes. We will summarize the measurements made at 4.2 K, i.e., at T about one-tenth T_c.

Below $H_t = 6$ G after ZFC (protocol 1), within the sensitivity of our apparatus, we were not able to detect any torque signal. On the other hand, the signal in curve A of Fig. 1, recorded after the same protocol with $H_t = 20$ G, shows a clear torque signal. This weak viscous signal changes little in intensity or form up to $H_t = 100$ G. Above $H_t = 120$ G (protocol 1) a dramatic increase of the torque intensity is observed, curve B of Fig. 1. Increasing H_t further up to our maximum field results in a continuous increase of the viscous torque signal. In agreement with the interpretation of magnetic hysteresis curves,[1] we have suggested that this behavior can be understood in a granular model[2,4] for the superconductivity. For fields between 10 and 120 G the flux lines have penetrated into the "weak link" structure connecting the strongly superconducting grains. Above 120 G some flux lines begin to penetrate the grains themselves irreversibly. This field can be considered as an "effective H_{c1}" for the grains.

Recordings following protocol 2 (after field cycling to 8.7 kG) show an "almost-rigid" signal for low turning fields, $H_t < 200$ G (curve C of Fig. 1), and again a fully developed

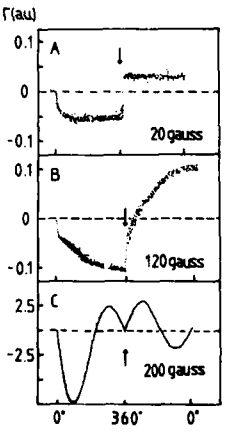


FIG. 1. Torque intensity (LaSrCuO sample) against the angle between the rotating magnetic field H_t and the initial direction, when the field is rotated at a constant rate. The arrows at 360° indicate that the sense of rotation of the field was reversed. Curve A: after ZFC, $H_t = 20$ G. Curve B: same as curve A with $H_t = 120$ G. Curve C: after field cycling to 8.7 kG and back to zero followed by rotation in turning fields $H_t = 200$ G.

 0021-8979/88/084173-03$02.40 © 1988 American Institute of Physics

viscous regime for $H_t > 1000$ G and $\theta \simeq 5$–$10°$. In parallel with this crossover the shape of the relaxation (protocol 3) also changes form,[5] Fig. 2(a). Relaxation in the almost-rigid regime cannot be parametrized over the whole time range as $\Gamma = A - B \ln t$ (Ref. 6), as is clearly shown by Fig. 2(b). A stretched exponential cannot fit the curve either over the full time range used, even for our relatively restricted time window 1–2500 s. Relaxation experiments on longer time scales are in progress. After field cooling (protocol 4), with H_a and H_t both equal to 100 G, we observed a "static" torque similar to, but less intense by a factor 10, than that we obtained after protocol 2 and $H_t = 200$ G. This can be understood as due to partial flux trapping in the grains during cooling in field through the transition temperature. Relaxation after FC is very weak up to $H_t = 200$ G and starts to be important for $H_t > 350$ G, indicating the crossover to a strong flux creep (viscous) regime.

We would like to stress that in LaSrCuO the relaxation rate can be very strong, with up to 40% loss of signal in 2500 s (after protocol 2 with $H_t = 1$ kG and 5° at 4.2 K). This result shows flux line pinning is weak and seems to us to rule out the use of this material as a high-intensity current carrier.

In the case of the YBaCuO sintered sample the picture is very close to that already described for LaSrCuO, but some elements seem to suggest that for this material the situation is not quite so bad.

(a) After protocol 2 with $H_t = 1.0$ kG it is still possible to observe a part of the flux strongly pinned; see Fig. 3(a). Preliminary results on single crystals in perpendicular geometry ($H \perp c$) show that the field needed to induce a fully viscous regime is as high as 3–5 kG.

(b) The signal decay in YBaCuO is slower than in LaSrCuO, Fig. 3(b); note that the comparison has been done at the same ratio T/T_c and probably at almost the same H/H_{c2}.

The situation is thus marginally better than for LaSrCuO, but there is considerable creep for rather low fields at T well below T_c. A possible explanation of the better results can be found in the role played by the observed twin boundaries[7] and in the suggestion that nonsuperconducting crystal planes can act as pinning centers.[8]

Let us now consider the consequences for the "glassy" state problem. Torque relaxations showing flux line creep (which has been considered the hallmark of a glassy state) were observed in the whole range of fields used for both samples. Following the interpretation given above, we are dealing with two different situations: (a) field penetration into the weak link structure ($H_t = 6$ to 100 G); (b) field penetration into the grains ($H_t > 120$ G). In the first case the weak links between superconductor grains are due to the intergranular material. In the second case there are two possibilities: (1) the grains are themselves inhomogeneous with flux creep paths constituted by the twin boundary regions (or less probably by other defects, like zones with different oxygen stoichiometry[9]), so we are dealing with defect properties that are extrinsic to the material; (2) flux creep paths

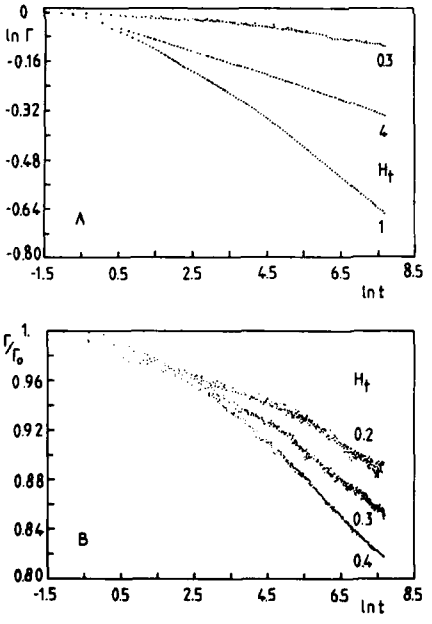


FIG. 2. (a) Torque (LaSrCuO sample) as a function of time on ln [$\Gamma(t)$] vs ln t plot at $T = 4.2$ K, $\theta = 5°$ for different values of field. (b) Torque Γ (normalized to Γ_0 the value at $t = 0$) against ln t, for different values of field.

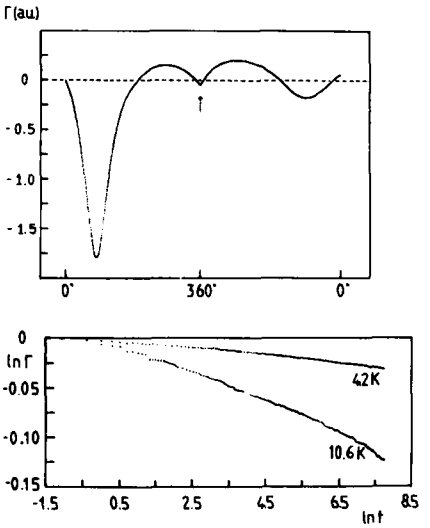


FIG. 3. (a) Same as curve C of Fig. 1 for YBaCuO sample with $H_t = 1$ kG. The y scale units are not comparable with those of Fig. 1. (b) Torque (YBaCuO sample) as a function of time as for Fig. 2(a) at $H_t = 1$ kG, $\theta = 5°$ for two different temperatures. Note that $T = 10.6$ K corresponds to the same T/T_c ratio as used for the LaSrCuO sample in Fig. 2(a).

are provided by specific crystal planes so the behavior found in these experiments is intrinsic to the two-dimensional (2D) structure.

The low-field intergranular glassy system is a 3D system while the high-field intragranular one could be basically 2D. As a consequence theoretical models should explain both regimes. A possible approach is through the analogy between the X-Y ferromagnet and the disordered junction array.[4]

[1]S. Senoussi, M. Oussena, M. Ribault, and G. Collin, Phys. Rev. B **36**, 4003 (1987).

[2]K. A. Müller, M. Takashige, and J. G. Bednorz, Phys. Rev. Lett. **58**, 1143 (1987).

[3]C. Giovannella, P. Rouault, I. A. Campbell, and G. Collin, J. Mod. Phys. B **1**, 1017 (1987).

[4]J. Rosenblatt, C. Lebeau, P. Peyral, and A. Raboutou, *Proceedings of the Workshop on Josephson Effects-Achievements and Trends* (ISI, Torino, 1985).

[5]C. Giovannella, G. Collin, P. Rouault, and I. A. Campbell, Europhys. Lett. **4**, 109 (1987).

[6]A. C. Mota, A. Pollini, P. Visani, K. A. Müller, and J. G. Bednorz, Phys. Rev. B **36**, 7 (1987); **36**, 4011 (1987).

[7]B. Raveau and C. Michel, Proceedings of the European Workshop on High T_c Superconductors and Potential Applications, Genoa, 1987, edited by the Commission of the European Communities (unpublished); G. Van Teneloo, H. W. Zandbergen, T. Okabe, M. Takeda, J. Van Landuyt, and S. Amelinckx, *ibid.*; G. Collin (unpublished).

[8]C. Chappert, C. Giovannella, P. Beauvillain, and G. Collin, J. Mod. Phys. B **1**, 993 (1987).

[9]H. Hervieu, B. Domenges, C. Michel, and B. Raveau, Europhys. Lett. **4**, 205 (1987); **4**, 211 (1987).

On the critical fields and current densities of $YBa_2Cu_3O_7$ and $La_{1.85}Sr_{0.15}CuO_4$ superconductors

S. Senoussi, M. Oussena, and S. Hadjoudj
Laboratoire de Physique des Solides, Université Paris-Sud, 91405 Orsay, France

We report a detailed investigation of the magnetic hysteresis of $YBa_2Cu_3O_7$ oxide in fields ranging from $\sim$0.2 Oe to 35 kOe and at different temperatures ($4.2<T<100$ K). It is shown that the magnetic behavior is that of a granular type-II superconductor in which strongly superconducting grains are coupled via less superconducting links. As a result, at low-H ($H\lesssim 20$ Oe at 4.2 K) the sample appears like a single superconducting filament while at high enough field ($H\gtrsim 5$ kOe) it behaves like a granular superconductor with most of the weak links being broken by the applied field. Five threshold fields are identified charaterizing the above magnetic regimes and the transition between them. It is concluded that the critical current density within the individual grains could attain 10^7 A/cm^2.

During the last few months there have been several but limited studies of the magnetic hysteresis cycle of the $YBa_2Cu_3O_7$ superconductor.[1-3] Very recently we reported[4,5] detailed investigations of the magnetic and transport properties of $La_{0.85}Sr_{0.15}CuO_4$ oxide in the superconducting state. One of the most significant results deduced from the magnetic data was that the critical current density in this material could attain 10^6 A/cm^2. It was also found that the macroscopic critical current was limited both by the microstructure (weak links) and by the size of the sample. We present an extensive investigation of the hysteresis cycle of $YBa_2Cu_3O_7$ at various temperatures ($4.2<T\leqslant 100$ K) and fields ($-35<H<35$ kOe). We find that the relationship M vs H evolves considerably with H exhibiting very different regimes characterized by five different threshold fields. As for the LaSrCuO system most of the data are analyzed in the framework of the phenomenological model of Bean[6-8] and are consistent with the picture that the present specimen is formed by strongly superconducting grains connected via less conducting (or weak) links. From the experimental point of view, at very low H, the distinction between the weak links and the basic grains is hard and the whole sample appears roughly like a single (but dirty) superconducting filament. On the other hand, at sufficiently high field ($H>5$ kOe at 4.2 K, for example) the superconducting behavior is that of a conventional granular superconductor. Moreover, it will be deduced from the present data that the critical current density within the grains could be as high as 10^5 to 10^7 A/cm^2.

The preparation of the $YBa_2Cu_3O_7$ material followed the same procedure as in Ref. 10. As in this case, x-ray diffraction analysis and scanning electron microscopy observation indicated that our materials are single phase and granular with grain size of the order of 1 to 100 μm. The sample was approximately cylindrical 6 mm long and 2.5 mm in diameter. Its magnetization was measured with a vibrating sample magnetometer as described in Refs. 4 and 5. The resistivity $\rho(T)$ ($4<T<300$ K) and the magnetoresistance $\rho(H)$ in very high pulsed fields up to 430 kOe of a specimen prepared in the same condition as the one considered have been reported in Ref. 10. It was inferred from those transport measurements that the upper critical field $H_{c2}(0)$ exceeded several MOe. It is to be stressed that in order to remove any magnetic memory acquired during previous field cyclings we have systematically heated our sample up to 110 K and then cooled it down in $H=0$ to the desired temperature prior to the measurement of the M-H curves.

Figure 1 shows a set of low-H cycles all plotted after zero-field cooling, following the above procedure, to the indicated temperatures. We note a global but gradual diminutive of the hysteresis effects with increasing temperature.

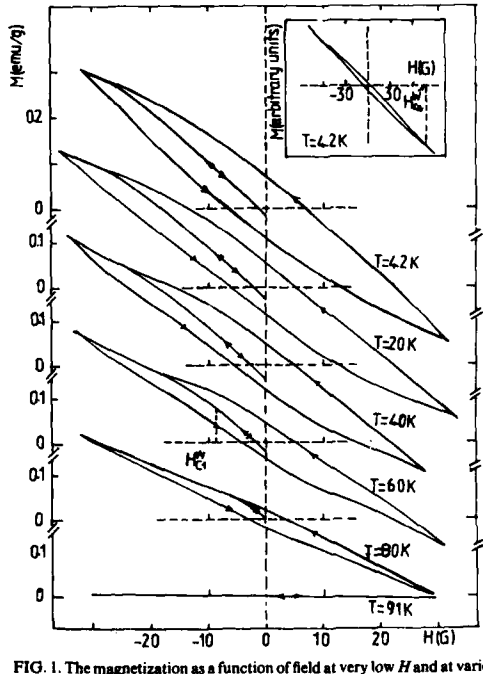


FIG. 1. The magnetization as a function of field at very low H and at various temperatures. The inset shows the M-H curve at a higher field and at 4.2 K. The small asymmetry of the initial branch is due to the earth field.

 0021-8979/88/084176-03$02.40 © 1988 American Institute of Physics

Starting from the origin and examining the initial branches of the cycles, we observe that the variation of M with H is quite linear and reversible up to a first (but ill-defined)[11] threshold field H_{c1}^{w}. Moreover, in this field region the sample exhibits perfect diamagnetism (i.e., $-4\pi M = H$) within the sensitivity ($\simeq 8\%$) of the magnetometer.

As H is further increased, marked departure from linearity together with a regime of weak irreversibilities set in. This behavior holds up to a second threshold field H_{c2}^{w} (also ill defined)[11] beyond which the irreversibilities decrease substantially whereas the M-H relationship becomes again approximately linear (see inset). As in Ref. 5 we shall call H_{c1}^{w} the first critical field of the weak links, since it is probably the field at which the first flux lines penetrate appreciably the sample through the weakest links.

The physical meaning of H_{c2}^{w} is less clear, but we tentatively propose that it could be the field limit where most of the weak links are broken. In this case, H_{c2}^{w} would represent a sort of second critical field for the weak links. The quasireversible behavior observed for $H > H_{c2}^{w}$ (see inset of Fig. 1) ceases at a third (also ill-defined) threshold field H_{c1}^{g} marking the onset of a regime of strong irreversibilities. This is illustrated in Fig. 2 at the appropriate field scale. As discussed earlier[5] H_{c1}^{g} would be associated with the first critical field of the superconducting grains and would therefore be a more intrinsic quantity of the $YBa_2Cu_3O_7$ system. However, it is to be noted that the individual crystallites of the polycrystalline $YBa_2Cu_3O_7$ are highly anisotropic[12] with $H_{c1}(\hat{H} \| \hat{C})/H_{c1}(\hat{H} \perp \hat{C}) \simeq 10$–15. Therefore the critical field H_{c1}^{g} and the critical current density in the grains would depend on the texture of the material and would be probably more typical of the crystallites. The c axis of which are perpendicular to the field H. Figure 3 shows that if the applied field is further increased the magnetization goes through a maximum at some field H_m and then decreases steadily with H. The examination of the high-temperature isotherms of Figs. 3 and 4 shows also that for high enough fields and temperature the M-H curves approaches once again, tangentially, a reversible behavior above some threshold field $H^{g}(T)$.

It is of interest to note that the same characteristic hysteresis loops and therefore the same threshold field were seen[5] in $La_{1.85}Sr_{0.15}CuO_4$ oxide except that the various threshold values were three to six times lower in this material. A possible interpretation of the field H^{g} is that it is the field above which the pinning forces F_p (Refs. 9 and 13) on the vortex lines within the grain become negligible compared to the magnetic driving forces so that the M vs H law would be governed principally by the equilibrium mixed state. To discuss further this point, let us assume[6,9] that the critical current density J_c (in A/cm^2), the radius R (in cm) of the grain, and the magnetization are related by the relationship

$$J_c = -15\ (M_+ - M_-)/R, \qquad (1)$$

where $M_+(H)$ and $M_-(H)$ refer to the algebraic values of the magnetization at H on the ascending and the descending branches, respectively, of the magnetic loop [i.e., $M_+(H) - M_-(H)$ is the distance between the two branches at H]. Then according to Eq. (1) above, the threshold field $H^{g}(T)$ is the limit above which the critical

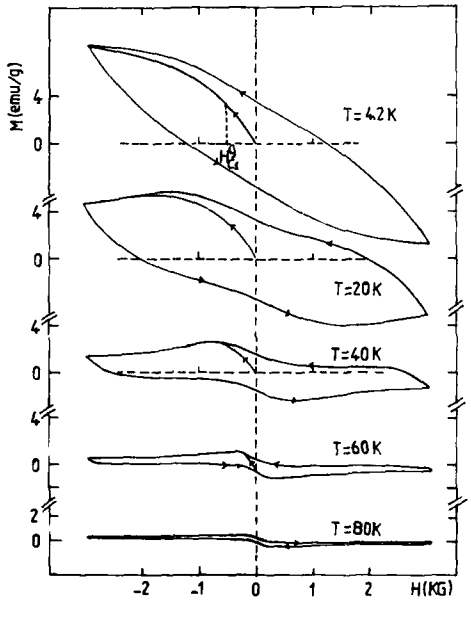


FIG. 2. A set of hysteresis cycles plotted at the same temperature as in Fig. 1 but the M and H scales are about 100 times larger here.

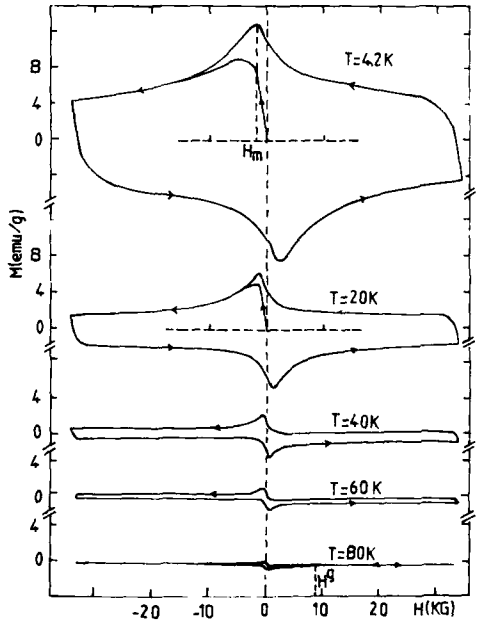


FIG. 3. The same M-H relationships and the same temperatures as in Figs. 1 and 2 but plotted at still higher fields.

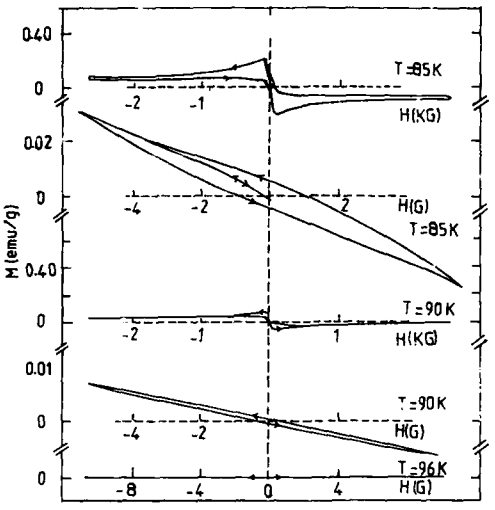


FIG. 4. Showing the evolution of the magnetic cycle near the transition temperature, note the expanded M and H scales with respect to the preceding figures.

current density J_c becomes practically zero (within the precision of the experimental data). Other possible interpretations of $H^g(T)$ in terms of a glassy behavior (an Almeida–Thouless-like line in the T-H plane) are discussed in Ref. 4. It is interesting to look at the evolution of the magnetic cycle in the transition region near 90 K. This is depicted in Fig. 4 where we have expanded the M and H scales with respect to Figs. 1–3. It is found that the diamagnetic cycle collapses at about 94 K in good agreement with the resistivity data.[10]

We believe that the magnetic measurements reported in this paper can be interpreted qualitatively as follows. First, since the magnetic screening is quasicomplete for $H \lesssim H_{c1}^w$, it is reasonable to assume that to a first approximation the whole sample behaves like a single but dirty filament up to $H \approx H_{c1}^w$, then, as the field is further increased a growing number of weak links are broken. As a consequence, at $H \gtrsim H_{c2}^w$ most of the superconducting grains are disconnected from each other and the magnetic behavior approaches that of a conventional granular superconductor in which the superconducting entities would coincide with the cystalline grains revealed by electron scanning microscopy and other microscopic techniques of observation. In other words, at the lowest field the superconducting order seems to be achieved by a coherent process, whereas at high enough field it is dominated by percolation phenomena.

Let us now try to calculate J_c at 4.2 K (Fig. 1) where the condition $H \ll H^g$ is certainly well fulfilled. Considering first the low-H limit ($H \lesssim H_{c2}^w \simeq 80$ G) above which the sample ceases to behave like a single filament of radius $R = 1.25$ mm. We find that this limit corresponds roughly to $J_c \approx 500$ A/cm^2. As discussed in more detail in Ref. 5, this value should coincide with those which could be deduced from resistivity measurements, provided that the sample is homogeneous and continuous at a scale much lower than its linear dimensions. We have carried out critical current measurements on several different $YBa_2Cu_3O_7$ samples immersed in liquid nitrogen and having approximately the same dimensions (~ 10 mm long, 4 mm diameter). We found that in some cases J_c exceeded 200 A/cm^2.

Second, considering the high-H limit such as $H > H_m$ (or $M \approx 30$ emu/cm^3 at 4.2 K, Fig. 3) and taking $R = 1$ to 100 μm for the grain radius we easily calculate that the current density within the grains would be of the order of 10^5 to 10^7 A/cm^2.

Finally, we emphasize that we have carried out measurements on many other granular $YBa_2Cu_3O_7$ from different sources. We generally observed the same characteristic behaviors marked by threshold fields (H_{c1}^w, H_{c2}^w, H_{c1}^g, H_m, and H^g) more or less comparable to the ones reported here.

[1] T. R. Dinger, T. K. Worthington, W. J. Gallagher, and R. L. Sandstrom, Phys. Rev. Lett. **58**, 2687 (1987).
[2] J. Z. Sun, D. J. Webb, M. Naito, K. Char, M. R. Hahn, J. W. P. Hsu, A. D. Kent, D. B. Mitzi, B. Oh, M. R. Beasley, T. H. Geballe, R. H. Hammond, and A. K. Kapitulink, Phys. Rev. Lett. **58**, 1574 (1987).
[3] D. A. Esparza, C. A. D'ovidio, J. Guimpel, E. Osquiguil, L. Civale, and F. de La Cruz, Solid State Commun. **63**, 137 (1987).
[4] M. Oussena, S. Senoussi, and G. Collin, Europhys. Lett. **4**, 625 (1987).
[5] S. Senoussi, M. Oussena, M. Ribault, and G. Collin, Phys. Rev. B **36**, 4003, (1987).
[6] C. P. Bean, Phys. Rev. Lett. **8**, 250 (1962); Rev. Mod. Phys. **36**, 31 (1964).
[7] Y. B. Kim, C. F. Hempstead, and A. R. Strnad, Phys. Rev. **129**, 528 (1963).
[8] P. W. Anderson, Phys. Rev. Lett. **9**, 309 (1962), J. Phys. **36**, 39 (1964).
[9] W. A. Fictz and W. W. Webb, Phys. Rev. **178**, 657 (1969).
[10] M. Oussena, S. Senoussi, G. Collin, J. M. Broto, H. Rakoto, S. Askenazy, and J. C. Ousset, Phys. Rev. B **36**, 4014 (1987).
[11] The threshold fields reported here are defined either by deviations from linearity of the M-H law or by the onset (or the vanishing) of the hysteresis effects. Both phenomena appear or disappear rather gradually as a function of H, making it very difficult to define the critical magnetic parameters with good precision. This is probably connected with the fact that the weak links and the grains considered here have many different sizes and shapes.
[12] T. R. Singer, T. K. Whorthington, W. J. Gallagher, and R. L. Sandstrom Phys. Rev. Lett. **58**, 2687 (1987).
[13] P. G. deGennes and J. Matricon, Rev. Mod. Phys. **36**, 45 (1964).

Constricted diamagnetic hysteresis loops observed for the high T_c superconductors

U. Atzmony,[a] R. D. Shull, C. K. Chiang, L. J. Swartzendruber, and L. H. Bennett
National Bureau of Standards, Gaithersburg, Maryland 20899

R. E. Watson
Brookhaven National Laboratory, Upton, New York 11973

Magnetic hysteresis loops, ac susceptibility, and resistivity measurements have been made on a $Ba_2YCu_3O_{7-x}$-type high-T_c superconductor. The shape of the hysteresis loops well below T_c are reminiscent of constricted hysteresis loops observed in certain ferromagnetic materials which are usually associated with magnetic aftereffects. Similar dynamic effects, with a time constant on the order of 10 s at 40 K, are shown to be present in the superconducting material. This dynamic magnetic viscosity effect is in addition to the flux creep observed for longer time periods.

INTRODUCTION

The application of the recently discovered high-temperature oxide superconductors[1,2] such as La-Sr-Cu-O and Y-Ba-Cu-O depends on details concerning their critical currents and response to applied magnetic fields. Magnetic hysteresis loops we have observed from these oxide superconductors have a shape which reminds one of the well-known constricted hysteresis loops[3] in certain ferromagnetic materials. Such loops are attributed to magnetic aftereffects (i.e., magnetic viscosity) in ferromagnets. Because of this similarity in the hysteresis loop shape, we measured time-dependent magnetization and found that, in addition to Anderson–Kim[4] flux creep which has a $\ln(t)$ behavior for times greater than about 100 s, a magnetic viscosity with a time constant on the order of 10 s is observed. When the measurement time is slow compared to the faster time constant, and fast compared to the flux creep, the hysteresis loop can be closely approximated by the Bean critical state model.[5,6]

SAMPLE PREPARATION

A number of oxide superconductors with varying composition and heat treatment were prepared and measured. We report here on one typical sample which was prepared from stoichiometric mixtures of $BaCO_3$, Y_2O_3, and CuO powders with 5 mol % of hafnium oxide added as a replacement for CuO. The powders were mixed mechanically and sintered at 690 °C for 10 h. The material was ground to powder and sintered again at 820 °C for 10 h. The last step was repeated at 910 °C before the powder was pressed into pellets approximately 12 mm in diameter. The pellets were fired at 960 °C for 12 h and cooled in steps of 50–100 to 150 °C. Holding time at each temperature step during the cooling was 2–6 h, except at 750 °C and 500 °C, which were 15 h and 11 h, respectively. All these processing steps were carried out in air.

RESISTIVITY AND ac SUSCEPTIBILITY

Resistivity and ac susceptibility measurements as a function of temperature are compared in Fig. 1. Both the real and imaginary component of the ac susceptibility are plotted. In Fig. 1 resistivity is given in mΩ cm and the susceptibility is given in rationalized units (equivalent to $4\pi M$ with M in emu/cm^3). The resistivity indicates an onset temperature of 92 ± 2 K and a zero resistivity at 86.5 ± 1 K. This can be considered representative of a typical sample of superconducting Y-Ba-Cu-O. The ac susceptibility also indicates an onset temperature of 92 ± 2 K.

From the ac susceptibility, the transition width (10%–90%) is approximately 15 K and the sample achieves nearly 100% superconductivity at low temperature. It is interesting to note that the transition width indicated by the ac susceptibility is much broader than the approximately 5 K width indicated by the resistivity. Further, zero resistivity is seen to occur near the temperature at which, according to the susceptibility measurement, the sample is approximately 50%

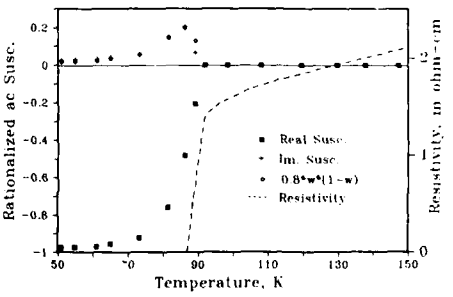


FIG. 1. Plot of the resistivity and complex ac susceptibility vs temperature for the Ba-Y-Cu-O type sample studied in this paper. Squares are the measured values for the real component of the susceptibility, crosses are the imaginary component of the susceptibility, and the dotted line is the resistivity (right scale). The diamonds are calculated points (see text).

[a] Permanent Address: Nuclear Research Centre–Negev, P.O. Box 9001, Beer-Sheva, Israel.

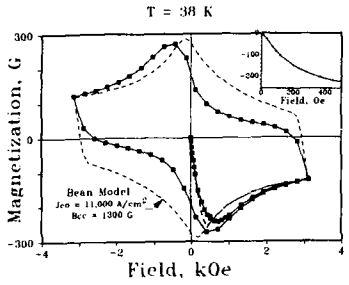


FIG. 2. Experimental (squares and solid line) and calculated (dotted line) hysteresis loops at 38 K for the sample studied in this paper. The inset gives an expanded view of the experimental virgin curve. The magnetization, given in G, represents $4\pi M$ where M is in emu/cm^3.

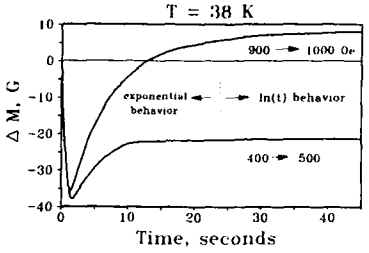


FIG. 3. Time dependence of change in sample magnetization for two steps in the applied magnetic field. The data were taken on the virgin curve. The magnetization change, ΔM, given in G represents 4π times the value in emu/cm^3. The top curve is for a sudden jump in applied field from 900 to 1000 Oe, and the bottom curve is for a sudden jump in applied field from 400 to 500 Oe. The dotted line represents, roughly, the transition between an exponential behavior and a $\ln(t)$ behavior.

superconducting, and the peak in the imaginary component of the susceptibility also occurs at this temperature.

From Fig. 1 it can be seen that the imaginary part of the susceptibility undergoes a peak near 85 K and does not reduce completely to zero at the lower temperatures. This same type of behavior has been noted for the La-Sr-Cu-O system by Oda *et al.*[7] Assuming that the energy loss arises primarily from eddy currents induced in the normal portion of the material, the peak in the energy loss can be understood roughly in terms of the Gorter–Casimir two-fluid model.[8] In this phenomenological model the electrons are divided into a fraction w of superconducting electrons, and a fraction $(1-w)$ of normal electrons. The changes in superconducting current induced by the magnetic field will cause dissipative eddy currents in the normal electrons. Thus the eddy-current losses will be roughly proportional to $n_e\mu w(1-w)$, where n_e is the density of electrons and μ is their mobility. This product, normalized to agree with the experimental data point at 80 K, is also plotted in Fig. 1. Good agreement with the observed values is obtained except very near the onset temperature.

HYSTERESIS MEASUREMENTS

A hysteresis loop obtained at 38 K for applied fields up to 3 kOe is shown in Fig. 2. The sample was cooled in zero field to obtain the virgin curve. At 38 K the ac susceptibility measurement indicates that the sample is almost completely superconducting and the initial slope of the magnetization versus applied field has a slope nearly equal to -1 (as expected for a nearly perfect diamagnet). From the inset in Fig. 2, which shows the virgin curve, it can be seen that M vs H begins to curve (flux begins to penetrate the sample) at a very low field, <80 Oe. A very large hysteresis is also seen at this temperature.

In Fig. 2 the measured hysteresis loop is compared with one calculated using the phenomenological model of Bean[5,6] for a plate geometry (the sample size used was 0.90 mm thick by 4.5 mm wide by 4.7 mm long with the field applied parallel to the surface of the plate). The variation in the critical current with field was assumed to have the form used by Kim, Hampstead, and Strnad,[9] i.e.,

$$J_c = J_{c0}/(1 + B/B_{cc}),$$

where J_c is the critical current at flux density B, J_{c0} is the critical current at zero flux density, and B_{cc} is a parameter representing the flux density at which the critical current is $\frac{1}{2}$ that at zero flux density. The value of J_{c0} used in Fig. 2 (11 000 A/cm^2) is approximately that which would be obtained by substituting the maximum observed magnetization in the formula given by Bean[6] for a plate geometry as $J_c = 40M/D$, where M is in emu/cm^3, J_c in A/cm^2, and D is the thickness in cm. This value for J_{c0} is considerably less than those found by Dinger *et al.*[10] for single-crystal $Y_1Ba_2Cu_3O_{7-x}$. These authors found, at 40 K, approximately 40 000 A/cm^2 for H parallel to the Cu-O planes, and 110 000 A/cm^2 for H perpendicular to the Cu-O planes. This reduced critical current for polycrystalline material has been attributed to the presence of "weak links" in the grain boundaries by McCallum *et al.*[11]

RELAXATION EFFECTS

There are interesting differences between the calculated and experimental loops of Fig. 2. The Bean model assumes that fluxoids, once formed by the application of magnetic fields, are pinned in place. If the fluxoids were free to move and obtain thermodynamic equilibrium, a magnetization curve with little or no hysteresis would result. Since the true picture appears intermediate to these two situations, the experimental hysteresis curve has less area, i.e., is more pinched, than the Bean-model loop. Further, due to relaxation effects in the fluxoid motion, the measured hysteresis loop will depend on the rate at which the loop is traversed. For the experimental hysteresis loop of Fig. 2 the time between experimental points was approximately 15 s.

The presence of Anderson–Kim flux creep in these superconductors has already been noted by a number of authors (see, e.g., Ref. 10). This creep, due to thermally activated jumping over flux pinning sites, has a $\ln(t)$ behavior and was observed in our samples for times greater than about 20

s. The above-mentioned analogy with pinched hysteresis loops in ferromagnets led us to look for dynamic effects at times shorter than 20 s. To observe such effects, the magnetic field was stepped in 100-G increments, with 90 s between steps, and the resultant magnetization followed on a recorder. The time constant for the field step was approximately 2 s and the response time of the magnetization measurement was 1 s. Two of the curves obtained are displayed in Fig. 3. One curve, labeled 400→500 Oe, is for the step occurring on the virgin curve just before the minimum in M. The second curve, labeled 900→1000 Oe, is for the step occurring after the minimum in M. The curves of Fig. 3 show that the initial change in magnetization upon a field step is nearly the same for both curves, in spite of the fact that the 900→1000-Oe step gives a final positive change and the 400→500-Oe step gives a final negative change. Two regions on the transient curves can be identified: the first region immediately following the step is a period of flux flow where the change in magnetization is exponential in character, and then a region at times longer than about 20 s where the magnetization follows the $\ln(t)$ behavior predicted by the Anderson–Kim[9,12] thermally activated flux-creep model.

The initial large transient diamagnetic effect might be explained in part by considering the large anisotropy of these materials. The sudden change of magnetization induces large supercurrents in the easy direction. Because of the random orientation of the grains, these initial fluxoids have a large energy because they lie at various angles to the net magnetic flux. These fluxoids then quickly relax to smaller values oriented in the direction of the flux density and therefore, on the average, in a less favorable direction to the crystallographic easy direction. The time constant for this relaxation at 38 K in the sample observed was ≈ 10 s. We have observed the same type of behavior in a number of samples processed in different ways, and more extensive measurements are underway to establish the temperature and sample dependence of the effect.

ACKNOWLEDGMENTS

We thank D. Mathews and R. Drew for technical assistance. One of us (R.E.W.) was supported by the U. S. Department of Energy under Contract No. DE-AC02-76CH00016.

[1] J. G. Bendnorz and K. A. Müller, Z. Phys. B **64**, 189 (1986).
[2] C. W. Chu, P. H. Hor, R. L. Meng, L. Gao, Z. J. Huang, and Y. W. Wang, Phys. Rev. Lett. **58**, 405 (1987).
[3] E.g., G. W. Rathenau, in *Magnetic Properties of Metals and Alloys* (American Society for Metals, Metals Park, OH, 1959), p. 168.
[4] P. W. Anderson and Y. B Kim, Rev. Mod. Phys. **36**, 39 (1964).
[5] C. P. Bean, Rev. Mod. Phys. **36**, 31 (1964).
[6] C.P. Bean, Phys. Rev. Lett. **8**, 250 (1962).
[7] Y. Oda, I. Nakada, T. Kohara, H. Fujita, T. Kaneko, H. Toyoda, E. Sakagami, and K. Asayama, Jpn. J. Appl. Phys. **26**, L481 (1987).
[8] See, for example, E. A. Lynton, *Superconductivity* (Methuen, London, 1969), p. 20.
[9] Y. B. Kim, C. F. Hempstead, and A. R. Strnad, Phys. Rev. **129**, 528 (1963).
[10] T. R. Dinger, T. K. Worthington, W. J. Gallagher, and R. L. Sandstrom, Phys. Rev. Lett. **58**, 2687 (1987).
[11] R. W. McCallum, J. D. Berhoeven, M. A. Noack, E. D. Gibson, F. C. Laabs, and D. K. Finnemore, *Ceramic Superconductors*, edited by D. R. Clarke and D. W. Johnson [Special issue of Advanced Ceramic Materials (to be published)].
[12] P. W. Anderson and Y. B. Kim, Rev. Mod. Phys. **36**, 39 (1964).

New glassy features in high-T_c superconductors

Y. Yeshurun[a)]
IBM Thomas J. Watson Research Center, Yorktown Heights, New York 10598

Y. Wolfus
Department of Physics, Bar-Ilan University, Ramat-Gan, Israel

I. Felner
Racah Institute of Physics, Hebrew University, Jerusalem, Israel

Magnetic measurements on a high-T_c superconductor $YBa_2Cu_3O_7$ reveal new spin-glass-like features. At low temperatures and low fields the irreversible part of the field-cooled magnetization M_{irr} rotates with the sample as a rigid entity. The rigidity is broken and part of M_{irr} disappears above an angle ϕ^* which decreases with increasing temperature or field. This behavior resembles that of spin glasses and differs qualitatively from the behavior found for Nb.

This paper was not proofread by the author; however, it has been proofread by one of the Publication Chairpersons.

In the effort to understand and characterize the features of the new superconductors, an enormous amount of work has been devoted to their magnetic properties. One of the intriguing features of their materials found in magnetic measurements[1-3] is the striking resemblance to the magnetic properties of spin glasses.[4] We have recently reported[2] on glassy features in $YBa_2Cu_3O_7$. Here we report on new features[5] which resemble those of spin glasses. We have studied the angular dependence of the field-cooled magnetization of $YBa_2Cu_3O_7$ by rotating the sample relative to the applied magnetic field. We find that at low temperatures and low fields the irreversible part of the magnetization M_{irr} rotates with the sample as a rigid entity. At higher fields and temperatures, the rigidity is broken and part of the M_{irr} disappears above an angle ϕ^* which decreases with increasing temperature or field. These results resemble the behavior in spin glasses[6-8] and are qualitatively different from those we observe in the ordinary type-II superconductor, Nb.

The sample was prepared from a mixture of $BaCO_3$, Y_2O_3, and CuO powders (at least 99.9% pure) in stoichiometric proportion according to the formula $YBa_2Cu_3O_7$. Finely ground powders were pressed into a pellet approximately 1.5 cm in diameter, and heated to 900 °C for 16 h in flowing oxygen. The product was then quenched to room temperature, reground, and heated again to 900 °C for 48 h, then cooled to ambient temperature. Powder x-ray diffraction shows that most of the observed lines could be indexed with an orthorhombic cell with lattice constants $a = 3.822$ Å, $b = 3.891$ Å, and $c = 11.67$ Å, in fair agreement with published data.[9]

The angular dependence of the magnetization was investigated via measurements of the magnetization on a vibrating sample magnetometer (VSM) with a 2π-rotating sample holder. The sample was cooled in an applied field H from well above the transition temperature T_c to the measuring temperature, which is stabilized to better than 0.1 K. With the same field on, the sample was rotated by an angle ϕ relative to the applied magnetic field. We then measured the magnetization M as a function of ϕ.

Figure 1 exhibits typical $M(\phi)$ data for various fields. The most obvious feature in this figure is the strong angular dependence of the magnetization. To understand this feature we recall that in VSM measurements the measured magnetization M is the projection of the total sample magnetization $\mathbf{m}$ in the direction of the field $\mathbf{H}$. The magnetization $\mathbf{m}$ is composed of reversible and irreversible components:

$$\mathbf{m} = \chi\mathbf{H} + \mathbf{M}_{irr}. \quad (1)$$

In the polycrystalline $YBa_2Cu_3O_7$ the bulk susceptibility is of course isotropic, and thus the reversible contribution χH is always in the direction of H. The irreversible part M_{irr}, on the other hand, might be coupled to the sample and rotate with it as a rigid entity. It should also be taken into account that as a result of the field M_{irr} might lag by an angle θ relative to the sample for a rotation ϕ of the sample. Thus, the measured contribution of the irreversible magnetization is expected to be $M_{irr}\cos(\phi - \theta)$ where $\theta \leqslant \phi$ and the measured magnetization is

$$M = \chi H + M_{irr}\cos(\phi - \theta). \quad (2)$$

Several features characterize the data of Fig. 1. Generally speaking, all curves exhibit the same shape. However, note that $M(2\pi) < M(0)$ and this difference is more pronounced for the higher fields. Moreover, irreversibility in $M(\phi)$ sets in at high angles. This is demonstrated in the lower part of Fig. 2 where we exhibit the angular dependence of the magnetization at 4 K for $H = 1500$ Oe. At an angle ϕ^* (which decreases with increasing field and temperature) there is a total breaking of the rigid moment and the signal is not recovered when the sample is rotated back from 2π to 0, demonstrating the complete disappearance of the original irreversibility.

In the low-field regime, the asymmetry in $M(\phi)$ is important only at a high angle of rotations. Thus, using Eq. (2), we can deduce M_{irr} directly from the raw data by taking $M_{irr} = [M(0) - M(\pi)]/2$. The inset of Fig. 1 exhibits the field dependence of M_{irr}. Note the resemblance of $M_{irr}(H)$ to the thermoremanent magnetization (TRM) in spin glasses.[4]

The effect of the field on the rigidity of M_{irr} is more dramatic at high temperatures. This is obvious from Fig. 2 where we demonstrate that the effect of 45 Oe at 67 K is

[a)] Permanent address: Department of Physics, Bar-Ilan University, Ramat-Gan, Israel.

 0021-8979/88/084182-03$02.40 © 1988 American Institute of Physics

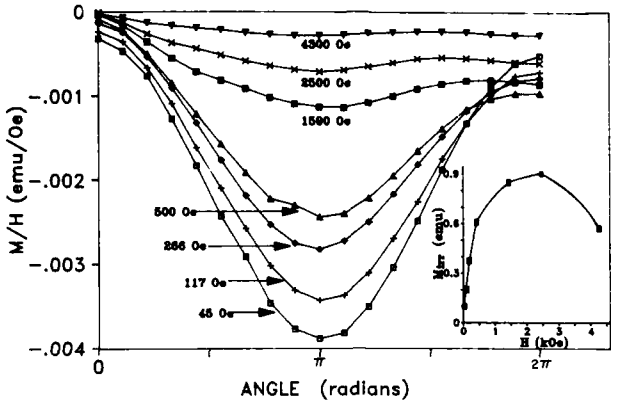


FIG. 1. Angular dependence of the field-cooled magnetization for $YBa_2Cu_3O_7$ at 4.2 K for various fields. The solid lines are a guide for the eye. Inset shows the field dependence of M_{irr} deduced from the angular dependence data (see text).

qualitatively similar to that of 1.5 kOe at 4.2 K. For higher fields the initial $\cos\phi$ dependence is abruptly interrupted at a relatively small angle ϕ^* which decreases with the increase of H.

To complete the experimental description, we compare the results with FC data for Nb (Fig. 3). The figure exhibits $M(\phi)$ dependencies for Nb which resemble those of $YBa_2Cu_3O_7$. There are, however, two important differences: (i) $M(\phi)/H$ curves for Nb coincide for the various fields for most of the angular span, as expected from type-II superconductors below H_{c1}. For $YBa_2Cu_3O_7$, on the other hand, the situation is completely different (see Fig. 1), implying that there is no true Meissner regime for this material. (ii) In the high-field regime we observe a plateau above an angle $\theta_c(H)$, implying that the magnetic moment is not capable of following the sample but the lag $\phi - \theta$ is a constant (see inset, Fig. 3). Very similar results, though on a limited angular span, were obtained by Heise[10] in his torque experiments. The plateau in high fields is limited to a small angular span and the overall shape of $M(\phi)$ is symmetric around π and is reversible, implying that M_{irr} is still a rigid body in spite of the fact that in this case $T/T_c \simeq 0.5$. This is to be contrasted with the asymmetry and the irreversibility for $YBa_2Cu_3O_7$ where the rigidity is broken and M_{irr} already vanishes for $T/T_c < 0.05$.

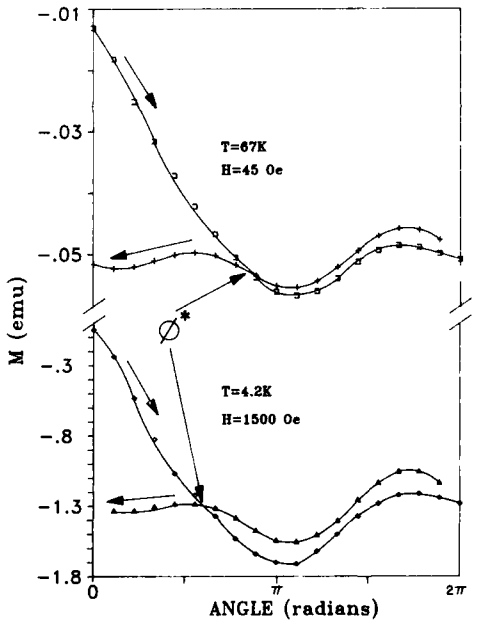


FIG. 2. Angular dependence of the field-cooled magnetization for $YBa_2Cu_3O_7$ at 4 K for 1.5 kOe and at 67 K for 45 Oe. Arrows indicate the direction of the rotation. The measurement starts at $\phi = 0$, the sample is rotated to 2π and back to zero. Note the break of rigidity at the critical angle ϕ^* denoted by the arrows and the irreversibility. The data taken from 2π to zero coincide with the (reversible) angular dependence of the zero-field-cooled magnetization. The lines are a guide to the eye.

Both Nb and $YBa_2Cu_3O_7$ are type-II superconductors characterized by a mixed phase above H_{c1} in which flux might be trapped and pinned to imperfections or dislocations. Pinned flux might explain the glassy features found in experiments[1-3] and it yields, in particular, a natural explanation for the present experiment: The trapped flux, which contributes a positive magnetization at $\phi = 0$, is rotated with the sample and generates a $\cos\phi$ shape. The fact that a $\cos\phi$ shape is found in the FC experiments for fields well below H_{c1} implies that flux is trapped during the cooling process, while crossing the mixed phase.

A different approach for the explanation of our results is based on recent superconducting glass models which have been suggested mainly for granular superconductors[11-13] but are quite appealing for the oxide superconductors because of their porous nature. In this picture the magnetic field induces frustration[14] by favoring nonuniform phase differences between neighboring grains which are weakly connected via a Josephson coupling. The concrete analogy between this frustrated phase and the magnetic spin-glass system yields a natural explanation for irreversible phenomena in the oxide superconductors. In this sense, the striking similarity between the results presented here and the experimental findings in spin glasses[6,7] lends much support to this approach.

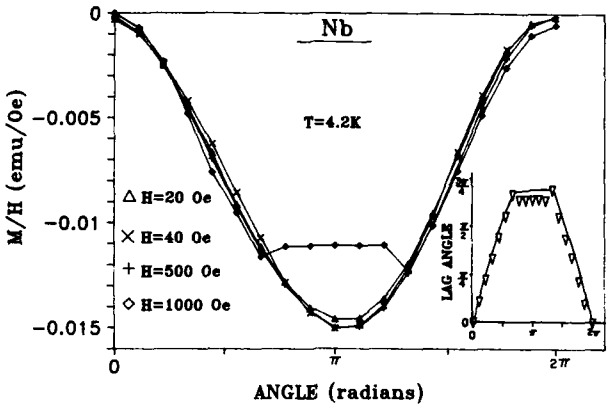


FIG. 3. Angular dependence of the field-cooled magnetization at 4.2 K for various fields for a Nb sample. Inset shows the lag $(\phi - \theta)$ as a function of the rotation angle ϕ for $H = 1$ kOe.

We are indebted to H. Sompolinsky for many illuminating discussions and suggestions. Useful discussions with S. Alexander and M. Gitterman are acknowledged. This work is supported in part by the Fund for Basic Research administered by the Israel Academy of Science and Humanities.

[a] Permanent address: Department of Physics, Bar-Ilan University, Ramat-Gan, Israel.

[1] K. A. Müller, M. Takashige, and J. G. Bednorz, Phys. Rev. Lett. **58**, 1154 (1987).
[2] Y. Yeshurun, I. Felner, and H. Sompolinsky, Phys. Rev. B **36**, 840 (1987).
[3] C. Giovannella, G. Collin, P. Rouault, and I. A. Campbell (unpublished).
[4] For a recent review of spin glasses, see K. Binder and P. Young, Rev. Mod. Phys. **58**, 801 (1986).
[5] Y. Wolfus, Y. Yeshurun, and I. Felner (unpublished).
[6] C. L. Henley, H. Sompolinsky, and B. I. Halperin, Phys. Rev. B **25**, 5849 (1982); W. M. Saslow, Phys. Rev. Lett. **48**, 505 (1982).
[7] A. Fert and P. M. Levy, Phys. Rev. Lett. **44**, 1538 (1980); A. Fert, A. Arvantis, and F. Hippert, J. Appl. Phys. **55**, 1640 (1984), and references therein; Y. Yeshurun and I. Felner, J. Magn. Magn. Mater. **54-57**, 215 (1986); Y. Yeshurun, I. Felner, and B. Wanklyn, Phys. Rev. Lett. **53**, 620 (1984) and references therein.
[8] A. Fert and F. Hippert, Phys. Rev. Lett. **49**, 1508 (1982); E. M. Gyorgy, L. R. Walker, and J. H. Wernick, *ibid.* **51**, 1684 (1983); J. B. Pastora, T. W. Adair, and D. P. Love, J. Phys. Lett. **44**, (1983).
[9] J. J. Capponi, C. Chaillout, A. W. Hewat, P. Lejay, M. Marezio, N. Nguyen, B. Raveau, J. L. Soubeyroux, J. L. Tholence and R. Tournier, Europhys. Lett. (to be published).
[10] B. H. Heise, Rev. Mod. Phys. **36**, 64 (1964).
[11] C. Ebner and A. Stroud, Phys. Rev. B **31**, 165 (1985); W. Y. Shih, C. Ebner, and D. Stroud, *ibid.* **30**, 134 (1984).
[12] G. Deutscher, I. Grave, and S. Alexander, Phys. Rev. Lett. **48**, 1497 (1982); G. Deutscher, Y. Imry, and L. Gunther, Phys. Rev. B **10**, 4598 (1974).
[13] P. G. DeGennes, C. R. Acad. Sci. Ser. B **292** (1981).
[14] G. Toulouse, Commun. Phys. **2**, 155 (1977).

Multiple coil pulsed NMR method for measuring the multipole moments of particle accelerator bending magnets

W. G. Clark, T. W. Hijmans, and W. H. Wong
Physics Department and Solid State Science Center, University of California at Los Angeles, Los Angeles, California 90024

An important step in the development and manufacture of the bending magnets for the proposed superconducting supercollider particle accelerator is measurement of the multipole moments of the magnetic field. This paper describes a method for doing so that makes use of the simultaneous pulsed NMR signal from a large number of coils placed on the diameter of a circle. From the value of the magnetic field thereby measured on the boundary, the multipole moments are obtained. Details of the basic concepts of the method are presented, along with some results of an early test of it.

I. INTRODUCTION

One of the technical challenges of the proposed Superconducting Supercollider (SSC) particle accelerator is the design, fabrication, and testing of long, high-field magnets whose homogeneity must meet stringent specifications.[1] In this paper, we describe a novel multiple coil pulsed magnetic resonance (MCPMR) method for testing such magnets. It uses a pulsed magnetic resonance signal that appears simultaneously in a large number of sample coils to map the field. These measurements are then used to calculate its multipole moments. Although the method is being developed for use with the SSC project, it should be useful as well in many other applications, such as other accelerator designs and magnetic resonance imaging magnets. The material presented here focuses almost exclusively on the SSC application. We describe the main principles and technical considerations, and include a brief report on the performance of our first prototype system.

The quantities needed in the SSC application are the multipole moments of the magnetic field in the region traversed by the particle beam. They determine the stability of the orbits, etc. The MCPMR method obtains this information by measuring the magnitude of the magnetic field at a discrete number of points on the boundary of a circle perpendicular to the beam path and centered on it. This is done by observing simultaneously the frequency of the free-induction decay signal from nuclear (or electron) spins in a large number of coils located on the circle. The multiplole moments are then calculated from these data.

II. MULTIPOLE MOMENTS AND HOW TO OBTAIN THEM

We begin with the definition of the multipole moments and show how they are related to the measurements made with the MCPMR method. We use the following coordinate system: The y axis is vertical, and is the direction of the large dipole field B_0 that bends the particle trajectories into a horizontal path. The z axis is horizontal and along the particle trajectory; the x axis is horizontal and perpendicular to it. The circular boundary upon which the field measurements will be made is centered at the origin and lies in the x-y plane. Points on the circle (radius R) are specified by the angle θ measured counterclockwise from the y axis. Since there are no sources of the magnetic field in this region, each Cartesion component of the magnetic field $\mathbf{B} = (B_x, B_y, B_z)$ satisfies Laplace's equation. Thus, if any component of $\mathbf{B}$ is specified on the boundary of a region (the circle), it is determined throughout the region (inside the circle). The solution of this boundary value problem gives

$$B_y(R,\theta) = B_0 + B_0 \sum_{n=1}^{\infty} R^n [b_n \cos(n\theta) - a_n \sin(n\theta)]. \tag{1}$$

The coefficients a_n and b_n are the multipole moments that are used for trajectory stability modeling. They are calculated using the Fourier inversion formulas:

$$b_n = \frac{1}{\pi B_0 R^n} \int_0^{2\pi} B_y(R,\theta)\cos(n\theta)d\theta, \quad n = 1,2,..., \tag{2}$$

$$a_n = \frac{-1}{\pi B_0 R^n} \int_0^{2\pi} B_y(R,\theta)\sin(n\theta)d\theta, \quad n = 1,2.... \tag{3}$$

The frequency of the magnetic resonance precession ω_L is given by the magnitude of B of the magnetic field, whereas Eqs. (1)–(3) refer only to its y component.[2] Since the field configuration of the SSC magnets involves only very small components B_x and B_z, and a small variation $B_0 - B_y$ along the y direction, the relation between ω_L, we expand the relation[2] between B and ω_L to first order in a Taylor series:

$$B = \frac{\omega_L(R,\theta)}{\gamma} = (B_x^2 + B_y^2 + B_z^2)^{1/2} \simeq B_0\left(1 - \frac{(B_0 - B_y)}{B_0}\right), \tag{4}$$

where $\omega_L(R,\theta)$ is the magnetic resonance frequency at R,θ on the circle and γ is the gyromagnetic ratio of the resonant spin. For the design goals of the SSC magnets,[1] the above approximation corresponds to an error of approximately 1 part in 10^6 for the determination of B_y. Examination of Eqs. (2)–(4) shows that from a measurement of ω_L at all points of the boundary, the multipole coefficients are determined.

One important point to note here is that within the framework of this approximation, only the variation of $\mathbf{B}$ along the y direction is measured [see Eq. (4)]. It is, never-

 0021-8979/88/084185-02$02.40 © 1988 American Institute of Physics

theless, sufficient to obtain the multipole coefficients. It does not, however, determine the *orientation* of the probe in the dipole field. For that, other means must be used, such as orientation via the null voltage from a Hall effect probe.

Equations (2)–(4) imply that ω_L is known everywhere on the circular boundary. Since it is not practical to measure it at all points, ω_L is measured instead at a discrete number of points. For this case, one then replaces the integrals in Eqs. (2)–(4) with discrete sums. We consider the case of M samples at the locations R, $2\pi m/M$ with m taking integral values between 0 and $M-1$. The result is

$$b_n = \frac{2}{M\langle\omega_L\rangle R^n}\sum_{m=0}^{M-1}\omega_L\left(R,\frac{2\pi m}{M}\right)\cos\left(\frac{2\pi mn}{M}\right), \tag{5}$$

$$a_n = \frac{-2}{M\langle\omega_L\rangle R^n}\sum_{m=0}^{M-1}\omega_L\left(R,\frac{2\pi m}{M}\right)\sin\left(\frac{2\pi mn}{M}\right), \tag{6}$$

where $\langle\omega_L\rangle$ is the average of ω_L over the circular boundary.

In applying Eqs. (5) and (6) it is important to make the number of probe positions M at least twice as large as the largest multipole index n to avoid the biasing that is inherent in discrete Fourier transforms. Also, going from the continuous case [Eqs. (2) and (3)] to the discrete case [Eqs. (5) and (6)] is an approximation, whose seriousness is easily modeled for a given situation.

III. PRACTICAL IMPLEMENTATION OF THE MCPMR METHOD

In this section we describe briefly some general considerations that apply to the MCPMR method in the context of the SSC application, describe a prototype working system that uses the MCPMR method, and comment on some possibilities for future development.

The design goals of the SSC magnets are operation from 0.3 T at particle injection to storage at 6.7 T with the magnets cooled to 4.5 K.[1] The typical mulitpole expansion coefficients are of order 1 or less in units of $10^{-4}B_0$. We take 1% of this as a target figure for the accuracy of each field measurement; i.e., ω_L should be determined at each point to 1 ppm. Here we adopt the very conservative estimate that the center of the resonance frequency can be determined to 10% of its width. It then follows that the width of the resonance line should not exceed 10^{-5} of its central frequency (or field).

This situation forces a compromise regarding the size of the individual samples. They must be small so that the linewidth associated with magnetic field inhomogeneities is still small (and so that its position is precisely determined), but they should be large to obtain a favorable signal-to-noise ratio. We have performed a detailed analysis of this situation. There is no space to present it here; we simply state that by using ^{3}He at 4.5 K as the working substance, it is predicted that the conditions for precision field measurement are readily satisfied over the range 0.3–6.7 T using surprisingly small samples. There are two advantages that follow from using small samples; many of them can be used in the restricted space available in the SSC bore, and very little pulsed rf power is needed to excite them.

Another important consideration is the method used to measure ω_L. In general, we have focused on pulsed magnetic resonance as it is capable of high sensitivity, is fast, and does not require auxiliary, time-dependent fields that are incompatible with the SSC configuration. A further advantage is that when measuring ω_L simultaneously in a large number of coils, one is rather insensitive to spurious drift or modulation of the magnetic field. The observed signal is the envelope of the free induction decay obtained with phase coherent detection.[3] It displays beats whose frequency Ω is the difference between ω_L (determined by the magnetic field) and that of the reference oscillator (ω_R) that governs the phase sensitive detection. This beat signal is digitally processed to extract the time interval T for N beats, and from that ω_L for each coil is determined.

We have constructed a prototype MCPMR system along the lines described above. A more detailed report on it will be published elsewhere. It has eight small magnetic resonance coils that are excited by a single transmitter. Each coil has its own receiver channel and digital processing to obtain Ω. Both protons in water at room temperature and ^{3}He gas at 4.2 K have been used as the working substance at $\omega_L/2\pi \approx 10$ MHz, which corresponds roughly to the SSC injection field. The digitized data are sent to a microcomputer. A single cycle of excitation, digitizing, and reading into the computer takes about 50 ms. Simple programs have been developed to perform the processing associated with Eqs. (5) and (6). In a relatively homogeneous field (free induction decay time of $\approx$1–2 ms), a field measurement good to about 1 ppm is obtained. Tests with time varying fields confirms that the field profile is accurately recorded even when the field is not static.

Several further developments of this system are planned for the near future. The number of coils will be increased to 32 to permit measurement of higher multipole moments. The operating frequency will be raised to 217 MHz to accommodate the 6.7-T storage field of the SSC. Finally, a material with a narrow electron-spin-resonance line, such as[4] (fluoroanthene)$_2$PF$_6$, will be used at 280 MHz to perform warm bore measurements at 0.01 T.

ACKNOWLEDGMENTS

This report is based upon work supported by the U.S. Department of Energy, Contract No. DE-AC02-87ER40350. One of us (W.G. C.) also expresses strong thanks to the Free University of Berlin and the Technische Hochschule Darmstadt for their hospitality while part of the work was being done, and to the Alexander von Humboldt-Stiftung for a U.S. Senior Scientist Award that helped to support it.

[1] "Conceptual Design of the Superconducting Super Collider," edited by J. D. Jackson, Report SSC-SR-2020, SSC Central Design Group, c/o Lawrence Berkeley Laboratory, 90-4040, 1 Cyclotron Road, Berkeley, CA 94720 (March 1986).
[2] C. P. Slichter, *The Principles of Magnetic Resonance*, 2nd ed. (Springer, Berlin, 1978).
[3] W. G. Clark, Rev. Sci. Instrum. 35, 316 (1964).
[4] E. Dormann, G. Sachs, W. Stöcklein, B. Bail, and M. Schwoerer, Appl. Phys. A 30, 227 (1983).

Superconducting and magnetic properties of $RBa_2Cu_3O_{7-x}$ compounds

S. A. Shaheen, N. Jisrawi, Y. H. Lee, M. Croft, and W. L. McLean
Serin Physics Laboratory, Rutgers University, Piscataway, New Jersey 08855-0849

H. Zhen, L. Rebelsky, and S. Horn
New York University, Department of Physics, 4 Washington Place, New York 10003

Superconducting properties of $RBa_2Cu_3O_{7-x}$ compounds (R = Y, La, Nd, Sm, Eu, Gd, Dy, Ho, Er, Tm, and Yb) have been studied by dc electrical resistivity and ac magnetic susceptibility techniques. Except for R = La, which is superconducting below 50 K, $RBa_2Cu_3O_{7-x}$ compounds exhibit sharp resistive and inductive transitions in the 90-K range. The nearly constant value of T_c for magnetic R ions indicates a very weak interaction between R ions, as anticipated from the known crystal structure of these materials. The effects of annealing in oxygen and argon, and air quenching, on the superconducting properties are also discussed.

The recent discoveries of superconductivity with critical transition temperatures T_c near 35 K (Refs. 1–3) and 90 K (Ref. 4) have stimulated unprecedented worldwide efforts for the preparation and characterization of $La_{2-x}(Ba,Sr)_xCuO_{4-x}$ compounds with the K_2NiF_4 structure and $RBa_2Cu_3O_{7-x}$ compounds (R = Y or a rare-earth element) with the $YBa_2Cu_3O_{7-x}$-type layered structure. These compounds are of great physical interest because of the occurrence of superconductivity at such high temperatures, and, additionally, they are of significant technological importance. With both these aspects in mind, we are preparing, characterizing, and studying the physical properties of the $RBa_2Cu_3O_{7-x}$ series.

Although it has been stated[5] that making the 90-K oxide superconductors is relatively easy, experienced scientists have found difficulties in producing the complete set of 90-K superconductors in the $RBa_2Cu_3O_{7-x}$ series.[6] The reason may lie in the fact that fabrication conditions which are appropriate for $YBa_2Cu_3O_{7-x}$ are not necessarily appropriate for its rare-earth analogues. In this paper we describe our optimized conditions for preparation of some individual members of the $RBa_2Cu_3O_{7-x}$ series and present electrical resistivity and magnetic susceptibility data on those members of the series that exhibit superconductivity above liquid-nitrogen temperature.

Several sets of $RBa_2Cu_3O_{7-x}$ samples were prepared by solid-state reaction of rare-earth oxides (or yttrium oxide), barium carbonate, and copper oxide powders in an alumina crucible using a standard procedure described in the literature[7] for $YBa_2Cu_3O_{7-x}$, i.e., by calcining in air, pelletizing, annealing in oxygen, and slow cooling. The calcining temperature of 950 °C is appropriate for $RBa_2Cu_3O_{7-x}$ compounds with R = Y, La, Pr, Nd, Sm, Gd, Dy and Ho, and 920–935 °C for the remaining members of the rare-earth series. The best results were obtained when materials were calcined for 16–24 h, and one or two intermediate grindings were applied. The pellets were pressed at 4 kbar, sintered at 900–930 °C in air or oxygen for at least 6 h, and slowly cooled in an oxygen atmosphere at a constant rate of 0.5 °C per minute in the range 630 °C–150 °C. Details of the experiment are given elsewhere.[8]

The x-ray diffraction patterns of the $RBa_2Cu_3O_{7-x}$ compounds revealed peaks characteristic only of the $YBa_2Cu_3O_{7-x}$-type structure (1:2:3 structure), except for R = Ce, Tb, Yb and Lu. All $RBa_2Cu_3O_{7-x}$ compounds forming the 1:2:3 structure were orthorhombic except for R = La and Pr, which were tetragonal within the resolution of the diffractometer. $YbBa_2Cu_3O_{7-x}$ and $LuBa_2Cu_3O_{7-x}$ did form the 1:2:3 structure, but also contained unknown impurity phases amounting to 5%–10% in Yb-based samples and 40%–60% in Lu-based samples. $CeBa_2Cu_3O_{7-x}$ formed an unknown structure. $TbBa_2Cu_3O_{7-x}$ did not form well in our three attempts and was not studied further.

Figure 1 shows the electrical resistivity (ρ) versus temperature data for the $RBa_2Cu_3O_{7-x}$ compounds with

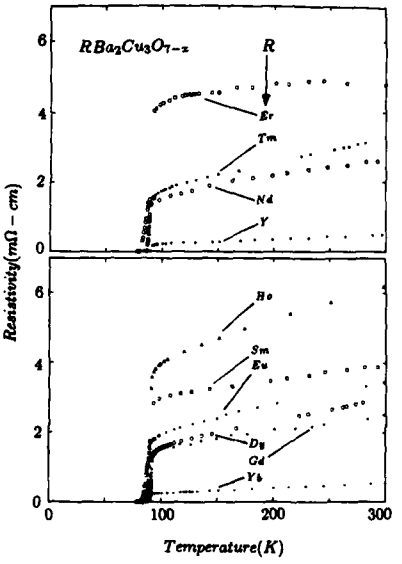


FIG. 1. Resistivity as a function of temperature for $RBa_2Cu_3O_{7-x}$ compounds (R = Y, or the rare-earth element indicated).

 0021-8979/88/084187-03$02.40 © 1988 American Institute of Physics

R = Y, Nd, Sm, Eu, Gd, Dy, Ho, Er, Tm, and Yb which exhibit superconductivity in the 90-K range. $LaBa_2Cu_3O_{7-x}$ was superconducting in the 70-K range. $CeBa_2Cu_3O_{7-x}$ and $PrBa_2Cu_3O_{7-x}$ were semiconducting or insulating down to 4.2 K. The highest observed value of T_c (where ρ drops to 50% of its extrapolated normal-state value) is 92.5 K for a $GdBa_2Cu_3O_{7-x}$ sample (not shown here). The width of the transition Δt (over which ρ drops from 90% to 10% of the extrapolated normal-state value) is typically 1–2 K. The $YBa_2Cu_3O_{7-x}$ and $YbBa_2Cu_3O_{7-x}$ samples exhibited the lowest resistivity and sharpest transitions ($\Delta t \sim 1.0$ K). Both these features are normally indicative of the good quality of the samples. However, our $YbBa_2Cu_3O_{7-x}$ sample was multiphase material. Similar observations were also made by others[7] for a multiphase $YbBa_2Cu_3O_{7-x}$ sample. This suggests that low resistivity and a sharp resistive transition may not necessarily indicate good sample quality for the oxide superconductors.

Some general trends were noted. The transition temperature for the superconducting compounds is nearly independent of the rare-earth element in the $RBa_2Cu_3O_{7-x}$ series. If R is taken from the middle of the rare-earth series, i.e., Eu, Gd, Dy, the single phase 1:2:3 structure is easily formed and sharp superconducting transitions above 90 K are observed. On the other hand, it is very hard to produce a single-phase $RBa_2Cu_3O_{7-x}$ compound with the end members of the rare-earth series, i.e., for R = Yb and Lu. The transition width Δt increases and T_c decreases in the $RBa_2Cu_3O_{7-x}$ series as one proceeds from R = Eu to R = La, i.e., from the middle to the beginning of the rare-earth series. Superconductivity is only observed if R is a trivalent ion. (R = Ce, Pr, and Tb are not trivalent under oxidizing conditions in the $RBa_2Cu_3O_{7-x}$ series.)

The normalized ac susceptibility data for some of the $RBa_2Cu_3O_{7-x}$ samples is displayed in Fig. 2. The noteworthy features are sharp transitions followed by a nearly-temperature-independent value below 77 K for all of these samples.

The effect of air quenching and Ar-annealing on $RBa_2Cu_3O_{7-x}$ samples was also investigated. The pellets of $RBa_2Cu_3O_{7-x}$ which were superconducting in the 90-K range were annealed in Ar and air at 900–930 °C for 6 h. Air-annealed pellets were then quenched by removal from the furnace at 900–930 °C. Ar-annealed pellets were cooled in an Ar atmosphere to room temperature by shutting off the furnace. X-ray spectra of air-quenched, oxygen-annealed, and argon-annealed $GdBa_2Cu_3O_{7-x}$ samples are shown in Fig.3. The spectra of the Ar-annealed samples clearly indicate the multiphase nature of the sample. The multiphase nature of the Ar-annealed samples was also apparent from the dirty green color of the crushed powders. There is very little difference between the spectra of the oxygen-annealed and air-quenched samples. The spectra are essentially characteristic of an orthorhombic 1:2:3 phase in both cases. A comparison of the superconducting properties of the air-quenched, Ar-annealed, and O_2-annealed $GdBa_2Cu_3O_7$ samples is made in Fig. 4. The Ar-annealed sample was insulating. The O_2-annealed sample showed a linear decrease in the normal-state resistivity on decreasing temperature and a sharp transition in the 92-K range. The air-quenched sample exhibited a slightly activated behavior before the onset of superconductivity in the 60-K range. The most striking difference between the O_2-annealed sample and the air-quenched sample is apparent from the static magnetic susceptibility data where Meissner effect is very tiny for the air-annealed sample as compared to the O_2-annealed sample. The Ar-annealed sample showed no evidence for superconductivity down to 4.2 K. The observed Meissner effect of $\sim 7\%$ for O_2-annealed sample is, in fact, somewhat underestimated because Curie-like paramagnetic susceptibility associated with the large magnetic moment of Gd atoms overshadows the Meissner signal, as is apparent from the upturn in the magnetic susceptibility at temperatures below the superconducting transitions. Using the measured effective paramagnetic moment of $7.65\mu_B$ corrections can be made. However, here we are concerned only with the relative magnitude of the Meissner signal for the air-quenched and oxygen-annealed samples. The magnitude of the Meissner signal in the air-quenched sample is so small that it can hardly account for a bulk superconductivity in this sample. This may mean that oxygen content is probably not homogen-

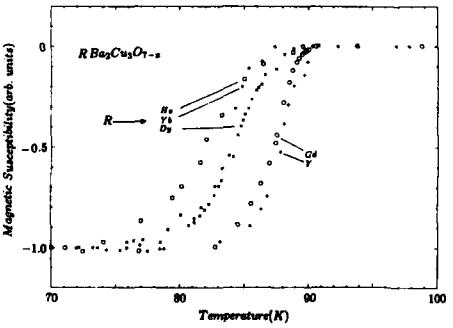


FIG. 2. Normalized ac susceptibility as a function of temperature for $RBa_2Cu_3O_{7-x}$ compounds (R = Y or a rare-earth ion).

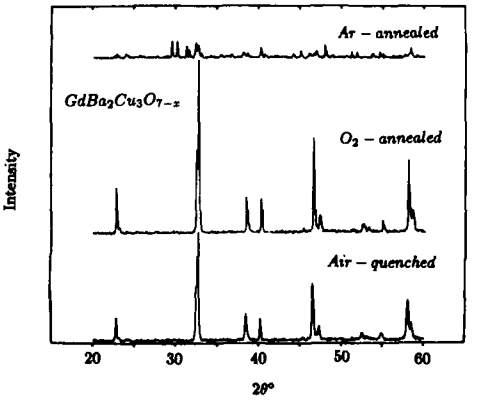


FIG. 3. X-ray spectra of air-quenched, Ar-annealed, and O_2-annealed $GdBa_2Cu_3O_{7-x}$ samples.

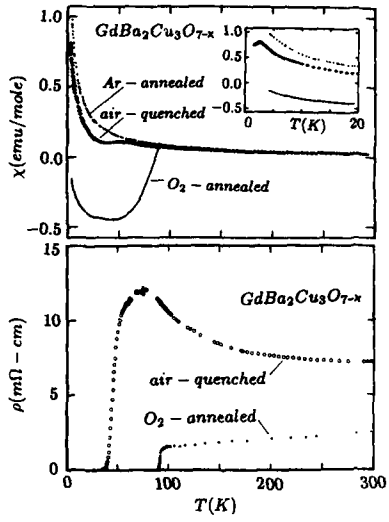


FIG. 4. Upper: the temperature dependence of the static magnetic susceptibility of the Ar-annealed, air-quenched, and O_2-annealed $GdBa_2Cu_3O_{7-x}$ samples. The inset shows the expanded view of the magnetic susceptibility data (in emu/mole units) between 0 and 20 K. Note the antiferromagnetic transition at 2.2 K. Lower: the electrical resistivity of the air-quenched and O_2-annealed $GdBa_2Cu_3O_{7-x}$ samples as a function of temperature.

eously distributed in the air-quenched sample. The experimental observations on this sample can be understood by visualizing that superconductivity emerges in the relatively oxygen-rich regions and activated normal-state resistivity is due to the more oxygen deficient regions of the samples. More systematic studies are needed to determine to what extent oxygen content and its homogeneous distribution are important for the bulk superconducting properties of these oxide superconductors.

In summary, we have shown that superconductivity in the $RBa_2Cu_3O_{7-x}$ series is observed only in those cases where the rare earths are trivalent. The transition temperature is nearly independent of the rare-earth ion, indicating a weak interaction between the rare-earth ions consistent with the 1:2:3 crystal structure. The amount of the oxygen content and its homogenous distribution in the lattice seems to be critically important for the bulk nature of the superconductivity in this class of materials.

This work was supported by Grants Nos. SNJCST 86-240040-13, SNJCST 87-240090-13, and DMR 85-11982.

[1]J. G. Bednorz, K. A. Müller, Z. Phys. B **64**, 189 (1986).
[2]S. Uchida, H. Takagi, K. Kitazawa, and S. Tanaka, Jpn. J. Appl. Phys. Lett. **26**, L1 (1987).
[3]R. J. Cava, B. Batlogg, R. B. van Dover, and E. A. Rietman, Phys. Rev. Lett. **58**, 408 (1987).
[4]M. K. Wu, J. R. Ashburn, C. J. Torng, P. H. Hor, R. L. Meng, L. Gao, Z. J. Haung, Y. Q. Wang, and C. W. Chu, Phys. Rev. Lett. **58**, 908 (1987).
[5]P. M. Grant, New Scientist **115**, 36 (1987)
[6]G. Kolata, Science **236**, 663 (1987).
[7]J. M. Tarascon, W. R. McKinnon, L. H. Greene, G. W. Hull, and E. M. Vogel, Phys. Rev. B **36**, 226 (1987).
[8]S. A. Shaheen, N. Jisrawi, Y. H. Lee, Y. Z. Zhang, M. Croft, W. L. McLean, H. Zhen, L. Rebelsky, and S. Horn, Phys. Rev. B **36**, 7214(1987).

X-ray absorption spectroscopy studies of high-T_c superconductors

Y. Jeon, F. Lu, H. Jhans, S. A. Shaheen, and M. Croft
Department of Physics, Rutgers University, Piscataway, New Jersey 08855-0849

P. H. Ansari
Seton Hall University, South Orange, New Jersey 07079

X-ray absorption spectroscopy measurements on rare-earth (R) and Ba sites in the new superconducting oxides and in binary rare-earth oxides are discussed. All of the near-edge spectra appear to manifest a continuum resonance feature whose energy is quantitatively well correlated with the R–O and Ba–O bond lengths. Evidence supporting a second such feature related to the R/Ba interatomic distance is also presented. Finally, simultaneous consideration of both of these features appears consistent with the inverse square-law expectation for the interatomic distance dependence of the energies of these spectra features.

The discovery of high-T_c superconductivity has stimulated a great deal of interest in oxide-based materials. X-ray absorption spectroscopy (XAS) has been used by a number of authors to probe valence states and local bond lengths in these new materials.[1–4] Here we are concerned with the interpretation of continuum resonance features occurring in the 60-eV range following an x-ray absorption edge in terms of local neighbor shell distances. We will address the interatomic distances surrounding the rare-earth (R) and Ba sites in R_2O_3, as well as in the superconducting $RBa_2Cu_3O_7$ (sometimes referred to as 123 compounds) materials.

A continuum resonance (CR) in an XAS near-edge spectrum occurs when: a local maximum in potential occurs in the vicinity of the atom being excited; and when the vestiges of a bound-localized state for this potential exists just above the escape threshold for photoelectrons.[5,6] This resonance in the free-photoelectron spectrum resembles the more simple case of an electron in a one-dimensional box where the first energy level (ϵ) is related to the box length L via the standing-electron wave condition, i.e., $\epsilon = (h^2/2m)/4L^2 = (151\ \text{eV Å}^2)/4L^2$.[6]

In the past, a number of studies have quantitatively related the energy of the continuum resonance above the K edges to the bond length for low-Z gas-phase molecules.[7–9] In these studies the electron count of the molecule introduced chemical shifts in the resonance energy versus bond-length correlations.[9] Continuum resonances have also been interpreted as occurring in materials where a metal atom sits in a shell of strongly electronegative ligand atoms.[10,11] In these cases, although the containment has a strong geometrical character the specific backscattering efficiency of different ligands should also play a role in the energy of the resonance through the backscattering phase factor.[11]

In Fig. 1 we show the R-L_3 and Ba-L_3 spectra of a series of cubic R_2O_3 and $RBa_2Cu_3O_7$ (R = Sm) compound. These heavy R_2O_3 compounds form in a cubic distorted florite structure,[12] and the orthorhombic oxygen-deficient 123 superconductor structure has been discussed extensively in the recent literature.[13–17] We have labeled three spectral features which recur in all of the spectra. The very stong feature a is the vestige of the $2p \rightarrow 5d$ atomic transition and is typically called a white-line (WL) feature.[18] We note that the WL feature provides the best empirically defined reference energy in the near-edge spectra and will be used as the common zero of energy in our discussion. Feature b is the weakest feature and will be discussed later. Feature c has been attributed previously to a continuum resonance caused by the oxygen ligands about the rare-earth site.[18]

It should be noted that feature c moves to higher energies (relative to the WL) as R moves to the right in the rare-earth row in the R_2O_3 compounds. By virtue of the lanthanide contraction, the R-O separation contracts uniformly in these cubic sesquioxides.[12] Thus, the CR feature responds to the decreasing size of the near-neighbor ligand cell as one would expect from the simple particle in a box analogy. The R-O relation in these cubic R_2O_3 compounds is related to that in the parent florite structure. The parent florite structure has the R sites in eightfold coordination with the O sites with the R–O bond length being $3a/4$, where a is the florite cell parameter. In the C-R_2O_3 structure two of the O neigh-

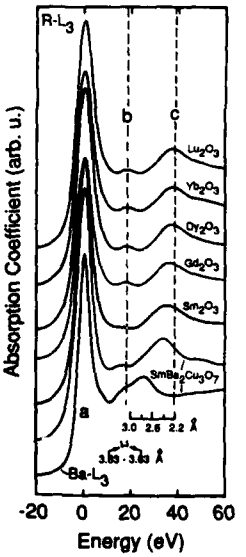


FIG. 1. Rare-earth (R) and Ba L_3 spectra in R_2O_3 and 123 superconducting oxides. Note feature: the labeled features in the spectra are as follows: a, a white line (WL) feature; c, a continuum resonance (CR) due to the oxygens ligands; and b, a feature interpreted here in terms of a CR caused by the more-distant R/Ba shell. The dashed verticle lines are included to help illustrate the energy shifts of the features. The scales at the bottom of the figure indicate the correlation between the energy of the spectra features b and c and the interatomic distances involved.

 0021-8979/88/084190-03$02.40 © 1988 American Institute of Physics

bors are removed from opposite sides of the R atoms and roughly sixfold (actually four plus two) coordination of R with O remains.[12] Alternation of which oxygens are removed also doubles the unit cell of the C-R_2O_3 structure relative to the parent florite structure. In Fig. 2 we have plotted the average florite-related R–O bond length versus the energy of the CR for the R_2O_3 compounds.

We turn now to the rare-earth sites in the 123 superconducting oxides. Referring to Fig. 1 it is clear that the R-L_3 is qualitatively quite similar in the sesquioxides and 123 oxides. The continuum resonance feature *c* is, however, shifted to lower energy in the 123 oxides. Hence, again using the quantum box analogy, the R environment might reasonably be expected to be expanded relative to that in the C-R_2O_3 compounds. The recent detailed structural work on the 123 oxides has shown that the R sites are eightfold coordinated to O with bond lengths in the 2.37–2.42-Å range—that is, expanded beyond the 2.25–2.37-Å range in the R_2O_3 compound.[17] We plot the energy of the R continuum resonance feature *c* versus the R-O separation (r) for a number of $RBa_2Cu_3O_7$ compounds in Fig. 2. The solid line in Fig. 2 is a least-squares fit to the combined sesquioxide and 123 oxide data. The empirical R–O bond-length relation $\Delta E = -23.6r(\text{eV/Å}) + 90.8$ (eV) would appear to hold true for all of these data.

Ba is the element immediately preceding the rare-earth series, hence its L_3 edge is closely related to the R-L_3 edges. Thus, it is not surprising to note in Fig. 1 that the Ba-L_3 edge shows a CR reminiscent of the R spectra and that this resonance is shifted toward lower energies (i.e., in an expanded environment). Due to oxygen deficiencies, and oxygen displacements, the Ba sites in the 123 oxides have four oxygen neighbors on one side at a distance 2.74–2.79 Å and six oxygen neighbors on the other side at a distance 2.90–3.02 Å. The energy of the CR peak for the Ba-L_3 spectrum is plotted in Fig. 2 versus this range of bond lengths. The nonsymmetrical environment of the Ba at present precludes a better determination of an average bond length. We note that the linear empirical relation derived above for the R sites would clearly underestimate the Ba–O bond length. Since the quantum box analogy would foreshadow such a deviation the Ba result would appear at first compatible with the common CR interpretation of feature *c* in all of these L_3 spectra.

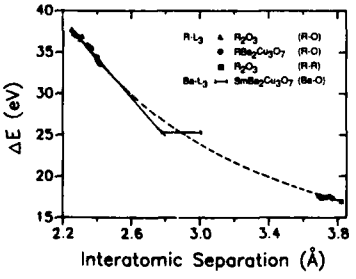


FIG. 2. The energy ΔE of spectral features *b* and *c* (see Fig. 1) plotted vs average interatomic separation of the shell we are associating with the respective features. The solid line is a linear fit of our R-O feature *c* results [$\Delta E = -23.6\,r(\text{eV/Å}) + 90.8$ (eV)]. The dashed line is adequate fit of all of the results to the equation $\Delta E = 162.1/r^2$ (eV/Å^2) + 5.9 (eV).

We will now consider several points regarding the weak feature *b* in the spectra in Fig. 1. First, we note that feature *b* appears to persist in all of the spectra. Second, we note that feature *b* appears to respond to local atomic volume changes between compounds in a manner qualitatively reminiscent of feature *c*. That is, across the R_2O_3 series feature *b* appears to move to higher energy with the lanthanide contraction, and feature *c* in the Sm 123 compound has moved in the lower-energy (volume expansion) direction relative to the C-R_2O_3 materials. Third, the rate at which feature *b* moves with atomic volume expansion is less than the rate with which feature *c* moves. Indeed, in the Ba-L_3 spectrum feature *b* has become an unresolved shoulder on the edge of the strongly red-shifted feature *c*. Finally, we note that if we were to try to apply the interatomic separation versus CR energy results we have obtained above (for feature *c*) to feature *b* we would have to consider atoms at distances strictly greater than 3.2 or 3.5 Å to explain feature *b*.

With the last point above in mind, it is important to realize that the R and Ba sites in all of these compounds will have direct line of sight coordination to eight R or Ba atoms with separations in the 3.68–4-Å range. By line of sight, we mean that no other atoms intervene. Thus, if neighbor backscattering from the highly coordinated O neighbors can induce a geometrical CR then, in principle a similar effect could occur from the R neighbors. The fact that the R neighbors are more distant and not strongly electronegative argue for a small effect, but that is what is observed. In Fig. 2, we have plotted the positions of the feature *c* versus average R–R and/or R–Ba bond lengths for those compounds. The smaller slope of ΔE versus distance relation noted qualitatively above is clear from the points. In making this plot, we are in effect *proposing* that features *b* be interpreted similar to feature *c*, but that it is the R (and Ba) shell of atoms about the R (or Ba) site that is the cause of the feature *b*. It is interesting to note that the calculations of Kutzler *et al.*[11,18] in which the ligand atoms only are included faithfully reproduce feature *c* but fail to produce feature *b*. This is at least consistant with our proposed action that it is the atomic shell beyond the ligand shell which produces this feature.

Three points motivate the notion to consider all of our results for feature *b* and feature *c* simultaneously: first is the expected $\epsilon \propto 1/L^2$ dependence from the quantum box analogy; second is the long-bond-length deviation of the Ba-feature-*c* result from the R-feature-*c* extrapolation; and third is the still stronger long-bond-length displacement of the feature-*b* results. Accordingly, we have fitted our interatomic separation r versus feature energy ΔE data in Fig. 2 to the relation $\Delta E = (h^2/2m)\,S/r^2 + \Delta E_0$ and obtain the dashed line displayed in Fig. 2 (with $S = 1.10$ and $\Delta E_0 = 5.9$ eV). By simultaneously fitting our R-R and R-O results we are assuming that the difference between backscattering from R and O is in some sense negligible at interatomic distance above 3.5 Å or so. This need not be true; however, the fact that the Ba-O deviation from the R-O results seem qualitatively consistent with the resulting fitted dashed line is encouraging. To summarize, we wish to note that we have put

forward a number of new ideas regarding the interpretation of XAS near-edge spectra. We wish to emphasize that these innovations should at this juncture be regarded strictly as proposals. We have, for example, considered CR features in the same spectrum caused by two different line-of-sight neighboring shells. At least one of these shells (the R shell) is not made up of strongly electronegative atoms. We have found an apparent correlation between R–O bond length and CR energy which spans dissimilar materials types. Finally, it may be that the oxygen-shell and R-shell results support (when considered together) the inverse distance squared relation expected for the distance dependence of the energy of a continuum resonance.

This work was supported by State of New Jersey Commission on Science and Technology Grants No. 86-240040-13 and No. 87-240090-13, and Department of Energy Grant No. De-F605-84-ER45081.

[1]J. M. Tranquada, S. M. Heald, A. R. Moodenbaugh, and M. Suenaga, Phys. Rev. B **35**, 7187 (1987).
[2]E. E. Alp, G. K. Shenoy, D. G. Hinks, D. W. Capone II, L. Soderholm, H.-B. Schuttler, J. Guo, D. E. Ellis, P. A. Montano, and M. Ramanathan, Phys. Rev. B **35**, 7199 (1987).
[3]J. B. Boyce, F. Bridges, T. Claeson, T. H. Geballe, C. W. Chu, and J. M. Tarascon, Phys. Rev. B **35**, 7203 (1987).
[4]Y. Jeon, F. Lu, H. Jhans, S. A. Shaheen, G. Liang, M. Croft, P. H. Ansari, K. V. Ramanujachary, E. A. Hayri, S. M. Fine, S. Li, H. Feng, M. Greenblatt, L. H. Greene, and J. M. Tarascon, Phys. Rev. B **36**, 3891 (1987).
[5]C. R. Natoli, in *EXAFS and Near Edge Structure III*, edited by K. O. Hodgson, B. Hedman, and J. E. Penner-Hahn (Springer, New York, 1984), p. 38.
[6]C. R. Natoli, in *EXAFS and Near Edge Structure*, edited by A. Bianconi, L. Incoccia, and S. Stipcich (Springer, New York, 1983), p. 43.
[7]A. P. Hitchcock, F. Sette, and J. Stohr, in Ref. 5, p. 43.
[8]F. Sette and J. Stohr, in Ref. 5, p. 250.
[9]F. Sette, J. Stohr, and A. P. Hitchcock, J. Chem. Phys. **81**, 4906 (1984).
[10]J. L. Dehmer, J. Chem. Phys. **56**, 4496 (1972).
[11]F. Kutzler, Ph. D. thesis, Stanford University, 1981.
[12]L. Eyring, in *Handbook on the Physics and Chemistry of Rare Earths*, edited by K. A. Gschneidner, Jr. and L. Eyring (North-Holland, Amsterdam, 1979), p. 337.
[13]P. H. Hor, R. L. Meng, Y. Q. Wang, L. Gao, Z. J. Huang, J. Bechtold, K. Forster, and C. W. Chu, Phys. Rev. Lett. **58**, 1891 (1987).
[14]T. Siegrist, S. Sunshine, D. W. Murphy, R. J. Cava, and S. M. Zahurak, Phys. Rev. B **35**, 7137 (1987).
[15]R. M. Hazen, L. W. Finger, R. J. Angel, C. T. Prewitt, N. L. Ross, H. K. Mao, C. G. Hadidiacos, P. H. Hor, R. L. Meng, and C. W. Chu, Phys. Rev. B **35**, 7238 (1987).
[16]Y. LePage, W. R. McKinnon, J. M. Tarascon, L. H. Greene, G. W. Hull, and D. M. Hwang, Phys. Rev. B **35**, 7245 (1987).
[17]J. M. Tarascon, W. R. McKinnon, L. H. Greene, G. W. Hull, and E. M. Vogel, Phys. Rev. B **36**, 226 (1987).
[18]F. Kutzler, K. Hodgson, D. Misemer, and S. Doniach, Chem. Phys. Lett. **92**, 626 (1982).

Correlation between electronic states of O, Cu, and Ba in several high-T_c superconductors

S. Horn and J. Cai
Department of Physics, New York University, 4 Washington Place, New York, New York 10003

S. A. Shaheen and M. Croft
Department of Physics, Rutgers University, Piscataway, New Jersey 08854

C. L. Chang and M. L. denBoer
Department of Physics, Hunter College of the City University of New York, New York, New York 10021

X-ray photoemission measurements of Y-, Sm-, Eu-, and Yb-based high-temperature superconductors show a clear correlation between Cu 2*p* satellite features, which previous work has shown are associated with materials which exhibit superconductivity, and a high-binding-energy peak in the O 1*s* spectrum. In samples with varying oxygen content the intensity of the Cu 2*p* satellites changes, reflecting the Cu valence which varies between 1 + and 2 + . The high-binding-energy O peak appears to track the Cu valence. This high-binding-energy peak may be indicative of the presence of O 2*p* holes, suggested in some models as necessary for superconductivity. The Ba 3*d* peak position also changes systematically with the Cu valence.

A number of core-level x-ray photoelectron spectroscopic studies of high-temperature superconductors of both the 40-K-type (generic formula $La_{2-x}Sr_xCuO_4$) and 90-K-type (modified perovskites with the generic formula $RBa_2Cu_3O_7$, where R can be Y or most rare earths) have been reported. This work has reached a reasonable consensus on the valence of the Cu; most x-ray photoelectron spectroscopies (XPS's) show that Cu in both types of systems is in a 2 + oxidation state. Fujimori *et al.*[1] observed satellites of the Cu 2*p* peaks, only present in materials which exhibited superconductivity, which resembled those observed in CuO, in which Cu has a formal 2 + valence. Similar observations were made by Horn *et al.*,[2] who concluded, by comparing superconductors and nonsuperconductors prepared by reducing the oxygen content and by substitution of Pr (valence greater than 3 +) for Y (formal valence 3 +), that Cu in materials which exhibited superconductivity was primarily in a 2 + formal oxidation state as in CuO. The correlation of superconductivity and divalent Cu was also observed by Shen *et al.*[3] and Bianconi *et al.*[4] on the basis of the Cu 2*p* spectra. Within the resolution of the XPS technique, there is no evidence for Cu in other oxidation states. Thus Steiner *et al.*[5] compared Cu in $LaSrCuO_4$ with materials in which Cu is formally divalent and trivalent, and concluded that at most 5% of the Cu was trivalent. These studies are directly relevant to determining the mechanism of high-temperature superconductivity, as several models predict charge fluctuations of the Cu ion between 2 + and 3 + . Other models emphasize the importance of both Cu 3*d* holes (hence Cu^{2+}) and O 2*p* holes in order to achieve the superconducting state. Thus a study of the electronic state of oxygen is necessary.

Unfortunately, there has been considerably less agreement on the charge state of the oxygen. Shen *et al.*[3] reported that before cleaning, $YBa_2Cu_3O_7$ showed split O 1*s* peaks, and the higher-binding-energy peak became smaller on cleaning, but published no spectra. Steiner *et al.*[6] also observed a split O 1*s* spectrum in $LaSrCuO_4$ and concluded by varying the takeoff angle that a peak at a binding energy of 531 eV was due to adsorbed O^- ions while another peak at 529 eV was a feature of the bulk. Kohiki, Hamada, and Wada[7] measured a similar spectrum in $YBa_2Cu_3O_7$ and found that the 531-eV peak decreased as the temperature decreased from 350 to 180 K. In contrast, Sarma *et al.*[8] found that the 529-eV peak decreased between 300 and 80 K, while a new peak appeared at 533 eV. They also concluded that the 531-eV peak was due to adsorbed O, as it increased with time after sample cleaning. On the other hand, Horn *et al.*[2] showed an O 1*s* spectrum with peaks at 529, 531, and 533 eV on an $YBa_2Cu_3O_7$ sample with reduced O content; only the 533-eV peak was present on a sample with higher O content which exhibited superconductivity at 90 K. This seems to support the notion that O 2*p* holes are present. The same conclusion was drawn by Thiry *et al.*,[9] who observed a resonance in valence-band features related to O at the O 2*s* binding energy. Some of these disagreements may be related to the experimental difficulties involved in measuring oxygen with XPS. Charging may occur in these poorly (normal) conducting materials, particularly before scraping off a surface layer which is produced in air and which we often find is insulating. Besides the sample, oxygen may be present on the sample holder, nearby chamber parts, and adsorbed in the form of CO or CO_2 on the surface or in grain boundaries. In this work, we study oxygen by observing correlations between features in the Cu 2*p* spectra already demonstrated to be related to superconductivity and associated features in the O 1*s* spectra, thus eliminating ambiguities due to spurious oxygen. We show that there is a high-binding-energy oxygen 1*s* peak which is clearly associated with superconductivity. We also find variations in the Ba 3*d* spectrum in these samples.

We have measured the XPS spectra of superconducting Y, Sm, Eu, and Yb perovskites both as initially introduced into the measurement chamber and after successive stages of

 0021-8979/88/084193-03$02.40 © 1988 American Institute of Physics

cleaning (by scraping with an Al_2O_3 file). Samples were prepared using sintering and oxygen annealing techniques by now well described in the literature. For comparison, an Y-based perovskite with a reduced oxygen content (achieved by rapid quenching from above 900 °C) which did not superconduct was also measured. The Y samples were measured soon after preparation, and portions of their XPS spectra have been previously reported;[2] however, the other samples were stored in air for as much as several weeks before measurement. All spectra were taken at room temperature in a previously described UHV system[2] equipped with a VSW 100-mm analyzer and a Mg$K\alpha$ x-ray source.

At the top of Fig. 1 we show that Cu $2p_{3/2}$ and O 1s spectra of the superconducting Y sample before scraping and corresponding spectra of the nonsuperconducting Y sample after cleaning. The satellite features of the Cu spectrum characteristic of Cu^{2+}, and corresponding to "well" and "poorly" screened final states,[10] are weakly evident in the latter, reinforced by the Mg$K\alpha$ high-energy satellites of the Cu $2p_{1/2}$ peak which have not been removed. On the unscraped sample, a single sharp O 1s peak at about 531 eV is apparent, while the nonsuperconducting sample exhibits a split O 1s spectrum with peaks at 529 and 531 eV and a weak shoulder at higher binding energy. Both the Eu- and Sm-based samples plotted below in Fig. 1 show almost no sign of the well-screened Cu 2p satellite, indicating that Cu in the surface region measured by XPS is not in the formally 2 + valence state of CuO. Correspondingly, the O 1s spectra show only two peaks at about 529 and 531 eV, with no sign of a high-binding-energy shoulder. In contrast, the Yb-based sample shows a noisy, but significant, Cu 2p satellite, and its O 1s spectrum shows, besides the low- and medium-binding-energy peaks at 529 and 531 eV, a high-binding-energy peak at about 533 eV. Finally, the superconducting Y-based sample shows a very prominent Cu 2p satellite, indicating in agreement with previous work[5] that the Cu is nearly divalent. The corresponding O 1s spectrum now consists of a single sharp peak at a high binding energy of 533 eV.

A similar systematic trend is also apparent in the Ba 3d spectra plotted in Fig. 2. The unscraped spectrum shows a single sharp $3d_{5/2}$ peak at a binding energy of 780.2 eV. In the nonsuperconducting Y and the Eu- and Sm-based samples, which have only weak Cu 2p satellites, the spectrum broadens and shifts about 0.5 eV to lower binding energy. In the Yb-based sample, in which the Cu satellites become significant, the spectrum shifts an additional 0.5 eV lower. In the superconducting Y-based sample in which the Cu satellites are most prominent, the spectrum has shifted a total of 1.5 eV to lower binding energy than in the unscraped surface.

In Table I we list the binding energy of the Cu $2p_{3/2}$, O 1s, and Ba $3d_{5/2}$ of the superconducting and nonsuperconducting Y-based samples. We also list the relative concentrations of each element at the surface region, estimated using the following procedure. First, we subtracted the background under a particular peak and integrated to find its total area. This was then corrected for the photoionization cross section of the particular level as tabulated by Ley and Cardona[11] and for the analyzer transmission function, which is inversely proportional to the electron kinetic energy. A value of 2 was assigned to the Ba $3d_{5/2}$ level. Previous experience has shown that this procedure is not usually accurate to better than 50%, although relative concentration determinations may be more precise.[12] Table I indicates reassuringly that the amount of each element in the surface region does not differ significantly from that expected from the bulk stoichiometry, with the principal difference between the superconducting and nonsuperconducting samples being the lower oxygen content of the latter.

The O 1s and Cu 2p results have important implications for the electronic structure of O in the high-temperature superconductors. Although we are unable to vary the takeoff angle, in agreement with other authors[6,8] we identify the medium-binding-energy 531-eV peak as an impurity due to species such as CO or OH^-, adsorbed on the surface or in grain boundaries of the sample, or originating from the sample holder. This is suggested both by its prominence on unscraped surfaces and by the observation that, if the superconducting Y-based sample is allowed to remain in the vacuum system for many hours, a shoulder at about 531 eV begins to form on the 533-eV peak. We identify the low-binding-ener-

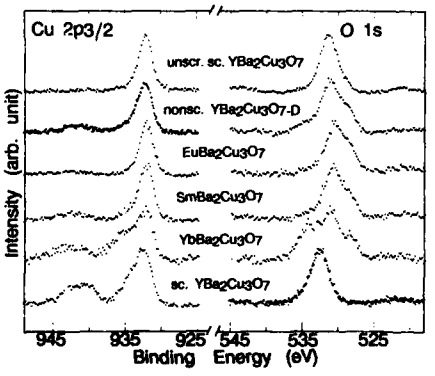


FIG. 1. X-ray photoelectron spectra (XPS) of the Cu $2p_{3/2}$ and O 1s core levels of a number of superconducting and nonsuperconducting oxide perovskites as labelled and discussed in the text. The high binding energy peak observed most prominently in superconducting $YBa_2Cu_3O_7$ is characteristic of Cu^{2+}, and is associated with a high binding energy feature in the O 1s spectrum.

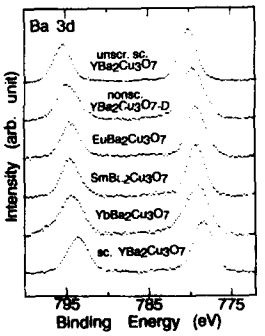


FIG. 2. X-ray photoelectron spectra (XPS) of Ba $3d_{3/2}$ and $3d_{5/2}$ core levels of several superconducting and nonsuperconducting oxide perovskites as noted and described in the text.

TABLE I. The binding energy (B.E.) and relative intensity (R.I.) of indicated peaks in the XPS spectra of the superconducting and nonsuperconducting $YBa_2Cu_3O_7$ samples. Relative intensity was estimated as described in the text, and normalized to make the Ba $3d_{5/2}$ intensity equal two. Although intensity estimates are subject to large errors, it is evident that there is more oxygen in the superconducting sample.

	Cu $2p_{3/2}$		O 1s		Ba $3d_{5/2}$	
	B.E.	R.I.	B.E.	R.I.	B.E.	R.I.
Superconducting	933.1	3.2	532.8	10.0	778.4	2.0
Nonsuperconducting	932.5	2.4	531.1	4.8	779.7	2.0

gy peak at 529 eV with bulk O^{2-}.

We tentatively suggest the following explanation of the high-binding-energy 533-eV O 1*s* peak. To our knowledge, this peak has not been observed by others at room temperature, although it might be related to the 533-eV peak observed below 90 K by Sarma *et al.*,[8] whose valence-band spectrum differs from others.[3,9] In the oxygen-deficient Y sample the Cu valence is less than 2 +, reflecting the ability of the bulk oxygen to remain in its preferred 2-formal valence state without fully oxidizing the Cu. On the other hand, in the Y-based material with a full oxygen content, there is insufficient valence electron charge (a "charge shortage") such that the Cu is fully oxidized to 2 +, and yet the oxygen must be content with a charge state less than 2 −, producing a single high-binding-energy O 1*s* peak. Since the Cu valence is not greater than 2 +,[5] simple charge counting arguments require that in a material with a full seven oxygen ions per unit cell those ions must have a formal charge less than 2 −. Thus this peak is direct evidence of unoccupied 2*p* levels in the oxygen. The Eu-, Sm-, and Yb-based samples then represent intermediate cases. Having been stored in air for some time, they may have lost oxygen. Changes in these high-temperature superconductors over time have been previously observed[13] and ascribed to loss of oxygen. For Yb, which may be somewhat more stable than the other two materials, this loss was less complete, so that some charge shortage remains, producing a weak Cu satellite and a high-binding-energy O 1*s* peak in the presence of low- and medium-binding-energy peaks representing, respectively, those oxygen ions in a more reduced state and adventitious oxygen. The latter is expected for the Yb-based sample as it was rather small and mounted on a Cu block, making it likely that some emission from the holder was included in the measurements. The same was true of the Sm- and Eu-based samples, while the Y-based sample was large and mounted on a small holder, so the x-ray source and analyzer measured only the sample surface. Other published work is likely affected by similar difficulties. The observed correlation between the Cu valence and the oxygen charge state is reasonable on physical grounds; it is to be expexted that an excess of oxygen, which produces a "charge shortage" in the material, will produce oxygen in a lower charge state and hence at a higher binding energy, while generating Cu in its higher 2 + valence state. The reduced oxygen charge in the superconducting materials, however, is also predicted by models of superconductivity which rely on O 2*p* holes.

A tentative interpretation of the Ba 3*d* spectra is on similar lines. Steiner *et al.* previously observed two Ba peaks on $La_{1.85}Ba_{0.15}CuO_4$ at 780.4 and 778.7 eV and, noting that the high-binding-energy feature increased with electron escape angle, concluded that it was due to O^{2-} defects associated with the Ba, of which there would be more present at the surface. On an unscraped surface, the high-binding-energy feature may also be due to formation of another Ba compound, such as BaO, at the surface. We then identify our higher-binding-energy peak observed on the unscraped surface with their 780.4-eV peak, and the low-binding-energy peak observed on superconducting Y with their 778.7-eV peak. The Sm-, Eu-, and, to a lesser extent Yb-, based samples represent intermediate cases between these extrema. The shift and broadening may then reflect the fact that we are unable to resolve the two peaks. As their relative proportion changes with oxygen concentration, the average peak position will shift accordingly.

This work was supported in part by the National Science Foundation under Grant No. DMR-8521561, by the Department of Energy under Grant No. DE-FG02-85ER45195, and by Grant No. 666450 from the PSC-CUNY Research Award Program of the City University of New York.

[1]A. Fujimori, E. Takayama-Muromachi, Y. Uchida, and B. Okai, Phys. Rev. B **35**, 8814 (1987).
[2]S. Horn, J. Cai, S. A. Shaheen, Y. Jeon, M. Croft, C. L. Chang, and M. L. denBoer, Phys. Rev. B **36**, 3895 (1987).
[3]Zhi-xun Shen, J. W. Allen, J. J. Yeh, J.-S. Kang, W. Ellis, W. Spicer, I. Lindau, M. B. Maple, Y. D. Dalichaouch, M. S. Torikachvili, and J. Z. Sun, Phys. Rev. B **36**, 8414 (1987).
[4]A. Bianconi, A. Congiu Castellano, M. De Santis, P. Delogu, A. Gargano, and R. Giorgi, Solid State Commun. **63**, 1135 (1987).
[5]P. Steiner, V. Kinsinger, I. Sander, B. Segwart, S. Hufner, C. Politis, R. Hoppe, and H. P. Muller, Z. Phys. B **67**, 497 (1987).
[6]P. Steiner, R. Courths, V. Kinsinger, I. Sander, B. Siegwart, S. Hufner, and C. Politis, Appl. Phys. A **44**, 75 (1987).
[7]S. Kohiki, T. Hamada, and T. Wada, Phys. Rev. B **36**, 2290 (1987).
[8]D. D. Sarma, K. Sreedhar, P. Ganguly, and C. N. R. Rao, Phys. Rev. B **36**, 2371 (1987).
[9]P. Thiry, G. Rossi, Y. Petroff, A. Revcolevshi, and Y. Jegoudez (unpublished).
[10]G. van der Laan, C. Westra, C. Haas, and G. A. Sawatsky, Phys. Rev. B **23**, 4369 (1981).
[11]M. Cardona and L. Ley, *Photoemission in Solids I: General Principles* (Springer, Berlin, 1978), p. 82.
[12]C. J. Powell, J. Vac. Sci. Technol. A **6**, 1532 (1986); C. J. Powell, N. E. Erickson, and T. E. Madey, J. Electron Spectrosc. Relat. Phenom. **17**, 361 (1979); **25**, 87 (1982); M. P. Seah, M. E. Jones, and M. T. Anthony, Surf. Interface Anal. **6**, 242 (1984).
[13]R. E. Walstedt, W. W. Warren, R. F. Bell, G. F. Brennert, G. P. Espinosa, J. P. Remeika, R. J. Cava, and E. A. Rietman Phys. Rev. B **36**, 5727 (1987).

Superconductivity and magnetism in transition-element-substituted $YBa_2Cu_3O_7$ compounds

Gang Xiao, F. H. Streitz, A. Gavrin, M. Z. Cieplak, and C. L. Chien
Department of Physics and Astronomy, The Johns Hopkins University, Baltimore, Maryland 21218

A. Bakhshai
Department of Physics, Goucher College, Towson, Maryland 21204

Superconducting properties of $YBa_2Cu_3O_7$ have been investigated by a systematic substitution of 3*d* transition elements for 10% of the Cu ions. Early transition elements Ti, V, and Cr affect the superconducting temperature of $YBa_2Cu_3O_7$ only slightly. Local magnetic moment formation is observed in Mn, Fe, Co, and Ni substituted compounds. T_c strongly correlates with the size of the paramagnetic moments, possibly due to scattering from the magnetic sites. Zn displays a phenomenal ability to suppress T_c because of the elimination of the 3*d* holes. The Zn compositional dependence of T_c indicates that the superconductivity completely disappears at 13–14 at. % of Zn. It is suggested that Zn preferentially substitutes the Cu(2) sites.

A number of theoretical and experimental studies[1-5] have indicated that both Cu and O are the crucial agents for high-T_c superconductivity in $YBa_2Cu_3O_7$. The low-dimensional character of the Cu-O planes and chains in the structure appears to be the critical feature sustaining the high transition temperature. The superconducting electrons come primarily from the *spd* hybridization states of the Cu and O ions.[6] An understanding of the Cu contribution to the superconductivity of $YBa_2Cu_3O_7$ should help to elucidate the nature of the superconducting mechanism. One approach to this problem is to partially substitute other 3*d* transition elements for Cu. Such substitution is facilitated by the fact that the ionic sizes of the 3*d* transition elements are similar to those of Cu. Changes are induced in the electronic structure at the Cu sites since the 3*d* elements allow a wide range of valence states and different occupations of the *d* band. In addition, some 3*d* transition elements such as Fe and Co possess a localized magnetic moment. The formation of a local magnetic moment can strongly affect superconductivity, providing clues as to the moment-induced pair-breaking mechanism. Partial substitution of Cu by other 3*d* transition metals is also of technical importance, as it allows us to ascertain which 3*d* elements are "friendly" to the $YBa_2Cu_3O_7$ compound and which elements should be avoided.

Using the $YBa_2Cu_3O_7$ compound a systematic substitution of the 3*d* elements for 10% of the Cu ions has been carried out. The samples are represented by $YBa_2(Cu_{0.9}A_{0.1})_3O_7$, where A = Ti, V, Cr, Mn, Fe, Co, Ni, Cu, and Zn. This level of substitution provides a sizable change in T_c in each case but is not large enough to destroy superconductivity. A strong correlation between superconductivity and the electronic and magnetic behavior of the substituting elements has been observed. Since Zn was found to have a strong effect on $YBa_2Cu_3O_7$, we have also studied the Zn compositional dependence of T_c for $YBa_2(Cu_{1-x}Zn_x)_3O_7$ ($0 \leqslant x \leqslant 0.20$).

Samples used in this study were prepared by using solid-state reaction methods. The sintering process was carried out at 950 °C in an oxygen atmosphere with a few intermediate grindings. The total firing time was about 50 h. The samples were furnace cooled very slowly in order to prevent an oxygen deficiency. The resistance of the samples was determined by using a standard four-probe method. T_c was chosen to be the midpoint of the resistive superconducting transition. Magnetic susceptibility was measured on a superconducting quantum interference device (SQUID) magnetometer in the temperature range 5–400 K. X-ray diffraction revealed that the samples were all single phase, with the same perovskite-type structure as the $YBa_2Cu_3O_7$ compound.[7,8] The fact that all of the samples in our substitution ranges are single phase supports the substitution of the Cu sublattices. Otherwise, if Y or Ba were replaced, the extra Y or Ba and deficient Cu atoms (comparing with the formula $YBa_2Cu_3O_7$) inevitably would lead to off-stoichiometry, resulting in multiphase samples with a high level of 10%–30% of extra phases. This would be clearly visible in the x-ray spectra.

In Fig. 1, the superconducting transition temperature T_c of $YBa_2(Cu_{0.9}A_{0.1})_3O_7$ is plotted against different 3*d* element substitutions. Also presented is the magnetic susceptibility at 100 K, which will be discussed later. In the early-transition-element region, (Ti, V, Cr, and Mn), T_c is only slightly reduced. There is a sizable dip in T_c in the mid-transition-element region (Fe, Co, and Ni); however, the most dramatic reduction in T_c occurs when Cu is substituted by Zn.

Among the transition elements, V has the smallest effect on the T_c of $YBa_2Cu_3O_7$. The temperature dependence of the normalized resistance of $YBa_2(Cu_{0.9}V_{0.1})_3O_7$ is displayed in Fig. 2, which shows a T_c of 91 K and a transition width of about 3 K. We attempted to substitute 50% of the Cu by V, but unfortunately the material was no longer single phase and became an insulator. Generally, impurities of early transition elements do not produce large effects on the superconductivity of $YBa_2Cu_3O_7$ and accordingly the early-transition-metal oxides can be used as substrates for $YBa_2Cu_3O_7$ thin films, since these oxides should in principle only slightly alter the properties of the superconducting film.

 0021-8979/88/084196-03$02.40 © 1988 American Institute of Physics

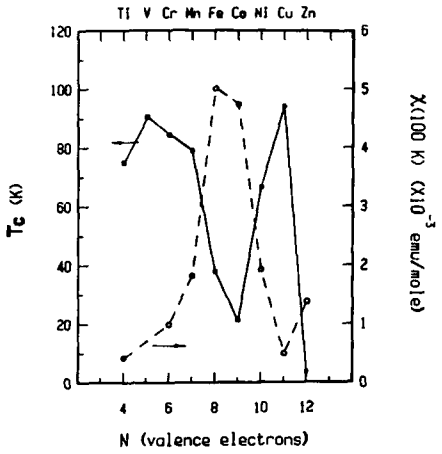


FIG. 1. T_c (solid line) and magnetic susceptibility at 100 K (dashed line) of $YBa_2(Cu_{0.9}A_{0.1})_3O_7$, where A is a 3*d* element, as a function of the number of valence electrons.

In the mid-3*d*-element region, where there is a large suppression of T_c, the magnetic susceptibility (χ) is greatly enhanced. Obviously, from Fig. 1, there is a strong anticorrelation between T_c and χ, with the exception of Zn, which will be discussed later. As we will show later, the enhancement of susceptibility is due to the appearance of a large local paramagnetic moment in the mid-3*d* elements. Most likely the T_c suppression arises from pair breaking by conduction and *d*-electron exchange scattering[9] at a paramagnetic site. This is to be contrasted with the rare-earth substitution results[10,11] in $YBa_2Cu_3O_7$ which show that the large localized moment of the rare-earth ions does not couple to the superconducting state. At the Cu sites, the *s-d* exchange interaction is much stronger, and the relatively large conduction-electron density at the Cu sites ensures that the superconductivity will be sensitive to the presence of magnetic ions on those sites.

All samples which are superconducting (except A = Zn) showed the Meissner effect at low temperatures. Magnetization and susceptibility data for the pure and substituted $YBa_2Cu_3O_7$ compounds as a function of temperature have been measured. Above T_c, the susceptibility becomes positive in every sample, and can be fitted very well by a Curie–Weiss law of the form

$$\chi = \chi_0 + Np_{\text{eff}}^2\mu_B^2/3k_B(T - T_0) . \quad (1)$$

Here χ_0 is temperature independent (resulting from diamagnetism and Pauli paramagnetism), N is the number of magnetic ions, p_{eff} is the effective magnetic moment in units of μ_B, and T_0 is the Curie–Weiss temperature. The analyses indicate that Cu ions carry a small paramagnetic moment of $0.22\mu_B$ with a small but positive Curie–Weiss temperature. When $YBa_2Cu_3O_7$ is alloyed with a 3*d* element, both the Cu and *A* sites should satisfy the following approximated relationship:

$$0.1p_A^2 + 0.9p_{Cu}^2 = p_{\text{eff}}^2 , \quad (2)$$

where p_{eff} is the measured magnetic moment from the Curie–Weiss law, p_A and p_{Cu} are the respective moments of A and Cu, and 0.1 and 0.9 are the relative concentrations of the A and Cu ions. Assuming $p_{Cu} \approx 0.22\mu_B$, we estimated the paramagnetic moment of Mn, Fe, Co, and Ni in the $YBa_2(Cu_{0.9}A_{0.1})_3O_7$ compounds. The values are $p_{Mn} \approx 2.01\mu_B$, $p_{Fe} \approx 3.61\mu_B$, $p_{Co} \approx 3.20\mu_B$, and $p_{Ni} \approx 2.05\mu_B$, whereas the paramagnetic moments for other transition elements are all less than $0.5\mu_B$.

Disorder induced by the substitution may also be a contributing factor affecting T_c but it probably is not the dominant mechanism. With the same level of substitution among the different 3*d* elements, there is a systematic change in T_c as shown in Fig. 1. The anticorrelation between T_c and magnetic susceptibility is difficult to reconcile with a disorder effect.

Another important factor which can influence the superconducting properties of these compounds is the valence state of the 3*d* element. In fact, even in pure $YBa_2Cu_3O_7$, the valence states of Cu remain controversial. If charge balance is assumed, Cu has an average valence of 2.3 +. It is generally accepted that the Cu(2) sites in the Cu-O_2 planes have valence 2 +. Then the Cu(1) sites should have valence 3 +. But photoemission data[12] show only Cu^{2+} states with little or no evidence of Cu^{3+} states. Other 3*d* elements could have rather different valence states. Furthermore, it has been known that the oxygen content plays an important role in $YBa_2Cu_3O_7$. Therefore, to understand the behavior of T_c in 3*d*-element-substituted $YBa_2Cu_3O_7$, it is important to determine the valence state of the 3*d* transition elements and the oxygen content. Further work along this line is being persued.

Of all the substituting 3*d* elements, Zn is unique. It has a definite valence state of 2 + and a filled 3*d* level ($3d^{10}$), therefore with no local moment. Indeed the Zn-substituted samples have low magnetic susceptibility as shown in Fig. 1. Surprisingly, the T_c suppressing power of Zn is even larger than that of Fe and Co. Intrigued by this finding, we have made a series of Zn-substituted samples represented by $YBa_2(Cu_{10-x}Zn_x)_3O_7$. Detailed x-ray diffraction mea-

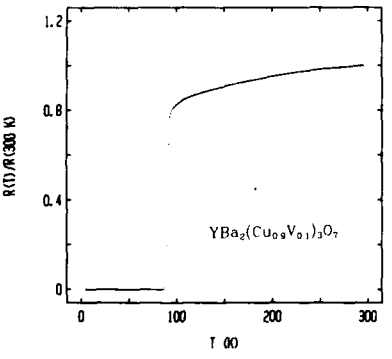


FIG. 2. Temperature dependence of the normalized resistance of $YBa_2(Cu_{0.9}V_{0.1})_3O_7$.

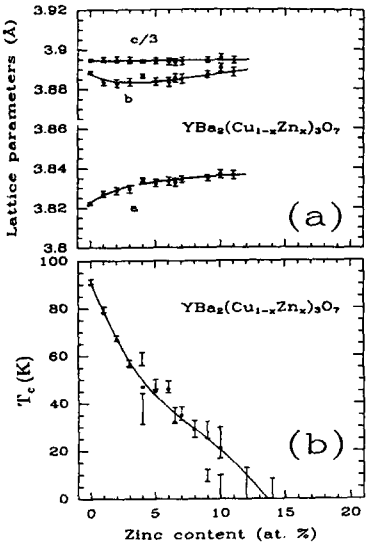


FIG. 3. (a) Lattice parameters of $YBa_2(Cu_{1-x}Zn_x)_3O_7$ as a function of Zn content. (b) Variation of T_c with Zn content. The solid dots are T_c's obtained from magnetization measurements under a field of 30 Oe, and the bars represent the resistive transition (90%–10%).

surements show that the structure remains orthorhombic throughout the composition range. The lattice parameters a, b, and c, as shown in Fig. 3(a), are very close to those of $YBa_2Cu_3O_7$. This indicates that the oxygen vacancy order or the linear chain structures of the Cu(1) sites remains intact. Cava *et al.*[13] have determined the lattice parameters of $YBa_2Cu_3O_{7-\delta}$ with various oxygen content ($0<\delta<0.7$). The lattice parameter c, most sensitive to δ, is linearly dependent on δ having a slope of $(1/c)(\Delta c/\Delta\delta) = -1.37\%/\text{O}$ atom. The c parameters of the Zn samples are essentially constant. We estimated the variation of oxygen content from the largest error bar of c, and δ came out to be ± 0.03, which should have a negligible effect on T_c.

The composition dependence of T_c is shown in Fig.3(b), where the solid circles represent the T_c obtained from magnetization measurements, and the bars are the transition widths from resistive measurements (90% to 10% resistance drop). The value of T_c reduces rapidly and monotonically with the Zn content. Superconductivity completely disappears around 13–14 at. % of Zn. The transition width also gradually broadens at higher Zn concentrations, caused by substitutional disorder.

Many theoretical models[1,2] have suggested that the crucial aspect of the high-T_c superconductors is the holes in the $3d$ bands of Cu^{2+}. The Zn^{2+} ions, with the same valence but one extra d electron, will eliminate the $3d$ holes upon substituting the Cu^{2+} ions. This accounts for the rapidly decreasing T_c caused by Zn substitution. Another important factor, as revealed by x-ray diffraction, is that the orthorhombic structure is unaffected, despite the large amount of Zn substitution. This indicates that Zn may be preferentially substituting the Cu(2) sites, thereby further amplifying the effect.

In conclusion, systematic variation of T_c with different $3d$-transition-element substitutions in $YBa_2Cu_3O_7$ have been studied. Formation of local magnetic moments in Mn, Fe, Co, and Ni suppresses T_c in accordance with the size of the magnetic moment. Such behavior can be best explained by a paramagnetic-moment-induced pair-breaking mechanism. Substitution of Cu by Zn negates the superconductivity of $YBa_2Cu_3O_7$ dramatically, which can be accounted for by Zn^{2+} filling the $3d$ holes of Cu^{2+}. We suggest that Zn is preferentially substituting the Cu(2) sites. Early transition elements Ti, V, and Cr seem to have a small effect on the T_c of $YBa_2Cu_3O_7$. It suggests that the oxides of the early transition elements may be used as substrates of the $YBa_2Cu_3O_7$ thin films because of their relative ineffectiveness in suppressing T_c.

This work was supported by National Science Foundation Grant No. DMR86-07150 and MEM87-18496.

[1]V. J. Emery, Phys. Rev. Lett. **58**, 2794 (1987).
[2]J. E. Hirsch, Phys. Rev. Lett. **59**, 228 (1987).
[3]Linus Pauling, Phys. Rev. Lett. **59**, 225 (1987).
[4]K. Kamaras, C. D. Porter, M. G. Doss, S. L. Herr, D. B. Tanner, D. A. Bonn, J. E. Greendan, A. H. O'Reilly, C. V. Stager, and T. Timusk, Phys. Rev. Lett. **59**, 919 (1987).
[5]H. Ihara, M. Hirabayashi, N. Terada, Y. Kimura, K. Senzaki, M. Akimoto, K. Bushida, F. Kawashima, and R. Uzuka, Jpn. J. Appl. Phys. **26**, L460 (1987).
[6]L. F. Mattheiss and D. R. Hamann, Solid State Commun. **63**, 395 (1987).
[7]R. J. Cava, B. Batlogg, R. B. van Dover, D. W. Murphy, S. Sunshine, T. Siegrist, J. P. Remeika, E. A. Rietman, S. Zahurak, and G. P. Espinosa, Phys. Rev. Lett. **58**, 1676 (1987).
[8]R. M. Hazen, L. W. Finger, R. J. Angel, C. T. Prewitt, H. K. Mao, C. G. Hadidiacos, P. H. Hor, R. L. Meng, and C. W. Chu, Phys. Rev. B **35**, 7238 (1987).
[9]S. V. Vonsovsky, Yu. A. Izyumov, and E. Z. Kurmaev, *Superconductivity of Transition Metals* (Springer, Berlin, 1982).
[10]P. H. Hor, R. L. Meng, Y. Q. Wang, L. Gao, Z. L. Huang, J. Bechtold, K. Forster, and C. W. Chu, Phys. Rev. Lett. **58**, 1891 (1987).
[11]Gang Xiao, F. H. Streitz, A. Gavrin, and C. L. Chien, Solid State Commun. **63**, 817 (1987).
[12]P. Steiner, V. Kinsinger, I. Scander, B. Siegwar, S. Hüfner, C. Politis, R. Hopp, and H. P. Müller, Z. Phys. B **67**, 497 (1987).
[13]R. J. Cava, B. Batlogg, C. H. Chen, E. A. Rietman, S. M. Zahurak, and D. Werder, Phys. Rev. B **36**, 5719 (1987).

Magnetic behavior of both superconducting thin films and their deposition targets

K. Moorjani, J. Bohandy, F. J. Adrian, and B. F. Kim
Applied Physics Laboratory, The Johns Hopkins University, Laurel, Maryland 20707

U. Atzmony,[a] R. D. Shull, C. K. Chiang, L. J. Swartzendruber, and L. H. Bennett
National Bureau of Standards, Gaithersburg, Maryland 20899

The superconducting properties of the bulk oxides $La_{1.85}Sr_{0.15}CuO_{4-x}$ and $Ba_2YCu_3O_{7-y}$ were investigated through their magnetic behavior by vibrating-sample magnetometry and complex ac susceptibility, and by dc resistivity and microwave response. These oxides were then used as targets in the preparation of thin films using a laser-ablation technique. The superconducting properties of the films were established through their microwave response. The *M-H* loops at low temperatures clearly establish the type-II behavior of the Ba-Y-Cu-O materials. The real part of the ac susceptibility showed the superconducting transition. Simultaneously, the imaginary part of the ac susceptibility showed the existence of nonsuperconducting portions in the samples which have a low enough resistivity to carry a significant amount of current. The novel method of microwave response was used to detect the superconductivity for both the bulk oxides and the thin films.

INTRODUCTION

Since the pioneering discovery of superconductivity at the amazingly high temperature of 30 K in the La-Ba-Cu-O system by Bednorz and Müller,[1] there has been an unprecedented amount of research devoted to the search for superconducting materials with even higher transition temperatures. A transition temperature of 40 K was soon found in the analogous system La-Sr-Cu-O (Refs. 2–4) and the superconducting phase stoichiometry was identified as $La_{1.85}Sr_{0.15}CuO_{4-x}$.[5,6] Subsequently, superconductivity was discovered at 90 K,[7] and the responsible phase identified as $Ba_2YCu_3O_{7-y}$.[8] Simultaneous with the search for new high-T_c superconducting materials there has been a parallel effort devoted to the preparation of these new superconducting oxides in thin-film form by a variety of techniques including sputtering,[9] electron-beam evaporation,[10,11] and laser evaporation.[12,13] Thin films are needed by the electronics industry for the construction of devices using the new materials. Because of the sensitivity of the superconducting transition temperature of the new materials to structure and composition, the preparation of thin films has not been easy, generally requiring great control over the processing variables. In this regard, the laser-ablation process[12] holds a certain attractiveness because it appears to be relatively insensitive to many of these processing variables. In this paper we will document the relationship between the thin films prepared by our novel laser ablation process and the bulk superconductors from which the films derive. In addition, we present *M*-vs-*H* hysteresis loops of the high-T_c superconductors used as the target material for the laser ablation.

RESULTS AND DISCUSSION

The bulk La-Sr-Cu-O laser target was prepared as follows: Initially, the appropriate amounts of blended $Ba(OH)_2$, $SrCO_3$, and CuO powder were sintered at 1000 °C in air. After an x-ray powder diffraction pattern verified that the majority of the material was $La_{1.85}Sr_{0.15}CuO_{4-x}$, the ceramic powder was compacted in a hydraulic press into a disk shape (~3.8 cm diameter) and then fired again at 1000 °C in air, furnace cooling the disk afterwards. A similar process was used to prepare the Ba-Y-Cu-O laser target: Initial sintering of the proper amounts of $BaCO_3$, Y_2O_3, and CuO powders was performed at 900 °C in air; the $Ba_2YCu_3G_{7-y}$ structure was verified by x-ray analysis; a disk (~6.2 cm in diameter) was hydraulically pressed; and a final firing at 950 °C in air followed by a slow stepwise cooling to 350 °C was performed.

Thin films of both $La_{1.85}Sr_{0.15}CuO_{4-x}$ and $Ba_2YCu_3O_{7-y}$ were prepared by laser ablation of the bulk superconducting oxide targets (described above) in vacuum using a pulsed eximer laser operating at 193 nm. A schematic of the apparatus is shown in Fig. 1. Either irradiation of a single spot on the target for 30–100 s using a pulse rate of 10 Hz (with an average energy per pulse between 120 and 170 mJ) or stepwise rastering the irradiation spot across the target for 30–100 s was used to deposit approximately 2-μm-thick films onto fused silica substrates (at ambient temperature) located in front of, but oriented at a 30° angle to the parent target. These two methods produced essentially equivalent results. These initial films, however, were not electrically conducting. Subsequently prepared thicker films are presently being analyzed by x rays.

The alternating-field reversible magnetic susceptibility of our target material was previously measured[12] in a Hartshorn-type bridge circuit. Both the real and imaginary components of the susceptibility were measured. Sharp drops in the real parts of the susceptibility at 41.5 and 94.5 K for

[a] Permanent address: NRCN, P. O. Box 9001, Beer-Sheva, Israel.

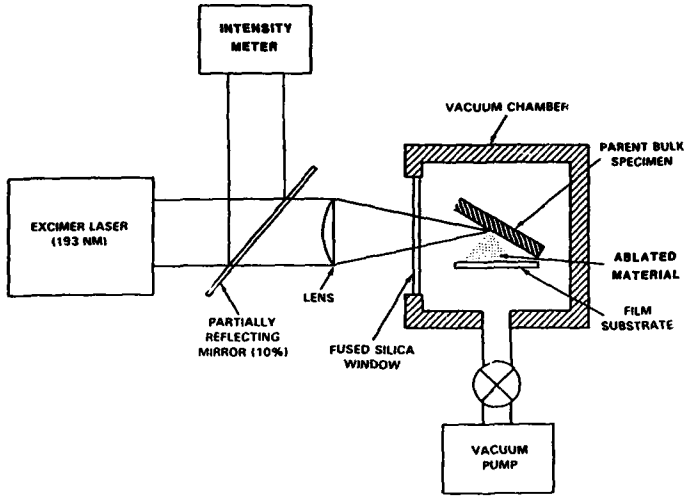


FIG. 1. Schematic of the laser-ablation process for creating thin films of the high-T_c superconductors.

$La_{1.85}Sr_{0.15}CuO_{4-x}$ and $Ba_2YCu_3O_{7-y}$, respectively, demonstrated the relative Meissner effect as the materials become superconducting (i.e., strongly diamagnetic) on decreasing temperature. The electrical resistivity (measured by a dc four-point probe method, with a measuring current of 1 mA, using Pt wires attached with silver paste) for the Ba-Y-Cu-O laser target exhibits metalliclike behavior between room temperature and T_c; and a sharp drop in electrical resistivity at 94.5 K agrees well with the T_c value determined previously[12] from the alternating-field susceptibility data. M-vs-H magnetic hysteresis loops were measured for the $Ba_2YCu_3O_{7-y}$ laser target at room temperature and 50 K using a vibrating-sample magnetometer. These show that at room temperature the magnetization of the Ba-Y-Cu-O material is positive and is not a linear function of the applied field. This material likely possesses a small amount of ferromagnetic impurity with a very small coercive field. The magnetic hysteresis loops measured on the same sample at 50 K (Fig. 2) show that the superconducting oxide $Ba_2YCu_3O_{7-y}$ displays type-II superconducting behavior. For these measurements, in order to eliminate the trapping of magnetic flux in the sample during cooling, the sample was first cooled to 50 K in zero field.

As seen in the inset in Fig. 2, the M-vs-H curve for small applied fields (less than about 100 Oe) is nearly linear. However, even for the lowest field loop taken, ∓ 50 Oe, the presence of hysteresis can be detected. This illustrates that flux penetration occurs at very low fields (i.e., H_{c1} is very small). For larger fields, the magnetization deviates strongly from linear behavior and goes through a minimum in magnitude as the field is increased further. From the flatness of the M-

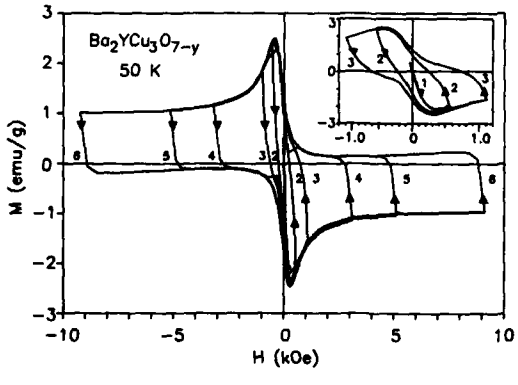


FIG. 2. Magnetization as a function of applied field isotherms (at 51 K) for the bulk $Ba_2YCu_3O_{7-y}$ target material. The magnetic field was cycled as indicated. The inset shows an expanded view of the low field loops.

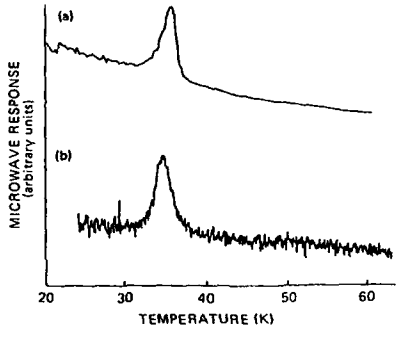


FIG. 3. Microwave signal vs temperature for $La_{1.85}Sr_{0.15}CuO_{4-x}$ in (a) bulk and (b) thin-film forms.

vs-H curves at the largest fields used in this study (9 kOe) it can be seen that H_{c2} is very large. The outer envelope of the hysteresis loops shown in Fig. 2 describes the M-H loop which would have been traced out for this superconductor in the absence of measuring the enclosed minor loops.

The superconducting transitions in the laser-ablated films (as well as in the bulk superconducting oxide targets) were detected by a novel method based on the microwave response of the specimen in a conventional homodyne-type ESR spectrometer operating at 9.1 GHz.[12] This method is essentially the observation of that part of the change in microwave loss which is produced by the application of a small alternating magnetic field (<5 Oe). As a material goes through a superconducting transition, there will be a maximum in the change in the microwave loss, as shown rather dramatically for pure niobium at 9.3 K in our earlier publication announcing this sensitive technique.[12] As shown in Fig. 3, both the laser-ablated film and the bulk target of $La_{1.85}Sr_{0.15}CuO_{4-x}$ display this absorption peak (at the same temperature) near this material's superconducting transition temperature (41.5 K) determined from the magnetic susceptibility data, thereby showing the laser-ablated film possesses the superconducting oxide. In addition, the equivalence of the microwave signatures for the bulk and thin-film material indicates the form of the superconducting oxide in the laser-ablated film must be nearly the same as that in the target. For the laser-prepared thin film and bulk $Ba_2YCu_3O_{7-y}$ the microwave absorption signatures were also observed.[12] Again the appearance of the absorption peaks for both materials near the T_c (94.5 K) determined resistively and magnetically proves the existence of the superconducting oxide phase in the thin film.

In conclusion, we have shown that for both $La_{1.85}Sr_{0.15}CuO_{4-x}$ and $Ba_2YCu_3O_{7-y}$, thin superconducting films may be prepared directly from a superconducting oxide target by a laser-ablation process without requiring any special environments or procedures to control the vapor composition, and without the necessity for any subsequent thermal treatment of the deposited film. Microwave absorption has been illustrated to be a fast and sensitive method for detecting the presence of a superconducting transition in the thin films. Finally, we have characterized the electric and magnetic behavior of the superconducting target material by measurements of magnetic hysteresis loops and electrical resistance.

[1] J. G. Bednorz and K. A. Müller, Z. Phys. B **64**, 189 (1986).
[2] C. W. Chu, P. H. Hor, R. L. Mong, L. Gao, Z. J. Huang, and Y. O. Wang, Phys. Rev. Lett. **58**, 405 (1987).
[3] R. J. Cava, R. B. van Dover, J. B. Batlogg, and E. A. Rietman, Phys. Rev. Lett. **58**, 408 (1987).
[4] J. M. Tarascon, L. H. Green, W. R. Mckinnon, G. W. Hull, and T. H. Geballe, Science **235**, 1373 (1987).
[5] H. Takagi, S. Uchida, K. Kitazawa, and S. Tanaka, Jpn. J. Appl. Phys. **26**, L123 (1987).
[6] R. J. Cava, A. Santoro, D. W. Johnson, Jr., and W. W. Rhodes, Phys. Rev. B **35**, 6716 (1987).
[7] M. K. Wu, J. R. Ashburn, C. J. Torng, P. H. Hor, R. L. Meng, L. Gao, A. J. Huang, Y. Q. Wang, and C. W. Chu, Phys. Rev. Lett. **58**, 908 (1987).
[8] R. J. Cava, B. Batlogg, R. B. van Dover, D. W. Murphy, S. Sunshine, T. Siegrist, J. P. Remeika, E. A. Rietman, S. Zahurak, and C. P. Espinosa, Phys. Rev. Lett. **58**, 1676 (1987).
[9] M. Kawasaki, M. Funabashi, S. Nagata, K. Fueki, and H. Koinuma, Jpn. J. Appl. Phys. **26**, L388 (1987).
[10] R. B. Laibowitz, R. H. Koch, P. Chaudhari, and R. J. Gambino, Phys. Rev. B **35**, 8821 (1987).
[11] M. Naito, R. H. Hammond, B. Oh, M. R. Hahn, J. W. T. Hsu, P. Rosenthal, A. F. Marshall, M. R. Beasley, T. H. Geballe, and A. Kapitulnik, J. Mater. Res. **2**, 713 (1987).
[12] K. Moorjani, J. Bohandy, F. J. Adrian, B. F. Kim, R. D. Shull, C. K. Chiang, L. J. Swartzendruber, and L. H. Bennett, Phys. Rev. B **36**, 4036 (1987).
[13] D. Dijkkamp, T. Venkatesan, X. D. Wu, S. A. Shaheen, N. Jisrawi, Y. H. Min-Lee, W. L. McLean, and M. Croft, Appl. Phys. Lett. **51**, 619 (1987).

EPR, magnetization, and resistivity studies in doped (4-*f* or 3-*d* ions) and undoped $RBa_2Cu_3O_y$ high T_C superconductors (R=Y,Pr,Nd,Eu,Gd,Ho,Er, or Yb) (abstract)[a]

D. C. Vier, J. F. Smyth, C. T. Salling, S. Schultz, Y. Dalichaouch, B. W. Lee, K. N. Yang, M. Torikachvili, and M. B. Maple
University of California, San Diego, La Jolla, California 92093

S. B. Oseroff
San Diego State University, San Diego, California 92182

Z. Fisk, J. D. Thompson, J. L. Smith, and E. Zirngiebl
Los Alamos National Laboratory, Los Alamos, New Mexico 87545

We have measured electron paramagnetic resonance (EPR), resistivity, and dc susceptibility from 2 to 300 K for the oxide high T_c superconductors $(R)Ba_2Cu_3O_y$ (R = Y,Pr,Nd,Eu,Gd,Ho,Er,Tm, or Yb). Selected systems were doped with 3-*d* ions (Cr,Mn,Fe,Ni,Co, or Zn) or 4-*f* ions (Gd or Er) which presumably substitute for the Cu or R site, respectively. In the systems studied we have observed an EPR line at low temperatures ($T < 40$ K), which exhibits an increase in intensity and decrease in field for resonance as the temperature is lowered. The ESR linewidth is also temperature dependent and exhibits a minimum at about 15 K. An additional EPR line that can be associated with a Gd^{3+}, Mn^{2+} or Er^{3+} ion was observed for those samples where these ions were present as dilute impurities. In some of the samples another EPR signal is observed with properties that depend on sample preparation conditions. The behavior and origin of all lines will be discussed. The variation of T_c with concentration of the added impurities over the range (1%–15%) will also be presented, and compared with previous studies in other superconducting systems.

[a] This work was supported by the National Science Foundation under Grants Nos. DMR-86-13858 and DMR-84-11839, the U.S. Department of Energy under Grant No. DE-FG03-86ER45230, and Los Alamos National Laboratories.

Magnetic ordering and crystal field effects in $REBa_2Cu_3O_{7-x}$ (RE=Gd, Dy, Ho, Er)[a] (abstract)

B. D. Dunlap, M. Slaski,[b] D. G. Hinks, C. Segre,[c] K. Zhang,[c] L. Soderholm, M. Beno, G. W. Crabtree, W. K. Kwok, S. K. Malik,[d] I. K. Schuller, J. D. Jorgensen, and Z. Sungaila
Argonne National Laboratory, Argonne, Illinois 60439

Heat capacity, resistivity and magnetic susceptibility data have been used to study electronic and magnetic properties of $REBa_2Cu_3O_{7-x}$ compounds. Neutron diffraction on the Ho compound shows identical crystal structure to $YBa_2Cu_3O_{6.8}$. All the compounds are superconducting at $T_c = (93 \pm 2)$ K. Magnetic transitions are observed in the heat capacity data at $T_m = 2.2$, 0.95, 0.17, and 0.59 K for RE = Gd, Dy, Ho, and Er, respectively, and the magnetically ordered state is found to coexist with superconductivity. Estimates have been obtained for the magnetic moment in the crystal field ground state and the energy splitting of the first excited state crystal field level.

[a] Work supported by the U.S. Department of Energy, BES-Materials Sciences and Chemical Sciences, under Contract No. W-31-109-ENG-38.
[b] Permanent address: Inst. Phys. Polytech., Krakow, Poland.
[c] Permanent address: Dept. Phys., Illinois of Technology, Chicago, IL 60680.
[d] Permanent address: Tata Inst. Fundamental Res., Bombay, India.

 0021-8979/88/084202-01$02.40 © 1988 American Institute of Physics

A new method for determining superconducting transition temperature T_c (abstract)

Ronghua Xue and Quan Lu
Department of Physics, Nanjing University, Nanjing, China

A new method for measuring superconducting transition temperature T_c is presented. In this method, the initial superconducting transition temperature T_c is determined by the temperature dependence of the voltage which is induced on a M pick-up coil and is proportional to the diamagnetic susceptibility of the superconducting sample. The alternating magnetic field for the measurement may be very low (down to 80 A/m) and only several milligrams of sample are needed. The experimental results show that this method is very sensitive and simple.

 0021-8979/88/084203-01$02.40 © 1988 American Institute of Physics

Magnetic behavior of Y-Ba-Cu-O superconductors prepared under different oxygen anneals

T. Datta, Carmen Almasan, and J. Estrada
University of South Carolina, Columbia, South Carolina 29208

C. E. Violet
Lawrence Livermore National Laboratory, Livermore, California 94550

D. U. Gubser and S. A. Wolf
Naval Research Laboratory, Washington, D.C. 20375

In our study of three YBa_2Cu_3 oxides prepared with different oxygen anneals, we observed that the temperature derivative of the magnetization or susceptibility $\chi(T)$ of these high-T_c superconductors has a maximum at approximately the transition temperature, T_c. This temperature as estimated by the peak value of $(\partial\chi/\partial T)_H$, ranged between 55 and 65 K. The most oxygen-poor sample showed the lowest T_c and the most oxygen-rich sample showed the highest T_c. In the subcritical region, a novel irreversibility is observed in the field-cooled warm-up and cool-down behaviors.

In this paper we describe the magnetic behavior of three $YBa_2Cu_3O_{7-x}$ specimens prepared under different oxygen annealing conditions. We also propose a novel analysis of the susceptometric data. Finally, we report on an unusual irreversible behavior of the field-cooled magnetization in the subcritical region.

The $YBa_2Cu_3O_{7-x}$ samples were produced by the well-known solid-state reaction of gravimetric amounts of pure powder oxides of Y, Ba, and Cu. Two specimens, A and B, were prepared at Lawrence Livermore National Laboratory,[1] and sample C was prepared at the Naval Research Laboratory.[2,3] Both A and B samples were sintered for 16 h at 950 °C. The resulting mass was x-ray analyzed, reground, and pelletized. The pellets were annealed at 950 °C for 5 h, cooled to 720° C, held for 12 h, and then cooled slowly (~ 1° C/min) to 200 °C and then removed from the furnace. For B the cool down was conducted in air, whereas A was cooled down with flowing oxygen. Sample C was prepared as follows: Mix powders of $BaCO_3$, CuO, and Y_2O_3, immerse mixture in alchohol, and pulverize loose agglomerates in an ultrasonic mixer, calcine for 6 h at 925–950 °C with intermediary grindings, grind and cold press into pellets and sinter in air at 925–950 °C for 12 h, and move into an oxygen furnace, heat to 950 °C for several hours and slow cool (1 °C/min). The specimen compositions were estimated by a microprobe technique. The oxygen content was lowest in sample B and highest in sample C. It has been shown that $YBa_2Cu_3O_{7-x}$ occurs in two forms with transition temperature of ≈ 60 and ≈ 90 K, which depends on the oxygen stoichiometry and ordering of the vacancies.[4,5]

The measurements were made with a computer-controlled variable-temperature superconducting quantum interference device (SQUID) (VTS) susceptometer. The specimens were small irregular $2\times2\times8$ mm^3 parallelpipeds. With both the specimen and the VTS cryostat in zero applied field and at room temperature, the samples were inserted into the cryostat and the temperature reduced to ≈ 5 K. The system was allowed to thermally equilibrate, and then the weak dc measurement field, B, was applied.

The magnetic moment $M(T)$ or susceptibility, $\chi(T)$, where $\chi \approx M/B$ per unit mass, was obtained[3] by holding B constant and increasing the sample temperature in a programmed sequence of steps until the preset maximum ($>T_c$) was reached. These data are termed zero-field-cooled warmup (ZFCW, or for brevity ZFC). At the end of a ZFC run, if desired, the temperature was cycled up and down in steps, to obtain the field-cooled (FC) and field-cooled warm-up (FCW) data. Three fields (0.1, 1.0, and 10 mT) were chosen, and typically the data were taken between 5 and 250 K.

Typical susceptibility data, $\chi(T)$, for specimens A and B are exhibited in Figs. 1(a) and 1(b). Both ZFC diamagnetic shielding and FC Meissner effect data are shown. An interesting property of these data is the flatness of χ above T_c. This suggests that the samples are relatively defect-free. Although not resolvable on the scale of the figure, a structureless weak paramagnetism was also observed above T_c. We observed that for $1 < B < 10$ mT, $\chi(T)$ was not sensitive to the applied field. Similar $\chi(T)$ data were also observed for specimen C. The data of Figs. 1(a) and 1(b) are similar to those reported in many other recent publications.[6-9]

The first and second derivatives of the susceptibility with respect to T, for specimens A and B, are shown in Figs. 2(a) and 2(b). In both cases a strong peak is observed in the first derivative. If we assume this peak temperature to be a close approximation to the transition temperature T_c we find for specimen A the value $T_c = 62$ K and for B $T_c = 55$ K. The onset temperature for both samples was 84 K. These values are consistent with those reported for oxygen-poor $YBa_2Cu_3O_{7-x}$ samples, i.e., $0.2<x<0.5$.[4] When analyzed by this derivative technique the data for higher fields also displayed equally convincing peaks at T_c. This is also true for specimen C, for which the T_c, as determined by the derivative technique, was 86 K; the onset temperature was 90 K. The width and asymmetry of the transitions, as well as the T_c could also be determined from the second derivatives which

 0021-8979/88/084204-03$02.40 © 1988 American Institute of Physics

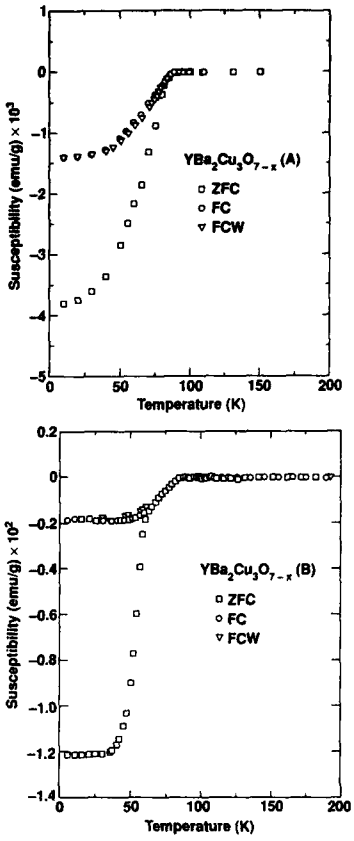


FIG. 1. (a) Magnetic susceptibility of sample A as a function of temperature. The zero-field-cooled data represent diamagnetic (flux) shielding and the field-cooled data represents Meissner effects or flux expulsion. (b) Magnetic susceptibility of sample B as a function of temperature. In this case the flux shielding is about 3 times stronger than in sample A; however, the flux explusion or the volume of perfect superconductivity is not increased as much.

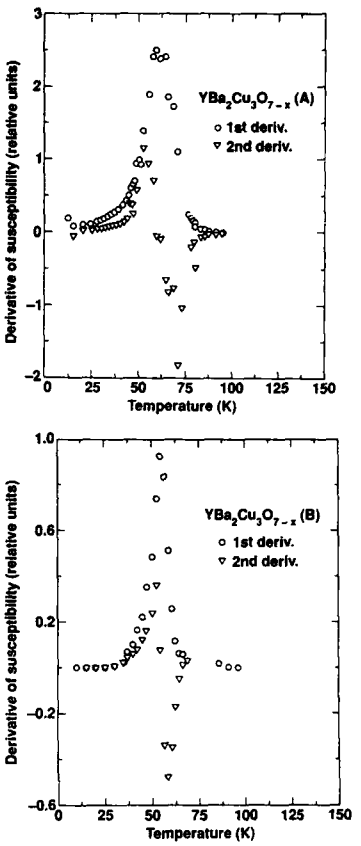


FIG. 2. (a) First- and second-temperature derivative analysis of the susceptibility data of Fig. 1(a). Notice the outstanding peak at 62 K in the first derivative. This is also the temperature where the second derivative crosses the baseline. (b) First- and second-temperature derivative analysis of the susceptibility data of Fig. 1(b). The peak temperature is 55 K. A smaller peak was observed between 60 and 90 K, but is not shown for clarity.

are included in Figs. 2(a) and 2(b). For accurate line-shape analysis and transition-width determination more data at smaller temperature intervals would be needed.

Müller, Takashige, and Bednorz[10] have reported the irreversible behavior of zero-field-cooled LaBaCuO. For our materials, we observe that even the field-cooled behavior is irreversible in the subcritical region. This behavior was most pronounced in specimen C. It was noticed that $\chi(\mathrm{FCW})$ and $\chi(\mathrm{FC})$ were not the same. In the $T_c - 20\ \mathrm{K} \lesssim T \lesssim T_c$ region, as shown in Fig. 3, $|\chi(\mathrm{FCW})| > |\chi(\mathrm{FC})|$. Also, $\Delta\chi(T) = \chi(\mathrm{FCW}) - \chi(\mathrm{FC})$ was irreversible under temperature cycling. This behavior is exhibited in Fig. 4. This irreversibility may be due to the time dependence of flux pinning or due to a spin-glass ordering in the material.

We suggest that the derivative analysis shown here may be fruitful for other physical properties such as resistivity. Furthermore, line-shape analysis of the first and second de-

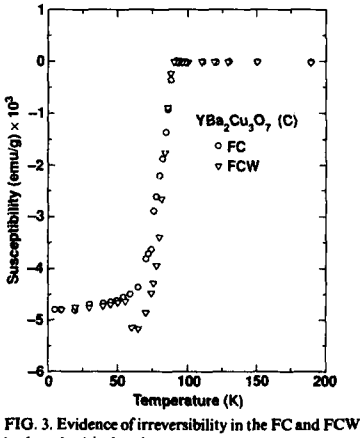


FIG. 3. Evidence of irreversibility in the FC and FCW data for specimen C, in the subcritical region.

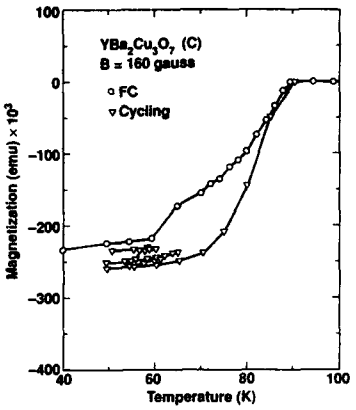


FIG. 4. Effect of temperature cycling on the irreversible diamagnetism in specimen C.

rivatives may provide information about the structure and energy-gap distribution of these granular superconductors.[11]

This work was supported by The University of South Carolina, Grant No. 1070K101, the U.S. Department of Energy, Lawrence Livermore National Laboratory, Contract No. W-7405-Eng-48, and the Naval Research Laboratory. Carmen Almasan acknowledges an Amelia Earhart Fellowship from Zonta International. We thank John Holthuis and James Wu of LBL for preparing the LLNL samples.

[1]H. M. Ledbetter, M. W. Austin, S. A. Kim, T. Datta, and C.E. Violet, J. Mater. Res. (to be published).
[2]J. J. Rhyne, D. A. Neuman, J. A. Gotaas, F. Beech, L. Toth, S. Lawrence, S. Wolf, M. Osofsky, and D. U. Gubser, Phys. Rev. B 36, 2294 (1987).
[3]T. Datta, C. Almasan, D. U. Gubser, S. A. Wolf, M. Osofsky, and L. E. Toth, *Novel Superconductivity*, edited by S. A. Wolf and V. Z. Kresin (Plenum, New York,1987), p. 817.
[4]R. J. Cava, B. Batlogg, C. H. Chen, E. A. Rietman, S. M. Zahurak, and D. Werder, Phys. Rev. B 36, 5719 (1987).
[5]J. D. Jorgensen, B. W. Veal, W. K. Kwok, G. W. Crabtree, A. Umezawa, L. J. Nowicki, and A. P. Paulikas, Phys. Rev. B 36, 5731 (1987).
[6]J. M. Tarascon, L. H. Greene, W. R. McKinnon, and G. W. Hull, Solid State Commun. 63, 499 (1987).
[7]R. L. Greene, H. Maletta, T. S. Plaskett, J. G. Bednorz, and K. A. Müller Commun. 63, 721 (1987).
[8]E. Zirngiebl, J. O. Willis, J. D. Thompson, C. Y. Huang, J. L. Smith, Z. Fisk, P. H. Hor, R. L. Meng, C. W. Chu, and M. K. Wu, Solid State Commun. 63, 721 (1987).
[9]Gang Xiao, F. H. Streitz, A. Gavin, and C. L. Chien, Solid State Commun. 63, 817 (1987).
[10]K. A. Müller, M. Takashige, and J.G. Bednorz, Phys. Rev. Lett. 58, 1143 (1987).
[11]T. Datta, C. P. Poole, H. A. Farach, C. Almasan, J. Estrada, D. U. Gubser, and S. A. Wolf (unpublished).

Effect of vacuum annealing on the superconducting transition temperature of the Y-Ba-Cu-O system

Dajian Wang, Guobin Wu, Shengtao Huang, and Chenghuan Tang
Department of Physics, Wuhan University, Wuhan, China

Wanqiu Cai and Peng Dan
Industrial University of Wuhan, Wuhan, China

The effect of vacuum annealing on the superconducting transition temperature T_c of the ceramic superconductor Y-Ba-Cu-O system with a perovskite-type structure has been investigated. For fixed annealing time, the resistivity increase and T_c decrease become larger for higher annealing temperature, and the crystallographic lattice parameters decrease slightly with increasing annealing temperature. This may be understood as the result of the introduction of oxygen vacancies in the basal plane of the CuO_6 octahedra. Therefore, it seems to be quite important to reduce the density of oxygen vacancies in the present system.

INTRODUCTION

Bednorz and Müller[1] have discovered the possibility of superconductivity around 35 K in the Ba-La-Cu-O system. Uchida and Takagi *et al.*[2,3] have observed the Meissner effect and established superconductivity in the system. Within a few months, several groups have reported additional results.[4–7] Chu *et al.*,[4] Hikami *et al.*,[8] and Zhao *et al.*[6] independently discovered the superconducting transition at 98 K in the Y-Ba-Cu-O system. We have prepared some $YBaCu_3O_{9-y}$ on nearly single-phase samples which exhibit superconductivity at 90–9[illegible] K and a transition width $\Delta T = 4$ K. We have studied the effect of vacuum annealing at elevated temperature on the value of T_c and crystallographic lattice parameters to obtain knowledge of the proper conditions for preparation. As reported by Michael and Raveau[9] and Siegrist *et al.*,[10] oxygen intercalation and disintercalation can take place easily for La-Sr-Cu-O and Y-Ba-Cu-O systems. According to their results, the oxygen vacancies are mainly distributed in the basal planes of the CuO_6 octahedra. Since the electron transport has a quasi-two-dimensional nature (as has been revealed by measurements of the superconducting critical magnetic field H_{c2} for single-crystal specimens), the conduction electrons are expected to stay mainly within the basal planes, and therefore oxygen vacancies may have an important effect on T_c.

EXPERIMENT

The experiment has been carried out in the following way. The single-phase samples of $YBa_2Cu_3O_{9-y}$ for the present experiment were prepared from a mixture of Y_2O_3, $BaCO_3$, and CuO with purities of 99.9%, 99.5%, 99.7%, respectively. Appropriate amounts of the well-mixed constituents were pressed into pellets, then heated at 960 °C for 16 h in atmosphere. The calcined powder was subsequently well ground, pressed into a disk-shaped form, and then sintered at 960 °C for 10 h in flowing O_2. After this procedure, the furnace was cooled down slowly to room temperature. The samples were then annealed at various temperatures in a vacuum of about 10^{-5} Torr for 2 h and quenched to room temperature. The resistivity measurements were carried out within a few hours after the above procedures. The resistivity data were taken with a standard four-probe technique. The resistivity of the single-phase samples in the normal state was a few hundreds of $\mu\Omega$ cm at room temperature; the current density used for measurement was 0.03 A/cm^2. The mutual-inductance method was adopted to measure the ac magnetic susceptibility. The powder x-ray analyses were performed on a nearly single-phase compound of $YBa_2Cu_3O_{9-y}$ after annealing at various temperatures.

RESULTS AND DISCUSSION

Figure 1 shows the temperature dependence of the resistivity for specimens annealed at various temperatures. The values of the resistivities are attached to the corresponding points. It is clear that the resistivity changes quite drastically with annealing temperature; for a fixed annealing time, the resistivity increase and the T_c decrease become larger at higher annealing temperature.

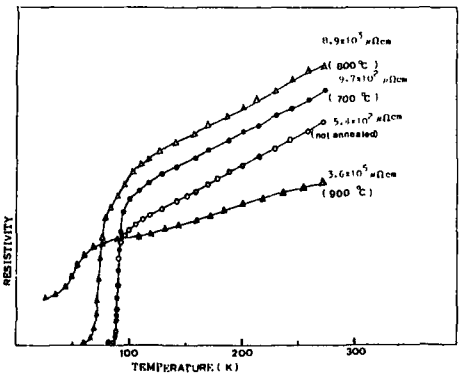


FIG. 1. Temperature dependence of the resistivity of the specimens of the Y-Ba-Cu-O system prepared by 2-h vacuum annealing. In the parentheses, the annealing temperatures are indicated. The values of the resistivities are attached to corresponding points.

 0021-8979/88/084207-02$02.40 © 1988 American Institute of Physics

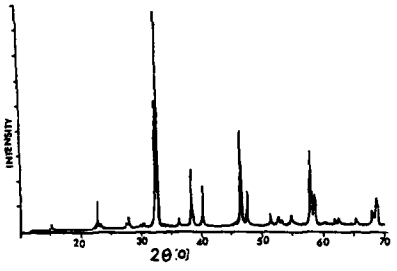


FIG. 2. X-ray powder diffraction pattern for stoichiometric single-phase $YBa_2Cu_3O_{9-y}$.

To confirm the superconductivity further, the ac susceptibility was measured. It was found that, compared with the unannealed sample, the amplitude of the ac signal at T_c becomes smaller, and the sharpness of the transition in the annealed samples becomes broader, with an increase of annealing temperature.

The x-ray powder diffraction pattern is shown in Fig. 2. According to a preliminary x-ray analysis of this single-phase compound $YBa_2Cu_3O_{9-y}$, it is suggested that the structure may be of an orthorhombic type with the crystallographic lattice constants $a = 3.828$ Å, $b = 3.896$ Å, $c = 11.687$ Å in the unannealed samples. This is consistent with the result reported by Kadowaki *et al.*[11] The oxygen content for the material annealed at various temperatures in a vacuum was determined by measuring the weight loss on reduction to Cu metal and Ba and Y oxides, yielding the values $y = 2.5, 2.9, 3.8, 5.1$, respectively. It appears that the lattice parameters are slightly dependent on the oxygen content. They also decrease slightly with annealing temperature in a vacuum. This appears to be in substantial disagreement with the work of Cava *et al.*[12] and Gallagher *et al.*[13] Both these papers report increases in the a and c lattice parameters and in the unit cell volume as the oxygen content is decreased; only the b parameter was found to increase. This is probably due to different sample conditions: the samples we measured were quenched, but their samples were annealed. We will clarify this in future work. More detailed investigations of the structure analysis are under way and will be presented later.

The changes of resistivity with annealing temperature in vacuum can be understood by the disintercalation of the oxygen in the basal planes. Due to the production of oxygen vacancies during annealing, randomness is introduced in the conduction path of the hole carrier and the density of hole carriers itself is reduced. As a result of these changes, the value of T_c also changes. The observed behavior reminds us of the theoretical predictions on the effect of randomness on superconducting T_c. However, we have not yet carried out a detailed analysis in the framework of electron localization due to randomness. This remains a future problem.

In summary, we have showed that T_c depends on vacuum annealing in a sensitive way. Therefore, it seems to be quite important to reduce the oxygen vacancy concentration in the present systems.

[1] J. G. Bednorz and K. A. Muller, Z. Phys. B **64**, 189 (1986).
[2] S. Uchida, H. Takagi, K. Kitazawa, and S. Tanaka (unpublished).
[3] H. Takagi, S. Uchida, K. Kitazawa, and S. Tanaka (unpublished).
[4] C. W. Chu, P. H. Hor, R. L. Meng, L. Gao, Z. J. Huang, Y. Q. Wang, J. Bechtold, D. Campbell, M. K. Wu, J. Ashburn, and C. Y. Huang, Phys. Rev. Lett. (to be published).
[5] R. J. Cava, R. B. Van Dover, B. Batlogg, and E. A. Rictman, Phys. Rev. Lett. **58**, 208 (1987).
[6] Z. Zhao, L. Chen, Q. Yang, Y. Huang, G. Chen, R. Tang, G. Lin, C. Cui, L. Chen, L. Wang, S. Guo, S. Li, and J. Bi, Nature (to be published).
[7] D. K. Finnemore, R. N. Shelton, J. R. Clem, R. W. Mccallum, H. C. Ku, R. E. McCarley, S. C. Chen, P. Klavins, and V. Kogan (unpublished).
[8] S. Hikami, T. Hirai, and S. Kagoshima (unpublished).
[9] C. Michel and B. Raveau, Rev. Chim. Miner. **21**, 407 (1984).
[10] T. Siegrist, S. Sunshine, D. W. Murphy, R. J. Cava, and S. M. Zahurak (unpublished).
[11] K. Kadowaki, Y. K. Huang, M. van Sprang, and A. A. Menovski (unpublished).
[12] R. J. Cava, B. Batlogg, C. H. Chen, E. A. Rietman, S. M. Zahurak, and D. Werder, AT&T Bell Labs preprint (July 1987).
[13] P. K. Gallagher, H. M. Bryan, S. A. Sunshine, and D. W. Murphy, AT&T Bell Labs preprint (July 1987).

Effective electron interactions due to virtual charge and spin excitations in an extended Hubbard model for Cu-O superconductors

H.-B. Schüttler
Center for Simulational Physics, Department of Physics and Astronomy, University of Georgia, Athens, Georgia 30602

A. J. Fedro
Northern Illinois University, DeKalb, Illinois 60115
and Materials Science Division, Argonne National Laboratory, Argonne, Illinois 60439

We have studied the effect of virtual Co-O charge and spin fluctuations in the perovskite high-T_c materials by applying a strong coupling expansion to an extended Hubbard model with hybridized Cu d orbitals and O p orbitals. Results for the charge and spin fluctuation-mediated effective interactions are derived and discussed.

Several nonphonon mechanisms of high-T_c superconductivity have recently been proposed for the copper oxide based perovskite materials. These mechanisms are based on the idea that attractive pairing interactions might be mediated by charge[1] or spin[2,3] fluctuations involving both the copper (Cu) and the oxygen (O) sites. Here we present further results which we have obtained from a strong coupling treatment of the simplest model Hamiltonian proposed to describe these effects. The model consists of a two-dimensional (2D) square network of hybridized copper (x^2-y^2) d orbitals and bond-parallel oxygen p orbitals[4] augmented by Hubbard-type Cu- and O-on-site interactions (U_d and U_p, respectively) and a nearest-neighbor Cu-O intersite repulsion (V) which leads to a Hamiltonian[1-3]:

$$H=\sum_{\langle ij\rangle}\left(\sum_{S} t_{ij}(c_{iS}^{\dagger}c_{jS}+\text{h.c.})+Vn_in_j\right)+\sum_i(\epsilon_i n_i+U_i n_{i\uparrow}n_{i\downarrow}). \tag{1}$$

Here, t_{ij} denotes the d-p hybridization strength (with $|t_{ij}|=t=\text{const}$). The first summation is over all Cu–O nearest-neighbor bonds $\langle ij\rangle$ and spin $S=\uparrow$ or $\downarrow$. The phase (sign) prefactors of the orbitals are chosen such that $t_{ij}=+t$ if $j=R+x$ or $R-y$, $t_{ij}=-t$ if $j=R-x$ or $R+y$, and $t_{ij}=0$, otherwise. Here, $i\equiv R$ denotes a Cu site and $j=R\pm x$, $R\pm y$ are its four nearest-neighbor oxygen sites along the x and y direction, respectively. The second sum is over all Cu and all O sites i with $\epsilon_i\equiv\epsilon_d$, $U_i\equiv U_d$, or $\epsilon_i\equiv\epsilon_p$, $U_i\equiv U_p$, respectively, where ϵ_d and ϵ_p denote the corresponding on-site energies for electrons (not holes). The operator $c_{iS}^{\dagger}$ creates an electron with spin S at a Cu or O site i; $n_{iS}\equiv c_{iS}^{\dagger}c_{iS}$ and $n_i\equiv n_{i\uparrow}+n_{i\downarrow}$ are the corresponding occupation numbers.

The model parameters are assumed to be such that for the "half-filled" system (corresponding to the undoped La_2CuO_4 material, for example), all d orbitals are singly occupied and all p orbitals are doubly occupied, if we let $t=0$ for the moment. This is equivalent to the ideal ionic configurations $Cu^{2+}(3d^9)$ and $O^{2-}(2p^6)$. If we remove a small number of electrons from such a half-filled "vacuum" state (e.g., by divalent doping in $La_{2-x}Sr_xCuO_4$), the extra holes can be accommodated either in Cu^{3+} or in O^- ionic configurations. The difference in energy between these two possible configurations is $E_x\equiv\epsilon_d-\epsilon_p-U_p+6V$. Thus, for $E_x>0$, Cu^{3+} is energetically favored, whereas for $E_x<0$, O^- is preferred. The case $E_x>0$ has already been discussed in Ref. 6. Here, we consider the case $E_x<0$, assuming again that the hybridization and the intersite repulsion are small, i.e., $|t|$, $V\ll|E_x|$, and $|t|$, $V\ll U_d+E_x>0$.

We focus on a subspace of low-lying states where all Cu ions are in the charge state Cu^{2+} whereas O ions a allowed to attain the charges O^0, O^-, O^{2-}. The hybridization term in (1) gives rise to transitions from such low-lying states into highly excited ones where one or more Cu ions have been promoted to charge states Cu^+ or Cu^{3+}. These virtual excitations are eliminated from the Hamiltonian by means of a canonical transformation, $H'=\exp(iS)\,H\exp(-iS)$, which is constructed such that the new Hamiltonian H' causes transitions only between the low-lying states. Our goal is then to determine H' perturbatively to order t^2. Although this can be accomplished, in principle, for the most general case defined by (1), our task is simplified considerably, if we do *not* include the p-orbital on-site repulsion U_p in the zeroth-order ($t=0$) Hamiltonian, but rather treat the U_p terms as a "small" perturbation, to be added to H', in addition to the perturbative t^2 terms arising from the canonical transformation. This approach is justified as long as $U_p\ll|E_x|$, U_d+E_x. In the following, we shall ignore these U_p terms altogether.

It is convenient to formulate the solution for H' in terms of appropriate linear combinations of the oxygen p orbitals surrounding a given Cu site i. These new oxygen orbitals correspond to new fermion operators given by $\hat{\phi}_{iS}=\hat{u}\hat{\psi}_{iS}$ and $\hat{\phi}_{iS}^{\dagger}=\hat{\psi}_{iS}^{\dagger}\hat{u}^{\dagger}$, where

$$\hat{u}=\frac{1}{2}\times\begin{bmatrix}1&-1&-1&1\\1&-1&1&-1\\\sqrt{2}&\sqrt{2}&0&0\\0&0&\sqrt{2}&\sqrt{2}\end{bmatrix} \tag{2}$$

is a unitary 4×4 matrix of c numbers, $\hat{\psi}_{iS}^{\dagger}$ and $\hat{\phi}_{iS}^{\dagger}$ are 1×4 matrices of the old and new p-electron operators, respectively, with components

 0021-8979/88/084209-03$02.40 © 1988 American Institute of Physics

$$\hat{\psi}^{\dagger}_{is} = [c^{\dagger}_{R+\frac{1}{2}x,s}\ c^{\dagger}_{R-\frac{1}{2}x,s}\ c^{\dagger}_{R+\frac{1}{2}y,s}\ c^{\dagger}_{R-\frac{1}{2}y,s}]$$

and

$$\hat{\phi}^{\dagger}_{is} = [D^{\dagger}_{is}\ S^{\dagger}_{is}\ A^{\dagger}_{is}\ B^{\dagger}_{is}],$$

defined for each Cu site $i \equiv R$ with nearest-neighbor O sites $j \equiv R \pm x, R \pm y$. $\hat{\psi}_{is}$ and $\hat{\phi}_{is}$ denote the 4×1 hermitian conjugates of $\hat{\psi}^{\dagger}_{is}$ and $\hat{\phi}^{\dagger}_{is}$, respectively. The new oxygen orbitals, corresponding to D_{is}, S_{is}, A_{is}, and B_{is}, have been chosen such that they transform like x^2-y^2, x^2+y^2, x, and y, respectively, under the symmetry operations of the point group of site i. Thus, the t_{ij} term in (1) hybridizes the (x^2-y^2) copper d orbital at site i (c_{is}) only with the oxygen D orbital, but not with the S, A, or B orbitals. Furthermore, without the U_p terms, the occupation numbers of the new orbitals, $n^{\alpha}_i \equiv n^{\alpha}_{i\uparrow} + n^{\alpha}_{i\downarrow}$ and $n^{\alpha}_{is} \equiv \alpha^{\dagger}_{is}\,\alpha_{is}$ ($\alpha \equiv D, S, A, B$; $s = \uparrow, \downarrow$), remain good quantum numbers of the zeroth-order ($t = 0$) Hamiltonian. Using these simplifications, H' (without U_p terms) can then be written in the following compact form:

$$H' = \sum_{i}{}' \left[e_D(n'_i) + \epsilon_D(n'_i) n^D_i + U_D(n'_i) n^D_{i\uparrow}\, n^D_{i\downarrow} + J_D(n'_i) \mathbf{S}^c_i \cdot \mathbf{S}^D_i \right]. \tag{3}$$

Here, the summation (Σ') is restricted to Cu sites i, $n'_i \equiv n^S_i + n^A_i + n^B_i$ is the total occupation number of nonhybridizing oxygen orbitals surrounding site i, and $\mathbf{S}^c_i$ and $\mathbf{S}^D_i$ denote, respectively, the spin operator of a copper d electron and of an oxygen D-electron at site i with components

$$S^{\alpha,\nu}_i = \sum_{ss'} \frac{1}{2}\, \alpha^{\dagger}_{is}\, \sigma^{\nu}_{ss'}\, \alpha_{is'} \quad (\alpha = c, D;\ \nu = x, y, z),$$

where σ^{ν} are the Pauli spin matrices. The operator functions e_D, ϵ_D, U_D, and J_D are given by

$$e_D(n'_i) = \tfrac{1}{2}(\epsilon_p + 2V) n'_i - 4t^2 g_4(n'_i), \tag{4}$$

$$\epsilon_D(n'_i) = \tfrac{1}{2}(\epsilon_p + 2V) - 2t^2 [\, g_2(n'_i) + g_3(n'_i) - 2g_4(n'_i)\,], \tag{5}$$

$$U_D(n'_i) = 4t^2 [\, g_2(n'_i) + g_3(n'_i) - g_1(n'_i) - g_4(n'_i)\,], \tag{6}$$

$$J_D(n'_i) = 8t^2 [\, g_2(n'_i) + g_3(n'_i)\,], \tag{7}$$

with energy denominators

$$1/g_1(n'_i) = U_d + E_x + (n'_i - 7)V, \tag{8}$$

$$1/g_2(n'_i) = U_d + E_x + (n'_i - 8)V, \tag{9}$$

$$1/g_3(n'_i) = -E_x - (n'_i - 6)V, \tag{10}$$

$$1/g_4(n'_i) = -E_x - (n'_i - 7)V, \tag{11}$$

and $E_x = \epsilon_d - \epsilon_p + 6V < 0$.

H' is restricted to the subspace of low-lying states where all Cu ions are in the charge state Cu^{2+}. H' conserves the total Cu-site occupation number $n_i = n_{i\uparrow} + n_{i\downarrow}$. However, we should stress that the oxygen orbital occupation numbers n^{α}_i ($\alpha = D, S, A, B$) or the total "on-site" spin $\mathbf{S}^T_i \equiv \mathbf{S}^c_i + \mathbf{S}^D_i$ are not conserved quantities in H'. This can be seen by expressing these operators (n^{α}_i, $\mathbf{S}^T_i$) in terms of the original p-electron operators c_{js}, $c^{\dagger}_{js}$, using Eq. (2). One then notices that two operators like, e.g., n^{α}_i and n^{β}_j ($\alpha, \beta = D, S, A, B$) do not in general commute with each other whenever i and l denote two nearest-neighbor Cu sites which share a common oxygen nearest-neighbor. Similarly, two fermion operators like $D^{\dagger}_{is}$ and A_{is}, for example, do not obey ordinary fermion anticommutation rules for a pair of nearest-neighbor Cu sites (i,l), since the set of all single electron orbitals corresponding to the operators D_{is}, S_{is}, A_{is}, and B_{is}, defined by Eq. (2), is nonorthogonal and overcomplete.

In the half-filled system, all p orbitals are fully occupied and hence all terms of order t^2 in H' vanish. The low-energy properties of the system are then governed by an order t^4 antiferromagnetic superexchange coupling of the form $J_c\ \mathbf{S}^c_i \cdot \mathbf{S}^c_l$ between nearest-neighbor Cu spins (i,l). Thus, the ground state is characterized by an antiparallel alignment of nearest-neighbor Cu spins. In the presence of a small concentration of holes in the oxygen p orbitals, however, the coupling J_D tends to locally align nearest-neighbor Cu spins in parallel if their common nearest-neighbor p orbital happens to be occupied by an unpaired electron, since the p-electron spin prefers to be aligned antiparallel to *both* nearest-neighbor Cu spins with a coupling constant $J_D \gg J_c$. By this mechanism,[2] doping with a small number of holes can suppress the antiferromagnetic order of the system.

Here, we would like to point out that the same mechanism, at larger dopant concentrations, may in fact give rise to a new type of magnetic order. In this new ordered state, which is dominated by the Cu-O exchange coupling J_D, the Cu- and the O-spin systems exhibit a ferrimagnetic alignment, with all Cu spins oriented in parallel, but opposite to all the (also parallel oriented) O spins. Analogous considerations apply if the Cu-O exchange is dominated by a direct (Heisenberg exchange) ferromagnetic contribution $J'_D < 0$ (with $J_D < |J'_D|$) between copper d and oxygen p orbitals, a possibility that has recently been discussed in the context of spin polaron formation.[7] In that case, ($J_D + J'_D < 0$), the magnetically ordered state at higher dopant levels would be ferromagnetic with all Cu and O spins aligned in parallel. We also note here that the ferri- or ferromagnetic spin fluctuations invoked in the foregoing discussion may give rise to attractive superconducting pairing interactions, between p electrons, similar to a recently discussed "double exchange" mechanism.[8] However, these spin fluctuation mediated interactions are likely to be attractive only in the triplet channel and would hence give rise to an odd-parity (anisotropic) superconducting order parameter.

To study the role of virtual Cu-O charge fluctuations in H', it is instructive to consider just a single CuO_4 cluster, and ignore, for the time being, the spin fluctuation (J_D) term in (3). The new oxygen orbital occupation numbers n^{α}_{is} ($\alpha = D, S, A, B$) are then conserved within the isolated cluster. To estimate the effective interactions between a pair of holes occupying one or two of these oxygen orbitals ($\alpha, \beta = D, S, A, B$), we compare the energies $\bar{\epsilon}_{\alpha}$ (needed to introduce a single hole into orbital α, starting from the half-filled "vacuum") with the energies $\bar{\epsilon}_{\alpha\beta}$ for introducing a pair of holes, one into α the other into β. The effective hole-hole interaction for such a pair of orbitals is then given by $\bar{U}_{\alpha\beta} = \bar{\epsilon}_{\alpha\beta} - \bar{\epsilon}_{\alpha} - \bar{\epsilon}_{\beta}$. Using Eqs. (4)–(11), we find that all $\bar{U}_{\alpha\beta}$ vanish for $V = 0$. Assuming $0 < V \ll E_0 \equiv \min(|E_x|, U_d + E_x)$,

we find that $\bar{U}_{DD} > 0$ is always repulsive and of order $\bar{U}_{DD} \sim t^2 V / E_0^2$ whereas, for $\alpha, \beta = S, A, B$ we always get an attraction $\bar{U}_{\alpha\beta} < 0$ of order $\bar{U}_{\alpha\beta} \sim -t^2 V^2 / E_0^3$ which is smaller by a factor $(V/E_0)^2$ than the exchange coupling $J_D \sim t^2/E_0$. Similarly, one can show that $\bar{U}_{D\beta}$ is smaller than J_D by at least a factor V/E_0. These results suggest that, at least in the parameter regime where our strong coupling expansion is valid, the pair-breaking effect of the Cu-O exchange coupling J_D is sufficiently strong to suppress charge fluctuation mediated superconducting pairing.

One of us (H.-B. S.) gratefully acknowledges fellowship support from the Advanced Computational Methods Center at the University of Georgia. This work was supported by the U. S. Department of Energy, BES-Materials Sciences, under Contract No. W-31-109-ENG-38.

[1] C. M. Varma, S. Schmitt-Rink, and E. Abrahams, Solid State Commun. **62**, 681 (1987); in Proceedings of the International Conference on Novel Mechanisms of Supeconductivity, Berkeley, CA, June 1987, edited by V. Kresin and S. Wolf (Plenum, New York, in press).
[2] V. Emery, Phys. Rev. Lett. **58**, 2794 (1987).
[3] J. E. Hirsch, Phys. Rev. Lett. **59**, 228 (1987).
[4] J. D. Jorgensen, H.-B. Schüttler, D. G. Hinks, D. W. Capone II, K. Zhang, M. B. Brodsky, and D. J. Scalapino, Phys. Rev. Lett. **58**, 1024 (1987); L. F. Mattheiss, *ibid.* **58**, 1028 (1987); J. Yu, A. J. Freeman, and J.-H. Xu, *ibid.* **58**, 1035 (1987).
[5] J. R. Schrieffer and P. A. Wolff, Phys. Rev. **149**, 491 (1966); A. B. Harris and R. V. Lange, *ibid.* **157**, 295 (1967); J. E. Hirsch, Phys. Rev. Lett. **54**, 1317 (1984).
[6] A. J. Fedro, H.-B. Schüttler, and S. K. Sinha, in Proceedings of the 18th Yamada Conference on Superconductivity in Highly Correlated Fermion Systems, 1987, Sendai, Japan.
[7] E. B. Stechel and D. R. Jennison (unpublished).
[8] P. G. deGennes (unpublished); V. Ambegaokar and P. G. deGennes (unpublished); D. J. Scalapino (private communication).

Magnetization of high-temperature superconductors (abstract)

Sang Boo Nam
University Research Center, Wright State University, Dayton, Ohio 45435

Superconducting Ba (X = Y, Nd, Sm, Gd, Dy, Er, Yb) CuO were made independently by the solid reaction method via mixing barium carbonate, (X) oxides, and copper oxide with atomic ion ratio Ba:X:Cu = R:1:R + 1 with R = 1 − 4, and sintering at 900–1000 °C for 24–72 h. (1) The best superconductor was found to be formed via R = 2 and sintering near 950 °C. All samples studied were found to have layered perovskite x-ray diffraction patterns. Samples via R = 1,3, and 4 were also found to have structures similar to those via R = 2, and found to have two phases by the x-ray diffraction. The temperature-dependent magnetizations M($\bar{T}$) were measured by using the BTi SQUID susceptometer. The transition temperature T_c was determined by extrapolating $M(T)$ and was found to be sensitive to the cooling rate of the sample during its synthesis. The Meissner effect was observed up to 78–92 K, and the fluxoids were found to be trapped while the samples cooled in a finite field at all temperatures below T_c. $M(T)$ was found to be of three types: type 1 being similar to that of Pb, type 2 having a knee perhaps due to the two crystal structures, and type 3 having zero slope near T_c, perhaps due to the sample crystal sizes being less than the effective penetration depth. Samples with large crystal sizes were found to be of type 1 or 2. The measured $M(T)$ can be understood in the framework of the BCS theory, and $2\Delta(0)/k\,T_c$ were deduced to be in the range of 3–4.4. However, the magnetic hysteresis was found to be present at even low field 30 G at 10 K, and $M(T)$ near T_c was found to be sensitive to thermal fluctuations. Various mechanisms for superconductivity in these systems will also be discussed.

---

[1]S. Nam, Videotape on High T_c Superconductors, APS Meeting, March 18, 1987; Videotape on High T_c Superconductors, MRS Meeting, April 23–24, 1987.

Correlation between the superconducting properties and the oxygen stoichiometry in $Y_1Ba_2Cu_3O_x$ (abstract)

J. F. Marucco, K. Wang, and P. Garoche
Laboratoire de Chimie des Solides, Université de Paris-Sud, 91405 Orsay Cedex, France and Laboratoire de Physique des Solides, Université de Paris-Sud, Bat. 510, 91405 Orsay Cedex, France

The phase diagram of the $Y_1Ba_2Cu_3O_x$ compound has been studied by thermogravimetric measurements. In order to reach the absolute value of the oxygen content, the starting oxides and carbonate were carefully weighted and reacted directly in the thermobalance. The temperature range for the respective formation of the $Y_1Ba_2Cu_3O_x$ and Y_2BaCuO_5 was determined; thus a single phase was obtained at high temperature. The phase diagram was constructed from the reacted material by a series of isothermal treatment under a precise partial pressure of oxygen. Step by step the oxygen partial pressure was reduced and both the kinetic of the reaction and the equilibrium value were monitored. For each step the oxygen partial pressure was cycled back and forward to insure a good equilibrium state. The change in the rate of evolution of the oxygen loss with temperature is possibly related to the orthorhombic to tetragonal structural transformation. The phases identified from the phase diagram where quenched and the correlation between the oxygen stoichiometry and superconducting properties established from the analysis of the low-temperature transport and calorimetric properties.

 0021-8979/88/084212-01$02.40 © 1988 American Institute of Physics

Are the high T_c superconducting materials bulk superconductors or grain boundary percolating network superconductors? (abstract)

N. Garcia, S. Vieira, A. M. Baro, J. Tornero, L. Vazquez, J. Gomez, A. Aguilo, S. Bourgeal, A. Buendia, M. Hortal, M. A. Lopez de la Torre, M. A. Ramos, and R. Villar
Universidad Autonoma de Madrid, Madrid, Spain

K. V. Rao, D-X. Chen, J. Nogues, and N. Karpe
Royal Institute of Technology, Stockholm, Sweden

We have studied the physical properties of high T_c Y-Ba-Cu-O_x superconducting materials with levitation, ac susceptibility, macroscopic resistivity, resistivity as measured by scanning tunneling microscopy (STM) and Hall effect. Levitation experiments show that the powder of the as-prepared material does not levitate at liquid nitrogen while pellets and powders that have been heated above 450 °C do levitate (are superconducting). These experiments seem to indicate that clustering and intimate contact of fine grains are necessary for levitating. The ac susceptibility experiments show that diamagnetism is extremely sensitive to pellet density. The higher the density and the smaller the field amplitude the less diamagnetic is the system. This is interpreted as evidence for a surface, not a bulk effect. Resistivity at 17 °C measured with macroscopic contacts is of the order of 10 Ω cm. When measured with microscopic STM contacts, a clear semiconducting behavior is observed. This observation does not preclude grain boundary regions with metallic conductivity. We conjecture that the bulk of the grain is semiconducting with a conducting percolative network of grain boundaries that is the source of the superconductivity. We propose a model of a superconductor-metal-superconductor percolative network based on the excitonic model of Allender, Bray, and Bardeen to explain the high values of T_c. Hall measurements show large effective masses in agreement with an excitonic model.

Properties of high T_c superconductors with modified compositions (abstract)

S. Jin, R. C. Sherwood, T. H. Tiefel, K. B. van Dover, R. A. Fastnacht, and M. Yan
AT&T Bell Laboratories, 600 Mountain Avenue, Murray Hill, New Jersey 07974

The recent discovery of high T_c superconductor materials such as $Ba_2YCu_3O_{9-x}$ stimulated worldwide interest in the subject. The interactions of the superconducting oxides with other oxides and metals are of considerable technical importance because of the need for (i) proper stabilizer for superconductor-normal metal composite wire, (ii) nonreactive crucible materials for crystal growth, and (iii) suitable substrate materials for thin-film/thick-film superconductor devices. In this paper, the effects of various metal and oxide additions (up to 10%–50% by weight) on superconducting transition properties have been investigated using magnetic susceptibility and resistivity measurement as a function of temperature. Fine particles of metals and oxides were intimately mixed with the $Ba_2YCu_3O_{9-x}$ powder, pressed into pellets, and then sintered at 900–1000 °C followed by slow cooling in oxygen atmosphere to achieve chemical homogeneity, desirable crystal structure and oxygen stoichiometry. Some of the oxides and metals were relatively benign and did not significantly affect the superconducting transition behavior, while others either caused less sharp transition (e.g., broad transition to below 77 K) or essentially eliminated the superconductivity. The experimental results and interpretations will be presented and their technical implications will be discussed.

 0021-8979/88/084213-01$02.40 © 1988 American Institute of Physics

Superconductivity above 110 K in the orthorhombic phase of the Y-Ba-Cu-O ceramic compounds (abstract)

J. Baszyński
Institute of Molecular Physics, Polish Academy of Sciences, 60-179 Poznań, Poland

We present the results of the study the crystalline structure of the high-temperature superconducting (above 110 K) phase in the ceramic compounds Y-Ba-Cu-O. These ceramics were prepared with nominal compositions represented by the formula $Y_{1.2}Ba_{0.8}CuO_{4-\delta}$.[1] From Fig. 1 it is evident that the diamagnetic shift starts at 126 K and at 112 K the air value of the solenoid inductance is achieved. The detailed HTS phase structure was evaluated from x-ray diffractograms (Fig. 2) which are obtained from the samples of the same chemical nominal compositions but have essentially diverse physical properties—see Fig. 2. We have concluded that the crystal symmetry of HTS phase is orthorhombic: $a = 3.756$ Å, $b = 3.45$ Å, and $c = 13.186$ Å with peculiar superstructure in plane (112), which could be also attributed to the plane (311) diamond type too.

This paper was not proofread by the author; however, it has been proofread by one of the Publication Chairpersons.

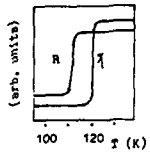


FIG. 1.

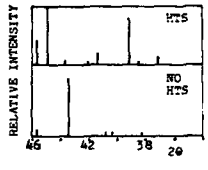


FIG. 2.

[1] M. K. Wu, J. R. Meng, L. Gao, Z. J. Huang, Y. Q. Wang, and C. W. Chu, Phys. Rev. Lett. **58**, 908 (1987).

Pairing and magnetic instabilities in high T_c systems with finite U (abstract)

A. J. Fedro[a)]
Northern Illinois University, DeKalb, Illinois 60115 and Argonne National Laboratory, Argonne, Illinois 60439

S. K. Sinha
Exxon Research and Engineering Company, Annandale, New Jersey 08801

We consider the Anderson lattice for finite U using a novel equation of motion technique. The method employs a truncation scheme based on a projection operator which projects out of any operator its exact thermal average in the space of *correlated* single-particlelike excitations, i.e., excitations both in the presence and absence of the opposite spin state. Thus, this method is good for all U. This is important in these superconducting transition metal oxide systems since experimental evidence has shown that the bandwidth/U is not small. For the single-particle spectrum we naturally generate the anomalous correction induced pairing and resulting gap equation for finite U, in contrast to previous treatments based on the large-U limit, where on-site double occupancy is excluded. The magnetic and pairing susceptibilities are calculated in a similar manner, again for finite U, and the competition between these instabilities will be discussed.

[a)] The work of A.J.F. was supported by the U.S. Department of Energy, BES-Materials Sciences, under Contract No. W-31-109-ENG-38.

 0021-8979/88/084214-01$02.40 © 1988 American Institute of Physics

Some novel melt-spun superconducting materials (abstract)

Akihisa Inoue,[a] Kunio Matsuzaki, and T. Masumoto
Institute for Materials Research, Tohoku University, Sendai 980, Japan

K. V. Rao, Han Zeng He, and D-X. Chen
Department of Solid State Physics, Royal Institute of Technology, Stockholm, Sweden

A new class of Fe-, Co-, Ni-, Cu-, and Ge-based ductile ribbons in which an amorphous matrix containing less than 12 vol. % of a fine dispersion of 0.1–3-μm size particles of immiscible elements M = Pb, Bi, Sn, or In have been produced by a modified melt-quenching technique. The Fe- and Co-based alloys containing Bi and Pb are found to be ferromagnetic above room temperature *and also superconducting* at temperatures in a range 7–9 K depending on the alloy. The saturation magnetization in these usual alloys range from 92 emu/gm for Co-Si-B-Pb-Bi to 15 emu/g for Fe-P-Pb-Bi at 77 K. At the superconducting transition the resistivity typically is found to drop by 2–3 orders of magnitude with a transition width $\sim$0.5 K before the "zero" resistance value is reached. In all the alloys studied the T dependence of the resistivity shows a typical metallic behavior despite its high magnitude (a few thousand $\mu\Omega$ cm in some cases). Extremely high values are found for the upper critical fields (1.6–1.72 T at 4.2 K) with critical current densities typically around 1.3×10^{7} A m^{-2} at 4.2 K. For Ge-Pb-Bi-Sn H_{c2} values of 5 T are obtained at 3 K. Along with detailed studies of magnetic and superconducting properties, extensive TEM, and x-ray characterization data will also be presented. Attempts to explain the above described behavior in terms of proximity, percolation, and surface properties at the dispersed Pb, Bi particles are found to be unsatisfactory. As far as we know there exists no theory that can explain the co-existence of ferromagnetism and superconductivity of the type described above. Time permitting, we will also discuss our recent work on high T_c oxide materials produced by melt-quenching techniques. Thus amorphous composite materials exhibiting unique and useful characteristics which cannot be achieved for homogeneous amorphous alloys can be produced by melt quenching. These materials are of importance both for scientific and engineering points of view.

This paper was not proofread by the author; however, it has been proofread by one of the Publication Chairpersons.

[a] Guest scientist at Royal Institute of Technology, Stockholm.

 0021-8979/88/084215-01$02.40 © 1988 American Institute of Physics

Studies at IBM on anisotropy in single crystals of the high-temperature oxide superconductor $Y_1Ba_2Cu_3O_{7-x}$ (invited)

W. J. Gallagher
IBM T. J. Watson Research Center, P.O. Box 218, Yorktown Heights, New York 10598

A series of studies carried out at IBM on the magnetic, transport, and optical properties of single crystal $Y_1Ba_2Cu_3O_{7-x}$ demonstrate the overriding importance of anisotropy in its superconducting and normal-state properties.

INTRODUCTION

An avalanche of scientific activity has followed the discovery of high-temperature superconductivity in La-Ba-Cu-O (Ref. 1) and the subsequent achievement of superconducting transition temperatures T_c in Y-Ba-Cu-O (Ref. 2) exceeding that at which nitrogen liquifies. Widespread applications of these new materials have been anticipated, although some aspects of the magnetic and electrical properties of the early ceramic materials were far from ideal and far from what would be adequate for many applications. For instance, resistive transitions in modest magnetic fields were very broad, indicating a rapid decrease of the temperature at which zero resistance was achieved, although some manifestations of superconductivity clearly remained in very high fields. Critical currents, even in zero field, were low ($<1000 A/cm^2$). Superconducting energy gap Δ measurements from tunneling and infrared reflectivity measurements spanned a range from $2\Delta/k_B T_c = 1.5$–11 or greater, with complicated structure showing up in the infrared data and multiple gaps indicated by some of the tunneling measurements. Recent measurements of single-crystal specimens have to a great extent implicated anisotropy as the explanation for these perplexing early results. This paper summarizes the results of recent low- and high-field magnetic measurements, transport measurements, and infrared reflectivity measurements made at IBM on high-quality single-crystal specimens[3] of $Y_1Ba_2Cu_3O_{7-x}$. (Restrictions of space and time prevent adequate referencing in this article of all the relevant activity inside and outside of IBM.)

CRYSTAL STRUCTURE AND CRYSTAL GROWTH

Studies by a number of groups[4] have resulted in the identification of the crystal structure of $Y_1Ba_2Cu_3O_{7-x}$ as an oxygen-defect layered perovskite with the superconducting properties optimized for oxygen stoichiometries approaching 7. The crystal structure for this oxygen stoichiometry, illustrated in Fig. 1, can be seen to consist of stacked perovskite blocks of BaCuO, YCuO, and BaCuO. The central plane of oxygen atoms is missing in the YCuO blocks and the CuO plane between the BaCuO blocks has half of its oxygen atoms missing. The resulting crystal structure thus has two-dimensional sheets of Cu-O surrounding the Y-atom planes and one-dimensional Cu-O chains between the Ba layers. Band-structure calculations indicate that the conduction electrons reside primarily in the planes, although the chains also make contributions to the electronic properties. Anisotropy investigations have thus looked for two-dimensional anisotropy that might be associated with the Cu-O planes as well as for further anisotropy that might be associated with the chains.

The paritectic decomposition of $Y_1Ba_2Cu_3O_{7-x}$ from the solid state makes the growing of large crystals difficult. Studies by Kaiser *et al.*[3] resulted in the identification of a set of conditions for Cu-O- and BaO-rich compositions in which crystals ranging in size from $<100\ \mu m$ to a few mm in size can be grown. After a subsequent oxygen anneal the crystals display sharp transitions near 92 K with ac susceptibilities having 10%–90% transitions widths of 0.12 to 0.15 K. Crystals grown by Kaiser *et al.*[3] were used in all of the studies summarized here with the exception of some of the early magnetization data taken on crystals grown by Dinger *et al.*[5] using a starting composition closer to that of $Y_1Ba_2Cu_3O_{7-x}$.

MAGNETIZATION MEASUREMENTS: CURRENT DENSITY AND LOWER CRITICAL FIELDS

Magnetization measured as a function of magnetic field provides a noncontact way of measuring lower critical fields and depinning current densities. As magnetic fields are ap-

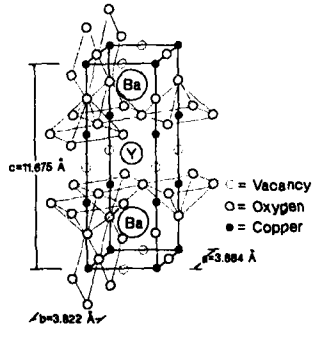


FIG. 1. Crystal structure of $Y_1Ba_2Cu_3O_{7-x}$.

 0021-8979/88/084216-04$02.40 © 1988 American Institute of Physics

plied to superconducting samples, the magnetization first increases in opposition to the applied field. The cancellation is perfect until the lower critical field H_{c1} is reached, above which flux begins to penetrate the sample. Pinning prevents the flux from immediately moving far in from the surface of the superconductor. The strength of the pinning will determine how large the surface screening currents can get before $\mathbf{J}\times\mathbf{B}$ forces cause flux bundles to jump further towards the sample center. Once the flux has penetrated to the sample center, there is a simple relationship[6] between the measured magnetization and the depinning critical current $J_c(B^{\text{eff}}) = 20M/r$, where $J_c(B^{\text{eff}})$ is the critical current at internal field B^{eff}, M is the sample magnetization, and r is the radius of the (cylindrically shaped) sample. Implicit in this relationship is an assumption that the pinning is uniform in the measured sample and that its field dependence is small.

Magnetization-versus-field hysteresis loops measured at 4.5 K by Dinger *et al.*[5] are shown in Fig. 2 for a crystal mounted with the CuO planes both perpendicular [Fig. 2(a)] and parallel [Fig. 2(b)] to the field lines as illustrated in the insets. The differences in the scale and in the shape of the curves for the two orientations are striking. [Note the ordinate scale in Fig. 2(b) is ten times smaller that that in Fig. 2(a).] The lower critical fields, $H_{c1}^{\perp}$ and $H_{c1}^{\parallel}$, for crystals oriented such that the applied field is perpendicular and parallel to the Cu-O planes, respectively, were determined from the point in the initial part of each loop at which the departure from linearity begins. Anisotropies in H_{c1} for two crystals were in excess of 10:1. The values for one crystal, corrected for the demagnetizing factors, are listed in Table I.

The difference in the magnitude of the hysteresis in the two loops in Fig. 2 indicates the substantial difference in pinning strength for the two orientations. The large magnetization loop in the perpendicular orientation indicates strong pinning for vortices that thread the Cu-O planes and thus high critical currents along the directions of the planes. In constrast, the smaller loop with the sharp break at $H_{c1}^{\parallel}$ in the parallel orientation is indicative of weak pinning between the planes and low critical currents between the planes. Figure 3

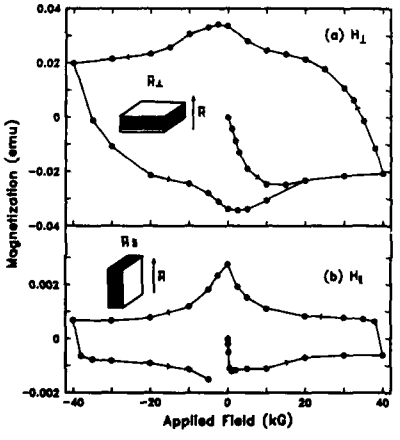


FIG. 2. Magnetization vs applied field hysteresis loops for a crystal oriented with the field (a) perpendicular and (b) parallel to the Cu-O planes.

TABLE I. Anisotropic parameters of $Y_1Ba_2Cu_3O_{7-x}$.

	$H_{\parallel}$	$H_{\perp}$
	Measured parameters	
T_c	92.4 K	
$-\frac{dH_{c2}(T_c)}{dT}$	3.8 T/K	0.54 T/K
H_{c1} (4.5 k)	<0.05 T	0.5 T
J_c(0 T, 4.5 K)	1.6×10^5 A/cm^2	3.2×10^6 A/cm^2
$\frac{2\Delta}{k_B T_c}$		~8
	Derived parameters	
$H_{c2}(0)$	240 T	34 T
$\xi(0)$	$\xi_Z = 4.3$ Å	$\xi_0 = 31$ Å
$H_c(0)$	2.8T	
$\lambda_{GL}(0)$	$\lambda_Z = 1800$ Å	$\lambda_0 = 270$ Å
κ	$\kappa_Z = 60$	$\kappa_0 = 8.6$

shows the field and temperature dependence of the critical current density as deduced using the Bean formula[6] from hysteresis curves like those shown in Fig. 2 but taken in addition at a number of higher temperatures. (Note that the curves in Fig. 3 are labeled according to the direction of the applied field. Thus, for example, the curves labeled with $H_{\perp}$ are for fields applied perpendicular to the Cu-O planes in which case the induced currents flow along the planes. The same convention is followed in Table I.) According to Fig. 3, the critical current anisotropy is ~7:1 at 4.5 K and zero field, increasing to ~20:1 at 4 T. It is significant to note that the critical current density along the Cu-O planes remains substantially in excess of 10^6 A/cm^2 out to 4 T and 4.5 K with no sign of a rapid fall-off. The anisotropy increases considerably at higher temperatures and fields as the fall-off of current density with field becomes more rapid first for the parallel orientation but eventually for both orientations. Measurements taken by Dinger *et al.*[5] on a second crystal confirmed the same general behavior and actually indicated a stronger anisotropy of 20:1 in the critical current density at low temperature and zero field ($J_c^{\perp} = 3.2\times10^6$ A/cm^2 and $J_c^{\parallel} = 1.6\times10^5$ A/cm^2).

Above H_{c1}, a slow relaxation of the magnetization in the

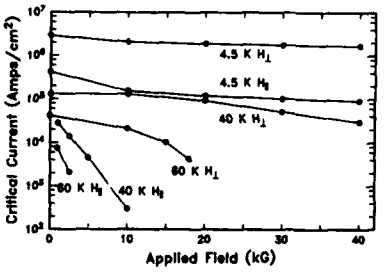


FIG. 3. Current density as a function of field at various temperatures for fields oriented parallel and perpendicular to the Cu-O planes.

single crystals was observed. This behavior is similar to that observed in $La_{2-x}Ba_xCuO_4$ polycrystalline samples by Müller, Takashige, and Bednorz.[7] Figure 4 reproduces a plot given by Worthington *et al.*[8] of the magnetization versus time for a field of 1 T applied perpendicular to the Cu-O planes. The magnetization can be seen to have changed by more than 20% and the time dependence to be consistent with logarithmic behavior for times longer than 1000 min. (For practical reasons, magnetization data like those reported in Fig. 2 are taken a few minutes after establishing the field.) Logarithmic time dependence has long been associated with flux creep in type-II superconductors. It is thus clear that the superconducting-glass-state behavior described by Müller, Takashige, and Bednorz[7] occurs within a single crystal above H_{c1}.

HIGH-FIELD DATA: UPPER CRITICAL FIELDS

To determine the upper critical field, H_{c2}, Worthington, Gallagher, and Dinger[9] measured the high-frequency ($\sim$1–100 MHz) ac susceptibility in field as a function of temperature. As the field increased the transitions were observed to broaden from their zero-field values, but they remained easy to pick out. Figure 5 shows data[10] for critical fields up to 23 T for fields applied parallel to the Cu-O layers and up to 15 T for those applied perpendicular to the layers. Except for temperatures very close to T_c, the data in each orientation are consistent with a linear temperature dependence as is expected from anisotropic Ginzburg–Landau theory. The slopes in the two orientations differ by a factor of 7. Extrapolation of the $H^{\parallel}_{c2}$ curve with a slope of -3.8 T/K back to zero field according to the dirty-limit isotropic formula (with no Pauli paramagnetism limiting effects) gave $H^{\parallel}_{c2}(0) = 240$ T. A linear extrapolation back to zero temperature, which might be more appropriate for an anisotropic superconductor, yielded instead 350 T. The perpendicular critical field extrapolated back to zero temperature according the dirty-limit isotropic formula gave $H^{\perp}_{c2}(0) = 34$ T. Data[9] taken on another crystal with a 2-K lower transition temperature displayed a slightly smaller anisotropy of 5:1 and gave an indication of an upward break in $H^{\perp}_{c2}$ occurring at $\sim$78 K. The break observed in $H^{\perp}_{c2}$ in that crystal was apparently not an intrinsic property of $Y_1Ba_2Cu_3O_{7-x}$.

Even though the crystals studied were twinned, if there were a strong uniaxial anisotropy associated with the Cu-O chains, it should be reflected in changes in the critical field of crystals rotated within the Cu-O planes. No change in the transition temperature of several crystals was seen by Worthington *et al.*[8,9] for rotations of 0°, 45°, and 90° in the *a-b* plane in several fields.

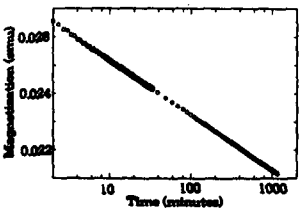


FIG. 4. Magnetization decay a function of time in 10 T applied perpendicular to the Cu-O planes.

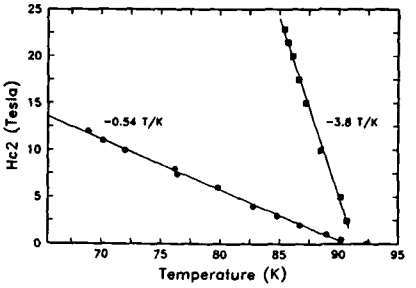


FIG. 5. Upper critical field of $Y_1Ba_2Cu_3O_{7-x}$ for field parallel and perpendicular to the Cu-O planes.

TRANSPORT MEASUREMENTS: RESISTIVITY AND HALL RESISTANCE ANISOTROPY

The most direct consequence of the conduction-electron density that is expected to reside mainly in the Cu-O planes in $Y_1Ba_2Cu_3O_{7-x}$ is an anisotropic conductivity. Because of difficulties in getting large crystals and in making contacts to them there are surprisingly few data on this. Tozer *et al.*[11] succeeded in making contacts to the corners of the 300×100-μm^2 *a-c* face of a $300\times300\times100$-μm^3 crystal. (The crystal was twinned so the labeling of the *a* and *b* directions is arbitrary.) Their resistivity data, reproduced in Fig. 6, show a linear decrease along the *a-b* planes (i.e., in ρ_{ab}) in agreement with the behavior seen in ceramic materials. Its magnitude just above the transition of $\sim$180 $\mu\Omega$ cm is roughly the same as that seen in the best ceramic samples, although it is about twice that seen in the best oriented film samples. (The reason for the larger resistivity value seen in this direction and also for the slightly depressed T_c could be a slight oxygen deficiency.) Along the *c*-axis direction, the magnitude of the resistivity is about 2 orders of magnitude larger than ρ_{ab} and its small, upward-curving temperature dependence suggests tendency toward semiconductive or localizing behavior at low temperatues. The ratio of the resistivities at $\sim$100 K is about 80, which is slightly larger than the

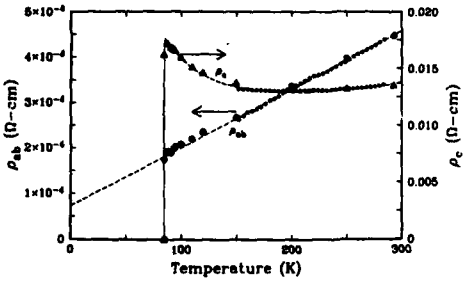


FIG. 6. Anisotropic resistivity of $Y_1Ba_2Cu_3O_{7-x}$.

value of 49 that is expected from the square of the critical field anisotropy. The only other data on resitivity anisotropy of which we are aware, those by Enomoto *et al.*[12] for a [011]-oriented thin film, showed a resistivity anisotropy ratio of about 40 just above T_c.

A nearly-temperature-independent and *electronlike* Hall constant was also measured by Tozer *et al.* for a field applied perpendicular to the contacted face. The magnitude of the Hall number obtained by normalizing the Hall conductance to the inverse of the unit-cell volume was in the range of 1.2–1.5 electrons per formula unit. (In a material with a complicated band structure like $Y_1Ba_2Cu_3O_{7-x}$, the normalization is more a convenience than something with physical significance.) Both the negative value for the Hall number and its termperature independence are in contrast to results measured for polycrystalline ceramics and for films oriented with their *c* axes perpendicular to the substrate and along the field direction of Hall measurements.

INFRARED DATA: ac CONDUCTIVITY AND ENERGY GAP

In infrared reflectivity studies of preferentially oriented films and then in a mosaic of aligned single crystals, Collins *et al.*[13] and Schlesinger *et al.*[14] convincingly observed a Drude-like normal-state reflectivity for electric fields in the metallic, *a-b* plane and superconducting-state behavior in good agreement with the Mattis–Bardeen expectations. The Mattis–Bardeen fits to the measured ratios of the crystal mosaic gave a very high gap value of $2\Delta/k_BT_c \simeq 8$. In the less perfectly aligned, though preferentially oriented films, and to a much greater extent in randomly oriented ceramics, they argued that low-reflectivity *c*-axis contributions tended to be heavily weighted in superconducting-state–normal-state reflectivity ratios. Earlier data on ceramic samples, dominated by low-reflectivity *c*-axis contributions, showed extremely complicated structure that often was thought to indicate anomalously small values of the energy gap. An attempt to observe gap anisotropy within the *a-b* plane gave no evidence of any such anisotropy, which might have been associated with the Cu-O chains.

SUMMARY AND CONCLUSIONS

Measurements on magnetic, transport, and optical properties of single-crystal $Y_1Ba_2Cu_3O_{7-x}$ show a strong anisotropy associated with the highly conductive Cu-O planes. Anisotropy in many cases explains initially puzzling features of early polycrystalline data, and certainly has consequences for many potential applications of this material. Values for some of the anisotropic parameters of $Y_1Ba_2Cu_3O_{7-x}$ are given in Table I along with derived low-temperature values for the anisotropic coherence lengths, ξ_Z and ξ_0, the Ginzburg–Landau penetration depths, λ_Z and λ_0, and the thermodynamic critical field, H_c. Here the subscripts Z and 0 refer, respectively, to values appropriate for directions perpendicular to the Cu-O planes and within the Cu-O planes. The quantities are derived from the measured quantities according to the methods described in Ref. 9 using the anisotropy ratio given by the ratios of dH_{c2}/dT near T_c and the standard isotropic dirty-limit extrapolation to get $H_{c2}(0)$. Obviously, use of the larger anisotropy observed for H_{c1} at lower temperatures or a different extrapolation method would alter the numerical results. We note that the zero-temperature coherence length perpendicular to the Cu-O layers, $\xi_Z = 4.3$ Å, is greater than the 3.9-Å spacing between the Cu-O layers adjacent to the Y layer, but it is significantly less than the spacing of the Cu-O planes separated by the one-dimensional Cu-O chains. According to the Josephson-coupled layer model,[15] the crossover to two-dimensional behavior is expected when $\xi_Z = s/\sqrt{2}$, where s is the effective interlayer spacing. If the effective interlayer spacing is governed by either the unit-cell *c* axis repeat distance or the separation due to the chain spacing, $Y_1Ba_2Cu_3O_{7-x}$ will clearly be two dimensional at low temperatures. If it is governed by the spacing between the planes separated by the Y layer, $Y_1Ba_2Cu_3O_{7-x}$ is just on the border of being two-dimensional at low temperatures.

[1] J. G. Bednorz and K. A. Müller, Z. Phys. B **64**, 189 (1986).
[2] M. K. Wu, J. Ashburn, C. J. Torng, P. H. Hor, R. L. Meng, L. Gao, Z. J. Huang, Y. Q. Wang, and C. W. Chu, Phys. Rev. Lett. **58**, 908 (1987).
[3] D. L. Kaiser, F. Holtzberg, B. A. Scott, and T. R. McGuire, Appl. Phys. Lett. **51**, 1040 (1987).
[4] See, for example, M. A. Beno, L. Soderholm, D. W. Capone II, D. G. Hinks, J. D. Jorgensen, I. K. Schuller, C. U. Segre, K. Zhang, and J. D. Grace, Appl. Phys. Lett. **51**, 57 (1987).
[5] T. R. Dinger, T. K. Worthington, W. J. Gallagher, and R. L. Sandstrom, Phys. Rev. Lett. **58**, 2687 (1987).
[6] C. P. Bean, Phys. Rev. Lett. **8**, 250 (1962).
[7] K. A. Müller, M. Takashige, and J. G. Bednorz, Phys. Rev. Lett. **58**, 1143 (1987).
[8] T. K. Worthington, W. J. Gallagher, T. R. Dinger, and R. L. Sandstrom, in *Novel Superconductivity*, edited by S. A. Wolf and V. Z. Kresin (Plenum, New York, 1987), pp. 781–786.
[9] T. K. Worthington, W. J. Gallagher, and T. R. Dinger, Phys. Rev. Lett. **59**, 1160 (1987).
[10] W. J. Gallagher, T. K. Worthington, T. R. Dinger, F. Holtzberg, D. L. Kaiser, and R. L. Sandstrom, Physica **148B**, 228 (1987).
[11] S. W. Tozer, A. W. Kleinsasser, T. Penney, D. Kaiser, and F. Holtberg, Phys. Rev. Lett. **59**, 1768 (1987).
[12] Y. Enomoto, T. Murakami, M. Suzuki, and K. Moriwaki, Jpn. J. Appl. Phys. **26**, L 1248 (1987).
[13] R. T. Collins, Z. Schlesinger, R. H. Koch, R. B. Laibowitz, T. S. Plasket, P. Freitas, W. J. Gallagher, R. L. Sandstrom, and T. R. Dinger, Phys. Rev. Lett. **59**, 704 (1987).
[14] Z. Schlesinger, R. T. Collins, D. L. Kaiser, and F. Holtzberg, Phys. Rev. Lett. **59**, 1958 (1987).
[15] R. A. Klemm, A. Luther, and M. R. Beasley, Phys. Rev. B **12**, 877 (1975).

Electronic structure, charge transfer excitations, and high-temperature superconducting oxides (invited)

A. J. Freeman, Jaejun Yu, S. Massidda, C. L. Fu,[a] and J. -H. Xu[b]
Materials Research Center, Northwestern University, Evanston, Illinois 60208 and Department of Physics and Astronomy, Northwestern University, Evanston, Illinois 60208

We present high-precision results on the electronic band structure and properties of $YBa_2Cu_3O_{7-\delta}$, $YB_2Cu_3O_6$, $GdBa_2Cu_3O_{7-\delta}$, and $La_{2-x}M_xCuO_4$ as obtained from highly precise state-of-the-art local density calculations. The results obtained demonstrate the close relation of the band structure to the structural arrangements of the constituent atoms and provide an integrated chemical and physical picture of the interactions and their possible relation to superconductivity. The ionic character of the Y is proven by similar detailed highly precise local density calculations for high T_C $GdBa_2Cu_3O_7$, and explains the coexistence of magnetism and superconductivity in the high T_C rare-earth superconductors. Surprising features are the low density of states (DOS) at E_F, especially for $\delta>0.1$ which is lower per Cu atom than that in $La_{2-x}Sr_xCuO_4$—in agreement with experiment and a relatively large magnetic Stoner factor. Strong indications are demonstrated for the inadequacy of a conventional phonon mechanism for obtaining the higher T_C. Charge transfer excitations of occupied Cu1 – O $dp\pi$ antibonding orbitals into their empty Cu1-O $dp\sigma$ antibonding orbital partners, result in poorly screened "Cu^{3+}-Cu^{4+}" -like charge fluctuations. These charge transfer excitations (excitons) thus lead to strong polarization effects in these poorly screened (highly ionic) materials and induce attractive interactions among the 2D electrons. Thus, these interactions via exchange of excitons enhance the electron pairing and serve to enhance the T_C proposed for the quasi-2D superconductors.

I. INTRODUCTION

The discovery of the high T_C superconductors $La_{2-x}M_xCuO_4$ (Ref. 1) and $YBa_2Cu_3O_{7-\delta}$ (Ref. 2) has generated excitement among scientists and technologists on an unprecedented scale. It has also led to considerable effort to understand the mechanism giving rise to their superconductivity. One of the starting points is certainly a detailed picture of the electronic structure of the compound, a goal which is achievable by present day supercomputers in combination with highly precise numerical methods to solve the local density (LD) Kohn–Sham equations in a self-consistent way. Even today, the origin of superconductivity in the new metallic oxides remains a challenge despite some intriguing hints obtained from experiment and electronic structure calculations. Still, it is now quite apparent that understanding the electronic structure and properties of the new high T_C superconductors is emerging. This is an important step towards achieving an understanding of the origin of their superconductivity. Detailed high-resolution local density band-structure results have served to demonstrate what has been our major emphasis, namely, the close relation of the physics (band structure) and chemistry (bonds and valences) to the structural arrangements of the constituent atoms, and may provide insight into the basis mechanism of their superconductivity. Results obtained on the systems we have studied—La_2CuO_4, $YBa_2Cu_3O_7$, $YBa_2Cu_3O_6$, and $GdBa_2Cu_3O_7$—indicate a number of common chemical and physical features, especially the role of oxygens (and oxygen vacancies), which bear further scrutiny. In this paper, we provide a brief summary of the results on the detailed electronic structures of the $La_{2-x}M_xCuO_4$ and $LnBa_2Cu_3O_{7-\delta}$ systems, compare them, and point out their relations to charge transfer excitations as a possible mechanism of superconductivity.

II. ELECTRONIC STRUCTURE AND PROPERTIES OF $La_{2-x}M_xCuO_4$

Early on, the results of highly precise all-electron local density full potential linearized augmented plane wave[3] (FLAPW) calculations of the energy band structure, charge densities, Fermi surface, etc., for $La_{2-x}M_xCuO_4$ (M = Sr,Ba)[4] demonstrated: (i) that the material consisted of metallic Cu-O(1) planes separated by insulating (dielectric) La-O(2) planes and (ii) that this 2D character and alternating metal/insulator planes would have, as some of their most important consequences, strongly anisotropic (transport, magnetic, etc.) properties. Thus, the calculated band structure along high symmetry directions in the Brillouin zone shows only flat bands, i.e., almost no dispersion, along the c axis, demonstrating that the interactions between the Cu,O(2), and La atoms are quite weak. However, along the basal plane directions there are very strong interactions between the Cu-O(1) atoms leading to large dispersions and a very wide bandwidth ($\sim$9 eV).

The band structure near E_F has a number of interesting features. What is especially striking is that, in contrast to the complexity of its structure, only a single free-electron-like

[a] Present address: Metals & Ceramics Division, ORNL, P. O. Box X, Oak Ridge, Tennessee 37831.
[b] Present address: Shanghai Institute of Metallurgy, Academy of Sciences of China, Shanghai, 200050 China.

 0021-8979/88/084220-06$02.40 © 1988 American Institute of Physics

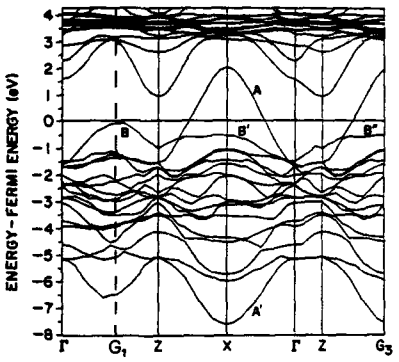


FIG. 1. Band structure of body-centered-tetragonal La_2CuO_4 along symmetry lines in the extended Brillouin zone. (See Ref. 4 for the notations used.)

band crosses E_F (cf., Fig. 1) and gives rise to a simple Fermi surface. Since this band A in Fig. 1 originates from the Cu $d_{x^2-y^2}$ — O(1) $p_{x,y}$ orbitals confined within the Cu-O(1) layer, it exhibits clearly all the characteristics of a two-dimensional electron system. Particularly striking is the occurrence of a van Hove saddle point singularity (SPS). Such an SPS is expected, and found (cf. Fig. 2), to contribute strongly, via a singular feature, to the density of states (DOS). As we shall see, this dominance of the DOS near E_F by the SPS contribution is responsible for many of the striking properties of this material with M_x additions.

The remarkable 2D nature of the electronic structure leads to a simple picture of the conductivity confined essentially to the metallic Cu-O(1) planes separated by insulating (ionic) planes of La-O(2). This picture is strongly confirmed by independent calculations[5] which model $La_{2-x}M_xCuO_4$ as a single slab consisting of a Cu-O(1) layer sandwiched by one La-O(2) layer on each side. (Note that such a slab has the correct stoichiometry and is charge neutral.) The electronic structure near E_F is dominated by the same single band of 2D p-d bounding character; the nesting feature[6] (with zone boundary spanning vector) and the van Hove SPS in the DOS are reproduced with this slab approach.

In the band structure shown in Fig. 1, the strongly dispersed band A along the Γ-X (110) direction has only a Cu $d_{x^2-y^2}$ — O(1) $p_{x,y}$ component, while band B along the Γ-G_1-Z (100) direction, especially at G_1 (i.e., the van Hove SPS point), is a mixture of Cu $d_{x^2-y^2}$ — O(1) $p_{x,y}$ and Cu d_{z^2} — O(2) p_z orbitals. Another notable feature in the band structure of La_2CuO_4 is that the character of the bonding partner (band A') of the antibonding Cu $d_{x^2-y^2}$ — O$p_{x,y}$ band A consists not only of the Cu $d_{x^2-y^2}$ — O$p_{x,y}$ orbitals but has a large contribution from Cu sp orbitals, as also described by others.[7] (Note that these results are significantly different from the two-dimensional tight binding model of Mattheiss,[8] where the antibonding band A and B, as well as the bonding band A, were regarded as having the same Cu $d_{x^2-y^2}$ — O$p_{x,y}$ orbital character.)

The quasi-2D properties of the electronic structure are also supported by plots of the charge densities of electrons at E_F (cf. Fig. 3). This charge density consists mainly of Cu $d_{x^2-y^2}$ and O(1) $p_{x,y}$ hybridized orbitals in the plane with some additional contribution of the Cu d_{z^2} and O(2) p_z components. There is essentially no electron density around the La site at E_F. This means that the La atoms do not contribute directly to the dynamical processes involving electrons near E_F. Further, an analysis of the band structure shows that the $5d$ level of La lies more than 1 eV above E_F; the $5p$ levels of La were found[4] to lie far below E_F ($\sim$15 eV). Thus, it is a fairly good approximation to consider the La atoms to be described in chemical terms as La^{3+} ions.

In view of the results presented above, we would expect—as a first approximation—that the introduction of divalent elements (e.g., M = Ba, Sr, etc.) as substitutional replacements for La would not change any major feature of the band structure, charge density, DOS, etc. Thus, the use of a rigid band approximation to treat the case of alloys, $La_{2-x}M_xCuO_4$, may be considered as a quite good first approximation when x is small ($\lesssim$0.3). (This has been confirmed by independent virtual crystal approximation calcu-

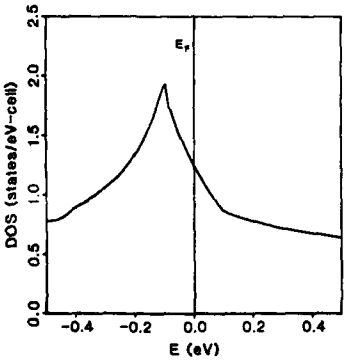


FIG. 2. Blow-up of the density of states near E_F for La_2CuO_4.

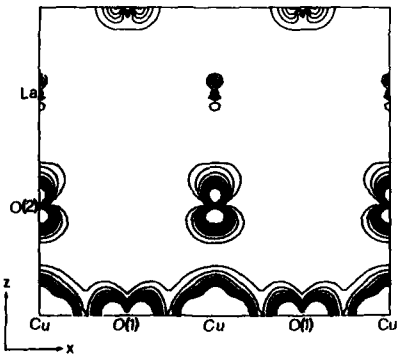


FIG. 3. Contour plot in the xz vertical plane of valence charge density at E_F for La_2CuO_4.

lations.[5]) Hence, in this spirit, the variation of composition x in $La_{2-x}M_xCuO_4$ can be taken into account simply as a change in the position of E_F, that is, $E_F = E_F(x)$. Further, since E_F lies very close to the SPS, $N(E_F)$ is extremely sensitive to the position of E_F relative to the singular point (cf. Fig. 2). As a function of x, $N(E_F)$ varies from 1.2 states/eV cell at $x = 0$ to 1.9 states/eV cell at $x = 0.16$. This large variation in $N(E_F)$ will immediately affect a number of properties such as the magnetic susceptibility, specific heat, etc.

One major effect of the van Hove singularity on the properties of the system is the anomalous behavior of T_C with varying composition x in $La_{2-x}M_xCuO_4$. With increasing x, the superconducting critical temperature T_C increases rapidly from 14 K for $x \simeq 0.05$ to a maximum of 37 K for $x \simeq 0.2$ but then drops sharply for larger x values. Under the condition that the pairing potential V, in the pairing interaction parameter $\lambda = N(E_F)V$, is constant, the change in T_C with the composition x is associated with a change of $N(E_F)$. In fact, recent reports[9] show a large variation of T_C vs x which rises sharply from 0 K at $x < 0.03$ to 22 K at $x = 0.08$, hits a maximum at $x \simeq 0.15$ and then drops off sharply. These results are very consistent with our picture. Thus, it is clear that the strong variation in $N(E_F)$, derived from the quasi-2D van Hove singularity, plays a dominant role in the anomalous behavior of T_C as a function of x.

In total energy frozen phonon calculations[5] on $La_{2-x}M_xCuO_4$, the role and effect of the optical breathing mode turned out to be significant. Since the breathing phonon mode involves the motion of oxygen atoms against the directional bonding of Cu d-O p in the plane, the in-plane Cu $d_{x^2-y^2}$-O(1) $p_{x,y}$ states of the 2D conduction bands are strongly affected by the breathing displacement. On the other hand, the out-of-plane Cu d_{z^2}-O(2) p_z orbitals, which are quite localized in the plane, are not much affected by the same breathing mode. But, because of the relative change of the Cu $d_{x^2-y^2}$-O(1) $p_{x,y}$ and Cu d_{z^2}-O(2) p_z, the charge fluctuations between Cu atoms, which can be as large as 0.3 electrons at the maximum of the O displacement, lead to transitions of the out-of-plane Cu d_{z^2}-O(2) p_z into the in-plane Cu $d_{x^2-y^2}$-O(1) $p_{x,y}$. Since the out-of-plane (antibonding) Cu d_{z^2}-O(2) p_z states near E_F are localized, we expect that the localized Cu d_{z^2}-O(2) p_z states, introduced by the charge fluctuation, may couple to the delocalized conduction electrons of the in-plane Cu $d_{x^2-y^2}$-O(1) $p_{x,y}$ orbital and possibly to form an excitonic state.[5] Thus, a key role in possible charge transfer excitations (CTE) is played by excitations between occupied localized Cu d_{z^2}-O(2) p_z and empty itinerant Cu $d_{x^2-y^2}$-O(1) $p_{x,y}$ states. We emphasized that these could couple resonantly with natural "Cu^{2+}-Cu^{3+}-like" charge fluctuations which exist in the $x > 0$ compounds, with important consequences for the superconductivity.

III. ELECTRONIC STRUCTURE AND PROPERTIES OF $YBa_2Cu_3O_7$

For the 90 K superconductor $YBa_2Cu_3O_{7-\delta}$, discovered by Chu *et al.*, we presented[10,11] detailed high-resolution results on the electronic band structure and density of states derived properties as obtained from the same highly precise state-of-the-art local density approach. These results demonstrated the close relation of the band structure to the structural arrangements of the constituent atoms and have helped to provide an integrated chemical and physical picture of the interactions.

The important structural features of the $YBa_2Cu_3O_{7-\delta}$ compounds arise from the fact that $(2+\delta)$ oxygen atoms are missing from the perfect triple perovskite, $YCuO_3(BaCuO_3)_2$. These vacancies arise from a total absence of O atoms in the Y-O planes (which seems to separate the Cu-Cu interactions across the Y plane) and an absence of O atoms in the Cu planes between the Ba-O planes (which leads to the formation of linear chains of Cu-O-Cu). As a result, there are two Cu ions (called Cu2) in five-coordinated positions, as shown in Fig. 4. Since the interatomic distance Cu2-O4 (2.303 Å) is much larger than Cu1-O4 (1.850 Å),[12] the Cu1 ions have a rather weak interaction with the Cu2 ions. The Cu2 ions are in the locally very strong tetragonal distortion and this yields a 2D structure for these planes similar to that of $La_{2-x}M_xCuO_4$. The additional distortions of the O2 and O3 ions (the so-called "dimpling") arises from the absence of O ions in the adjacent Y-O plane. From the contour plots of the valence charge density of $YBa_2Cu_3O_7$ on two vertical planes cutting the Cu-O bonds, it is apparent that there is an overall two-dimensionality to this system; the three horizontal Cu planes of the unit cell form, in fact, separated entities which do not interact with the neighboring entities along the c axis.

The calculated valence-band structure of stoichiometric $YBa_2Cu_3O_7$ along high symmetry directions in the bottom ($k_z = 0$) plane of the orthorhombic BZ is shown in Fig. 5. The very close similarity in the band structure for the $k_z = 0$ and $k_z = \pi/c$ planes[10] indicates the highly 2D nature of the band structure.

It is seen from Fig. 5, that as in the case of La_2CuO_4, a remarkably simple band structure near E_F emerges from this

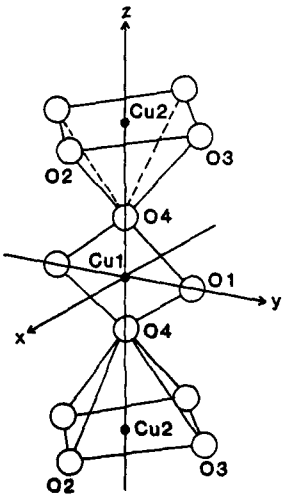


FIG. 4. A local environment for the Cu1 and Cu2 atoms in $YBa_2Cu_3O_7$, following the Y-Cu2-Ba-Cu1-Ba-Cu2-Y ordering along z.

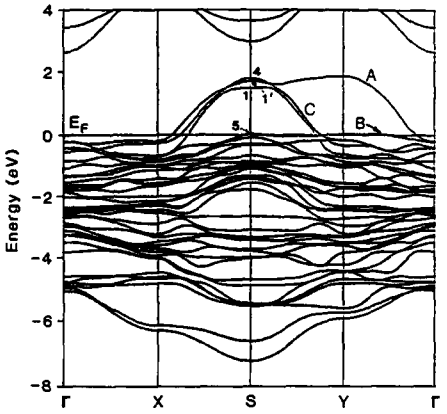


FIG. 5. Band structure of $YBa_2Cu_3O_7$ along symmetry directions in the $k_z = 0$ plane of the orthorhombic Brillouin zone.

complex set of 36 bands (originating from three Cu ($3d$) and seven O($2p$) atoms]. Four bands—two each consisting of Cu2($3d$)-O2(p)-O3(p) orbitals and Cu1(d)-O1(p)-O4(p) orbitals—cross E_F. Two strongly dispersed bands C (S_1' and S_4 in Fig. 5; the labelling is given by their character at S) consist of Cu2($d_{x^2-y^2}$)-O2(p_x)-O3(p_y) combinations and have the 2D character which proved so important for the properties of $La_{2-x}M_xCuO_4$. The symmetry allowed interactions of the Cu2 bands with the Cu1 band result in a complicated dispersion for the Cu2 bands (as occupied bands) along Γ-X and Γ-Y. Note that the S_1 and S_1' states have the same symmetry and so can interact (anticrossing) and disperse along the S-Y direction. Significantly, the Cu1($d_{x^2-y^2}$)-O1(p_y)-O4(p_z) antibonding band A (S_1 in Fig. 5) shows the (large) 1D dispersion expected from the Cu1-O1-Cu1 linear chains but is almost entirely unoccupied. This band is in sharp contrast to the π-bonding band B [formed from the Cu1(d_{xy})-O1(p_z)-O4(p_y) orbitals] which is almost entirely occupied in the stoichiometric ($\delta = 0$) compound and becomes fully occupied for the superconducting materials ($\delta > 0.1$). We will soon see that since this almost flat π-bonding band B (the states S_5 in Fig. 5) lies just below and crosses E_F (for $\delta = 0$) along S-Y, it gives rise to peaks in the DOS near E_F making the DOS at E_F sensitive to the position of E_F (i.e., to δ).

In our calculation for $\delta = 0$, the DOS at E_F, $N(E_F)$, is 1.13 states/eV Cu atom, which is comparable to the 1.2 and 1.9 states/eV Cu atom found earlier for $La_{2-x}M_xCuO_4$ at $x = 0$ and at the peak at $x = 0.16$, respectively. For increasing δ values (hence increasing E_F), $N(E_F)$ decreases sharply. Thus, for $\delta = 0.1$, $N(E_F) = 0.87$ states/eV Cu atom while, for $\delta = 0.2$, $N(E_F) = 0.52$ states/eV Cu atom (after which the DOS remains roughly constant). This means that the $N(E_F)$ per Cu atom values in the high T_C superconductor, $YBa_2Cu_3O_{7-\delta}$, are significantly lower than was found earlier (either experimentally or theoretically) for the (lower) high T_C superconductor, $La_{2-x}M_xCuO_4$. This result—which agrees with the conclusion of a recent experiment[13]—has a number of important possible consequences for DOS derived properties and superconductivity, including reduced screening, an increased role for the polarization of ionic constituents, lowered conductivity (and reduced superconducting current carrying capacity), etc.

IV. THE ROLE OF OXYGEN VACANCIES: $YBa_2Cu_3O_7$ vs $YBa_2Cu_3O_6$

Recently, several neutron experiments[14] showed that the oxygen vacancies concentrate on the O1 sites and change the composition and symmetry from orthorhombic (in $YBa_2Cu_3O_7$) to tetragonal (in $YBa_2Cu_3O_6$). The absence of oxygens on the O1 site destroys the 1D chain structure in the $YBa_2Cu_3O_6$. The additional oxygen vacancies, therefore, change the local symmetry as well as the electronic configuration around the Cu1 sites. In this geometry, each Cu1 ion would be completely isolated from the other Cu1 ions in the Cu1 plane (having no oxygens lying between the Cu1's) and remain as Cu^+ ions with a completely filled d shell. Hence, the d-orbital states of Cu1 are expected to be very localized in the Cu1 plane. One notable consequence of the change of structure is that the Cu1-O4 distance in $YBa_2Cu_3O_6$ is even shorter than in $YBa_2Cu_3O_7$.

To examine these expectations and to provide insight into the possible role[11] of the CTE in the 1D chains of $YBa_2Cu_3O_{7-\delta}$, we compare the results of calculations[15] for both $YBa_2Cu_3O_7$ and $YBa_2Cu_3O_6$, focussing on the roie of chains versus planes. The calculated band structure (near E_F) of tetragonal $YBa_2Cu_3O_6$ and orthorhombic $YBa_2Cu_3O_7$ both exhibit two strongly dispersed 2D bands crossing E_F consisting of Cu2($d_{x^2-y^2}$)-O2(p_x)-O3(p_y) orbitals in the 2D Cu2-O planes. However, the dominant 1D electronic structure, arising from the linear chains in $YBa_2Cu_3O_{7-\delta}$, is completely absent in $YBa_2Cu_3O_6$. Instead of the 1D structure of $dp\sigma$ and $dp\pi$ states from the Cu1-O1-O4 chains, the O_6 compound has two bands consisting of Cu1 $d_{yz}(d_{zx})$-O4$p_y(p_x)$ orbitals and are degenerate at the points Γ and M in the BZ.

In addition to the two conduction bands crossing E_F, there is a very small contribution to $N(E_F)$ from the Cu1 complex in the linear chains; therefore, the DOS at E_F of $YBa_2Cu_3O_6$ is reduced to 0.67 states/eV Cu atom, which is smaller than that of $YBa_2Cu_3O_7$. In addition to the reduction of $N(E_F)$, there is a strong hybridization of the Cu2-O2(3) $dp\sigma$ bands and the Cu1-O4 $dp\pi$ bands along the ΓM direction.

V. STONER FACTORS AND MAGNETISM IN Y AND Gd TRANSITION-METAL OXIDES

In considering magnetic properties, we calculated[11] the Stoner factors for both $YBa_2Cy_3O_6$ and $YBa_2Cu_3O_7$. We found a surprisingly large Stoner factor. $S = N(E_F)I$, $S = 1.12$, for $YBa_2Cu_3O_{7-\delta}$ at $\delta = 0$ (indicating a possible magnetic instability), with the largest contribution to S coming from the O1 and O4. As δ becomes greater than 0.1, the Fermi level E_F increases and moves above the flat $dp\pi$ band formed mostly by the 01, 04, and Cu1 orbitals, and S drops sharply to 0.86 for $\delta = 0.1$ and 0.52 for $\delta = 0.2$. In contrast, the Stoner factor for $YBa_2Cu_3O_6$, $S = 1.38$, is even

larger. Further, the dominant contribution to S comes from the 2D layers of Cu2 and O2(3) where the 2D conduction bands originate. This suggests a possible magnetic ordering in the 2D Cu2-O2(3) conducting layer, as a result of localization of the Cu2-O2(3) hybridized states within each 2D layer due to the isolation of Cu1 ions, which may relate to its observed semiconductivity. These results appear to be consistent with the recent susceptibility experiments[16] on both orthorhombic $YBa_2Cu_3O_{7-\delta}$ and tetragonal $YBa_2Cu_3O_6$. In the experiment, $YBa_2Cu_3O_{7-\delta}$ shows Pauli susceptibility, but $YBa_2Cu_3O_6$ shows a Curie–Weiss behavior.

Charge density calculations[10,11] reflect the structural properties of the material. Charge density plots for the individual states near E_F demonstrate the 2D nature of Cu2-O2-O3 $dp\sigma$ bands and the 1D nature of the Cu1-O1-O4 $dp\sigma$ bands. The ionic Y (or R = rare earth) atoms act as electron donors and do not otherwise participate. Also, the partial DOS at E_F for Y give extremely low values for the conduction electrons (the same is true for Gd). These results give an immediate explanation for the observed[17] coexistence of the high T_C superconductivity and magnetic ordering in the $RBa_2Cu_3O_{7-\delta}$ structures. The lack of conduction electron density around the R site[18] means that the unpaired rare-earth f electrons are decoupled from the Cooper pairs (i.e., magnetic isolation) and so cannot pair break.

VI. EXCITONIC MECHANISM OF SUPERCONDUCTIVITY

We have made crude estimates[11] of the electron-phonon interaction in $YBa_2Cu_3O_{7-\delta}$, using the rigid muffin-tin approximation (RMTA) to calculate the McMillan–Hopfield constant η and the electron-phonon coupling constant λ. Surprisingly, by far the largest contribution to η comes from the O1 atoms, again indicating the important role played by the "metallized" oxygens. We find that the calculated T_C, even for the assumed Debye temperature $\theta_D = 100$ K, cannot exceed the value of ~ 32 K—a similar limit found previously in $La_{2-x}M_xCuO_4$.[19] Despite the crudeness of the RMTA approach, it is expected that this estimate cannot be so far off (i.e., a factor of 3) and so casts doubt on a purely electron-phonon explanation of the observed high T_C.

Many authors have discussed the excitonic mechanism[20] of superconductivity, in which the effective attractive interaction between conduction electrons originates from virtual excitations of excitons rather than phonons. The basic idea of the models proposed is that conduction electrons residing on the conducting filament (or plane) induce electronic transitions on nearby easily polarizable molecules (or complexes), which result in an effective attractive interaction between conduction electrons. As perhaps a striking realization of the excitonic mechanism of superconductivity, $YBa_2Cu_3O_{7-\delta}$ has two 2D conduction bands and additional highly polarizable 1D electronic structure between the two conduction planes.

We previously discussed[11] the importance of the 1D feature in the electronic structure near E_F, pointing out the possible role played by charge transfer excitations ("exitons") of occupied (localized) Cu1-O $dp\pi$ orbitals into their empty (itinerant) Cu1-O $dp\sigma$ antibonding partners. As shown schematically in Fig. 6, we can characterize the 1D

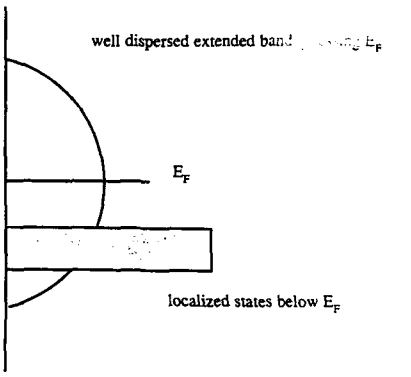


FIG. 6. Schematic drawing of the 1D electronic structure of $YBa_2Cu_3O_7$.

electronic structure with two types of electronic states in it, one free-electron-like (the well-dispersed $dp\sigma$ band) and the other localized (the almost flat $dp\pi$ state). When the localized hole is created (effectively a "Cu^{+4} complex") due to the excitation, a strong attractive correlation between the hole and excited electron may lead to an electron-hole bound state ("exciton"). Hence, this excitation of the localized $dp\pi$ to the extended $dp\sigma$ with the electron-hole correlation in the 1D electronic structure will give rise to a strong polarization in the 1D chains between two conduction planes and couple to the 2D conduction electrons, which carry most of the superconductivity.

We can draw an analogy between the electronic structures near E_F of La_2CuO_4 and $YBa_2Cu_3O_7$; we find the electronic structure of a well-dispersed $d_{x^2-y^2}$-$p_{x,y}$ band and a fairly localized d_{z^2}-p_z state in the 2D Cu plane of La_2CuO_4 corresponding to that of a strongly dispersed Cu1-O1-O4 $dp\sigma$ band and a localized Cu1-O1-O4 $dp\pi$ state in the 1D chain of $YBa_2Cu_3O_7$. In fact, the 2D $dp\sigma$ conduction bands in the Cu2 plane of $YBa_2Cu_3O_7$ are well separated at E_F from 1D bands, while the 2D conduction bands of the $d_{x^2-y^2}$-$p_{x,y}$ orbitals in La_2CuO_4 show a hybridization with the localized d_{z^2}-p_z orbitals along the (100) direction.

For $La_{2-x}M_xCuO_4$, we discussed the importance of "Cu^{2+}-Cu^{3+}-like" charge fluctuations in connection with the possible role played by charge transfer excitations (CTE) in superconductivity. Concerning the superconductivity in $YBa_2Cu_3O_7$, it is expected that the Cu1-O1-O4 chain can play a critical role. A simple rigid band treatment of the band results[11] suggests that the Cu1(d_{xy})-O1(p_z)-O4(p_y) ($dp\pi$ antibonding) band becomes fully occupied for $\delta \geq 0.1$. Hence, excitations to its (almost) empty Cu1 ($d_{z^2-y^2}$)-O1(p_y)-O4(p_z) ($dp\sigma$ antibonding) partner band can create strong polarization fields because the $dp\pi$ state is highly localized spatially whereas the $dp\sigma$ state is fairly itinerant along Cu1-O1 chains. As a result of the difference in the bonding character of the $dp\pi$ and $dp\sigma$ states, a "local" charge transfer excitation (CTE) from the $dp\pi$ state to $dp\sigma$ state may lead to significant electronic polarization. Incorporating the interactions between

the 2D Cu *d*-O*p* conduction electrons and the charge transfer excitations (excitons), could produce the pairing interactions, via an exchange of excitons, which would enhance the T_C.

Finally, we should note that while we discussed the CTE based upon the excitations of occupied *localized* $dp\pi$ states into the empty *itinerant* $dp\sigma$ antibonding band, Varma *et al.*[21] proposed a charge transfer resonance mechanism by considering excitations of the bonding Cu $d_{x^2-y^2}$-p_x-p_y $dp\sigma$ state (β) and into its antibonding (conduction) $dp\sigma$ band (α) partner. Starting from the particle-hole excitation $\beta \rightarrow \alpha$, they argued that a sharp excitonic resonance from the $\alpha\beta$ transitions can happen if the $\alpha\beta$ particle holes have Coulomb attractions strong enough to cancel the $\alpha\beta$ interband transition gap, which is more than 6 eV.[10] However, it appears unreasonable to neglect the presence of the $dp\pi$ orbital states which lie near E_F, and hence $dp\pi \rightarrow dp\sigma$ particle-hole excitation must be included in the CTE model. Similarly, in the case of $La_{2-x}Sr_xCuO_4$, we again note than similarly the "Cu^{2+}-Cu^{3+}-like" resonant charge fluctuations induced by the optic breathing mode were shown[5] to lead to transitions between the in-plane $d_{x^2-y^2}$ orbitals and localized out-of-plane d_{z^2} orbital states located just below E_F to the itinerant in-plane $d_{x^2-y^2}$ orbitals. Finally, the special role of O-*p* electrons involved in the photoemission process (which may relate to the excitonic mechanism) has been discussed in detail for both the $La_{2-x}M_xCuO_4$ (Ref. 22) and $YBa_2Cu_3O_{7-\delta}$ (Ref. 23) cases.

ACKNOWLEDGMENTS

Work supported by NSF (through the Northwestern University Materials Research Center, Grant No. DMR85-20280). We are grateful to NASA Ames personnel in the NAS program for help with the use of their Cray 2. We thank our collaborators, D. D. Koelling and J. R. Anderson.

[1] J. G. Bednorz and K. A. Müller, Z. Phys. B **64**, 189 (1986).
[2] M. K. Wu, J. R. Ashburn, C. J. Torng, P. H. Hor, R. L. Meng, L. Gao, Z. J. Huang, Y. Q. Wang, and C. W. Chu, Phys. Rev. Lett. **58**, 908 (1987).
[3] H. J. F. Jansen and A. J. Freeman, Phys. Rev. B **30**, 561 (1984); E. Wimmer *et al.*, Phys. Rev. B **24**, 864 (1981).
[4] J. Yu, A. J. Freeman, and J. -H. Xu, Phys. Rev. Lett. **58**, 1035 (1987); A. J. Freeman, J. Yu, and C. L. Fu, Phys. Rev. B **36**, 7111 (1987).
[5] C. L. Fu and A. J. Freeman, Phys. Rev. B **35**, 8861 (1987).
[6] J. -H. Xu, T. J. Watson-Yang, J. Yu, and A. J. Freeman, Phys. Lett. A **120**, 489 (1987).
[7] K. Takegahara, H. Harima, and A. Yanase, Jpn. J. Appl. Phys. **26**, L352 (1987); T. Oguchi, Jpn. J. Appl. Phys. **26**, L417 (1987).
[8] L. F. Mattheiss, Phys. Rev. Lett. **58**, 1028 (1987).
[9] S. Kanbe, K. Kishio, K. Kitazawa, K. Fueki, H. Takagi, and S. Tanaka, Chem. Lett., 547 (1987); R. B. van Dover, R. J. Cava, B. Batlogg, and E. A. Rietman, Phys. Rev. B **35**, 5337 (1987).
[10] S. Massidda, J. Yu, A. J. Freeman, and D. D. Koelling, Phys. Lett. **122**, 198 (1987).
[11] J. Yu, S. Massidda, A. J. Freeman, and D. D. Koelling, Phys. Lett. **122**, 203 (1987).
[12] M. A. Beno, L. Soderholm, D. W. Capone, II, D. G. Hinks, J. D. Jorgensen, J. D. Grace, I. K. Schuller, C. U. Segre, and K. Zhang, Appl. Phys. Lett. **51**, 57 (1987).
[13] R. J. Cava, B. Batlogg, R. B. van Dover, D. W. Murphy, S. Sunshine, T. Siegrist, J. P. Remeika, E. A. Rietman, S. Zahurack, and G. P. Espinosa, Phys. Rev. Lett. **58**, 1676 (1987); D. G. Hinks, G. Soderholm, D. W. Capone, II, J. D. Jorgensen, I. K. Schuller, C. U. Segre, K. Zhang, and J. D. Grace, Appl. Phys. Lett. **50**, 1688 (1987).
[14] A. Santoro, S. Miraglia, F. Beech, S. A. Sunshine, D. W. Murphy, L. F. Schneemeyer and J. V. Waszczak, Mater. Res. Bull. **22**, 1007 (1987); J. D. Jorgensen, B. W. Veal, W. K. Kwok, G. W. Crabtree, A. Umezawa, L. J. Nowicki, and A. P. Paulikas, (unpublished); I. K. Schuller, D. G. Hinks, M. A. Beno, D. W. Capone, II, L. Soderholm, J. -P. Locquet, Y. Bruynseraede, C. U. Segre, and K. Zhang, Solid State Commun. **63**, 385 (1987).
[15] J. Yu and A. J. Freeman (to be published).
[16] M. Ishikawa, T. Takabatake, and Y. Nakazawa (unpublished).
[17] J. O. Willis, Z. Fisk, J. D. Thompson, S. -W. Cheong, R. M. Aikin, J. L. Smith, and E. Zirngiebl, J. Magn. Magn. Mater **67**, L139 (1987).
[18] J. Yu and A. J. Freeman (to be published).
[19] J. Yu and A. J. Freeman (unpublished); W. E. Pickett, H. Krakauer, D. A. Papaconstantopoulos, and L. L. Boyer, Phys. Rev. B **35**, 7252 (1987).
[20] W. A. Little, Phys. Rev. **134**, A1416 (1964); V. L. Ginzburg, Sov. Phys. JETP **46**, 397 (1964).
[21] C. M. Varma, A. Schmitt-Rink, and E. Abrahams, Solid State Commun. **62**, 681 (1987).
[22] J. Redinger, J. Yu, A. J. Freeman, and P. Weinberger, Phys. Lett. A **124**, 463 (1987).
[23] J. Redinger, A. J. Freeman, J. Yu, and S. Massidda, Phys. Lett. A **124**, 469 (1987).

One-dimensional Hubbard model with first- and second-neighbor hopping

T. A. Kaplan
Department of Physics and Astronomy and Center for Fundamental Materials Research, Michigan State University, East Lansing, Michigan 48824

The one-dimensional Hubbard model with first- and second-neighbor hopping, t_1 and t_2, with $t_2 \approx t_1/\sqrt{2}$ and large repulsion U, is proposed as a testing ground of Anderson's idea that the existence of an resonating valence bond ground state in the half-filled-band case will show superconductivity when a finite concentration of holes is introduced. Interestingly, our preliminary calculations in the $U=\infty$ limit for small chains have revealed a *new* mechanism for enhancement of singlet pairing: We find that for $t_2<0$ the ground state is a singlet, and, for $t_2<0$ and $|t_2/t_1| \ll 1$, the nearest-neighbor extended-singlet-pairing correlation function becomes enhanced appreciably as the temperature decreases below t_2.

Anderson has recently proposed[1] a novel and attractive mechanism for high-T_c superconductivity based on the idea of resonating valence bond (RVB) states.[2] See also Refs. 3 and 4. We argue here that this RVB state is somewhat ill defined, we note that a definition which was probably intended and which is in accord with that of a number of other authors[5,6] does not apply to the two lattices thought to be pertinent to the recently discovered high-T_c superconductors, and we point out that there is a model to which the RVB idea does apply. The latter is the one-dimensional Hubbard model with first- and second-neighbor hopping, t_1 and t_2, with $t_2 \approx t_1/\sqrt{2}$ and large repulsion U. In the course of the first step in an investigation of this model, namely, a study of the *infinite-U* case, we have found an entirely *different* mechanism for singlet-pairing enhancement, which occurs for a possibly realistic situation; these results will be described.

Early papers which discuss valence bond (VB) states and their linear combinations[7-9] argue that a certain class of VB states (noncrossing Lewis diagrams) are independent and their number equals the number of singlets for the number of (spin-$\frac{1}{2}$) particles being considered; i.e., these VB states span the space of singlets. (By a singlet I mean a state with $S^2=0$, where S is the total spin.) Anderson[1] seems to define an RVB state as any state with such an expansion, but ascribes special physical properties to such states: they are liquidlike[1,2] and there is no long-range order.[10] However, one can show that a singlet state can have long-range order (LRO), as can readily be seen[11] in the ground state of a model of Lieb and Mattis.[12] That state is a singlet (for the antiferromagnetic case) and the correlation function $\langle \mathbf{S}_i \cdot \mathbf{S}_j \rangle$ for spins at sites i and j is *identical*,[11] in the thermodynamic limit, to that of the famous antiferromagnetic Neel state where the spins on one sublattice are described by the "up"-state α, the rest by β. In fact, singlet ground states can have widely varying properites such as the following, for example: a Neel-type antiferromagnet, as above; a Heisenberg AF with LRO but large zero-point fluctuations, as expected for the square lattice with nearest-neighbor (NN) interactions[13]; the NN-interaction AF spin-$\frac{1}{2}$ Heisenberg chain with its quasi long-range order[14]; the simple Fermi sea, which is liquidlike. Hence, to attach any special physics to a general expansion in singlet states, one must limit that expansion in some way. Following Oguchi[5] and Sutherland,[6] as well as Anderson's physical requirements,[1,2] I will assume that an RVB state has in its expansion, states with only short-range bonds. But then it cannot represent the above Heisenberg chain with its quasi-LRO, nor, probably, the ground state of the same model for the square lattice with its LRO.

As Majumdar has shown,[15] the spin-$\frac{1}{2}$ Heisenberg chain with the ratio of second- to first-neighbor interactions $J_2/J_1=\frac{1}{2}$, both being antiferromagnetic, has as its ground state *precisely* such a short-range bond VB or RVB state. Namely, $\cdots[12][34][56]\cdots$, where $[ij]$ is the familiar two-particle singlet. (The RVB state is a linear combination of this VB state with its degenerate counterpart $\cdots[23][45]\cdots$.) And in view of the recent calculations of Tonegawa and Harada,[16] the bonds probably remain short ranged for J_2/J_1 near $\frac{1}{2}$. Since the half-filled-band Hubbard model with large repulsion U and parameters t_{ij} for hopping between sites i and j corresponds to a Heisenberg model with exchange parameters $J_{ij}=2t_{ij}^2/U$, we see that the Majumdar condition is established when $t_2=t_1/\sqrt{2}$. Thus, the notion[1-4] that when some electrons are removed from the $\frac{1}{2}$-filled band, these singlet pairs would tend to move as units, giving rise to superconductivity, could be tested within this Hubbard model. Of course, this is one-dimensional, so no phase transition could occur at nonzero temperature T; however, one could see if pairing fluctuations or correlations were enhanced by the existence of the VB pairs.

The Hamiltonian of interest is then

$$H = t_1 \sum a_{i,\sigma}^{\dagger} a_{i+1,\sigma} + t_2 \sum a_{i\sigma}^{\dagger} a_{i+2,\sigma} + \text{h.c.} + U \sum n_{i\uparrow} n_{i\downarrow}. \quad (1)$$

Here $a_{i,\sigma}$ destroys an electron at site i with spin σ, and $n_{i,\sigma}=a_{i,\sigma}^{\dagger}a_{i,\sigma}$. Let N,N_S be the number of electrons and number of sites, respectively. We are interested in perturbation theory when $U \gg |t_1|,|t_2|$. As is known, a convenient approach is through an effective Hamiltonian—see, e.g., Refs. 17–19. I will follow Hirsch's notation fairly closely. I consid-

 0021-8979/88/084226-03$02.40 © 1988 American Institute of Physics

er $N/N_S \ll 1$. The effective Hamiltonian is

$$H_{\text{eff}} = P\left(t_1 \sum a^\dagger_{i,\sigma} a_{i+1,\sigma} + t_2 \sum a^\dagger_{i,\sigma} a_{i+2,\sigma}\right) P + \text{h.c.} + O(t_i t_j/U), \quad (2)$$

where P is the projection on to the unperturbed states, i.e., the states with no doubly occupied sites.[20] The terms of $O(t_1^2/U)$ were written by Hirsch[19]; they contain the exchange terms plus second-neighbor hopping terms, with and without spin flip. There are similar terms for t_2^2/U, with fourth-neighbor replacing second-neighbor hopping; also first- and third-neighbor hopping terms $\propto t_1 t_2/U$.

Clearly, the first question that must be addressed is "what are the eigenstates of H_{eff} when $U = \infty$?" In other words, what are the eigenstates of just the sum of the first two hopping terms in Eq. (2)? For the case $t_2 = 0$, thermodynamic quantities[21,22] as well as energy eigenvalues and eigenstates[22] are known. I give a somewhat different formulation of the latter. Define the N-fermion states

$$|j_1\sigma_1, j_2\sigma_2, \ldots, j_N\sigma_N\rangle = a^\dagger_{j_1\sigma_1} a^\dagger_{j_2\sigma_2} \cdots a^\dagger_{j_N\sigma_N}|0\rangle, \quad (3)$$

where $|0\rangle$ is the vacuum. Call the first term in Eq. (2) $t_1 h_1$. And consider *chains* first (open ends). Choosing basis states as in (3) but with a fixed ordering of the j's, for example, $j_1 < j_2 < \cdots < j_N$ (for uniqueness of the signs of the basis states), it is clear that because of the projection operator, the order of the σ's along the chain can not be changed by application of h_1. That is, there is no matrix element of h_1 between basis states with different spin configurations, $\{\sigma_1, \sigma_2, \ldots, \sigma_N\} = \{\sigma\}$. Furthermore, the submatrix of h_1 for a given $\{\sigma\}$ is clearly *independent of* $\{\sigma\}$: The matrix elements are either 0 or 1, and they depend only on the sets of *positions* $\{j_1, \ldots\}$ and $\{j_1', \ldots\}$ in the initial and final states. It follows that each energy eigenvalue has (at least) the total spin degeneracy 2^N. Also, the solution for the case of equal spins is just that of the noninteracting spinless fermion problem. Since the energies for a *chain* of such fermions are nondegenerate, we see that the degeneracy of each level is 2^N. Writing the l th eigenstate of the spinless fermion problem as

$$\sum C_l(j_1, j_2, \ldots)|j_1, j_2, \ldots\rangle,$$

in an obvious notation, we see that the eigenstates of our $t_2 = 0$, $U = \infty$ problem can be written

$$\psi_l(\sigma_1, \sigma_2, \ldots, \sigma_N) = \sum_{j_1 < j_2 < \cdots} C_l(j_1, j_2, \ldots)|j_1\sigma_1, j_2\sigma_2, \ldots\rangle. \quad (4)$$

Of course the $C_l(j_1, j_2, \ldots)$ are just Slater determinants of the one-particle eigenfunctions evaluated at the positions $j_1, \ldots$.

For *rings*, the above argument does not hold, since the spin configuration can be changed (e.g., by hopping a particle from site N_S to site 1, in which case there is also a sign change for even N). The implied removal of the spin degeneracy can be checked easily for two electrons and three sites.[23,24] It is also clear that introduction of the second-neighbor hopping $t_2 h_2$ can change the spin configuration, so this is expected to remove the spin degeneracy. To get rid of the spurious, boundary-condition-dependent splitting caused by periodic boundary conditions, I decided to work with chains in studies of finite systems.

TABLE I. Energies, expectation values of the square of the angular momentum, and the $r = 1$ singlet and triplet propagators for the eight lowest eigenstates of H. $t_1 = -1$, $t_2 = -0.1$, number of electrons $= 4$, number of sites $= 7$.

Energy	S^2	Singlet propagator	Triplet propagator
−4.1801	0.0000	0.2362	0.0180
−4.1189	2.0000	0.1722	0.0863
−4.0505	2.0000	0.1013	0.0895
−4.0179	0.0000	0.0680	0.0697
−3.9839	2.0000	0.0312	0.0925
−3.9550	6.0000	0.0000	0.1814
−3.3605	0.0000	0.1314	0.0065
−3.3300	2.0000	0.1015	0.0362

Using binary arithmetic to represent and manipulate the states (3) plus a diagonalization routine,[25] I diagonalized the $U = \infty$ effective Hamiltonian for small systems. I considered the cases $N = 2$, $N_S = 3,4,\ldots,10$, and $N = 4$, $N_S = 5,6,7$. Use was made of only S_z as a good quantum number. The largest matrix handled was 210×210, which occurred for the case $N, N_S = 4,7$. Results for this case, with $t_1 = -1$, $t_2 = -0.1$, are given as an example, in Table I, where various properties of the lowest eight energy eigenstates with $S_z = 0$ are shown. There are six $S_z = 0$ spin states for four electrons; among these the eigenstates of S^2 must include two singlets, three triplets, and one quintet. The latter are seen among the six lowest states, which are split by about 5% of the central value; also these are rather close compared to the jump in going from state 6 to 7—quite reasonable from our discussion and considering the value of t_2/t_1. The ground state is seen to be a singlet. I found for all cases considered that the ground state is a singlet for $t_2 < 0$, while for $t_2 > 0$, the state of highest multiplicity is lowest.

Also shown in Table I are the singlet and triplet propagators, defined as follows, using a notation similar to Hirsch.[19] Let

$$P_0(r) = 1/(N_S - r - 1) \sum_i \langle 0_i^\dagger 0_{i+r}\rangle \quad (5)$$

be the propagator as a function of r corresponding to the pair destruction operators

$$0_i = a_{i\uparrow} a_{i+1\downarrow} - a_{i\downarrow} a_{i+1\uparrow} \quad \text{(SP)},$$
$$0_i = a_{i\uparrow} a_{i+1\downarrow} + a_{i\downarrow} a_{i+1\uparrow} \quad \text{(TP)}, \quad (6)$$

for singlet pairing (SP) and triplet pairing (TP). $\langle\ \rangle$ denotes the average in a given eigenstate. These are quite similar to the extended singlet and triplet pairing correlation functions defined by Hirsch,[19] the closer analogy being the thermal average, which is discussed below. So far I have only calculated $P_0(1) = P_0$, and this is shown in the table. The maximum propagator is the ground-state value of P_{SP}. The most interesting aspect of these results is the fact that the values of P_{SP} in the ground state is appreciably larger than the average of the P_{SP} values over the six low-lying states,

$(P_{SP})_{av}$. This is measured by the factor

$$f = (P_{SP})_0/(P_{SP})_{av}, \tag{7}$$

where $(P_{SP})_0$ is the ground-state value. The results in the table give $f = 3.3$ [the multiplicities $2S+1$ must be included in calculating $(P_{SP})_{av}$]. It changes by very little as N_S goes from 5 to 7, or when t_2 decreases (even to the limit 0), for $N = 4$. The interesting implication is that the thermal average $(P_{SP})_T$ at temperature T will increase by about the factor f as decreases from a value higher than the splitting of the low-lying levels ($O(t_2)$) to a much lower value. But rough ball-park values are $|t_1| \approx 1$ eV, and $t_2 \approx 0.1$–$0.1t_1$, which might put the temperatures at which the model is producing "action," i.e., appreciable enhancement of the singlet pairing correlations, in the range of the high T_c's recently observed (≈ 100 K). Further, linear chains of Cu and O exist in these materials and seem to be fundamental to the high T_c's found.[26,27]

Clearly further studies of this model are warranted. The most immediate directions are to get results for larger N and N_S, find the pairing propagators for larger r and the more general functions of three distances (still with four field operators), and to calculate the thermal averages indicated. Also the spin-spin and charge-charge correlations need to be calculated. These are in progress.

An interesting theoretical approach is the next level of perturbation theory, still within the $U = \infty$ model, considering t_2/t_1 as small, so the $t_2 = 0$ eigenfunctions (4) are the unperturbed eigenstates.[28] Again, we have a degenerate perturbation theory, the degeneracy being precisely the spin degeneracy 2^N. The new effective Hamiltonian will have the matrix representation

$$\langle \sigma_1' \cdots \sigma_N' | \tilde{H}_{\text{eff}} | \sigma_1 \cdots \sigma_N \rangle = \langle \psi_0(\sigma_1' \cdots \sigma_N') | t_1 h_1 | \psi_0(\sigma_1 \cdots \sigma_N) \rangle, \tag{8}$$

where $\psi_0(\sigma_1 \cdots)$ are the lowest unperturbed eigenfunctions. Hence, $\tilde{H}_{\text{eff}}$ is a function of the N spin-$\frac{1}{2}$ operators $\mathbf{s}_\nu$ associated with N pseudosites $\nu = 1,\ldots,N$. (These are clearly *not* the lattice sites for our Hubbard model.) Symmetry tells us that this must be invariant under uniform spin rotations. As a start, I worked this out for $N = 2$, arbitrary N_S, in which case symmetry gives $\tilde{H}_{\text{eff}} = A + B\mathbf{s}_1 \cdot \mathbf{s}_2$. I won't write down the somewhat cumbersome expressions for the constants A and B. The important points are (i) $B = \beta t_2$ where $\beta < 0$, in agreement with the exact diagonalization results that a singlet (triplet) is lowest when $t_2 < 0$ (> 0), and (ii) contributions to B from the various terms in Eq. (8) when the expansion (4) is used occur only when two electrons are nearest neighbors and are bordered by an empty site.

The latter gives, perhaps, some insight into the cause of the singlet-pairing enhancement found above. Extension of this to larger N is in progress. I also note that convergence questions that will occur for large enough N_S will have to be considered.

I thank Dr. S. D. Mahanti, Dr. Kenn Kubo, Dr. M. Challa, Dr. R. Day, Dr. J. Borysowicz, Dr. M. Thorpe, and Mr. Joel Gales for many helpful discussions.

[1] P. W. Anderson, Science **235**, 1196 (1987).
[2] P. W. Anderson, Mater. Res. Bull. **8**, 153 (1973).
[3] G. Baskaran, Z. Zou, and P. W. Anderson, Solid State Commun. **63**, 973 (1987).
[4] P. W. Anderson, G. Baskaran, Z. Zou, and T. Hsu, Phys. Rev. Lett. **58**, 2790 (1987).
[5] T. Oguchi, J. Phys. Soc. Jpn. **55**, 323 (1986).
[6] B. Sutherland, preprint.
[7] G. Rumer, Nachr. Ges. Wiss. Gottingen, Math.-Phys. Kl. 337 (1932).
[8] L. Pauling, J. Chem. Phys. **1**, 280 (1933).
[9] L. Hulthen, Ark. Mat. Astron. Fys. **26A**, 11 (1938).
[10] P. W. Anderson (private communication).
[11] T. A. Kaplan (unpublished).
[12] E. Lieb and D. Mattis, J. Math. Phys. **3**, 749 (1962).
[13] J. Oitmaa and D. D. Betts, Can. J. Phys. **56**, 897 (1978); J. E. Hirsch, Phys. Rev. Lett. **51**, 1900 (1983).
[14] The correlation function $\to 0$ as $i - j \to \infty$, but *slowly*: A. Luther and I. Peschel, Phys. Rev. B **12**, 3908 (1975). Sufficiently slowly that the structure factor *diverges* (at the antiferromagnetic wave vector); this is hardly liquidlike behavior.
[15] C. K. Majumdar, J. Phys. C **3**, 911 (1970). See also P. M. van den Broek, Phys. Lett. **77A**, 261 (1980).
[16] T. Tonegawa and I. Harada (unpublished).
[17] E. C. Kemble, *The Principles of Quantum Mechanics* (McGraw-Hill, New York, 1937) (reprinted by Dover, New York, 1958), Sec. 48C.
[18] A. B. Harris and R. V. Lange, Phys. Rev. **157**, 295 (1967).
[19] J. E. Hirsch, Phys. Rev. Lett. **54**, 1317 (1985).
[20] This projection, crucial to the whole idea, seems to have been omitted in a recent work: J. Parmenter, Phys. Rev. Lett. **59**, 923 (1987).
[21] G. Beni, T. Holstein, and P. Pincus, Phys. Rev. B **125**, 164 (1973).
[22] Z. G. Zoos and D. J. Klein, J. Chem. Phys. **55**, 3284 (1971); D. J. Klein, Phys. Rev. B **8**, 3452 (1973); D. J. Klein, W. A. Seitz, *ibid.* **10**, 3217 (1974).
[23] J. H. Van Vleck, *Quantum Theory of Atoms, Molecules, and Solids* (Academic, New York, 1966), p. 475.
[24] The conclusion of total spin degeneracy was first reached by J. Sokoloff, Phys. Rev. B **2**, 779 (1970). However, he claimed it for rings; the correct statement concerning boundary-condition effects was made by Zoos and Klein, J. Chem. Phys. **55**, 3284 (1971). The difference is important, of course, only for finite systems.
[25] IMSL routine EIGRS, ISML Library, Addition 9.2, revised Nov. 1984.
[26] I. K. Schuller, D. G. Hinks, M. A. Beno, D. W. Capone II, L. Soderholm, J. -P. Locquet, Y. Bruynseraede, C. U. Segre, and K. Zhang, Solid State Commun. **63**, 385 (1987).
[27] W. W. Warren, Jr., R. E. Walstedt, G. F. Brennert, G. P. Espinosa, and J. P. Remeika, Phys. Rev. Lett. **59**, 1860 (1987).
[28] This approach was used in Refs. 22 for the case $t_2 = 0$, U large and finite.

Magnetic susceptibility of rapidly solidified $YBa_2Cu_3O_{7-x}$ superconductors

M. E. McHenry, J. McKittrick, S. Sasayama, V. Kwapong, R. C. O'Handley, and G. Kalonji

Department of Materials Science and Engineering, Massachusetts Institute of Technology, Cambridge, Massachusetts 02139

The superconducting $YBa_2Cu_3O_{7-x}$ phase has been produced through a novel rapid solidification processing route yielding a high-quality granular superconducting phase. Features in the magnetic susceptibility as measured at various fields can be attributed to important transitions in the superconducting behavior of these materials. At low fields ($\sim$20 Oe) anomalies in the susceptibility arise from decoupling of the grains in these polycrystalline materials. Susceptibility response at higher fields ($\sim$100 Oe) is representative of randomly oriented superconducting grains which show local superconducting current densities comparable to those of single crystals. At even higher fields features consistent with Muller's superconducting glass state model are observed.

INTRODUCTION

The discovery of high-temperature superconductivity in oxide materials[1] led to a torrent of activity in investigating and attempting to understand their properties. Central to the demonstration of bulk superconductivity in these materials is the observation of a significant Meissner effect. With this torrid activity in high-temperature oxide superconductivity has come a wealth of magnetic susceptibility data often with anomalous features and sometimes with ambiguous interpretation. In this paper we discuss the physical origins of some anomalous magnetic susceptibility data we have observed in the study of our materials. Our results show the need to view susceptibility data with the same caution with which resistance measurements are viewed.

EXPERIMENTAL PROCEDURE

We have undertaken a novel rapid solidification processing route to prepare high-quality polycrystalline samples of the high T_c $YBa_2Cu_3O_{7-x}$ phase. A variety of metastable phases have been produced in this way and reported elsewhere.[2-3] The step most critical to producing high-temperature superconductors involves annealing of the rapidly solidified oxide precursors at 950 °C in oxygen with subsequent slow cooling to produce the now famous orthorhombic 123 phase. The use of rapid solidification of the oxide material allows for notable chemical homogeneity as well as for latitude in controlling the microstructure of these materials. The melt extraction technique employed for rapid solidification of these alloys yielded flakes of material typically $\sim 50\,\mu$m in thickness which after annealing yielded the 123 phase with grains typically $\sim 10\,\mu$m long and $\sim$2–5 μm in width. These flakes were subsequently crushed into powder and compacted into pellets. The resulting material was confirmed by x-ray diffraction and TEM to be of single phase. Resistance measurements revealed a T_c of 91 K with a $\Delta T_c \approx 1$ K (measured between 10% and 90% of the resistive transition). Magnetic measurements have been performed at fields up to 50 kOe using a SQUID magnetometer at the Francis Bitter National Magnet Lab.

RESULTS AND DISCUSSION

The diamagnetic response of our polycrystalline YBaCuO superconductors below H_{c1} is not uniform. A transition from nearly perfect diamagnetism [$\chi = -1/(4\pi)$] at $H \sim 0$ to a lower constant value of χ occurs at $H_d \sim 25$ Oe. This transition has been attributed to grain decoupling[3,4] and is shown for our materials in Fig. 1(a) where the magnetization as a function of low applied fields is depicted at 10 K. Figure 1(a) shows this decoupling phenomenon to be a source of hysteresis in these materials as is evident in the irreversibility of the magnetization with increasing and decreasing fields. When the bulk intragranular linear response is subtracted from the data in Fig. 1(a) it can be seen that the decoupling event magnetization behavior mimics that typical of dirty type II superconductors for fields extending well above H_{c1} but on a greatly reduced field scale as shown in

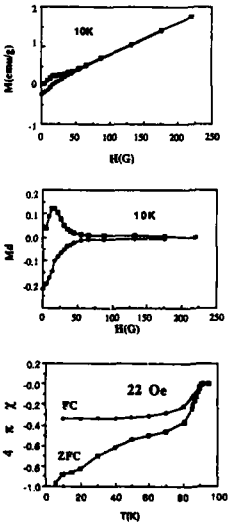


FIG. 1. (a) Field dependence of diamagnetic response at 10 K for 123 compound in increasing (open symbols) and decreasing (closed symbols) fields. (b) Same as (a) with linear response subtracted. (c) Temperature dependence of susceptibility $4\pi M/H$ at 22 Oe for field cooled (FC) and zero-field cooled (ZFC) conditions.

 0021-8979/88/084229-03$02.40 © 1988 American Institute of Physics

Fig. 1(b). As discussed in a previous paper[3] this grain decoupling phenomenon displays a unique temperature dependence. For our material the field H_d at which grain decoupling occurs decreases with increasing temperature, with the grains being nearly completely decoupled at zero applied field for temperatures greater than ~ 50 K.

With this behavior in mind it is possible to understand the anomalies in the low field susceptibility data as shown in Fig. 1(c). This figure shows the susceptibility as a function of temperature for an applied field of 22 Oe. This field was chosen so as to be in the middle of a low field transition from high initial susceptibility to lower values [Fig. 1(a)]. The zero field cooled (ZFC) susceptibility for $H < H_d$ (corrected for sample demagnetization effects) reflects 100% of ideal diamagnetic shielding [$\chi = -1/(4\pi)$]. In Fig. 1(c) for temperatures less than ~ 5 K the 22-Oe applied field does not exceed H_d and this ideal susceptibility is attained. Between 10 and 50 K the 22-Oe applied field is greater than H_d and thus represents a field on the decaying portion of the grain decoupling magnetization curve. This explains the nonsaturating nature of the ZFC susceptibility observed in this temperature range. The branch of the susceptibility curve above 50 K saturates at a value of $\sim 60\%$ of ideal diamagnetic response.

The initial magnetic response of Fig. 1(a) reflects persistent currents which arise so as to shield the entire macroscopic sample. Above H_d flux begins to penetrate the grain boundary regions which to this point have acted as weak Josephson links coupling the superconducting grains of the material. Above ~ 50 K the grains are nearly completely decoupled even at zero applied field and the ZFC susceptibility represents the response of a randomly oriented aggregate of uncoupled superconducting grains. The saturating nature of the branch of the susceptibility curve above 50 K and the limiting value of the susceptibility which it approaches are influenced by several features of this uncoupled aggregate. The shape of the grains now determines the demagnetization effects (whereas the sample shape does for $H < H_d$). The uniaxial anisotropy of these materials[5] decreases the susceptibility by a factor of three for randomly oriented grains. Finally, any preferred orientation to the grains will further complicate this issue. A susceptibility 50% of that of an ideal diamagnet has been estimated for a random aggregate of spherical grains in which the individual grains display uniaxial anisotropy.[4] The value of 60% we have attained is possibly reflective of the nonspherical shapes of our grains.

We believe that this grain decoupling phenomenon may be the source of much of the disparity which exists in the reported values of the diamagnetic susceptibilities of these materials. This points to the necessity of examining complete magnetization versus field curves in understanding the response of these materials. Specifically, low-field ac and dc susceptibility results displaying large diamagnetic response should be viewed as possibly arising from weakly coupled grains; the low-field response may not be representative of the material's response at slightly higher fields. It is also clear from the literature that different temperature dependencies for the decoupling event exist for materials made by different processes. Anomalies in low field susceptibility measurements have been noted by Gallagher *et al.*[6] who observe a discontinuity at 60 K in the ZFC susceptibility measured at 0.01 Oe while Grant *et al.*[7] have noted similar behavior in their materials between 40 and 70 K for susceptibility measurements at 20 Oe. On the other hand, Kwak *et al.*[4] have noticed the grain decoupling phenomenon at 77 K at ~ 25 Oe while Ginley *et al.*[8] and Schirber *et al.*[9] notice discontinuities in the diamagnetic shielding at ~ 88 K for fields of 3 and 2.5 Oe, respectively. If all of these susceptibility anomalies are due to grain decoupling, these results suggest that this phenomenon may be controllable by processing.

The importance of grain decoupling is further emphasized by comparing the critical current densities derived from the remanences of two M-H curves. Figure 1(b) reveals a remanent magnetization of ~ 0.22 emu/g which corresponds to a critical current density[10] of $J_c \sim 30 M_r/R \sim 500$ A/cm^2. This value is typical of polycrystalline samples[11] and thus implies that the most important determinant of critical current densities in polycrystalline superconductors may be the strength of the grain boundary Josephson junctions. Figure 2 shows a typical magnetization versus field curve for this sample at 5 K driving the materials to $H = 25$ kOe then reversing the field. Note that on this large field scale the grain decoupling is not noticeable and the magnetization reflects intragranular processes. The remanent magnetization for this loop can be used to calculate J_c where in this case the pertinent dimension would be the grain size. Using these parameters a $J_c \sim 2 \times 10^6$ A/cm^2 at 5 K can be calculated. This intragranular critical current density is reflective of what may be expected of single crystals or of polycrystalline samples with strongly coupled grains. Indeed this critical current density is comparable to those being reported for single crystal samples.[12] Anomalies in the temperature dependence of the critical fields, current densities and penetration depth were also noted in these materials and are discussed in more detail in Ref. 3. In that reference a microscopic model of flux pinning of the twin boundaries in these materials is offered to explain some aspects of the data.

Figure 3(a) shows the susceptibility as a function of temperature for an applied field of 100 Oe for our sample. Over the entire temperature range the ZFC susceptibility is

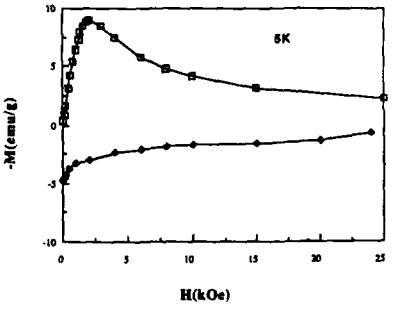


FIG. 2. Diamagnetic response of 123 material at 5 K in increasing (open symbols) and decreasing (closed symbols) fields. Note the magnitude of the applied field relative to that used in Fig. 1.

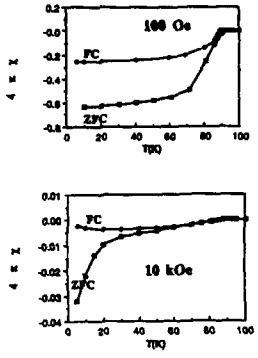


FIG. 3. Temperature dependence of the magnetic susceptibility for zero field cooled (ZFC) and field cooled (FC) conditions. (a) $H = 100$ Oe, (b) $H = 10$ kOe.

smooth indicating that by this field the grains are decoupled and the sample is behaving as an aggregate of randomly oriented noninteracting grains. The susceptibility is seen to saturate at a value of 62% of ideal diamagnetism which is similar to the value attained in the decoupled branch of Fig. 1(c). The high-field susceptibility [Fig. 3(b)] also displays the onset of reentrant paramagnetic behavior at low temperatures. This behavior is manifested in the turning of the Meissner (FC) susceptibility toward zero at low temperature. This reentrance is interpreted as a simple consequence of the superposition paramagnetism (presumably due to moments on the Y sites) on the superconducting states diamagnetism in the temperature region where these paramagnetic local moments become appreciable.

Figure 3(a) also illustrates a feature common to all the susceptibility curves measured at various fields, namely the departure of the ZFC susceptibility from the FC susceptibility at a temperature T^*. For the small (100 Oe) applied field of Fig. 3(a) the value of T^* is 87 K, close to the transition temperature of 91 K. As shown in Fig. 3(b) the value T^* is reduced to ~ 75 K for an applied field of 10 kOe. This behavior has been described by Muller *et al.*[13] in their superconductive glass state model. The deviation of the ZFC response as compared to the FC response also marks the point of departure of the dc and ac susceptibilities[14] which are defined as M/H and dM/dH, respectively. This point of departure (T^*, H^*), which defines a phase boundary between ergodic and nonergodic behavior, has been shown by Muller *et al.*[13] to obey a spin-glass-like transition temperature dependence in samples of Ba-doped La_2CuO_4. From a limited set of (T^*, H^*) points we have determined that our material obeys the $H^* \sim k(T^*/T_c)^{3/2}$ dependence noted by Muller but with a proportionality constant k which is an order of magnitude larger than that reported in Ref. 13 for La_2CuO_4:Ba. This larger proportionality constant is consistent with the sharp onset of superconductivity and large diamagnetism of our samples.

In conclusion we note that YBa_2CuO_{7-x} has been produced through a novel rapid solidification processing route to yield a high-quality superconducting material. This material displays low field grain decoupling phenomena which illustrate the origin of important limitations on the current carrying capacity of these polycrystalline materials. The bulk magnetization versus field behavior shows the limiting response which could be expected of single crystals or of strongly coupled polycrystalline materials. The high-field response of these materials shows features consistent with the superconducting glass state model but with parameters consistent with the stronger superconductivity.

ACKNOWLEDGMENT

This work was supported in part by funding from the Center for Materials Science and Engineering at MIT.

[1]G. J. Bednorz and K. A. Muller, Z. Phys. B **64**, 189 (1986).
[2]J. McKittrick, L. Q-. Chen, S. Sasayama, M. E. McHenry, G. Kalonji, and R. C. O'Handley, Adv. Cer. Mater. **2**, 353 (1987).
[3]M. E. McHenry, J. McKittrick, S. Sasayama, V. Kwapong, R. C. O'Handley, and G. Kalonji, Phys. Rev. B **37**, 623 (1988).
[4]J. R. Kwak, E. L. Venturini, D. S. Ginley, and W. Fu, in *Novel Superconductivity*, edited by S. A. Wolf, and V. Z. Kresin (Plenum, New York, 1987), p. 983.
[5]T. K. Worthington, W. J. Gallagher, and T. R. Dinger, Phys. Rev. Lett. **59**, 1160 (1987).
[6]W. J. Gallagher, R. L. Sandstrom, T. R. Dinger, T. M. Shaw, and D. A. Chance, Solid State Commun. **63**, 147 (1987).
[7]P. M. Grant, R. B. Beyers, E. M. Engler, G. Lim, S. S. P. Parkin, M. L. Ramirez, V. Y. Lee, A. Nazzal, J. E. Vazquez, and R. J. Savoy, Phys. Rev. B **35**, 7242 (1987).
[8]D. S. Ginley, E. L. Venturini, J. F. Kwak, R. J. Baughman, B. Morosin, and J. E. Schirber, Phys. Rev. B **36**, 829 (1987).
[9]J. E. Schirber, D. S. Ginley, E. L. Venturini, and B. Morosin, Phys. Rev. B **35**, 8709 (1987).
[10]C. P. Bean, Phys. Rev. Lett. **8**, 250 (1962).
[11]R. J. Cava, B. Batlogg, R. B. van Dover, D. W. Murphy, S. Sunshine, T. Siegrist, J. P. Remeika, E. A. Rietman, S. Zahurak, and G. P. Espinosa, Phys. Rev. Lett. **58**, 1676 (1987).
[12]T. R. Dinger, T. K. Worthington, W. J. Gallagher, and R. L. Sandstrom, Phys. Rev. Lett. **58**, 2687 (1987).
[13]K. A. Muller, M. Takashige, and J. G. Bednorz, Phys. Rev. Lett. **58**, 1143 (1987).
[14]C. Ebner and A. Stroud, Phys. Rev. B **31**, 165 (1985).

Field ion microscopy of the high T_c superconductor $Ba_2YCu_3O_{7-x}$ (abstract)

A. J. Melmed, R. D. Shull, C. K. Chiang, and H. A. Fowler
National Bureau of Standards, Gaithersburg, Maryland 20899

Field ion microscopy (FIM) observations (using either hydrogen or neon gas) were performed on both the high T_c superconducting oxide $Ba_2YCu_3O_{7-x}$ ($0<x<0.5$) and the related nonsuperconducting oxide $Ba_2YCu_3O_6$. For the superconducting material, ac magnetic susceptibility measurements determined a transition temperature of 92 K. At 30 K strong preferential images of atomic or molecular layers were observed for $Ba_2YCu_3O_{7-x}$ perpendicular to the long c axis, but not for $Ba_2YCu_3O_6$. The preferential field evaporation or field ionization responsible for the layered images (possessing a spacing of approximately 12 Å which is equivalent to the c-axis lattice parameter) in the superconducting oxide below its transition temperature is interpreted as possible evidence for the existence of relatively highly conducting atomic layers in the unit cell of this material at low temperatures. Computer simulations of FIM images expected under various assumptions of preferential imaging are most consistent with the layered images being due to the copper-oxygen end planes (those located between the planes of Ba atoms). FIM observations of $Ba_2YCu_3O_{7-x}$ performed above the superconducting transition temperature (at 100 K) showed primarily a highly intense disordered image similar to that obtained for the structurally related nonsuperconducting oxide $Ba_2YCu_3O_6$ at low temperatures, and faintly discernible parallel rows of atoms. Both twins and grain boundaries in $Ba_2YCu_3O_{7-x}$ have been observed in the FIM at low temperatures; and no special images related to the superconducting state have been found to be associated with these structural features. To date, consistent observations have been performed on approximately 100 specimens, thereby assuring that the present observations are not artifacts, but representative of the bulk material. Similar FIM observations have also been obtained for the related high T_c superconductor $Ba_2YbCu_3O_{7-x}$.

The following papers were also presented:

Spin excitations in La_2CuO_4

C. Peters
Massachusetts Institute of Technology, Cambridge, Massachusetts 02139

Electronic anisotropy and magnetism in $Y_1Ba_2Cu_3O_7$ and $La_{2-x}Sr_xCuO_4$ measured using the techniques of muon spin rotation and positron annihilation

D. Harshman
AT&T Bell Labs, Murray Hill, New Jersey 07974

Observation of hexagonally ordered flux quanta on $YaBa_2Cu_3O_7$

D. J. Bishop, P. L. Gammel, G. J. Dolan, J. R. Kwo, C. A. Murray, L. F. Schneemeyer, and J. V. Waszczak
AT&T Bell Labs, Murray Hill, New Jersey 07974

Resonating valence bands and *d*-wave superconductivity

G. Kotliar
Department of Physics, Massachusetts Institute of Technology, Cambridge, Massachusetts 02139

Superconductivity and magnetic ordering in the $YBa_2(Cu_{1-x}Fe_x)_3O_{9-\delta}$ system

Z. Q. Qiu, H. Tang, Y. W. Du, and J. C. Walker
Department of Physics, Johns Hopkins University, Baltimore, Maryland 21218
K. Moorjani, J. S. Morgan, and W. A. Bryden
Applied Physics Laboratory, Johns Hopkins University, Laurel, Maryland 20707

Metallic, but not superconducting, La-Ba (and La-Sr) copper oxides

J. B. Torrance, Y. Tokura, A. Nazzal, and S. S. P. Parkin
IBM Almaden Research Center, San Jose, California 95120

 0021-8979/88/084233-01$02.40 © 1988 American Institute of Physics

Macroscopic quantum tunneling in single domain magnetic particles

A. DeFranzo, I. Klik, and L. Gunther
Tufts University, Medford, Massachusetts 02155
A. G. Swanson and J. S. Brooks
Boston University, Boston, Massachusetts 02215

Since the 1950's there have been a number of experimental observations involving small single domain (SD) magnetic particles ($\lesssim 200$ Å diameter) which have been attributed to what we'd today call "macroscopic quantum tunneling" (MQT) of the magnetization in its switching from one easy axis direction to another. A comprehensive study of this phenomenon is not only of great interest for the sake of fundamental physics: It is of utmost practical importance in that *MQT sets a limit on the lifetime of information storage* on magnetic tapes and films. In this paper we present a brief summary of some of the latest results of our theoretical and experimental studies of this phenomenon.

I. BACKGROUND

The relaxation time τ of the magnetization M in small ($\lesssim 200$ Å) single domain (SD) magnetic particles is strongly dependent upon temperature because of the barrier U_B due to anisotropy energy. Numerous experiments measuring τ either directly[1] or indirectly through an analysis of Mössbauer spectra[2] have exhibited Arrhenius behavior, $\tau^{-1} = \nu_0 \times \exp(-\beta U_B)$, indicative of switching by thermal activation (TA). Here ν_0 is a frequency typically $O(10^9$–$10^{10}\,\mathrm{s}^{-1})$ and $\beta = (kT)^{-1}$. However, some experiments indicate that τ may be finite as $T \to 0$ K (instead of ∞ as expected). Such behavior has been attributed to "quantum tunneling" of the magnetization in its switching from one easy axis direction to another. Since the magnetization is a macroscopic variable representing the correlated behavior of many electrons [typically greater than $O(10^4)$], such tunneling is an example of what has come to be referred to as "macroscopic quantum tunneling", or simply MQT.[3–5] To date, clearcut evidence of MQT has been seen only in Josephson junctions.[6]

The finiteness of τ at $T = 0$ K is extremely important in the field of information storage: In order to increase the density of information storage in magnetic tapes and films, SD particles will have to made smaller. Since U_B decreases with decreasing particle size, the temperature will have to be lowered to keep τ long enough. However, there exists a crossover temperature T_0 from classical Arrhenius behavior to MQT, below which τ saturates to its zero temperature value. Theoretical estimates[7] of T_0 range from about 50 mK to a few degrees K, dependent upon the switching mechanism and the material.

II. EXISTING EXPERIMENTAL EVIDENCE FOR MQT IN SD PARTICLES

In 1954, Weil[8] found that particles in a sample of nickel powder failed to reach their blocking temperature[9] down to 4.2 K. Subsequently, Bean and Livingston[10] suggested quantum tunneling as a possible explanation.[11] Neither idea was pursued further, to our knowledge.

In 1973, Bostanjoglo and Gemünd[12] suggested quantum tunneling explicitly as a mechanism to account for their observation that the velocity of extraordinary viscous wall motion in 83% Ni-17% Fe films reached a constant value below temperatures on the order of 10 K. Switching in small occluded oxide particles was assumed to dominate viscous drag on wall motion in the film matrix.

Recently, Uehara and Barbara[13] have observed anomalous behavior in the relaxation time for magnetization reversal of chemically disordered $SmCo_{3.5}Cu_{1.5}$. They claim evidence for a crossover to wall jumping via a quantum tunneling process below a temperature of about 10 K. We believe that their explanation requires further study for three reasons: First, the crossover temperature is too large from a theoretical standpoint. Second, a distribution of volumes for their activation process can account for their experimental results. Third, the temperatures studied weren't low enough to see a leveling off as $T \to 0$ K.

III. SOME THEORETICAL CONSIDERATIONS

There are two basic mechanisms which have been considered for magnetization switching in SD particles—wall switching and rotation in unison. In the case of wall switching, a wall is nucleated on one side of the particle and sweeps across the particle. MQT for this mechanism was first considered by Stauffer[14] in the absence of an applied magnetic field and neglecting the effect of dissipation on the quantum tunneling rate ν_{QT}. He obtained in the WKB approximation

$$\nu_{QT} = A \exp(-B), \tag{1}$$

where A is a frequency prefactor estimated by Stauffer as $(N^2\sigma_w^2/\hbar m_w)^{1/3}$ and B is the WKB exponent given by $B \sim v(m_w\sigma_w)^{1/2}/\hbar$. N is the number of elemental spins, σ_w is the

 0021-8979/88/084234-03$02.40 © 1988 American Institute of Physics

energy per unit area of a wall, m_w is the mass per unit area of a wall and v is the particle volume. Alternatively, we can write

$$B \sim v\sqrt{K}/\mu, \tag{2}$$

where K is the anisotropy constant and $\mu = \hbar$ (gyromagnetic ratio) $= \hbar g$.

We wish to note here that wall switching requires a wall thickness $\ll$ particle radius and hence is restricted to materials with very large anisotropy, such as the rare-earth alloy $SmCo_{3.5}Cu_{1.5}$.

The case of *rotation in unison* is more complicated: First, we have *two* coordinates specifying the state of a particle, say the spherical coordinates θ and ϕ, giving the direction of the magnetization M within a given particle. Second, there is the important question of the source of an effective inertia, associated with the polar angle θ.

For magnetic films, the Landau–Lifshitz equation or its improved version, the Gilbert equation,[15] has been found to describe experiments reasonably well. The latter reads

$$\frac{d\mathbf{M}}{dt} \equiv \dot{\mathbf{M}} = -\frac{g}{M}\mathbf{M}\times\nabla u - \frac{\alpha}{M}\mathbf{M}\times\dot{\mathbf{M}}. \tag{3}$$

Here u is the energy density as a function of (θ,ϕ) and α is a dimensionless parameter reflecting dissipation, being typically of order 10^{-3}–10^{-2}. In the case of a SD particle with simple uniaxial anisotropy in an external magnetic field H parallel to the z axis, we might have approximately

$$u = -MH\cos\theta - K\cos^2\theta. \tag{4}$$

In 1958, Smith[16] applied the Gilbert equation to a thin film with weak uniaxial anisotropy in the plane of the film (so that $K \ll 4\pi M^2$) and $\alpha \ll 1$, showing that θ satisfies the equation

$$\ddot{\theta} + 4\pi\alpha g M\dot{\theta} + 4\pi g^2\frac{\partial u}{\partial\theta} = 0. \tag{5}$$

It is apparent that demagnetization energy generates an effective moment of inertia $I = v/4\pi g^2$.[17,18] If we calculate the WKB exponent neglecting dissipation using Eq. (4) for the energy density u, we find for H close to the critical field $H_0 \equiv 2K/M$ above which the barrier vanishes

$$B \simeq B_0(1-h)^{3/2}, \tag{6}$$

where $h \equiv H/H_0$ and $B_0 \sim v\sqrt{K}/\mu$ exactly as in the case of wall switching. The crossover temperature is estimated by setting $B_0 = \beta U_B(h=0) = Kv/kT_0$. This leads to $T_0 = \mu\sqrt{K}/k$, which is explicitly independent of volume. When $v \sim 10^{-19}$ cm^3 (corresponding to particle radius of 30 Å), $K \sim 10^6$ ergs/cm^3 (corresponding to magnetite), and $\mu \sim \mu_B$, we have $B_0 \sim 1\times10^4$ and $T_0 \sim 60$ mK.

IV. A HEAT BATH OF MAGNETIC OSCILLATORS AND THE EFFECTIVE LAGRANGIAN

Quantum tunneling of a macroscopic variable has been shown to be sensitive to dissipation. Furthermore, quantization of a classical system with dissipation is not straightforward. Fortunately, it is often possible to quantize a dissipative system by modeling the source of dissipation as a reversibly dynamical coupling of the system to a set of harmonic oscillators.[4] The sets of masses m_α, frequencies ω_α, and coupling constants c_α for the oscillator coordinates x_α are chosen so as to reproduce the classical equation for the dissipative macroscopic coordinate(s). Then the entire set of coordinates can be quantized in the usual way. For a SD particle, we have considered two sorts of heat baths—a set of magnetic field oscillators and phonons coupled magnetoelastically. Here we discuss only the former.

Suppose we add to the external field acting on M a fluctuating field $\mathbf{h}$ (cf. Brown[19]), setting $\mathbf{h} = \Sigma_\alpha c_\alpha \mathbf{x}_\alpha$. If the spectral function[4]

$$J(\omega) \equiv (\pi/2)\sum_\alpha (c_\alpha^2/m_\alpha\omega_\alpha)\delta(\omega-\omega_\alpha) \tag{7}$$

is chosen to equal $(\alpha/Mg)\omega$, it is easy to show that we obtain the Gilbert equation. Thus, this heat bath model is reasonable for a magnetic system whose classical behavior follows the Gilbert equation. (We cannot assume *a priori* that such is the case for SD particles.) It is then straightforward to derive the *effective action*[4] in *imaginary time* τ used to calculate ν_{QT}, starting with the Gilbert Lagrangian.[20] With the energy density given by Eq. (4) we obtain

$$S_{\text{eff}} = \int_0^{\beta\hbar} v\,d\tau\,[-M\{(i\dot{\phi}/g)+H\}(1+\cos\theta)+K\sin^2\theta + \frac{\alpha M}{\pi g}\int_0^{\beta\hbar} d\tau'(\tau-\tau')^{-2}\left(\sin^2\frac{(\theta-\theta')}{2} + \sin\theta\sin\theta'\sin^2\frac{(\phi-\phi)'}{2}\right)\Big]. \tag{8}$$

V. A SPIN DYNAMICS APPROACH

As an alternative approach, the magnetization can be treated as a large spin. Equation (4) is then represented by the Hamiltonian

$$H = -\hbar\omega\hat{S}_z - \kappa\hat{S}_z^2 - \mathbf{h}\cdot\hat{\mathbf{S}}, \tag{9}$$

where $\omega = gH$ is the Larmor frequency, $\kappa = K\mu^2/M^2v$, $\hat{S}_z$ is the spin component in the external field direction and $\mathbf{h}$ is the fluctuating field of Sec. IV. This model is a trivial example of quantization of a macroscopic variable.

Now let $\mathbf{h} = 0$ in this Hamiltonian. Then the spectrum consists of $2S+1$ energy levels $E_m = -\omega m - \kappa m^2$, $-S \leqslant m \leqslant S$. If $-S < \omega/2\kappa < S$, then there exists a barrier in the *total* energy separating the spin-up and spin-down states. The problem is to determine how the presence of the barrier influences the relaxation process as compared to the $\kappa = 0$ case. The problem is solved by applying to it the theory of the time-convolutionless master equation[21] for the density matrix $\sigma(t)$. It is assumed that the time scale of the heat bath is much shorter than that of the spin. For a spin of magnitude S, the master equation results in a linear system of $2S+1$ equations for the diagonal elements of the density matrix. The case $S = 1/2$ is trivial, but the $S = 1$ case is easily solved[21] to yield for the diagonal elements of σ $(i = 1,2,3)$:

$$\sigma_{ii}(t) = A_{ii} + B_{ii}\exp(-\lambda_1 t) + C_{ii}\exp(-\lambda_2 t). \tag{10}$$

The decay rates $\lambda_{1,2}$ are not in the Arrhenius form. However, the form of the solution changes dramatically in the classical limit $(S\to\infty, \beta\to 0, \kappa\to 0)$. It is obtained by using the spin coherent states representation in trigonometric parametri-

zation.[21] The resultant equation reproduces essentially the Fökker–Planck equation of Brown,[19] only the temperature dependence and physical origin of the diffusion coefficient are specified. Brown[19] and Aharoni[22] determined from this equation the decay rate in the Arrhenius form.

VI. EXPERIMENTAL STUDIES

Experiments on samples having a distribution of occlusions or local inhomogeneities (such as those of Refs. 12 and 13) have the disadvantage that the single domain regions or particles, in which switching across a barrier takes place, are not only difficult to characterize, but also are describable by parameters such as size which are widely distributed. It would be useful to study a sample of SD particles whose characteristics are better controlled. An example is a ferrofluid of magnetite. Fractionation using gel chromatography can produce a narrow distribution of particle sizes, thus aiding in the characterization of the particles[23] and simplifying the analysis of low-temperature data. By cooling such a ferrofluid in the presence of a huge magnetic field, M will line up with H. If the fluid remains amorphous to absolute zero and has a viscosity which doesn't get too large, ($\lesssim 10^7$ P) down to a temperature of ~ 100 K, we end up with a suspension of SD particles all with an easy axis lined up with the field. The *derivative of the hysteresis curve* with respect to the field H is analogous to the "switching distribution" $P(I)$ (Ref. 6) of the bias current which switches a Josephson junction from a zero voltage state to a nonzero voltage state. With such an experiment in mind, we considered a magnetite ferrofluid for future MQT studies. One of the problems with magnetite is that in the bulk, it undergoes a crystalline phase transition, the Verwey transition.[24] Its occurrence in small particles would clearly strongly affect the course of low-temperature measurements of the sort envisioned. We were able to make use of the availability at the National Magnet Laboratory of high magnetic fields and low temperatures to obtain the first clearcut evidence of the occurrence of the Verwey transition in samples of magnetite ferrofluid.[25,26]

VII. DISCUSSION

We hope that we have convinced our readers that the subject of MQT in SD particles is an exciting subject warranting much further study. We believe that much needs to be done in the areas of dissipation and effective inertia. The spin-density matrix formalism must be studied at low temperatures. A Heisenberg model of ferromagnetism with magnetoelastic coupling should prove very useful. Previous experiments indicating MQT should be continued down to lower temperatures. Finally, experiments of the sort outlined in Sec. VI should be carried out.[31]

Note Added in Proof: Soon after this paper was submitted for publication, E. Chudnovsky and L. Gunther developed a theory of MQT in ferromagnets which was applied to a model with transverse anisotropy, wherein a term $K'v \times \sin^2\theta \sin^2\phi$ is added to the Lagrangian in Eq. (8). This term produces an effective inertia $M'^2v/2g^2K'$ as anticipated in Ref. 17. For small $\delta \equiv 1 - h$, we find $B \sim N(K/K')^{1/2}\delta^{3/2}$ and a corresponding crossover temperature $T_0 \sim g\hbar(KK')^{1/2}/kM$. This model should be reasonable for magnetite, for which $K \sim K' \sim 10^6$ ergs/cm^3 and $M \sim 500$ G. For a 60-Å-diam particle of magnetite, $B \sim 6000\,\delta^{3/2}$ and $T_0 \sim 0.1$ K, so that MQT should be readily observable. Soon thereafter, the theory was extended to deal with quantum nucleation in bulk samples. Both works have been accepted for publication.

ACKNOWLEDGMENTS

We have been fortunate to have Professor Eugene Chudnovsky recently join us at Tufts University in our study of this problem. Conversations with him regarding our work have been invaluable. L. G. is grateful to Ami Berkowitz for his frequent advice and strong encouragement.

[1] I. S. Jacobs and C. P. Bean, in *Magnetism*, edited by T. Rado and H. Suhl (Academic, New York, 1963), Vol. III, Chap. 6.
[2] P. Roggwiller and W. Kündig, Solid State Commun. **12**, 901 (1973); S. Morup and H. Topsoe, J. Magn. Magn. Mater. **31–34**, 953 (1983).
[3] A. J. Leggett, Suppl. Prog. Theor. Phys. **69**, 80 (1980).
[4] A. O. Caldeira and A. J. Leggett, Phys. Rev. Lett. **46**, 211 (1981).
[5] A. I. Larkin and Yu. N. Ovchinnikov, Pisma Zh. Eksp. Teor. Fiz. **37**, 322 (1983) [JETP Lett. **37**, 382 (1983)].
[6] S. Washburn, R. A. Webb, and S. M. Faris, Phys. Rev. Lett. **54**, 2712 (1985); J. M. Martinus, M. M. Devoret, and J. E. Lukens, Phys. Rev. Lett. **55**, 1547 (1985).
[7] E. Chudnovsky and L. Gunther (unpublished).
[8] L. Weil, J. Chim. Phys. **51**, 715 (1954).
[9] The "blocking temperature" is that temperature below which the relaxation time τ exceeds experimental time scales, usually set at 100 s.
[10] See, e.g., C. P. Bean and J. D. Livingston, J. Appl. Phys. **30**, 1205 (1959).
[11] "Clumping of particles" was also a suggested possibility.
[12] O. Bostanjoglo and H. P. Gemünd, Phys. Status Solidi **17**, 115 (1973).
[13] M. Uehara and B. Barbara, J. Phys. (Paris) **47**, 235 (1986).
[14] D. Stauffer, Solid State Commun. **18**, 533 (1976). Domain wall tunneling in bulk specimens was earlier studied by T. Egami [Phys. Status Solidi B **57**, 211 (1973); Phys. Status Solidi A **20**, 157 (1973)].
[15] T. H. O'Dell, *Ferromagnetodynamics* (Wiley, New York, 1981).
[16] D. O. Smith, J. Appl. Phys. **29**, 264 (1958).
[17] We would expect that for a pancake-shaped particle or for a spherical particle with strong transverse anisotropy (with respect to ϕ), qualitatively similar results should be obtained.
[18] See the note added in proof.
[19] W. F. Brown, Jr., Phys. Rev. **130**, 1677 (1963).
[20] W. F. Brown, Jr., *Magnetostatic Principles in Ferromagnetism* (North-Holland, Amsterdam, 1962); T. L. Gilbert, Ph.D. thesis.
[21] F. Shibata, J. Phys. Soc. Jpn. **49**, 15 (1980).
[22] A. Aharoni, Phys. Rev. **133**, A447 (1964); *ibid.* **177**, 793 (1969).
[23] We thank Tony Nunes for discussions regarding this problem.
[24] E. J. Verwey, Nature **144**, 327 (1939).
[25] A. DeFranzo, L. Gunther, J. S. Brooks, and A. G. Swanson, Bull. Am. Phys. Soc. **32**, 846 (1987); Proceedings of Low Temperature Physics Conference XVIII, Kyoto (1987). We are grateful to the Ferrofluidics Corp., Nashua, NH, for providing us with sample.
[26] In a different but related area our Tufts group is also examining MQT in magnetic bubbles. Preliminary studies indicate this to be an important phenomenon at low temperatures.

Hysteresis of submicron permalloy particulate arrays

J. F. Smyth and S. Schultz
University of California, San Diego and Center for Magnetic Recording Research, La Jolla, California 92093

D. Kern, H. Schmid, and Dennis Yee
IBM Thomas J. Watson Research Center, Yorktown Heights, New York 10598

We have prepared controlled arrays of submicron permalloy particles as part of a program to determine the magnetic properties of verifiable single-domain particles (SDP) and the effects of interactions between SDPs. We have measured the hysteresis loops of these arrays as a function of size, aspect ratio, and spacing. The arrays are fabricated utilizing electron beam lithography and liftoff techniques. Each array consists of approximately 10^6 identical particles with identical spacing between the particles. Particle size and spacing [center-to-center distance (ccd)], vary from $5\ \mu m \times 15\ \mu m$ (width by length) with ccd of $25\ \mu m$ to $0.07\ \mu m \times 0.1\ \mu m$ with ccd of $0.25\ \mu m$. The thickness of the films varied from 0.072 to 0.049 μm. Hysteresis loops are obtained utilizing a SQUID magnetometer. For well-separated particles we observe an order of magnitude increase in H_c with decreasing particle size, and then a subsequent decrease in H_c as the ccd is reduced. However, even for the smallest particles, the ratio of the remanence to saturation magnetization indicates that they are not single domain, and the loop shape is not indicative of Stoner–Wohlfarth behavior.

I. INTRODUCTION

An accurate description of the magnetic properties of strongly interacting superparamagnetic particles remains an unsolved problem. If the properties of the individual particles are specified, numerical simulation techniques should be applicable, and considerable progress along that direction has been reported.[1] In principle, it would be desirable to determine the complete microscopic status of an interacting spin system, but the experimental problems are quite formidable. Suitable samples require a knowledge (and control) of the particles' size, shape, morphology, magnetic properties, and their relative orientations and spacings. Attempts at such studies by using magnetic tape media and varying packing fraction have been hampered by particle clustering, lack of controlled orientation, and a lack of accurate knowledge of the magnetic behavior of the individual constituent particles. To overcome these difficulties we have prepared controlled arrays of permalloy particles utilizing ultrahigh-resolution electron beam lithography, which we then study with SQUID magnetometry. In addition to serving as a suitable material for these controlled interaction studies, the use of permalloy is of interest in its own right, as we believe these experiments represent measurement of controlled particle moments several orders of magnitude smaller than has hitherto been reported.

The ideal magnetic particle, from a theoretical perspective, is an ellipsoid whose magnetization would be uniform under all applied fields and which would switch via coherent rotation as discussed by Stoner and Wohlfarth[2] (SW). It is generally accepted that, in principle, barring effects due to surface spin pinning, a sufficiently small, homogeneous, isolated particle should exhibit such behavior. While it would be preferable, at least initially, to be able to produce such particles and demonstrate SD behavior, it is really not necessary for the purpose of making progress on the question of the nature of the interaction field, and the magnetic properties of strongly interacting particle arrays. If the magnetic hysteresis behavior of isolated individual particles could be determined, whatever it turned out to be, then one could subsequently investigate the effects of interactions by varying the particle spacing. The results of measurements on such suitably prepared samples could then be compared with numerical simulations.

II. SAMPLE PREPARATION

The particle arrays were made utilizing ultrahigh-resolution electron-beam lithography and liftoff techniques de-

TABLE I. Representative array parameters.

Array	Thickness (Å)	Particle size $a \times b$(μm)	ccd-a[a] (μm)	ccd-b[b] (μm)	Total number of particles	Squareness ratio M_r/M_s	Coercivity H_c (Oe)
A	515	5×15	20	30	16 100	0.78	6
B	735	1×3	8	10	99 680	0.11	25
C	735	0.3×0.9	3.5	4.3	3 149 410	0.12	50
D	515	0.072×0.143	0.3	0.4	12 755 510	0.32	120
E-1	650	0.21×0.41	1.7	2.2	11 672 500	0.10	50
E-2	650	0.21×0.41	0.8	1.0	11 672 500	0.05	35
E-3	650	0.21×0.41	0.5	0.6	11 672 500	0.03	30

[a] ccd-a is the center-to-center distance along the a direction.
[b] ccd-b is the center-to-center distance along the b direction.

 0021-8979/88/084237-03$02.40 © 1988 American Institute of Physics

signed especially or nanolithography.[3,4] Representative array parameters are presented in Table I. In Fig. 1 we present a scanning elecron microscopy (SEM) picture for array *E*-3, illustrating the quality of the arrays and particles. The magnetization measurements were made utilizing a SQUID magnetometer[5] which is crucial to this work, as the total number of particles need to form a detectable moment, and also the physical size of the arrays, become limiting factors when particle dimensions are $\sim 0.1\ \mu$m. The largest center-to-center distances (ccd) between the particles (for a given sized particle) were chosen to be the farthest apart the particles could be placed without making the sample too large for the SQUID measurements. For arrays *B*, *C*, and *E*-1, the field at the center of a particle due to the nearest neighbor (approximated as a point dipole) was less than 1 Oe; for arrays *D* and *E*-2, ~ 10 Oe; and for array *E*-3 ~ 50 Oe. The use of pure Si substrates is important, and the diamagnetic susceptibility has been subtracted from the hysteresis loop data when appropriate.

III. EXPERIMENT

In Figs. 2(a)–2(d) we present hysteresis loop data taken for the arrays indicated with the dc field in the plane of the substrate and parallel to the particle long direction. The arrays for this series were all made with large interparticle spacings, which were chosen so that the hysteresis loop parameters would be a measure of the individual noninteracting particle properties. Array *A*, with $5\times 15\ \mu$m particles, has an $H_c \sim 6$ Oe that is still comparable with that of the bulk film as-deposited, which had an $H_c \sim 2$ Oe. As the particle size is reduced (arrays B–C–D), we find there is an increase in H_c, and the changes in squareness as noted in Table I.

In Figs. 3(a)–3(c) we present hysteresis loop data, taken as for Fig. 2, but where the array samples are all for the same particle size, and where the interparticle spacings were reduced for the purpose of increasing the interactions. We note that while the values of H_c (defined as the field for which the magnetization equals zero) do indeed decrease with decreasing particle spacing, there are other changes in the general shape of the loops which clearly indicate that such a simple description is inadequate to parametrize the magnetic properties of these systems.

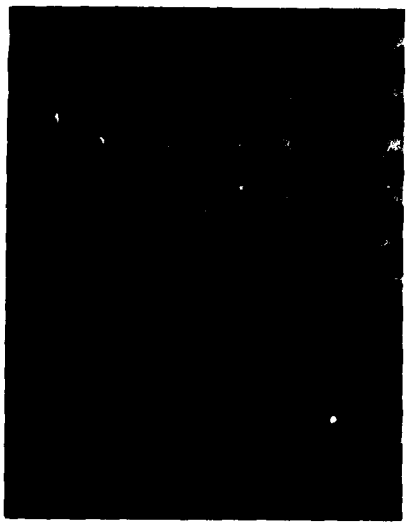


FIG. 1. An SEM display of array *E*-3 (described in Table I) taken at 20 KV, X70 000. The permalloy particles are $0.21\times 041\ \mu$m. A magnetization samples consists of approximately 10^7 such particles.

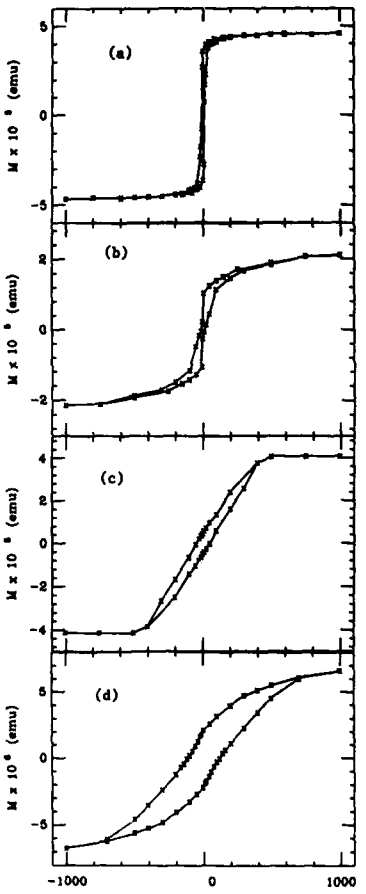


FIG. 2. Hysteresis loops for arrays with parameters as described in Table I. The interparticle spacings were chosen to as large as possible so as to allow the measurement of the magnetization behavior of the isolated particles. (a) Array *A*, particles $5\times 15\ \mu$m with a coercivity H_c comparable to the bulk film. (b) Array *B*, particles $1\times 3\ \mu$m. (c) Array *C*, particles 0.3×0.9 μm; and (d) Array *D*, particles $0.07\times 0.14\ \mu$m. We note there is an increase in H_c with decreasing particle size.

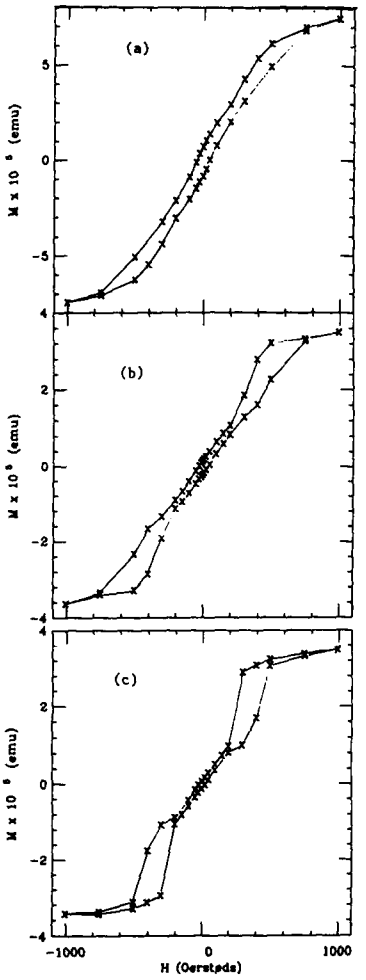


FIG. 3. Hysteresis loops for arrays with parameters as described in Table I. In this series the particle size was held constant at 0.21×0.41 μm and the interparticle spacings were varied as follows: (a) Array *E*-1, (b) array *E*-2, and (c) array *E*-3. We note that although the coercivity (taken as usual where $M = 0$) does decrease with decreasing particle spacing, the other changes in the loop indicate a complicated magnetic behavior.

We have also measured the ferromagnetic resonance (FMR) of these arrays. The angular dependence of the field for resonance of the fundamental mode is in qualitative agreement with the particle shape anisotropy.[6] Details of this experiment will be published elsewhere.

In his pioneering papers,[7] Brown addressed the question as to the critical size of a spherical particle below which the magnetization is uniform. Recently, Aharoni[8] has extended this work to include ellipsoids of arbitrary aspect ratio, and when we apply his criterion to our material we find that one should not expect fully single-domain behavior even for our smallest particles. However, the same criterion predicts that particles with an aspect ratio of 10/1 with our smallest widths (~ 0.07 μm) should definitely be single domain, and we are in the process of preparing a new series of arrays which will encompass this range of parameters.

ACKNOWLEDGMENTS

We thank Dr. Grant Wilson and Dr. T. H. P. Chang for their interest and encouragement of this project, and Dr. Steve Rishton for his help with the nanolithography. This work was supported by the Center for Magnetic Recording Research, University of California, San Diego, and IBM Thomas J. Watson Research Center, Yorktown Heights.

[1] Ching-Ray Chang and D. R. Fredkin, IEEE Trans. Magn. **MAG-22**, 391 (1986).
[2] E. C. Stoner and E. P. Wohlfarth, Trans. R. Soc. London, Ser. A **240**, 599 (1948).
[3] D. P. Kern, P. J. Houzego, P. J. Coane, and T. H. P. Chang, J. Vac. Sci. Technol. B **1**, 1096 (1983).
[4] S. A. Rishton, H. Schmid, D. P. Kern, H. E. Luhn, T. H. P. Chang, G. A. Sai-Halasz, M. R. Wordeman, E. Ganin, and M. Polcari, J. Vac. Sci. Technol. Ser. B (to be published).
[5] Biomagnetic Technologies, Inc., 4174 Sorrento Valley Blvd., P. O. Box 210079, San Diego CA 92121.
[6] C. Kittel, Phys. Rev. **71**, 270 (1947); **73**, 155 (1948).
[7] W. F. Brown, Jr., J. Appl. Phys. **39**, 993 (1968); Ann. N. Y. Acad. Sci. **147**, 461 (1969).
[8] A. Aharoni, these proceedings.

Particle size dependence of the magnetic properties of ultrafine granular films

S. H. Liou[a] and C. L. Chien
Department of Physics and Astronomy, The Johns Hopkins University, Baltimore, Maryland 21218

Magnetic granular solids consist of ultrafine metal granules of nanometer sizes embedded in an insulating medium. The magnetic properties are dictated by the microstructure such as particle size, metal volume fraction, which are process controlled. We report the results of a series of granular $Fe_{60}(SiO_2)_{40}$ films in which the particle size has been systematically varied. The magnetic coercivity, ranging from 500 to 2200 Oe, increases with particle size. The ferromagnetic-superparamagnetic transition had been studied by SQUID magnetometry and Mössbauer spectroscopy. The value of the magnetic anisotropy energy is found to be much larger than that due to magnetocrystalline anisotropy.

INTRODUCTION

Granular metal films are small metal particles of nanometer size embedded in an insulating matrix. The persistent interest in this class of composite material is due primarily to their unusual transport, optical, and superconducting properties.[1-3] The magnetic properties of granular Ni-(SiO_2,Al_2O_3), Co-SiO_2, Fe-SiO_2, etc.,[4-7] have also been reported.

The magnetic properties of granular solids are determined by the intrinsic properties and the volume fraction of the metal, as well as the granule size. The main features of the magnetic behavior of these films are the presence of a ferromagnetic-superparamagnetic transition and high coercivity.

The investigations of the granular films so far have been emphasized mostly on the properties affected by the metal volume fraction in the films. However, for a given process condition, the average size of the metal particles in granular films has been found also to depend on the metal volume fraction. This means that the physical properties discussed are affected by *both* the particle size and the volume fractions. There are very few systematic studies of the magnetic properties affected only by the different granular sizes.

In this paper we investigate the magnetic properties, and specifically, the particle size effects of granular $Fe_{60}(SiO_2)_{40}$, with a Fe volume fraction of $p = 0.29$. We have chosen the volume fraction of $p = 0.29$, which is much less than the percolation threshold ($p_c \simeq 0.6$), so that isolated granules can be assured. The magnetic properties have been found to depend sensitively on the particle size.

EXPERIMENT

The granular metal films were made by using a high-rate magnetron sputtering device. The vacuum prior to sputtering was in the 10^{-8} Torr range with a LN_2 cold trap in the chamber. The granular metal film about 3–6 μm thick were prepared by rf sputtering at an argon pressure of 4×10^{-3} Torr from composite targets of Fe and SiO_2. The composition of films, was determined by atomic absorption and fluorescence x-ray spectroscopy. The composition of the films were found to be very close to that of the sputtering targets (within 5 at. %). The microstructure of film was studied by transmission electron microscopy (TEM) and electron and x-ray diffractions. The magnetic properties were determined by SQUID magnetometry and Mössbauer spectroscopy.

RESULTS AND DISCUSSIONS

The morphology of the composites was revealed by TEM. Figure 1 shows typical bright-field TEM images of $Fe_{60}(SiO_2)_{40}$ ($p = 0.29$) with different deposition conditions. By varying the substrate temperature from 300 to 875 K, the size of the granules increases from 30 to 50 Å. The ability to control particle size with a fixed metal volume fraction is clearly demonstrated by the data shown in Fig. 1. The particles are nearly equiaxial with small aspect ratios.

X-ray diffraction was used to examine the crystal struc-

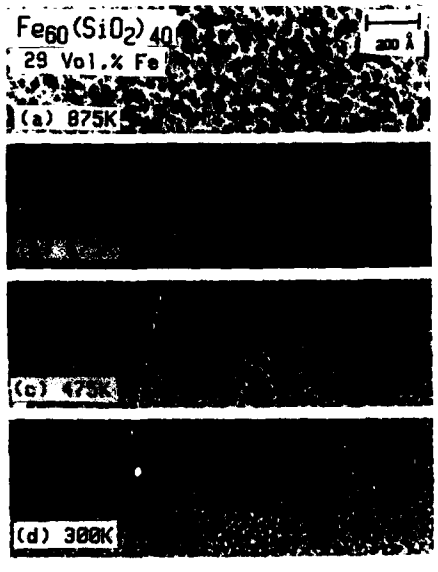


FIG. 1. TEM micrograph of granular $Fe_{60}(SiO_2)_{40}$ (29 vol. % Fe) films prepared at various substrate temperatures: (a) 875 K, (b) 675 K, (c) 475 K, (d) 300 K.

[a] Present address: AT&T Bell Laboratories, Murray Hill, NJ 07974.

 0021-8979/88/084240-03$02.40 © 1988 American Institute of Physics

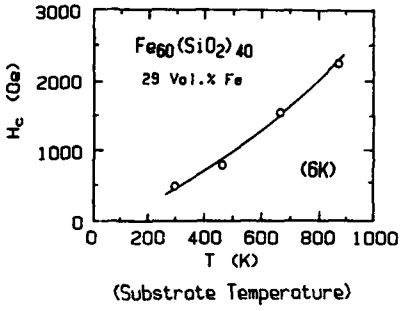


FIG. 2. Variation of coercivity of $Fe_{60}(SiO_2)_{40}$, 29 vol. % Fe, at 6 K with substrate temperatures.

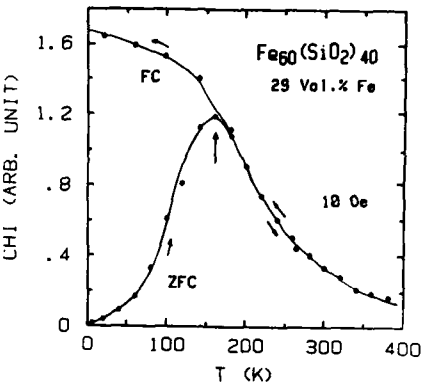


FIG. 3. Zero-field-cooled and field-cooled magnetic susceptibility vs temperature with an applied field of $H_a = 10$ Oe of $Fe_{60}(SiO_2)_{40}$ deposited at 675 K. The arrow indicates the blocking temperature of T_{B1}.

ture of the Fe particles. For the samples prepared at low substrate temperatures, the x-ray diffraction pattern of films can be consistently indexed to α-Fe and the amorphous SiO_2 matrix. This is also confirmed by Fe^{57} Mössbauer spectroscopy. However, there is an asymmetric broadening of the main x-ray diffraction peak, the (110) peak, suggesting the possibilities of other phases in the film. The asymmetric broadening is more pronounced for the film prepared at higher temperatures. The detail of this asymmetric broadening is still being investigated.

The magnetic coercivity (H_c) at 6 K versus the substrate temperature is shown in Fig. 2. The value of H_c increases dramatically from 500 to 2200 Oe when the substrate temperature is increased from 300 to 875 K. Since higher substrate temperature produces larger granules, H_c is evidently size dependent. For single domain small particles, there are a number of possible contributions (magnetocrystalline, shape, stress, surface, etc.) to H_c. In the case of Fe particles, the magnetocrystalline contribution, assuming it is the same as that of bulk Fe, is about 600 Oe, which is much smaller than the H_c found in the films prepared at higher substrate temperatures. Effects due to stress, surface, and possibly long-range interaction between the particles cannot be easily delineated. Almost all the existing models of H_c assume free-standing particles or particles dispersed in a nonbonding medium.[8] In granular Fe-SiO_2 films, the particles are strongly bonded to the matrix, probably under large stresses. A significant portion of the Fe atoms are also at or near the particle surface. Further investigations are needed to clarify the importance of these contributions.

Coercivity, remanence, and other magnetic properties of ultrafine single-domain magnetic particles decrease rapidly with temperature due to superparamagnetic relaxation. Assuming a simple Arrhenius law, the superparamagnetic relaxation time is[8]

$$\tau = \tau_0 \exp(CV/k_B T), \tag{1}$$

where C is the total magnetic anisotropy energy per volume, V is the particle volume, and τ_0 is related to the natural gyromagnetic precession time, estimated to be in the range of 10^{-9}–10^{-13} s. Superparamagnetic behavior can be observed by using an instrument with a characteristic measuring time (τ_i) and at temperatures above the blocking temperature (T_{Bi}), defined by

$$T_{Bi} = CV/k_B[\ln(\tau_i/\tau_0)]\,. \tag{2}$$

At $T > T_{Bi}$, the relaxation time of the magnetic moment vectors is shorter than τ_i, hence the specimen appears to be paramagnetic even though each granule remains magnetically ordered. Superparamagnetism and the associated blocking phenomenon have been observed in magnetic granular materials by several techniques.[6,9,10] The two techniques we employed were SQUID magnetometry and ^{57}Fe Mössbauer spectroscopy with characteristic times of $\tau_1 = 10$ s and $\tau_2 = 10^{-8}$ s, respectively. Such a large difference in characteristic times enables us to determine separately the relaxation time constant τ_0, and the magnetic anisotropy energy (CV) of the granules. A significant advantage of using two measuring techniques is that the ratio of the measured blocking temperatures

$$T_{B1}/T_{B2} = \ln(\tau_2/\tau_0)/\ln(\tau_1/\tau_0) \tag{3}$$

is *independent* of sample. From Eq. (2), using the values of τ_1, τ_2, T_{B1}, and T_{B2} one can obtain the magnetic anisotropy energy via

$$CV = k_B T_{B1}[\ln(\tau_2/\tau_1)/(1 - T_{B1}/T_{B2})]\,. \tag{4}$$

For the $Fe_{60}(SiO_2)_{40}$ sample deposited at 675 K, the magnetization under an applied field of 10 Oe is shown in Fig. 3, where the zero-field-cooled (ZFC) and field-cooled (FC) data are shown. $T_{B1} = 160$ K is chosen to be the cusp below which irreversible behavior is observed. The granular sample was then measured by ^{57}Fe Mössbauer spectroscopy. At temperatures above the blocking temperature (T_{B2}), i.e., in the superparamagnetic regime, only a central peak was observed with no magnetic hyperfine splitting. At lower temperatures, magnetic hyperfine splitting appears, whose intensity increases at the expense of that of the central peak. The value of $T_{B2} = 450$ K can be conveniently determined using a zero-velocity thermal scan method, in which the in-

tensity of the central peak is measured as the sample temperature is varied. For other samples, of course the values of T_{B1} and T_{B2} will be different, but the ratio of T_{B1}/T_{B2} remains the *same* at 0.35. It is clear from Eq. (4), since the terms within the brackets are independent of samples, CV scales with the blocking temperature. The average diameter of the small particles obtained from TEM (Fig. 1) is 45 Å for $Fe_{60}(SiO_2)_{40}$ prepared at 675 K. Consequently the magnetic anisotropy constant (C) is 1.5×10^7 erg/cm^3. This value is about two orders of magnitude larger than bulk magnetocrystalline anisotropy of Fe (1×10^5 erg/cm^3),[4] indicating that the magnetocrystalline anisotropy energy is not the main contribution in ultrafine single-domain particles.

In summary, we have synthesized Fe-SiO_2 granular films with different particle sizes by changing the substrate temperature. The much enhanced magnetic coercivity has been found to scale with the particle size. The ferromagnetic-superparamagnetic transition has been studied by both SQUID magnetometry and Mössbauer spectroscopy. From the measured blocking temperatures, whose ratio is found to be independent of samples, we have determined the magnetic anisotropy energy. The anisotropy constant is much larger than that due to magnetocrystalline anisotropy.

ACKNOWLEDGMENT

This work was supported by ONR Contract No. N0001485-K-0175.

[1] B. Abeles, P. Sheng, M. D. Couts, and Y. Arie, Adv. Phys. **24**, 407 (1975).
[2] Ping Sheng, Phys. Rev. B **31**, 4906 (1985).
[3] D. Shoenberg, *Superconductivity* (Cambridge University Press, London, 1962).
[4] J. J. Hauser, Solid State Commun. **37**, 349 (1981).
[5] J. I. Gittleman, Y. Goldstein, and S. Bozowski, Phys. Rev. B **5**, 3609 (1972).
[6] J. I. Gittleman, B. Abeles, and S. Bozowski, Phys. Rev. B **9**, 3891 (1974).
[7] S. Barzilai, Y. Goldstein, and I. S. Helman, Phys. Rev. B **23**, 1809 (1981).
[8] I. S. Jacobs and C. P. Bean, in *Magnetism III*, edited by G. T. Rado and H. Suhl (Academic, New York, 1963), p. 275.
[9] J. L. Dormann, D. Fiorani, J. L. Tholence, and C. Sella, J. Magn. Magn. Mater. **35**, 119 (1983); D. Fiorani, J. L. Dormann, J. L. Tholence, L. Bessais, and D. Villers, J. Magn. Magn. Mater. **54–57**, 173 (1986).
[10] S. Morup, H. Topsoe, and B. S. Clausen, Phys. Scr. **25**, 713 (1982).

Preparation and properties of sputter-deposited crystalline ultrafine particles

S. Ohnuma and A. Kunimoto
The Research Institute of Electric and Magnetic Alloys, Sendai 982, Japan
T. Masumoto
Institute for Materials Research, Tohoku University, Sendai 980, Japan

The composition and size dependence of the magnetic properties of crystalline Fe-Co and Ni ultrafine particles has been investigated. Samples were prepared by sputter deposition onto sputter-etched polyimide substrates. Little difference between the magnetic properties of crystalline and amorphous particles was found in Fe-rich alloys, but we found a greater influence of magnetocrystalline anisotropy in Co-rich alloys. When the particles are larger than 2500 Å, the samples have negative anisotropy K_u (easy direction parallel to the substrate plane). As the particle diameter decreases, K_u becomes positive, and the coercive field H_c increases from a few hundred oersteds to a maximum of more than 1000 Oe. Below a particle diameter of about 1000 Å, M_s, K_u, and H_c all drop rapidly toward zero, presumably due to the appearance of superparamagnetism. Annealing above about 200 °C leads to significant increases in H_c, K_u, and M_s, and also to significant changes in the line shapes of the x-ray diffraction patterns, as a result of stress relaxation. A low-temperature diffusion process leading to changes in the morphology of the subparticles may also be a cause of the increment of magnetic properties on annealing.

INTRODUCTION

We have previously reported a method for producing a planar array of elongated ultrafine amorphous particles (UFAP).[1] The particles were elongated fingerlike projections in a perpendicular array on the polymer substrate, and were mostly isolated from one another. They had a magnetic easy axis perpendicular to the substrate surface, attributed to the shape anisotropy of the particles, and coercive fields as high as 700 Oe.[2] Very recently, the first attempt to use these UFAP as perpendicular recording media has been carried out.[3]

The same technique can be used to prepare arrays of crystalline particles. This paper reports the composition and size dependence of magnetic properties of crystalline Fe-Co particles covering the entire composition range, and also of pure Ni particles, as well as the effects of annealing on the magnetic properties.

EXPERIMENT

All the samples in this work were made by rf sputtering from homogeneous arc-melted alloy targets, using essentially the same preparation technique described previously.[1,3] The particles were examined by scanning electron microscopy (SEM), and the crystalline structure was confirmed by x-ray diffraction. Annealing treatments were carried out in vacuum (10^{-6} Torr) at temperatures up to 500 °C. The magnetic hysteresis loop at room temperature was measured with a vibrating sample magnetometer at a maximum applied field of 9 kOe to give the total magnetization, the magnetic anisotropy, and coercive fields parallel and perpendicular to the substrate plane.

RESULTS AND DISCUSSION

As in the case of amorphous ultra fine particles,[1-3] the samples have the geometrical form of conventional thin films, but the surfaces are dull black with very low reflectivity. The particle size and shape were kept similar for samples over the full range of composition studied.

X-ray diffraction shows a bcc structure from $x = 0.0$ to 0.8 in $Fe_{1-x}Co_x$ UFP. hcp and fcc structures are found in Co and Ni UFP, respectively. Each line of these diffraction patterns was considerably broadened from the stress which appears during the deposition.

Figure 1 shows the composition dependence of the mag-

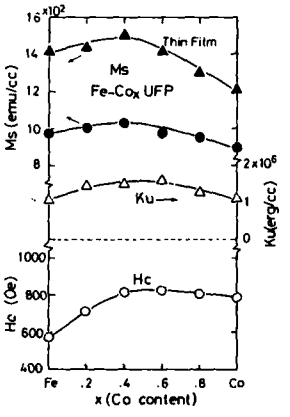


FIG. 1. Composition dependence of magnetic properties of as-deposited Fe UFP. Curve labelled "Thin Film" is for samples deposited on glass substrates at the same time as the corresponding UFP samples.

 0021-8979/88/084243-03$02.40 © 1988 American Institute of Physics

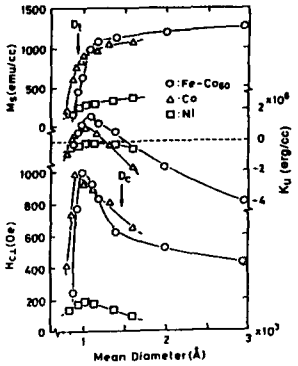


FIG. 2. Change in magnetic properties with mean diameter of $Fe_{40}Co_{60}$, Co, and Ni particles.

netic properties of as-deposited Fe-Co UFP, with a diameter of about 1000 Å and an aspect ratio of about 4. Measurement techniques are described in Ref. 1. The variation of the magnetization is similar to that of bulk samples and of continuous (nonparticle) thin films. However, the absolute value of M_s is lower; this will be discussed later. Perpendicular anisotropy larger than 10^6 erg/cm^3 is seen in all compositions, with composition dependence almost the same as that of M_s. Coercive field increases with increasing Co content, has a broad maximum around $x = 0.6$, and then decreases very slightly.

The fact that the measured coercivity remains high while the magnetization decreases in Co-rich particles means that the anisotropy cannot be due solely to shape anisotropy. Co has strong uniaxial magnetocrystalline anisotropy; therefore, crystalline anisotropy can contribute to H_c in single-crystal Co-rich particles. This interpretation is supported by the behavior of amorphous $(Fe\text{-}Co)_{80}B_{20}$ UFP,[2] which have no magnetocrystalline anisotropy; in these materials, H_c and K_u show a sharp decrease at high Co contents.

Particle size effects on magnetic properties are shown in Figs. 2 and 3. The particle size was controlled by varying the deposition time, with other preparation conditions fixed. Below a critical value of diameter (D_T = 800–1000 Å), M_s, K_u, and H_c all drop rapidly toward zero. This is attributed to the onset of superparamagnetic behavior. The reduced absolute value of M_s in UFP is attributed to the morphology of UFP. The fingerlike particles are subdivided into smaller particles of about 100–300 Å, some of which may be superparamagnetic.[2] [See Fig. 5(a).]

As the particle diameter increases, the easy magnetization axis rotates to be parallel to the sample surface, as shown by the anisotropy data in Fig. 2. This result is strongly related to the morphology of particles[2]; with longer sputtering time, the individual fingers grow together at their tips and eventually the surface becomes a continuous film.

The particle size dependence of H_c is also shown in Fig. 2. A maximum coercive field greater than 1000 Oe is obtained at the critical diameter D_T for the $Fe_{40}Co_{60}$ alloy. The rapid drop in H_c above D_T is attributed to the size effect in single domain particles. The slower decrease in H_c above 2500 Å may be due to domain wall nucleation. The arrow labelled D_C in Fig. 2 indicates the calculated critical diameter where a domain wall could be nucleated in these particles, approximated by Kittel's method; the calculated D_C is near the diameter where H_c begins to decrease. The properties of Ni particles depend less strongly on particle diameter.

However, SEM observation of the particles and the behavior of K_u show that the decrease in H_c begins at the diameter at which the particle tips start to join together. Therefore, Néel's model[5] may also have to be considered.

Figure 3 summarizes the effects of successive 20-min annealing treatments on the magnetic properties of Co and Ni UFP. The coercive field of the annealed samples is greater than 1000 Oe for all compositions in the Fe-Co series. The saturation magnetization of Co UFP increases by more than 50% after annealing. The improvement is interpreted in

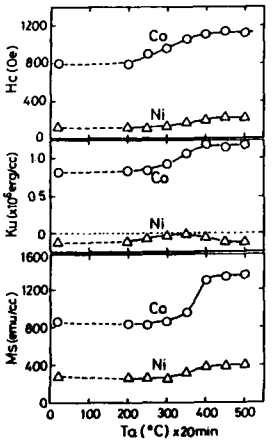


FIG. 3. Effect of annealing on magnetic properties of Co and Ni particles.

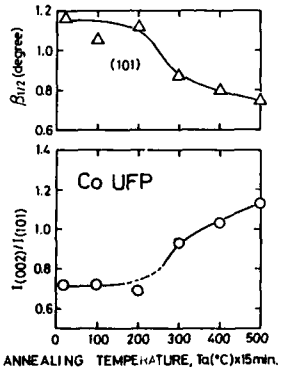


FIG. 4. Dependence of x-ray linewidth and intensity on annealing temperature of Co UFP.

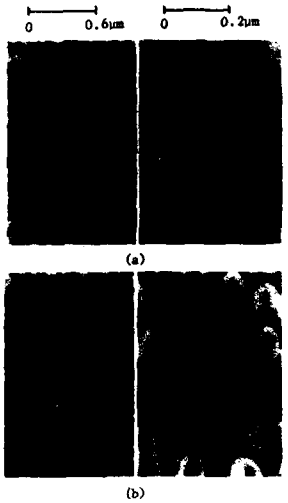


FIG. 5. SEM photograph of $Fe_{40}Co_{60}$ UFP before (a) and after (b) annealing.

terms of structural relaxation and of low-temperature diffusion processes leading to changes in particle morphology. Figure 4 shows the result of x-ray diffraction analysis of Co ultrafine particles. With annealing temperatures over 150 °C, the x-ray linewidth decreases, suggesting stress relaxation or grain growth. Also, the relative intensity $I_{(002)}/I_{(101)}$ increases, indicating crystal orientation. Furthermore, high magnification SEM examination shows that the surface of each particle after annealing above about 300 °C changes from bumpy to very smooth (Fig. 5). This change can be explained by assuming that small secondary smaller particles diffuse together at quite low temperature, thus changing from superparamagnetic to ferromagnetic.

ACKNOWLEDGMENTS

We would like to thank M. Saito of the Research Institute of Electric and Magnetic Alloys and M. Yamada of Hitachi Co. for SEM observations. C. D. Graham, Jr. helped with the preparation of the manuscript.

[1] S. Ohnuma, Y. Nakanouchi, C. D. Graham, Jr., and T. Masumoto, IEEE Trans. Magn. MAG-21, 2038 (1985).
[2] S. Ohnuma, Y. Nakanouchi, C. D. Graham, Jr., and T. Masumoto, IEEE Trans. Magn. MAG-22, 1098 (1986).
[3] A. Kunimoto, M. Kato, T. Masuda, S. Ohnuma, and T. Masumoto, IEEE Trans. Magn. (to be published).
[4] C. Kittel, Rev. Mod. Phys. 21, 541 (1949).
[5] L. Néel, C. R. Acad. Sci. 224, 1550 (1947).

Variation of magnetic properties with composition in $(Fe\text{-}Ni)_{76}Si_8B_{16}$ amorphous ultrafine particles

S. Ohnuma and M. Mitera
The Research Institute of Electric and Magnetic Alloys, Sendai 982, Japan

C. D. Graham, Jr.
Department of Materials Science and Engineering, University of Pennsylvania, Philadelphia, Pennsylvania 19104

T. Masumoto
Institute for Materials Research, Tohoku University, Sendai 980, Japan

The composition dependence of magnetic properties in ultrafine $(Fe_{1-x}Ni_x)_{76}Si_8B_{16}$ amorphous particles has been investigated. Samples were prepared by sputter deposition onto sputter-etched polyimide substrates. The particle diameter was held constant at about 800 Å, and the L/D ratio was approximately 4. The room-temperature saturation magnetization (M_s) decreases with increasing Ni content and extrapolates to zero at about $x = 0.9$. All the samples showed positive anisotropy (K_u). This anisotropy varied linearly with M_s^2, suggesting that its origin is largely the shape anisotropy of the particles. Furthermore, the measured perpendicular coercive field varied linearly with K_u/M_s, as predicted by a simple Stoner–Wohlfarth single domain model. However, the absolute value of H_c and its angular dependence cannot be explained by the coherent rotation model.

INTRODUCTION

A planar array of elongated ultrafine particles can be prepared by sputter deposition onto a sputter-etched polymer substrate.[1] The long axis of the particles is perpendicular to the plane of the substrate, and the particle diameter can range from a few hundred to a few thousand angstroms, with length-to-diameter ratios up to about 5. The arrays have a magnetic easy axis perpendicular to the substrate surface with $K_u/2M_s^2 = 0.1$ to 0.2, attributed to the shape anisotropy of the particles, and coercive fields as high as 650 Oe (Ref. 2); however, there is limited information on this topic.

In this paper we report on the preparation of ultrafine $(Fe_xNi_{1-x})_{76}Si_8B_{16}$ amorphous particles made in this way. We also describe the composition dependence of magnetic properties over the range $x = 0$ to 0.7, and compare the high coercivity with a Stoner–Wohlfarth model. We chose this alloy system because its magnetization is easily controllable and its magnetic anisotropy is negligible.

EXPERIMENTAL PROCEDURE

Sample preparation was essentially the same as described previously.[1] A polyimide substrate was sputter etched to produce a densely packed array of needlelike projections on its surface. The sputtering targets were homogeneous arc-melted disks of high-purity $(Fe\text{-}Ni)_{76}Si_8B_{16}$. The deposition was carried out at room temperature in Ar at a pressure of 6 mTorr. The presputtering background pressure was in the 10^{-7} Torr range.

The morphology of the particles was examined by scanning electron microscopy (SEM), and x-ray diffraction was used to confirm the amorphous structure. The value of room-temperature saturation magnetization (M_s) was obtained from the field required to saturate the magnetization in a direction perpendicular to the film plane, using a vibrating sample magnetometer. Coercive fields, H_c, parallel and perpendicular to the substrate, and magnetic anisotropy, K_u, were obtained from the hysteresis loop. The effective thickness of the magnetic layer was estimated by direct thickness measurements of continuous (nonparticle) films deposited on glass during the same deposition run as the ultrafine amorphous particle (UFAP) samples. All data presented in this paper are for as-deposited particles.

RESULTS AND DISCUSSION

The samples have the geometrical form of conventional thin films, but the surfaces are dull black with very low reflectivity. Examination of the samples in the scanning elec-

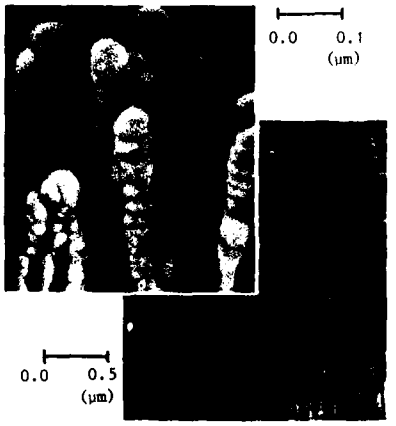


FIG. 1. SEM photographs of sputter-deposited ultrafine amorphous $(Fe_{0.6}Ni_{0.4})_{76}Si_8B_{16}$ particles.

 0021-8979/88/084246-03$02.40 © 1988 American Institute of Physics

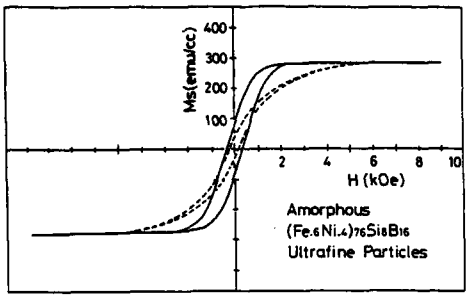


FIG. 2. Hysteresis loops of $(Fe_{0.6}Ni_{0.4})_{76}Si_8B_{16}$ UFAP measured parallel and perpendicular to the substrate plane.

tron microscope shows that elongated fingers of amorphous alloy have grown from the projections on the substrate (Fig. 1). X-ray diffraction reveals a typical amorphous structure for all the compositions studied.

Magnetic properties of ferromagnetic ultrafine particles strongly depend on the size, shape, volume fraction, and size dispersion of the particles. One of the important advantages of this preparation method is the ease of controlling the size and shape of the particles,[1] which are distributed uniformly on the substrate (Fig. 1). The size and shape of the particles could therefore be kept similar for samples over the full range of compositions studied.

Figure 2 shows a typical example of measured hysteresis loops parallel and perpendicular to the substrate. As described previously,[1,2] they have an easy axis of magnetization perpendicular to the substrate plane and a large coercive field, in spite of having an amorphous structure. Figure 3 shows the composition dependence of the magnetic properties of $(Fe_{1-x}Ni_x)_{76}Si_8B_{16}$ UFAP. The value of M_s decreases with increasing Ni content, consistent with earlier data on rapidly quenched amorphous ribbons and with measurements on continuous (nonparticulate) sputtered amorphous films, and extrapolates to zero at about $x = 0.9$. All

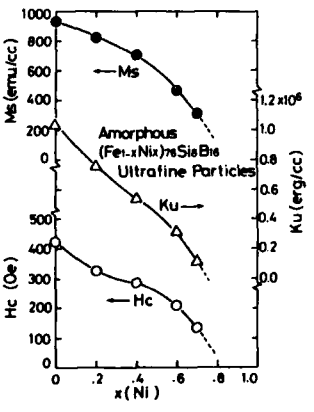


FIG. 3. Composition dependence of magnetic properties of $(Fe_{1-x}Ni_x)_{76}Si_8B_{16}$ UFAP.

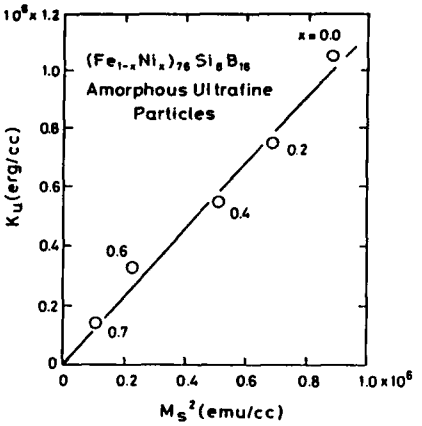


FIG. 4. Perpendicular anisotropy vs square of magnetization for $(Fe_{1-x}Ni_x)_{76}Si_8B_{16}$ UFAP.

the samples showed positive anisotropy K_u, meaning that the easy direction of magnetization is perpendicular to the plane of the substrate. The coercive field also decreases with increasing Ni content in almost the same manner as K_u, and extrapolates to zero at about $x = 0.8$.

Figure 4 shows the measured anisotropy plotted against the square of magnetization over almost the entire composition range. The relationship is linear with relatively little scatter, suggesting that these UFAP samples are behaving as a collection of single-domain particles whose anisotropy is controlled by their shape.

Figure 5 shows that the measured coercive field varies linearly with the saturation magnetization for samples of all compositions. This result indicates that the coercive field can be attributed to the shape anisotropy of the particles, and also suggesting that the particles are single domain particles.

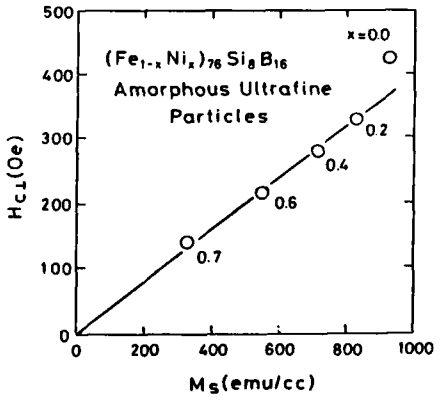


FIG. 5. Coercive field vs saturation magnetization for $(Fe_{1-x}Ni_x)_{76}Si_8B_{16}$ UFAP.

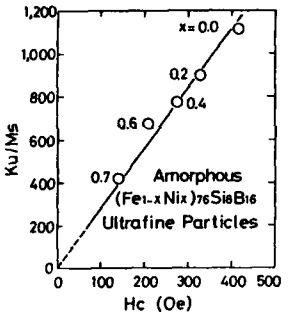


FIG. 6. Ratio of anisotropy to magnetization vs coercive field for $(Fe_{1-x}Ni_x)_{76}Si_8B_{16}$ UFAP.

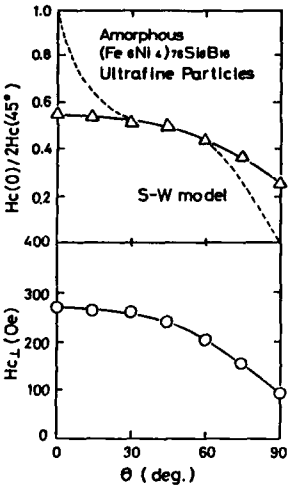


FIG. 7. Angular dependence of coercive field for $(Fe_{0.6}Ni_{0.4})_{76}Si_8B_{16}$ UFAP.

Furthermore, according to the well-known Stoner–Wohlfarth coherent rotation model, the coercive field is known to be proportional to the ratio of anisotropy to magnetization. As shown in Fig. 6, the measured perpendicular coercive field of the UFAP varies linearly with K_u/M_s, as predicted by Stoner and Wohlfarth.

Although the magnetic properties agree qualitatively with the coherent rotation model, if we calculate the shape anisotropy the absolute value of H_c is about one-fifth of the single-domain value. And the data for the angular dependence of coercive field (Fig. 7) do not fit the coherent rotation model. The discrepancies are presumably due to particle interaction effects,[5] plus the effect of the complex but unknown morphology where the magnetic material is attached to the substrate projections. Some magnetic material is deposited in the valleys between the substrate projections and may act as domain nucleation sites.

ACKNOWLEDGMENTS

Helpful discussions with K. Shirakawa and A. Kunimoto are gratefully acknowledged. We also would like to acknowledge M. Yamada at Hitachi, Ltd. for his assistance with the SEM measurements.

[1] S. Ohnuma, Y. Nakanouchi, and T. Masumoto, Proceedings of the 5th International Conference on Rapidly Quenched Metals, 1117 (1984); S. Ohnuma, Y. Nakanouchi, C. D. Graham, Jr., and T. Masumoto, IEEE Trans. Magn. MAG-21, 2038 (1985).
[2] S. Ohnuma, Y. Nakanouchi, C. D. Graham, Jr., and T. Masumoto, IEEE Trans Magn. MAG-22, 1098 (1986).
[3] T. Masumoto, K. Watanabe, M. Mitera, and S. Ohnuma, in *Amorphous Magnetism II*, edited by R. A. Levy and R. Hasegawa (Plenum, New York, 1977), p. 369.
[4] E. C. Stoner and E. P. Wohlfarth, Trans. R. Soc. London Ser. A 240, 599 (1948).
[5] L. Néel, C. R. Acad. Sci. 224, 1550 (1947).

Particulate metallic glass composite magnetostrictors for interferometric magnetometry

D. Brugel, M. R. J. Gibbs, and P. T. Squire
School of Physics, University of Bath, Bath, BA2 7AY, United Kingdom

The design of sensor heads for fiber optic interferometric magnetometers is critical when sub-nano-Tesla fields are to be measured. Magnetically soft metallic glasses can exhibit large magnetostrictions and are candidates as materials for this application. However, their usefulness is limited at high frequencies through eddy current losses in bulk materials. This paper discusses the use of particulate metallic glasses in an inert binder. Measurements are presented on magnetization and magnetostriction of these composite materials in the quasi-dc regime. Their dynamic behavior when used as magnetic field sensors is also described.

I. INTRODUCTION

The use of magnetostrictive particles as sensor head constituents for interferometric magnetometers (for principle, see, for example, Ref. 1) has the potential of partly overcoming sensitivity reductions at high frequencies due to eddy current loss.

A preliminary study of the magnetization loop and magnetostriction of Metglas 2605SC (Ref. 2) in a platelet state is presented. The specimens are a composite of the magnetic material in platelet form embedded in a binder.

A number of parameters may be influential in the achievement of a useful magnetostriction value (at least a few ppm). They fall into two related categories: (a) those which affect the magnetostriction and magnetization of individual platelets: platelet size, shape, and annealing conditions; and (b) those which control the magnetization of the specimen and its (engineering) magnetostriction λ: platelet orientation, packing factor, voids volume fraction, and mechanical properties of the matrix. The importance of each of these parameters (except platelet geometry, over which we have at present no control, and voids volume fraction for which results are not available at the time of writing) is discussed on the basis of systematic measurements of M-H and λ-H loops after a section on the production of platelets and preparation of specimens. In the light of these results an attempt is made to use the optimum composite as a magnetic sensor head constituent in an all-fiber Mach-Zehnder interferometer.

II. PLATELET PRODUCTION AND SPECIMEN PREPARATION

25-mm-wide Metglas 2605SC was embrittled in air at 450 °C for 10 min. The strip was then cut into 50–75 mm lengths for a ball mill which was run for 24 h at approximately 60 rpm. This produced platelets having a range of sizes after sieving: <53, 90–150, and 180–250 μm. It should be noted that these sizes are well above the critical dimension for single domain behavior. X-ray diffraction did not reveal any sign of crystallization.

The magnetic material was mixed by hand in the selected binder: epoxy, cement, or engineering adhesive.[3] The composite was then placed in a jig for curing. Specimens of 5 cm $\times$ 1–2 mm diameter were thus produced.

III. INFLUENCE OF SELECTED FACTORS ON dc MAGNETIZATION LOOPS AND MAGNETOSTRICTION

For sensor applications one objective is a large gradient of magnetostriction with applied field ($\Delta\lambda/\Delta H$). This requires a large magnetization change with the applied field, both at dc and modulation frequencies. The factors mentioned in the Introduction were taken in turn and the magnetization and magnetostriction loops were measured using the apparatus described in Refs. 4 and 5, respectively.

Figure 1 shows the effect of platelet size range on the following properties: (a) magnetization at the maximum field available (9000 A/m), (b) coercive field (H_c) corresponding to a minor loop (9000 A/m is not sufficient to take any specimen to saturation), and (c) magnetostriction (obtained between 0 and 6000 A/m).

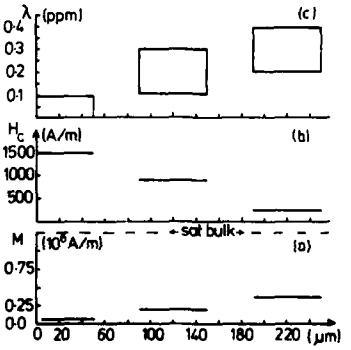


FIG. 1. Magnetization at 9 kA/m (a) coercive field (b), and dc magnetostriction (c) as a function of platelet size range. The Metglas 2605SC (Ref. 1) platelets were packed at 70% of total weight in an epoxy matrix (GY250/HY837) (Ref. 2).

 0021-8979/88/084249-03$02.40 © 1988 American Institute of Physics

For 70% weight of magnetic material in an epoxy binder, the change in magnetization is roughly fivefold (from 75 to 390 kA/m) for platelet sizes varying from 50 to 250 μm but may vary according to other factors. The specimens have low susceptibility and the magnetization at 9000 A/m is well below the bulk magnetization at this level of drive field. On the other hand, H_c varies from a few thousand to a few hundred A/m as size increases, but is still well above the bulk value.

The magnetostriction values for all the ranges of platelet size are of the order of 0.1 ppm, much smaller than that of the bulk value (30 ppm) for the as-received state. However, despite a spread of results reflecting the variations between nominally identical samples, Fig. 1 shows an upward trend for the magnetostriction as the platelet size increases; maximum values of 0.4 ppm were obtained for the larger sizes.

The effect of annealing was investigated on platelets of $< 53\ \mu$m; these were annealed prior to immersion in the epoxy matrix at 380 °C for 10 min in a flow of argon pressurized at 1/2 atm. A reduction in H_c was observed (1.5 kA/m down to 0.6 kA/m) and also an increase in the magnetization (52–80 kA/m). The magnetostriction of the epoxy composites with preannealed platelets was not distinguishable from unannealed ones.

In order to investigate platelet orientation, two epoxy composite specimens with their long axes orthogonal were placed for curing in a field of 0.4 T parallel to one of the long axes. The hysteresis loops were then measured and the change in their shape suggests orientation of the platelets (Fig. 2). Any coercive field change was undetected, and the magnetostriction values lie in the range of results of Fig. 1.

The magnetic material concentration was stepped from 70% to 85% by weight in an epoxy matrix for the size range 90–150 μm. Figure 3 shows an increase in the magnetization at 9000 A/m. A possible change in coercive field was again not detected, and the magnetostriction is small.

To assess the role of the matrix, the platelets ($< 53\ \mu$m) were immersed in the unactivated resin GY250 (viscosity of 22–28 Pa s at 21 °C). Another specimen was prepared in the usual way, with a hardener. The results were a decrease in magnetization from 87 to 75 kA/m going from the soft to the hard matrix; the coercive field underwent the same trend,

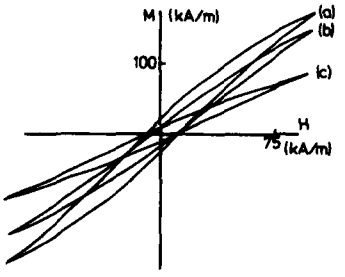


FIG. 2. Effect of curing in a 0.4 T magnetic field on the hysteresis loop. The specimens were 90–150-μm platelets of Metglas 2605SC (Ref. 1) embedded in an epoxy matrix (GY250/HY837) (Ref. 2) and packed at 70% of specimen weight. (a) Field parallel to specimen axis, (b) no field, (c) field ⊥.

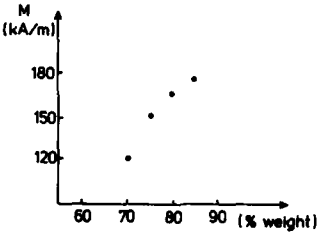


FIG. 3. Effect of platelet concentration (% of specimen weight) on magnetization at 9 kA/m for 90–150-μm Metglas (2605SC) platelets (Ref. 1) in an epoxy matrix (GY250/HY837) (Ref. 2).

from 2.7 kA/m down to 1.5 kA/m. This was also observed for thermally treated (preannealed) platelets and gave a decrease of magnetization form 139 to 80 kA/m; the coercive field was down from 830 to 530 A/m. The comparison between various cured binders never exhibited such a change. In this case the importance of the binder lies rather on its effect on the magnetostriction, easiness of platelet orientation, and high achievable packing factor. For orientation, we need a low initial viscosity matrix; for a high magnetostriction, experience shows that the epoxy binder inhibited the specimen expansion less than cement (Autostic) and engineering adhesive (Rocksett).[3] If a thermal treatment is required, we need a binder with high-temperature capabilities. These requirements are not always compatible.

IV. OPTIMUM MATERIAL FOR A MAGNETIC SENSOR

The composite chosen was an 80% weight concentration of 190–250 μm thermally treated (380 °C, 10 mins in $\frac{1}{2}$ atm argon) platelets oriented along the length of a GY250-HY1341GB matrix specimen. The magnetization at 9000 A/m, the coercive field, and the dc magnetostriction were 290 kA/m, 340 A/m, and 0.43 ppm, respectively. The response at 1 kHz of this sensor head and a strip of bulk material were measured in a standard all-fiber Mach-Zehnder interferometer.[1]

The output was obtained as a function of dc bias field. For comparison, the rms value of the ac field was taken to be half the coercive field of the sample studied, i.e., 3.1 A/m for the Metglas strip and 170 A/m for the composite. In this condition and in the linear region of the curves the ratio of the slopes ($d\phi/dH$) between composite- and strip-based sensors outputs was 0.01 to 0.02. This shows the difficulty of the composite to be magnetized at ac as well. The extent of the quasi-linear region for the composite sensor is about 15 kA/m against 1.7 kA/m for the Metglas strip. 20 kHz was the upper limit for a response of the composite to a 1 kHz, 80 A/m (rms) field whereas the strip reacted to 3.1 A/m (rms) at 100 kHz.

V. DISCUSSION

The coercive field of the composites is very much larger than in the bulk material, but annealing can lead to partial recovery. H_c decreases with increased platelet size both in

the unannealed and annealed states. There is no detected packing factor dependence of coercive field.

These results indicate that the magnetization process in the composite materials is governed by the magnetic properties of the individual platelets. Optical microscopy reveals ploughing and bending of the platelets, and Gibbs *et al.*[4] have demonstrated the increase of H_c on inhomogeneous deformation and its recovery by annealing. Therefore, the increased H_c (compared to annealed platelets) is ascribed to inhomogenous plastic deformation of the platelets during ball milling. Maximum domain wall pinning comes when the pinning center is spatially of the order of the domain wall width.[6] Given that there is no observable packing factor dependence of H_c, we assume that there are no domain structures larger than the platelet size, and hence that the domain wall pinning centers are within each platelet. The shear bands and their associated strain fields are therefore the likely cause of domain wall pinning in the individual platelets.

After annealing, the irregular surface topology may provide the difference from the bulk material and explain the size dependence of H_c as the surface-to-volume ratio increases with decreasing size.

Figure 1 shows the magnetization increasing as the particle size increases. Also, annealing increases the magnetization in the maximum field. We therefore assume that the magnetization attained is again determined by the individual platelets. Inhomogeneous deformation increases magnetization energy because the smaller the platelet the greater the degree of deformation, explaining the subsequent reduction in magnetization observed. Annealing reduces the stress in the platelets and leads to a reduction of magnetization energy and an increase in magnetization. Curing the epoxy matrix does decrease the magnetization, showing that there is an interaction between the platelets and matrix.

Figure 2 reveals a decrease of the spread in platelet orientation with respect to the specimen long axis. This is supported by optical observation and results in the increase in the magnetization. There is some magnetostatic interplatelet interaction as there is a packing factor dependence of magnetization (Fig. 3).

The magnetostrictions achieved are all very low compared to bulk material. The magnetization energies and coercive fields are large, and in the fields available the magnetization change, and hence magnetostriction, is small. Also the matrix may constrain the material or give poor strain transfer. More importantly, the gradient of magnetostriction with applied field, the crucial parameter for sensors, is very low, and this is reflected in the interferometer results.

VI. CONCLUSIONS

In general, for metallic glass platelet composites, the magnetization, coercive field, and engineering magnetostriction were severely degraded compared to results on ribbon material of the same composition.

Consequently, the performance of the composite as a magnetic sensor head in a Mach-Zehnder interferometer was also worse than for ribbon form material: the ac (1 kHz) field-induced electrical output phase change with dc field was 2% of the as-received sensor response. The primary cause of this is the low susceptibility of the composite giving little magnetization change, and hence a small magnetostrictive response.

ACKNOWLEDGMENTS

We acknowledge the award of an S.E.R.C. cooperative grant with S.T.C. Technology Ltd. for this program.

[1] A. Dandridge, A. B. Tveten, G. H. Sigel, Jr., E. J. West, and T. G. Giallorenzi, Electron. Lett. **16**, 508 (1980).
[2] Metglas is a registered trademark of the Allied Corporation.
[3] Epoxy Resin GY250; hardeners HY837 or HY1341GB [Ciba Geigy (UK), Ltd.]. Autostic: industrial adhesive/cement, Rocksett: engineering adhesive (Carlton Brown and Partners, Ltd.).
[4] M. R. J. Gibbs, J. E. Evetts, and N. J. Shah. J. Appl. Phys. **50**, 7642 (1979).
[5] P. T. Squire and M. R. J. Gibbs, J. Phys. E **20**, 499 (1987).
[6] B. D. Cullity, *Introduction to Magnetic Materials* (Addison Wesley, Reading, MA, 1972), p. 320.

Enhanced magnetic coercivity in magnetic granular solids

Gang Xiao and C. L. Chien
Department of Physics and Astronomy, The Johns Hopkins University, Baltimore, Maryland 21218

We have fabricated magnetic granular Fe-SiO_2 solids over a wide metal volume fraction range 15%–100%. The microstructure of the samples has been characterized by using transmission electron spectroscopy, electron diffraction, and Mössbauer spectroscopy. Giant magnetic coercivity, as high as 2500 Oe, has been observed in samples with nanometer particle size. The behaviors of coercivity across the metal volume fraction range are attributed to the change of particle size and percolation effect.

I. INTRODUCTION

Magnetic fine particles in the size range of a few to a few tens of nanometers have been of persistent scientific interest and of technological importance.[1-3] This is the size range near or below the critical size for the formation of single-domain particles in which superior magnetic properties, unattainable in bulk solids, are realized. Chemical methods (e.g., forced hydrolysis) are often used to produce relatively large (hundreds of nanometer) and free-standing particles. The fine particles must be prevented from coalescing into large aggregates, and in the case of metal particles, from oxidizing. This necessitates the use of an inert medium in which the fine particles are dispersed as evenly as possible through nontrivial processes.

A different, and in many respects, superior method for making ultrafine magnetic particles is the vapor deposition of metal-insulator composites. These granular metal films consist of ultrafine metal particles of only a few nanometers in size with rather uniform sizes and dispersion. It should be noted that in the vapor deposition method, the fabrication, the dispersion of the ultrafine particles, as well as coating onto a desirable surface are achieved simultaneously without additional processing.

Because of the unique microstructure of ultrafine particles, unusual properties have been realized in granular metal films.[1-3] In this paper, we will describe the fabrication and characterization of a magnetic granular system Fe-(SiO_2) where the ultrafine Fe particles are embedded in an amorphous SiO_2 matrix. A dramatically enhanced magnetic coercivity, as high as 2500 Oe, achieved in this granular system will be reported. Such coercivity is about 50 times higher than that of the bulk Fe.

II. EXPERIMENTS

The granular Fe-(SiO_2) samples were fabricated by using a high-rate rf magnetron sputtering system. Samples over a large Fe volume fraction range (p) of 15%–100% have been made. The sputtering targets were composite targets of pure Fe and SiO_2 with appropriate composition. The presputtering pressure in the vacuum chamber was in the 10^{-8} Torr range. Care was taken in maintaining constant sputtering conditions to assure a uniform size of the ultrafine granules. The samples, with thicknesses of 2–5 μm, were deposited onto various substrates kept at room temperature. The composition of the samples was crosschecked with atomic absorption, x-ray fluorescence analysis, and target composition, with general agreement within 5 at. %.

The microstructures of the samples were examined by transmission electron microscopy (TEM), electron and x-ray diffraction, and complimented by ^{57}Fe Mössbauer spectroscopy. Magnetic measurements were performed by using a SQUID magnetometer. The coercivity was determined from either a complete or a portion of a hysteresis loop with magnetic fields up to 50 kOe. Measurements were made at various temperatures from 2 to 400 K.

III. RESULTS AND DISCUSSIONS

Inherent to granular metal systems is the phenomenon of percolation. The percolation threshold (p_c), above which a connecting network of granules exist, is usually near a metal volume fraction (p) of about 50%–60%.[1] This is illustrated by the TEM micrographs shown in Fig. 1, where the structures of two samples, $Fe_{90}(SiO_2)_{10}$ and $Fe_{60}(SiO_2)_{40}$,

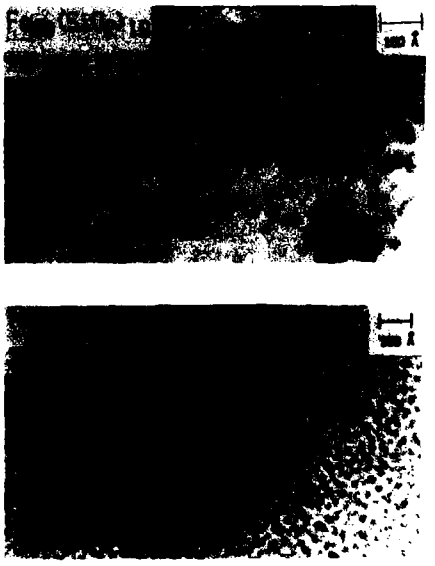


FIG. 1. TEM micrograph of granular $Fe_{90}(SiO_2)_{40}$ (70 vol. % Fe) and $Fe_{60}(SiO_2)_{40}$ (29 vol. % Fe) films.

 0021-8979/88/084252-03$02.40 © 1988 American Institute of Physics

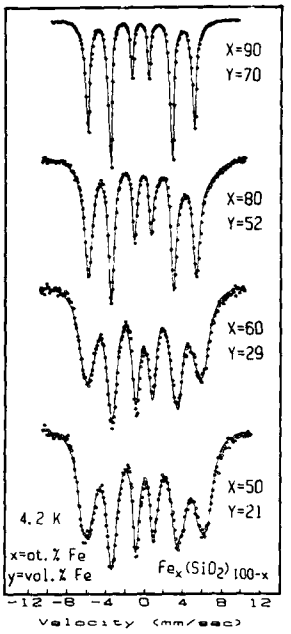


FIG. 2. Mössbauer spectra of various granular Fe-SiO_2 solids at $T = 4.2$ K.

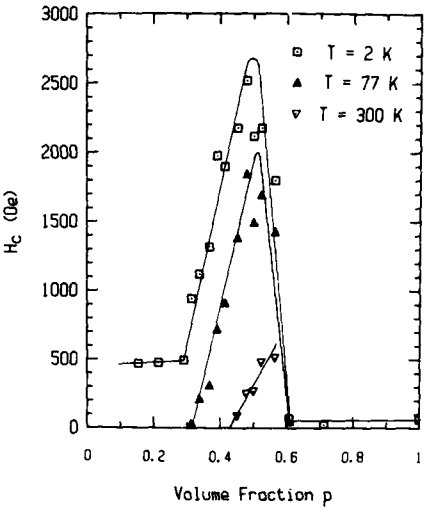


FIG. 3. Magnetic coercivities measured at $T = 2$, 77, and 300 K of Fe-SiO_2 granular films as a function of Fe volume fraction.

with respective Fe volume fractions of 70% and 29% (which are above and below the percolation threshold), are clearly displayed. The $Fe_{90}(SiO_2)_{10}$ sample consists of large connecting granules, while the small Fe granules are well separated in $Fe_{60}(SiO_2)_{40}$. With room-temperature substrates, we observed a monotonic increase of granule size with Fe volume fraction. Specifically, we obtained average granule sizes of 17, 38, 50, and 70 Å for samples with $p = 14\%, 29\%, 38\%$, and 70%, respectively. These approximately equiaxial granules exist in magnetic single-domain form because their sizes are smaller than the critical size for single-domain Fe partic[1] (~ 200 Å).[4]

Electron diffraction established that, for samples with relatively large particles whose diffraction patterns are not excessively broad, the granules have a bcc structure, the same as α-Fe. Further confirmation came from ^{57}Fe Mössbauer spectroscopy. Figure 2 shows the Mössbauer spectra of a number of granular samples at 4.2 K. For sample with smaller granular sizes, as realized in samples with lower volume fraction, the spectra lines are broader as expected. The line positions are slightly different from that of bulk Fe. It is also apparent that there are no evidence of large contributions from Fe oxides. From these results one c ın conclude that the granules are essentially pure Fe granules.

In Fig. 3, the coercivity (H_c) data of the Fe-(SiO_2) system at 2, 77, and 300 K are presented as a function of the Fe volume fraction p. The results at 2 K are close to the ground-state properties, in which one observes a giant enhancement of H_c. Spectacular changes of H_c occur in the range of $29\% \leqslant p \leqslant 60\%$. Keeping in mind that H_c of bulk Fe is less than 50 Oe due to magnetic multidomain structure, we find that the granular Fe sample has an H_c as high as 2500 Oe at $p = 46\%$. Then H_c precipitously drops to a value of about $H_c \sim 50$ Oe, which is close to the value of the sputtered bulk pure Fe, and remains at that value from $p = 60\%$ to 100%. The precipitous decrease in H_c is attributed to the percolation effect. As p approaches the percolation threshold, formation of a connecting network of small granules starts to occur. As a result, magnetic coercivity reduces substantially.

As shown in Fig. 3, H_c decreases as temperature increases due to superparamagnetism.[4,5] According to Kneller

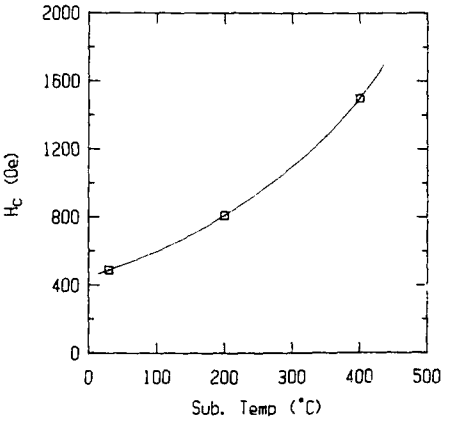


FIG. 4. Magnetic coercivity as a function of sample deposition temperature for a Fe-(SiO_2) sample with a volume fraction of 28%.

and Luborsky,[6] the temperature dependence of coercivity for noninteracting uniform particles is

$$H_c = H_{c0}(1 - \sqrt{T/T_g}), \quad (1)$$

where T_g is the onset temperature for superparamagnetism which is proportional to the magnetic anisotropy energy KV, with K being the anisotropy constant and V the granular volume.

For samples deposited at room temperature, larger particle sizes are realized in samples with higher values of p as mentioned earlier. This would normally result in a stronger dipole-dipole interaction, which tends to decrease H_c as established both theoretically[7] and experimentally.[8] Therefore, the observed increase of H_c must be associated with the effects due to the increase of particle size. This indeed is supported by the following experiment. We deposited three samples with the same volume fraction (29%) at three different temperatures 30, 200, and 400 °C. The high substrate temperature effectively enlarges the particle size. In Fig. 4, H_c is plotted against the substrate temperature. Clearly, high H_c is a result of enlarged particle size. It is noted that the strength of the dipole-dipole interaction in samples with the same volume fraction is about the same.

There are two essential features of the behavior of H_c in the granular Fe-SiO_2 system. First, H_c increases dramatically with particle size. Such a phenomenon, observed at 2 K, is not a thermal artifact due to magnetic relaxation,[5] but intrinsic to Fe-SiO_2. The second is the extremely high H_c values (at least 2500 Oe) achieved in the granular system.

According to conventional theories,[9] for Fe particles with sizes less than 120 Å, the rotation-in-unison mode of magnetization reversal is more favorable than bucking and curling modes. In this mode, the zero-temperature coercivity H_{c0} is $2K/M$, where M is the magnetization and K is the effective anisotropy constant from various contributions such as magnetocrystalline, shape, strain, etc.,[4] which are largely independent of size. Since the magnetization remains relatively constant in our Fe-SiO_2 system, the effective K would necessarily be size dependent in order to account for the experimental results. Further difficulties are encountered when very large H_c values are to be accommodated in various models. Both the magnetocrystalline anisotropy and the maximum strain induced coercivity of bulk Fe are only of the order of 600 Oe.[4] In the rotation-in-unison model, H_c was predicted to be as high as 5000 Oe but only for particles with an extremely large aspect ratio.[4] The chain-of-spheres fanning model[9] indicates a maximum H_c of 2700 Oe for an infinitely long chain in a random system. These extreme particle shapes and morphology were not revealed in our TEM micrographs, although there are evidences of neighboring granules in contact for samples near p_c. It should be pointed out that the enhancement of H_c is not due to the particles in contact near p_c where one may imagine the existence of some chain-of-spheres-like arrangement. Particle size is the dominant factor affecting H_c. One of the ample evidences is shown in Fig. 4, where H_c is enhanced with particle size. In these samples the volume fraction is much below p_c where particles are well isolated from each other. Other evidences can also be found in a related publication.[10] The fact that in ultrafine granules H_c is size dependent cannot be satisfactorily accounted for by existing models.

However, it must be recognized that the above-mentioned models, and indeed almost all the existing models, assume free-standing particles or particles dispersed in a nonbonding medium. In the granular Fe-SiO_2 system, the particles are strongly bonded to the insulating matrix and may be subjected to very larger stresses. For small particles, a large portion of the Fe atoms are at or near the surface. The number of surface atoms increases with particle size. The metal-insulator interfaces may dominate the coercivity in such systems. Under a reversing field, the moment reversal may well begin first at the surface and then propagate throughout the particle.

IV. SUMMARY

Granular Fe-SiO_2 solids over a large metal volume fraction range (15%–100%) have been made with a magnetron sputtering system. The granular nature of the samples has been characterized by transmission electron microscopy, electron diffraction, and ^{57}Fe Mössbauer spectroscopy. A giant magnetic coercivity of 2500 Oe is observed at 46% metal volume fraction. The H_c of the samples with higher volume fractions drops to the bulk Fe value. The observed behaviors of H_c are due to changes of particle size and percolation effect.

ACKNOWLEDGMENT

This work was supported by the Office of Naval Research Contract No. N0001485-K-0175.

[1] B. Abeles, in *Applied Solid State Science: Advances in Materials and Device Research*, edited by R. Wolfe (Academic, New York, 1976), p.1.
[2] J. A. A. J. Perenboom, P. Wyder, and F. Meier, Phys. Rep. **78**, 173 (1981).
[3] W. P. Halperin, Rev. Mod. Phys. **58**, 533 (1986).
[4] A. H. Morrish, *The Physical Principles of Magnetism* (Wiley, New York, 1965).
[5] J. I. Gittleman, B. Abeles, and S. Bozowski, Phys. Rev. B **9**, 3891 (1974).
[6] E. F. Kneller and F. E. Luborsky, J. Appl. Phys. **34**, 656 (1963).
[7] E. P. Wohlfarth, Proc. R. Soc. London Ser. A **232**, 208 (1955).
[8] A. H. Morrish and S. P. Yu, J. Appl. Phys. **26**, 1049 (1955).
[9] I. S. Jacobs and C. P. Bean, Phys. Rev. **100**, 1060 (1955); E. H. Frei, S. Shtrikman, and D. Treves, Phys. Rev. **106**, 446 (1957); I. S. Jacobs and C. P. Bean, in *Magnetism III*, edited by G. T. Rado and H. Suhl (Academic, New York, 1963), p. 275.
[10] S. H. Liou and C. L. Chien (these proceedings).

Magnetic properties of gas atomized powders of $Al_{74}Mn_{20}Si_6$

M. E. McHenry, R. A. Dunlap,[a] R. Chatterjee, A. Chow, and R. C. O'Handley
Department of Materials Science and Engineering, Massachusetts Institute of Technology, Cambridge, Massachusetts 02139

Rapidly quenched powders of $Al_{74}Mn_{20}Si_6$ were prepared by the ultrasonic gas atomization technique. Particles ranged from less than 40 μm to greater than 150 μm. The smaller particles were found to be primarily of the icosahedral phase. Larger powders showed an increasing proportion of the β-Al-MnSi phase. There was no evidence for the presence of α-AlMnSi commonly found in crystallized icosahedral AlMnSi alloys. Magnetic measurements showed the existence of a local Mn moment in all alloys. This moment was found to be 1.27 μ_B for the icosahedral phase and 0.63 μ_B for the β phase.

I. INTRODUCTION

A quasicrystalline phase with icosahedral symmetry was first reported by Shechtman *et al.*[1] in $Al_{86}TM_{14}$ (TM = Cr,Mn,Fe) alloys. This phase coexisted with a matrix of fcc Al. Subsequently it was found[2] that the addition of Si to Al-Mn has several positive effects on the formation of the icosahedral phase: (1) a sharpening of the electron diffraction spots and the x-ray diffraction peaks for this phase, (2) an elimination of the fcc Al phase, and (3) an increase in the stability of the icosahedral phase as suggested by an increase in the crystallization temperature. A close association of the icosahedral Al-Mn-Si structure and crystalline α-AlMnSi has been suggested[3] and Audier and Guyot[4] have proposed an icosahedral structure based on an interconnection of the McKay icosahedra which make up the α-AlMnSi structure.[5]

Although the exact structure of the icosahedral phase is not known for certain, a comparison of experimental magnetic data[6–8] with model calculations of the electronic structure (e.g., Ref. 9 and references therein) provides insight into the effects of icosahedral symmetry. It is important as well to consider data on icosahedral alloys in the context of results on similar alloys with known crystal structures. The present measurements on ultrasonic gas atomized powders of various sizes allows for the comparison of the magnetic properties of alloys with varying proportions of the icosahedral phase of AlMnSi and crystalline (hexagonal) β-AlMnSi. Results for single-phase icosahedral AlMnSi prepared by melt spinning or splat quenching and single-phase β-AlMnSi prepared by spray deposition are presented as well.

II. EXPERIMENTAL METHODS

Samples of $Al_{74}Mn_{20}Si_6$ were quenched using the following techniques: (1) Two samples were prepared by quenching from the melt onto the surface of a single Cu roller. In one case the surface speed of the roller was ~60 m/s and the alloy was quenched in air. For the second sample the roller surface speed was ~30 m/s and quenching was performed in He. No evidence of excessive surface oxidation was observed in the air-quenched sample. (2) A sample was splat quenched by melting in an arc furnace under an atmosphere of He and splatting using a hammer-anvil method. (3) A powder sample was prepared by ultrasonic gas atomization. The powder was quenched in an argon atmosphere and the various size particles were separated by sieving. (4) A sample was prepared by spray depositing ultrasonic gas atomized particles onto a Cu substrate. Quenching was performed under argon.

X-ray diffraction measurements were performed on a Rigaku RU300 rotating anode diffractometer using Cu$K\alpha$ radiation. Scanning electron microscopy (SEM) measurements were made on a Hitachi S-800 SEM. Magnetic susceptibility measurements were made on a S.H.E. VTS905 SQUID susceptometer.

III. RESULTS

A. X-ray diffraction measurements

Characteristic x-ray diffraction patterns are illustrated in Fig. 1. Both melt-spun samples as well as the splat-quenched sample were found to show x-ray diffraction patterns which are characteristic of the icosahedral phase with no evidence of the presence of any significant quantity of a second phase. The 44-μm powder showed primarily diffraction peaks due to the icosahedral phase. Peaks which were indexed as β-AlMnSi with an intensity of about 20% of the icosahedral peaks also are observed in this diffraction pattern. An increasing proportion of β-AlMnSi relative to icosahedral AlMnSi is observed in alloys quenched at progressively lower rates. The 150-μm powder (not shown in Fig. 1) shows predominantly the β-AlMnSi phase and a smaller quantity of icosahedral AlMnSi. The spray-deposited sample shows the presence of only β-AlMnSi.

B. SEM measurements

SEM photographs of a small particle (~10 μm diameter) and a larger particle (~150 μm diameter) both prepared by gas atomization are illustrated in Fig. 2. The small icosahedral particle shows crystallite growth with the fivefold symmetry characteristic of the symmetry of the domi-

[a] On leave from Department of Physics, Dalhousie University, Halifax, Nova Scotia B3H 3J5, Canada.

 0021-8979/88/084255-03$02.40 © 1988 American Institute of Physics



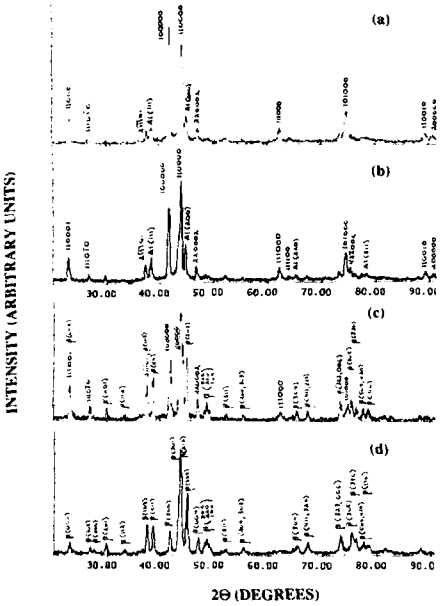


FIG. 1. X-ray diffraction patterns (Cu$K\alpha$) for (a) melt-spun sample (60 m/s), (b) splat-quenched sample, (c) ultrasonic gas atomized powder ($\sim 44\ \mu$m diameter particles), and (d) spray deposited sample.

nant phase. On the other hand, the crystallite growth on the 150-μm particle [Fig. 2(b)] shows the hexagonal symmetry of the dominant hcp β-AlMnSi phase. Sectioned powder particles revealed dendritic growth in the smaller icosahedral particles. From the spacing of the secondary dendrite arms[11] it was possible to estimate the cooling rate of these particles as shown in Table I.

C. Magnetic susceptibility measurements

The temperature dependence of the magnetic susceptibility of the single-phase icosahedral and β-phase samples (melt spun and spray deposited, respectively) is illustrated in Fig. 3. These and the other alloys show a susceptibility above about 5 K which exhibits a Curie-like behavior. These data are described by a Curie temperature θ and a susceptibility χ as

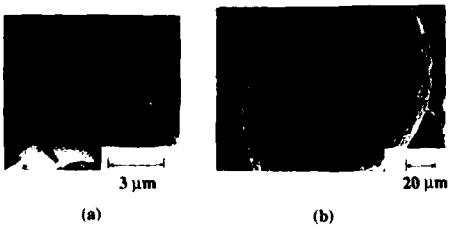


FIG. 2. SEM photographs of ultrasonic gas atomized particles of (a) ~ 10 μm diameter and (b) $\sim 150\ \mu$m diameter. Note the pentagonal and hexagonal facets in the (a) icosahedral-rich and (b) β-rich particles, respectively.

TABLE I. Parameters obtained from magnetic susceptibility measurements of rapidly quenched $Al_{74}Mn_{20}Si_6$ alloys. The quench rate was estimated on a basis of sample preparation parameters and secondary dendrite arm spacings.

Sample	dT/dt (°C/s)	μ_{eff} (μ_B)	χ_0 (cm^3/g)	θ (K)
Melt spun (60 m/s)	4×10^6	1.30	2.00×10^{-6}	3.8
Melt spun (30 m/s)	2×10^6	~1.3	...	...
Splat quenched	5×10^5	1.27	1.98×10^{-6}	3.6
44-μm powder	2×10^5	1.22	5.40×10^{-6}	4.1
150-μm powder	$\sim10^4$	1.04	2.71×10^{-6}	1.2
Spray deposited	$\sim10^1-10^2$	0.63	2.41×10^{-6}	3.5

$$\chi-\chi_0=C/(T-\theta), \tag{1}$$

where the constant C is given in terms of an effective paramagnetic moment μ_{eff} as

$$C=n\mu_{eff}^2/3k_B. \tag{2}$$

n is the concentration of magnetic ions (Mn) per unit volume. Parameters obtained for the susceptibility data for the AlMnSi samples are given in Table I. We should stress that the values of μ_{eff} are average Mn moments as it is not yet clear if all Mn carry the same moment in these alloys.

The sign of the parameter θ given in Table I for these alloys suggests the presence of antiferromagnetic coupling between moments. The insert in Fig. 1, illustrating the susceptibility of zero-field and field-cooled samples, shows the onset of spin-glass behavior below about 5 K as a result of this distribution of magnetic interactions.

There is growing evidence of two distinct transition-metal sites in icosahedral alloys[12] although there is no reason based on structural models that these sites exist in proportions given by the golden mean. It has been suggested that Mn only carries a moment on one of the sites.[2,8] Mössbauer measurements clearly indicate a relatively low symmetry for the transition-metal sites[12–14] and have been interpreted[12] in terms of two distinct sites on the outer shell of a MacKay cluster. It is clear from the present measurements that the crystalline β phase shows a much smaller average Mn moment than the icosahedral phase. As β-AlMnSi (and α-

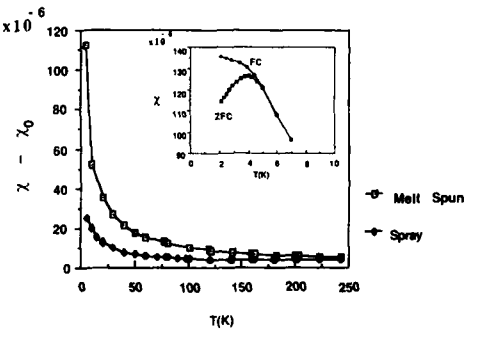


FIG. 3. SQUID susceptibility measurements of (a) melt-spun sample (60 m/s) obtained in an applied field of 20 kOe with insert showing low-temperature susceptibility measured at 100 Oe for a sample initially cooled in zero field (ZFC) and a sample cooled in 100 Oe (FC).

AlMnSi as well) contain no Mn-Mn nearest neighbors and no Mn on icosahedral sites (where we would expect the formation of a large moment[9]) we would not expect it to have a large average magnetic moment. If we accept the usual structural models of the icosahedral phase in which building blocks based on the crystalline materials are interconnected in some way to preserve fivefold rotational symmetry, then it is necessary to account in some way for the increase in the Mn moment.

The rapid quenching necessary to produce the icosahedral phase is most likely responsible for the introduction of disorder in these alloys. This can explain the magnetic data in one of two ways: (1) average Mn-Mn distances are decreased as a result of the disorder or (2) in the icosahedral phase some small percentage of Mn occupies the high symmetry icosahedral site. A combination of these two effects may be present as well. Mössbauer measurements can provide some important information concerning this problem but unfortunately have not as yet provided an answer. The distinction between magnetic and nonmagnetic Mn sites on the outer shell of a MacKay icosahedron is not inconsistent with the picture of an increased Mn moment due to a reduction in the average Mn-Mn distance. It is likely that the distinction between magnetic and nonmagnetic sites[12] arises not because of the distinction between vertex and edge sites in the MacKay cluster but because of distinctions in the Mn atom's role in bonding to adjacent clusters. In a recent model Nanao[15] has decorated a three-dimensional Penrose tiling in such a way that a small but significant fraction of the Mn are in icosahedral sites. If we assume that the predominant reason for an increase in the average Mn moment is due to icosahedral-site Mn we can estimate the percentage of Mn at this site. Taking the calculated moment for Mn on this site to be $3.6\,\mu_B^0$, we find that the increase in μ_{eff} between the crystalline and quasicrystalline phases can be accounted for by 20% of the Mn in the high symmetry icosahedral environment. Certainly we would expect that if Fe substituted randomly for Mn in icosahedral alloys then this icosahedral site should be seen as a low quadrupole split component in the Mössbauer spectra. Dunlap *et al.*[12] have suggested that Fe does not substitute randomly for Cr in icosahedral Al-Cr alloys but has a particular site preference. There is therefore no reason to assume *a priori* that Fe should substitute randomly for Mn in icosahedral Al-Mn-Si. The lack of a corresponding component in the Fe Mössbauer spectrum is therefore not conclusive evidence that Mn does not exist in a high symmetry site.

IV. CONCLUSIONS

Rapidly quenched $Al_{74}Mn_{20}Si_6$ alloys are found to be either of the icosahedral structure or of the β-AlMnSi phase or a combination of these two. A quench rate on the order of $\sim 10^5$ K s^{-1} is necessary to completely eliminate the β phase and a quench rate below $\sim 10^2$ K s^{-1} is necessary to remove all traces of the icosahedral phase. No evidence was seen in the x-ray patterns of any of the alloys for the presence of the α-AlMnSi phase as is often seen in recrystallized icosahedral AlMnSi alloys.[16] Gas atomized particles are seen to exhibit crystallite growth which is characteristic of the symmetry of the crystal structure.

The magnetic moment of Mn in the icosahedral phase is found to be significantly larger than in crystalline β phase. This may be explained in terms of the introduction of disorder as a result of the rapid solidification process resulting in either Mn-Mn nearest neighbors or Mn atoms at icosahedral sites. The precise details of the icosahedral structure are not yet known. The icosahedral phase of Al-Mn-Si shows spin-glass behavior below about 5 K.

[1] D. Shechtman, I. Blech, D. Gratias, and J. W. Cahn, Phys. Rev. Lett. **53**, 1951 (1984).
[2] C. H. Chen and H. S. Chen, Phys. Rev. B **33**, 2814 (1986).
[3] V. Elser and C. L. Henley, Phys. Rev. Lett. **55**, 2883 (1985).
[4] M. Audier and P. Guyot, Philos. Mag. B **53**, L43 (1986).
[5] M. Cooper, Acta Crystallogr. **20**, 614 (1966).
[6] S. E. Youngquist, P. F. Miceli, D. G. Wiezler, H. Zabel, and H. L. Fraser, Phys. Rev. B **34**, 2960 (1986).
[7] S. J. Poon, A. J. Drehman, and K. R. Lawless, Phys. Rev. Lett. **55**, 2324 (1985).
[8] J. J. Hauser, H. S. Chen, and J. V. Wasczak, Phys. Rev. B **33**, 3577 (1986).
[9] M. E. McHenry and R. C. O'Handley, Mater. Sci. Eng. (1988).
[10] V. Anand, A. J. Kaufman, and N. J. Grant, in *Rapid Solidification Processing II*, edited by R. Mohrabian, B. Kear, and M. Cohen (Claitors, Baton Rouge, LA, 1980), p. 273.
[11] N. J. Grant, in *Advances in Powder Metallurgy*, edited by G. Y. Chin (ASM, Metals Park, OH, 1982).
[12] R. A. Dunlap, D. W. Lawther, and D. J. Lloyd (to be published).
[13] M. Eibschutz, H. S. Chen, and J. J. Hauser, Phys. Rev. Lett. **56**, 169 (1986).
[14] L. J. Swartzendruber, D. Shechtman, L. Bendersky, and J. W. Cahn, Phys. Rev. B **32**, 1383 (1985).
[15] S. Nanao (private communication).
[16] R. A. Dunlap and K. Dini, J. Mater. Res. **1**, 415 (1986).

Noncollinear magnetic structure of $CoFe_2O_4$ small particles

K. Haneda[a] and A. H. Morrish
Department of Physics, University of Manitoba, Winnipeg, Manitoba, R3T 2N2 Canada

The magnetic structure of small $CoFe_2O_4$ particles has been investigated as a function of the particle size. Samples (in the 10–100 nm size range and up) were prepared by chemical precipitation followed by a heat treatment at relatively low temperatures. Mössbauer spectra of the ^{57}Fe nuclei, obtained with a longitudinal magnetic applied field, unambiguously establish that a noncollinear structure exists that is most pronounced for the smallest particles. The analysis indicates that a surface effect of the crystallites that make up a particle is the origin of this phenomenon. A model is proposed in which the $CoFe_2O_4$ crystallites that make up a particle consist of a core with the usual spin arrangement and a boundary surface layer with atomic moments inclined to the direction of the net magnetization. The temperature dependency of this structure is also examined.

INTRODUCTION

Cobalt ferrite ($CoFe_2O_4$) is a spinel and is usually assumed to have a collinear ferrimagnetic spin structure. This spinel was shown to be partially inverse with the formula $(Co_xFe_{1-x})[Co_{1-x}Fe_{1+x}]O_4$, where the round and square brackets indicate A and B sites, respectively. The ratio, $Fe(A)/Fe(B)$, has been found to vary from 0.61 ± 0.04 to 0.87 ± 0.04 for two extremes—quenched (q) and slowly cooled samples (s.c.), respectively.[1,2] For both ionic distributions, a magnetic moment of more than 3 μ_B per unit chemical formula or 71.5 emu/g is anticipated assuming 5 μ_B for Fe^{3+} and 3 μ_B for Co^{2+} ions. The values observed, 3.4 μ_B for s.c. and 3.9 μ_B for q, respectively, confirm this expectation.[1]

Several authors, using large applied fields, have found that the saturation magnetization of $CoFe_2O_4$ small particles diminishes rapidly with decreasing particle size.[3–5] Such a phenomenon has been interpreted consistently in terms of our previous Mössbauer studies of small $CoFe_2O_4$ particles where it has been found that a noncollinear spin arrangement exists, possibly at or near the surface of $CoFe_2O_4$ particles.[6] This conclusion was based upon the presence of the second and fifth lines of the ^{57}Fe Mössbauer spectra obtained with a large magnetic field applied along the propagation direction of the γ ray. A noncollinear structure has been found near the surface for various materials in fine particle form, such as γ-Fe_2O_3, $NiFe_2O_4$, and CrO_2.[7] Furthermore, it has been analyzed that the particle morphology or a boundary surface layer of the crystallites that make up a particle is an important factor influencing the noncollinear magnetic structure in fine particles. As a natural extension, in order to examine if such an analysis is applicable to $CoFe_2O_4$ small particles, a similar investigation by using Mössbauer spectroscopy has been made for additional samples of $CoFe_2O_4$ with different sizes, and is the subject of this report. In addition, the temperature dependency of this structure is also explored.

EXPERIMENT

Small particles of $CoFe_2O_4$ (in the 10–100 nm size range and up) were prepared by chemical precipitation and subsequent heat treatment at relatively low temperatures for extended periods of time. Three samples, each with different particle sizes, and labelled A, B, and C, were made by changing the thermal conditions during the heat treatment for the dried precipitates. Electron-microscope photographs, EPMA composition measurements, room-temperature x-ray diffraction patterns, and Mössbauer spectra at 4.2 and 300 K taken with a $^{57}Co/Rh$ source driven by a triangular wave form were obtained. Absorbers were made by dispersing and binding the particles in benzophenone. Mössbauer spectra were also taken with a large magnetic field applied along the propagation direction of the γ rays at 4.2 K and temperatures up to 150 K. The data were analyzed with a least-squares computer program that assumed the line shapes were Lorentzian.

RESULTS AND DISCUSSION

A typical example of the electron-microscope photographs is shown in Fig. 1 for sample B. In any given sample the particles are fairly uniform in size. The median size for each sample is listed in Table I. X-ray diffraction of all samples showed only the spinel phase; an example of these data is shown in Fig. 2 for sample B. Information on the crystallite size was deduced from x-ray line broadening using the Sher-



FIG. 1. Electron photomicrograph of small $CoFe_2O_4$ particles (sample B).

[a] Present address: Research Institute for Scientific Measurements, Tohoku University, Sendai, Japan.

 0021-8979/88/084258-03$02.40 © 1988 American Institute of Physics

TABLE I. Data for $CoFe_2O_4$ samples A, B, and C.

Sample	Particle size (Å)	Crystallite size (Å)
A	300 ± 50	200
B	500 ± 150	240
C	3500 ± 400	420

rer formula, and is also given in Table I. The chemical composition, particularly the ratio of Co to Fe ions, as determined by EPMA measurements, was close to the nominal value for all samples.

The Mössbauer spectrum obtained at 4.2 K is shown for sample B in Fig. 3. There is not much difference to note among the absorption profiles at 4.2 K for these samples. Two overlapping six-line hyperfine patterns corresponding to the ^{57}Fe in *B* and *A* sites have been fitted. Although visually the sixth *B*-site line seems to be smaller than the *A*-site line for every sample, the spectra in an applied field for these samples will reveal that the *B*-site area is indeed larger than that corresponding to ^{57}Fe in *A* sites; the feature is consistent with that observed for bulk $CoFe_2O_4$.[1,2] This implies that there must be a large distribution of *B*-site hyperfine fields in small $CoFe_2O_4$ particles. Further, the hyperfine field for some of the ^{57}Fe in *B* sites must be nearly the same as that for ^{57}Fe in *A*-sites. The shoulder at the sixth *B*-site line becomes less visible at 300 K for every sample, indicating a more rapid decrease in hyperfine field with increasing temperature at the *B* site than at the *A* site.

Mössbauer spectra taken with a longitudinal 50 kOe magnetic field at 4.2 K are shown in Fig. 4. Not only are the *A*- and *B*-site patterns separated, but also the magnetic structure is revealed. In a collinear magnetic system, the atomic moments lie along the direction of the external magnetic field, and the polarization conditions require the disappearance of the $\Delta m = 0$ lines (2,5 lines) in the hyperfine pattern. For simplicity the data were fitted with a total of only two six-line patterns, one with normal line broadening for *A*-site cations, and the other with fairly large line broadening for *B*-site cations. Some parameters obtained are summarized in Table II. The ratio of the *A*- to *B*-site patterns is approximately 0.5–0.6, which is somewhat less than the minimum reported for ceramic samples.[1,2] The difference in the preparation methods and in the particle sizes may be

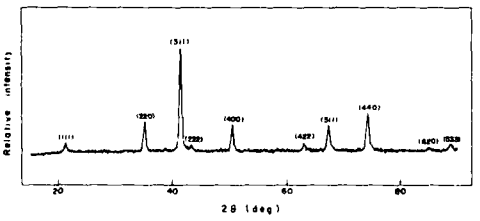


FIG. 2. X-ray diffraction patterns taken using Co$K\alpha$ radiation for $CoFe_2O_4$ particles (sample B). Here 2θ is twice the Bragg angle.

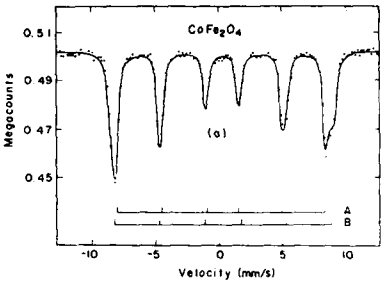


FIG. 3. Mössbauer spectra of small $CoFe_2O_4$ particles (sample B) taken at 4.2 K.

responsible. The Fe spins in small $CoFe_2O_4$ particles are canted with respect to the direction of the external magnetic field since substantial second and fifth absorption lines are obviously present. The average spin-canting angle Θ between the direction of the external magnetic field and the direction of the magnetization is evaluated and is given in Table II. This trend increases in smaller particles and is less pronounced in larger particles.

It is pertinent to examine the data in terms of the particle morphology, if the relationship between the crystallite size and the spin structure exists. From the value of the relative intensity of the 2,5 line areas compared to the 1,6 line areas, the thickness of the spin-canted surface layer of each crystallite was evaluated assuming a spherical shape, no cavities, and random canting angles between 0° and 90°, the maintenance of local magnetic order, and a 3:2:1 line area ratio. The

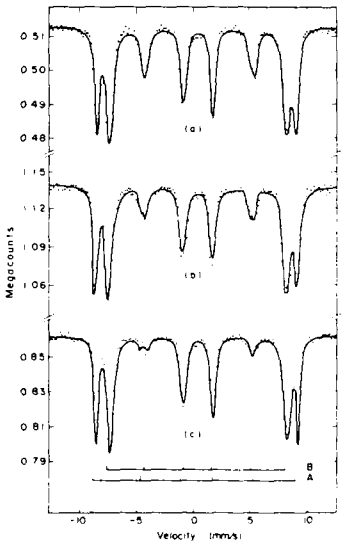


FIG. 4. Mössbauer spectra of small $CoFe_2O_4$ particles taken at 4.2 K in a longitudinal external magnetic field of 50 kOe for (a) sample A, (b) sample B, and (c) sample C.

TABLE II. Parameters deduced from Mössbauer spectra of small $CoFe_2O_4$ particles in a longitudinal magnetic field of 50 kOe at 4.2 K.

Sample	Area ratio (A/B)	$H_{hf}(A)$ (kOe)	$H_{hf}(B)$ (kOe)	Average canting angle (deg)			$A_{2.5}(A,B)$ / $A_{1.6}(A,B)$	Canted-layer thickness (Å)
				A site	B site	Both sites		
A	0.607	551	484	35	36	36	0.272	16
B	0.523	553	489	26	28	27	0.159	10
C	0.511	553	483	22	20	21	0.092	11

random-angle assumption is equivalent to an average canting angle of 54.5°, which is consistent with earlier results.[8] The values of the canted-layer thickness deduced (Table II) are remarkably similar considering the experimental errors.

An analysis based on particle size does not give consistent results for the thickness of the canted layer. Hence the data imply that the crystallite rather than the particle size is the important factor for spin canting. Therefore, $CoFe_2O_4$ crystallites that make up a particle may be visualized as having a core with the normal (bulk) spin arrangement and a boundary surface layer in which the spin arrangement takes a noncollinear structure.

Finally, something about the temperature dependency of this magnetic structure will be mentioned. Mössbauer spectra at $T = 100$ and 150 K in a magnetic field of 50 kOe taken under the same geometrical arrangement as was used in Fig. 4 are shown in Fig. 5 for sample B. The average spin canting angle, 27° at $T = 100$ K and 21° at $T = 150$ K, has been found to change only slightly with the temperature; the phenomenon is slightly more pronounced at the lower temperatures.

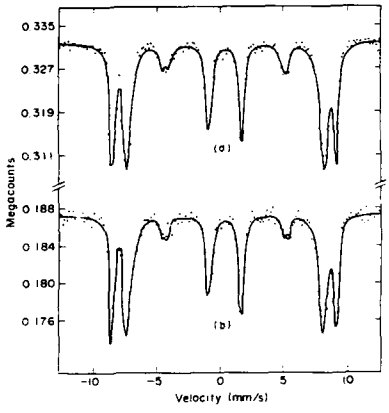


FIG. 5. Mössbauer spectra of small $CoFe_2O_4$ particles (sample B) taken in a longitudinal external magnetic field of 50 kOe (a) at $T = 100$ K and (b) at $T = 150$ K.

[1] G. A. Sawatzky, F. van der Woude, and A. H. Morrish, J. Appl. Phys. **39**, 1204 (1968).
[2] G. A. Sawatzky, F. van der Woude, and A. H. Morrish, Phys. Rev. **187**, 747 (1969).
[3] P. Mollard, P. Germi, and A. Rousset, Physica **86–88B**, 1393 (1977).
[4] A. E. Berkowitz, J. A. Lahut, and C. E. VanBuren, IEEE Trans. Magn. **MAG-16**, 184 (1980).
[5] R. E. Vandenberghe, R. Vanleerberghe, E. DeGrave, and G. Robbrecht, J. Magn. Magn. Mater. **15–18**, 1117 (1980).
[6] K. Haneda and A. H. Morrish, *Proceedings of the International Symposium on the Physics of Magnetic Materials* (World Scientific, Singapore, 1987), pp. 214–217.
[7] A. H. Morrish and K. Haneda, J. Magn. Magn. Mater. **35**, 105 (1983).
[8] A. H. Morrish, K. Haneda, and P. J. Schurer, J. Phys. (Paris) **37**, C6-301 (1976).

Magnetic properties of thin-film Ag + iron-oxide granular metals

R. D. Shull, U. Atzmony,[a] A. J. Shapiro, L. J. Swartzendruber, and L. H. Bennett
National Bureau of Standards, Gaithersburg, Maryland 20899

W. J. Green and K. Moorjani
The Johns Hopkins University, Applied Physics Laboratory, Laurel, Maryland 20707

The magnetic properties of iron-oxide particulates dispersed in silver (prepared by rf diode sputtering silver and iron oxide over a wide composition range) have been investigated using the Mössbauer effect, electron microscopy, and vibrating sample magnetometry. The sputtered films are nanocrystalline mixtures of immiscible particles of the two constituents (even when only a very small amount of silver is present). At room temperature, the Mössbauer effect data show that for most compositions (even those with low silver content) the majority of the film is superparamagnetic, with the fraction of material in the superparamagnetic state increasing with increasing Ag content. Consistent with these results, very narrow hysteresis loops were observed. On decreasing the temperature to near 100 K, the fraction of material in the superparamagnetic state decreased and the magnetically ordered component increased. Electron diffraction patterns clearly showed the presence of polycrystalline Ag and Fe_3O_4 in the films, but composition analysis (0.03 μm resolution) was unable to separate these regions.

INTRODUCTION

When two immiscible constituents, one a metal and the other a nonmetal, are simultaneously condensed from the vapor, the resulting thin-film deposit often has a unique morphology.[1,2] This composite material, characterized as an intimate mixture of granules of the two constituents having a size on the order of nanometers, is generally referred to as a granular metal. If the metallic constituent possesses a magnetic moment, the magnetic properties of the composite material have been found to be a strong function of the relative amounts of the two phases.[3–5] For example, in the Ni-SiO_2 granular metal system,[3,4] the material is ferromagnetic at room temperature for the very Ni-rich compositions and becomes superparamagnetic on addition of SiO_2 in excess of 40% (by volume). In a very narrow composition range near 40% SiO_2, on cooling, the superparamagnetic material becomes ferromagnetic at a characteristic temperature which decreases with increasing SiO_2 content. For higher SiO_2 contents, superparamagnetic behavior is observed at all temperatures. In the Co-SiO_2 (Ref. 6) and Fe-SiO_2 (Ref. 7) granular metal systems, similar magnetic behavior has been observed; but the composition region in which the superparamagnetic-ferromagnetic transition occurs is shifted to a higher SiO_2 volume percentage. By analogy, it might be expected that for granular metal systems in which the nonmetallic component is the only constituent possessing a permanent magnetic moment (so that there still only exist magnetic interactions between chemically similar entities), similar magnetic behavior would be displayed. The present investigation of the Ag + iron-oxide system provides information to test this hypothesis and provides a basis for the understanding of the magnetic behavior in a granular metal system comprised of constituents in which both components possess a magnetic moment.

EXPERIMENTAL PROCEDURE

Thin films of interspersed silver and iron-oxide particulates were prepared by rf diode sputtering over a wide range of compositions. Sputtering was performed upward with the target, which consisted of mechanical mixtures of high-purity needle silver and iron-oxide powders, located approximately 8 cm below the fused silica substrates. A sputtering gas pressure of 6 μm (high-purity argon) was standard for all the runs, as was the application of 400 W rf power to the electrodes. Our typical specimens (1–2 μm thick) were obtained after sputtering for 7 h. Both commercially obtained Fe_2O_3 and the Fe_3O_4 iron-oxide powders were used in the initial sputtering targets. Qualitatively, we did not observe any major difference in the magnetic behavior of the thin films prepared from the two oxide forms. Apparently, during the sputtering process under our conditions the iron-oxide phase is broken up and subsequently reforms. All data (except that for sample C) reported here are for sputtering deposits derived from the use of the commercial Fe_3O_4 oxide powder. Since the composition of the thin-film deposit was not the same as the composition of the powder mixture in the sputtering target, the specimen notation used in this paper denotes the qualitative composition of the thin films, identified by letters in ascending order of increasing silver content. Compositions were quantitatively determined by using energy dispersive x-ray analysis in a scanning electron microscope. Transmission electron microscopy observations of the specimens were performed using a high-resolution 300-kV microscope. Separately deposited very thin samples (requiring no additional thinning) were prepared for the TEM observations, since conventional electrochemical or ion thinning processes created uncontrolled artifacts. Mössbauer effect measurements were performed using the sample as the absorber and a 0.5 mCi ^{57}Co in Rh source. The equipment was calibrated using an Fe_2O_3 powder sample. The zero of velocity for the Mössbauer spectra herein is tak-

[a] Permanent address: NRCN, P. O. Box 9001, Beer-Sheva, Israel.

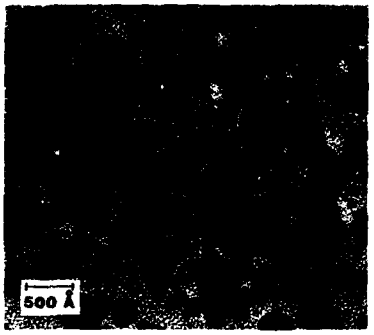


FIG. 1. Transmission electron micrograph for a thin sputtered film of Ag + iron oxide containing approximately 18 wt. % Ag.

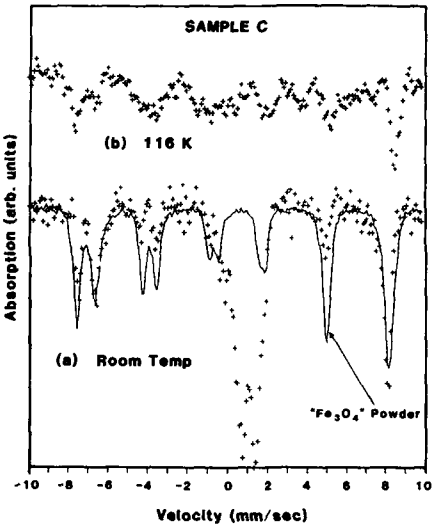


FIG. 2. Mössbauer effect spectrum (a) measured for a sputtered film of Ag + iron oxide containing 5 wt. % Ag (crosses) and for the starting commercial Fe_3O_4 powder (solid line) at room temperature and (b) measured for the 5 wt. % Ag composite at 116 K.

en as the center of a pure Fe room-temperature spectrum. For each spectrum, the typical data accumulation period was 5 days and the maximum effect was typically 0.1%. Due to the small sample volumes used in this study, saturation effects were not important. Magnetic susceptibility and hysteresis measurements were made using a vibrating sample magnetometer.

RESULTS AND DISCUSSION

Transmission electron microscopy of thin films prepared by cosputtering silver and iron-oxide powders directly onto carbon-coated TEM grids showed that the deposits possessed a granular morphology with nanometer-sized particles. An example is shown in Fig. 1. The same Ag/Fe ratio was measured for the two distinct features in this picture (i.e., the large dark circular areas and the lighter matrix). Electron diffraction patterns for this material could be indexed by the superposition of diffraction rings for Fe_3O_4 and Ag. We believe that the large dark regions in this picture are not chemically different from the matrix, but are thicker (less transparent) conglomerated regions in the deposit. We have been unable to image any regions with distinctly different composition and, consequently, tentatively conclude that the small amount of silver in the deposit is located in the boundary regions (dark in contrast) between the light-colored nanometer-sized Fe_3O_4 cells.

The room-temperature Mössbauer effect data for a thin film of silver + iron oxide with ~5 wt. % silver is shown in Fig. 2(a). This spectrum appears to be a superposition of two components: (1) a multiple line spectrum extending to large velocities indicative of magnetically ordered Fe_3O_4 and (2) a larger intensity central doublet spectrum centered near 1 mm/s, indicating superparamagnetism similar to that reported by Kundig *et al.*[8] for submicron particles of α-Fe_2O_3. The relative intensities of the spectral components show that only small amounts of silver are required to break up the Fe_3O_4 into superparamagnetic regions. Comparison of the Mössbauer effect data of Fig. 2(a) with that displayed in Fig. 3 for a thin film sputtered using only the commercial Fe_3O_4 powder target proves that sputtering without silver does not result in the deposition of superparamagnetic iron. Similarly, if the pure Fe_2O_3 oxide form is sputtered by itself under the same conditions, only a magnetically split spectrum, although indicating a combination of Fe_2O_3 and Fe_3

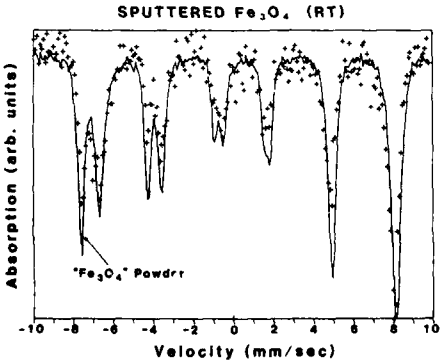


FIG. 3. Room temperature Mössbauer effect spectrum for a powder sample (solid line) and for a sputtered film (crosses) of commercial Fe_3O_4.

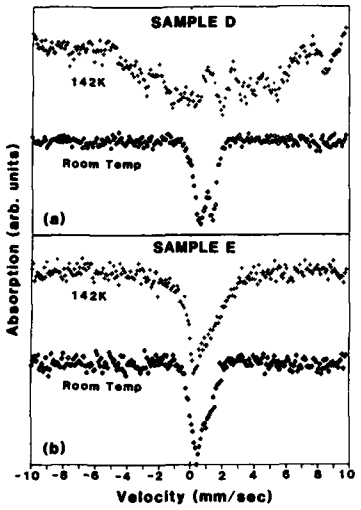


FIG. 4. Mössbauer effect spectra for sputtered films of Ag + iron oxide containing (a) 18 wt. % Ag (sample D) and (b) 80 wt. % Ag (sample E), measured at the indicated temperatures.

O_4 environments, is observed in the thin-film deposit. The magnetically split spectrum in Fig. 2(a) indicates that the magnetically ordered material in the Ag + iron-oxide granular metal is primarily Fe_3O_4 with some admixture of γ-Fe_2O_3. Comparison of the unpolarized spectrum from the commercial Fe_3O_4 powder (note this material also contains some admixed Fe_2O_3 as indicated by the enclosing quotation marks in the figure) with the granular metal spectrum in Fig. 2(a) also suggests the Ag + iron-oxide thin sputtered film possesses a magnetic polarization. Since the propagation direction of the γ radiation is perpendicular to the plane of the film in our experiments, the smaller intensities of the second and fifth absorption lines of the granular metal indicate the magnetic polarization must be out of the thin-film plane. There may be applications of this in the high density vertical recording industry. After cooling this sample to low temperatures, the Mössbauer effect spectrum shown in Fig. 2(b) was measured. At 116 K the superparamagnetic portion of the sample which was responsible for the intense central doublet in the room-temperature spectrum has become magnetically ordered. This is consistent with a distribution of particle sizes in the sample, each size with its own characteristic magnetic blocking temperature.[9] A similar change in the Mössbauer pattern on cooling was observed by Xiao *et al.*[7] for a granular metal of Fe + SiO_2 containing 60 at. % Fe.

As more Ag is added to the deposits the proportion of material in the granular metal that is magnetically ordered at room temperature decreases, while the amount of superparamagnetic material increases (see Fig. 4). With increasing Ag content either the distance between the iron-oxide particles increases (thereby, decreasing the magnetic interaction between particles) or the already very small iron oxide particles become even smaller (which also decreases the superparamagnetic blocking temperature), or both. In the Fe-SiO_2 system, the transition between superparamagnetic and ferromagnetic behavior was attributed to a size reduction of isolated magnetic particles.[7] In the present study, we have not measured the Mössbauer data at a sufficient number of temperatures to determine the relative importance of the interparticle/intraparticle interactions.

The very small proportion of magnetically ordered material at room temperature in sample D (indicated by the Mössbauer data in Fig. 4) was consistent with the measurement of only a very narrow magnetic hysteresis loop at this temperature. On decreasing the temperature to below 140 K, the area of the hysteresis loop significantly increased. Sample E (Fig. 4) shows the temperature dependence of the Mössbauer effect data for a specimen containing much more Ag ($\sim$80 wt. %) than any of the other samples. No magnetically ordered material is observed at room temperature; and after cooling the sample to $\sim$140 K, there is no appreciable change in the Mössbauer pattern. Presumably, for sample E the iron oxide particle size is so small that the blocking temperature lies below 142 K.

In conclusion, cosputtering Ag and iron oxide has been found to form a granular metal over a wide composition range. There are many similarities between the magnetic behavior of these granular metals and the behavior previously observed for conventional granular metals whose magnetic constituent was the metal. Nonetheless, superparamagnetic behavior is observed in this granular metal at surprisingly low concentrations ($\sim$5 wt. %) of the nonmagnetic component. This result may be due to a difference in the relative importance of the interparticle magnetic interaction.

[1]B. Abeles, P. Sheng, M. D. Coutts, and Y. Arie, Adv. Phys. **24**, 407 (1975).
[2]B. Abeles, Appl. Solid State Sci. **6**, 1 (1976).
[3]Y. Goldstein and J. I. Gittleman, Solid State Commun. **9**, 1197 (1971).
[4]J. I. Gittleman, Y. Goldstein, and S. Bozowski, Phys. Rev. B **5**, 3609 (1972).
[5]J. L. Dormann, P. Gibart, C. Suran, J. L. Tholence, and C. Sella, J. Magn. Magn. Mater. **15–18**, 1121 (1980).
[6]S. Barzilai, Y. Goldstein, I. Balberg, and J. S. Helman, Phys. Rev. B **23**, 1809 (1981).
[7]Gang Xiao, S. H. Liou, A. Levy, J. N. Taylor, and C. L. Chien, Phys. Rev. B **34**, 7573 (1986).
[8]W. Kundig, H. Bommel, G. Constabaris, and R. Lindquist, Phys. Rev. **142**, 327 (1966).
[9]*Applications of Mössbauer Spectroscopy*, edited by R. L. Cohen (Academic, New York, 1976), Vol. 1.

The application of sodium amalgam to prepare ferrofluids containing iron particles in mercury

L. Takács[a)]
Department of Physics, Clark University, Worcester, Massachusetts 01610

Mercury-based ferrofluids are prepared by using sodium amalgam to reduce iron into mercury while agitating mechanically and magnetically by an ordinary magnetic stirrer. The field dependence of the room-temperature magnetization is measured and used to determine the particle size distribution and its aging behavior. Samples prepared by the conventional method of electroplating into a mercury cathode are also studied for comparison. It is shown that the samples prepared by the two methods are very similar and the small amount of sodium remaining in the samples prepared from sodium amalgam can enhance the stability.

INTRODUCTION

Most ferrofluids consist of small single-domain magnetic particles dispersed in water or organic solvents. Such ferrofluids are commercially available and have several technical applications.[1] Ferrofluids based on mercury as a carrier liquid are of special interest because of their high electrical and thermal conductivities. The main problem here is the agglomeration of the magnetic metal particles into larger ones. This process can be greatly reduced but not completely avoided by additives such as tin and sodium.[2,3] Our current research goal is to study the metallurgy and magnetic properties of ferrofluids containing iron particles in mercury.

The standard procedure to prepare these materials is to electroplate iron into a mercury cathode from an aqueous solution. Continuous mechanical and magnetic agitation is necessary to avoid the formation of dendrites instead of small spherical particles.[4] A much simpler approach, utilizing the reducing ability of sodium amalgam instead of using direct current, is also possible.[5] This is attractive as sodium itself has been shown to improve stability.[3] Several samples were prepared by both methods. The field dependence of the magnetization was measured and used to determine the particle size distribution both immediately after preparation and after aging at room temperature.

SAMPLE PREPARATION

Samples were prepared by both electroplating and from sodium amalgam. To prepare the electrolytic samples, a cell similar to that used by van Wonterghem *et al.*[4] was constructed. Usually an aqueous solution of $FeCl_3$ was used as the electrolyte. The composition of the ferrofluid samples is determined by the amount of iron dissolved in the electrolyte. Our samples contained about 0.5 at. % iron.

Although the method using electrolysis is fairly simple, an even simpler method which can be performed in any chemistry laboratory without prior preparation is possible utilizing sodium amalgam. This method was used to prepare iron amalgams in connection with the development of permanent magnets several years ago.[5] Sodium amalgam can be prepared by dissolving metallic sodium in mercury, a very exothermic process best performed under inert gas atmosphere. The required amount of sodium amalgam is poured into a beaker and put onto a magnetic stirrer. The quickly rotating stirring bar and the rotating magnetic field produces enough mechanical and magnetic agitation to prevent the growth of dendrites. To conserve sodium a ferrous solution is preferred as electrolyte. This is poured onto the mercury with the stirrer running. Usually, it takes about 3 h to oxidize most of the sodium solved in the mercury. If slow production of hydrogen bubbles can be observed with the stirring stopped momentarily, a substantial amount of sodium is still present in the mercury and the preparation process can be continued. At the end of the process, the iron amalgam produced is pipetted out and washed with acetone. This method is less controllable than that using electrolysis, especially because the speed of the reaction depends on the area of the interface between the amalgam and the eletrolyte. Usually, the mercury falls into droplets as a result of the stirring, the size of the droplets and the area of the interface being quite unpredictable. However, as the properties of the samples are not very sensitive to the conditions of the preparation, the method can still be advantageous when quick production of a small amount is necessary.

The maximum solubility of sodium in mercury is about 5 at. % at room temperature. The amalgam used in this study contained 4 at. % sodium. As two sodium atoms are needed to reduce a ferrous ion, the highest iron content possible is 2 at. %. As part of the sodium reduces hydrogen instead of iron, the actual iron content is less than that, usually below 1 at. %.

EXPERIMENTAL METHOD

The field dependence of the room-temperature magnetization was measured to determine the size distribution of the iron particles. Measurements were performed immediately after preparation and after aging at room temperature for several days. Control samples kept frozen at dry ice temperature were also measured and showed no significant changes. The measurements were carried out in a vibrating sample magnetometer at room temperature up to a field of 1 T. Sam-

[a)] On leave from the Central Research Institute for Physics, Budapest, Hungary.

 0021-8979/88/084264-03$02.40 © 1988 American Institute of Physics

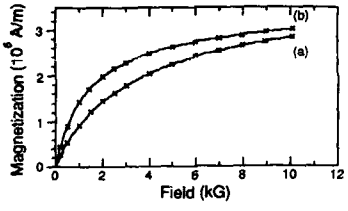


FIG. 1. Magnetization curve of sample B (prepared from sodium amalgam) immediately after preparation (a) and after aging for 42 days at room temperature (b).

ple masses of about 1.5 g were used giving large, well measurable magnetic signals. Some typical magnetization curves are shown in Fig. 1.

The ferrofluid samples are superparamagnets consisting of freely rotating single-domain magnetic particles embedded in liquid mercury. As the magnetic moment of the particles is large, the problem can be treated classically. The contribution to the magnetization is described by a different Langevin function for each particle, the exact field dependence being determined by the magnetic moment of the actual particle. The total magnetization of a sample is given by the sum of the contributions from the individual particles. In the reverse direction, the probability distribution of magnetic moments can be determined by decomposing the measured field dependence into a linear combination of Langevin functions. Assuming that the magnetization of the particles equals to the room-temperature magnetization of bulk iron and the particles are approximately spherical, the distribution of magnetic moments can be converted into the distribution of particle diameters.

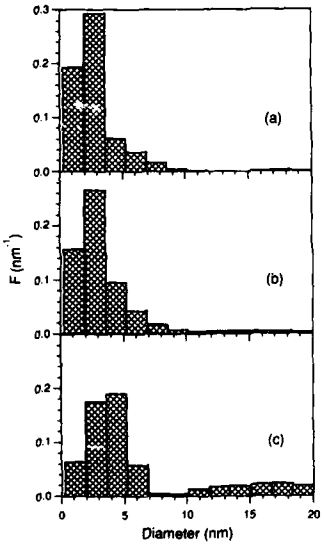


FIG. 2. Particle size distribution of sample A (electroplated) after preparation (a) and after aging at room temperature for 4 days (b) and 42 days (c). $F(D)dD$ is defined as the volume fraction of the particles with diameters between D ...d $D + dD$.

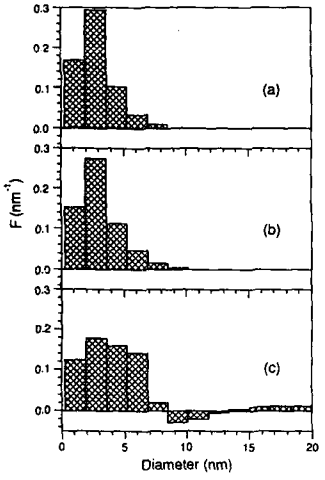


FIG. 3. Particle size distribution of sample B (prepared from sodium amalgam) after preparation (a) and after aging at room temperature for 4 days (b) and 42 days (c).

To perform this procedure, a computer program similar to that described by Weser and Stierstadt[6] was applied. Demagnetization effects were treated in the mean field approximation using a combined demagnetization factor to take into consideration the shape of both the sample as a whole and the individual particles. Although the particle size distribution is sensitive to the demagnetization factor assumed and the shape of the particles can be nonspherical especially after aging, we have no means to distinguish changes of the demagnetization factor from changes of the particle size distribution.

RESULTS

Several samples were prepared using both electrolysis and sodium amalgam. The average particle size of the as-prepared samples varied from 2.4 to 4.3 nm. In the present paper, the particle size distribution and its aging behavior is shown for two typical samples prepared in different ways but having very similar characteristics. One of them was prepared by electroplating iron into a mercury cathode from $FeCl_3$ solution (sample A). The other was made from sodium amalgam using $FeCl_2$ as an electrolyte (sample B). The iron concentrations estimated from the saturation magnetization are 0.4 and 0.9 at. %, respectively.

The particle size distribution is shown for sample A on Fig. 2. Shortly after the preparation, the average particle diameter obtained is 3 nm and the number of particles larger than 8 nm is negligible. During the first four days, the average particle diameter increases to 3.5 nm. After 42 days, the distribution of the particle diameters splits into two regions: The small size region below 8 nm shows the steady increase

of the particle size. At the same time, a substantial fraction of much larger particles appears. Although large particles can be formed by the agglomeration of much smaller ones, this result can also be an artifact. Some particles can become elongated changing the demagnetizing effects. As the samples were aged in the sample holders, the formation of agglomerates at the walls of the sample holders is also possible. This possibility is underlined by the fact that a small hysteresis effect is observed indicating a ferromagnetic contribution to the magnetization.

Similar results are shown on Fig. 3 for sample B. The average particle diameter in the as-prepared state is again nearly 3 nm. However, the size increase on aging is somewhat less, to only 3.2 nm in four days. As compared to sample A, the presence of very large particles is much less clear after 42 days. On the other hand, a region with unphysical negative probability can be observed between 8 and 13 nm indicating that the assumptions of the data evaluation are not completely satisfied.

CONCLUSIONS

It has been shown that mercury-based ferrofluids can be prepared from sodium amalgam with extremely simple means. The samples so produced are very similar to others prepared by the conventional method of electroplating. A slightly smaller aging effect was seen in the sample prepared from sodium amalgam, probably because of the stabilizing effect of sodium remaining in the sample.

ACKNOWLEDGMENTS

The author expresses his thanks to Dr. C. Landee for the permission to use his magnetometer and for his helpful comments. He also acknowledges the encouraging discussions with Dr. C. Hohenemser. The technical help and comments of R. Greeney and N. Rosov were invaluable.

[1]R. L. Bailey, J. Magn. Magn. Mater. **39**, 178 (1983).
[2]R. B. Falk and F. E. Luborsky, Trans. Met. Soc. AIME **233**, 2079 (1965).
[3]S. W. Charles and J. Popplewell, IEEE Trans. Magn. **MAG-12**, 795 (1976).
[4]J. van Wonterghem, S. Morup, S. W. Charles, and J. Popplewell, J. Magn. Magn. Mater. **65**, 276 (1987).
[5]A. Mayer and E. Vogt, Z. Naturforsch. **7a**, 334 (1952).
[6]T. Weser and K. Stierstadt, Z. Phys. B **59**, 253 (1985).

Effect of magnetic field cooling and magnetization anomaly in magnetic fluids near melting point

H. Miyajima, N. Inaba, S. Taketomi, M. Sakurai, and S. Chikazumi
Department of Physics, Faculty of Science and Technology, Keio University, Hiyoshi 3-14-1, Yokohama 223, Japan

The magnetization process of ferrofluids with carrier fluids of water, paraffin, and alkylnaphtalene was investigated in a temperature range from 77 to 300 K as functions of the freezing rate and the intensity of cooling magnetic fields. A uniaxial magnetic anisotropy is induced by field cooling in frozen ferrofluids. This induced anisotropy which is caused by the formation of clustering of magnetic particles disappears on heating near the melting point. The magnetization of the frozen fluids exhibits an anomalous increase below the melting point of the carrier fluids. In a frozen state, no relative motion of particles, such as Brownian motion, occurs. With increasing temperature, the inhibited motion will be released gradually by the recovery of viscosity. The anomaly may be related to glassy transition and premelting. These magnetic properties are discussed in terms of mesoscopic phase transition between liquid and solid.

INTRODUCTION

Magnetic fluid that is a suspension of colloidal particles dispersed in a carrier fluid exhibits ferromagnetism of fluidal state and possesses many kinds of characteristic phenomenon like optical birefringence.[1] Usually these particles are subject to Brownian motion in the liquid. However, when the magnetic fluid is frozen below the melting point of the carrier fluid, no relative motion is allowed. With gradually increasing temperature, the inhibited motion will be released above some temperature, say, the glass transition temperature. Therefore, a transition of the physical properties between solid and liquid can be observed by using the magnetic fluid as a magnetic probe. Recently, Hoon *et al.* observed below the melting point of water that the magnetic torque amplitude for a water-based magnetic fluid after freezing in a magnetic field of 8.4 kOe shows some anomalies which may be attributable to the premelting of the particle surfactants.[2]

In this paper phase transitions of magnetic fluids between solid and liquid are discussed in terms of magnetic field cooling and size distribution of particles.

EXPERIMENTAL PROCEDURE AND RESULTS

Three kinds of magnetic fluid containing Fe_3O_4 particles whose carrier fluids are water, paraffin, and alkylnaphtalene were prepared. The values of viscosity of these solvents are 1.002×10^{-2} P (water, 20 °C), 93.6×10^{-2} P (alkylnaphtalene, 20 °C), 37.2×10^{-2} P (alkylnaphtalene, 38 °C), 3.53×10^{-2} P (paraffin, 20 °C), and 3.06×10^{-2} P (paraffin, 40 °C). The melting temperature T_m was determined to be about 268, 196, and 265 K for water, paraffin, and alkylnaphtalene, respectively. These values are somewhat lower than those of pure fluids because of the presence of surfactants in the solution. The magnetization and the torque of these magnetic fluids were measured in a temperature range from 77 to 300 K as a function of the intensity of cooling magnetic field H_f.

The magnetization curve for paraffin-based fluid frozen in $H_f \simeq 3.5$ kOe is shown in Fig. 1 for two directions of cooling field relative to the external field H_e. The difference between the two curves is caused by the magnetic anisotropy induced by field cooling. The magnitude of the induced anisotropy K_u at 77 K was evaluated as 4.0×10^3 and 8.2×10^3 erg/cm^3 for water- and paraffin-based magnetic fluids, respectively. These values depend strongly on the intensity of cooling field. The magnetic fluid frozen without H_f naturally showed an isotropic magnetization curve and no induced anisotropy.

The magnetization at constant fields varied with temperature rather complicatedly. Figure 2 shows the temperature dependence of the magnetization for water-based fluids. As seen in the figure, the field cooling seems to strongly affect the magnetization near the melting point T_m. That is, the magnetization after cooling without H_f exhibited anomalous variation near T_m, especially in a low magnetic field of 0.5 kOe, while the magnetization observed after field cooling

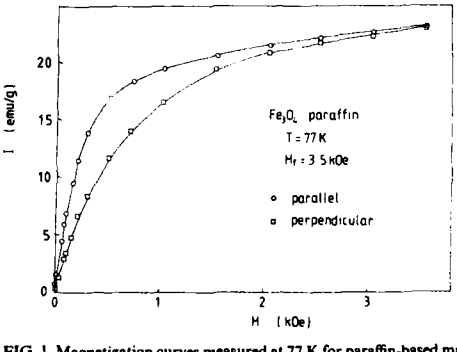


FIG. 1. Magnetization curves measured at 77 K for paraffin-based magnetic fluid frozen in $H_f = 3.5$ kOe. Two curves were obtained by applying magnetic field parallel and perpendicular to the cooling field.

 0021-8979/88/084267-03$02.40 © 1988 American Institute of Physics

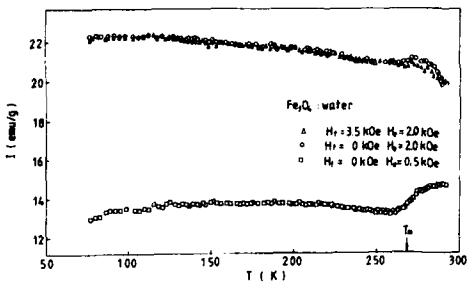


FIG. 2. Temperature dependence of magnetization for water-based magnetic fluid. The notation H_f and H_e represent the cooling and the external magnetic field, respectively.

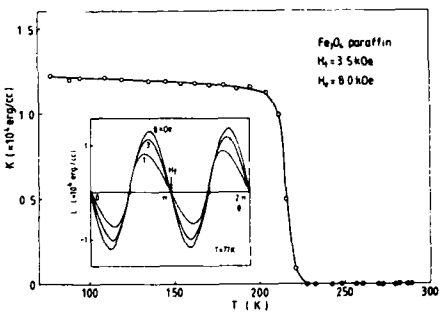


FIG. 4. Temperature dependence of the induced anisotropy for a paraffin-based ferrofluid frozen in $H_f = 3.5$ kOe and measured in $H_e = 8$ kOe. The inset shows the magnetic field dependence of the torque curve at 77 K.

varied rather smoothly near T_m. Figures 3(a), 3(b), and 3(c) show the variations of magnetization for water-, paraffin-, and alkylnaphtalene-based fluids in 0.5 kOe after cooling without H_f, respectively. It should be noted that such an unusual behavior in a lower field is commonly observed in any magnetic fluids and also that they occurred not at the melting point but below this point (in the case of paraffin- and alkylnaphtalene-based fluids) or above (water-based fluid).

Figure 4 shows the temperature dependence of the induced anisotropy constant K_u for the paraffin-based ferrofluid. The value of K_u decreased linearly with increasing temperature below about 180 K and somewhat bent away from the straight line between 180 and 200 K. The value of K_u decreased abruptly at about 200 K, which corresponds to T_m, and finally down to a very small value of the order of 10^2 erg/cm^3 or less above about 230 K. The insert shows a torque curve from which K_u was determined.

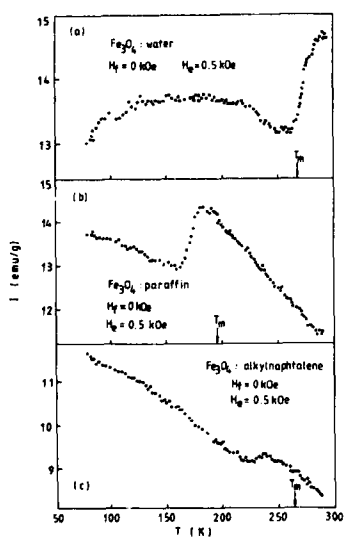


FIG. 3. Temperature dependence of magnetization in $H_e = 0.5$ kOe for magnetic fluid frozen without H_f. (a), (b), and (c) show water-, paraffin-, and alkylnaphtalene-based magnetic fluids, respectively. The arrow indicates the melting point of the solvent.

DISCUSSION

The size distribution of magnetic colloid is known to take a logarithmic normal distribution function[3] given by

$$f(r) = 1/[\sqrt{2\pi}\sigma r_0 \exp(\sigma^2/2)] \times \exp[-(\ln r - \ln r_0)^2/2\sigma^2], \quad (1)$$

where r is the radius of the particle, r_0 the average radius of the particle, and σ the standard deviation of the distibution. By using the relationships proposed by Chantrell *et al.*,[4] the mean radius and the standard deviation for the paraffin-based fluid are estimated to be 31 Å and 0.23, respectively. Therefore, the average energy of single particle $K_a V$ is evaluated to be 1.6×10^{-14} erg, where K_a is the anisotropy constant of Fe_3O_4 and V is the average volume of the particle.

It is considered that the magnetic particles in a magnetic fluid form clusters elongated along the applied field. These clusters are solidified by cooling below T_m. The shape anisotropy of the cluster assumed to form an ellipsoid can be calculated, but the magnitude is smalller than that of observed one by one-fifth. The dipole-dipole interaction energy E_d between the colloidal particles which form into a line parallel to the magnetic field direction is given by

$$E_d = NM_0 \int_0^{\theta} H(\theta')\sin\phi(\theta')d\theta' \quad (2)$$

$$\sim 3.6 I_s M_0/d_0^3 \sin^2\theta, \quad (3)$$

where d_0 is the average distance between particles, I_s the saturation magnetization of a ferrofluid, M_0 the average magnetic moment of single particle, H the molecular field given by dipole moments, θ the tilting angle of the magnetic moment from the chain axis, and ϕ is the angle between the magnetic moment and the external magnetic field. By using r_0 and σ for the paraffin-based ferrofluid obtained in the above section, the anisotropy energy constant caused by this interaction is estimated to be about 1.9×10^4 erg/cm^3 at 77

K by assuming that the particles are almost contacted. The evaluated value is slightly larger than the observed one shown in Fig. 4. This may be caused by the following situation: The cluster formed only one linear chain. The interaction between clusters was ignored. The average particle size and the average distance between particles were used. The colloidal particles were assumed to obtain dipole magnetic moments and high-order interactions between the particles were ignored. The induced anisotropy is, however, considered to be mainly caused by the dipole-dipole interaction. Further investigation on this point will be needed.

As mentioned above, the magnetization measured under a constant field exhibits unusual behavior near T_m. The alignment of the magnetic moments of colloidal particles in ferrofluids under the applied magnetic field is caused by the following two processes: namely, the direction of the moment in the particle is changed against the magnetic anisotropy of the particle, and also the moment can be aligned by the rotation of the particle. When the colloidal particles are frozen without H_f, their magnetic moments are directed randomly in space without forming clusters. In the frozen state below T_g, which is some temperature related to the viscosity, there is neither induced magnetic anisotropy nor relative motion, such as Brownian motion or rotation. The variation of net magnetization of ferrofluids is produced only through the former process. Therefore, especially under a low magnetic field, it is difficult to align the moments, so that the net magnetization is small. With increasing temperature below T_g the net magnetization of ferrofluids was gradually decreased since the thermal agitation of magnetic moments in particles is increased. With increasing temperature above T_g but below T_m, the viscosity of the ferrofluid is decreased gradually, so that the inhibited motion is released gradually, and the colloidal particles turn not only to form chainlike clusters but also to align the easy direction toward the magnetic field. The alignment of the magnetic moments toward the applied field is easier than below T_g. As a result the magnetization is increased gradually. Under a low magnetic field like 0.5 kOe as shown in Fig. 3, this variation was clearly observed. On the contrary, when the ferrofluid is heated up above T_m and recovers large fluidity as a liquid, the magnetization is decreased with increasing temperature by the thermal agitation of magnetic moments and violent Brownian motion of particles. On the other hand, when a magnetic field H_f is applied, the chainlike cluster is formed along this field and solidified below T_m. Because of the dipole-dipole interaction between colloidal particles, both thermal agitation of magnetic moments and Brownian motion of the particles have a small effect on the variation of net magnetization near the melting point. Therefore, the magnetization varies smoothly near T_m.

The physical meaning of T_g is not yet fully understood, but there are some papers on this points. O'Grady *et al.* measured the temperature dependence of the initial susceptibility for a toluene-based ferrofluid of Co particles.[5] They found that the $1/\chi - T$ plot in a freezing region bends at about 200 K which is lower than T_m by 40 K. Hoon *et al.* suggested that the local regulation under the effect of local pressure or premelting may be responsible.[2] While Soeffge and Schmidbauer studied on a diester-based Fe_3O_4 ferrofluid over a wide temperature range from 4.2 to 380 K by measuring ac susceptibility,[6] and they found that spin-glass-like behaviors in a frozen state, that is, χ in a solid state, takes a maximum at a temperature which depends strongly on external magnetic fields. In present investigations, the magnetization anomaly caused by the recovery of viscosity was observed near T_m. It is considered that T_g is similar to the glassy transition temperature which often observed in amorphous semiconductors and metallic alloys. The effect of freezing conditions on T_g and the x-ray analysis of the structure at about T_m are now being investigated.

ACKNOWLEDGMENT

This work was partially supported by Yamada Science Foundation.

[1]S. Chikazumi, S. Taketomi, S. Ukita, T. Mizukami, M. Setogawa, and Y. Kurihara, J. Magn. Magn. Mater. **65**, 245 (1987).
[2]S. R. Hoon, B. K. Tanner, and M. Kilner, J. Magn. Magn. Mater. **39**, 30 (1983).
[3]C. G. Granqvist and R. A. Buhrman, J. Appl. Phys. **47**, 2200 (1976).
[4]R. W. Chantrell, J. Popplewell, and S. W. Charles, IEEE Trans. Magn. MAG-14, 975 (1978).
[5]K. O'Grady, A. Bradbury, S. W. Charles, S. Menear, J. Popplewell, and R. W. Chantrell, J. Magn. Magn. Mater. **31–34**, 958 (1983).
[6]F. Soeffge and E. Schmidbauer, J. Magn. Magn. Mater. **24**, 54 (1981).

Magnetotransport: An ideal probe of anisotropy energies in epitaxial films (invited)

E. Dan Dahlberg and Kevin Riggs
School of Physics and Astronomy, University of Minnesota, Mineapolis, Minnesota 55455

G. A. Prinz
Naval Research Laboratories, Washington, DC 20375-5000

Magnetotransport measurements provide an ideal probe to determine the various anisotropy energies in epitaxial magnetic films. The extraordinary Hall effect (EHE) can be used to determine the perpendicular or surface anisotropy energy while the anisotropic magnetoresistance (AMR) can be used to investigate the in-plane anisotropy energies. The advantage of magnetotransport over more tranditional measurement techniques used to determine these anisotropy energies is the ease of the technique, the lack of a need for sophisticated equipment, and the insensitivity of the techniques to the magnetic properties of a semiconducting or insulating substrate. Both the EHE and the AMR have been used to study the magnetic properties of epitaxial iron films grown on GaAs substrates. The results of the EHE and the AMR study and how the various anisotropy energies compare with those determined by the more traditional techniques of ferromagnetic resonance and vibrating sample magnetometry will be discussed.

I. INTRODUCTION

The recent application of molecular-beam epitaxy (MBE) to the manufacture of thin magnetic films has provided a number of interesting phenomena for study[1–4] and certainly more surprises are forthcoming. However, associated with the advances in this area resides the difficulty of measuring the magnetic properties of films which range in thickness from submonolayer to 100's of nm in thickness. For the study of the anisotropy energies in these materials one normally considers the use of a SQUID or vibrating sample magnetometer (VSM). In this paper we will discuss another technique, magnetotransport, which provides information on the various anisotropy energies of thin MBE films grown on semiconducting or insulating substrates. Also included are some magnetotransport study results of MBE grown iron films. The data have been accumulated from iron films of 4–20 nm in thickness grown on {110} surfaces of GaAs.

Some advantages of magnetotransport to determine anisotropy energies of MBE films as compared to the above techniques are the insensitivity to a semiconducting or insulating substrate, the simplicity of the experimental setup and the relative low cost of the equipment. The first is probably the most important reason for considering magnetotransport to study MBE films since in either a VSM or SQUID magnetometer it is difficult to subtract the magnetic contribution of the substrate from the data whereas in magnetotransport it is only the metallic portion of the sample (the thin film) which is measured. All the anisotropy energies may be determined by measuring the magnetotransport properties of the films in two different applied magnetic field geometries. In one the magnetic field is applied perpendicular to the plane of the film and in the second it is applied parallel to the plane of the film.

Considering the former geometry first, with the magnetic field applied perpendicular to the plane of the film, the off diagonal resistivity or the voltage perpendicular to the current is measured [see Fig. 1(a)]. This geometry is the usual one for the ordinary Hall effect (OHE). Our interest will be in the magnetic contribution to the measured voltage which is referred to as either the extraordinary Hall effect (EHE) or the anomalous Hall effect in the literature.

The EHE voltage or resistance is linearly proportional to the component of the magnetization perpendicular to the plane of the film, M_z. For this reason the EHE varies with an applied perpendicular magnetic field only if M_z is less than the saturation magnetization of the film. The magnitude of the applied magnetic field necessary to saturate the EHE

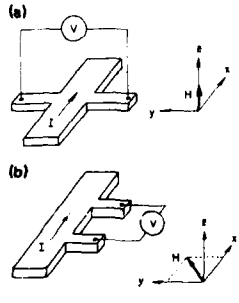


FIG. 1. The different magnetic field geometries for the magnetotransport measurements are shown. In (a) the magnetic field is applied perpendicular to the plane of the film with mesurements of the transverse resistivity. This is the geometry for the EHE. In (b) the magnetic field is in the plane of the film for measurements of the longitudinal resistivity. This geometry is used to measure the AMR.

 0021-8979/88/084270-06$02.40 © 1988 American Institute of Physics

signal is related to the perpendicular or surface ansiotropy energy. In general the importance of determining the perpendicular anisotropy energy may be realized by considering the recent theoretical prediction[5] and experimental confirmation[3] that for iron films grown on the {100} plane of Ag possess a surface anisotropy energy sufficiently strong to overcome the demagnetization energy and orient the magnetization perpendicular to the plane of the films. Although one does not expect this situation to occur in all MBE films it does suggest the possibility should not be overlooked.

When the applied magnetic field is in the plane of the film the diagonal resistivity or the voltage parallel to the current is measured [see Fig.1(b)]. Assuming that the magnetization is uniform then the measured resistance depends only upon the angle between the magnetization and the current in the sample. This effect is known as the anisotropic magnetoresistance (AMR). Clearly if the magnitude of the AMR is known (which is defined as the resistance of the film with the magnetization parallel to the current minus the resistance with the magnetization perpendicular to the current) then a measure of the resistance of a film determines the projection of the magnetization on the current direction. For different crystallographic directions one may determine the magnitude of the field necessary to saturate or rotate the magnetization to the selected direction. With this information and utilizing an analysis similar to that used in a vibrating sample or SQUID magnetometer measurement one may determine the various crystalline anisotropy energies.[6]

Two final comments before proceeding are that the samples will be considered to have a uniform magnetization and the magnetoresistance associated with nonmagnetic effects will be considered to be either nonexistant or negligible. In practice, effects from both of the above are present but for the following reasons they will be negected. First, contributions from them are usually easy to separate from the quantities of interest (as will be born out by the examples of data shown here). Second, their neglect greatly simplifies the discussion of the magnetotransport properties. In the next two sections we will discuss in greater detail the two measurements described above and review some of the results which we have obtained using these measures on MBE grown iron films. In the last section is discussed other potential uses of the magnetotransport data.

II. EXTRAORDINARY HALL EFFECT

As stated above, using the Hall geometry with the magnetic field applied perpendicular to the plane of the film one may determine the presence and magnitude of a surface anisotropy energy. In this geometry it is the off-diagonal component of the resistivity which is measured just as in the ordinary Hall effect. The origin of the EHE is, however, very different than the OHE. The EHE arises from an asymetry in the right-left scattering of the conduction electrons from the component of the magnetization perpendicular to the current. Physically it is the spin-orbit coupling which links spin-space to real space and provides this scattering asymetry. There are two theroretical models which provide the necessary scattering asymmetry in magnetic systems. One is referred to as skew scattering whereas the other is called the side-jump. Here the details of the two models will not be discussed and the interested reader is referred to Ref.7 for a very useful comparison of the two models. For the present discussion only the fact that the two models may be distinguished by measuring the magnitude of the EHE and comparing it to the resistivity of the materials is necessary. In the case of the skew scattering model the magnitude of the EHE should scale with the resistivity ρ whereas the side-jump mechanism predicts the magnitude to be proportional to the square of the resistivity. Although not developed in detail in this paragraph, one should accept that a Hall-type measurement in a magnetic system can probe the component of the magnetization perpindicular to the plane of the film. What is now necessary to consider is how this perpendicular component varies as a function of an applied magnetic field.

Normally the magnetization of a thin magnetic film is assumed to lie in the plane of the film due to the demagnetization energy in the absence of any external magnetic fields. The interaction energy of the magnetization with a field applied perpendicular to the plane of the film (H_z) can rotate the magnetization such that it develops a component normal to the plane. Considering only these two energies (which usually are dominant) to be present in the film then the energy of the film per unit of area is given by

$$F = (4\pi t M_z^2/2) - (tM_z H_z), \tag{1}$$

where 4π is the demagnetization factor appropriate for a thin film, t is the thickness of the film, and M_z is the z component of the magnetization.

If a large surface anisotropy energy is present it also must be considered. The possibility of a surface anisotropy energy due to the reduced local symmetry was first introduced by Neel[8] and to lowest order is given by

$$F_s = K_s(M_z^2/M_s^2), \tag{2}$$

where K_s is the surface anisotropy constant. Considering all the energies in Eqs. (1) and (2) to be present one may show the equilibrium value of M_z in an arbitrary perpendicular magnetic field to be

$$M_z = (4\pi + 2K_s/M_s^2 t)^{-1} H_z. \tag{3}$$

Obviously this equation is valid only if $M_z < M_s$ and it is this requirement which provides the signature in the EHE data necessary in the analysis of the data for the determination of K_s.

From Eq. (3) ones sees the value of M_z to be linear in the applied magnetic field until the magnetization saturates. Any measurement sensitive to M_z will therefore vary linearly in the applied field and then abruptly stop changing as the magnetization saturates. The magnetic field where the saturation occurs (H_s) can be calculated by substituting M_s for M_z in Eq. (3) and solving for H_s. This operation results in an H_s given by

$$H_s = 4\pi M_s + 2K_s/M_s t. \tag{4}$$

Based upon the discussion thus far one would expect the magnetic field dependence of the Hall resistance for a perfect sample [defect and strain free and with only the energies described in Eqs. (1) and (2) present] to have a steep initial slope consisting almost entirely of the EHE followed by a

more modest slope associated with the OHE. The field at which the slope of the Hall resistance changes corresponds to a value of the applied field which is of sufficient strength to saturate the magnetization of the film in the perpendicular direction. Above this field value there is no change in the value of M_z, assuming the sample is well below the Curie temperature, and therefore the magnitude of the asymmetric scattering is constant beyond this point and also the Hall resistance associated with the EHE. At higher field values the Hall resistance is only that due to the OHE. The magnitude of the EHE or what is known as the spontaneous Hall resistivity, R_s, is the Hall resistivity at the saturation field minus the resistivity of the ordinary Hall effect. Although functionally this is straight forward, in practice it requires a knowledge of the internal field for a correct subtraction of the OHE resistivity. Also, in a real sample things are more complicated as shown in Fig. 2 which shows the Hall voltage of a 16-nm-thick film as a function of applied magnetic field. One notices that there is not an abrupt crossover from the low field regime to the high field regime. For this reason an operational definition must be made for both the saturation field and the Hall voltage at saturation. This is most simply done by performing a least-squares fit to the initial data and the data taken in the largest applied fields. Then the intercept of the two lines defines the saturation field and Hall voltage at saturation.

For the epitaxial iron films we have studied the Hall data have been analyzed in the above manner. In discussing the results we would first like to address the origin of the EHE in these films. As mentioned previously the two theoretical models can be distinguished by comparing the magnitude of the EHE to the resistivity of the films. For the iron films we have studied the resistivity of the films depend upon the thickness of the films as expected due to surface scattering. This distribution of resistivities allows a comparison between the resistivity and R_s with the results shown in Fig. 3. A least-squares fit to the data is shown in the figure and its slope is consistent with the side-jump mechanism proposed

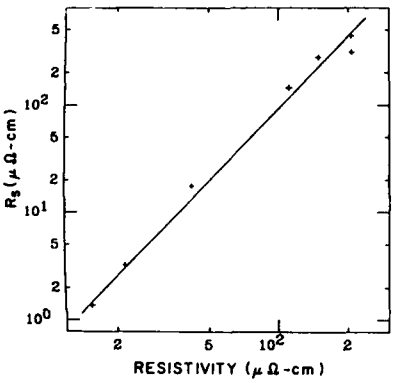


FIG. 3. A log-log plot of the EHE magnitude or R_s vs the resistivity for the different film thicknesses. The data were taken with the current in the ⟨100⟩ direction and from the slope of the line shown in this figure indicate the side jump mechanism as dominating the EHE.

by Berger[9] which predicts the magnitude of the EHE should be proportional to the square of the resistivity.

We turn now to the other and for the purposes of this paper the more germane aspect of the EHE data, the saturation field of the magnetization. Figure 4 shows how the field defined as H_s varies as a function of film thickness. Comparison of this figure with Eq. (4) would suggest that a surface anisotropy energy does play a role in these films. However, Eq. (4) assumes the magnetization of the films is independent of the thickness of the films. In the case of the iron films we have studied experimental measurements of the saturation magnetization[10] reveal the above film thickness dependence of H_s may be entirely explained by variations of the saturation magnetization, i.e., the data are consistent with $K_s = 0$. The fact that a large surface anisotropy is not present indicates that the phenomena predicted[5] and observed[3] is not necessarily common.

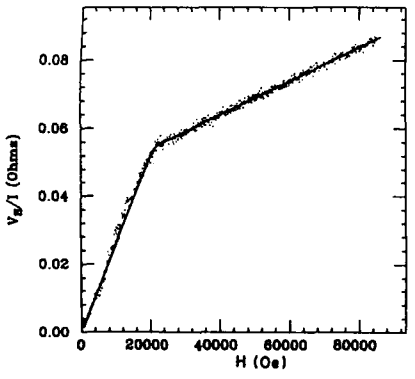


FIG. 2. The measured Hall voltage of a 16-nm-thick film. The saturation field H_s is defined as the field given by the intersection of a straight line fit to the low- and high-field data.

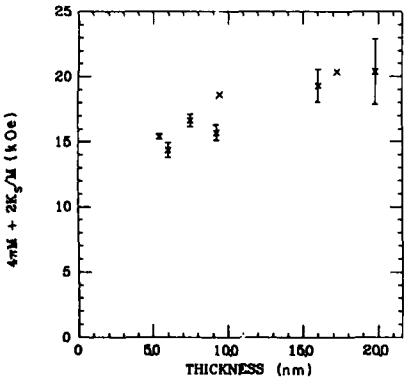


FIG. 4. The variation of the saturation field H_s with film thickness. The variation stems from the thickness dependence of the magnetization and not a surface anisotropy energy.

An interesting feature of this work is a comparison of the EHE study with a study on similar films using ferromagnetic resonance (FMR).[11] The FMR work included films with an iron oxide coating and others with an overcoating of Al. The EHE study included only oxide covered films. The results of the EHE data were consistent not with the oxide covered film FMR data but instead with the AL covered film data. This surprising result was attributed to a coupling of the iron resonance to the oxide.

In concluding this section we would like to emphasize the ease in making the above measurements we have discussed. The necessary ingredients are to have a film thick enough to be continuous (probably only a few atomic layers dependent upon the substrate quality), leads attached to the sample (five are a minimum for four terminal measurements) and a magnetic field of sufficient strength to orient the saturation magnetization in a direction perpendicular to the plane of the film. In all probability it is the last requirement which most experimentalists will find most difficult to accomplish for *in situ* measurements.

III. ANISOTROPIC MAGNETORESISTANCE

Studies of the anisotropic magnetoresistance entail measurements of the diagonal resistivity [as in Fig. 1(b)] as a function of the angle between the magnetization and the current (Θ). As a rule the resistance is a minimum when the current is perpendicular to the magnetization and a maximum when it is parallel however exceptions are known.[12] Since the applied magnetic field lies in the plane of the film the magnetic fields necessary for the measurement need only to be sufficient to overcome the crystalline anisotropy energies of the bulk film and need not be as large as in the EHE case. Just as in the EHE, it is the spin-orbit coupling which gives rise to the AMR. Theoretically the correlation between the AMR and the spin-orbit coupling has been worked out by several researchers[13–16] and the interested reader is refered to these references. An important point to make, however, is the AMR is not a measure of the magnetoresistance one normally associates with a nonmagnetic material. The AMR is associated with the magnetic state of the sample and is independent of the orientation of the current with respect to the crystallographic axes. It is this fact which allows one to utillize the AMR of polycrystalline films in technological applications.

As we have stated, the power of an AMR measurement of an MBE single-crystal film is that it provides a sensitive measure of the direction of the saturation magnetization in the plane of the film. If the magnetization makes an angle theta with respect to the current then the resistivity one measures is given by

$$\rho = \rho_0 + \Delta\rho(1 - \cos^2\Theta), \tag{5}$$

where ρ_0 is the isotropic resistivity (not the residual or zero temperature resistivity) and $\Delta\rho$ is defined as the difference between the resistivities measured with the magnetization parallel and perpendicular to the current. It is clear that in a magnetic field large enough to maintain the saturation magnetization in the direction of the applied field the measured resistance should oscillate with a period of twice Θ as the magnetic field is rotated in the plane of the film. This effect is shown in Fig. 5 for a film 9 nm thick in an applied field of 10 kOe. As shown in this figure the resistivity of the film varies as the square of the angle between the magnetic field and the current direction in the film. Of course, if the applied field is insufficient to overcome the crystalline anisotropy energies of the film then the magnetization will not remain parallel to the applied field. One could, in principle, use this fact to determine the anisotropy energies by making a large number of measurements of the resistance as a function of angle in various magnetic fields. Fortunately there is an easier way to determine the anisotropy energies with magnetoresistance.

If a field is applied parallel to a hard axis the resistance will vary smoothly with increasing field until the magnetization is saturated along the hard axis. The shape of the observed magnetoresistance is very similar to what one observes in a *B-H* loop experiment and the analysis of the data to determine the anisotropy energy is the same. In continuing the analogy with a *B-H* loop measurement if the the external field is applied along the easy axis of a demagnetized sample then as a function of applied field the data are again very similar to those obtained from a *B-H* loop measurement, i.e., the resistance changes rapidly in modest fields, as the sample becomes a single domain, and then saturates. However, the analogy to a *B-H* loop study no longer holds if one reverses the magnetic field direction and tries to measure the coercive field. As shown in Eq. (5) the resistance depends on the $\cos^2(\Theta)$ and therefore if the magnetization reverses by 180° the resistance will have the same value. For this reason coercive fields cannot be determined by magnetoresistance.

The above experimental procedure may be applied in the simple case where in the plane of the film there is only hard and easy axes. A more interested situation arises when there is a hard axis, an easy axis, and an intermediate axis in the plane of the film. This is the situation which occurs for the iron films we have studied which were grown on the {110} surface of GaAs. The iron films grow in a [110] direction which results in an easy axis (the ⟨100⟩ direction), a

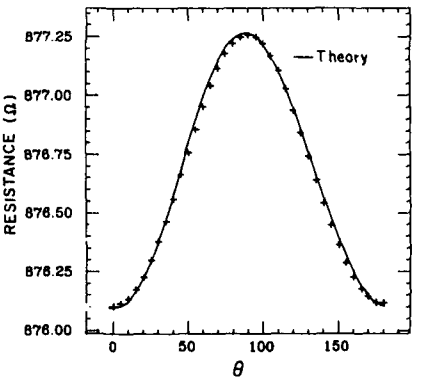


FIG. 5. The resistance of a 9-nm-thick film as a function of the angle an applied field of 10 kOe makes with the current direction.

hard axis (the ⟨111⟩ direction), and an intermediate axis (the ⟨110⟩ direction) in the plane of the film[17] with the hard axis direction between the easy and intermediate directions. Because of the large demagnetization energy of the thin films the magnetization lies in the plane of the film for all magnetic fields applied in the plane of the films. This means for the magnetization to rotate from the easy direction to the intermediate direction it must rotate pass the hard axis direction. This has interesting consequences if one considers in detail how the magnetization rotates from the easy axis to the intermediate axis.

If the field is applied parallel to the intermediate axis the magnetization rotates to a position closer to the hard axis. Once the component of this field in the hard axis direction is of sufficient strength for the magnetization to pass the hard axis the magnetization will abruptly rotate into the intermediate or ⟨110⟩ direction. This situation is analogous to a first order transition where the applied magnetic field plays the role of temperature. The abruptness of the transition is shown in Fig. 6 where the magnetoresistance of a 16-nm-thick film with the current in the ⟨110⟩ direction or intermediate axis is shown. Also in this figure one will note the presence of hysteresis in the transition which is dominated by the energetics of the domain patterns and motions in the films.

Thus far the discussion has been limited to fields applied parallel to the intermediate axis. In practice one may use fields applied anywhere in the plane of the film between the intermediate and hard axis directions. Of course, with the field applied parallel to the hard axis there is no longer a first-order transition but more a situation as described previously when only a hard and an easy axis were considered. It is clear then that the magnitude of the abrupt magnetization rotation depends upon the crystallographic direction of the applied magnetic field. This is analogous to the thermodynamic situation of a phase diagram with a first-order transition line terminated by a critical point and one may construct a phase diagram by plotting the field components parallel to both the easy and intermediate axes where the transition occurs. In other words the magnetic field direction in the plane is fixed and as the field is varied the components of the magnetic field in the crystallographic directions when the transition occurs is measured. An example of this analysis is shown in Fig. 7. In this figure is plotted the transition in both increasing and decreasing field for a 17-nm-thick film. The point at which the two curves intersect coincides with the critical point where the transition becomes second order. From analysis of the data such as shown in this figure one may determine the appropriate anisotropy energies. For the iron films we have investigated a uniaxial anisotropy energy not occuring in bulk iron must be considered. Although this is somewhat surprising the magnetoresistance analysis[6] is consistent with an analysis based on ferromagnetic resonance data.[18]

IV. CONCLUSIONS

We have shown how simple magnetotransport measurements may be used to determine the various anisotropy energies in MBE grown films. As compared to other techniques used for analysis of MBE films the magnetotransport is simpler and less expensive as a rule and possibly most important the magnetotransport measurements are insensitive to the presence of a semiconducting or insulating substrate. In addition, when used in conjunction with the more traditional measurement techniques magnetotransport may indicate the presence of unsuspected phenomena occuring in MBE films.[11] Also the magnetotransport data may be useful as a measure of the spin-orbit coupling in MBE films. As was pointed out in the discussions both the EHE and the AMR theories rely on the spin-orbit coupling for connecting spin space to real space. As yet a systematic investigation of this type has not been carried out. A final point is the magnetotransport properties also contain other useful information such as band structure information from measures of the

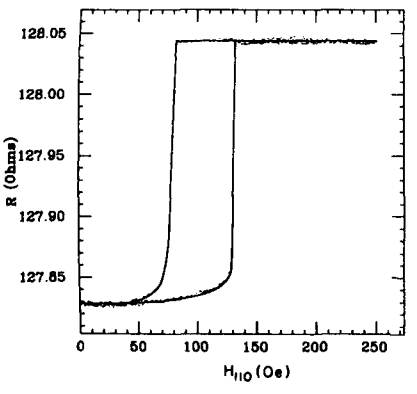


FIG. 6. The resistance of a 16-nm-thick iron with an applied magnetic field parallel to the intermediate axis (the ⟨110⟩ direction). The curve to the right is in increasing magnetic field whereas the one on the left is in decreasing field.

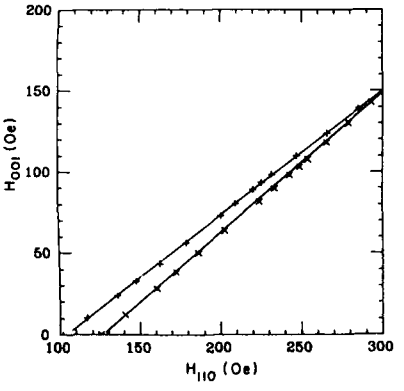


FIG. 7. The components of the applied field along the ⟨100⟩ axis versus the ⟨110⟩ for the first-order magnetoresistance transition of a 17-nm-thick film. The data were taken for various angles between the applied field and the crystallographic axes. At each angle there are two data points; one associated with increasing field and another with decreasing field.

OHE with the current in various crystallographic directions. The iron films grown on GaAs are strained by the mismatch in lattice parameters. This strain reduces the iron from cubic sysmetry which results in the ordinary Hall resistance being different in different crystallographic directions. For thicker iron films the strain is lessened and the asymetry in the Hall resistance is less. At the present time a detailed model for this behavior is lacking.

ACKNOWLEDGMENTS

The authors would like to express their graditude to the AFOSR and the Control Data Corp. for support of the work accomplished at the University of Minnesota (Grant Nos. AFOSR-86-0201 and 86M101, respectively) and the ONR for the work done at the Navel Research Laboratory.

[1]A. S. Arrott, B. Heinrich, S. T. Purcell, J. F. Cochran, and K. B. Urquhart, J. Appl. Phys. **61**, 3721 (1987).
[2]S. D. Bader and E. R. Moog, J. Appl. Phys. **61**, 3729 (1987).
[3]B. T. Jonker, K.-H. Walker, E. Kisker, G. A. Prinz, and C. Carbone, Phys. Rev. Lett. **57**, 142 (1986).
[4]S. Schultz, D. Youm, A. F. Starr, and J. P. Armstrong, J. Appl. Phys. **61**, 3366 (1087).
[5]J. G. Gay and Roy Richter, J. Appl. Phys. **61**, 3362 (1987).
[6]K. T. Riggs, E. Dan Dahlberg, and G.A. Prinz (unpublished).
[7]L. Berger and Gerd Bergmann, in *The Hall Effect and Its Applications*, edited by C. L. Chien and C. R. Westgate (Plenum, New York, 1980), pp. 55–76.
[8]L. Neel, Cont. Rend. **237**, 1468 (1953).
[9]L. Berger, Phys. Rev. B **2**, 4559 (1970).
[10]T. R. McGuire, J. J. Krebs, and G. A. Prinz, J. Appl. Phys. **55**, 2505 (1984).
[11]K. T. Riggs, E. Dan Dahlberg, and G. A. Prinz, J. Magn. Magn. Mater. (to be published).
[12]T. M. McGuire and R. I. Potter, IEEE Trans. Magn. **MAG-11**, 1018 (1975).
[13]J. Smit, Physica **16**, 612 (1951).
[14]Vu Dinh Ky, Physica **82B**, 339 (1976).
[15]O. Jaoul, I. A. Campbell, and A. Fert, J. Magn. Magn. Mater. **5**, 23 (1977).
[16]A. Malozemoff, Phys. Rev. B **32**, 6080 (1985).
[17]For films of thicknesses less than 5 nm the easy axis is the ⟨110⟩ and not the ⟨100⟩. For a discussion of this behavior see G. A. Prinz, G. A. Rado, and J. J. Krebs, J. Appl. Phys. **53**, 2087 (1982).
[18]J. J. Krebs, F. J. Rachford, P. Lubitz, and G. A. Prinz, J. Appl. Phys. **53**, 8058 (1982).

Exchange forces between domain wall and electric current in permalloy films of variable thickness

C.-Y. Hung and L. Berger
Physics Department, Carnegie-Mellon University, Pittsburgh, Pennsylvania 15213

Wall displacements are induced by large current pulses crossing a wall, in $Ni_{81}Fe_{19}$ films. In films of thickness $w < 35$ nm containing Néel walls, the sense of wall motion is found to be independent of the magnetization sense in the two domains adjacent to the wall, and is identical to the sense of motion of the electronlike charge carriers. This shows that the wall motion is not caused by stray magnetic fields, but rather by *s-d* exchange forces generated by conduction electrons. The value $\simeq 5\times 10^{7}$ A cm^{-2} of the needed current density agrees with predictions of a theory based on *s-d* exchange. In the case of cross-tie walls in films with 35 nm $< w <$ 86 nm, the sense of wall motion does depend on the sense of the domain magnetizations. The force of the circumferential magnetic field of the current is probably important, here.

INTRODUCTION

In a recent theoretical paper,[1] we proposed the existence of an interaction between a magnetic domain wall and an electric current, arising from the *s-d* exchange and spin-orbit interactions. This "exchange-drag" force would be dominant in metallic films of thickness $w < 0.1\ \mu$m, while hydromagnetic "domain-drag" forces[2] associated with the Hall effect are important in thicker samples. The exchange-drag force per unit wall area is predicted to have the form

$$F_x = 2M_s\mu_i^{-1}(\beta_1 v_e - v_w)\ , \tag{1}$$

where M_s is the saturation magnetization, v_e the electron drift speed assumed normal to the wall, v_w the wall velocity, μ_i the intrinsic wall mobility, and β_1 a correction coefficient of order unity. The current density j_x is related to v_e through the carrier density n_e and the carrier charge $e^* = \pm 1.60\times 10^{-19}$ C:

$$j_x = n_e e^* v_e\ . \tag{2}$$

Preliminary experimental data[3] for $Ni_{81}Fe_{19}$ films of thickness $w \simeq 30$–40 nm suggest that the exchange-drag force exists, and yield $\beta_1 \simeq +1.8$. Current pulses $I \lesssim 45$ A, of duration $\simeq 1\ \mu$s, are used. They have the shape of a decreasing exponential. Current-induced wall displacements are observed with a polarizing microscope, through the Faraday effect. The critical current density j_c for wall motion is measured, and is 1–2×10^{11} A m^{-2} in samples of wall coercive field $\mu_0 H_c \simeq 50\ \mu$T.

The fact[3] that the experimental value of β_1 is of order unity means that the current-induced drive force [v_e term in Eq. (1)] is described by the same mobility μ_i as the more familiar intrinsic damping force acting on a moving wall [term in v_w in Eq. (1)]. In turn, this suggests that the damping force in Ni-Fe films has the same physical origin as the drive force, namely an interaction of magnetic spins with conduction electrons.

The purpose of the present paper is to confirm these early results, and to study the influence of parameters such as the film thickness and the sense of the domain magnetization.

EXPERIMENTAL TECHNIQUE

As in Ref. 3, Ni-Fe films are prepared by vacuum deposition. Most have the nominal composition $Ni_{81}Fe_{19}$, a few $Ni_{78}Fe_{22}$ or $Ni_{85}Fe_{15}$. A magnetic field is applied during deposition to induce an in-plane easy axis z. Walls are parallel to this axis, and normal to the current [Fig. 1(a)]. Sample and current leads must be as coplanar as possible, in order to minimize the force on the walls associated with stray magnetic fields generated by the current in the leads. Therefore, the silver-paint leads used in Ref. 3 are replaced by thinner leads made of Ni-Fe film, which are merely an extension of the sample itself [Fig. 1(a)]. For similar reasons, the curvature of the Corning 7059 glass substrates has been measured by optical interference methods. During currents equal to a typical value for wall motion, the easy-axis component of the total stray field, averaged over film thickness, is calculated to be less than 3% of the average coercive field $\mu_0 H_c \simeq 160\ \mu$T of our samples.

In order to extend the range of critical current densities j_c which can be determined experimentally, a constant magnetic field H_z parallel to the easy axis is applied. It produces a force parallel to the exchange-drag force. For a given j_x value, the field H_z is increased gradually until a given wall is seen to move during current pulses. This determines one point P_1 in the (H_z, j_x) phase diagram [Fig. 1(b)]. Then another j_x value is chosen, and the procedure is repeated, giving a point P_2. In that manner, the boundary line between regions of static walls and of moving walls can be found [Fig. 1(b)]. By using Eqs. (1) and (2), the equation giving this phase boundary is predicted to be

$$H_z = \pm H_c - (\beta_1/n_e e^* \mu_i) j_x\ . \tag{3}$$

If H_c is assumed to be independent of j_x, Eq. (3) predicts the boundary to be composed to two parallel straight lines [see curves labeled "const. H_c" on Fig. 1(b)]. The intercepts of these lines on the H_z axis are $\pm H_c$. The intercepts on the j_x axis are $\pm j_c$. Even if the part of the boundary close to the j_x axis corresponds to too high currents to be found directly, the intercepts $\pm j_c$ can still be determined by linear extrapolation of the known part of the boundary [Fig. 1(b)]. This is the so-called "field-assisted" method to find j_c.

 0021-8979/88/084276-03$02.40 © 1988 American Institute of Physics

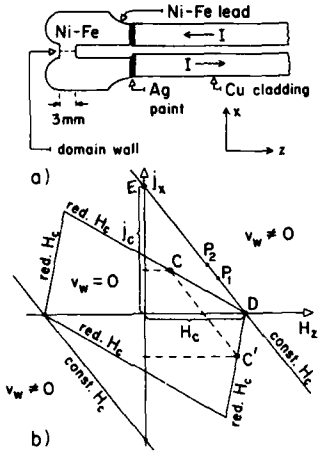


FIG. 1. (a) Nickel-iron thin-film sample, with coplanar current leads. (b) Phase diagram in (H_z, j_x) plane, for experiments assisted by a field H_z. The two solid lines labeled "const. H_c" are the predicted phase boundary for incipient wall motion, under the assumption of constant H_c. The four solid lines labeled "red. H_c" are the experimental phase boundary, where H_c is reduced for increasing current.

EXPERIMENTAL RESULTS

The films range between 14 and 86 nm in thickness. Wall displacements induced by a current are observed in all 42 samples studied. Because of local H_c variations, only a part of the wall actually moves. As stated above, a constant field H_z is used to assist the exchange-drag force. However, wall displacements were observed in some samples even without field assistance, because of an especially low value of j_c.

For each sample, a phase diagram like Fig. 1(b) is drawn. However, in contradiction with the assumption of constant H_c, the experimental phase boundary for incipient wall motion is usually bent sharply at the point D where it crosses the H_z axis [see curves labeled "red. H_c" in Fig. 1(b)]. A likely explanation is that the short current pulses "shake" the wall, excite modes of wall oscillations, and cause a reduction of pinning forces. In other words, the coercive field is a decreasing function $H_c(j_x)$ of the current density. We expect this function to satisfy $H_c(-j_x) = H_c(j_x)$. Because of this evenness, a graphical construction [Fig. 1(b)] can be used to find what the phase boundary would have been in the absence of this "H_c-reduction effect." Select two opposite values j_x and $-j_x$. The corresponding points on the experimental phase boundary are C and C'. Draw the straight line CC'. Draw a straight line DE through point D, parallel to CC'. It is the corrected phase boundary, and its intercept on the j_x axis is j_c. Values of j_c range between 2.3×10^{11} and 360×10^{11} A m^{-2}. A simplified model of wall modes based on the harmonic oscillator predicts that H_c is a linear function of $|j_x|$, in agreement with our experimental findings.

Calculations of heat diffusion through sample and substrate indicate that Joule heating causes a sample temperature increase $\Delta T \simeq 200$ °C. However, most of this increase happens at the end of each exponential pulse, when the current has already passed its maximum. Hence, the resulting resistivity increase and H_c reduction probably do not affect much the measured j_c values.

Since $j_c > 0$ by definition, we introduce a quantity j_{c+-}, with $j_{c+-} = j_c$ when walls move at $H_z = 0$ in the same sense as j_x, and $j_{c-+} = -j_c$ when they move in the opposite sense. In the case $v_e \neq 0$, $v_w \simeq 0$, one can show from Eqs. (1)–(3) that $F_x/j_x = 2M_sH_c/j_{c+-}$. Hence, the quantity $2M_sH_c/j_{c+-}$ has the meaning of a drive force per unit current. On Fig. 2(a) we plot $2M_sH_c/j_{c+-}$ versus thickness w for all samples. We assume $M_s = 1.1$ T, a value derived from measurements of anomalous Hall effect in our films. Also, the phase boundary has been corrected for the H_c reduction.

We distinguish between walls of "type" 1 and type 2, depending on the sense of the magnetization in the two domains adjacent to the wall (see insert of Fig. 2). Wall type can be determined by moving the wall with a field H_z. If the exchange-drag force of Eq. (1) were the only force exerted by the current on the wall, M_sH_c/j_{c+-} would be independent of wall type at all thicknesses. The domain-drag force[2] is also independent of wall type, but is small in films as thin as ours. However, the sample current produces a circumferential (or "global") magnetic field, which runs in closed loops around the sample. The field component along the easy axis z has opposite signs at the top and bottom of the film. If the current density is uniform, the change of sign takes place exactly at the median plane of the film, and the net force on the wall vanishes.[4] On the other hand, a variation of electrical resistivity of a few percent across the film thickness results in a nonuniform current, and in a significant net force on the wall. This "global-field force" has opposite sign for walls of types 1 and 2.

At thicknesses smaller than $\simeq 35$ nm, M_sH_c/j_{c+-} has approximately the same value for walls of both types [Fig.

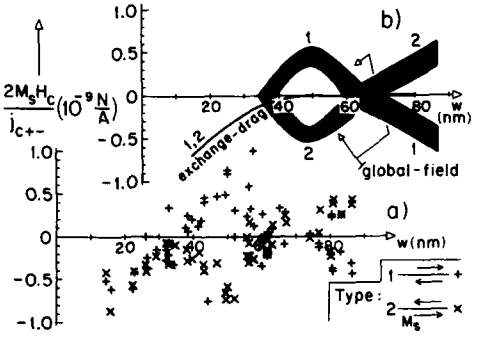


FIG. 2. (a) The quantity $2M_sH_c/j_{c+-}$, which is the same as the drive force per unit current, is plotted versus sample thickness w. Two kinds of symbols correspond to different wall "types," i.e., different senses of the domain magnetization. (b) Rough decomposition of the drive force on a wall into an exchange-drag part, which is independent of wall type, and a global-field part, which changes sign between walls of types 1 and 2.

2(a)]. This indicates that exchange-drag is dominant in this thickness range. At $w > 35$ nm, the value of $M_s H_c / j_{c+-}$ for type 1 walls is found [Fig. 2(a)] to have a sign opposite to that for walls of type 2. This indicates that the global-field force becomes important in this thickness range.

Now, we attempt a rough separation into exchange-drag and global-field forces. The combination

$$[(2M_s H_c / j_{c+-})_1 + (2M_s H_c / j_{c+-})_2]/2$$

of experimental values for walls of type 1 and 2 at the same thickness represents the type-independent part of $2M_s H_c / j_{c+-}$. Hence, it is to be identified with the exchange-drag force [Fig. 2(b), curve labeled "exchange drag"]. Similarly

$$\pm [(2M_s H_c / j_{c+-})_1 - (2M_s H_c / j_{c+-})_2]/2$$

is the global-field force for walls of types 1 and 2 [see corresponding curves on Fig. 2(b)].

The exchange-drag force has the largest absolute magnitude [Fig. 2(b)] at $w \simeq 15$ nm, with

$$2M_s H_c / j_{c+-} \simeq -0.6 \times 10^{-9}\ \mathrm{N\,A^{-1}}.$$

Using this value and the expression

$$j_{c+-} = n_e e^* \mu_i H_c / \beta_1$$

derived from Eq. (3), and assuming

$$R_0 = (n_e e^*)^{-1} = -1.4 \times 10^{-10}\ \mathrm{m^3\,C^{-1}}$$

from measurements of ordinary Hall coefficient R_0 in our films, and $\mu_i \simeq 1.5\ \mathrm{m^2\,C^{-1}}$ from Ref. 3, we obtain $\beta_1 \simeq +2.9$. This is to be compared to the earlier experimental value $\beta_1 \simeq +1.8$ quoted in Ref. 3. Exchange-drag theory[1] gives

$$\beta_1 = d(\ln \sigma_1)/d(\ln n_1),$$

where σ_1 is the conductivity arising from a band of carriers of concentration n_1. Hence, β_1 is expected to be positive and of order unity if a simple parabolic band is assumed. This agrees with our experimental findings. The fact that β_1 is positive means that the wall moves in the same sense as the electron-like carriers. Permalloy films of this thickness have[5] 180° Néel walls, made of a "core" of thickness $\simeq 100$ nm surrounded by a much broader "tail." The exchange-drag force depends[1] on the spatial rate of change $d\theta/dx$ of the direction of the magnetization, which is largest in the core. Films with $w > 30$ nm contain[5] very broad cross-tie walls, where $d\theta/dx$ is smaller. This may explain why the absolute magnitude of the exchange-drag force decreases towards zero between 15 and 40 nm [Fig. 2(b)].

On the basis of anomalous Hall-effect measurements, the hydromagnetic domain-drag force[2] is expected to be positive and small in our samples. Its value is predicted in the "single-wall" model to be proportional to thickness, and equivalent to

$$2M_s H_c / j_{c+-} \simeq +0.09 \times 10^{-9}\ \mathrm{N\,A^{-1}}$$

at $w = 65$ nm. This is almost negligible.

The global-field force seems to vanish for the thinnest samples [Fig. 2(b)]. This is what is expected if the resistivity difference across the film thickness is assumed not to exceed a finite value as the thickness is reduced. At 35 nm $< w <$ 65 nm, the sign of the force for a given wall type indicates that the resistivity is maximum at the film bottom. This is consistent with the fact[6] that crystal-grain boundaries and voids are more numerous at the bottom surface than at the top of a film exhibiting columnar structure.

At larger thickness $w > 65$ nm, the sign of the global-field force for given wall type is reversed (Fig. 2), indicating that the resistivity is maximum at the film top. This might be caused by a small but increasing oxygen or carbon contamination as the vacuum degrades during film deposition ($p \lesssim 1.5 \times 10^{-6}$ Torr). However, Auger analysis shows no such gradient of oxygen or carbon concentration across the film thickness.

ACKNOWLEDGMENTS

We are thankful to the Magnetics Technology Center and to the Center for the Study of Materials at Carnegie-Mellon University for the use of their facilities. This work was supported by the National Science Foundation under Grant No. DMR-84-19980.

[1] L. Berger, J. Appl. Phys. **55**, 1954 (1984).
[2] L. Berger, J. Phys. Chem. Solids **35**, 947 (1974).
[3] P. P. Freitas and L. Berger, J. Appl. Phys. **57**, 1266 (1985).
[4] H. J. Williams and W. Shockley, Phys. Rev. **75**, 178 (1949).
[5] S. Methfessel, S. Middelhoek, and H. Thomas, IBM J. Res. Dev. **4**, 96 (1960); R. Kirchner and W. Doring, J. Appl. Phys. **39**, 855 (1968).
[6] S. Nakahara, Thin Solid Films **45**, 421 (1977). See Fig. 9(a).

Electrical and magnetic properties of semiconducting ternary U compounds: UTSn and UTSb

T. T. M. Palstra,[a] G. J. Nieuwenhuys, R. F. M. Vlastuin, and J. A. Mydosh
Kamerlingh Onnes Laboratorium der Rijks-Universiteit Leiden, 2300 RA Leiden, The Netherlands
K. H. J. Buschow
Philips Research Laboratories, 5600 JA Eindhoven, The Netherlands

We have measured the electrical-transport and magnetic properties of several intermetallic compounds UTSn and UTSb, where T is a transition metal. The electrical resistivity is up to three orders of magnitude larger than usually found for U-based compounds. This is ascribed to the occurrence of a spin polarized energy gap related to the MgAgAs-type crystal structure. For UNiSn at least one spin band closes at low temperature, resulting in half-metallic behavior. Interestingly, the magnetic properties exhibit Kondo-lattice character and weak-moment ordering.

I. INTRODUCTION

Since the discovery of the half-metallic ferromagnets[1] there is a growing interest in the Heusler compounds of the MgAgAs-type structure. This activity stems from the remarkable fact that 100% spin polarization occurs at the Fermi surface, resulting from a semiconducting energy gap in the minority-spin band at the Fermi level, whereas the majority-spin band exhibits normal metallic behavior. This phenomenon was studied first for 3*d*-band compounds, like NiMnSb. Because of our general interest in the magnetic and electrical transport properties of U-based compounds, we have investigated whether such behavior could also be established for 5*f*-band compounds.

For that purpose we have prepared the systems UTSn and UTSb, with T being a transition metal. Most compounds crystallize in the hexagonal Fe_2P- or $CaIn_2$-type structure, which are characterized by normal metallic conduction and local moment behavior, as has been discussed extensively elsewhere.[2] Still, a few compounds adopt the desired MgAgAs-type ($C1_b$) crystal structure, like UNiSn, URhSb, and UPtSn. Interestingly, these compounds exhibit semiconducting-like behavior in the transport properties, and a magnetic behavior reminiscent of Kondo-lattice systems. Since this combination is highly anomalous we have extended our studies of the magnetic and transport properties by measuring and comparing the electrical resistivity, Hall resistivity, magnetization and specific heat of these compounds, and their nonmagnetic (Th, Hf, Zr, Ti) T (Sn, Sb) reference materials.

II. EXPERIMENTAL PROCEDURES AND RESULTS

For sample preparation and experimental procedures we refer to Ref. 2. In Fig. 1 we show the electrical resistivity of the three U-based compounds UNiSn, URhSb, and UPtSn. These compounds exhibit a low-temperature resistivity increase, beyond which an exponential decrease is observed. Fitting the data in the temperature interval $500 < T < 1000$ °C (not shown) to the formula appropriate for semiconductors $\rho \sim \exp(E_{gap}/2k_B T)$, we obtain a value of $E_{gap} = 0.12$, 0.44, and 0.34 eV for UNiSn, URhSb, and UPtSn, respectively. Note that the absolute value of the resistivity is up to three orders of magnitude larger than usually found for intermetallic compounds. In addition the resistivity of the nonmagnetic materials is very high. The highest value was observed for TiPtSn, which has a residual resistivity of $6.3 \times 10^{+5}$ $\mu\Omega$ cm.

Figure 2 shows the temperature dependence of the magnetization of the U-based compounds. At high-temperature Curie–Weiss behavior is observed with effective moments of 3.08, 3.25, and 3.55 μ_B/f.u. and large negative Curie–Weiss temperatures of -75, -111, and -100 K for UNiSn, URhSb, and UPtSn, respectively. In spite of these effective moments with large antiferromagnetic interactions, no clear antiferromagnetic ordering is observed at low temperature. UNiSn has a change of slope in the M-T curve at 47 K, URhSb exhibits a broad maximum with an inflection point at 37 K and UPtSn only shows a leveling off of the Curie–Weiss increase of the magnetic susceptibility below about 75 K. The two small steplike anomalies in the M-T curve of UPtSn at about 5 and 25 K can probably be ascribed to the presence of 0.3% of the binary compound UPt, which is

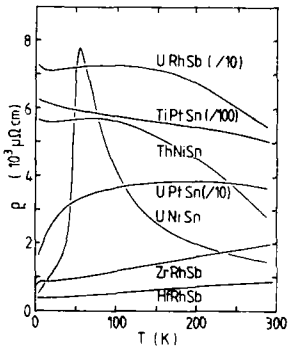


FIG. 1. Temperature dependence of the electrical resistivity of (U, Th) NiSn, (U, Th) PtSn and (U, Hf, Zr) RhSb.

[a] Present address: AT&T Bell Laboratories, Murray Hill, NJ 07974.

 0021-8979/88/084279-03$02.40 © 1988 American Institute of Physics

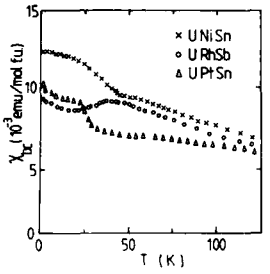


FIG. 2. Temperature dependence of the dc susceptibility of UNiSn, URhSb, and UPtSn.

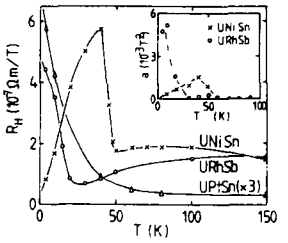


FIG. 4. Temperature dependence of the Hall resistivity of UNiSn, URhSb, and UPtSn. The inset shows the temperature dependence of the magnetoresistivity coefficient a(see text).

ferromagnetic ($T_C = 27$ K).

In Fig. 3 we show the specific heat of several compounds plotted as C/T vs T^2. For the U-based compounds a λ-like anomaly is clearly observable at 48 K for UNiSn and at 35 K for URhSb and UPtSn. The nonmagnetic materials exhibit low values for the specific-heat coefficient $\gamma < 2$ mJ/mol f.u. K^2, and Debye temperatures (calculated for $T < 10$ K) ranging from 185 to 310 K.

We plotted in Fig. 4 the Hall resistivity R_H of UNiSn, URhSb, and UPtSn. For UNiSn the λ-like anomaly in the specific heat and resistivity peak at 48 K is reflected in a sharp wedge-shaped maximum of R_H at 40 K. However, for URhSb and UPtSn not such pronounced anomalies are present at the temperature at which the specific-heat anomaly is observed. Nevertheless, the specific-heat anomalies are still reflected in the field-dependence of the transport properties for these compounds. In the inset of Fig. 4 we plotted the (transverse) magnetoresistivity coefficient, $a(T)$, defined as

$$[\rho(H) - \rho(0)]/\rho(0) = a(T)H^2.$$

Here an abrupt increase of the coefficient $a(T)$ occurs below 60 K for UNiSn and below 30 K for URhSb.

III. DISCUSSION

A salient feature of our experimental results is the extremely high electrical resistivity of these compounds, being up to 3 orders of magnitude larger than usually found for intermetallic compounds. The exponential decrease of the resistivity at high temperature indicates that these compounds are semiconductors. This is confirmed by the relatively large values of the Hall resistivity, which is inversely proportional to the carrier concentration. The semiconducting properties cannot be ascribed to ionic or covalent bonds, but rather to the fact that the valence band is completely filled. This property seems to be closely related to the band structure of the MgAgAs-type crystal structure,[3] since high resistivity values were also observed for binary Mg_2(Si,Ge,Sn,Pb) (Ref. 4) and ternary AsAgMg and SbAgMg,[5] all crystallizing in the MgAgAs-type crystal structure or the related CaF_2-structure.

Still, the exponential decrease of the resistivity with increasing temperature is only observed at high temperature, whereas the resistivity remains rather constant below room temperature. This must probably be ascribed to impurity band conduction. However, for the U-based compounds the resistivity even decreases with decreasing temperature at lower temperature. For UNiSn a dramatic decrease of the resistivity is observed below 55 K and a residual resistivity of 413 $\mu\Omega$ cm is attained, comparable to typical values for other intermetallic compounds. We believe that this decrease in the resistivity of the U-based compounds is caused by a decrease in the size of the energy gap, probably induced by magnetic interactions and ordering. For UNiSn the energy gap in (at least) one of the spin bands disappears below 55 K, resulting in metallic conduction.

This interpretation is in keeping with recent band structure calculations,[6] which show (at $T = 0$) that UNiSn belongs to the class of half metallic ferromagnets, i.e., the majority spin band exhibits metallic conduction, whereas the minority spin band has an energy gap at the Fermi level. It should be mentioned that these band structure calculations give no information about the type of magnetic interactions (ferro- or antiferromagnetic), although it was clearly established that the magnetic properties are related to the U bands, as the Ni d bands are almost completely filled. This means that with UNiSn we have found an analogue for NiMnSb, where the conduction band is 100% spin polarized. Furthermore, this interpretation requires that the conduction band is strongly hybridized with the 5f band. This has also been suggested from recent XPS measurements,[7] which show that the 5f band is very near the Fermi level. For URhSb and UPtSn a much larger energy gap is present at high temperature and consequently the band gap fails to completely close at lower temperature. Nevertheless for UPtSn some closure of the band begins below 100 K and results in a resistivity decrease of a factor two.

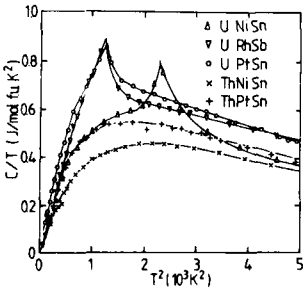


FIG. 3. Temperature dependence of the specific heat of (U, Th) NiSn, (U,Th) PtSn, and URhSb plotted as C/T vs T^2.

A second remarkable property of these compounds is the magnetic behavior. Magnetization measurements at high temperature reveal effective moments of 3.0–3.5μ_B/f.u., which agree with typical values of local U moments. Local-moment magnetism is in keeping with the Hill criterion, which predicts local moment magnetism for U-U spacings larger than 3.6 Å as is the case for these compounds.[2] Also the band structure calculations[6] show that the magnetism in these compounds originates from the U 5*f* electrons. Yet, in spite of the high-temperature moments and large antiferromagnetic interactions, no standard local moment magnetic ordering is observed. Instead, weak anomalies are observed in the magnetization measurements (Fig. 2), with corresponding anomalies in the specific heat (Fig. 3), indicating some sort of phase transition and/or crystal field effects.

The overall behavior of the magnetization is reminiscent of spin-fluctuation behavior, as observed for heavy-electron systems.[8] Here also large effective moments with large negative Curie–Weiss temperatures were observed at high temperature, turning to weakly magnetic systems at low temperature. This correspondence is most remarkable because of the greatly reduced number of conduction electrons in the cases of URhSb and UPtSn. Still, the linear specific heat coefficient, γ, has a value comparable to values of metallic systems, e.g., $\gamma = 10.9$ mJ/mol K^2, whereas the residual resistivity, $\rho_0 = 19\,000\ \mu\Omega$ cm, is orders of magnitude higher than in metallic systems. Speculatively, we suggest that this γ-value results from a hybridization of the impurity band with the nearby lying 5*f* band. This could result in an enhancement of the γ value with respect to the low-temperature density of states value expected from the residual resistivity. Accordingly, ThPtSn has a six times smaller γ value, in spite of a seven times higher conductivity.

IV. CONCLUSION

The electrical transport properties of the compounds UTSn, UTSb, and their nonmagnetic reference materials are governed by an energy gap at the Fermi level, resulting in semiconducting behavior. At lower temperature the gap is strongly influenced by the magnetic behavior and for UNiSn one spin band gap closes below 55 K. Hence, this compound belongs to the class of half-metallic magnets, due to the presence of the 5*f* electrons of U. The magnetic ground state is highly complex and a complete understanding requires further study, including the optical behavior. If the spin orbit coupling is important, then a large magneto-optical (Kerr) effect should be observed.

ACKNOWLEDGMENTS

We acknowledge the support of J. van den Berg. This work is in part supported by the Nederlandse Stichting voor Fundamenteel Onderzoek der Materie (FOM).

[1] R. A. de Groot, F. M. Mueller, P. G. van Engen, and K. H. J. Buschow, Phys. Rev. Lett. **50**, 2024 (1983).
[2] T. T. M. Palstra, G. J. Nieuwenhuys, R. F. M. Vlastuin, J. van den Berg, J. A. Mydosh, and K. H. J. Buschow, J. Magn. Magn. Mater. **67**, 331 (1987).
[3] S. H. Wei and A. Zunger, Phys. Rev. Lett. **56**, 528 (1986).
[4] A. F. Wells, in *Structural Inorganic Chemistry* (Oxford Press, London, 1984), p. 1315.
[5] W. B. Pearson, in *The Crystal Chemistry and Physics of Metals and Alloys* (Wiley, New York, 1972), p. 207.
[6] R. C. Albers, A. M. Boring, G. H. O. Daalderop, and F. M. Mueller, Phys. Rev. B **36**, 3661 (1987).
[7] H. Hoechst, K. Tan, and K. H. J. Buschow, J. Magn. Magn, Mater. **54-57**, 545 (1986).
[8] See, e.g., G. R. Stewart, Rev. Mod. Phys. **56**, 755 (1984).

The electrical resistance of Cr films

J. A. J. Lourens, S. Arajs, H. F. Helbig, L. Cheriet, and El-Sayed A. Mehanna[a)]
Department of Physics and Center for Advanced Materials Processing, Clarkson University, Potsdam, New York 13676

Measurements of the thickness dependence of the electrical resistance of two very thin Cr films deposited at substrate temperatures of 385 and 360 °C and pressures of 4×10^{-7} and 10^{-6} Torr are reported. Preliminary measurements of the thickness dependence of the Néel temperature (T_N) of the film deposited at 360 °C at thicknesses >10 nm are also presented. In these two films the resistance in the thickness region $2<d<7.5$ nm can be very well described by $R\propto[(d/d_c)^{-1}]^{-t}$ with d_c equal to 1.64 ± 0.20 and 1.03 ± 0.20 nm, respectively, and $t=1.34\pm0.11$. The Néel temperatures show a turning point around 14 nm in agreement with the known thickness dependence of the stress. dT_N/dS_i has been found to be ~100 K/kbar where S_i is the internal tensile stress in the film.

INTRODUCTION

Using Monte Carlo methods, Zabolitzky[1] calculated the conductivity of a random network of resistors in two dimensions and found the finite-size conductivity exponent t/ν to be 0.973 ± 0.005 in very good agreement with the results of other researchers (references cited in Ref. 1). Since the generally accepted value of the coherence length exponent ν is $\frac{4}{3}$, $t=1.297\pm0.005$. Experimental confirmation of this value of t has so far involved model percolating systems only. For example, in a recent investigation Dubson and Garland[2] measured the resistance of a percolating pattern on an aluminized plate and fitted their results to the power law $R\propto(f_c-f)^{-t}$ where f is the fraction of the sample area covered by holes in the sheet and f_c is the critical hole fraction. These authors found that $t=1.29\pm0.03$ for site percolation on the square lattice and 1.34 ± 0.07 for random-void continuum percolation, proving that t depends only on the dimensionality of the system.

Various conduction mechanisms exist in real two-dimensional systems. Near the onset of conduction at very low average film thicknesses highly activated conduction mechanisms between isolated islands occur.[3,4] As the islands start coalescing with increasing thickness continuous metallic paths are formed and the system undergoes a metal-insulator transition. As the thickness increases further the conductivity is influenced by grain boundary, surface, and roughness scattering. One purpose of the present investigation was to see if the critical exponent t associated with conductivity can be determined in the presence of other conducting mechanisms in very thin films. Measurements of the resistance of two Cr films, one in the thickness region $0<d<26$ nm and the other in $0<d<10$ nm, have been carried out under slightly different deposition conditions. For very thin films it is reasonable to expect that $R\propto(d-d_c)^{-t}$ where d is the average thickness of the film. A direct experimental determination of the critical thickness d_c which marks the onset of the metal-insulator region is precluded by the highly activated conduction mechanisms at very low film thicknesses. It has nevertheless been found that d_c can be indirectly inferred from the measurements and that t can be determined with an accuracy of $\pm8\%$ in Cr films.

The second objective of this investigation is concerned with the effects of film stresses on the Néel temperature (T_N) of thin Cr films. It has been found by Mehanna[5] *et al.* that Cr films having thicknesses of 70–100 nm deposited on Corning glass (no. 7059) substrates at a substrate temperature of 400 °C show well-defined anomalies in the electrical resistivity versus temperature curves at T_N. A direct correlation with the stress vs thickness curves of Abermann and Martinz[6] could, however, not be carried out in the absence of a 400 °C isotherm in the stress-thickness figure of these authors. It was therefore decided to measure T_N of Cr films deposited at 360 °C for which a stress-thickness relation exists. A tensile stess maximum occurs near a film thickness of ~14 nm followed by a compressive maximum near ~50 nm. According to the model of Abermann and Martinz,[6] the maximum at 14 nm indicates the end of the coalescence stage of film growth and hence also the end of the formation of continuous metallic paths as mentioned above.

RESULTS AND DISCUSSION

With a view to extracting the critical exponent t we first present and discuss the results of observations on two Cr films. Film 1 was deposited on a Corning glass (no. 7059) substrate at a temperature of 385 °C, a deposition rate of 0.1 nm s^{-1} and a pressure of $\lesssim4\times10^{-7}$ Torr. The corresponding parameters for film 2 are 360 °C, 0.7 nm s^{-1} and $\lesssim1\times10^{-6}$ Torr. The resistances of films 1 and 2 as a function of average film thickness in the region $0<d<10$ nm are shown in Fig. 1. Conduction in film 1 starts at a thickness of about 1 nm. Hereafter R decreases rapidly by a factor of $\sim10^3$ as the thickness changes from 1 to ~3 nm. Conduction in film 2 appears at ~0.2 nm which points to the effect of the deposition parameters in determining the size of the islands in the two films. The initial rapid decrease in resis-

a) Present address: Military College, Cairo, Egypt.

 0021-8979/88/084282-03$02.40 © 1988 American Institute of Physics

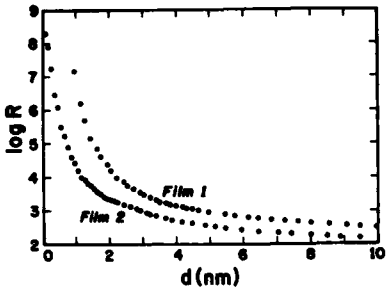


FIG. 1. The log of the resistance, R, vs film thickness, of Cr films 1 and 2.

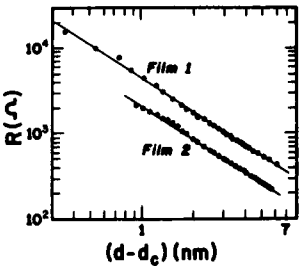


FIG. 3. The resistance, R, of Cr films 1 and 2 vs $d - d_c$ in the metal-insulator region. The straight lines have a slope of -1.31 and d_c equals 1.68 and 1.11 nm for the two films, respectively.

tance below ~ 2 nm is believed to arise from activated conduction mechanisms which exist at thicknesses close to the onset of conduction and the formation of continuous metallic paths at the slightly higher critical thicknesses of 1.03 and 1.64 nm as found below. This is indicated in region A of Fig. 2 which shows the conductivity of the two films as a function of film thickness. The conductivity increases rapidly in region B and then much more slowly in region C.

In analyzing these results the relation[7] $Rd = K_0 + K_1/d + K_3/d^3$ was fitted to the measurements on film 1 in region C of Fig. 2 where the conductivity is apparently influenced by grain boundary and roughness scattering as described by the second and third terms of this equation. In the thickness region from 7.6 to 13.5 nm $\Delta R^2 = (R - R_{\rm fit})^2$ is always smaller than 2.5 Ω^2 which implies a rather good fit to the data. At a thickness of 7.4 ± 0.2 nm ΔR^2 starts to incease rapidly with decreasing thickness reaching a value of ~ 180 Ω^2 at 6.5 nm. Hence, application of the scaling law becomes physically meaningless for values of d exceeding 7.6 nm. A fit of the above relation in the region $2 < d < 8$ nm produced $K_1 < 0$ which is physically unacceptable. If only the first two terms are fitted, i.e., with $K_3 = 0$, a very bad fit is obtained. A least squares fit of $R \propto (d - d_c)^{-t}$ to the data on film 1 in region B of Fig. 2 using the critical thickness d_c as a variable revealed that $1.3 < d_c < 2.6$ nm, the experimental points displaying a distinct concave upward and downward feature near the beginning of the fits for d_c equal to 1.3 and 2.6 nm, respectively. A similar analysis pointed to the existence of a critical thickness in film 2. Sliding least squares fits were subsequently performed on sets of data each spanning 5.5 nm of thickness for each film, starting at thicknesses in the range $0.5 < d_s < 3.5$ (e.g., with $d_s = 2$ nm, a fit would cover the range $2 < d < 7.5$ nm). It was found that t decreases for each film from about 1.8 to 1 with increasing d_s. However, χ^2 increased rapidly from $\sim 8 \times 10^{-4}$ to more that ten times this value at $t = 1.52$ in the case of film 1. A similar behavior was displayed by film 2. Hence, the upper limit of the critical exponent is taken to occur at $t = 1.45$. The rapid increase in χ^2 above this value is attributed to the effects of the activated conduction mechanisms. Application of the scaling law to values of $d < 7.6$ nm yielded a lower limit of $t = 1.23$. Therefore $t = 1.34 \pm 0.11$ with corresponding critical thicknesses of 1.64 ± 0.20 and 1.03 ± 0.20 nm for films 1 and 2, respectively. Figure 3 shows the resistance versus $d - d_c$ for the two films in the region where the conductivity is dominated by the formation of continuous metallic paths. For these fits the error in t amounts to only ± 0.005 (two standard deviations), the much larger error of ± 0.11 reflecting the over-

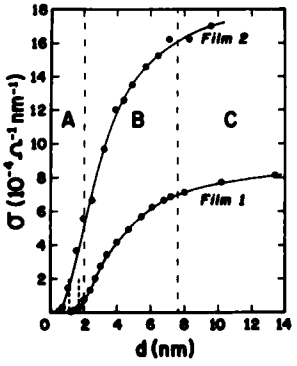


FIG. 2. The conductivity, σ, of Cr films 1 and 2 vs d. Not all the experimental points are shown. Regions A, B, and C are referred to in the text. The vertical dashed lines below 2 nm indicate the critical thickness of each film.

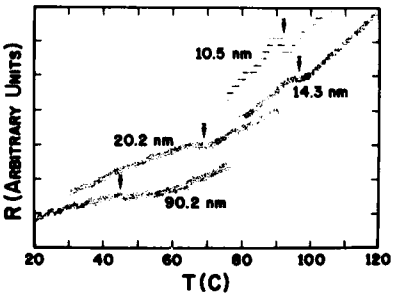


FIG. 4. The resistance of Cr firms of various thicknesses vs temperature. Néel temperatures are indicated by an arrow. For each curve the resistance is in arbitrary units.

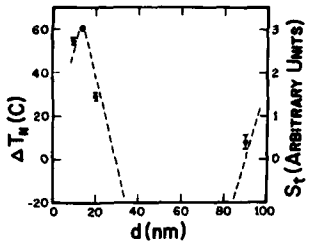


FIG. 5. The shift, ΔT_N, from the value in bulk Cr as a function of film thickness d. The dashed line indicates the stress vs thickness variation[6] where stress is plotted on an arbitrary scale.

lapping effects of the other conduction mechanisms into the metal-insulator region.

A search for the Néel temperature in film 2 which had a thickness of 10.5 nm when the first deposition was terminated at a substrate temperature of 360 °C, revealed that $T_N = 366$ K, 55 K higher than the value in bulk Cr. Depositing an additional 3.8 nm of Cr on this film raised the Neel temperature to 371 K while a decrease to 340 K was observed for a film of total thickness of 14.3 nm. Figure 4 illustrates the anomalies in R as a function of T and Fig. 5 the shift in T_N as a function of film thickness together with the expected variation according to the internal stress measurements of Abermann and Martinz[6] who employed a cantilever method to measure the stress. We emphasize that our measurements are preliminary in the sense that film thicknesses were obtained additively. Furthermore, extensions to our equipment are being made to locate anomalies below room temperature.

The maximum in ΔT_N occurring at a thickness of ~ 14 nm agrees with the stress vs thickness measurements of Abermann and Martinz[6] (cf. Fig. 5), thus confirming the end of the coalescence stage around this thickness. If we assume a force per unit film width of 0.8 N m^{-1} for Cr[6] at 14 nm, then $dT_N/dS_t \simeq 10^2$ K/kbar where S_t is the tensile stress in the film. In bulk Cr, $dT_N/d_p \sim -5$ K/kbar. It appears that in thin films rather large shifts in T_N due to film stresses can be observed which would render the determination of the critical exponent associated with the shift in the absence of stress rather difficult.

CONCLUSIONS

We have identified a percolating region in Cr films which can be reasonably well described by $R \propto (d - d_c)^{-t}$ with $t = 1.34 \pm 0.11$. In agreement with stress vs thickness curves,[6] a maximum shift in T_N occurs near a film thickness of 14 nm. $dT_N/dS_t \simeq 10^2$ K/kbar where S_t is the internal tensile stress in the film.

ACKNOWLEDGMENTS

One of us (J.A.J.L.) thanks the RAU and FRD for financial support and Clarkson University for its warm hospitality.

[1] J. G. Zabolitzky, Phys. Rev. B **30**, 4077 (1984).
[2] M. A. Dubson and J. C. Garland, Phys. Rev. B **32**, 7621 (1985).
[3] C. N. Neugebauer and M. B. Webb, J. Appl. Phys. **33**, 74 (1962).
[4] C. J. Adkins, J. Phys. C **15**, 7143 (1982).
[5] El-Sayed A. Mehanna, S. Arajs, and H. F. Helbig, J. Appl. Phys. **61**, 4273 (1987).
[6] R. Abermann and H. P. Martinz, Thin Solid Films **115**, 185 (1984).
[7] H.-U. Finzel and P. Wissmann, Ann. Phys. **43**, 5 (1986).

Magnetic properties across the metal-insulator transition (invited)

Subir Sachdev
Center for Theoretical Physics, P. O. Box 6666, Yale University, New Haven, Connecticut 06511
R. N. Bhatt and M. A. Paalanen
AT&T Bell Laboratories, Murray Hill, New Jersey 07974

We review recent theoretical and experimental work on the metal to insulator transition in doped semiconductors. The spin excitations on the insulating side of the transition can be described in terms of a spin-$\frac{1}{2}$ Heisenberg antiferromagnet with the spins randomly located in space. Numerical analysis of this Hamiltonian has led to a fairly complete understanding of the static spin susceptibility and the electron spin resonance spectrum. The physics on the metallic side far from the transition is also fairly well understood in terms of a recently developed theory of the disordered Fermi liquid. The physics near the transition point is, however, still not clear. All the experimental evidence indicates the presence of local electronic moments on the metallic side of the transition. Recent theoretical work and open problems in the description of such a metallic phase are briefly discussed.

I. INTRODUCTION

This paper presents a review of recent theoretical and experimental work on the study of the metal-insulator transition in doped semiconductors. We will focus, in particular, on phosphorus silicon (Si:P) as a prototype system on which a large body of experiments have been performed recently.[1] Although the original studies on this system were performed two decades ago,[2] there remain gaps in our understanding of the physics, especially at doping concentrations n which are close to the metal-insulator transition density n_c.

We begin by presenting an overview of the properties of doped semiconductors as a function of doping concentration. The physics is best understood by considering three regions of dopant concentration: (i) insulating, (ii) transitional, and (iii) metallic. These regions are discussed briefly below, with the details being relegated to the subsequent sections.

At very low phosphorus doping concentrations the extra electron carried by phosphorus remains bound to the excess positive charge carried by the phosphorus nucleus. The strong Coulomb interactions between electrons coupled with the strong positional disorder prevent any charge transport and the system is an insulator.[3] However, the weak orbital overlap between neighboring electrons leads to an antiferromagnetic interaction which dominates the magnetic properties.[4] A good model for the low-lying excitations is therefore a spin-$\frac{1}{2}$ Heisenberg Hamiltonian with the spins located randomly in space. At high temperatures the electron spins fluctuate independently of one another and yield a Curie susceptibility. As the temperature is lowered, the spin fluctuations are gradually quenched and only a smaller number of spin degrees of freedom remain active. In Sec. II we briefly discuss a simple picture of condensation of electrons into tightly bound singlet pairs which gives a satisfactory explanation of the experimental data.

With an increase in phosphorus density, the overlap between the electron orbitals increases and the system undergoes an insulator to metal transition. Stress-tuning experiments[5] have established that this transition is continuous, i.e., the conductivity σ increases continuously from zero as n goes above n_c: $\sigma \sim (n - n_c)^{\mu}$. The exponent μ is expected to be a *universal* feature of the transition: in other words, it is independent of the details of the microscopic interactions and just a property of the scale-invariant critical point describing the transition. Experimentally μ has been found to be near 0.5 in uncompensated semiconductors like Si:P but its value in compensated semiconductors (e.g., silicon doped with a donorlike phosphorus and an acceptorlike boron) is near 1.[6] A number of theoretical works have addressed the question of the exponents but have not been successful in clarifying the experimental situation. In comparing theory to experiments it is important to keep in mind that the finite-temperature experiments may not be measuring the true asymptotic critical behavior of the putative zero temperature scale–invariant theory. If this is the case, then it is clearly necessary to focus on the "nonuniversal" finite temperature thermodynamic and magnetic properties in the transitional region for a complete understanding of the physics.

As one increases the density further, the system goes into a noncritical metallic phase. This region can be described by a disordered version of Landau's Fermi liquid theory.[7–10] The properties of this Fermi liquid theory are very similar to those of the conventional Fermi liquid theory of clean metals. Charge, spin, and energy diffusion occurs by the excitation of long-lived quasiparticles. Theoretical calculations of the thermodynamic and magnetic properties of the system are possible in this region: the dimensionless parameter measuring the strength of the disorder is small and can form the basis of an expansion in perturbation theory. Further details on this point of view and comparison with experiments are discussed in Sec. III.

The theoretical challenge that remains is to come up with a theory of the transition region which is capable of explaining the transport (conductivity), thermodynamic (specific heat and spin susceptibility), and dynamic spin (electron spin resonance and nuclear magnetic resonance) properties. The transition region is bracketed by two differ-

 0021-8979/88/084285-06$02.40 © 1988 American Institute of Physics

ent types of behavior, both of which are amenable to description by a simple intuitive picture: antiferromagnetically interacting electron local moments on the insulating side and non-plane-wave quasiparticles on the metallic side. The transition region exhibits features of both quasiparticle and local moment like behavior. In particular, as we shall discuss in Sec. IV, the experiments now appear to present unambiguous evidence of the presence of local electron moments on the metallic side of the transition. The interaction of the itenerant quasiparticles with the local moments needs to be understood in greater detail. The problem is clearly enormously complicated: the interaction of a signal local moment with electrons in a clean metal is by itself nontrivial[11] and the present situation involves many local moments interacting with electrons in a dirty metal. Nevertheless, some progress can be made at a phenomenological level, leading to experimentally testable predictions. Recent attempts by one of us[12] in this direction are described in Sec. IV.

The remainder of the paper is organized as follows: Sec. II reviews work on the insulating side of the transition while Sec. III does the same for the metallic side of the transition. Section IV presents a discussion of the theoretical implications of experiments in the transition region and a brief discussion of a phenomenological theory of this phase.[12]

II. THE INSULATING PHASE

This section will be brief because the situation on the insulating side of the transition has recently been reviewed in separate articles.[13,14] We only present enough details to place the discussion on the metallic side of the transition in context.

Since there is no charge transport in the insulating phase, it is useful to focus solely on the spin excitations of the system. These can be described by the Hamiltonian

$$H = \sum_{i \neq j} J_{ij}\, \mathbf{S}_i \cdot \mathbf{S}_j \,, \tag{1}$$

where $\mathbf{S}_i$ is a spin-$\frac{1}{2}$ operator for the electron localized around the impurity phosphorus nucleus at $\mathbf{R}_i$. The exchange constant J_{ij} is positive and depends exponentially upon the distance between $\mathbf{R}_i$ and $\mathbf{R}_j$.[4] The positions of the impurity nuclei $\mathbf{R}_i$ are assumed to be distributed randomly in the silicon crystal. This random Heisenberg Hamiltonian has formed the basis of our understanding of many experiments on the insulator.

An important experimental probe is electron spin resonance (ESR). The total weight under the ESR peak gives the electron spin paramagnetic susceptibility. In Fig. 1 we show the electron spin susceptibility measured in this manner for a variety of dopant concentrations n. We focus on concentrations $n < n_c$ in this section. The temperature dependence of the susceptibility $\chi(T)$ is described very well by the phenomenological equation

$$\chi(T) = A(n) T^{-\alpha} \,, \tag{2}$$

where $A(n)$ depends on the density and the exponent $\alpha \approx 0.6$.

This temperature dependence of the paramagnetic susceptibility can be understood in terms of a gradual freezeout

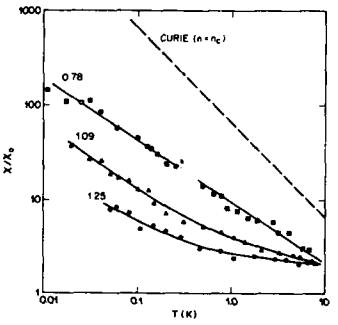


FIG. 1. Temperature dependence of the paramagnetic spin susceptibility of Si:P for different values of the phosphorus concentration n/n_c. The metal-insulator transition occurs at n_c.

of the electron moments due to their mutual exchange interactions. As the temperature is lowered an increasing number of electrons condense into tightly bound singlet pairs with their nearest neighbors; only the unbound spins contribute a Curie-type susceptibility ($\chi \sim 1/T$). The decrease in the number of unbound spins with temperature is therefore the reason for the slower than $1/T$ temperature dependence of Eq. (2). A computer renormalization group calculation by Bhatt and Lee[15] has put this picture on a more rigorous foundation and also yielded results for $\chi(T)$ which have temperature dependence similar to Eq. (2).

In addition to the variation in the total spin susceptibility, the ESR linewidth and resonance field also exhibit nontrivial dependence on temperature and frequency.[16] This can be understood in terms of a slowing down of the diffusion of spin excitations which must accompany the condensation of the singlet pairs.[17] Over the timescale probed by ESR, the small diffusion coefficient localizes the electronic excitations on small clusters (sizes <20). On such small clusters the secular approximation for evaluating the ESR spectrum breaks down. It is necessary to resort to computer diagonalizations of the spin Hamiltonian; these are fortunately tractable because of the small cluster sizes. The results fit the experiments well, confirming the localized nature of the spin excitations.

III. THE METALLIC PHASE

On the metallic side of the metal-insulator transition powerful analytic methods are available for the calculation of the magnetic, transport, and thermodynamic properties of the system.[7,8] All these methods rely upon a perturbation expansion in the disorder present in the system. Deep on the metallic side of the transition, where the large number of dopant electrons raises the Fermi energy E_F, it can be shown that E_F is the largest energy in the problem rather than disorder and electron-electron interactions; consequently the perturbation expansion may be expected to work reasonably. As we shall discuss in this section, it is in this region that the analytic methods have been most sucessful. The perturbation methods can also be combined with renormalization-

group methods to make predictions all the way up to the metal-insulator transition but these have been far less successful.

The zeroth-order description for the metallic side of the transition is the system with no disorder. This system is assumed to be described completely by Fermi liquid theory. Spin, charge, and energy transport in the system occurs via movement of quasiparticle excitations. The quasiparticles have mass m^* interact with each other via the Fermi liquid constants A_l^s and A_l^a in the density and spin channels respectively. The usual Landau interaction constants F_l^s and F_l^a are related to these by

$$F_l^s = A_l^s/[1 - A_l^s/(2l+1)] \tag{3}$$

and similarly for F_l^a. For technical reasons, the A parameters are more convenient in disordered systems. Performing and physically interpreting a consistent perturbation theory about this state is not easy; although the initial insights for Altshuler and Aronov[18] came eight years ago, it is only recently that a proper physical understanding of the structure of the perturbation theory has emerged.[7,8,10] The perturbation expansion is easiest to organize in two dimensions where one obtains logarithmically divergent terms involving the infrared cutoff (the larger of the temperature T or measurement frequency ω). Keeping terms to leading order in powers of $|\ln T\tau|/(E_F\tau)$, where τ is the elastic scattering time, it is then argued that a resummation of these same terms capture the important physics in $2+\epsilon$ dimensions. Following the example of classical phenomena, it is hoped that this will yield useful results in three dimensions. Such a procedure yields a description of the metallic state in terms of a disordered Fermi liquid. This Fermi liquid has several features which are identical with the clean system: the low-lying excitations are quasiparticle and quasihole-like states which are responsible for charge, spin, and energy *diffusion*. The quasiparticle wave functions, however, are no longer planewave-like: the elastic scattering from the impurities yields wave functions which average over the nonzero angular momenta interaction constants and only the A_0^a and A_0^s terms survive. Another important feature of this disordered Fermi liquid is that the interaction constants and the quaisparticle weights are now *scale* dependent; the temperature T (frequency ω) defines relevant length scale of the system $\sqrt{D/T}$ ($\sqrt{D/\omega}$) where D is the diffusion constant.

Far away from the metal-insulator transition this theory can be used to make definite predictions. The conductivity $\delta(T)$ is predicted to have the temperature dependence[19–21]

$$\frac{\sigma(T)}{\sigma_0} = 1 + \frac{\beta}{(2E_F\tau)^{1+\epsilon}}\left(4 - 3\frac{1+|A_0^a|}{|A_0^a|}\ln(1+|A_0^a|)\right)(T\tau)^{\epsilon/2} \tag{4}$$

in a space of dimension $2+\epsilon$ where σ_0 is the conductivity and A_0^a a Fermi liquid interaction constant of the clean Fermi liquid, and β is phase-space factor of order unity. We replace ϵ by 1 in the above expression to get an estimate of the conductivity in three dimensions. The resulting $\sqrt{T}$ term in the conductivity can have either sign depending upon the magnitude of A_0^a. This expression has been fit successfully to the temperature dependence of the conductivity in Ge:Sb.[22] The coefficient of the $\sqrt{T}$ term is arbitrary in the fit and can be used to determine the value of the Fermi liquid interaction constant. A more stringent test would require the use of this known interaction constant in some other experiment, but this has not been done for Ge:Sb. In Si:P, the physics is complicated by the presence of six valleys in the conduction band and the scattering of electrons between the valleys. The valley scattering rate is an additional parameter which affects the conductivity and makes a determination of the coefficient of the $\sqrt{T}$ term from first principles difficult.[23]

In a similar manner the spin susceptibility $\chi_s(T)$ is found to have the enhancement[8,24–26]

$$\frac{\chi_s(T)}{\chi_0} = 1 + \frac{\gamma}{(2E_F\tau)^{1+\epsilon}}2|A_0^a|(T\tau)^{\epsilon/2}, \tag{5}$$

where γ is a phase space factor of order unity. Examining Fig. 1 again we see that in the region $n \gg n_c$ the spin susceptibility does have a weak upturn at low temperatures which can be fit to a $\sqrt{T}$ term. However, an n approaches n_c, the spin susceptibility increases much more rapidly at low temperature, and smoothly crosses over the $T^{-\gamma}$ dependence upon the insulating side of the transition. This rapid increase is clearly beyond the applicability of the perturbation theory expression in Eq. (5). The spin diffusivity has corrections which are exactly the inverse of the spin susceptibility, as might be expected in any Fermi liquid.

Another magnetic property which is correlated with the spin susceptibility is the ESR linewidth.[27] As on the insulating side of the transition, the hyperfine interaction of the electrons with the phosphorus nuclei is an important source of spin dephasing, although certain spin-orbit scattering processes may also be significant. Here we only treat the hyperfine term for simplicity. In the clean Fermi liquid the linewidth is given by a spin relaxation time $1/\tau_s = 2\pi N_0 A^2$, where N_0 is the density of states at the Fermi level. In the disordered system the suppresion of spin diffusivity leads to a decrease in the amount motional narrowing and a broadening of the line. A direct calculation shows[25,26]

$$\frac{1}{\tau_s} = \frac{1}{(\tau_s)_0}\left(1 + \frac{2\gamma}{(2E_F\tau)^{1+\epsilon}}[2\ln(1+|A_0^a|) - |A_0^a|](T\tau)^{\epsilon/2}\right). \tag{6}$$

For small A_0^a Eqs. (5) and (6) predict that the enhancement of the susceptibility and the linewidth are identical. Experimentally this prediction is borne out by the experiments on Si:P.[27] In actuality the proportionality between the electron spin susceptibility and the ESR linewidth persists all the way to n_c; this cannot be understood in the framework of this perturbation theory. This proportionality is an important constraint which should be satisfied by any theory of the

transitional phase in uncompensated semiconductors.

Mention was made earlier of the valley structure of the silicon conduction band which complicated effects in the comparison of the theory with the data on Si:P. It was shown in Ref. 28, however, that this valley structure can be turned into an advantage by making experimentally testable predictions which are a nontrivial consequence of the structure of the disordered Fermi liquid theory. Using an analogy between the valley and spin quantum numbers, it was noted that the decrease in spin diffusivity with falling temperatures should have a parallel in the temperature dependence of the *valley* diffusivity. The valley diffusivity measures the rate at which a polarization of the electron population in the valley configuration would diffuse. Such a polarization is dynamically created by an ultrasonic wave propagating through the silicon crystal. It is therefore not surprising that the attenuation rate of the ultrasonic wave is proportional to a valley relaxation time. This valley relaxation time is the analog of the spin relaxation time that is measured in an ESR experiment. Reasoning in analogy with the spin relaxation time we can therefore conclude that the ultrasonic attenuation in multivalley doped semiconductor like Si:P should have a temperature dependent increase at low temperatures which can be correlated with the broadening of the ESR line. This temperature dependence of the ultrasonic attenuation has a clear signature in its dependence on the direction of propagation and polarization of the ultrasonic wave. An experimental measurement of the ultrasonic attenuation should therefore provide a rather unambiguous test of the applicability of the disordered Fermi liquid theory in Si:P.

IV. THE TRANSITION REGION

In this section we discuss the region just around n_c. As noted in the introduction, no complete theory of this region exists. We will discuss a few significant experiments and present recent theoretical attempts in understanding this region.

Reexamining Fig. 1 we see that the spin susceptibility gradually crosses over from a weak $\sqrt{T}$ correction at high densities to the almost Curie-type behavior in the insulating phase. A remarkable feature of the data is that on the metallic side of the transition (at a density of $1.09n_c$) the susceptibility at 50 mK is over ten times larger than that at 10 K. This clearly cannot be explained by the expression in Eq. (5). A similar point is made by Fig. 2: in this figure we have plotted the temperature dependent susceptibility as a function of the conductivity for two different metallic samples ($n = 1.09n_c$ and $1.25n_c$). The almost vertical slope of the line clearly indicates that the temperature dependence of the susceptibility is far stronger than that of the conductivity. This disagrees with Eqs. (4) and (5) which predict a change in the conductivity and susceptibility of the same order of magnitude. We also show in Fig. 2 the results of a renormalization group calculation[28,29] for the temperature dependence of the susceptibility and conductivity. This calculation can be interpreted as a resummation of an infinite number of terms in the weak disorder perturbation theory; Eqs. (4) and (5) contain only the leading order terms in this series.

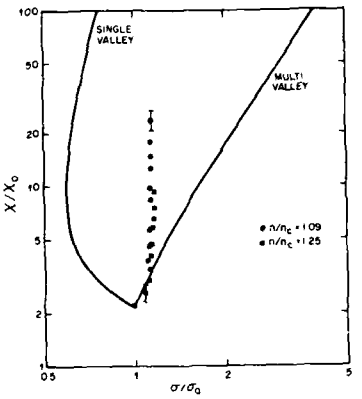


FIG. 2. Spin susceptibility (χ) and conductivity (σ) for two different metallic samples of Si-P. The suceptibility is normalized to the susceptibility (χ_0) of a free Fermi gas, while the conductivity is normalized to the conductivity of the sample at 10 K (σ_0). The solid lines represent theoretical renormalization-group calculations of two versions of the disordered Fermi liquid theory. The two versions differ in their treatment of the valley index of the conduction band. There is only one adjustable parameter in the theoretical calculations, and it is used to fix the high-temperature point common to the two solid curves and the experimental points.

The results of this calculation depend upon whether the disordered Fermi liquid preserves the many-valley structure of the underlying conduction band or averages over it; both cases are presented in Fig. 2. As plotted in Fig. 2, there is only one adjustable Fermi liquid constant which determines the theoretical curves. This constant is used to fix the high-temperature starting point of the renormalization-group calculation; this is the point at which the two theoretical curves intersect in Fig. 2. The lack of any correspondence between the theoretical and experimental curves indicates the inapplicability of the disordered Fermi liquid theory. Neither of the theoretical curves is close to vertical as the conductivity and susceptibility vary on the same temperature scale. To get better agreement with the experiment it is then clearly necessary to introduce a different model which treats the spin excitations and charge transport differently from one another.

Before abandoning the Fermi liquid description at densities close to n_c, it is of interest to examine whether its general physical framework is useful, independent of the validity of perturbation theory. The disordered Fermi liquid theory framework allows one to make phenomenological scaling ansatzes for the frequency, density and temperature dependences of the thermodynamic quantities of the system. For example, it states that asymptotically close to n_c, the conductivity should satisfy the following equation[10]:

$$\sigma(n,T) = (n - n_c)^{\mu}\Phi\left[T^{x}(n - n_c)\right], \tag{7}$$

where Φ is smooth function of its arguments. Attempts to fit the data in Si:P to Eq. (7) have not been successful[29] indicating that the corrections to scaling terms in the experimental region of interest are so large that the scaling concept is not very useful.

Two recent nuclear magnetic resonance (NMR) experiments[30,31] have provided important clues about the nature of this intermediate phase. The first by Paalanen *et al.*[30] measured T_1 relaxation times of Si^{29} nuclei. They found strong enhancements over the Korringa relaxation rate present in a clean metal. In addition, the T_1 relaxation rates were strongly dependent upon the magnitude of the magnetic field. These results were explained by Gan and Lee[32] using a simple two fluid model of the electrons. The electron liquid was assumed to be made divided into two mutually independent components: (i) a disordered Fermi liquid which was responsible for the charge transport and (ii) electron local moments, which were precursors of the spins on the insulating side of the transition and were responsible for the large spin susceptibility. The local moments were necessary in the model of Gan and Lee[32] to explain the magnetic field dependence of T_1. The second experiment by Alloul *et al.*[31] measured the NMR signal from P nuclei. The interaction of the P nuclei with the electrons leads to a shift in resonance frequency of NMR (the Knight shift). If the electron is in a localized bound state near a nucleus, then the shift is so large that the NMR signal from the nucleus becomes part of the background. The NMR experiment therefore only measures the signal from the P nuclei which interact with itinerant electrons. The experiment found an abrupt decrease in the Knight shift as the doping density was changed from $1.1n_c$ to n_c. This can be interpreted as the transformation of the itinerant quasiparticle spectral weight into local moments. This transformation occurs while the system still has a nonzero conductivity at zero temperature.

The two-fluid model discussed by Gan and Lee[32] is actually a very old one and was also used by Quirt and Marko[33] in their early experiments on the magnetic properties of doped semiconductors. At its simplest level the model can be taken as a phenomenological description of the electronic states as being made up of two independent fluids: a Fermi fluid with extended quasiparticle-like excitations which carry charge, spin, and energy and a configuration of localized moments which consist of electrons singly occupying localized states and contributing a large spin susceptibility. To go beyond this model it is obviously necessary to introduce an interaction between the two components. Such a program would have to ultimately show the correlation between the decrease in the quasiparticle weight in Fermi fluid and the increase in the weight of the local moment spectrum. In the remaining part of this section we summarize the result of a recent attempt by one of us[12] to develop a theory of the interaction between the local moments and the Fermi liquid.

The Hamiltonian describing the interactions of the Fermi liquid and the local moments can be written as follows:

$$H = H_{\rm fl} + \sum_{i \neq j} J_{ij}\, \mathbf{S}_i \cdot \mathbf{S}_j + \sum_{\mathbf{k},\mathbf{q}} \sum_{\alpha,\beta} \sum_{i} K_i\, \mathbf{S}_i\, c^{\dagger}_{\mathbf{k}+\mathbf{q},\alpha}\, \sigma_{\alpha,\beta}\, c_{\mathbf{k},\beta}\, e^{i\mathbf{q}\cdot\mathbf{R}_i}, \quad (8)$$

where $H_{\rm fl}$ is the Fermi liquid Hamiltonian for the quasiparticles, $c^{\dagger}$ is a quasiparticle creation operator, $\mathbf{S}_i$ are local electron spins interacting with each other with exchange J_{ij} and with the extended quasiparticles with exchange K_i. An issue that arises at the outset is the lack of an analytical description of the spatial and dynamical correlations in the local moment susceptibility. In Ref. 12 a simple phenomenological description of the local moments is assumed. All spatial correlations are ignored and the local moments are assumed to be randomly located. After averaging over the locations of the moments, this leads to a momentum independent local moment susceptibility $\chi(\omega_n)$. It is assumed that the spectral weight in χ is zero above a spin-fluctuation frequency ω_s, with ω_s satisfying $\omega_s \ll E_F$. Then to second order in coupling K between the local moments and the conduction electrons several important features of the properties of the system can be understood which are independent of the spectral shape of $\chi(\omega_n)$. At any finite temperature T the self-energy $\Sigma(\omega)$ of the electrons in the Fermi liquid has the form

$$\Sigma(\mathbf{k},\omega) = \Sigma_C(\mathbf{k},\omega) + \omega(1-Z) - \frac{i}{2\tau_{\rm in}}\,\mathrm{sgn}(\omega)\,. \quad (9)$$

Here Σ_C is the Fermi liquid self-energy from the Coulomb interactions between the itinerant electrons and remaining terms arise from the interaction with the local moments. The only wave-vector dependence in Σ is contained in Σ_C. The frequency renormalization factor Z can be shown to arise from the local moment spectral weight in the region $\omega > T$ and the inelastic scattering from the local moment spectral weight in the region $\omega < T$. It is shown in Ref. 12 that the renormalization factor Z cancels in the expression for the compressibility and conductivity, but yields an enhancement of the spin susceptibility. The local moment inelastic scattering (described by the term $\tau_{\rm in}$), however, leads to a decrease in the conductivity. Using a local sum rule on the magnitude of the local-moment spin at each site it can be shown to exponential accuracy in T/ω_s that

$$1/2\tau_{\rm in} \sim TK^2 N \chi_s(T)\,, \quad (10)$$

where $\chi_s(T)$ is the *static* local moment susceptibility. Assuming that the spin susceptibility of the itenerant electrons is negligible compared to that of the local moments this immediately leads to an experimentally testable connection between the temperature dependence of the spin susceptibility and the conductivity. As discussed elsewhere[12] this correlation is found to be consistent with experiments except *very* close to the metal insulator transition.

As an aside we note that although the inelastic spin-flip rate $\tau_{\rm in}$ will modify all the quantum interference effects in the disordered Fermi liquid, it will not show up as an additional linewidth in the ESR experiment. In particular $\tau_{\rm in}$ will be relevant in choosing between the various renormalization group fixed points of Finkelstein.[7,8] The reason it does not contribute to the ESR linewidth is simple: the ESR experiment measures the *total* electron spin susceptibility while $\tau_{\rm in}$ represents relaxation of spin between different parts of the electron system. An analytic calculation describing this phenomena in detail can be found in Ref. 12.

The results that emerge out of this analysis of the interactions between the local moments and the disordered Fermi liquid are therefore very simple. The dominant effect of the local moments on the Fermi liquid is to introduce a frequency renormalization factor and a strongly temperature depen-

dent inelastic scattering rate. The inelastic scattering leads to a temperature dependent conductivity and also cuts off all the quantum interference effects which were responsible for the scaling behavior.

V. CONCLUSIONS

We have presented a review of experimental and theoretical work on the metal insulator transition in doped semiconductors, especially Si:P. While considerable progress has been made in the understanding of the insulating and metallic phases, there are still many unresolved issues on the physics of the transition between the two regions. There appears to be a decoupling of the charge and spin degrees of freedom in the transition region between the metal and insulator. While the conductivity vanishes at a critical density n_c, there is clear experimental evidence for the appearance of local electron moments at densities greater than n_c. Although a complete understanding of this unusual phase is still lacking, phenomenological approaches[12] have recently had some success in understanding the interaction between extended disordered quasiparticles and local moments.

On the experimental front, most work on magnetic properties has so far concentrated on uncompensated semiconductors. An important future direction is therefore the measurement of magnetic properties of compensated materials. The measurement of the conductivity exponent μ has already indicated differences from the uncompensated semiconductors. The magnetic properties of compensated semiconductors will undoubtedly yield important clues about the value of μ and the physics of metal-insulator transition.

[1]R. F. Milligan, T. F. Rosenbaum, R. N. Bhatt, and G. A. Thomas, in *Electron-Electron Interactions in Disordered Systems*, edited by A. L. Efros and M. Pollak (North-Holland, Amsterdam, 1985).
[2]L. R. Friedman and D. P. Tunstall, Eds., *The Metal Non-Metal Transition in Disordered Systems* (SUSSP Publ., Edinburgh, 1978).
[3]N. F. Mott, *Metal-Insulator Transitions* (Taylor and Francis, London, 1974).
[4]C. Herring, in *Magnetism*, edited by G. T. Rado and H. Suhl, (Academic, New York, 1966), Vol. IIB, pp. 1–181; C. Herring and M. Flicker, Phys. Rev. **134**, A362 (1964).
[5]T. F. Rosenbaum, K. Andres, G. A. Thomas, and R. N. Bhatt, Phys. Rev. Lett. **45**, 1723 (1980).
[6]G. A. Thomas, Philos. Mag. B **52**, 479 (1985).
[7]A. M. Finkelstein, Zh. Eksp. Teor. Fiz. **84**, 166 (1983) [Sov. Phys. JETP **57**, 97 (1983)].
[8]A. M. Finkelstein, Z. Phys. B **56**, 189 (1984).
[9]C. Castellani, C. DiCastro, P. A. Lee. and M. Ma, Phys. Rev. B **30**, 527 (1984).
[10]C. Castellani, B. G. Kotliar, and P. A. Lee, Phys. Rev. Lett. **56**, 1179 (1986).
[11]This is the well-studied Kondo problem. See, e.g., K. Wilson, Rev. Mod. Phys. **47**, 773 (1975).
[12]S. Sachdev (unpublished).
[13]R. N. Bhatt, Phys. Scr. **T14**, 7 (1986).
[14]S. Sachdev and R. N. Bhatt, J. Appl. Phys. **61**, 4366 (1987).
[15]R. N. Bhatt and P. A. Lee, Phys. Rev. Lett. **48**, 344 (1982).
[16]C. T. Murayama, W. G. Clark, and J. Sanny, Phys. Rev. B **29**, 6063 (1984).
[17]S. Sachdev and R. N. Bhatt, Phys. Rev. B **34**, 4898 (1986).
[18]B. L. Altshuler and A. G. Aronov, Solid State Commun. **30**, 115 (1979).
[19]B. L. Altshuler and A. G. Aronov, Solid State Commun. **46**, 429 (1983).
[20]B. L. Altshuler, A. G. Aronov, and P. A. Lee, Phys. Rev. Lett. **44**, 1288 (1980).
[21]H. Fukuyama, J. Phys. Soc. Jpn. **48**, 2169 (1980).
[22]C. Castellani, C. DiCastro, H. Fukuyama, P. A. Lee, and M. Ma, Phys. Rev. B **33**, 7277 (1986).
[23]R. N. Bhatt and P. A. Lee, Solid State Commun. **48**, 755 (1983).
[24]C. Castellani, C. DiCastro, P. A. Lee, M. Ma, S. Sorella, and E. Tabet, Phys. Rev. B **30**, 1596 (1984).
[25]S. Sachdev, Phys. Rev. B **34**, 6069 (1986).
[26]S. Sachdev, Phys. Rev. B **35**, 7558 (1987).
[27]M. A. Paalanen, S. Sachdev, R. N. Bhatt, and A. E. Ruckenstein, Phys. Rev. Lett. **57**, 2061 (1986).
[28]S. Sachdev, Phys. Rev. Lett. **58**, 2590 (1987).
[29]S. Sachdev (unpublished).
[30]M. A. Paalanen, A. E. Ruckenstein, and G. A. Thomas, Phys. Rev. Lett. **54**, 1295 (1985).
[31]H. Alloul and P. Dellouve, Phys. Rev. Lett. **59**, 578 (1987).
[32]Z. Z. Gan and P. A. Lee, Phys. Rev. Lett. B **33**, 3595 (1986).
[33]J. D. Quirt and J. R. Marko, Phys. Rev. B **7**, 3842 (1973).

Electrical transport properties of thin epitaxially grown iron films on GaAs

F. J. Rachford, M. Rubinstein, and G. A. Prinz
Naval Research Laboratory, Washington, DC 20375

We have determined the components of the magnetoresistance tensor through fifth order in the magnetic direction cosines for four epitaxially grown iron films with thicknesses between 200 and 60 Å at 300, 77, and 4.2 K. We have also determined their magnetic anisotropy parameters from ferromagnetic resonance at 300 K. These phenomenological parameters provide an excellent description of the magnetic field dependence of the planar magnetoresistivity for electric current directed along the [001], [1$\bar{1}$0], and [1$\bar{1}\sqrt{2}$] directions and the applied fields necessary to produce spin flops.

There have been many recent papers on the properties of epitaxially grown iron films.[1] In an attempt to further investigate the properties of these films, we have conducted electrical transport measurements on samples with iron film thicknesses between 200 and 60 Å.

Thin iron films were grown on GaAs substrates by MBE techniques. As in previously reported samples, the substrate orientation was chosen to be a (110) face. GaAs was chosen as the substrate because its nearest-neighbor distances are close (within -1.4%) to that of bcc iron, and also because magnetic films deposited on semiconductors have application potential.

In order to make transport measurements on the iron films, it was necessary to use a highly insulating GaAs substrate. The (110) substrates were prepared using conventional polishing and annealing procedures. The film thicknesses were measured by x-ray fluorescence after the samples had been grown and removed from the vacuum chamber. The samples were then photolithographically etched with a pattern of three conducting strips, one along the magnetically easy [001] axis, one along the [1$\bar{1}$0] axis and a third along an intermediate direction [1$\bar{1}\sqrt{2}$] at 45° from the [001] axis. A strip of iron film was also left intact for subsequent analysis by FMR. The samples were allowed to oxidize in air. It is believed that this produces a stable oxide surface of 30–35 Å, removing approximately 15 Å of metallic iron.

Four samples, 200, 160, 90, and 60 Å $\pm$ 5 Å thick, were analyzed by FMR using the methods explained in previous publications.[1] The 200- and 160-Å samples were found to have their easy direction of magnetization along the [001] axis, while the two thinner samples have their easy axis along the [1$\bar{1}$0] direction. The samples are single domain, and their magnetization lies in the plane of the film. In order to analyze the observed anisotropy of the FMR spectra, the following energy density expression was employed:

$$E = -HM + 2\pi M^2 + K_1(\alpha_1^2\alpha_2^2 + \alpha_2^2\alpha_3^2 + \alpha_3^2\alpha_1^2) + K_u \sin^2\Theta + K_u' \sin^4\Theta + K_\perp (M_\perp/M)^2, \quad (1)$$

where Θ is the angle between M and [001] in the (110) plane, the α's are the direction cosines of M with respect to the cubic crystalline axes, and $M_\perp$ is the component of M normal to the surface. K_u and K_u' are the epitaxy-induced uniaxial in-plane anisotropy constants, and $K_\perp$ is the perpendicular anisotropy constant. Table I displays the room-temperature resistivity, the magnetic anisotropy and magnetization parameters deduced from FMR for these four films, and those for bulk iron. Their dependence on film thickness are in agreement with the previous studies. In particular, we note (1) the existence of a large uniaxial anisotropy attributed to the lattice mismatch between the GaAs and the Fe film, (2) the change in the easy direction of magnetization from the [001] to the [1$\bar{1}$0] when the sample thickness is less than 100 Å indicated by the change in sign of K_u, and (3) the low magnetization of the iron films compared to the magnetization of bulk iron at room temperature ($4\pi M \cong 21$ kOe).

Previous magnetometry and FMR studies have shown the existence of a first-order magnetic phase transition in (110) iron films with a {001} easy axis.[2] This transition occurs when a magnetic field is applied in the (110) plane of the iron film and aligned near the hard [1$\bar{1}$0] axis. A sudden spin flop occurs with increasing field as the magnetization abruptly realigns from a direction near the [001] to a position near the [1$\bar{1}$0] axis. In this paper we report this transition plus a new transition observed by monitoring the resistivity or the planar Hall effect. The measurements are sensitive to such transitions due to the small but easily observed magnetoresistive anisotropy in the films. The new transition is closely related to the old, and involves two successive spin flops. The double transitions can be calculated from a knowledge of the magnetocrystalline anisotropy parameters derived from the FMR experiments.

In Fig. 1(a) we have plotted the electrical resistance measured in the 160-Å-thick iron film as a function of applied magnetic field for a series of fixed angular orientations

TABLE I. Phenomenological magnetic and electrical transport parameters for several thin iron films used in this study assuming $K_\perp/M = 0.27$ kOe.

Thickness (Å)	$4\pi M$ (kOe)	K_u/M (kOe)	K_u'/M (kOe)	ρ (300 K) ($\mu\Omega$ cm)
bulk	21	0	0	9.71
200	17.6	−0.22	+0.009	23.0
160	16.5	−0.05	+0.15	30.9
90	12.6	+0.35	−0.1	68.1
77				73.3
60	11.4	+0.63	−0.16	177.5

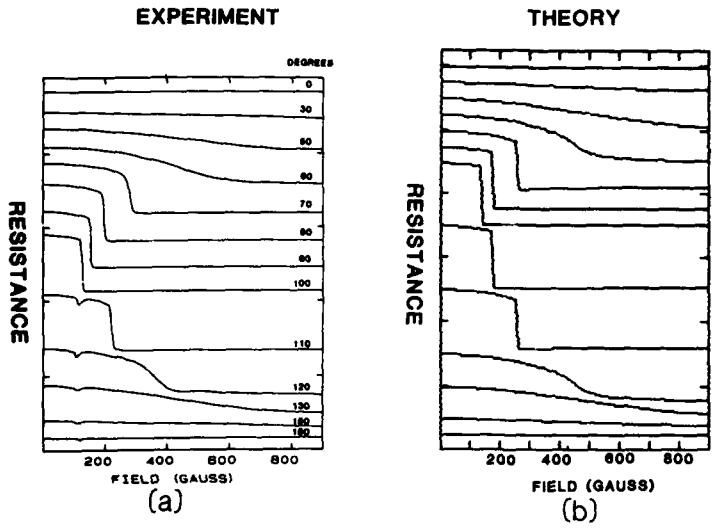


FIG. 1. (a) Experimentally determined resistivity vs applied magnetic field for various angles of the applied magnetic field. (b) Theoretical family of magnetization curves as shown in (a).

of the applied field with respect to the crystalline axis of the film. The direction of the current is along the $[1\bar{1}0]$ axis. The angles indicated are for the direction of the magnetic field with respect to its initial direction along the [001] easy axis in the (110) plane of the film. Initially the film is magnetized with a strong magnetic field along the [001] axis, i.e., 0° in Fig. 1(a).

For this film, abrupt changes in the resistivity as a function of applied field are observed whenever the field angle $\theta > 63°$. These changes are caused by spin-reorientation transitions which produce a sudden change in the electrical resistance because of a small (0.3%) anisotropic magnetoresistance in these iron films.

In order to reproduce the actual data traces we need to find the magnetoresistance tensor for the film. We do this by measuring the resistance in a saturating field as a function of angle in the (110) plane assuming perfect alignment of M and H and negligible "forced" magnetoresistance. The high field data is fit to a fourth-order expansion of the cubic and orthorhombic magnetoresistance tensor in the direction cosines of the current direction and the direction cosines of the magnetization with respect to the crystalline axis.[3] With a knowledge of the magnetocrystalline anisotropy constants (obtained from FMR), we can reproduce the detailed shape of the resistance (and planar Hall effect) curves as a function of magnetic field. Figure 1(b) shows the "theoretical" results for this sample while the experimental results are shown in Fig. 1(a).

When $90° < \theta < 120°$ for this film, two magnetic-field-induced spin-reorientation transitions are seen, and when $\theta > 120°$, only a single transition is observed. The behavior of the transition when $0° < \theta < 90°$ has already been discussed previously.[1,2]

In Fig. 2 we plot the magnetic fields at which these transitions occur versus field angle in the (110) plane for the 160-Å-thick iron film. The solid line is the theoretical prediction. The crosses are the experimentally observed values of the spin flop. The theory numerically calculates the magnetic energy [Eq. (1)] as a function of initial magnetization state, field amplitude and orientation, and predicts the orientation of the magnetization. The regime of double spin flops, cross hatched in the diagram, extends from $> 90°$ to $< 120°$ in this sample.

To illustrate the origin of the spin flops and to relate the transition for $90° < \theta < 120°$ to the previously studied case where $63° < \theta < 90°$ we present a contour mapping of the energy surface for the magnetization of the 160-Å sample as a function of magnetization angle in the (110) plane (relative to [001] and the applied field) for the two symmetric cases where the external field is applied at 70° [Fig. 3(a)] and at 110° [Fig. 3(b)]. At zero field minima occur at the 0° and

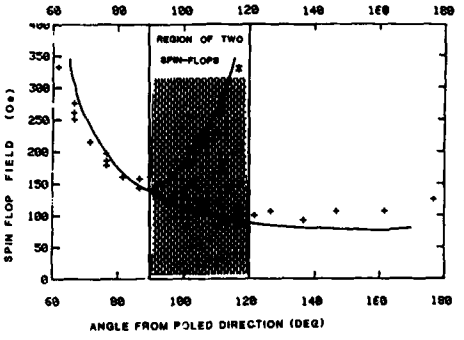


FIG. 2. Magnetic field amplitude, in Oersteds, at which spin flops are observed to occur for the 160-Å-thick iron film as a function of the field angle.

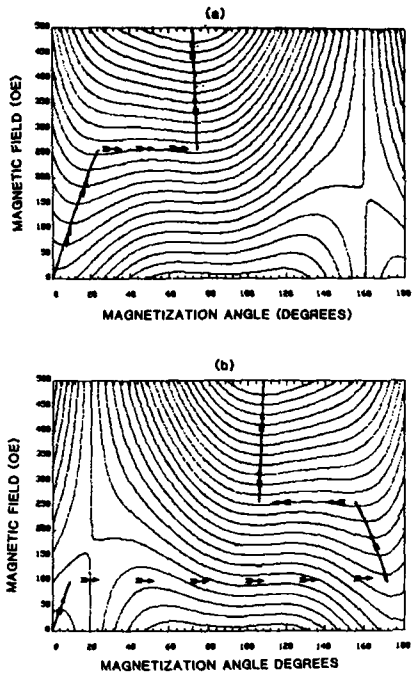


FIG. 3. The contours of energy vs magnetization angle and applied field orientations in the (110) plane: (a) H applied at 70° from the [001] and (b) H applied at 110° from the [001].

180° positions corresponding to the equivalent cases where the magnetization is oriented along the [001] or the [00$\bar{1}$]. The magnetization is assumed to be initially directed along the [001]. In Fig. 3(a), as the magnetic field is increased, the magnetization slowly rotates as the energy minimum shifts to a larger angle. The trajectories of magnetization are indicated by directed lines intersecting the contours. At about 260 G the energy for an orientation at approximately 74° becomes less than the minimum near 24° and the magnetization suddenly reorients. Here we have neglected the domain wall nucleation energy, and the magnetization reorientation trajectory is theoretically reversible in applied fields. Experimentally, a small hysteresis is noted. This is an example of the previously studied magnetization reorientation transition,[2] and indicates that wall reorientation proceeds by domain wall formation and motion.

In Fig. 3(b) we plot the case where the external field is applied at 110° to the [001]. The energy contours are mirror reflected about 90° from those of the previous example. The magnetization is initially directed along the [001]. As soon as a magnetic field is applied, the global energy minimum is found near 180°, [00$\bar{1}$]. We experimentally find that the magnetization does not immediately reorient to the global minimum but remains in the local minimum near [001] as in the first example until a transition to the local energy minimum near the [1$\bar{1}$0] becomes energetically favorable. At this point, we assume two $\sim$90° walls are generated and sweep through the sample reorienting the magnetization to the global minimum near the [1$\bar{1}$0]. As the field increases further, the magnetization follows a trajectory which is the mirror image of the previous case [Fig. 3(a)]. The transition at $\sim$100 G is not reversible and the magnetization rotates to the [00$\bar{1}$] as the field is subsequently reduced to zero.

Since reorientation is delayed until $\sim$90° rotations are energetically favorable we conclude that the reorientations of angles greater than 90° occur by a two step process and that large reorientations do not occur until "90° walls" can be generated. In this calculation, we assume that the sample is single domain except during the magnetization reorientations, when one or two $<$90° domain walls are generated and rapidly sweep through the sample.

Thus, using Eq. (1), the parameters obtained from fitting the FMR data on each sample and the experimentally determined magnetoresistivity tensor for each film, we can numerically calculate the magnetic energy and generate an acceptable fit to the transition data and the nonsaturated magnetoresistance curves.

[1] J. J. Krebs, B. T. Jonker, and G. A. Prinz, J. Appl. Phys. **61**, 3744 (1987) and references therein.
[2] K. B. Hathaway and G. A. Prinz, Phys. Rev. Lett. **47**, 1761 (1981).
[3] R. S. Birss, *Symmetry and Magnetism* (North-Holland, Amsterdam, 1964).

Magnetothermal conductivity of $ErAl_2$ for cryogenic applications

C. B. Zimm, C. K. Campenni, and J. A. Barclay
Astronautics Technology Center, Madison, Wisconsin 53716

The thermal conductivity K of rare-earth intermetallic compounds with magnetic ordering temperatures T_0 below 100 K is a key parameter affecting their use in magnetic refrigerators and regenerators. We have measured the thermal conductivity of $ErAl_2$, $T_0 = 12$ K, between 5 and 170 K in 0- and 7-T applied magnetic fields. The zero-field results show a strong, 20-K-wide minimum in the thermal conductivity near the ordering temperature. The results at 7 T indicate that the magnetic field eliminates the minimum and produces a monotonic temperature dependence. We attribute these effects to magnetic scattering of electrons.

INTRODUCTION

Magnetic refrigeration technology currently under development for use above 20 K typically uses as a refrigerant a ferromagnetic rare-earth (RE) intermetallic compound operating near its Curie point T_C. The heat transfer from the magnetic refrigerant is a critical part of the thermodynamic cycle; hence the thermal conductivity K of intermetallics in the presence of an applied magnetic field B_a is a key parameter needed for designing magnetic refrigerators.

Unfortunately, measurements of thermal conductivity for RE intermetallic compounds below 100 K are sparse, and we know of none in high magnetic fields. This is not because the magnetic component of the thermal resistivity ($1/K$) is negligible. Indeed, a strong correlation of the thermal resistivity of $REAl_2$ compounds with the de Gennes factor, $(g-1)^2J(J+1)$, suggests a strong magnetic component of the thermal resistivity in temperatures up to 270 K.[2,3] A sharp anomaly in thermal conductivity has also been observed for $GdAl_2$ at its 160-K Curie point.[4]

The electrical and thermal resistivities normally show similar behavior, conventionally described by the Wiedemann–Franz relation. Field-dependent magnetic scattering in electrical resistivity is illustrated by measurements on Gd, coupled with an excellent correlation between the field dependence of the specific heat and the field dependence of the temperature derivative of the resistivity.[5] Simple theory predicts[2] that the phonon scattering of the electrons carrying heat should drop faster with declining temperature T than the magnetic scattering, provided $T_c < T < \theta_D$, where θ_D is the Debye temperature. Hence the magnetic scattering component of thermal conductivity for $ErAl_2$, a Laves phase ferromagnetic with a Curie temperature of 12 K, should be strong. With the above motivation, we have measured the thermal conductivity of $ErAl_2$ for $B_a = 0$ and 7 T.

EXPERIMENTAL METHOD

The $ErAl_2$ sample used for this study was made by the Materials Preparation Center of Ames Laboratory, at Iowa State University. The erbium used was of true 99.9% atomic purity with respect to nonmetallic elements and approximate 99.999% purity with respect to metals, including other rare earths. The aluminum was 99.999% pure. The constituents were arc-melted and then arc-cast in an argon atmosphere. The polycrystalline single-phase nature of the sample was verified by metallography. The sample was cut to form a rectangular rod of 3 mm × 4 mm × 30 m size.

Thermal conductivity was measured using a steady-state, longitudinal heat-flow design, as described by Arenz, Clark, and Lawless.[6] The configuration is nontypical in that a single thermometer is used to determine the thermal conductivity of the material between two heaters. Use of a single thermometer to measure a temperature difference cancels out much of the thermometer calibration error that can occur in the conventional dual-thermometer, single-heater configuration.

Figure 1 shows a cross section of the apparatus, which includes a vacuum chamber with a pumping tube at the top and an oxygen-free high-conductivity (OFHC) copper base (62 mm o.d.). The base contains electrical feed-throughs to

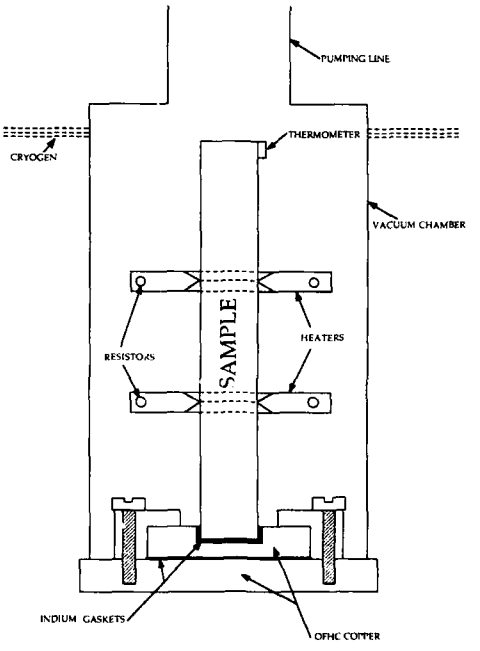


FIG. 1. Schematic of the thermal-conductivity apparatus.

 0021-8979/88/084294-03$02.40 © 1988 American Institute of Physics

enable cryogenic heat sinking of the electrical leads. The sample is held in place in an OFHC copper support which is secured to the base. Indium gaskets are used between the sample, the support, and the base; the seal between the base and vacuum chamber is an indium O-ring. For field-dependent studies, an 8-T superconducting solenoid that surrounds the vacuum chamber is used to apply field parallel to the long axis of the sample. The vacuum chamber is surrounded by a boiling cryogen (helium or nitrogen) that serves as a heat sink.

Each heater consists of an OFHC copper split clamp tightened onto the sample with screws. Two ¼-W, 510-Ω metal film resistors, connected in parallel are potted inside each heater with epoxy. The total change in resistance was less than 0.2% between 4.5 and 300 K. The heaters are tapered to approach line contact with the sample so that the distance between the locations of heat input can be precisely measured.

The thermometer is attached to the side of the sample near the non-heat-sunk end using shrink-wrap tubing and dental floss. Copper-filled grease is used to ensure effective thermal contact between the sample and the thermometer. A silicon (Si) diode is used to measure the sample temperature in zero field. Due to the strong field dependence of the silicon diode, a bismuth ruthenium oxide (BRO) resistor, which exhibits only a 75-mK field dependence at 4 K, is used for field-dependent studies. Zero-field thermal-conductivity data were obtained between 4.5 and 35 K using the BRO resistor; this data agreed with the data obtained using the Si diode. The thermometers were calibrated against a carbon-glass thermometer calibrated by Lakeshore, Inc. The nonlinearity of the BRO resistor required fitting of the calibration data.

The dual-heater, single-thermometer design effectively measures the thermal conductivity of the sample between the two heaters. Initially a power is applied to the lower heater ($\dot{Q}$), and the steady-state temperature (T_1) is recorded. A portion of the applied power ($\Delta\dot{Q}$) is then applied to the upper heater while reducing the lower heater power by $\Delta\dot{Q}$; the total power applied to the sample is thereby held constant as the subsequent steady-state temperature (T_2) is recorded. The thermal conductivity at $T_{\text{avg}} = (T_2 - T_1)/2$ is then given for a sample of constant cross section A by

$$K = (\Delta\dot{Q})(L)/(T_2 - T_1)(A)\,,$$

where L is the distance between the two heaters. A computer system controlled the heaters and acquired the data. To minimize averaging the thermal conductivity over wide temperature spans, the system monitored the temperature rise ($T_2 - T_1$) at each data point and adjusted the subsequent $\Delta\dot{Q}$ to maintain a temperature rise of less than 2 K. Steady-state temperatures were recorded when the rate of temperature change was less than 3 mK/min.

Optimization of procedures and verification of calibration of the thermal-conductivity apparatus was accomplished through analysis of two National Bureau of Standards (NBS) standards: sintered tungsten (NBS Research Material No. 8422) and austenitic stainless steel (NBS Standard Reference Material No. 1460). The thermal conductivity of both test samples measured in our apparatus generally agreed to within 5% of the NBS reported results. Measurement using boiling N_2 below 80 K and boiling He below 7 K are less accurate due to the small heat loads used. The apparatus has the capability of measuring thermal conductivity over a large range of values. For instance, measurements on $ErAl_2$ were obtained between 4.5 and 175 K by varying the total applied power between 0.01 and 4.12 W.

RESULTS AND DISCUSSION

Figure 2 shows our measured zero-field thermal-conductivity data for $ErAl_2$. Also shown for comparison are the published measurement of Bauer, Gratz, and Adam.[3] The large minimum near 12 K was reproduced over several runs using two different types of thermometers.

We ascribe the large difference between our measurements and those of Bauer and co-workers to sample purity. Our samples were made from rare earths of 99.9% atomic purity with respect to all elements including oxygen and hydrogen. Most commercial sources of rare earths of nominal 99.9% purity with respect to other metals contain a few atomic percent of oxygen and hydrogen. Such impurities may serve as effective scatterers of electrons, thereby decreasing K at low temperature.

Application of a 7-T magnetic field produces a large change in thermal conductivity near the Curie point of $ErAl_2$ (Fig. 3). The effect fades with increasing temperature, becoming barely resolvable above 25 K.

The RE Laves phases are very brittle and prone to cracking. We noted that presence of at least one microcrack on our sample. Such cracks should not change the temperature or field dependences of K, but our measured values might differ from that of a completely crack free and void-free specimen by a constant scaling factor.

A simple theory gives a qualitative understanding of the above thermal-conductivity results. First, note that heat may be carried by both electrons and phonons. Arguments have been made[3] that the phonon conductivity in RE Laves phase compounds around 20 K is quite small; moreover, thermal conductivity of the magnetic insulators $Gd_2(SO_4)_3 \cdot 8H_2O$ and $Dy_2Ti_2O_7$ show no field depend-

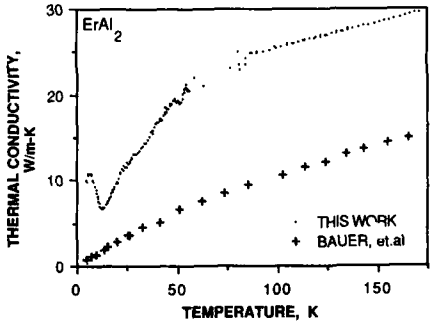


FIG. 2. Measured thermal conductivity of $ErAl_2$ in zero applied field.

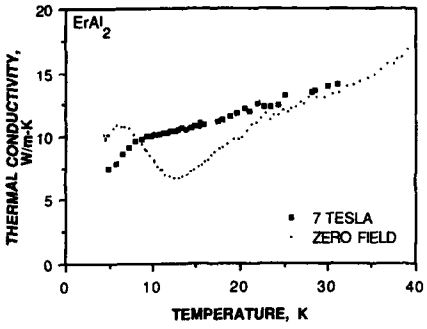


FIG. 3. Measured thermal conductivity of $ErAl_2$ in 0- and 7-T applied magnetic fields. The Curie point of $ErAl_2$ is 12 K.

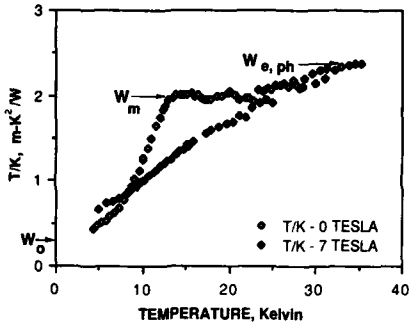


FIG. 4. Temperature divided by the measured thermal conductivity of $ErAl_2$. Three types of electronic scattering are evident: W_0 (impurity scattering), W_m (spin scattering), and $W_{e,ph}$ (phonon scattering).

ence.[8] Hence consider only the electronic contribution to the thermal conductivity. Using the thermal equivalent of Matthiesson's rule, the electronic thermal resistivity can be written as[2] $W_e = W_{e,0} + W_{e,\mathrm{mag}} + W_{e,\mathrm{ph}}$ where $W_{e,0}$ is due to the scattering of electrons by impurities and defects, $W_{e,\mathrm{mag}}$ is the scattering by spins, and $W_{e,\mathrm{ph}}$ is the scattering by phonons. A linearized Boltzmann equation approach[2] predicts for $B_a = 0$ the following temperature dependence for each of the scattering terms multiplied by the temperature:

$$TW_{e,0} = W_0 ,$$

$$TW_{e,\mathrm{mag}} = \begin{cases} W_m , & T > T_c \\ 0 , & T = 0 , \end{cases}$$

$$TW_{e,\mathrm{ph}} \sim \begin{cases} T , & T \sim \theta_D \\ T^3 , & T \ll \theta_D . \end{cases}$$

By plotting $T \cdot W (= T/K)$ vs T (Fig. 4), we indeed see, for $B_a = 0$, a nonzero $T = 0$ intercept, W_0; a higher constant value just above T_C, $W_0 + W_m$; and a gradual increase due to $W_{e,\mathrm{ph}}$ well above T_C. The constant value of T/K above T_C occurs because the spin system becomes entirely disordered above T_C for $B_a = 0$. As the spin system orders for $T < T_C$, the magnetic scattering drops. A magnetic field extends the magnetic order to temperatures above T_C; hence the 7-T applied field washes out the sharp transition at T_C. We have measured the magnetization of $ErAl_2$ for $B_a = 7$ T, confirming that 7 T nearly saturates the spin system at T_C, but not at 30 K.

We have observed that the thermal conductivity of $ErAl_2$ is strongly temperature and field dependent in a 10-K region about T_C. Such effects, arising from the magnetic scattering of electrons, must be considered when designing or modeling thermomagnetic devices using rare-earth intermetallic compounds.

ACKNOWLEDGMENTS

Work sponsored by Flight Dynamics Laboratory, Air Force Wright Aeronautical Laboratories, Aeronautical Systems Division (AFSC) United State Air Force, Wright-Patterson AFB, OH 45433-6533, under Contract No. F33615-86-C-3431. Funding is provided by the Strategic Defense Initiative Organization (SDIO).

[1] J. A. Barclay, *Advances in Cryogenic Engineering* (Plenum, New York, in press), Vol. 33.
[2] E. Gratz, E. Bauer, and H. Nowotny, J. Magn. Magn. Mater. **70**, 18 (1987).
[3] E. Bauer, E. Gratz, and G. Adam, J. Phys. **16**, 493 (1986).
[4] J. B. Sousa, R. P. Pinto, M. M. Amado, M. E. Braga, and J. Sukurai, J. Magn. Magn. Mater. **28**, 29 (1982).
[5] D. S. Simons and M. B. Salamon, Phys. Rev. **10**, 4680 (1974).
[6] R. W. Arenz, C. F. Clark, and W. N. Lawless, Phys. Rev. B **26**, 2727 (1982).
[7] K. A. Gschneidner, Jr., *Science and Technology of Rare Earth Materials* (Academic, New York, 1980), p. 29.
[8] J. A. Barclay, L. Paterson, D. Bingham, and O. Moze, Cryogenics **18**, 535 (1978).

Enhanced spin-density waves in Co-Cr superlattices

Shihui Ge[a] and M. B. Stearns
Department of Physics, Arizona State University, Tempe, Arizona 85287

The electrical resistivity of a series of Co-Cr multilayered thin films (MLS) of equal layer thickness of ~30–30 Å made at various substate temperatures and deposition rates of 0.5 and 2 Å/s was measured over the temperature range of 4.2–350 K. The most striking feature seen in several of these MLS was that the bump near the Néel temperature T_N of the spin-density wave (SDW) of Cr was 2–4 times greater than that seen in *Cr*Co alloys. The bump in the MLS is also much sharper than that of the alloys. The resistivity bump and an increase in T_N in the alloys has been attributed to an enhancement of the SDW due to the exchange interaction between the Co moments and the SDW. It is proposed that the even larger enhancement of the SDW in the MLS is due to the superlattice structure of the MLS. This changes the Cr Fermi surface by introducing new Brillouin zones and thus increases the nesting which gives rise to the SDW. The variation of the T_N values of the MLS varies systematically with the substrate temperature. Other similarities and differences between the MLS and the alloys resistivity behavior are discussed.

INTRODUCTION

Because of their application as a recording and storage media the properties of thin films of Co-Cr alloys have been studied extensively in recent years. Since thin multilayered structures (MLS) allow the opportunity of achieving greater structural variety than alloys, MLS of Co-Cr are of special interest for both their potential practical use as well as for their inherent scientific behavior. The magnetic and structural properties of Co-Cr MLS have been previously studied by x-ray scattering,[1,2] magnetization measurements,[1,3] and ferromagnetic resonance (FMR).[4] Here we report on the unusual resistivity behavior found in certain MLS of layer thicknesses of about 30 Å Co–30 Å Cr, indicating the presence of enhanced spin-density waves.

Since the 1960s several groups have extensively studied the resistivity of Co-Cr alloys.[5–10] The magnetic contribution is manifest as a bump in the resistivity near the Néel temperature T_N. Defining T_N to be the inflection point in this bump it was found[7,8] that, upon the addition of Co to Cr, T_N first decreases up to ~2 at. % Co; it then increases up to ~4 at. % Co after which it again decreases. It has been proposed[10] that the oscillatory behavior of T_N is due to competition between scattering by the magnetic impurities (which decrease T_N) and an exchange enhancement of the electron-hole pairing or nesting of the Fermi surface by the exchange coupling between the magnetic impurity moments and the SDW (which increases T_N). Susceptibility measurements indicate that the magnetic moment of Co is strongly coupled to the SDW.[11]

Other workers[9,12] have attributed the rise in T_N above 2 at. % Co to the increased stability of the SDW with Co content since neutron scattering experiments have shown[13] that the SDW becomes commensurate at Co concentrations greater than 2 at. % Co.

We have found a similar, but greatly enhanced bump in the resistivity for several MLS. A comparison between the resistivity behavior of the MLS and alloys is discussed below.

SAMPLE PREPARATION AND MEASUREMENTS

The Co-Cr MLS were prepared by evaporation in a UHV system having two water-cooled, shrouded *e*-beam guns and a reciprocating shutter.[1,13] A high-speed 8-in. Varian cryopump provides a base pressure of $\sim 5\times 10^{-10}$ Torr. The ambient pressure during deposition depends on the deposition rate and is typically about 10^{-8} Torr at a rate of ~1 Å/s. The materials used in the evaporization were 99.95% pure cubes of the elements ~1 cm on a side. The films were deposited onto *p*-type oxidized single-crystal (100) Si substrates. The temperature of the substrate, T_s, was varied between 173 and 573 K and the deposition rates used were 0.5 and 2 Å/s. The resistivity samples were prepared in the shape of a dumbbell having a small connecting area. In order to investigate the deposition distribution and the reproducibility of the measurements, two resistivity specimens were fabricated in each sample fabrication. As seen below, the two specimens gave similar resistivity behavior.

The resistivity was measured on the dumbbell-shaped samples using the standard four-terminal method. A sample holder incorporating four spring-loaded probes provided good, reproducible contacts to the MLS. The profile of the cross-sectional rod of the sample was determined using a DEKTAK II profilometer. The center rod of the dumbbell which defines the geometry of the sample had typical dimensions of a length of 3.5 mm with a width of 1 mm and a thickness of ~3000 Å. The errors in widths and thicknesses could be quite large so that it is estimated that the cross-sectional area was known to only ~10%–20%. Thus the absolute resistivies are less well known compared to the relative resistivities which are estimated to be known within 0.5%. The temperature of the sample was varied from 4.2 to 300 K in a Janis Supervaritemp Dewar. The sample was placed in an oven for higher-temperature measurements. We limited the temperature to 350 K since we did not want to

[a] This work was done when on leave from Department of Physics, Lanzhou University, Lanzhou, Gansu, People's Republic of China.

 0021-8979/88/084297-03$02.40 © 1988 American Institute of Physics

TABLE I. Summary of fabrication conditions and T_N, T_{max}, $\rho(77\,K)$, and $\Delta\rho/\rho_{max}$ values for nominally 30–30 Å Co-Cr MLS. (RT denotes room temperature.)

MLS	T_s (K)	T_N (K)	$T_N - T_{max}$ (K)	$\rho(77\,K)$ ($\mu\Omega$ cm)	$\Delta\rho/\rho_{max}$ (%)
		Deposition rate of 2 Å/s			
CO44	573	260	24	52.5	6.6
CO43-1	523	262	24	53	4.9
CO43-2	523	258	21	58 (RT)	4.9
CO42	473	295	18	49	2.9
CO41	423	307	9	52	0.7
CO40-1	373	327		44	None
CO40-2	373	312	9	46	0.3
CO36-1	313	311	43	94	12.5
CO36-2	313	314	38	73	9.8
CO37-1	313	298	12	47	3.6
CO37-2	313	285	12	47	1.3
CO39-1	273	270		43.5	None
CO39-2	273	283		50 (RT)	None
		Deposition rate of 0.5 Å/s			
CO31	523	281	30	62	9.8
CO29	473	293	9	36	0.7
CO28	423	312	11	41.5	1.2
CO30	373	322	25	58	5.3
CO33	273	281	23	58	1.2
CO32	173	291	41	104	3.3

diffuse the interfaces of the MLS. We had determined that this was a safe temperature from FMR measurements and magnetization measurements.

RESULTS AND DISCUSSION

The values of T_s, T_N, the difference between T_N and the temperature at which ρ_{max} occurs, $T_N - T_{max}$, the resistivity at 77 K, $\rho(77\,K)$ and the size of the bump, $B = (\rho_{max} - \rho_{min})/\rho_{max}$ are tabulated in Table I. The T_N values were determined, as usual, from the minimum of the derivative of the resistivity with respect to temperature, i.e., the inflection point. The most striking feature is the size of the bump in the resistivity of several of the MLS. To put this in perspective it is of interest to compare this size with those of Co*Cr* alloys[5–9] listed in Table II, where it is seen that the maximum value of B for the alloys is 3.3. This is similar to the size of the bump in CO42 which is shown in Fig. 1. As seen in Table I and Fig. 1 the bumps in several of the Co-Cr MLS are 2–4 times larger than those seen in Co-Cr alloys.

In order to compare various other features of the MLS with those of the alloys we list some properties of the alloys in Table II. We see that the $\rho(77\,K)$ values of the MLS are comparable to those of alloys containing 5–8 at. % Co while the $T_N - T_{max}$ values of the MLS are more similar to those of alloys containing 3 at. % Co or less. Thus the bumps in the MLS are much sharper than those of the alloys and the behavior of the MLS is quite different from the alloys in many details.

In column 3 of Table I we list the T_N values as a function of T_s. It is seen that they have a systematic variation with T_s, maximizing slightly above the T_N of pure Cr for a T_s of

TABLE II. Relative bump height, $\Delta\rho/\rho_{max}$, and $\rho(77\,K)$ for Co-Cr alloys.

at. % Co	T_N (K)	T_{max} (K)	$T_N - T_{max}$ (K)	$\rho(77\,K)$ ($\mu\Omega$ cm)	$\Delta\rho/\rho_{max}$ (%)	Reference
0	313			1.0	0.8	6
1	290	280	10	9.6	1.0	8
3	304	280	26	24.5	2.4	8
3.4	304	275	29		1.65	9
3.5	316	275	41	29.0	2.3	6
4.4	308	260	48	35.3	3.1	6
4.4	301	265	36		2.3	9
5	247	235	62	49.9	3.3	8
6.2	290	220	70	44.5	3.0	6
6.5	267	218	49		3.2	9
8	250	180	70	50.8	3.3	6
8	260	190	70	53.0	3.3	8

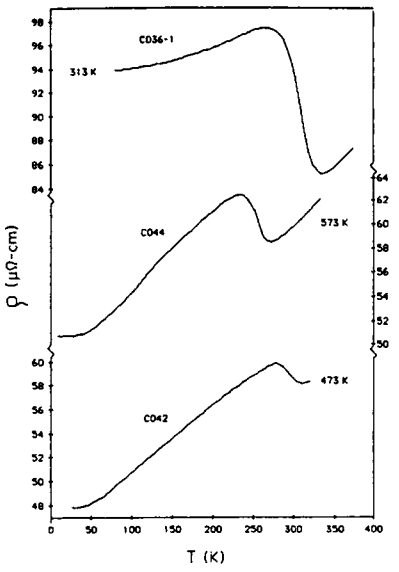


FIG. 1. Temperature dependence of the resistivity of a series of nominally 30 Å Co–30 Å Cr MLS made at different substrate temperatures at a deposition rate of 2 Å/s.

~373 K. The variation is seen to be similar for the two deposition rates. The range of T_N values is similar to that seen in Co*Cr* alloys.

There is often a low-temperature inflection point near 100 K in the slope $\Delta\rho/\Delta T$. This may simply be caused by the conductivity at low temperatures being limited by interfacial scattering. Or it could be due to the planar geometry of the Cr layers in the MLS which might strongly enhance the difference in scattering from the longitudinal and transverse SDW's. Neutron scattering experiments should be able to determine which mechanism is occurring.

As seen from Table I there seems to be no correlation of the size of the bump B with T_s or T_N. However there does seem to be some correlation with the magnitude of ρ(77 K), i.e., the MLS having larger ρ tend to have larger B values. We have recently been able to completely characterize the structure of the MLS by modeling the large-angle x-ray θ-2θ scattering spectra of the MLS. This procedure will be described elsewhere. Such analyses show that these nominally 30-Å/30-Å MLS are composed of aggregates of three types of small crystallites having lengths and orientations in the direction of growth of ~150 Å with layers of [110]Cr and [10.1]Co, ~50 Å (for 2 Å/s) and ~100 Å (for 0.5 Å/s) of pure [00.2]Co and/or [110]Cr crystallites, and ~25 Å of [10.0] Co. The columnar structure of the MLS has also been seen in high-resolution TEM images of one of these MLS.[2] Thus the rather random occurrence of samples having large values of B is believed to be due to the chance formation of regions of connected layered structures across the neck of the dumbbell. Any crystallites of pure material will tend to short out the higher resistance of the MLS unless an MLS region exists completely across the width of the neck of the sample. Thus the samples having larger values of B should have higher resistivities as observed. We have also found that we do not get large B values in any samples having neck widths of greater than 1 mm. If this is the correct explanation of the random occurrence of high B values it is likely that we have thus far only seen quite reduced values from those present in the MLS. We expect to see even greater resistivity bumps in MLS having narrower necks. Moreover, from the structural computer analysis of the x-ray scattering spectra of Co-Cr MLS of various thicknesses we have found that MLS having layer thicknesses of 15–20 Å grow with both superior alignment of the MLS and much fewer pure crystallites present. Thus MLS of these thicknesses should also give higher B values. We are in the process of verifying this explanation by both reducing the neck width of present samples by ion milling and by growing new samples with reduced neck widths and layer thicknesses ~15–20 Å.

The enhancement of the SDW in alloys, over that in pure Cr, has been attributed to the effects of the exchange interaction between the Co moments and the SDW.[10] Such an effect would also be expected to occur in the MLS due to the proximity of the ferromagnetic Co to the Cr layers. It is proposed that the increased enhancement of the SDW in some of the MLS, over that in the alloys, is due to the superlattice structure which introduces new Brillouin zones and thus causes an increased nesting of the Fermi surface of Cr. Thus this effect is of special interest since it would be one of the few cases in which real superlattice effects are seen in metallic multilayer systems.

ACKNOWLEDGMENTS

We wish to acknowledge that the MLS samples were fabricated by C.H. Lee. Partial support of this work was given by Energy Conversion Devices, Inc. of Troy, MI. This work was also partially supported by the National Science Foundation, Grant No. DMR-8610863.

[1]M. B. Stearns, C. H. Lee, and S. P. Vernon, J. Magn. Magn. Mater. **54-57**, 791 (1986).
[2]M. B. Stearns, C. H. Lee, C.-H. Chang, and A. K. Petford-Long, in *Metallic Multilayers and Epitaxy*, edited by M. Hong (TMS, Warrendale, PA, 1987).
[3]A. Walmsley, J. Thompson, D. Friedman, R. M. White, and T. H. Geballe, IEEE Trans. Magn. **MAG-19**, 1992 (1983).
[4]B. L. Ramakrishna, C. H. Lee, Y. Cheng, and M. B. Stearns, J. Appl. Phys. **61**, 4290 (1987).
[5]S. Arajs, G. R. Dunmyre, and S. J. Dechter, Phys. Rev. **154**, 448 (1967).
[6]S. Arajs and G. R. Dunmyre, J. Appl. Phys. **38**, 1157 (1967).
[7]S. Arajs, K. V. Rao, H. U. Astrom, and T. F. De Young, Phys. Scr. **8**, 109, 1973.
[8]S. Katano, M. Mori, and K. Nakayama, J. Phys. Soc. Jpn. **48**, 192 (1980).
[9]L. De Koning, H. L. Alberts, and S. J. Burger, Phys. Status Solidi A **62**, 371 (1980).
[10]M. M. Antonoff, J. Magn. Magn. Mater. **15-18**, 277 (1980).
[11]F. T. Hedgcock, J. O. Strom-Olsen, and D. F. Wilford, J. Phys. F **7**, 855 (1977).
[12]Y. Endoh, Y. Ishikawa, and H. Ohno, J. Phys. Soc. Jpn. **24**, 263 (1968).
[13]C. H. Lee, Ph.D. thesis, Arizona State University, 1987.

Magnetoresistance of very thin cobalt-gold multilayers with perpendicular anisotropy

C. Dupas, J. P. Renard, J. Seiden, and E. Vélu
Institut d'Electronique Fondamentale, Centre National de la Recherche Scientifique UA 22, Bât. 220, Université Paris-Sud, 91405, Orsay Cédex, France

D. Renard
Institut d'Optique, Centre National de la Recherche Scientifique UA 14, Bât. 503, Université Paris-Sud, 91405, Orsay Cédex, France

We report magnetoresistance (MR) measurements on Au/Co/Au sandwiches and Au/Co/Au multilayers, deposited on polished glass substrates in ultrahigh vacuum, with Co thickness ranging between 3 and 30 Å. The experiments were performed at room temperature in the field range 0–0.8 T and at low temperature 1.3–4.2 K in the field range 0–5 T for different field orientations with respect to the film and to the current. For Co thickness below 11 Å, the experimental data are consistent with an easy axis perpendicular to the film, in agreement with previous ferromagnetic resonance and magnetization measurements. From the hysteretic behavior of the MR, coercive fields of a few 10^2 Oe at room temperature are observed. In Co bilayers, the MR is enhanced with respect to the MR of simple sandwiches and indicates a square hysteresis loop. The abnormally large MR of the ultrathin Co films is attributed to a Co/Au interface resistance related to walls between Co domains with alternating perpendicular magnetization.

We present here magnetoresistance studies of ultrathin films of cobalt, consisting of a few atomic layers sandwiched between thicker gold layers which extend our previous work on three samples.[1] Previous SQUID measurements of remanent magnetization parallel and perpendicular to the film plane[2,3] and ferromagnetic resonance (FMR) experiments[3,4] have shown that the Au/Co/Au (111) sandwiches with a cobalt thickness less than 11 Å have an easy axis perpendicular to the film plane. This interesting feature is not usual for ferromagnetic films. Indeed, the magnetization is generally parallel to the film in order to minimize the demagnetizing field. In our Co films, out-of-plane interface magnetic anisotropy overcomes the shape anisotropy which favors the in-plane magnetization, when the Co thickness becomes smaller than 11 Å.

The aim of this work is to confirm the perpendicular orientation of the spontaneous magnetization of ultrathin Co films by magnetoresistance (MR), which is a simple technique well suited to metallic magnetic thin films[5] and to obtain information on some important characteristics of the films such as the coercive field. The experiments were performed on simple sandwiches Au/Co/Au with Co thickness t_{Co} ranging from 3.2 to 30 Å and on Co bilayers Au/Co/Au/Co/Au with $t_{Co} \simeq 8$ and 30 Å and gold interlayer spacing t_{Au} ranging from 15 to 400 Å. The samples are prepared by slow evaporation in ultrahigh vacuum (starting pressure of about 10^{-10} Torr) onto a glass substrate with very small surface roughness (5 Å). The film thickness is monitored by a quartz oscillator during deposition. The first Au layer (thickness 250 Å) consists of large polycrystals (typical lateral dimensions 2000–3000 Å) with random orientations in the plane of the film but with a (111)-oriented surface. The surface exhibits terraces with monoatomic steps. The characterization of these sandwiches is performed by *in situ* resistivity, followed by post-deposition grazing x-ray diffraction and by transmission electronic microscopy (TEM). The TEM results obtained on a 80-Å-thick Co film show that the Co film on Au(111) is hcp with the c axis perpendicular to the film.[6] The sandwiches have sharp interfaces and good crystallinity. The upper Au layer (250 Å thick) protects the sample against oxidation. In order to measure their resistance R, the samples were cut to the following dimensions: 1×10 mm^2. Electrical contacts were made by sticking gold leads with silver paint on the top gold covering. Four-points measurements were performed with an ac bridge operating at low frequency (32 Hz), with very weak power dissipation (10^{-8}–10^{-9} W and high precision ($\delta R/R = 10^{-5}$–10^{-6}). The MR was measured both at room temperature in the field range 0–0.8 T and at low temperature (1.3–4.2 K) for magnetic fields in the range 0–5 T. Several field orientations with respect to the film plane and the electric current could be obtained. In this article, we will use the following notations: $H_\perp$ for a field perpendicular to the film plane, and H_t for a transversal fields, i.e., in the film plane but perpendicular to the electric current.

In the samples studied, the electrical conductivity is mainly determined by the gold layers which are much thicker than the cobalt layers. Indeed, the room-temperature value of the resistance before any thermal cycling is close (to within 10%) to that of a pure gold sample having the same geometry. Owing to this fact, it is very suprising that the magnetic behavior of the cobalt layers (first magnetization curve, hysteresis) is clearly seen in the MR. The MR of sandwiches with $t_{Co} < 8$ Å is rather different for $H_\perp$ and H_t. A marked hysteresis in $R(H)$ is observed, as shown in Fig. 1. R reaches a maximum value, which is slightly smaller than the initial value in zero field, at a field which is likely close to the coercive field H_c. At low temperature, for fields much larger than H_c, a parabolic dependence $R^*(H) = R(0) + aH^2$, classical for a metal, is observed. Co contri-

 0021-8979/88/084300-03$02.40 © 1988 American Institute of Physics

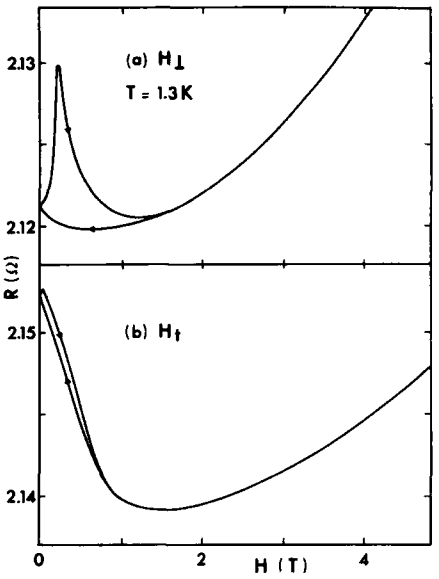


FIG. 1. Magnetoresistance of a Au/Co/Au sandwich with $t_{Co} = 7.6$ Å at 1.3 K for magnetic fields (a) perpendicular ($H_\perp$) and (b) transversal ($H_\parallel$). In high field, $H > 2$ T, the parabolic magnetoresistance of gold is observed.

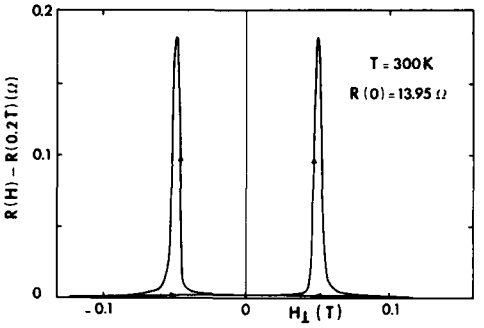


FIG. 2. Room-temperature perpendicular magnetoresistance of a Co bilayer, Au/Co/Au/Co/Au with $t_{Co} = 7.5$ Å and $t_{Au} = 30.4$ Å. The coercive field is $H_c = 493$ Oe and $\Delta R(H_c)/R(0) = 1.3$ %.

bution to the magnetoresistance can be obtained as $\Delta R(H) = R(H) - R^*(H)$. An estimation of the magnitude of the Co MR contribution is given by the ratio $\Delta R_{max}/R(0)$ of the maximum of ΔR at $H = H_c$, to $R(0)$. This ratio can reach a few percent, as shown in Table I, for sandwiches with very thin Co layers and for Co bilayers with $t_{Co} \simeq 8$ Å and $t_{Au} = 30$ and 127 Å. In these bilayers, the hysteretic behavior of $R(H)$ is spectacular since the peaks of R at $H = H_c$ are very narrow, especially at room temperature (Fig. 2). Furthermore, the zero-field Co contribution $\Delta R(0)$, after having put the sample in a high field, is close to zero. These features strongly suggest that the perpendicular magnetization has a perfectly square hysteresis loop, which is characteristic of ferromagnets with strong uniaxial anisotropy. In constrast, for the same samples, the MR in field $H_\parallel$ parallel to the film plane shows a smooth field variation and little hysteresis (Figs. 1 and 3). This clearly confirms the perpendicular orientation of the spontaneous magnetization in the thinnest Co films.

Some general trends can be inferred from Tables I and

TABLE I. Low-temperature main characteristics of the thin Co films magnetoresistance. The data are given at 4.2 K except for the two thinnest films with 3.2 and 3.7 Å, for which the data are at 1.3 K. Notice the decrease of the cobalt contribution to MR and the decrease of the coercive field H_c with increasing the cobalt thickness t_{Co}.

	t_{Co} (Å)	t_{Au} (Å)	$\Delta R_{max}/R(0)$	H_c (Oe)
Sandwiches	3.2		2.2×10^{-2}	5380
Au/Co/Au	3.7		1.4×10^{-2}	4730
	7.5		5.3×10^{-3}	2180
	8.1		5×10^{-3}	4300
	30		3.2×10^{-4}	140
Bilayers	8.2	7.7	1.1×10^{-3}	930
Au/Co/Au/Co/Au	7.5	30.4	3×10^{-2}	1650
	33	15	3×10^{-3}	137

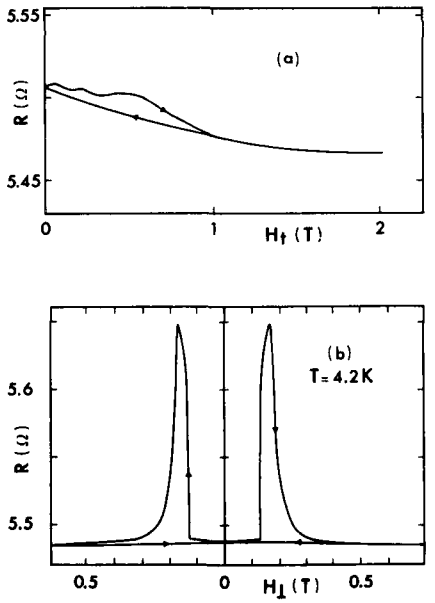


FIG. 3. Magnetoresistance of a Co bilayer Au/Co/Au/Co/Au with $t_{Co} = 7.5$ Å and $t_{Au} = 30.4$ Å at 4.2 K for (a) $H_\parallel$ and (b) $H_\perp$. Notice the square hysteresis for perpendicular field orientation and the large MR of this sample $\Delta R_{max}/R(0) = 3\%$.

TABLE II. Main characteristics of the thin Co films magnetoresistance at room temperature. The $\Delta R_{max}/R(0)$ values for sandwiches are approximative because the MR peaks around H_c are broad and the field range too restricted for allowing the accurate determination of the high-field MR behavior.

	t_{Co} (Å)	t_{Au} (Å)	$\Delta R_{max}/R(0)$	H_c (Oe)
Sandwiches	8.1		3×10^{-4}	600
Au/Co/Au	11.1		2×10^{-4}	430
	30		8×10^{-5}	56
Bilayers	8	15	5.3×10^{-4}	520
Au/Co/Au/Co/Au	7.5	30.4	1.3×10^{-2}	490
	8	127	8.3×10^{-3}	430
	10.3	410	1.2×10^{-3}	520
	33	15	1.3×10^{-3}	60

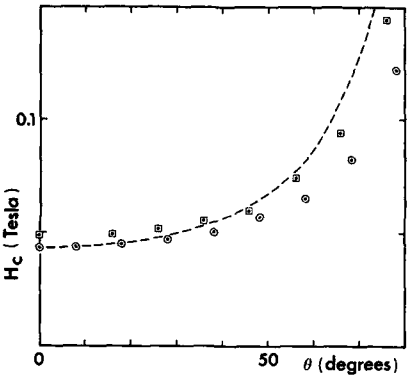


FIG. 4. Angular dependence of the coercive field of two Co bilayers with $t_{Co} = 7.5$ Å, $t_{Au} = 30.4$ Å and with $t_{Co} = 8$ Å, $t_{Au} = 127$ Å at room temperature. $\theta = 0$ corresponds to perpendicular orientation. The dashed curve is $H_c(\theta) = 0.043\times(\cos\theta)^{-1}$.

II, in which the main characteristics of the samples are reported:

(i) For the simple sandwiches, the Co contribution to MR decreases with increasing Co thickness and becomes very small for the films with parallel orientation of the spontaneous magnetization (for $t_{Co} \geqslant 11$ Å).

(ii) In Co bilayers with $t_{Co} \simeq 8$ Å, a Co MR much larger than in simple sandwiches with the same t_{Co} is observed for gold interlayer thicknesses $t_{Au} = 30$ and 127 Å; this "*bilayer enhancement*" is also observed in the sample with $t_{Co} = 33$ Å and $t_{Au} = 15$ Å (Tables I and II).

(iii) The coercive field H_c, at low temperature, is a decreasing function of t_{Co} for small thicknesses. It exhibits the expected decrease with increasing the temperature.

Finally, we show in Fig. 4 the angular variation of the coercive field of two Co bilayers at room temperature. H_c is minimum for perpendicular orientation of the field, $\theta = 0$, which again confirms the perpendicular anisotropy of the films. However the data cannot be perfectly fitted to the simple law $H_c(\theta) = H_c(0)\ (\cos\theta)^{-1}$ which would hold if the parallel field component had no effect on the magnetization.

There is no straightforward explanation for the large MR of the ultrathin Co films embedded in gold. The deviation of the current lines by the alternating induction induced in gold by the Co domains with perpendicular magnetization gives a contribution to MR which is at least 2 orders of magnitude smaller than the experimental data.[1] We suggest that the large Co MR results from a gold-wall interface resistance due to either the deformation by magnetostriction of the atomic array induced by the large magnetic induction in the Co walls, or to an abnormally large density of $3d$ electron virtual bound states near the gold Fermi level, generated by the Co atoms in walls. These mechanisms which will be discussed in details in a forthcoming paper, lead to the following MR contribution:

$$\Delta R/R \sim (\lambda/t)[\Lambda_W/(\Lambda_D + \Lambda_W)] \times |\langle\cos\theta_D - \cos\theta_W\rangle|, \quad (1)$$

where t is the whole thickness of the sample, θ_D and θ_W the average deviation of an electron crossing, respectively, a domain and a wall, Λ_D and Λ_W the respective lateral size of a domain and a wall, and λ the electron mean free path.

Assuming physically reasonable values for the parameters: $\Lambda_D = 2000$ Å, $\Lambda_W = 20$ Å and $|\langle\cos\theta_D - \cos\theta_W\rangle| \simeq 0.5$, relation (1) gives $\Delta R/R \simeq 10^{-2}$, which can account for the experimental results.

In conclusion, we have confirmed by magnetoresistance measurements the perpendicular anisotropy of the ultrathin hcp Co films on Au(111), and we have determined the coercive field of these films. The strong contribution of Co to MR is probably related to the walls between the Co domain with alternating perpendicular magnetization. This assumption has to be checked by further experiments on other metallic multilayers such as fcc Co/Cu for which the perpendicular anisotropy is smaller than for Co/Au (111).[7,8]

[1] E. Vélu, C. Dupas, D. Renard, J. P. Renard, and J. Seiden, Phys. Rev. B (to be published).

[2] C. Chappert, D. Renard, P. Beauvillain, J. P. Renard, and J. Seiden, J. Magn. Magn. Mater **54-57**, 795 (1986); C. Chappert, Ph.D thesis, Université Paris-Sud, Orsay, 1985 (unpublished).

[3] C. Chappert, K. Le Dang, P. Beauvillain, H. Hurdequint, D. Renard, and C. Marlière, *Proceedings of the Conference on Magnetic Thin Films*, Strasbourg, 1986 (Les Editions de Physique, Les Ulis, France, 1986), p. 59.

[4] C. Chappert, K. Le Dang, P. Beauvillain, H. Hurdequint, and D. Renard, Phys. Rev. B **34**, 3192 (1986).

[5] T. R. McGuire and R. I. Potter, IEEE Trans. Magn. **MAG-11**, 1018 (1975).

[6] C. Cesari, G. Nihoul, and D. Renard, Proceedings of the Conference on Magnetic Thin Films, Strasbourg, 1986, Ref. 3, p. 55; D. Renard and G. Nihoul, Philos. Mag. B **55**, 75 (1987).

[7] D. Pescia, G. Zampieri, M. Stampanoni, G. L. Bona, R. F. Willis, and F. Meier, Phys. Rev. Lett. **58**, 933 (1987).

[8] J. P. Renard and P. Beauvillain, Proceedings of the 7th General Conference of the Condensed Matter Division of the European Physical Society, Pisa, 1987 [Phys. Scr. **T19**, 405 (1987)].

Transport and magnetic properties of amorphous $Fe_{80-x}M_xB_{14}Si_6$ (M = Mn, V, Cr)

S. U. Jen and S. M. Yang
Institute of Physics, Academia Sinica, Taipei, Taiwan, Republic of China

A series of amorphous $Fe_{80-x}M_xB_{14}Si_6$ (M = Mn, V, Cr, and $x = 2$, 4, 6, 8, 10, 12, and 14 at. %) alloys have been made by the spinning-wheel method. We have measured the density δ, saturation magnetization M_s, electrical resistivity ρ_0, Hall resistivity ρ_H, and magnetoresistance $\Delta\rho/\rho_0$ of each sample at room temperature. The anomalous Hall coefficient R_s is determined from the relation $\rho_H = R_0B + R_sM_s$. R_s is found to vary as $R_s = A\rho_0^{1.7}$. The density, magnetization, and magnetoresistance are all decreasing functions of x. The Curie temperature T_C is determined from the low-field thermomagnetization data and the Arrott plot. The positive forced magnetoresistivities are discussed from the viewpoint of the current models.

I. INTRODUCTION

In the past, most of the papers dealing with transport and magnetic properties of ferromagnetic metallic glasses are associated with the alloys on the right-hand side of the Slater–Pauling curve.[1-3] In this paper we shall qualitatively discuss the experimental results of a few metallic glasses on the left-hand side. These include amorphous $Fe_{80-x}M_xB_{14}Si_6$ with M = Mn,V,Cr.

For the anomalous Hall effect, the results will be discussed from the viewpoint of the side-jump mechanism.[4] The quantities, such as magnetization, ferromagnetic anisotropic resistance (FAR), and Curie temperature, are all decreasing functions when plotted versus x. The positive forced magnetoresistivities are discussed with comparison of the current models.[5,6] All results presented here are limited to data taken at room temperature, although some of the data at low or high temperatures are also available.

II. EXPERIMENT

A series of amorphous $Fe_{80-x}M_xB_{14}Si_6$(M = Mn,V, Cr,and x = 2,4,6,8, 10, 12, and 14 at. %) alloys have been made by the rapid-quench method. For $x > 14$ at. %, Fe-M alloys are nonferromagnetic at room temperature.

For the electrical resistivity and FAR measurements, the standard four-point technique was employed. We used a stable dc current source (North Hills CS-12) to supply current, and a Keithley 181 nanovoltmeter to measure voltages. Thermoelectric voltages were eliminated by reversing the current and by taking the average. The applied magnetic field in either the perpendicular or the parallel direction was as large as 6 kOe. The FAR is defined as $\Delta\rho/\rho_0 = (\rho_\parallel - \rho_\perp)/(\frac{1}{3}\rho_\perp + \frac{1}{3}\rho_\parallel)$,[7] where $\rho_\perp$ is the saturation value of the resistivity in perpendicular field, and $\rho_\parallel$ is that in parallel field. The forced magnetoresistivities $1/\rho(\partial\rho/\partial B)_\perp$ and $1/\rho(\partial\rho/\partial B)_\parallel$ are determined from the slopes of each $\rho_\perp$ and $\rho_\parallel$ versus external field ($B = \mu_0 H$) plot.

For the Hall-effect measurements, all leads were welded on the top surface and an additional Hall probe was used with a potentiometer to eliminate misalignment voltages. The measurements of Hall voltage V_H is repeated after reversing B and I. Then, the Hall resistivity is calculated as[8]

$$\rho_H = (wt/4Id)[V_H(+B,+I) - V_H(+B,-I) - V_H(-B,+I) + V_H(-B,-I)], \quad (1)$$

where w and t are the thickness and the width of the sample, and d is the separation between Hall probes. Both t and d are measured with a micrometer and a translation stage, and w is calculated from the density and the mass of each sample. From the ρ_H-vs-B curve, we determined the anomalous Hall coefficient R_s by extrapolation of the relation $\rho_H = R_0B + R_sM_s$ back to $B = 0$. Because the field was not sufficiently large ($B < 18$ kG), R_0 was left undetermined. The Hall conductivity is defined as $\gamma_H \equiv \rho_H/\rho_0^2$.

The magnetic moment of each sample was measured with a vibrating sample magnetometer. For high-temperature measurements an oven assembly (model 151) was used. Each sample was in an argon atmosphere and the heating rate is about 1 K/min. In principle, the Curie temperature of each sample was determined from each corresponding low-field thermomagnetic curve. At one point, we have also performed more-detailed measurements and the Arrott plot was used to determine the Curie point of one of the samples.

TABLE I. The density δ and the electrical resistivity ρ_0 of $Fe_{80-x}M_xB_{14}Si_6$(M = Mn,Cr,V) glasses at room temperature.

x	δ(g/cm^3)			ρ_0 ($\mu\Omega$ cm)		
(at. %)	Mn	Cr	V	Mn	Cr	V
2	7.55	7.4	6.5	168.93	120.01	140.78
4	7.54	7.4	···	138.71	118.97	···
6	7.53	7.39	6.1	167.03	125.74	160.01
8	···	7.39	5.9	···	118.46	146.59
10	7.51	7.39	5.7	164.61	121.44	220.13
12	7.50	7.2	···	147.12	125.15	···
14	7.49	···	5.5	111.30	···	158.87

 0021-8979/88/084303-03$02.40 © 1988 American Institute of Physics

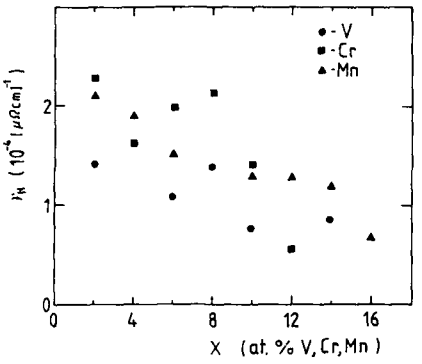


FIG. 1. Hall conductivities for amorphous $Fe_{80-x}M_xB_{14}Si_6$ at room temperature.

III. RESULTS AND DISCUSSIONS

Table I shows the density and the electrical resistivity of each sample at room temperature. The density is, in general, a decreasing function of x. However, there does not seem to exist a definite relationship between ρ_0 and x. The uncertainty of ρ_0 may still result from the sample thinness, about 10–15 μm, and from residual irregular surface.

The compositional dependence of γ_H at room temperature is shown in Fig. 1 for each series of M = Mn,Cr,V glasses. γ_H roughly varies from 2.0 to 1.0×10^{-4} $(\mu\Omega\ \mathrm{cm})^{-1}$. γ_H reported here for the $x\simeq0$ at. % glass is smaller than $\gamma_H\simeq5\times10^{-4}$ $(\mu\Omega\ \mathrm{cm})^{-1}$ quoted from Ref. 1. Since our measurements were carried out at room temperature, the side-jump mechanism[4] is expected to dominate over the skew scattering mechanism. According to the theory of the former mechanism, the anomalous Hall coefficient $R_s = A\rho_0^2$. For our case, ρ_0 of each series of glasses is varied not through a temperature effect but by changing the solute concentration, since in metallic glasses R_s and ρ_0 are almost temperature independent.[9,10] Then, a constant γ_H would imply that A and M_s vary with the alloy compositions. Figure 2 shows data points for varying impurity concentrations of M = Mn,Cr,V. They are fitted with an empirical formula:

$$R_s = A\rho_0^n \qquad (2)$$

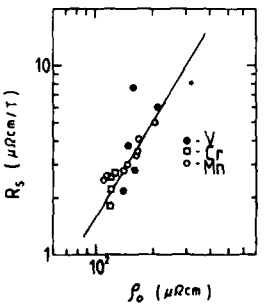


FIG. 2. Double logarithmic plot of the anomalous Hall coefficient R_s vs the electrical resistivity of $(FeM)_{80}B_{14}Si_6$ glasses at room temperature.

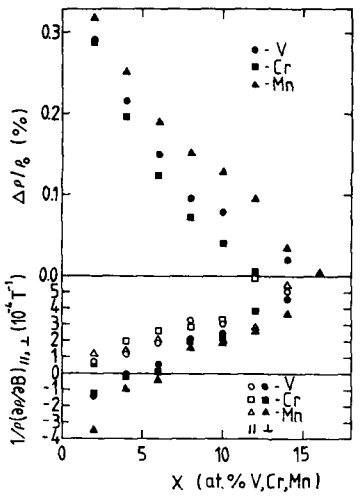


FIG. 3. The FAR ($\Delta\rho/\rho_0$) and the forced magnetoresistivities as a function of concentration X in $Fe_{80-x}M_xB_{14}Si_6$ glasses ($T = 295$ K).

on a double logarithmic plot. Then, from the slope of the fitting straight line $n = 1.7$, close to the value of 2.

Figure 3 shows the summarized results of magnetoresistance data, including the FAR and the forced magnetoresistivities, of each sample at room temperature. The FAR for each series of alloys is seen to decrease with increasing x.

Generally speaking, the $\rho_\perp$ and $\rho_\parallel$ obtained are typical in

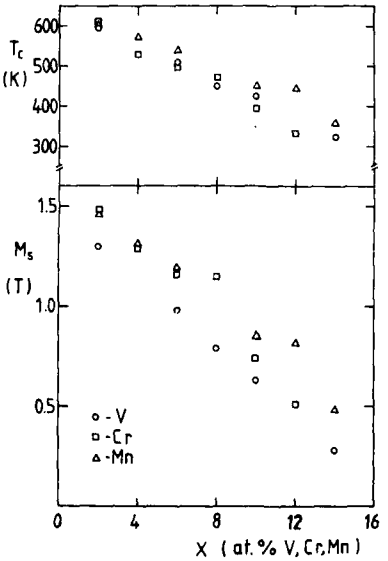


FIG. 4. The magnetization and the Curie temperature of each series of $Fe_{80-x}M_xB_{14}Si_6$ glasses (M = Mn,Cr,V).

that $\rho_\perp$ saturates around $H_d = 1.5$ kOe, $\rho_\parallel$ saturates around $H_d = 0.6$ kOe, and for $B_E > \mu_0 H_d$ a linear field dependence of $\rho_\perp$ and $\rho_\parallel$ is found. Before saturation, the influence on $\rho_\perp$ and $\rho_\parallel$ is purely ferromagnetic in origin in that the actual domain configuration and the intrinsic anisotropic scattering play a role.[11,12] After saturation, we find the values of $1/\rho(\partial\rho/\rho B)_\perp$ are not the same as $1/\rho(\partial\rho/\rho B)_\parallel$. However, the general trend of $1/\rho(\partial\rho/\rho B)$ is the same in that $1/\rho(\partial\rho/\partial B)$ becomes more positive and increases with the concentration as shown in Fig. 3. Since we have made thermal expansion tests on these glasses,[13] together with other evidence,[14] we find that $x < 6$ at. %, Fe-M alloys are Invar alloys. However, because the Invar anomaly disappears for $x > 6$ at. % samples, and $1/\rho(\partial\rho/\partial B)$ increases even for paramagnetic glasses,[15] the forced magnetostriction mechanism does not seem to explain the whole situation of our cases.[5] A member of mechanisms affect $\partial\rho/\partial B$, including the ordinary magnetoresistivity due to the Lorentz force, the eletron-magnon scattering, and the susceptibility related mechanisms.[6] The Lorentz force contribution is positive. However, because of short mean free path in glassy materials, its effect may be small. Because of less electron-magnon scattering with increasing field, $1/\rho(\partial\rho/\partial B)$ is negative. This may explain the negative $1/\rho(\partial\rho/\partial B)$ observed in Fig. 3. Although our field is not large enough to ensure the values of the high-field susceptibility, we do obtain relatively large susceptibility at $B = 5$ kG for these glasses. Then, it is known that Zeeman energy shifts the Fermi levels $\epsilon_F^\uparrow$ and $\epsilon_F^\downarrow$ with increasing field. Similar to Pauli paramagnetism, when the spin-up band is full, $\chi_{HF} = 0$, and when the spin-up band is not, $\chi_{HF}^{-1} \propto D_\uparrow^{-1}(\epsilon_F) + D_\downarrow^{-1}(\epsilon_F)$. Therefore, when adding Mn,Cr,V, the spin-up band becomes more empty (weak ferromagnetic), and χ_{HF} increases with x. This may explain our observation that $1/\rho(\partial\rho/\partial B)$ increases with x. The detailed conditions require the band structure of these materials.

For magnetization data, Fig. 4 shows that both the magnetization M_s and the Curie temperature T_C decreases with increasing x as expected. The Curie temperature is determined from the low-field thermomagnetization curve and, in principle, it is not as accurate as that from the Arrott-plot method. We have noticed that when Arrott plots are used T_C is slightly different for the heating runs and for the cooling runs which may be due to crystallization or structural relaxation.

IV. CONCLUSIONS

We have studied the transport properties, such as the Hall and the magnetoresistance effects, and the magnetic properties, such as magnetization and Curie temperature of $(FeM)_{80}B_{14}Si_6$ metallic glasses (M = Mn,Cr,V). It is concluded that the side-jump mechanism dominates for these materials and is mainly responsible for the anomalous Hall effects. The magnetoresistivity observed has also been qualitatively examined. Further studies require careful annealing for the materials and using sufficiently strong fields.

ACKNOWLEDGMENTS

This work is supported in part by the National Science Council of the Republic of China. Helpful discussions with Dr. L. Berger are mostly acknowledged.

[1] R. C. O'Handley, Phys. Rev. **18**, 2577 (1978).
[2] A. K. Nigam and A. K. Majumdar, Physica **95B**,385 (1978).
[3] Z. Marohnic, E. Babic, and D. Pavuna, Phys. Lett. **63A**, 348 (1977).
[4] L. Berger and G. Bergman, *The Hall Effect and Its Application*, edited by C. L. Chien and C. R. Westgate (Plenum, New York, 1980).
[5] K. Fukamichi, R. J. Gambino, and T. R. McGuire, in Proceedings of the 4th International Conference on Rapidly Quenched Metals, Sendai, 1981, p.835.
[6] A. Hamzic, S. Senoussi, I. A. Campbell, and A. Fert, J. Phys. F **8**, 1947 (1978).
[7] J. P. Jan, in *Solid State Physics*, edited by F. Seitz and D. Turnbull (Academic, New York, 1957), Vol. 5.
[8] A. K. Agarwala, Ph.D. thesis, Carnegie-Mellon University, 1985.
[9] J. Ivkov, Z. Marohnic, E. Babic, and P. Dubcek, J. Phys. F **14**, 3023 (1984).
[10] N. Teoh, W. Teoh, and S. Arajs, J. Phys. Chem. Solids **38**, 919 (1977).
[11] A. K. Agarwala and L. Berger, IEEE Trans. Magn. **MAG-22**, 544 (1986).
[12] A. P. Malozemoff, Phys. Rev. B **32**, 6080 (1985).
[13] Data to be published.
[14] J. Kamarad and Z. Arnold, J. Magn. Magn. Mater. **23**, 69 (1981).
[15] R. Kern, M. Naka, and U. Gonser, Proceedings on the 4th International Conference on Rapidly Quenched Metals, Sendai, 1981, p.847.

A new type of high-resistive soft magnetic amorphous films utilized for a very high-frequency range

H. Karamon
Sony Magnetic Products, Research and Deve' opment Division, Tagajo, Miyagi 985, Japan

A new type of high-resistivity soft magnetic amorphous alloy film with a very fine two-phase heterostructure was found in cosputtered Fe-B-C films. These amorphous films are found to have a number of superior properties in the high-frequency range (over ~ 10 MHz) over not only regular amorphous films, but also sendust film cores, which have already been applied to high-density recording media having high coercivity. They were found to exhibit unique isotropic soft magnetic B-H curves with high B_s ($\sim$15 000 G), low H_c ($\sim$0.3 Oe), and high ρ ($\sim$300 $\mu\Omega$ cm), and the reduced magnetization versus reduced temperature curve was almost the same as the $j = \infty$ curve of the Brillouin function. A very high permeability with less core loss, especially in the high-frequency range, was also experimentally observed in those amorphous films.

INTRODUCTION

There has long been an interest in high-density recording technology, but recently this topic has become the subject of intensive study. In the field of magnetic recording, ferrite heads, connected with oxide media, have been in great use for a long period of time. On the other hand, metal heads[1,2] for use with high H_c metal media,[3,4] utilizing metallic materials such as sputtered sendust and single-phase amorphous films (regular type), have only recently been introduced in order to achieve high-density recording. Recently, the trend in magnetic recording technology is shifting away from the familiar analog recording to digital recording in order to obtain a higher recording density and higher performance. Accordingly, it is necessary to operate over the approximately 50 MHz range at the shortest wavelength because of the tendency towards higher frequency and higher recording density, employed in the digital recording system (Digital High Definition VTR, for example).[5] There exists a great deal of core loss in such a high-frequency range, and the metal heads, which have already been introduced, show a large amount of reduction in the reproduced characteristics. On the other hand, ferrite heads have an associated problem when applied to high-density recording technology, that is, the low B_s of soft magnetic ferrites makes them incompatible with metal media. In order to solve those two major problems, a new type of high-resistive metal film with high B_s, coupled with a small core loss in the high-frequency range, was developed for high-density digital recording. These high-resistive metal films possess a very fine two-phase heteroamorphous structure, combining properties such as high B_s and high permeability in the high-frequency range. Some of the unique properties of the new type of two-phase heteroamorphous films, compared with the regular single-phase amorphous films, will be reported in the next section.

EXPERIMENTAL PROCEDURE

Amorphous Fe-B-C films were deposited by rf magnetron cosputtering onto fotoceram substrates, using $5\times5\times2$ mm^3 boron carbide (B_4C) chips placed on a 100 mmϕ pure iron target. The system was initially evacuated down to approximately 1×10^{-6} Torr before introducing Ar gas, and setting the sputtering Ar gas pressure to a required pressure in the range between 1 and 7×10^{-2} Torr. The vertical distance between the water-cooled electrodes was 40 mm. The rf power and Ar mass flow were kept constant at 300 W and 1 cm^3/min, respectively. The saturation magnetic induction (B_s) and coercivity (H_c) were measured by a vibrating sample magnetometer and the temperature dependence of saturation magnetization in the range 77–900 K was obtained with a Faraday-type magnetic balance. The crystalli-

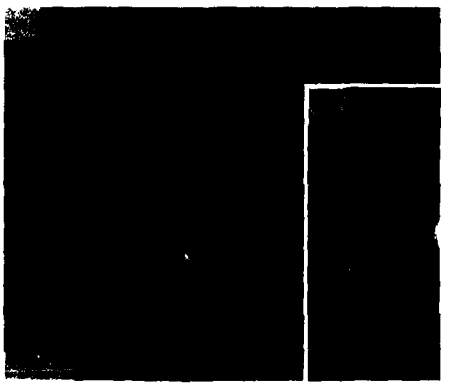


FIG. 1. Lorentz electron micrographs of a $Fe_{80}B_{14}C_6$ heteroamorphous film. (Accelerating voltage 200 kV.) (a) Dark-field image. (b) Diffraction pattern.

 0021-8979/88/084306-03$02.40 © 1988 American Institute of Physics

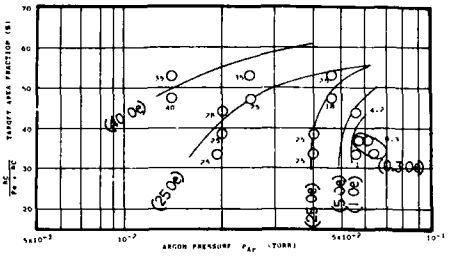


FIG. 2. Variation of coercivity (H_c) of the sputtered two-phase heteroamorphous films (Fe-B-C) with Ar pressure and target area fraction.

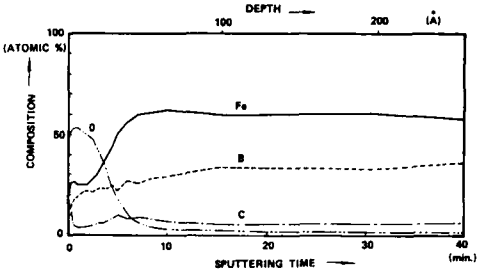


FIG. 4. A depth profile of the particular sample showing remarkably soft magnetic properties ($B_r = 14\,500$ G, $H_c = 0.3$ Oe, $\rho = 400\ \mu\Omega$ cm).

zation and Curie temperature were also derived from the above data. Specific resistivities (ρ) were measured by the four-probe method. X-ray diffraction with Co$K\alpha$, ESCA, and transmission electron microscopy were employed to determine and analyze the amorphous structure. The frequency dependence of the effective permeability for the thin-film samples was plotted by a high-frequency permeance meter.[6,7] In the analysis of the amorphous structure owing to the extremely small size of the metal and nonmetal phase regions (~ 50 Å in size), which is beyond the limits of the presently available technology, it was impossible to separately analyze the boron content in the metal phase and the B/C ratio in the nonmetal phase. Therefore, the compositions reported are of the overall composition of both phases.

RESULTS AND DISCUSSION

In the earlier studies we reported that the cosputtered amorphous Fe-B-N films[8] consist of two extremely fine amorphous phases (~ 50 Å in size). Identical structures were also observed in cosputtered amorphous Fe-B-C films, as shown in Fig. 1. Their coercivity and specific resistivity measured for a wide variety of sputtering conditions are shown in Figs. 2 and 3. We report here that the unique soft magnetic properties emerge at some particular data points in the figures. Those values of B_s, H_c, and ρ were measured to be 14 500 G, 0.3 Oe, and 400 $\mu\Omega$ cm, respectively, for the film shown in Fig. 1. The increase of resistivity seems to originate through the coexistence of both very fine nonmetallic and metallic amorphous phases, as shown in Figs. 1 and 3. The appearance of soft magnetic properties with a comparatively small coercivity indicates to us that the movement of magnetic walls is fairly smooth in the case where the nonmetallic amorphous regions are extremely small in size, as shown in Figs. 1 and 2. The crystallization temperature (T_x) and Curie temperature (T_c) determined at this composition are approximately 775 and 715 K, respectively. In addition to this, it is found that T_x is always greater than T_c throughout the range of sputtering conditions. The composition of the remarkably soft magnetic film was determined to be approximately $Fe_{60}B_{34}C_6$ (atomic concentration) from the depth profile of the sample examined by ESCA, as shown in Fig. 4. Figure 5 exhibits a typical B-H curve of the amorphous $Fe_{60}B_{34}C_6$ sample, showing an isotropic nature. The unique isotropic B-H curve seems to be caused by isotropic wall nucleation, originating from the very fine two-phase heteroamorphous structures. Curves of reduced magnetization $M(T)/M(0)$ against reduced temperature T/T_c derived from the Brillouin function $j = \frac{1}{2}$ and ∞ are shown in Fig. 6. As is well known, for large values ($j = \infty$) the expression is the same as the Langevin function, indicating the system behaves in a totally classical manner. For the indicated sample, the experimental curve closely follows the $j = \infty$ curve ($\times$ indication), if we allow a rough extrapolation of the data points from 77 K. It may be said that the result can be caused by the appearance of the unique amorphous structure.

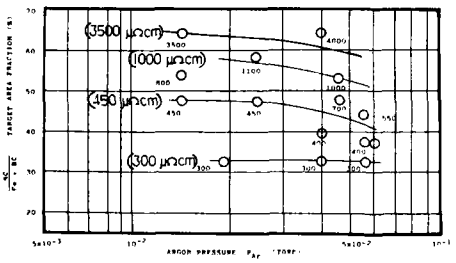


FIG. 3. Variation of specific resistivity (ρ) of the sputtered two-phase heteroamorphous films (Fe-B-C) with Ar pressure and target area fraction.

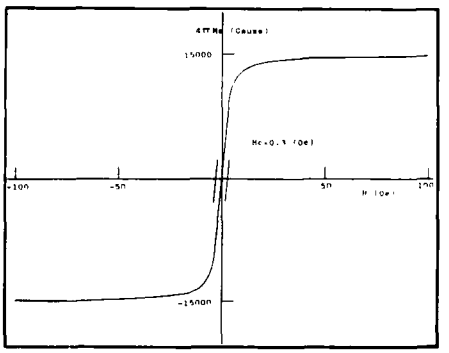


FIG. 5. Typical B-H curve of the two-phase heteroamorphous film indicated in Fig. 4. Those soft magnetic amorphous films show an isotropic nature in B-H curve.

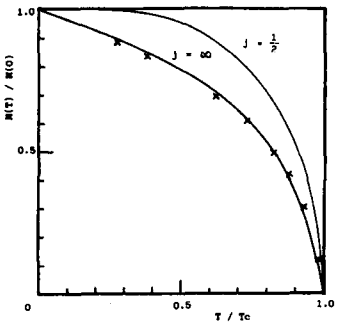


FIG. 6. Curves of reduced magnetization vs reduced temperature derived from the Brillouin function $J = \frac{1}{2}$ and ∞. Those $\times$ indications in this figure represent the same sample exhibited in Figs. 1, 4, 5, and 7.

Figure 7 shows the high-frequency dependence of the permeability. The soft amorphous ribbon and sputtered sendust film, already utilized for metal heads, are employed as a comparison with our unique amorphous films. The best performance on permeability with lowest core loss especially in the high-frequency range can be observed in the new type of amorphous films in the figure.

CONCLUSION

The relation between B_s and ρ for typical low H_c soft magnetic materials utilized for magnetic head cores is shown

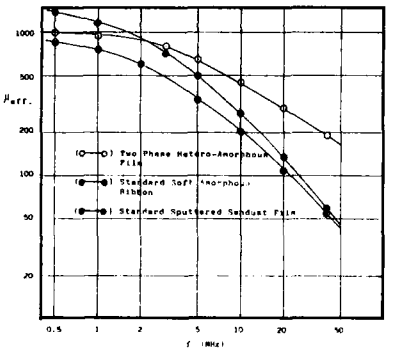


FIG. 7. High-frequency dependence of the effective permeability (measured in the direction of hard axis). (O—O) Sputtered two-phase hetero-amorphous film ($Fe_{60}B_{34}C_6$), 27 μm thick, $B_s = 14\,500$ G, $H_c = 0.3$ Oe. Rotating field annealing (650 K, 15 min, 100 rpm, 6 kG in N_2 gas). (●—●) Standard amorphous ribbon ($Fe_{4.25}Co_{70.25}Si_{12.5}B_9Cr_4$) 27 μm thick, $B_s = 8200$ G, $H_c = 0.02$ Oe. (◎—◎) Standard sputtered sendust film, 27 μm thick, $B_s = 10\,000$ G, $H_c = 0.25$ Oe (annealed at 825 K, 1 h in vacuum).

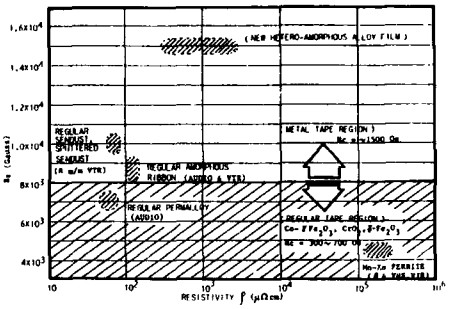


FIG. 8. Collection of data on the typical low H_c soft magnetic materials utilized for head cores, referring to their B_s and ρ properties.

collectively in Fig. 8. To increase the value of B_s, materials are usually required to be metallic, and nonmetallic materials tend to have low B_s. They are, in general, contrary to each other. The new materials, however, fall outside these categories, combining high ρ with high B_s, as shown in Fig. 8. The new amorphous alloy films possessing high B_s and ρ are sufficient enough to satisfy the metal media region, and to perform with an excellent, low core loss capability in the high-frequency range. The process of developing metal heads and utilizing those unique materials is in progress.

ACKNOWLEDGMENTS

The author would like to thank his colleagues at Sony Magnetic Products, R&D Division, Electronic Components Division, and Sony Research Center for many valuable assistance and suggestions. The encouragement provided by the Masumoto Amorphous Project of Research and Development Corp. of Japan is also appreciated.

[1] T. Kobayashi, M. Kubota, H. Satoh, T. Kumura, K. Yamauchi, and S. Takahashi, IEEE Trans. Magn. MAG-21, 1536 (1985).
[2] K. Takahashi, K. Ihara, S. Muraoka, H. Yohda, E. Sawai, and N. Kaminaka, IEEE Trans. Magn. MAG-23, 2928 (1987).
[3] H. Shibaya and I. Fukuda, IEEE Trans. Magn. MAG-13, 1005 (1977).
[4] R. Chubachi and N. Tamagawa, IEEE Trans. Magn. MAG-20, 45 (1984).
[5] Y. Hashimoto, IEEE Trans. Magn. MAG-23, 3167 (1987).
[6] P. A. Calcagno and D. A. Thompson, Rev. Sci. Instrum. 46, 904 (1975).
[7] M. Hayakawa, Sony Res. Bull. 52, 12 (1986).
[8] H. Karamon, T. Masumoto, and Y. Makino, J. Appl. Phys. 57, 3527 (1985).

Effects of hydrogen and nitrogen ion bombardments on soft magnetism of iron films during double-ion-beam sputtering

M. Nagakubo, T. Yamamoto, and M. Naoe
Department of Physical Electronics, Tokyo Institute of Technology, 2-12-1 Oh-okayama Meguro-ku, Tokyo 152, Japan

The dependence of the crystal structure and magnetic properties of iron films on preparation conditions has been investigated in detail by using a double-ion-beam sputtering system. During sputtering of an iron target by argon ions, the growing surfaces of iron films were bombarded by nitrogen or hydrogen ions with different kinetic energies below 500 eV. It has been found that these ions changed significantly the film structure and magnetic properties through the process of collision and reaction with iron atoms at the surface layer of growing film. As a result, the small amount of hydrogen or nitrogen added into iron films by ion bombardment improved effectively the soft magnetic properties of iron films. The iron films with saturation magnetization $4\pi M_s$ as large as 22 kG and coercive force H_c as low as about 5 Oe were prepared by adjusting the accelerating voltage in the range of 100–300 V and the partial pressure of hydrogen or nitrogen in the range of 10^{-4}–10^{-5} Torr.

I. INTRODUCTION

Recently, it has been found that a magnetic layer with large saturation magnetization $4\pi M_s$ and low coercive force H_c is required in the thin-film type of head for achieving high density in a perpendicular magnetic recording system.[1] Pure iron is one of the most suitable materials for such a high-performance head because it has a $4\pi M_s$ as large as 21.5 kG and permeability as high as several hundreds.

However, the magnetic properties are remarkably affected even by the small amount of gaseous and metallic elements included in the films. Therefore, the apparatus with good controllability for the content of these elements in films is necessary for improving the soft magnetic properties of iron thin films. For this propose, the double-ion-beam sputtering method is much more useful than conventional sputtering methods because it can control the ions for sputtering the target and ones for bombarding the film surface, independently and separately.[2,3]

In this study, both hydrogen and nitrogen were used as additional elements for bombarding the growing surface layer separately. Hydrogen is very interesting as an additional element because of its active deoxidization and small radius, leading to a large diffusion constant in iron. On the other hand, nitrogen is necessary for synthesizing the iron-nitride such as γ'-Fe_4N and Fe_8N with $4\pi M_s$ larger than that of pure iron.[4,5]

Therefore, the effects of bombardment and addition of these elements to the crystal structure and magnetic properties of iron thin films have been investigated in detail.

II. EXPERIMENT

Figure 1 shows the schematic diagram of the double-ion-beam sputtering apparatus used in this study. The ion sources are Kaufman type with two grids. Pure argon was introduced through the main ion source into the chamber to the pressure of 1×10^{-4} Torr. The main ion source sputtered a pure iron target with 99.99% purity under the conditions of a constant accelerating voltage V_{mg} of 500 V and a constant ion current of 4 mA. The deposition rate under these conditions was 14 Å/min. All films were deposited without a magnetic field. The auxiliary ion source bombarded the growing film surface on the water-cooled glass slides at various accelerating voltages V_{ag} below 500 V. Either a mixture of argon and hydrogen ($Ar + H_2$) or argon and nitrogen ($Ar + N_2$) was introduced to the pressure of 1.8×10^{-4} Torr. The ratio in percentage of hydrogen and nitrogen partial pressure to total pressure of gas mixture will be represented by R_{H_2} and R_{N_2}, respectively. In order to control the nitrogen content in iron films, R_{N_2} was changed from 10% to 100% under the condition of current density I_d of 20 μA/cm^2. On the other hand, in order to investigate the bombarding effect of argon and hydrogen ions, I_d was ranged at 10, 20, and 100 μA/cm^2 under the condition of R_{H_2} of 50%.

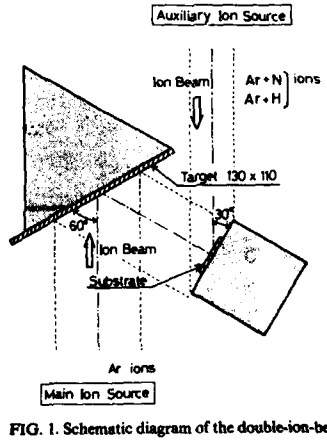


FIG. 1. Schematic diagram of the double-ion-beam sputtering apparatus.

 0021-8979/88/084309-03$02.40 © 1988 American Institute of Physics

The thickness of specimen films was approximately 3000 Å. The composition and crystal structures of the films were analyzed by means of x-ray diffractometry and XMA, respectively. $4\pi M_s$ and H_c were determined on the hysteresis loops observed by using VSM.

III. RESULTS AND DISCUSSION

A. Films bombarded by argon and hydrogen ions

Figure 2 shows the dependencies of saturation magnetization $4\pi M_s$ and coercive force H_c on accelerating voltage V_{sg}. The magnetic properties of iron thin films changed significantly with V_{sg} and current density of argon and hydrogen ions bombarding the film surface I_d.

$4\pi M_s$ took the maximum value of about 21 kG when I_d was 20 μA/cm^2. The films bombarded by only argon ions ($R_{H_2} = 0\%$) and the films bombarded by argon and hydrogen ions at I_d of 100 μA/cm^2 showed $4\pi M_s$ below 20 kG.

H_c of the films bombarded by only argon ions was about 6.5 Oe and did not apparently depend on V_{sg}. On the other and, when R_{H_2} and I_d were 50% and 100 μA/cm^2, respectively, H_c increased monotonicaly with V_{sg}. However, when I_d was 20 and 10 μA/cm^2 at R_{H_2} of 50%, H_c took the minimum value below 5 Oe at V_{sg} of 100 and 300 V, respectively.

Each of the films having a different H_c also showed different x-ray diffraction diagrams. H_c looked to be in proportion to the intensity of the diffraction peak from (110) plane of α-Fe. The films with the lower H_c showed the x-ray diffraction diagrams with the broader and smaller peaks.

The iron thin films with a minimum H_c of below 5 Oe and maximum $4\pi M_s$ of 21 kG have been prepared at an I_d of 20 μA/cm^2 and V_{sg} of 100 V when R_{H_2} was 50%. These results suggest that the bombardment of a proper amount of hydrogen ions with moderate energy to the growing film surface is useful for improving the soft magnetic properties of iron thin films.

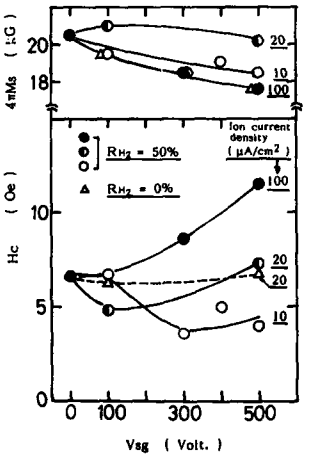


FIG. 2. Dependence of $4\pi M_s$ and H_c on accelerating voltage V_{sg} for films bombarded by argon and hydrogen ions.

B. Films bombarded by argon and nitrogen ions

Nitrogen is one of the well-known active elements for iron. The double-ion-beam sputtering system is capable of changing the nitrogen content in iron films by adjusting the conditions of bombarding nitrogen ions such as R_{N_2} and V_{sg}. Figure 3 shows the dependencies of the interplanar spacing d of the iron-nitride crystallites on V_{sg} and R_{N_2}, where values of d were calculated from the position of the highest peak in x-ray diffraction diagrams. All the iron-nitride films deposited on the substrates at room temperature showed only one diffraction peak, and the strongest diffraction intensity was obtained in the films at V_{sg} of 150–300 V.

The nitrogen content in films increased monotonically to about 21 at. % with R_{N_2}, as shown in Fig. 3. In this case, the argon content in the film at R_{N_2} of 100% was approximately 10 times as large as that in the film at R_{N_2} of 10% in spite of the lower argon partial pressure in the auxiliary ion source. Also the argon content in films increased with V_{sg} for all of the bombarding ions. These results may indicate that the argon atoms ejected from the main ion source and then repelled by the target occupy the vacancies in films by bombardment of energetic nitrogen ions or hydrogen ions.[6]

For R_{N_2} of 100% and 50%, the orthorhombic phase ζ-Fe_2N and the hexagonal phase Fe_3N, respectively, were synthesized in films with higher nitrogen contents. For R_{N_2} of 20% and 10%, a small amount of nitrogen atoms may enter into the interstices among the iron atoms, expanding and distorting the lattice of iron crystallites, as shown in Fig. 3. For the films bombarded by argon and hydrogen ions, the change of d was less pronounced. This may be due to the difference of atomic size between hydrogen and nitrogen.

Figure 4 shows the dependence of $4\pi M_s$ and H_c of these iron-nitride films on V_{sg}. When R_{N_2} was 100% and 50%, $4\pi M_s$ took the minimum values 1 and 10 kG, respectively, at V_{sg} of 150 V. Also, the H_c of these higher nitriding films increased drastically with V_{sg} in the region of 0–150 V. These results can be attributed to the well crystallization of ζ-Fe_2N and Fe_3M grains, because ζ-Fe_2N is nonmagnetic at room temperature and Fe_3N has a much smaller $4\pi M_s$ than α-Fe.

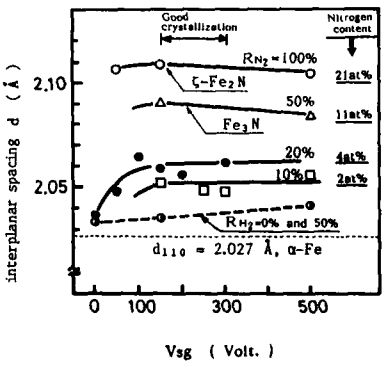


FIG. 3. Dependence of interplanar spacing d on V_{sg}.

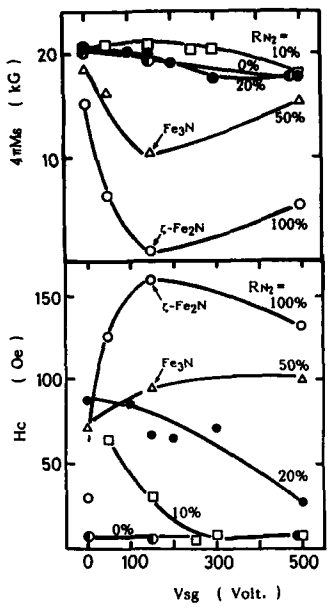


FIG. 4. Dependence of $4\pi M_s$ and H_c on V_{sg} for films bombarded by argon and nitrogen ions.

On the other hand, for R_{N_2} of 20% and 10%, the change of $4\pi M_s$ with an increase of V_{sg} was not so remarkable. And the H_c decreased with increase of V_{sg}, opposite those for R_{N_2} of 100% and 50%. Especially, at R_{N_2} of 10% and V_{sg} of 250 V, $4\pi M_s$ and H_c took a maximum value of above 22 kG and a minimum value below 5 Oe, respectively.

The iron content in the films and the ferromagnetic exchange force among iron atoms are considered the main factors for determining the value of $4\pi M_s$. Therefore, it may imply that the small amount of nitrogen atoms in the interstices among iron increase the exchange force without a significant decrease of $4\pi M_s$ due to a decrease of iron packing density in the films, improving the microscopic uniformity in films.[7]

IV. CONCLUSION

Iron thin films have been deposited by means of the double-ion-beam sputtering apparatus with an iron target of 99.99% purity. The effects of bombardment of hydrogen and nitrogen ions to the surface layer of growing film on their crystal structure and magnetic properties has been investigated.

The bombardment of argon and hydrogen ions with proper kinetic energy gave rise to an improvement of microscopic uniformity, making the crystallites in the films finer. Consequently, $4\pi M_s$ and H_c of these films were 21 kG and below 5 Oe, respectively, at V_{sg} of 100 V and I_d of 20 $\mu A/cm^2$.

As for the films bombarded by argon and nitrogen ions, the semihard compounds of ζ-Fe_2N and Fe_3N were synthesized in the films with higher nitrogen content. On the other hand, for lower nitrogen content, the films exhibited large $4\pi M_s$ above 22 kG and low H_c of 5 Oe by adjusting the nitrogen percentage to 10% and the accelerating voltage to about 250 V.

It has been found that the double-ion-beam sputtering method is a very useful technique for controlling the magnetic properties of iron thin films, especially by bombarding proper ions with moderate energy to a growing film surface.

[1]Y. Niimura, S. Nakagawa, Y. Kitamoto, and M. Naoe, J. Appl. Phys. 61, 3152 (1987).
[2]M. Naoe, M. Yamaga, and N. Terada, IEEE Trans. Magn. MAG-21, 1900 (1985).
[3]N. Terada and M. Naoe, Mater. Res. Soc. Symp. Proc. 58, 37 (1986).
[4]T. K. Kim and M. Takahashi, Appl. Phys. Lett. 20, 492 (1972).
[5]N. Terada, Y. Hoshi, M. Naoe, and S. Yamanaka, IEEE Trans. Magn. MAG-20, 1451 (1984).
[6]B. O. Johansson, H. T. G. Hentzell, J. M. E. Harper, and J. J. Cuomo, J. Mater. Res. 1, 442 (1986).
[7]Y. Nagai, A. Tago, K. Yanagisawa, and T. Toshima, J. Appl. Phys. 61, 3481 (1987).

Effects of boron implantation in films of iron-nickel

J. Ryu, K. Castell, W. Nowak, and C. Vittoria
Northeastern University, Boston, Massachusetts 02115

We have implanted boron ions into films of Fe-Ni alloy composition. A homogeneous distribution of boron was determined from the sputter Auger analysis with a concentration of 18% and 34% for low- and high-dose implantation, respectively. The resistivity of film was increased by a factor of 2 and 4 as a result of low- and high-dose implantation, respectively. The magnetic properties of these films are studied as a function of annealing temperature by using FMR measurements. Both the uniaxial anisotropy field and FMR linewidth are dramatically decreased as a result of annealing at elevated temperatures. The changes of effective magnetization of these films are strongly dependent on implanted boron concentration.

I. INTRODUCTION

A number of techniques, such as melt quenching,[1] vapor condensation in thermal evaporation,[2] or sputtering[3] process and ion implantation,[4] have been employed to produce amorphous alloys. Ion implantation is a process that can be used to introduce controlled amounts of foreign atoms into a layer adjacent to a material surface. This technique has been extensively used in magnetic bubble technology, since the first discovery of altering the magnetic anisotropy in garnet crystals.[5] In this study, we have produced amorphous Fe-Ni-B alloys via ion implanting boron into crystalline Fe-Ni films and investigated the changes in magnetic properties of these films after ion implantation and post-annealing treatment. Ferromagnetic resonance (FMR), resistivity, and Auger analysis were performed to characterize the films.

II. EXPERIMENTAL PROCEDURE

Thin films of $Fe_{20}Ni_{80}$ and $Fe_{70}Ni_{30}$ were thermally evaporated in thicknesses ranging from 1400 to 3100 Å on a quartz or slide glass substrate. The substrate was heated at 250 °C using a quartz lamp heater. The pressure of the chamber was initially 1×10^{-6} Torr, but increased to 1×10^{-5} Torr during deposition. Boron was implanted into these films at an ambient substrate temperature. The implantation conditions in terms of dose and energy were $4\times10^{16}/cm^2$ at 20 keV, $5.7\times10^{16}/cm^2$ at 40 keV, and $9.7\times10^{16}/cm^2$ at 80 keV for lower-dose implantation and $1.2\times10^{17}/cm^2$ at 20 keV, $1.7\times10^{17}/cm^2$ at 40 keV, and $2.9\times10^{17}/cm^2$ at 80 keV for high-dose implantation. The concentration and distribution of boron was determined after implantation by using a sputter-Auger technique. The depth distribution of boron was deduced from the sputtering rate which was determined by measuring the depth of the crater after sputtering in a given time. The structure of the films after implantation was determined by using reflection electron deflection (RED) at a beam energy of 50 keV. The implanted films were annealed in 5×10^{-6} Torr vacuum at temperatures from 100 to 350 °C in 50 °C intervals. The annealing period was 30 min at each annealing temperature. Resistivity and ferromagnetic resonance (FMR) measurements were performed on films in the as-deposited, implanted, and annealed state. Resistivity of the film was measured using a four-probe technique. The magnetic properties, effective saturation magnetization ($4\pi M_{eff}$), FMR linewidth (ΔH), and anisotropy field (H_A) were determined using the standard in-plane FMR analysis.[6] The FMR experiment was performed in a microwave cavity tuned to 9.5 GHz. In this measurement, a dc magnetic field was applied parallel to the film plane.

III. RESULTS AND DISCUSSION

The depth distribution of the implanted boron was obtained by using the sputter-Auger technique, as shown in Fig. 1. Boron was uniformly distributed in ranges of 200–2400 Å from the film surface. The concentration of boron was 34% (peak at 1000–1400 Å) and 18% (peak at 750 Å) for high- and low-dose implantation, respectively. Clearly, the distribution of boron is more homogeneous in the high-dose implanted sample. Further, reflection electron deflection(RED) analysis revealed that complete amorphous and highly damaged (diffused ring pattern) structure in high- and low-dose implanted samples, respectively.

The changes in resistivity of implanted samples after annealing are shown in Fig. 2. As expected, the values of resistivity are increased four and two times in the high- and

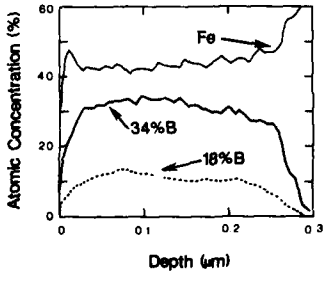


FIG. 1. Depth distribution of implanted boron in $Fe_{70}Ni_{30}$ thin films. The thickness of the film was 3100 Å.

 0021-8979/88/084312-03$02.40 © 1988 American Institute of Physics

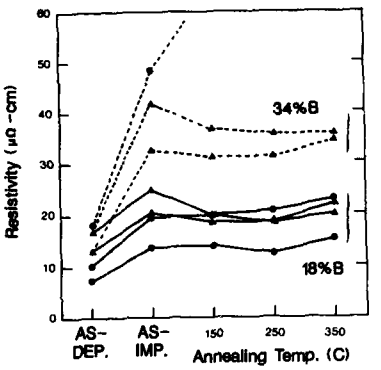


FIG. 2. Changes in resistivity as functions of implantation and annealing conditions. The solid circle and triangle represent $Fe_{20}Ni_{80}$ and $Fe_{70}Ni_{30}$ thin films, respectively. Note that the resistivity of high-dose boron implanted $Fe_{20}Ni_{80}$ film was increased abnormally after post-annealing.

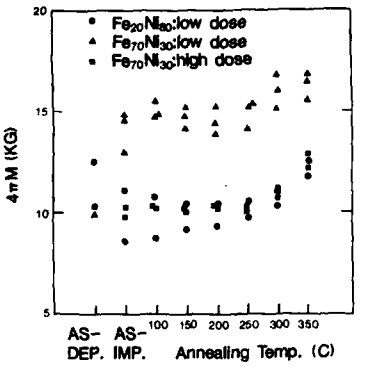


FIG. 4. Changes in effective magnetization $4\pi M$ as functions of ion implantation and post-annealing treatment.

low-dose implanted sample, respectively. Annealing of these films at elevated temperature resulted in slow decrease in resistivity. However, the resistivities of films annealed at 350 °C were still higher than the resistivities of as-grown films. It has to be mentioned that the resistivity of some of high-dose implant samples, especially in permalloy composition, are dramatically increased after annealing. We could not observe ferromagnetic resonance in these samples. Thus, we believed that these samples are magnetically disordered or paramagnetic in these high-dose levels (34% B).

The changes in anisotropy field (H_A) are relatively independent of alloy composition or implanted boron concentration, as is shown in Fig. 3. The values of H_A are decreased in all samples as a result of ion implantation and annealing at elevated temperatures. In low-dose implanted permalloy ($Fe_{20}Ni_{80}$) films, the H_A are minimum after annealing at 150–200 °C. Annealing these films above 200 °C resulted in a slight increase in H_A. In $Fe_{70}Ni_{30}$ composition films, the H_A of both high- and low-dose implants show a minimum after annealing films at 200 °C. Annealing these samples above 200 °C resulted in a rapid increase in H_A.

A typical plot of effective saturation magnetization ($4\pi M$) as a function of annealing temperature is shown in Fig. 4. The changes in $4\pi M$ are strongly dependent on the alloy composition as well as boron concentration. Thermal post-annealing has little effect on effective magnetization at temperatures lower than 200 °C. Annealing these films above 300 °C resulted in a gradual increase in $4\pi M$. Comparing the values of $4\pi M$ for high- and low-dose implanted $Fe_{70}Ni_{30}$ films, it is clear that high-dose boron implantation reduces the effective magnetization. The reduction in $4\pi M$ may be related to a new magnetic ordering or presence of paramagnetic phase. The results of FMR measurements for as-deposited, ion-implanted, and annealed films at 200 °C are summarized in Table I.

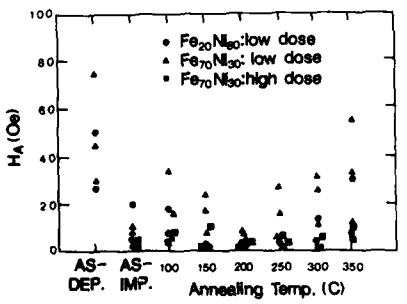


FIG. 3. Changes in anisotropy field H_A as results of ion implantation and post-annealing treatment. A minimum value of H_A is obtained after annealing at 200 °C for all samples.

IV. CONCLUSION

Amorphous thin films of Fe-Ni-B were produced via the ion implantation technique. Uniform distribution of boron

TABLE I. Results of FMR measurements for films of $Fe_{20}Ni_{80}$ and $Fe_{70}Ni_{30}$ composition in as-deposited, boron-implanted, and annealed ($T_A = 200$ °C) states.

	$Fe_{20}Ni_{80}$ (3100 Å)			$Fe_{70}Ni_{30}$ (2500 Å)		
	As-dep.	Low-dose implant	High-dose implant	As-dep.	Low-dose implant	High-dose implant
$4\pi M$ (kG)	10.3	10.6	···	9.5(?)	15.1	10.4
H_A (Oe)	50	6	···	75	6	5
ΔH (Oe)	62	29	···	176	98	41

was obtained by implanting this species in three different doses and energies. The minimum values of H_A and ΔH were obtained after post-annealing these films at temperatures of 200–250 °C. The annealing results were independent of alloy composition. Typically, the values of H_A were measured to be in the range of 2–7 Oe and ΔH in the order of 30–50 Oe after annealing the films at 200 °C. The value of $4\pi M$ is strongly dependent on alloy composition and relatively independent on annealing treatment temperatures below 300 °C. The low value of $4\pi M$ in high-dose implant $Fe_{70}Ni_{30}$ films may indicate the presence of the paramagnetic phase in high boron concentration samples.

ACKNOWLEDGMENTS

We are grateful to Dr. Dean Casy of GTE Laboratories for help with ion implanting boron in this research.

[1] R. C. O'Handley, R. Hasegawa, R. Ray, and C.-P. Chou, Appl. Phys. Lett. **29**, 330 (1976).
[2] A. G. Dirks and J. R. M. Gijsbers, Thin Solid Films **58**, 333 (1979).
[3] R. J. Kobliska, J. A. Aboaf, A. Gangulee, J. J. Cuomo, and E. Klokholm, Appl. Phys. Lett. **33**, 473 (1978).
[4] P. Zieman, Mater. Sci. Eng. **69**, 95 (1985).
[5] R. Wolf, J. C. North, R. L. Barns, M. Robinson, and H. J. Levinstein, Appl. Phys. Lett. **19**, 298 (1971).
[6] Ronald F. Soohoo, *Magnetic Thin Films* (Harper & Row, New York, 1965).

Magnetic properties of ion-beam sputter-deposited Fe-Ni-B-Si films

J. Ryu, Y. Huang, and C. Vittoria
Center for Electromagnetics Research, Northeastern University, Boston, Massachusetts 02115

We have produced Fe_x-Ni_{80-x}-B_{15}-Si_5 ($x = 20$, 40, and 75) and permalloy thin films on a silicon substrate using ion-beam sputtering technique. Four-point probe measurement indicated that quarternary films had 3–4 times higher resistivity than permalloy films, and this ratio was not changed after thermal annealing. The values of saturation magnetization were determined to be 5–13 kG depending on Fe concentration. The anisotropy fields of these films were in the ranges of 2–15 Oe after deposition, however, these values were reduced by more than 50% after annealing with field. The lowest value of the anisotropy field was 1.3 Oe for the permalloy film after thermal annealing without field.

I. INTRODUCTION

High saturation magnetization ($4\pi M_s$) and low uniaxial anisotropy field (H_K) are essential for microwave frequency application of magnetic materials. Magnetic oxide films have been used extensively for microwave devices. The values of saturation magnetization of the oxide films are typically only half those of the metal films. Recently, high $4\pi M$, low H_K, and relatively high-resistivity amorphous Fe-Ni-B-Si ribbons[1] were prepared in various compositions by using the melt-quench technique. For microwave device application, it may be essential to develop these materials in thin-film form. In this study, we have produced thin films of Fe-Ni-B-Si alloy on a Si substrate via the ion-beam sputtering technique. In addition, permalloy films (Fe_{20}-Ni_{80}) were prepared for the purpose of comparison.

II. EXPERIMENTAL PROCEDURE

An apparatus as shown in Fig. 1 was used for deposition of Fe-Ni-B-Si as well as Fe-Ni films. The target of desired composition was mounted on a water-cooled holder and a 3-cm beam diameter Kaufman-type ion source was used for sputter deposition. The compositions of the targets used are Fe_{20}-Ni_{80} and Fe_x-Ni_{80-x}-B_{15}-Si_5 ($x = 20$, 40, and 75) in atomic percent. Since the film composition was not determined, compositions described in this paper referred to the target composition. The deposition chamber was initially pumped down to lower than 2×10^{-6} Torr, then purified Ar gas was introduced into the ion source. The pressure of the chamber during growth was maintained at 3×10^{-4} Torr. Silicon substrate was mounted parallel to the target at a 4 in. distance. The substrate was not heated, but was rotated at 2 rpm speed to enhance the uniformity of the film. The voltage and current of the ion beam were 1 keV and 50–60 mA, respectively. Under these conditions, the deposition rate was 3–4 Å/s. The thickness of the film, measured by using a surface profilometer, was in the range of 2400–2800 Å. After deposition, one set of films was annealed in vacuum lower than 2×10^{-5} Torr at 275 °C for 30 min using a quartz lamp heater. The other set of films was annealed in a magnetic field of 300 Oe applied along the hard axis of the film which was determined from vibrating sample magnetometer (VSM) measurement. For resistivity and magnetic property measurements, specimens were cut into disk shape (6 mm in diameter). Resistivity of the film was measured by the four-point probe technique. The saturation magnetization and the coercive field H_c were measured with a vibrating sample magnetometer. In addition, the magnetic anisotropy was determined by measuring the VSM hysteresis loops along both easy and hard axis and corroborated by FMR technique.

III. RESULTS AND DISCUSSION

Typical hysteresis loops of the permalloy and Fe-rich ($x = 75$) quarternary films in the as-deposited state are shown in Fig. 2. Although these two films have nearly the same coercive field, permalloy film has much smaller anisot-

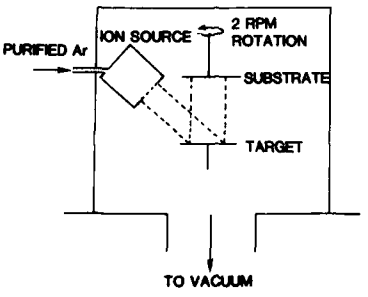


FIG. 1. Schematic diagram of the ion-beam sputter-deposition system.

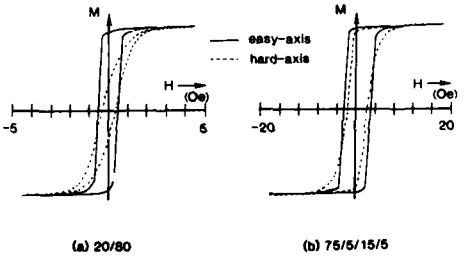


FIG. 2. Typical hysteresis loops of the as-deposited (a) permalloy and (b) Fe-rich quarternary films.

 0021-8979/88/084315-03$02.40 © 1988 American Institute of Physics

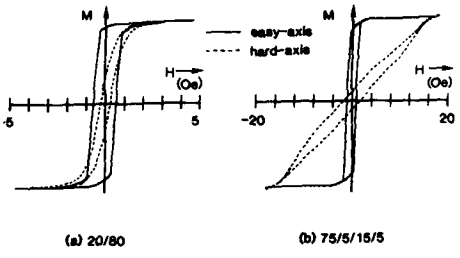


FIG. 3. Typical hysteresis loops of the annealed (a) permalloy and (b) Fe-rich quarternary films. Note the squareness (M_r/M_s) of the Fe-rich films is greatly increased as a result of field annealing.

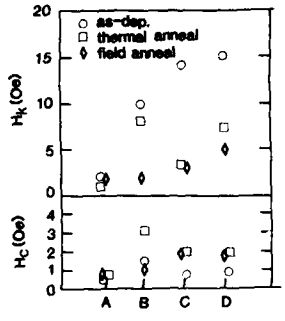


FIG. 5. Values of coercive field (H_c) and anisotropy field (H_k) as functions of alloy composition and annealing condition. A, B, C, and D represent $Fe_{20}Ni_{80}$, $Fe_{20}Ni_{60}B_{15}Si_5$, $Fe_{40}Ni_{40}B_{15}Si_5$, and $Fe_{75}Ni_5B_{15}Si_5$ films, respectively.

ropy field. In Fig. 3, the hysteresis loops for the same samples after 275 °C annealing in a magnetic field of 300 Oe along the hard axis are shown. Comparing Figs. 2 and 3, the hysteresis loops for the as-deposited and the annealed permalloy film are almost identical. However, in the Fe-rich ($x = 75$) quarternary film, the squareness (M_r/M_s) of hysteresis loops increased remarkably as a result of field annealing. This increase in squareness of the hysteresis loop was observed in all quarternary films. The highest M_r/M_s values obtained for the $Fe_{40}Ni_{40}B_{15}Si_5$ films after annealing were 98% and 88% along the easy and hard axis, respectively. Furthermore, in some Ni-rich ($x = 20$) films, square-shaped hysteresis loops were obtained in all orientations of applied magnetic field. No particular easy or hard axis of magnetization existed in these films. One notable feature observed was that annealing the film at 275 °C in a magnetic field of 300 Oe along the hard axis resulted in a complete rotation of magnetic easy axis in all samples.

The values of $4\pi M_s$ and resistivity as functions of nominal film compositions as well as annealing conditions are plotted in Fig. 4. As expected, the Fe-rich ($x = 75$) film showed the highest $4\pi M_s$. After annealing without field, the values of $4\pi M_s$ for all but permalloy films increased slightly, and this trend was more significant in the Fe-richer films. The highest value of $4\pi M_s$ is 13 300 G, obtained for the $Fe_{75}Ni_5B_{15}Si_5$ film after thermal annealing without field. The resistivity of all but the Ni-rich ($x = 20$) films was not sensitive to annealing treatment. In the Ni-rich film ($x = 20$), the resistivity decreased from 44 to 32 $\mu\Omega$ cm as a result of annealing. Generally, the resistivities of the quarternary films, in as-deposited as well as annealed states, were 3–4 times higher than that of permalloy film. However, the resistivity of our quarternary films (about 40 $\mu\Omega$ cm) is much less than the values obtained from the amorphous ribbons ($\rho = 100$–200 $\mu\Omega$ cm) (Ref. 2) or the amorphous films[3] of similar compositions. This low-resistivity value indicates that our films may contain cyrstalline structure, although they have a high concentration (20%) of glass-forming elements, boron and silicon.

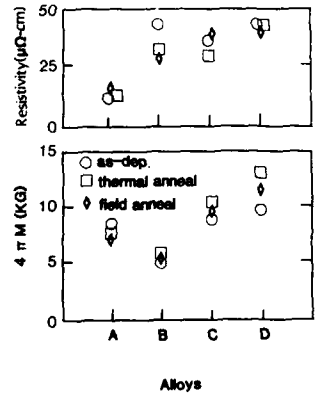


FIG. 4. Values of saturation magnetization ($4\pi M_s$) and resistivity (ρ) as functions of alloy composition and annealing condition. A, B, C, and D represent $Fe_{20}Ni_{80}$, $Fe_{20}Ni_{60}B_{15}Si_5$, $Fe_{40}Ni_{40}B_{15}Si_5$, and $Fe_{75}Ni_5B_{15}Si_5$ films, respectively.

The values of coercive field (H_c) and H_K were determined from the hysteresis loops. The results are shown in Fig. 5. While the change in H_c for the permalloy films is negligible, H_c in all the quarternary films increased about 100% as a result of annealing. An increase in H_c of the quarternary films tends to indicate that crystallization occurred during annealing. The value of H_K for the permalloy films was not changed after anneal with field, however, this value decreased 30% after annealing without field. In all quarternary films, the values of H_K drastically decreased as a result of annealing.

IV. CONCLUSION

The Fe-Ni-B-Si system exhibits the following properties: (1) The saturation magnetization, $4\pi M_s$, can vary between 10 000 and 13 000 G for the iron-rich ($x = 75$) films. This is to be compared to 7000–8000 G for the permal-

loy film. (2) The H_K values for the as-deposited films are always higher than H_K values obtained for annealed films. The lowest values of H_K are 1.3 and 5 Oe for the permalloy and the iron-rich ($x = 75$) quarternary films, respectively. The system also exhibits square loop properties. The remanence magnetization is relatively high and is in the order of 94%–98% after field annealing. (3) Finally, we observed complete rotation of magnetic easy axis as a result of annealing the films in a magnetic field along the hard axis of magnetization.

[1]L. T. Kabacoff, M. Wun-Fogel, and F. Bucholtz, IEEE Trans. Magn. MAG-21, 2014 (1985).
[2]R. Hasegawa and J. A. Dermon, Phys. Lett. 42A, 407 (1973).
[3]R. J. Kobliska, J. A. Aboaf, A. Gangulee, J. J. Cuomo, and E. Klokholm, Appl. Phys. Lett. 33, 473 (1978).

Induced magnetic anisotropy related to the local atomic order: A study in amorphous Co-Zr and Co-Zr-M thin films

G. Suran, M. Naili, and J. Sztern
CNRS, Laboratoire de Magnétisme, 92195 Meudon Cedex, France

The in-plane uniaxial anisotropy K_u, induced by a magnetic field applied during the deposition, was investigated in amorphous thin films of $Co_{1-x}Zr_x$ and $Co_{1-x-y}Zr_x M_y$ (M = Ti, Nb, and Pt) obtained by rf sputtering. For a given concentration K_u presents a bell-shaped variation as a function of Ar pressure P_{Ar}. The critical pressure for which the maximum value of K_u is obtained and the absolute value of $(K_u)_{max}$ changes for the various alloys. These results and the high value of $(K_u)_{max}$ are explained by a model where $(K_u)_{max}$ is related to the local anisotropy via the local structure upon the nonmagnetic metal. $(K_u)_{min}$ is essentially related to a pseudodipolar short-range order.

INTRODUCTION

$Co_{1-x}M_x$ amorphous alloys, where M is a nonmagnetic early transition-metal (ETM) like Zr, Ti, or Nb, are promising materials for application as thin-film recording heads.[1] A high permeability could be obtained only in thin films which possess a small but well-defined uniaxial anisotropy field H_k. In films prepared by sputtering a more on less well-defined H_k field is formed spontaneously during the deposition process and it is necessary to adjust the magnitude of H_k by a post-deposition annealing treatment.[2]

We recently performed a study[3] on $Co_{1-x}Ti_x$ amorphous films where we tried to control the magnitude of H_k by applying a dc magnetic field during the deposition. Our experiments showed that for a given concentration the value of $K_u = H_k M_s/2$ could be largely varied by changing the pressure of the sputtering gas P_{Ar}. The results were explained by a model, based upon a detailed structural investigation, where it is assumed that K_u is related to the local anisotropy of Co atoms.

Here we report an extension of the previous work to amorphous $Co_{1-x}Zr_x$ and $Co_{1-x-y}Zr_xM_y$ thin films with M = Nb, Ti, and Pt.

EXPERIMENT

The *a*-$Co_{1-x}M_x$ films were deposited by rf sputtering onto water-cooled glass substrates. We used Ar as a sputtering gas. During the deposition process a dc magnetic field of 700 Oe was applied parallel to the substrate surface.[4] We used a vacuum-melted target (150 mm diam) of $Co_{94}Zr_6$ on which small triangular-shaped plates of Zr, Nb, Ti, and/or Pt were disposed in a regular way. The concentration range investigated is reported in Table I. The lowest amount of ETM necessary to obtain an amorphous $Co_{1-x}M_x$ alloy is for M = Zr and corresponds to $x = 0.05$. The presence of Zr in the ternary alloys permitted to obtain the amorphous state in all the compositions investigated (Table I). The thickness of the films was in the range of 0.1–0.3 μm.

The coercive field H_c and the uniaxial anisotropy field H_k were deduced respectively from the hysteresis loop detected along the in-plane easy and hard axis. The FMR measurements were performed at 9.8 GHz with the external field both perpendicular to the film plane and parallel to the in-plane easy and in-plane hard axes. From the three resonance fields we computed $4\pi M_s$, H_k, and the g factor. The value of H_k determined by the two techniques generally agreed within $\pm$ 5%. The characteristics of the FMR spectra also gave a valuable indication regarding the magnetic homogeneities of the samples.

RESULTS AND DISCUSSION

The variations of H_c and H_k were studied systematically as a function of the main deposition parameters, which are P_{Ar} and the rf input power W_{rf}. For a given composition the value of K_u is essentially related to P_{Ar}. Figure 1 shows the typical variation of K_u as a function of P_{Ar} in *a*-$Co_{1-x}Zr_x$ thin films. For a given concentration K_u follows a bell-shaped-like variation as a function of P_{Ar} with a well-defined maximum value $(K_u)_{max}$. In a given alloy $Co_{1-x}M_x$, $(K_u)_{max}$ occurs always for the the same pressure $(P_{Ar})_{cr}$ independent of the concentration. At a given concentration the smallest value of K_u, $(K_u)_{min}$, is always obtained for the lowest pressure used which in the present experiments is $P_{Ar} = 2\times10^{-3}$ Torr. The FMR measurements confirmed the high magnetic uniformity of the thin films independently from the composition. For perpendicular resonance on all the alloy systems investigated we obtained a spin-wave spectrum, the various modes nicely following a quadratic dispersion law.

In Fig. 2 is shown $(K_u)_{max}$ as obtained on all the alloys investigated. In the alloys containing only NTM, $(K_u)_{max}$ decreases continuously when the total amount of the NTM $x + y$ increases. Another characteristic is the absolute overall value of $(K_u)_{max}$, which is exceptionally high, almost an

TABLE I. Composition of the various deposit and concentration range investigated.

Composition	*Concentration range investigated*	
	x	y
$Co_{1-x}Zr_x$	$0.052 \leq x \leq 0.16$	...
$Co_{1-x-y}Zr_xNb_y$	0.055	$0.025 \leq y \leq 0.075$
$Co_{1-x-y}Zr_xTi_y$	0.048	$0.04 \leq y \leq 0.105$
$Co_{1-x-y}Zr_xPt_y$	0.065	$0.1 \leq y \leq 0.175$

 0021-8979/88/084318-03$02.40 © 1988 American Institute of Physics

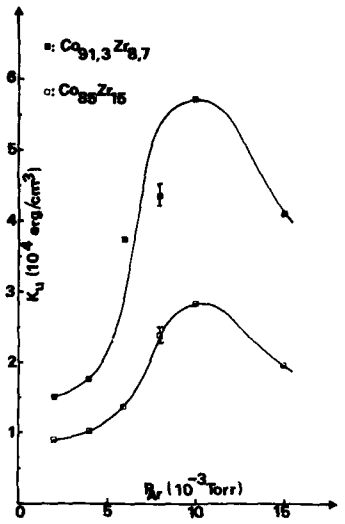


FIG. 1. Variation of K_u as a function of Ar pressure in $Co_{1-x}Zr_x$ amorphous thin films.

order of magnitude higher than that obtained when K_u is related to a mono- (or diatomic) directional order via pseudodipolar interaction. These overall results are qualitatively similar to that obtained on a-$Co_{1-x}Ti_x$ and we explain them by using the model proposed for a-$Co_{1-x}Ti_x$.[3]

The main assumption is that the structure of a-$Co_{1-x}M_x$ alloys films is formed of a random continuous

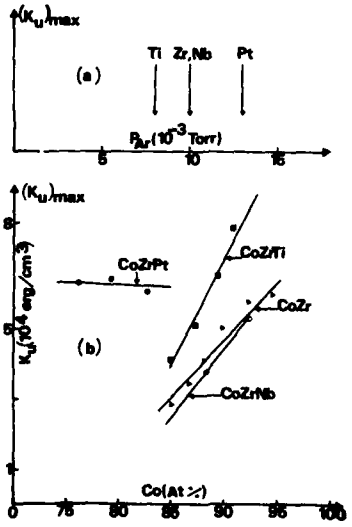


FIG. 2. (a) Location of $(K_u)_{max}$ for the various alloys. (b) Maximum induced anisotropy $(K_u)_{max}$ as a function of Co concentration for the various alloys.

matrix of clusters with trigonal (hcp like), octahedral (fcc like), and icosahedral symmetries. Similar to crystalline Co-rich alloys, a-$Co_{1-x}M_x$ exhibits a structural transformation around a critical temperature T_{cr} which requires a well-defined activation energy $Q_0 \approx 0.15$ eV.[5] The high anisotropy state corresponds to the transformation of octahedrallike clusters to trigonal ones, the high value of $(K_u)_{max}$ being related to the local anisotropy of Co atoms located in trigonal-type clusters, K_u being maximum when the probability is highest that these clusters are oriented along the applied field.

Based on these hypotheses, the variation of K_u as a function of P_{Ar} is explained as follows: the energy E^f of the sputtered atoms as they arrive on the substrate is related to P_{Ar} and can be computed using a formula of the literature.[6] At low Ar pressure (i.e., $P_{Ar} = 2\times10^{-3}$ Torr) the values of E^f and Q are high ($Q = 1$–1.5 eV following the metal) so the films are built up essentially of icosahedral and low anisotropy octahedral clusters. For high P_{Ar} (i.e., $P_{Ar} = 15$ mT) the sputtered atoms are thermalized to the temperature of the plasma, $T_p \sim 400$ K. Now E^f is low so a significant amount of trigonal-type clusters are formed which explains that the value of K_u is much higher than for low P_{Ar}, but these clusters are oriented more or less randomly. When $K = (K_u)_{max}$, $P_{Ar} = (P_{Ar})_{cr}$ and the as-computed value of E^f is close to 0.15 eV. The phase transformation is the largest so part of octahedral clusters will be transformed to trigonal (or icosahedral) ones and the easy axis of the trigonal clusters will be oriented along the applied field in order to minimize the total energy acting upon the films.

As shown in Fig. 2(a), $(P_{Ar})_{cr}$ is different for the various alloys. The energy loss of a sputtered atom is related to the ratio of atomic mass of the sputtered atoms to the Ar particles, so for a metal with higher atomic mass a higher P_{Ar} is necessary in order to obtain the same E^f. $(P_{Ar})_{cr}$ increases with the atomic mass of the various metals M in $Co_{1-x}M_x$ as expected from the computation. The decrease of $(K_u)_{max}$ with increasing NTM content is believed to be related to the increasing disorder in the local structure: the trigonal (and octahedral clusters) progressively lose their bond orientational order so the corresponding local anisotropy decreases.[3]

The definition of the local structure for a given concentration is related to the particular NTM. The main parameters are believed to be the minimum NTM metal content x_0 corresponding to the amorphous state and the structure of the crystalline phase. Among the NTM investigated x_0 is highest for Ti($x_0 = 0.14$). Ti and Zr possess a hcp structure while Nb has a bc one. For a given concentration in layers containing Ti the trigonal-like clusters are better defined, while the inclusion of Nb should favor the formation of the octahedral clusters. This explains that for a given concentration $x + y$ $(K_u)_{max}$ is respectively the highest and lowest for CoZrTi and CoZrNb.

The concentration dependence of $(K_u)_{max}$ in $Co_{1-x-y}Zr_xPt_y$ alloy is different from the previous ones. The results can be explained by assuming that the amount and definition of the trigonal-type clusters does not change when one increases the Pt content in the films.[7]

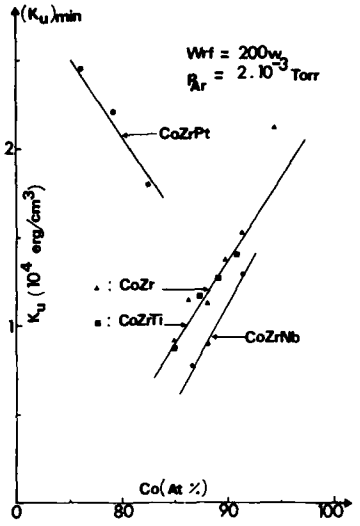


FIG. 3. Minimum induced anisotropy $(K_u)_{min}$, for $P_{Ar} = 2\times10^{-3}$ Torr, in the various alloys.

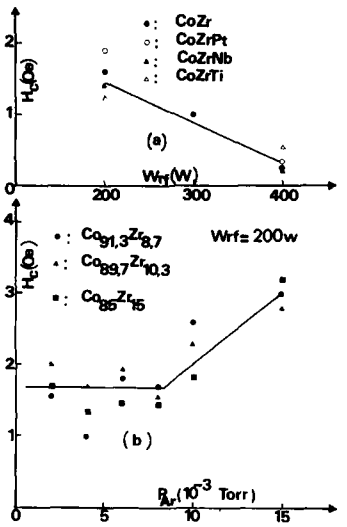


FIG. 4. Variation of H_c with deposition parameters. (a) Variation of H_c with rf input power W_{rf}. The value of H_c reported for each composition corresponds to a typical sample. (b) Variation of H_c with P_{Ar} in a-$Co_{1-x}Zr_x$ thin films.

In Fig. 3 are reported the variations of $(K_u)_{min}$ with Co content for the various alloys. In alloys containing only NTM for a given concentration $x + y$, the value of $(K_u)_{min}$ is practically same. This result is believed to be related to the fact that the physical origin of $(K_u)_{min}$ is now essentially due to a pseudodipolar directional short-range order, so it is independent of the nature of the NTM. The magnetic annealing performed on a-$Co_{1-x}Ti_x$ films showed[8] that on samples deposited at $P_{Ar} < 3\times10^{-3}$ Torr when K_u was smaller than 10^4 erg/cm^3, it could be suppressed by annealing in a rotating magnetic field, while $(K_u)_{max}$ remained unchanged.

The variations of the coercive field H_c with the deposition parameters are shown in Fig. 4. The absolute value of H_c and the trend of its variation were the same for the various alloys for a given set of deposition parameters. H_c decreases with increasing W_{rf} [Fig. 4(a)]. W_{rf} determines the deposition rate; the decrease of H_c is probably due to a lower amount of nonmagnetic defects, like rare-gas incorporation, when the deposition rate increases. Dependence of H_c upon P_{Ar} for $Co_{1-x}Zr_x$ is shown in Fig. 4(b). H_c is practically constant for $P_{Ar} < (P_{Ar})_{cr}$ and increases slightly but significantly for $P_{Ar} > (P_{Ar})_{cr}$. This result is related to the contribution of the local anisotropy to H_c via the development of the randomly distributed trigonal-like clusters.

In conclusion, when a-$Co_{1-x}M_x$ thin films—where M is a glass-forming transition metal (NTM)—are deposited by rf sputtering in the presence of a dc magnetic field, the trend in the variations of the in-plane uniaxial anisotropy K_u as a function of deposition parameters and concentration are the same. The values of K_u change with the pressure of the sputtering gas showing a maximum $(K_u)_{max}$ for a critical pressure. $(K_u)_{max}$ is related to the local anisotropy K_1 of the Co atoms located in trigonal-like clusters.

[1] H. Fujimori, N. Kazama, K. Hirose, J. Zhang, H. Morita, I. Sato, and H. Sugarawa, J. Appl. Phys. **55**, 1769 (1983).
[2] Y. Shimada and N. Saito, Jpn. J. Appl. Phys. **25**, 419 (1986); H. Sakakima, IEEE Trans. Magn. **MAG-19**, 131 (1983).
[3] G. Suran, K. Ounadjela, and F. Machizaud, Phys. Rev. Lett. **57**, 3109 (1986).
[4] K. Ounadjela, G. Suran, and J. Sztern, Thin Solid Films **151**, 397 (1987).
[5] B. W. Corb, R. C. O'Handley, J. Magesar, and N. J. Grant, Phys. Rev. Lett. **51**, 1386 (1983).
[6] F. J. Cadieu and N. Chencinski, IEEE Trans. Magn. **MAG-11**, 227 (1975).
[7] G. Suran, K. Ounadjela, F. Machizaud, and J. Sztern, IEEE Trans. Magn. **MAG-22**, 585 (1986).
[8] A. Materne and G. Suran (to be published).

Perturbations to the Stoner–Wohlfarth threshold in 2×20 μm *M-R* memory elements

C. S. Comstock, H. Y. Yoo, and A. V. Pohm
Department of Electrical and Computer Engineering, and Engineering Research Institute, Iowa State University, Ames, Iowa 50011

Perturbations to the Stoner–Wohlfarth threshold in 2×20 μm *M-R* memory elements have been examined experimentally and analytically. For the small dimensioned elements studied the perturbations are large. The thresholds were reduced up to 50% for transverse elements and increased 10% or more for longitudinal elements.

I. INTRODUCTION

Magnetoresistive memory elements have been studied by the authors for memory applications requiring nondestructive readout, nonvolatility, integrated circuit compatibility, and high density. In general, the integrated circuit and high density requirements dictated that the elements be of small dimension. At these small dimensions, demagnetizing effects and exchange significantly perturb the Stoner–Wohlfarth threshold; these effects have been examined experimentally and analytically.

II. EXPERIMENTAL STUDIES

8×8 test arrays of 2×20 μm memory elements were used to make the experimental measurements. The elements were made from two layers of 150-Å-thick ternary alloy (65% Ni, 15% Fe, 20% Co) separated by a 50-Å nonmagnetic layer. (In our laboratory Ta typically is used for the separation layer. The test elements were prepared by Honeywell Inc.)

The uniaxial anisotropy axis was either parallel or perpendicular to the long dimension of the element. Those elements with the easy axis perpendicular to the long dimension were labeled transversed elements and those with the easy axis parallel to the long dimension longitudinal elements. The elements are depicted in Fig. 1.

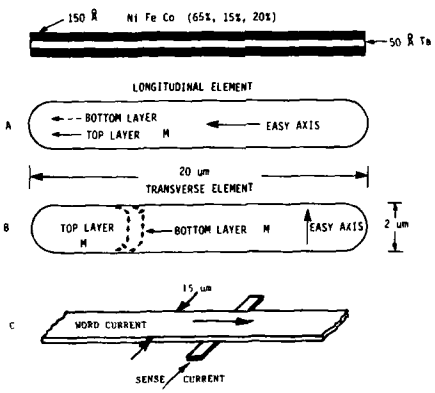


FIG. 1. Longitudinal and transverse magnetoresistive memory elements.

The bulk ternary double-layer material before etching typically had an anisotropy constant of 18 ± 3 Oe and a coercive force of 0.3–0.8 Oe. This ternary alloy has an anisotropy constant substantially larger than 80–20 permalloy. Switching fields were provided by sense currents through the *M-R* elements and word currents through orthogonal, 15-μm-wide word lines [Fig. 1(c)]. Nominal sense currents were 3–4 mA and nominal word currents were 15–30 mA. The material had a resistance of 7–10 Ω/□ and a magnetoresistive coefficient ($\Delta R/R$) of 2.4% ± 0.3%.

Figures 2(a) and 2(b) depict the 60-Hz switching behavior for both transverse (a) and longitudinal elements (b). The longitudinal elements thresholds were determined for the memory mode[1] in which the interior of thinner layer is switched to change state. Output from the elements were 1–4 mV for nominal drive conditions. A strong field was used to initially align the magnetization at the edges ($H > 200$ Oe). In Fig. 2(a) the small difference in the required word current to switch the element from one state to the other indicates a slight amount of skew.

Figure 3 depicts the switching threshold for a transverse element with little skew. The indicated error in H_L is a consistent one arising from the error in the sense line width

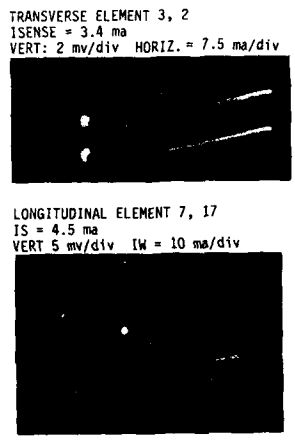


FIG. 2. Element switching.

 0021-8979/88/084321-03$02.40 © 1988 American Institute of Physics

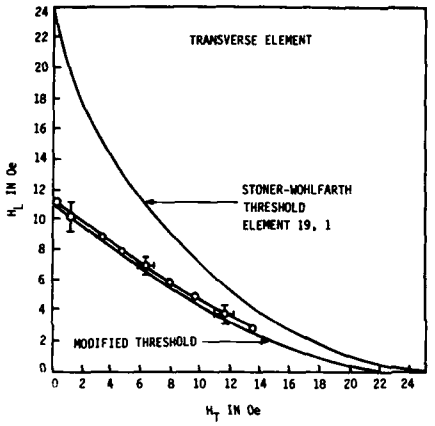


FIG. 3. Transverse element threshold.

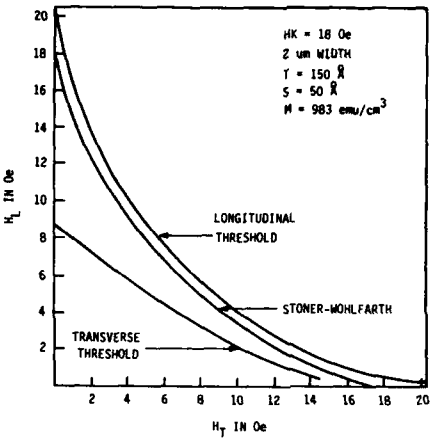


FIG. 5. Theoretical thresholds.

$(2 \pm 0.2\,\mu\text{m})$. In Fig. 3 the assumed H_K value for the theoretical curve was selected so that the theoretical curve matched the experimental data at the point the H_L and H_T values were equal. The transverse field H_T was provided by the sense current and the longitudinal field H_L was provided by the word current.

Figure 4 depicts the threshold characteristics of a small skew, longitudinal element. The transverse field was provided by the sense current and the longitudinal field by the word current in this case. Again, most measurement error arose from the error in the element width. The theoretical curve was matched to the experimental data at the point where H_T and H_L were equal by adjusting the value of H_K.

III. THEORETICAL STUDIES

As previously reported[2] for flat double-layer structures where the top and bottom layer magnetizations rotate away from the easy axis equally in opposite directions (θ), a simple one-dimensional torque differential equation can be derived which describes the average rotation of the magnetization within the layer. For longitudinal elements, this equation is as follows:

$$2A\frac{d^2\theta}{dx^2} + MH_L \sin\theta + MH_T \cos\theta + 2\pi M^2 TS' \cos\theta \frac{d^2(\sin\theta)}{dx^2} = MH_K \sin\theta\cos\theta,$$

where θ is the angle of rotation, M is the magnetization, A is the exchange constant, T is the thickness of a single magnetic layer, and S' is the effective separation of the two layers as given below:

$$S' = S + \frac{1}{\alpha^2 T}\left(\frac{\cosh\alpha T/2 - 1}{\cosh\alpha T/2 - (1/\alpha T)\sinh\alpha T/2}\right),$$

$$\alpha = \sqrt{4\pi M^2/2A}\ .$$

The quantity S is the separation from the bottom of one magnetic layer to the top of the other. The equation for the transverse elements is similar except the demagnetizing term involves the $\cos\theta$ rather than $\sin\theta$.

The magnetization was assumed to be parallel to the edges at the edges. For field values below the threshold, two solutions exist. One solution corresponds to the zero torque, stable solution; the other corresponds to the zero torque solution at the point of unstable equilibrium. When the two solutions coincide, the threshold is reached.

This equation was solved numerically by an iterative procedure. Figure 5 illustrates the resulting transverse and longitudinal thresholds for a sample with $H_K = 18$ Oe, $T = 150$ Å, width $= 2\,\mu$m, $s = 50$ Å, and $M_S = 983$ emu/cm^3.

For the transverse elements, the magnetization curls to be parallel with the edges. Both exchange and demagnetizing fields arising from the curling at the edge provide torques aiding the switching, as evidenced by the reduced threshold

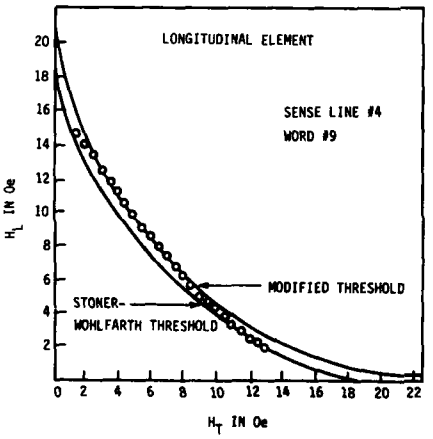


FIG. 4. Longitudinal element threshold.

in Fig. 5. For the longitudinal elements as the magnetization is rotated, the edge curling and demagnetizing fields provide retarding torques and consequently increase the threshold.

To estimate the demagnetizing effects in the long dimension for the finite length 20-μm sample, an ellipsoidal approximation was used. Longitudinal demagnetization for the 20-μm-long elements increased the effective H_K for transverse elements by 7 Oe and reduced the H_K value for the longitudinal elements by 7 Oe. The true demagnetizing field is nonuniform because the shape is not ellipsoidal. A smaller demag ıetizing is expected in the center of the element.

To compare theoretical predictions to the experimental data, the assumed value of H_K for the theoretical model was adjusted until the theoretical curve matched the experimental data at the point where H_L and H_T were equal. As seen in Figs. 3 and 4, the theoretical curves agreed with the experimental data within experimental error. Independent measurements of H_K in the individual elements were not available.

IV. SUMMARY AND CONCLUSIONS

For the 2-μm-wide elements studies, exchange and demagnetization fields significantly perturbed the Stoner–Wohlfarth threshold. The analytical model employing a one-dimensional torque differential equation was found to give results which agreed with experimental results within experimental error if demagnetizing effects in the long dimension were included. The model was found to be a useful tool for fine tuning values of material parameters such as H_K and device parameters such as thickness and separation.

Experimentally and analytically it was found that the threshold diminished for elements with their easy directions perpendicular to the long dimension. The magnetization curls to be parallel with the edges. Both exchange and demagnetizing fields reduce the threshold field values in this case. For elements with the easy axis in the long dimension, the thresholds are increased.

ACKNOWLEDGMENTS

The authors would like to thank Jeanne Cacavas for typing the manuscript and Katherine Trahanovsky for making the measurements and reducing the data. This work was supported by grants from Honeywell, Inc. and Control Data Corp.

[1]A. V. Pohm, J. M. Daughton, C. S. Comstock, H. Y. Yoo, and J. Hur, IEEE Trans. MAG-23, 2575 (1987).
[2]A. V. Pohm and C. S. Comstock, J. Magn. Magn. Mater. 54–57, 1667 (1986).

On the pinning of domain walls in low magnetization materials

C. H. Wörner and J. E. Valdés[a)]
Instituto de Física, Universidad Católica de Valparaíso, Casilla 4059, Valparaíso 2, Chile

The proposal of an interaction potential between 180° Bloch walls and nonmagnetic obstacles, precipitates or pores, is presented. Use is made of the analogy between this phenomenon and the pinning of grain boundaries in polycrystalline materials. The model takes into account the increase of energy due to the flexibility of the boundary and it is applicable to low magnetization materials. Using this approach it is possible to calculate the coercive force and to compare it with early findings. The numerical values obtained are in agreement with the values we find in the literature with the advantage that the proposed potential is expressed in a simple analytical form.

INTRODUCTION

The determination of the coercive force in ferromagnetic materials is a problem of considerable interest, both theoretical and practical. The first model that describes that behavior was proposed by Kersten.[1] He assumed that coercivity was due to the pinning of Bloch walls by second-phase particles, considered the walls as rigid walls and calculated the area decrement to obtain an expression for the surface energy density, which allowed him to determine the coercive force.

The analogy between this problem and the calculus of the yield stress in two-phase alloys was pointed out by Gaunt.[2] He used this insight for modeling the pinning phenomenon, the Bloch wall bowing, in a manner similar to the mechanical problem of dislocation bowing due to pinning centers.

Another approach which takes into account the flexibility of Bloch walls was developed by Della Torre *et al.*[3–5] They used a numerical model considering the wall energy and the magnetic interaction between the pinning obstacle and the Bloch wall to obtain its shape.

The pinning of domain walls by nonmagnetic second-phase particles by pores is similar to the pinning effect of precipitates that impede grain growth in polycrystalline materials, a phenomenon known as the Zener drag.[6]

After the Zener treatment, there have been several works concerning the grain-boundary pinning problem. Gladman[7] treats the problem as one of a planar boundary and Hellman and Hillert[8] consider the growth as due to a curved boundary. Comments on the validity of these models of grain growth inhibition has been recently presented.[9,10]

Gladman's model, although it includes a superflous parameter, is specially well suited for describing the growth of a 180° domain wall, since it considers the movement of a plane unperturbed boundary.

In this paper we modify Gladman's proposal, inspired by the dislocation pinning analogy developed by Gaunt, and we develop and apply it to the phenomenon of migration of a 180° domain wall pinned by an array of nonmagnetic particles or pores.

THE MODIFIED GLADMAN'S MODEL

The model proposed by Gladman considered the displacement of a planar boundary along its normal direction when it is pinned by a spherical inclusion of radius R. Let us fix the origin of our coordinate system in the center of the particle; a plane parallel to the YZ plane contains the unperturbed boundary (see Fig. 1).

Gladman assumed that the perturbed boundary is an hyperboloid of revolution. In a plane through its symmetry axis (plane XY in Fig. 1), the hyperbola has the equation

$$y = (\xi/2)(R^2 - \xi^2/4)^{1/2}/(\xi - x), \qquad (1)$$

where ξ is the distance between the unperturbed boundary and the inclusion. It is to be noted that Eq. (1) implies that the hyperbola has asymptotes for $x = \xi$ and $y = 0$, and also that it intersects the spherical inclusion at right angles.

For different positions of the unperturbed boundary wall, the hyperbolic profiles of the perturbed wall are shown in Fig. 2.

At this point we depart from Gladman's treatment, and we calculate the area variation of the boundary due to the pinning effect of the inclusion. Let us consider Fig. 3; the length element over the hyperboloid is $dl = (d\rho^2 + dx^2)^{1/2}$, $d\rho$ being the corresponding element over the asymptotic plane. Hence, the area variation is

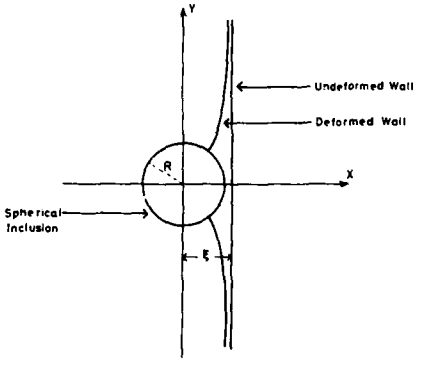


FIG. 1. A cut of the pinned boundary. The growing boundary moves in the $+X$ direction.

a) Present address: Departamento de Física, Universidad de Santiago de Chile, Casilla 5659, Santiago 2, Chile.

 0021-8979/88/084324-03$02.40 © 1988 American Institute of Physics

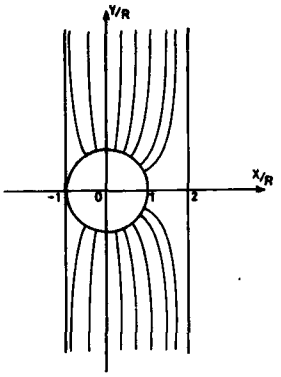


FIG. 2. Wall profiles.

$$\Delta A' = 2\pi \int_{y_0}^{\infty} \rho(dl - d\rho),$$

where y_0 is the ordinate of the contact point between the hyperbola and the inclusion.

Using Eq. (1) the following is obtained:

$$\Delta A' = \pi y_0 [\, y_0 - R + (\xi/4) \times \ln|(2R+\xi)/(2R-\xi)|\,]. \tag{2}$$

It is easy to show that

$$y_0 = (R^2 - \xi^2/4)^{1/2}, \tag{3}$$

hence,

$$\Delta A' = \pi\left(R^2 - \frac{\xi^2}{4}\right)\left[\left(R^2 - \frac{\xi^2}{4}\right)^{1/2} + \left(\frac{\xi}{4}\right)\ln\left|\frac{R+\xi/2}{R-\xi/2}\right| - R\right]. \tag{4}$$

The total area variation, ΔA, is obtained by subtracting from $\Delta A'$ the area of the circle of radius y_0; that is,

$$\Delta A = \Delta A' - \pi(R^2 - \xi^2/4). \tag{5}$$

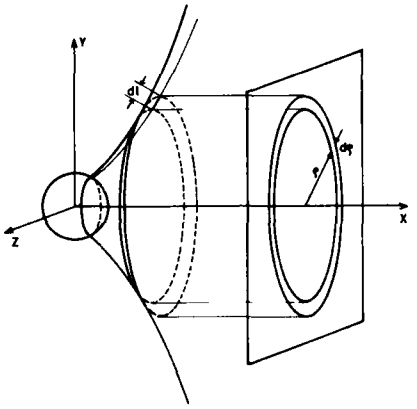


FIG. 3. Same as Fig. 1 but showing the area projection.

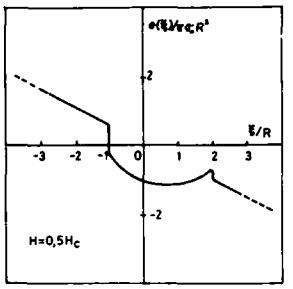


FIG. 4. Interaction energy for the wall-particle system vs undeformed boundary position.

We apply these findings to the pinning of a 180° domain wall growing in the $+x$ direction. Considering that the material at the left-hand side of the wall (Fig. 1) is magnetized in the $-y$ direction and the material at the right-hand side is magnetized in $+y$ direction, an external field H pointing in the $+y$ direction causes the wall movement in the indicated $+x$ direction.

The increase in energy of the wall by the phenomenon of pinning is assumed as the product of a constant energy surface density, σ_0, times the increase in area as calculated in Eq. (5). Then, the energy of the wall one-particle system can be written as

$$U(\xi) = \begin{cases} \pi\sigma_0 R^2\left(1 - \dfrac{\xi^2}{4R^2}\right)^{1/2}\left(\dfrac{\xi}{4R}\ln\left|\dfrac{1+\xi/2R}{1-\xi/2R}\right| - 1\right), \\ \qquad -R < \xi < 2R, \\ 0, \text{ otherwise.} \end{cases} \tag{6}$$

We assume that the pinning centers are distributed in an equivalent simple cubic lattice, with concentration N. Using this distribution we further assume that, for a macroscopic description, the energy per area of the wall boundary associated to each pinning center is

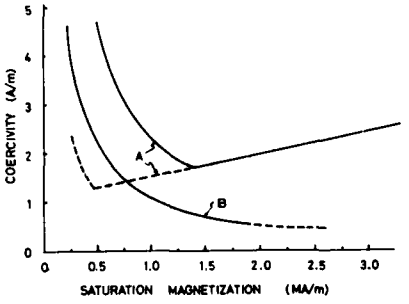


FIG. 5. Coercivity vs saturation magnetization curves. (a) Sukienniki and Della Torre results, P and P' separate regions of low and high magnetization; (b) our results.

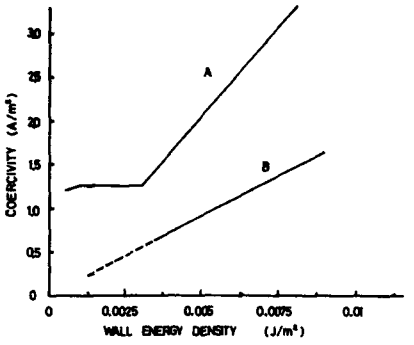


FIG. 6. Coercivity vs wall energy density. (a) Sukienniki and Della Torre results; (b) our results.

$$u(\xi) = U(\xi)/N^{2/3}. \tag{7}$$

As usual,[11] we estimate the coercive field by means of the expression

$$H_c = (2\mu_0 M_s)^{-1}\left(\frac{\partial u}{\partial \xi}\right)_{\max}, \tag{8}$$

where μ_0 is the permeability of free space and M_s is the magnetization at the saturated state. Then, a numerical calculation allows us to write for the coercive field

$$H_c = K(\pi\sigma_0 R/2\mu_0 M_s)N^{2/3}, \tag{9}$$

with $K = 1.09$. Kernsten's finding[1] was roughly one half of the value we obtained.

The total surface density energy of the wall-particle system in the external fields H is

$$e(\xi) = u(\xi) - 2\mu_0 M_s H\xi. \tag{10}$$

This is displayed in Fig. 4, showing a local maximum at $\xi = 1.98R$. The gradient of this energy density gives us the pressure on the wall.

It is to be noted (Fig. 2) that the sequences of wall profiles are not symmetrical respect to the Y axis. Just after the wall touches the precipitate ($\xi = -R$), a suction force appears over the wall; this force changes its direction at $\xi = 0$. For $0 < \xi < 1.98R$, the force slows down the movement of the wall and the subsequent change in the force direction produces the detachment of the wall from the pinning centers.

DISCUSSION

In the present treatment, the magnetic interaction between the nonmagnetic particles or pores with the magnetized material has been neglected. Since this mechanism is considered a significant component in the coercivity of high magnetic materials, our model is suitable for low magnetization materials.

We use the material's parameters employed by Sukienniki and Della Torre[5] to compute coercivity versus saturation magnetization and coercivity versus wall energy density. Ours and their results are shown in Figs. 5 and 6, respectively. We observe that our curve in Fig. 5 lies between the two proposals of these authors. The curves in Fig. 6 show a linear dependence between coercivity and wall energy density, differing in slope.

Furthermore, using the values for magnetic garnets cited in Ref. 4, we obtain a coercive force of 5.5 A/m. It has the same order of magnitude (3.1 A/m) reported in that work.

In the present work the domain is modeled as a surface with no structure. However, we think that more realistic results could be obtained by first considering the magnetic dipole effect before including the domain wall width.

In summary, we have proposed a simple analytical expression for the interaction energy between a domain wall and a precipitate. The application of the proposed potential, already discussed, is in good agreement with the cited numerical findings.

[1]M. Kersten, *Grundlangen einer Theorie der Ferromagntischen und der Koerzitivkraft* (Hirzel, Leipzig, 1943).
[2]P. Gaunt, Philos. Mag. **48**, 261 (1983).
[3]E. Della Torre and M. Torfeh-Isfahani, J. Appl. Phys. **53**, 4309 (1982).
[4]E. Della Torre, J. Kulhanek, and A. Sukiennicki, IEEE Trans. Magn. MAG-19, 2004 (1983).
[5]A. Sukienniki and E. Della Torre, J. Appl. Phys. **55**, 3739 (1984).
[6]C. Zener quoted by C. S. Smith, Trans. AIME **175**, 15 (1948).
[7]T. Gladman, Proc. R. Soc. London Ser. A **294**, 298 (1966).
[8]P. Hellman and M. Hillert, Scan. J. Metall. **4**, 211 (1975).
[9]C. H. Wörner and A. Cabo, Scr. Metall. **18**, 565 (1984).
[10]C. H. Wörner, A. Cabo, and M. Hillert, Scr. Metall. **20**, 829 (1986).
[11]C. Kittel, Rev. Mod. Phys. **21**, 541 (1949).

Period competition in a stripe domain structure subjected to a periodic field

P. Molho, J. L. Porteseil, and Y. Souche
Laboratoire Louis Néel, C.N.R.S.-U.S.T.M.G., 166 X, 38042 Grenoble Cedex, France

The behavior of a parallel array of stripe domains subjected to a periodic field was studied. Experiments were performed on a layer of single-crystal ferrimagnetic garnet (bubble material) featuring in zero field a periodic pattern of parallel stripe domains. The layer was applied to a magnetic tape on which a sinusoidal waveform was recorded. The garnet-tape distance, and hence the interaction strength, could be varied. The resulting domain patterns were observed in polarized light. We present results obtained for a recorded wavelength (66 μm) equal to six times the natural domain period (11 μm). The domain structure adapted itself by reducing the number of stripes, in particular by means of dislocation glide in the stripe array. This resulted in various modulated stripe patterns. The transitions between structures with different stripe numbers could be observed. These were achieved by local distortions of the parallel array around dislocations. The total energy of the garnet layer was calculated as the sum of magnetostatic, wall, and interaction energies for various interaction strengths. The equilibrium domain configuration could be deduced by minimizing the energy with respect to wall positions. The calculated modulated domain structures are in agreement with the observed one.

I. INTRODUCTION

Much attention has been paid in the past few years to period competition effects which occur when a periodic system is subjected to a perturbation of different wavelength.[1] Quasi-periodic patterns were observed in a convecting nematic liquid crystal subjected to spatially periodic forcing.[2,3] We report here similar experiments on a periodic domain structure (DS) in a garnet layer (bubble material) subjected to the periodic field created by a magnetic tape on which a sine signal was recorded. Such a setup was already used to study the feasibility of magneto-optically reading magnetic media, and it was observed that the DS in the garnet could reproduce the recorded wave in a certain wavelength range.[4–8] We deal here with the evolution of the DS when the garnet-tape interaction increases, which is achieved by decreasing the air gap between them, when the recorded wavelength is large with respect to the natural period of the DS.

II. EXPERIMENT

The sample was a 5.3-μm-thick garnet layer of formula $(YLuBi)_3(FeGa)_5O_{12}$, epitaxially deposited on a 111-oriented GGG substrate. Its saturated flux density $4\pi M_S$ was 188 G, and its equilibrium period (twice the width of a single "up" or "down" stripe) was 11 μm.

The magnetic tape was a regular, longitudinal recording audio tape. The wavelength of the recorded sine wave, and hence of the field which acted upon the garnet, was 66 μm.

The garnet was held parallel to the tape as indicated by Fig. 1, the parallel stripes of the initial DS being oriented across the tape axis. The tape-garnet distance h could be varied, and domain observations were performed by means of a polarizing microscope using the magneto-optical Faraday effect.

Figure 2 shows some stages in the evolution of the DS, from the initial structure made of equal parallel stripes, as h decreased. The first stage (a) consisted of modulated stripe widths, the number of stripes being preserved. In the next step (b), dislocations appeared in the stripe array and allowed for collapse of some stripes. This collapse did not take place in an homogeneous fashion (may be due to imperfect tape-garnet parallelism) and showed progressive accommodation of the DS to the recorded period. This mechanism continued as h was further decreased (c) until the final state (d) obtained for maximum interaction ($h = 0$), which was again made of parallel but fewer stripes with modulated widths.

III. THEORY

The above patterns were interpreted by calculating the energy of the DS as a function of h, including the dipolar energy of the magnetic layer, the wall energy, and the interaction with the tape. Let D_0 be the initial period of the DS, D_1 the period of a hypothetical undeformed DS after suppressing a certain number of stripes, D_2 the recorded period, and

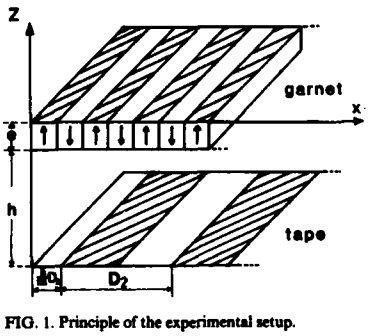


FIG. 1. Principle of the experimental setup.

 0021-8979/88/084327-03$02.40 © 1988 American Institute of Physics

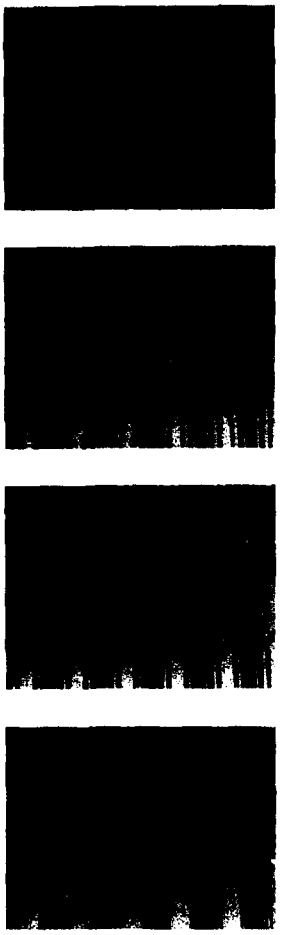


FIG. 2. Evolution of the domain pattern as the interaction strength is increased.

N_1 and N_2 the smallest integers such that $N_1D_1 = N_2D_2 = D$ period of the overall system.

The DS can be assimilated to a sequence of magnetization steps (Fig. 3). A period D contains $2N_1$ steps (stripes); the k th step is located a distance l_k away from the origin and has a width $l_{k+1} - l_k$.

The z component of the field created inside the garnet layer by the magnetic poles on the upper face of the layer can be expressed by the Fourier series[9]:

$$H_z(x,z) = -2\pi M_S\left(\sum_{k=1}^{2N_1} a_{0k} + \sum_{k=1}^{2N_1}\sum_{j=1}^{\infty}(a_{jk}\cos j2\pi x/D \times \exp j2\pi z/D + b_{jk}\sin j2\pi x/D \times \exp j2\pi z/D)\right), \quad (1)$$

with

$$a_{0k} = (-1)^{k+1}D/2\pi,$$

$$a_{jk} = (-1)^{k+1}(2/D)\int_{l_k}^{l_{k+1}}\cos j2\pi x/D\,dx$$

$$= (-1)^{k+1}/j\pi(\sin j2\pi l_{k+1}/D - \sin j2\pi l_k/D) \quad (j>1),$$

$$b_{jk} = (-1)^{k+1}(2/D)\int_{l_k}^{l_{k+1}}\sin j2\pi x/D dx$$

$$= (-1)^{k}/j\pi(\cos j2\pi l_{k+1}/D - \cos j2\pi l_k/D) \quad (j>1).$$

Let

$$A_0 = \sum_{k=1}^{2N_1} a_0k,$$

$$A_j = j\pi/2\sum_{k=1}^{2N_1} a_{jk} = \sum_{k=1}^{2N_1}(-1)^k\sin j2\pi l_k/D,$$

$$B_j = j\pi/2\sum_{k=1}^{2N_1} b_{jk} = \sum_{k=1}^{2N_1}(-1)^k\cos j2\pi l_k/D.$$

Then

$$H_z(x,z) = -2\pi M_S\left(A_0 + \sum_{j=1}^{\infty}(2/j\pi)(A_j\cos j2\pi x/D + B_j\sin j2\pi x/D)\exp j2\pi z/D\right), \quad (2)$$

and similarly, the magnetization in the layer is

$$M(x) = M_S\left(A_0 + \sum_{j=1}^{\infty}(2/j\pi)(A_j\cos j2\pi x/D + B_j\sin j2\pi x/D)\right). \quad (3)$$

Taking into account both faces of the layer, the demagnetizing energy per unit area of layer is

$$E_p = (2/D)(-1/2)\int\int M(x)H(x,z)dx\,dz$$

$$= (2M_S^2D/\pi^2)\sum_{j=1}^{\infty}(A_j^2 + B_j^2)/j^3. \quad (4)$$

The field created by the tape is[9]

$$H_{ext} = H_0\sin(2\pi x/D_2 + \delta)\exp(-2\pi z/D_2), \quad (5)$$

where δ is the phase shift of the recorded periodic signal with respect to the origin of the x axis (see Fig. 1). H_0 depends on

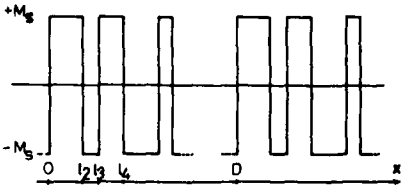


FIG. 3. Representation of the domain structure by a sequence of period D of magnetization steps. The distance of the k th step to the origin is l_k ($l_1 = 0$).

TABLE I. Configurations (N_1,N_2) corresponding to the values of D_1 for which the energy minimization was performed, and values of the interaction field H_1 (see text) for which every configuration is the lower-energy state.

$D_1(\mu m)$	11	11.65	13.2	14.67	16.5	18.86	22	33	66
N_1	6	17	5	9	4	7	3	2	1
N_2	1	3	1	2	1	2	1	1	1
H_1 (Oe)	0	45	100	115	125	135	145	···	···

the remanent magnetization of the tape. The interaction energy per unit area reads

$$E_i = -1/D \int_{x=0}^{D} \int_{z=h}^{h+e} M(x) H_{\text{ext}}(x,z)\,dx\,dz. \qquad (6)$$

All contributions cancel out in the integration over a period D, except that of the N_2th harmonic:

$$E_i = -(D_2/N_2)(M_S H_0/2\pi^2)\exp(-2\pi h/D_2) \times [1-\exp(-2\pi e/D_2)](A_{N_2}\sin\delta + B_{N_2}\cos\delta). \qquad (7)$$

Finally the wall energy per unit area of layer is

$$E_w = \sigma e 2N_1/D, \qquad (8)$$

σ being the superficial energy density of domain walls.

Given D_1, which fixed the values of N_1, N_2, and D $(N_1D_1 = N_2D_2 = D)$, we calculated the set of l_k which minimized the total energy $E_T = E_p + E_i + E_w$ as a function of the parameter h. We performed this minimization for values of D_1 corresponding to small integers N_1 and N_2. Thus we obtained the dependence of the l_k at equilibrium on h, together with the energy E_T at equilibrium. From these data, one can plot the energy versus D_1. The curves show a minimum which yields the equilibrium value of D_1 for given h. For better physical understanding, the results are given in terms of the interaction field

$$H_1 = H_0 \exp(-2\pi h/D_2)[1-\exp(-2\pi e/D_2)] \times \exp(2\pi e/D_2)$$

rather than h (Table I). This effective field takes in account the unknown remanent magnetization of the tape, and the distance h which is also not precisely known.

IV. ANALYSIS OF OBSERVATIONS AND CONCLUSION

Due to the nonuniformity of the field on the sample (there is a gradient perpendicular to the x axis) we can observe several states of the domain structure on the same picture (Fig. 4). In the top of that picture, we see a periodic structure. The period is equal to $D_2 = 66\ \mu m$ and contains six black stripes plus six white stripes. The observed widths agree with those calculated for $N_1 = 6$, $N_2 = 1$, $H_1 = 80$ Oe, as shown on the figure.

Lower in that picture we see stripe collapse (three stripes merge into one) at the approximative rate of one collapse per period D_2: the configuration is now defined by $(N_1 = 5, N_2 = 1)$. The observed l_k are again in agreement with calculations for $H_1 = 100$ Oe which is the equilibrium field for that configuration (Table I). In the lower part of Fig. 4, the structure locks to $(N_1 = 4, N = 1)$ and the l_k correspond to $H_1 = 125$ Oe, also the equilibrium field for that configuration (Table I).



FIG. 4. Calculated stripe widths compared to the observed ones; upper: $N_1 = 6, N_2 = 1, H_1 = 80$ Oe; center: $N_1 = 5, N_2 = 1, H_1 = 100$ Oe (equilibrium); lower: $N_1 = 4, N_2 = 1; H_1 = 125$ Oe (equilibrium).

It can be concluded that the DS adjusts its period to the interaction by locking to the recorded wavelength. The pattern $(N_1 = 6, N_2 = 1)$ persists over an extended interaction range due to the energy barrier which prevents stripe collapse. On the contrary, the patterns $(N_1 = 5, N_2 = 1)$ and $(N_1 = 4, N_2 = 1)$ can be observed only in a reduced region in which they are close to the equilibrium state, because of easy motion of the dislocation which have appeared. The transition regions are complex, may be of very big period, and exhibit considerable distortion of the stripe array around dislocations. The final pattern (maximum interaction) is essentially homogeneous, but it is difficult to say if it is periodic due to limited observation field. We can only say that motifs of configurations $(N_1 = 4, N_2 = 1)$, $(N_1 = 3, N_2 = 1)$, $(N_1 = 2, N_2 = 1)$, appear in that structure.

ACKNOWLEDGMENTS

Thanks are due to P. Coullet for suggesting this type of experiment, and L. Arnaud for giving us the sample.

[1] P. Coullet and D. Repoux, Europhys. Lett. 3, 573 (1987).
[2] M. Lowe, J. P. Gollub, and T. C. Lubensky, Phys. Rev. Lett. 51, 786 (1983).
[3] M. Lowe and J. P. Gollub, Phys. Rev. A 31, 3893 (1985).
[4] T. Yamada, H. Matsuda, Y. Makino, and M. Himuro, Proceedings of the 3rd International Conference on Ferrites, Kyoto, 1980, p. 751.
[5] T. Nomura, IEEE Trans. Magn. MAG-21, 1545 (1985).
[6] T. Nomura, IEEE Trans. Magn. MAG-23, 1923 (1987).
[7] E. Huijer, J. C. Lehureau, and J. P. Castera, IEEE Trans. Magn. MAG-23, 1919 (1987).
[8] J. C. Lehureau, J. P. Castera, and J. M. Desvignes, Proceedings of Intermag, Tokyo, 1987.
[9] See, for example, A. Herpin, *Theorie du Magnetisme* (Bibliotheque des Sciences et Techniques Nucleaires, 1968).

A theory of the three-dimensional solenoidal magnetization configurations in ferro- and ferrimagnetic materials

R. Vlaming
University of Technology, Delft, The Netherlands
H. A. M. van den Berg
Siemens, P. O. Box 3240, Erlangen, Federal Republic of Germany

A method for constructing three-dimensional solenoidal magnetization distributions, with invariant magnitude of $\mathbf{m}$, in arbitrarily shaped objects is presented. The formalism harks back to the theory developed by van den Berg for two-dimensional $\mathbf{m}$ distributions. The space within a general object Ω is partitioned into i subspaces Ω_i, described by a family of surfaces to which the magnetization is tangent. A characteristic equation which defines the course of $\mathbf{m}$ at each of the surfaces is derived. A boundary condition for $\mathbf{m}$ arises naturally, or can be chosen to determine $\mathbf{m}$ at the surface. Within the above framework an infinite number of solutions are generated that, in general, exhibit singularities. Special attention, also from the topological point of view, is paid to the $\mathbf{m}$ distributions having point defects only.

INTRODUCTION

Landau and Lifshitz[1] founded the basis of the micromagnetic theory, which was further developed into a self-consistent mathematical framework by Brown. Explicit solutions of the magnetic dipole distribution in three-dimensional objects could be formulated in a few special cases only, owing to the strong nonlinearity of the equations. In this paper, again, a special situation is treated because we confine ourselves to ideally soft-magnetic objects of sufficient dimensions to which no fields are applied. The magnetostatic energy dominates the magnetization distribution and can be minimized by taking a solenoidal configuration, e.g., $\nabla\cdot\mathbf{m}=0$ and $\mathbf{m}$ parallel to the object boundary. The most important exchange interaction is included in the ferromagnetic condition $\mathbf{m}\cdot\mathbf{m}=m_s^2$. Hubert[2] and Arrott[3] attempted to solve this problem by taking $\mathbf{m}$ equal to $\mathbf{m}=\text{rot}\,\mathbf{A}$, however, a third-order differential equation in $\mathbf{A}$ was obtained, which could only analytically be solved for a few special cases.

In this paper an analytic method is presented that generates solenoidal three-dimensional magnetization distributions. In principle, it is an elaboration of the two-dimensional theory of van den Berg.[4] This method will be developed in the first part, while, subsequently, a few examples will be discussed. Special attention will be paid to the $\mathbf{m}$ distributions with singular points only, because they are expected to possess the minimum energy.

THEORY

In order to give a proper description of the magnetization distribution within a general object it is necessary to decompose the object space Ω into i subspaces Ω_i, which satisfy:

$$\Omega_i\cap\Omega_j=0 \quad \text{for} \quad i\neq j \quad \text{and} \quad \cup\Omega_i=\Omega\,. \tag{1}$$

At the boundary $\delta\Omega_i$ of Ω_i, $\mathbf{m}$ is required to be tangent to $\mathbf{m}$. In each Ω_i, a solenoidal $\mathbf{m}$ distribution will be derived. The $\mathbf{m}$ distributions in the various subspaces Ω_i constitute the total vector field in Ω, which is always a valid solution of the stated problem. To derive a solenoidal $\mathbf{m}$ field in Ω_i, a family of unbounded surfaces $f_i(\mathbf{q})=0$ whose members have no point of intersection inside Ω_i is defined. The magnetization is required to be tangent to the surfaces at the surfaces. On each f_i, $\mathbf{m}$ will be determined by the characteristic equations and the complementary boundary conditions. The distributions at the surfaces f_i constitute the total vector field in Ω_i. There are two situations for every surface f_i. First, f_i has at most points of contact with the boundary $\delta\Omega_i$ and, second, one or more lines of intersection with $\delta\Omega_i$ exist. In the latter case a boundary condition for $\mathbf{m}$ is created in a natural fashion, which might lead to a line singularity, as described later on.

As outlined above, the determination of $\mathbf{m}$ at each f_i, constitutes an essential step in our framework. For simplicity, we define an orthonormal coordinate system with variables q^1, q^2, and q^3 where q^1 and q^2 determine the positions at each f_i, at which each f_i is defined by a specific q^3. Obviously, $m^3=0$ since $\mathbf{m}$ is tangent to f_i. Thus, we have transformed the three-dimensional problem into a two-dimensional one without loss of generality, which is governed by the following equations:

$$\nabla\cdot\mathbf{m}=0, \tag{2}$$

$$\mathbf{m}\cdot\mathbf{m}=m_s^2=(m^1)^2+(m^2)^2\,, \tag{3}$$

$$\mathbf{m}\cdot\mathbf{n}=0 \quad (\mathbf{n}\text{ normal to }\delta\Omega). \tag{4}$$

By defining a new variable,

$$\xi=m^2/m^1, \tag{5}$$

all the $\mathbf{m}$ components can be eliminated from relations (2) and (3) in an orthonormal curvelinear system. The ultimate partial differential equation solved by the method of characteristics (see Sneddon[5]) yields the system

$$\frac{dq^1}{dt}=h_2h_3\xi\,, \tag{6a}$$

$$\frac{dq^2}{dt}=-h_1h_3\,, \tag{6b}$$

 0021-8979/88/084330-03$02.40 © 1988 American Institute of Physics

$$\frac{d\xi}{dt} = (1+\xi^2)\left(\frac{\partial h_2 h_3}{\partial q^1} + \xi \frac{\partial h_1 h_3}{\partial q^2}\right), \tag{6c}$$

where t is a position parameter along the characteristic and the coefficients h_j are the fundamental transformation functions.[6] This system generates curves, called characteristics, to which the magnetization is perpendicular. The complementary boundary condition is defined at curve Γ_i not perpendicular to $\mathbf{m}$ at which $\mathbf{m}$ is given. In general, the characteristics intersect and mostly ambiguities in $\mathbf{m}$ arise at these points. To stave off these ambiguities, mathematical singularities have to be allowed at points and along lines at f_i. In two dimensions, these lines represent domain walls as van den Berg[4] demonstrated. This two-dimensional method will be transposed to the three-dimensional case. In three dimensions a point singularity and line defects at each f_i generally pile up to line and surface defects (domain walls), respectively.

Evidently, the initial curve Γ_i plays an important role in determining the magnetization on f_i. If a line of intersection between $\delta\Omega_i$ and a specific f_i exists, this boundary naturally forms the curve Γ_i at which $\mathbf{m}$, and thus ξ, is prescribed. When f_i is a closed surface inside $\delta\Omega_i$ the boundary Γ_i on f_i can be freely chosen; however, it should be emphasized that this freedom, in general, does not exist when f_i belongs to the class of generalized tori. This class has specific significance for $\mathbf{m}$ distributions that contains point singularities only.

Let's introduce a classification of the surfaces f_i that are completely located in Ω_i. Within Ω_i, the surfaces f_i are closed (compact and having no boundary) if they do not intersect with $\delta\Omega_i$. All two-dimensional, orientable, and closed surfaces can be topologically classified according to the genus number g, simply meaning the number of "holes" in the surface. This number is related to the Euler–Poincaré characteristic χ (see Dubrovin[7]) by $\chi = 2 - 2g$. χ is related to the number and nature of the signularities. For example, a nonvanishing continuous vector field tangent to a sphere ($g = 0$) must be singular at least two points. The only category of surfaces that need not have singular points is the one with $\chi = 0$ and $g = 1$. The only surfaces with $\chi = 0$ that are orientable and suit our purposes is the torus and the surfaces homeomorphic to it, called generalized tori. The family f_i should merely consist of these tori when an $\mathbf{m}$ distribution with the smallest number of defects possible is aimed at.

Let's consider such an $\mathbf{m}$ distribution in the simply connected subspace Ω_i. At least two singular points lie at the "axis" of the tori system, which is formed by the degenerated "outermost" torus that asymptotically approaches to $\delta\Omega_i$.

Another useful topological concept is that of the winding number n, described by Mermin.[8] A point singularity at a surface is characterized by it and it can be found by taking a null-homotipic curve (a curve that can continuously be deformed to a point without leaving the surface) around the singularity and calculating:

$$\frac{1}{2\pi}\oint d\phi = n\,, \tag{7}$$

in which ϕ is the angle of $\mathbf{m}$ with respect to a reference direction. From this winding-number conservation law (7), it is obvious that at least one singular point at f_i exists when f_i intersects $\delta\Omega_i$ along one single line (Fig. 1).

EXAMPLES

A physical meaning can be attributed to the coefficients h_j in Eq. (6). Let's take q^1 along the $\mathbf{m}$ lines ($\xi = 0$), which is always locally possible. From (6c), it follows

$$\frac{\partial h_2 h_3}{\partial q^1} = 0\,. \tag{8}$$

In other words, the cross section $h_2 h_3$ of the tube bounded by $\mathbf{m}$ lines is constant, e.g., the flux is conserved (see Fig. 2). Let's subsequently pose the following extra limitation:

$$h_2 = h_2(q^2,q^3); \quad h_3 = h_3(q^2,q^3)\,. \tag{9}$$

A moving Serret–Frenet frame can be introduced[9] for each of the parameter curves. The tangential $\mathbf{t}$ and the principal normal $\mathbf{n}$ are indexed with the corresponding parameter number. Then

$$\mathbf{t}_2 \cdot \mathbf{t}_1 = 0 \tag{10}$$

holds. Let $\mathbf{r}$ denote the position of the characteristic curve; then relation (10) leads to

$$\frac{\partial^2 \mathbf{r}}{\partial q^2\,\partial q^1}\frac{\partial \mathbf{r}}{\partial q^2} + \frac{\partial \mathbf{r}}{\partial q^1}\frac{\partial^2 \mathbf{r}}{(\partial q^2)^2} = 0\,. \tag{11}$$

From Eq. (9) and the definition of h_2, it follows that

$$\frac{\partial^2 \mathbf{r}}{\partial q^2\,\partial q^1}\frac{\partial \mathbf{r}}{\partial q^2} = 0\,. \tag{12}$$

This means that the second term in (11) is zero and $\mathbf{n}_2 \cdot \mathbf{t}_1 = 0$.

Thus, the principal normal from the characteristic is perpendicular to the surface and therefore each characteristic is a so-called geodesic curve at the surface. The physical interpretation of it can be found in the geodesic parallels[9] which coincide with the $\mathbf{m}$ lines. This means that the shape of the cross section of the magnetic flux tubes (see Fig. 2) does not change along a particular $\mathbf{m}$ line. Corresponding q_1 lines

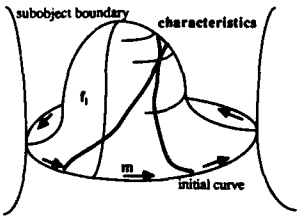


FIG. 1. Surface f_i that intersects Ω_i at the initial curve Γ_i.

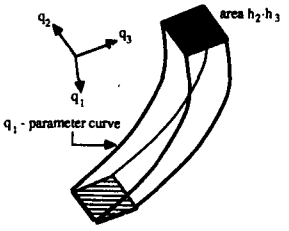


FIG. 2. Infinitesimal tube in which the flux is captured. Shaded area is constant.

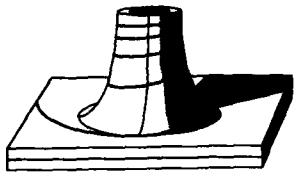


FIG. 3. Global impression of three f_i's near Arrott's singular point. The thick line is a characteristic.

on the surfaces f_i and f_{i+di} are parallel in the geodesic sense. The surfaces f_i are parallel everywhere, when, in addition, h_3 is independent of q^2.

As a special case of the above simple situation, the magnetic distributions in plane parallel thin-film objects considered by van den Berg[4] can be mentioned. Here, the family f_i has only one member: a plane. Formally this situation can be continued in the third dimension obtaining parallel surfaces. The geodesics on the plane are straight lines perpendicular to Γ_i and $\mathbf{m}$ and which intersect one another. Lines of discontinuity in $\mathbf{m}$, e.g., domain walls, should arise[4] to stave off ambiguities in $\mathbf{m}$. The inevitability of singularities at these planes also follow from the topological relation (7).

The cylinder solution described by Arrott[3] is another example. The cylinder contains only two point singularities and it is therefore expected that the associated surface system consists of the generalized tori. The problem of constructing these tori is simplified by the fact that the object possesses rotational symmetry. First, a better understanding of the singularity is required. Therefore, a family f_i of noncompact surfaces that is developed about the defect located at the origin is introduced:

$$f_i(r,\theta,\phi) = r\sin\theta\sqrt{\cos\theta} + i = 0\,, \tag{13}$$

where r,θ,ϕ are spherical coordinates. For convenience, a nonorthogonal system is defined:

$$x = u\cos v, \tag{14a}$$

$$y = u\sin v, \tag{14b}$$

$$z = w^2u/\sqrt{u^4 - w^4}\,, \tag{14c}$$

where q^1,q^2 are replaced by u and v, respectively. The equivalent equations to Eq. (6) yield

$$\xi = \frac{\pm u^5}{(u^4 - w^4)^{3/2}}\sqrt{C(s,w) + \frac{w^4(2u^4 - 5w^4)}{u^8}} + \xi_0(s,w)\,, \tag{15}$$

where s denotes the position parameter along Γ_i. When we put $C(s,w) = 3$, $\xi(s,w) = 0$, and sign $(\xi) = -1$, Arrott's "simplest" point singularity in a field of constant magnitude is obtained. The course of the corresponding characteristic is given in Fig. 3. $\mathbf{m}$ for the above values is given by

$$m_u = -\left[(u^4 - w^4)^{3/2}/2u^6\right], \tag{16a}$$

$$m_v = \frac{(u^4 - w^4)^{3/2}}{2u^6}\left(\frac{u\sqrt{3u^4 + 5w^4}}{(u^4 - w^4)}\right), \tag{16b}$$

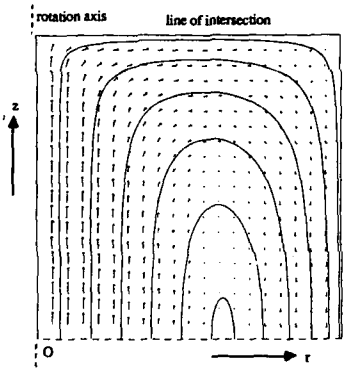


FIG. 4. Cylinder solution of Arrott projected on the plane $\phi = 0$, $z > 0$. The lines of intersection of the above plane and the tori are indicated by the drawn lines.

or, in spherical coordinates,

$$m_r = \tfrac{1}{2}(3\cos^2\theta - 1)\,, \tag{16c}$$

$$m_\theta = -\sin\theta\cos\theta\,, \tag{16d}$$

$$m_\phi = \tfrac{1}{2}\sin\theta\sqrt{5\cos^2\theta + 3}\,. \tag{16e}$$

Unfortunately, the magnetization on the cylinder casing cannot be covered by one single analytic expression, but numerical integration shows the tori that exist in the cylinder. It has to be pointed out that the magnetization lines are of infinite length on these tori and not periodic! Figure 4 shows the magnetization in the upper quadrant of the cylinder. Also some tori are plotted. The magnetization patterns all have more or less the same structure, a fact already recognized by Arrott, due to the rotational symmetry and the fact that tori system must converge to the cylinder surface $\delta\Omega$. The interesting question of whether Arrott's solution with only point singularities can be generalized for arbitrary objects will be the subject of a forthcoming paper.

[1] L. Landau and E. Lifshitz, Phys. Z. Sowjetunion 8, 153 (1935).
[2] A. Hubert, Phys. Status Solidi 32, 519 (1969).
[3] A. S. Arrott, B. Heinrich, and A. Aharoni, IEEE Trans. Magn. MAG-15, 1228 (1979).
[4] H. A. M. van den Berg, J. Appl. Phys. 61, 4194 (1987).
[5] I. N. Sneddon, *Elements of Partial Differential Equations* (McGraw-Hill, Tokyo, 1957).
[6] J. A. Stratton, *Electromagnetic Theory* (McGraw-Hill, New York, 1941).
[7] B. A. Dubrovin, A. T. Fomenko, and S. P. Novikov, *Modern Geometry, Methods and Applications II* (Springer, New York, 1985).
[8] N. D. Mermin, Rev. Mod. Phys. 51, 591 (1979).
[9] T. J. Willmore, *Differential Geometry* (Oxford University Press, Oxford, 1983).

Effect of preannealing on the kinetics of the reorientation of the field-i: duced anisotropy in CoZr thin films (abstract)

Tomasz Jagielinski
Diversified Technologies Group-Research Laboratories, Eastman Kodak Company, San Diego, California 92121

In this paper, we will analyze the changes in the kinetics of the induced anisotropy due to preannealing in 300-Å and 1-μm-thick $Co_{94}Zr_6$ amorphous films. Samples were prepared by a dc sputtering method. A silicon wafer with SiO_2 overcoat was used as a substrate material, and a field of 200 Oe was applied during the deposition to induce uniaxial anisotropy. Based on x-ray data and resistivity measurements, the films were considered amorphous. The samples were annealed in a magnetic field at temperatures up to 500 °C, and the annealing time was varied from 0.5 to 400 h. As previously reported, the anisotropy, K_u, in as-deposited samples is a function of sample thickness and varied from 1.6×10^4 ergs/cm^3 for 300-Å film to $\sim1\times10^4$ ergs/cm^3 for 1-μm films [T. Jagielinski, J. Appl. Phys. **61**, 3237 (1987)]. It was found that the K_u in thick films is reversible, and the kinetics can be fully explained by the anelasticity model [T. Egami, Rep. Prog. Phys. **47**, 1601 (1984)]. The mean value of the activation energy is ~2 eV for samples preanneled at 375 °C. However, in the case of thin films, an additional irreversible component of anisotropy, always along the direction of the field applied during the deposition, is observed. The magnitude is a growing function of annealing temperature, and is as large as 3×10^4 ergs/cm^3 for a 300-Å sample preanneled at 400 °C. The origin of the irreversible component of the anisotropy is not well understood. Based on x-ray data, we concluded that this effect is not related to crystallization. However, since anisotropy is thickness dependent, the structure of the film-substrate interface seems to be responsible for the irreversible part. The reversible parts of anisotoropy behave similarly in both thin and thick films and are 1.6×10^4 ergs/cm^3 and 8×10^3 ergs/cm^3 for 300-Å and 1-μm films, respectively.

 0021-8979/88/084333-01$02.40 © 1988 American Institute of Physics

$Rb_2Cu_{1-x}Co_xF_4$, a two-dimensional Ising spin glass

C. Dekker, A. F. M. Arts, and H. W. de Wijn
Fysisch Laboratorium, Rijksuniversiteit Utrecht, P. O. Box 80.000, 3508 TA Utrecht, The Netherlands

We report on the dc susceptibility of the insulating spin glass $Rb_2Cu_{1-x}Co_xF_4$, with $x = 0.22$. This model compound is a realization of the two-dimensional short-range Edwards–Anderson model, which has competing nearest-neighbor Ising interactions. Below a frequency-dependent freezing temperature spin-glass behavior is observed for longitudinal spin components only. The nonlinear part of the susceptibility is found to excellently obey static $T_c = 0$ scaling with $\beta = 0.0 \pm 0.1$ and $\Delta = 3.2 \pm 0.2$, in conformity with the Monte Carlo results for the two-dimensional Edwards–Anderson model, $T_c = 0$, $\beta = 0$, and $\Delta = 3.5 \pm 0.5$. These findings thus provide experimental evidence for the lower critical dimensionality for Ising spin glasses to exceed 2.

INTRODUCTION

A consensus has been reached that the lower critical dimensionality d_l for Ising spin glasses is between two and three.[1,2] Extensive Monte Carlo (MC) simulations as well as various theoretical arguments have convincingly shown that the three-dimensional ($d = 3$) Ising spin glass (SG) enters an ordered phase at a finite critical temperature T_c, while for $d = 2$ order is not achieved until $T_c = 0$.[2–4] As concerns the experiments performed up till now, a vast number of three-dimensional SG systems have been studied, but data for $d = 2$ systems are still scarce. Besides, the few reports on the latter[5] all concern planar spin ordering, rather than spin ordering along an easy axis, such as considered in the MC and theoretical calculations on Ising SG systems.

In this paper, for the first time experimental data on a $d = 2$ Ising SG, viz., $Rb_2Cu_{1-x}Co_xF_4$, are presented. This model compound closely conforms to the characteristics of the $d = 2$ short-range Edwards–Anderson (EA) model,[6] i.e., Ising anisotropy, a square lattice, and a distribution of ferro- and antiferromagnetic nearest-neighbor interactions. As it appears below, our results are strikingly similar to those from MC simulations of the $d = 2$ EA model, culminating in an excellent $T_c = 0$ scaling of the nonlinear susceptibility.

MAGNETIC STRUCTURE OF $Rb_2Cu_{1-x}Co_xF_4$

The crystal structure of $Rb_2Cu_{1-x}Co_xF_4$ is, as that of the pure end members, of the K_2NiF_4 type. The magnetic ions are situated on a simple square lattice within widely separated layers, with the intralayer exchange at least three orders stronger than the interlayer exchange. Rb_2CoF_4 is an archetypal $d = 2$ Ising antiferromagnet, ordering with the spins along the tetragonal axis below $T_N = 103.0$ K.[7] The magnetic properties of Rb_2CuF_4 presumably are quite similar to those of the extensively studied $d = 2$ ferromagnet K_2CuF_4, which has predominant Heisenberg exchange with small ($\sim 1\%$) XY anisotropy such as to leave the spins within the plane.[8] Our magnetization experiments on Rb_2CuF_4 indeed establish planar ferromagnetic ordering, and further yield $T_c = 6.0 \pm 0.1$ K. Because the uniaxial single-ion anisotropy of Co^{2+} is so strong, Co substituted for Cu directs the spins along the c axis already for small Co concentrations x. In fact, for $x = 0.06$ we find that the system essentially behaves as a uniaxial ferromagnet.

Randomizing Co and Cu spins over the square lattice leads to a distribution of nearest-neighbor exchange interactions that is special in that it tends to bond randomness. As has been pointed out,[9] in the Cu compounds the arrangement of the Cu^{2+} $d_{z^2-x^2}$ and $d_{z^2-y^2}$ ground-state orbitals is such that they alternate along the crystallographic [100] and [010] axes, leading to a ferromagnetic Cu – Cu exchange. As illustrated in Fig. 1, the substitution of Co for Cu then results in two possible Cu – Co exchange interactions, depending on the orientation of the Cu^{2+} orbital relative to the Cu–Co bond. The exchange is antiferromagnetic in case the d orbital lobe points towards the Co ion, and ferromagnetic otherwise.[10] In $Rb_2Cu_{1-x}Co_xF_4$, we thus have two ferromagnetic (Cu – Cu and Cu – Co) and two antiferromagnetic interactions (Cu – Co and Co – Co). By virtue of the high uniaxial Co anisotropy the Co-Co and the Cu-Co interactions are expected to be Ising-type in character. The phase diagram of $Rb_2Cu_{1-x}Co_xF_4$ contains a SG region for $0.2 < x < 0.4$, bordered by ferromagnetic and antiferromagnetic phases.[11] In this range of concentrations,

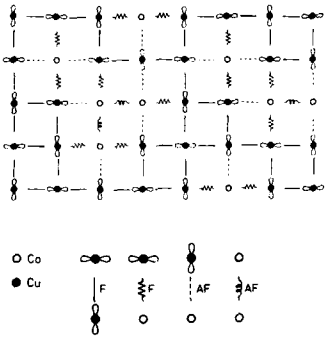


FIG. 1. Distribution of ferromagnetic (F) Cu-Cu and Cu-Co and antiferromagnetic (AF) Co-Co and Cu-Co exchange interactions in $Rb_2Cu_{1-x}Co_xF_4$ for $x = 0.22$. Also indicated are the in-layer d orbital lobes of Cu^{2+}.

 0021-8979/88/084334-03$02.40 © 1988 American Institute of Physics

$Rb_2Cu_{1-x}Co_xF_4$ may thus serve as an experimental realization of the $d = 2$ EA model.

EXPERIMENTAL RESULTS

Single crystals of $Rb_2Cu_{1-x}Co_xF_4$ over the entire concentration range were grown from a stochiometric melt of RbF, CuF_2, and CoF_2 with the Czochralski pulling technique. Here, we focus upon the results for a good-quality sample with $x = 0.22$, as determined with atomic absorption spectroscopy. The sample was shaped roughly to the form of an ellipsoid with dimensions $7.0 \times 3.9 \times 1.3$ mm^3. Magnetic moments were measured with a vibrating-sample magnetometer with a sensitivity of 10^{-5} emu. External fields up to 12.5 kG were applied. All fields were corrected for demagnetization effects. In zero field, the earth magnetic field was compensated by a pair of Helmholz coils. The sample was oriented to within 2° with its c axis parallel or perpendicular to the field direction. Below 4.25 K, the temperature was stabilized to within 0.01 K by controlled pumping of a liquid helium bath. Above 4.25 K, temperatures were maintained with a servostabilized He gas flow to an accuracy of 0.1 K.

Two different experimental procedures were used: (i) field cooling (FC), where the field was turned on at high temperature, say 20 K, and the magnetization $M(T)$ was measured after slow cooling (typical cooling rate of 5 mK/s), and (ii) zero-field cooling (ZFC), where the sample was slowly cooled in zero field to the temperature of interest, at which the field was switched on and $M(T)$ was monitored as a function of the time.

In Fig. 2, the temperature dependences of the FC and ZFC magnetizations are shown in an external field $H = 10.0$ G. For $\mathbf{H} \| \mathbf{c}$ a SG-like maximum in $M^{ZFC}(T)$ is observed near 3 K, which is accompanied with the onset of strong hysteresis in FC and ZFC magnetizations. For $\mathbf{H} \perp \mathbf{c}$ (inset of Fig. 2), the FC and ZFC data are essentially indistinguishable, demonstrating that the freezing is restricted to longitudinal spin components only. Taking the peak position of $M^{ZFC}(T)$ as a phenomenological definition of a freezing temperature T_f, we observe strong dynamical effects, i.e., a decrease of T_f from 3.10 K at 10 s to 2.97 K at 90-s observation time. Both for $\mathbf{H} \| \mathbf{c}$ and $\mathbf{H} \perp \mathbf{c}$ the FC magnetization increases with decreasing temperature down to the lowest temperature reached. In other words, we do not observe the characteristic plateau in $M^{FC}(T)$ below T_f seen in metallic spin glasses, such as CuMn,[12] as well as in insulating spin glasses, such as $Fe_{0.5}Mn_{0.5}TiO_3$.[13] Rather than attributing this to an effect of the dimensionality, we believe this to be caused by a reduction of local magnetizations by low-lying thermal excitations residing on the percolating Cu backbone. Below approximately 3 K, the FC magnetization appears to be dependent on the cooling rate. Apparently, at these low temperatures the FC magnetization deviates from the equilibrium magnetization.

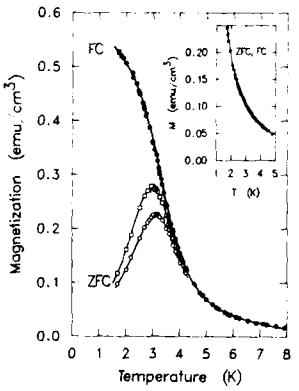


FIG. 2. Field-cooled (filled symbols) and zero-field-cooled (open symbols) magnetizations of $Rb_2Cu_{0.78}Co_{0.22}F_4$ vs temperature in a field of 10.0 G along the c axis. The ZFC magnetizations were taken at 10 s (circles) and 90 s (squares) after switching on the field. Inset shows the coincident FC and ZFC magnetizations vs temperature for $\mathbf{H} \perp \mathbf{c}$.

Upon lowering the temperature, the magnetization becomes increasingly nonlinear with the field. In order to examine this in detail, we have measured $M^{FC}(T)$ curves such as in Fig. 2 for as many as 35 fields ranging from 1.0 to 12 500 G at 19 discrete temperatures between 1.67 and 4.25 K. From these data $M^{FC}(H)$ isotherms were deduced.

STATIC SCALING

In case a phase transition occurs at zero temperature, the dependence of the nonlinear part of the magnetization on field and temperature can be cast into a scaling relation of the form[3]

$$1 - (TM/H) = T^{\beta} f(H/T^{\Delta}) , \tag{1}$$

where β and Δ are critical exponents, and $f(x)$ is a scaling function, which asymptotically behaves as $f(x) = cx^2$ for $x \to 0$, and as $f(x) \to 1$ for $x \to \infty$. In Eq. (1) it is implicitely assumed that the linear part χ_0 of the susceptibility follows the simple Curie behavior appropriate to systems with a symmetric distribution of exchange interactions, i.e., $\chi_0 = C/T$, with $C = 1$ in the notation of Ref. 3. In real systems, however, the interactions generally do not average out to zero. In $Rb_2Cu_{0.78}Co_{0.22}F_4$, the high-temperature data in fact follow the Curie–Weiss law $\chi_0 = C/(T-\theta)$, with $\theta = 5.1 \pm 0.2$ K, a value *above* the freezing temperature T_f. This implies that in the temperature regime of our analysis, $3.20\ \text{K} \leqslant T \leqslant 4.25$ K, short-range ferromagnetic correlations result in an anomalous $\chi_0(T)$, and further affect the nonlinear part of the magnetization.[2] To account for this, we follow Omari *et al.*[14] by choosing $\chi_0 H$ and T rather than H and T as the scaling fields. This leads to

$$1 - (M/\chi_0 H) = T^{\beta} f(\chi_0 H/T^{\Delta - 1}). \tag{2}$$

Figure 3 shows our FC data scaled according to Eq. (2) for temperatures ranging from 3.20 to 4.25 K and fields ranging from 1.0 G to 12.5 kG. Here, values of χ_0 as obtained from the linear part of the $M^{FC}(H)$ isotherms have been inserted. The noteworthy result is that this set of data can be brought to conformity with $T_c = 0$ scaling. The critical exponents obtained are $\beta = 0.0 \pm 0.1$ and $\Delta = 3.2 \pm 0.2$. It is known that critical exponents from scaling may suffer from deviations when using too large a field or temperature range.[15] Essentially the same results are, however, obtained when restricting the data set to fields so small that the nonlinear part of $M(H)$ is less than 10% of χ_0. Inclusion of temperatures lower than 3.20 K leads to a deterioration of

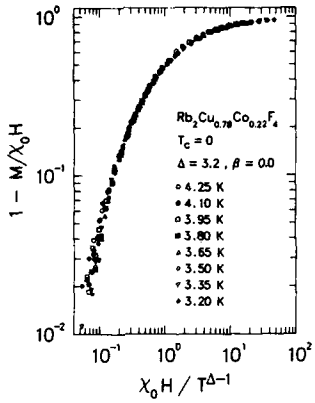


FIG. 3. $T_c = 0$ scaling plot of the FC magnetization data of $Rb_2Cu_{0.78}Co_{0.22}F_4$.

the fit, presumably because the small but finite cooling rate prevents the system from reaching equilibrium. A second noteworthy point is that the values for β and Δ deduced from the experiments compare excellently with the results of MC simulations for the $d = 2$ EA model, i.e., $\beta = 0$ and $\Delta = 3.5 \pm 0.5$.[3] Here, it is remarked that the MC simulation data have been taken at both sides of the freezing temperature T_f, whereas the experimental data pertain to the regime above T_f only. Apparently, the critical regime is quite broad.

A remarkable feature of the MC simulation data for the $d = 2$ EA model is that they could equally well be scaled to a $d = 3$ scaling expression with a nonzero transition temperature T_c, although ample evidence is available that $T_c = 0$ for the $d = 2$ EA model. To show that the present data on $Rb_2Cu_{0.78}Co_{0.22}F_4$ exhibit an entirely similar behavior, we have scaled them to the $d = 3$ analogue of Eq. (2),

$$1 - (M/\chi_0 H) = \tau^{\beta} f(\chi_0 H / \tau^{(1/2)(\gamma+\beta)}) , \qquad (3)$$

in which $\tau = (T - T_c)/T$, $f(x)$ behaves as $x^{2/\delta}$ in the high-x limit, and β, γ, and δ are critical exponents. For the range of T_c from 3.0 down to 0.5 K, fits of a quality comparable with the fit of Eq. (2) are obtained. We find $\delta = 21.0 \pm 0.2$, and, with decreasing T_c, γ varying from 0.8 to 23, and β from 0.04 to 1.1. There, however, appears to be a small but definite trend towards better fits the lower T_c, suggestive of $T_c = 0$ K.

In conclusion, we have shown that experimental data on the static magnetization of $Rb_2Cu_{0.78}Co_{0.22}F_4$ are consistent with a $T_c = 0$ scaling. This verifies the MC results on the $d = 2$ EA model, and provides experimental evidence for a d_l larger than 2. A more extensive report, including the ac susceptibility, will be published elsewhere.

ACKNOWLEDGMENT

The authors thank M. van Eekhout for his competent assistance in the experiments.

[1]M. B. Salamon, J. Appl. Phys. **61**, 4228 (1987).
[2]K. Binder and A. P. Young, Rev. Mod. Phys. **58**, 801 (1986).
[3]W. Kinzel and K. Binder, Phys. Rev. B**29**, 1300 (1984).
[4]R. N. Bhatt and A. P. Young, Phys. Rev. Lett. **54**, 924 (1985); A. T. Ogielski and I. Morgenstern, *ibid.* **54**, 928 (1985); J. Appl. Phys. **57**, 3382 (1985).
[5]K. Katsumata, T. Nire, M. Tanimoto, and H. Yoshizawa, Phys. Rev. B **25**, 428 (1982); Y. Kimishima, H. Ikeda, A. Furukawa, and H. Nagano, J. Phys. Soc. Jpn. **55**, 3574 (1986).
[6]S. F. Edwards and P. W. Anderson, J. Phys. F**5**, 965 (1975).
[7]E. J. Samuelsen, Phys. Rev. Lett. **31**, 936 (1973); J. Phys. Chem. Solids **35**, 785 (1974).
[8]I. Yamada, J. Phys. Soc. Jpn. **33**, 979 (1972).
[9]D. I. Komskii and K. I. Kugel, Solid State Commun. **13**, 763 (1973).
[10]P. W. Anderson, in *Magnetism*, edited by G. T. Rado and H. Suhl (Academic, New York, 1963), Vol. *I*, p. 25.
[11]C. Dekker, A. F. M. Arts, and H. W. de Wijn (unpublished).
[12]S. Nagata, P. H. Keesom, and H. R. Harrison, Phys. Rev. B **19**, 1633 (1979).
[13]A. Ito, H. Aruga, E. Torikai, M. Kikuchi, Y. Syono, and H. Takei, Phys. Rev. Lett. **57**, 483 (1986).
[14]R. Omari, J. J. Prejean, and J. Souletie, J. Phys. (Paris) **44**, 1069 (1983).
[15]H. Bouchiat, J. Phys. (Paris) **47**, 71 (1986).

Spin-glass behavior in mixed metal oxides with a rutile-type structure

A. Labarta, X. Obradors, and J. Tejada
Facultat de Fisica, Universitat de Barcelona, Diagonal 647, 08028 Barcelona, Spain
F. J. Berry and M. Sarson
Department of Chemistry, University of Birmingham, P. O. Box 363, Birmingham B15 2TT, United Kingdom

We report here on the magnetic properties of compounds of composition $Fe_{1-x}Cr_xSbO_4$ and $Fe_{1-x}Ga_xSbO_4$. The introduction of paramagnetic Cr^{3+} and diamagnetic Ga^{3+} into the rutile-related iron antimonate lattice does not destroy the antisite atomic ordering which exists in iron antimonate of composition $FeSbO_4$. The initial slope of the Curie temperature dependence on x is similar in both series, indicating that Fe^{3+}-Cr^{3+} interactions are very small. The magnetic susceptibility measurements recorded from the compounds of composition $Fe_{1-x}Cr_xSbO_4$, $x<0.4$, and $Fe_{0.9}Ga_{0.1}SbO_4$ show them to behave as spin glasses at low temperatures. The inhibition of compounds of the type $Fe_{1-x}Cr_xSbO_4$, $x>0.4$, and $Fe_{1-x}Ga_xSbO_4$, $x>0.1$ to undergo a spin-glass transition above 4.2 K is associated with a dilution effect.

INTRODUCTION

We have recently reported[1] on the observation of spin-glass behavior in the rutile-related iron antimonate of composition $FeSbO_4$, which contains a superlattice,[2] and have associated the spin-glass transition with antisite atomic ordering.[1] We are currently accumulating experimental data to increase the general understanding of the mechanisms involved in spin-glass behavior, in this paper we describe the changes in the magnetic properties of this rutile-related material which result from the substitution of the Fe^{3+} species by paramagnetic Cr^{3+} and diamagnetic Ga^{3+}.

EXPERIMENT

The compounds of composition $Fe_{1-x}Cr_xSbO_4$ ($x=1$, 0.7, 0.6, 0.4, 0.1) and $Fe_{1-x}Ga_xSbO_4$ ($x=0.7$, 0.5, 0.3, 0.1) were prepared by coprecipitation techniques.

^{57}Fe and ^{121}Sb Mössbauer spectra were recorded at various temperatures between 77 and 298 K with a microprocessor controlled Mössbauer spectrometer using $^{57}Co/Rh$ and $Ca^{121}SnO_3$ sources. All the spectra were computer fitted. The magnetic susceptibility measurements were performed in the temperature range between 1.7 and 80 K with a SHE SQUID magnetometer with applied fields up to 100 Oe, and with a Faraday balance in the temperature range between 80 and 1000 K with applied fields up to 5000 Oe.

RESULTS AND DISCUSSION

The magnetic susceptibility data recorded between 1.7 and 1000 K for the compounds of composition $Fe_{0.9}Ga_{0.1}SbO_4$ and $Fe_{0.6}Cr_{0.4}SbO_4$ are shown in Figs. 1 and 2, respectively. The maximum in the zero-field-cooled (ZFC) magnetic susceptibility recorded from

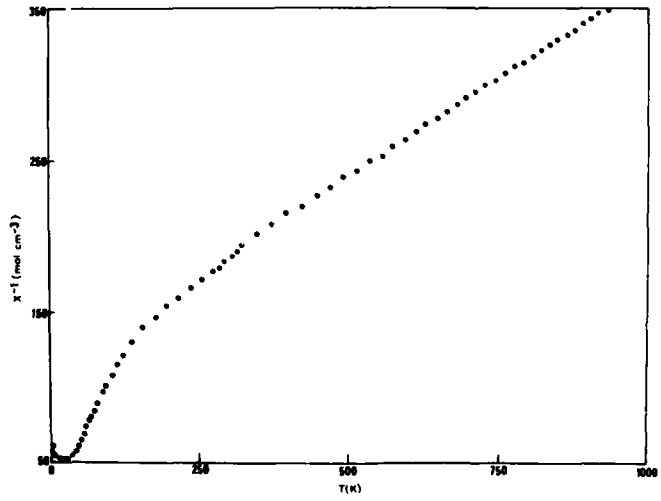


FIG. 1. Temperature dependence of the inverse of the magnetic susceptibility of the compound $Fe_{0.9}Ga_{0.1}SbO_4$.

 0021-8979/88/084337-03$02.40 © 1988 American Institute of Physics

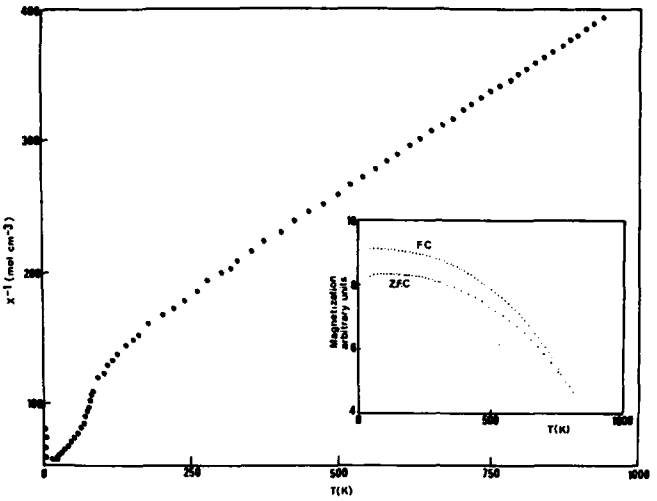


FIG. 2. Temperature dependence of the inverse of the magnetic susceptibility of the compound $Fe_{0.6}Cr_{0.4}SbO_4$. The inset shows the irreversible zero-field-cooled and field-cooled susceptibilities.

$Fe_{1-x}Cr_xSbO_4$ ($x = 0.1$, 0.4) and $Fe_{0.9}Ga_{0.1}SbO_4$ at low temperatures, together with the irreversible ZFC and FC magnetic susceptibilities at 1000 Oe, suggest that these three compounds behave as spin glasses. Compounds in which the Cr^{3+} concentration exceeds 0.4, or those in which the concentration of Ga^{3+} is larger than 0.1 show no minimum in the low-temperature susceptibility data which suggests the disappearance of the spin-glass behavior or a decrease of the spin-freezing temperature below 4.2 K (Fig. 3).

The ^{57}Fe Mössbauer spectra recorded at 298 and 77 K from the compounds in the series $Fe_{1-x}Ga_xSbO_4$ and $Fe_{1-x}Cr_xSbO_4$ were all similar (Fig. 4) and show the presence of high-spin Fe^{3+} cations. The similarities between the chemical isomer shift and quadrupole splitting data recorded from the two series of mixed oxides are consistent with the antisite atomic ordering which exists in iron antimonate being conserved when Cr^{3+} and Ga^{3+} enter the lattice. The ^{121}Sb Mössbauer spectra recorded at 298 K from all the samples were characteristics of Sb^{5+}. The observation of broadened lines in the spectra recorded at 77 K is indicative of the presence of a supertransferred magnetic hyperfine field at the ^{121}Sb nuclei.[2]

The magnetic susceptibility data recorded from all the compounds in the high-temperature regime, i.e., $T > 300$ K, obey Curie-Weiss laws which allow an evaluation of both the Curie temperature θ and the effective dipolar magnetic moment μ_{eff}. The results are collected in Table I. The θ value increase with decreasing values of x, and the effective dipolar magnetic moment varies within each series according to the concentration of paramagnetic Fe^{3+} and Cr^{3+} ions or dia-

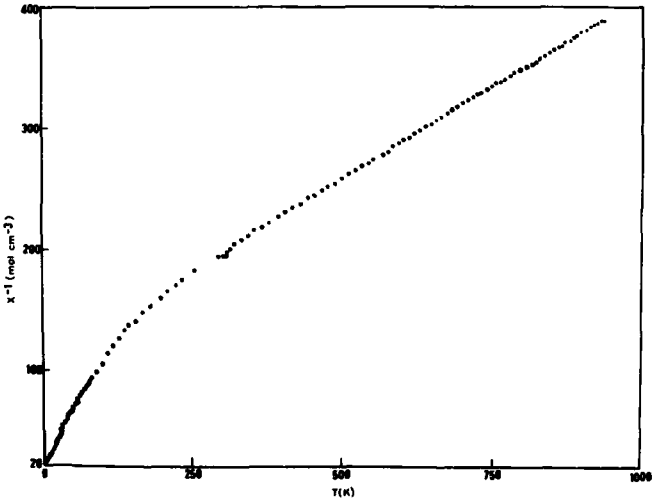


FIG. 3. Temperature dependence of the inverse of the magnetic susceptibility of the compound $Fe_{0.7}Ga_{0.3}SbO_4$.

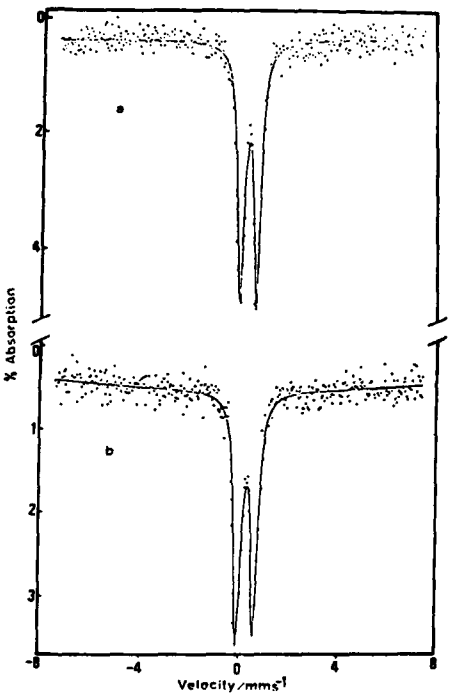


FIG. 4. ^{57}Fe Mössbauer spectra recorded from $Fe_{0.6}Cr_{0.4}SbO_4$ at (a) 298 K and (b) 77 K.

magnetic Ga^{3+} ions. The initial slopes of the $\theta(x)$ curves are similar for the two series showing that the magnetic interactions between Cr^{3+} and Fe^{3+} and between Cr^{3+} and Cr^{3+} are very small. Although the results obtained in this high-temperature regime are characteristic of pure paramagnetic behavior, the large values of θ indicate that strong antiferromagnetic interactions exist between the spins. The paramagnetic behavior in both series is conserved until a temperature of 80 K is attained for compounds in which the iron concentration is less than 0.6, i.e., $x > 0.4$. The magnetic susceptibility data for compounds in which $x < 0.4$ begins to deviate from the Curie-Weiss behavior at temperatures below 200 K. The decrease of the effective paramagnetic moment in this regime is indicative of onset of clustering between the individual Fe^{3+} species at these temperatures. However, after a regime in which the data follow a Curie-type dependence on temperature a new straight line relationship with smaller magnetic moments is observed which corresponds to the formation of clusters with antiferromagnetic correlations. The positive θ values of this new Curie–Weiss behavior may be related with ferromagnetic interactions between clusters. In the final temperature regime, i.e., $T < 20$ K, a minimum is observed in the ZFC susceptibility which corresponds to the freezing of the spins. The freezing temperature decreases when x increases, and no minimum in the ZFC susceptibility is observed above 4.2 K in compounds in which $x > 0.4$.

TABLE I. Effective magnetic moments per formula unit and Curie temperatures for compounds of composition $Fe_{1-x}Cr_xSbO_4$ and $Fe_{1-x}Ga_xSbO_4$ deduced from the high-temperature regime ($T > 300$ K).

x	μ_{eff} (Bohr magnetons)	θ (K)
	$Fe_{1-x}Cr_xSbO_4$	
1	4.01	108
0.7	4.62	189
0.6	4.86	250
0.4	5.29	356
0.1	5.73	446
	$Fe_{1-x}Ga_xSbO_4$	
0.7	3.05	99
0.5	4.09	210
0.3	4.96	347
0.1	5.62	447

Despite evidence of the cluster formation below 200 K, the Mössbauer data above 77 K do not show any slow relaxation phenomena. The results indicate that the relaxation times of the short-range magnetically ordered clusters are significantly faster than the Mössbauer time scale τ_M.[3] Further Mössbauer spectroscopic experiments below 77 K are currently in progress to examine the variation of the relaxation times with temperature. In this respect it is pertinent to note that the broad-lined unresolved ^{57}Fe Mössbauer spectrum recorded[1] at 77 K from iron antimonate, $FeSbO_4$, shows that at this lower temperature some of the short-range magnetically ordered clusters have a relaxation time τ comparable to the Mössbauer time scale. It therefore appears that although the introduction of Cr^{3+} and Ga^{3+} into the rutile-type structure does not affect the occurrence of cluster formation, the relaxation times at given temperatures of the clusters in the $Fe_{1-x}Cr_xSbO_4$ and $Fe_{1-x}Ga_xSbO_4$ systems are faster than both τ and τ_M as a consequence of the decrease in the cluster-cluster magnetic correlation.

[1] F. J. Berry, M. Sarson, A. Labarta, X. Obradors, R. Rodriquez, and J. Tejada, J. Solid State Chem. (to be published).
[2] F. J. Berry, J. G. Holden, and M. H. Loretto, J. Chem. Soc. Faraday Trans. 1 **83**, 615 (1987).
[3] J. A. Mydosh, in *Heidelberg Colloquium in Spin Glasses*, edited by J. L. Van Hemmen and I. Morgenstern (Springer, Berlin, 1983), p. 79, and references therein.

Spin-glass behavior of cubic $Tb_{0.3}Y_{0.7}Ag$: A scaling of the thermoremanence

M. R. Said and J. S. Kouvel
Department of Physics, University of Illinois, Chicago, Illinois 60680
T. O. Brun
Materials Science Division, Argonne National Laboratory, Argonne, Illinois 60439

Magnetization-versus-temperature (M-vs-T) measurements in a fixed field on cubic pseudobinary $Tb_{0.3}Y_{0.7}Ag$ show that M for increasing and then decreasing T bifurcates at the antiferromagnetic Néel point ($T_N = 36$ K), where M is maximum. The resulting thermoremanence (M_R), which decays very slowly with time, diminishes with increasing T and vanishes at T_N. Thus, the long-range antiferromagnetism appears to coexist with spin-glass ordering. Measurements of M_R with increasing T were also made for different cooling fields (H_{cl}) The changes of M_R with H_{cl} and T are found to reduce to a universal relationship between the temperature-normalized quantities, $m = M_R/M_0(T)$ and $h = H_{cl}/H_0(T)$. Setting both the initial slope of m vs h and the saturation m at high h equal to unity, we determine that $M_0(T) = M_0(0)\exp(-T/T_0)$, with $M_0(0) = 0.82\mu_B$/Tb atom and $T_0 = 4.3$ K, and that $H_0(T)$ varies analogously, with $H_0(0) = 225$ kOe and the same T_0. A similar temperature scaling of M_R vs H_{cl}, with similar exponential forms for $M_0(T)$ and $H_0(T)$, has been deduced earlier for Ag-Mn and other canonical spin glasses.

While many chemically disordered systems at certain compositions are known to undergo "reentrant" transitions from ferromagnetism to a spin-glass-like phase upon cooling (as evidenced by the onset of magnetic irreversibilities and time dependencies), there have been no reported examples of analogous transitions from long-range antiferromagnetism (AFM), except for $(Fe,Mg)Cl_2$.[1] However, a case that relates to the latter is that of disordered Tb_xY_{1-x}, where the $x = 0.05$ alloy was found[2] to have both a long-range (helical) AFM and a spin-glass-like irreversibility of the magnetization that persists up to the susceptibility-peak temperature, which presumably is the antiferromagnetic Néel point; thus, there appears to be a coexistence of AFM and spin-glass (SG) ordering. An AFM-SG coexistence may also be occurring in disordered Gd_xY_{1-x} alloys, where recent neutron diffraction work[3] has revealed a helical AFM for x down to 0.015, which is well into the dilute composition regime characterized as SG from the resistivity behavior[4] (though not so from the susceptibility behavior[5]).

We have recently begun to investigate the nature of the breakdown of the long-range AFM in the pseudobinary compounds, $Tb_xY_{1-x}Ag$ and $Gd_xY_{1-x}Ag$, whose high crystal symmetry (cubic CsCl-type) is expected to allow the breakdown to occur more readily (i.e., at larger x) than in the hexagonal Tb_xY_{1-x} and Gd_xY_{1-x} alloys, thus making it easier to study in detail. Consistent with this expectation, our preliminary results for both series of compounds are showing that even at x as large as 0.5 field cooling produces a thermoremanence which decays logarithmically with time, indicating that some SG order may be accompanying the long-range AFM. In this paper, we will present our most complete magnetization results to date, which are for the compound $Tb_{0.3}Y_{0.7}Ag$.

Our sample compounds were prepared by arc-melting together 99.95% pure metals under argon; the buttons were flipped over and remelted several times to ensure chemical homogeneity. A thin rod sample ($\sim 1\times1\times8$ mm^3) was spark-cut from each polycrystalline button and annealed successively at 500, 400, and 300 °C for 3, 2, and 1 day(s), respectively. Magnetizations were measured with a vibrating-sample magnetometer at temperatures down to 4.2 K in fields up to 56 kOe.

Some of the basic magnetic properties of our $Tb_{0.3}Y_{0.7}Ag$ sample are displayed in Fig. 1. After zero-field cooling to 4.2 K, its magnetization (M) was measured in a fixed field (H) of 10 kOe as the temperature (T) was raised up to ~ 140 K and then lowered slowly back to 4.2 K. We see that M has a pronounced peak at 36 K, above which M vs T is reversible, but immediately below which the two M-vs-T curves bifurcate, the curve for decreasing T lying increasing-

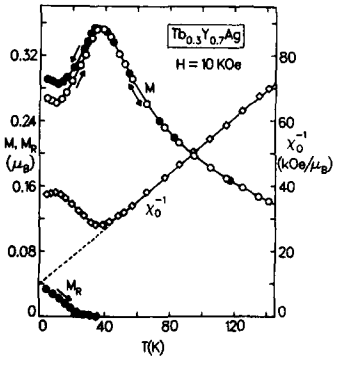


FIG. 1. Magnetization (M) of $Tb_{0.3}Y_{0.7}Ag$ measured in a 10-kOe field (after zero-field cooling) as temperature (T) is raised (open circles) and then lowered (closed circles). Thermoremanence (M_R) then measured with increasing T. Inverse initial susceptibility (χ_0^{-1}) also shown vs T. M and M_R in units of μ_B per Tb atom.

 0021-8979/88/084340-03$02.40 © 1988 American Institute of Physics

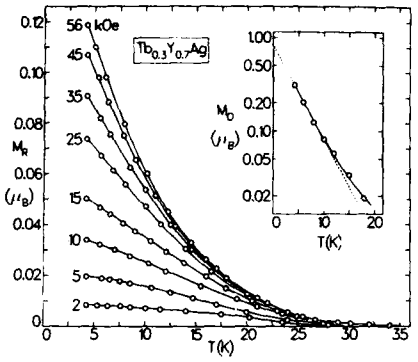


FIG. 2. Thermoremanence (M_R) of $Tb_{0.3}Y_{0.7}Ag$ measured with increasing temperature (T) after cooling to 4.2 K in various fields, as labeled. [Inset: M_0 (log scale) vs T.] M_R and M_0 in units of μ_B per Tb atom.

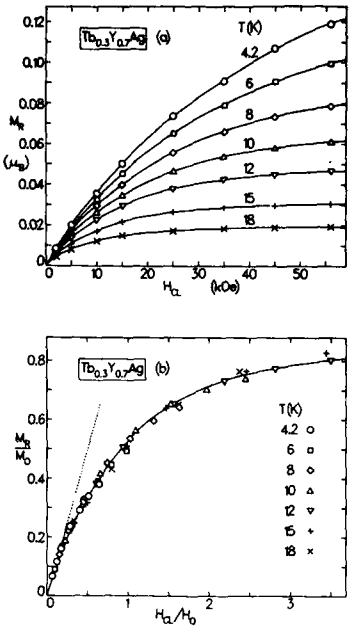


FIG. 3. (a) Thermoremanence (M_R) of $Tb_{0.3}Y_{0.7}Ag$ vs cooling field (H_{cl}) at various temperatures (T). M_R in units of μ_B per Tb atom. (b) Universal plot of M_R/M_0 versus H_{cl}/H_0 for various T. Initial slope (dashed line) and saturation level of M_R/M_0 are both scaled to unity.

ly above the other as T approaches 4.2 K. When the temperature cycle was completed, H was removed and a thermoremanence (M_R) was observed. Upon subsequent warming in zero H, M_R decreases monotonically and vanishes at or very near the temperature of maximum M. Figure 1 also shows the variation with T of the inverse initial susceptibility χ_0^{-1}. Above its minimum at 36 K, χ_0^{-1} vs T exhibits a linear (Curie–Weiss) behavior, whose T-axis intercept gives $\theta = -22.5$ K and whose slope gives an effective paramagnetic moment (μ_p) of 10.23 μ_B per Tb atom, which is consistent with the theoretical μ_p value of 9.72 μ_B for Tb^{3+} plus some conduction-band polarization.

The susceptibility-peak temperature (36 K) is clearly associated with magnetic ordering, and very recent neutron diffraction work at the National Bureau of Standards[6] on an identically prepared sample of $Tb_{0.3}Y_{0.7}Ag$ shows that this temperature is the Néel point for a modulated variant of the $\pi\pi 0$ antiferromagnetic configuration found earlier[7] in TbAg. Since this temperature also marks the onset of a SG-like irreversibility in M, it appears to represent where AFM and SG order set in coexistently. Our observation that the thermoremanence which persists up to this temperature, decays logarithmically with time, further supports this interpretation.

The time decay of the thermoremanence (M_R), though an important feature, is too small (about 5% in 1 h) to affect significantly the measured temperature dependence of M_R shown in Fig. 1. Hence, we decided to extend our study of M_R vs T to different cooling fields (H_{cl}). By cooling our $Tb_{0.3}Y_{0.7}Ag$ sample from above 36 K slowly down to 4.2 K in various H_{cl}, then removing H_{cl} and measuring the changes of M_R as T was raised, we obtained the results shown in Fig. 2. For each H_{cl}, M_R decreases monotonically with increasing T, and although its relative rates of decrease are smaller for lower H_{cl}, M_R vanishes in each case essentially at the Néel point (T_N) of 36 K.

Points taken from the curves in Fig. 2 at different temperatures up to 18 K (above which the relative errors are prohibitive) produce the isotherms of M_R vs H_{cl} shown in Fig. 3(a). From the latter, we see that M_R approaches a high-H_{cl} saturation level that rises as the approach to saturation slows down with decreasing T. Indeed, the very systematic changes in the shapes of these curves suggest that they may all be related through a simple temperature scaling. We tested this possibility and succeeded in finding temperature-normalizing quantities for which the points of $M_R/M_0(T) \equiv m$ vs $H_{cl}/H_0(T) \equiv h$ closely follow a universal curve for all T. The absolute scales of $M_0(T)$ and $H_0(T)$ were fixed by setting both the initial slope of m vs h and the saturation level of m at high h equal to unity. The final results of this procedure are given by the m-vs-h plot in Fig. 3(b), which clearly displays the universality referred to above. The values of $M_0(T)$ that we used are plotted logarithmically against T in the inset of Fig. 2. The linear behavior of this plot below 12 K gives $M_0(T) = M_0(0)\exp(-T/T_0)$, with $M_0(0) = 0.82\ \mu_B$ per Tb atom and $T_0 = 4.3$ K. Analogously, the $H_0(T)$ values that we used are found to obey (again below 12 K) the relation, $H_0(T) = H_0(0)\exp(-T/T_0)$, with $H_0(0) = 225$ kOe and again $T_0 = 4.3$ K. A similar temperature scaling of M_R vs H_{cl} (but restricted to the initial slopes and the saturation M_R values) with similar exponential forms for $M_0(T)$ and $H_0(T)$, has previously been deduced for Ag-Mn and other canonical SG

systems.[8] This detailed similarity is further evidence that the thermoremanence of $Tb_{0.3}Y_{0.7}Ag$ derives from SG ordering, which from the fairly sizable value of $M_0(0)$ would appear to be competing very effectively with the coexistent long-range AFM. How this SG-AFM competition evolves with changes of x in $Tb_xY_{1-x}Ag$ and $Gd_xY_{1-x}Ag$ is presently under study.

We are grateful to Dr. J. A. Gotaas of the National Bureau of Standards for a preliminary report on his neutron diffraction results for $Tb_{0.3}Y_{0.7}Ag$. The work at the University of Illinois at Chicago was supported by the National Science Foundation under Grant No. DMR84-06898 and the work at the Argonne National Laboratory by the U. S. Department of Energy, BES–Material Science, under Contract No. W-31-109-Eng-38.

[1]Po-zen Wong, S. von Molnar, T. T. M. Palstra, J. A. Mydosh, H. Yoshizawa, S. M. Shapiro, and A. Ito, Phys. Rev. Lett. 55, 2043 (1985).
[2]L. J. P. Ketelsen and M. B. Salamon, Solid State Commun. 55, 237 (1985).
[3]L. E. Wenger, G. W. Hunter, J. A. Mydosh, J. A. Gotaas, and J. J. Rhyne, Phys. Rev. Lett. 56, 1090 (1986).
[4]B. V. B. Sarkissian and B. R. Coles, Commun. Phys. 1, 17 (1976).
[5]P. Pureur, A. Fert, R. Wendler, and K. Baberschke, J. Appl. Phys. 57, 3230 (1985).
[6]J. A. Gotaas (private communication).
[7]J. W. Cable, W. C. Koehler, and E. O. Wollan, Phys. Rev. 136, A240 (1964).
[8]H. Bouchiat and P. Monod, J. Magn. Magn. Mater. 30, 175 (1982), and references therein.

Nonstationary spin glass dynamics from susceptibility and noise measurements

Ph. Refregier, M. Ocio, J. Hammann, and E. Vincent
Département de Physique Générale, Service de Physique du Solide, et de Résonance Magnétique, Centre d'Études Nucléaires de Saclay, 91191 Gif-sur-Yvette Cedex, France

Nonstationary dynamics has been observed in very-low-frequency (10^{-2}–10^{-1} Hz) ac susceptibility and noise measurements on the thiospinel $CdCr_{1.7}In_{0.3}S_4$ spin glass. The time relaxation of the ac susceptibility yields a large decrease of the out-of-phase component χ'' towards a finite stationary value. The relaxation of the spectral density of the magnetization derived from zero-field noise measurements is in remarkable agreement with the behavior of χ''. The observed time dependence compares well with the predictions from the thermoremanent magnetization decay analyses. In the range of times of χ'' measurements, the linear-response theory applies to the nonstationary dynamics.

Nonstationary dynamics has been found in various spin glass systems whether they are metallic like Cu:Mn[1] and Ag:Mn[2,3] or insulating like $CsNiFeF_6$ and $CdCr_{1.7}In_{0.3}S_4$.[4] The compound $Eu_{0.4}Sr_{0.6}S$ is an exception among the currently studied spin glasses where no aging effects could be detected in the limit of small applied fields.[5] The nonstationary dynamics was mostly evidenced in the time decay of the thermoremanent magnetization (TRM). The decay was found to depend on the time t_w the system has spent below the freezing temperature T_g before the field is switched off. This waiting time dependence (aging effect) has already been extensively studied. Two main regimes were distinguished. As long as t_w remains smaller or of the same order as the observation time t_{obs} ($t_{obs}=0$ at the field removal), the nonstationary contribution dominates the response function,[3,4] but a stationary contribution can be defined in the limit of large values of t_w as compared to t_{obs}. The experimental conditions prevailing in most TRM decay measurements ($t_{obs}>0.1$ s, $100<t_w<10^5$ s) make them especially suitable to study the nonstationary dynamics. They cannot give detailed information on the stationary part. The situation is reversed in susceptibility or noise measurements which are indeed made at constant frequency ν, i.e., at a constant observation time of order $1/\nu$. The waiting time t_w is, in these experiments, the time t the sample has spent at the working temperature (i.e., the age of the system). It is always larger than t_{obs}. ac susceptibility and noise experiments have been widely used to study the stationary dynamics. However, even in these experiments, nonstationary effects may be important at very small frequencies.[6,7]

In this paper, we show evidence for a large time dependence of the ac susceptibility measured at 10^{-2} Hz and 8×10^{-2} Hz in the thiospinel spin glass $CdCr_{1.7}In_{0.3}S_4$. The results are compared to those of noise experiments and to the behavior expected from a previous quantitative analysis of the TRM decay. The linear-theory approach is found to be valid in the range of times of susceptibility and noise experiments.

LOW-FREQUENCY SUSCEPTIBILITY AND NOISE

In Figs. 1 and 2, we show the time dependences of the out-of-phase susceptibility χ'' and of the in-phase susceptibility χ' at a temperature $T=12$ K ($T/T_g=0.72$). The main figures correspond to a frequency $\nu=10^{-2}$ Hz, the insets to $\nu=8\times10^{-2}$ Hz. The experimental points have been obtained from SQUID measurements in an applied field of about 1 mOe using a digital method. Each experimental point is taken over two periods $1/\nu$ of the ac signal. The time scale covers a range of 20 h for the results at 10^{-2} Hz. The origin of the scale is taken from the time the sample has reached the working temperature of 12 K after a rapid cooling from above T_g.

Both components of the susceptibility decrease as a function of time towards a finite stationary value which is given in the figures by the dashed lines. However, the variation is ten times larger for χ'' than for χ'. After 10 min (three first experimental points), χ'' is still 50% larger than its equilibrium value at $\nu=10^{-2}$ Hz, whereas at the same time χ' exceeds only by 5% its equilibrium value. At such a low frequency a very long waiting time is needed in order to get the correct value of the stationary response. The value indicated in the figures is obtained after an experiment of 15

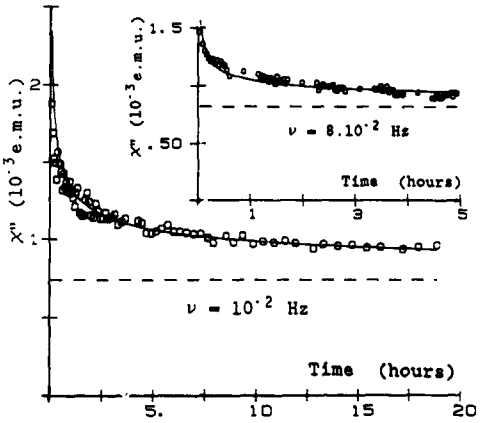


FIG. 1. Out-of-phase susceptibility χ'' as a function of the time spent at the working temperature $T/T_g=0.72$ for $\nu=10^{-2}$ Hz. The inset shows the results for $\nu=8\times10^{-2}$ Hz. The dashed line represents the equilibrium value, and the solid line corresponds to the values calculated from the proposed expression for the relaxation function.

 0021-8979/88/084343-03$02.40 © 1988 American Institute of Physics

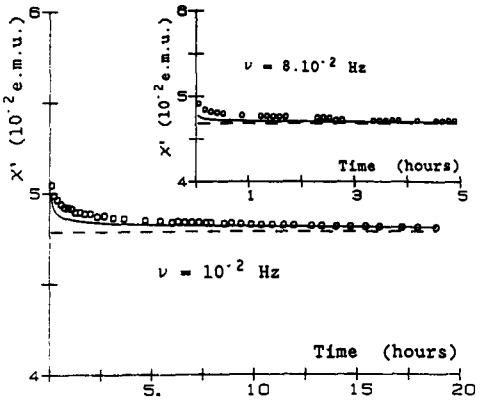


FIG. 2. In-phase susceptibility χ' as a function of the time spent at $T/T_g = 0.72$ for $\nu = 10^{-2}$ Hz. The inset shows the results for $\nu = 8\times10^{-2}$ Hz. The symbols are the same as in Fig. 1.

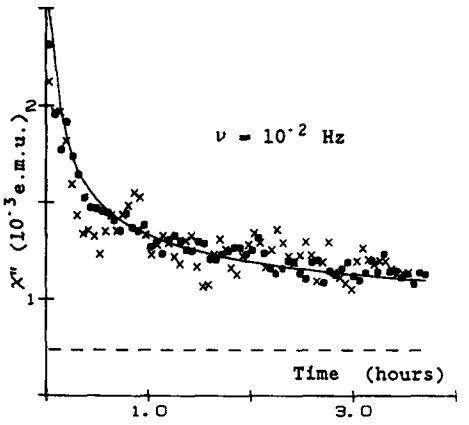


FIG. 3. Out-of-phase susceptibility χ'' as a function of time at $T/T_g = 0.72$ and $\nu = 10^{-2}$ Hz in a reduced time scale. The full points correspond to the measured χ'' values, the crosses to the normalized values of the spectral density of the magnetization $\langle M^2(\nu,t)\rangle$, and the solid line to the values calculated from the proposed expression for the relaxation function. The dashed line gives the equilibrium value.

days.[8] The same amount of variation is observed at $\nu = 8\times10^{-2}$ Hz in a much shorter time scale. The rate of decay increases as the frequency increases.

A more-detailed representation of the time dependence of χ'' at $\nu = 10^{-2}$ Hz is given in Fig. 3 for the first four hours of the measurement. The χ'' values (full circles) are compared to values derived from a noise measurement (crosses) and from the TRM decay measurements (solid line).

In the noise experiments, one measures the flux fluctuations which are induced by the sample in a pick-up coil coupled to a SQUID magnetometer. These fluctuations are proportional to the magnetization fluctuations in the sample. In the present experiment, no magnetic field was applied (H residual <1 mOe). The sample was rapidly cooled down to 12 K and the experimental points were determined as a function of the time t spent at this constant temperature. For each point the noise signal was recorded over 200 s and the module of the Fourier component at 10^{-2} Hz was calculated; the whole process was repeated 64 times in order to determine the mean value of this component. The results proportional to $\langle M^2(\nu,t)\rangle$ are represented in Fig. 3, their average level being normalized to that of the χ'' values. The time dependence of $\langle M^2(\nu,t)\rangle$ at 10^{-2} Hz is the same as that of χ''. This is an indication for the validity of the relationship between these two quantities as derived from the fluctuation-dissipation theorem (FDT).

COMPARISON WITH THE ANALYSIS OF THE TRM DECAY

Our suggestion to quantitatively analyze the TRM decay in the whole range of times investigated was to introduce an effective time λ defined by

$$d\lambda = [t_w/(t_{\rm obs}+t_w)]^{\mu} dt_{\rm obs},$$

where μ is an aging parameter.[3,4] In this approach, the decay can be represented by a relaxation function at constant age:

$$\sigma = \sigma_0 \lambda^{-\alpha} \exp[-(\lambda/\tau)^{\beta}], \quad \tau \propto t_w^{\mu}. \tag{1}$$

In the limit of ac and noise measurements i.e., $t_{\rm obs} < t_w$, $\lambda \approx t_{\rm obs}$ and the exponential in σ can be expanded to first order:

$$\sigma \approx \sigma_0 t_{\rm obs}^{-\alpha}[1-(t_{\rm obs}/\tau)^{\beta}], \quad \tau \propto t_w^{\mu}. \tag{2}$$

The stationary contribution ($t_{\rm obs}^{-\alpha}$) has already been extensively studied and compared to the stationary susceptibility. In particular, at 12 K, χ' and χ'' were found to display a power-law dependence of the frequency ν. A discrepancy was noted between the exponent a of this power law and the exponent α of the TRM decay[4] though the linear theory was previously shown to be valid.[4,9] A detailed analysis of the equilibrium values of χ' and χ'' revealed that χ_0 the extrapolated value of χ' to zero frequency, was 35% lower than the dc field-cooled susceptibility $\chi_{\rm FC}$. Therefore, according to linear theory, the stationary contribution in the relaxation function must be more properly written as $\sigma_{\rm st} = \chi_{\rm FC} - \chi_0 + A t_{\rm obs}^{-\alpha}$ where A and χ_0 are completely determined from the frequency dependence of the stationary values of χ' and χ''. It has been verified that within our experimental time range the variation of $\sigma_{\rm st}$ cannot be distinguished from that of $t_{\rm obs}^{-\alpha}$ which was the simplified expression used in the analysis of the TRM measurements.

With the stationary contribution derived from the equilibrium susceptibility and the nonstationary contribution derived from the long-time TRM decay, the relation (2), updated, can now be analytically Fourier transformed and the time dependencies of χ' and χ'' evaluated within the framework of linear theory. The solid lines in Figs. 1–3 correspond to this evaluation. From Figs. 1 and 3, it appears that very good agreement with the experimental values is found for χ''. This agreement is observed not only for $\nu = 10^{-2}$ Hz but also for $\nu = 8\times10^{-2}$ Hz where the values

of t_{obs}/t_w are much smaller and out of the fitting range of relation (1). In the case of χ', the expected decrease as a function of time is always much faster than the observed one, but the discrepancy is probably not significant owing to the very small variation of χ' ($\approx 5\%$).

The above comparisons confirm our analysis of the TRM relaxation function. Aging phenomena, which had up to now mostly been evidenced in the $t_{obs} > t_w$ range, appear to play also a significant role in the $t_{obs} < t_w$ range of times. It implies that the TRM relaxation function indeed includes an aging contribution in the whole time range, even at the very short times when the stationary part becomes predominant.

On the other hand, it appears that the linear theory can be applied in the study of the nonstationary dynamics, at least in the limit $t_{obs} < t_w$.

SUMMARY

In the thiospinel spin-glass compound $CdCr_{1.7}In_{0.3}S_4$, a large time dependence of the out-of-phase susceptibility χ'' has been found for $\nu = 10^{-2}$ Hz and $T/T_g = 0.72$. The observed behavior is another evidence for the importance of the nonstationary dynamics which was otherwise extensively studied by TRM decay measurements. The reported time dependence of χ'' is shown to be in remarkable agreement with that of the spectral density of the magnetization $\langle M^2(\nu,t)\rangle$ derived from a zero-field noise experiment at the same frequency. It can be concluded that the relationship between χ'' and $\langle M^2(\nu,t)\rangle$ derived from the FDT remains valid in the case of the nonstationary dynamics as it was in the case of the stationary one.

The measured time dependence of χ' and χ'' has also been compared to that calculated from a previously proposed expression for the relaxation function. This expression was first derived from a detailed analysis of TRM decay measurements. Its final quantitative determination for $T/T_g = 0.72$ was obtained by deriving the stationary part from the frequency dependence of the equilibrium values of both components of the ac susceptibility at the considered temperature. Good agreement is found for the time dependence of χ''. A discrepancy is noted in the case of χ'; it is believed to be nonsignificant owing to the very small variation of χ'.

The results suggest that the linear-response theory can be applied to the nonstationary dynamics. It must be stressed, however, that the present conclusion only corresponds to the limit $t_{obs} < t_w$. In our approach the limit is equivalent to $\lambda \simeq t_{obs}$ which defines the range of times where the measurements are made at constant age. In other words, the system does not change during the time of the observation and the derived response function, though it is not the equilibrium response, describes the dynamics of a system frozen at a given stage of its evolution. Our analysis in terms of λ is meant to describe the same frozen dynamics in the range where t_{obs} becomes larger than t_w and where the state of the system changes continuously during the observation. It is therefore very interesting to check the validity of the linear theory in this extended range.

A measurement of the magnetization relaxation induced by different variations of the applied field has shown the validity of the superposition principle even in the regime of long observation times. It would be of interest to also check the validity of the FDT in this regime by deriving the autocorrelation function from noise experiments, and comparing it to the relaxation function.

[1] L. Lundgren, P. Svedlindh, P. Nordblad, and O. Beckman, Phys. Rev. Lett. **51**, 911 (1983).
[2] R. V. Chamberlin, Phys. Rev. B **30**, 5393 (1984).
[3] M. Alba, M. Ocio, and J. Hammann, Europhys. Lett. **2**, 45 (1986).
[4] M. Alba, J. Hammann, M. Ocio, Ph. Refregier, and H. Bouchiat, J. Appl. Phys. **61**, 3683 (1987).
[5] N. Bontemp, and R. Orbach (unpublished).
[6] L. Lundgren, P. Svedlindh, and O. Beckman, J. Magn. Magn. Mater. **31-34**, 1349 (1983).
[7] Ph. Refregier, E. Vincent, J. Hammann, and M. Ocio, J. Phys. (Paris) **48**, 1533 (1987).
[8] In Ref. 4 we published values of the exponent α for the power-law frequency dependence of χ'' which were smaller at 10^{-1} Hz than at 10 Hz. This discrepancy was the result of a too short value of the waiting time. At equilibrium α remains constant in the frequency range published and equal to its value at 10 Hz.
[9] W. Reim, R. H. Koch, A. P. Malozemoff, M. B. Ketchen, and H. Maletta, Phys. Rev. Lett. **57**, 905 (1986).
[10] L. Lundgren, P. Nordblad, and L. Sandlund, Europhys. Lett. **1**, 529 (1986).

Isothermal anisotropy rotation in a Au-Fe spin-glass alloy

Kh. Ziq and J. S. Kouvel
Department of Physics, University of Illinois, Chicago, Illinois 60680

Magnetization-vector measurements were made on a slowly rotating disk sample of $Au_{85}Fe_{15}$ after cooling to 4.2 K from above T_g (= 52 K) in a 15-kOe field that saturates the thermoremanence. For M_T, the magnetization component transverse to the applied field H, results are shown as HM_T vs θ, the sample-rotation angle relative to H, for θ cycled between 0° and 180° at each value of H. For $H \lesssim 0.1$ kOe, HM_T varies nearly reversibly in simple accord with an anisotropy field $\mathbf{H}_K$ (0.41 kOe in size) that rotates rigidly with the sample. At higher H, the rotational hysteresis grows rapidly until, for $H \gtrsim 0.4$ kOe, another simple but highly irreversible behavior is observed. From this behavior, it is deduced that $\mathbf{H}_K$ rotates relative to the sample isothermally when the torque on it exerted by the sample magnetization reaches the magnitude of a frictional torque. The frictional-torque coefficient is seen to decrease steadily with increasing H, as confirmed by direct measurements of the rotations of the remanence that result from sample rotations in various H at 4.2 K.

The spin-glass (SG) alloys of Mn in Cu, Ag, or Ni are known to exhibit a unique characteristic behavior when cooled in a magnetic field (H_{c1}) to well below the SG-freezing temperature (T_g). The magnetic anisotropy then seen is almost purely unidirectional, the single easy direction being that of $\mathbf{H}_{c1}$, and any subsequent isothermal changes of the magnetization (M) in moderate fields (H) are nearly elastic, as manifested in narrow displaced hysteresis loops.[1] This behavior has been shown theoretically[2] to be consistent with the notion that the randomly oriented atomic spins are exchange coupled so strongly that their rotation against relatively weak Dzyaloshinsky-Moriya-type forces is essentially rigid. This notion was further supported by our recent measurements of the components of M parallel and perpendicular to H in which a field-cooled Ni-Mn sample is slowly rotated at 4.2 K.[3] Basically, our results showed that M rotates elastically under the combined influence of H and a unidirectional anisotropy field ($\mathbf{H}_K$) whose orientation in the rotating sample remains fixed.

Subsequently, by similar magnetization-vector measurements, we have been examining several situations in which the orientation of $\mathbf{H}_K$ in a field-cooled SG sample does not remain fixed but changes irreversibly as the sample rotates in a stationary field. We first encountered this phenomenon in the same Ni-Mn sample but at higher temperatures (nearer yet still below T_g), which is where a "redefinition of the direction of the anisotropy axis" was previously observed by torque measurements on dilute *Cu*Mn.[4] However, our most complete results to date regarding this phenomenon are for Au-Fe well below T_g, and they will be described in this paper.

For our magnetization-vector study of Au-Fe, a circular-disk sample (5 mm diam, 0.5 mm thick) was cut from an alloy ingot of 15 at. % Fe, kindly supplied to us by Dr. H. Claus. The sample was annealed for 3 h at 600 °C and water quenched. Consistent with this thermal treatment,[5] the temperature dependence of the low-field magnetization showed a peak at $T_g = 52$ K, below which the magnetization is irreversible with field and temperature. Conventional measurements with a vibrating-sample magnetometer also showed that field cooling to 4.2 K results in a M-vs-H hysteresis loop that is symmetric about the origin and fairly broad; for $H_{c1} = 15$ kOe, which is sufficient to saturate the thermoremanence ($M_R = 9.8$ emu/g), the coercivity is 0.48 kOe. Qualitatively, this behavior (where M_R decays slowly with time) is typical of Au-Fe and other SG systems that do not clearly manifest a unidirectional anisotropy even after field cooling to well below T_g.

Using the quadrature arrangement of magnetometer pickup coils described previously,[3] we measured both M_L and M_T, the sample magnetization components longitudinal and transverse to the applied field H in the plane of the sample disk rotated about its axis. The $Au_{85}Fe_{15}$ sample was initially cooled from above T_g down to 4.2 K in $H_{c1} = 15$ kOe. Starting at the lowest H of 0.05 kOe, M_L and M_T were measured as the sample was rotated in progressive angular steps from $\theta = 0°$ to $\theta = 180°$ and back to $\theta = 0°$, the initial field-cooled position. These measurements were then repeated at successively higher H up to 2 kOe. However, before each change of H, the sample at $\theta = 0$ was subjected to a 15-kOe field, which restored the thermoremanence to its original saturated value isothermally, thus removing the need for additional field cooling.

In Fig. 1, our results for each H are displayed as a plot of HM_T versus increasing and then decreasing θ. Theoretically, the θ dependence of HM_T (the magnitude of the magnetic torque) is predictably simple if the anisotropy field $\mathbf{H}_K$ produced by $\mathbf{H}_{c1}$ is fixed in the sample, so that θ_K, the rotation angle of $\mathbf{H}_K$, equals the sample-rotation angle θ. In that case, since the equilibrium condition for the sample magnetization M is

$$HM_T \equiv HM \sin\phi = H_K M \sin(\theta_K - \phi), \qquad (1)$$

where ϕ is the rotation angle of M, it follows that HM_T is zero at $\theta = 0°$ and 180°, between which HM_T varies reversibly through a maximum, whose value rises linearly with H until it reaches $H_K M$ at $H = H_K$, where it remains for all $H > H_K$. Our results appear to follow this simple behavior but only at 0.05 kOe and (though less ideally) at 0.1 kOe, where the rotational hysteresis is fairly small—which agrees

 0021-8979/88/084346-03$02.40 © 1988 American Institute of Physics

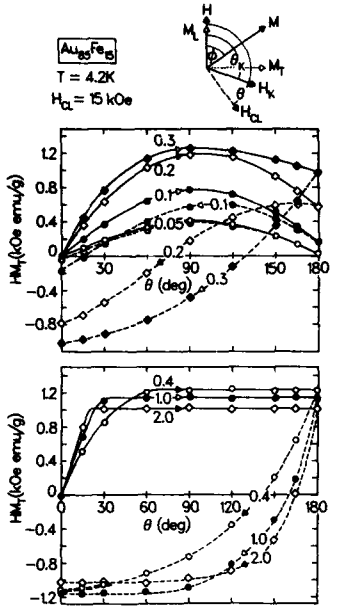


FIG. 1. $Au_{85}Fe_{15}$ cooled to 4.2 K in 15 kOe at $\theta = 0°$. Variation of HM_T with increasing and then decreasing θ (sample-rotation angle relative to field H) for various H (in kOe), where M_T is magnetization component transverse to H. Vector diagram at top shows sample magnetization M, anisotropy field $\mathbf{H}_K$, and rotated cooling-field direction in sample ($\mathbf{H}_{c1}$) relative to fixed applied field H.

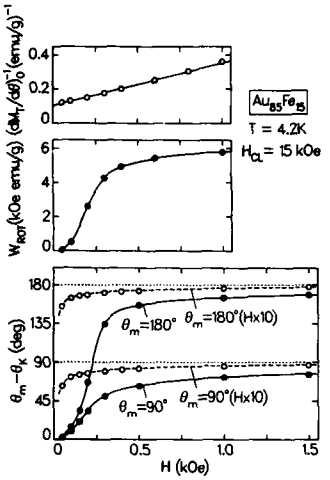


FIG. 2. $Au_{85}Fe_{15}$ cooled to 4.2 K in 15 kOe. Field dependence of $(dM_T/d\theta)_0^{-1}$ and of rotational hysteresis energy per cycle (W_{rot}), as derived from results in Fig. 1. Field dependence of $\theta_m - \theta_K$, where θ_m is sample-rotation angle of 90° or 180° and θ_K is rotation angle of remanent magnetization, both relative to field H. For open circles, the H scale is multiplied by 10.

with the reversible low-H regime seen in recent torque measurements on $Au_{82}Fe_{18}$.[6] At higher H, the rotational hysteresis clearly becomes a dominant effect, which for $H > 0.4$ kOe results in another simple but highly irreversible regime, where HM_T rises to a flat plateau with increasing θ and then descends with decreasing θ to a negative plateau of about the same magnitude.

However, even for this high-H regime, the initial rise of HM_T from zero at $\theta = 0°$ is reversible. Hence, it is still valid to deduce from Eq. (1) with $\theta_K = \theta$ that

$$(dM_T/d\theta)_0^{-1} = M^{-1}(1 + H/H_K), \tag{2}$$

for the inverse initial slope of M_T vs θ. Our experimental values for this quantity are plotted against H in Fig. 2; from the linearity of this plot we find via Eq. (2) that $M = 10.2$ emu/g and $H_K = 0.41$ kOe. The product, $H_K M = 4.18$ kOe emu/g, is the peak value of HM_T predicted for reversible behavior, and it is clearly much larger than the plateau levels at which HM_T is truncated in Fig. 1. Hence, with reference to the vector diagram in this figure, we deduce that $\mathbf{H}_K$ and therefore M remain fixed relative to H when the sample-rotation angle θ exceeds some critical value θ_c; in the sample frame, the orientation of $\mathbf{H}_K$ changes such that θ_K stays equal to θ_c. Analogously, as θ is lowered from 180°, the orientation of $\mathbf{H}_K$ in the sample changes when θ decreases below $180° - 2\theta_c$ and θ_K stays equal to $-\theta_c$, thus producing the observed negative plateaus of HM_T.

The phenomenological rationale implicit in this description is that the torque on $\mathbf{H}_K$ exerted by M, which from Eq. (1) equals HM_T, is opposed by a frictional torque having a certain maximum value (to be called $H_K M\alpha$). Since HM_T cannot exceed $H_K M\alpha$, it levels off upon reaching that value (or its negative), and the subsequent frictional rotation of $\mathbf{H}_K$ in the sample produces the observed rotational hysteresis (whose energy per cycle, W_{rot}, is plotted versus H in Fig. 2). Equating the plateau levels of HM_T in Fig. 1 to $H_K M\alpha$, we obtain $\alpha = 0.297$, 0.275, and 0.244, respectively, for $H = 0.4$, 1, and 2 kOe.

To see how the frictional-torque coefficient α changes at higher H, we performed another experiment, which would also check directly the rotations of $\mathbf{H}_K$ in the sample at 4.2 K. Namely, we rotated our field-cooled $Au_{85}Fe_{15}$ sample from $\theta = 0$ to $\theta = \theta_m$ ($= 90°$ or 180°) in various H up to 15 kOe, then removed H and measured the orientation of the remanence, which corresponds to the orientation of $\mathbf{H}_K$ (whose shift from the $\mathbf{H}_{c1}$ direction in the sample is $\theta_m - \theta_K$). Our results in Fig. 2 show for both θ_m values that $\theta_m - \theta_K$ remains small up to $H = 0.1$ kOe, which is also the approximate threshold field for the rotational hysteresis. At higher H, $\theta_m - \theta_K$ rises rapidly, then gradually approaches θ_m. For $H \gg H_K$, when ϕ in Eq. (1) is very small, it follows that $\alpha \approx \sin\theta_K$, and we find from $\theta_m - \theta_K$ for both θ_m values that $\alpha = 0.216$, 0.087, and 0.044, respectively, for $H = 2$, 8, and 15 kOe. Thus, α continues to decrease steadily with increasing H.

In a future report, we will compare our Au-Fe results in greater detail with the frictional anisotropy model, which was first invoked for the anisotropy rotations seen in an XY spin glass (YTb),[7] and which appears to pertain to previous torque data for CuMn.[4] The latter also revealed time-dependent (viscous) anisotropy changes, which our measure-

ments on Au-Fe find to be very small relative to the nearly instantaneous frictional changes. Our detailed report on Au-Fe will include our results for the longitudinal magnetization component M_L, which do not bear significantly on the results presented here for M_T, except in the threshold region near $H = 0.2$ kOe.

This work was supported by the National Science Foundation under Grant No. DMR84-06898.

[1]J. S. Kouvel, J. Phys. Chem. Solids **21**, 57 (1961); P. A. Beck, *Magnetism in Alloys* (TMS-AIME, New York, 1972), p. 211; P. Monod, J. J. Prejean, and B. Tissier, J. Appl. Phys. **50**, 7324 (1979); J. S. Kouvel, W. Abdul-Razzaq, and Kh. Ziq, Phys. Rev. B **35**, 1768 (1987).
[2]P. M. Levy, C. Morgan-Pond, and A. Fert, J. Appl. Phys. **53**, 2168 (1982); C. L. Henley, H. Sompolinsky, and B. I. Halperin, Phys. Rev. B **25**, 5849 (1982); W. M. Saslow, *ibid.* **27**, 6873 (1983).
[3]Kh. Ziq and J. S. Kouvel, J. Appl. Phys. **61**, 3625 (1987).
[4]J. B. Pastora, T. W. Adair, and D. P. Love, J. Phys. (Paris) Lett. **44**, L-859 (1983).
[5]S. Crane. D. W. Carnegie, and H. Claus, J. Appl. Phys. **53**, 2179 (1982).
[6]I. A. Campbell, H. Hurdequint, and F. Hippert, Phys. Rev. B **33**, 3540 (1986).
[7]S. E. Inderhees, M. B. Salamon, and L. J. P. Ketelsen, J. Appl. Phys. **61**, 3628 (1987).

Torque relaxation in a CuMn spin glass

C. Giovannella[a] and I. A. Campbell
Physique des Solides, Université Paris Sud, 91405 Orsay, France

Torque relaxation data on a Cu 5-at. % Mn sample at different temperatures are presented. The relaxations after field cooling and after zero-field cooling are different at each temperature, implying that the in-field states of the sample after these two procedures are different. Torque data for the effective anisotropy K are compared with values from experiments having shorter time windows so as to obtain information on relaxation over a very wide time spectrum. The estimated effective T_g values tend to a frequency-independent limit at low frequencies.

Relaxation in spin glasses has been studied principally through magnetization measurements, first from relatively high fields and more recently by very precise low-field SQUID experiments.[1] These have been analyzed phenomenologically using a combination of power-law and stretched exponential decay functions. One can also use torque measurements to see transverse relaxation after the direction of the field has been changed.[2,3] The field rotation tends to turn the spin system against the anisotropy axes and so in a different perturbation from a change of the strength of the applied field.

We have made measurements on a Cu 5-at. % Mn sample with a T_g value of 28 K, using a capacity cell torquemeter. Experiments following different protocols have been reported[3] [e.g., turning the field after field cooling (FC) to T, or alternatively zero-field cooling (ZFC) to T followed by ramping up and then turning the field]. The results showed that for given H and T the torque decay varied substantially depending on the previous magnetic history of the sample, i.e., the internal state of the sample was strongly history dependent. Here we give data on the same sample at different temperatures.

First, in Figs. 1 and 2, we show decay curves for the torque signal (normalized each time to the value immediately after turning the field) for a field of 8.7 kG and a turning angle of 5°, at various temperatures. The curves in Fig. 1 correspond to measurements in the FC condition; and in Fig. 2 after ZFC followed by field ramping up to the same field value before turning. It can be seen that relaxation becomes more rapid as the temperature is raised; the relaxation after the ZFC procedure is at each temperature substantially faster than after the FC procedure. We can compare with magnetic data. Remanent magnetizations are conventionally measured with the field reduced to zero either after FC or ZFC, giving thermoremanent magnetization (TRM) and isothermal remanent magnetization (IRM), respectively. It is well established that at a given T, TRM equals IRM when the magnetizing field used is greater than a value referred to as H_s (see inset to Fig. 2).[4] The natural implication of these results is that the state of the sample is the same after FC or ZFC if a field $H > H_s$ is applied. For our sample, H_s is about 25, 11, and 2.5 kg at 4.2, 8.6, and 16 K, respectively. Figures 1 and 2 thus correspond to measurements made with H less than, of the order of, and greater than H_s. In the three cases the relaxation patterns after FC and ZFC are far from identical, so even in a field H greater than H_s the internal state of the sample still depends on its magnetic history. The fact that when the field is subsequently reduced to zero, TRM and IRM are equal, means that the ramping down procedure modifies the state of the sample and to a certain extent smudges out previous magnetic history. The well-known standard TRM and IRM curves (Fig. 2 inset) are thus not characteristic of the state of the sample in field, but of a state modified by field ramping.

We can also use the torque data in combination with results from other techniques to obtain informations on the relaxation over a very wide time scale. EPR,[5,6] ac transverse susceptibility,[6] and torque are all analyzed in terms of effective values of the anisotropy constant K, for which the accepted mechanism is that of triad anisotropy arising from the Dzaloshinsky-Moriya interaction.[7] The appropriate time window in which the value of K is "measured" for the two former experiments can be considered to be their inverse frequencies, i.e., about 10^{-10} s and 3×10^{-2} s, respectively. We can then plot on the same figure the anisotropy at each temperature measured at 10^{-10} s from EPR, at $\cdot\times10^{-2}$ s from transverse susceptibility, and from 1 s to 2×10^{3} s from

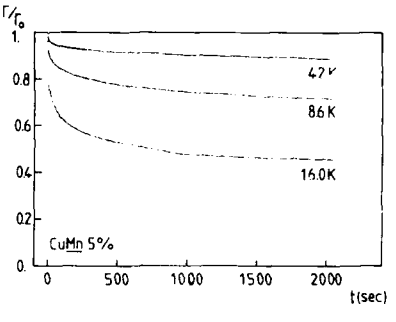


FIG. 1. Relaxation of the torque signal after FC in a field of 8.7 kG to 4.2, 8.6, and 16.0 K and turning angle of 5°. Torque normalized to the value immediately after turning.

[a] Permanent address: Dipartimento di Fisica, II Universita degli Studi di Roma, 00173 Italy.

 0021-8979/88/084349-02$02.40 © 1988 American Institute of Physics

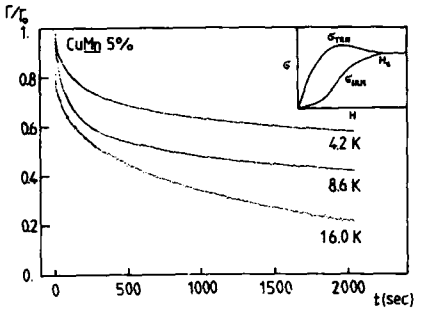


FIG. 2. Same as for Fig. 1 but following ZFC to the same temperatures. Inset: schematic TRM and IRM curves, following Ref. 4.

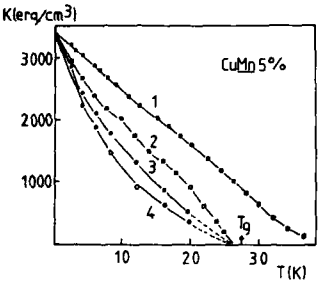


FIG. 3. Comparison of effective anisotropy values K from different experiments. Curves 1 and 2 are data for EPR and transverse susceptibility at 30 Hz, respectively, from Ref. 6. Curves 3 and 4 are FC torque values, H, equal to 2 kG, taken 1 s and 2000 s after turning. The normalization constant for all the torque data has been adjusted so that the extrapolations at zero temperature coincide with those for the other results.

the torque (giving us a total range of 13 decades in time!) All these experiments are performed in fields of the order of a kilogauss. In fact, none of these experiments is strictly measuring K, as the observed signals will be reduced by a rotation of the triad anisotropy axes during the experiment (this is directly observed in torque[2]). It is legitimate to compare the three experiments but keeping in mind that the effective K is a convenient but loose way of expressing the data.

Figure 3 shows that in the range of time scales from 3×10^{-2} s to 2×10^{3} s the temperature T_g^K at which K goes to zero by extrapolation is slightly lower than the cusp value T_g^0 and is independent of frequency within the accuracy of the extrapolation. (The difference between T_g^K and T_g^0 has been discussed in Ref. 8.) On the contrary the "EPR" value of T_g^K is about 30% higher. The effective T_g is thus frequency dependent at high frequencies, but as the frequency is lowered the effective value of T_g tends to a constant rather than going to zero. This is a further indication that the ordering in a canonical Heisenberg spin glass is not simply a dynamical effect but that the limit $T_g(\omega\to0)$ is well defined. Note that these are measurements on a spin glass *in a field* not in the usual zero-field condition. The high-frequency effect leading to the shift of the EPR T_g^K can be pictured as a trapping of the system within a restricted part of phase space on time scales up to 10^{-10} s for temperatures well above T_g.[9]

The form of the relaxation is strongly nonexponential, as in the case of magnetization relaxation.[1] If we restrict ourselves to the time scale accessible in our experiment, the curves can be parametrized by products of power laws ($t^{-\alpha}$) and stretched exponentials [$\exp(-t^{\beta})$].

The fact that we obtain relaxation faster than a power law in our time range is not a waiting time effect[1] (we find no observable waiting time dependence of FC relaxation) but may well be because we perturb the sample rather too violently by turning the field through 5° (giving a transverse field of up to 750 G), so we are not strictly observing relaxation associated with spontaneous equilibrium fluctuations. If we plot our results together with EPR and transverse susceptibility values for K with the appropriate time windows as a function of log t, the data suggest that the relaxation over the range 10^{-10} s to a few seconds can be parametrized by a power law, with α varying from a value of about 0.05 at 20 K to about 0.01 at 4 K. These numbers are similar to those estimated from magnetization decay at much longer times, and can be compared with the intrapolations between neutron spin echo and magnetization which cover a similar time window.[10] On the other hand, a careful comparison between Mn NMR frequency and temperature dependence of TRM at temperatures below the cooling temperature in *Cu*Mn (Ref. 11) gives results in which at $T\ll T_g$ there is only weak relaxation concentrated at high frequency. The temperature at which the applied field is modified in strength (or direction) clearly plays a vital role in the form of subsequent relaxation.

These results give an indication of the form of the transverse relaxation over a very wide time spectrum for a spin glass in a field and at temperatures below T_g. A great deal remains to be understood, even on a phenomenological level, concerning the relaxation in even the canonical spin glasses.

[1] R. V. Chamberlin, G. Mozurkewich, and R. Orbach, Phys. Rev. Lett. **52**, 867 (1984); P. Norblad, P. Svedlindh, L. Lundgren, and L. Sandlund, Phys. Rev. B **33**, 645 (1986); M. Ocio, M. Alba, and J. Hammann, J. Phys. (Paris) Lett. **46**, L1101 (1985); M. Ocio, H. Bouchiat, and P. Monod, J. Magn. Magn. Mater. **54-57**, 11 (1986).

[2] J. B. Pastora, T. W. Adair, and D. P. Love, J. Phys. Lett. **44**, L859 (1983); D. Avanitis, Doctorate thesis, Orsay, 1984.

[3] C. Giovannella, I. A. Campbell, and F. Hippert, Phys. Rev. Lett. **59**, 1030 (1987).

[4] H. Bouchiat and P. Monod, J. Magn. Magn. Mater. **30**, 175 (1982).

[5] S. Schultz, E. M. Gullikson, D. R. Fredkin, and M. Tovar, Phys. Rev. Lett. **45**, 1508 (1980).

[6] D. Youm and S. Schultz, Phys. Rev. B **34**, 7958 (1986).

[7] A. Fert and P. Levy, Phys. Rev. Lett. **44**, 1538 (1980); A. Fert and F. Hippert, *ibid.* **49**, 1508 (1982).

[8] N. de Courtenay, A. Fert, and I. A. Campbell, Phys. Rev. B **30**, 6791 (1984).

[9] I. A. Campbell, Phys. Rev. B **33**, 3587 (1986).

[10] F. Mezei, A. P. Murani, and J. L. Tholence, Solid State Commun. **45**, 411 (1983).

[11] H. Alloul, P. Mendels, P. Beauvillain, and C. Chappert, Europhys. Lett. **1**, 595 (1986).

Spin-glass dynamics in $Fe_{2-x}Ti_{1+x}O_5$

R. L. Lichti and S. Kumar,
Texas Tech University, Lubbock, Texas 79409

C. Boekema
San Jose State University, San Jose, California 95192

Zero-field muon-spin-relaxation (μSR) and X-band ESR have been used to study the spin-freezing dynamics in single crystals of the Ising spin glass $Fe_{2-x}Ti_{1+x}O_5$. Parameters obtained for the power-law and Vogel–Fulcher descriptions of the critical slowing are consistent with other methods for $x = 0$ and indicate significantly slower freezing in Ti-rich samples. Interpretation of cluster effects, observed in $x = 0.25$-μSR data, as a Griffiths-like phase yields an estimate of 61 ± 1 K for the Néel temperature in site-ordered Fe_2TiO_5.

INTRODUCTION

The effects related to formation of a spin glass extend well into the paramagnetic phase and are easily observed in experiments sensitive to spin dynamics. Measurements of spin-correlation times show increasing correlations starting at temperatures several times the spin-glass temperature T_g, and in some cases indicate a divergence as T_g is approached from above. A number of mathematical expressions have been used to describe the spin-freezing process. Those most frequently applied are the phenomenological Vogel–Fulcher law

$$\tau = \tau_0 \exp[E/k(T - T_0)] \quad (1)$$

adopted from the field of structural glasses, and a power law of the form

$$\tau = \tau_0 [T/(T - T_0)]^{z\nu} \quad (2)$$

derived from mean-field theory. The T_0 in these expressions is a critical temperature associated with the spin-glass transition, distinguished from an experimentally defined freezing temperature T_g, and τ_0 is the characteristic spin-correlation time.

In the region just above T_g, small clusters of spins may freeze into a "glassy" state while the rest of the sample remains paramagnetic. Such cluster formation can be treated as inhomogeneous freezing with some (cluster) fraction of the sample in the spin-glass state at a given temperature, thus yielding a distribution in T_g. Spin dynamics should then take on a nonexponential character due to slow paramagnetic-like response of small frozen clusters.[1,2] Randeria *et al.*[3] suggest that this case, where long-time dynamics may be dominated by cluster effects, is similar to the Griffiths phase of a diluted ferromagnet and can be identified as a separate intermediate phase between the paramagnetic and spin-glass states.

We have performed zero-field muon-spin-relaxation (μSR) and X-band ESR linewidth measurements on the anisotropic spin-glass system $Fe_{2-x}Ti_{1+x}O_5$ using single-crystal samples.[4-6] Here we concentrate on the spin-freezing parameters for the power law and Vogel–Fulcher descriptions, and on the presence of cluster effects in the spin dynamics.

EXPERIMENTAL RESULTS

A single-crystal sample of composition $Fe_{1.75}Ti_{1.25}O_5$ was investigated using μSR measurements in zero applied field. As previously reported,[4,5] the dominant feature in the relaxation rate versus temperature curve is a sharp peak at T_g (see inset, Fig. 1). This peak is accompanied by a drop in relative asymmetry to one third. At temperatures below the peak the relaxation is best fitted by an exponential square-root time dependence associated with a spin-glass state having fast-fluctuation modes.[7,8] The simultaneous occurrence of these three signatures identifies T_g as 43.5 ± 0.5 K for this oxide spin glass. Above 60 K, the relaxation exhibits single exponential behavior expected for spin dynamics in a paramagnetic system.

The data between T_g and 60 K clearly show nonexponential behavior but are poorly fit by the exponential square-

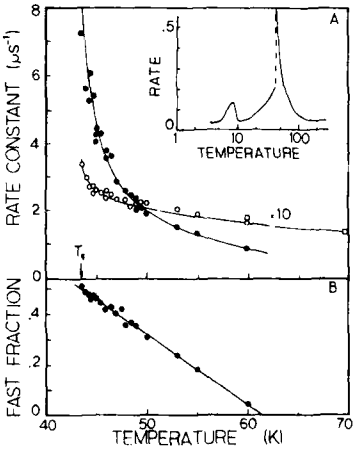


FIG. 1. Two exponential analysis of zero-field μSR data in $Fe_{1.75}Ti_{1.25}O_5$ for $43.5 < T < 60$ K. (a) Rate constants: (●) fast relaxing μSR component, (○) slow-relaxing μSR component (×10). Insert shows full temperature dependence for a single component analysis. (b) Fractional strength of fast-relaxing μSR component.

 0021-8979/88/084351-03$02.40 © 1988 American Institute of Physics

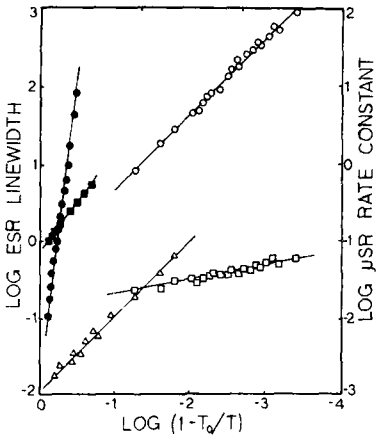


FIG. 2. Power-law description of spin freezing in $Fe_{2-x}Ti_{1-x}O_5$. Open symbols are μSR results for $x = 0.25$: (○) fast-relaxing μSR component $T < 60$ K, (□) slow-relaxing μSR component $T < 60$ K, (△) single component $T > 60$ K. Filled symbols are ESR results: (●) $x = 0$, (■) $x = 0.20$.

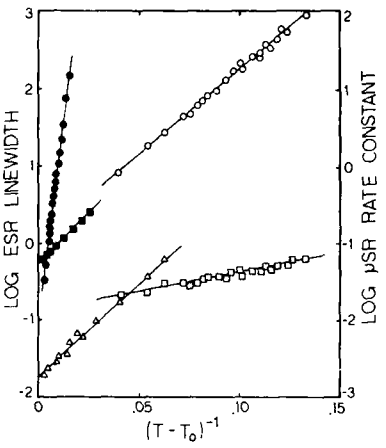


FIG. 3. Vogel–Fulcher description of spin freezing in $Fe_{2-x}Ti_{1-x}O_5$. Open symbols are μSR results for $x = 0.25$: (○) fast-relaxing μSR component $T < 60$ K, (□) slow-relaxing μSR component $T < 60$K, (△) single component $T > 60$ K. Filled symbols are ESR results: (●) $x = 0$, (■) $x = 0.20$.

root time dependence observed for $T < T_g$. The analysis reported is a sum of two exponentials, selected to minimize the number of fitting parameters. Figure 1 displays the temperature dependence of the two rate constants and the fractional strength of the fast-relaxing μSR component.

In order to compare spin-freezing parameters from the μSR data with those obtained by other methods, separate fits to power and Vogel–Fulcher laws were performed for the single exponential rate constant for $T > 60$ K and to both rate constants for $43.5 < T < 60$ K. These fits are shown in Figs. 2 and 3 along with those from the ESR measurements discussed below. Tholence *et al.*[9] determined the power-law exponent and Vogel–Fulcher energy paramet . for spin freezing in Fe_2TiO_5 (i.e., $x = 0$) from the dependence of T_g on probe frequency using susceptibility and neutron scattering data. A comparison (see Table I) of their results and our μSR results for $T > 60$ K ($x = 0.25$) show nearly an order of magnitude diffrence in these parameters.

Two single-crystal samples of composition $Fe_{2.0}Ti_{1.0}O_5$ and $Fe_{1.80}Ti_{1.20}O_5$ were studied from 77 to 400 K using *X*-band ESR. The line shapes were well approximated as Lorentzian at higher temperatures but became progressively more asymmetric at lower temperatures. The derivative peak-to-peak width used here provides a general width determination. This approach works well down to approximately $2T_g$, where fits to the freezing laws were terminated. Typical fits for a single-temperature cycle of each sample are plotted (filled symbols) in Figs. 2 and 3.

DISCUSSION

Fe_2TiO_5 (pseudobrookite) was initially chosen for a study of spin-freezing dynamics in insulating short-range spin glasses because its highly anisotropic magnetic character represents an excellent experimental approximation to the Ising model. The stoichiometric compound shows uniaxial spin-glass behavior with a cusp in the low-frequency susceptibility at ~55 K along the orthorhombic *c* axis, while transverse components remain paramagnetic to much lower temperature,[10] ordering below 10 K.[4–11] Random mixing of Ti^{4+} ions into the nominally Fe^{3+} sites of the pseudo-

TABLE I: Spin-freezing parameters for $Fe_{2-x}Ti_{1-x}O_5$ using power-law and Vogel–Fulcher descriptions.

Concentration	Power law		Vogel–Fulcher		
x	T_0 (K)	$z\nu$	T_0 (K)	E/k (K)	Method
(0)	47.4	9.5	43.5	170	T_g vs f*
0.0	47 ± 1	7.8 ± 1	43 ± 2	170 ± 7	ESR ($T > 110$ K)
0.20	42 ± 2	1.4 ± 0.2	37 ± 1	30 ± 3	ESR ($T > 80$ K)
0.25	41 ± 1	1.0 ± 0.2	36 ± 2	25 ± 5	μSR ($T > 60$ K)
	41.8 ± 0.4	0.9 ± 0.2	36 ± 1	23 ± 2	μSR (43–60 K) fast component
	~41	~0.2	~35	~6	μSR (43–60 K) slow component

*J. L. Tholence *et al.*, J. Magn. Magn. Mater. **54,57**, 203 (1986).

brookite structure causes this system to become a spin glass rather than an antiferromagnet. Introduction of additional Ti^{4+}, necessary in order to obtain large single crystals for the μSR work, forces some of the iron ions to become Fe^{2+} and introduces additional randomness.

A comparison of the parameters shown in Table I indicates agreement between the ESR results for $x = 0$ and those obtained by Tholence *et al.* Furthermore, the μSR results for $x = 0.25$ ($T > 60$ K) and the ESR results for $x = 0.20$ are compatible. One may conclude that these various methods are probing the spin freezing in a similar manner. The aim here is not to argue that ESR or μSR data should be treated using specific functional forms, but rather to compare parameters from several methods using the more commonly applied spin-freezing descriptions.

The combination of magnetic probes applied to $Fe_{2-x}Ti_{1+x}O_5$ yields a consistent picture of the effect of increasing titanium content on the spin dynamics of that system. The observed decrease in critical temperature with dilution is a common feature of paramagnetic to ordered or spin-glass phase boundaries. Perhaps more interesting are changes in the power-law exponent and Fulcher energy parameter, which measure how rapidly fluctuations slow with decreasing temperature. The factor of 5 to 8 decrease in these parameters in going from $x = 0$ to 0.25 indicates much less rapid spin freezing in the diluted pseudobrookites.

The appearance of cluster effects just above the spin-glass temperature effectively precluded the possibility of making a choice of spin-freezing descriptions based on the $x = 0.25$ μSR data. Theoretical predictions generally agree that spin dynamics with clusters present will have a nonexponential time dependence; however, the exact form will certainly be model dependent. The two-exponential treatment of the μSR data provides a satisfactory fit while minimizing the number of parameters. There are, however, serious inconsistencies in that treatment, and another approach more directly related to a detailed physical model is being pursued. The major conflict is that while the rate constant from the single exponential above 60 K matches that for the slowly relaxing μSR component below 60 K, the spin-freezing parameters above 60 K match those for the rapidly relaxing μSR component whose intensity increases from zero below 60 K. Based on the agreement of the magnitude of the rate constants and relative strengths of two components one is tempted to assign the slow-relaxing μSR component to paramagnetic spins. However, the excellent agreement of the spin-freezing parameters indicates that the short-time, fast-relaxing μSR component is a continuation of the higher temperature paramagnetic dynamics. Theoretical models place cluster effects at long times consistent with the latter assignment. Pinkvos *et al.*[12] have treated similar μSR data from single crystal *Cu*Mn as inhomogeneous spin freezing. Their results indicated the coexistence just above T_g of spatial regions having fast spin fluctuations with regions of more strongly correlated spins.

Assumption of the existence of a Griffiths-like phase implies a critical temperature for cluster formation. The onset of two-component relaxation in the μSR data for $Fe_{1.75}Ti_{1.25}O_5$ places that temperature at 61 ± 1 K. That value should apply to all concentrations since theoretically it is the ordering temperature of the undiluted system. It thus may represent the Néel temperature at which antiferromagnetic ordering should take place in Fe_2TiO_5 if site mixing did not occur.

In conclusion, cluster effects have been observed in the spin-freezing dynamics of the Ising spin-glass system $Fe_{2-x}Ti_{1+x}O_5$ in zero-field μSR relaxation measurements just above T_g. Interpreting these effects as a Griffiths phase yields an estimate of 61 K for the critical temperature in site-ordered Fe_2TiO_5. ESR and μSR data on titanium-rich samples indicate less rapid freezing in the diluted pseudobrookites and yield power-law and Vogel–Fulcher parameters consistent with other methods.

ACKNOWLEDGMENTS

We wish to thank V. A. M. Brabers (Technical University of Eindhoven) and J. P. Remeika (AT&T Bell Laboratories) for providing the single-crystal samples used in this work, and members of the LAMPF μSR collaboration for their involvement in the collection and analysis of the μSR data. C.B. acknowledges NATO and San Jose State University Foundation Grants.

[1] K. L. Ngai, Comments Solid State Phys. **9**, 127 (1979)
[2] R.G. Palmer *et al.*, Phys. Rev. Lett. **53**, 958 (1984).
[3] M. Randeria *et al.*, Phys. Rev. Lett. **54**, 1321 (1985).
[4] C. Boekema *et al.*, Hyperfine Interact. **31**, 369 (1986).
[5] V. A. M. Brabers *et al.*, J. Appl. Phys. **61**, 4086 (1987).
[6] S. Kumar, Masters thesis, Texas Tech University, 1987.
[7] Y. J. Uemura, Solid State Commun. **36**, 369 (1980); Hyperfine Interact. **8**, 739 (1981).
[8] A. T. Fiory, Hyperfine Interact. **8**, 777 (1981).
[9] J. L. Tholence *et al.*, J. Magn. Magn. Mater. **54-57**, 203 (1986).
[10] U. Atzmony *et al.*, Phys. Rev. Lett. **43**, 782 (1979).
[11] Y. Yeshurun and H. Sompolinsky, Phys. Rev. B **31**, 3191 (1985).
[12] H. Pinkvos *et al.*, Hyperfine Interact. **31**, 363 (1986).

Energy gap in concentrated spin glasses

S. B. Liao and S. M. Bhagat
Department of Physics, University of Maryland, College Park, Maryland 20742

M. A. Manheimer
Laboratory for Physical Science, College Park, Maryland 20740

K. Moorjani
Applied Physics Laboratory, Johns Hopkins University, Laurel, Maryland 20707

Using magnetic resonance data at several frequencies, we have obtained the temperature dependence of the field-induced magnetization (M) in three concentrated spin glasses. At every frequency, M is independent of T for $T \lesssim T_{SG}$ and drops linearly with T at higher temperatures. $[M(0) - M(T)]/M(0)$ is closely represented by the function $[\exp(\Delta/T) - 1]^{-1}$, where Δ is a characteristic gap energy with values close to the corresponding Curie–Weiss temperatures θ_p but much larger than the respective spin-glass transition temperatures T_{SG}.

Recently,[1] two of us have reported on the temperature dependence of the field-induced magnetization (M), derived from magnetic resonance measurements at 35 GHz (~ 10 kOe), in a number of reentrant ferromagnets (REE) and one concentrated spin glass (SG), belonging to the series $(Fe_pNi_{1-p})_{75}P_{16}B_6Al_3$. It was found that in the REEs the variation of M with T shows marked deviations from the simple $T^{3/2}$ law at *low* temperatures while in the SG, *M is constant below T_{SG} and drops linearly with T for $T \gtrsim T_{SG}$*. The observations were interpreted by (i) introducing an energy gap Δ in the excitation spectrum, i.e., $\epsilon = \Delta + Dq^2$, and (ii) providing a nonzero density of states (DOS) at the gap energy Δ in addition to recognizing that in REE at low T, and in concentrated spin glasses, the usual spin-wave integral is cut off at the lower limit (due to break up or nonexistence of the infinite cluster) and only the term corresponding to excitations at the gap energy survives thereby yielding (cf. Fig. 4, Ref. 1).

$$\frac{M_0 - M(T)}{M_0} = \frac{\delta M}{M_0} = \frac{C}{\exp(\Delta/T) - 1} \qquad (1)$$

for $0 < T < T_m$, $T_m = \Delta/\ln(1 + C)$. Further, M_0 is the 0-K value of M and C is a measure of the DOS at Δ. For $(Fe_{0.16}Ni_{0.84})_{75}G_{25}$, the SG discussed in Ref. 1, $\Delta \simeq (145 \pm 5)$ K at 35 GHz and its closeness to the paramagnetic Curie temperature, $\theta_p = (140 \pm 10)$ K was used to suggest that Δ was a measure of the intracluster exchange. The main idea is that in the presence of a magnetic field the magnetization induced in a concentrated SG reduces with increasing T as a consequence of the break up of spin clusters and Δ is the characteristic energy for this process. Here, we present further evidence in support of this contention. We have reanalyzed our previous data[2,3] on the temperature dependence of M in three concentrated spin glasses

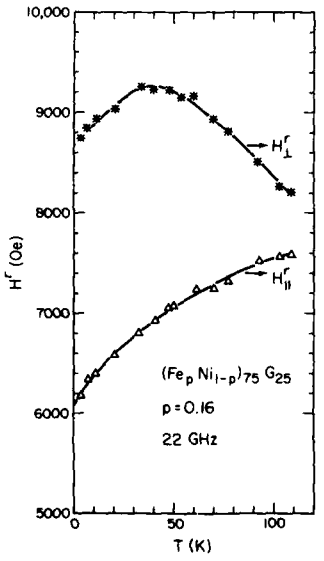


FIG. 1. Temperature dependencies of the observed magnetic fields for resonance in $(Fe_{0.16}Ni_{0.84})_{75}G_{25}$. Note that these values have to be corrected for lineshape effects (Refs. 2 and 3) prior to substitution in Eq. (2).

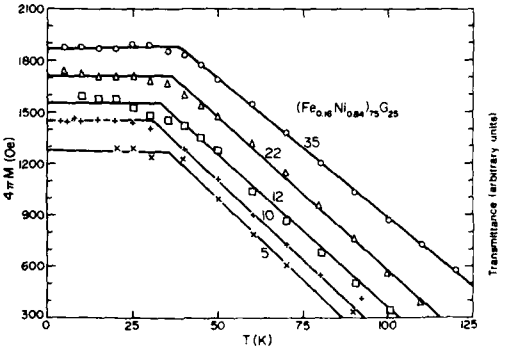


FIG. 2. Variation of field-induced magnetization, with temperature, in $(Fe_{0.16}Ni_{0.84})_{75}G_{25}$. The data are labelled by the frequency (in GHz).

 0021-8979/88/084354-03$02.40 © 1988 American Institute of Physics

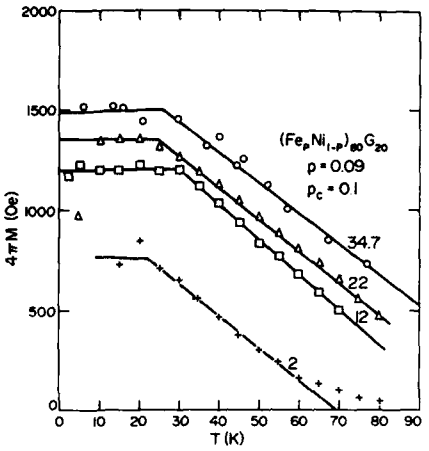


FIG. 3. Same as Fig. 2 for $(Fe_{0.09}Ni_{0.91})_{80}G_{20}$.

$(Fe_{0.16}Ni_{0.84})_{75}G_{25}$, (I), $(Fe_{0.09}Ni_{0.91})_{80}G_{20}$ (II), and a-$Mn_{48}B_{52}$ (III). Recall that M is derived from parallel (magnetic field in sample plane) and perpendicular (field normal to sample) resonance data at several frequencies between 35 and 2 GHz. To recapitulate, a typical set of data showing the T dependencies of the observed resonance fields are in Fig. 1. The linewidths being large, detailed calculations[2,3] were necessary to obtain the "true" resonance fields which will satisfy the Kittel equations:

$$\omega/\gamma = H_\perp - 4\pi M_\perp + H_{an}$$
$$= [(H_\parallel + H_{an})(H_\parallel + H_{an} + 4\pi M_\parallel)]^{1/2}. \quad (2)$$

We set $M_\perp = M_\parallel = M(\omega)$, assumed γ to be independent of T, and found that $H_{an} \neq 0$ at low T and increases rapidly as T drops below T_{SG}. Details on H_{an} have been presented elsewhere.[2,3] Here, we concentrate on the T dependence of $M(\omega)$. The explicit dependence on ω is stated merely to assert that we are discussing T dependence of a field-induced M. Figures 2, 3, and 4 show $4\pi M$, as a function of T, for various frequencies, corresponding to I, II, and III, respectively. In every case, it is noted that M is relatively flat at low T but drops linearly with T at $T \gtrsim T_{SG}$. As seen from the normalized plot in Fig. 5, this is precisely in accord with Eq. (1). The values of Δ required to explain the data in terms of Eq. (1) are in Table I. Δ is relatively insensitive to frequency. In Table I we have also listed values of the other two characteristic temperatures, T_{SG} (the zero-field spin-glass transition temperature) and θ_p (the paramagnetic Curie temperature obtained from low-field susceptibility studies at high T).[4] In every case, Δ is much larger than T_{SG} but of the same order as θ_p further supporting the suggestion in Ref. 1, that T_{SG} measures the intercluster coupling while θ_p and Δ describe the intracluster interactions. It should be recalled[4] that in all these SGs the low-field susceptibility does not exhibit Curie–Weiss behavior except at rather high T ($\gtrsim 10T_{SG}$). Thus, they are *not* conventional paramagnets over a wide range of temperatures above T_{SG}. This, combined with the near equivalence of Δ and θ_p, strongly suggests the picture proposed in Ref. 1. To reiterate, as the temperature is lowered below the paramagnetic region, stable spin clusters are nucleated and the susceptibility deviates from the Curie law. The characteristic energy for the formation of clusters is the intracluster coupling represented, on the average, by θ_p. At the opposite end, starting at $T = 0$, application of a magnetic field causes the cluster moments to orient along the applied field giving rise to the sizeable values for $4\pi M_0$ in Figs. 2–4. Note that the clusters are likely to be

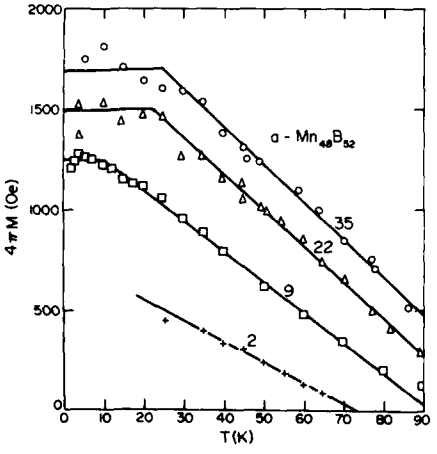


FIG. 4. Same as Fig. 3 for a-$Mn_{48}B_{52}$.

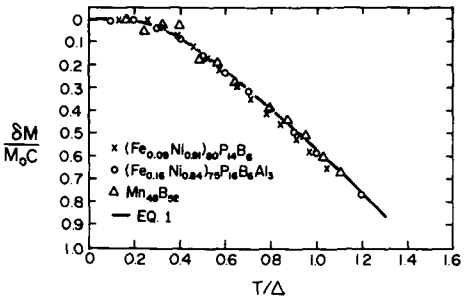


FIG. 5. Normalized plot showing comparison of Eq. (1), full line, with experimental points: $(Fe_{0.16}Ni_{0.84})_{75}P_{16}B_6Al_3$, 35 GHz, $C = 1.75$; $(Fe_{0.09}Ni_{0.84})_{80}P_{14}B_6$, 22 GHz, $C = 1$; $Mn_{48}B_{52}$, 22 GHz, $C = 0.85$.

TABLE I. Characteristic temperatures for concentrated spin glasses.

Sample	T_{SG} (K)	θ_p (K)	Δ (K)
$(Fe_{0.16}Ni_{0.89})_{75}G_{25}$	29	140	130 ± 20
$(Fe_{0.09}Ni_{0.91})_{80}G_{20}$	16	140	100 ± 20
$Mn_{48}B_{52}$	18	100	80 ± 20

quite large[5] because p is rather close to the percolation concentration. As the temperature is raised, the reduction in M occurs via the breakup of these spin clusters which again brings into play an intracluster interaction energy, namely Δ. The third characteristic temperature T_{SG} is measured at or near zero field. It provides a measure of the intercluster coupling which is understandably weaker than the interactions necessary for the formation of the clusters in the first place.

The work performed at A. P. L. was supported by the Department of the Navy under Contract No. N00039-87-C-5301. One of us (S.B.L.) is thankful to the NSF for support under the US/China cooperative program.

[1]S. B. Liao and S. M. Bhagat, Solid State Commun. (in press).
[2]S. B. Liao, S. M. Bhagat, M. A. Manheimer, and M. J. Park, Solid State Commun. **63**, 119 (1987).
[3]M. J. Park, S. M. Bhagat, M. A. Manheimer, and K. Moorjani, J. Magn. Magn. Mater. **59**, 287 (1986).
[4]P. Mazumdar and S. M. Bhagat, J. Magn. Magn. Mater. **66**, 263 (1987).
[5]M. F. Sykes, D. S. Gaunt, and M. Glen, J. Phys. A **9**, 1705 (1976).

Spin-density wave in spin glasses (*Cu*Mn) and other dilute alloys (*Y*Gd) (invited) (abstract)[a]

J. A. Mydosh
Kamerlingh Onnes Laboratorium, Rijks-Universiteit Leiden, 2300 RA Leiden, The Netherlands

Spin glasses have been of particular interest in magnetism for the past 15 years. Their present theoretical description, based upon a simple physical model, requires a fundamentally new type of statistical mechanics for its solution. Most experimental interpretations have attempted to follow this approach, although its physical meaning and direct comparison are partially obscured and somewhat strained. Almost 30 years ago Overhauser proposed a spin-density-wave (SDW) model which endeavored to explain the "antiferromagnetic" behavior in dilute alloys such as *Cu*Mn. In the intervening period the spin-glass phenomenon has mainly evolved unconnected with the SDW approach. However, in recent times a series of neutron-scattering experiments has renewed the connection and introduced the distinction between a "long-range" SDW as found in *Y*Gd and the "short-range" SDW of the spin glasses, e.g., *Cu*Mn. It is the purpose of this paper to review the available evidence for a SDW mechanism in these dilute alloys relying not only on neutron-scattering data, but also on macroscopic measurements such as specific heat, magnetization, and susceptibility. Here clear-cut differences arise between the long-range and short-range SDW's which are related to the glassy dynamics of the latter systems.

[a] A full length paper will appear in an upcoming issue of J. Appl. Phys.

Magnetic susceptibility in the spin glass system, $[(CH_3)_3NH]Co_{1-x}Ni_xCl_3\,2H_2O$ (abstract)[a]

Gerald V. Rubenacker, Donald N. Haines, and John E. Drumheller
Physics Department, Montana State University, Bozeman, Montana 59717

The pseudo-one-dimensional mixed system $[(CH_3)_3NH]Co_{1-x}Ni_xCl_3\,2H_2O$ was found to exhibit spin-glass behavior below a characteristic temperature evidenced by the onset of time-dependent thermoremanent magnetization. In order to confirm the spin-glass behavior we now have studied the ac susceptibility of this series in zero field using an ac SQUID susceptometer. Along the weak ferromagnetic axis (a axis), the ac susceptibility shows a cusp at the spin-glass transition temperature. Increasing the measurement frequency from 80 to 160 Hz increases the slope of the susceptibility below the transition temperature but no significant shift in the transition temperature itself is seen for this small frequency range. Spin-glass behavior is seen only along the a axis and a typical antiferromagnetic transition is seen along the c axis.

[a] This work was supported by NSF grant DMR-8702933.

 0021-8979/88/084357-01$02.40 © 1988 American Institute of Physics

Asymmetric hysteresis cycles as a probe of local fields in metallic spin glasses (abstract)

Laurent P. Lévy, and Hélène Bouchiat
AT&T Bell Laboratories, 600 Mountain Avenue, Murray Hill, New Jersey 07974

We have studied the magnetization in the spin-glass phase of *Ag*Mn under the repetitive application of a small ($10\ \text{Oe} < h < 50\ \text{Oe}$) magnetic field [assymetric hysteresis cycles (L. Néel, in Proceedings of the R. A. Welch Foundation Conference on Chemical Res. II, Atomic Structure, Houston, Texas, 1958)] after the sample has been cooled in a static field H ($0 < H < 1.1$ kOe). When $H = 0$, the magnetization m_n in the field off state ($h = 0$) grows as the logarithm of the number of cycles (n), while the magnetization in the on state ($h \neq 0$) M_n *decreases* with cycle number. This weaker response reflects an increase of the stiffness of the spin system after each cycle. At low temperature m_n grows linearly with temperature, reaches a maximum around $T \sim 0.6\ T_g$ and decreases as T_g is approached. The effects are larger when the system is prepared in a nonequilibrium state (rapid thermal quenching, or removal of the static field H). The irreversible growth of the magnetization m_n scale linearly with T_g (i.e., exchange) for samples of 0.5 and 2.6 at. % Mn concentration. We find that m_n grows as the value of H is increased, reaches a maximum around $H \sim T_g/15$ and decreases slowly at higher fields. We suggest as a possible interpretation of this phenomenon, the existence of a cavity in the distribution of local fields acting on the low temperature excitations. Additional information on the role of anisotropic forces will also be presented.

 0021-8979/88/084358-01$02.40 © 1988 American Institute of Physics

AUTHOR INDEX

Abe, M. – (8) 3642, 3774
Abernathy, S. M. – (8) 4133
Abosf, J. A. – (8) 3227
Acet, M. – (8) 3921
Achard, J. C. – (8) 3236, 4121
Adrian, F. J. – (8) 4161, 4199
Aeppli, G. – (8) 3902
Agarwala, Ashok K. – (8) 3645
Aguilo, A. – (8) 4213
Ahmed, M. R. – (8) 3016
Ahmed, S. – (8) 3560
Aidun, R. – (8) 3239
Aikin, R. – (8) 3405
Aitken, R. G. – (8) 4096
Alberts, H. L. – (8) 3609, 3913
Ali, Naushad – (8) 3583
Aliev, F. – (8) 3414
Almasan, Carmen – (8) 4204
Altounian, Z. – (8) 3330
Aly, S. H. – (8) 3704
Amano, E. – (8) 3391
Amemiya, M. – (8) 3443
Anandaraj, A. W. – (8) 3387
Anderson, E. E. – (8) 3561
Andreev, A. V. – (8) 3070
Andrés, Mercedes – (8) 3575
Andricacos, P. C. – (8) 4036
Ansari, P. H. – (8) 3503, 4190
Aoyama, S. – (8) 3443
Arajs, S. – (8) 3239, 4282
Arajs, Sigurds – (8) 3561
Argyle, B. E. – (8) 4033, 4036
Arko, A. J. – (8) 3680
Arnaud, L. – *(8) 3153*
Arrott, A. S. – (8) 3043, 3863, 4029
Artman, J. O. – (8) 2917, 3808
Arts, A. F. M. – (8) 4334
Asada, H. – (8) 3171
Atzmony, U. – (8) 3223, 3620, 4179, 4199, 4261
Awschalom, D. D. – (8) 3285
Axe, J. D. – (8) 3580
Aylesworth, K. D. – (8) 3218, 3699
Azaria, P. – (8) 3758

Bach, H. – (8) 3933
Bagus, P. S. – (8) 2962
Bai, Gui-Ru – (8) 3076
Bakhshai, A. – (8) 4196
Ballou, R. – (8) 3487
Balucani, U. – (8) 3820
Bancel, P. A. – (8) 4070
Bang-Zheng, L. – (8) 3620
Banhart, J. – (8) 4130
Barbara, B. – (8) 4091
Barclay, J. A. – (8) 4294
Baro, A. M. – (8) 4213
Barrault, J. – (8) 3236
Baselgia, L. – (8) 4157
Baszyński, J. – (8) 4214
Batail, P. – (8) 2962
Batra, A. P. – (8) 3398
Batra, Inder P. – (8) 3049
Batra, S. – (8) 3662, 3672
Baum, H.-P. – (8) 3420, 3686
Baumgart, P. – (8) 3880
Bayinqilao – (8) 3967
Beardsley, I. A. – (8) 3278
Becerra, C. C. – (8) 3092
Beck, Paul A. – (8) 4099
Becker, K. W. – (8) 3673
Bedrosian, G. – (8) 3019
Belaiche, M. – (8) 3551
Bell, Alan E. – (8) 3648
Benayad, N. – (8) 4001
Bennett, L. H. – (8) 3136, 3223, 3620, 4179, 4199, 4261
Beno, M. – (8) 4202
Benyoussef, A. – (8) 4001
Berger, L. – (8) 4276
Bernards, J. P. C. – (8) 2897
Berry, F. J. – (8) 4337
Bertram, H. Neal – (8) 3248
Bhagat, S. M. – (8) 4089, 4354
Bhatt, R. N. – (8) 4285
Bilotte, J. – (8) 4086
Binder, K. – (8) 3077
Bird, R. – (8) 3958
Bishop, D. J. – (8) 4233
Bland, J. A. C. – (8) 4051
Blazej, M. – (8) 4002
Bloomberg, Dan S. – (8) 3381
Blums, E. – (8) 3561
Bluncson, C. – (8) 4133
Boccara, N. – (8) 4001
Boekema, C. – (8) 4351
Bohandy, J. – (8) 4161, 4199
Bohn, H. G. – (8) 3089
Bohr, J. – (8) 3447
Boileau, F. – (8) 3153
Boltich, E. B. – (8) 3124, 3964
Bond, Marcus R. – (8) 3028
Böni, P. – (8) 3089, 3447
Bonner, J. C. – (8) 3560, 4160
Bonner, Jill C. – (8) 3543, 4144
Booth, J. G. – (8) 3344, 3817
Borchers, J. – (8) 3461
Borchers, J. A. – (8) 3458
Borg, R. J. – (8) 3398
Borges, H. – (8) 3405
Borsa, F. – (8) 3095, 3563
Bouchand, J. C. – (8) 3961
Bouchiat, Hélène – (8) 4358
Boufelfel, A. – (8) 3221, 3221, 3880
Boumazouza, D. – (8) 4099
Bourgeal, S. – (8) 4213
Bowen, Samuel P. – (8) 3402
Brauer, J. R. – (8) 3197, 3200
Bredl, C. D. – (8) 3405
Brener, N. E. – (8) 4057
Brewer, Earl G. – (8) 3528
Bridenbaugh, P. – (8) 3291
Bridger, K. – (8) 3233, 3786
Brooks, J. S. – (8) 4234
Brown, P. J. – (8) 3601, 3606
Brown, R. D. – (8) 3537
Brück, E. – (8) 3417
Brug, J. A. – (8) 4039
Brugel, D. – (8) 4249
Brun, T. O. – (8) 4340
Bruno, A. B. – (8) 3197, 3200
Bryden, W. A. – (8) 4233
Buchkov, D. T. – (8) 3247
Budnick, J. I. – (8) 3222, 3719
Buendia, A. – (8) 4213
Bührer, W. – (8) 3399
Burke, P. E. – (8) 3016, 3194
Burkhardt, G. L. – (8) 3930
Burriel, R. – (8) 3575
Buschow, K. H. J. – (8) 3130, 3586, *4113, 4116, 4279*
Bush, G. G. – (8) 3768
Bush, Gary G. – (8) 3765, 3798
Bykovetz, N. – (8) 4127

Cable, J. W. – (8) 3447
Cadieu, F. J. – (8) 3589, 3696
Cadogan, J. M. – (8) 3713
Cagan, V. – (8) 3955
Cai, J. – (8) 4193
Caillé, A. – *(8) 3098*
Calabrese, Joseph C. – (8) 2949
Calkins, J. – *(8) 3630*
Callaway, J. – (8) 3496, 4057
Calvayrac, Y. – (8) 4070
Calvo, Miguel – (8) 3073
Campbell, I. A. – (8) 4173, 4349
Campenni, C. K. – (8) 4294
Canaperi, D. F. – (8) 4036
Capasso, C. – (8) 3680
Carbone, C. – (8) 3499
Carley, L. Richard – (8) 3254
Carlin, R. L. – (8) 3551
Carlin, Richard L. – (8) 3566, 3572, *3575, 3576*
Carlson, J. M. – (8) 4001
Casabo, Jaime – (8) 3566
Caspari, R. – (8) 3405
Castell, K. – (8) 4312
Castillo, Gilbert – (8) 3272, 3275
Causa, M. T. – (8) 4164
Cei, Wanqiu – (8) 4207
Celasco, M. – (8) 2983
Chakrabarti, Amitabha – (8) 3735
Chakraborty, A. – (8) 2952
Chan, C. H. – (8) 3446
Chang, C. L. – (8) 4193
Chang, Ching-Ray – (8) 3435
Chang, L. L. – (8) 3285
Chang, W. C. – (8) 3531
Chang, Wen Cheng – (8) 3993
Charap, S. H. – (8) 3378
Chari, M. V. K. – (8) 3019
Chatterjee, R. – (8) 4255
Chayes, J. T. – (8) 4001
Chayes, L. – (8) 4001
Chen, C. J. – (8) 3786
Chen, D-X. – (8) 4213, 4215
Chen, H. S. – (8) 4063
Chen, H. Y. – (8) 3969
Chen, J. K. – (8) 3334
Chen, Kan – (8) 3903
Chen, Liang – (8) 2974
Chen, M. M. – (8) 3801
Chen, Mao-Min – (8) 3272, 3275, 4020
Chen, Swe-Kai – (8) 3981
Cheng, Ben-pei – (8) 3702
Cheriet, L. – (8) 4282
Chiang, C. K. – (8) 4179, 4199, 4232
Chiang, Da-Pun – (8) 3993
Chien, C. L. – (8) 3233, 3447, 4196, 4240, 4252
Chikazumi, S. – (8) 3316, 3614, 4267
Ching, W. Y. – (8) 3297, 3716
Chittipeddi, Sailesh – (8) 2952
Chow, A. – (8) 4255
Chow, Lee – (8) 3098
Christner, J. A. – (8) 2902, 2920, 3260
Chubb, S. R. – (8) 3493
Cieplak, M. Z. – *(8) 4196*
Clark, A. E. – (8) 3910
Clark, W. G. – (8) 3890, 4185
Clarke, John P. – (8) 3991
Claus, H. – (8) 4170
Cochran, J. F. – (8) 3464, 3811, 3814, 3863
Coey, J. M. D. – (8) 3649, 3713
Cohen, P. I. – (8) 3662, 3672
Coles, B. R. – (8) 4094
Collin, G. – (8) 4173
Comstock, C. S. – (8) 3149, 3151, 4321
Condon, J. – (8) 3041
Cooper, B. R. – (8) 3683
Cooper, Bernard R. – (8) 3826
Corb, B. W. – (8) 2941
Coronado, E. – (8) 3551
Cort, B. – (8) 3598
Corti, M. – (8) 3563
Cost, J. R. – (8) 3537
Coughlin, T. M. – (8) 3375
Coutinho-Filho, M. D. – (8) 3755
Cox, D. L. – (8) 3896
Crabtree, G. W. – (8) 3893, 4170, *4202*
Croft, M. – (8) 3503, 3692, 4187, 4190, 4193
Cross, L. E. – (8) 3789
Crow, J. E. – (8) 4127
Crowley, C. W. – (8) 3025
Cullen, J. R. – (8) 3649

Dahlberg, E. D. – (8) 3672
Dahlberg, E. Dan – (8) 2920, 3662, 4270
Dai, S. – (8) 3722
Dai, Z. – (8) 3446
d'Albuquerque e Castro, J. – (8) 3408, 3830
Dale, B. – (8) 3224
Dalichaouch, Y. – (8) 4202
Dan, Peng – (8) 4207
Dandridge, A. – (8) 3915
Daneshvar, K. – (8) 4096
Das, B. N. – (8) 3139
Dassonvalle, P. – (8) 3043
Datta, T. – (8) 4204
de Boer, F. R. – (8) 3064, 3067, 3070, 3417
DeFotis, G. C. – (8) 3569
DeFranzo, A. – (8) 4234
De Gasperis, P. – (8) 3107, 3306, 3335, 4136
de Jonge, W. J. M. – (8) 3479
Dekker, C. – (8) 4334
del Giudice, M. – (8) 3680
Della Torre, Edward – (8) 3001, 3004
Demczyk, B. G. – (8) 2905
den Boer, M. L. – (8) 3692, 4193

den Broeder, F. J. A. – (8) 3479
Deportes, J. – (8) 3487
Devlin, G. – (8) 3291
de Wijn, H. W. – (8) 4334
Diep, H. T. – (8) 3036, 3758
Dionne, Gerald F. – (8) 3777
Dmowski, W. – (8) 3397, 4070
Doetsch, H. – (8) 4157
Dolan, G. J. – (8) 4233
Dong, X. Y. – (8) 3560
Donovan, M.M. – (8) 3669
Doyle, W. – (8) 2948
Draaisma, H. J. G. – (8) 3479
Dragieva, I. D. – (8) 3247
Drillon, M. – (8) 3551
Drumheller, John E. – (8) 3028, 3031, 3034, 4357
Du, R. – (8) 3458, 3461
Du, Y. W. – (8) 3657, 3659, 4100, 4161, 4233
Du, Y.-W. – (8) 4105
Duh, Young Mouh – (8) 3356
Dunham, W. R. – (8) 4133
Dunlap, B. D. – (8) 3680, 4202
Dunlap, R. A. – (8) 4255
Dupas, C. – (8) 4300
Dutcher, J. R. – (8) 3464, 3814, 3863
Dutrús, S. M. – (8) 4164

Ebert, H. – (8) 3052, 3055, 4130
Echols, K. R. – (8) 3569
Edelstein, A. S. – (8) 3689
Edwards, D. M. – (8) 3830
Egami, T. – (8) 4070
Egamov, Shoukhrat – (8) 3116
Egelhoff, W. F., Jr. – (8) 3464, 3863
Eibschütz, M. – (8) 4063
Eisaki, H. – (8) 4009
Elmers, H. J. – (8) 3664
Emad, F. P. – (8) 3188
Emerson, K. – (8) 3034
Emrick, R. M. – (8) 3221
Emrick, Roy M. – (8) 3221
Emtage, P. R. – (8) 3817
Endoh, M. – (8) 3510
Engdahl, G. – (8) 3924
Engemann, J. – (8) 3159
England, C. D. – (8) 3227
Epstein, A. J. – (8) 2952
Epstein, Arthur J. – (8) 2949
Erber, T. – (8) 3952
Erdmann, K. – (8) 4113, 4116
Erkelens, W. A. C. – (8) 3538
Erwin, R. W. – (8) 3458, 3461, 4080, *4099*
Escorne, M. – (8) 3236, 4121
Estrada, J. – (8) 4204
Evans, B. J. – (8) 4133

Fadley, C. S. – (8) 3506
Faini, G. – (8) 3058, 3061
Fainstein, C. – (8) 4164
Falco, C. M. – (8) 3227, 3880
Falco, Charles M. – (8) 3221, 3221
Fan, Kang-Ming – (8) 3993
Farrell, J. N. – (8) 4108
Fastnacht, R. A. – (8) 4213
Federighi, A. – (8) 3820
Fedro, A. J. – (8) 4209, 4214
Felcher, G. P. – (8) 3247
Feldmann, P. – (8) 3104
Felner, I. – (8) 4182
Fermin, José R. – (8) 3300
Fernandez, Julio F. – (8) 3738
Fernandez-Baca, J. A. – (8) 3749, 4080
Fernandez-de-Castro, J. J. – (8) 3165
Ferrari, R. L. – (8) 3025
Fierz, Ch. – (8) 3899
Finkelstein, B.I. – (8) 3441
Fischer, P. – (8) 3399
Fish, G. E. – (8) 2986, 3749, 4080, 4083
Fisher, David – (8) 3098
Fisher, Michael E. – (8) 3082, 3994
Fisk, Z. – (8) 3890, 3893, 4202
Flanders, P. J. – (8) 3940
Fleming, R. M. – (8) 3447
Florczak, J. – (8) 3662
Flouquet, J. – (8) 3899
Flynn, C. P. – (8) 3458, 3461
Foiles, C. L. – (8) 3209
Fong, C. Y. – (8) 3046, 3049
Forsyth, J. B. – (8) 3606
Fourmeaux, R. – (8) 4086
Fowler, H. A. – (8) 4232
Frankel, R. B. – (8) 4063
Fratello, V. J. – (8) 3099
Fredkin, D. R. – (8) 3179, 3435
Freeman, A. J. – (8) 3655, 4220
Freitas, P. P. – (8) 3746
Friedberg, S. A. – (8) 3557
Friedlaender, F. J. – (8) 3165
Froning, M. H. – (8) 3522
Fry, J. L. – (8) 4057, 4060
Fu, C. L. – (8) 3655, 4220
Fueki, K. – (8) 4009
Fuerst, C. D. – (8) 3119, 3324, 3725
Fujikura, M. – (8) 3507
Fujimoto, K. – (8) 3171
Fujiwara, H. – (8) 2908
Fukushima, K. – (8) 3174
Fulde, P. – (8) 3673
Furdyna, J. K. – (8) 3297
Fuster, G. – (8) 4057
Fütterer, H. – (8) 3933

Galam, Serge – (8) 3758, 3760
Galera, R. M. – (8) 3580
Gallagher, W. J. – (8) 4216
Gammel, P. L. – (8) 4233
Garcia, N. – (8) 2947
Garcia, N. – (8) 4213
Garoche, P. – (8) 3058, 3061, 4070, 4212
Gau, J.-S. – (8) 3278
Gauder, D. R. – (8) 3522
Gavigan, J. P. – (8) 3713
Gavrin, A. – (8) 4196
Gay, J. C. – (8) 3341
Ge, Shihui – (8) 4297
Geballe, T. H. – (8) 4003
Geick, R. – (8) 3729
Geisau, O. V. – (8) 3347
Geiss, R. H. – (8) 3835
George, B. – (8) 4099
George, P. K. – (8) 3257
Geri, A. – (8) 3191
Geschwind, S. – (8) 3231
Ghazali, A. – (8) 3036
Ghemawat, A. Mitra – (8) 3388
Gibbs, Doon – (8) 3447
Gibbs, M. R. J. – (8) 4249
Giebultowicz, T. M. – *(8) 3297*
Gill, H. S. – (8) 4039
Giorgi, A. L. – (8) 3604
Giovannella, C. – (8) 4173, 4349
Givord, D. – (8) 3713
Glatzhofer, Daniel T. – (8) 2949
Godlieb, W. F. – (8) 3841, 3847
Goldman, Alan I. – (8) 3447
Goldstone, J. A. – (8) 3604
Gomes, A. A. – (8) 3408
Gomez, J. – (8) 4213
Gomi, M. – (8) 3642, 3774
Gong, W. – (8) 3513
Goodman, G. L. – (8) 3598
Gotaas, J. A. – (8) 3577
Gradmann, U. – (8) 3652, 3664
Graham, C. D., Jr. – (8) 3534, 4246
Green, W. J. – (8) 4261
Greidanus, F. J. A. M. – (8) 3841, *3847*
Grimm, H. – (8) 3447
Grünberg, P. – (8) 3473
Grütter, P. – (8) 2947
Grynszpan, R. I. – (8) 3043
Gu, Dong-mei – (8) 3702
Gu, Zong-Quan – (8) 3716
Gualtieri, D. M. – (8) 3795
Gubser, D. U. – (8) 4204
Guillot, M. – (8) 3104
Gunapala, S. – (8) 3692
Gunnarsson, O. – (8) 3676
Gunther, L. – (8) 4234
Güntherodt, G. – (8) 3880
Güntherodt, H.-J. – (8) 2947
Guo, C. – (8) 3327
Guo, Wei – (8) 3896
Guthrie, M. S. – (8) 3537
Guyot, M. – (8) 3955
Gyorffy, B. L. – (8) 3052, 3055
Gyorgy, E. M. – (8) 3247

Hadjipanayis, G. C. – (8) 3224, 3513, 3699, 3704, 3978
Hadjipanayis, George C. – (8) 3310
Hadjoudj, S. – (8) 4086, 4176
Hahn, H. T. – (8) 3768
Haines, Donald N. – (8) 3031, 4357
Hairston, D. K. – (8) 3621
Halchin, David J. – (8) 3338
Hammann, J. – (8) 4343
Hammond, E. C. – (8) 3620
Hanazono, M. – (8) 3470
Haneda, K. – (8) 4258
Haque, M. F. – (8) 3239, 3561
Harada, H. – (8) 3321, 3510
Harnden, J. – (8) 3041
Harris, A. B. – (8) 3083
Harshman, D. – (8) 4233
Hasegawa, R. – (8) 2986
Hasegawa, Ryusuke – (8) 2989
Hathaway, K. B. – (8) 3649
Havela, L. – (8) 3064, 3067, 3070
Hayano, S. – (8) 3174, 3366, 3369
He, Han Zeng – (8) 4215
Hegarty, J. – (8) 3291
Hegde, H. – (8) 3696
Heger, G. – (8) 3729
Heh, Shiang-Jiun – (8) 3981
Heidmann, J. – (8) 3159
Heim, D. E. – (8) 4026
Heiney, P. A. – (8) 4070
Heinrich, B. – (8) 3464, 3811, 3863
Heinzelmann, H. – (8) 2947
Helbig, H. F. – (8) 4282
Hellman, F. – (8) 3247
Hennion, B. – (8) 4071
Hennion, M. – (8) 4071, 4077
Henry, Warren E. – (8) 3422
Herbst, J. F. – (8) 3324
Herman, D. A. – (8) 4033
Herman, D. A., Jr. – (8) 4036
Herman, Warren N. – (8) 4127
Hermsmeier, B. D. – (8) 3506
Hicken, R. J. – (8) 3885
Hidber, H. R. – (8) 3045
Hijmans, T. W. – (8) 4185
Hikosaka, K. – (8) 3595
Hillebrands, B. – (8) 3880
Hillebrecht, F. U. – (8) 3676
Hilleke, R. O. – (8) 3247
Hilscher, G. – (8) 3070
Hinchey, L. – (8) 3473
Hines, W. A. – (8) 3890
Hinks, D. – (8) 3420
Hinks, D. G. – (8) 4202
Hinks, D. H. – (8) 3686
Hippert, F. – (8) 4071, 4077
Hirosawa, S. – (8) 3316, 3319, 3713
Ho, H.-M. – (8) 3278
Ho, Wing Kei – (8) 2944
Höck, K.-H. – (8) 3482
Holtz, R. L. – (8) 3689
Holtzberg, F. – (8) 4167
Homma, Hitoshi – (8) 4066
Homma, M. – (8) 3707
Hong, J. M. – (8) 3285
Hong, M. – (8) 3447, 3453, 3627
Hong, Soon C. – (8) 3655
Hood, Kevin – (8) 3098
Hoole, N. Ratnasuneeran *G. – (8) 3022*
Hoole, S. Ratnajeevan H. – (8) 3010, 3013, 3022, 3384, 3387
Horn, S. – (8) 3405, 4187, 4193
Hortal, M. – (8) 4213
Howard, J. K. – (8) 3263
Hsieh, T. C. – (8) 3447
Hu, B. P. – (8) 3722
Hu, Gong-Jia – (8) 3826
Hu, Q. – (8) 3327
Huan, C. H. A. – (8) 3904
Huang, Shengtao – (8) 4207
Huang, Y. – (8) 4315
Huber, D. L. – (8) 3297, 4151
Humphrey, F. B. – (8) 3168, 3949
Humphrey, Floyd B. – (8) 2944
Hung, C.-Y. – (8) 4276
Hunter, D. – (8) 3043
Hur, J. H. – (8) 3149
Hutton, Stuart L. – (8) 3028
Hwang, Cherngye – (8) 3272
Hwang, U. – (8) 2914, 2929

Ida, N. – (8) 3989
Ida, Nathan – (8) 3007
Idzerda, Y. U. – (8) 4069
Ikeguchi, S. – (8) 3369
Inaba, N. – (8) 4267
Inoue, A. – (8) 3397
Inoue, Akihisa – (8) 4215
Ishibashi, K. – (8) 2914, 2929
Ito, H. – (8) 3850
Itoh, T. – (8) 3774
Iwayama, K. – (8) 2966, 2971

Jaccard, D. – (8) 3899
Jackson, E. M. – (8) 4089
Jagielinski, Tomasz – (8) 4333
Jayakumaran, S. – (8) 3015
Jayanetti, J. K. D. – (8) 3696
Jayaprakash, C. – (8) 3903
Jeanniot, D. – (8) 3961
Jee, Chan-Soo – (8) 4127
Jefferson, C. Michael – (8) 3278
Jehanno, G. – (8) 4121
Jen, S. U. – (8) 4303
Jeon, Y. – (8) 4190
Jérome, D. – (8) 4005
Jhans, H. – (8) 4190
Jiang, S. Y. – (8) 3972
Jiles, D. C. – (8) 2980, 3930, 3946
Jin, C. – (8) 3667
Jin, S. – (8) 4213
Jisrawi, N. – (8) 4187
Johannsen, I. – (8) 2962
Johnson, D. D. – (8) 3490
Johnson, Mark – (8) 3934
Johnston, D. C. – (8) 4015
Jones, B. A. – (8) 3902

Jonker, B. T. – (8) 3303, 3309, 3467, 3869, 4069
Jorgensen, J. D. – (8) 3604, 4202
Joshi, Sushama – (8) 3792
Joss, W. – (8) 3893
Jouret, P. – (8) 4086

Kádár, György – (8) 3001, 3004
Kaindl, G. – (8) 3728
Kaiser, D. L. – (8) 4167
Kalonji, G. – (8) 4229
Kamprath, N. – (8) 3589, 3696
Kanetkar, S. M. – (8) 3792
Kang, W. – (8) 4005
Kanno, F. – (8) 2908
Kano, H. – (8) 3639
Kaplan, T. A. – (8) 4226
Karamon, H. – (8) 4306
Karpe, N. – (8) 4213
Kasiraj, P. – (8) 2938
Kasuya, T. – (8) 3580
Katriel, J. – (8) 3042
Katti, R. R. – (8) 3378
Katti, Romney R. – (8) 3254
Kaufman, Charles – (8) 4154
Kawamoto, A. – (8) 3853, 3856
Kawamura, H. – (8) 3949
Kawamura, Hikaru – (8) 3086, 3997
Kelly, J. R. – (8) 3146
Kern, D. – (8) 4237
Kern, S. – (8) 3598
Ketterson, J. B. – (8) 3420, 3686
Kim, A. – (8) 3310
Kim, A. S. – (8) 3519, 3975
Kim, B. F. – (8) 4161, 4199
Kioussis, N. – (8) 3683
Kishan, P. – (8) 3780
Kishimoto, M. – (8) 3443
Kishino, Y. – (8) 3174
Kishio, K. – (8) 4009
Kisker, E. – (8) 3499
Kistenmacher, T. J. – (8) 4124
Kitakami, O. – (8) 2908
Kitamoto, Yoshitaka – (8) 2911
Kitamura, N. – (8) 3636, 3850
Kitazawa, K. – (8) 4009
Klaasse, J. C. P. – (8) 3064, 3417
Klik, I. – (8) 4234
Kobayashi, H. – (8) 2966
Kobayashi, Toshio – (8) 3203
Koehler, T. R. – (8) 3179
Koelling, D. D. – (8) 3680
Koeppe, P. V. – (8) 4042
Kogekar, M. V. – (8) 3771
Komiya, M. – (8) 3507
Komsa, M. L. – (8) 4036
Komuro, M. – (8) 3470
Kong, Lin-shu – (8) 3702
Konishi, S. – (8) 3171
Koon, N. C. – (8) 3139, 3303, 3728, 3869
Koshino, N. – (8) 3639
Koshizuka, N. – (8) 3113
Kotiuga, P. R. – (8) 3357, 3360
Kotliar, G. – (8) 4233
Kouvel, J. S. – (8) 4340, 4346
Kovachik, V. – (8) 3414
Kozono, Y. – (8) 3470
Krause, H. – (8) 3159
Krebs, J. J. – (8) 3303, 3309, 3467, 3829, 3869, 4069
Krishnamurthy, H. R. – (8) 3903
Krishnan, R. – (8) 2992, 4119
Krongelb, S. – (8) 4036
Krounbi, M. – (8) 2938
Kryder, M. H. – (8) 3378, 3621, 3624, 3844, 4042
Krzeminski, S. – (8) 4002
Kuanr, B. K. – (8) 3780
Kübler, J. – (8) 3482
Kugiya, F. – (8) 2908
Kumano, T. – (8) 2971
Kumar, N. – (8) 3780
Kumar, R. – (8) 3725
Kumar, S. – (8) 4351
Kumasaka, Noriyuki – (8) 3203
Kunii, S. – (8) 3580
Kunimoto, A. – (8) 4243
Kuzuo, R. – (8) 3853
Kventsel, G. F. – (8) 3042
Kwapong, V. – (8) 4229
Kwo, J. – (8) 3447, 3453
Kwo, J. R. – (8) 4233
Kwok, W. K. – (8) 4170, 4202
Kwun, H. – (8) 3930

Labarta, A. – (8) 3041, 3206, 4091, 4337
Lahoz, Fernando – (8) 3575
Lallemand, P. – (8) 3036
Lamas, A. C. – (8) 3548
Lamloumi, J. – (8) 4121
Lan, M. D. – (8) 3890
Landau, D. P. – (8) 3039, 3077
Landee, C. P. – (8) 3548
Landenburger, L. – (8) 3034
Lander, G. H. – (8) 3598, 3601
Langlois, P. – (8) 3043
Lashmore, D. – (8) 3223
LaTourette, D. – (8) 2948
Laughlin, D. E. – (8) 2905, 3266, 3624
Lavender, W. – (8) 3795
Lavers, J. D. – (8) 3016, 3194
Lawson, A. C. – (8) 3604
Layadi, A. – (8) 3808
Le Dang, K. – (8) 2992, 4119
Lederer, P. – (8) 3076
Lee, B. W. – (8) 4202
Lee, Hyung J. – (8) 3269
Lee, J. I. – (8) 2920, 3260
Lee, J.-W. – (8) 2905, 3266, 3624, 3808
Lee, K. M. – (8) 3740
Lee, Robert W. – (8) 3528
Lee, Rod E. – (8) 4020
Lee, Y. H. – (8) 4187
Le Gall, H. – (8) 3104
Leidecker, H. – (8) 3041
Lemaire, R. – (8) 3487
Lequien, S. – (8) 4071, 4077
Leupold, H. A. – (8) 3987
Leupold, Herbert A. – (8) 3991
Lévy, Laurent P. – (8) 4358
Levy, M. – (8) 3420, 3686, 3927
Levy, P. M. – (8) 3896
Li, D. – (8) 3984
Li, Fulin – (8) 2974
Li, H. S. – (8) 3713
Li, Zhenchun – (8) 2974
Lian, M. R. – (8) 3168
Liang, G. – (8) 3503
Liao, S. B. – (8) 4089, 4354
Lichti, R. L. – (8) 4351
Lim, S. P. – (8) 4151
Lin, C.-J. – (8) 3835
Lin, C. L. – (8) 4127
Lin, Chin – (8) 3592, 3967
Lin, Jiang-Ching – (8) 3993
Lin, Judy – (8) 3275
Lin, Wan Ke – (8) 3034
Lin, Ying-Chun – (8) 3993
Lind, D. M. – (8) 4069
Lines, M. E. – (8) 4063
Liou, S. H. – (8) 4240
Liu, J. Z. – (8) 4170
Liu, Jian-Min – (8) 4144
Liu, K. S. – (8) 3531
Liu, N. C. – (8) 3589, 3696
Liu, Puru – (8) 2974
Liu, S. – (8) 3516
Liu, X. – (8) 3309
Liu, Zun-Xiao – (8) 3967
Lo, Jerry – (8) 4020
Long, Jerome R. – (8) 3031
Loong, C. K. – (8) 3598
Lopez, O. – (8) 2902
López, R. A. – (8) 3617
Lopez de la Torre, M. A. – (8) 4213
Lottis, D. K. – (8) 3662, 3672
Lottis, Daniel K. – (8) 2920
Lou, Zheng-Hua – (8) 3592, 3967
Lourens, J. A. J. – (8) 3913, 4282
Lowe, Carol – (8) 3576
Lowther, D. A. – (8) 3363, 3375
Lu, F. – (8) 3503, 3692, 4190
Lu, Quan – (8) 4203
Lubitz, P. – (8) 3223
Luitjens, S. B. – (8) 2897
Lynn, J. W. – (8) 3749, 4083

Ma, B. M. – (8) 3333, 3334
MacLaughlin, D. E. – (8) 3890
Maeda, Takeshi – (8) 3862
Majkrzak, C. F. – (8) 3447, 3453
Majkrzak, Charles – (8) 3221
Makous, J. L. – (8) 3221
Maletta, H. – (8) 3067
Malik, S. K. – (8) 4202
Mälmhäll, R. – (8) 3949
Malozemoff, A. P. – (8) 3874
Mancini, Jay D. – (8) 3402
Mangin, P. – (8) 4099
Manheimer, M. A. – (8) 4089, 4354
Mansuripur, M. – (8) 3831
Maple, M. B. – (8) 4202
Marabelli, F. – (8) 3422
Marcelli, R. – (8) 3335, 4136
Marchand, A. – (8) 3104
Marcus, P. M. – (8) 4045
Markham, D. – (8) 2948
Marro, J. – (8) 3041
Martin, Y. – (8) 2948
Martinez, B. – (8) 3041
Martinez, B. – (8) 3206
Marucco, J. F. – (8) 4212
Maruyama, H. – (8) 3713
Maruyama, T. – (8) 4023
Masoero, A. – (8) 2983
Massidda, S. – (8) 4220
Masumoto, T. – (8) 3397, 4215, 4243, 4246
Matsuki, H. – (8) 3394
Matsumoto, F. – (8) 3507
Matsumoto, M. – (8) 3230, 4119
Matsuo, Y. – (8) 2966
Matsuyama, K. – (8) 3171
Matsuzaki, Kunio – (8) 4215
Mauger, A. – (8) 3236, 4121
Mayergoyz, I. D. – (8) 2995, 3188, 3381
Mazzetti, P. – (8) 2983
McCally, R. L. – (8) 4124
McDaniel, T. W. – (8) 3831, 3859
McFee, S. – (8) 3363
McGhee, E. M. – (8) 3569
McGlashan-Powell, M. – (8) 3099
McGuire, T. R. – (8) 3746, 4167
McGurn, A. R. – (8) 3560
McHenry, M. E. – (8) 3388, 4229, 4255
McKittrick, J. – (8) 4229
McLean, W. L. – (8) 4187
McMasters, O. D. – (8) 3910
McWhan, D. B. – (8) 3447
Mehandiev, D. R. – (8) 3247
Mehanna, El-Sayed A. – (8) 4282
Meisner, G. P. – (8) 3119
Melamud, M. – (8) 3136
Melmed, A. J. – (8) 4232
Meng-Zhao, L. – (8) 3620
Menovsky, A. A. – (8) 3414
Merabet, K. E. – (8) 3566, 3575
Merceron, T. – (8) 3955
Mermelstein, M. D. – (8) 3915
Meyer, E. – (8) 2947
Miccoli, G. – (8) 3335, 4136
Migliano, A. C. – (8) 3092
Mildrum, H. F. – (8) 3321, 3516, 3984
Miller, Joel S. – (8) 2949, 2952
Miltat, J. – (8) 3153
Ming, Y. – (8) 4157
Mirebeau, I. – (8) 4071, 4077
Mishra, Raja K. – (8) 3528
Mitchell, A. W. – (8) 3680
Mitchell, P. V. – (8) 2917
Mitchell, T. B. – (8) 3162
Mitera, M. – (8) 4246
Mittag, M. – (8) 3586
Miyajima, H. – (8) 3316, 3614, 4267
Miyazawa, H. – (8) 3394
Moi, K. – (8) 3949
Molho, P. – (8) 4327
Moncton, D. E. – (8) 4015
Montenegro, F. C. – (8) 3755
Montes de Oca, R. – (8) 3391
Moon, Jaekyun J. – (8) 3254
Moorjani, K. – (8) 4124, 4161, 4199, 4233, 4261, 4354
Moreu, M. A. – (8) 3206
Morgan, J. S. – (8) 4124, 4233
Morgan, W. – (8) 3620
Mori, N. – (8) 3595, 3611
Morisako, A. – (8) 3230, 4119
Morón, Mary C. – (8) 3566
Morris, J. – (8) 3598
Morrish, A. H. – (8) 3722, 4258
Moruzzi, V. L. – (8) 4045, 4060
Moshchalkov, V. V. – (8) 3414
Mountfield, K. R. – (8) 2905, 2917, 3266
Moyer, C. – (8) 3239
Moyer, C. A. – (8) 3561
Müller, G. – (8) 3560
Müller, Gerhard – (8) 4154
Muniz, R. Bechara – (8) 3408, 3830
Murakami, K. – (8) 3394
Muraleedharan, K. – (8) 3728
Murdock, E. – (8) 4039
Murray, C. A. – (8) 4233
Musal, H. M., Jr. – (8) 3768
Mycielski, Andrzej – (8) 3279
Mydosh, J. A. – (8) 3414, 3577, 4279, 4357
Myrtle, K. – (8) 3811

Naberhuis, S. – (8) 4039
Nafis, S. – (8) 3218, 3743
Nagai, A. – (8) 3636
Nagakubo, M. – (8) 4309
Nagato, K. – (8) 3853, 3856
Nahm, K. – (8) 3933
Naili, M. – (8) 4318
Nakagawa, Shigeki – (8) 2911
Nakahara, S. – (8) 3627
Nakamura, K. – (8) 3171
Nakao, Takeshi – (8) 3862
Nakatani, Ryoichi – (8) 3203
Nakayama, H. – (8) 2971
Nam, Sang Boo – (8) 4212

Naoe, M. – (8) 3230, 3636, 3850, 4119, 4309
Naoe, Masahiko – (8) 2911, 3212
Narishige, S. – (8) 3470
Nazareth, A. – (8) 3978
Naziripour, G. A. – (8) 3771
Nazzal, A. – (8) 4233
Nazzal, A. I. – (8) 2962
Nelson, J. S. – (8) 3046, 3049
Netzelmann, U. – (8) 3347
Neuenschwander, J. – (8) 3399
Newnham, R. E. – (8) 3789
Nieuwenhuys, G. J. – (8) 4279
Niimura, Yoshiro – (8) 2911
Nogues, J. – (8) 4213
Noques, J. – (8) 3398
Norman, M. R. – (8) 3903
Novotny, M. A. – (8) 3546
Novotny, P. M. – (8) 2977
Nowak, W. – (8) 4312
Nozawa, T. – (8) 2966

Obermyer, R. T. – (8) 3964
Obradors, X. – (8) 3206, 4091, 4337
O'Brien, T. – (8) 3453
Ocio, M. – (8) 4343
Ogale, S. B. – (8) 3792
Ogawa, S. – (8) 3639
Ogielski, A. T. – (8) 3291
O'Handley, R. C. – (8) 3388, 3669, 4229, 4255
Ohkoshi, Masatoshi – (8) 2926
Ohmukai, M. – (8) 4023
Ohnuma, S. – (8) 4243, 4246
Ohta, Norio – (8) 3633, 3838, 3862
Ohtsuka, S. – (8) 3595
Ojima, Masahiro – (8) 3838
Okada, M. – (8) 3707
Okamine, Shigenori – (8) 3862
Oliker, J. – (8) 3042
Oliveira, N. F., Jr. – (8) 3092
Oliver, F. W. – (8) 3620
Oliver, S. A. – (8) 3802, 3829
Ootomo, Shigekazu – (8) 3203
Ortiz, C. – (8) 3801
Oseroff, S. B. – (8) 2923, 3446, 4202
O'Shea, M. J. – (8) 3740, 374
Ostergaard, Dale F. – (8) 3185
Osterman, D. P. – (8) 3580
Osterwalder, J. – (8) 3506
Otani, Y. – (8) 3316
Ott, H. R. – (8) 3890
Ouladdiaf, B. – (8) 3487
Ounadjela, K. – (8) 3244
Oussena, M. – (8) 4176

Paalanen, M. A. – (8) 4285
PaiVerneker, V. – (8) 3786
Palacio, Fernando – (8) 3566, 3575
Palanisamy, R. – (8) 3182
Paleari, A. – (8) 3563
Palstra, T. T. M. – (8) 3414, 4279
Panissod, P. – (8) 3719
Papaconstantopoulos, D. A. – (8) 4060
Papaefthymiou, G. – (8) 4063
Pardavi-Horváth, M. – (8) 3107, 3110, 3306
Parker, G. – (8) 3998
Parkin, S. S. P. – (8) 2962, 4005, 4233
Parkinson, J. B. – (8) 3560, 4160
Parkinson, John B. – (8) 3543
Parra, R. E. – (8) 3617
Patil, K. C. – (8) 3789
Pattnaik, P. C. – (8) 4060
Patton, C. E. – (8) 3344, 3771, 3817, 4160
Paul, D. I. – (8) 3441
Paul-Boncour, V. – *(8) 3236*
Pawlowska, Z. – (8) 3042
Pearey, L. A. – (8) 3149
Pedziwiatr, A. T. – (8) 3710, 3719
Pelzl, J. – (8) 3347, 3933
Peng, J. P. – *(8) 3372*
Percheron-Guegan, A. – (8) 3236, *4121*
Perez, I. – (8) 3503
Perlov, C. M. – (8) 2902, *3046*
Pernet, M. – (8) 4091
Perscheid, B. – (8) 3728
Pesty, F. – (8) 3058, 3061
Petek, B. – (8) 4033, 4036
Peters, C. – (8) 4233
Peterson, R. L. – (8) 2920, 3260
Petrou, A. – (8) 3309
Peuzin, J. C. – (8) 3341
Phase, D. M. – (8) 3792
Pickett, W. E. – (8) 3493
Pillmayr, N. – (8) 3070
Pinchuk, A. R. – (8) 3025
Pinkerton, F. E. – (8) 3119, 3333
Pinski, F. J. – (8) 3490
Plaskett, T. S. – (8) 3746
Plumer, M. L. – (8) 3098
Pohm, A. V. – (8) 3149, 3151, 4321
Poilblanc, D. – (8) 3076
Pommier, J. – (8) 3036
Pons, Josefina – (8) 3566
Pont, Montse – (8) 3397
Porter, C. – (8) 4133
Porteseil, J. L. – (8) 4327
Potenziani II, E. – (8) 3719, 3987
Pourarian, F. – (8) 3964, 3972
Prasad, S. – (8) 3762
Prinz, G. A. – (8) 3303, 3309, 3467, 3829, 3869, 4069, 4270, 4291
Przybylski, M. – (8) 3652
Purcell, S. T. – (8) 3863
Puźniak, R. – (8) 3397

Qadri, S. B. – (8) 3303
Qi, B. – (8) 3503
Qian, Y. J. – (8) 3420, 3686
Qiu, Z. Q. – (8) 3657, 3659, 4100, 4161, 4233
Qiu, Z.-Q. – (8) 4105

Rachford, F. J. – (8) 4291
Rado, G. T. – (8) 3885
Rakers, L. D. – (8) 4099
Ramesh, R. – (8) 3333, 3334
Ramos, M. A. – (8) 4213
Ranjan, R. – (8) 3260
Rao, K. V. – (8) 3397, 3398, 4213, 4215
Rao, S. L. N. – (8) 3780
Rastelli, E. – *(8) 3083, 3823*
Rath, D. L. – (8) 4036
Rau, C. – (8) 3667
Ravindranathan, P. – (8) 3789
Ray, A. E. – (8) 3516, 3522
Ray, R. – (8) 3525
Re, M. E. – (8) 4033, 4042
Rebelsky, L. – (8) 3405, 4187
Rebizant, J. – (8) 3601
Reddy, P. Venugopal – (8) 3783
Refregier, Ph. – (8) 4343
Regnault, L. P. – (8) 3538
Reiff, William Michael – (8) 2957
Reilly, K. – *(8) 3405*
Ren, Y. G. – (8) 3699
Renard, D. – (8) 4300
Renard, J. P. – (8) 3538, 4300
Rezende, S. M. – *(8) 3755*
Rhyne, J. J. – (8) 3297, 3458, 3461, *3577, 3749,* 3752, 4080, 4083, 4099
Ribas, J. – (8) 3538
Rigamonti, A. – (8) 3095, 3563
Riggs, Kevin – (8) 4270
Riseborough, P. S. – (8) 3695
Riseborough, Peter S. – (8) 4141
Robert, M. – (8) 3667
Roemer, L. E. – (8) 3989
Romankiw, L. T. – (8) 4036
Rosenberg, M. – (8) 3586, 4113, 4116
Rosenthaler, L. – (8) 2947
Rossat-Mignod, J. – (8) 3538
Rouault, P. – (8) 4173
Roy, R. – (8) 3789
Roy, S. B. – (8) 4094
Ruane, M. F. – (8) 3630
Rubenacker, Gerald V. – (8) 3028, *3034, 4357*
Rubins, R. S. – (8) 3028
Rubinstein, M. – (8) 3223, 4291
Ruby, S. L. – (8) 3795
Rudd, J. M. – (8) 3811
Ruigrok, J. J. M. – (8) 3847
Rusek, P. – (8) 3496, 4002
Ryan, D. H. – (8) 3330
Ryan, P. J. – (8) 3162
Ryu, J. – (8) 4312, 4315
Ryu, J. S. – (8) 3805

Sáblik, M. J. – (8) 3930
Sachdev, Subir – (8) 4285
Sache, G. – (8) 3961
Sáenz, J. J. – (8) 2947
Sagawa, M. – (8) 3316, 3319, 3713
Said, M. R. – (8) 4340
Saint-Paul, M. – (8) 4091
Saito, Y. – (8) 3174, 3366, 3369
Sakamoto, H. – (8) 3507
Sakurai, M. – (8) 4267
Salamon, M. B. – (8) 3458, 3461
Salling, C. T. – (8) 4202
Salmeron, M. – (8) 3801
Salva, H. R. – (8) 4164
Sankar, S. G. – (8) 3710, 3789, 3964, 3969, 3972
Sarma, B. K. – (8) 3686
Sarma, Bimal K. – (8) 3420
Sarma, D. D. – (8) 3676
Sarson, M. – *(8) 4337*
Sasayama, S. – (8) 4229
Saslow, W. M. – (8) 3998
Sato, Noboru – (8) 3476
Sato, T. – (8) 3856
Satoh, K. – (8) 3642
Saurenbach, F. – (8) 3473
Scalapino, D. J. – (8) 4019
Schenstrom, A. – (8) 3420, 3686
Schloemann, E. – (8) 3802
Schloemann, Ernst – (8) 3140
Schmid, H. – (8) 4237
Schneemeyer, L. F. – (8) 4233
Scholte, P. M. L. O. – (8) 3841
Schönhammer, K. – (8) 3676
Schrauwen, C. P. G. – (8) 2897
Schuller, I. K. – (8) 4202
Schuller, Ivan K. – (8) 4066
Schultz, M. D. – (8) 3844
Schultz, S. – (8) 2923, 3446, 4202, 4237
Schüttler, H.-B. – (8) 4209
Schwarzacher, W. – (8) 4051
Schweiss, P. – (8) 3729
Sechovsky, V. – (8) 3064, 3067, 3070
Seddon, K. R. – (8) 3576
Segmüller, Armin – (8) 3285
Segre, C. – (8) 4202
Seiden, J. – (8) 4300
Sellmyer, D. J. – (8) 3215, 3218, 3699, 3704, 3743
Senoussi, S. – (8) 4086, 4176
Seo, A. – (8) 3595
Sethna, J. P. – (8) 4001
Shaheen, S. A. – (8) 3411, 4187, 4190, 4193
Shan, Z. S. – (8) 3218
Shapiro, A. J. – (8) 4261
Shaw, T. M. – (8) 4167
Shen, Guo-Yin – (8) 3076
Sherif, M. A. – (8) 3188
Sherwood, R. C. – (8) 4213
Shi, Longpei – *(8) 3241*
Shieh, H-P. D. – (8) 3624, 3627, 3844
Shimizu, R. – (8) 3319
Shin, Sung-Chul – (8) 3645
Shinde, S. – (8) 4167
Shirane, G. – (8) 3089, 4015
Shoji, M. – (8) 3636
Shono, K. – (8) 3639
Shull, R. D. – (8) 4179, 4199, 4232, 4261
Shum, Danny – (8) 3572
Sieger, D. – (8) 3729
Sierro, J. – (8) 3899
Silber, L. M. – *(8) 3350, 3353*
Silsbee, R. H. – (8) 3934
Silvester, P. P. – (8) 3025
Simizu, Satoru – (8) 3557
Simmons, R. – (8) 4039
Singh, P. K. – (8) 3762, 3780
Singh, Prabhat K. – (8) 3762, 3780
Singh, Rajiv R. P. – (8) 3082, 3994
Singleton, E. – (8) 3699, 3704
Sinha, S. K. – (8) 4015, 4214
Sinkovic, B. – (8) 3506
Sinn, Ekk – (8) 3572
Slaski, M. – (8) 4202
Slaughter, J. M. – (8) 3209
Slavcheva, M. S. – (8) 3247
Smit, P. – (8) 3609
Smith, J. L. – (8) 3890, 4202
Smith, N. – (8) 2948, 3958
Smith, Neil – (8) 2932
Smyth, J. F. – (8) 4202, 4237
Soderholm, L. – (8) 4202
Sohal, G. S. – (8) 3499
Soohoo, R. F. – (8) 3829
Souche, Y. – (8) 4327
Spano, M. L. – (8) 3752
Speliotis, D. E. – (8) 2908, 3429, 3432
Spinolo, G. – (8) 3563
Spirlet, J. C. – (8) 3601
Spruit, J. H. M. – (8) 3847
Squire, P. T. – (8) 4249
Srinivasan, G. – (8) 3344, 3817, 4160
Srinivasan, T. T. – (8) 3789
Srivastava, G. P. – (8) 3780
Srivastava, Niraj – (8) 4154
Stadelmaier, H. H. – (8) 3589
Stamm, W. – (8) 3921
Stankiewicz, Jolanta – (8) 3300
Stassis, C. – (8) 4015
Stearns, M. B. – (8) 3222, 4297
Steigerwald, D. A. – (8) 3464, 3863
Stepanescu, A. – (8) 2983
Steren, L. B. – (8) 4164
Stern, G. P. – (8) 3657, 3659
Sticht, J. – (8) 3482
Stirling, W. G. – (8) 3538
Stocks, G. M. – (8) 3490
Stoffel, N. G. – (8) 3692
Strange, P. – (8) 3052, 3055

Streitz, F. H. – (8) 4196
Strnat, K. J. – (8) 3321, 3516, 3984
Ström-Olsen, J. O. – (8) 3330
Strzeszewski, J. – (8) 3224, 3699, 3978
Su, James L. – (8) 4020
Sugimoto, S. – (8) 3707
Sugita, Y. – (8) 3470
Suhl, H. – (8) 3257, 4147
Suit, J. C. – (8) 3835
Suits, F. – (8) 4033
Sukeda, Hirofumi – (8) 3838
Sumide, Makoto – (8) 2911
Sumiya, K. – (8) 3443
Sun, S. W. – (8) 3669
Sun, Shu-he – (8) 3702
Sun, Yun-Xi – (8) 3592, 3967
Sungaila, Z. – (8) 4202
Suran, G. – (8) 3244, 4318
Suryanarayana, Darbha – (8) 4110
Suzuki, M. – (8) 2908
Suzuki, T. – (8) 2914, 2929, 3171
Suzuki, Yoshio – (8) 3633
Svensson, L. – (8) 3924
Swanson, A. G. – (8) 4234
Swartzendruber, L. J. – (8) 3223, 3620, 4179, 4199, 4261
Sztern, J. – (8) 4318

Tagami, Katsumichi – (8) 3438
Taher Ahmed, M. – (8) 3194
Takács, L. – (8) 4264
Takagi, H. – (8) 4009
Takahashi, H. – (8) 3595
Takahashi, K. – (8) 3230, 3366
Takahashi, Masahiko – (8) 3838, 3862
Takahashi, N. – (8) 2966
Takahashi, T. – (8) 3611
Takamure, H. – (8) 3949
Takeda, Takayuki – (8) 3438
Taketomi, S. – (8) 4267
Tamaura, Y. – (8) 3774
Tanaka, Masaichi – (8) 3212
Tanaka, S. – (8) 4009
Tanemura, Masaharu – (8) 3997
Tang, Chenghuan – (8) 4207
Tang, H. – (8) 3657, 3659, 4100, 4105, 4161, 4233
Tarnopolsky, G. – (8) 4039
Tasset, F. – (8) 3606
Tassi, A. – (8) 3823
Tatsumi, T. – (8) 4023
Taylor, R. D. – (8) 3398, 4108
Tejada, J. – (8) 3041, 3206, 4091, 4337
Teter, J. P. – (8) 3910
Thavendrarajah, A. – (8) 3107
Thayamballi, P. – (8) 3143
Thiaville, A. – (8) 3153
Tholence, J. L. – (8) 3893, 4091
Thomas, G. – (8) 3278, 3333, 3334
Thompson, J. D. – (8) 3405, 3880, 4202
Thorpe, A. – (8) 3620
Thouless, D. J. – (8) 4001
Tiefel, T. H. – (8) 4213
Tietze, H. – (8) 3729
Tiwald, Thomas E. – (8) 3215
Tobin, V. M. – (8) 3446
Tobise, M. – (8) 3669
Tognetti, V. – (8) 3820
Tokunaga, M. – (8) 3321, 3510
Tokura, Y. – (8) 4233
Tsrikachvili, M. – (8) 4202
Tornero, J. – (8) 4213
Torrance, J. B. – (8) 2962, 4233
Torre, S. – (8) 3095
Tovar, M. – (8) 4164
Treutmann, W. – (8) 3729
Troper, A. – (8) 3408
Trouilloud, P. L. – (8) 4036
Trout, S. R. – (8) 3510
Tsang, C. – (8) 2938
Tsantes, E. – (8) 3350
Tsoukatos, A. – (8) 3224
Tsubokawa, Y. – (8) 3319
Tsushima, K. – (8) 311°
Tsuya, N. – (8) 3174
Tu, Guo-hau – (8) 3330
Tustison, R. W. – (8) 3802
Tustison, Randal – (8) 3140
Tuszyński, J. A. – (8) 3918

Uchida, S. – (8) 4009
Uchiyama, Y. – (8) 2914, 2929
Ueno, K. – (8) 2971
Ukai, T. – (8) 3595, 3611
Umezawa, A. – (8) 4170
Umezawa, H. – (8) 3113
Urai, H. – (8) 4023
Urquhart, K. B. – (8) 3811, 3863
Ushioda, A. – (8) 3669

Vaia, R. – (8) 3820
Vaknin, D. – (8) 4015
Valdés, J. E. – (8) 4324
Valenzuela, R. – (8) 3391
van den Berg, H. A. M. – (8) 4330
Vander Heiden, R. H. – (8) 3197
van Deursen, A. P. J. – (8) 3893
van Dover, K. B. – (8) 4213
Van Hook, H. J. – (8) 3802
Van Hook, H. Jerrold – (8) 3140
van Ruitenbeek, J. M. – (8) 3893
van Sprang, M. – (8) 3417
Varitimos, Thomas – (8) 3140
Varner, J. R. – (8) 3372
Varonis, O. J. – (8) 3182
Vazquez, L. – (8) 4213
Veca, G. M. – (8) 3191
Veenhuizen, P. A. – (8) 3064, 3067, 3070
Veillet, P. – (8) 2992, 4119
Vélu, E. – (8) 4300
Verdaguer, M. – (8) 3538
Vértesy, G. – (8) 3110
Vettier, C. – (8) 3538
Victora, R. H. – (8) 3423
Vidyasagar, Samuel – (8) 3010, 3384
Vieira, S. – (8) 4213
Vier, D. C. – (8) 4202
Villar, R. – (8) 4213
Vincent, E. – (8) 4343
Violet, C. E. – (8) 3398, 4204
Vittoria, C. – (8) 3802, 3805, 3829, 4312, 4315
Vlaming, R. – (8) 4330
Vlastuin, R. F. M. – (8) 4279
Vogt, O. – (8) 3601
Voitländer, J. – (8) 4130
Volin, K. – (8) 4070
Volin, K. J. – (8) 3604
Volkening, F. – (8) 3303
Volkening, F. A. – (8) 3869
Vurens, G. – (8) 3801

Wachter, P. – (8) 3399, 3422
Waite, R. I. – (8) 3151
Waldner, F. – (8) 4157
Walikainen, D. – (8) 3927
Walker, I. R. – (8) 4029
Walker, J. C. – (8) 3657, 3659, 4100, 4105, 4161, 4233
Wallace, W. E. – (8) 3710, 3719, 3964, 3969, 3972
Walz, U. – (8) 3473
Wang, Dajian – (8) 4207
Wang, Guiqin – (8) 3116
Wang, Hao – (8) 3116
Wang, K. – (8) 4070, 4212
Wansleben, S. – (8) 3039
Warnock, J. – (8) 3309
Wassermann, E. F. – (8) 3499, 3921
Waszczak, J. V. – (8) 4063, 4233
Watanabe, Takaaki – (8) 3438
Watson, R. E. – (8) 3136, 3223, 4179
Watts, J. – (8) 3233
Webb, Bucknell C. – (8) 2923
Webb, J. P. – (8) 3363
Weber, M. J. – (8) 3118
Weeber, Konrad – (8) 3010, 3022, 3384
Weinberger, P. – (8) 4130
Weinstock, H. – (8) 3952
Weissman, Jehoshua – (8) 3140
Welker, E. E. – (8) 3537
Wenger, L. E. – (8) 3577
White, R. J. – (8) 3522
White, R. M. – (8) 2920
Wickramasekara, L. – (8) 3589, 3696
Wickramasinghe, H. K. – (8) 2948
Wiegert, R. F. – (8) 3927
Wiese, R. S. – (8) 3569
Wiesen, K. C. – (8) 3378
Wiesler, D. G. – (8) 3554
Wigen, P. E. – (8) 3107, 3110, 3306, 4157
Wilber, W. D. – (8) 3353
Willett, R. D. – (8) 3028
Williams, A. R. – (8) 3482
Williams, C. M. – (8) 3139
Willis, J. O. – (8) 3405
Willis, R. F. – (8) 4051
Wills, J. M. – (8) 3683
Winzer, S. R. – (8) 3786
Wolf, S. A. – (8) 4204
Wolf, W. P. – (8) 3904
Wolfe, R. – (8) 3099
Wolfus, Y. – (8) 4182
Wong, W. H. – (8) 3890, 4185
Woods, J. – (8) 3669
Woollam, John A. – (8) 3215
Wörner, C. H. – (8) 4324
Wortmann, G. – (8) 3728
Wowchak, A. M. – (8) 3662, 3672
Wu, Guobin – (8) 4207
Wu, T. B. – (8) 3531
Wu, Tsai-Wei – (8) 3275
Wulff, M. – (8) 3601

Xia, J. – (8) 3805
Xia, Qing – (8) 4141
Xiao, Gang – (8) 4196, 4252
Xiao, Y. – (8) 3516
Xu, Chang-qing – (8) 3076
Xu, J.-H. – (8) 4220
Xu, M.-F. – (8) 3420, 3686
Xue, Ronghua – (8) 4203

Yafet, Y. – (8) 3447, 3453
Yamada, K. – (8) 4023
Yamada, O. – (8) 3713
Yamamoto, Hiroshi – (8) 3212
Yamamoto, T. – (8) 3394, 4309
Yamasaki, J. – (8) 3949
Yamauchi, T. – (8) 3614
Yan, M. – (8) 4213
Yang, C. J. – (8) 3525
Yang, K. N. – (8) 4202
Yang, Kai-Yueh – (8) 4066
Yang, S. M. – (8) 4303
Yang, Ying-chang – (8) 3702
Yee, Dennis – (8) 4237
Yelon, W. B. – (8) 3119, 3725
Yeshurun, Y. – (8) 4182
Yohannes, T. – (8) 3933
Yokoyama, Y. – (8) 3113
Yoo, H. Y. – (8) 4321
Yorozu, T. – (8) 3853, 3856
Yoshida, N. – (8) 2929
Yoshida, Y. – (8) 2908
Yoshitomi, Y. – (8) 2971
Yu, Jaejun – (8) 4220
Yu, S. C. – (8) 4083
Yuan, S. H. – (8) 3306
Yuen, T. – (8) 4127

Zabel, H. – (8) 3554
Zähres, H. – (8) 3921
Zalyaljutdinov, M. – (8) 3414
Zaspel, C. E. – (8) 3028
Zhai, Hongru – (8) 3116
Zhang, K. – (8) 4202
Zhang, S. G. – (8) 3722
Zhang, Shiyuan – (8) 3116
Zhang, X. Y. – (8) 3257, 4147
Zhang, Y. D. – (8) 3222, 3719
Zhang, Y. T. – (8) 4160
Zhao, Y. Z. – (8) 4057, 4060
Zhao, Z. R. – (8) 3699, 3704
Zhen, H. – (8) 4187
Zhou, S. Z. – (8) 3327, 3534
Zhou, X. Z. – (8) 3722
Zhou, Y. X. – (8) 3534
Zhu, Jian-Gang – (8) 3248
Zieren, V. – (8) 2897
Zimm, C. B. – (8) 4294
Zinn, W. – (8) 3089, 3473
Ziolo, J. – (8) 3095, 3563
Ziq, Kh. – (8) 4346
Zirngiebl, E. – (8) 3880, 4202
Zora, J. A. – (8) 3576
Zysler, R. – (8) 4164

American Institute of Physics Conference Proceedings 135.
Proceedings of a conference held at the Congressional Office of Technology Assessment in Washington, D.C., April 1985.

New technological ideas in energy conservation . . .

ENERGY SOURCES
Conservation and Renewables

Edited by David Hafemeister, Henry Kelly, and Barbara Levi

Packed with ideas that point the way to future advances, this important volume surveys energy-conservation technology in buildings, windows, lighting, appliances, HVAC, industry, automobiles, electrical generation, and more.

Applications of the most advanced research

Leading experts from national laboratories, industry, and academia detail recent achievements and future options, including . . .

- smart meters to "spot price" electricity
- off-peak cooling to reduce peak power demands
- prism method of conservation scorekeeping
- passive solar heating and passive cooling systems in buildings
- controls for indoor air quality
- steam-injected, gas turbine cogeneration
- photovoltaic technologies
- applications of maximally concentrating optics for solar energy collection
- wind turbines
- hydro-power
- liquid and gaseous fuels from biomass
- DOE-2 Computer Program for Thermal Simulations

Sound technical options

Energy Sources: Conservation and Renewables analyzes specific techniques to enhance end-use efficiency. Reviewing the past decade's technical progress, it shapes the discussion of energy options and planning for the coming years.

"The ideas discussed in these chapters are too numerous to summarize, but together they give a clear signal that there are soundly based technical options which can continue to reduce America's energy consumption in the future."

The Editors

682 pages • Clothbound • 6¼" × 9¼" •
1985 • ISBN 0-88318-334-X • LC 85-73019
$55.00 (20% discount available to members of AIP Member Societies)

= AMERICAN INSTITUTE OF PHYSICS =

Send your order with payment to:
American Institute of Physics
Marketing Services
335 East 45 Street
New York, NY 10017

Amex, Visa & MC accepted:
To place your credit card order:
call 1-800-AIP-PHYS;
In New York State,
call 212-661-9404

Available now from the
American Institute of Physics

ANNALS OF THE ISRAEL PHYSICAL SOCIETY

This series of hardbound conference proceedings promotes interaction within the international scientific community. If your library does not automatically receive each release, it may enroll in the standing order plan by simply sending a purchase order. We will supply all requested back volumes and send upon publication each new volume billed to the purchase order number.

Annals 1
ATOMIC PHYSICS IN NUCLEAR EXPERIMENTATION
Editors: *Baruch Rosner and Rafael Kalish, Technior—Israel Institute of Technology, Haifa.*

Focuses on atomic phenomena related to ion solid interaction, such as slowing down, charge exchange, and atomic excitation processes, as well as various aspects of ion surface interaction phenomena. 638 pages. 1977. $35.00 Clothbound. ISBN: 0-85274-355-6. ISSN: 0309-8710.

Annals 3
GROUP THEORETICAL METHODS IN PHYSICS
Editors: *L. Horwitz and Y. Ne'eman, University of Tel Aviv.*

Provides a joint forum for theoretical physicists working in various fields, such as nuclear, particle, solid state and condensed matter, atomic and molecular, relativity and mathematical physics and for mathematicians sharing an interest in the development of group theoretical methods. Topics covered include: group theory in condensed matter, linear and affine groups, exceptional groups, classification and gauge theory, nuclear theory, covariant relativistic and quantum mechanics. 417 pages. 1980. $45.00 Clothbound. ISBN: 0-85274-424-2. ISSN: 0309-8710.

Annals 4
MOLECULAR IONS, MOLECULAR STRUCTURE AND INTERACTION WITH MATTER
Editor: *Baruch Rosner, Technion—Israel Institute of Technology, Haifa*

Develops common ground opened for scientists in a variety of disciplines by research with molecular beams processed in particle accelerators. Examines advances in the study of molecular structures and the study of the forces acting on atoms traveling at high speed through a solid. 290 pages. 1981. $40.00 Clothbound. ISBN: 0-82574-441-2. ISSN: 0309-8710.

Annals 5
PERCOLATION STRUCTURE AND PROCESSES
Editors: *G. Deutscher, Tel Aviv University; R. Zallen, Xerox; and J. Adler, Technion—Israel Institute of Technology, Haifa*

Presents a review of topical papers highlighting recent developments in the area of percolation research. Applications of percolation include: flow of liquid in porous medium, spread of disease in a population, communication or resistor networks, conductor–insulator composite materials, composite superconductor–metal materials, discontinuous metal films, star formation in spiral galaxies, and polymer gelation. 660 pages. 1984. $60.00 Clothbound. ISBN: 0-85274-447-3. ISSN: 0309-8710.

Annals 6
VACUUM ULTRAVIOLET RADIATION PHYSICS VUV VII
Editors: *A. Weinreb and A. Ron, Hebrew University, Jerusalem*

Provides comprehensive treatment of research on instrumentation and experimentation techniques, atoms, molecules, condensed matter, luminescence phenomena, multiphoton processes and selected topics in the forefront of UV radiation physics. 623 pages. 1983. $60.00 Clothbound. ISBN: 0-85274-760-8. ISSN: 0309-8710.

Annals 7
ELECTROMAGNETIC PROPERTIES OF HIGH SPIN NUCLEAR LEVELS
Editors: *Gvirol Goldring and Michael Hass*

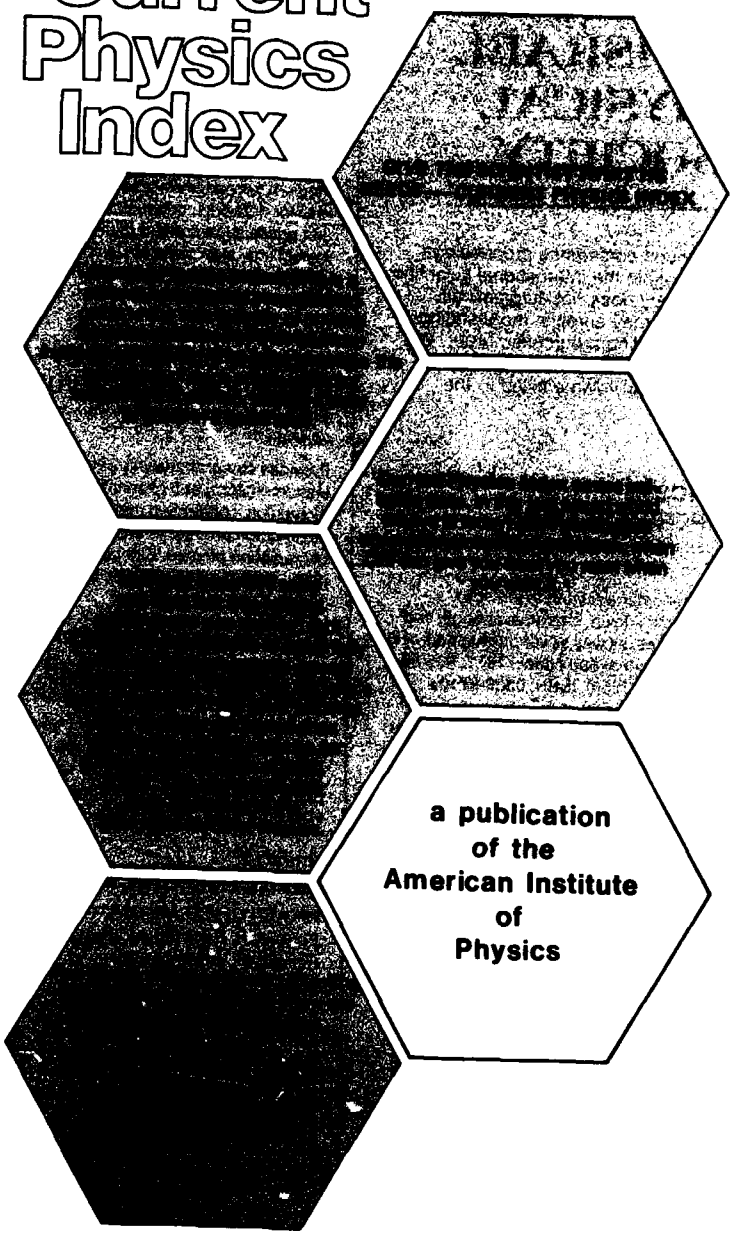
Presents the full range of recent work on nuclear moments and transition strengths within the general context of nuclear high spin physics. Consistently and clearly discusses future plans and directions. 347 pages. 1984. $45.00 Clothbound. ISBN: 0-85274–775–6. ISSN: 0309-8710.

Annals 8
FRAGMENTATION, FORM AND FLOW IN FRACTURED MEDIA
Editors: *R. Englman and Z. Jaeger—Soreq Nuclear Research Center, Yavne*

Materials engineers and scientists with fragmentation experience combine with physicists for a multidisciplinary approach to issues connected with fracture. Structural characterization, statistical models, rock blasting, fracture theories, elastic failure, waves, flow, fast effects, shear effects, and recent acquisitions are covered. 628 pp. $75.00. Clothbound. ISBN: 0-85274-578-8. ISSN: 0309-8710.

Send orders to: **American Institute of Physics**
Marketing Services
335 East 45th Street
New York, NY 10017
To place credit card orders, call 1-800-AIP-PHYS; in New York State, call 212-661-9404.

Current Physics Index



a publication
of the
American Institute
of
Physics

PHYSICS BRIEFS ...

A Comprehensive Physics Abstracts Journal at a Realistic Price!

PHYSICS BRIEFS is a comprehensive abstracts journal covering the fields of physics and related topics. It is published completely—100%—in English, but follows the long tradition of excellence established by the German publication, *Physikalische Berichte*, which it superseded in 1979.

PHYSICS BRIEFS is published in cooperation with the American Institute of Physics.

But more important to you ...

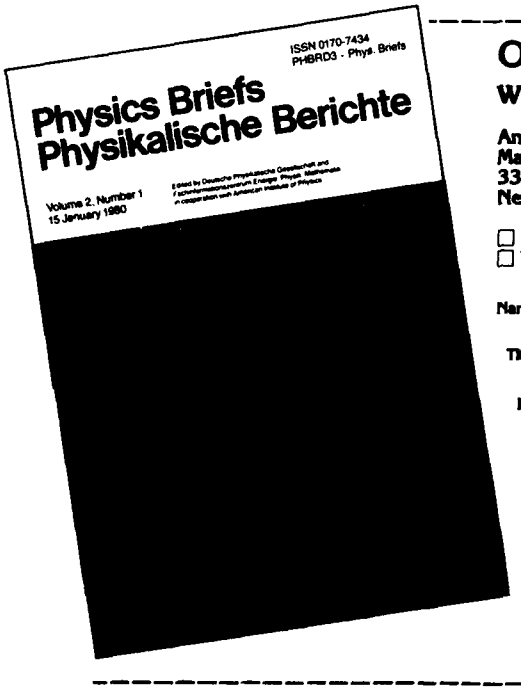
PHYSICS BRIEFS covers all fields of physics. The information is extracted from serial and non-serial literature published in all countries and all languages. This includes journals, books, patents, reports, theses and conference papers—derived from approximately 2,800 different periodicals and series. More than 500 core journals in physics are abstracted completely.

PHYSICS BRIEFS is complete. It contains a greater quantity of items per year than any other physics abstracts publication.

PHYSICS BRIEFS is timely. Information from AIP publications is entered into **PB**'s computerized data base directly from the computer-readable magnetic tape used by the AIP to produce its primary journals.

PHYSICS BRIEFS saves you money. In addition to receiving 24 semimonthly issues, semiannual author and subject indexes are included in an annual subscription—all for the low price of $2175 (U.S. & Possessions) and $2190 (Canada & Mexico).

Subscribe Now To PHYSICS BRIEFS



Order your FREE issue with this coupon today!

American Institute of Physics
Marketing Services
335 East 45 Street
New York, NY 10017

☐ **Yes, send me a FREE issue of PHYSICS BRIEFS.**
☐ **Yes, enter a 1988 subscription to PHYSICS BRIEFS.**

Name _____

Title _____

Institution/firm _____

Address _____

_____

City _____ **State** _____

Zip Code _____



Review of Scientific Instruments — Keeps You Abreast With the Latest Principles, Devices and Techniques in Scientific Instrumentation

Published primarily for experimental physical scientists engaged in research and development, this monthly journal is a fact-filled collection of original articles that provides you with:

- Detailed information on the construction of new apparatus
- References to various commercially available instruments and materials used in the experiment
- Sections reporting on new instruments, materials, and components
- Over 2700 pages of original research annually
- Editorial coverage of over 100 subjects

Review of Scientific Instruments is a valuable and convenient source for researchers active in atomic/molecular physics, chemical physics, electromagnetic/optical properties, laser technology, nuclear physics, plasma physics, surface science/vacuum technology, thermal/mechanical physics.

Take advantage of our FREE SAMPLE COPY OFFER! Receive your free sample copy of **Review of Scientific Instruments** by completing and returning the attached form at right

OR. . .

Start your 1988 Subscription to **Review of Scientific Instruments** today!

*Reduced rates are available for individuals. For details, please call (212) 661-9404, and ask for Marketing Services.

ORDER FORM

☐ Please send me a free sample copy of **Review of Scientific Instruments**

☐ **ORDER**

Subscription Prices	
☐ **Domestic**	**$395.00**
☐ **Foreign (surface mail)**	**$415.00**
☐ **Optional Airfreight Europe**	**$440.00**
☐ **Optional Airfreight Asia**	**$440.00**

Name

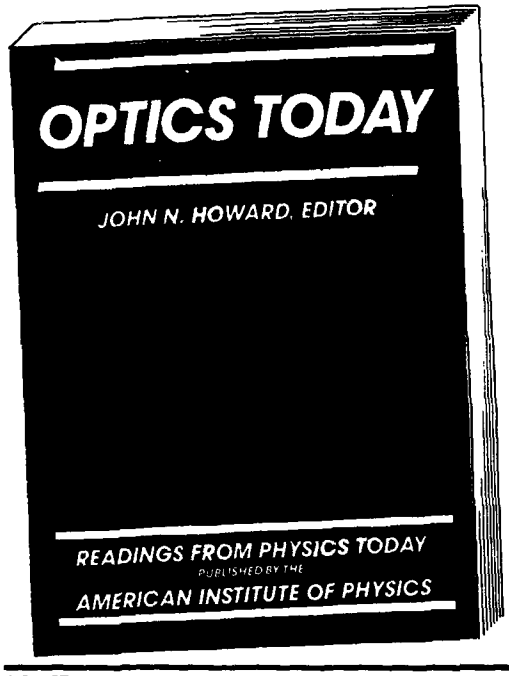
Address

City State

ZIP Code Country

FREE SAMPLE

Send to:
American Institute of Physics, Marketing Services
335 East 45 Street, New York, NY 10017



"These articles are, without exception, of high quality . . . this well-organized book is a valuable reference, and I highly recommend it it to professionals with an interest in optics."

Science Books and Films
November/December, 1987

OPTICS TODAY

EDITED BY JOHN N. HOWARD

More than a review of recent optics research, *Optics Today* enables you to relive the dramatic progress of the past dozen years with over fifty articles and news items from *Physics Today*

Distinguished contributors include leading researchers and science writers, such as **Nicolaas Bloembergen, Solomon J. Buchsbaum, Arthur L. Schawlow, Steven Weinberg, Lowell Wood,** and more. Writing about the frontiers of research for a news magazine, they address a general scientific audience and convey the vitality of the moment.

Optics Today is the third volume in the series, "Readings from *Physics Today*," which includes *Astrophysics Today* and *History of Physics*.

1986 • 384 pp • illustrations • photos • ISBN 0-88318-499-0
• Hardbound: $35.00 nonmembers/$28.00 members
• Softbound: $25.00 nonmembers/$20.00 members

CONTENTS

OPTICS YESTERDAY AND TOMORROW
The electric lamp: 100 years of applied physics, John M. Anderson and John S. Saby; **Physics looks at solar energy,** Aden Baker Meinel and Marjorie Pettit Meinel; **Solar photovoltaic energy,** Henry Ehrenreich and John H. Martin; **Infrared interferometer to measure size and shape of stars,** Gloria B. Lubkin; **Correcting for atmospheric distortion in telescopes,** Barbara G. Levi; **Solar Optical Telescope will orbit space shuttle,** Bertram M. Schwarzschild; **Ultraviolet, optical and infrared astronomy,** E. Joseph Wampler; **A look at photon detectors,** Robert J. Keyes and Robert H. Kingston; **Quantum wells for photonics,** Daniel S. Chemla; **Optics: an ebullient revolution,** Peter Franken.

LASER PHYSICS: HIGHER POWER, HIGHER FREQUENCY, AND ULTRASHORT
Frontiers of laser development, John L. Emmett; **Rare-gas halide lasers,** James J. Ewing; **New sources of high-power coherent radiation,** Phillip Sprangle and Timothy Coffey; **Coherent sources of extreme uv,** Bertram M. Schwarzschild; **X-ray lasers,** George Chapline and Lowell Wood; **Livermore group reports soft x-ray laser,** Barbara G. Levi; **Prospects for a gamma-ray laser,** G.C. Baldwin and R.V. Khoklov; **Ultrashort phenomena,** Robert R. Alfano and Stanley L. Shapiro; **Sub-picosecond spectroscopy,** Erich P. Ippen and Charles V. Shank; **30-femtosecond light pulses at Bell Labs,** Bertram M. Schwarzschild

LASER SPECTROSCOPY
Nobel Physics Prize to Bloembergen, Schawlow and Siegbahn, Gloria B. Lubkin; **High-resolution spectroscopy of atoms and molecules,** Theodor W. Hansch; **Coherent Raman spectroscopy,** Marc D. Levenson; **Coherent optical transients,** Richard G. Brewer; **Laser linewidth,** Aram Mooradian; **Tunable coherent infrared techniques show progress,** Gloria B. Lubkin; **Lasers and physics: a pretty good hint,** Arthur L. Schawlow

HOLOGRAPHY AND PHASE CONJUGATION
Nobel prizes: physics to Gabor, chemistry to Herzberg, Gloria B. Lubkin; **Progress in holography,** Emmett N. Leith and Juris Upatnieks; **Optics as scattering,** Giuliano Toraldo di Francia; **Applications of optical phase conjugation,** Concetto R. Giuliano

LIGHTWAVE COMMUNICATIONS, FIBER AND INTEGRATED OPTICS
Lightwave communications: An overview, Solomon J. Buchsbaum; **Light sources,** Henry Kressel, Ivan Ladany, Michael Ettenberg, and Harry Lockwood; **Advances in semiconductor lasers,** Yasuharu Suematsu; **Novel laser for fiber-optic communication,** Bertram M. Schwarzschild; **The fiber lightguide,** Alan G. Chynoweth; **Lightwave telecommunication,** Tingye Li; **Detectors for lightwave communication,** Hans Melchior; **Integrated optics,** Esther M. Conwell; **Observation of optical bistability confirms prediction,** H. Richard Leuchtag; **Sensitive fiber-optic gyroscopes,** Bertram M. Schwarzschild.

LASER IN CHEMISTRY AND INDUSTRY
Laser selective chemistry—is it possible?, Ahmed H. Zewail; **Laser-induced chemical processes,** V.S. Letokhov; **Laser annealing of silicon,** John M. Poate and Walter L. Brown; **Infrared laser-induced unimolecular reactions,** Nicolaas Bloembergen and Eli Yablonovitch; **Laser-induced thermonuclear fusion,** John Nuckolls, John Emmett, and Lowell Wood; **Shiva moves closer to laser fusion,** Bertram M. Schwarzschild

X RAYS AND TOMOGRAPHY
Computerized tomography: taking sectional x rays, William Swindell and Harrison H. Barrett; **The physics of medical imaging,** Paul R. Moran, R. Jerome Nickles, and James A. Zagzebski; **Nobel Prize to Cormack and Hounsfield for medicine,** Bertram M. Schwarzschild; **Interest grows in synchrotron-radiation sources,** Gloria B. Lubkin; **The renaissance of x-ray optics,** James H. Underwood and David T. Attwood

CONCEPTS AND EPILOGUE
The concept of the photon, Marlan O. Scully and Murray Sargent III; **Light as a fundamental particle,** Steven Weinberg; **Epilogue,** John N. Howard

Please send me____copy(ies) of OPTICS TODAY. (20% discount available to members of AIP Member and Affiliated Societies)
Hardbound: ☐ $35.00 nonmembers ☐ $28.00 members
Softbound: ☐ $25.00 nonmembers ☐ $20.00 members

Method of Payment
☐ Check enclosed (payable in U.S. dollars to the American Institute of Physics, drawn on a bank in the U.S.) in the amount of $_____
☐ Charge my credit card: ☐ AMEX ☐ Visa ☐ MasterCard

Account No _____ Exp. date _____
Signature _____
Name _____ Title _____
Organization _____
Address _____
City _____ State _____ Zip _____

Please send orders to the American Institute of Physics, Marketing Services, 335 East 45th Street, New York, NY 10017.
REMITTANCE MUST ACCOMPANY ALL ORDERS.

NOW WEEKLY!

even more

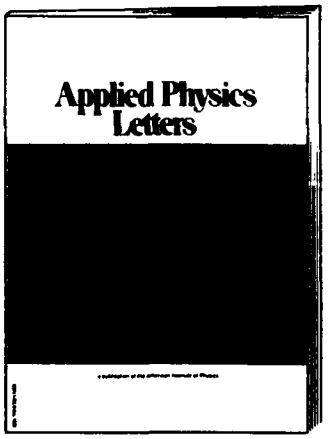
Keep current with APPLIED PHYSICS LETTERS

Now published weekly, **Applied Physics Letters** offers timely reports on the latest developments in . . .

- **Semiconductor properties and devices**
- **Crystal growth and characterization**
- **Superconductivity**
- **Lasers and their applications**
- **Luminescence**
- **Nonlinear optics and guided waves**
- **Structure, properties, and preparation of materials**
- **Defects and irradiation effects in solids**
- **Optoelectronics**
- **Properties and uses of plasmas**

. . . and more.

If your library has not yet taken advantage of **APL's** coverage of the most recent developments, check a box below to receive your FREE sample issue or to begin your subscription.



ORDER FORM

☐ Yes! Send me a FREE sample issue of **APL**

☐ Enter a 1988 subscription for my institution/company:*

☐ Domestic	$425.00
☐ Foreign (surface mail)	$460.00
☐ Optional Airfreight Europe	$485.00
☐ Optional Airfreight Asia	$485.00

Organization _____ Attn: _____

Address _____

City/State/Zip _____

Country _____ Telephone No. _____

Purchase Order No. _____

Send orders and inquiries to: **AMERICAN INSTITUTE OF PHYSICS**
Marketing Services
335 East 45th Street
New York, NY 10017

*Reduced rates are available for individuals. For details, please call (212) 661-9404, and ask for Marketing Services.

Inquiries from Japan should be directed to Kinokuniya Co., Ltd.

Remittance must accompany all orders. Foreign payments must be made by check payable in U.S. dollars and drawn on a U.S. bank.

From The Institute of Physics (U.K.)

Inverse Problems

The International Journal of Inverse Problems, Inverse Methods and Computerized Inversion of Data.

This new journal combines theoretical and mathematical papers on inverse problems with numerical and practical approaches to their solution. INVERSE PROBLEMS includes contributions on:

- General Theory
- Inverse Source Problems
- Electromagnetic Inverse Problems
- Elastic Wave Inverse Problems
- Potential Inverse Problems
- Quantum Wave Inverse Problems
- Excited Source Inverse Problems
- Mathematical Application of Inversion Methods
- Interpretation Theory and Other Non-destructive Methods
- Inverse Chemistry and Geochemistry Problems
- Inverse Hydrogeologic Problems
- Inverse Tsunami Problems

If you're a physicist or mathematician (pure or applied), INVERSE PROBLEMS keeps you current in an expanding field of special importance to workers in geophysics, optics, radar, acoustics, communication theory or signal processing. INVERSE PROBLEMS emphasizes original contributions to methods of solving mathematical, physical and applied problems.

INVERSE PROBLEMS
1988 Volume 4
4 issues (February, May, August, November)
ISSN 0266-5611 Coden INPEEY
Subscription rates: $305.00;
$183.00 Microfiche

Please return completed order form to:
American Institute of Physics, Marketing Services,
335 East 45th Street, New York, NY 10017.

☐ YES, Enter my subscription to INVERSE PROBLEMS, Volume 4 ☐ $305.00 ☐ $183.00 Microfiche

Method of Payment:
☐ Check enclosed (payable in U.S. dollars to American Institute of Physics drawn on a bank in the U.S.)
☐ Use purchase order number_____
☐ Bill my organization (billing charge is $2.00)

Name
Title
Organization
Address
City
State Zip
Country
Telephone Number

For subscriptions outside of North America contact:
Institute of Physics, Techno House, Redcliffe Way,
Bristol BS1 6NX, England.

AMERICAN INSTITUTE OF PHYSICS
335 EAST 45th STREET, NEW YORK, NY 10017 · (212) 661-9404

Under U.S. copyright law, the transfer of copyright from the author(s) should be explicitly stated to enable the publisher to disseminate the work to the fullest extent. The following transfer must be signed and returned to the Editor's office before the manuscript can be accepted for publication. Please note that if the manuscript has been prepared as a Work Made For Hire, the transfer should be signed by both employer and employee. Address requests for further information or exceptions to the Office of Rights and Permissions, AIP, 335 East 45th Street, New York, New York 10017 (212) 661-9404.

TRANSFER OF COPYRIGHT AGREEMENT

Copyright to the unpublished and original article, including copyright to the abstract forming part thereof, entitled

_____

submitted by the following author(s) (names of all authors) _____

_____

is hereby transferred to AIP for the full term thereof throughout the world, BUT SUBJECT to the following rights reserved to the author(s) and to acceptance of the article for publication in

_____
Name of Journal

AIP shall have the right to register copyright to the article and the accompanying abstract in its name as claimant, whether separately or as part of the journal issue or other medium in which such work is included.

The author(s) reserve the following rights:

(1) All proprietary rights other than copyright, such as patent rights.
(2) The right, after publication by AIP, to grant or refuse permission to third parties to republish all or part of the article or translations thereof. In the case of whole articles, such third parties must obtain AIP's written permission as well. However, such permission will not be refused by AIP except at the direction of the author. AIP may grant rights with respect to journal issues as a whole.
(3) The right, after publication by AIP, to use all or part of the article and abstract in compilations or other publications of the author's own works, and to make copies of all or part of such material for the author's use for lecture or classroom purposes.
(4) If the article has been prepared by an employee within the scope of his or her employment, the employer reserves the right to make copies of the work for its own internal use. If the article was prepared under a U.S. Government contract, the government shall have the rights under the copyright to the extent required by the contract.

The author(s) agree that all copies of the whole article or abstract made under any of the above reserved rights shall include notice of the AIP copyright. If each author's signature does not appear below, the signing author(s) represent that they sign this agreement as authorized agents for and on behalf of all the authors, and that this agreement and authorization is made on behalf of all the authors.

_____
Signature Date

_____
Name (print)

If the manuscript has been prepared as a Work Made For Hire, the transfer should be signed by the employee (above) and by the employer (below):

_____
Name of Employer (print)

_____
Signature Name (print) Title Date

A work prepared by a U.S. Government officer or employee as part of his or her official duties is not eligible for U.S. copyright. If at least one of the authors is *not* in this category, that author should sign above. If all the authors are in this category, check the box here and return this form unsigned. ☐

3/87

American Institute of Physics

335 East 45 Street, New York, NY 10017

The American Institute of Physics was founded in 1931. It is chartered as a membership corporation with leading societies in the fields of physics and astronomy as members. The Institute combines into one operating agency those functions which can best be done by the societies jointly. Its purpose is the advancement and diffusion of the knowledge of physics and its application to human welfare.

The Institute publishes scientific journals; provides abstracting and indexing services; serves the public by making available to the press and other channels of public information reliable communications on physics and astronomy and their progress; carries on extensive manpower activities; maintains projects directed toward providing information about physics and astronomy education to students, teachers, and academic departments; encourages and assists in the documentation and study of the history and philosophy of recent physics; cooperates with local, national, and international organizations devoted to physics and related sciences; and fosters the relations of the science of physics to other sciences and to the arts and industries.

Member Societies

The American Physical Society
W. W. Havens, Jr., Executive Secretary
335 East 45 Street, New York, NY 10017

Optical Society of America
Jarus W. Quinn, Executive Director
1816 Jefferson Pl. N.W., Washington, DC 20036

Acoustical Society of America
Murray Strasberg, Secretary
500 Sunnyside Blvd., Woodbury, NY 11797

The Society of Rheology
D. G. Baird, Secretary
Polymer Materials & Interfaces Lab.
Virginia Polytechnic Institute & State University
Blacksburg, VA 24061-6496

American Association of Physics Teachers
Jack M. Wilson, Executive Officer
Dept. of Physics & Astronomy
University of Maryland
College Park, MD 20742

American Crystallographic Association
William L. Duax, Executive Officer
P.O. Box 96, Endicott Station
Buffalo, NY 14205-0096

American Astronomical Society
Peter B. Boyce, Executive Officer
2000 Florida Avenue, N.W.
Suite 300
Washington, DC 20009

American Association of Physicists in Medicine
Guy H. Simmons, Secretary
VA Medical Center
Nuclear Medicine
Cooper Drive
Lexington, KY 40511

American Vacuum Society
William D. Westwood, Secretary
Bell-Northern Research, Ltd.
P.O. Box 3511, Station C
Ottawa, Ontario K1Y4H7, Canada

American Geophysical Union
A. F. Spilhaus, Jr., Executive Director
2000 Florida Avenue, N.W.
Washington, DC 20009

Affiliated Societies

American Institute of Aeronautics and Astronautics, American Meteorological Society, American Nuclear Society, ASM International, Division of Physical Chemistry of ACS, Electron Microscopy Society of America, Engineering Information, Inc., The Geological Society of America, Instrument Society of America, International Association of Mathematical Physicists, Materials Research Society, Nuclear and Plasma Sciences Society of IEEE, The Philosophical Society of Washington, Physics Club of Milwaukee, Physics Section of AAAS, Society for Applied Spectroscopy, Society of Photo-Optical Instrumentation Engineers.

Corporate Associates: 110 leading corporations, by their membership, participate in and contribute to the support of AIP.

Publications

Physical Review A · Benjamin Bederson, *Editor*, Physics Dept., N.Y.U., New York, NY 10003
Physical Review B · P.D. Adams, *Editor*, The American Physical Society, 1 Research Rd., Box 1000, Ridge, NY 11961
Physical Review C · Sam Austin, *Editor*, Cyclotron Labs., Michigan State University, E. Lansing, MI 48824
Physical Review D · Lowell S. Brown, Stanley G. Brown, and D.L. Nordstrom, *Editors*, APS, 1 Research Rd., Box 1000, Ridge, NY 11961
Physical Review Abstracts · Margaret Judd, *Editor*, APS
Physical Review Letters · G. Baabas, S.G. Brown, and G.L. Wells, *Editors*, APS
Bulletin of The American Physical Society · W.W. Havens, Jr., *Editor*, APS
Reviews of Modern Physics · David Pines, *Editor*, Loomis Lab. of Physics, 1110 W. Green St., Urbana, IL 61801
The Journal of the Acoustical Society of America · Daniel W. Martin, *Editor-in-Chief*, 7349 Clough Pike, Cincinnati, OH 45244
American Journal of Physics · John S. Rigden, *Editor*, Physics Dept., University of Missouri, St. Louis, MO 63121
The Astronomical Journal · Paul W. Hodge, *Editor*, Astronomy Dept. FM-20, University of Washington, Seattle, WA 98195
Bulletin of the American Astronomical Society · Peter B. Boyce, *Editor*, AAS
The Astrophysical Journal · Helmut A. Abt, *Managing Editor*, Kitt Peak National Observatory, Box 26732, Tucson, AZ 85726
Journal of Materials Research · Walter L. Brown, *Editor-in-Chief*, AT&T Bell Laboratories, 600 Mountain Ave., Murray Hill, NJ 07974
The Journal of Chemical Physics · J.C. Light, *Editor*, James Franck Institute, The University of Chicago, Chicago, IL 60637
Journal of Mathematical Physics · L.C. Biedenharn, Jr., *Editor*, Dept. of Physics, Duke University, Science Drive, Durham, NC 27706
The Physics of Fluids · A. Acrivos, *Editor*, The Levich Institute for PCH, Room 202, Steinman Hall, CCNY, Convent Ave. at 138 St., New York, NY 10031. F.L. Ribe, *Editor*, College of Engineering, 356 Benson Hall, BF-20, University of Washington, Seattle, WA 98195
Journal of Applied Physics · Lester Guttman, *Editor*, Argonne Natl. Lab., Box 8296, Argonne, IL 60439-8296
Applied Physics Letters · Gilbert J. Perlow, *Editor*, Argonne Natl. Lab., Box 8296, Argonne, IL 60439-8296
Review of Scientific Instruments · Thomas H. Braid, *Editor*, Argonne Natl. Lab., Box 8293, Argonne, IL 60439-8293
Journal of Physical and Chemical Reference Data · David R. Lide, Jr., *Editor*, Natl. Bur. Std., Gaithersburg, MD 20899
Physics Today · Gloria B. Lubkin, *Editor*, AIP
Computers in Physics · Robert R. Borchers, *Editor-in-Chief*, Lawrence Livermore Natl. Lab., P.O. Box 808-L-668, Livermore, CA 94550
Journal of Vacuum Science and Technology A · Gerald Lucovsky, *Editor*, Dept. of Physics, N. Carolina State Univ., Raleigh, NC 27650
Journal of Vacuum Science and Technology B · Thomas Mayer, *Editor*, Dept. of Chemistry, Univ. of N. Carolina, Chapel Hill, NC 27514
Medical Physics · J.S. Laughlin, *Editor*, Memorial Sloan-Kettering Cancer Center, 1275 York Ave., New York, NY 10021
AAPT Announcer · Jack M. Wilson, *Editor*, Dept. of Physics & Astronomy, University of Maryland, College Park, MD 20742
The Physics Teacher · Donald F. Kirwan, *Editor*, Dept. of Physics, University of Rhode Island, Kingston, RI 02881
Journal of Rheology · Arthur B. Metzner, *Editor*, Center for Composite Materials, University of Delaware, Newark, DE 19716
Journal of the Optical Society of America A · Harrison H. Barrett, *Editor*, Optical Sciences Center, Univ. of Ariz., Tucson, AZ 85721
Journal of the Optical Society of America B · Willes H. Weber, *Editor*, S-3078 Research Labs., Ford Motor Co., Dearborn, MI 48121-2053
Applied Optics · William T. Rhodes, *Editor*, Georgia Institute of Technology, School of Electr. Engin., Atlanta, GA 30332
Optics Letters · Paul L. Kelley, *Editor*, C174 Lincoln Lab., Lexington, MA 02173-0073
Optics News · J.N. Howard, *Editor*, 7 Norman Rd., Newton Highlands, MA 02161
Journal of Lightwave Technology · T.G. Giallorenzi, *Editor*, Naval Research Laboratory, Code 6500, Washington, DC 20375
The Journal of Undergraduate Research in Physics · R.E. Adelberger, *Editor*, Physics Dept., Guilford College, Greensboro, NC 27410
AIP Conference Proceedings

Soviet Journal of Low Temperature Physics	Soviet Physics-Acoustics	Soviet Physics-Semiconductors	Soviet Astronomy
Soviet Journal of Nuclear Physics	Soviet Physics-Crystallography	Soviet Physics-Solid State	Soviet Astronomy Letters
Soviet Journal of Optical Technology	Soviet Physics-Doklady	Soviet Physics-Technical Physics	Chinese Physics
Soviet Journal of Particles and Nuclei	Soviet Physics-JETP	Soviet Physics-Uspekhi	Chinese Physics-Lasers
Soviet Journal of Plasma Physics	JETP Letters	Soviet Technical Physics Letters	
Soviet Journal of Quantum Electronics	Optics and Spectroscopy		

Current Physics Index (CPI), quarterly and annual subject index with abstracts to all the above journals.
General Physics Advance Abstracts (GPAA), semimonthly advance abstracts of AIP-published physics literature
Searchable Physics Information Notices (SPIN), monthly computer-readable tape of abstracts.
Current Physics Microform (CPM), monthly microfilm edition of all the above journals.
Current Physics Reprints (CPR), on-demand copies of any article in any of the above journals.
Physics Briefs (PB), semimonthly comprehensive index with abstracts to the world literature of physics.
PI-NET, an online physics information network.

Governing Board

*Hans Frauenfelder, *Chair*
Orson L. Anderson
Robert S. Bauer
Peter M. Bell
Robert T. Beyer
*Peter B. Boyce
Praveen Chaudhari
Alex Dalgarno
William L. Duax
Frederick H. Fisher
*Kenneth W. Ford—*ex officio*
Judy R. Franz
Thomas E. Graedel
*Roderick M. Grant—*ex officio*
Robert G. Greenler
*William W. Havens, Jr.
Donald F. Holcomb
Herwig Kogelnik
James A. Krumhansl
Arlo U. Landolt
*David Lazarus
Harry Lustig
Eugen Merzbacher
James S. Murday
*James A. Purdy
Jarus W. Quinn
Robert Resnick
Joseph M. Reynolds
Jean St. Germain
*F. Dow Smith
A. F. Spilhaus, Jr.
Murray Strasberg
*Martin Walt
*Jack M. Wilson
Gerald Wheeler
Kurt F. Wissbrun
Jerry M. Woodall

**executive committee*

AIP Officers

Hans Frauenfelder, *Chair*
Kenneth W. Ford, *Executive Director*
Roderick M. Grant, *Secretary*
Gerald F. Gilbert, *Treasurer*
John S. Rigden, *Managing Director of Physics Programs*

Publishing Services

John T. Scott, *Director Publishing I Branch*
Lawrence Feinberg, *Manager Production I Division*
Irving Lieblich, *Manager Scientific Classification Division*
Leon Benedict, *Manager Composition I Division*
Darlene Carlin, *Director Publishing II Branch*
James J. Donohue, *Manager Production II Division*
Gogo Lewis, *Manager Composition II Division*
Edward P. Greeley, *Manager Advertising Division*
Kita G. Lerner, *Manager Books Division*
S. Jeffrey Howitt, *Manager Marketing Division*
Geraldine Bindert, *Manager Publication Billing*
John DiCaro, *Manager Subscription Fulfillment*

4/86